Echocardiography

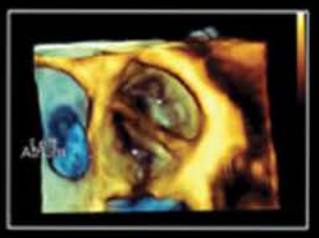
in Pediatric and Congenital Heart Disease

z.f

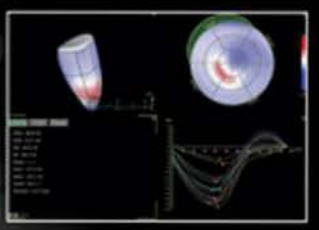
From Fetus to Adult

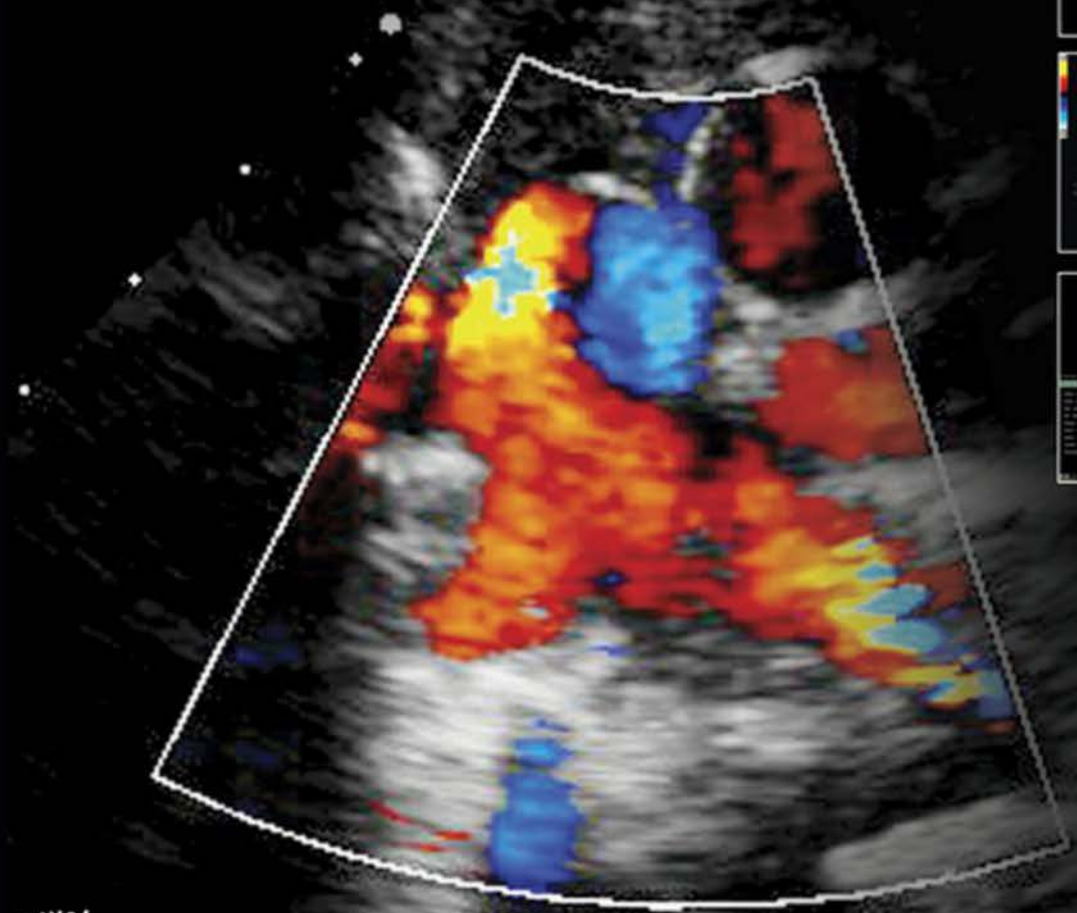
Edited by Wyman W. Lai, Luc L. Mertens
Meryl S. Cohen, Tal Geva

SECOND EDITION









with website

WILEY Blackwell

Echocardiography in Pediatric and Congenital Heart Disease

Dedications

To my parents, CheToo and SoFa Lai; my wonderful wife, Lydia; and my children, Justin and Amanda.

Wyman W. Lai

To my wife Benedikte, my daughter Virginie and my son Francis. For all the time I could not spend with them.

Luc L. Mertens

To my husband Bruce Randazzo and my children Jake, Isabel and Ethan for supporting me always.

Meryl S. Cohen

To my wife Judith and sons Omri and Alon with Love.

Tal Geva

Echocardiography in Pediatric and Congenital Heart Disease

From Fetus to Adult

Second Edition

Edited by

Wyman W. Lai MD, MPH

Professor of Pediatrics at CUMC
Columbia University Medical Center;
Director, Noninvasive Cardiac Imaging
Morgan Stanley Children's Hospital of NewYork-Presbyterian
New York, NY, USA

Luc L. Mertens MD, PhD

Section Head, Echocardiography
The Hospital for Sick Children;
Professor of Pediatrics
University of Toronto
Toronto, ON, Canada

Meryl S. Cohen MD

Professor of Pediatrics
Perelman School of Medicine, University of Pennsylvania;
Medical Director, Echocardiography
Program Director, Cardiology Fellowship
The Cardiac Center
The Children's Hospital of Philadelphia
Philadelphia, PA, USA

Tal Geva MD

Professor of Pediatrics
Harvard Medical School;
Chief, Division of Noninvasive Cardiac Imaging
Department of Cardiology
Boston Children's Hospital
Boston, MA, USA

WILEY Blackwell

This edition first published 2016 © 2016 by John Wiley & Sons Ltd.
First edition published 2009 © 2009 by John Wiley & Sons Ltd.

Registered office: John Wiley & Sons, Ltd, The Atrium, Southern Gate, Chichester, West Sussex, PO19 8SQ, UK

Editorial offices: 9600 Garsington Road, Oxford, OX4 2DQ, UK
The Atrium, Southern Gate, Chichester, West Sussex, PO19 8SQ, UK
111 River Street, Hoboken, NJ 07030-5774, USA

For details of our global editorial offices, for customer services and for information about how to apply for permission to reuse the copyright material in this book please see our website at www.wiley.com/wiley-blackwell

The right of the author to be identified as the author of this work has been asserted in accordance with the UK Copyright, Designs and Patents Act 1988.

All rights reserved. No part of this publication may be reproduced, stored in a retrieval system, or transmitted, in any form or by any means, electronic, mechanical, photocopying, recording or otherwise, except as permitted by the UK Copyright, Designs and Patents Act 1988, without the prior permission of the publisher.

Designations used by companies to distinguish their products are often claimed as trademarks. All brand names and product names used in this book are trade names, service marks, trademarks or registered trademarks of their respective owners. The publisher is not associated with any product or vendor mentioned in this book. It is sold on the understanding that the publisher is not engaged in rendering professional services. If professional advice or other expert assistance is required, the services of a competent professional should be sought.

The contents of this work are intended to further general scientific research, understanding, and discussion only and are not intended and should not be relied upon as recommending or promoting a specific method, diagnosis, or treatment by health science practitioners for any particular patient. The publisher and the author make no representations or warranties with respect to the accuracy or completeness of the contents of this work and specifically disclaim all warranties, including without limitation any implied warranties of fitness for a particular purpose. In view of ongoing research, equipment modifications, changes in governmental regulations, and the constant flow of information relating to the use of medicines, equipment, and devices, the reader is urged to review and evaluate the information provided in the package insert or instructions for each medicine, equipment, or device for, among other things, any changes in the instructions or indication of usage and for added warnings and precautions. Readers should consult with a specialist where appropriate. The fact that an organization or Website is referred to in this work as a citation and/or a potential source of further information does not mean that the author or the publisher endorses the information the organization or Website may provide or recommendations it may make. Further, readers should be aware that Internet Websites listed in this work may have changed or disappeared between when this work was written and when it is read. No warranty may be created or extended by any promotional statements for this work. Neither the publisher nor the author shall be liable for any damages arising herefrom.

Library of Congress Cataloging-in-Publication Data

Echocardiography in pediatric and congenital heart disease : from fetus to adult / edited by Wyman W. Lai, Luc L. Mertens, Meryl S. Cohen, Tal Geva. – Second edition.
p. ; cm.
Includes bibliographical references and index.
ISBN 978-0-470-67464-2 (cloth)
I. Lai, Wyman W., editor. II. Mertens, Luc, editor. III. Cohen, Meryl, editor. IV. Geva, Tal, editor.
[DNLM: 1. Heart Defects, Congenital–ultrasonography. 2. Echocardiography–methods. 3. Heart Defects, Congenital–diagnosis. WG 141.5.E2]
RJ423.5.U46
618.92′1207543–dc23

2015033801

A catalogue record for this book is available from the British Library.

Wiley also publishes its books in a variety of electronic formats. Some content that appears in print may not be available in electronic books.

Cover images: Reproduced from images within the book.

Set in 9.5/12pt MinionPro by Aptara Inc., New Delhi, India

1 2016

Contents

Contributors, vii

Preface, xi

About the Companion Website, xii

Part I Introduction to Cardiac Ultrasound Imaging

1 Ultrasound Physics, 3
Jan D'hooge and Luc L. Mertens

2 Instrumentation, Patient Preparation, and Patient Safety, 19
Stacey Drant and Vivekanand Allada

3 Segmental Approach to Congenital Heart Disease, 31
Tal Geva

4 The Normal Pediatric Echocardiogram, 44
Wyman W. Lai and H. Helen Ko

Part II Quantitative Methods

5 Structural Measurements and Adjustments for Growth, 63
Thierry Sluysmans and Steven D. Colan

6 Hemodynamic Measurements, 73
Mark K. Friedberg

7 Systolic Ventricular Function, 96
Luc Mertens and Mark K. Friedberg

8 Diastolic Ventricular Function Assessment, 132
Peter C. Frommelt

Part III Anomalies of the Systemic and Pulmonary Veins, Septa, and Atrioventricular Junction

9 Pulmonary Venous Anomalies, 157
David W. Brown

10 Systemic Venous Anomalies, 180
Leo Lopez and Sarah Chambers

11 Anomalies of the Atrial Septum, 197
Tal Geva

12 Ventricular Septal Defects, 215
Shobha Natarajan and Meryl S. Cohen

13 Ebstein Anomaly, Tricuspid Valve Dysplasia, and Right Atrial Anomalies, 231
Frank Cetta and Benjamin W. Eidem

14 Mitral Valve and Left Atrial Anomalies, 243
James C. Nielsen and Laurie E. Panesar

15 Common Atrioventricular Canal Defects, 259
Meryl S. Cohen

Part IV Anomalies of the Ventriculo-arterial Junction and Great Arteries

16 Anomalies of the Right Ventricular Outflow Tract and Pulmonary Valve, 281
Matthew S. Lemler and Claudio Ramaciotti

17 Pulmonary Atresia with Intact Ventricular Septum, 297
Jami C. Levine

18 Abnormalities of the Ductus Arteriosus and Pulmonary Arteries, 317
Bhawna Arya and Craig A. Sable

19 Anomalies of the Left Ventricular Outflow Tract and Aortic Valve, 336
John M. Simpson and Owen I. Miller

20 Hypoplastic Left Heart Syndrome, 357
David J. Goldberg and Jack Rychik

21 Aortic Arch Anomalies: Coarctation of the Aorta and Interrupted Aortic Arch, 382
Jan Marek, Matthew Fenton, and Sachin Khambadkone

22 Tetralogy of Fallot, 407
Shubhika Srivastava, Wyman W. Lai, and Ira A. Parness

23 Truncus Arteriosus and Aortopulmonary Window, 433
Timothy C. Slesnick, Ritu Sachdeva, Joe R. Kreeger, and William L. Border

24 Transposition of the Great Arteries, 446
Luc Mertens, Manfred Vogt, Jan Marek, and Meryl S. Cohen

25 Double-Outlet Ventricle, 466
Leo Lopez and Tal Geva

26 Physiologically "Corrected" Transposition of the Great Arteries, 489
Erwin Oechslin

Part V Miscellaneous Cardiovascular Lesions

27 Hearts with Functionally One Ventricle, 511
Stephen P. Sanders

28 Echocardiographic Assessment of Functionally Single Ventricles after the Fontan Operation, 541
Marc Gewillig and Luc Mertens

29 Cardiac Malpositions and Heterotaxy Syndrome, 558
Irene D. Lytrivi and Wyman W. Lai

30 Congenital Anomalies of the Coronary Arteries, 584
J. René Herlong and Piers C. A. Barker

31 Vascular Rings and Slings, 609
Andrew J. Powell

32 Connective Tissue Disorders, 624
Julie De Backer

33 Cardiac Tumors, 641
Michele A. Frommelt

Part VI Anomalies of Ventricular Myocardium

34 Dilated Cardiomyopathy, Myocarditis, and Heart Transplantation, 653
Renee Margossian

35 Hypertrophic Cardiomyopathy, 677
Colin J. McMahon and Javiar Ganame

36 Restrictive Cardiomyopathy and Pericardial Disease, 694
Cecile Tissot and Adel K. Younoszai

37 Other Anomalies of the Ventricular Myocardium, 719
Rebecca S. Beroukhim and Mary Etta E. King

Part VII Acquired Pediatric Heart Disease

38 Kawasaki Disease, 739
Erik C. Michelfelder and Allison Divanovic

39 Rheumatic Fever and Rheumatic Heart Disease, 750
Bo Reményi, Andrew Steer, and Michael Cheung

40 Infective Endocarditis, 763
Manfred Otto Vogt and Andreas Kühn

Part VIII Special Techniques and Topics

41 Transesophageal and Intraoperative Echocardiography, 777
Owen I. Miller, Aaron J. Bell, and John M. Simpson

42 3D Echocardiography, 791
Folkert Jan Meijboom, Heleen van der Zwaan, and Jackie McGhie

43 Pregnancy and Heart Disease, 815
Anne Marie Valente

44 Fetal Echocardiography, 834
Darren P. Hutchinson and Lisa K. Hornberger

45 The Echocardiographic Assessment of Pulmonary Arterial Hypertension, 872
Lindsay M. Ryerson and Jeffrey F. Smallhorn

APPENDIX Normal Echocardiographic Values for Cardiovascular Structures, 883

Index, 903

Contributors

Vivekanand Allada MD
Professor of Pediatrics
University of Pittsburgh School of Medicine
Director of Clinical Services, Pediatric Cardiology
Children's Hospital of Pittsburgh of UPMC
Heart Institute
Pittsburgh, PA, USA

Bhawna Arya MD
Assistant Professor
Department of Pediatrics
University of Washington School of Medicine
Seattle Children's Hospital
Seattle, WA, USA

Piers C.A. Barker MD
Associate Professor of Pediatrics and Obstetrics/Gynecology
Duke University Medical Center
Durham, NC, USA

Aaron J. Bell MD
Department of Congenital Heart Disease
Evelina London Children's Hospital;
Guy's & St Thomas' NHS Foundation Trust
London UK

Rebecca S. Beroukhim MD
Director, Fetal Echocardiography
Instructor in Pediatrics
Massachusetts General Hospital
Boston, MA, USA

William L. Border MBChB, MPH, FASE
Director of Noninvasive Cardiac Imaging
Medical Director, Cardiovascular Imaging Research Core (CIRC)
Children's Healthcare of Atlanta Sibley Heart Center;
Associate Professor
Emory University School of Medicine
Atlanta, GA, USA

David W. Brown MD
Assistant Professor of Pediatrics
Department of Cardiology
Boston Children's Hospital;
Department of Pediatrics
Harvard Medical School
Boston, MA, USA

Frank Cetta MD
Professor of Medicine and Pediatrics
Mayo Clinic
Rochester, MN, USA

Sarah Chambers MD
The Pediatric Heart Center at the Children's Hospital at Montefiore
New York, NY, USA

Michael Cheung BSc, MB ChB, MRCP(UK), MD
Associate Professor
Head of Cardiology
Royal Children's Hospital;
Department of Paediatrics
University of Melbourne;
Heart Research Group
Murdoch Childrens Research Institute
Melbourne, VIC, Australia

Meryl S. Cohen MD
Professor of Pediatrics
Perelman School of Medicine, University of Pennsylvania;
Medical Director, Echocardiography
Program Director, Cardiology Fellowship
The Cardiac Center
The Children's Hospital of Philadelphia
Philadelphia, PA, USA

Steven D. Colan MD
Professor of Pediatrics
Harvard Medical School;
Boston Children's Hospital
Boston, MA, USA

Julie De Backer MD, PhD
Senior Lecturer
Department of Cardiology and Medical Genetics
University Hospital Ghent
Ghent, Belgium

Jan D'hooge MD
Professor
Department of Cardiovascular Sciences
Catholic University of Leuven;
Medical Imaging Research Center
University Hospital Gasthuisberg
Leuven, Belgium

Allison Divanovic MD
Assistant Professor of Pediatrics
University of Cincinnati College of Medicine
The Heart Institute
Cincinnati Children's Hospital Medical Center
Cincinnati, OH, USA

Stacey Drant MD
Associate Clinical Professor
Director, Pediatric Echocardiography Laboratory
Children's Hospital of Pittsburgh
Pittsburgh, PA, USA

Benjamin W. Eidem MD, FACC, FASE
Professor of Pediatrics and Medicine
Mayo Clinic
Rochester, MN, USA

Matthew Fenton MB, BS, BSc
Consultant Paediatric Cardiologist
Cardiothoracic Unit
Great Ormond Street Hospital for Children and Institute of Cardiovascular Sciences
London, UK

Mark K. Friedberg MD
Associate Professor of Pediatrics
The Labatt Family Heart Center
The Hospital for Sick Children
University of Toronto
Toronto, ON, Canada

Peter C. Frommelt MD
Professor of Pediatrics
Director of Echocardiography
Division of Pediatric Cardiology
Medical College of Wisconsin
Children's Hospital of Wisconsin
Milwaukee, WI, USA

Michele A. Frommelt MD
Associate Professor of Pediatrics
Children's Hospital of Wisconsin
Milwaukee, WI, USA

Javiar Ganame MD, PhD
Department of Medicine
Division of Cardiology
McMaster University
Hamilton, ON, Canada

Tal Geva MD
Professor of Pediatrics
Harvard Medical School;
Chief, Division of Noninvasive Cardiac Imaging
Department of Cardiology
Boston Children's Hospital
Boston, MA, USA

Marc Gewillig MD, PhD, FESC, FACC, FSCAI
Professor Paediatric & Congenital Cardiology
University Hospitals Leuven
Leuven, Belgium

David J. Goldberg MD
Assistant Professor
Division of Pediatric Cardiology
The Children's Hospital of Philadelphia;
Perelman School of Medicine, University of Pennsylvania
Philadelphia, PA USA

J. René Herlong MD
Associate Clinical Professor of Pediatric Cardiology
Sanger Heart and Vascular Institute
Levine Children's Hospital
Charlotte, NC, USA

Lisa K. Hornberger MD
Professor of Pediatrics and Obstetrics & Gynecology
Director, Fetal and Neonatal Cardiology Program
Section Head, Pediatric Echocardiography
Stollery Children's Hospital
Edmonton, AB, Canada

Darren P. Hutchinson MBBS, FRACP
Fetal & Pediatric Cardiologist
Department of Pediatric Cardiology
The Royal Children's Hospital
Melbourne, VIC, Australia

Sachin Khambadkone MD
Paediatric and Adolescent Cardiology, Interventional Cardiologist
Great Ormond Street Hospital for Children and Institute of Cardiovascular Sciences
London, UK

Mary Etta E. King MD
Associate Professor of Pediatrics
Massachusetts General Hospital
Boston, MA, USA

H. Helen Ko BS, RDMS, RDCS
Mount Sinai Medical Center
New York, NY, USA

Joe R. Kreeger RCCS, RDCS
Technical Director, Echocardiography
Children's Healthcare of Atlanta Sibley Heart Center
Atlanta, GA, USA

Andreas Kühn MD
Department of Pediatric Cardiology and Congenital Heart Disease
Deutsches Herzzentrum München
Technische Universität München
Munich, Germany

Wyman W. Lai MD, MPH
Professor of Pediatrics at CUMC
Columbia University Medical Center;
Director, Noninvasive Cardiac Imaging
Morgan Stanley Children's Hospital of NewYork-Presbyterian
New York, NY, USA

Matthew S. Lemler MD
Professor of Pediatrics
Division of Cardiology
University of Texas Southwestern;
Director, Echocardiography Laboratory
Children's Medical Center of Dallas
Dallas, TX, USA

Jami C. Levine MS, MD
Associate in Cardiology
Assistant Professor of Pediatrics
Boston Children's Hospital
Boston, MA, USA

Leo Lopez MD
Associate Professor of Clinical Pediatrics
The Pediatric Heart Center
Children's Hospital at Montefiore
New York, NY, USA

Irene D. Lytrivi MD
Assistant Professor of Pediatrics
Icahn School of Medicine at Mount Sinai
Division of Pediatric Cardiology
Mount Sinai Medical Center
New York, NY, USA

Jan Marek MD, PhD
Associate Professor of Cardiology
Institute of Child Health
University College London;
Director of Echocardiography
Consultant Pediatric and Fetal Cardiologist
Great Ormond Street Hospital for Children
London, UK

Renee Margossian MD
Assistant Professor of Pediatrics
Harvard Medical School
Department of Cardiology
Boston Children's Hospital
Boston, MA, USA

Jackie McGhie
Congenital Cardiac Ultrasound Specialist
Department of Cardiology
Erasmus University Rotterdam
Rotterdam, The Netherlands

Colin J. McMahon MB, BCh, FRCPI, FAAP
Consultant Paediatric Cardiologist
Department of Paediatric Cardiology
Our Lady's Hospital for Sick Children
Crumlin, Ireland

Folkert Jan Meijboom MD, PhD
Staff Physician
Department of Pediatrics and Cardiology
Academic Medical Centre Utrecht
Utrecht, The Netherlands

Luc L. Mertens MD, PhD
Section Head, Echocardiography
The Hospital for Sick Children;
Professor of Pediatrics
University of Toronto
Toronto, ON, Canada

Erik C. Michelfelder MD
Associate Professor of Pediatrics
University of Cincinnati College of Medicine
The Heart Institute
Cincinnati Children's Hospital Medical Center
Cincinnati, OH, USA

Owen I. Miller FRACP, FCSANZ, FRCPCH
Head of Service/Clinical Lead, Congenital Heart Disease
Consultant in Pediatric and Fetal Cardiology
Evelina London Children's Hospital;
Guy's & St Thomas' NHS Foundation Trust;
Honorary Senior Lecturer, Kings College London
London, UK

Shobha Natarajan MD
Assistant Professor of Clinical Pediatrics
The University of Pennsylvania School of Medicine
Division of Cardiology
The Children's Hospital of Philadelphia
Philadelphia, PA, USA

James C. Nielsen MD
Associate Professor of Pediatrics and Radiology
Chief, Division of Pediatric Cardiology
Stony Brook Children's
Stony Brook, NY, USA

Erwin Oechslin MD, FRCPC, FESC
Director, Toronto Congenital Cardiac Centre for Adults
The Bitove Family Professor of Adult Congenital Heart Disease;
Professor of Medicine, University of Toronto
Peter Munk Cardiac Centre
University Health Network/Toronto General Hospital
Toronto, ON, Canada

Laurie E. Panesar MD
Assistant Professor of Pediatrics
Director, Fetal and Pediatric Echocardiography
Stony Brook Children's
Stony Brook, NY, USA

Ira A. Parness MD
Professor of Pediatrics
Division of Pediatric Cardiology
Mount Sinai Medical Center
New York, NY, USA

Andrew J. Powell MD
Department of Cardiology, Boston Children's Hospital;
Associate Professor of Pediatrics
Department of Pediatrics, Harvard Medical School
Boston, MA, USA

Claudio Ramaciotti MD
Professor of Pediatrics
Division of Cardiology
University of Texas Southwestern;
Children's Medical Center of Dallas
Dallas, TX, USA

Bo Remenyi MD
Menzies School of Health Research
Charles Darwin University
Darwin, NT, Australia

Jack Rychik MD
Professor of Pediatrics
Division of Pediatric Cardiology
The Children's Hospital of Philadelphia;
Perelman School of Medicine, University of Pennsylvania
Philadelphia, PA USA

Lindsay M. Ryerson MD, FRCPC
Assistant Clinical Professor
University of Alberta;
Division of Pediatric Cardiology
Stollery Children's Hospital
Edmonton, AB, Canada

Craig A. Sable MD
Director, Echocardiography and Telemedicine
Children's National Medical Center
Washington, DC, USA

Ritu Sachdeva MD
Medical Director, Cardiovascular Imaging Research Core
Children's Healthcare of Atlanta Sibley Heart Center;
Associate Professor of Pediatrics
Emory University School of Medicine
Atlanta, GA, USA

Stephen P. Sanders MD
Professor of Pediatrics (Cardiology)
Harvard Medical School;
Director, Cardiac Registry
Departments of Cardiology, Pathology, and Cardiac Surgery
Boston Children's Hospital
Boston, MA, USA

John M. Simpson MD, FRCP, FESC
Consultant in Fetal and Paediatric Cardiology
Department of Congenital Heart Disease
Evelina Children's Hospital;
Guy's and St Thomas' NHS Foundation Trust
London, UK

Timothy C. Slesnick MD
Director of Cardiac MRI
Children's Healthcare of Atlanta Sibley Heart Center;
Assistant Professor of Pediatrics
Emory University School of Medicine
Atlanta, GA, USA

Thierry Sluysmans MD, PhD
Professor of Pediatrics
Université Catholique de Louvain;
Director, Cliniques Universitaires Saint Luc
Brussels, Belgium

Jeffrey F. Smallhorn MBBS, FRACP, FRCPC
Professor of Pediatrics
University of Alberta;
Division of Pediatric Cardiology
Stollery Children's Hospital
Edmonton, AB, Canada

Shubhika Srivastava MBBS
Associate Professor of Pediatrics
Division of Pediatric Cardiology
Mount Sinai Medical Center
New York, NY, USA

Andrew Steer MD
Department of General Medicine and Centre for International Child Health
Department of Paediatrics
Royal Children's Hospital
Melbourne, VIC;
Group A Streptococcal Research Group, Murdoch Childrens Research Institute
Melbourne, VIC, Australia

Cécile Tissot MD
Attending Physician
Pediatric Cardiology Unit
The University Children's Hospital of Geneva
Geneva, Switzerland;
The Heart Institute
Children's Hospital Colorado
Aurora, CO, USA

Anne Marie Valente MD
Associate Professor of Pediatrics and Internal Medicine
Department of Cardiology, Department of Pediatrics
Boston Children's Hospital;
Division of Cardiology, Department of Medicine
Brigham and Women's Hospital;
Harvard Medical School
Boston, MA, USA

Heleen van der Zwaan MD, PhD
Department of Cardiology
Erasmus University Rotterdam
Rotterdam, The Netherlands

Manfred Otto Vogt MD, PhD
Professor of Pediatric Cardiology
Department of Pediatric Cardiology and Congenital Heart Disease
Deutsches Herzzentrum München
Technische Universität München
Munich, Germany

Adel K. Younoszai MD
Associate Professor, University of Colorado Denver
Director of Cardiac Imaging and Fetal Cardiology
The Heart Institute
Children's Hospital Colorado
Aurora, CO, USA

Preface

For the first edition of this textbook, we had set out to fill a void for an updated comprehensive resource on all aspects related to echocardiography in patients with congenital heart disease, from the fetus to the adult. We felt it was important to include detailed information about the anatomy and pathophysiology of each lesion and to describe the goals and techniques of the echocardiographic examinations for diagnosis, guidance of treatment, and monitoring after intervention. In addition to diagrams and still images, hundreds of videos were provided to illustrate key anatomic and functional issues mentioned in the text. We were pleased by the overwhelmingly positive response that the first edition of this book received.

In this second edition, we made improvements in multiple areas. The discussion of fundamental concepts of echocardiography and the sections on imaging techniques were updated to include advances in knowledge and improvements in ultrasound technology. Our coverage of congenital lesions was expanded to include separate chapters on the post-Fontan patient and on pregnancy and heart disease. Each of the lesion chapters now has a section highlighting the *Key elements* of the echocardiogram(s). Finally, all of the figures and videos were reviewed with the goal of upgrading and standardizing image quality and display technique.

The field of echocardiography remains dynamic and constantly evolving. Nevertheless, the mainstay for education in clinical echocardiography continues to be the written text illustrated with images. As we try to expand the resources available to trainees, practitioners, and educators, we are constrained by the publishing format currently available for textbooks. Therefore, our second edition remains mostly accessible in print or PDF format. The videos have moved from being primarily available on DVD to a companion website. Future efforts will no doubt benefit from greater electronic access to the text and images.

As with the first edition, this book is the product of many excellent contributions from the best physician and sonographer experts in the field. We are indebted to their dedication to the field and their commitment to education. We remain grateful to our mentors and colleagues, and we continue to be inspired by our trainees. The staff at Wiley-Blackwell have been truly supportive, and the professional appearance of this book is due to their many contributions. Finally, this and all projects in which the editors are involved remain possible only with the unwavering support of our families and friends.

Wyman W. Lai, MD, MPH
Luc L. Mertens, MD
Meryl S. Cohen, MD
Tal Geva, MD

About the Companion Website

This book is accompanied by a companion website:



www.lai-echo.com

The companion website includes over 580 video clips, referenced at the end of the chapters throughout the book.

PART I

Introduction to Cardiac Ultrasound Imaging

CHAPTER 1

Ultrasound Physics

Jan D'hooge[1] and Luc L. Mertens[2]

[1]Department of Cardiovascular Sciences, Catholic University of Leuven; Medical Imaging Research Center, University Hospital Gasthuisberg, Leuven, Belgium
[2]Cardiology, The Hospital for Sick Children; Department of Pediatrics, University of Toronto, Toronto, ON, Canada

Physics and technology of echocardiography

Echocardiography is the discipline of medicine in which images of the heart are created by using ultrasound waves. Knowledge of the physics of ultrasound helps us to understand how the different ultrasound imaging modalities operate and also is important when operating an ultrasound machine to optimize the image acquisition.

This section describes the essential concepts of how ultrasound waves can be used to generate an image of the heart. Certain technological developments will also be discussed as well as how systems settings influence image characteristics. For more detailed treatment of ultrasound physics and imaging there is dedicated literature, to which readers should refer, for example [1,2].

How the ultrasound image is created

The pulse–echo experiment

To illustrate how ultrasound imaging works, the acoustic "pulse–echo" experiment can be used:

1 A short electric pulse is applied to a piezoelectric crystal. This electric field will induce a shape change of the crystal through reorientation of its polar molecules. In other words, due to application of an electric field the crystal will momentarily deform.
2 The deformation of the piezoelectric crystal induces a local compression of the tissue with which the crystal is in contact: that is, the superficial tissue layer is briefly compressed resulting in an increase in local pressure; this is the so-called acoustic pressure (Figure 1.1).
3 Due to an interplay between tissue elasticity and inertia, this local tissue compression (with subsequent decompression, i.e., rarefaction) will propagate away from the piezoelectric crystal at a speed of approximately 1530 m/s in soft tissue (Figure 1.2). This is called the acoustic wave. The rate of compression/decompression determines the frequency of the wave and is typically 2.5–10 MHz (i.e., 2.5–10 million cycles per second) for diagnostic ultrasonic imaging. As these frequencies cannot be perceived by the human ear, these waves are said to be "ultrasonic." The spatial distance between subsequent compressions is called the wavelength (λ) and relates to the frequency (f) and sound velocity (c) as: $\lambda f = c$. During propagation, acoustic energy is lost mostly as a result of viscosity (i.e., friction) resulting in a reduction in amplitude of the wave with propagation distance. The shorter the wavelength (i.e., the higher the frequency), the faster the particle motion and the larger the viscous effects. Higher frequency waves will thus attenuate more and penetrate less deep into the tissue.
4 Spatial changes in tissue density or tissue elasticity will result in a disturbance of the propagating compression (i.e., acoustic) wave and will cause part of the energy in the wave to be reflected. These so-called "specular reflections" occur, for example, at the interface between different types of tissue (e.g., blood and myocardium) and behave in a similar way to optic waves in that the direction of the reflected wave is determined by the angle between the reflecting surface and the incident wave (cf. reflection of optic waves on a water surface). When the spatial dimensions of the changes in density or compressibility become small relative to the wavelength (i.e., below ~100 μm), these inhomogeneities will cause part of the energy in the wave to be scattered, that is, retransmitted in all possible directions. The part of the scattered energy that is retransmitted back into the direction of origin of the wave is called *backscatter*. Both the specular and backscattered reflections propagate back towards the piezoelectric crystal.
5 When the reflected (compression) waves impinge upon the piezoelectric crystal, the crystal deforms. This results in relative motion of its (polar) molecules and generation of an electric field, which can be detected and measured. The amplitude of this electric signal is directly proportional to the amount of compression of the crystal, that is, the amplitude of the reflected/backscattered wave. This electric signal is called

Echocardiography in Pediatric and Congenital Heart Disease: From Fetus to Adult, Second Edition. Edited by Wyman W. Lai, Luc L. Mertens, Meryl S. Cohen and Tal Geva.
© 2016 John Wiley & Sons, Ltd. Published 2016 by John Wiley & Sons, Ltd.
Companion website: www.lai-echo.com

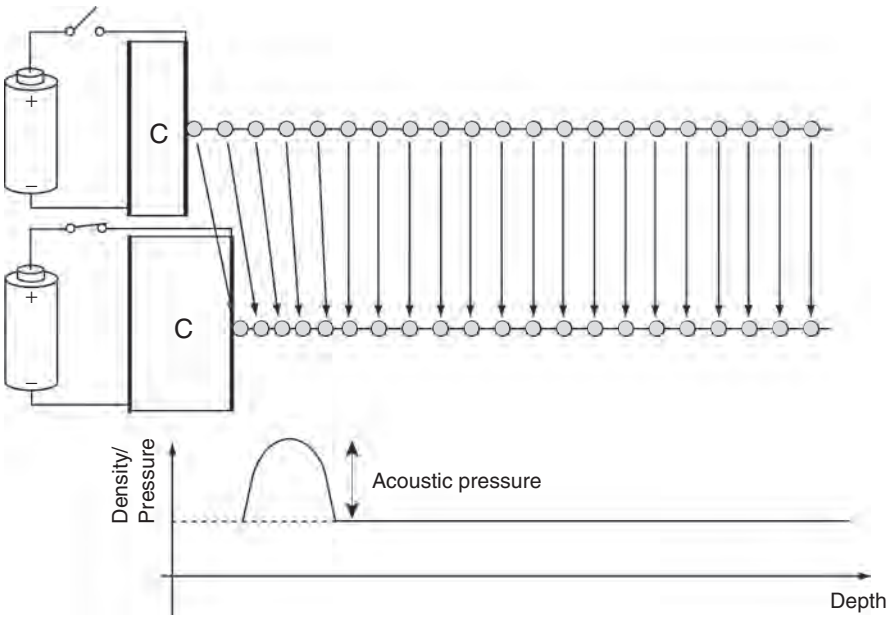


Figure 1.1 Local tissue compression due to deformation of the piezoelectric crystal when applying an electric field.

the radio-frequency (RF) signal and represents the amplitude of the reflected ultrasound wave as a function of time (Figure 1.3). Because reflections occurring further away from the transducer need to propagate further, they will be received later. As such, the time axis in Figure 1.3 can be replaced by the propagation distance of the wave (i.e., depth). The signal detected by the transducer is typically electronically amplified. The amount of amplification has a preset value but can be modified on an ultrasound system by using the "gain" button (typically the largest button on the operating panel). Importantly, the overall gain will amplify both the signal and potential measurement noise and will thus not affect the signal-to-noise ratio.

In the example shown in Figure 1.3, taken from a water tank experiment, two strong specular reflections can be observed (around 50 and 82 μs, respectively) while the lower amplitude reflections in between are scatter reflections. In clinical echocardiography, the most obvious specular reflection is the strong reflection coming from the pericardium observed in the parasternal views as a consequence of its increased stiffness with

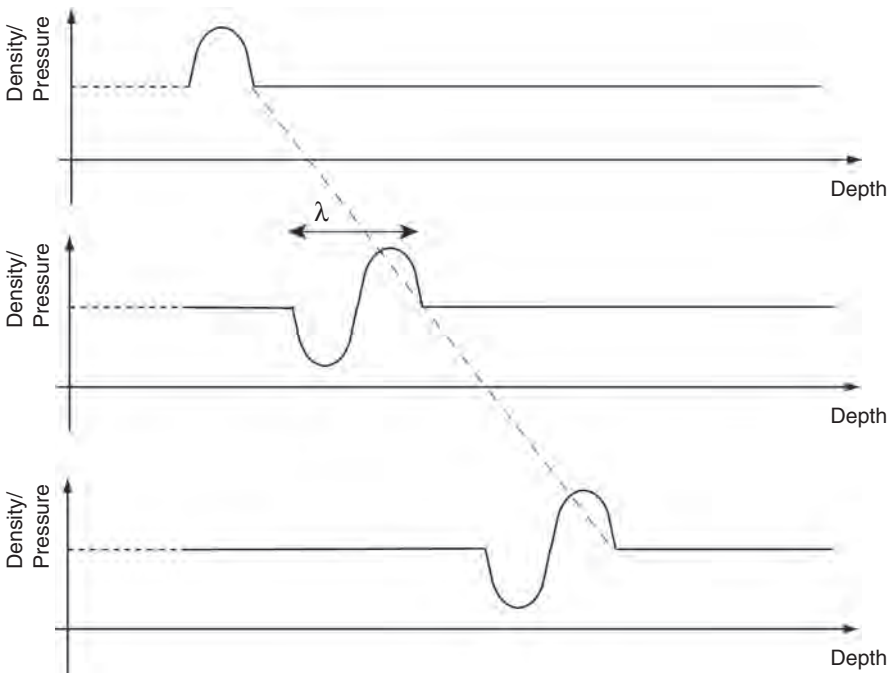


Figure 1.2 The local tissue compression/decompression propagates away from its source at a speed of approximately 1530 m/s in soft tissue.

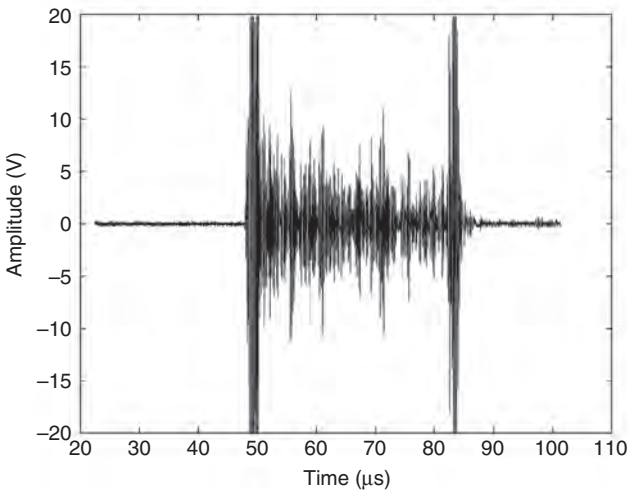


Figure 1.3 The reflected amplitude of the reflected ultrasound waves as a function of time after transmission of the ultrasound pulse is called the radio-frequency (RF) signal.

respect to the surrounding tissues. The direction of propagation of the specular reflection is determined by the angle between the incident wave and the reflecting surface. Thus, the strength of the observed reflection will depend strongly on the exact transducer position and orientation with respect to the pericardium. Indeed, for given transducer positions/orientations, the strong specular reflection might propagate in a direction not detectable by the transducer. For this reason, the pericardium typically does not show as bright in the images taken from an apical transducer position. In contrast, scatter reflections are not angle dependent and will always be visible for a given structure independent of the exact transducer position.

The total duration of the above described "pulse–echo" experiment is about 100 μs when imaging at 5 MHz. The reflected signal in Figure 1.3 is referred to as an A-mode image ("A" referring to "Amplitude") and is the most fundamental form of imaging given that it tells us something about the acoustic characteristics of the materials in front of the transducer. For example, Figure 1.3 clearly shows that at distance of ~3.7 cm in front of the transducer the propagation medium changes density and/or compressibility with a similar change occurring at a distance of ~6.3 cm (these distances correspond to 50/82 μs × 1530 m/s – which is the total propagation distance of the wave – divided by two as the wave has to travel back and forth). The 2.6 cm of material in between these strong reflections is acoustically inhomogeneous (i.e., shows scatter reflections) and thus contains local (very small) fluctuations in mass density and/or compressibility while the regions closer and further away from the transducer do not cause significant scatter and would thus be acoustically homogeneous. Indeed, this A-mode image was taken from a 2.6 cm thick tissue-mimicking material (i.e., gelatin in which small graphite particles were dissolved) put in a water tank.

Grayscale encoding

Since the A-mode image presented above is not visually attractive, the RF signal resulting from a pulse–echo experiment is processed in the following manner:

1 *Envelope detection:* The high-frequency information of the RF signal is removed by detecting the envelope of the signal (Figure 1.4). This process is also referred to as "demodulation."
2 *Grayscale encoding:* The signal is subdivided as a function of time in small intervals (i.e., pixels). Each pixel is attributed a number, defined by the local amplitude of the signal, ranging between 0 and 255 (2^8 or 8-bit image). "0" represents "black;" "255" represents "white;" a value in between is represented by a grayscale. By definition, bright pixels correspond to high-amplitude reflections. This process is illustrated in Figure 1.4. Please note that a different kind of color encoding is also possible simply by attributing different colors to the range of values between 0 and 255. For example, shades of blue or bronze are also popularly used. The choice of the color map used to display an image is a matter of preference and can easily be changed on all ultrasound systems. Nowadays, most ultrasound systems have 12- or 16-bit resolution images (i.e., encoding 4096 or 65536 gray/color levels).
3 *Attenuation correction*: As wave amplitude decreases with propagation distance due to attenuation (mostly due to conversion of acoustic energy to heat), reflections from deeper structures are intrinsically smaller in amplitude and therefore show less bright. In order to give identical structures located at different distances from the transducer a similar gray value (i.e., reflected amplitude), compensation for this attenuation must occur. Thus, an attenuation profile as a function of distance from the transducer is assumed, which allows for automatic amplification of the signals from deeper regions – the so-called *automated* time-gain compensation (TGC), also referred to as depth-gain compensation. As the pre-assumed attenuation profile might be incorrect, sliders on the ultrasound scanner (TGC toggles) allow for manual correction of the automatic compensation and will result in more or less local amplification of the received signal as required to obtain a more homogenous brightness of the image. In this way, the operator can optimize local image brightness. It is recommended to start scanning using a neutral setting of these sliders, as attenuation characteristics will be patient and view specific. For each view the TGC can be optimized manually.
4 *Log-compression*: In order to increase the image contrast in the darker (i.e., less bright) regions of the image, gray values in the image may be redistributed according to a logarithmic curve (Figure 1.5). The characteristics of this compression (i.e., local contrast enhancement) can be changed through settings on the ultrasound scanner. They will not change the ultrasound acquisition as such (and thus impact image quality) but will merely influence the visual representation of the resulting image. This is similar to what is nowadays very common in digital photography, where ambient lighting

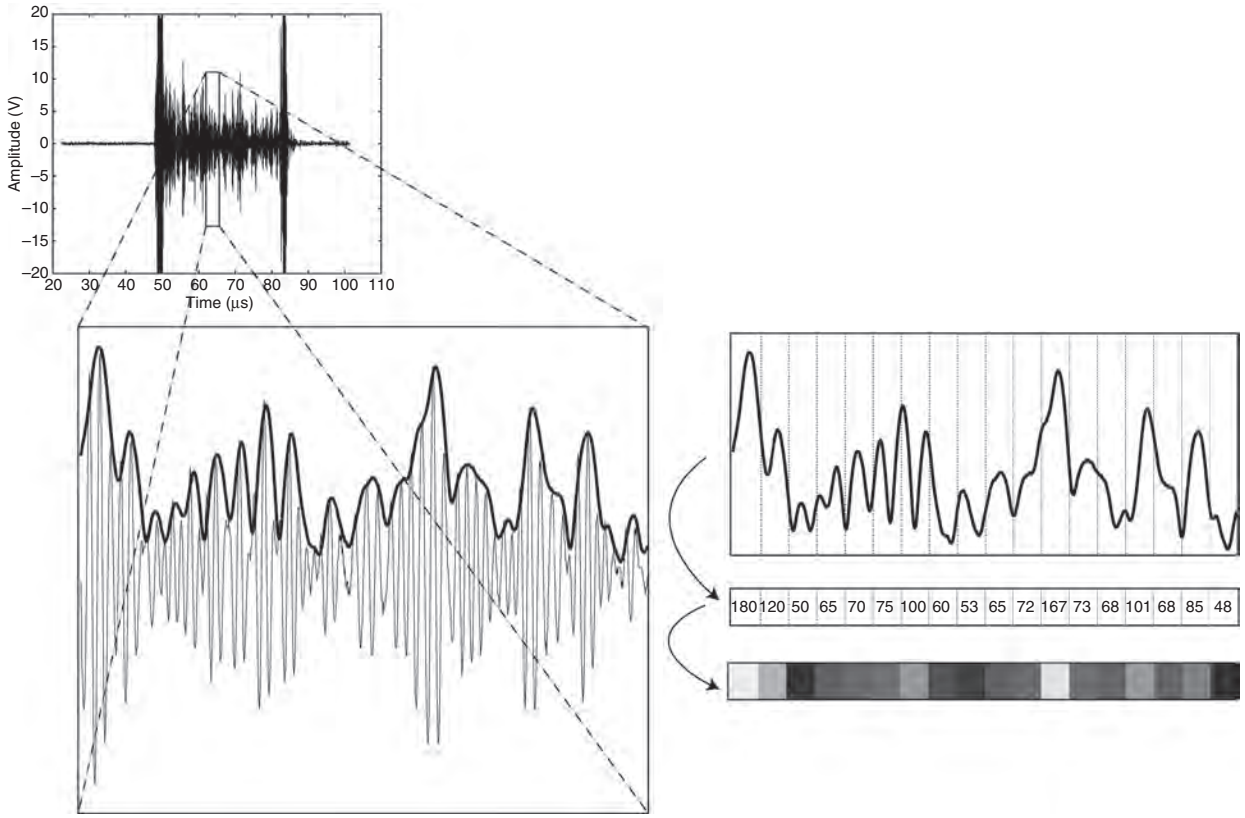


Figure 1.4 The RF signal is demodulated in order to detect its envelope. This envelope signal (bold) is color encoded based on the local signal amplitude.

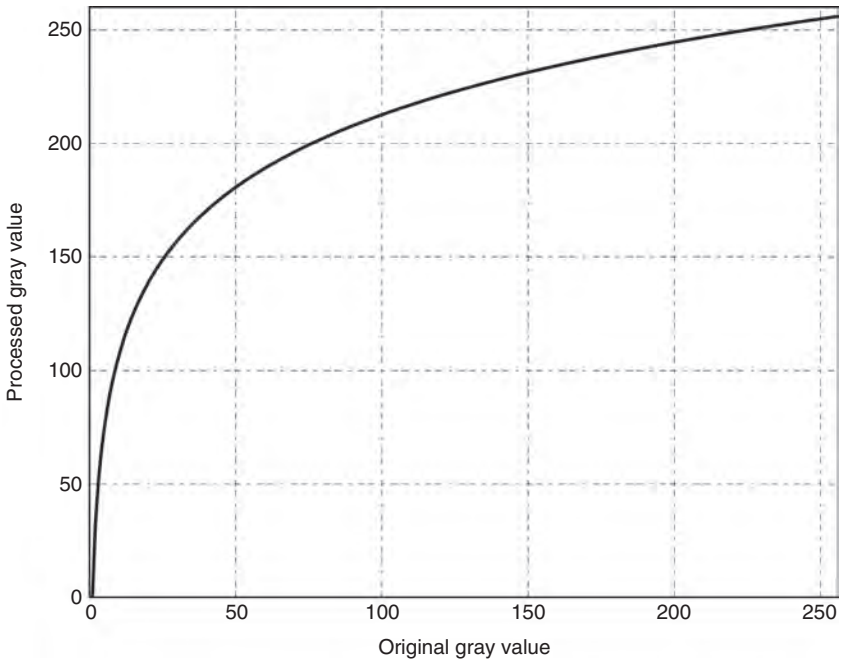


Figure 1.5 The logarithmic compression curve.

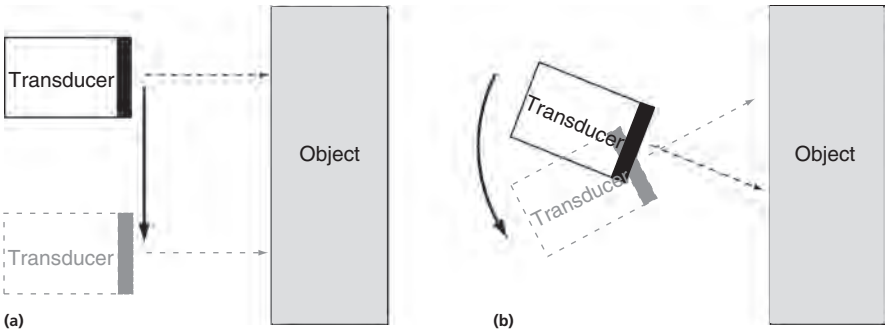


Figure 1.6 Translation of the ultrasound source results in a linear image format **(a)** whereas pivoting results in sector images **(b)**.

and/or contrast can be retrospectively enhanced. The setting on the system impacting the visual aspect of the image is the so-called "dynamic range" which will change the number of gray values used and will therefore result in "hard" (i.e., almost black-and-white images without much gray) or "soft" images for low and high dynamic range, respectively.

Image construction

In order to obtain an ultrasound image, the above procedures of signal acquisition and post-processing are repeated.

For conventional B-mode imaging ("B" referring to "brightness" mode), the transducer can either be translated (Figure 1.6a) or tilted (Figure 1.6b) within a plane between two subsequent "pulse–echo" experiments. In this way, a conventional 2D cross-sectional image is obtained. The same principle holds for 3D imaging by moving the ultrasound beam in 3D space between subsequent acquisitions.

Alternatively, the ultrasound beam is transmitted into the same direction for each transmitted pulse. In that case, an image line is obtained as a function of time, which is particularly useful to look at motion. This modality is therefore referred to as M-mode (motion-mode) imaging.

Image artifacts

Side lobe artifacts

In the construction of an ultrasound image, the assumption is made that all reflections originate from a region directly in front of the transducer. Although most of the ultrasound energy is indeed centered on an axis in front of the transducer, in practice part of the energy is also directed sideways (i.e., directed off-axis). The former part of the ultrasound beam is called the main lobe whereas the latter is referred to as the side lobes (Figure 1.7).

Because the reflections originating from these side lobes are much smaller in amplitude than the ones coming from the main lobe, they can typically be neglected. However, image artifacts can arise when the main lobe is in an anechoic region (i.e., a cyst or inside the left ventricular cavity) causing the relative contribution of the side lobes to become significant. In this way, a small cyst or lesion may be more difficult to detect, as it appears brighter than it should due to spillover of (side-lobe) energy from neighboring regions. Similarly, when using contrast agents (see later) the reflections resulting from small side lobes may still become significant as these agents reflect energy strongly. As such, increased brightness may appear in regions adjacent to regions filled with contrast without contrast being present in the region itself.

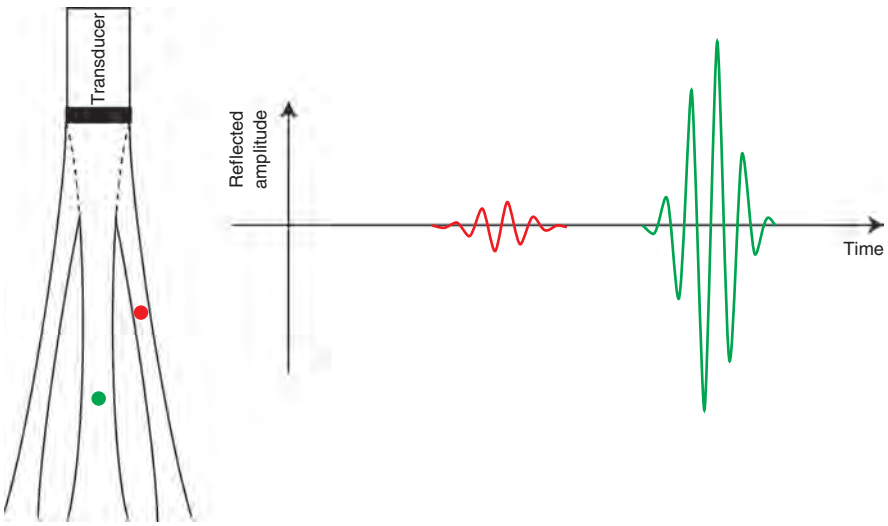


Figure 1.7 Reflections caused by side lobes (red) will induce image artifacts because all reflections are assumed to arrive from the main ultrasound lobe (green).

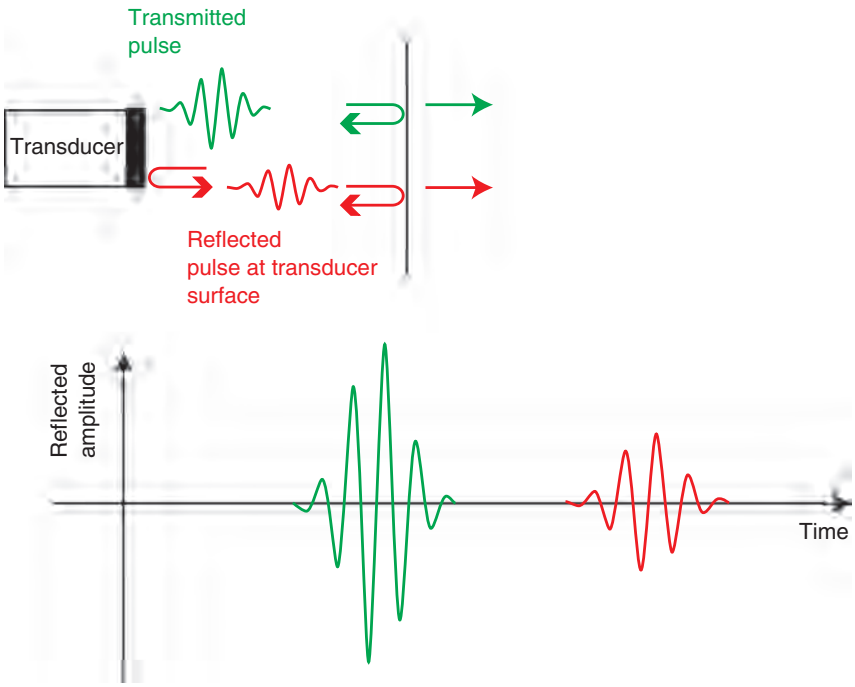


Figure 1.8 A transmitted wave (green) will reflect and result in an echo signal (green). The reflected wave will, however, partially reflect at the transducer surface (red) and generate secondary signals (red).

Reverberation artifacts

When the reflected wave arrives at the transducer, part of the energy is converted to electrical energy as described in the previous section. However, another part of the wave is simply reflected on the transducer surface and will start propagating away from the transducer as if it were another ultrasound transmission. This secondary "transmission" will propagate in a way similar to that of the original pulse, which means that it is reflected by the tissue and detected again (Figure 1.8).

These higher-order reflections are called reverberations and give rise to ghost (mirror image) structures in the image. These ghost images typically occur when strongly reflecting structures such as ribs or the pericardium are present in the image. Similarly, as the reflected wave coming from the pericardium is very strong, its backscatter (i.e., propagating again towards the pericardium) will be sufficiently strong as well. This wave will reflect on the pericardium and can be detected by the transducer after the actual pericardial reflection arrives. In clinical practice, this causes a ghost image to be created behind the pericardial reflection that typically appears as a mirror image of the left ventricle around the pericardium in a parasternal long-axis view.

Shadowing and dropout artifacts

When perfect reflections occur, no acoustic energy is transmitted to more distal structures and – as a consequence – no reflections from these distal structures can be obtained. As a result, a very bright structure will appear in the image followed by a signal void, that is, an acoustic shadow. For example, when a metallic artificial valve has been implanted, the metal (being very dense and extremely stiff) can cause close to perfect ultrasound reflections resulting in an apparently anechoic region distal to the valve. This occurs because no ultrasound energy reaches these deeper regions. Similarly, some regions in the image may receive little ultrasound energy due to superficial structures blocking ultrasound penetration. Commonly, ribs (being more dense and stiff than soft tissue) are fairly strong reflectors at cardiac diagnostic frequencies and can impair proper visualization of some regions of the image. These artifacts are most commonly referred to as "dropout" and can only be avoided – if at all – by changing the transducer position/orientation.

When signal dropout occurs at deeper regions only, the acoustic power transmitted can be increased. This will obviously result in more energy penetrating to deeper regions and will increase the overall signal-to-noise ratio of the image (in contrast to increasing the overall gain of the received signals as explained earlier). However, the maximal transmit power allowed is limited in order to avoid potential adverse biological effects. Indeed, at higher energy levels, ultrasound waves can cause tissue damage either due to cavitation (i.e., the formation of vapor cavities that subsequently implode and generate very high local pressures and temperatures) or tissue heating. The former risk is quantified in the "mechanical index" (MI) and should not pass a value of 1.9 while the latter is estimated through a "thermal index" (TI). Both parameters are displayed on the monitor during scanning and will increase with increasing power output. The operator thus has to find a compromise between image quality (including penetration depth) and the risk of adverse biological effects. In case penetration is not appropriate at maximal transmit power, the operator has to choose a transducer with lower transmit frequency (see earlier).

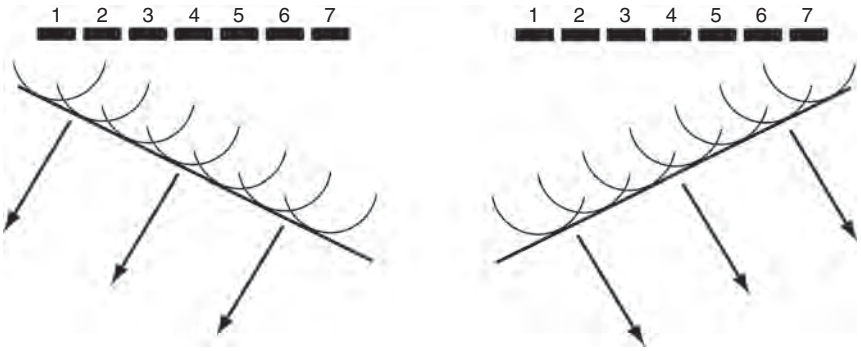


Figure 1.9 An array of crystals can be used to steer the ultrasound beam electronically by introducing time delays between the activation of individual elements in the array.

Ultrasound technology and image characteristics

Ultrasound technology

Phased array transducers

Rather than mechanically moving or tilting the transducers, as in early generation ultrasound machines, modern ultrasound devices use electronic beam steering. To do this an array of piezoelectric crystals is used. By introducing time delays between the excitation of different crystals in the array, the ultrasound wave can be sent in a specific direction without mechanical motion of the transducer (Figure 1.9). The RF signal for a transmission in a particular direction is then simply the sum of the signals received by the individual elements. These individual contributions can be filtered, scaled, and time-delayed separately before summing. This process is referred to as *beam-forming* and is a crucial element for obtaining high-quality images. The scaling of the individual contributions is typically referred to as *apodization* and is critical in suppressing side lobes and thus avoiding the associated artifacts.

This concept can be generalized by creating a 2D matrix of elements that enables steering of the ultrasound beam in three dimensions. This type of transducer is referred to as a matrix array or 2D array transducer. Because each of the individual elements of such an array needs electrical wiring, manufacturing such a 2D array remained technically challenging for many years, in part because of the limitation of the thickness of the transducer cable. Generally, these obstacles have been overcome and 2D arrays are now readily available.

Second harmonic imaging

Wave propagation as illustrated in Figure 1.2 is only valid when the amplitude of the ultrasound wave is relatively small (i.e., the acoustic pressures involved are small). Indeed, when the amplitude of the transmitted wave becomes significant, the shape of the ultrasound wave will change during propagation, as illustrated in Figure 1.10. This phenomenon of wave distortion during propagation is referred to as nonlinear wave propagation. It can be shown that this wave distortion causes harmonic frequencies (i.e., integer multiples of the transmitted frequency) to be

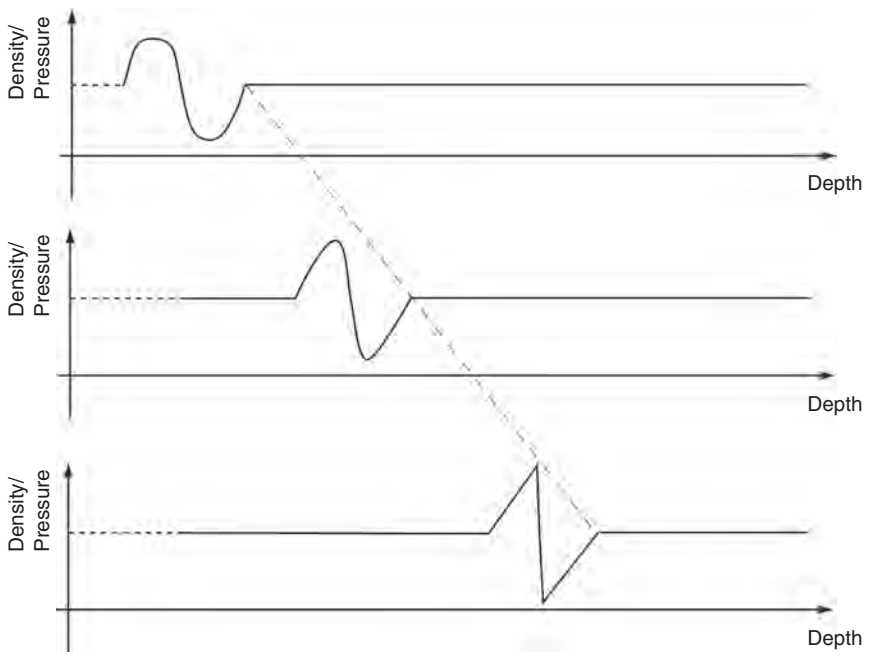


Figure 1.10 Nonlinear wave behavior results in changes in shape of the waveform during propagation.

generated. Transmitting a 1.7-MHz ultrasound pulse will thus result in the spontaneous generation of frequency components of 3.4, 5.1, 6.8, 8.5 MHz, and so on. These harmonic components will grow stronger with propagation distance. The rate at which the waveform distorts for a specific wave amplitude is tissue dependent and characterized by a nonlinearity parameter, β (or the so-called "B/A" parameter).

The ultrasound scanner can be set up to receive only the second harmonic component through filtering of the received RF signal. If further post-processing of the RF signal is done in exactly the same way as described earlier, a second harmonic image is obtained. Such an image typically has a better signal-to-noise ratio by avoiding clutter noise due to (rib) reverberation artifacts. This harmonic image is commonly used in patients with poor acoustic windows and poor penetration. Although harmonic imaging increases signal-to-noise, it has intrinsically poorer axial resolution as elucidated later. Please note that higher harmonics (i.e., third, fourth, etc.) are present but typically fall outside the bandwidth of the transducer and thus remain undetected. Harmonic imaging has become the default cardiac imaging mode for adult scanning on many systems. It is typically unnecessary to use harmonic imaging in young infants but is often required to enhance the image in the older patient. Switching between conventional and harmonic imaging is done by changing the transmit frequency of the system. For lower frequency transmits, it will automatically enter a harmonic imaging mode, which is indicated on the display by showing both transmit and receive frequencies (i.e., 1.7/3.4 MHz). When a single frequency is displayed, the scanner is in a conventional (i.e., fundamental) imaging mode. For pediatric scanning, especially in smaller infants, fundamental imaging is the preferred mode due to its better spatial resolution.

Contrast imaging

As blood reflects little ultrasound energy it shows dark in the image. For some applications (such as myocardial perfusion assessment) it can be useful to artificially increase the blood reflectivity. This can be achieved using an ultrasound contrast agent. As air is an almost perfect reflector of ultrasound energy given it is very compressible and has a low density compared to soft tissue, it often is used as a contrast agent. As such, the injection of small air bubbles (of diameter similar to that of red blood cells) will increase blood reflectivity. This can be done using agitated saline or by using ultrasound contrast agents that encapsulate air bubbles in order to limit diffusion of the air (or a heavier gas) in blood. Contrast imaging can be used to help in visualizing the endocardial border by enhancing the difference in gray value between the myocardium and the blood pool (i.e., left ventricular opacification) or to detect shunts. Similarly, contrast agents can be used to increase the brightness of perfused (myocardial) tissue although artifacts become more prominent and may make interpretation less obvious. At present, different contrast agents are commercially available for clinical use but none of them have been approved for pediatric use. Especially in the presence of right-to-left shunting, contrast agents should be used carefully.

Image resolution

Resolution is defined as the shortest distance at which two adjacent objects can be distinguished as separate. The spatial resolution of an ultrasound image varies depending on the position of the object relative to the transducer. Also the resolution in the direction of the image line (range or *axial* resolution) is different from the one perpendicular to the image line within the 2D image plane (azimuth or *lateral resolution*), which is different again from the resolution in the direction perpendicular to the image plane (*elevation resolution*).

Axial resolution

In order to obtain an optimal axial resolution, a short ultrasound pulse needs to be transmitted. The length of the transmitted pulse is mainly determined by the characteristics of the transducer. Current transducers can generate multiple frequencies influencing axial resolution by selecting different frequencies. The bandwidth is most commonly expressed relative to the center frequency of the transducer. A typical value would be 80% implying that for a 5-MHz transducer the absolute bandwidth is about 4 MHz. This type of transducer can thus generate/receive frequencies in the range of 3–7 MHz. The absolute transducer bandwidth is typically proportional to the mean transmission frequency. A higher frequency transducer will thus produce shorter ultrasound pulses and thus, better axial resolution. Unfortunately, higher frequencies are attenuated more by soft tissue and are impacted by depth (see earlier). As such, a compromise needs to be made between image resolution and penetration depth (i.e., field of view). In pediatric and neonatal cardiology, higher frequency transducers can be used that increase image spatial resolution. Generally, for infants 10–12-MHz transducers are used resulting in a typical axial resolution of the order of 250 μm.

Most systems allow changing the transmit frequency of the ultrasound pulse within the bandwidth of the transducer. As such, a 5-MHz transducer can be used to transmit a 3.5-MHz pulse which can be practical when penetration is not sufficient at 5 MHz. The lower frequency will result in a longer transmit pulse with a negative impact on axial resolution. Similarly, for second harmonic imaging a narrower band pulse needs to be transmitted, as part of the bandwidth of the transducer needs to be used to be able to receive the second harmonic. As such, in harmonic imaging mode, a longer ultrasound pulse is transmitted (i.e., less broadband) resulting in a worse axial resolution of the second harmonic image despite improvement of the signal-to-noise ratio. Therefore, some of the cardiac structures appear thicker, especially valve leaflets. This should be considered when interpreting the images.

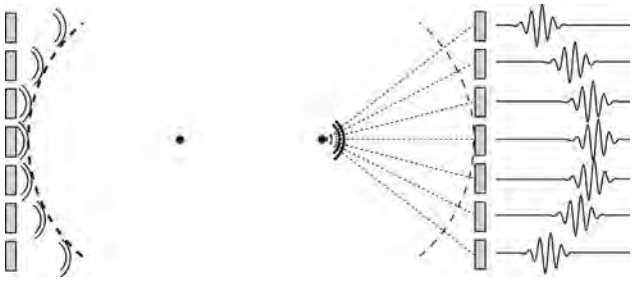


Figure 1.11 Introducing time delays during transmission of individual array elements (left) allows for all wavelets to arrive at a particular point (focus) simultaneously. Similarly, received echo signals can be time delayed so that they constructively interfere (receive focus).

Lateral resolution

Lateral resolution is determined by the width of the ultrasound beam (i.e., the width of the main lobe). The narrower the ultrasound beam, the better the lateral resolution. In order to narrow the ultrasound beam, several methods can be used but the most obvious one is focusing. This is achieved by introducing time delays between the firing of individual array elements (similar to what is done for beam steering) in order to assure that the transmitted wavelets of all individual array elements arrive at the same position at the same time and will thus constructively interfere (Figure 1.11). Similarly, time delaying the reflections of the individual crystals in the array will make sure that reflections coming from a particular point in front of the transducer will sum in phase and therefore create a strong echo signal (Figure 1.11). Because the sound velocity in soft tissue is known, the position from which reflections can be expected is known at each time instance after transmission of the ultrasound pulse. As such, the time delays applied in receive can be changed dynamically in order to move the focus point to the appropriate position. This process is referred to as *dynamic (receive) focusing*. In practice, dynamic receive focusing is always used and does not need adjustments by the operator in contrast to the transmit focus point whose position should be set manually. Obviously, to resolve most morphologic detail, the transmit focus should always be positioned close to the structure/region of interest. Most ultrasound systems allow selecting multiple transmit focal points. In this setting, each image line will be created multiple times with a transmit pulse at each of the set focus positions and the resulting echo signals will be combined in order to generate a single line in the image. Although this results in a more homogeneous distribution of the lateral resolution with depth, this obviously implies that it takes more time to generate a single image and thus will result in lowering the frame rate (i.e., temporal resolution).

The easiest way to improve the focus performance of a transducer is by increasing its size (i.e., aperture). Unfortunately, the footprint needs to fit between the patient's ribs, thereby limiting the size of the transducer and thus limiting lateral resolution of the imaging system. For an 8-MHz pediatric transducer, realistic numbers for the lateral resolution of the system are depth dependent and are approximately 0.3 mm at 2 cm going up to 1.2 mm at 7 cm depth.

Elevation resolution

For elevation resolution, the same principles hold as for lateral resolution in the sense that the dimension of the ultrasound beam in the elevation direction will be determinant. However, most ultrasound devices are still equipped with 1D array transducers. As such, focusing in the elevation direction needs to be done by the use of acoustic lenses (similar to optic lenses acoustic lenses concentrate energy in a given spatial position), which implies that the focus point is fixed in both transmit and receive (i.e., dynamic focusing is not possible in the elevation direction). This results in a resolution in the elevation direction that is worse than the lateral resolution. The homogeneity of the resolution is also worse with depth. Moreover, transducer aperture in the elevation direction is typically somewhat smaller (in order to fit in between the ribs of the patient) resulting in a further decrease of elevation resolution compared to the lateral component. Newer systems with 2D array transducer technology have more similar lateral and elevation image resolution. Matrix array transducers not only create 3D images but also allow generating 2D images of higher/more homogeneous spatial resolution.

Temporal resolution

Typically, a 2D pediatric cardiac image consists of 300 lines. The construction of a single image thus takes about 300 × 100 μs (the time required to acquire one line as explained earlier) or 30 ms. About 33 images can be produced per second, which is sufficient to look at motion (e.g., standard television displays only 25 frames per second). With more advanced imaging techniques such as parallel beam forming, higher frame rates can be obtained (70–80 Hz). In order to increase frame rate, either the field of view can be reduced (i.e., a smaller sector will require fewer image lines to be formed and will thus speed up the acquisition of a single frame) or the number of lines per frame (i.e., the line density) can be reduced. The latter comes at the cost of spatial resolution, as image lines will be further apart. There is thus an intrinsic trade-off between the image field-of-view, spatial resolution and temporal resolution. Most systems have a "frame rate" button nowadays that allow changing the frame rate although this always comes at the expense of spatial resolution. Higher frame rates are important when the heart rate is higher as is often the case in pediatric patients and when you want to study quickly moving structures like valve leaflets or myocardial wall motion.

Image optimization in pediatric echocardiography

All the aforementioned principles can be used to optimize image acquisition in the pediatric population. As children are smaller, less penetration is required. The heart rates are higher

requiring higher temporal resolution and, as structural heart disease is more common in the pediatric age group spatial resolution needs to be optimized to obtain the best possible diagnostic images. Image optimization will always be a compromise between spatial and temporal resolution. A few general recommendations can be made which can help in image optimization:

1. Always use the highest possible transducer frequency to optimize spatial resolution. For infants high-frequency probes (8–12 MHz) must be available and used. Often different transducers have to be used for different parts of the exam. So, for instance, for subcostal imaging in a newborn, a 5- or 8-MHz probe can be used while for the apical and parasternal windows a 10–12-MHz probe often provides better spatial resolution. For larger children and young adults 5-MHz and rarely 2.5–3.5-MHz probes can be used, although for the parasternal windows the higher-frequency probes generate good quality images also in this population.
2. Especially in smaller children harmonic imaging does not necessarily result in better image quality due to its intrinsically lower axial resolution. In general, fundamental frequencies provide good-quality images. Harmonic imaging is generally more useful in larger children and adults.
3. Gain and dynamic range settings are adjusted to optimize image contrast so that the structures of interest can be seen with the highest possible definition. TGCs are used to make the images as homogeneous as possible at different depths. Image depth and focus are always optimized to image the structures of interest.
4. For optimizing temporal resolution the narrowest sector possible is to be used.
5. Depth settings are minimized to include the region of interest.

Doppler imaging

Continuous-wave Doppler

When an acoustic source moves relative to an observer, the frequencies of the transmitted and the observed waves are different. This phenomenon is known as the Doppler effect. A well-known example is that of a whistling train passing a static observer: the observed pitch of the whistle is higher when the train approaches than when it moves away.

The Doppler phenomenon can be used to measure tissue and blood velocities by comparing the transmitted to the received ultrasound frequency. Indeed, when ultrasound scattering occurs at stationary tissues, the transmitted and reflected frequencies are identical. This statement is only true when attenuation effects are negligible. In soft tissue there will be an intrinsic frequency shift due to frequency-dependent attenuation. When scattering occurs at tissue in motion (Figure 1.12), a (additional) frequency shift – the Doppler shift (f_D) – will be induced that is

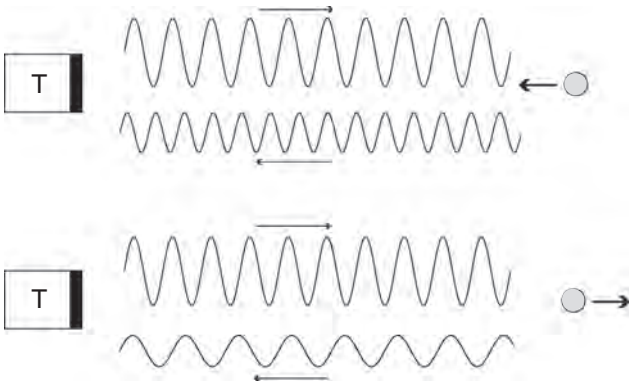


Figure 1.12 The Doppler effect will induce a frequency shift of the transmitted ultrasound wave when the reflecting object is in motion.

directly proportional to the velocity (v) by which the tissue is moving:

$$f_D = -2v\cos\theta f_T/c$$

where f_T is the transmit frequency, θ is the angle between the direction of wave propagation and the tissue motion, and c is the velocity of sound in soft tissue (i.e., 1530 m/s). Note that for motion orthogonal to the image line, θ = 90° and the Doppler shift is zero regardless of the amplitude of the tissue velocity v. The Doppler phenomenon thus only allows measuring the magnitude of the velocity along (parallel to) the image line (i.e., motion towards or away from the transducer) while motion orthogonal (perpendicular) to the line is not detected. In practice, an angle up to 20° is considered acceptable in order to obtain clinically relevant Doppler measurements. Ideally, the angle should always be minimized by selecting the proper image line for the Doppler recording or by repositioning the ultrasound transducer. Notably, the velocities cannot be overestimated due to angle dependency; thus, the highest value recorded is closest to the true one. Moreover, in case the angle between the flow and the ultrasound line is known (i.e., θ in the above equation), the velocity estimate can be corrected for this angle. Although this is possible in laminar flow conditions (such as flow in a nonstenosed vessel), the flow direction is typically not known in cardiac applications. Angle correction is therefore typically not made in cardiac ultrasound and should be used with care when applied.

In order to make a Doppler measurement, one piezoelectric crystal is used for transmitting a continuous wave of a fixed frequency and a second crystal is used to continuously record the reflected signals. Both crystals are embedded in the same transducer, and the frequency difference, that is, the Doppler shift, is continuously determined. The instantaneous shift in frequency is converted to a velocity according to the Doppler equation and is displayed as a function of time in a so-called *spectrogram*. However, because different velocities are present within

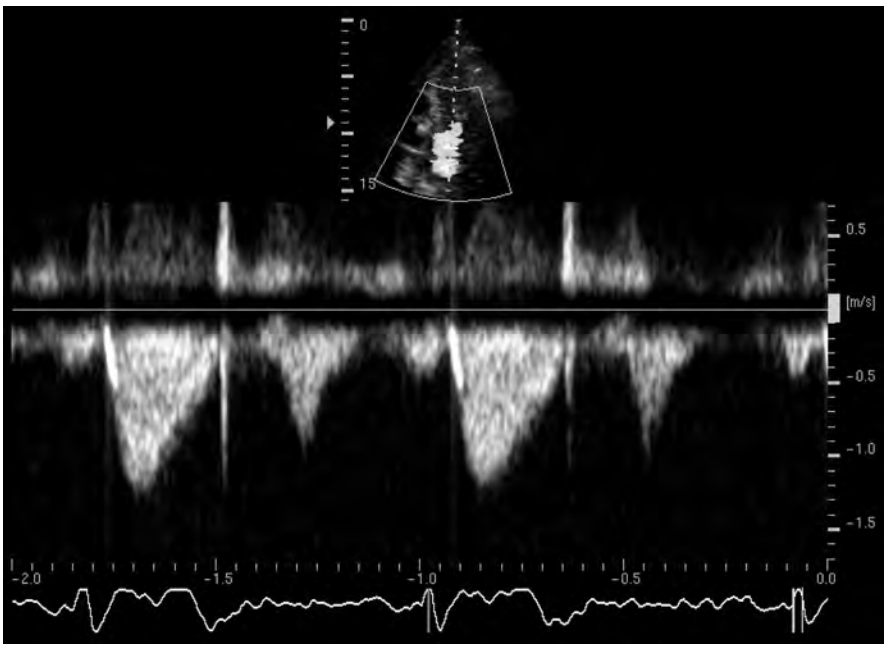


Figure 1.13 Example of a continuous-wave Doppler spectrogram of the left ventricular outflow tract.

the ultrasound beam for any given time instance during the cardiac cycle, a range of Doppler frequencies is typically detected. Thus, there is a spectrum of Doppler shifts measured and displayed in the spectrogram (Figure 1.13) – hence the name "spectral Doppler" often encountered in literature. Depending on the clinical application, the speed at which the spectrogram is updated can be modified (i.e., the sweep speed). For example, to look at beat-to-beat variations during the respiratory cycle, a low sweep speed can be used while a high sweep speed is needed when looking at flow characteristics within a single cardiac cycle.

Finally, as typical blood velocities cause a Doppler shift in the sonic range (20 Hz to 20 kHz), the Doppler shift itself can be made audible to the user. A high pitch (large Doppler shift) corresponds to a high velocity whereas a low pitch (small Doppler shift) corresponds to a low velocity. As such, the user gets both visual (spectrogram) and aural information on the velocities instantaneously present in the ultrasound beam.

The system described earlier is referred to as the continuous-wave (CW) Doppler system. As an ultrasound wave is transmitted continuously, no spatial information is obtained. Indeed, all velocities occurring anywhere within the ultrasound beam (i.e., on the selected ultrasound line of interrogation) will contribute to the reflected signal and appear in the spectrogram. In fact, as the ultrasound signal weakens with depth due to attenuation, velocities close to the transducer will intrinsically contribute more than the ones occurring further away. For most applications CW Doppler is combined with 2D imaging which allows the operator to align the Doppler signal based on the anatomical information. Sometimes the relatively large footprint of the probe does not allow a good Doppler alignment and the use of a small blind probe can help with obtaining better Doppler alignment. This can be used, for instance, for measurement of a peak gradient across the aortic valve in case of aortic valve stenosis.

Optimization of CW Doppler

1. Alignment with the direction of the measured velocity should be optimized.
2. The gain control affects the ratio of the output signal strength to the input signal strength. The gain controls should be manipulated to produce a clean uniform profile without any "blooming." The gain controls should be turned up to overemphasize the image and then adjusted down. This will prevent any loss of information due to too little gain.
3. The compress control assigns the varying amplitudes a certain shade of gray. If the compress control is very low or high the quality of the spectral analysis graph will be affected and this may lead to erroneous interpretation.
4. The reject button eliminates the smaller amplitude signals that are below a certain threshold level. This will help to provide a cleaner image and may make measurements more obvious.
5. The filter is used to reduce the noise that occurs from reflectors that are produced from walls and other structures that are within the range of the ultrasound beam.

Pulsed-wave Doppler

The "pulse–echo" measurement described previously can be repeated along a particular line in the ultrasound image at a given repetition rate (referred to as the "pulse repetition frequency," or PRF). Rather than acquiring the complete RF signal as a function of time, in pulsed-wave Doppler mode, a single sample of each reflected pulse is taken at a fixed time after the transmission of the pulse (the so-called range gate or sample volume). Assuming the position of the scattering sites relative to the

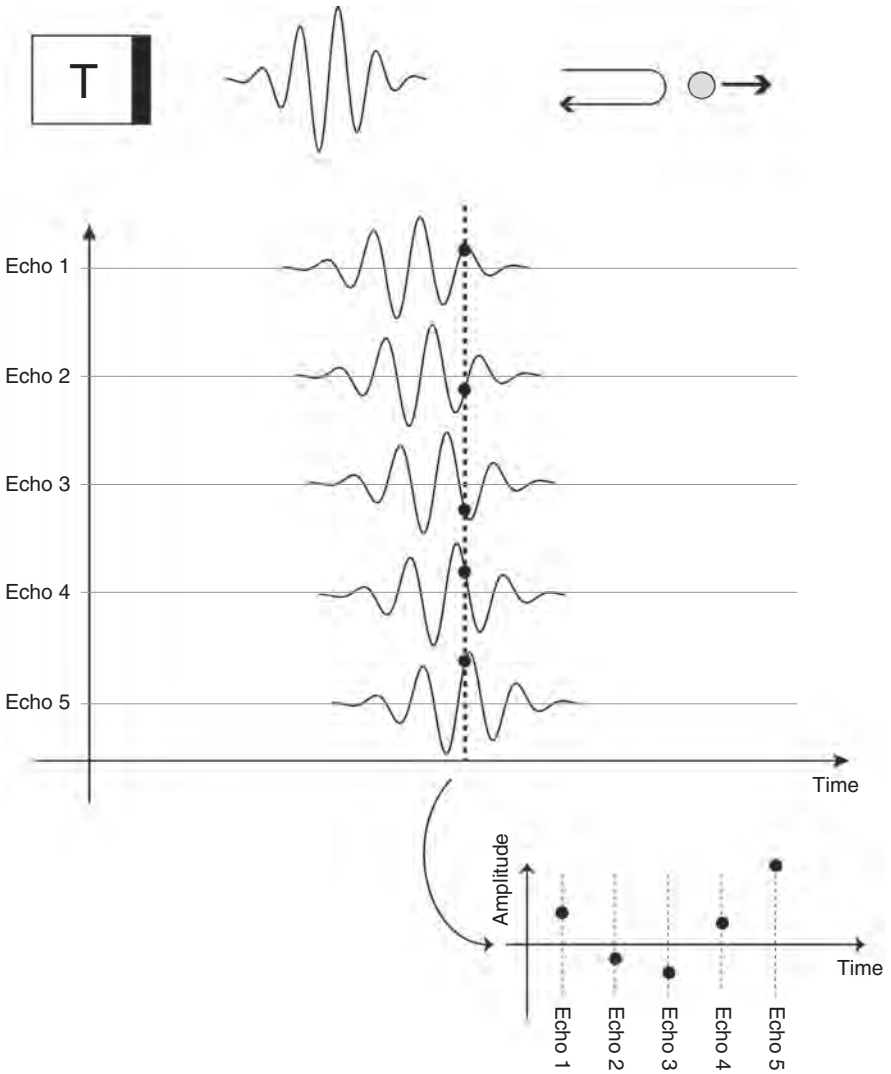


Figure 1.14 Schematic illustration of the principle of the pulsed-wave Doppler system.

transducer remains constant over time, all reflections (therefore all samples taken at the range gate) will be identical. However, when the tissue is moving relative to the transducer, the ultrasound wave will have to travel further (motion away from the transducer) or less far (motion toward the transducer) between subsequent acquisitions. As a result, the reflected signal will shift in time and the sample taken at the range gate will change (Figure 1.14).

It can be demonstrated that the frequency of the signal constructed in this way is directly proportional to the velocity of the reflecting object following the same mathematical relationship that is given in the Doppler equation. For this reason, this imaging mode is referred to as pulsed-wave (PW) *Doppler* imaging despite the fact that the Doppler phenomenon as such is not exploited.

Note that motion orthogonal to the direction of wave propagation will not induce a significant change in propagation distance for the ultrasound wave; it will not result in a significant time shift of the reflected signal and will thus not be detected by the system.

For a PW Doppler system, velocities are displayed as a function of time in a spectrogram similar to what is done for the CW Doppler system (Figure 1.15). However, the velocities displayed in a PW spectrogram are occurring within a specific region (the sample volume) within the 2D image.

In practice, more than one sample is taken at the range gate. Moreover, it can be demonstrated that the accuracy of the velocity estimate is better for narrow band pulses (i.e., ultrasound pulses containing relatively few frequencies). By changing the size of the range gate, the bandwidth of the transmitted pulse can be changed. A larger range gate (i.e., a longer or more narrow band transmit pulse) will improve the accuracy of the velocity estimate and will improve the signal-to-noise ratio of the spectrogram but will obviously result in a less localized measurement. The operator can change the size of the range gate as appropriate.

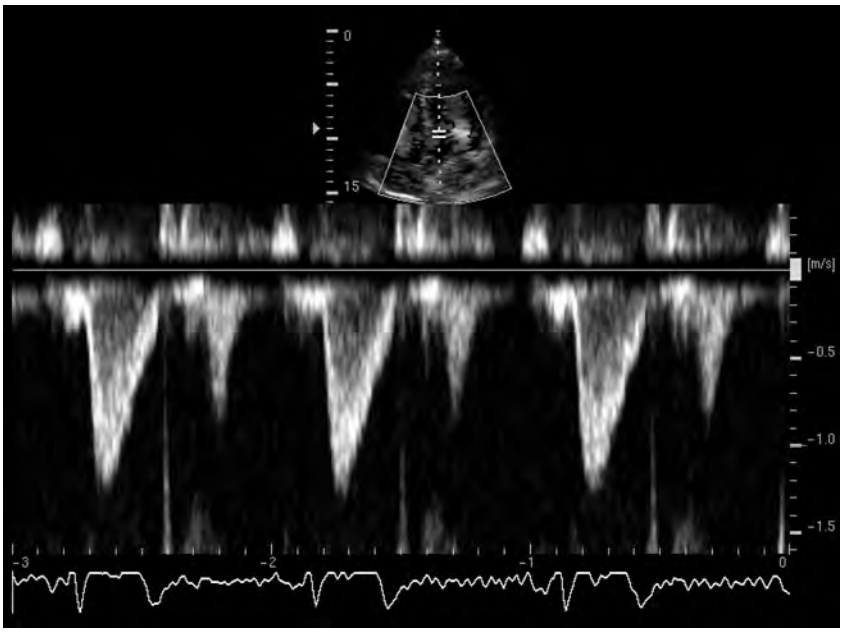


Figure 1.15 Example of a pulsed-wave Doppler spectrogram of the left ventricular outflow tract.

As explained earlier, blood is relatively poorly echogenic making it appear dark in the B-mode image. As a result, echo signals obtained from the blood are sensitive to, for example, side lobe artifacts and may thus contain echo signals coming from the wall. In order to avoid displaying these "spilled over" velocities in the spectrogram, low velocities are removed from the spectrogram using a high pass filter typically referred to as the "wall filter." The cut-off frequency of this high pass filter can be manually selected and should be chosen such that strong, low-amplitude velocities from the wall are adequately removed without significantly impacting the velocity spectrum of the blood itself.

Aliasing

If the velocity of the scattering object is relatively large and the shift between two subsequent acquisitions is larger than half a wavelength, the PW Doppler system cannot differentiate this high velocity (Figure 1.16a – red signal) from a low velocity (Figure 1.16a – green signal) because the extracted samples at the range gate are identical. This effect is known as aliasing, and a clinical example is given in Figure 1.16b. To avoid aliasing, either the PRF needs to be increased or the transmit frequency needs to be decreased. The latter option is not commonly used in practice while the former can be adjusted as required. Depending on the system, the PRF setting is referred to as "Nyquist velocity," "Scale," or "Velocity range." Moreover, in case the direction of flow is known, most systems allow shifting the baseline of the spectrogram thereby increasing the maximal velocity that can be measured without introducing aliasing.

Velocity resolution

A high PRF will ensure that aliasing will not occur when the maximal detectable velocity is high. However, as the ultrasound

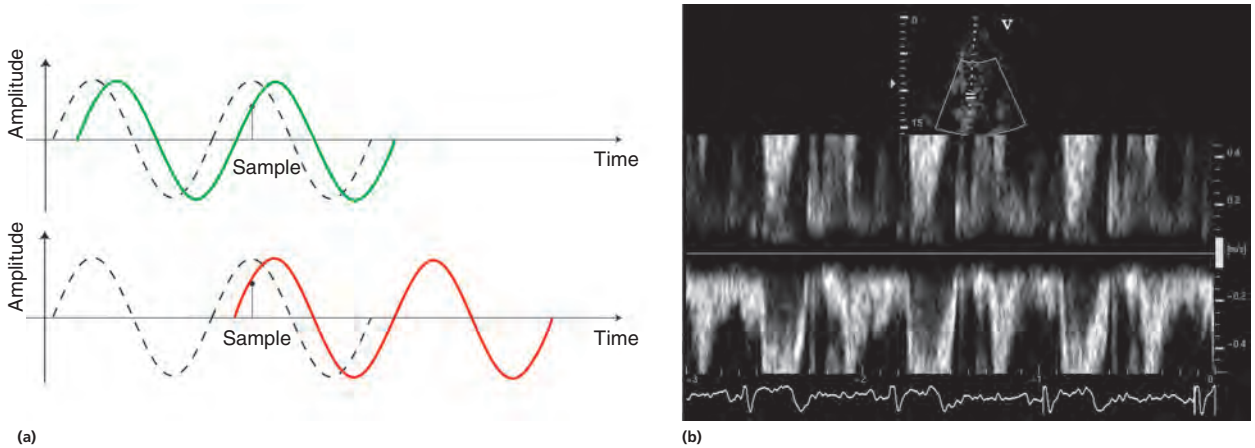


Figure 1.16 Principle of aliasing in Doppler acquisitions **(a)** and a practical example **(b)**.

system can only measure a fixed number of velocity amplitudes, the smallest difference between two velocity amplitudes detectable by the system will decrease with increasing PRF. As such, a compromise needs to be made between velocity resolution and maximal detectable velocity. For this reason, it is important in practice to keep the PRF as small as possible while still avoiding aliasing in order to have maximal accuracy of the velocity measurement. When the maximum velocity is high, PW Doppler will not be able to detect the highest velocity without aliasing and CW Doppler will be required to measure true peak velocities. Thus, in turbulent flow, both PW and CW Doppler interrogation is needed to make an accurate interpretation of location and maximum velocity. The velocity amplitude at which PW Doppler is no longer capable of measuring the velocity without aliasing is dependent on the transmit frequency, the PRF, and the depth at which these velocities occur (the closer to the transducer, the higher the maximal velocity that can correctly be measured).

Optimizing PW Doppler signals

1 As for any Doppler technique, alignment with the direction of the velocity is important.
2 The gain control, compress, filter settings are similar compared to CW Doppler.
3 Baseline: shift of the baseline allows the whole display to be used for either forward or reverse flow, which is useful if the flow is only in one direction.
4 The Nyquist limit should always be optimized and be set no higher or lower than necessary to display the measured flow velocities.
5 Sample volume: increase in sample volume increases the strength of the signal and more velocity information at the expense of a lower spatial resolution. In general the smallest sample volume that results in adequate signal-to-noise ratio should be used.

Color flow imaging

The PW Doppler measurement can be implemented for several range gates along the image line and can be repeated for each image line in order to obtain velocity information within a 2D region of interest. However, many ultrasound pulses need to be transmitted to reconstruct a single image line (as explained earlier), therefore the temporal resolution of such a system would be extremely poor (a maximal frame rate of a few Hertz is obtained). In order to overcome this problem, color flow (CF) imaging has been developed. CF imaging allows estimation of the flow velocity based on only two ultrasound transmissions in the same direction. Although in theory two pulses are indeed sufficient, in practice more pulses are used to improve the quality of the measurement. Indeed, similar to PW Doppler, motion of the scattering sites between acquisitions will result in a time delay between both reflected signals if motion of the tissue is present (Figure 1.17). By measuring this time delay between both reflections, the amount of tissue displacement between both acquisitions is obtained. The local velocity is then simply calculated as this displacement divided by the time interval between both acquisitions (= 1/PRF).

This procedure can be applied along the whole RF line in order to obtain local velocity estimates along the line (from close to the transducer to the deepest structures). Moreover, it is repeated between subsequent image lines within the 2D image. In this way, CF imaging can visualize the spatial distribution of the velocities by means of color superimposed onto the grayscale image. By convention, red represents velocities toward the transducer and blue represents velocities away from the transducer whereby different shades of red/blue indicate different velocity amplitudes. High variance of the velocity estimate measured in a given pixel is typically encoded by adding yellow or green to the color in this pixel. In this way, regions with high variance in the velocity estimate are highlighted as they indicate disturbed (i.e., turbulent) flow.

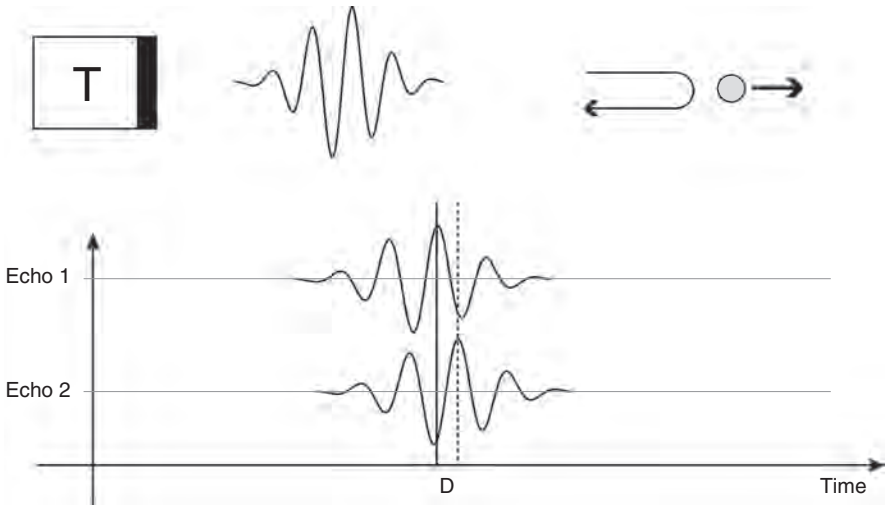


Figure 1.17 Principle of color flow imaging.

Similar to the PW Doppler technique, aliasing can occur with CF imaging and can be reduced by increasing PRF (allowing less time for motion between the two acquisitions) or reducing the transmission frequency. However, PRF settings are linked to the velocity resolution in the same way as for the PW Doppler system. An important difference with the PW Doppler technique is that the local average velocity rather than the local spectrum in velocities is measured. Peak velocity values measured with both techniques will thus be different with CF imaging giving lower peak values.

Finally, it should be noted that creating a CF image takes more time than creating a B-mode image, as several pulses need to be sent along each image line. In order to keep the temporal resolution of the CF data set acceptable, the region in which velocities are effectively estimated should be minimized to the anatomically relevant region only. All systems enable this by buttons affecting the size of the so-called "color box."

Optimizing color Doppler imaging

1 Use the smallest color Doppler sector as necessary. Large sector color Doppler has lower temporal resolution.
2 Gain settings should be adjusted until background noise is detected in the color image and then reducing it so that the background noise disappears.
3 Nyquist limit (scale): should be adapted depending on the velocities of the flows measured. When looking at high velocity flows, the scale should be adjusted so a high Nyquist limit is chosen. When low velocities are studied (coronary flow, venous flows), the scale needs to be lowered to allow the display of these lower velocities.

Myocardial velocity imaging

Doppler myocardial imaging

The exact same Doppler systems as described earlier can be used to measure myocardial velocities rather than blood velocities. The only difference is related to filtering: when imaging blood velocities the goal is to filter out slowly moving, strongly reflecting structures (i.e., velocities originating from the myocardium) whereas myocardial velocity imaging requires filtering structures that are moving at high velocity and which have low scattering power (i.e., the blood). On occasion, Doppler myocardial imaging displays slowly moving blood as these velocities do not only fall within the typical myocardial velocity range but also have brightness similar to that of myocardium due to blood aggregation. To measure tissue Doppler velocities, both PW Doppler and color Doppler can be used. For both techniques optimization of the Doppler beam alignment with the direction of motion is important. As color Doppler velocities do not represent peak velocities, the velocities measured are generally lower compared to the velocities measured by PW Doppler. As in the pediatric heart tissue Doppler velocities can be higher than in the adult population, attention should be paid to avoid aliasing during the image acquisition. Also for color tissue Doppler, acquiring at the highest possible frame rates, is important. This can be achieved by reducing the sector width and by using the frame rate button, which reduces the number of echo beams used to generate the images in turn reducing spatial resolution.

Estimation of motion in 2D: speckle tracking

A limitation of the conventional Doppler techniques (CW, PW, and CF) is that they only detect motion along the image line. Indeed, motion perpendicular to the image line will not be detected.

In order to overcome this limitation several methods have been proposed, but a very popular one is a technique commonly referred to as "speckle tracking." The principle of "speckle tracking" is very simple: a particular segment of tissue is displayed in the ultrasound image as a pattern of gray values (Figure 1.18). Such a pattern, resulting from the spatial distribution of gray values, is commonly referred to as a "speckle pattern." This pattern characterizes the underlying myocardial tissue acoustically and is (assumed to be) unique for each tissue segment. It can therefore serve as a fingerprint of the tissue segment within the ultrasound image.

If the position of the tissue segment within the ultrasound image changes, we can assume that the position of its acoustic fingerprint will change accordingly. Tracking of the acoustic pattern during the cardiac cycle thus allows detection of the motion of this myocardial segment within the 2D image. The

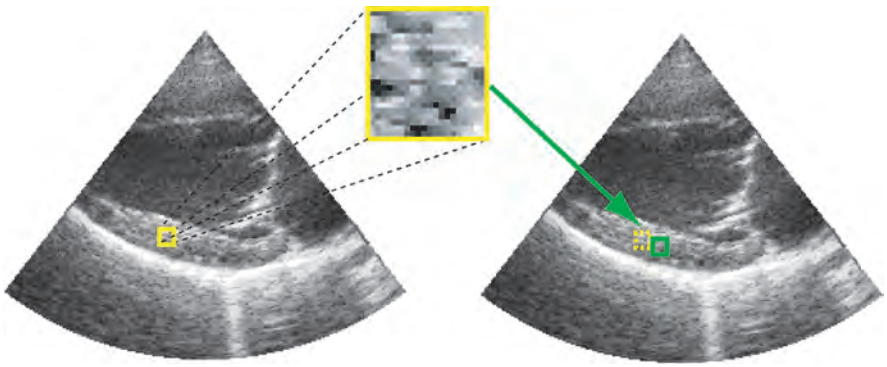


Figure 1.18 A particular segment of soft tissue (i.e., the heart) results in a specific spatial distribution of gray values (i.e., speckle pattern) in the ultrasound image. This pattern can be used as an acoustic marker of the tissue.

same approach can be taken when 3D datasets are available. Fundamental to this methodology is that speckle patterns are preserved between image frames. It can be shown that this is indeed the case if tissue rotation, deformation and out-of-plane motion between subsequent image frames are limited. An obvious way to achieve this is by acquiring grayscale data at a sufficiently high frame rate in order to make the time interval between subsequent image acquisitions short and as such avoid the above effects.

Although these methods were initially proposed to measure 2D myocardial velocities, they have more recently also been applied to measure 2D blood flow patterns using ultrasound contrast agents [3]. More information on ultrasound velocity estimation methodologies can be found in [4].

References

1 Suetens P. *Fundamentals of Medical Imaging*. Cambridge, UK: Cambridge University Press, 2002, Chapter 7: Ultrasonic imaging, pp. 145–183.
2 Szabo T. *Diagnostic Ultrasound Imaging: Inside Out*. London: Elsevier Academic Press, 2004.
3 Zheng H, Liu L, Williams L, et al. Real time multicomponent echo particle image velocimetry technique for opaque flow imaging. *Appl Phys Lett* 2006;**88**:261915.
4 Jensen JA. *Estimation of Blood Velocities Using Ultrasound*. Cambridge, UK: Cambridge University Press, 1996.

CHAPTER 2

Instrumentation, Patient Preparation, and Patient Safety

Stacey Drant and Vivekanand Allada
Pediatric Cardiology, Children's Hospital of Pittsburgh of UPMC, Pittsburgh, PA, USA

Introduction

With continued advances in ultrasound technology and accreditation requirements, establishing and maintaining a pediatric echocardiography laboratory (echo lab) has become progressively more complex. Echo labs have become increasingly "digital" requiring sophisticated information technology for digital acquisition, reporting and archiving. Lab accreditation has become more widespread to establish consistency within and between pediatric echo labs in an effort to assure quality. Guidelines and recommendations for pediatric echo labs have been published and incorporated into the requirements for accreditation. This chapter serves as a reference guide to establishing and maintaining a pediatric echo lab.

A variety of published recommendations exist pertaining to the organization and function of a pediatric echo lab from several medical societies including the American College of Cardiology (ACC), American Heart Association (AHA), American Academy of Pediatrics (AAP), and the American Society of Echocardiography (ASE). These recommendations have substantial overlap and form the basis for the requirements of the Intersocietal Accreditation Commission (IAC) necessary to achieve accreditation of a pediatric echo lab. For more detailed information, readers are referred to the applicable references and websites cited.

Structure and organization

Pediatric echo labs vary substantially in size and composition of the staff from individual office practices performing outpatient echocardiograms to large hospital-based labs that combine inpatient and outpatient imaging. In general, pediatric echo labs include physical space, ultrasound machines, pediatric cardiologists, and sonographers. They usually have a Medical and/or Technical Director to provide administrative functions.

Personnel and supervision

Physicians: The performance and interpretation of transthoracic echocardiograms is a requirement for cardiology fellowship training. Echocardiography is an operator-dependent imaging technique that requires skill in both performance and interpretation of studies. The recommendations of the ACC/AHA/AAP Clinical Competency and Training Statement on Pediatric Cardiology represent the most recent guidelines for echocardiography training [1]. These guidelines describe two levels of expertise, core and advanced, that are appropriate for different career goals. Core level training should be achieved by all pediatric cardiology fellows during their 3-year cardiology fellowship. Physicians with core level training are not expected to develop expertise in transesophageal and fetal echocardiography, though many fellows become competent in these areas. Advanced fellowship (generally requiring an additional year of training) allows for the development of skill and expertise in transthoracic, transesophageal, and fetal echocardiography and is often obtained when a faculty position in academic echocardiography is the goal. The specific minimum procedure numbers, knowledge base, and skills for the core and advanced levels of training are listed in Tables 2.1–2.3 [2]. At present in North America, there is no formal examination that can be used to determine competency in pediatric echocardiography; thus evaluation is based solely upon an assessment of the trainee's skills during fellowship training. Continued performance and interpretation of echocardiograms and participation in intramural conferences and continuing medical education is necessary to maintain clinical competency. In order to be accredited by the IAC in pediatric echocardiography, the medical staff of the lab are required to meet the training guidelines outlined above as well as demonstrate continuing medical education specific to pediatric echocardiography. IAC requires that each member of the medical staff should interpret a minimum of 300 pediatric studies annually [3].

Echocardiography in Pediatric and Congenital Heart Disease: From Fetus to Adult, Second Edition. Edited by Wyman W. Lai, Luc L. Mertens, Meryl S. Cohen and Tal Geva.
© 2016 John Wiley & Sons, Ltd. Published 2016 by John Wiley & Sons, Ltd.
Companion website: www.lai-echo.com

Table 2.1 Pediatric echocardiography training: recommended minimum procedure numbers

Core training	Number of studies
TTE perform and interpret	150 (50 <1 year of age)
TTE review	150
Advanced training*	
TTE perform and interpret	200 (50 <1 year of age)
TTE review	200
TEE perform and interpret	50
Fetal echocardiogram	50

*Numbers are in addition to those obtained during core training.
TEE, transesophageal echocardiogram; TTE, transthoracic echocardiogram
Source: Saunders et al. 2005 [1]. Reproduced with permission of American Heart Association.

Table 2.2 Required knowledge base for core and advanced levels of expertise in pediatric echocardiography for physicians

Core training

- Understanding of the basic principles of ultrasound physics
- Knowledge of the indications for transthoracic echocardiography in pediatric patients
- Knowledge of common congenital heart defects and surgical interventions
- Knowledge of Doppler methods and their application for assessment of blood flow and prediction of intracardiac pressures
- Knowledge of the limitations of echocardiography and Doppler techniques
- Knowledge of alternative diagnostic imaging techniques
- Knowledge of standard acoustic windows and transducer positions
- Knowledge of image display and orientation used in pediatric echocardiography
- Ability to recognize normal and abnormal cardiovascular structures by 2-dimensional imaging and to correlate the cross-sectional images with anatomic structures
- Familiarity with standard echocardiographic methods of ventricular function assessment
- Familiarity with major developments in the field of noninvasive diagnostic imaging

Advanced (in addition to the knowledge base required in the core level)

- In-depth knowledge of ultrasound physics
- Ability to recognize and characterize rare and complex congenital and acquired cardiovascular abnormalities in a variety of clinical settings
- In-depth understanding of Doppler methods and their application to the assessment of cardiovascular physiology
- Familiarity with all echocardiographic methods available for assessment of global and regional ventricular function and knowledge of the strengths and weaknesses of these techniques
- Up-to-date knowledge of recent advances in the field of noninvasive cardiac imaging, including ability to review critically published research that pertains to the field
- Knowledge of current training guidelines and regulations relevant to pediatric echocardiography

Source: Lai et al. 2006 [2]. Reproduced with permission of Elsevier.

Sonographers: The technique of performing a pediatric echocardiogram has become increasingly sophisticated due to continued advances in cardiac ultrasound and its application to the pediatric population. This places added educational and professional demands on sonographers. The American Society of Echocardiography (ASE) has published minimum qualifications for cardiac sonographers [4,5], which are reflected in the IAC standards for technical staff summarized in Table 2.4. The current standards recognize that training in cardiac sonography has historically been heterogeneous. More recently, the importance of a formal verifiable education in cardiac sonography has been emphasized to guarantee that new sonographers have adequate knowledge and technical skills to be competent in contemporary pediatric echocardiography. Current guidelines recommend that each sonographer achieves and maintains minimum standards in education and credentialing in pediatric and/or fetal echocardiography within 2 years of the start of employment [6]. Requirements for credentialing and maintenance of competence are listed in Table 2.5.

Facility

The facility must meet the standards set forth by the Occupational Safety and Health Administration and by the Joint Commission where applicable.

Space requirements: The ASE [6] and the IAC [3] recommend that echo laboratories should be large enough to accommodate an area for scanning, designated space for the interpretation and preparation of reports, and space for the storage of images and reports to remain compliant with state laws (Figure 2.1). The scanning space needs to be large enough to accommodate a patient bed that allows for position changes, an echo imaging system, and patient privacy; a scanning room is generally recommended to be at least 150 square feet [7]. In addition, a sink and antiseptic soap must be readily available and used for hand washing in accordance with the infection control policy of the facility. For the practice of transesophageal echocardiography, space must be available to perform high-level disinfection and to store transesophageal echocardiography probes.

Equipment: Pediatric echo labs require a variety of equipment to function effectively. In addition to the ultrasound systems, other equipment is needed (Table 2.6) including a specialized bed, gel warmer, and blood pressure machine. Forms of distraction such as DVD players or televisions are also recommended to entertain young children during the performance of the studies. All imaging equipment should be tested on a regular basis; the manufacturer's recommendations regarding preventative maintenance should be followed. Echo labs that perform special procedures, including TEE, stress echo and sedated echocardiograms, should also have written procedures in place to handle acute medical emergencies including maintaining a

Table 2.3 Required skills for core and advanced levels of expertise in pediatric echocardiography for physicians

Core training
Ability to safely, properly, and efficiently use cardiac ultrasound equipment
Ability to perform a complete transthoracic echocardiographic examination with proper use of M-mode, 2-dimensional, and Doppler techniques in normal pediatric patients and in those with heart disease, with consultation as needed
Advanced training (in addition to the skills required in the core level)
Ability to perform independently a complete transthoracic echocardiographic examination with proper use of all available ultrasound techniques in patients with all types of congenital heart disease
Ability to assess cardiovascular physiology and global and regional ventricular function using a variety of ultrasound techniques
Ability to supervise and teach pediatric echocardiography to sonographers, pediatric cardiology fellows, and other physicians

Source: Lai et al. 2006 [2]. Reproduced with permission of Elsevier.

fully equipped crash cart and other pediatric specific medical equipment in a variety of sizes to accommodate patients of varying sizes [3].

Ultrasound systems: Ultrasound systems dedicated to echocardiography must include the hardware and software to perform M-mode, two-dimensional (2D) imaging, color flow and spectral Doppler along with ECG gating [2,3,6]. There should also be a system setting for tissue Doppler imaging [3]. The image display may include the name of the institution, patient name, date and time of the study, the ECG tracing, and range and depth markers. Echocardiography has specific transducer requirements, including the ability for the transducer head to fit in between rib spaces for a variety of patient sizes as well as the wedge-shaped sector display. Transducers ranging from 2.0–12 MHz providing both low and high frequency imaging are required for pediatric imaging due to the range in patient size from premature infants to adults with congenital heart disease. In addition, a dedicated nonimaging continuous-wave Doppler transducer (Pedoff) must be available. All machines should have harmonic imaging capability and other instrument settings that enable the optimization of both standard and contrast-enhanced ultrasound exams.

Echo lab personnel, including sonographers, trainees, and physicians must be able to adjust the system settings for image optimization; thus an in-depth familiarity with each system is ideal. Pediatric echocardiography often incorporates significantly more vascular imaging than adult labs to evaluate the systemic venous return, pulmonary veins, branch pulmonary arteries, coronary arteries, and the aortic arch. These static structures benefit from different system settings than the more

Table 2.4 ASE guidelines for pediatric cardiac sonographer

Comprehensive understanding of:
Cardiovascular and thoracic anatomy, pathophysiology, hemodynamics, and embryology
Congenital and acquired heart defects
Segmental approach to the diagnosis of congenital heart defects
Surgical procedures for repair and palliation of congenital heart defects
Ultrasound physics
Instrumentation
Tissue characteristics
Biological effects of ultrasound
Measurements of cardiac structures and blood flow
Making appropriate quantitative calculations from echo measurements
Communication and safety-related skills:
Ability to interact and communicate effectively both orally and in writing
Be well versed in medical terminology
Capable of explaining the purpose of the echo exam to the patient and answer questions
Utilize proper infection control procedures
Comply with patient confidentiality and privacy laws
Competent in first aid and basic life support
Familiar with other types of diagnostic tests

Table 2.5 ASE guidelines for credentialing and maintenance of competence in pediatric echocardiography

Credentialing and education
• Credentialing recognized by ASE
RDCS: Registered Diagnostic Cardiac Sonographer
RDMS: American Registry for Diagnostic Medical Sonography in adult, pediatric, or fetal echocardiography
RCS: Registered Cardiac Sonographer by CCI, Cardiovascular Credentialing International
• Formal education
At least 12 months of full-time echocardiography education in a program recognized by ASE*
Additional 6 months (minimum) clinical instruction in a primary pediatric setting recommended for comprehensive training in pediatric echocardiography
Technical expertise
• Must be able to properly display cardiac and/or vascular structures and blood flow in each of the imaging views within a standardized protocol
• Proficiency in 2D, M-mode, and Doppler echocardiography
• Ability to accurately document abnormal echocardiography and Doppler velocities indicative of abnormal cardiovascular pathophysiology
• Demonstrate knowledge and competency in specialty areas of echocardiography when required in practice
Maintenance of competence
• Perform a minimum of 100 pediatric echocardiograms annually
• Document at least 15 hours of echocardiography-related CME over a period of 3 years; 10 of these must be relevant to pediatric echocardiography

*For new cardiac sonographers entering the field



Figure 2.1 Echocardiography reading room with live imaging displayed on wall screens and dual screen work stations for efficient review of images and reporting.

mobile intracardiac structures and thus the ability to readily adjust the depth and gain along with the persistence, log compression, sector angle, gate, and Doppler filters becomes imperative. Most vendors have systems specialists who can provide training in the utilization and adjustment of the system settings in order to create optimal preset packages for each machine according to the institutional preferences.

Scheduling

Sufficient time should be allotted for each study according to the procedure type. Performance time for an uncomplicated complete pediatric transthoracic echocardiogram is generally 45–60 minutes from patient encounter to departure. Additional time may be required for (i) patients with complex disease, (ii) when other modalities such as three-dimensional (3D) imaging or speckle tracking imaging are required, or (iii) studies performed on sedated patients. An "urgent" study must be performed in the next available time slot while a "stat" study must be performed as soon as possible, pre-empting routine studies. Qualified personnel and equipment must be available for urgent or "stat" studies outside normal working hours in inpatient facilities or where appropriate [2,3,6]. Many busy pediatric echo labs have systems that schedule patients in time slots during the course of the day while others use a "first come, first served" type of schedule.

Table 2.6 Pediatric echocardiography laboratory equipment

- Ultrasound system
 - Hardware and software to perform M-mode, 2D, Doppler (including color, spectral [pulsed wave and continuous wave] and tissue Doppler modalities)
 - Image display including name of institution, patient name, date and time of study, ECG tracing, range and depth markers
 - Transducers
 - Frequency range 2.0–12.0 MHz
 - Dedicated nonimaging continuous-wave Doppler (Pedoff)
 - Transesophageal probes (if performed in the lab)
- Digital image storage method
- Imaging bed with dropout section of mattress
- Gel warmer
- Blood pressure machine (including age-appropriate cuff sizes)
- Distraction equipment (e.g., TV, DVD player, music player)
- Contrast agents and intravenous supplies
- Equipment to treat medical emergencies (suction, oxygen, code cart)

Storage

A permanent record of both echocardiographic images and the final echocardiographic report must be produced and retained in accordance with applicable state and federal guidelines. Federal guidelines fall under the *Healthcare Insurance Portability and Accountability Act* passed in 1996 and directs that facilities retain records for 6 years from the date of creation [8]. State laws also govern the length of time medical records need to be retained and vary from state to state; however, HIPAA requirements supersede state laws if the state law requires shorter retention periods.

Images must be archived as moving images in the original format that they were acquired. The current standard format has changed from analog media utilizing videotape to digital storage. The ASE has published guidelines for digital echocardiography [9] which describe digital archiving in detail. The DICOM (Digital Imaging and Communications in Medicine) standard was created through a collaboration of the National Electrical Manufacturers' Association and various professional organizations and serves to standardize the exchange of digital images allowing interoperability within and between echo labs. In order

to accommodate the large storage requirements, both clinical and digital compression is often required. Clinical compression is at the discretion of the imager and can be accomplished by limiting the time length of a clip or the number of clips. Digital compression is accomplished utilizing JPEG compression, currently the only compression approved by the DICOM committee, which provides more efficient storage of individual frames and loops without significant distortion of the images. Quantitative image analysis has shown little degradation at compression ratios as high as 20 : 1 [10]. DICOM standards now also need to be applied to 3D echocardiograms. Thus the DICOM Working Group is rewriting the standard to allow exchange of multidimensional data sets.

Optimal transfer of images for interpretation and archiving is performed using high-speed networks with a minimum speed of 100 megabits per second; heavily trafficked lines benefit from gigabit per second capacity. Echo data should initially be stored locally on a high capacity hard disk array that supports rapid access to handle both recent studies and returning patients. A long-term archive is needed, which may take the form of a jukebox of optical disks, CD ROMs, DVDs, digital linear tape, advanced intelligent tape, or videotape. The archive should simultaneously generate a second copy of each study to serve as a back-up which should be stored in a separate location to provide recovery in case of archive failure.

Software systems that connect the echocardiographic reports to the hospital information systems for scheduling, reporting, and billing are becoming more common. As more hospitals move toward electronic scheduling, registration, and medical record keeping, the ability to interface information electronically between the hospital system and the echocardiography machine has become a reality. DICOM worklists allow patient demographics to directly populate the echo machine, eliminating the risk of manual entry errors.

Patient preparation and safety

Proper patient preparation is an essential step to ensure a quality echocardiogram; this is particularly important in the pediatric population where lack of cooperation can be a major obstacle to obtaining adequate images. A system for transferring patients to and from the echo lab should be a part of the manual of operations. A parent or guardian should accompany a minor to and from the echo lab and be present during the study, except where privacy issues supersede. Having a brief discussion with the patient and family to explain the procedure helps to guide expectations and allay fears. ECG leads can be placed during this discussion. The importance of patient position for optimal imaging can also be explained (Figure 2.2). In addition, the caretaker can be asked to help calm or distract their child during the procedure. A calm environment sometimes helps avoid the need for sedation in young children. Each echo room should use dimmed lighting, use warmed ultrasound gel, and provide visual distractions (e.g., bubbles, toys, television, DVD player). In some cases, bundling (in neonates) or a parent lying on the bed next to their child can help keep the child still for the study. Moreover, small rewards (such as a sticker), are often used as positive reinforcement.

Sedation

The performance of high-quality transthoracic echocardiography is more likely to yield the necessary diagnostic information when the patient does not move and when any associated anxiety is effectively controlled. This has become increasingly important because the initial diagnosis of both structural and functional cardiac abnormalities are generally made by echocardiography and a substantial percentage of interventional decisions rely solely upon this data. Most sedation for pediatric



Figure 2.2 Pediatric echocardiograms are performed in rooms with enough space for the ultrasound machine and for the sonographer to have comfortable seating. During the examination, the patient is often required to move into various positions including left decubitus position as seen here. An apical 4-chamber view is being performed in this study.

outpatient echocardiography is performed in a hospital setting, which can provide the necessary trained personnel and equipment. Each echo lab requires a written policy for sedation protocols and appropriate staff for the performance of sedation is required based on hospital policies. A search for the most efficacious method of sedation that can be used in the outpatient setting [11,12], has revealed no clear consensus among pediatric cardiologists; in fact, a variety of approaches have been advocated. In the past decade, interest in procedural sedation has moved beyond the mainstay of chloral hydrate, expanding the menu to include oral pentobarbital [13], intranasal medications such as midazolam [14,15] or dexmedetomidine [16,17,18], and face-mask general anesthesia [19]. Table 2.7 lists some of the medications used for procedural sedation in pediatrics along with their advantages and disadvantages [11–22]. For all of these approaches the balance between length and depth of sedation and the risk of deleterious side effects and cost vary with patient age and acuity and will likely require that most echo labs have multiple patient-specific approaches.

There has been recent interest in nonpharmacologic approaches to aid in lessening patient anxiety using distraction methods and even massage [23–26]. Each lab must use its own resources to provide safe and effective distraction, anxiolysis and/or sedation to assure that the necessary information is obtained from the study.

Examinations and procedures

Transthoracic echocardiography

The standard pediatric echocardiogram involves 2D imaging of all cardiac structures along with spectral and color Doppler hemodynamic assessment of the valves and vessels and an evaluation of ventricular function. A protocol should be in place that defines the components of the standard examination including the order in which the imaging planes will be interrogated, the structures to be examined, and the measurements to be made. It is helpful to have a list of structures to be interrogated within each imaging plane. Optimally, recorded images are a combination of complete sweeps and selected single planes to assure that the segmental anatomy of the heart is accurately determined. Guidelines for a standard pediatric transthoracic echocardiogram protocol have been published by the Task Force of the Pediatric Council of the ASE [2] and are used by the IAC for pediatric accreditation. If a required element cannot be adequately imaged, it should be documented in the report. Due to the complexity of congenital heart disease, a complete examination may require custom planes to completely display and interrogate an abnormality.

Transesophageal echocardiography

Detailed description of and guidelines for the performance of transesophageal echocardiography (TEE) in pediatric patients with acquired and congenital heart disease have been published [27,28] and are described in detail in Chapter 41. The purpose of this section is to focus on the practical aspects of echo lab requirements to perform TEE in pediatric patients or adult patients with congenital heart disease within a facility. The location and indication for pediatric TEE often differ from those performed in adult labs and require a specialized fund of knowledge and skills. Pediatric TEEs are occasionally performed in an outpatient setting; however, the majority of these studies are performed in the operating room, cardiac catheterization lab, intensive care unit, or a sedation unit. These type of studies require ongoing communication and close collaboration with surgeons, interventionalists, anethesiologists, and intensivists.

The knowledge, skill, and training needed to perform a pediatric TEE are quite different from those required to perform TEE in the adult patient. Comprehensive knowledge of congenital heart disease and surgical repairs as well as experience in TEE imaging are crucial to adequately demonstrate and interrogate structures in the nonstandard views necessary. Thus, it is recommended that physicians who perform TEE independently on pediatric or adult patients with congenital heart disease achieve additional training and experience as outlined in Table 2.8 [27]. IAC certification exists for pediatric TEE [3] and these requirements are outlined in Table 2.9. Because TEE is an invasive procedure, an explanation of the procedure along with indications, risks, and benefits should be provided to the patient and/or their legal guardian and informed consent obtained. If the TEE is being performed in conjunction with a surgical or catheterization procedure, the consent may be obtained and documented with the consent for the primary procedure or anesthesia. Probe size is largely determined by patient size; each probe comes with guidelines regarding use based on weight of the patient.

TEE probe disinfection and maintenance are integral to assure patient safety. Integrity of the insulating layers of the transducer must be routinely checked before and after each use. Probe cleaning technique and specific brands of disinfectants are recommended by probe manufacturers and a policy should be in place to follow these guidelines. In addition to cleaning, it is recommended that the TEE probe be intermittently tested for electrical safety utilizing a saline bath connected to a leakage current analyzer. Guidelines, similar to those in place for gastrointestinal endoscopy, have recently been published by the British Society of Echocardiography in 2011 [29] and provide detailed information regarding TEE probe decontamination.

Fetal echocardiography

A detailed description of and guidelines for the performance of a fetal echocardiogram have been published [30]. Fetal echocardiography is described in detail in Chapter 44. Fetal echocardiography requires additional knowledge to pediatric echo including understanding of maternal–fetal physiology, fetal anatomic and physiologic changes throughout gestation, and fetal arrhythmias. Advanced training is recommended for fetal echocardiography. IAC certification exists for performance of fetal echocardiograms [3] and these requirements are outlined

Table 2.7 Common agents used in pediatric procedural sedation

Method	Medication	Route	Dose	Onset	Duration	Advantage	Disadvantage
Distraction	N/A	N/A	N/A	Immediate	Indefinite	No risk	Labor intensive Variable results
Anxiolysis	Midazolam	IN	0.2–0.3 mg/kg Repeat × 1	10 min	60 min	Minimal monitoring No IV	Effectiveness 80% Mild negative inotrope
Sedation	Chloral hydrate	PO PR	50–100 mg/kg Max 2.0 gm	15–60 min	1–4 hour	Little hemodynamic effects	Prolonged onset of sedation Emesis Respiratory depression Obstructive sleep apnea Paradoxical reaction Sedation failure Decreased availability due to lack of production
	Pentobarbital	PO	5.0 mg/kg	10–20 min	45–100 min	Rapid onset of sedation	Longer recovery time Emesis Paradoxical reaction
	Etomidate	IV	0.2 mg/kg	1–3 min	35 min	Rapid onset of sedation Minimal physiologic effects	Requires IV Myoclonus
	Dexmedetomidine	IN	1.0–2.0 μg/kg	45–60 min		No IV	Little experience with echo
General anesthesia	Sevoflurane	Inhalation	Per anesthesia	Immediate	As needed	Predictability Safety Short recovery time Usually no IV	Requires anesthesiology staff Physiologic effects Expense
Propofol		IV	Loading dose: Infant/young child 2 mg/kg Older child/teenager 1 mg/kg Subsequent infusion 100 μg/kg/min titrating to effect	Immediate	Variable	Short recovery time	Requires anesthesia staff Respiratory depression/apnea Painful injection Contraindicated if egg or soy allergy

IN, intranasal; IV, intravenous; PO, by mouth; PR, per rectum.

Table 2.8 Guidelines for training and maintenance of competence in transesophageal echocardiography (TEE) in pediatric and congenital heart disease

Component	Objective	Duration	Number of cases
Echocardiography (Level 2)	Prior experience in perform/ interpreting TTE	6 mo or equivalent	400: ≥200 <1 y
Esophageal intubation	TEE probe insertion	Variable	25 cases (12 <2 y)
TEE exam	Perform and interpret with supervision	Variable	50 cases
Ongoing TEE experience (Level 3)	Maintenance of competency	Annual	50 cases; or achievement of laboratory-established outcome variables

TEE, transesophageal echocardiography; TTE, transthoracic echocardiography.
Source: Ayres et al. 2005 [27]. Reproduced with permission of Elsevier.

Table 2.9 Pediatric transesophageal echocardiography: IAC requirements summary

- Ordering and scheduling
 - Process in place for obtaining and recording indication for test
 - Order must be present in the patient's medical record and include
 - Type of study to be performed
 - Reason for the study
 - Clinical question to be answered
 - Scheduling
 - Uncomplicated complete study (outside the OR) – 45–60 min
 - Complicated studies – additional 15–30 min
 - Time for adequate post sedation monitoring should be included
 - Urgent or stat – studies performed as soon as possible
 - Availability for emergencies: qualified personnel and equipment should be available outside of normal working hours
- Training: See Table 2.8, Guidelines for training and maintenance of competence
- Components of transesophageal echocardiograms
 - Technical personnel – to assist the physician and may include
 - Sonographer
 - Nurse
 - Trainee
 - Preparation of the patient
 - Consent must be obtained
 - Safety guidelines (including intravenous access, cardiac monitor with ECG telemetry, pulse oximetry, oxygen with appropriate delivery devices)
 - Conscious sedation: Written policies must exist for the use of conscious sedation including
 - Type of sedatives and appropriate dosing
 - Monitoring during and after the examination
 - Monitoring the patient: Facility guidelines for the monitoring of patients who receive anesthetic agents are required.
 - Recovery of the patient: The patient must be monitored for sufficient time to assure that no complications have arisen from the procedure or the sedation used.
 - Components of the examination: Protocol must be in place defining standard views and components of a comprehensive TEE examination.
- Procedure volumes
 - Facility: minimum of 50 pediatric TEE annually
 - Medical staff: minimum 50 TEE annually for each member who performs/interprets TEE
 - Facilities or individuals who do not meet these procedure volumes will be required to demonstrate competence through submission of additional case studies and quality assurance documentation
- Probe safety and maintenance
- A list of peri-procedural complications must be maintained
- Reporting – report must include
 - Complications of the procedure, if any
 - Components of the procedure (2D, color Doppler, spectral Doppler)
 - Comment on all structures evaluated in the examination
 - Note any structure not well visualized
 - Note if examination is abbreviated for any reason
 - Summary of the examination including pertinent positive and negative findings

in Table 2.10. Space, ultrasound equipment, information technology, and staff requirements are similar to those required for pediatric echo. Many fetal echocardiography laboratories are housed within the pediatric echo lab. Others are located in areas that perform other types of fetal imaging (i.e., maternal–fetal medicine units).

Intracardiac echocardiography

One of the more recent applications of echocardiography, intracardiac echocardiography (ICE), has become integral to many cardiac catheterization interventions including device placement, mitral valve interventions, and electrophysiology procedures. Current guidelines for use of ICE in catheter interventions have been published by the ASE [31]. The advantage of ICE over TEE in the adult population is that it obviates the need for general anesthesia. Moreover, ICE catheters are manipulated by the interventionalist so that an echocardiography physician is not always needed during the procedure. ICE has been utilized sparingly in pediatrics primarily due to the limitations imposed by patient size; ICE catheters range in size from 8–10F and require a 10F venous sheath. Current ICE catheters are steerable and employ a monoplane 64-element phased array transducer with grayscale, color, spectral, and tissue Doppler capabilities. Views are obtained by rotating the catheter within the right atrium or right ventricle and steering the catheter tip. ICE catheters are also expensive and have only a single use. In the adult population this cost is offset by avoiding the costs for an anesthesiologist and an echocardiography physician; however, it is unclear whether this can be duplicated in the pediatric population. Currently, ICE is being used in pediatrics primarily for atrial septal defect device closure and evaluation of percutaneous Melody pulmonary valve placement [32]. ICE catheters have also been used as TEE probes in very small infants. In one adult study, ICE catheters were used as a nasogastric TEE probe to image the atria in patients being evaluated for intracardiac thrombus prior to cardioversion [33]. The use of ICE during interventional and electrophysiology procedures has been published [34,35].

Table 2.10 Fetal echocardiography: IAC requirements summary

- A technical protocol must be written and adhered to in the facility including
 - Components of the examination
 - Indications for performance of a fetal echocardiogram
- Complete examination – standard views from multiple planes including views of all cardiac and selected extracardiac structures and may include:
 - Presence of single or multiple gestations and locations of fetuses relative to the mother and one another
 - Survey of fetal lie and position defining fetal orientation
 - Measurement to estimate fetal size/gestational age (e.g., biparietal diameter or head circumference, abdominal circumference, femur length)
 - Fetal cardiac position and visceral situs
 - Measurement of chest and heart circumference and area for calculation of size ratios
 - Assessment of fetal heart rate and rhythm using M-mode and Doppler techniques
 - Short-axis view of umbilical cord vasculature with spectral Doppler evaluation of flow in the umbilical vessels and ductus venosus
 - Imaging of pericardial and pleural space, abdomen, and skin for fluid or edema
 - Imaging and Doppler/color flow of systemic veins, their course, and cardiac connection
 - Imaging and Doppler/color flow of pulmonary veins, their course, and cardiac connection
 - Multiple imaging planes of and Doppler assessment of flow direction and velocity of:
 - Atria
 - Atrial septum
 - Foramen ovale
 - Ductus arteriosus
 - Ventricular septum
 - Atrioventricular valves
 - Ventricular outflow tracts
 - Semilunar valves
 - Four-chamber and short-axis view of the heart for assessment of cardiac chamber size and function
 - Short- and long-axis views of:
 - Ascending, descending, and transverse arch of the aorta
 - Ductus arteriosus
 - Main and proximal branch pulmonary arteries
 - Additional fetal elements
 - Middle cerebral arterial blood flow
- Report components – must include but may not be limited to
 - Measurements performed where normal values are known
 - Interpretation of measurements appropriate to the area of abnormality or clinical issue
 - Doppler values both normal and abnormal appropriate to the area of abnormality or clinical issue
 - Text must include comment on
 - Components of procedure
 - All structures evaluated in the exam (as specified above)
 - Text must be consistent with quantitative and Doppler data including localization and quantification of abnormal findings
 - Notation of structures that were not well visualized
- Procedure volumes
 - Facility: minimum of 50 fetal echocardiograms annually
 - Staff: minimum 25 fetal echocardiograms annually for each member that performs or interprets fetal echocardiograms
 - Facilities or individuals who do not meet these procedure volumes will be required to demonstrate competence through submission of additional case studies and quality assurance documentation

Research protocols

Research activities that require echocardiography are common in academic centers. In general, single-center investigator-initiated research studies are organized within the laboratory structure and do not require oversight outside of the local institutional review board (IRB). If a specific protocol is being utilized, there may be designated sonographers and physicians who obtain and interpret the images and make the necessary measurements or calculations. In larger multicenter studies, a core lab is often utilized. Core labs provide image storage, consistency in measurements, quality assurance, and feedback to participating echo labs to achieve the highest quality echo studies. Guidelines for echocardiography in clinical trials has been published by ASE and serves to outline the different levels of core lab requirements. These guidelines also provide recommendations regarding study design, image analysis, data management, quality assurance, statistical analysis plan, and regulatory considerations [36].

Telemedicine

Telemedicine is the use of telecommunication and information technology to provide echocardiography services at a distance. Echocardiograms performed on pediatric patients at one site can be transferred electronically to another site for interpretation by an experienced pediatric echocardiographer. This allows for more efficient use of the physician's time by obviating the need for travel between different locations to read echocardiograms. Telemedicine also allows for after-hours review by on-call cardiologists from their homes. After-hours echocardiography review is accomplished by direct digital transfer utilizing network connections.

Telemedicine places significant demands on hospital-based networks. The speed of transfer is often dependent upon the network speed of the transferring facility. Some examples of modes of transmission include ISDN phone lines, DSL, cable modem, T1 lines, and fiber optic cable. The rate of transfer for a T1 line is 1.5 Mbps while that of fiber optic cable is often 50–100 Mbps. Actual rates of transfer may be significantly slower depending upon other network traffic. The rate of transfer of an entire study can be improved utilizing incremental transfer of each image as it is captured from the echo machine rather than downloading the entire study at its conclusion [9].

Indications/reporting/billing

The indications for performing a pediatric transthoracic echocardiogram were published by the ACC/AHA/ASE Association Task Force on Practice Guidelines in 1997 [37] and were updated in 2003 [38]. Echocardiography is increasingly being utilized to screen, diagnose, and monitor patients with

Table 2.11 Definitions of complete and limited echocardiograms

Complete study

- CPT definition: A comprehensive procedure that includes two-dimensional and, when performed, selected M-mode examination of the left and right atria, left and right ventricles, the aortic, mitral, and tricuspid valves, the pericardium, and adjacent portions of the aorta in addition to spectral and color flow Doppler providing information regarding intracardiac blood flow and hemodynamics.
- ICAEL definition: Imaging study that defines the cardiac and visceral position and a complete segmental image analysis of the heart from multiple views and also defines the cardiac anatomy and physiology as fully as possible using imaging and Doppler modalities.

Limited or follow-up study

- CPT definition: An examination that does not evaluate or document or attempt to evaluate all the structures that comprise the complete echocardiographic exam. Typically limited to, or performed in follow-up of a focused clinical concern.
- ICAEL definition: A study that generally examines a specific region of interest of the heart and/or addresses a defined clinical question.

congenital or acquired heart disease; it is also being used to assess those at risk for the development of myocardial dysfunction and pulmonary hypertension. Requirements for the reporting of a pediatric echocardiogram are dictated not only by the clinical question but also by the requirements for echo lab accreditation (IAC) as well as billing (CPT codes). The indication for an echocardiogram, regardless of modality, must be verified prior to performing the study to appropriately direct the examination. The echocardiogram order must clearly indicate the type of study to be performed, the reason for the study, underlying diagnosis, and the clinical question(s) to be answered.

The definition of a complete and a limited study based on CPT and IAC criteria is outlined in Table 2.11. The distinction is often ambiguous; a focused question may require a thorough evaluation of multiple structures and thus meet the definition of a complete echocardiogram. From a billing standpoint, the CPT codes for complete and limited echocardiograms are divided into noncongenital and congenital designations; however, these definitions are not always explicitly differentiated. Echo reporting guidelines and requirements have been published by the Task Force of the Pediatric Council of ASE [2] as well as IAC [3] in an attempt to improve quality and consistency. Descriptions of an abnormality of a cardiac structure should include comments on both anatomy and function (if appropriate). The interpretation summary should highlight the key abnormalities and compare to prior studies (if appropriate) to determine if findings are unchanged, progressive, or improved. The final report must be reviewed and signed by the interpreting physician and include the date and time of the signature. Amended reports must include the time and date of the amendment and action taken if there was a significant change from the original study. Timeliness of reporting has specific requirements for accreditation; (i) routine inpatient echocardiograms must be interpreted by the medical staff within 24 hours of completion of the exam, (ii) outpatient studies must be interpreted by the end of the next business day, and (iii) the report must be signed and verified within 48 hours of the interpretation.

Preliminary findings on urgent studies should be immediately available and the final report should be available by the end of the next business day. A policy and procedure must be in place for reporting and documentation of critical values including documentation of physician-to-physician communication. Preliminary reports should be prepared under IAC guidelines. Sufficient support staff should be available to assist with scheduling and distribution of finalized echocardiography reports.

IAC accreditation

The Intersocietal Accreditation Commission (IAC) provides accreditation for a variety of cardiovascular testing including echocardiography. This organization is sponsored by the ASE, ACC, Society of Diagnostic Medical Sonography (SDMS), and Society of Pediatric Echocardiography (SOPE) with a mission to improve health care through accreditation. The IAC provides accreditation in specific areas of pediatric echocardiography including transthoracic, TEE, and fetal echocardiography. The American Society of Echocardiography states that "existing echo labs should be accredited by the IAC" while new labs should be expected to submit applications within 2 years of the onset of operation. Increasingly, IAC accreditation has become linked to reimbursement for Medicare and Medicaid as well as many private insurers. Completion of the application requires both detailed information of echo lab operations as well as submission of case studies for review. This process requires facilities to adopt or revise policies and protocols, ensure adequate personnel training and expertise, and validate quality improvement (QI) programs. Once accredited, reaccreditation is required every 3 years with demonstration of compliance with updated standards. The IAC Standards and Guidelines for Pediatric Echocardiography Accreditation are available for download on the IAC website and define the minimum requirements for all echocardiography facilities [3]. Case studies for submission can be identified prospectively or retrospectively. The review process generally takes approximately 12–16 weeks. Audits of institutions may occur at any time during accreditation.

Quality improvement

Establishment and maintenance of a robust quality improvement program is essential to maintaining quality and consistency in any pediatric echo lab. The process encourages continuous feedback for the lab as a unit as well as for each individual sonographer and physician. Along with continued

Table 2.12 IAC quality improvement measures

- Variability
 - Physician interpretation variability – must be assessed on a minimum of two cases per modality per quarter for:
 - Ejection fraction
 - Degree of valve regurgitation/stenosis
 - VSD gradients
 - Sonographer performance – two cases per modality must be reviewed and discrepancies reconciled for:
 - Image quality
 - Completeness of the study
 - Adherence to facility protocol
- Report review – a minimum of 10 random reports per quarter for:
 - Report components
 - Demographics (including height, weight, blood pressure)
 - 2D and/or M-mode numeric data
 - Doppler evaluation
 - Report text comments
 - Interpretation time
 - Final report generation
- Correlation will be performed on a minimum of two per modality per quarter with other imaging modalities for:
 - Ejection fraction
 - Degree of valve regurgitation/stenosis
 - VSD gradients
 - Patients sent for surgical repair based upon echo data alone must be compared to the operative findings

Table 2.13 Quality improvement correlation requirements

- Transthoracic echocardiograms:
 - Correlate with
 - Other diagnostic procedures
 - Cardiac catheterization
 - MRI
 - CT
 - Surgical intervention
 - Postmortem examination
 - Components for correlation include
 - Semilunar valve stenosis
 - Selected anomalies of functional evaluation of diagnostic interest to the facility
- Transesophageal echocardiograms (if performed)
 - Correlate with
 - Other diagnostic procedures
 - Surgical repair
 - Components for correlation include
 - Left ventricular function and regional wall motion analysis
 - Left or right ventricular function
 - Presence and severity of valvar dysfunction
 - Defects of atrial and ventricular septation
 - Presence or absence of thrombi or vegetations
 - Presence or absence of anomalous venous connections
- Fetal echocardiograms (if performed)
 - Correlate with
 - Postnatal transthoracic echocardiogram
 - Postnatal cardiac catheterization
 - Postmortem examination

medical education, the quality improvement process also serves an educational role. The quality improvement requirements for the IAC reflect recommendations published in the ASE publications "Recommendations for Quality Echocardiography Laboratory Operations" in 2011 [6] and "Recommendations and Guidelines for Continuous Quality Improvement in Perioperative Echocardiography" [28]. Of note, the latter recommendations are not specific to pediatrics.

The IAC requirements are briefly summarized in Table 2.12. Each facility must have a quality improvement program in place. Quarterly meetings are required and minutes of the meetings must be maintained and made available to all personnel. A policy to address discrepancies must be in place. All medical and technical staff are required to attend at least two of the four quarterly meetings. Correlation and confirmation of results must be maintained for each physician and each modality. Correlation with other modalities or with surgical or autopsy findings is generally warranted as outlined in Table 2.13. Guidelines published by the ASE in 2011, "American Society of Echocardiography Recommendations for Quality Echocardiography Laboratory Operations," include quality assessment recommendations. The goal of these recommendations is "to provide feedback to the lab members in the spirit of learning and quality improvement while keeping in mind that reasonable and equally competent people can sometimes differ in their review of echocardiographic results."

References

1 Saunders SP, Colan SD, Cordes TM, et al. ACCF/AHA/AAP Recommendations for Training in Pediatric Cardiology. Task Force 2: Pediatric Training Guidelines for Noninvasive Cardiac Imaging. *Circulation* 2005;**112**:2555–2580.

2 Lai WW, Geva T, Shirali GS, et al. Guidelines and standards for performance of a pediatric echocardiogram. *J Am Soc Echocardiogr* 2006;**19**:1413–1430.

3 The IAC Standards and Guidelines for Pediatric Echocardiography Accreditation Updated 8/2012. www.intersocietal.org/echo/main/echo_standards.htm (accessed February 24, 2015).

4 Ehler D, Carney DK, Dempsey AL, et al. Guidelines for cardiac sonographer education. *J Am Soc Echocardiogr* 2001;**14**:77–84.

5 Bierig SM, Ehler D, Knoll ML, Waggoner AD. ASE Minimum Standards for the Cardiac Sonographer: A Position Paper. 2005; http://www.asecho.org/wordpress/wp-content/uploads/2013/05/Minimum-Standards-for-the-Cardiac-Sonographer.pdf (accessed February 24, 2015).

6 Picard MH, Adams D, Bierig SM, et al. American Society of Echocardiography recommendations for quality echocardiography laboratory operations. *J Am Soc Echocardiogr* 2011;**24**:1–10.

7 Kisslo J, Byrd BF, Geiser EA, et al. Recommendations for continuous quality improvement in echocardiography. *J Am Soc Echocardiog* 1995;**8**:S1–S28.

8 45 CFR 164.316(b)(2) at http://www.ecfr.gov/cgi-bin/text-idx?tpl=/ecfrbrowse/Title45/45cfr164_main_02.tpl(accessed February 24, 2015).

9 Thomas JD, Adams DB, DeVries S, et al. Guidelines and recommendations for digital echocardiography. *J Am Soc Echocardiogr* 2005;**18**:287–297.

10 Karson TH, Zepp RC, Chandra S, et al. Digital storage of echocardiograms offers superior image quality to analog storage, even with 20:1 digital compression: results of the Digital Echo Record Access Study. *J Am Soc Echocardiogr* 1996;**9**:769–778.

11 Macias CG, Chumpitazi CE. Sedation and anesthesia for CT: emerging issues for providing high-quality care. *Pediatr Radiol* 2011;**41**: S517–S522.

12 Di Liddo L, D'Angelo A, Nguyen B, et al. Etomidate versus midazolam for procedural sedation in pediatric outpatients: a randomized controlled trial. *Ann Emerg Med* 2006;**48**:433–440.

13 Warden CN, Bernard PK, Kimball TR. The efficacy and safety of oral pentobarbital sedation in pediatric echocardiography. *J Am Soc Echocardiogr* 2010;**22**:33–37.

14 Lazol JP, DeGroff CG. Minimal sedation second dose strategy with intranasal midazolam in an outpatient pediatric echocardiographic setting. *J Am Soc Echocardiogr* 2009;**22**:383–387.

15 Chiaretti A, Barone G, Rigante D, et al. Intranasal lidocaine and midazolam for procedural sedation in children. *Arch Dis Child* 2011;**96**:160–163.

16 Yuen VM, Hui TW, Irwin MG, et al. A comparison of intranasal dexmedetomidine and oral midazolam for premedication in pediatric anesthesia: a double-blinded randomized controlled trial. *Anesth Analg* 2008;**106**:1715–1721.

17 Cooper L, Candiotti K, Gallagher C, et al. A randomized, controlled trial on dexmedetomidine for providing adequate sedation and hemodynamic control for awake, diagnostic transesophageal echocardiography. *J Cardiothorac Vasc Anesth* 2011;**25**: 233–237.

18 Talon MD, Woodson LC, Sherwood ER, et al. Intranasal dexmedetomidine premedication is comparable with midazolam in burn children undergoing reconstructive surgery. *J Burn Care Res* 2009;**30**:599–605.

19 Nicholson SC, Montenegro LM, Cohen MS, et al. A comparison of the efficacy and safety of chloral hydrate versus inhaled anesthesia for sedating infants and toddlers for transthoracic echocardiograms. *J Am Soc Echocardiogr* 2010;**23**:38–42.

20 Roach CL, Husain N, Zabinsky J, et al. Moderate sedation for echocardiography of preschoolers. *Pediatr Cardiol* 2010;**31**:469–473.

21 Heistein LC, Ramaciotti C, Scott WA, et al. Chloral hydrate sedation for pediatric echocardiography: physiologic responses, adverse events, and risk factors. *Pediatrics* 2006;**117**:e434–441.

22 Sahyoun C, Krauss B. Clinical implications of pharmacokinetics and pharmacodynamics of procedural sedation agents in children. *Curr Opin Pediatr* 2012;**24**:225–232.

23 Stouffer JW, Shirk BJ, Polomano RC. Practice guidelines for music interventions with hospitalized pediatric patients. *J Pediatr Nurs* 2007;**22**:448–456.

24 Walworth DD. Procedural-support music therapy in the healthcare setting: a cost-effectiveness analysis. *J Pediatr Nurs* 2005;**20**:276–284.

25 McGee K. The role of a child life specialist in a pediatric radiology department. *Pediatr Radiol* 2003;**33**:467–474.

26 Etzel-Hardman D, Kapsin K, Jones S, et al. Sedation reduction in a pediatric radiology department. *J Healthc Qual* 2009;**31**: 34–39.

27 Ayres NA, Miller-Hance W, Fyfe DA, et al. Indications and guidelines for performance of transesophageal echocardiography in the patient with pediatric acquired or congenital heart disease. *J Am Soc Echocardiogr* 2005;**18**:91–98.

28 Mathew JP, Glas K, Troianos CA, et al. American Society of Echocardiography/Society of Cardiovascular Anesthesiologists recommendations and guidelines for continuous quality improvement in perioperative echocardiography. *J Am Soc Echocardiogr* 2006;**19**:1303–1313.

29 Kanagala P, Bradley C, Hoffman P, et al. Guidelines for transoesophageal echocardiographic probe cleaning and disinfection from the British Society of Echocardiography. *Eur J Echocardiogr* 2011;**12**:17–23.

30 Rychik J, Ayres N, Cuneo B, et al. American Society of Echocardiography guidelines and standards for performance of the fetal echocardiogram. *J Am Soc Echocardiogr* 2004;**17**:803–810.

31 Silvestry FE, Kerber RE, Brook MM, et al. Echocardiography-guided interventions. *J Am Soc Echocardiogr* 2009;**22**:213–231.

32 Baker PC. Intracardiac echocardiography in congenital heart disease. *J Cardiovasc Trans Res* 2009;**2**:19–23.

33 Schuster P, Chen J, Hoff PI. TEE time? ICE TEE time! IntraCardiac Echocardiography probe used for TransoEsophageal Echocardiography. *Europace* 2010;**12**:1787–1788.

34 Hijazi ZM, Shivkumar K, Sahn DJ. Intracardiac echocardiography during interventional and electrophysiological cardiac catheterization. *Circulation* 2009;**119**:587–596.

35 Kliger C, Cruz-Gonzalez I, Ruiz CE. The present and future of intracardiac echocardiography for guiding structural heart disease interventions. *Rev Esp Cardiol* 2012;**65**:791–794.

36 Douglas PS, DeCara JM, Devereux RB, et al. Echocardiographic imaging in clinical trials: American Society of Echocardiography standards for echocardiography core laboratories. *J Am Soc Echocardiogr* 2009;**22**:755–764.

37 Cheitlin MD, Alpert JS, Armstrong WF, et al. ACC/AHA Guidelines for the Clinical Application of Echocardiography: A Report of the American College of Cardiology/American Heart Association Task Force on Practice Guidelines (Committee on Clinical Application of Echocardiography). *Circulation* 1997;**18**:1686–1744.

38 Cheitlin MD, Armstrong WF, Aurigemma GP, et al. ACC/AHA/ASE 2003 Guideline Update for the Clinical Application of Echocardiography Summary Article. *J Am Soc Echocardiogr* 2003;**16**:1091–1110.

CHAPTER 3

Segmental Approach to Congenital Heart Disease

Tal Geva
Division of Noninvasive Cardiac Imaging, Department of Cardiology, Boston Children's Hospital and Harvard Medical School, Boston, MA, USA

Before the advent of surgical treatment for patients with congenital heart disease (CHD), physicians generally regarded these conditions as hopeless. In 1936, Dr. Maude Abbott, who worked at McGill University, published the first systematic classification of CHD based on a study of 1000 heart specimens [1]. Two years later in 1938, Dr. Robert Gross, who worked at Boston Children's Hospital, performed the first successful cardiovascular operation – ligation of a patent ductus arteriosus in a 7.5-year-old girl [2]. This breakthrough procedure was followed by Blalock and Taussig's landmark establishment of a systemic-to-pulmonary artery shunt to alleviate cyanosis in tetralogy of Fallot [3]; resection of aortic coarctation by Gross and Hufnagel and by Crafoord and Nylin; and the first open heart surgery to close an atrial septal defect by Gibbons in 1953 [4]. These and other landmark advances in the treatment of patients with CHD during the 1940s and 1950s inspired interest in the study of CHD morphology and stimulated the development of several taxonomies for its classification.

The highly variable spectrum of congenital anomalies of the cardiovascular system presents a challenge for those who care for these patients. A comprehensive classification scheme of CHD based on clear and internally consistent nomenclature is, therefore, essential for diagnosis, management, research, and education. The goals of any CHD taxonomy are:

1. to provide a consistent nomenclature based on readily identifiable anatomic-morphologic features of the cardiac chambers;
2. to devise a systematic analytical approach that produces a specific and unique set of diagnoses for each cardiac malformation;
3. to be applicable to all forms of CHD, including cardiac malformations that have not yet been described;
4. to promote understanding and exchange of data among clinicians and researchers.

This chapter describes a segment-by-segment approach, known as the *segmental approach to congenital heart disease*, to the classification and nomenclature of congenital anomalies of the heart and great vessels. Inspired by Dr. Maurice Lev, Van Praagh and his colleagues originally proposed this classification system in the 1960s and early 1970s [5–7] and have since refined it [8,9]. Importantly, notable modifications and alternative taxonomies have been proposed by pathologists, geneticists, embryologists, cardiologists, cardiovascular surgeons, radiologists, and others [9–22]. In particular, many practitioners favor the nomenclature advocated by Anderson and colleagues [23]. However, despite numerous efforts by individuals and professional groups to advocate the use of a single classification system, none has achieved uniform acceptance. A potentially more successful approach, currently being developed, is to acknowledge the major taxonomies and to create a system that cross-links individual malformations and therapeutic procedures to common codes [24–26]. Although this chapter emphasizes the taxonomy advocated by Van Praagh et al., readers should also familiarize themselves with Anderson's nomenclature and, most importantly, maintain a clear and consistent method of communication within their institutions.

Segmental analysis of congenital heart disease

Analysis of CHD is based upon an understanding of the developmental, morphologic and segmental anatomy of the heart and great vessels. The cardiac segments are the anatomic and embryologic "building blocks" that form the mammalian heart (Figure 3.1). The three main segments are: (i) veins and atria; (ii) ventricles; and (iii) great arteries. There are two connecting segments between the main segments: (i) the atrioventricular (AV) canal; and (ii) the conus or infundibulum. The AV canal consists of the AV valves (the mitral and tricuspid valves in normally formed hearts) and the atrioventricular septum. The infundibulum (or conus) is the connecting segment between the ventricles and the great arteries. In normally formed hearts, the infundibulum consists of a circumferential subpulmonary myocardium shaped like a prolate cone (as viewed externally; hence conus) or

Echocardiography in Pediatric and Congenital Heart Disease: From Fetus to Adult, Second Edition. Edited by Wyman W. Lai, Luc L. Mertens, Meryl S. Cohen and Tal Geva.
© 2016 John Wiley & Sons, Ltd. Published 2016 by John Wiley & Sons, Ltd.
Companion website: www.lai-echo.com

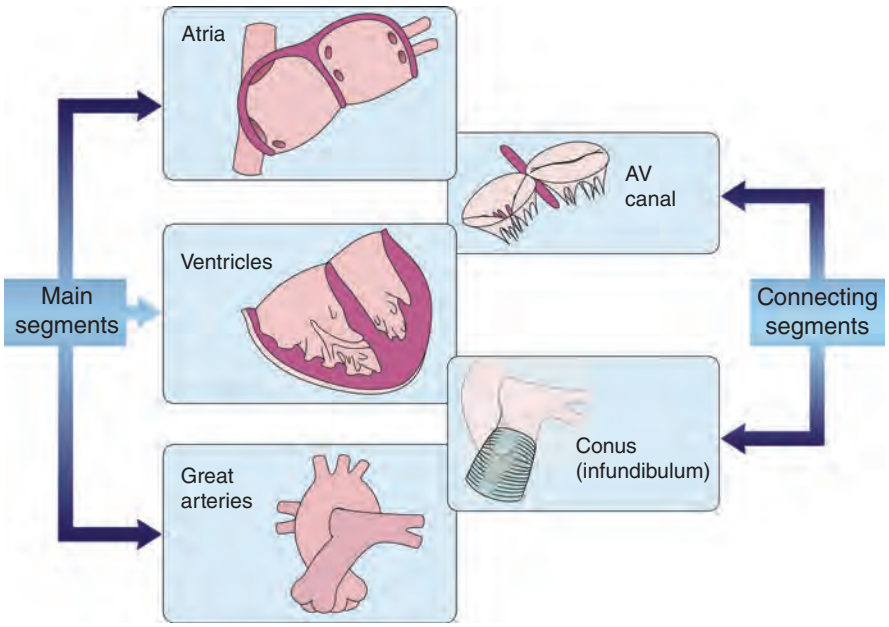


Figure 3.1 Anatomic segments of the heart. The three main cardiac segments are the atria, ventricles, and great arteries. There are two connecting segments: the atrioventricular (AV) canal (including the AV valves, the interatrial and interventricular components of the AV canal septum), and the conus (or infundibulum). The connecting segments may be viewed as multidirectional joints between the main cardiac segments allowing infinite possibilities of atrioventricular and ventriculo-arterial alignments. In the segmental approach to congenital heart disease it is essential that each cardiac segment is analyzed separately and independent of adjacent segments.

a funnel (as viewed internally; hence infundibulum). The normal subpulmonary infundibular myocardium separates the pulmonary and tricuspid valves. The normal subaortic infundibulum consists mostly of a conal septum (the myocardium that separates the left and right ventricular outflow tracts). The posterior aspect of the subaortic infundibular free wall is normally absent, resulting in fibrous continuity between the left and noncoronary aortic valve leaflets and the anterior leaflet of the mitral valve.

The fundamental principle of segmental analysis of CHD is to analyze each of the aforementioned components of the heart in a sequential step-by-step fashion. First, the anatomical pattern (i.e., situs) of the abdominal and thoracic organs is defined and the position of the heart is described. Then, each of the main cardiac segments is examined, described, and assigned a designation based upon its unique morphologic features, independent of neighboring segments (Figure 3.2). For example, each ventricle is defined according to its intrinsic morphology and not by the entering atrioventricular valve or the exiting great artery. Analysis of the main cardiac chambers – veins and atria, ventricles, and great arteries – involves two steps. First, the *identity* of the chamber or great vessel is determined based upon its morphology and intrinsic myocardial architecture. Second, the *situs* of the cardiac segment is determined. In the case of the atria, their situs may be solitus (normal), inversus (mirror image of solitus), or ambiguous (indeterminate, or having anatomic features of both atria). Once the three main cardiac segments are characterized according to their unique morphologic features, the connecting segments are evaluated and defined. Finally, a complete set of diagnoses is formulated by combining the five cardiac segments and all associated cardiovascular anomalies as described in the following section.

Step-by-step segmental analysis

The following 10 steps are taken as part of the segmental analysis of CHD:

1 **Thoraco-abdominal situs** (Figure 3.3). Before analyzing intracardiac anatomy, the situs of the thoracic and abdominal organs is determined to provide an "anatomic framework" for further analysis. Normally, the visceral organs are "lateralized." In other words, the pattern of anatomic organization of the abdominal organs, tracheo-bronchial tree, and lungs is asymmetric. In *situs solitus* (normal arrangement), the spleen, pancreas, stomach, and sigmoid colon are left-sided, and the liver, cecum, and appendix are right-sided. The left lung comprises two lobes and the left mainstem bronchus is longer, more horizontal, and hyparterial (courses inferior to the left pulmonary artery) (Figure 3.4). The right lung comprises three lobes and the right mainstem bronchus is shorter and eparterial (courses posterior to the right pulmonary artery). In visceral *situs inversus*, the spatial organization of the abdominal and thoracic organs is the mirror image of normal. In other words, there is complete left–right reversal of the position and orientation of the organs. It is worth noting that in visceral situs inversus the pattern of anatomic organization is asymmetric similar to situs solitus but in mirror image. Ciliary disorders are often associated with situs inversus. In *situs ambiguous*, the spatial position and orientation of the abdominal and thoracic organs are abnormally symmetrical and inconsistent. For example, the spleen may be absent, the liver is often midline, both lungs may have two or three lobes, and the bronchi may be similar to each other in length and orientation. Situs ambiguous is typically associated with heterotaxy syndrome, a condition characterized

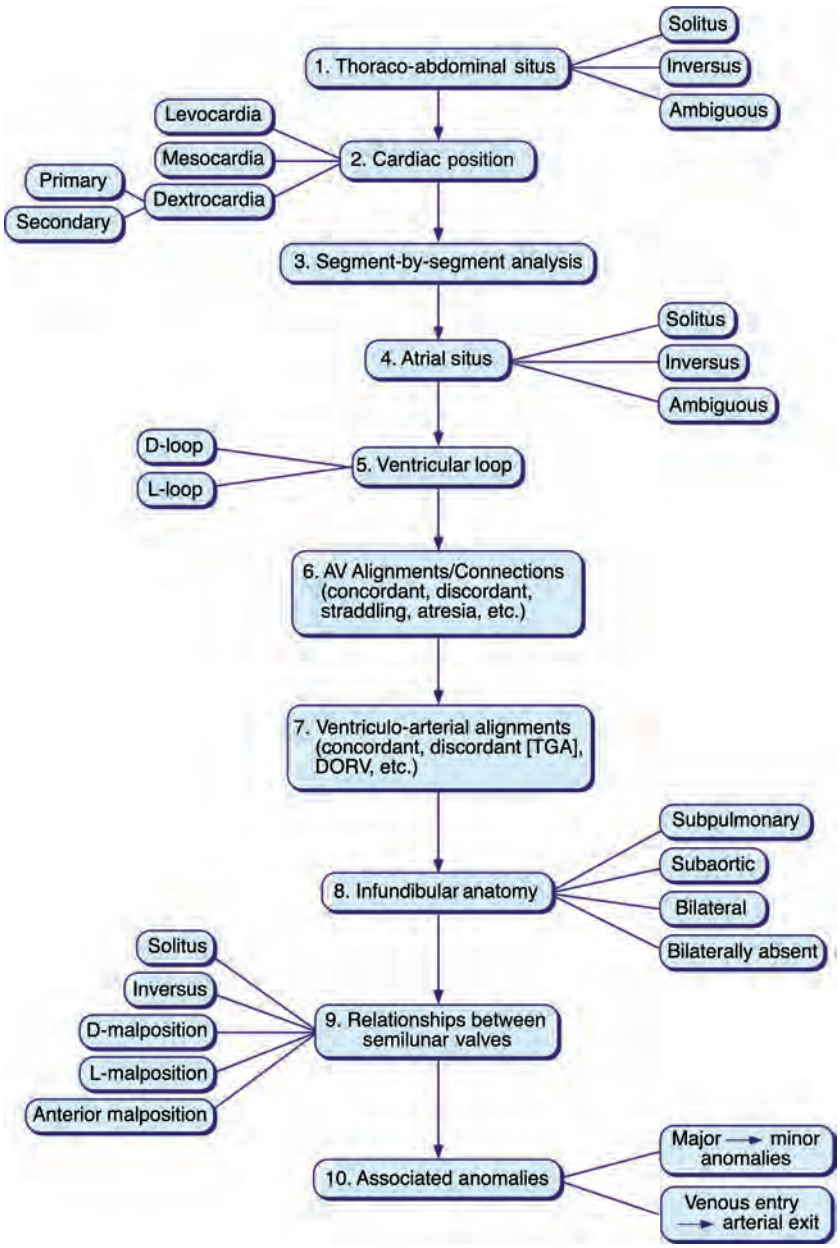


Figure 3.2 The 10 steps of the segmental approach to diagnosis of congenital heart disease. Before analyzing intracardiac anatomy, the situs of the thoracic and abdominal organs and cardiac position within the thorax are determined to provide an "anatomic framework" for further analysis (steps 1 and 2). When describing cardiac anatomy, the following principles apply: (i) Each cardiac segment must be described in terms of its own unique anatomic features and not according to those of adjacent segments (steps 3–9). For example, the left ventricle is determined according to its internal morphology, particularly its smooth superior septal surface, and not according to the AV valve that connects it with the atria (usually it is the mitral valve but it may be both mitral and tricuspid valves, as in double-inlet left ventricle, or it may be a common AV valve or even a tricuspid valve). (ii) For each cardiac segment, both its situs and connections must be described specifically and not inferred from each other. (iii) Associated malformations (step 10) may be described in order of their hemodynamic importance or in an anatomic order (progressing from the venous entry to the arterial exit of the heart). DORV, double-outlet right ventricle; TGA, transposition of the great arteries.

by partial or complete lack of lateralization of the visceral organs leading to an abnormal degree of symmetry, anomalies of the spleen (e.g., polysplenia, asplenia), congenital heart disease, and extracardiac anomalies [27–29]. In many patients with heterotaxy syndrome, visceral situs cannot be clearly designated as solitus or inversus, hence the term *situs ambiguous* is used. However, the anatomic organization of the visceral organs in these patients is often partially lateralized, allowing for determination of a "predominant situs." For example, when the stomach is right-sided and the inferior vena cava is left-sided, the predominant abdominal situs is inversus even though the liver may be midline.

2 **Cardiac position** (Figure 3.5): The position of the heart within the thorax can be described as levocardia, mesocardia, or dextrocardia. This designation is based on the spatial location of the majority of the cardiac mass relative to a sagittal plane that crosses the thoracic midline from the sternum to the spine. In addition, the orientation of the long axis of the heart (the orientation of the axis connecting the AV junction and the ventricular apex) should be described. Although the position of the heart within the thorax and the orientation of the base-to-apex axis are often concordant (e.g., levocardia and a leftward pointing apex), occasional exceptions occur (e.g., dextrocardia and a leftward pointing apex).

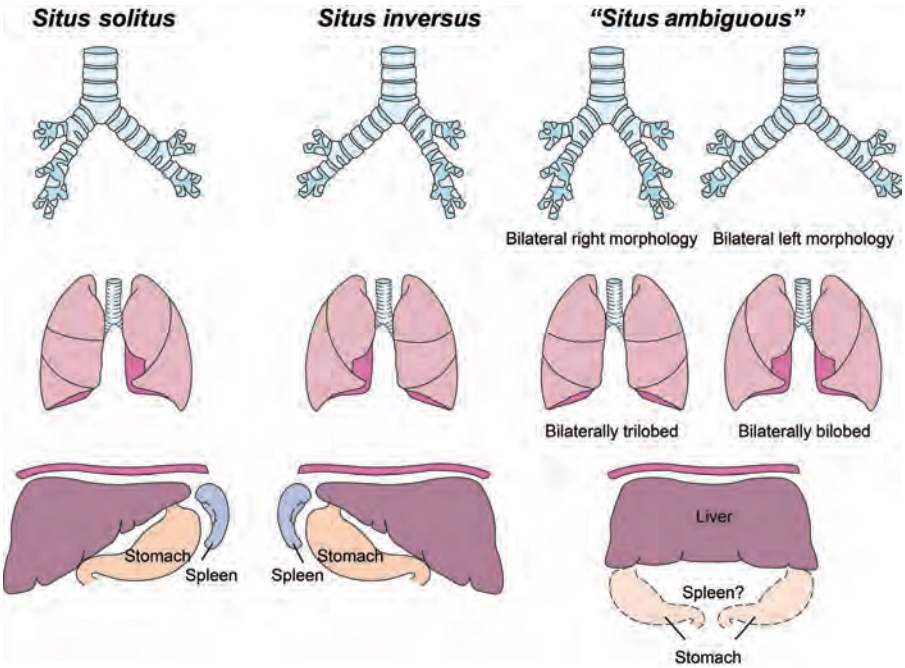


Figure 3.3 Thoraco-abdominal situs. Top panel: Morphology of the tracheo-bronchial tree. In situs solitus, the right mainstem bronchus is short and eparterial (its branch for the right upper lobe is over the second branch of the right pulmonary artery) and the left mainstem bronchus is longer and hyparterial (it courses underneath the left pulmonary artery). In situs inversus, there is mirror-imaging of the anatomy seen in situs solitus. In situs ambiguous the bronchi can have a bilaterally right or bilaterally left morphology. Bilaterally hyparterial left bronchial morphology is often seen in patients with heterotaxy syndrome and polysplenia, whereas bilaterally eparterial right bronchial morphology is often seen in patients with heterotaxy syndrome and asplenia. Middle panel: Lung lobation. A bilobed left lung and a trilobed right lung are typical in situs solitus. In situs inversus, the right lung is bilobed and the left lung is trilobed. As with the tracheo-bronchial tree, in situs ambiguous the lungs may be bilaterally bilobed or bilaterally trilobed. Lower panel: In visceral situs solitus the liver is right-sided and the stomach and spleen are left-sided. Incomplete lateralization of the abdominal organs with a midline liver and stomach may be seen in patients with heterotaxy syndrome. Splenic anomalies (asplenia, polysplenia, hyposplenia and a single right-sided spleen) and complex cardiac anomalies are frequent. In patients with heterotaxy syndrome and visceral situs ambiguous, the disposition of the abdominal situs predicts atrial situs less reliably than bronchial anatomy.

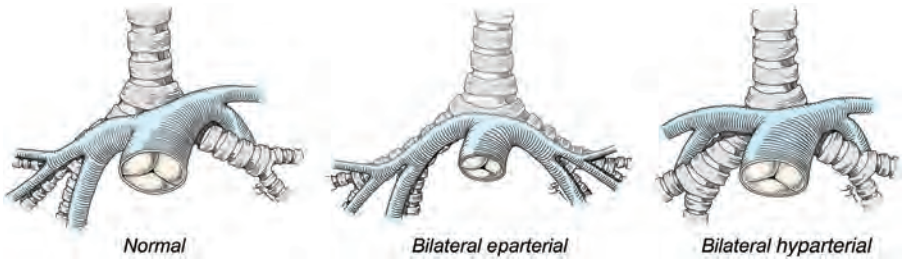


Figure 3.4 Relationships between the main stem bronchi and the pulmonary arteries. In normal anatomy (left panel), the right pulmonary artery courses anterior to the right main stem bronchus (the bronchus is said to be eparterial) and left pulmonary artery courses over the left main stem bronchus (the bronchus is said to be hyparterial). In the majority of patients with asplenia syndrome both main stem bronchi are eparterial and in most patients with polysplenia syndrome both main stem bronchi are hyparterial.

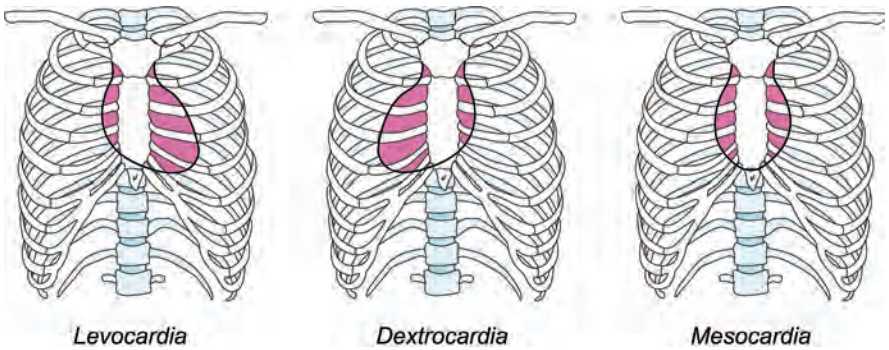


Figure 3.5 Cardiac position within the thorax. In levocardia, the heart is predominantly in the left hemithorax. In dextrocardia, the heart is predominantly in the right hemithorax. In mesocardia, the heart is midline and the apex typically points anteriorly or inferiorly. The orientation of the apex should be explicitly described because the position of the heart within the thorax and the orientation of the apex may not be concordant (e.g., dextrocardia with a leftward pointing apex).

In levocardia, the heart is positioned predominantly in the left hemithorax. In dextrocardia, the heart is predominantly in the right hemithorax. In mesocardia, the heart is midline with approximately equal proportions of the cardiac mass on each side of the sternum. The base-to-apex axis in mesocardia is usually oriented anteriorly or sometimes inferiorly. The terms *primary* and *secondary* dextrocardia are used to distinguish between cardiac malposition related primarily to cardiac anomalies and secondary to noncardiac anomalies. *Primary dextrocardia* is defined as a condition in which the heart is in the right hemithorax in association with a structural congenital heart defect. In primary dextrocardia the apex usually points to the right. *Secondary dextrocardia* is a condition in which the heart is either "pushed" or "pulled" toward the right hemithorax due to extracardiac abnormalities. Examples of circumstances where the heart is "pushed" to the right hemithorax include left-sided tension pneumothorax, left congenital lobar emphysema, and left-sided diaphragmatic hernia. Conditions where the heart is pulled toward the right hemithorax include hypoplasia or agenesis of the right lung. In secondary dextrocardia the cardiac apex may point to the left or anteriorly. Leftward malposition of the heart occurs in patients with right diaphragmatic hernia or hypoplasia or agenesis of the left lung. In the latter condition, the heart is displaced toward the left-superior hemithorax and the base-to-apex orientation points toward the left axilla.

In addition to malposition of the heart within the thorax, the heart can rarely be partially or completely exteriorized, a condition termed *ectopia cordis*. The extent of the midline defect that allows the heart to be partially or completely outside the thoracic cavity varies. A known association of anomalies, of which ectopia cordis is a component, is termed *pentalogy of Cantrell*. This group of defects includes: deficiency of the anterior diaphragm; a midline supra-umbilical abdominal wall defect; a defect in the diaphragmatic pericardium; congenital cardiac abnormalities; and a defect of the lower sternum [30].

3 **Segment-by-segment analysis of cardiac anatomy** (Figure 3.2). At this stage of the segmental analysis, the three main segments and the two connecting segments are analyzed individually (steps 4–9 below).

4 **Atrial situs** (Figures 3.6 and 3.7). The first step in determining atrial situs is to identify the atria according to their morphologic characteristics (Table 3.1, Figure 3.6a,b). The atria are not designated based on systemic and/or pulmonary

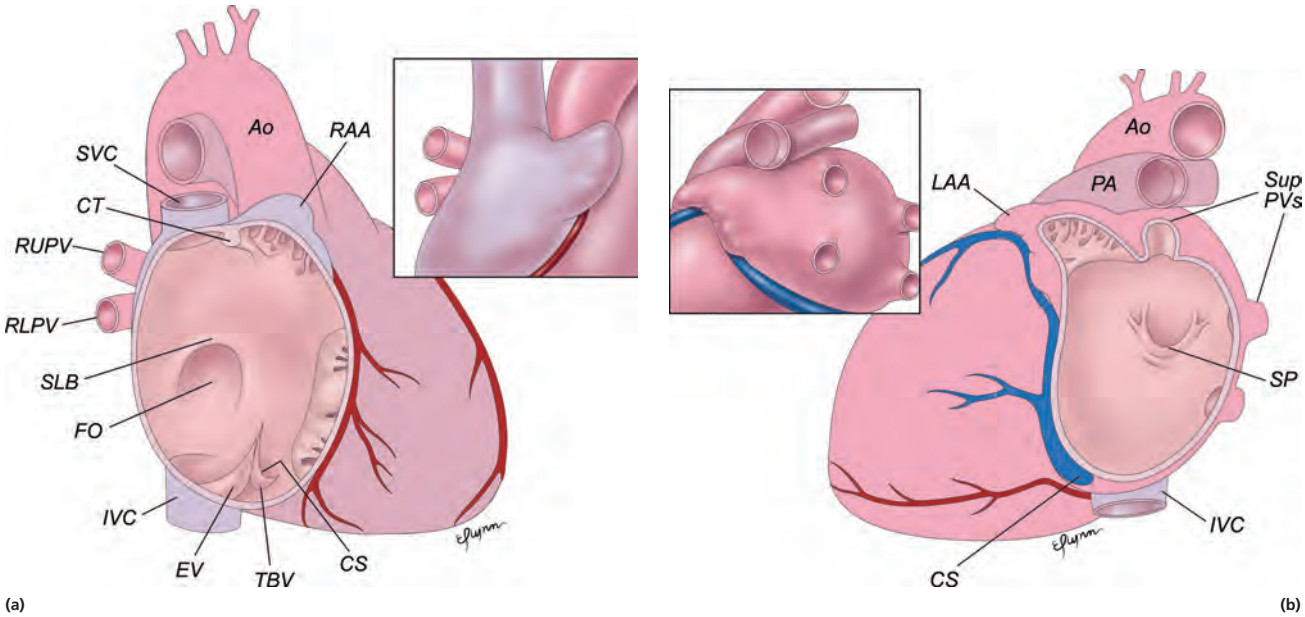


Figure 3.6 Atrial morphology. **(a)** Right atrial morphology: The right atrium (RA) can be divided into three components: (i) *Sinus venosus*, including the orifices of the inferior vena cava (IVC), superior vena cava (SVC), and coronary sinus (CS), and is characterized by its smooth surface (absence of muscular trabeculations). The sinus venosus is partially separated from the other components of the right atrium by remnants of the embryonic right venous valve system, which includes the Thebesian valve (TBV) of the coronary sinus and the Eustachian valve (EV) of the inferior vena cava. (ii) The *right atrial appendage* (RAA) is characterized by a broad-based triangular shape and coarse trabeculations (pectinate muscle). The crista terminalis (CT) is a prominent muscle bar that separates the sinus venosus component of the RA from the trabeculated right atrial appendage and is the site of the sinoatrial node. (iii) The *interatrial portion of the AV canal* includes the base of the atrial septum and the tricuspid valve annulus. The fossa ovalis (FO) forms the right atrial side of the interatrial septum and is characterized by an oval-shaped muscular boundary (termed *septum secundum* or *limbus of the fossa ovalis*) whereas the floor of the fossa is covered by septum primum. **(b)** Left atrial morphology. Similar to the right atrium, the left atrium can also be divided into three components: (i) a pulmonary venous component; (ii) a left atrial appendage (LAA), which is narrow-based and elongated; and (iii) the AV canal region, which is bordered distally by the mitral valve annulus. Note the attachments of septum primum (SP) are located on the left atrial septal surface.

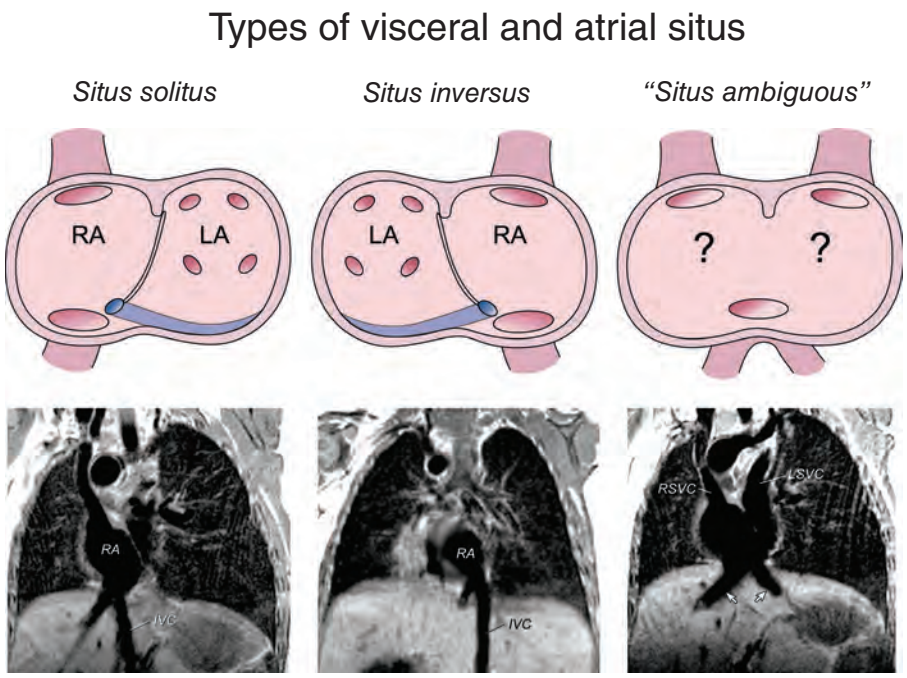


Figure 3.7 Diagram of atrial situs. Upper panel: In *atrial situs solitus*, the right-sided right atrium (RA) receives the major horn of the sinus venosus, including the superior vena cava, inferior vena cava and the orifice of the coronary sinus. The left-sided left atrium (LA) normally receives the pulmonary veins, its septum features septum primum (the flap valve of the foramen ovale) and a narrow-based, elongated and posterior appendage (Table 3.1). In *atrial situs inversus*, the right atrium is left-sided and the left atrium is right-sided. In *atrial situs ambiguous*, typically seen in patients with heterotaxy syndrome, the anatomic landmarks characteristics of the right and left atria are not sufficient to determine situs (either situs solitus or situs inversus). Commonly in this situation, the atria are in common with absence (or presence of only remnants) of the atrial septum, the inferior vena cava may be interrupted between the renal and hepatic segments, there may be bilateral superior vena cavae and the coronary sinus may be unroofed or absent. The atrial appendages may be quite similar to each other. Lower panel: Coronal plane spin echo magnetic resonance imaging (MRI) in patients with heterotaxy syndrome and atrial situs solitus (left panel), atrial situs inversus (central panel), and atrial situs ambiguous (right panel). IVC, inferior vena cava; LSVC, left superior vena cava; RA, right atrium; RSVC, right superior vena cava

venous connections because these can be variable. Instead, the atria are defined by their intrinsic anatomy. The right atrial myocardium includes the crista terminalis and tinea sagittalis (Figure 3.6a). The septal surface of the right atrium features the superior and inferior limbic bands of the fossa ovale. The right atrial appendage is typically broad-based, it has a triangular shape, and its position is anterior relative to the left atrial appendage. The pectinate muscles of

Table 3.1 Morphologic criteria for identification of right atrium and left atrium

	Right atrium	Left atrium
Myocardial features	Crista terminalis, tinea sagittalis, extension of pectinate muscles toward AV valve	Pectinate muscles confined to appendage*
Appendage	Broad-based, triangular, anterior	Long and narrow (finger-like), posterior
Septum	Septum secundum (limbus of the fossa ovale)	Septum primum (valve of the foramen ovale)
Veins	Receives the right and left terminations of the sinus venosus: IVC†, SVC‡, CS§	Normally receives all pulmonary veins¶

CS, coronary sinus; IVC, inferior vena cava; SVC, superior vena cava
*When a persistent left superior vena cava (LSVC) drains directly into the left atrium a muscle bar similar to a crista terminalis may be present in the LSVC–LA junction.
†In cases with interrupted IVC: the right atrium receives the CS.
‡The SVC is not a reliable marker of the right atrium because a persistent left superior vena cava may drain directly into the left atrium [39].
§When the coronary sinus is unroofed, the drainage site of the IVC may incorrectly identify the right atrium. In such circumstance, drainage of the IVC to the unroofed coronary sinus creates the appearance of IVC-to-left atrium connection. When the CS is unroofed and the IVC is interrupted, the shape, size, and location of the atrial appendages may be used for identification of atrial situs.
¶The pulmonary veins are not a reliable marker of the left atrium due to their potential for variable connections.

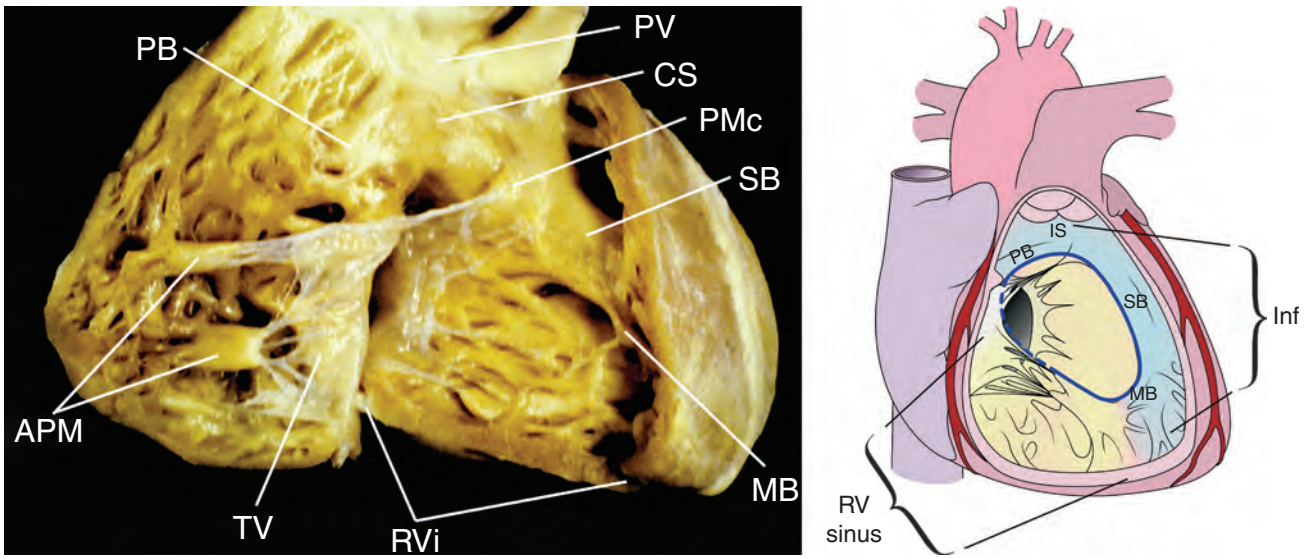


Figure 3.8 Right ventricular morphology. **(a)** Anatomic specimen showing normal right ventricular (RV) morphology. Note the coarse trabeculations and the chordal attachments of the tricuspid valve (TV) to the trabeculated septal surface. **(b)** The normal right ventricle comprises two distinct chambers, which are well incorporated into each other: the right ventricular (RV) sinus, and the infundibulum (Inf). The boundary between the RV sinus and the infundibulum is termed the *proximal os infundibulum* (shown as a dark ring) and comprises the parietal band (PB), infundibular septum (IS), septal band (SB), moderator band (MB), and the anterior papillary muscle of the tricuspid valve (APM). The RV sinus may be subdivided into two parts: (i) an atrioventricular (AV) canal portion (underneath the septal leaflet of the tricuspid valve); and (ii) the trabecular portion, which extends to the RV apex. The infundibulum may be similarly subdivided into two components: (i) a distal (subpulmonary) segment, which includes the distal portion of septal band, infundibular septum, and parietal band; and (ii) the proximal infundibulum, which is typically trabeculated and has its own apex located anterior to the RV sinus apex. CS, conal septum; PMc, papillary muscle of the conus; RVi, right ventricular inflow (sinus).

the right atrial appendage extend toward the AV valve annulus and the Eustachian valve. The left atrium is characterized by an elongated, narrow appendage (Figure 3.6b). The left atrial appendage is located posterior relative to the right atrial appendage. In contrast to the right atrial appendage, the pectinate muscles of the left atrium are confined to the appendage. The left atrial septal surface features septum primum (the valve of the foramen ovale).

In atrial situs solitus (Figure 3.7), the right atrium is right-sided whereas in atrial situs inversus it is left-sided. In individuals with normal anatomy, the right atrium receives the right and left horns of the sinus venosus, including the superior vena cava, inferior vena cava and the orifice of the coronary sinus (the cardiac termination of the left horn of the sinus venosus). The left atrium normally receives the pulmonary veins. In atrial situs ambiguous, typically seen in patients with heterotaxy syndrome, the anatomic landmarks characteristic of the right and left atria are not sufficient to determine situs (either situs solitus or situs inversus). Variations of anatomy may include a common atrium with absence (or presence of only remnants) of the atrial septum, interruption of the inferior vena cava between the renal and hepatic segments, bilateral superior venae cavae, and an unroofed or absent coronary sinus. The atrial appendages can be similar to each other; however, in most cases of heterotaxy syndrome the atrial appendages are not identical (i.e., they are not "isomeric"). Although the distribution of the pectinate muscles has been proposed as a useful marker of atrial identity [31], imaging of the pectinate muscle in living patients has not been consistently achieved.

5 **Ventricular loop** (Figure 3.8). The first step in determining the ventricular loop (situs) is to identify the left and right ventricles. It is important to recognize that between the atrioventricular and the semilunar valves (what is generally considered the ventricular mass of the heart) there are three distinct chambers: the left ventricle, the right ventricular sinus, and the infundibulum (or conus) [6,7,32,33]. The normal right ventricle comprises two distinct chambers, which are well incorporated into each other: the right ventricular sinus, and the infundibulum. Externally, the normal right ventricle is triangular in shape and the diaphragmatic (inferior) wall makes an acute angle with the anterior wall. Internally, the normal right ventricle is characterized by septal attachments of the tricuspid valve, coarse trabeculations, and a distinct septal surface that includes the septal and moderator bands (Figure 3.8a). The infundibulum is normally well incorporated with the right ventricular sinus, such that their separate identities may be obscured (Figure 3.8a,b). However, these chambers have different embryologic and developmental origins. Moreover, in several congenital cardiac anomalies the infundibulum is either poorly incorporated with the right ventricular sinus (e.g.,

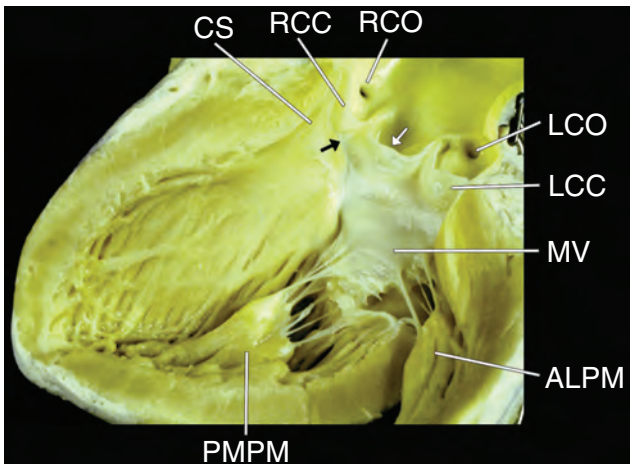


Figure 3.9 Left ventricular morphology. The most reliable morphologic feature of the left ventricle is its smooth superior septal surface. In the normal left ventricle, the finely trabeculated apex (trabeculae carneae) are quite characteristic. However, in a markedly hypertrophied left ventricle, or in double- or common-inlet left ventricle, the apical trabeculations may be prominently hypertrophied (similar to the trabeculations seen in the right ventricle). In the normal left ventricle, the mitral valve (MV) attaches to two large groups of papillary muscles, which attach to the left ventricular free wall. The aortic valve is in fibrous continuity with the mitral valve due to absence of an intervening conal musculature in this region. More anteriorly, under the right coronary cusp of the aortic valve, conal musculature comprises the infundibular septum (CS). The black arrow denotes the location of the membranous septum under the right noncoronary commissure. The white arrow denotes the noncoronary cusp of the aortic valve. ALPM, antero-lateral papillary muscle; LCC, left coronary cusp, LCO, left coronary orifice; MV, mitral valve; PMPM, postero-medial papillary muscle; RCO, right coronary orifice; RCC, right coronary cusp.

double-chambered right ventricle [34]) or is completely dissociated from the right ventricular sinus and completely associated with the left ventricle (e.g., anatomically corrected malposition of the great arteries and transposition of the great arteries with posterior aorta [32,35]).

The anatomic features of the normal left ventricle are illustrated in Figure 3.9. Externally, the shape of the normal left ventricle approximates that of a cone. Internally, the myocardial architecture exhibits fine apical trabeculations, and attachments of the mitral valve to two distinct papillary muscles that attach to the left ventricular free wall without attachments to the interventricular septum. The aortic valve is in fibrous continuity with the mitral valve due to absence of an intervening conal musculature in this region. It is important to recognize, however, that variations in anatomy and physiology can greatly alter left ventricular morphology, and many of the morphologic characteristics of the normal left ventricle can be altered. For example, in a markedly hypertrophied left ventricle, or in double- or common-inlet left ventricle, the apical trabeculations may be prominently hypertrophied, similar to the trabeculations of the right ventricle. Also, the normal attachments of the mitral valve to the left ventricular free wall papillary muscles are usually altered in common AV canal defects, straddling mitral valve, and other malformations. Therefore, the most reliable morphologic feature of the left ventricle is its smooth superior septal surface.

Once ventricular identity has been established based on morphologic criteria, the type of ventricular loop can be determined (Figure 3.10a,b). The type of ventricular loop is clinically relevant in that it determines the pattern of coronary artery distribution, the disposition of the conduction system, and the internal organization of the ventricular myocardium. Furthermore, L- (or levo-) ventricular loop is associated with increased risks of atrioventricular block (either congenital or acquired), Ebstein-like malformation of the left-sided tricuspid valve, and hypoplasia of the left-sided right ventricular sinus. Because the spatial position of the ventricles varies widely, a right–left location relative to each other cannot be used reliably to determine the ventricular loop [36,37]. Instead, the principle of *chirality* is used. This method can be applied regardless of the spatial position of the ventricles and requires only the identification of the inflow, outflow, and septal surface of one of the ventricles (Figure 3.10a,b). The only circumstance where the type of ventricular loop cannot be reliably determined is in anatomically single right ventricle without a recognizable left ventricle or an interventricular septum.

6 **Atrioventricular alignments and connections** (Figure 3.11). Once the identity and situs of the atria and the ventricles have been established, attention is then focused on the first connecting segment, the AV canal. Figure 3.11 illustrates several representative types of AV alignments and connections. However, it is important to recognize that these examples are only samples of an anatomic continuum. Moreover, AV valve type generally goes with the ventricle to which it connects excepting the case of AV canal and double inlet ventricle.

7 **Ventriculo-arterial alignments** (Figure 3.12). Next, the outflow of the heart is examined to determine from which cardiac chamber each great artery originates. Ventriculo-arterial alignment describes how the semilunar valves and their respective great vessels align with the underlying ventricles. Figure 3.12 illustrates several representative types of ventriculo-arterial alignments. However, as with atrioventricular alignments, it is important to recognize that the spectrum of possible alignments between the great arteries and the underlying ventricles is a continuum and sometimes difficult to determine. Classification of ventriculo-arterial alignment into discrete groups requires drawing sharp borders within transition zones, which inevitably leave certain anatomic variations straddling between categories. The preferred approach is to assign a great vessel to an underlying ventricle when it completely or nearly completely relates to that chamber. In cases where a semilunar valve significantly overrides the ventricular septum the preferred approach is to describe the anatomy (e.g., right ventricular origin of

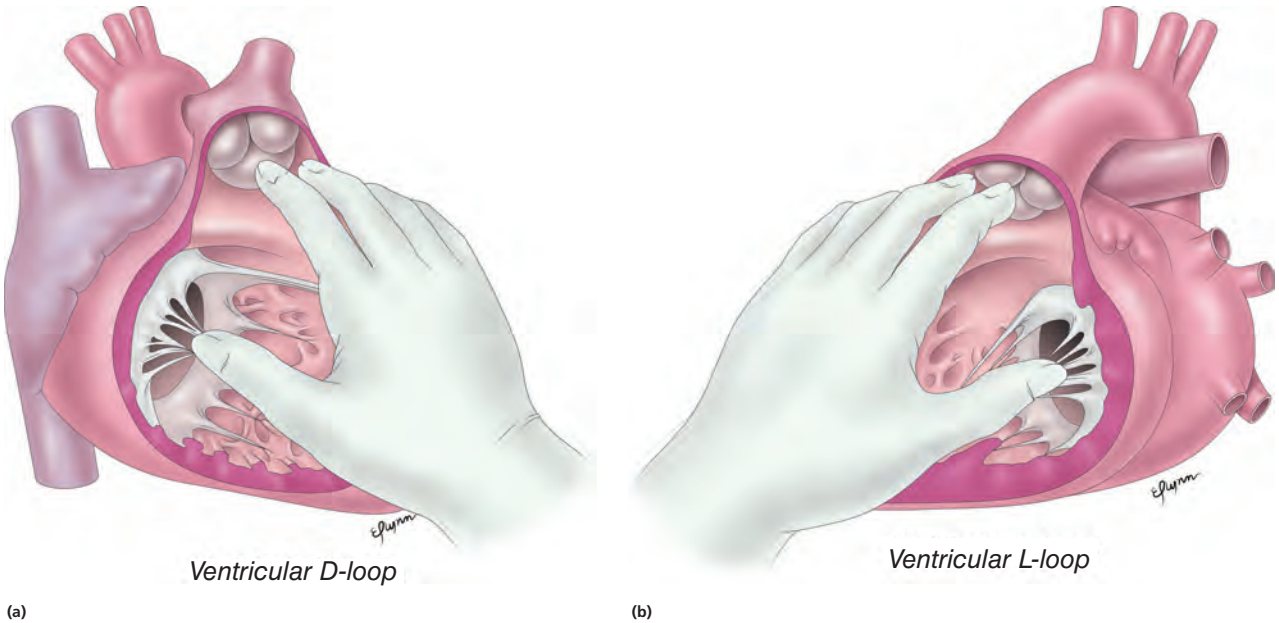


Figure 3.10 Determination of ventricular situs. **(a)** In ventricular D-loop the palmar aspect of the right hand is placed over the right ventricular septal surface with the thumb in the tricuspid valve, the fingers in the right ventricular outflow and the dorsum of the right hand facing the right ventricular free wall. **(b)** In ventricular L-loop the palmar aspect of the left hand faces the right ventricular septal surface with the thumb in the tricuspid valve (or inflow), the fingers in the right ventricular outflow and the dorsum of the left hand facing the right ventricular free wall. Using this principal, ventricular situs can be determined regardless of ventricular position in the chest. The same principle also applies to the left ventricle. When using the left ventricle, a right-handed left ventricle will be L-looped and a left-handed left ventricle will be D-looped.

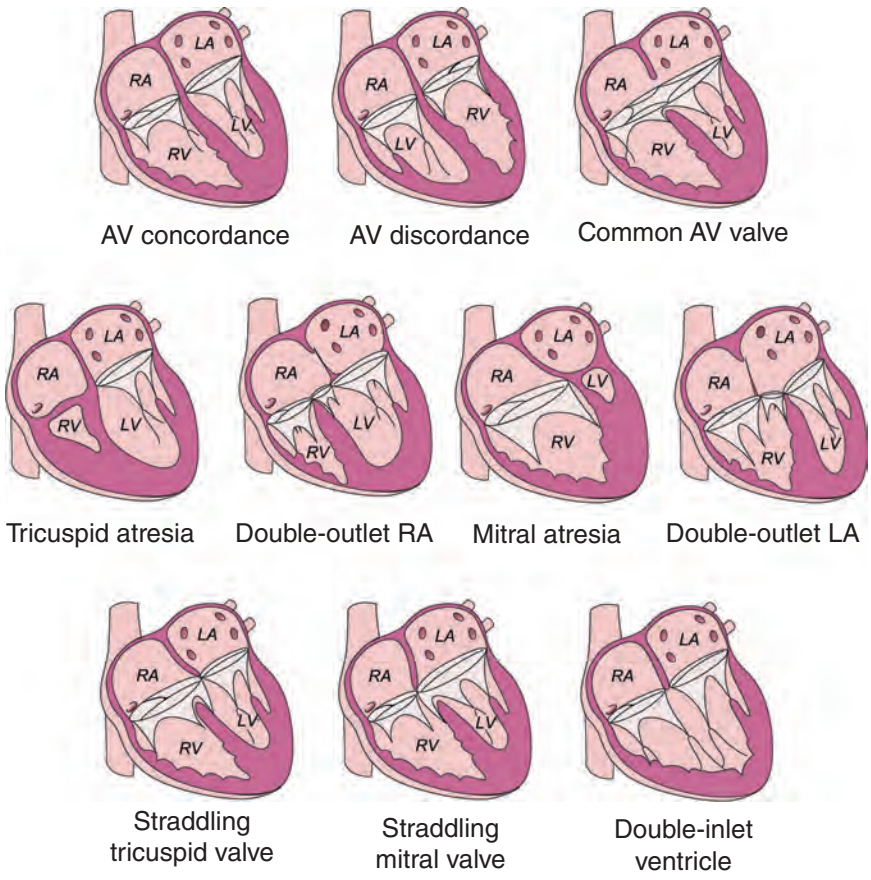


Figure 3.11 Diagram illustrating some of the possible atrioventricular (AV) alignments and connections. This step in the segmental approach to congenital heart disease follows identification of atrial and ventricular morphology and situs. RA, right atrium; LA, left atrium; RV, right ventricle; LV, left ventricle.

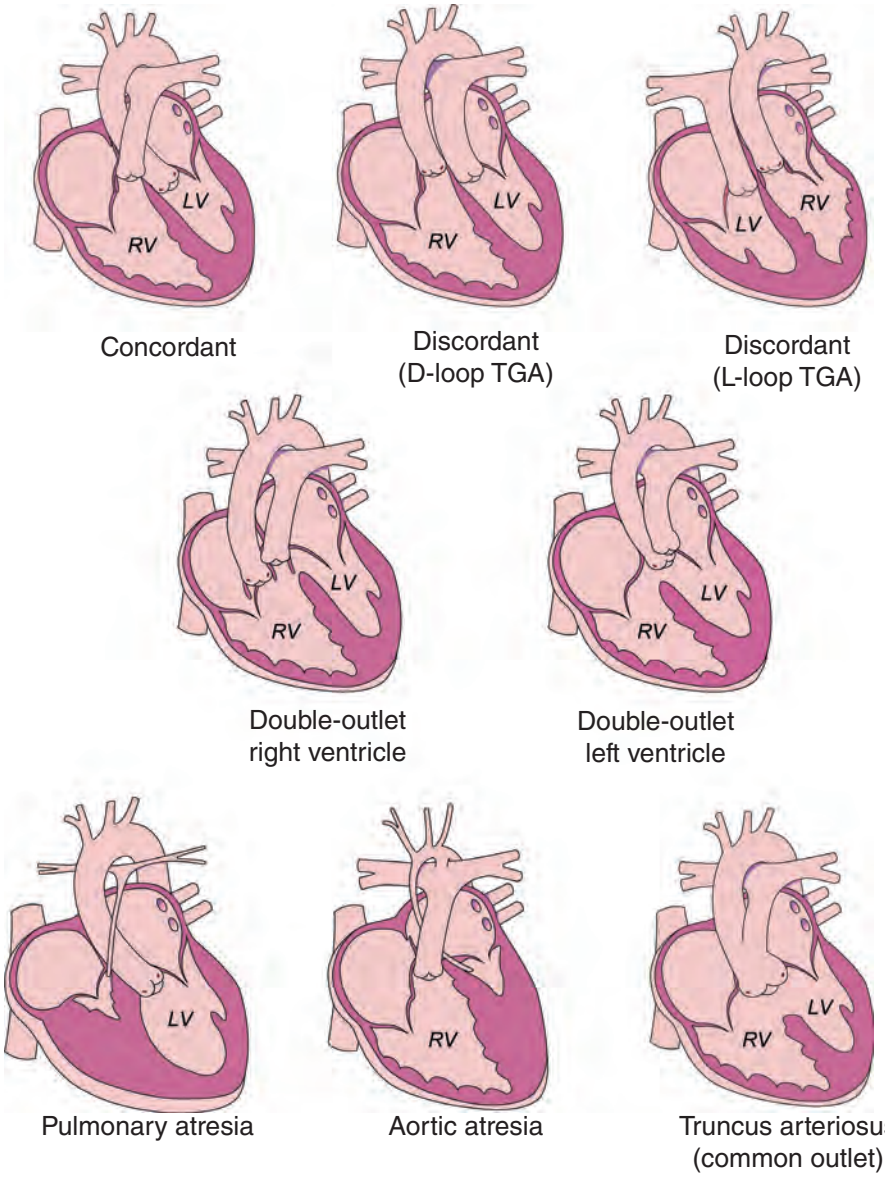


Figure 3.12 Diagram illustrating some of the possible ventriculo-arterial (VA) alignments and connections. Note that the type of ventriculo-arterial alignment is determined by which great artery arises entirely or predominantly from which ventricle. It is clinically impractical to accurately and reproducibly determine great arterial origin from either ventricle in terms of percent origin. Specifically, the so-called "50% rule" is not applicable in vivo. This is due to complex three-dimensional relations between the ventricles and the great arteries, the complex geometric nature of the ventricular septum and cardiac motion in systole and diastole and with respiration. TGA, transposition of the great arteries; RV, right ventricle; LV, left ventricle.

the aorta and biventricular origin of the main pulmonary artery). Specifically, the so-called "50% rule" is not practicably applicable in vivo due to complex three-dimensional relations between the ventricles and the great arteries, the curved geometry of the ventricular septum, and rotational and translational cardiac motion. It is important to note that determination of ventriculo-arterial alignment is based on the spatial relationships between the semilunar valves and the underlying ventricles and is not based on the type of infundibulum present (see next paragraph).

8 **Type of infundibulum (conus)** (Figure 3.13). The infundibulum is the connecting segment between the ventricles and the great arteries. In normal anatomy, there is a complete *subpulmonary conus* with muscular separation between the pulmonary and the AV valves (Figure 3.8), whereas the subaortic conus is incomplete, allowing fibrous continuity between the left and noncoronary cusps of the aortic valve and the anterior leaflet of the mitral valve (Figure 3.9). Part of the subaortic conus is normally present in the form of a conal septum represented by the myocardium that separates the anterolateral aspect of the left ventricular outflow (the myocardium under the right coronary cusp of the aortic valve) and the right ventricular outflow tract. In some patients, there is an increased distance between the left coronary cusp and the anterior mitral leaflet due to elongation of the intervalvular fibrosa. In this circumstance, the aortic and mitral valves are said to have fibrous contiguity as opposed to fibrous continuity.

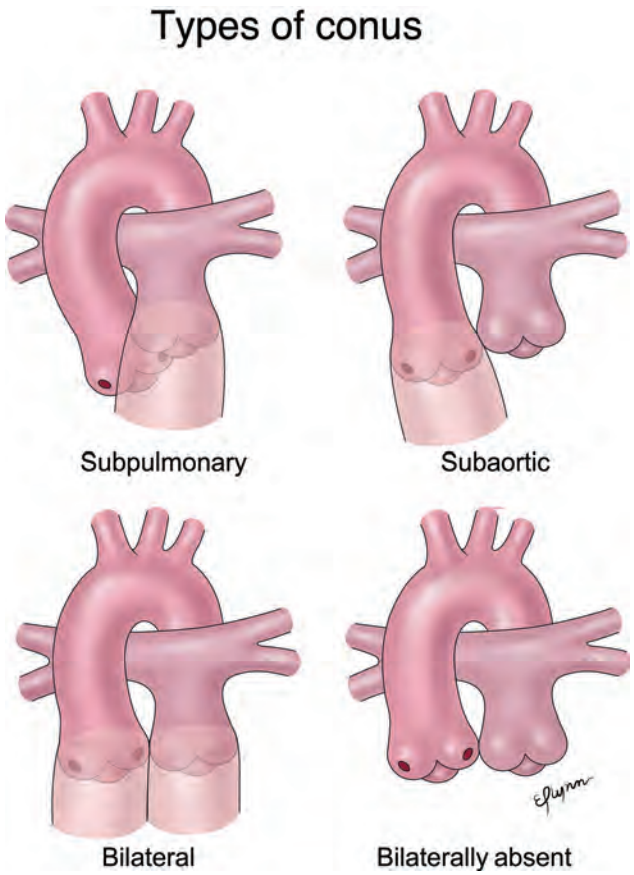


Figure 3.13 Type of infundibulum. In general, there are four types of conus (or infundibulum): (i) *subpulmonary* with absence of subaortic infundibular free wall (found in the normal heart); (ii) *subaortic* with absence of subpulmonary infundibular free wall (often found in transposition of the great arteries); (iii) *bilateral conus* (commonly found in patients with double-outlet right ventricle, but can be rarely found in patients with TGA and even in patients with normally related great arteries); (iv) *bilaterally absent* (found in some patients with double-outlet left ventricle).

Normal conal anatomy is termed *subpulmonary conus* indicating presence of a complete subpulmonary infundibular myocardium and partial absence of the subaortic infundibular free wall. Abnormal conal anatomy includes complete *subaortic conus*, *bilateral conus*, and *bilaterally absent conus*. A *subaortic conus* is present when the aortic valve is entirely supported by infundibular myocardium completely separating it from the AV valve(s). The subpulmonary conus is incomplete with absence of infundibular myocardium between the pulmonary and AV valve(s). A subaortic conus is often found in transposition of the great arteries. However, it is important to recognize that (i) transposition of the great arteries is a specific type of ventriculo-arterial alignment (which great artery originates from which ventricle?) and is not defined by the type of conus; and (ii) any type of conus may be present in transposition of the great arteries or in any other type of ventriculo-arterial alignment (other than normal) [38].

Bilateral conus is present when both semilunar valves are completely separated from the AV valve(s) by infundibular myocardium. Although a bilateral conus is commonly associated with double-outlet right ventricle, it is important to recognize that, similar to transposition, (i) double-outlet right ventricle is a specific type of ventriculo-arterial alignment (which great artery originates from which ventricle?) and is not defined by the type of conus; and (ii) any type of conus may be present in double-outlet right ventricle.

Bilaterally absent conus is the least common type of infundibular anatomy. It is present when both semilunar valves are in direct fibrous continuity with the AV valve(s) and in direct fibrous continuity with each other as a result of absence of infundibular myocardium. It is the rarest type of conal anatomy and most commonly seen in double-outlet left ventricle.

9 **Relationship between semilunar valves** (Figure 3.14). This step in the segmental approach to congenital heart disease describes the spatial relationships between the aortic and pulmonary valves. Although the spatial relationships between the semilunar valves are often associated with predictable patterns of ventriculo-arterial alignments, there are many exceptions to these rules. Moreover, it is important to recognize that the designation of "D" and "L" to describe the spatial relationships between the semilunar valves does not provide information regarding the anterior–posterior and the superior–inferior orientations. Therefore, it is important to provide this additional information as part of comprehensive description of the anatomy.

10 **Associated anomalies**. Once the three main cardiac segments and the two connecting segments have been evaluated and categorized, all associated cardiovascular anomalies

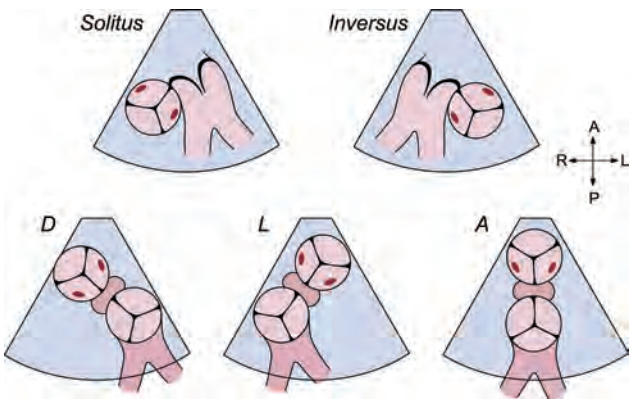


Figure 3.14 Relationships between semilunar valves. The diagram illustrates several common interrelations between the semilunar valves as seen by a transthoracic echocardiographic parasternal short-axis view. It must be recognized, however, that the interrelations between the semilunar valves form an anatomic continuum. D, dextro (rightward); L, levo (leftward); A, anterior; L, left; P, posterior; R, right.

are systematically examined and described. To provide a logical and consistent description of all associated anomalies, they can either be described in order of their hemodynamic importance (from major to minor anomalies) or in an anatomic order (progressing from the venous entry to the arterial exit of the heart) (Figure 3.2).

Conclusion

The above-described segmental approach to anatomic analysis of congenital heart disease allows accurate description of all known forms of cardiac anomalies and can be applied to patients of all ages using diagnostic imaging modalities such as echocardiography, angiography, computed tomography, and magnetic resonance imaging. In rare circumstances when the morphology does not conform to a clearly defined diagnostic category, it is essential to provide an accurate detailed description of the anatomy using tools provided by the segmental approach to CHD.

References

1 Abbott ME. *Atlas of Congenital Cardiac Disease*. New York, NY: The American Heart Association, 1936.
2 Gross RE. Surgical management of the patent ductus arteriosus: with summary of four surgically treated cases. *Ann Surg* 1939;**110**: 321–356.
3 Blalock A, Taussig HB. Landmark article May 19, 1945: The surgical treatment of malformations of the heart in which there is pulmonary stenosis or pulmonary atresia. By Alfred Blalock and Helen B. Taussig. *JAMA* 1984;**251**:2123–2138.
4 Gibbon JH, Jr. Application of a mechanical heart and lung apparatus to cardiac surgery. *Minn Med* 1954;**37**:171–185; passim.
5 Van Praagh R. The segmental approach to diagnosis of congenital heart disease. In: *Birth Defects: Original Article Series*. Baltimore, MD: Williams & Wilkins, 1972, pp. 4–23.
6 Van Praagh R, Van Praagh S, Vlad P, Keith JD. Anatomic types of congenital dextrocardia: diagnostic and embryologic implications. *Am J Cardiol* 1964;**13**:510–531.
7 Van Praagh R, Van Praagh S. Isolated ventricular inversion. A consideration of the morphogenesis, definition and diagnosis of nontransposed and transposed great arteries. *Am J Cardiol* 1966;**17**: 395–406.
8 Van Praagh R, Santini F, Geva T. Segmental situs in congenital heart disease: a fundamental concept. *G Ital Cardiol* 1990;**20**:246–253.
9 Van Praagh R. The segmental approach clarified. *Cardiovasc Intervent Radiol* 1984;**7**:320–325.
10 Lev M. Some newer concepts of the pathology of congenital heart disease. *Med Clin North Am* 1966;**50**:3–14.
11 Lev M, Liberthson RR, Golden JG, et al. The pathologic anatomy of mesocardia. *Am J Cardiol* 1971;**28**:428–435.
12 de la Cruz MV, Nadal-Ginard B. Rules for the diagnosis of visceral situs, truncoconal morphologies, and ventricular inversions. *Am Heart J* 1972;**84**:19–32.
13 Stanger P, Rudolph AM, Edwards JE. Cardiac malpositions. An overview based on study of sixty-five necropsy specimens. *Circulation* 1977;**56**:159–172.
14 Rao PS. Dextrocardia: systematic approach to differential diagnosis. *Am Heart J* 1981;**102**:389–403.
15 Freedom RM. The "anthropology" of the segmental approach to the diagnosis of complex congenital heart disease. *Cardiovasc Intervent Radiol* 1984;**7**:121–123.
16 Shinebourne EA, Macartney FJ, Anderson RH. Sequential chamber localization – logical approach to diagnosis in congenital heart disease. *Br Heart J* 1976;**38**:327–340.
17 Tynan MJ, Becker AE, Macartney FJ, et al. Nomenclature and classification of congenital heart disease. *Br Heart J* 1979;**41**:544–553.
18 Anderson RH, Becker AE, Freedom RM, et al. Sequential segmental analysis of congenital heart disease. *Pediatr Cardiol* 1984;**5**:281–287.
19 Anderson RH, Becker AE, Tynan M, et al. The univentricular atrioventricular connection: getting to the root of a thorny problem. *Am J Cardiol* 1984;**54**:822–828.
20 Weinberg PM. Systematic approach to diagnosis and coding of pediatric cardiac disease. *Pediatr Cardiol* 1986;**7**:35–48.
21 Van Praagh R. Diagnosis of complex congenital heart disease: morphologic-anatomic method and terminology. *Cardiovasc Intervent Radiol* 1984;**7**:115–120.
22 Van Praagh R. The importance of segmental situs in the diagnosis of congenital heart disease. *Semin Roentgenol* 1985;**20**:254–271.
23 Anderson RH, Razavi R, Taylor AM. Cardiac anatomy revisited. *J Anat* 2004;**205**:159–177.
24 Beland MJ, Franklin RC, Jacobs JP, et al. Update from the International Working Group for Mapping and Coding of Nomenclatures for Paediatric and Congenital Heart Disease. *Cardiol Young* 2004;**14**:225–229.
25 Jacobs JP, Franklin RC, Jacobs ML, et al. Classification of the functionally univentricular heart: unity from mapped codes. *Cardiol Young* 2006;**16**:9–21.
26 Bergersen L, Everett AD, Giroud JM, et al. Report from The International Society for Nomenclature of Paediatric and Congenital Heart Disease: cardiovascular catheterisation for congenital and paediatric cardiac disease (Part 1 – Procedural nomenclature). *Cardiol Young* 2011;**21**:252–259.
27 Geva T, Vick GW, 3rd, Wendt RE, Rokey R. Role of spin echo and cine magnetic resonance imaging in presurgical planning of heterotaxy syndrome. Comparison with echocardiography and catheterization. *Circulation* 1994;**90**:348–356.
28 Van Praagh R, Van Praagh S. Atrial isomerism in the heterotaxy syndromes with asplenia, or polysplenia, or normally formed spleen: an erroneous concept. *Am J Cardiol* 1990;**66**:1504–1506.
29 Sutherland MJ, Ware SM. Disorders of left-right asymmetry: heterotaxy and situs inversus. *Am J Med Genet C* 2009;**151C**:307–317.
30 Cantrell JR, Haller JA, Ravitch MM. A syndrome of congenital defects involving the abdominal wall, sternum, diaphragm, pericardium, and heart. *Surg Gynecol Obstet* 1958;**107**:602–614.
31 Uemura H, Ho SY, Devine WA, Anderson RH. Analysis of visceral heterotaxy according to splenic status, appendage morphology, or both. *Am J Cardiol* 1995;**76**:846–849.
32 Van Praagh R, Van Praagh S. Anatomically corrected transposition of the great arteries. *Br Heart J* 1967;**29**:112–119.

33 Geva T, Powell AJ, Crawford EC, et al. Evaluation of regional differences in right ventricular systolic function by acoustic quantification echocardiography and cine magnetic resonance imaging. *Circulation* 1998;**98**:339–345.
34 Wong PC, Sanders SP, Jonas RA, et al. Pulmonary valve-moderator band distance and association with development of double-chambered right ventricle. *Am J Cardiol* 1991;**68**:1681–1686.
35 Van Praagh R, Perez-Trevino C, Lopez-Cuellar M, et al. Transposition of the great arteries with posterior aorta, anterior pulmonary artery, subpulmonary conus and fibrous continuity between aortic and atrioventricular valves. *Am J Cardiol* 1971;**28**:621–631.
36 Geva T, Van Praagh S, Sanders SP, et al. Straddling mitral valve with hypoplastic right ventricle, crisscross atrioventricular relations, double outlet right ventricle and dextrocardia: morphologic, diagnostic and surgical considerations. *J Am Coll Cardiol* 1991;**17**:1603–1612.
37 Geva T, Sanders SP, Ayres NA, et al. Two-dimensional echocardiographic anatomy of atrioventricular alignment discordance with situs concordance. *Am Heart J* 1993;**125**:459–464.
38 Pasquini L, Sanders SP, Parness IA, et al. Conal anatomy in 119 patients with d-loop transposition of the great arteries and ventricular septal defect: an echocardiographic and pathologic study. *J Am Coll Cardiol* 1993;**21**:1712–1721.
39 Van Praagh S, Geva T, Lock JE, et al. Biatrial or left atrial drainage of the right superior vena cava: anatomic, morphogenetic, and surgical considerations – report of three new cases and literature review. *Pediatr Cardiol* 2003;**24**:350–363.

CHAPTER 4

The Normal Pediatric Echocardiogram

Wyman W. Lai[1] and H. Helen Ko[2]
[1]Division of Pediatric Cardiology, Columbia University Medical Center, New York, NY, USA
[2]Mount Sinai Medical Center, New York, NY, USA

Examination principles

The basic elements of a standard transthoracic examination are two-dimensional (2D) images supplemented by Doppler and color Doppler information in multiple orthogonal imaging planes [1]. The use of M-mode echocardiography is reserved primarily for the assessment of ventricular function [2], although some current pediatric recommendations call for 2D assessment of left ventricular size and function [3]. Any laboratory performing a pediatric echocardiogram should have a written examination protocol that outlines the views to be obtained, the imaging modalities to be deployed for each view, and the preferred methods for recording and display. Whenever possible, the initial pediatric echocardiogram should be a complete study. A list of the structures to be examined with each view is helpful, and the required versus optional measurements should be clearly defined. A complete transthoracic pediatric echocardiogram should include a quantitative assessment of left ventricular size and systolic function (see later) [4].

The pediatric echocardiogram is organized by acoustic "windows" from which the heart is examined. Many pediatric echocardiography laboratories begin the examination with subxiphoid, or subcostal, imaging instead of left parasternal views. This allows for the determination and display of visceral situs (site or location) at the beginning of an examination. Regardless of where the examination starts, the segmental approach is used to describe all of the major cardiovascular structures in sequence [5–7].

Complete sweeps of the heart should be made during the examination to rule out abnormalities at its base or apex or on one of its surfaces. The study information may be recorded as complete sweeps, multiple selected single planes, or with a combination of both techniques [8–10]. Most ultrasound systems are configured so that a notch, or some other marking, on the side of a transducer corresponds to the side of a symbol displayed at the top of the image sector, usually to the right side of the screen. Therefore, when the transducer is positioned with the notch to the patient's left (at the 3 o'clock position), the left side of the patient will be displayed on the right of the screen. When the transducer is clockwise rotated so that the notch is directed inferiorly (at 6 o'clock), the inferior structures are displayed on the right side of the screen. In the course of a routine sweep, the transducer notch position is held in a fixed position, and the transducer is angled to obtain a series of images in the desired imaging plane.

Because of the wide range of complex pathology that may be seen on a pediatric echocardiogram, images should be shown in their correct spatial, or "anatomically correct," position on the display screen. Therefore, the anterior and superior structures are displayed at the top of the screen, and the rightward structures are generally placed on the left side of the image display (with the exception being the parasternal long-axis view where the cardiac apex is displayed by convention on the left of the screen).

The diagnostic accuracy of an examination depends greatly on the image quality. Technical adjustments should be made throughout the examination by the operator to improve signal-to-noise ratio and image resolution. The appropriate probe and optimal transducer frequency are selected to image the structures in question, and adjustments of the electronic (acoustic) focus depth are made throughout the study as necessary. Centering of structures of interest, using an appropriate degree of magnification, and optimizing of windows for imaging and Doppler interrogation are critical for image quality. The optimal window should allow the ultrasound beam to be directed perpendicularly to structures of interest for imaging and parallel to flow jets for Doppler interrogation and color flow mapping. Patient position, comfort, and level of anxiety are important considerations during the examination.

In the usual performance of an echocardiogram, the goals from each view should be (i) imaging of cardiovascular structures; (ii) color and/or spectral Doppler interrogation of each valve and other major cardiovascular structures; and (iii) a complete evaluation of any suspicious chamber, vessel, or flow jet

Echocardiography in Pediatric and Congenital Heart Disease: From Fetus to Adult, Second Edition. Edited by Wyman W. Lai, Luc L. Mertens, Meryl S. Cohen and Tal Geva.
© 2016 John Wiley & Sons, Ltd. Published 2016 by John Wiley & Sons, Ltd.
Companion website: www.lai-echo.com

Table 4.1 Structures viewed from subxiphoid (subcostal) views

Inferior vena cava
Hepatic veins
Abdominal aorta
Diaphragm
Superior vena cava
Left atrium
Right atrium
Atrial septum
Coronary sinus
Pulmonary veins
Mitral valve
Tricuspid valve
Left ventricle
Right ventricle
Ventricular septum
Left ventricular papillary muscles
Aortic valve
Pulmonary valve
Ascending aorta
Coronary arteries
Main and branch pulmonary arteries
Pericardium

identified during the course of the examination. Tables 4.1–4.5 list the structures that should be visualized from the standard examination views. During the progress of a pediatric echocardiogram, the sonographer or echocardiographer must keep in mind the indications for the study and the need to address potential issues that may affect treatment. A complete examination may require that custom, or "in-between," planes be used to investigate or display an abnormality.

Extracardiac structures are also visualized during a standard transthoracic examination. Mediastinal abnormalities such as masses or cysts, if present, should be noted [11,12]. The presence or absence of the thymus may be seen in young children. Careful attention to symmetry and amplitude of diaphragm motion and screening for pleural effusions from subxiphoid and flank windows (see later) is particularly important in postoperative cardiac patients.

Table 4.2 Structures viewed from apical views

Inferior vena cava
Left atrium
Right atrium
Atrial septum
Coronary sinus
Selected pulmonary veins
Mitral valve
Tricuspid valve
Left ventricle
Right ventricle
Ventricular septum
Left ventricular papillary muscles
Aortic valve
Pulmonary valve
Ascending aorta
Main and branch pulmonary arteries

Table 4.3 Structures viewed from left parasternal views

Inferior vena cava
Superior vena cava
Left atrium
Right atrium
Atrial septum
Coronary sinus
Pulmonary veins
Mitral valve
Tricuspid valve
Left ventricle
Right ventricle
Ventricular septum
Left ventricular papillary muscles
Aortic valve
Pulmonary valve
Ascending aorta
Coronary arteries
Main and branch pulmonary arteries
Pericardium

Standard orthogonal imaging views

The five standard views of a pediatric echocardiogram, as defined by the American Society of Echocardiography, are all employed as part of a routine examination: subxiphoid (subcostal), apical, parasternal (left parasternal), suprasternal notch, and right parasternal [13]. These imaging planes provide unique information regarding cardiovascular malformations that are often seen in childhood. A complete examination requires that the cardiovascular structures be imaged from multiple orthogonal planes. This practice minimizes artifacts due to false

Table 4.4 Structures viewed from suprasternal notch views

Superior vena cava
Left atrium
Pulmonary veins
Ascending aorta
Superior thoracic aorta
Main and branch pulmonary arteries
Aortic arch
Proximal brachiocephalic arteries
Left innominate vein

Table 4.5 Structures viewed from right parasternal views

Inferior vena cava
Superior vena cava
Right atrium
Atrial septum
Right pulmonary veins
Ascending aorta
Right pulmonary artery

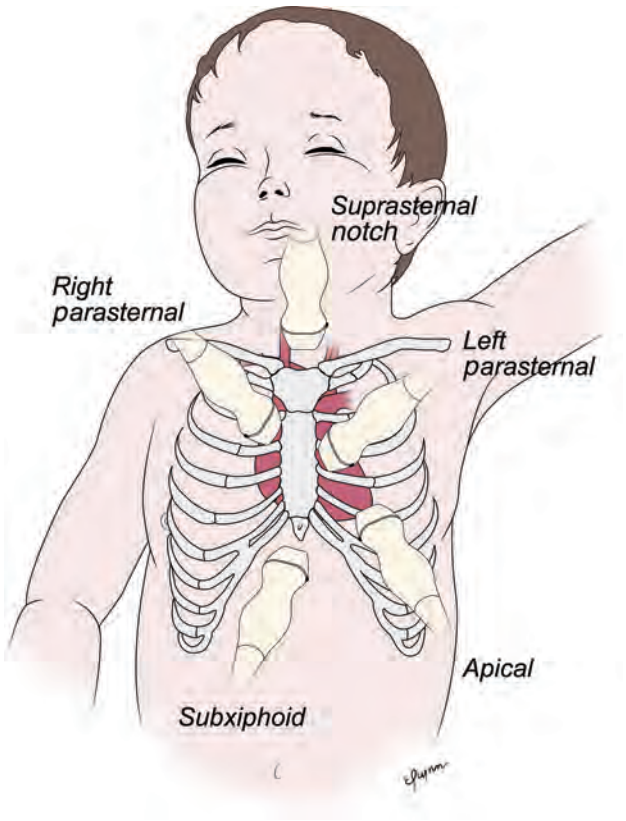


Figure 4.1 Line drawing of transducer locations for standard imaging windows.

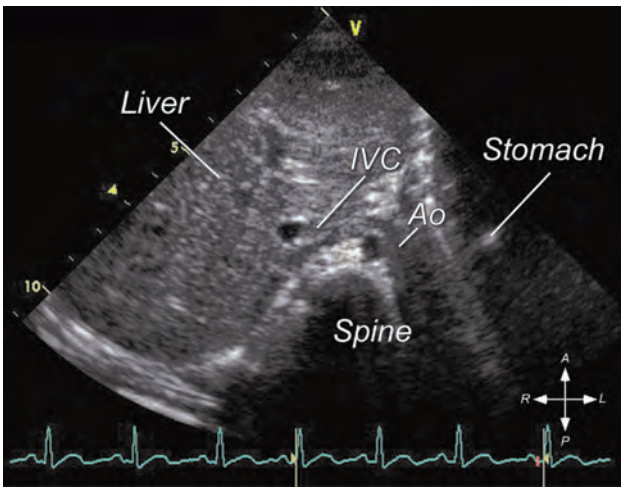


Figure 4.2 Axial image of a child with normal abdominal visceral situs. Ao, aorta; IVC, inferior vena cava.

"dropout" of structures imaged parallel to the beam of interrogation, "shadowing" from reflective structures proximal to the area of interest, or "mirroring" from the reflection of ultrasound on tissue layers.

The imaging planes are identified by transducer location (subxiphoid, apical, parasternal, suprasternal notch, and right parasternal) and by the plane of examination relative to the heart (4-chamber, 2-chamber, long-axis, and short-axis) (Figure 4.1). In addition, imaging planes may be described as anatomic planes (sagittal, transverse/axial, or coronal). The views and structures presented in the following sections are described as seen in a patient with normal or near-normal cardiovascular anatomy.

Subxiphoid (subcostal) views

Subxiphoid imaging [14–16] begins with the determination of abdominal visceral situs in the transverse plane. The transducer is positioned with the notch at the 3 o'clock position as viewed from inferiorly with anterior structures displayed at the top of the screen. In addition to visualization of the liver and stomach, the spleen should be sought in patients with suspected abnormal abdominal visceral situs. The location of the hepatic segment of the inferior vena cava and descending aorta in relation to the midline and one another are determined from this view (Figure 4.2). The patency, size, and collapsibility of the inferior vena cava should be documented in its long axis (the transducer is rotated clockwise so that the notch is at the 6 o'clock position), and the abdominal descending aorta should also be demonstrated (Figure 4.3). If a dilated azygos vein is seen posterior to the descending aorta, interruption of the inferior vena cava should be suspected. Inadvertent compression of the inferior vena cava, mimicking interruption, may be avoided by reducing the amount of abdominal pressure used to obtain the image.

The imaging plane is then inverted so that the superior structures are displayed at the top of the screen. As the plane of imaging is angled from the abdomen to the thorax, the connections of the hepatic veins to the inferior vena cava are visualized, followed by the connection of the inferior vena cava to the right atrium. The descending aorta at the level of the diaphragm should be identified, and any additional vascular structures crossing the diaphragm should be fully investigated by 2D imaging and color flow mapping. It is useful to visualize both hemi-diaphragms at the same time in the subxiphoid long-axis (transverse) view to document normal diaphragmatic motion with respiration.

The subxiphoid long-axis (coronal, frontal) sweep begins in the transverse plane and utilizes the liver as an acoustic window to the heart (Figure 4.4; Video 4.1). The connections of the hepatic veins to the inferior vena cava should be documented, as well as the entrance of the inferior vena cava to the right atrium. As the sweep passes the inferior/posterior surface of the heart, the coronary sinus is often well visualized along the left posterior atrioventricular groove, and the posterior descending coronary artery may be seen in the posterior interventricular groove. The long-axis view allows for good visualization of the atrial septum and characterization of right versus left atrial and ventricular morphology. As imaging transitions into a nearly coronal plane, the ventricular outflow tracts are well displayed, as is the right atrial appendage and the proximal portion of the normal right

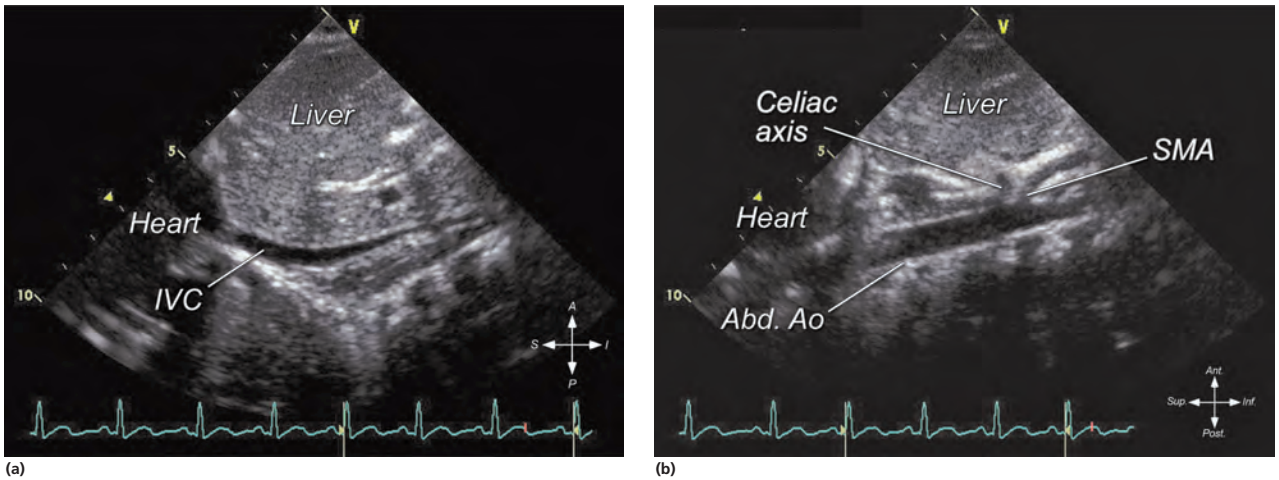


Figure 4.3 Long-axis composite image of uninterrupted inferior vena cava and descending aorta. **(a)** IVC, inferior vena cava. **(b)** Abd. Ao, abdominal aorta; SMA, superior mesenteric artery.

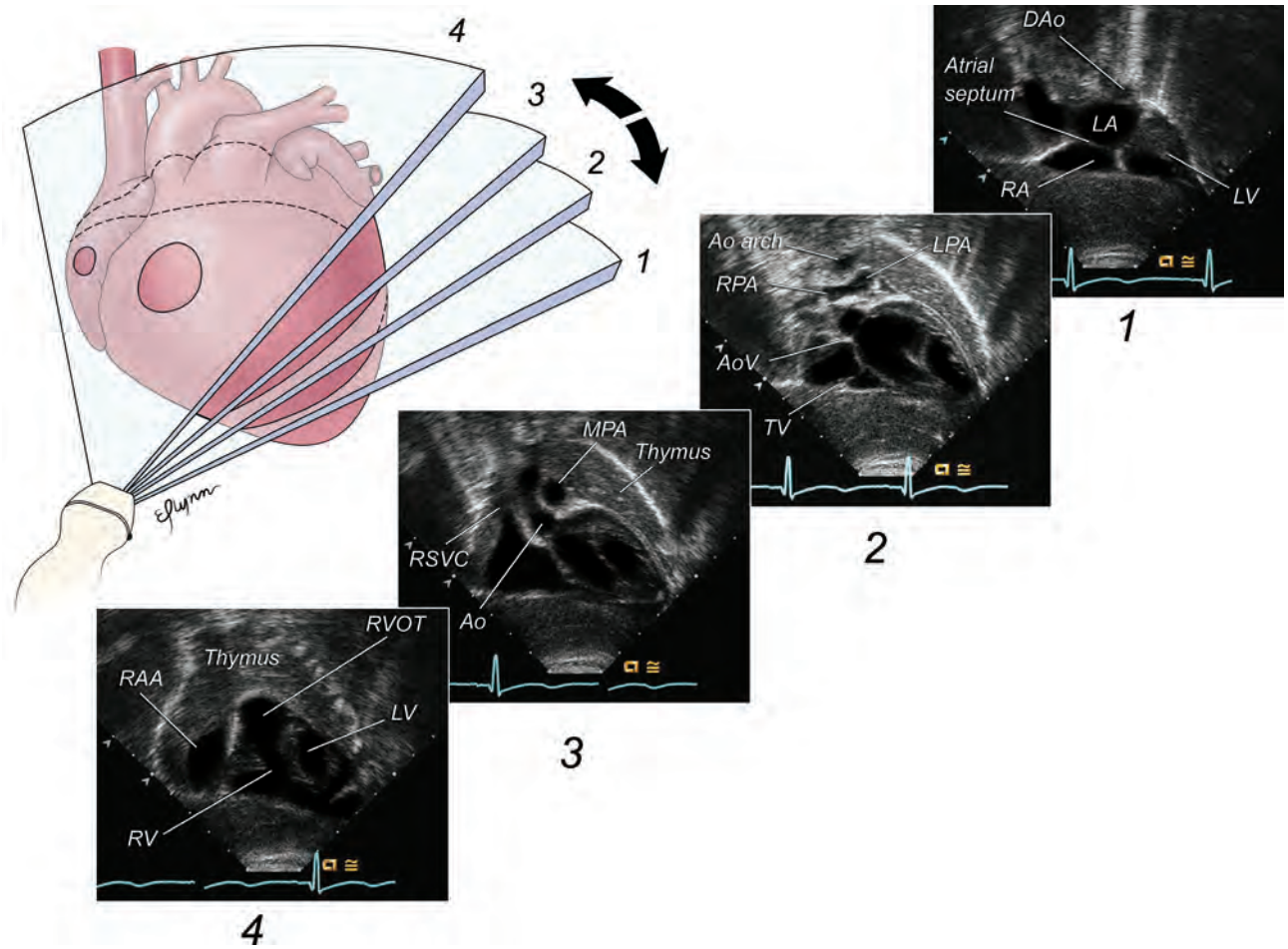


Figure 4.4 Line drawings and serial images of subxiphoid long-axis (frontal) sweep. **(1)** DAo, descending aorta; LA, left atrium; LV, left ventricle; RA, right atrium. **(2)** Ao arch, aortic arch; AoV, aortic valve; LPA, left pulmonary artery; RPA, right pulmonary artery; TV, tricuspid valve. **(3)** Ao, aorta; MPA, main pulmonary artery; RSVC, right superior vena cava. **(4)** LV, left ventricle; RAA, right atrial appendage; RV, right ventricle; RVOT, right ventricular outflow tract.

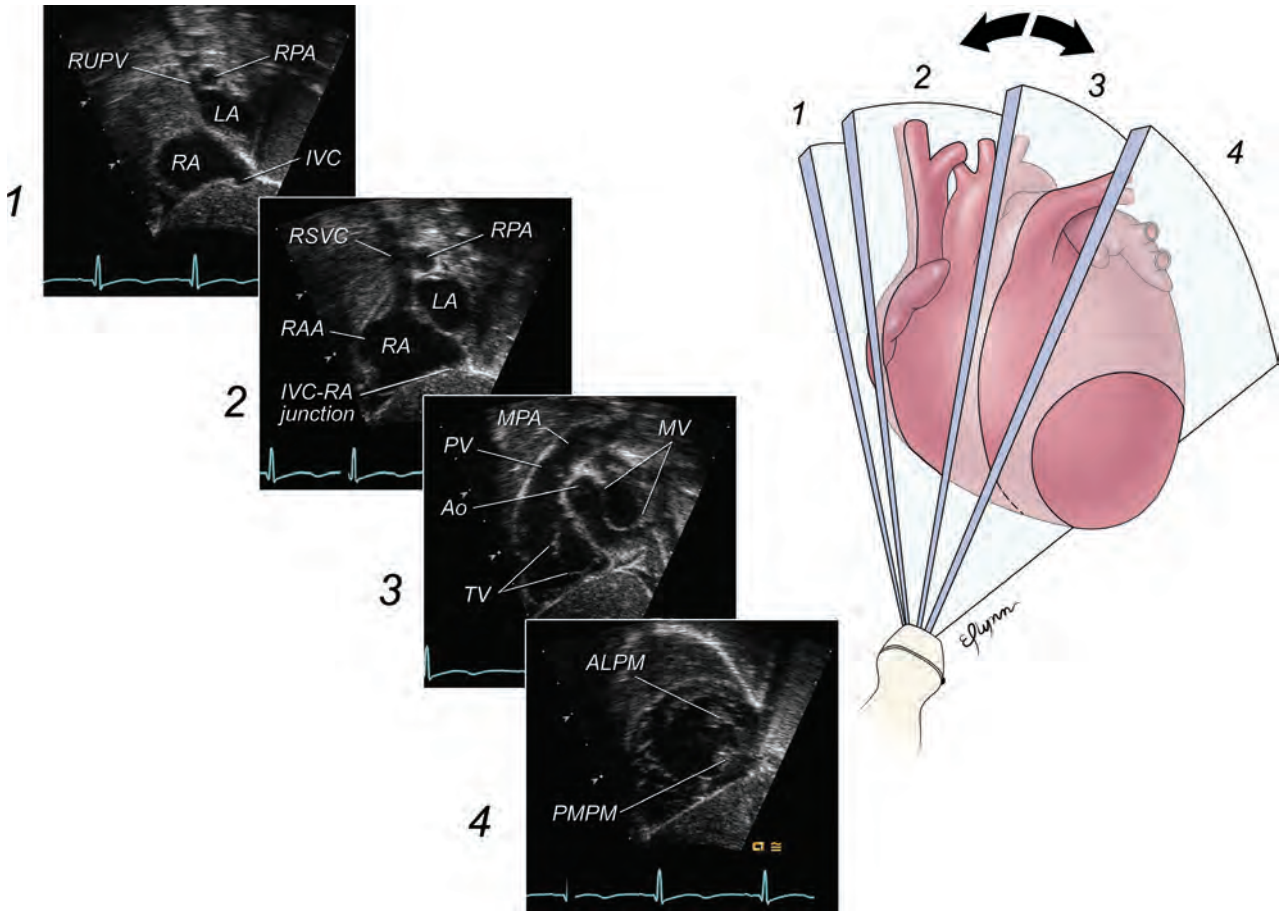


Figure 4.5 Line drawings and serial images of subxiphoid short-axis (sagittal) sweep. **(1)** IVC, inferior vena cava; LA, left atrium; RA, right atrium; RPA, right pulmonary artery; RUPV, right upper pulmonary vein. **(2)** IVC-RA junction, inferior vena caval–right atrial junction; LA, left atrium; RA, right atrium; RAA, right atrial appendage; RPA, right pulmonary artery; RSVC, right superior vena cava. **(3)** Ao, aorta; MPA, main pulmonary artery; MV, mitral valve; PV, pulmonary valve; TV, tricuspid valve. **(4)** ALPM, antero-lateral papillary muscle; PMPM, postero-medial papillary muscle.

superior vena cava to the right of the ascending aorta. The position of the left coronary artery ostium may be visualized as the sinuses of Valsalva and ascending aorta are imaged. The bifurcation of the main pulmonary artery into the branch pulmonary arteries should be documented during the sweep. Color flow mapping in the subxiphoid long axis may be advantageous for interrogation of the atrial septum and the anterior muscular septum. To visualize the true long axis of the atrial septum, the transducer should be rotated in between the subxiphoid long- and the short-axis views. Sweeping from this plane can further elucidate defects in the inferior atrial septum that might be underappreciated in the standard subxiphoid views.

The subxiphoid short-axis (sagittal) sweep (Figure 4.5; Videos 4.2 and 4.3) starts in a sagittal plane with the transducer notch positioned inferiorly (6 o'clock). The short-axis "reference view" includes the atria (including the right atrial appendage), the atrial septum, and the superior and inferior venae cavae. The Eustachian valve – the venous valve of the inferior vena cava – is frequently seen in this view as an extension of the anterior wall of the inferior vena cava and should not be confused with the atrial septum [17]. The imaging sweep normally begins to the right, allowing visualization of the right upper pulmonary vein as it passes lateral and posterior to the superior vena cava and then proceeds from the base to the apex of the heart. The right pulmonary artery is seen in cross-section posterior to the superior vena cava and above the roof of the left atrium. The arch of the azygos vein above the right pulmonary artery and into the superior vena cava may also be visualized in this sweep. Atrial septal morphology, including the apposition of septum primum and septum secundum, is often well seen in the short-axis plane. The tricuspid valve is imaged before the mitral valve as the transducer passes from right to left. The morphology of the atrioventricular valves, including fibrous continuity between the atrioventricular and aortic valves, can be identified as the imaging plane passes the atrioventricular canal region. The transducer position may need to be repositioned during the sweep (generally more rightward on the abdomen, taking advantage of the right-sided liver as an acoustic window) to maintain a short-axis imaging plane as the apex of the heart is visualized. A list of structures that should be identified on the subxiphoid

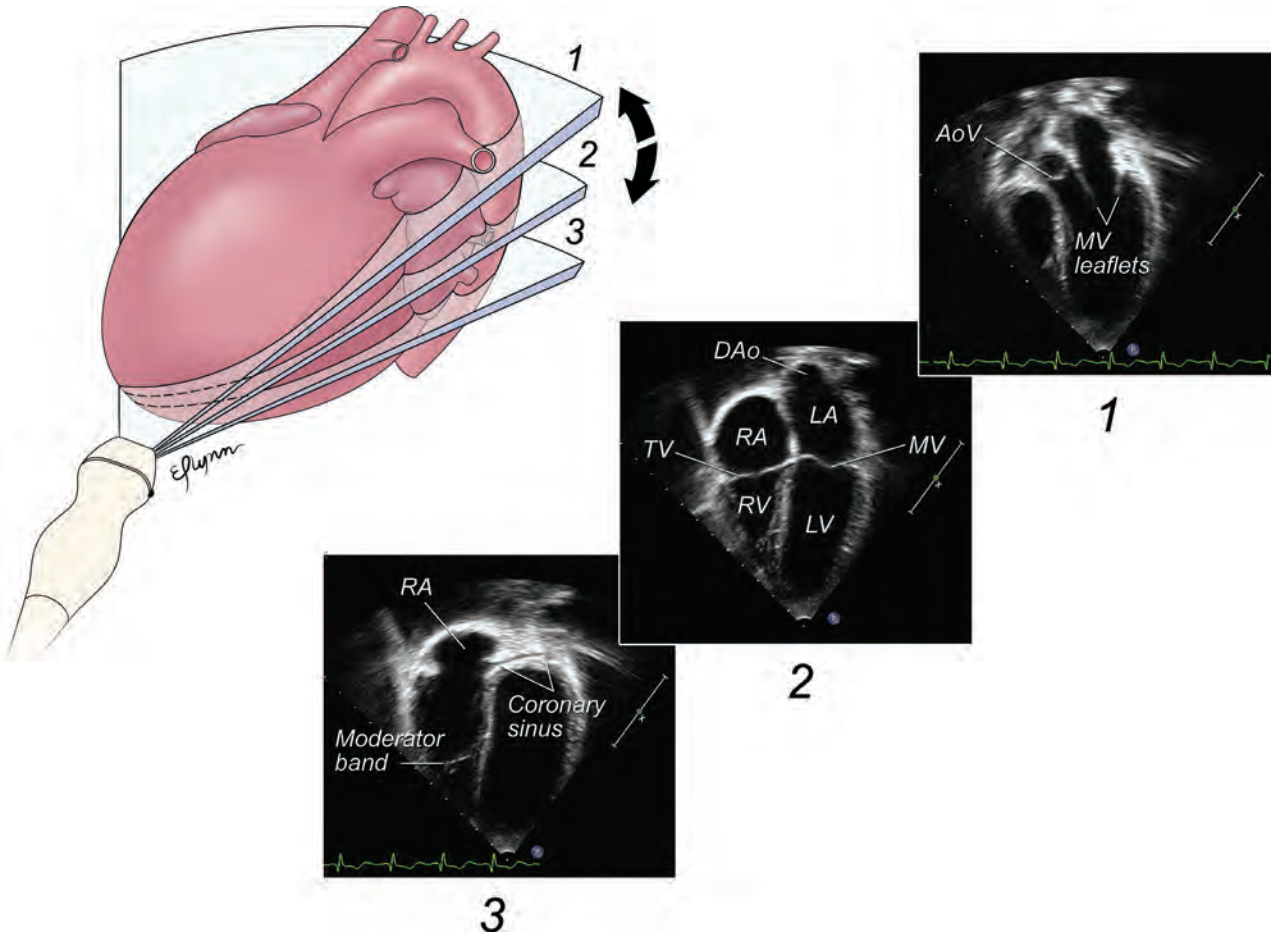


Figure 4.6 Line drawings and serial images of apical 4-chamber sweep. **(1)** AoV, aortic valve; MV leaflets, mitral valve leaflets. **(2)** DAo, descending thoracic aorta; LA, left atrium; LV, left ventricle; MV, mitral valve; RA, right atrium; RV, right ventricle; TV, tricuspid valve. **(3)** RA, right atrium.

views is provided in Table 4.1. Color flow mapping of the atrial and ventricular septa, particularly in smaller children, is often best visualized in the subxiphoid short-axis sweep. It is important to lower the color flow Doppler scale due to the poor angle of interrogation for flow across parts of the ventricular septum. Doppler interrogation of the descending aorta at the level of the diaphragm is recommended as part of a complete examination in all patients.

Apical views

Standard apical [18] 4-chamber and long-axis ("3-chamber") – as well as, in some laboratories, apical 2-chamber – views are obtained. The child is placed in a partial left lateral decubitus position with the left arm raised to bring the apex of the heart closer to the chest wall, and the apical impulse may be palpated for transducer placement. The notch of the transducer is directed toward the left axilla, at the 2–3 o'clock position as viewed from the apex. The apical 4-chamber reference view allows for the spectral and color Doppler interrogation of the atrioventricular valves and characterization of ventricular morphology. With the proper adjustments, the apical displacement of the normal tricuspid annulus relative to the mitral annulus, ventricular trabeculations and the moderator band may be well visualized. The 4-chamber sweep (Figure 4.6; Videos 4.4 and 4.5) begins posteriorly to demonstrate the coronary sinus [19], the entrance of the inferior vena cava into the right atrium bordered anteriorly/inferiorly by the Eustachian valve, and the thoracic descending aorta posterior to the left atrium in the nearly transverse plane. The sweep covers the anterior surface of the heart after passing through the "5-chamber view," which highlights the left ventricular outflow tract and ascending aorta (Table 4.2). The ventricular apex may be magnified in the 4-chamber view for careful color Doppler mapping of the apical muscular septum. This view should not be used to interrogate the atrial septum as it is parallel to the ultrasound beam and false dropout can occur.

At the end of the 4-chamber sweep, repositioning of the transducer medially toward the lower left sternal border and moving up one or two rib spaces brings the right ventricular inflow and right ventricular free wall more into alignment with the beam of interrogation. Superior and anterior angulation from this position brings the right ventricular outflow tract into alignment and

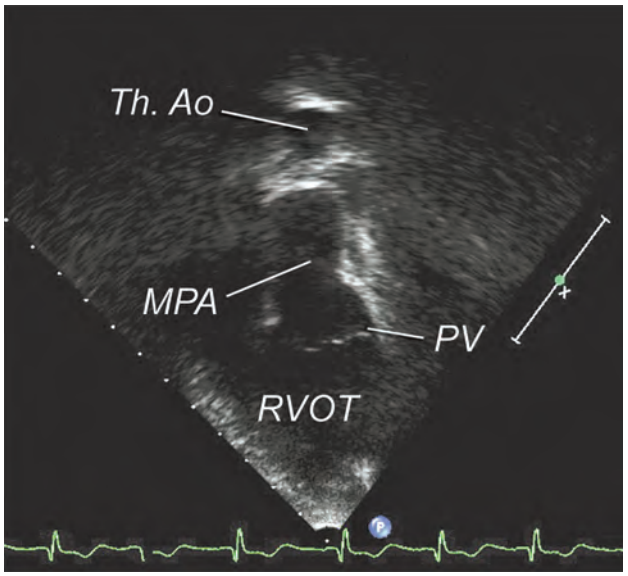


Figure 4.7 Image of modified apical view demonstrating the right ventricular outflow tract. MPA, main pulmonary artery; PV, pulmonary valve; RVOT, right ventricular outflow tract; Th. Ao, thoracic aorta.

often offers an optimum angle for Doppler interrogation of the right ventricular outflow tract and color flow mapping of the pulmonary valve (Figure 4.7).

The apical long-axis ("3-chamber") view is obtained by rotation of the transducer clockwise approximately 60° from the 4-chamber view (Figure 4.8), with the transducer notch at 4 o'clock. Imaging of the left ventricular outflow tract from the apex allows for visualization of subaortic structures oriented perpendicular to the plane of insonation [20]. The long-axis view allows for optimal Doppler interrogation of the left ventricular outflow tract and ascending aorta as well as color flow mapping of the aortic valve. Modified views foreshortening the left ventricle may allow clearer visualization of the left ventricular outflow tract.

The 2-chamber view is utilized for quantification of left atrial size, global left ventricular function [21], or assessment of regional wall motion. This view is obtained by rotation of the transducer counterclockwise approximately 60° from the 4-chamber view, with the transducer notch at 12–1 o'clock. The anterior wall is displayed on the right side of the screen and inferior wall on the left (Figure 4.9).

Parasternal (left parasternal) views

With the child still in a partial left lateral decubitus position, the transducer is placed on the upper to mid left sternal border with the transducer notch directed toward the right shoulder (10 o'clock) to provide a parasternal [19,22] long-axis view. The long-axis reference view is obtained with the transducer positioned over the left ventricular outflow tract (Figure 4.10; Videos 4.6 and 4.7), allowing visualization of the aortic valve, mitral valve, and the basal to mid inferolateral wall of the left ventricle. The fibrous continuity between the mitral and aortic valves is easily demonstrated, and the phasic motion of the valve leaflets is well visualized. The transducer is tilted toward the right hip to visualize the tricuspid valve and right ventricular inflow. The coronary sinus ostium may also be visualized with this posterior sweep. The transducer is then tilted anteriorly toward the left shoulder to visualize the right ventricular outflow tract, pulmonary valve, and main pulmonary artery. Color flow mapping of each of the valves should be performed

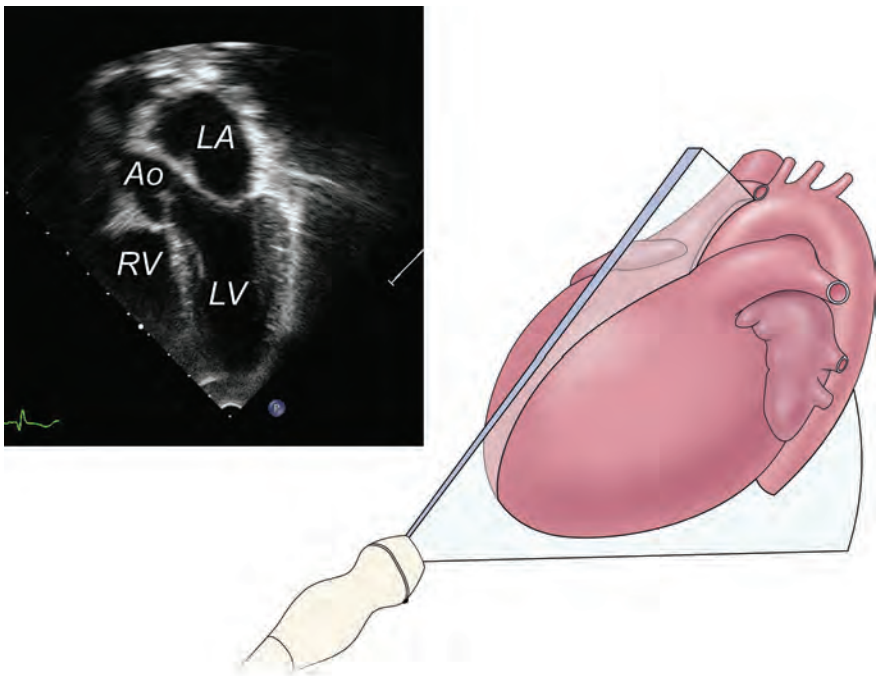


Figure 4.8 Line drawing and image of apical long-axis view. Ao, aorta; LA, left atrium; LV, left ventricle; RV, right ventricle.

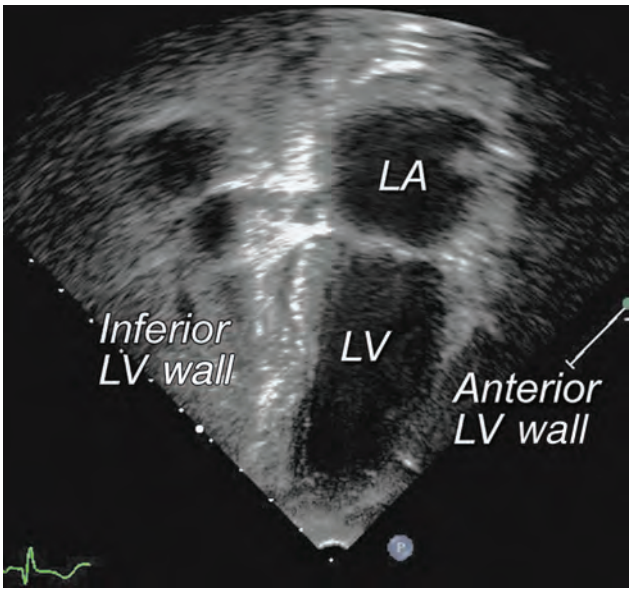


Figure 4.9 Image of apical 2-chamber view. LA, left atrium; LV, left ventricle.

from the parasternal window. Repositioning of the transducer superiorly may be required to provide a long-axis or sagittal oblique view of the aorta, which best demonstrates the proximal ascending aorta in its long axis for diameter measurement and also allows for visualization of the right coronary artery ostium relative to the sinotubular junction.

The parasternal short-axis view (Figure 4.11; Videos 4.8 and 4.9) at the base of the heart can provide detailed imaging of aortic valve morphology [23] as well as views of the right ventricular infundibulum (conus) and pulmonary valve. From the long-axis view, the transducer is clockwise rotated so that the transducer notch is directed toward the left shoulder (2 o'clock). The short-axis reference view consists of: the aorta centered in the imaging sector; the right ventricular inflow; the right ventricular outflow tract and main pulmonary artery; and the atria. Although relatively parallel to the beam of insonation, the atrial septum may be visualized in a modified short-axis view obtained by slight clockwise rotation (3 o'clock) and repositioning the transducer one or two rib notches inferiorly; this view may be especially useful in larger children with poor subxiphoid windows. Examination of the coronary artery ostia should be obtained from the short-axis views, as well as imaging and color flow mapping of

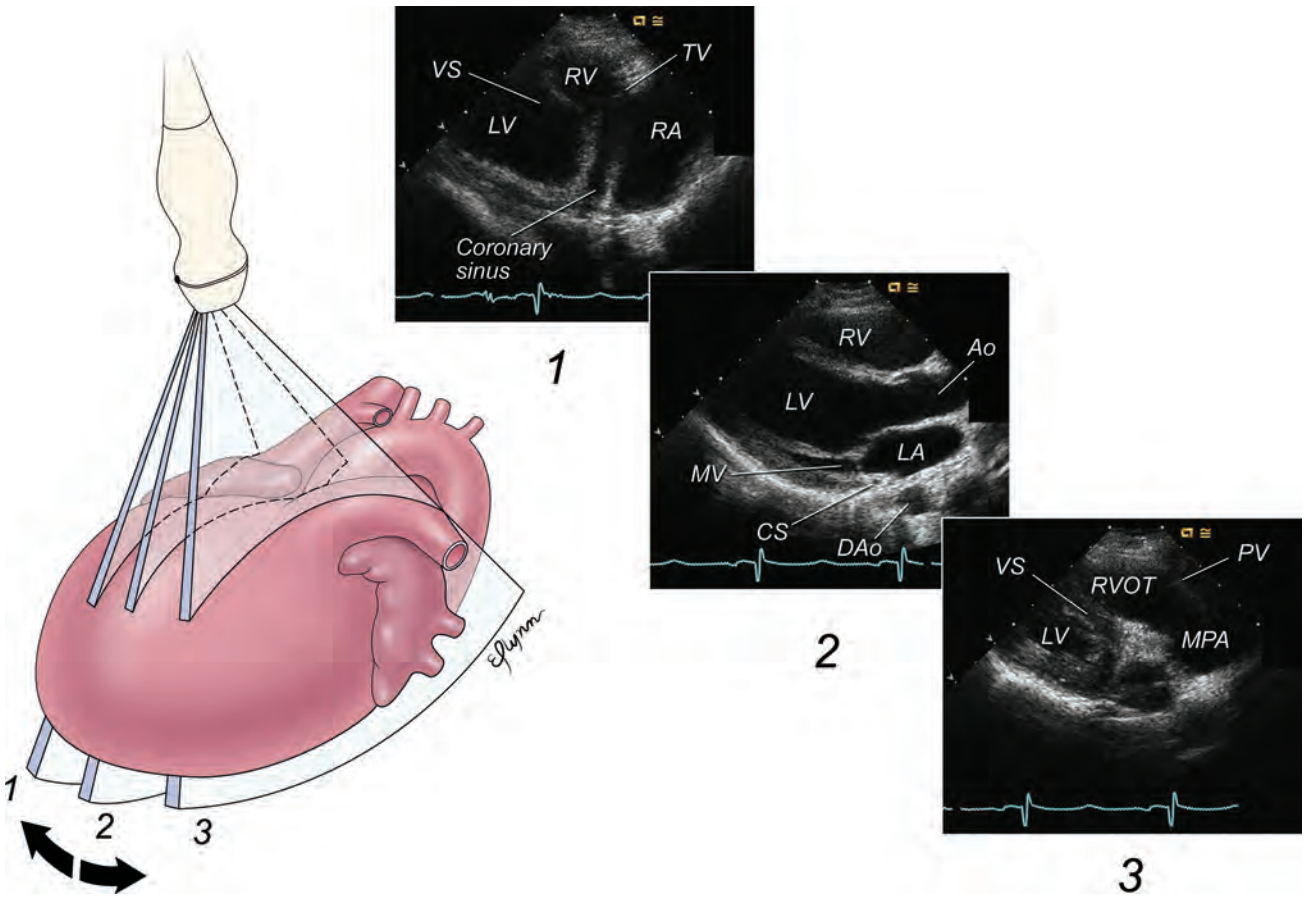


Figure 4.10 Line drawings and serial images of parasternal long-axis sweep. **(1)** LV, left ventricle; RA, right atrium; RV, right ventricle; TV, tricuspid valve; VS, ventricular septum. **(2)** Ao, aortic valve; CS, coronary sinus; DAo, descending aorta; LA, left atrium; LV, left ventricle; MV, mitral valve, RV, right ventricle. **(3)** LV, left ventricle; MPA, main pulmonary artery; PV, pulmonary valve; RVOT, right ventricular outflow tract; VS, ventricular septum.

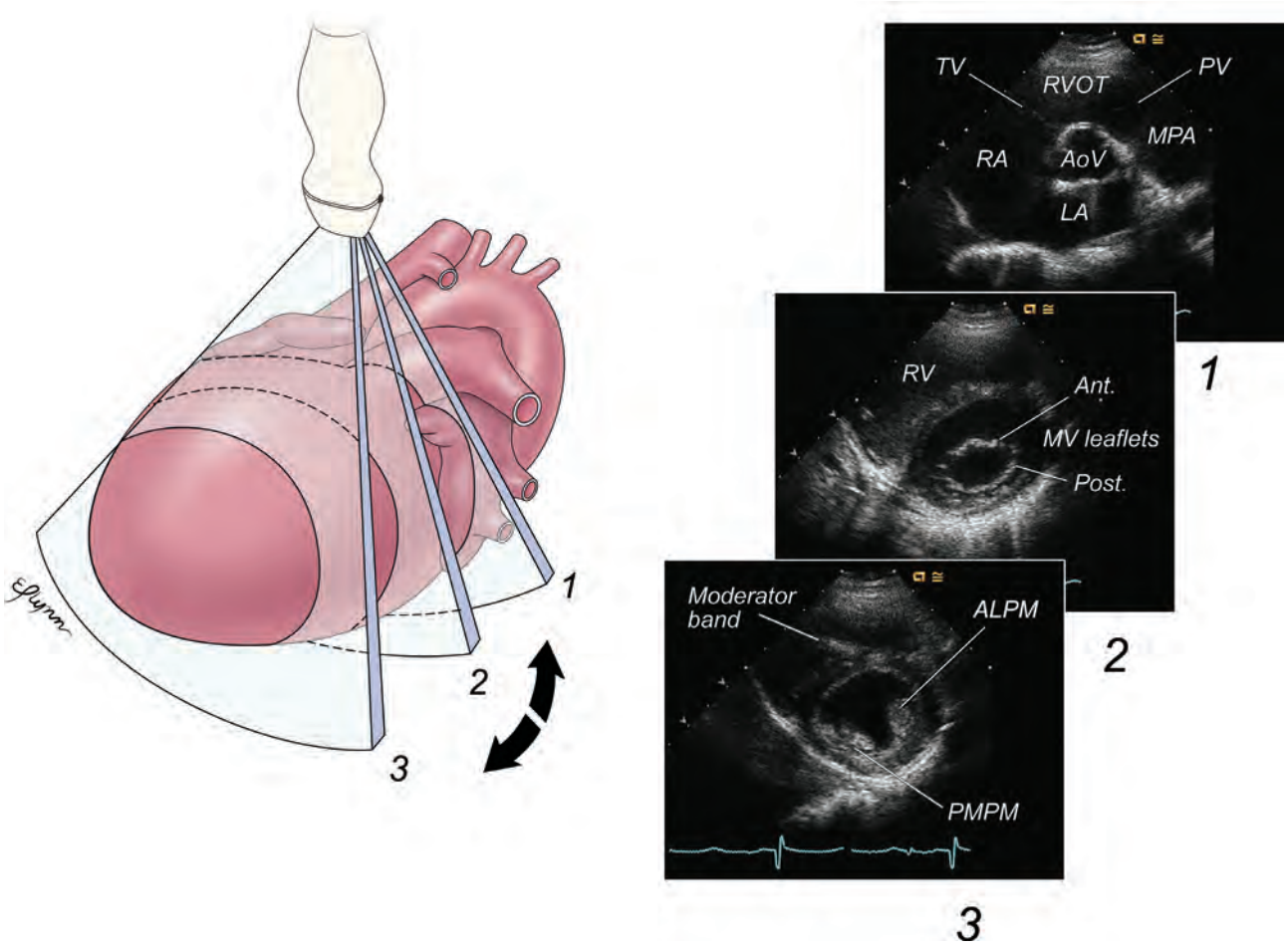


Figure 4.11 Line drawings and serial images of parasternal short-axis sweep. **(1)** AoV, aortic valve; LA, left atrium; MPA, main pulmonary artery; PV, pulmonary valve; RA, right atrium; RVOT, right ventricular outflow tract; TV, tricuspid valve. **(2)** Ant. MV, anterior mitral valve; Post. MV, posterior mitral valve; RV, right ventricle. **(3)** ALPM, anterolateral papillary muscle; PMPM, posteromedial papillary muscle.

the proximal coronary arteries (Figures 4.12 and 4.13; Videos 4.10 and 4.11) [24–26]. Clockwise rotation of the transducer (also 3 o'clock) into a transverse view elongates the left main and anterior descending coronary arteries, and often demonstrates the bifurcation of the left main coronary artery. The great cardiac vein may also be well visualized from this transverse left parasternal window [27]. Slight counterclockwise rotation (1 o'clock) may elongate the right coronary artery and improve its visualization.

The parasternal short-axis sweep begins with the transducer tilted toward the right shoulder to demonstrate better the main and branch pulmonary arteries. Detailed imaging of the pulmonary valve and proximal main pulmonary artery may require repositioning of the transducer inferiorly, as well as tilting and clockwise rotation (to 3 o'clock) to provide a nearly coronal plane of imaging directed superiorly. Imaging of the pulmonary valve in this angled short-axis view should be optimized for pulmonary annulus diameter measurement. The parasternal short-axis sweep progresses from the base of the heart to the apex. On the left border of the heart at the base, the sweep shows the branch pulmonary arteries, followed by the left atrial appendage positioned anterior to the left upper pulmonary vein, and then the left lower pulmonary vein proximal to the atrioventricular groove. The right lower pulmonary vein is found near the entrance of the inferior vena cava separated by the atrial septum. Color and spectral Doppler are often helpful in distinguishing the left atrial appendage from the left upper pulmonary vein. The morphology of the mitral leaflets and valve apparatus, including the position of the left ventricular papillary muscles, is often best seen on short-axis views of the ventricles. In larger hearts, color flow mapping of the ventricular septum may require separate sweeps of the anterior and posterior portions of the septum to assess for muscular ventricular septal defects. Examination of the apical muscular septum may require repositioning of the transducer toward the apex during the short-axis sweep. A list of structures that should be identified on the left parasternal views is provided in Table 4.3.

A "ductal view" is obtained from imaging in a parasagittal plane from a high left parasternal window, with the transducer notch at 12 o'clock. This window lines up the ultrasound beam

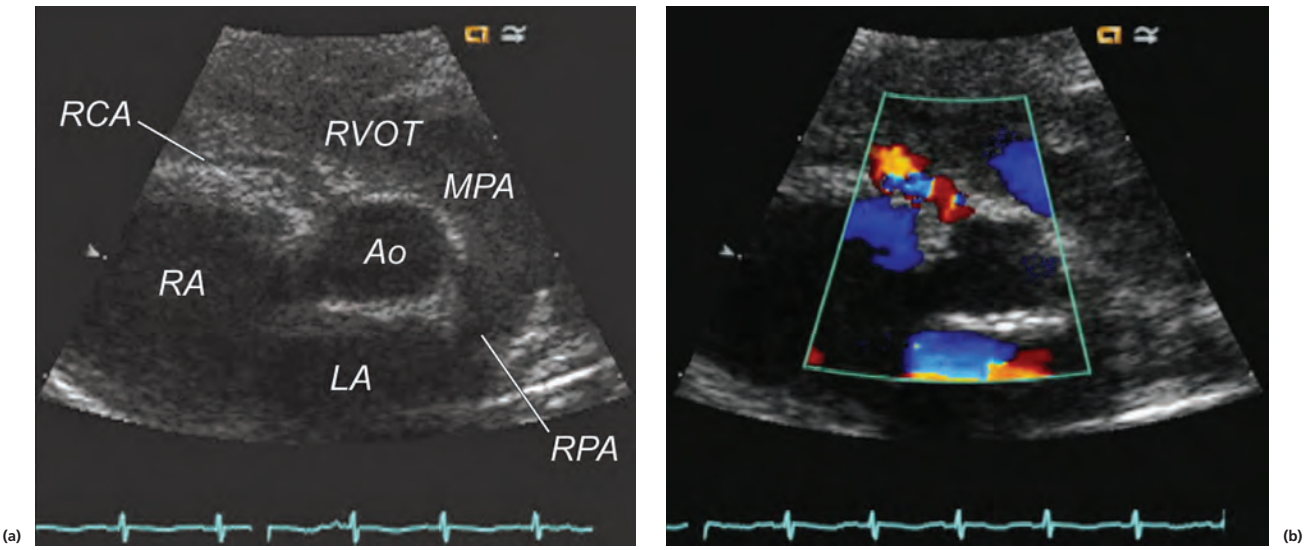


Figure 4.12 **(a)** Parasternal short-axis 2D and **(b)** color Doppler images of axial right coronary artery. Ao, aorta; LA, left atrium; MPA, main pulmonary artery; RA, right atrium; RCA, right coronary artery; RPA, right pulmonary artery; RVOT, right ventricular outflow tract.

with the main pulmonary artery–ductus–descending aorta continuum and allows for exclusion of a normally located small patent ductus arteriosus (Figure 4.14; Videos 4.12 and 4.13). On a larger patient, the position of the transducer may need to be adjusted to a lower window. The distal aortic arch and superior thoracic aorta may also be visualized through the heart and the main pulmonary artery, and, in larger individuals, the aortic isthmus is sometimes best seen from this position. The heart may be used as an acoustic window for the rest of the thoracic descending aorta. Clockwise rotation of the transducer to a high left sternal border transverse plane (transducer notch at 3 o'clock) may better demonstrate the left pulmonary veins in some larger individuals.

Suprasternal notch views

The child is placed in a supine position, and the neck and upper back may be slightly arched with the assistance of a rolled towel or pillow under the shoulders. Imaging from the suprasternal notch [28–30] includes positioning of the transducer in the right supraclavicular region and occasionally in the left supraclavicular region. In the coronal, or short-axis plane with the transducer notch at 3 o'clock, the connection or absence of the left innominate vein to the right superior vena cava may be visualized. The leftward extent of the left innominate vein should be examined by color flow mapping to exclude a left superior vena cava or an anomalous pulmonary venous connection. Infrequently, small tributaries of the left innominate vein, such as the left superior

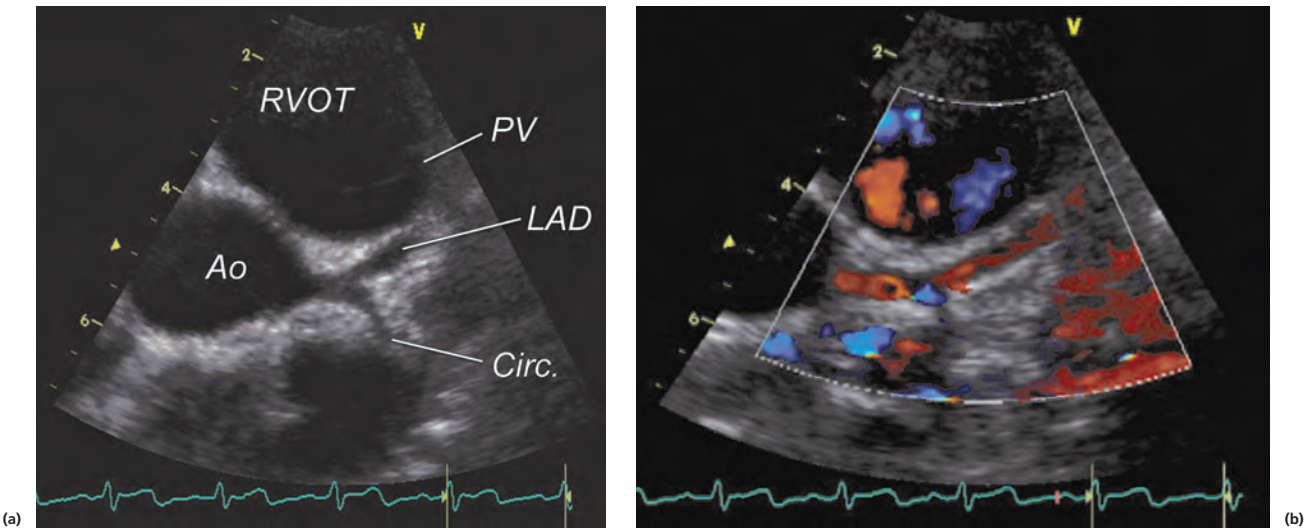


Figure 4.13 **(a)** Parasternal short-axis 2D and **(b)** color Doppler images of axial left coronary artery. Ao, aorta; Circ., circumflex; LAD, left anterior descending; PV, pulmonary valve; RVOT, right ventricular outflow tract.

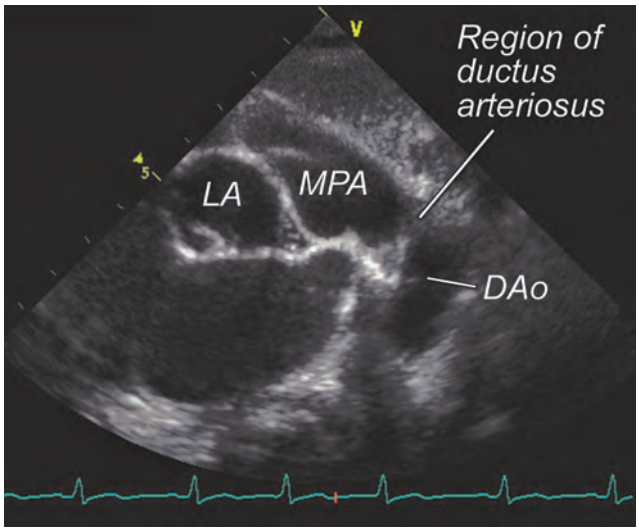


Figure 4.14 Image of high parasternal "ductal" view. DAo, descending aorta; LA, left atrium; MPA, main pulmonary artery.

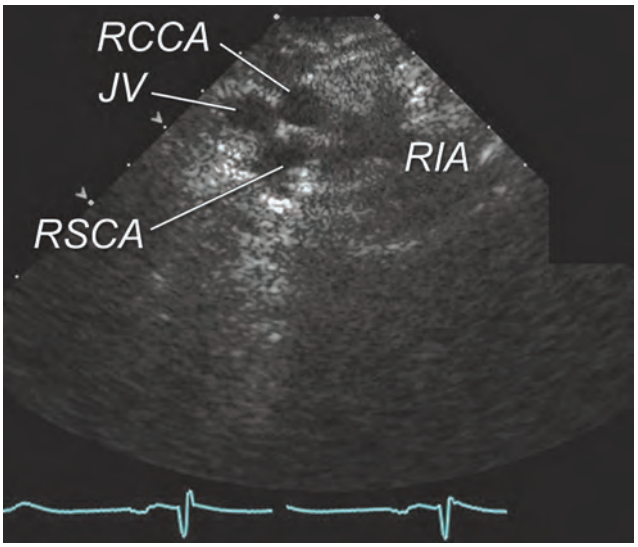


Figure 4.15 Image of suprasternal notch short-axis sweep. JV, jugular vein; RCCA, right common carotid artery; RIA, right innominate artery; RSCA, right subclavian artery.

intercostal vein or left internal thoracic vein, may be seen draining normally by color flow mapping.

From the suprasternal notch short-axis view, superior (cranial) angulation of the transducer demonstrates the branching pattern of the aorta (Figure 4.15; Videos 4.14 and 4.15) [31]. The sidedness of the aortic arch may be determined in almost all cases as opposite of the direction, or sidedness, of the first brachiocephalic artery. Visualization of the aorta relative to the trachea or acoustic shadowing from the tracheal air column may help confirm arch sidedness. A normal branching pattern of the aortic arch should be documented by demonstration of a normally bifurcating first brachiocephalic artery; if the first branch does not bifurcate normally and/or the first and second branches are the same size, an aberrant origin of the subclavian artery should be suspected.

Demonstration of the left aortic arch in its long axis (Figure 4.16; Video 4.16) is achieved by counterclockwise rotation, resulting in a transducer notch position of 1–2 o'clock from the coronal plane in the suprasternal notch window. The axis is from

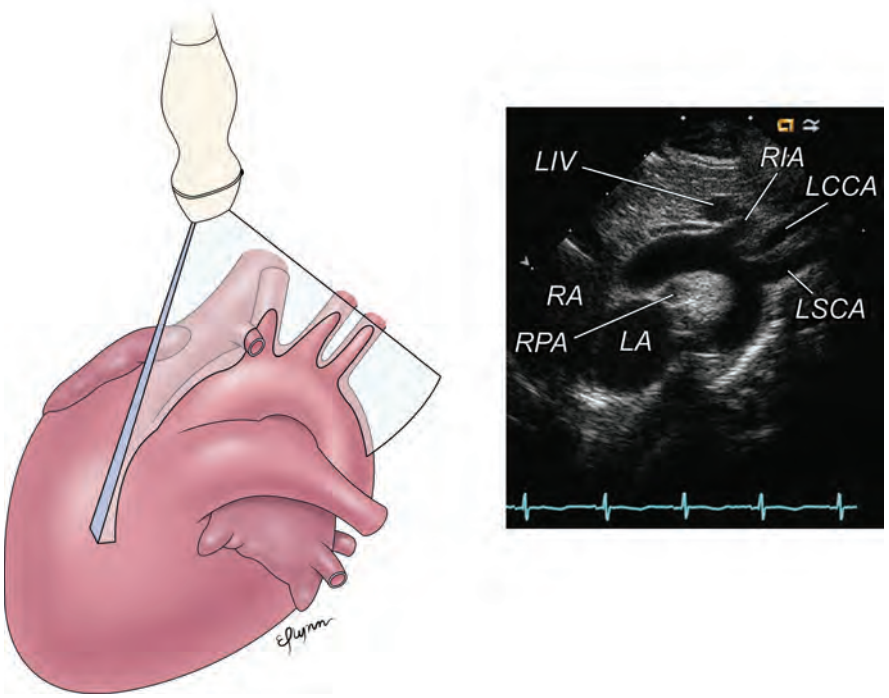


Figure 4.16 Line drawing and image of suprasternal notch aortic arch view. LA, left atrium; LCCA, left common carotid artery; LIV, left innominate vein; LSCA, left subclavian artery; RA, right atrium; RIA, right innominate artery; RPA, right pulmonary artery.

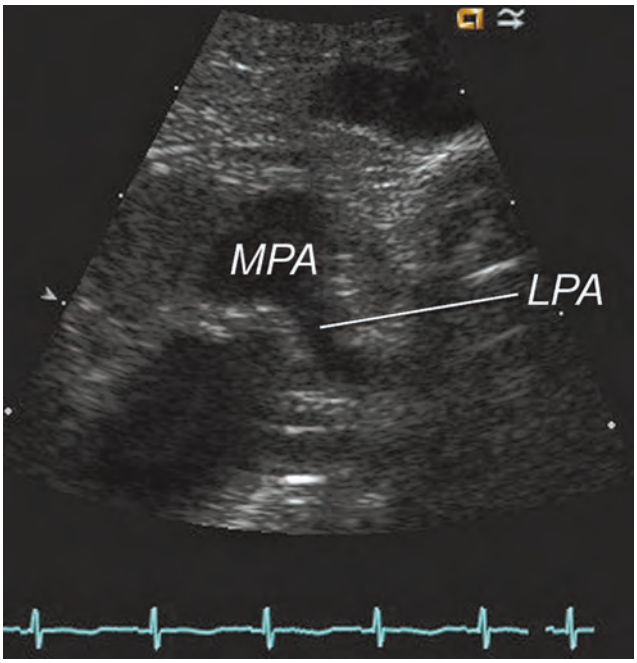


Figure 4.17 Image of suprasternal notch left pulmonary artery view. LPA, left pulmonary artery; MPA, main pulmonary artery.

left shoulder to right anterior hip. As noted earlier, the distal aortic arch and aortic isthmus are sometimes best seen from a "ductal view." Further leftward angulation often best demonstrates the left pulmonary artery (Figure 4.17; Video 4.17). A list of structures that should be identified on the suprasternal notch views is provided in Table 4.4.

With the transducer in a nearly coronal plane (transducer notch at 3 o'clock) using an increased depth of field, the right pulmonary artery is demonstrated in its long axis. In smaller individuals, both the right and left pulmonary venous connections to the left atrium are well visualized in the far field of the suprasternal notch or left infraclavicular transverse view ("crab view") (Figure 4.18; Video 4.18). Repositioning the transducer over the right supraclavicular or infraclavicular regions may better reveal the right pulmonary artery or right pulmonary veins. Flow in the superior vena cava may also be best seen in this plane.

Right parasternal views

The rightward extent of the atrial septum and nearby structures may be well visualized in a parasagittal imaging plane from the right parasternal border with the transducer notch at 12 o'clock (Table 4.5) [32]. Positioning of the patient in a right lateral decubitus position with the right arm raised above the head is often helpful. From a window at the mid to upper right sternal border (Figure 4.19), the structures imaged are similar to the subxiphoid short-axis reference view, including the atria, the atrial septum, and the superior and inferior venae cavae. The unique feature of the right parasternal window is that the atrial septum is oriented perpendicular to the plane of insonation, resulting in less "dropout" artifact. This view is therefore useful to assess for a sinus venosus defect. A sweep is made initially toward the right to demonstrate the rightward extent of the atrial septum and the right upper pulmonary vein. The azygos vein is often seen by imaging and color flow mapping as it arches over the right pulmonary artery and connects to the superior vena cava. The sweep then is directed leftward to image and color-flow-map the overlapping septum primum and septum secundum (Videos 4.19 and 4.20). Doppler interrogation of the left ventricular outflow tract can also be performed from the superior right upper parasternal window if indicated. In larger children, a separate inferior window one or two rib spaces lower may be utilized to demonstrate the more inferior structures at the rightward extent of the heart.

Rotation into a short-axis (transverse) imaging plane from a superior right parasternal window, with the transducer notch then positioned at 3 o'clock, allows visualization and color flow mapping of the right upper pulmonary vein. Sweeping from cranial to caudal, the relative positions of the right superior vena cava and ascending aorta are seen, followed by the right pulmonary artery in its long axis. The right upper pulmonary vein is visualized just below the right pulmonary artery bifurcation. Frequently, three separate right pulmonary veins can be demonstrated by imaging or color flow mapping (Figure 4.20; Videos 4.21 and 4.22).

Additional or supplemental imaging views

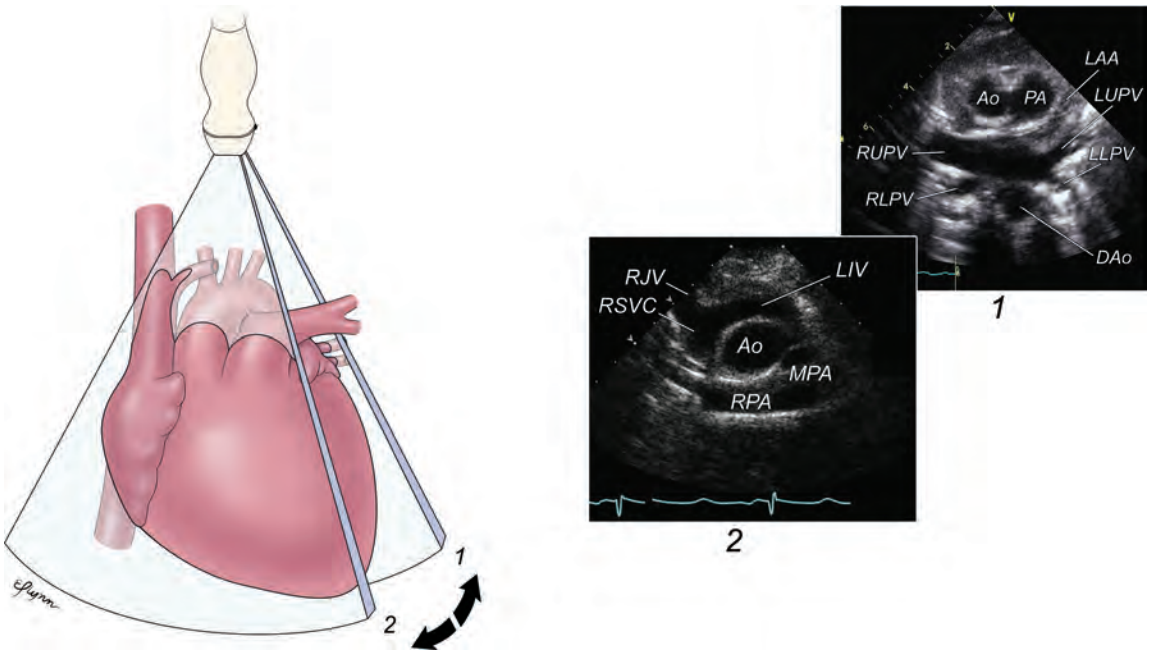
In some pediatric echocardiography laboratories, "in-between" imaging views are routinely performed as part of a normal echocardiogram. Two of these in-between views may be described as analogs of the right anterior oblique and the left anterior oblique, or long axial oblique, angiographic views used in cardiac catheterization procedures. The performance of these views is particularly important when cardiovascular malformations are suspected in the regions of interest.

Right anterior oblique view

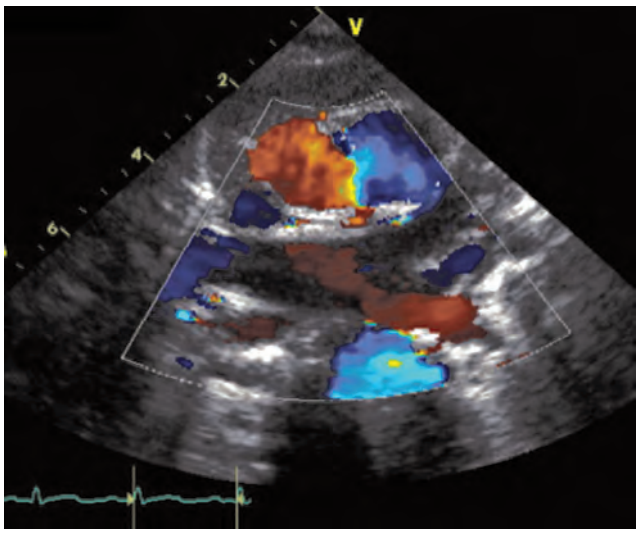
The right anterior oblique view [33,34] is acquired by rotation of the transducer approximately 45° counterclockwise from the standard subxiphoid long-axis view, resulting in the transducer notch being positioned at 1–2 o'clock (Figure 4.21). This plane simultaneously images the inflow and outflow portions of the right ventricle and highlights abnormalities of conal septum, particularly when there is anterior malalignment. It also demonstrates the right ventricular outflow tract and the connection to the branch pulmonary arteries. No sweep is involved with this view.

Left anterior oblique view

The left anterior oblique view [35–37] is a sweep acquired by rotation of the transducer approximately 30–45° clockwise from the standard subxiphoid long-axis view, resulting in the transducer notch being positioned at 4–5 o'clock, and scanning from base to apex (normally from right hip to left shoulder) (Figure 4.22; Video 4.23). This plane produces an en face view of



(a)



(b)

Figure 4.18 Line drawing, 2D image **(a)** and color Doppler image **(b)** of suprasternal view of pulmonary veins. **(1)** Ao, aorta; DAo, descending aorta; LAA, left atrial appendage; LLPV, left lower pulmonary vein; LUPV, left upper pulmonary vein; PA, pulmonary artery; RLPV, right lower pulmonary vein; RUPV, right upper pulmonary vein. **(2)** Ao, aorta; LIV, left innominate vein; MPA, main pulmonary artery; RJV, right jugular vein; RPA, right pulmonary artery; RSVC, right superior vena cava.

the atrioventricular valves that best demonstrates any abnormal attachment of the atrioventricular valve leaflets and the chordal and papillary muscle positions.

"Flank" views

Supplemental imaging from the "flanks" is indicated when early postoperative examinations are performed. These views are obtained along the right and left posterior axillary lines near the level of the diaphragm with the transducer notch at 12 o'clock, resulting in a coronal imaging plane (with the superior structures to the right of the display screen and the inferior structures to the left) (Figure 4.23). Whenever possible, the liver or the spleen should be used as an acoustic window in order to visualize the costophrenic margin and beyond to observe diaphragmatic motion as well as to rule out pleural effusion.

Measurements

The measurement of cardiac structures and flows is critical to the interpretation of a pediatric echocardiogram. An abnormally

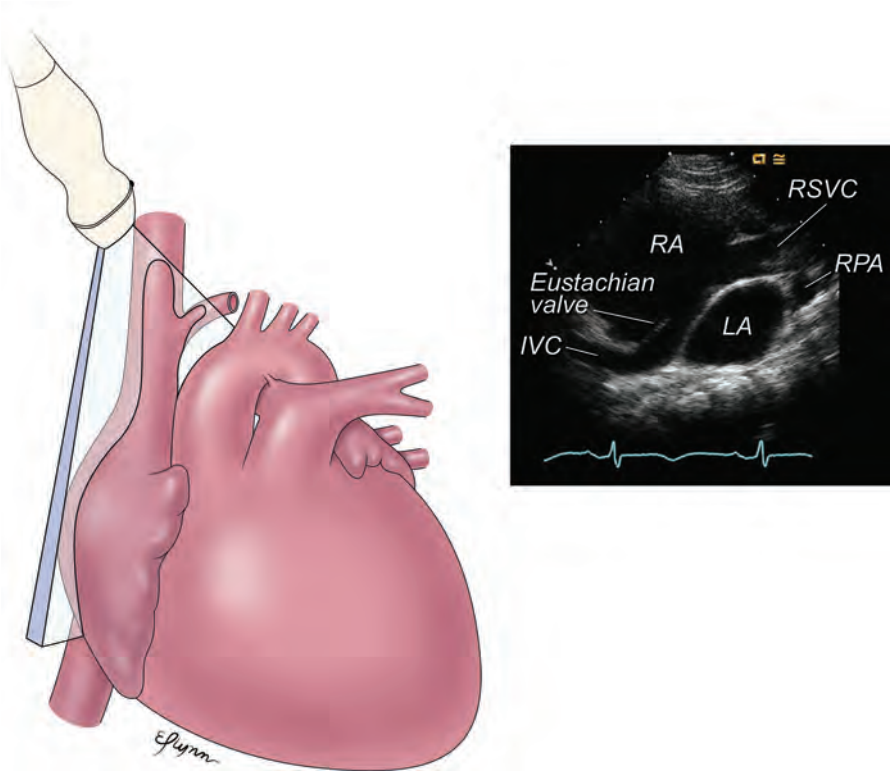


Figure 4.19 Line drawing and image of right parasternal longitudinal view. IVC, inferior vena cava; LA, left atrium; RA, right atrium; RPA, right pulmonary artery; RSVC, right superior vena cava.

small or large structure can be a clue to otherwise silent pathology, and is important to the planning of surgical procedures. Mild forms of obstruction can be diagnosed only by accurate measurement of flow velocities.

In general, it is recommended that all relevant measurements be made as part of a complete pediatric echocardiogram, as outlined in Chapters 5–8 on quantitative methods. Recommendations for quantification methods for a pediatric echocardiogram have been published [3]. In addition, guidelines have been published for the echocardiographic assessment of valvar regurgitation [38] and quantitative methods in adult patients [21]. The measurements that are "relevant" in pediatric patients, however, will vary depending upon the specifics of their cardiovascular anatomy. The examination protocol of a laboratory should specify which measurements to perform and the laboratory procedure for obtaining each measurement for internal consistency.

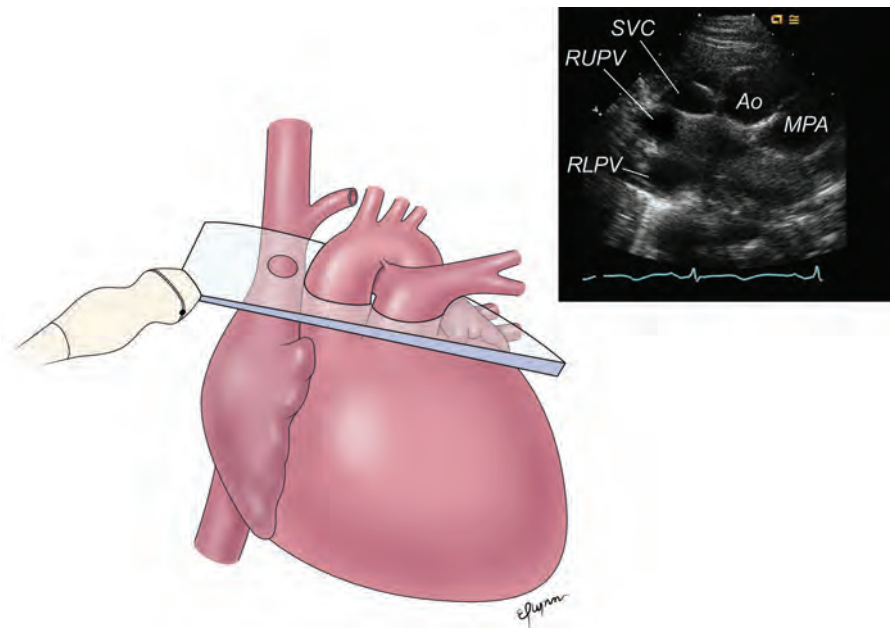


Figure 4.20 Line drawing and image of right parasternal short-axis view. Ao, aorta; MPA, main pulmonary artery; RLPV, right lower pulmonary vein; RUPV, right upper pulmonary vein; SVC, superior vena cava.

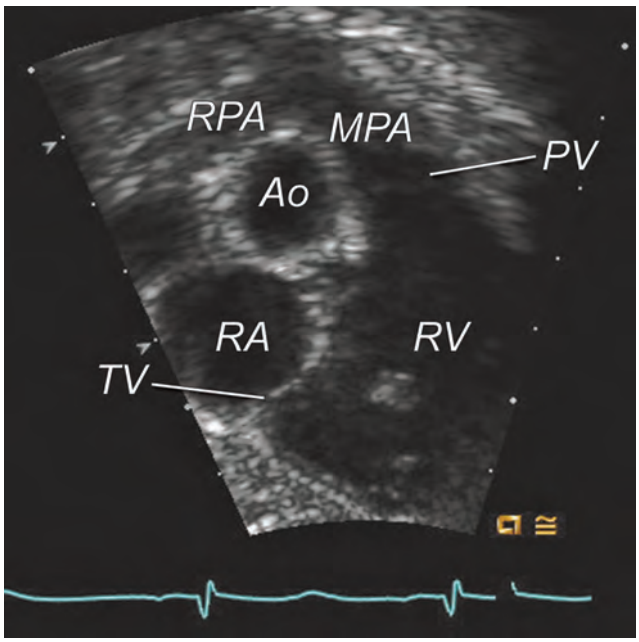


Figure 4.21 Image of subxiphoid right anterior oblique view. Ao, aorta; MPA, main pulmonary artery; PV, pulmonary valve; RA, right atrium; RPA, right pulmonary artery; RV, right ventricle; TV, tricuspid ventricle.

Recommended measurements may be grouped into measurements of cardiovascular structures, ventricular size and function measurements, hemodynamic measurements, and miscellaneous/pathology-related measurements. The reader is referred to the appropriate sections of this textbook for a discussion of each of these measurement categories.

Reporting

The minimum elements of a pediatric echocardiography report have been defined in guidelines published by the American Society of Echocardiography [13] and in the accreditation standards of the Intersocietal Accreditation Commission [4]. An adapted version of the reporting requirements is provided in Table 4.6. Basic identifier information should be listed, and a statement relating to the indication for study is required. Appointment information, including the indications for the study, should be provided. The patient's height and weight should be recorded for body surface area calculation. Conveyance of the echocardiographic findings in a clear and cogent manner is important. The final report must be completely typewritten, and must include the name of the sonographer, ordering physician, and interpreting physician. Abbreviations should be generally avoided or, when used, should be clearly noted and/or unambiguous.

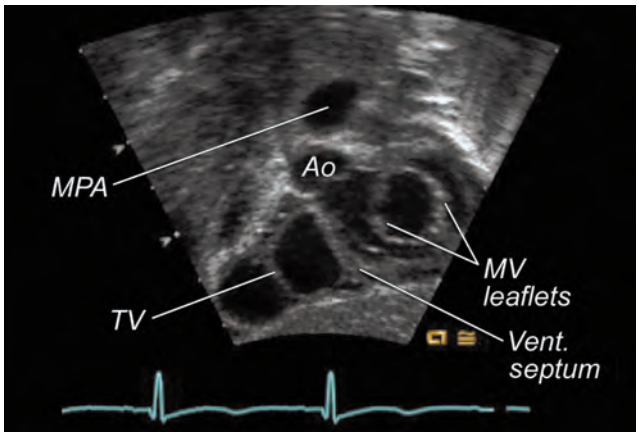


Figure 4.22 Image of subxiphoid left anterior oblique view. Ao, aorta; MPA, main pulmonary artery; MV leaflets, mitral valve leaflets; TV, tricuspid valve; Vent. Septum, ventricular septum.

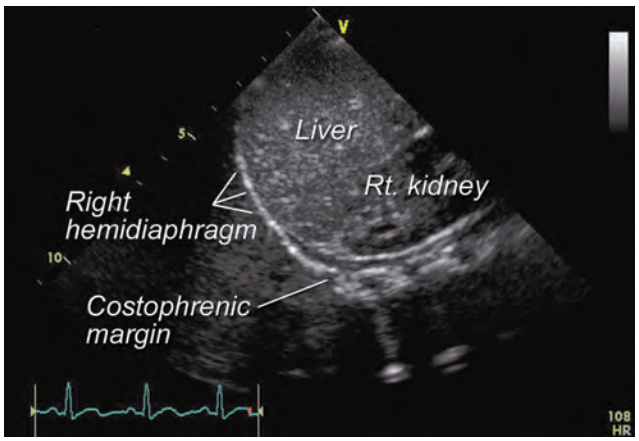


Figure 4.23 Flank view. Rt., right.

The report findings section can be configured in a variety of ways but should include information on (i) structural findings, (ii) measurements of cardiovascular structures made, (iii) Doppler echocardiographic data, and (iv) ventricular function assessment. Positive findings and pertinent negative findings should be listed.

Information pertaining to cardiovascular anatomy and structure can be conveyed utilizing the segmental approach. In addition to reporting the absolute values, it is useful to report quantitative measures within the context of age- or size-appropriate norms (e.g., z-score values) [39–41].

The hemodynamic and ventricular function measurements are discussed in other sections of this textbook. Relevant Doppler information concerning the atrioventricular valves, semilunar valves, and any shunt sites should be provided. Quantitative Doppler and ventricular function information, when appropriate, should be included in the report.

A summary section should be provided, including any pertinent positive or negative findings. If possible, important changes from the previous study should be noted. Any technical or other limitations – such as lack of patient cooperation – that might compromise the diagnostic accuracy of the echocardiographic examination should be specified in the report. Examples include

Table 4.6 Minimal elements for a pediatric echocardiography report

Demographic data
Name
Date of birth
Gender
Medical record identifier
Appointment information
Date of study
Location of study
Performing sonographer
Referring physician
Sedation used
Clinical data
Study indications
Patient height and weight (for body surface area calculation)
Blood pressure
Findings section
Structural features (morphologic diagnoses)
Measurements of cardiovascular structures (with z-scores for comparison with normal data), including aortic root dimension
Doppler (hemodynamic) findings
Ventricular function assessment, including quantitative assessment of left ventricular dimensions; wall thickness or mass; and systolic function (with some exceptions)
Summary section
Summary of the results, including any pertinent positive and negative findings

suboptimal acoustic windows, heart rate constraints, and excessive patient motion during the examination.

Videos

To access the videos for this chapter, please go to www.laiecho.com.

Video 4.1 Subxiphoid long-axis imaging sweep.

Video 4.2 Subxiphoid short-axis imaging sweep.

Video 4.3 Subxiphoid short-axis color Doppler sweep.

Video 4.4 Apical 4-chamber imaging sweep.

Video 4.5 Apical 4-chamber color Doppler clips.

Video 4.6 Parasternal long-axis imaging sweep.

Video 4.7 Parasternal long-axis color Doppler sweep.

Video 4.8 Parasternal short-axis imaging sweep.

Video 4.9 Parasternal short-axis color Doppler sweep.

Video 4.10 Parasternal right coronary artery imaging and color Doppler sweeps.

Video 4.11 Parasternal left coronary artery imaging and color Doppler sweeps.

Video 4.12 Parasternal "ductal view" imaging sweep.

Video 4.13 Parasternal "ductal view" color Doppler sweep.

Video 4.14 Suprasternal notch short-axis imaging sweep.

Video 4.15 Suprasternal notch short-axis color Doppler sweep.

Video 4.16 Suprasternal notch imaging and color Doppler of aortic arch.

Video 4.17 Suprasternal notch imaging of left pulmonary artery.

Video 4.18 Suprasternal imaging and color Doppler of pulmonary veins.

Video 4.19 Right parasternal longitudinal imaging sweep.

Video 4.20 Right parasternal longitudinal color Doppler sweep.

Video 4.21 Right parasternal short-axis imaging sweep.

Video 4.22 Right parasternal short-axis color Doppler sweep.

Video 4.23 Left anterior oblique imaging view.

References

1 Henry WL, DeMaria A, Gramiak R, et al. Report of the American Society of Echocardiography Committee on Nomenclature and Standards in Two-dimensional Echocardiography. *Circulation* 1980;**62**:212–217.

2 Snider AR, Serwer GA, Ritter SB. *Echocardiography in Pediatric Heart Disease*, 2nd edn. St. Louis, MO: Mosby, 1997.

3 Lopez L, Colan SD, Frommelt PC, et al. Recommendations for quantification methods during the performance of a pediatric echocardiogram: a report from the Pediatric Measurements Writing Group of the American Society of Echocardiography Pediatric and Congenital Heart Disease Council. *J Am Soc Echocardiogr* 2010;**23**:465–495.

4 The IAC Standards and Guidelines for Pediatric Echocardiography Accreditation, Intersocietal Accreditation Commission, July 2014. www.intersocietal.org/echo/standards/IACPedEchoStandardsJuly2014.pdf (accessed February 24, 2015).

5 Lev M. Pathologic diagnosis of positional variations in cardiac chambers in congenital heart disease. *Lab Invest* 1954;**3**:71–82.

6 Van Praagh R. Diagnosis of complex congenital heart disease: morphologic-anatomic method and terminology. *Cardiovasc Intervent Radiol* 1984;**7**:115–120.

7 Anderson RH, Becker AE, Freedom RM, et al. Sequential segmental analysis of congenital heart disease. *Pediatr Cardiol* 1984;**5**:281–287.

8 Thomas JD, Adams DB, Devries S, et al. Guidelines and recommendations for digital echocardiography. *J Am Soc Echocardiog* 2005;**18**:287–297.

9 Frommelt PC, Whitstone EN, Frommelt MA. Experience with a DICOM-compatible digital pediatric echocardiography laboratory. *Pediatr Cardiol* 2002;**23**:53–57.

10 Mathewson JW, Dyar D, Jones FD, et al. Conversion to digital technology improves efficiency in the pediatric echocardiography laboratory. *J Am Soc Echocardiog* 2002;**15**:1515–1522.

11 Chandraratna PA, Littman BB, Serafini A, et al. Echocardiographic evaluation of extracardiac masses. *Br Heart J* 1978;**40**:741–749.

12 O'Laughlin MP, Huhta JC, Murphy DJ, Jr. Ultrasound examination of extracardiac chest masses in children. Doppler diagnosis of a vascular etiology. *J Ultrasound Med* 1987;**6**:151–157.

13 Lai WW, Geva T, Shirali GS, et al. Guidelines and standards for performance of a pediatric echocardiogram: a report from the Task Force of the Pediatric Council of the American Society of Echocardiography. *J Am Soc Echocardiog* 2006;**19**:1413–1430.

14 Bierman FZ, Williams RG. Subxiphoid two-dimensional imaging of the interatrial septum in infants and neonates with congenital heart disease. *Circulation* 1979;**60**:80–90.

15 Lange LW, Sahn DJ, Allen HD, Goldberg SJ. Subxiphoid cross-sectional echocardiography in infants and children with congenital heart disease. *Circulation* 1979;**59**:513–524.

16 Sanders SP, Bierman FZ, Williams RG. Conotruncal malformations: diagnosis in infancy using subxiphoid 2-dimensional echocardiography. *Am J Cardiol* 1982;**50**:1361–1367.

17 Limacher MC, Gutgesell HP, Vick GW, et al. Echocardiographic anatomy of the Eustachian valve. *Am J Cardiol* 1986;**57**:363–365.

18 Silverman NH, Schiller NB. Apex echocardiography. A two-dimensional technique for evaluating congenital heart disease. *Circulation* 1978;**57**:503–511.

19 Tajik AJ, Seward JB, Hagler DJ, et al. Two-dimensional real-time ultrasonic imaging of the heart and great vessels. Technique, image orientation, structure identification, and validation. *Mayo Clin Proc* 1978;**53**:271–303.

20 DiSessa TG, Hagan AD, Isabel-Jones JB, et al. Two-dimensional echocardiographic evaluation of discrete subaortic stenosis from the apical long axis view. *Am Heart J* 1981;**101**:774–782.

21 Lang RM, Badano LP, Mor-Avi V, et al. Recommendations for cardiac chamber quantification by echocardiography in adults: an update from the American Society of Echocardiography and the European Association of Cardiovascular Imaging. *J Am Soc Echocardiogr* 2015;**28**:1–39.e14.

22 Tanaka M, Neyazaki T, Kosaka S, et al. Ultrasonic evaluation of anatomical abnormalities of heart in congenital and acquired heart diseases. *Br Heart J* 1971;**33**:686–698.

23 Zema MJ, Caccavano M. Two dimensional echocardiographic assessment of aortic valve morphology: feasibility of bicuspid valve detection. Prospective study of 100 adult patients. *Br Heart J* 1982;**48**:428–433.

24 Jureidini SB, Marino CJ, Waterman B, et al. Transthoracic Doppler echocardiography of normally originating coronary arteries in children. *J Am Soc Echocardiog* 1998;**11**:409–420.

25 Zeppilli P, dello Russo A, Santini C, et al. In vivo detection of coronary artery anomalies in asymptomatic athletes by echocardiographic screening. *Chest* 1998;**114**:89–93.

26 Clouse M, Cailes C, Devine J, et al. What is the feasibility of imaging coronary arteries during routine echocardiograms in children? *J Am Soc Echocardiog* 2002;**15**:1127–1131.

27 Harada K, Tamura M, Toyono M, Takada G. Noninvasive visualization and measurement of great cardiac vein flow by transthoracic Doppler echocardiography in normal children. *Am J Cardiol* 2001;**88**:710–713.

28 Allen HD, Goldberg SJ, Sahn DJ et al. Suprasternal notch echocardiography. Assessment of its clinical utility in pediatric cardiology. *Circulation* 1977;**55**:605–612.

29 Sahn DJ, Allen HD, McDonald G, Goldberg SJ. Real-time cross-sectional echocardiographic diagnosis of coarctation of the aorta: a prospective study of echocardiographic-angiographic correlations. *Circulation* 1977;**56**:762–769.

30 Snider AR, Silverman NH. Suprasternal notch echocardiography: a two-dimensional technique for evaluating congenital heart disease. *Circulation* 1981;**63**:165–173.

31 Murdison KA. Ultrasonic imaging of vascular rings and other anomalies causing tracheobronchial compression. *Echocardiography* 1996;**13**:337–356.

32 McDonald RW, Rice MJ, Reller MD, et al. Echocardiographic imaging techniques with subcostal and right parasternal longitudinal views in detecting sinus venosus atrial septal defects. *J Am Soc Echocardiog* 1996;**9**:195–198.

33 Marino B, Ballerini L, Marcelletti C, et al. Right oblique subxiphoid view for two-dimensional echocardiographic visualization of the right ventricle in congenital heart disease. *Am J Cardiol* 1984;**54**:1064–1068.

34 Isaaz K, Cloez JL, Danchin N, et al. Assessment of right ventricular outflow tract in children by two-dimensional echocardiography using a new subcostal view. Angiocardiographic and morphologic correlative study. *Am J Cardiol* 1985;**56**:539–545.

35 de Leva F, Caso P, Calabro R, et al. Tetralogy of Fallot. Subcostal approach in bidimensional echocardiography. *G Ital Cardiol* 1984;**14**:113–120.

36 Chin AJ, Yeager SB, Sanders SP, et al. Accuracy of prospective two-dimensional echocardiographic evaluation of left ventricular outflow tract in complete transposition of the great arteries. *Am J Cardiol* 1985;**55**:759–764.

37 Cohen MS, Jacobs ML, Weinberg PM, Rychik J. Morphometric analysis of unbalanced common atrioventricular canal using two-dimensional echocardiography. *J Am Coll Cardiol* 1996;**28**:1017–1023.

38 Zoghbi WA, Enriquez-Sarano M, Foster E, et al. Recommendations for evaluation of the severity of native valvular regurgitation with two-dimensional and Doppler echocardiography. *J Am Soc Echocardiog* 2003;**16**:777–802.

39 Fisher SD, Easley KA, Orav EJ, et al. Mild dilated cardiomyopathy and increased left ventricular mass predict mortality: the prospective P2C2 HIV Multicenter Study. *Am Heart J* 2005;**150**:439–447.

40 Daubeney PE, Blackstone EH, Weintraub RG, et al. Relationship of the dimension of cardiac structures to body size: an echocardiographic study in normal infants and children. *Cardiol Young* 1999;**9**:402–410.

41 Sluysmans T, Colan SD. Theoretical and empirical derivation of cardiovascular allometric relationships in children. *J Appl Physiol* 2005;**99**:445–457.

PART II

Quantitative Methods

CHAPTER 5

Structural Measurements and Adjustments for Growth

Thierry Sluysmans[1] and Steven D. Colan[2]
[1]Cliniques Universitaires Saint Luc, Brussels, Belgium
[2]Harvard Medical School; Boston Children's Hospital, Boston, MA, USA

Introduction

Observations of the developing cardiovascular system date from antiquity, with Aristotle's description of the beating heart in a chicken egg. However, quantitative description of the cardiovascular system, an essential part of William Harvey's method, was a key step on the path to modern cardiology. The development of measurement techniques, beginning in the 19th century, combined with the ability to treat heart lesions beginning in the mid-20th century, spurred interest in accurate diagnosis and in methods correlating physiology with clinical outcome.

Determination of the dimensions of the heart and great arteries is mandatory for adequate diagnosis and treatment of congenital heart diseases [1]. For many cardiac disorders, these quantitative variables are highly predictive of outcome and provide critical information about response to therapy, timing of intervention and, most importantly, which type of intervention is likely to have the optimum outcome. Invariably, changes in the size and shape of cardiovascular structures can be secondary to factors other than the disease process, and methods are therefore required to differentiate these potential confounders from the disease process. These issues are particularly evident in children, where diagnostic evaluation is subject to the need to differentiate between disease or treatment effects and the effects of age and somatic growth. Because all cardiovascular structures increase in size in conjunction with growth, comparison of subjects whose body size is not identical requires some method of adjusting for this effect.

Recommendations for standardization of measurements in children were published in 2010 by the American Society of Echocardiography [2]. These recommendations incorporate the requirement for reporting the size of cardiovascular structures as z-scores relative to body size. The Appendix to this textbook contains a set of normative values for echocardiographic measurements that are derived from data collected at Boston Children's Hospital, measured in accordance with the American Society of Echocardiography recommendations. The methods of data collection and analysis have been previously published [3,4]. Here we present a general discussion of the issues surrounding adjustment of cardiovascular structures for age and body size and the methods that were used in the derivation of the models that are provided in the Appendix.

Allometric modeling

Many disease processes result in a change in the size of cardiovascular structures, and these changes are often diagnostically and prognostically useful. For example, the magnitude of left ventricular (LV) dilation in patients with aortic regurgitation is useful in determining the severity of regurgitation and is also useful in predicting outcome after surgery. However, the usefulness of this variable is limited by the confounding effects of other factors that influence left ventricular size. In general, cardiovascular structures are highly plastic, remodeling in response to sustained changes in the hemodynamic state related to many interacting factors including growth, development, exercise participation, genetics, body composition, basal metabolic rate and hematocrit, in addition to many environmental factors such as altitude and ambient temperature. Adjustment for these confounders improves the utility of these measurements. Body size and age are two of the most potent confounders, particularly in children, and considerable effort has been devoted by many investigators to identification of the relationship between body size and the size of cardiovascular structures. The relative growth of a part of an organism in relation to the growth of the entire organism is known as allometry, and therefore here we are concerned with cardiovascular allometry.

In addition to the implications of allometry for patient care, adjustment for the effects of changes in body size also has

Echocardiography in Pediatric and Congenital Heart Disease: From Fetus to Adult, Second Edition. Edited by Wyman W. Lai, Luc L. Mertens, Meryl S. Cohen and Tal Geva.
© 2016 John Wiley & Sons, Ltd. Published 2016 by John Wiley & Sons, Ltd.
Companion website: www.lai-echo.com

important implications for clinical research. Although many clinical trials attempt to avoid potential confounders by selection of a properly matched control group, if the disease or the therapeutic intervention can impact growth then detection of beneficial effects due to the therapeutic intervention can still be confounded by differential growth in the treated and untreated groups. For example, consider a study undertaken to determine if a novel medical therapy can favorably alter the severity of left ventricular dilation in infants with dilated cardiomyopathy. The typical study design would include active and placebo treated cohorts matched for age and body surface area at the time of study enrollment, thereby in theory permitting direct comparison of ventricular size between groups without the need to account for differences in body size. If growth during the treatment period was similar in children in both cohorts, comparison of the change in size of the LV between groups would address the study question. However, if active treatment influences somatic growth either directly or secondary to improved cardiovascular status, the impact of somatic growth on left ventricular size could confound the interpretation of the direct effects of disease treatment on left ventricular size. Thus, directly adjusting for the effects of growth would improve the ability to accurately detect therapeutic effects.

The fallacy of indexing for BSA: the so-called "per-BSA method"

Historically, the most common approach to the problem of adjusting cardiovascular structures for body size has been to express them as their ratio relative to body surface area (BSA). For example, "cardiac index" is usually calculated as cardiac output (CO) divided by BSA, and "ventricular mass index" is calculated as ventricular mass divided by BSA. The continued common reliance on such "per-surface area standards" [5] despite their lack of validity, particularly in children, justifies a critical discussion of the deficiencies in this method prior to an exploration of alternative approaches to this problem [6–8].

The genesis of the per-BSA approach is the observation that in numerous intra- and inter-species studies, body heat production and CO are linearly related to BSA over a broad range of body size [9,10]. Consequently, cardiac index (CO/BSA) has been adopted as a reasonably valid method of comparing the CO of individuals of varying BSA. Next, based on regression models that found a nearly linear relationship between CO and the size of other cardiac and vascular structures, the per-BSA method was extrapolated and adopted by many as a general method for adjusting for the effects of growth on all cardiovascular structures.

Unfortunately, although the relationship between two variables can often be described as linear, this does not mean that this is the best descriptor of their relationship. The mathematical inadequacy of this method can be readily recognized by a simple example. There are many studies documenting a statistically significant linear relationship between left ventricular volume and BSA, and a statistically significant linear relationship between left ventricular short-axis dimension and BSA. However, volume and dimension are related by a cubic function, and it is therefore mathematically impossible for both volume and dimension to have a true linear relationship to BSA. The delusion that the per-BSA provides an adequate method of adjusting for the effects of body size is based on excess reliance on simple regression analysis performed over short ranges of the independent variable (BSA) in the absence of critical examination of how well the mathematical model actually describes the data, particularly in the absence of any meaningful theoretical basis [11].

It is reasonably straightforward to statistically test whether an allometric model provides an adequate description of the relationship between body size and the size of the body part. The intent of "indexing" or "normalizing" a variable such as CO for BSA is to permit valid comparisons between individuals of differing BSA by eliminating any residual dependence of the indexed variable on BSA. Therefore, if the method of indexing or adjusting for body size fully accounts for the effect of body size on the cardiovascular measurement, then the indexed variable will have the same mean value and the same distribution regardless of body size. From a statistical point of view, the mean and standard deviation of a variable "indexed" to BSA should be constant across the range of BSA.

It is worth considering a concrete example of how easily one can be misled by a high correlation coefficient obtained by linear regression. Figure 5.1 presents the strong linear relationship ($r = 0.92$) between the diameter of the aortic valve annulus (AoV) and BSA in 550 normal children varying in age from newborn to 18 years of age [3]. Such observations, in the absence of careful testing for whether this linear model eliminates residual dependence of AoV on BSA, has led to the common method of a per-BSA standard approach where "indexed AoV" is calculated as AoV divided by BSA.

Does the per-BSA method fully account for the effect of body size? As noted earlier, this would imply that firstly, there should be no significant residual correlation between BSA and BSA-adjusted AoV, and secondly, BSA-adjusted AoV should have the

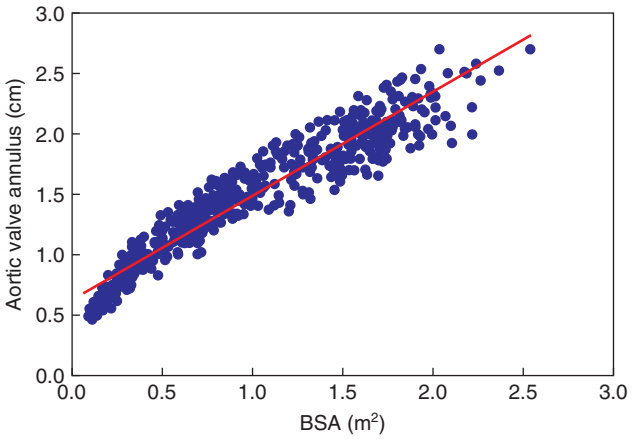


Figure 5.1 Graph of aortic valve annulus dimension versus body surface area (BSA) in 550 normal children. The linear regression line is also shown.

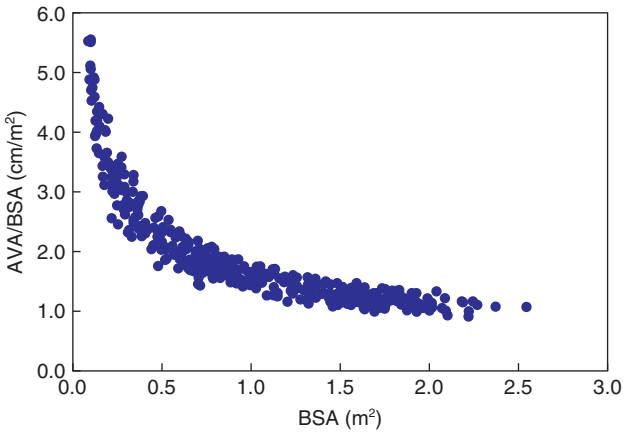


Figure 5.2 Graph of AVA/BSA versus BSA in 550 normal children. AVA, aortic valve annulus dimension; BSA, body surface area.

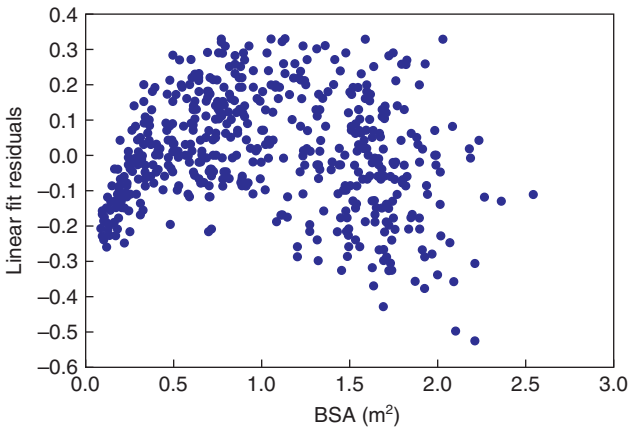


Figure 5.3 Graph of the residuals of the linear regression of aortic valve annulus dimension versus body surface area (BSA) in 550 normal children. The residuals of the linear regression deviate from zero such that for low and high BSA values the residuals are skewed below zero whereas in the mid-range the data are skewed above zero, indicating that the relationship is not linear.

same mean value and distribution regardless of BSA. Figure 5.2 presents the relationship of AoV/BSA ("indexed aortic valve annulus diameter") to BSA demonstrating that the relationship is curvilinear and the linear fit has a significantly non-zero slope value, failing the first of the foregoing requirements. In addition, the mean ± standard deviation (SD) of the "indexed aortic valve annulus diameter" for a BSA of 1.8 m^2 is 1.2 ± 0.2 cm/m^2, whereas for a BSA of 0.2 m^2 the mean ± SD is 3.5 ± 0.75 cm/m^2, indicating that this approach to normalization also fails the second requirement.

For the mathematically inclined, it is relatively easy to determine the circumstances under which the per-BSA method will fail. In order for the per-BSA method of indexing to work, three assumptions must be met. The relationship to BSA must be linear, the intercept of the regression line must be zero, and the variance must be constant over the range of BSA. The first two assumptions arise mathematically as follows. For any variable such as AoV, if the "indexed AoV" (AoVi) is calculated as AoVi = AoV/BSA, then this relationship can be rearranged as AoV = AoVi × BSA. This rearrangement reveals that the relationship has the equation of a line (y = mx + b) where the intercept (b) is zero and the line has a slope (m) equal to AoVi. If we look back at Figure 5.1, the regression line does not pass through the intercept (AoVi = 0.65 when BSA = 0) and although the regression has a high correlation, the data deviate from the regression line such that at low and high BSA values the data points are skewed below the regression line whereas in the mid-range the data are skewed above the regression line, indicating that the relationship is not truly linear. The failure of the linear fit to adequately describe the data can also be detected by examining the residuals of the linear regression, shown in Figure 5.3. A statistically significantly better fit ($r = 0.96$) can be achieved with a nonlinear model of the form $y = mx^a + b$, as shown in Figure 5.4. The superiority of the nonlinear regression is shown in Figure 5.5, where the residuals of the nonlinear regression are seen to have no significant residual relationship to BSA. The failure to meet the third assumption (constant variance) is also shown in Figures 5.1 and 5.3, where the data spread around the regression line is seen to increase as BSA increases, which is to say the variance is not constant over the range of BSA. This pattern of having the variance rise as a function of BSA (nonconstant variance, or heteroscedasticity) is observed for virtually all cardiovascular parameters [11–15] and, as shown in Figure 5.5, it is not eliminated by the nonlinear regression. Heteroscedasticity is a common statistical observation in almost all growth models in biology and economics [11] and can be explained by the BSA- and age-related increase in the inter-individual variation in other factors that influence the size of these structures, such as blood pressure, adiposity, and habitual activity level.

Alternative "indexing" methods

The inadequacy of the per-BSA method has led investigators to evaluate other approaches to adjusting for the effect of body size on the size of cardiovascular structures. The first and simplest is

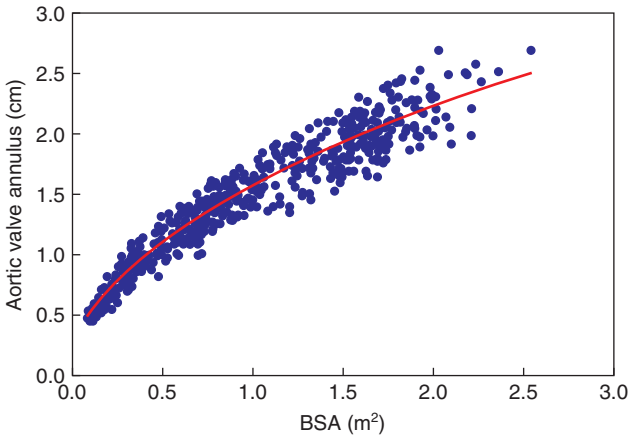


Figure 5.4 Nonlinear regression of the form $y = ax^b + c$ for aortic valve annulus dimension versus body surface area (BSA) in 550 normal children.

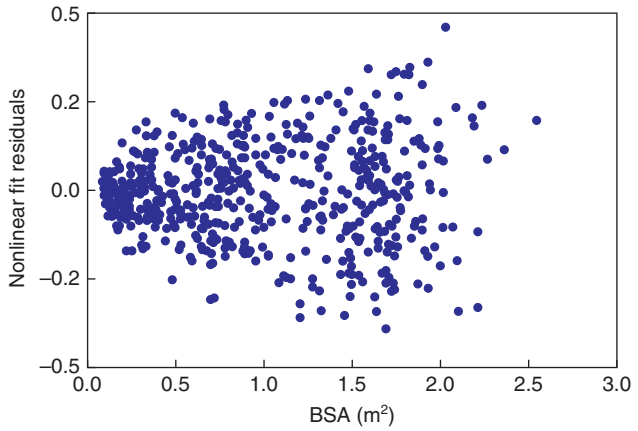


Figure 5.5 Graph of the residuals of the nonlinear regression of aortic valve annulus dimension versus body surface area (BSA) in 550 normal children. The residuals of the nonlinear regression have no significant residual relationship to BSA, although the magnitude of the residuals varies as a function of BSA (heteroscedasticity).

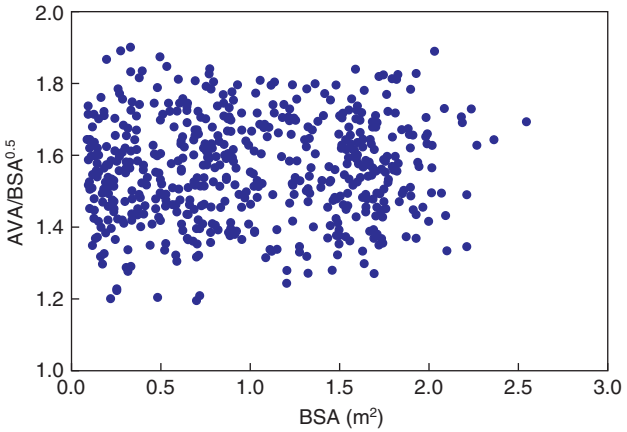


Figure 5.7 Graph of the relationship between AVA/BSA$^{0.5}$ versus BSA in 550 normal children. AVA, aortic valve annulus dimension; BSA, body surface area; BSA$^{0.5}$ = square root of BSA.

to attempt to linearize the relationship by transforming either the cardiovascular structure or the BSA. Several authors have noted that the areas of cardiovascular structures relate linearly to BSA, whereas their diameters relate linearly to the square root of BSA (BSA$^{0.5}$). It has in fact been suggested that this approach can be generalized [3] such that linear measurements should be normalized to BSA$^{0.5}$, area measurements should be normalized to BSA, and volume measurements should be normalized to BSA$^{1.5}$. In general, fully normalized variables should be dimensionless, and this method indeed results in dimensionless normalized variables because cm/(m^2)$^{0.5}$, cm^2/m^2 and cm^3/(m^2)$^{1.5}$ all reduce to units of m/m.

If we explore this option with regard to the relationship of AoV versus BSA$^{0.5}$ (Figure 5.6), the regression is indeed highly linear with a zero intercept, meeting two of the requirements for an adequate method of "indexing." The graph of AoV/BSA$^{0.5}$ versus BSA is shown in Figure 5.7, and there is no significant relationship between the two. However, examination of the residuals of the relationship between AoV/BSA$^{0.5}$ and BSA (Figure 5.8) demonstrates that the data spread still varies as a function of BSA, thereby failing to meet the third criterion for an adequate method of "indexing." Besides failing to deal with heteroscedasticity, the approach of indexing to fixed (0.5, 1, 1.5) powers of BSA has not been uniformly successful in fully eliminating residual variance between BSA and certain cardiovascular structures, such as left ventricular dimension, volume and mass [4]. Similarly, the annuli of the tricuspid and mitral valves are usually elliptical such that the annulus area indeed relates to BSA but the major and minor diameters do not relate to BSA$^{0.5}$ [3].

Z-score methods

The failure of these simpler methods has resulted in the growing dependence of the pediatric community on the use of *z-scores*, also known as *normal deviates* or *standard scores*, to adjust for the effect of age and/or body size on the size of cardiovascular structures [16]. The z-score of a variable is the position,

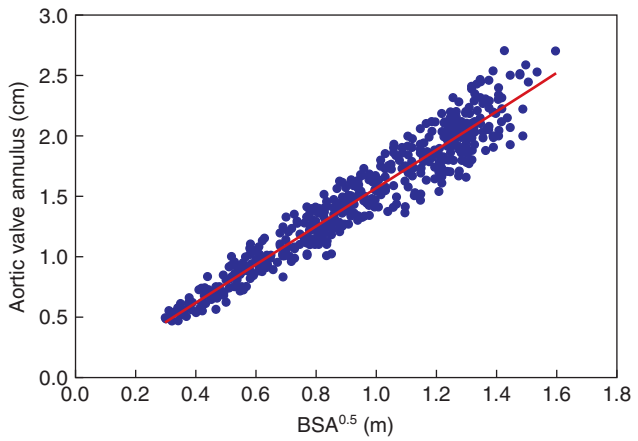


Figure 5.6 Graph of aortic valve annulus dimension versus the square root of body surface area (BSA$^{0.5}$) in 550 normal children.

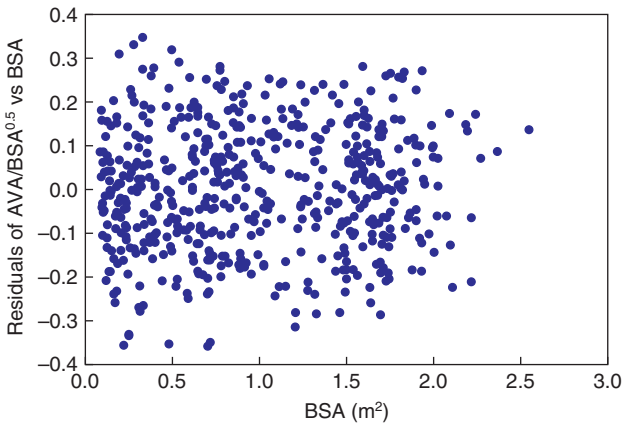


Figure 5.8 Graph of residuals of the regression shown in Figure 5.7 (AVA/BSA$^{0.5}$ versus BSA) in 550 normal children. AVA, aortic valve annulus dimension; BSA, body surface area; BSA$^{0.5}$ = square root of BSA.

expressed in standard deviations, of the observed case relative to the mean of the population distribution. For cardiovascular structures, the calculation of z-scores is performed relative to the distribution of the structure in the normal population in order to adjust for the normal relationship to age or body size. Again, an example helps to illustrate this approach. For a given variable such as AoV the relationship versus BSA must first be determined directly in a large population of normal subjects and both the mean and standard deviation of the normal distribution are obtained as functions of BSA. For any new observation, the position of the variable within the normal distribution for that patient's BSA is then determined as the number of standard deviations from the normal population mean. For a patient who has an observed AoV = AoV_O, the BSA-appropriate mean value (AoV_N) and standard deviation (SD_N) of that parameter BSA in the normal population are used to calculate the z-score as $(AoV_O - AoV_N)/SD_N$.

Z-scores are normalized variables, which means that a z-score of zero represents a value at the normal population mean and a z-score of 1 or −1 represents a value that is 1 standard deviation above or below the normal mean, respectively. The interpretation of z-scores is exactly parallel to the use of percentiles to express age-adjusted height and weight relative to the normal population. In the case of height and weight, calculation of percentiles adjusts for the normally expected age-related change in height or weight, permitting comparison of subjects at varying ages. Although z-scores can be readily converted to percentiles, their use is often preferable as they avoid range compression in the higher and lower ranges. For example, a z-score of 4 (4 standard deviations above the normal population mean) has a percentile of 99.8, whereas a z-score of 10 (10 standard deviations above the population mean) has a percentile of 99.9. At values outside of the normal range, it is much easier to appreciate the magnitude of abnormality of a structure when it is expressed as a z-score. The z-score approach represents the most powerful and flexible approach to normalizing cardiovascular parameters for the effects of age and BSA and has therefore become the standard approach in pediatric cardiology [16].

Several caveats concerning the determination of z-scores are in order. A number of recent publications have documented large differences in the z-score systems that have been published and have noted a failure on the part of some of the systems to meet criteria for clinical and statistically validity [17]. There are several important issues that arise in the determination of valid normative z-scores:

1 Selecting an appropriate population for determination of "normal" values is obviously critical, including assurance by means other than a "normal" echocardiogram that the patient is free of systemic disorders.
2 The population needs to include an appropriate range for BSA and age as well as consideration of other potential demographic confounders such as sex and race.
3 The method of calculating BSA must be the method that correlates most closely with the size of cardiovascular structures and must be the same as that used in the derivation of the z-scores, a requirement that is often neglected. There are a number of published methods for calculating BSA and they yield different results, particularly at lower values. The formula with the soundest experimental basis is that of Haycock et al. [18]. In a systematic analysis of the normative data at Boston Children's Hospital, in which we compared the amount of variance of the cardiovascular structures relative to BSA that could be explained by each of these formulas, we found the Haycock formula to have the best performance [3].
4 The method of measurement must be the same for the normal population and new cases. For example, it is clear from a number of publications that differences between echocardiographic and magnetic resonance imaging values for left ventricular volume derived from magnetic resonance imaging are systematically larger than those for echocardiography, precluding use of a common set of normative values [19]. Other differences in practice include reliance on M-mode versus two-dimensional (2D) left ventricular dimension data, diastolic (the standard in adult labs) versus systolic (the standard in pediatric labs) measurement of aortic dimensions, leading-edge versus inner-edge to inner-edge measurements, and several different algorithms for left ventricular mass and volumes that yield different values.
5 The resulting z-score algorithms need to optimize the quality of the data fit and nonconstant variance (heteroscedasticity) must be eliminated. If possible, solutions that have both a physiologic justification and statistical validity are preferable over those that are based on statistical considerations alone, because they are the most likely to be extensible beyond the observational cohort. These two issues (physiologic validity and heteroscedasticity) are discussed in more detail in the following section.

Choice of normalizing variable

The selection of which parameter of body size, such as height, weight or BSA, is optimal for the purposes of normalizing the size of cardiovascular structures has been controversial [20,21]. We found that in normal children, BSA performed better than height or weight [3]. The controversy concerning which variable is appropriate has arisen primarily in the discussion surrounding the correct method of adjusting for the effect of body size on left ventricular mass [22,23]. Concern has been expressed that use of BSA as the normalizing variable can result in underdetection of left ventricular hypertrophy in the presence of obesity. Physiologically, adipose tissue is less metabolically active than other tissues and therefore requires less blood flow [24], implying that the normal relationship between BSA and CO could be disrupted in the presence of obesity. The recommendation has therefore been put forward that left ventricular mass should be adjusted for height instead of BSA. However, there are substantial differences in lean body mass between individuals independent

of adiposity, and obesity is associated with an increase in lean body mass as well as adipose tissue. Adjustment for height alone ignores these differences. Alternatively, stroke volume and CO have been reported to relate more closely to fat-free mass [25], and therefore fat-free mass has been suggested as a potential allometric scaling variable [21]. However, fat-free mass is not generally measured in clinical practice and normative data relative to this variable are not available. Furthermore, although the blood flow requirement of adipose tissue is less than lean tissue, adipose tissue is not inert and therefore the impact of adipose tissue on cardiac output should not be totally neglected. It is likely that some adjustment for the relative amounts of fat-free mass versus adipose tissue will provide the most accurate method of incorporating body mass into the allometric scaling process. Work in this area has been stymied in part because of the absence of an accurate, inexpensive, and easily deployed method for measuring adiposity, a technique that would no doubt be of great utility in other aspects of medicine as well.

Heteroscedasticity

Another caveat concerning the development of z-score systems is that nonconstant variance with respect to both age and body size has been demonstrated for virtually all echocardiographic measurement. Although the term "heteroscedasticity" is unfamiliar to most clinicians, the concept is not. As shown in Figures 5.4 and 5.5, the data range increases as the absolute value of BSA increases. This phenomenon is one type of heteroscedasticity, and follows the pattern seen with virtually all anatomic measurements, where the data spread increases progressively in conjunction with increasing values for the independent variable (age, height, weight, BSA, etc.).

Statistical methods for dealing with this phenomenon have received considerable attention, as discussed in some detail by Abbott and Gutgesell [11]. There are several statistical methods that can be used to reduce nonconstant variance when constructing confidence and prediction intervals. These methods include multiple regression techniques [26], variance stabilizing transformations [11,16,26–28] and weighted least squares analysis [29]. Such statistical methods, although improving the accuracy of prediction intervals, are invariably ad hoc and lack a sound physiologic basis for choosing one method over another. In heart growth, data are skewed to the right, and logarithmic transformation is probably the most common type of transformation used in medical research for correcting heteroscedasticity and rightwardly skewed data [11]. For residuals that demonstrate a reasonably regular relationship to the independent variable, the method of Altman [30] has particular appeal of simplicity both in terms of calculation and interpretation. Regardless of the method that is selected, the end result must be tested to confirm that the final model results in an equal and constant distribution around the mean value over the full range of the independent variable, and that 96% of all data are included in the interval going from −2SD to +2SD.

Parametric versus statistical derivation of z-scores

The methods described in the foregoing are based on the assumption that it is possible to define a continuous parametric equation that adequately describes the relationship between the size of the cardiovascular structure and either age or a measure of body size over the full range of the independent variable. This approach has the unique advantage of permitting conclusions concerning the nature of the physiologic relationship between somatic and cardiovascular growth. This is discussed in more detail later, but briefly, the fact that the cross-sectional areas of the central arteries and cardiac valves are highly correlated with BSA, and that BSA is highly correlate with cardiac output, supports the concept that flow is a primary and reproducibly constant determinant of the growth of these structures. An alternative to this "physiologic" approach that has also been pursued is a purely statistical description of the data, which permits derivation of z-scores but does not provide any implications concerning the underlying physiologic mechanisms. Perhaps the best known of these approaches is the lambda-mu-sigma (LMS) method that has been used to calculate the z-scores and percentiles for height and weight data that are used in the Centers for Disease Control and Prevention (CDC) and World Health Organization growth charts for children [31–34]. The LMS method evaluates the population distribution over discrete intervals of the independent variable and then applies a smoothing function to the derived ranges to yield a description of the data that is a continuously varying function over the range of the independent variable. The complex relationships between height and weight lend themselves well to this approach. This technique is most advantageous when the determinates of growth are sufficiently heterogeneous that a single, physiologically based relationship that adequately describes the data over the full range of the independent variable cannot be identified. The other advantage is that the variance of the data is determined locally rather than as a global function and nonconstant variance can be correctly reflected in the confidence intervals.

In some instances, an adequate parametric model can be identified that fully describes the mean behavior of the population, but heteroscedasticity invalidates the resulting confidence intervals. For example, we found that although an exponential growth model of the form $y = ax^b + c$ fully describes the mean relationship between BSA and left ventricular mass over the full range of BSA, it was not possible to identify a method of calculating the standard deviation as a continuous function of BSA that resulted in confidence intervals that adequately described the data at both the upper and lower ends of the BSA range. The LMS method overcomes this issue [35], albeit at the cost of eliminating any physiologic implications for the regression model. Nevertheless, for the explicit purposes of calculating normative data ranges, this approach appears to represent the best approach for those variables for which an explicit parametric approach fails to adequately describe the data.

Physiologic principles underlying cardiovascular dimensions

The relation of cardiovascular dimensions and body size can be observed empirically and analyzed statistically, as described from echocardiographic measurements of cardiac and vascular dimensions. The relation can also be predicted theoretically from one or more basic physical principles or design characteristics. These two approaches can be used for purposes of reciprocal verification. That is, a higher level of confidence can be attached to conclusions that are achieved through both theoretical and empirical methods. We performed such a comprehensive analysis [3] and present the results in brief here.

The development and maintenance of optimum geometric properties of the vascular pathways is essential to provide adequate blood flow over a wide range of body activities, while simultaneously avoiding excess hemodynamic stress. Optimized design of biological structures as a result of the environmental pressure exerted by natural selection is an established principle of biology that explains the curvilinear relation of the weight of a tree and the size of its branches [36], the relation between the diameters of pulmonary bronchi and bronchial air flow [37,38], or the shape of eggs [39]. It is believed that the driving principle underlying the optimization of vascular dimensions is to minimize the energy required to propel blood in the vascular system by optimizing the interrelation between vessel radius and flow rates. Theoretical foundations of the principle of minimum work [40,41] and theoretical studies of optimality of the vascular system [42–47] have been validated by the quantitative studies of coronary [48] and cerebral artery dimensions [49]. The theoretical aspects and details of the calculations have been presented [42,48,49].

The principle of minimum work

The energy cost of phasic blood flow is determined by two components. Viscous energy loss [50,51] is related to friction at the vessel–blood interface and decreases with increasing vessel radius. This is a geometric relationship related to the fact that the volume of contained blood increases as the cube of the radius whereas the surface area increases in proportion to the square of the radius. Therefore, the proportion of the blood that encounters a viscous interface decreases as the radius increases, which means there is proportionally less resistance to flow in large vessels. The second component of energy loss is due to the oscillatory nature of blood flow in the central vasculature. The oscillatory component of energy loss, related to the need to accelerate flow with every beat, increases as the blood column and the vessel radius gets larger and the inertia of the blood increases. The optimal vascular dimension is that at which the sum of these two energy demands is minimized (Figure 5.9). We estimated the viscous energy loss and the inertial energy content of blood flow for the aorta and the main pulmonary artery over the typical range of body size (0.2–1.8 m^2 BSA) and over the range of CO encountered during physical activity (from 3.5 L/min/m^2 to 17.5 L/min/m^2) in order to determine the optimal vessel size [3]. We found that the size of the aorta that we observed in our normal population corresponded to the theoretical optimal value in terms of energy dissipation for CO up to two times the resting CO in infants, increasing to values that were optimal for three to four times the resting CO for older children (Figure 5.10). Data obtained from athletes and hypertensive subjects indicate that cardiac structures adapt to peak levels of pressure and volume demand. Heart rate response is the primary determinant of CO increase with exertion, and infants have an approximate twofold magnitude of heart rate reserve, a value that increases to

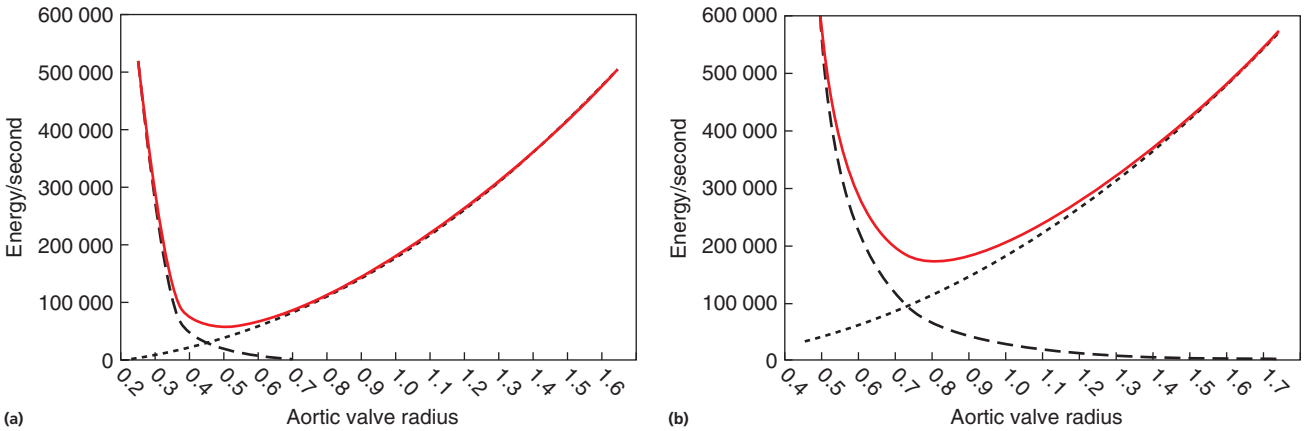


Figure 5.9 Optimal aortic valve radius calculated according to the principle of minimal work for two levels of cardiac output. Energy loss per second (erg/s) because of viscous friction (long-dashed line) is plotted against the radius of the aortic valve (cm). On the same scale, the inertial energy content of blood (short-dashed line) and total energy loss calculated as the sum of viscous energy loss and inertial energy content loss (continuous line) are plotted for theoretical cardiac outputs of 3.5 L/min **(a)** and 17.5 L/min **(b)**, representing the theoretical cardiac output at rest and at maximal exercise of a normal subject with a body surface area (BSA) of 1 m^2. The least amount of total energy loss per unit time corresponds to the minimum of the total energy loss curve. The corresponding radius for 3.5 L/min flow is 0.45 cm, whereas it is 0.8 cm for 17.5 L/min. These values represent the theoretical range of normal optimal aortic valve radius for this BSA. Source: Sluysmans and Colan 2005 [3]. Reproduced with permission from the American Physiologic Society.

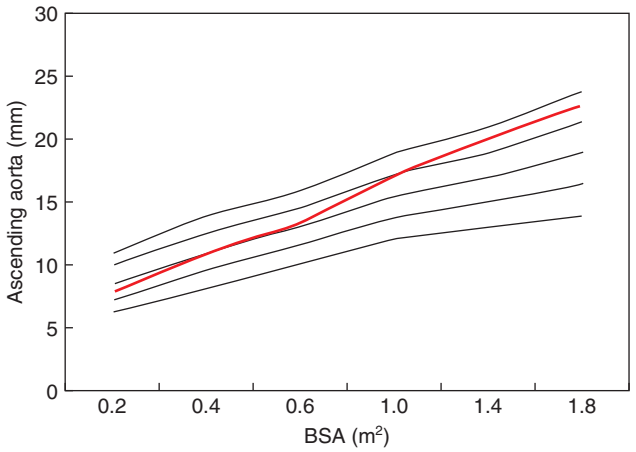


Figure 5.10 Principle of minimum work: comparison of optimal dimensions and observed dimensions of vascular pathways. Comparison of the optimal valve and vascular diameters derived from the theoretical principle of minimal work and calculated for cardiac output of 1 × 3.5, 2 × 3.5, 3 × 3.5, 4 × 3.5, and 5 × 3.5 L/min, respectively (thin lines, from low to high values) with the mean observed values (thick line) of the ascending aorta in normal subjects. The normal mean diameters are optimal in terms of energy dissipation for cardiac output equivalent to twice the cardiac output at rest in infants and approximately four times the cardiac output at rest for older children, corresponding to the progressively higher peak activity level and heart rate reserve associated with growth. Vascular dimensions appear optimized to accommodate the cardiac output associated with peak normal activity. Source: Sluysmans and Colan 2005 [3]. Reproduced with permission from the American Physiologic Society.

three- to fourfold in older children and young adults. Thus the difference between observed diameters that are optimal in terms of energy dissipation in infants versus children corresponds to the expected difference in CO associated with age-appropriate physical activity and range of intensity of exertion.

Adjustment of ventricular size for somatic growth

Both empiric and theoretical approaches have found that cross-sectional area of the cardiac valves and vessels relate most closely to BSA, and consequently semilunar valve and great vessel diameters relate most closely with $BSA^{0.5}$. Although atrioventricular valve areas manifest the same linear relationship to BSA, their diameters do not because these valves have a noncircular orifice. However, when this simple paradigm is applied to the size of the left ventricle, it fails. Numerous investigations have found that left ventricular end-diastolic volume, determined according to several different algorithms, related most closely to BSA^b where mean b = 1.38 (range 1.34–1.4, reviewed in [3]) and our empiric observation in this study similarly found that LV volume varies as a function of $BSA^{1.35}$ [3]. The failure of ventricular volume to follow the same allometric pattern of vascular size, which predicts that ventricular volume should relate to $BSA^{1.5}$, was found to relate to the nonlinear decrease in heart rate that is seen with an increase in body size. Heart rate is proportional to $BSA^{-0.4}$ in normal human subjects [3]; and in various series evaluating different species of mammals with a 1800- to 500,000-fold increase of body weight. It is also clear that when factors other than BSA influence basal heart rate, the relationship between BSA and ventricular size can be expected to change. Two examples of this are complete heart block and training-induced bradycardia, both of which are associated with ventricular volumes larger than would be predicted for BSA. Less well-investigated and outside the scope of this discussion is whether the normal age-related fall in heart rate in adults similarly influences the relationship between heart rate and ventricular size, creating a need for adjusting ventricular size for either age or heart rate independent of BSA.

Conclusion

The progress in therapeutic options available to the pediatric cardiology community has made it requisite that we identify meaningful risk and outcome variables for evaluating our interventions, which often requires the ability to differentiate between the effects of body size and the effects of disease. Echocardiographic imaging techniques have made this information available on an unprecedented scale, enabling analyses that permit both improved understanding of the control mechanisms in the growth of cardiovascular structures and the routine application of normative data to clinical practice. Advances in information technology have permitted incorporation of calculation of these normative data into routine laboratory reporting. The intersection of these driving forces makes universal adoption of the z-score techniques requisite for optimal care delivery.

References

1 Lipshultz SE, Miller TL. Establishing norms for echocardiographic measurements of cardiovascular structures and function in children. *J Appl Physiol* 2005;**99**:386–388.
2 Lopez L, Colan SD, Frommelt PC, et al. Recommendations for quantification methods during the performance of a pediatric echocardiogram: a report from the Pediatric Measurements Writing Group of the American Society of Echocardiography Pediatric and Congenital Heart Disease Council. *J Am Soc Echocardiogr* 2010;**23**: 465–495.
3 Sluysmans T, Colan SD. Theoretical and empirical derivation of cardiovascular allometric relationships in children. *J Appl Physiol* 2005;**99**:445–457.
4 Colan SD, Parness IA, Spevak PJ, Sanders SP. Developmental modulation of myocardial mechanics: age- and growth-related alterations in afterload and contractility. *J Am Coll Cardiol* 1992;**19**: 619–629.
5 Tanner JM. Fallacy of per-weight and per-surface area standards, and their relation to spurious correlation. *J Appl Physiol* 1949;**2**: 1–15.

6 Graham TP, Jr., Jarmakani JM, Canent RV, Jr., Morrow MN. Left heart volume estimation in infancy and childhood. Reevaluation of methodology and normal values. *Circulation* 1971;**43**:895–904.

7 Gutgesell HP, Rembold CM. Growth of the human heart relative to body surface area. *Am J Cardiol* 1990;**65**:662–668.

8 Henry WL, Ware J, Gardin JM, et al. Echocardiographic measurements in normal subjects. Growth-related changes that occur between infancy and early adulthood. *Circulation* 1978;**57**: 278–284.

9 Grollman A. Physiologic variations in the cardiac output in man. *Am J Physiol* 1929;**90**:210–217.

10 Lange PE, Onnasch DG, Schaupp GH, et al. Size and function of the human left and right ventricles during growth. Normative angiographic data. *Pediatr Cardiol* 1982;**3**:205–211.

11 Abbott RD, Gutgesell HP. Effects of heteroscedasticity and skewness on prediction in regression: modeling growth of the human heart. *Methods in Enzymology* 1994;**240**:37–51.

12 El Habbal M, Somerville J. Size of the normal aortic root in normal subjects and in those with left ventricular outflow obstruction. *Am J Cardiol* 1989;**63**:322–326.

13 King DH, Smith EO, Huhta JC, Gutgesell HP. Mitral and tricuspid valve anular diameter in normal children determined by two-dimensional echocardiography. *Am J Cardiol* 1985;**55**:787–789.

14 Gutgesell HP, French M. Echocardiographic determination of aortic and pulmonary valve areas in subjects with normal hearts. *Am J Cardiol* 1991;**68**:773–776.

15 Lester LA, Sodt PC, Hutcheon N, Arcilla RA. M-mode echocardiography in normal children and adolescents: some new perspectives. *Pediatr Cardiol* 1987;**8**:27–33.

16 Kirklin JW, Blackstone EH, Jonas RA, Kouchoukos NT. Anatomy, dimensions, and terminology. In: Kirklin JW, Barrat-Boyes BG (eds.) *Cardiac Surgery*. New York, NY: Churchill Livingstone, 1993, pp. 21–60.

17 Cantinotti M, Scalese M, Molinaro S, et al. Limitations of current echocardiographic nomograms for left ventricular, valvular, and arterial dimensions in children: a critical review. *J Am Soc Echocardiogr* 2012;**25**:142–152.

18 Haycock GB, Schwartz GJ, Wisotsky DH. Geometric method for measuring body surface area: a height-weight formula validated in infants, children, and adults. *J Pediatr* 1978;**93**:62–66.

19 Leonardi B, Margossian R, Colan SD, Powell AJ. Relationship of magnetic resonance imaging estimation of myocardial iron to left ventricular systolic and diastolic function in thalassemia. *JACC Cardiovasc Imaging* 2008;**1**:572–578.

20 Winter EM, Brooks GA. From euclid to molecular biology and gene expression: where now for allometric modeling? *Exerc Sport Sci Rev* 2007;**35**:83–85.

21 Batterham AM, George KP, Whyte G, et al. Scaling cardiac structural data by body dimensions: a review of theory, practice, and problems. *Int J Sports Med* 1999;**20**:495–502.

22 De Simone G, Daniels SR, Devereux RB, et al. Left ventricular mass and body size in normotensive children and adults: assessment of allometric relations and impact of overweight. *J Am Coll Cardiol* 1992;**20**:1251–1260.

23 Daniels SR, Kimball TR, Morrison JA, et al. Indexing left ventricular mass to account for differences in body size in children and adolescents without cardiovascular disease. *Am J Cardiol* 1995;**76**: 699–701.

24 Frayn KN, Karpe F, Fielding BA, et al. Integrative physiology of human adipose tissue. *Int J Obes Relat Metab Disord* 2003;**27**: 875–888.

25 Collis T, Devereux RB, Roman MJ, et al. Relations of stroke volume and cardiac output to body composition: The Strong Heart Study. *Circulation* 2001;**103**:820–825.

26 Bates DM, Watts DG. *Nonlinear Regression Analysis and Its Applications*. New York, NY: John Wiley & Sons, Inc., 1988.

27 Zar JH. *Biostatistical Analysis*, 2nd edn. Englewood Cliffs, NJ: Prentice-Hall, 1974, p. 261.

28 Montgomery DC, Peck EA. *Introduction to Linear Regression Analysis*, 2nd edn. New York, NY: John Wiley & Sons, Inc., 1992.

29 Theil H. *Principles of Econometrics*. New York, NY: John Wiley & Sons, 1971, p. 244.

30 Altman DG. Construction of age-related reference centiles using absolute residuals. *Stat Med* 1993;**12**:917–924.

31 Ward R, Schlenker J, Anderson GS. Simple method for developing percentile growth curves for height and weight. *Am J Phys Anthropol* 2001;**116**:246–250.

32 Flegal KM. Curve smoothing and transformations in the development of growth curves. *Am J Clin Nutr* 1999;**70**:163S–165S.

33 Cole TJ, Freeman JV, Preece MA. British 1990 growth reference centiles for weight, height, body mass index and head circumference fitted by maximum penalized likelihood. *Stat Med* 1998;**17**: 407–429.

34 Cole TJ, Green PJ. Smoothing reference centile curves: the LMS method and penalized likelihood. *Stat Med* 1992;**11**:1305–1319.

35 Foster BJ, Mackie AS, Mitsnefes M, et al. A novel method of expressing left ventricular mass relative to body size in children. *Circulation* 2008;**117**:2769–2775.

36 Murray CD. A relationship between circumference and weight in trees and its bearing on branching angles. *J Gen Physiol* 1927;**11**:431–441.

37 Horsfield K. Diameters, generation, and orders in the bronchial tree. *J Appl Physiol* 1990;**68**:457–461.

38 Weibel ER. *Morphometry of the Human Lung*. Heidelberg/New York: Springer Verlag/Academic Press, 1963.

39 Thompson DW. On the shape of eggs and on certain other hollow structures. In: Cambridge University Press (ed.) *On Growth and Form*. New York, NY: Macmillan, 1943, pp. 935–957.

40 Murray CD. The physiologic principle of minimal work applied to the angle of branching arteries. *J Gen Physiol* 1926;**6**: 835–841.

41 Murray CD. The physiologic principle of minimum work: I. The vascular system and the cost of blood volume. *Proc Natl Acad Sci U S A* 1926;**12**:207–214.

42 Pollanen MS. Dimensional optimization at different levels of the arterial hierarchy. *J Theor Biol* 1992;**159**:267–270.

43 Kamiya A, Togawa T. Optimal branching structures of the vascular tree. *Bull Math Biophys* 1972;**34**:431–438.

44 Kamiya A, Togawa T. Theoretical relationship between the optimal models of the vascular tree. *Bull Math Biophys* 1974;**36**:311–323.

45 Zamir M. The role of shear forces in arterial branching. *J Gen Physiol* 1976;**67**:213–222.

46 Uylings HBM. Optimization of diametres and bifurcation angles in lungs and vascular tree structures. *Bull Math Biol* 1977;**39**: 509–520.

47 Sherman TF. On connecting large vessels to small: the meaning of Murray's law. *J Gen Physiol* 1981;**78**:431–453.
48 Seiler C, Kirkeeide RL, Gould KL. Basic structure–function relations of the epicardial coronary vascular tree: basis of quantitative coronary arteriography for diffuse coronary artery disease. *Circulation* 1992;**85**:1987–2003.
49 Rossitti S, Löfgren J. Vascular dimensions of the cerebral arteries follow the principle of minimum work. *Stroke* 1993;**24**:371–377.
50 Caro CC, Pedley TJ, Schroter RC, Seed WA. Flow in pipes and around objects. In: Caro CG, Pedley TJ, Schroter RC, Seed WA (eds.) *The Mechanics of the Circulation*. New York, NY: Oxford University Press, 1978, pp. 44–78.
51 Yoganathan AP, Cape EG, Sung H-W, Williams FP, Jimoh A. Review of hydrodynamic principles for the cardiologist: applications to the study of blood flow and jets by imaging techniques. *J Am Coll Cardiol* 1988;**12**:1344–1353.

CHAPTER 6

Hemodynamic Measurements

Mark K. Friedberg
The Labatt Family Heart Center, The Hospital for Sick Children, The University of Toronto, Toronto, ON, Canada

Introduction

Hemodynamics refers to the physiology of blood flow. Although neither pressure nor flow can be measured directly by echocardiography, their assessment is commonly used in clinical echocardiography to evaluate ventricular performance and pressure, shunt lesions, valvar and vascular stenosis, and valvar regurgitation. Hemodynamic assessment by echocardiography is very useful to diagnose, follow and manage children with congenital and acquired heart disorders. In this chapter, the principles underlying the clinical use of Doppler echocardiography as well as its important limitations are reviewed. Hemodynamic measurements to evaluate ventricular systolic and diastolic function as well as hemodynamic assessment of specific lesions are covered in the chapters pertaining to those subjects.

Table 6.1 lists the abbreviations used in this chapter.

Blood flow and its assessment by Doppler echocardiography

Blood flow refers to the amount of blood passing a given point during a specified length of time and is expressed as units of volume per unit of time, for example, liters/minute. Flow velocity refers to the rate at which the blood changes position, and is expressed in distance per unit time, for example, meters/second. Laminar flow refers to flow that occurs at a relatively homogeneous velocity and direction across the vessel. Acceleration refers to the rate of change in flow velocity, expressed as units of distance per time squared, for example, meters/second^2 [1,2]. Blood flow velocity can be measured noninvasively using Doppler, but both flow and acceleration must be calculated and cannot be directly measured by echocardiography.

The periodic nature of the cardiac cycle has a number of implications for blood flow in the heart and central vasculature. The rise in pressure caused by the heart's contraction generates the force that accelerates the blood and generates flow. Because of inertial effects, the increase in flow velocity lags behind the pressure event. Doppler flow across the mitral valve, with a simultaneous pressure recording in the left atrium and ventricle, provides a good illustration of this phenomenon (Figure 6.1). When pressure in the left ventricle falls below that in the left atrium, the pressure difference between the left atrium and ventricle drives flow acceleration into the left ventricle. The flow accelerates as long as pressure is higher in the atrium than in the ventricle. However, peak velocity actually occurs when the pressure has already equalized in both chambers. When the pressure gradient reverses and becomes lower in the atrium, flow decelerates. For a period of time the inertial forces cause blood to flow against the pressure difference, from the atrium into the ventricle.

The Doppler insonation angle

The Doppler insonation angle is the angle between the ultrasound beam and the direction of blood flow. To reliably measure flow velocity by Doppler the insonation angle should be as narrow as possible, that is, the ultrasound beam must be oriented as closely as possible to the direction of flow. When the direction of flow is not parallel to the insonation angle, the flow velocity will be underestimated as a function of the cosine of the insonation angle. When the Doppler beam is at 90° to the direction of flow, the detected flow velocity is zero and therefore invisible to the ultrasound. It is theoretically possible to calculate the true velocity of flow by correcting for the angle between the ultrasound beam and direction of flow. In practice, however, the calculation is suboptimal, and it is far preferable to align the ultrasound beam with the direction of flow. This is facilitated by using color Doppler flow to visualize the flow orientation before placing the pulsed- or continuous-wave Doppler sample. For clinical practice, angles of less than 15–20° between the insonation beam and blood flow are acceptable. In addition, multiple views should be obtained to ensure that the optimal insonation angle and highest velocity are captured.

Blood flow profiles

Blood flow is calculated as the product of the average velocity and cross-sectional area (CSA) of the vessel. If flow was constant,

Echocardiography in Pediatric and Congenital Heart Disease: From Fetus to Adult, Second Edition. Edited by Wyman W. Lai, Luc L. Mertens, Meryl S. Cohen and Tal Geva.
© 2016 John Wiley & Sons, Ltd. Published 2016 by John Wiley & Sons, Ltd.
Companion website: www.lai-echo.com

Table 6.1 Symbols and abbreviations for hemodynamic variables and other parameters

2D – two-dimensional
3D – three-dimensional
C_c – coefficient of contraction
E – energy
g – gravitational constant
h – height
m – mass
P – pressure
ρ – density of blood
v – velocity
AOA – anatomic orifice area
CSA – cross-sectional area
CW – continuous wave
EOA – effective orifice area
EROA – effective regurgitant orifice area
LV – left ventricle or left ventricular
LVOT – left ventricular outflow tract
MR – mitral regurgitation
PAH – pulmonary arterial hypertension
PISA – proximal isovelocity surface area
PRF – pulse repetition frequency
PW – pulsed wave
Qp/*Qs* – ratio of pulmonary to systemic flow
RA – right atrium or right atrial
ROA – regurgitant orifice area
RF – regurgitant flow
RV – right ventricle or right ventricular
TVI – time–velocity integral

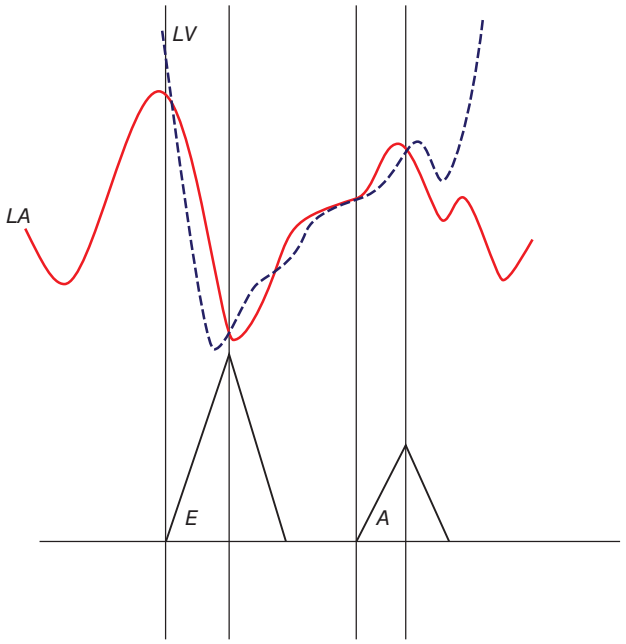


Figure 6.1 The relationship between the mitral inflow velocity and the pressure difference between the left atrium (LA) and left ventricle (LV). Flow acceleration of the E wave on the mitral inflow Doppler tracing begins with the first pressure crossover and corresponds with a period when LV pressure is higher than pressure in the LA. Peak velocity of the E wave corresponds to the second pressure crossover and the deceleration phase of the E wave corresponds to flow against the pressure gradient when LA pressure is higher than LV. This pattern is repeated during the A wave.

laminar, and homogenous across the vessel this would be relatively easy to do. However, in the cardiovascular system, flow is pulsatile and the flow velocity varies across the cross-section of the vessel or orifice. The distribution of flow velocities across the vessel is called the flow velocity profile. In a straight, rigid tube with steady laminar flow, flow velocities are highest in the center and lowest in the periphery. This yields a parabolic velocity profile across the vessel with the highest velocities in the center of the spectral Doppler envelope and the lowest velocities at its edges. In contrast, flow entering a tube from a reservoir has a relatively flat velocity profile at the vessel inlet, that is, all velocities are similar across the vessel cross-sectional area. The flat flow velocity profile at the inlet of the vessel gradually becomes parabolic as flow propagates through the vessel. Because the velocity profile at the vessel inlet is flat, spectral Doppler measurement of the peak velocity at the vessel inlet is more representative of the average velocity. The transition from a flat to parabolic velocity profile occurs because of the viscous drag between the vessel wall and the adjacent fluid with concomitant acceleration of flow in the center of the vessel. Consequently, when the velocity profile is parabolic, the maximum velocity significantly overestimates the mean velocity, which is the parameter needed to calculate flow. For example, in the branch pulmonary arteries, the flow velocity profile is parabolic and a three-dimensional assessment would be required to derive the true average velocity for flow calculations [1,2]. Likewise, a small Doppler sample volume that captures local velocities may not represent the average velocity across the entire cross-sectional area of the vessel if it is placed either in a region of local turbulence or in a region of local high-velocity laminar flow. One can picture this as a river with fast flow in the center and slow flow at the edges. Sampling the flow in one region will not reflect the average velocity across the entire width of the river. Likewise sampling flow velocity in a region where the water is turbulent due to rocks does not represent the average velocity of the river across its width.

Other factors also influence flow profiles. At vascular bifurcations, such as the carotid artery bifurcation [3], the greater central velocity in the carotid artery results in a skewed velocity profile in the internal carotid artery, with greater velocity flow adjacent to the bifurcation. In curved vessels, such as the aortic arch, the flow profile in the curved segment depends on the flow profile at the entrance to the curve. If parabolic, the maximum velocity is shifted toward the outer wall with flow velocity slowing along the inner wall and vortex development or even flow reversal [4] (Video 6.1). In contrast, if the flow profile is flat at the entrance to the curve, centrifugal forces produce higher pressure (lower velocities) at the outer aspect of the curve, and lower pressures (higher velocities) at the inner curvature of the vessel. For example, the flow profile in the ascending aorta is generally flat (velocities are equal across the whole cross-sectional area), and therefore the flow velocities are generally highest along the inner curvature of the aortic arch.

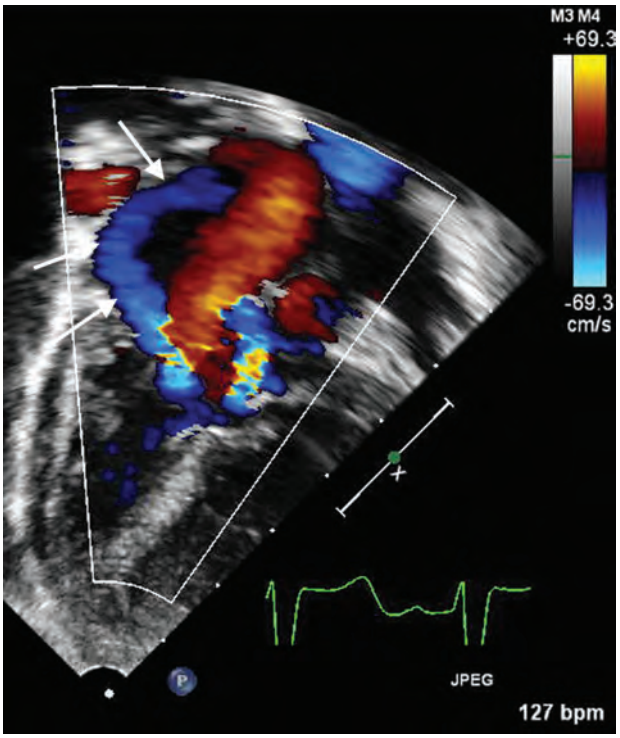


Figure 6.2 Left atrioventricular valve regurgitation on an apical 3-chamber (long-axis) view with color flow Doppler in a patient after repair of atrioventricular septal defect. Note the eccentric regurgitant jet going away from the transducer (blue) which then tracks along the left atrial wall (arrows) due to the Coanda effect.

The Coanda effect

The Coanda effect is a specific flow profile where the tendency of a stream of fluid is to follow a convex surface, rather than a straight line. In the heart, the Coanda effect causes jets to adhere to the chamber or vessel wall and can significantly affect Doppler assessment of valvar regurgitation and shunts. Examples include aortic regurgitation jets that track along the valve cusp or the ventricular septal surface and mitral regurgitation jets that hug the atrial wall (Figure 6.2; Video 6.2). The Coanda effect is actually a manifestation of the Bernoulli principle, which is described in further detail later. The larger decrease in flow velocity along the inner surface of the jet, away from the vessel wall, increases the pressure relative to the outer surface of the jet where velocities are higher, thereby pushing the jet toward the vessel wall. Because of the Coanda effect, and in general because of eccentric jets, multiple echocardiographic views should be obtained in order to achieve the narrowest insonation angle between the ultrasound beam and direction of flow and hence capture the highest velocity.

Characteristics of flow through a narrow orifice, the vena contracta, and the phenomenon of pressure recovery

When flow approaches a narrowing, the flow streamlines converge to enter the orifice. This pushes the streamlines close together so that the diameter of the jet passing through the orifice is smaller than the size of the anatomical orifice itself [known as the *anatomic orifice area* (AOA)]. The narrowest region of the jet at or immediately after it emerges from the orifice is called the *vena contracta*. Because the vena contracta is the smallest CSA through which the flow passes it is also known as the *effective orifice area* (EOA). The flow velocity is highest and pressure lowest at this point. It is the EOA and not the AOA that determines the hemodynamic importance of a narrowing. Therefore, the hemodynamic effect of a stenosis can be significantly greater than would be predicted on the basis of the actual orifice size. The size of the vena contracta is relatively independent of flow rate and driving pressure for a fixed orifice [5]. The vena contracta is measured from color Doppler [6–8], correlates closely with the actual EOA [9] and severity of valve regurgitation [10], and is therefore used to judge the severity of valvar regurgitation. Downstream of the vena contracta, the streamlines begin to diverge at the periphery of the jet, forming a central core of laminar flow that persists for a variable distance (Figure 6.3).

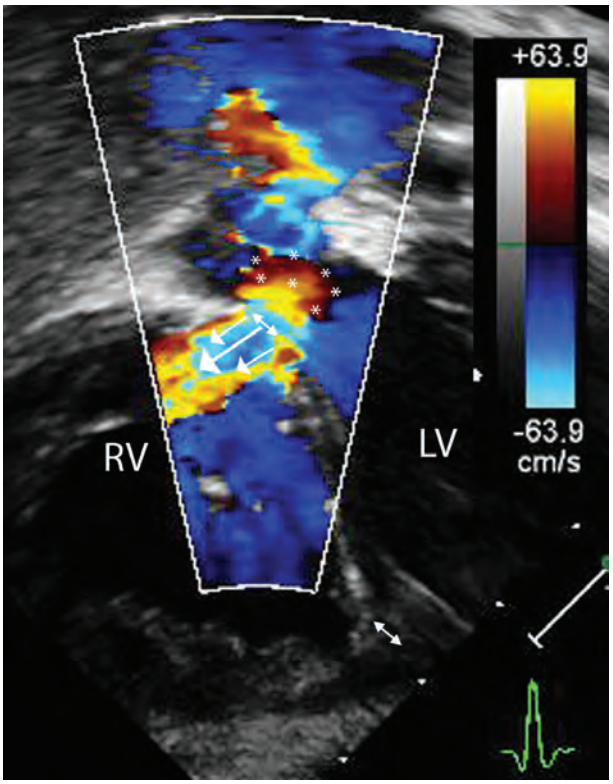


Figure 6.3 Color flow Doppler of shunting through a ventricular septal defect (VSD) depicting flow characteristics of a jet. Proximal to the VSD in the left ventricle (LV), flow is seen converging onto the VSD orifice in concentric semicircles of increasing velocity [proximal isovelocity surface acceleration (PISA)] (asterisks). The jet streamlines form the narrowest diameter at or just beyond the anatomical orifice of the VSD – at the vena contracta (double-headed arrow). Distal to the VSD orifice, the jet is seen with the highest velocity at its center (long arrow) and lower velocities at its edges (short arrows). More distally the flow re-laminarizes and can be seen as the solid orange color at the edge of the sample box in the right ventricle (RV).

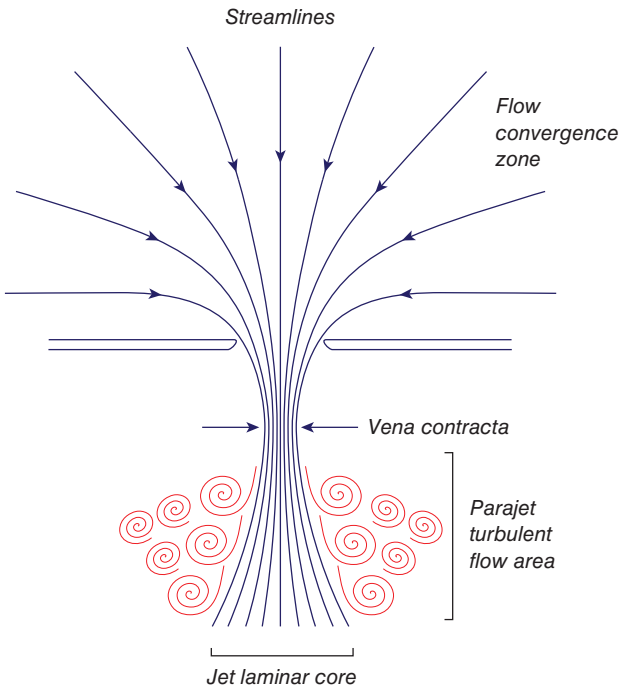


Figure 6.4 Flow through an orifice in a flat surface. The flow convergence area is characterized by nonturbulent flow that follows streamlines converging in a symmetric pattern. The inertial forces of the peripheral streamlines are directed toward the center of the orifice and exert forces in a direction that narrows the jet to a minimum cross-sectional area at the level of the vena contracta; the streamlines then diverge in the jet laminar core. The parajet area is characterized by turbulent flow eddies.

The high-velocity edges of the central core shear against the stagnant flow around the central jet, creating eddies that gradually engulf the central core and the surrounding area (Figure 6.4). A common error is to assume that aliasing of the color Doppler signal distal to the orifice implies turbulence when in reality it is the turbulent flow of the parajet region creating the aliasing, not high flow velocity. More distally in the vessel, downstream from the stenotic orifice, the phenomenon of pressure recovery becomes important. Let us dwell on this for a moment as pressure recovery impacts Doppler measurements. The Bernoulli equation, which is subsequently discussed, implies that the conversion of pressure to velocity is reversible, and that velocity can be converted to pressure. When blood flows across a narrow orifice, velocity rises and pressure falls, with the lowest pressure associated with the narrowest portion of the jet at the vena contracta. Distal to this point, as the flow stream widens and the flow velocity diminishes, the pressure rises again, a phenomenon known as pressure recovery [11]. In essence, pressure recovery occurs because not all kinetic energy across the stenosis is dissipated as turbulence, and some of the flow becomes laminar again. However, pressure recovery is always incomplete because some energy is lost due to friction along the boundaries of the outflow jet (Figure 6.5). The amount of energy lost in this transition depends on the shape of the outlet chamber and can be clinically significant. For example, in aortic stenosis

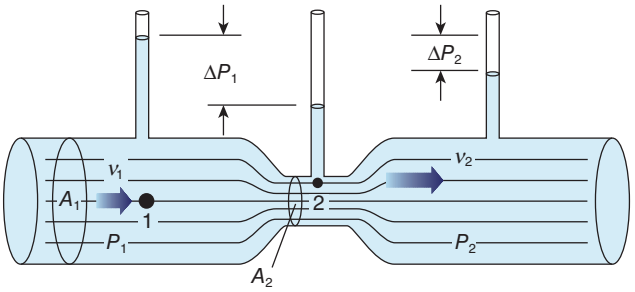


Figure 6.5 The Venturi tube (after Giovanni Venturi, 1746–1822) is a cylindrical pipe with a streamlined constriction designed to minimize energy losses in the fluid flowing through it. The pressure drop between the inlet and area of greatest constriction (ΔP_1) can be used to calculate flow and is the basis of the Venturi meter. The shape of the outlet is optimized to avoid turbulence. With optimal geometry of the tube, pressure recovery can lead to a net loss of pressure as small as 10% (ΔP_2) if turbulent flow is avoided and the only energy loss is due to the viscous effects at the walls of the chamber. A_1 and A_2 are the initial and minimum cross-sectional areas, v_1 and v_2 are the initial and final velocities, and P_1 and P_2 are the initial and final pressures.

there is an inverse relationship between the size of the aortic root (which is often dilated) and the amount of pressure recovery distal to the stenotic aortic valve [12]. The larger the aortic root, the less the pressure recovery, and the higher the gradient across the valve. Similarly, pressure recovery is less in eccentric jets [12] (Video 6.1) Therefore, for any given orifice size, the functional severity of stenosis is greater in eccentric jets, both because of a greater pressure loss (smaller effective orifice area) and because of diminished pressure recovery.

When a Doppler sample is placed at, or immediately distal to the vena contracta, pressure recovery has not yet occurred and even though the measured gradient is true, it will overestimate the net gradient. The more clinically relevant parameter is the actual pressure in the vessel that incorporates the recovered pressure. Hence, due to pressure recovery the net gradient from the left ventricle to the aorta will be lower than that measured at the vena contracta, where pressure recovery has not yet occurred. Accordingly, the left ventricular pressure will not be as elevated as would be expected from the measured Doppler gradient. Therefore, a large gradient measured at the vena contracta of the aortic valve may not be hemodynamically important if the left ventricular systolic pressure is not significantly elevated. Other factors can influence the prediction of stenosis severity based on the vena contracta. Gilon et al. [13] showed that doming stenotic aortic valves have a much smaller impact on the reduction in valve area at the level of the vena contracta than flat valves.

Quantification of blood flow and the measurement of cardiac output

Calculation of cardiac output, its change over time and its response to intervention is potentially useful, especially in critically ill patients. There are two methods commonly used to measure blood flow and specifically stroke volume by

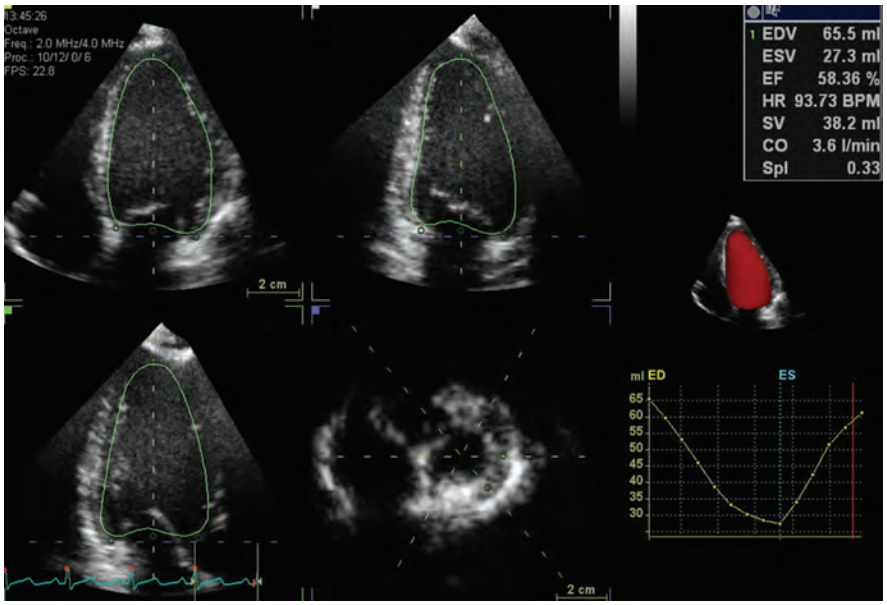
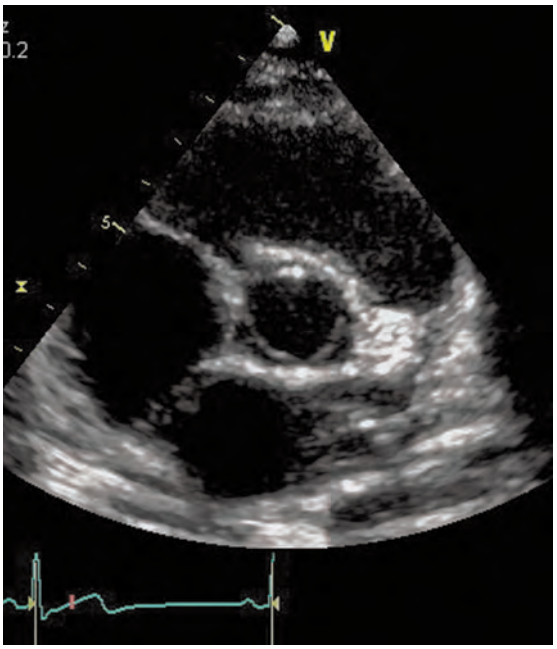


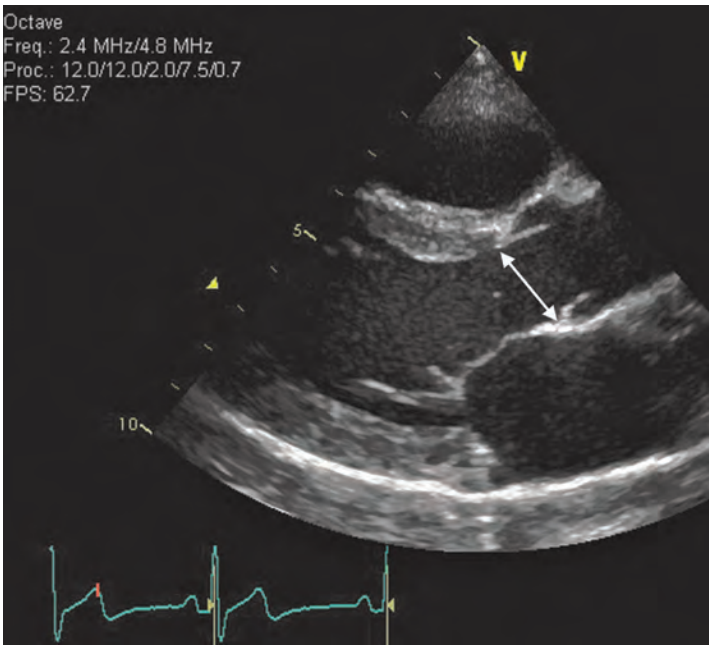
Figure 6.6 Calculation of cardiac output using volumetry. In this example, three-dimensional (3D) echocardiography is used to calculate the left ventricular end-diastolic (ED) and end-systolic (ES) volumes. These can also be obtained from 2D or M-mode techniques. A 3D full-volume acquisition of the left ventricle from the apical view is automatically sectioned into a 4-, 3- and 2-chamber view and ventricular volumes calculated. In the absence of valvar regurgitation or intracardiac shunts, the difference between the end-diastolic and end-systolic volumes is the stroke volume, which is 38.2 mL in this example. The stroke volume times the heart rate (94 beats per minute in this example) yields the cardiac output (3.6 L/min in this example). The cardiac output can be indexed to body surface area to yield the cardiac index.

echocardiography. The first uses M-mode, two-dimensional (2D) or three-dimensional (3D) echocardiography to calculate the change in chamber volume between end-diastole and end-systole to yield the stroke volume (Figure 6.6). The stroke volume multiplied by heart rate yields cardiac output, which can be indexed to body surface area to yield cardiac index. Alternatively, as previously mentioned, blood flow can be quantified as the product of the average flow velocity and the CSA of the vessel or structure. The flow velocity is obtained by Doppler and the CSA is obtained by M-mode, 2D or 3D echocardiography. As previously mentioned, it is the average velocity that is required to calculate flow. If blood flow is laminar and the flow velocity profile flat, then the average velocity is relatively easy to calculate. However, because blood flow is pulsatile and because the velocity flow profile is often parabolic, all velocities within the Doppler spectral envelope must be summed and integrated to yield the average velocity. Integrating all flow velocities across the Doppler spectral envelope is called the time velocity integral (TVI). The integration of velocity yields the stroke distance, that is, the distance the column of blood has moved in one heartbeat. The TVI multiplied by the CSA of the vessel or valve yields the flow (TVI × CSA). Although this sounds complex, in practice this is relatively easy to do with digital echocardiography. A Doppler sample is placed at the structure of interest [e.g., left ventricular outflow tract (LVOT)], a pulsed spectral Doppler is acquired and the average flow velocity across the CSA is calculated by integrating all the velocities encapsulated in the Doppler spectral display. This is achieved by digitally tracing the Doppler spectral envelope (Figure 6.7c). To simplify the calculation, the CSA is usually calculated as a circle (πr^2). Cardiac output is most commonly measured at the aortic valve as the normal aortic valve annulus diameter can be measured with good accuracy and reproducibility, and the true CSA is relatively close to being a circle (Figure 6.7a). Pulsed-wave (PW) Doppler rather than continuous-wave (CW) Doppler should be used to ensure that the velocity sample is obtained in the LVOT or at the annulus where the flow profile is relatively flat (Figure 6.7c). Otherwise, more distal flow acceleration may be captured by the CW sample resulting in spuriously high flow velocities and erroneously high calculation of the cardiac output. The Doppler sample is placed in the LVOT a few millimeters below the valve in an apical 5-chamber, 3-chamber, or subcostal view. The aortic valve diameter can be measured from these positions, although usually the parasternal long-axis view is used (Figure 6.7b). Because the aortic annulus diameter does not vary much through the cardiac cycle, the timing of the measurement is not crucial, although is usually performed in mid-systole when the aortic leaflets are open and the attachment of the valve cusps to the vessel wall (the hinge points) can be discerned (Figure 6.7b). The flow across the aortic valve (the product of CSA and TVI) in one cardiac cycle yields the stroke volume, which multiplied by heart rate provides the cardiac output. The cardiac output can be further indexed to body surface area to yield the cardiac index.

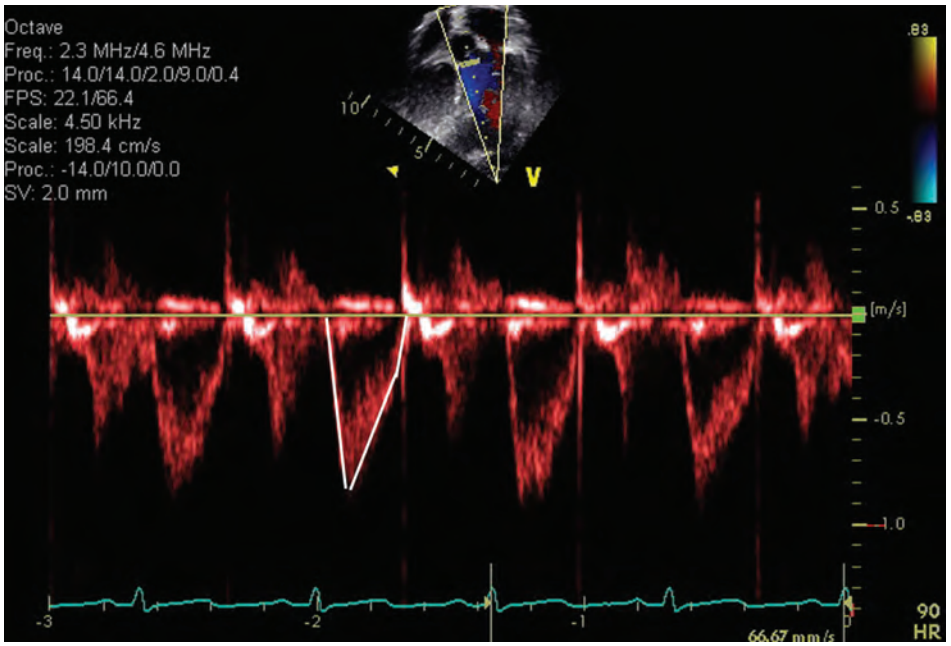
In theory, flow at other locations can be sampled in a similar fashion, but measurements are less accurate than at the aortic valve. For example, when the pulmonary valve annulus can be seen clearly from subcostal or parasternal short-axis views, right ventricular (RV) stroke volume and hence pulmonary flow can be calculated by measuring the pulmonary annulus and by placing a PW Doppler sample in the RV outflow tract. Calculation of pulmonary flow in addition to aortic flow should permit calculation of the pulmonary versus aortic flow ratio (Qp/Qs) to evaluate the magnitude of intracardiac shunts. In practice, measurement of the pulmonary valve area is subject to error due to poorer visualization of the pulmonary valve, which leads to inaccurate measurements of the pulmonary annulus diameter.



(a)



(b)



(c)

Figure 6.7 Computation of cardiac output by Doppler. The cross-section of the aortic valve is approximated as a circle **(a)**. The cross-sectional area is computed using the diameter of the valve measured from the parasternal long-axis view **(b)**. The time velocity integral (TVI) is computed by tracing the spectral Doppler envelope from a pulsed-wave Doppler placed in the left ventricular outflow tract in the apical 5-chamber view **(c)**. Tracing the spectral Doppler integrates (averages) all velocities during ejection to yield the distance the blood has been displaced over the cardiac cycle. The TVI times the aortic cross-sectional area yields the stroke volume, which multiplied by the heart rate yields cardiac output.

Because the annulus diameter is squared to calculate the CSA, a small measurement error of the annulus diameter will result in a large error when calculating the CSA. This error is further amplified if the measurement is used to calculate a ratio such as *Q*p/*Q*s. Consequently, relatively small measurement errors by echocardiography can have a large impact on cardiac output measurements or derived ratios such as the *Q*p/*Q*s. Because much of the error stems from inaccuracies in measurement of the valve diameter some authors have suggested using simplifications of this principle to approximate the *Q*p/*Q*s using just the

ratio of the peak velocities and ratio of the annulus diameters of the pulmonary and aortic valves as follows [14]:

$$Qp/Qs \sim [PkV_{PA}/PkV_{AO}] \times [D_{PA}/D_{AO}]^2 \quad (6.1)$$

In practice, due to the inaccuracies of calculating Qp/Qs by echocardiography this measurement is not routinely used. Rather, considerations such as the patient's clinical status and left-sided chamber enlargement determine clinical decisions such as the need to close a ventricular septal defect. Similarly, measurement of flow across the atrioventricular valves would be useful to calculate the severity of valve regurgitation. However, measurement accuracy is limited by the elliptical shape of the atrioventricular valve annuli, the change in their shape over the cardiac cycle, and the large magnitude of atrioventricular valve motion relative to the ultrasound transducer.

Because a large source of error in calculating blood flow/stroke volume by echocardiography is the calculation of the CSA, some have proposed using the TVI alone to assess relative changes in cardiac output. If we assume that the CSA of the aortic or pulmonary valves, for example, remain relatively constant over the cardiac cycle and relatively constant from one examination to the next over short periods of time, then any change in the TVI should reflect a change in cardiac output. This method has been used in a number of clinical situations. For example, in pulmonary hypertension, assessment of the TVI serially over time can reflect changes in cardiac output. This imperfect measure of RV performance has been shown in some studies to correlate with patient outcomes in pulmonary arterial hypertension (PAH) [15]. The change in TVI as a measure of change in cardiac output can also be used to optimize pacemaker settings during cardiac resynchronization therapy. Multiple measurements of the TVI at different pacemaker settings are made at the same session in a relatively short period of time. The change in TVI between settings allows evaluation of which pacemaker setting yields the highest cardiac output [16]. One should be cognizant, however, of the important factors influencing TVI. Just as stroke volume is highly influenced by preload and afterload, TVI is similarly influenced by loading conditions. Likewise, cardiac output is the product of heart rate and stroke volume. Therefore, a change in TVI when heart rate has changed may not in itself reflect a change in cardiac output.

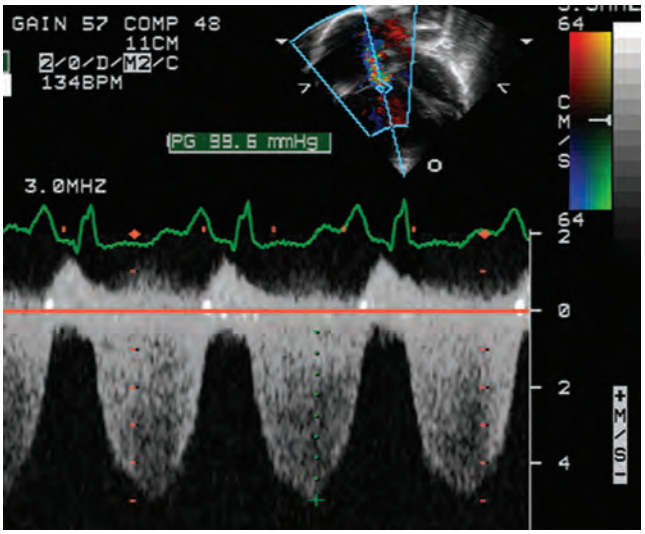


Figure 6.8 Spectral Doppler display of a continuous-wave Doppler sample of tricuspid regurgitation in a child with severe pulmonary arterial hypertension. The TR velocity is close to 5 m/s translating to a right ventricle to right atrial gradient of nearly 100 mmHg using the modified Bernoulli equation. To obtain the absolute right ventricular pressure, the right atrial pressure would have to be added to this gradient. Note the relatively dense and triangular configuration of the Doppler spectral envelope suggesting a significant volume of regurgitation. Also apparent is the prolonged duration of systole (the duration of the tricuspid regurgitation) versus the shortened duration of diastole (the time between two regurgitant jets) which has been found to correlate with outcomes in children with pulmonary hypertension [42].

Estimation of pressure gradients and the Bernoulli equation

One of the key and most common hemodynamic assessments in clinical practice is the measurement of pressure gradients across valves or vessels. Common examples in pediatric cardiology include measurement of pressure gradients across stenotic valves (e.g., aortic or pulmonary valve stenosis), assessment of pressure gradients across a ventricular septal defect to determine whether it is restrictive to pressure, and measurement of the pressure gradient from the RV to the right atrium (RA) across the tricuspid valve to assess RV systolic pressures (Figure 6.8). Measurement of pressure gradients by echocardiography is done by measuring flow velocities, which are then translated into pressure gradients using the Bernoulli principle. It is important to remember, regardless of the particular example, that echocardiography cannot measure absolute pressures and that only the difference in pressures across a structure (i.e., the pressure gradient) is measured. For example, if the gradient across an atrial septal defect is low, this does not automatically imply that left atrial pressure is low, as RA pressure may be elevated. The absolute pressures in the left and right atria remain unknown and can only be estimated by echocardiography using indirect methods which will not be discussed here.

The Bernoulli equation is based on the principle of conservation of energy, that is, the total amount of energy at all points within a closed system must be constant. Applied to blood flow this means that if a valve or vessel area decreases, the flow velocity must increase. Again, think of the example of a river. If the river narrows, the flow quickens to maintain the same flow volume. Although in clinical echocardiography we almost always use a condensed, boiled-down version of the full Bernoulli equation, it is worthwhile discussing the elements that make up the full equation as they explain some of the common pitfalls encountered when using the simplified version. The

$$\Delta P = \underbrace{\frac{1}{2}\rho(v_2^2 - v_1^2)}_{\text{Convective acceleration (kinetic) component}} + \underbrace{\rho\int_1^2 \frac{dv}{dt}\,ds}_{\text{Local acceleration (inertial) component}} + \underbrace{R(\mu,v)}_{\text{Viscous (shear stress) component}}$$

Figure 6.9 The complete Bernoulli equation. P = pressure, ρ = fluid density, v = velocity, t = time, s = distance, and $R(\mu,v)$ is shear force expressed as a function of velocity (v) and position (μ).

full Bernoulli equation incorporates three elements: (i) convective (kinetic) acceleration; (ii) flow acceleration; and (iii) viscous friction (Figure 6.9). Convective (kinetic) acceleration describes the increase in flow velocity between two points. The velocities at these two points are the v_1 (proximal) and v_2 (distal) in the Bernoulli equation. Acceleration of any mass requires force, and in the circulation, the force accelerating blood is largely supplied by contraction of the myocardium. The direct "force" accelerating blood through a narrowing is provided by the pressure drop across the narrowing. A constriction in a blood vessel causes acceleration of blood flow through the narrowing and a change in its kinetic energy proportional to the square of the velocity. The increase in kinetic energy is associated with a concomitant decrease in potential energy. This component of the Bernoulli equation is the one most important to clinicians and is encapsulated in the simplified Bernoulli equation used in clinical practice. The second component in the complete Bernoulli equation is flow acceleration. When flow is pulsatile the flow velocity at any given location will increase and decrease with each heartbeat, with some energy loss due to viscous friction. However, when matched for phase, the velocity at a location varies little from beat to beat, and this component of the Bernoulli equation is disregarded in the modified version used in clinical practice. The third component of the complete Bernoulli equation relates to energy lost due to viscous forces. Viscous friction is the resistance that slows blood flow due to friction between blood layers and between blood and the vessel wall (imagine squeezing through a narrow tunnel). Although the true magnitude of viscous losses is difficult to estimate, when the velocity is high enough, or the structure large enough, the viscous losses may be neglected and are dropped from the modified Bernoulli equation. When estimating gradients across valves for example, viscous friction can be neglected. In contrast, the viscous friction component can be important in small or stenotic vessels. Therefore, the simplified Bernoulli equation does not perform well when calculating gradients across a small vessel such as a Blalock–Taussig shunt.

The condensed and simplified Bernoulli equation,

$$\Delta P = 4v_2^2 \tag{6.2}$$

most commonly used in clinical practice, therefore takes only the first component of the full equation into account. The "4" is a rounded-up conversion factor that converts velocity into pressure units of mmHg. It is also important to note that the simplified equation only includes v_2, or the blood flow velocity distal to the narrowing. For large pressure differences, the initial velocity (v_1) is small compared with the distal velocity (v_2), and can be ignored. However, when v_1 is relatively large compared to the distal velocity (i.e., when it is 2 m/s or more) it should be accounted for and the modified equation should be (Figure 6.10):

$$\Delta P = 4\left(v_2^2 - v_1^2\right) \tag{6.3}$$

Likewise, the simplified Bernoulli equation cannot be used to quantify intraventricular flow or flow across unobstructed left ventricular inflow or outflow tracts [17]. The Bernoulli equation performs best across discrete stenoses. When there is a long-segment narrowing, the simplified Bernoulli equation will overestimate the gradient. This can be commonly seen, for example, when assessing gradients across long-segment narrowing in the aortic isthmus (i.e., diffuse aortic coarctation). Other technical factors can be important sources of error. Beyond the alignment of the ultrasound beam with the direction of the blood flow, the image quality will influence the spectral Doppler measurement and hence the estimation of peak velocity. A common example in clinical practice is underestimating the peak velocity and hence RV systolic pressure when the tricuspid regurgitation spectral envelope is incomplete. Careful adjustment of gain and reject settings, as well as sampling the jet from multiple views to ensure the highest velocity is paramount. Contrast with agitated saline can be used to enhance the spectral display intensity, although this necessitates placement of an intravenous catheter. One must also be cognizant of where the Doppler sample is placed and if there is more than one jet, which jet is being sampled. For example, when trying to sample the LVOT in hypertrophic cardiomyopathy, the mitral regurgitation jet, which is in close proximity, must be avoided. Similarly a jet across a ventricular septal defect can contaminate the estimation of RV systolic pressure using the tricuspid regurgitation jet. This can also be a problem when trying to determine the pressure gradient across RV muscle bundles associated with a ventricular septal defect where a high-velocity ventricular septal defect jet can contaminate the flow acceleration across the closely related muscle bundles (Video 6.3).

The configuration of the spectral jet can also provide clues not only on the severity of the obstruction in terms of peak velocity, but also to its mechanism. Dynamic muscular obstructions often have a curved, dagger-like profile. Sometimes, multiple contours can be seen simultaneously pointing to multilevel obstruction. This is commonly seen in multilevel right ventricular obstruction in unrepaired tetralogy of Fallot (Figure 6.11; Videos 6.4 and 6.5). Gradients should be obtained at a stable heart rate. The presence of premature beats affects filling and hence stroke volume and can lead to errors in assessment of the true gradient (Figure 6.12a,b).

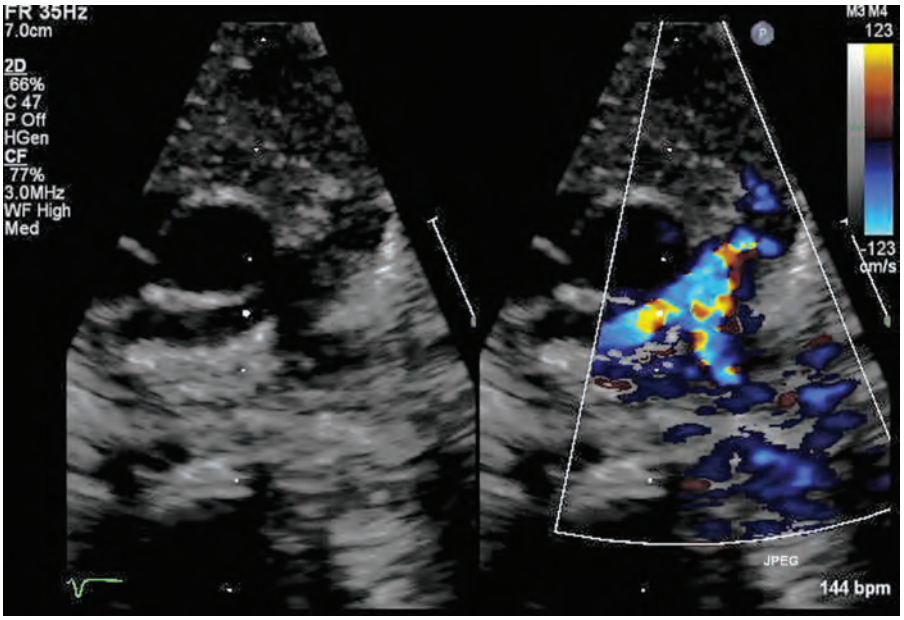


Figure 6.10 Two-dimensional echocardiography (left panel) with corresponding color flow Doppler (right panel) of the branch pulmonary arteries in a patient with tetralogy of Fallot. Note the small branch pulmonary arteries. Calculation of pressure gradients into the branches is limited by a number of factors. Flow profiles are not flat at the entrance to the branch pulmonary arteries (see text for details). In addition there is flow acceleration at the entrance to the vessel because of more proximal right ventricular outflow tract obstruction. Therefore, the proximal flow velocity cannot be disregarded and V_1 would have to be incorporated into the modified Bernoulli equation. Also note the suboptimal Doppler insonation angle to the right pulmonary artery which may lead to significant underestimation of the true gradient.

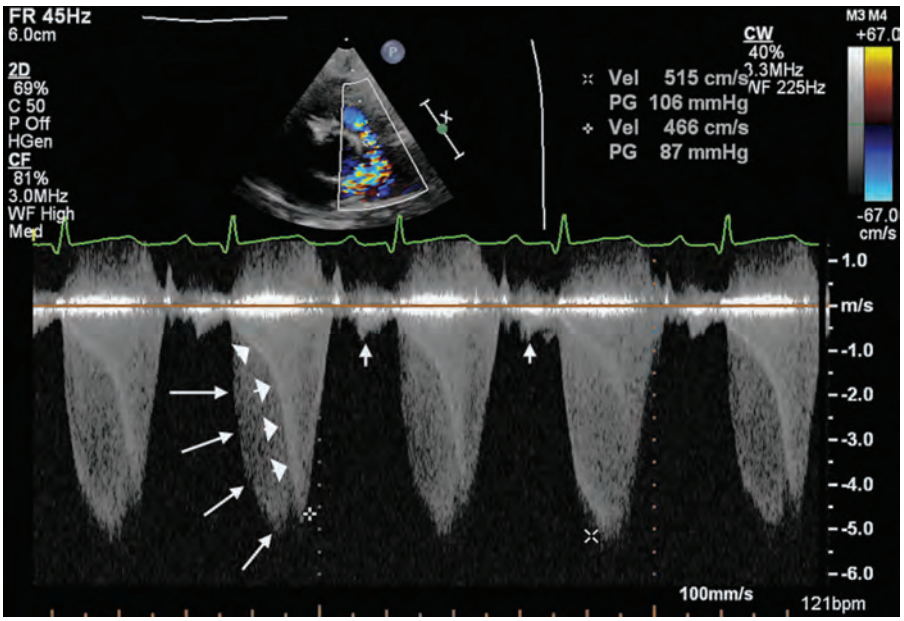
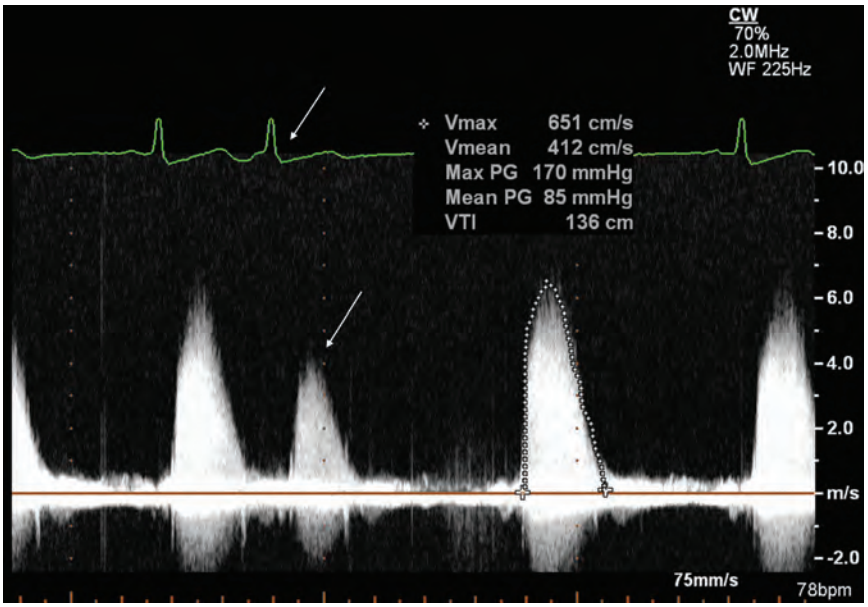
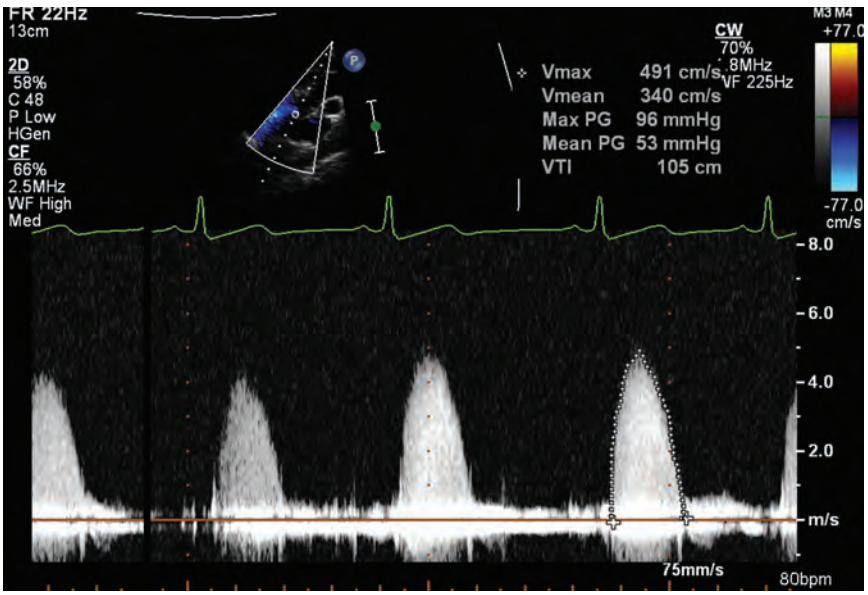


Figure 6.11 Right ventricular outflow tract continuous-wave Doppler in an infant with unrepaired tetralogy of Fallot. A double contour beneath the baseline is readily seen in the spectral display. Infundibular stenosis yields the "dagger shape" contour typical of dynamic muscular obstruction (arrowheads) while fixed obstruction at the pulmonary valve level creates a triangular contour (long arrows). Also noted in this patient is antegrade flow at end-diastole, after the ECG P wave, consistent with restrictive right ventricular physiology (small arrows).



(a)



(b)

Figure 6.12 Continuous-wave Doppler obtained from the suprasternal notch position in a child with aortic valve stenosis (**a**). The spectral envelope is traced to yield peak and mean velocities, which are transformed to peak and mean pressure gradients using the modified Bernoulli equation. In this example, the complex following a premature beat (arrows) is traced. This can lead to overestimation of the true gradient as following the premature beat there is a compensatory pause which allows more ventricular filling, a larger stroke volume and hence a larger gradient on the subsequent ejection. By the same token, it can be seen that the premature beat causes incomplete ventricular filling and consequently lower stroke volume (TVI) and lower velocity across the valve. Therefore Doppler assessment of gradients across stenoses should be obtained under stable conditions and during a regular heart rhythm as demonstrated in (**b**).

Differences in catheter and Doppler measured pressure gradients

Calculation of pressure differences based on Doppler measurement of flow velocities has become a staple of patient care. However, the conversion of velocity to pressure using the modified Bernoulli equation is imperfect. Likewise, there are several factors that contribute to differences in the pressure gradient measured invasively in the catheterization laboratory versus those assessed noninvasively by Doppler. It is worthwhile to consider these briefly.

1 *Velocity measurement error*. As previously discussed, Doppler measures only the component of velocity in the direction of the ultrasound beam. Therefore, an off-angle Doppler sample results in underestimation of the true velocity.
2 *Pressure measurement error in the catheterization lab*. Inadequately calibrated pressure transducers, disturbance of the flow by the catheter itself, and measurement of stagnation pressure can each lead to pressure measurement errors at cardiac catheterization and therefore differences between echocardiographic and catheter measurements (even the "gold-standard" of catheter measurements is imperfect!).
3 *Physiologic differences in the patient state between studies*. The interval between the echocardiographic study and

catheterization as well as differences in the hemodynamic state of a fasting, sedated patient in the catheterization laboratory compared with the awake and sometimes uncooperative child having an echocardiogram will influence measurements of gradients. Doppler gradients in the awake child are usually higher than in the sedated child in the catheterization lab.

4 *Peak-to-peak versus peak pressure differences*. Catheter calculations are generally based on the peak pressure difference between two chambers even though these occur at different times. Doppler measurements, on the other hand, estimate the peak instantaneous pressure drop. These values are different, and this becomes important predominantly in mild stenosis.

5 *Pressure recovery*. The phenomenon of pressure recovery has been discussed previously. Because Doppler techniques do not detect pressure recovery, they may overestimate pressure gradients [18]. In contrast, a catheter positioned downstream from a stenotic valve measures recovered pressure, but measuring the maximum pressure drop within the vena contracta is generally not possible [19]. Similarly, if the catheter is positioned close to the vena contracta, the pressure gradient may be overestimated as pressure recovery, which can continue for 5–10 cm downstream, has not fully occurred. Also, smaller peak velocities are associated with a greater degree of pressure recovery, resulting in greater relative differences between catheter and Doppler estimates of pressure differences even though the absolute differences tend to be small.

6 *Inaccuracies introduced by use of the simplified Bernoulli equation*. As previously discussed, use of the simplified Bernoulli equation assumes that the proximal velocity is negligible and that viscous effects are small. Tunnel-like stenoses, eccentric jets, and prosthetic valves are all subject to greater viscous effects and the simplified Bernoulli equation may be inaccurate in these situations.

Although it is theoretically possible to estimate the catheter peak-to-peak gradient based on the peak instantaneous echocardiographic Doppler gradient using regression equations derived from comparative studies [20], in practice most laboratories do not do so.

Assessment of valvar stenosis and regurgitation in clinical practice

Valve stenosis imposes a pressure load on the pumping chamber. The severity of this load is proportional to the magnitude of the stenosis and therefore quantifying valvar stenosis is important. In valvar regurgitation, the regurgitant volume influences the ventricular response and is the parameter of interest. In both valvar stenosis and regurgitation, the ventricular response to the abnormal loading is the key parameter that determines clinical decision making and is therefore an integral part of the hemodynamic assessment. Consequently, assessment of ventricular hypertrophy, enlargement, and function are more important in aortic stenosis and regurgitation than quantitative assessment of the stenosis or regurgitant volume themselves. Nonetheless, in asymptomatic children with preserved ventricular function and dimensions, the severity of stenosis is used to decide on the timing of intervention, both for the aortic and pulmonary valves. Although Doppler echocardiography is a valuable tool to assess valvar stenosis and regurgitation, it is important to recognize the many limitations to these methods. It is equally important to remember that sometimes simple clues can provide useful information on the severity of a hemodynamic lesion. For example, a pulsatile abdominal aorta on 2D imaging suggests that more proximal arch obstruction or aortic coarctation is not severe. Likewise, flow reversal in the abdominal aorta suggests that aortic regurgitation is at least of moderate severity or that flow across a patent arterial duct is substantial. The key points in the assessment of native valvar stenosis and regurgitation are summarized in Table 6.2.

Table 6.2 Assessment of native valvar stenosis and regurgitation

- In children valve gradients rather than valve areas are generally used to describe the hemodynamic severity of stenosis.
- Physiologic and methodologic differences account for differences in catheter versus Doppler assessment of stenosis.
- The peak pressure gradient is generally used to assess ventricular outflow obstruction, whereas mean gradient is generally usually used to assess ventricular inflow obstruction.
- Specifically in aortic stenosis, the mean Doppler instantaneous gradient empirically correlates better with the catheter measured peak-to-peak gradient.
- Multiple parameters should be used to judge the severity of regurgitant lesions as use of any individual parameter may be unreliable. These include M-mode, 2D or 3D measurements as well as Doppler parameters of the vena contracta, the regurgitant jet area and flow convergence; among others.
- Technical factors such as Nyquist limit and gain are crucial to correct assessment of valvar regurgitation.
- In the asymptomatic patient, the ventricular response to stenosis or regurgitation remains the single most important factor in assessment of valvar hemodynamic lesions.

Assessment of native valvar stenosis

There are several Doppler echocardiography methods to judge the severity of valvar stenosis. One of these is to measure the stenotic valve area relative to body surface area. This theoretically can be achieved by direct planimetry of the valve area from 2D images and perhaps more accurately by 3D echocardiography [21]. However, direct measurement of the AOA is often not possible or reliable. Moreover, even if the actual AOA could be accurately measured, this would still underestimate the severity of the stenosis, because, as previously detailed, the effective orifice area and not the anatomic orifice area determines the severity of the stenosis. Therefore, assessment of valvar stenosis using the CSA area has largely relied on measurement of blood flow using the continuity equation rather than on direct measurement. The continuity equation is commonly used in adult cardiology, but is less commonly used in pediatric laboratories for reasons that will be subsequently detailed. The continuity equation is based on the dictum that if there are no intracardiac shunts or valvar regurgitation, flow across all four cardiac valves is equal

and, specifically, flow across the aortic and mitral valves is equal; otherwise blood would rapidly accumulate in the left ventricle. Therefore, based on the calculation of blood flow we detailed previously, the continuity equation for the left-sided valves is

$$CSA_{aortic} \times TVI_{aortic} = CSA_{mitral} \times TVI_{mitral}. \quad (6.4)$$

Let us assume that we wish to know the CSA of the mitral valve to determine if there is mitral stenosis. We have already established that this measurement is difficult to determine directly. However, as can be seen from the equation, if the aortic CSA (more easily measured directly) and TVI are known, the mitral valve TVI can be easily obtained from a mitral inflow Doppler, so that the mitral valve CSA can be calculated as

$$CSA_{mitral} = (CSA_{aortic} \times TVI_{aortic})/TVI_{mitral}. \quad (6.5)$$

Similarly, the continuity equation can be used to estimate regurgitant volumes across valves. In the absence of an interventricular communication, the difference in antegrade flow volume across the aortic and mitral valves represents additional flow from aortic or mitral regurgitation. The continuity equation also forms the basis for calculations of regurgitant flow volume using the proximal isovelocity area (PISA) method, which will be detailed subsequently. Incidentally, the Gorlin equation, which is used for estimation of valve areas in the catheterization lab, is a special case of the continuity equation where flow velocity is replaced by the square root of the pressure drop. However, in contrast to the continuity equation, the Gorlin calculation provides an estimate of AOA, not EOA.

Although calculation of the valve area is the most accepted approach to assessment of valvar stenosis in adults, in pediatric cardiology most clinical decisions are based on measurement of pressure gradients alone [22]. Arguments can be made in favor of either approach. Valve area is potentially advantageous over Doppler gradients as it is not influenced by the volume of blood flow and hence by factors such as tachycardia and anemia. Measurement of pressure, however, is more accurate than measurement of flow. Therefore, the assumption is generally made in pediatrics that incorporation of flow measurement across the valve orifice is more likely to increase rather than decrease the error in the estimate of hemodynamic severity. Although variation in flow can contribute substantially to variation in gradient, marked reduction in cardiac output is common in adults with valvar heart disease, but is very unusual in children. For example, in adults, severe aortic valve stenosis may be accompanied with a low gradient across the valve due to decreased ventricular function. This is generally not the case in children, although there are exceptions, such as critical aortic stenosis of the newborn.

As pressure gradients are generally used in children to assess the severity of stenosis, it can be debated whether the peak or mean gradient across a stenotic valve should be reported. Clinically, the peak pressure gradient is generally used to assess ventricular outflow obstruction, whereas mean gradient is usually used to assess ventricular inflow obstruction (although there are exceptions). For virtually all types of obstruction, peak gradients correlate poorly to the valve area whereas mean gradients are used calculate the valve area (e.g., the Gorlin formula). However, the hemodynamic importance of outflow obstruction is its impact on the ventricle, which is more closely related to peak pressure than to mean pressure. Specifically, the risk for subendocardial ischemia, arrhythmias, and sudden death relate more closely to the peak gradient than the mean gradient as does the development of ventricular hypertrophy which relates more closely to peak wall stress than mean wall stress [23]. In aortic stenosis, the mean Doppler instantaneous gradient empirically correlates better to the catheter measured peak-to-peak gradient (which historically was used for clinical decision making) than the peak Doppler instantaneous gradient. It is therefore our practice to report both the mean and the peak gradients across the aortic valve/LVOT (Figure 6.12b). For the pulmonary valve/RVOT we report the peak gradient.

Assessment of native valvar regurgitation

Two-dimensional echocardiography

Two-dimensional echocardiography can provide clues to the presence and severity of valvar regurgitation. For example, the LV is expected to be large and appear hyperdynamic on 2D imaging when mitral regurgitation is present. The atrium gradually dilates to accommodate the regurgitant volume and this can be measured by M-mode, 2D or 3D echocardiography. The use of 2D or 3D echocardiography is particularly important to ascertain the mechanism and cause of regurgitation. A flail leaflet is usually associated with severe mitral regurgitation. Conversely, it is unusual to have severe mitral regurgitation if the mitral valve and its support apparatus are anatomically normal. The presence of a coaptation defect readily visible by 2D echocardiography usually indicates a significant degree of regurgitation. In mitral regurgitation, pulmonary artery pressure may rise in response to both the chronic mildly elevated left atrial pressure seen with chronic mitral regurgitation or in response to acute severe elevation with acute mitral regurgitation. When left atrial pressure is chronically elevated, pulmonary vascular resistance may increase and affect RV function.

Volumetric assessment

Volumetric assessment of valvar regurgitation is based on measurement of stroke volume in two regions of the heart. The stroke volume in one region includes the regurgitant volume, while the other region includes only the systemic stroke volume [24]. The difference between the two represents the regurgitant volume. For example, in mitral regurgitation, one can measure the stroke volume across the mitral valve (which includes the regurgitant volume) and the stroke volume across the left ventricular outflow tract (the systemic stroke volume). Subtracting the LVOT stroke volume from the mitral stroke volume will yield the mitral regurgitant volume. The stroke volumes can be obtained in a variety of ways. Flow through the left ventricular outflow tract can be calculated by multiplying the CSA by

the PW Doppler velocity time velocity integral as previously detailed. Stroke volume can also be obtained from 2D or 3D echocardiography by subtracting LV end-systolic volume from end-diastolic volume. While the volumetric methods are theoretically attractive, they are not widely used in clinical practice due to a number of limitations. They are time consuming and require multiple measurements and calculations which likely reduces their reliability [25]. Moreover, they are prone to errors in the primary measurements, which are then amplified in the subsequent calculations. The potential for error is further compounded by the need to subtract two large numbers from each other to obtain a smaller number, that is, the regurgitant volume.

Doppler echocardiography

Pulsed-wave Doppler

Significant valvar regurgitation creates a larger inflow volume across the valve in the subsequent cardiac cycle thereby increasing the velocity of atrioventricular early diastolic inflow. Consequently it is unlikely to have severe mitral regurgitation if the early diastolic inflow wave (E wave) is not elevated (>1.5 m/sec with normal pressure half-time in adults).

The characteristics of the regurgitant spectral display can also provide clues to the severity of the regurgitation. For example, in mild mitral or tricuspid regurgitation, the spectral recording of the jet has a soft density with a parabolic, rounded contour whereas in severe MR, the jet is dense with a triangular, early peaking velocity. In mild mitral regurgitation, pulmonary vein flow is normal with antegrade systolic flow. In contrast, in severe mitral regurgitation pulmonary vein systolic flow reversal may be present.

Color Doppler

Color flow Doppler is widely used to detect valvar regurgitation and to semiquantitatively assess its severity through measurement of the regurgitation jet width at the vena contracta, the regurgitant jet area in the atrium and by the assessment of flow convergence into the regurgitant orifice (Figure 6.13; Video 6.6).

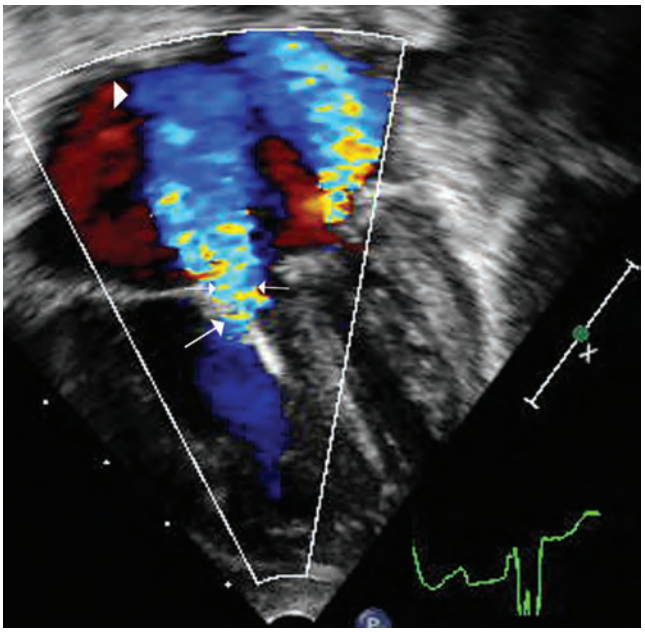


Figure 6.13 Severe right atrioventricular valve regurgitation in a child after repair of a complete atrioventricular septal defect. Depicted are several features used to assess valvar regurgitation. Proximal convergence is seen as the flow approaches the regurgitant orifice (single, thick arrow). The vena contracta, the narrowest portion of the jet is seen in the region of the regurgitant orifice (bounded by the two narrow arrows). Note that in this example it is difficult to accurately determine the location and width of the vena contracta. The exit jet area is large and reaches to the back of the atrium (arrowhead).

Jet area

A larger regurgitant jet area in the atrium implies more severe regurgitation. Some authors have proposed refining this method by using the ratio of the regurgitant jet area to atrial area as a measure of the severity of the regurgitation. This too is limited, however, as chronic severe regurgitation will lead to atrial enlargement and hence a lower jet-to-atrial area ratio. Regardless of whether the absolute jet area or its ratio to atrial area is measured, this parameter can be very misleading due to the many technical physiologic and anatomic factors that affect the size of the regurgitant jet area. The most important technical factors are the pulse repetition frequency (PRF) (Nyquist limit) and color gain. The jet area is inversely proportional to PRF and directly proportional to color gain; that is, the lower the Nyquist limit and the higher the gain, the larger the jet area. Therefore it is optimal for each lab to use standard settings and to use similar settings from one study to the next so that changes can be more readily appreciated. Gain should be set so that random color speckles are eliminated from nonmoving regions. Nonetheless, even with standardization, substantial error and variability can be introduced by the technical settings and it is unreliable to use jet area as the sole parameter for assessment of regurgitation severity. Moreover, eccentric, wall-hugging jets appear smaller than centrally directed jets of similar hemodynamic severity because they flatten against the atrial wall due to the previously detailed Coanda effect. When an eccentric jet is seen, a structural abnormality, often opposite to the jet direction, such as a prolapsing leaflet or cleft left atrioventricular valve, should be sought (Figure 6.14; Video 6.7).

Vena contracta

The vena contracta is the narrowest portion of a jet that occurs at or immediately downstream from the orifice. The CSA of the vena contracta represents a measure of the effective regurgitant orifice area (EROA), which is the narrowest area of actual flow. The vena contracta method has been used to determine severity of aortic regurgitation, mitral regurgitation, and in pediatric cardiology, the severity of tricuspid regurgitation in hypoplastic left heart syndrome [26–28]. In children, the ratio of the vena contracta to aortic valve diameter has been proposed as a measure of aortic regurgitation severity [29]. Nonetheless, if

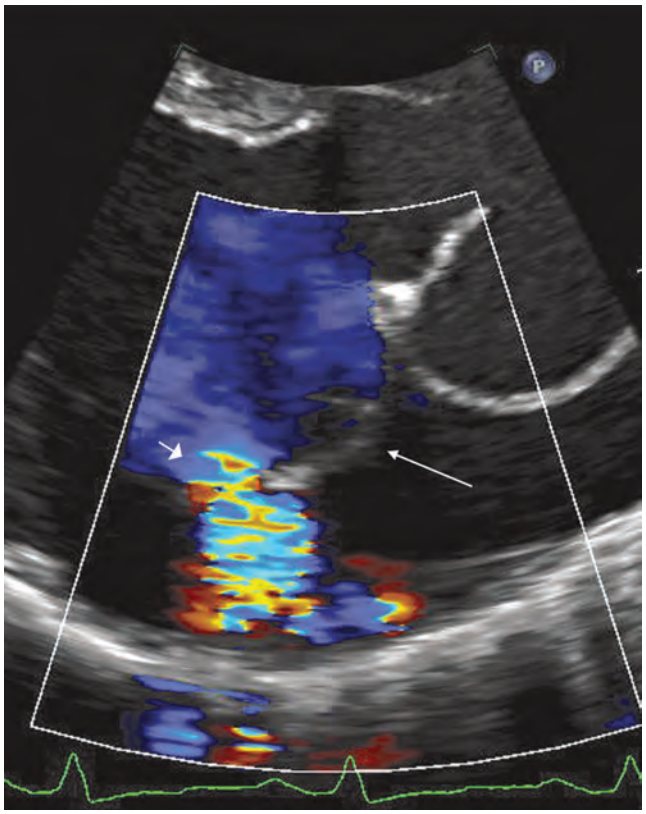


Figure 6.14 Mitral valve prolapse with mitral regurgitation. The prolapsing anterior leaflet (long arrow) prevents formation of a complete PISA hemisphere (short arrow) which complicates calculation of the mitral regurgitant volume by PISA. Although there are calculations that theoretically can correct for these factors, these are cumbersome, can be inaccurate and are not routinely used in pediatric laboratories. Note the eccentric posteriorly directed jet.

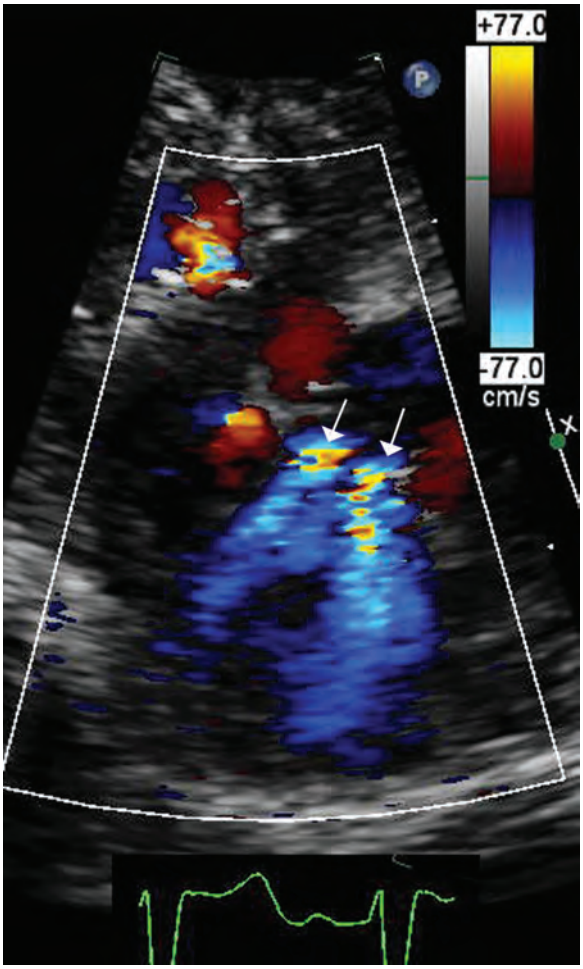


Figure 6.15 Two jets of left atrioventricular valve regurgitation in a child after repair of an atrioventricular septal defect. Theoretically the regurgitation severity can be assessed by summing the regurgitant volume from each jet based on the proximal convergence (arrows) or by summing the vena contracta of each individual jet. In practice this is rarely done in pediatric laboratories although these factors are qualitatively assessed by the reader and incorporated into the judgement of regurgitation severity.

the regurgitant orifice is dynamic, the vena contracta may change with changing hemodynamics or during the cardiac cycle [30]. Because the vena contracta has high velocities, it is less sensitive to technical factors than the regurgitant jet area. To image the vena contracta and to differentiate it from the more proximal flow acceleration and from the jet expansion distally, it may be necessary to angulate the transducer out of the regular imaging plane. Because the vena contracta is narrow its measurement is limited by the lateral resolution of color Doppler and small measurement errors can lead to a significant error in judging the severity of the regurgitation. Zoom mode can be used to better visualize the vena contracta and to facilitate more accurate measurement of its width. For optimal lateral and temporal resolution, the color flow sector should be adjusted to be as narrow as possible and depth as shallow as possible. The vena contracta method is also inaccurate when multiple jets are present, even though theoretically, the vena contracta of individual jets can be summed (Figure 6.15). Three-dimensional echocardiography has been proposed to assess the vena contracta area to increase measurement accuracy and to allow evaluation of jets where geometric assumptions may not be applicable [31]. The 3D dataset is manually cropped by an image plane perpendicularly oriented to the jet direction up to the narrowest cross-sectional area of the jet. The effective regurgitant orifice area (EROA)-3D is then measured by manual planimetry of the color Doppler signal in an "en face" view of the jet. This methodology has recently been demonstrated for children with aortic regurgitation [32].

Proximal isovelocity surface area (PISA), or flow convergence method

When flow converges on a narrow orifice it forms a flow pattern of a series of isovelocity lines of progressively higher velocity, which are used in PISA calculations (Figure 6.16; Video 6.8). The surface area of the PISA can be used to determine the flow

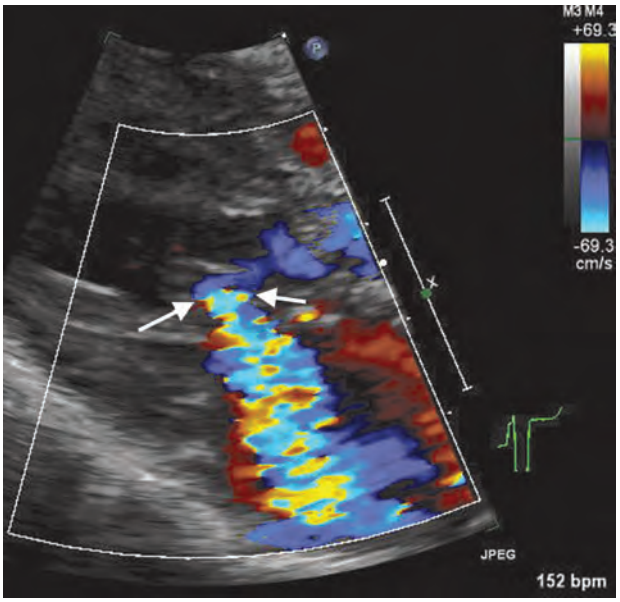


Figure 6.16 Left atrioventricular regurgitation in a patient after repair of atrioventricular septal defect. The blood approaching the relatively narrow regurgitant orifice forms lines of increasing velocity in the form of a hemisphere. The surface area of the hemisphere can be calculated from its radius, which is the distance from the regurgitant orifice to the aliasing boundary (Nyquist limit) (arrows) of 69.3 cm/s in this case. The product of the surface area of the hemisphere and Nyquist limit provides the regurgitant volume. Note, however, that it is difficult to determine exactly where the regurgitant orifice is, complicating this calculation. See text for further details.

volume through the valve and hence the severity of valvar regurgitation. For a circular orifice, the isovelocity lines converge on the orifice in the form a hemisphere. One may imagine this phenomenon as a crowd of spectators outside a sport stadium converging on a narrow turnstile to enter the stadium. Outside the stadium the spectators form a half circle and move progressively faster in concentric lines towards the narrow turnstile, akin to PISA. Once through the turnstile they are ejected into the stadium in a narrow stream (akin to the vena contracta), and then once inside the stadium they disperse after a variable distance (credits to Dr. Norman Silverman for this analogy). The surface area of the PISA is that of a hemisphere ($2\pi r^2$). The regurgitant flow volume is then calculated as flow velocity × PISA. The PISA method has been used to estimate aortic and mitral regurgitation with reasonable correlation with other methods. Practical steps to measure a regurgitant volume using the PISA method:

1 Turn on color Doppler through the regurgitant orifice;
2 Reduce the velocity scale (Nyquist limit) until an aliasing boundary forms near to the orifice;
3 Measure the distance between the aliasing boundary and the flow orifice (this is the radius (r) of the hemisphere);
4 Calculate the PISA surface area as $2\pi r^2$;
5 Calculate peak regurgitant flow as PISA × aliasing velocity. The aliasing velocity is the Nyquist limit where the aliasing boundary was measured.

The PISA method can also be combined with the continuity equation to calculate the regurgitant orifice area (ROA) as a measure of the regurgitation severity:

$$\text{ROA} = \text{regurgitant flow (by PISA)}/V_{\max}, \quad (6.6)$$

where $V_{\max}$ is the maximum flow velocity through the regurgitant orifice. The regurgitant volume can be calculated as ROA × TVI, where TVI is the time–velocity integral of the flow across the regurgitant orifice.

Although theoretically sound and attractive, in reality there are a number of important factors that limit the applicability of the PISA method in clinical practice. In a significant number of patients, aliasing boundaries proximal to the regurgitant orifice cannot be identified, either because the required flow conditions are not present or because the echocardiographic image is inadequate. When an aliasing boundary is identified, it is often difficult to identify the position of the regurgitant orifice in order to measure the distance between the orifice and the aliasing boundary (Figure 6.13). Furthermore, one of the assumptions that underlie the PISA calculation is that of a hemispheric PISA. However, often the shape of the PISA is distorted by proximal structures [33] such as the ventricular wall or a flail leaflet within the proximal convergence area that prevents formation of full hemispheric contours (Figure 6.14; Video 6.7). Even in unbounded flow, the PISA is hemispheric only for a specific portion of the flow convergence area with the flow contours flattening towards the orifice [34,35]. Using 3D echocardiography, one study found that the PISA shape was not hemispheric in almost 90% of children with mitral regurgitation [36]. Likewise, the regurgitant orifice is not always constant. For example, patients with mitral valve prolapse may have substantial variation in the ROA over the course of systole. Similarly, the tricuspid valve has a large ROA in early systole that nearly disappears by the end of systole. If there is significant variation in the ROA over the cardiac cycle, the calculation of the regurgitant volume using PISA will be inaccurate. Due to these substantial limitations, in many pediatric laboratories, PISA is not used as a routine technique to assess severity of regurgitation.

Other specific parameters for assessment of valvar regurgitation

Two additional parameters may be useful to assess the severity of aortic regurgitation. The aortic pressure half-time is obtained from the CW Doppler recording of reversed flow across the aortic valve in diastole and is measured as the time required for the peak velocity to decline by a factor of $1/\sqrt{2}$ (Figure 6.17). The time required for the aorta-to-left ventricle pressure gradient to fall is indicative of the regurgitation severity [37]. A shorter pressure half-time indicates more severe regurgitation with values less than 200–250 ms generally indicating severe regurgitation, between 200–400 moderate regurgitation, and higher than 400 ms, mild regurgitation. However, the pressure half-time is influenced by multiple factors other than the

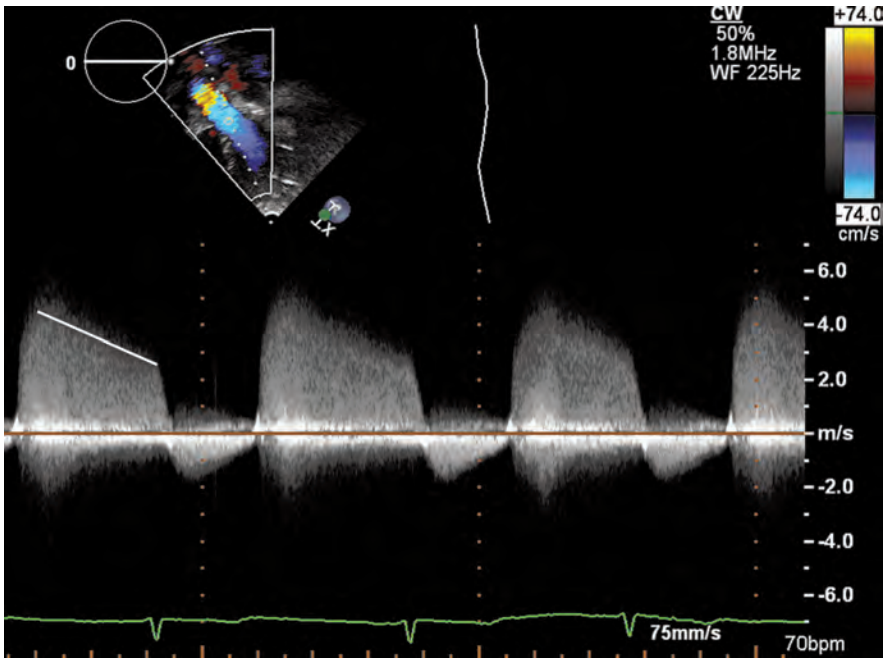


Figure 6.17 Continuous-wave spectral Doppler envelope of aortic regurgitation in a teenager with severe aortic regurgitation. Tracing of the pressure half-time slope is depicted by the white line.

severity of regurgitation, such as ventricular compliance and whether the regurgitation is acute or chronic. Acute aortic regurgitation is associated with much shorter pressure half-time values as the ventricle is not dilated and is less compliant. In chronic regurgitation where the ventricle has dilated and has become more compliant, the pressure half-time will be longer for the same degree of regurgitation. Likewise, systemic vascular resistance and medications that affect it will also affect the pressure half-time. In addition, measurements of slopes in echocardiography are subject to poor reproducibility [25].

As previously mentioned, when aortic regurgitation is hemodynamically significant, there will be flow reversal in the aortic arch and descending aorta [38]. Although the ratio of the reversed to forward flow velocity time integral has been proposed as a quantitative measure of the aortic regurgitant fraction, we use the presence of holo-diastolic flow reversal in the descending aorta as a qualitative, albeit very important measure of at least moderate aortic regurgitation (Figure 6.18; Video 6.9). Akin to this parameter, flow reversal in the pulmonary artery can be used to qualitatively judge the severity of pulmonary valve regurgitation. With mild pulmonary regurgitation there is no flow reversal in the pulmonary artery. Moderate pulmonary regurgitation is associated with flow reversal in the main pulmonary artery, while severe pulmonary regurgitation is associated with flow reversal in the branch pulmonary arteries [39]. Similar to the pressure half-time for aortic valve regurgitation, the pattern of the spectral Doppler envelope can assist in judging the severity of pulmonary regurgitation. When the regurgitation is severe, pressure between the pulmonary artery and RV equalizes rapidly resulting in a rapid down-sloping Doppler envelope. When regurgitation is mild, after an initial pressure peak in early diastole there will be a plateau before the velocity equalizes. The hemodynamics of valvar regurgitation has other important implications for patient management. Changes in the size of the regurgitant orifice have far more impact on the severity of regurgitation than changes in the pressure difference across the orifice. In fact, manipulation of blood pressure has minimal effect on regurgitant volume. For example, it is unusual for afterload reduction therapy to induce a fall of more than 10% in mean arterial pressure, and yet even this relatively robust clinical response would result in only a 3% fall in regurgitant volume. This may explain why use of medications that decrease left ventricular afterload such as angiotensin-converting enzyme receptor inhibitors may not significantly affect atrioventricular valve regurgitation.

It is apparent that one should use multiple parameters to judge the severity of regurgitant lesions as use of any individual parameter may be unreliable. In a given patient, the clinician's assessment by synthesizing the clinical status in combination with echo assessment of the ventricular response and echo parameters of the regurgitation severity will determine the management. In adults and adolescents, guidelines exist to assist the clinician with these decisions [40].

Hemodynamic assessment of flow through prosthetic valves

Echocardiographic evaluation of prosthetic valves is an extensive topic. Echocardiographic evaluation of the prosthetic valve begins before its implantation in assessing the indications for a prosthetic valve versus the prospects of repairing the native valve; determining the prospects for an appropriately sized prosthesis; and intraoperatively assessing its implantation. Following implantation, assessment of prosthesis function, pannus formation, thrombus and vegetations are part of the

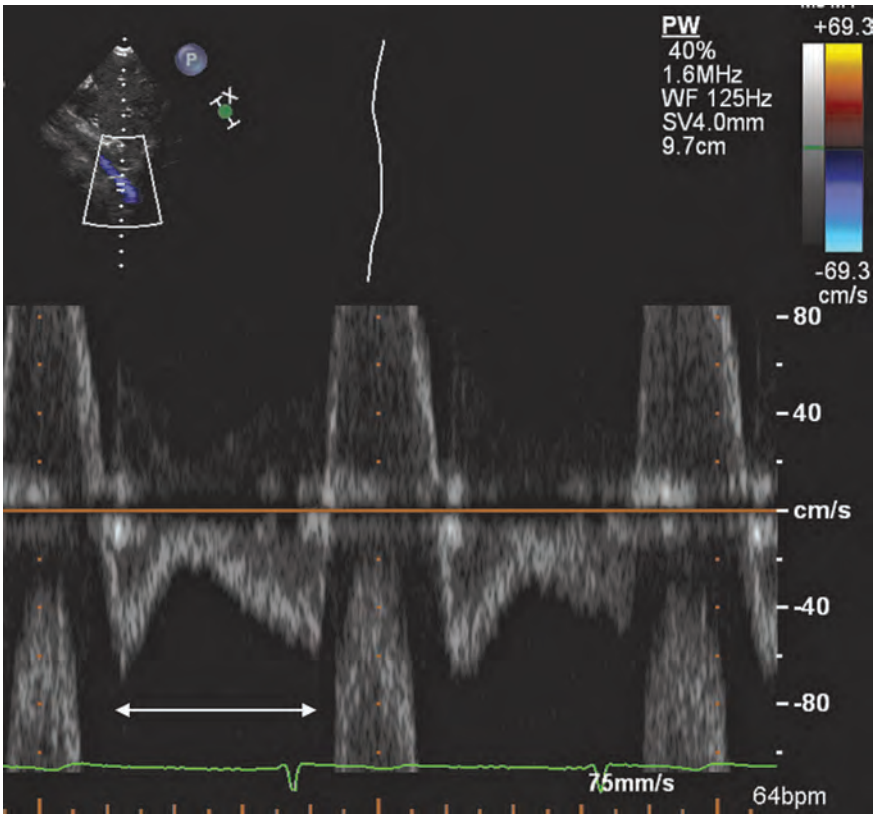
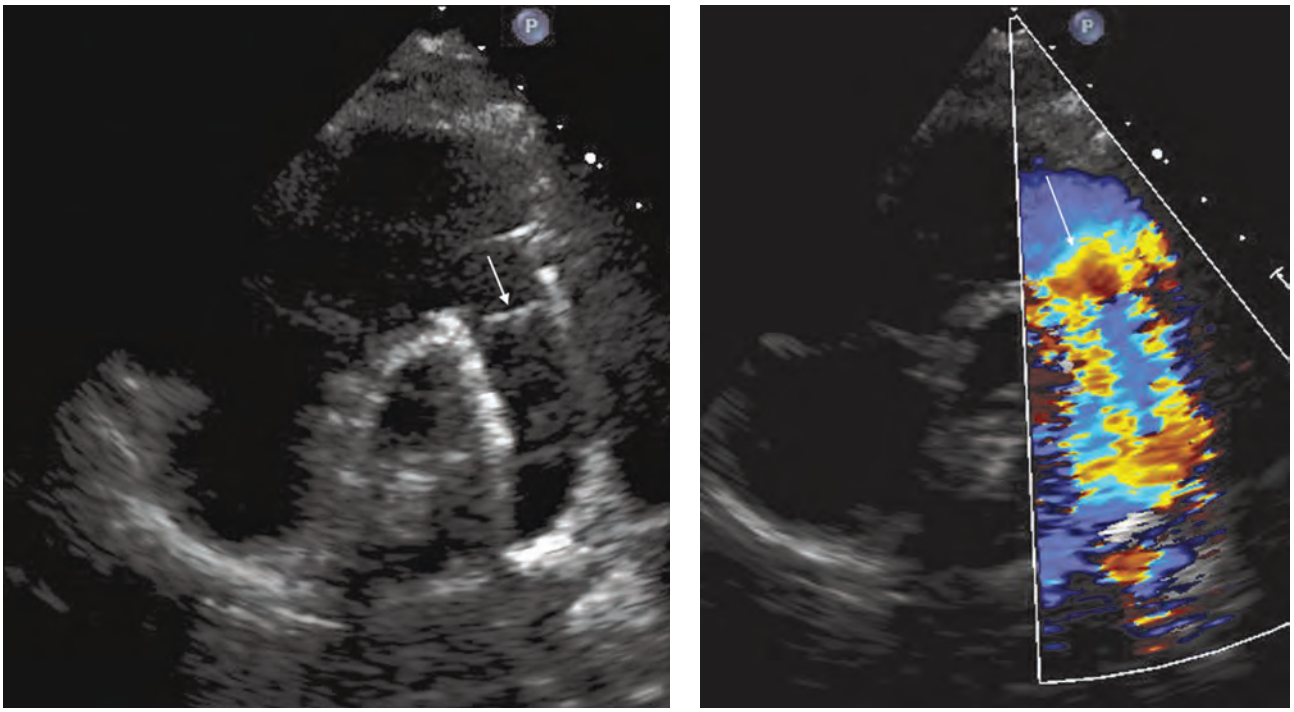


Figure 6.18 A pulsed-wave Doppler is placed in the descending aorta at the level of the diaphragm in a patient with aortic insufficiency. Holo-diastolic flow reversal is seen beneath the Doppler baseline (doubleheaded arrow) and signifies significant (at least moderate) aortic regurgitation.

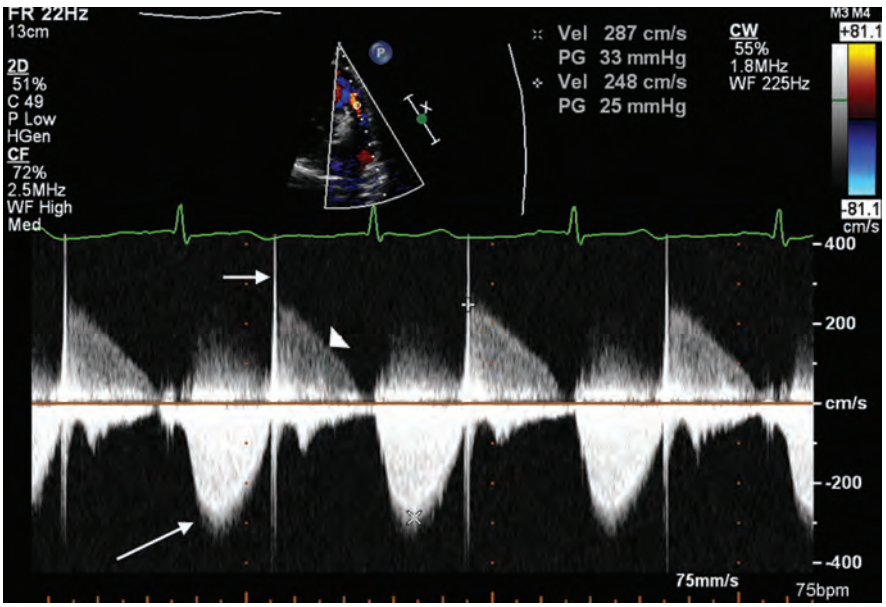
routine echocardiographic assessment of prosthetic valves. With the increase in catheter implantation of stented bioprosthetic valves in the pulmonary position in children with congenital heart disease and RVOT dysfunction, echocardiographic assessment of prosthetic valves in children is becoming more common (Figure 6.19a–c). In this section we will focus on the hemodynamic assessment of prosthetic valves. Prosthetic valves, either mechanical or bioprosthetic, differ in size, shape and number of orifices from native valves leading to differences in blood flow. These differences can affect hemodynamic assessment of prosthetic valves, which is often difficult. For example, a bileaflet prosthetic tilting disc valve has three orifices (Video 6.10). Flow is highest through the central rectangular orifice, and lower through the two peripheral semicircular orifices (Figure 6.20a; Video 6.11). However, the true net gradient through the valve is determined by flow through all three orifices. Therefore, sampling of flow through the central orifice will overestimate the true net gradient. In another example, in caged ball valves, flow travels around the occluding device rather than through a defined orifice complicating Doppler assessment. In these valves turbulence is created by the occluding ball in the center of the stream and by eddies of circulating backflow around the occluding ball leading to overestimation of pressure gradients through these valves. Assessment of the prosthetic valve with color Doppler flow can assist in determining the number of orifices and flow pattern through the valve. Pulsed- and continuous-wave Doppler can then be used to define the valve gradients in the same manner as for native valves. Prosthetic valves, especially in the inflow position may be seated differently from the native inflow and the blood flow can have eccentric orientation. Accordingly, the echocardiographic views may need to be modified to align the Doppler beam as closely as possible with the direction of flow (Figure 6.20b). As with native valves, multiple views should be obtained to ensure the highest velocity is recorded, especially in eccentric jets. A CW Doppler should be obtained and the peak and mean gradients reported (Figure 6.20c).

Prosthetic valves are inherently stenotic. The sewing ring may be too small relative to the flow volume through the valve, even if the valve functions well. This condition is termed prosthesis–patient mismatch and is a problem in growing children with an increasing stroke volume. Conversely, in infancy, the smallest available prosthetic valve size may be too large. In addition, the effective valve orifice is always smaller than the sewing ring, effectively increasing the stenosis. Even in stented bioprosthetic valves, the valve leaflets are less compliant than native leaflets, which increases resistance to flow. Over time, bioprosthetic leaflets tend to thicken and become fibrotic with the risk of increasing stenosis and regurgitation. Likewise, the flow profile through a bioprosthesis is often triangular and smaller than the anatomic valve area.

Pressure recovery also affects the hemodynamic assessment of gradients through prosthetic valves. This is most clinically relevant in the aortic position. Immediately distal to the prosthesis central orifice, flow is high and pressure has not yet



(a) (b)



(c)

Figure 6.19 Two-dimensional image of a stented bioprosthesis in the pulmonary position in a patient after surgical repair of tetralogy of Fallot **(a)**. The valve leaflets are in the closed position (arrow). The bright echos of the stent are visible. In systole there is mild flow acceleration starting at the valve leaflets **(b)**. The spectral envelope of a continuous Doppler signal **(c)** reveals a peak velocity of 287 cm/s translating into a peak gradient of 33 mmHg (long arrow). Above the baseline, there is mild pulmonary regurgitation (arrowhead). The linear echo of the prosthetic leaflet closure is apparent (short arrow).

recovered. Further downstream in the aorta, pressure recovery occurs thereby leading to a lower net gradient between the LV and aorta. Sampling close to the valve will therefore reflect a higher (albeit true) local gradient which overall overestimates the net physiologic LV to aorta gradient. As for native valves, pressure recovery will be larger with larger valve areas and in larger aortic roots.

The peak and mean gradient through the prosthetic valve can be obtained by Doppler, but different patterns may be observed depending on which opening in the valve is sampled.

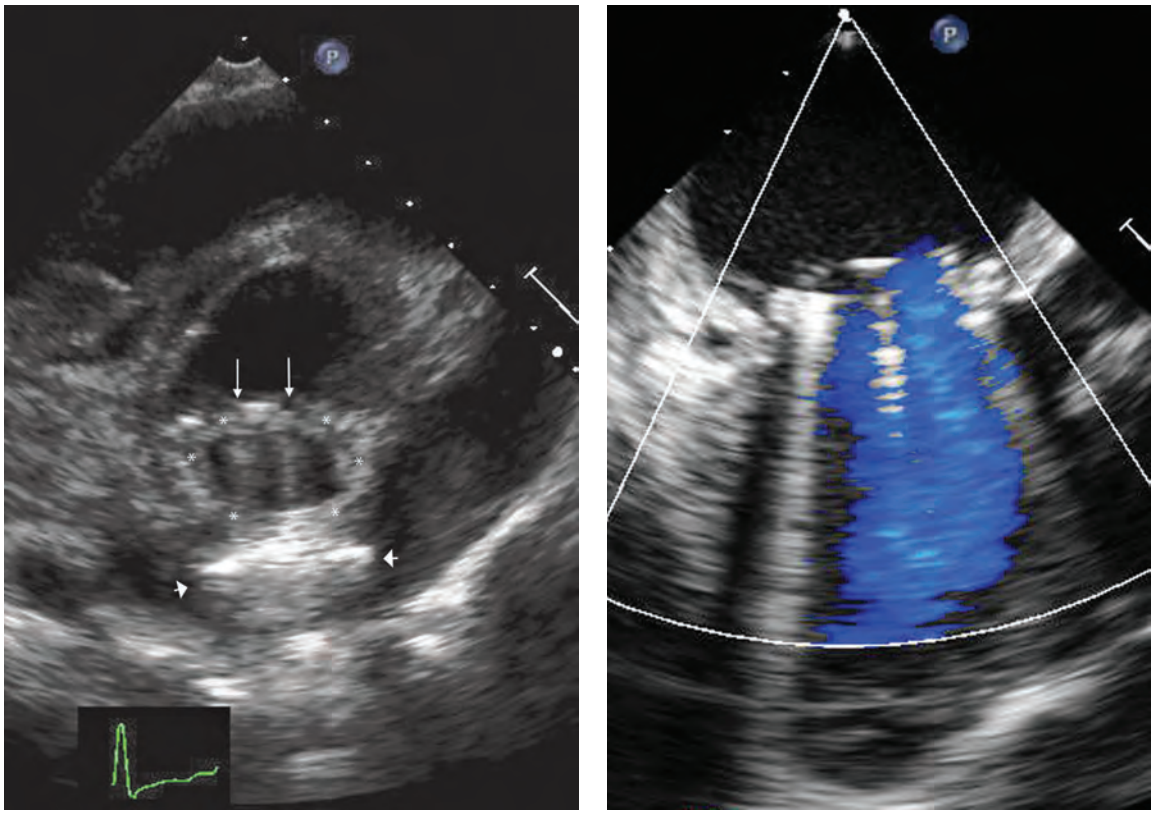


Figure 6.20 Two-dimensional diastolic image of a mechanical disc prosthesis in the mitral position **(a)**. The oval sewing ring is demarcated by the asterisks. The two discs are open and are seen as linear echogenicities (arrows). The central square orifice and two peripheral semi-oval orifices can be seen. A strong echogenic artefact from the device is seen posterior to the valve (arrowheads). In **(b)** a transesophageal echocardiographic mid-esophageal 4-chamber view shows two laminar inflow jets. The third jet is not visible in this plane. In **(c)** a spectral Doppler of the prosthetic inflow is seen taken from a transthoracic 4-chamber view. Note the strong linear echogenicities of the discs opening and closing (arrows). There is no obstruction to flow through the prosthesis with a mean gradient of 3 mmHg.

Gradients through prosthetic valves are usually higher than through native valves and depend on the type and size of the valve. For example, a 19 mm St. Jude prosthesis may normally have a peak flow velocity of 4.5 m/s, which is quite abnormal for a native aortic valve. Therefore, it is helpful to consult tables that report expected gradients through prosthetic valves according to their type and size. It is especially useful to record the baseline gradient after valve implantation so that changes over time can be assessed and recognized. For this purpose an adequate baseline study before discharge from the hospital and in the first 2–3 months after prosthesis implantation should be obtained. If an elevated or increasing gradient is detected the mechanism of stenosis should be evaluated and the motion of the valve occluding mechanism (most often two tilting discs in the mitral position (Video 6.10) should be evaluated. This can be facilitated using M-mode. In some children, assessment of the leaflet motion can be very difficult by transthoracic echocardiography due to the strong echos generated by the prosthesis (Figure 6.20a; Video 6.10) and difficult imaging windows in patients who have undergone repeated surgery. Transesophageal echo and especially cine fluoroscopy are useful to confirm opening and closing of both discs, especially when thrombus is suspected. As for native valves, the physiologic consequences of valvar stenosis are central to clinical management. For example, when there is an increased gradient across a mitral prosthesis, RV systolic pressures should be assessed to evaluate whether pulmonary pressures are increased. Although the continuity equation can be used to determine the effective orifice area of prosthetic valves, as for native valves, this method is not usually used in pediatric laboratories. Rather, changes in the valve gradient on serial assessment, combined with assessment of effects on cardiac and patient status is more practical. An additional practical approach to assessing gradients through aortic prostheses is use of the Doppler velocity index: the ratio between the outflow tract velocity and the maximal velocity through the valve. Because all prosthetic valves are stenotic to some degree, the expected ratio is less than 1 (usually between 0.35–0.5), use of the TVI has been proposed in place of the peak velocity to avoid errors that can occur in the peak velocity in small or bileaflet valves as previously discussed. Whether the peak velocity or TVI is used, the higher the Doppler velocity index, the larger the valve area. Conversely, the smaller the index, the smaller the valve area. One advantage of using the Doppler velocity index is that as a ratio it corrects variations in flow rates and the patient serves as his/ her own reference. In adult studies the pressure half-time has been proposed to assess prosthetic mitral valve stenosis, with the same limitations pertaining to native valves such as the effects of chamber compliance. In adults, the mitral valve area is often approximated by the pressure half-time principle using the empirical formula of

$$\text{mitral valve area (cm}^2\text{)} = 220/\text{pressure half-time (ms)}. \quad (6.7)$$

Although this method can be applied to prosthestic valves in the mitral position, it is not commonly used in pediatric laboratories even for native valves, and will overestimate the effective valve area for prosthetic valves. Likewise, this method applies only when the valve is actually stenotic and cannot be used to follow nonstenotic valves. Nonetheless, a prolonged pressure half-time in relation to previous measurements in the same patient suggests increasing stenosis or obstruction.

In addition to being inherently stenotic, prostheses are also inherently regurgitant. Indeed, some degree of regurgitation may be part of the valve design in order to "wash" the valve and reduce the risk of thrombus. Assessment of valve regurgitation and visualization of the regurgitant jet can be complicated by shadowing and reverberations from the prosthesis. The pattern of "normal" prosthetic regurgitation is dependent on the type of valve and must be distinguished from abnormal regurgitation. In general there are two categories of normal prosthetic valve regurgitation. Closure backflow is the mechanism by which regurgitant flow closes the valve in early systole or diastole (depending on whether the valve is an inflow or outflow valve), and ends once the occluding mechanism is seated in the sewing ring. Backflow leakage occurs after the discs have closed or occluding mechanism is seated in the sewing ring and is usually seen as small puffs of regurgitation between the valve discs and seating ring (Figure 6.21; Video 6.12). These backflow jets are short in duration, narrow, symmetric in bileaflet prostheses, and of low velocity. In contrast, regurgitation between the

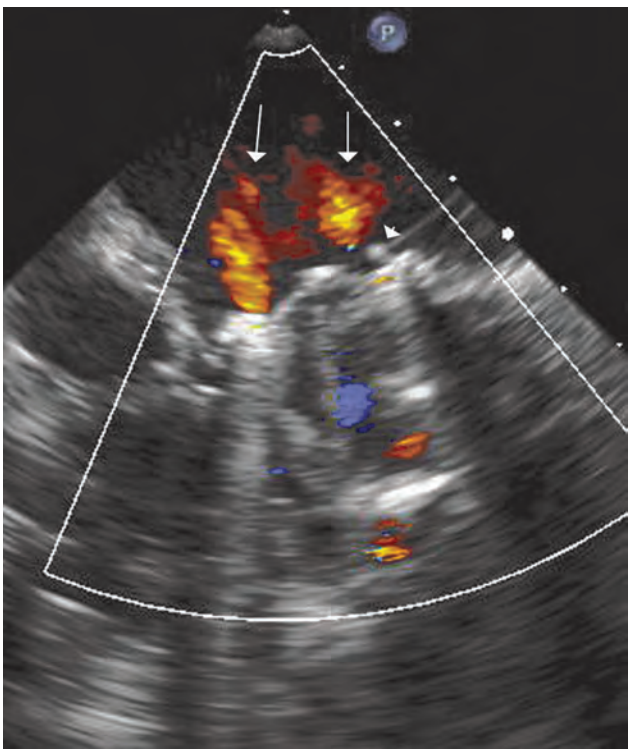


Figure 6.21 Color Doppler in a 4-chamber view demonstrating normal seating puffs (arrows) of mild prosthetic regurgitation. These are small in area and clearly originate between the discs and the sewing ring (arrowhead).

Table 6.3 Assessment of prosthetic valves

- Echocardiographic evaluation of the prosthetic valve is important before, during, and after its implantation.
- Prosthetic valves differ in size, shape, and number of orifices from native valves complicating hemodynamic assessment. Imaging difficulties further hinder assessment of prosthetic valve function.
- Within known pitfalls and limitations, the Doppler techniques to assess prosthetic valve hemodynamics are similar to that for native valves.
- Various factors cause prosthetic valves to be inherently stenotic as well as regurgitant.
- Cine fluoroscopy should be used to confirm opening and closing of tilting disc prostheses when thrombus is suspected.
- Changes in the valve gradient on serial assessment, combined with assessment of effects on cardiac and patient status is the most practical way to assess prosthesis function and stenosis.
- Normal prosthesis regurgitation jets are short in duration, narrow, symmetric in bileaflet prostheses, and of low velocity. Regurgitation between the seating ring and tissue is abnormal and should be suspected when there is more than a mild degree of regurgitation such as that extending far into the receiving chamber, wide, large, high velocity, asymmetrical (across the valve area), eccentric and wall-hugging jets.

seating ring and tissue is abnormal and implies valve dehiscence or dislodgement. Abnormal regurgitation should be suspected when there is more than a mild degree of regurgitation such as that which extends far into the receiving chamber, wide, large, high velocity, asymmetrical (across the valve area), eccentric and wall-hugging jets. Color M-mode can help in determining the timing and duration of both native valve and prosthesis regurgitation. Normal bioprosthetic valves also often exhibit mild central regurgitation. The majority of patients after transcatheter implantation of a bioprosthetic valve in the right ventricular outflow tract position show no or trivial pulmonary regurgitation by echocardiography over the first 2 years [41]. The key points in the assessment of prosthetic valves are summarized in Table 6.3.

Acknowledgment

I would like to acknowledge the contribution of Steven Colan, MD who wrote the "Hemodynamics assessment" chapter in the previous edition of this book. That material forms the basis for the current document.

Videos

To access the videos for this chapter, please go to www.laiecho.com.

Video 6.1 Color Doppler flow across a stenotic aortic valve sampled from the subcostal coronal view. The jet across the aortic valve is oriented towards the wall of the aorta. The high flow velocity creates a region of low pressure adjacent to the vessel wall. At the inner curvature of the aorta there is slower flow velocity with development of flow reversal (orange flow towards the transducer).

Video 6.2 Color Doppler flow on an apical 3-chamber (long-axis) view depicting left atrioventricular valve regurgitation in a child after repair of an atrioventricular septal defect. The eccentric regurgitant jet [travelling away from the transducer (blue color)] tracks along the left atrial posterior wall due to the Coanda effect.

Video 6.3 Subcostal sagittal view with color Doppler flow. There is flow acceleration into the right ventricular outflow tract from right ventricular muscle bundles. However, interrogating the gradient across this region may yield inaccurate measurements due to flow from a closely associated perimembranous ventricular septal defect. The two jets would have to be clearly differentiated in order to reliably interrogate the gradient across the right ventricular outflow tract.

Video 6.4 Two-dimensional subcostal sagittal view of the right ventricle and right ventricular outflow tract in an infant with tetralogy of Fallot.

Video 6.5 Color flow across the right ventricular outflow tract. The ventricular septal defect is seen. Note the dynamic narrowing of the right ventricular outflow tract and the flow acceleration that begins in the infundibulum, well below the pulmonary valve. Together with the narrow pulmonary valve this creates the double-contour spectral Doppler shown in Figure 6.11.

Video 6.6 Subcostal coronal echo showing color Doppler across the aortic valve in a child with severe aortic regurgitation. Note the proximal convergence of the regurgitant flow which forms isovelocity lines (PISA) as it approaches the regurgitant orifice from the aorta. The vena contracta can be seen as the narrowest region of the regurgitant jet at the regurgitant orifice. The relatively large width of the vena contracta in this patient is consistent with severe regurgitation. The regurgitant jet is large and extends far into the left ventricle. Note that the jet is eccentric and the regurgitation is more severe than depicted by jet area alone.

Video 6.7 Mitral valve prolapse with mitral regurgitation in an adolescent with Marfan syndrome. The prolapsing anterior leaflet prevents formation of a complete PISA hemisphere which complicates calculation of the mitral regurgitant volume by PISA. Although there are calculations that theoretically can correct for these factors, these are cumbersome, can be inaccurate and are not routinely used in pediatric laboratories. Note the eccentric posteriorly directed jet.

Video 6.8 Tricuspid regurgitation in a child with pulmonary atresia and intact ventricular septum. Note the proximal isovelocity surface acceleration as the regurgitant jet approaches the regurgitant orifice. Lines of increasing velocity are seen as aliasing of the color flow (dark blue to light blue). The surface area of the PISA hemisphere times the Nyquist limit (73.2 cm/s in this example) can be used to approximate the regurgitant volume.

Video 6.9 Prominent diastolic flow reversal (blue color depicting flow away from the transducer) in the abdominal aorta at the level of the diaphragm in a child with aortic regurgitation. The

presence of flow reversal in the abdominal aorta is consistent with at least a moderate degree of regurgitation.

Video 6.10 Tilting disc prosthesis in the mitral position seen from a parasternal short-axis view. The motion of both discs is clearly seen. When open, this prosthesis forms three orifices, a central square orifice flanked by two semicircular orifices. Note the strong echogenic artifact created by the metallic prosthesis behind the valve.

Video 6.11 Color flow Doppler through a tilting disc prosthesis in the mitral position seen from an apical view. The three inflow jets are seen as orange flow depicting flow towards the transducer. There is flow acceleration as the flow traverses the valve orifices.

Video 6.12 Color Doppler in a 4-chamber view during transesophageal echocardiography demonstrating normal seating puffs of mild prosthetic regurgitation seen as small orange jets entering the left atrium. These originate between the discs and the sewing ring.

References

1 Poulsen JK, Kim WY. Measurement of volumetric flow with no angle correction using multiplanar pulsed Doppler ultrasound. *IEEE Trans Biomed Eng* 1996;**43**:589–599.

2 Shiota T, Jones M, Aida S, et al. Calculation of aortic regurgitant volume by a new digital Doppler color flow mapping method: an animal study with quantified chronic aortic regurgitation. *J Am Coll Cardiol* 1997;**30**:834–842.

3 Hyun S, Kleinstreuer C, Archie JP, Jr. Computational particle-hemodynamics analysis and geometric reconstruction after carotid endarterectomy. *Comput Biol Med* 2001;**31**:365–384.

4 Myers LJ, Capper WL. Analytical solution for pulsatile axial flow velocity waveforms in curved elastic tubes. *IEEE Trans Biomed Eng* 2001;**48**:864–873.

5 Baumgartner H, Schima H, Kuhn P. Value and limitations of proximal jet dimensions for the quantitation of valvular regurgitation: an in vitro study using Doppler flow imaging. *J Am Soc Echocardiogr* 1991;**4**:57–66.

6 Tribouilloy CM, Enriquez-Sarano M, Bailey KR, et al. Assessment of severity of aortic regurgitation using the width of the vena contracta: a clinical color Doppler imaging study. *Circulation* 2000;**102**:558–564.

7 Ishii M, Jones M, Shiota T, et al. Quantifying aortic regurgitation by using the color Doppler-imaged vena contracta: a chronic animal model study. *Circulation* 1997;**96**:2009–2015.

8 Mascherbauer J, Rosenhek R, Bittner B, et al. Doppler echocardiographic assessment of valvular regurgitation severity by measurement of the vena contracta: an in vitro validation study. *J Am Soc Echocardiogr* 2005;**18**:999–1006.

9 Tribouilloy C, Shen WF, Quere JP, et al. Assessment of severity of mitral regurgitation by measuring regurgitant jet width at its origin with transesophageal Doppler color flow imaging. *Circulation* 1992;**85**:1248–1253.

10 Evangelista A, del Castillo HG, Calvo F, et al. Strategy for optimal aortic regurgitation quantification by Doppler echocardiography: agreement among different methods. *Am Heart J* 2000;**139**:773–781.

11 Garcia D, Pibarot P, Dumesnil JG, et al. Assessment of aortic valve stenosis severity: A new index based on the energy loss concept. *Circulation* 2000;**101**:765–771.

12 Richards KE, Deserranno D, Donal E, et al. Influence of structural geometry on the severity of bicuspid aortic stenosis. *Am J Physiol Heart Circ Physiol* 2004;**287**:H1410–1416.

13 Gilon D, Cape EG, Handschumacher MD, et al. Effect of three-dimensional valve shape on the hemodynamics of aortic stenosis: three-dimensional echocardiographic stereolithography and patient studies. *J Am Coll Cardiol* 2002;**40**:1479–1486.

14 Silverman NH. *Pediatric Echocardiography*. Baltimore, MD: Williams and Wilkins, 1993.

15 Galie N, Hinderliter AL, Torbicki A, et al. Effects of the oral endothelin-receptor antagonist bosentan on echocardiographic and Doppler measures in patients with pulmonary arterial hypertension. *J Am Coll Cardiol* 2003;**41**:1380–1386.

16 Gorcsan J, 3rd, Abraham T, Agler DA, et al. Echocardiography for cardiac resynchronization therapy: recommendations for performance and reporting–a report from the American Society of Echocardiography Dyssynchrony Writing Group endorsed by the Heart Rhythm Society. *J Am Soc Echocardiogr* 2008;**21**:191–213.

17 Thomas JD, Popovic ZB. Intraventricular pressure differences: a new window into cardiac function. *Circulation* 2005;**112**:1684–1686.

18 Gjertsson P, Caidahl K, Svensson G, et al. Important pressure recovery in patients with aortic stenosis and high Doppler gradients. *Am J Cardiol* 2001;**88**:139–144.

19 Heinrich RS, Fontaine AA, Grimes RY, et al. Experimental analysis of fluid mechanical energy losses in aortic valve stenosis: importance of pressure recovery. *Ann Biomed Eng* 1996;**24**:685–694.

20 Baumgartner H, Stefenelli T, Niederberger J, et al. "Overestimation" of catheter gradients by Doppler ultrasound in patients with aortic stenosis: a predictable manifestation of pressure recovery. *J Am Coll Cardiol* 1999;**33**:1655–1661.

21 Fang L, Hsiung MC, Miller AP, et al. Assessment of aortic regurgitation by live three-dimensional transthoracic echocardiographic measurements of vena contracta area: usefulness and validation. *Echocardiography* 2005;**22**:775–781.

22 Vlahos AP, Marx GR, McElhinney D, et al. Clinical utility of Doppler echocardiography in assessing aortic stenosis severity and predicting need for intervention in children. *Pediatr Cardiol* 2008;**29**:507–514.

23 Colan S. Ventricular function in pressure overload lesions. In: Fogel MA (ed.) *Ventricular Function and Blood Flow in Congenital Heart Disease*. Malden, MA: Blackwell Publishing, 2005, pp. 187–204.

24 Enriquez-Sarano M, Bailey KR, Seward JB, et al. Quantitative Doppler assessment of valvular regurgitation. *Circulation* 1993;**87**:841–848.

25 Colan SD, Shirali G, Margossian R, et al. The ventricular volume variability study of the Pediatric Heart Network: study design and impact of beat averaging and variable type on the reproducibility of echocardiographic measurements in children with chronic dilated cardiomyopathy. *J Am Soc Echocardiogr* 2012;**25**:842–854.e846.

26 Perry GJ, Helmcke F, Nanda NC, et al. Evaluation of aortic insufficiency by Doppler color flow mapping. *J Am Coll Cardiol* 1987;**9**:952–959.

27 Hall SA, Brickner ME, Willett DL, et al. Assessment of mitral regurgitation severity by Doppler color flow mapping of the vena contracta. *Circulation* 1997;**95**:636–642.

28 Ohye RG, Sleeper LA, Mahony L, et al. Comparison of shunt types in the Norwood procedure for single-ventricle lesions. *N Engl J Med* 2010;**362**:1980–1992.

29 Tani LY, Minich LL, Day RW, et al. Doppler evaluation of aortic regurgitation in children. *Am J Cardiol* 1997;**80**:927–931.

30 Kizilbash AM, Willett DL, Brickner ME, et al. Effects of afterload reduction on vena contracta width in mitral regurgitation. *J Am Coll Cardiol* 1998;**32**:427–431.

31 Marsan NA, Westenberg JJ, Ypenburg C, et al. Quantification of functional mitral regurgitation by real-time 3D echocardiography: comparison with 3D velocity-encoded cardiac magnetic resonance. *JACC Cardiovasc Imaging* 2009;**2**:1245–1252.

32 Bharucha T, Fernandes F, Slorach C, et al. Measurement of effective aortic valve area using three-dimensional echocardiography in children undergoing aortic balloon valvuloplasty for aortic stenosis. *Echocardiography* 2012;**29**:484–491.

33 Anayiotos AS, Fan P, Perry GJ, et al. Analysis of the proximal orifice flowfield under pulsatile flow conditions and confining wall geometry: implications in valvular regurgitation. *Echocardiography* 1998;**15**:219–232.

34 Rodriguez L, Anconina J, Flachskampf FA, et al. Impact of finite orifice size on proximal flow convergence. Implications for Doppler quantification of valvular regurgitation. *Circ Res* 1992;**70**:923–930.

35 Nozaki S, Shandas R, DeMaria AN. Requirement for accurate measurement of regurgitant stroke volume by the combined continuous-wave Doppler and color Doppler flow convergence method. *Am Heart J* 1997;**133**:19–28.

36 Ziani AB, Latcu DG, Abadir S, et al. Assessment of proximal isovelocity surface area (PISA) shape using three-dimensional echocardiography in a paediatric population with mitral regurgitation or ventricular shunt. *Arch Cardiovasc Dis* 2009;**102**:185–191.

37 Teague SM, Heinsimer JA, Anderson JL, et al. Quantification of aortic regurgitation utilizing continuous wave Doppler ultrasound. *J Am Coll Cardiol* 1986;**8**:592–599.

38 Reimold SC, Maier SE, Aggarwal K, et al. Aortic flow velocity patterns in chronic aortic regurgitation: implications for Doppler echocardiography. *J Am Soc Echocardiogr* 1996;**9**:675–683.

39 Goldberg SJ, Allen HD. Quantitative assessment by Doppler echocardiography of pulmonary or aortic regurgitation. *Am J Cardiol* 1985;**56**:131–135.

40 Nishimura RA, Carabello BA, Faxon DP, et al. ACC/AHA 2008 guideline update on valvular heart disease: focused update on infective endocarditis: a report of the American College of Cardiology/American Heart Association Task Force on Practice Guidelines: endorsed by the Society of Cardiovascular Anesthesiologists, Society for Cardiovascular Angiography and Interventions, and Society of Thoracic Surgeons. *Circulation* 2008;**118**:887–896.

41 McElhinney DB, Hellenbrand WE, Zahn EM, et al. Short- and medium-term outcomes after transcatheter pulmonary valve placement in the expanded multicenter US melody valve trial. *Circulation* 2010;**122**:507–516.

42 Alkon J, Humpl T, Manlhiot C, et al. Usefulness of the right ventricular systolic to diastolic duration ratio to predict functional capacity and survival in children with pulmonary arterial hypertension. *Am J Cardiol* 2010;**106**:430–436.

CHAPTER 7

Systolic Ventricular Function

Luc Mertens and Mark K. Friedberg
The Labatt Family Heart Center, The Hospital for Sick Children, The University of Toronto, Toronto, ON, Canada

Introduction

Evaluation of systolic function is an essential part of every echocardiographic examination. Too often this is based on subjective evaluation of global and regional myocardial function. Various echocardiographic techniques allow quantification of ventricular performance. However, the acquisition and interpretation of the various measurements can be challenging especially in patients with congenital heart disease due to variability in ventricular size, geometry, and loading conditions. In this chapter we review the echocardiographic assessment of left and right ventricular (LV and RV, respectively) systolic function.

The mechanics of cardiac systolic function

The heart is a volume pump that must generate sufficient cardiac output to provide oxygen supply to the tissues commensurate with the oxygen demand. Cardiac pump function is dependent on active force development in the myocytes resulting in pressure development in the ventricle. Once the semilunar valve opens, myocardial fiber shortening and wall deformation leads to ejection of the blood from the ventricle. Hence, cardiac function can be assessed by studying the relationship between force development and myocardial deformation at the different levels of cardiac organization: the myocyte, myocardial wall, and whole ventricle, as illustrated in Figure 7.1 [1]. At the myocyte, or fiber, level, sarcomere activation results in active myocardial force development and fiber shortening. At the level of the myocardial wall, segmental force development increases regional wall stress and causes myocardial shortening and thickening during ejection. On the ventricular level, the increase in ventricular cavity pressure above aortic or pulmonary pressure during early systole leads to semilunar valve opening. The subsequent contraction of the myocardial segments results in the displacement of blood volume. The relationship between cavity pressure changes and volume changes has been studied invasively by pressure-volume loops. The end-systolic pressure–volume relationship, or elastance, is considered the gold standard for evaluating contractile function as this parameter corrects for loading conditions, thereby representing intrinsic myocardial contractility.

Fiber organization and wall mechanics

The complex structural organization of myofibers in different layers is one of the basic determinants of cardiac mechanics. In the normal heart sarcomere shortening is approximately 15%. This relatively small shortening percentage results in a 35–40% wall thickening and ejection of 55–60% of LV blood volume in each systole [2,3]. In contrast to skeletal muscle fibers, cardiac fibers do not assemble in parallel arrays but bifurcate and recombine to form a complex three-dimensional (3D) network. In the subepicardium, myofibers are organized in a left-handed obliquely oriented spiral, changing to a more circumferential orientation in the LV mid-wall and to a right-handed spiral of more obliquely and longitudinally oriented fibers in the subendocardial layer. Myocardial function is most commonly described in a spatial reference frame of the three major axes (longitudinal, circumferential, and radial; Figure 7.2). The complex 3D myocardial fiber organization results in significant fiber interaction and shear forces during systole. When myofibers shorten and thicken they compress each other. This process, called cross-fiber shortening, is responsible for the amplification of the effects of myofiber shortening, thickening, and twisting. In the LV, the mid-wall layer is the most prominent explaining the predominant circumferential shortening and radial thickening in the LV. The more longitudinally oriented subepicardial and subendocardial fibers cause longitudinal shortening with displacement of the atrioventricular annular plane in the direction of the relatively stationary apex. Radial thickening results from the combined effects of circumferential and longitudinal shortening. While in the LV circumferential shortening predominates during ejection, in the RV longitudinal shortening is the dominant myocardial motion during ejection. In the LV, the opposite spiraling of the oblique subendocardial and subepicardial

Echocardiography in Pediatric and Congenital Heart Disease: From Fetus to Adult, Second Edition. Edited by Wyman W. Lai, Luc L. Mertens, Meryl S. Cohen and Tal Geva.
© 2016 John Wiley & Sons, Ltd. Published 2016 by John Wiley & Sons, Ltd.
Companion website: www.lai-echo.com

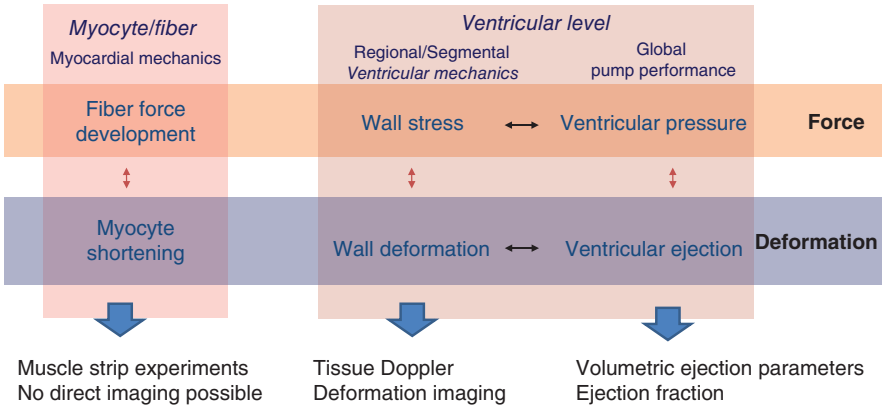


Figure 7.1 Cardiac function can be studied at different levels (myocyte, segment, ventricle as a whole). At each level force development results in myocardial deformation resulting in ventricular output.

fibers cause a torsional motion of the heart caused by counterclockwise rotation at the apex (Video 7.1) and clockwise rotation at the base (Video 7.2) when viewed from the apex. This wringing motion of the heart contributes to cardiac output and is an important component of cardiac mechanics. For a detailed overview on the basics of cardiac mechanics related to echocardiography, we refer the reader to two comprehensive reviews on the topic [4,5]. An understanding of cardiac mechanics is required to understand myocardial deformation imaging using newer speckle-tracking echocardiography (STE) technologies [6].

Cardiac function at the ventricular level

Global ventricular performance is the ability of the heart to develop force and deform so that it can eject blood. Ventricular performance can be assessed by measuring the stroke volume, which is the blood volume ejected by the heart with each heartbeat. The resulting cardiac output is the product of stroke volume and heart rate. Cardiac output depends on preload, afterload, heart rate, and intrinsic contractility. *Preload* is the load present at end-diastole before the onset of cardiac contraction. It is best defined in the isolated muscle strip model as end-diastolic fiber length. Through the Frank–Starling relationship, up to a certain point, higher preload results in higher force generation. Consequently, an acute increase in preload leads to increased systolic function and increased stroke volume while reduced preload leads to lower stroke volume and ejection fraction (Frank–Starling relationship). In the intact organ end-diastolic fiber length cannot be measured and LV end-diastolic volume or pressure are usually used as surrogate markers, albeit imperfect, for fiber length. In patients with chronic volume load, end-diastolic volume is an inaccurate measurement of preload as ventricular remodeling with eccentric hypertrophy changes the resting length of the myofibers and reduces end-diastolic fiber stress. In patients with a large left-to right shunt eccentric remodeling can normalize preload. Therefore, preload and volume loading should not be confused. Likewise, end-diastolic pressure does not accurately reflect preload as it is influenced by ventricular compliance and does not directly reflect fiber length. For example, in a stiffer ventricle a higher end-diastolic pressure does not necessarily represent a higher preload.

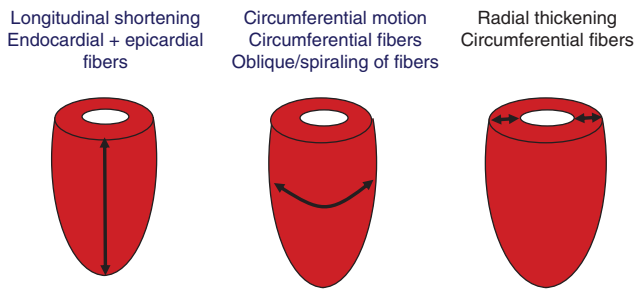


Figure 7.2 Myocardial fiber orientation and myocardial deformation. Longitudinal fibers cause longitudinal shortening; circumferential fibers cause circumferential shortening and radial thickening. Spiraling of the fibers is responsible for the rotational motion with clockwise rotation of the base and counterclockwise motion of the apex.

Afterload in an isolated muscle strip is the force resisting shortening after the onset of systole. Increased afterload reduces myocardial shortening which should be taken into account when interpreting systolic functional indices especially during the ejection phase. Important determinants of afterload are peak arterial pressure, arterial compliance, and vascular resistance. In the intact organ afterload is best defined as the resistance against which the ventricle contracts, or the wall stress [7]. Wall stress is determined by intracavitary pressure, cavity dimension, and wall thickness (Laplace's law; Figure 7.3):

$$\text{wall stress} = \text{pressure} \times \text{radius}/(2 \times \text{wall thickness}).$$

Wall stress varies throughout systole. Peak systolic wall stress is the highest wall stress during systole and is the trigger for the development of concentric hypertrophy. Total systolic wall stress (time–stress integral) determines oxygen consumption. End-systolic wall stress is the afterload at the end of systole at the time of aortic valve closure and determines the degree of total systolic shortening. Wall stress is a force, which means that it can be considered as a vector with components in different

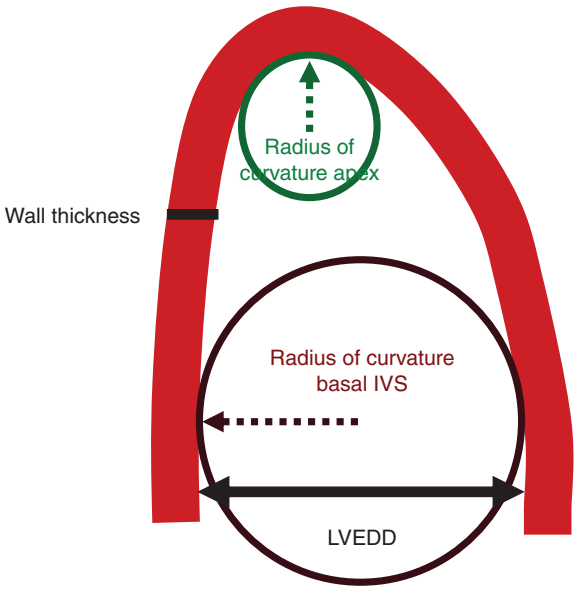


Figure 7.3 Definition of wall stress by the Laplace formula. Global LV wall stress increases with intracavitary pressure and with an increase of left ventricular end-diastolic dimension (LVEDD), and with decrease of wall thickness. Regional wall stress is influenced by the curvature of the wall defined by the radius of curvature. This is the radius of the circle that fits the local wall curvature. At the apex of the radii of curvature are small myofibers resulting in lower local wall stress. The flat wall at the base of the interventricular septum has the largest radius of curvature resulting in higher wall stress.

directions. The cardiac coordinate system can be used as the reference with circumferential stress (short axis), meridional stress (long axis), and radial stress (transmural) as the 3D stress vector components. However, due to the organization and orientation of the myofibers, stress on the fibers is not identical to stress in the direction of the cardiac coordinate system [7]. Therefore, although ideally fiber stress is the best parameter to reflect afterload it is difficult to measure. Consequently, ventricular systolic pressure is often used as a surrogate for afterload. However, this is a gross simplification as pressure is only one of several parameters in the Laplace formula. An acute increase in systolic pressure will result in an acute increase in wall stress but chronic pressure loading will cause concentric ventricular remodeling. This reduces wall stress and thus afterload [8]. As cavity size influences wall stress, ventricular dilatation in the absence of a concentric hypertrophic response increases afterload [9,10]. The diminished mass-to-volume ratio increases fiber stress throughout systole. As such, depressed contractility resulting in LV dilatation increases afterload even when blood pressure is normal or reduced. Because of concentric remodeling, it is important to distinguish between chronic pressure loading and changes in afterload.

Beyond preload and afterload, *heart rate* is an important determinant of cardiac performance. Up to a point, an increased heart rate enhances the force of ventricular contraction. This phenomenon, termed the "force–frequency relationship," is thought to be due to increased myocardial intracellular calcium concentrations at higher heart rates [11]. When the heart rate becomes too high (>180 beats/min for the adult heart), contractile force decreases again. In isolated muscle strips obtained from failing ventricles, the force–frequency response is blunted [12]. In the intact heart, the influence of the decreased duration of ventricular filling at high heart rates opposes the force–frequency effect on cardiac output. Nevertheless, the effect of heart rate on contractility should be taken into account when interpreting ventricular function.

Intrinsic contractility refers to the ability of the cardiac muscle to generate force and to shorten independent of preload, afterload, and heart rate. In the isolated myocardial fiber, increased contractility results in a higher shortening velocity and total shortening. In the past, several attempts have been made to transfer this physiologic concept to the intact in vivo beating heart. However, measuring intrinsic contractility independent from loading conditions and heart rate is extremely difficult. Hence, loading conditions influence the vast majority of echocardiographic parameters used to assess cardiac function. Invasive recording of pressure–volume loops combined with preload manipulation can provide information on intrinsic myocardial contractility but this is an invasive technique not routinely used for clinical follow-up [13,14].

Echocardiographic assessment of left ventricular systolic function

A wide variety of echocardiographic measurements have been proposed as indices of LV function. One group of measurements is based on changes in chamber size or wall dimensions during systole, including fractional shortening, ejection fraction, and myocardial deformation. A second group of measurements is based on Doppler and includes timing measurements such as peak dP/dt, the myocardial performance index and velocity measurements such as peak systolic tissue Doppler velocities. Most echocardiographic parameters quantify global myocardial function and assessment of regional or segmental myocardial function has traditionally been based on subjective scoring of regional wall motion. More recently, techniques such as measurement of tissue velocities and myocardial deformation or strain imaging, allow quantification of regional myocardial function, although they are also used in the assessment of global ventricular function. Regional wall motion abnormalities are very common in ischemic heart disease, but can also be detected in cardiomyopathies, valvar disease, and congenital heart disease. These methods also allow investigation of segmental interaction and especially the coordination of contraction between different segments, which is an important determinant of optimal global pump performance. Mechanical dyssynchrony can result from electrical conduction delays such as left bundle branch block or from regional myocardial dysfunction. Mechanical dyssynchrony causes mechanical inefficiency and

can contribute to ventricular dysfunction and heart failure. It can be studied by measuring the timing of systolic mechanical activation in different myocardial segments by various techniques including color tissue Doppler or myocardial deformation [15]. In appropriately selected cases, cardiac resynchronization therapy can result in improvement of cardiac function in adults as well as in children [16].

The timing of contraction is important for effective cardiac performance. In the normal heart, force development starts prior to ejection and peaks in the first 1/3rd of systole. The time between electrical activation and the opening of the semilunar valve is called the pre-ejection period and the time between opening and closing of the semilunar valve the ejection phase. Echocardiographic systolic measurements can measure the pre-ejection phase (pre-ejection period, isovolumic acceleration) but most echocardiographic parameters are measured during ejection and are ejection phase parameters (e.g., ejection fraction). The potential advantage of pre-ejection parameters is that they are less dependent on afterload compared with ejection phase parameters.

When using functional parameters in clinical practice and in research, the feasibility, reliability and accuracy of the measurements should be considered. The *feasibility* of a measurement reflects whether a measurement is technically possible. For example, due to limitations in echocardiographic windows, the feasibility of a 3D volumetric acquisition is generally lower than a 2D acquisition, especially in obese or postoperative patients with poor ultrasound windows. Measurement feasibility is determined by technical limitations. The *reliability* of a measurement is represented by its reproducibility. When the same measurement is repeated by the same observer, this is the intraobserver variability, which is generally lower than the interobserver variability, that is, the variability between different observers. Knowing the variability of a measurement is crucial to be able to interpret when a measurement difference can be considered as reflecting a true change in function (minimal relevant difference) versus when measurement differences arise from variability alone. For example, if a 10% decrease in ejection fraction is measured by the biplane Simpson's method, the measurement variability must be known in order to determine whether this difference is related to measurement variability or whether this reflects a true change in function. Measurement variability can be reduced by standardization of acquisition and analysis techniques. The published quantification guidelines can be used as an important tool for standardizing scanning protocols and measurements. However, each echocardiographic laboratory should ideally define standard scanning protocols and evaluate its own reliability. The *accuracy* of a measurement reflects whether the measurement indicates what it is supposed to measure. The accuracy of a measurement can be determined by validating the technique against a gold-standard method. For example, the validation of LV echocardiographic 3D volumetric measurements against volumetric measurements derived from the "gold-standard" of magnetic resonance imaging (MRI).

Systolic function derived from dimensional changes

Fiber shortening during ejection results in displacement of blood and dimensional changes both within the cavity and within the myocardial walls. Traditionally, the assessment of global systolic function has been based on measuring changes in ventricular size and volume during the systolic ejection phase from apical and short-axis views. Measurement of dimensional changes can be based on 1D (M-mode), 2D (biplane Simpson's method), and more recently, 3D measurements (Table 7.1). The American Society of Echocardiography (ASE) has published separate guideline papers on the quantification of chamber sizes and dimensions in the adult [17] and pediatric age groups [18]. There are no specific guidelines for adults with congenital heart disease.

LV dimensions and shape representing LV remodeling

LV dysfunction is commonly associated with LV remodeling and measurement of LV dimensions should be a routine part of systolic functional assessment. Typically, progressive LV dysfunction causes LV dilation, which is a mechanism for maintaining stroke volume, as a larger ventricle needs to contract less to pump the same blood volume. LV dilatation causes a more spherical LV wall configuration, which results in increased wall stress or afterload, especially in the apical segments. Therefore, diagnosis of LV dysfunction requires investigation of LV dimensions and remodeling. Typically, this involves measuring the LV end-diastolic dimension (LVEDD z-score) and the LV septal and posterior wall thickness (LVPWT z-score) from a parasternal short-axis view using M-mode or 2D measurements (Figure 7.4). The LV length can be measured from an apical 4-chamber or subcostal long-axis view. Derived parameters include the sphericity index and the thickness-to-dimension ratio. The sphericity index can be defined as the LV minor or short-axis dimension divided by the LV major axis dimension or LV length. At end-diastole this parameter is normally 0.6–0.7 but approaches 1 as the ventricle becomes more spherical as typically occurs in dilated cardiomyopathy [19]. In patients after anthracycline exposure the thickness-to-dimension ratio has been described to change before variations occur in myocardial performance thereby reflecting myocardial remodeling [20]. Progressive LV dilatation, wall thinning and a more spherical configuration represent unfavorable ventricular remodeling while the opposite is seen in reverse remodeling. These parameters can be useful in defining disease progression.

Dimensional changes in systole representing LV performance

The most commonly used parameters for assessing left ventricular function are based on changes in chamber size from end-diastole to end-systole. End-diastole is best defined as the

Table 7.1 Left ventricular systolic function derived from dimensional changes

	Strengths	Weaknesses
Dimensional changes		
Shortening fraction by M-mode	• Ease of measurement	• Only reflects basal regional function • Influenced by abnormal septal motion • Does not measure longitudinal shortening • Load-dependent • Geometry-dependent
Shortening fraction by 2DE	• Less dependent on probe positioning on chest and angulation than M-mode	• Reflects basal regional function • Influenced by abnormal septal motion • Does not measure longitudinal shortening • Load-dependent • Geometry-dependent
Ejection fraction by biplane Simpson	• Is a global parameter as it takes regional function into account	• Endocardial border detection can be challenging • Load-dependent
Ejection fraction by 5/6 area*length	• Endocardial border detection in short axis easier than biplane Simpson method	• Geometry-dependent • Load-dependent
Ejection fraction by 3DE	• More accurate than 2DE EF methods	• Load-dependent
MAPSE by M-mode	• Ease of measurement • Measures longitudinal function	• Load-dependent • Influenced by valve regurgitation
Vcfc	• Relatively preload-independent	• Based on geometric assumptions • Afterload-dependent

2DE, two-dimensional echocardiography; 3DE, three-dimensional echocardiography; MAPSE, mitral annular plane systolic excursion; *Vcfc*, velocity of circumferential fiber shortening corrected for heart rate.

image frame before mitral valve closure and end-systole as the frame before mitral valve opening. M-mode echocardiography was one of the first techniques available for assessing LV dimension changes. Either a long-axis or short-axis cut through the LV just below the mitral valve leaflet tips is obtained. A short-axis cut is our method of choice as it is easier to evaluate whether the imaging plane is truly perpendicular to the LV long axis with the LV appearing as a circular structure in systole and the RV projecting anteriorly to the LV (Figure 7.4). This requires an optimal parasternal position of the transducer with a scanning plane perpendicular to the plane of interest. M-mode echocardiography has the advantage of having a very high temporal resolution compared to 2D imaging. The spatial resolution of 2D echocardiography, however, is better. Two-dimensional imaging allows for direct assessment of the segments being measured, and it also has the ability to evaluate for in-plane motion

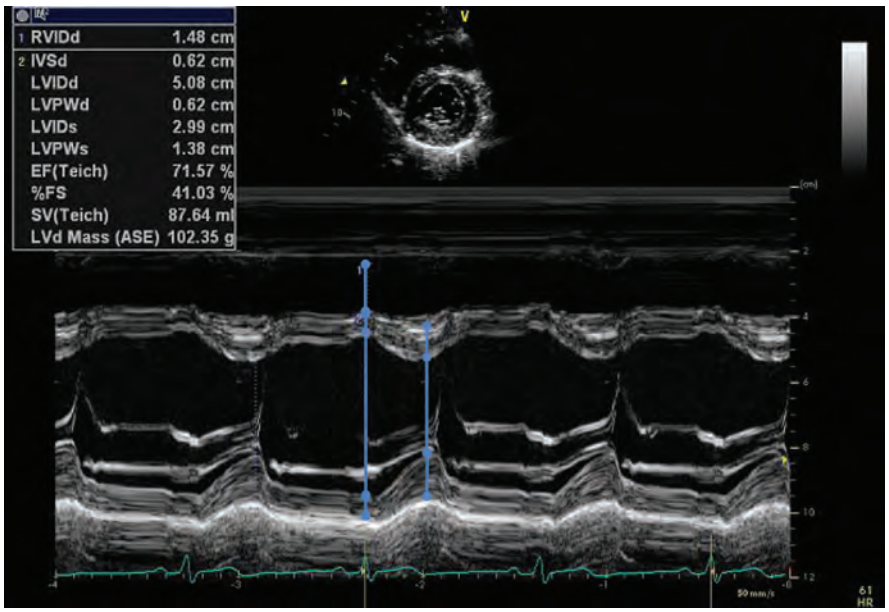


Figure 7.4 M-mode calculation of LV shortening fraction. From an M-mode obtained at the basal level of the left ventricle just distal to the mitral valve leaflet tips, LV end-diastolic and end-systolic dimensions can be measured and shortening fraction can be calculated.

artifact. Therefore, the American Society of Echocardiography pediatric guideline recommendations call for using a 2D short-axis view at the level of the papillary muscles for the measurement of LV cavity dimensions [18]. Most normal reference data, however, are based on M-mode measurements, and we employ both M-mode and 2D in our laboratory. *Shortening fraction* (SF) is defined as the percent change in left ventricular dimension from end-diastole to end-systole based on either M-mode or 2D imaging acquired just below the level of the mitral valve leaflet tips. SF represents the degree of apposition of the basal LV posterior wall to the basal ventricular septum. As the mitral valve cannot be viewed on the short-axis cut, the left ventricular cavity is measured at the end of diastole defined as the onset of the QRS-complex (left ventricular end-diastolic dimension, LVEDD) and at end-systole, which is the closest point of apposition between the septum and the posterior wall (left ventricular end-systolic dimension, LVESD). Shortening fraction (SF) is expressed as a percent and is calculated as:

$$SF\% = (LVEDD - LVESD)/LVEDD \times 100.$$

Shortening fraction normally varies between 28 and 38%. Values below 28% suggest reduced systolic LV function, while values above 38% indicate hyperdynamic LV function. The popularity of this measurement (in particular the M-mode measurement) is largely due to the ease with which it can be obtained. There are, however, important limitations to its use. One limitation is that SF reflects thickening of the basal part of posterior wall and ventricular septum and thus by definition is a regional parameter which is used to assess global LV function. Thus SF only reflects global pump function in the absence of regional wall motion abnormalities. However, the basal ventricular septum in particular can be influenced by different factors. A typical example is the septal dyskinesia in the presence of right ventricular volume loading (as occurs in atrial septal defects). This can be associated with a paradoxical systolic motion of the ventricular septum, which moves away from the posterior wall during systole (Figure 7.3). In this instance SF cannot be used to assess LV systolic function. Similarly, immediately after cardiopulmonary bypass, septal hypokinesia or dyskinesia are common findings, and SF often underestimates true LV systolic performance in the immediate postoperative period. When regional myocardial function is preserved in the septum and posterior walls but reduced in other segments, SF overestimates global LV performance. Likewise, SF mainly reflects circumferential fiber shortening and as such does not account for longitudinal shortening. Loading conditions should also be taken into account when interpreting SF measurements. As an ejection phase parameter, SF is influenced by changes in volume and pressure loading. Volume loading will generally result in increased SF. In the presence of chronic mitral or aortic regurgitation, a normal – and certainly a reduced – SF should be considered as a possible sign of underlying LV dysfunction. Increased afterload results in a decrease in SF. A typical example is a hypertensive crisis, which causes an acute increase in arterial pressure and LV afterload, which typically results in an acute reduction in SF. This is not due to intrinsic myocardial dysfunction but is related to changes in loading conditions. Decreasing the blood pressure will often result in a complete normalization of pump performance. An additional limitation is the dependency of SF measurements on LV geometry. Typically LV hypertrophy without LV dilatation, as occurs in hypertrophic cardiomyopathy, results in a smaller LV cavity. In this context, changes in LV dimensions during systole result in overestimation of LV systolic function. Thus, in addition to loading conditions, geometry should also be accounted for when interpreting SF. Data are available on the reliability of SF measurements. In a multicenter study, Lipshultz et al. compared M-mode measurements obtained in local laboratories with core lab measurements [21]. They found the highest interclass correlations for LV end-diastolic dimension (ICC 0.97) but a lower value for SF (ICC = 0.64). This is not surprising as SF measurements are based on measurement of two parameters (end-diastolic and end-systolic dimension) increasing measurement variability. Geelhoed et al. demonstrated that rigorous standardization can significantly improve measurement reproducibility to yield a high ICC and narrow limits of agreement between two observers. No validation studies of 2D measurements are available, although a study in patients with dilated cardiomyopathy showed that measurement of dimensions were generally more variable compared with measurement of areas [22].

A second parameter based on measurement of dimension changes is the measurement of LV *ejection fraction* (EF); defined as the percentage change in LV volume from end-diastole to end-systole. Its calculation requires measurement of LV volumes:

$$EF(\%) = (LVEDV - LVESV)/LVEDV \times 100$$

where LVEDV is the LV volume at end-diastole and LVESV the LV volume at end-systole.

LV volumes can be calculated by various methods. The first is based on measurement of LV dimensions using M-mode echocardiography. Quinones et al. [23] proposed a simplified formula to calculate EF by measuring internal LV dimensions and based on simplified geometrical assumptions of LV shape. This method has all the limitations of M-mode echocardiography outlined in the previous paragraph; the most important being that it measures changes in only two segments. The pediatric guidelines recommend two different methods based on 2D echocardiography to measure LV volumes and EF. The method most commonly used and also recommended by the American Society of Echocardiography adult guidelines is the modified Simpson's or disk summation method [24,25]. In this method two orthogonal planes from the apical view are used (apical 4-chamber and apical 2-chamber view). The LV is divided into a number (n) of cylinders or disks of equal height. The height of each cylinder is determined by dividing the total length of the

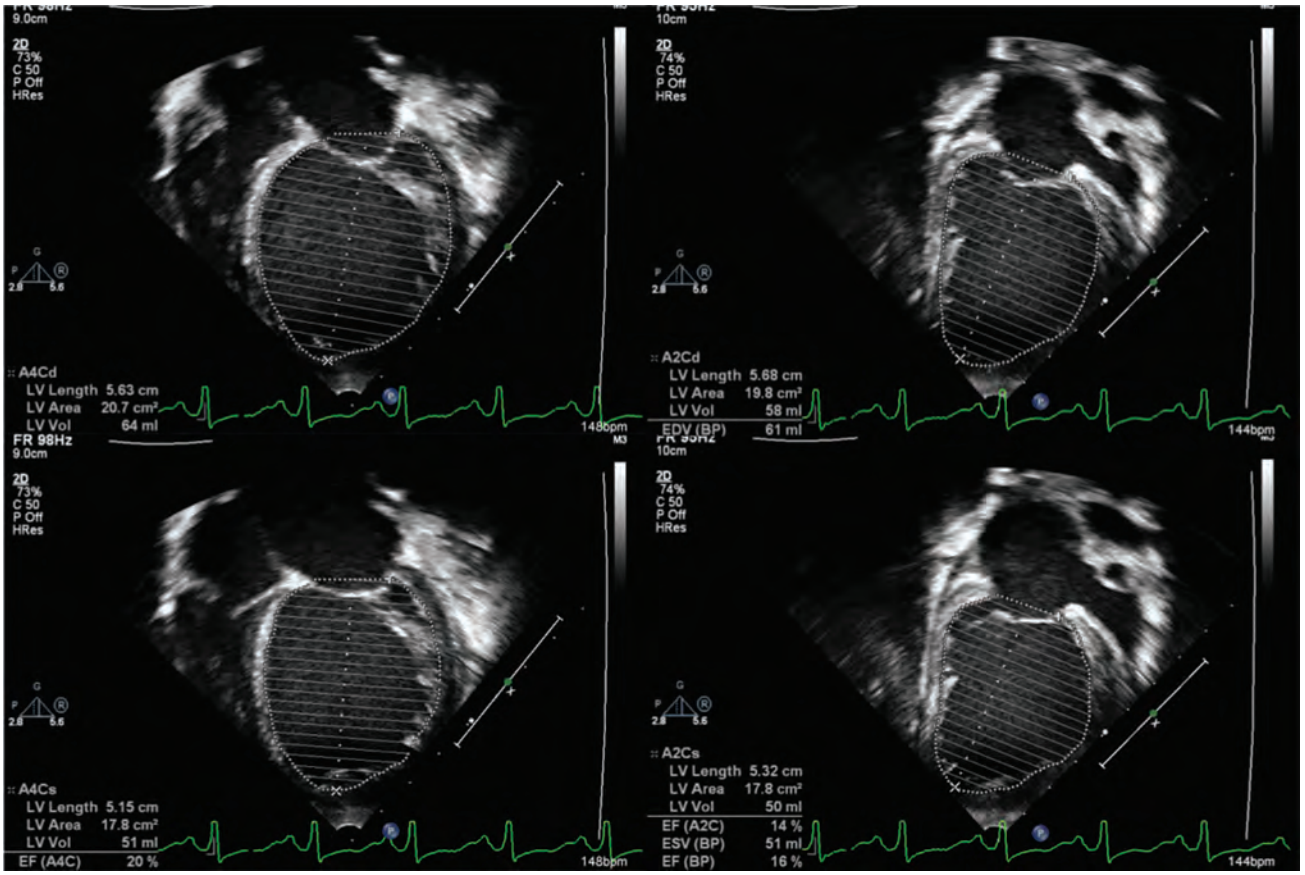


Figure 7.5 Biplane modified Simpson's calculation of LV ejection fraction. In the apical 4- and 2-chamber views, the endocardial borders are manually traced. End-diastolic volume, end-systolic volumes and ejection fraction are calculated using the modified Simpson's algorithm.

LV cavity (L) by the number of cylinders (L/n). The volume of each cylinder is calculated from the diameter of the cylinders (ai and bi) obtained in the two planes. The LV volume is the sum of the volumes of the individual cylinders using the formula:

$$V = \pi/4 \sum (a\text{i} \times b\text{i}) \times L/n.$$

The summation of discs method is probably the most reliable for calculating ejection fraction, but also the most time consuming in clinical practice because it requires LV endocardial border tracing at end-diastole and end-systole in two apical views (Figure 7.5). In patients with poor echocardiographic windows and also in severely dilated ventricles, endocardial border detection and tracing can be challenging. The LV lateral and anterior walls can be especially difficult to trace. This influences both the feasibility and the reliability of this method. Other simplified methods for calculating LV volumes are the bullet, or area-length, method. This method is possibly more reproducible than the biplane Simpson's method, but it is influenced by changes in LV shape. The area-length method requires measuring the short-axis basal LV area and the LV length. The LV basal area can be obtained from a parasternal or subcostal short-axis view (Figure 7.6). LV length can be measured from the apical 4-chamber or the subcostal long-axis views. LV volume can then be calculated using the formula:

$$\text{LV volume} = 5/6 \times \text{short-axis basal area} \times \text{LV length}.$$

The measurements need to be repeated in end-diastole and end-systole. The preferred method for measurement of LVEF is currently uncertain and largely dependent on individual laboratory experience. For both methods optimal 2D images of the LV are required and foreshortening of the LV cavity should be avoided. Generally, the variability of the measurements is within the 10–15% range. A reduction in EF of >10% in the normal range (>55%) and >5% if <55%, is considered clinically significant. Automated border detection algorithms have been developed to reduce measurement variability arising from manual border tracing [26,27]. These methods utilize the differences in ultrasound reflective properties between blood and tissue. Both Kimball [28] and Mahle [29] have shown that this method can also be used in children with hypoplastic left heart syndrome to evaluate right ventricular function through the different stages of palliation.

The more recent versions of the automated methods are based on STE technology and use apical 4-chamber, 2-chamber, and 3-chamber views (Figure 7.7). In adults, these automated

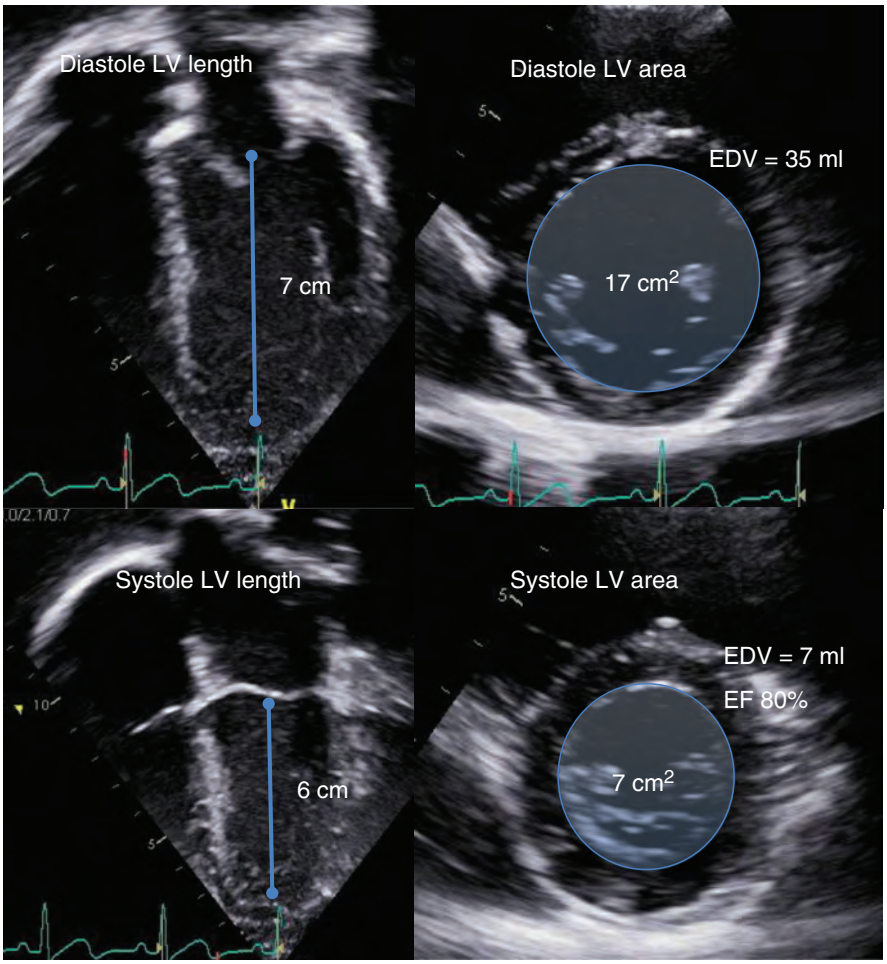


Figure 7.6 Area-length method for calculation of LV ejection fraction. In this method LV basal areas are measured from the subcostal or parasternal basal short-axis views while LV length can be measured from the apical 4-chamber or subcostal long-axis views. The measurements are obtained in end-systole and end-diastole and ejection fraction is calculated using the 5/6 area-length formula.

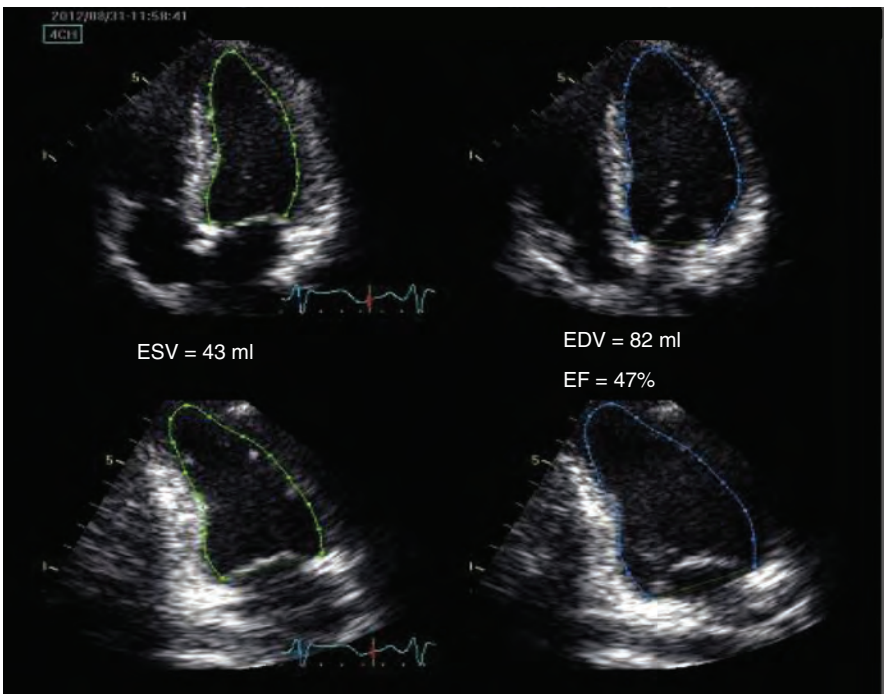


Figure 7.7 Automated border-detection methods for LV EF calculations. Instead of manual tracing of the borders in the apical 2- and 4-chamber views, an automated border-detection method is used to calculate LV volumes and ejection fraction.

methods significantly reduce interobserver variability and post-processing times [30]. Three-dimensional echocardiography has recently been introduced and the availability of high-frequency matrix transducers allow the acquisition of high-resolution full volumetric datasets in children [31]. The analysis of 3D datasets for EF is currently based on automated border detection methods with manual correction thereby reducing measurement variability and increasing accuracy, as measurements are not based on geometric assumptions (Video 7.3). LV 3D volumes have also been demonstrated to be more accurate than 2D when compared with LV volumes measured by MRI [32]. The advantage of 2D and 3D EF calculations is that they account for regional wall motion abnormalities and are the methods of choice so long as image quality is adequate. However, it should be remembered that whatever method is used, EF is load-dependent and 2D-based methods especially are dependent on ventricular geometry [33–36].

Longitudinal LV function

Because fractional shortening mainly assesses circumferential fiber shortening, a separate assessment of longitudinal fiber shortening provides additional information on LV function. In the normal LV, the circumferentially oriented fibers predominate over the longitudinal fibers and short-axis shortening exceeds long-axis shortening. Therefore, LV sphericity normally decreases during contraction as the LV short axis decreases more than its long axis. Long-axis function is, however, an important contributor to LV ejection and global function. As subendocardial fibers contribute to longitudinal contraction, subendocardial dysfunction or fibrosis will affect longitudinal LV function more than circumferential contraction. Pressure loading also affects longitudinal function more than circumferential function. Both factors probably explain why patients with aortic valve stenosis have more significant abnormalities in longitudinal than radial function [37]. Different techniques can be used to quantify longitudinal LV function. The easiest measurement is the *displacement of the mitral valve annulus, also called mitral annular plane systolic excursion* (MAPSE). MAPSE can be obtained from the apical 4-chamber and 2-chamber views by M-mode echocardiography (Figure 7.8). An M-mode cursor can be placed through the lateral, septal, anterior and/ or posterior walls [38]; although generally either the septum or the lateral walls are preferred. The systolic excursion is measured from the lowest point in diastole to aortic valve closure. In adults, MAPSE ranges between 10 and 15 mm and a value <8 mm is considered abnormal. MAPSE is heart-size dependent and unfortunately pediatric normal values are not available limiting its use in younger children. In patients with increased LV afterload, including arterial hypertension and aortic stenosis, reduced longitudinal function can be present despite a preserved ejection fraction, suggesting that reduced longitudinal function may be an early sign of ventricular dysfunction. Diseases associated with increased mass-to-volume ratio (such as arterial hypertension, aortic stenosis or hypertrophic cardiomyopathy) are associated with increased short-axis shortening and decreased long-axis function. MAPSE is load-dependent, is influenced by valve regurgitation and by translational motion as the heart moves in the chest during contraction. Newer methods such as tissue Doppler and longitudinal strain measurements also provide measurements of LV longitudinal function and will be discussed later in this chapter. For a complete LV functional assessment, at least one of these techniques to assess longitudinal LV function should be performed.

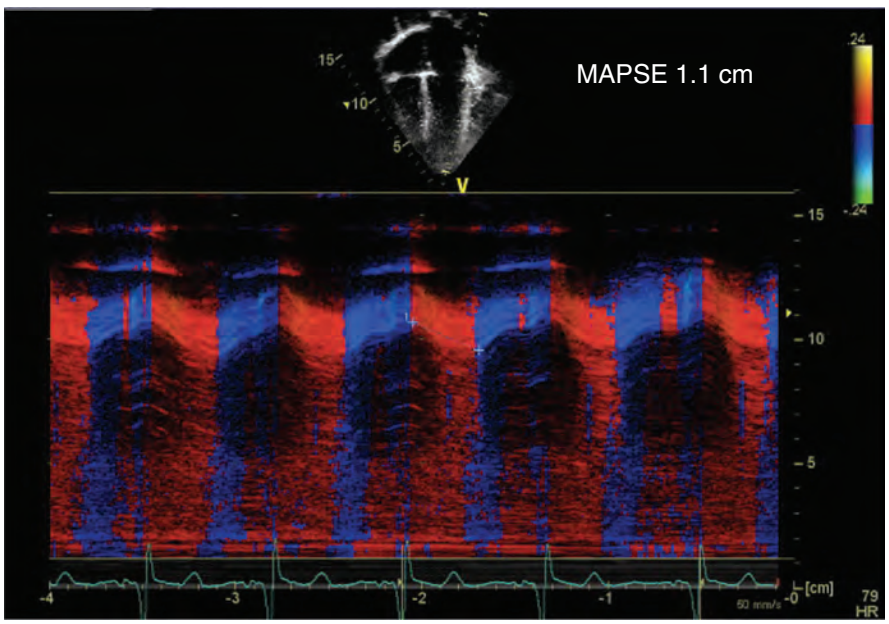


Figure 7.8 Mitral annular plane systolic excursion (MAPSE). An M-mode cursor is placed through the mitral annulus aligned with the longitudinal motion of the annulus during systole. The excursion of the annulus during systole is measured. We use color tissue Doppler to help with the timing of the measurements.

Correcting dimensional changes for afterload

To overcome some of the problems associated with load-dependency of SF and EF, methods correcting dimensional changes for afterload have been developed. One of these measures the *velocity of circumferential fiber shortening* (*V*cf), that is, the velocity of LV dimension change during ejection calculated by dividing the FS by the LV ejection time (VCF = FS/Ejection time). Therefore, *V*cf is an estimate of the average rate of change of the LV diameter per unit of time. Typically, ejection time is calculated from an M-mode through the aortic valve thereby utilizing the very high temporal resolution of M-mode.

This measurement reflects the speed at which shortening occurs. As a timing parameter, it has to be corrected for heart rate which can be done by dividing the SF measurement by the square root of the preceding R-R interval (Bazett's correction).

$$VcFc = [(SF)/(ET)] \text{ divided by } (RR)^{0.5}$$
$$= [(SF) \times (RR)^{0.5}]/(ET).$$

The corrected *V*cfc is relatively insensitive to preload changes but is influenced by afterload [39]. If corrected for afterload, *V*cfc can be used as a parameter of contractility. Colan et al. [39] used this principle and calculated end-systolic meridional wall stress (longitudinal) as a measure of afterload. Wall stress is defined by the formula:

$$ESWS\ (g/cm^2) = [(1.35)\ (Pes)\ (LVESD)]: [(4)\ (hes)\ (1 + hes/LVESD)]$$

where Pes is end-systolic pressure (in mmHg), LVESD is the LV end-systolic internal diameter (in cm) and hes is the LV end-systolic posterior wall thickness. In the original description of the methodology, ventricular dimensions were obtained from an M-mode through the LV. The challenging part of this method is defining LV end-systolic pressure. The forearm systolic and diastolic blood pressures were measured and using a tonometry device the carotid pulse tracing was recorded together with the M-mode tracing. On the carotid tracing, the dicrotic notch caused by aortic valve closure identifies end-systole. End-systolic blood pressure could then be extrapolated on the indirect arterial pressure waveform by measuring the height from the baseline to the dicrotic notch. A phonogram-derived signal is superimposed on the M-mode image and the end-systolic LV dimension and posterior wall thickness are measured at aortic valve closure (first component of the second heart sound). Colan et al. [39] found a linear negative correlation between *V*cfc and end-systolic meridional wall stress and published the normal range of the *V*cfc and end-systolic wall stress relationship. Abnormal LV contractility is defined as values for wall stress versus *V*cfc below the normal expected range. While conceptually sound, the complexity of the measurements and other fundamental methodological limitations probably explain why this method never became a standard echocardiographic technique and has remained mainly a research tool. One of the assumptions is the linearity of the *V*cfc–wall stress relationship, which has been questioned, especially in younger children [40,41]. Gentles et al. demonstrated that wall stress, as calculated by the formula, misrepresents afterload in children and young adults with abnormal left ventricular geometry [42]. In that study wall stress was compared to fiber stress. Likewise, efforts have been made to reduce the complexity of the measurements. A simplified method was proposed using mean arterial pressure instead of end-systolic pressure [41]. This facilitates its clinical integration in the echocardiography laboratory, but scientific evidence is lacking that afterload correction actually helps in better predicting clinical outcomes.

Blood pool Doppler indices of ventricular function

Methods measuring ventricular dimensions for assessing function are geometry-dependent which limits their use in congenital heart disease and in growing children. Doppler methods are attractive, as they are not influenced by ventricular geometry or morphology. Various Doppler-based methods for assessing cardiac function have been proposed (Table 7.2). The first is echocardiographic estimation of d*P*/d*t*. The peak velocity in pressure rise occurs very early after electrical activation mainly during the isovolumic contraction period and reflects how rapidly pressure builds in the LV cavity. Peak d*P*/d*t* can be measured invasively by calculating the first temporal derivative of the ventricular pressure curve. As it occurs during the isovolumic contraction period when the aortic valve is still

Table 7.2 Blood pool Doppler indices of left ventricular function

	Strengths	Weaknesses
Blood pool Doppler indices		
d*P*/d*t*	• Geometry-independent • Afterload-independent	• Preload-dependent • Clear continuous-wave Doppler tracing required • Very short time interval limits reproducibility
PEP/ET	• Geometry-independent	• ET is afterload-dependent • Conduction delay prolongs PEP
Myocardial performance index (MPI)	• Geometry-independent	• Measures both systolic and diastolic function • Load-dependent
Systolic/Diastolic (S/D) duration ratio	• Geometry-independent	• Heart rate-dependent

d*P*/d*t*, ratio of change in pressure over change in time; PEP/ET, ratio of pre-ejection period over ejection time.

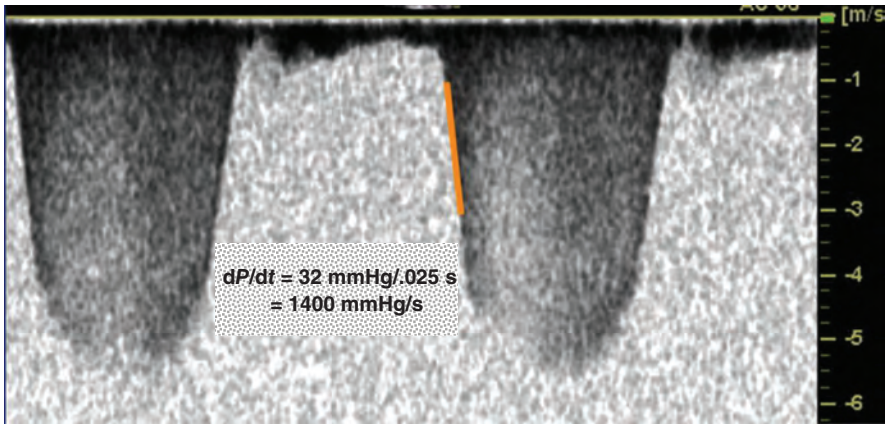


Figure 7.9 Measurement of d*P*/d*t* measured by obtaining a mitral regurgitant jet continuous-wave Doppler. The time it takes for the velocity to go up from 1 m/s to 3 m/s is measured and this time difference is used to calculate d*P*/d*t*.

closed, it is afterload-independent but is influenced by ventricular size and preload. Two different echocardiographic methods have been proposed to estimate d*P*/d*t*. The first requires a continuous-wave (CW) Doppler tracing of the mitral regurgitation jet and measures the mean increase in mitral regurgitant Doppler velocity (Figure 7.9). As LA pressure does not change significantly during the isovolumic contraction period, the rise in mitral regurgitation velocity during this period reflects d*P*/d*t*. The method consists of measuring the time interval between 1 m/s and 3 m/s on the mitral regurgitation Doppler trace. The pressure difference between those two points is 32 mmHg as calculated by the Bernoulli equation. The d*P*/d*t* can then be calculated as:

$$dP/dt = 32 \text{ mmHg/time interval (s)}.$$

For the normal LV, d*P*/d*t* is 1200 mmHg/s or higher. The method requires a clear CW tracing of the mitral regurgitation jet, which is not always available. Likewise, the calculation is dependent on the measurement of a very short time interval on a spectral Doppler signal, which influences its reproducibility. Although no good reliability data are available in pediatrics, Colan et al. showed that in general, the reproducibility of measuring time intervals is relatively poor [22]. An alternative method for calculating d*P*/d*t* is based on the measurement of the isovolumic contraction time (ICT) [43]. The pressure difference between the aortic diastolic pressure and the LV end-diastolic pressure reflects the pressure rise during the ICT. Diastolic pressure can be measured by blood pressure measurement and LVEDP is estimated at 5 mmHg for the calculation. ICT can be measured by blood pool Doppler or by tissue Doppler.

Mean d*P*/d*t* = (aortic diastolic pressure − LVEDP)/ICT. The variability of this method seems low in patients with a single ventricle with an interclass correlation of 0.95 for interobserver variability [44]. The usefulness of this method requires further investigation, but in general d*P*/d*t* measurements seem to be too variable to be used in clinical practice. The main problem for both methods to calculate d*P*/d*t* is that they are based on the measurement of very short time intervals and a small measurement error will result in a large difference in the calculated d*P*/d*t*.

Aortic blood flow velocities can be measured using pulsed- or continuous-wave Doppler signals through the ascending aorta or the left ventricular outflow tract. Systolic time intervals can be measured and used to assess ventricular function [45]. One of the indices that gained some interest is the ratio of the pre-ejection period (PEP) to the left ventricular ejection time (ET). The pre-ejection period is the time from the onset of the electrocardiogram QRS complex to the onset of ejection. This method is poorly validated in children and is very afterload-dependent, as ET is very sensitive to changes in afterload. Likewise, the presence of conduction delays will prolong PEP. Currently, this method is not widely used in clinical practice.

The *myocardial performance index* (MPI) is another Doppler-based timing parameter that was introduced by Tei et al. as an index for global ventricular function combining systolic and diastolic time intervals [46–48]. It measures the time the heart spends in isovolumic periods, adding the isovolumic contraction and relaxation time (ICT and IRT, respectively), and correcting the sum for the ejection time (ET). The formula is:

$$\text{MPI} = (\text{ICT} + \text{IRT})/\text{ET}.$$

The time intervals can be calculated relatively easily using a pulsed Doppler trace placed at the region of fibrous continuity between the mitral and aortic valves that simultaneously captures LV inflow and outflow (Figure 7.10). Systolic dysfunction results in prolongation of the ICT and shortens the ET. Early diastolic dysfunction (relaxation abnormality) prolongs the IRT. More advanced diastolic dysfunction and an increase in LV filling pressures shortens the IRT. Normal MPI values for the left ventricle are 0.35 ± 0.03. Ventricular dysfunction generally prolongs the MPI. The main advantage of this index is that it does not rely on geometric assumptions and thus can be used in patients with abnormal geometry [49,50]. One of its main limitations is that the MPI does not differentiate between systolic and diastolic dysfunction. Moreover, there is a paradoxical effect of

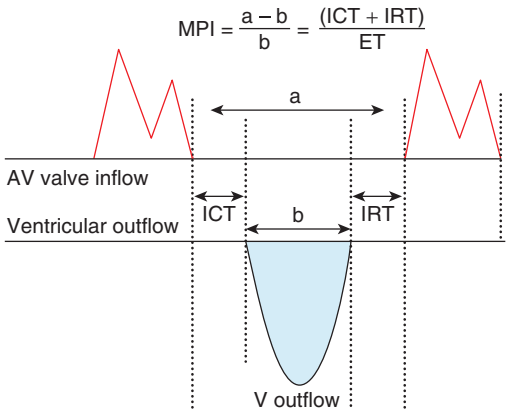


Figure 7.10 Measurement of myocardial performance index. A Doppler sample between the LV inflow and outflow is obtained. The time between mitral valve closure and mitral valve opening (a) and the ejection time (b) are measured. MPI can be calculated as (a – b)/b.

increased filling pressures on MPI as more severe diastolic dysfunction shortens the MPI while ventricular function is actually deteriorating. When patients are treated with diuretics, and filling pressures are reduced in the context of heart failure, the MPI worsens even though the patient is clinically improving. MPI is a very general marker for cardiac dysfunction. It can be considered as the "C-reactive protein" of cardiac function: when abnormal, it indicates that something is wrong with ventricular function, which then needs further definition using other techniques. The second limitation is the load-dependency of the myocardial performance index as shown by Cheung et al. [51]. ICT, IRT, and ET are influenced by changes in preload and afterload, thereby affecting the MPI. In children this load-sensitivity did not seem to significantly influence MPI measurements when the effect of acute volume or pressure changes were evaluated [49]. Theoretically, MPI should be very sensitive to almost any change or abnormality in contractility, loading and relaxation. As a combined parameter the MPI has prognostic value.

Doppler methods to assess timing of cardiac events have also been used to measure the ratio of systolic to diastolic duration (S/D ratio). This can be measured by obtaining a CW Doppler through the mitral valve regurgitation jet (Figure 7.11). The systolic duration is defined by the duration of regurgitant flow and the diastolic phase by the diastolic inflow duration. As the ventricle becomes progressively dysfunctional, it spends more time in systole, which shortens diastole. Although ejection time gets shorter, the time the heart spends in systole (defined as the period of atrioventricular valve regurgitation) lengthens, resulting in a shortened diastole (forward filling from opening to closure of the atrioventricular valve). An elevated LV S/D ratio has been found in patients with restrictive and dilated cardiomyopathy [52], and an elevated RV S/D ratio has been found in children with hypoplastic left heart syndrome [53] and in those with pulmonary hypertension [54]. The S/D ratio is heart rate-dependent and for the right ventricle normal values have been published recently for different heart rates [55]. Interestingly, systolic duration shortens linearly with heart rate while the relationship between diastolic duration and heart rate is exponential. Shortening the inflow duration with progressive disease influences cardiac filling and through this mechanism reduces cardiac output. Further study of this method is needed in both children and adults.

Problems with reliability of measuring Doppler-derived time intervals, dependency on the presence of high-quality Doppler traces, and the load and heart rate dependency of the methods limit the clinical use of blood pool-derived Doppler indices.

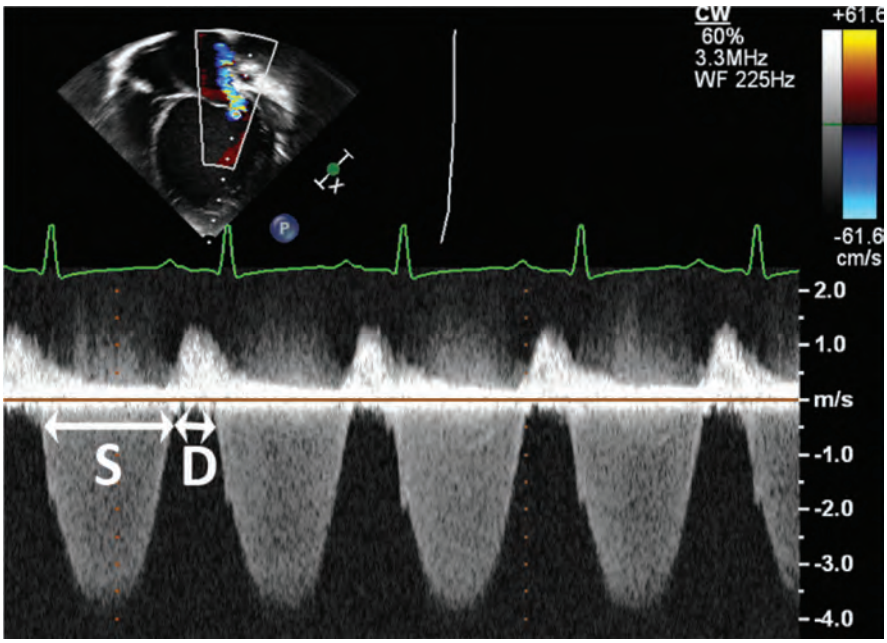


Figure 7.11 S/D ratio. The ratio between the duration of systole and diastole can be calculated by obtaining a continuous-wave Doppler through the mitral regurgitant jet. Systolic duration is defined by the duration of the regurgitant jet. Diastolic duration is defined as the duration of mitral inflow.

	Strengths	Weaknesses
Tissue Doppler indices		
Systolic annular tissue velocity (S′)	• Geometry-independent	• Tissue velocities influenced by cardiac translation and tethering • Angle-dependent • Heart rate-dependent • Load-dependent
Myocardial acceleration during isovolumic contraction (IVA)	• Geometry-independent • Relatively afterload-independent • Allows studying force–frequency relationships	• Influenced by preload, especially when filling pressures are increased • Very short time interval limits reproducibility • Angle-dependent
Myocardial performance index (MPI) by TDI	• Geometry-independent	• Measures both systolic and diastolic function • Load-dependent
Systolic/Diastolic (S/D) duration ratio	• Geometry-independent	• Heart rate-dependent

Table 7.3 Tissue Doppler imaging for the evaluation of left ventricular myocardial function

Tissue Doppler imaging for the evaluation of left ventricular myocardial function

Most of the previously discussed methods indirectly assess myocardial function through dimension changes or blood pool Doppler time intervals. When assessing myocardial function, it makes sense to directly interrogate the myocardium and measure how the cardiac muscle itself changes during the cardiac cycle. This became possible with the introduction of tissue Doppler and myocardial deformation imaging. In this section we will introduce tissue Doppler measurements (Table 7.3), while in the next section we will focus on myocardial deformation, or strain, imaging. In a recent joint statement paper by the American Society of Echocardiography and the European Association for Echocardiography, both technologies were described as "evolving techniques" [6]. The applications of tissue Doppler and strain imaging are evolving quickly, however, also in pediatric and congenital disease with increasing clinical use of these methodologies [56,57].

Tissue Doppler imaging (TDI), also known as Doppler myocardial imaging or myocardial velocity imaging, is a technique that measures segmental myocardial velocities [58]. In the late 1980s and early 1990s, the use of adapted thresholds and filters made it possible to distinguish between the poorly reflective and rapidly moving blood (range 50–150 cm/s) and the highly reflective and slower myocardium (3–25 cm/s). These technical adaptations allowed interrogation of segmental myocardial velocities [59,60]. After its initial description, experimental studies confirmed that, for normal myocardium, changes in segmental systolic velocities are closely linked to changes in contractility [61]. This resulted in numerous clinical studies investigating the value of regional myocardial velocities in various diseases such as ischemic heart disease, aortic insufficiency, and hypertrophic cardiomyopathy [62,63].

The introduction of TDI into the comprehensive echocardiographic evaluation of children with acquired or congenital heart disease has also been enthusiastic. Tissue Doppler imaging provides a geometry-independent quantitative measure of systolic and diastolic function that is easy to obtain and is highly reproducible [64]. Our group validated tissue Doppler measurements in children defining the feasibility and reliability using different ultrasound systems [65]. Myocardial velocities can be measured with either pulsed-wave or color Doppler methodologies. For clinical use longitudinal velocities are measured at the mitral annulus or at the basal segments of the LV walls just below the annulus. With *pulsed-wave TDI*, a sample volume of 2–5 mm is placed within the myocardium. As translational cardiac motion is more pronounced in children, we prefer to place the sample volume at the basal LV wall just below the mitral annulus. This reduces contamination by velocities from atrial motion. As with all Doppler techniques, the ultrasound beam should be well aligned with the direction of myocardial motion. The resulting velocity waveform represents the peak instantaneous velocity in that area throughout the cardiac cycle; providing a real-time display of myocardial velocities at high temporal resolution (250–300 frames/sec). The spatial resolution is limited because the myocardial wall moves in relation to a fixed sample volume. Likewise, only one sample volume can be placed at a given time, limiting the use of pulsed tissue Doppler. A normal pulsed-wave TDI trace obtained in the basal septum (Figure 7.12) is characterized by an initial short and sharp isovolumic contraction peak, followed by a systolic peak of longer duration that corresponds to a base-to-apex motion of the myocardium during systole. This is followed by another brief isovolumic relaxation peak. The systolic events are followed by early and late diastolic waves. These reflect the opposite motion of the atrioventricular valve plane towards the base in diastole when the LV fills. By convention, motion towards the transducer is represented as a positive wave and motion away from the transducer as a negative wave. When well-standardized (e.g., sample volume, alignment, etc.), pulsed tissue Doppler velocities are highly reproducible in adults as well as in children. *Color Doppler myocardial imaging* (CDMI) is a color Doppler technique measuring mean rather than peak velocities. Consequently, CDMI-derived myocardial velocities are 15–20% lower than pulsed-wave (PW)

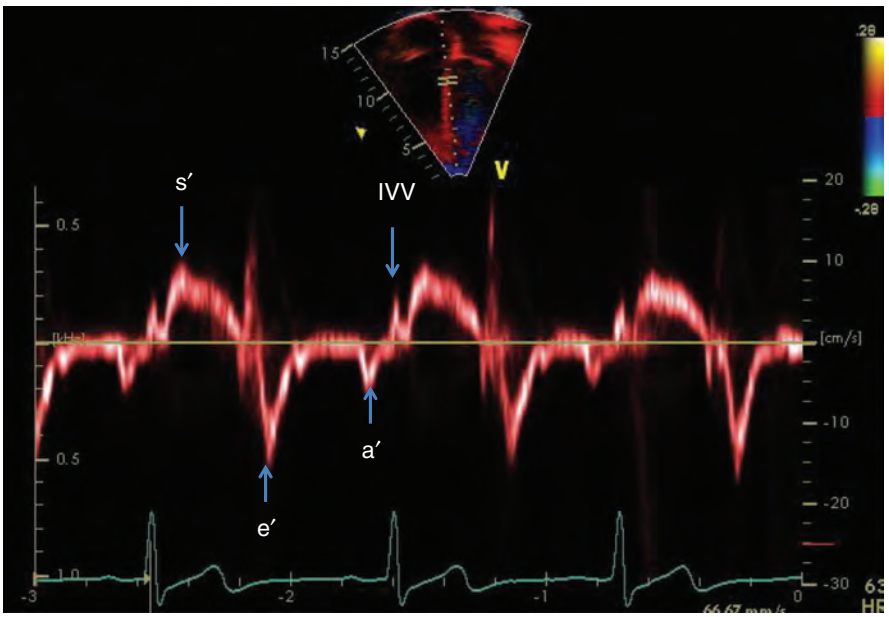


Figure 7.12 Pulsed tissue Doppler tracing obtained in the basal part of the interventricular septum. A pulsed-wave Doppler sample is put into the basal segment. Different velocities can be measured: peak early systolic (s′), peak velocity during the isovolumic contraction period (IVV), early diastolic velocity (e′), and diastolic velocity during atrial contraction (a′).

Doppler velocities in the same segment [66]. As for blood pool Doppler imaging, myocardial motion towards the transducer is coded red, while motion away from the transducer is coded blue. Using post-processing software, myocardial velocity curves can be obtained anywhere in the myocardium (Figure 7.13). As for PW Doppler, the ultrasound beam should be well aligned with the direction of myocardial motion. Reducing the sector width and decreasing the beam density enables higher temporal resolution and usually frame rates of >180 frames/s. An important advantage of CDMI is that velocities can be measured simultaneously in multiple myocardial segments, thereby allowing comparison of myocardial velocities between different myocardial segments in the same cardiac cycle. This can be useful in certain clinical applications such as the assessment of mechanical dyssynchrony.

The velocity at which a myocardial segment moves is influenced by various factors and does not directly represent the segment's intrinsic myocardial contractility. First, tissue velocities are influenced by the overall motion of the heart in the chest during the cardiac cycle (cardiac translation). Second, in the

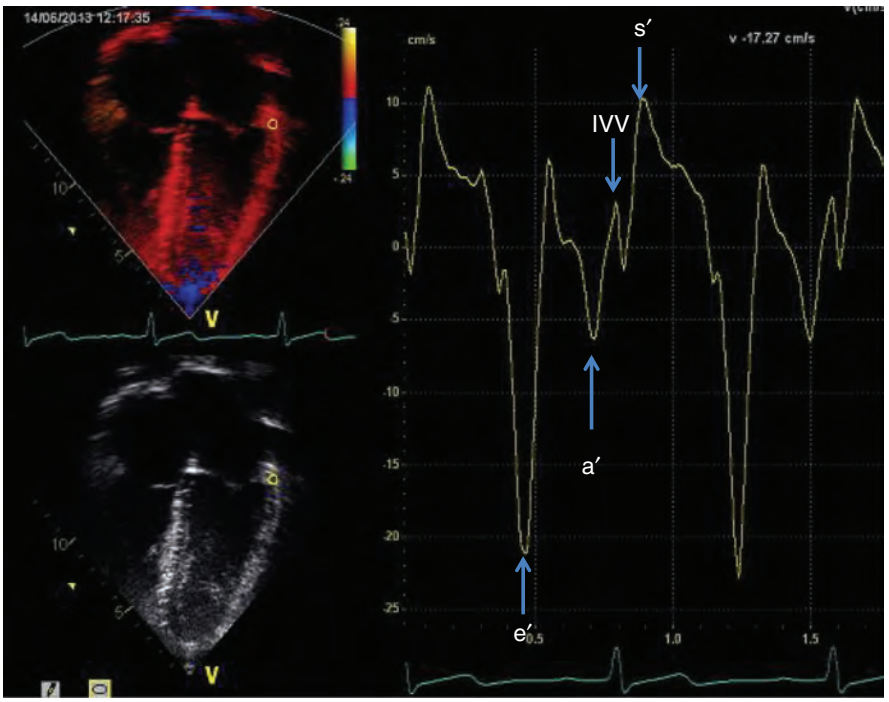


Figure 7.13 Myocardial velocity profile measured in the lateral mitral annulus derived from color Doppler myocardial imaging. The curve represents the mean velocities in the sample volume placed in the myocardial velocity map. As on the pulsed Doppler tracing peak early systolic (s′), peak velocity during the isovolumic contraction period (IVV), early diastolic velocity (e′), and diastolic velocity during atrial contraction (a′) can be measured.

presence of regional dysfunction, a healthy segment will pull on a noncontractile segment and cause it to move, even though the interrogated segment itself is not contracting (tethering). Third, as for most functional parameters, tissue Doppler velocities are influenced by changes in loading: increased afterload will lead to decreased peak systolic tissue Doppler velocities, with the opposite effect following increased preload. Moreover, tissue Doppler velocities are regional measurements and vary with the direction of motion. Therefore, longitudinal velocities in the same segment differ from radial velocities. Even within the same direction of motion, myocardial velocities differ along the ventricular wall. Longitudinal velocities are higher in the basal segments and decrease progressively towards the apex, which remains almost stationary during the cardiac cycle [67]. Similarly, in the radial direction, myocardial velocities are higher in the endocardium compared with the epicardium [68]. Finally, tissue Doppler velocities are influenced by heart size and therefore age- or body size-corrected reference values should be used. This is particularly important in pediatric patients.

Clinical use of tissue Doppler velocities for the assessment of systolic function

Given the aforementioned limitations of tissue Doppler imaging, as well as the subsequent development of myocardial deformation imaging, it is perhaps not surprising that clinical use of tissue Doppler velocities has lost some of its initial traction. Currently, tissue velocities are mainly used in the assessment of diastolic function and in the assessment of mechanical dyssynchrony, although even for this application its use is diminishing.

Use of tissue Doppler velocities in children

As tissue Doppler velocities are influenced by heart size, it became necessary to establish age-related normal reference values in children [69–72]. Eidem et al. published the largest cohort of normal data, including 325 children of different ages [67]. These data showed that peak pulsed tissue Doppler velocities are influenced by LV end-diastolic dimensions and LV mass. This implies that ventricular size should be taken into account when interpreting a measurement. One of the problems of the published normal values is that the variability of the measurements resulted in a wide range of normal values, particularly in younger children. This can partially be explained by the retrospective data collection, which likely influenced measurement variability. Nonetheless, the wide variability of the published normal values significantly limits the diagnostic utility of tissue Doppler measurements in children as it substantially decreases the sensitivity of the measurement to identify abnormal values. Our group tried to approach this problem using prospective standardized data collection. This substantially narrowed the normal range of values and also allowed us to study the relationship between tissue Doppler measurements and body size (see appendix). Loading conditions also influence tissue Doppler measurement. While initial studies suggested that tissue Doppler velocities were relatively load-independent [73], later experimental studies demonstrated that acute changes in loading influence tissue Doppler velocities [74]. There are, however, important differences between acute and chronic effects of volume and pressure loading. In chronic loading, cardiac remodeling can result in normalization of myocardial velocities. Studies including children with chronic volume and pressure loading documented only minimal changes in tissue Doppler velocities in patients with a ventricular septal defect or mild to moderate aortic stenosis [75,76].

Performing measurements during the isovolumic contraction period avoids the influence of afterload and forms the basis for measuring *myocardial acceleration during the isovolumic contraction period* (IVA). This parameter was proposed as a relatively load-independent index of contractility. IVA is calculated as the average rate of myocardial acceleration peak during the isovolumic contraction period (Figure 7.14) [77]. This velocity peaks at a time when the myofibers develop force and likely reflects the velocity of LV shape change. As IVA occurs when the aortic valve is closed, it is afterload-independent. However, subsequent studies have shown it to be influenced by preload, particularly when filling pressures are increased [78]. As isovolumic contraction is a short-lived event (30–40 ms), measurement of IVA requires imaging at very high temporal resolution (>200 frames/s). Typically we measure IVA in the basal segment of the LV lateral wall using a narrow-sector color tissue Doppler image. In experimental studies using pressure-volume loops, IVA has been validated as a sensitive, noninvasive index of LV contractility which is relatively unaffected by load-dependency within a physiologic range [79]. As IVA is a rapid event and it requires measuring a slope, its measurement variability can be high. IVA is highly dependent on heart rate, which is thought to reflect the physiologic force–frequency relationship. Consequently, its measurement has been applied clinically to measure the force–frequency response using pacing [80] and supine bicycle exercise testing [81]. Due to its variability and heart rate dependency, the clinical utility of IVA is limited, and it is still predominantly used as a research tool. We do not routinely measure IVA in our clinical functional protocol but use it to study force–frequency relationship during exercise.

As previously discussed, developments in myocardial deformation imaging and the limitations associated with the use of tissue Doppler measurements for the assessment of LV systolic function explain why use of systolic tissue Doppler velocities in the assessment of LV function is limited. We use systolic tissue Doppler velocities in the serial follow-up of several patient groups including children who have undergone heart transplant or those exposed to anthracyclines. If loading conditions are relatively similar, a decrease in peak systolic tissue velocity generally indicates a change in ventricular performance. This may allow detection of more subtle changes in cardiac performance. In pediatric patients with cardiomyopathy, tissue Doppler velocities have been shown to have prognostic value [82–84], but further prospective data are needed.

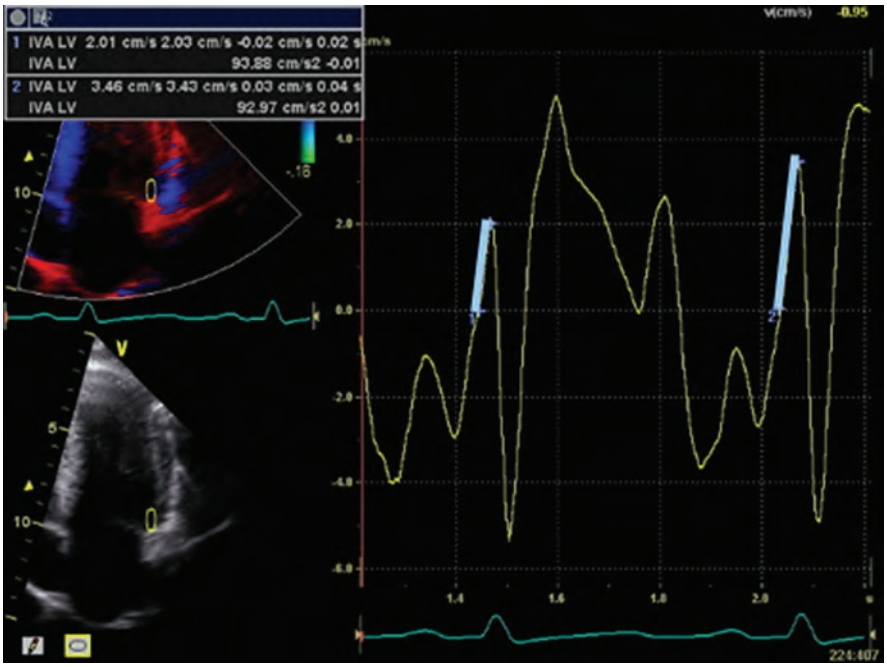


Figure 7.14 Measurement of myocardial acceleration during the isovolumic contraction period. This is measured from a color tissue Doppler-derived velocity tracing obtained in the basal part of the LV lateral wall. The acceleration is measurement as the mean acceleration (change in velocity divided by time of acceleration) of the IVV spike during the isovolumic period.

Deformation imaging in pediatric and congenital heart disease

As tissue Doppler velocities are influenced by global cardiac motion and translation, they do not accurately reflect segmental myocardial function. This is one of the major reasons why myocardial deformation imaging has largely replaced tissue Doppler measurements to assess systolic function. Myocardial deformation is measured by assessing segmental strain and strain rate. *Strain* is a dimensionless unit and represents the percent change in the dimension (deformation) of a myocardial segment. Typically end-systolic or peak systolic strain is measured. *End-systolic strain* corresponds to the maximal deformation measured in a certain direction at the time of aortic valve closure, thereby representing deformation during the ejection period. *Peak systolic strain* is the highest strain value measured in the contractile cycle, which can be measured after aortic valve closure in the case of post-systolic shortening. Certain conditions are associated with persistent myocardial shortening and thickening in certain segments after the aortic valve closes. This phenomenon is more pronounced in the presence of regional differences in function (e.g., ischemic heart disease) and when afterload is increased (e.g., early aortic valve closure). Review of the mechanisms underlying post-systolic shortening or thickening is beyond the scope of this chapter [85], but the differences between the two measurements are important when used clinically. *Strain rate* represents the velocity of deformation and is expressed as (/s).

Peak systolic strain rate occurs early during the cardiac cycle in the normal heart as normally peak force develops in the muscle in the first third of the cardiac cycle. Strain is influenced by afterload while strain rate measurements more accurately reflect myocardial contractility [86]. During the cardiac cycle, myocardial segments deform in different directions (Figure 7.15). Deformation is generally studied in the conventional cardiac reference system measuring longitudinal, circumferential, and radial deformation. In the longitudinal direction, as measured from apical views, the wall shortens in systole and lengthens in diastole. By convention, shortening is expressed as a negative value. Hence, longitudinal systolic strain values are negative. Circumferential shortening (strain) during systole can be measured from short-axis views at different levels: the basal level (just below the mitral valve), the papillary muscle level, and at the apical level, and is expressed as a negative value. Cardiac rotation and torsion can also be measured from the short-axis view. Rotation at the base is predominantly clockwise while at the apex it is counterclockwise (Figure 7.16). Rotation is expressed in degrees. The net difference between apical and basal rotation is called torsion or LV twist [87]. Recoil is the opposite movement to rotation while untwist is the opposite motion to twist.

Two different echocardiographic techniques allow measurement of regional myocardial deformation or strain. The initial technique was based on the calculation of tissue Doppler velocity gradients (TDI-based strain techniques) while more recent techniques are based on grayscale imaging using STE technology. Tissue Doppler-derived strain calculation measures the velocity gradient from the base to the apex in the longitudinal direction and from endocardium to epicardium in the radial direction [68,88]. Regional strain rate can be measured as the velocity difference between two segments of myocardium divided by the distance between them (= area of computation).

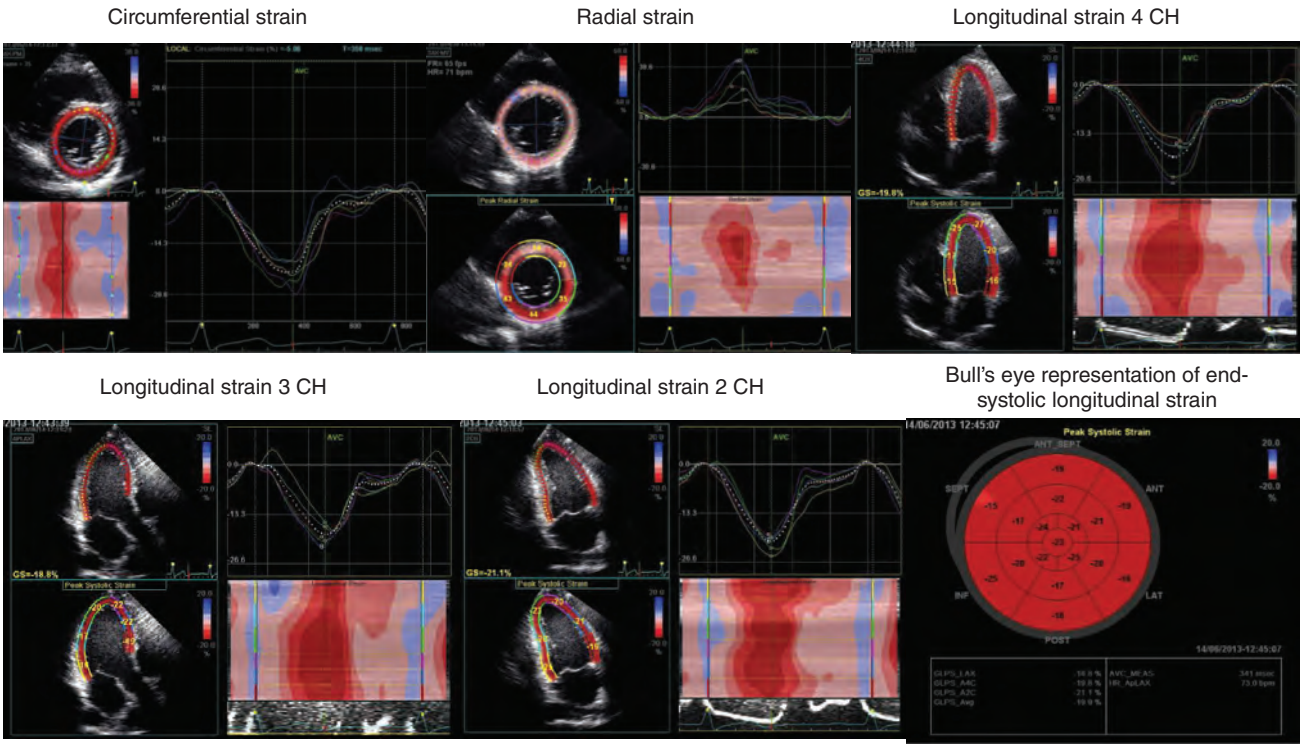


Figure 7.15 Myocardial strain calculations in different directions. Using speckle-tracking technology, LV circumferential, radial, and longitudinal myocardial deformation can be measured in the different myocardial segments. Global strain in a certain direction (such as global longitudinal stain) represents the average of the end-systolic strain measurements. In each segment end-systolic strain measurements are obtained and the number is represented on the segment. For each analysis strain curves are generated.

When integrating the strain rate curve over time, regional myocardial strain can be measured based on the strain rate curves (Figure 7.17). In pediatrics we use computational distances of 4–5 mm in the radial direction and 8–9 mm for the longitudinal direction. The tissue Doppler-based technique has all the disadvantages of conventional Doppler techniques, particularly the angle-dependency which increases measurement variability. This also limits the number of segments that can be analyzed for radial strain. Measurement of circumferential strain by tissue Doppler is possible but is prohibitively difficult

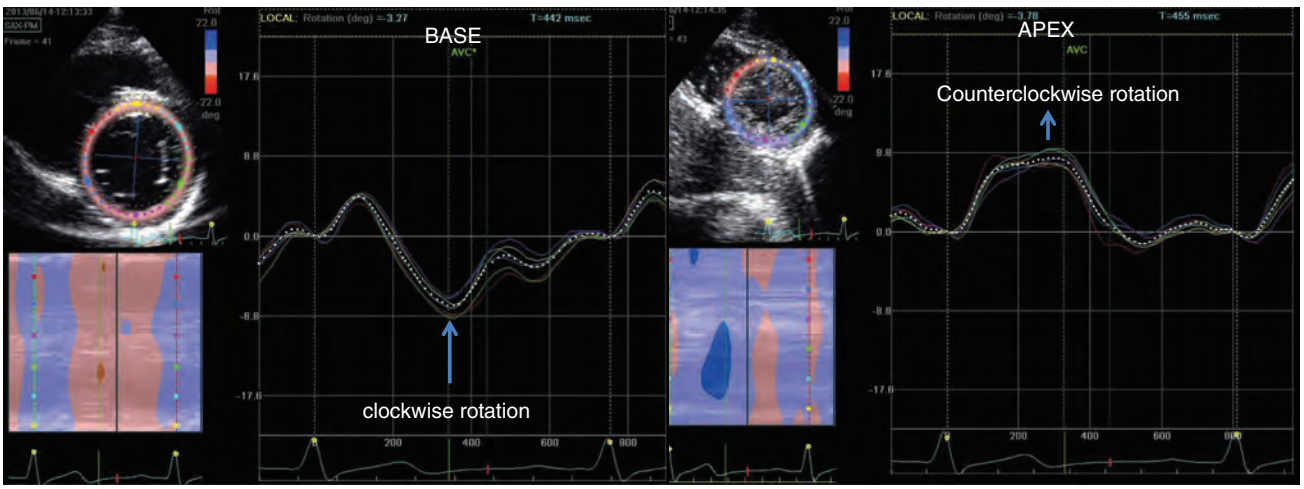


Figure 7.16 Myocardial rotation. From short-axis views obtained at the LV and apex, myocardial rotation can be quantified. By convention, clockwise rotation is negative and counterclockwise rotation is positive. At the base there is an early counterclockwise rotation followed by a clockwise rotation during ejection. The apical rotation is counterclockwise during systole. End-systolic rotation can be measured as well as derived parameters like rotation rate and recoil rate. Twist is the difference between apical and basal rotation.

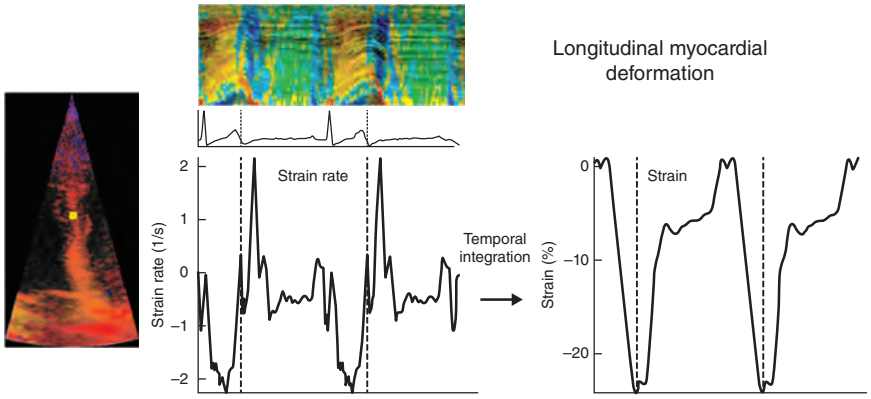


Figure 7.17 Strain measurements obtained from color tissue Doppler imaging. Velocity gradients can be measured in a myocardial segment, which represent myocardial strain rate; temporal integration of the myocardial strain rate curves represents myocardial strain. This method is angle-dependent and more variable compared with the speckle-tracking method, which has become the method used more commonly in clinical practice.

to allow its use in clinical practice. Furthermore, post-processing can be time consuming. Strain rate curves are based on velocity curves and tend to be very noisy which complicates identification of peak values. The advantage of tissue Doppler-based analysis is the very high frame rates which facilitate more accurate measurements; this is particularly important for strain rate calculations. Accordingly, strain rate measurements are approximately twice as high on tissue Doppler-derived images compared with speckle-tracking analysis [89]. Another limitation is that TDI-derived calculations allow strain to be calculated in only one direction (unidimensional). Since 2004, deformation imaging has become clinically more accessible with the introduction of 2D STE. This method is based on 2D grayscale imaging where myocardial deformation is measured by tracking myocardial reflectors (i.e., speckles) in a myocardial segment through the cardiac cycle. Myocardial deformation is then calculated based on the motion of the speckles (Figure 7.18). Different software packages are available to calculate myocardial deformation parameters using semi-automated tracking algorithms. As STE is a 2D technique, it is not angle-dependent and deformation can be derived in two dimensions from the same image. Hence longitudinal and radial (transverse strain) can be calculated from the apical views, while circumferential and radial strain, as well as rotation and torsion, can be ascertained from the short-axis views (Videos 7.4 and 7.5). Averaging the regional values for the 17 LV segments from the apical views results in global longitudinal LV strain. Compared to TDI-derived strain, speckle-tracking methodologies require less post-processing time and the software is generally more user-friendly. The frame rates currently are between 50–100 frames/s. Our group has demonstrated that in children, measurement reliability is good for longitudinal and circumferential strain (between 10–15%), but radial strain measurements are less reproducible and on some systems are highly variable [89]. We also noted differences between different vendors when the same measurement is repeated in the same subject using different ultrasound systems and analysis software. These differences are probably due to technical variability in the analysis algorithms used. Industry standardization is needed to improve the accuracy of the technology [89,90]. More recently 3D strain technology has been developed using full-volume acquisition [91]. This allows calculation of myocardial deformation in the same cardiac cycle in all myocardial segments. The disadvantage seems to be the lower frame rate, the higher variability, and the reliance on very good quality 3D data sets, all of which limit the current feasibility of the technology. While STE is still considered an emerging technology, technical improvements have allowed more widespread access to myocardial deformation imaging, which has resulted in a sizeable number of studies on this topic in general and specifically in pediatric and

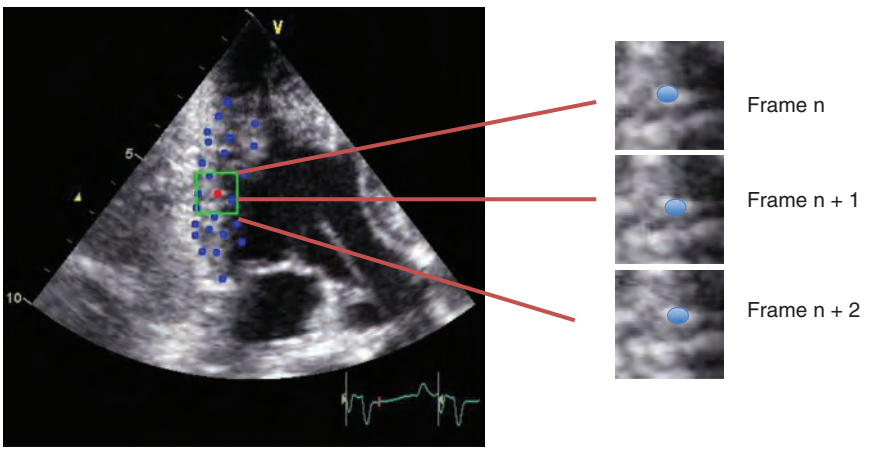


Figure 7.18 Two-dimensional speckle-tracking echocardiography. Speckles are echocardiographic reflectors within the myocardium, which can be tracked frame-by-frame throughout the cardiac cycle. The relative change of position of the speckles can be used to calculate myocardial strain.

Table 7.4 Left ventricular deformation imaging

	Strengths	Weaknesses
Deformation imaging		
2D Strain by TDI	• Geometry-independent • Ability to detect regional differences • High frame rates	• One-dimensional • Angle-dependent • Load-dependent
2D Strain rate by TDI	• Same as above	• High variability • Low signal-to-noise ratio
2D Strain by STE	• Ability to detect regional differences • Angle-independent • Two-dimensional • Short post-processing time • Assessment of longitudinal function • Assessment of circumferential strain, rotation, and torsion	• Radial strain measurements less reproducible • Load-dependent
2D Strain rate by STE	• Same as above	• Lower frame rates than TDI-derived SR • More variable
3D Strain by STE	• Ability to calculate strain in all directions • Measurements in a single heartbeat	• Lower frame rate • Higher variability • Reliance on very good quality 3D data sets • Load-dependent
3D Strain rate by STE	• Same as above	• Low frame rates are a major limitation

2D, two-dimensional; 3D, three-dimensional; SR, strain rate; STE, speckle-tracking echocardiography; TDI, tissue Doppler imaging.

congenital heart disease [56,92]. Currently, the main clinical applications of deformation imaging are quantification of regional myocardial dysfunction, early detection of myocardial dysfunction, and evaluation of mechanical dyssynchrony (Table 7.4).

Clinical applications in children

As with any new method, normal values have to be defined for the pediatric population. Due to continuing changes in technology as well as differences between available software packages, this has proven to be a challenging endeavor. The first paper on normal strain rate and strain data in children was based on TDI-derived measurements which are now all but obsolete in the clinical setting [93]. Boettler et al. compared strain values in different age groups and demonstrated that strain and strain rate values are influenced by heart rate [94]. More recent papers studied normal strain values obtained by STE [95,96]. The two studies used different speckle-tracking techniques, which resulted in slightly different values and normal ranges. While most data seem to suggest that strain values are relatively independent of age and heart size, Marcus et al. reported higher strain values in adolescence and suggested that age-appropriate measurements are required. In our laboratory we have established our own normal values, which are included in the appendix to this chapter.

Clinical applications of myocardial deformation imaging in the assessment of LV function

The use of deformation imaging is still not widespread and is not generally accepted in routine clinical practice. In our laboratory it has become part of a full functional LV assessment. Some of its current applications include the following.

Quantification of regional left ventricular function

This is an obvious indication in patients with coronary artery disease, which is less common in the pediatric compared with the adult population. Coronary artery problems can be present in patients with Kawasaki disease, congenital abnormalities of the coronary artery origins, or in patients after surgical coronary transfer or reimplantation such as after the arterial switch procedure. Traditionally, detection of regional myocardial dysfunction has largely been based on qualitative assessment of regional wall motion. This requires specific training and expertise. In practice a standard 17-segment model of the LV is used and an experienced reader qualitatively assesses function in each and every segment [97]. The 17 segments can be displayed in a circumferential polar plot also called a bull's eye plot (Figure 7.19). For subjective visual analysis a numeric scoring system has been developed based on the evaluation of systolic thickening in each segment. A higher score indicates more severe wall motion abnormalities (1 – normal, 2 – hypokinesis, 3 – akinesis, 4 – dyskinesis, and 5 – aneurysm). This scoring system can be used at rest as well as during exercise or pharmacologic stress. Despite its subjective nature, the diagnostic accuracy of this method is good in the hands of experienced readers. Nevertheless, availability of a quantitative method such as calculation of regional strain could decrease variability that stems from subjective assessment and improve diagnostic accuracy. Using the apical 2-, 3- and 4-chamber views, a full 17-segment longitudinal strain analysis can easily be performed. Figure 7.19 shows an

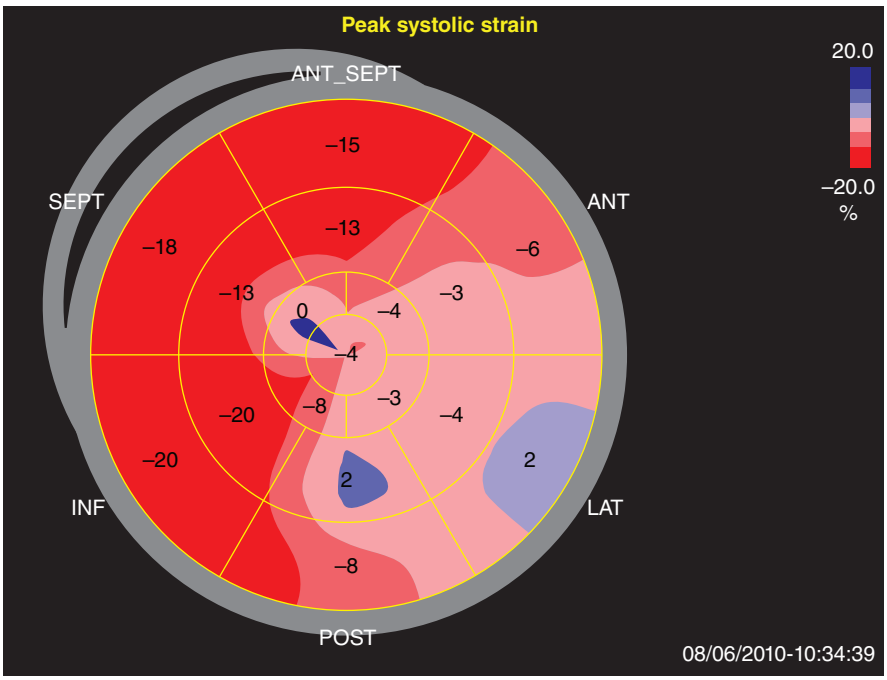


Figure 7.19 Regional myocardial end-systolic longitudinal strain map in an 11-year-old girl with myocardial infarction related to abnormal origin of the left coronary artery from the right cusp with posterior looping behind the aorta. The extent of the myocardial infarction can be easily displayed using the bull's eye representation of the myocardial segments.

example of a pediatric patient with a myocardial infarction based on an abnormal origin of the left coronary artery from the right coronary cusp running posteriorly to the aorta. The bull's eye plot represents the segmental distribution of the myocardial infarction.

Apart from being useful in the detection of coronary artery disease, strain methodology is capable of detecting subtle abnormalities in regional myocardial function that are not obvious to the human eye. In hypertrophic cardiomyopathy for instance, it was thought that systolic myocardial function is preserved and that obvious regional wall motion abnormalities are absent. However, using regional wall deformation, it is apparent that wall segments that are most hypertrophied also have the lowest longitudinal strain values [98,99]. Likewise, in patients with aortic stenosis and preserved ejection fraction, regional differences in wall motion are not detected visually in most patients. In contrast, when myocardial deformation parameters are quantified, reduced longitudinal deformation, particularly at the LV septum, is detected. This regional dysfunction can persist even after successfully relieving the aortic valve stenosis [100,101]. Reduced longitudinal function in the presence of preserved circumferential and radial function has also been found in patients after coronary reimplantation for abnormal origin of the left coronary artery from the pulmonary artery [102]. In this patient population this phenomenon is probably related to damage caused to the subendocardial fibers resulting in decreased longitudinal function. As opposed to the traditional reliance on assessment of global radial and circumferential function by measures such as shortening fraction, these data suggest that assessment of longitudinal function is a potentially important component in the assessment of ventricular function, which could potentially have important prognostic and therapeutic implications.

Detection of early myocardial dysfunction

Heart failure is a progressive disease and myocardial dysfunction can be difficult to detect in the early stages of the disease especially when using ejection fraction. In the presence of mild dysfunction, the heart employs several compensation mechanisms to maintain cardiac output. Early changes can be difficult to detect. In young patients with Duchenne muscular dystrophy and normal LV EF, we found subtle abnormalities in myocardial deformation, particularly in the inferior and inferolateral LV segments [103]. These segments seem vulnerable to early damage as reflected by reduced radial and longitudinal strain (Figure 7.20). We and others have detected regional and global myocardial deformation abnormalities in patients after anthracycline exposure with normal ejection fraction [104–106]. In a pediatric age range the prognostic value of these subtle changes is still unknown. In women treated for breast cancer with a highly cardiotoxic combination of anthracyclines and trastuzumab, changes in myocardial deformation were detectable prior to changes in EF; and, in combination with changes in biomarkers, changes in deformation were highly sensitive and specific in predicting later changes in EF [107–109]. There are limited data suggesting that this approach may also be useful when monitoring pediatric patients exposed to anthracyclines [110]. These data require further validation, but in our laboratory we routinely include longitudinal strain measurements in the follow-up of this patient population. Whether serial

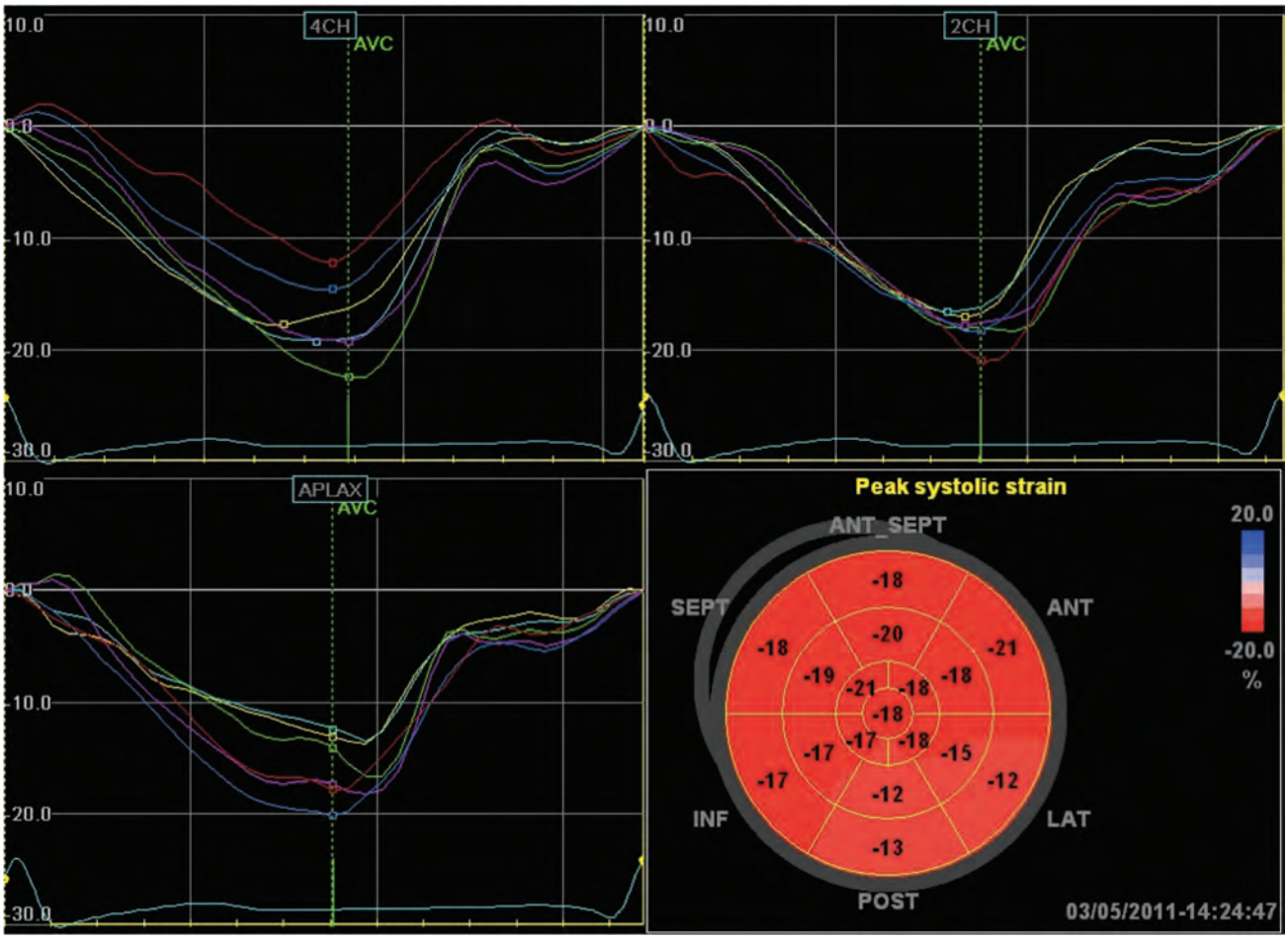


Figure 7.20 Early detection of regional myocardial dysfunction in a 10-year-old boy with Duchenne muscular dystrophy with normal ejection fraction. A reduction in longitudinal deformation can be observed in the lateral and posterior wall segments.

changes in strain can help to detect patients at risk for developing cardiomyopathy remains to be proven.

Detection of mechanical dyssynchrony

An important component of myocardial function is the synchronous contraction of the various segments during the cardiac cycle. If mechanical activation is delayed in certain segments, the efficiency of contraction decreases and can cause progressive myocardial dysfunction. Electrical conduction delays, such as left bundle branch block, pacing and regional myocardial fibrosis, can cause delays in myocardial mechanical activation. Cardiac resynchronization therapy can be a very efficient treatment for this condition but the indications for its use are still controversial, particularly in children with congenital heart disease with variable morphology. There is an extensive literature on the role of echocardiographic measurements to help identify patients with mechanical dyssynchrony, the discussion of which goes beyond the scope of this chapter. We refer the reader to recent reviews on this topic pertaining to the pediatric population [15,16] as well as to the guidelines published by the American Society of Echocardiography [111]. In our laboratory we combine different methodologies and our protocol includes storage of all raw echocardiographic data for offline mechanical dyssynchrony analysis. The various echocardiographic techniques are used to study the timing of activation of different wall segments and for identifying abnormal early activation of certain segments with delayed activation of others. The methods include visual assessment of the 2D images, M-mode, color tissue Doppler, and STE. M-mode is used to identify septal-to-posterior wall motion delay and for the presence of a septal flash (early contraction followed by immediate septal stretch) (Figure 7.21). Color tissue Doppler data from the apical 4-chamber, 2-chamber, and 3-chamber views are stored for offline analysis. We measure the time-to-peak systolic tissue Doppler velocities in the basal and mid segments of the six walls, calculate the largest difference in time-to-peak between 12 segments and also calculate the standard deviation of the 12 measurements (Yu-index). These timing indices can be very challenging to measure and were shown to be highly variable and not predictive of the response to resynchronization therapy in a randomized trial

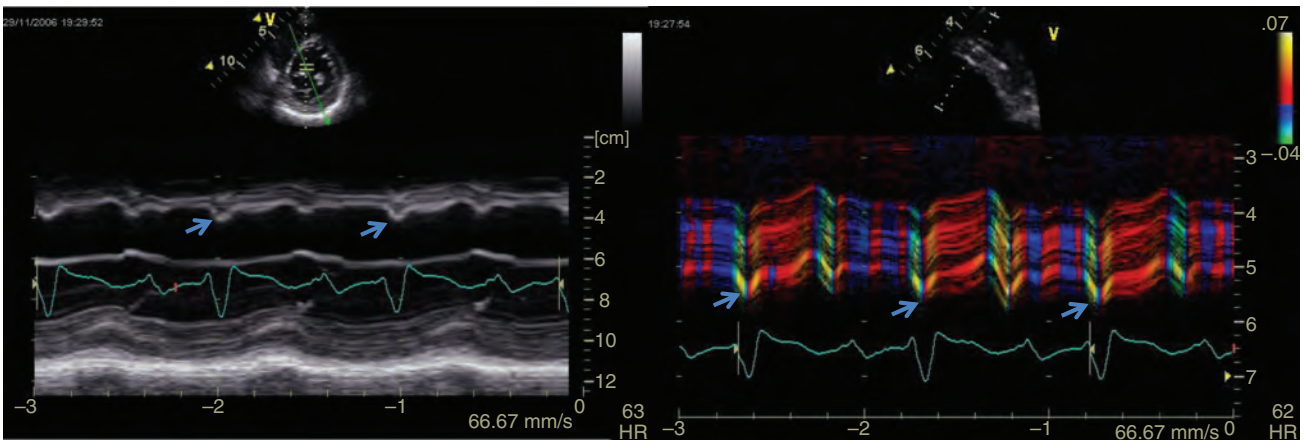


Figure 7.21 Myocardial dyssynchrony in a patient with left bundle branch block. A typical septal pattern with early activation of the basal part of the interventricular septum with subsequent lengthening of this segment as it is stretched by the activation of the LV lateral wall. This phenomenon is called the septal flash and has been described to be a good predictor for the response to cardiac resynchronization therapy.

[112]. Consequently, we now rely less on this methodology. Finally, we include longitudinal strain analysis in our assessment to evaluate segmental activation patterns. In particular, we evaluate for pre-activation of some segments, with concurrent stretching of others, followed by (relatively) strong contraction of pre-stretched segments. For this purpose a 17-segment longitudinal strain analysis from the apical views is used. If dyssynchrony is suspected on the longitudinal strain curves, we perform further offline analysis studying circumferential and occasionally radial strain patterns, looking for segments with early and late mechanical activation. We have found these techniques to be particularly helpful in identifying the detrimental effects of single-site, RV pacing-induced dyssynchrony and dysfunction in some children, sometimes leading to upgrade of the pacing system to a biventricular pacemaker. Normative data for timing differences have been published and could potentially be used for identifying pediatric patients with mechanical dyssynchrony [113].

With chronic resynchronization therapy (CRT), echocardiography can be used to guide lead implantation and assess the acute effect of different pacing sites on cardiac function. The effect on mechanical coordination can be studied and evaluating A-V and V-V synchrony can be used to optimize CRT. As experience is relatively new in children, we routinely repeat evaluation and pacer optimization at 3–6 months after implantation. To assess the effect of CRT, visual assessment, ventricular dimensions, volumes, EF and strain parameters can be combined using a complete functional assessment including myocardial mechanics.

Summary: Echocardiographic assessment of LV function in practice

In the previous section, we provided an overview of the various echocardiographic methods that can be used to assess LV function. Each method has its advantages and disadvantages and no single parameter can reliably define LV systolic function. It is integrating the information from different parameters and defining consistency in the findings that help with interpretation. A good example is the early detection of rejection after cardiac transplantation. Noninvasive follow-up requires a consistent imaging protocol, as the initial echocardiographic signs of rejection can be subtle. These changes can include a mild increase in wall thickness (inflammatory response), a mild increase in AV-valve regurgitation, mild changes in diastolic properties, a mild reduction in tissue Doppler velocities and strain measurements, and the presence of pericardial effusion. The evidence for early rejection becomes stronger if the different parameters change at the same time. The concept of multiparametric functional assessment forms the basis of echocardiographic rejection scoring systems, which have been proposed for clinical use. This concept can be expanded to any functional assessment and forms the foundation of our functional protocol, which can be considered as a segmental approach to LV systolic function. Our laboratory's functional protocol is detailed in the appendix but its outline includes:

- Assessment of *LV dimensions and wall thickness* (cardiac remodeling).
- Assessment of *global pump performance*
 - M-mode based %FS
 - Biplane Simpson's EF
 - 3D EF.
- Assessment of *regional myocardial function*
 - Pulsed-wave tissue Doppler measurements at the basal segments (longitudinal function)
 - Color tissue Doppler acquisitions
 - 2D grayscale acquisitions for strain analysis (RAW–DICOM format)
 - Some vendors allow easy post-processing of longitudinal strain on the machines and representation of the measurements in a 17-segment model.

- If indicated, offline assessment of *mechanical dyssynchrony.*
- *Afterload assessment*. In the morphologically normal LV, we obtain data for calculation of wall stress and *V*cfc.

The echocardiographic assessment of right ventricular function

Echocardiographic assessment of RV function is an important topic in congenital heart disease as the RV is affected by multiple structural defects. The echocardiographic quantification of RV function is challenging and in most echocardiographic laboratories assessment of RV function is limited to subjective visual evaluation ("eyeballing"). In recent years several quantitative techniques have been developed that provide more objective measures of RV function [114,115]. As for the LV, we believe that there is no single parameter that fully describes RV function, but that useful quantitative information can be obtained by combining multiple parameters. Ultimately, it is our hope that more consistent use of these measurements will provide the necessary information for patient management but this still requires further prospective evaluation.

The RV is more difficult to evaluate than the LV because of its more complex geometry, its anterior position in the chest and its different physiology and mechanics. The RV has a complex 3D shape with a triangular appearance in the sagittal plane and a crescent shape in the coronal plane. As the RV inflow and outflow are positioned in different planes, they are difficult to image simultaneously by 2D techniques. The normal RV is thin-walled (around 3–5 mm in the adult) and has prominent trabeculations, which complicate wall detection and endocardial definition. The apical trabeculations form a complex network of muscle which blood enters in diastole and is squeezed out in systole. This trabecular network functions as a sponge and seems important for maintenance of RV output. The anterior position of the RV in the chest limits echocardiographic visualization due to limited spatial resolution in the near field of the ultrasound beam. Finally, lung interference can further limit echocardiographic windows. This can be especially problematic in patients with lung disease in whom evaluation of RV function can be important. Following the predominantly longitudinal orientation of the RV fibers, normal RV contraction is characterized by longitudinal motion of the base towards the apex, and less circumferential and rotational motion. Additionally, RV contraction is characterized by a bellow-like motion of the free wall towards the septum and bulging of the ventricular septum into the RV cavity. The normal RV pressure-volume loop has a trapezoidal shape with poorly defined isovolumic periods. This is in contrast to the typical rectangular LV pressure-volume loop, which has clearly defined isovolumic contraction and relaxation phases. RV output is highly sensitive to increased afterload and a relatively mild acute increase in afterload will lead to reduced RV output.

As for the LV, assessment of RV function starts with measurement of RV dimensions. The American Society of Echocardiography published recommendations for standardized 2D RV measurements [116].

Various 2D echocardiographic views should be obtained to allow full coverage of the RV, including its inlet, trabecular and outlet segments. This requires measurements obtained from apical, parasternal long-axis, short-axis, and subcostal views (Figure 7.22). Normal RV dimensions are available for the adult

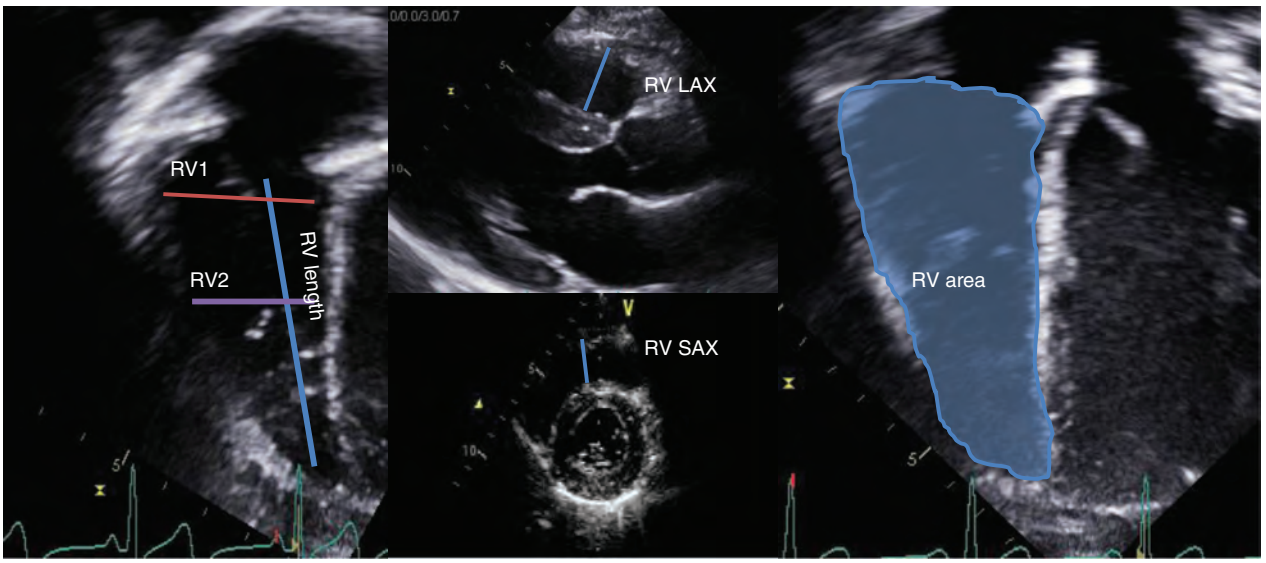


Figure 7.22 Measuring RV dimensions. Right ventricular dimensions can be measured from the apical RV-centric view (RV1 = transverse dimension of the RV just below the tricuspid valve, RV2 = transverse RV dimension at mid RV level, RV length measured from the tricuspid annulus to the RV apex. The RV dimensions are also measured from the parasternal short-axis and long-axis views. The RV end-diastolic area as obtained from the RV-centric view has been shown to have the highest correlation with RV volumetric measurements by magnetic resonance imaging.

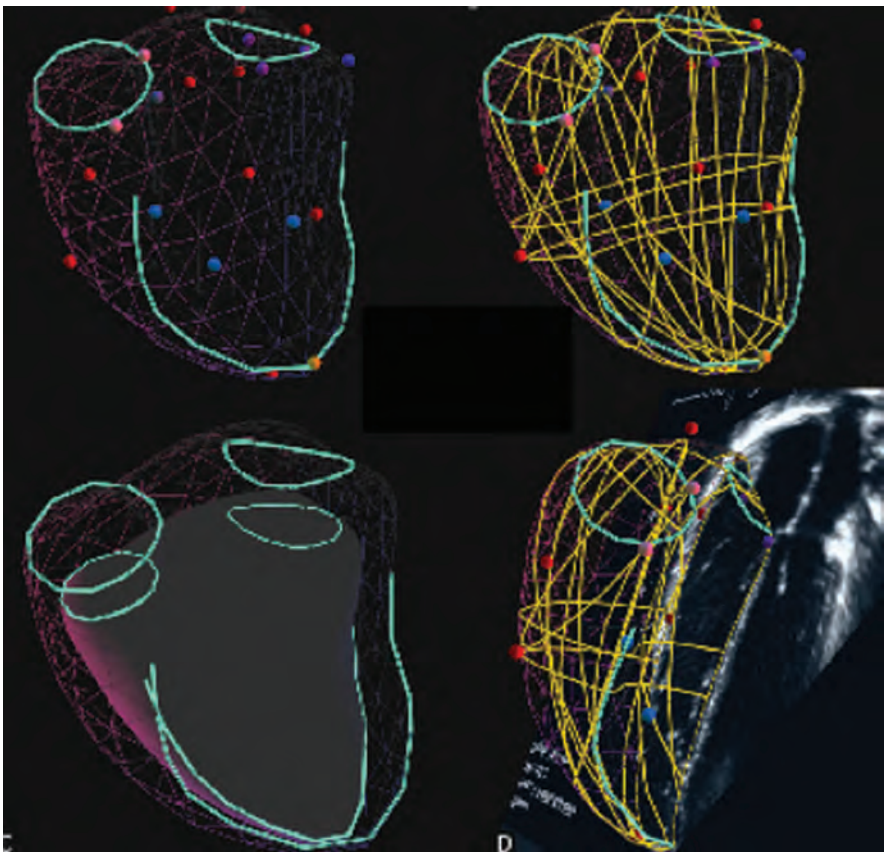


Figure 7.23 Two-dimensional-based 3D reconstruction of RV volumes. This method uses 2D images that are obtained with a magnetic tracker attached to the probe. On the 2D images, anatomic landmarks are identified (tricuspid annulus, pulmonary valve, septum, RV endocardium) and the RV volumes are reconstructed based on an online database of RV shapes.

population. However, for the pediatric population z-scores are not available for all recommended measurements. Two-dimensional measurements are reliable if well standardized and can be used for monitoring changes in RV size during serial follow-up. Several complicated formulae have been proposed to calculate RV volumes based on 2D measurements, but none have accurately predicted RV volumes when validated against cardiac MRI [117]. Therefore, this approach has largely been abandoned. Amongst the different 2D measurements to predict RV volumes, the end-diastolic RV area as measured from the apical 4-chamber view correlates best with RV volumes measured by MRI [118,119]. Based on these findings it is suggested that indexed (for body surface area) RV end-diastolic area is probably the best 2D substitution for RV volume or could at least be used to determine which patients require additional imaging. When using this method, it is important to obtain a good RV-centered apical 4-chamber view without foreshortening the RV. We include the RV trabeculations in the RV area, as this is the method used by our MRI specialists when measuring RV volumes (Figure 7.23). The main limitation of the RV area method is that currently there are no normal pediatric z-scores available for this measurement. We recently validated a 2D-based 3D reconstruction method. Using a magnetic tracker, 2D echocardiography images can be located in 3D space [120,121]. Anatomic landmarks (points) are then marked on the 2D images and the 3D volume reconstructed using a catalogue of reference RV shapes (Figure 7.23). The method has proven to be very reliable and measurements correlate well with MRI measurements, but the need for a magnetic tracking device and dedicated equipment limits its clinical use. Three-dimensional echocardiography allows full volumetric data acquisition and subsequent offline analysis of RV volumes using dedicated software (Figure 7.24; Video 7.5). However, 3D

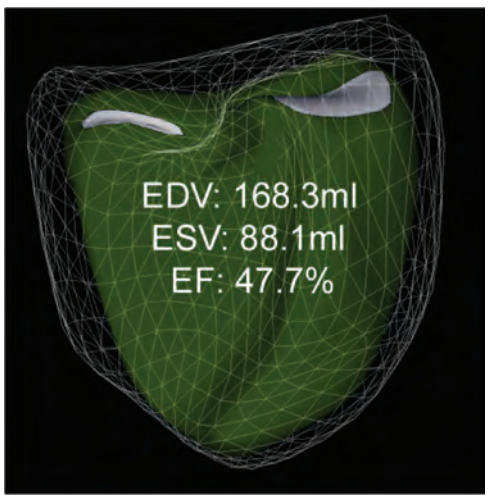


Figure 7.24 Three-dimensional echocardiography can be used for measuring RV volumes using dedicated analysis software.

	Strengths	Weaknesses
Dimensional changes		
Fractional area change	• Correlates with RV EF	• Geometry-dependent – does not assess the RV outflow tract • Variability due to difficulty of tracing RV endocardial border at end-systole • Load-dependent
Ejection fraction by 3DE	• More accurate than 2DE EF methods	• Reliance on very good quality 3D data sets • Load-dependent
TAPSE by M-mode	• Ease of measurement • Correlates with RV FAC and EF if no regional dysfunction • Highly reproducible	• Regional parameter • Load-dependent • Influenced by valve regurgitation

2DE, two-dimensional echocardiography; 3DE, three-dimensional echocardiography; EF, ejection fraction; TAPSE, tricuspid annular plane systolic excursion.

Table 7.5 Right ventricular systolic function derived from dimensional changes

echocardiography for assessing RV volumes has two important limitations. The first is the limited feasibility of the method. Full, high-quality 3D data sets of the RV can be difficult to obtain particularly when the RV is dilated and in postoperative patients [122]. A second limitation is the observation that 3D echocardiographic RV volumes are generally 15–34% lower compared with MRI volumes [122–124]. This discrepancy may be related to difficulties in echocardiographic acquisition (with the RV not completely included in the data sets) and in RV endocardial border detection and definition. In various studies the intra- and interobserver variability of 3D volumetric measurements varied between 10 and 20%, which needs to be taken into consideration for the interpretation of serial measurements.

RV functional parameters

RV functional parameters from dimension changes

As for the LV, the most commonly used quantitative methods to assess RV function are based on measuring dimension changes (Table 7.5). Due to its complex geometry and longitudinal contraction pattern, simple 1D or 2D techniques such as SF and the biplane Simpson's or area-length methods that rely on geometric assumptions are not applicable to the RV. Calculation of *fractional area change* from the RV-centric apical 4-chamber view is a viable alternative. This method measures RV end-diastolic (RVEDA) and end-systolic (RVESA) areas from the apical 4-chamber view (Figure 7.25).

$$\text{RV FAC (\%)} = [(\text{RVEDA} - \text{RVSA})/\text{RVEDA}] \times 100.$$

A normal FAC value is >40%. This method requires a good quality apical view and we trace the RV endocardium at the base of the trabeculations. Feasibility is dependent on the quality of the echocardiographic windows, but in our experience FAC measurement is feasible in most patients. The variability of the FAC measurement seems to be mainly related to the difficulty of measuring RVESA as the endocardial border is difficult to identify at end-systole. FAC only measures dimensional changes in the inflow and trabecular portions of the RV, which may result in overestimation of RVEF in the presence of right ventricular outflow tract dysfunction as may occur in postoperative tetralogy of Fallot patients. Despite these limitations, FAC correlates well with RV EF. In our practice we consider it a useful tool, which is easy to integrate into clinical practice. If available, 2D-based 3D reconstruction or other 3D techniques can be used to measure RVEF in select patients.

As longitudinal shortening is the predominant vector determining RV output, assessment of longitudinal function is an important component of RV functional assessment. This easiest method is measurement of the *tricuspid annular plane systolic excursion* (TAPSE), which is obtained by placing an M-mode

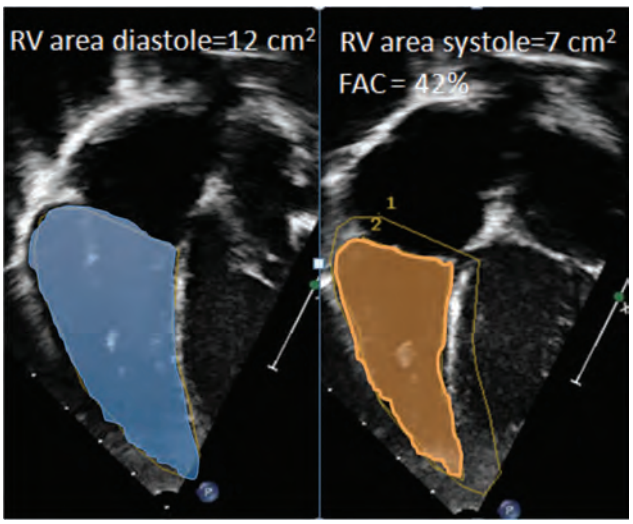


Figure 7.25 RV fractional area change. From an apical RV centric view RV end-diastolic and end-systolic area are measured and the fractional area change is calculated.

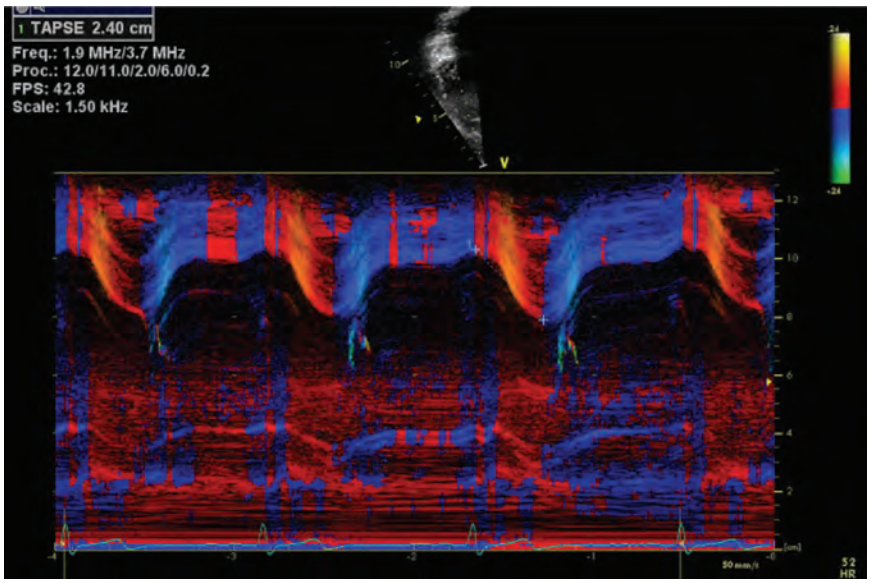


Figure 7.26 Tricuspid annular plane systolic excursion (TAPSE). An M-mode cursor is placed through the tricuspid annulus aligned with the longitudinal motion of the annulus during systole. The excursion of the annulus during systole is measured. We use color tissue Doppler to help with the timing of the measurements.

cursor through the tricuspid lateral annulus (Figure 7.26). We use color Doppler M-mode to define the onset of systole and the point of maximal systolic excursion. TAPSE measures the distance the RV annulus travels during systole, which is normally >1.5 cm in adults. Because TAPSE is dependent on cardiac size, normal pediatric data should be used in children [125]. TAPSE has been found to correlate well with RVEF and fractional area change (FAC%). It is, however, a regional parameter measuring longitudinal shortening only in the RV lateral free wall. In patients after tetralogy of Fallot repair who have regional dysfunction in the RV outlet secondary to outflow tract surgery, TAPSE has been found to correlate weakly with global RVEF [126,127]. Because TAPSE is easy to measure, is highly reproducible and normal values are available in children, we consider it a useful quantitative parameter to serially assess RV longitudinal function in patients with right heart disease.

Data on the use of RV systolic velocities (tricuspid annular velocities) to quantify RV longitudinal function have also been published and will be discussed later.

Doppler indices: the myocardial performance index

Because RV physiology is characterized by very short or absent isovolumic events (especially isovolumic relaxation), the use of isovolumic time intervals to assess RV function is not intrinsically logical. Nevertheless the myocardial performance index has been applied to the RV, based on measurements of tricuspid inflow patterns and the pulmonary artery blood pool Doppler. However, due to RV geometry these Doppler signals cannot be measured simultaneously, which increases measurement variability. Although the normal RV has little if any isovolumic periods, in the presence of RV dysfunction, the isovolumic time intervals prolong and the ejection time shortens resulting in a prolonged MPI. Apart from the conceptual problem of applying this principle to the RV, MPI is highly sensitive to changes in loading conditions [51]. As for the LV, an abnormal MPI can reflect changes in either systolic or diastolic function (or both) and in loading conditions. MPI derived from tissue Doppler was found to correlate well with pulmonary vascular pressures and resistance in pulmonary arterial hypertension (PAH) before and after surgery for thrombo-embolic pulmonary vascular disease [128]. After surgery, the absolute change in MPI correlated well with the concomitant change in PVR. This likely reflects the prolongation of the isovolumic relaxation period with increased PVR. Indeed, the ratio of the isovolumic relaxation to ejection period has been used as a noninvasive marker of pulmonary pressures and does not in itself reflect inherent RV contractile function. As a combined ventricular–vascular index, MPI was shown to be a strong prognostic factor in patients with primary pulmonary hypertension [129].

In congenital heart disease MPI has been used as a geometry-independent indicator of RV performance after tetralogy of Fallot repair. In this patient group MPI correlated well with RVEF measured by CMR; an MPI > 0.40 predicted an RVEF < 35% with good sensitivity and specificity [130]. However, the use of the MPI in repaired tetralogy of Fallot patients is even more counterintuitive as due to the relatively high prevalence of pulmonary regurgitation and restrictive physiology, true isovolumic events are uncommon. Because the MPI lacks a physiologic basis in these conditions, we have not included it in our laboratory's RV functional protocol (Table 7.6).

Tissue Doppler and myocardial deformation imaging

Tissue Doppler velocities measured in the basal part of the RV free wall measure the velocity of longitudinal motion. These are

	Strengths	Weaknesses
Blood pool and tissue Doppler indices		
d*P*/d*t*	• Geometry-independent • Afterload-independent	• Preload-dependent • Clear continuous-wave Doppler tracing required • Very short time interval limits reproducibility • More difficult to measure for RV than for LV
Myocardial performance index (MPI) by pulsed wave and TDI	• Geometry-independent • TDI-derived MPI correlates with PVR • Correlates with RV EF	• Tricuspid inflow and pulmonary artery Doppler velocities not measured simultaneously (which is why TDI measurement is preferred) • Load-dependent
Myocardial acceleration during isovolumic contraction (IVA)	• Geometry-independent • Relatively afterload-independent • Heart rate dependence allows for study of force–frequency relationship	• Influenced by preload, especially when filling pressures are increased

d*P*/d*t*, ratio of change in pressure over change in time; TDI, tissue Doppler imaging.

Table 7.6 Blood pool and tissue Doppler indices of right ventricular function

easily obtained and reproducible measurements that are useful for quantifying longitudinal function and can be used in the serial follow-up of patients (Figure 7.27). As for the LV, disadvantages of tissue Doppler measurements at the basal RV free wall include their angle and load dependency, the influence of translational motion, and the effect of segmental interactions. RV longitudinal tissue velocities are higher than those obtained in the LV. As for LV velocities, heart size influences the velocities and age-adjusted measurements should be used (see appendix). To overcome the load-dependency of peak systolic velocities, RV isovolumic acceleration (IVA) was proposed as an alternative measurement. Normal values of IVA measured in the basal segment of the RV free wall are >1.1 m/s^2. Isovolumic acceleration has been shown to be a good method to investigate contractile reserve using dobutamine in patients after atrial switch repair for TGA. The change in IVA before and after dobutamine correlated well with the change in end-systolic elastance [131]. Isovolumic acceleration is strongly dependent on heart rate and has been used to study the force–frequency relationship in patients after congenital heart surgery [80]. Frigiola et al. demonstrated an inverse relationship between baseline IVA measurements and the severity of pulmonary regurgitation [132]. However, measurement variability and heart rate dependency limit its use in clinical practice.

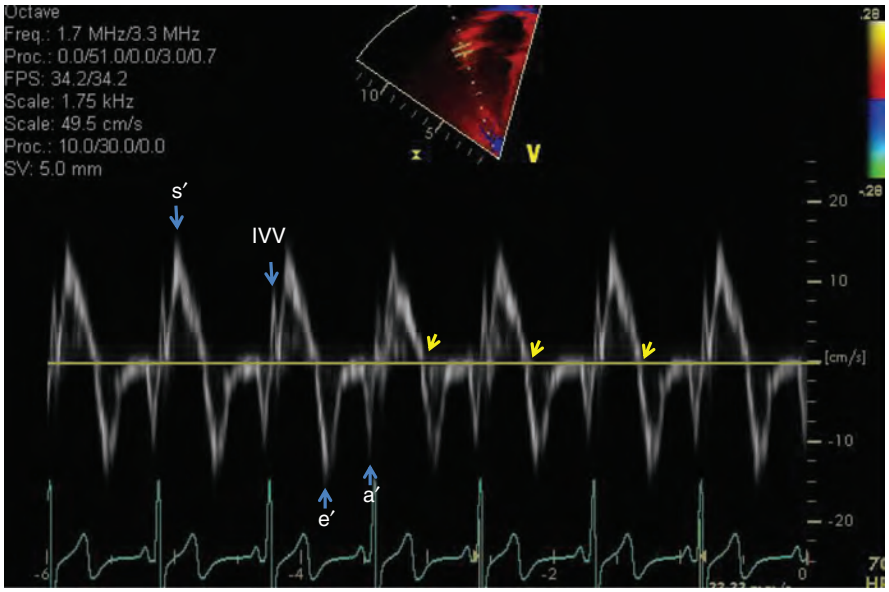


Figure 7.27 Pulsed tissue Doppler of the RV lateral basal segment. Compared with the mitral annulus tracing the absence of an isovolumic relaxation period can be noted on the trace. The velocity continues from end-systole into early diastole (yellow arrows). This is typical for a normal RV.

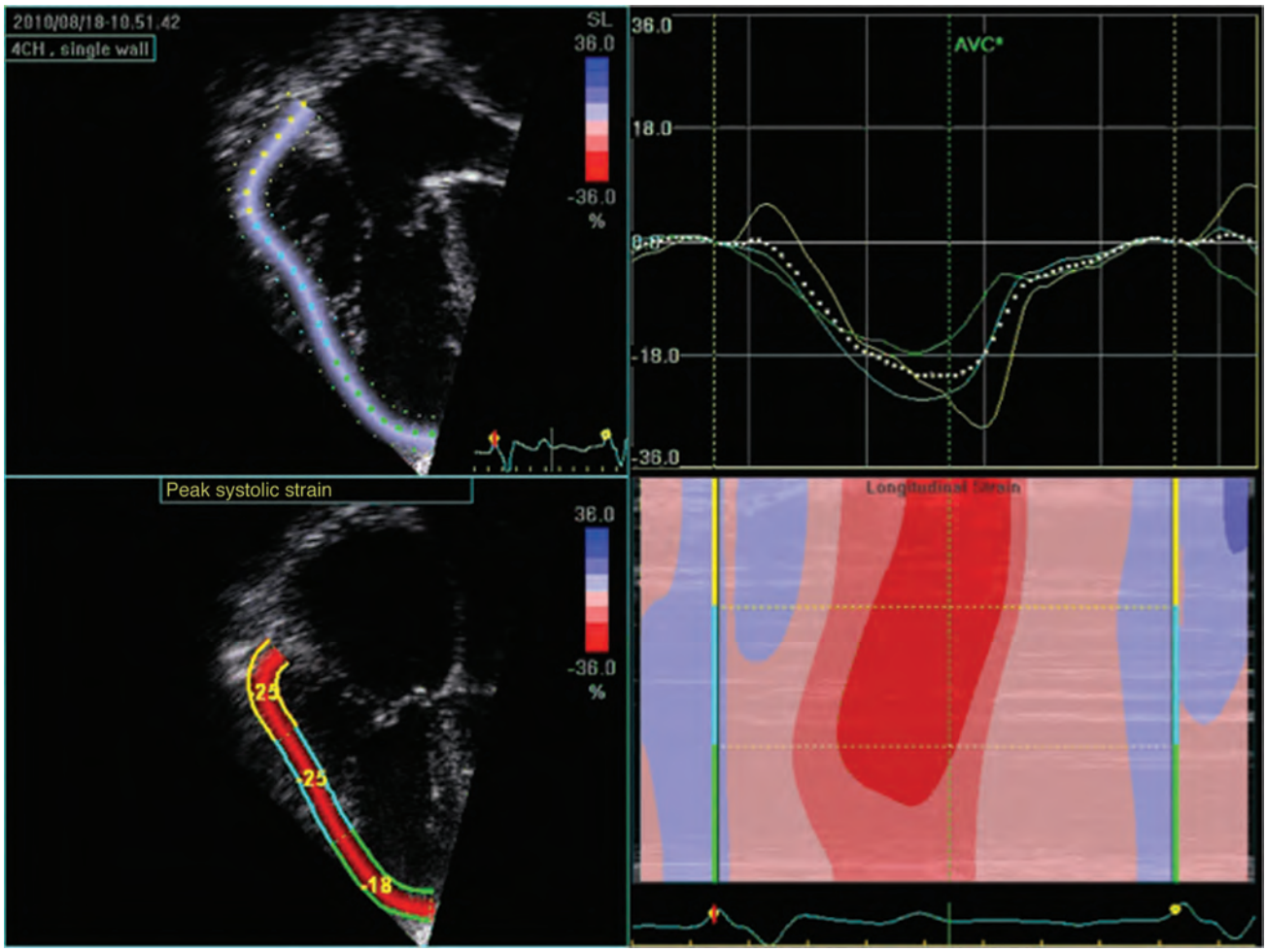


Figure 7.28 RV longitudinal strain measurements in a patient after tetralogy of Fallot repair. Typically in this patient population longitudinal strain is lower in the RV apical segments.

Tissue Doppler-derived strain measurements and speckle-tracking methodologies can also be used to measure RV myocardial deformation and mechanics (Figure 7.28) (Table 7.7). The number of studies investigating RV function using strain and strain rate imaging is growing rapidly. Normal RV strain values for children and adults are available. Due to limitations in echocardiographic windows, it is not possible to image all RV segments. Generally RV strain analysis is limited to the assessment of longitudinal strain in the RV free wall imaged from the apical 4-chamber view. Due to the thin RV walls, radial contraction is not measurable and too variable; and, as there are few circumferential fibers in the normal RV, the circumferential contribution to RV ejection is limited. This may differ in the systemic RV in which RV hypertrophy seems to cause more circumferential shortening and radial thickening with relatively decreased longitudinal deformation [133]. In patients with global RV dysfunction, longitudinal strain measurements correlate well with RV EF as an ejection parameter [134]. This relationship is weaker when regional dysfunction is present such as in patients after tetralogy of Fallot repair [135]. Our group also demonstrated important regional differences within the RV free wall, with decreased RV apical deformation relative to basal longitudinal strain in patients after tetralogy of Fallot repair. Very few data are available on the prognostic value of reduced strain measurements. In patients with PAH, both tissue velocities and RV longitudinal strain measurements are reduced in the RV free wall. Sachdev et al. recently demonstrated that a global longitudinal strain >12.5% was a strong predictor for clinical right heart failure, clinical deterioration, and mortality [136,137]. In this study, and in others, a more significant reduction in apical longitudinal strain values was observed, which suggests that the RV apex plays an important role in maintaining RV output in various diseases. The role of strain imaging in congenital RV diseases needs further study, but quantification of regional RV function by strain measurements is a promising emerging technique that requires further evaluation.

Table 7.7 Right ventricular deformation imaging

	Strengths	Weaknesses
Deformation imaging		
2D Strain by TDI	• Geometry-independent • Ability to detect regional differences	• Usually not possible to visualize all RV segments • Thin-walled RV • Limited to longitudinal strain in normal RV • One-directional • Angle-dependent • Load-dependent • Tethering
2D Strain rate by TDI	• Same as above • Higher frame rate than STE	• Same as above
2D Strain by STE	• Geometry-independent • Ability to detect regional differences • Angle-independent • Multidirectional • Less post-processing time • More user-friendly software	• Usually not possible to visualize all RV segments • Thin-walled RV • Limited to longitudinal strain in normal RV • Radial strain measurements less reproducible • Load-dependent
2D Strain rate by STE	• Same as above	• Same as above
3D Strain by STE	• Ability to calculate strain in all directions	• Lower frame rate • Higher variability • Reliance on very good quality 3D data sets • Load-dependent
3D Strain rate by STE	• Same as above	• Same as above

2D, two-dimensional; 3D, three-dimensional; STE, speckle-tracking echocardiography; TDI, tissue Doppler imaging.

Right ventricular dyssynchrony and ventricular–ventricular interactions

To date, the vast majority of research into mechanical dyssynchrony has focused on left ventricular dyssynchrony. However, RV dysfunction has been found to be associated with mechanical dyssynchrony. In the normal RV, there are regional differences in mechanical activation between the different parts of the RV (inflow and outflow) with the RV infundibulum contracting after the RV inflow [138]. As this is more difficult to study, most studies on RV mechanical dyssynchrony have focused on the delay in time to peak systolic motion or deformation between the RV lateral wall and the ventricular septum [139]. In adults with pulmonary hypertension the delay between time to peak strain at the lateral wall and septum was significantly increased compared to controls, as was interventricular dyssynchrony (delay between time to peak strain between the LV and RV lateral wall). Both RV delay and interventricular dyssynchrony were strongly associated with RV FAC% and RV dyssynchrony is linked to disease severity and functional class in this population [140,141]. RV intraventricular and interventricular delay by strain imaging have also been associated with low RVEF and low oxygen consumption during exercise in patients with a systemic RV after atrial switch operation for transposition of the great arteries [142]. RV intra- and interventricular dyssynchrony may also impact RV function and exercise tolerance after repair of tetralogy of Fallot [143]. In PAH, interventricular dyssynchrony, caused by prolonged RV contraction and measured by CMR circumferential strain, has been proposed to impair LV filling via septal shift and reduced RV ejection due to inefficient contraction and postsystolic shortening, overall leading to reduced cardiac output [144]. The prolonged RV contraction is not caused by bundle branch block, as is typical for LV dyssynchrony in adults, but by prolongation of RV wall tension development [144]. In addition to decreased cardiac output that results directly from RV failure, RV dilatation displaces the ventricular septum leftward and impedes LV filling. This secondary LV geometrical change, easily measured from the ratio of the long axis-to-short axis of the LV by 2D echo or CMR imaging, is linearly related to cardiac output, whereas RV end-diastolic volume, in and of itself, was not related to cardiac output [145]. Although ejection duration is shortened in PAH, RV contraction is prolonged. Consequentially, RV diastolic duration and filling time are shortened, compromising RV and LV filling and filling rate, further reducing cardiac output. These temporal phenomena are further impacted by heart rate, and children with PAH have a marked logarithmic decrease in diastolic duration and increase in the systolic-to-diastolic duration ratio when their heart rate increases as compared with controls. The systolic-to-diastolic duration ratio, which reflects both the overall prolonged systole and decreased ventricular filling, is easily measured from the Doppler signal of the tricuspid regurgitation jet, and is linked to death or need for lung transplantation in children with PAH [146].

Summary: Echocardiographic assessment of RV function

RV functional assessment should extend beyond subjective "eyeballing" alone. We suggest the following approach to the echocardiographic assessment of RV function.

1 Assess RV dimensions and RVEDA using 2D echocardiography.
2 Assess RV volumes in those patients with increased RV dimensions. For this purpose we propose either:
 a 2D-based 3D reconstruction
 b 3D echocardiography.
3 Assess Fractional Area Change (%FAC).
4 Measure TAPSE.
5 Measure tissue Doppler velocities in the basal part of the RV.
6 Measure longitudinal strain using STE if available.

These methods should help to determine whether a patient has RV dysfunction. The role of the echocardiographer is to interpret and integrate these methods in assessment of the individual patient.

Conclusion

Multiple techniques are available for the assessment of systolic ventricular function in children. No single technique or number completely reflects LV or RV systolic function. We therefore propose a multiparametric approach and suggest the introduction of a functional assessment protocol that integrates the different available methods.

Videos

To access the videos for this chapter, please go to www.lai-echo.com.

Video 7.1 Short-axis view at the base of the heart demonstrating the clockwise rotation during systole.

Video 7.2 Short-axis view at the LV apex demonstrating the counterclockwise rotation of the LV apex during systole.

Video 7.3 Speckle-tracking analysis of LV longitudinal function. From the apical 4-chamber view, longitudinal systolic strain is analyzed using speckle-tracking echocardiography. Shortening is represented by red and lengthening by blue. By convention systolic shortening is shown as a negative value.

Video 7.4 Speckle-tracking echocardiography analysis of LV radial function. From the parasternal short axis speckle tracking is used to calculate radial LV thickening. Red represents thickening and blue thinning. By convention thickening is shown as a positive value.

Video 7.5 Three-dimensional echocardiography used to calculate LV ejection fraction. A 3D volume is obtained from the LV apex and an automated LV segmentation program is used to calculate LV ejection fraction.

References

1 Sutherland G, Hatle L, Claus P, et al. *Doppler Myocardial Imaging. A Textbook*. Hasselt, Belgium: BSWK, 2006.
2 MacGowan GA, Shapiro EP, Azhari H, et al. Noninvasive measurement of shortening in the fiber and cross-fiber directions in the normal human left ventricle and in idiopathic dilated cardiomyopathy. *Circulation* 1997;**96**:535–541.
3 Rademakers FE, Rogers WJ, Guier WH, et al. Relation of regional cross-fiber shortening to wall thickening in the intact heart. Three-dimensional strain analysis by NMR tagging. *Circulation* 1994;**89**:1174–1182.
4 Sengupta PP, Korinek J, Belohlavek M, et al. Left ventricular structure and function: basic science for cardiac imaging. *J Am Coll Cardiol* 2006;**48**:1988–2001.
5 Sengupta PP, Krishnamoorthy VK, Korinek J, et al. Left ventricular form and function revisited: applied translational science to cardiovascular ultrasound imaging. *J Am Soc Echocardiogr* 2007;**20**:539–551.
6 Mor-Avi V, Lang RM, Badano LP, et al. Current and evolving echocardiographic techniques for the quantitative evaluation of cardiac mechanics: ASE/EAE Consensus Statement on Methodology and Indications endorsed by the Japanese Society of Echocardiography. *Eur J Echocardiogr* 2011;**12**:167–205.
7 Regen DM. Calculation of left ventricular wall stress. *Circ Res* 1990;**67**:245–252.
8 Hein S, Arnon E, Kostin S, et al. Progression from compensated hypertrophy to failure in the pressure-overloaded human heart: structural deterioration and compensatory mechanisms. *Circulation* 2003;**107**:984–991.
9 Hara Y, Hamada M, Hiwada K. Left ventricular end-systolic wall stress is a potent prognostic variable in patients with dilated cardiomyopathy. *Jpn Circ J* 1999;**63**:196–200.
10 Laskey WK, Sutton MS, Zeevi G, et al. Left ventricular mechanics in dilated cardiomyopathy. *Am J Cardiol* 1984;**54**:620–625.
11 Piot C, Lemaire S, Albat B, et al. High frequency-induced upregulation of human cardiac calcium currents. *Circulation* 1996;**93**:120–128.
12 Meyer M, Keweloh B, Guth K, et al. Frequency-dependence of myocardial energetics in failing human myocardium as quantified by a new method for the measurement of oxygen consumption in muscle strip preparations. *J Mol Cell Cardiol* 1998;**30**:1459–1470.
13 Kass DA, Maughan WL, Guo ZM, et al. Comparative influence of load versus inotropic states on indexes of ventricular contractility: experimental and theoretical analysis based on pressure-volume relationships. *Circulation* 1987;**76**:1422–1436.
14 Suga H. Paul Dudley White International Lecture: Cardiac performance as viewed through the pressure-volume window. *Jpn Heart J* 1994;**35**:263–280.
15 Friedberg MK, Mertens L. Echocardiographic assessment of ventricular synchrony in congenital and acquired heart disease in children. *Echocardiography* 2013;**30**:460–471.

16 Mertens L, Friedberg MK. Echocardiography and cardiac resynchronization therapy in children and patients with congenital heart disease. *Minerva Pediatr* 2012;**64**:451–460.
17 Lang RM, Bierig M, Devereux RB, et al. Recommendations for chamber quantification: a report from the American Society of Echocardiography's Guidelines and Standards Committee and the Chamber Quantification Writing Group, developed in conjunction with the European Association of Echocardiography, a branch of the European Society of Cardiology. *J Am Soc Echocardiogr* 2005;**18**:1440–1463.
18 Lopez L, Colan SD, Frommelt PC, et al. Recommendations for quantification methods during the performance of a pediatric echocardiogram: a report from the Pediatric Measurements Writing Group of the American Society of Echocardiography Pediatric and Congenital Heart Disease Council. *J Am Soc Echocardiogr* 2010;**23**:465–495; quiz 576–577.
19 Tani LY, Minich LL, Williams RV, Shaddy RE. Ventricular remodeling in children with left ventricular dysfunction secondary to various cardiomyopathies. *Am J Cardiol* 2005;**96**:1157–1161.
20 Lipshultz SE, Lipsitz SR, Sallan SE, et al. Chronic progressive cardiac dysfunction years after doxorubicin therapy for childhood acute lymphoblastic leukemia. *J Clin Oncol* 2005;**23**:2629–2636.
21 Lipshultz SE, Easley KA, Orav EJ, et al. Reliability of multicenter pediatric echocardiographic measurements of left ventricular structure and function: the prospective P(2)C(2) HIV study. *Circulation* 2001;**104**:310–316.
22 Colan SD, Shirali G, Margossian R, et al. The ventricular volume variability study of the Pediatric Heart Network: study design and impact of beat averaging and variable type on the reproducibility of echocardiographic measurements in children with chronic dilated cardiomyopathy. *J Am Soc Echocardiogr* 2012;**25**:842–854.e6.
23 Quinones M, Waggoner A, Reduto LA, et al. A new, simplified and accurate method for determining ejection fraction with two-dimensional echocardiography. *Circulation* 1981;**64**:744–753.
24 Schiller NB, Shah PM, Crawford M, et al. Recommendations for quantitation of the left ventricle by two-dimensional echocardiography. American Society of Echocardiography Committee on Standards, Subcommittee on Quantitation of Two-Dimensional Echocardiograms. *J Am Soc Echocardiogr* 1989;**2**:358–367.
25 Lang R, Bierig M, Devereux R, et al. Recommendations for chamber quantification. *Eur J Echocardiogr* 2006;**7**:79–108.
26 Hashimoto I, Ichida F, Miura M, et al. Automatic border detection identifies subclinical anthracycline cardiotoxicity in children with malignancy. *Circulation* 1999;**99**:2367–2370.
27 Kuhl HP, Schreckenberg M, Rulands D, et al. High-resolution transthoracic real-time three-dimensional echocardiography: quantitation of cardiac volumes and function using semi-automatic border detection and comparison with cardiac magnetic resonance imaging. *J Am Coll Cardiol* 2004;**43**:2083–2090.
28 Kimball TR, Witt SA, Khoury PR, Daniels SR. Automated echocardiographic analysis of systemic ventricular performance in hypoplastic left heart syndrome. *J Am Soc Echocardiogr* 1996;**9**:629–636.
29 Mahle WT, Coon PD, Wernovsky G, Rychik J. Quantitative echocardiographic assessment of the performance of the functionally single right ventricle after the Fontan operation. *Cardiol Young* 2001;**11**:399–406.
30 Szulik M, Pappas CJ, Jurcut R, et al. Clinical validation of a novel speckle-tracking-based ejection fraction assessment method. *J Am Soc Echocardiogr* 2011;**24**:1092–1100.
31 Riehle TJ, Mahle WT, Parks WJ, et al. Real-time three-dimensional echocardiographic acquisition and quantification of left-ventricular indices in children and young adults with congenital heart disease: comparison with magnetic resonance imaging. *J Am Soc Echocardiogr* 2008;**21**:78–83.
32 van den Bosch AE, Robbers-Visser D, Krenning BJ, et al. Real-time transthoracic three-dimensional echocardiographic assessment of left ventricular volume and ejection fraction in congenital heart disease. *J Am Soc Echocardiogr* 2006;**19**:1–6.
33 Silverman NH, Hudson S. Evaluation of right ventricular volume and ejection fraction in children by two-dimensional echocardiography. *Pediatr Cardiol* 1983;**4**:197–203.
34 Trowitzsch E, Colan SD, Sanders SP. Two-dimensional echocardiographic estimation of right ventricular area change and ejection fraction in infants with systemic right ventricle (transposition of the great arteries or hypoplastic left heart syndrome). *Am J Cardiol* 1985;**55**:1153–1157.
35 Trowitzsch E, Colan SD, Sanders SP. Two-dimensional echocardiographic evaluation of right ventricular size and function in newborns with severe right ventricular outflow tract obstruction. *J Am Coll Cardiol* 1985;**6**:388–393.
36 Friedberg MK, Rosenthal DN. New developments in echocardiographic methods to assess right ventricular function in congenital heart disease. *Curr Opin Cardiol* 2005;**20**:84–88.
37 Weidemann F, Herrmann S, Stork S, et al. Impact of myocardial fibrosis in patients with symptomatic severe aortic stenosis. *Circulation* 2009;**120**:577–584.
38 Stoylen A, Skjaerpe T. Systolic long axis function of the left ventricle. Global and regional information. *Scand Cardiovasc J* 2003;**37**:253–258.
39 Colan SD, Borow KM, Neumann A. Left ventricular end-systolic wall stress-velocity of fiber shortening relation: a load-independent index of myocardial contractility. *J Am Coll Cardiol* 1984;**4**:715–724.
40 Banerjee A, Brook MM, Klautz RJ, Teitel DF. Nonlinearity of the left ventricular end-systolic wall stress-velocity of fiber shortening relation in young pigs: a potential pitfall in its use as a single-beat index of contractility. *J Am Coll Cardiol* 1994;**23**:514–524.
41 Rowland DG, Gutgesell HP. Noninvasive assessment of myocardial contractility, preload, and afterload in healthy newborn infants. *Am J Cardiol* 1995;**75**:818–821.
42 Gentles TL, Colan SD. Wall stress misrepresents afterload in children and young adults with abnormal left ventricular geometry. *J Appl Physiol* 2002;**92**:1053–1057.
43 Rhodes J, Udelson JE, Marx GR, et al. A new noninvasive method for the estimation of peak dP/dt. *Circulation* 1993;**88**:2693–2699.
44 Rhodes J, Margossian R, Sleeper LA, et al. Non-geometric echocardiographic indices of ventricular function in patients with a Fontan circulation. *J Am Soc Echocardiogr* 2011;**24**:1213–1219.
45 Ahmed SS, Levinson GE, Schwartz CJ, Ettinger PO. Systolic time intervals as measures of the contractile state of the left ventricular myocardium in man. *Circulation* 1972;**46**:559–571.

46 Tei C, Dujardin KS, Hodge DO, et al. Doppler index combining systolic and diastolic myocardial performance: clinical value in cardiac amyloidosis. *J Am Coll Cardiol* 1996;**28**:658–664.

47 Tei C, Ling LH, Hodge DO, et al. New index of combined systolic and diastolic myocardial performance: a simple and reproducible measure of cardiac function – a study in normals and dilated cardiomyopathy. *J Cardiol* 1995;**26**:357–366.

48 Tei C, Nishimura RA, Seward JB, Tajik AJ. Noninvasive Doppler-derived myocardial performance index: correlation with simultaneous measurements of cardiac catheterization measurements. *J Am Soc Echocardiogr* 1997;**10**:169–178.

49 Eidem BW, O'Leary PW, Tei C, Seward JB. Usefulness of the myocardial performance index for assessing right ventricular function in congenital heart disease. *Am J Cardiol* 2000;**86**:654–658.

50 Eidem BW, Tei C, O'Leary PW, et al. Nongeometric quantitative assessment of right and left ventricular function: myocardial performance index in normal children and patients with Ebstein anomaly. *J Am Soc Echocardiogr* 1998;**11**:849–856.

51 Cheung MM, Smallhorn JF, Redington AN, Vogel M. The effects of changes in loading conditions and modulation of inotropic state on the myocardial performance index: comparison with conductance catheter measurements. *Eur Heart J* 2004;**25**:2238–2242.

52 Friedberg MK, Silverman NH. The systolic to diastolic duration ratio in children with heart failure secondary to restrictive cardiomyopathy. *J Am Soc Echocardiogr* 2006;**19**:1326–1331.

53 Friedberg MK, Silverman NH. The systolic to diastolic duration ratio in children with hypoplastic left heart syndrome: a novel Doppler index of right ventricular function. *J Am Soc Echocardiogr* 2007;**20**:749–755.

54 Alkon J, Humpl T, Manlhiot C, et al. Usefulness of the right ventricular systolic to diastolic duration ratio to predict functional capacity and survival in children with pulmonary arterial hypertension. *Am J Cardiol* 2010;**106**:430–436.

55 Sarnari R, Kamal RY, Friedberg MK, Silverman NH. Doppler assessment of the ratio of the systolic to diastolic duration in normal children: relation to heart rate, age and body surface area. *J Am Soc Echocardiogr* 2009;**22**:928–932.

56 Forsey J, Friedberg MK, Mertens L. Speckle tracking echocardiography in pediatric and congenital heart disease. *Echocardiography* 2013;**30**:447–459.

57 Friedberg MK, Mertens L. Tissue velocities, strain, and strain rate for echocardiographic assessment of ventricular function in congenital heart disease. *Eur J Echocardiogr* 2009;**10**:585–593.

58 Sutherland GR, Di Salvo G, Claus P, et al. Strain and strain rate imaging: a new clinical approach to quantifying regional myocardial function. *J Am Soc Echocardiogr* 2004;**17**:788–802.

59 McDicken WN, Sutherland GR, Moran CM, Gordon LN. Colour Doppler velocity imaging of the myocardium. *Ultrasound Med Biol* 1992;**18**:651–654.

60 Isaaz K, Thompson A, Ethevenot G, et al. Doppler echocardiographic measurement of low velocity motion of the left ventricular posterior wall. *Am J Cardiol* 1989;**64**:66–75.

61 Gorcsan J, 3rd, Strum DP, Mandarino WA, et al. Quantitative assessment of alterations in regional left ventricular contractility with color-coded tissue Doppler echocardiography. Comparison with sonomicrometry and pressure-volume relations. *Circulation* 1997;**95**:2423–2433.

62 Derumeaux G, Ovize M, Loufoua J, et al. Doppler tissue imaging quantitates regional wall motion during myocardial ischemia and reperfusion. *Circulation* 1998;**97**:1970–1977.

63 Vinereanu D, Ionescu AA, Fraser AG. Assessment of left ventricular long axis contraction can detect early myocardial dysfunction in asymptomatic patients with severe aortic regurgitation. *Heart* 2001;**85**:30–36.

64 Mertens L, Ganame J, Eyskens B. What is new in pediatric cardiac imaging? *Eur J Pediatr* 2008;**167**:1–8.

65 Koopman LP, Slorach C, Manlhiot C, et al. Myocardial tissue Doppler velocity imaging in children: comparative study between two ultrasound systems. *J Am Soc Echocardiogr* 2010;**23**:929–937.

66 Kukulski T, Voigt JU, Wilkenshoff UM, et al. A comparison of regional myocardial velocity information derived by pulsed and color Doppler techniques: an in vitro and in vivo study. *Echocardiography* 2000;**17**:639–651.

67 Eidem BW, McMahon CJ, Cohen RR, et al. Impact of cardiac growth on Doppler tissue imaging velocities: a study in healthy children. *J Am Soc Echocardiogr* 2004;**17**:212–221.

68 Uematsu M, Miyatake K, Tanaka N, et al. Myocardial velocity gradient as a new indicator of regional left ventricular contraction: detection by a two-dimensional tissue Doppler imaging technique. *J Am Coll Cardiol* 1995;**26**:217–223.

69 Kapusta L, Thijssen JM, Groot-Loonen J, et al. Tissue Doppler imaging in detection of myocardial dysfunction in survivors of childhood cancer treated with anthracyclines. *Ultrasound Med Biol* 2000;**26**:1099–1108.

70 Rychik J, Tian ZY. Quantitative assessment of myocardial tissue velocities in normal children with Doppler tissue imaging. *Am J Cardiol* 1996;**77**:1254–1257.

71 Hiarada K, Orino T, Yasuoka K, et al. Tissue doppler imaging of left and right ventricles in normal children. *Tohoku J Exp Med* 2000;**191**:21–29.

72 Roberson DA, Cui W, Chen Z, et al. Annular and septal Doppler tissue imaging in children: normal z-score tables and effects of age, heart rate, and body surface area. *J Am Soc Echocardiogr* 2007;**20**:1276–1284.

73 Sohn DW, Chai IH, Lee DJ, et al. Assessment of mitral annulus velocity by Doppler tissue imaging in the evaluation of left ventricular diastolic function. *J Am Coll Cardiol* 1997;**30**:474–480.

74 Missant C, Rex S, Claus P, et al. Load-sensitivity of regional tissue deformation in the right ventricle: isovolumic versus ejection-phase indices of contractility. *Heart* 2008;**94**:e15.

75 Eidem BW, McMahon CJ, Ayres NA, et al. Impact of chronic left ventricular preload and afterload on Doppler tissue imaging velocities: a study in congenital heart disease. *J Am Soc Echocardiogr* 2005;**18**:830–838.

76 Kiraly P, Kapusta L, Thijssen JM, Daniels O. Left ventricular myocardial function in congenital valvar aortic stenosis assessed by ultrasound tissue-velocity and strain-rate techniques. *Ultrasound Med Biol* 2003;**29**:615–620.

77 Vogel M, Schmidt MR, Kristiansen SB, et al. Validation of myocardial acceleration during isovolumic contraction as a novel noninvasive index of right ventricular contractility: comparison with ventricular pressure-volume relations in an animal model. *Circulation* 2002;**105**:1693–1699.

78 Lyseggen E, Rabben SI, Skulstad H, et al. Myocardial acceleration during isovolumic contraction: relationship to contractility. *Circulation* 2005;**111**:1362–1369.
79 Vogel M, Cheung MM, Li J, et al. Noninvasive assessment of left ventricular force-frequency relationships using tissue Doppler-derived isovolumic acceleration: validation in an animal model. *Circulation* 2003;**107**:1647–1652.
80 Cheung MM, Smallhorn JF, Vogel M, et al. Disruption of the ventricular myocardial force-frequency relationship after cardiac surgery in children: noninvasive assessment by means of tissue Doppler imaging. *J Thorac Cardiovasc Surg* 2006;**131**:625–631.
81 Roche SL, Vogel M, Pitkanen O, et al. Isovolumic acceleration at rest and during exercise in children normal values for the left ventricle and first noninvasive demonstration of exercise-induced force-frequency relationships. *J Am Coll Cardiol* 2011;**57**:1100–1107.
82 McMahon CJ, Nagueh SF, Eapen RS, et al. Echocardiographic predictors of adverse clinical events in children with dilated cardiomyopathy: a prospective clinical study. *Heart* 2004;**90**:908–915.
83 McMahon CJ, Nagueh SF, Pignatelli RH, et al. Characterization of left ventricular diastolic function by tissue Doppler imaging and clinical status in children with hypertrophic cardiomyopathy. *Circulation* 2004;**109**:1756–1762.
84 McMahon CJ, Pignatelli RH, Nagueh SF, et al. Left ventricular noncompaction cardiomyopathy in children: characterisation of clinical status using tissue Doppler-derived indices of left ventricular diastolic relaxation. *Heart* 2007;**93**:676–681.
85 Claus P, Weidemann F, Dommke C, et al. Mechanisms of postsystolic thickening in ischemic myocardium: mathematical modelling and comparison with experimental ischemic substrates. *Ultrasound Med Biol* 2007;**33**:1963–1970.
86 Ferferieva V, Van den Bergh A, Claus P, et al. The relative value of strain and strain rate for defining intrinsic myocardial function. *Am J Physiol Heart Circ Physiol* 2012;**302**:H188–195.
87 Takahashi K, Al Naami G, Thompson R, et al. Normal rotational, torsion and untwisting data in children, adolescents and young adults. *J Am Soc Echocardiogr* 2010;**23**:286–293.
88 Heimdal A, Stoylen A, Torp H, Skjaerpe T. Real-time strain rate imaging of the left ventricle by ultrasound. *J Am Soc Echocardiogr* 1998;**11**:1013–1019.
89 Koopman LP, Slorach C, Hui W, et al. Comparison between different speckle tracking and color tissue Doppler techniques to measure global and regional myocardial deformation in children. *J Am Soc Echocardiogr* 2010;**23**:919–928.
90 Koopman LP, Slorach C, Manlhiot C, et al. Assessment of myocardial deformation in children using Digital Imaging and Communications in Medicine (DICOM) data and vendor independent speckle tracking software. *J Am Soc Echocardiogr* 2011;**24**:37–44.
91 Jasaityte R, Heyde B, D'Hooge J. Current state of three-dimensional myocardial strain estimation using echocardiography. *J Am Soc Echocardiogr* 2013;**26**:15–28.
92 Friedberg MK, Mertens L. Deformation imaging in selected congenital heart disease: is it evolving to clinical use? *J Am Soc Echocardiogr* 2012;**25**:919–931.
93 Weidemann F, Eyskens B, Sutherland GR. New ultrasound methods to quantify regional myocardial function in children with heart disease. *Pediatr Cardiol* 2002;**23**:292–306.
94 Boettler P, Hartmann M, Watzl K, et al. Heart rate effects on strain and strain rate in healthy children. *J Am Soc Echocardiogr* 2005;**18**:1121–1130.
95 Lorch SM, Ludomirsky A, Singh GK. Maturational and growth-related changes in left ventricular longitudinal strain and strain rate measured by two-dimensional speckle tracking echocardiography in healthy pediatric population. *J Am Soc Echocardiogr* 2008;**21**:1207–1215.
96 Marcus KA, Mavinkurve-Groothuis AM, Barends M, et al. Reference values for myocardial two-dimensional strain echocardiography in a healthy pediatric and young adult cohort. *J Am Soc Echocardiogr* 2011;**24**:625–636.
97 Cerqueira MD, Weissman NJ, Dilsizian V, et al. Standardized myocardial segmentation and nomenclature for tomographic imaging of the heart: a statement for healthcare professionals from the Cardiac Imaging Committee of the Council on Clinical Cardiology of the American Heart Association. *Circulation* 2002;**105**:539–542.
98 Weidemann F, Eyskens B, Mertens L, et al. Quantification of regional right and left ventricular function by ultrasonic strain rate and strain indexes in Friedreich's ataxia. *Am J Cardiol* 2003;**91**:622–626.
99 Ganame J, Mertens L, Eidem BW, et al. Regional myocardial deformation in children with hypertrophic cardiomyopathy: morphological and clinical correlations. *Eur Heart J* 2007;**28**:2886–2894.
100 Marcus KA, de Korte CL, Feuth T, et al. Abnormal two-dimensional strain echocardiography findings in children with congenital valvar aortic stenosis. *Ultraschall Med* 2012;**33**:E283–292.
101 Marcus KA, de Korte CL, Feuth T, et al. Persistent reduction in left ventricular strain using two-dimensional speckle-tracking echocardiography after balloon valvuloplasty in children with congenital valvular aortic stenosis. *J Am Soc Echocardiogr* 2012;**25**:473–485.
102 Di Salvo G, Eyskens B, Claus P, et al. Late post-repair ventricular function in patients with origin of the left main coronary artery from the pulmonary trunk. *Am J Cardiol* 2004;**93**:506–508.
103 Mertens L, Ganame J, Claus P, et al. Early regional myocardial dysfunction in young patients with Duchenne muscular dystrophy. *J Am Soc Echocardiogr* 2008;**21**:1049–1054.
104 Ganame J, Claus P, Uyttebroeck A, et al. Myocardial dysfunction late after low-dose anthracycline treatment in asymptomatic pediatric patients. *J Am Soc Echocardiogr* 2007;**20**:1351–1358.
105 Mavinkurve-Groothuis AM, Groot-Loonen J, Marcus KA, et al. Myocardial strain and strain rate in monitoring subclinical heart failure in asymptomatic long-term survivors of childhood cancer. *Ultrasound Med Biol* 2010;**36**:1783–1791.
106 Mavinkurve-Groothuis AM, Marcus KA, Pourier M, et al. Myocardial 2D strain echocardiography and cardiac biomarkers in children during and shortly after anthracycline therapy for acute lymphoblastic leukaemia (ALL): a prospective study. *Eur Heart J Cardiovasc Imaging* 2013;**14**:562–569.
107 Fallah-Rad N, Walker JR, Wassef A, et al. The utility of cardiac biomarkers, tissue velocity and strain imaging, and cardiac magnetic resonance imaging in predicting early left ventricular dysfunction in patients with human epidermal growth factor receptor

II-positive breast cancer treated with adjuvant trastuzumab therapy. *J Am Coll Cardiol* 2011;**57**:2263–2270.
108 Sawaya H, Sebag IA, Plana JC, et al. Early detection and prediction of cardiotoxicity in chemotherapy-treated patients. *Am J Cardiol* 2011;**107**:1375–1380.
109 Sawaya H, Sebag IA, Plana JC, et al. Assessment of echocardiography and biomarkers for the extended prediction of cardiotoxicity in patients treated with anthracyclines, taxanes, and trastuzumab. *Circ Cardiovasc Imaging* 2012;**5**:596–603.
110 Poterucha JT, Kutty S, Lindquist RK, et al. Changes in left ventricular longitudinal strain with anthracycline chemotherapy in adolescents precede subsequent decreased left ventricular ejection fraction. *J Am Soc Echocardiogr* 2012;**25**:733–740.
111 Gorcsan J, 3rd, Abraham T, Agler DA, et al. Echocardiography for cardiac resynchronization therapy: recommendations for performance and reporting – a report from the American Society of Echocardiography Dyssynchrony Writing Group endorsed by the Heart Rhythm Society. *J Am Soc Echocardiogr* 2008;**21**:191–213.
112 Chung ES, Leon AR, Tavazzi L, et al. Results of the Predictors of Response to CRT (PROSPECT) trial. *Circulation* 2008;**117**:2608–2616.
113 Marcus KA, Janousek J, Barends ME, et al. Synchronicity of systolic deformation in healthy pediatric and young adult subjects: a two-dimensional strain echocardiography study. *Am J Physiol Heart Circ Physiol* 2012;**302**:H196–205.
114 Mertens LL, Friedberg MK. Imaging the right ventricle–current state of the art. *Nat Rev Cardiol* 2010;**7**:551–563.
115 Valsangiacomo Buechel ER, Mertens LL. Imaging the right heart: the use of integrated multimodality imaging. *Eur Heart J* 2012;**33**:949–960.
116 Rudski LG, Lai WW, Afilalo J, et al. Guidelines for the echocardiographic assessment of the right heart in adults: a report from the American Society of Echocardiography endorsed by the European Association of Echocardiography, a registered branch of the European Society of Cardiology, and the Canadian Society of Echocardiography. *J Am Soc Echocardiogr* 2010;**23**:685–713; quiz 86–88.
117 Helbing WA, Bosch HG, Maliepaard C, et al. Comparison of echocardiographic methods with magnetic resonance imaging for assessment of right ventricular function in children. *Am J Cardiol* 1995;**76**:589–594.
118 Alghamdi MH, Grosse-Wortmann L, Ahmad N, et al. Can simple echocardiographic measures reduce the number of cardiac magnetic resonance imaging studies to diagnose right ventricular enlargement in congenital heart disease? *J Am Soc Echocardiogr* 2012;**25**:518–523.
119 Greutmann M, Tobler D, Biaggi P, et al. Echocardiography for assessment of right ventricular volumes revisited: a cardiac magnetic resonance comparison study in adults with repaired tetralogy of Fallot. *J Am Soc Echocardiogr* 2010;**23**:905–911.
120 Dragulescu A, Grosse-Wortmann L, Fackoury C, Mertens L. Echocardiographic assessment of right ventricular volumes: a comparison of different techniques in children after surgical repair of tetralogy of Fallot. *Eur Heart J Cardiovasc Imaging* 2012;**13**:596–604.
121 Dragulescu A, Grosse-Wortmann L, Fackoury C, et al. Echocardiographic assessment of right ventricular volumes after surgical repair of tetralogy of Fallot: clinical validation of a new echocardiographic method. *J Am Soc Echocardiogr* 2011;**24**:1191–1198.
122 Khoo NS, Young A, Occleshaw C, et al. Assessments of right ventricular volume and function using three-dimensional echocardiography in older children and adults with congenital heart disease: comparison with cardiac magnetic resonance imaging. *J Am Soc Echocardiogr* 2009;**22**:1279–1288.
123 van der Zwaan HB, Geleijnse ML, McGhie JS, et al. Right ventricular quantification in clinical practice: two-dimensional vs. three-dimensional echocardiography compared with cardiac magnetic resonance imaging. *Eur J Echocardiogr* 2011;**12**:656–664.
124 van der Zwaan HB, Helbing WA, Boersma E, et al. Usefulness of real-time three-dimensional echocardiography to identify right ventricular dysfunction in patients with congenital heart disease. *Am J Cardiol* 2010;**106**:843–850.
125 Koestenberger M, Ravekes W, Everett AD, et al. Right ventricular function in infants, children and adolescents: reference values of the tricuspid annular plane systolic excursion (TAPSE) in 640 healthy patients and calculation of z-score values. *J Am Soc Echocardiogr* 2009;**22**:715–719.
126 Koestenberger M, Nagel B, Avian A, et al. Systolic right ventricular function in children and young adults with pulmonary artery hypertension secondary to congenital heart disease and tetralogy of Fallot: tricuspid annular plane systolic excursion (TAPSE) and magnetic resonance imaging data. *Congenit Heart Dis* 2012;**7**:250–258.
127 Morcos P, Vick GW, 3rd, Sahn DJ, et al. Correlation of right ventricular ejection fraction and tricuspid annular plane systolic excursion in tetralogy of Fallot by magnetic resonance imaging. *Int J Cardiovasc Imaging* 2009;**25**:263–270.
128 Blanchard DG, Malouf PJ, Gurudevan SV, et al. Utility of right ventricular Tei index in the noninvasive evaluation of chronic thromboembolic pulmonary hypertension before and after pulmonary thromboendarterectomy. *JACC Cardiovasc Imaging* 2009;**2**:143–149.
129 Yeo TC, Dujardin KS, Tei C, et al. Value of a Doppler-derived index combining systolic and diastolic time intervals in predicting outcome in primary pulmonary hypertension. *Am J Cardiol* 1998;**81**:1157–1161.
130 Schwerzmann M, Samman AM, Salehian O, et al. Comparison of echocardiographic and cardiac magnetic resonance imaging for assessing right ventricular function in adults with repaired tetralogy of fallot. *Am J Cardiol* 2007;**99**:1593–1597.
131 Vogel M, Derrick G, White PA, et al. Systemic ventricular function in patients with transposition of the great arteries after atrial repair: a tissue Doppler and conductance catheter study. *J Am Coll Cardiol* 2004;**43**:100–106.
132 Frigiola A, Redington AN, Cullen S, Vogel M. Pulmonary regurgitation is an important determinant of right ventricular contractile dysfunction in patients with surgically repaired tetralogy of Fallot. *Circulation* 2004;**110**:II153–157.
133 Pettersen E, Helle-Valle T, Edvardsen T, et al. Contraction pattern of the systemic right ventricle shift from longitudinal to circumferential shortening and absent global ventricular torsion. *J Am Coll Cardiol* 2007;**49**:2450–2456.
134 Eyskens B, Weidemann F, Kowalski M, et al. Regional right and left ventricular function after the Senning operation: an ultrasonic study of strain rate and strain. *Cardiol Young* 2004;**14**:255–264.

135 Dragulescu A, Grosse-Wortmann L, Redington A, et al. Differential effect of right ventricular dilation on myocardial deformation in patients with atrial septal defects and patients after tetralogy of Fallot repair. *Int J Cardiol* 2013;**168**:803–810.
136 Hardegree EL, Sachdev A, Villarraga HR, et al. Role of serial quantitative assessment of right ventricular function by strain in pulmonary arterial hypertension. *Am J Cardiol* 2013;**111**:143–148.
137 Sachdev A, Villarraga HR, Frantz RP, et al. Right ventricular strain for prediction of survival in patients with pulmonary arterial hypertension. *Chest* 2011;**139**:1299–1309.
138 Geva T, Powell AJ, Crawford EC, et al. Evaluation of regional differences in right ventricular systolic function by acoustic quantification echocardiography and cine magnetic resonance imaging. *Circulation* 1998;**98**:339–345.
139 Hui W, Slorach C, Bradley TJ, et al. Measurement of right ventricular mechanical synchrony in children using tissue Doppler velocity and two-dimensional strain imaging. *J Am Soc Echocardiogr* 2010;**23**:1289–1296.
140 Lopez-Candales A, Dohi K, Bazaz R, Edelman K. Relation of right ventricular free wall mechanical delay to right ventricular dysfunction as determined by tissue Doppler imaging. *Am J Cardiol* 2005;**96**:602–606.
141 Lopez-Candales A, Dohi K, Rajagopalan N, et al. Right ventricular dyssynchrony in patients with pulmonary hypertension is associated with disease severity and functional class. *J Cardiovasc Ultrasound* 2005;**3**:23.
142 Chow PC, Liang XC, Lam WW, et al. Mechanical right ventricular dyssynchrony in patients after atrial switch operation for transposition of the great arteries. *Am J Cardiol* 2008;**101**:874–881.
143 Friedberg MK, Fernandes FP, Roche SL, et al. Relation of right ventricular mechanics to exercise tolerance in children after tetralogy of Fallot repair. *Am Heart J* 2013;**165**:551–557.
144 Marcus JT, Gan CT, Zwanenburg JJ, et al. Interventricular mechanical asynchrony in pulmonary arterial hypertension: left-to-right delay in peak shortening is related to right ventricular overload and left ventricular underfilling. *J Am Coll Cardiol* 2008;**51**:750–757.
145 Gan CT, Lankhaar JW, Marcus JT, et al. Impaired left ventricular filling due to right-to-left ventricular interaction in patients with pulmonary arterial hypertension. *Am J Physiol Heart Circ Physiol* 2006;**290**:H1528–1533.
146 Alkon J, Humpl T, Manlhiot C, et al. Usefulness of the right ventricular systolic to diastolic duration ratio to predict functional capacity and survival in children with pulmonary arterial hypertension. *Am J Cardiol* 2010;**106**:430–436.

Appendix: The Functional Protocol at The Hospital for Sick Children

Parasternal Long-Axis View (PLAX)
PLAX in 2D
Color aortic valve, mitral valve
2D RV inflow / color / Doppler
 Estimate RV systolic pressure from peak TR jet using CW 2D
RV outflow / color / Doppler
 Estimate mean pulmonary artery pressure from peak PI jet
M-mode LVET / R-R measurements
Measure LA dimension by M-mode, ensure cursor is perpendicular to LA, z-score

Parasternal Short-Axis View (PSAX)
M-mode with measurements (just below MV annulus)
 Record RV and LV dimensions with z-scores, include z-scores for wall thicknesses
 LV FS and EF, LV *V*cf and *V*cfc
 ∗Include LV PW in systole – required for wall stress calculation
 LV mass and LV mass index
PSAX in 2D at each level
 Base / Mid LV / Apex (Ensure your LV basal level is below the MV annulus)
2D PSAX at aortic valve level
Color TV / aortic valve / pulmonary valve
PW Doppler main PA just distal to PV leaflets
CW RVOT
 Estimate mean PAp from peak early PI jet

Apical 4-Chamber View (A4C), Both Ventricles Together
A4C view in 2D, include both ventricles and both atria
Color tissue Doppler, wide sector, highest FR possible
 Ensure RV free wall, IVS and LV lateral wall are included together
 Ensure TDI color scale is set just high enough to prevent aliasing
Tissue Doppler PW of the basal segments: RV free wall / IVS / LV lateral wall
 Measure e′, a′, s′ tissue velocities for all three walls

Apical 4-Chamber View, Focused on Left Ventricle (LV)
Color mitral valve / PW for diastolic function
 Align cursor parallel to flow
 Place sample volume at the leaflet tips
 Measure E, A velocities, DT, A-wave duration
Color M-mode of LV inflow
 Color scale set to ~one-half of the peak E velocity
PW IVRT, measure (sample volume between LV inflow and outflow)
PW pulmonary vein
 Place sample volume 0.5 to 1.0 cm into the vein
 Measure S, D velocities, A-wave reversal, A-wave duration

LV Apical 5-Chamber View (A5C)
2D apical 5-chamber
Color LVOT / PW / CW
 PW velocity of LVOT
 CW Doppler through LVOT

LV Apical 2-Chamber View (A2C)
LV apical 2-chamber
Color MV
Wide-sector color TDI – maximum FR

PW tissue Doppler PW of the basal segments:
LV anterior wall and LV inferior wall
Measure e′, a′, s′

LV Apical 3-Chamber View (A3C)
A3C LV apical 3-chamber view in 2D, include LA
color MV / AoV
Wide-sector color TDI – maximum FR
Tissue Doppler PW of LV inferolateral wall basal segment
Measure e′, a′, s′ tissue velocities

Apical 4-Chamber View – Focused on Right Ventricle (RV)
Apical view of RV
Measure FAC
Color TV / CW / PW
Estimate RVSp from peak TR jet
Measure TV E-wave velocity from PW
M-mode TV annulus with TDI color map for TAPSE

LV 3D Full Volume (frame rate one-half to one-third of patient's HR)
Calculate 3D EF

Subcostal View
Hepatic vein / color / PW (place sample volume 0.5 to 1.0 cm into the vein)
Abdominal aorta / color / PW

Suprasternal Notch View
SVC in 2D / color / PW
Aortic arch only if previous coarctation and/or abnormal abdominal Ao flow profile

Right arm BP + Wall stress
Record BP and calculate wall stress

Biplane Simpson's and/or Auto EF when:
Visual assessment of function is abnormal M-mode EF is <55% In the presence of RWMA Paradoxical motion of the IVS
Abnormal geometry, Dilated LV
Reminder: Four beat loops for
2D short-axis levels, 2D apical views, wide-sector TDI of apical views

CHAPTER 8

Diastolic Ventricular Function Assessment

Peter C. Frommelt
Medical College of Wisconsin, Children's Hospital of Wisconsin, Milwaukee, USA

Introduction

Echocardiography is the primary tool in the diagnosis and assessment of pediatric heart disease, including abnormalities of ventricular function. The initial focus when assessing myocardial function has traditionally centered on systolic function. Diastolic dysfunction, although recognized as a component of pediatric heart disease, has been less well understood and investigated. There are several reasons for this: (i) diastolic disease is felt to be relatively rare in pediatric patients; (ii) there is no single measure that adequately describes diastolic function (in contrast to ejection fraction, which is a simple method to characterize systolic function); (iii) echocardiographic techniques that help understand diastolic disease are not routinely applied in children; and (iv) Doppler patterns that characterize diastolic function vary significantly with age and heart rate in children in the absence of diastolic disease. Despite these challenges, there has been a recent evolution in diastolic assessment of children using echocardiography, and this chapter focuses on the current techniques of diastolic function assessment.

Definition and physiology of diastole

Diastole is the phase of the cardiac cycle during which ventricular filling occurs (Figure 8.1). It is defined as the time period beginning at end-ejection (closure of the semilunar valves) and extending until the atrioventricular (AV) valves are closed. Diastole can be further divided into four components:

1. Isovolumic relaxation – defined as the time from semilunar valve closure to onset of flow across the AV valve.
2. Rapid filling – starts when ventricular pressure after systolic contraction decreases to a value less than atrial pressure. As ventricular pressure continues to fall during early diastole, a pressure difference is generated between the atrium and ventricle. Blood flows across the AV valve because of this pressure difference and ventricular filling begins. This early diastolic flow, which can be detected by pulsed Doppler in the AV valve orifice, is called the early filling, or "E" velocity, wave. The E velocity peaks in early diastole, generally at the time of ventricular pressure minimum, and decelerates as ventricular pressure begins to increase with continued ventricular filling.
3. Diastasis – occurs in mid-diastole when atrial and ventricular pressures equalize after early filling, so that little flow passes across the AV valve.
4. Atrial contraction – in late diastole atrial pressure suddenly increases and again exceeds ventricular pressure, generating a second wave of flow across the AV valve. This late diastolic velocity profile is called the atrial contraction or "A" wave.

Many factors influence ventricular diastolic filling, including ventricular systolic function, AV valve function, rate of ventricular relaxation, the passive compliance or stiffness of the atrial and ventricular muscle, atrial systolic function, the loading or volume conditions of the two chambers, intrathoracic pressure changes with respiration, and heart rate and rhythm. All of these factors influence the observed diastolic velocity profile, and so must be considered in the analysis of these Doppler waveforms.

Atrial filling has also been analyzed using Doppler echocardiography. Systemic and pulmonary venous inflow is pulsatile and can generally be separated into systolic and diastolic phases. The systolic phase occurs during ventricular systole when atrial pressure drops as the atria relax after atrial contraction. In addition, there is active apical displacement of the AV valve annulus during ventricular systole, which creates a suction effect in the atria, with resultant augmentation of venous emptying into the atria. As atrial filling continues in later systole against a closed AV valve, atrial pressures rise and venous inflow decelerates. The diastolic phase of venous inflow is initiated with AV valve opening in early diastole, as this causes a sudden decrease in atrial pressure. During this phase, the atria act as a conduit from the veins to the ventricles. Diastolic venous inflow begins to decrease with increasing ventricular pressure as the ventricular chambers fill. With atrial contraction, there is a sudden increase in atrial pressure and cessation of venous inflow. If atrial

Echocardiography in Pediatric and Congenital Heart Disease: From Fetus to Adult, Second Edition. Edited by Wyman W. Lai, Luc L. Mertens, Meryl S. Cohen and Tal Geva.
© 2016 John Wiley & Sons, Ltd. Published 2016 by John Wiley & Sons, Ltd.
Companion website: www.lai-echo.com

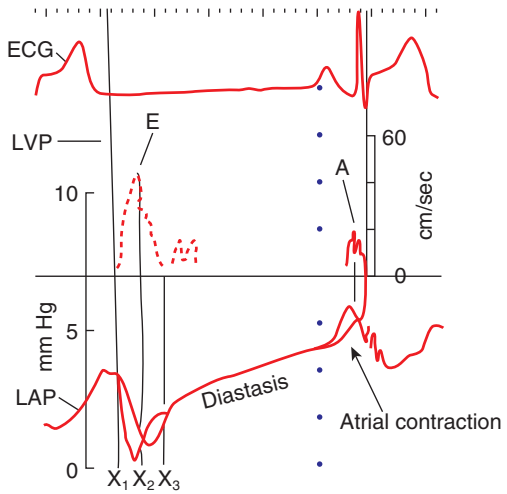


Figure 8.1 Simultaneous recordings of left atrial pressure (LAP), left ventricular pressure (LVP) and mitral valve Doppler inflow tracings in open-chested dogs. When left ventricular pressure decreases to a value equal to left atrial pressure (the first crossover point shown as X_1), the mitral valve opens and the onset of flow occurs on the mitral valve Doppler trace. Both pressures decrease rapidly after mitral valve opening, with a short duration of transvalvular pressure difference. The peak E velocity (E) occurs at the second crossover point X_2, which corresponds closely in time with the left ventricular minimum pressure. Deceleration from the peak E velocity begins with the onset of the increase in left ventricular diastolic pressure (the rapid filling wave) and ends at the third crossover point X_3. In mid-diastole, the two pressures appear to be equal, increasing slowly together (diastasis), and there is no flow across the mitral valve. Left atrial pressure increases and exceeds left ventricular pressure with atrial contraction, producing flow across the mitral valve at the A wave of the Doppler trace. ECG, electrocardiogram. Source: Courtois et al. 1988 [1]. Reproduced with permission of Wolters Kluwer.

pressures are elevated at the time of atrial contraction, significant reversal of flow from the atria into the veins can be seen and has been described as the atrial reversal phase of venous inflow. The same factors that influence ventricular filling are important in atrial filling as well; in addition, AV valve competence and venous vessel compliance play a significant role.

Echocardiographic techniques for assessing diastolic function

Doppler echocardiography

The current understanding of diastolic function and characterization of diastolic disease have mostly developed through investigation of intracardiac diastolic blood flow patterns using Doppler echocardiography [1]. The majority of work done on both adults and children has involved analysis of mitral and pulmonary venous inflow Doppler patterns [2–5], although interest in right ventricular diastolic function has grown recently.

Mitral inflow

Technique

Pulsed Doppler analysis of mitral inflow velocities is straightforward and easily incorporated into a routine complete echocardiographic study (Table 8.1). The best position for Doppler analysis is the apical 4-chamber view, where the Doppler signal can be aligned nearly parallel to mitral inflow, allowing accurate quantitation of peak velocities. Sample volume position is also critical, with the peak velocities generally best recorded distal to the mitral annulus near the tips of the valve leaflets. Both peak E and peak A velocities are significantly decreased as the sample

Table 8.1 Mitral inflow and pulmonary venous Doppler indices

	Strengths	Weaknesses
Mitral inflow Doppler indices		
Isovolumic relaxation time (IVRT)	• Relatively heart rate independent • Prolongation is a good marker of early mild diastolic disease	• Poor discriminator of more severe forms of diastolic disease
E-wave deceleration time	• Easy to obtain • Varies with progressive diastolic disease	• Heart rate dependent
E/A ratio	• Easy to obtain • Varies with progressive diastolic disease	• Requires sinus rhythm • Affected by mitral valve disease • Preload dependent • Age-dependent normal values • Diastolic disease can be associated with a "pseudonormal" pattern • Fusion with increased HR
Pulmonary venous Doppler indices		
Systolic/Diastolic (S/D) ratio	• Easy to obtain • Varies with progressive diastolic disease	• Requires sinus rhythm • Affected by mitral valve disease • Age-dependent normal values
A-wave duration (relative to mitral inflow)	• Important discriminator of normal vs. "pseudonormal" mitral inflow patterns	• Requires sinus rhythm • Varies with position within the pulmonary vein

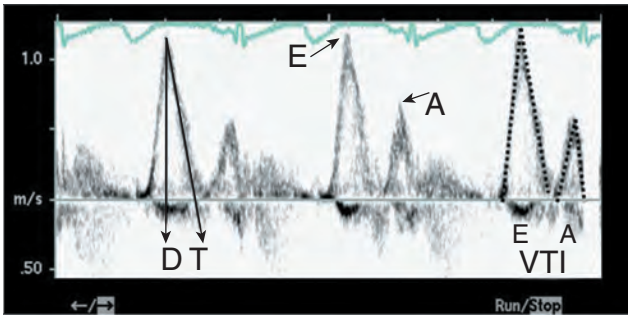


Figure 8.2 Typical mitral inflow Doppler during childhood. Note the dominant peak E and smaller peak A velocities. The velocity time integrals of the E wave (E VTI) and A wave (A VTI) are outlined. Deceleration time (DT) is measured from the peak E velocity to cessation of early diastolic flow (arrows).

volume is moved into the left atrium. The use of color Doppler can help better align both the Doppler cursor and sample volume positions.

Measurements

Several different indices of left ventricular diastolic function can be derived from the mitral valve Doppler inflow trace (Figure 8.2) [6]. These include diastolic time intervals, peak velocities during early filling and with atrial contraction, area filling fractions, velocity and area ratios, and peak filling rate. The most commonly used diastolic time interval is the isovolumic relaxation time (IVRT), which is the time from aortic valve closure to the initiation of diastolic flow across the mitral valve. It can be measured from the aortic closure component of the second heart sound as recorded on a phonocardiogram to the onset of diastolic flow velocity from the mitral valve Doppler tracing. It is also possible to measure this interval using continuous-wave (CW) Doppler positioned at the apex with the Doppler cursor angled to record both left ventricular outflow tract velocities in systole and left ventricular inflow velocities simultaneously from a 5-chamber view. The time from cessation of aortic forward flow to the onset of diastolic mitral inflow is the IVRT. This index is regarded as relatively heart rate independent. In patients with impaired left ventricular relaxation, IVRT is prolonged; conversely, in patients with abnormal left ventricular compliance and elevated left atrial pressures, it may be shortened. The deceleration time during early filling from peak E velocity to cessation of flow has also been used to describe the time course of relaxation, with more prolonged deceleration correlating with delayed relaxation. The duration of diastolic flow varies with heart rate, however, so deceleration time shortens with increasing heart rate irrespective of the diastolic properties of the heart [7] and is generally not a clinically useful measure in tachycardic infants and children.

Recommendations for measures to assess AV valve inflow include E-wave and A-wave velocities, A-wave duration, deceleration time, IVRT, and calculation of the E/A ratio [8].

Pulmonary venous inflow

Technique

Studies using pulsed-wave (PW) Doppler to assess pulmonary venous inflow have described a variety of patterns in different disease states; information obtained using this technique appears complementary to mitral inflow Doppler analysis and has added to the understanding of left ventricular diastolic function (Table 8.1) [9–12]. To obtain pulmonary venous inflow Doppler measurements, the PW sample volume is placed in the right or left upper pulmonary vein from an apical 4-chamber window. From this view, flow as it enters the left atrium can be aligned parallel to the Doppler beam using color Doppler. The sample volume should be placed as far distally into the vein as possible, preferably 1–2 cm distal to the orifice, for the most accurate and reproducible data. The closer the sample volume is placed to the orifice of the vein, the more turbulent and less distinct the Doppler signal becomes. In the uncommon pediatric patient with a suboptimal apical 4-chamber view, the parasternal, subcostal and/or suprasternal views may provide visualization and alignment with pulmonary venous inflow. Transesophageal imaging also provides an excellent window for evaluation of pulmonary venous inflow.

Measurements

Measurements performed on the pulmonary venous inflow Doppler trace include peak systolic (S wave) velocity, peak diastolic (D wave) velocity, the velocity time integral during the systolic and diastolic phases compared with the total area under the curve, and systolic/diastolic velocity and velocity time integral ratios (Figure 8.3). The systolic pulmonary venous flow is frequently biphasic in infants and young children and likely represents dissociation between atrial relaxation and mitral annular displacement (Figure 8.4). The highest systolic velocity is usually measured. Finally, the velocity and duration of atrial reversal (Ar wave) have been measured and found to be important in differentiating diastolic Doppler patterns in the face of elevated left atrial and left ventricular end-diastolic pressure (see later section "Patterns of diastolic dysfunction").

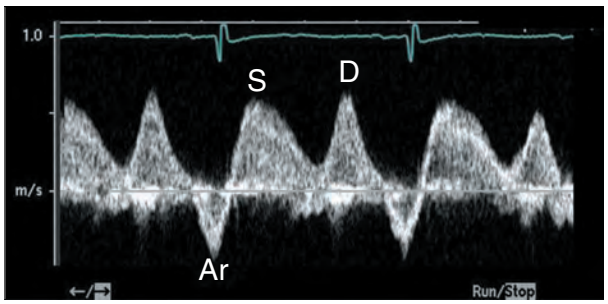


Figure 8.3 Pulmonary venous inflow Doppler. Phasic flow is characteristically seen with peaks in diastole (D) and systole (S) and deceleration of flow at end-systole and end-diastole. Atrial reversal of flow (Ar) can be seen in late diastole with atrial contraction and may reflect elevated left ventricular end-diastolic filling pressure.

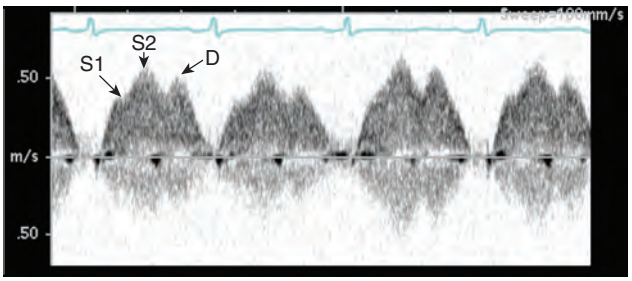


Figure 8.4 Pulmonary venous inflow Doppler in an infant with triphasic peaks during left atrial filling. There are two peaks in systole and one peak in diastole (D). The initial systolic peak (S1) likely represents atrial relaxation in early systole, whereas the second systolic peak (S2) is associated with augmented atrial filling secondary to mitral annular displacement toward the apex during ventricular contraction; this pattern is a normal variant and not characteristic of diastolic disease.

Tricuspid and systemic venous inflow

Right heart filling can also be assessed by Doppler echocardiography. Indices of diastolic function used for mitral and pulmonary vein inflow can be applied to the tricuspid and systemic venous inflow Doppler patterns, and appropriate positioning of the Doppler cursor remains important. Right ventricular diastolic function can be difficult to assess by inflow Doppler analysis of tricuspid and systemic venous inflow, however, because of variable preload with normal respiration. There can be dramatic variations in right ventricular filling with changes in intrathoracic pressure during the respiratory cycle. Inspiration lowers intrathoracic pressure and augments systemic venous emptying into the right atrium, and this alters the patterns of both systemic venous emptying and tricuspid inflow that are unrelated to the diastolic properties of the right ventricle. Forward systemic vein inflow is augmented and tricuspid inflow velocities increased with inspiration, and these flows are decreased with exhalation/positive-pressure ventilation when intrathoracic pressure increases. The tricuspid inflow peak E velocity increases by 26% and peak A by 20% with inspiration in normal children.

Caveats

Inflow Doppler patterns are influenced by AV valve stenosis, AV valve insufficiency, pulmonary/systemic venous obstruction, and arrhythmias. When these are present, assessment of the diastolic properties of the ventricle using inflow Doppler becomes difficult and should be made with caution.

Tissue Doppler Imaging

Changes in inflow Doppler tracings may not reflect alterations in the intrinsic diastolic properties of the ventricular muscle, as they are frequently influenced by myocardial loading conditions. The development of ultrasonic quantitative imaging of myocardial motion has improved understanding of myocardial diastolic function in both normal children and children with heart disease. The technique that has been the focus of the majority of investigation, called tissue Doppler imaging (TDI), allows regional assessment of myocardial wall velocities throughout the cardiac cycle. Specifically, pulsed Doppler assessment of longitudinal mitral, septal, and tricuspid annular motion has yielded important new observations in both children and adults, and has become a complementary technique to standard diastolic indices of function using echocardiography. Application of this technique in the analysis of mitral annular motion has provided additional insight in the noninvasive assessment of left ventricular diastolic function [13–17]. Similarly, tricuspid annular motion as an assessment tool for diastolic right ventricular function has been described [17,18]. Importantly, there is no significant variation in tricuspid annular motion with respiration, suggesting that this technique, unlike tricuspid inflow, is relatively preload independent [18]. The mitral early diastolic annular velocity also appears to be relatively preload independent, so that changes in intravascular volume have little effect on that velocity [19]. This is in striking contrast to mitral inflow velocities, which can change dramatically with changes in intravascular volume [20]. Given the variable volume loads that return to the heart in children with congenital heart disease, it appears that pulsed TDI may be a helpful load-independent technique in assessing ventricular diastolic function in pediatric echocardiography (Table 8.2).

Ventricular myocardial contraction and expansion occur along the major (apex to base) and minor (anterior to posterior) axes. AV valve annular motion occurs along the long axis of the ventricle as the annulus is displaced toward the apex in systole and away from the apex in diastole. Early diastolic motion of the annulus appears to reflect recoil of the ventricle from a contracted state and has correlated well with other indices of relaxation in clinical studies [13,15], whereas late diastolic annular motion is likely affected by both ventricular diastolic and atrial systolic function. The apical echocardiographic window appears to be an ideal view to assess annular motion because the motion is parallel to the apex, allowing well-aligned Doppler interrogation throughout the cardiac cycle. In addition, the apex and crux of the heart are relatively fixed in position with little translational (i.e., rocking) motion of the heart throughout the cardiac cycle.

Technique

Doppler assessment of annular motion requires a modified wall filter and decreased overall gains to display the low-velocity, high-amplitude signals of the myocardium while avoiding blood flow detection. This modification is available from most commercial ultrasound vendors. Annular pulsed TDI recordings are best obtained from an apical 4-chamber view with the patient in the left lateral decubitus position (Figure 8.5). Transducer angulation and position changes to maximize parallel alignment of the Doppler cursor with the plane of maximal annular motion are frequently required. The pulsed Doppler cursor generally provides the best annular velocity signals when the sample volume gate is 3–5 mm in children. In order to visualize clearly the

Table 8.2 Tissue Doppler indices

	Strengths	Weaknesses
Tissue Doppler indices		
Isovolumic relaxation time (IVRT)	• Easy to obtain • Relatively heart rate independent • Prolongation is a good marker of early mild diastolic disease	• Poor discriminator of more severe forms of diastolic disease
e′/a′ ratio	• Easy to obtain • Geometry independent • Less load dependent than inflow Doppler • Varies with progressive diastolic disease	• Requires sinus rhythm • Age-dependent normal values • Fusion with increased HR • Tissue velocities angle dependent and influenced by overall motion of the heart (cardiac translation)
E/e′ ratio	• Easy to obtain • Helps discriminate normal vs. "pseudonormal" mitral inflow patterns	• Requires sinus rhythm • Affected by mitral valve disease • Not accessible at higher HR (fusion) • Insensitive marker in children because of wide variation in normal ranges

low-velocity spectral Doppler patterns, the Nyquist limits should be decreased to 15–30 cm/s while using the lowest wall filter settings. It is also helpful to lower the dynamic range to 30–35 dB and decrease overall gains to minimize noise around the signal. Recordings should be made with a simultaneous ECG display to correlate timing of annular motion with cardiac electrical events. Doppler tracings should be displayed at a sweep speed of 100–150 mm/s to separate waveforms better and assess temporal changes in myocardial wall motion.

The mitral and tricuspid annuli have circumferential attachments to the ventricular myocardium. Mitral annular motion at the septal–annular junction is easily obtained because the transducer can be best maintained parallel to annular motion at the septum. It may not completely reflect left ventricular dynamics, however, because of the influence of right ventricular function on septal motion. Lateral–annular motion probably provides a better assessment of left ventricular myocardial function, but it is harder to maintain a parallel transducer position when assessing the lateral–annular junction because of translational shifts in cardiac position during the cardiac cycle. Tricuspid annular motion, as a reflection of right ventricular longitudinal function, is best assessed at the medial–annular (i.e., nonseptal) junction. All three positions can provide high-quality spectral Doppler tracings that can be easily recorded and interpreted.

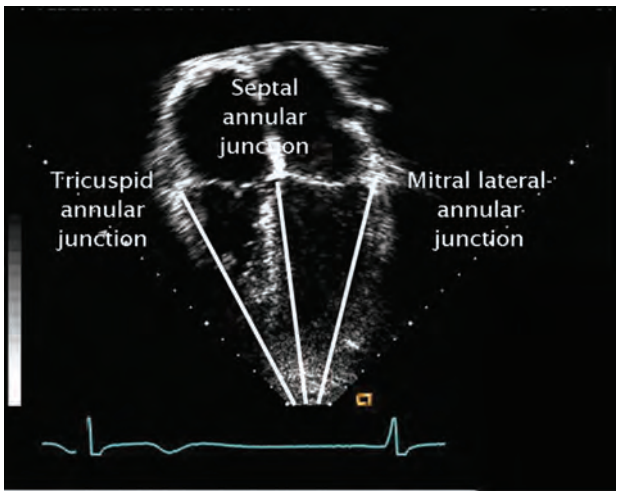


Figure 8.5 Apical 4-chamber image of Doppler cursor position to obtain pulsed tissue Doppler imaging (TDI) recordings from the mitral septal–annular and mitral lateral–annular junctions and the tricuspid annular (nonseptal) junction.

Measurements

Several diastolic measurements can be obtained from the pulsed TDI tracings of annular motion (Figure 8.6). Two diastolic waveforms are usually seen, much like the E and A waves on

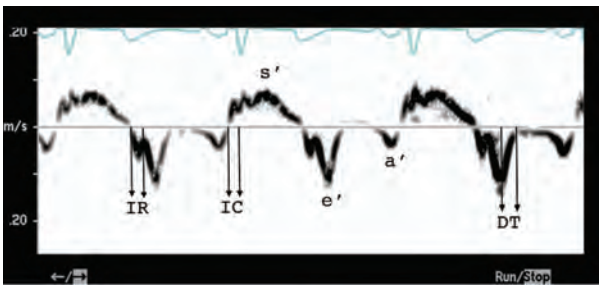


Figure 8.6 A typical pulsed tissue Doppler imaging (TDI) tracing from the mitral annulus showing the different measures that can be obtained. Two diastolic waveforms are usually seen below the baseline: the annular velocity during early diastole (e′), and the annular velocity during atrial contraction (a′). The deceleration time (DT) is the interval from the peak e′ velocity until cessation of early diastolic annular motion. The systolic annular velocity (s′) is the dominant waveform above the baseline, starting shortly after the QRS complex. The isovolumic relaxation time (IR, measured as the time from the end of the systolic waveform to the beginning of the early diastolic velocity) and the isovolumic contraction time (IC, measured as the time from the end of the diastolic waveform with atrial contraction to initiation of the systolic velocity) are identified with arrows. Small, low-velocity waveforms are commonly seen during isovolumic relaxation and likely represent translational changes in annular position.

Table 8.3 Other diastolic function indices

	Strengths	Weaknesses
Other indices		
Color M-mode flow propagation	• Correlates with tau • Preload independent	• Angle and HR dependent
LA diameter (M-mode)	• Easy to obtain	• Less accurate in LA size assessment than volumes
LA volume (biplane Simpson or area–length method)	• Established normative data • Likely best marker of chronic diastolic disease • More accurate than diameter by M-mode	• Affected by mitral valve disease and intracardiac shunts • Requires precise techniques

inflow Doppler, that represent the early diastolic annular velocity (called the e′ or E_a wave) and diastolic velocity with atrial contraction (called a′ or A_a wave). These waveforms are seen below the baseline as the annulus moves away from the apex in diastole. A third distinct waveform is seen above the baseline during systole and represents systolic mitral annular motion toward the apex (called s′ or S_a wave). Diastolic time intervals can also be measured. Isovolumic relaxation, the time from the end of systolic motion to the initiation of early diastolic motion, can frequently be identified. It may be associated with very low-velocity signals that likely represent translational shifts in heart position with the transition from systole to diastole.

Limitations

Although pulsed TDI of both tricuspid and mitral annular motion have been found to be clinically useful, some caveats are important to remember when applying this technique. TDI velocities, just like blood flow velocities, are dependent on the angle of insonation; it is critical to interrogate the myocardial segment parallel to the wall motion in order to obtain the true peak velocities. Some myocardial segments have very low-velocity motion, and it sometimes can be difficult to separate this motion from translational shifts in the cardiac mass during the cardiac cycle. Finally, it is important to remember that segmental wall motion patterns may not reflect global myocardial function.

Color M-mode flow propagation

The pattern of ventricular filling can be visualized by M-mode assessment of early diastolic flow propagation velocity from AV valve to apex using color Doppler (Table 8.3). The color M-mode tracing is obtained from the apical 4-chamber view with the cursor aligned parallel with diastolic inflow. The area of color Doppler interrogation is manipulated to obtain the longest column of flow from the AV annulus to the apex of the ventricle. The M-mode cursor is positioned through the center of the color signal. This index can be useful in the routine clinical evaluation of LV diastolic function as it provides an estimate of ventricular filling that appears to correlate well with the time constant of LV relaxation (τ) [21]. Studies have found that color M-mode Doppler is not affected by preload alterations and is most strongly influenced by LV relaxation both in experimental models during varying lusitropic conditions [22] and in humans with heart disease [23]. As relaxation becomes abnormal, the rate of early diastolic flow propagation into the ventricle slows. This decrease in flow propagation can be measured as the slope (described as the flow propagation velocity, or V_p) of the line drawn from apex to base on the color tracing (Figure 8.7). The slope of flow propagation can be best seen by decreasing the color Nyquist limit to display the first color aliasing velocity (usually at Nyquist velocity about 75% of the peak E-wave velocity). The higher the slope, the faster the flow propagation and more rapid the ventricular relaxation.

Myocardial deformation imaging

Strain rate/strain imaging

Strain rate and strain imaging appear to be important new methods for the quantification of both left ventricular and right ventricular function. Assessment of myocardial mechanics is now available echocardiographically for quantification of regional myocardial function. Importantly, myocardial strain and strain rate quantify myocardial deformation while negating the effects of cardiac translational motion and local tethering effects that complicate pulsed Doppler analysis of annular motion [24–26]. Regional strain rate corresponds to the rate of deformation of a specific segment of the myocardium. Strain rate curves are calculated from tissue velocity data, where the strain rate is the difference of two velocities in the segment of interest

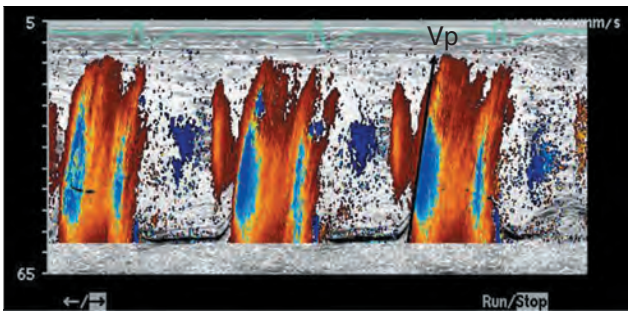


Figure 8.7 M-mode color Doppler image of the flow propagation velocity of mitral inflow. The M-mode cursor is directed apex to base through the left ventricular inflow from a 4-chamber view, and the color Doppler Nyquist limit is dropped until a clear linear aliasing envelope is seen in the color Doppler tracing. The propagation velocity (*V*p) is the slope of the line drawn parallel to the aliasing envelope (arrow). Steeper slopes correlate with more rapid diastolic relaxation in the ventricle.

divided by the distance between those two velocity points. Strain is calculated by integrating strain rate over time and is expressed as a percentage. Limitations related to angle dependence as well as signal noise have compromised the clinical acceptance of TDI-derived strain and strain rate measurements, and therefore a Doppler-independent technique is attractive. Speckle tracking echocardiography (STE) is a Doppler-independent technique to derive directionally unconstrained imaging of the myocardial motion. Speckles are ultrasound reflectors within tissue and are highly reproducible. This technique computes and displays multiple derivative parameters of diastolic function, including diastolic velocities, diastolic strain rate, and times to peak for these parameters from the tracked endocardial contour by advanced analyses (Figure 8.8) [25]. The load dependency [20] and influence of heart rate [27] on strain and strain rate have also been investigated, but application of STE in the assessment of diastolic function in children has been limited.

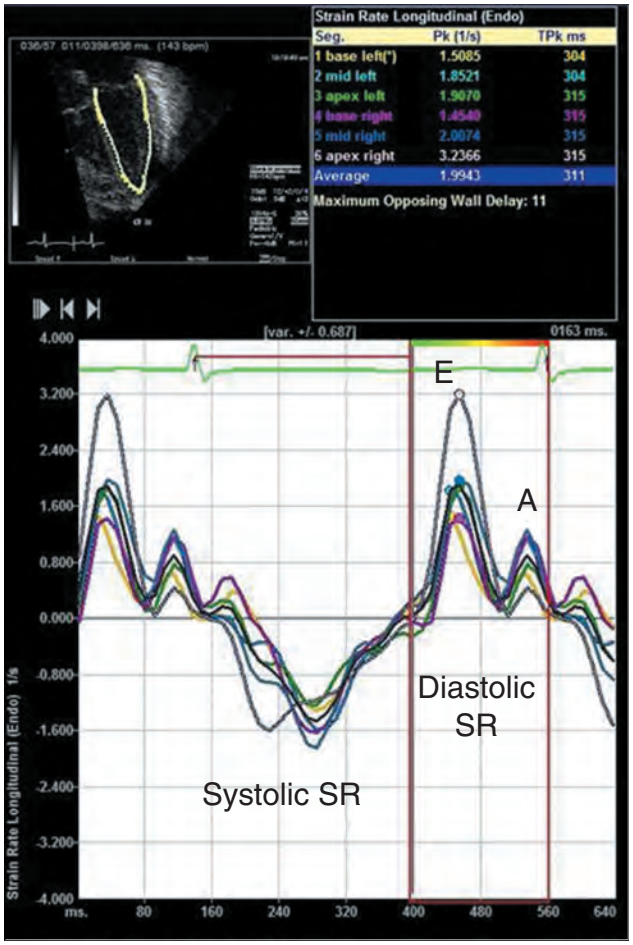


Figure 8.8 Longitudinal strain rate graph from the endocardium of the left ventricle in a child with normal intracardiac anatomy and function. The ventricle is divided into six segments as described in the table above the graph (base left, mid left, apex left, base right, mid right and apex right), and strain rate from the different segments is calculated using speckle tracking. The linear graph colors correspond to the segments represented, and the strain rate (SR) throughout the cardiac cycle is displayed. Systolic SR is negative because the distance between the two points interrogated is shortening, whereas diastolic SR is positive as the distance is lengthening in the normal heart. Two distinct diastolic curves are seen, representing early (E) filling and filling with atrial contraction (A). Notice that the E and A diastolic SR peaks occur at similar intervals from QRS activation of the ventricle, and the time to peak (TPk) for diastolic SR from the different segments is provided in the table as a gauge of synchrony. Pk, peak.

Left atrial volume

Left atrial (LA) volume appears to be a reliable marker of duration and severity of left ventricular diastolic disease. It is attractive because whereas Doppler indices describe diastolic function at one moment in time, LA volumes reflect chronic cumulative filling pressures over time. LA volume has been well correlated with the severity of diastolic dysfunction as estimated by Doppler echocardiographic methods in the elderly; only 9% of the population with evidence of normal diastolic function had LA enlargement (defined as $\geq$30 cm^3/m^2 in women and $\geq$33 mL/m^2 in men) whereas 100% of those with estimated severe dysfunction had a significantly enlarged LA [28]. Left atrial enlargement, as evidenced by an indexed volume of $\geq$32 cm^3/m^2, has also been shown to be a risk factor for a first cardiovascular event (atrial fibrillation, stroke, heart failure) in elderly adults [29]. Finally, LA enlargement has been correlated with survival in the elderly, with those patients with the largest atria having the poorest survival. This measure has not been routinely utilized in children, although normal values have been established and appear to vary with patient size. Healthy children and young adults were divided into five groups according to body surface area: 0.5–0.75 m^2, 0.75–1.0 m^2, 1.0–1.25 m^2, 1.25–1.5 m^2 and >1.5 m^2; mean left atrial maximum volume/body surface area as estimated by three-dimensional (3D) echocardiography was 19.6, 21.7, 22.0, 24.5, and 27.4 mL/m^2, respectively [30]. Unfortunately, normal values for right atrial volumes in children have not been established.

The size of the LA varies during the cardiac cycle and only maximum LA volume is routinely measured in clinical practice. This is best assessed at mitral valve opening. The minimum volume can also be measured and is best estimated at mitral valve closure at end-diastole. The LA can be assessed by the phasic functions of the chamber during diastole: these can be described by the total LA emptying volume as an estimate of reservoir volume, which is calculated as the difference between maximum and minimum LA volumes; the LA passive emptying volume (calculated as the difference between maximal LA volume and the LA volume preceding atrial contraction); LA active emptying (contractile) volume (calculated as the difference between pre-atrial contraction LA volume and minimum LA volume); and LA conduit volume (calculated as the difference between LV stroke volume and the total LA emptying volume). Not surprisingly, phasic contributions vary with the degree of diastolic dysfunction, with the relative contribution of the reservoir, conduit and contractile function of the LA to the filling of the LV in normal adults estimated at 40%, 35%, and 25%, respectively

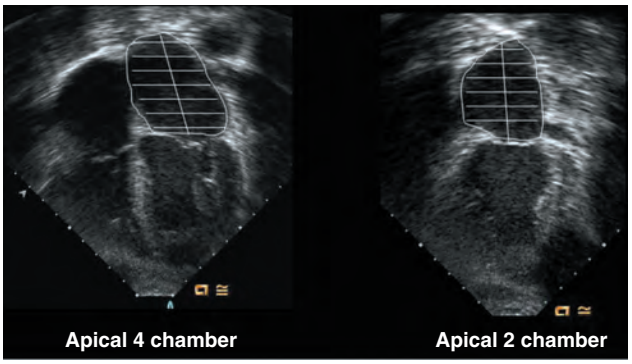


Figure 8.9 Calculation of left atrial volume using the biplane method of disks (modified Simpson's rule) from orthogonal apical 4-chamber and 2-chamber images with the left atrium traced at its maximum volume at end-systole immediately before mitral valve opening.

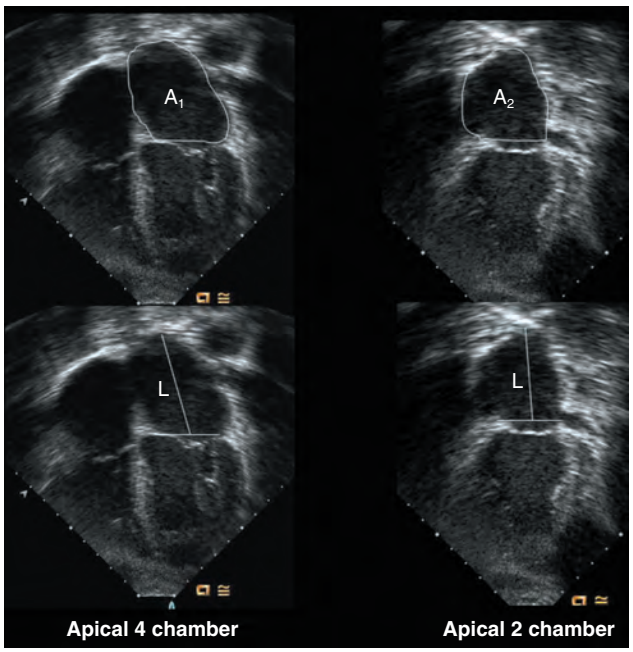


Figure 8.10 Calculation of left atrial volume using the biplane area–length method from orthogonal apical 4-chamber and 2-chamber images with the left atrium traced at its maximum volume at end-systole immediately before mitral valve opening. The formula for LA volume is $8/3\pi[(A_1)(A_2)/(L)]$ where L is the shortest of either the apical 4- or 2-chamber length. Note that the length is measured from the back wall to the hinge point of the mitral annulus, not the mitral leaflets.

[31]. With abnormal LV relaxation, the relative contribution of LA reservoir and contractile function increases and conduit function decreases. However, as LV filling pressure progressively increases with advancing diastolic dysfunction, the LA serves predominantly as a conduit.

Many methods exist to estimate LA size, including M-mode assessment of diameter. The American Society of Echocardiography has recommended quantification of LA size by biplane two-dimensional (2D) echocardiography using either the method of disks (by Simpson's rule) (Figure 8.9) or the area–length method (Figure 8.10) [8] (Table 8.3). Both methods have been validated and appear to be more accurate than M-mode estimates of LA size. Both techniques underestimate LA volume compared with magnetic resonance and computed tomography methods. It is important to remember certain caveats to improve accuracy of the measure:

- the LA can be foreshortened by inappropriate transducer position; the length measure of the two orthogonal planes utilized should not differ by more than 5 mm;
- the maximal LA volume should be measured; this is the frame immediately before mitral valve opening; and
- the LA border should be consistently measured; the inferior border of the LA is the mid-point of the mitral annulus (not the leaflet tips), and the tracing of the border should exclude the appendage and pulmonary venous confluence.

Diastolic disease

Patterns of diastolic dysfunction

Because of the many physiologic variables that determine atrial and ventricular filling, simple analysis of pulmonary venous and mitral inflow Doppler patterns as the sole means of diagnosing diastolic dysfunction can be limited. Elegant studies by Appleton and colleagues, however, have provided significant insight into the etiology of commonly identified Doppler patterns seen in a variety of disease states [32,33]. They identified Doppler patterns of mitral and pulmonary venous inflow that appear to correlate more with myocardial function and hemodynamic status than the disease process itself. They proposed a dynamic continuum of abnormal Doppler patterns that varied with changes in left atrial pressure, rate of relaxation of the left ventricle and compliance of the ventricle (Table 8.4).

Abnormal relaxation with normal atrial pressure

The mildest form of diastolic dysfunction is abnormal ventricular relaxation, when the active uncoupling of the ventricular muscle after systolic contraction is delayed. Diastolic dysfunction is initially manifested by impaired left ventricular relaxation; because ventricular compliance is unaffected, normal left atrial pressure is maintained. In this pattern, a slower rate of ventricular pressure fall after ventricular contraction results in later AV valve opening and a longer isovolumic relaxation time. Delayed relaxation also causes a reduced early diastolic pressure gradient across the AV valve so that the peak E velocity is decreased. Relaxation continues during early diastole and delays the ventricular pressure rise during rapid filling, prolonging the E-wave deceleration time. With less filling in early diastole, the percentage of filling with atrial contraction will likely be increased as a compensatory mechanism to maintain cardiac output, resulting in an increased A-wave velocity, decreased

Table 8.4 Classification of left ventricular diastolic function

	Mitral inflow	Pulmonary venous flow	TDI septal
Normal	E/A 2.3 ± 0.6 109 ms ≤ DT ≤ 216 ms	S < D MVA_{dur} > PVA_{dur}	E/e′ < 10
Abnormal relaxation	E/A ≤ 1.0 DT age/HR dependent	S > D MVA_{dur} > PVA_{dur}	E/e′ < 10
Pseudo-normal	E/A similar to normal DT similar to normal	S < D MVA_{dur} < PVA_{dur}	E/e′ > 10
Restrictive physiology	E/A > 1.5 DT < 150 ms	S < D MVA_{dur} < PVA_{dur}	E/e′ > 10

A, mitral velocity at atrial contraction; D, pulmonary venous diastolic velocity; DT, mitral deceleration time; TDI, tissue Doppler imaging; E, mitral inflow E-wave velocity; e′, mitral early diastolic septal annular velocity; MVA_{dur}, duration of mitral A-wave velocity; PVA_{dur}, duration of pulmonary venous atrial reversal velocity; S, pulmonary venous systolic velocity.

early filling fractions and decreased E-wave/A-wave velocity and VTI ratios (Figure 8.11). In addition, atrial emptying is slower during early diastole in these patients with a resultant decrease in diastolic venous inflow and dominant systolic venous velocities (Figure 8.12). Because atrial pressures are generally not significantly elevated in these patients, there is little reversal of vein flow with atrial contraction. The presence of a mid-diastolic filling wave is occasionally seen in patients with abnormal relaxation and slower heart rates; this "L" wave (as characterized by Keren et al. [34]) appears to reflect markedly delayed relaxation that creates a mid-diastolic pressure gradient across the mitral valve with resultant additional filling during the diastasis phase between the E and A waves (Figure 8.13).

Abnormal relaxation with elevated atrial pressure

As diastolic disease progresses, an intermediate or "pseudo-normal" inflow pattern is seen in patients with abnormal ventricular relaxation in association with a moderate increase in atrial pressure [32,33]. Worsening diastolic disease results in reduced ventricular compliance and an increase in atrial diastolic pressure, which normalizes the early diastolic gradient from atrium to ventricle with resultant normalization of the E-wave velocity and E/A velocity ratio. In these patients, the increase in atrial pressure masked relaxation abnormalities by normalizing the early diastolic pressure gradient across the AV valve. An inflow tracing that is indistinguishable from normal results (the "pseudo-normal" pattern). This limits the utility of inflow Doppler as an effective screen for diastolic disease. Because of this, it has been recognized that analysis of pulmonary venous inflow patterns is a useful adjunct in the assessment of left ventricular diastolic disease in children and adults. Most importantly, prolonged reversal of pulmonary vein flow with atrial contraction (PV Ar wave) has been identified as a sensitive and specific sign of elevated left ventricular filling pressure. Because normal children and adults can have some reflux of blood into the pulmonary veins with atrial contraction, the key feature of the PV Ar wave is that its duration is prolonged compared with the duration of A-wave filling on the mitral inflow Doppler tracing. A pediatric study from the Mayo Clinic documented a sensitivity and specificity of approximately 90% for elevated LV end-diastolic pressure when the ratio of the PV A-wave duration to the mitral A-wave duration is greater than 1.2, and when the difference between the PV Ar-wave duration and the mitral inflow A-wave duration exceeds 29 ms [7]. Identification of prolonged atrial reversal in the pulmonary veins appears to be the most sensitive indicator of LV diastolic disease available from Doppler inflow analysis (Figure 8.14).

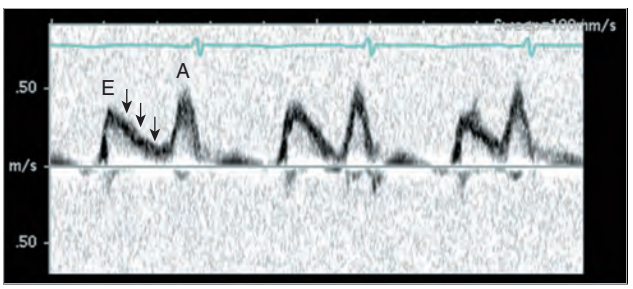


Figure 8.11 Mitral inflow Doppler in a child with abnormal relaxation. Note the decreased early diastolic (E) velocities and increased velocities with atrial contraction (A). Deceleration time of the E-wave velocity is also prolonged (arrows) and reflects the delay in relaxation into mid-diastole.

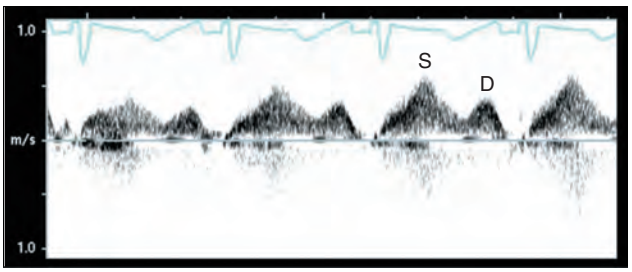


Figure 8.12 Pulmonary venous inflow Doppler in a child with abnormal relaxation. Note the decreased diastolic (D) velocities compared with the systolic (S) velocities. No reversal of flow with atrial contraction is seen, suggesting that end-diastolic left ventricular pressure is not increased.

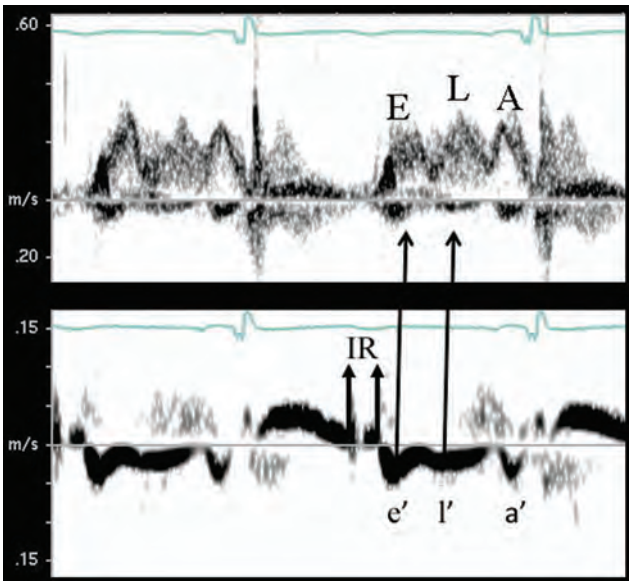


Figure 8.13 Mitral inflow Doppler (top panel) and septal annular pulsed tissue Doppler imaging (TDI; bottom panel) recordings from a child with abnormal left ventricular relaxation. The mitral inflow is unusual with decreased early diastolic velocities (E) and a prominent mid-diastolic filling wave (L). The mitral annular TDI tracing mimics this pattern with significantly decreased early annular (e′) velocities and mid-diastolic annular motion (l′); these waves appear to initiate the early and mid-diastolic inflow waves on the mitral inflow trace (arrows) and likely represent delayed and prolonged ventricular relaxation. Not surprisingly, isovolumic relaxation (IR) is also prolonged. Annular motion with atrial contraction (a′) and inflow with atrial contraction (A) appear unaffected.

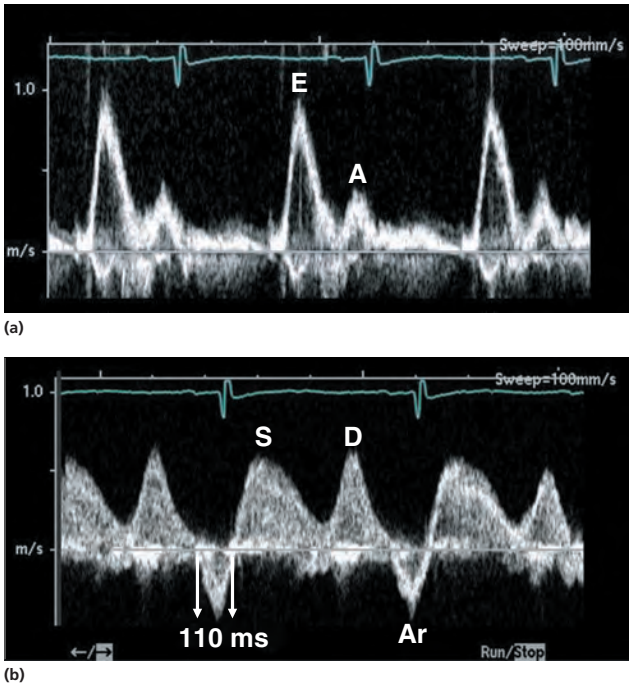


Figure 8.14 Mitral inflow Doppler **(a)** and pulmonary venous inflow Doppler **(b)** tracings from a child with diastolic disease characterized by pseudo-normal left ventricular filling. The mitral inflow tracing appears normal because the early diastolic filling (E) velocity has been "pseudo-normalized" by elevated left atrial pressures with poor left ventricular (LV) compliance. The pulmonary venous inflow tracing shows prolonged atrial reversal (Ar) with atrial contraction, and the Ar duration (120 ms) exceeds the A duration (80 ms) from the mitral tracing. This finding correlates with elevated end-diastolic ventricular pressure and helps to discriminate that the mitral pattern is "pseudo-normal." D, diastolic velocities; S, systolic velocities.

The utility of diastolic annular TDI patterns as a marker of abnormal relaxation has been well demonstrated. The early diastolic mitral TDI velocity (e′ wave) has also been found to be significantly lower in patients with abnormal relaxation compared with normal subjects. Importantly, however, this decrease in e′ persisted in patients with a pseudo-normal mitral inflow Doppler pattern and elevated left atrial pressure [15,16]. These findings suggest that the early diastolic annular velocity may be a more sensitive indicator of abnormal relaxation, and invasive studies have shown a good inverse correlation between e′ and the time constant of left ventricular pressure decay, tau. The early diastolic annular velocity also appears to be relatively preload independent, with no significant change during volume loading [19,20]. This contrasts with mitral inflow velocities, which have been shown to vary significantly with changes in volume status and preload. Because mitral inflow E-wave velocity increases whereas mitral annular e′-wave velocity remains low with increasing left atrial pressure in patients with diastolic dysfunction, the E/e′ ratio appears be a useful noninvasive predictor of increased left atrial pressure (Figure 8.15). A hemodynamic study correlated an E/e′ ratio >10 with pulmonary capillary wedge pressure >12 mmHg in adults [15].

Color M-mode assessment of LV flow propagation has been used to differentiate patients with normal from those with "pseudo-normal" filling, and to estimate the effect of LV filling pressure when combined with pulsed Doppler indices. Decreased rates of flow propagation (V_p) correlate with delayed relaxation, and this persists in the face of increasing left atrial pressure. A study in children used color M-mode Doppler to assess diastolic function and found that the ratio of the mitral inflow E-wave velocity to V_p was a good predictor of elevated LV end-diastolic pressure. A ratio of E/V_p >2.0 predicted an LV end-diastolic pressure ≥15 mmHg with a sensitivity of 100% and a specificity of 77% [21]. In addition, color M-mode flow propagation, like early annular diastolic velocities, appears to be preload independent [22]. This is another tool for the identification of "pseudo-normal" LV filling.

Abnormal ventricular compliance

The most severe form of diastolic disease is seen in patients with poor ventricular compliance and markedly elevated atrial pressures. Because of increased ventricular stiffness to filling, atrial pressures are elevated and generate an increased early pressure gradient across the AV valve. An increase in peak E-wave velocity results as blood rapidly fills the ventricle. Because of

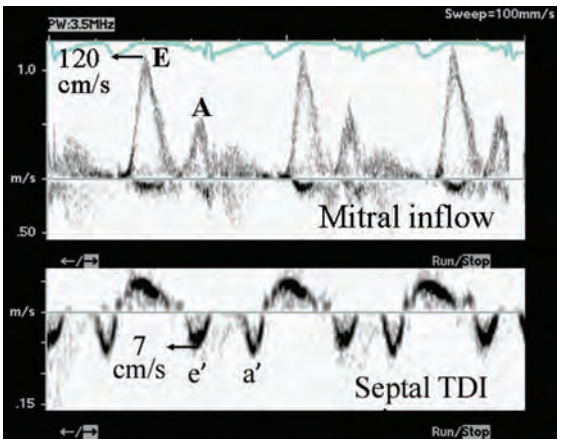


Figure 8.15 Mitral inflow Doppler (top panel) and septal annular pulsed TDI (bottom panel) recordings from a child with pseudo-normal left ventricular filling. The mitral inflow tracing appears normal because the early diastolic filling (E) velocity has been "pseudo-normalized" by elevated left atrial pressures with altered LV compliance. The mitral annular TDI tracing shows a significantly decreased early annular (e′) velocity, however, reflecting abnormal diastolic relaxation that is unaffected by the elevation in filling pressure. Because the E-wave velocity normalizes with increasing filling pressure while the e′ velocity remains decreased as diastolic disease progresses, the E/e′ ratio can be used to identify diastolic disease. In this example, the E/e′ ratio is 120/7 = 17.1, which is clearly above the normal range of 7.0 ± 1.9 in children.

abnormal ventricular compliance, however, ventricular pressure rises rapidly with small changes in volume. This abrupt increase in ventricular diastolic pressure during rapid filling causes premature cessation of E-wave flow and a short deceleration time (Figure 8.16). Ventricular pressures are markedly elevated in late diastole, resulting in a decreased or absent peak A-wave velocity because only a slight additional pressure gradient can be generated across the AV valve with atrial contraction. High atrial pressure also results in early AV valve opening during ventricular relaxation, and this can be identified by a shortened isovolumic relaxation time. Venous inflow Doppler shows rapid

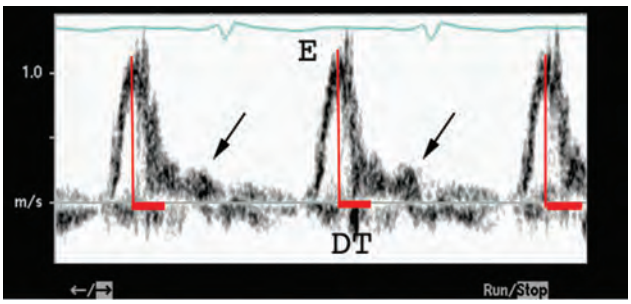


Figure 8.16 Mitral inflow Doppler in a child with abnormal ventricular compliance. Note the increased early diastolic (E) velocities and rapid deceleration time (DT) of the E-wave velocity secondary to the poor compliance as ventricular pressure rises rapidly during early filling, abolishing the early transvalvar gradient across the mitral valve. In late diastole, ventricular pressures have risen to the point where very little additional filling occurs with atrial contraction (arrows).

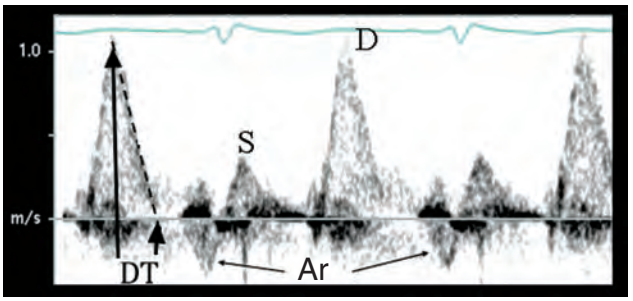


Figure 8.17 Pulmonary venous inflow Doppler in a child with abnormal ventricular compliance. Note the increased diastolic (D) velocities compared with the systolic (S) velocities, with rapid deceleration of the diastolic wave in mid-diastole (DT), reflecting the rapid increase in left ventricular pressure during early filling with a resultant increase in diastolic left atrial pressure and abrupt cessation of pulmonary venous emptying. Atrial reversal of flow with atrial contraction is seen (Ar), reflecting the marked increase in end-diastolic left ventricular pressure as an additional sign of poor compliance. Systolic venous inflow is blunted because of the chronic left atrial hypertension and distension.

atrial filling in early diastole with AV valve opening as the high-pressure atrium empties; this flow decelerates in mid-diastole as ventricular pressures rise abruptly with filling (Figure 8.17). There frequently is prolonged reversal of venous inflow with atrial contraction because of the dramatic increase in both atrial and ventricular pressure at end-diastole. Systolic venous inflow is blunted because of chronic atrial hypertension and distension.

As with pulmonary venous inflow, identification of high-velocity reversal of inferior vena cava inflow with atrial contraction suggests poor right ventricular compliance and has been used to identify elevated right atrial filling pressures in adults. Specifically, reversal velocities during atrial contraction that exceed forward velocities have been correlated with central venous pressures greater than 15 mmHg (Figure 8.18) [35]. This finding has not been corroborated in children and is likely

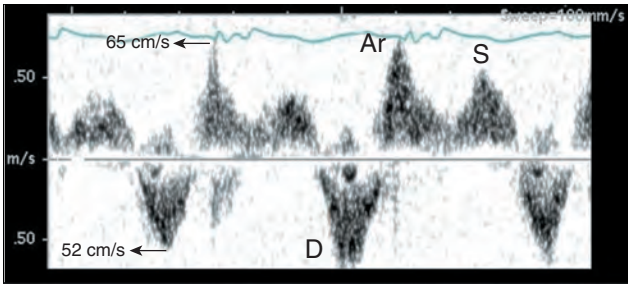


Figure 8.18 Hepatic venous inflow Doppler in a child with abnormal right ventricular compliance. Early diastolic (D) velocities are seen below the baseline, reflecting forward flow into the right atrium. However, there is marked reversal of flow with atrial contraction (Ar), with a peak velocity that exceeds the forward diastolic peak velocity (65 vs. 52 cm/s), reflecting markedly elevated right atrial end-diastolic pressure. In addition, there is significant tricuspid insufficiency in the patient, with resultant reversal of flow during systole as well (S).

Table 8.5 Normal inflow Doppler values in infants and children

Demographics	<1 year	1–5 y	6–9 y	10–13 y	14–18 y	Total
N	63	68	55	58	81	325
Male	29	39	27	38	44	177
Age (y)	0.40 ± 0.30	3.05 ± 1.51†	7.91 ± 1.12†	11.99 ± 1.11†	16.0 ± 1.40†	78 ± 6.0
Weight (kg)	6.6 ± 2.7	15.1 ± 5.4†	33.8 ± 14.9†	47.2 ± 16.3†	66.1 ± 15.5†	33.3 ± 25.2
BSA (m^2)	0.34 ± 0.08	0.62 ± 0.14†	1.07 ± 0.27†	1.37 ± 0.29†	1.73 ± 0.25†	1.0 ± 0.6
HR (bpm)	124 ± 16	105 ± 17†	80 ± 11†	75 ± 12	69 ± 16	90 ± 26
Echocardiographic						
LV EDD (cm)	2.3 ± 0.3	3.1 ± 0.4†	3.9 ± 0.4†	4.3 ± 0.4†	4.7 ± 0.4†	3.6 ± 1.0
LV ESD (cm)	1.4 ± 0.2	1.9 ± 0.3†	2.4 ± 0.3†	2.7 ± 0.3†	3.0 ± 0.4†	2.3 ± 0.6
LV PWT (cm)	0.4 ± 0.1	0.6 ± 0.1†	0.7 ± 0.1*	0.8 ± 0.1*	0.9 ± 0.2	0.7 ± 0.2
LV SWT (cm)	0.5 ± 0.1	0.6 ± 0.1†	0.8 ± 0.1†	0.8 ± 0.2	1.0 ± 0.2†	0.7 ± 0.2
LV mass (g/m^2)	18.9 ± 6.5	43.6 ± 16.4†	82.3 ± 28.3†	110.1 ± 32.9†	158.4 ± 48.5†	81.8 ± 58.9
Mitral E velocity	79.7 ± 18.8	95.2 ± 19.5†	94.4 ± 14.8	94.5 ± 16.0	90.3 ± 17.8	90.8 ± 18.5
Mitral A velocity	65.3 ± 13.3	61.3 ± 12.1	49.4 ± 12.5†	49.5 ± 13.8	45.5 ± 13.2	54.4 ± 15.0
Mitral E/A ratio	1.24 ± 0.30	1.60 ± 0.46†	1.99 ± 0.51†	2.02 ± 0.58	2.13 ± 0.65	1.79 ± 0.61
PV S-wave velocity	44.6 ± 10.3	48.0 ± 8.9	50.7 ± 11.3	49.0 ± 11.1	47.7 ± 7.3	48.7 ± 9.2
PV D-wave velocity	46.0 ± 9.5	54.5 ± 11.0†	53.3 ± 11.4	58.4 ± 12.1	57.9 ± 15.0	54.6 ± 12.9
PV A-reversal velocity	16.4 ± 6.3	20.6 ± 4.3†	20.2 ± 3.8	21.2 ± 4.9	20.0 ± 5.2	20.5 ± 5.1
Tricuspid E velocity	53.3 ± 12.3	61.6 ± 12.5*	60.5 ± 13.9	59.6 ± 11.4	60.4 ± 10.9	59.2 ± 12.4
Tricuspid A velocity	53.2 ± 13.0	48.3 ± 12.3*	42.4 ± 10.8*	39.2 ± 11.3	34.5 ± 11.2*	43.3 ± 13.5
Tricuspid E/A ratio	1.01 ± 0.38	1.27 ± 0.31†	1.49 ± 0.40†	1.61 ± 0.47*	1.88 ± 0.56†	1.47 ± 0.53
SF (%)	38.9 ± 4.1	38.0 ± 3.6	37.4 ± 3.8	37.4 ± 4.2	36.4 ± 4.3	37.6 ± 4.1
LV MPI	0.33 ± 0.08	0.34 ± 0.07	0.32 ± 0.06	0.34 ± 0.06	0.34 ± 0.08	0.33 ± 0.08
RV MPI	0.29 ± 0.09	0.28 ± 0.07	0.29 ± 0.08	0.28 ± 0.08	0.29 ± 0.08	0.28 ± 0.08

A, atrial; BSA, body surface area; D, diastolic; E, early diastolic velocity; EDD, end-diastolic dimension; ESD, end-systolic dimension; HR, heart rate; LV, left ventricular; MPI, myocardial performance index; PV, pulmonary venous; PWT, posterior wall thickness; S, systolic; SF, shortening fraction; SWT, systolic wall thickness.
*$p < 0.05$, †$p < 0.01$ compared with preceding column.
Data expressed as mean ± SD.
Doppler velocities expressed as cm/s.
Source: Eidem et al. 2004 [36]. Reproduced with permission of Elsevier.

to be invalid when positive-pressure ventilation or airway disease is present secondary to the associated dramatic changes in intrathoracic pressure.

Diastolic function in pediatric patients without heart disease

Age-related changes in diastolic filling

Doppler patterns of left atrial and left ventricular filling have identified variable pulmonary venous and mitral inflow patterns that appear to correlate and change with increasing age in the pediatric patient. The greatest change appears to occur during infancy, when both fetal and neonatal Doppler patterns show predominant ventricular filling during atrial contraction with decreased peak E-wave velocity and decreased E-wave/A-wave velocity and velocity time integral ratios compared with older children. The infant mitral pattern is consistent with altered ventricular relaxation and a decreased early transmitral pressure gradient. This is also reflected in the pulmonary venous Doppler patterns seen in young infants, with increased peak systolic velocities, decreased peak diastolic velocities, and increased systolic/diastolic velocity and velocity time integral ratios compared with older children. These patterns of altered filling seen in infancy likely reflect differences in the diastolic properties of immature myocardium, but they are also influenced by changes in heart rate and loading conditions. With increasing age, there is a shift in LV filling from late to early diastole, and a shift in LA filling from systole to diastole during the first year of life; in general, older children and adolescents have pulmonary venous and mitral inflow Doppler patterns that are similar to patterns seen in healthy young adults. Characterization of inflow Doppler (Table 8.5) and annular TDI velocities (Table 8.6) in normal neonates, children and adults has provided reference values for future investigations in children and adults with congenital and acquired heart disease. Interestingly, the patterns of filling described in infants recur in the elderly adult as part of the "normal" process of myocardial aging.

Healthy children/athletes

Diastolic properties of the LV and RV have been recently characterized in healthy children using inflow Doppler [10,36] and pulsed annular Doppler tissue imaging [17,18,36]. Mitral inflow parameters are remarkably stable from age 3 years through

Table 8.6 Normal annular tissue Doppler imaging values in infants and children

Age group	*N*	e′-wave velocity	a′-wave velocity	s′-wave velocity	ICT	IRT	E/E′ ratio
Mitral annular							
<1 y	63	9.7 ± 3.3 (8.8–10.5)	5.7 ± 1.8 (5.3–6.2)	5.7 ± 1.6 (5.3–6.1)	77.4 ± 18.4 (72.7–82.0)	57.0 ± 14.8 (53.1–60.8)	8.8 ± 2.7 (8.1–9.5)
1–5 y	68	15.1 ± 3.4† (14.3–15.4)	6.5 ± 1.9 (6.1–7.0)	7.7 ± 2.1† (7.2–8.2)	76.9 ± 15.9 (72.8–80.9)	62.1 ± 13.2 (58.9–65.4)	6.5 ± 2.0† (6.0–7.0)
6–9 y	55	17.2 ± 3.7† (16.2–18.3)	6.7 ± 1.9 (6.2–7.3)	9.5 ± 2.1† (8.9–10.1)	77.9 ± 18.9 (72.4–83.4)	62.9 ± 11.9 (59.5–66.3)	5.8 ± 1.9 (5.3–6.4)
10–13 y	58	19.6 ± 3.4† (18.7–20.5)	6.4 ± 1.8 (5.9–6.9)	10.8 ± 2.9* (10.0–11.5)	76.6 ± 16.2 (72.4–80.9)	62.6 ± 12.4 (59.4–65.9)	4.9 ± 1.3 (4.6–5.2)
14–18 y	81	20.6 ± 3.8 (19.7–21.4)	6.7 ± 1.6 (6.3–7.1)	12.3 ± 2.9† (11.6–12.9)	78.9 ± 15.4 (75.4–82.3)	69.5 ± 15.5* (66.1–73.0)	4.7 ± 1.3 (4.4–5.0)
Total	325	16.5 ± 5.3 (16.0–17.1)	6.4 ± 1.9 (6.2–6.6)	9.3 ± 3.4 (8.9–9.7)	77.5 ± 16.7 (75.7–79.5)	63.2 ± 14.4 (61.7–64.9)	6.1 ± 2.4 (5.9–6.4)
Septal							
<1 y	63	8.1 ± 2.5 (7.5–8.7)	6.1 ± 1.5 (5.7–6.4)	5.4 ± 1.2 (5.1–5.7)	77.5 ± 17.5 (73.0–82.0)	53.0 ± 11.7 (50.0–56.0)	10.3 ± 2.7 (9.7–11.0)
1–5 y	68	11.8 ± 2.0† (11.3–12.3)	6.0 ± 1.3 (5.7–6.4)	7.1 ± 1.5† (6.8–7.5)	80.1 ± 15.5 (76.3–83.9)	59.8 ± 12.0 (56.9–62.7)	8.1 ± 1.8† (7.7–8.5)
6–9 y	55	13.4 ± 1.9† (12.8–13.9)	5.9 ± 1.3 (5.5–6.3)	8.0 ± 1.3 (7.6–8.4)	82.8 ± 15.3 (78.4–87.2)	65.6 ± 10.7 (62.5–68.7)	7.2 ± 1.6 (6.8–7.7)
10–13 y	58	14.5 ± 2.6 (13.8–15.2)	6.1 ± 2.3 (5.6–6.7)	8.2 ± 1.3 (7.9–8.5)	87.9 ± 16.4* (83.6–92.2)	72.5 ± 12.3 (69.3–75.8)	6.6 ± 1.4 (6.3–7.0)
14–18 y	81	14.9 ± 2.4 (14.3–15.4)	6.2 ± 1.5 (5.9–6.6)	9.0 ± 1.5 (8.7–9.3)	88.4 ± 15.6 (84.9–91.9)	77.5 ± 14.5 (74.3–80.8)	6.4 ± 1.5 (6.1–6.8)
Total	325	12.6 ± 3.4 (12.2–13.0)	6.1 ± 1.6 (5.9–6.3)	7.6 ± 1.9 (7.4–7.8)	83.5 ± 16.5 (81.7–85.4)	66.1 ± 15.3 (64.4–67.9)	7.7 ± 2.3 (7.5–8.0)
Tricuspid annular							
<1 y	63	13.8 ± 8.2 (11.7–15.9)	9.8 ± 2.4 (9.1–10.5)	10.2 ± 5.5 (8.8–11.7)	68.7 ± 18.2 (63.9–73.5)	52.0 ± 12.9 (48.5–55.4)	4.4 ± 2.3 (3.8–5.0)
1–5 y	68	17.1 ± 4.0† (16.1–18.1)	10.9 ± 2.7 (10.2–11.6)	13.2 ± 2.0† (12.7–13.7)	77.7 ± 15.0 (73.9–81.5)	59.0 ± 13.9 (55.4–62.5)	3.8 ± 1.1 (3.5–4.1)
6–9 y	55	16.5 ± 3.0 (15.7–17.4)	9.8 ± 2.7 (9.0–10.6)	13.4 ± 2.0 (12.8–14.0)	91.8 ± 21.5† (85.5–98.0)	58.5 ± 17.5 (53.4–63.6)	3.6 ± 0.8 (3.4–3.9)
10–13 y	58	16.5 ± 3.1 (15.7–17.4)	10.3 ± 3.4 (9.3–11.2)	13.9 ± 2.4 (13.2–14.5)	98.1 ± 21.7 (92.2–103.9)	61.7 ± 19.9 (56.4–67.1)	3.5 ± 1.4 (3.2–3.9)
14–18 y	81	16.7 ± 2.8 (16.0–17.3)	10.1 ± 2.6 (9.5–10.7)	14.2 ± 2.3 (13.7–14.7)	101.9 ± 20.4 (97.2–106.6)	62.9 ± 18.9 (58.5–67.3)	3.7 ± 1.0 (3.5–3.9)
Total	325	16.1 ± 4.7 (15.6–16.7)	10.2 ± 2.8 (9.9–10.5)	13.0 ± 3.4 (12.6–13.4)	88.2 ± 23.1 (85.6–90.8)	59.0 ± 17.2 (57.0–60.9)	3.8 ± 1.4 (3.6–4.0)

A, Late diastolic velocity; a′, late diastolic annular velocity; ICT, isovolumic contraction time; E, early diastolic inflow Doppler velocity; e′, early diastolic annular velocity; IRT, isovolumic relaxation time; S, systolic velocity; s′, systolic annular velocity.
*$p < 0.05$; †$p < 0.01$ compared with preceding age group.
Data expressed as mean ± SD (95% confidence interval). Doppler tissue imaging velocities are expressed in cm/s. Time intervals are expressed in milliseconds.
Source: Eidem et al. 2004 [36]. Reproduced with permission of Elsevier.

17 years, with similar E-wave velocities, A-wave velocities, E-wave/A-wave velocity ratio and isovolumic relaxation time; only deceleration time changes significantly, and this is most likely related to the effect of decreasing heart rate with age. TDI measures correlated significantly with age and parameters of cardiac growth [36], but were not influenced by gender, heart rate, or respiration. Research studies have also focused on the influence of diastolic function with exercise in healthy adolescents and young adults. Diastolic function appears well preserved in elite female and male athletes [37] despite significant changes in LV wall thickness and ventricular dimensions. It appears that diastolic function has a significant impact on peak exercise

oxygen uptake, with a strong correlation identified between diastolic flow propagation into the LV using color M-mode and peak oxygen consumption with exercise. In fact, it appears that assessment of diastolic function measured at rest using echocardiography may be a useful predictor of better adaptation of myocardial performance during exercise with a positive impact on peak oxygen consumption. Finally, a study has identified pathologic alterations in LV diastolic relaxation following marathon running in recreational runners independent of the predicted change in preload, suggesting the phenomenon of exercise-induced cardiac fatigue [38]. In some of the runners, these changes correlated with elevations in cardiac troponin-T, suggesting exercise-induced cardiac damage. It certainly raises the question of how much is too much when considering exercise as a good thing.

Diastolic disease in pediatric patients with primary myocardial disease

Hypertrophic cardiomyopathy

Diastolic abnormalities have been consistently identified in both children and adults with hypertrophic cardiomyopathy. Mitral inflow Doppler patterns in children with nonobstructive hypertrophic cardiomyopathy are consistent with abnormal relaxation. Diastolic TDI patterns in patients with hypertrophic cardiomyopathy have also correlated with abnormal relaxation, and have been used to predict elevations in LV filling pressure using the E/e′ ratio when pseudo-normalization of the mitral inflow occurs [39]. Doppler tissue imaging patterns also have identified dyssynchronous diastolic function in children with hypertrophic cardiomyopathy (Figure 8.19) and have been used to assess the benefit of calcium channel blocker therapy in improving diastolic function [40]. Importantly, TDI patterns of annular motion have been utilized to predict functional class and exercise capacity in children [41,42] and adults with this disease. A study in children with hypertrophic cardiomyopathy identified annular TDI patterns that were predictive for adverse outcomes, including death, cardiac arrest, and ventricular tachycardia [41]. The most sensitive indicator was the ratio of the early transmitral E velocity/septal annular e′ velocity ratio, which was increased in the at-risk children (median ratio 13.7 with 25th to 75th percentile range 12.3–15.1) compared with those without adverse events (median ratio 8.5 with 25th to 75th percentile 7.4–11.2). In addition, this ratio was significantly higher in children with symptoms (median 11.9 vs. 8.1) and correlated inversely with peak oxygen consumption during exercise testing. Finally, diastolic annular TDI patterns, isovolumic relaxation time and LA volume [43] have identified hypertrophic cardiomyopathy in the absence of pathologic hypertrophic changes, suggesting that this technique may identify a genetic predilection for the disease before phenotypic expression can be identified by 2D imaging. Differentiation of hypertrophic cardiomyopathy and the appropriate physiologic hypertrophy seen in well-trained athletes is also possible using TDI; early annular diastolic velocities are always normal to increased in athletes and consistently decreased in those with hypertrophic cardiomyopathy. In one series, an é/á ratio <1 was commonly encountered in the mutation-positive hypertrophic population and never seen in the athletes [44].

Dilated cardiomyopathy

Dilated cardiomyopathy, in which the predominant abnormality is decreased systolic LV function with left heart chamber dilation, has also been associated with diastolic dysfunction. Although indices of systolic function appear to be most predictive of outcome, abnormalities in inflow Doppler patterns consistent with more severe diastolic disease also correlate with symptoms in adults with dilated cardiomyopathy. Patients with the most severe symptoms had changes on inflow Doppler

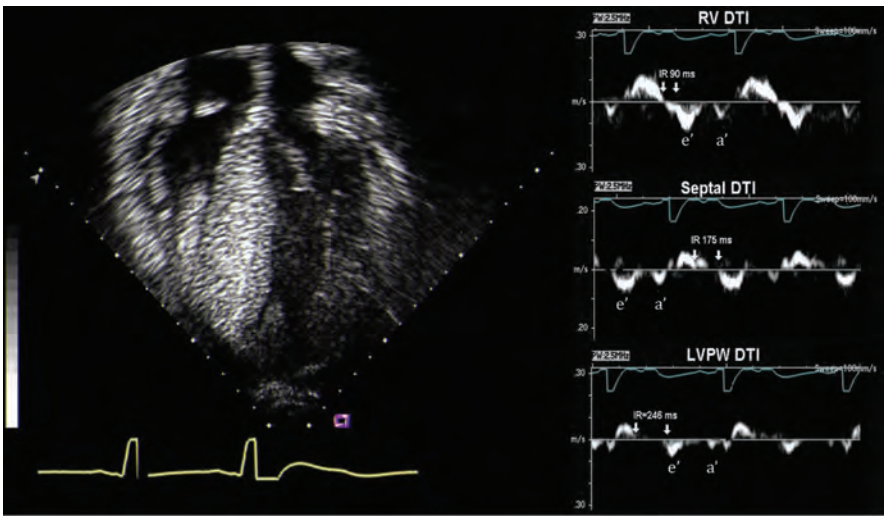


Figure 8.19 Apical 4-chamber image and pulsed tissue Doppler imaging (TDI) recordings from the left ventricular posterior wall (LVPW), ventricular septum and right ventricular (RV) free wall in a child with hypertrophic cardiomyopathy. Although on 2D imaging the septum appears most affected, diastolic dysfunction is identified by TDI in all three areas interrogated with prolonged isovolumic relaxation (IR) and decreased early diastolic annular (e′) velocities compared with normals. The dyssynchronous diastolic relaxation properties of different segments of the myocardium in this disease are also evident by the variable IR (90 ms in the RV compared with 246 ms in the LVPW) and variable e′ velocities found at each site. a′, diastolic annular velocity with atrial contraction.

consistent with poorer ventricular compliance (shorter isovolumic relaxation time, higher peak E velocity, increased E/A ratio, shorter deceleration time) compared with those who were less symptomatic. In addition, those with ejection fractions less than 25% and deceleration times less than 130 ms had the worst 2-year survival [45]. This is in contrast to mitral inflow patterns in children with dilated cardiomyopathy, which do not appear to discriminate the incidence of symptoms or poorer outcome. Tissue Doppler imaging studies have identified a decrease in mitral, septal, and tricuspid annular velocities compared with findings in normal children. Surprisingly, the mitral and septal TDI patterns were not predictive of adverse outcome (hospitalization, transplantation or death) in children with dilated cardiomyopathy, but the tricuspid e′ velocities had excellent specificity for identifying patients at risk [46]. The combination of a left ventricular ejection fraction of less than 30% and a tricuspid e′ velocity of less than 8.5 cm/s had 100% specificity and 44% sensitivity in identifying those at increased risk.

Diastolic function assessment may also have a role in identifying myocardial dysfunction and predicting the development of dilated cardiomyopathy in children with Duchenne muscular dystrophy (DMD) [47,48]. In one study, all indices of diastolic function measured were significantly abnormal for boys with DMD when compared with a normal control group in the absence of systolic dysfunction. Abnormalities were present for both ventricular relaxation (mitral E/A ratio, mitral annular e′/a′ ratio, isovolumic relaxation time, velocity of flow propagation) and ventricular compliance (mitral E deceleration time, prolonged pulmonary venous reversal wave at atrial contraction, mitral E/annular é ratio, and mitral E/velocity of flow propagation ratio) indices. In addition, boys who subsequently went on to develop dilated cardiomyopathy had significantly worse diastolic indices at baseline compared with those who did not [48].

Restrictive cardiomyopathy

A restrictive cardiomyopathy is characterized predominantly by an abnormality in ventricular diastolic compliance with very stiff ventricular muscle and a rapid increase in ventricular pressures during diastolic filling. Isolated restrictive cardiomyopathy is rare and frequently fatal; it can be idiopathic, associated with congenital endocardial fibroelastotic changes in the ventricle or infiltrative processes like amyloidosis. Restrictive cardiomyopathy must be considered when 2D imaging identifies marked atrial enlargement with normal ventricular size and ventricular systolic function in the absence of significant AV valve insufficiency (Figure 8.20). The mitral inflow trace is characteristic, with an increased E-wave velocity with rapid E-wave deceleration and a small or absent A wave, consistent with the abnormal compliance pattern described previously (Figure 8.16) [49]. Because of the rapid increase in ventricular pressure during early diastolic filling, ventricular pressures can exceed atrial pressure, and mid-diastolic mitral insufficiency can be seen by both pulsed-wave and color Doppler. Mid-diastolic insufficiency is generally only seen with severe restrictive cardiomyopathy. Because of poor atrial emptying in this condition, systolic pulmonary venous forward flow is blunted; the majority of pulmonary vein flow is seen in early diastole with rapid deceleration of flow in mid-diastole associated with the rapid increase in ventricular diastolic pressures (Figure 8.17). Dramatic reversal of flow with atrial contraction is usually seen, although some of these patients develop atrial systolic dysfunction secondary to the marked dilation with a trivial or absent reversal wave in late diastole.

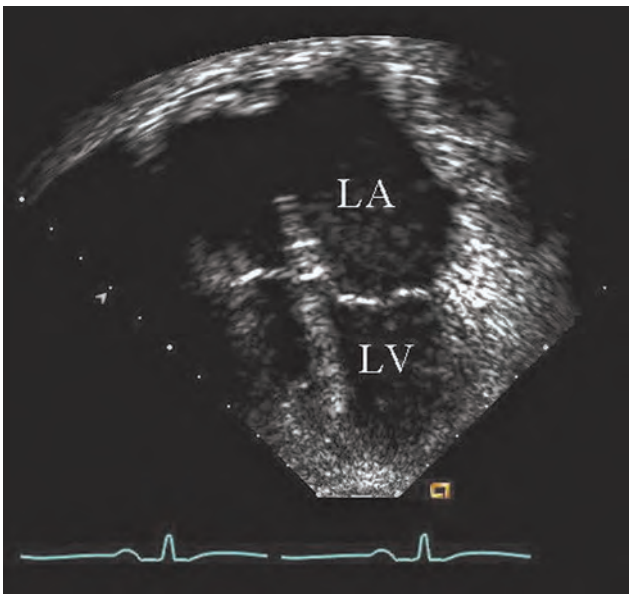


Figure 8.20 Apical 4-chamber image in a child with restrictive cardiomyopathy. The left atrium (LA) is markedly dilated relative to the size of the left ventricle (LV).

Left ventricular noncompaction is a heterogeneous form of cardiomyopathy characterized by prominent endocardial trabeculations. This disease process can have variable systolic function, but it appears to be consistently associated with diastolic dysfunction. In milder forms, and as an additional diagnostic tool, abnormal relaxation is found using annular TDI with decreased e′ velocities and abnormal diastolic strain patterns [50,51]. More severe forms can manifest findings consistent with restrictive disease and end-stage heart failure.

Pediatric patients with acquired heart disease/systemic disease states

Left ventricular hypertrophy

Many studies have documented a common pattern of mitral inflow associated with left ventricular hypertrophy that appears specific to the hypertrophy rather than the disease process that caused it. Diastolic filling abnormalities were found in 36% of the children with essential hypertension, and approximately one-third of those patients had patterns consistent with altered

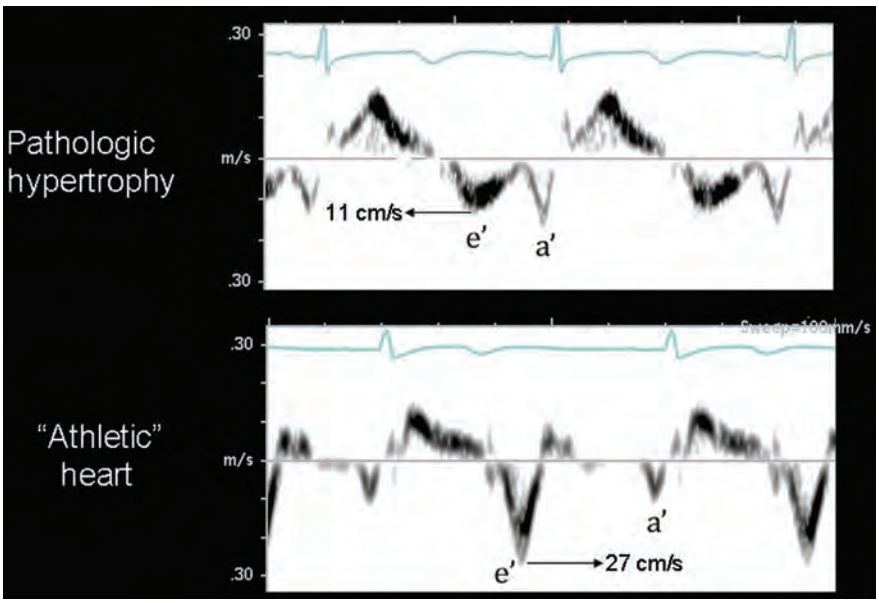


Figure 8.21 Mitral annular pulsed tissue Doppler imaging (TDI) recordings from an adolescent with pathologic left ventricular hypertrophy (top panel) and an athletic adolescent with increased left ventricular mass reflecting an "athletic" heart. The pathologic hypertrophy patient has decreased early diastolic annular velocities (a′) and reversed e′/a′ ratio, whereas the athletic heart has "supranormal" early diastolic annular velocities with an é velocity of 27 cm/s, consistent with the rapid and exaggerated ventricular relaxation seen in athletes.

relaxation, and one-third had patterns consistent with altered compliance. Elevated ventricular mass was found to be the most significant independent predictor of pathologic diastolic function [52]. Mitral annular TDI assessment has been shown to be useful in both children and adults with pathologic hypertrophy and is helpful in differentiating pathologic hypertrophy from the physiologic hypertrophy commonly seen in competitive high-school and college athletes (Figure 8.21) The "athletic" heart has normal e′ velocities, isovolumic relaxation and mitral E/e′ ratios, and these findings can be an important adjunct in assessing the hypertrophied heart [44].

Chronic renal disease

Children and adolescents with chronic renal failure appear to have abnormal diastolic function, much like their adult counterparts. By observing mitral inflow and mitral annular velocities, children with mild to moderate chronic renal failure were found to have decreased early annular velocities and higher early mitral inflow velocity to mitral annular early diastolic velocity ratios with increased LA dimensions compared with normal children, all suggestive of abnormal LV relaxation and compliance [53]. Importantly, the children on dialysis had worse diastolic disease that appeared to correlate with the degree of LV hypertrophy, despite normal LV systolic function [54].

Obesity

Obese children have been found to have increased LV mass, and this puts them at risk for diastolic dysfunction. Several studies have identified abnormal LV diastolic function in obese children and adults using imaging and inflow Doppler parameters. This abnormality is characterized by increased LA dimensions, prolonged isovolumic relaxation time, and prolonged early diastolic deceleration time in association with increased LV dimension and mass that correlates with body mass index [55]. A study that compared obese children with normal controls using TDI [56] found that the obese subjects exhibited evidence of abnormal LV diastolic function, with a decrease in the peak early diastolic mitral annular velocity measured at the ventricular septum and a significant increase in the peak diastolic annular velocity with atrial contraction at the ventricular septum, LV lateral wall, and LV posterior wall. The obese group also had significantly lower early to late diastolic annular velocity ratios at the ventricular septum, of a degree that was inversely related to body mass index, implying that pathologic diastolic changes correlate and progress with the degree of obesity. Strain rate imaging has also been used to discriminate diastolic function in obese children. Those meeting criteria for obesity had a shift to increased late diastolic myocardial motion and decreased systolic strain compared with normal-weight children [57]. These abnormalities are likely subtle markers for early cardiac disease.

Type 1 diabetes mellitus

Studies using inflow Doppler techniques have identified left ventricular diastolic dysfunction in the absence of systolic changes in children and young adults with type 1 diabetes [58–60]. These abnormalities were consistent with abnormal relaxation and decreased early diastolic LV filling with a compensatory increase in filling with atrial contraction. Duration and severity of disease appeared to be associated with these filling changes. More recently, the diastolic properties of the LV were analyzed using pulsed TDI in a large cohort of children and adolescents with stable type 1 diabetes and compared with age- and gender-matched controls [60]. Both boys and girls had significantly prolonged isovolumic relaxation times, consistent with delayed myocardial relaxation. The girls also had additional abnormalities as measured by pulsed TDI

indices of diastolic function despite the absence of correlations in these findings with duration of diabetes or hemoglobin HbA_{1c} levels. These early changes emphasize the risk for cardiac complications associated with this disease state. The gender predilection warrants additional investigation.

Obstructive sleep apnea

Obstructive sleep apnea has generally been associated with RV dysfunction secondary to altered pulmonary vascular resistance. Echocardiographic characterization of LV diastolic function in children with obstructive sleep apnea identified significant diastolic dysfunction in the absence of clinically apparent heart disease [61]. Importantly, there was a significant correlation between the severity of the obstructive sleep apnea and the degree of LV diastolic disease, which was independent of obesity, blood pressure, or LV mass. This study also demonstrated that the pathologic LV diastolic changes improved when the obstructive sleep apnea was treated effectively. Although no assessment of RV function or pulmonary hypertension was provided in this study, it was postulated that LV diastolic dysfunction in this disease may negatively impact pulmonary vascular resistance and contribute to the development of cor pulmonale.

Anthracycline cardiotoxicity

Anthracyclines are commonly used in the treatment of childhood malignancies, and there is a clear association between cumulative anthracycline dose and the development of LV systolic dysfunction. Diastolic dysfunction has also been identified [62–66], and a relationship between anthracycline dose and a decrease in mitral early diastolic inflow velocity with a prolongation in isovolumic relaxation time has been seen [64]. This suggests that high doses of anthracycline may be a risk factor for the development of impaired left ventricular relaxation. There did not appear to be a correlation between diastolic abnormalities and subsequent development of systolic dysfunction, although the observation that cumulative doses under 250 mg/m^2 did not appear to be associated with diastolic deterioration again supports the concept of dose monitoring of these chemotherapeutic agents. Importantly, however, children with low cumulative doses of anthracycline (<250 mg/m^2) demonstrated adverse changes in diastolic longitudinal function characterized by decreased early annular tissue Doppler velocities with a compensatory increase in late diastolic velocities (and decreased e′/a′ ratio) in both the RV and LV that persisted at later follow-up in the absence of systolic dysfunction [66].

Pediatric patients with congenital heart disease

Tetralogy of Fallot

Echocardiography frequently identifies abnormal RV diastolic function as a sequela of primary tetralogy of Fallot repair. This has been coined RV "restrictive physiology" [67–75]. Restrictive physiology is characterized echocardiographically by the pulmonary artery Doppler pattern of antegrade diastolic main pulmonary artery flow with atrial contraction, which occurs only if the right ventricle has become a stiff noncompliant conduit between the right atrium and pulmonary artery with transmission of the atrial contraction filling wave into the pulmonary arteries (Figure 8.22) [67,68]. The identification of restrictive physiology by main pulmonary artery Doppler has become a useful index for identifying abnormal right ventricular diastolic compliance. This finding is recognized as a predictor of poorer initial recovery from surgical repair [67,69–71,75]. RV diastolic dysfunction is demonstrable by Doppler echocardiography early after surgery and tends to be worse with transannular patch placement [69,74,75]. Restrictive physiology predicts longer duration of inotropic support, prolonged ventilator support, prolonged intensive care unit (ICU) and hospital stay, and higher doses of diuretics during postoperative recovery. The presence of early restrictive physiology appears to predict restriction at later follow-up: one study demonstrated that 56% of patients with early restriction also had restriction at follow-up, whereas only 6% of patients without early restrictive RV physiology developed restriction later. In fact, early restriction was the only independent variable predictive of late restriction [73].

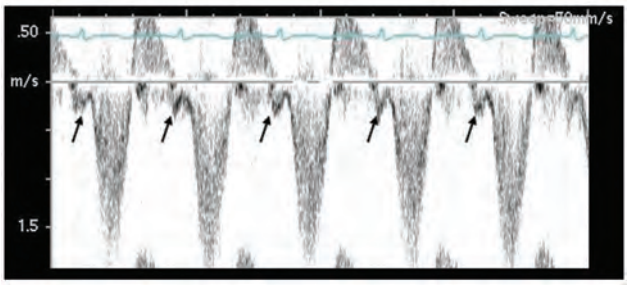


Figure 8.22 Main pulmonary artery (MPA) pulsed Doppler tracing in a child with tetralogy of Fallot after repair. Antegrade diastolic flow is seen in the MPA with atrial contraction (arrows), consistent with restrictive right ventricular physiology.

The importance of the currently accepted strategy of complete repair at a younger age, generally during infancy, likely also influences the development of restriction, because later age at surgery has been found to correlate with subsequent development of restriction [72]. Ten percent of the patients repaired before 6 months of age had evidence of restrictive physiology at follow-up, increasing to 38% with repair after 9 months. Restrictive RV physiology was found to be inversely related to age at repair and independent of type of outflow tract repair. Surprisingly, restrictive physiology appears to be favorable late after repair because it is associated with less pulmonary regurgitation, better exercise tolerance, decreased RV size, less QRS prolongation and fewer symptomatic ventricular arrhythmias [68,74]. The "benefit" of restrictive physiology late into adulthood after repair is controversial, however, given its association

with pathologically abnormal RV compliance, and the impact of this finding on clinical decision-making (particularly timing of pulmonary valve replacement) remains unclear.

Several studies have used newer echocardiographic techniques to assess RV diastolic function late after surgical repair of tetralogy of Fallot, specifically focusing on Doppler tissue imaging. There appears to be a significant decrease in tricuspid annular and regional RV velocities in both early diastole and with atrial contraction in children following tetralogy of Fallot repair at intermediate follow-up [76–78]. These findings suggest delayed RV relaxation and restrictive RV filling, and they have been correlated with pathologic electrocardiographic changes, suggesting that TDI patterns may also be predictive of higher-risk outcomes late after surgery. These diastolic abnormalities are also associated with prolongation in isovolumic relaxation and isovolumic contraction times as well as depressed systolic annular velocities, implying that both systolic and diastolic function are affected. Systolic and diastolic abnormalities of wall motion of the RV, characterized by reversal of velocity direction in the mid and apical segments (from the normally apically directed systolic velocity and basally directed early and late diastolic velocities), were detected in 65% of adolescents and young adults following repair of tetralogy of Fallot [78]. There was no correlation between the incidence of wall-motion abnormalities and age at time of examination, degree of pulmonary insufficiency, or type of surgical technique. The patients with reversed systolic and/or diastolic myocardial velocities in the RV free wall had more abnormal electrocardiogram (ECG) changes, with a longer QRS duration and greater QT and JT dispersion, than those with normal wall motion, suggesting pathologic mechanoelectrical interactions that may impact outcome.

Using strain and strain rate imaging, evaluation of patients after more than a year following surgical repair of tetralogy of Fallot found reduced systolic strain rate and strain as well as poorer early diastolic strain rate that correlated with depressed RV ejection fraction [79]. Abnormalities in strain and strain rate indices were not appreciated in the intraventricular septum, suggesting that septal myocardial function may be preserved during childhood as a compensatory mechanism for the RV free wall dysfunction in those patients. Given the risk of late RV failure after tetralogy of Fallot repair, particularly in the presence of significant pulmonary insufficiency, these tools provide additional and important information about the health of the RV and the timing/need for pulmonary valve replacement.

Single ventricle physiology

Ventricular diastolic function in the patient with a functional single ventricular chamber is frequently abnormal when assessed by Doppler echocardiography. Atrioventricular and pulmonary venous Doppler patterns tend to be much more variable in this patient population because the source of pulmonary blood flow, and thus the loading conditions, vary depending on the lesion and form of palliation [80]. Some patients have pulsatile antegrade systolic pulmonary flow from the single ventricle, some have continuous pulsatile flow from an aortopulmonary shunt, and others have passive low-velocity flow from direct systemic venous-to-pulmonary artery anastomoses. These patients are frequently palliated by separation of the systemic and pulmonary circulation using the Fontan operation. Studies have documented inflow Doppler patterns in patients following the Fontan procedure that again are consistent with impaired ventricular relaxation, decreased peak E velocities, mid-diastolic filling waves, decreased E/A velocity and area ratios, and decreased normalized peak filling rates compared with normal children [81–86]. This impairment in ventricular relaxation has also been observed in invasive studies using the time constant, tau, and normalized peak filling rate [87]. However, by contrast, the invasive studies found that there was little difference in diastolic passive chamber stiffness between the Fontan group and the control group, and that the Fontan group had normal net chamber filling at rest. Echo studies agree that these abnormalities appear to be mild at early and intermediate follow-up, with one study documenting that the AV valve inflow E/A ratio remains greater than 1 and isovolumic relaxation time is within the normal range. Pulmonary venous inflow patterns are also different compared with normals, with predominant systolic pulmonary venous emptying, again consistent with delayed relaxation and resultant decreased diastolic emptying of the pulmonary veins. Prolonged reversal of pulmonary vein flow with atrial contraction has not been identified [82]. This suggests that although delayed relaxation is a constant feature of Fontan physiology at rest, its effect on overall diastolic filling is minimal. Length of time after Fontan palliation also had a negative impact on early diastolic velocities, however, suggesting that diastolic function progressively deteriorates as the patient ages [88]. Again, these techniques may provide early insight into ventricular dysfunction and the opportunity for medical intervention to preserve ventricular function before more global heart failure and systolic dysfunction develop.

Strategy for the echocardiographic assessment of diastolic function in children

The earlier discussion suggests that a new paradigm is needed to better assess diastolic function in pediatric patients echocardiographically (Figure 8.23). This approach must include the routine screening of mitral, tricuspid, pulmonary and systemic vein inflow in all children. In addition, all children should have TDI assessment of tricuspid annular motion as well, because tricuspid inflow Doppler patterns can vary so dramatically with respiration. LA volumes and mitral TDI assessment should be obtained in all children who have abnormal mitral/pulmonary venous inflow patterns and/or have known heart disease. Similarly, right atrial volumes and main pulmonary artery Doppler assessment should be obtained in all children who have

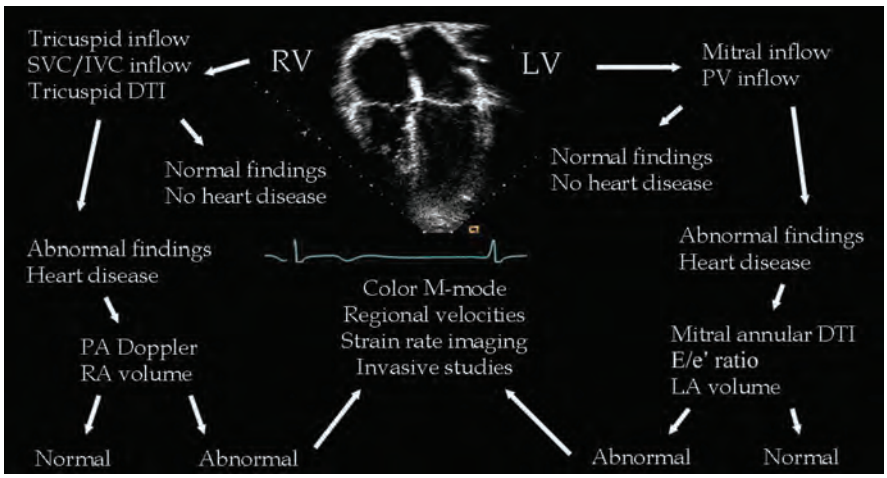


Figure 8.23 Proposed schematic flowchart for the assessment of diastolic function in pediatric patients using echocardiography. TDI, tissue Doppler imaging; E, early diastolic filling velocity; e′, early annular velocity; IVC, inferior vena cava; LA, left atrium; LV, left ventricle; PA, pulmonary artery; RA, right atrium; RV, right ventricle; SVC, superior vena cava.

abnormal tricuspid inflow/TDI patterns and/or have known heart disease. Serial evaluations, additional echocardiographic techniques and/or invasive testing should be done in those identified with diastolic disease.

Conclusions

Diastolic function can be assessed by Doppler echocardiography in pediatric patients and should be part of the routine echocardiographic exam.

- Mitral and pulmonary venous inflow Doppler patterns can identify abnormal LV relaxation and compliance as well as an elevation in LA pressure.
- Age-related differences in inflow Doppler patterns are important to recognize in the pediatric patient, because a shift in ventricular filling from late to early diastole is expected during infancy in normal children.
- Tissue Doppler imaging analysis of mitral and tricuspid diastolic annular motion can significantly augment the identification of diastolic disease in children.
- Ventricular hypertrophy from any cause, cardiomyopathies, children with tetralogy of Fallot after repair, and children with single ventricle physiology are at significant risk for diastolic disease and should be assessed carefully.
- Newer techniques, including color M-mode Doppler, myocardial deformation imaging and assessment of atrial volumes, may add to the echocardiographic assessment of diastolic disease and should also be applied in children.

References

1 Courtois M, Kovacs S, Ludbrook P. Transmitral pressure-flow velocity relation. Importance of regional pressure gradients in the left ventricle during diastole. *Circulation* 1988;**78**:661–671.

2 Snider AR, Serwer GA, Ritter SB. Methods for obtaining quantitative information from the echocardiographic examination. In: *Echocardiography in Pediatric Heart Disease*. St. Louis, MO: Mosby, 1997, pp. 133–234.

3 Oh JK, Appleton CP, Hatle LK, et al. The noninvasive assessment of left ventricular diastolic function with two-dimensional and Doppler echocardiography. *J Am Soc Echocardiog* 1997;**10**:246–270.

4 Nishimura RA, Housamans PR, Hatle LK, et al. Assessment of diastolic function of the heart: background and current applications of Doppler echocardiography. Part I. Physiology and pathophysiologic features. *Mayo Clin Proc* 1989;**64**:71–81.

5 Nishimura RA, Abel MD, Hatle LK, et al. Assessment of diastolic function of the heart: background and current applications of Doppler echocardiography. Part II. Clinical studies. *Mayo Clin Proc* 1989;**64**:181–204.

6 Snider A, Serwer G, Ritter S. *Echocardiography in Pediatric Heart Disease*, 2nd edn. St. Louis, MO: Mosby, 1997.

7 O'Leary PW, Durongpisitkul K, Cordes T, et al. Diastolic ventricular function in children: a Doppler echocardiographic study establishing normal values and predictors of increased ventricular end-diastolic pressure. *Mayo Clin Proc* 1998;**73**:616–628.

8 Lopez L, Colan SD, Frommelt PC, et al. Recommendations for quantification methods during the performance of a pediatric echocardiogram: a report from the Pediatric Measurements Writing Group of the American Society of Echocardiography Pediatric and Congenital Heart Disease Council. *J Am Soc Echocardiogr* 2010;**23**:465–495.

9 Keren G, Sherez J, Megidish B, et al. Pulmonary venous flow pattern – its relationship to cardiac dynamics. *Circulation* 1985;**71**:1105–1112.

10 Smallhorn H, Freedom R, Olley P. Pulsed Doppler echocardiographic assessment of extraparenchymal pulmonary vein flow. *J Am Coll Cardiol* 1987;**9**:573–579.

11 Klein A, Tajik A. Doppler assessment of pulmonary venous flow in healthy subjects and in patients with heart disease. *J Am Soc Echocardiogr* 1991;**4**:379–392.

12 Adurrahman L, Hoit B, Banerjee A, et al. Pulmonary venous flow Doppler velocities in children. *J Am Soc Echocardiogr* 1998;**11**:132–137.

13 Nagueh S, Sun, H, Kopelen H, et al. Hemodynamic determinants of the mitral annulus diastolic velocities by tissue Doppler. *J Am Coll Cardiol* 2001;**37**:277–285.
14 Frommelt PC. Pulsed Doppler tissue imaging of mitral annular motion: a new technique in the non-invasive assessment of diastolic function. *Prog Pediatr Cardiol* 1999;**10**:75–82.
15 Nagueh SF, Middleton KJ, Kopelen HA, et al. Doppler tissue imaging: a noninvasive technique for evaluation of left ventricular relaxation and estimation of filling pressures. *J Am Coll Cardiol* 1997;**30**:1527–1533.
16 Sohn DW, Chai IH, Lee DJ, et al. Assessment of mitral annulus velocity by Doppler tissue imaging in the evaluation of left ventricular diastolic function. *J Am Coll Cardiol* 1997;**30**:474–480.
17 Rychik J, Tian ZY. Quantitative assessment of myocardial tissue velocities in normal children with Doppler tissue imaging. *Am J Cardiol* 1996;**77**:1254–1257.
18 Frommelt PC, Ballweg JA, Whitstone BN, et al. Usefulness of Doppler tissue imaging analysis of tricuspid annular motion for determination of right ventricular function in normal infants and children. *Am J Cardiol* 2002;**89**:610–613.
19 Eidem B, McMahon C, Ayres N, et al. (2005) Impact of chronic left ventricular preload and afterload on Doppler tissue imaging velocities: a study in congenital heart disease. *J Am Soc Echogardiogr* 2005;**18**:830–838.
20 Abali G, Tokgozoglu L, Ozcebe OI, et al. Which Doppler parameters are load independent? A study in normal volunteers after blood donation. *J Am Soc Echocardiogr* 2005;**18**:1260–1265.
21 Border WL, Michelfelder EC, Glascock BJ, et al. Color M-mode and Doppler tissue evaluation of diastolic function in children: simultaneous correlation with invasive indices. *J Am Soc Echocardiogr* 2003;**16**:988–994.
22 Garcia MJ, Smedira NG, Greenberg NL, et al. Color M-mode Doppler flow propagation velocity is a preload insensitive index of left ventricular relaxation: animal and human validation. *J Am Coll Cardiol* 2000;**35**:201–208.
23 Stugaard M, Brodahl U, Torp H, et al. Abnormalities of left ventricular filling in patients with coronary artery disease: assessment by color M-mode Doppler technique. *Eur Heart J* 1994;**15**:318–327.
24 Sutherland GR, Di Salvo G, Claus P, et al. Strain and strain rate imaging: a new clinical approach to quantifying regional myocardial function. *J Am Soc Echocardiogr* 2004;**17**:788–802.
25 Marwick TH. Measurement of strain and strain rate by echocardiography: ready for prime time? *J Am Coll Cardiol* 2006;**47**:1313–1327.
26 Weidemann F, Eyskens B, Jamal F, et al. Quantification of regional left and right ventricular radial and longitudinal function in healthy children using ultrasound-based strain rate and strain imaging. *J Am Soc Echocardiogr* 2002;**15**:20–28.
27 Boettler P, Hartmann M, Watzl K, et al. Heart rate effects on strain and strain rate in healthy children. *J Am Soc Echocardiogr* 2005;**18**:1121–1130.
28 Tsang TS, Barnes ME, Gersh BJ, et al. Left atrial volume as a morphophysiologic expression of left ventricular diastolic dysfunction and relation to cardiovascular risk burden. *Am J Cardiol* 2002;**90**:1284–1289.
29 Pritchett AM, Mahoney DW, Jacobsen SJ, et al. Diastolic dysfunction and left atrial volume: a population-based study. *J Am Coll Cardiol* 2005;**45**:87–92.
30 Poutanen T, Jokinen E, Sairanen H, Tikanoja T. Left atrial and left ventricular function assessed by three-dimensional echocardiography. *Heart* 2003;**89**:544–549.
31 Abhayaratna WP, Seward JB, Appleton CP, et al. Left atrial size: physiologic determinants and clinical applications. *J Am Coll Cardiol* 2006;**47**:2357–2363.
32 Appleton CP, Hatle LK, Popp RL. Relation of transmitral flow velocity patterns to left ventricular diastolic function: new insights from a combined hemodynamic and Doppler echocardiographic study. *J Am Coll Cardiol* 1988;**12**:426–440.
33 Appleton CP, Hatle LK. The natural history of left ventricular filling abnormalities: assessment by two-dimensional and Doppler echocardiography. *Echocardiography* 1990;**9**:453–462.
34 Keren G, Meisner JS, Sherez J, et al. Interrelationship of mid-diastolic mitral valve motion, pulmonary venous flow, and transmitral flow. *Circulation* 1986;**74**:36–44.
35 Ommen SR, Nishimura RA, Hurrell DG, et al. Assessment of right atrial pressure with 2-dimensional and Doppler echocardiography: a simultaneous catheterization and echocardiographic study. *Mayo Clin Proc* 2000;**75**:24–29.
36 Eidem BW, McMahon CJ, Cohen RR, et al. Impact of cardiac growth on Doppler tissue imaging velocities: a study in healthy children. *J Am Soc Echocardiogr* 2004;**17**:212–221.
37 Nottin S, Nguyen L-D, Terbah, M, et al. Left ventricular function in endurance trained children by tissue Doppler imaging. *Med Sci Sports Exerc* 2004;**36**:1507–1513.
38 Whyte G, George K, Shave R, et al. Impact of marathon running on cardiac structure and function in recreational runners. *Clin Sci* 2005;**108**:73–80.
39 Nagueh SF, Bachinski LL, Meyer D, et al. Tissue Doppler imaging consistently detects myocardial abnormalities in patients with hypertrophic cardiomyopathy and provides a novel means for an early diagnosis before and independently of hypertrophy. *Circulation* 2000;**104**:128–130.
40 Pacileo G, De Cristofaro M, Russo MG, et al. Hypertrophic cardiomyopathy in pediatric patients: effect of verapamil on regional and global left ventricular diastolic function. *Can J Cardiol* 2000;**16**:146–152.
41 McMahon CJ, Nagueh SF, Pignatelli RH, et al. Characterization of left ventricular diastolic function by tissue Doppler imaging and clinical status in children with hypertrophic cardiomyopathy. *Circulation* 2004;**109**:1756–1762.
42 Yetman AT, Gow RM, Seib P, et al. Exercise capacity in children with hypertrophic cardiomyopathy and its relation to diastolic left ventricular function. *Am J Cardiol* 2001;**87**:491–493.
43 Poutanen T, Tikanoja T, Jaaskelainen P, et al. Diastolic dysfunction without left ventricular hypertrophy is an early finding in children with hypertrophic cardiomyopathy-causing mutations in the beta-myosin heavy chain, alpha-tropomyosin, and myosin-binding protein C genes. *Am Heart J* 2006;**151**:725.
44 Cardim N, Oliveira AG, Longo S, et al. Doppler tissue imaging: regional myocardial function in hypertrophic cardiomyopathy and in athlete's heart. *J Am Soc Echocardiogr* 2003;**16**:223–232.
45 Rihal CS, Nishimura RA, Hatle LK, et al. Systolic and diastolic dysfunction in patients with clinical diagnosis of dilated cardiomyopathy. Relation to symptoms and prognosis. *Circulation* 1994;**90**:2772–2779.
46 McMahon CJ, Nagueh SF, Eapen RS, et al. Echocardiographic predictors of adverse clinical events in children with dilated

cardiomyopathy: a prospective clinical study. *Heart* 2004;**90**:908–915.
47 Bahler R, Mohyuddin T, Finkelhor S, et al. Contribution of Doppler tissue imaging and myocardial performance index to assessment of left ventricular function in patients with Duchenne's muscular dystrophy. *J Am Soc Echocardiogr* 2005;**18**:666–673.
48 Markham LW, Michelfelder EC, Border WL, et al. Abnormalities of diastolic function precedes dilated cardiomyopathy associated with Duchenne muscular dystrophy. *J Am Soc Echocardiogr* 2006;**7**:865–871.
49 Cetta F, O'Leary PW, Seward JB, et al. Idiopathic restrictive cardiomyopathy in childhood: diagnostic features and clinical course. *Mayo Clin Proc* 1995;**70**:634–640.
50 McMahon CJ, Pignatelli RH, Nagueh SF, et al. Left ventricular noncompaction cardiomyopathy in children: characterization of clinical status using tissue Doppler-derived indices of left ventricular diastolic relaxation. *Heart* 2007;**93**:676–681.
51 Fazio G, Pipitone S, Iacona MA, et al. Evaluation of diastolic function by the tissue Doppler in children affected by non-compaction. *Int J Cardiol* 2007;**116**:e60–62.
52 Border WL, Kimball TR, Witt SA, et al. Diastolic filling abnormalities in children with essential hypertension. *J Pediatr* 2007;**150**:503–509.
53 Mitsnefes MM, Kimball TR, Border WL, et al. Impaired left ventricular diastolic function in children with chronic renal failure. *Kidney Int* 2004;**65**:1461–1466.
54 Goren A, Glaser J, Drukker A. Diastolic function in children and adolescents on dialysis and after kidney transplantation: an echocardiographic assessment. *Pediatr Nephrol* 1993;**7**:725–728.
55 DiSalvo G, Pacileo G. Abnormal myocardial deformation properties in obese, non-hypertensive children: an ambulatory blood pressure monitoring, standard echocardiographic, and strain rate imaging study. *Eur Heart J* 2006;**27**:2689–2695.
56 Mehta SK, Holliday C, Hayduk L, et al. Comparison of myocardial function in children with body mass indexes ≥25 versus those <25 kg/m^2. *Am J Cardiol* 2004;**93**:1567–1569.
57 Lorch SM, Sharkey A. Myocardial velocity, strain, and strain rate abnormalities in healthy obese children. *J Cardiometab Syndr* 2007;**2**:30–34.
58 Albanna II, Eichelberger SM, Khoury PR, et al. Diastolic dysfunction in young patients with insulin dependent diabetes mellitus as determined by automated border detection. *J Am Soc Echocardiogr* 1998;**11**:349–355.
59 Schannwell CM, Schneppenheim M, Perings S, et al. Left ventricular diastolic dysfunction as an early manifestation of diabetic cardiomyopathy. *Cardiology* 2002;**98**:33–39.
60 Suys BE, Katier N, Rooman R, et al. Female children and adolescents with type 1 diabetes have more pronounced early echocardiographic signs of diabetic cardiomyopathy. *Diabetes Care* 2004;**27**:1947–1953.
61 Amin RS, Kimball TR, Kalra M, et al. Left ventricular function in children with sleep-disordered breathing. *Am J Cardiol* 2005;**95**:801–804.
62 Bu'Lock FA, Mott MG, Oakhill A, et al. Left ventricular diastolic filling patterns associated with progressive anthracycline-induced myocardial damage: a prospective study. *Pediatr Cardiol* 1999;**20**:252–263.
63 Kapusta L, Thijssn JM, Groot-Loonen J, et al. Tissue Doppler imaging in detection of myocardial dysfunction in survivors of childhood cancer treated with anthracyclines. *Ultrasound Med Biol* 2000;**26**:1099–1108.
64 Dorup I, Levitt G, Sullivan I, et al. Prospective longitudinal assessment of late anthracycline cardiotoxicity after childhood cancer: the role of diastolic function. *Heart* 2004;**90**:1214–1216.
65 Ganame J, Claus P, Uyttebroeck A, et al. Myocardial dysfunction late after low-dose anthracycline treatment in asymptomatic pediatric patients. *J Am Soc Echocardiogr* 2007;**20**:1351–1358.
66 Stapleton G, Stapleton S, Martinez A, et al. Evaluation of longitudinal ventricular function with tissue Doppler echocardiography in children treated with anthracyclines. *J Am Soc Echocardiogr* 2007;**20**:492–497.
67 Cullen S, Shore D, Redington A. Characterization of right ventricular diastolic performance after complete repair of tetralogy of Fallot. Restrictive physiology predicts slow postoperative recovery. *Circulation* 1995;**91**:1782–1789.
68 Gatzoulis MA, Clark AL, Cullen S, et al. Right ventricular diastolic function 15 to 35 years after repair of tetralogy of Fallot. Restrictive physiology predicts superior exercise performance. *Circulation* 1995;**91**:1775–1781.
69 Sachdev MS, Bhagyavathy A, Varghese R, et al. Right ventricular diastolic function after repair of tetralogy of Fallot. *Pediatric Cardiology* 2006;**27**:250–255.
70 Rathore KS, Gupta N, Kapoor A, et al. Assessment of right ventricular diastolic function: does it predict post-operative course in tetralogy of Fallot. *Indian Heart J* 2004;**56**:220–224.
71 Chaturvedi RR, Shore DF, Lincoln C, et al. Acute right ventricular restrictive physiology after repair of tetralogy of Fallot: association with myocardial injury and oxidative stress. *Circulation* 1999;**100**:1540–1547.
72 Munkhammar P, Cullen S, Jogi P, et al. Early age at repair prevents restrictive right ventricular (RV) physiology after surgery for tetralogy of Fallot (TOF): diastolic RV function after TOF repair in infancy. *J Am Coll Cardiol* 1998;**32**:1083–1087.
73 Norgard G, Gatzoulis MA, Josen M, et al. Does restrictive right ventricular physiology in the early postoperative period predict subsequent right ventricular restriction after repair of tetralogy of Fallot? *Heart* 1998;**79**:481–484.
74 Norgard G, Gatzoulis MA, Moraes F, et al. Relationship between type of outflow tract repair and postoperative right ventricular diastolic physiology in tetralogy of Fallot. Implications for long-term outcome. *Circulation* 1996;**94**:3276–3280.
75 Eroglu AG, Sarioglu A, Sarioglu T. Right ventricular diastolic function after repair of tetralogy of Fallot: its relationship to the insertion of a 'transannular' patch. *Cardiol Young* 1999;**9**:384–391.
76 Toyono M, Harad K, Tamura M, et al. Myocardial acceleration during isovolumic contraction as a new index of right ventricular contractile function and its relation to pulmonary regurgitation in patients after repair of tetralogy of Fallot. *J Am Soc Echocardiogr* 2004;**17**:332–337.
77 Yasuoka K, Harada K, Toyono M, et al. Tei index determined by tissue Doppler imaging in patients with pulmonary regurgitation after repair of tetralogy of Fallot. *Pediatr Cardiol* 2004;**25**:131–136.
78 Vogel M, Sponring J, Cullen S, et al. Regional wall motion and abnormalities of electrical depolarization and repolarization in patients after surgical repair of tetralogy of Fallot. *Circulation* 2001;**103**:1669–1673.
79 Solarz DE, Witt SA, Glascock BJ, et al. Right ventricular strain rate and strain analysis in patients with repaired tetralogy of Fallot:

possible interventricular septal compensation. *J Am Soc Echocardiogr* 2004;**17**:338–344.

80 Rychik J, Fogel M, Donofrio M, et al. Comparison of patterns of pulmonary venous blood flow in the functional single ventricle heart after operative aortopulmonary shunt versus superior cavopulmonary shunt. *Am J Cardiol* 1997;**80**:922–926.

81 Frommelt PC, Snider AR, Meliones JN, et al. Doppler assessment of pulmonary artery flow patterns and ventricular function after the Fontan operation. *Am J Cardiol* 1991;**68**:1211–1217.

82 Olivier M, O'Leary PW, Pankratz VS, et al. Serial Doppler assessment of diastolic function before and after the Fontan operation. *J Am Soc Echocardiogr* 1991;**16**:1136–1143.

83 Penny DJ, Rigby ML, Redington AN. Abnormal patterns of intraventricular flow and diastolic filling after the Fontan operation: evidence for incoordinate ventricular wall motion. *Br Heart J* 1991;**63**:375–380.

84 Cheung YF, Penny DJ, Redington AN. Serial assessment of left ventricular diastolic function after Fontan procedure *Heart* 2000;**83**:420–424.

85 Mahle WT, Coon PD, Wernovsky G, et al. Quantitative echocardiographic assessment of the performance of the functionally single right ventricle after the Fontan operation. *Cardiol Young* 2001;**11**:399–406.

86 Border WL, Syed AU, Michelfelder EC, et al. Impaired systemic ventricular relaxation affects postoperative short-term outcome in Fontan patients. *J Thorac Cardiov Surg* 2003;**26**:60–64.

87 Redington A, Chan K, Carvalho J, et al. Early diastolic clicks after the Fontan procedure for double inlet left ventricle: anatomical and physiological correlates. *Br Heart J* 1990;**63**:304–307.

88 Vitarelli A, Conde Y, Cimino E, et al. Quantitative assessment of systolic and diastolic ventricular function with tissue Doppler imaging after Fontan type of operation. *Int J Cardiol* 2005;**102**:61–69.

PART III

Anomalies of the Systemic and Pulmonary Veins, Septa, and Atrioventricular Junction

CHAPTER 9

Pulmonary Venous Anomalies

David W. Brown
Department of Cardiology, Children's Hospital Boston; Department of Pediatrics, Harvard Medical School, Boston, MA, USA

Definition

Pulmonary venous anomalies include many anatomic variations, with a wide range of clinical presentations and outcomes. The anomalies may be grouped into four categories:

1 *abnormal numbers* of pulmonary veins
2 normal pulmonary venous connections with *anomalous drainage*
3 *stenotic connections*
4 *anomalous connections*.

The presentation ranges from normal, in those with variations on the normal number of pulmonary veins, to life-threatening disease in the neonate with obstructed total anomalous pulmonary venous connection. Fortunately, the vast majority of pulmonary venous anomalies may now be readily and rapidly diagnosed by echocardiography.

Incidence

The incidence of pulmonary venous anomalies varies widely according to the anomaly observed. Abnormal number of pulmonary veins is commonly encountered; a single right or single left pulmonary vein is present in nearly 25% of the population in anatomic studies [1], and a third pulmonary vein is present on either side in 1.6–2% [1]. Cor triatriatum, an example of stenotic pulmonary venous connection due to incomplete incorporation of the common pulmonary vein into the left atrium, occurs in 3 in 100,000 of the population [2]. Partial anomalous pulmonary venous connection (PAPVC) has been described in autopsy series in 400 to 700 in 100,000 specimens [1], with isolated PAPVC in 160 of 100,000. Total anomalous pulmonary venous connection (TAPVC) has been described in 9 in 100,000 of the population [3,4].

Etiology

Most cases of pulmonary venous anomalies are sporadic. However, there are known syndromic associations for PAPVC, most notably Turner and Noonan syndromes [5,6]. TAPVC similarly has syndromic associations including cat-eye, Holt–Oram, and the asplenia syndromes. Numerous case reports of nonsyndromic familial cases suggest a heritable genetic cause, with heterogeneous genetic loci reported; one gene for familial total anomalous pulmonary venous return in a large Utah kindred was mapped to chromosome 4p13-q12 [7].

Morphology and classification

Developmental considerations

The classification of pulmonary venous anomalies is based on an understanding of the embryological development of the pulmonary veins, and the relationships between the pulmonary veins, systemic veins, and the atria. The lungs and tracheobronchial tree are derived from the foregut, and the pulmonary vascular bed is formed by a portion of the splanchnic plexus. Thus, early in gestation, the primitive lung drains via the splanchnic venous plexus into the systemic circulation via the umbilicovitelline and cardinal venous systems. At 32–33 days of gestation, the pulmonary veins subsequently establish a communication with the common pulmonary vein, which becomes incorporated into the posterior aspect of the developing left atrium.

The precise origin and site of development of the common pulmonary vein has been controversial, with some believing this derives from an evagination in the sinoatrial region of the heart that grows out toward the lungs [8], others that the common vein arises from the pulmonary venous plexus confluence and grows toward the heart [1]. More recent work that includes analysis of embryologic cell expression markers suggests that the common pulmonary vein derives from the midpharyngeal endothelial strand, a structure in the dorsal mesocardium that from early stages connects the endocardium of the primitive heart tube to the splanchnic venous plexus. This structure subsequently lumenizes to form the common pulmonary vein, but appears to be connected to the endothelium of the heart from the beginning

Echocardiography in Pediatric and Congenital Heart Disease: From Fetus to Adult, Second Edition. Edited by Wyman W. Lai, Luc L. Mertens, Meryl S. Cohen and Tal Geva.
© 2016 John Wiley & Sons, Ltd. Published 2016 by John Wiley & Sons, Ltd.
Companion website: www.lai-echo.com

[9–11]. The common pulmonary vein becomes incorporated into the posterior aspect of the left atrium, between the left and right horns of the sinus venosus, superior to the coronary sinus, and leftward of septum primum; ultimately two right and two left pulmonary veins connect directly to the left atrium. Once the communication of the common pulmonary vein with the left atrium has become established, the primitive connections of the pulmonary venous system to the systemic venous system are no longer necessary, and typically regress [12]. Nearly all of the pulmonary venous anomalies considered in this chapter may be seen as a result of abnormal development of the common pulmonary vein and varying patterns of persistence of embryologic pulmonary-to-systemic venous connections.

Anatomy

Abnormal number of pulmonary veins

An abnormal number of pulmonary veins results from irregular incorporation of the common pulmonary vein into the left atrium. With normal incorporation of the common pulmonary vein, two right and two left pulmonary veins connect directly and separately to the left atrium. When incomplete incorporation of either the right or left side occurs, a single pulmonary vein may drain that lung; a single left pulmonary vein is more frequently observed than a single right [1]. More rarely, a common pulmonary vein accepts veins from both sides and then drains into the left atrium, seen most often in those with asplenia forms of heterotaxy [1]. When more than typical incorporation occurs, a third pulmonary vein on either the right or left side is observed [1].

Normal pulmonary venous connections with anomalous drainage

This results when the common pulmonary vein incorporates normally into the left atrium, resulting in normally positioned pulmonary venous connections, but due to interatrial anatomy the pulmonary venous inflow is directed into the morphologic right atrium. Most commonly this is due to anatomically leftward *malposition or malattachment of septum primum*, which can result in partial or total anomalous pulmonary venous drainage, depending upon the degree of malposition and number of veins affected (Figure 9.1). This is commonly encountered in those with polysplenia syndrome due to absence of septum secundum and resulting anatomic leftward malposition of septum primum [13]. Another frequently encountered example is *common atrium* as also observed in the heterotaxy syndromes, where virtual absence of the atrial septum results in ipsilateral drainage of the pulmonary veins into respective sides of the common atrium.

Sinus venosus defect (SVD)

Sinus venosus defect is a type of anomalous pulmonary venous drainage with normal connections that occurs due to "unroofing" or absence of the sinus venosus tissue between the right pulmonary veins and the superior vena cava or right atrium [14,15]. This topic is covered in detail in Chapter 11, "Anomalies of the Atrial Septum." It is important to note that despite the absence of sinus venosus septum, the pulmonary veins remain normally connected to the left atrium.

Stenotic connections

Stenotic connections may be seen in individual pulmonary veins with normal connections to the heart, in anomalously connecting veins, or as stenosis of the common pulmonary vein, which manifests as *cor triatriatum sinister*. Stenosis of the individual pulmonary veins is a rare disorder that may result from abnormal incorporation of the common pulmonary vein into the left atrium [16]; trauma or manipulation provoking inflammation may be antecedent events. Pulmonary vein stenosis can be found in otherwise structurally normal hearts, or in association with congenital heart defects, commonly atrial or ventricular septal defects [17], or less often with complex heart disease such as the heterotaxy syndromes [18]. The stenosis can be extraparenchymal, with obstruction at the pulmonary vein/left atrial junction, intraparenchymal with diffuse involvement of the smaller pulmonary veins in the lung, or both. Recent investigations have implicated intimal proliferation of abnormal myofibroblasts in the pathology of this disease [19,20]. Finally, stenosis of anomalously connecting pulmonary veins is commonly encountered, particularly in those with total anomalous pulmonary venous connection below the diaphragm.

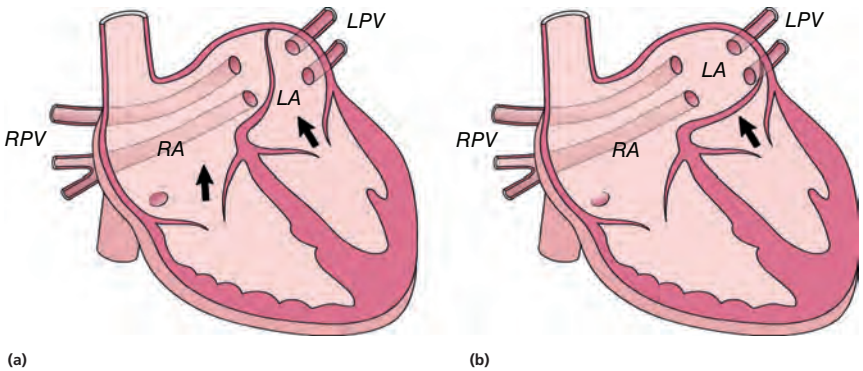


Figure 9.1 Malposition of septum primum. **(a)** Mild leftward malposition with normal pulmonary venous connections results in anomalous drainage of the right upper and lower pulmonary veins to the right atrium. **(b)** With more severe malposition of septum primum, drainage of all four pulmonary veins is directed anomalously into the right atrium. Note the absence of a well-developed septum secundum; this is common in patients with the polysplenia forms of heterotaxy syndrome. LA, left atrium; LPV, left pulmonary veins; RA, right atrium; RPV, right pulmonary veins.

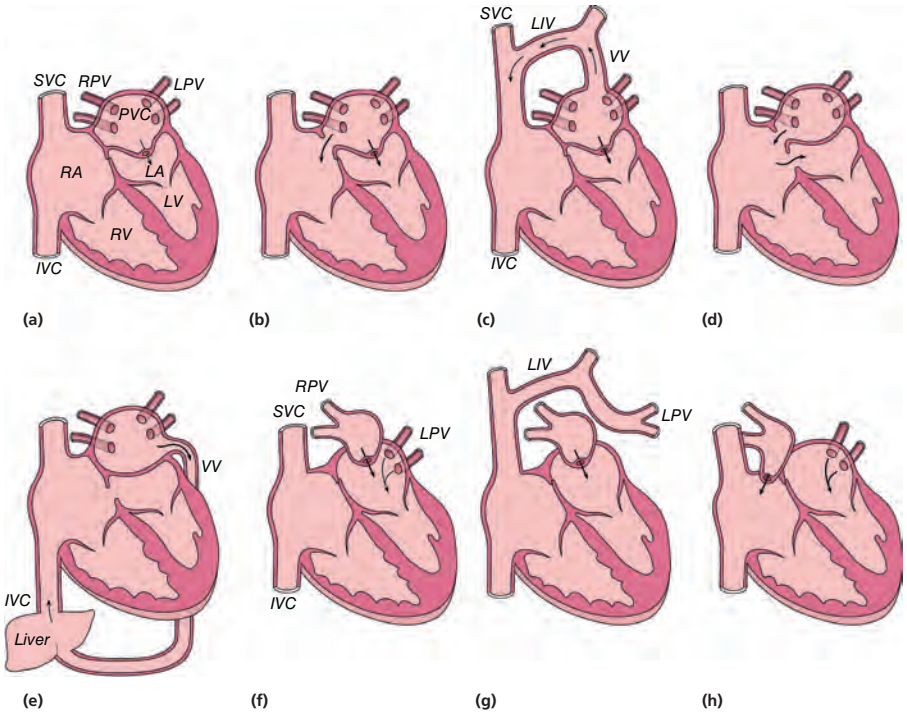


Figure 9.2 Cor triatriatum variants. **(a)** Classic cor triatriatum. Right and left pulmonary veins (RPV, LPV) drain to the pulmonary venous confluence (PVC), with discrete membrane between the PVC and true left atrium (LA); the only egress for blood is through the opening in the membrane. **(b)** Cor triatriatum with defect between the PVC and the right atrium (RA), which allows for decompression of pulmonary venous blood. **(c)** Cor triatriatum with decompressing vertical vein (VV) to the left innominate vein (LIV), which allows for decompression of the PVC. **(d)** Pulmonary venous return decompresses via a communication between the PVC and right atrium, and then crosses to the true left atrium via a patent foramen ovale. **(e)** Decompressing vertical vein that descends below the diaphragm to connect to the systemic venous circulation via the hepatic or portal veins. **(f)** "Partial" or subtotal cor triatriatum with normally draining left pulmonary veins; the right pulmonary veins communicate with the true left atrium via a stenotic orifice. **(g)** Subtotal cor triatriatum of the right pulmonary veins along with partial anomalous venous return of the left pulmonary veins via the left innominate vein. **(h)** Subtotal cor triatriatum of the right pulmonary veins to the right atrium (RA) with normal drainage of the left pulmonary veins to the left atrium. IVC, inferior vena cava; LV, left ventricle; RV, right ventricle; SVC, superior vena cava.

Cor triatriatum sinister

This results from incomplete incorporation of the common pulmonary vein into the posterior aspect of the left atrium. Cor triatriatum has many variations, the classic form consisting of a membranous partition that divides the left atrium into a chamber that receives the pulmonary veins posteriorly, and a chamber that communicates with the mitral valve anteriorly and inferiorly (Figure 9.2a). A communicating orifice of varying size is typically present, the atrial septum is usually intact, and the left atrial appendage is on the distal side of the cor triatriatum membrane as a feature of the anatomic left atrium [21]. Variations include the presence of an atrial septal defect, which communicates between the right atrium and either the pulmonary venous chamber or the distal true left atrial chamber; decompressing anomalous venous connections; "subtotal" cor triatriatum, which can involve the veins from only one side of the lung; and atresia of the dividing membrane, termed "complete" cor triatriatum (Figure 9.2).

Atresia of the common pulmonary vein

This is a rare disorder, with functionally no communication present between the pulmonary venous confluence and the heart or the systemic veins; a blind-ending pouch is present at the confluence of the pulmonary veins with no outlet to flow [22].

Partial anomalous pulmonary venous connection (PAPVC)

This occurs with one or more (but not all) pulmonary venous connections to the systemic venous circulation, with a wide anatomic spectrum of variations possible (Figure 9.3). As mentioned previously, PAPVC must be considered distinct from cases of partial anomalous pulmonary venous *drainage*. Left-sided pulmonary veins typically form anomalous connections to left cardinal vein derivatives (such as the left innominate vein and coronary sinus), and right-sided veins typically connect to derivatives of the right cardinal system (superior and inferior vena cavae), although crossed drainage across the midline is possible as the splanchnic venous plexus is a midline structure. With reclassification of many cases previously considered PAPVC to the superior vena cava and right atrium as sinus venosus defects or malposition of septum primum, the most common form of PAPVC is the left pulmonary veins to the left innominate vein, followed by right pulmonary venous connections to the inferior vena cava.

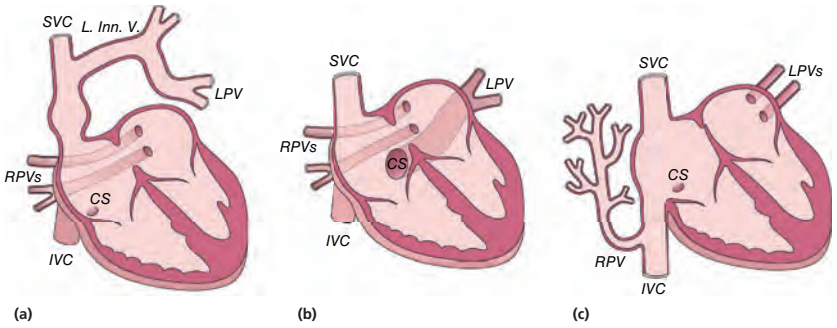


Figure 9.3 Partial anomalous pulmonary venous connection: variants. **(a)** Anomalous connection of the two left pulmonary veins (LPV) to the left innominate vein to the superior vena cava (SVC); the right pulmonary veins (RPV) connect normally to the left atrium. **(b)** Anomalous connection of the left pulmonary veins to the coronary sinus (CS). **(c)** Anomalous connection of the right pulmonary veins to the inferior vena cava (IVC) to right atrium (RA) junction; in association with right lung hypoplasia this is termed "scimitar syndrome." See text for more details.

With left-sided pulmonary venous connection to the left innominate vein, one or more left pulmonary veins connect to the innominate vein by a persistent embryologic vein, named a *vertical vein* due to its orientation (Figure 9.3a); an atrial septal defect is commonly present. Other less common sites of left-sided connection include to a persistent left superior vena cava, to a coronary sinus (Figure 9.3b), or to right-sided venous structures such as the superior vena cava, the azygous vein, and the inferior vena cava [23].

Anomalous right pulmonary venous connection of all or some of the right pulmonary veins to the inferior vena cava is frequently encountered as part of a malformation termed *scimitar syndrome* (Figure 9.3c). This term was coined to describe the crescent-shaped (Turkish scimitar "sword-like") shadow seen on roentgenogram in the right lower lung field, projected by the right pulmonary vein as it courses to join the inferior vena cava at or just below the diaphragm [24]. This syndrome is frequently associated with other anomalies of right lung development, including hypoplasia of the right lung and right pulmonary artery, secondary dextrocardia, bronchial abnormalities, anomalous arterial connection to the right lung from the aorta, and pulmonary sequestration [24,25].

Total anomalous pulmonary venous connection (TAPVC)

This occurs with all pulmonary venous connections to the systemic venous circulation. Embryologically, TAPVC results from failure to establish a normal connection between the pulmonary venous plexus and the common pulmonary vein before the connections with the splanchnic venous system have regressed. The most commonly used anatomic classification [26] of TAPVC is based on the site of connection(s) between the pulmonary and systemic veins:

Type I – with anomalous connections at the *supracardiac* level.
Type II – the *cardiac* type, with anomalous connections to the coronary sinus.
Type III – the *infradiaphragmatic* type, with anomalous connections below the diaphragm.
Type IV – with *mixed* types of connections.

With all types, an interatrial communication to allow blood to enter the systemic circulation is necessary to sustain life, so that a patent foramen ovale or atrial septal defect is considered part of the malformation.

Supracardiac TAPVC (Figure 9.4a) is the most common type (47% in the largest published series [27]), and among this group the most common site of connection is to the leftward aspect of the innominate vein (36% of all cases of TAPVC [27]). A pulmonary venous confluence is typically present posterior to the left atrium that drains via a left-sided ascending vertical vein to the innominate vein. This vertical vein usually passes anterior to the left pulmonary artery and mainstem bronchus, although occasionally this will pass *between* these structures which usually results in clinically significant obstruction to pulmonary venous flow. Supracardiac TAPVC with right-sided connections to the right superior vena cava or azygous vein occur, but are less common; a similar but right-sided vertical vein is observed, which typically courses anterior to the hilum of the right lung.

Cardiac TAPVC (Figure 9.4b) occurs in 16% of cases [27,28], and involves anomalous connection between the pulmonary venous confluence and the coronary sinus, with a venous vessel connecting typically in the region of the left atrioventricular groove. The coronary veins drain normally into the proximal end of the coronary sinus, and the typically severely dilated coronary sinus drains normally into the right atrium; the coronary sinus septum is usually intact.

Infradiaphragmatic TAPVC (Figure 9.4c) occurs in 13–23% [27,28] with anomalous connection typically to the umbilicovitelline system below the diaphragm. A descending vertical vein typically originates from the confluence of pulmonary veins to course below the diaphragm (just anterior to the esophagus in the esophageal hiatus) to form connections with the portal venous system (most common), the ductus venosus, hepatic vein, or inferior vena cava. Obstruction is frequently present with infradiaphragmatic forms of TAPVC for a number of reasons, most commonly due to intrinsic narrowing of the connecting vessel, the interposition of the hepatic sinusoids between the pulmonary venous drainage and the heart for those that drain via the portal vein, and constriction of the ductus venosus.

Mixed TAPVC (Figure 9.4d) is the least common type (7–10% [27,28]) with often complex variations of the above forms of venous connections represented.

Pathophysiology

The pathophysiology of the various forms of pulmonary venous anomalies depends entirely upon the nature of the anomaly, the degree of mixing of systemic and pulmonary venous blood, and

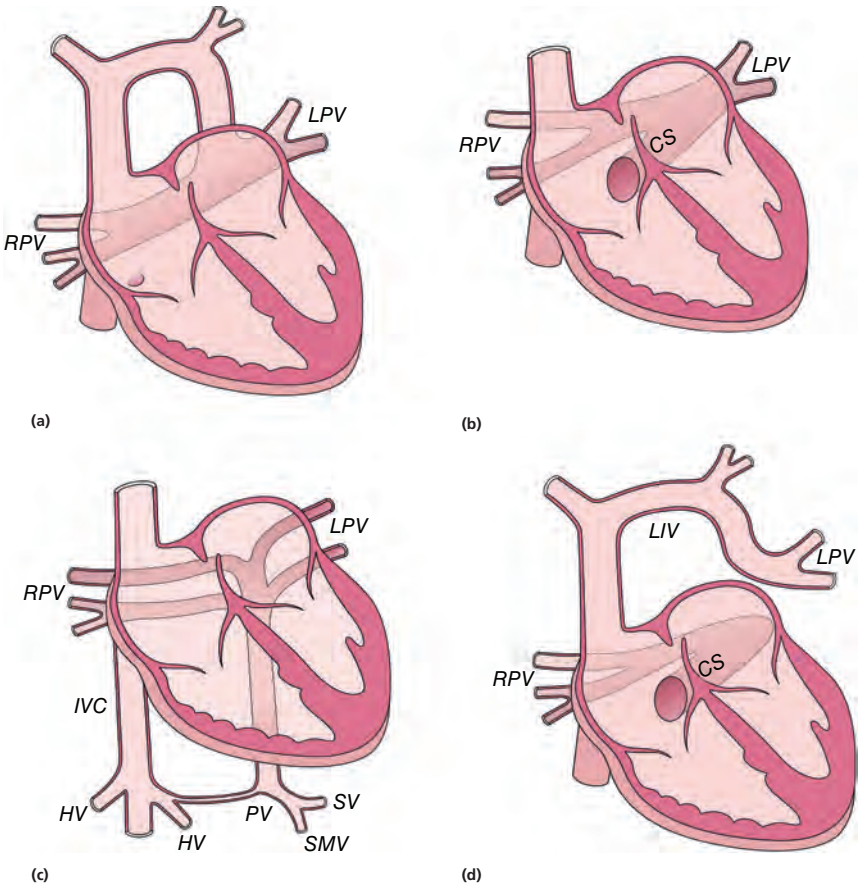


Figure 9.4 Variants of total anomalous pulmonary venous connection. **(a)** Supracardiac: both right (RPV) and left (LPV) pulmonary veins join a common pulmonary venous confluence behind the heart, which drains via a vertical vein to the undersurface of the left innominate vein, and thence to the right atrium. **(b)** Cardiac: the pulmonary venous confluence connects to the coronary sinus (CS), and thence to the right atrium via the coronary sinus ostium. **(c)** Infradiaphragmatic: the pulmonary venous confluence drains inferiorly via a vertical vein to the portal vein (PV) or hepatic veins (HV) and thence to the right atrium. **(d)** Mixed connections: left pulmonary veins drain to the left innominate vein (LIV), and right pulmonary veins to the coronary sinus in this example. SMV, superior mesenteric vein; SV, splenic vein.

the presence or absence of obstruction to pulmonary venous flow.

Anomalies that result in pulmonary venous obstruction cause pulmonary venous hypertension in the affected lobe or lobes. With an increase in the number of lobes affected and worsening obstruction, the pulmonary venous hypertension is transmitted back through the vascular bed of the lung, to result in pulmonary capillary and pulmonary artery hypertension. A cascade of effects on the pulmonary vasculature results, from acute changes such as pulmonary edema and reflex pulmonary vasoconstriction, to chronic alterations in pulmonary vascular resistance, vessel reactivity, and vascular remodeling. The effects of this dramatic increase in afterload on the right side of the heart include initially compensatory right ventricular hypertrophy, subsequent chamber enlargement, contractile dysfunction, and eventual right heart failure.

The pathophysiology of most of the various forms of PAPVC is similar to that of an atrial septal defect, with increased pulmonary blood flow due to recirculation of oxygenated blood through the lungs; this is dependent upon the extent of the pulmonary vascular bed drained by the anomalously connecting vein(s), as well as the status of the atrial septum. The excess flow through the right heart and lungs leads to dilation of the right atrium, right ventricle, and pulmonary vascular bed. With PAPVC of a single pulmonary vein and an intact atrial septum, typically the anomalous blood flow is 20–25% of total pulmonary blood flow [29], which is rarely clinically apparent. With PAPVC of an entire lung with an intact atrial septum, due to the greater compliance of the right atrium and right ventricle relative to the left side of the heart, the anomalously draining blood usually represents 66% rather than 50% of pulmonary venous drainage. When encountered with forms of scimitar syndrome (Figure 9.3c), the net shunt tends to be lower (24–32% of pulmonary blood flow) due to abnormalities of the right lung parenchyma and pulmonary vasculature [30]. The subsequent development of pulmonary vascular disease with PAPVC is rare, but has been reported [31].

If a small atrial septal defect is present with PAPVC, the pathophysiology is similar to that discussed earlier; if a large atrial septal defect is present, the degree of left-to-right shunt is often significantly increased, with pulmonary recirculation not only of blood from the anomalously draining lung but also half or more of the normally connecting lung's blood via the atrial septal defect. Partial anomalous pulmonary venous *drainage* shares similar pathophysiology to PAPVC, with the degree of left-to-right shunt dependent upon the number of pulmonary veins redirected to the right atrium by the malpositioned septum.

The pathophysiology seen with TAPVC depends greatly upon the presence or absence of pulmonary venous obstruction, as well as the adequacy of the interatrial defect to allow flow to the systemic circulation. In the absence of pulmonary venous obstruction, there is complete mixing of systemic and

pulmonary venous blood in the right atrium; as the resistance to pulmonary blood flow is significantly lower than that of the systemic circulation, there is significant pulmonary overcirculation (often 3–5 times normal) and the systemic saturation may be 90% or higher (resulting often in clinically inapparent cyanosis). Right ventricular dilation and hypertrophy frequently occur, along with varying degrees of pulmonary hypertension.

The size of the interatrial communication with TAPVC plays a critical role; with worsening restriction to flow across the atrial septum, there is not only a dramatic increase in pulmonary overcirculation (and worsening pulmonary hypertension) but diminished systemic output. Similarly, with extrinsic or intrinsic obstruction to pulmonary venous flow, the cascade of pulmonary vascular changes discussed earlier may occur. Infants with obstructed TAPVC typically present in the first month of life, with a rapid and fulminant progression of dyspnea to cardiorespiratory failure [32].

Imaging

Any detailed assessment of the pulmonary venous connections and drainage must by necessity include an assessment of the systemic venous anatomy, right and left atria, and the atrial septum. These structures are imaged from multiple acoustic windows, including the subcostal, apical, left parasternal, high right parasternal, and suprasternal notch. Two- (2D) and three-dimensional (3D) imaging along with careful color and spectral Doppler techniques are used to render complete imaging of these structures. As the majority of pulmonary venous anomalies are diagnosed in infants and children, transthoracic echocardiography is the preferred modality and can yield a diagnosis in the vast majority of cases; however, transesophageal echocardiography (TEE) may be a helpful adjunct diagnostic modality in the older patient with poor transthoracic acoustic windows. Cardiac magnetic resonance imaging with angiography is an excellent alternative modality for delineation of both systemic and pulmonary venous anatomy in those in whom a complete diagnosis cannot be obtained with echocardiographic techniques [33,34].

Goals of the examination

Preoperative examination

In all cases, complete anatomic and functional examination by 2- and 3D imaging, as appropriate, and by color and spectral Doppler. In addition, the following elements of cardiovascular anatomy and function should be evaluated in detail and be given priority:

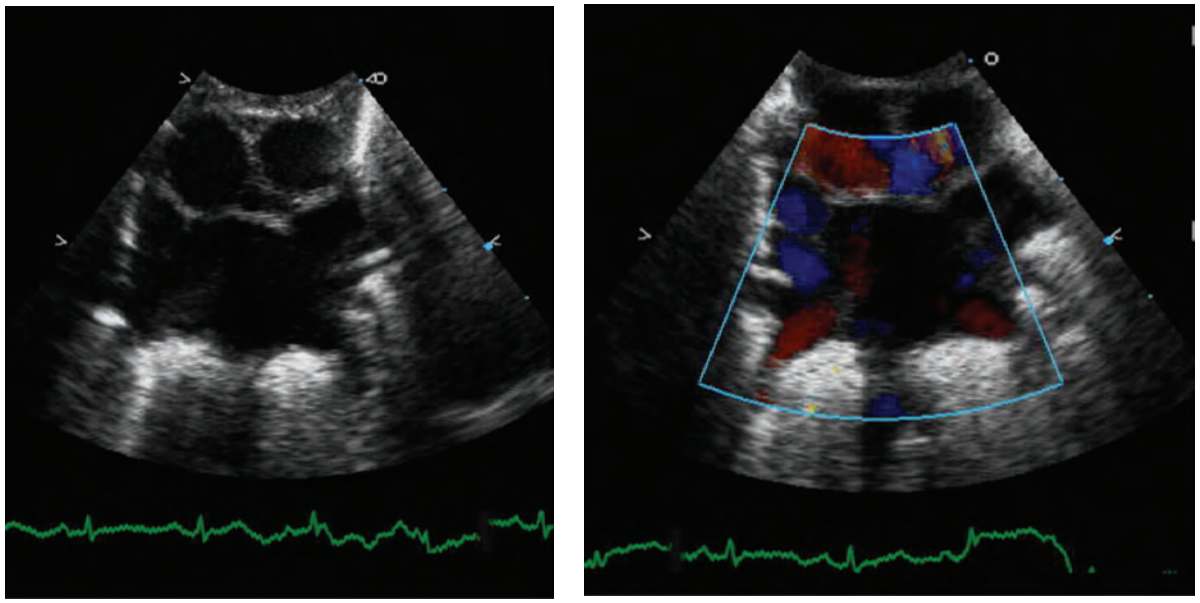
- Identify each pulmonary vein and its connection site by 2D and color Doppler. Do not assume two veins from each lung; the number of individual pulmonary veins varies, and additional vein(s) with separate connection(s) to a systemic vein (e.g., left innominate vein, azygous vein, IVC, SVC) should be excluded.
- Follow each anomalously connecting pulmonary vein from its origin to its connection to the systemic vein from multiple views by continuous 2D and by color Doppler sweeps.
- Interrogate each pulmonary vein by spectral Doppler and record mean gradients; interrogate by spectral Doppler and record mean gradient in every site where flow velocity accelerates and the lumen narrows by color Doppler.
- In TAPVC: measure the diameters of each pulmonary vein and the smallest diameter of the pulmonary venous confluence.
- Image the anatomic relationship between the pulmonary venous confluence and the left atrium.
- Rule out mixed drainage (make sure no additional pulmonary veins enter a systemic vein separately).
- Rule out anomalous systemic venous connections.
- Assess atrial septum, direction of atrial shunt, and evaluate for restriction to flow (color and spectral Doppler).
- Assess presence and degree of right ventricular volume load (TV annulus diameter; diastolic septal flattening; qualitative assessment of RV size; RV volume by 3D, if feasible).
- Assess RV pressure by tricuspid and pulmonary regurgitation jet velocities and by systolic septal configuration.
- Measure LA and LV volumes.
- Exclude associated cardiovascular anomalies.

Postoperative examination

- Identify each pulmonary vein and its connection site by 2D and color Doppler.
- Interrogate each pulmonary vein by spectral Doppler and record mean gradients.
- Measure the left-to-right and the superior-to-inferior diameters of the anastomosis between the pulmonary venous confluence and the left atrium.
- Assess atrial septum and the direction of atrial shunt (color AND spectral Doppler).
- Assess RV pressure by tricuspid regurgitation jet velocity and systolic septal configuration.
- Assess presence and degree of right ventricular volume load (TV annulus diameter; diastolic septal flattening; qualitative assessment of RV size; RV volume by 3D, if feasible).

Imaging of abnormal number of pulmonary veins

The subcostal window is ideal for the evaluation of pulmonary veins in infants and young children. The parasternal, subclavicular, and suprasternal views are more useful in older patients. In older patients, the right parasternal and subcostal windows can often provide better imaging of the connection of the right upper pulmonary vein than the left parasternal view. In both long- and short-axis subcostal views the right upper pulmonary vein can be imaged entering the left atrium superiorly and just posterior to the right superior vena cava. The suprasternal notch view is particularly helpful in infants, where the so-called "crab view" can frequently demonstrate the drainage of all four pulmonary veins (Figure 9.5). TEE can be helpful in patients with suboptimal transthoracic acoustic windows.

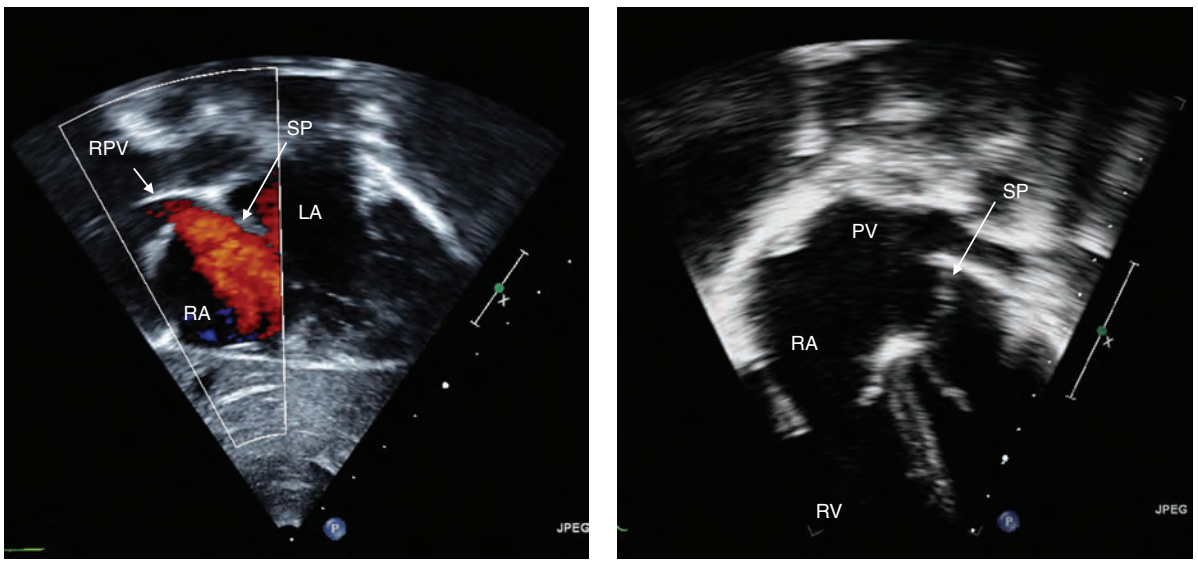


(a) (b)

Figure 9.5 Normal pulmonary venous connection. Suprasternal notch view of the pulmonary veins and left atrium with 2D imaging **(a)** and color Doppler flow mapping **(b)** shows the "crab" view. Two left and two right pulmonary veins drain normally into the left atrium – the "legs" of the crab; the right superior vena cava and left atrial appendage are the "claws."

Imaging of normal pulmonary vein connections with anomalous drainage

The typical acoustic views for establishing this diagnosis are the subxiphoid, apical, and high parasternal short-axis views, all of which can demonstrate the site of connection of the pulmonary veins to the posterior aspect of the anatomic left atrium, as well as establish the plane of septum primum and demonstrate any attachments to the wall of the left atrium (Figure 9.6). In older patients, a low parasternal short-axis window (Figure 9.7; Video 9.1) is frequently the most helpful, as the views from subxiphoid and suprasternal notch are typically not adequate to demonstrate the position of septum primum.



(a) (b)

Figure 9.6 Anomalous pulmonary venous drainage. **(a)** Partial. Subxiphoid long-axis image in this patient with mild leftward malposition of septum primum (SP) demonstrates flow from the normally connecting right pulmonary veins (RPV) into the right atrium (RA). **(b)** Total. Apical 2D image in this patient with severe leftward malposition of septum primum shows the lack of septum secundum superiorly, normal pulmonary venous connections to the posterior aspect of the left atrium (LA), and leftward malposition of SP resulting in total anomalous pulmonary venous drainage. PV, pulmonary veins; RV, right ventricle.

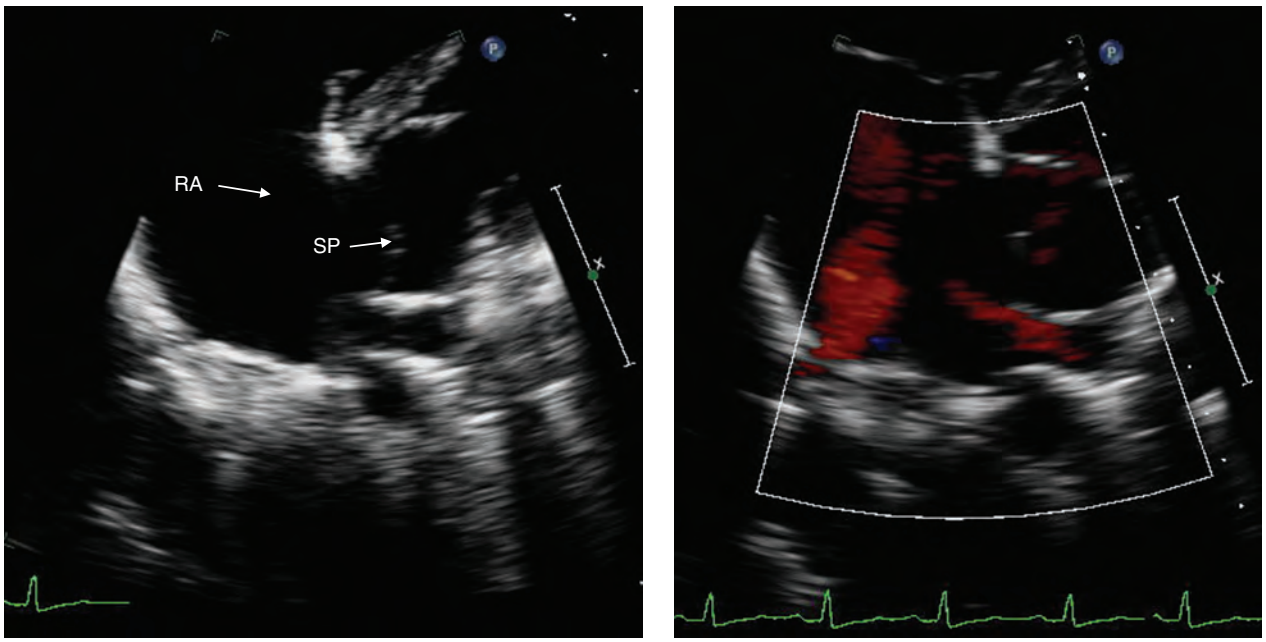


Figure 9.7 Total anomalous pulmonary venous drainage: parasternal short-axis view. Parasternal short-axis image with 2D **(a)** and color Doppler flow mapping **(b)** in this patient with severe leftward malattachment of septum primum (SP). Note the normal connection of the pulmonary veins posteriorly, with flow directed to the right atrium (RA).

In addition to 2D imaging, color Doppler is critical in demonstrating the anomalous drainage toward the anatomic right atrium. Due to the absence of septum secundum encountered in patients with polyspenia syndrome, establishing the landmarks of the anatomic left atrium is important to distinguish this entity from "ipsilateral" pulmonary veins, in which true anomalous connection of the right pulmonary veins occurs to the anatomic right of the right horn of the sinus venosus. Pulsed- and continuous-wave spectral Doppler may be helpful in demonstrating any restriction to flow of the anomalously draining pulmonary veins due to restricting attachments of septum primum, although this is rarely encountered clinically.

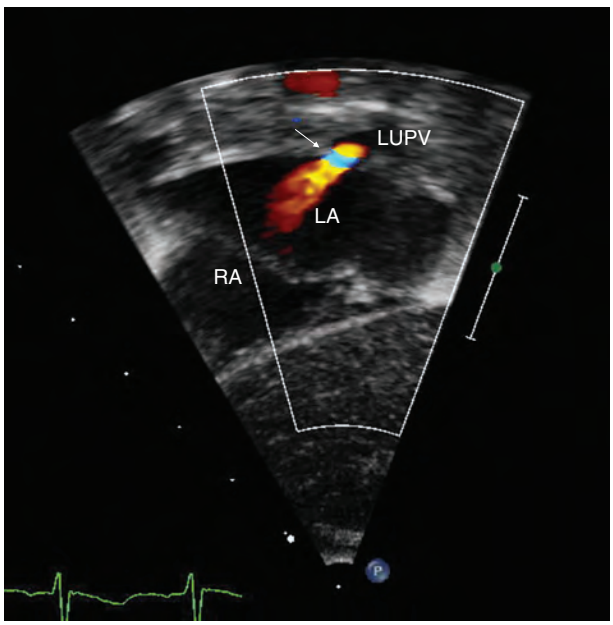
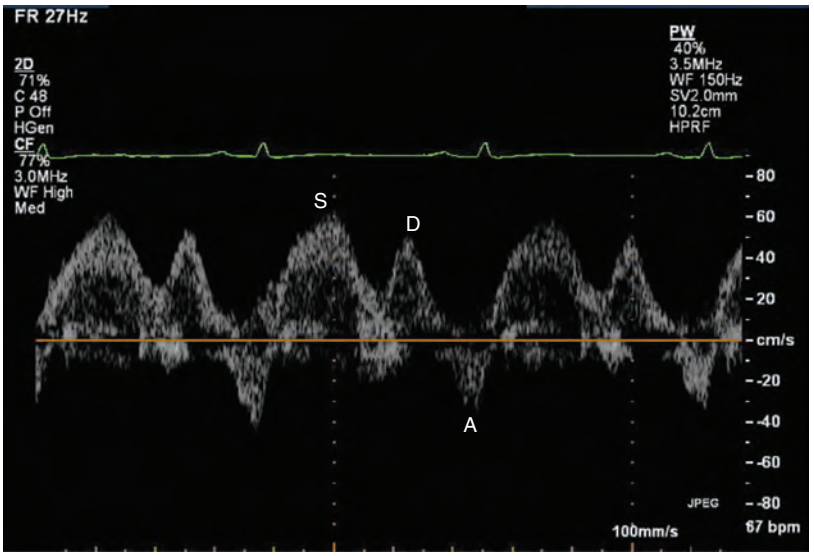


Figure 9.8 Pulmonary vein stenosis: subxiphoid view. Subxiphoid long-axis image of the left atrium (LA) with color Doppler flow mapping shows discrete stenosis of the left upper pulmonary vein (LUPV) at its junction with the LA (arrow). Note the dilation of the vein proximal to the obstruction. RA, right atrium.

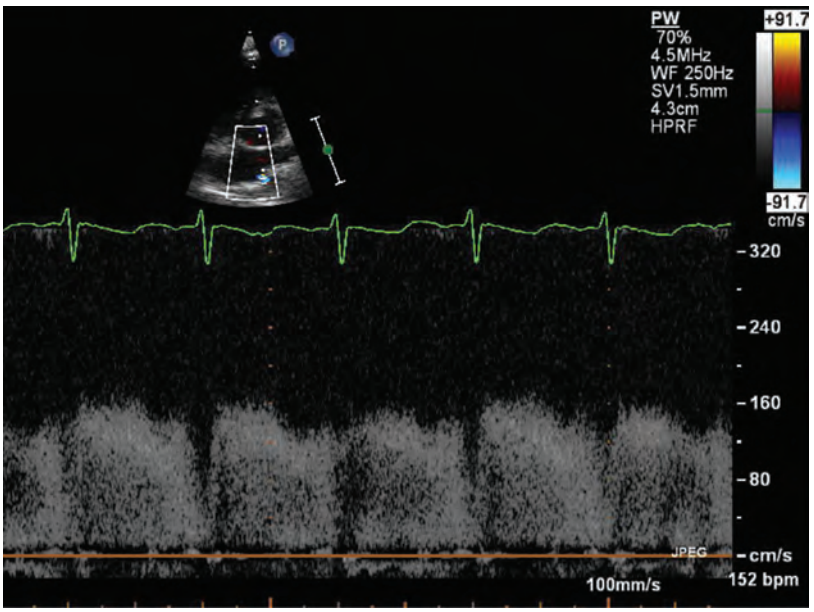
Imaging of pulmonary vein stenosis

Stenosis of individual pulmonary veins is best imaged from high parasternal windows, and in younger patients from suprasternal and subxiphoid views. Careful evaluation of all four pulmonary veins and their respective orifices is required by 2D imaging. Color Doppler and pulsed- and continuous-wave spectral Doppler techniques are necessary to evaluate the presence and severity of obstruction (Figure 9.8). Normal pulmonary venous Doppler flow patterns are typically laminar, low velocity, and phasic, with a short flow reversal during atrial systole (the retrograde "A" wave). With increasing degrees of obstruction, the retrograde A wave is absent, velocities increase, and phasicity of flow is lost (Figure 9.9). In practice, care must be taken to obtain accurate spectral Doppler tracings, which is made more difficult by the fact that the direction of inflow from the pulmonary vein orifices is rarely parallel to the interrogating transducer from any of the usual views; modified or off-axis views are frequently required.

Due to acoustic dropout from lung tissue, typically only stenoses of the distal pulmonary veins and their respective



(a)



(b)

Figure 9.9 Pulmonary vein Doppler patterns. **(a)** Spectral Doppler pulsed-wave interrogation of the right upper pulmonary vein from apical imaging demonstrates the normal phases of pulmonary venous flow. Flow is laminar and low velocity, with retrograde flow noted in atrial systole (A wave). D, diastolic wave; S, systolic wave. **(b)** Pulmonary vein stenosis Doppler pattern. Spectral Doppler pulsed-wave interrogation of the left lower pulmonary vein (LLPV) from parasternal short-axis view in a patient with discrete stenosis of the LLPV at its junction with the left atrium. Note the high velocity and increased turbulence of venous flow, loss of phasic variation, and absence of the retrograde "A" wave relative to the normal pattern.

orifices are able to be imaged by echocardiography; more long-segment stenosis that extends back into the hilum of the lungs is better imaged by other modalities such as cardiac magnetic resonance, cardiac CT, or by catheter angiography. Other clues to the diagnosis of pulmonary vein stenosis include evidence from parasternal short-axis views of pulmonary hypertension in response to pulmonary venous inflow obstruction, such as dilation of the right atrium, right ventricle, and pulmonary artery, along with systolic flattening of the ventricular septum indicative of right ventricular hypertension.

Imaging of cor triatriatum

The cor triatriatum membrane is often easily demonstrated from apical views as a curvilinear membrane in the mid-portion of the left atrium, separating the pulmonary venous portion of the left atrium from the true anatomic left atrium (Figure 9.10; Video 9.2). The membrane is often thin, and may move throughout the cardiac cycle in response to changes in atrial filling pressures and flows. Parasternal short-axis and subxiphoid imaging is important in demonstrating the relationship of the cor triatriatum membrane to the left atrial appendage, as well as the position of septum primum. Malposition and/or malattachment of septum primum can be easily confused with cor triatriatum from some views; one of the keys in establishing the diagnosis of cor triatriatum is that the left atrial appendage is invariably on the distal or "low-pressure" side of the membrane, and the position of septum primum is often normal. A supramitral stenosing ring, in contrast, is located on the immediate atrial side of the

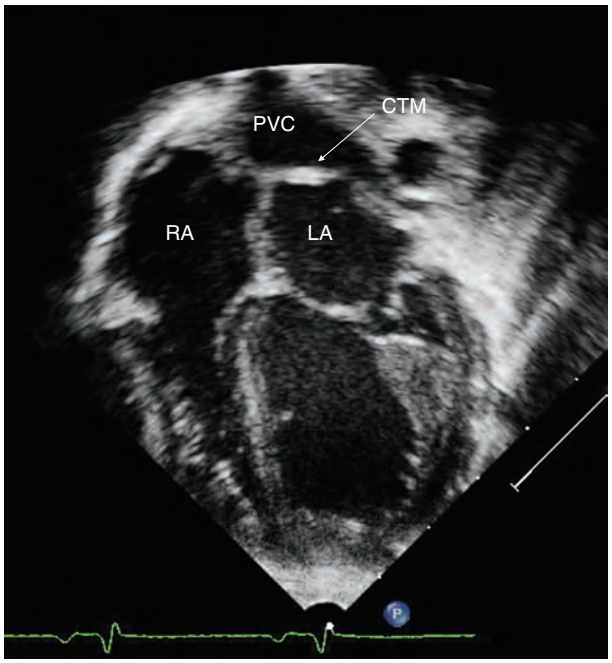


Figure 9.10 Classic cor triatriatum sinister. Apical 4-chamber view example of the "classic" form of cor triatriatum, with a discrete "membrane" (arrow) seen between the pulmonary venous confluence (PVC) and the anatomic left atrium (LA). The only egress for pulmonary venous blood is through the membrane orifice. RA, right atrium.

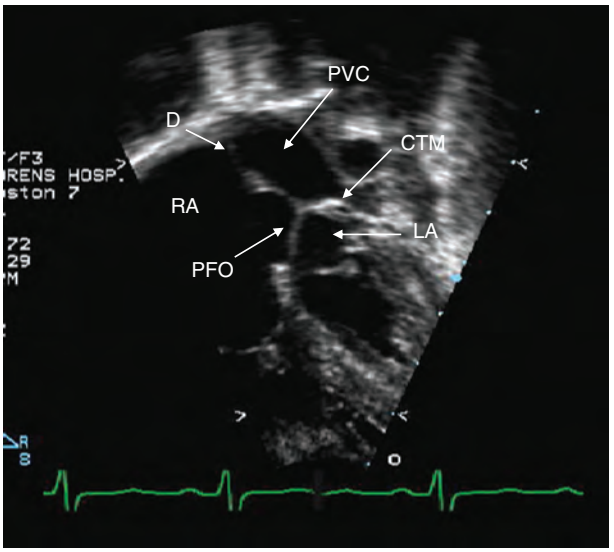


Figure 9.11 Cor triatriatum with patent foramen ovale (PFO) in hypoplastic left heart syndrome (HLHS). Off-axis apical 2D image in an infant with HLHS and cor triatriatum. Note the defect (D) between the pulmonary venous confluence (PVC) and the right atrium (RA) superiorly, as well as the flap of septum primum inferiorly which allows a PFO communication with the true left atrium (LA). CTM, cor triatriatum membrane.

mitral annulus, does not encompass the left atrial appendage, is frequently more immobile, and may cause restriction of mitral leaflet excursion due to valvar attachments.

Careful evaluation of the atrial septum from subxiphoid and parasternal short-axis views is necessary to elucidate the nature of an interatrial communication, if present (Figure 9.11). In addition, the course and drainage of each of the pulmonary veins should be evaluated, since partial forms of cor triatriatum can occur (Figure 9.12), as well as anomalous pulmonary venous connection in some variants (Figure 9.2) [35,36]. The presence or absence of obstruction across the cor membrane is often best confirmed from the apical view, even in older patients, as the flow jet is often directed toward the mitral valve (Figure 9.13). Color Doppler interrogation along with pulsed- and continuous-wave spectral Doppler can provide information regarding direction of flow and degree of obstruction, along with estimates of the peak and mean pressure gradient across a stenotic orifice.

Imaging of PAPVC

The diagnosis of PAPVC is established through careful assessment of the pulmonary venous connections as well as the systemic venous anatomy. The systemic vein distal to the connection of the pulmonary vein is often dilated, which is frequently the first clue that PAPVC may be present (Figures 9.14 and 9.15). Anomalous connection of pulmonary veins to the innominate vein or SVC is best evaluated from high parasternal views (Figure 9.14; Video 9.3), both short and long axis, as well as the suprasternal notch; in infants and young children, PAPVC may be imaged even from subcostal windows. Care must be taken to distinguish normal systemic venous structures (e.g., azygous vein, superior intercostal vein) from PAPVC, with clues such as

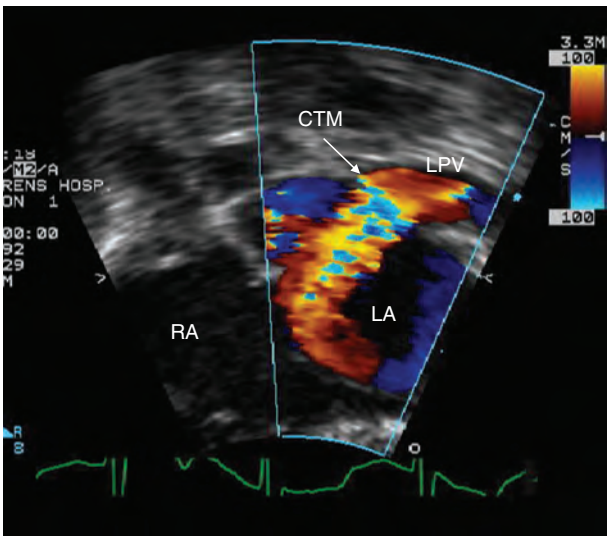


Figure 9.12 Partial cor triatriatum. Off-axis apical view of the left atrium (LA) with color Doppler flow mapping shows a left-sided partial cor triatriatum, with a "membrane" (CTM) between the confluence of left pulmonary veins (LPV) and the LA. Note the obstruction by color Doppler flow. RA, right atrium.

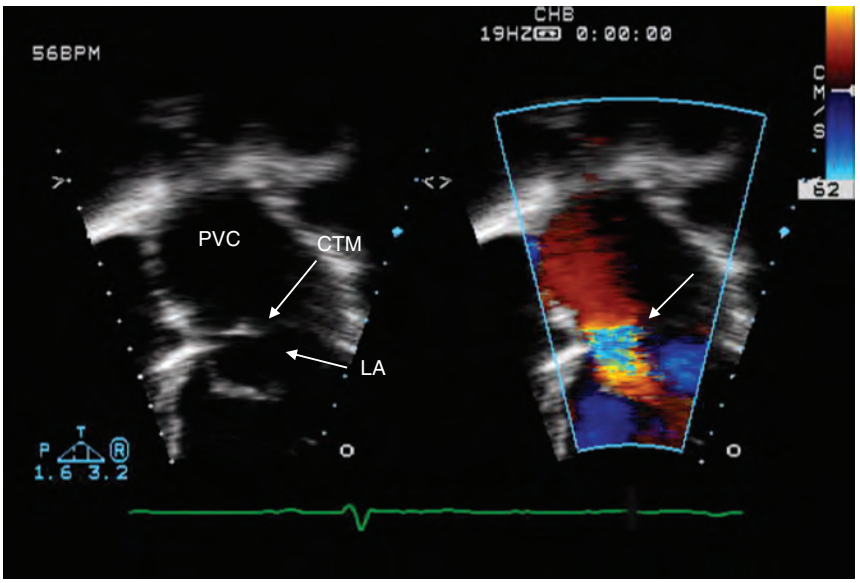


Figure 9.13 Classic cor triatriatum with obstruction. Apical view with 2D and color Doppler mapping shows an example of a more "distal" cor triatriatum membrane (CTM) in an adult patient with pulmonary hypertension. The orifice that allows pulmonary venous inflow is medial in this case, with flow acceleration by color Doppler (arrow). LA, left atrium; PVC, pulmonary venous confluence.

the absence of normally connected pulmonary veins to the left atrium, dilation of the innominate vein and superior vena cava, and evidence of right ventricular volume overload by diastolic septal flattening helpful in establishing the diagnosis.

PAPVC to the coronary sinus is best imaged from subcostal (particularly in infants and children) and parasternal views, but also from apical views. The coronary sinus is typically severely dilated, necessitating an evaluation of the presence or absence of a persistent left superior vena cava.

PAPVC to the inferior vena cava, which usually establishes the diagnosis of scimitar syndrome, is most easily imaged from the subcostal window. Both short- and long-axis imaging of the inferior vena cava is naturally best accomplished through this window, and frequently anomalously connecting veins can be seen by 2D and color Doppler connecting to the inferior vena cava just proximal to the junction with the right atrium (Figure 9.16; Video 9.4). Careful evaluation with pulsed- and continuous-wave spectral Doppler can establish the presence or absence of stenosis of the anomalously connecting pulmonary veins. The rightward border of the left atrium typically has an abnormally "blunted" contour consistent with the diagnosis. The presence of abnormal cardiac position (mesocardia or dextrocardia) and hypoplasia of the right pulmonary artery are often further clues to the diagnosis.

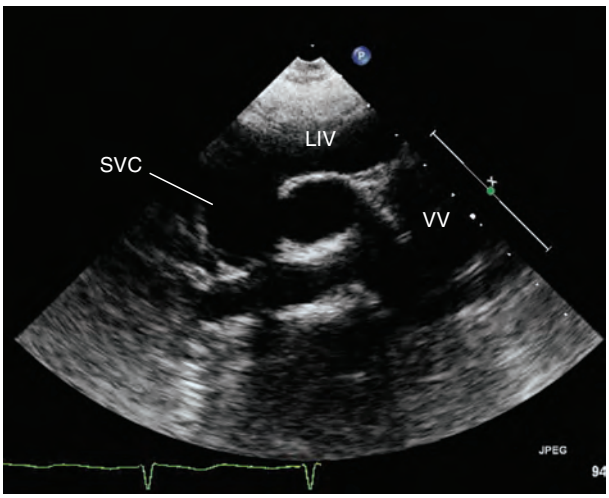


Figure 9.14 Partial anomalous pulmonary venous connection (PAPVC): left upper pulmonary vein to innominate vein. Suprasternal notch short-axis 2D image in this patient with PAPVC of the left upper pulmonary vein to the innominate vein shows the dilated left innominate vein (LIV) and right superior vena cava (SVC). VV, vertical vein.

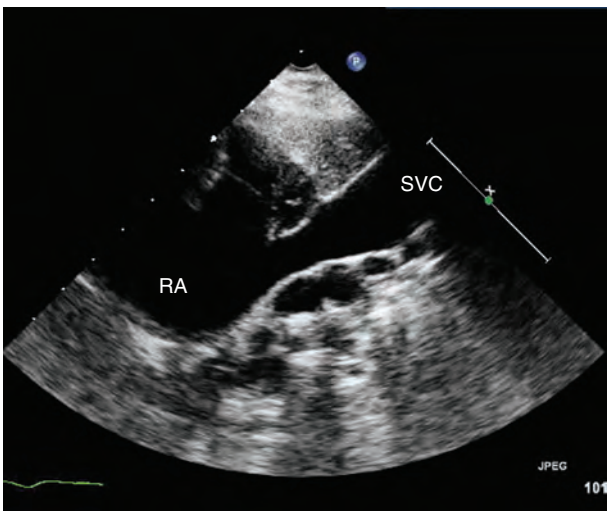


Figure 9.15 Partial anomalous pulmonary venous connection (PAPVC): dilated superior vena cava (SVC). High right parasternal long-axis image in this patient with PAPVC of the left pulmonary veins to the innominate vein demonstrates marked dilation of the SVC, consistent with significantly increased venous return through this vessel. RA, right atrium.

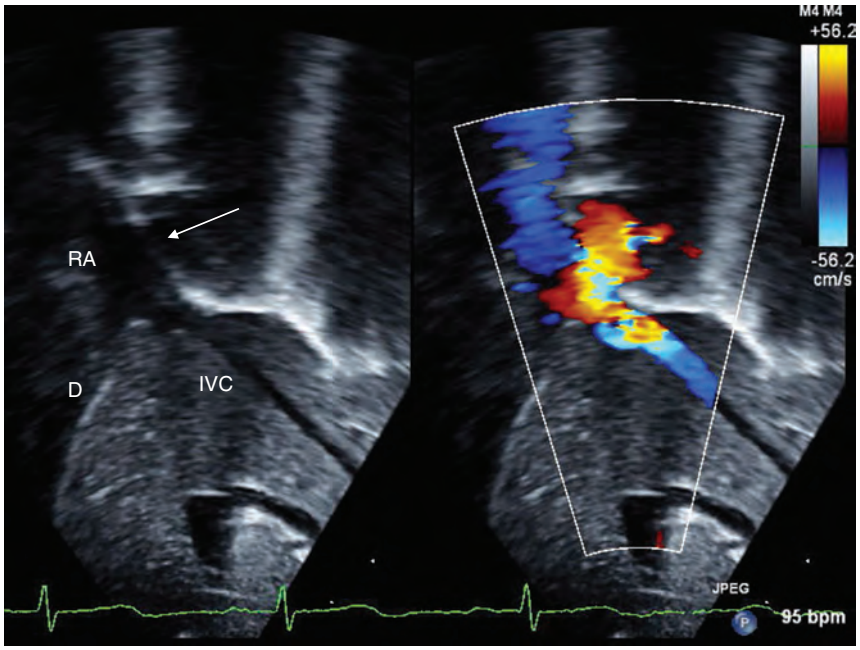
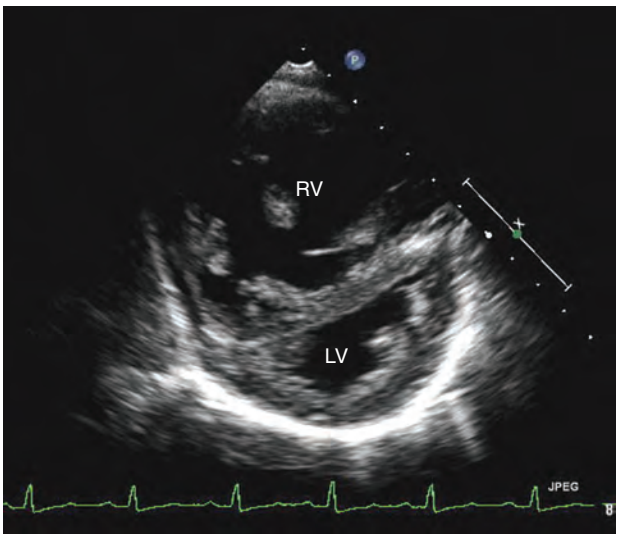


Figure 9.16 Partial anomalous pulmonary venous connection (PAPVC): scimitar syndrome. Subxiphoid short-axis image with color Doppler flow mapping in this patient with scimitar syndrome demonstrates PAPVC of right pulmonary veins to the inferior vena cava (IVC) at its junction with the right atrium (RA). Note the mild flow acceleration by color Doppler (arrow). D, diaphragm.

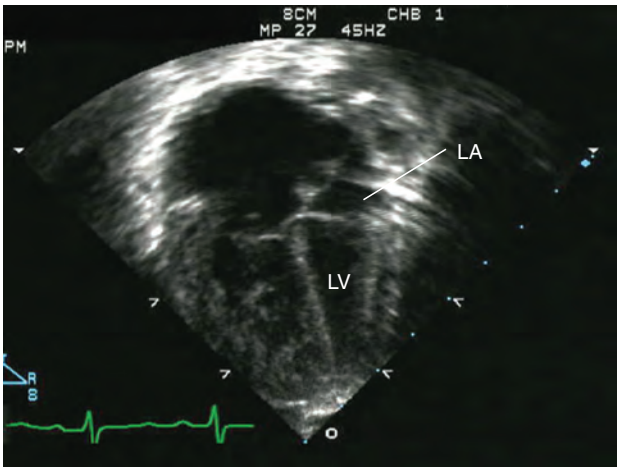
Imaging of TAPVC

As with PAPVC, the echocardiographic assessment of TAPVC requires a careful step-by-step analysis of the anatomy from multiple imaging views. The right atrium is frequently dilated, and the atrial septum bows into the left atrium. The right ventricle is dilated, and in addition to volume overload, right ventricular hypertension is often present; the ventricular septum often bows into the left ventricle (Figure 9.17a). Concomitantly, the left-sided heart structures are frequently mildly hypoplastic (although rarely too hypoplastic to support a two-ventricle circulation for isolated forms of TAVPC, Figure 9.17b). The first clues to the diagnosis include a large right-to-left shunt across the interatrial septum, as well as the inability to image the pulmonary veins draining into the left atrium, along with a hypoplastic left atrial chamber. Typically the pulmonary venous confluence is noted as an echo-free space behind the left atrium.

The challenge with cases of TAPVC is to image each of the four major pulmonary veins and to determine the size,



(a)



(b)

Figure 9.17 Total anomalous pulmonary venous connection (TAPVC): **(a)** right ventricular hypertension. Left parasternal short-axis image of the ventricles shows the dilation of the right ventricle (RV) relative to the left ventricle (LV), as well as the flat septal position in systole consistent with systemic right ventricular pressures in this patient with TAPVC. **(b)** Left heart hypoplasia. Apical view in this patient with supracardiac TAPVC demonstrates the relative hypoplasia of the left atrium (LA), mitral valve, and left ventricle relative to the corresponding right heart structures.

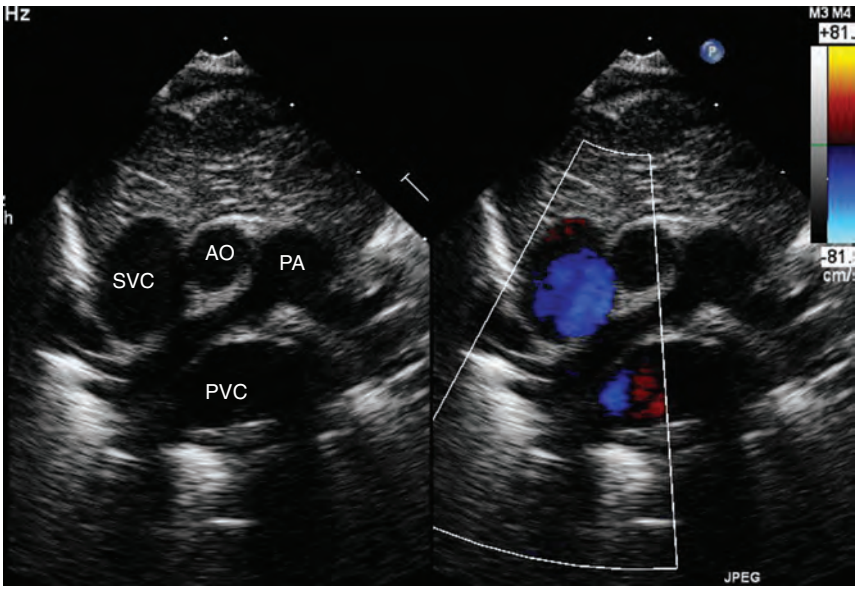


Figure 9.18 Supracardiac total anomalous pulmonary venous connection (TAPVC): high parasternal short-axis view. High parasternal imaging in short axis in this patient with supracardiac TAPVC shows the severely dilated right superior vena cava (SVC), the first clue to the diagnosis from this view. Note the pulmonary venous confluence (PVC) appears relatively normally positioned in this plane posterior to the pulmonary artery bifurcation. AO, ascending aorta; PA, pulmonary artery.

course, and drainage of each of these veins. This is particularly important as "mixed" forms of TAPVC occur and can significantly complicate the surgical management. The size of the individual pulmonary veins has been determined to be an independent risk factor for the development of recurrent obstruction in TAPVC following surgical repair [37], and thus this should be one of the goals of the evaluation. The most helpful views are typically the subxiphoid, parasternal, and suprasternal notch views; evaluation includes both 2D imaging and color Doppler flow mapping. The size, orientation (horizontal or vertical), and position of the pulmonary venous confluence relative to the left atrial chamber is crucial information for the surgeon, as well as the course and ultimate connection of the venous channel draining the pulmonary venous blood into the systemic circulation.

With supracardiac TAPVC, the vertical vein is frequently imaged to the left of the midline, with venous flow ascending to join most commonly into the leftward aspect of the innominate vein (Video 9.5). The innominate vein and superior vena cava are usually severely dilated (Figure 9.18). Despite the venous connections that are typically high in the chest, the individual pulmonary veins and location and course of the vertical vein in supracardiac TAPVC are often well imaged from subxiphoid views in infants (Figure 9.19; Video 9.6). The

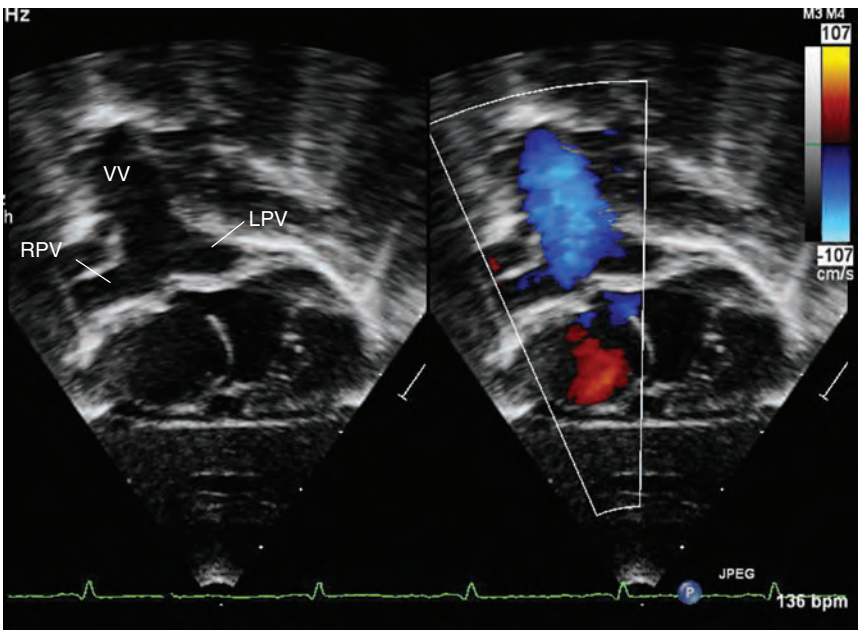


Figure 9.19 Supracardiac total anomalous pulmonary venous connection (TAPVC): subxiphoid long-axis view. Subxiphoid 2D and color Doppler flow mapping in this patient with supracardiac TAPVC shows flow from both right (RPV) and left pulmonary veins (LPV) into a large, superiorly draining vertical vein (VV). Note the obligate right-to-left shunt across the secundum atrial septal defect.

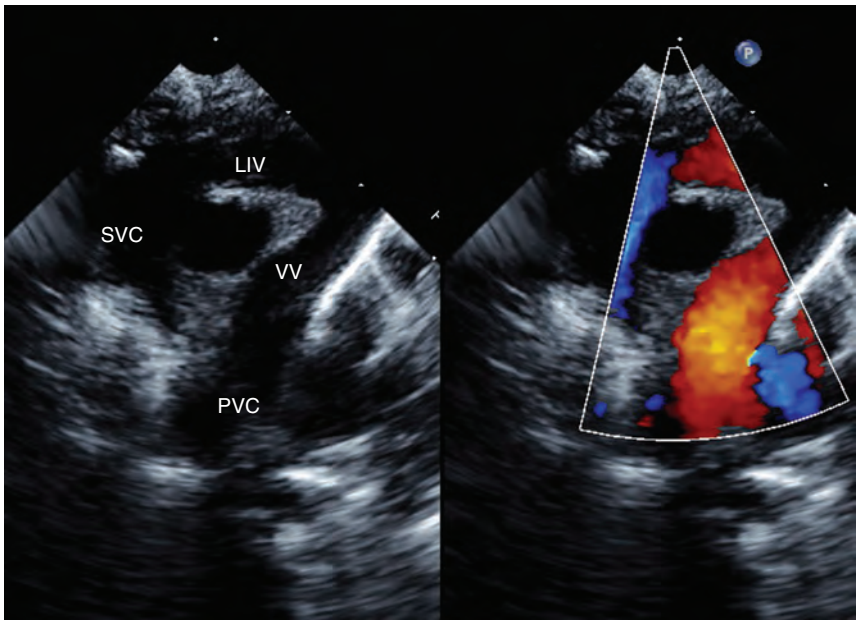


Figure 9.20 Supracardiac total anomalous pulmonary venous connection (TAPVC). Parasternal short-axis view with color Doppler flow mapping in this patient with supracardiac TAPVC to the left innominate vein (LIV) shows the pulmonary venous confluence (PVC) that drains via the vertical vein (VV) toward the leftward aspect of the innominate vein. SVC, superior vena cava.

connection between the vertical vein and the systemic venous system is frequently easily imaged from high parasternal short-axis and suprasternal notch views, with color Doppler flow mapping important to ascertain the direction of venous flow and the presence of any degree of obstruction (Figures 9.20 and 9.21). The vertical vein most commonly ascends anterior to both the left pulmonary artery and the left mainstem bronchus; however, this vessel may pass *between* the left pulmonary artery and the bronchus, which results in extrinsic compression of the vessel and obstruction to pulmonary venous return (Figure 9.22 ; Video 9.7). In addition to color Doppler, pulsed- and continuous-wave spectral Doppler from high parasternal and suprasternal notch views are crucial in demonstrating the presence and severity of obstruction; severe obstruction to pulmonary venous flow is considered an urgent if not emergent indication for surgical repair. Other evidence of pulmonary hypertension, such as dilation of right-heart structures and systolic flattening of the ventricular septum as noted from short-axis views, is frequently present (Figure 9.17a). Other forms of supracardiac connections that may be present include right-sided connections to the right superior vena cava or azygous vein (Figure 9.23; Video 9.8); obstruction can occur in

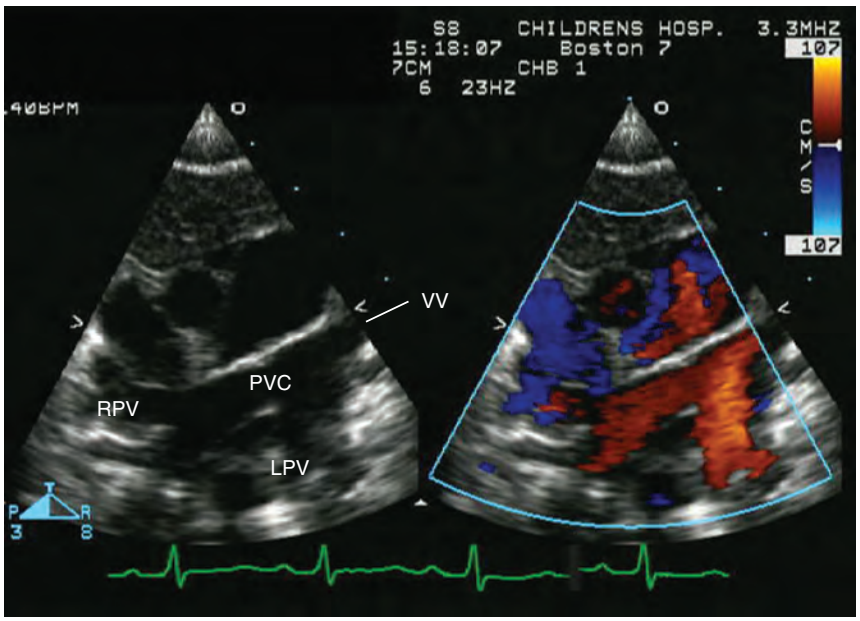


Figure 9.21 Total anomalous pulmonary venous connection (TAPVC): supracardiac to the left innominate vein. Parasternal short-axis imaging in this patient with TAPVC via a left-sided vertical vein (VV) to the left innominate vein. Note the horizontal configuration of the pulmonary venous confluence (PVC). LPV, left pulmonary veins; RPV, right pulmonary veins.

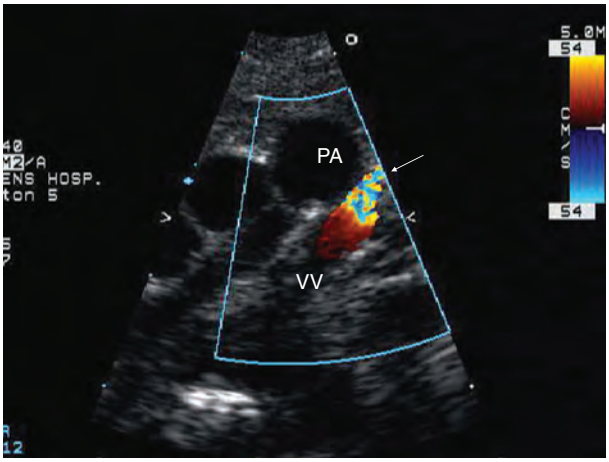


Figure 9.22 Total anomalous pulmonary venous connection (TAPVC): supracardiac to the left innominate vein. Parasternal short-axis imaging with color Doppler flow mapping in a patient with supracardiac TAPVC and obstruction of the left-sided vertical vein (VV) as it courses in between the left pulmonary artery and the left mainstem bronchus (arrow). This patient had a mean gradient of ~14 mmHg at this site by Doppler and suprasystemic right ventricular pressure. PA, pulmonary artery.

these forms as well, if the ascending vertical vein passes between the right pulmonary artery and the trachea or right mainstem bronchus.

"Cardiac" TAPVC is typically associated with a severely dilated coronary sinus, which can be noted from multiple views along the posterior left atrioventricular groove; this structure is best imaged from subcostal (particularly in infants and children) (Figure 9.24) and parasternal views (Figure 9.25), but also easily noted from apical views even in larger adult patients (Figure 9.26). Two-dimensional and color Doppler imaging of each of the pulmonary veins is best performed from high parasternal short-axis views, suprasternal notch imaging, and subxiphoid long-axis imaging when possible (Figure 9.24b). Other causes of a dilated coronary sinus include a persistent left superior vena cava and partial anomalous pulmonary venous connection to the coronary sinus, and these must be confirmed or excluded. The orifice of the coronary sinus is typically quite large. Obstruction to pulmonary venous flow in this form of TAPVC, either at the venous channel draining into the coronary sinus, or at the level of the coronary sinus ostium, is rare, but can be excluded with color and pulsed Doppler assessment of these structures (Figure 9.27; Video 9.9). As with other forms of TAPVC, other evidence of the presence of this defect includes dilation of the right heart structures and evidence of some degree of pulmonary and right ventricular hypertension.

Infradiaphragmatic TAPVC is associated with a high incidence of obstruction to pulmonary venous drainage. The pulmonary venous confluence is often positioned posterior to the left atrium, with a draining vertical vein that descends through the esophageal hiatus of the diaphragm (just anterior to the esophagus, Figure 9.28) to connect with the portal venous system (most common), the ductus venosus, hepatic vein, or inferior vena cava (Figure 9.29; Video 9.10). The individual veins joining the confluence may be imaged from high parasternal and suprasternal notch views (Figure 9.30), although subxiphoid imaging is crucial in demonstrating the location, size, and course of the draining vertical vein, as well as the ultimate connection(s) to the systemic venous system below the diaphragm. Careful color, pulsed-wave (PW), and continuous-wave (CW) Doppler

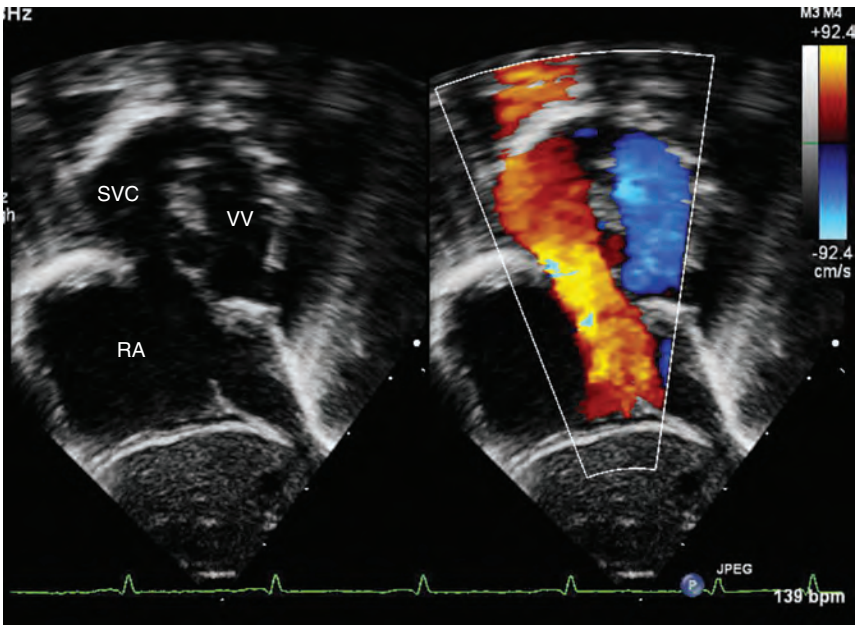
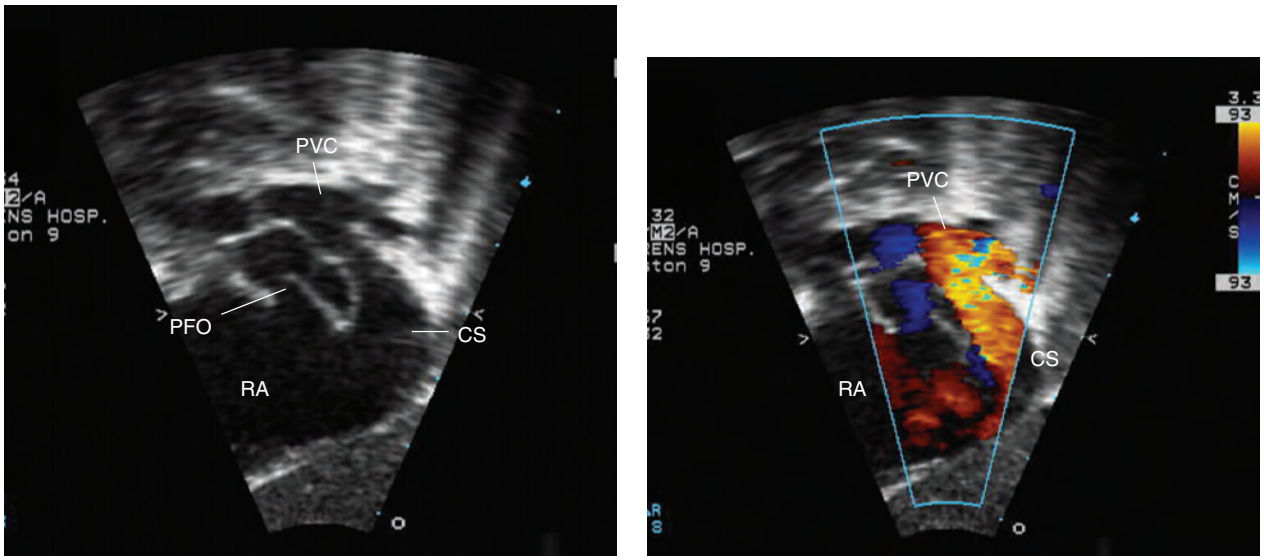


Figure 9.23 Total anomalous pulmonary venous connection (TAPVC): supracardiac to the right superior vena cava (SVC). Subxiphoid short-axis 2D and color Doppler flow mapping in this patient with TAPVC to the right SVC shows the large vertical vein (VV) that courses posterior to the right pulmonary artery and mainstem bronchus, to arch and join the right SVC at the level of the azygous vein. RA, right atrium.



(a) (b)

Figure 9.24 Cardiac total anomalous pulmonary venous connection (TAPVC). Subxiphoid short-axis 2D view in this patient with TAPVC to the coronary sinus by 2D imaging **(a)** and color Doppler **(b)** demonstrates the typical "whale's tail" view of the pulmonary venous confluence (PVC) draining via a communicating vein to the severely dilated coronary sinus (CS). Note the relative hypoplasia of the left atrium and the obligate open position of the patent foramen ovale (PFO) which allows filling of the left heart. RA, right atrium.

evaluation are mainstays in determining the site of connection as well as the presence and degree of venous obstruction. Obstruction most often occurs at the junction between the vertical vein and the portal vein, ductus venosus, or hepatic vein, and Doppler tracings are characterized by an increase in absolute venous velocities and a loss of phasicity (Figure 9.31). Pulmonary hypertension in this setting is the rule and is often severe; evaluation of other structures such as the patent ductus arteriosus (if present) can assist in assessing the degree of pulmonary hypertension (Figure 9.32).

As the interatrial communication is life-sustaining in TAPVC, a thorough evaluation of the atrial septum is necessary to determine the type and size of the communication, and the presence or absence of obstruction to flow. The most helpful views of the atrial septum are obtained from subxiphoid long- and short-axis views, as the plane of the atrial septum is typically en face to the

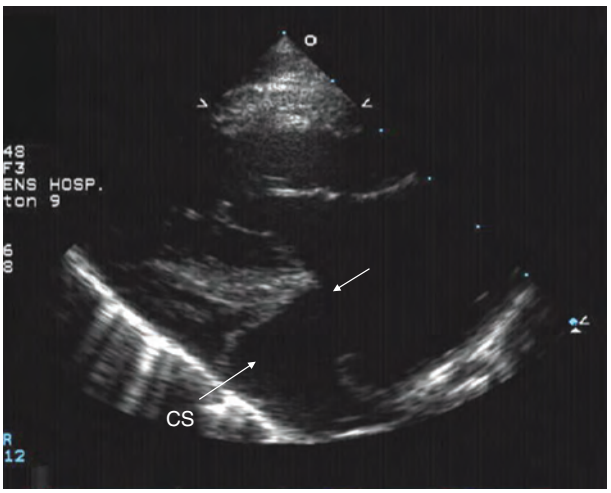


Figure 9.25 Cardiac total anomalous pulmonary venous connection (TAPVC): parasternal long-axis view. Parasternal long-axis 2D imaging in this patient with total anomalous pulmonary venous connection (TAPVC) to the coronary sinus (CS) shows a severely dilated CS and coronary sinus ostium (arrow).

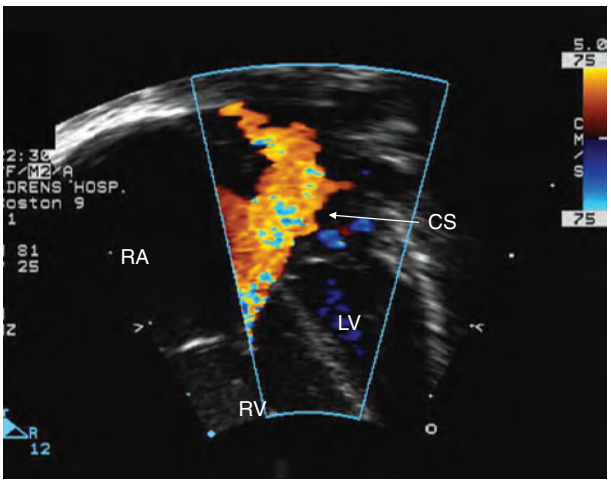


Figure 9.26 Cardiac total anomalous pulmonary venous connection (TAPVC): apical view. Apical view with color Doppler flow mapping in this patient with TAPVC to the coronary sinus (CS) demonstrates all pulmonary venous flow directed via the dilated CS into the right atrium (RA). LV, left ventricle; RV, right ventricle.

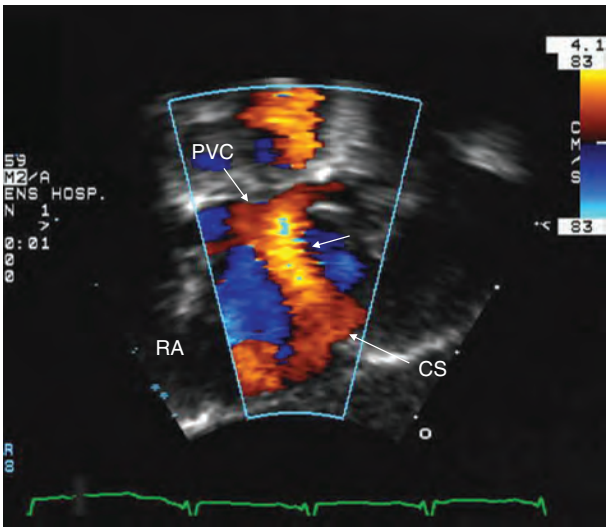


Figure 9.27 Cardiac total anomalous pulmonary venous connection (TAPVC): subxiphoid long-axis view with obstruction. Subxiphoid long-axis imaging in this patient with TAPVC to the coronary sinus (CS) shows mild flow acceleration in the connecting vein between the pulmonary venous confluence (PVC) and the CS (arrow). The mean gradient in this patient by spectral Doppler estimate was only ~3 mmHg. RA, right atrium.

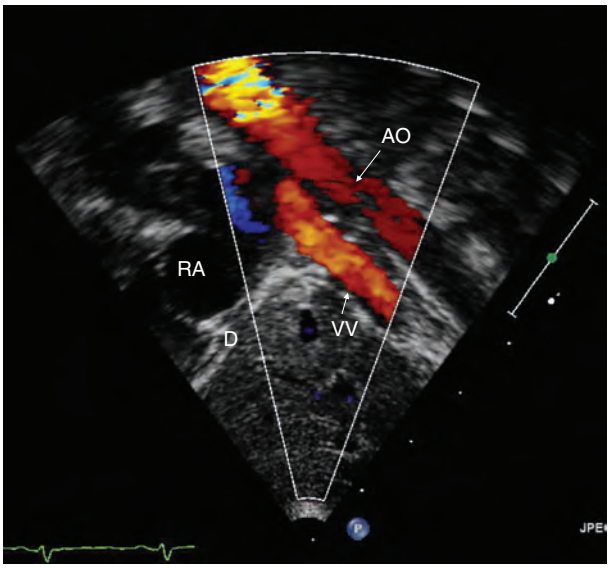


Figure 9.28 Infradiaphragmatic total anomalous pulmonary venous connection (TAPVC). Subxiphoid short-axis imaging with color Doppler mapping in this patient with infradiaphragmatic TAPVC shows a large vertical vein (VV) coursing inferiorly from behind the heart through the diaphragm (D); this is anterior to the aorta (AO). Flow is toward the probe (red) in both vessels. RA, right atrium.

interrogating probe. Parasternal short-axis views are also helpful; color Doppler and spectral Doppler techniques are helpful in determining the size of the flow jet and any degree of obstruction to flow.

Prenatal assessment

Due to the small amount of pulmonary blood flow and resulting pulmonary venous return to the left heart in utero (roughly 7% of fetal combined ventricular output [38]), the diagnosis of pulmonary venous anomalies by fetal echocardiography is challenging, particularly partial anomalous pulmonary venous return, which is infrequently diagnosed in utero [39,40]. Indirect clues that suggest the diagnosis of partial or total anomalous pulmonary venous connections, such as dilation of the right heart structures, disproportion of the great arteries, or mild hypoplasia of the left atrium [41], should lead to as complete an evaluation of pulmonary venous return as possible, although such

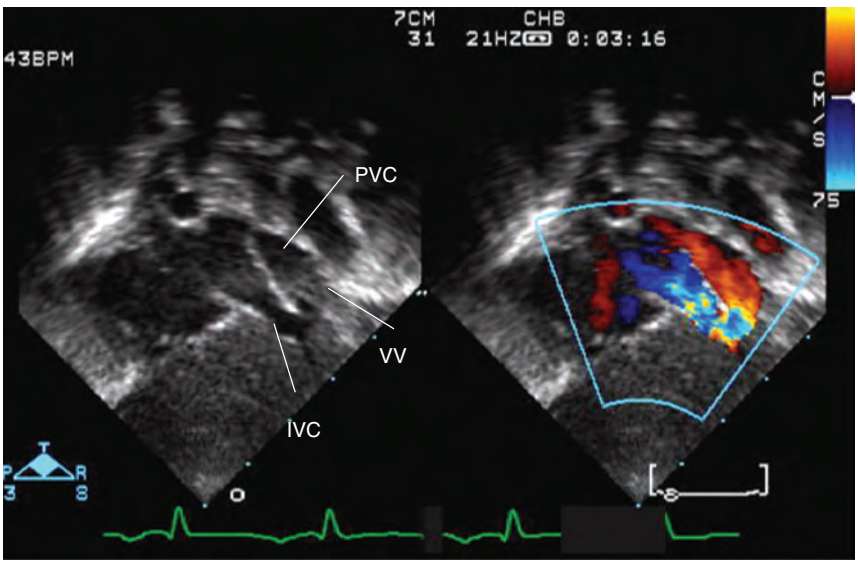


Figure 9.29 Infradiaphragmatic total anomalous pulmonary venous connection (TAPVC): subxiphoid short-axis view. The subxiphoid short-axis view in this patient with infradiaphragmatic TAPVC with 2D and color Doppler flow mapping shows the vertical vein (VV) descending just below the level of the diaphragm, and then coursing anteriorly to drain directly into the inferior vena cava (IVC). Note the color flow acceleration at the connection to the IVC. PVC, pulmonary venous confluence.

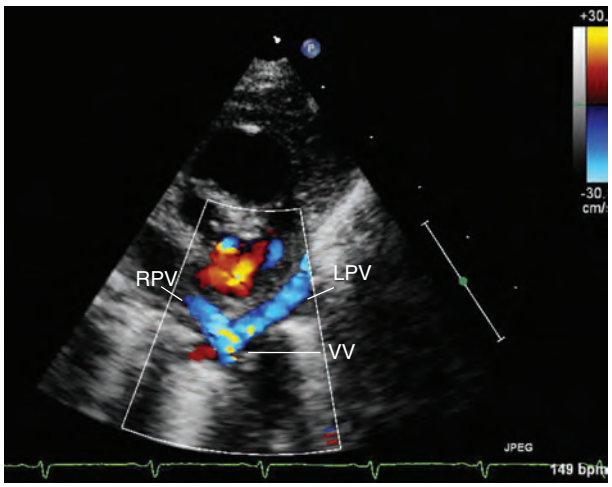
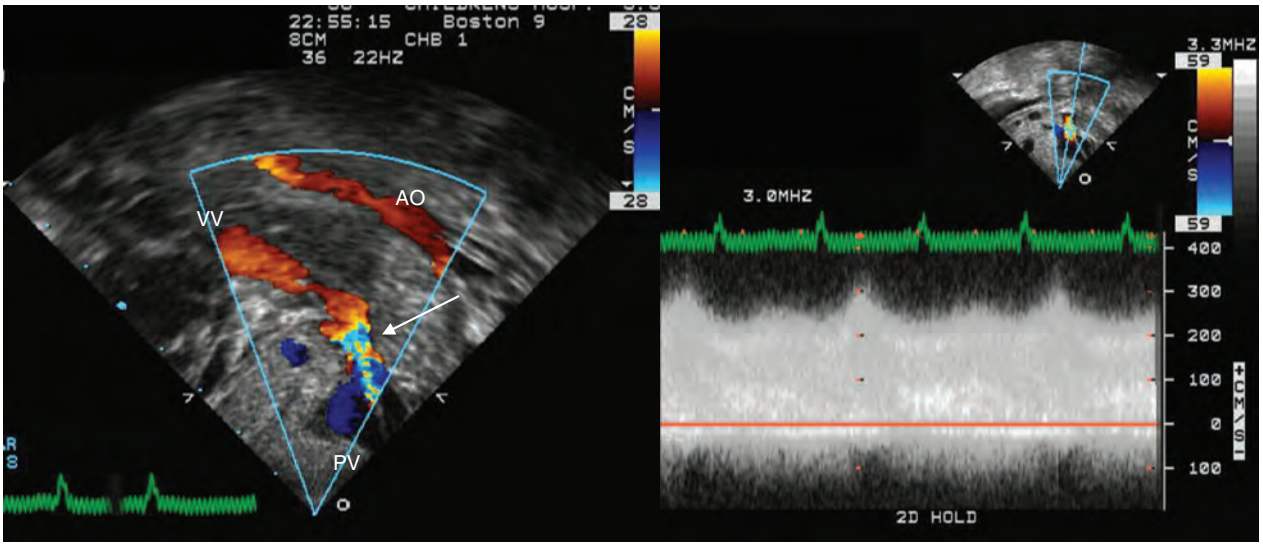


Figure 9.30 Infradiaphragmatic total anomalous pulmonary venous connection (TAPVC): parasternal short-axis view. Parasternal short-axis view with color Doppler flow mapping in this patient with infradiaphragmatic TAPVC shows right (RPV) and left (LPV) pulmonary veins coursing posteriorly to meet and descend via a vertical vein (VV) below the diaphragm.

clues are nonspecific and can also be associated with coarctation of the aorta, other left-sided obstructive lesions, or arteriovenous malformation. Visualization of a venous confluence behind the left atrium (Figure 9.33) as well as the visualization of a vertical vein are common findings associated with fetal cases of TAPVC; obstruction to pulmonary venous flow has also been reported [40]. Findings suggestive of scimitar syndrome with PAPVC include dextrocardia and hypoplasia of the right pulmonary artery [40]. Some diagnoses, such as malposition of the atrial septum with anomalous pulmonary venous drainage, are extremely difficult to establish in utero due to the normal deviation of septum primum into the left atrium, although other findings suggestive of heterotaxy syndrome with polysplenia would heighten the suspicion of this potential diagnosis. Pulmonary veins are seen best from the fetal 4-chamber view as well as short-axis views; color and PW Doppler mapping is of great utility in confirming the presence of normal or abnormal pulmonary venous drainage.

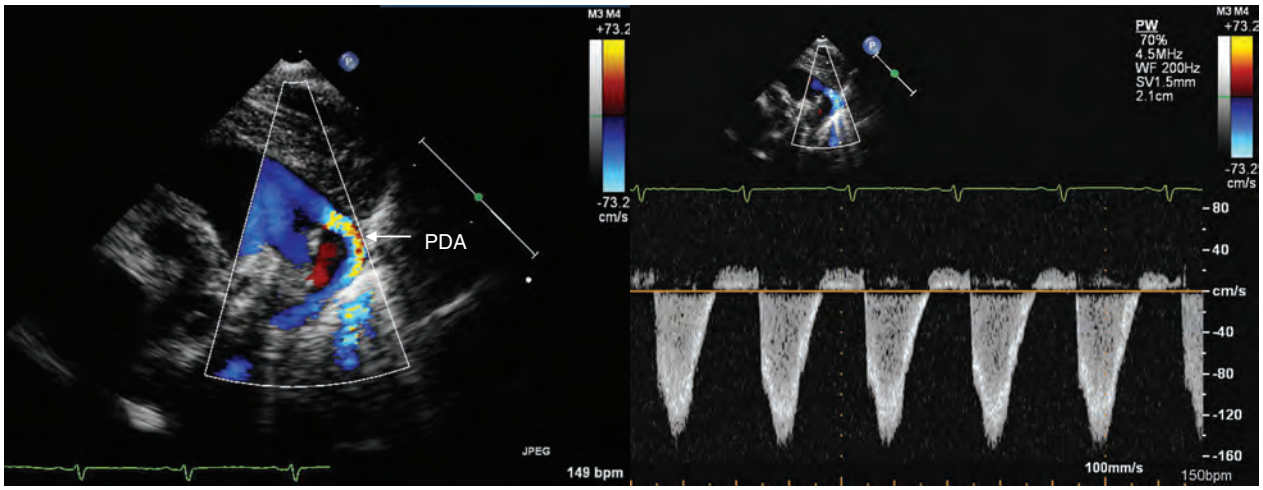
Imaging of the adult

The diagnosis of pulmonary venous anomalies in the adult patient is difficult due to technical limitations. Adequate 2D imaging and Doppler signals are difficult to obtain from subcostal and suprasternal views due to increased distance from the probe. For larger patients, the high parasternal short-axis view is often the most helpful, which allows assessment of the atrial septum as well as the lower pulmonary veins and frequently the left upper pulmonary vein as well. The right upper pulmonary vein is difficult to image from this vantage point in larger patients, although the high right sternal border view is often helpful in these situations to exclude a sinus venosus defect. Indirect evidence of anomalous pulmonary venous drainage may be seen in even the largest patients, including enlargement of the right heart chambers and diastolic flattening of the ventricular septum, typically from parasternal short-axis views.



(a) (b)

Figure 9.31 Infradiaphragmatic total anomalous pulmonary venous connection (TAPVC) with obstruction. **(a)** Subxiphoid short-axis image with color Doppler flow mapping in this patient with infradiaphragmatic TAPVC shows severe obstruction of the vertical vein (VV) at the site of entry (arrow) into the portal vein (PV), which is markedly dilated. **(b)** Continuous-wave spectral Doppler tracing from the same patient, demonstrating continuous, high-velocity flow with complete loss of phasic variation. The mean gradient estimate across this region of obstruction was ~28 mmHg. AO, descending aorta.



(a) (b)

Figure 9.32 Total anomalous pulmonary venous connection (TAPVC): pulmonary hypertension with obstructed veins. **(a)** Parasternal imaging with color flow Doppler shows the patent ductus arteriosus (PDA) (arrow) in this patient with obstructed infradiaphragmatic TAPVC. **(b)** Spectral Doppler pattern of the ductus arteriosus in the same patient. Pulmonary artery pressure is suprasystemic in systole (below the baseline).

Transesophageal echocardiography (TEE) provides an excellent alternative in these situations; TEE allows for clear imaging of the atria, atrial septum, pulmonary veins, and the vena cavae from multiple imaging planes. Nearly all pulmonary venous anomalies, including cor triatriatum, sinus venosus defect and partial anomalous pulmonary venous return, may be readily diagnosed by TEE [42–44]. A potential drawback, however, is the inability to completely image the connections between the pulmonary and systemic venous system, which may be high in the mediastinum or below the diaphragm. Cardiac magnetic resonance imaging is an excellent alternative to TEE in children and adults with suspected pulmonary venous anomalies, allowing clear visualization of the atria, atrial septum, pulmonary and systemic veins, and accurate quantification of right ventricular size, function, and pulmonary to systemic venous flow ratio [34,45,46].

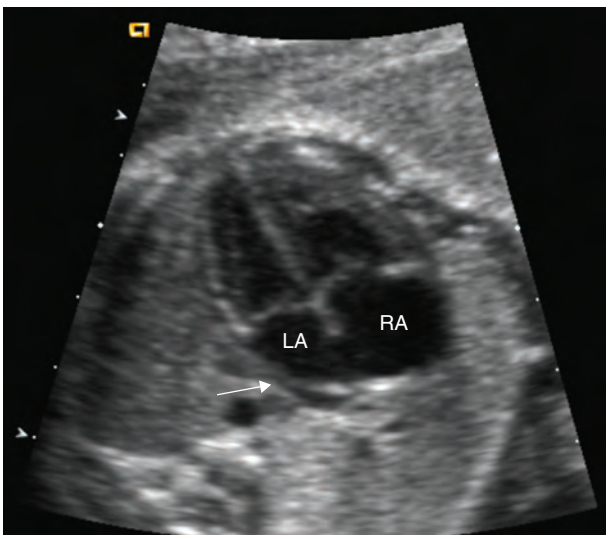


Figure 9.33 Prenatal diagnosis of total anomalous pulmonary venous connection (TAPVC). Four-chamber view of this fetus at 28 weeks gestation with TAPVC shows the subtle findings of an absence of a connection (arrow) between the pulmonary veins and the posterior aspect of the left atrium (LA), along with mild dilation of the right atrium (RA) and right ventricle.

Echocardiographic guidance of transcatheter and surgical treatment

The treatment of the vast majority of pulmonary venous anomalies, where treatment is indicated, is surgical. For congenital or acquired pulmonary vein stenosis, transcatheter techniques have been described, with treatment options varying from simple balloon dilation [47,48], to cutting balloon dilation [49,50], stent placement [51,52], and even drug-eluting stents. While such transcatheter interventions have proven helpful in acutely relieving obstruction in congenital pulmonary vein stenosis, the disease tends to be progressive and frequently recurs (Figure 9.34). Surgical intervention, similarly, has been largely unsuccessful long term, although more recently the "sutureless" operative technique has had perhaps more success at reducing recurrence of pulmonary vein stenosis [53–55]. As this disease tends to affect the young infant and the intervention is typically a vascular procedure, intraprocedural imaging in the catheterization laboratory is typically by angiography, and echocardiography has been more often used for following the status of the pulmonary veins noninvasively in follow-up after the procedure, along with the degree of right ventricular and pulmonary artery hypertension by Doppler assessment. TEE may be helpful to the surgeon in demonstrating the acute relief of pulmonary vein stenosis in the operating room, and is the mainstay of

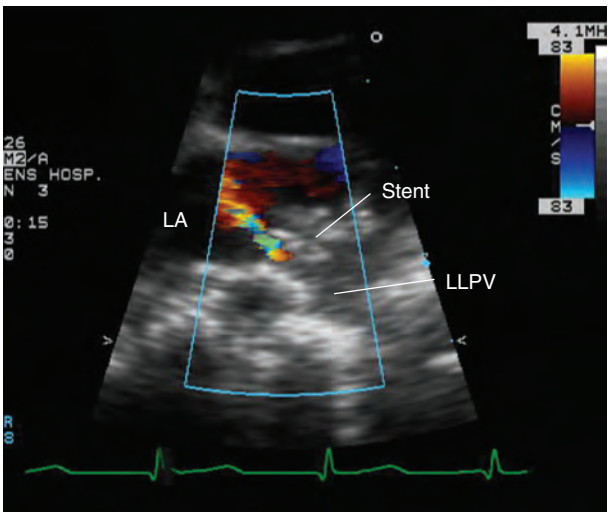


Figure 9.34 Pulmonary vein in-stent restenosis. Parasternal short-axis image with color Doppler flow mapping in this patient with severe, recurrent pulmonary vein stenosis shows a small jet of accelerated pulmonary venous inflow in the left lower pulmonary vein (LLPV). Note the gap between the color flow jet and the edges of the stent consistent with in-stent restenosis. LA, left atrium.

noninvasive evaluation over the weeks and months following repair as surveillance for recurrence.

Intraoperative TEE is considered quite helpful during repair of sinus venosus defects or other forms of partial anomalous venous return, cor triatriatum, and total anomalous pulmonary venous return (Figure 9.35; Video 9.11) [56,57]. Three-dimensional TEE probes are now becoming available to assist with intraoperative evaluation as well (Figure 9.36; Video 9.12). Complex venous baffling may be required for repair of partial

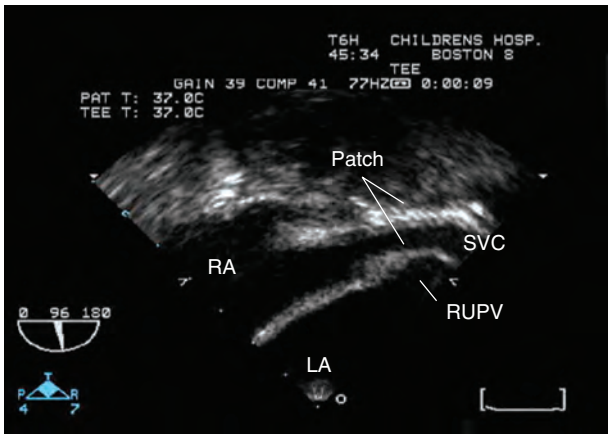


Figure 9.35 Postoperative transesophageal echocardiography (TEE) after superior sinus venosus repair. Long-axis (bicaval) TEE view following "two-patch" repair of the unroofing defect between the right upper pulmonary vein (RUPV) and the superior vena cava (SVC), as well as patch augmentation of the SVC anteriorly. The SVC is mildly narrow but unobstructed. LA, left atrium; RA, right atrium.

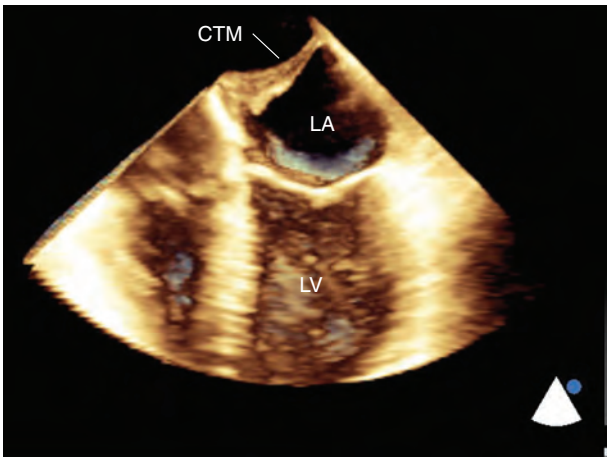


Figure 9.36 Three-dimensional transesophageal echocardiogram. Preoperative image with 3D probe demonstrates a thick cor triatriatum "membrane" (CTM) within the left atrium (LA). LV, left ventricle.

anomalous pulmonary venous return, and TEE is excellent for evaluating the patency of the pulmonary and systemic venous pathways as well as residual leaks. TEE evaluation of repair of TAPVC, however, may be more challenging as the surgical anastomosis is often directly anterior to the esophagus, at times too close to the interrogating probe to allow for complete color and pulsed Doppler interrogation. In small infants, as well, the possibility of probe-related distortion or compression of the pulmonary venous pathway must be considered. Epicardial intraoperative imaging is an option in this situation, which allows for imaging of the venous anastomosis without the potential for such distortion; this is also a good option for infants less than 3 kg, for whom the passage of a TEE probe may be difficult. Regardless of the technique, the goals of post-cardiopulmonary bypass imaging include evaluation of the repair, exclusion of residual lesions, and functional assessment including the AV valves, right heart pressures by Doppler estimate, and ventricular function.

Postoperative assessment

The goals of longer term postoperative imaging are determined in many respects by the nature of the repaired lesion. Congenital or acquired pulmonary vein stenosis is discussed in some detail in the preceding section. Resection of cor triatriatum has a high success rate, with excellent survival and long-term results [58]; follow-up evaluation includes comprehensive imaging of the left atrium and any residual membrane tissue, color and spectral Doppler evaluation of flow in the pulmonary veins and left atrium, evaluation of any residual interatrial defects, and assessment of right heart pressure, size, and function.

Following repair of sinus venosus defect, obstruction of both the pulmonary venous pathway and the superior vena cava have been described [59]. In repaired partial anomalous pulmonary venous return, echocardiographic follow-up evaluation should

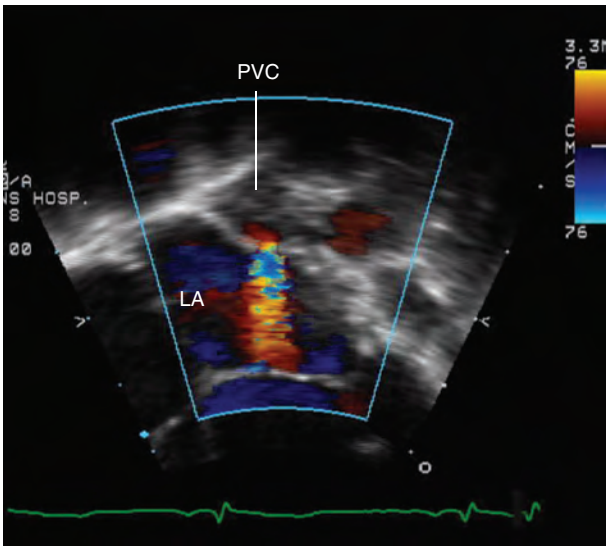


Figure 9.37 Recurrent obstruction after repair of total anomalous pulmonary venous connection (TAPVC). Apical view with color Doppler flow mapping in this patient after repair of infradiaphragmatic TAPVC shows severe obstruction at the anastomosis between the pulmonary venous confluence (PVC) and the left atrium (LA).

include assessment for any stenosis of the venous baffle to the left atrium, residual leaks, presence of any stenosis of the systemic vein, and assessment of right heart pressure, size, and function.

Repair of total anomalous pulmonary venous return is associated with a significant risk of recurrent pulmonary venous obstruction, both at the level of the anastomosis of the confluence to the left atrium, as well as at the level of the individual pulmonary veins. The risk of recurrence of obstruction across all types of TAPVC repair is 11–17% [60,61]. Goals for the echocardiographic assessment of these patients must include careful assessment of the dimensions and flow characteristics, by both color and spectral Doppler, of the pulmonary venous confluence anastomosis as well as the individual pulmonary veins. Subxiphoid imaging in conjunction with high parasternal and suprasternal notch imaging is helpful for the delineation of the individual pulmonary veins; frequently the apical view is best for evaluation of the pulmonary venous confluence, as the orifice is usually directed at the left atrial outlet and parallel to the interrogating transducer in this view (Figure 9.37). Evaluation of the right heart size, pressure, and function are important to exclude pulmonary hypertension and ventricular dysfunction in this setting.

Videos

To access the videos for this chapter, please go to www.laiecho.com.

Video 9.1 Total anomalous pulmonary venous drainage: parasternal short-axis view. Parasternal short-axis image with color Doppler flow mapping in this patient with severe leftward malattachment of septum primum. Note the normal connection of the pulmonary veins posteriorly, with flow directed to the right atrium.

Video 9.2 Apical view of "classic" cor triatriatum with color Doppler interrogation demonstrates the cor triatriatum "membrane" with a large orifice allowing unobstructed pulmonary venous inflow from the pulmonary venous confluence and the true left atrium.

Video 9.3 Partial anomalous pulmonary venous connection (PAPVC): left upper pulmonary vein to innominate vein. High parasternal short-axis view with color Doppler flow mapping in this patient with PAPVC of the left upper pulmonary vein to the left innominate vein shows a large vertical vein connecting with the caudal aspect of the dilated innominate vein.

Video 9.4 Partial anomalous pulmonary venous connection (PAPVC): scimitar syndrome. Subxiphoid short-axis image with color Doppler flow mapping in this patient with scimitar syndrome demonstrates PAPVC of right pulmonary veins to the inferior vena cava at its junction with the right atrium. Note the mild flow acceleration by color Doppler and the flow directed caudally toward the transducer, which in this view is always an abnormal finding.

Video 9.5 Supracardiac total anomalous pulmonary venous connection (TAPVC). Parasternal short-axis view with color Doppler flow mapping in this patient with supracardiac TAPVC to the left innominate vein shows the pulmonary venous confluence that drains cephalad via the vertical vein toward the leftward aspect of the innominate vein. Note the dilated superior vena cava.

Video 9.6 Supracardiac total anomalous pulmonary venous connection (TAPVC): subxiphoid long-axis view. Subxiphoid two-dimensional and color Doppler flow mapping in this patient with supracardiac TAPVC shows flow from both right and left pulmonary veins into a large, superiorly draining vertical vein. Note the obligate right-to-left shunt across the secundum atrial septal defect.

Video 9.7 Total anomalous pulmonary venous connection (TAPVC): supracardiac to the left innominate vein. Parasternal short-axis imaging with color Doppler flow mapping in a patient with supracardiac TAPVC and obstruction of the left-sided vertical vein as it courses in between the left pulmonary artery and the left mainstem bronchus. This patient had a mean gradient of ~14 mmHg at this site by Doppler and suprasystemic right ventricular pressure.

Video 9.8 Total anomalous pulmonary venous connection (TAPVC): supracardiac to the right superior vena cava (SVC). Subxiphoid short-axis two-dimensional and color Doppler flow mapping in this patient with TAPVC to the right SVC shows the large vertical vein that courses posterior to the right pulmonary artery and mainstem bronchus, to arch and join the right SVC at the level of the azygous vein.

Video 9.9 Cardiac total anomalous pulmonary venous connection (TAPVC): subxiphoid short-axis view. Subxiphoid short-axis view in this patient with TAPVC to the coronary sinus demonstrates the typical "whale's tail" of pulmonary venous flow directed into the right atrium via the severely dilated coronary sinus (CS).

Video 9.10 Infradiaphragmatic total anomalous pulmonary venous connection (TAPVC): subxiphoid short-axis view. The subxiphoid short-axis view in this patient with infradiaphragmatic TAPVC with two-dimensional and color Doppler flow mapping shows the vertical vein descending just below the level of the diaphragm, and then coursing anteriorly to drain directly into the inferior vena cava (IVC). Note the color flow acceleration at the connection to the IVC.

Video 9.11 Postoperative transesophageal echocardiography (TEE) after superior sinus venosis repair. Long-axis (bicaval) TEE view following "two-patch" repair of the unroofing defect between the right upper pulmonary vein (RUPV) and the superior vena cava (SVC), as well as patch augmentation of the SVC anteriorly. The SVC is mildly narrow but unobstructed.

Video 9.12 TEE. Three-dimensional, preoperative cor triatriatum. Preoperative image with 3D transesophageal imaging probe demonstrates a thick cor triatriatum "membrane" within the left atrium, immediately anterior to the imaging probe (apex of the pyramidal data set).

References

1 Healy JE, Jr. An anatomic survey of anomalous pulmonary veins: their clinical significance. *J Thorac Surg* 1952;**23**:433–444.
2 Ostman-Smith I, Silverman NH, Oldershaw P, et al. Cor triatriatum sinistrum. Diagnostic features on cross sectional echocardiography. *Br Heart J* 1984;**51**:211–219.
3 Ferencz C, Rubin JD, McCarter RJ, et al. Congenital heart disease: prevalence at livebirth. The Baltimore-Washington Infant Study. *Am J Epidemiol* 1985;**121**:31–36.
4 Hoffman JI, Kaplan S. The incidence of congenital heart disease. *J Am Coll Cardiol* 2002;**39**:1890–1900.
5 Moore JW, Kirby WC, Rogers WM, Poth MA. Partial anomalous pulmonary venous drainage associated with 45,X Turner's syndrome. *Pediatrics* 1990;**86**:273–276.
6 van Wassenaer AG, Lubbers LJ, Losekoot G. Partial abnormal pulmonary venous return in Turner syndrome. *Eur J Pediatr* 1988;**148**:101–103.
7 Bleyl S, Nelson L, Odelberg SJ, et al. A gene for familial total anomalous pulmonary venous return maps to chromosome 4p13-q12. *Am J Hum Genet* 1995;**56**:408–415.
8 Neill CA. Development of the pulmonary veins; with reference to the embryology of anomalies of pulmonary venous return. *Pediatrics* 1956;**18**:880–887.
9 Douglas YL, Mahtab EA, Jongbloed MR, et al. Pulmonary vein, dorsal atrial wall and atrial septum abnormalities in podoplanin knockout mice with disturbed posterior heart field contribution. *Pediatr Res* 2009;**65**:27–32.
10 Jongbloed MR, Vicente-Steijn R, Douglas YL, et al. Expression of Id2 in the second heart field and cardiac defects in Id2 knock-out mice. *Dev Dyn* 2011;**240**:2561–2577.
11 Douglas YL, Jongbloed MR, Deruiter MC, Gittenberger-de Groot AC. Normal and abnormal development of pulmonary veins: state of the art and correlation with clinical entities. *Int J Cardiol* 2011;**147**:13–24.
12 Rammos S, Gittenberger-de Groot AC, Oppenheimer-Dekker A. The abnormal pulmonary venous connexion: a developmental approach. *Int J Cardiol* 1990;**29**:285–295.
13 Moller JH, Nakib A, Anderson RC, Edwards JE. Congenital cardiac disease associated with polysplenia. A developmental complex of bilateral "left-sidedness". *Circulation* 1967;**36**:789–799.
14 Blom NA, Gittenberger-de Groot AC, Jongeneel TH, et al. Normal development of the pulmonary veins in human embryos and formulation of a morphogenetic concept for sinus venosus defects. *Am J Cardiol* 2001;**87**:305–309.
15 Van Praagh S, Carrera ME, Sanders SP, et al. Sinus venosus defects: unroofing of the right pulmonary veins–anatomic and echocardiographic findings and surgical treatment. *Am Heart J* 1994;**128**:365–379.
16 Edwards JE. Congenital stenosis of pulmonary veins. Pathologic and developmental considerations. *Lab Invest* 1960;**9**:46–66.
17 Sade RM, Freed MD, Matthews EC, Castaneda AR. Stenosis of individual pulmonary veins. Review of the literature and report of a surgical case. *J Thorac Cardiovasc Surg* 1974;**67**:953–962.
18 Rubino M, Van PS, Kadoba K, et al. Systemic and pulmonary venous connections in visceral heterotaxy with asplenia. Diagnostic and surgical considerations based on seventy-two autopsied cases. *J Thorac Cardiovasc Surg* 1995;**110**:641–650.
19 Riedlinger WF, Juraszek AL, Jenkins KJ, et al. Pulmonary vein stenosis: expression of receptor tyrosine kinases by lesional cells. *Cardiovasc Pathol* 2006;**15**:91–99.
20 Sadr IM, Tan PE, Kieran MW, Jenkins KJ. Mechanism of pulmonary vein stenosis in infants with normally connected veins. *Am J Cardiol* 2000;**86**:577–579, A10.
21 Niwayama G. Cor triatriatum. *Am Heart J* 1960;**59**:291–317.
22 Dudell GG, Evans ML, Krous HF, et al. Common pulmonary vein atresia: the role of extracorporeal membrane oxygenation. *Pediatrics* 1993;**91**:403–410.
23 Juraszek AL, Cohn H, Van PR, Van PS. Isolated left-sided scimitar vein connecting all left pulmonary veins to the right inferior vena cava. *Pediatr Cardiol* 2005;**26**:846–847.
24 Neill CA, Ferencz C, Sabiston DC, Sheldon H. The familial occurrence of hypoplastic right lung with systemic arterial supply and venous drainage "scimitar syndrome". *Bull Johns Hopkins Hosp* 1960;**107**:1–21.
25 Gao YA, Burrows PE, Benson LN, et al. Scimitar syndrome in infancy. *J Am Coll Cardiol* 1993;**22**:873–882.
26 Craig JM, Darling RC, Rothney WB. Total pulmonary venous drainage into the right side of the heart; report of 17 autopsied cases not associated with other major cardiovascular anomalies. *Lab Invest* 1957;**6**:44–64.
27 Burroughs JT, Edwards JE. Total anomalous pulmonary venous connection. *Am Heart J* 1960;**59**:913–931.
28 Lucas RV, Jr., Adams P, Jr., Anderson RC, et al. Total anomalous pulmonary venous connection to the portal venous system: a cause of pulmonary venous obstruction. *Am J Roentgenol Radium Ther Nucl Med* 1961;**86**:561–575.

29 Tajik AJ, Gau GT, Ritter DG, Schattenberg TT. Echocardiographic pattern of right ventricular diastolic volume overload in children. *Circulation* 1972;**46**:36–43.

30 Fiandra O, Barcia A, Cortes R, Stanham J. Partial anomalous pulmonary venous drainage into the inferior vena cava. *Acta Radiol* 1962;**57**:301–310.

31 Saalouke MG, Shapiro SR, Perry LW, Scott LP, III. Isolated partial anomalous pulmonary venous drainage associated with pulmonary vascular obstructive disease. *Am J Cardiol* 1977;**39**:439–444.

32 Delisle G, Ando M, Calder AL, et al. Total anomalous pulmonary venous connection: report of 93 autopsied cases with emphasis on diagnostic and surgical considerations. *Am Heart J* 1976;**91**:99–122.

33 Geva T, Greil GF, Marshall AC, et al. Gadolinium-enhanced 3-dimensional magnetic resonance angiography of pulmonary blood supply in patients with complex pulmonary stenosis or atresia: comparison with X-ray angiography. *Circulation* 2002;**106**:473–478.

34 Greil GF, Powell AJ, Gildein HP, Geva T. Gadolinium-enhanced three-dimensional magnetic resonance angiography of pulmonary and systemic venous anomalies. *J Am Coll Cardiol* 2002;**39**:335–341.

35 Geggel RL, Fulton DR, Rockenmacher S. Nonobstructive cor triatriatum in infancy. *Clin Pediatr (Phila)* 1999;**38**:489–491.

36 Wolf WJ. Diagnostic features and pitfalls in the two-dimensional echocardiographic evaluation of a child with cor triatriatum. *Pediatr Cardiol* 1986;**6**:211–213.

37 Jenkins KJ, Sanders SP, Orav EJ, et al. Individual pulmonary vein size and survival in infants with totally anomalous pulmonary venous connection. *J Am Coll Cardiol* 1993;**22**:201–206.

38 Rudolph AM, Heymann MA. The circulation of the fetus in utero. Methods for studying distribution of blood flow, cardiac output and organ blood flow. *Circ Res* 1967;**21**:163–184.

39 Driggers RW, Spevak PJ, Crino JP, et al. Fetal anatomic and functional echocardiography: a 5-year review. *J Ultrasound Med* 2003;**22**:45–51.

40 Valsangiacomo ER, Hornberger LK, Barrea C, et al. Partial and total anomalous pulmonary venous connection in the fetus: two-dimensional and Doppler echocardiographic findings. *Ultrasound Obstet Gynecol* 2003;**22**:257–263.

41 Allan LD, Sharland GK. The echocardiographic diagnosis of totally anomalous pulmonary venous connection in the fetus. *Heart* 2001;**85**:433–437.

42 Jean D, Girard F, Couture P, et al. Transesophageal echocardiographic diagnosis of sinus venosus-type atrial septal defect associated with partial anomalous venous connections during cardiac surgery in adults. *J Cardiothorac Vasc Anesth* 1995;**9**:438–441.

43 Sunaga Y, Hayashi K, Okubo N, et al. Transesophageal echocardiographic diagnosis of coronary sinus type atrial septal defect. *Am Heart J* 1992;**124**:1657–1659.

44 Watanabe F, Takenaka K, Suzuki J, et al. Visualization of sinus venosus-type atrial septal defect by biplane transesophageal echocardiography. *J Am Soc Echocardiogr* 1994;**7**:179–181.

45 Powell AJ, Tsai-Goodman B, Prakash A, et al. Comparison between phase-velocity cine magnetic resonance imaging and invasive oximetry for quantification of atrial shunts. *Am J Cardiol* 2003;**91**:1523–1525, A9.

46 Valente AM, Sena L, Powell AJ, et al. Cardiac magnetic resonance imaging evaluation of sinus venosus defects: comparison to surgical findings. *Pediatr Cardiol* 2007;**28**:51–56.

47 Driscoll DJ, Hesslein PS, Mullins CE. Congenital stenosis of individual pulmonary veins: clinical spectrum and unsuccessful treatment by transvenous balloon dilation. *Am J Cardiol* 1982;**49**:1767–1772.

48 Singh H, Singh C, Aggarwal N, Kumar A. Angioplasty of congenital pulmonary vein stenosis. *Indian Heart J* 2005;**57**:709–712.

49 Bromberg-Marin G, Tsimikas S, Mahmud E. Treatment of recurrent pulmonary vein stenoses with endovascular stenting and adjuvant oral sirolimus. *Catheter Cardiovasc Interv* 2007;**69**:362–368.

50 Seale AN, Daubeney PE, Magee AG, Rigby ML. Pulmonary vein stenosis: initial experience with cutting balloon angioplasty. *Heart* 2006;**92**:815–820.

51 Cook AL, Prieto LR, Delaney JW, Rhodes JF. Usefulness of cutting balloon angioplasty for pulmonary vein in-stent stenosis. *Am J Cardiol* 2006;**98**:407–410.

52 Tomita H, Watanabe K, Yazaki S, et al. Stent implantation and subsequent dilatation for pulmonary vein stenosis in pediatric patients: maximizing effectiveness. *Circ J* 2003;**67**:187–190.

53 Spray TL, Bridges ND. Surgical management of congenital and acquired pulmonary vein stenosis. *Semin Thorac Cardiovasc Surg Pediatr Card Surg Annu* 1999;**2**:177–188.

54 Azakie A, Lavrsen MJ, Johnson NC, Sapru A. Early outcomes of primary sutureless repair of the pulmonary veins. *Ann Thorac Surg* 2011;**92**:666–671; discussion 71–72.

55 Yanagawa B, Alghamdi AA, Dragulescu A, et al. Primary sutureless repair for "simple" total anomalous pulmonary venous connection: midterm results in a single institution. *J Thorac Cardiovasc Surg* 2011;**141**:1346–1354.

56 Rosenfeld HM, Gentles TL, Wernovsky G, et al. Utility of intraoperative transesophageal echocardiography in the assessment of residual cardiac defects. *Pediatr Cardiol* 1998;**19**:346–351.

57 Stevenson JG, Sorensen GK, Gartman DM, et al. Transesophageal echocardiography during repair of congenital cardiac defects: identification of residual problems necessitating reoperation. *J Am Soc Echocardiogr* 1993;**6**:356–365.

58 Alphonso N, Norgaard MA, Newcomb A, et al. Cor triatriatum: presentation, diagnosis and long-term surgical results. *Ann Thorac Surg* 2005;**80**:1666–1671.

59 Stewart RD, Bailliard F, Kelle AM, et al. Evolving surgical strategy for sinus venosus atrial septal defect: effect on sinus node function and late venous obstruction. *Ann Thorac Surg* 2007;**84**:1651–1655.

60 Hancock Friesen CL, Zurakowski D, Thiagarajan RR, et al. Total anomalous pulmonary venous connection: an analysis of current management strategies in a single institution. *Ann Thorac Surg* 2005;**79**:596–606.

61 Seale AN, Uemura H, Webber SA, et al. Total anomalous pulmonary venous connection: outcome of postoperative pulmonary venous obstruction. *J Thorac Cardiovasc Surg* 2013;**145**:1255–1262.

CHAPTER 10

Systemic Venous Anomalies

Leo Lopez and Sarah Chambers
The Pediatric Heart Center at the Children's Hospital at Montefiore, New York, NY, USA

Introduction

The development of and variations in the systemic venous return have been the object of study for many years [1,2]. Systemic venous anomalies can occur in isolation, often with little hemodynamic significance, or in association with other structural heart defects. With the increasing utility of catheterization and surgical intervention in patients with congenital heart disease, prior identification and analysis of systemic venous anomalies can prevent significant morbidity and mortality, and echocardiography has become an essential tool in the diagnosis and management of these patients [3–6]. Because of the wide variability within this class of anomalies, evaluation of the systemic venous return must involve a systematic approach with a comprehensive description of each individual segment: the superior vena cava (SVC), the inferior vena cava (IVC), the azygos and hemiazygos veins, the hepatic veins, the coronary sinus (CS), and the innominate vein.

Atrial situs is a key variable in the understanding of the systemic veins [7]. If there is lateralized situs (situs solitus or situs inversus), the CS is usually present, and systemic venous anomalies are few, rare, and fairly predictable. The most common anomaly in situs solitus is a persistent left SVC connecting to the CS. In situs inversus, the systemic venous return is usually a mirror image of the normal pattern. If there is abnormal situs as in heterotaxy syndrome (right isomerism or left isomerism), there is often a common atrium with fundamentally flawed venous segments [8–12]. The anomalies are complex and frequent, but they can be predictable based on the type of isomerism, or, in other words, on whether the heterotaxy syndrome is of the asplenia type or the polysplenia type [3,13]. In right isomerism (asplenia type), the CS is almost always absent, and there are usually bilateral SVCs connecting to the atria without a connecting vein. In left isomerism (polysplenia type), many abnormalities can coexist, including anomalous hepatic venous connection, interrupted IVC with azygos continuation, and bilateral SVCs with the left SVC connecting either directly to the left-sided atrium or to the CS if present.

Systemic venous anomalies can have important implications in the management of any patient who requires cardiac catheterization or surgical intervention and cardiopulmonary bypass, since the systemic venous return is cannulated in these procedures. Preoperative identification and complete characterization of any abnormalities in systemic venous return is also crucial in patients with single ventricle circulation, because their surgical palliation ultimately requires connection of the systemic venous return directly into the pulmonary arteries.

Prevalence

Systemic venous anomalies are uncommon in isolation, and their frequency is higher in association with other structural heart defects. A persistent left SVC, the most common systemic venous anomaly, occurs in 0.3–0.5% of the general population [14–16], whereas its frequency in patients with congenital heart diseases is as high as 2–10% [17–20]. In the setting of heterotaxy syndrome, which has an incidence of 10/100,000 livebirths [21] and a frequency of 0.8% in patients with congenital heart disease [13], systemic venous anomalies occur in more than 70% of cases [13,22].

Etiology and embryology

With increasing knowledge pertaining to the development of abnormal visceroatrial situs, systemic venous anomalies represent one component of the morphologically diverse lesions that comprise heterotaxy syndrome. It remains unknown, however, whether heterotaxy syndrome and the development of bilateral isomeric atrial appendages are predetermined in the genetic code. There is a trend toward persistence of the bilateral venous return, and this is present early in gestation. Whether the regularity of venous anomalies in isomerism is due to local effects after differentiation or to a separate but related early genetic signal is not known.

Echocardiography in Pediatric and Congenital Heart Disease: From Fetus to Adult, Second Edition. Edited by Wyman W. Lai, Luc L. Mertens, Meryl S. Cohen and Tal Geva.
© 2016 John Wiley & Sons, Ltd. Published 2016 by John Wiley & Sons, Ltd.
Companion website: www.lai-echo.com

Table 10.1 Embryologic origins of the major systemic veins

Systemic vein	Embryologic origin
Superior vena cava	Right anterior cardinal vein
Left innominate vein	Persistent connection between the anterior cardinal veins after regression of the left anterior cardinal vein
Coronary sinus	Left common cardinal vein (left sinus horn)
Inferior vena cava	Right vitelline vein, right hepatocardiac vein, right subcardinal vein, caudal segment of the right supracardinal vein
Hepatic veins	Vitelline veins, omphalomesenteric veins
Azygos vein	Right supracardinal vein
Hemiazygos vein	Left supracardinal vein

The embryologic origins of the major systemic veins are outlined in Table 10.1, and the embryologic origins of common systemic venous anomalies are outlined in Table 10.2. There are three separate venous systems in the early human embryo that contribute to the systemic venous return: the umbilical, vitelline, and cardinal veins. The paired umbilical veins (from the chorionic villi) and the paired vitelline veins (from the yolk sac) appear during the third week of gestation (13-somite stage). The sinus venosus develops by enlargement of the confluence of the umbilical veins and communicates with the atrial heart segment through the sinoatrial foramen [23]. The vitelline veins then join the umbilical veins as they drain into the rightward and leftward aspect of the developing sinus venosus, thus forming the right and left horns of the sinus venosus.

The anterior and posterior cardinal veins appear during the fourth week of gestation (20-somite stage). The anterior cardinal veins appear first, draining blood from the cranial end of the embryo and the developing central nervous system. The posterior cardinal veins appear shortly thereafter, lateral to the spinal cord, draining blood from the caudal end of the embryo. The anterior and posterior cardinal veins converge into the common cardinal veins that join the umbilical and vitelline veins as they drain into the right and left horns of the sinus venosus.

At around the same time, rightward lateralization of the systemic venous return ensues. First, there is invagination of the junction between the left horn of the sinus venosus and the common atrium, separating the left horn from the left atrium (LA). This is followed by a rightward shift of the sinus venosus to commit the three paired venous systems to the right atrium (RA). Now that the systemic venous return has lateralized to drain into the RA, the formation of the individual systemic veins begins.

Table 10.2 Embryologic origins of common systemic venous anomalies

Systemic venous anomaly	Embryologic origin
Left SVC	Persistence of the left anterior cardinal vein
Connecting vein between bilateral SVCs	Formation of connection between anterior cardinal veins
Atretic right SVC	Regression of right anterior cardinal vein
Left SVC to LA	Failure of infolding between left sinus horn and LA (absent CS), persistence of left anterior cardinal vein versus extensive unroofing of the CS
Levoatrial cardinal vein	Persistent connection between primordial common pulmonary vein and cardinal veins
Right SVC to LA or to both atria	Leftward superior displacement of right sinus horn versus unroofed right pulmonary veins near SVC–RA junction
Interrupted IVC	Failure of connection between right hepatocardiac veins and right subcardinal veins; prominent right supracardinal vein becomes azygos continuation or prominent left supracardinal vein becomes hemiazygos continuation
Bilateral IVCs	Persistence of caudal segment of left supracardinal vein
Left IVC to RA	Persistence of left supracardinal vein and regression of right supracardinal vein
Retroaortic innominate vein	Formation of alternate connection between anterior cardinal veins

CS, coronary sinus; IVC, inferior vena cava; LA, left atrium; RA, right atrium; SVC, superior vena cava.

SVC and coronary sinus

The proximal segments of the right anterior cardinal and right common cardinal veins form the right SVC, which connects the left innominate, right jugular, and right subclavian veins to the RA. The left innominate vein develops during the seventh week of gestation as an enlargement of a connection between the anterior cardinal veins. This is followed by the involution of the left anterior cardinal vein, which remains as the ligament of Marshall and left superior intercostal vein. Finally, the left horn of the sinus venosus and the left common cardinal vein become the coronary sinus, draining the cardiac veins into the RA.

IVC and hepatic veins

The hepatic veins develop during the fourth and fifth weeks of gestation from the confluence of the left and right omphalomesenteric veins, a network of sinusoids which evolves from and between the vitelline veins then lateralizes to join the RA via the right horn of the sinus venosus. The development of the IVC is a complex process involving multiple embryologic venous systems that contribute to different IVC segments. Between the sixth and eighth weeks of gestation, the subcardinal veins develop medially to the posterior cardinal veins, connections form between the posterior cardinal veins and the subcardinal veins (forming the subcardinal sinus), and the posterior cardinal veins regress so that the blood from the posterior part of the embryo now returns to the heart via the subcardinal veins.

As the caudal segment of the posterior cardinal veins regresses, anastomoses between the right and left subcardinal veins develop, the left subcardinal vein regresses, and the right subcardinal system becomes the suprarenal segment of the IVC. The increased volume of blood flow through the subcardinal veins stimulates the development of an unpaired venous channel that becomes the hepatic segment of the IVC and connects the subcardinal sinus to the hepatic veins and the ductus venosus as they drain to the RA [23]. As this is happening, another paired venous system (the supracardinal veins) forms dorsally to the subcardinal sinus. These veins connect the subcardinal veins to the distal cranial segment of the posterior cardinal vein and to the iliac veins. Thus, the right supracardinal vein becomes the infrarenal segment of the IVC and the azygos vein, and the left supracardinal vein becomes the hemiazygos vein.

Superior vena caval anomalies

The right SVC receives blood from the upper half of the body via the two brachiocephalic or innominate veins. It also receives the azygos vein and several small veins from the pericardium and other mediastinal structures.

Left SVC to the coronary sinus (bilateral SVC)

A persistent left SVC is the most common systemic venous anomaly. It occurs in 20% of patients with tetralogy of Fallot and 8% of those with Eisenmenger syndrome [24]. A persistent left SVC drains into the RA via the CS in 92% of cases (Figure 10.1a). In the remaining 8% of cases, it drains into the LA either directly because of absence or unroofing of the CS (Figure 10.1c) or via a left pulmonary vein (partially persistent left SVC) [25,26].

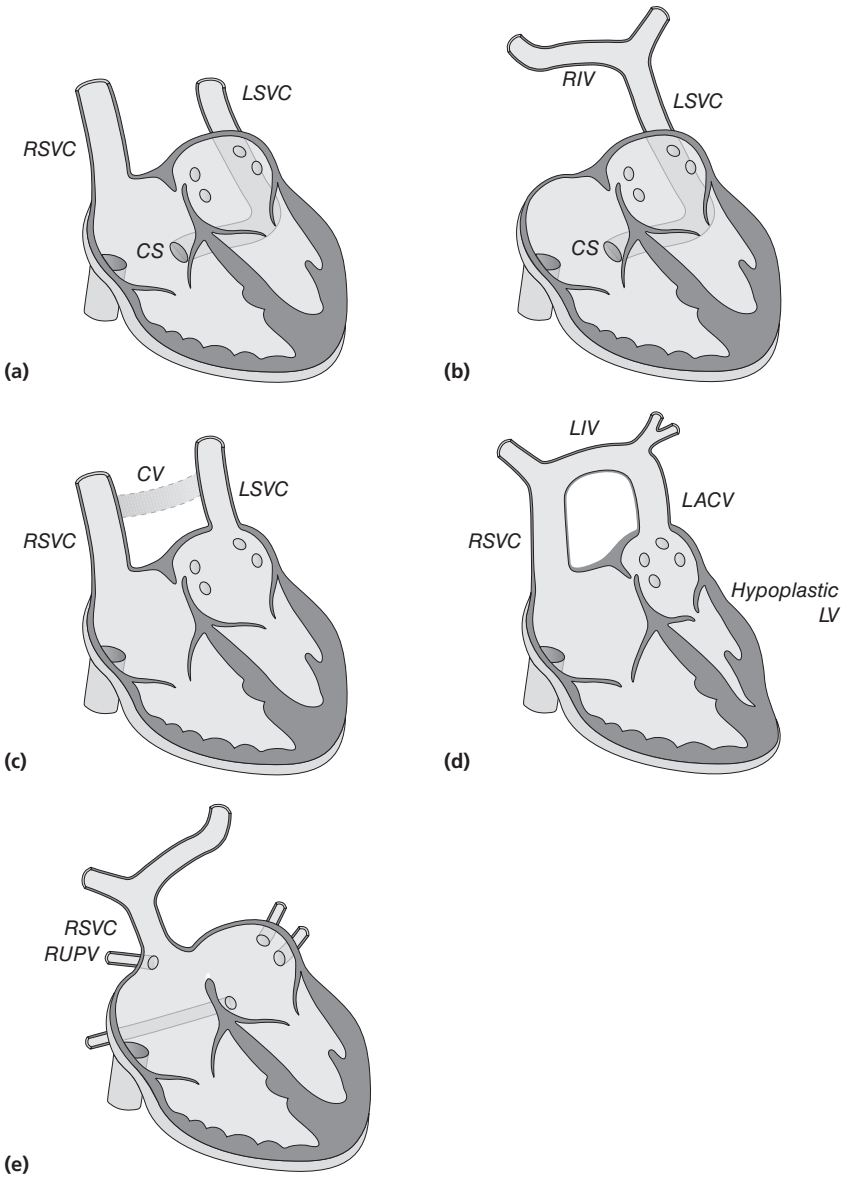


Figure 10.1 Anomalies of the superior vena cava: **(a)** persistent left superior vena cava draining into a dilated coronary sinus without a connecting vein between the bilateral superior venae cavae; **(b)** atretic right superior vena cava with a persistent left superior vena cava draining into a dilated coronary sinus; **(c)** left superior vena cava draining directly into the left atrium, occasionally with a connecting vein between the bilateral superior venae cavae; **(d)** hypoplastic left heart syndrome with a restrictive patent foramen ovale and a levoatrial cardinal vein connecting from the left atrium into the left innominate vein; **(e)** biatrial connection of the right superior vena cava in a sinus venosus defect with partially anomalous drainage of the right upper pulmonary vein into the right atrium. CS, coronary sinus; CV, connecting vein; LACV, levoatrial cardinal vein; LIV, left innominate vein; LSVC, left superior vena cava; LV, left ventricle; RIV, right innominate vein; RSVC, right superior vena cava; RUPV, right upper pulmonary vein.

Embryologically, this anomaly results from failure of regression of the left anterior cardinal and left common cardinal veins. If a connection forms between the right and left anterior cardinal veins, it can persist as a connecting vein, as seen in 60% of cases with bilateral SVCs [18]. In general, the size of the connecting vein is inversely proportional to the size of the persistent left SVC [17,18]. A persistent left SVC normally courses anteriorly to the left pulmonary artery and aortic arch, between the LA appendage and left pulmonary veins, and into the CS as it traverses the left atrioventricular groove. Occasionally, it courses behind the left pulmonary artery with potential for obstruction as it passes between the left pulmonary artery and the left bronchus, an area that has been referred to as the "anatomic vise."

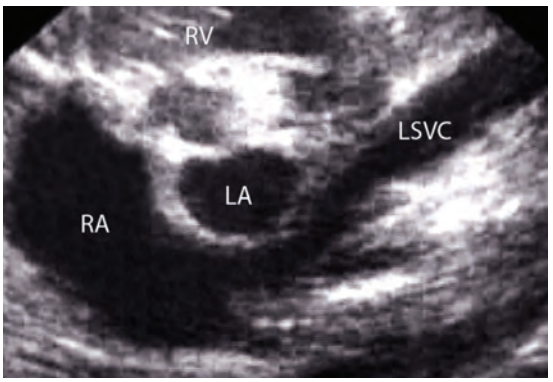


Figure 10.2 High left parasagittal view of a persistent left superior vena cava draining via a dilated coronary sinus into the right atrium. LA, left atrium; LSVC, left superior vena cava; RA, right atrium; RV, right ventricle.

Pathophysiology and clinical significance

In bilateral SVCs with the left SVC to an intact CS, all the systemic venous return still drains into the RA so there is no hemodynamic significance. From a practical standpoint, identification of bilateral SVCs prior to surgical intervention can have significant impact on the cannulation approach during initiation of cardiopulmonary bypass support [27]. In addition, identification of a well-developed connecting vein can allow for surgical ligation of the left SVC in the operating room if necessary. The accidental insertion of a percutaneous venovenous cannula into a persistent left SVC has also been reported in a patient undergoing liver transplantation, resulting in a left hemothorax, systemic hypertension, and performance of the procedure without venovenous bypass [28]. In patients with a functionally single ventricle, staged surgical intervention involves a bidirectional superior cavopulmonary anastomosis (bidirectional Glenn procedure). Bilateral SVCs without a connecting vein may require bilateral bidirectional superior cavopulmonary anastomoses or, occasionally, surgical ligation of the left SVC [29]. Failure to identify the persistent left SVC would ultimately result in a persistent right-to-left shunt and decreased oxygen saturation.

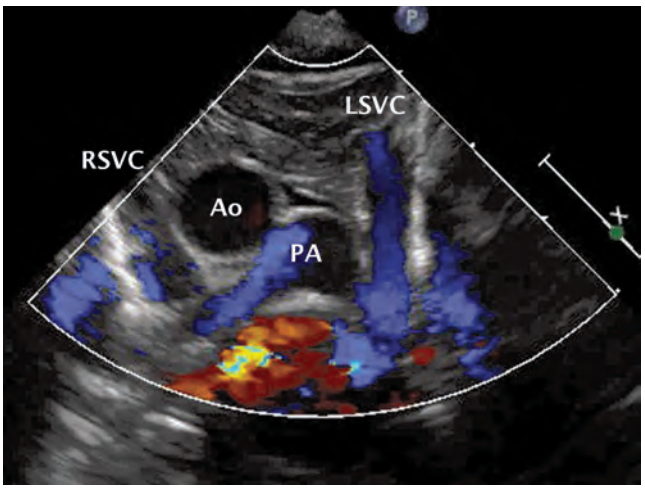


Figure 10.3 Suprasternal short-axis (transverse) view of bilateral superior venae cavae without a connecting vein. Ao, aorta; LSVC, left superior vena cava; PA, pulmonary artery; RSVC, right superior vena cava.

Imaging

The persistent left SVC can be detected by echocardiography with a sensitivity of 95–100% [3]. A high left parasagittal view in a nearly vertical orientation can delineate most of the left SVC and its continuity with the CS (Figure 10.2; Video 10.1). A suprasternal short-axis (transverse) view can display both SVCs and their relationship to the ascending aorta (Figure 10.3; Video 10.2). In addition, a connecting vein, if present, can usually be visualized in this view, particularly with the use of low-scale color mapping. Color mapping sweeps in a subcostal short-axis (sagittal) view can also show the supero-inferior flow from both SVCs into the heart. A persistent left SVC is the most common cause of a dilated CS, which can be seen during the posterior-to-anterior sweep of a subcostal long-axis view, during the posterior sweep of an apical 4-chamber view (Figure 10.4; Video 10.3), and in the posterior atrioventricular groove in a

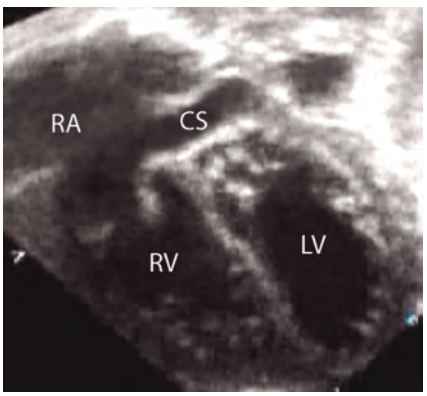


Figure 10.4 Posterior sweep in an apical 4-chamber view reveals a dilated coronary sinus. CS, coronary sinus; LV, left ventricle; RA, right atrium; RV, right ventricle.

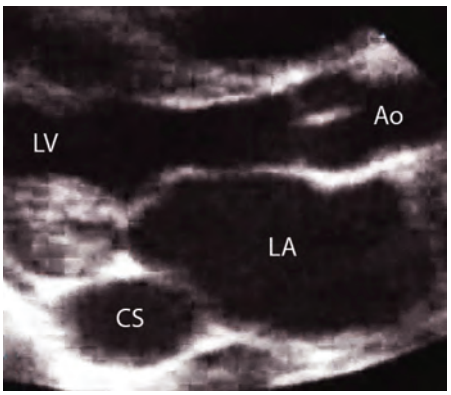


Figure 10.5 Parasternal long-axis view of a dilated coronary sinus in cross-section as it traverses along the posterior left atrioventricular groove. Ao, aorta; CS, coronary sinus; LA, left atrium; LV, left ventricle.

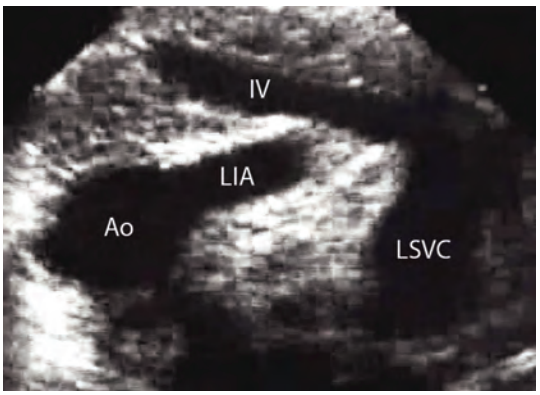


Figure 10.6 Suprasternal short-axis (transverse) view of an atretic right superior vena cava with drainage of the right innominate vein via the left superior vena cava and coronary sinus into the right atrium; the patient also has a right aortic arch whose first branch is the left innominate artery. Ao, aorta; IV, innominate vein; LIA, left innominate artery; LSVC, left superior vena cava.

parasternal long-axis image [30] (Figure 10.5; Video 10.4). If the left SVC cannot be delineated easily by imaging and/or color mapping, saline contrast injection into the left arm will result in the presence of contrast in the dilated CS before its presence in the RA. Prenatal diagnosis of a persistent left SVC usually involves a dilated CS as seen during the posterior sweep in 4-chamber views and in the long-axis view of the left ventricle in the area of the left atrioventricular groove [31]. The persistent left SVC itself can be identified in cross-section as an additional vessel to the left of the pulmonary artery on a prenatal 3-vessel view [32], and its long axis can be seen with leftward sagittal sweeps of the heart.

Left SVC to the coronary sinus with an atretic right SVC

Rarely a persistent left SVC occurs without a right SVC because of regression of the right anterior cardinal vein [33,34], and this has been associated with an increased incidence of arrhythmias such as sinus node dysfunction, Wolff-Parkinson-White syndrome, third-degree atrioventricular block, atrioventricular nodal reentrant tachycardia, and atrial fibrillation [35].

In this anomaly, the right-sided head and neck vessels drain via the right innominate vein into the left SVC, which in turn drains via a dilated CS into the RA (Figure 10.1b). Echocardiographic imaging reveals absence of a right SVC connecting to the RA in the subcostal short-axis view. The dilated CS and the left SVC are then visualized with the same techniques described earlier. The suprasternal short-axis (transverse) view can also display the left SVC and absent right SVC (Figure 10.6; Video 10.5).

Left SVC to the left atrium

A persistent left SVC drains directly into the LA in 8% of patients (Figure 10.7; Video 10.6) [25]. The vessel runs anteriorly to the left pulmonary artery and connects directly to the LA between the left upper pulmonary vein and the LA appendage [36,37]. It has been suggested that this anomaly results from failure of the invagination between the left sinus horn and the LA (with consequent failure of development of the CS) and from

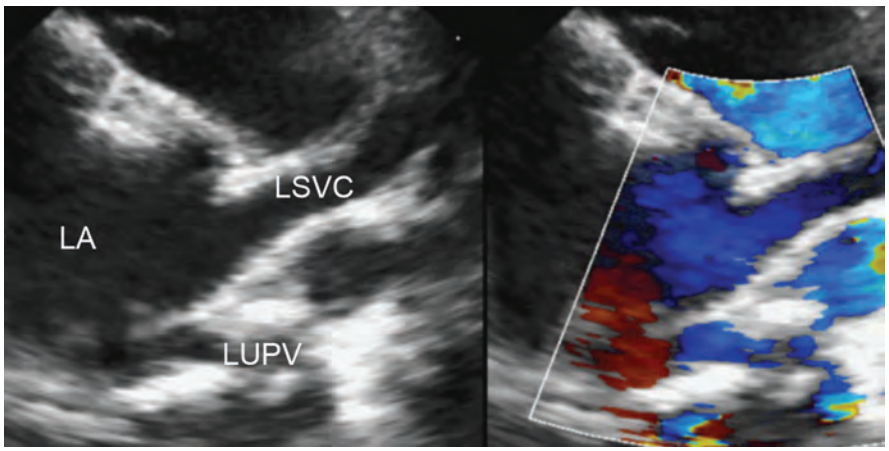


Figure 10.7 Modified high left parasagittal view without and with color depicting a left superior vena cava draining directly into the left atrium. LA, left atrium; LSVC, left superior vena cava; LUPV, left upper pulmonary vein.

persistence of the left anterior cardinal vein (Raghib anomaly) [38]. Another theory suggests that the anomaly results from extensive unroofing of the CS [39,40]. Nevertheless, the most common scenario involving direct connection of a left SVC to the LA is in isomeric right or left atrial appendages with drainage of bilateral SVCs into both sides of the atrial mass. The CS is usually absent with abnormal situs, so an embryologic explanation may not be relevant.

Pathophysiology and clinical significance

When there is no connecting vein between the bilateral SVCs and no interatrial communication, patients with a left SVC to the LA will present early in infancy with decreased oxygen saturation and usually no cardiac murmur. If there is a connecting vein between the bilateral SVCs and a small or absent interatrial communication, however, the left SVC and connecting vein decompress the LA blood into the right SVC and RA (which has a lower pressure than the LA). Color mapping will reveal retrograde (cephalad) flow along the left SVC (Figure 10.8; Video 10.7). Hemodynamically, this anomaly represents a left-to-right shunt similar to an atrial septal defect or partial anomalous pulmonary venous return and can cause right ventricular volume overload. Surgical repair of this anomaly is often indicated. If there is a connecting vein or if the upper venous pressure is less than 15 mmHg with test occlusion of the left SVC, surgical treatment involves ligation of the left SVC [29]. Alternatively, the left SVC can be reimplanted into the RA or the pulmonary artery [41,42]. More recently, the preferred surgical approach involves creation of an intra-atrial baffle to direct the flow from the left SVC across a surgically created atrial septal defect into the RA [43]. A persistent left SVC to the LA can cause cyanosis after a Fontan procedure, and interventional catheterization with coil occlusion of the vein can be beneficial and preclude the need for another operation.

Imaging

The diagnosis of a persistent left SVC with direct connection to the LA can be made by echocardiography using the same high left parasagittal and suprasternal short-axis views discussed previously. In the absence of a connecting vein between the bilateral SVCs, there is obligate flow from the left SVC into the LA, and color mapping will reveal antegrade flow along the left SVC. Saline contrast injection into the left arm will result in the appearance of contrast in the LA. Radionuclide studies can also be used to detect the early appearance of systemic venous blood in the LA [44,45]. More recently, computed tomography and magnetic resonance angiography have been used to delineate the abnormal vasculature.

Levoatrial cardinal vein

The levoatrial cardinal vein is an embryologic connection between the capillary plexus of the embryonic foregut (the origin of the pulmonary veins) and the cardinal venous system. Elevated LA pressures in the setting of LA outlet obstruction early in gestation may result in persistence of the levoatrial cardinal vein in order to decompress the LA into the left innominate vein or right SVC (Figure 10.1d) [46].

Pathophysiology and clinical significance

LA outlet obstruction occurs with mitral stenosis or atresia (with or without hypoplastic left heart syndrome) and an intact atrial septum or restrictive atrial septal defect (Figure 10.9; Video 10.8). Decompression of the LA via a levoatrial cardinal vein allows for drainage of oxygenated pulmonary venous return into the right heart. Unlike the course of a persistent left SVC, a levoatrial cardinal vein usually courses behind the left pulmonary artery and in front of the left bronchus, the "anatomic vise" which can cause compression or obstruction of the vessel as it traverses the area.

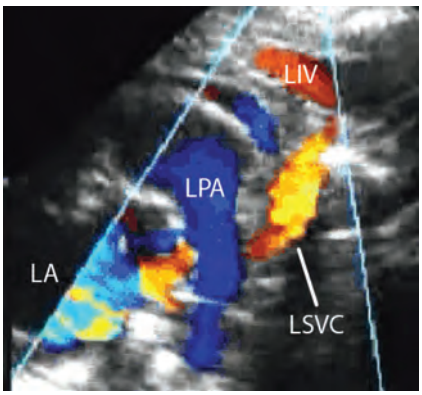


Figure 10.8 Suprasternal short-axis (transverse) view with color mapping of a left superior vena cava connecting directly to the left atrium; in the setting of a connecting (left innominate) vein between the bilateral superior venae cavae, there is retrograde flow along the left superior vena cava from the left atrium. LA, left atrium; LIV, left innominate vein or connecting vein between the bilateral superior venae cavae; LPA, left pulmonary artery; LSVC, left superior vena cava.

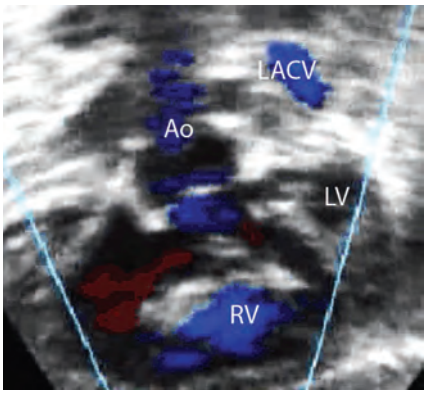


Figure 10.9 Subcostal short-axis (sagittal) view with color mapping of a levoatrial cardinal vein in a patient with small restrictive atrial septal defects, mitral atresia, left ventricular hypoplasia, ventricular septal defect, and double outlet right ventricle; the flow in the levoatrial cardinal vein is away from the heart into the left innominate vein. Ao, aorta; LACV, levoatrial cardinal vein; LV, left ventricle; RV, right ventricle.

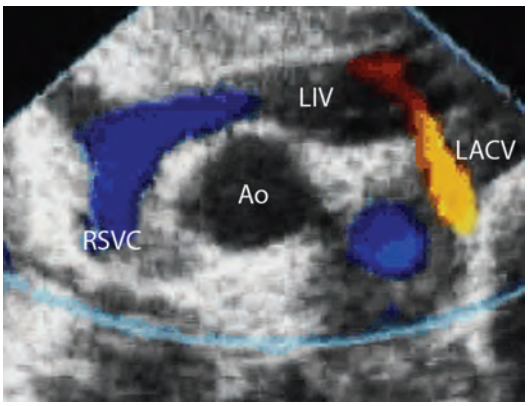


Figure 10.10 Suprasternal short-axis (transverse) view with color mapping of a levoatrial cardinal vein in a patient with small restrictive atrial septal defects, mitral atresia, left ventricular hypoplasia, ventricular septal defect, and double outlet right ventricle; the flow in the levoatrial cardinal vein is away from the heart into the left innominate vein. Ao, aorta; LACV, levoatrial cardinal vein; LIV, left innominate vein; RSVC, right superior vena cava.

Imaging

When LA outlet obstruction is seen in the subcostal long-axis sweep, a levoatrial cardinal vein appears as an abnormal vessel draining superiorly into the thorax away from the heart. Suprasternal short-axis views can show the retrograde flow within the decompressing vessel from the LA or left pulmonary vein into the left innominate vein or right SVC (Figure 10.10; Video 10.9).

Right SVC to the left atrium or to both atria

Direct connection of the right SVC to the LA is a rare anomaly and has been attributed to leftward and superior displacement of right sinus horn [47–49]. The development of a superior sinus venosus defect has also been attributed to this embryologic event, and connection of the right SVC to both atria (Figure 10.1e) is a hallmark finding of a superior sinus venosus defect, suggesting that both anomalies are variants of the same lesion. More recent reports suggest that both lesions result from unroofing of the right pulmonary veins at or above the junction between the right SVC and the RA [50]. In other words, the usual partition between the posterior aspect of the right SVC and the anterior aspect of the right pulmonary veins is absent. Hemodynamically, decreased oxygen saturation results from direct connection to the LA, and right ventricular volume overload results from biatrial connection. By echocardiography, the relationship of the right SVC to both atria is best delineated from the subcostal short-axis (sagittal) view (Figure 10.11; Video 10.10) or the right sternal border long-axis view (Figure 10.12; Video 10.11).

Other SVC anomalies

Congenital SVC obstruction in isolation is extremely rare. Occasionally, SVC obstruction can result from compression by a tumor or from thrombus formation. In the setting of congenital heart disease, postoperative SVC obstruction can occur after an atrial switch procedure for transposition of the great arteries and after repair of a sinus venosus defect with partially anomalous return of the right upper pulmonary vein. It can

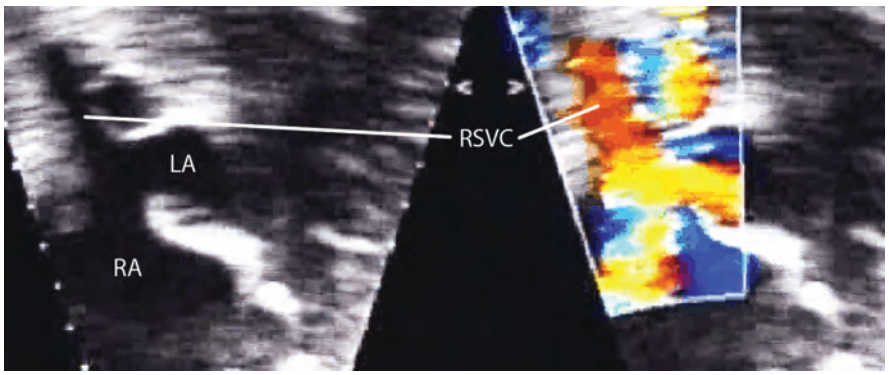


Figure 10.11 Subcostal short-axis (sagittal) view with color mapping of a right superior vena cava with biatrial connection. LA, left atrium; RA, right atrium; RSVC, right superior vena cava.

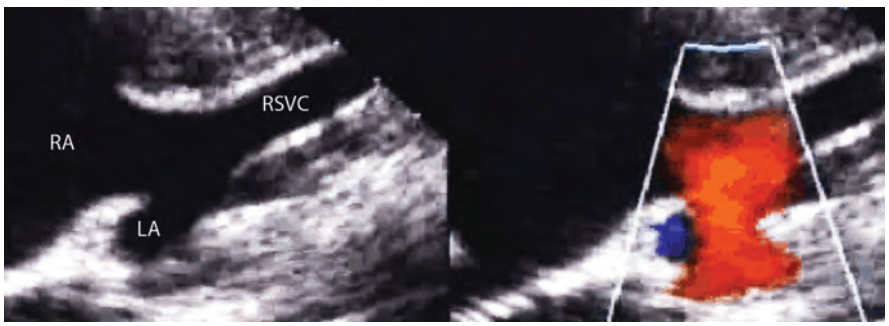


Figure 10.12 Right sternal border long-axis view with color mapping of a right superior vena cava with biatrial connection. LA, left atrium; RA, right atrium; RSVC, right superior vena cava.

also occur after orthotopic heart transplantation with bicaval anastomoses. Management of SVC obstruction can involve balloon dilation during cardiac catheterization [51] or surgical revision. Echocardiographic diagnosis of SVC obstruction usually involves subcostal, right sternal border, and suprasternal imaging and color mapping, though occasionally a transesophageal echocardiogram is necessary since prior surgery often results in poor transthoracic echocardiographic windows. Doppler interrogation of SVC flow can estimate the gradient across the obstruction.

Complete absence of both right and left SVCs has been reported in a patient with tetralogy of Fallot, wherein bilateral jugular and subclavian veins drain into dorsally located vessels joining above the diaphragm behind the heart, course caudally along the left side of the spine, cross to the right side at the level of the left kidney, and drain anteriorly into the IVC and RA [52]. The authors postulate that failure of the development of the anterior cardinal system has resulted in persistence of the supracardinal veins as a means of decompressing the upper half of the body into the heart.

Inferior vena caval anomalies

There is wide variation in the arrangement of the inferior systemic veins below the level of the renal veins. However, the progressively anterior location of the ascending IVC as it receives the hepatic veins and connects to the RA is fairly constant and can be seen in at least 97% of the general population [3]. In heterotaxy syndrome, the spatial relationship between the IVC and descending aorta may be abnormal [53], and echocardiography can usually delineate this relationship [5], especially with subcostal views [7] (Figure 10.13).

The common azygos trunk is formed from paravertebral drainage of the right ascending lumbar vein, subcostal vein, and lumbar azygos vein if present; ascends along the rightward posterior aspect of the mediastinum to the level of the fourth thoracic vertebra; arches anteriorly at this level above the root of the right lung; and drains into the SVC just before it pierces the pericardium. The azygos vein is joined by the right superior intercostal vein at its junction with the SVC, representing the confluence of the second, third, and fourth posterior intercostal veins. In contrast, the hemiazygos vein drains the left renal vein, lumbar azygos, lumbar veins, and the lower three posterior intercostal veins; ascends along the left side of the vertebrae (similar to the azygos vein); crosses the midline across the anterior surface of the eighth vertebral body; and connects to the azygos vein on the right at this level.

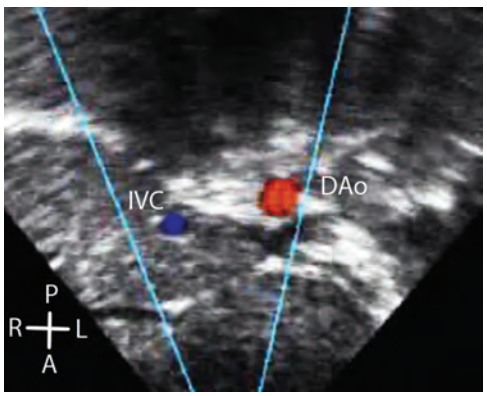


Figure 10.13 Subcostal long-axis (transverse) view with color mapping displaying the spatial relationship between the inferior vena cava and the descending aorta just below the level of the diaphragm; the inferior vena cava is rightward and anterior in location with respect to the descending aorta. A, anterior; Dao, descending aorta; IVC, inferior vena cava; L, left; P, posterior; R, right.

Interrupted IVC with azygos/hemiazygos continuation

Interrupted IVC with azygos continuation (also known as absent hepatic segment of the IVC with azygos continuation) (Figure 10.14a) occurs in up to 84% of patients with left isomerism or polysplenia syndrome [54], but it may also occur in patients with situs solitus [3] and rarely in patients with right isomerism or asplenia syndrome [55]. It has a prevalence of approximately 0.6% among patients with congenital heart disease [56] and less than 0.3% among those without other heart defects [15,16]. Embryologically, failure of the right subcardinal vein to connect to the right vitelline and right hepatocardiac veins results in absence of the hepatic segment of the IVC. The right supracardinal vein enlarges and ultimately becomes the azygos continuation to the right SVC. If there is a left SVC and no right SVC, the left supracardinal vein enlarges to become the hemiazygos continuation of an interrupted IVC. In either arrangement, the hepatic veins maintain their connection to the floor of the atrial mass [3,57,58]. One unusual case report describes an interrupted IVC with continuation to an accessory hemiazygos vein, to the superior intercostal vein, and ultimately to the brachiocephalic vein [59].

Pathophysiology and clinical significance

Because an interrupted IVC is usually seen in the setting of heterotaxy syndrome, its hemodynamic significance is usually determined by the associated intracardiac anomalies. It is important to diagnose azygos continuation of the IVC by echocardiography because cardiac catheterization and intraoperative venous cannulation may be difficult in these patients [27,60,61]. In addition, patients with left isomerism and an interrupted IVC are at increased risk for complete heart block [62], and emergency placement of a pacemaker can be difficult to place via an azygos vein. In patients with single ventricle circulation, the timing for staged palliation is affected by an interrupted IVC since a bidirectional superior cavopulmonary anastomosis will result in connection of the entire systemic venous system except for the hepatic veins to the pulmonary arteries (Kawashima procedure) [63].

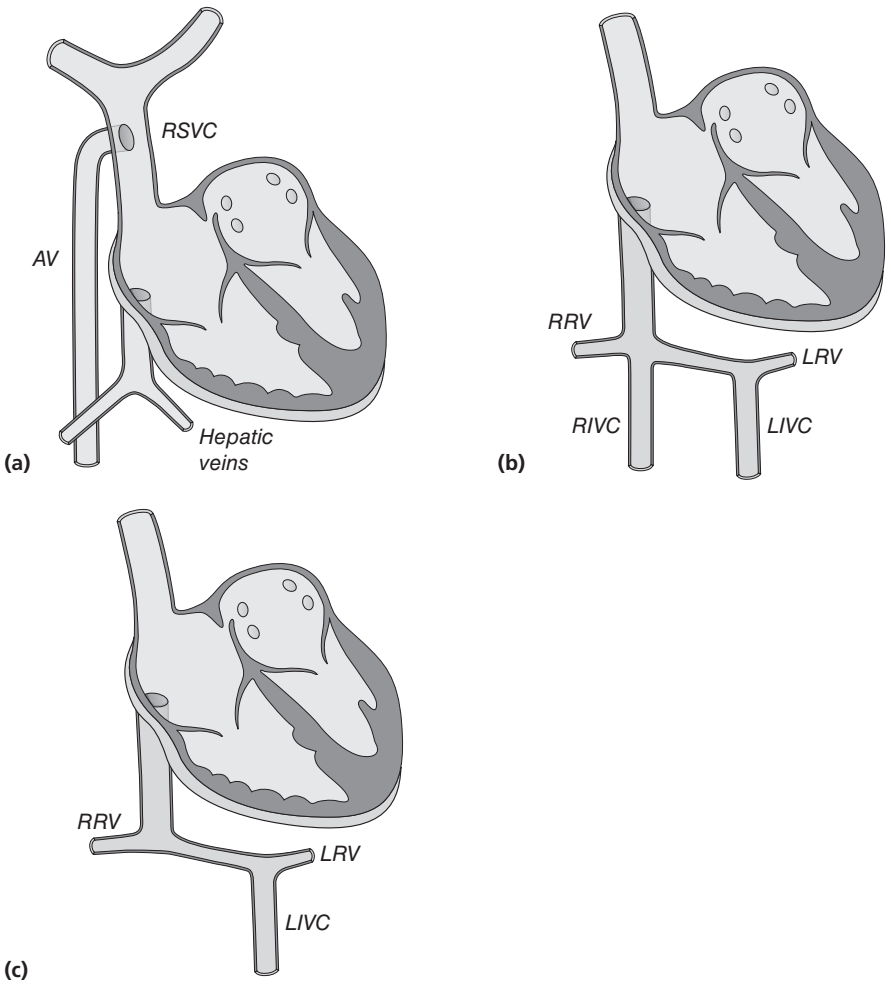


Figure 10.14 Anomalies of the inferior vena cava: **(a)** interrupted inferior vena cava with azygos continuation to the right superior vena cava; **(b)** bilateral inferior venae cavae which converge into a common right-sided inferior vena cava at the level of the renal veins; **(c)** left inferior vena cava connecting to the right inferior vena cava at the level of the renal veins with an atretic subrenal segment of the right inferior vena cava. AV, azygos vein; LIVC, left inferior vena cava; LRV, left renal vein; RIVC, right inferior vena cava; RRV, right renal vein; RSVC, right superior vena cava.

Imaging

Subcostal short-axis (sagittal) and long-axis (transverse) views with posterior angulation usually demonstrate hepatic venous drainage to the RA without IVC connection to the RA. Subcostal short-axis (sagittal) views are especially useful in delineating the following anatomic features:

- The length of the IVC from the level of the kidneys to its junction with the RA to avoid erroneously identifying a prominent hepatic vein as the IVC;
- A prominent azygos vein coursing parallel to and along the rightward and posterior aspect of the descending aorta (a prominent hemiazygos vein courses along the leftward and posterior aspect of the descending aorta);
- Opposite direction of flow in the azygos or hemiazygos vein and the descending aorta by color mapping (Figure 10.15; Video 10.12).

Right sternal border long-axis (parasagittal) and the suprasternal long-axis views can also demonstrate the arch of the azygos vein as it connects to the posterior aspect of the right SVC (Figure 10.16; Video 10.13). Fetal echocardiography usually reveals absence of the full length of the IVC during

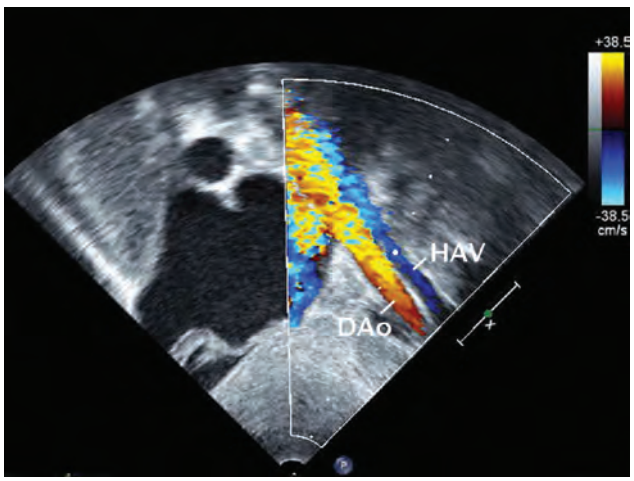


Figure 10.15 Subcostal short-axis (sagittal) view with color mapping of an interrupted inferior vena cava with hemiazygos continuation into the left superior vena cava; the hemiazygos vein is parallel and posterior to the descending aorta. Dao, descending aorta; HAV, hemiazygos vein.

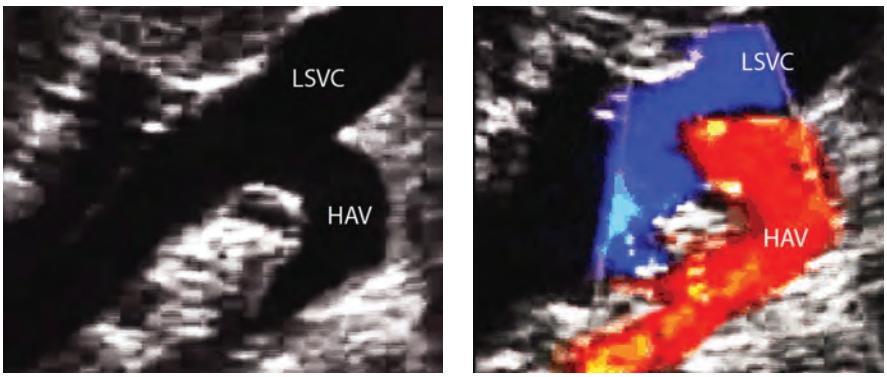


Figure 10.16 Modified high left parasagittal view **(a)** without and **(b)** with color mapping of an interrupted inferior vena cava with hemiazygos continuation into the left superior vena cava. HAV, hemiazygos vein; LSVC, left superior vena cava.

sagittal sweeps of the fetal chest and abdomen. Identification of the prominent azygos vein behind and to the right of the descending aorta is often the first clue to an interrupted IVC in utero [31].

Bilateral IVCs (duplication of the IVC)

Because the hepatic segment of the IVC is unpaired, complete bilateral IVCs do not exist. However, duplication of certain segments of the IVC is seen in 0.2–0.3% of the general population [64]. This results from persistence of both supracardinal veins, which is rare and can occur in patients with and without abnormal situs [65]. In these cases, the left IVC ends at the level of the renal veins, crosses in front of the descending aorta, and joins the right IVC at the level of the kidneys (Figure 10.14b). Connection of bilateral IVCs may occur at other levels, and the practical significance of this rare anomaly depends on exactly where the two IVCs join (Figure 10.17). Echocardiographic diagnosis of this defect is extremely difficult.

Left IVC to the right atrium (absent right IVC)

A left IVC connecting to the RA is a rare anomaly that occurs in 0.2–0.5% of the general population [64]. It results from regression of the right supracardinal vein and persistence of the left supracardinal vein. In this arrangement, the hepatic segment of the right IVC (including the hepatic veins) maintains its connection to the RA. The caudally located left IVC can cross in front of the descending aorta at or above the level of the renal veins before connecting to the right IVC (Figure 10.14c) or it can drain into a prominent hemiazygos vein. Subcostal long-axis (transverse) imaging and color mapping sweeps (at a low color mapping scale) can sometimes display the left IVC as it crosses the midline in front of the descending aorta before connecting with the hepatic segment of the right IVC (Figure 10.18; Video 10.14).



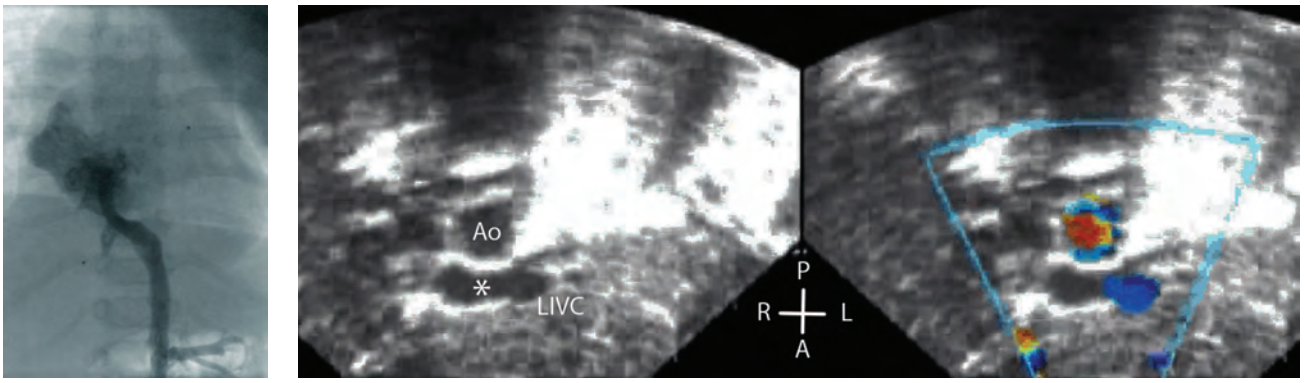
Figure 10.17 Magnetic resonance angiogram of bilateral inferior venae cavae (stars) converging into a common inferior vena cava just below the diaphragm. Source: Dr. Tal Geva from Children's Hospital Boston, MA, USA. Reproduced with permission of Dr. Geva.

Right IVC to the left atrium

There have been few reports of anomalous drainage of the IVC into the LA with an intact atrial septum [66–68]. Some have suggested that these cases are related to persistence of the embryonic valves of the sinus venosus in the setting of an atrial septal defect [69] or to errors in pathologic description [23]. A complete embryologic explanation for direct connection of an IVC to the LA is not currently available. Preoperative diagnosis of these lesions is especially important to prevent iatrogenic diversion of IVC flow to the LA during surgical closure of an atrial septal defect [70]. In the absence of an interatrial communication, these patients have an obligatory right-to-left shunt and therefore have lower oxygen saturation. In the presence of an interatrial communication, biatrial connection of the IVC may be a result of an inferior secundum atrial septal defect that is confluent with the IVC or an inferior sinus venosus defect. Echocardiographic evaluation involves careful color mapping of IVC flow in subcostal and right sternal border views (Figure 10.19; Video 10.15). Saline contrast injection into a lower extremity systemic vein can confirm the diagnosis with the immediate appearance of contrast in the LA.

Hepatic vein anomalies

Normal hepatic venous drainage occurs from both hepatic lobes directly into the IVC, and abnormal drainage can involve some



(a) (b)

Figure 10.18 **(a)** Angiogram of a left inferior vena cava which crosses the midline just below the diaphragm before draining into the right atrium; **(b)** subcostal long-axis (transverse) view with color mapping of a left inferior vena cava at the level where it crosses in front of the descending aorta (star) before draining into the right atrium. A, anterior; Ao, aorta; L, left; LIVC, left inferior vena cava; P, posterior; R, right.

or all of the hepatic veins. Anomalous hepatic venous connection directly to the heart occurs in up to 28% of patients with right isomerism or asplenia syndrome [13], although it may also occur in situs solitus or situs inversus [3,71,72]. Anomalous hepatic venous connection to the atrial mass via a single trunk also occurs in left isomerism. In left isomerism or polysplenia syndrome, two or more separate hepatic venous connections are often seen in association with an interrupted IVC. Recognition of anomalous hepatic venous drainage in patients with single ventricle circulation and in patients undergoing liver transplantation is critical in determining the appropriate surgical intervention. For example, failure to identify a separate accessory hepatic vein prior to a Fontan procedure can result in the inadvertent exclusion of this vessel with decompression from the Fontan pathway via the accessory hepatic vein into the atrial mass; this, in turn, results in significant progressive cyanosis after the operation [73,74]. Lastly, some or all of the hepatic veins can drain anomalously into the CS, resulting in a dilated CS as discussed later [75]. Echocardiographic evaluation of the IVC and hepatic veins should be performed during the posterior sweep in subcostal long-axis (transverse), apical, parasternal, and even suprasternal views (Figure 10.20; Video 10.16).

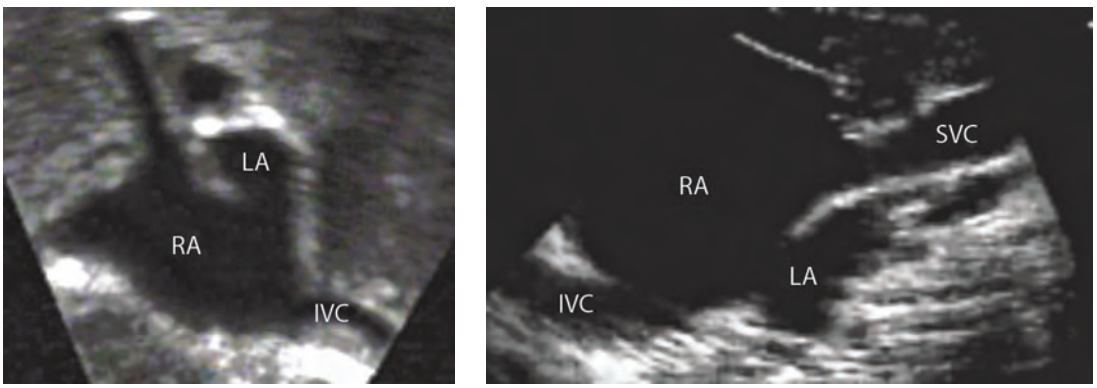
Coronary sinus anomalies

Although the CS drains into the RA, some consider it a structure associated with the LA since it courses along the posterior aspect of the left atrioventricular groove, accounting for its absence in right isomerism. It represents the left horn of the sinus venosus after leftward invagination of the junction between the left sinus horn and the common atrium. Aside from a dilated CS, other anomalies of the CS are rare [76].

Dilated coronary sinus

The CS becomes dilated as a result of abnormally increased flow or pressure. Some causes of the increased flow in the CS include:

- Persistent left SVC to the CS
- Coronary sino-septal defect (partial or complete unroofing of the CS)



(a) (b)

Figure 10.19 Biatrial connection of an inferior vena cava secondary to an atrial septal defect which is confluent with the inferior vena cava in **(a)** a subcostal short-axis (sagittal) view, and **(b)** a right sternal border long-axis view. IVC, inferior vena cava; LA, left atrium; RA, right atrium; SVC, superior vena cava.

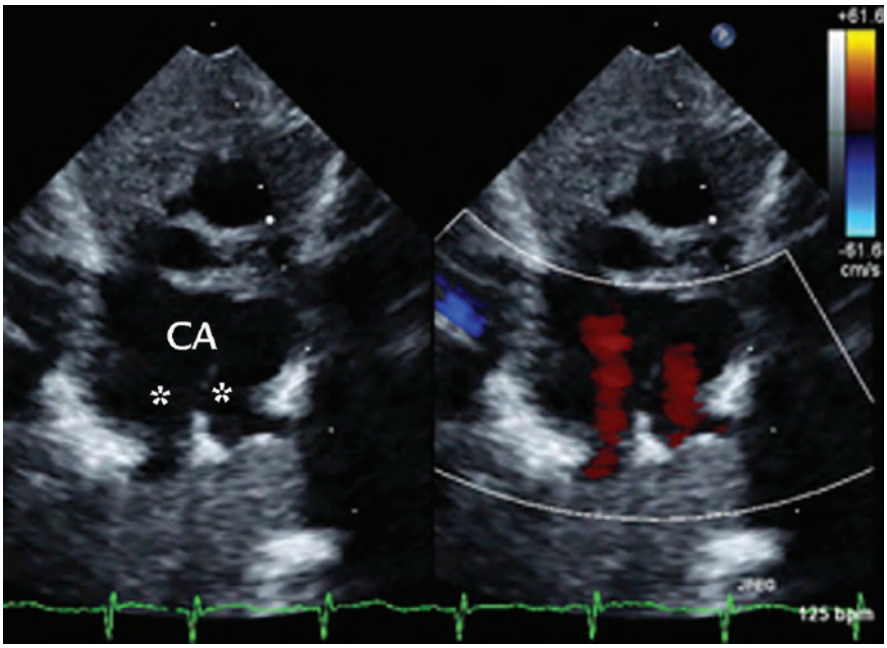


Figure 10.20 Suprasternal short-axis view of separate hepatic venous connections (stars) to the common atrium of a patient with heterotaxy syndrome. CA, common atrium.

- Partially or totally anomalous pulmonary venous drainage into the CS
- Partially or totally anomalous hepatic venous drainage into the CS [75].

Increased pressure in the CS results primarily from RA hypertension, particularly in the setting of the classic Fontan procedure involving direct anastomosis of the RA appendage to the pulmonary artery.

As discussed previously, a dilated CS can be seen by echocardiography during the posterior-to-anterior sweep of a subcostal long-axis view, during the posterior sweep of an apical 4-chamber view (Figure 10.4; Video 10.3) and along the posterior atrioventricular groove in a parasternal long-axis image [30] (Figure 10.5; Video 10.4). When a dilated CS is seen, a systematic approach should include evaluation of the left innominate vein, the individual pulmonary veins, the hepatic veins, and the roof of the CS. It is especially important to evaluate the CS with views wherein the roof is perpendicular to the ultrasound beam; these include the posterior sweep of an apical view as well as a high left parasagittal view with the probe in a nearly vertical orientation. A coronary sino-septal defect (partial or complete unroofing of the CS) is often associated with a left SVC, is located along the superior aspect of the CS as it passes behind the LA, can present like a left SVC to the LA, and may or may not be associated with an additional interatrial communication. Saline contrast injection into the left arm may result in the appearance of contrast in the LA.

Coronary sinus ostium atresia or stenosis

Atresia or stenosis of the CS ostium is extremely rare, and the obstruction is thought to result from a prominent Thebesian valve. Decompression of coronary venous blood usually occurs via a persistent left SVC, although occasionally decompression occurs via a prominent Thebesian vein, a coronary sino-septal defect, or a connection with the IVC [69]. In these instances, the anomaly has no hemodynamic significance and the clinical course is usually benign. Absence of adequate decompression is generally associated with poor outcome, emphasizing the critical importance of even a small left SVC in these cases. Suprasternal short-axis views with color mapping can demonstrate retrograde flow from the left SVC into the connecting vein in most of these cases. It is important to distinguish this anomaly from the normal drainage of a prominent superior intercostal vein or internal thoracic vein into the left innominate vein in the setting of a small CS. It is especially critical to identify this anomaly prior to surgical intervention because ligation of a left SVC in the setting of CS ostium atresia or stenosis may lead to severe myocardial ischemia or sudden cardiac arrest [77,78].

Other coronary sinus anomalies

Absence of the CS is common in the setting of abnormal atrial situs with isomerism and is distinctly uncommon in the setting of lateralized atrial situs [3]. Rarely the coronary sinus connects to the IVC instead of the RA [79].

Innominate vein anomalies

The normal left innominate vein

- originates from the persistent connection between the anterior cardinal veins after regression of the left anterior cardinal vein;
- represents the systemic venous drainage from the left subclavian and left common jugular veins;
- courses in front of the aortic arch and ascending aorta before draining into the right SVC.

Retroaortic innominate vein

In this rare anomaly, the innominate vein courses behind the ascending aorta and below the aortic arch before draining into the right SVC at a level below the connection of the azygos vein. It occurs in 1% of patients with congenital heart disease [80] and in at most 0.008% of the general population [23]. It is most commonly seen in patients with tetralogy of Fallot or truncus arteriosus and a right aortic arch [80–82]. Embryologically, some have suggested that this anomaly results from failure of development of the usual connection between the anterior cardinal veins and formation of an alternative connection in a different location [82].

Pathophysiology and clinical significance

Although there is no hemodynamic significance to this lesion, it can have an effect during venous cannulation [27] and during a bidirectional superior cavopulmonary anastomosis procedure. When the innominate vein is absent, it usually represents the presence of bilateral SVCs without a connecting vein. However, a retroaortic innominate vein may also occur in this setting.

Imaging

Echocardiographic evaluation involves suprasternal short-axis (transverse) and long-axis (sagittal) views. Suprasternal short-axis (transverse) imaging of a normal left innominate vein reveals its course in front of the ascending aorta, usually just below the origin of the first aortic arch branch. With a retroaortic innominate vein, short-axis sweeps can reveal two separate and parallel vessels (representing the right pulmonary artery and the retroaortic innominate vein) coursing behind the ascending aorta (Figure 10.21; Video 10.17). Occasionally, the right pulmonary artery is small, and the problem may not be recognized if the retroaortic innominate vein is erroneously identified as a normal-sized right pulmonary artery. In long-axis (sagittal) views, two circles are seen below the transverse aortic arch, the superior one representing the cross-section of the retroaortic innominate vein and the inferior one representing the cross-section of the right pulmonary artery (Figure 10.22).

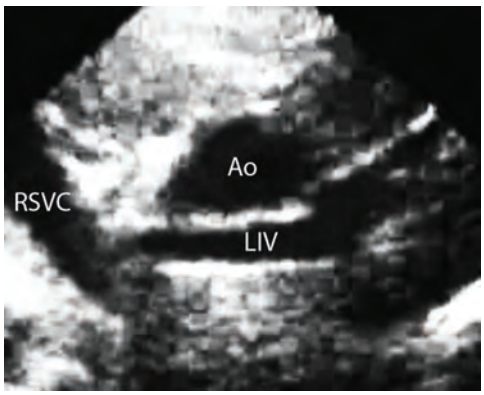


Figure 10.21 Suprasternal short-axis view of a retroaortic innominate vein. Ao, aorta; LIV, left innominate vein; RSVC, right superior vena cava.

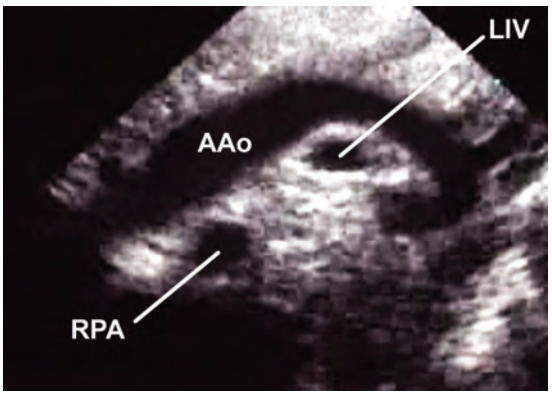


Figure 10.22 Suprasternal long-axis view of a retro-aortic innominate vein as it courses below the aortic arch and above the right pulmonary artery. AAo, ascending aorta; LIV, left innominate vein; RPA, right pulmonary artery.

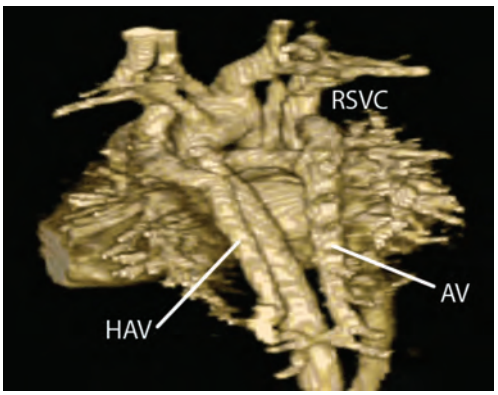


Figure 10.23 Posterior view during magnetic resonance 3D reconstruction of an absent left innominate vein; the left head and neck vessels drain into the hemiazygos vein which, in turn, connects to the azygos vein below the diaphragm with subsequent drainage via the azygos vein into the right superior vena cava. AV, azygos vein; HAV, hemiazygos vein; RSVC, right superior vena cava. Source: Dr. Tal Geva from Children's Hospital Boston, MA, USA. Reproduced with permission of Dr. Geva.

Other innominate vein anomalies

Other extremely rare anomalies of the innominate vein include duplication of the left innominate vein [23] and absent left innominate vein (Figure 10.23; Video 10.18).

Videos

To access the videos for this chapter, please go to www.lai-echo.com.

Video 10.1 High left parasagittal view of persistent left superior vena cava. High left parasagittal view without and with color mapping of a persistent left superior vena cava draining via a dilated coronary sinus into the right atrium.

Video 10.2 Suprasternal short-axis view of bilateral superior venae cavae. Suprasternal short-axis (transverse) view with color mapping of bilateral superior venae cavae without a connecting vein.

Video 10.3 Apical 4-chamber sweep showing a dilated coronary sinus. Posterior sweep in an apical 4-chamber view reveals a dilated coronary sinus along the posterior left atrioventricular groove.

Video 10.4 Parasternal long-axis view of a dilated coronary sinus. Parasternal long-axis view of a dilated coronary sinus in cross-section as it traverses along the posterior left atrioventricular groove.

Video 10.5 Suprasternal short-axis view of a persistent left superior vena cava. Suprasternal short-axis (transverse) view without and with color mapping of an atretic right superior vena cava with drainage of the right innominate vein via the left superior vena cava and coronary sinus into the right atrium; the patient also has a right aortic arch whose first branch is the left innominate artery.

Video 10.6 Modified high left parasagittal view without and with color depicting a left superior vena cava draining directly into the left atrium.

Video 10.7 Suprasternal short-axis view of left superior vena cava to left atrium with retrograde flow. Suprasternal short-axis (transverse) view with color mapping of a left superior vena cava connecting directly to the left atrium; in the setting of a connecting (left innominate) vein between the bilateral superior venae cavae, there is retrograde flow along the left superior vena cava from the left atrium.

Video 10.8 Subcostal short-axis sweep demonstrating a levoatrial cardinal vein. Subcostal short-axis (sagittal) sweep with color mapping in a patient with small restrictive atrial septal defects, mitral atresia, left ventricular hypoplasia, ventricular septal defect, and double outlet right ventricle; the left atrium decompresses into a levoatrial cardinal vein with flow away from the heart into the left innominate vein.

Video 10.9 Suprasternal short-axis view of a levoatrial cardinal vein. Suprasternal short-axis (transverse) view with color mapping of a levoatrial cardinal vein in a patient with small restrictive atrial septal defects, mitral atresia, left ventricular hypoplasia, ventricular septal defect, and double outlet right ventricle; the flow in the levoatrial cardinal vein is away from the heart into the left innominate vein.

Video 10.10 Subcostal short-axis view of a right superior vena cava with biatrial connection. Subcostal short-axis (sagittal) view with color mapping of a right superior vena cava with biatrial connection (superior sinus venosus defect).

Video 10.11 Right sternal border long-axis view of a right superior vena cava with biatrial connection. Right sternal border long-axis view without and with color mapping of a right superior vena cava with biatrial connection (superior sinus venosus defect).

Video 10.12 Subcostal short-axis view of an interrupted inferior vena cava. Subcostal short-axis (sagittal) view with color mapping of an interrupted inferior vena cava with hemiazygos continuation into the left superior vena cava; the hemiazygos vein is parallel and posterior to the descending aorta; there is diastolic reversal of flow in the descending aorta, presumably secondary to a patent ductus arteriosus.

Video 10.13 High left parasagittal view of the hemiazygos vein to left superior vena cava. Modified high left parasagittal view without and with color mapping of an interrupted inferior vena cava depicting the arch of the hemiazygos vein as it connects to the left superior vena cava.

Video 10.14 Subcostal long-axis sweep demonstrating a left inferior vena cava to right atrial connection. Subcostal long-axis (transverse) sweep with color mapping of a left inferior vena cava that crosses in front of the descending aorta before draining into the right atrium.

Video 10.15 Subcostal short-axis sweep of an inferior vena cava with biatrial connection. Subcostal short-axis (sagittal) sweep of an inferior vena cava with biatrial connection (atrial septal defect that is confluent with the inferior vena cava).

Video 10.16 Supasternal short-axis sweep showing separate hepatic venous connections. Suprasternal short-axis color compare sweep showing separate hepatic venous connections to a common atrium and infra-diaphragmatic total anomalous pulmonary venous return in a patient with heterotaxy syndrome.

Video 10.17 Suprasternal short-axis view demonstrating a retroaortic innominate vein. Suprasternal short-axis view with color mapping of a retroaortic innominate vein as it courses inferior of the transverse aortic arch to the right superior vena cava.

Video 10.18 Magnetic resonance 3D reconstruction of an absent left innominate vein. Magnetic resonance 3D reconstruction of an absent left innominate vein; the left head and neck vessels drain into the hemiazygos vein which, in turn, connects to the azygos vein below the diaphragm with subsequent drainage via the azygos vein into the right superior vena cava. Source: Dr. Tal Geva from Children's Hospital Boston, MA, USA. Reproduced with permission of Dr. Geva.

References

1 McClure CFW, Butler EG. The development of the vena cava inferior in man. *Am J Anat* 1925;**35**:331–383.
2 Seib GA. The azygos system of veins in American whites and American negroes, including observations on the inferior caval venous sytem. *Am J Phys Anthropol* 1934;**19**:29.
3 Huhta JC, Smallhorn JF, Macartney FJ, et al. Cross-sectional echocardiographic diagnosis of systemic venous return. *Br Heart J* 1982;**48**:388–403.

4 Foale R, Bourdillon PD, Somerville J, Rickards A. Anomalous systemic venous return: recognition by two-dimensional echocardiography. *Eur Heart J* 1983;**4**:186–195.
5 Slovis TL, Clapp SK, Farooki ZQ. Noninvasive evaluation of the inferior vena cava. The value of sonography. *Am J Dis Child* 1984;**138**:277–280.
6 Tacy TA, Silverman NH. Systemic venous abnormalities: embryologic and echocardiographic considerations. *Echocardiography* 2001;**18**:401–413.
7 Huhta JC, Smallhorn JF, Macartney FJ. Two dimensional echocardiographic diagnosis of situs. *Br Heart J* 1982;**48**:97–108.
8 Ivemark BI. Implications of agenesis of the spleen on the pathogenesis of conotruncus anomalies in childhood; an analysis of the heart malformations in the splenic agenesis syndrome, with fourteen new cases. *Acta Paediatrica* 1955;**44**:7–110.
9 Ongley PA, Titus JL, Khoury GH, et al. Anomalous connection of pulmonary veins to right atrium associated with anomalous inferior vena cava, situs inversus and multiple spleens: a developmental complex. *Mayo Clin Proc* 1965;**40**:609–624.
10 Rastelli GC, Rahimtoola SH, Ongley PA, McGoon DC. Common atrium: anatomy, hemodynamics, and surgery. *J Thorac Cardiovasc Surg* 1968;**55**:834–841.
11 Van Mierop LHS, Gessner JH, Schiebler GL. Asplenia and polysplenia syndromes. *Birth Defects* 1972;**8**:36–44.
12 Krayenbuhl CU, Lincoln JC. Total anomalous systemic venous connection, common atrium, and partial atrioventricular canal. A case report of successful surgical correction. *J Thorac Cardiovasc Surg* 1977;**73**:686–689.
13 Van Praagh S. Cardiac malpositions and the heterotaxy syndromes. In: Keane JF, Lock JE, Fyler DC (eds.) *Nadas' Pediatric Cardiology*. Philadelphia, PA: Saunders Elsevier, 2006, pp. 675–695.
14 Abbott ME. *Atlas of Congenital Cardiac Disease*. New York, NY: AHA, 1936.
15 Papez JW. Two cases of persistent left superior vena cava in man. *Anat Rec* 1938;**70**:191–198.
16 Sanders JM. Bilateral superior vena cava. *Anat Rec* 1946;**94**:657.
17 Campbell M, Deuchar DC. The left-sided superior vena cava. *Br Heart J* 1954;**16**:423–439.
18 Winter FS. Persistent left superior vena cava: survey of world literature and report of thirty additional cases. *Angiology* 1954;**5**:90–132.
19 Cha EM, Khoury GH. Persistent left superior vena cava. Radiologic and clinical significance. *Radiology* 1972;**103**:375–381.
20 Kula S, Cevik A, Sanli C, et al. Persistent left superior vena cava: experience of a tertiary health-care center. *Pediatr Int* 2011;**53**:1066–1069.
21 Fyler DC, Bucklet LP, Hellenbrand WE, Cohn HE. Report of the New England Regional Infant Cardiac Program. *Pediatrics* 1980;**65**:375–461.
22 Rubino M, Van Praagh S, Kadoba K, et al. Systemic and pulmonary venous connections in visceral heterotaxy with asplenia. Diagnostic and surgical considerations based on seventy-two autopsied cases. *J Thorac Cardiovasc Surg* 1995;**110**:641–650.
23 Geva T, Van Praagh S. Abnormal systemic venous connections. In: Allen HD, Driscoll DJ, Shaddy RE, Feltes TF (eds.) *Moss and Adams' Heart Disease in Infants, Children and Adolescents: Including the Fetus and Young Adult*, 7th edn. Philadelphia, PA: Lippincott Williams & Wilkins, 2007, pp. 792–817.
24 Wood P. *Diseases of the Heart and Circulation*, 2nd edn. Philadelphia, PA: JB Lippincott, 1956.
25 Meadows WR, Sharp JT. Persistent left superior vena cava draining into the left atrium without arterial oxygen unsaturation. *Am J Cardiol* 1965;**16**:273–279.
26 Looyenga DS, Lacina SJ, Gebuhr CJ, Stockinger FS. Persistent left superior vena cava communicating with the left atrium through a systemic-pulmonary venous malformation. *J Am Coll Cardiol* 1986;**8**:621–626.
27 Bosher LH, Jr. Problems in extracorporeal circulation relating to venous cannulation and drainage. *Ann Surg* 1959;**149**:652–663.
28 Schreiber KL, Matsusaki T, Bane BC, et al. Accidental insertion of a percutaneous venovenous cannula into the persistent left superior vena cava of a patient undergoing liver transplantation. *Can J Anesth* 2011;**58**:646–649.
29 Freed MD, Rosenthal A, Bernhard WF. Balloon occlusion of a persistent left superior vena cava in the preoperative evaluation of systemic venous return. *J Thorac Cardiovasc Surg* 1973;**65**:835–839.
30 Snider AR, Ports TA, Silverman NH. Venous anomalies of the coronary sinus: detection by M-mode, two-dimensional and contrast echocardiography. *Circulation* 1979;**60**:721–727.
31 Hornberger LK. Abnormalities of systemic and pulmonary venous connections. In: Allan L, Hornberger LK, Sharland G (eds.) *Textbook of Fetal Cardiology*. London: Greenwich Medical Media, 2000, pp. 103–114.
32 Galindo A, Gutierrez-Larraya F, Escribano D, et al. Clinical significance of persistent left superior vena cava diagnosed in fetal life. *Ultrasound Obstet Gynecol* 2007;**30**:152–161.
33 Karnegis JN, Wang Y, Winchell P, Edwards JE. Persistent left superior vena cava, fibrous remnant of the right superior vena cava and ventricular septal defect. *Am J Cardiol* 1964;**14**:573–577.
34 Choi JY, Anderson RH, Macartney FJ. Absent right superior caval vein (vena cava) with normal atrial arrangement. *Br Heart J* 1987;**57**:474–478.
35 Ratnasamy C, Idriss SF, Carboni MP, Kanter RJ. Arrhythmias in children having a single left superior vena cava and minimal structural heart disease. *J Cardiovasc Electrophysiol* 2009;**20**:182–186.
36 Horwitz S. Clinical diagnosis of persistent left superior vena cava draining into left atrium. *Jpn J Thorac Surg* 1974;**27**:647–651.
37 Taybi H, Kurlander GJ, Lurie PR, Campbell JA. Anomalous systemic venous connection to the left atrium or to a pulmonary vein. *Am J Roentgenol Radium Ther Nucl Med* 1965;**94**:62–77.
38 Raghib G, Ruttenberg HD, Anderson RC, et al. Termination of left superior vena cava in left atrium, atrial septal defect, and absence of coronary sinus; a developmental complex. *Circulation* 1965;**31**:906–918.
39 Davis WH, Jordaan FR, Snyman HW. Persistent left superior vena cava draining into the left atrium, as an isolated anomaly. *Am Heart J* 1959;**57**:616–622.
40 Fischer DR, Zuberbuhler JR. Anomalous systemic venous return. In: Anderson RH, Baker EJ, Macartney FJ, et al. (eds.) *Paediatric Cardiology*, 2nd edn. London: Churchill Livingstone, 2002, pp. 851–865.
41 Shumacker HB, Jr., King H, Waldhausen JA. The persistent left superior vena cava. Surgical implications, with special reference to caval drainage into the left atrium. *Ann Surg* 1967;**165**:797–805.

42 Foster ED, Baeza OR, Farina MF, Shaher RM. Atrial septal defect associated with drainage of left superior vena cava to left atrium and absence of the coronary sinus. *J Thorac Cardiovasc Surg* 1978;**76**:718–720.

43 de Leval MR, Ritter DG, McGoon DC, Danielson GK. Anomalous systemic venous connection. Surgical considerations. *Mayo Clin Proc* 1975;**50**:599–610.

44 Konstam MA, Levine BW, Strauss HW, McKusick KA. Left superior vena cava to left atrial communication diagnosed with radionuclide angiocardiography and with differential right to left shunting. *Am J Cardiol* 1979;**43**:149–153.

45 Park HM, Smith ET, Silberstein EB. Isolated right superior vena cava draining into left atrium diagnosed by radionuclide angiocardiography. *J Nucl Med* 1973;**14**:240–242.

46 Bernstein HS, Moore P, Stanger P, Silverman NH. The levoatriocardinal vein: morphology and echocardiographic identification of the pulmonary-systemic connection. *J Am Coll Cardiol* 1995;**26**:995–1001.

47 Kirsch WM, Carlsson E, Hartmann AF, Jr. A case of anomalous drainage of the superior vena cava into the left atrium. *J Thorac Cardiovasc Surg* 1961;**41**:550–556.

48 Braudo M, Beanlands DS, Trusler G. Anomalous drainage of the right superior vena cava into the left atrium. *Can Med Assoc J* 1968;**99**:715–719.

49 Shapiro EP, Al-Sadir J, Campbell NP, et al. Drainage of right superior vena cava into both atria. Review of the literature and description of a case presenting with polycythemia and paradoxical embolization. *Circulation* 1981;**63**:712–717.

50 Van Praagh S, Geva T, Lock JE, et al. Biatrial or left atrial drainage of the right superior vena cava: anatomic, morphogenetic, and surgical considerations–report of three new cases and literature review. *Pediatr Cardiol* 2003;**24**:350–363.

51 Ali MK, Ewer MS, Balakrishnan PV, et al. Balloon angioplasty for superior vena cava obstruction. *Ann Int Med* 1987;**107**:856–857.

52 Krasemann T, Kehl G, Vogt J, Asfour B. Unusual systemic venous return with complete absence of the superior caval veins. *Pediatr Cardiol* 2003;**24**:397–399.

53 Elliott LP, Cramer GG, Amplatz K. The anomalous relationship of the interior vena cava and abdominal aorta as a specific angiocardiographic sign in asplenia. *Radiology* 1966;**87**:859–863.

54 Van Praagh S. Cardiac malpositions and the heterotaxy syndromes. In: Keane JF, Lock JE, Fyler DC (eds.) *Nadas' Pediatric Cardiology*, 2nd edn. Philadelphia, PA: Saunders Elsevier, 2006, pp. 675–695.

55 Ruscazio M, Van Praagh S, Marrass AR, et al. Interrupted inferior vena cava in asplenia syndrome and a review of the hereditary patterns of visceral situs abnormalities. *Am J Cardiol* 1998;**81**:111–116.

56 Anderson RC, Adams P, Jr., Burke B. Anomalous inferior vena cava with azygos continuation (infrahepatic interruption of the inferior vena cava). Report of 15 new cases. *J Pediatr* 1961;**59**:370–383.

57 Haswell DM, Berrigan TJ, Jr. Anomalous inferior vena cava with accessory hemiazygos continuation. *Radiology* 1976;**119**:51–54.

58 Floyd GD, Nelson WP. Developmental interruption of the inferior vena cava with azygos and hemiazygos substitution. Unusual radiographic features. *Radiology* 1976;**119**:55–57.

59 Puchalski MD, Williams RV, Minich LL. An unusual variant of anomalous systemic venous return. *Cardiol Young* 2003;**13**:563–564.

60 Huhta JC, Smallhorn JF, Macartney FJ. Cross-sectional echocardiographic diagnosis of azygos continuation of the inferior vena cava. *Catheter Cardiovasc Diagn* 1984;**10**:221–232.

61 Wolfhard U, Splittgerber FH, Gocke P, Reidemeister JC. Bilateral inferior vena cava with azygos continuation but without congenital heart disease complicates routine venous cannulation for cardiopulmonary bypass in an adult. *The Thoracic and Cardiovascular Surgeon* 1997;**45**:40–42.

62 Wren C, Macartney FJ, Deanfield JE. Cardiac rhythm in atrial isomerism. *Am J Cardiol* 1987;**59**:1156–1158.

63 Kawashima Y, Kitamura S, Matsuda H, et al. Total cavopulmonary shunt operation in complex cardiac anomalies. A new operation. *J Thorac Cardiovasc Surg* 1984;**87**:74–81.

64 Bass JE, Redwine MD, Kramer LA, et al. Spectrum of congenital anomalies of the inferior vena cava: cross-sectional imaging findings. *Radiographics* 2000;**20**:639–652.

65 Gladstone RJ. Development of the inferior vena cava in the light of recent research, with especial reference to certain abnormalities, and current descriptions of the ascending lumbar and azygos veins. *J Anat* 1929;**64**:70–93.

66 Meadows WR, Bergstrand I, Sharp JT. Isolated anomalous connection of a great vein to the left atrium. The syndrome of cyanosis and clubbing, "normal" heart, and left ventricular hypertrophy on electrocardiogram. *Circulation* 1961;**24**:669–676.

67 Gardner DL, Cole L. Long survival with inferior vena cava draining into left atrium. *Br Heart J* 1955;**17**:93–97.

68 Black H, Smith GT, Goodale WT. Anomalous inferior vena cava draining into the left atrium associated with intact interatrial septum and multiple pulmonary arteriovenous fistulae. *Circulation* 1964;**29**:258–267.

69 Lucas RV, Krabill KA. Abnormal systemic venous connections. In: Emmanoulides GC, Rreimenschneider TA, Allen HD, Gutgesell HP (eds.) *Moss and Adams' Heart Disease in Infants, Children, and Adolescents: Including the Fetus and Young Adult*, 5th edn. Baltimore, MD: Williams & Wilkins, 1995, pp. 874–902.

70 Mustard WT, Firor WB, Kidd L. Diversion of the venae cavae into the left atrium during closure of atrial septal defects. *J Thorac Cardiovasc Surg* 1964;**47**:317–324.

71 Georghiou GP, Erez E, Bruckheimer E, et al. Anomalous hepatic venous drainage. *Ann Thorac Surg* 2005;**80**:1113–1115.

72 Stoller JK, Hoffman RM, White RD, Mee RB. Anomalous hepatic venous drainage into the left atrium: an unusual cause of hypoxemia. *Respir Care* 2003;**48**:58–62.

73 Fernandez-Martorell P, Sklansky MS, Lucas VW, et al. Accessory hepatic vein to pulmonary venous atrium as a cause of cyanosis after the Fontan operation. *Am J Cardiol* 1996;**77**:1386–1387.

74 Yoshimura N, Yamaguchi M, Oshima Y, et al. Intrahepatic venovenous shunting to an accessory hepatic vein after Fontan type operation. *Ann Thorac Surg* 1999;**67**:1494–1496.

75 Sanders SP. Anomalous hepatic venous connection to the coronary sinus diagnosed by two-dimensional echocardiography. *Am J Cardiol* 1984;**54**:458–459.

76 Mantini E, Grondin CM, Lillehei CW, Edwards JE. Congenital anomalies involving the coronary sinus. *Circulation* 1966;**33**:317–327.

77 Prows MS. Two cases of bilateral superior vena cava, one draining a closed coronary sinus. *Anat Rec* 1943;**87**:99–106.

78 Edwards JE. Malformations of the thoracic veins. In: Gould SE, Thomas CC (eds.) *Pathology of the Heart*, 2nd edn. Springfield, IL: Charles C. Thomas, 1960.
79 Brickner ME, Eichhorn EJ, Netto D, et al. Left-sided inferior vena cava draining into the coronary sinus via persistent left superior vena cava: case report and review of the literature. *Cathet Cardiovasc Diagn* 1990;**20**:189–192.
80 Choi JY, Jung MJ, Kim YH, et al. Anomalous subaortic position of the brachiocephalic vein (innominate vein): an echocardiographic study. *Br Heart J* 1990;**64**:385–387.
81 Smallhorn JF, Zielinsky P, Freedom RM, Rowe RD. Abnormal position of the brachiocephalic vein. *Am J Cardiol* 1985;**55**:234–236.
82 Gerlis LM, Ho SY. Anomalous subaortic position of the brachiocephalic (innominate) vein: a review of published reports and report of three new cases. *Br Heart J* 1989;**61**:540–545.

CHAPTER 11

Anomalies of the Atrial Septum

Tal Geva
Division of Noninvasive Cardiac Imaging, Department of Cardiology, Boston Children's Hospital and Harvard Medical School, Boston, MA, USA

Definition

Defects that allow interatrial communication can result from openings in the atrial septum (defined as *atrial septal defect*, or ASD), or from defects in the sinus venosus component of the atria (defined as *sinus venosus defect*), or in the tissue that separates the coronary sinus from the left atrium (defined as *coronary sinus defect*). Patent foramen ovale is an interatrial communication that exists normally in the fetus and in most newborns, but because of its clinical importance in certain congenital heart defects and in older patients with paradoxical emboli and stroke, it is discussed in this chapter. Atrial septal defects are further classified into secundum and primum defects. Ostium primum atrial septal defect – a defect that results from abnormal formation of the embryonic endocardial cushions – is discussed in Chapter 15.

Incidence

Defects of the atrial septum comprise the third most common type of congenital heart disease, with an estimated incidence of 56 per 100,000 live births [1]. This estimate represents the median incidence based on analysis of 43 published articles spanning many decades. With improved recognition of clinically silent defects by echocardiography, recent estimates are approximately 100 per 100,000 live birth live births [2].

Etiology

Most cases of secundum ASD are sporadic; however, several investigators reported familial clusters with different modes of inheritance as well as an association with conduction defects. Examples include mutations in the cardiac transcription factor gene *NKX2.5* [3–5], mutations in the *GATA4* gene [6,7], a mutation in the myosin heavy chain 6 gene located on chromosome 14q12 [8], as well as several other mutations [9–11]. Secundum ASD is also frequently associated with genetic syndromes such as Holt–Oram, Noonan, Down, Budd–Chiari, and Jarcho–Levine, to mention just a few [12–19].

Morphology and classification

Developmental considerations

The classification of interatrial communications is based on understanding of atrial septation and the relationships between the pulmonary veins, the systemic veins, and the atria. Atrial septation involves the following structures:

- septum primum
- septum secundum
- atrioventricular (AV) canal septum
- sinus venosus
- coronary sinus.

Detailed description of atrial septation can be found in several publications [20–23]. Briefly, septum primum – the first septum to appear in the developing atria at approximately 28 days of development – grows as a crescent-shaped structure toward the developing endocardial cushions (Figure 11.1a). Its leading edge is covered by a layer of mesenchymal cells (mesenchymal cap) [23]. The space between the developing septum primum and the closing endocardial cushions is termed *foramen primum* or the *primary foramen*. Septum secundum, also called the *limbus of the fossa ovalis*, is a crescent-shaped muscular infolding of the atria wall that develops to the right of septum primum (Figure 11.1b). Foramen primum closes as a result of fusion between the mesenchymal cap of septum primum and the now fused superior and inferior endocardial cushions (Figure 11.1c). Foramina secundi (secondary foramina) form at the same time as coalescing fenestrations within septum primum (Figure 11.1b,c).

The AV canal septum is formed, at least in part, by the superior and inferior endocardial cushions and contributes to septation of the outlet portion of the atria and the inlet portion of the ventricles (Figure 11.1). Normal development of the atrial

Echocardiography in Pediatric and Congenital Heart Disease: From Fetus to Adult, Second Edition. Edited by Wyman W. Lai, Luc L. Mertens, Meryl S. Cohen and Tal Geva.
© 2016 John Wiley & Sons, Ltd. Published 2016 by John Wiley & Sons, Ltd.
Companion website: www.lai-echo.com

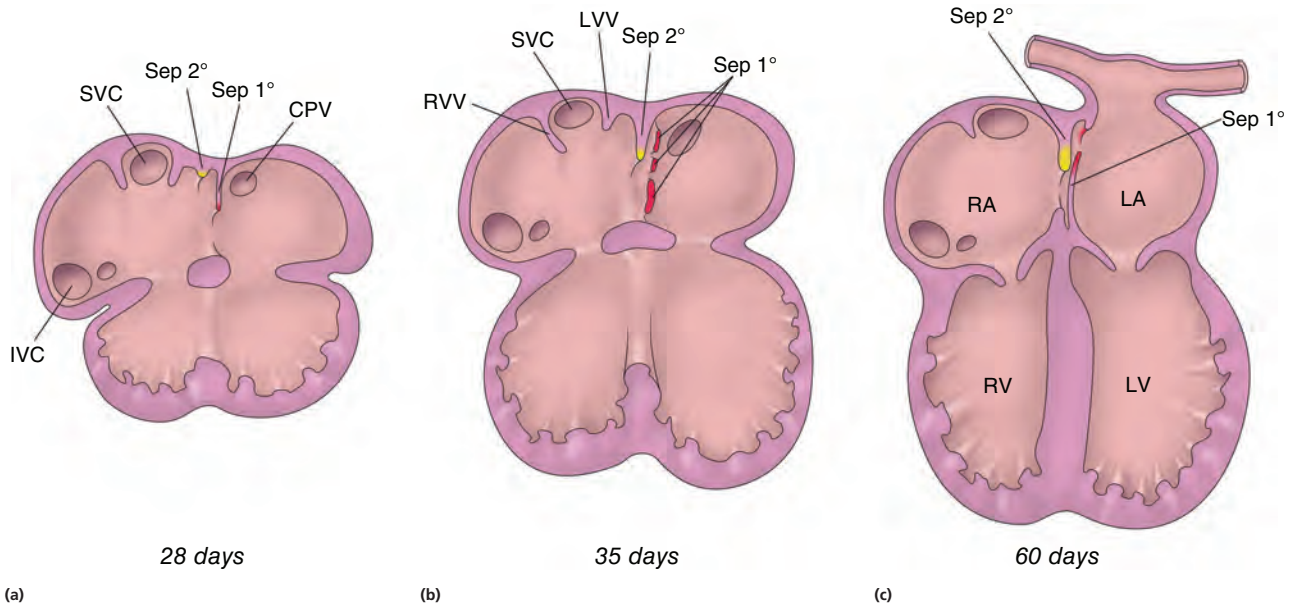


Figure 11.1 Diagram showing development of the atrial septum. **(a)** At 28 days after gestation, septum primum (Sep 1^0) develops as a crescent-shape structure with a layer of mesenchymal cells at the leading edge (red color). The space between the developing septum primum and the developing endocardial cushions is called *foramen primum* or *ostium primum*. Septum secundum (Sep 2^0) appears shortly thereafter to the right of septum primum. **(b)** At 35 days, both septum primum and septum secundum continue to develop. The openings within septum primum are called *foramina secundi*. **(c)** At 60 days, the atrial septum is nearly fully formed and the foramina secundi close by way of coalescing fenestrations within septum primum. The foramen ovale remains patent throughout pregnancy. CPV, common pulmonary vein; IVC, inferior vena cava; LA, left atrium; LV, left ventricle; LVV, left venous valve; RA, right atrium; RV, right ventricle; RVV, right venous valve; SVC, superior vena cava.

septum results in formation of the fossa ovalis, which includes two anatomic elements: (i) muscular boundaries contributed by *septum secundum*; and (ii) the valve of the fossa ovalis, which attaches on the left atrial (LA) aspect of the septum – *septum primum*. The atrial component of the AV canal septum lies anterior and inferior to the fossa ovalis, separating it from the tricuspid and mitral valve annuli – the *AV canal septum* (Figure 11.2). The tissue that separates the right pulmonary veins from the superior vena cava (SVC) and from the posterior and inferior aspects of the right atrial (RA) free wall is termed *sinus venosus* [24–26]. The tissue that separates the coronary sinus from the left atrium (LA) is termed *coronary sinus septum* [27].

Anatomy

Patent foramen ovale (PFO)

This is the space between a well-developed (valve-competent) septum primum and a normally formed septum secundum (Figure 11.3). PFO is a normal interatrial communication during fetal life, characterized by streaming of flow from the ductus venosus and, to a lesser extent, from the inferior vena cava, through the foramen ovale to the LA (Figure 11.4a; Video 11.1). After birth, LA pressure normally exceeds RA pressure and, as a result, septum primum apposes septum secundum (the superior limbic band of the fossa ovalis) and the foramen ovale narrows (Figure 11.4b; Videos 11.2 and 11.3). A PFO is seen in almost all newborns, but its frequency decreases with advancing age [28–30]. Complete anatomic closure of the foramen ovale occurs in 70–75% of adults [31].

Secundum ASD

This is a defect within the fossa ovalis, usually due to a single or multiple defects within septum primum (Figure 11.5). Septum secundum is usually well formed. Most secundum ASDs are not confluent with the venae cavae, right pulmonary veins, coronary sinus, or the AV valves. With the exception of PFO, secundum ASD is the most common cause of an atrial-level shunt. The size of secundum ASDs varies from several millimeters to 2–3 centimeters. Large defects are usually associated with marked deficiency, or even complete absence, of septum primum. Rarely, a secundum ASD results from deficiency of septum secundum (the muscular limb of the fossa ovalis). In such cases, the superior border of the defect can reach the SVC–RA junction ("high" secundum defect) but, in contrast to a sinus venosus defect, does not involve the right upper pulmonary vein.

Primum ASD

Primum ASD is an endocardial cushion defect with an interatrial communication located between the anterior-inferior margin of the fossa ovalis and the AV valves. It is considered a form of partial AV canal defect with two separate AV valve annuli and no ventricular septal defect of the AV canal type (Figure 11.1 and Chapter 15).

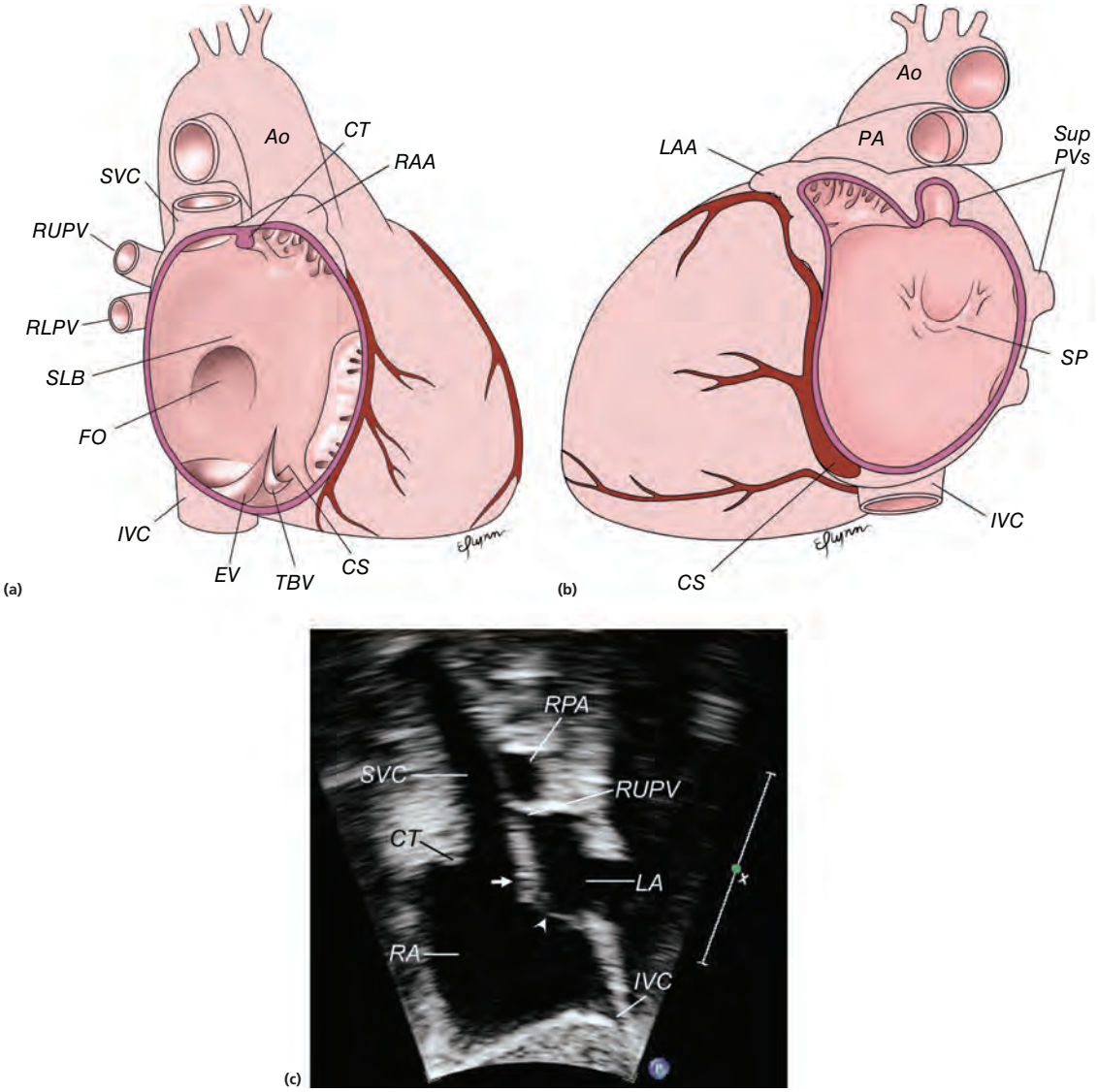


Figure 11.2 Diagram showing the anatomy of the atrial septum and neighboring structures. **(a)** Right atrial aspect; **(b)** left atrial aspect; **(c)** echocardiographic view. Ao, aorta; CS, coronary sinus; CT, crista terminalis; EV, Eustachian valve; FO, foramen ovale; IVC, inferior vena cava; LAA, left atrial appendage; PA, (main) pulmonary artery; RAA, right atrial appendage; RLPV, right lower pulmonary vein; RUPV, right upper pulmonary vein; SLB, superior limbic band (septum secundum); SP, septum primum; SVC, superior vena cava; TBV, Thebesian valve.

Sinus venosus defect (SVD)

This is a communication between one or more of the right pulmonary veins and the cardiac end of the SVC and/or the posterior-inferior wall of the right atrium (RA) (Figure 11.5) [24,26]. SVDs comprise approximately 4–11% of ASDs [32]. From an anatomic standpoint, SVD is not an atrial septal defect because it does not allow direct communication between the left and right atria. Instead, the interatrial communication is through one or more systemic and pulmonary veins. The most common location of a SVD (approximately 87% [24]) is between the right upper pulmonary vein and the superior vena cava, below the insertion of the azygos vein (SVC-type SVD). The defect results from partial or complete absence of the sinus venosus tissue that separates the anterior aspect of the right upper pulmonary vein from the posterior wall of the SVC [24,25]. The deficiency of the sinus venosus tissue can extend peripherally to involve secondary branches of the right pulmonary veins, resulting in drainage of several pulmonary veins to the SVC. The LA orifice of the right upper pulmonary vein is usually widely patent, allowing for a communication between the LA and the cardiac end of the SVC. The combination of an interatrial shunt through the LA orifice of the right upper pulmonary vein (LA-to-SVC-to-RA) and drainage of right upper pulmonary vein blood to the RA through the SVC typically result in a large left-to-right shunt and marked right ventricular volume overload [33].

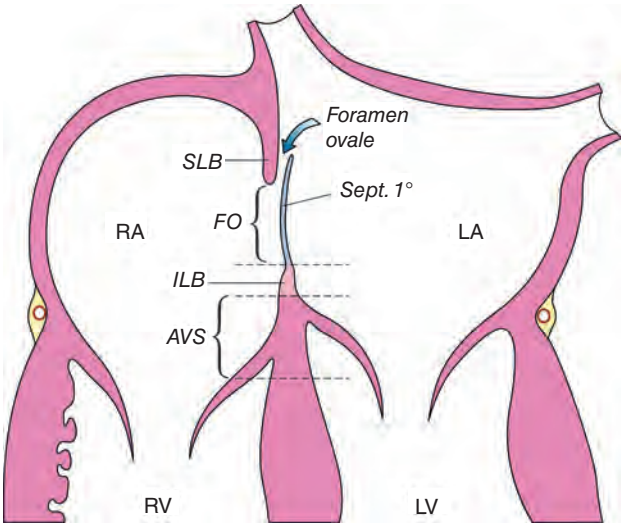


Figure 11.3 Diagram of atrial septal components showing patent foramen ovale (PFO) (arrow). AVS, atrioventricular septum; FO, foramen ovale; ILB, inferior limbic band; LA, left atrium; LV, left ventricle; RA, right atrium; RV, right ventricle; Sept. 1^0, septum primum; SLB, superior limbic band (septum secundum).

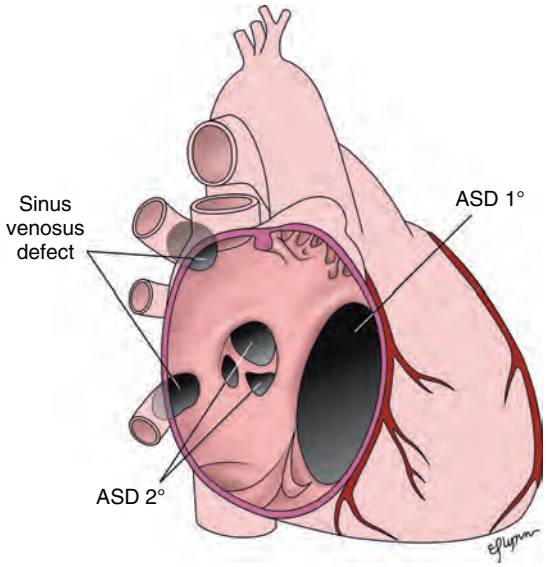
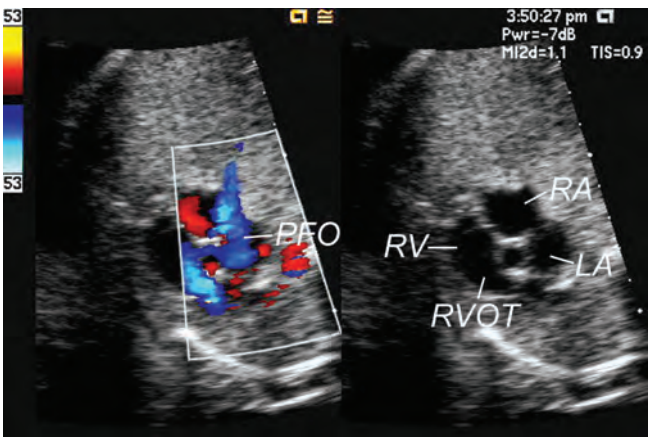


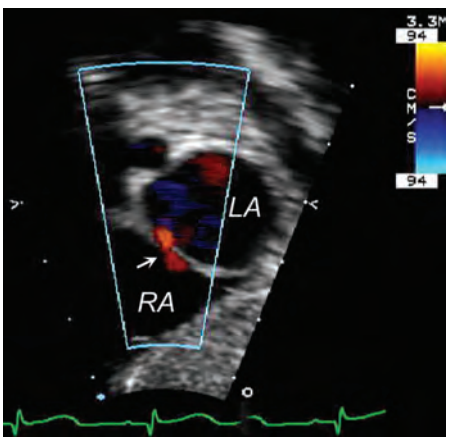
Figure 11.5 Diagram showing types of interatrial communications. ASD 1^0, primum atrial septal defect; ASD 2^0, secundum atrial septal defect.

Less frequently, the defect also involves the right lower and/or middle pulmonary veins and the middle or inferior aspects of the RA (Figure 11.6). This type of sinus venosus defect has been called IVC-type although direct involvement of the inferior vena cava is extremely rare. For that reason, the term *sinus venosus defect of the right atrial type* is preferred [24]. In the study of Banka et al. [26], RA-type SVD accounted for 1.2% of cases with an isolated interatrial communication. Anatomic characteristics of RA-type SVD include (i) posterior and/or inferior defect confluent with the posterior wall of the atria with no posterior and/or inferior rim; (ii) confluence of the defect with the right pulmonary veins(s) or with the IVC–RA junction; and (iii) presence of a well-developed septum primum covering the fossa ovale (Figure 11.6) [26]. Rarely, both SVC- and RA-types coexist, resulting in drainage of all right pulmonary veins draining to the right heart. This should be distinguished from leftward malposition of septum primum resulting in anomalous drainage of the right pulmonary veins to the RA.

It is important to recognize that although the right pulmonary veins in SVD almost always drain anomalously, their anatomic connections with the LA are usually normal, through their native orifices. In the rare circumstance when the LA orifice of the right upper pulmonary vein is atretic, there is no interatrial communication and the anatomic appearance is that of partially anomalous pulmonary venous connection of the right upper pulmonary vein to the SVC.



(a)



(b)

Figure 11.4 Patent foramen ovale. **(a)** Fetal echocardiogram at 18 weeks' gestation showing right-to-left flow from the ductus venosus to the left atrium (LA) through a patent foramen ovale (PFO). **(b)** Patent foramen ovale with left-to-right flow (arrow) in a newborn. LA, left atrium; RA, right atrium; RV, right ventricle; RVOT, right ventricular outflow tract.

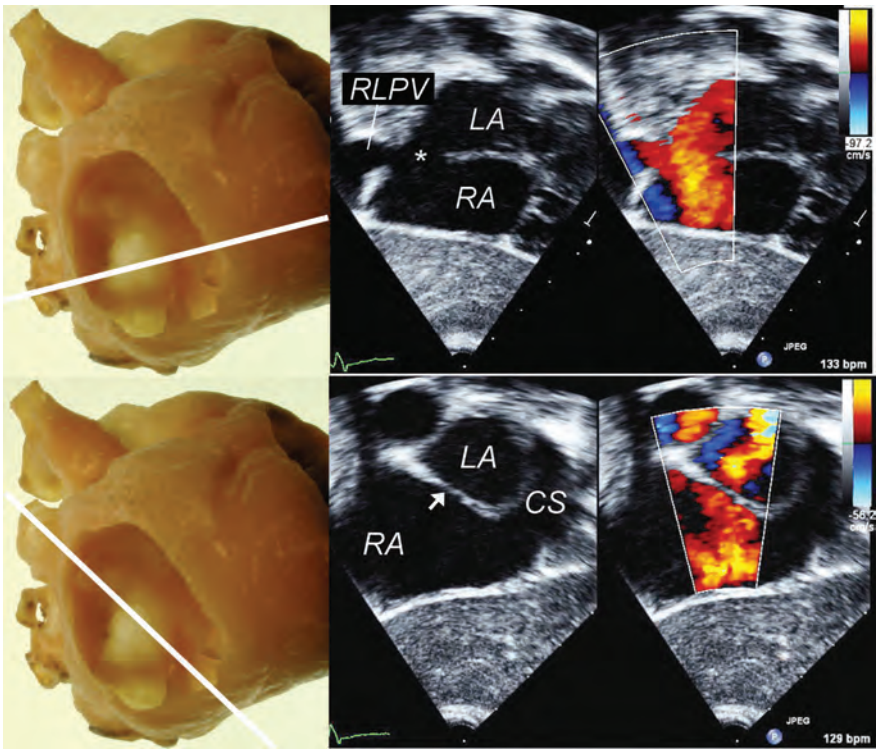


Figure 11.6 Echocardiographic 2D and color Doppler images in a subcostal long-axis plane (top) show the typical appearance of a RA-type SVD (star). Imaging in the subcostal short-axis plane (bottom) demonstrates an intact fossa ovalis and septum primum (arrow) in the same patient. CS, coronary sinus; LA, left atrium; RA, right atrium; RLPV, right lower pulmonary vein. Source: Banka et al. 2011 [26]. Reproduced with permission of Elsevier.

Coronary sinus defect

This is an uncommon anomaly that results from partial or complete unroofing of the tissue separating the coronary sinus from the LA, allowing the right and left atria to communicate through the defect and the coronary sinus orifice (Figure 11.7). The orifice of the coronary sinus in this anomaly is usually large as a result of the left-to-right shunt, resulting in a sizeable defect in the inferior aspect of the atrial septum near the entry of the inferior vena cava. The association of a coronary sinus septal defect and persistent left superior vena cava is termed *Raghib syndrome* [34]. When the coronary sinus is completely unroofed, the left superior vena cava enters the left superior corner of the LA, anterior to the orifice of the left upper pulmonary vein and posterior to the LA appendage.

Common atrium

Common atrium is present when septum primum, septum secundum, and the AV canal septum are absent (usually in patients with heterotaxy syndrome). Remnants of atrial septal tissue can sometime be recognized in these patients, such as a fibromuscular strand that crosses the inferior aspect of the

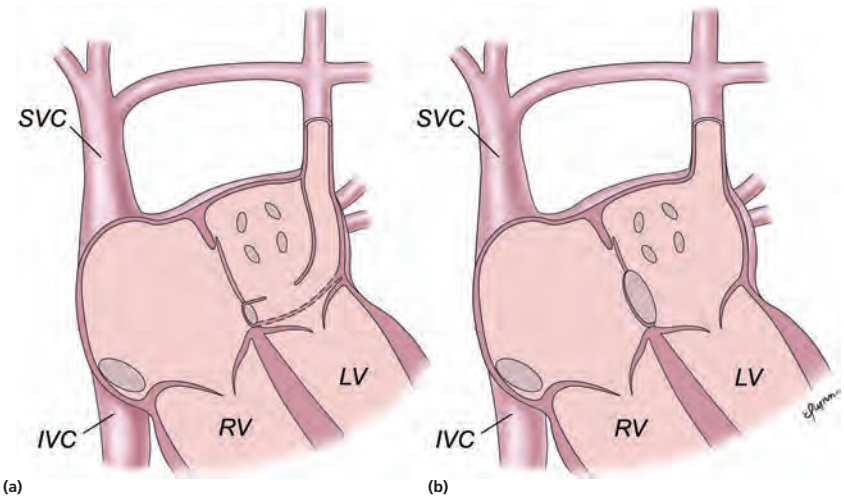


Figure 11.7 Diagram of coronary sinus septal defect. **(a)** Small coronary sinus septal defect associated with left superior vena cava-to-coronary sinus. **(b)** Unroofed coronary sinus associated with left superior vena cava (Raghib syndrome). Note the large interatrial communication through the coronary sinus ostium. IVC, inferior vena cava; LV, left ventricle; RV, right ventricle; SVC, superior vena cava.

common atrium (inferior limbic band of the fossa ovalis) or remnants of venous valve tissue.

Pathophysiology

Regardless of the specific anatomic type and assuming no AV valve stenosis or hypoplasia, the amount of shunting through an interatrial communication is determined by the defect size and relative compliance of the right and left ventricles. Over the first few months of life, right ventricular compliance typically rises leading to an increasing left-to-right shunt. In adults, left ventricular compliance normally decreases, further augmenting the left-to-right flow. Shunt flow through the right heart and lungs leads to dilation of the RA, right ventricle, pulmonary arteries, and pulmonary veins. Most young children tolerate this increased pulmonary blood flow well and are asymptomatic; a few develop dyspnea or growth failure [35,36]. Defects in this age group are typically detected after auscultation of a heart murmur or incidentally when a chest radiogram, an electrocardiogram, or an echocardiogram is obtained for other indications. The risk of pulmonary arterial hypertension increases with age and up to 5–10% of patients with significant left-to-right shunts may develop pulmonary vascular disease by adulthood [37]. Adults with unrepaired ASDs are also at risk for exercise intolerance, atrial arrhythmias, and paradoxical emboli [38,39]. Small secundum ASDs (≤5 mm) may close spontaneously or become smaller in the first few years of life; thereafter, defects tend to become larger with time [40,41]. By contrast, primum ASDs, sinus venosus septal defects, and coronary sinus septal defects almost never become smaller with time.

Imaging

The atrial septum is imaged from multiple acoustic windows, including the subcostal, apical, left parasternal, and high right parasternal. Two-dimensional (2D) and three-dimensional (3D) imaging as well as color and spectral Doppler techniques are used in concert for comprehensive evaluation of the fossa ovalis, sinus venosus, and coronary sinus. If a defect is seen from one acoustic window, its presence must be confirmed from other windows. Transesophageal echocardiography (TEE) – often used during surgical and transcatheter closure of ASDs (see later) – is also performed as a diagnostic procedure in patients with suboptimal transthoracic windows and inconclusive diagnosis. In such cases, cardiac magnetic resonance imaging (MRI) can be considered as a noninvasive alternative [33,42,43]. Contrast echocardiography is another helpful technique in certain patients [e.g., poor acoustic windows, diagnosis of left superior vena cava associated with coronary sinus septal defect (Raghib syndrome)] [44].

Key elements

Preoperative examination

In all cases, complete anatomic and functional examination by 2D and 3D imaging, as appropriate, and by color and spectral Doppler. In addition, the following elements of cardiovascular anatomy and function should be evaluated in detail:

- Atrial septal imaging: subcostal short-axis, long-axis, and in-between views; apical 4-chamber view; parasternal short-axis view; right sternal border. When feasible, 3D imaging with en face views of the atrial septum from the perspectives of the RA and LA.
- Size, location, and number of defects by imaging and color Doppler
 - Measurement of defect(s) diameter from all views
 - Measurement of septal rims and total atrial septal length:
 - Superior and inferior rims from subcostal and right sternal border bicaval views; anterior (retroaortic) and posterior rims from parasternal short-axis views;
 - Total septal length from subcostal in-between and short-axis (bicaval) view, right sternal border bicaval view, and apical 4-chamber view.
- ASD flow by color Doppler all views.
- In views with acceptable interrogation angle, assess ASD flow with spectral Doppler. Measure mean transseptal pressure gradient if high-velocity flow is noted.
- Visualization of pulmonary venous return, including high right parasternal window (long- and short-axis) to rule out accessory connections to the SVC. Exclude partially anomalous pulmonary venous connection to a systemic vein.
- Estimation of right ventricular pressure by tricuspid regurgitation and pulmonary regurgitation jet velocities and by systolic ventricular septal configuration (Chapter 45).
- Evaluation of right ventricular size and function with particular attention to evidence of dilatation and volume overload (Chapter 7).

Postoperative and postdevice examination

- Imaging of the atrial septum from multiple planes for evaluation of patch position.
- Rule-out residual ASD by color Doppler from multiple acoustic windows.
- After device closure of ASD, evaluate device position with particular attention to visualization of the left and RA arms or disks.
- Rule-out impingement of the device on neighboring structures, including systemic and pulmonary veins, AV valves, and aortic root.
- Rule-out intracardiac thrombus or vegetation with particular attention to the ASD patch or device.
- Estimation of right ventricular pressure by tricuspid regurgitation and pulmonary regurgitation jet velocities and by systolic ventricular septal configuration (Chapter 45).

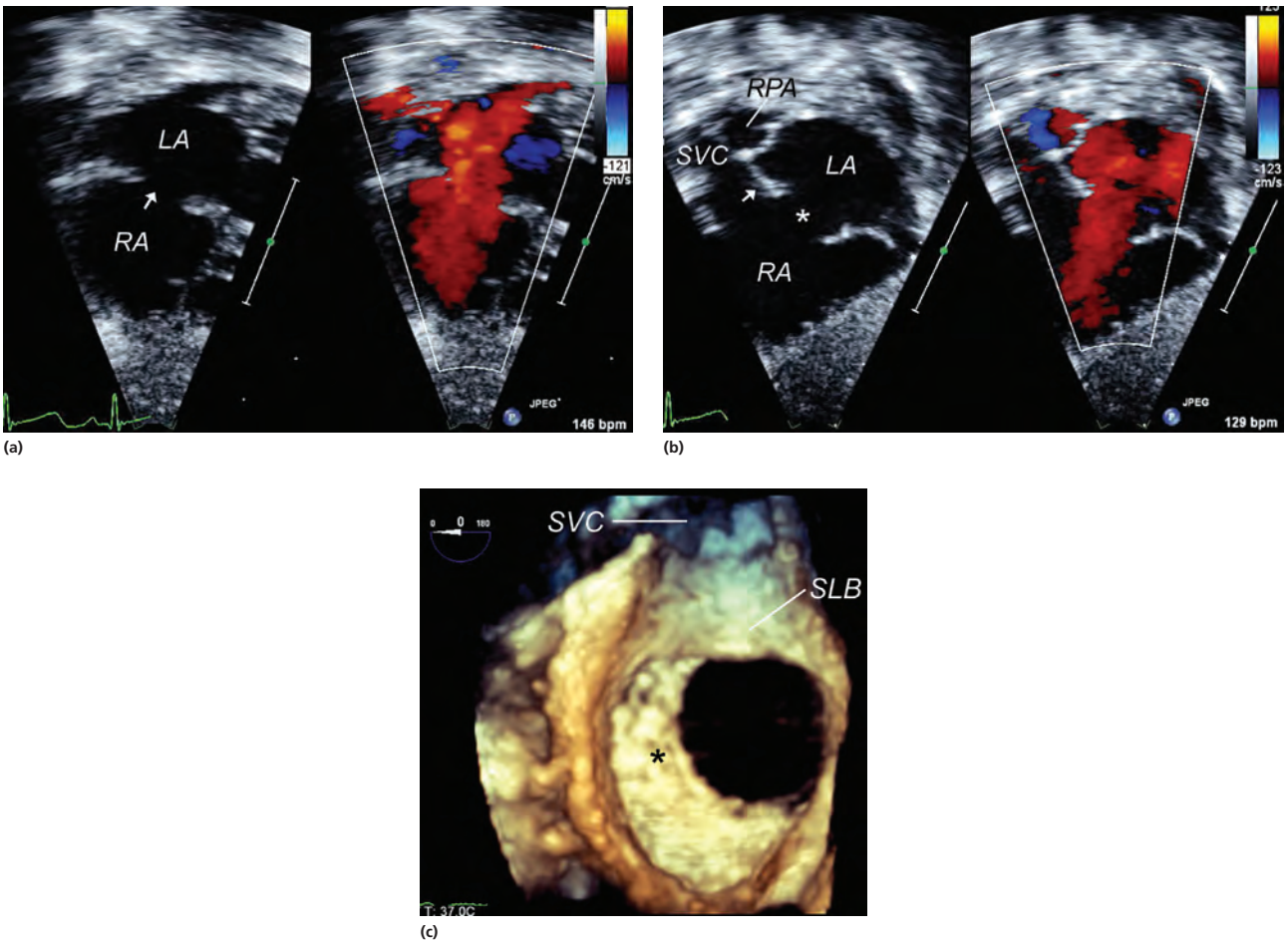


Figure 11.8 Imaging of secundum ASD from the subxiphoid window: **(a)** Long-axis view showing 2D and color Doppler flow mapping. The arrow points to the secundum atrial septal defect. **(b)** Short-axis view. The asterisk indicates secundum atrial septal defect; arrow denotes superior limbic band (septum secundum). **(c)** Real-time 3D imaging (right atrial view) showing a large secundum ASD associated with deficient septum primum (asterisk). LA, left atrium; RA, right atrium; RPA, right pulmonary artery; SLB, superior limbic band; SVC, superior vena cava

- Evaluation of right ventricular size and function with particular attention to evidence of dilatation and volume overload (Chapter 7).

Imaging of secundum ASDs

The subcostal acoustic window is ideally suited for evaluation of the fossa ovalis because the normally oriented septum is relatively echo-reflective from that position (Figure 11.8). This minimizes the likelihood of false dropout of acoustic signals, which can lead to erroneous diagnosis of an ASD. Imaging is performed in the long- and short-axis views and the use of "in-between" transducer angle is encouraged. A secundum ASD is seen as a defect within the fossa ovalis, confirmed by evidence of transseptal flow by color Doppler (Figure 11.8a–d; Video 11.4). In the subcostal long-axis view, a secundum ASD is not contiguous with the posterior RA free wall or with the right pulmonary veins. Such findings are suggestive of a SVD of the RA type. In the subcostal short-axis view, the superior limbic band of the fossa ovalis separates a secundum ASD from the SVC and the right upper pulmonary vein. The subcostal short-axis view is also optimal for assessment of right ventricular volume load (right ventricular enlargement and diastolic septal flattening) and right ventricular hypertension (systolic septal flattening).

The apical window is not ideally suited for evaluation of the fossa ovalis due to risk of false dropout of acoustic signal as a result of the parallel orientation of the ultrasound beam relative to the atrial septum. However, this view is helpful for measurement of the tricuspid regurgitation jet velocity for estimation of right ventricular systolic pressure. The apical window is also helpful for detection of acoustic signals during a contrast echocardiogram (Figure 11.9). The imager is looking for the appearance of acoustic reflective signals ("bubbles") in the LA and left ventricle (representing right-to-left flow) or a negative jet effect in the RA representing left-to-right flow.

The parasternal window is helpful, especially in the short-axis plane, for imaging of the atrial septum. A low left parasternal short-axis view can often provide adequate imaging of the atrial septum, even in patients with suboptimal subcostal

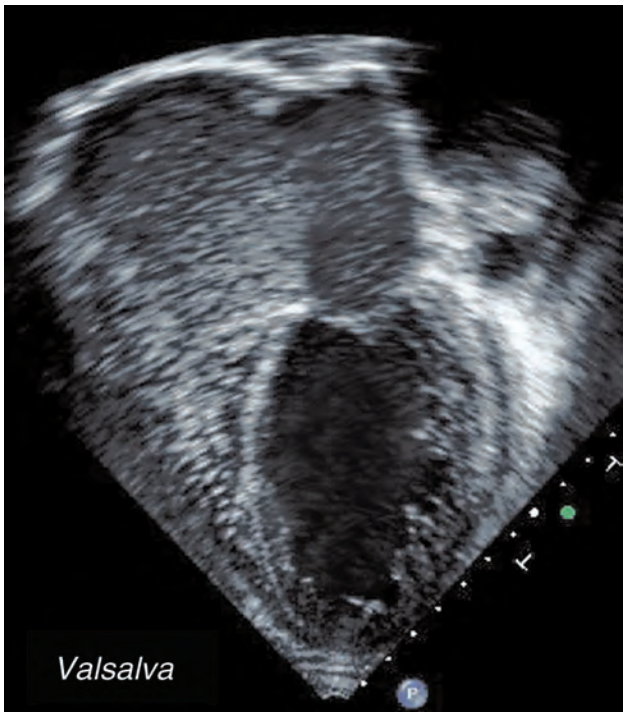


Figure 11.9 Contrast echocardiogram in a patient with secundum ASD. During a Valsalva maneuver, contrast crosses the atrial septum and appears in the left heart.

windows (Figure 11.10). This view is helpful for measurement of the antero-posterior diameter of the defect. The presence or absence of right ventricular volume and pressure loads is also evaluated from the parasternal short-axis view.

The high right parasternal window is also ideally suited for assessment of the fossa ovalis and the superior sinus venosus area as a result of the perpendicular orientation of these structures relative to the ultrasound beam. Placing the patient in the right lateral decubitus position facilitates imaging from this acoustic window.

Three-dimensional imaging provides en face views of the defect from the perspectives of the right and left atria (Figure 11.8d; Video 11.5). These views provide enhanced depth perception of the ASD and its relation to neighboring structures. It also demonstrates the dynamic nature of the defect's size throughout the cardiac cycle. Although restricted acoustic windows hinder transthoracic 3D imaging of the atrial septum in some patients, transesophageal echocardiography usually provides excellent 3D image quality in patients who can accommodate a 3D transesophageal probe.

Imaging of sinus venosus defects

SVC-type SVD is seen best from the subcostal short-axis and high right parasternal views as a communication between the right upper corner of the LA at the usual location of the right upper pulmonary vein and the SVC just above its RA junction (Figure 11.11; Videos 11.6, 11.7, and 11.8). The cross-section of the right pulmonary artery is seen in these views as an oval-shaped vessel crossing just above the defect, behind the SVC. Color-coded Doppler flow mapping shows flow from the LA through the SVC to the RA and confirms the pulsatile nature of the flow in the right pulmonary artery. Imaging in the transverse plane of the chest from either left or right parasternal windows at the level of the cardiac end of the SVC is helpful in showing the unroofed sinus venosus septum, seen as absence of the tissue separating the right upper pulmonary vein from the SVC (Figure 11.12; Video 11.9). This view also shows the communication between the LA and the SVC, the site of the LA orifice of the right upper pulmonary vein. Evaluation of the hemodynamic burden associated with SVD defect is similar to that of secundum ASD.

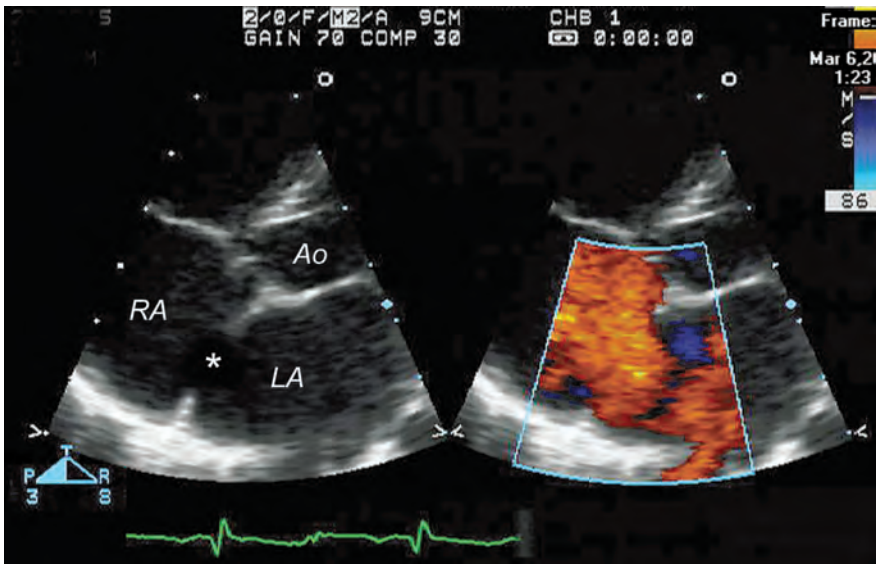
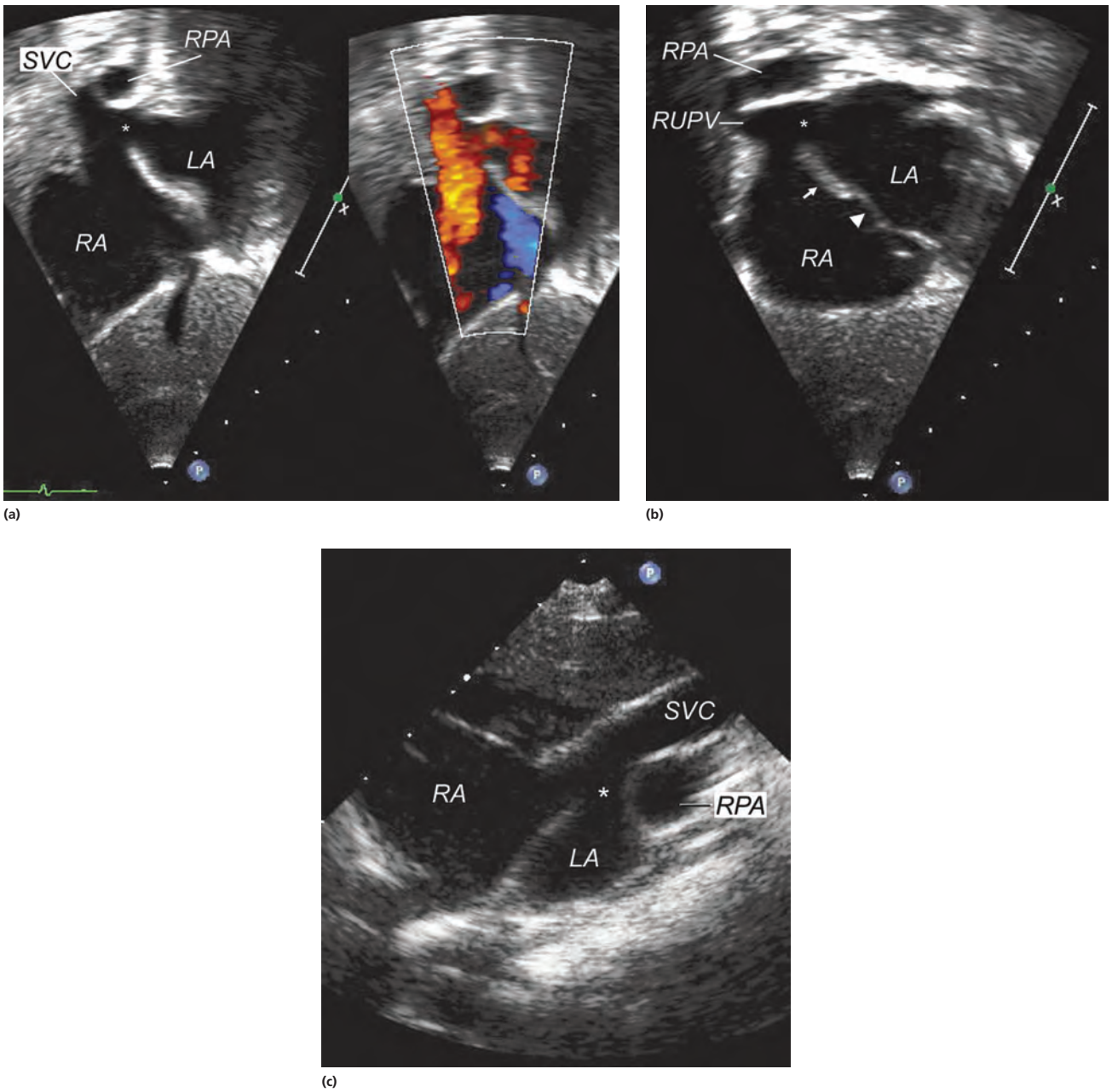


Figure 11.10 Imaging of secundum ASD from the parasternal short-axis view. Left panel depicts a 2D image of the defect (∗). The right panel shows flow from the left atrium to the right atrium through the defect.



(a) (b) (c)

Figure 11.11 Imaging of superior vena cava (SVC)-type sinus venosus defect. **(a)** Imaging from the subxiphoid short-axis view. Note the location of the defect (∗) cranial to the superior limbic band of the fossa ovalis and its communication with the cardiac end of the superior vena cava (SVC). Blood flows from the left atrium (LA) to the SVC through the left atrial orifice of the right upper pulmonary vein and sinus venosus defect. Note the absence of direct interatrial communication; hence, sinus venosus defect is NOT an atrial septal defect. **(b)** Imaging from the subxiphoid long-axis view. The arrowhead points to the fossa ovalis, which is covered by septum primum. The full arrow points to the superior limbic band of the fossa ovalis. Note the interatrial communication (∗) via the enlarged left atrial orifice of the right upper pulmonary vein (RUPV). **(c)** Imaging from the high right parasternal view. Note the location of the defect (∗) just below the right pulmonary artery (RPA). RA, right atrium.

Right atrial-type SVD is seen best from the subxiphoid long-axis and from the parasternal short-axis views, appearing as a posterior-inferior atrial defect with no posterior margins (Figure 11.13; Video 11.10). The defect is flushed with the posterior-inferior atrial free wall, may involve the atrial orifices of the right lower and middle pulmonary veins, or may be inferior to the right pulmonary veins and above the IVC–RA junction. In some cases the defect results in drainage of the right middle and lower pulmonary veins to the RA. The fossa ovalis is not involved in the defect.

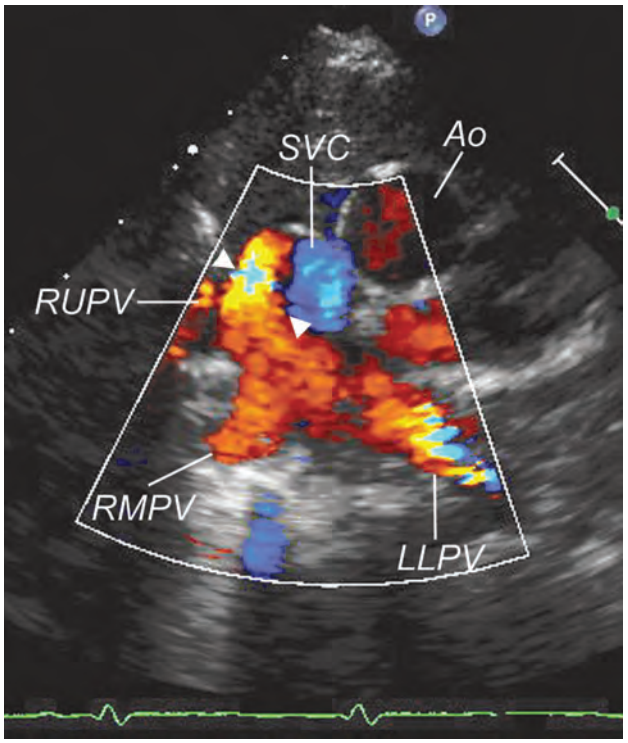


Figure 11.12 Imaging of superior vena cava-type sinus venosus defect from the parasternal short-axis view. The arrowheads mark the margins of the defect, which results from deficiency in the tissue that separates the posterior wall of the superior vena cava (SVC) from the anterior wall of the right upper pulmonary vein (RUPV). Flow from the left atrium into the superior vena cava (and then to the right atrium) is through the left atrial orifice of the right upper pulmonary vein (RUPV). Ao, ascending aorta; LLPV, left lower pulmonary vein; RLPV, right lower pulmonary vein; RMPV, left middle pulmonary vein.

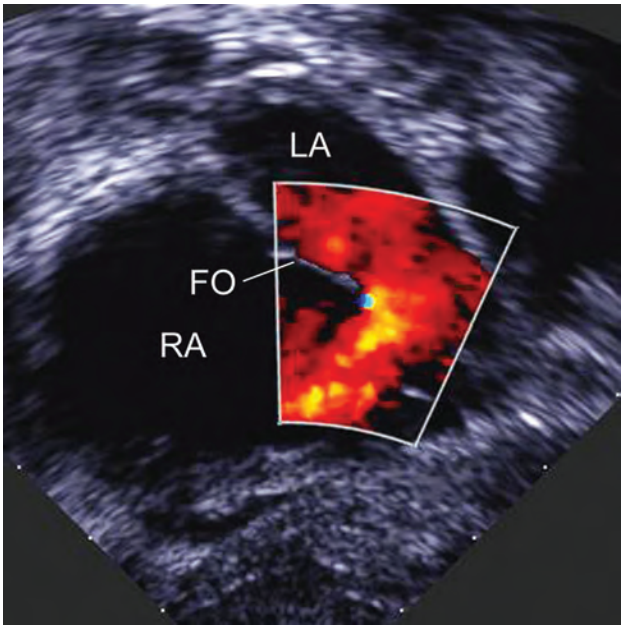


Figure 11.14 Coronary sinus septal defect. Blood flows from the left atrium (LA) through the unroofed coronary sinus into the right atrium (RA) through the enlarged coronary sinus ostium. Note the inferior-posterior location of the coronary sinus ostium and its relation to the intact fossa ovalis (FO).

Imaging of coronary sinus defects

The diagnosis of a coronary sinus septal defect is often first suspected in a patient with ASD physiology and an enlarged coronary sinus ostium (Figure 11.14; Video 11.11). The dilated coronary sinus ostium is seen as an inferior interatrial communication, just above and slightly anterior to the IVC–RA junction. The defect might be confused with an ostium primum ASD,

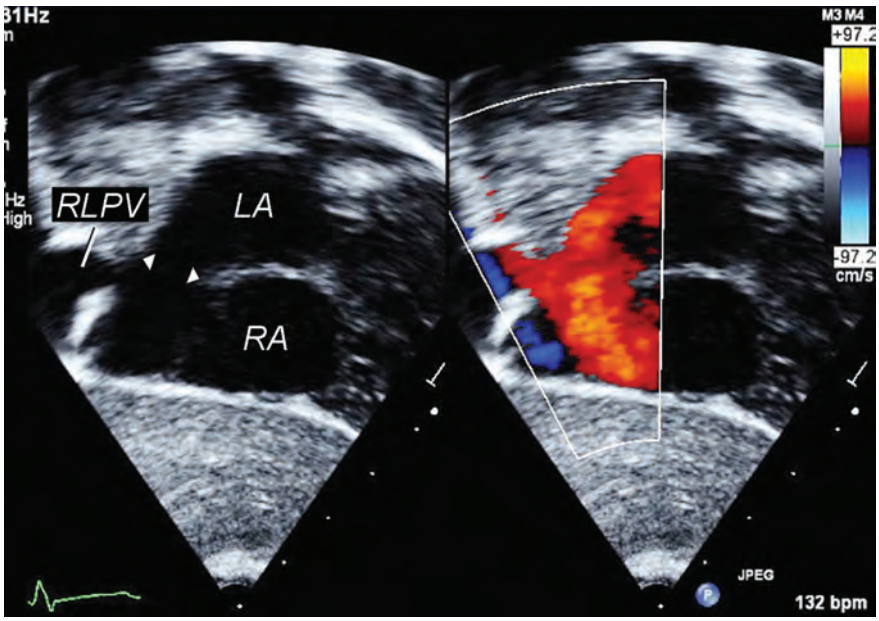


Figure 11.13 Right atrial-type sinus venosus defect. Subxiphoid long-axis view showing a large defect between the posterior wall of the right atrium (RA) and the anterior wall of the right lower pulmonary vein (RLPV). The interatrial communication (arrowheads) is via the left atrial (LA) orifice of the right lower pulmonary vein. This illustrates anomalous drainage of the RLPV to the RA but with normal connection. Note the flow from the right lower pulmonary vein and from the left atrium to the right atrium.

except for the intact anterior mitral leaflet and absence of other features of AV canal defect. Once the enlarged coronary sinus ostium is recognized, the coronary sinus is imaged in detail from multiple views. Absence of a visible coronary sinus indicates complete lack of sinoatrial septal tissue (the wall separating the coronary sinus from the LA); a condition known as completely unroofed coronary sinus. In a partially unroofed coronary sinus, part of the sinoatrial septal tissue is seen and the coronary sinus is recognizable. The presence or absence of a persistent left superior vena cava must be ascertained. When present, (Raghib syndrome [34]), the LA termination of the left superior vena cava is anterior to the left upper pulmonary vein and posterior to the LA appendage. Remnants of coronary sinus septum might be visualized within the LA at the entrance of the left superior vena cava. Injection of agitated saline through an intravenous cannula placed in the left arm, while imaging from the apical 4-chamber window, demonstrates the appearance of the contrast in the left upper corner of the LA with subsequent appearance in the RA. Rarely, the ostium of the coronary sinus is stenotic or atretic, in which case the interatrial shunt is small or absent and the coronary sinus septal defect allows drainage of cardiac venous return directly to the LA. In patients with typical Raghib syndrome, the fossa ovalis is usually small and displaced superiorly. An associated secundum ASD is unusual.

Prenatal assessment

Detailed evaluation of the atrial septum is integral to a comprehensive fetal echocardiogram. Two-dimensional and Doppler (spectral and color flow mapping) ultrasound are used to evaluate the anatomic components of the septum – septum primum and septum secundum – and the pattern of interatrial blood flow. In the normal fetus, oxygenated blood from the placenta flows through the umbilical vein to the ductus venosus, streaming through the foramen ovale to the LA. The direction of flow is in a caudal–cephalad direction, which is best imaged in the sagittal plane of the fetus (Figure 11.4a). A restrictive septum or intact atrial septum are important fetal cardiac abnormalities often associated with other congenital heart defects (e.g., transposition of the great arteries, hypoplastic left heart syndrome, tricuspid atresia) and are discussed in their respective chapters.

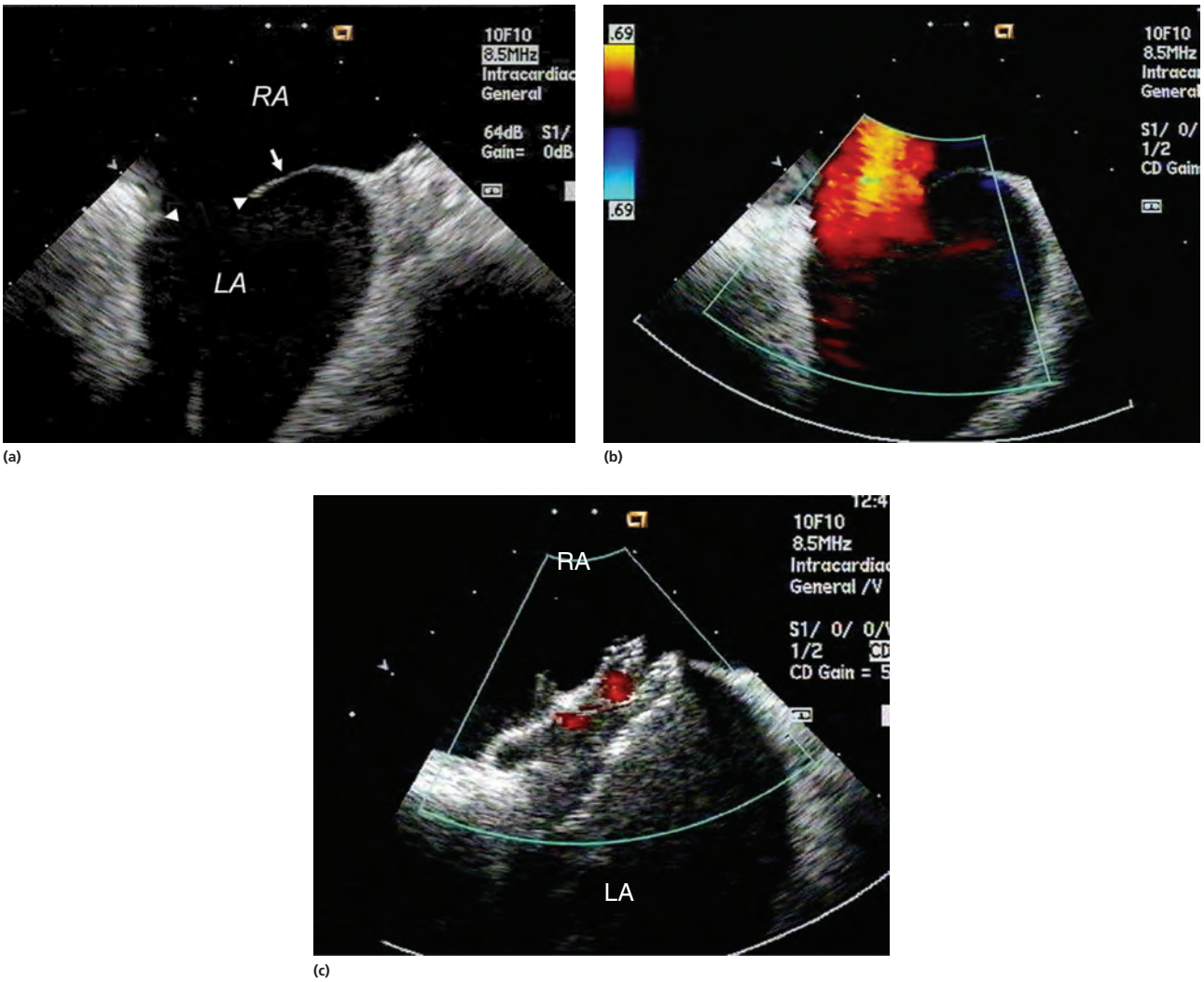
Prenatal diagnosis of an atrial septal defect is challenging. In contrast to primum ASD, which can be reliably diagnosed in most cases, the diagnosis of a secundum ASD is less reliable, especially in the absence of associated congenital heart defects. For example, Driggers et al. found that the agreement between pre- and postnatal echocardiograms for diagnosing secundum ASDs was only modest (kappa = 0.6) [45]. This known limitation of fetal echocardiography is due to the difficulty in distinguishing small-moderate secundum ASDs from the normal flow through a patent foramen ovale. With regard to prenatal diagnosis of sinus venosus or coronary sinus septal defects, the data published to date are scant. However, it is worth noting that the study of Driggers and colleagues demonstrated a weak ability to diagnose partially anomalous pulmonary venous connections by fetal echocardiography [45].

Imaging of the adult

The main challenge in the evaluation of the atrial septum in the adult is technical, relating to difficulties in obtaining clear images and Doppler signals from subcostal or transthoracic acoustic windows. The ability of transthoracic echocardiography (TTE) to diagnose sinus venosus defect in adults is even poorer with only one in four cases correctly diagnosed [46]. Enlargement of right heart chambers associated with flattening of the interventricular septum during diastole indicative of right ventricular volume overload should prompt suspicion of atrial-level shunting. Therefore, when clinical, electrocardiographic, radiographic, and/or echocardiographic evidence suggests an intracardiac shunt and TTE is inconclusive, further evaluation is warranted. Transesophageal echocardiography (TEE) provides an excellent alternative to transthoracic imaging, allowing for clear imaging of the fossa ovalis, sinus venosus septum, cardiac ends of the pulmonary veins, and the coronary sinus [46–57]. Cardiac MRI provides a noninvasive alternative to TEE in adults with suspected ASDs, allowing clear visualization of the anatomic elements of the atrial septum as well as accurate quantification of right ventricular size and function and the ratio of pulmonary-to-systemic flow [33,58–60]. Advantages of MRI over TEE include avoidance of sedation or anesthesia, which is required for TEE, visualization of extracardiac anatomy (e.g., systemic and pulmonary veins), and hemodynamic assessment of the right heart volume load. The advantage of TEE over MRI is its superior spatial resolution allowing it to clearly visualize small secundum ASDs and to evaluate the presence of absence of a PFO.

Echocardiographic guidance of transcatheter ASD closure

The limited ability of X-ray fluoroscopy to image the atrial septum renders echocardiographic guidance essential for transcatheter closure of secundum ASD and PFO. Transesophageal echocardiography has been used to guide transcatheter device placement since the 1980s [49,61–63]. Technological advances, including miniaturization and development of high-resolution multiplane and 3D probes, have greatly enhanced the clinical utility of TEE in patients with congenital heart disease. More recently, intracardiac echocardiography (ICE) has been advocated as an alternative to TEE (Figure 11.15; Videos 11.12 and 11.13) [64–70]. Although extensive experience with TEE during transcatheter closure of ASDs has demonstrated its usefulness [49], the procedure is usually performed under general anesthesia with endotracheal intubation to protect the airways and to provide adequate ventilation. An expert echocardiographer usually performs imaging, and this adds to the cost and personnel associated with the procedure. Although, ICE requires the use of an expensive disposable imaging catheter, which increases the cost of the procedure, the catheterization



(a) (b) (c)

Figure 11.15 Intracardiac echocardiographic imaging of secundum ASD. **(a)** The arrowheads point to the margins of the defect. The white arrow points to septum primum. **(b)** Color Doppler flow mapping showing flow from the left atrium to the right atrium. **(c)** After deployment of an atrial septal defect occluding device, no left-to-right flow is seen. LA, left atrium; RA, right atrium.

team can perform imaging. In a study that compared the hospital charges and costs of 20 TEE-guided ASD closures with 20 ICE-guided procedures, Alboliras and Hijazi found that on average, ICE was more expensive than TEE [71]. Therefore, the choice of transesophageal versus intracardiac echocardiographic guidance of transcatheter closure of ASDs depends on institutional experience, availability of resources (e.g., anesthesia support and expert echocardiographers), and future technological advances (e.g., miniaturization of real-time 3D imaging probes).

Echocardiographic support for transcatheter ASD or PFO closure can be divided into three phases – before, during, and after device deployment.

1 **Before device deployment:** Imaging of the location and size of the defect(s) and its relationships with neighboring structures, including the AV valves, venae cavae, and right pulmonary veins (Figure 11.16). Identification of multiple defects is particularly important for planning the procedure. The margins (rims) of the defect are measured as well as the total septal length. Many centers also measure the stretched diameter of the defect based on echocardiographic and fluoroscopic measurements of a balloon inflated across the defect (Figure 11.17). Color and spectral Doppler are used to evaluate the transseptal shunt. The pulmonary veins are imaged to exclude partially anomalous pulmonary venous connection and the degree of AV valve regurgitation is evaluated as baseline for comparison after device deployment. In patients with associated congenital heart disease, a comprehensive TEE is recommended before device deployment.
2 **During device deployment:** First, the course and position of the sheath are ascertained. Next, the LA arms or disc are released. The catheter and device are then retracted to approximate the LA arms/disc against the LA septal surface with

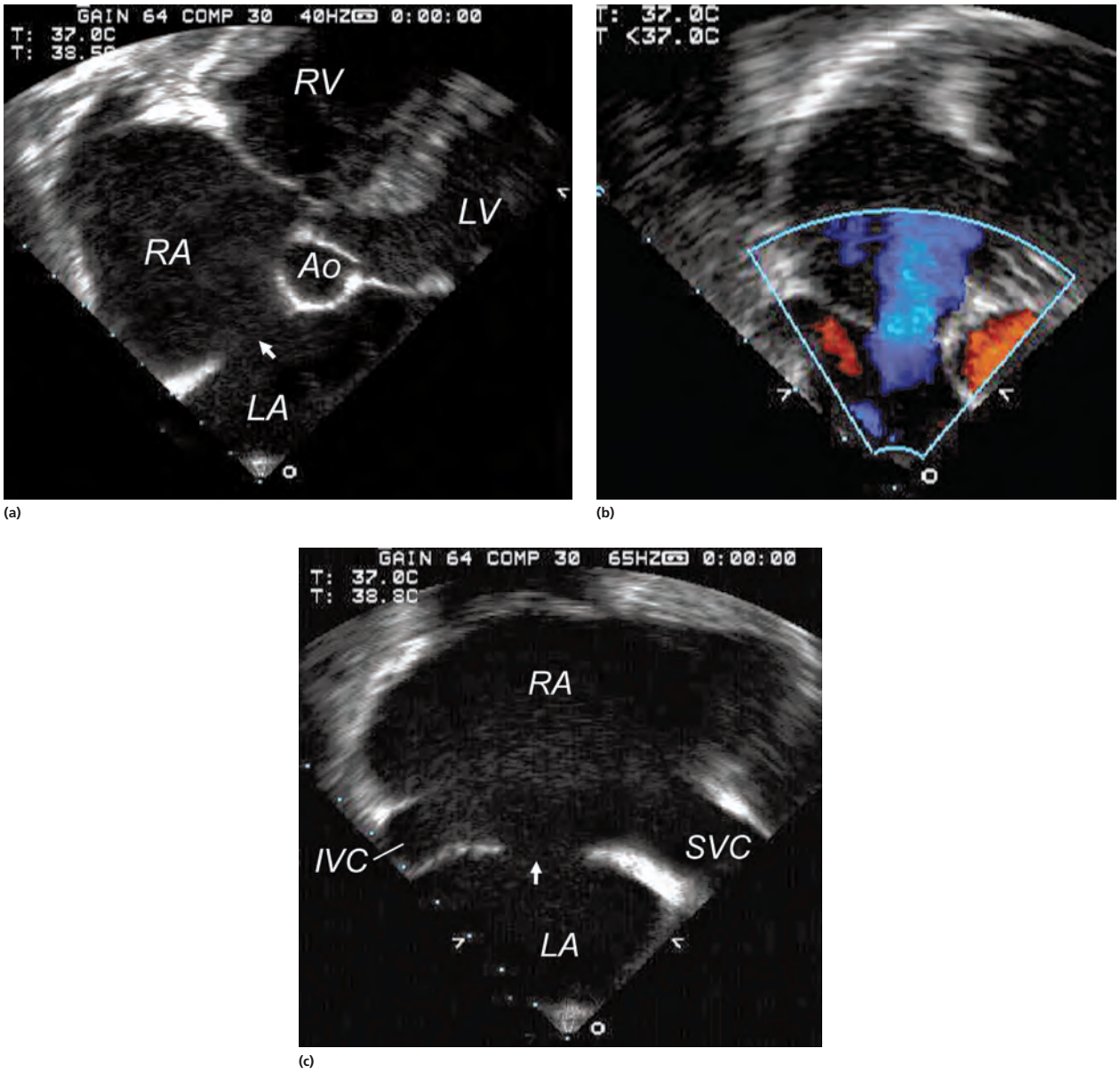


Figure 11.16 Transesophageal echocardiographic imaging of secundum atrial septal defect. **(a)** Horizontal plane image showing a moderate-sized secundum atrial septal defect (arrow). Note the retroaortic (Ao) location of the defect. **(b)** Color Doppler flow mapping showing flow from the left atrium (LA) to the right atrium (RA). **(c)** Vertical plane image showing the superior-inferior dimension of the secundum defect (arrow). IVC, inferior vena cava; SVC, superior vena cava.

particular attention to the orientation of the device relative to the atrial septal plane (Figure 11.18a). Once the device is in proper position, the RA arms/disc are released (Figure 11.18b). Again, proper position is ascertained before the device is released (Figure 11.18c; Video 11.14).

3 **After deployment:** Imaging aims to evaluate the proper and stable device position across the atrial septum, the presence, location, and extent of residual transseptal flow, device impingement on neighboring structures (SVC, IVC, coronary sinus, pulmonary veins, or AV valves), and any adverse change that might be related to the procedure.

Key to a successful procedure is effective communication between the imaging, catheterization, and anesthesia teams. The echocardiographic images should be clearly available to the catheterization team, preferably through a dedicated high-resolution screen mounted beside the fluoroscopy and the physiologic monitoring screens.

Intraoperative assessment

Although intraoperative echocardiography can be used during surgical closure of ASD, its utility varies according to defect type and associated anomalies. Randolph et al. demonstrated a

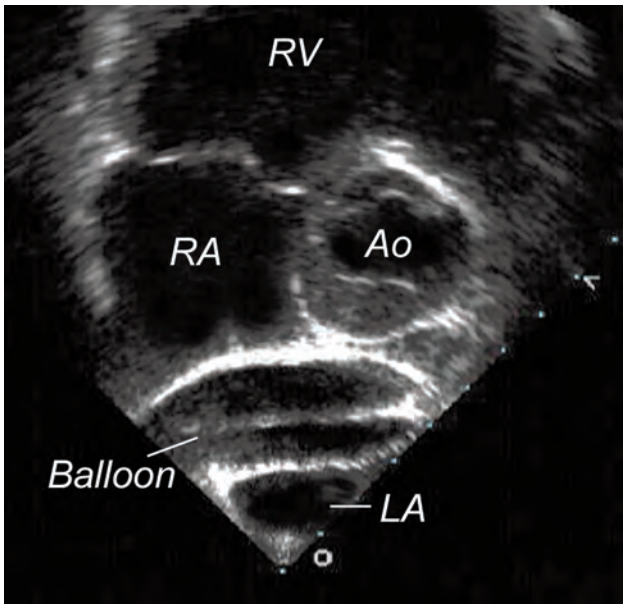


Figure 11.17 Balloon sizing of secundum atrial septal defect. Ao, aortic root; LA, left atrium; RA, right atrium; RV, right ventricle.

low rate of major findings before and after surgical closure of secundum ASD [72]. However, intraoperative TEE is considered helpful during repair of sinus venosus defects, coronary sinus septal anomalies, complex intra-atrial baffles, use of minimal access approach, and primum ASD surgery [72–78]. The transesophageal approach is generally preferred because it does not interfere with the surgical field, provides a wider field of view, and often yields superior image quality as compared with epicardial imaging. Miniaturization of multiplane TEE probes has allowed transesophageal imaging in most infants weighing ≥3 kg. Epicardial imaging should be considered in patients in whom TEE is contraindicated or considered hazardous [79], and in circumstances where real-time 3D imaging is desirable. Goals of the pre-cardiopulmonary bypass examination include confirmation of the preoperative diagnosis and refinement of surgical planning. After cardiopulmonary bypass, imaging is performed to evaluate the integrity of the repair, for the exclusion of residual lesions, and for functional assessment (e.g., ventricular function, AV valve regurgitation). An agitated saline contrast study through a venous cannula placed in a lower extremity can help to exclude inadvertent misplacement of an atrial septal patch incorporating the inferior vena cava into the LA, which usually results from mistaking a prominent Eustachian valve as the inferior margin of the atrial septum [80].

Follow-up assessment

Continued echocardiographic surveillance is important after transcatheter and surgical treatment of all forms of interatrial communications. Although residual transseptal shunts are commonly seen by TEE or ICE immediately after device deployment, their frequency decreases substantially over time with reports indicating 1–2% residual leaks [81–83]. It is worth noting, however, the lower sensitivity of transthoracic color Doppler echocardiography in detecting residual atrial-level shunts as compared with TEE or agitated saline contrast studies [84,85]. A key element of echocardiographic surveillance after transcatheter closure of ASDs is monitoring of the device for late complications, including obstruction of neighboring structures [86], fractures and change in device configuration [87], late migration or embolization of the device [88,89], thrombus formation [90,91], inflammatory reaction leading to abscess formation or local erosion [92,93], and perforation or rupture of cardiac structures [94–96].

Detailed echocardiographic assessment should be performed after surgical repair of ASD to exclude residual shunts, confirm remodeling of the right ventricle and resolution of right heart volume load, and rule out pericardial effusion in the early postoperative period. In patients after repair of sinus venosus and coronary sinus septal defects, the evaluation also includes assessment of the systemic and pulmonary venous pathways. Assessment of biventricular function and valve function, and noninvasive assessment of right ventricular systolic pressure are integral to the echocardiographic follow-up of all patients with repaired ASDs, regardless of the closure technique.

Videos

To access the videos for this chapter, please go to www.lai-echo.com.

Video 11.1 Imaging of normal flow across a patent foramen ovale in an 18-weeks gestation fetus. Note the flow from the ductus venosus through the right atrium and foramen ovale into the left atrium (blue-encoded flow jet).

Video 11.2 Subxiphoid long-axis view showing a patent foramen ovale with a small left–right flow in a newborn.

Video 11.3 Subxiphoid short-axis view showing a patent foramen ovale with a small left–right flow jet in a newborn.

Video 11.4 Subxiphoid long-axis view showing a moderate-sized secundum atrial septal defect due to deficient septum primum.

Video 11.5 Three-dimensional cine loop showing en face view of a secundum atrial septal defect from the right atrium.

Video 11.6 Cine loop of superior vena cava-type sinus venosus defect imaged from the subxiphoid short-axis view. Note the location of the defect above the junction between the superior vena cava and the right atrium.

Video 11.7 Cine loop of superior vena cava-type sinus venosus defect imaged from the subxiphoid short-axis view with color Doppler.

Video 11.8 Cine loop of superior vena cava-type sinus venosus defect imaged from the subxiphoid long-axis view.

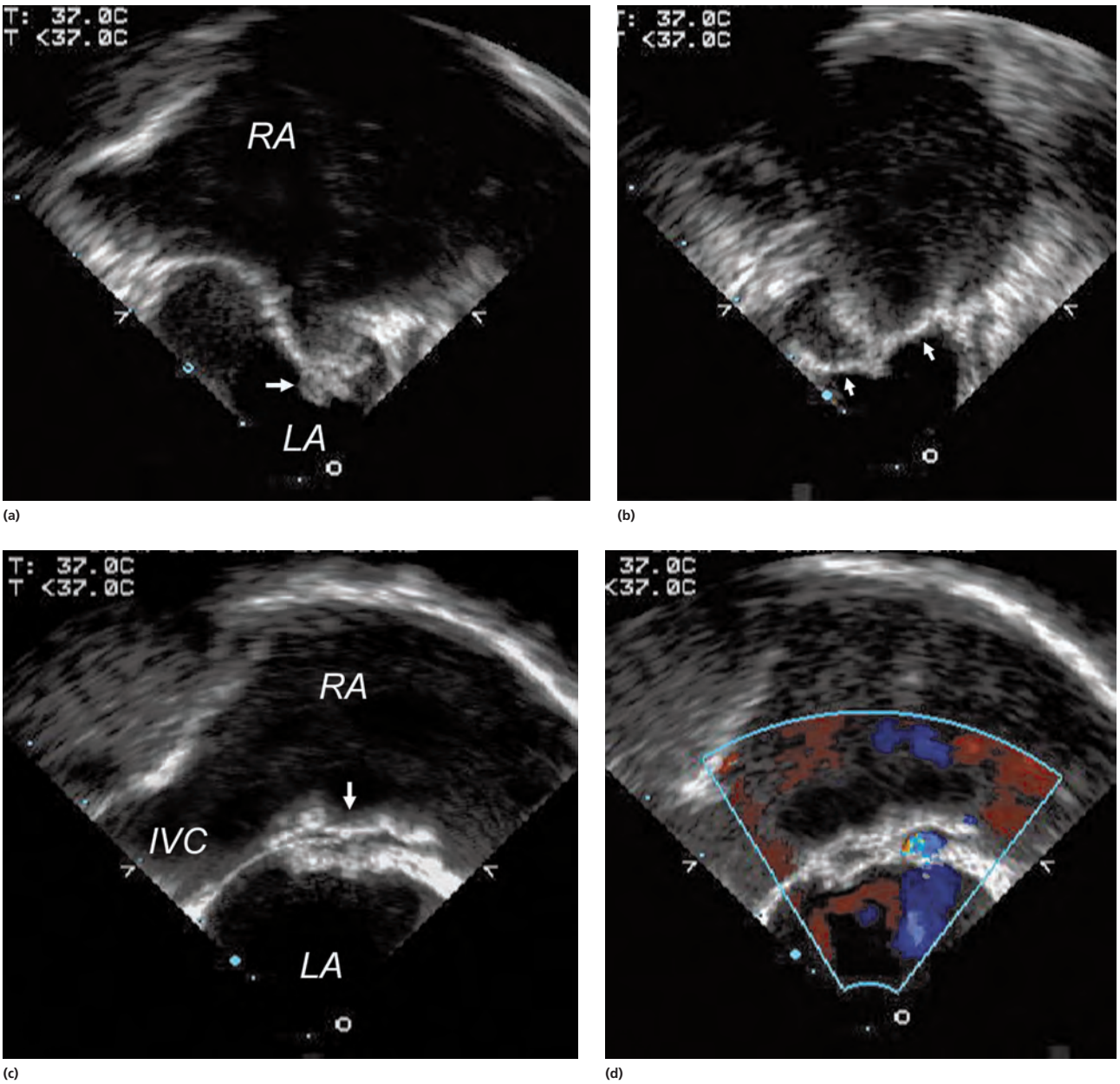


Figure 11.18 Transesophageal echocardiographic guidance of transcatheter device closure of secundum atrial septal defect: **(a)** The device (arrow) is advanced into the left atrium (LA). **(b)** The left atrial arms are opened (arrows) and the device is retracted until the arms are flushed against the left atrial septal surface. **(c)** Vertical plane image showing the deployed device with the left and right atrial arms flushed against the atrial septum. **(d)** Color Doppler flow mapping shows a small amount of flow between the arms of the device but no residual atrial septal defect. IVC, inferior vena cava; RA, right atrium.

Video 11.9 Cine loop of superior vena cava-type sinus venosus defect imaged from the high parasternal short-axis (transverse) view with color Doppler flow mapping. The defect is between the posterior wall of the superior vena cava and the anterior wall of the right upper pulmonary vein.

Video 11.10 Cine loop of right atrial-type sinus venosus defect imaged from the subxiphoid long-axis view. Note large defect between the posterior wall of the right atrium and the anterior wall of the right lower pulmonary vein. The interatrial communication is via the left atrial orifice of the right lower pulmonary vein. This illustrates anomalous drainage of the RLPV to the RA but with normal connection. Note the flow from the right lower pulmonary vein and from the left atrium to the right atrium.

Video 11.11 Cine loop of coronary sinus septal defect with color Doppler flow mapping.

Video 11.12 Intracardiac echocardiogram showing secundum atrial septal defect. LA, left atrium; RA, right atrium.

Video 11.13 Intracardiac echocardiogram showing color Doppler flow mapping through secundum atrial septal defect. LA, left atrium; RA, right atrium.

Video 11.14 Intracardiac echocardiogram showing an occluding device across a secundum atrial septal defect. LA, left atrium; RA, right atrium.

References

1 Hoffman JI, Kaplan S. The incidence of congenital heart disease. *J Am Coll Cardiol* 2002;**39**:1890–1900.
2 Botto LD, Correa A, Erickson JD. Racial and temporal variations in the prevalence of heart defects. *Pediatrics* 2001;**107**:E32.
3 Schott JJ, Benson DW, Basson CT, et al. Congenital heart disease caused by mutations in the transcription factor NKX2-5. *Science* 1998;**281**:108–111.
4 Benson DW, Silberbach GM, Kavanaugh-McHugh A, et al. Mutations in the cardiac transcription factor NKX2.5 affect diverse cardiac developmental pathways. *J Clin Invest* 1999;**104**:1567–1573.
5 McElhinney DB, Geiger E, Blinder J, et al. NKX2.5 mutations in patients with congenital heart disease. *J Am Coll Cardiol* 2003;**42**:1650–1655.
6 D'Amato E, Giacopelli F, Giannattasio A, et al. Genetic investigation in an Italian child with an unusual association of atrial septal defect, attributable to a new familial GATA4 gene mutation, and neonatal diabetes due to pancreatic agenesis. *Diabetic Med* 2010;**27**:1195–1200.
7 Chen Y, Han ZQ, Yan WD, et al. A novel mutation in GATA4 gene associated with dominant inherited familial atrial septal defect. *J Thorac Cardiovasc Surg* 2010;**140**:684–687.
8 Ching YH, Ghosh TK, Cross SJ, et al. Mutation in myosin heavy chain 6 causes atrial septal defect. *Nat Genet* 2005;**37**:423–438.
9 Okubo A, Miyoshi O, Baba K, et al. A novel GATA4 mutation completely segregated with atrial septal defect in a large Japanese family. *J Med Genet* 2004;**41**:e97.
10 Ikeda Y, Hiroi Y, Hosoda T, et al. Novel point mutation in the cardiac transcription factor CSX/NKX2.5 associated with congenital heart disease. *Circ J* 2002;**66**:561–563.
11 Hosoda T, Komuro I, Shiojima I, et al. Familial atrial septal defect and atrioventricular conduction disturbance associated with a point mutation in the cardiac homeobox gene CSX/NKX2-5 in a Japanese patient. *Jpn Circ J* 1999;**63**:425–426.
12 Strauss RM, Ferguson AD, Rittey CD, Cork MJ. Microcephaly-lymphoedema-chorioretinal-dysplasia syndrome with atrial septal defect. *Pediatr Dermatol* 2005;**22**:373–374.
13 Yoshihara K, Ozawa T, Sakuragawa H, et al. [Noonan syndrome associated with atrial septal defect, pulmonary stenosis, and completely unroofed coronary sinus without LSVC: a case report.] *Kyobu Geka* 1999;**52**:134–137.
14 Cunningham ET, Jr., Eliott D, Miller NR, et al. Familial Axenfeld-Rieger anomaly, atrial septal defect, and sensorineural hearing loss: a possible new genetic syndrome. *Arch Ophthalmol* 1998;**116**:78–82.
15 Diegeler A, Van Son JA, Mohr FW. Budd-Chiari syndrome as late complication of secundum atrial septal defect closure. *Eur J Cardiothorac Surg* 1997;**12**:501–503.
16 Shimizu K, Arai H, Sakamoto T, Sunamori M, Suzuki A. Jarcho-Levin syndrome associated with atrial septal defect and partial anomalous pulmonary venous return: a case report. *J Card Surg* 1997;**12**:198–200.
17 Aynaci FM, Ozdemir M, Isik Y. Atrial septal defect in Hallermann Streiff syndrome. *Genet Couns* 1997;**8**:145–146.
18 Holt M, Oram S. Familial heart disease with skeletal malformations. *Br Heart J* 1960;**22**:236–242.
19 Ganie MA, Laway BA, Ahmed S, et al. Mayer-Rokintansky-Kuster-Hauser syndrome associated with atrial septal defect, partial anomalous pulmonary venous connection and unilateral kidney–an unusual triad of anomalies. *J Pediatr Endocrinol Metab* 2010;**23**:1087–1091.
20 Anderson RH, Brown NA, Webb S. Development and structure of the atrial septum. *Heart* 2002;**88**:104–110.
21 Dalgleish AE. The development of the septum primum relative to atrial septation in the mouse heart. *J Morphol* 1976;**149**:369–382.
22 Mommersteeg MT, Soufan AT, de Lange FJ, et al. Two distinct pools of mesenchyme contribute to the development of the atrial septum. *Circ Res* 2006;**99**:351–353.
23 Wessels A, Anderson RH, Markwald RR, et al. Atrial development in the human heart: an immunohistochemical study with emphasis on the role of mesenchymal tissues. *Anat Rec* 2000;**259**:288–300.
24 Van Praagh S, Carrera ME, Sanders SP, et al. Sinus venosus defects: unroofing of the right pulmonary veins–anatomic and echocardiographic findings and surgical treatment. *Am Heart J* 1994;**128**:365–379.
25 Blom NA, Gittenberger-de Groot AC, Jongeneel TH, et al. Normal development of the pulmonary veins in human embryos and formulation of a morphogenetic concept for sinus venosus defects. *Am J Cardiol* 2001;**87**:305–309.
26 Banka P, Bacha E, Powell AJ, et al. Outcomes of inferior sinus venosus defect repair. *J Thorac Cardiovasc Surg* 2011;**142**:517–522.
27 Chin AJ, Murphy JD. Identification of coronary sinus septal defect (unroofed coronary sinus) by color Doppler echocardiography. *Am Heart J* 1992;**124**:1655–1657.
28 Hagen PT, Scholz DG, Edwards WD. Incidence and size of patent foramen ovale during the first 10 decades of life: an autopsy study of 965 normal hearts. *Mayo Clin Proc* 1984;**59**:17–20.
29 Connuck D, Sun JP, Super DM, et al. Incidence of patent ductus arteriosus and patent foramen ovale in normal infants. *Am J Cardiol* 2002;**89**:244–247.
30 Fisher DC, Fisher EA, Budd JH, et al. The incidence of patent foramen ovale in 1,000 consecutive patients. A contrast transesophageal echocardiography study. *Chest* 1995;**107**:1504–1509.
31 Schneider B, Zienkiewicz T, Jansen V, et al. Diagnosis of patent foramen ovale by transesophageal echocardiography and correlation with autopsy findings. *Am J Cardiol* 1996;**77**:1202–1209.
32 Attenhofer Jost CH, Connolly HM, Danielson GK, et al. Sinus venosus atrial septal defect: long-term postoperative outcome for 115 patients. *Circulation* 2005;**112**:1953–1958.
33 Valente AM, Sena L, Powell AJ, et al. Cardiac magnetic resonance imaging evaluation of sinus venosus defects: comparison to surgical findings. *Pediatr Cardiol* 2007;**28**:51–56.
34 Raghib G, Ruttenberg HD, Anderson RC, et al. Termination of left superior vena cava in left atrium, atrial septal defect, and absence of coronary sinus; a developmental complex. *Circulation* 1965;**31**:906–918.

35 Phillips SJ, Okies JE, Henken D, et al. Complex of secundum atrial septal defect and congestive heart failure in infants. *J Thorac Cardiovasc Surg* 1975;**70**:696–700.

36 Weinberg M, Jr., Miller RA, Hastreiter AR, et al. Congestive heart failure in children with atrial septal defect. *J Thorac Cardiovasc Surg* 1966;**51**:81–87.

37 Engelfriet P, Meijboom F, Boersma E, et al. Repaired and open atrial septal defects type II in adulthood: an epidemiological study of a large European cohort. *Int J Cardiol* 2008;**126**:379–385.

38 Saxena A, Divekar A, Soni NR. Natural history of secundum atrial septal defect revisited in the era of transcatheter closure. *Indian Heart J* 2005;**57**:35–38.

39 Shah D, Azhar M, Oakley CM, et al. Natural history of secundum atrial septal defect in adults after medical or surgical treatment: a historical prospective study. *Br Heart J* 1994;**71**:224–227; discussion 8.

40 Hanslik A, Pospisil U, Salzer-Muhar U, et al. Predictors of spontaneous closure of isolated secundum atrial septal defect in children: a longitudinal study. *Pediatrics* 2006;**118**:1560–1565.

41 Cockerham JT, Martin TC, Gutierrez FR, et al. Spontaneous closure of secundum atrial septal defect in infants and young children. *Am J Cardiol* 1983;**52**:1267–1271.

42 Holmvang G, Palacios IF, Vlahakes GJ, et al. Imaging and sizing of atrial septal defects by magnetic resonance. *Circulation* 1995;**92**:3473–3480.

43 Durongpisitkul K, Tang NL, Soongswang J, et al. Predictors of successful transcatheter closure of atrial septal defect by cardiac magnetic resonance imaging. *Pediatr Cardiol* 2004;**25**:124–130.

44 Rosenzweig BP, Nayar AC, Varkey MP, Kronzon I. Echo contrast-enhanced diagnosis of atrial septal defect. *J Am Soc Echocardiogr* 2001;**14**:155–157.

45 Driggers RW, Spevak PJ, Crino JP, et al. Fetal anatomic and functional echocardiography: a 5-year review. *J Ultrasound Med* 2003;**22**:45–51; quiz 2–3.

46 Kronzon I, Tunick PA, Freedberg RS, et al. Transesophageal echocardiography is superior to transthoracic echocardiography in the diagnosis of sinus venosus atrial septal defect. *J Am Coll Cardiol* 1991;**17**:537–542.

47 Tempe DK, Sharma S, Banerjee A, et al. The utility of transesophageal echocardiography for detecting residual shunt in a patient undergoing atrial septal defect repair. *Anesth Analg* 2007;**104**:777–778.

48 Trinca M, Caeiro A, Fernandes R, Semedo P, Jara A. Sinus venosus atrial septal defect in an adult, diagnosed by transesophageal echocardiography. *Rev Port Cardiol* 2006;**25**:369–370.

49 Kleinman CS. Echocardiographic guidance of catheter-based treatments of atrial septal defect: transesophageal echocardiography remains the gold standard. *Pediatr Cardiol* 2005;**26**:128–134.

50 Pascoe RD, Oh JK, Warnes CA, et al. Diagnosis of sinus venosus atrial septal defect with transesophageal echocardiography. *Circulation* 1996;**94**:1049–1055.

51 Oh JK, Seward JB, Khandheria BK, et al. Visualization of sinus venosus atrial septal defect by transesophageal echocardiography. *J Am Soc Echocardiogr* 1988;**1**:275–277.

52 Mehta RH, Helmcke F, Nanda NC, et al. Transesophageal Doppler color flow mapping assessment of atrial septal defect. *J Am Coll Cardiol* 1990;**16**:1010–1016.

53 Hausmann D, Daniel WG, Mugge A, et al. Value of transesophageal color Doppler echocardiography for detection of different types of atrial septal defect in adults. *J Am Soc Echocardiogr* 1992;**5**:481–488.

54 Lin SL, Ting CT, Hsu TL, et al. Transesophageal echocardiographic detection of atrial septal defect in adults. *Am J Cardiol* 1992;**69**:280–282.

55 Sunaga Y, Hayashi K, Okubo N, et al. Transesophageal echocardiographic diagnosis of coronary sinus type atrial septal defect. *Am Heart J* 1992;**124**:1657–1659.

56 Watanabe F, Takenaka K, Suzuki J, et al. Visualization of sinus venosus-type atrial septal defect by biplane transesophageal echocardiography. *J Am Soc Echocardiogr* 1994;**7**:179–181.

57 Jean D, Girard F, Couture P, et al. Transesophageal echocardiographic diagnosis of sinus venosus-type atrial septal defect associated with partial anomalous venous connections during cardiac surgery in adults. *J Cardiothorac Vasc Anesth* 1995;**9**:438–441.

58 Durongpisitkul K, Tang NL, Soongswang J, et al. Cardiac magnetic resonance imaging of atrial septal defect for transcatheter closure. *J Med Assoc Thai* 2002;**85**:S658–666.

59 Taylor AM, Stables RH, Poole-Wilson PA, Pennell DJ. Definitive clinical assessment of atrial septal defect by magnetic resonance imaging. *J Cardiovasc Magn Reson* 1999;**1**:43–47.

60 Holmvang G. A magnetic resonance imaging method for evaluating atrial septal defects. *J Cardiovasc Magn Reson* 1999;**1**:59–64.

61 Hellenbrand WE, Fahey JT, McGowan FX, et al. Transesophageal echocardiographic guidance of transcatheter closure of atrial septal defect. *Am J Cardiol* 1990;**66**:207–213.

62 Hijazi Z, Wang Z, Cao Q, et al. Transcatheter closure of atrial septal defects and patent foramen ovale under intracardiac echocardiographic guidance: feasibility and comparison with transesophageal echocardiography. *Catheter Cardiovasc Interv* 2001;**52**:194–199.

63 Latiff HA, Samion H, Kandhavel G, et al. The value of transesophageal echocardiography in transcatheter closure of atrial septal defects in the oval fossa using the Amplatzer septal occluder. *Cardiol Young* 2001;**11**:201–204.

64 Baglini R. Intracardiac echocardiography in monitoring atrial septal defect percutaneous closure: initial experience in an adult laboratory. *Int J Cardiol* 2007;**114**:274–276.

65 Zanchetta M, Rigatelli G, Pedon L, et al. Transcatheter atrial septal defect closure assisted by intracardiac echocardiography: 3-year follow-up. *J Interv Cardiol* 2004;**17**:95–98.

66 Zanchetta M. On-line intracardiac echocardiography alone for Amplatzer Septal Occluder selection and device deployment in adult patients with atrial septal defect. *Int J Cardiol* 2004;**95**:61–68.

67 Earing MG, Cabalka AK, Seward JB, et al. Intracardiac echocardiographic guidance during transcatheter device closure of atrial septal defect and patent foramen ovale. *Mayo Clin Proc* 2004;**79**:24–34.

68 Zanchetta M, Pedon L, Rigatelli G, et al. Intracardiac echocardiography evaluation in secundum atrial septal defect transcatheter closure. *Cardiovasc Intervent Radiol* 2003;**26**:52–57.

69 Zanchetta M, Onorato E, Rigatelli G, et al. Intracardiac echocardiography-guided transcatheter closure of secundum atrial septal defect: a new efficient device selection method. *J Am Coll Cardiol* 2003;**42**:1677-82.

70 Butera G, Chessa M, Bossone E, et al. Transcatheter closure of atrial septal defect under combined transesophageal and intracardiac echocardiography. *Echocardiography* 2003;**20**:389–390.

71 Alboliras ET, Hijazi ZM. Comparison of costs of intracardiac echocardiography and transesophageal echocardiography in monitoring percutaneous device closure of atrial septal defect in children and adults. *Am J Cardiol* 2004;**94**:690–692.
72 Randolph GR, Hagler DJ, Connolly HM, et al. Intraoperative transesophageal echocardiography during surgery for congenital heart defects. *J Thorac Cardiovasc Surg* 2002;**124**:1176–1182.
73 Muhiudeen Russell IA, Miller-Hance WC, Silverman NH. Intraoperative transesophageal echocardiography for pediatric patients with congenital heart disease. *Anesth Analg* 1998;**87**:1058–1076.
74 O'Leary PW, Hagler DJ, Seward JB, et al. Biplane intraoperative transesophageal echocardiography in congenital heart disease. *Mayo Clin Proc* 1995;**70**:317–326.
75 Rosenfeld HM, Gentles TL, Wernovsky G, et al. Utility of intraoperative transesophageal echocardiography in the assessment of residual cardiac defects. *Pediatr Cardiol* 1998;**19**:346–351.
76 Stevenson JG. Role of intraoperative transesophageal echocardiography during repair of congenital cardiac defects. *Acta Paediatr Suppl* 1995;**410**:23–33.
77 Stevenson JG. Utilization of intraoperative transesophageal echocardiography during repair of congenital cardiac defects: a survey of North American centers. *Clin Cardiol* 2003;**26**:132–134.
78 Bichell DP, Geva T, Bacha EA, et al. Minimal access approach for the repair of atrial septal defect: the initial 135 patients. *Ann Thorac Surg* 2000;**70**:115–118.
79 Ayres NA, Miller-Hance W, Fyfe DA, et al. Indications and guidelines for performance of transesophageal echocardiography in the patient with pediatric acquired or congenital heart disease: report from the task force of the Pediatric Council of the American Society of Echocardiography. *J Am Soc Echocardiogr* 2005;**18**:91–98.
80 Beitzke D, Koestenberger M, Knez I, Beitzke A. Anomalous connection of the inferior vena cava to the left atrium: a surgical error in closing an atrial septal defect. *Clin Res Cardiol* 2008;**97**:191–193.
81 Nugent AW, Britt A, Gauvreau K, et al. Device closure rates of simple atrial septal defects optimized by the STARFlex device. *J Am Coll Cardiol* 2006;**48**:538–544.
82 Hijazi ZM, Cao Q, Patel HT, et al. Transesophageal echocardiographic results of catheter closure of atrial septal defect in children and adults using the Amplatzer device. *Am J Cardiol* 2000;**85**:1387–1390.
83 Spies C, Timmermanns I, Schrader R. Transcatheter closure of secundum atrial septal defects in adults with the Amplatzer septal occluder: intermediate and long-term results. *Clin Res Cardiol* 2007;**96**:340–346.
84 Belkin RN, Pollack BD, Ruggiero ML, et al. Comparison of transesophageal and transthoracic echocardiography with contrast and color flow Doppler in the detection of patent foramen ovale. *Am Heart J* 1994;**128**:520–525.
85 Waggoner AD, Davila-Roman VG, Hopkins WE, et al. Comparison of color flow imaging and peripheral venous saline contrast during transesophageal echocardiography to evaluate right-to-left shunt at the atrial level. *Echocardiography* 1993;**10**:59–66.
86 Soo AW, Healy DG, Walsh K, Wood F. Inferior vena cava and coronary sinus obstruction after percutaneous atrial septal defect device closure requiring surgical revision. *J Thorac Cardiovasc Surg* 2006;**131**:1405–1406.
87 Spence MS, Qureshi SA. Complications of transcatheter closure of atrial septal defects. *Heart* 2005;**91**:1512–1514.
88 Hsiao JF, Hsu LA, Chang CJ, et al. Late migration of a sideris septal occluder device for closure of atrial septal defect into the left atrium with mitral valve obstruction. *Am J Cardiol* 2007;**99**:1479–1480.
89 Cotts T, Strouse PJ, Graziano JN. Late migration of a Sideris buttoned device for occlusion of atrial septal defect. *Catheter Cardiovasc Interv* 2006;**68**:754–757.
90 Clarke AC, Hirsch KJ, Kells CM, Howlett J. Thrombus formation on an atrial septal defect closure device. *Can J Cardiol* 2005;**21**:68–70.
91 Divchev D, Schaefer A, Fuchs M, et al. Thrombus formation on an atrial septal defect closure device: a case report and review of the literature. *Eur J Echocardiogr* 2007;**8**:53–56.
92 Divchev D, Podewski EK, Mengel M, et al. Inflammatory, abscess-forming foreign body reaction mimics a thrombus formation on an atrial septal defect closure device: a commented case report. *Eur J Echocardiogr* 2007;**8**:298–302.
93 Meier B. Iatrogenic atrial septal defect, erosion of the septum primum after device closure of a patent foramen ovale as a new medical entity. *Catheter Cardiovasc Interv* 2006;**68**:165–168.
94 Baykut D, Doerge SE, Grapow M, et al. Late perforation of the aortic root by an atrial septal defect occlusion device. *Ann Thorac Surg* 2005;**79**:e28.
95 Divekar A, Gaamangwe T, Shaikh N, et al. Cardiac perforation after device closure of atrial septal defects with the Amplatzer septal occluder. *J Am Coll Cardiol* 2005;**45**:1213–1218.
96 Amin Z, Hijazi ZM, Bass JL, et al. Erosion of Amplatzer septal occluder device after closure of secundum atrial septal defects: review of registry of complications and recommendations to minimize future risk. *Catheter Cardiovasc Interv* 2004;**63**:496–502.

CHAPTER 12

Ventricular Septal Defects

Shobha Natarajan and Meryl S. Cohen
The Children's Hospital of Philadelphia, Philadelphia, PA, USA

Definition

A ventricular septal defect (VSD) is defined as a communication between the left and right ventricles or between the left ventricle and the right atrium. VSDs are amongst the most common abnormalities of the heart. They can be present in isolation or in association with other congenital cardiac abnormalities. In fact, a VSD is a major component of such abnormalities as tetralogy of Fallot, double outlet ventricle, truncus arteriosus, and common atrioventricular (AV) canal defect. VSDs are also frequently seen in association with transposition of the great arteries and arch anomalies. This chapter describes VSDs that occur in the setting of normally related great arteries. VSDs in association with conotruncal anomalies are described in other chapters.

Incidence

The reported incidence of VSD has varied widely, due at least in part to varying diagnostic methodologies and the natural history of VSD. Large population-based studies provide sufficient live births (denominators) at the expense of an inability to detect all with congenital heart disease (numerators), whereas intensive, sensitive studies usually cannot be done on very large populations [1]. Given the high propensity of VSDs to close spontaneously, starting as early as in utero, the incidence of VSD would be much higher if all fetuses were examined, somewhat lower if all newborns were examined, even lower if only those newborns with murmurs were examined, and lower still if subjects were first evaluated at 1 year of age [2]. Prior to the wide availability of echocardiography, the incidence of VSD was reported between 30 and 240 per 100,000 births [3–5]. More recently, a higher incidence of VSD has been reported, particularly in premature infants [6–10]. Utilizing screening echocardiography in neonates, a muscular ventricular septal defect was diagnosed in 5320 and 5660 per 100,000 term and preterm babies, respectively [8,9]. Groups reporting a high incidence have also reported high rates of spontaneous closure of these defects. The perceived increase in the incidence of VSD may be due to increased sensitivity of perinatal and neonatal surveillance rather than to a true increase in incidence. Between 10,000 and 11,000 infants with an isolated VSD are diagnosed annually in the United States [5,11,12]. Between 15% and 20% of these patients require surgery [13]. If VSD in association with other congenital heart anomalies were included, the incidence of VSD would be much higher.

Etiology

Like other congenital heart defects, the etiology of VSD is multifactorial. Moreover, different types of VSDs likely arise from different developmental abnormalities. VSDs are quite prevalent in association with genetic syndromes, especially in trisomy 13, 18, or 21 as well as other less common syndromes [14–16]. In the autosomal dominant Holt–Oram syndrome, both atrial and ventricular septal defects are inherited in association with limb deformities as a result of mutations in the gene encoding the transcription factor TBX5 [17]. The Baltimore-Washington Infant Study has reported an association between paternal use of marijuana and cocaine and paternal occupation such as jewelry making and paint stripping with the occurrence of VSDs in their offspring [18,19].

Morphology and classification

Development

Detailed description of the development of the human heart is provided elsewhere [20–31]. Septation of the ventricles involves a complex series of events. The transitional zone between the embryonic left and right ventricles (LV and RV) is characterized by the expression of "neuromuscular" markers, and forms a ring around the primary interventricular foramen, termed the "primary ring" [26,32–34]. This ring separates the upstream portion (the atrium and LV) from the downstream portion (the RV

Echocardiography in Pediatric and Congenital Heart Disease: From Fetus to Adult, Second Edition. Edited by Wyman W. Lai, Luc L. Mertens, Meryl S. Cohen and Tal Geva.
© 2016 John Wiley & Sons, Ltd. Published 2016 by John Wiley & Sons, Ltd.
Companion website: www.lai-echo.com

ISNPCHD*	Van Praagh, Weinberg	Anderson	Other
Central	Conoventricular membranous	Perimembranous	Paramembranous Infracristal
Inlet	Atrioventricular canal type	Perimembranous inlet**	
Outlet	Conal septal, conal septal hypoplasia	Doubly committed subarterial	Subpulmonary defect Juxta-arterial defect Supracristal
Outlet	Malalignment, Conoventricular with malalignment	Perimembranous with malalignment	
Trabecular	Muscular (with naming location: anterior, mid, posterior, apical)	Muscular (with naming inlet, outlet, trabecular, apical)	Trabecular

*International Society for Nomenclature of Paediatric and Congenital Heart Disease
**Distinction is made between the VSD in an atrioventricular canal defect and the VSD in a patient with straddling tricuspid valve (malalignment of the ventricular septum).

Table 12.1 Glossary of terms used to describe ventricular septal defects

and outflow tract) of the heart. Myocardialization and fusion of the endocardial cushions in the outflow tract (outflow-tract ridges) leads to the formation of a muscular outlet (or conal) septum [35]. The muscular interventricular septum is formed from three components: (i) the primary, or trabecular, component that arises from the septum separating the trabeculated cavities of the developing RV and LV and becomes the muscular septum; (ii) the AV canal or inlet component that develops from the AV cushions; and (iii) the conal septum or outlet portion that develops from the outflow-tract ridges. The muscular septum is identifiable between the trabecular portions of both ventricles at 5 weeks' gestation. The fibrous membranous septum is formed by the fused major (superior and inferior) AV cushions and the mesenchymal cap of the primary atrial septum. The bifurcation of the ventricular conduction system is the landmark that separates the contribution of the AV cushions and the outflow-tract ridges to septation [21].

Anatomy

A thorough understanding of the anatomy of the ventricular septum is critical to fully describe and categorize VSDs and optimize treatment strategies. The natural history and prognosis of VSDs vary according to the location of the defect(s). Treatment choices are expanding for some types of VSDs to include transcatheter and innovative surgical options. Several schemes for nomenclature and classification have been proposed and debated. Further discussion about this nomenclature is beyond the scope of this chapter. For the purposes of echocardiography, we choose to define VSDs primarily by their geographic location rather than by their surrounding structures. However, both components are important for complete characterization of the VSD. Thus, for each VSD type, several of the names that are in common usage will be discussed and are listed in Table 12.1. Recently, the International Society for Nomenclature of Paediatric and Congenital Heart Disease has come to a consensus about categorization of VSDs using geographical location as the initial point in the hierarchy but also emphasizing whether there are fibrous or muscular borders to the defects. The four geographical regions include central defects (e.g., perimembranous or conoventricular VSD), inlet defects (atrioventricular canal type with or without malalignment of the ventricular septum or posterior muscular VSD), outlet defects (conal septal or doubly committed subarterial with or without malalignment), and trabecular defects (defects exclusively in the muscular septum).

Anatomy of the ventricular septum

Viewed from the RV, the ventricular septum may be divided into four zones: (i) AV canal (inlet), (ii) muscular (trabecular) or ventricular sinus septum, (iii) septal band, and (iv) parietal band (Figure 12.1) [36,37]. The smooth-walled AV canal (inlet) septum extends inferiorly and posteriorly adjacent to the septal leaflet of the tricuspid valve to the distal septal attachments of the tricuspid valve papillary muscles. Extending inferiorly and anteriorly is the muscular (trabecular) septum, which is characterized by coarse trabeculations on the RV aspect and includes

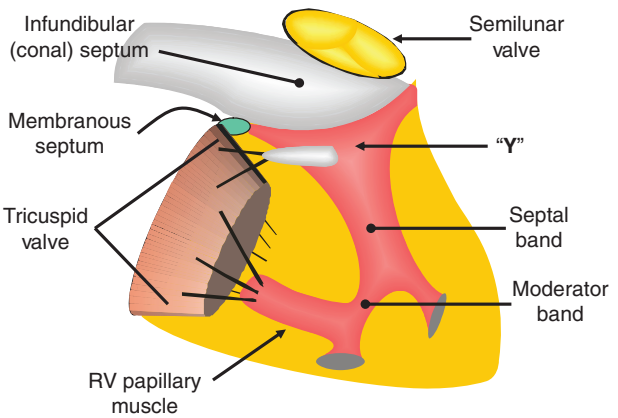


Figure 12.1 Pictorial view of the normal right ventricular (RV) septal wall demonstrates normal landmarks of the ventricular septum. The "Y" indicates the "Y" configuration of the septal band to help define ventricular septal defect (VSD) location.

the moderator band. The muscular (trabecular) septum is separated from the smooth-walled conal (infundibular, outlet) septum by the septal band (septo-marginal trabeculation), which courses superiorly and posteriorly from the mid-portion of the ventricular septum. The septal band divides into an antero-superior limb, which courses superiorly toward the pulmonary valve and blends into the subpulmonary conus (infundibulum), and a postero-inferior limb, which courses towards the RV free wall, where it merges with the parietal band (septo-parietal trabeculation). The conal (infundibular) septum sits within the "Y" of the septal band and in the normal heart is difficult to distinguish from the conal free wall (it becomes more clearly recognized when it is displaced from the "Y" of the septal band). The membranous septum, the fibrous component of the ventricular septum, sits at the inferior edge of the conal septum just superior to the atrioventricular canal (inlet) septum. The membranous septum is divided by the septal leaflet of the tricuspid valve such that a portion sits on the right atrial side (a defect in this area results in the rare left ventricular to right atrial defect, the Gerbode defect [38]) while the other portion is interventricular and is in continuity with all other components of the ventricular septum. On the LV side, the membranous septum sits adjacent to the right coronary-noncoronary commissure of the aortic valve. The conduction tissue, consisting of the AV conduction bundle, the branching bundle and left bundle branch, courses in the posterior-inferior border of the membranous septum.

Conoventricular or perimembranous VSD

A conoventricular defect is the most common type of VSD that requires surgical closure. It is in the central location of the ventricular septum. This defect carries various other names including perimembranous VSD and paramembranous VSD because of its close proximity to or inclusion of the membranous septum. However, many other defects (including atrioventricular canal defects, and malalignment defects) are also located adjacent to the membranous septum. Thus, the terms "perimembranous" or "paramembranous" are nonspecific with regard to location but are better used to describe borders. That being said, the term "perimembranous" is part of the cardiology vernacular. Conoventricular defects are located between the conal (infundibular) septum and the muscular (trabecular) septum near the septal/anterior commissure of the tricuspid valve (Figure 12.2a,b). These defects are typically in fibrous continuity with the tricuspid valve and aortic valve but in some cases, are only in continuity with the tricuspid valve. The tricuspid valve frequently has attachments to the margins of the defect, partially or completely restricting the ventricular level shunt. In some cases, adherence of the tricuspid valve leaflets to the edges of the VSD may cause shunting from the LV directly into the right atrium (not to be confused with a true Gerbode defect). On the LV side, conoventricular VSDs lie adjacent to the commissure between the right and noncoronary cusps of the aortic valve; thus in some cases, a portion of an aortic valve leaflet (most commonly from the right coronary cusp) may prolapse into the VSD and cause aortic regurgitation. Conoventricular VSDs may also be associated with the late development of muscle bundles in the RV outflow tract, so-called double-chambered RV and subaortic membranes.

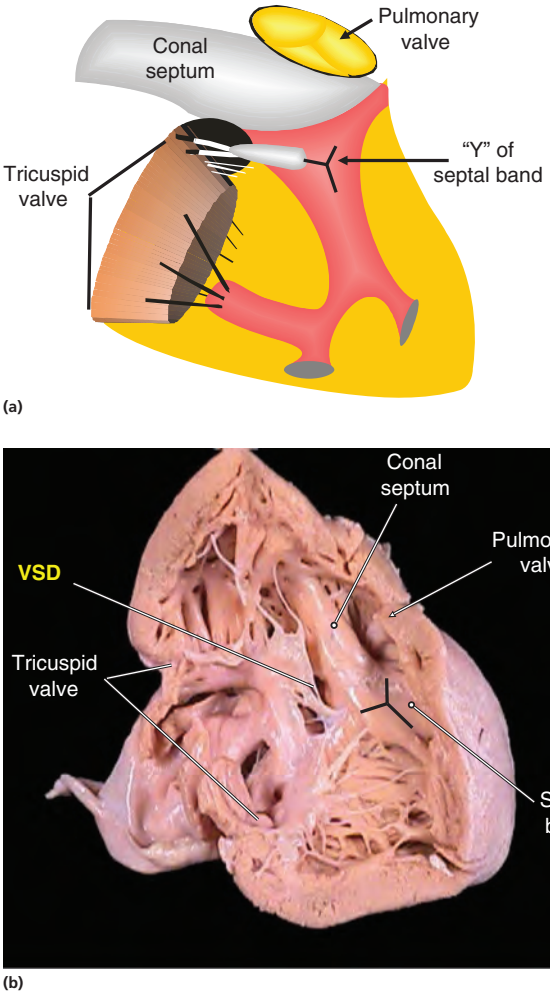
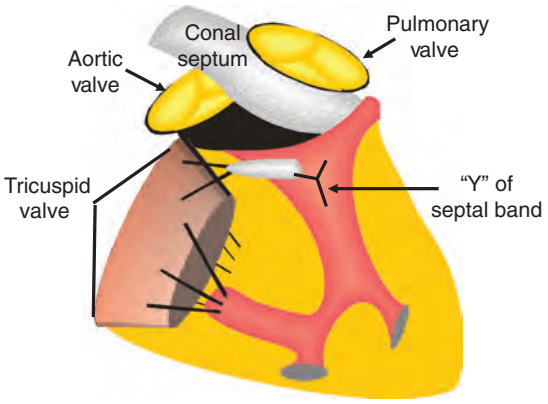


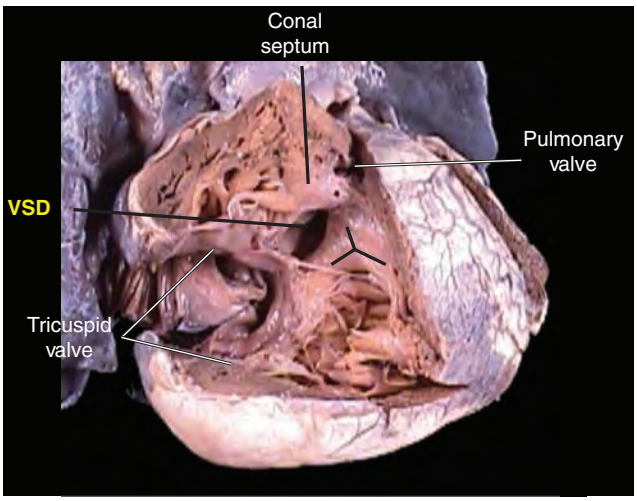
Figure 12.2 **(a)** Pictorial view of the RV septal wall shows a conoventricular type VSD (in black). The defect is seen in proximity to the septal leaflet of the tricuspid valve and usually encompasses the membranous septum as well. **(b)** A pathologic specimen in the same view of the RV septal wall shows a conoventricular type VSD (indicated in yellow) sitting under tricuspid valve septal attachments. The "Y" of septal band is represented by the black Y to show the relationship to the defect.

Malalignment VSD

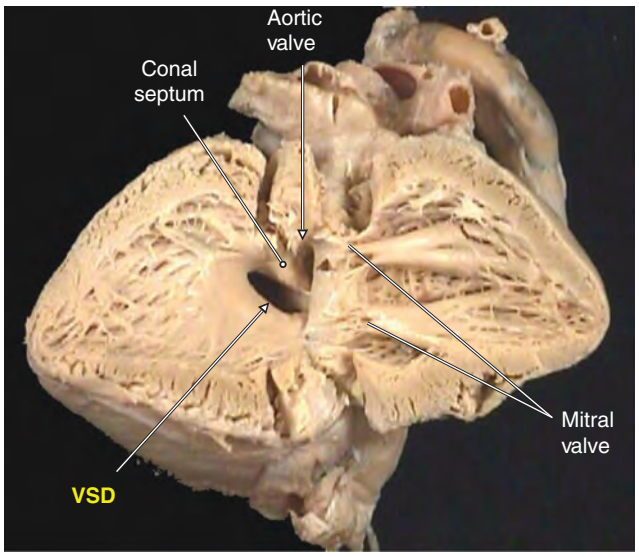
Malalignment defects are defined by the orientation of the conal (infundibular) septum. As such, they are defects in the outlet portion of the ventricular septum. In malalignment defects, the conal septum which normally sits in the "Y" of the septal band, is positioned out of that plane either toward the right ventricular outflow tract (i.e., tetralogy of Fallot) or toward the left ventricular outflow tract (associated with subaortic narrowing) (Figure 12.3a,b). Some refer to malalignment defects as



(a)



(b)



(c)

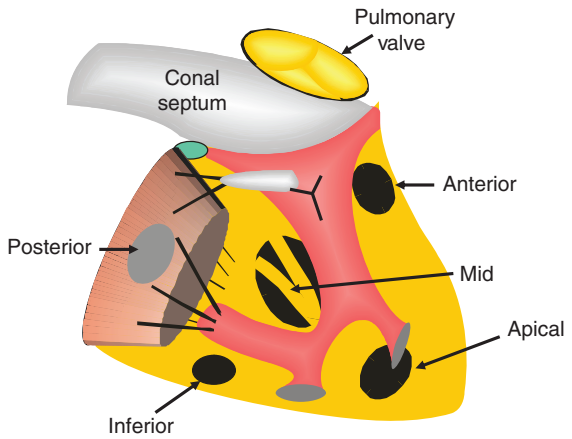
"conoventricular or perimembranous defects with malalignment." Importantly, malalignment defects almost never close spontaneously and generally do not have tricuspid valve tissue attached to the margins of the defect. In rare circumstances, AV valve tissue may be "pulled" into the defect, obstructing ventricular level flow and potentially obstructing an outflow tract. Malalignment defects are commonly associated with other conotruncal malformations such as double outlet ventricle or transposition of the great arteries. In the setting of normally related great arteries, anterior malalignment makes the conal septum an exclusively RV structure that impinges on the subpulmonary region resulting in (i) subpulmonary obstruction, (ii) the aorta positioned over the ventricular septum (overriding aorta), and (iii) right ventricular hypertrophy. These components in addition to the VSD itself make up the diagnosis of tetralogy of Fallot although all are the result of the malaligned conal septum. When anterior malalignment is severe, the conal septum may fuse with the free wall of the right ventricular outflow tract resulting in pulmonary atresia. In cases of mild anterior malalignment, there may be no significant pulmonary outflow tract obstruction; these defects are called "Eisenmenger type" VSDs because the pulmonary vascular bed is not protected from increased flow [39].

In posterior malalignment, the conal septum becomes an exclusively LV structure; as a result, the aorta sits entirely above the LV (Figure 12.3c). It is almost always associated with subaortic narrowing and usually associated with coarctation of the aorta or interruption of the aortic arch. When posterior malalignment is severe, aortic atresia may be present.

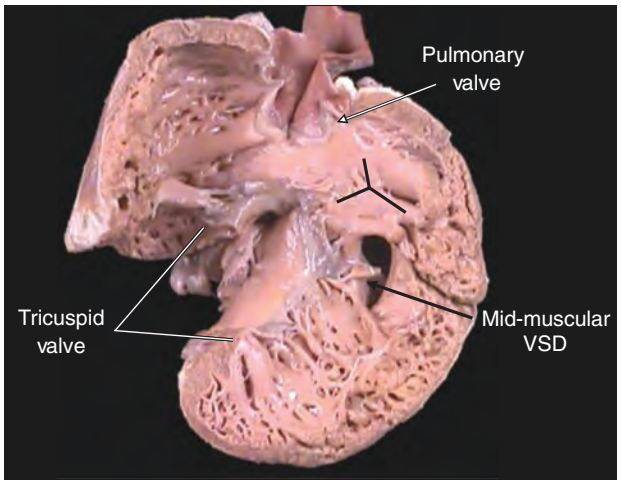
Muscular VSD

Muscular VSDs are the most common defects seen in the fetus and newborn. There is little controversy with regard to name. When small, many muscular VSDs will close spontaneously without intervention. Muscular defects are present in the trabecular portion of the ventricular septum and are entirely surrounded by muscle. Typical designations of more specific location include anterior, posterior, mid-muscular, inferior, and apical (Figure 12.4a,b). In autopsy specimens, muscular VSDs are readily seen on the LV septal surface because of

Figure 12.3 **(a)** Pictorial view of the RV septal wall shows a malalignment type VSD (in black). In this example, anterior malalignment of the conal septum is depicted. The aortic valve is shown in this figure because it is overriding the ventricular septum (tetralogy of Fallot). **(b)** A pathologic specimen in the same view of the RV septal wall shows an anterior malalignment type VSD (indicated in yellow). The conal septum is seen deviated toward the pulmonary valve which is small (i.e., tetralogy of Fallot). The "Y" of septal band is represented by the black Y to show the relationship to the defect. **(c)** A pathologic specimen of the left ventricular septal wall shows a posterior malalignment type VSD (indicated in yellow). The conal septum is seen projecting into the left ventricular outflow tract with a small aortic valve.

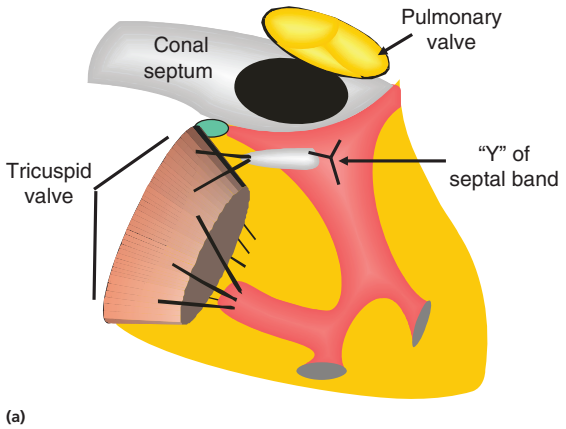


(a)

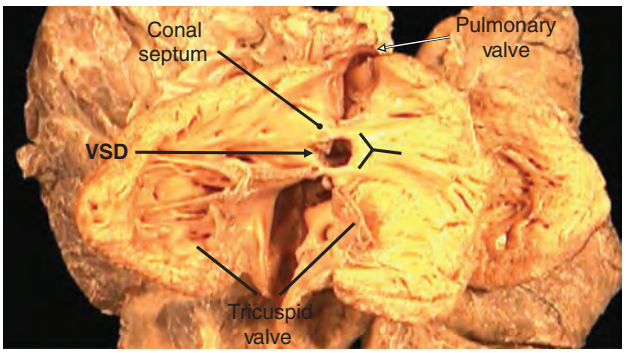


(b)

Figure 12.4 **(a)** Pictorial view of the RV septal wall shows multiple locations of muscular type VSDs (in black). All possible locations of muscular defects are labeled including the posterior muscular defect that sits behind the tricuspid valve. **(b)** A pathologic specimen in the same view of the RV septal wall shows a large mid-muscular type VSD.



(a)



(b)

Figure 12.5 **(a)** Pictorial view of the RV septal wall shows a conal septal type VSD (in black). A portion of the conal septum is absent. The defect is adjacent to the pulmonary valve. Notice that the membranous septum is intact. **(b)** A pathologic specimen in the same view of the RV septal wall shows a conal septal type VSD. Notice its close proximity to the pulmonary valve and that the defect is just above the "Y" of septal band.

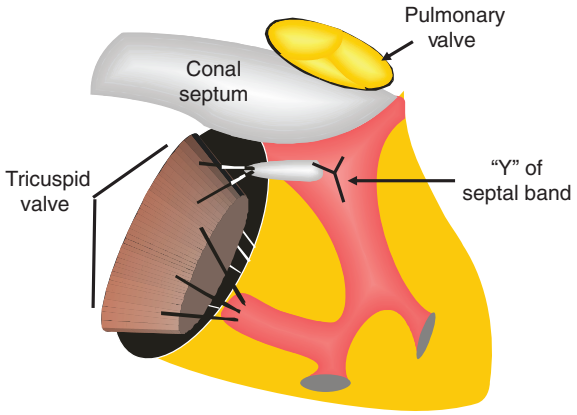
the fine trabeculations but they may be covered by dense and coarse trabeculations on the RV side, giving the appearance of multiple defects – the so-called "Swiss-cheese" septum [40]. Multiple defects in the same patient are also common. Accurate echocardiographic location of these defects is important if surgical or catheter-directed closure is considered.

Conal septal VSD

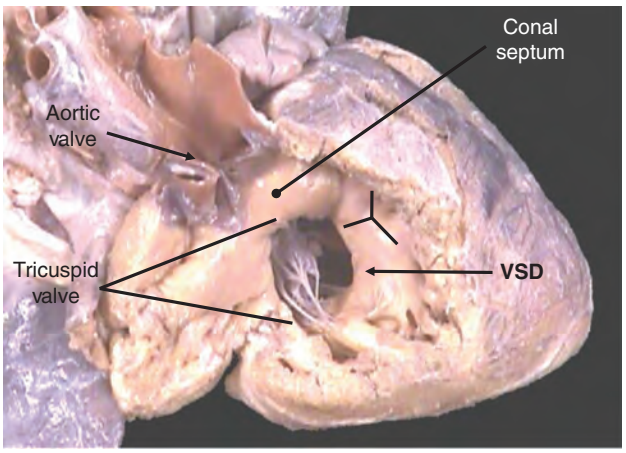
A conal septal VSD occurs in the outlet portion of the ventricular septum and is defined as complete or partial absence of muscle in the conal septum (Figure 12.5a,b). Many other names have been used to describe this type of VSD including doubly committed subarterial defect, subpulmonary defect, juxta-arterial defect, and supracristal defect. This type of defect occurs more frequently in the Asian population. It is important to distinguish conal septal defects from conoventricular defects though they are relatively close in location. Conal septal defects do not close spontaneously and often require a surgical approach through the pulmonary valve for closure. With complete absence of the conal septum, there is fibrous continuity between the adjacent cusps of the aortic and pulmonary valves. Due to the close proximity of these defects to the right coronary cusp of the aortic valve and the lack of support to the aortic valve from below, there is a strong tendency for the right coronary cusp of the aortic valve to prolapse into the VSD resulting in partial or complete closure. Conal septal defects can be seen in combination with malalignment.

Atrioventricular canal VSD

AV canal type VSD occurs in the inlet portion of the ventricular septum and is seen under the entire length of the AV valve (Figure 12.6a,b). The distinction between an AV canal type VSD



(a)



(b)

Figure 12.6 **(a)** Pictorial view of the RV septal wall shows an atrioventricular canal type VSD (in black). Notice that the defect sits along the entire length of the tricuspid valve and that the conoventricular portion of the ventricular septum is also included in the defect. **(b)** A pathologic specimen in the same view of the RV septal wall shows an atrioventricular canal type VSD. Notice that the tricuspid valve is straddling the defect.

and a posterior muscular defect is that the AV canal type VSD has no superior muscular rim between the AV valve and the defect. Both, however, are inlet defects. Importantly, in an AV canal type VSD the conduction tissue courses posterior to the defect resulting in the typical counterclockwise loop on electrocardiogram [41]. Though typically large, AV valve tissue may partially or completely fill in these defects. AV canal type VSDs are most commonly seen in association with the spectrum of common AV canal defects (with ostium primum atrial septal defects and a common AV valve and annulus). However, they can also be seen in patients who have distinct tricuspid and mitral valves. Tricuspid valves straddle exclusively through AV canal type VSDs. This straddling is associated with malalignment between the atrial and ventricular septum with variable degrees of RV hypoplasia [42].

Gerbode type VSD

The Gerbode defect is defined as a communication between the left ventricle and the right atrium in the membranous portion of the ventricular septum that sits above the tricuspid valve [38]. True Gerbode defects (in contrast to defects that result from adherence of the tricuspid valve commissure to the VSD rim) are extremely rare.

Pathophysiology

A VSD may have two closely related adverse consequences: altered hemodynamics due to a left-to-right shunt, and alteration of the pulmonary vascular resistance.

Left-to-right shunt

Left-to-right shunting across a VSD leads to increased pulmonary blood flow. The magnitude of the left-to-right shunt depends on VSD size and the resistance in the pulmonary vascular bed. Based on both these factors, VSDs are broadly divided into three categories: small, moderate, and large [43]. Small VSDs are variably pressure-restrictive, preventing transmission of systemic pressure and usually maintaining a normal RV pressure. Of note, a substantial left-to-right shunt can occur through smaller, pressure-restrictive defects as the pulmonary vascular resistance drops over the first weeks of life. A moderate VSD usually provides some resistance to pressure but little resistance to flow. As a result, this defect leads to variable elevation of RV pressure, and hemodynamically significant left-to-right ventricular shunting. Large VSDs offer little restriction to pressure or flow such that the RV pressure is usually at systemic levels and the left-to-right shunt is large.

Left-to-right shunting across a VSD may lead to three adverse hemodynamic consequences: (i) LV volume overload, (ii) pulmonary overcirculation, and (iii) potentially compromised systemic cardiac output. The increased volume load on the LV leads to dilation, which produces elevation of end-diastolic pressure via the length–tension relationship [44]. LV hypertrophy develops as a compensatory mechanism to minimize the increase in wall tension, but it also decreases ventricular compliance, thus further aggravating the increase in end-diastolic pressure [45]. This elevation in end-diastolic pressure is reflected in increased left atrial and pulmonary venous pressure. The subsequent increase in hydrostatic pressure of the pulmonary capillary bed, leads to the development of pulmonary interstitial fluid and even pulmonary edema [46]. Pulmonary compliance and gas exchange may be altered as a result. Tachypnea is a common symptom of this phenomenon.

Alteration of pulmonary vascular resistance

A hemodynamically significant VSD leads to a "common ejectile force," where RV and pulmonary arterial systolic pressure are systemic. Increased pulmonary blood flow and increased pulmonary arterial pressure may alter the normal maturation of

the pulmonary vascular bed [47]. As the pulmonary resistance drops over the first few weeks after birth, left-to-right shunting of blood increases, leading to pulmonary overcirculation. Heart failure symptoms develop with tachypnea, tachycardia, diaphoresis with feeds, and failure to thrive in infants. Without intervention, this pulmonary overcirculation leads to changes in the pulmonary vascular bed, limiting the left-to-right shunt and decreasing symptoms [48]. The pulmonary arteriole vessel transitions from having a reactive muscular wall to one with potentially irreversible structural changes consisting of medial hypertrophy and intimal proliferation, leading to elevated pulmonary vascular resistance. Eventually, pulmonary vascular resistance elevates to the point of exceeding systemic vascular resistance, leading to right-to-left shunting across the VSD and cyanosis, the so-called Eisenmenger syndrome.

Associated defects

VSDs often occur in isolation. However, in surgical series, nearly 50% of all patients with a VSD have an additional cardiac anomaly [49]. Atrial septal defects, pulmonary stenosis, and a persistent left superior vena cava are seen in up to 13%, 15%, and 8% of VSD patients, respectively [50]. Patent ductus arteriosus in association with VSD is also seen frequently. Conotruncal anomalies such as tetralogy of Fallot, truncus arteriosus or double outlet ventricle almost invariably have a VSD. Double-chambered RV and subaortic stenosis, either separately or in combination, have been reported in up to 10% of patients with a conoventricular VSD in surgical series [51,52].

Aortic regurgitation is an acquired and frequently progressive lesion in some patients with VSD [53]. It develops in association with conoventricular or conal septal type VSDs. The conal septal VSD lies directly below the right coronary cusp of the aortic valve, accounting for the strong tendency of this cusp to prolapse into the VSD. Prolapse of the right coronary cusp of the aortic valve leads to defective apposition of the leaflets. In addition, absence of the conal septum may cause deficient support for the valve apparatus from below. In contrast, the conoventricular VSD lies below both the right and noncoronary cusps of the aortic valve. Aortic regurgitation in this setting has been attributed to prolapse of either of these cusps [54]. Leaflet deformities include elongation, and thickened and rolled edges. The left coronary cusp of the aortic valve is distant from the ventricular septum, and prolapse of this leaflet into a VSD is quite uncommon.

Imaging

Key elements

A complete anatomic and hemodynamic examination with two-dimensional (2D) (and 3D, when appropriate) imaging as well as color and spectral Doppler should be performed to evaluate the VSD and its associated abnormalities. The following elements of the anatomy and physiology should be given priority:

Preoperative examination

- Anatomic assessment
 - Determine VSD type, location, size, and number
 - Demonstrate the relationship of the VSD with adjacent structures (e.g., tricuspid, aortic, and pulmonary valves)
 - Measure defect margins (assessment of suitability for transcatheter closure)
- Hemodynamic assessment
 - Assess direction of flow across defect and document with spectral Doppler
 - Assess degree of restriction across the VSD and RV systolic pressure estimate with the peak velocity and direction of VSD shunt (by color and spectral Doppler)
 - Estimate RV systolic pressure with tricuspid regurgitation peak velocity and ventricular septal curvature at end-systole
 - Determine the degree of volume load to the left side of the heart with LA and LV size and LV systolic and diastolic performance
- Evaluate for associated lesions.

Postoperative/follow-up examination

- Assess for residual/additional VSDs
- Assess TR jet or residual VSD jet velocity to estimate RV pressure
- Evaluate for abnormalities of adjacent valves either involved in the VSD or manipulated during the surgical approach
- Monitor ventricular function and aneurysm formation if the surgical approach involved a ventriculotomy
- Monitor for long-term associations with VSD:
 - Double chamber right ventricle
 - Subaortic membrane/stenosis
 - Aortic insufficiency secondary to valve prolapse.

Transthoracic imaging

Echocardiography has evolved into a universally applicable modality for the comprehensive diagnosis of VSD, including anatomic and hemodynamic assessments [55]. Two-dimensional echocardiography, utilizing a combination of multiple imaging windows, planes, and sweeps, is the mainstay for complete examination of the ventricular septum. As the subxiphoid long-axis sweep progresses superiorly, it profiles the AV canal septum and membranous septum. Advancing superiorly and anteriorly, this sweep demonstrates the muscular septum. The subxiphoid short-axis sweep demonstrates the conal (outlet) septum as well as the muscular septum.

The apical 4-chamber sweep starts posteriorly in the plane of the coronary sinus and the AV valves. This view demonstrates the AV canal septum above, and the posterior and mid-muscular septum below. As the plane of this sweep proceeds anteriorly, the membranous septum comes into view at the septal/anterior commissure of the tricuspid valve.

The parasternal long-axis view transects the aorta and the LV in the long axis and demonstrates the mid and apical muscular septum. Tilting the transducer to the tricuspid inflow and the

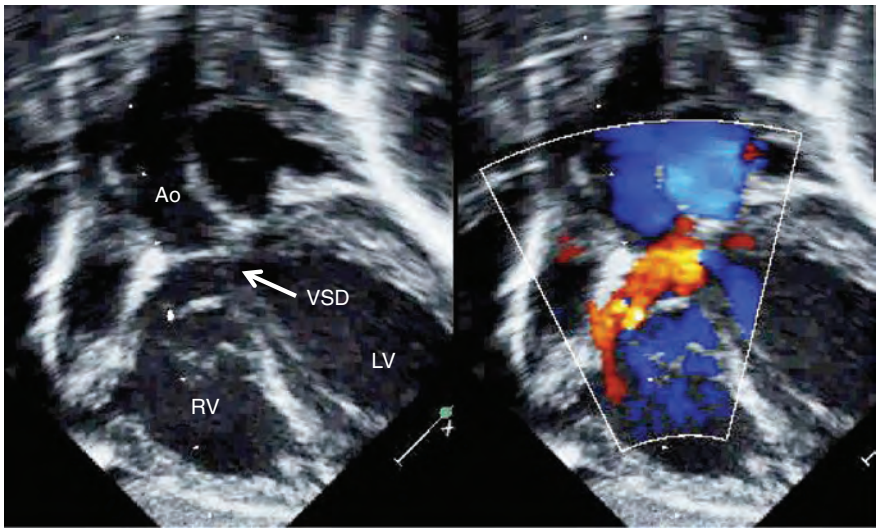


Figure 12.7 Subxiphoid frontal view in color compare mode demonstrates a conoventricular VSD adjacent to the tricuspid and aortic valves with left-to-right shunt by color Doppler.

pulmonary outflow tract demonstrates the membranous septum and conal septum, respectively.

The parasternal short-axis view at the base of the heart demonstrates the membranous septum between the tricuspid valve hinge point (9 o'clock) and 11 o'clock positions. Conal septum is seen between 11 o'clock and the hinge of the pulmonary valve (2 o'clock). As this sweep progresses towards the apex, the muscular septum is profiled well.

Conoventricular VSD

Conoventricular VSDs (also named perimembranous or paramembranous defects) are visualized adjacent to the septal/anterior commissure of the tricuspid valve on the RV side and the commissure between the right and noncoronary cusps of the aortic valve on the LV side. Two-dimensional and color Doppler subxiphoid frontal sweeps provide anatomic visualization of the defect size and degree of restriction to flow (Figure 12.7). The defect can also be visualized in the apical 4-chamber view with anterior angulation between the septal leaflet of the tricuspid valve and the aortic valve. In the parasternal short-axis view at the base of the heart, conoventricular defects are visualized between the tricuspid valve annulus and 11 o'clock (Figure 12.8).

Oftentimes, tissue from the septal leaflet of the tricuspid valve can shroud a conoventricular VSD and restrict the ventricular level shunt (Video 12.1). This tissue can mask the defect and underestimate its true measurement by 2D imaging. Subxiphoid sagittal and right anterior oblique views aid in the assessment of double-chamber RV, when associated with a conoventricular VSD (Video 12.2). Another associated finding with the VSD, prolapse of the right or noncoronary cusp with aortic insufficiency, can be assessed in the parasternal long-axis view at the

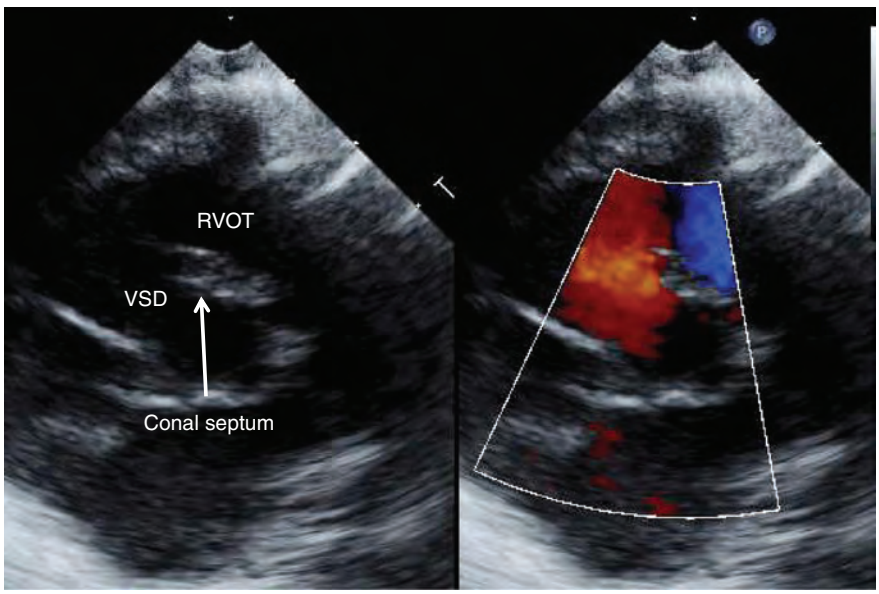


Figure 12.8 Parasternal short-axis view in color compare mode at the base of the heart demonstrates the conoventricular VSD between the septal leaflet of the tricuspid valve and 11 o'clock with left-to-right shunt by color Doppler.

level of the LV outflow tract and in the parasternal short-axis view at the base (see Video 12.8 for an example of aortic valve prolapse into a conal septal VSD). When the aortic valve prolapses, the cusp appears distorted and slips into the defect, at times significantly restricting the shunt.

Malalignment VSD

Anterior deviation of conal septum is readily visualized in many views. With subxiphoid imaging, the anteriorly malaligned conal septum can be seen impinging on the anterior outflow tract in the right anterior oblique or sagittal views (Figure 12.9). In the parasternal short-axis view at the base of the heart, the conal septum can be seen out of line with the aorta, shifted anteriorly and narrowing the right ventricular outflow tract (Video 12.3). With subtle forms of malalignment, size discrepancy between the aorta and pulmonary artery may be helpful; in a normal heart, the pulmonary artery is slightly larger than the aorta but in tetralogy of Fallot, the pulmonary artery is usually smaller than the aorta.

In posterior malalignment defects, deviation of the conal septum may be subtle. In the subxiphoid views, hypoplasia of the aortic valve (in normally related great vessels) in association with a VSD is often the first clue that posterior malalignment of the conal septum is present. Abnormally positioned conal septum may be visualized in the left anterior oblique view (Video 12.4). In the normal heart, the apical 5-chamber and parasternal long-axis views of the LV outflow tract demonstrate that the aortic valve slightly overrides the ventricular septum. In posterior malalignment defects, the aortic valve is typically positioned completely over the LV and the conal septum can be seen in the left ventricular outflow tract; this finding is an additional clue that the conal septum is malaligned and can be seen in apical and parasternal long-axis views (Figure 12.10a,b).

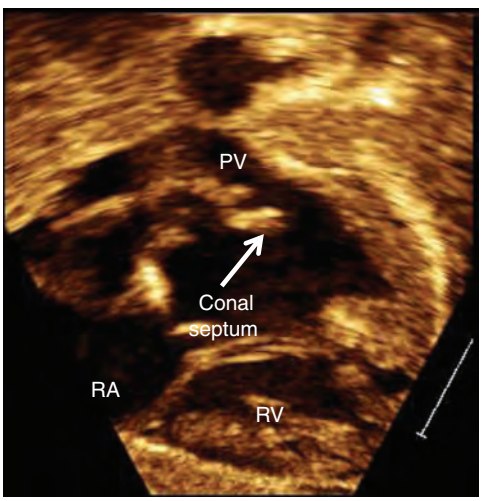
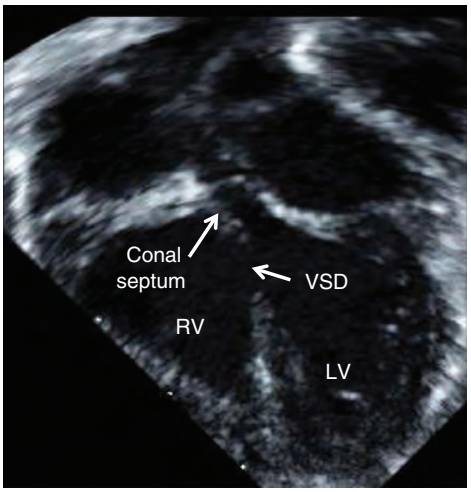
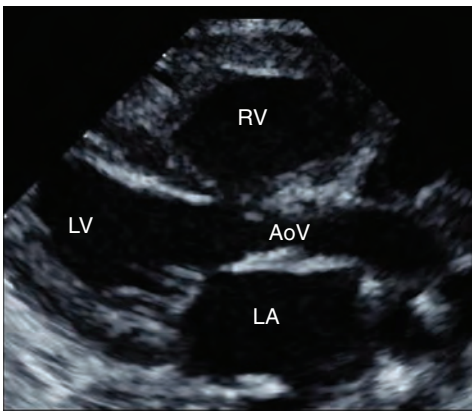


Figure 12.9 Subxiphoid right anterior oblique view demonstrates anterior and superior deviation of conal septum with pulmonary outflow tract obstruction in a patient with tetralogy of Fallot.



(a)



(b)

Figure 12.10 **(a)** Apical 4-chamber view with anterior angulation demonstrates a large VSD with posterior malalignment of conal septum. The aortic valve is aligned entirely over the left ventricle without the normal slight override above the ventricular septum and is hypoplastic. This patient also had coarctation of the aorta. **(b)** Parasternal long-axis view demonstrates a posterior malalignment VSD with a hypoplastic aortic valve. Again note that the aorta is located entirely over the LV without normal override of the ventricular septum. Often the conal septum is small in these cases.

Although the VSD can be seen between 10 and 12 o'clock in the parasternal short-axis view, the malposition of the conal septum can only be appreciated when sweeping to the left ventricular outflow tract. Aside from aortic valve hypoplasia, a narrowed subaortic region, bicuspid aortic valve, and aortic arch obstruction are common associated anomalies with posterior malalignment defects. Mitral valves straddle exclusively through malalignment defects.

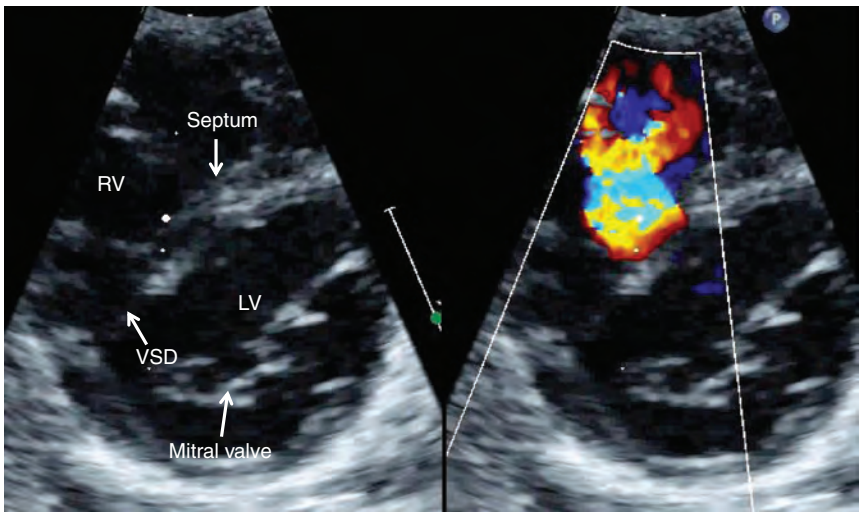
Muscular defects

Muscular VSDs can be variable in size and multiple. Since these defects are surrounded by muscle and can narrow during systole, they are often difficult to visualize by 2D imaging. Color Doppler

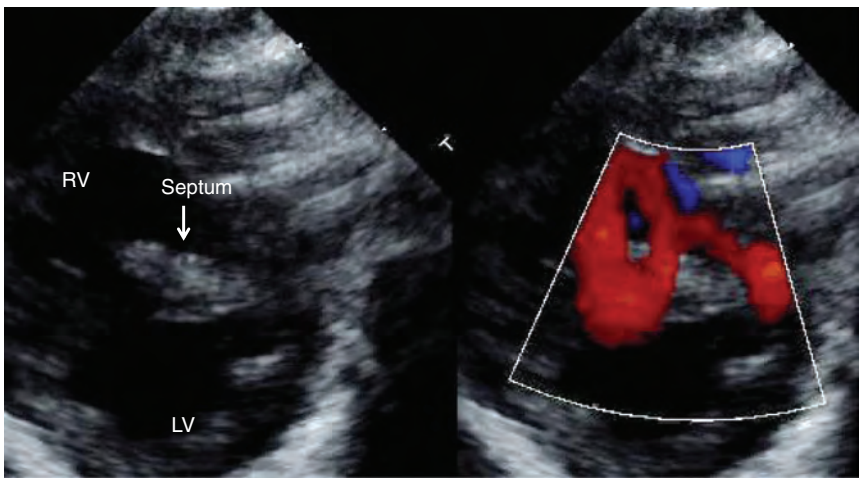
interrogation can greatly assist in identifying the location and number of defects. Larger muscular defects are readily identified without color. In order to confirm a shunt by color Doppler, the color jet must traverse the septum from one ventricle to the other. Multiple muscular defects often appear as a "Swiss cheese" septum on echocardiographic imaging [56] (Video 12.5). In subxiphoid views, a sagittal sweep can scan the muscular septum for defects. Sweeps of the septum in apical views can also demonstrate defects either in posterior, mid, or apical muscular septum. As the parasternal short-axis sweep progresses from base to apex, posterior muscular VSDs appear between 7 and 10 o'clock, mid-muscular VSDs appear between 10 and 12 o'clock, and anterior muscular VSDs appear between 12 and 2 o'clock (Figure 12.11a,b). Of note, it is important to ensure the color box covers the most anterior portion of the septum to identify anterior muscular defects. Muscular defects in association with other larger VSDs can be difficult to visualize because there is no pressure gradient across the defects. They are sometimes missed on preoperative imaging [57].

Conal septal defects

Also named doubly committed or subarterial VSDs, these defects are well seen on subxiphoid sagittal views, with flow directed from the LV directly into the main pulmonary artery (Figure 12.12; Video 12.6). Because of the absence of conal septum, the aortic and pulmonary valves will appear at the same level in this view. In the apical and parasternal long-axis views, the location of the defect appears similar to a conoventricular VSD. The parasternal short-axis view at the level of the aortic valve offers one of the best ways to distinguish a conal septal defect from a conoventricular defect: echocardiographic dropout from conal septal VSD is located between 12 and 2 o'clock (Video 12.7). Conal septal defects can be associated with prolapse of the right coronary cusp into the defect, possibly restricting the degree of ventricular level shunting and also leading to aortic insufficiency (Figure 12.13; Video 12.8) This finding can be seen best in the parasternal long- and short-axis views of the base of the heart. These VSDs can also be seen in association with malalignment and valvar obstruction (e.g.,



(a)



(b)

Figure 12.11 **(a)** Parasternal short-axis view in color compare mode at the level of the mitral valve demonstrates a posterior muscular VSD (between 7 and 10 o'clock) with left-to-right shunt by color Doppler. **(b)** Parasternal short-axis view in color compare mode at the level of the mitral valve papillary muscles demonstrates a mid-muscular VSD (between 10 and 12 o'clock) and an anterior muscular VSD (between 12 and 2 o'clock) with left-to-right shunt by color Doppler.

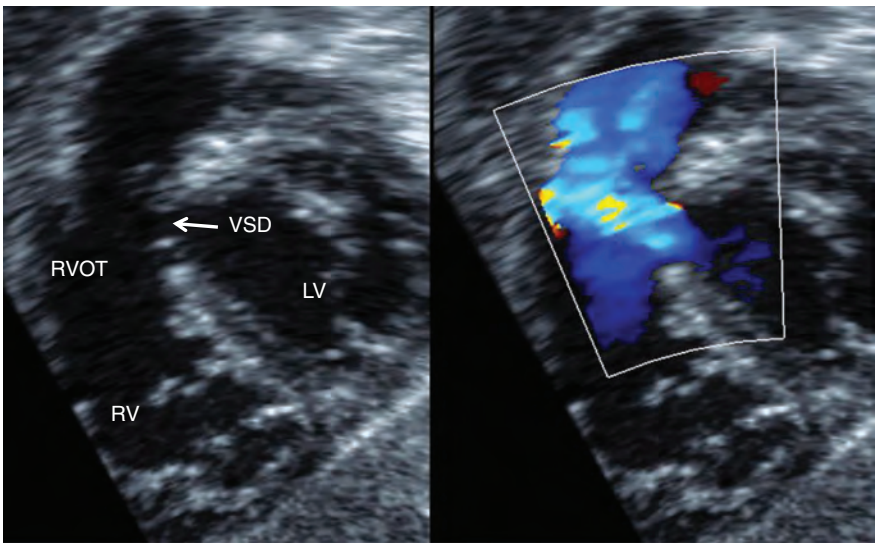


Figure 12.12 Subxiphoid left anterior oblique view in color compare mode demonstrates a conal septal VSD just under the pulmonary valve with color Doppler left-to-right shunt from the LV directly into the pulmonary artery.

tetralogy of Fallot) and therefore, assessment of valvar anatomy and function is important (Figure 12.14). Some conal septal VSDs are perforations within the conal septum rather than complete absence. Aortic prolapse can still occur in this setting. In contrast to conoventricular VSDs, these defects do not close with tricuspid valve tissue.

Atrioventricular (AV) canal defects

AV canal defects (inlet defects) are located in the posterior muscular septum but the lack of muscular rim between the tricuspid valve and the defect distinguishes the AV canal type defect from a posterior muscular defect. On subxiphoid sweeps, the defect is visualized below the AV valves. However, subxiphoid imaging often does not show the entire defect because the plane of ultrasound sweeps through the defect. In apical 4-chamber view, the defect is posterior and the normal offset between the mitral and tricuspid valves is absent (Figure 12.15). In parasternal short-axis sweep from base to apex, AV-canal type VSDs appear in the posterior part of the ventricular septum between 7 and 9 o'clock at the level of the tricuspid and mitral valves (Video 12.9).

Physiologic assessment of VSDs must accompany the anatomic assessment. Direction of flow across the VSD is determined by color Doppler interrogation within the defect. The degree of pressure restriction across the defect is estimated by measurement of the peak velocity across the shunt (the higher the velocity, the higher the pressure gradient across

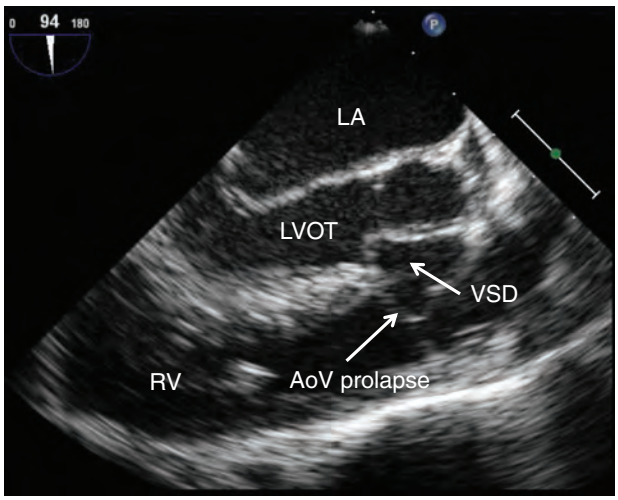


Figure 12.13 Long-axis TEE view at 90 degrees demonstrates aortic valve cusp prolapse into a conal septal VSD

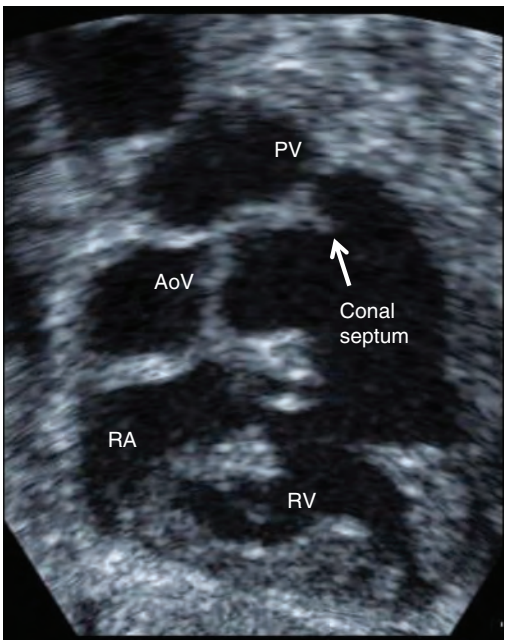


Figure 12.14 Subxiphoid right anterior oblique echocardiographic view demonstrates a combination of anterior malalignment and conal septal defect in a patient with tetralogy of Fallot.

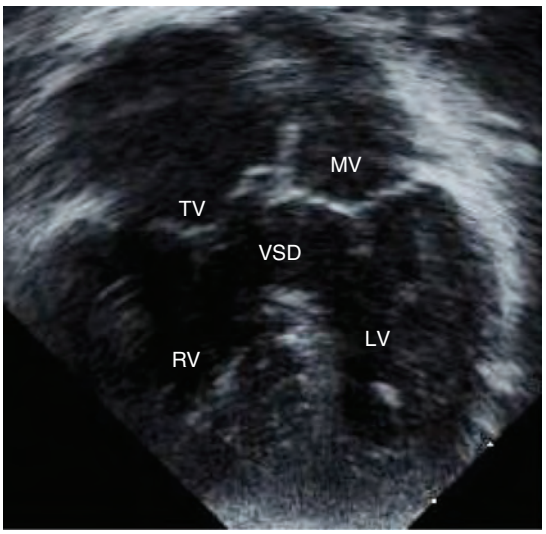


Figure 12.15 Apical 4-chamber view demonstrates a large AV canal VSD (in a patient with common atrioventricular canal) in the posterior aspect of the ventricular septum, just below the AV valves. Note that the atrioventricular valves are at the same level.

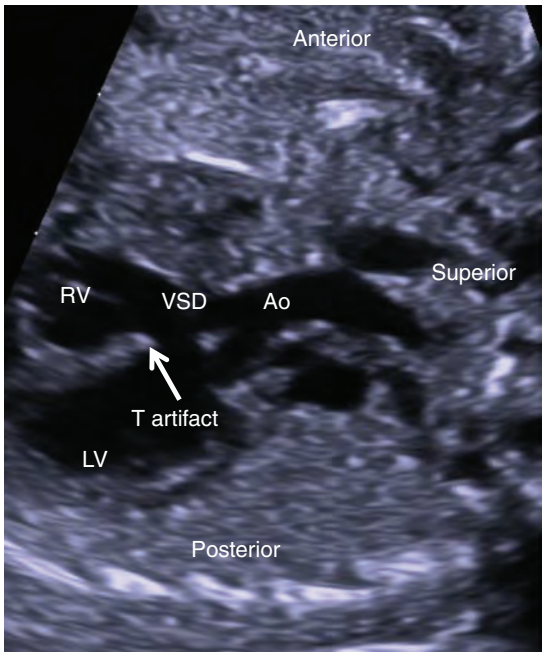


Figure 12.16 Long-axis fetal view demonstrates a large VSD. A "T artifact" at the edge of the defect helps to confirm a true defect versus echocardiographic dropout that can mimic the presence of a VSD.

the defect and the lower the RV pressure). Positioning of the Doppler beam should be as parallel to the direction of VSD flow as possible to obtain the highest velocity. While the velocity across the defect gives an estimation of RV pressure, it is also important to determine RV pressure by tricuspid regurgitation velocity, curvature of the ventricular septum at end-systole, RV size and degree of hypertrophy, and RV function. The magnitude of the shunt and impact on the left heart can be estimated by assessing LA and LV size as well as LV systolic and diastolic function.

Prenatal assessment

Although VSD is the most common CHD diagnosed during the first year of life, its detection in the fetus can be challenging. Fetal movement limits the ability to acquire and maintain optimal imaging planes to identify VSDs. Analogous fetal views to those mentioned in TTE can be used to assess the number, size, and location of VSDs. In the 4-chamber view with the imaging beam parallel to the plane of the ventricular septum, VSDs can be distinguished from artifact or dropout by the appearance of a "T" artifact (echo-dense areas at the blood–tissue interface of a true VSD) [58] (Figure 12.16). Care must be taken when interrogating the membranous septum because this region is particularly thin and produces dropout that can mimic the appearance of a defect. Aligning the septum in a perpendicular orientation allows the use of color Doppler to assist in the detection of true defects. Decreasing the color scale is helpful in detecting low-velocity ventricular shunting. Since the right and left ventricular pressures are equal in the fetus, overlying tissue may completely obscure even a large conoventricular defect in utero. The association of chromosomal abnormalities such as trisomy 18 or 21 should increase the level of suspicion of associated VSDs, especially malalignment and AV canal types, respectively [2]. Isolated VSDs rarely cause a problem in utero or in the neonatal period. In fact, some muscular defects close by the time of birth. It is important to determine whether other significant hemodynamic abnormalities are present to appropriately plan fetal and neonatal management.

Imaging of the adult

Imaging of the adult with a VSD can be problematic, as a larger body habitus and adult-specific lung disease (such as emphysema) often contribute to poor acoustic windows. Adequate visualization of the defect is paramount in the surveillance of this growing patient population for the development of potential hemodynamically important associated lesions, such as aortic insufficiency in conoventricular VSDs with aortic cusp prolapse, double-chambered right ventricle, and subaortic membrane development, in addition to progressive left ventricular dilation and endocarditis [59]. Eisenmenger syndrome most typically presents in adolescence or early adulthood with reversal of flow across the VSD, elevated RV pressure hypertrophy and flattened ventricular septum and associated cyanosis (Video 12.10). Transesophageal echocardiography can be quite useful in detecting these lesions when TTE imaging is suboptimal. Often in the adult, TEE can be performed with moderate sedation obviating the need for the general anesthesia that is frequently necessary in the pediatric population.

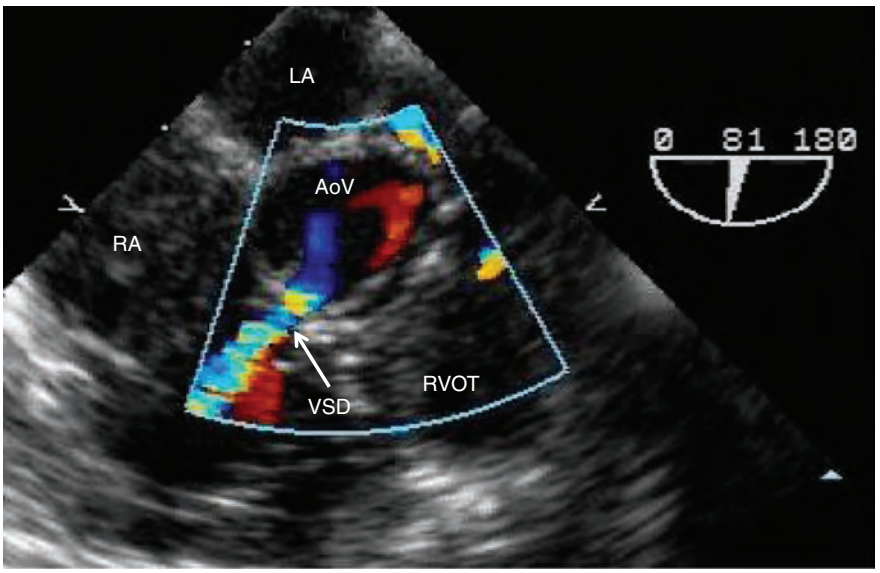


Figure 12.17 Short-axis TEE view at 80 degrees with color demonstrates a residual VSD after surgical patch closure.

Preoperative/intraoperative imaging

Preoperative assessment of VSD can include both TTE and TEE. The goals and techniques of transthoracic imaging are described in detail earlier. Transesophageal echocardiography is often used in the operating room to confirm anatomic details of the VSD and associated defects preoperatively. Postoperatively, cardiothoracic surgery teams often request TEE after the patient is weaned from cardiopulmonary bypass to assess the surgical repair prior to chest closure. In addition to evaluating for residual/additional VSDs, postoperative TEE should also assess for residual abnormalities that may be associated with the surgical approach: (i) tricuspid valve regurgitation or stenosis following detachment of the septal leaflet (for better defect exposure) followed by re-suspension of the leaflet, (ii) pulmonary/aortic valve regurgitation/stenosis if there was a transvalvar approach to the defect, or (iii) RV function following an approach through a ventriculotomy. Postoperatively, TEE findings have been shown to change the surgical management, including the return to cardiopulmonary bypass for repair of significant residual defects [60] (Figure 12.17; Video 12.11). Further, medical management of the patient immediately after cardiopulmonary bypass can be altered based on TEE findings, such as the addition of inotropes and volume in response to decreased ventricular function or abnormal filling, or removal of intracardiac air noted on TEE. This modality has been shown to be safe in regards to ventilation in babies as small as 2 kg, the patient population at highest risk of having residual postoperative defects [61].

Echocardiographic guidance of transcatheter VSD closure

Transcatheter device closure of VSDs has growing clinical relevance. Muscular defects, in particular, can be challenging to visualize and close surgically due to dense trabeculations of the right ventricular aspect of the septum. Transcatheter techniques have developed over recent years to facilitate safe, effective ways of closing these types of defects. Conoventricular defects are closed by this method in some cases as well [62]. These procedures can be performed via access through the femoral vessels or via a hybrid procedure with a perventricular approach. Transesophageal echocardiography plays a critical role to help guide device placement. TEE is used for sizing of the defect to ensure selection of the appropriate device as well as for the assessment of residual defects or impingement on AV or aortic valves upon deployment [63] (Figure 12.18; Video 12.12). More recently, intracardiac echocardiography (ICE) has been shown to be effective in the guidance of transfemoral VSD device

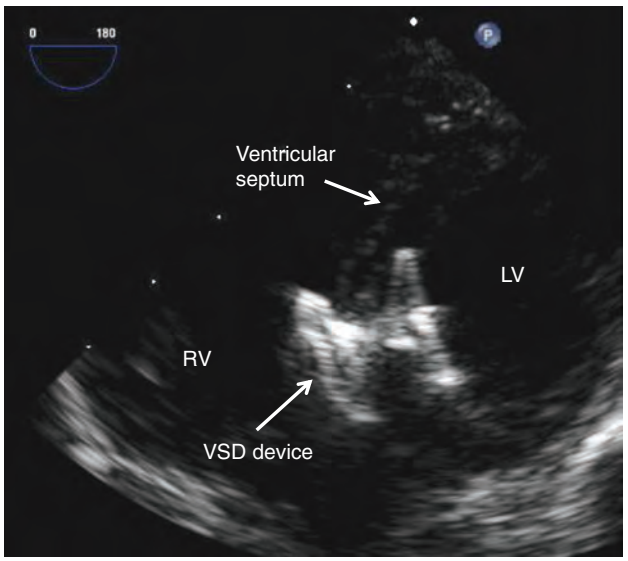


Figure 12.18 Transgastric short-axis TEE view at 0 degrees demonstrates a device placed in a muscular VSD that appears to be well-seated across the ventricular septum.

occlusion. Although the catheters are expensive, require a fairly large sheath (8–10.5 Fr), and have a learning curve secondary to novel imaging planes, ICE offers the possibility of performing the procedure without subjecting the patient to general anesthesia [64].

Postoperative assessment

The primary objective in the echocardiographic assessment of the postoperative patient following isolated VSD closure is the evaluation for residual ventricular-level shunts. Residual defects can easily be detected by TTE along the margins of the VSD patch. Up to 38% of patients have echocardiographic evidence of residual ventricular-level shunting in the peripatch area [65]. However, if the color jet diameter is less than 4 mm, spontaneous resolution of the residual VSD can be expected in approximately 65% of cases within 1 year of repair. In addition to assessment for residual VSDs, it is important to evaluate the septum for smaller additional defects remote from the VSD repair site; in some cases these VSDs are not appreciated on preoperative examination due to elevated RV pressure and limited ventricular level shunt. These additional defects may become more obvious postoperatively after RV pressure has decreased.

Structures adjacent to the repair site and those regions involved in the surgical approach need to be fully interrogated for residual abnormalities. In the current era, the preferred route for repair of most VSDs is via a right atriotomy. A subset of these patients will require detachment of the tricuspid valve anterior leaflet, septal leaflet, or both for better defect exposure, with subsequent re-suspension of the leaflets after VSD closure [66]. Although the documented incidence of stenosis and/or regurgitation is low following this approach, interrogation of the tricuspid valve is important. In large VSDs with systemic RV pressure preoperatively, an RV pressure estimate should be attempted by tricuspid regurgitation jet velocity or residual VSD velocity to assure that the RV pressure has normalized.

Repair via ventriculotomy, either right or left, is rarely required save for specific circumstances, such as repair of apical or otherwise inaccessible muscular VSDs. However, surveillance for ventricular dysfunction and aneurysm development following this approach should be performed via serial echocardiograms indefinitely.

The postoperative evaluation of patients following repair of VSDs with aortic cusp prolapse and resultant aortic regurgitation should involve a thorough evaluation of the valve for residual incompetence either as a result of the surgical repair or from pre-existing damage to the valve. Even when valvuloplasty is performed at the time of VSD closure, aortic insufficiency may progress postoperatively. Predictors of the need for subsequent aortic valve replacement following initial surgical closure of a VSD with aortic cusp prolapse include patient age greater than 15 years and at least moderate insufficiency preoperatively [67]. This subset of patients should be followed serially with specific scrutiny of the aortic valve. Patients with conoventricular defects can develop double-chambered RV and subaortic membrane even after surgical closure of the VSD. These patients should be followed routinely over time to screen for these associated abnormalities.

Acknowledgment

We would like to acknowledge Dr. Paul M. Weinberg who generously provided the pictorial images and pathologic specimens for this chapter as well as providing guidance on how to describe the anatomy of ventricular septal defects.

Videos

To access the videos for this chapter, please go to www.lai-echo.com.

Video 12.1 Parasternal short-axis clip with color compare demonstrates tricuspid valve tissue within the conoventricular VSD restricting the degree of shunting.

Video 12.2 Subxiphoid right anterior oblique clip in color compare mode demonstrates an RV muscle bundle under the pulmonary valve producing turbulent flow and forming a double-chamber RV in association with a conoventricular VSD. The color Doppler VSD jet is directed into the RV chamber proximal to the RV muscle bundle obstruction.

Video 12.3 Parasternal short-axis view at the base of the heart demonstrates tetralogy of Fallot in which the conal septum is positioned out of line with the aorta, more anteriorly and impinging on the right ventricular outflow tract.

Video 12.4 Subxiphoid left anterior oblique sweep demonstrates a large VSD with posterior malalignment of conal septum with potential for subaortic obstruction and associated aortic valve hypoplasia.

Video 12.5 Parasternal long-axis clip in color compare mode demonstrates multiple muscular VSDs with left-to-right shunt by color Doppler.

Video 12.6 Subxiphoid left anterior oblique clip demonstrates a conal septal VSD just under the pulmonary valve and aortic valve with complete absence of conal septum.

Video 12.7 Parasternal short-axis clip demonstrates a conal septal VSD located between 12 and 2 o'clock. Note that the membranous septum between 9 and 11 o'clock is intact.

Video 12.8 Parasternal long-axis clip with color compare demonstrates that the prolapsed aortic valve cusp is restricting the left-to-right shunt through the conal septal VSD.

Video 12.9 Parasternal short-axis sweep in color compare mode demonstrates an AV canal VSD in the posterior ventricular septum

at the level of the AV valves with a predominantly left-to-right shunt by color Doppler.

Video 12.10 Parasternal short-axis clip demonstrates a moderate anterior muscular VSD with a predominantly right-to-left color Doppler shunt and a flattened ventricular septum in systole, indicating markedly elevated RV pressure in a patient with Eisenmenger syndrome.

Video 12.11 Long-axis TEE clip at 120 degrees in color compare mode demonstrates a residual VSD just below the aortic valve after repair of tetralogy of Fallot.

Video 12.12 Long-axis TEE clip at 0 degrees with color Doppler demonstrates no residual VSD around an Amplatzer device in the ventricular septum.

References

1 Hoffman JIE, Kaplan S. The incidence of congenital heart disease. *J Am Coll Cardiol* 2002;**39**:1890–1900.
2 Paladini D, Palmieri S, Lamberti A, et al. Characterization and natural history of ventricular septal defects in the fetus. *Ultrasound Obstet Gynecol* 2000;**16**:118–122.
3 Fyler DC, Buckley LP, Hellenbrand WE, et al. Report of the New England Regional Infant Care Program. *Pediatrics* 1980;**6**:375–461.
4 Dickinson DF, Arnold R, Wilkinson JL. Ventricular septal defect in children born in Liverpool 1960 to 1969. *Br Heart J* 1981;**46**:47–54.
5 Mitchell SC, Korones SB, Berendes HW. Congenital heart disease in 56,109 births. *Circulation* 1971;**43**:323–332.
6 Mehta AV, Chidambaram B. Ventricular septal defect in the first year of life. *Am J Cardiol* 1992;**70**:364–366.
7 Meberg A, Otterstad JE, Froland G, et al. Increasing incidence of ventricular septal defects caused by improved detection rate. *Acta Paediatr* 1994;**83**:653–700.
8 Du ZD, Roguin N, Barak M, et al. High prevalence of muscular ventricular septal defect in preterm neonates. *Am J Cardiol* 1996;**78**:1183–1185.
9 Roguin N, Du ZD, Barak M, et al. High prevalence of muscular ventricular septal defect in neonates. *J Am Coll Cardiol* 1995;**26**:1545–1548.
10 Sands AJ, Casey FA, Craig BG, et al. Incidence and risk factors for ventricular septal defect in "low risk" neonates. *Arch Dis Child-Fetal* 1999;**81**:F61–F63.
11 Arias E, MacDorman MF, Strobino DM, et al. Annual summary of vital statistics–2002. *Pediatrics* 2003;**112**:1215–1230.
12 Hoffman JIE, Christianson R. Congenital heart disease in a cohort of 19,502 births with long-term follow-up. *Am J Cardiol* 1978;**42**:641–647.
13 Keith JD. Ventricular septal defect. In: Keith JD, Rowe RD, Vlad P (eds.) *Heart Disease in Infancy and Childhood*. New York, NY: Macmillan, 1978, pp. 320–379.
14 Nora JJ, Fraser FLC. *Medical Genetics*. Philadelphia, PA: Lea & Febiger, 1974, p. 334.
15 Musewe NN, Alexander DJ, Teshima I, et al. Echocardiographic evaluation of the spectrum of cardiac anomalies associated with trisomy 13 and trisomy 18. *J Am Coll Cardiol* 1990;**15**:673–677.
16 Marino B, Papa M, Guccione P, et al. Ventricular septal defect in Down syndrome. Anatomic types and associated malformations. *Am J Dis Child* 1990;**144**:544–545.
17 Vaughan CJ, Basson CT. Molecular determinants of atrial and ventricular septal defects and patent ductus arteriosus. *Am J Med Genet* 2000;**97**:304–309.
18 Correa-Villasenor A, Ferencz C, Loffredo C, et al. Paternal exposures and cardiovascular malformations. The Baltimore-Washington Infant Study Group. *J Expo Anal Environ Epidemiol* 1993;**3**:173–185.
19 Ewing CK, Loffredo CA, Beaty TH. Paternal risk factors for isolated membranous ventricular septal defects. *Am J Med Genet* 1997;**71**:42–46.
20 De la Cruz MV, Markwald RR. *Living Morphogenesis of the Heart*. Boston, MA: Birkhäuser, 1998.
21 Lamers WH, Moorman AFM. Cardiac septation. A late contribution of the embryonic primary myocardium to heart morphogenesis. *Circ Res* 2002;**91**:93–103.
22 de Jong F, Virágh S, Moorman AFM. Cardiac development: a morphologically integrated molecular approach. *Cardiol Young* 1997;**7**:131–146.
23 Christoffels VM, Habets PEMH, Franco D, et al. Chamber formation and morphogenesis in the developing heart. *Dev Biol* 2000;**223**:266–278.
24 Moorman AFM, Schumacher CA, de Boer PAJ, et al. Presence of functional sarcoplasmic reticulum in the developing heart and its confinement to chamber myocardium. *Dev Biol* 2000;**223**:279–290.
25 Moorman AFM, Lamers WH. Development of the conduction system of the vertebrate heart. In: Harvey RP, Rosenthal N (eds.) *Heart Development*. San Diego, CA: Academic Press, 1999, pp. 195–207.
26 Wessels A, Markman MWM, Vermeulen JLM, et al. The development of the atrioventricular junction in the human heart. *Circ Res* 1996;**78**:110–117.
27 Wessels A, Markwald RR, Webb S, et al. Atrial development in the human heart: an immunohistochemical study with emphasis on the role of mesenchymal tissues. *Anat Rec* 2000;**259**:288–300.
28 Mjaatvedt CH, Yamamura H, Wessels A, et al. Mechanisms of segmentation, septation, and remodeling of the tubular heart: endocardial cushion fate and cardiac looping. In: Harvey RP, Rosenthal N (eds.) *Heart Development*. San Diego, CA: Academic Press, 1999, pp. 159–177.
29 Moorman AFM, van den Hoff MJB, de Jong F, et al. Myocardialization: a novel mechanism of cardiac septation. In: Clark EB, Nakazawa M, Takao A (eds.) *Etiology and Morphogenesis of Congenital Heart Disease: Twenty Years of Progress in Genetics and Developmental Biology*. Armonk, NY: Futura, 2000, pp. 131–135.
30 Kruithof BPT, van den Hoff MJB, Wessels A, et al. Cardiac muscle cell formation after development of the linear heart tube. *Dev Dyn* 2003;**227**:1–13.
31 Van den Hoff MJB, Kruithof BPT, Moorman AFM, et al. Formation of myocardium after the initial development of the linear heart tube. *Dev Biol* 2001;**240**:61–76.
32 Ikeda T, Iwasaki K, Shimokawa I, et al. Leu-7 immunoreactivity in human and rat embryonic hearts, with special reference to the development of the conduction tissue. *Anat Embryol* 1990;**182**:553–562.
33 Lamers WH, Wessels A, Verbeek FJ, et al. New findings concerning ventricular septation in the human heart. Implications for maldevelopment. *Circulation* 1992;**86**:1194–1205.

34 Wessels A, Vermeulen JL, Verbeek FJ, et al. Spatial distribution of "tissue-specific" antigens in the developing human heart and skeletal muscle. III. An immunohistochemical analysis of the distribution of the neural tissue antigen GlN2 in the embryonic heart: implications for the development of the atrioventricular conduction system. *Anat Rec* 1992;**232**:97–111.

35 Lamers WH, Virágh SS, Wessels A, et al. Formation of the tricuspid valve in the human heart. *Circ Res* 1995;**91**:111–121.

36 Van Praagh R, Geva T, Kreutzer J. Ventricular septal defects: how shall we decribe, name and classify them? *J Am Coll Cardiol* 1989;**14**:1298–1299.

37 Jacobs JP, Burke RP, Quintessenza JA, et al. Congenital Heart Surgery Nomenclature Database Project: ventricular septal defect. *Ann Thorac Surg* 2000;**69**:S25.

38 Gerbode F, Hultgren H, Melrose D, Osborn J. Syndrome of left ventricular-right atrial shunt: successful surgical repair of defect in five cases with observation of bradycardia on closure. *Ann Surg* 1958;**148**:433–436.

39 Oppenheimer-Dekker A, Gittenberger-de Groot AC, Bartelings MM, et al. Abnormal architecture of the ventricles in hearts with an overriding aortic valve and a perimembranous ventricular septal defect ("Eisenmenger VSD"). *Int J Cardiol* 1985;**9**:341–355.

40 Macé L, Dervanian P, Le Bret E, et al. "Swiss cheese" septal defects: surgical closure using a single patch with intermediate fixings. *Ann Thorac Surg* 1999;**67**:1754–1758.

41 Thiene G, Wenink AC, Frescura C, et al. Surgical anatomy and pathology of the conduction tissues in atrioventricular defects. *J Thorac Cardiovasc Surg* 1981;**82**:928–937.

42 Pessotto R, Padalino M, Rubino M, et al. Straddling tricuspid valve as a sign of ventriculoatrial malalignment: a morphometric study of 19 postmortem cases. *Amer Heart J* 1999;**138**:1184–1195.

43 Van Hare GF, Soffer LJ, Sivakoff MC, et al. Twenty-five-year experience with ventricular septal defect in infants and children. *Am Heart J* 1987;**114**:606–614.

44 Braunwald E, Ross J, Jr., Sonnenblick EH. Mechanisms of contraction of the normal and failing heart. *N Engl J Med* 1967;**227**:853–862.

45 Jarmakani MM, Graham TP, Jr., Canent RV, Jr., et al. Effect of site of shunt on left heart volume characteristics with ventricular septal defect and patent ductus arteriosus. *Circulation* 1969;**40**:411–418.

46 Vincent RN, Lang P, Elixon EM, et al. Extravascular lung water in children immediately after operative closure of either isolated atrial septal defect or ventricular septal defect. *Am J Cardiol* 1987;**56**:536–539.

47 Dammann JF, Jr., Ferencz C. The significance of the pulmonary vascular bed in congenital heart disease. III. Defects between the ventricles or great vessels in which both increased pressure and blood flow may act upon the lungs and in which there is a common ejectile force. *Am Heart J* 1956;**52**:210–231.

48 Lucas RV, Jr., Adams P, Jr., Anderson RC, et al. The history of isolated ventricular septal defect. A serial physiologic study. *Circulation* 1961;**24**:1372–1387.

49 Blackstone EH, Kirklin JW, Bradley EL, et al. Optimal age and results in repair of large ventricular septal defects. *J Thorac Cardiovasc Surg* 1976;**72**:661–679.

50 Kouchoukos NT, Blackstone EH, Doty DB, et al. Ventricular septal defect. In: *Kirklin/Barratt-Boyes Cardiac Surgery*. Philadelphia, PA: Churchill Livingstone, 2003, pp. 850–909.

51 Simpson WF, Jr., Sade RM, Crawford FA, et al. Double-chambered right ventricle. *Ann Thorac Surg* 1987;**44**:7–10.

52 Baumstark A, Fellows KE, Rosenthal A. Combined double-chambered right ventricle and discrete subaortic stenosis. *Circulation* 1978;**57**:299–303.

53 Rhodes LA, Keane JF, Keane JP, et al. Long follow-up (to 43 years) of ventricular septal defect with audible aortic regurgitation. *Am J Cardiol* 1990;**66**:340–345.

54 Keane JF, Plauth WH, Nadas AS. Ventricular septal defect with aortic regurgitation. *Circulation* 1977;**56**:72–77.

55 Cheatham JP, Latson LA, Gutgesell HP. Ventricular septal defect in infancy: detection with two-dimensional echocardiography. *Am J Cardiol* 1981;**47**:85–89.

56 Ludomirsky A, Huhta JC, Vick GW, 3rd, et al. Color Doppler detection of multiple ventricular septal defects. *Circulation* 1986;**74**:1317–1322.

57 Chin AJ, Alboliras ET, Barber G, et al. Prospective detection by color Doppler flow imaging of additional defects in infants with a large ventricular septal defect. *J Am Coll Cardiol* 1990;**15**:1637–1642.

58 Canale JM, Sahn DJ, Allen HD, et al. Factors affecting real-time, cross-sectional echocardiographic imaging of perimembranous ventricular septal defect. *Circulation* 1981;**63**:689–697.

59 Hoffman P, Wojcik AW, Rozanski J, et al. The role of echocardiography in diagnosing double-chambered right ventricle in adults. *Heart* 2004;**90**:789–793.

60 Roberson DA, Muhiudeen IA, Cahalan MK, et al. Intraoperative transesophageal echocardiography of ventricular septal defect. *Echocardiography* 1991;**8**:687–697.

61 Andropoulos DB, Ayres NA, Stayer SA, et al. The effect of transesophageal echocardiography on ventilation in small infant undergoing cardiac surgery. *Anesth Analg* 2000;**90**:47–49.

62 Oses P, Hugues N, Dahdah N, et al. Treatment of isolated ventricular septal defects in children: Amplatzer versus surgical closure. *Ann Thorac Surg* 2010;**90**:1593–1598.

63 Carminati M, Gianfranco B, Chessa M, et al. Transcatheter closure of congenital ventricular septal defect with Amplatzer septal occluders. *Am J Cardiol* 2005;**96**:52L–58L.

64 Cao Q-L, Zabal C, Koenig P, et al. Initial clinical experience with intracardiac echocardiography in guiding transcatheter closure of perimembranous ventricular septal defects: feasibility and comparison with transesophageal echocardiography. *Catheter Cardiovasc Interv* 2005;**66**:258–267.

65 Rychik J, Norwood WI, Chin AJ. Doppler color flow mapping assessment of residual shunt after closure of large ventricular septal defects. *Circulation* 1991;**84**:III153–161.

66 Bol-Raap G, Weerheim J, Kappetein AP, et al. Follow-up after surgical closure of congenital ventricular septal defect. *Eur J Cardiothoracic Surg* 2003;**24**:511–515.

67 Chiu S, Wang JK, Lin MT, et al. Progression of aortic regurgitation after surgical repair of outlet-type ventricular septal defects. *Am Heart J* 2007;**153**:336–342.

CHAPTER 13

Ebstein Anomaly, Tricuspid Valve Dysplasia, and Right Atrial Anomalies

Frank Cetta and Benjamin W. Eidem
Mayo Clinic, Rochester, MN, USA

Introduction and incidence

Ebstein anomaly and tricuspid valve dysplasia are the two most common congenital malformations of the tricuspid valve. Ebstein anomaly was initially described in 1866 after an autopsy by Wilhelm Ebstein showed a unique abnormality of the tricuspid valve [1]. The reported prevalence of Ebstein anomaly is 1–5 per 100,000 live births with an equal distribution between the sexes [2–4]. Yet, it was not until 1950 that Ebstein anomaly was clinically recognized [5].

Morphology and development

The tricuspid valve is composed of three leaflets, the anterior, septal, and inferior (a.k.a. posterior) leaflets. As the name implies, the septal leaflet has connections to the ventricular septum. It is typically displaced toward the cardiac apex in Ebstein anomaly when compared to the normal heart. The anterior leaflet is usually large and redundant and has been described as "sail-like" (Figure 13.1). The inferior leaflet is positioned along the inferior aspect of the right ventricular cavity. It lies adjacent to the diaphragmatic surface of the heart (Figures 13.2 and 13.3).

In Ebstein anomaly there is failure of proper delamination of the tricuspid valve leaflets from the ventricular myocardium. Although Ebstein anomaly is considered a disorder of the tricuspid valve leaflets, it is more accurately described as an aberration in myocardial development and essentially is a cardiomyopathy [4]. The right ventricle in Ebstein anomaly rarely has normal morphology or function.

The hallmark anatomic feature of Ebstein anomaly is displacement of the septal and inferior leaflets away from the crux of the heart and the atrioventricular junction (Videos 13.1 and 13.2). During cardiac development, leaflet displacement results from failure to fully separate from the underlying ventricular wall. The normal leaflet separation process is referred to as "delamination." Normal delamination begins at the tips of the embryonic leaflets and proceeds toward the base of the leaflet at the atrioventricular junction. The normal delaminated tricuspid valve leaflet will have a hinge point near the true anatomic annulus (Figure 13.4).

Due to the arrest in proper delamination of the tricuspid valve leaflets, patients with Ebstein anomaly have varying degrees of apical displacement of the septal leaflet with accompanying anterior rotation of leaflet tissue towards the right ventricular outflow tract. The displacement seen in Ebstein anomaly is not simply a linear shift of the tricuspid valve towards the apex but actually a spiral rotation of the leaflets anteriorly towards the right ventricular outflow tract (Figure 13.5) [6]. In hearts with Ebstein anomaly the septal and inferior leaflets are usually the most dramatically involved. In contrast, the anterior leaflet is formed at a different stage in cardiac development. As a result, the junctional hinge point of the anterior leaflet usually remains at the true anatomic annulus. However, the anterior leaflet is far from normal and is usually very large and "sail-like" (Video 13.3). In cases of Ebstein anomaly that are associated with pulmonary atresia with intact ventricular septum, the anterior leaflet may appear to be more normal. More commonly, the anterior leaflet has attachments to the free wall of the right ventricle resulting in varying degrees of tethering. These attachments may be thin chordae or they may be heavily muscularized. These attachments play an important role in the novel repair techniques wherein the surgeon tries to mobilize the leaflet tissue and reattach it to the anatomic annulus.

The distance that the septal leaflet is displaced from the true anatomic annulus towards the apex of the right ventricle can be quantitated echocardiographically. This measurement (Figure 13.6) has been referred to as the "displacement index." Although hearts afflicted by Ebstein anomaly have many other leaflet and myocardial abnormalities, the displacement of the septal leaflet has become the hallmark, although not exclusive,

Echocardiography in Pediatric and Congenital Heart Disease: From Fetus to Adult, Second Edition. Edited by Wyman W. Lai, Luc L. Mertens, Meryl S. Cohen and Tal Geva.
© 2016 John Wiley & Sons, Ltd. Published 2016 by John Wiley & Sons, Ltd.
Companion website: www.lai-echo.com

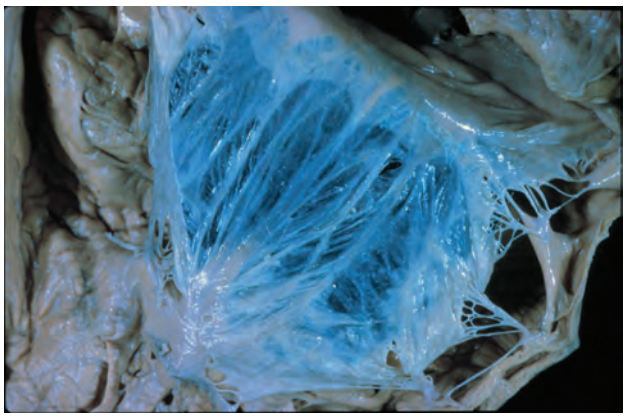


Figure 13.1 Pathologic specimen demonstrating a "sail-like" anterior leaflet of the tricuspid valve in Ebstein anomaly. Note the translucent nature of the leaflet, its large size and the multiple cordal attachments to the free wall of the right ventricle. Source: Courtesy of Dr. William Edwards, copyright Mayo Clinic Foundation, all rights reserved.

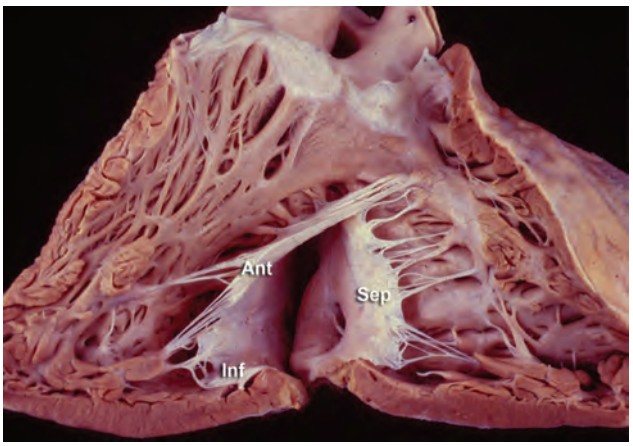


Figure 13.3 Pathologic specimen of the right ventricular aspect of the tricuspid valve demonstrating anterior (Ant), inferior (Inf), and septal (Sep) leaflets. Note the multiple chordal attachments to the septum. Source: Courtesy of Dr. William Edwards, copyright Mayo Clinic Foundation, all rights reserved.

feature in the diagnosis of Ebstein anomaly. This is discussed further in the Echocardiographic Assessment section of this chapter.

Pathophysiology

Patients with Ebstein anomaly present at many ages. The most severely affected will present in the newborn period. Newborns with severe Ebstein anomaly have massive cardiomegaly and significant cyanosis due to right-to-left shunting at the level of the atrial septum [7,8]. Neonates with Ebstein anomaly can be difficult to manage due to increased pulmonary vascular

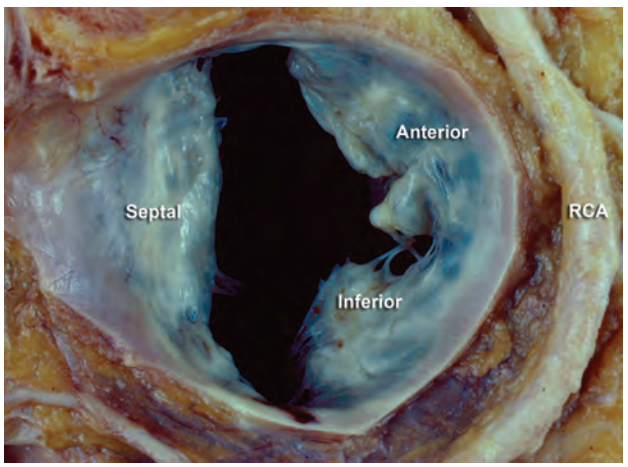


Figure 13.2 Right atrial view of a tricuspid valve demonstrating the normal position of the anterior, inferior and septal leaflets. Also note the proximity of the right coronary artery (RCA) as it traverses the right atrioventricular groove. Source: Courtesy Dr. William Edwards, copyright Mayo Clinic Foundation, all rights reserved.

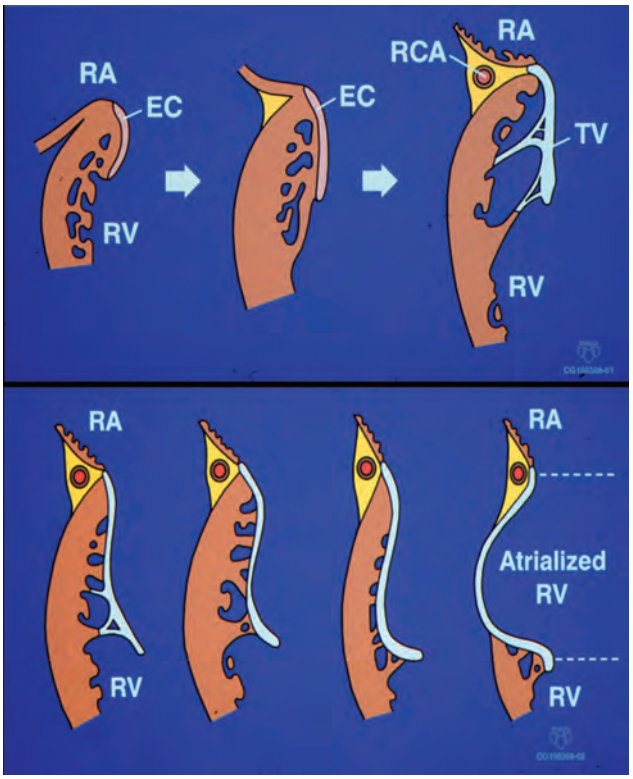


Figure 13.4 **(Top panel)** Diagram of normal delamination from the myocardium of the tricuspid leaflet at the level of the endocardial cushion (EC). RA, right atrium; RCA, right coronary artery; RV, right ventricle; TV, tricuspid valve. **(Bottom panel)** Diagram demonstrating failed or incomplete delamination of the TV leaflets present in Ebstein anomaly. The lower panel demonstrates the "atrialized" right ventricle. This is below the level of the true anatomic annulus and above the level of coaptation of the leaflets. Source: With permission, copyright Mayo Clinic Foundation, all rights reserved.

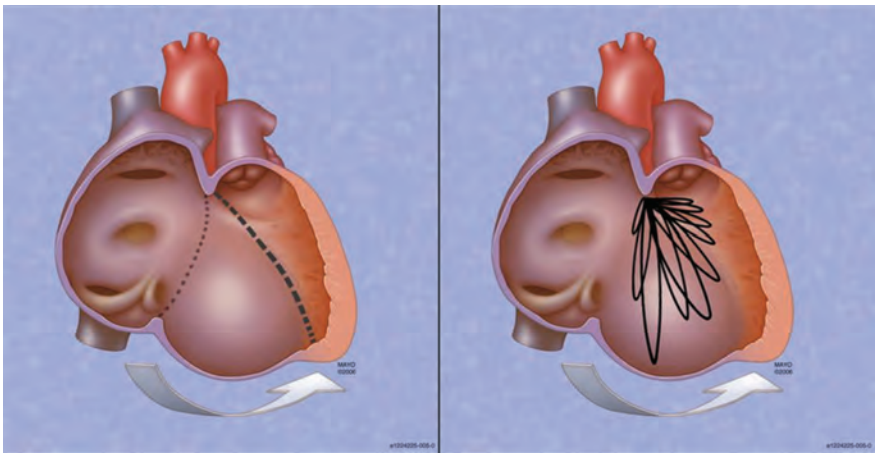


Figure 13.5 Diagram demonstrating several positions of tricuspid valve coaptation in Ebstein anomaly. Note in panel B the rotation of the coaptation point anteriorly into the right ventricular outflow tract. Source: Courtesy Dr. Robert Anderson, copyright Mayo Clinic Foundation, all rights reserved.

resistance. In the most severe cases, the dysfunctional right ventricle cannot generate enough pressure to adequately open the pulmonary valve resulting in functional pulmonary atresia [9,10]. This leaves the patient extremely cyanotic due to right-to-left shunting across the patent foramen ovale.

As the pulmonary vascular resistance drops, antegrade flow across the pulmonary valve occurs. The cyanosis will steadily improve due to less tricuspid insufficiency and less right-to-left shunting at the atrial level. In rare cases of neonates with pulmonary valve regurgitation, a "circular circulation" is established which increases cyanosis and worsens prognosis.

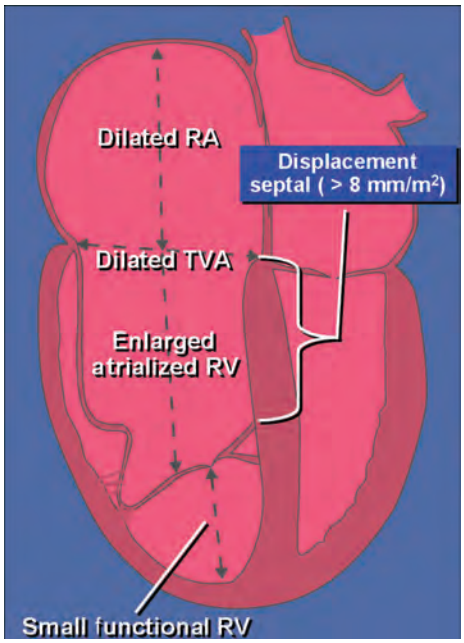


Figure 13.6 Diagram of the "displacement index." The distance from the hinge point of the anterior mitral leaflet is measured to the hinge point of the delaminated septal tricuspid leaflet. This measurement divided by the body surface area is the displacement index. A displacement index >8 mm/m^2 is diagnostic of Ebstein anomaly. A small functional right ventricle is present inferior to the coaptation point of the tricuspid valve. RA, right atrium; RV, right ventricle; TVA, tricuspid valve annulus. Source: With permission, copyright Mayo Clinic Foundation, all rights reserved.

Depending on the associated anomalies, infants with Ebstein anomaly typically do not need surgical intervention in the newborn period. On the other hand, those patients with the most severe forms of Ebstein anomaly with severe tricuspid regurgitation or severe right ventricular obstruction or atresia will need intervention. In these cases, palliation with a systemic-to-pulmonary arterial shunt can allow the patient to grow [11]. Oversewing the tricuspid valve with a fenestration (Starnes procedure) in conjunction with a central shunt has also been used for palliation [12]. Novel tricuspid valve repair techniques may have a role in these patients but to date most neonates with severe Ebstein anomaly have had a poor outcome. Cardiac transplantation is another consideration for the most severe cases.

Clinical presentation

Ebstein anomaly can be readily diagnosed in utero with fetal echocardiography utilizing the 4-chamber view that delineates abnormalities of the tricuspid valve (Video 13.4). Echocardiography has impacted the age of diagnosis for patients with Ebstein anomaly. In 1979, Guiliani et al. reported that one-third of patients with Ebstein anomaly were diagnosed before 4 years of age [13]. Another 40% of patients were diagnosed by age 19 years. However, cases have been reported of >60-year-old patients who were misdiagnosed with "mitral valve prolapse" based on clinical exam alone. Ultimately these patients had an echocardiogram, and the diagnosis was revised to Ebstein anomaly.

The clinical examination of a child with Ebstein anomaly can vary. The cardiac impulse is normal in patients with milder forms of tricuspid malformation and laterally displaced in more severe forms. With severe tricuspid regurgitation a holosystolic

murmur is usually present along the left lower sternal border. An ejection murmur of right ventricular outflow obstruction may be present. Patients with mild Ebstein anomaly have normal first and second heart sounds. However, split first and second sounds and/or third or fourth heart sounds may be present [12,13]. The typical auscultation of the patient with Ebstein anomaly has been described as a "multiplicity of sounds." Cyanosis may be evident but is subtle. Jugular venous distension is not common because the large right atrium and atrialized right ventricle dissipate the "V" wave. However, sometimes the accentuated jugular venous V wave is observed in patients with severe tricuspid regurgitation without an interatrial shunt. Hepatomegaly is uncommon except in patients with advanced right heart failure.

The electrocardiogram in these patients will demonstrate right atrial enlargement with large P waves, PR interval prolongation and a right bundle branch pattern. Wolff–Parkinson–White (WPW) with overt preexcitation evident on the surface electrocardiogram is present in up to 15% of patients with Ebstein anomaly. Supraventricular tachycardia (SVT) in patients with WPW and Ebstein anomaly is common.

Chest radiography can appear normal in mild forms of Ebstein anomaly. In contrast, in neonates with massive cardiomegaly, the heart can occupy the majority of the chest (Figure 13.7). This can occur in severe cases of Ebstein anomaly and tricuspid valve dysplasia where tricuspid regurgitation is the major hemodynamic abnormality. Impressive right ventricular enlargement is observed echocardiographically. Indications for operation in patients with Ebstein anomaly are summarized in Table 13.1.



Figure 13.7 Anterior/posterior chest radiograph from an infant with severe Ebstein anomaly demonstrating massive cardiomegaly. Source: With permission, copyright Mayo Clinic Foundation, all rights reserved.

Table 13.1 Indications for operation in Ebstein anomaly

– Decreased exercise tolerance, especially when associated with cyanosis
– Progressive RV dilation
– Prior to significant RV systolic dysfunction
– Onset or progression of atrial arrhythmia
– Earlier operation if valve morphology is favorable for repair
– Prior to LV systolic dysfunction

Associated features with Ebstein anomaly

Ventricular septal defects, tetralogy of Fallot, coarctation of the aorta, and patent ductus arteriosus have all been described with Ebstein anomaly. Left-sided cardiac anomalies, specifically mitral valve prolapse and noncompaction of the left ventricle, have also been described [14]. In 1987, Benson et al. proposed that the morphology and function of the right heart in Ebstein anomaly alters the left ventricular geometry and in turn its function [15]. It has been shown in neonates with Ebstein anomaly that increased fibrosis is present in the left ventricular myocardium [16]. Therefore, left ventricular dysfunction in Ebstein anomaly is likely a combination of both mechanisms.

Functional pulmonary valve atresia or stenosis may be found in up to one-third of neonates presenting with Ebstein anomaly. In severe Ebstein anomaly the massive cardiac size compresses the lungs and causes pulmonary hypoplasia. This contributes to the clinical instability of these newborns.

Imaging

Echocardiographic features of Ebstein anomaly

Echocardiography has been considered the gold standard for the diagnostic evaluation of patients with Ebstein anomaly [17,18]. The internal cardiac crux, as imaged in the 4-chamber view, is the most consistent imaging landmark in the human heart (Figure 13.8; Video 13.1). The 4-chamber view permits assessment of the septal hinge points of the mitral and tricuspid leaflets. The most sensitive and specific diagnostic feature in Ebstein anomaly is the displacement of the annular hinge point of the septal leaflet (Video 13.2) [19]. This displacement is appreciated by comparison of the annular hinge point of the anterior mitral valve leaflet to that of the septal leaflet of the tricuspid valve. In normal hearts, there invariably is slight apical displacement of the hinge point of the tricuspid septal leaflet as compared to the mitral anterior leaflet (Figure 13.9). However, in Ebstein anomaly, due to the failure of leaflet delamination, the septal leaflet hinge point is displaced inferiorly towards the apex. The distance between the valve hinge points can typically be measured in either systolic or diastolic still frames in the apical 4-chamber plane. The distance from the hinge point of the anterior leaflet of the mitral valve to the hinge point of the septal leaflet of the tricuspid valve is divided by the body surface area measured in square meters. This is known as the "displacement

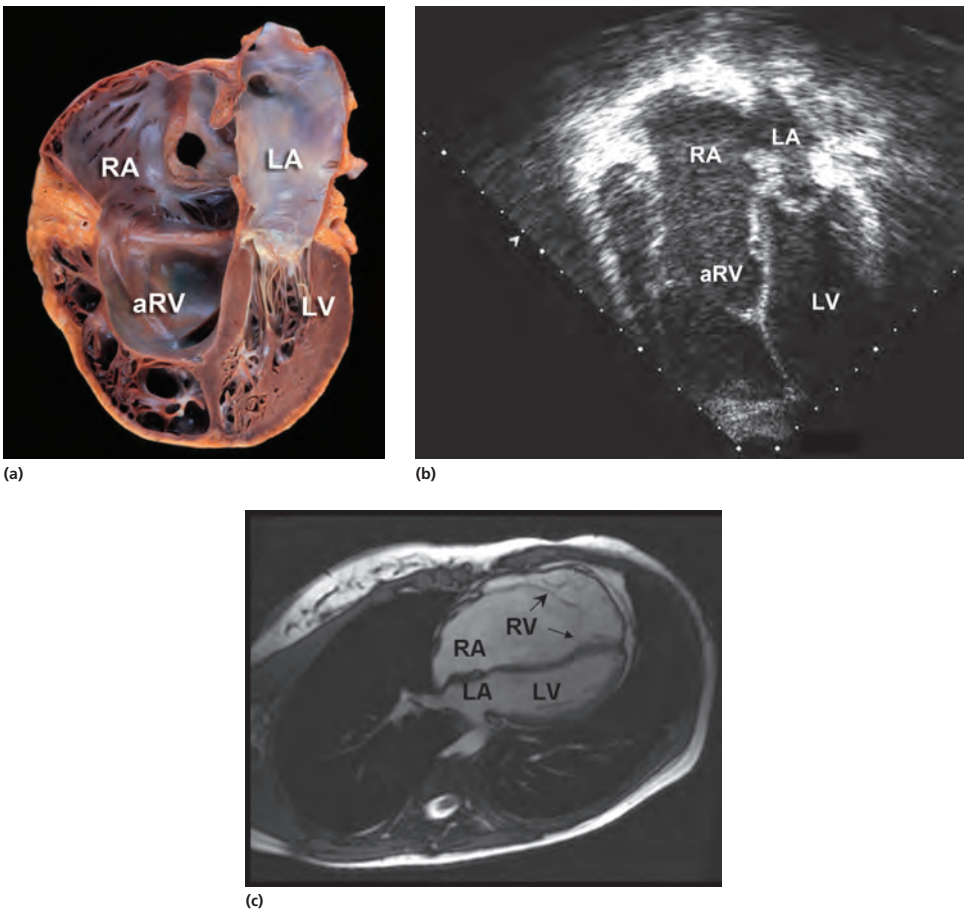
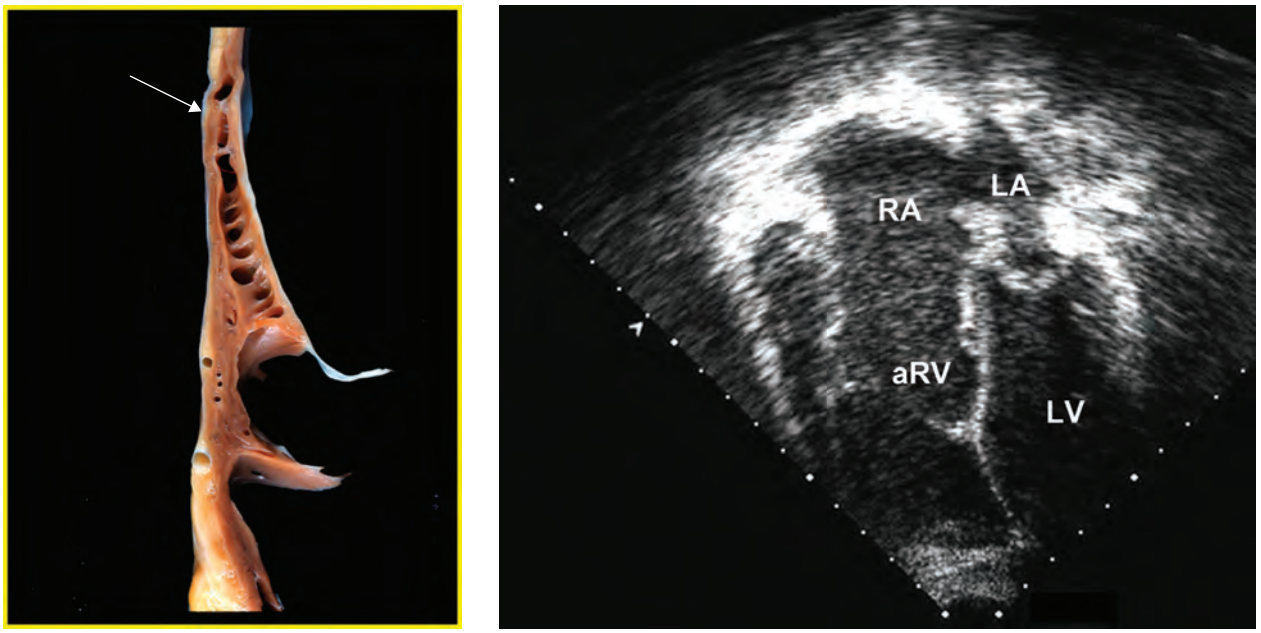


Figure 13.8 Pathologic specimen **(a)**, apical 4-chamber echocardiographic image **(b)**, and cardiac MRI **(c)**, in severe Ebstein anomaly. All three images show severe displacement of the tricuspid valve leaflets into the apex of the right ventricle with severe enlargement of the right atrium and atrialized portion of the right ventricle. The left ventricle is compressed due to the massive right-sided volume overload. The anterior TV leaflet has multiple muscular tethering points along its length. The septal leaflet is not delaminated in all three images. aRV, atrialized right ventricle; LA, left atrium; LV, left ventricle; RA, right atrium. Source: With permission, copyright Mayo Clinic Foundation, all rights reserved.

index." A displacement index exceeding 8 mm/m^2 is a reliable feature to distinguish hearts with Ebstein anomaly from other forms of RV volume overload. In the most severe cases of Ebstein anomaly, the hinge point of the septal leaflet is not visualized in the 4-chamber imaging plane (Video 13.5). This is because the septal leaflet has been rotated anteriorly into the right ventricular outflow tract (Figure 13.5). In these cases, the displacement index is considered infinite (Figure 13.10).

The displacement index is a simple quantitative measurement to assist in the diagnosis of Ebstein anomaly; but it is not the entirety of the diagnosis. As previously mentioned, patients with Ebstein anomaly have failure of delamination of the inferior and anterior leaflets. These leaflets have abnormal tethering and muscularization of the chordal apparatus. In some cases there may appear to be complete absence of the septal and inferior leaflets. Ebstein anomaly is a disease of the right ventricular myocardium and careful assessment of the structure, size and function of the right ventricle is important, in addition to detailed interrogation of the leaflet morphology.

Echocardiography is uniquely suited for evaluation of the tricuspid valve apparatus and support structures. However, assessment of the severity of tricuspid regurgitation in Ebstein anomaly has multiple pitfalls. Tricuspid regurgitation has been quantitated utilizing criteria established for normal adult hearts [20]. However, quantification of tricuspid regurgitation in patients with Ebstein anomaly is not as straightforward. For example, measurement of the vena contracta in patients with Ebstein anomaly can be difficult. Right ventricular systolic pressure in these patients is usually normal. Therefore, the tricuspid regurgitation jet will appear laminar when evaluated with color flow Doppler. This can be deceptive and cause the observer to underestimate the severity of tricuspid regurgitation due to the lack of an "aliased" region where it is easy to measure the vena contracta (Figure 13.11). The valve leaflets in Ebstein anomaly may have multiple fenestrations and therefore multiple jets of tricuspid regurgitation. This creates further pitfalls in evaluation and quantification of tricuspid regurgitation. Most importantly, the orientation of the valve leaflets is not normal. Many



(a) (b)

Figure 13.9 **(a)** Pathologic specimen demonstrating the true anatomic annulus (arrow) at the hinge point of the anterior TV leaflet. Note in this specimen the failed delamination of the anterior leaflet until the very tip of the leaflet which is present deep in the apex of the right ventricle near the level of the moderator band. Source: Courtesy of Dr. William Edwards, copyright Mayo Clinic Foundation, all rights reserved. **(b)** Apical 4-chamber echo image demonstrating a patient with Ebstein anomaly. A displacement index >8 mm/m^2 is a consistent hallmark of Ebstein anomaly. aRV, atrialized right ventricle; LV, left ventricle; RA, right atrium; LA, left atrium. Source: With permission, copyright Mayo Clinic Foundation, all rights reserved.

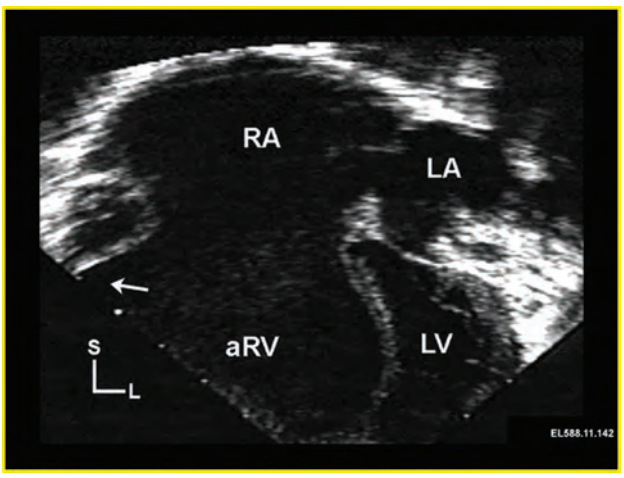


Figure 13.10 Apical 4-chamber image demonstrating a severe form of Ebstein anomaly. In this image, there appears to be no delamination of the septal leaflet. The anterior leaflet has dense attachments to the free wall of the right ventricle (arrow). In the apical 4-chamber image, it appears that the right ventricle is entirely "atrialized." The left ventricle is compressed due to the right-sided volume overload. There is massive right atrial enlargement. aRV, atrialized right ventricle; LA, left atrium; LV, left ventricle; RA, right atrium. Source: With permission, copyright Mayo Clinic Foundation, all rights reserved.

patients with Ebstein anomaly have rotation of the leaflets into the right ventricular outflow tract. This causes the orientation of the tricuspid regurgitation jet to be unusual. Therefore, the tricuspid regurgitation jet may not be adequately evaluated in the apical 4-chamber view. Instead, the best view of the tricuspid

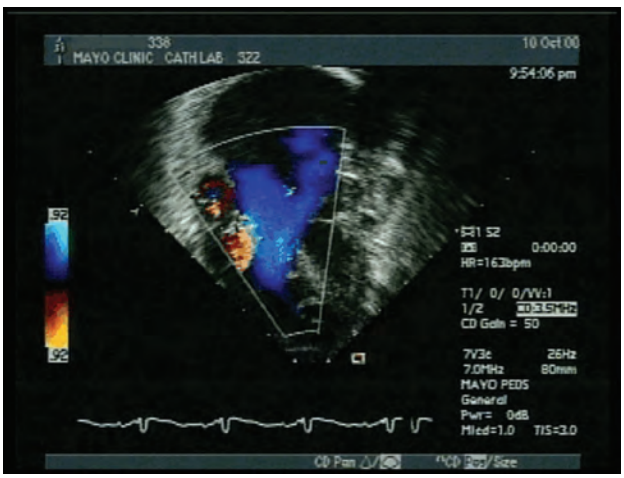


Figure 13.11 Apical 4-chamber view demonstrating a patient with Ebstein anomaly and severe tricuspid regurgitation. Note the laminar tricuspid regurgitation color flow due to the wide vena contracta and low velocity. Source: With permission, copyright Mayo Clinic Foundation, all rights reserved.

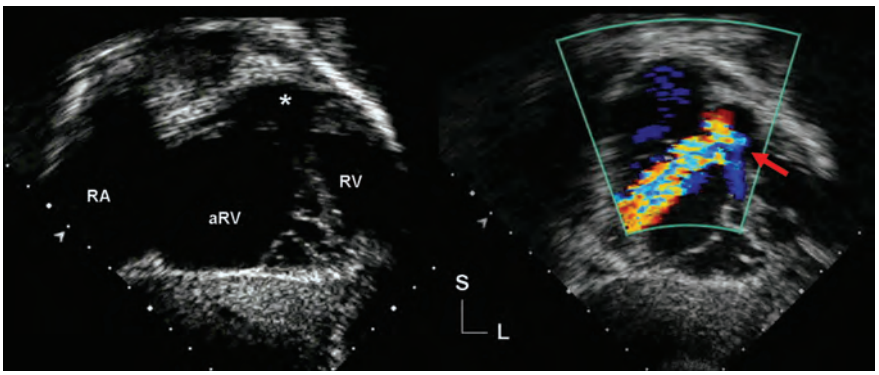


Figure 13.12 Subcostal images from an infant with severe Ebstein anomaly. The functional orifice is also the origin of a single broad jet of regurgitation. This jet begins near the right ventricular outflow tract and is oriented inferiorly toward the diaphragm. aRV, atrialized right ventricle; L, left; RA, right atrium; RV, right ventricle; S, superior. Source: With permission, copyright Mayo Clinic Foundation, all rights reserved.

regurgitation jet will be in a modified right ventricular outflow tract view (Figure 13.12). Many components of the traditional echocardiographic assessment of tricuspid regurgitation in the normal heart may not be as useful in the evaluation of tricuspid regurgitation in Ebstein anomaly. The echocardiographer must be astute and utilize multiple imaging planes to adequately assess tricuspid regurgitation in these patients.

In 1992 Celermajer proposed an echocardiographic technique that measured the size of the right atrium (defined as the area above the tricuspid valve coaptation) and divided this by the combined area of the right ventricle below the level of coaptation + left atrium area + left ventricle area (Figure 13.13) [21]. If this index exceeded 1.0, it was a poor prognostic factor [16]. This index has been utilized in neonates and small children; its applicability in older children and adults has not been rigorously studied. The importance of the Celermajer index emphasizes that the right atrium is severely enlarged in many patients with Ebstein anomaly. The area below the true anatomic annulus but above the level of coaptation of the valve leaflets has been referred to as the "atrialized right ventricle" (Figure 13.12). This area of the right heart will have right atrial pressure if one places a pressure transducer in this location. However, since it lies below the anatomic tricuspid valve annulus, the action potential and electrocardiographic signals in this area are those of ventricular myocardium. Recruitment of this area of the right ventricle is one of the benefits of the cone repair technique.

Impact of echocardiography on tricuspid valve repair

The traditional monoleaflet repair technique, introduced by Gordon Danielson at the Mayo Clinic in the 1970s, served many patients with Ebstein anomaly well for decades. When data from these patients were re-evaluated at the Mayo Clinic, 40–50% of patients received a repair that was durable for 15–20 years [22]. However, nearly 60% of patients operated in that era had a valve replacement. Preoperative echocardiography was highly predictive of surgical ability to repair the tricuspid valve with the monoleaflet approach. The most important feature predictive of a durable monoleaflet repair was the mobility of the anterior leaflet. It was critical for at least one-half of the leaflet to be

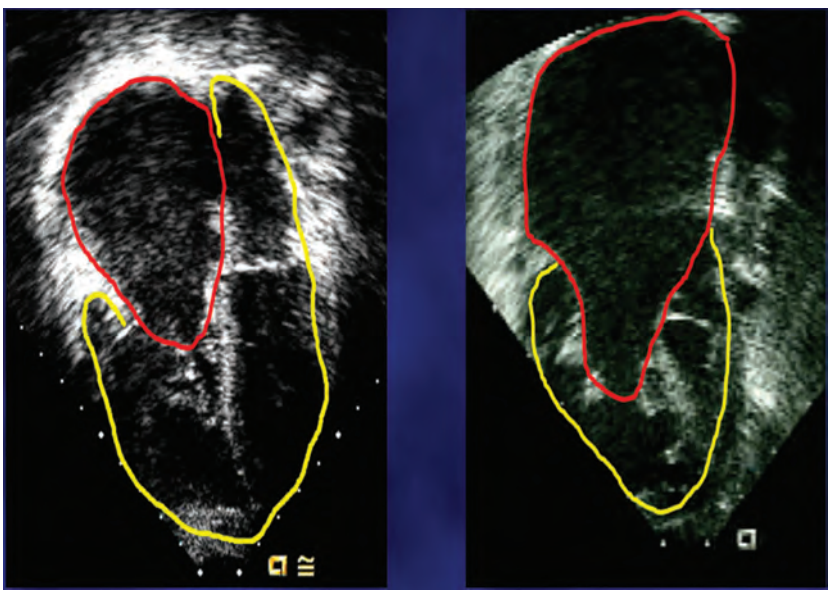


Figure 13.13 Apical 4-chamber views that demonstrate the Celermajer index in two patients with Ebstein anomaly. In the left panel the area of the left atrium + left ventricle + right ventricle below the level of tricuspid valve coaptation is larger than the area of the right atrium + atrialized right ventricle. The Celermajer index in this patient would be <1.0. In contrast, the patient in the right panel has a Celemajer index >1.0. The area of the right atrium + atrialized right ventricle is larger than the other chambers of the heart. A Celermajer index >1.0, in neonates, correlates with poor prognosis. Source: With permission, copyright Mayo Clinic Foundation, all rights reserved.

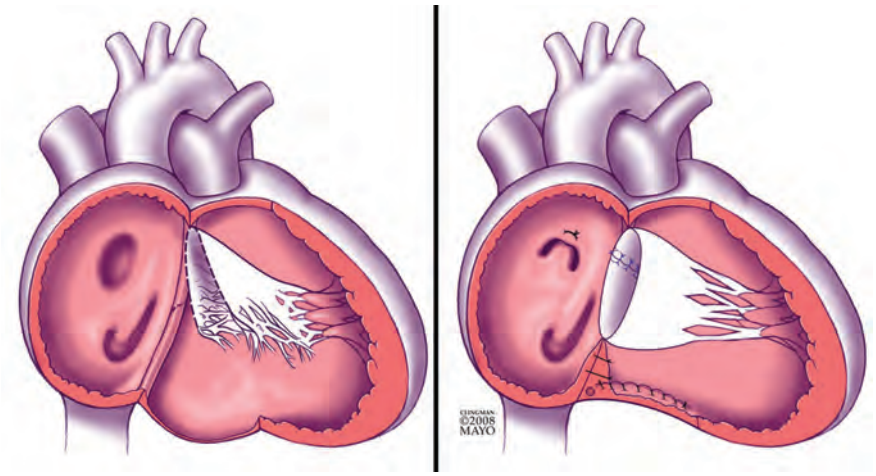


Figure 13.14 Diagrams demonstrating the cone repair for Ebstein anomaly of the tricuspid valve. In the left panel, note that the leaflets are surgically delaminated and brought to the level of the true anatomic annulus. In the right panel, a reduction of the atrialized right ventricle has been performed and the valve is reconstructed to form the shape of a cone. Source: Courtesy of Dr. Joseph Dearani, copyright Mayo Clinic Foundation, all rights reserved.

mobile, free of major tethering to the myocardium, and have a leading edge that would freely coapt with the ventricular septum post repair (Videos 13.6 and 13.7). With this monocusp repair, no attempt was made to delaminate the septal leaflet or form a functionally coapting valve. Instead the "sail-like" qualities of the anterior leaflet were utilized to create a monoleaflet repair. Unfortunately, the more severe forms of Ebstein anomaly were not amenable to this repair technique. Specifically, when leaflet tissue was rotated anteriorly into the right ventricular outflow tract, that tissue could not be mobilized to form adequate coaptation at the level of the true tricuspid valve annulus. Many patients with severe forms of Ebstein anomaly had valve replacement in the era prior to the cone repair (Videos 13.8 and 13.9).

In the modern era with the "cone technique" originally introduced in Brazil by José DaSilva and extensively utilized by Joseph Dearani at the Mayo Clinic, the majority of patients with Ebstein anomaly are now amenable to a successful repair technique. Recent data from the Mayo Clinic demonstrated that in patients less than 21 years of age, greater than 95% of patients had valve repair regardless of leaflet morphology [23]. One important issue that needs to be addressed for prediction of reparability with the cone technique is muscularization of the leaflet and its support apparatus. The surgeon is able to successfully "delaminate" much of the septal, inferior, and anterior leaflets. Thick muscular chordal attachments to the anterior leaflet and muscularization of the leaflet itself are features that predict a less than acceptable repair. Partial annuloplasty rings are applied to most cone repairs. Unlike the monoleaflet repair, the cone reconstruction permits repair of the valve at the true anatomic annulus (Figures 13.14 and 13.15; Videos 13.10–13.13). The surgeon delaminates the valve tissue preserving much of the right ventricular myocardium. Supplementation of the leaflets with GORE-TEX® sutures and patch material are adjuncts. Great care is taken to avoid the right coronary artery and the conduction tissue when the mobilized valve leaflets are attached at the atrioventricular junction. The cone reconstruction dramatically decreases the amount of tricuspid regurgitation in most patients and restores the hinge point of the repaired tricuspid valve to its normal anatomic position.

After the cone repair, many of the tricuspid valve leaflets appear thickened when imaged with surface echocardiography. Despite this leaflet thickening, tricuspid valve stenosis has not been a major problem in these patients. In patients with significant right ventricular dilation and dysfunction, a cavopulmonary connection is added to a cone repair in order to reduce the volume load on the RV. This cavopulmonary connection was not utilized as frequently in the era of the monoleaflet repair. However, in the current age, it is employed in 15–20%

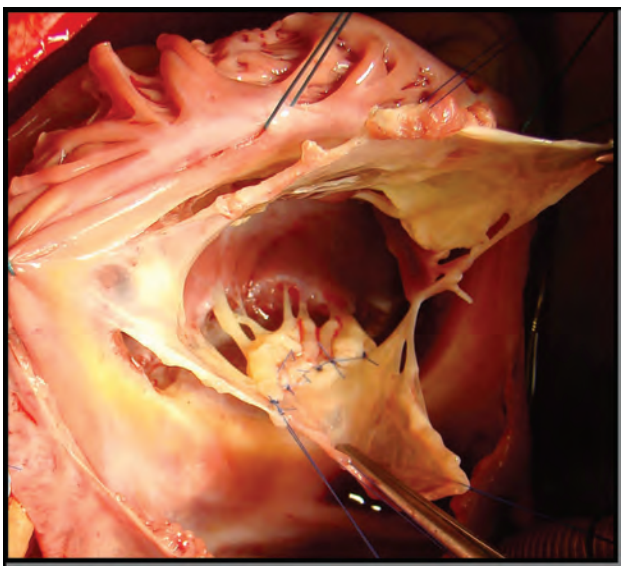


Figure 13.15 Intraoperative right atrial view during a cone repair for Ebstein anomaly. Note that all three leaflets of the tricuspid valve have been mobilized and are being extended to the level of the true anatomic annulus. Source: Courtesy of Dr. Joseph Dearani, copyright Mayo Clinic Foundation, all rights reserved.

of patients, specifically those with significant right ventricular systolic dysfunction.

In older patients (>50 years of age), there is a lower threshold for tricuspid valve replacement with a bioprosthesis. Valve replacement should also be considered, if more than half of the anterior leaflet has failed to delaminate, or if the leading edge of the anterior leaflet has dense attachments to the right ventricle [24]. In a large series from Mayo Clinic prior to the cone reconstruction experience, there was no difference in long-term survival or freedom from reoperation between those patients who had valve repair versus those with replacement [22]. Thus, in older patients, tricuspid valve replacement is a reasonable option. Need for reoperation at 20 years postoperative is approximately 50%. Mechanical prosthetic valves are usually avoided in Ebstein anomaly unless the patient has an additional reason for chronic anticoagulation. The most recent intervention for these patients is percutaneous valve-in-valve therapy in those with a dysfunctional bioprosthesis [25]. Use of percutaneous valve technology will hopefully obviate the need for further surgery in many patients (Videos 13.14 and 13.15).

Patients experiencing arrhythmias usually have an electrophysiology study with ablation, prior to surgical intervention. A Maze procedure can be completed at the time of the tricuspid valve surgery. However, recurrence of atrial arrhythmias after a surgical Maze procedure for patients with Ebstein anomaly is high (50%). Cardiac transplantation in patients with Ebstein anomaly is reserved for the most severe cases and when there is concurrent severe left ventricular dysfunction.

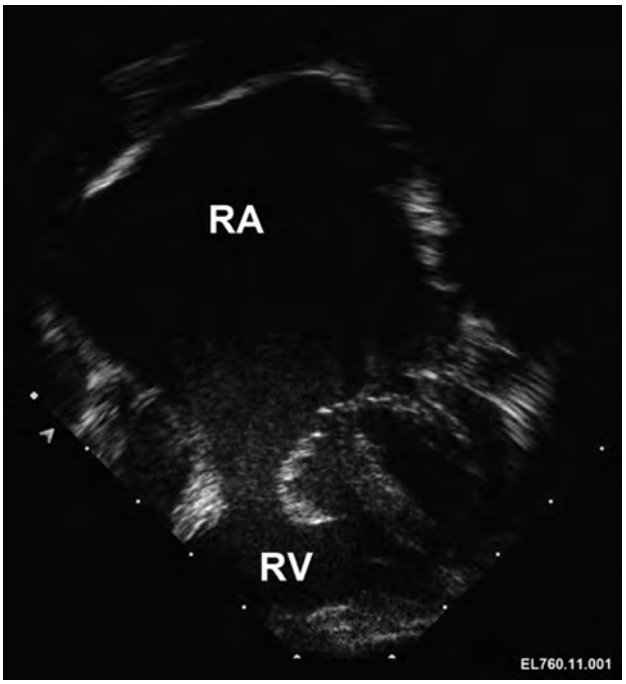


Figure 13.16 Apical 4-chamber echocardiograph demonstrating severe tricuspid valve dysplasia. Note that the hinge points of the tricuspid leaflets are at the level of the anatomic annulus. There is no displacement into the body of the right ventricle. However, the leaflets are very abnormal and the tips are thickened. There is restricted movement and consequently severe tricuspid regurgitation. Note the severe right atrial enlargement. RA, right atrium; RV, right ventricle. Source: With permission, copyright Mayo Clinic Foundation, all rights reserved.

Key elements

Preoperative examination

- Determine displacement index of the annular hinge point of the septal leaflet on apical 4-chamber view
- Evaluate septal and posterior leaflet mobility and support structures; rule out dysplasia
- Assess mobility and degree of tethering of the anterior leaflet
- Assess severity of tricuspid regurgitation and rule out tricuspid stenosis
- Measure Celermajer index
- Evaluate functional RV morphology, size, and function
- Evaluate LV morphology, size, and function
- Assess for commonly associated lesions, including patent foramen ovale or atrial septal defect; pulmonary stenosis or functional pulmonary atresia; ventricular septal defect; and patent ductus arteriosus.

Tricuspid valve dysplasia

Congenital dysplasia of the tricuspid valve is another abnormality which can cause severe tricuspid regurgitation and clinically important symptoms. In tricuspid valve dysplasia the hinge point of the leaflets is not displaced from the level of the true tricuspid annulus (Videos 13.16 and 13.17). The leaflets are thickened and the chordal apparatus is foreshortened. This causes large gaps in coaptation of the tricuspid leaflets resulting in significant tricuspid regurgitation. Segments of the tricuspid leaflets may be flail with broken chordae (Figure 13.16). Contrary to Ebstein anomaly, in tricuspid valve dysplasia, the myocardium of the right ventricle typically is normal. Right ventricular systolic function is preserved until more advanced stages of the disease. The leaflets of a dysplastic tricuspid valve may not be as amenable to repair as in Ebstein anomaly. Insertion of a partial annuloplasty ring can reduce the size of the annulus and hopefully improve coaptation resulting in less tricuspid regurgitation.

The consequences of severe tricuspid regurgitation are similar to those seen in Ebstein anomaly: progressive right atrial enlargement, right ventricular dilation with eventual reduction in systolic function, and right-to-left shunting at the level of the atrial septum. However, the low pressure volume load of isolated tricuspid regurgitation is usually well tolerated through early childhood. The anatomic and echocardiographic criteria that were listed earlier in this chapter help to distinguish Ebstein anomaly from tricuspid valve dysplasia. The displacement index is <8 mm/m^2 in tricuspid valve dysplasia and the 2D appearance of the right ventricle is more normal. However, tricuspid valve

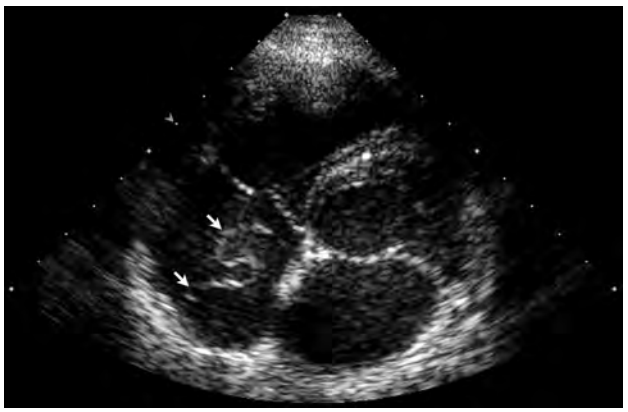


Figure 13.17 Subcostal scan demonstrating redundant Eustachian valve (arrows) within the right atrium.

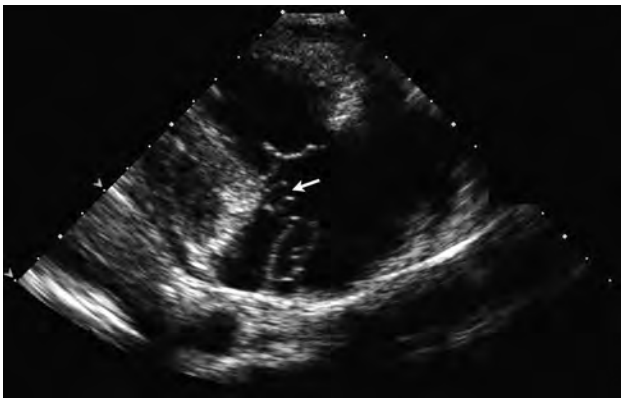


Figure 13.18 Parasternal long-axis scan angled into the RV inflow view. Note the prominent Chiari network (arrow) emanating from the os of the coronary sinus.

dysplasia and Ebstein anomaly may represent a disease spectrum and, at times, are difficult to distinguish echocardiographically from one another.

Systemic venous valves and right atrial anomalies

Embryonic regression of the right sinus venosus valve results in the formation the Eustachian and Thebesian valves. Incomplete regression of the fetal right sinus valve results in the persistence of membranous structures within the right atrium, most notably the Chiari network and cor triatriatum dextrum.

Eustachian valve

The Eustachian valve originates from the inferior vena cava and attaches to the limbus of the fossa ovalis. During fetal life, this structure directs the highly oxygenated blood returning from the maternal placenta across the fossa ovalis into the left atrium. Postnatally, this valve is present within the right atrium and can be readily imaged by echocardiography. Imaging is optimal from the subcostal and parasternal windows (Figure 13.17; Videos 13.18 and 13.19). This valve tissue can often be prominent or redundant but is rarely obstructive.

Thebesian valve

The Thebesian valve is present within the coronary sinus and is not readily imaged in the majority of normal hearts.

Chiari network

The Chiari network is a fine "lattice-like" or "serpentine" fenestrated membrane found on the floor of the right atrium. This network extends from the Thebesian or Eustachian valve and attaches to the wall of the right atrium or directly to the atrial septum. It can be quite mobile and even prolapse into the tricuspid valve orifice. While rarely obstructive, this membrane can be a nidus for thrombus or endocarditis as well as stroke. It can be imaged best from the RV inflow view in parasternal long-axis scan plane but also in short-axis or apical 4-chamber orientations (Figure 13.18; Videos 13.20 and 13.21).

Cor triatriatum dextrum

The Eustachian membrane may be very thickened and effectively divide the right atrium into two distinct chambers: (1) a posteromedial venous chamber that includes the connections of the caval veins and coronary sinus, and (2) an anterolateral chamber with the right atrial appendage and vestibule of the tricuspid valve. This membrane has variable size, redundancy, and number of fenestrations resulting in a variable degree of inflow obstruction to the right atrium and tricuspid valve. The presence of a patent foramen ovale or atrial septal defect is also variable and may be located either proximal or distal to this membrane. When present, this atrial defect can act as a pop-off valve allowing right-to-left shunting in patients with significant obstruction.

Imaging of cor triatriatum dextrum is best facilitated in the subcostal imaging planes as well as the parasternal short-axis orientation. From the subcostal short-axis imaging plane, this membrane can be demonstrated originating from the IVC and connecting distally to the interatrial septum, separating the right atrium into a true double chamber with the vena cavae located proximal to the membrane and the atrial appendage and tricuspid valve located distally. The location of the coronary sinus and atrial septal defect can be variable, but both are most commonly located proximal to this membrane.

Videos

To access the videos for this chapter, please go to www.lai-echo.com.

Video 13.1 Apical 4-chamber orientation demonstrating the normal cardiac crux. Note the normal offset of the atrioventricular

valves with the mitral valve inserted more basally in the ventricular septum than the tricuspid valve.

Video 13.2 Apical 4-chamber orientation in a child with Ebstein anomaly. Note the prominent apical displacement of the septal tricuspid leaflet compared to the mitral valve insertion in the ventricular septum.

Video 13.3 Apical 4-chamber view demonstrating the large sail-like anterior leaflet in Ebstein anomaly. Also note the attachments of the anterior leaflet to the underlying right ventricular (RV) myocardium.

Video 13.4 Fetal echocardiogram in Ebstein anomaly. Note the severe right atrial and right ventricular enlargement resulting in significant cardiomegaly and pulmonary compression.

Video 13.5 Apical 4-chamber view demonstrating the lack of septal leaflet in this imaging plane. The orifice of the tricuspid valve has been significantly rotated into the right ventricular outflow tract (RVOT) resulting in a lack of tricuspid tissue in this scan.

Video 13.6 Monocusp Danielson repair: two-dimensional imaging demonstrated excellent repair with coaptation of the anterior leaflet with the ventricular septum.

Video 13.7 Monocusp Danielson repair: color Doppler demonstrates mild residual tricuspid regurgitation and no significant stenosis.

Video 13.8 Prosthetic tricuspid tissue valve replacement in Ebstein anomaly. Two-dimensional imaging demonstrates good leaflet mobility and coaptation.

Video 13.9 Prosthetic tricuspid tissue valve replacement in Ebstein anomaly. Color Doppler demonstrates normal antegrade flow across the prosthesis and a trivial degree of prosthetic regurgitation.

Video 13.10 Cone repair: preoperative two-dimensional imaging in an apical 4-chamber orientation demonstrates the classic features of Ebstein anomaly with a sail-like anterior leaflet with multiple areas of tethering to the underlying RV myocardium and a dilated true anatomic tricuspid annulus. Note the prominent apical displacement of the septal leaflet attachment of the tricuspid valve.

Video 13.11 Cone repair: preoperative color Doppler evaluation demonstrates a broad medial jet of tricuspid regurgitation.

Video 13.12 Cone repair: postoperative two-dimensional imaging demonstrates the post-repair tricuspid orifice is now at the true tricuspid annulus. This reconstructed tricuspid annulus has been decreased in size allowing improved leaflet coaptation.

Video 13.13 Cone repair: postoperative color Doppler interrogation demonstrates an excellent cone repair with minimal stenosis and mild residual regurgitation.

Video 13.14 Two-dimensional imaging by intracardiac echocardiography of the Melody valve in the tricuspid position.

Video 13.15 Color Doppler by intracardiac echocardiography demonstrating normal flow across the Melody valve in the tricuspid position.

Video 13.16 Apical 4-chamber view demonstrating tricuspid valve dysplasia. Note the normal insertion of the septal tricuspid leaflet at the cardiac crux and the lack of central valve leaflet coaptation.

Video 13.17 Apical 4-chamber view demonstrating very mild Ebstein anomaly. Note the exaggerated offset of the AV valve insertions at the cardiac crux due to apical displacement of the septal leaflet of the tricuspid valve. There is very mild right atrial and right ventricular chamber dilatation.

Video 13.18 Parasternal long-axis orientation with posterior angulation into the tricuspid inflow view. Note the prominent redundant Eustachian valve in this view.

Video 13.19 Subcostal view demonstrating Eustachian valve within the right atrium with its connection to the atrial septum.

Video 13.20 Parasternal long-axis orientation with posterior angulation into the tricuspid inflow view. Note the prominent redundant Chiari network in this view.

Video 13.21 Apical 4-chamber view demonstrating Chiari network within the right atrium emanating from the coronary sinus.

References

1 Ebstein W. Uber einen sehr seltenen fall von insufficienz der valvula tricuspidalis, bedingt durch eine angeborene hochgradige misshildung derselben. *Arch Anat Physiol* 1866;**33**:238–254.

2 Fyler DC, Buckley LP, Hellenbrand WE. Report of the New England regional infant cardiac program. *Pediatrics* 1980;**65**:375–461.

3 Attenhofer Jost CH, Connolly HM, Dearani JA, et al. Ebstein's anomaly. *Circulation* 2007;**115**:277–285.

4 Edwards WD. Embryology and pathologic features of Ebstein's anomaly. *Prog Pediatr Cardiol* 1993;**2**:5–15.

5 Blount SG, Jr., Gelb IJ, McCord MC. Ebstein's anomaly. *Circulation* 1957;**15**:210–224.

6 Anderson KR, Zuberbuhler JR, Anderson RH, et al. Morphologic spectrum of Ebstein's anomaly of the heart: a review. *Mayo Clin Proc* 1979;**54**:174–180.

7 Hornberger LK, Sahn DJ, Kleinman CS, et al. Tricuspid valve disease with significant tricuspid insufficiency in the fetus: diagnosis and outcome. *J Am Coll Cardiol* 1991;**17**:167–173.

8 Oberhoffer R, Cook AC, Lang D, et al. Correlation between echocardiographic and morphological investigations of lesions of the tricuspid valve diagnosed during fetal life. *Br Heart J* 1992;**68**:580–585.

9 Newfeld EA, Cole RB, Paul MH. Ebstein's malformation of the tricuspid valve in the neonate. Functional and anatomic pulmonary outflow tract obstruction. *Am J Cardiol* 1967;**19**:727–731.

10 Smallhorn JF, Izukawa T, Benson L, Freedom RM. Noninvasive recognition of functional pulmonary atresia by echocardiography. *Am J Cardiol* 1984;**54**:925–926.

11 Knott-Craig CJ, Goldberg SP. Management of neonatal Ebstein's anomaly. *Semin Thorac Cardiovasc Surg Pediatr Card Surg Annu* 2007:112–116.
12 Starnes VA, Pitlick PT, Bernstein D, et al. Ebstein's anomaly appearing in the neonate. A new surgical approach. *J Thorac Cardiovasc Surg* 1991;**101**:1082–1087.
13 Giuliani ER, Fuster V, Brandenburg RO, Mair DD. Ebstein's anomaly: the clinical features and natural history of Ebstein's anomaly of the tricuspid valve. *Mayo Clin Proc* 1979;**54**:163–173.
14 Attenhofer Jost CH, Connolly HM, O'Leary PW, et al. Left heart lesions in patients with Ebstein anomaly. *Mayo Clin Proc* 2005;**80**:361–368.
15 Benson LN, Child JS, Schwaiger M, et al. Left ventricular geometry and function in adults with Ebstein's anomaly of the tricuspid valve. *Circulation* 1987;**75**:353–359.
16 Celermajer DS, Dodd SM, Greenwald SE, et al. Morbid anatomy in neonates with Ebstein's anomaly of the tricuspid valve: pathophysiologic and clinical implications. *J Am Coll Cardiol* 1992;**19**:1049–1053.
17 Ports TA, Silverman NH, Schiller NB. Two-dimensional echocardiographic assessment of Ebstein's anomaly. *Circulation* 1978;**58**:336–343.
18 Shiina A, Seward JB, Edwards WD, et al. Two-dimensional echocardiographic spectrum of Ebstein's anomaly: detailed anatomic assessment. *J Am Coll Cardiol* 1984;**3**:356–370.
19 Seward JB. Ebstein anomaly. Ultrasound imaging and hemodynamic evaluation. *Echocardiography* 1993;**10**:641–664.
20 Guidelines for the echocardiographic assessment of the right heart in adults. *J Am Soc Echocardiographr* 2010;**23**:685–713.
21 Celermajer DS, Cullen S, Sullivan ID, et al. Outcome in neonates with Ebstein's anomaly. *J Am Coll Cardiol* 1992;**19**:1041–1046.
22 Brown ML, Dearani JA, Danielson GK, et al. The outcomes of operations for 539 patients with Ebstein anomaly. *J Thorac Cardiovasc Surg* 2008;**135**:1120–1136.
23 Dearani JA, Said SM, Burkhart HB, et al. Anatomic repair of Ebstein's malformation: early results of cone reconstruction. *Abstract presented at 48th STS Annual Meeting, Ft*. Lauderdale, FL, USA, 2012.
24 Dearani JA, Danielson GK. Surgical management of Ebstein's anomaly in the adult. *Semin Thorac Cardiovasc Surg* 2005;**17**:148–154.
25 Roberts PA, Boudjemline Y, Cheatham JP, et al. Percutaneous tricuspid valve replacement in congenital and acquired heart disease. *J Am Coll Cardiol* 2011;**58**:117–122.

CHAPTER 14

Mitral Valve and Left Atrial Anomalies

James C. Nielsen[1] and Laurie E. Panesar[2]

[1]Division of Pediatric Cardiology, Stony Brook Children's, Stony Brook, NY, USA
[2]Fetal and Pediatric Echocardiography, Stony Brook Children's, Stony Brook, NY, USA

Definitions

Mitral valve prolapse (MVP) occurs when there is systolic extension of a leaflet segment beyond the annular plane. Historically, the definition of MVP has varied considerably resulting in diagnostic confusion [1]. Defining MVP as classic or nonclassic forms is supported by adult outcome studies [1,2]. Classic MVP is defined as systolic leaflet displacement of >2 mm and diastolic leaflet thickness exceeding 5 mm; nonclassic MVP exists when the systolic displacement is >2 mm with leaflet thickness <5 mm. Borderline displacement <2 mm is considered a normal variant and is not associated with morbidity or progression [1].

Cleft mitral valve is present when the anterior leaflet remains divided into two separate leaflet components, each of which attach to a separate papillary muscle group. *Isolated cleft mitral valve* (ICMV), the subtype addressed in this chapter, is a cleft not associated with an ostium primum defect. ICMV frequently coexists with other congenital heart lesions – the term "isolated" refers only to the lack of an ostium primum defect.

Straddling mitral valve (SMV) is defined as the presence of chordal attachments on both sides of the ventricular septum, and by definition can only occur in the presence of a ventricular septal defect (VSD) [3–5]. In SMV the anterior leaflet is frequently divided [6], leading to a separate commissure and thus a trileaflet MV; this arrangement, however, is not, strictly speaking, a cleft because chordae tendineae from two separate leaflets join a single (or closely spaced) papillary muscle group(s). It is appropriately termed a commissure.

Double orifice mitral valve (DOMV) is defined as two separate orifices each supported by its own chordae and papillary muscles.

Congenital mitral stenosis (MS) is defined as an abnormality at any level of the mitral valve apparatus that results in restriction of diastolic filling.

Isolated congenital giant left atrium (GLA) is defined as left atrial enlargement out of proportion to the hemodynamic load on the left atrium in the absence of rheumatic heart disease. It is frequently referred to as congenital left atrial aneurysm or left atrial appendage aneurysm [7,8].

Incidence

Initial reports describing the prevalence of MVP showed it to be as high as 5–15%. The results of these studies were affected by selection bias and the lack of a clear definition of MVP [9]. More recent studies in unselected individuals [1,10] report a much lower prevalence of 0.6 to 2.4%. The true incidence of ICMV, DOMV and SMV are yet to be determined [11,12]. Pathologic studies from large congenital cardiac registries have reported ICMV in 41/3369 (1.2%) [12], DOMV in 28/2733 (1.0%) [13], and SMV in 8/2200 (0.4%) [4]. Congenital MS is an equally rare condition that occurs in approximately 0.4% of patients with congenital heart disease [14]. Worldwide, the prevalence of acquired rheumatic mitral stenosis exceeds that of congenital MS; however, in developed nations congenital MS is more common. Congenital GLA is very rare, with <20 pediatric cases reported in the literature [7,8,15–25].

Etiology

In primary classic MVP there is myxomatous degeneration of the valve without an identifiable connective tissue disorder. Familial inheritance can be present in an autosomal dominant fashion [25]. Secondary MVP is histologically identical to primary, but is present with connective tissue disease (e.g., Marfan or Ehlers–Danlos syndromes). ICMV with normally related great arteries (NRGA) and DOMV have in common abnormal development of the embryonic endocardial cushions and, therefore, can be seen with increased frequency in trisomy 21 [12,13]. The rarity of SMV [4] and its association with other complex anatomic lesions [6] makes it difficult to ascribe a specific etiology to SMV. Similarly, congenital MS typically involves

Echocardiography in Pediatric and Congenital Heart Disease: From Fetus to Adult, Second Edition. Edited by Wyman W. Lai, Luc L. Mertens, Meryl S. Cohen and Tal Geva.
© 2016 John Wiley & Sons, Ltd. Published 2016 by John Wiley & Sons, Ltd.
Companion website: www.lai-echo.com

disruption of several components of the valve apparatus, hypoplasia of additional left-sided structures and other complex cardiac lesions, which makes the determination of specific etiology equally challenging. In contrast to idiopathic giant right atrium (see Chapter 13) [26], which is by definition truly "isolated," congenital GLA has most frequently been reported in the setting of some degree of mitral valve disease [27]. The exact etiology of congenital GLA is obscure. Surgical and histological examinations have demonstrated extremely thin atrial wall and fibrosis [8,18,19]. Authors have proposed fetal viral infection or focal developmental error leading to lack of myoblasts and loss of wall integrity [16,17].

Morphology and classification

Developmental considerations

The atrioventricular (AV) valve leaflets, chordae tendineae, and the myotendinous junction are derived from the endocardial cushions, with some contribution of myocardial cells [28–30]. The complex process of normal morphogenesis of the AV junction and AV valve is under investigation [31–33]. The rarity of SMV, DOMV, ICMV and congenital MS, together with their frequent association with other abnormalities, makes defining their developmental basis extremely challenging. Recent advancements in the understanding of complex signaling pathways and epithelial to mesenchymal transition provide new insight into the mysteries of cardiac embryogenesis [34]. On a basic level, the lower aspect of the endocardial cushions, through a poorly understood interaction with myocardial cells, forms freely mobile "mature" leaflets through delamination (detachment) from the myocardial wall, eventually leaving only the chordae tendineae attached to both leaflet and papillary myocardium [31,33]. How interruption of this process leads to these complex anomalies is yet to be defined. For ICMV it is generally recognized that failure of fusion of the left ventricular aspect of the superior and inferior endocardial cushions results in a cleft in the anterior leaflet [33]. Of note, the portion of the endocardial cushions that participates in the final step of ventricular septation eventually leads to the formation of both the membranous septum and the anterior MV leaflet [31–33], which fits with the anatomic observation (see "Anatomy" later) that the cleft attachments in ICMV with NRGA are always near the membranous septum [12]. SMV in the setting of crossed AV inflows, superior-inferior ventricles, and right ventricular (RV) sinus hypoplasia is thought to be related to a post-looping abnormal clockwise rotation (twisting) that brings the infundibular chamber in close proximity to the leftward aspect of the developing AV canal, allowing the MV to straddle into the infundibular chamber [5]. Congenital MS can develop from an abnormality of one or more of the components. The narrowing of the supravalvular area, annulus, and valve leaflets often extends distally with additional subvalvar obstruction from hypertrophied or misplaced papillary muscles and abnormal chordae. Four common anatomic subtypes have been described: typical congenital MS, parachute MV, supravalvar mitral ring, and hypoplastic MS. The last subtype will be addressed in Chapter 20 [35]. By limiting flow to distal structures during embryologic development, MS may play a role in the hypoplasia or stenosis of downstream structures [36].

Anatomy

Mitral valve prolapse

The mitral valve annulus is divided into anterior and posterior components. The anterior mitral annulus is in continuity with the aortic annulus through a region termed the aortomitral curtain which extends between the left and right fibrous trigones. This region is well supported and less prone to distortion and remodeling compared to the posterior mitral annulus which is adjacent to a rim of discontinuous fibrous tissue and fat. The annular shape is likened to a hyperbolic paraboloid or "saddle" (Figure 14.1) with the most superior aspect of the annulus located anteriorly and the most inferior aspect located laterally at the commissures (Figure 14.2). This morphology has been shown to reduce stress on the mitral leaflets during systole [37] and has implications for design of annuloplasty rings [38,39]. During the cardiac cycle, annular movement is dependent on contraction of adjacent muscular structures and is threefold-translational (toward and away from the apex), circumferential and "folding" across the intercommissural axis [40]. The nonplanar shape of the mitral annulus is particularly important to appreciate when imaging and defining what constitutes MVP [2,27].

Normally, the leaflet edges are thrust together during ventricular systole along a 2–4 mm coaptation zone (zona coapta) at the leaflet tips. MVP results when a leaflet edge slips past this coaptation zone. More significant MVP (classic) usually results from excessive leaflet tissue (redundancy), myxomatous proliferation of the spongiosa, and elongation of the chordal apparatus [41]. These abnormalities lead to a more fundamental

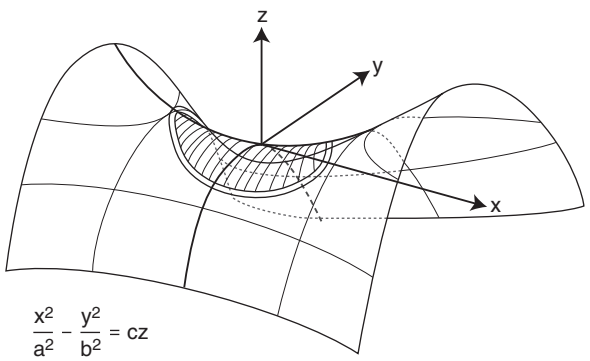


Figure 14.1 Schematic of an idealized "saddle-shaped" surface – hyperbolic paraboloid – which is concave downward in one direction (parallel to the yz plane) and upward in a perpendicular direction (parallel to the xz plane). The symbols a, b, and c denote constants that determine the shape of the structure. Source: Levine RA, et al. 1987 [67]. Reproduced with permission of Wolters Kluwer Health.

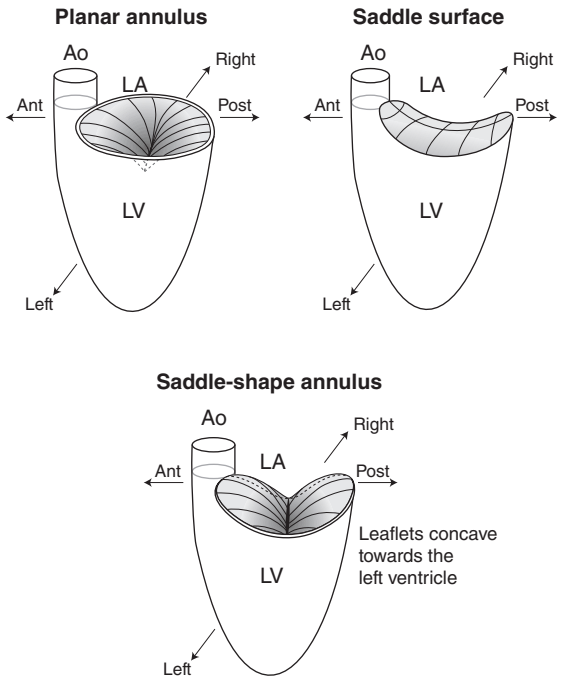


Figure 14.2 (Top left) Diagram of the model in vitro with a planar annulus and leaflets curving downward toward the zone of coaptation. Adjacent cardiac structures are also diagrammed. Ant., anterior; Ao, aorta; LA, left atrium; LV, left ventricle; Post., posterior. (Top right) Diagram of the model in vitro with the leaflets and annulus shaped to lie on a saddle surface. (Bottom) The model restructured with leaflets concave toward the left ventricle, reflecting its systolic pressure, but not protruding above the anterior and posterior high points of the saddle-shaped annulus. Source: Levine RA, et al. 1987 [67]. Reproduced with permission of Wolters Kluwer Health.

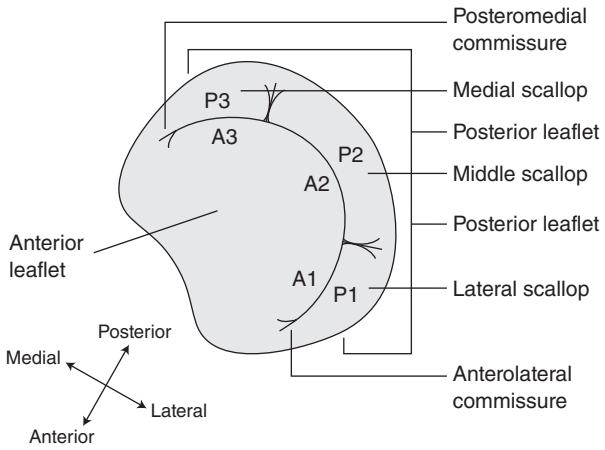


Figure 14.3 Nomenclature used to describe the anatomy of the MV leaflets segments and commissures (surgical view from the left atrium). A1, lateral segment; A2, middle segment; A3, medial segment; P1, lateral scallop; P2, middle scallop; P3, medial scallop. Source: Shanewise JS, et al. ASE/SCA guidelines for performing a comprehensive intraoperative multiplane transesophageal echocardiography examination: recommendations of the American Society of Echocardiography Council for Intraoperative Echocardiography and the Society of Cardiovascular Anesthesiologists Task Force for Certification in Perioperative Transesophageal Echocardiography. *J Am Soc Echocardiogr* 1999;**12**(10):884–900. Reproduced with permission of Elsevier.

failure of MV function, significant prolapse, mitral regurgitation (MR), and rarely chordal rupture.

A standard nomenclature of leaflet segments provides consistency when describing the location of isolated prolapsing segments (Figure 14.3). In a large adult surgical series on MVP, isolated posterior and bileaflet prolapse, with a prevalence of 52% and 33%, respectively, were the more common patterns of mitral leaflet prolapse. In comparison, the prevalence of isolated anterior leaflet prolapse was 15% [42].

Isolated cleft mitral valve

By definition, ICMV exists without an ostium primum defect. Within this definition, there are two separate categories, which were characterized in a large anatomic investigation [12]. When ICMV coexists with an abnormal conotruncus the cleft attachments are to the subarterial left ventricular (LV) myocardium, in a more vertical location. This morphology is important to define and recognize because it can lead to LV outflow tract obstruction [12,43,44]. In addition, ICMV with an abnormal conotruncus is notable for having no features similar to AV canal defects – namely a normal ventricular inlet/outlet ratio [45] and no association with trisomy 21. This differs from ICMV with normally related great arteries (NRGA), where the cleft attachments are more horizontal to the ventricular septum. In ICMV with NRGA, trisomy 21 is more frequent and a reduced inlet/outlet ratio is present [12,46]. Prior to this insight there had been debate about whether ICMV was related in some manner to AV canal defects [47–49]. To sort this out, investigators examined the location of the cleft attachments, papillary muscle location and inlet/outlet ratio, producing different conclusions [44–50]. The recognition of two distinct groups – NRGA and abnormal conotruncus – was key to explaining the vertical location of the cleft attachment [12]. In ICMV with NRGA the cleft attachments are to the membranous septum (when intact) or to the crest of the ventricular septum when a VSD is present. Functionally, the attachment appears to "migrate" superiorly when the membranous septum is intact resulting in a cleft location that is in between horizontal and vertical.

Straddling mitral valve

SMV occurs when MV chordal attachments are present within the right ventricle. Straddling is across the anterior (outlet) septum and differs from a straddling tricuspid valve which crosses the inlet septum [51]. The attachments of a SMV are to a single papillary muscle or closely spaced papillary muscle groups within the infundibulum to either the conal septum, septal band or the free wall, and can involve the anterior leaflet or both mitral valve leaflets. This lesion is always associated with a VSD and an abnormal conotruncus, either double-outlet right ventricle (DORV) or transposition of the great arteries (TGA) [6]. When SMV is present in the setting of {S,D,L} or {S,L,D}

segmental sets there are invariably crossed AV valve inflows, superior-inferior ventricles, and hypoplasia of the RV sinus [5]. Major straddling occurs when greater than one-half of the MV is related to the infundibulum. Typically the MV orifice is adequately sized and rarely more than mildly incompetent. Outflow obstruction from the attachments is rare. Risk factors for survival are related to the presence of multiple or noncommitted (remote) ventricular septal defects [43].

Double-orifice mitral valve

In its most frequent form, DOMV exists with two discrete orifices, each with its own chordal support and papillary muscles. The orifices are frequently divided by a "fibrous ridge," which is actually normal MV leaflet tissue [52,53]. This separation can either be limited to the tips of the respective orifices, sparing the more basal aspects, or extend along the entire length of the leaflets [53]. Another much less common anatomic variation is a muscular separation of the orifices associated with papillary muscle abnormality [53]. The size of the papillary muscles varies directly with the size of the orifice that they subtend. At one end of the spectrum is a chordal ring, a tiny anterolateral orifice without papillary support inserting directly into the LV wall. More typically, the valves are relatively equal in size. When DOMV is present with an AV canal defect, it is often characterized by a smaller posteromedial orifice. A recent report indicates that DOMV is more prevalent in partial AVC defects (64%) versus complete AVC defects (34%) or transitional AVC defects (2%) [54].

Mitral stenosis

Typical congenital MS involves thickened and rolled leaflets, shortened chordae tendineae with absence of the interchordal spaces (as seen in anomalous mitral arcade), and underdeveloped papillary muscles, which may be closely spaced [29]. Typical MS has also been termed "symmetric" [55], implying equal distribution of chordae to each papillary muscle and equal papillary muscle size. Asymmetric papillary muscle location, size, and distribution of chordal attachments is common (found in approximately 30% of a large cross-sectional study) [56], and in the extreme results in a true parachute MV [57] with all chordae inserting into a single papillary muscle – typically the anterolateral papillary muscle is absent [35,57]. Congenital MS is strongly associated with obstructive left-sided lesions including pulmonary vein stenosis, supravalvar and valvar aortic stenosis, parachute mitral valve, supravalvar mitral ring, subaortic membrane and coarctation of the aorta – the last four lesions together were originally described by Shone et al. [14]. Supravalvar mitral ring is an important subtype of MS characterized by a membranous tissue growth from the left atrial side of the mitral leaflets that results in a variable degree of stenosis. Two types of congenital mitral rings exist. The much more common "intramitral" ring consists of a thin membrane adherent to the atrial surface of the valve leaflets, and it is more commonly associated with Shone complex. The "supramitral" ring is a shelf-like membrane at or just above the mitral annulus, and this less common form of ring is usually associated with a normal subvalvular apparatus [58]. Congenital mitral ring can be progressive and is optimally treated surgically [55,56,58].

Congenital giant left atrium

The morphology of congenital GLA is fairly consistent [7,8,59], with a globally enlarged left atrial cavity and more focal aneurysmal enlargement of the atrial wall adjacent to the appendage. Typically the atrial cavity extends apically along the anterior and lateral left ventricular wall (Figure 14.4). The mass effect can lead to compression of the left ventricular free wall, right atrium and adjacent thoracic structures, including the esophagus, left bronchus, and recurrent laryngeal nerve.

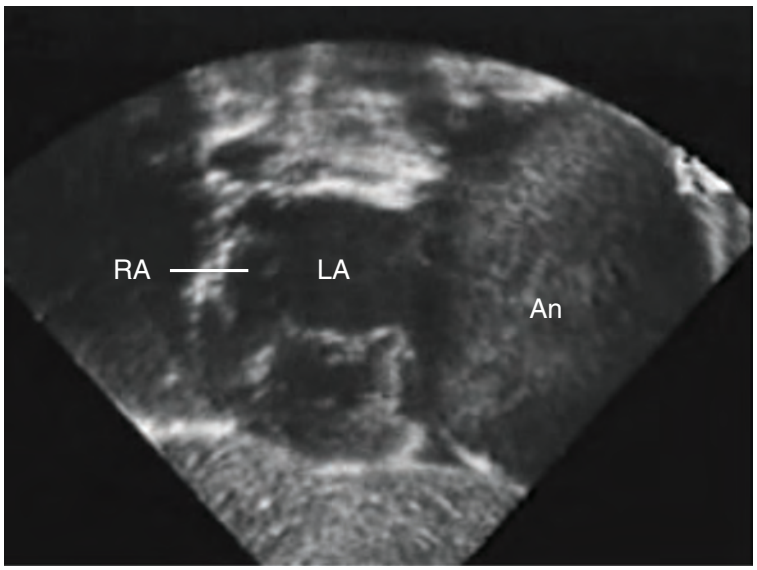


Figure 14.4 Apical 4-chamber view demonstrating the massively dilated left atrial appendage in a patient with "giant left atrium." An, aneurysm; LA, left atrium; RA, right atrium.

Pathophysiology

The pathophysiology associated with either abnormal MV development (cleft, straddling, parachute, or double orifice) or abnormal MV apparatus function (MVP) is predominantly a function of the competence of the valve (regurgitation) and the adequacy of the flow orifice (stenosis). An additional factor specific to ICMV with abnormal conotruncus and SMV is the location of the attachments relative to the potential pathway from the LV to the outflow and whether this pathway is adequate for a biventricular repair [43,60,61].

Chronic MR can develop in classic MVP and in general is well tolerated with minimal symptoms. The indications for surgical MV plasty are related to the exact mechanism and location of prolapse, the integrity of the MV apparatus, degree of MR, age, and LV size. Preservation of long-term LV function is the rationale behind early surgical intervention [42]. Recently, a study in adults showed that patients with a lower ejection fraction (<64%) and higher end-systolic dimension by M-mode (>37 mm) preoperatively were more likely to develop LV systolic dysfunction following mitral valve repair for MVP compared to patients with a higher EF and smaller LVESD [62]. Acute chordal or papillary muscle rupture, resulting in a flail leaflet, and acute MR is poorly tolerated, producing acute left atrial and pulmonary artery hypertension. In general, flail involving the posterior leaflet is more amenable to surgical repair.

ICMV frequently results in MR due to the lack of adequate coaptation zone along the cleft. The outcome following plasty, which basically involves suture plasty of the cleft to improve coaptation, is a trade-off between better coaptation and adequacy of the flow orifice with good mid-term outcomes [63,64].

DOMV without associated lesions occurs rarely (7% of all DOMV cases) [52], which is likely an underestimate because when DOMV is present in isolation, the valve typically is functioning well and is clinically silent. The pathophysiology is generally not related to dysfunction of the DOMV, but rather the morbidity of the associated lesions – frequently AV canal defects, stenosis of the aggregate flow orifice, or obstructive left-sided lesions [13,52,54]. In DOMV with an AV canal defect, if regurgitation is present, the posteromedial orifice is frequently the culprit. Significant mitral stenosis of a DOMV is often present and is amenable to balloon valvuloplasty in selected patients [56]. Successful surgical management of DOMV with AVC defects involves complete closure of the accessory orifice if it is contributing to MR. However, competent accessory orifices are often left alone. Of note, if the accessory orifice is closed, modification to the surgical closure of the cleft is usually required to avoid creating mitral stenosis [54].

The hemodynamic burden of mitral stenosis, and therefore symptoms, depends upon the flow orifice size and the cardiac output. As heart rate increases, diastole is shortened more than systole and the mean gradient across the valve increases, even at a fixed cardiac output. To maintain a given cardiac output, a greater mean pressure gradient is required. For severe stenosis, a small increase in flow rate necessitates a large increase in the pressure gradient [65]. The elevated left atrial pressure results in left atrial dilation, elevated pulmonary venous pressures, pulmonary edema, and dyspnea. Pulmonary hypertension in moderate or severe MS is secondary to transmission of pressure to the pulmonary bed, reactive vasoconstriction, and vessel wall changes [66]. Severe pulmonary hypertension can in turn lead to right ventricular dysfunction and tricuspid regurgitation. Left atrial dilation is a powerful substrate for atrial fibrillation, which increases the risk of thromboembolic events.

Imaging

Key elements

The key elements of the echocardiographic examination in the setting of mitral valve anomalies can be summarized as follows:

- Assessment of mitral valve apparatus morphology and function, including:
 - the integrity of chordal and leaflet support structures;
 - length of the chordae;
 - chordal attachments and papillary muscle – location and number;
 - careful definition of the annular plane;
 - identification of MVP;
 - localization of the prolapsing leaflet segment (Figure 14.3);
 - identification of MV cleft attachment location;
 - identification of SMV – major versus minor;
 - identification of associated conotruncal and atrioventricular canal lesions;
 - feasibility of biventricular repair by visualizing the pathway from LV to outflow as it relates to the ICMV or SMV attachments.
- Full interrogation of all MR jets:
 - localize the regurgitation orifice;
 - assess the degree of MR using multiple methods to overcome limitations of each:
 - color flow mapping (spatial distribution);
 - width of the jet at the vena contracta;
 - continuous-wave Doppler with analysis of the spectral pattern;
 - pulsed-wave spectral Doppler of pulmonary veins;
 - consider quantification of the regurgitant volume.
- Anatomic and hemodynamic assessment of the MV flow orifice:
 - annulus size – dimensions in two orthogonal planes;
 - assessment of anatomic flow orifice by two-dimensional (2D) imaging;
 - recognize physiology that leads to reduced orifice flow – atrial septal defect (ASD) and/or reduced cardiac output;
 - Doppler interrogation.
- Left atrial size
- Left ventricular size

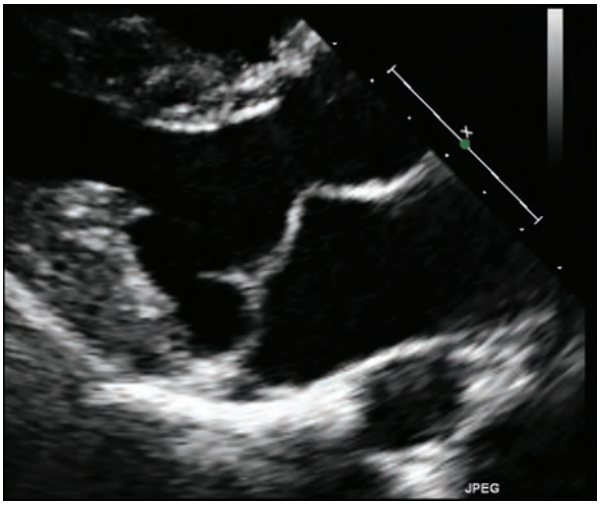


Figure 14.5 Systolic frame from a standard parasternal long-axis view showing mild mitral valve prolapse. Note the displacement of both the anterior and posterior leaflets beyond the annular plane. (Video 14.1).

- Estimation of right ventricular pressure by tricuspid regurgitation and/or ventricular septal configuration
- Ventricular function.

As the above goals highlight, imaging of the MV is an involved process, which is best accomplished within the framework of a normal thorough congenital examination utilizing slow sweeps of the cardiac anatomy from multiple acoustic windows. Imaging tips specific to each lesion and the details of the hemodynamic assessment of stenosis are discussed in the following sections.

Mitral valve prolapse (MVP)

In its more subtle form, MVP can be erroneously missed or diagnosed when not present. This is mainly due to failure to account for the nonplanar anatomy of the annulus [67]. The leaflets of a normal MV move beyond the annular level in standard 2- and 4-chamber views where the annular edge extends more inferiorly (closer to the LV apex) and can be mistaken for MVP; therefore MVP should be diagnosed from ventricular long-axis, or 3-chamber, views (Figure 14.5; Video 14.1). Isolated MVP of the posterior leaflet is best seen from the long-axis views (P2) and 2-chamber views (P1 and P3). Isolated posterior leaflet prolapse is particularly important to recognize because the outcome of surgical plasty is excellent [42], which may alter the threshold for recommending repair.

Isolated cleft mitral valve (ICMV)

Visualization of the cleft attachments is best from a subxiphoid short-axis view (Figure 14.6; Video 14.2). ICMV with an abnormal conotruncus has more vertically positioned cleft attachments near the LV outflow. Examination of ICMV is focused on determining if outflow tract obstruction is present and if the cleft interferes with the potential pathway from the LV to the great artery (either aorta or pulmonary); it is best accomplished from the modified subxiphoid windows (Figure 14.7; Video 14.3) that

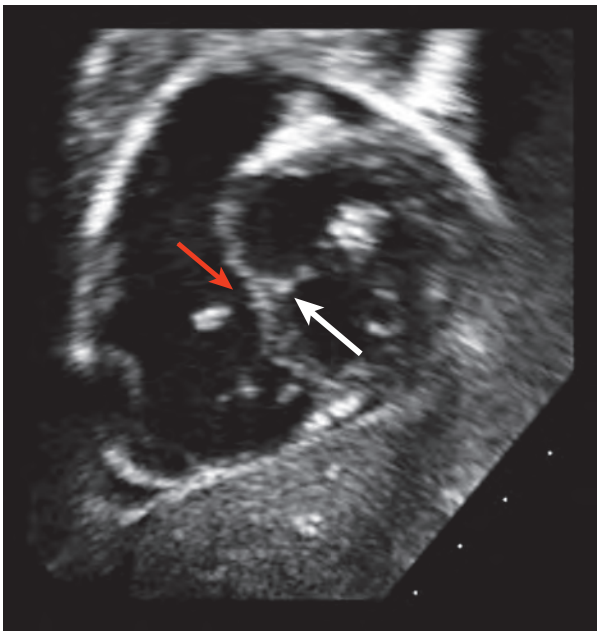


Figure 14.6 Systolic frame from a modified short-axis view obtained from a subxiphoid window profiling an isolated cleft of the mitral valve in a young child. From the subxiphoid window the chordae of the cleft (white arrow) are perpendicular to plane of interrogation which provides better visualization compared to the parasternal short-axis window. Note the characteristic location of the attachments near the membranous septum – which is marked by the anteroseptal commissure of the tricuspid valve (red arrow). (Video 14.2).

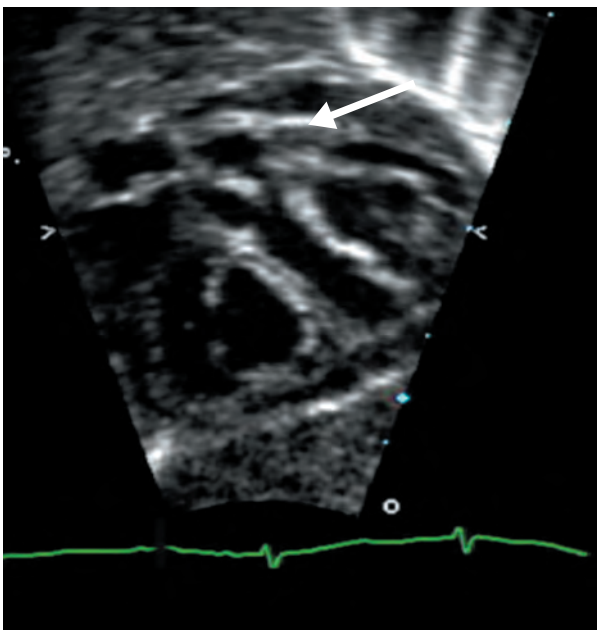


Figure 14.7 Diastolic frame from a modified view obtained from a subxiphoid window profiling an isolated cleft of the mitral valve (ICMV) in an infant with D-transposition of the great arteries {S,D,D}. Note the vertical orientation (arrow) of the cleft attachments, typical for ICMV with transposition or double-outlet right ventricle (see text). The cleft attaches to the leftward aspect of the left ventricular outflow. (Video 14.3).

profile each respective structure of interest. One often needs to rotate the transducer from standard long- and short-axis views to visualize these pathways better [6]. In addition, sweeping this anatomy once the modified view is found is crucial to understanding the adequacy of the pathway and degree of potential outflow obstruction.

Straddling mitral valve (SMV)

Imaging of SMV is focused on first identifying major straddling (Figures 14.8 and 14.9; Video 14.4 and 14.5), which usually precludes biventricular repair. When straddling is minor, similar to ICMV, standard and modified subxiphoid views provide visualization of the straddling chordae and papillary muscles, their exact attachment location and the feasibility of VSD closure or baffle repair. Parasternal imaging provides enhanced visualization of the chordal attachments within the infundibulum (free wall, septal band or conal septum) in SMV or within the LV outflow in ICMV (Figure 14.10; Videos 14.6 and 14.7).

Double-orifice mitral valve (DOMV)

The mitral valve orifices are best visualized from an apical view, rotating the transducer counterclockwise to image each orifice in its long-axis plane. Standard short-axis views from either parasternal or subxiphoid windows (Figure 14.11; Video 14.8) provide imaging of the double orifice en face, and sweeping the MV in this plane defines the extent of the fibrous ridge, the adequacy of each orifice and the competency of the valve [53].

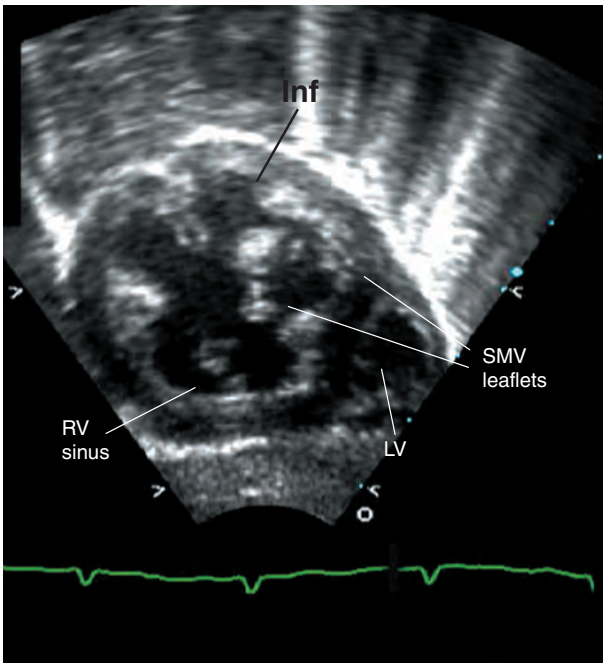
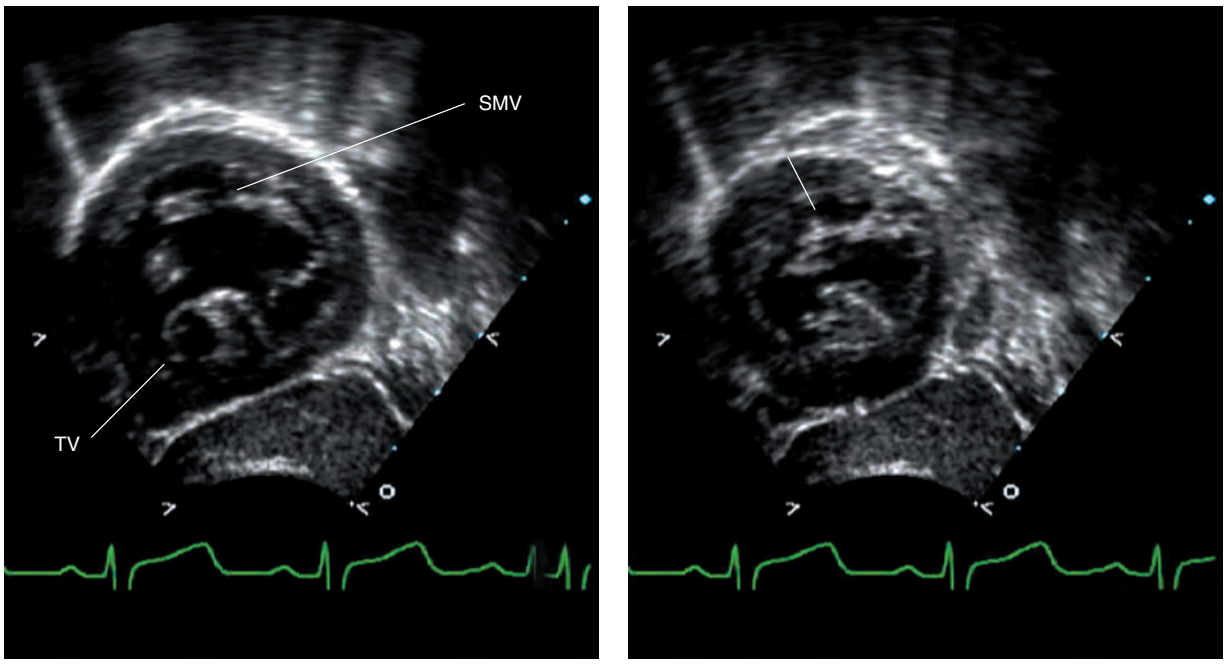
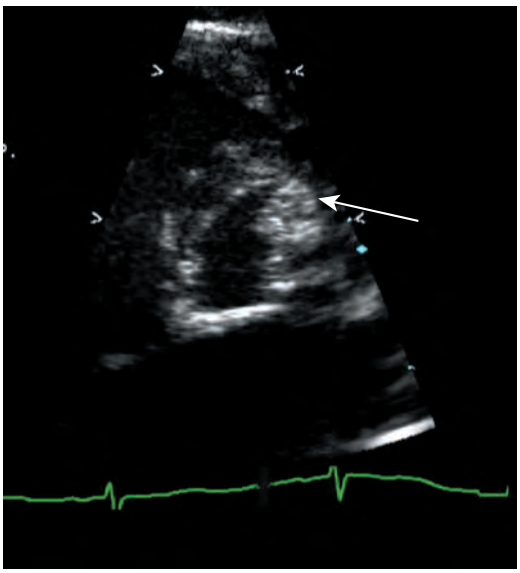


Figure 14.8 Diastolic frame from a modified long-axis view obtained from a subxiphoid window profiling major straddling of the mitral valve in an infant with double-outlet right ventricle (DORV) {S,D,D}. Note the commissure of the straddling valve with attachments within the infundibulum and the marked degree of straddling that would complicate biventricular repair. Inf, infundibulum; RV, right ventricular; LV, left ventricle; SMV, straddling mitral valve. (Video 14.4).

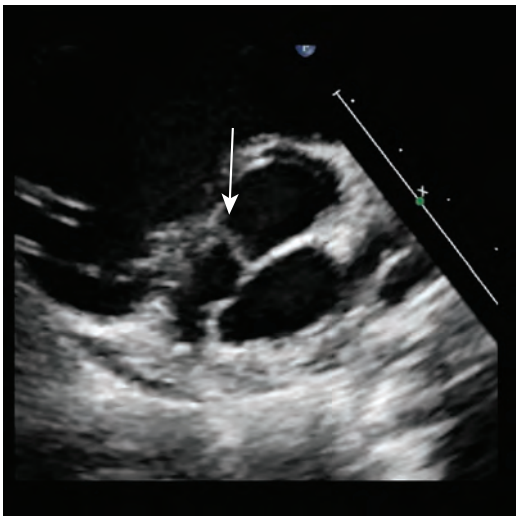


(a) (b)

Figure 14.9 Diastolic **(a)** and systolic **(b)** frames from a modified short-axis view obtained from a subxiphoid window profiling major straddling of the mitral valve (SMV) in an infant with TGA {S,D,D} pulmonary stenosis. Note the inferiorly positioned tricuspid valve (TV) inflow and the mitral straddling via the anterior (outflow) aspect of the ventricular septum. Systolic frame **(b)** shows the coapting commissure (arrow) of the straddling valve. (Video 14.5).



(a)



(b)

Figure 14.10 **(a)** Systolic frame from a standard short-axis plane profiling the exact location (arrow) of the cleft attachments to the leftward aspect of the left ventricular outflow tract (LVOT) in the same infant as shown in Figure 14.9 with D-transposition of the great arteries {S,D,D} and isolated cleft of the mitral valve. **(b)** Systolic frame from a standard short-axis plane demonstrating cleft attachments to the rightward aspect of the LVOT – typical for ICMV with normally related great arteries in the same patient as seen in Figure 14.6. (Videos 14.6 and 14.7).

Supravalvar mitral ring

Supravalvar mitral ring is a challenging lesion to image [58,68] and requires a high index of suspicion and diligence on the part of the imager. One should suspect this lesion in the setting of congenital MS with an increasing degree of stenosis over time. The membrane is thin and often adherent to the atrial side of the leaflet with frequently only its edge visible. The 4-chamber apical views provide an interrogation angle perpendicular to the membrane, thereby enhancing visualization. Careful sweeps utilizing appropriate gain and compression settings, transducer selection and targeted magnification of the leaflets is key (Figure 14.12a,b; Video 14.9). Any uncertainty about the presence or absence of this diagnosis following a thorough transthoracic examination should prompt a transesophageal echocardiogram (Figure 14.13).

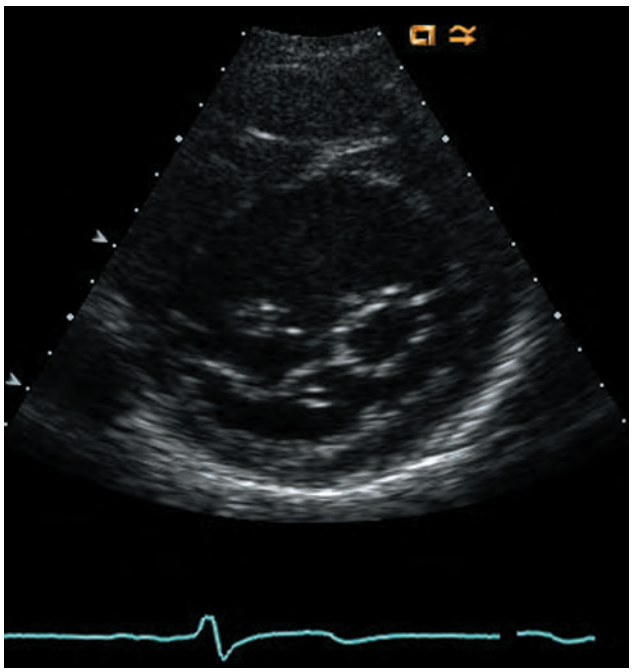


Figure 14.11 Diastolic frame from a parasternal short-axis plane demonstrating a double-orifice mitral valve. Note the equal size of each orifice and their location above their respective papillary muscle groups. (Video 14.8).

Typical congenital MS and parachute mitral valves

Congenital MS and parachute mitral valves are best imaged in the apical (Figure 14.14a–c; Videos 14.10 and 14.11), and ventricular long- and short-axis planes. The subxiphoid window in infants and younger children typically gives a higher yield than the parasternal window. Slow, targeted sweeps of the mitral apparatus utilizing magnification mode provide optimal visualization to differentiate subtypes of mitral stenosis (Figure 14.15a,b; Videos 14.12 and 14.13).

Congenital giant left atrium (GLA)

Imaging is focused on assessing the overall size of the left atrium, distortion of other cardiac structures including the atrial septum and ventricular septum, and narrowing of the inferior vena cava or superior vena cava. The left atrial size is best assessed from the apical 4-chamber view. It is important to image the full extent of the left atrial cavity with slow sweeps. Measurements of size should be performed in similar imaging planes for a given patient to limit variability. The morphology and function of the mitral and aortic valves should be thoroughly examined given the frequent association of GLA with rheumatic heart disease.

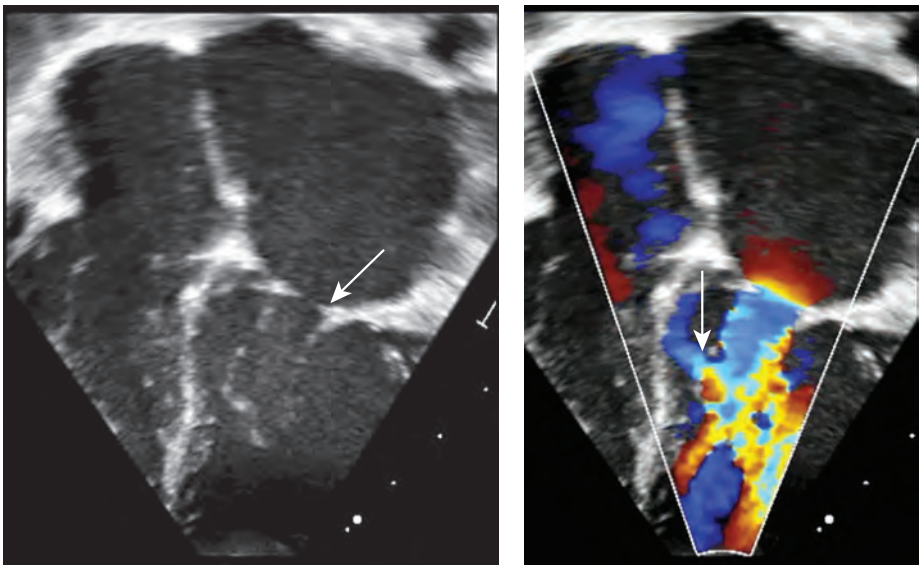


Figure 14.12 **(a)** Diastolic frame from an apical window demonstrating congenital mitral stenosis and a supravalvar mitral ring (SVMR). Note the prominent papillary muscle that extends further toward the annulus than in a normal apparatus, the accompanying shortened chordae and hypoplasia of the annulus. The membranous SVMR (arrow) is seen as a thin projection from the atrial side of the leaflet, extending from the annulus into the supravalvar flow orifice. **(b)** Color Doppler in the same imaging plane demonstrating flow acceleration beginning just prior to the annulus – a characteristic finding in SVMR. When present this should prompt the imager to undertake an extensive search for an unrecognized SVMR. Note the additional egress from the inflow (arrow) directed medially via an abnormal intrachordal space. This type of complex inflow orifice makes accurate measurement of the flow orifice area particularly challenging (see text). (Video 14.9).

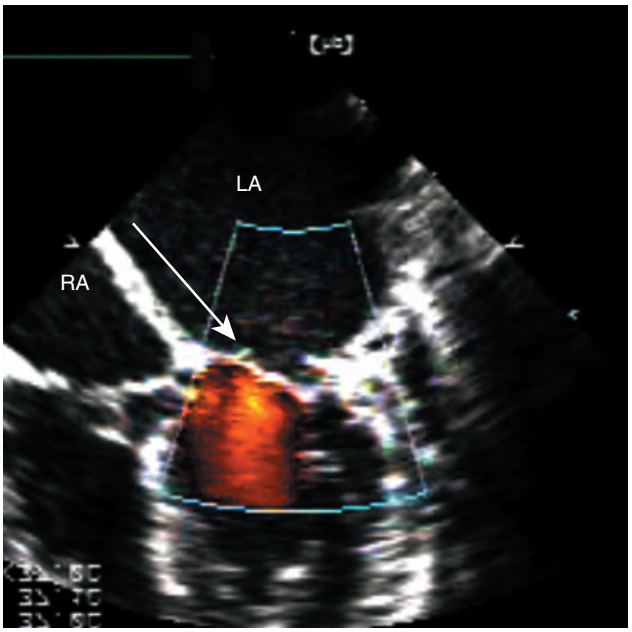


Figure 14.13 Systolic frame from a transesophageal echocardiogram, mid-esophageal 4-chamber view in the same patient as seen in Figure 14.12. Note the enhanced visualization of the supravalvar mitral ring provided by TEE. The membrane is now conspicuous, extending from both the lateral aspect of the atrial side of the leaflet and the medial aspect (arrow).

Mitral stenosis (MS) – flow orifice assessment

In general, the challenge of defining and grading the degree of stenosis is a significant one that is best addressed utilizing all available clinical (signs and symptoms), hemodynamic, and imaging data. Similar to other congenital lesions, a single echocardiographic parameter that accurately characterizes the degree of stenosis does not exist. Flow orifice area (effective valve area) is the best available measure of stenosis. In many types of congenital MS, however, defining the minimal flow orifice is not possible due to the complex anatomy of the flow orifice, which is often not the mitral valve annulus [35]. This is particularly true of lesions addressed in this chapter – MS that is not associated with annular hypoplasia. Nevertheless, annular dimensions appropriately adjusted for body surface area (see Chapter 5) and expressed as a z-score have been shown to predict outcome [69] and should be obtained using magnified diastolic frames from the apical 4-chamber (lateral dimension) and parasternal long-axis views (antero-posterior dimension). Calculation of the mitral valve area using planimetry is a well-established technique in adults [70,71] and has shown good agreement with anatomic measurements from explanted intact mitral valves [72]. The valve is imaged in the parasternal short-axis view and the maximal orifice is planimetered to calculate the area; again, indexing to body surface area is critical. It

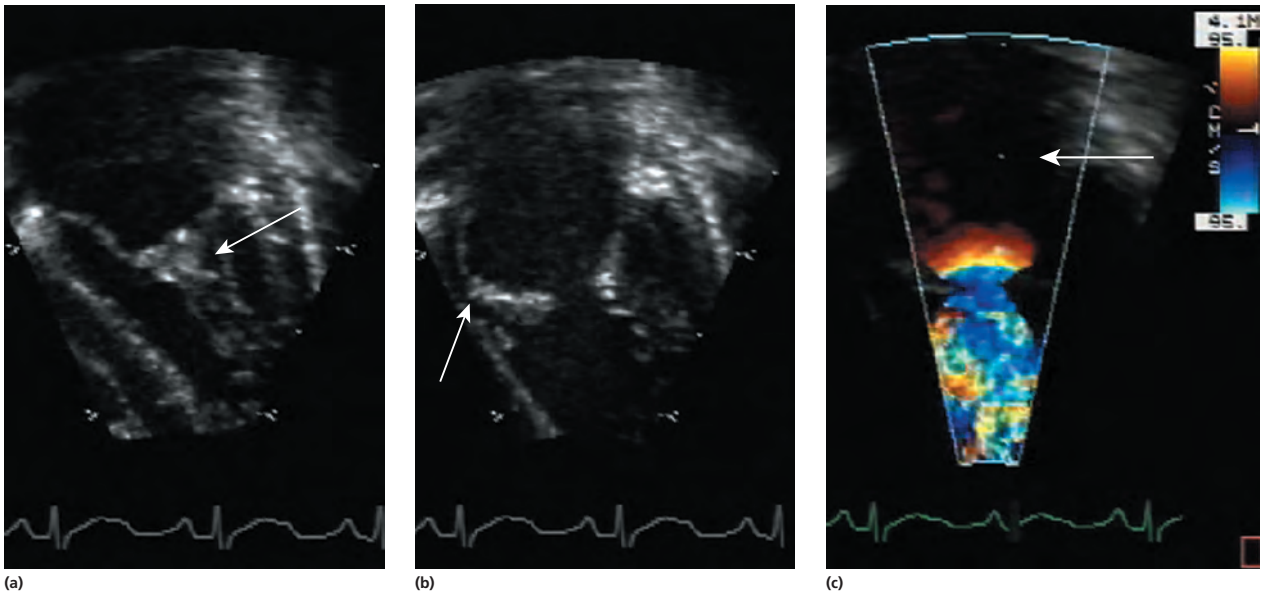


Figure 14.14 **(a)** A late-systolic frame in typical congenital mitral stenosis from an apical 4-chamber view. Note the thickened and short chordae (arrow). **(b)** An early diastolic frame – note the rolled and thickened leaflet tips, the reduced orifice size and doming of the middle aspect of the anterior leaflet (arrow). **(c)** Color Doppler with flow acceleration in the distal aspect of the inflow (arrow indicates the annulus level). Note the proximal isovelocity surface area (PISA) aliased lines representing increasing velocity "shells" as the flow approaches the small orifice. (Videos 14.10 and 14.11).

is crucial that careful attention is given to the acoustic window that profiles the mitral inflow cone in its short axis, which may be off-angle relative to the left ventricular short axis, and then defining the smallest flow orifice with careful sweeping. Figure 14.16 (Videos 14.10 and 14.12) demonstrates the potential limitations of this technique in congenital MS. Although three-dimensional (3D)-echocardiography promises better definition of the minimal flow orifice [73] in adults and older children, the underlying complex anatomy and the high heart rates of infants challenge the special and temporal resolution of current 3D technology.

Surrogate parameters to flow orifice area can be divided into two main categories:

1 those based on the continuity principle (flow orifices in continuity with one another must handle equal total flow in a given short time interval) – this includes Doppler-derived

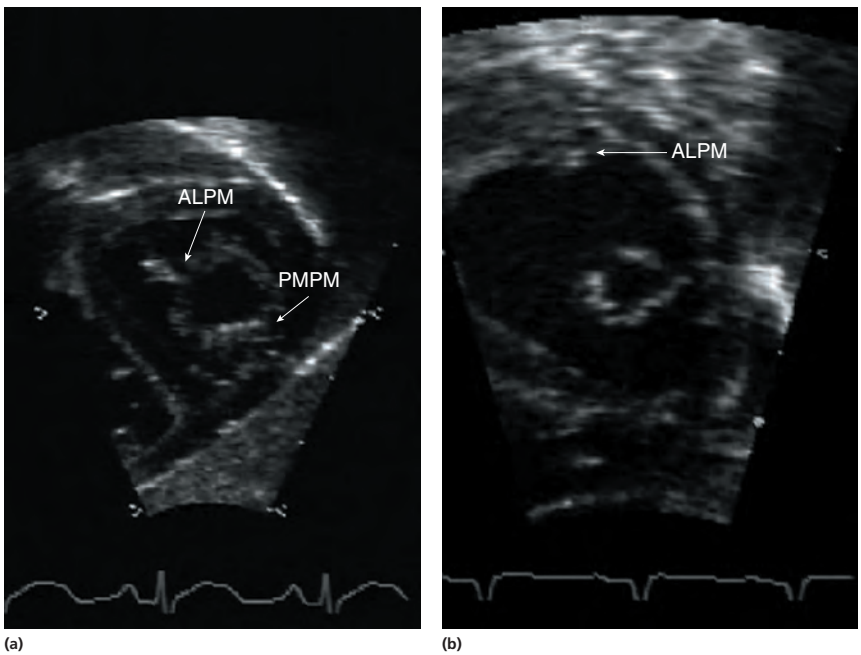


Figure 14.15 **(a)** Diastolic frame short-axis plane from a subxiphoid window in typical congenital mitral stenosis. Note separate well-spaced papillary muscle groups (arrows). **(b)** Diastolic frame, short-axis plane from a subxiphoid window demonstrating a parachute mitral valve. Note the presence of a hypoplastic anterolateral papillary muscle (arrow) that receives no chordae, which is the most common arrangement in the parachute lesion (see text). ALPM, anterolateral papillary muscle group; PMPM, posteromedial papillary muscle group. (Videos 14.12 and 14.13).

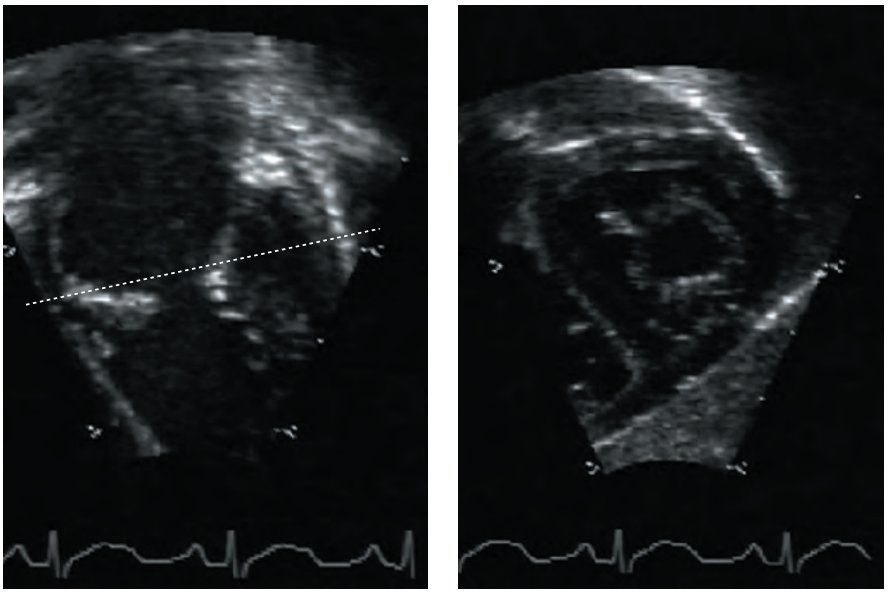


Figure 14.16 Diastolic frames in an apical 4-chamber plane **(a)** and subxiphoid short-axis plane **(b)** in the same patient as seen in Figure 14.15a. Note that the orifice appears falsely adequate in the short-axis view, due to the relationship of the distal aspect of the leaflets to the orifice – the leaflet adjacent to the orifice runs nearly parallel to the orifice (a). When imaging in the orthogonal plane (white dashed line) it is difficult to locate this exact plane, thus the orifice is inadequately characterized and appears larger. (Videos 14.10 and 14.12).

continuity equation and flow convergence zone analysis (proximal isovelocity surface area, or PISA; see Chapter 6);

2 the pressure response to flow across a narrowed orifice – which includes Doppler-obtained pressure gradient and pressure half-time (PHT).

Both categories require obtaining accurate instantaneous peak velocities by spectral Doppler. Proper alignment of the range-gated Doppler beam (cursor) with the MV inflow is the first step in accurately characterizing the velocity. This is achieved by interrogation of the mitral valve flow orifice from an acoustic window that provides adequate spectral Doppler signal at the optimal angle of interrogation; this acoustic window is optimal for Doppler interrogation, and may be different than the optimal acoustic window for 2D visualization of anatomy and measurement of structures. Typically, this is a modified apical window, but restricting oneself to a standard view is a mistake that can lead to a misrepresentation of the gradient.

The mean MV gradient is a useful surrogate to mitral valve area [74,75]. It is obtainable in most patients, even in those with poor acoustic windows. When compared with simultaneous catheterization, the mean Doppler gradient shows good agreement [76], with a mean difference of 0.2 ± 1.2 mmHg. As detailed previously, the dependence of gradient on cardiac output is strong and explains why nonsimultaneous comparison with an invasive gradient yields poor agreement, both in large studies of adult subjects [77] and in smaller pediatric cohorts [55,56,78]. Recording the heart rate as a measure of cardiac output is useful for serial comparison. The presence of less than a full systemic cardiac output (ASD or low cardiac output state) needs to be recognized when using flow-based measures of mitral stenosis. Limited published data exist on what level of gradient constitutes significant stenosis. A mean gradient >3 mmHg [68] or peak >12 mmHg [55] has been used as the definition of significant mitral stenosis in native valves; and a peak >19 mmHg as severe MS following MV replacement [79].

Doppler-derived PHT is based on the principle that the rate of pressure gradient decline varies with the degree of obstruction. Its utility in congenital MS is limited. With increasing obstruction the pressure gradient across the valve is maintained for a longer time. The PHT is the time needed for the initial peak pressure gradient to decrease by half. The relationship proposed by Hatle et al. [80] is MV area (cm^2) = 220/PHT (ms). The constant 220 is empirically derived based on adults using the Gorlin [81,82] method of value area as the reference standard. Many studies in adults have examined this correlation [71]; however, only one investigation utilized the more robust reference standard of direct anatomic measurement of explanted valves [72,83]. In that study, PHT showed reasonable correlation ($r = 0.80$) with explanted MV areas. Of note, the same investigation showed 2D-echocardiographic planimetry had significantly better correlation ($r = 0.95$), with a mean difference near zero and limits of agreement of –0.21 to +0.29 cm^2 [84]. PHT is also dependent on both atrial and ventricular compliance, the initial transmitral pressure gradient and the heart rate [84,85], all of which are dynamic variables in normal growing children and markedly altered in congenital heart disease. In addition, as shown in a Doppler study on newborns [86], diastolic filling is shifted to later in diastole with increasing heart rate, which alters the PHT independent of the flow orifice area. Given the above, PHT has little role in congenital MS and its use should be reserved for adult-sized pediatric patients, and always assessed in the context of other measures of stenosis.

Prenatal assessment

Typically, only severe cases of MVP (as in neonatal Marfan syndrome) will be diagnosed prenatally. However, it is possible

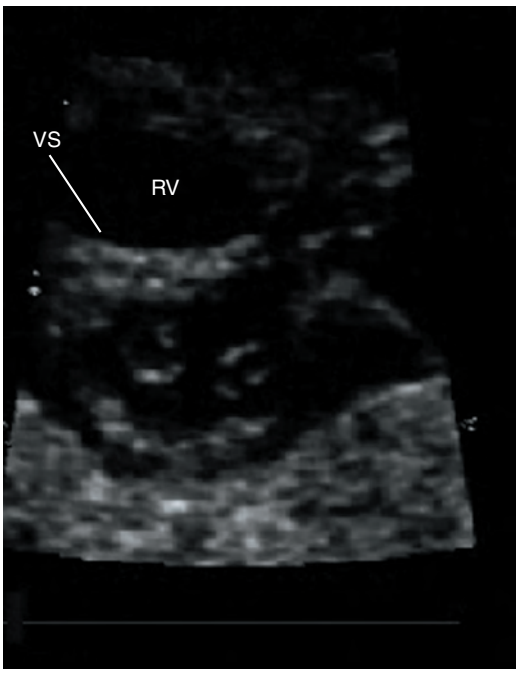


Figure 14.17 Diastolic frame in a short-axis plane in a fetus of 31-week gestation, demonstrating a double-orifice mitral valve. RV, right ventricle; VS, ventricular septum; (Video 14.14).

to diagnose ICMV, SMV, mitral stenosis, and DOMV (Figure 14.17; Video 14.14) by fetal echocardiography. In general, these rare lesions are diagnosed by interrogating the MV apparatus from all available acoustic windows, which allows identification of the chordal and papillary muscle positions, leaflet number, presence of a cleft, and valve size [1] and integrity. When an abnormal conotruncus is found, a diligent search for ICMV and SMV in the context of an assessment of possible biventricular repair is critical. Given the current spatial and temporal resolution of fetal imaging, subtle forms of the above lesions, such as nonclassic MVP, ICMV with NRGA and no VSD, and DOMV with a chordal ring, may go undetected. As with any fetal examination, the impact of missing these lesions needs to be appreciated in the context of their overall favorable prognosis. The hemodynamic significance of mitral stenosis can be difficult given the redundancy of the fetal circulation at the atrial septal and ductal levels, which can lead to less than full cardiac output traversing the mitral valve. Defining the MV apparatus as above, including careful measurement of the annulus and a thorough Doppler interrogation of ascending aorta, transverse arch, ductus, and foramen ovale, provides insight into the physiology and aids in characterizing the degree of stenosis.

Echocardiographic guidance of transcatheter and surgical treatment

The surgical advances made in the last two decades in MV plasty [42] have added considerable complexity to the perioperative transesophageal echocardiographic (TEE) interrogation of MV anatomy and function [87,88]. Critical to this success is an accurate assessment of the exact mechanism underlying the MV dysfunction, which requires a systematic, thorough interrogation of the MV apparatus and, importantly, effective communication between the imaging team and surgeon. This interchange is dynamic and ongoing during surgical MV plasty. The en face view of the valve (Figure 14.3) provides a foundation for the nomenclature as well as a vantage point for systematic interrogation. Briefly, the esophageal 4-chamber view is obtained with minimal transducer angulation (0–15 degrees); the mitral valve is then scanned from the superior, mid and lower esophageal locations, which typically profiles the A1–P1, A2–P2 and A3–P3 segment coaptation, respectively. The commissural view from the mid-esophagus with 45–70 degrees of angulation and the transgastric en face view (0–10 degrees of angulation with anteflexion) provide additional views to verify which leaflet segments are dysfunctional. This interrogation method provides a foundation that can be modified to evaluate the more complex lesions of ICMV, SMV, DOMV, and congenital MS.

Balloon valvuloplasty for congenital mitral stenosis is utilized when the mitral disease is the predominant lesion (i.e., not hypoplastic left heart syndrome), other surgically correctable lesions are absent and the anatomy of the valve narrowing is favorable [55,56,89]. Importantly, a supravalvar mitral ring must be definitively excluded as balloon valvuloplasty of this lesion has poor outcomes compared with surgery [56]. As the long-term morbidity following mitral valve replacement in growing children is significant [79], palliative valvuloplasty is an option in selected patients.

Imaging of the adult and postoperative assessment

Transthoracic echocardiography (TTE) in adults with SMV, DOMV and ICMV is typically limited by poor acoustic windows – especially from the subxiphoid views, which are critical in ICMV and SMV. As the ventricular long-axis views are standard in adult imaging and MVP is diagnosed from this plane, the previously discussed issues around MVP and imaging approach to evaluate MVP is well suited to the adult patient. TTE assessment of the hemodynamic severity of MS using color and spectral Doppler in adults is typically achievable, even in those with poor acoustic windows; however, the details of the morphology and exact mechanism of the mitral valve apparatus dysfunction are often incompletely characterized with TTE alone. Transesophageal echocardiography (discussed earlier) is, in general, ideally suited to image the MV due to the close proximity of the probe to the MV apparatus. Surgical repair has been advocated for congenital GLA due to the frequent morbidities of atrial tachycardia [16] and compressive effects [7,17,18]. Imaging following resection is straightforward as therapy is generally curative [8,18].

Postoperatively, there are numerous potential issues surrounding the above lesions, but the basic aspects of valvar competence (regurgitation) and the adequacy of the flow orifice

(stenosis) are central. Following mitral valve repair or replacement, a thorough evaluation of residual MS, mitral regurgitation, paravalvar leaks, and normal motion of prosthetic valves is performed. Serial mean gradients from appropriately obtained spectral Doppler interrogation provide a repeatable, consistent, and simple means of follow-up. As mentioned previously, the limitation of gradient should be noted and heart rate during interrogation recorded.

Videos

To access the videos for this chapter, please go to www.lai-echo.com.

Video 14.1 Parasternal long-axis view showing mild bileaflet mitral valve prolapse. Note the displacement of both the anterior and posterior leaflets beyond the annular plane.

Video 14.2 Subxiphoid short-axis sweep showing isolated cleft of the mitral valve anterior leaflet. Note the horizontal orientation of the cleft attachments in this patient with normally related great arteries.

Video 14.3 Modified view obtained from a subxiphoid window profiling an isolated cleft of the mitral valve (ICMV) in an infant with D-transposition of the great arteries {S,D,D}. Note the vertical orientation of the cleft attachments, typical for ICMV with transposition or double-outlet right ventricle. The cleft attaches to the leftward aspect of the left ventricular outflow.

Video 14.4 Modified long-axis view obtained from a subxiphoid window profiling major straddling of the mitral valve in an infant with double-outlet right ventricle (DORV) {S,D,D}. Note the commissure of the straddling valve with attachments within the infundibulum and the marked degree of straddling that would complicate biventricular repair.

Video 14.5 A modified short-axis view obtained from a subxiphoid window profiling major straddling of the mitral valve (SMV) in an infant with TGA {S,D,D} pulmonary stenosis. Note the inferior positioned tricuspid valve (TV) inflow and the straddling via the anterior (outflow) aspect of the ventricular septum.

Video 14.6 Parasternal short-axis plane profiling the exact location of the cleft attachments to the leftward aspect of the left ventricular outflow tract (LVOT) in D-transposition of the great arteries {S,D,D} and isolated cleft of the mitral valve.

Video 14.7 Parasternal short-axis plane demonstrating cleft attachments to the rightward aspect of the LVOT – typical for ICMV with normally related great arteries.

Video 14.8 A parasternal short-axis plane demonstrating a double-orifice mitral valve. Note the equal size of each orifice and their location above their respective papillary muscle groups.

Video 14.9 Apical window demonstrating congenital mitral stenosis and a supravalvar mitral ring (SVMR). Note the prominent papillary muscle that extends further toward the annulus than in a normal apparatus, the accompanying shortened chordae and hypoplasia of the annulus. The membranous SVMR is seen as a thin projection from the atrial side of the leaflet, extending from the annulus into the supravalvar flow orifice. Color Doppler in the same imaging plane demonstrating flow acceleration beginning just prior to the annulus – a characteristic finding in SVMR, which if present should prompt the imager to undertake an extensive search for an unrecognized SVMR. Note the additional egress from the inflow directed medially via an abnormal intrachordal space. This type of complex inflow orifice makes accurate measurement of the flow orifice area particularly challenging (see text).

Video 14.10 Typical congenital mitral stenosis from an apical 4-chamber view. Note the thickened and short chordae, the rolled and thickened leaflet tips, the reduced orifice size and the diastolic doming of the middle aspect of the anterior leaflet.

Video 14.11 Color Doppler of typical congenital mitral stenosis from an apical 4-chamber view. Note the flow acceleration in the distal aspect of the inflow with the proximal isovelocity surface area (PISA) aliased lines representing increasing velocity "shells" as the flow approaches the small orifice.

Video 14.12 A short-axis plane from a subxiphoid window in typical congenital mitral stenosis. Well-spaced papillary muscle groups are readily appreciated in this short-axis plane – excluding parachute mitral valve morphology (Video 14.13). Note that the orifice appears falsely adequate in the short-axis view, due to the relationship of the distal aspect of the leaflets to the orifice – the leaflet adjacent to the orifice runs nearly parallel to the orifice. This aspect of the anatomy is only appreciated in orthogonal views (apical 4-chamber, Video 14.10).

Video 14.14 A short-axis plane in a fetus of 31 weeks' gestation demonstrating a double-orifice mitral valve.

References

1 Freed LA, Levy D, Levine RA, et al. Prevalence and clinical outcome of mitral-valve prolapse. *N Engl J Med* 1999;**341**(1):1–7.

2 Levine RA, Handschumacher MD, Sanfilippo AJ, et al. Three-dimensional echocardiographic reconstruction of the mitral valve, with implications for the diagnosis of mitral valve prolapse. *Circulation* 1989;**80**(3):589–598.

3 Liberthson RR, Paul MH, Muster AJ, et al. Straddling and displaced atrioventricular orifices and valves with primitive ventricles. *Circulation* 1971;**43**(2):213–226.

4 Freedom RM, Bini R, Dische R, Rowe RD. The straddling mitral valve: morphological observations and clinical implications. *Eur J Cardiol* 1978;**8**(1):27–50.

5 Geva T, Van Praagh S, Sanders SP, et al. Straddling mitral valve with hypoplastic right ventricle, crisscross atrioventricular relations,

double-outlet right ventricle and dextrocardia: morphologic, diagnostic and surgical considerations. *J Am Coll Cardiol* 1991; **17**(7):1603–1612.
6 Fraisse A, del Nido PJ, Gaudart J, Geva T. Echocardiographic characteristics and outcome of straddling mitral valve. *J Am Coll Cardiol* 2001;**38**(3):819–826.
7 Hougen TJ, Mulder DG, Gyepes MT, Moss AJ. Aneurysm of the left atrium. *Am J Cardiol* 1974;**33**(4):557–561.
8 Morales JM, Patel SG, Jackson JH, et al. Left atrial aneurysm. *Ann Thorac Surg* 2001;**71**(2):719–722.
9 Levy D, Savage D. Prevalence and clinical features of mitral valve prolapse. *Am Heart J* 1987;**113**(5):1281–1290.
10 Flack JM, Kvasnicka JH, Gardin JM, et al. Anthropometric and physiologic correlates of mitral valve prolapse in a biethnic cohort of young adults: the CARDIA study. *Am Heart J* 1999;**138**(3 Pt 1):486–492.
11 Hoffman JI, Kaplan S. The incidence of congenital heart disease. *J Am Coll Cardiol* 2002;**39**(12):1890–1900.
12 Van Praagh S, Porras D, Oppido G, et al. Cleft mitral valve without ostium primum defect: anatomic data and surgical considerations based on 41 cases. *Ann Thorac Surg* 2003;**75**(6):1752–1762.
13 Bano-Rodrigo A, Van Praagh S, Trowitzsch E, Van Praagh R. Double-orifice mitral valve: a study of 27 postmortem cases with developmental, diagnostic and surgical considerations. *Am J Cardiol* 1988;**61**(1):152–160.
14 Shone JD, Sellers RD, Anderson RC, et al. The developmental complex of "parachute mitral valve," supravalvular ring of left atrium, subaortic stenosis, and coarctation of aorta. *Am J Cardiol* 1963;**11**:714–725.
15 Zimand S, Frand M, Hegesh J. Congenital giant left atrial aneurysm in an infant. *Eur Heart J* 1997;**18**(6):1034–1035.
16 Varghese PJ, Simon AL, Rosenquist GC, et al. Multiple saccular congenital aneurysms of the atria causing persistent atrial tachyarrhythmia in an infant. Report of a case successfully treated by surgery. *Pediatrics* 1969;**44**(3):429–433.
17 Mansour E, Aldousany A, Arce O, et al. Recurrent congenital left atrial aneurysm in a newborn. *Pediatr Cardiol* 1998;**19**(2):165–167.
18 Kadowaki MH, Berger S, Shermeta DW, et al. Congenital left atrial aneurysm in an infant. *J Pediatr Surg* 1989;**24**(3):306–308.
19 Fountain-Dommer RR, Wiles HB, Shuler CO, et al. Recognition of left atrial aneurysm by fetal echocardiography. *Circulation* 2000;**102**(18):2282–2283.
20 Lu W-WY. Giant congenital left atrial aneurysm in an 11-year-old boy. *Circulation* 2012;**125**(14):1818–1820.
21 Bhattarai A. Congenital giant aneurysm of the left atrial appendage in an infant. *Cardiol Young* 2011;**21**(6):697.
22 Dumitrescu AA. Giant left atrial appendage with a common ventricular-appendicular wall and an abnormal course of the circumflex coronary artery in an asymptomatic 18-month-old girl. *Pediatr Cardiol* 2008;**29**(2):431–433.
23 McGuinness J, Kindawi A, Tajri S, et al. Surgical management of giant left atrial diverticulum. *J Thorac Cardiovasc Surg* 2007;**133**(3):820–822.
24 Wang D, Holden B, Savage C, et al. Giant left atrial intrapericardial aneurysm: noninvasive preoperative imaging. *Ann Thorac Surg* 2001;**71**(3):1014–1016.
25 Devereux RB, Brown WT, Kramer-Fox R, Sachs I. Inheritance of mitral valve prolapse: effect of age and sex on gene expression. *Ann Intern Med* 1982;**97**(6):826–832.
26 Sumner RG, Phillips JH, Jacoby WJ, Jr., Tucker DH. Idiopathic enlargement of the right atrium. *Circulation* 1965;**32**(6):985–991.
27 Apostolakis E, Shuhaiber JH. The surgical management of giant left atrium. *Eur J Cardiothorac Surg* 2008;**33**(2):182–190.
28 Kanani M, Moorman AF, Cook AC, et al. Development of the atrioventricular valves: clinicomorphological correlations. *Ann Thorac Surg* 2005;**79**(5):1797–1804.
29 De la Cruz MV, Gimenez-Ribotta M, Saravalli O, Cayre R. The contribution of the inferior endocardial cushion of the atrioventricular canal to cardiac septation and to the development of the atrioventricular valves: study in the chick embryo. *Am J Anat* 1983;**166**(1):63–72.
30 Oosthoek PW, Wenink AC, Vrolijk BC, et al. Development of the atrioventricular valve tension apparatus in the human heart. *Anat Embryol (Berl)* 1998;**198**(4):317–329.
31 Wessels A, Sedmera D. Developmental anatomy of the heart: a tale of mice and man. *Physiol Genomics* 2003;**15**(3):165–176.
32 Lincoln J, Alfieri CM, Yutzey KE. Development of heart valve leaflets and supporting apparatus in chicken and mouse embryos. *Dev Dyn* 2004;**230**(2):239–250.
33 Wessels A, Markman MW, Vermeulen JL, et al. The development of the atrioventricular junction in the human heart. *Circ Res* 1996;**78**(1):110–117.
34 von Gise A, Pu WT. Endocardial and epicardial epithelial to mesenchymal transitions in heart development and disease. *Circ Res* 2012;**110**(12):1628–1645.
35 Ruckman RN, Van Praagh R. Anatomic types of congenital mitral stenosis: report of 49 autopsy cases with consideration of diagnosis and surgical implications. *Am J Cardiol* 1978;**42**(4):592–601.
36 Rudolph AM, Heymann MA, Spitznas U. Hemodynamic considerations in the development of narrowing of the aorta. *Am J Cardiol* 1972;**30**(5):514–525.
37 Salgo IS, Gorman JH, 3rd, Gorman RC, et al. Effect of annular shape on leaflet curvature in reducing mitral leaflet stress. *Circulation* 2002;**106**(6):711–717.
38 Tibayan FA, Rodriguez F, Langer F, et al. Annular remodeling in chronic ischemic mitral regurgitation: ring selection implications. *Ann Thorac Surg* 2003;**76**(5):1549–1554; discussion 1554–1555.
39 Gorman JH, 3rd, Gorman RC, Jackson BM, et al. Annuloplasty ring selection for chronic ischemic mitral regurgitation: lessons from the ovine model. *Ann Thorac Surg* 2003;**76**(5):1556–1563.
40 Silbiger JJ. Anatomy, mechanics, and pathophysiology of the mitral annulus. *Am Heart J* 2012;**164**(2):163–176.
41 Marks AR, Choong CY, Sanfilippo AJ, et al. Identification of high-risk and low-risk subgroups of patients with mitral-valve prolapse. *N Engl J Med* 1989;**320**(16):1031–1036.
42 Suri RM, Schaff HV, Dearani JA, et al. Survival advantage and improved durability of mitral repair for leaflet prolapse subsets in the current era. *Ann Thorac Surg* 2006;**82**(3):819–826.
43 Fraisse A, Massih TA, Vouhe P, et al. Management and outcome of patients with abnormal ventriculo-arterial connections and mitral valve cleft. *Ann Thorac Surg* 2002;**74**(3):786–791.
44 Moene R. Congenital mitral valve anomalies in transposition of the great arteries. *Am J Cardiol* 1982;**49**(8):1972.
45 Penkoske P. Further observations on the morphology of atrioventricular septal defects. *J Thorac Cardiovasc Surg* 1985;**90**(4):611.
46 DiSegni E. Cleft anterior leaflet of the mitral valve with intact septa. A study of 20 cases. *Am J Cardiol* 1983;**51**(6):919.

47 Sigfusson G, Ettedgui JA, Silverman NH, Anderson RH. Is a cleft in the anterior leaflet of an otherwise normal mitral valve an atrioventricular canal malformation? *J Am Coll Cardiol* 1995;**26**(2):508–515.

48 Smallhorn JF, de Leval M, Stark J, et al. Isolated anterior mitral cleft. Two dimensional echocardiographic assessment and differentiation from "clefts" associated with atrioventricular septal defect. *Br Heart J* 1982;**48**(2):109–116.

49 Anderson R. Of clefts, commissures, and things. *J Thorac Cardiovasc Surg* 1985;**90**(4):605.

50 Disegni E. Two-dimensional echocardiography in detection of endocardial cushion defect in families. *Am J Cardiol* 1985;**55**(13 Pt 1):1649.

51 Pessotto R, Padalino M, Rubino M, et al. Straddling tricuspid valve as a sign of ventriculo-atrial malalignment: a morphometric study of 19 postmortem cases. *Am Heart J* 1999;**138**(6 Pt 1):1184–1195.

52 Zalzstein E, Hamilton R, Zucker N, et al. Presentation, natural history, and outcome in children and adolescents with double orifice mitral valve. *Am J Cardiol* 2004;**93**(8):1067–1069.

53 Trowitzsch E, Bano-Rodrigo A, Burger BM, et al. Two-dimensional echocardiographic findings in double orifice mitral valve. *J Am Coll Cardiol* 1985;**6**(2):383–387.

54 Sharma V, Burkhart HM, Schaff HV, et al. Double-orifice left atrioventricular valve in patients with atrioventricular septal defects: surgical strategies and outcome. *Ann Thorac Surg* 2012;**93**(6):2017–2020; discussion 2020–2021.

55 Moore P, Adatia I, Spevak PJ, et al. Severe congenital mitral stenosis in infants. *Circulation* 1994;**89**(5):2099–2106.

56 McElhinney DB, Sherwood MC, Keane JF, et al. Current management of severe congenital mitral stenosis: outcomes of transcatheter and surgical therapy in 108 infants and children. *Circulation* 2005;**112**(5):707–714.

57 Oosthoek PW, Wenink AC, Macedo AJ, Gittenberger-de Groot AC. The parachute-like asymmetric mitral valve and its two papillary muscles. *J Thorac Cardiovasc Surg* 1997;**114**(1):9–15.

58 Toscano A, Pasquini L, Iacobelli R, et al. Congenital supravalvar mitral ring: an underestimated anomaly. *J Thorac Cardiovasc Surg* 2009;**137**(3):538–542.

59 Park JS, Lee DH, Han SS, et al. Incidentally found, growing congenital aneurysm of the left atrium. *J Korean Med Sci* 2003;**18**(2):262–266.

60 Serraf A, Nakamura T, Lacour-Gayet F, et al. Surgical approaches for double-outlet right ventricle or transposition of the great arteries associated with straddling atrioventricular valves. *J Thorac Cardiovasc Surg* 1996;**111**(3):527–535.

61 Anderson R. Which hearts are unsuitable for biventricular correction? *Ann Thorac Surg* 1998;**66**(2):621.

62 Tribouilloy C, Rusinaru D, Szymanski C, et al. Predicting left ventricular dysfunction after valve repair for mitral regurgitation due to leaflet prolapse: additive value of left ventricular end-systolic dimension to ejection fraction. *Eur J Echocardiogr* 2011;**12**(9):702–710.

63 Perier P, Clausnizer B. Isolated cleft mitral valve: valve reconstruction techniques. *Ann Thorac Surg* 1995;**59**(1):56–59.

64 Tamura M, Menahem S, Brizard C. Clinical features and management of isolated cleft mitral valve in childhood. *J Am Coll Cardiol* 2000;**35**(3):764–770.

65 Rahimtoola SH, Durairaj A, Mehra A, Nuno I. Current evaluation and management of patients with mitral stenosis. *Circulation* 2002;**106**(10):1183–1188.

66 Otto CM, Davis KB, Reid CL, et al. Relation between pulmonary artery pressure and mitral stenosis severity in patients undergoing balloon mitral commissurotomy. *Am J Cardiol* 1993;**71**(10):874–878.

67 Levine RA, Triulzi MO, Harrigan P, Weyman AE. The relationship of mitral annular shape to the diagnosis of mitral valve prolapse. *Circulation* 1987;**75**(4):756–767.

68 LaCorte M, Harada K, Williams RG. Echocardiographic features of congenital left ventricular inflow obstruction. *Circulation* 1976;**54**(4):562–566.

69 Schwartz ML, Gauvreau K, Geva T. Predictors of outcome of biventricular repair in infants with multiple left heart obstructive lesions. *Circulation* 2001;**104**(6):682–687.

70 Nichol PM, Gilbert BW, Kisslo JA. Two-dimensional echocardiographic assessment of mitral stenosis. *Circulation* 1977;**55**(1):120–128.

71 Gonzalez MA, Child JS, Krivokapich J. Comparison of two-dimensional and Doppler echocardiography and intracardiac hemodynamics for quantification of mitral stenosis. *Am J Cardiol* 1987;**60**(4):327–332.

72 Faletra F, Pezzano A, Jr., Fusco R, et al. Measurement of mitral valve area in mitral stenosis: four echocardiographic methods compared with direct measurement of anatomic orifices. *J Am Coll Cardiol* 1996;**28**(5):1190–1197.

73 Chen Q, Nosir YF, Vletter WB, et al. Accurate assessment of mitral valve area in patients with mitral stenosis by three-dimensional echocardiography. *J Am Soc Echocardiogr* 1997;**10**(2):133–140.

74 Hatle L, Brubakk A, Tromsdal A, Angelsen B. Noninvasive assessment of pressure drop in mitral stenosis by Doppler ultrasound. *Br Heart J* 1978;**40**(2):131–140.

75 David D, Lang RM, Marcus RH, et al. Doppler echocardiographic estimation of transmitral pressure gradients and correlations with micromanometer gradients in mitral stenosis. *Am J Cardiol* 1991;**67**(13):1161–1164.

76 Nishimura RA, Rihal CS, Tajik AJ, Holmes DR, Jr. Accurate measurement of the transmitral gradient in patients with mitral stenosis: a simultaneous catheterization and Doppler echocardiographic study. *J Am Coll Cardiol* 1994;**24**(1):152–158.

77 Otto CM, Davis KB, Holmes DR, Jr., et al. Methodologic issues in clinical evaluation of stenosis severity in adults undergoing aortic or mitral balloon valvuloplasty. The NHLBI Balloon Valvuloplasty Registry. *Am J Cardiol* 1992;**69**(19):1607–1616.

78 Banerjee A, Kohl T, Silverman NH. Echocardiographic evaluation of congenital mitral valve anomalies in children. *Am J Cardiol* 1995;**76**(17):1284–1291.

79 Beierlein W, Becker V, Yates R, et al. Long-term follow-up after mitral valve replacement in childhood: poor event-free survival in the young child. *Eur J Cardiothorac Surg* 2007;**31**(5):860–865.

80 Hatle L, Angelsen B, Tromsdal A. Noninvasive assessment of atrioventricular pressure half-time by Doppler ultrasound. *Circulation* 1979;**60**(5):1096–1104.

81 Gorlin R, Gorlin SG. Hydraulic formula for calculation of the area of the stenotic mitral valve, other cardiac valves, and central circulatory shunts. *I. Am Heart J* 1951;**41**(1):1–29.

82 Cohen MV, Gorlin R. Modified orifice equation for the calculation of mitral valve area. *Am Heart J* 1972;**84**(6):839–840.
83 Flachskampf FA, Klinghammer L. Determination of stenotic mitral valve area: new, old, and gold standards. *Eur J Echocardiogr* 2008;**9**(3):321.
84 Karp K, Teien D, Bjerle P, Eriksson P. Reassessment of valve area determinations in mitral stenosis by the pressure half-time method: impact of left ventricular stiffness and peak diastolic pressure difference. *J Am Coll Cardiol* 1989;**13**(3):594–599.
85 Thomas JD, Weyman AE. Doppler mitral pressure half-time: a clinical tool in search of theoretical justification. *J Am Coll Cardiol* 1987;**10**(4):923–929.
86 Harada K, Takahashi Y, Shiota T, et al. Effect of heart rate on left ventricular diastolic filling patterns assessed by Doppler echocardiography in normal infants. *Am J Cardiol* 1995;**76**(8):634–636.
87 Stewart WJ, Currie PJ, Salcedo EE, et al. Intraoperative Doppler color flow mapping for decision-making in valve repair for mitral regurgitation. Technique and results in 100 patients. *Circulation* 1990;**81**(2):556–566.
88 Kawano H, Mizoguchi T, Aoyagi S. Intraoperative transesophageal echocardiography for evaluation of mitral valve repair. *J Heart Valve Dis* 1999;**8**(3):287–293.
89 Kveselis DA, Rocchini AP, Beekman R, et al. Balloon angioplasty for congenital and rheumatic mitral stenosis. *Am J Cardiol* 1986;**57**(4):348–350.

CHAPTER 15

Common Atrioventricular Canal Defects

Meryl S. Cohen
The Children's Hospital of Philadelphia, Philadelphia, PA, USA

Definition

The term common atrioventricular canal describes a group of cardiac defects characterized by abnormalities of the structures derived from the endocardial cushions during embryologic development of the heart. In these lesions, both atria are connected to a common (single) atrioventricular valve. Typically there are deficiencies in the atrial and ventricular septa as well as abnormalities of the atrioventricular valves. Of note, there are several different terms used to describe the atrioventricular canal including endocardial cushion defect, atrioventricular septal defect, common atrioventricular orifice, and atrioventricularis communis. For the remainder of this chapter the term common atrioventricular canal defect (CAVC) will be used because it is anatomically correct and is inclusive of the abnormality of the atrioventricular valve.

There is a spectrum of disease from an exclusive atrial communication to a large ventricular communication that usually dictates the physiology and the clinical course of CAVC. There is also a range of abnormalities of the common atrioventricular valve and incompetence of the valve is the norm. CAVC defects are commonly associated with Down syndrome. At least 40% of children with Down syndrome have congenital heart disease and of those, CAVC is one of the most common lesions seen along with isolated ventricular septal defect (VSD) [1].

Incidence

The incidence of CAVC is approximately 34.8 per 100,000 live births (range 24.2 to 39.6 per 100,000 live births), representing the ninth most common congenital heart lesion [2]. The incidence is likely higher in the fetal population since termination of pregnancy is sometimes performed if congenital heart disease or a chromosomal abnormality such as Down syndrome is detected before birth.

Etiology

A strong link exists between CAVC and Down syndrome (trisomy 21). In fact, the risk of CAVC is 1000-fold compared to those with normal chromosomes. Despite this known association, the responsible gene on chromosome 21 has yet to be identified. Recently, DSCAM (Down syndrome cell adhesion molecule) has been proposed as a possible candidate gene [3]. CAVC can also have an autosomal dominant pattern of inheritance or occur sporadically [4]. An association with chromosome 8p deletion and familial clusters with different modes of inheritance have also been reported [5,6]. CAVC is also seen frequently in association with the heterotaxy syndrome, particularly the asplenia (right isomerism) type.

Morphology and classification

Developmental considerations

Prior to the formation of the endocardial cushions, cardiac jelly expands in the region between the atria and the primitive ventricles, the so-called atrioventricular canal. The endocardial cushions are the primordia of the valves and septa of the developed heart which form as a result of epithelial-to-mesenchymal transformation [7]. Embryos that fail to develop these cushions experience demise once a fully functional heart is required in late gestation. The endocardial cushions are made up of mesenchymal tissue and are divided into superior, inferior, right, and left cushions. The atrioventricular canal septum is formed, at least in part, by the superior and inferior endocardial cushions which contribute to septation of the outlet portion of the atria and the inlet portion of the ventricles. If the endocardial cushions fail to fuse, likely as a result of abnormal migration of mesenchymal cells, the canal portions of the atrial and ventricular septa do not develop. In addition, abnormalities of atrioventricular valve development occur, particularly affecting the septal leaflet of the tricuspid valve and the anterior leaflet of the mitral valve. Detailed description of development of the endocardial cushions can be found in several publications [7–9].

Echocardiography in Pediatric and Congenital Heart Disease: From Fetus to Adult, Second Edition. Edited by Wyman W. Lai, Luc L. Mertens, Meryl S. Cohen and Tal Geva.
© 2016 John Wiley & Sons, Ltd. Published 2016 by John Wiley & Sons, Ltd.
Companion website: www.lai-echo.com

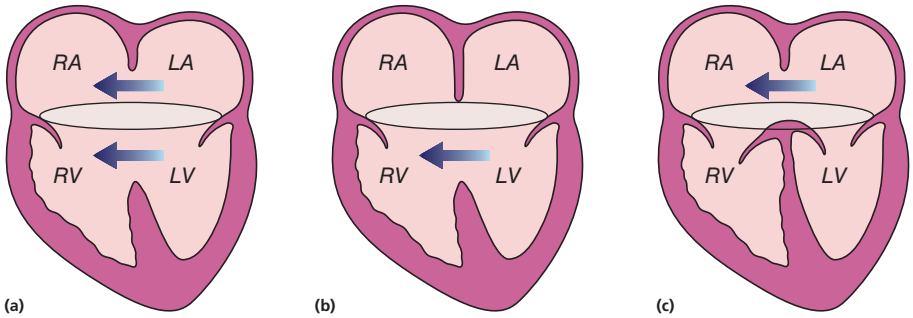


Figure 15.1 **(a)** Diagram showing the complete form of CAVC with a large atrial and large ventricular communication and a common atrioventricular valve orifice over both ventricles. **(b)** Diagram showing the rare form of CAVC with no atrial communication but a large ventricular septal defect. The atrioventricular valve sits more superior in the defect closing off the atrial communication. **(c)** Diagram of the incomplete form of CAVC with a large atrial communication, no ventricular communication, and two atrioventricular valve orifices. The atrioventricular valve sits more inferiorly and adheres to the ventricular septum closing off the ventricular communication. LA, left atrium; LV, left ventricle; RA, right atrium; RV, right ventricle.

Anatomy

CAVC is categorized in several ways. The deficiency in the atrioventricular septum is the same in all forms with the relationship of the atrioventricular valve within that defect being variable. Indeed, if the atrioventricular valve leaflets are removed in a heart specimen with CAVC, it is not possible to distinguish between the various subtypes. The complete form of CAVC (Figures 15.1a and 15.2a) is characterized by an interatrial communication antero-inferior to the margin of the fossa ovalis and adjacent to the atrioventricular valves, along with a large posterior VSD along the septal leaflet of the atrioventricular valve extending into the vicinity of the membranous septum, giving the ventricular septum a scooped-out appearance (Figures 15.2a and 15.3). Instead of two distinct atrioventricular valves, there is a common atrioventricular valve with a common annulus. Typically there is at least one mural, or lateral, leaflet positioned exclusively over the right ventricle and one mural leaflet positioned exclusively over the left ventricle that can be variable in size [10]. Moreover, in contrast to the normal tricuspid and mitral valves, there are two leaflets that bridge the crest of the ventricular septum in the superior and inferior position (Figures 15.3 and 15.4a,b). The superior bridging leaflet distorts the atrioventricular junction and subsequently causes superior displacement ("unwedging") of the aortic outflow tract; thus the aortic annulus no longer sits between the normal tricuspid and mitral valves (Figure 15.4b). As a result, the length of the left ventricle from the atrioventricular valve annulus to the apex is foreshortened and the length from the apex to the aortic valve annulus is elongated (typically these measures are equal in length in the normal heart) (Figure 15.5) [11]. The inferior bridging leaflet has extensive chordal attachments to the crest of the ventricular septum while the chordal attachments of the superior leaflet are variable and have been subclassified by Rastelli and colleagues (Figure 15.6) [12]. In Rastelli type A, the superior bridging leaflet is divided at the level of the ventricular septum (Figure 15.7). In type B arrangement, the rarest form, division of the superior bridging leaflet occurs at a right ventricular papillary muscle. In type C, the superior bridging leaflet is undivided or "free floating"; this is the most rudimentary form of CAVC and common in Down syndrome (Figure 15.8). Rastelli type A

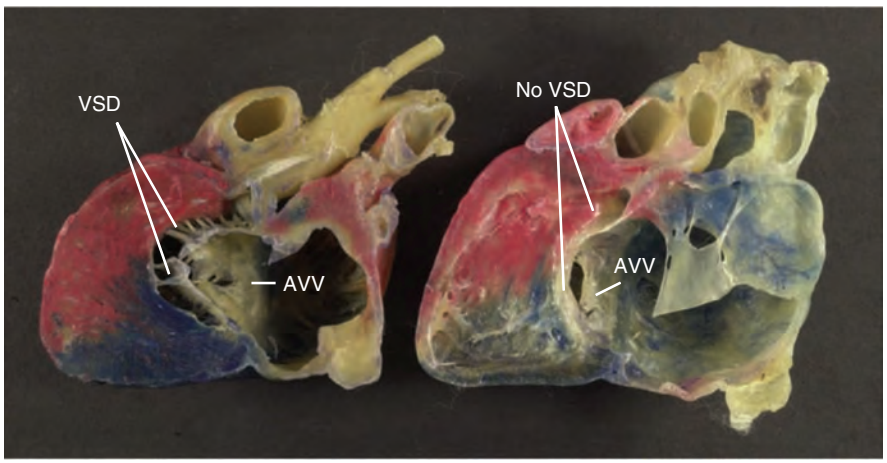


Figure 15.2 **(a)** Waxed anatomic specimen of a left ventricular view of the ventricular septum in the complete form of CAVC demonstrating the scooped-out appearance of the ventricular septum from the VSD with some choral attachments of the atrioventricular valve (AVV) to the crest of the septum. **(b)**The same view in a waxed anatomic specimen of incomplete CAVC demonstrating that the atrioventricular valve (AVV) is adherent to the crest of the ventricular septum with no VSD component. The scooped-out appearance of the ventricular septum is still present despite no ventricular level shunting.

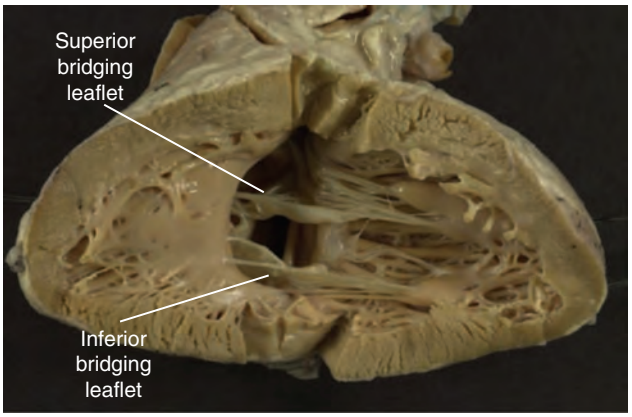


Figure 15.3 An anatomic specimen of complete CAVC in the left ventricular view of the ventricular septum shows the superior and inferior bridging leaflets crossing the ventricular septum into the left ventricle and the scooped-out appearance of the ventricular septum.

is more commonly associated with preoperative left ventricular outflow obstruction in part because of increased elongation of the outflow tract [13]. The complete form of CAVC is typically seen in children with Down syndrome. In a more unusual form of complete CAVC, the atrioventricular valve leaflets sit superiorly in the atrioventricular defect such that the atrial communication is trivial or absent and the ventricular communication is large (Figure 15.1b). Even rarer is the CAVC defect where atrioventricular valve tissue fills in the atrial and ventricular communications and there is no shunting whatsoever.

The incomplete (also known as partial) form of CAVC is characterized by an interatrial communication in the canal portion of the atrial septum (located between the antero-inferior margin of the fossa ovalis and the atrioventricular valves) with a common atrioventricular annulus in association with two atrioventricular valve orifices (Figure 15.1c). This form is often called ostium primum atrial septal defect. However, this term does not describe the atrioventricular valve abnormality or the fact that the defect

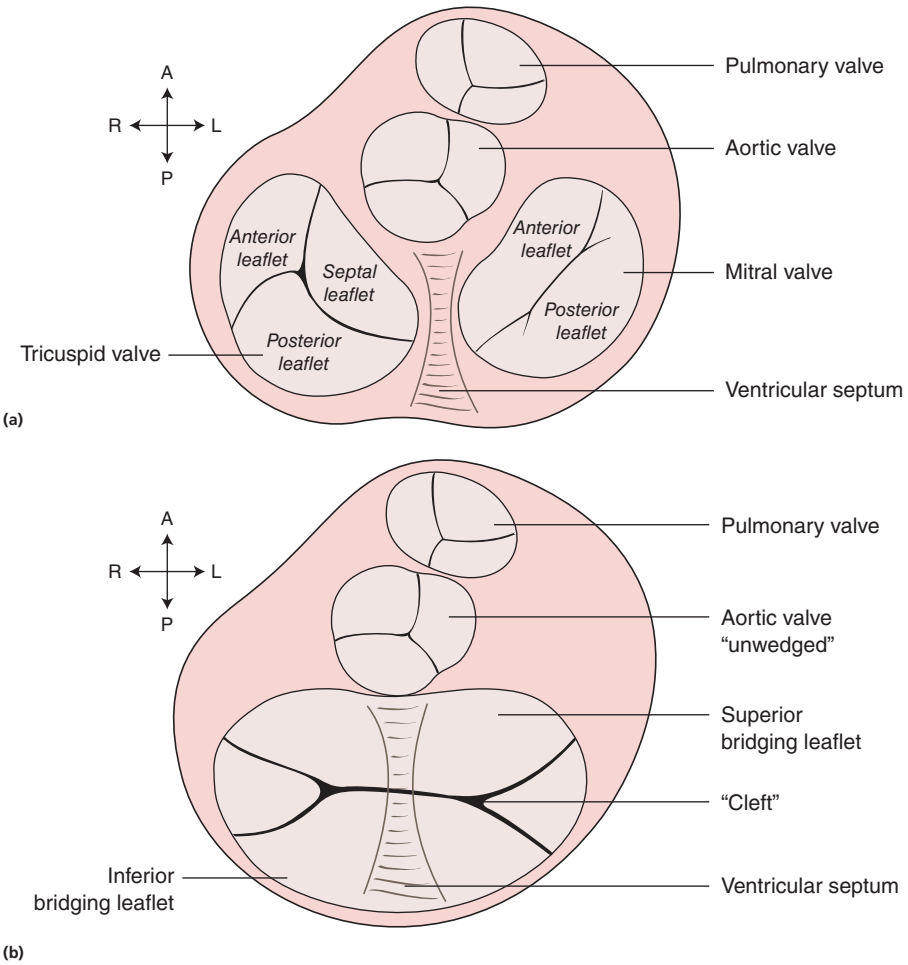


Figure 15.4 **(a)** Diagram depicting the relationship of the mitral and tricuspid valves to the aortic valve in a normal heart. The aortic valve sits wedged between the two atrioventricular valves. **(b)** The same view is depicted in this diagram of CAVC. The superior and inferior bridging leaflets are demonstrated with the "cleft" where the two bridging leaflets come together at the ventricular septum. The aortic valve is unwedged anteriorly as a result of the position of the superior bridging leaflet.

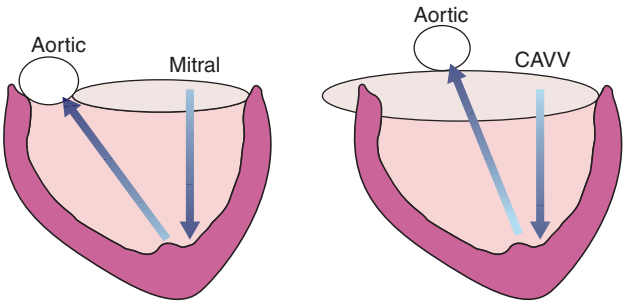


Figure 15.5 Diagram showing that the length of inflow and outflow are the same in the left ventricle of the normal heart. In CAVC, the outflow length is elongated because of the unwedged aortic valve.

in the atrioventricular septum is the same as in the complete form of CAVC. The distinction is that the atrioventricular valve tissue is adherent to the crest of the ventricular septum forming a connecting tongue, thus allowing no ventricular level shunt (Figures 15.2b and 15.9). Though the two orifices are separate, the valves do not resemble normal tricuspid and mitral valves, and thus the term mitral valve "cleft" is a misnomer. In fact the so-called "cleft" is the deficit of atrioventricular valve tissue where the superior and inferior bridging leaflets meet at the ventricular septum (Figure 15.10). Atrioventricular valve regurgitation at the level of apposition of the superior and inferior bridging leaflets in CAVC is the norm.

There is an intermediate form in the spectrum of CAVC known as transitional type typified by significant chordal attachments of the superior bridging leaflet to the ventricular septum with some shunting through these chordae at the ventricular

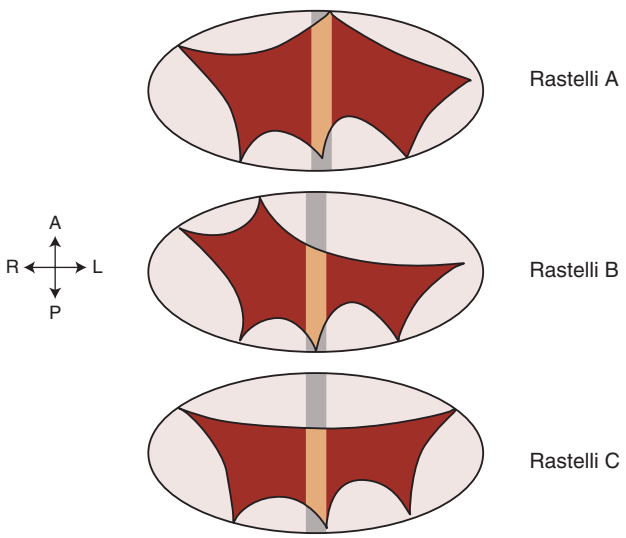


Figure 15.6 Rastelli classification. Type A: The superior bridging leaflet is divided at the level of the ventricular septum, Type B: Division of the superior bridging leaflet occurs to a right ventricular papillary muscle, Type C: The superior bridging leaflet is undivided or "free floating."

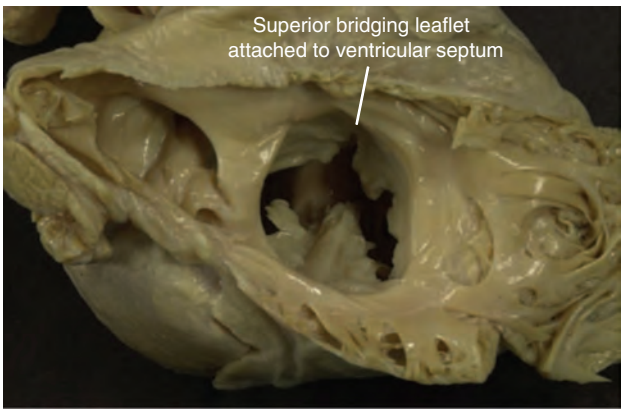


Figure 15.7 Anatomic specimen showing the right atrial view looking down toward common atrioventricular valve. This view demonstrates Rastelli type A anatomy with division of the superior bridging leaflet at the ventricular septum.

level. The VSD component is typically restrictive with subsystemic pulmonary artery pressure.

In CAVC, the relationship of the atrial septum to the common atrioventricular valve may be balanced or unbalanced. In the balanced form, the atrial septum sits over the ventricular septum with relatively equal distribution of atrial inflow to the right and left side of the atrioventricular valve. Rarely, the atrial septum is malaligned in relation to the ventricular septum (also known as "double-outlet atrium") such that the atrial septum is deviated predominantly towards the left atrial inflow (double-outlet right atrium) or the right atrial inflow (double-outlet left atrium) (Figure 15.11a,b). Inflow into the contralateral ventricular can be obstructed in some cases.

Maldistribution of the atrioventricular valve over the ventricles occurs much more commonly than double-outlet atrium and accounts for 10% of all cases of CAVC [14]. When the atrioventricular valve sits more over one ventricle than the

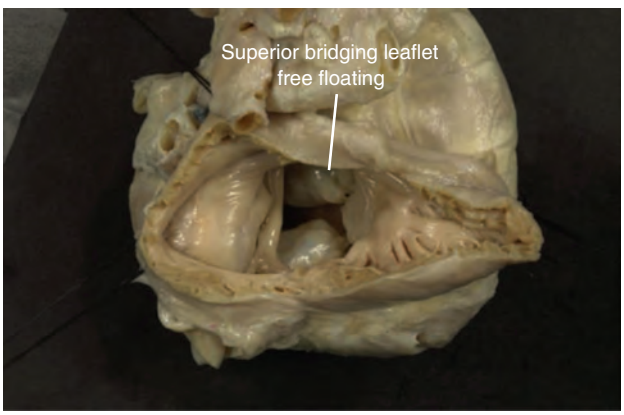


Figure 15.8 Anatomic specimen showing the right atrial view looking down toward common atrioventricular valve. This view demonstrates Rastelli type C anatomy with a free-floating superior bridging leaflet.

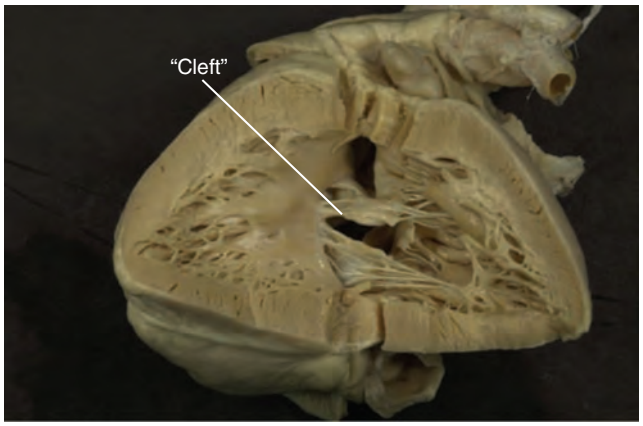


Figure 15.9 Anatomic specimen of incomplete CAVC in the left ventricular view of the ventricular septum demonstrating the scooped-out appearance of the ventricular septum with the atrioventricular valve adherent to the septum and no VSD component. This view highlights the "cleft" of the left-sided atrioventricular valve.

other, the contralateral ventricle is typically hypoplastic (Figures 15.11c,d and 15.12a,b). Unbalance to the right (with left ventricular hypoplasia) is more common and is often associated with other levels of left-sided obstruction, including coarctation of the aorta. In its most extreme form, unbalance to the right is a variant of hypoplastic left heart syndrome, sometimes with no left ventricular cavity seen. Unbalance to the left (with right ventricular hypoplasia) can be associated with pulmonary outflow

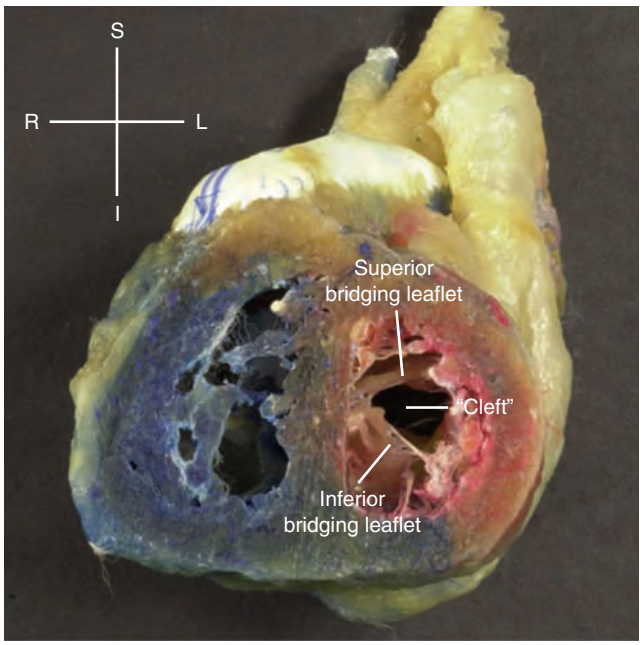


Figure 15.10 Waxed specimen cut in the subcostal sagittal echocardiographic view showing that the orientation of the "cleft" is perpendicular to the ventricular septum. The normal anterior leaflet is more parallel to the ventricular septum.

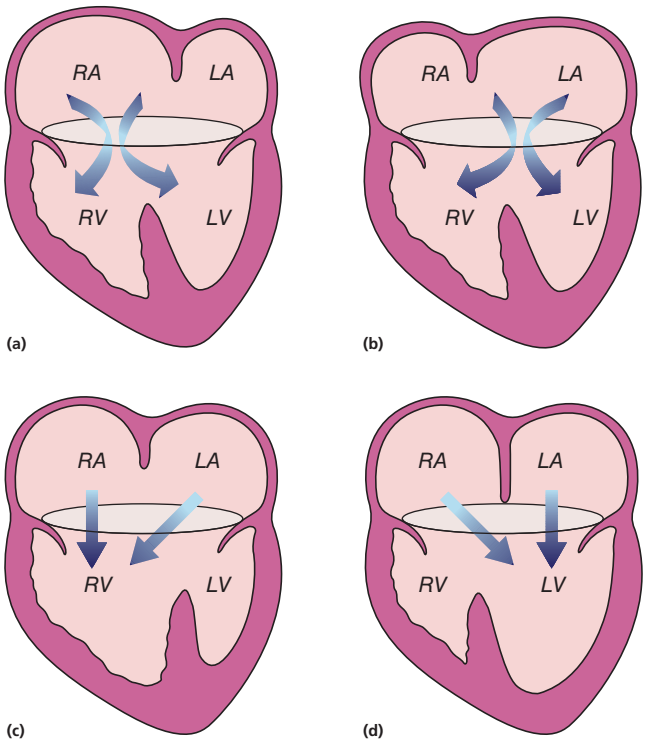
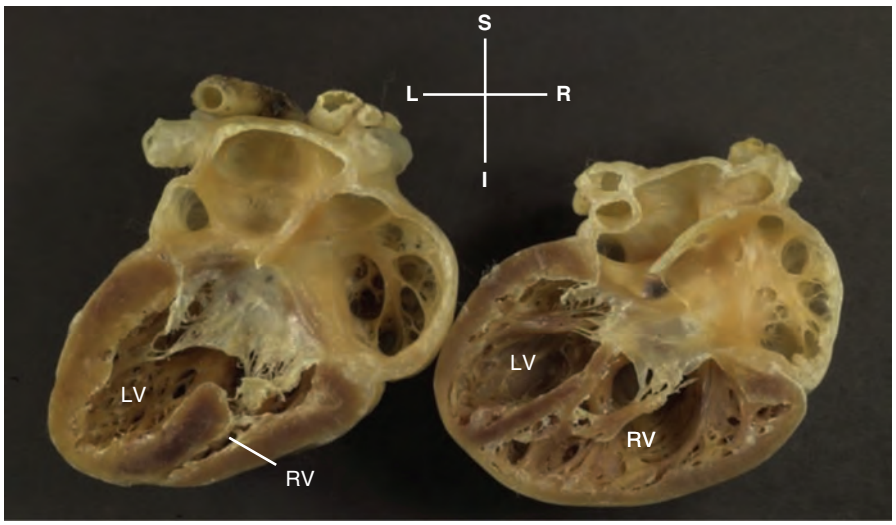


Figure 15.11 **(a)** Diagram showing double-outlet right atrium with malalignment of the atrial septum toward the left atrium. **(b)** Diagram showing double-outlet left atrium with malalignment of the atrial septum toward the right atrium. **(c)** Diagram showing unbalanced CAVC to the right with concomitant left ventricular hypoplasia. **(d)** Diagram showing unbalanced CAVC to the left with concomitant right ventricular hypoplasia. LA, left atrium; LV, left ventricle; RA, right atrium; RV, right ventricle.

obstruction and tetralogy of Fallot. Unbalance of the atrioventricular valve in relationship to the ventricular septum can occur in all forms of CAVC.

In CAVC, the left ventricular anterolateral papillary muscles are often more closely spaced than normal [15]. Left atrioventricular valve abnormalities can also be seen in approximately 5% of CAVC, most typically double orifice or single papillary muscle (parachute) [15–17]. These lesions are more common in incomplete CAVC and can also be seen in association with unbalanced defects to the right with concomitant left ventricular hypoplasia. Such valve abnormalities may complicate surgical repair with possible residual left atrioventricular valve regurgitation, stenosis, or both [17,18].

CAVC frequently has associated lesions including tetralogy of Fallot (usually seen in children with Down syndrome), patent ductus arteriosus, coarctation of the aorta, and left ventricular outflow tract obstruction. Secundum type atrial septal defects and additional VSDs can also be seen. In heterotaxy syndrome, CAVC is common particularly in the asplenia (right isomerism) type.



(a) Unbalanced CAVC to left (b) Balanced CAVC

Figure 15.12 Anatomic wax specimens cut in the apical 4-chamber view. **(a)** Looking toward the superior bridging leaflet, the specimen demonstrates unbalance of the atrioventricular valve to the left with right ventricular hypoplasia. **(b)** A specimen in the same view with a common atrioventricular valve that is well balanced over both ventricles. LA, left atrium; LV, left ventricle; RA, right atrium; RV, right ventricle.

Atrioventricular canal type VSD (otherwise known as inlet type VSD) can exist as an entity without a common atrioventricular junction. These are defects along the septal leaflet of the tricuspid valve often with straddling of the tricuspid valve chordae into the left ventricle. Often the ventricular septum is malaligned in these cases with concurrent right ventricular hypoplasia. These defects are frequently seen in association with complex congenital heart disease. Further detail about this type of VSD can be found in Chapter 12.

Pathophysiology

The clinical course of a patient with CAVC defect is variable and depends on the magnitude of atrial and ventricular level shunting, the severity of atrioventricular valve regurgitation, the degree of unbalance at the level of the ventricles if present, and other associated lesions. In the balanced form of CAVC, ventricular level left-to-right shunting is determined almost exclusively by the pulmonary vascular resistance since the defect is large and unrestrictive with right ventricular and pulmonary artery pressure at systemic level. In the early newborn period, symptoms are few but as the pulmonary vascular resistance decreases over the first 6–8 weeks of life, the amount of left-to-right ventricular shunting increases with a concomitant increase in pulmonary blood flow and volume overload to the left atrium and ventricle. If left uncorrected, this defect will result in symptoms of congestive heart failure including growth failure, respiratory symptoms, and tachycardia.

When the atrial septal defect is the predominant lesion, the left-to-right shunt is determined by the relative compliance of the right and left ventricles. Shunting increases over the first few months of life as right ventricular compliance increases. Atrial level shunting causes dilation of the right atrium, right ventricle and pulmonary arteries. If atrial level shunting is in isolation, most young children tolerate this increased pulmonary blood flow well and are asymptomatic but dyspnea or growth failure can occur in some cases [19]. In those with transitional type of CAVC, restrictive ventricular level shunting is seen in combination with the atrial level shunt. Depending on the magnitude of the ventricular level shunting, some will have evidence of heart failure while others with smaller shunts will not. Atrioventricular valve regurgitation particularly of the left atrioventricular valve can also cause an undue volume burden on the left atrium and ventricle resulting in cardiomegaly and symptoms of heart failure.

If CAVC is not surgically addressed, pulmonary vascular disease will likely ensue. This will occur earlier (within the first year of life) in those with large ventricular communications but can also occur in those with exclusive atrial communication in later decades of life. Though the restrictive VSD in the transitional type of CAVC can close over time with atrioventricular valve tissue, the ostium primum atrial septal defect and the large CAVC type VSD do not typically close spontaneously.

Those children with Down syndrome and CAVC are at higher risk for the development of pulmonary vascular obstructive disease within the first year of life [16]. Studies of children with and without Down syndrome have demonstrated that those with Down syndrome are more likely to have elevated pulmonary vascular resistance at the time of surgical repair [16]. Noncardiac issues may come into play in Down syndrome including chronic airway obstruction and central hypoventilation.

Imaging

CAVC is imaged from multiple acoustic windows. Two-dimensional (2D) imaging provides excellent visualization of the

anatomy in CAVC and is utilized along with color and spectral Doppler techniques to perform a comprehensive anatomic and physiologic evaluation of the defect. Three-dimensional (3D) echocardiography augments 2D imaging by demonstrating details of atrioventricular valve anatomy and function as well as assessment of the left ventricular outflow tract. Transesophageal echocardiography (TEE) often used to assess surgical repair of CAVC, can be utilized as a diagnostic tool in patients with suboptimal transthoracic windows or inconclusive diagnosis. Rarely, cardiac catheterization is required before surgery to augment the information provided by the echocardiogram.

Key elements

Preoperative imaging:

- Determination of atrial septal defect size and additional defects
- Determination of ventricular septal defect size, and additional defects
- Anatomy of atrioventricular annulus, valve(s), and chordal attachments
 - Rastelli classification
 - Assessment of atrioventricular valve leaflet anatomy and size
 - Assessment for left (parachute, double orifice) and right (Ebstein anomaly) atrioventricular valve anomalies
 - Assessment of number and spacing of the left ventricular papillary muscles
- Assessment for atrial or ventricular level unbalance
 - Relationship of atrial septum to inlet and ventricular septum
 - Distribution of atrioventricular valve over the ventricles (subxiphoid view)
 - Assessment of atrioventricular valve annulus and inflow into the ventricle by color in unbalanced CAVC (apical 4-chamber view)
 - Determination of severity of ventricular hypoplasia
- Assessment of etiology of left ventricular outflow tract obstruction if present
- Hemodynamic assessment
 - Flow direction of atrial and ventricular septal defect (by color and spectral Doppler)
 - Peak instantaneous pressure gradient across the VSD (if present) to estimate right ventricular pressure by continuous-wave (CW) Doppler
 - Assessment of severity of atrioventricular valve regurgitation by color flow mapping
 - Evidence of hemodynamic load to the left or right ventricle (dilation, increased flow across pulmonary outflow, and left atrioventricular valve inflow)
 - Estimation of right ventricular systolic pressure based on tricuspid regurgitation jet velocity by CW Doppler (in cases of restrictive or no VSD)
 - Assessment of severity of left ventricular or right ventricular outflow tract obstruction if present
- Measures of systolic and diastolic biventricular function
- Detection of associated lesions, particularly patent ductus arteriosus, coarctation of the aorta, secundum type atrial septal defect, additional VSD, or tetralogy of Fallot

Postoperative imaging:

- Assessment for residual atrial or ventricular level shunting
- Size of residual atrial septal defect or VSD, if present
- Direction of flow in residual defects
- Assessment of atrioventricular valve function
 - Atrioventricular valve regurgitation
 - Atrioventricular valve stenosis, if present (mean gradient in mmHg)
 - Estimate of right ventricular pressure by right atrioventricular valve regurgitation jet
- Measures of biventricular systolic and diastolic function
- Assessment of left ventricular outflow tract for subaortic stenosis.

Transthoracic imaging

Complete CAVC

Subxiphoid imaging provides excellent windows to evaluate the atrial septum and the relationship of the common atrioventricular valve to the septum. In particular, the subxiphoid frontal (long-axis) (Video 15.1) view and the "in-between" left anterior oblique (LAO) acoustic sweep demonstrate the size of the ostium primum type atrial septal defect (Figure 15.13a; Video 15.2). Additional atrial communications are seen in these planes as well. Color Doppler in subxiphoid frontal or LAO view shows atrial level shunt direction (Figure 15.13b; Video 15.3). The subxiphoid frontal view also demonstrates the unwedging of the aortic outflow and abnormal elongation of the left ventricular outflow tract with the resultant curve in the ascending aorta, the so-called "goose-neck deformity" (Figures 15.14 and 15.15; Video 15.1). The subxiphoid LAO view is ideal to image the common atrioventricular valve "en face" to assess how much is apportioned to each ventricle (i.e., determination of balance, Figure 15.16) [20]. The subxiphoid sagittal (short-axis) view can also be utilized to assess the anatomy of the atrioventricular valve; chordal attachments of the atrioventricular valve to the ventricular septum can be seen in this view and can determine Rastelli classification. Often, the size of the ventricular septal defect is difficult to determine in subxiphoid imaging because the probe sweeps through the defect without highlighting its edges. The papillary muscles can be identified in subxiphoid sagittal view and are often located counterclockwise to their position in a normal heart. The presence of a solitary papillary muscle and an eccentric orifice of the valve should be highlighted as a complicating factor for the repair of the left atrioventricular valve [15].

The apical window is not ideally suited for evaluation of the atrial septum because of false dropout of the acoustic signal from the parallel orientation of the ultrasound beam relative to the atrial septum. However, the 4-chamber view is extremely

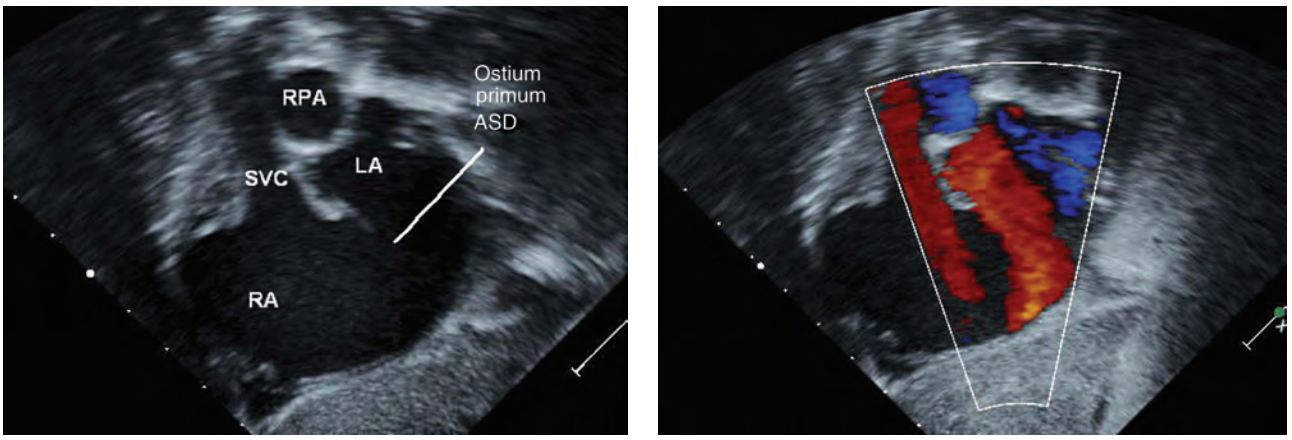


Figure 15.13 **(a)** Subxiphoid left anterior oblique view demonstrating a large ostium primum atrial septum defect. LA, left atrium; RA, right atrium; RPA, right pulmonary artery; SVC, superior vena cava. **(b)** Same view with color flow mapping showing left-to-right shunting at the ostium primum atrial septal defect.

useful when imaging CAVC because it displays the orientation of the atrioventricular valve within the atrioventricular septal defect, thus helping to determine the size of the atrial and ventricular communication (Figure 15.17; Video 15.4). In rare cases, the AV valve is attached to the atrial septum, and there is only a VSD component (Video 15.5). Chordal attachments in relation to the ventricular septum can also be demonstrated in this plane. Tilting of the transducer from posterior to anterior in this view often reveals the full scope of the VSD and helps diagnose additional septal defects [21]. In addition, this view best demonstrates atrioventricular valve inflow and valve

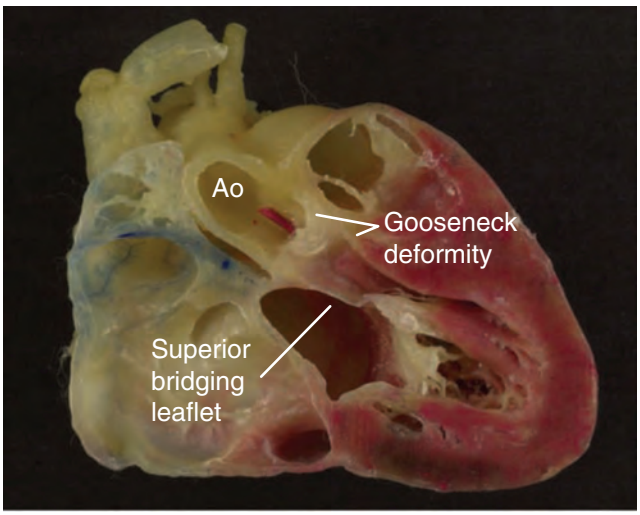


Figure 15.14 Anatomic specimen cut in subcostal frontal view demonstrating how the superior bridging leaflet in CAVC causes the displacement of the left ventricular outflow tract This anatomic finding has been called a "gooseneck deformity," pathognomonic for this lesion. Ao, aorta.

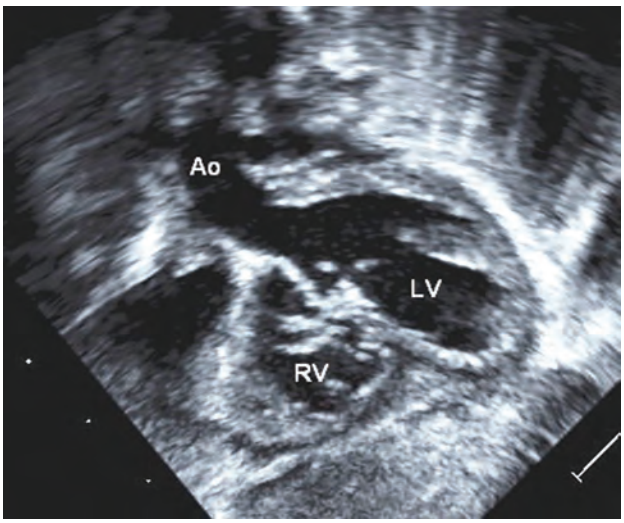


Figure 15.15 Subxiphoid frontal view demonstrating the "gooseneck deformity" of the left ventricular outflow tract in CAVC. Ao, aorta; LV, left ventricle; RV, right ventricle.

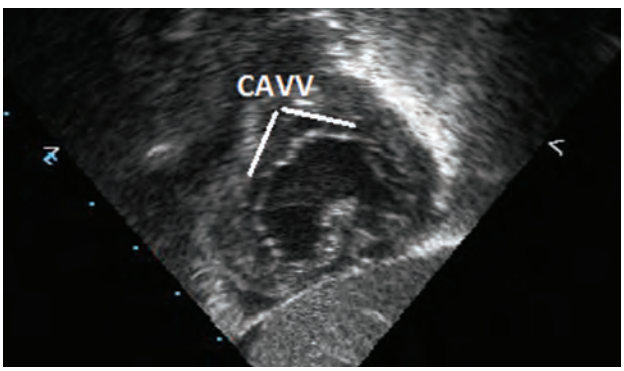


Figure 15.16 Subxiphoid left anterior oblique view of the common atrioventricular valve seen "en face" in the open position. This view can be used to assess the severity of unbalance of the valve over the ventricles.

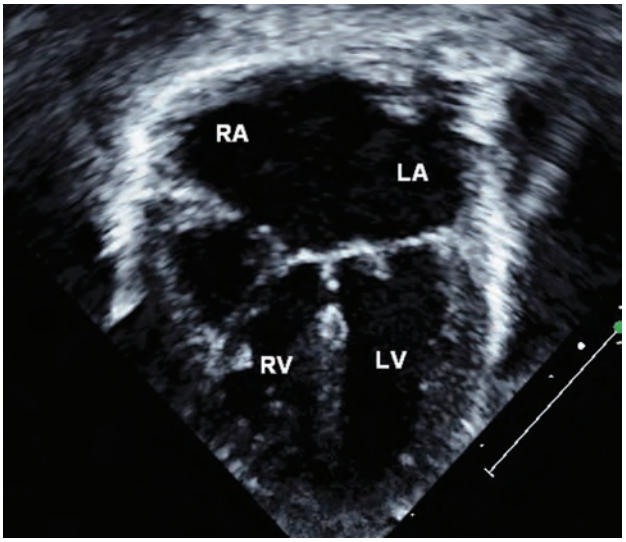


Figure 15.17 Apical 4-chamber view demonstrating a large atrial and large ventricular communication in this patient with complete CAVC. The common AV valve is closed but can be identified as a single common valve. More superior or inferior location of the valve alters the size of the atrial and ventricular communications. LA, left atrium; LV, left ventricle; RA, right atrium; RV, right ventricle.

regurgitation (Figure 15.18). Subjective and quantitative measures of atrioventricular valve regurgitation can be performed using this view as well. The apical 5-chamber view helps identify left ventricular outflow tract obstruction with quantitation of severity by pulsed-wave (PW) and continuous-wave (CW) Doppler.

Parasternal long-axis view helps in the estimation of the severity of atrioventricular valve regurgitation. A low left parasternal short-axis view can often provide additional imaging of the atrial septum, particularly in patients with suboptimal subxiphoid windows. In addition, it is important to distinguish between atrial and ventricular level shunting in this view based on location and timing of color Doppler flow (Figure 15.19a,b). Parasternal short-axis plane at the level of the ventricular septum highlights the VSD (Video 15.6). It also identifies additional muscular defects. The superior and inferior bridging leaflets of the left atrioventricular valve are also demonstrated often with atrioventricular valve regurgitation through the "cleft" (Figure 15.20; Video 15.7). Papillary muscle orientation is also seen in this view.

Incomplete and transitional CAVC

Imaging goals are similar for the incomplete and transitional forms of CAVC. Subxiphoid LAO and sagittal views are particularly useful to demonstrate that the two atrioventricular valves are anatomically abnormal with bridging of the superior leaflet across the ventricular septum. In fact, the subxiphoid sagittal view often helps clinch the diagnosis of CAVC because a normal anterior leaflet of the mitral valve is parallel to the ventricular septum while the "cleft" in an incomplete CAVC has a perpendicular orientation to the ventricular septum (Figure 15.21a,b). LAO view highlights the ostium primum atrial septal defect well. (Figure 15.13a,b; Videos 15.2 and 15.3). Double-orifice mitral valve and other left atrioventricular valve abnormalities are more common in the incomplete form and therefore should be ruled out in all cases (Video 15.8). Three-dimensional imaging can be very helpful in the diagnosis of left atrioventricular valve abnormalities such as double-orifice (Figure 15.22; Video 15.8) and parachute valves (Video 15.9).

Apical 4-chamber demonstrates nicely the position of the atrioventricular valve and its close proximity to the ventricular septum. Often there is atrioventricular valve tissue under the AV valve "filling in" the VSD component and some would consider this a transitional AV canal even if there is no longer VSD flow present (Figure 15.23). In incomplete forms of the defect, the AV

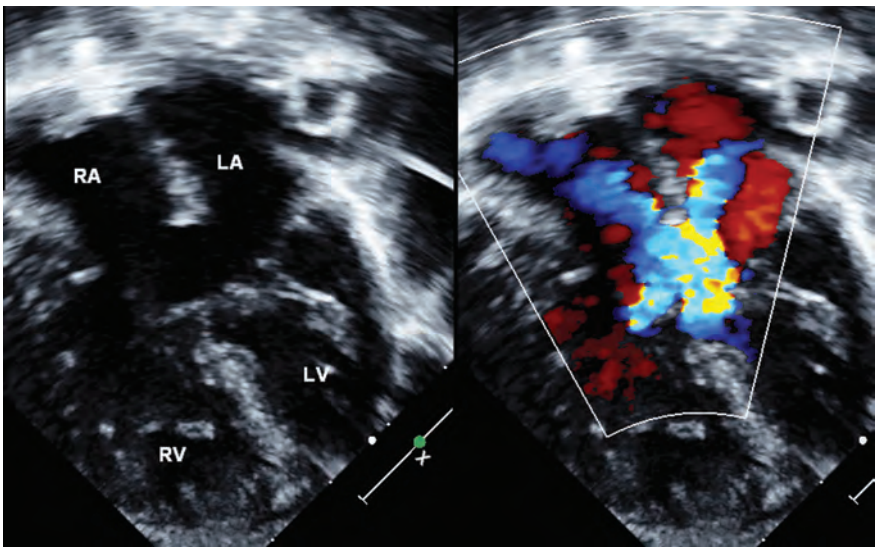
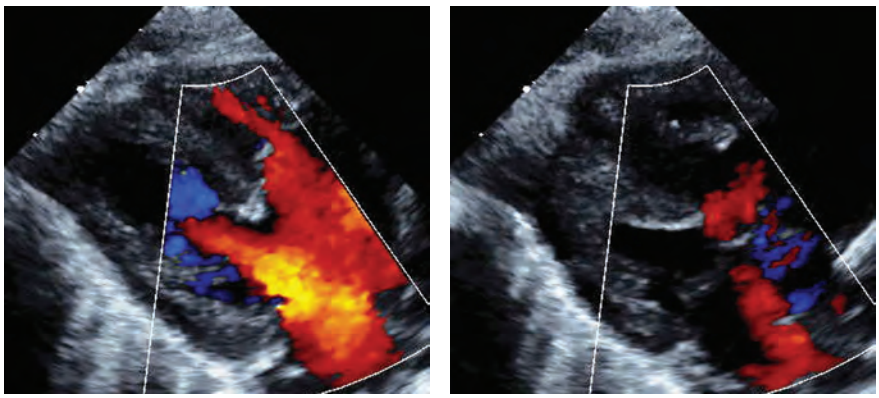


Figure 15.18 Apical 4-chamber view in color compare mode of a patient with complete CAVC demonstrating a large ostium primum ASD and significant common AV valve regurgitation which tracks along both sides of the atrial septum. LA, left atrium; LV, left ventricle; RA, right atrium; RV, right ventricle.



(a) (b)

Figure 15.19 **(a)** Parasternal long-axis view with color flow in diastole demonstrates the atrial level left-to-right shunting in a patient with complete CAVC. This flow is often confused with ventricular level shunting. **(b)** Color flow in systole in the same patient shows the ventricular level shunting underneath the AV valve.

valve is typically completely adherent to the ventricular septum (Figure 15.24). Apical 4-chamber view also helps identify atrioventricular valve regurgitation (usually through the left-sided "cleft") (Video 15.10). Ventricular level shunting, if identified, can often be seen in this view including shunting from the left ventricle to the right atrium (Figure 15.25; Video 15.10). In transitional CAVC, the amount of ventricular level shunting may be minimal; color Doppler is useful to detect a small defect. Parasternal short-axis can be used to align the spectral Doppler for quantitative estimate of the pressure gradient across the VSD.

Left ventricular outflow tract

With the left ventricular outflow tract elongation of CAVC, obstruction can occur both before and after surgical intervention. Outflow obstruction is more common in the incomplete form and in Rastelli A subtype. Etiology of outflow tract obstruction varies and includes abnormal chordal attachments to the left ventricular side of the septum, discrete subaortic membrane, septal hypertrophy, and anomalous or prominent anterolateral papillary muscle [22]. The apical 5-chamber view displays the left ventricular outflow tract well. It also allows for an appropriate angle of interrogation to identify obstruction by Doppler. The parasternal long-axis view also displays the left ventricular outflow tract well and identifies cause of obstruction at this level (Figure 15.26; Video 15.11).

Unbalanced CAVC

Unbalance at the level of the atria is quite rare. When suspected, it is best seen in the apical 4-chamber view (Figure 15.27a). Atrial inflow can be evaluated with color Doppler (Figure 15.27b). PW and CW Doppler performed in this view can help determine if there is obstruction across the atrioventricular valve inlet and the severity of that obstruction (by measurement of the mean inflow gradient). The contralateral atrium may appear hypoplastic.

When there is unbalance at the level of the ventricle, the subxiphoid LAO or sagittal view help determine how much of the valve is apportioned to each ventricle (Figure 15.28) [20]. Apical 4-chamber view provides additional information because the severity of ventricular hypoplasia is usually best exhibited in

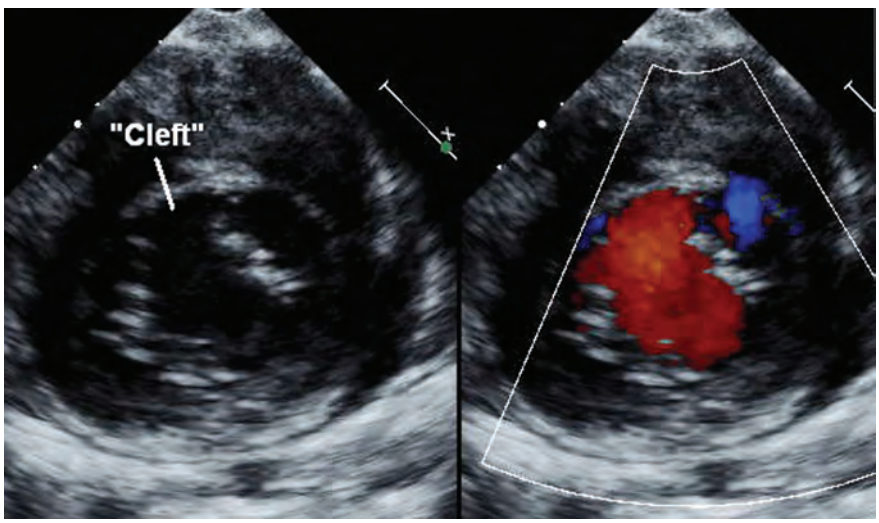


Figure 15.20 Parasternal short-axis view at the level of the left AV valve demonstrates the "cleft" associated with CAVC. The superior and inferior bridging leaflets cross the ventricular septum in a perpendicular fashion. This view typically shows atrioventricular valve regurgitation through the "cleft."

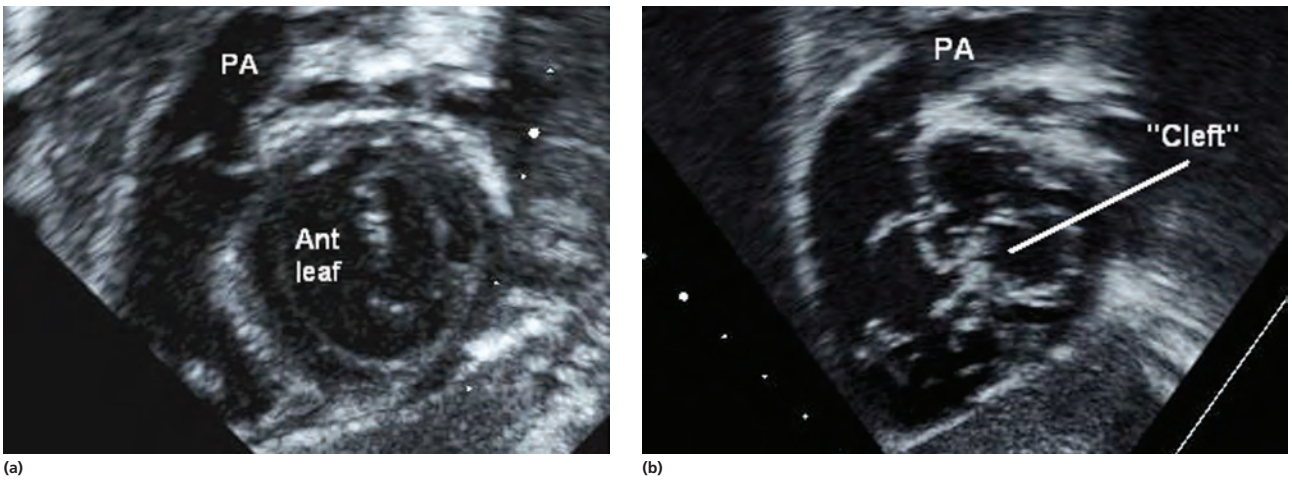


Figure 15.21 **(a)** Subxiphoid sagittal view in a normal heart exhibiting the anterior leaflet (ant leaf) in parallel with the ventricular septum. PA, pulmonary artery. **(b)** The same view in CAVC demonstrates that the superior and inferior bridging leaflets are perpendicular to the ventricular septum.

this plane (Figure 15.29a,b; Videos 15.12 and 15.13). In addition, color flow in diastole can demonstrate how much inflow (if any) crosses into the hypoplastic ventricle by measuring the secondary color Doppler inflow diameter (Figure 15.30; Video 15.14). In right dominant unbalanced CAVC, limited inflow into the left ventricle is a risk factor for poor outcome of biventricular repair [23]. Other echocardiographic features of left ventricular adequacy can also be used to help determine whether biventricular repair can be successfully performed including direction of flow at the VSD in systole (right-to-left flow is a risk factor for poor outcome) and direction of flow in the transverse aortic arch (retrograde flow is a risk factor for poor outcome) [20]. Moreover, right dominant unbalanced CAVC can be associated with a hypoplastic left mural leaflet (Figure 15.31; Video 15.15). If the mural leaflet is small, the "cleft" makes up the primary commissure of the left AV valve which may result in significant AV valve regurgitation after biventricular repair. Assessment for distal levels of obstruction, particularly at the outflow tract and the arch (unbalance to the right) are also important components of the echocardiographic assessment of unbalanced CAVC.

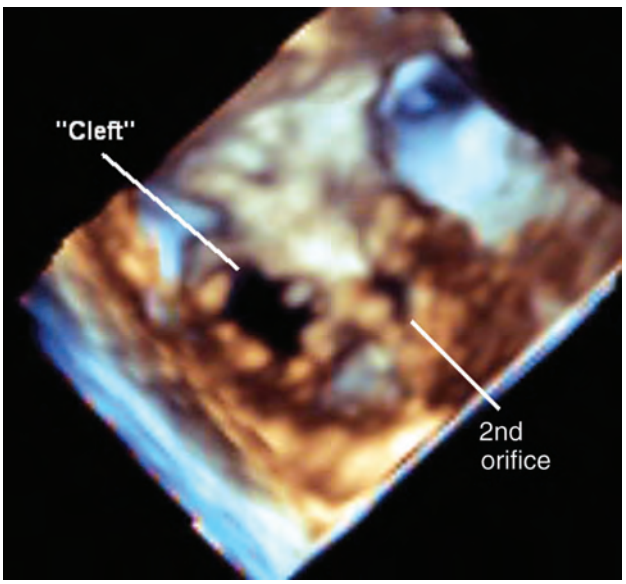


Figure 15.22 Three-dimensional image (from LV to left atrium) of a patient with incomplete CAVC who also has double-orifice left AV valve. There is a cleft in the large orifice and a smaller second orifice seen in the open position.

Additional defects

Defects commonly associated with CAVC are generally discussed in other chapters. However, certain lesions deserve mention. Subxiphoid imaging, 4-chamber and parasternal views help confirm the association of CAVC with tetralogy of Fallot (Video 15.16). In this combination of defects, anterior malalignment of the conal septum is seen in association with the features of complete CAVC (usually with Rastelli type C).

A patent ductus arteriosus should always be ruled out in CAVC, particularly in children with Down syndrome. The high parasternal view ("ductal" view) is used to confirm its presence. Suprasternal imaging is used to determine arch sidedness, to rule out coarctation of the aorta, and to confirm normal systemic and pulmonary venous connections (of particular importance in those with heterotaxy syndrome).

Prenatal assessment

In fetal echocardiography, the 4-chamber view readily identifies most of the anatomic features of CAVC including the common atrioventricular valve and its position within the atrioventricular defect, the size of the atrial communication and the size of the VSD (Figure 15.32; Video 15.17). Gooseneck deformity can be

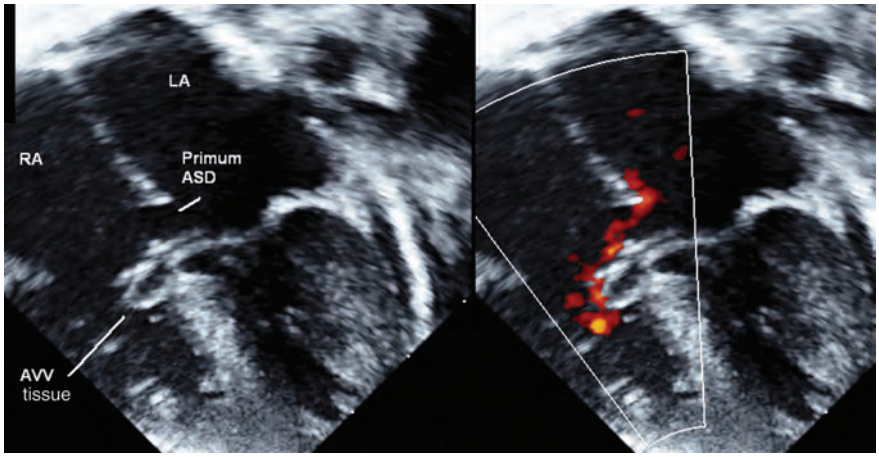


Figure 15.23 Apical 4-chamber view in color compare mode demonstrates a small ostium primum ASD with left-to-right flow. AV valve tissue is seen filling in the VSD thus there is no ventricular level shunting. Though there is no VSD shunting, some would still define this as a transitional CAVC. LA, left atrium; RA, right atrium.

seen on fetal echocardiography as well (Video 15.18). A short-axis sweep of the heart may demonstrate the common atrioventricular valve straddling the ventricular septum or the view of the "cleft" similar to the postnatal view (Video 15.19). This is especially useful in fetuses with a small or no ventricular septal defect. Color Doppler is used to identify direction of flow in the defects but is dependent on the angle of interrogation. Fetal flow patterns are demonstrated including right-to-left atrial level shunting and bidirectional flow at the VSD. Common atrioventricular valve regurgitation if present can also be seen. Severe atrioventricular valve regurgitation is poorly tolerated by the fetus and can result in heart failure and hydrops fetalis. Unbalance of the atrioventricular valve over the ventricles can also be seen with concomitant hypoplasia of the contralateral ventricle. CAVC with heterotaxy syndrome is suspected in prenatal diagnosis if the associated findings are identified such as systemic venous anomalies, conotruncal abnormalities, or anomalous pulmonary venous connection [24]. Complete heart block is sometimes seen in association with CAVC in the fetus and outcome in this group of patients is uniformly quite poor [24]. Serial fetal echocardiography is suggested if the diagnosis of CAVC is made before birth to observe for progression of disease. When counseling families with this fetal diagnosis, amniocentesis is suggested since there is a significant association of CAVC with Down syndrome.

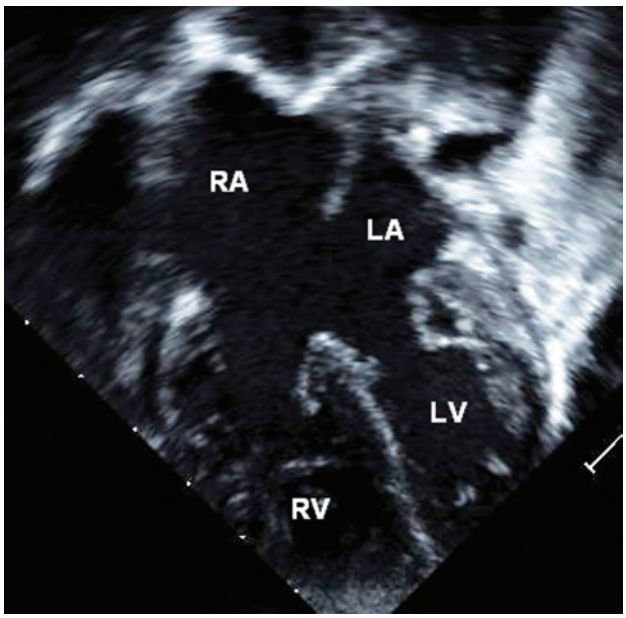


Figure 15.24 Apical 4-chamber view demonstrates an incomplete CAVC. There is a large ostium primum ASD and the right atrium is dilated from the atrial level shunt. The AV valves are in the open position (at the same level) and are adherent to the ventricular septum. LA, left atrium; LV, left ventricle; RA, right atrium; RV, right ventricle.

Imaging of the adult

Imaging the adult with CAVC can be quite challenging, particularly in those with Down syndrome. The subxiphoid acoustic window is typically not feasible in the adult patient because of limited ultrasound penetration at that distance from the heart. Thus, accurate assessment of the atrial communication (ostium primum defect) may be difficult. In contrast, the apical window provides much information in the adult with CAVC, including relative size and dilation of the ventricles, subjective assessment of biventricular shortening, the relationship of the atrioventricular valve within the defect, and severity of atrioventricular valve regurgitation. Importantly, right ventricular pressure estimate can be performed in this view to help determine if pulmonary artery pressure is elevated. Most adults with unrepaired complete CAVC will have evidence of pulmonary vascular disease and may even demonstrate signs of Eisenmenger syndrome with right-to-left shunting at the ventricular level (Figure 15.33). Incomplete CAVC is occasionally diagnosed in adulthood because symptoms may not occur until the third or fourth decade of life. Similar views to those used for complete CAVC are required to make the diagnosis. The full extent of the ostium primum atrial communication may not be appreciated

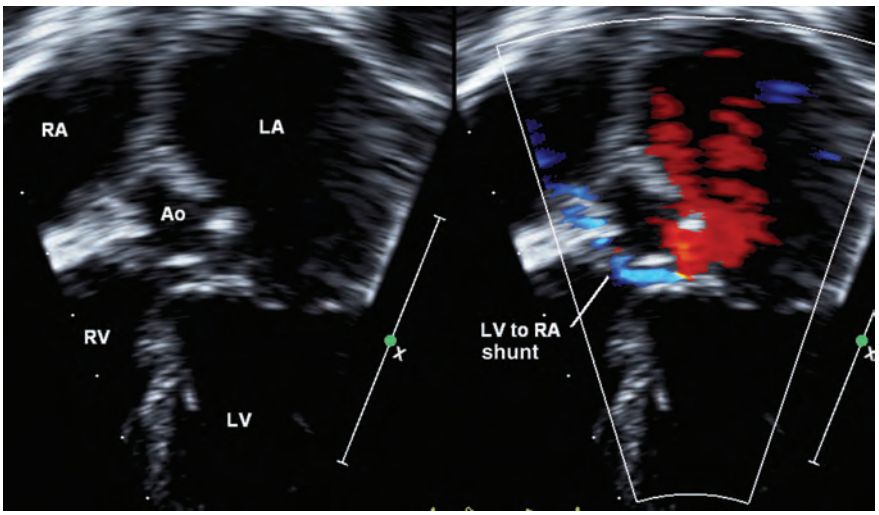


Figure 15.25 Apical 4-chamber view in color compare mode of a transitional CAVC demonstrates a small left ventricle to right atrial shunt through the atrioventricular valve. Ao, aorta; LA, left atrium; LV, left ventricle; RA, right atrium; RV, right ventricle.

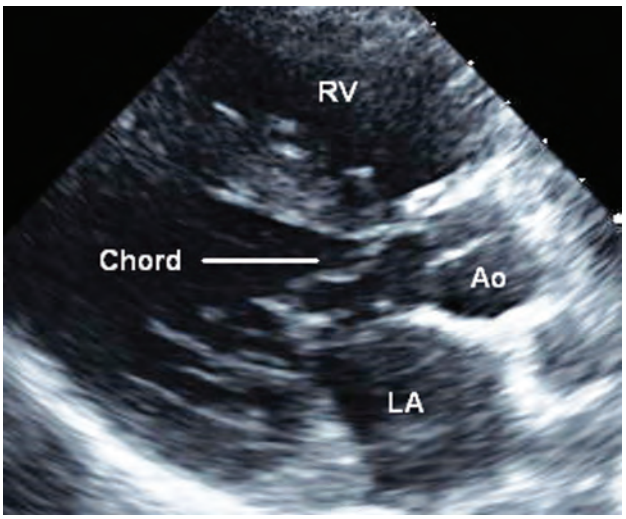
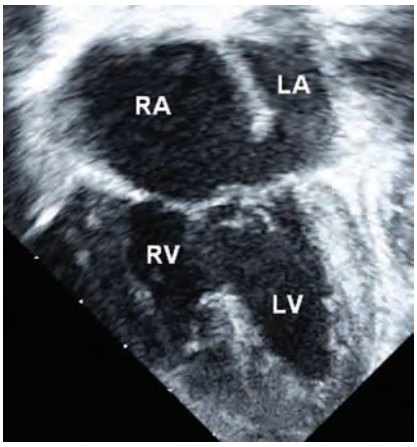


Figure 15.26 Parasternal long-axis view of a patient with incomplete CAVC demonstrating left AV valve chord crossing the left ventricular outflow tract causing obstruction. Ao, aorta; LA, left atrium; RV, right ventricle.

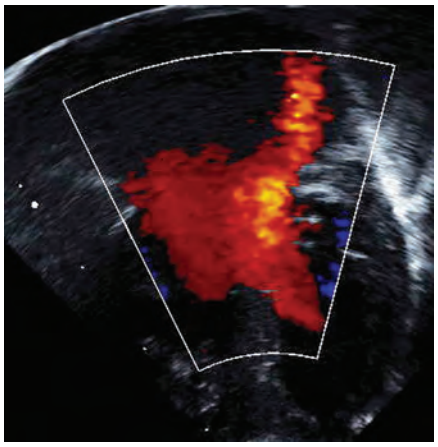
on transthoracic imaging. Transesophageal echocardiography (TEE) provides an excellent alternative to transthoracic imaging, particularly in adults with poor acoustic windows. The probe is in close proximity to the atrial septal structures and atrioventricular valves and imaging of these regions is improved. Cardiac magnetic resonance imaging can offer a noninvasive alternative to TEE in adults with suspected CAVC.

Intraoperative assessment

Intraoperative imaging to assess the CAVC repair is typically performed using TEE. Epicardial imaging should be considered in patients in whom TEE is contraindicated or considered hazardous (e.g., very small infant or esophageal disease). Preoperative TEE imaging, if performed, confirms the diagnosis and may enhance or alter surgical planning (Video 15.20). Though transthoracic imaging provides most of the information required for surgical intervention, preoperative TEE can help identify atrioventricular valve morphology and the etiology of atrioventricular valve regurgitation. Postoperative TEE



(a)



(b)

Figure 15.27 **(a)** Apical 4-chamber view of a patient with complete CAVC shows double-outlet right atrium (RA) with malalignment of the atrial septum in relationship to the ventricular septum. The left atrium (LA) is small and the right ventricle (RV) is also hypoplastic because the AV valve is mildly malaligned toward the left ventricle (LV). There is a large ASD and VSD component in this patient. **(b)** Color flow in the same patient demonstrates a narrow jet from the left atrium into the ventricles.

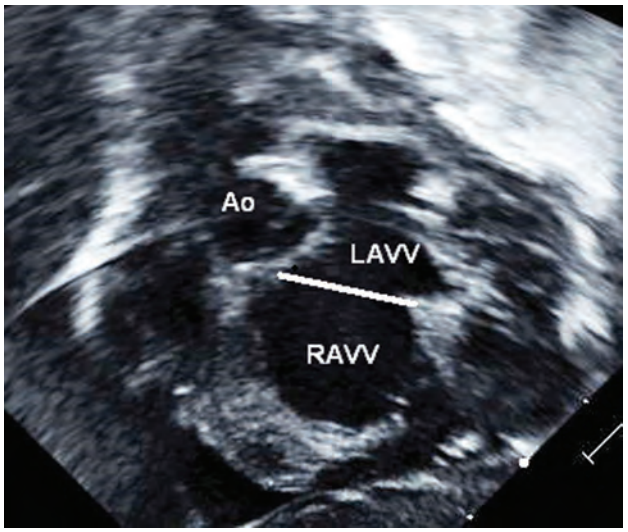


Figure 15.28 Subcostal left anterior oblique view demonstrating mild unbalance of the common atrioventricular valve to the right. More of the valve opens into the right ventricle (RAVV) than the left ventricle (LAVV). Ao, aorta.

imaging is performed as the patient is weaned from cardiopulmonary bypass to assess adequacy of the repair (Video 15.21). The procedure identifies residual atrial and ventricular septal defects, severity of residual atrioventricular valve regurgitation (Figure 15.34a), and the potential development of atrioventricular valve stenosis (Figure 15.34b). Global assessment of ventricular function is also performed. Determination of the significance of residual VSDs can be challenging. In general, a residual defect less than 3 mm at its greatest diameter will not require surgical re-intervention while defects greater than 4 mm will require immediate re-operation. In borderline cases or in very small infants, intraoperative hemodynamic assessment of the residual shunt (by measuring Qp:Qs via oxygen saturation measurements) can help in the decision process [25].

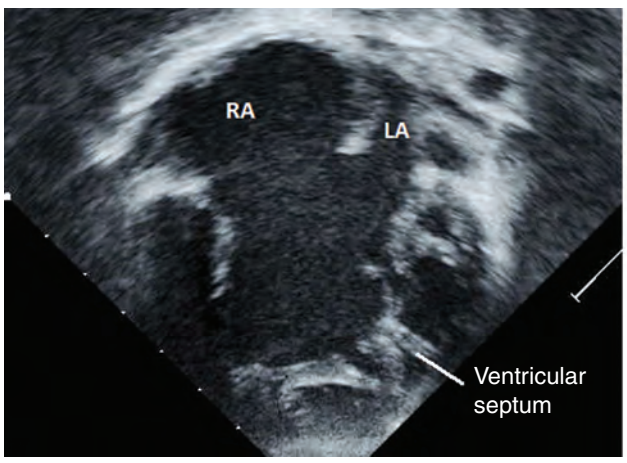
Underestimation of the severity of atrioventricular valve regurgitation on intraoperative TEE compared to postoperative transthoracic assessment is common [26,27]. These differences are likely related to alterations in preload, afterload and inotropic support from the immediate post-bypass period to the more stable postoperative state. Moreover, color Doppler assessment may be interpreted differently with TEE in comparison to transthoracic echocardiography. Despite these limitations, intraoperative TEE is a useful screening tool to determine whether immediate re-intervention is necessary.

Three-dimensional assessment

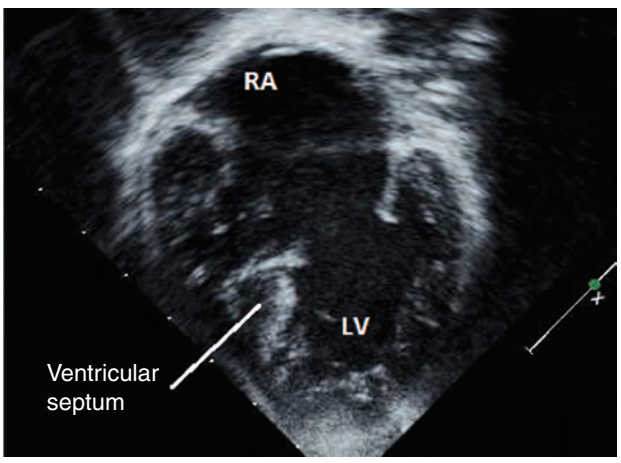
CAVC is the ideal lesion to image using 3D echocardiography. Three-dimensional planes can be used to identify the atrioventricular valve anatomy and highlight the "cleft" (Figure 15.35) as well as anomalies such as double-orifice left atrioventricular valve or parachute valve (Figure 15.22; Videos 15.8 and 15.9). These distinctions are important to identify prior to surgical intervention and alter the risk of the repair. Three-dimensional imaging can also demonstrate the magnitude of the atrioventricular septal defect and its relationship to the atrioventricular valve. A newer technology of 3D, 3D color, should help quantitate severity of atrioventricular valve regurgitation.

Follow-up assessment

Follow-up echocardiographic assessment is an important component of the long-term care of the patient with CAVC. Except in unusual circumstances, surgical intervention is almost always recommended for this defect. At present, there are no viable medical or catheter-directed therapeutic options for this lesion. Repair of CAVC generally involves patch closure of the atrial and ventricular communication (if present) using a one-patch or



(a)



(b)

Figure 15.29 **(a)** Apical 4-chamber view showing severe right dominant unbalanced complete CAVC with left ventricular hypoplasia. The atrioventricular valve sits almost entirely over the right ventricle. **(b)** The same view showing left dominant unbalanced complete CAVC with marked right ventricular hypoplasia.

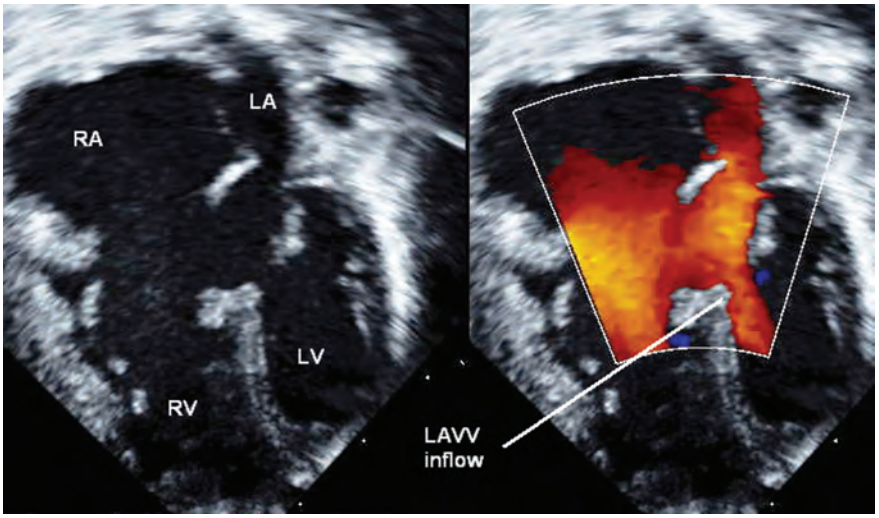


Figure 15.30 Apical 4-chamber view in color compare mode demonstrating a right dominant unbalanced CAVC with narrowed inflow into the left ventricle (LV) compared to flow from the right atrium (RA) to the right ventricle (RV). There is a large atrial communication and flow can be seen from the left atrium (LA) to the RV. LAVV, left atrioventricular valve; RA, right atrium.

two-patch technique with suture approximation of the superior and inferior bridging leaflets on the left ventricular side (Figure 15.36) [28].

Surveillance soon after repair includes assessment for residual atrial and ventricular communications, residual atrioventricular valve regurgitation as well as assessment for pericardial effusion. Residual atrial septal defects are unusual but can occur. Small residual ventricular septal defects are common [25,29]. Color Doppler is a very sensitive technique to assess for residual shunts. VSDs less than 2 mm in diameter will often close spontaneously after CAVC repair [30]. CW Doppler can be used to measure the peak velocity of the VSD jet and help estimate right ventricular pressure, particularly when there is no right atrioventricular valve regurgitation. Assessment for resolution of pulmonary hypertension by estimation of right ventricular pressure is also important, particularly in those with complete CAVC, Down syndrome, or late diagnosis.

Assessment of left atrioventricular valve function is one of the most important components of the postoperative evaluation of CAVC. This evaluation includes assessment of degree of atrioventricular valve regurgitation. Most repairs of CAVC include at least partial closure of the left atrioventricular valve "cleft" to enhance left atrioventricular valve function (Video 15.22). Left-sided atrioventricular valve regurgitation is the primary indication for re-operation in patients with repaired CAVC (Video 15.23). Significant atrioventricular valve regurgitation seen on the preoperative echocardiogram is a risk factor for severe regurgitation on the postoperative study [31,32].

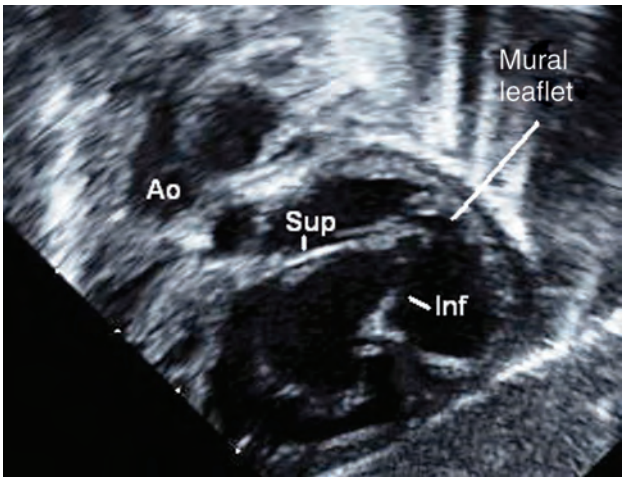


Figure 15.31 Subxiphoid left anterior oblique view showing a right dominant unbalanced CAVC with a small left-sided mural leaflet. Note that the commissure between the superior (sup) bridging leaflet and the inferior (inf) bridging leaflet makes up the majority of the valve and is at risk for significant regurgitation after biventricular repair. Ao, aorta.

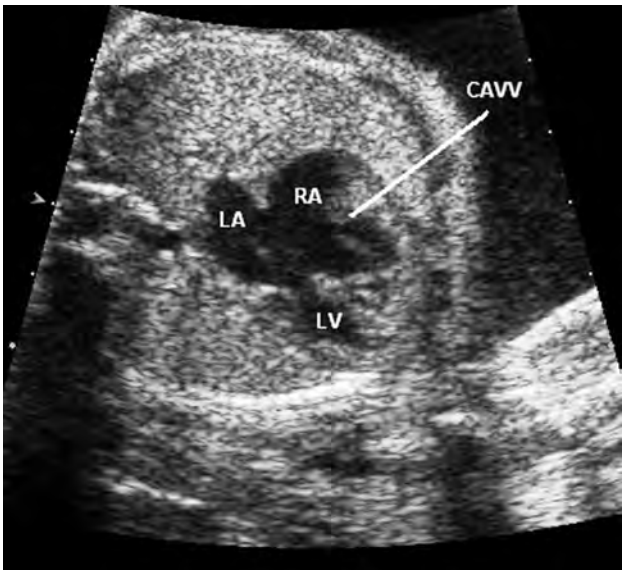


Figure 15.32 Fetal echocardiogram demonstrates a fetus with a complete CAVC. Note the opened common atrioventricular valve (CAVV). Ao, aorta; LA, left atrium; LV, left ventricle; RA, right atrium.

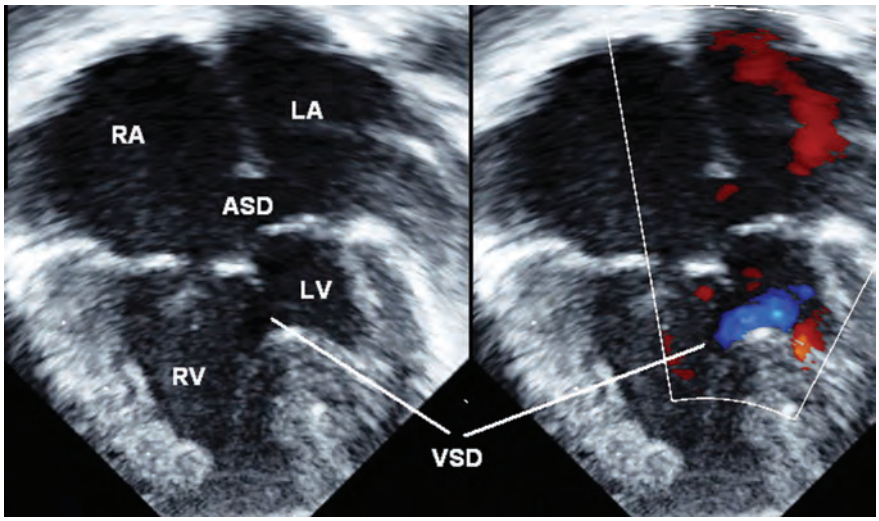


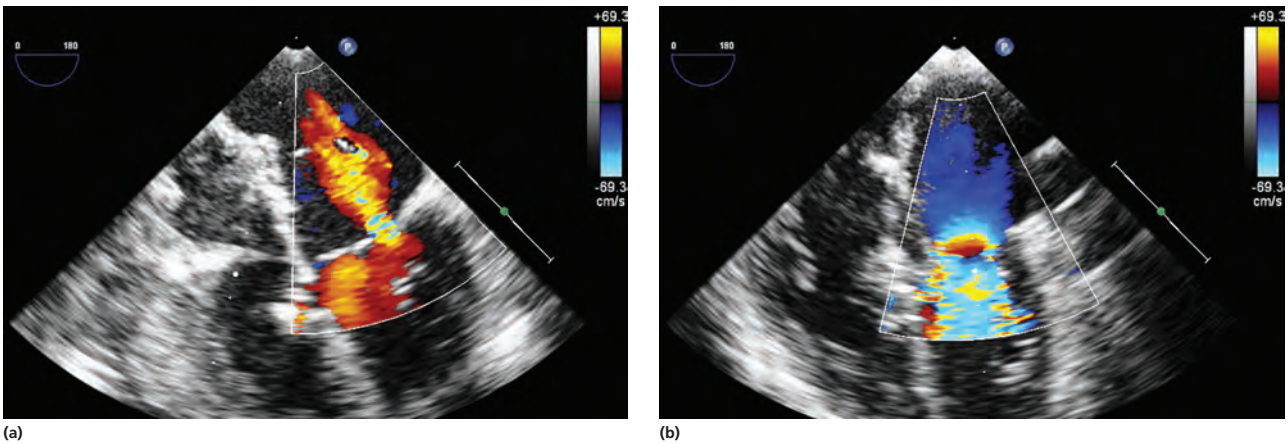
Figure 15.33 Apical 4-chamber view in color compare mode of a patient with complete CAVC and Eisenmenger syndrome. Note that the VSD jet is shunting right-to-left and the right ventricle (RV) is significantly hypertrophied. LA, left atrium; LV, left ventricle; RA, right atrium.

Residual or recurrent left atrioventricular valve regurgitation typically occurs at the interface of the superior and inferior bridging leaflets but can occur at the other commissures as well. Three-dimensional echocardiography can help determine the location and etiology of left atrioventricular valve regurgitation after repair [33]. Early primary repair, before significant atrioventricular valve regurgitation develops, may help prevent reoperation in some cases [34,35].

Postoperative assessment for left atrioventricular valve stenosis is important as well. Left atrioventricular valve leaflet motion may be limited by "cleft" closure (Figure 15.37; Video 15.24). More severe stenosis can occur with suture closure of the cleft in those with smaller valves preoperatively. It can also been seen in those with single papillary muscles or maldistribution of the common atrioventricular valve during surgical division.

Long-term assessment of CAVC repair includes surveillance for progression of left atrioventricular valve regurgitation or stenosis. In addition, evaluation of ventricular function and estimation of pulmonary artery pressure remain important. Left ventricular outflow tract obstruction, if present preoperatively, may progress in the long term and may impact aortic valve function. In some cases, subaortic stenosis may occur months to years after repair (Video 15.25).

Many techniques have been developed to assess left atrioventricular valve regurgitation. Importantly, no method is gold standard especially in the pediatric population. Both qualitative and quantitative methods exist and all have limitations. The majority of echocardiographers continue to utilize the qualitative method of estimating the left atrioventricular valve regurgitation jet area compared to the left atrium area [36]. This method has been reported in correlation with angiographic grading in children [37]. It does not require complicated calculation and can be performed serially in the same patient to assess for progression over time. A recent study suggests that all quantitative methods of



(a) (b)

Figure 15.34 **(a)** TEE image in 4-chamber view in a patient after repair of complete CAVC shows significant left AV valve regurgitation. Note the patch across the atrioventricular septum. **(b)** Inflow during diastole in the same patient shows acceleration of flow across the left AV valve suggesting stenosis of this valve likely from cleft closure.

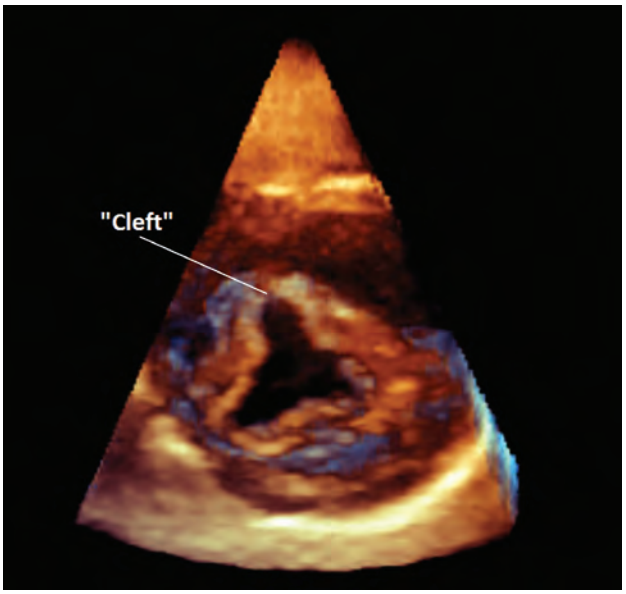


Figure 15.35 Three-dimensional image of the left atrioventricular valve in a patient with incomplete CAVC highlighting the trifoliate orientation of the valve and the cleft directed toward the ventricular septum.

assessing severity of atrioventricular valve regurgitation in the CAVC population are flawed with significant intraobserver variability [38]. The hemodynamic impact of valve regurgitation can also be assessed. Left atrial and left ventricular dilation are common when atrioventricular regurgitation is severe. Other quantitative methods include proximal isovelocity surface area (PISA), vena contracta (regurgitant jet area), and assessment of severity pulmonary venous flow reversal [39]. Discussion of these methods can be found in Chapters 6 and 14.

Echocardiography demonstrates most of the important characteristics of all forms of CAVC defects. Diagnostic cardiac catheterization for these lesions is usually not required unless there is concern for increased pulmonary vascular resistance. Postoperative echocardiographic surveillance helps diagnose residual or recurrent abnormalities that may require intervention.

Acknowledgments

I would like to acknowledge and thank Dr. Paul M. Weinberg for his assistance and guidance in the writing of this manuscript as well as the contribution of his photographs of the pathologic specimens.

Videos

To access the videos for this chapter, please go to www.lai-echo.com.

Video 15.1 Subxiphoid frontal view in a patient with complete CAVC. The large ostium primum ASD is seen with anterior sweep followed by the common AV valve and the VSD is seen underneath the valve.

Video 15.2 Subxiphoid left anterior oblique view demonstrating a large ostium primum atrial septal defect. Note that the right pulmonary artery posterior to the superior vena cava is dilated from the atrial level left-to-right shunt. At the end of the clip, there is acceleration of flow across the pulmonary valve likely from the large atrial level left-to-right shunt.

Video 15.3 Subxiphoid left anterior oblique view with color Doppler in the same patient as Video 15.2 showing left-to-right shunting at the ostium primum atrial septal defect.

Video 15.4 Apical 4-chamber view in color compare mode of a patient with a complete CAVC. Note the large atrioventricular communication and the common AV valve. With color Doppler, small multiple jets of AV valve regurgitation can be seen.

Video 15.5 Apical 4-chamber view in color compare mode of a patient with the rare form of CAVC where the AV valve is adherent

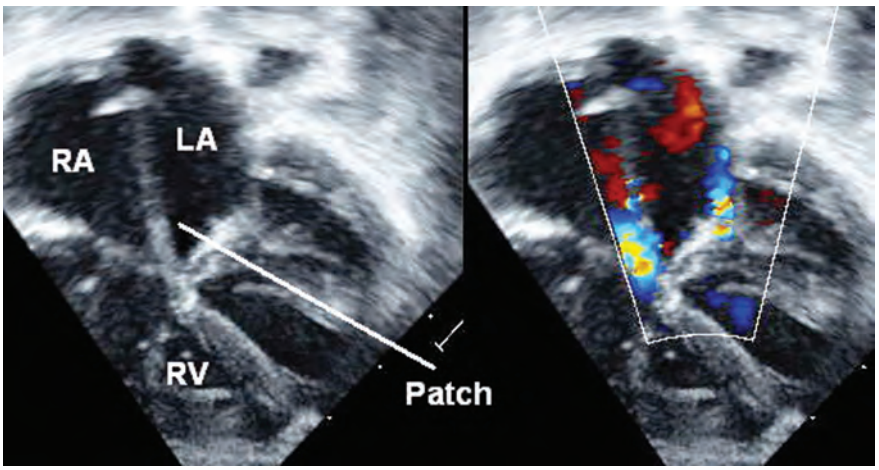


Figure 15.36 Apical 4-chamber view in color compare mode in a postoperative patient with complete CAVC demonstrating a single patch closing the atrial and ventricular septal defects. The patch also divides the common atrioventricular valve into a right and left atrioventricular valve. Note the minimal residual left and right AV valve regurgitation. LA, left atrium; RA, right atrium; RV, right ventricle.

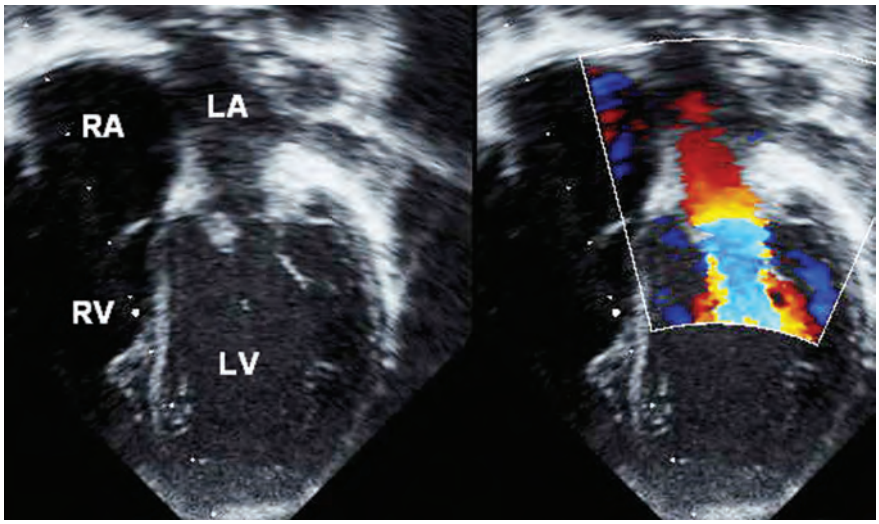


Figure 15.37 Apical 4-chamber view in color compare mode demonstrates limited excursion of the left AV valve leaflets. Color Doppler demonstrates inflow acceleration and mild left AV valve stenosis after "cleft" closure. LA, left atrium; LV, left ventricle; RA, right atrium; RV, right ventricle.

to the atrial septum such that there is no atrial communication but a large VSD. There is still a common AV valve annulus in these cases with a "cleft" of the left-sided AV valve.

Video 15.6 Parasternal short-axis view in color compare mode of a patient with complete CAVC. A sweep through the ventricular septum demonstrates the posterior location of the VSD. The bridging leaflets of the common AV valve can be seen as the sweep is directed toward the base of the heart. A small patent ductus arteriosus is also present.

Video 15.7 Parasternal short-axis view in color compare mode of a patient with complete CAVC. This clip highlights the "cleft" between the superior and inferior bridging leaflets. The large AV canal type VSD with left-to-right flow is also seen.

Video 15.8 Three-dimensional echocardiography clip in parasternal short-axis (from LV to left atrium) of a patient with incomplete CAVC who also has double-orifice left AV valve. The white arrows indicate the two openings. A cleft is seen in the larger orifice.

Video 15.9 Three-dimensional echocardiography clip in parasternal short-axis (from LV to left atrium) of a patient with incomplete CAVC who also has a parachute left AV valve. The small, eccentric orifice is seen.

Video 15.10 Apical 4-chamber view in color compare mode of a transitional CAVC demonstrates a small left ventricle to right atrial shunt through the atrioventricular valve. Left AV valve regurgitation is also seen through the "cleft."

Video 15.11 Parasternal long-axis view in a patient with incomplete CAVC demonstrates subaortic stenosis caused by left AV valve chordal tissue attaching to the ventricular septum.

Video 15.12 Apical 4-chamber view showing severe right dominant unbalanced complete CAVC with left ventricular hypoplasia. The atrioventricular valve sits almost entirely over the right ventricle.

Video 15.13 Apical 4-chamber view showing left dominant unbalanced complete CAVC with right ventricular hypoplasia. The atrioventricular valve sits almost entirely over the left ventricle.

Video 15.14 Apical 4-chamber view in color compare mode of severe right dominant unbalanced CAVC with the common atrioventricular valve emptying almost exclusively into the right ventricle. Color Doppler inflow (in red) enters exclusively into the right ventricle with no inflow seen into the left ventricle because the common AV valve obstructs flow into the left ventricle in the open position.

Video 15.15 Three-dimensional echocardiography clip in parasternal short-axis view showing a small left-sided mural leaflet. The "cleft" makes up the majority of the left AV valve and is at risk for regurgitation.

Video 15.16 Subxiphoid sagittal view with color Doppler demonstrating a patient with complete CAVC with tetralogy of Fallot. The common AV valve is seen and the conal septum is seen malaligned anteriorly resulting in subpulmonary stenosis.

Video 15.17 Fetal 4-chamber view demonstrates a complete CAVC with a large atrial and ventricular communication and a common AV valve.

Video 15.18 Fetal image of complete CAVC demonstrates the left ventricular outflow tract which has a "gooseneck" deformity.

Video 15.19 Fetal short-axis view of incomplete CAVC demonstrates the "cleft" of the left AV valve directed toward the ventricular septum.

Video 15.20 Transesophageal echocardiogram (TEE) with color Doppler in the 4-chamber view of a patient with complete CAVC. There is a large atrial and ventricular communication. There is a trivial amount of AV valve regurgitation.

Video 15.21 Intraoperative transesophageal echocardiogram (TEE) with color Doppler in the 4-chamber view of a patient with

complete CAVC after two-patch repair. The atrial and ventricular septal defect patches are seen. There is minimal right and left AV valve regurgitation. There is a small residual peripatch ventricular septal defect.

Video 15.22 Parasternal short-axis view in color compare mode of a patient who has undergone cleft closure. There is minimal left AV valve regurgitation through the residual cleft.

Video 15.23 Apical 4-chamber view in color compare mode demonstrating severe left AV valve regurgitation after complete CAVC repair. The left atrium is severely dilated.

Video 15.24 Apical 4-chamber view in color compare mode of a patient with repaired complete CAVC after left AV valvuloplasty. There is mild residual left AV valve stenosis and mild residual left AV valve regurgitation.

Video 15.25 Apical 5-chamber view in color compare mode zoomed into the left ventricular outflow tract. There is a chord across the subaortic region causing obstruction and there is mild aortic regurgitation.

References

1 Marx GR, Fyler DC. Endocardial cushion defects. In: Keane JF, Lock JE, Fyler DC (eds.) *Nadas' Pediatric Cardiology*. Philadelphia, PA: Saunders Elsevier, 2006, pp. 663–674.

2 Hoffman JI, Kaplan S. The incidence of congenital heart disease. *J Am Coll Cardiol* 2002;**39**:1890–1900.

3 Barlow GM, Chen XN, Shi ZY, et al. Down syndrome and congenital heart disease: a narrowed region and a candidate gene. *Genet Med* 2001;**3**:91–101.

4 Maslen CL. Molecular genetics of atrioventricular septal defects. *Curr Opin Cardiol* 2004;**19**:205–210.

5 Kumar A, Williams CA, Victorica BE. Familial atrioventricular septal defect: possible genetic mechanisms. *Br Heart J* 1994;**71**:79–81.

6 Devriendt K, Van Schoubroeck D, Eyskens B, et al. Prenatal diagnosis of a terminal short arm deletion of chromosome 8 in a fetus with an atrioventricular septal defect. *Prenat Diagn* 1998;**18**:65–67.

7 Loewy Kirby M. *Endocardium, Cardiac Cushions, and Valve Development in Cardiac Development*. New York, NY: Oxford University Press, 2007, pp. 119–131.

8 Butcher J, Markwald RR. Valvulogenesis: the moving target. *Phil Trans R Soc B* 2007;**2130**:1–15.

9 Eisenberg LM, Markwald RR. Molecular regulation of atrioventricular valvuloseptal morphogenesis. *Circ Res* 1995;**77**:1–6.

10 Barrea C, Levasseur S, Roman K et al. Three-dimensional echocardiography improves the understanding of left atrioventricular valve morphology and function in atrioventricular septal defects undergoing patch augmentation. *J Thorac Cardiovasc Surg* 2005;**129**:746–753.

11 Anderson RH, Ho SY, Falcao S, et al. The diagnostic features of atrioventricular septal defect with common atrioventricular junction. *Cardiol Young* 1998;**8**:33–49.

12 Rastelli GC, Ongley PA, Kirklin JW, McGoon DC. Surgical repair of complete form of persistent common atrioventricular canal. *J Thorac Cardiovasc Surg* 1968;**55**:299–308.

13 Mahle WT, Shirali GS, Anderson RH. Echo-morphological correlates in patients with atrioventricular septal defect and common atrioventricular junction. *Cardiol Young* 2006;**16**(Suppl. 3):43–51.

14 Bharati S, Lev M. The spectrum of common atrioventricular orifice (canal). *Am Heart J* 1973;**86**:553–561.

15 Kohl T, Silverman NH. Comparison of cleft and papillary muscle position in cleft mitral valve and atrioventricular septal defect. *Am J Cardiol* 1996;**77**:164–169.

16 Clapp S, Perry BL, Farooki ZQ, et al. Down syndrome, complete atrioventricular canal and pulmonary vascular obstructive disease. *J Thorac Cardiovasc Surg* 1990;**100**:115–121.

17 Ilbawi MN, Idriss FS, DeLeon SY, et al. Unusual mitral valve abnormalities complicating surgical repair of endocardial cushion defects. *J Thorac Cardiovasc Surg* 1983;**85**:697–704.

18 Michielon G, Stellin G, Rizzoli G, et al. Left atrioventricular valve incompetence after repair of common atrioventricular canal defects. *Ann Thorac Surg* 1995;**60**(6 Suppl.): S604–609.

19 Weinberg M, Jr., Miller RA, Hastreiter AR, et al. Congestive heart failure in children with atrial septal defect. *J Thorac Cardiovasc Surg* 1966;**51**(1):81–87.

20 Cohen MS, Jacobs ML, Weinberg PM, Rychik J. Morphometric analysis of unbalanced common atrioventricular canal using two-dimensional echocardiography. *J Am Coll Cardiol* 1996;**28**:1017–1023.

21 Silverman NH, Zuberbuhler JR, Anderson RH. Atrioventricular septal defects: cross-sectional echocardiographic and morphologic comparisons. *Int J Cardiol* 1986;**13**:309–331.

22 Draulans-Noe H, Weinink ACG. Anterolateral muscle bundle of the left ventricle in atrioventricular septal defect: left ventricular outflow tract and subaortic stenosis. *Pediatr Cardiol* 1991;**12**:83–88.

23 Szwast AL, Marino BS, Rychik J, et al. Usefulness of left ventricular inflow index to predict successful biventricular repair in right-dominant unbalanced atrioventricular canal. *Am J Cardiol* 2011;**107**:103–109.

24 Cohen MS. Clarifying anatomical complexity: diagnosing heterotaxy syndrome in the fetus. *Prog Pediatr Cardiol* (J Rychik (ed.)) 2006;**22**:61–70.

25 Yang SG, Novello R, Nicolson SC, et al. Evaluation of ventricular septal defect repair using intraoperative transesophageal echocardiography: frequency and significance of residual defects in infants and children. *Echocardiography* 2000;**17**:681–684.

26 Lee HR, Montenegro LM, Nicolson SC, et al. Usefulness of intraoperative transesophageal echocardiography in predicting the degree of mitral regurgitation secondary to atrioventricular defect in children. *Am J Cardiol* 1999;**83**:750–753.

27 Kim HK, Kim WH, Hwang SW, et al. Predictive value of intraoperative transesophageal echocardiography in completer atrioventricular septal defect. *Ann Thorac Surg* 2005;**80**:56–59.

28 Castaneda AR, Jonas RA, Mayer JE, et al. Atrioventricular canal defect. In: *Cardiac Surgery of the Neonate and Infant*. Philadelphia, PA: W.B. Saunders Company, 1994, pp. 167–186.

29 Rychik J, Norwood WI, Chin AJ. Doppler color flow mapping assessment of residual shunt after closure of large ventricular septal defects. *Circulation* 1991;**84**:153–161.

30 Dodge-Khatami A, Knirsch W, Tomaske M, et al. Spontaneous closure of small residual ventricular septal defects after surgical repair. *Ann Thorac Surg* 2007;**83**:902–905.

31 Ten Harkel AD, Cromme-Dijkhuis AH, Heinerman BC, et al. Development of left atrioventricular valve regurgitation after correction

of atrioventricular septal defect. *Ann Thorac Surg* 2005;**79**:607–612.

32 Murashita T, Kubota T, Oba J, et al. Left atrioventricular valve regurgitation after repair of incomplete atrioventricular septal defect. *Ann Thorac Surg* 2004;**77**:2157–2162.

33 Takahashi K, Guerra V, Roman KS, et al. Three-dimensional echocardiography improves the understanding of the mechanisms and site of left atrioventricular valve regurgitation in atrioventricular septal defect. *J Am Soc Echocardiogr* 2006;**19**:1502–1510.

34 Suzuki K, Tatsuno K, Kikuchi T, Mimori S. Predisposing factors of valve regurgitation in complete atrioventricular septal defect. *J Am Coll Cardiol* 1998;**32**:1449–1453.

35 Boening A, Scheewe J, Heine K, et al. Long-term results after surgical correction of atrioventricular septal defects. *Eur J Cardiothorac Surg* 2002;**22**:167–173.

36 Helmcke F, Nanda NC, Hsiung M, et al. Color Doppler assessment of mitral regurgitation with orthogonal planes. *Circulation* 1987;**75**:175–183.

37 Wu YT, Chang AC, Chin AJ. Semiquantitative assessment of mitral regurgitation by Doppler color flow imaging in patients aged <20 years. *Am J Cardiol* 1993;**71**:727–732.

38 Prakash A, Lacro RV, Sleeper LA, et al. Challenges in echocardiographic assessment of mitral regurgitation in children after repair of atrioventricular septal defect. *Pediatr Cardiol* 2012;**33**:205–214.

39 Khanna D, Miller AP, Nanda NC, et al. Transthoracic and transesophageal echocardiographic assessment of mitral regurgitation severity: usefulness of qualitative and semi-quantitative techniques. *Echocardiography* 2005;**22**:748–769.

PART IV

Anomalies of the Ventriculo-arterial Junction and Great Arteries

CHAPTER 16

Anomalies of the Right Ventricular Outflow Tract and Pulmonary Valve

Matthew S. Lemler and Claudio Ramaciotti
Children's Medical Center of Dallas, Dallas, TX, USA

Malformation of the pulmonary valve

Malformation affecting the pulmonary valve can lead to pulmonary stenosis and/or regurgitation.

Incidence of pulmonary valve stenosis

Pulmonary valve stenosis is defined as an obstruction at the level of the pulmonary valve. It is the fourth most common congenital heart lesion, occurring in approximately 53 (range 35–83) per 100,000 live births [1]. The valve abnormality is virtually always congenital, although acquired cases due to carcinoid disease and rheumatic heart disease can rarely occur [2]. Presentation is determined by the degree of obstruction, and can range from in utero or neonatal diagnosis in severe cases to discovery in the older patient evaluated for an asymptomatic murmur. Stenosis of the pulmonary valve is usually found in isolation. However, when the valve is dysplastic, there is an increased incidence of additional cardiac and noncardiac malformations [3]. Syndromes that are commonly associated with dysplastic pulmonary valve stenosis include Noonan, congenital rubella, Williams and Alagille syndromes [4,5].

Morphology and classification

The normal pulmonary valve consists of three leaflets supported in a semilunar fashion within the sinuses of the pulmonary trunk. The free edges of each leaflet are appreciably longer than the chord of the sinus that supports it. This arrangement permits the leaflets to fit snugly together in the closed position [6]. Morphologic types of pulmonary valve stenosis can be divided into three categories:

1 The most common form is the dome-shaped valve. Fusion, underdevelopment, or absence of the commissures result in a small central opening. The degree of fusion determines the size of the orifice. The valve leaflets remain mobile [3,6].
2 Thickened and mucoid leaflets with poor mobility are typical of dysplastic pulmonary valves. The thickened, dysplastic leaflets are characteristically associated with a narrowed sinotubular junction [6,7].
3 Unicuspid and bicuspid pulmonary valves rarely occur in isolation, and are classically associated with more complex lesions such as tetralogy of Fallot [7]. Bicuspid and quadricuspid pulmonary valves occur in 0.1–0.2% of the general population [8]. Only 4% of quadricuspid pulmonary valves result in clinically important pathology; of these 33% result in stenosis and 67% cause regurgitation [9].

Poststenotic dilation of the main pulmonary artery is common in patients with pulmonary valve stenosis. However, it does not occur in patients with dysplastic pulmonary valves. Additionally, the degree of stenosis does not correlate with the size of the main pulmonary artery.

Pathophysiology

The clinical consequences of pulmonary valve stenosis are typically related to the degree of obstruction and the effect on the right ventricle (RV). Normal or only mild RV hypertrophy occurs in response to mild or moderate pulmonary valve stenosis. Marked RV hypertrophy develops as a consequence of increased wall stress associated with severe stenosis (Figure 16.1a–c; Videos 16.1 and 16.2). Infundibular hypertrophy may lead to anatomic and/or dynamic subvalvar obstruction. Severe RV hypertrophy leads to reduced end-systolic deformation of the RV, diminished elastic recoil in early diastole and elevated RV pressure in early diastole [10]. Significant elevation of RV diastolic pressures results in the elevation of right atrial pressure and dilation of the right atrium. Right-to-left shunting may then occur in the presence of an atrial septal defect (ASD) or a patent foramen ovale (PFO) (Figure 16.1d).

Echocardiography in Pediatric and Congenital Heart Disease: From Fetus to Adult, Second Edition. Edited by Wyman W. Lai, Luc L. Mertens, Meryl S. Cohen and Tal Geva.
© 2016 John Wiley & Sons, Ltd. Published 2016 by John Wiley & Sons, Ltd.
Companion website: www.lai-echo.com

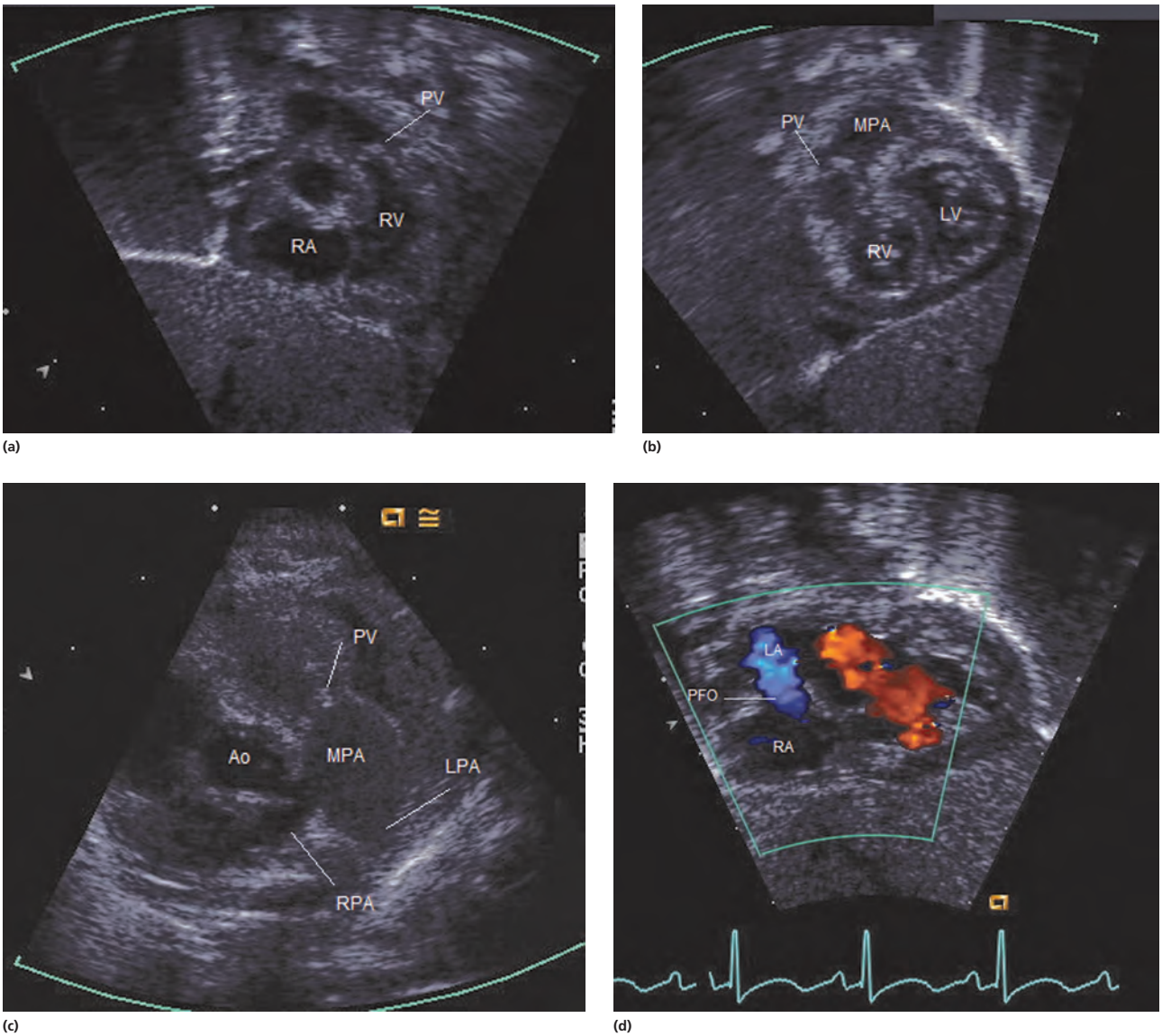


Figure 16.1 Term infant with critical pulmonary valve stenosis prior to intervention. **(a)** Subcostal long-axis view: dysplastic pulmonary valve with systolic doming. **(b)** Subcostal short-axis view: systolic frame showing subvalvar narrowing secondary to dyanamic compression of hypertrophied muscle bundles, the intraventricular septum deviates towards the left ventricle, indicative of supra-systemic right ventricular systolic pressure. **(c)** Parasternal short-axis view: dilated main and proximal left pulmonary arteries. **(d)** Subcostal long-axis view: right-to-left flow across a patent foramen ovale. Ao, aorta; LPA, left pulmonary artery; LV, left ventricle; MPA, main pulmonary artery; PV, pulmonary valve; RA, right atrium; RPA, right pulmonary artery; RV, right ventricle.

Both severe and critical pulmonary valve stenosis in a neonate will result in systemic or supra-systemic RV pressures. Critical pulmonary stenosis occurs when the RV is unable to maintain systemic arterial saturations above 90% in the absence of a patent ductus arteriosus (PDA) [11]. When the RV is unable to eject the entire systemic return across the pulmonary valve, nonoxygenated blood crosses the PFO causing systemic arterial desaturation [11]. Adequate pulmonary blood flow then becomes dependent on left-to-right shunting across the PDA. This causes a volume load on the left ventricle (LV), which is already facing the increased afterload that occurs during the neonatal transitional period. Poor biventricular function ensues. When critical pulmonary valve stenosis occurs in the presence of severe tricuspid valve regurgitation, the RV suffers from both a pressure and volume load resulting in increased right-to-left atrial shunting.

Progression of pulmonary valve stenosis is common in the neonatal period, partially due to normal hemodynamic changes, including increased cardiac output [12], decreased pulmonary vascular resistance [13], and closure of the PDA. The rate of progression tapers off during infancy, and is uncommon beyond the first year of life.

Imaging

Key elements

- Define the morphology of the pulmonary valve with particular attention to leaflet number, mobility and thickness
 - Confirm site of stenosis to be at the level of the valve
 - Determine the presence or absence of additional sites of stenosis
 - infundibular
 - supravalvar.
- Measure the diameters of the pulmonary valve annulus, main pulmonary artery and branches and report z-scores.
- Measure the Doppler estimated peak and mean gradients across the valve from multiple views
 - continuous-wave (CW) Doppler to assess severity
 - pulsed-wave (PW) Doppler to assess location
 - confirm pulmonary gradient with estimated right ventricle pressure from the tricuspid regurgitation jet.
- Assess pulmonary valve regurgitation
 - precise location
 - grade severity.
- Evaluate the right ventricle
 - size
 - function
 - hypertrophy
 - dilation
 - systolic pressure.
- Assess the tricuspid valve
 - annulus diameters and z-scores
 - morphology (leaflets, chordae tendineae, and papillary muscles)
 - stenosis
 - regurgitation.
- Assess size of the right atrium.
- Evaluate the atrial septum: if defect present, measure the size and determine the direction of flow by color and spectral Doppler.
- Determine the presence of a PDA; if present, determine direction and velocity of flow.
- Determine the presence of associated defects.

Prenatal assessment

Isolated pulmonary valve stenosis can be diagnosed in the fetus. In patients with mild or moderate pulmonary valve stenosis the cardiac chambers tend to be normal in size. Additionally, the PDA demonstrates normal antegrade right-to-left flow. Therefore, the examiner must rely on the size, morphology and flow acceleration across the pulmonary valve [14]. In fetuses with severe or critical pulmonary valve stenosis the morphology of the RV is determined by the degree of tricuspid valve regurgitation. The RV is dilated and the ventricular wall is normal or thin in the presence of severe regurgitation, whereas in patients without tricuspid regurgitation, the RV is hypertrophied with various degrees of cavity hypoplasia (Figure 16.2; Video 16.3). The degree of enlargement of the right atrium correlates with the degree of tricuspid valve regurgitation [15]. In patients with critical pulmonary valve stenosis flow across the PDA is retrograde from the aorta into the pulmonary arteries. Serial evaluations of the fetus diagnosed with pulmonary stenosis are important because progression from mild to critical pulmonary stenosis or even atresia has been well documented [15].

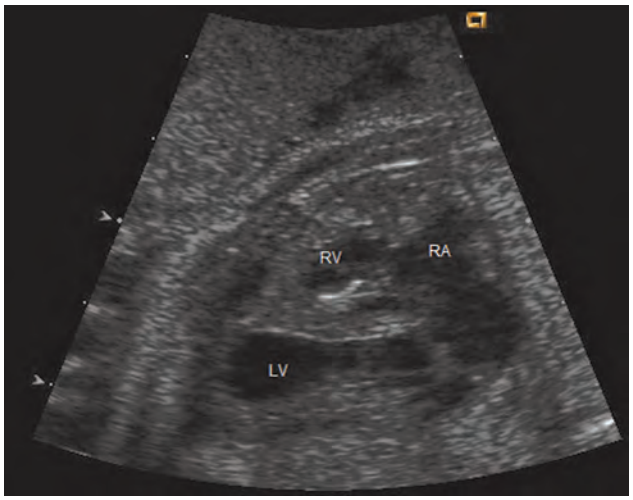


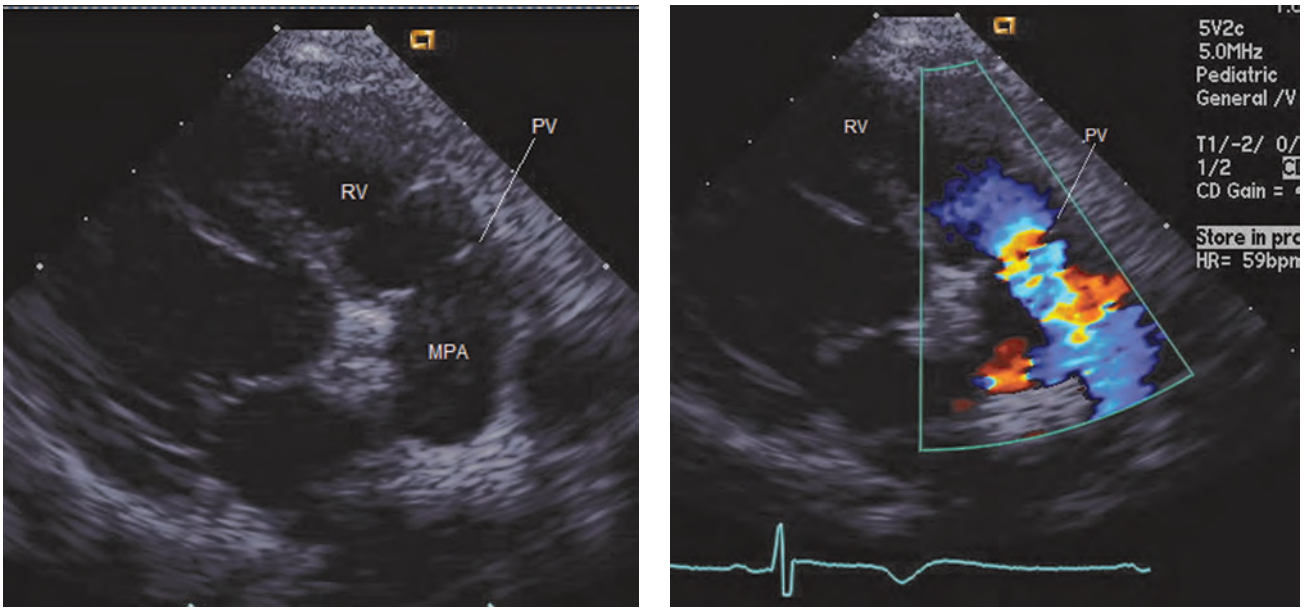
Figure 16.2 Fetus with severe/critical pulmonary valve stenosis. The 4-chamber view demonstrates a severely hypertrophied right ventricle. LV, left ventricle; RA, right atrium; RV, right ventricle.

It is important to assess flow across the PFO, as the fetuses with severe pulmonary stenosis and PFO restriction are at high risk of developing hydrops [16]. As a result of decreased preload, the LV is unable to generate adequate cardiac output. However, restrictive right-to-left shunting across the foramen ovale is difficult to diagnose because the imager cannot rely on increase in velocity to identify the restriction [17]. Therefore, it is imperative to look for signs of impending hydrops fetalis, including increased cardiothoracic ratio, pericardial effusion, holosystolic tricuspid valve regurgitation and abnormal venous Doppler flow [16].

In the study of Gomez-Montes et al. [18], a tricuspid-to-mitral valve diameter ratio ≤0.83, pulmonary-to-aortic valve diameter ratio ≤0.75, tricuspid inflow duration/cardiac cycle length ≤36.5%, and RV-to-LV length ratio ≤0.64 were associated with a univentricular repair after birth. Having three out of the four markers was 100% sensitive and 92% specific whereas the presence of all four markers was 100% sensitive and specific in the second trimester of pregnancy. In addition to the tricuspid-to-mitral valve diameter ratio, tricuspid and pulmonary valve z-scores were associated with a single ventricle outcome but cut-offs and reliability vary with gestational age [19].

Postnatal assessment

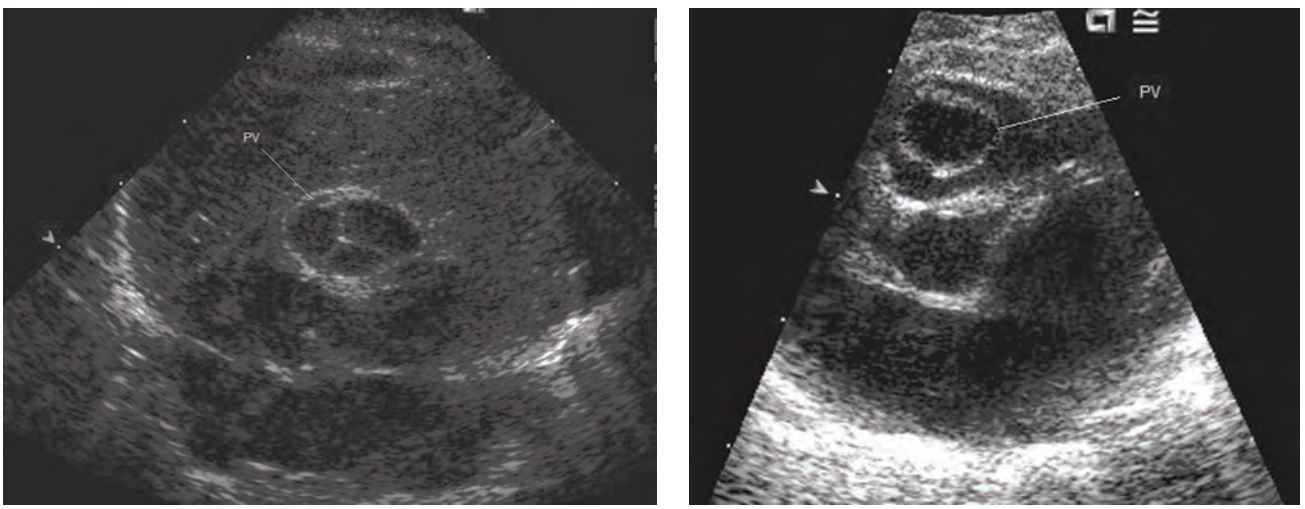
Pulmonary valve anatomy and physiology are well defined by two-dimensional (2D) imaging. The pulmonary valve is appreciated in the parasternal long-axis view by tilting the transducer



(a) (b)

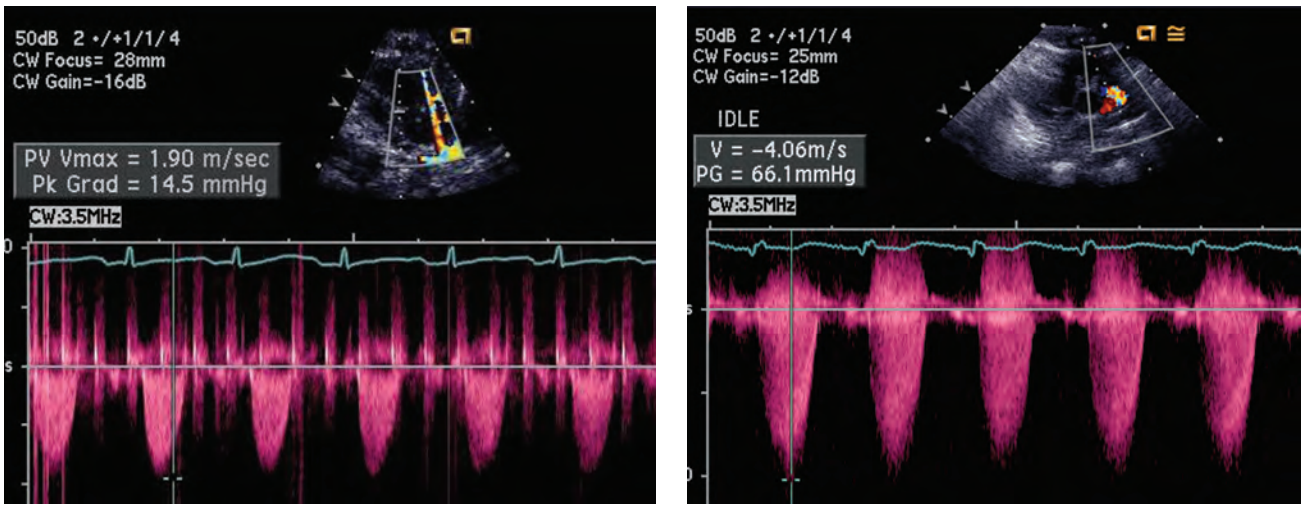
Figure 16.3 **(a)** Parasternal long-axis view performed by tilting the transducer towards the patient's left shoulder. **(b)** Color flow mapping demonstrates turbulence across a stenotic pulmonary valve. MPA, main pulmonary artery; PV, pulmonary valve; RV, right ventricle.

toward the patient's left shoulder (Figure 16.3a,b; Videos 16.4 and 16.5) and in the parasternal short-axis view at the base of the heart (Figure 16.1c). In addition to the morphology of the valve, the subcostal short-axis and right anterior oblique views provide an excellent opportunity to assess additional levels of obstruction (Figure 16.1a,b; Videos 16.1 and 16.2). In infants and young children, the apical 4-chamber view can be adapted by sweeping anterior and clockwise to include the pulmonary valve and subvalve region. Using standard echocardiography views, the pulmonary valve is imaged in its longitudinal axis. However, using a high left parasternal view, a cross-sectional image of the pulmonary valve can be obtained by visualizing the short axis of the aortic valve and rotating the transducer clockwise ~10–20° (Figure 16.4a,b; Videos 16.6 and 16.7) [20]. The cross-sectional view of the pulmonary valve can also be successfully performed with three-dimensional (3D) imaging in about 60–70% of patients (Video 16.8) [21]. Three-dimensional imaging has the potential to enhance the details of the pulmonary valve morphology; however, the incremental benefit has yet to be established.



(a) (b)

Figure 16.4 High parasternal view shows a cross-section of the pulmonary valve (PV). **(a)** Normal trileaflet valve in diastole. **(b)** Bicuspid valve in systole.



(a) (b)

Figure 16.5 Doppler pattern across the pulmonary valve in an infant who presented with critical pulmonary valve stenosis with severe tricuspid regurgitation and right ventricular dysfunction. **(a)** At presentation there is only a trivial increase in velocity across the pulmonary valve. **(b)** After stabilization with recovery of right ventricular function, significant pulmonary valve stenosis was unmasked.

The degree of valve thickness and dysplasia should be assessed. It is typical to see doming of the pulmonary valve noting restrictive motion when stenosis is present. A variable degree of poststenotic dilation of the main pulmonary artery may be noted.

Quantification of pulmonary valve stenosis is performed primarily by PW and CW Doppler. The estimated systolic pressure gradient is derived from the trans-pulmonary velocity flow curve using the simplified Bernoulli equation:

$$\Delta \text{ Pressure} = 4v_2^2.$$

Doppler will underestimate a catheter measured gradient if there is a high divergence (>20%) between the ultrasound beam and the direction of blood flow [22]. To ensure accuracy it is important to line up the Doppler sample volume parallel to the direction of flow with the aid of color flow mapping. This must be performed in multiple views; including the parasternal short-axis, subcostal and modified 5-chambered views [23]. Although Doppler-derived peak instantaneous gradients are often higher than the peak-to-peak gradient measured in the cardiac catheterization laboratory, the literature supports the accuracy of Doppler-derived gradients to predict catheter-derived maximum instantaneous gradients [23–25].

The Bernoulli equation is most accurate in patients with discrete stenosis and becomes less reliable in patients with long-segment stenosis or multiple levels of obstruction in series. In contrast, Silvilairat et al. reported that outpatient mean Doppler gradients more accurately predict catheter peak-to-peak gradients in both isolated pulmonary valve stenosis [26] and in complex pulmonary outflow stenosis [27]. Therefore we recommend obtaining both peak instantaneous and mean gradients when assessing the severity of pulmonary valve stenosis. It is important to utilize PW Doppler to detect different levels of obstruction in the outflow tract [28].

When evaluating a patient with pulmonary valve stenosis by Doppler, it is important to understand that pressure gradients depend on both the effective valve orifice area and the flow rate across the valve [29]. Conditions that reduce the flow across the valve will underestimate the degree of obstruction. This includes severe tricuspid valve regurgitation, and RV dysfunction. Additionally, with pulmonary artery hypertension or a large PDA, the distal pulmonary artery pressure is elevated, thus masking the true impediment to flow. Therefore, it is possible to have severe stenosis with little or no gradient (Figure 16.5a,b; Video 16.9). In fact, critical pulmonary valve stenosis can sometimes only be distinguished from pulmonary valve atresia by the presence of a trivial quantity of pulmonary regurgitation, when the RV is unable to eject blood across the dysplastic valve. Similarly, additional flow across the pulmonary valve as occurs with other left-to-right intracardiac shunts will cause overestimation of gradients.

RV wall thickness and the degree of systolic flattening of the ventricular septum are additional semiquantitative methods to evaluate the degree of obstruction across the pulmonary valve. When possible, it is important to confirm RV systolic pressure estimates by measuring the tricuspid regurgitation velocity.

The anterior location of the pulmonary valve may limit the value of transesophageal echocardiography. The pulmonary valve and the right ventricular outflow tract may be imaged from a mid-esophageal or a transgastric window by rotating the transducer 50–90 degrees [28]. Gradients across the pulmonary valve are best obtained by rotating the transducer to 0 degrees, maximally flexing the probe and turning slightly counterclockwise.

Pulmonary valve regurgitation

Trivial to mild pulmonary valve regurgitation is common and can be considered a normal variant when accompanied by normal valve morphology. More severe regurgitation occurs with dysplastic valves, and most commonly after intervention for valve stenosis. Acquired forms of pulmonary regurgitation are rare and include pulmonary artery hypertension, endocarditis, carcinoid, and rheumatic heart disease [30].

Many studies analyzing the long-term effects of pulmonary regurgitation have used either subjective or semiquantitative methods to evaluate the degree and the consequences of pulmonary regurgitation. Detection and grading of pulmonary regurgitation is performed principally with color flow mapping and spectral Doppler. Functional regurgitation is characterized by a small, short, central jet. Pathologic regurgitation is distinguished from physiologic regurgitation by a longer duration of flow. In severe or "free" pulmonary regurgitation, equalization of diastolic pulmonary artery and right ventricular pressures occur early in diastole, thus shortening the jet. The phenomena can mimic mild regurgitation. One must use additional methods such as jet width, diastolic retrograde flow in the distal pulmonary arteries, and the presence of right ventricular dilation to distinguish mild from severe pulmonary regurgitation.

Grading of pulmonary regurgitation by color Doppler has been poorly validated. Methods include determination of overall jet size, depth of penetration of color flow Doppler into the RV, width of the vena contracta, or overall width of the jet in relation to the width of the RV outflow tract [31]. The maximum color jet width measured immediately below the pulmonary valve suffers from high intraobserver variability; however, a jet width that occupies >65% of the right ventricular outflow width is associated with severe pulmonary regurgitation [30]. Spectral Doppler can be used to measure the end-diastolic pressure difference between the RV and the pulmonary artery. A "no flow time" (diastolic period – duration of pulmonary regurgitation) >80 ms and a pressure half-time <100 ms distinguished angiographic severe pulmonary regurgitation from milder forms of disease [32].

RV dilation secondary to volume overload should be sought as indirect evidence of significant regurgitation. Williams et al. used a ratio of the pulmonary regurgitation color jet width to the pulmonary valve annulus of 0.4 (measured in early diastole in the parasternal short-axis plane) to differentiate between ≤1+ and ≥2+ angiographic grade pulmonary regurgitation. In the same study, indexed RV end-diastolic diameter correlated with angiographic pulmonary regurgitation. Nonetheless, there was significant overlap between angiographic grades. Retrograde diastolic flow in the branch pulmonary arteries was also statistically significant in separating the degrees of pulmonary regurgitation [33].

Pulmonary regurgitation is dependent on both downstream and upstream components. Elevated RV diastolic pressure and restrictive physiology will decrease the amount of pulmonary regurgitation. In the pulmonary arteries, higher proximal compliance and lower distal compliance will increase regurgitation. Meanwhile valve obstruction will decrease regurgitation, while distal obstruction will increase the severity of the regurgitation.

Three-dimensional imaging offers the potential, but still unproven improvement in quantification of pulmonary regurgitation. Three-dimensional color Doppler allows the cropping plane to be positioned exactly parallel to the vena contracta, which then can be planimetered and can be used to calculate the severity of pulmonary regurgitation [21]. In reality, poor visualization of the pulmonary valve has limited progress in developing 3D algorithms for quantification of pulmonary regurgitation [34].

Transcatheter and surgical treatment

Catheter balloon dilation is the primary modality for treatment of pulmonary valve stenosis. Surgical intervention is reserved for patients with multiple levels of obstruction, dysplastic pulmonary valves, and hypoplastic pulmonary valve annulus. Echocardiography is the most important diagnostic modality for planning catheterization and surgical interventions. Indications for balloon dilation of pulmonary valve stenosis remain controversial. The excellent results and low morbidity of the procedure have led to use of balloon valvuloplasty even in patients with mild obstruction. Mullins has recommended balloon valvuloplasty for patients with Doppler-measured peak instantaneous gradients as low as 35 mmHg, along with other objective signs of RV hypertrophy by echocardiography or electrocardiography [35]. Others feel that the RV systolic pressure should exceed 55–60 mmHg [6]. In the presence of severe tricuspid regurgitation or RV dysfunction, the gradient across the pulmonary valve cannot be relied upon to determine need for intervention. Measurement of the diameter of the pulmonary annulus is required to plan adequately for the catheterization procedure. Echocardiography very closely approximates the catheter measurement of the pulmonary valve [22]. Typically the balloon size used for valvuloplasty is 1.1–1.2 times the size of the pulmonary annulus, with a maximum balloon-to-annulus diameter ratio of 1.4.

Postprocedure assessment and long-term sequelae

Since its original description in 1982, balloon valvuloplasty has become the treatment of choice for patients with congenital pulmonary valve stenosis [36]. Balloon valvuloplasty is highly successful at reducing the gradient across the valve with long-term success in >95% of cases [22,37,38]. It is important to identify the site and type of residual obstruction in patients after balloon valvuloplasty. It is common for infundibular gradients to increase immediately after intervention; however, the gradient improves during the first 18 months of follow-up [38]; by contrast, patients with residual gradients across the valve do not improve [39]. Patients with Noonan syndrome have higher residual gradients compared with nonsyndromic patients

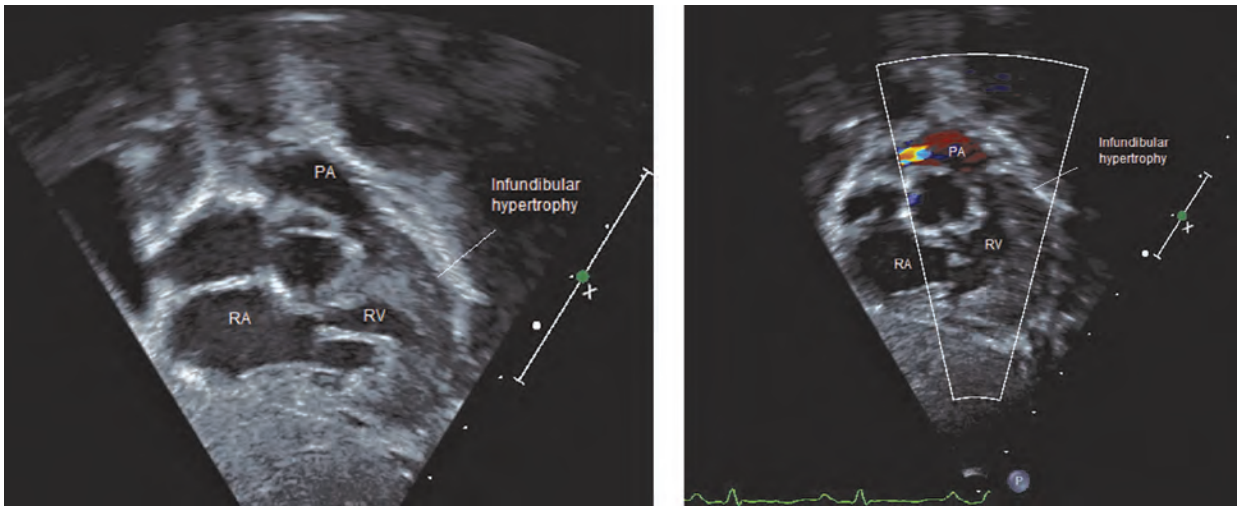


Figure 16.6 **(a)** Subgastric view of the right ventricular outflow tract demonstrating severe dynamic infundibular obstruction after pulmonary valvuloplasty. **(b)** Color flow Doppler demonstrates limited flow across the right ventricular outflow tract and the pulmonary valve. PA, pulmonary artery; RA, right ventricle; RV, right ventricle.

[40], leading some physicians to advocate surgical repair of pulmonary valve stenosis in patients with Noonan syndrome.

Acutely after the procedure it is important to recognize complications of angioplasty including: perforation of the pulmonary valve leaflets or annulus, tricuspid valve injury, perforation of the right ventricular outflow tract, disruption of the pulmonary trunk, and cardiac tamponade [22].

Significant pulmonary valve regurgitation occurs in 33% of patients undergoing balloon angioplasty, occurring more frequently in patients who presented with more severe pulmonary valve stenosis [22]. Clinically, pulmonary regurgitation is mild in the first few months after valvuloplasty, secondary to right ventricular hypertrophy and low compliance; however, it is thought that as RV compliance improves the pulmonary regurgitation becomes more evident [41].

Prior to the development of balloon valvuloplasty, surgical valvuloplasty was the treatment of choice. At a median follow-up of 34 years, 43% of patients had moderate to severe pulmonary valve regurgitation, 16% had moderate to severe tricuspid valve regurgitation, 63% had moderate to severe RV dilation, and 10% had moderate to severe RV systolic dysfunction [42].

Patients with critical pulmonary valve stenosis can undergo pulmonary valve balloon dilation in the cardiac catheterization laboratory with less than a 3% failure rate. Of patients with successful angioplasty 21% required additional procedures; including repeat valvuloplasty, surgical enlargement of the RVOT, or a systemic-to-pulmonary arterial shunt [43]. After pulmonary valve balloon dilation the tricuspid valve, pulmonary valve and RV have all been documented to increase in size at or above the rate of somatic growth [44,45]. Most patients have adequate systemic oxygen saturations after balloon valvuloplasty. However, patients with hyperdynamic RV outflow tracts can develop infundibular obstruction (so-called "suicide" RV), causing inadequate flow across the RV outflow tract (Figure 16.6a,b; Video 16.10). Other patients remain cyanotic secondary to right-to-left shunting across the PFO due to poor RV compliance or RV hypoplasia [46]. It is important to recognize these physiologic states by echocardiography, because both may require resumption of prostaglandin therapy. While the dynamic infundibular stenosis usually improves within several days, a poorly compliant RV may take several weeks to improve. In such cases, surgical creation of a systemic-to-pulmonary artery shunt should be entertained. In patients with a diminutive pulmonary annulus a systemic-to-pulmonary shunt may be required in addition to a transannular patch across the RV outflow tract [47].

In the presence of significant pulmonary valve regurgitation, there is a risk of blood flow regurgitating back into the RV from either a PDA or systemic-to-pulmonary artery shunt through the pulmonary valve. This phenomenon, known as a "circular shunt," is more severe in cases with important tricuspid valve regurgitation. A circular shunt must be excluded in any patient with metabolic acidosis or cyanosis in the post-interventional period.

Subpulmonary stenosis, including double-chambered right ventricle

Subvalvular pulmonary stenosis includes infundibular pulmonary stenosis and double-chambered right ventricle (DCRV). Infundibular stenosis can be primarily caused by a discrete fibromuscular obstruction or hypertrophic cardiomyopathy. Secondary forms include an aneurysm of the ventricular septum, an aneurysm of the sinus of Valsalva, accessory tricuspid valve tissue, cardiac tumors, and RV hypertrophy secondary to pulmonary valve stenosis. Hypertrophic cardiomyopathy and

the secondary forms will not be discussed in this chapter. Discrete fibromuscular subpulmonary obstruction is described as a ring or fibromuscular diaphragm with an orifice located at the infundibular ostium or within the RV infundibulum. DCRV encompasses conditions in which the muscular structures comprising the proximal infundibular ostium create a division within the right ventricle, resulting in muscular narrowing between the RV sinus (inflow) and the infundibulum (outflow). Patients with this abnormality are also categorized as having anomalous RV muscle bundles. The progressive obstruction divides the right ventricle into a proximal high-pressure RV sinus chamber and a low-pressure infundibular chamber distal to the muscular structures.

The incidence of discrete fibromuscular obstruction has been reported to vary between 0.2% and 8% of all cases of pulmonary stenosis [48,49]. The incidence of DCRV is not accurately known. Due to its progressive nature, this lesion is more easily detected after the first months of life. It has been suggested that 3–7% of patients with a ventricular septal defect (VSD) will acquire pulmonary outflow obstruction [50,51]. Among all patients with a VSD seen at Boston Children's Hospital between 1973 and 2002, 0.04% developed a double-chambered right ventricle [52]. Simpson et al. reported 10% prevalence in children undergoing VSD repair [53], and Moran et al. noted development of DCRV in 3.1% of patients undergoing tetralogy of Fallot repair before the age of 2 years [54]. In a series from Spain, 0.75% of all cardiac defects repaired in childhood included DCRV [55].

The embryologic mechanism suggested for the development of discrete fibromuscular obstruction is a defect in absorption of the anterolateral conus or pulmonary infundibulum [56]. There is no consensus about the origin of the anomalous muscle bundles that make up a DCRV. Some have suggested that the anomaly arises from high takeoff of the moderator band with acquired hypertrophy of the muscle bundles of the proximal os infundibulum, including septal, moderator, and parietal bands [57]. It has also been proposed that the anomaly is due to persistence of prominent septal-parietal trabeculations [58–62]. Possible relationships between DCRV and Down syndrome [63] and Noonan syndrome [64] have been proposed. In addition, Lougheed et al. have reported the development of RV outflow tract obstruction in almost 10% of recipients of fetal twin-to-twin transfusion [65].

Morphology and classification

In its more common form, the obstruction caused by anomalous RV muscle bundles is not present in the first months of life. The muscle bundles become more prominent as the patient grows, and the obstruction is usually progressive [61]. However, rates of progression vary considerably [53,66]. In addition, several authors have described various forms of obstruction within the RV that are different from typical DCRV. These include an anomalous apical shelf with or without an associated Ebstein anomaly; an apical shelf confluent with the outlet septum that can give the impression of double-outlet LV; and a circumferential muscular diaphragm in the presence of tetralogy of Fallot [67–69].

Subpulmonary obstruction caused by a discrete fibromuscular ridge usually begins at the lower portion of the infundibulum. RV cavity division by anomalous muscle bundles usually occurs at the junction between the sinus (inlet) and the infundibular (outlet) components of the RV. The anomalous muscle bundles have also been described to develop proximal to the usual RV outflow obstruction found in tetralogy of Fallot [54]. It may also occur in patients with other conotruncal lesions such as D- or L-loop transposition of the great arteries or double-outlet RV [70]. Membranous VSD is the cardiac anomaly most commonly associated with DCRV, although muscular and malalignment defects are also found. Another common association is between DCRV with or without a membranous VSD and discrete subvalvar aortic stenosis [71]. The development of left ventricular outflow tract obstruction has been reported to occur before, concomitant with, or even years after surgical repair of DCRV.

Pathophysiology

In the majority of patients the obstruction caused by anomalous muscle bundles is progressive [61], but rates of progression vary considerably [53,66]. Progressive RV outflow obstruction causes an increase in the pressure gradient measured within the RV cavity. In our experience, in most cases the VSD communicates with the proximal high-pressure RV sinus chamber [72]. The progression of obstruction in such patients causes a decrease in the amount of left-to-right shunting. In the most severe cases of DCRV the shunt across the VSD can reverse. Although some of these patients have been considered to have a form of tetralogy of Fallot, the two conditions are part of a continuum. However, spontaneous closure of the VSD and left ventricular outflow abnormalities are more frequently associated with DCRV whereas pulmonary annular hypoplasia, right aortic arch, and pulmonary artery abnormalities are typical in patients with tetralogy of Fallot.

In patients with DCRV the VSD may undergo spontaneous closure. It is widely believed that cases that present with an intact ventricular septum may actually have had spontaneous closure of a VSD. Right ventricular dysfunction, a late finding, is more commonly seen in patients with restrictive or even closed VSD and markedly elevated RV pressure.

Imaging

Key elements

- Define the site and severity of obstruction(s) within the RV cavity.
- Define the type of subpulmonary stenosis.
- Determine the morphology of the anomalous muscle bundle/subpulmonary obstruction in relation to the tricuspid and pulmonary valves.
- Determine the presence of an associated VSD, its relation to the obstruction site, flow direction, and the pressure gradient across the defect.

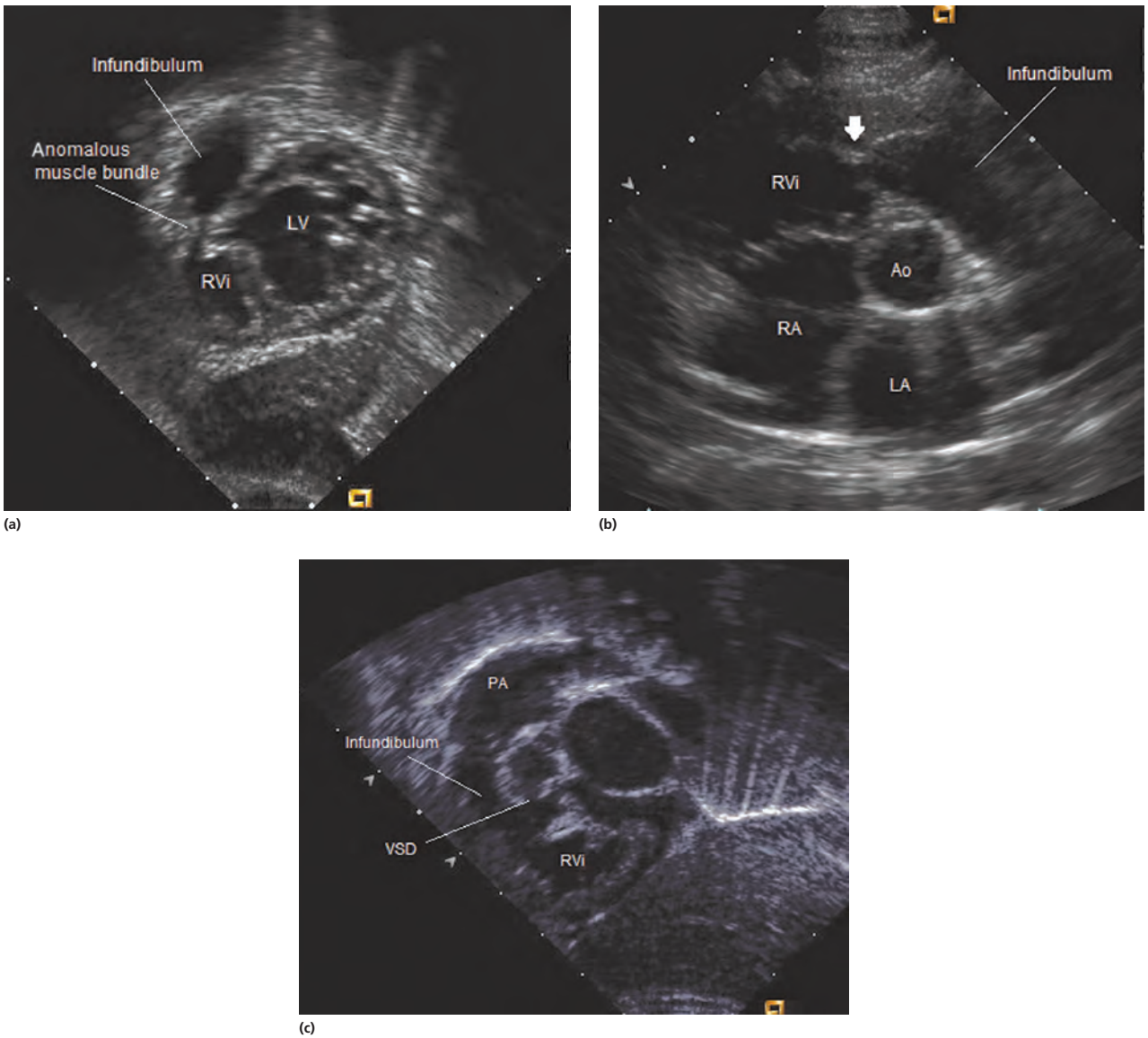


Figure 16.7 Double-chambered right ventricle with a prominent anomalous muscle bundle producing narrowing of the proximal os infundibulum. **(a)** Subcostal short-axis view. **(b)** Parasternal short-axis view. **(c)** Double-chambered right ventricle – prominent anomalous muscle bundle causing narrowing proximal to the ventricular septal defect – subcostal oblique view. Ao, aorta; LA, left atrium; LV, left ventricle; PA, pulmonary artery; RA, right atrium; RVi, right ventricular inlet; VSD, ventricular septal defect.

- Determine the presence of associated left ventricular outflow tract obstruction.
- Assess the degree of tricuspid regurgitation and determine proximal chamber pressure.
- Evaluate RV function.

Prenatal assessment

DCRV is rarely present in newborns, and the diagnosis is infrequently made in utero [73,74]. RV outflow tract obstruction has been associated with twin-to-twin transfusion. The recipient twin may develop infundibular or valvar stenosis in utero with the potential to progress to pulmonary atresia [65].

Preoperative assessment

The anatomy of subpulmonary obstruction can be systematically determined by a comprehensive echocardiographic examination. In patients with discrete subpulmonary stenosis, a nonmobile, thick ridge is seen at the level of the proximal infundibular ostium. This structure is best visualized in subcostal short-axis, long-axis, and oblique views as well as the parasternal short-axis view. Similar views are used to demonstrate anomalous muscle bundles in DCRV (Figure 16.7a–c; Videos 16.11, 16.12, and 16.13). Color Doppler flow mapping helps to highlight their existence even in the presence of a mild gradient. The RV inflow and outflow are visualized in the same

plane in the subcostal oblique view. This view also permits measurement of the distance from anomalous muscle bundles to the tricuspid and pulmonary valves. Subcostal views usually provide optimal angles for measurement of flow velocities within the RV cavity. Useful anatomic information and gradient estimation of the RV outflow obstruction can also be obtained by anteriorly angling the transducer from a modified apical view. This view can be obtained by sliding the transducer rightward and superior from the apical 4-chamber view. Subcostal and parasternal short-axis sweeps from apex to base allow similar assessment of the RV. Obstruction caused by a fibromuscular ridge located immediately below the pulmonary valve may be difficult to differentiate from isolated valvar stenosis. Therefore, special attention should be paid to leaflet motion, presence of leaflet fluttering and presence of early valvar closure.

Complete evaluation of the ventricular septum by 2D imaging and color flow mapping is important to evaluate the presence and location of a VSD. Special attention to the relationship of the defect to the anomalous muscle bundles is required. In the presence of a high-pressure proximal RV chamber, a low gradient across the VSD is expected even in the presence of significant restriction. Imaging of the left ventricular outflow tract from apical and parasternal views, in addition to a subcostal approach, should focus upon the possible presence of discrete subaortic stenosis.

Estimation of RV pressure based on the tricuspid regurgitation jet velocity confirms the elevated systolic pressure in the proximal chamber. Agreement of pressure estimation in the RV proximal and distal chambers based on measurement of flow velocities across the VSD, RV outflow and tricuspid regurgitation jet solidifies understanding of hemodynamic status.

Wong and colleagues suggested that the degree of superior displacement of the moderator band could identify patients at risk for development of DCRV [57]. The distance from the pulmonary valve to the moderator band was measured from subcostal views and normalized for the size of the tricuspid valve annulus. Alva et al. challenged the prognostic value of the moderate band displacement measurements, as they believed that the abnormal muscle bundle probably represents accentuated septal-parietal trabeculations [62]. There have been no published studies addressing the additional value of 3D echocardiography in the diagnosis of DCRV.

Echocardiographic guidance of surgical treatment

Treatment of discrete subpulmonary obstruction and DCRV is surgical. Operations are usually performed beyond infancy, with low mortality and good results. Most patients are referred for surgery based only on echocardiographic findings. The details about location of obstruction, its relation to tricuspid and pulmonary valves, and relative position of the VSD are helpful for surgical planning. Preoperative transesophageal echocardiography can confirm these details, particularly in larger patients. The RV cavity with the anomalous muscle bundles and the relationship to the ventricular septal defect are usually best demonstrated in a 45–80° "RV inflow-outflow view." The subpulmonary ridge can be viewed from 30 to 90° depending on the spatial orientation of the RV outflow tract.

Postoperative assessment

Echocardiographic assessment starts in many cases as the patient is weaned from cardiopulmonary bypass. Evaluation of residual obstruction within the RV cavity in the early postoperative period should take into consideration intravascular volume status and inotropic support. A decrease in RV volume caused by low intravascular volume and a hyperdynamic ventricle will exaggerate the residual gradient. Follow-up of patients with DCRV should include assessment of the left ventricular outflow tract, as Vogel et al. have demonstrated that the subaortic obstruction can develop after surgical correction of DCRV [71].

RV dysfunction that is present preoperatively usually improves after relief of the obstruction. In 1984, Kveselis et al. reported the long-term follow-up of 20 patients. After a mean follow-up of 19 years, five developed aortic regurgitation and two had mild RV outflow tract obstruction [75]. In 2000, Galal and colleagues reported follow-up of 73 patients after repair of DCRV [76]. A small residual VSD was present in seven, and there were no other residual lesions. Recurrent obstruction related to anomalous muscle bundles has not been reported as a significant long-term complication. Said et al. reported the outcomes of surgical repair of DCRV performed at the Mayo Clinic [77]. Over 38 years, 61 patients were repaired (median age 13 years, interquartile range 2 months to 64 years); there were two early deaths due to persistent low cardiac output, and the late survival was 90% at 10 years. There were two late deaths related to heart failure and one sudden death. No patients required reoperation for residual or recurrent obstruction. Telagh et al. reported the postoperative results of 35 patients (median age at operation 21.3 years, range 4 to 69 years), with no hospital or late death (postoperative interval 2 months to 41 years) and no reoperations. The authors concluded that surgical repair of DCRV yields excellent hemodynamic and functional results over the mid to long term [78].

Imaging of the adult

The best views to evaluate subpulmonary obstructions are the subcostal long-axis, short-axis and oblique views as well as the parasternal short-axis view. However, in adult patients subcostal images are more difficult to acquire, and the relevant anatomy is usually seen best from the parasternal approach. Adult patients with DCRV commonly present with high gradients and either a restrictive VSD or intact ventricular septum. Therefore, color Doppler flow mapping is particularly helpful even in the presence of poor echocardiographic windows.

Absent pulmonary valve with intact ventricular septum

Absent pulmonary valve is a rare lesion characterized by complete absence of or rudimentary pulmonary valve leaflets

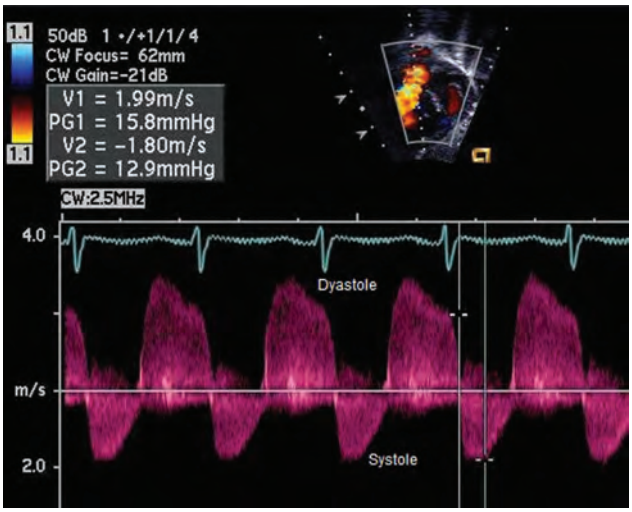


Figure 16.8 Doppler pattern across the fibrous ring in a patient with absent pulmonary valve syndrome with mild stenosis and severe regurgitation.

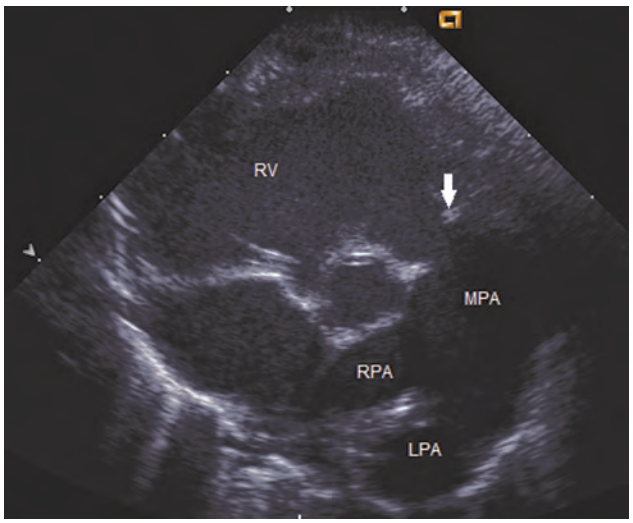


Figure 16.9 Absent pulmonary valve with intact ventricular septum seen from the parasternal short-axis view. Note the unguarded pulmonary valve (arrow) dilated right ventricle (RV), and dilated main pulmonary artery (MPA), left pulmonary artery (LPA), and right pulmonary artery (RPA).

resulting in severe regurgitation and a variable degree of stenosis (Figure 16.8; Videos 16.14 and 16.15). Absent pulmonary valve occurs in two distinct phenotypes. The more common type occurs with a malalignment conoventricular septal defect, typical of tetralogy of Fallot. A PDA is rarely present with the occurrence of a VSD. Absent pulmonary valve with an intact ventricular septum is rarer, and typically occurs with a PDA.

Absent pulmonary valve syndrome occurs in 1% of fetuses diagnosed with congenital heart disease with only 10% occurring in association with intact ventricular septum. However, due to the high rate fetal demise in those with a VSD, the incidence of absent pulmonary valve syndrome and intact ventricular septum is higher (40%) after birth. The clinical presentation of patients with intact ventricular septum is highly variable; patients may be asymptomatic during infancy and childhood and are diagnosed during a workup for a murmur [79]. Other patients are cyanotic at birth and may require intervention in the neonatal period.

Pathophysiology

The right ventricle, main pulmonary artery and branch pulmonary arteries become dilated from the increased volume and pressure load (Figure 16.9). Patients with an intact ventricular septum characteristically develop less severe dilation of the pulmonary arteries as compared to those associated with a VSD. The etiology of this is not well understood but has been speculated to occur because the presence of a patent ductus arteriosus in utero provides a pathway for runoff into the systemic circulation [80,81]. On the other hand, persistent patency of a ductus arteriosus after birth can lead to increased right ventricular stroke volume, further pulmonary dilation and right heart failure [79,82]. When the branch pulmonary arteries are significantly dilated, patients will often present with airway obstruction [81].

Imaging

Prenatal assessment

Several series have documented the ability to correctly diagnose absent pulmonary valve with and without a VSD in the fetus [80,81,83]. The characteristic findings of enlargement of the central pulmonary arteries and dilated RV are uncommon until gestation reaches 22 weeks. However, the diagnosis can still be made based on the presence of severe pulmonary regurgitation (Video 16.16) [84]. It is important to determine the presence of a VSD or a PDA, which rarely occur together. The risk of fetal and neonatal loss associated with absent pulmonary valve makes it imperative to perform frequent follow-up examinations that include measurements of fetal well-being. Serial measurements of the cardiothoracic ratio, diameters of the pulmonary trunk and branches, and Doppler velocities across the RV outflow and main pulmonary artery are important as well as frequent assessments for signs of hydrops fetalis.

Preoperative assessment

Echocardiography should provide all the essential information necessary to manage patients with absent pulmonary valve. An echo-bright fibrous ring occupying the location of the pulmonary valve can be identified in the parasternal short- and long-axis views and in the subcostal coronal, short-axis and oblique views (Figure 16.10). Thickened, dysplastic valve remnants can sometimes be identified as part of the lesion. The degree of stenosis depends on the size of the valve annulus. Subvalvar and supravalvar obstruction are rarely part of this lesion, but must be excluded. The RV is characteristically dilated and hypertrophied. It is important to measure the diameters of the main and distal pulmonary arteries. This can be accomplished in the parasternal short-axis and suprasternal views. Size discrepancies between the right and left pulmonary arteries have

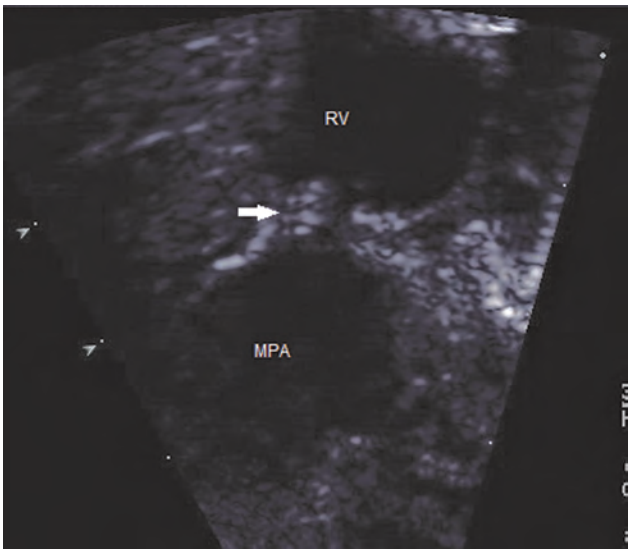


Figure 16.10 Echo-bright fibrous ring occupying the location of the pulmonary valve (arrow) in patient with absent pulmonary valve with intact ventricular septum identified in the parasternal short-axis view. MPA, main pulmonary artery; RV, right ventricle.

been reported [85]. Additional abnormalities are rare although severe tricuspid valve stenosis and atresia have been reported [86]. Serial examinations are important to follow the degree of RV outflow tract obstruction, size and function of the RV, and growth of the main and distal pulmonary arteries.

Main pulmonary artery stenosis

Obstruction distal to the pulmonary valve can occur at the level of the main pulmonary artery and/or pulmonary artery branches. These lesions are found in 2–3% of patients with congenital heart disease in association with various cardiovascular anomalies [87]. In this chapter we will only discuss lesions of the main pulmonary artery. Lesions of the branch pulmonary arteries are discussed in Chapter 18.

The embryologic mechanisms involved in the development of supravalvar pulmonary stenosis are not known. This anomaly has been associated with Williams, DiGeorge, Alagille, Keutel and congenital rubella syndromes. Congenital obstruction at the level of the main pulmonary artery can be caused by a discrete ridge or by a diffusely hypoplastic segment. The ridge can be located immediately distal to the pulmonary valve, at the midportion of the main pulmonary artery, or close to the bifurcation. Acquired lesions are seen after surgical intervention. Surgical banding of the main pulmonary artery is a palliative therapeutic option used to prevent pulmonary overcirculation and detrimental alteration of the pulmonary vasculature. In patients who have undergone main pulmonary artery banding, a poststenotic dilation can be seen. Imaging at regular intervals is needed for early diagnosis of migration of the surgical band, which can cause encroachment on the branch pulmonary arteries. The encroachment can interfere with branch pulmonary artery growth and cause stenosis and hypoplasia. Obstruction at the level of the neo-main pulmonary artery has also been reported after the arterial switch operation, due to manipulation and positioning for the LeCompte maneuver.

Imaging

Stenosis of the main pulmonary artery can be visualized from parasternal long- and short-axis views (Figures 16.11 and 16.12; Video 16.17). The anatomy can be demonstrated in young patients by anteriorly angling the transducer from a modified apical view and from subcostal short-axis and right anterior

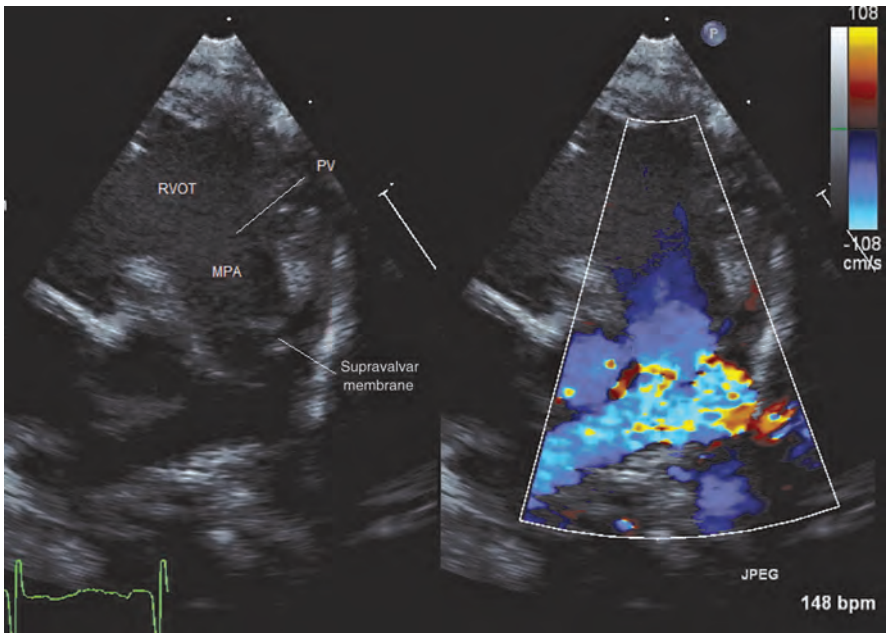


Figure 16.11 Supravalvar pulmonary stenosis – parasternal short-axis view showing a membranous diaphragm causing narrowing distal to the pulmonary valve with and without color flow mapping. MPA, main pulmonary artery; PV, pulmonary valve; RVOT, right ventricular outflow tract.

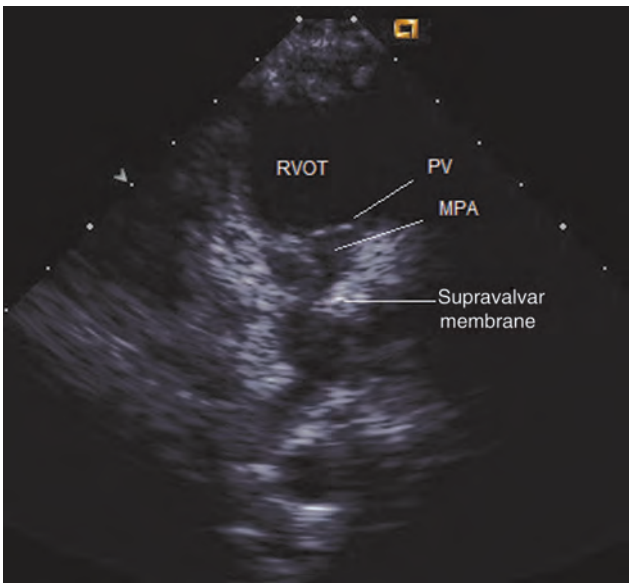


Figure 16.12 Supravalvar pulmonary stenosis – parasternal short-axis view showing a membranous diaphragm causing narrowing distal to the pulmonary valve. MPA, main pulmonary artery; PV, pulmonary valve; RVOT, right ventricular outflow tract.

oblique views. Maximum instantaneous and mean gradients across the main pulmonary artery are determined by PW and CW Doppler interrogation of flow from each view. When using CW Doppler, jets originating at other levels of obstruction can mask the actual gradient across the main pulmonary artery.

Videos

To access the videos for this chapter, please go to www.lai-echo.com.

Video 16.1 Subcostal right anterior oblique view in an infant with severe/critical pulmonary valve stenosis. There is severe right ventricular hypertrophy.

Video 16.2 Subcostal right anterior oblique view in an infant with severe/critical pulmonary valve stenosis. Significant obstruction with mild insufficiency is demonstrated by color flow Doppler.

Video 16.3 Fetus with severe/critical pulmonary valve stenosis. There is severe right ventricular hypertrophy and significant flow disturbance across a dysplastic pulmonary valve, as demonstrated by color flow Doppler.

Video 16.4 Thickened dysplastic pulmonary valve seen in the parasternal long-axis view.

Video 16.5 Bicuspid pulmonary valve demonstrated in a high parasternal view.

Video 16.6 Dysplastic pulmonary valve with limited mobility is seen in the high parasternal view.

Video 16.7 Bicuspid pulmonary valve noted in the high parasternal view with 3D imaging.

Video 16.8 Infant with severe pulmonary valve stenosis and no significant gradient across the pulmonary valve secondary to elevated pulmonary vascular resistance and poor RV function. The apical 4-chamber view demonstrates right ventricle dysfunction and severe tricuspid insufficiency.

Video 16.9 Infant with severe pulmonary valve stenosis and no significant gradient across the pulmonary valve secondary to elevated pulmonary vascular resistance and poor RV function. Parasternal long-axis view demonstrates only mild turbulence across the pulmonary valve.

Video 16.10 Subcostal right anterior oblique view demonstrates severe infundibular dynamic obstruction. Color Doppler fails to demonstrate flow across the right ventricular outflow tract.

Video 16.11 Double-chambered right ventricle – prominent anomalous muscle bundle causing narrowing proximal to the ventricular septal defect – subcostal short-axis view.

Video 16.12 Double-chambered right ventricle with a prominent anomalous muscle bundle producing narrowing of the proximal os infundibulum, with color flow mapping showing the level of obstruction – parasternal short-axis view.

Video 16.13 Double-chambered right ventricle with a prominent anomalous muscle bundle producing narrowing of the proximal os infundibulum with color flow mapping showing the level of obstruction – subcostal short-axis view.

Video 16.14 Absent pulmonary valve syndrome with rudimentary pulmonary valve apparatus is seen in the parasternal short-axis view.

Video 16.15 Color Doppler demonstrates free pulmonary regurgitation. The parasternal short-axis view also shows the dilated right ventricle and pulmonary arteries.

Video 16.16 Free pulmonary regurgitation in the fetus is indicative of absent pulmonary valve syndrome.

Video 16.17 Supravalvar pulmonary stenosis – imaging of a membranous diaphragm causing narrowing distal to the pulmonary valve, followed by superimposed color flow mapping – parasternal short-axis view.

References

1 Hoffman JIE, Kaplan S. The incidence of congenital heart disease. *J Am Coll Cardiol* 2002;**39**:1890–1900.
2 Bruce CJ, Connolly HM. Right-sided valve disease deserves a little more respect. *Circulation* 2009;**119**:2726–2734.
3 Freedom RM, Benson L. Congenital pulmonary stenosis and isolated congenital pulmonary insufficiency. In: Freedom RM, Yoo SJ, Mikailian H, Williams WG (eds.) *The Natural and Modified*

History of Congenital Heart Disease, 1st edn. New York, NY: Blackstone Publishing, 2004, pp. 107–118.
4 Bertola DR, Kim CA, Sugayama SMM, et al. Cardiac findings in 31 patients with Noonan's syndrome. *Arq Bras Cardiol* 2000;**75**:409–412.
5 Dore A. Pulmonary stenosis. In: Gatzoulis MA, Webb GD, Daubeney PEF (eds.) *Diagnosis and Management of Adult Congenital Heart Disease*. Edinburgh: Elsevier, 2003, pp. 299–303.
6 Tynan M, Anderson RH. Pulmonary stenosis. In: Anderson RH, Baker EJ, MacCarthy FJ, et al. (eds.) *Pediatric Cardiology*, 2nd edn. London: Harcourt, 2002, pp. 1461–1479.
7 Bashore TM. Adult congenital heart disease: right ventricular outflow tract lesions. *Circulation* 2007;**115**:1933–1947.
8 Jashari R, Van Hoeck B, Goffin Y, Vanderkelen A. The incidence of congenital bicuspid or bileaflet and quadricuspid or quadrileaflet arterial valves in 3,861 donor hearts in the European homograft bank. *J Heart Valve Dis* 2009;**18**:337–344.
9 Hurwitz LE, Roberts WC. Quadracuspid semilunar valve. *Am J Cardiol* 1973;**31**:623–626.
10 Vermilion RP, Snider AR, Bengur R, Meliones JN. Long-term assessment of right ventricular diastolic filling in patients with pulmonic valve stenosis successfully treated in childhood. *Am J Cardiol* 1991;**68**:648–652.
11 Artman M, Mahony L, Tietel DF. *Neonatal Cardiology*. New York, NY: McGraw-Hill Medical, 2011.
12 Mandelbaum VH, Alverson DC, Kirchgessner A, Linderkamp O. Postnatal changes in cardiac output and haemorrheology in normal neonates born at full term. *Arch Dis Child* 1991;**66**:391–394.
13 Emmanouilides GC, Moss AJ, Duffie ER, Adams FH. Pulmonary arterial pressure changes in human newborn infants from birth to 3 days of age. *J Pediatr* 1964;**65**:327–333.
14 Fouron JC. Anomalies of the right heart. In: Yagel S, Silverman N, Gembruch U (eds.) *Fetal Cardiology*. London: Martin Dunitz, 2003.
15 Todros T, Paladini D, Chiappa E, et al. Pulmonary stenosis and atresia with intact ventricular septum during prenatal life. *Ultrasound Obstet Gynecol* 2003;**21**:228–233.
16 Huhta J, Quintero RA, Suh E, Bader R. Advances in fetal cardiac intervention. *Curr Opin Pediatr* 2004;**16**:487–493.
17 Giardina A, Schmitt B, Azakie A, Tacy TA. Effect of chamber capacitance on Doppler flow pattern across restrictive defects in obligatory atrial-level shunts. *J Am Soc Echocardiogr* 2004;**17**:1286–1291.
18 Gomez-Montes E, Herraiz I, Mendoza A, et al. Pulmonary atresia/critical stenosis with intact ventricular septum: prediction of outcome in the second trimester of pregnancy. *Prenatal Diagnosis* 2011;**31**:372–379.
19 Gardiner HM, Belmar C, Tulzer G, et al. Morphologic and functional predictors of eventual circulation in the fetus with pulmonary atresia or critical pulmonary stenosis with intact septum. *J Am Coll Cardiol* 2008;**51**:1299–1308.
20 McAleer E, Kort S, Rosenzweig BP, et al. Unusual echocardiographic views of bicuspid and tricuspid pulmonic valves. *J Am Soc Echocardiogr* 2001;**14**:1036–1038.
21 Lang RM, Tsang W, Weiner BS. Valvular heart disease: the value of 3-dimensional echocardiography. *JACC* 2011;**58**:1933–1944.
22 Werynski P, Rudzinski A, Krol-Jawien W, Kuzma J. Percutaneous balloon valvuloplasty for the treatment of pulmonary valve stenosis in children–a single centre experience. *Kardiologia Polska* 2009;**67**:369–375.
23 Frantz EG, Silverman NH. Doppler ultrasound evaluation of valvar pulmonary stenosis from multiple transducer positions in children requiring pulmonary valvuloplasty. *Am J Cardiol* 1988;**61**:844–849.
24 Aldousany AW, DiSessa TG, Dubois R, et al. Doppler estimation of pressure gradient in pulmonary stenosis: maximal instantaneous vs peak-to-peak, vs mean catheter gradient. *Pediatr Cardiol* 1989;**10**:145–149.
25 Lima CO, Sahn DJ, Valdes-Cruz LM, et al. Noninvasive prediction of transvalvular pressure gradient in patients with pulmonary stenosis by quantitative two-dimensional echocardiographic Doppler studies. *Circulation* 1983;**67**:866–871.
26 Silvilairat S, Cabalka AK, Cetta F, et al. Echocardiographic assessment of isolated pulmonary valve stenosis: which outpatient Doppler gradient has the most clinical validity? *J Am Soc Echocardiogr* 2005;**18**:1137–1142.
27 Silvilairat S, Cabalka AK, Cetta F, et al. Outpatient echocardiographic assessment of complex pulmonary outflow stenosis: Doppler mean gradient is superior to the maximum instantaneous gradient. *J Am Soc Echocardiogr* 2005;**18**:1143–1148.
28 Baumgartner H, Hung J, Bermejo J, et al. Echocardiographic assessment of valve stenosis: EAE/ASE recommendations for clinical practice. *J Am Soc Echocardiogr* 2009;**22**:1–23.
29 Snider AR, Sewer GA, Ritter SB. *Echocardiography in Pediatric Heart Disease*, 2nd ed. St Louis, MO: Mosby, 1990.
30 Lancellotti P, Tribouilloy C, Hagendorff A, et al. European Association of Echocardiography recommendations for the assessment of valvular regurgitation. Part 1: aortic and pulmonary regurgitation (native valve disease). *Eur J Echocardiogr* 2010;**11**:223–244.
31 Feigenbaum H, Armstrong WF, Ryan T. *Echocardiography*, 6th edn. Philadelphia, PA: Lippincott Williams & Wilkins, 2005.
32 Yang H, Pu M, Chambers CE, et al. Quantitative assessment of pulmonary insufficiency by Doppler echocardiography in patients with adult congenital heart disease. *J Am Soc Echocardiogr* 2008;**21**:157–164.
33 Williams RV, Minich LL, Shaddy RE, et al. Comparison of Doppler echocardiography with angiography for determining the severity of pulmonary regurgitation. *Am J Cardiol* 2002;**89**:1438–1440.
34 Cai Q, Ahmad M. Three-dimensional echocardiography in valvular heart disease. *Echocardiography* 2012;**29**:88–97.
35 Mullins CE. *Cardiac Catheterization in Congenital Heart Disease*. Oxford: Blackwell Futura, 2006, pp. 430–440.
36 Kan JS, White RI, Mitchell SE, Gardner TJ. Percutaneous balloon valvuloplasty: a new method for treating congenital pulmonary valve stenosis. *N Engl J Med* 1982;**307**:540–542.
37 Lee M, Peng J, Tu G, et al. Major determinants and long-term outcomes of successful balloon dilation for the pediatric patients with isolated native valvular pulmonary stenosis: a 10-year institutional experience. *Yonsei Med J* 2008;**49**:416–421.
38 Cheragh H, Mahmood UH, Mohamad H, Adnan MG. Outcome of balloon pulmonic valvuloplasty with 18 months follow up. *J Ayub Med Coll Abbottabad* 2009;**21**:95–98.
39 Gupta D, Saxena A, Kothari SS, Juneja R. Factors influencing late course of residual valvular and infundibular gradients following pulmonary valve balloon dilation. *Int J Cardiol* 2001;**79**:143–149.
40 Masura J, Burch M, Deanfield JE, Sullivan ID. Five-year follow-up after balloon pulmonary valvuloplasty. *J Am Coll Cardiol* 1993;**21**:132–136.

41 Latson LA. Balloon pulmonary valvuloplasty, pulmonary regurgitation, and exercise capacity: the good, the bad, and the not yet clear. *JACC* 2010;**55**:1048–1049.

42 Earing MG, Connolly HM, Dearani JA, et al. Long-term follow-up of patient after surgical treatment for isolated pulmonary valve stenosis. *Mayo Clin Proc* 2005;**80**:871–876.

43 Gudausky TM, Beekman RH. Current options and long term results for interventional treatment of pulmonary valvar stenosis. *Cardiol Young* 2006;**16**:418–427.

44 Kovalchin JP, Forbes TJ, Nihill MR, Geva T. Echocardiogrphic determinants of clinical course in infants with critical and severe pulmonary valve stenosis. *J Am Coll Cardiol* 1997;**29**:1095–1101.

45 Gildein HP, Kleiner S, Goh TH, et al. Pulmonary valve annulus grows after balloon dilation of neonatal critical pulmonary valve stenosis. *Am Heart J* 1998;**136**:276–280.

46 Sommer RJ, Rhodes JR, Parness IA. Physiology of critical pulmonary valve obstruction in the neonate. *Catheter Cardio Interv* 2000;**50**:473–479.

47 Hanley FL, Sade RM, Freedom RV, et al. Outcomes in critically ill neonates with pulmonary stenosis and intact ventricular septum: a multi-institutional study. *J Am Coll Cardiol* 1993;**22**:183–192.

48 Castaneda-Zuniga WR, Formanek A, Ampaltz K. Radiologic diagnosis of different types of pulmonary stenoses. *Cardiovasc Radiol* 1978;**1**:45–57.

49 Rowe RD. Pulmonary stenosis with normal aortic root. In: Keith JD, Rowe RD, Vlad P (eds.) *Heart Disease in Infancy and Childhood*, 3rd edn. New York, NY: Macmillan, 1978, pp. 761–788.

50 Weidman WH, Blount SG, DuShane JW, et al. Clinical course in ventricular septal defect. *Circulation* 1977;**56**(1 Suppl.):I56–69.

51 Corone P, Dovon F, Gaudeau S, et al. Natural history of ventricular septal defect. A study involving 790 cases. *Circulation* 1977;**55**:908–915.

52 Keane JF, Fyler DC. Ventricular septal defect. In: Keane JF, Lock JE, Fyler DC (eds.) *Nadas' Pediatric Cardiology*, 2nd edn. Philadelphia, PA: Saunders Elsevier, 2006, pp. 527–547.

53 Simpson WF, Jr., Sade RM, Crawford FA, et al. Double-chambered right ventricle. *Ann Thorac Surg* 1987;**44**:7–10.

54 Moran AM, Hornberger LK, Jonas RA, Keane JF. Development of a double-chambered right ventricle after repair of tetralogy of Fallot. *J Am Coll Cardiol* 1998;**31**:1227–1233.

55 Cabrera A, Martinex P, Rumoroso JR, et al. Double-chambered right ventricle. *Eur Heart J* 1995;**16**:682–686.

56 Valdes-Cruz LM, Cayre RO. Anomalies of the right ventricular outflow tract and pulmonary arteries. In: Valdes-Cruz LM, Cayre RO (eds.) *Echocardiographic Diagnosis of Congenital Heart Disease. An Embryologic and Anatomic Approach*. Philadelphia, PA: Lippincott-Raven, 1999, pp. 325–348.

57 Wong PC, Sanders SP, Jonas RA, et al. Pulmonary valve-moderator band distance and association with development of double-chambered right ventricle. *Am J Cardiol* 1991;**68**:1681–1686.

58 Hartman AF, Jr., Goldring D, Carlsson E. Development of right ventricular obstruction by aberrant muscle bands. *Circulation* 1964;**30**:679–685.

59 Lintermans JP, Roberts DB, Gunteroth WG, Figley MM. Two-chambered right ventricle without outflow obstruction in ventricular septal defect. *Am J Cardiol* 1968;**21**:582–587.

60 Rowland TW, Rosenthal A, Castaneda AR. Double-chamber right ventricle: experience with 17 cases. *Am Heart J* 1975;**89**:455–462.

61 Pongiglione G, Freedom RM, Cook D, Rowe RD. Mechanism of acquired right ventricular outflow tract obstruction in patients with ventricular septal defect: an angiocardiographic study. *Am J Cardiol* 1982;**50**:776–780.

62 Alva C, Ho SY, Lincoln CR, et al. The nature of the obstructive muscular bundles in double-chambered right ventricle. *J Thorac Cardiovasc Surg* 1999;**117**:1180–1189.

63 Eltohami EA, Hajar HA, Folger GM. Double-chambered right ventricle and Down's syndrome: a proposed new association. *Angiology* 1994;**45**:119–123.

64 Ozkutlu S, Cil E, Pasaoglu I, Saraclar M. Noonan syndrome with double-chambered right ventricle. *Pediatr Cardiol* 1996;**17**:251–253.

65 Lougheed J, Sinclair BG, Fung Kee Fung K, et al. Acquired right ventricular outflow tract obstruction in the recipient twin in twin-twin transfusion syndrome. *J Am Coll Cardiol* 2001;**38**:1533–1538.

66 Oliver JM, Garrido A, Gonzalez A, et al. Rapid progression of mid-ventricular obstruction in adults with double-chambered right ventricle. *J Thorac Cardiovasc Surg* 2003;**126**:711–717.

67 Restivo A, Cameron AH, Anderson RH, Allwork SP. Divided right ventricle: a review of its anatomical varieties. *Pediatr Cardiol* 1984;**5**:197–204.

68 Yoo S-J, Kim YM, Bae EJ, et al. Rare variants of divided right ventricle with sequestered apical trabecular component. *Int J Cardiol* 1997;**60**:249–255.

69 Karczenski K. Double-chambered right ventricle. *Perspect Pediatr Pathol* 1988;**12**:115–127.

70 Freedom RM, Mawson J, Yoo S-J, Benson LN. The divided right ventricle; anomalous right ventricular muscle bundles and other entities. In: Freedom RM, Mawson J, Yoo S-J, Benson LN (eds.) *Congenital Heart Disease: Textbook of Angiocardiography*. Armonk, NY: Futura, 1997, pp. 389–407.

71 Vogel M, Smallhorn JF, Freedom RM, et al. An echocardiographic study of the association of ventricular septal defect and right ventricular muscle bundles with a fixed subaortic abnormality. *Am J Cardiol* 1988;**61**:857–860.

72 Hubail Z, Ramaciotti C. Spatial relationship of the VSD to the anomalous muscle bundle in double-chambered right ventricle. *Congenital Heart Dis* 2007;**2**:421–423.

73 Leandro J, Dyck JD, Smallhorn JF. Intra-utero diagnosis of anomalous right ventricular muscle bundle in association with a ventricular septal defect: a case report. *Pediatr Cardiol* 1994;**15**:46–48.

74 Marton T, Hajdu J, Papp Z. A rare case of non-immune hydrops fetalis: double-chambered right ventricle. A case report. *Fetal Diagn Ther* 2001;**16**:251–253.

75 Kveselis D, Rosenthal A, Ferguson P, et al. Long-term prognosis after repair of double-chamber right ventricle with ventricular septal defect. *Am J Cardiol* 1984;**54**:1292–1295.

76 Galal O, Halees Z, Solymar L, et al. Double-chambered right ventricle in 73 patients: spectrum of the disease and surgical results of transatrial repair. *Can J Cardiol* 2000;**16**:167–174.

77 Said SM, Burkhart HM, Dearani JA, et al. Outcomes of surgical repair of double-chambered right ventricle. *Ann Thorac Surg* 2012;**93**:197–200.

78 Telagh R, Alexi-Meskishivili V, Hetzer R, et al. Initial clinical manifestations and mid- and long-term results after surgical repair of double-chambered right ventricle in children and adults. *Cardiol Young* 2008;**18**:268–274.

79 Zucker N, Rozin I, Levitas A, Zalzstein E. Clinical presentation, natural history, and outcome of patients with the absent pulmonary valve syndrome. *Cardiol Young* 2004;**14**:402–408.
80 Volpe P, Paladini D, Maasini M, et al. Characteristics, associations and outcome of absent pulmonary valve syndrome in the fetus. *Ultrasound Obstet Gynecol* 2004;**24**:623–628.
81 Yeager SB, Van Der Velde ME, Waters BL, Sanders SP. Prenatal role of the ductus arteriosus in absent pulmonary valve syndrome. *Echocardiography* 2002;**19**:489–493.
82 Grotenhuis HB, Nijveld A, Backx A. Absent pulmonary valve syndrome with intact ventricular septum and patent ductus arteriosus: report of two cases and a short review of the literature. *Ann Thorac Surg* 2003;**75**:280–282.
83 Nørgaard MA, Alphonso N, Newcomb AE, et al. Absent pulmonary valve syndrome. Surgical and clinical outcomes with long-term follow-up. *Eur J Cardio-Thorac Surg* 2006;**29**:682–687.
84 Galindo A, Gutieree-Larray F, Martinez JM, et al. Prenatal diagnosis and outcome for fetuses with congenital absence of the pulmonary valve. *Ultrasound Obstet Gynecol* 2006;**28**:32–39.
85 Marek J, Skovranek J, Povysilova V. Congenital absence of aortic and pulmonary valve in a fetus with severe heart failure. *Heart* 1996;**75**:98–100.
86 Joshi AN, Rane HS, Kamble RC, et al. Prenatal diagnosis of absent pulmonary valve syndrome. Report of 2 cases, most common and most rare presentations. *J Ultrasound Med* 2010;**29**:823–829.
87 Trivedi KR, Benson LN. Peripheral pulmonary artery stenosis. In: Freedom RM, Yoo SJ, Mikailian H, Williams WG (eds.) *The Natural and Modified History of Congenital Heart Disease*, 1st edn. New York, NY: Blackstone Publishing, 2004, pp. 119–134.

CHAPTER 17

Pulmonary Atresia with Intact Ventricular Septum

Jami C. Levine
Boston Children's Hospital, Boston, MA, USA

Definition

Pulmonary atresia with intact ventricular septum (PA/IVS) is a relatively uncommon congenital heart disease characterized by luminal discontinuity between the right ventricular outflow tract and the main pulmonary artery in the absence of a ventricular septal defect.

Historical background

Peacock published the first case series of patients with PA/IVS in 1869 [1]. This included a historical review in which he credits John Hunter for the first description of this anomaly in 1783. Grant first described the associated coronary artery abnormalities in 1926 [2]. There were anecdotal case reports in the mid-1900s, including a series of 10 cases described by Maude Abbot in her seminal atlas of congenital heart disease [3]. Glaboff et al. published the first detailed description of PA/IVS with a dilated right ventricle (RV) in 1950 [4]. From 1955 through 1970, a number of reports described the anatomic features of PA/IVS [5–12]. The first attempts at surgical palliation were reported in the 1960s [6,8,13]. Initially, surgical therapy was technically successful but did not significantly improve outcome. Over the ensuing decades, the diagnostic evaluation has become more refined and the treatment plans more tailored to the anatomic variants, resulting in dramatically improved prognosis for infants with PA/IVS [14,15].

Incidence

In the New England Regional Infant Cardiac Program, 75 of 2251 infants (3.3%) had PA/IVS, and 85% of these were diagnosed in the first week of life [16]. Estimates of the incidence of PA/IVS vary from 1 in 8000 live births [17] to 1 in 144,000 live births [16]. Without treatment, 50% of infants die within 2 weeks, and 85% die by 6 months of age [7,17–20]. Death is typically due to complications of cyanosis secondary to insufficient pulmonary blood flow.

Etiology

Both genetic and environmental factors have been implicated in the etiology of PA/IVS, but little is known about specific contributing factors. It is likely that genetic factors, when important, are multifactorial. From empiric data, it appears that PA/IVS is not one of the more heritable forms of congenital heart disease [21] and is only occasionally associated with specific chromosomal anomalies. There are, however, anecdotal reports of pedigrees that include more than one family member with PA/IVS, including a few reports of affected siblings [22,23].

The role of environmental factors in the etiology of PA/IVS is also unknown. Evidence that environmental factors can directly influence the development of the right heart comes from a report by Baetz-Greenwalt et al. [24]. This paper described 14 infants with right heart hypoplasia, all diagnosed within a 2-year period in a small area of Ohio. Of this group, 79% had extracardiac anomalies, prompting speculation that an environmental exposure in the second month of pregnancy may have produced a new syndrome, which included abnormalities of right heart growth.

There are several theories about the morphogenesis of pulmonary valve atresia [9,25–27]. Most popular is the flow theory, which assumes that an anatomic abnormality early in development decreases blood flow through the right heart, resulting in diminished growth of right heart structures. The lack of growth leads to further decrease in flow through the right heart. Eventually, this cycle ends in acquired atresia of the pulmonary valve. Several structural defects have the potential to disrupt flow through the right ventricle, including primary abnormalities of the foramen ovale, Eustachian valve, tricuspid valve, and pulmonary valve. It is likely that the timing of valve atresia is important and that infants with the smallest right heart structures are the ones who experienced the earliest progression to

Echocardiography in Pediatric and Congenital Heart Disease: From Fetus to Adult, Second Edition. Edited by Wyman W. Lai, Luc L. Mertens, Meryl S. Cohen and Tal Geva.
© 2016 John Wiley & Sons, Ltd. Published 2016 by John Wiley & Sons, Ltd.
Companion website: www.lai-echo.com

atresia, whereas those with dilated right hearts may have had antegrade flow for a longer period, thus allowing for more in utero growth of the right heart. It is worth noting, however, that the cause and effect of diminished flow through the right heart and its etiologic association with PA/IVS have not been established.

Morphology

There is significant morphologic heterogeneity among patients with PA/IVS [7,9,11,14,25–32]. Initial anatomic studies suggested that patients could be divided into two relatively distinct groups depending on the size of their right heart structures [5,7–9,25–31]. Those with pulmonary atresia and hypoplasia of the RV were designated as type I, whereas those with pulmonary atresia and normal or enlarged right heart structures were designated as type II. Type I patients had small, abnormal tricuspid valves, severe right ventricular hypertrophy and coronary artery fistulae, whereas type II patients were more likely to have severe tricuspid regurgitation, a thin-walled and dilated right ventricle, and a massively enlarged right atrium, but no significant coronary artery fistulae. It is clear from more contemporary anatomic studies that there is a continuum with respect to right heart disease, yet the majority of patients tend to have features that grossly fit into one of these two subtypes.

Pulmonary atresia with RV hypoplasia

Right atrium

The vast majority of patients have a patent foramen ovale, although ~20% of patients have a secundum atrial septal defect (ASD) [9]. The right atrium and its associated caval connections may be dilated and the right atrial wall is hypertrophied, although this is probably dependent on the amount of tricuspid regurgitation, the size of the foramen ovale, and the length of time that the hemodynamic abnormalities were present.

Right ventricle and tricuspid valve

The size of the tricuspid valve correlates with the size of the right ventricle [25–27,30–33]. Studies suggest that 70–90% of patients with PA/IVS have hypoplasia of both tricuspid valve and right ventricle, with up to 60% of patients having severe right ventricular hypoplasia [14,26,28,30,33]. Hypoplasia typically involves all segments of the right ventricle, although some portions may be so underdeveloped as to be absent [34]. The right ventricular sinus (inlet) is often foreshortened (Figures 17.1 and 17.2). The moderator band and tricuspid valve papillary muscles may be poorly defined, although when present they can be severely hypertrophied. The infundibular portion is frequently hypoplastic, and in about 10–25% of patients it is atretic [31,32,34]. The ventricular endocardium is typically fibrotic and in some cases there may be diffuse endocardial fibroelastosis as well as myocardial fiber disarray [25,35–38].

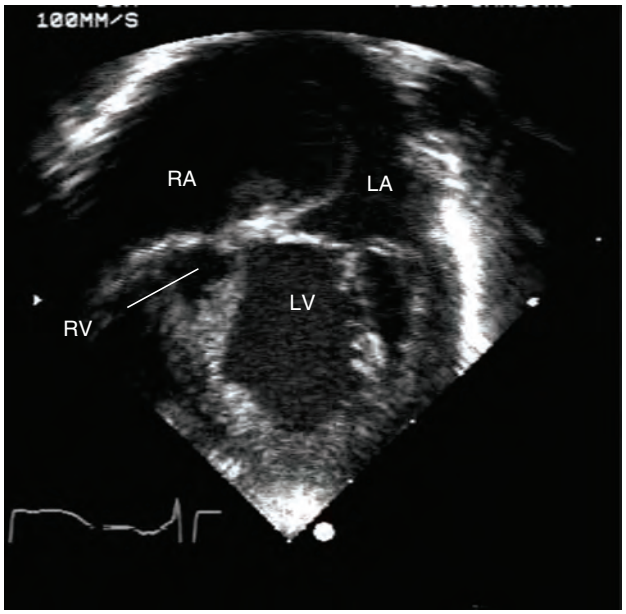


Figure 17.1 Severely hypoplastic right ventricle (RV) in pulmonary atresia with intact ventricular septum. Four-chamber view from the apical window demonstrates a diminutive right ventricular cavity and a hypoplastic tricuspid valve annulus. LA, left atrium; LV, left ventricle; RA, right atrium.

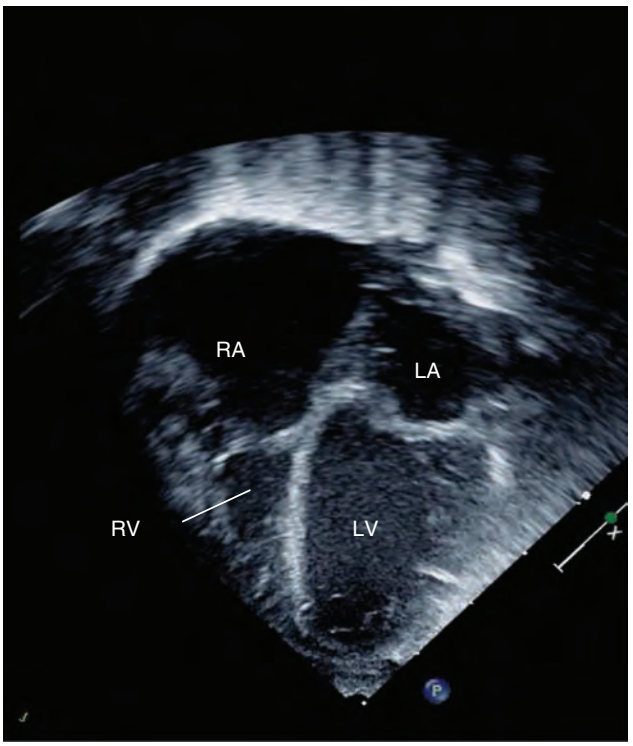


Figure 17.2 Moderately hypoplastic right ventricle in pulmonary atresia with intact ventricular septum seen from the apical 4-chamber view. Note the nearly normal-sized tricuspid valve annulus. The right ventricle is about two-thirds the length of the left ventricle. LA, left atrium; LV, left ventricle; RA, right atrium; RV, right ventricle.

Typically, the valve annulus is small and the leaflets and supporting apparatus are morphologically abnormal. The Congenital Heart Surgeons' Society (CHSS) multicenter study found that the tricuspid valve annulus diameter z-score is less than –2 in 50% of patients and less than –5 in 10% of patients [14]. In addition to annular hypoplasia, the leaflets are often thickened, especially at their edges, the chordae tendineae are short and the papillary muscles are small. These abnormalities often result in tethered leaflets with reduced mobility [6,7,9,15,25,32,39].

Coronary arteries

Abnormalities of the coronary arteries and the presence of right ventricular sinusoids are common in PA/IVS [14,25,27,32,40–43]. Right ventricular sinusoids are endothelial-lined channels within the myocardium that communicate with the cavity. These are remnants of the sinusoidal spaces that nourish the myocardium in early fetal life. When they persist in postnatal life, they can be a site of communication between the right ventricular cavity and the coronary arteries. These fistulous communications are found in as many as 50% of patients with small, hypertensive right ventricles and may provide the only source of egress of blood from the RV [14,28,40–45]. Their prevalence increases with increased right ventricular pressure and correlates inversely with the size of the tricuspid valve and right ventricular cavity.

The epicardial coronary arteries may also be abnormal, exhibiting intimal proliferation, nodularity or endarteritis [28,37,45,46]. Stenotic lesions within the coronary arteries or atresia of the coronary artery ostium at the aortic root can be present. These types of severe coronary abnormalities are more common in those with muscular atresia of the infundibulum [47]. Severe coronary artery stenoses and/or ostial atresia disrupt the flow of oxygenated blood from the aortic root to the myocardium. The myocardium that does not receive antegrade flow from the epicardial coronary arteries may be perfused entirely with blood from the right ventricle through persistent fistulous communications [42,43,48]. This condition is known as a right ventricular-dependent coronary circulation (Figures 17.3 and 17.4; Video 17.1) and is present in 10–20% of patients with PA/IVS [14,31,40,42,45,49–51].

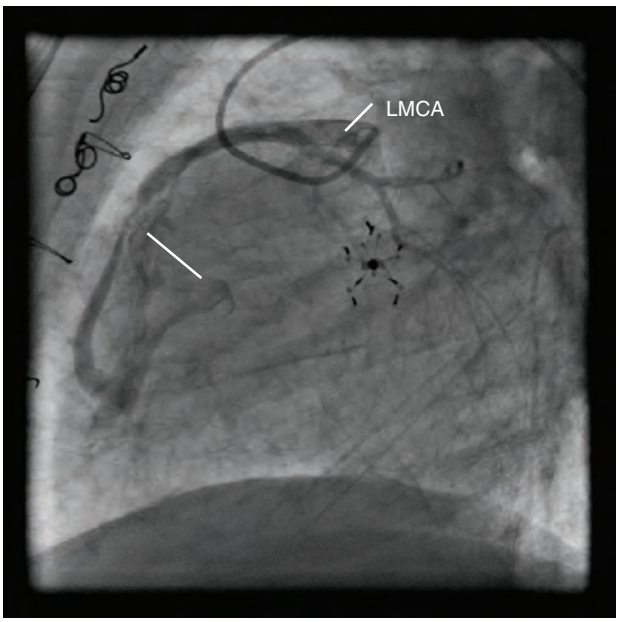


Figure 17.3 Coronary fistula in right ventricular-dependent coronary circulation. Angiography is done in the aortic root. The left coronary can be seen proximally and the stenosis is seen in the mid portion of the left anterior descending. The aneurysm is not obvious at this stage of the cardiac cycle. LMCA, left main coronary artery.

Pulmonary valve and arteries

By definition, there is luminal discontinuity between the right ventricle and the main pulmonary artery. In almost all cases the pulmonary valve is atretic. Approximately 70–80% of the patients have a small but patent infundibulum and membranous atresia of the valve, often with recognizable pulmonary valve tissue and definable commissures [20,25,27] (Figures 17.5 and 17.6; Video 17.2). The remainder have muscular infundibular atresia with or without overlying fibrous valve tissue [14,18] (Figure 17.7; Video 17.3). Rarely, the infundibulum is atretic and the pulmonary valve is patent [52]. The atretic pulmonary valve annulus diameter may be normal or mildly hypoplastic. The main and branch pulmonary arteries are usually normal in size [9,18]. In the CHSS database, only 6% of patients had significant pulmonary artery hypoplasia [14]. Rarely, the main pulmonary artery is absent. An absent main pulmonary artery is much more likely if there is muscular atresia of the right ventricular infundibulum [47]. Pulmonary blood flow is almost always through a patent ductus arteriosus [45,46].

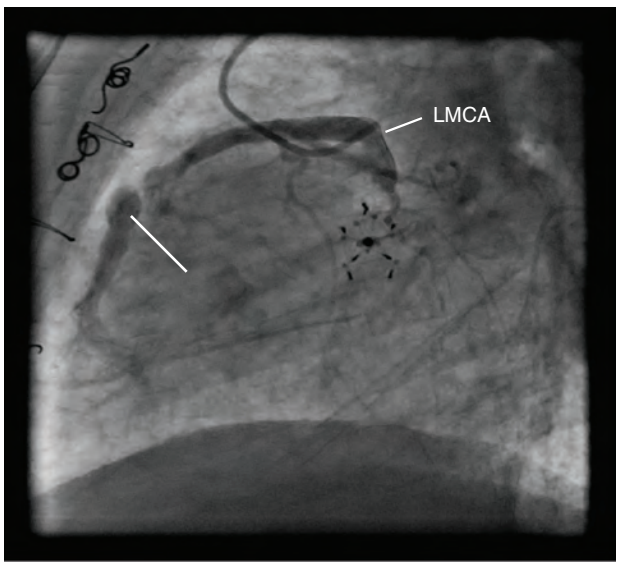


Figure 17.4 Coronary fistula in right ventricular-dependent coronary circulation. This image is identical to that in Fig. 17.3, but depicts a different phase of the cardiac cycle. Now the aneurysm of the coronary artery is easily visualized just distal to the stenotic area. LMCA, left main coronary artery.

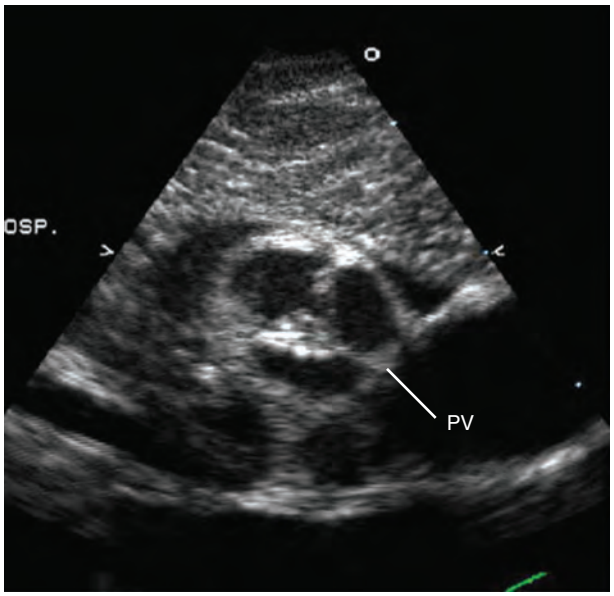


Figure 17.5 Pulmonary valve morphology in pulmonary atresia with intact ventricular septum. This en face image is taken from the high left parasternal window with the marker pointing straight left. The main pulmonary artery sinuses appear essentially normal. The commissures are well delineated, but thickened. This morphology is often seen in patients with membranous pulmonary valve atresia. PV, pulmonary valve.

Pulmonary atresia with RV dilation

The right ventricle is dilated in ~5–10% of patients with PA/IVS [14,28,31,32]. Right ventricular enlargement may be mild, but patients in this group can have massive cardiac enlargement due to severe right atrial dilatation.

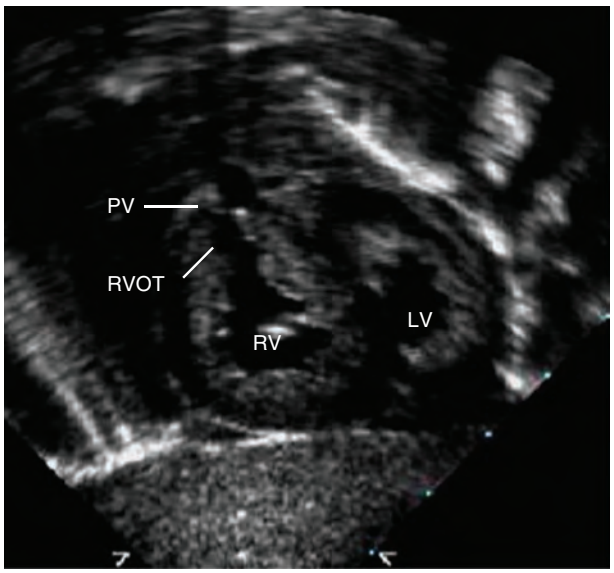


Figure 17.6 Right ventricular outflow tract (RVOT) in membranous pulmonary atresia seen from the subcostal short-axis view of the outflow tract. Note the small but well-formed right ventricular outflow with a good-sized pulmonary valve (PV) annulus. LV, left ventricle; RV, right ventricle.

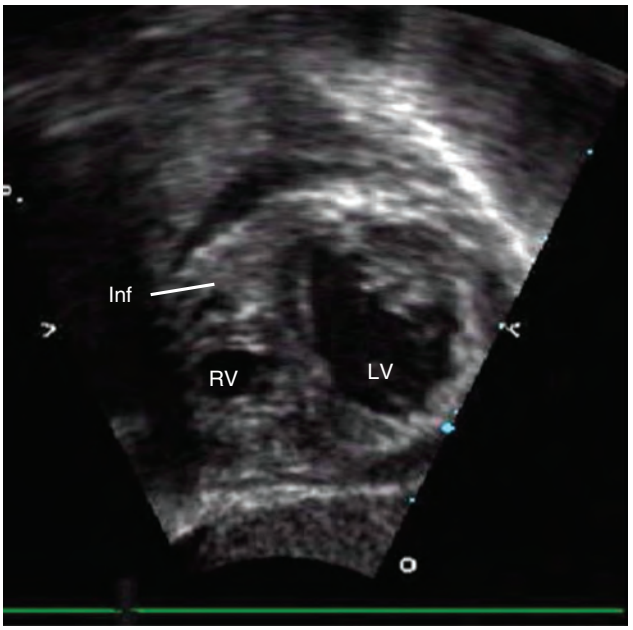


Figure 17.7 Right ventricular outflow tract in muscular pulmonary atresia. This subcostal short-axis view demonstrates a short right ventricular outflow tract with no obvious infundibular cavity. Instead there is muscular obliteration of the outlet and no identifiable pulmonary annulus. Inf, infundibulum; LV, left ventricle; RV, right ventricle.

Right atrium

In contrast to the patients with right ventricular hypoplasia, patients in this group typically have severe tricuspid regurgitation. The right atrium is often severely dilated and there may be associated dilation of the venae cavae. The patent foramen ovale is often stretched with right-to-left atrial-level shunt.

Right ventricle and tricuspid valve

The tricuspid valve annulus and right ventricle are both larger than normal. In many, the right heart becomes so dilated that it compresses the left heart, compromising cardiac output (Figure 17.8). The heart may have a "wall-to-wall" appearance on chest radiography, similar to severe Ebstein anomaly (Figure 17.9). In some of these patients, Ebstein anomaly coexists, with significant apical displacement of the septal leaflet, leading to poor coaptation and severe tricuspid regurgitation [29,32,34,53,54]. In others, the tricuspid valve is hinged normally at the annulus but the leaflets are redundant, dysplastic and sail-like. Because of the tricuspid regurgitation, the right ventricle is unlikely to be hypertensive and endocardial fibroelastosis is uncommon. The right ventricle tends to be thin-walled and dilated. Uhl anomaly of the right ventricle is uncommon, but has been reported [55]. Patients with a dilated right ventricle typically have membranous atresia of the pulmonary valve, although rarely they may have an associated muscular atresia of the infundibulum.

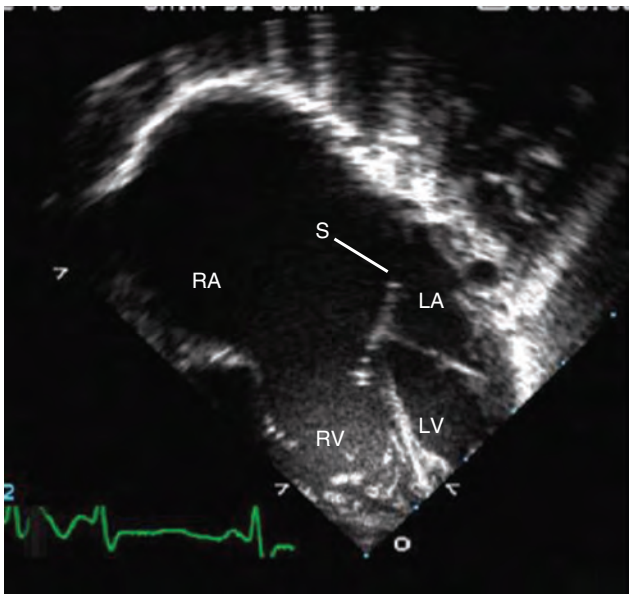


Figure 17.8 Severely dilated right ventricle (RV) and right atrium (RA) in pulmonary atresia with intact ventricular septum seen from the apical window. The tricuspid valve annulus is severely dilated and the tricuspid valve leaflets are elongated. The RV is significantly larger than the left ventricle (LV). The RA is severely dilated and the atrial septum deviates leftward, making the left atrium (S) appear much smaller than usual. LA, left atrium.

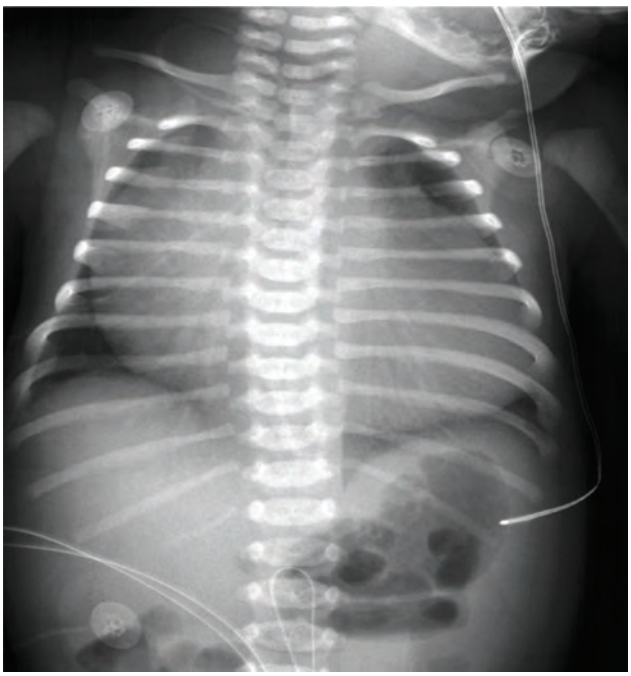


Figure 17.9 Chest radiograph in newborn with severe right heart dilation and pulmonary atresia with intact ventricular septum. Note that the borders of the cardiac silhouette extend from the right chest wall to the left chest wall.

Coronary arteries

Because the right ventricle in this group of patients decompresses during systole through tricuspid regurgitation, significant right ventricular hypertension is uncommon and anomalies of the coronary arteries are rare.

Pulmonary valve and arteries

Similar to the right ventricular hypoplasia group, the pulmonary valve annulus, main pulmonary artery and branch pulmonary arteries are likely to be normal in size or mildly undersized. It is unusual for them to be diminutive, discontinuous or absent.

Associated structural heart disease

Normal cardiac position and segmental anatomy are present in ~98% of patients with PA/IVS. There have been reports of associated morphologic abnormalities of the left heart, but hemodynamically significant left heart disease is rare [31,56,57].

Pathophysiology

Preoperative

Before birth, PA/IVS with severe tricuspid regurgitation and massive dilation of the right heart can result in low cardiac output, hydrops, and intrauterine death. Fetuses with PA/IVS and normal-sized or hypoplastic right ventricles usually survive pregnancy.

After birth, the systemic venous return crosses the atrial septum through the foramen ovale and mixes with the pulmonary venous return in the left atrium, which results in cyanosis. The ductus arteriosus remains the only source of pulmonary blood flow, and survival depends on maintaining ductal patency.

The systolic pressure in the right ventricle depends on the pathways available for blood to exit the chamber. In the presence of a competent tricuspid valve the systolic pressure is usually very high, whereas in those with severe tricuspid regurgitation the pressure may be normal or only mildly elevated. In the postnatal circulation, coronary artery abnormalities can become important in a number of ways. In those with right ventricular-dependent coronary artery circulation, oxygen delivery to the myocardium depends on the perfusion pressure and oxygen content in the right ventricle. If either of these falls significantly, myocardial ischemia can result. With or without right ventricle-dependent coronary circulation, increased intracavitary pressure may lead to chronic subendocardial ischemia. Finally, the presence of right ventricle-to-coronary artery communications can allow for a right-sided circular shunt [46]. Blood can go from RV to coronary artery to coronary vein to coronary sinus to right atrium to right ventricle without passing through the systemic capillary bed. Any or all of these factors can cause chronic and/or intermittent ischemia, which can adversely affect both systolic and diastolic myocardial properties [56,58–61].

Postoperative

Postoperative physiology varies greatly depending on the operation performed. The most dramatic changes are those occurring after decompression of the right ventricle. As right ventricular pressure falls, myocardium that was perfused through sinusoids may experience at least a transient decrease in blood flow, leading to myocardial ischemia. The degree of ischemia depends on the extent to which blood from the aortic root can reach those myocardial segments through the epicardial coronary arteries. If there are significant coronary artery stenoses, the myocardial segments distal to those stenoses may become profoundly ischemic and severe ventricular dysfunction may ensue [49,50]. Even without coronary stenoses, if there are large coronary-cameral fistulae, then these may cause "steal" of blood flow from the coronary arteries as right ventricular pressure falls [58,59]. Ventricular dysfunction can be transient, although for some patients it is profound and irreversible.

Treatment

Prenatal

Accurate early diagnosis offers parents the option to consider fetal therapy. Evidence from prenatal studies indicates that early atresia of the pulmonary valve can be associated with an arrest of right heart growth in utero [63]. This observation has led to speculation that in utero restoration of antegrade pulmonary blood flow may stimulate growth of the right ventricle and tricuspid valve. Over the past decade, reports of successful in utero pulmonary valve dilation have been published [62,63]. Although in some cases growth of the right ventricle, tricuspid valve, and outflow tract has been observed after the intervention, this was not seen in other cases [63–66]. At present, selection criteria identifying fetuses likely to benefit from intrauterine intervention remains unknown. As the techniques used for in utero balloon valvuloplasty continue to improve and experience with this intervention accumulates, it is reasonable to expect that better information will become available concerning the risks, benefits and criteria for patient selection.

PA/IVS with RV hypoplasia

The goal of treatment is to achieve a biventricular circulation in as many infants as possible without compromising myocardial perfusion [14,67–89].

Patients with right ventricular-dependent coronary circulation are at risk for myocardial ischemia and death if the right ventricle is decompressed. Therefore, a single ventricle management strategy is pursued. The first step is to create a stable source of pulmonary blood flow by a systemic-to-pulmonary artery shunt. Eventually, palliation is achieved with a Fontan-type circulation in the first few years of life [14,90,91]. Without establishment of antegrade pulmonary blood flow, there is no growth of the right ventricle and it usually remains hypoplastic and hypertensive. There is a paucity of long-term outcome data in these patients, but follow-up of patients up to 10 years after surgery suggests that the overall survival in patients with PA/IVS and a single ventricle circulation is ~80% [90,91].

For the majority of infants, coronary flow is not dependent on the right ventricle and a biventricular repair can be considered. The first step is creation of antegrade pulmonary blood flow. This can be achieved by placement of a right ventricular outflow tract patch, surgical valvotomy, or by transcatheter perforation and balloon dilation of the valve [67,83,88,89,92,93]. The hope is that restoring antegrade pulmonary blood flow can stimulate right heart growth, ultimately giving the patient a right ventricle that can carry a full cardiac output.

If antegrade flow is established and significant cyanosis persists, an alternate source of pulmonary blood flow may be needed. This is most commonly achieved by placement of a Blalock–Taussig shunt or stenting of the ductus arteriosus [88,94–96]. Once stable pulmonary blood flow is established, patients are followed with noninvasive imaging to assess tricuspid valve and right ventricular growth. If the right ventricle grows sufficiently, then an attempt is made to occlude or ligate any accessory sources of pulmonary blood flow and close any existing atrial level shunts, either surgically or with an implantable occlusion device.

In many case series, there is a subset of patients who thrive after a right ventricular outflow tract procedure and a shunt, yet fail attempts to remove accessory sources of pulmonary blood flow from the circulation and close the atrial communication(s). In some of these patients a strategy has been pursued in which the atrial communication is closed and a bidirectional Glenn shunt is performed (called 1.5-ventricle repair). This allows inferior vena caval flow to be carried by the right ventricle while flow from the superior vena cava is delivered directly to the pulmonary vascular bed [97–99].

PA/IVS with RV dilation

Management of patients with PA/IVS and massive right ventricular dilation is challenging. This group has higher rates of in utero demise, newborn morbidity, and postoperative mortality. There have been some successful attempts at creating a biventricular circulation by performing tricuspid valvuloplasty in addition to placement of a right ventricular outflow tract patch. In some cases, this may be done in association with a surgical reduction in the size of the RV and/or right atrium. Rarely, pulmonary valvotomy or a right ventricular outflow tract patch alone is sufficient.

Imaging

PA/IVS was first diagnosed by M-mode echocardiography in the late 1970s [100,101]. By the mid-1980s, two-dimensional (2D) echocardiography had supplanted M-mode, increasing the available anatomic detail [102,103]. With the addition of color and spectral Doppler technology, noninvasive evaluation has

become more detailed and increasingly important for diagnosis and assessment of prognosis.

Prenatal assessment

Increasingly, the diagnosis of PA/IVS is being made in utero. Echocardiographic details are used to assess candidacy for fetal balloon valvuloplasty and can also be important tools for judging overall prognosis [104–115]. Because this lesion frequently causes a change in chamber size, it is relatively easy to identify on an obstetrical screening exam. Unfortunately, right ventricular hypoplasia may not be obvious early in the second trimester, and screening ultrasound at 14–18 weeks of gestation may only identify the most severe cases. Early diagnosis can be made more often if color Doppler is used to evaluate tricuspid valve function, flow through the right ventricular outflow tract and pulmonary valve, and the direction of ductal flow.

Fetal evaluation includes detailed assessment of the right heart structures, including tricuspid valve size and function; right ventricular morphology, size and function; presence of coronary artery fistulae; morphology of the right ventricular outflow tract and the pulmonary arteries. Evaluation of the tricuspid valve includes measurements of the annulus diameter in the 4-chamber and long-axis planes and depiction of the valvar and subvalvar apparatus anatomy (Figures 17.10–17.12; Videos 17.4 and 17.5). Color Doppler is used to assess valve inflow and regurgitation (Video 17.6). Spectral Doppler is used to assess the

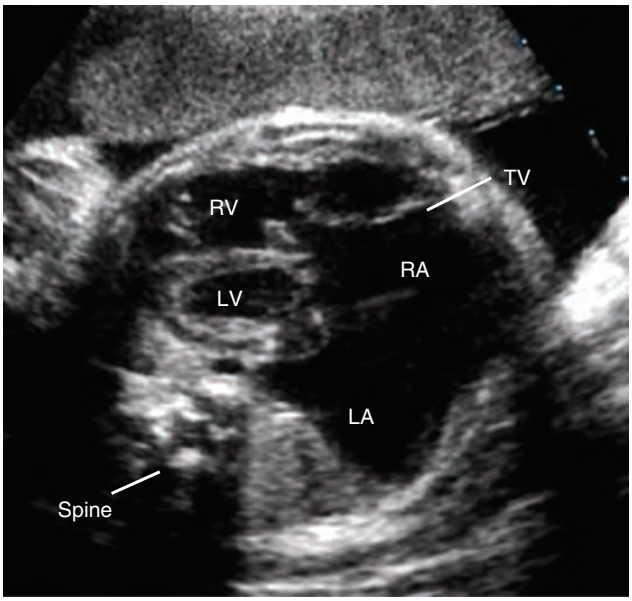


Figure 17.11 Fetal heart in pulmonary atresia with intact ventricular septum and right ventricular dilation. The image illustrates that the heart spans the entire width of the chest. It also extends posteriorly, although one can see small amounts of lung tissue behind the left atrium and left ventricle. The tricuspid valve annulus is dilated and the leaflets are redundant. LA, left atrium; LV, left ventricle; RA, right atrium; RV, right ventricle; TV, tricuspid valve.

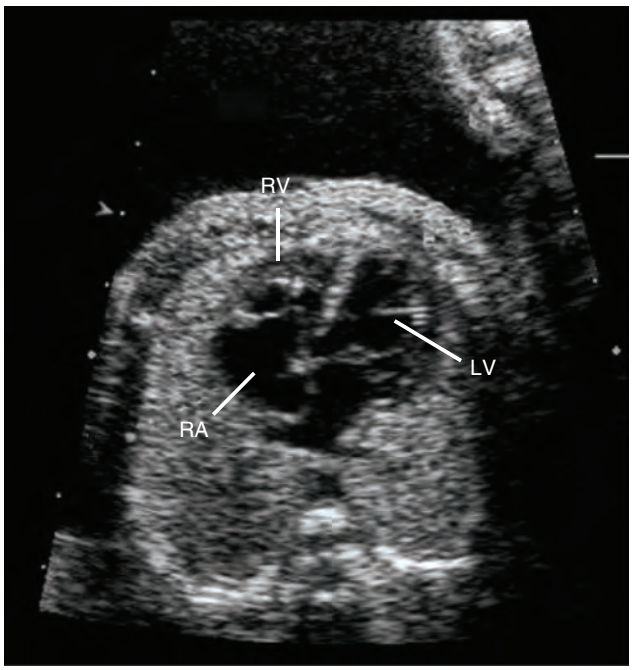


Figure 17.10 Fetal heart in pulmonary atresia with intact ventricular septum and right ventricular hypoplasia. Note that the right ventricular cavity is markedly hypoplastic and the right ventricular apex does not reach the left ventricular apex. The tricuspid valve annulus diameter is roughly half that of the mitral valve and the atrial septum deviates into the left atrium. LV, left ventricle; RA, right atrium; RV, right ventricle.

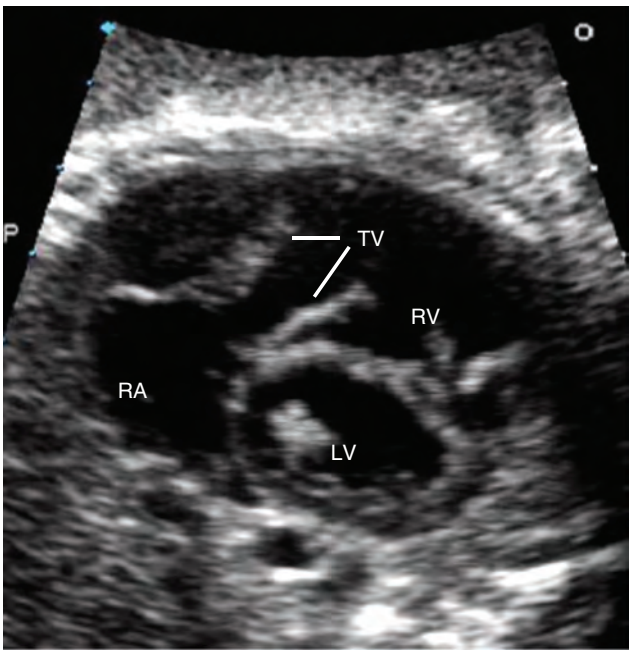


Figure 17.12 Tricuspid valve in fetus with pulmonary atresia and intact ventricular septum. This coronal view shows massive dilation of the right ventricle as well as the redundant, sail-like tricuspid valve leaflets. LV, left ventricle; RA, right atrium; RV, right ventricle; TV, tricuspid valve leaflet.

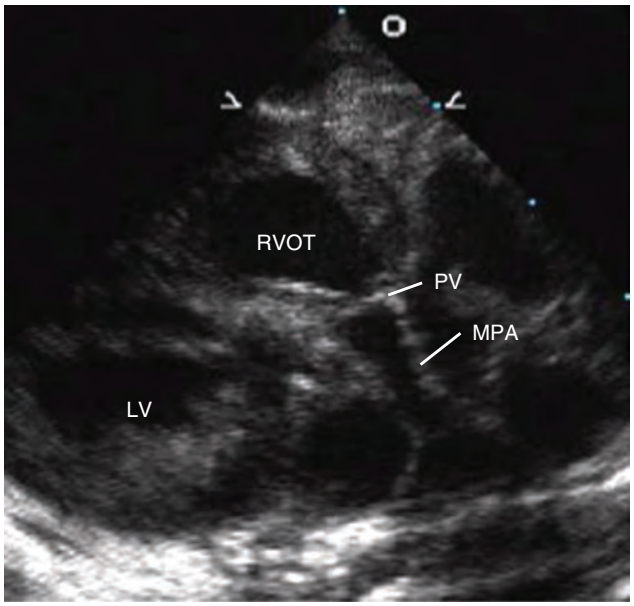


Figure 17.13 Right ventricular outflow tract evaluation in a fetus with membranous pulmonary atresia. This long-axis view of the right ventricular outflow tract demonstrates a patent infundibulum, an atretic pulmonary valve, and a good-sized main pulmonary artery. LV, left ventricle; MPA, main pulmonary artery; PV, pulmonary valve; RVOT, right ventricular outflow tract.

inflow pattern and to estimate right ventricular systolic pressure when a regurgitation jet is present. The right ventricle should be evaluated in all views with attention to length, degree of hypertrophy and degree of systolic dysfunction. Color Doppler is used to screen for coronary artery fistulae. Magnifying the right ventricle and interrogating the cavity and myocardium by color Doppler with a low Nyquist limit allows visualization of coronary artery fistulae in some fetuses. Fistulae are seen as streams of color signals within the myocardium and jets into the cavity during diastole (Video 17.7). The right ventricular outflow tract and main pulmonary artery are imaged to evaluate pulmonary annulus size and outflow tract patency (Figure 17.13). Color Doppler is used to determine presence or absence of flow across the pulmonary valve. In the presence of flow from the aorta to the pulmonary artery through the ductus arteriosus, the pulmonary valve may not open even when it is not anatomically atretic (functional atresia). In this case, detection of pulmonary regurgitation excludes pulmonary valve atresia. The main and branch pulmonary artery anatomy and size are documented. The ductus arteriosus is evaluated with 2D imaging and color Doppler. In PA/IVS, flow is from the aorta to the pulmonary arteries, the reverse of normal flow direction (Video 17.8). The atrial septum is evaluated to document unrestrictive right-to-left flow at the atrial level. As with all fetuses, the echocardiogram includes an evaluation of left heart anatomy and function as well as Doppler evaluation of the umbilical vessel, ductus venosus, and inferior vena cava. The flow profile in the umbilical vessels and hepatic veins can be markedly

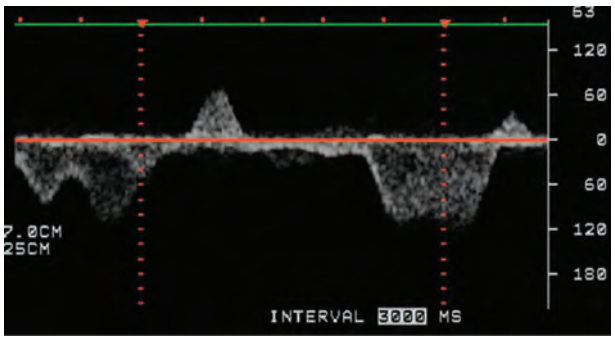


Figure 17.14 Spectral Doppler in the hepatic veins in a fetus with pulmonary atresia and intact ventricular septum. Flow below the baseline is toward the heart and flow above the baseline is away from the heart. This tracing shows a prolonged period of no flow in the hepatic veins as well as a short period of retrograde flow (away from the heart). Typically, hepatic venous flow is toward the heart, occasionally with very short periods of no flow. This tracing is consistent with severe tricuspid regurgitation.

abnormal in the presence of significant tricuspid regurgitation (Figure 17.14).

Studies in fetuses with PA/IVS show that a smaller tricuspid valve diameter and right ventricular size are predictive of worse hypoplasia of the right heart at birth, and are associated with a lower likelihood of achieving a biventricular outcome [109–112]. Sequential prenatal echocardiograms are important in that they add potentially valuable prognostic information about growth velocity of the tricuspid valve and right ventricle, as well as progression of tricuspid regurgitation [109]. Although no studies have documented that prenatal diagnosis of PA/IVS leads to improved postnatal outcome, some studies of other duct-dependent congenital heart disease have suggested decreased morbidity and neurologic sequelae in prenatally diagnosed patients [116–118].

Preoperative imaging

Similar to the prenatal evaluation, the postnatal echocardiogram includes a comprehensive anatomic survey with particular attention to the right-sided structures. Every effort should be made to optimize conditions for high-quality imaging, including adjustment of lighting, use of high-frequency transducers, and minimization of patient movements.

Key elements

In all cases, complete anatomic and functional examination by 2D and 3D imaging, as appropriate, and by color and spectral Doppler. In addition, the following elements of cardiovascular anatomy and function should be evaluated in detail and be given priority.

Preoperative examination:

- Imaging of the atrial septum with documentation of flow direction by color Doppler and velocity by spectral Doppler. If restrictive, measure mean gradient.
- Measurements of tricuspid valve annulus diameters in the apical 4-chamber and parasternal long-axis views.

- Evaluation of tricuspid valve morphology by 2D and 3D imaging, including leaflets, chordae tendineae, and papillary muscles. Note leaflet thickness and motion, tethering, and displacement.
- Evaluation of tricuspid valve stenosis and regurgitation by color and spectral Doppler. If tricuspid regurgitation is present, document peak velocity for assessment of right ventricular systolic pressure along with contemporaneous systemic blood pressure.
- Image the RV with particular attention to chamber size, thickness, and myocardial architecture (e.g., excessive muscle bundles). Note the morphology of the sinus (inflow) and infundibular (outflow) portions of the ventricle.
- Assessment of right ventricular function.
- Evaluation of the RV outflow tract. Note muscular versus membranous atresia.
- When present, measure pulmonary valve annulus diameter.
- Measurements of main and branch pulmonary arteries diameters.
- Evaluation of the ductus arteriosus with documentation of smallest size and direction of flow.
- Imaging of the origins and flow in the proximal coronary arteries. Document flow from the aortic root into the proximal left and right coronary arteries.
- Evaluation of right ventricle-to-coronary artery fistulae by color and, when feasible, spectral Doppler.
- Evaluation of global and regional left ventricular function. Note any regional wall motion abnormalities.
- Evaluation of associated cardiovascular anomalies.

The ability of the right ventricle to fill and, therefore, to grow depends on the size of the tricuspid valve and on the size and compliance of the inflow portion. Numerous studies have demonstrated that tricuspid valve annulus diameter predicts outcome after catheter-based or surgical treatment of PA/IVS [14,110–112,119–122]. Therefore, it is of utmost importance to obtain clear images of the tricuspid valve and its supporting apparatus and to measure the annulus diameters in orthogonal views. The apical 4-chamber view depicts the lateral diameter (Figures 17.1 and 17.2) and the parasternal long-axis angled towards the right hip shows the anterior–posterior diameter (Figure 17.15). An annulus diameter z-score of less than –3 is associated with a lower likelihood of tolerating right ventricular decompression as the sole intervention [14]. The subvalvar apparatus can be difficult to image due to right ventricular hypertrophy (Figure 17.16). It is often best seen in the short-axis sweeps from the parasternal and the subcostal acoustic windows. Three-dimensional imaging of the subvalvar apparatus can help clarify the anatomy in some patients. Color and spectral Doppler are used to assess inflow and regurgitation (Figure 17.17; Video 17.9).

The right ventricular inflow is best imaged in the 4-chamber and subcostal long-axis views (Figures 17.1 and 17.2), allowing measurements of chamber length. The outflow portion of the right ventricle is visualized from the subcostal short-axis

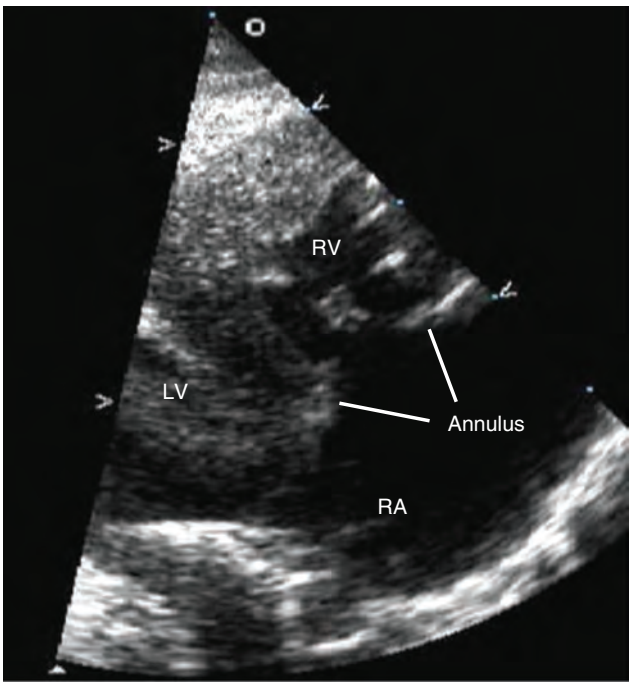


Figure 17.15 Parasternal long-axis view of the tricuspid valve and right ventricular inflow. The transducer is angled toward the right. This is a standard view for measuring the tricuspid valve annulus (in addition to the 4-chamber view). The hinge points of the tricuspid valve are noted. The valve annulus is measured at the hinge points of the leaflets, not at the functional orifice. LV, left ventricle; RA, right atrium; RV, right ventricle.

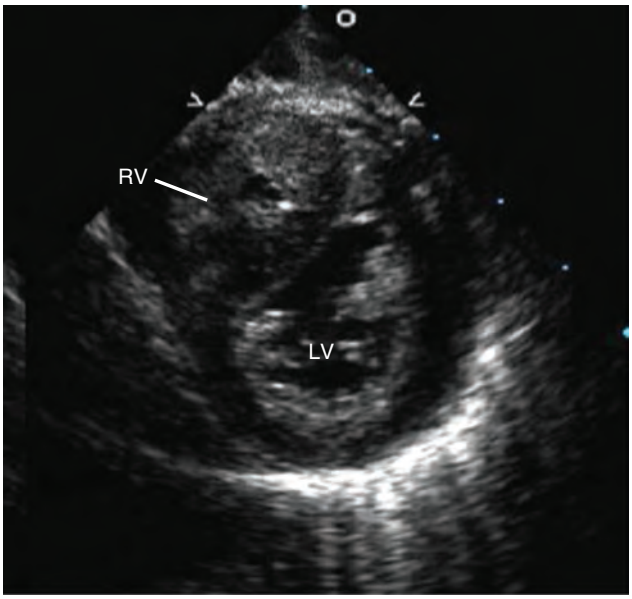


Figure 17.16 Parasternal short-axis imaging of the ventricles during systole at the level of the left ventricular papillary muscles. Note that only a small amount of right ventricular cavity is visualized at this level. There is severe hypertrophy of the right ventricular wall as well as septal bowing toward the left ventricle, consistent with suprasystemic right ventricular pressure. LV, left ventricle; RV, right ventricle.

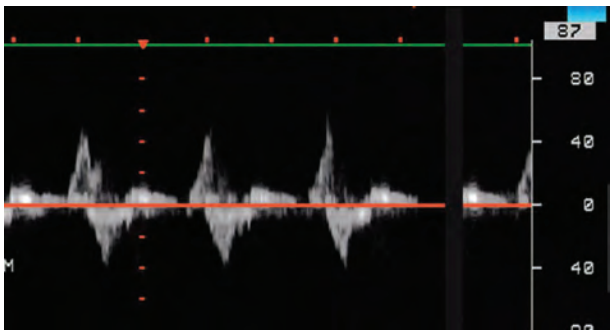


Figure 17.17 Doppler tracing of the tricuspid valve inflow recorded from the apical 4-chamber view in a patient with pulmonary atresia and intact ventricular septum. Note the very short period of low-velocity antegrade flow across the valve (above the baseline). The flow below the baseline will vary depending on the amount of tricuspid regurgitation.

view (Figures 17.6 and 17.7; Videos 17.2 and 17.3), from the parasternal long-axis view with the transducer angled toward the left shoulder and from the parasternal short-axis view with the transducer focused on the area anterior to the aortic root (Figure 17.18; Video 17.10). These views are excellent for evaluating the anatomy of the infundibulum and for color Doppler interrogation of the pulmonary valve. As with the prenatal echocardiogram, detection of a tiny antegrade jet through the pulmonary valve may be difficult to visualize in the presence of retrograde ductal flow into the main pulmonary artery. Therefore, detection of even the smallest jet of pulmonary regurgitation indicates that the pulmonary valve is not atretic.

The diameters of the pulmonary valve annulus and main and branch pulmonary arteries are measured from the parasternal images, although sometimes they are also clearly seen from a modified apical view with the transducer angled anteriorly. The pulmonary artery branches are best seen from a high parasternal short-axis view with the transducer placed just below the left

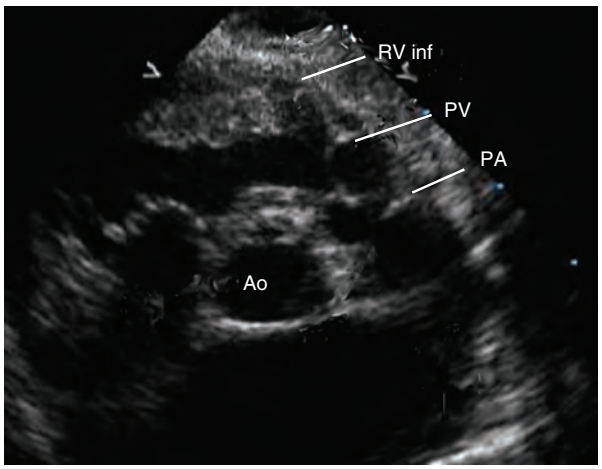


Figure 17.18 Parasternal short-axis image of the right ventricular outflow tract demonstrating a patent infundibulum. The pulmonary valve tissue is clearly seen but there is no functional orifice. The pulmonary valve annulus is well developed. Ao, aorta; PA, main pulmonary artery; PV, pulmonary valve; RV inf, right ventricular infundibulum.

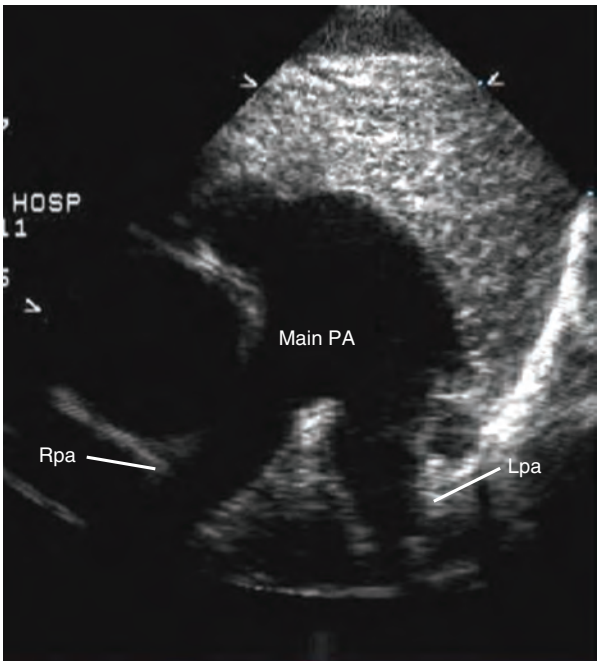


Figure 17.19 Branch pulmonary arteries in a patient with membranous pulmonary atresia. The image is from a high left parasternal imaging window with the marker oriented to the left. The main and branch pulmonary arteries are normal in size and appearance. Lpa, left pulmonary artery; Main PA, main pulmonary artery; Rpa, right pulmonary artery.

clavicle (Figures 17.19 and 17.20). The main pulmonary artery is evaluated in this view as well as from the parasternal long- or lower short-axis views.

The presence and size of an atrial-level shunt are evaluated from the subcostal long- and short-axis views (Figure 17.21;

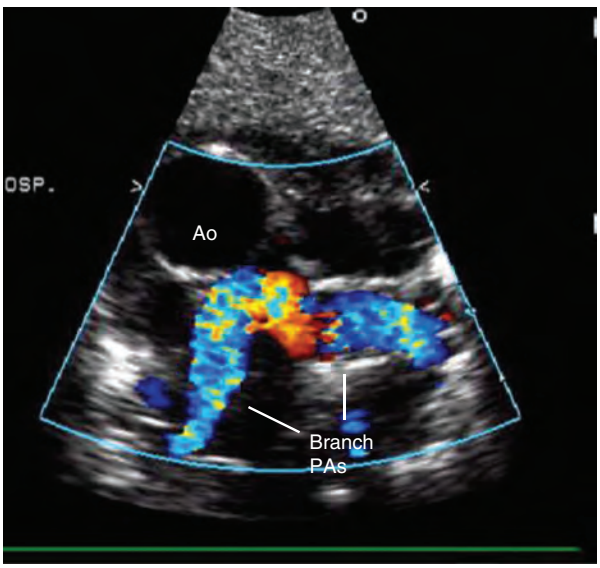


Figure 17.20 Branch pulmonary arteries in a patient with muscular pulmonary atresia. The image is from a high left parasternal imaging window with the marker oriented to the left. The pulmonary arteries are confluent and normally located, but no main pulmonary artery is present. Ao, aorta; PA, pulmonary artery.

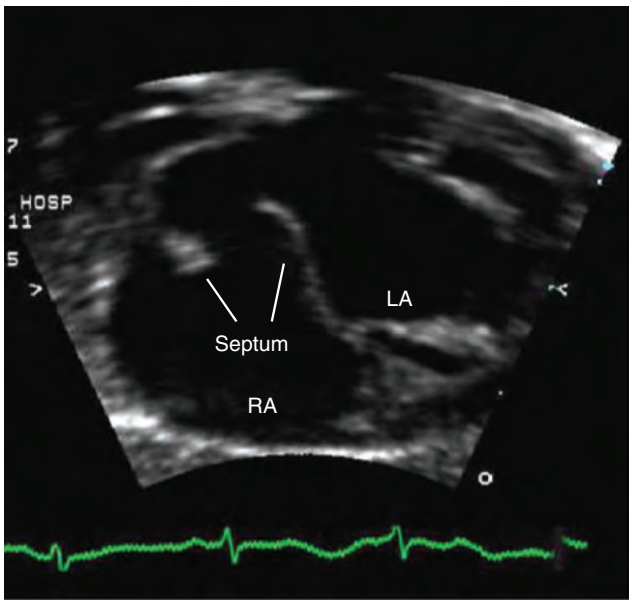


Figure 17.21 Patent foramen ovale in newborn with pulmonary atresia and intact ventricular septum imaged from the subcostal long-axis window. The image shows the widely sprung foramen ovale with the basal portion of the septum swung toward the left atrium. This appearance is typical in all forms of pulmonary atresia with intact ventricular septum. LA, left atrium; RA, right atrium.

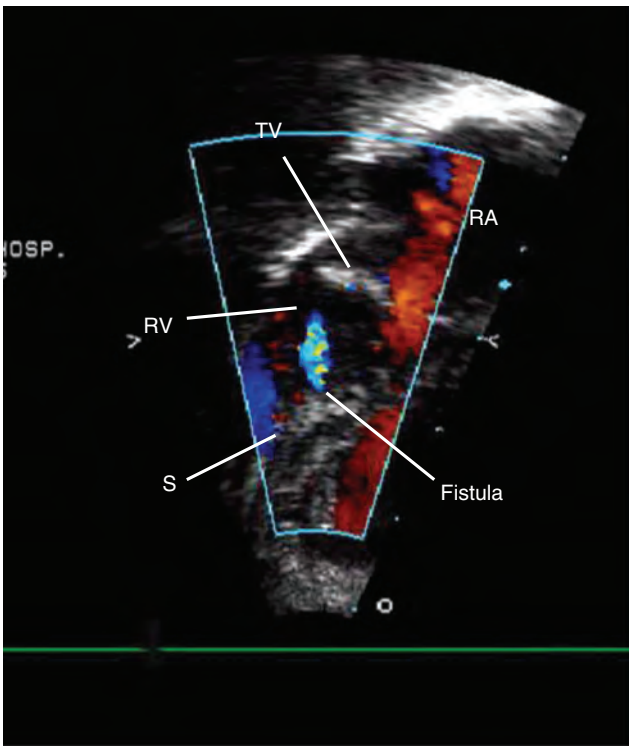


Figure 17.22 Fistula from the coronary artery to the right ventricle. This is a magnified image of the small right ventricle taken from the apical 4-chamber view. Note the prominent color jet in the middle of the right ventricle. This represents flow from an apical sinusoid into the right ventricle. RA, right atrium; RV, right ventricle; S, septum; TV, tricuspid valve.

Video 17.11). One expects to see predominantly right-to-left shunting at the atrial level. In the rare event of a restricted atrial shunt, it manifests as turbulent flow demonstrated by color and spectral Doppler of the right-to-left flow jet. The mean gradient is recorded.

The ductus arteriosus is imaged from a high left parasternal view. In most patients, the pulmonary arteries are supplied by a patent ductus arteriosus. Rarely aorto-pulmonary collateral vessels are present and a thorough evaluation of the mid-thoracic descending aorta to detect these vessels should be done. The mid-thoracic aorta can be imaged from the subcostal view, but parasternal windows can be used as well.

Detailed evaluation of the coronary arteries is particularly important in patients with PA/IVS. Right ventricular sinusoids and coronary artery fistulae are evaluated by color Doppler [123–125.]. The ventricular cavity and myocardium are interrogated by color Doppler with a low Nyquist limit from the 4-chamber, parasternal, and subcostal views (Figure 17.22; Videos 17.12–17.14). Coronary–cameral fistulae manifest as flow signal within the myocardium, communicating with the right ventricular cavity. The ostia and proximal segments of the left and right coronary arteries are evaluated from the parasternal short-axis view. The coronary artery origins are identified by 2D imaging and, importantly, flow from the root into the coronary arteries is then documented by color Doppler. Rarely, coronary ostial atresia can be present [47,126]. Although echocardiography can document the presence of coronary fistulae and/or sinusoids, cardiac catheterization and angiography remain the gold standard for the assessment of a right ventricular-dependent coronary circulation. Finally, detailed assessment of left ventricular size and function is important, with particular attention to the presence of any regional wall motion abnormalities.

For those with a dilated right ventricle, the echocardiogram proceeds in a similar fashion but with particular attention directed toward the anatomy and function of the tricuspid valve and the subvalvar apparatus (Video 17.15). Three-dimensional echocardiography can be helpful in evaluating the tricuspid valve in these patients.

Intraoperative imaging

The role of imaging in the operating room varies depending on the operation performed. In the setting of shunt placement, there is usually little need for imaging support, although some surgeons request an evaluation of ventricular function once shunt flow commences. In patients undergoing right ventricular decompression, imaging is useful for assessing both right and left ventricular function after the procedure. In addition, echocardiography can document patency of the right ventricular outflow tract. The RV and the outflow tract can be evaluated by



Figure 17.23 Transgastric view of the ventricles. The esophageal probe is in the stomach and anteflexed maximally to achieve this view. It should be possible to sweep from right to left and visualize most of the left ventricle. The anterior portion of the right ventricle is seen as well, but other segments may be difficult to image. LV, left ventricle; RV, right ventricle.

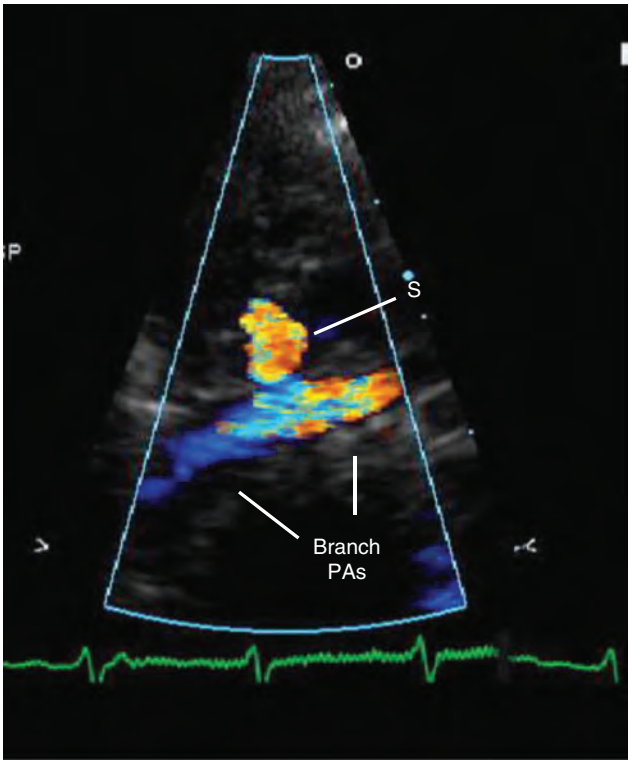


Figure 17.25 Blalock–Taussig shunt. Image of the distal end of a right Blalock–Taussig shunt taken from a high left parasternal view. The marker is pointed to the left and the transducer is angled slightly toward the right chest to find the distal end of the shunt. PA, pulmonary arteries; S, shunt.

epicardial imaging techniques, but transesophageal echocardiography (TEE) is often preferred because of the wider field of view and because it avoids interference with the surgical field. Ventricular function can be assessed by TEE from all views, but is often best demonstrated from transgastric views (Figure 17.23). In these views, the ventricles can be imaged in short-axis with a sweep from the base of the heart to the apex. Further assessment is done in the 4-chamber view with attention to both global function and regional wall motion abnormalities.

In patients with PA/IVS and dilated right ventricle, the first operation often involves right ventricular decompression, tricuspid valve plasty, and a procedure to decrease the size of the right heart chambers. In these patients, TEE can be used to assess tricuspid valve and right ventricular function in addition to left ventricular function. In general, the tricuspid valve is best imaged from the 4-chamber view (Video 17.16) and from short-axis views obtained from the mid-esophagus. This is done with the imaging plane at a 90–110° orientation with the probe turned toward the patient's right.

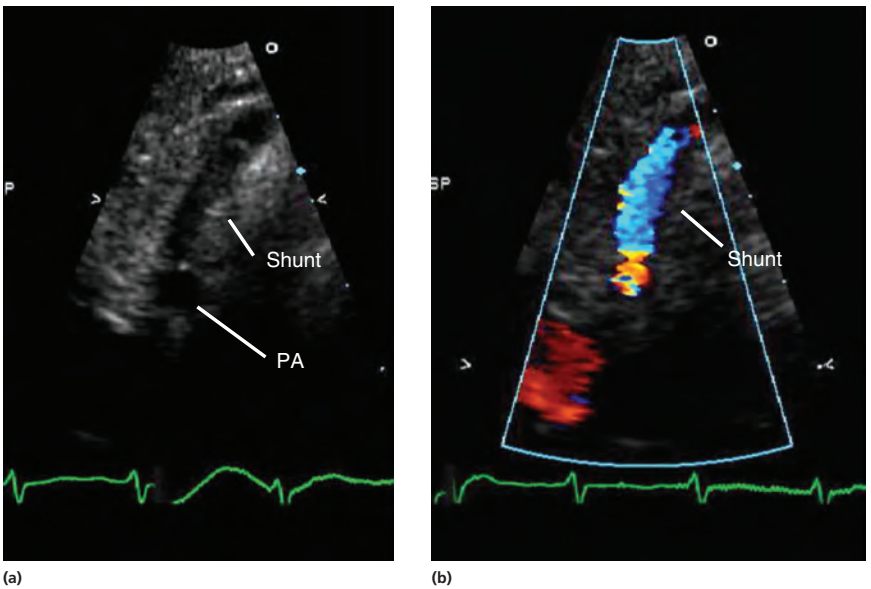
Postoperative imaging

Goals for follow-up echocardiography vary with the surgical strategy being pursued. In children with a systemic-to-pulmonary artery shunt, the shunt can be imaged from the high parasternal views (Figures 17.24a,b and 17.25). The shunt can also be imaged from the subcostal views. If shunt occlusion is suspected, the descending aorta is interrogated by Doppler for evidence of diastolic flow reversal due to runoff through the shunt (Figure 17.26). For those patients who have been palliated with stenting of the duct, the high left parasternal views of the duct and descending arch are used to document stent patency and direction of flow (Video 17.17).

Key elements

Postoperative examination after RV decompression procedure:

- Imaging of the atrial septum with documentation of flow direction by color Doppler and velocity by spectral Doppler. If restrictive, measure mean gradient.
- Measurements of tricuspid valve annulus diameters in the apical 4-chamber and parasternal long-axis views.
- Assessment of TV inflow by color and spectral Doppler. Document mean inflow gradient.
- Assessment of RV systolic pressure by TR jet velocity.
- If significant TR, assessment of mechanism; consider 3D imaging.
- Assessment of RV size, morphology, and function; consider 3D imaging.
- Evaluation of the right ventricular outflow tract for subvalvar stenosis using color and spectral Doppler.
- Rule-out aneurysm of the right ventricular outflow tract.
- Evaluation of pulmonary valve stenosis and/or regurgitation.
- Measurement of pulmonary valve annulus diameter.
- Measurements of main and branch pulmonary arteries diameters.



(a) (b)

Figure 17.24 Long-axis views of the Blalock–Taussig shunt. The transducer is positioned just to the left of the upper sternum with the marker oriented superiorly or slightly to the left. The examiner sweeps toward the right to get into the plane of the shunt. **(a)** The shunt with color Doppler. **(b)** The shunt by 2D imaging. The entire length of the shunt is visualized. These views are used to evaluate the shunt for thrombus or focal stenosis. PA, pulmonary artery.

- Measurements of left ventricular size and function. Note any regional wall motion abnormalities.
- If procedure was RV decompression with a shunt or stented ductus arteriosus to augment pulmonary blood flow, the following are assessed:
 - Evaluation of shunt/ductus by 2D, color, and spectral Doppler
 - Spectral Doppler in the descending aorta for diastolic run-off.

After a procedure to decompress the right ventricle, follow-up echocardiography is used to evaluate the right ventricular outflow tract and pulmonary valve for obstruction and regurgitation. Both color and spectral Doppler are used to assess blood flow across the outflow tract and pulmonary artery (Figure 17.27). It is important to note the degree and mechanism of obstruction to blood flow. Echocardiography is also important for assessing tricuspid valve size and function, right ventricular size and function, the direction of flow across the atrial septum, and global and regional left ventricular function [127]. Right ventricular systolic pressure is evaluated based on the tricuspid regurgitation jet velocity. In some patients, abnormalities of the right ventricular myocardial architecture persist despite adequate chamber growth (Figure 17.28). Similarly, persistent structural abnormalities of the tricuspid valve are common and may be the substrate for hemodynamically important stenosis and/or regurgitation. Diastolic flattening of the interventricular septum is a common finding and suggests right ventricular volume overload from pulmonary and/or tricuspid valve regurgitation (Figure 17.29).

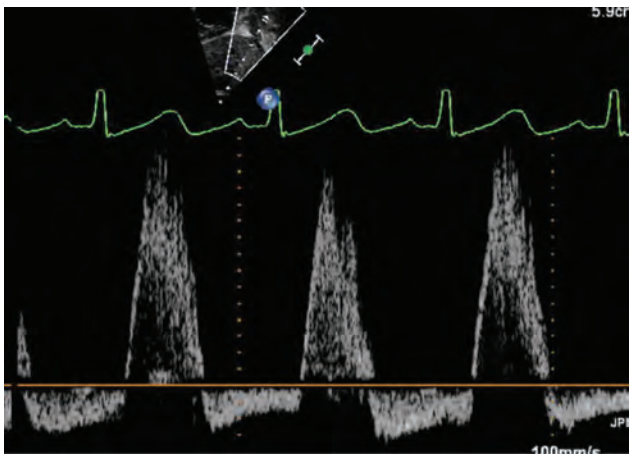


Figure 17.26 Spectral Doppler in the descending aorta recorded from the subcostal window with the cursor aligned with the descending aorta. Note the normal systolic flow profile toward the diaphragm as well as holodiastolic flow going away from the diaphragm. This diastolic flow is typical for a patient with an aorto-pulmonary shunt.

In patients managed with a single ventricle strategy, echocardiography focuses on the elements relevant to a successful Fontan operation. Follow-up echocardiography includes detailed evaluation of left ventricular size and function, atrioventricular valve regurgitation and pulmonary artery growth. Each follow-up study should document unrestrictive flow across the atrial septum. In patients undergoing a modified Fontan operation, the right ventricle usually remains hypoplastic and hypertensive and the septum bows into the left ventricle (Figures 17.30 and 17.31).

In patients with PA/IVS and abnormal coronary arteries (e.g., fistulae, stenoses), long-term follow-up of myocardial function is warranted. In addition to standard assessment of global and regional left ventricular function at rest, stress echocardiography can provide information about myocardial segments at risk for ischemia. To date, experience with this patient group is limited and the optimal strategy for evaluating myocardial ischemia in this population (e.g., stress echocardiography, nuclear

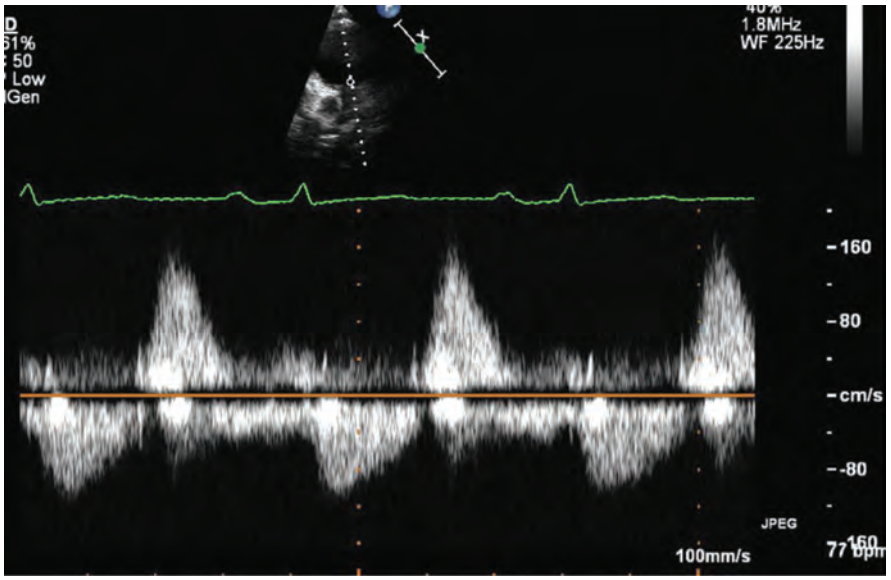


Figure 17.27 Spectral Doppler of the right ventricular outflow tract. The signal below the baseline represents antegrade systolic flow across the pulmonary annulus. The signal above the baseline represents retrograde diastolic flow in the right ventricular outflow tract from pulmonary regurgitation.

techniques, magnetic resonance perfusion and viability) awaits further studies.

Cardiac magnetic resonance imaging (MRI) can be used during follow-up of patients with PA/IVS when quantification of antegrade blood flow into the pulmonary artery is important in deciding treatment strategy. In older patients in whom echocardiography cannot adequately image the right ventricle or pulmonary arteries, this modality offers a noninvasive

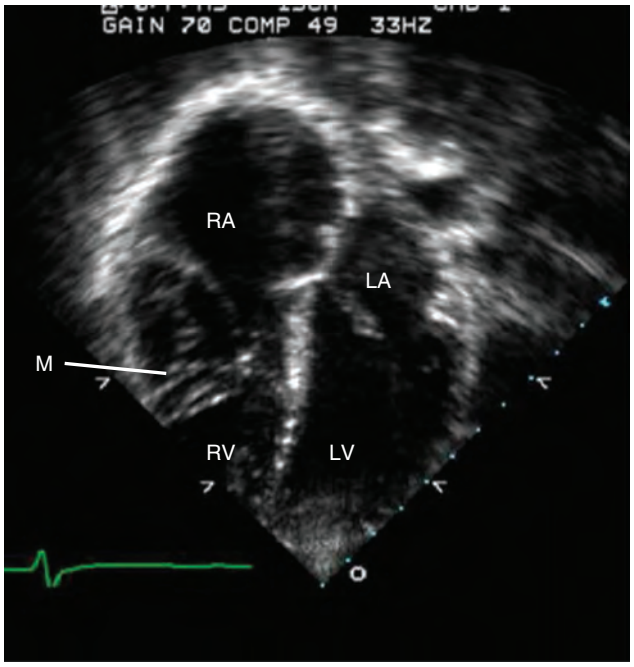


Figure 17.28 Right ventricular growth, 6 years after biventricular repair. This is a 4-chamber view in a patient with pulmonary atresia with intact ventricular septum status post-pulmonary valve dilation and placement of a Blalock–Taussig shunt followed by shunt ligation and atrial septal defect closure at age 1 year. The right ventricle is nearly normal in length, but still has abnormal myocardial architecture. Note the large mid-ventricular muscle bar. LA, left atrium; LV, left ventricle; M, muscle bar; RA, right atrium; RV, right ventricle.

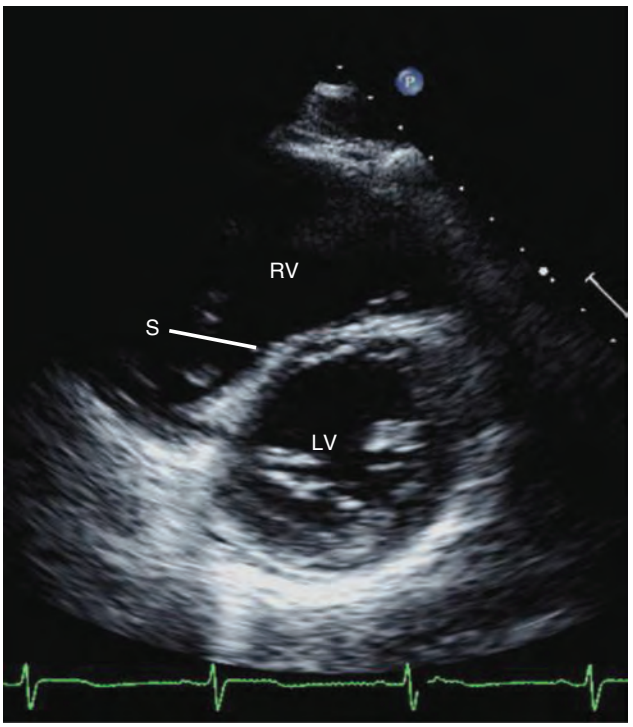


Figure 17.29 Right ventricle after pulmonary valve dilation. This is a parasternal short-axis image showing the right ventricle several years after pulmonary valve dilation. Compared with the newborn period, the right ventricle is less hypertrophied and the cavity is larger. There is diastolic septal flattening consistent with right ventricular volume load from pulmonary regurgitation. LV, left ventricle; RV, right ventricle; S, septum.

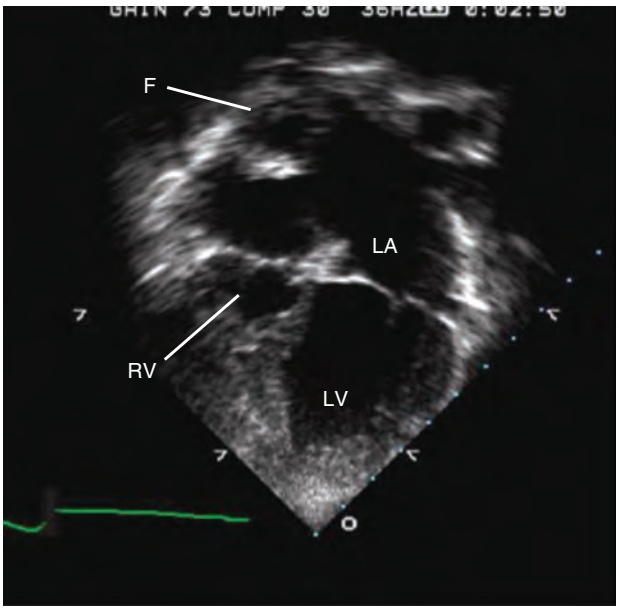


Figure 17.30 Lateral tunnel style of Fontan operation seen from the apical 4-chamber view in a patient with moderate right ventricular hypoplasia. The hypoplastic tricuspid valve and right ventricle are seen. As expected without antegrade flow through the right ventricular outflow tract, no right ventricular growth has taken place. The Fontan tunnel is identified in the posterior portion of the right atrium. F, Fontan pathway; LA, left atrium; LV, left ventricle; RV, right ventricle.

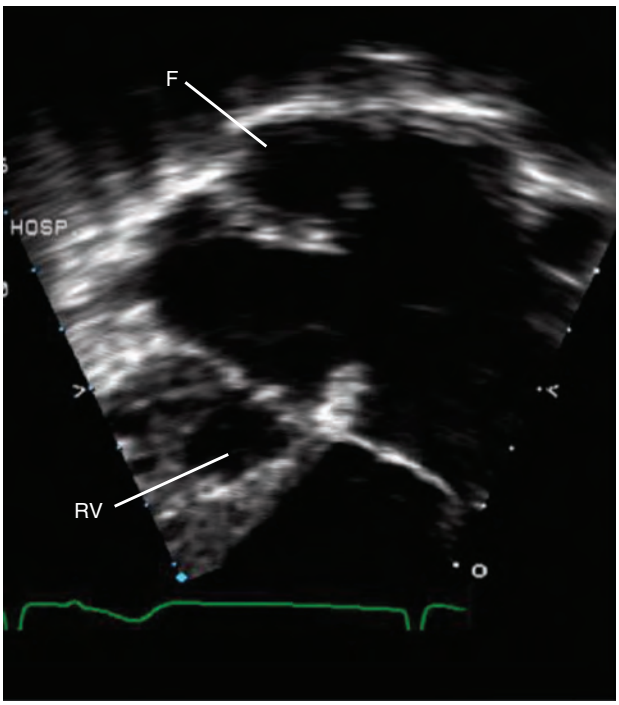


Figure 17.31 Fontan pathway. This is a magnified image from the 4-chamber view of the right atrium in a patient with a lateral tunnel style of Fontan pathway. This is an excellent view for evaluating the tunnel, any fenestrations in the tunnel, right-sided pulmonary venous flow around the tunnel and the tricuspid valve function. F, Fontan pathway; RV, right ventricle.

alternative. MRI can also be used to answer questions related to RV fibrosis, delayed enhancement of myocardium and global systolic function [99,128–130].

Videos

To access the videos for this chapter, please go to www.lai-echo.com.

Video 17.1 Coronary artery stenosis by angiography. Angiogram of a patient with right ventricular-dependent coronary arteries. This injection into the left main coronary artery shows a prominent aneurysm in the mid portion of the vessel, just distal to a very tight area of vessel stenosis.

Video 17.2 Subcostal short-axis sweep in pulmonary atresia with intact ventricular septum. This video is focused on the right ventricle and shows how well one can image the right ventricular outflow from this view, particularly in infants. This is an excellent view for evaluating tricuspid valve tissue and papillary muscles (seen in the caudal aspect of the right ventricular image, just to the right of the septum).

Video 17.3 Subcostal long-axis sweep in pulmonary atresia with intact ventricular septum. This clip shows how well one can image both the inflow and outflow portions of the right ventricle as the sweep progresses from posterior to anterior.

Video 17.4 Prenatal evaluation in a mid-trimester fetus with moderate hypoplasia of the right ventricle and tricuspid valve. Note the hypertrophied right ventricular apex and poor movement of the tricuspid valve during the cardiac cycle.

Video 17.5 Prenatal evaluation in fetus with pulmonary atresia with intact ventricular septum and RV dilation. This fetus has dilation of the RV and a severely dysplastic tricuspid valve; note that the heart is "wall to wall." The cardiac silhouette reaches from one ribcage to the other and there is diminished room for the lung tissue. The right atrium is much larger than the left atrium due to the tricuspid regurgitation, leading to left atrial compression.

Video 17.6 Fetal tricuspid regurgitation. This is an evaluation of tricuspid regurgitation in a mid-trimester fetus with pulmonary atresia and intact ventricular septum who has severe RV dilation and a very dysplastic tricuspid valve. This is a magnified image of the dysplastic tricuspid valve. The severe tricuspid regurgitation results in massive dilation of the right atrium.

Video 17.7 Coronary artery fistula in fetal life. There is a small coronary-cameral fistula entering the right ventricle of a fetus with pulmonary atresia and intact ventricular septum associated with severe right ventricular hypoplasia. These can be difficult to see in the fetus. Note that the Nyquist limit is decreased in an attempt to find low-velocity diastolic flow.

Video 17.8 Prenatal evaluation of the ductus arteriosus in a fetus with pulmonary atresia with intact ventricular septum. The duct is

well seen in the arch view. Typically ductal flow is towards the aorta in the normal fetus. In this fetus, flow is towards the pulmonary artery as expected in the setting of pulmonary atresia.

Video 17.9 Color Doppler evaluation of the tricuspid valve from the apical view. Note that there is very little antegrade tricuspid valve flow and very little tricuspid valve motion. This illustrates the low volume to-and-from flow that is characteristic of patients with pulmonary atresia.

Video 17.10 Parasternal imaging of the right ventricular outflow tract. This composite image shows how well one can evaluate the infundibulum, valve tissue and proximal main pulmonary artery from the parasternal acoustic window. These images are taken from a mid to high parasternal window with the transducer "dot" almost straight leftward. The color Doppler portion of the composite reveals the lack of antegrade or retrograde flow across fairly thin valve tissue. Note that though there is membranous atresia, the valve sinuses are well formed and the annulus looks normal in size.

Video 17.11 Evaluation of atrial septum. This is a subcostal long-axis image of the atrial septum. The color Doppler reveals that there is a right-to-left shunt at the atrial level, typical of pulmonary atresia and intact ventricular septum. This is an example of a widely sprung foramen ovale.

Video 17.12 Right ventricular-coronary artery fistula. This is a magnified image of the right ventricular outflow tract from the subcostal acoustic window. The arrow is delineating a color jet of to-and-from flow within the myocardium and right ventricular cavity. This is the typical appearance of a low velocity fistula due to intramyocardial sinusoids which communicate with both the coronary arteries and the ventricular cavity.

Video 17.13 Coronary sinusoid and associated aneurysm. This is a magnified image taken from the parasternal short-axis window. The aorta is in the center of the screen. The arrow delineates an echo-free space within the myocardium anterior to the aorta. This space looks very dilated during a portion of the cardiac cycle and much more like a mildly ectatic vessel in other portions of the cardiac cycle. This is an aneurysm of the intramyocardial sinusoid associated with a coronary artery stenotic lesion.

Video 17.14 Color Doppler of coronary sinusoid and associated aneurysm. This is the same image as in Video 17.13, but with color Doppler. The color makes it easy to see the to-and-from flow in the aneurysmal vessel. This particular patient had complete atresia of the coronary ostia, though that is not obvious from this clip.

Video 17.15 Two-dimensional imaging and color Doppler evaluation of a dysplastic tricuspid valve in pulmonary atresia with intact ventricular septum and a dilated right ventricle. This is a very abnormal-appearing tricuspid valve and subvalvar apparatus.

Video 17.16 Intraoperative TEE. Evaluation in a patient with pulmonary atresia and intact ventricular septum who has moderate hypoplasia of the tricuspid valve. TEE typically gives excellent views of the annulus size and is a good modality for evaluating tricuspid valve function. This example shows that there is some antegrade tricuspid valve flow, though with a narrowed inflow jet, and no significant tricuspid regurgitation.

Video 17.17 Evaluation of a stent in the ductus arteriosus in an infant with pulmonary atresia and intact ventricular septum. The stent is well seen in the high left parasternal image. This dual view suggests that there is no significant thrombus and robust flow through the stent with the majority of the flow going towards the pulmonary artery, as expected.

References

1 Peacock TB. Malformation of the heart, atresia of the orifice of the pulmonary artery, aorta communicating with both ventricles. *Trans Pathol Soc London* 1869;**20**:61–86.
2 Grant RT. An unusual anomaly of the coronary vessels in the malformed heart of a child. *Heart* 1926;**13**:273–283.
3 Abbott ME. *Atlas of Congenital Cardiac Disease*. New York, NY: American Heart Association, 1936.
4 Glaboff J, Gohmann J, Little J. Atresia of the pulmonary artery with intact ventricular septum. *J Pediatr* 1950;**37**:396–399.
5 Greenwold W, DuShane J, Burchell H, et al. Congenital pulmonary atresia with intact ventricular septum: two anatomic types. *Proceedings of the 29th Scientific Session*. American Heart Association, 1956, pp. 51.
6 Paul MH, Lev M. Tricuspid stenosis with pulmonary atresia, a cineangiographic pathologic correlation. *Circulation* 1960;**22**:198–203.
7 Davignon AL, Greenwold WE, DuShane JW, Edwards JE. Congenital pulmonary atresia with intact ventricular septum: clinicopathologic correlation of two anatomic types. *Am Heart J* 1961;**62**:591–602.
8 Benton JW, Elliott LP, Adams P, et al. Pulmonary atresia and stenosis with intact ventricular septum. *Am J Dis Child* 1962;**104**:161–168.
9 Elliott LP, Adams P, Edwards JE. Pulmonary atresia with intact ventricular septum. *Br Heart J* 1963;**25**:489–501.
10 Morgan BC, Stacy GS, Dillard DH. Pulmonary valvular and infundibular atresia with intact ventricular septum. *Am J Cardiol* 1965;**16**:746–750.
11 Cole RB, Alexander JM, Lev M, Paul MH. Pulmonary atresia with intact ventricular septum. *Am J Cardiol* 1968;**21**:23–31.
12 Bowman FO, Malm JR, Hayes CJ, et al. Pulmonary atresia with intact ventricular septum. *J Thorac Cardiovasc Surg* 1971;**61**:85–95.
13 Gersony WM, Bernhard WF, Nadas AS, Gross RE. Diagnosis and surgical treatment of infants with critical pulmonary outflow obstruction: study of thirty-four infants with pulmonary stenosis or atresia, and intact ventricular septum. *Circulation* 1967;**35**:765–776.
14 Hanley FL, Sade RM, Blackstone EH, et al. Outcomes in neonatal pulmonary atresia with intact ventricular septum. A multi-institutional study. *J Thorac Cardiovasc Surg* 1993;**105**:406–423.

15 Reddy M, Ungerleider R, Hanley F. Pulmonary valve atresia with intact ventricular septum. In: Garson A, Bricker TJ, Fisher DJ, Neish SR (eds.) *Science and Practice of Pediatric Cardiology*, 2nd edn. Baltimore, MD: Williams and Wilkins, 1998, pp. 1563–1577.

16 Fyler DC, Buckley LP, Hellenbrand WE, et al. Report of the New England Regional Infant Cardiac Program. *Pediatrics* 1980;**65**:375–461.

17 Mitchell SC, Korones SB, Berends HW. Congenital heart disease in 56,109 births. *Circulation* 1971;**43**:323–332.

18 Buckley LP, Dooley KJ, Fyler DC. Pulmonary atresia and intact ventricular septum in New England. *Am J Cardiol* 1976;**37**:124.

19 Dhanavaravibul S, Nora JJ, McNamara DG. Pulmonary atresia with intact ventricular septum: problems in diagnosis and results of treatment. *J Pediatr* 1970;**77**:1010–1016.

20 de Leval M, Bull C, Hopkins R, et al. Decision making in the definitive repair of the heart with a small right ventricle. *Circulation* 1985;**72**(Suppl. 2):52–60.

21 Nora JJ, Nora AH. Update on counseling the family with a first-degree relative with a congenital heart defect. *Am J Med Genet* 1988;**29**:137–142.

22 Chitayat D, McIntosh N, Fouron JC. Pulmonary atresia with intact ventricular septum: a single gene disorder. *Am J Med Genet* 1992;**42**:304–306.

23 Erikson NL, Buttino LJ, Juberg RC. Congenital pulmonary atresia and patent ductus arteriosus in two sibs. *Am J Med Genet* 1989;**32**:187–188.

24 Baetz-Greenwalt B, Ratliff NB, Moodie DS. Hypoplastic right-sided heart complex: a cluster of cases with associated congenital birth defects: a new syndrome? *J Pediatr* 1983;**103**:399–401.

25 Zuberbuhler JR, Anderson RH. Morphological variations in pulmonary atresia with intact ventricular septum. *Br Heart J* 1979;**41**:281–288.

26 Kutsche LM, van Mierop LHS. Pulmonary atresia with and without ventricular septal defect: a different etiology and pathogenesis for the atresia in the 2 types? *Am J Cardiol* 1983;**51**:932–935.

27 Freedom RM, Mawson JB, Yoo S-J, Benson LN. Pulmonary atresia and intact ventricular septum. In: Freedom RM, Mawson JB, Yoo S-J, Benson LN (eds.) *Congenital Heart Disease Textbook of Angiography*. New York, NY: Futura Publishing, 1997, pp. 617–662.

28 Van Praagh R, Ando M, van Praagh S, et al. Pulmonary atresia: anatomic considerations. In Kidd BSL, Rowe RD (eds.) *The Child with Congenital Heart Disease after Surgery*. New York, NY: Futura Publishing, 1976, pp. 103.

29 Freedom RM, Dische MR, Rowe RD. The tricuspid valve in pulmonary atresia and intact ventricular septum: a morphological study of 60 cases. *Arch Pathol Lab Med* 1978;**102**:28–31.

30 Bull C, de Leval MR, Mercanti C, et al. Pulmonary atresia and intact ventricular septum: a revised classification. *Circulation* 1982;**66**:266–272.

31 Daubeny PE, Delaney DJ, Anderson RH, et al. Pulmonary atresia with intact ventricular septum. Range of morphology in a population-based study. *J Am Coll Cardiol* 2002;**39**:1670–1679.

32 Freedom RM. The morphological variations of pulmonary atresia and intact ventricular septum: guidelines for surgical intervention. *Pediatr Cardiol* 1983;**4**:183–188.

33 Choi YH, Seo JW, Choi JY, et al. Morphology of tricuspid valve in pulmonary atresia with intact ventricular septum. *Pediatr Cardiol* 1998;**19**:381–389.

34 Dyamenahalli U, McCrindle B, McDonald C, et al. Pulmonary atresia with intact ventricular septum: management of, and outcomes for, a cohort of 210 consecutive patients. *Cardiol Young* 2004;**12**:299–308.

35 Bryan CS, Oppenheimer EH. Ventricular endocardial fibroelastosis. Basis for its presence or absence in cases of pulmonic or aortic atresia. *Arch Pathol* 1969;**87**:82–86.

36 Essed CE, Klein HW, Kredict P. Coronary and endocardial fibroelastosis of the ventricles in the hypoplastic left and right heart syndromes. *Virchows Arch* 1975;**368**:87–97.

37 O'Connor WN, Cottril CM, Johnson CL, et al. Pulmonary atresia with intact ventricular septum and ventriculocoronary communications: surgical significance. *Circulation* 1982;**65**:805–809.

38 Bulkley BH, D'Amico B, Taylor AL, et al. Extensive myocardial fiber disarray in aortic and pulmonary atresia. Relevance to hypertrophic cardiomyopathy. *Circulation* 1983;**67**:191–198.

39 Silver MD, Lam JHC, Ranganathan N, Wigle ED. Morphology of the human tricuspid valve. *Circulation* 1971;**43**:333–348.

40 Lauer RM, Fink HP, Petry EL, et al. Angiographic demonstration of intramyocardial sinusoids in pulmonary valve atresia with intact ventricular septum and hypoplastic right ventricle. *N Engl J Med* 1964;**271**:68–72.

41 Williams RR, Kent GB, Edwards JE. Anomalous cardiac blood vessel communicating with the right ventricle. Observations in a case of pulmonary atresia with an intact ventricular septum. *Arch Path* 1951;**52**:480–487.

42 Freedom RM, Harrington DP. Contribution of intramyocardial sinusoids in pulmonary atresia and intact ventricular septum to a right-sided circular shunt. *Br Heart J* 1974;**36**:1061–1065.

43 Lenox CC, Briner J. Absent proximal coronary arteries associated with pulmonic atresia. *Am J Cardiol* 1972;**30**:666–669.

44 Cornell SH. Myocardial sinusoids in pulmonary valvular atresia. *Radiology* 1966;**86**:421–424.

45 Patel RG, Freedom RM, Moes CA, et al. Right ventricular volume determinations in 18 patients with pulmonary atresia and intact ventricular septum. Analysis of factors influencing right ventricular growth. *Circulation* 1980;**61**:428–440.

46 Oppenheimer EH, Esterly JR. Some aspects of cardiac pathology: eleven cases of unusual coronary endarteritis with congenital cardiac malformations. *Bull Johns Hopkins Hosp* 1966;**119**:343.

47 Kipps AK, Powell AJ, Levine JC. Muscular infundibular atresia is associated with coronary otial atresia in pulmonary atresia with intact ventricular septum. *Congenit Heart Dis* 2011;**6**(5):444–450.

48 Selamet SE, Hsu DT, Thaker HM, Gersony WM. Complete atresia of coronary ostia in pulmonary atresia and intact ventricular septum. *Pediatr Cardiol* 2004;**25**:67–69.

49 Giglia TM, Mandell VS, Connor AR, et al. Diagnosis and management of right ventricular dependent coronary circulation in pulmonary atresia with intact ventricular septum. *Circulation* 1992;**86**:1516–1528.

50 Tanoue Y, Kado H, Maeda T, et al. Left ventricular performance of pulmonary atresia with intact ventricular septum after right heart bypass surgery. *J Thorac Cardiovasc Surg* 2004;**128**:710–717.

51 Gittenberger-De Groot AC, Sauer U, Bindl L, et al. Competition of coronary arteries and ventriculocoronary arterial communications in pulmonary atresia with intact ventricular septum. *Int J Cardiol* 1988;**18**:243–258.

52 Geva T, Van Praagh S, Van Praagh R. Thoracoabdominal ectopia cordis with isolated infundibular atresia. *Am J Cardiol* 1960;**66**: 891–893.

53 Newfeld EA, Cole RB, Paul MH. Ebstein's malformation of the tricuspid valve in the neonate. Functional and anatomic pulmonary outflow tract obstruction. *Am J Cardiol* 1967;**19**:727–731.

54 Freedom R, Anderson R, Perrin D. The significance of ventriculocoronary arterial connections in the setting of pulmonary atresia with an intact ventricular septum. *Cardiol Young* 2005;**15**:447–468.

55 Cote M, Davignon A, Fouron JC. Congenital hypoplasia of the right ventricular myocardium Uhl's anomaly associated with pulmonary atresia in a newborn. *Am J Cardiol* 1973;**31**:658–661.

56 Akiba T, Becker AD. Disease of the left ventricle in pulmonary atresia with intact ventricular septum. *J Thorac Cardiovasc Surg* 1994;**108**:1–8.

57 Sholler GF, Colan SD, Sanders SP. Effect of isolated right ventricular outflow obstruction on left ventricular function in infants. *Am J Cardiol* 1988;**62**:778–784.

58 Gentles TL, Colan SD, Giglia TG, et al. Right ventricular decompression and left ventricular function in pulmonary atresia with intact ventricular septum. The influence of less extensive coronary anomalies. *Circulation* 1993;**88**:183–188.

59 Akagi T, Benson LN, Williams WG, et al. Ventriculo-coronary arterial connections in pulmonary atresia with intact ventricular septum, and their influences on ventricular performance and clinical course. *Am J Cardiol* 1993;**72**:586–590.

60 Hausdorf G, Gravinghoff L, Deck EW. Effects of persisting myocardial sinusoids on left ventricular performance in pulmonary atresia with intact ventricular septum. *Eur Heart J* 1987;**8**:291–296.

61 Sideris EB, Olley PM, Spooner E, et al. Left ventricular function and compliance in pulmonary atresia with intact ventricular septum. *J Thorac Cardiovasc Surg* 1982;**84**:192–199.

62 Gómez Montes E, Herraiz I, Mendoza A, Galindo A. Fetal intervention in right outflow tract obstructive disease: selection of candidates and results. *Cardiol Res Pract* 2012;**2012**:592403.

63 Tworetzky, W, McElhinney D, Marx G, et al. In utero valvuloplasty for pulmonary atresia with hypoplastic right ventricle: techniques and outcomes. *Pediatrics* 2009;**124**:e510–518.

64 Tulzer G, Arzt W, Franklin RC, et al. Fetal pulmonary valvuloplasty for critical pulmonary stenosis or atresia with intact septum. *Lancet* 2002;**360**:1567–1568.

65 Tworetzky W, Marchall AC. Fetal interventions for cardiac defects. *Pediatr Clin N Am* 2004;**51**:1503–1513.

66 Tworetzky W, Wilkins-Haug L, Jennings RW, et al. Balloon dilation of severe aortic stenosis in the fetus: potential for prevention of hypoplastic left heart syndrome: candidate selection, technique and results of successful intervention. *Circulation* 2004;**110**:2125–2131.

67 Hawkins JA, Thorne JK, Boucek MM, et al. Early and late results in pulmonary atresia and intact ventricular septum. *J Thorac Cardiovasc Surg* 1990;**100**:492–497.

68 Leung MP, Mok CK, Lee J, et al. Management evolution of pulmonary atresia and intact ventricular septum. *Am J Cardiol* 1993;**71**:1331–1336.

69 Mainwarning RD, Lamberti JJ. Pulmonary atresia with intact ventricular septum. Surgical approach based on ventricular size and coronary anatomy. *J Thorac Cardiovasc Surg* 1993;**106**:733–738.

70 Lewis AB, Wells W, Lindesmith GG. Evaluation and surgical treatment of pulmonary atresia and intact ventricular septum in infancy. *Circulation* 1983;**67**:1318–1323.

71 McAffrey FM, Leatherbury L, Moore HV. Pulmonary atresia and intact ventricular septum. Definitive repair in the neonatal period. *J Thorac Cardiovasc Surg* 1991;**57**:551–556.

72 Shaddy RE, Sturtevant JE, Judd VE, McGough EC. Right ventricular growth after transventricular pulmonary valvotomy and central aortopulmonary shunt for pulmonary atresia and intact ventricular septum. *Circulation* 1990;**82**(Suppl. 4):157–163.

73 Luckstead EF, Mattioli L, Crosby I, et al. Two-stage palliative surgical approach for pulmonary atresia with intact ventricular septum (Type I). *Am J Cardiol* 1972;**29**:490–496.

74 Sano S, Ishino K, Kawada M, et al. Staged biventricular repair of pulmonary atresia or stenosis with intact ventricular septum. *Ann Thorac Surg* 2000;**70**:1501–1506.

75 Yoshimura N, Yamaguchi M, Ohashi H, et al. Pulmonary atresia with intact ventricular septum: strategy based on right ventricular morphology. *J Thorac Cardiovasc Surg* 2003;**126**:1417–1426.

76 Pawade A, Capuani A, Penny DJ, et al. Pulmonary atresia with intact ventricular septum. Surgical management based on right ventricular infundibulum. *J Cardiac Surg* 1993;**8**:371–383.

77 Latson LA. Nonsurgical treatment of a neonate with pulmonary atresia and intact ventricular septum by transcatheter puncture and balloon dilation of the atretic valve membrane. *Am J Cardiol* 1991;**68**:277–279.

78 Agnoletti G, Piechaud JF, Bonhoeffer P, et al. Perforation of the atretic pulmonary valve: long-term follow-up. *J Am Coll Cardiol* 2003;**41**:1399–1403.

79 Alwi M, Geetha K, Bilkis A, et al. Pulmonary atresia with intact ventricular septum: percutaneous radiofrequency-assisted valvotomy and balloon dilation versus surgical valvotomy and Blalock–Taussig shunt. *J Am Coll Cardiol* 2000;**35**:468–476.

80 Humpl T, Soderberg B, McCrindle B, et al. Percutaneous balloon valvotomy in pulmonary atresia with intact ventricular septum: impact on patient care. *Circulation* 2003;**108**:826–832.

81 Ovaert C, Qureshi SA, Rosenthal E, et al. Growth of the right ventricle after successful transcatheter pulmonary valvotomy in neonates and infants with pulmonary atresia and intact ventricular septum. *J Thorac Cardiovasc Surg* 1998;**115**:1055–1062.

82 Weber H. Initial and late results after catheter intervention for neonatal critical pulmonary valve stenosis and atresia with intact ventricular septum: a technique in continual evolution. *Cathet Cardiovasc Intervent* 2002;**56**:394–399.

83 Graham TP, Bender HW, Atwood GF, et al. Increase in right ventricular volume following valvulotomy for pulmonary atresia or stenosis with intact ventricular septum. *Circulation* 1974;**49**(Suppl. 11):69–79.

84 Squittieri C, di Carlo D, Giannico S, et al. Tricuspid valve avulsion or excision for right ventricular decompression in pulmonary atresia with intact ventricular septum. *J Thorac Cardiovasc Surg* 1989;**97**:779–784.

85 Laks H, Gates RN, Grant PW, et al. Aortic to right ventricular shunt for pulmonary atresia with intact ventricular septum. *Ann Thorac Surg* 1995;**59**:342–347.

86 Williams WG, Burrows P, Freedom RM, et al. Thrombo-exclusion of the right ventricle in children with pulmonary atresia and intact ventricular septum. *J Thorac Cardiovasc Surg* 1991;**101**:222–229.

87 Jahangiri M, Zurakowski D, Bichell D, et al. Improved results with selective management in pulmonary atresia with intact ventricular septum. *J Thorac Cardiovasc Surg* 1999;**118**:1046–1055.

88 Chubb H, Pesonen E, Sivasubramanian S, et al. Long-term outcome following catheter valvotomy for pulmonary atresia with intact ventricular septum. *J Am Coll Cardiol* 2010;**59**:1468–1476.

89 Hoashi T, Kagisaki K, Kitano M, et al. Late clinical features of patients with pulmonary atresia or critical pulmonary stenosis with intact ventricular septum after biventricular repair. *Ann Thorac Surg* 2012:**94**(3):833–841.

90 Najm HK, Williams WG, Coles JG, et al. Pulmonary atresia with intact ventricular septum: results of the Fontan procedure. *Ann Thorac Surg* 1997;**63**:669–675.

91 Powell AJ, Mayer JE, Lang P, Lock JE. Outcome in infants with pulmonary atresia, intact ventricular septum and right ventricle-dependent coronary circulation. *Am J Cardiol* 2000;**86**:1272–1274.

92 Giglia TM, Jenkins KJ, Matitiau A, et al. Influence of right heart size on outcome in pulmonary atresia with intact ventricular septum. *Circulation* 1993;**88**(Suppl. 1):2248–2256.

93 Shaath G, Al Mutairi M, Tamimi O, et al. Predictors of reintervention in neonates with critical pulmonary stenosis or pulmonary atresia with intact ventricular septum. *Catheter Cardiovasc Interv* 2012;**79**(4):659–664.

94 Alwi M, Choo KK, Latiff HA, et al. Initial results and medium-term follow-up of stent implantation in patent ductus arteriosus in duct dependent pulmonary circulation. *J Am Coll Cardiol* 2004;**44**:438–445.

95 Sivakumar K, Bhagyavathy A, Coelho R, et al. Longevity of neonatal ducal stenting for congenital heart diseases with duct-dependent pulmonary circulation. *Congenit Heart Dis* 2012;Epub Apr 30.

96 Li S, Chen W, Zhang Y, et al. Hybrid therapy for pulmonary atresia with intact ventricular septum. *Ann Thorac Surg* 2011;**91**(5):555–560.

97 Takayama H, Sekiguchi A, Chikada M. Update: Pulmonary atresia with intact ventricular septum: long-term results of "one and a half ventricular repair". *Ann Thorac Surg* 2001;**72**:2178–2179.

98 Muster AJ, Zales VR, Ilbawi MN, et al. Biventricular repair of hypoplastic right ventricle assisted by pulsatile bidirectional cavopulmonary anastomosis. *J Thorac Cardiovasc Surg* 1993;**105**:112–119.

99 Uribe S, Bächler P, Valverde I, et al. Hemodynamic assessment in patients with one-and-a-half ventricle repair revealed by four-dimensional flow magnetic resonance imaging. *Pediatr Cardiol* 2013;**34**:447–451.

100 Meyer RA, Kaplan S. Echocardiography in the diagnosis of hypoplasia of the left or right ventricles in the neonate. *Circulation* 1972;**46**:55–64.

101 Lewis, BS, Amitai N, Simcha A, et al. Echocardiographic diagnosis of pulmonary atresia with intact ventricular septum. *Am Heart J* 1979;**97**:92–95.

102 Trowitsch E, Colan SD, Sanders SP. Two-dimensional echocardiographic evaluation of right ventricular size and function in newborns with severe right ventricular outflow tract obstruction. *J Am Coll Cardiol* 1985;**6**:388–393.

103 Silove ED, DeGiovanni JV, Shiu MF, Myint YM. Diagnosis of right ventricular outflow tract obstruction in infants by cross sectional echocardiography. *Br Heart J* 1983;**50**:416–420.

104 Sharland GK, Chita SK, Allan LD. Tricuspid valve dysplasia or displacement in intrauterine life. *J Am Coll Cardiol* 1991;**17**:944–949.

105 Daubeny PEF, Sharland GK, Cook AC, et al. Pulmonary atresia with intact ventricular septum. Impact of fetal echocardiography on incidence at birth and postnatal outcome. *Circulation* 1998;**98**:562–566.

106 Todros T, Paladini D, Chiapppa E, et al. Pulmonary stenosis and atresia with intact ventricular septum during prenatal life. *Ultrasound Obstet Gynecol* 2003;**21**:228–233.

107 Allan LD, Cook A. Pulmonary atresia with intact ventricular septum in the fetus. *Cardiol Young* 1992;**2**:367–376.

108 Maeno YV, Boutin C, Hornberger LK, et al. Prenatal diagnosis of right ventricular outflow tract obstruction with intact ventricular septum and detection of ventriculo-coronary connections. *Heart* 1999;**81**:661–668.

109 Peterson R, Levi D, Williams R, et al. Echocardiographic predictors of outcome in fetuses with pulmonary atresia with intact ventricular septum. *J Am Society of Echocardiogr* 2006;**19**:1393–1400.

110 Salvin J, Colan SD, McElhinney DB, et al. Fetal tricuspid valve annulus as a predictor of single vs. biventricular outcome in pulmonary atresia with intact ventricular septum. *Pediatrics* 2006;**118**:415–420.

111 Satou GM, Perry SB, Gauvreau K, Geva T. Echocardiographic predictors of coronary artery pathology in pulmonary atresia with intact ventricular septum. *Am J Cardiol* 2000;**85**:1319–1324.

112 Minich LL, Tani LY, Ritter S et al. Usefulness of the preoperative tricuspid/mitral valve ratio for predicting outcome in pulmonary atresia with intact ventricular septum. *Am J Cardiol* 2000;**85**:1325–1328.

113 Tworetzky W, Reddy VM, Brook MM, et al. Improved surgical outcome after fetal diagnosis of hypoplastic left heart syndrome. *Circulation* 2001;**103**:1269–1273.

114 Tuo G, Volpe P, Bondanza S, et al. Impact of prenatal diagnosis on outcome of pulmonary atresia and intact ventricular septum. *J Matern Fetal Neonatal Med* 2012;**25**(6):669–674.

115 Gomez-Montes E, Herraiz I, Mendoza A, et al. Pulmonary atresia/critical stenosis with intact ventricular septum: prediction of outcome in the second trimester of pregnancy. *Prenat Diagn* 2011;**31**(4):372–379.

116 Sandor G, Cook A, Sharland G, et al. Coronary arterial abnormalities in pulmonary atresia with intact ventricular septum diagnosed during fetal life. *Cardiol Young* 2002;**12**:436–444.

117 Mahle WT, Clancy RR, McGaurn SP, et al. Impact of prenatal diagnosis on survival and early neurologic morbidity in neonates with the hypoplastic left heart syndrome. *Pediatrics* 2001;**107**;1277–1282.

118 Verheijen PM, Lisowski LA, Stoutenbeek P, et al. Prenatal diagnosis of congenital heart disease affects preoperative acidosis in the newborn patient. *J Thorac Cardiovasc Surg* 2001;**123**:798–803.

119 Daubeny P, Wand D, Delany D, et al. Pulmonary atresia with intact ventricular septum: predictors of early and medium-term outcome in a population-based study. *J Thorac Cardiovasc Surg* 2005;**130**:1071–1078.

120 Odim J, Laks H, Plunkett M, Tung T. Successful management of patients with pulmonary atresia with intact ventricular septum

using a three tier grading system for right ventricular hypoplasia. *Ann Thorac Surg* 2006;**81**:678–684.

121 Cleuziou J, Schreiber C, Eicken A, et al. Predictors for biventricular repair in pulmonary atresia with intact ventricular septum. *Thorac Cardiovasc Surg* 2010;**58**(6):339–344.

122 Drighil A, Alijufan M, Slimi A, et al. Echocardiographic determinants of successful balloon dilation in pulmonary atresia with intact ventricular septum. *Eur J Echocardiogr* 2011;**11**(2):172–175.

123 Sanders SP, Parness IA, Colan SD. Recognition of abnormal connections of coronary arteries with the use of Doppler color flow mapping. *J Am Coll Cardiol* 1989;**13**:922–926.

124 Velvis H, Schmidt KG, Silverman NH, Turley K. Diagnosis of coronary artery fistula by two-dimensional echocardiography, pulsed Doppler ultrasound and color flow imaging. *J Am Coll Cardiol* 1989;**14**:968–976.

125 Garcia J, Zellers TM, Weinstein EM, Mahoney L. Usefulness of Doppler echocardiography in diagnosing right ventricular coronary arterial communications in patients with pulmonary atresia and intact ventricular septum and comparison with angiography. *Am J Cardiol* 1998;**81**:103–104.

126 Wald R, Juraszek A, Pigula F, Geva T. Echocardiographic diagnosis and management of bilateral coronary ostial atresia in a patient with pulmonary atresia and intact ventricular septum. *J Am Soc Echocardiogr* 2006;**19**:939.e1–e3.

127 Huang SC, Ishino K, Kashahara S, et al. The potential of disproportionate growth of tricuspid valve after decompression of the right ventricle in patients with pulmonary atresia and intact ventricular septa. *J Thorac Cardiovasc Surg* 2009;**138**(5):1160–1166.

128 Liang XC, Lam WW, Cheung EW, et al. Restrictive right ventricular physiology and right ventricular fibrosis as assessed by cardiac magnetic resonance and exercise capacity after biventricular repair of pulmonary atresia and intact ventricular septum. *Clin Cardiol* 2010;**33**(2):104–110.

129 Roomeih S, Groenink M, Roest AA, et al. Exercise capacity and cardiac reserve in children and adolescents with corrected pulmonary atresia with intact ventricular septum. *J Thorac Cardiovasc Surg* 2012;**143**(3):569–575.

130 Bautista-Hernandez V, Hasan BS, Harrild DM, et al. Late pulmonary valve replacement in patients with pulmonary atresia and intact ventricular septum: a case-matched study. *Ann Thorac Surg* 2011;**91**(2):555–560.

CHAPTER 18

Abnormalities of the Ductus Arteriosus and Pulmonary Arteries

Bhawna Arya[1] and Craig A. Sable[2]
[1]University of Washington School of Medicine, Seattle Children's Hospital, Seattle, WA, USA
[2]Children's National Medical Center, Washington, DC, USA

Abnormalities of the ductus arteriosus

Definition

The ductus arteriosus (DA) is a normal vascular structure in the human fetus. It normally connects the main pulmonary artery (MPA) to the descending aorta, allowing most of the blood from the right ventricle (RV) to bypass the fetus's fluid-filled lungs and high-resistance pulmonary vascular bed. In a left aortic arch, the DA inserts into the proximal descending aorta at the junction with the aortic isthmus, distal to the origin of the left subclavian artery. In a right aortic arch, there are three types of DA insertion from the MPA to the aorta: (1) directly into the right descending aorta (right DA); (2) directly into the proximal left subclavian artery (left DA); or (3) both (bilateral DA). Normally, the DA closes during the first hours to days of life. Persistence of ductal blood flow is termed patent ductus arteriosus (PDA).

Incidence

The incidence of persistent PDA without additional cardiac anomalies varies greatly depending on the postnatal age of the patients and their degree of prematurity. The overall incidence of PDA is inversely related to increasing gestational age and birth weight [1]. PDA is common in preterm infants and is considered a functional abnormality as opposed to a structural congenital cardiac anomaly. In full-term infants, the DA may remain patent for several days after birth. Doppler echocardiogram studies in healthy newborn infants have demonstrated closure of the DA in nearly all subjects by 4–7 days after birth [2,3]. Based on a review of 40 published articles over several decades, it has been estimated that the median incidence of PDA in term infants is 56.7 per 100,000 live births [4].

Etiology

The etiology of isolated PDA in full-term infants older than one week of age is not well understood. PDA can be a result of environmental exposure before birth, isolated genetic mutations, or genetic syndromes. Congenital rubella is associated with a high incidence of PDA [5–7]. Patients at high altitude are at increased risk for PDA, likely due to chronic hypobaric hypoxia, as oxygen saturation and arterial oxygen pressure are lower [8]. Recent investigations have identified the genes that affect the development of the fourth and sixth pharyngeal arches, and noted their association with cardiovascular defects similar to those observed in chromosome 22q11 deletions [9]. Char syndrome is a familial form of PDA with characteristic facial dysmorphisms and hand anomalies [10].

Morphology

Embryologic considerations

The normal anatomy and congenital malformations of the DA and branch pulmonary arteries (PAs) are determined by the development of the embryonic sixth aortic arches (see Chapter 31). The human embryo has two dorsal aortas, which communicate with the aortic sac via several branchial arch arteries. During normal development, there is systematic appearance and regression of the six pairs of primitive aortic arches. Both the ductus arteriosus and the branch PAs are derived from the fourth and sixth arches. The left fourth arch becomes the distal left aortic arch (between the left common carotid and left subclavian artery). The right fourth arch persists as the innominate artery and proximal right subclavian artery. The left dorsal aorta persists as the segment that extends from the left subclavian artery to the aortic isthmus, or site of entrance of the ductus arteriosus. The right dorsal aorta involutes. The proximal portions of the right and left sixth arches form the proximal portions of the right and left PAs, respectively. The distal left sixth arch forms the ductus arteriosus and the distal right sixth arch regresses [11].

Pathophysiology

The pathophysiology of PDA depends on several factors, including patient age, associated congenital heart disease, and hemodynamic and anatomic factors. In preterm infants, presence of

Echocardiography in Pediatric and Congenital Heart Disease: From Fetus to Adult, Second Edition. Edited by Wyman W. Lai, Luc L. Mertens, Meryl S. Cohen and Tal Geva.
© 2016 John Wiley & Sons, Ltd. Published 2016 by John Wiley & Sons, Ltd.
Companion website: www.lai-echo.com

a PDA is common and associated with increase morbidity. It is considered a functional abnormality in this population. In full-term infants and children, PDA likely results from a significant structural abnormality. The flow pattern and hemodynamic consequences of an isolated PDA depend on resistance to flow through the duct, as well as the pulmonary and systemic vascular resistances. The PDA resistance is determined by the smallest cross-sectional area, length, and its configuration. In the setting of normal pulmonary vascular resistance (PVR), an isolated PDA demonstrates left-to-right flow, resulting in increased pulmonary blood flow and left heart volume overload. The left atrium and ventricle will dilate and mitral regurgitation may develop. Left ventricular systolic function is usually preserved. A large PDA with significant left-to-right flow leads to pulmonary overcirculation, respiratory distress, poor growth, and eventually pulmonary vascular disease [5]. The diastolic blood pressure in the aorta decreases owing to diastolic "runoff" through the PDA, potentially resulting in decreased coronary perfusion pressure. This feature, coupled with increased intramyocardial tension from left ventricular dilation and increased oxygen demand, may result in subendocardial ischemia [12]. Conversely, a small PDA is usually not associated with significant hemodynamic effects. PDA carries an increased risk of infective endocarditis, which is estimated at ~1% per year [5].

In patients with elevated PVR, ductal flow is either bidirectional (right-to-left during systole) or exclusively right-to-left. In patients who have associated right heart obstructive lesions, a PDA provides a source of pulmonary blood flow. Conversely, in patients with obstructive left heart lesions, a PDA provides a source of systemic perfusion through the right heart. Congenital heart disease in which either the pulmonary or systemic circulation is dependent on blood flow via the PDA for survival is termed a "ductal-dependent lesion."

PDA with left aortic arch

In this abnormality, the PDA represents a persistent vascular connection between the aortic isthmus and the superior aspect of the proximal left pulmonary artery (LPA) (Figures 18.1 and 18.2). In the absence of right ventricular outflow obstruction, the course of the PDA is similar to that of the aortic arch. However, the ductal arch can be easily distinguished from the aortic arch with the following features: (i) the ductal arch is inferior to the aortic arch; (ii) the ductal arch does not give rise to head vessels; (iii) in postnatal life with normal PVR, the ductal flow is directed from the aorta to the MPA, while the aortic flow is in the reverse direction.

PDA with a right aortic arch

Right aortic arch occurs in approximately 0.1% of the population and is more common among patients with tetralogy of Fallot, truncus arteriosus, and tricuspid atresia. It is also associated with chromosome 22q11 deletion [13–16]. In individuals with normal intracardiac anatomy, a right aortic arch is often associated with aberrant origin of the left subclavian artery from the right descending aorta with a retro-esophageal course [15]. The most common form of the right aortic arch is with mirror image branching of the head vessels and a left-sided DA [17]. Recognizing the location of the DA in a right aortic arch is especially important, as it may result in a vascular ring (see Chapter 31) [18].

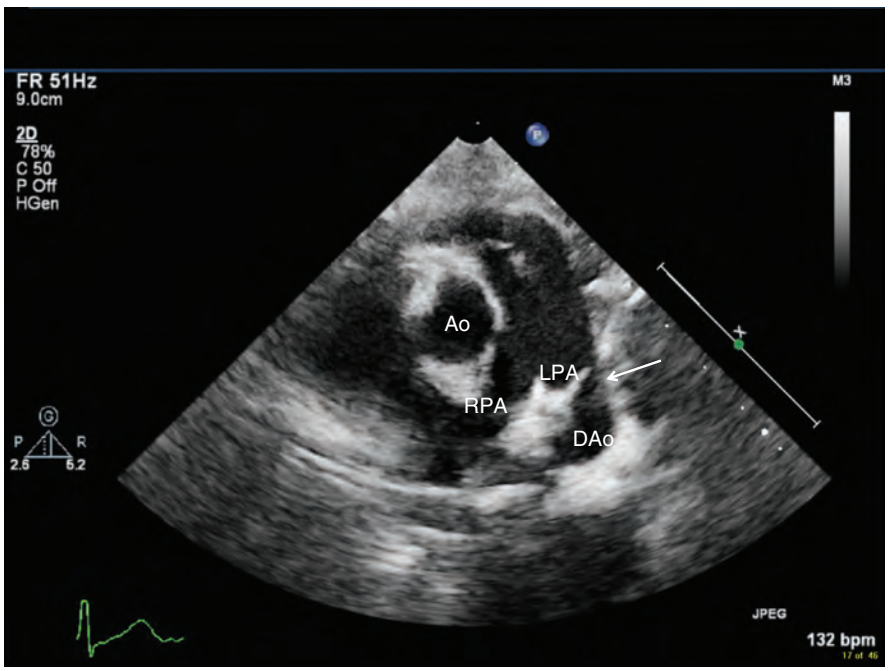


Figure 18.1 Parasternal short-axis image of a small patent ductus arteriosus (arrow) that is conical in shape and funnels at the pulmonary end. Ao, aorta; Dao, descending aorta; LPA, left pulmonary artery; RPA, right pulmonary artery

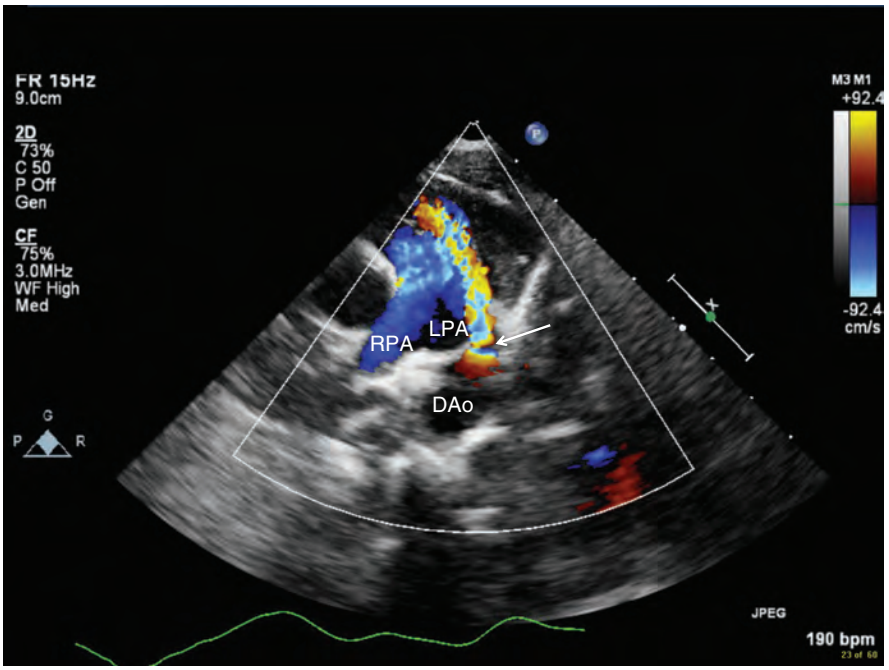


Figure 18.2 Parasternal short-axis color Doppler image of a small patent ductus arteriosus (arrow). Dao, descending aorta; LPA, left pulmonary artery; RPA, right pulmonary artery.

Reverse-oriented PDA

In normal fetal development, blood flow is directed from the MPA to the descending aorta through the DA. The right-to-left flow directionality results in a configuration of the ductal arch with its concave portion facing downward. In circumstances when there is decreased or no flow across the right ventricular outflow tract in fetal life, blood flow is reversed in the DA and is directed from the descending aorta to the MPA. When the flow in the DA originates from the aorta, the DA is long and tortuous, and the abnormal left-to-right flow directionality results in a configuration of the ductal arch with its concave portion facing upward. This ductal course is often referred to as a "reverse-oriented" or "vertical" DA. Reverse-oriented DA is commonly seen in critical right heart obstruction including tricuspid atresia, pulmonary atresia/intact ventricular septum, and tetralogy of Fallot with severe pulmonary stenosis or atresia [19].

Bilateral ductus arteriosi

Bilateral DA may be present in the setting of right aortic arch as described earlier, often with an aberrant left subclavian. Rarely, bilateral DA occurs as an isolated anomaly. Bilateral DA is also associated with congenital heart defects. In one study over two decades, 55% of bilateral DA had their origin from bilateral non-confluent branch PAs to the aorta. This anomaly is likely a result of interruption in the development of the proximal sixth aortic arches (branch PAs), with persistence of both distal sixth aortic arches (bilateral ductus) and continuity with the proximal arches. Bilateral DA has also been associated with interruption of the aortic arch with isolation of the subclavian artery and interruption of the aortic arch in which bilateral DA supports the entire systemic circulation [20].

Ductal aneurysm

Ductal aneurysm is a rare congenital anomaly defined as marked dilation of the DA. The reported incidence varies from 0.8% at neonatal autopsy [21] to 1.5% in a prenatal series [22]. A study in term neonates demonstrated an incidence of 8.8% [23,24]. There is a strong association with chromosomal abnormalities or syndromes (25%) as well as with connective tissue disorders (13%) [22]. An increased incidence of ductal aneurysm has also been noted in infants of diabetic mothers [23]. The variability in reported incidence may be explained by the inconsistent diagnostic criteria and variable age at examination of ductal aneurysms [25,26].

The clinical course for ductal aneurysm is usually benign with closure in approximately 70% by 3 days of age [23]. Symptoms are uncommon and likely occur due to compression of adjacent structures, thrombus formation and extension, or erosion into the airways. Surgical resection is indicated for aneurysms persisting beyond the neonatal period or for those that develop complications [27].

Imaging

In infancy, one of the most common indications for an echocardiogram is to screen for PDA. Echocardiography is necessary for early diagnosis of a PDA, especially in the preterm infant, due to the management implications of this finding [28,29].

Goals of the examination

The objectives of echocardiography in the setting of PDA include:

- Demonstrate the position, size, and course of the PDA with two-dimensional (2D) and color Doppler (Figures 18.1 and 18.2).

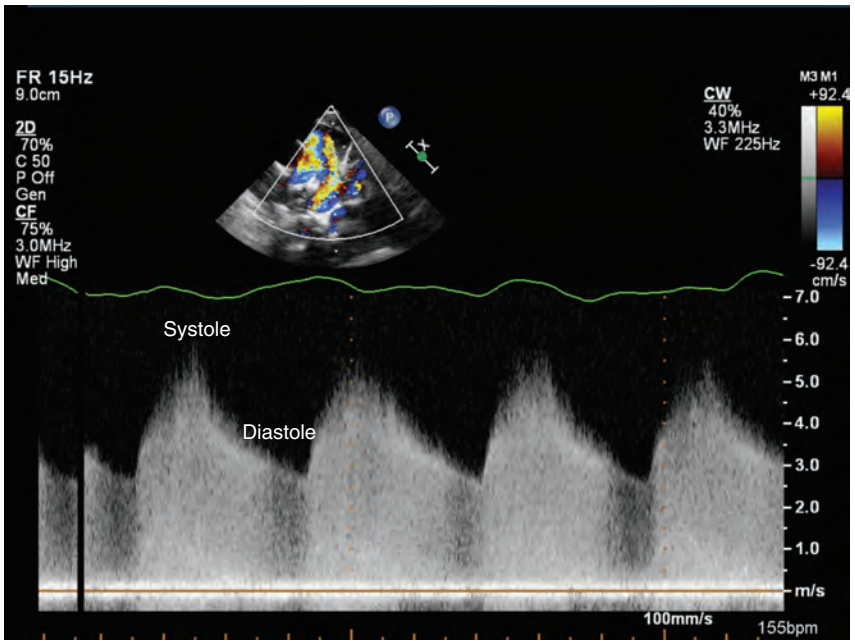


Figure 18.3 Continuous-wave spectral Doppler interrogation of a small restrictive patent ductus arteriosus with a peak velocity of 5 m/sec in systole.

- Measure the narrowest diameter of the PDA on 2D and color Doppler.
- Determine the direction of ductal flow by color and spectral Doppler (Figures 18.2 and 18.3).
- Measure the peak systolic velocity of flow though the PDA. This can be utilized as an estimate of PA pressure (record contemporaneous systemic blood pressure).
- Demonstrate arch sidedness and head vessel branching.
- Assess for potential aortic coarctation. Include transverse arch, isthmus, and descending aorta measurements. Also assess the origin of the left subclavian artery.
- Evaluate the flow profile in the abdominal aorta with color and spectral Doppler for diastolic flow reversal.
- Evaluate branch PAs. Assess for stenosis, especially of the LPA.
- Evaluate left atrial size and left ventricular size and function.
- Demonstrate any associated lesions.

Doppler examination

The most accurate Doppler signal of the PDA flow is often obtained from the high left parasternal window, because this is the view where the transducer is nearest to the PDA. The direction and timing of ductal flow are valuable tools for assessing PA pressure. Three ductal Doppler flow patterns are possible, depending on PA pressure and associated heart lesions:

1 A dominant left-to-right shunt is present in isolated PDA without significant LV outflow tract obstruction or pulmonary hypertension (PVR < systemic vascular resistance) (Figure 18.2; Videos 18.1 and 18.2). Continuous left-to-right flow with a late systolic peak velocity is the characteristic Doppler pattern (Figures 18.3 and 18.4).
2 A bidirectional shunt involves right-to-left flow in systole and left-to-right flow in diastole (Figure 18.5; Video 18.3). Systolic right-to-left flow via a PDA always corresponds to the presence of significant LV outflow tract obstruction, arch obstruction, or significant pulmonary hypertension.
3 A dominant right-to-left shunt is present in the setting of significant LV outflow tract obstruction (ductal-dependent lesion) or severe pulmonary hypertension (PVR ≥ systemic vascular resistance). Continuous or near continuous right-to-left flow with early systolic peak velocity is the characteristic Doppler pattern (Figure 18.6).

Assessment of the clinically significant left-to-right PDA shunt

Once a PDA has been identified, it is important to determine whether the shunt is clinically significant. As the PVR falls after birth, left-to-right shunting via the PDA increases, resulting in increased pulmonary venous return. This eventually leads to left atrial and left ventricular enlargement. In the preterm infant, the following echocardiographic criteria may aid in recognizing a clinically significant left-to-right PDA [30]:

- Smallest PDA diameter ≥1.4 mm/kg
- Left ventricular dilation
- Holodiastolic flow reversal in the descending aorta
- Increase pulmonary blood flow resulting in increased antegrade diastolic flow in the branch PAs, with mean flow velocity ≥0.5 m/s
- Increase velocity of flow in pulmonary veins (with normal phasic pattern on Doppler).

Considerations for the right-to-left PDA shunt

A PDA with right-to-left flow can be difficult to identify because the flow profile through the duct appears similar to the flow in the descending aorta or LPA. Anatomic assessment by 2D imaging accompanied by color Doppler is most important in these

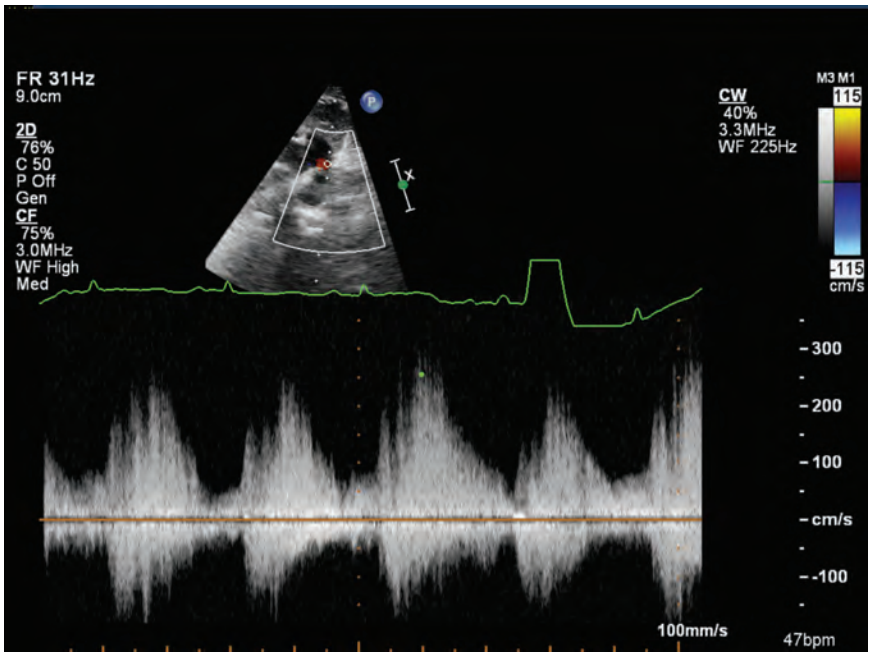


Figure 18.4 Continuous-wave spectral Doppler interrogation of a moderate-size patent ductus arteriosus with left-to-right shunting and peak velocity of 2.5 m/sec in systole.

cases. Detection of a right-to-left PDA can be supported by the presence of severe pulmonary hypertension (see Chapter 45) and arterial oxygen saturation differential between the upper and lower extremities (upper extremities > lower extremities). If there is restriction to a right-to-left ductus, the Doppler flow profile resembles that of coarctation of the aorta. A restrictive right-to-left PDA can be differentiated from coarctation by: (i) imaging an unobstructed aortic arch and isthmus; (ii) clear imaging of flow originating in the MPA and coursing to the descending aorta via a PDA; (iii) evidence of severe pulmonary hypertension (see Chapter 45); and (iv) clinical correlation (normal lower extremity pulses and absence of blood pressure gradient from upper to lower extremities).

Infants with profound pulmonary vascular disease may rarely develop systolic and diastolic flow reversal in the aortic arch. This is due to low cardiac output secondary to low pulmonary blood flow. In this situation, flow from the RV aids systemic perfusion via the PDA and is an indication of decreased left ventricular outflow and worsening clinical status [31,32].

PDA with left aortic arch

In most infants with a PDA, ductal flow can be visualized by color Doppler from the subcostal, apical, parasternal, and suprasternal notch views. Transthoracic imaging in older children may be difficult due to poor acoustic windows (see "Imaging in the adult" later). High left parasternal and suprasternal

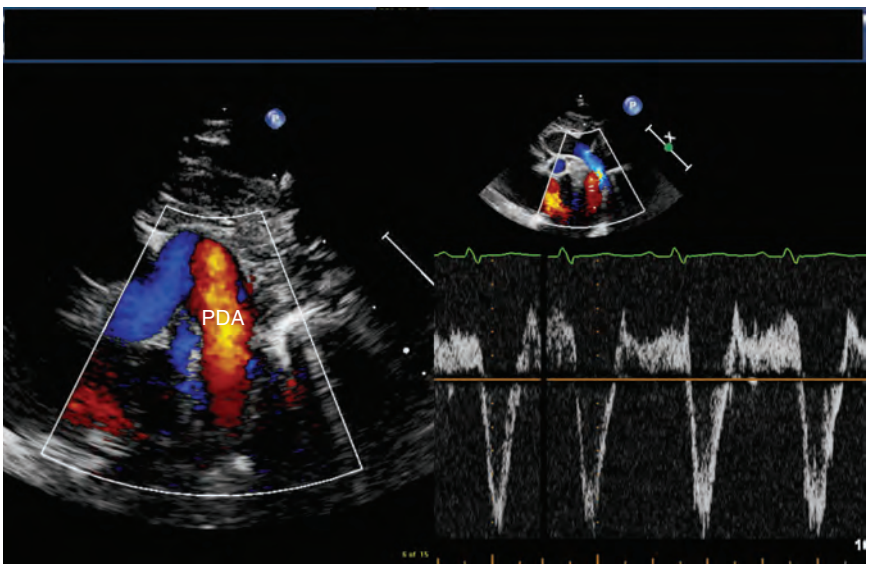


Figure 18.5 Color and pulsed-wave spectral Doppler image from suprasternal notch of a large patent ductus arteriosus with bidirectional shunting; left-to-right in diastole (color image) and right-to-left in systole.

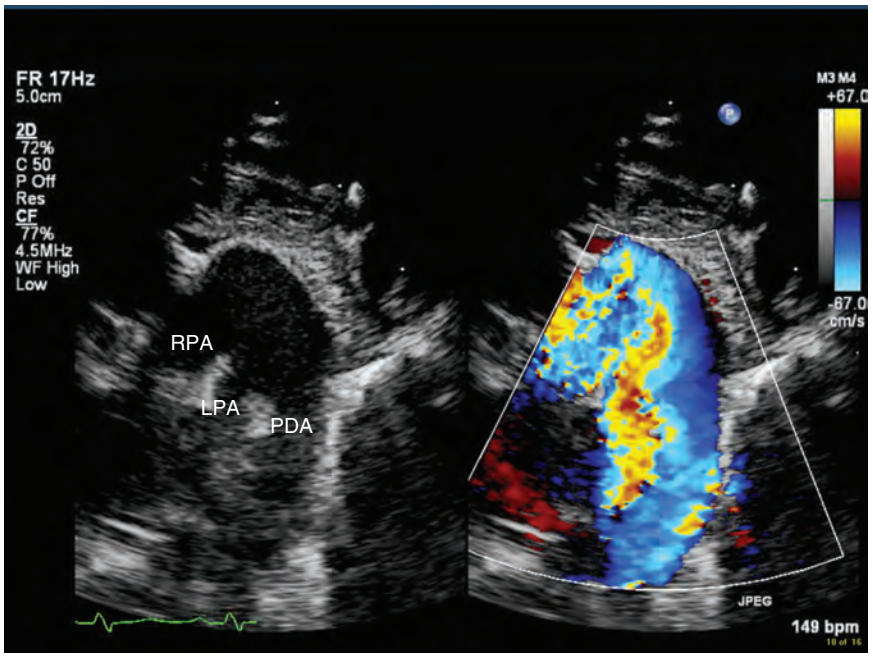


Figure 18.6 Doppler color compare image from suprasternal notch of a large patent ductus with right-to-left shunting. LPA, left pulmonary artery; PDA, patent ductus arteriosus; RPA, right pulmonary artery.

notch views are the best windows for evaluation of a PDA in older children.

Parasternal views

In the parasternal long-axis view, ductal flow can be demonstrated with the transducer angled leftward and superiorly toward the distal portion of the RV outflow tract and MPA. This acoustic window is only useful if the extension of the jet from the PDA to the MPA is relatively long. In the parasternal short-axis view, the PDA is visualized by 2D along the left lateral border of the MPA, usually leftward of the LPA. Cranial tilt of the transducer demonstrates the PDA. In the setting of a typical left-to-right PDA, flow is directed toward the transducer. Movement of the transducer superiorly to the high left parasternal window and clockwise rotation allows for visualization of the pulmonary artery (PA) bifurcation. From this view, counterclockwise rotation of the transducer toward 12 o'clock demonstrates the entire length of the PDA with its connection from the underside of the descending aorta to the LPA. This view is often called the "ductal view."

It is not uncommon to see a color Doppler flow pattern in normal individuals that can be confused for PDA flow. In the parasternal short-axis view, a flow signal directed toward the transducer can sometimes be seen along the medial aspect of the MPA in early systole. This flow pattern most likely represents helical flow within the MPA, a consequence of flow in a curved tube [30]. The medial location and systolic timing of the flow distinguish this flow profile from typical left-to-right ductal flow.

Suprasternal window

With the aortic arch in view, a slight leftward tilt of the transducer demonstrates the LPA. A slight clockwise rotation of the transducer will reveal the LPA and the descending aorta in the same plane. Once both of these vessels are imaged simultaneously, the PDA, if present, will be visualized in this plane.

PDA with right aortic arch

Evaluation of a PDA associated with a right aortic arch begins with determination of arch sidedness. The suprasternal coronal view is the best acoustic window for assessing arch sidedness and brachiocephalic vessel branching order. With the transducer rotated toward 3 o'clock (coronal plane), sweeps should progress from anterior–inferior to superior–posterior. The transducer is initially angled to visualize the ascending aorta in cross-section. Angling the transducer superiorly, the ascending aorta can be followed to the level of the transverse arch, and the innominate vein is visualized anterior to the distal ascending aorta. Just posterior to the innominate vein, the first brachiocephalic artery branches from the aortic arch. The direction of the first branch, the innominate artery, is opposite to the arch side.

Once the side of the first brachiocephalic artery is determined, the next step is to determine whether this artery bifurcates. This is evaluated by following the vessel as it courses towards the neck. If it does not bifurcate, this branch is most likely the ipsilateral carotid artery, which can be confirmed by following it to the neck. In such circumstance, an aberrant origin of the subclavian artery from the proximal descending aorta is suspected. The aberrant subclavian artery is often visualized with the use of color Doppler inferior and separate from the carotid artery. Alternatively, the origin of the aberrant subclavian artery from the proximal descending aorta can be visualized from the suprasternal coronal view. The descending aorta is evaluated by 2D and color Doppler for an artery that courses medially and superiorly in the posterior mediastinum. In young patients the

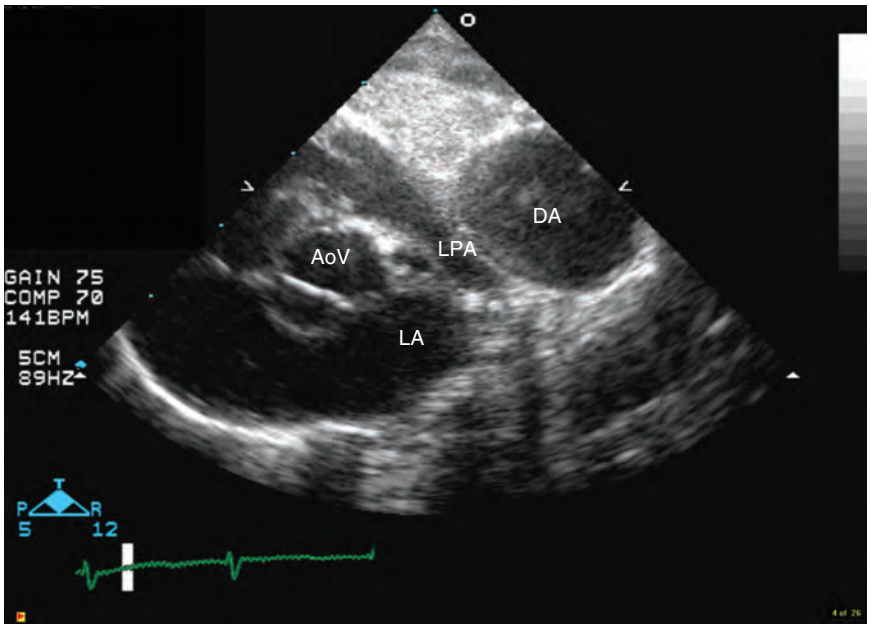


Figure 18.7 Parasternal short-axis image of a large ductal aneurysm. AoV, aortic valve; DA, ductal aneurysm; LA, left atrium; LPA, left pulmonary artery.

proximal descending aorta can be evaluated for an aberrant subclavian artery from the subcostal windows.

Assessment of PDA course

The PDA in a right aortic arch can originate from the proximal descending aorta and/or the base of the left subclavian artery. Both of these sites must be interrogated with 2D, color and spectral Doppler for potential arterial flow heading toward the PA, consistent with a PDA. The PDA is visualized in its entirety, to determine its course. This can be achieved from a high parasternal view or suprasternal view. A right-sided PDA courses from the proximal descending aorta to the origin of the right pulmonary artery (RPA). A left-sided PDA courses from the left subclavian artery to the origin of the LPA. Demonstration of a right aortic arch, aberrant left subclavian artery, and a left-sided PDA confirms the diagnosis of a vascular ring (see Chapter 31).

Reverse-oriented PDA

A reverse-oriented PDA arises from the underside of the aortic isthmus, and its tortuous course is best seen during visualization of the aortic arch in the suprasternal long-axis view (Videos 18.4 and 18.5). Following the length of the PDA with color Doppler interrogation demonstrates its entire course. Often it is difficult to visualize the entire length of the PDA in a single plane due to its tortuosity. If a reverse-oriented PDA is identified, detailed assessment of the RV outflow tract and PAs is imperative to exclude stenosis or atresia of these segments. In particular, the PA segment at or just distal to the duct insertion site should be imaged in detail for discrete stenosis or luminal discontinuity.

Bilateral PDA

Imaging of bilateral DA requires a high index of suspicion and familiarity with the anatomic possibilities. Accurate diagnosis requires interrogation of the aortic isthmus and ipsilateral branch PA as well as the base of the innominate artery or proximal subclavian artery on the opposite side. The possibility of bilateral PDA should be investigated in the setting of a right aortic arch with aberrant origin of the left subclavian artery, in congenitally absent mediastinal branch PA, discontinuous branch PAs associated with other congenital heart disease such as tetralogy of Fallot, interrupted aortic arch type B, isolation of a subclavian artery, and other. Echocardiographic evaluation, especially with color Doppler, of all possible sites of ductal insertion is required to exclude the presence of bilateral PDA (Video 18.6).

Ductal aneurysm

Parasternal view

When imaging from the high left parasternal transverse (short-axis) view, ductal aneurysm is suspected when unusual flow is noted from the PDA to the MPA. A large vessel is visualized leftward and superior to the LPA with the restricted portion of the duct at its insertion into the MPA. Thus, three large vessels are seen from medial to left lateral position: the ascending aorta, MPA, and ductal aneurysm (Figures 18.7 and 18.8; Videos 18.7 and 18.8).

Suprasternal view

A characteristic image of ductal aneurysm is visualized from a suprasternal short-axis view. Angling the transducer posteriorly to image the descending aorta, the "rabbit-ear sign" is seen. The right-sided ear is the transverse aortic arch and the descending aorta and the left-sided ear comprises the ductal aneurysm. Ductal aneurysm generally demonstrates saccular dilation with a maximal internal diameter larger than that of the adjacent transverse arch or descending aorta [23]. Images that mimic ductal aneurysm include mirror image aliasing of the PA, normal soft

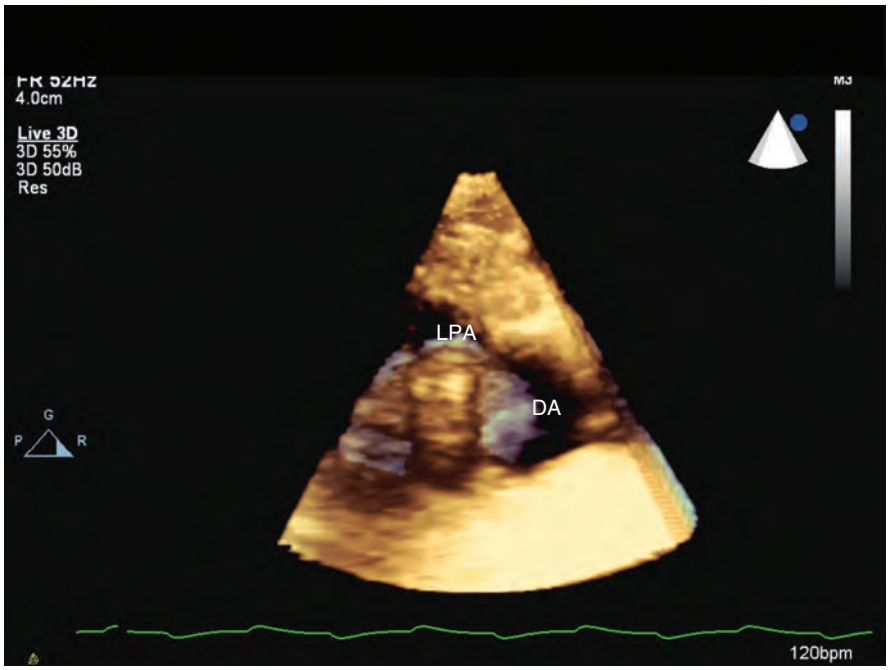


Figure 18.8 Parasternal short-axis three-dimensional image of a large ductal aneurysm. DA, ductal aneurysm; LPA, left pulmonary artery.

tissue shadow of the superior portion of the PDA, left superior vena cava, dilated left atrial appendage, and a vertical duct.

Prenatal assessment

A PDA is a normal structure in the fetus (see detailed discussion in Chapter 44).

Imaging in the adult

PDA is uncommon in adults; however, when present it is associated with several complications including calcification, endocarditis, aneurysm formation, dissection, rupture, left heart volume overload, and pulmonary vascular disease. Transthoracic echocardiographic imaging of PDA in adults is challenging due to restricted acoustic windows. Imaging is best performed from the suprasternal view, using techniques similar to those described in pediatric patients. Cardiac computed tomography and magnetic resonance imaging (MRI) provide noninvasive evaluation of the PDA when echocardiographic evaluation is inconclusive. Cardiac MRI is preferred due to its ability to not only visualize the PDA, but also to assess its hemodynamic effects, including biventricular size and function and estimation of pulmonary-to-systemic flow ratio.

Echocardiographic assessment during and after PDA closure

Preterm infants

In preterm infants PDA closure can be induced by pharmacologic means. However, even after documentation of cessation of ductal flow, recurrence can occur. When medical therapy fails, surgical ligation and division via lateral thoracotomy is usually performed if the PDA is hemodynamically significant. Echocardiography is performed to assess the status of the ductal flow before and after treatment.

Older children and adults

In older patients, closure of the PDA can be performed via surgical ligation and division or by minimally invasive thoracoscopic clipping. In recent years, transcatheter occlusion has become the treatment of choice when feasible [5]. Transcatheter closure is achieved by endoluminal placement of a coil or occluding device into the PDA. After surgical or transcatheter PDA occlusion, echocardiography is utilized to assess for residual ductal shunt and/or inadvertent impingement of the LPA or descending aorta. In patients after transcatheter PDA closure, echocardiography is also useful in identifying device position and inadvertent migration (Figures 18.9 and 18.10; Videos 18.9 and 18.10) [33].

Echocardiographic assessment during and after PDA stenting

Stenting of the PDA in duct-dependent cyanotic congenital cardiac anomalies has become a nonsurgical alternative to conventional systemic-to-PA shunt surgery. In cases where ductal stenting is considered, echocardiographic evaluation of PDA origin from the aorta, site of insertion into the PA and its course (long and tortuous versus short and straight) is imperative. Accurate description of the PDA aids in determination of the feasibility of successful stent placement. Echocardiographic imaging following stent placement initially assesses for inadvertent occlusion of the PA or descending aorta by the stent (Figure 18.11; Video 18.11). These patients are followed closely

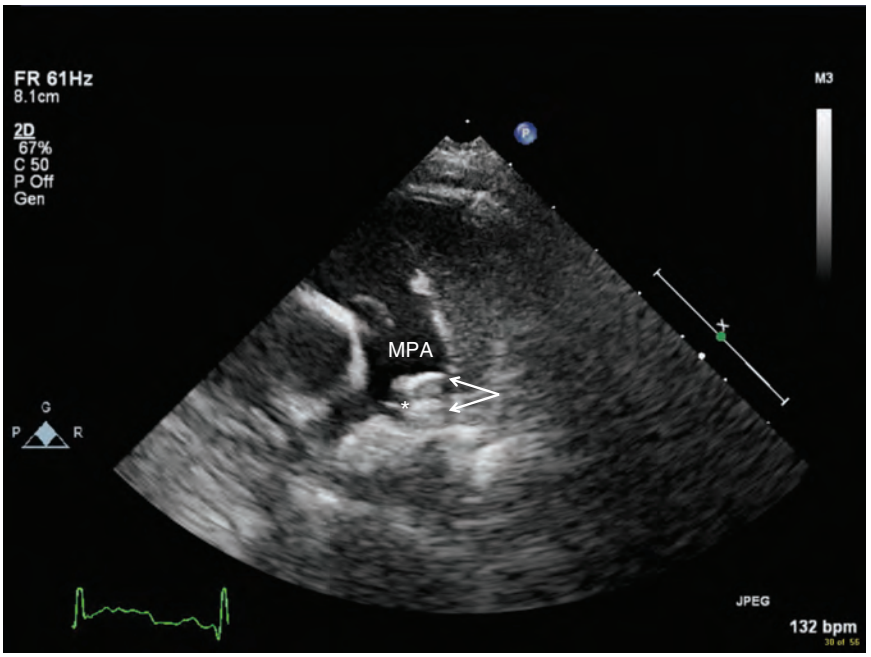


Figure 18.9 Parasternal short-axis image of a ductal occluder device (double arrow) causing near complete occlusion of the proximal left pulmonary artery (∗). MPA, main pulmonary artery.

with echocardiography to exclude stent occlusion by thrombus formation or neointimal proliferation [34–36].

Abnormalities of the pulmonary arteries

Definition

In normal anatomy, the MPA emanates from the right ventricle supported by an infundibulum and travels to the left of the ascending aorta in the direction of the left shoulder. As it bifurcates, the LPA continues as a smooth arch and courses over the left bronchus. The RPA arises at an acute angle and courses posterior to the ascending aorta and superior vena cava. Congenital anomalies of the PAs include branch PA stenosis, hypoplasia, discontinuity, absence, and abnormal origin (e.g., from the ascending aorta).

Morphology

Embryologic considerations

The MPA and its branches have their origins from three separate vascular components. The proximal portion of the pulmonary

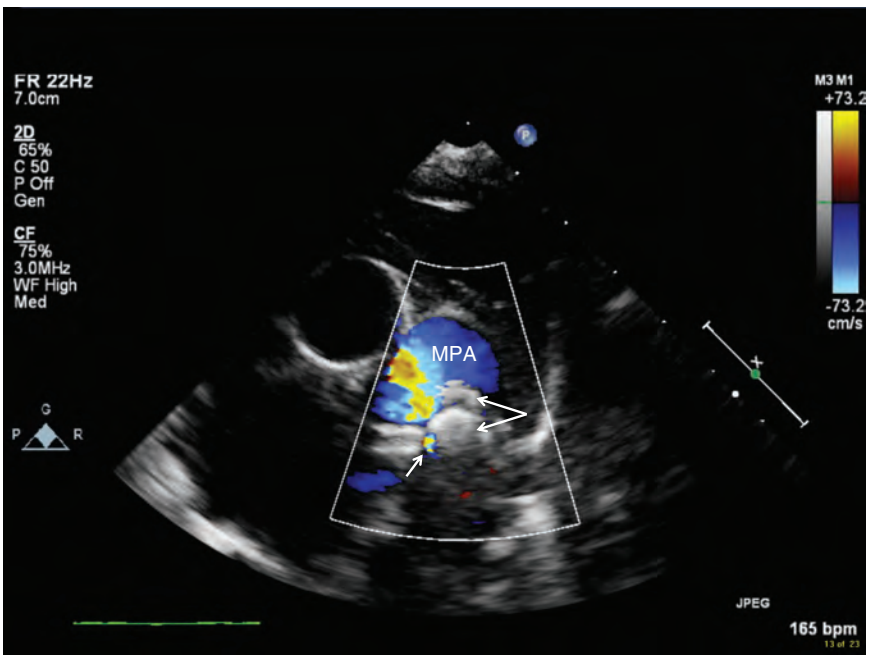


Figure 18.10 Parasternal short-axis color Doppler image of a ductal occluder device (double arrow) causing near complete occlusion of the proximal left pulmonary artery (single arrow) with minimal color flow around device. MPA, main pulmonary artery.

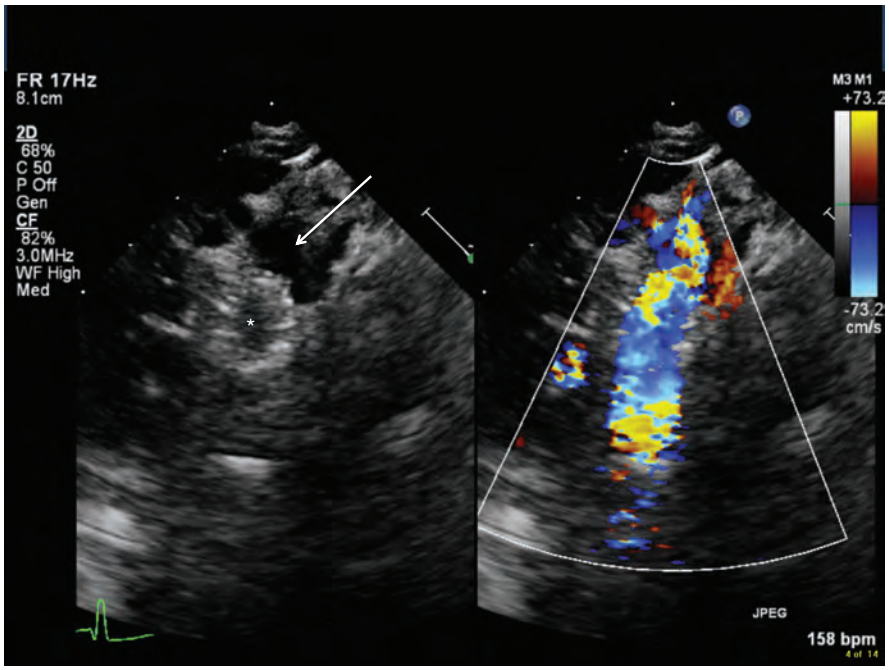


Figure 18.11 Doppler color compare image from suprasternal notch of a ductal stent placed as part of a hybrid procedure for hypoplastic left heart. Ductal stent (∗) allows for unobstructed flow into native aortic arch (arrow).

trunk develops from the cranial end of the bulbus cordis (conus cordis) and the distal portion of the pulmonary trunk is derived from division of the truncus arteriosus into the MPA and ascending aorta. The proximal portions of the right and left PAs are formed from the proximal portions of the right and left sixth arches. The distal portions of the pulmonary artery branches arise from the postbranchial pulmonary vascular plexus [11].

Congenital branch pulmonary artery stenosis

Incidence and etiology

Congenital stenosis of the pulmonary arteries, isolated or in association with other cardiac defects or genetic syndromes occurs in 2–3% of all patients with congenital heart disease [4]. The pathogenesis of branch PA stenosis is not completely understood. It appears that multiple factors and many types of pathologic changes may produce narrowing of the branch PAs. When intracardiac anomalies are associated, the pathogenesis is likely developmental in origin. Certain teratogenic agents may interfere with the development of any of the components of the PA tree and may lead to stenosis, hypoplasia, or atresia. Specific genetic abnormalities associated with PA branch stenosis have also been identified [37].

Pathophysiology

The physiology associated with branch PA stenosis depends on the severity and distribution of the stenoses, and may result in elevated RV and PA (proximal to stenosis) systolic pressure. In most cases, the obstruction is central. Bilateral branch PA stenosis results in right ventricular pressure overload and hypertrophy.

Physiologic branch pulmonary artery stenosis

Branch pulmonary stenosis may be mild and transient in the neonate. Physiologic branch PA stenosis in infants is a common cause of functional murmur and sometimes results in referral for echocardiographic evaluation. It is characterized by a mild increase in branch PA flow velocity, less than 2 m/s, in the absence of discrete anatomic narrowing or hypoplasia. The PA stenosis in these cases usually resolves within several months as the PAs remodel [38]. The flow velocity may also be increased in the presence of high cardiac output states and atrial level shunts.

Isolated branch pulmonary artery stenosis

Isolated branch PA stenosis is characterized by diffuse arterial involvement generally affecting the main and lobar arteries. When severe, it produces symptoms of RV failure [35,36]. Isolated branch PA stenosis is often associated with a congenital syndrome, the most common being Alagille (often a JAG1 mutation) and Williams–Beuren (caused by a microdeletion at chromosome 7q11.23) syndromes [39–42]. In Alagille syndrome, branch PA stenosis is found in 76% of patients, 10% have tetralogy of Fallot [42]. Approximately 50% of patients with Williams–Beuren syndrome have peripheral pulmonic stenosis, which can be progressive [43]. Isolated branch PA stenosis has also been associated with Noonan syndrome, cutis laxa, Ehlers–Danlos, Silver–Russell syndrome, and congenital rubella [6,7,44,45]. Although rare, familial and nonfamilial cases of isolated branch PA stenosis with no underlying syndrome have also been described [46].

Branch pulmonary artery stenosis associated with congenital heart disease

Branch PA stenosis associated with congenital heart disease, especially conotruncal anomalies, is discussed in the respective chapters.

Unilateral branch pulmonary artery stenosis

An important cause of unilateral branch PA stenosis, termed PA coarctation, is likely caused by PDA tissue encircling the origin of the branch PA. The stenosis is discrete, and often the proximal portion of the affected PA is distorted. This abnormality is present in 67% and 10% of patients with pulmonary atresia and pulmonary stenosis, respectively [47]. Early identification of this anomaly is imperative, as early correction greatly impacts future PA growth [48]. When the stenosis is unilateral, RV pressure remains normal, because the normal contralateral branch PA can accommodate the cardiac output without pressure increase. Flow to the stenotic side is reduced and the systolic pressure difference tends to underestimate the severity of the obstruction.

Discontinuous branch pulmonary arteries

Congenitally discontinuous branch PAs may be due to regression of the proximal sixth arch segment as part of a conotruncal anomaly [20]. The incidence of chromosome 22q11 deletion is increased in these patients (45%), as compared to patients with normal left aortic arch with normal branching (3%) [49,50]. Discontinuous branch PAs with bilateral ductus arteriosus are present in up to 16% of patients [51–53].

Anatomic variants of discontinuous PAs include: (i) both branch PAs discontinuous with each other and with the RV outflow tract – each PA is supplied by either a PDA or an aortopulmonary collateral vessel; (ii) branch PAs discontinuous with each other – one PA is continuous with the RV outflow tract and the other PA is supplied by either a PDA or a collateral vessel [54]. Early diagnosis is important as growth of the affected branch PA is most successful with early surgical recruitment and establishment of antegrade flow [49,55].

Congenital absence of a branch pulmonary artery

Congenital absence of a branch PA is a rare anomaly most frequently associated with other congenital heart disease, especially tetralogy of Fallot. Other cardiac anomalies that have been associated with absent branch PA include coarctation of the aorta, subvalvar aortic stenosis, transposition of the great arteries, and Taussig–Bing malformation. A few cases of isolated congenital absence of a branch PA have also been reported [56]. The absent mediastinal PA is usually contralateral to the side of the aortic arch. In fetal life and in neonates, the distal branches of the absent PA are supplied by a PDA or aortopulmonary collateral. The PDA usually arises from the base of the subclavian artery contralateral to the side of the aortic arch and terminates on the side of the absent PA at or near the hilum of the affected lung. Upon closure of the PDA, a dimple is seen at the base of the subclavian artery [57]. Although some patients with isolated congenital absence of a branch PA are completely asymptomatic, others may have severe pulmonary hypertension and congestive heart failure [58].

Origin of branch pulmonary artery from the ascending aorta

Origin of a branch PA from the ascending aorta is a rare congenital cardiac abnormality. The developmental etiology of this anomaly is not well understood, but several theories exist. One consideration is incomplete migration of the affected branch PA towards the contralateral PA. Alternatively, the defect may result from failure of fusion of one of the sixth arches with the MPA [59]. Ascending aortic origin of a branch PA is often associated with other cardiac anomalies, including tetralogy of Fallot, pulmonary atresia and interrupted aortic arch [59–61]. It has also been associated with chromosome 22q11 microdeletion [61,62].

Typically, the anomalous branch pulmonary artery arises from the posterolateral wall of the ascending aorta above the aortic sinus. Alternatively, the PA can originate distally from the ascending aorta near the origin of the innominate artery [61,63,64]. Origin of the RPA from the ascending aorta occurs more commonly than origin of the LPA. Anomalous origin of the RPA is invariably associated with a left aortic arch, and usually a left-sided PDA. Anomalous origin of the LPA from the ascending aorta is rare and is usually associated with a right aortic arch [59] and right-sided PDA. In the setting of tetralogy of Fallot, the anomalous branch PA is often larger than branch PA that arises normally from the MPA [60].

Physiologically, the lesion may result in abnormal pulmonary vasculature in the associated lung [60]. Stenosis of the affected branch PA is unusual. Coronary ischemia is a reported adverse outcome, likely related to steal phenomenon or low aortic diastolic pressure [61]. Irrespective of the mechanism, early diagnosis and surgical repair is important to prevent the development of irreversible pulmonary vascular disease [60,65].

In the past, origin of a branch PA from the ascending aorta was referred to as a "hemitruncus." This anomaly is distinct from truncus arteriosus embryologically and morphologically, as it occurs in the setting of normal separation of the aortic and pulmonary valves. Aortic origin of a branch PA should be distinguished from other cardiac defects associated with abnormal aortopulmonary flow such as PDA, major aortopulmonary collaterals, truncus arteriosus, or discontinuous branch PA with ductal connection to the aorta.

Crossed pulmonary arteries

Normally, the RPA originates from the MPA lower than the LPA. In crossed PAs, the LPA ostium lies rightward and superior to the RPA ostium. As a result, the branch PAs must cross each other proximally as they course to their respective lungs [66,67]. Despite the anomalous course of the crossed PAs, a PDA usually arises from its normal position, at the base of the LPA. A variation of this entity, PA malposition, occurs when the ostium of the LPA is located directly superior to the RPA without

crossing of the proximal branch PAs. Crossed PAs may be confused with a left PA sling, but can be distinguished by the posterior course of the LPA to the left of the trachea in crossed PAs [68]. In one study, approximately 50% of patients with either crossed or malposed PAs had deletion of chromosome 22q11 [67]. When crossed PAs are associated with truncus arteriosus, there also tends to be an interruption of the aortic arch [69].

Imaging

All patients referred for an echocardiogram due to suspected congenital heart disease or associated syndromes should undergo careful evaluation of the main and branch pulmonary arteries. Early identification of congenital abnormalities of the PAs results in early surgical and/or transcatheter intervention and increased potential for PA growth and improved right heart hemodynamics [48,49]. Careful examination of the PAs is imperative after surgical repair involving manipulation of the MPA or branches, such as in the LeCompte maneuver for arterial switch operation. Swirling of color flow in the MPA is a normal variant that is characterized by systolic reversal of flow, usually in the rightward aspect of the MPA.

Goals of imaging

- Demonstrate the morphology (position and size) of the MPA and branch pulmonary arteries with 2D and color Doppler from multiple views (parasternal long- and short-axis, suprasternal long- and short-axis).
- Measure the MPA prior to its bifurcation at the largest internal diameter and the branch PAs just beyond their bifurcation on 2D and color Doppler.
- Evaluate for stenosis or long-segment hypoplasia by 2D and measure at the narrowest diameter.
- Assess the direction of flow (i.e., forward versus reversal) by color and spectral Doppler, especially when distal stenosis is suspected.
- Measure the peak systolic flow velocity in the main and branch PAs. Both pulsed- (PW) and continuous-wave (CW) Doppler should be utilized.

Branch pulmonary artery stenosis

Branch PA stenosis can be subtle, and both 2D and color Doppler assessment are necessary to adequately assess for narrowing. Careful attention to the Doppler color scale is important to not over- or underestimate the degree of branch stenosis. The branch PAs are imaged from the parasternal and suprasternal windows (Figure 18.12; Video 18.12). From the suprasternal window, with the transducer turned toward 3 o'clock, the greatest length of the LPA and RPA is visualized. Evaluation by 2D imaging includes determination of the extent of stenosis, measurement of the narrowest diameter, and assessment of poststenotic dilation. Note that measurements derived from color Doppler images often overestimate the PA diameter.

When color Doppler is employed, any flow reversal should be noted, as this is suggestive of pulmonary regurgitation, distal

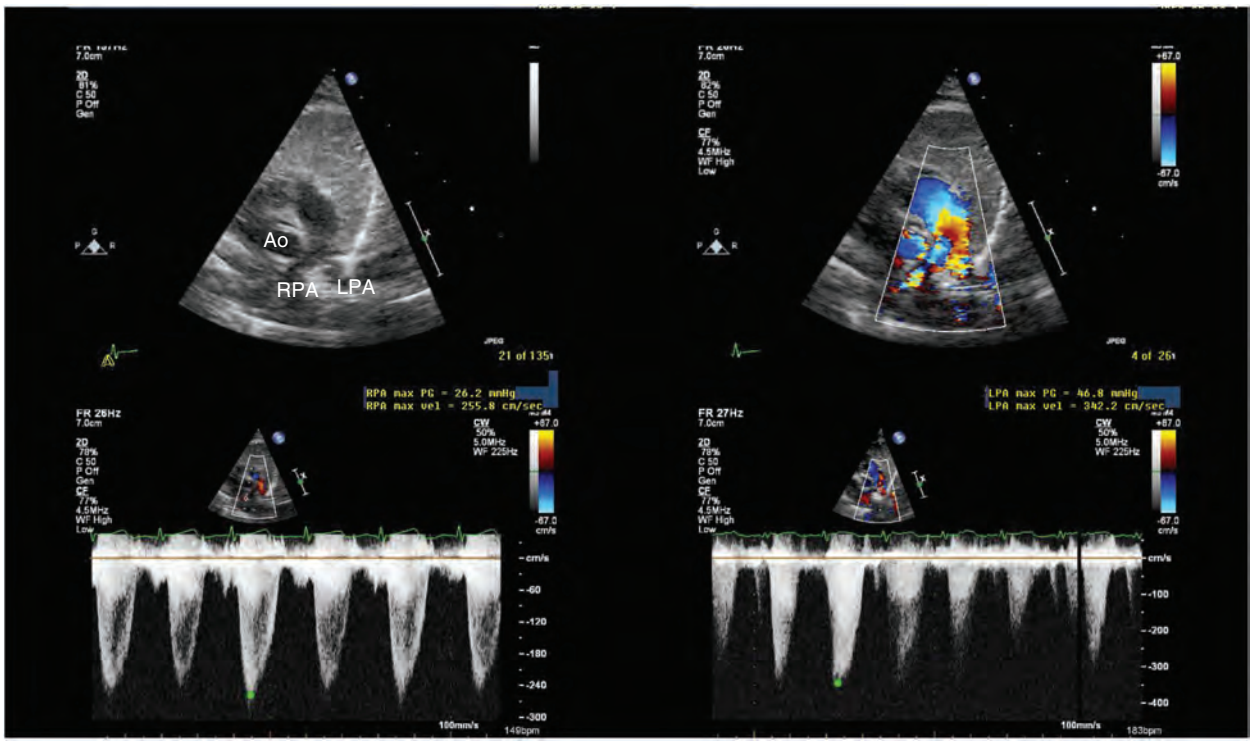


Figure 18.12 Parasternal short-axis color compare and spectral Doppler images of mild bilateral pulmonary artery stenosis. Ao, aorta; LPA, left pulmonary artery; RPA, right pulmonary artery.

stenosis, increased stiffness, or elevated resistance. Discrete narrowing may be masked by the systolic color flow, but can be identified in diastole when reversed flow is noted. If any pulmonary regurgitation is noted with reversal in the branch PAs, the diameter of reversed flow through the stenotic area will demonstrate more stenosis than the systolic forward color flow.

In the setting of unilateral branch PA stenosis, flow may be diverted from the stenotic branch to the normal branch, which results in decreased flow to the stenotic branch. Doppler evaluation of peak flow velocity can underestimate the degree of obstruction in these cases. Due to low flow rate across the stenotic artery, the spectral Doppler may demonstrate normal flow velocity (no gradient) across the affected artery. Due to increased flow across the normal contralateral branch PA, the spectral Doppler may demonstrate increased flow velocity in that vessel. Thus, Doppler evaluation of branch PA stenosis should be done in the context of flow rate in both PAs.

Spectral Doppler-derived peak systolic and mean gradients are calculated. The peak systolic gradient by Doppler correlates well with the catheter-derived peak-to-peak pressure gradient and catheter-derived maximal instantaneous pressure gradient. Still, the Doppler-derived peak gradient tends to overestimate the peak-to-peak catheter gradient by as much as 25–40% [70,71]. Echocardiographic evaluation of the severity of branch PA stenosis relies on careful assessment of the PA anatomy by 2D and estimation of RV pressure (tricuspid regurgitant gradient, RV hypertrophy, and ventricular septal configuration). Lung perfusion scan and MRI are useful for quantifying differential pulmonary blood flow, and may aid in echocardiographic evaluation of branch pulmonary stenosis.

Discontinuous pulmonary arteries

The diagnosis of discontinuous PAs should be considered during echocardiographic evaluation of all patients with conotruncal anomalies (especially in the setting of pulmonary atresia) and/or chromosome 22q11 deletion. If a patient has bilateral ductus arteriosus with tetralogy of Fallot, the likelihood of discontinuous PAs is high.

The imaging technique for identifying discontinuous PAs is similar to that described for imaging the PDA and branch PA stenosis. The RV outflow, MPA, and bifurcation of each branch PA are assessed from multiple views. The high left parasternal and suprasternal views are often most useful in identifying discontinuous PAs. From the high left parasternal view, continuation of the branch PAs from the MPA can appear falsely normal because the LPA and RPA overlap each other in their course. Furthermore, the walls that separate the branch PAs may be difficult to visualize, as they are parallel to the ultrasound beam. By moving the transducer slightly clockwise and rightward, toward the PA bifurcation, any walls separating the PAs into two vessels can be seen. If PA discontinuity is suspected, it is important to scan each site of possible ductal origin for evidence of a PDA as previously described. Again, the presence of bilateral PDA increases the likelihood of discontinuous branch PAs. In infants and young children, a small PDA supplying the distal aspect of the discontinuous branch PA may be seen by color Doppler. Subcostal sagittal imaging of the aortic arch and descending aorta is also useful to identify aortopulmonary collateral vessels. Coronal subcostal imaging may help to identify the pulmonary branches.

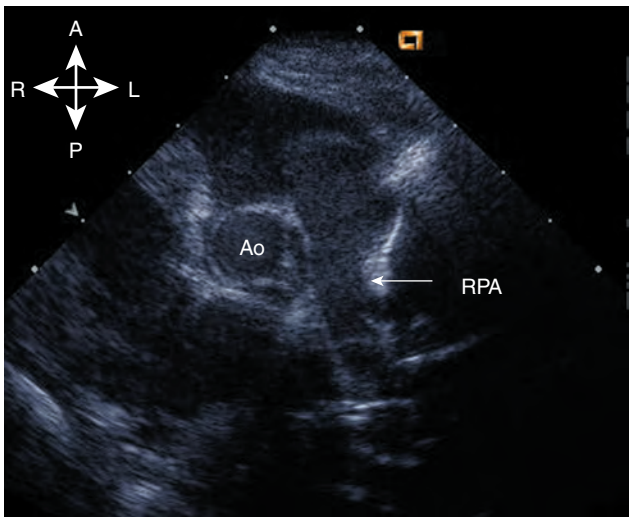
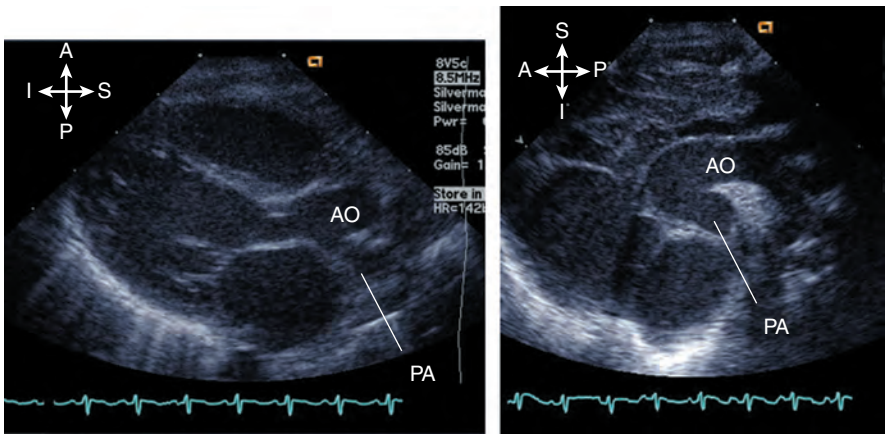


Figure 18.13 Imaging of congenitally absent right pulmonary artery (RPA) from the high left parasternal view. Note the normally located main and left pulmonary arteries, absence of pulmonary artery bifurcation, and no right pulmonary artery coursing posterior to the ascending aorta. Ao, aorta.

Congenital absence of a branch pulmonary artery

When one of the branch PAs is not visualized after careful evaluation from multiple acoustic windows, congenitally absent branch PA is suspected, especially in the setting of other congenital heart disease (Figure 18.13). When congenital absence of a branch PA is an isolated finding without additional cardiac anomalies, the absent branch PA is usually contralateral to the side of the aortic arch [56]. In infants and young children, as previously described in the evaluation of discontinuous branch PAs, a small PDA may be seen supplying the distal branches of the absent PA. Usually the PDA arises from the base of the subclavian artery contralateral to the side of the arch and terminates on the side of the absent PA at or near the hilum of the affected lung. All possible sites of ductal origin should be imaged, beginning with the subclavian artery on the side of the absent PA. In the presence of a ductus arteriosus, pulsed-wave Doppler demonstrates normal pulsatile flow in the normal branch PA, and continuous flow in the branch PA arising from the PDA.

Echocardiographic assessment should also include evaluation for RV hypertrophy, pulmonary hypertension, and presence of aortopulmonary collaterals to the affected lung. Further noninvasive imaging via cardiac computed tomography or magnetic resonance imaging will confirm the diagnosis and delineate the pulmonary artery anatomy and aortopulmonary collaterals if present.



(a) (b)

Figure 18.14 Origin of the right pulmonary artery (PA) from the proximal ascending aorta. This patient has otherwise normal cardiac anatomy. **(a)** Parasternal long-axis view demonstrating the origin of the right PA from the posterior aspect of the ascending aorta. **(b)** Suprasternal notch view of arch demonstrating the origin of the right PA from the posterior aspect of the aorta. AO, aorta.

Aortic origin of a branch pulmonary artery

Echocardiographic evaluation of aortic origin of a branch PA begins with identification of two separate outflow tracts and semilunar valves and absence of the usual MPA bifurcation. The unaffected branch pulmonary artery arises normally from the MPA; the affected branch PA originates from the ascending aorta (Figure 18.14). The branch PAs are discontinuous and the arch sidedness and PDA are usually contralateral to the anomalous PA. The ascending aorta is imaged in multiple views, including subxiphoid long- and short-axis, apical 5-chamber, parasternal long- and short-axis, and suprasternal long-axis. The abnormally connected branch PA is often seen originating from the posterolateral aspect of the proximal ascending aorta. Less commonly, the anomalous PA arises from the distal portion of the ascending aorta, proximal to the origin of the innominate artery. Echocardiographic assessment for pulmonary hypertension reveals systemic pulmonary pressure.

Anomalous branch PA arising distally from the ascending aorta can be confused with congenitally absent branch PA with PDA supply to the intrapulmonary branches. As previously described, the PDA of an absent branch PA originates from the base of the subclavian artery ipsilateral to the absent PA. Anomalous aortic origin of the branch PA is from the ascending aorta proximal to the innominate artery. Aortopulmonary window should also be considered in the differential diagnosis during echocardiographic imaging. Aortopulmonary window has normal PA bifurcation, and is best seen from a high left parasternal view. Anomalous aortic origin of a branch PA will not demonstrate normal PA bifurcation from any view.

Crossed pulmonary arteries

Crossed pulmonary arteries can be diagnosed by identification of the LPA originating superior to the RPA without overlapping of the branch PAs (Figure 18.15). The best window for visualization of the branching of both PAs is in the high left parasternal view. Normally the bifurcation is seen in the same plane, but in crossed pulmonary arteries, the branching of both PAs cannot be seen in one view. A sweep from inferior to superior reveals the abnormal branching of the LPA and RPA. Beginning inferiorly, first the origin of the RPA from the left side of the MPA is seen. Sweeping superiorly, the RPA is no longer visualized, and the LPA is seen arising from the right side of MPA, coursing leftward toward the left lung (Video 18.13).

Postprocedural echocardiographic assessment of the pulmonary arteries

Patients with branch pulmonary artery stenosis, congenital or acquired, may require surgical correction with pulmonary arterioplasty or transcatheter correction with balloon angioplasty or stenting [72,73]. Postprocedural assessment includes evaluation of the site of repair or stent placement by 2D and Doppler for residual stenosis. When transcatheter stenting is utilized, it is important to assess for thrombus or neointimal proliferation resulting in obstruction to flow (Figure 18.16; Video 18.14). Three-dimensional imaging can help to define the origins en face as well as display cine-angiographic simulation as shown in Figure 18.17 and in Videos 18.15 and 18.16.

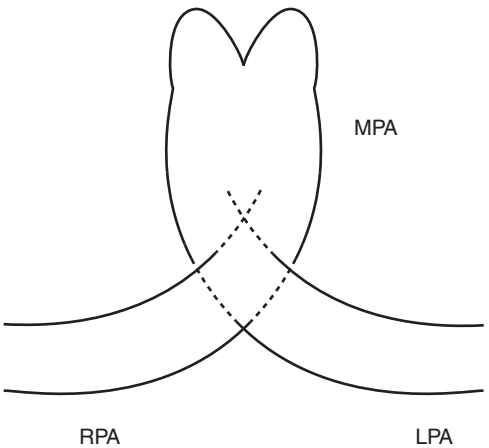
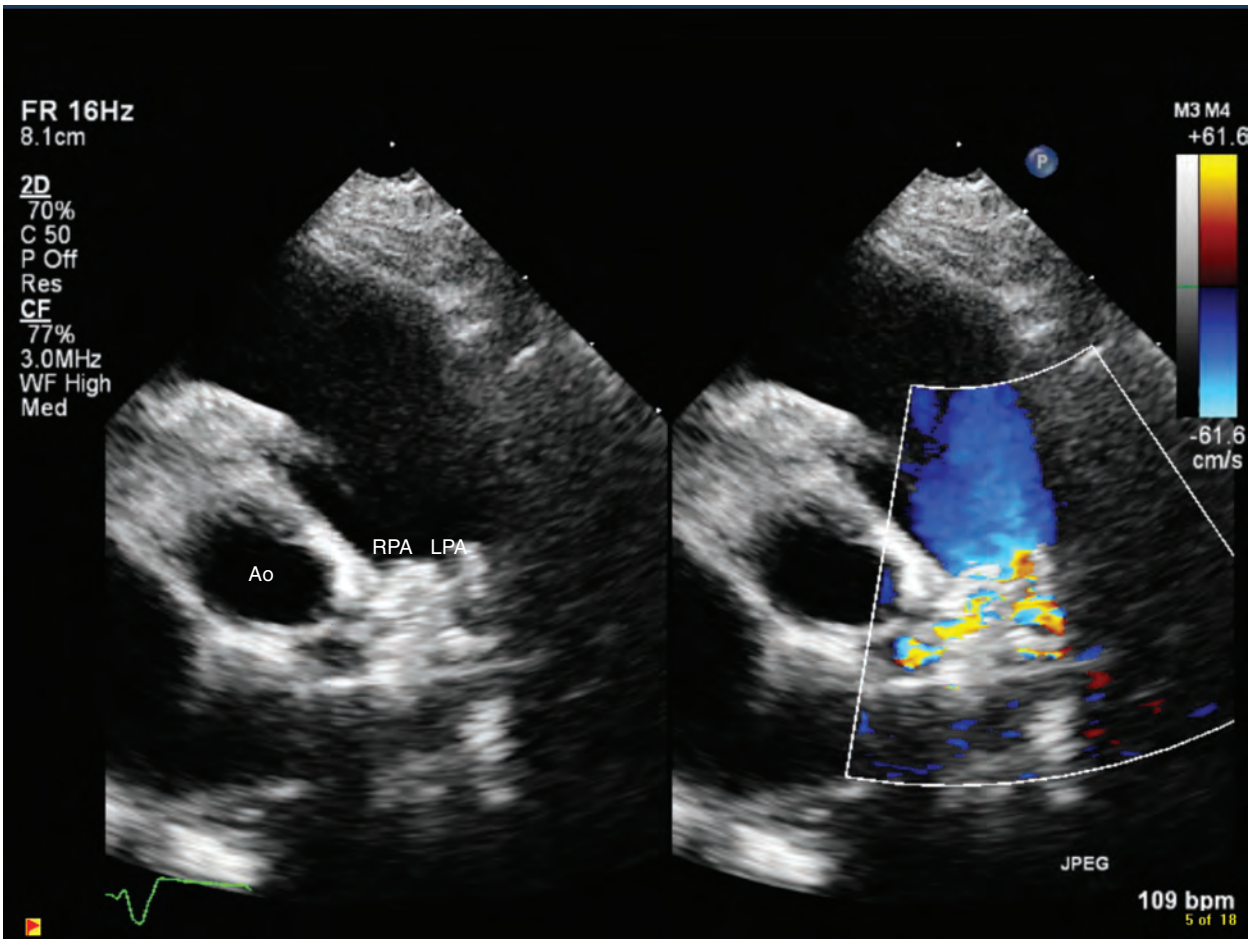
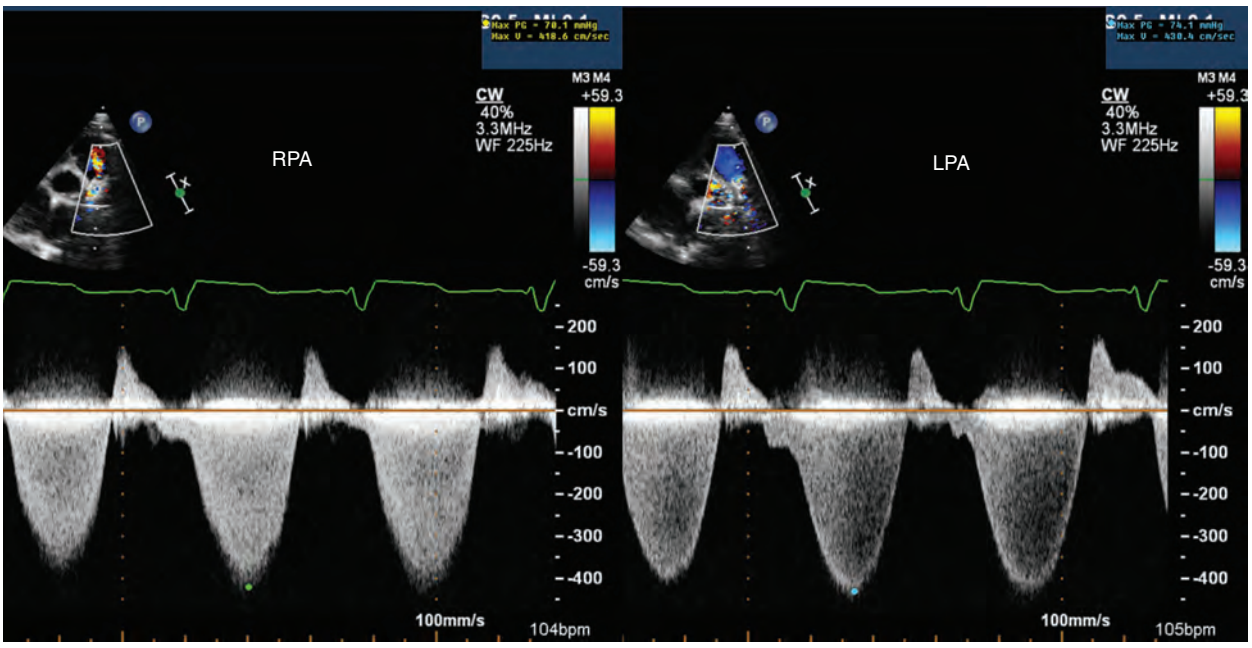


Figure 18.15 Diagram showing crossed pulmonary arteries. The right pulmonary artery (RPA) is inferior and arises from the leftward aspect of the main pulmonary artery (MPA). The left pulmonary artery (LPA) is superior and arises from the rightward aspect of the MPA.

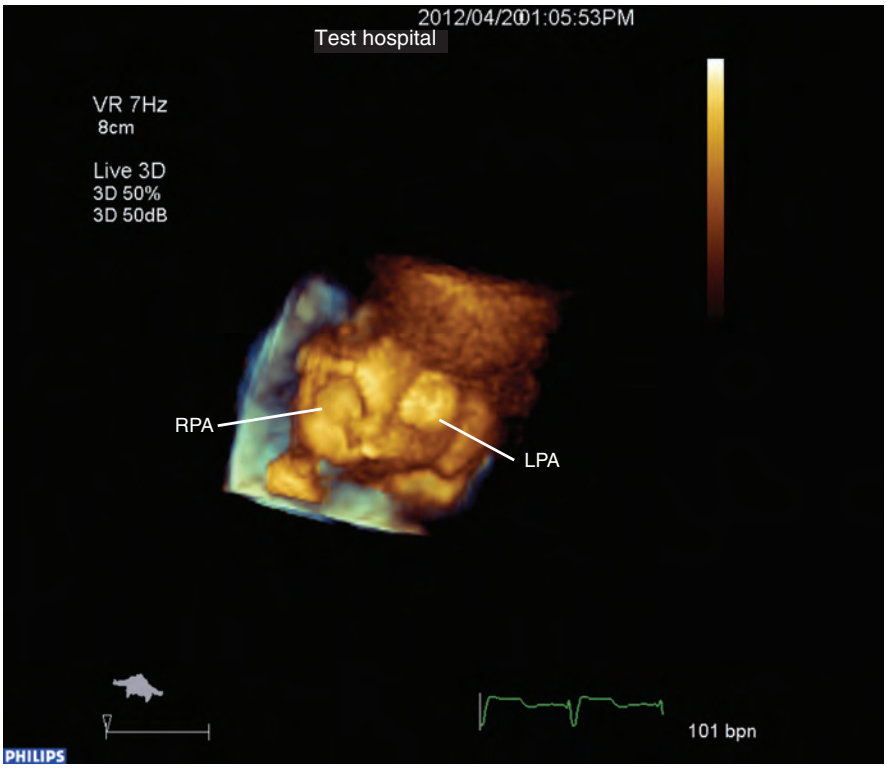


(a)

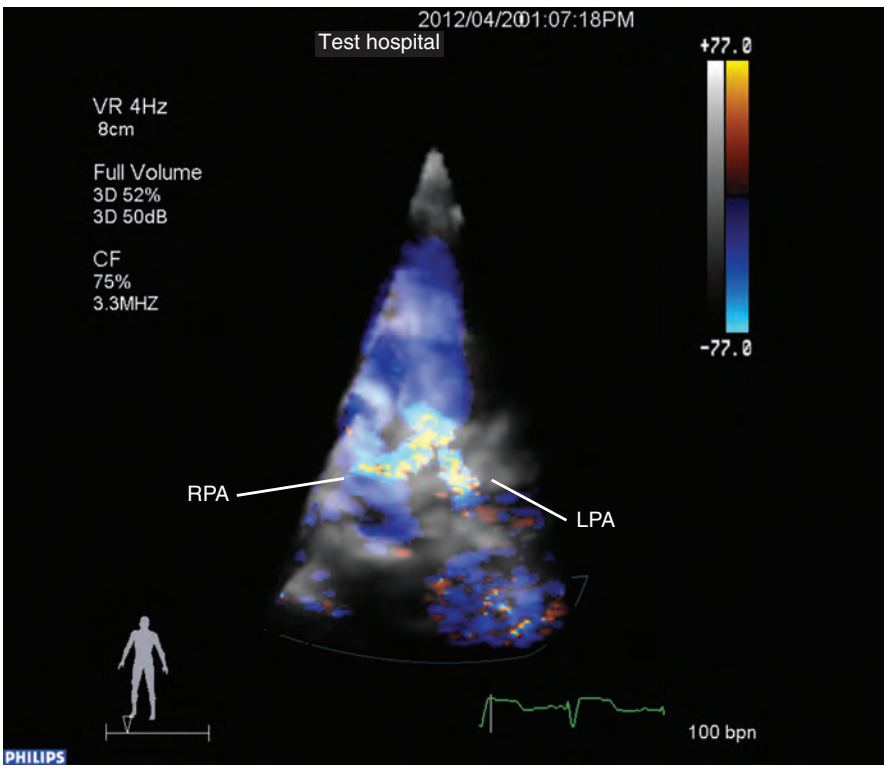


(b)

Figure 18.16 **(a)** Parasternal short-axis color compare Doppler image of bilateral pulmonary artery stents and severe pulmonary artery branch stenosis. **(b)** Spectral Doppler image of severe bilateral pulmonary artery branch stenosis. Ao, aorta; LPA, left pulmonary artery; RPA, right pulmonary artery.



(a)



(b)

Figure 18.17 **(a)** Three-dimensional black and while en fosse image of pulmonary arteries/stents in same patient as Figure 18.16. **(b)** Three-dimensional color Doppler image of pulmonary arteries/stents in same patient as Figure 18.16. LPA, left pulmonary artery; RPA, right pulmonary artery.

Echocardiographic evaluation of the PAs after the arterial switch operation is discussed in Chapter 24.

Videos

To access the videos for this chapter, please go to www.laiecho.com.

Video 18.1 Small patent ductus. Parasternal short-axis color Doppler video of a small patent ductus arteriosus that is conical in shape and funnels at the pulmonary end.

Video 18.2 Moderate patent ductus. Parasternal short-axis color Doppler compare video of a moderate patent ductus arteriosus.

Video 18.3 Large patent ductus. Parasternal short-axis color Doppler compare video of a large patent ductus arteriosus with bidirectional shunting.

Video 18.4 Vertical patent ductus. Suprasternal notch color Doppler compare video of a moderate serpiginous patent ductus arteriosus with left-to-right shunting in a patient with pulmonary atresia.

Video 18.5 Vertical patent ductus/3D. Suprasternal notch color three-dimensional "color angio" video of a moderate serpiginous patent ductus arteriosus in a patient with pulmonary atresia.

Video 18.6 Bilateral ducti. Doppler color video from suprasternal notch of bilateral ducti in a patient with discontinuous pulmonary arteries. The right ductus arises from the right innominate artery and the left ductus arises from the proximal descending aorta.

Video 18.7 Ductal aneurysm/black and white. Parasternal short-axis video of a large ductal aneurysm with mild compression of left pulmonary artery and spontaneous contrast in ductal aneurysm.

Video 18.8 Ductal aneurysm/color. Parasternal short-axis color Doppler video of a large ductal aneurysm with mild compression of left pulmonary artery and small amount of flow into ductus aneurysm.

Video 18.9 Ductal device occluding LPA/black and white. Parasternal short-axis video of a ductal occluder device causing near complete occlusion of the proximal left pulmonary.

Video 18.10 Ductal device occluding LPA/color. Parasternal short-axis video of a ductal occluder device causing near complete occlusion of the proximal left pulmonary with minimal color flow into left pulmonary artery.

Video 18.11 Hybrid. Doppler color compare video from suprasternal notch of a ductal stent placed as part of a hybrid procedure for hypoplastic left heart. Flow enters the ascending aorta without obstruction.

Video 18.12 Mild PABS. Parasternal short-axis color compare video and spectral Doppler images of mild bilateral pulmonary artery stenosis.

Video 18.13 Crossing pulmonary arteries. High parasternal short-axis color compare video of crossing pulmonary arteries with right pulmonary artery coursing inferior to left pulmonary artery.

Video 18.14 Severe PABS with stents. Parasternal short-axis color compare Doppler video of bilateral pulmonary artery stents and severe pulmonary artery branch stenosis.

Video 18.15 Severe PABS with stents/3D. Parasternal short-axis three-dimensional video of bilateral pulmonary artery stents showing ostia of both pulmonary arteries en fosse.

Video 18.16 Severe PABS with stents/3D color. Parasternal short-axis color three-dimensional "color angio" video of bilateral pulmonary artery stents and severe pulmonary artery branch stenosis. The color "hologram" setting and "3D swivel" provides detailed anatomic information.

References

1 Siassi B, Blanco C, Cabal LA, Coran AG. Incidence and clinical features of patent ductus arteriosus in low-birthweight infants: a prospective analysis of 150 consecutively born infants. *Pediatrics* 1976;**57**:347–351.

2 Reller MD, Ziegler ML, Rice MJ, et al. Duration of ductal shunting in healthy preterm infants: an echocardiographic color flow Doppler study. *J Pediatr* 1988;**112**:441–446.

3 Lim MK, Hanretty K, Houston AB, et al. Intermittent ductal patency in healthy newborn infants: demonstration by colour Doppler flow mapping. *Arch Dis Child* 1992;**67**:1217–1218.

4 Hoffman JI, Kaplan S. The incidence of congenital heart disease. *J Am Coll Cardiol* 2002;**39**:1890–1900.

5 Schneider DJ, Moore JW. Patent ductus arteriosus. *Circulation* 2006;**114**:1873–1882. [Review]

6 Rowe RD. Cardiovascular disease in the rubella syndrome. *Cardiovasc Clin* 1973;**5**:61–80.

7 Hastreiter AR, Joorabchi B, Pujatti G, et al. Cardiovascular lesions associated with congenital rubella. *J Pediatrics* 1967;**71**:59–65.

8 Freudenthal FP, Heath A, Villanueva J, et al. Chronic hypobaric hypoxia, patent arterial duct and a new interventional technique to close it. *Cardiol Young* 2012;**22**:128–135.

9 Kochilas L, Merscher-Gomez S, Lu MM, et al. The role of neural crest during cardiac development in a mouse model of DiGeorge syndrome. *Dev Biol* 2002;**251**:157–166.

10 Satoda M, Zhao F, Diaz GA, et al. Mutations in TFAP2B cause Char syndrome, a familial form of patent ductus arteriosus. *Nat Gen* 2000;**25**:42–46.

11 Moore K. The circulatory system. In: Moore K (ed.) *The Developing Human: Clinically Oriented Embryology*, 3rd edn. Philadelphia, PA: WB Saunders, 1982, pp. 298–338.

12 Hoffman JI, Buckberg GD. Regional myocardial ischemia–causes, prediction and prevention. *Vasc Surg* 1974;**8**:115–130.

13 Momma K, Matsuoka R, Takao A. Aortic arch anomalies associated with chromosome 22q11 deletion (CATCH 22). *Pediatr Cardiol* 1999;**20**:97–102. [Review]
14 Luetmer PH, Miller GM. Right aortic arch with isolation of the left subclavian artery: case report and review of the literature. *Mayo Clin Proc* 1990;**65**:407–413.
15 Knight L, Edwards JE. Right aortic arch. Types and associated cardiac anomalies. *Circulation* 1974;**50**:1047–1051.
16 Stewart JR, Kincaid OW, Titus JL. Right aortic arch: plain film diagnosis and significance. *Am J Roent Rad Ther Nucl Med* 1966;**97**:377–389.
17 Hastreiter AR, D'Cruz IA, Cantez T, et al. Right-sided aorta. I. Occurrence of right aortic arch in various types of congenital heart disease. II. Right aortic arch, right descending aorta, and associated anomalies. *Br Heart J* 1966;**28**:722–739. [Review]
18 McElhinney DB, Tworetzky W, Hanley FL, Rudolph AM. Congenital obstructive lesions of the right aortic arch. *Ann Thorac Surg* 1999;**67**:1194–1202.
19 Berning RA, Silverman NH, Villegas M, et al. Reversed shunting across the ductus arteriosus or atrial septum in utero heralds severe congenital heart disease. *J Am Coll Cardiol* 1996;**27**:481–486.
20 Freedom RM, Moes CA, Pelech A, et al. Bilateral ductus arteriosus (or remnant): an analysis of 27 patients. *Am J Cardiol* 1984;**53**:884–891.
21 Falcone MW, Perloff JK, Roberts WC. Aneurysm of the nonpatent ductus arteriosus. *Am J Cardiol* 1972;**29**:422–426.
22 Dyamenahalli U, Smallhorn JF, Geva T, et al. Isolated ductus arteriosus aneurysm in the fetus and infant: a multi-institutional experience. *J Am Coll Cardiol* 2000;**36**:262–269.
23 Jan SL, Hwang B, Fu YC, et al. Isolated neonatal ductus arteriosus aneurysm. *J Am Coll Cardiol* 2002;**39**:342–347.
24 Jan SL, Hwang B, Fu YC, Chi CS. Prediction of ductus arteriosus closure by neonatal screening echocardiography. *Int J Cardiovasc Imaging* 2004;**20**:349–356.
25 Hornberger LK. Congenital ductus arteriosus aneurysm. *J Am Coll Cardiol* 2002;**39**:348–350.
26 Acherman RJ, Siassi B, Wells W, et al. Aneurysm of the ductus arteriosus: a congenital lesion. *Am J Perinatol* 1998;**15**:653–659.
27 Jan SL, Hwang B, Fu YC, Chi CS. Initial clinical experience of real-time three-dimensional echocardiography in neonates with isolated congenital ductus arteriosus aneurysm. *Int J Cardiol* 2005;**105**:300–305.
28 Alagarsamy S, Chhabra M, Gudavalli M, et al. Comparison of clinical criteria with echocardiographic findings in diagnosing PDA in preterm infants. *J Perinat Med* 2005;**33**:161–164.
29 Hamrick SE, Hansmann G. Patent ductus arteriosus of the preterm infant. *Pediatrics* 2010;**125**:1020–1030.
30 El Hajjar M, Vaksmann G, Rakza T, et al. Severity of the ductal shunt: a comparison of different markers. *Arch Dis Child Fetal Neonatal Ed* 2005;**90**:F419–422.
31 Khongphatthanayothin A, Lane J, Wong PC, Acherman RJ. Severe pulmonary hypertension as a cause of reverse aortic arch flow in the neonate: report of two cases. *J Am Soc Echocardio* 1996;**9**:915–917.
32 Lane J, Acherman RJ, Khongphattanayothin A, et al. Reverse aortic arch flow secondary to severe pulmonary hypertension in the neonate. *Am J Perinatol* 1999;**16**:143–149.
33 Ali Khan MA, al Yousef S, Mullins CE, Sawyer W. Experience with 205 procedures of transcatheter closure of ductus arteriosus in 182 patients, with special reference to residual shunts and long-term follow-up. *J Thorac Cardiovasc Surg* 1992;**104**:1721–1727.
34 Gibbs JL, Uzun O, Blackburn ME, et al. Fate of the stented arterial duct. *Circulation* 1999;**99**:2621–2625.
35 Hosking MC, Benson LN, Musewe N, et al. Transcatheter occlusion of the persistently patent ductus arteriosus. Forty-month follow-up and prevalence of residual shunting. *Circulation* 1991;**84**:2313–2317.
36 Thanopoulos BD, Hakim FA, Hiari A, et al. Further experience with transcatheter closure of the patent ductus arteriosus using the Amplatzer duct occluder. *J Am Coll Cardiol* 2000;**35**:1016–1021.
37 Pierpont ME, Basson CT, Benson DW, Jr., et al. Genetic basis for congenital heart defects: current knowledge: a scientific statement from the American Heart Association Congenital Cardiac Defects Committee, Council on Cardiovascular Disease in the Young: endorsed by the American Academy of Pediatrics. *Circulation* 2007;**115**:3015–3038.
38 Rodriguez RJ, Riggs TW. Physiologic peripheral pulmonic stenosis in infancy. *Am J Cardiol* 1990;**66**:1478–1481.
39 Wang CC, Hwu WL, Wu ET, et al. Outcome of pulmonary and aortic stenosis in Williams-Beuren syndrome in an Asian cohort. *Acta Paediatr* 2007;**96**:906–909.
40 Beuren AJ, Schulze C, Eberle P, et al. The syndrome of supravalvular aortic stenosis, peripheral pulmonary stenosis, mental retardation and similar facial appearance. *Am J Cardiol* 1964;**13**:471–483.
41 Alagille D, Odievre M, Gautier M, Dommergues JP. Hepatic ductular hypoplasia associated with characteristic facies, vertebral malformations, retarded physical, mental, and sexual development, and cardiac murmur. *J Pediatrics* 1975;**86**:63–71.
42 McElhinney DB, Krantz ID, Bason L, et al. Analysis of cardiovascular phenotype and genotype-phenotype correlation in individuals with a JAG1 mutation and/or Alagille syndrome. *Circulation* 2002;**106**:2567–2574.
43 Scheiber D, Fekete G, Urban Z, et al. Echocardiographic findings in patients with Williams-Beuren syndrome. *Wien Klin Wochenschr* 2006;**118**:538–542.
44 Noonan JA. Hypertelorism with Turner phenotype. A new syndrome with associated congenital heart disease. *Am J Dis Child* 1968;**116**:373–380.
45 Hayden JG, Talner NS, Klaus SN. Cutis laxa associated with pulmonary artery stenosis. *J Pediatrics* 1968;**72**:506–509.
46 Matsumoto AH, Delany DJ, Parker LA, Ney KA. Massive hemoptysis associated with isolated peripheral pulmonary artery stenosis. *Cathet Cardiovasc Diagn* 1987;**13**:313–316.
47 Elzenga NJ, von Suylen RJ, Frohn-Mulder I, et al. Juxtaductal pulmonary artery coarctation. An underestimated cause of branch pulmonary artery stenosis in patients with pulmonary atresia or stenosis and a ventricular septal defect. *J Thorac Cardiovasc Surg* 1990;**100**:416–424.
48 Shinkawa T, Yamagishi M, Shuntoh K, et al. Pulmonary arterial reconstruction for pulmonary coarctation in early infancy. *Ann Thorac Surg* 2007;**83**:188–192.
49 Murphy DN, Winlaw DS, Cooper SG, Nunn GR. Successful early surgical recruitment of the congenitally disconnected pulmonary artery. *Ann Thorac Surg* 2004;**77**:29–35.
50 McElhinney DB, Driscoll DA, Levin ER, et al. Chromosome 22q11 deletion in patients with ventricular septal defect: frequency and associated cardiovascular anomalies. *Pediatrics* 2003;**112**:e472.

51 Shimazaki Y, Maehara T, Blackstone EH, et al. The structure of the pulmonary circulation in tetralogy of Fallot with pulmonary atresia. A quantitative cineangiographic study. *J Thorac Cardiovasc Surg* 1988;**95**:1048–1058.

52 Robin E, Silberberg B, Ganguly SN, Magnisalis K. Aortic orgin of the left pulmonary artery. Variant of tetralogy of Fallot. *Am J Cardiol* 1975;**35**:324–329.

53 Formigari R, Vairo U, de Zorzi A, et al. Prevalence of bilateral patent ductus arteriosus in patients with pulmonic valve atresia and asplenia syndrome. *Am J Cardiol* 1992;**70**:1219–1220.

54 Castaner E, Gallardo X, Rimola J, J, et al. Congenital and acquired pulmonary artery anomalies in the adult: radiologic overview. *Radiographics* 2006;**26**:349–371.

55 Stamm C, Friehs I, Zurakowski D, et al. Outcome after reconstruction of discontinuous pulmonary arteries. *J Thorac Cardiovasc Surg* 2002;**123**:246–257.

56 Ten Harkel AD, Blom NA, Ottenkamp J. Isolated unilateral absence of a pulmonary artery: a case report and review of the literature. *Chest* 2002;**122**:1471–1477.

57 Pfefferkorn JR, Loser H, Pech G, et al. Absent pulmonary artery. A hint to its embryogenesis. *Pediatr Cardiol* 1982;**3**:283–286.

58 Toews WH, Pappas G. Surgical management of absent right pulmonary artery with associated pulmonary hypertension. *Chest* 1983;**84**:497–499.

59 Aru GM, English WP, Gaymes CH, Heath BJ. Origin of the left pulmonary artery from the aorta: embryologic considerations. *Ann Thorac Surg* 2001;**71**:1008–1010.

60 Fong LV, Anderson RH, Siewers RD, et al. Anomalous origin of one pulmonary artery from the ascending aorta: a review of echocardiographic, catheter, and morphological features. *Br Heart J* 1989;**62**:389–395.

61 Peng EW, Shanmugam G, Macarthur KJ, Pollock JC. Ascending aortic origin of a branch pulmonary artery–surgical management and long-term outcome. *Eur J Cardiothorac Surg* 2004;**26**:762–766.

62 Pahlajani DB, Pantvaidya SH, Pandit S, et al. Anomalous origin of right pulmonary artery from ascending aorta with right ventricular endocardial fibroelastosis. *Pediatr Cardiol* 1985;**6**:47–49.

63 Nakamura Y, Yasui H, Kado H, et al. Anomalous origin of the right pulmonary artery from the ascending aorta. *Ann Thorac Surg* 1991;**52**:1285–1291.

64 Kutsche LM, Van Mierop LH. Anomalous origin of a pulmonary artery from the ascending aorta: associated anomalies and pathogenesis. *Am J Cardiol* 1988;**61**:850–856.

65 Mair DD, Ritter DG, Danielson GK, et al. Truncus arteriosus with unilateral absence of a pulmonary artery. Criteria for operability and surgical results. *Circulation* 1977;**55**:641–647.

66 Galinanes M, Stanley P, Guerin R, et al. Pulmonary banding complicated by low origin of right pulmonary artery. *Tex Heart Inst J* 1993;**20**:238–240.

67 Recto MR, Parness IA, Gelb BD, et al. Clinical implications and possible association of malposition of the branch pulmonary arteries with DiGeorge syndrome and microdeletion of chromosomal region 22q11. *Am J Cardiol* 1997;**80**:1624–1627.

68 Zimmerman FJ, Berdusis K, Wright KL, Alboliras ET. Echocardiographic diagnosis of anomalous origins of the pulmonary arteries from the pulmonary trunk (crossed pulmonary arteries). *Am Heart J* 1997;**133**:257–260.

69 Becker AE, Becker MJ, Edwards JE. Malposition of pulmonary arteries (crossed pulmonary arteries) in persistent truncus arteriosus. *Am J Roentgenol Radium Ther Nucl Med* 1970;**110**:509–514.

70 Aldousany AW, DiSessa TG, Dubois R, et al. Doppler estimation of pressure gradient in pulmonary stenosis: maximal instantaneous vs peak-to-peak, vs mean catheter gradient. *Pediatr Cardiol* 1989;**10**:145–149.

71 Frank DU, Minich LL, Shaddy RE, Tani LY. Is Doppler an accurate predictor of catheterization gradients for postoperative branch pulmonary stenosis? *J Am Soc Echocardiogr* 2002;**15**:1140–1144.

72 Fraser CD, Jr., Latson LA, Mee RB. Surgical repair of severe bilateral branch pulmonary artery stenosis. *Ann Thorac Surg* 1995;**59**:738–740.

73 Bacha EA, Kreutzer J. Comprehensive management of branch pulmonary artery stenosis. *J Interv Cardiol* 2001;**14**:367–375.

CHAPTER 19

Anomalies of the Left Ventricular Outflow Tract and Aortic Valve

John M. Simpson and Owen I. Miller
Evelina London Children's Hospital, Guy's and St Thomas' NHS Foundation Trust, London, UK

This chapter addresses anomalies of the left ventricular outflow tract, with emphasis on echocardiographic evaluation. In general, lesions are divided into those causing obstruction of the left ventricular outflow tract and those involving the aortic root, such as sinus of Valsalva aneurysm, aortic valve cusp prolapse and aortico–left ventricular tunnel.

Definitions

Obstruction of the left ventricular outflow tract may occur below the level of the aortic valve (*subaortic stenosis*), at the level of the aortic valve (*valvar aortic stenosis*), or above the aortic valve, typically at the level of the sinotubular junction (*supravalvar aortic stenosis*). When there is a ventricular septal defect immediately below the aortic valve there is the potential for one of the aortic cusps (usually the right coronary cusp) to prolapse into the ventricular septal defect, which can lead to regurgitation of the aortic valve. A sinus of Valsalva aneurysm refers to abnormal dilation of the aortic root wall or scalloped area of the cusps of the aortic valve. This condition can be complicated by rupture of the affected sinus into an adjacent area of the heart. An aortico–left ventricular tunnel is a lesion where there is abnormal communication between the ascending aorta and the left ventricle through an abnormal pathway ("tunnel"), which has the hemodynamic effect of severe aortic regurgitation.

Incidence

The incidence of aortic valve stenosis in liveborn infants is around 0.4 per 1000 live births [1]. The incidence of bicuspid aortic valve is approximately 13.5 per 1000 live births [1]. In a cross-sectional study, Kitchiner et al. [2] described an incidence of subvalvar aortic stenosis of 0.09 per 1000, whereas that of supravalvar aortic stenosis was 0.05 per 1000. Sinus of Valsalva aneurysm and aortico–left ventricular tunnel are rare lesions without large reported numbers to give an accurate estimation of population incidence.

Etiology

There is good evidence that cardiac defects causing left heart obstruction have a significant genetic component [3,4]. Aortic valve stenosis is seldom associated with major chromosomal abnormalities [5], but empiric studies of familial patterns of recurrence [3] suggest a significant genetic influence. Recent work has implicated the NOTCH pathway and genes such as *KCNJ2* and *NKX2*-5 [6]. Bicuspid aortic valve has a definite genetic component [7] and may coexist with other forms of left heart obstruction such as coarctation of the aorta. This has led professional groups to recommend family screening where left ventricular outflow tract obstruction, particularly bicuspid aortic valve, has been identified in the index case [8,9]. Supravalvar aortic stenosis is most characteristically associated with Williams–Beuren syndrome, which is due to a deletion in the elastin gene on chromosome 7q11.23 [10]. Familial occurrence of supravalvar aortic stenosis has been observed without the characteristic phenotype or gene deletion found in Williams–Beuren syndrome and may be due to other mutations in the elastin gene [11]. Subaortic stenosis may be familial [12] but in most cases is felt to be the result of the interaction of a number of factors. These factors include abnormal morphologic findings such as ventricular septal defect, and abnormal aorto-septal angle producing increased septal shear stress, which in susceptible individuals leads to abnormal cellular proliferation causing subaortic obstruction [13,14].

Echocardiography in Pediatric and Congenital Heart Disease: From Fetus to Adult, Second Edition. Edited by Wyman W. Lai, Luc L. Mertens, Meryl S. Cohen and Tal Geva.
© 2016 John Wiley & Sons, Ltd. Published 2016 by John Wiley & Sons, Ltd.
Companion website: www.lai-echo.com

Subaortic stenosis

Morphology and classification

Subaortic stenosis may occur in isolation or in association with other congenital heart defects such as ventricular septal defect, atrioventricular septal (canal) defect, bicuspid (bicommissural) aortic valve, aortic valve stenosis, coarctation of the aorta, interruption of the aortic arch, and double-chambered right ventricle [15–17]. In addition, subvalvar aortic stenosis may accompany conotruncal anomalies and complex anomalies, including transposition of the great arteries, double-outlet right ventricle and single ventricle. Abnormalities of the insertion of the mitral valve or accessory mitral valve tissue may also coexist [18]. Variation in the morphology of the left ventricular outflow tract obstruction can have several causes:

1 Hypertrophic cardiomyopathy: hypertrophy of the ventricular septum can result in muscular obstruction of the left ventricular outflow tract. This may be accompanied by abnormal systolic anterior motion of the mitral valve. This is dealt with in more detail in Chapter 34.
2 Discrete "membranous" subaortic stenosis (Figures 19.1 and 19.2; Videos 19.1 and 19.2): this form of subaortic stenosis usually manifests during childhood and is rare during infancy [19]. The morphology of the left ventricular outflow is characterized by a steeper angle between the plane of the ventricular septum and the aortic root (aorto-septal angle), elongation of the intervalvular fibrosa between the anterior mitral leaflet and the aortic valve, and an exaggerated aortic override above the ventricular septal crest [20]. There is a frequent association with a membranous ventricular septal defect, and abnormal shear stresses have been implicated, by causing abnormal proliferation of fibrous tissue. Although such discrete obstruction is amenable to surgical repair, regrowth of tissue may lead to recurrence of subaortic obstruction [21–24]. Note that the obstructive subaortic tissue may not be limited to the ventricular septum and may extend onto the anterior leaflet of the mitral valve (Figure 19.2; Video 19.2) as well as the ventricular aspect of the aortic valve leaflets.
3 "Tunnel-type" subaortic stenosis (Figure 19.3; Video 19.3): as the name implies, this form of subaortic stenosis involves a long segment of narrowing of the left ventricular outflow tract and is often caused by muscle. The muscular narrowing can involve an accessory anterolateral papillary muscle, septal hypertrophy, or a combination of the above. This form of obstruction frequently occurs early in life and is often associated with other forms of left heart obstruction. The clinical

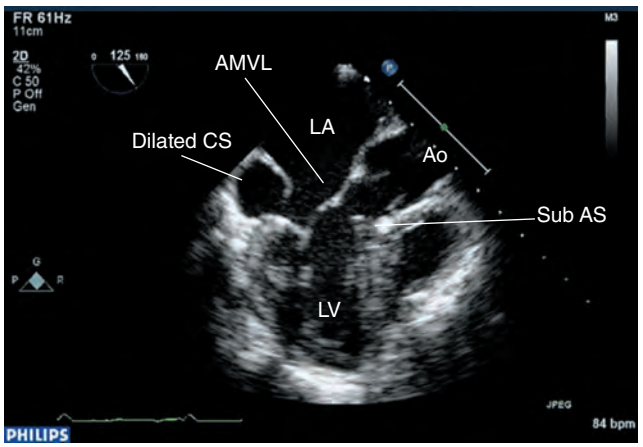


Figure 19.2 Transesophageal echocardiogram of subaortic stenosis. This patient has a persisting left superior vena cava draining to the coronary sinus, which explains the dilated coronary sinus. The extension of the subaortic tissue onto the anterior leaflet of the mitral valve is well demonstrated. AMVL, anterior mitral valve leaflet; Ao, aorta; CS, coronary sinus; LA, left atrium; LV, left ventricle; Sub AS, subaortic stenosis.

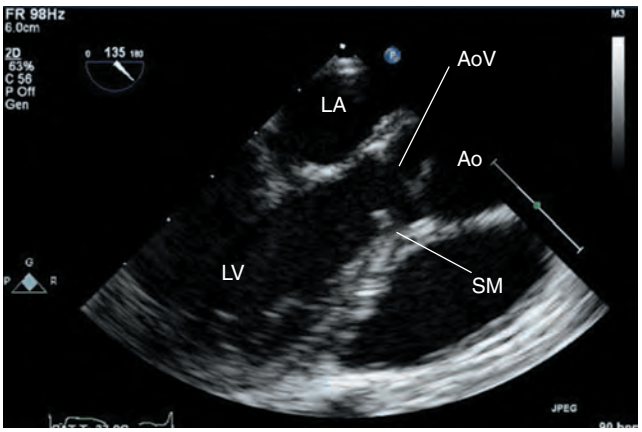


Figure 19.1 Transesophageal echocardiogram of a patient with "membranous" subaortic stenosis. There is a discrete area of stenosis below the aortic valve. The aortic valve itself is of normal size. Ao, aorta; AoV, aortic valve; LA, left atrium; LV, left ventricle; SM, subaortic membrane.

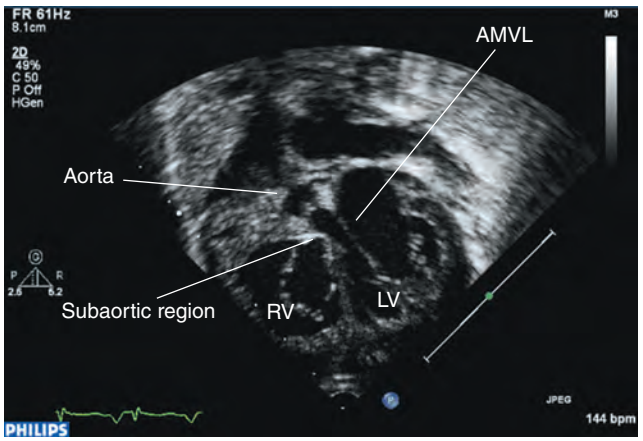


Figure 19.3 Subcostal view of an infant with coarctation of the aorta and "tunnel"-type subaortic stenosis. There is no discrete "membrane" but the subaortic region is diffusely hypoplastic with the potential for a long segment of obstruction to the left ventricular outflow tract. AMVL, anterior mitral valve leaflet; LV, left ventricle; RV, right ventricle.

implication is that a more extensive type of surgical repair will be required compared with repair of the discrete fibrous form of obstruction [25,26].

4 Posterior deviation of the outlet (infundibular) septum may cause subaortic obstruction [27]. This typically occurs in association with conditions such as type B interruption of the aortic arch or, less commonly, coarctation of the aorta with ventricular septal defect, where the aortic valve and ascending aorta may be hypoplastic.

Pathophysiology

The development of subaortic stenosis is thought to be due to abnormal shear forces in the left ventricular outflow tract, leading to abnormal growth of fibrous tissue [13,28]. Such shear forces are increased in the presence of an abnormal aorto-septal angle and other lesions such as a ventricular septal defect. The obstruction to the left ventricular outflow tract leads to compensatory ventricular hypertrophy. Contractile function of the left ventricle is usually well maintained initially but may worsen with time if severe outflow tract obstruction is not relieved. The fibrous tissue below the aortic valve may extend onto the aortic valve leaflets and contribute to obstruction of the left ventricular outflow tract. The turbulent jet across the subaortic region may also interfere with optimal motion of the aortic valve and may contribute to aortic valve regurgitation. Consequently, some centers have advocated early surgical resection of the subaortic lesion to reduce aortic regurgitation [22,23], a strategy that has not been consistently adopted [28,29]. There is a clear indication for surgical intervention where there is severe left ventricular outflow tract obstruction. The indications for intervention in children with relatively mild outflow tract obstruction are less clear-cut. As a minimum, serial echocardiographic examination is required because rapid progression of subaortic stenosis may occur in infancy and early childhood [23]. For adults with relatively low Doppler-derived gradients (<50 mmHg) a conservative approach may be adopted although progression may occur during adult life, albeit more slowly than in infancy and early childhood [23,30].

Imaging

The goals of echocardiographic assessment of subvalvar aortic stenosis are to comprehensively characterize the morphologic features of the obstructive lesion, to evaluate the hemodynamic severity, and to delineate associated anomalies.

Key elements

In all cases, complete anatomic and functional examination by two-dimensional (2D) and 3D imaging, as appropriate, and by color and spectral Doppler. In addition, the following elements of cardiovascular anatomy and function should be evaluated in detail and be given priority.

- Delineation of the morphology of the left ventricular outflow tract and the type of subaortic obstruction by 2D and 3D imaging from the subcostal, apical, and parasternal windows.
- Measurement of the distance between the obstructive subaortic tissue from the aortic valve hinge in systole.
- Measurements of aortic valve annulus, root, and ascending aorta diameters from the parasternal long-axis view in systole.
- Assessment of aortic valve morphology.
- Assessment of the severity of left ventricular outflow tract obstruction by pulsed- (PW) and continuous-wave (CW) Doppler.
- Evaluation of aortic valve regurgitation.
- Quantitative assessment of left ventricular size and function.
- Identification of associated abnormalities.

The assessment of severity of left ventricular outflow tract obstruction can be done in a manner analogous to that of aortic valve stenosis (see "Aortic valve stenosis" later). Muscular subaortic obstruction may be accompanied by an increase in the Doppler velocity in late systole leading to an asymmetric Doppler trace consistent with dynamic obstruction. To obtain optimal Doppler signals, imaging is undertaken from the apical and from the suprasternal notch views. Pulsed Doppler is helpful to localize flow acceleration and, in patients with several levels of obstruction, to determine the contribution of each location to the total estimated pressure drop. The maximum instantaneous and mean gradients across the left ventricular outflow are also recorded from both transducer positions by CW Doppler, with particular attention to optimization of the alignment between the ultrasound beam and the direction of flow. A detailed discussion of the principles of assessing stenosis by Doppler can be found in Chapter 6.

Imaging of the morphology of the left ventricular outflow tract is crucial for planning management. In the membranous form of subaortic stenosis the full extent of the fibrous membrane should be defined, as such membranes vary in their distance from the aortic valve itself, and some extend circumferentially to involve the anterior leaflet of the mitral valve. This assessment is best achieved from the parasternal long- and short-axis views. Three-dimensional imaging allows en face views of the subaortic obstruction from the left ventricular cavity and through the aortic valve (Figure 19.4; Video 19.4). In some patients, accessory tissue related to the mitral valve attaches to the subaortic septum, producing or contributing to subaortic stenosis [31]. The aortic valve may be intrinsically abnormal or be restricted in its motion due to encroachment of fibrous tissue onto the ventricular aspect of the leaflets. The aortic valve leaflets may "flutter" during systole as they are hit by the turbulent jet from the subaortic region (Figure 19.5).

Comprehensive echocardiographic evaluation is crucial for planning subaortic stenosis surgery. Discrete "membranous" subaortic stenosis may be resected with preservation of the native aortic valve. However, "tunnel" forms of subaortic stenosis may not be able to be managed by resection of a localized area of tissue and may require a more extensive resection [21,25,26,32]. It is therefore essential to have all anatomic information before surgical repair. In the tunnel type of subaortic obstruction, the left ventricular outflow tract is often hypoplastic

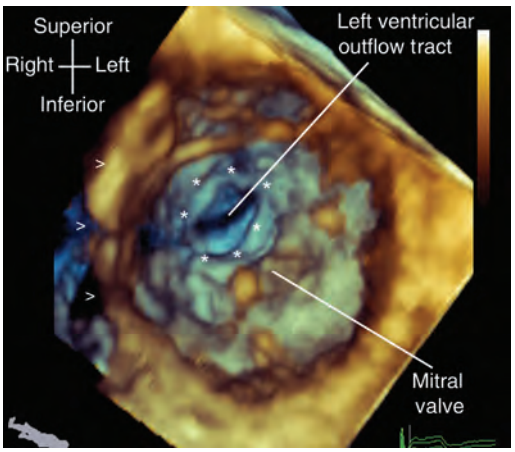


Figure 19.4 Three-dimensional echocardiogram demonstrating an en face view of circumferential subaortic obstruction viewed from the left ventricle. The subaortic obstruction is indicated by the asterisks (∗) and the ventricular septum by the open-headed arrows (>).

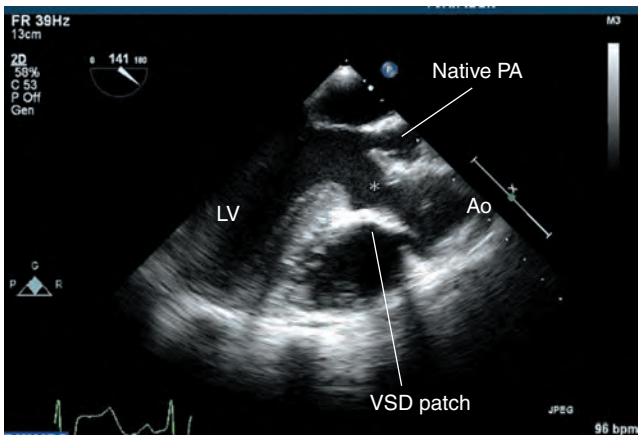


Figure 19.6 Transesophageal echocardiogram of a patient with subaortic obstruction following a "Rastelli" repair of transposition of the great arteries with an associated ventricular septal defect (VSD) and pulmonary stenosis. The outflow of the left ventricle is across the VSD. This leads to a tortuous subaortic area, and in this example there is stenosis between the native pulmonary artery and the VSD patch. The asterisk (∗) denotes the area of subaortic narrowing. Ao, aorta; LV, left ventricle; PA, pulmonary artery.

including the aortic valve annulus. In selected patients, extensive subaortic resection may have to be combined with insertion of the patient's pulmonary valve into the aortic position (Ross–Konno operation) [33,34]. In small infants, transthoracic echocardiographic imaging is usually all that is necessary to plan treatment, but in older children and adults, transesophageal echocardiography (TEE) may be necessary to gain all relevant information. In some patients, subaortic obstruction follows repair of more complex forms of congenital heart disease [35]. An example of this would be subaortic obstruction following a "Rastelli" type of repair for conditions such as transposition of the great arteries with a ventricular septal defect and pulmonary stenosis. In this repair, the outflow from the left ventricle is baffled to the aorta via the ventricular septal defect, using a patch. The tortuous outflow tract is a substrate for subaortic obstruction (Figure 19.6). Subaortic stenosis may also develop following complete repair of an atrioventricular septal (canal) defect which may be related the unwedged position of the native aorta and elongation of the left ventricular outflow tract (Figure 19.7; Video 19.5). Other examples include conditions such as double-inlet left ventricle with transposition of the great arteries, where the outlet of the left ventricle to the ascending aorta is through a bulboventricular foramen, which, if restrictive, effectively causes subaortic obstruction.

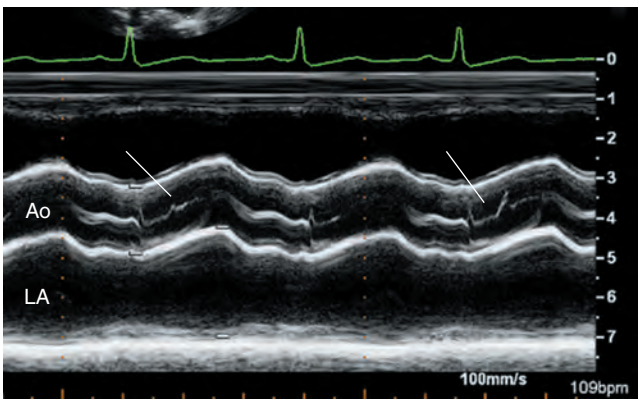


Figure 19.5 M-mode echocardiogram of the long-axis aortic valve. "Fluttering" of the aortic valve leaflets is indicated by the arrows and is due to the turbulent subaortic jet striking the aortic valve leaflets. Ao, aorta; LA, left atrium.

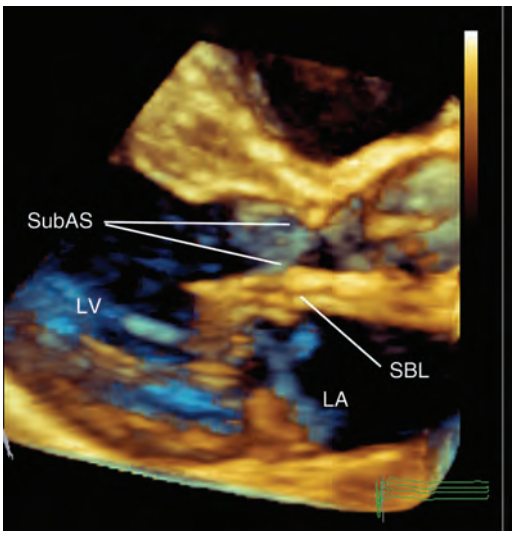


Figure 19.7 Parasternal long-axis 3D echocardiogram of subaortic stenosis following repair of an atrioventricular septal defect. This technique allows a depth of view to assist in delineating the extent of the fibrous subaortic stenosis, in this case extending onto the repaired superior bridging leaflet. LA, left atrium; LV, left ventricle; SBL, superior bridging leaflet; SubAS, subaortic stenosis.

At the authors' center, intraoperative imaging, either by an epicardial or transesophageal approach, is done in all cases of subaortic stenosis, whatever the anatomic substrate, to confirm adequacy of the surgical relief of obstruction. Alignment of the Doppler cursor to the direction of flow is typically best achieved by a transgastric transesophageal approach but this can be difficult or impossible when the chest is open during surgery. The severity of aortic regurgitation should be assessed because this can occasionally worsen following removal of fibrous subaortic obstruction, particularly in cases where fibrous tissue has extended onto the aortic valve leaflets themselves. The mitral valve should be imaged for evidence of mitral valve regurgitation as damage to the anterior leaflet may occur if a circumferential subaortic "membrane" has had to be surgically resected from the anterior mitral valve leaflet. Finally, it is necessary to guard against iatrogenic creation of a ventricular septal defect due to inadvertent perforation of the ventricular septum.

In the longer term, sequential echocardiography is indicated to exclude recurrence of subaortic stenosis, which can occur even after initial apparent complete resection of the obstructive tissue. The risk of recurrence is higher when the subaortic "membrane" is closer to the aortic valve and in patients with severe preoperative obstruction [24]. Aortic regurgitation should be assessed semiquantitatively and chamber dimensions, wall thickness, and contractile function should be measured.

Aortic valve stenosis

Morphology

Aortic valve stenosis in children is due to a congenitally abnormal aortic valve rather than degeneration of a morphologically normal valve as may occur in late adult life. Morphologically, the anomaly may be due to commissural underdevelopment, myxomatous thickening of the valve leaflets, annular hypoplasia, or a combination of these elements. As a result of commissural underdevelopment, the aortic valve may be unicuspid (when only one commissure, usually the left-noncoronary commissure, is well-formed), bicuspid (when one commissure is underdeveloped and the other two are well formed), tricuspid (all three commissures are well developed) or, rarely, quadricuspid (when an extra commissure is present). Three-dimensional echocardiography has the potential to assist in defining valve morphology by permitting display of a depth of field so that both cusps can be visualized. (Figure 19.8; Video 19.6). In some cases, particularly in infancy, it may be difficult to identify true separate cusps, with the appearance of a single central or eccentric orifice, which has been likened to a "volcano"-type orifice [36]. In some patients the valve may be incompetent and stenotic. Aortic regurgitation is invariably present following balloon valvuloplasty, either surgical or transcatheter. Poststenotic dilation of the proximal ascending aorta also occurs due to the high-velocity, turbulent and often eccentric jet through the valve.

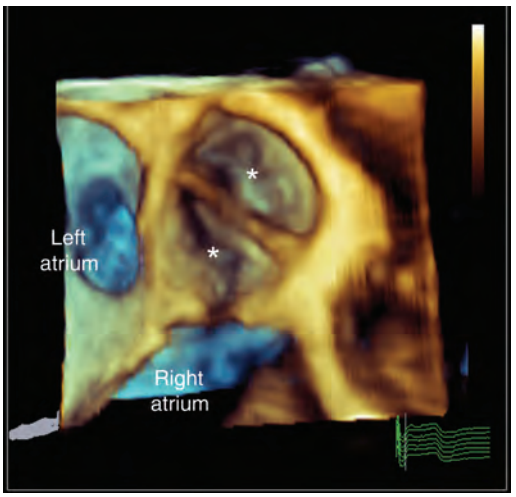


Figure 19.8 Three-dimensional echocardiogram of a bicuspid aortic valve viewed from the aortic side. In this example there was coexisting subaortic stenosis. The two cusps of the aortic valve are marked by the asterisks (*).

Pathophysiology

Obstruction to the left ventricular outflow tract results in an increased afterload on the left ventricle. The myocardial response to the excess load depends on the stage of development at which it occurs. During fetal life, mild stenosis of the aortic valve is usually well tolerated with good contraction of the left ventricle and normal development of left heart structures. In fetuses with severe aortic valve stenosis the left ventricle dilates, contractile function decreases and endocardial fibroelastosis often develops [37]. As gestational age advances, growth of the left ventricle and aorta is subnormal in the majority of cases so that, by term, the left ventricle and aorta are hypoplastic and postnatal management is more akin to that of hypoplastic left heart syndrome [37,38]. Such progression of aortic stenosis provides the rationale for intrauterine intervention to prevent progression of aortic valve stenosis to hypoplastic left heart syndrome, with the potential to improve the likelihood of a biventricular repair postnatally [39–41].

Following birth, once the arterial duct closes, the systemic arterial circulation has to be supported entirely by left heart structures. If there is severe aortic stenosis with significant left ventricular dysfunction and/or underdevelopment of left heart structures, then the left heart may be unable to support the circulation and the infant will present with cardiovascular collapse. In such circumstances, administration of prostaglandin E is life-saving, by reopening the arterial duct and permitting the right heart structures to support the systemic circulation. The term "critical" aortic stenosis is commonly applied to infants where the systemic circulation is dependent on the maintenance of ductal patency. In less severe cases, closure of the arterial duct does not lead to left ventricular failure because the left ventricle hypertrophies in response to left ventricular outflow tract obstruction and maintains an adequate cardiac output. Such

infants and children may remain asymptomatic early in life and present for other reasons such as cardiac murmur, reduced exercise tolerance, or exercise-induced syncope. In adults, aortic valve stenosis may develop due to degeneration of an aortic valve that was not previously stenotic. Individuals with a congenitally bicuspid aortic valve have a higher risk of late degeneration of the valve than if the valve is tricuspid [42].

Imaging

The goals of echocardiographic assessment of aortic valve stenosis are to comprehensively characterize the morphologic features of the obstructive lesion, to evaluate the hemodynamic severity, and to delineate associated anomalies.

Key elements

In all cases, complete anatomic and functional examination by 2D and 3D imaging, as appropriate, and by color and spectral Doppler. In addition, the following elements of cardiovascular anatomy and function should be evaluated in detail and be given priority.

- 2D imaging of the aortic valve from subcostal, apical, and parasternal views with focus on the subvalvar area, annulus, leaflets and commissures, root, sinotubular junction, and ascending aorta.
- 3D imaging of aortic valve morphology with emphasis on en face views of the valve from the left ventricular outflow and from aortic root.
- Note underdevelopment of commissures, size of leaflets, leaflet thickness and doming, leaflet prolapse, subvalvar stenosis, and supravalvar stenosis.
- Measurements of the following aortic dimensions in the parasternal long-axis view in systole: aortic valve annulus, root, sinotubular junction, and ascending aorta at the level of the right pulmonary artery.
- Evaluation of maximum instantaneous and mean Doppler gradients across the aortic valve from the subcostal, apical, and suprasternal/high right parasternal windows.
- Quantitative assessments of left ventricular size and systolic and diastolic functions.
- If present, note presence of endocardial fibroelastosis.
- Evaluate for pulmonary hypertension.
- Left atrial volume measurements.

The severity of aortic valve stenosis is estimated by measurement of the Doppler-derived maximum instantaneous and mean pressure drop across the aortic valve. Classification by Doppler-derived pressure drop is only valid if left ventricular function is well preserved and cardiac output is normal. Assuming this to be the case, and beyond the neonatal age range, mild aortic valve stenosis may be defined as a peak Doppler velocity of less than 3 m/s; moderate aortic valve stenosis has a peak velocity of 3–4 m/s, and severe aortic stenosis is characterized by a peak velocity of more than 4 m/s. Color Doppler flow mapping is extremely helpful to observe the direction of the flow jet, which may be eccentric, and allows optimal alignment of the Doppler cursor with the jet (Figure 19.9; Video 19.7). Imaging from the suprasternal notch often has the best alignment with the direction of flow. Use of the low-frequency CW nonimaging Doppler probe is recommended as it provides optimal access to the suprasternal notch, particularly in smaller children. In infants and children an apical 3-chamber projection provides an excellent window for Doppler interrogation of the left ventricular outflow tract. CW Doppler is optimal to determine the maximum instantaneous and mean Doppler-derived pressure drop, but PW Doppler is extremely helpful in patients with multiple levels of left ventricular outflow tract obstruction because "step

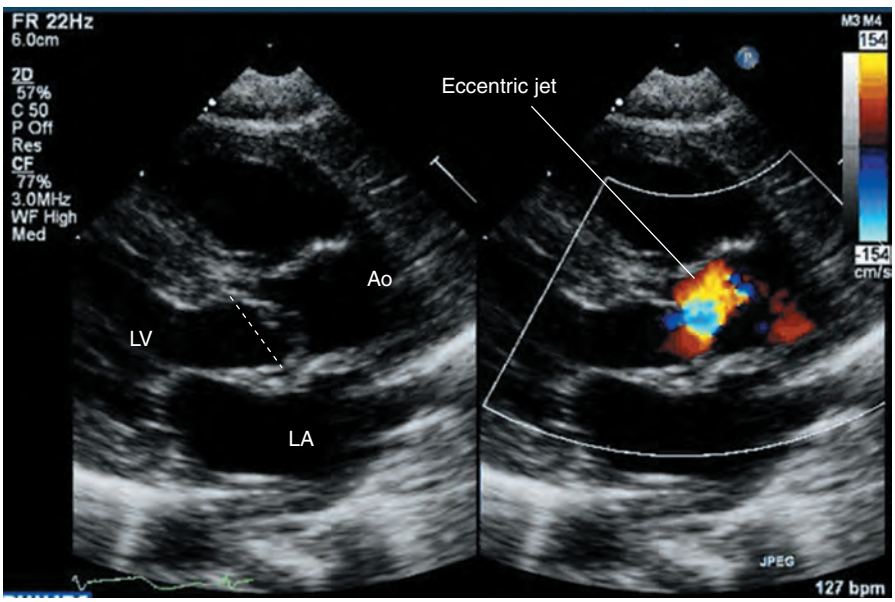


Figure 19.9 Long-axis view of the left ventricle demonstrating aortic valve stenosis with an eccentric jet across the aortic valve. Use of color flow Doppler permits optimization of the angle of insonation to obtain the most accurate values of pressure drop across the valve. The dashed line represents the distance between the hinge points of the aortic valve, which is employed for balloon sizing for aortic valvuloplasty. Ao, aorta; LA, left atrium; LV, left ventricle.

up" in velocity at different sites may be observed and allow determination of the relative contribution of the different levels of obstruction.

In older children and in young adults with congenital aortic valve stenosis, an assessment of valve area can be made by employing the continuity equation [43,44] or other formulas [45,46]. In adults with mild aortic valve stenosis, the effective orifice area is >1.4 cm^2; in moderate aortic valve stenosis it is 1.0–1.4 cm^2, and in severe aortic valve stenosis it is <1.0 cm^2 [47]. One important group has relatively low "gradients" across the aortic valve due to reduced left ventricular ejection fraction resulting in a reduced cardiac output. In this group, severe aortic valve stenosis coexists with a relatively low Doppler velocity across the aortic valve. Dobutamine stress echocardiography examines for increases in effective orifice area, contractile function and pressure gradient under stress conditions, permitting stratification of risk for surgery [47].

The morphology of the aortic valve is best seen with a short-axis view of the aortic valve. The diameter of the aortic valve annulus is measured during systole from the parasternal long-axis view. If there is aortic regurgitation, the parasternal short-axis view is ideal for determining the site of regurgitation through the valve. Three-dimensional echocardiography can provide further information because the depth of field permits visualization of the whole cusp rather than the single cut plane of cross-sectional techniques (Figure 19.10; Video 19.8). Assessment of aortic regurgitation is discussed in detail in Chapter 6. Briefly, the severity can be assessed by the width of the vena contracta of the aortic regurgitation jet using color flow mapping from the parasternal long axis, relative to the aortic annulus diameter. CW Doppler interrogation of the regurgitant jet can be used to estimate the pressure half-time, and the degree and duration of reversal of flow in the distal aortic arch or descending aorta during diastole can be helpful to give a semiquantitative assessment of the degree of aortic valve regurgitation [48].

In all cases of left ventricular outflow tract obstruction at any level, left ventricular dimensions and wall-thickness should be measured. These measurements can be obtained by cross-sectional or M-mode echocardiography of the left ventricle at the level of the tips of the mitral valve in either a long- or a short-axis projection of the left ventricle. Alternatively, left ventricular volume, mass and systolic function can be measured by 2D or 3D techniques (see Chapter 7 for further details). It is essential that Doppler-derived pressure drop across a stenotic aortic valve is interpreted in light of left ventricular contractile function and blood flow rate. An example of this occurs in small infants with severe aortic stenosis in whom left ventricular contractile function may be so poor that only low-velocity jets are observed across a critically stenotic aortic valve.

A thorough examination of all left heart structures is essential when aortic valve stenosis is diagnosed. Aortic valve stenosis may coexist with other types of left heart obstruction including supramitral membrane, mitral valve stenosis, subaortic stenosis, and coarctation of the aorta. In infancy, critical aortic stenosis is frequently accompanied by hypoplasia of left heart structures including the mitral valve, left ventricle and aorta (Figures 19.11–19.13; Videos 19.9 and 19.10). Endocardial fibroelastosis is observed as a brightly echogenic lining to the left ventricle; in its mildest form this may involve only the papillary muscles but in its severest form it may line the entire left ventricular cavity (Figures 19.12 and 19.13). Estimation of the extent and severity of endocardial fibroelastosis may be assisted by magnetic resonance imaging (MRI) (Figure 19.14). In severely affected infants it may be difficult to judge whether

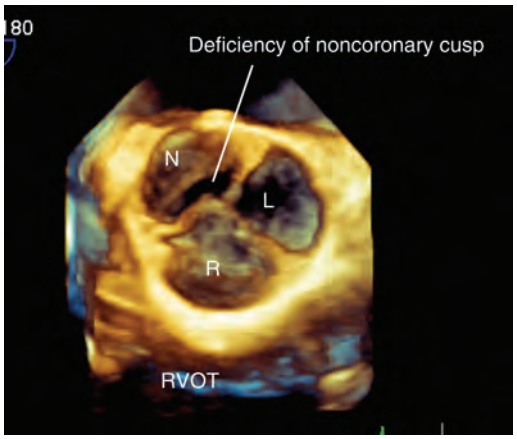


Figure 19.10 Three-dimensional transesophageal echocardiogram of an abnormal aortic valve from a patient who had undergone previous balloon dilatation of the aortic valve. The noncoronary cusp (N) is deficient, whereas the left coronary cusp (L) and right coronary cusp (R) are more normal. RVOT, right ventricular outflow tract.

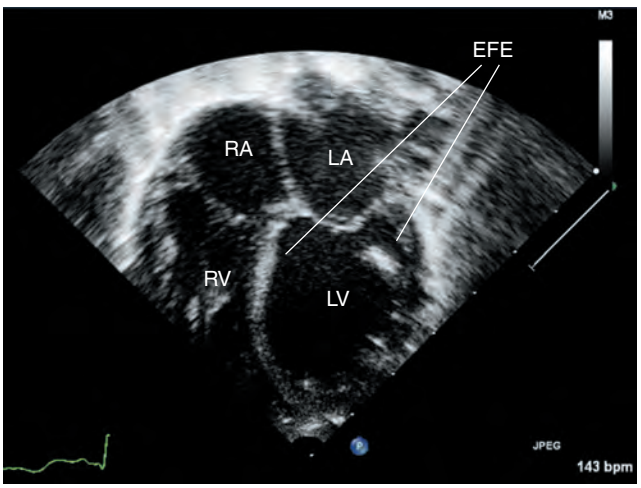


Figure 19.11 Four-chamber view of a newborn with critical aortic stenosis. In this example the left ventricle is dilated and more globular than normal. There is endocardial fibroelastosis affecting mainly the papillary muscle apparatus and the ventricular septum. EFE, endocardial fibroelastosis; LA, left atrium; LV, left ventricle; RA, right atrium; RV, right ventricle.

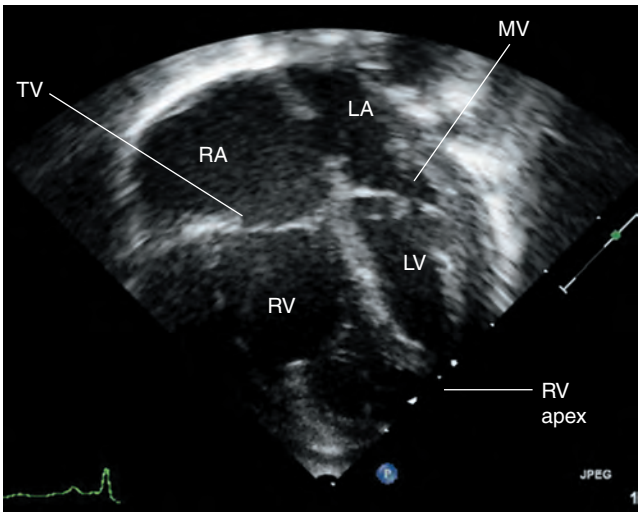


Figure 19.12 Four-chamber view of a newborn with critical aortic stenosis with associated hypoplasia of the left ventricle and mitral valve. The left ventricle no longer forms the apex of the heart, which is now formed by the apex of the right ventricle. LA, left atrium; LV, left ventricle; MV, mitral valve; RA, right atrium; RV, right ventricle; TV, tricuspid valve.



Figure 19.14 Magnetic resonance imaging may assist in delineating the extent of endocardial fibroelastosis (EFE) in infants with severe aortic stenosis. In this example late gadolinium enhancement has been used to demonstrate the EFE. LA, left atrium; LV, left ventricle; RA, right atrium; RV, right ventricle.

left heart structures are capable of supporting the systemic arterial circulation or not. This poses a major challenge in terms of management because if left heart structures are judged adequate, an intervention to relieve the aortic valve stenosis may be attempted. However, if left heart structures are judged inadequate to support cardiac output a single-ventricle ("Norwood") palliation might be adopted. Echocardiographic criteria have been developed to aid in decision-making in this regard [49–51] and an online calculator developed by the Congenital Heart Surgeons' Society is available (http://www.chssdc.org/content/chss-score-neonatal-critical-aortic-stenosis).

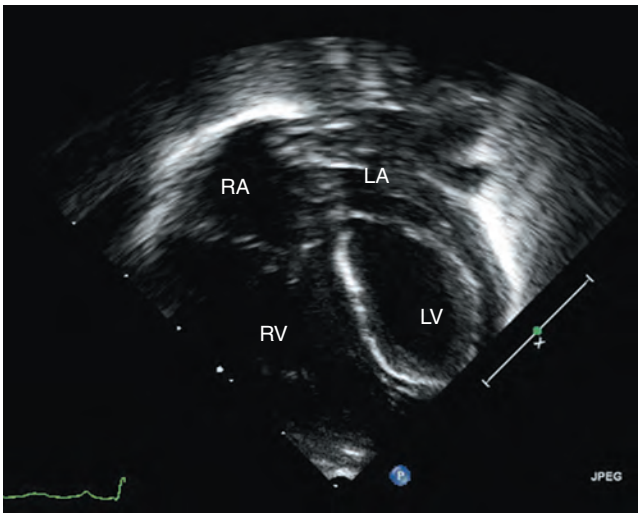


Figure 19.13 An example of an infant with critical aortic stenosis and severe endocardial fibroelastosis accounting for the bright echogenicity of the entire left ventricle. Such extensive endocardial fibroelastosis is regarded as an adverse prognostic sign for a biventricular repair. LA, left atrium; LV, left ventricle; RA, right atrium; RV, right ventricle.

Echocardiographic evaluation before, during and after intervention for aortic valve stenosis

In the preoperative assessment of the aortic valve, the echocardiographer should focus on the morphology of the aortic valve, noting the number of aortic valve leaflets, the morphology of the commissures and whether or not any leaflets are fused. An accurate measurement of the aortic valve at the hinge points of the leaflets is essential for selection of the appropriate balloon size for valvuloplasty (Figure 19.9; Video 19.7). In addition, the degree of aortic regurgitation should be carefully documented as an increase in the degree of regurgitation may occur following intervention.

In most units, balloon aortic valvuloplasty is favored as the initial intervention to relieve critical aortic stenosis. Thus, accurate measurement of the hinge points of the aortic valve is important to guide optimal balloon sizing. Echocardiography may be undertaken during the procedure if a complication is suspected, such as perforation of the left ventricle with a guidewire or damage to the aortic valve. At the authors' center, echocardiography is not routinely performed during the interventional procedure unless a major complication is suspected but is performed shortly after the procedure to assess residual gradients across the aortic valve and to judge the severity of aortic valve regurgitation. Judging the severity of aortic valve regurgitation early after balloon valvuloplasty may be difficult because of reduced compliance of the left ventricle related to muscle hypertrophy or

endocardial fibroelastosis, which may lead to underestimation of the degree of aortic regurgitation.

Follow-up echocardiography is indicated in all patients who have had intervention or surgery on the aortic valve. This is to evaluate restenosis of the aortic valve, particularly with growth, and to review the severity of aortic regurgitation, which is almost invariable following balloon aortic valvuloplasty or surgical valvotomy.

Aortic valve stenosis in the fetus

Aortic valve stenosis may be diagnosed accurately during fetal life and the echocardiographic findings have been reported [37–39]. In mild cases of aortic stenosis, there is an increased Doppler velocity across the aortic valve with good left ventricular function and antegrade flow around the aortic arch. Growth of left heart structures is well maintained with advancing gestational age. Sequential echocardiography is indicated during fetal life to monitor for progression of aortic valve stenosis, as some fetuses will demonstrate progressively increased severity of left ventricular outflow tract obstruction.

In severe cases of aortic stenosis diagnosed during fetal life, the left ventricle is typically dilated early in gestation with reduced systolic function (Figure 19.15). Endocardial fibroelastosis is a frequent association, although the severity may vary. This appears as a bright echogenic lining of the left ventricular cavity. Mitral valve regurgitation may occur and, if severe, is associated with poor prognosis [52,53] (Figure 19.16; Video 19.11). The interatrial communication, which normally permits right-to-left flow, may reverse due to left heart inflow obstruction. In some cases the atrial septum may be highly restrictive or even intact (Figures 19.17 and 19.18). Doppler interrogation of the pulmonary veins, with particular attention to the degree and duration of flow reversal during atrial contraction, is extremely helpful in determining the degree of restriction of the atrial septum (Figure 19.19). With advancing gestational age, growth of left heart structures is almost always subnormal so that by term, the aorta, left ventricle and mitral valve are severely hypoplastic. Judging which fetuses will be managed toward a biventricular circulation versus those that will be managed toward a single ventricle physiology is often difficult. The relative diameters and lengths of the right and left ventricles, presence of endocardial fibroelastosis, degree of mitral valve regurgitation, hypoplasia of the aorta and direction of flow in the distal aortic arch may all help in prognostication [39]. Fetuses at the severe end of the

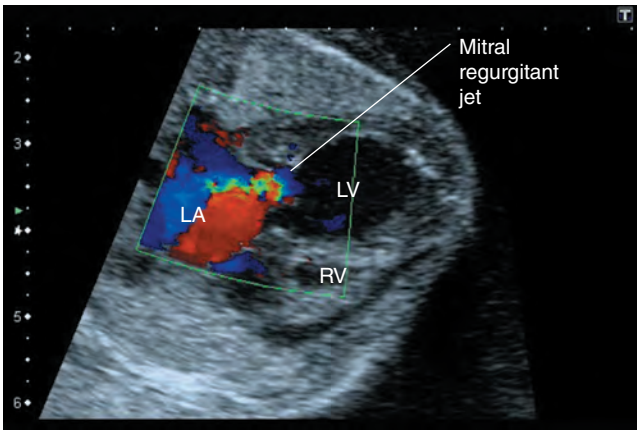


Figure 19.16 Fetal echocardiogram demonstrating severe mitral valve regurgitation in a fetus with critical aortic stenosis. There is a broad jet of mitral valve regurgitation, which fills a large portion of the dilated left atrium. LA, left atrium; LV, left ventricle; RA, right atrium.

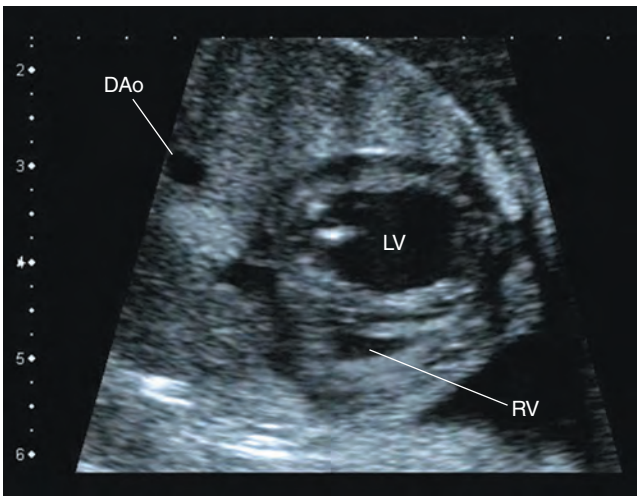


Figure 19.15 Fetal echocardiogram of a fetus with severe aortic stenosis. The left ventricle is dilated and compresses the right ventricle. Growth of the left ventricle is subnormal in the majority of cases so that by late gestation the appearances are more akin to classical hypoplastic left heart syndrome. DAo, descending aorta; LV, left ventricle; RV, right ventricle.

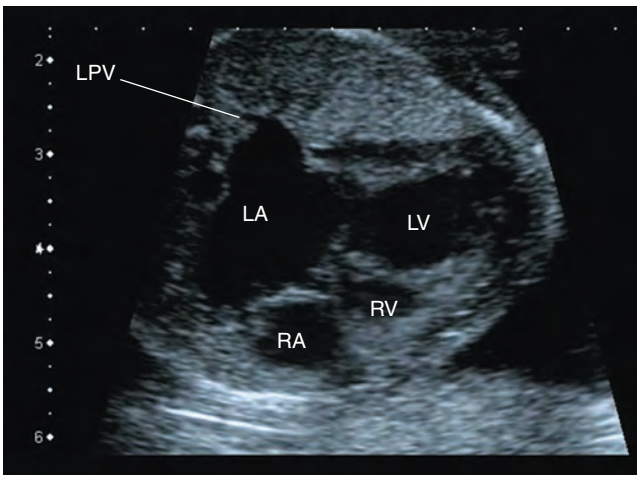


Figure 19.17 Severe dilation of the left atrium in a fetus with critical aortic stenosis, severe mitral valve regurgitation, and a restrictive interatrial communication. Note the pronounced dilation of the left pulmonary veins and bowing of the atrial septum from left to right. LA, left atrium; LPV, left pulmonary veins; LV, left ventricle; RA, right atrium; RV, right ventricle.

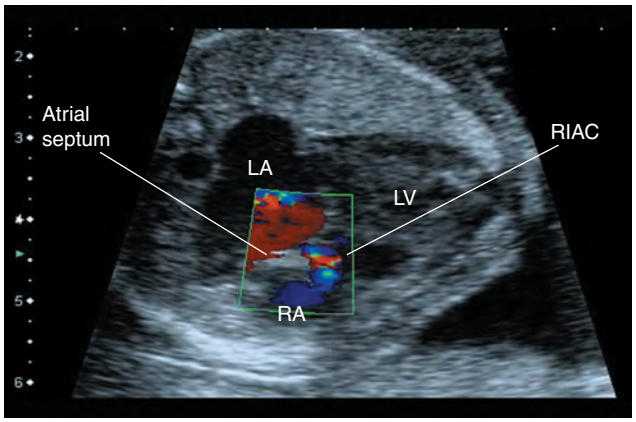
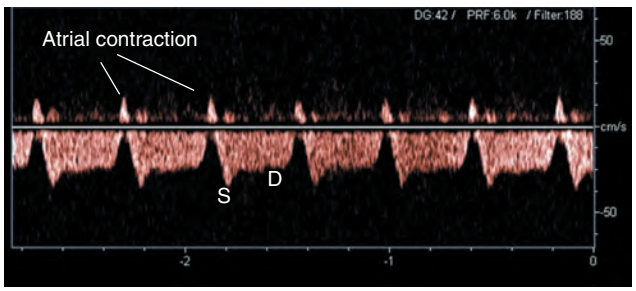
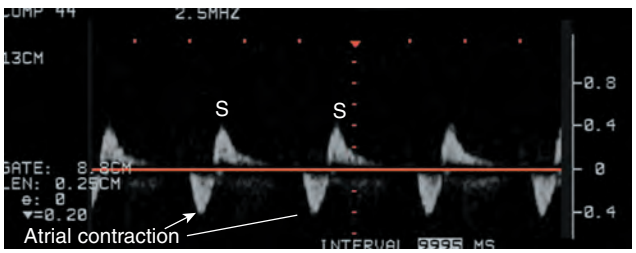


Figure 19.18 Restriction interatrial communication in a fetus with critical aortic stenosis. There is a narrow turbulent jet of blood from the left atrium to the right atrium representing the only point of decompression of the left atrium. LA, left atrium; LV, left ventricle; RA, right atrium; RIAC, restrictive interatrial communication.

spectrum will often require management with a single-ventricle palliation using a Norwood strategy rather than balloon dilation of the aortic valve or surgical valvotomy. It is the progression of aortic valve stenosis to a situation analogous to hypoplastic left heart syndrome that has led to prenatal intervention being considered for affected fetuses [39–41].



(a)



(b)

Figure 19.19 Interrogation of the pulmonary veins can be helpful to assess the degree of restriction of the atrial septum in the context of severe left heart obstruction. In **(a)** there is flow into the left atrium during ventricular systole (S) and diastole (D) with only a short low-velocity period of flow reversal during atrial contraction. In **(b)** there is a short period of normal flow into the left atrium during early ventricular systole only, with major reversal of flow during atrial systole. This represents the findings where the atrial septum is highly restrictive.

The echocardiographic approach during fetal life includes all of the assessments listed above but in addition should also include:

- Diameters of left and right ventricles
- Lengths of right and left ventricles
- Diameters of the mitral and tricuspid annuli
- Severity of mitral valve regurgitation
- Diameters of aortic valve annulus and aortic arch
- Direction of systolic flow in the distal aortic arch (antegrade versus retrograde)
- Direction of flow across the atrial septum
- Flow profile in the pulmonary veins.

Supravalvar aortic stenosis

Morphology

Supravalvar aortic stenosis typically occurs at the sinotubular junction and is characterized by discrete narrowing of the aortic lumen at this point (Figures 19.20 and 19.21; Video 19.12). This condition is most often seen due to defects in the elastin gene [54]. Marked thickening of the aortic media at the sinotubular junction produces the narrowing. The sinuses of Valsalva may be enlarged below the level of stenosis (Figure 19.21), and tethering of the aortic valve leaflets and stenosis of the coronary ostia are frequent associations. In addition to narrowing at the level of the sinotubular junction there may be varying degrees of hypoplasia of the ascending aorta, aortic arch and stenoses of head and neck vessels [55]. The extent of stenoses affecting other vessels or hypoplasia of the aortic arch may be assessed by MRI (Figure 19.22) as well as echocardiography.

Pathophysiology

Supravalvar aortic stenosis is extremely rare during fetal and early postnatal life but can become progressively more severe with age. It leads to increased afterload on the left ventricle and is associated with left ventricular hypertrophy when outflow tract obstruction is significant. In addition to the narrowing at the level of the sinotubular junction, the anomaly can involve the aortic valve with tethering and restricted leaflet motion. This can contribute further to the increased afterload on the left ventricle. Coronary ostial stenoses can occur in association with supravalvar aortic stenosis, which can lead to a precarious balance of coronary supply to the myocardium in the face of increased myocardial oxygen demand. Hypoplasia of the aortic arch and stenoses of the head and neck vessels can further increase the afterload on the left ventricle [55,56]. The abnormal composition of the vessel wall leads to increased medial hypertrophy and reduced elasticity of the vessel wall, which places further load on the left ventricle.

Imaging

The goals of echocardiographic assessment of supravalvar aortic stenosis are to comprehensively characterize the morphologic

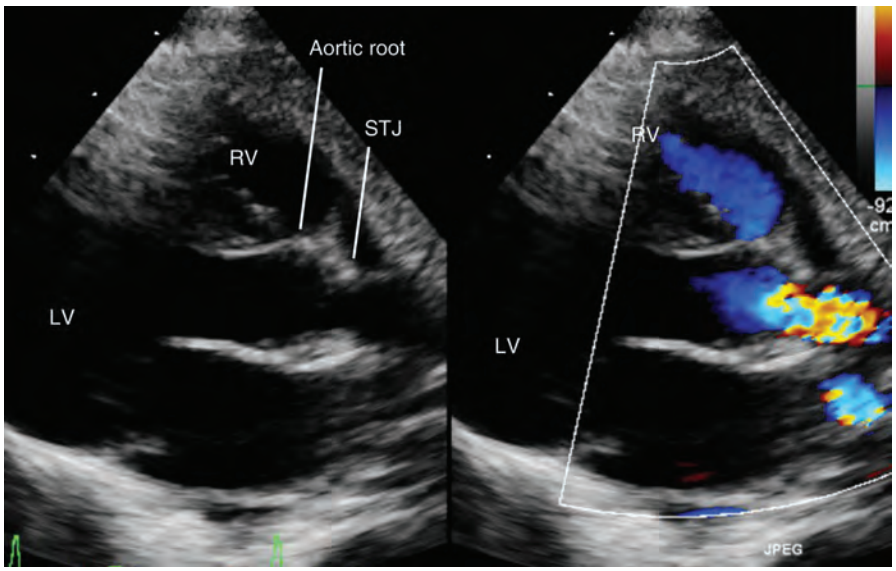


Figure 19.20 Supravalvar aortic stenosis. Parasternal long-axis view demonstrating "pinching" of the aorta at the level of the sinotubular junction. Color flow mapping confirms that turbulence of blood flow originates in the supravalvar region. LV, left ventricle; RV, right ventricle; STJ, sinotubular junction.

features of the obstructive lesion, to evaluate the hemodynamic severity, and to assess the entire thoracic aorta.

Key elements

In all cases, complete anatomic and functional examination by 2D and 3D imaging, as appropriate, and by color and spectral Doppler. In addition, the following elements of cardiovascular anatomy and function should be evaluated in detail and be given priority.

- Delineation of the morphologic features of the aortic root, sinotubular junction, and aortic valve morphology by 2D and 3D imaging.
- Measurements of the aortic valve annulus, root, sinotubular junction, and ascending aorta diameters in systole.
- Doppler evaluation of the severity of obstruction to blood flow from the subcostal, apical, and suprasternal/high right parasternal views.
- Assessment of the anatomy of the aortic arch and evaluation of flow around the aortic arch by Doppler.
- Visualization of the head and neck vessels to identify stenosis.
- Measurements of left ventricular size and function.

The imaging planes used to assess severity of obstruction are similar to those for aortic valve stenosis; imaging from the high right parasternal and suprasternal notch acoustic windows is particularly helpful. Although obtaining good acoustic windows to evaluate the ascending aorta can be difficult,

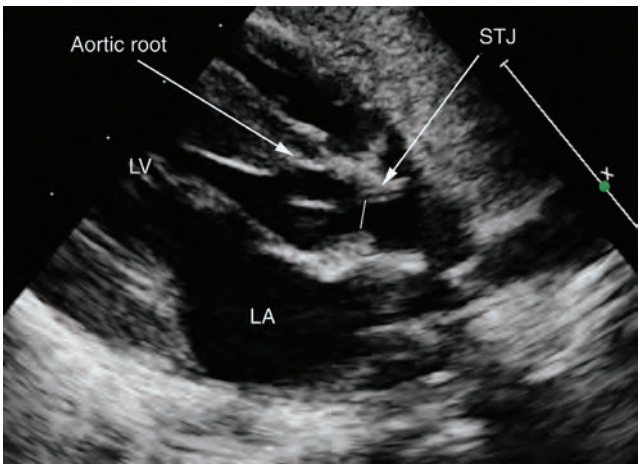


Figure 19.21 Parasternal long-axis view of a patient with supravalvar aortic stenosis. The line represents the dimension of the narrowest region of the aorta at the level of the sinotubular junction. LA, left atrium; LV, left ventricle; STJ, sinotubular junction.

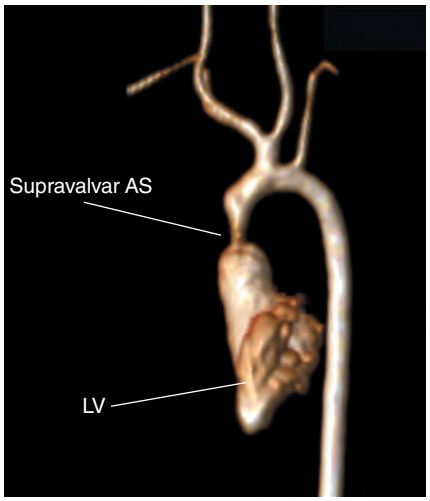


Figure 19.22 Magnetic resonance imaging of the ascending aorta, aortic arch, and head and neck vessels. This form of imaging is extremely helpful in planning the surgical approach for repair of supravalvar aortic stenosis and to identify occult stenoses in other vessels. AS, aortic stenosis; LV, left ventricle.

positioning the patient in a left or a right lateral decubitus can be helpful. Long-axis views of the left ventricle can be adapted to include the affected area at the sinotubular junction (Figures 19.20 and 19.21). Careful assessment of the aortic arch and head and neck vessels is essential because there may be generalized hypoplasia of the arch, coarctation of the aorta, and stenoses of the head and neck vessels, particularly at their origin from the aortic arch. If supravalvar aortic stenosis is considered severe enough to merit surgery, MRI is desirable to supplement echocardiography (Figure 19.22). During surgery, TEE or epicardial imaging is useful to confirm relief of obstruction and to image the aortic valve and origins of the coronary arteries.

Follow-up echocardiography is important for any patient with supravalvar aortic stenosis. This is performed to evaluate progression of the severity of stenosis both before and after surgery. In some patients, the entire aortic arch is hypoplastic, and relief of supravalvar aortic stenosis at the level of the sinotubular junction simply exposes pressure drops elsewhere in the aorta. The degree of aortic regurgitation should also be assessed because the aortic valve leaflets are frequently tethered at the level of the sinotubular junction and surgery occasionally results in worsening of the degree of aortic valve regurgitation.

Bicuspid (bicommissural) aortic valve

Morphology

In around 0.8–1.0% of individuals the aortic valve is made up of two rather than three cusps [1,57]. This is due to underdevelopment of one of the three commissures that define the aortic valve leaflets. The commissure can be absent, resulting in a truly bicuspid valve, or it may exhibit varying degrees of underdevelopment, a circumstance that has been described as "functionally bicuspid (or bicommissural) valve." It is worth noting that even when the commissure is absent, a raphe is typically present, marking the location of the commissure. One of the fused cusps is frequently hypoplastic. Although some bicuspid aortic valves may exhibit stenosis or, less frequently, regurgitation during infancy and childhood, many others function normally for decades. There is, however, an increased likelihood of degeneration with acquired stenosis and/or regurgitation later in life. Bicuspid aortic valve is more common in males (approximately 70%) and follows a genetic predisposition [7].

Dilation of the ascending aorta has been increasingly recognized as an accompaniment, which has been linked to structural abnormalities of the aortic wall similar to that seen in cystic medial necrosis associated with Marfan syndrome and other connective tissue disorders. This dilation has been linked to an increased risk of aortic dissection later in life [42,58,59]. Importantly, the sites of aortic dilation in bicuspid aortic valve and Marfan syndrome are different. The mid-ascending aorta is the site most involved in bicuspid aortic valve, whereas the sinuses of Valsalva (i.e., aortic root) are most commonly involved in Marfan syndrome. Recent data have confirmed a progressive increase in the aortic diameter z-score of children followed sequentially for a bicuspid aortic valve [60–62].

The morphology of the bicuspid aortic valve has clinical and prognostic implications. In ~60–70% of patients the intercoronary commissure is underdeveloped, leading to fusion of the left and right coronary cusps. In ~28–37% of patients the right noncoronary commissure is underdeveloped, leading to fusion of the right and noncoronary cusps. The left noncoronary commissure is underdeveloped in only 2–4% of cases with fusion of the left and noncoronary cusps [63,64]. Compared with other morphologies of the bicuspid aortic valve, underdevelopment of the intercoronary commissure is more often associated with coarctation of the aorta and other congenital heart disease, whereas underdevelopment of the right noncoronary commissure is more often associated with aortic valve dysfunction (stenosis and regurgitation) and with more severe dilation of the ascending aorta [63,65]. Associated congenital cardiac anomalies include, among others, coarctation of the aorta, interrupted aortic arch, hypoplastic left heart syndrome, atrioventricular canal defect, Ebstein anomaly, partially and totally anomalous pulmonary venous connection, tetralogy of Fallot, double-outlet right ventricle, and transposition of the great arteries.

Imaging

Bicuspid aortic valves should be evaluated in a manner analogous to that used for aortic valve stenosis (Figure 19.8; Video 19.6). In childhood there may be no evidence of obstruction at the valvar level, but bicuspid valves have a high likelihood of developing stenosis during adulthood. In some patients, the bicuspid valve exhibits mostly regurgitation. Thus, surveillance of aortic valve function is indicated in patients with bicuspid aortic valve. Three-dimensional echocardiography may assist in defining the precise morphology of the bicuspid aortic valve [66]. The echocardiographic evaluation should also include measurements of the ascending aorta and root due to the risk of progressive aortic dilation. Quantitative measurements of left ventricular size and function are essential in patients with abnormal aortic valve function. Because the aortic valve is bicuspid in ~30% of children with coarctation of the aorta, the finding of a bicuspid valve should prompt a detailed assessment of the aortic arch. In young children, short-axis views by a transthoracic approach are adequate to image the aortic valve, but in older children and adults, TEE may be required to obtain adequate image quality, particularly if surgery is being considered.

Aortic cusp prolapse

Morphology

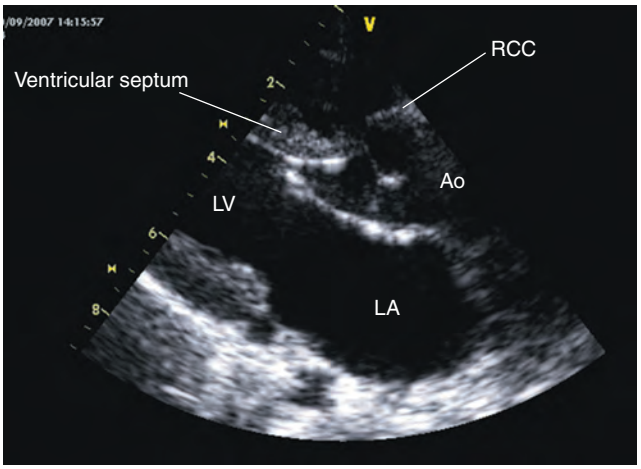
Aortic cusp prolapse occurs when one of the leaflets, usually the right coronary cusp, prolapses into a ventricular septal defect, which may be either a membranous or doubly committed subarterial (conal septal) defect [67,68]. Such prolapse of an aortic

valve leaflet often leads to partial or complete occlusion of the ventricular septal defect and is associated with aortic regurgitation in most cases. The mechanism of prolapse is thought to be related to the flow dynamics across a restrictive ventricular septal defect. The high-velocity jet across the ventricular septum leads to a low-pressure area (known as the Venturi effect), which has the effect of drawing the coronary cusp into the ventricular septal defect [69]. The site of aortic regurgitation may be central or through a commissure between the aortic cusps, most commonly between the right and noncoronary cusps. If aortic regurgitation is moderate or worse, surgical intervention to restore aortic valve function is indicated. In cases with mild or no aortic regurgitation, serial echocardiography is indicated to monitor for worsening aortic regurgitation [70–72]. Detailed visualization of the aortic valve is mandatory prior to surgical repair, with transesophageal echocardiography being the technique of choice [73].

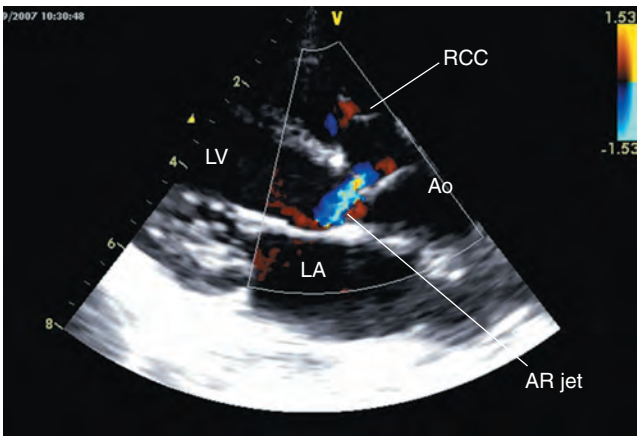
Imaging

Parasternal long-axis views show the prolapse of the cusp and the aortic regurgitant jet (Figure 19.23a–c; Video 19.13). The ventricular septum is aligned to the "belly" of the aortic valve leaflet rather than to the anterior wall of the aortic root. Short-axis views of the aortic valve demonstrate the location of any residual ventricular septal defect and the site of aortic regurgitation. Three-dimensional echocardiography can assist management by permitting accurate identification of the prolapsing leaflet and unique views from the right ventricle, which emulates the surgical view during repair (Figure 19.24 a–c; Videos 19.14–19.16).

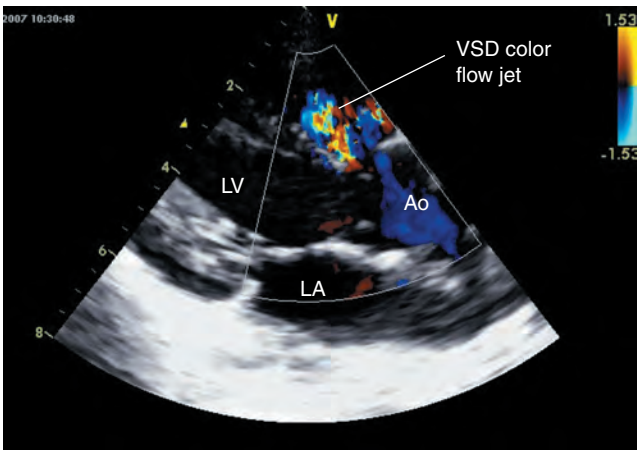
Transesophageal echocardiography is the technique of choice to document the anatomy when transthoracic imaging is insufficient and is indicated in most children being considered for surgical repair. Three-dimensional transesophageal imaging provides further definition particularly by creating novel views of the defect from the transaortic surgical view and from the right ventricular aspect (Figure 19.24 a–c; Videos 19.14–19.16). Surgical repair involves resuspension of the affected aortic valve cusp and closure of the ventricular septal defect. Intraoperative TEE is extremely helpful in monitoring the effectiveness of the repair and documenting aortic regurgitation, which may persist postoperatively. Follow-up echocardiography is mandatory, mainly to check for progression of aortic regurgitation following surgery. In some patients with aortic cusp prolapse, a conservative approach may be adopted if aortic regurgitation is absent or mild, without evidence of progression over sequential echocardiographic assessments.



(a)



(b)



(c)

Figure 19.23 Aortic cusp prolapse. **(a)** Parasternal long-axis view demonstrating prolapse of the right coronary cusp into a membranous ventricular septal defect (VSD). Note that the "belly" of the right coronary cusp is abnormally aligned to the crest of the ventricular septum. **(b)** The eccentric jet of aortic valve regurgitation is clearly seen, directed toward the anterior leaflet of the mitral valve. **(c)** The color flow jet of the restrictive membranous VSD can be readily visualized just below the right coronary cusp. Ao, aorta; AR, aortic regurgitation; LA, left atrium; LV, left ventricle; RCC, right coronary cusp.

Sinus of Valsalva aneurysm

Morphology

The aortic sinus of Valsalva is defined as the part of the aortic root that is delineated proximally by the attachments of the

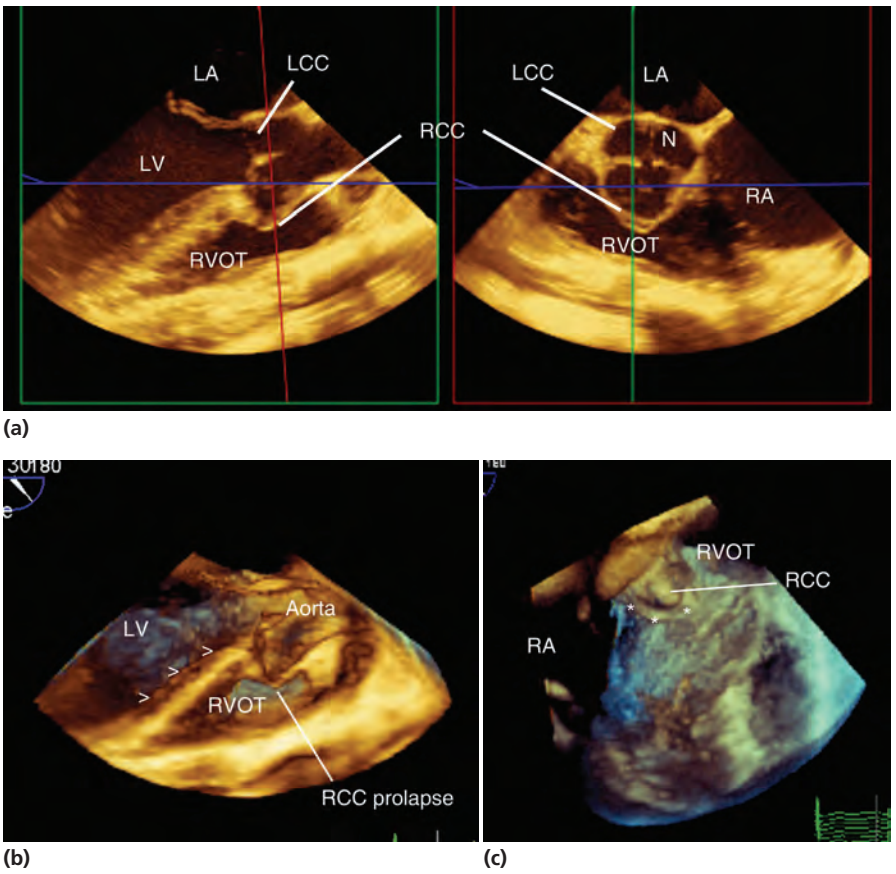


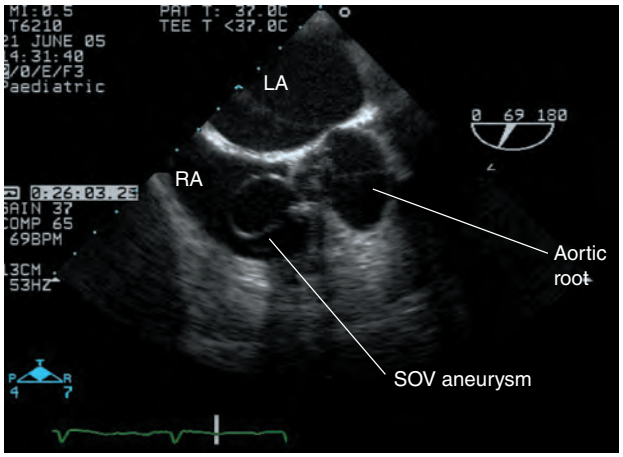
Figure 19.24 Three-dimensional (3D) echocardiogram from a patient with right coronary cusp prolapse into a membranous ventricular septal defect. **(a)** Multiplanar reformatted approach to identification of the prolapsing cusp. The red, green, and blue planes are centered over the prolapsing right coronary cusp. **(b)** Rendered 3D projection of the right coronary cusp prolapsing into the ventricular septal defect. The ventricular septum is indicated by the open-headed arrows (>). **(c)** Three-dimensional projection from the right ventricle where the prolapsing right coronary cusp can be visualized from the right ventricular aspect. The margins of the ventricular septal defect are indicated by the asterisks (∗). This type of projection is not achievable by 2D techniques and mirrors the view of the surgeon during repair. LA, left atrium; LCC, left coronary cusp; LV, left ventricle; N, noncoronary cusp; RA, right atrium; RCC, right coronary cusp; RVOT, right ventricular outflow tract.

aortic valve leaflet and distally by the sinotubular ridge [74]. Aneurysms of the sinus of Valsalva may occur in isolation or in association with other cardiac lesions such as a ventricular septal defect, subaortic stenosis, tetralogy of Fallot, or aortic valve abnormalities [75]. The aneurysm may originate from any one of the sinuses and the site of rupture may vary. Figure 19.25 shows a case where the aneurysm originated from the noncoronary sinus and ruptured to the right atrium (Video 19.17). Most cases affect the right coronary sinus, with the most frequent site of rupture being into the right ventricle (Figure 19.26) [76]. Three-dimensional echocardiography can project the abnormality to illustrate the aortic valve morphology and site of rupture in a single projection (Figure 19.27; Video 19.18). Although such aneurysms may occur in the context of congenital heart disease, they may also occur in other conditions that weaken the wall of the aortic root, such as Marfan syndrome, syphilis, Behçet disease, endocarditis, and trauma [75,76] . Presentation is most commonly with shortness of breath during exercise, but chest pain, congestive cardiac failure, syncope, and an asymptomatic cardiac murmur are all recognized modes of presentation [75,76].

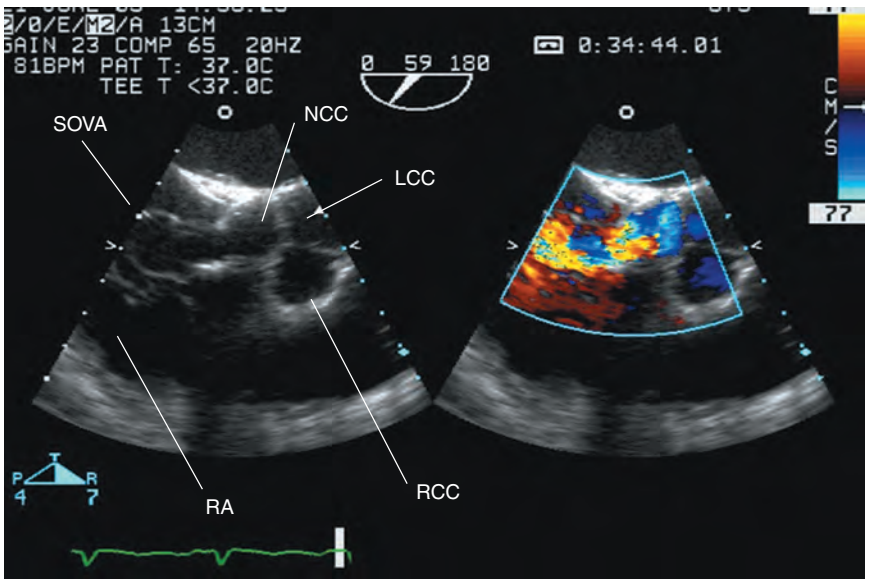
An aneurysm of the sinus of Valsalva may lead to aortic valve regurgitation, causing volume loading of the left ventricle. This may be asymptomatic while left ventricular function is maintained, but with increased volume loading symptoms such as exercise limitation and dyspnea may become more prominent. As mentioned earlier, the most frequent site of rupture of a sinus of Valsalva is from the right coronary cusp to the right ventricle [76]. This leads to a combination of regurgitation through the sinus and a left-to-right shunt as the blood flows from the systemic arterial circulation to the right ventricle and hence to the pulmonary circulation. In this clinical situation, symptoms of congestive heart failure are more pronounced, and urgent repair is indicated.

Imaging

Sinus of Valsalva aneurysm occurs mainly in older children and adults. The aims of the echocardiographic study are to determine which sinus of Valsalva and aortic valve leaflet are affected and, if ruptured, to determine the site of rupture. The most common site of rupture is from the right coronary cusp to the right ventricle, followed in incidence by rupture of either the right or noncoronary cusp to the right atrium. The noncoronary cusp occasionally ruptures, but involvement of the left coronary cusp is rare. Associated findings include aortic valve regurgitation in almost half of patients, and around one-third of patients have an associated ventricular septal defect. Other associated anomalies include Marfan-like habitus, bicuspid aortic valve, coarctation of



(a)



(b)

Figure 19.25 Sinus of Valsalva aneurysm from noncoronary sinus to right atrium. **(a)** Transesophageal echocardiogram demonstrating the classic "windsock" appearance of a sinus of Valsalva aneurysm originating from the noncoronary cusp and entering the right atrium. **(b)** This dual projection image clearly shows the aneurysm of the sinus of Valsalva originating from the noncoronary sinus. The aneurysm has ruptured into the right atrium. LA, left atrium; LCC, left coronary cusp of the aortic valve; NCC, noncoronary cusp; RA, right atrium; RCC, right coronary cusp; SOVA, sinus of Valsalva aneurysm.

the aorta, tetralogy of Fallot, mitral valve regurgitation, tricuspid valve regurgitation, Ebstein anomaly, and atrial septal defect [76,77].

In patients with suboptimal transthoracic acoustic windows, TEE provides excellent imaging of the aortic root to define the anatomy of the affected sinus of Valsalva and to determine where the ruptured sinus is draining. In a minority of cases, other techniques such as cardiac catheterization may be necessary to delineate the aneurysm, but MRI is proving increasingly helpful [77, 78]. Intraoperative TEE is helpful to confirm adequacy of surgical repair or to guide selected catheter intervention for device closure in selected cases [79,80] (Figure 19.28; Video 19.19).

Aortico–left ventricular tunnel

Morphology

Aortico–left ventricular tunnel is a rare congenital lesion characterized by an abnormal communication between the ascending aorta, at or above the level of the sinotubular junction, and the left ventricle [81]. The aortic origin of the tunnel is usually located above the right coronary ostium. The tunnel then passes in the tissue plane between the aorta and the posterior aspect of the subpulmonary infundibulum. The ventricular end of the tunnel occupies the same area as the fibrous triangle between the right and noncoronary leaflets of the aortic valve [82,83]. An aortico–left ventricular tunnel permits systemic arterial blood from the ascending aorta to regurgitate back into the left ventricle via the tunnel (Figures 19.29 and 19.30). This has an identical physiologic effect to that of severe aortic valve regurgitation with volume loading and potential dysfunction of the left ventricle. Aortico–ventricular tunnels are thought to represent a developmental abnormality, having been described during fetal life [84,85]. The outcome for cases diagnosed early in fetal and neonatal life is guarded because of the effects on left ventricular function, but successful surgery has been reported [86].

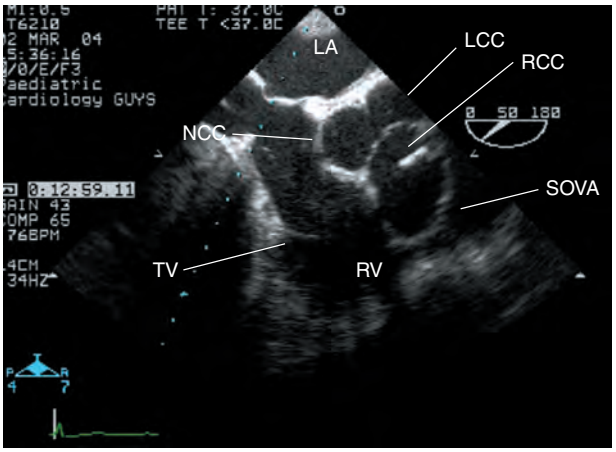


Figure 19.26 (Left) Sinus of Valsalva aneurysm from right coronary sinus to right ventricular outflow tract. There is a "windsock" of the sinus of Valsalva aneurysm extending into the right ventricular outflow tract. This is the most common site of origin and rupture of such aneurysms. LA, left atrium; LCC, left coronary cusp; NCC, noncoronary cusp; RCC, right coronary cusp; RV, right ventricle; SOVA, sinus of Valsalva aneurysm; TV, tricuspid valve.

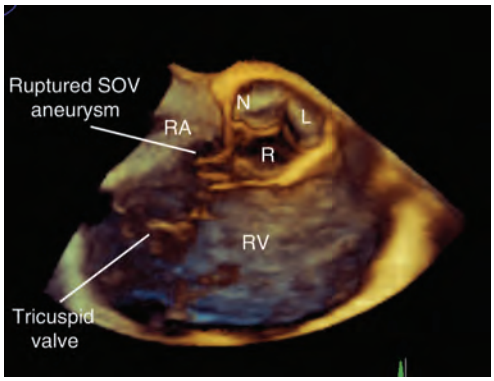


Figure 19.27 Three-dimensional echocardiogram of an aneurysm of the sinus of Valsalva of the right coronary cusp which has ruptured into the right atrium. There is a classic "windsock" appearance in this example. L, left coronary cusp; N, noncoronary cusp; R, right coronary cusp; RA, right atrium; RV, right ventricle; SOV, sinus of Valsalva.

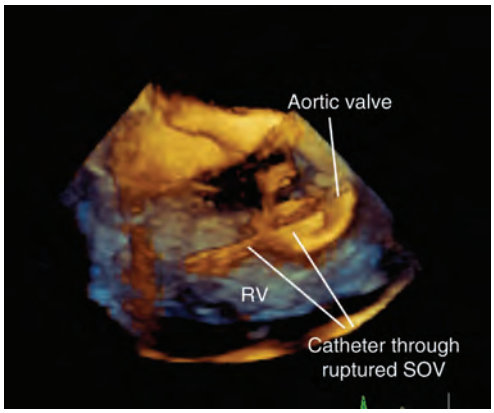
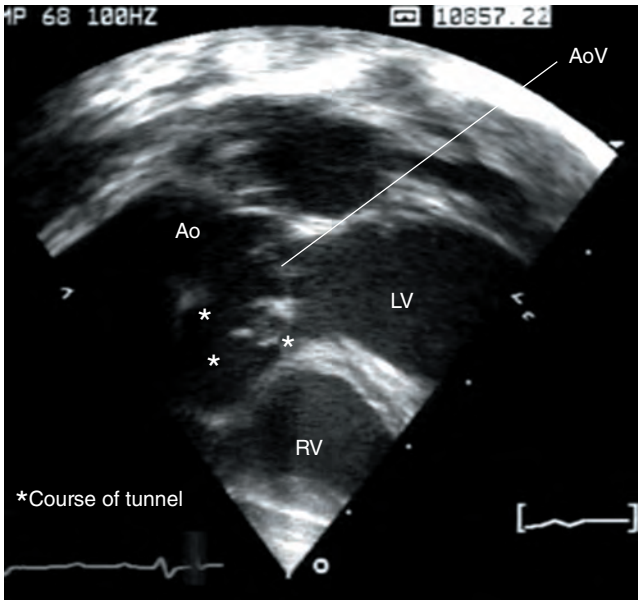
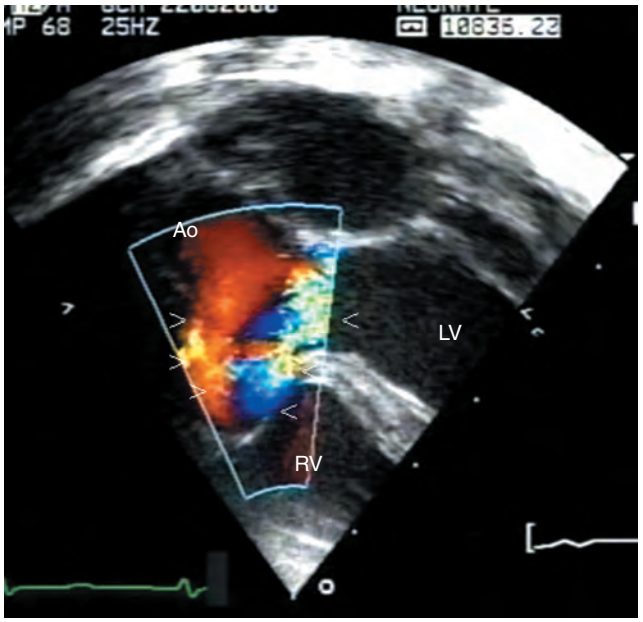


Figure 19.28 Three-dimensional echocardiography can be utilized to guide device closure of a ruptured sinus of Valsalva aneurysm. This example shows a catheter passing from the aorta to the right ventricle through a ruptured sinus of Valsalva. RV, right ventricle; SOV, sinus of Valsalva.

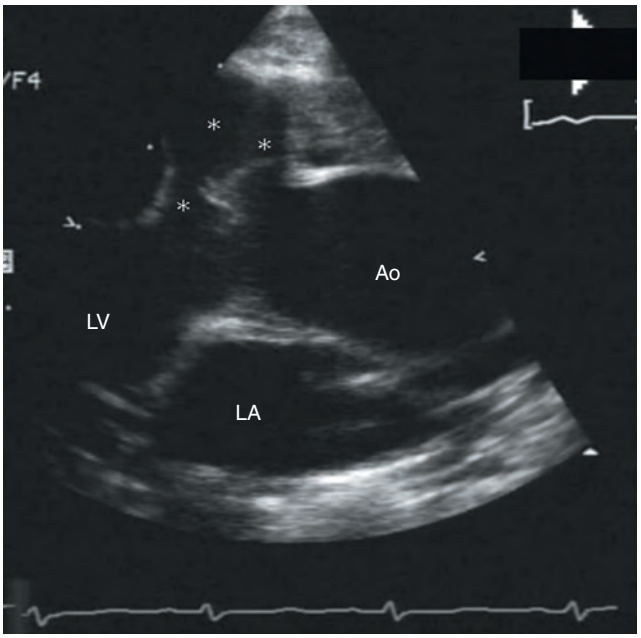


(a)

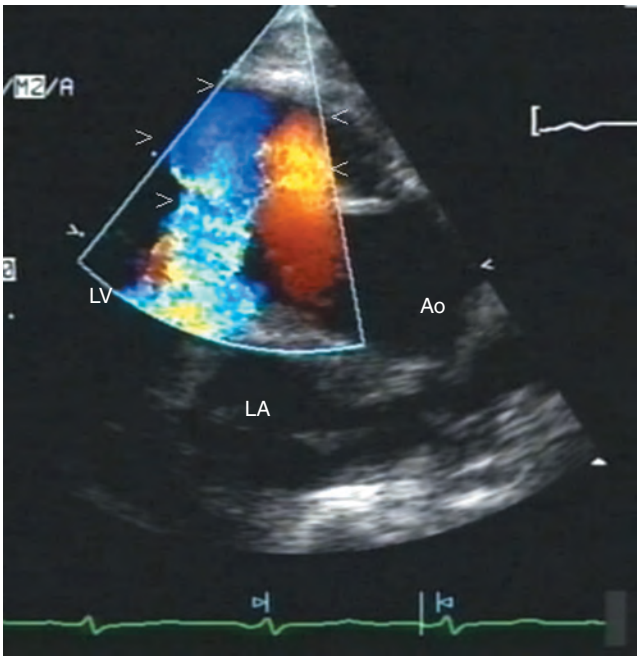


(b)

Figure 19.29 Aortico–left ventricular tunnel. **(a)** Foreshortened apical view of an aortico–left ventricular tunnel in an infant in whom the lesion was identified prenatally. The course of the tunnel is shown by the asterisks. **(b)** Color flow Doppler mapping demonstrates the course of the tunnel and the free regurgitation of blood from the ascending aorta to the left ventricle. The asterisks (∗) mark the course of the tunnel on the cross-sectional image. The arrowheads (< and >) mark the color flow jet through the tunnel. Ao, aorta; AoV, aortic valve; LV, left ventricle; RV, right ventricle.

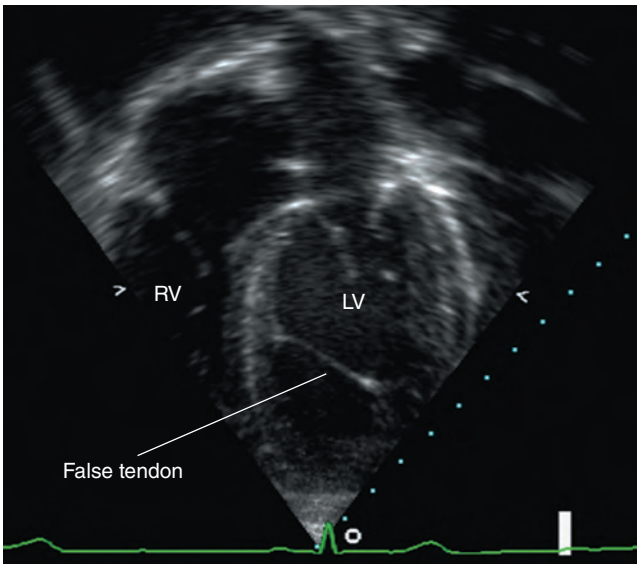


(a)

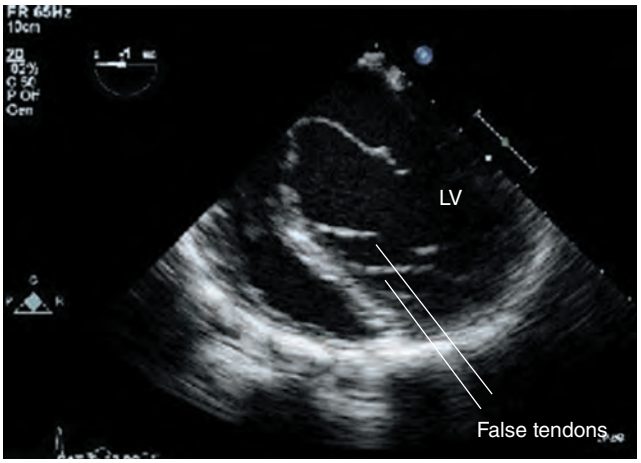


(b)

Figure 19.30 Aortico–left ventricular tunnel, long-axis views from the same infant as depicted in Fig. 19.29. **(a)** The tunnel can be seen to take a tortuous route from the aorta to the left ventricle. **(b)** Color flow Doppler mapping of the aortico–left ventricular tunnel with a broad jet passing from the aorta into the left ventricle; this has a hemodynamic effect analogous to that of severe aortic valve regurgitation. The asterisks (*) mark the course of the tunnel on the cross-sectional image. The arrowheads (< and >) mark the color flow jet through the tunnel. Ao, aorta; LV, left ventricle; RV, right ventricle.



(a)



(b)

Figure 19.31 **(a)** False tendon in the left ventricle of an asymptomatic child. **(b)** Transesophageal echocardiogram of a child with two false tendons. This child had a ventricular septal defect and aortic regurgitation, which prompted the examination. LV, left ventricle; RV, right ventricle.

Imaging

The aims of echocardiographic evaluation of aortico–left ventricular tunnel are to delineate the anatomy of the tunnel and to assess the effect of severe volume loading on the left ventricle in terms of its size and contractile function. The aortic origin, the course, and the left ventricular exit site of the tunnel can be imaged from the parasternal window through a combination of long- and short-axis views. Color Doppler flow mapping is particularly helpful to delineate the tunnel, which is characterized by antegrade flow from the left ventricle to the ascending aorta during systole and retrograde flow through the tunnel during diastole. Spectral Doppler is helpful to determine the direction and timing of the to-and-from flow through the tunnel [87]. In contrast to aortic regurgitation, the flow from the ascending

aorta to the left ventricle during diastole does not cross the aortic valve. A fistula between the right coronary artery and the left ventricle is excluded based on imaging of an uninvolved proximal right coronary artery.

False tendons

False tendons are occasionally observed within the cavity of the left ventricle and may run transversely or obliquely from the interventricular septum to the free wall (Figure 19.31a,b). These relatively thin muscle bundles have been implicated in the causation of the innocent vibratory murmur prevalent during childhood, although recent data suggest that they are no more prevalent in children with murmurs than in a control group without murmurs [88]. Pathologic examination has confirmed that such "tendons" may involve the conduction system [89]. The possibility of a link to ventricular extrasystoles [90] and an association with ventricular tachycardia in a subgroup of patients has been suggested [91,92].

Acknowledgement

I would like to acknowledge the contributions of Alexandra Savis, Kelly Peacock, and Karolina Bilska to the preparation of some of the echocardiographic images used in this chapter.

Videos

To access the videos for this chapter, please go to www.lai-echo.com.

Video 19.1 Subaortic stenosis. Transesophageal echocardiogram of membranous subaortic stenosis. The fluttering of the aortic valve leaflets is clearly demonstrated.

Video 19.2 Subaortic stenosis. Transesophageal echocardiogram of the left ventricular outflow tract demonstrating subaortic stenosis. Note that the obstructive subaortic ridge extends onto the anterior leaflet of the mitral valve.

Video 19.3 Subaortic stenosis. "Tunnel"-type of subaortic stenosis in an infant. There is a long segment of narrowing of the left ventricular outflow tract, which contrasts with the more discrete forms of obstruction illustrated in Videos 19.1 and 19.2.

Video 19.4 Three-dimensional echocardiogram demonstrating an en face view of circumferential subaortic obstruction viewed from the left ventricle. The mitral valve is seen to open and close in the near field and the gray-blue membrane is seen in the far field.

Video 19.5 Parasternal long-axis three-dimensional echocardiogram of subaortic stenosis which has developed following repair of an atrioventricular septal defect.

Video 19.6 Three-dimensional echocardiogram of a bicuspid aortic valve viewed from the aortic side. In this example the aortic valve leaflets flutter due to coexisting subaortic stenosis. The aortic valve leaflets are thin and the subaortic stenosis can be visualized through the aortic valve.

Video 19.7 Aortic valve stenosis. There is an eccentric color flow jet across the stenotic aortic valve. Use of color flow mapping assists in Doppler interrogation of the blood flow velocity.

Video 19.8 Three-dimensional transesophageal echocardiogram of an abnormal aortic valve. This patient had undergone previous balloon dilatation of the aortic valve.

Video 19.9 Neonatal aortic valve stenosis. This infant has severe aortic valve stenosis with an underdeveloped mitral valve and left ventricle. The right ventricle forms the cardiac apex. Subnormal growth of left heart structures is a frequent accompaniment of aortic valve stenosis during fetal life.

Video 19.10 Neonatal aortic valve stenosis. This infant has a hypoplastic left ventricle with severe endocardial fibroelastosis affecting the entire left ventricle.

Video 19.11 Fetal aortic valve stenosis. The left ventricle is severely dilated and poorly contractile. Right ventricular contractile function is well preserved.

Video 19.12 Parasternal long-axis view of supravalvar aortic stenosis. The thickening of the aortic wall at the level of the sinotubular junction and the narrowing at this level can be seen.

Video 19.13 Parasternal long-axis view demonstrating prolapse of the right coronary leaflet into a perimembranous ventricular septal defect. Note that the "belly" of the right coronary leaflet is abnormally aligned to the crest of the ventricular septum.

Video 19.14 Multiplanar reformatted three-dimensional echocardiography demonstrating prolapse of the right coronary leaflet. Note that placing the intersection of the red, green, and blue planes can assist in accurate diagnosis of the prolapsing leaflet (upper left and upper right panes). The rendered view of the prolapsing leaflet is shown in the lower right pane.

Video 19.15 Three-dimensional TEE-rendered video of right coronary cusp prolapse into a restrictive perimembranous ventricular septal defect. The depth of the leaflet can be appreciated. Acquisition at a TEE angle of 120 degrees provides optimal visualization of this lesion.

Video 19.16 Three-dimensional (3D) TEE view of right coronary cusp prolapse into a perimembranous ventricular septal defect. This is a uniquely 3D view produced by cropping away the right ventricular free wall looking en face at the ventricular septum. The motion of the cusp into the defect can be readily visualized.

Video 19.17 Aneurysm of the sinus of Valsalva. This is a short-axis view of the aortic valve obtained by transesophageal echocardiography. There is a classic "windsock" appearance of the aneurysm,

which arises from the noncoronary cusp and has ruptured into the right atrium.

Video 19.18 Rendered three-dimensional TEE view of the aortic valve, tricuspid valve and right ventricular outflow tract. The depth of field means that the ruptured right coronary sinus of Valsalva into the right atrium can be seen in a single projection.

Video 19.19 Rendered three-dimensional echocardiographic view of a catheter through a ruptured sinus of Valsalva. In this case, the right coronary sinus has ruptured into the right ventricular outflow tract.

References

1 Hoffman JI, Kaplan S. The incidence of congenital heart disease. *J Am Coll Cardiol* 2002;**39**:1890–900.
2 Kitchiner D, Jackson M, Malaiya N, et al. Incidence and prognosis of obstruction of the left ventricular outflow tract in Liverpool (1960–91): a study of 313 patients. *Br Heart J* 1994;**71**:588–595.
3 Gill HK, Splitt M, Sharland GK, Simpson JM. Patterns of recurrence of congenital heart disease: an analysis of 6,640 consecutive pregnancies evaluated by detailed fetal echocardiography. *J Am Coll Cardiol* 2003;**42**:923–929.
4 McBride KL, Pignatelli R, Lewin M, et al. Inheritance analysis of congenital left ventricular outflow tract obstruction malformations: segregation, multiplex relative risk, and heritability. *Am J Med Genet A* 2005;**134**:180–186.
5 Allan LD, Sharland GK, Milburn A, et al. Prospective diagnosis of 1,006 consecutive cases of congenital heart disease in the fetus. *J Am Coll Cardiol* 1994;**23**:1452–1458.
6 Garg V. Molecular genetics of aortic valve disease. *Curr Opin Cardiol* 2006;**21**:180–184.
7 Cripe L, Andelfinger G, Martin LJ, et al. Bicuspid aortic valve is heritable. *J Am Coll Cardiol* 2004;**44**:138–143.
8 Hiratzka LF, Bakris GL, Beckman JA, et al. 2010 ACCF/AHA/AATS/ACR/ASA/SCA/SCAI/SIR/STS/SVM guidelines for the diagnosis and management of patients with Thoracic Aortic Disease: a report of the American College of Cardiology Foundation/American Heart Association Task Force on Practice Guidelines, American Association for Thoracic Surgery, American College of Radiology, American Stroke Association, Society of Cardiovascular Anesthesiologists, Society for Cardiovascular Angiography and Interventions, Society of Interventional Radiology, Society of Thoracic Surgeons, and Society for Vascular Medicine. *Circulation* 2010;**121**:e266–369.
9 Kerstjens-Frederikse WS, Du Marchie Sarvaas GJ, Ruiter JS, et al. Left ventricular outflow tract obstruction: should cardiac screening be offered to first-degree relatives? *Heart* 2011;**97**:1228–1232.
10 Morris CA, Mervis CB. Williams syndrome and related disorders. *Annu Rev Genomics Hum Genet* 2000;**1**:461–484.
11 Park S, Seo EJ, Yoo HW, Kim Y. Novel mutations in the human elastin gene (ELN) causing isolated supravalvular aortic stenosis. *Int J Mol Med* 2006;**18**:329–332.
12 Richardson ME, Menahem S, Wilkinson JL. Familial fixed subaortic stenosis. *Int J Cardiol* 1991;**30**:351–353.
13 Cape EG, Vanauker MD, Sigfusson G, et al. Potential role of mechanical stress in the etiology of pediatric heart disease: septal shear stress in subaortic stenosis. *J Am Coll Cardiol* 1997;**30**:247–254.
14 Sigfusson G, Tacy TA, Vanauker MD, Cape EG. Abnormalities of the left ventricular outflow tract associated with discrete subaortic stenosis in children: an echocardiographic study. *J Am Coll Cardiol* 1997;**30**:255–259.
15 Oztunc F, Ozme S, Ozkutlu S, et al. Fixed subaortic stenosis in childhood. Medical and surgical course in 90 patients. *Jpn Heart J* 1992;**33**:327–335.
16 Reeder GS, Danielson GK, Seward JB, et al. Fixed subaortic stenosis in atrioventricular canal defect: a Doppler echocardiographic study. *J Am Coll Cardiol* 1992;**20**:386–394.
17 Silverman NH, Gerlis LM, Ho SY, Anderson RH. Fibrous obstruction within the left ventricular outflow tract associated with ventricular septal defect: a pathologic study. *J Am Coll Cardiol* 1995;**25**:475–481.
18 Marasini M, Zannini L, Ussia GP, et al. Discrete subaortic stenosis: incidence, morphology and surgical impact of associated subaortic anomalies. *Ann Thorac Surg* 2003;**75**:1763–1768.
19 Kleinert S, Ott DA, Geva T. Critical discrete subaortic stenosis in the newborn period. *Am Heart J* 1993;**125**:1187–1189.
20 Kleinert S, Geva T. Echocardiographic morphometry and geometry of the left ventricular outflow tract in fixed subaortic stenosis. *J Am Coll Cardiol* 1993;**22**:1501–1508.
21 van Son JA, Schaff HV, Danielson GK, et al. Surgical treatment of discrete and tunnel subaortic stenosis. Late survival and risk of reoperation. *Circulation* 1993;**88**:II159–69.
22 Coleman DM, Smallhorn JF, McCrindle BW, et al. Postoperative follow-up of fibromuscular subaortic stenosis. *J Am Coll Cardiol* 1994;**24**:1558–1564.
23 Gersony WM. Natural history of discrete subvalvar aortic stenosis: management implications. *J Am Coll Cardiol* 2001;**38**:843–845.
24 Geva A, McMahon CJ, Gauvreau K, et al. Risk factors for reoperation after repair of discrete subaortic stenosis in children. *J Am Coll Cardiol* 2007;**50**:1498–1504.
25 Serraf A, Zoghby J, Lacour-Gayet F, et al. Surgical treatment of subaortic stenosis: a seventeen-year experience. *J Thorac Cardiovasc Surg* 1999;**117**:669–678.
26 Caldarone CA. Left ventricular outflow tract obstruction: the role of the modified Konno procedure. *Semin Thorac Cardiovasc Surg Pediatr Card Surg Annu* 2003;**6**:98–107.
27 Choi JY, Sullivan ID. Fixed subaortic stenosis: anatomical spectrum and nature of progression. *Br Heart J* 1991;**65**:280–286.
28 McMahon CJ, Gauvreau K, Edwards JC, Geva T. Risk factors for aortic valve dysfunction in children with discrete subvalvar aortic stenosis. *Am J Cardiol* 2004;**94**:459–464.
29 Drolet C, Miro J, Cote JM, et al. Long-term pediatric outcome of isolated discrete subaortic stenosis. *Can J Cardiol* 2011;**27**:389 e19–24.
30 Oliver JM, Gonzalez A, Gallego P, et al. Discrete subaortic stenosis in adults: increased prevalence and slow rate of progression of the obstruction and aortic regurgitation. *J Am Coll Cardiol* 2001;**38**:835–842.
31 Bezold LI, Smith EO, Kelly K, et al. Development and validation of an echocardiographic model for predicting progression of discrete subaortic stenosis in children. *Am J Cardiol* 1998;**81**:314–320.
32 Gaynor JW, Elliott MJ. Congenital left ventricular outflow tract obstruction. *J Heart Valve Dis* 1993;**2**:80–93.

33 Jahangiri M, Nicholson IA, del Nido PJ, et al. Surgical management of complex and tunnel-like subaortic stenosis. *Eur J Cardiothorac Surg* 2000;**17**:637–642.

34 Wilson WR, Greer GE, Durzinsky DS, Curtis JJ. Ross procedure for complex left ventricular outflow tract obstruction. *J Cardiovasc Surg (Torino)* 2000;**41**:387–392.

35 Belli E, Serraf A, Lacour-Gayet F, et al. Biventricular repair for double-outlet right ventricle. Results and long-term follow-up. *Circulation* 1998;**98**:II360–365; discussion II365–367.

36 Anderson RH. Morphology of critically stenotic aortic valves. *J Thorac Cardiovasc Surg* 1995;**110**:565.

37 Simpson JM, Sharland GK. Natural history and outcome of aortic stenosis diagnosed prenatally. *Heart* 1997;**77**:205–210.

38 McCaffrey FM, Sherman FS. Prenatal diagnosis of severe aortic stenosis. *Pediatr Cardiol* 1997;**18**:276–281.

39 Makikallio K, McElhinney DB, Levine JC, et al. Fetal aortic valve stenosis and the evolution of hypoplastic left heart syndrome: patient selection for fetal intervention. *Circulation* 2006;**113**:1401–1405.

40 Marshall AC, Tworetzky W, Bergersen L, et al. Aortic valvuloplasty in the fetus: technical characteristics of successful balloon dilation. *J Pediatr* 2005;**147**:535–539.

41 Tworetzky W, Wilkins-Haug L, Jennings RW, et al. Balloon dilation of severe aortic stenosis in the fetus: potential for prevention of hypoplastic left heart syndrome: candidate selection, technique, and results of successful intervention. *Circulation* 2004;**110**:2125–2131.

42 Ward C. Clinical significance of the bicuspid aortic valve. *Heart* 2000;**83**:81–85.

43 Grayburn PA, Smith MD, Harrison MR, et al. Pivotal role of aortic valve area calculation by the continuity equation for Doppler assessment of aortic stenosis in patients with combined aortic stenosis and regurgitation. *Am J Cardiol* 1988;**61**:376–381.

44 Zoghbi WA, Farmer KL, Soto JG, et al. Accurate noninvasive quantification of stenotic aortic valve area by Doppler echocardiography. *Circulation* 1986;**73**:452–459.

45 Hakki AH, Iskandrian AS, Bemis CE, et al. A simplified valve formula for the calculation of stenotic cardiac valve areas. *Circulation* 1981;**63**:1050–1055.

46 Gorlin R, Gorlin SG. Hydraulic formula for calculation of the area of the stenotic mitral valve, other cardiac valves, and central circulatory shunts. *I. Am Heart J* 1951;**41**:1–29.

47 Chambers J. Low "gradient", low flow aortic stenosis. *Heart* 2006;**92**:554–558.

48 Beroukhim RS, Graham DA, Margossian R, et al. An echocardiographic model predicting severity of aortic regurgitation in congenital heart disease. *Circ Cardiovasc Imaging* 2010;**3**:542–549.

49 Rhodes LA, Colan SD, Perry SB, Jonas RA, Sanders SP. Predictors of survival in neonates with critical aortic stenosis. *Circulation* 1991;**84**:2325–2335.

50 Colan SD, McElhinney DB, Crawford EC, et al. Validation and re-evaluation of a discriminant model predicting anatomic suitability for biventricular repair in neonates with aortic stenosis. *J Am Coll Cardiol* 2006;**47**:1858–1865.

51 Kovalchin JP, Brook MM, Rosenthal GL, et al. Echocardiographic hemodynamic and morphometric predictors of survival after two-ventricle repair in infants with critical aortic stenosis. *J Am Coll Cardiol* 1998;**32**:237–244.

52 Vogel M, McElhinney DB, Wilkins-Haug LE, et al. Aortic stenosis and severe mitral regurgitation in the fetus resulting in giant left atrium and hydrops: pathophysiology, outcomes, and preliminary experience with pre-natal cardiac intervention. *J Am Coll Cardiol* 2011;**57**:348–355.

53 Rogers LS, Peterson AL, Gaynor JW, et al. Mitral valve dysplasia syndrome: a unique form of left-sided heart disease. *J Thorac Cardiovasc Surg* 2011;**142**:1381–1387.

54 Smoot LB. Elastin gene deletions in Williams syndrome. *Curr Opin Pediatr* 1995;**7**:698–701.

55 Stamm C, Friehs I, Ho SY, et al. Congenital supravalvar aortic stenosis: a simple lesion? *Eur J Cardiothorac Surg* 2001;**19**:195–202.

56 Stamm C, Li J, Ho SY, et al. The aortic root in supravalvular aortic stenosis: the potential surgical relevance of morphologic findings. *J Thorac Cardiovasc Surg* 1997;**114**:16–24.

57 Nistri S, Basso C, Marzari C, et al. Frequency of bicuspid aortic valve in young male conscripts by echocardiogram. *Am J Cardiol* 2005;**96**:718–721.

58 Davies RR, Kaple RK, Mandapati D, et al. Natural history of ascending aortic aneurysms in the setting of an unreplaced bicuspid aortic valve. *Ann Thorac Surg* 2007;**83**:1338–1344.

59 Yap SC, Takkenberg JJ, Witsenburg M, et al. Aortic stenosis at young adult age. *Expert Rev Cardiovasc Ther* 2005;**3**:1087–1098.

60 Warren AE, Boyd ML, O'Connell C, Dodds L. Dilatation of the ascending aorta in paediatric patients with bicuspid aortic valve: frequency, rate of progression and risk factors. *Heart* 2006;**92**:1496–1500.

61 Holmes KW, Lehmann CU, Dalal D, et al. Progressive dilation of the ascending aorta in children with isolated bicuspid aortic valve. *Am J Cardiol* 2007;**99**:978–983.

62 Beroukhim RS, Kruzick TL, Taylor AL, et al. Progression of aortic dilation in children with a functionally normal bicuspid aortic valve. *Am J Cardiol* 2006;**98**:828–830.

63 Ciotti GR, Vlahos AP, Silverman NH. Morphology and function of the bicuspid aortic valve with and without coarctation of the aorta in the young. *Am J Cardiol* 2006;**98**:1096–1102.

64 Fernandes SM, Sanders SP, Khairy P, et al. Morphology of bicuspid aortic valve in children and adolescents. *J Am Coll Cardiol* 2004;**44**:1648–1651.

65 Fernandes SM, Khairy P, Sanders SP, Colan SD. Bicuspid aortic valve morphology and interventions in the young. *J Am Coll Cardiol* 2007;**49**:2211–2214.

66 Sadron Blaye-Felice MA, Seguela PE, Arnaudis B, et al. Usefulness of three-dimensional transthoracic echocardiography for the classification of congenital bicuspid aortic valve in children. *Eur Heart J Cardiovasc Imaging* 2012;**13**:1047–1052.

67 Craig BG, Smallhorn JF, Burrows P, et al. Cross-sectional echocardiography in the evaluation of aortic valve prolapse associated with ventricular septal defect. *Am Heart J* 1986;**112**:800–807.

68 Menahem S, Johns JA, del Torso S, et al. Evaluation of aortic valve prolapse in ventricular septal defect. *Br Heart J* 1986;**56**:242–249.

69 Tweddell JS, Pelech AN, Frommelt PC. Ventricular septal defect and aortic valve regurgitation: pathophysiology and indications for surgery. *Semin Thorac Cardiovasc Surg Pediatr Card Surg Annu* 2006:147–152.

70 Tomita H, Fuse S, Chiba S. Is early surgery always necessary in patients with aortic valve prolapse complicating an Eisenmenger-type ventricular septal defect? *Acta Paediatr Jpn* 1998;**40**:232–235.

71 Tomita H, Yamada O, Kurosaki K, et al. Eccentric aortic regurgitation in patients with right coronary cusp prolapse complicating a ventricular septal defect. *Circ J* 2003;**67**:672–675.
72 Butter A, Duncan W, Weatherdon D, et al. Aortic cusp prolapse in ventricular septal defect and its association with aortic regurgitation–appropriate timing of surgical repair and outcomes. *Can J Cardiol* 1998;**14**:833–840.
73 de Waroux JB, Pouleur AC, Goffinet C, et al. Functional anatomy of aortic regurgitation: accuracy, prediction of surgical repairability, and outcome implications of transesophageal echocardiography. *Circulation* 2007;**116**:I264–269.
74 Sutton JP, 3rd, Ho SY, Anderson RH. The forgotten interleaflet triangles: a review of the surgical anatomy of the aortic valve. *Ann Thorac Surg* 1995;**59**:419–427.
75 Vural KM, Sener E, Tasdemir O, Bayazit K. Approach to sinus of Valsalva aneurysms: a review of 53 cases. *Eur J Cardiothorac Surg* 2001;**20**:71–76.
76 Moustafa S, Mookadam F, Cooper L, et al. Sinus of Valsalva aneurysms–47 years of a single center experience and systematic overview of published reports. *Am J Cardiol* 2007;**99**:1159–1164.
77 Feldman DN, Roman MJ. Aneurysms of the sinuses of Valsalva. *Cardiology* 2006;**106**:73–81.
78 Schuster A, Hedstrom E, Blauth C, et al. Ruptured aneurysm of the sinus of valsalva insights from magnetic resonance first-pass myocardial perfusion imaging. *J Am Coll Cardiol* 2012;**59**:538.
79 Sarupria A, Kapoor PM, Makhija N, Kiran U. Trans-esophageal echocardiography: an indispensible guide for transcatheter device closure of ruptured sinus of Valsalva aneurysm. *Ann Card Anaesth* 2012;**15**:156–157.
80 Arora R, Trehan V, Rangasetty UM, et al. Transcatheter closure of ruptured sinus of valsalva aneurysm. *J Interv Cardiol* 2004;**17**:53–58.
81 Levy MJ, Schachner A, Blieden LC. Aortico-left ventricular tunnel: collective review. *J Thorac Cardiovasc Surg* 1982;**84**:102–109.
82 Ho SY, Muriago M, Cook AC, et al. Surgical anatomy of aorto-left ventricular tunnel. *Ann Thorac Surg* 1998;**65**:509–514.
83 Cook AC, Fagg NL, Ho SY, et al. Echocardiographic-anatomical correlations in aorto-left ventricular tunnel. *Br Heart J* 1995;**74**:443–448.
84 Pascoli I, Cester M, Nanhorngue K, Paternoster DM. Aortico-left ventricular tunnel diagnosed prenatally: case report. *Prenat Diagn* 2007;**27**:1263–1265.
85 Kenny D, Chen Q, Uzun O. Antenatal diagnosis of aortico-left ventricular tunnel. *Pediatr Cardiol* 2007;**28**:241–242.
86 Kolcz J, Januszewska K, Malec E. Successful repair of aorto-left ventricular tunnel diagnosed prenatally. *Cardiol Young* 2005;**15**:219–222.
87 Humes RA, Hagler DJ, Julsrud PR, et al. Aortico-left ventricular tunnel: diagnosis based on two-dimensional echocardiography, color flow Doppler imaging, and magnetic resonance imaging. *Mayo Clin Proc* 1986;**61**:901–907.
88 Van Oort A, Hopman J, De Boo T, et al. The vibratory innocent heart murmur in schoolchildren: a case-control Doppler echocardiographic study. *Pediatr Cardiol* 1994;**15**:275–281.
89 Abdulla AK, Frustaci A, Martinez JE, et al. Echocardiography and pathology of left ventricular "false tendons". *Chest* 1990;**98**:129–132.
90 Suwa M, Hirota Y, Kaku K, et al. Prevalence of the coexistence of left ventricular false tendons and premature ventricular complexes in apparently healthy subjects: a prospective study in the general population. *J Am Coll Cardiol* 1988;**12**:910–914.
91 Thakur RK, Klein GJ, Sivaram CA, et al. Anatomic substrate for idiopathic left ventricular tachycardia. *Circulation* 1996;**93**:497–501.
92 Suwa M, Yoneda Y, Nagao H, et al. Surgical correction of idiopathic paroxysmal ventricular tachycardia possibly related to left ventricular false tendon. *Am J Cardiol* 1989;**64**:1217–1220.

CHAPTER 20

Hypoplastic Left Heart Syndrome

David J. Goldberg and Jack Rychik
Division of Pediatric Cardiology, The Children's Hospital of Philadelphia, Philadelphia, PA; Perelman School of Medicine at the University of Pennsylvania, Philadelphia, PA, USA

Definition

Hypoplastic left heart syndrome (HLHS) describes a collection of heterogeneous congenital heart anomalies in which the left ventricle (LV), by virtue of structural abnormalities, is incapable of providing adequate systemic perfusion. HLHS may include abnormalities such as mitral stenosis or atresia, LV hypoplasia, aortic valve stenosis or atresia, and ascending aortic hypoplasia (Figure 20.1; Video 20.1). The syndrome was first reported by Lev in 1952, and the term HLHS was first described by Noonan and Nadas [1,2]. It is one of the most severe forms of congenital anomalies and accounts for 20–25% of all mortality in infants born with congenital heart disease.

Incidence and associated anomalies

The incidence of HLHS is 266 per 1 million live births; hence approximately 2000 affected infants are born each year in the United States [3]. The prevalence of HLHS in the population ranges from 0.02% to 0.08%, but continues to increase as the accuracy of diagnosis and successful management strategies are increasing survival.

Autopsy series in patients with HLHS have described a prevalence of extracardiac anomalies or genetic/chromosomal syndromes of up to 28% [4]. In particular, Turner syndrome (XO) has been well described in association with HLHS and should be investigated in every female infant with this form of heart disease [5]. Other syndromes reported in association with HLHS include Smith–Lemli–Opitz, Holt–Oram, and Jacobsen. As genetic testing becomes more refined, it is likely that additional genetic influences will be identified.

Much attention has been focused on the relationship between the central nervous system and HLHS. Congenital brain anomalies that have been identified in association with HLHS include agenesis of the corpus callosum, holoprosencephaly and more subtle findings including abnormal appearance of the cortical mantle on autopsy examination [6]. Magnetic resonance imaging (MRI) of the brain in hemodynamically stable infants with HLHS prior to surgery demonstrates a high frequency of periventricular leukomalacia and an overall immature appearance to the brain [7,8]. The exact relationship between HLHS and these findings is unclear, but they may be a consequence of altered prenatal blood flow patterns inherent in HLHS or they may occur simply as an associated congenital malformation.

Etiology

The precise cause of HLHS is unknown. Because the disease phenotype is heterogeneous, there are probably a variety of different developmental origins. Altered flow into the developing LV due to mitral or aortic valve stenosis and/or hypoplasia has been implicated as one explanation. Aortic stenosis with an initially dilated LV has been observed during fetal life to evolve into postnatal HLHS, presumably through the process of decreased transventricular blood flow and arrest of LV development [9]. Another hypothesis proposes that abnormalities of the atrial septum limit right-to-left flow early in gestation leading to reduced filling of the LV and resultant hypoplasia. Intrinsic abnormality of LV myocardial development may be another mechanism of HLHS.

Although the disease etiology is likely multifactorial, HLHS is clearly a heritable disorder with a strong genetic influence. Mutations associated with HLHS have been reported in the genes *NKX2-5*, connexin 43, and *NOTCH1* [10–12]. Studies have shown that anywhere from 5–19% of first-degree relatives of infants with HLHS also have congenital heart defects, with the dominant lesion being left-sided obstruction (bicuspid aortic valve or coarctation of the aorta) [13,14]. More recent research efforts have focused on family-based linkage analysis in order to identify loci harboring HLHS-causing genes [15].

Echocardiography in Pediatric and Congenital Heart Disease: From Fetus to Adult, Second Edition. Edited by Wyman W. Lai, Luc L. Mertens, Meryl S. Cohen and Tal Geva.
© 2016 John Wiley & Sons, Ltd. Published 2016 by John Wiley & Sons, Ltd.
Companion website: www.lai-echo.com

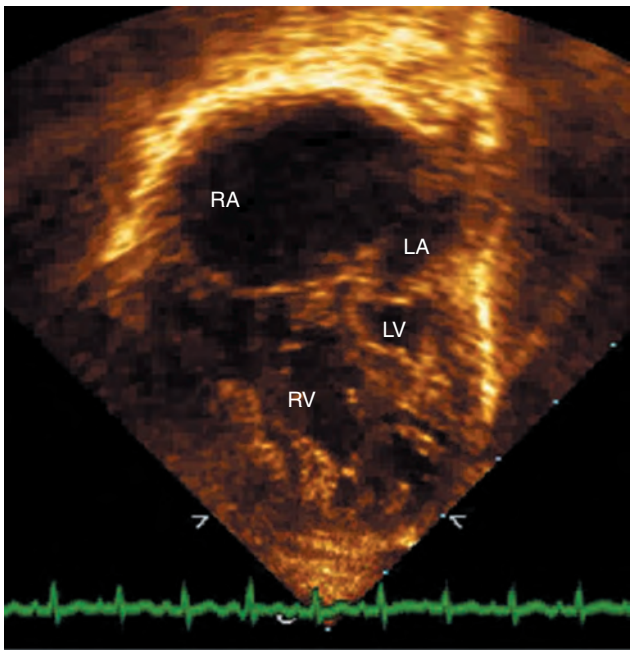


Figure 20.1 An apical 4-chamber view of hypoplastic left heart syndrome (HLHS). The left-sided structures are small and incapable of contributing to systemic output. LA, left atrium; LV, left ventricle; RA, right atrium; RV, right ventricle.

Morphology and classification

Types

Hypoplastic left heart syndrome can be roughly divided into the following major anatomic groups based on the size and functionality of the mitral and aortic valves.

1 mitral and aortic stenosis
2 mitral stenosis and aortic atresia
3 mitral and aortic atresia.

While there is no definite difference in terms of outcomes among the subtypes, some centers have reported that the mitral stenosis and aortic atresia subtype is at an increased risk of mortality. It is in this group that coronary cameral fistulae are sometimes observed and some have felt that these fistulae are a risk factor for coronary ischemia and subsequent ventricular dysfunction or acute arrhythmia leading to hypoperfusion and/or sudden cardiac arrest.

Anatomy

Systemic veins

In HLHS the right superior vena cava (RSVC) and the inferior vena cava (IVC) return to the right atrium normally. A review of pathology specimens with HLHS found that 5% had a left superior vena cava (LSVC) [16]. In the initial surgical management of HLHS, the presence of an LSVC can alter the technique of placement on cardiopulmonary bypass. In the second stage of palliation, the presence of a LSVC without a left innominate vein requires anastomosis of the LSVC to the left pulmonary artery. In the presence of a bridging left innominate vein, the LSVC may be ligated.

Right atrium

The right atrium is generally unaffected in HLHS, although it may be dilated to accommodate both systemic and pulmonary blood flows.

Left atrium

In patients with HLHS the left atrium is often small. However, if there is any restriction to flow across the atrial septum, the left atrium may become hypertensive and distended. Often, the finger-like left atrial appendage is easily visualized because of this distention. This finding may help to identify patients who are at high risk of early morbidity and mortality and would benefit from fetal or early postnatal intervention.

Atrial septum

Abnormalities of the atrial septum are common in HLHS and may include primum and secundum atrial septal defects or abnormal position and attachment of septum primum to the atrial wall [17,18] (Figure 20.2). However, it is those patients with an intact atrial septum (6% of all cases between 1990 and 1997 at our institution) who are at greatest risk of a poor outcome [19]. In a cohort review of 38 patients with a very restrictive or intact atrial septum, there was only a 68% 30-day survival. Survival decreased to 38% in those with a completely intact atrial septum and inadequate decompression [20], well below the survival numbers for HLHS as a whole.

Pulmonary veins

The entry of the pulmonary veins into the left atrium is an important part of the overall characterization of HLHS and important for the purpose of surgical planning. Even when the veins seem to enter the left atrium normally, care should be taken to distinguish anomalous pulmonary venous *drainage* from anomalous pulmonary venous *connection* [21]. If the pulmonary veins enter the left atrium but there is a decompressing vein, this indicates anomalous drainage in the setting of normal venous connection. The decompressing vein, or "levoatriocardinal vein," is thought to be a remnant of the cardinal venous system that persists in the face of increased left atrial pressure [22,23]. This vein is distinct from a LSVC, which can be seen as a separate structure even in the presence of a decompressing vein [22].

Mitral valve and left ventricle

The mitral valve in HLHS may be stenotic or atretic. This difference is important for a variety of reasons. First, the presence of a patent mitral valve implies the presence of an associated LV cavity. Such a cavity will be limited in its contribution to systemic perfusion, will contract poorly, may have endocardial

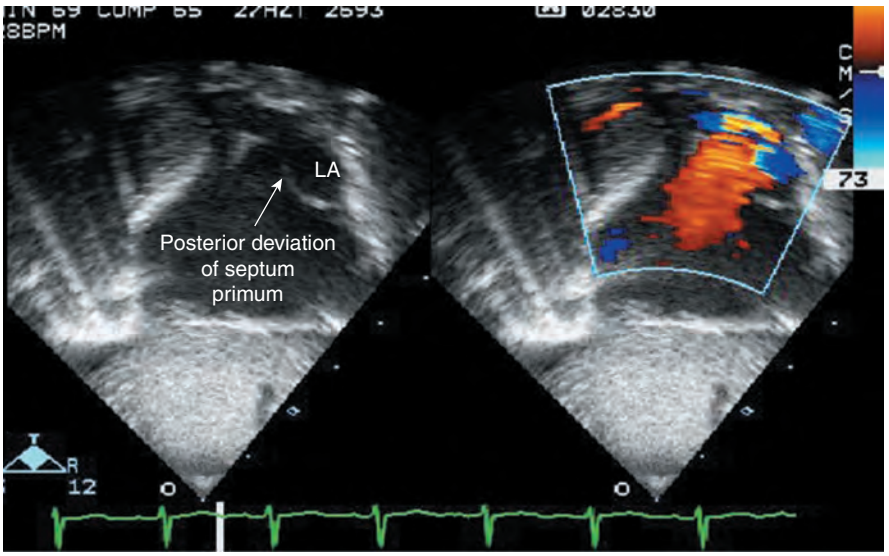


Figure 20.2 Subcostal view demonstrating posterior deviation of septum primum (arrow). LA, left atrium.

fibroelastosis, will exist under high, perhaps suprasystemic pressure, and may adversely influence RV mechanics [24]. Second, investigators have reported on the possibility of an increased risk of mortality in patients falling within the HLHS subcategory of mitral stenosis, aortic atresia, particularly in those patients with left ventricular–coronary connections [25–27].

Tricuspid valve and right ventricle

Morphologic abnormalities of the tricuspid valve are relatively common in HLHS and may play an important role in short- and long-term survival [28–30]. However, some studies have not shown that tricuspid regurgitation (TR) is necessarily a risk factor [28,31,32]. In patients with HLHS, 7–12% may have a bileaflet tricuspid valve, and 35% may have significant tricuspid valve dysplasia (Figure 20.3; Videos 20.2 and 20.3) [16,33]. In patients with severely dysplastic and regurgitant tricuspid valves, a primary transplant strategy may be considered as an alternative to a high-risk staged reconstruction [34,35]. It is important to keep in mind that in the unoperated, neonatal state and following initial first-stage palliation there is a volume load on the RV as it supports both systemic and pulmonary blood flows. Such volume load may alter annular dimensions leading to incomplete leaflet coaptation. This, in combination with the anatomic variability of the tricuspid valve in HLHS, may influence the degree of regurgitation. However, when the volume load on the RV is reduced after the superior cavopulmonary anastomosis and Fontan completion operations, TR may improve [36–38]. RV dysfunction is sometimes noted in association with the volume-loaded state after Stage 1. While the TR may improve as a result of improved coaptation of the valve, RV function may also improve after superior cavopulmonary anastomosis, possibly related to diminished wall stress from the reduction of the volume load [39].

Aorta, coronary arteries, and ductus arteriosus

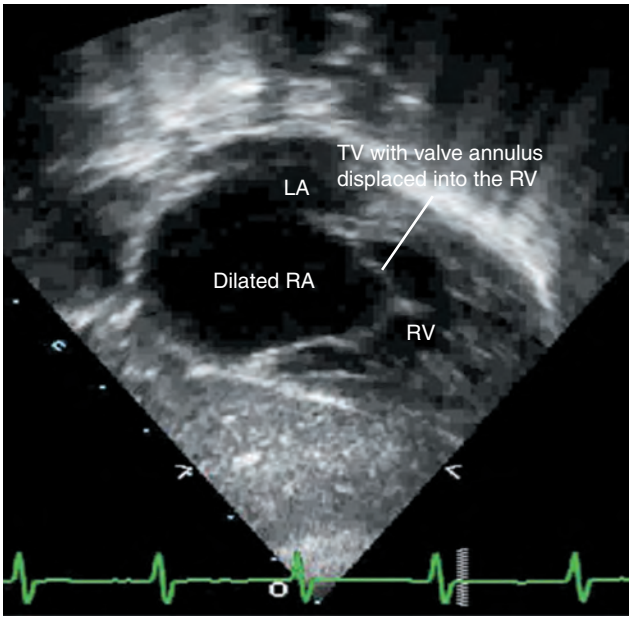
In HLHS a patent ductus arteriosus (PDA) is necessary for survival. In the fetus with HLHS, the PDA is the predominant avenue for systemic flow, and the ductal arch consequently develops with a continuous, smooth transition into the descending aorta.

The ascending aorta in HLHS varies in size and is related to the degree of antegrade flow. In cases of aortic atresia, the ascending aorta may be markedly hypoplastic (diameter 1–2 mm) and may serve as a "common coronary artery" carrying blood in a retrograde manner from the PDA to the aortic root and into the left and right coronary arteries (Figure 20.4; Video 20.4). In cases of aortic stenosis, the ascending aorta may be larger depending on the ratio of antegrade flow from the LV to retrograde flow from the PDA. The transverse aortic arch often exhibits varying degrees of hypoplasia and elongation.

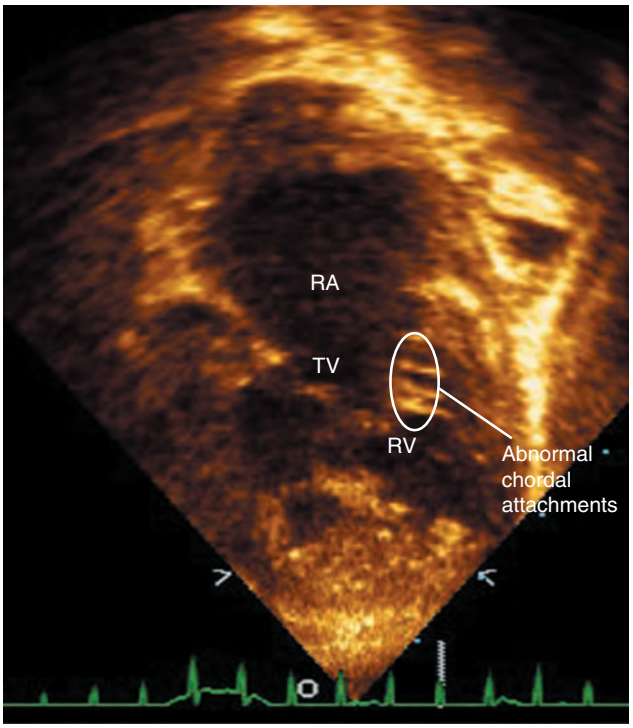
Coarctation of the aorta is common in HLHS [40]. Presumably this is related to flow dynamics as blood leaves the PDA and splits to supply the aortic arch and the descending aorta. This "branch-point" is often the site of coarctation. Histologic studies have demonstrated ductal tissue in the juxtaductal area, tissue that may play a role in coarctation [41]. The extreme form of coarctation, interrupted aortic arch, has also been reported in HLHS [42]. In such cases, coronary perfusion and survival depend on sufficient antegrade flow across the aortic valve.

The descending aorta beyond the ductal arch is generally of normal caliber as it carries the normal systemic output to the lower half of the body.

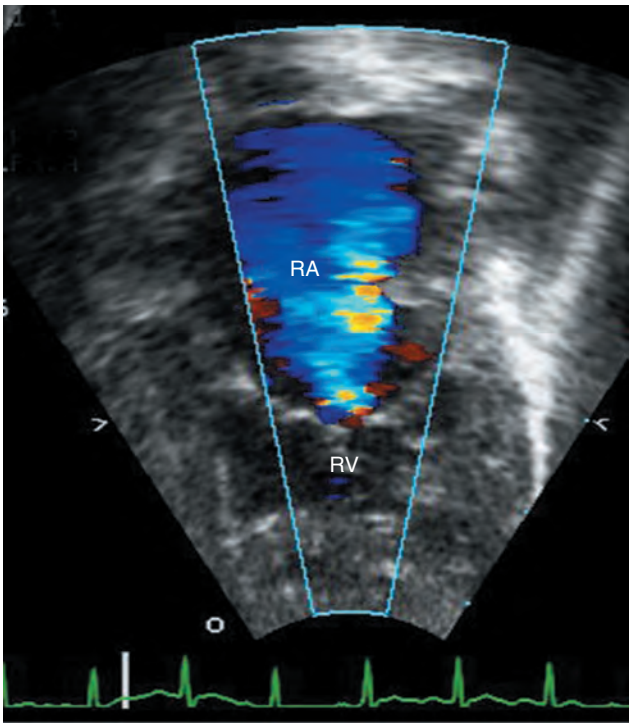
The coronary arteries in HLHS typically have normal ostia, arise normally from the aortic root, and follow a normal course [43]. However, cases of anomalous origin of a coronary artery from the main and the right pulmonary arteries have been reported [44,45]. In the subset of HLHS characterized by mitral



(a)



(b)



(c)

Figure 20.3 The effective orifice of this tricuspid valve is displaced into the right ventricle. **(a)** The displacement from a subcostal frontal view. **(b)** An apical 4-chamber view showing abnormal chordal attachment of the septal leaflet "tethering" the leaflet to the ventricular septum and limiting excursion. **(c)** Severe tricuspid regurgitation due to the abnormal tricuspid valve. LA, left atrium; RA, right atrium; RV, right ventricle; TV, tricuspid valve.

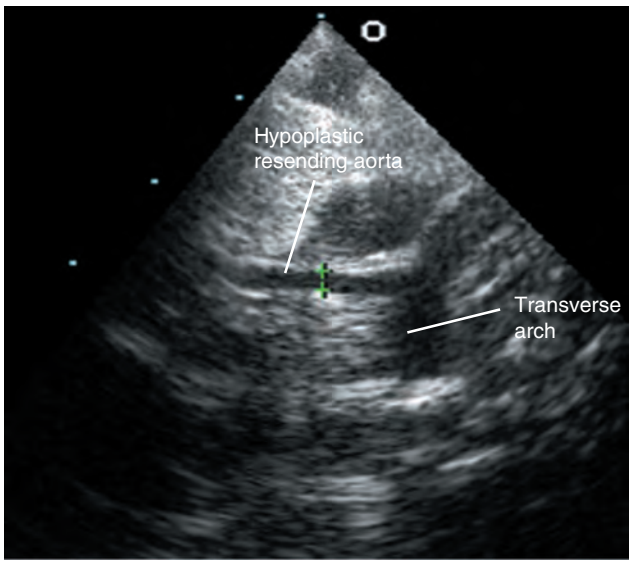


Figure 20.4 Markedly hypoplastic ascending aorta in a newborn with aortic atresia. This vessel carries blood retrogradely from the aortic arch to the coronary arteries.

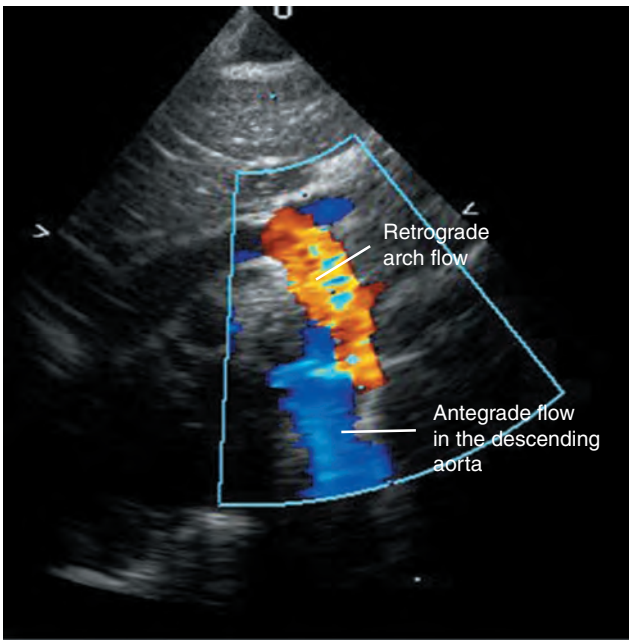


Figure 20.5 Suprasternal sagittal view demonstrating retrograde flow in the aortic arch from the patent ductus arteriosus.

stenosis and aortic atresia, patients may be at risk of fistulous connections, with or without stenoses, from the left ventricle to the coronary arteries. These may place them at higher risk for morbidity and mortality than the HLHS population as a whole [25,46].

Pathophysiology

Infants with HLHS typically manifest tachypnea and cyanosis at birth. Peripheral pulses may be weak, with cool extremities due to poor perfusion. Chest radiograph will usually reveal a large heart with increased pulmonary vascular markings. Postnatal survival depends upon patency of the PDA, which supplies the systemic circulation. Once the PDA begins to constrict, blood supply to the body decreases and an increasing amount of blood is driven into the pulmonary circulation, resulting in improved oxygenation but at the cost of hypotension and circulatory shock. When HLHS is identified, prostaglandin E_1 infusion should be initiated immediately in order to maintain patency of the PDA. Increasingly, prenatal diagnosis of HLHS and prompt initiation of prostaglandin E_1 infusion in the delivery room allows avoidance of neonatal shock as the presenting symptom.

An open PDA supplies most, if not all, of the blood flow to the body. Depending on the anatomic type of HLHS, retrograde flow through the PDA into the aortic arch may also be the major or only source of blood supply to the upper extremities, head and coronary arteries (Figure 20.5; Video 20.5). Because there is limited or no contribution to systemic blood flow from the LV, flow through the PDA will be from the pulmonary artery to the aorta during systole. However, during diastole it is the ratio of vascular resistances between the pulmonary and systemic circuits that dictates flow. With pulmonary vascular resistance normally lower than systemic vascular resistance following birth, diastolic flow across the PDA is typically left-to-right (aorta-to-pulmonary artery), creating a degree of systemic steal. In conditions in which the pulmonary vascular resistance is abnormally elevated – such as in the presence of a very restrictive or intact atrial septum, lung parenchymal disease, persistent pulmonary hypertension, or lung prematurity – the left-to-right shunt in diastole may be minimized or completely eliminated [47]. Such infants will manifest severe cyanosis. Alternatively, if pulmonary vascular resistance is very low relative to systemic vascular resistance, then diastolic flow from left to right may be substantial resulting in a significant systemic hypoperfusion.

Management

The approach to palliation for HLHS is variable. Since Norwood's initial reports of successful palliation [48], substantial improvements in survival have taken place. Currently, there are a number of strategies available for the neonate with HLHS.

Primary cardiac transplantation is practiced at a small number of institutions in the United States, with good results [49]. However, limited donor availability has curtailed the widespread use of this practice as a primary means of therapy. As outcomes following staged reconstructive surgery have continued to improve, many centers have reserved primary transplantation

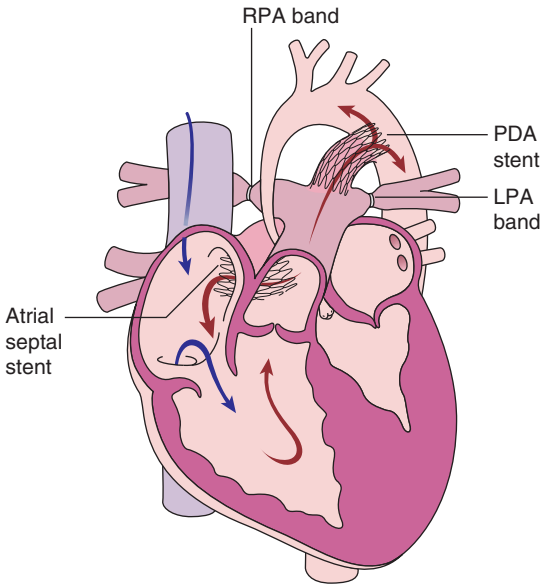
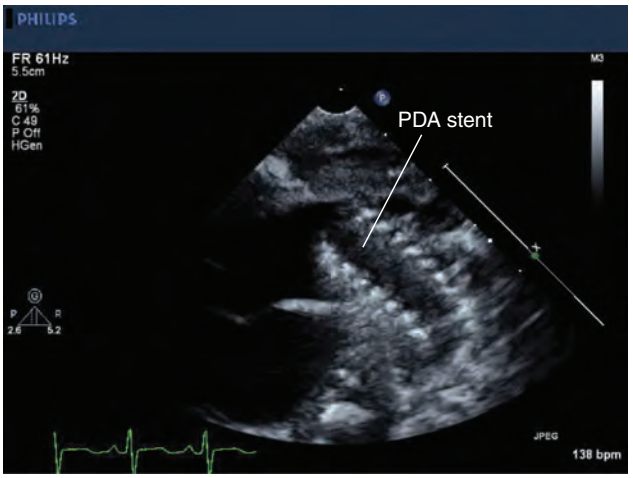


Figure 20.6 Schematic representation of the "hybrid procedure." In this procedure stents are placed across the atrial septum and the ductus arteriosus and bands are placed across the branch pulmonary arteries. LPA, left pulmonary artery; PDA, patent ductus arteriosus; RPA, right pulmonary artery. Source: Galantowicz M, Cheatham JP. Lessons learned from the development of a new hybrid strategy for the management of hypoplastic left heart syndrome. *Pediatric Cardiology* 2005;**26**:190–199. Reproduced with kind permission of Springer Science and Business Media.

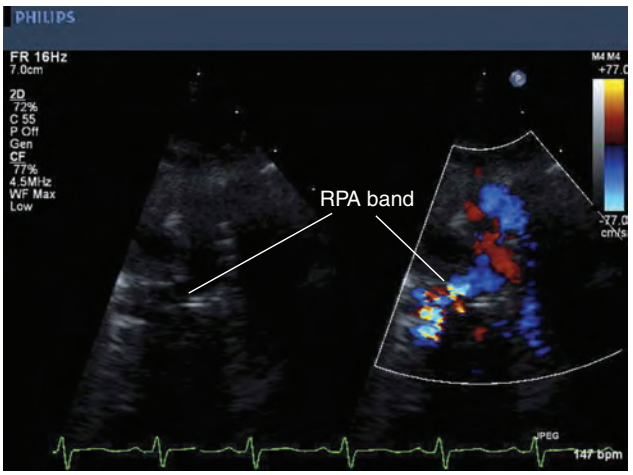
for high-risk infants such as those with dysplasia of the tricuspid valve and severe regurgitation, and/or marked RV dysfunction.

Because mortality for neonatal Norwood reconstruction remains relatively high in comparison with surgery for other forms of congenital heart disease, some investigators have moved toward the development of strategies that avoid a major surgical operation in the neonatal period. By placing a stent in the PDA and banding the branch pulmonary arteries, it is possible to create a desirable physiologic situation in which the single RV supplies the systemic and pulmonary circulations with unimpeded flow to the descending aorta and in which pulmonary blood flow is limited and the pulmonary vasculature is protected (Figures 20.6 and 20.7; Videos 20.6–20.8) [50]. This "hybrid approach" involves both a cardiac catheter-driven procedure and surgical technique, and achieves physiologic goals that are similar to the Norwood first-stage reconstruction, but without the performance of a challenging neonatal operation [51]. Ultimately, arch reconstruction takes place in conjunction with a superior cavopulmonary anastomosis at a later time, typically at age 6 months. Although this technique is now common at a number of institutions, the outcome of this strategy has not been demonstrated to be significantly different from the more common surgical approaches [52].

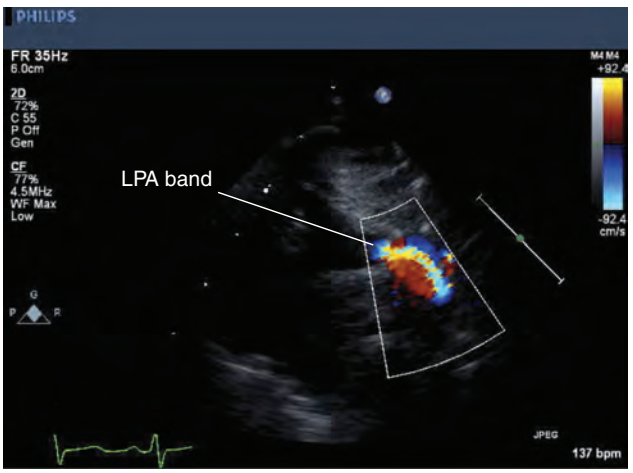
While transplant and the "hybrid" approach are performed at some facilities, the most common palliation for HLHS continues to be the stage 1 reconstruction, also known as the Norwood



(a)



(b)



(c)

Figure 20.7 In this example of the "hybrid procedure," **(a)** the struts of the ductal stent can be seen as can the bands constricting the **(b)** right pulmonary artery and **(c)** left pulmonary artery. LPA, left pulmonary artery; RPA, right pulmonary artery.

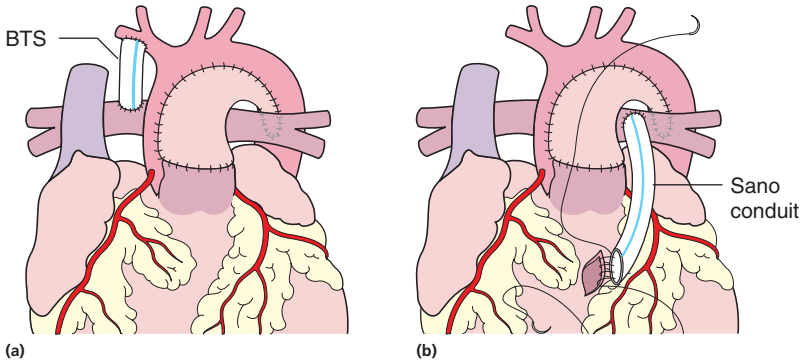


Figure 20.8 Two common variations of the first-stage palliation for hypoplastic left heart syndrome. **(a)** Diagram of the Norwood procedure with a modified Blalock–Taussig shunt (BTS) connecting the systemic circulation to the pulmonary circulation. **(b)** Diagram of the Norwood procedure with the Sano modification: RV-to-PA conduit in place of the modified Blalock–Taussig shunt. Source: Gardner TJ, Spray TL (eds.) *Operative Cardiac Surgery*, 5th edn. London: Arnold Publishers, 2004. Reproduced with permission of CRC Press.

procedure. This operation consists of an atrial septectomy, transection of the pulmonary artery with oversewing of the distal stump, construction of a neo-aorta using the incised native aorta augmented with a homograft patch sewn to the native proximal pulmonary artery, ligation of the PDA, and the establishment of secure pulmonary blood flow using a modified Blalock–Taussig (BT) shunt [48]. The Sano modification, an alternative to a BT shunt in which pulmonary blood flow is secured using a RV-to-pulmonary artery conduit, has been used by some centers with good success (Figure 20.8) [53–55]. In high-volume centers, the outcome for the Norwood procedure can be quite good with greater than 90% survival for standard risk patients [56].

A large multicenter trial was recently completed, which evaluated the outcomes of the Norwood operation. In this Single Ventricle Reconstruction (SVR) Trial, infants were randomized to a BT shunt or a Sano modification for pulmonary blood flow [57] and outcomes were assessed over the first year of life. Initial reports from the SVR Trial demonstrated an early survival advantage for the Sano modification. However, longer-term follow-up data suggests that the survival advantage is lost after one year of age as there may be mid- and long-term morbidities preferentially associated with the Sano.

Imaging

Once HLHS is suspected in the neonate, a detailed echocardiographic evaluation is undertaken, including 2D, color and spectral Doppler imaging. A segmental approach to analyzing this complex anomaly is performed in a systematic manner by the echocardiographer.

Goals of the initial evaluation

In the setting of HLHS, the initial echocardiographic evaluation has the following main objectives:

- Determination of the anatomic components of the HLHS: left atrium, mitral valve, left ventricular cavity, aortic valve, ascending aorta, aortic arch, and isthmus.
- Size of the interatrial communication and Doppler evaluation of flow restriction.
- Assessment of tricuspid valve morphology and function.
- Evaluation of RV size and function.
- Evaluation of the pulmonary valve and right ventricular outflow tract.
- Evaluation of the ductus arteriosus for size and flow characteristics.
- Assessment of the aorta including (ascending aorta, transverse arch, and aortic isthmus).
- Imaging of the coronary arteries; note presence of LV–coronary fistulae.
- Detection of associated lesions (e.g., levoatrial cardinal vein).

Preoperative imaging

Right atrium and systemic veins

The right atrium is well seen from a variety of views. It is usually dilated and hypertrophied due to the volume load from obligate prenatal left-to-right shunting. Subcostal long- and short-axis imaging delineates the systemic venous connections. In HLHS, the RSVC and the IVC typically have a normal course and entry into the right atrium, although an absent or underdeveloped Eustachian valve may be noted [58]. Anomalous systemic venous return has been reported and should be explicitly excluded [59].

Persistent LSVC to coronary sinus can be reliably identified by echocardiography and should be ruled in or out in all cases of HLHS. Visualization of a dilated coronary sinus from the subcostal, apical, and parasternal windows provides a clue that a LSVC is present. In the suprasternal view, the LSVC can be directly visualized and should course from superior to inferior, anterior to the left pulmonary artery. A LSVC should be distinguished from other venous structures such as a persistent levoatrial cardinal vein, which is a more posterior venous structure. Doppler interrogation demonstrating a low-velocity venous flow pattern confirms the presence of the LSVC and distinguishes it from other structures in the general vicinity, such as a branch pulmonary artery or the left atrial appendage. Whereas flow through a LSVC usually drains into the right atrium via the coronary sinus, there have been reports of coronary sinus ostial atresia with coronary venous decompression and retrograde flow through a LSVC to the innominate vein [60,61]. The direction of flow through the LSVC can be confirmed using color and PW Doppler. If a cephalad direction of blood flow is noted through

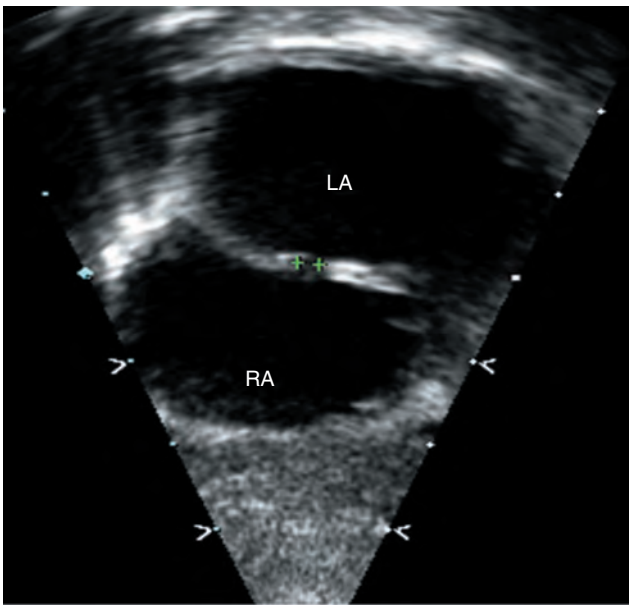
a LSVC, then further investigation of the nature of the coronary venous drainage should be undertaken as any manipulation of the LSVC in this circumstance could deleteriously impact coronary perfusion.

Atrial septum

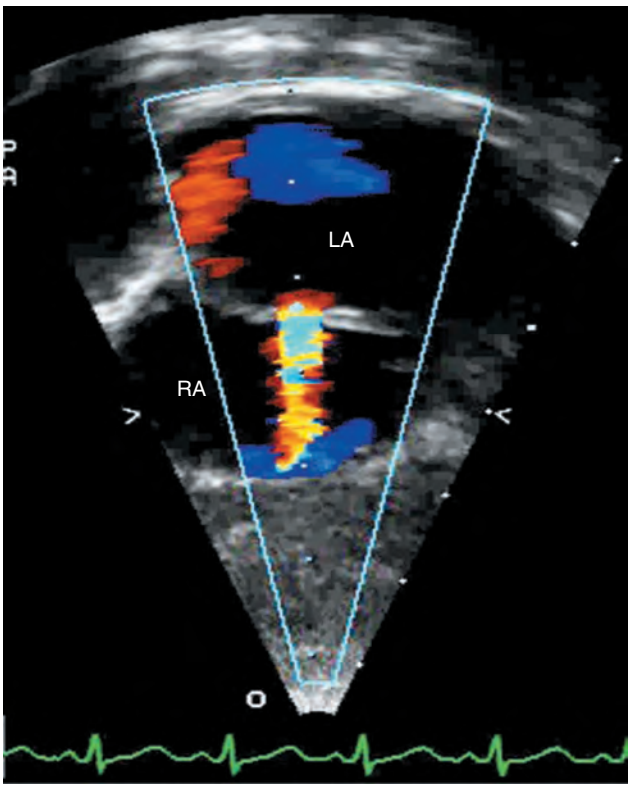
A rapid and accurate assessment of the atrial septum is crucial for decision making about disposition in the immediate postnatal period. The specific anatomy of the atrial septum can be quickly and accurately diagnosed from subcostal imaging, particularly from long-axis, short-axis and in-between views. Acceleration across the atrial septum can be seen using color or PW Doppler (Figure 20.9).

Levoatrial cardinal vein and other decompressing veins

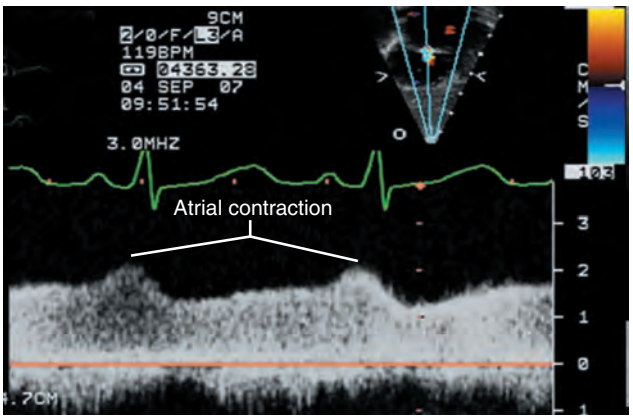
The presence of a decompressing vein can be confirmed using color Doppler from the subcostal and suprasternal views, although other views may also be helpful to trace the entire course and anatomy of the vein. A levoatrial cardinal vein usually connects the left upper pulmonary vein to the left innominate vein, but other decompressing veins entering the RSVC, the IVC, or the azygous vein can be found. In the setting of a decompressing vein, obstruction may be seen anywhere along the course of the vein, hence a full view of its connection from the left atrium to the insertion into the systemic vein is important. A decompressing vein can be difficult to distinguish from the pulmonary arteries and other vascular structures coursing



(a)



(b)



(c)

Figure 20.9 Restrictive atrial septum in hypoplastic left heart syndrome. **(a)** Two-dimensional image from the subcostal view profiling a 2-mm atrial communication. **(b)** The flow jet from the left atrium (LA) to the right atrium (RA) is profiled. The jet is aliased and splays out on the back wall of the right atrium. **(c)** Continuous-wave Doppler interrogation across the atrial communication. The velocity remains elevated throughout the cardiac cycle without the normal return to baseline.

in the region above the heart but may be identified by the low-velocity continuous flow pattern seen by color or CW Doppler.

Pulmonary veins

The connections and drainage of all pulmonary veins must be visualized by 2D and color Doppler. Although the pulmonary veins can be seen from subcostal imaging, they are more reliably seen with color Doppler from the suprasternal frontal view. Spectral Doppler is important to assess for pulmonary vein stenosis, which manifests as high-velocity turbulent flow with diminished or absent phasic variations.

Mitral valve and left ventricle

The mitral valve is evaluated for patency (stenosis versus atresia) and morphology. The dimensions of the mitral valve are measured in both the apical 4-chamber view (lateral diameter) and the parasternal long-axis view (antero–posterior diameter). The inflow pattern into the LV and the degree of mitral regurgitation should be documented using color and PW Doppler. The presence of inflow into the LV, without evidence for mitral regurgitation, should alert the echocardiographer to the likelihood of ventriculo-coronary connections as a means for decompressing the LV when there is aortic atresia. Color Doppler interrogation of the LV free wall, apex, and septum with a low Nyquist limit is performed in search of such connections.

Examination of the LV itself is best accomplished from the apical 4-chamber view, but imaging from the subxiphoid and parasternal windows is complementary. The presence of an echo-bright endocardium, which may represent endocardial fibroelastosis, should be noted. Rarely, the LV may contain calcifications, although these are not usually of hemodynamic significance.

Tricuspid valve and right ventricle

The tricuspid valve is imaged from multiple views and angles. The subcostal oblique view demonstrates the tricuspid valve inflow and the pulmonary outflow in one plane. The apical 4-chamber and parasternal long-axis views are optimal for showing the morphology of the tricuspid valve and the subvalvar apparatus. Leaflet displacement and abnormal chordal or papillary attachments can be well seen from the apical view. It is important to identify and to quantify TR. This is best done from apical 4-chamber and parasternal windows using color Doppler interrogation. Three-dimensional echocardiography (3D) is emerging as a newer tool to evaluate the tricuspid valve morphology and may be particularly helpful in identifying the mechanism of regurgitation [62].

Aorta and ductus arteriosus

The aortic and ductal arches are well seen from suprasternal oblique sagittal imaging, and the ascending aorta by itself may be seen from parasternal long-axis views. The presence or absence of flow across the aortic valve can be seen by color Doppler

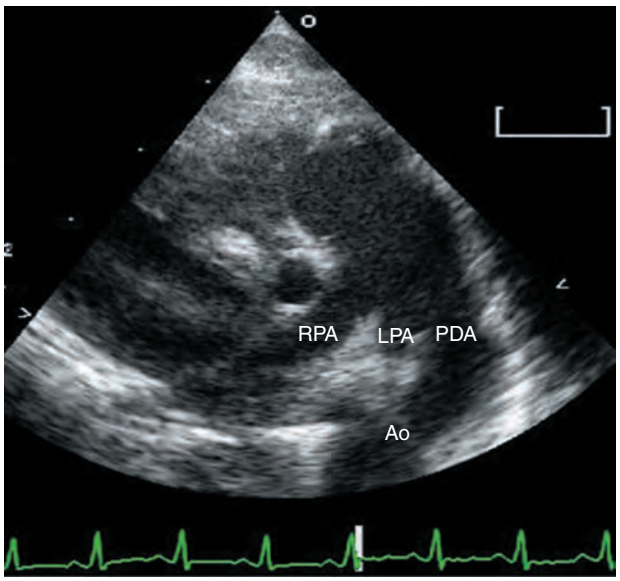


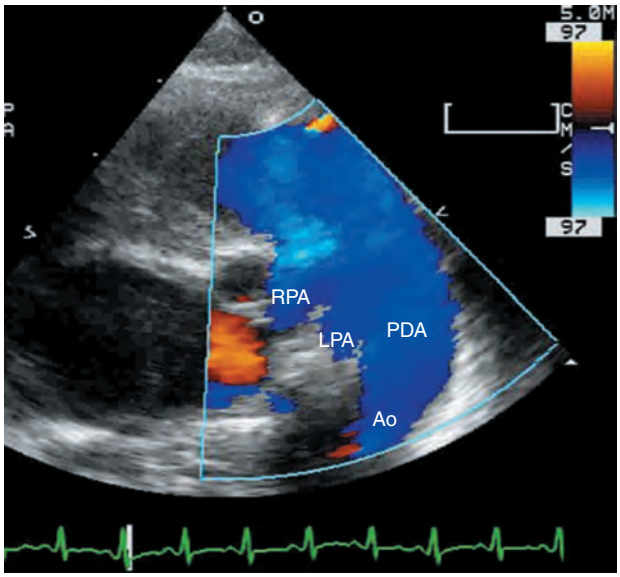
Figure 20.10 Ductal view from the high parasternal window. This view delineates the branch pulmonary arteries as well as the course of the patent ductus arteriosus (PDA) from the main pulmonary artery to the aorta. Ao, aorta; LPA, left pulmonary artery; RPA, right pulmonary artery.

interrogation in parasternal long- and short-axis views as well as the apical and high right parasternal views.

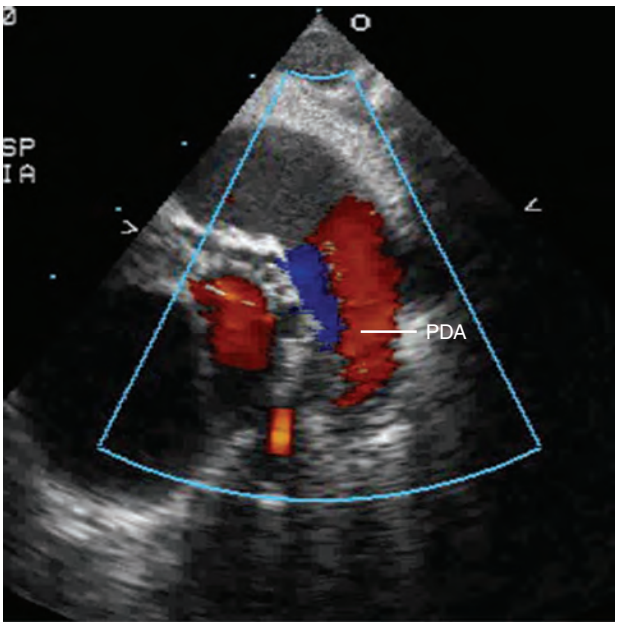
The full extent of the PDA is best evaluated from a high parasternal sagittal view. In the ideal "ductal view," the origin of both the right and left pulmonary arteries can be seen along with the insertion of the PDA (Figure 20.10; Videos 20.9 and 20.10). With very slight manipulations of the tail of the transducer, it is usually possible to see the full course of the ductus from the pulmonary artery to its insertion into the aorta. In HLHS, the PDA can be quite large and describes a smooth, curved trajectory with easy transition into the descending aorta. With the probe in the suprasternal sagittal position a similar image can be obtained and the ductal and aortic arches can be compared with mild left–right tilting. The aortic arch frequently has a more acute curve than normal and frequently appears as a "branch" off the larger ductal arch. The direction of flow in the ductus arteriosus is determined with color and PW Doppler from the suprasternal or high left subclavicular sagittal views. Doppler sampling in the distal aspect of the aortic arch and aortic isthmus reveals the retrograde nature of the flow in systole up into the transverse aortic arch, with antegrade forward steal into the PDA and pulmonary vascular bed in diastole (Figure 20.11). Placement of the Doppler cursor in the descending aorta distal to the PDA will reveal a flow pattern similar to that seen in the ductus arteriosus itself with antegrade flow in systole, and retrograde flow in diastole.

Coronary arteries

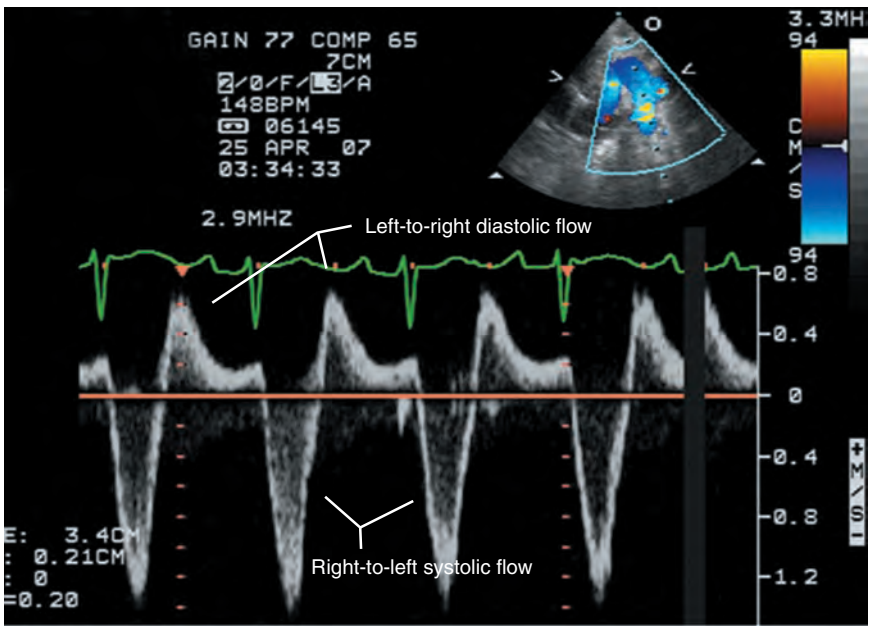
The coronary arteries arise from the small aortic root, and typically have a normal distribution. Their origins and course are



(a)



(b)



(c)

Figure 20.11 Doppler evaluation of the ductus arteriosus from a high parasternal position. **(a)** Color Doppler flow mapping in systole demonstrating flow from the main pulmonary artery to the aorta. **(b)** In diastole, flow across the duct is retrograde from the aorta to the main pulmonary artery. **(c)** Spectral Doppler demonstrating right-to-left flow during systole and left-to-right flow in diastole. The laminar pattern indicates no obstruction to flow. Ao, aorta; LPA, left pulmonary artery; PDA, patent ductus arteriosus; RPA, right pulmonary artery.

best visualized in the parasternal short-axis view, with focus on the region of the aorta just above the level of the aortic valve. The right coronary artery may be more prominent than the left as it perfuses the systemic, dominant ventricle; however, if there are significant coronary-to-left ventricle fistulous connections, then the left coronary artery may appear enlarged. The right and left coronary artery distribution can also be appreciated from a modified apical view angled anteriorly and superiorly toward the outflow tract.

Prenatal assessment

Hypoplastic left heart syndrome is readily diagnosed in the fetus and is one of the most frequently detected forms of congenital heart disease prior to birth. It can be easily identified by the

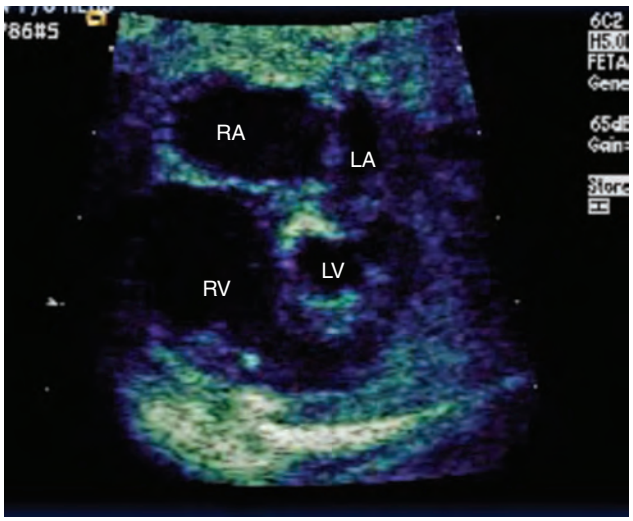


Figure 20.12 A 4-chamber view of a fetus with hypoplastic left heart syndrome (HLHS) and a restrictive atrial septum. The atrial septum bulges toward the right atrium and the pulmonary veins are noticeably dilated. LA, left atrium; PV, pulmonary valve; RA, right atrium; RV, right ventricle.

abnormal chamber morphology at the time of screening prenatal ultrasound. A detailed fetal echocardiographic examination delineates the anatomic details of HLHS, including the morphology of the left heart structures and associated cardiovascular anomalies. Because of the association with extracardiac anomalies and various syndromes, it is advisable for all fetuses with HLHS to have careful obstetrical ultrasound evaluation for other defects and amniocentesis for genetic/chromosomal abnormalities.

Blood flow patterns in the fetus with HLHS are different than normal. In HLHS the systemic and umbilical venous returns undergo mixing in the right atrium due to the hypoplastic left heart structures. The pulmonary venous return to the left atrium must traverse the atrial septum and drain to the right atrium. The presence of such a left-to-right atrial-level shunt is an important parameter, which defines the inadequacy of the left-sided structures. In addition to defining the direction of flow, the size of the interatrial communication is important. Patency of the interatrial communication is critical for normal lung development. A restrictive or intact atrial septum impairs pulmonary venous drainage and impacts pulmonary vascular development. Without an open atrial communication, blood returning from the lungs has no egress from the left atrium causing increased left atrial pressure. This increased pressure is transmitted back to the pulmonary vasculature, leading to pulmonary vein dilation and smooth muscle proliferation in the walls of the pulmonary veins (Figures 20.12 and 20.13; Videos 20.11 and 20.12) [19,63]. In some cases, severe restriction to atrial flow necessitates postnatal catheter-based intervention or open surgical septectomy to relieve left atrial obstruction [64,65] (Figure 20.14; Videos 20.13 and 20.14). In these cases, prenatal identification of atrial-level restriction and immediate postnatal access to the cardiac catheterization laboratory or the operating room are essential.

The magnitude of atrial-level restriction is assessed by direct inspection of the atrial septum on 2D imaging as well as by color Doppler flow mapping. An apparently small interatrial communication should raise suspicion of a restrictive septum, even in the absence of increased flow velocity. Although of no immediate clinical consequences in utero, a restrictive or intact atrial septum complicates the postnatal course. Pulsed Doppler interrogation of the pulmonary veins is important for assessing the degree of restriction to left atrial egress and should be performed in every fetus with HLHS (Figure 20.15) [66,67]. The greater the degree of reversal of pulmonary venous flow with atrial contraction, the greater is the degree of impediment to left atrial egress. The magnitude of flow reversal relates to the severity

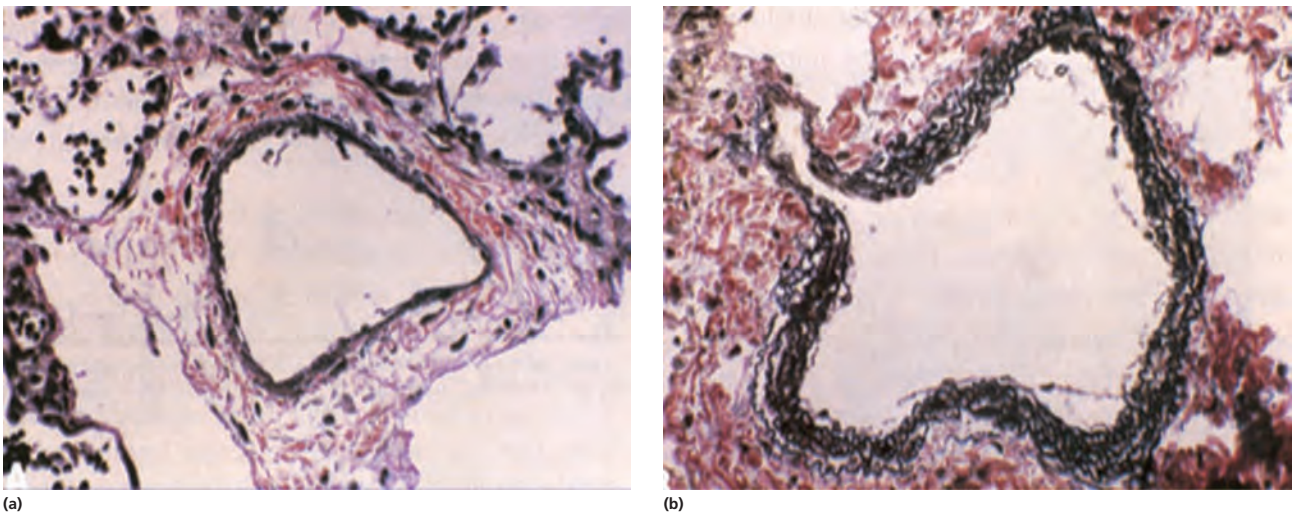
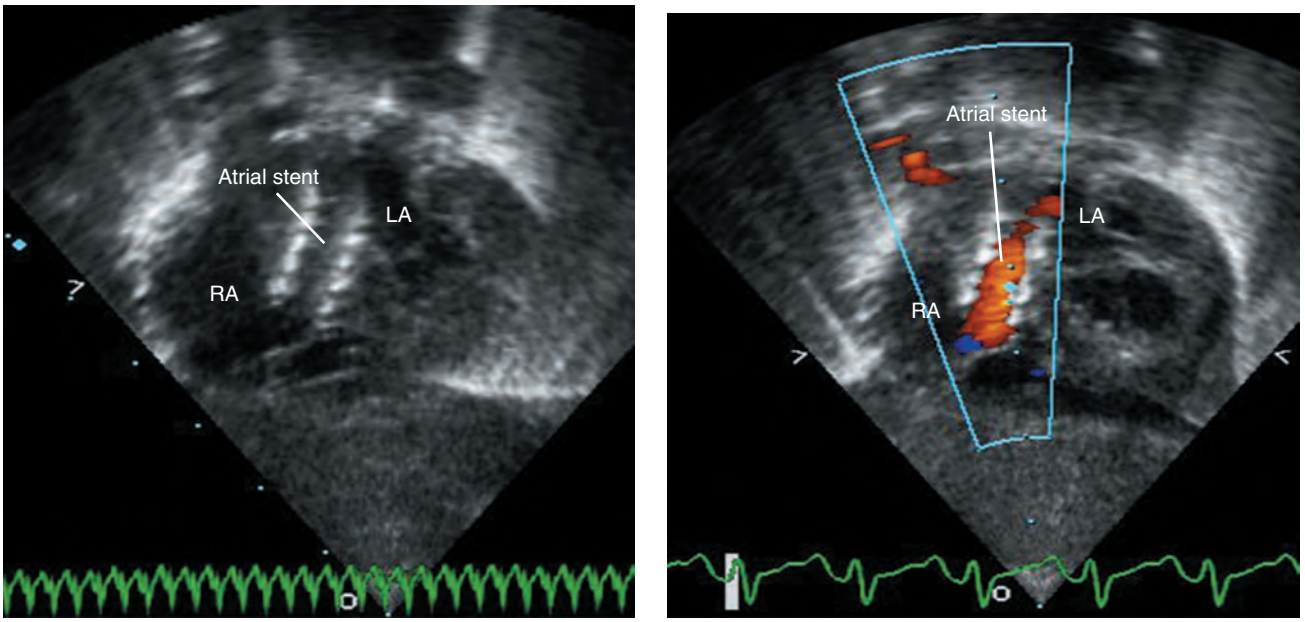

(a) (b)

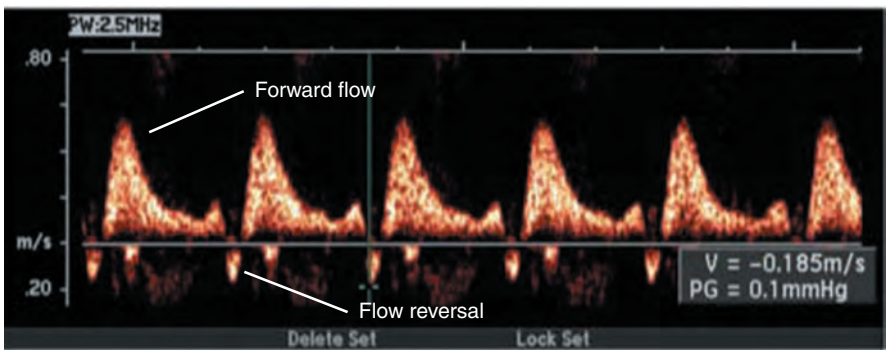
Figure 20.13 Normal pulmonary venous histology has a relative paucity of smooth muscle **(a)**. Infants with hypoplastic left heart syndrome and an intact atrial septum have an increased presence of smooth muscle in the walls of the pulmonary veins **(b)**.



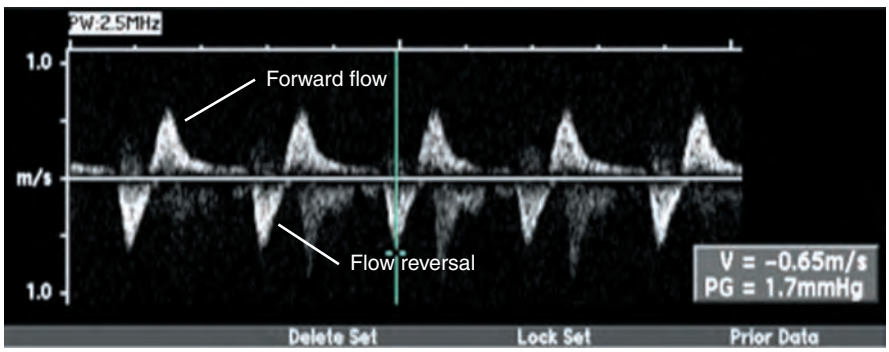
(a) (b)

Figure 20.14 **(a)** Subcostal two-dimensional image of a stent deployed across a restrictive atrial septum. The effective size of the atrial communication is equal to the diameter of the stent. **(b)** Color flow Doppler showing non-aliased flow through the atrial stent from the left atrium (LA) to the right atrium (RA).

of pulmonary vascular disease and predicts the early postnatal course. The detection of important obstruction at the atrial level with significant pulmonary venous flow reversal should prompt consideration of prenatal intervention to open the atrial septum [68]. The effectiveness and optimal timing for such intervention have not yet been determined. Techniques for fetal atrial decompression include fetal balloon atrial septostomy and deployment and expansion of a stent in the fetal atrial septum (Figures 20.16 and 20.17; Videos 20.15 and 20.16). Given the high mortality rates that currently exist despite timely postnatal intervention,



(a)



(b)

Figure 20.15 Pulmonary venous Doppler pattern in the fetus. **(a)** Normal flow characterized by predominantly antegrade flow with only a small amount of retrograde flow during atrial contraction. **(b)** Hypoplastic left heart syndrome with a restrictive atrial septum. Note the much greater degree of retrograde flow implying impedance to flow across the atrial septum.

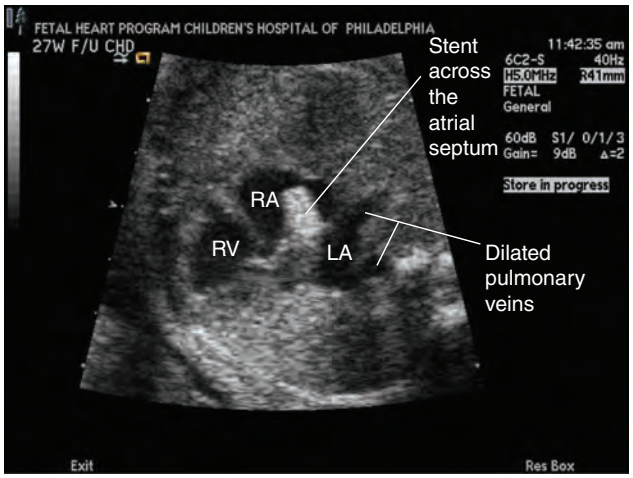


Figure 20.16 A stent across the atrial septum in a fetus who has undergone fetal intervention. The stent was advanced through a catheter that was advanced through the maternal uterine wall, then through the fetal chest wall, and finally into the fetal heart where it was positioned across the atrial septum to allow for successful stent deployment. LA, left atrium; RA, right atrium; RV, right ventricle.

fetal interventions should be considered in the setting of HLHS with an intact atrial septum. In the absence of fetal therapy, plans should be made for delivery at a site where immediate intervention at birth can take place to open the atrial septum either via catheter or surgical technique.

Other important variables to evaluate in the fetus with HLHS are the presence and degree of TR and RV function. Mild TR is common and is usually tolerated well. However, moderate or severe TR may lead to fetal hydrops and indicate a poor prognosis (Figure 20.18). Tricuspid valve incompetence may also worsen when transitioning from prenatal to postnatal life as RV

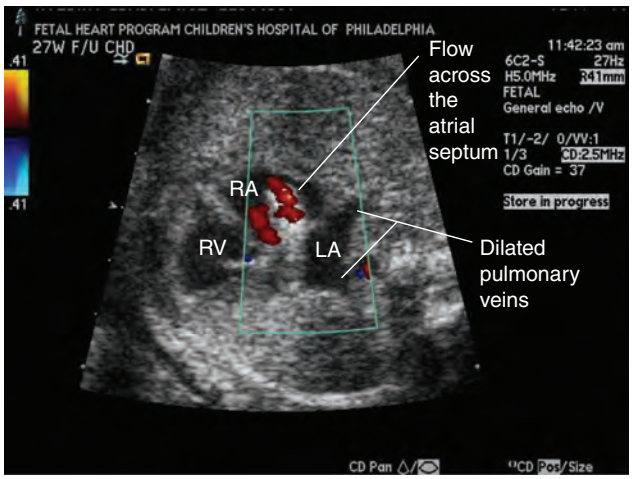
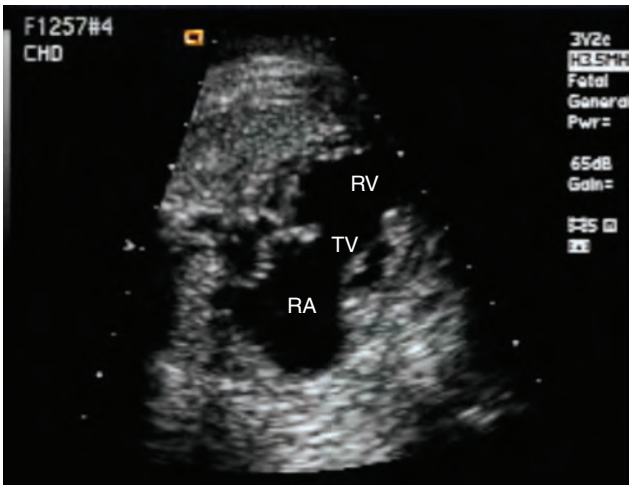
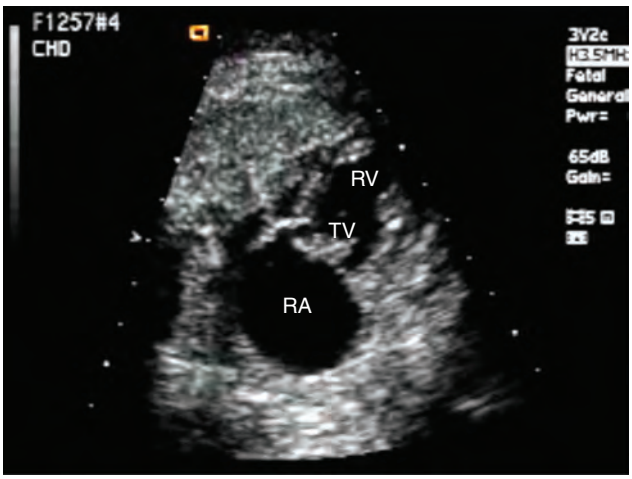


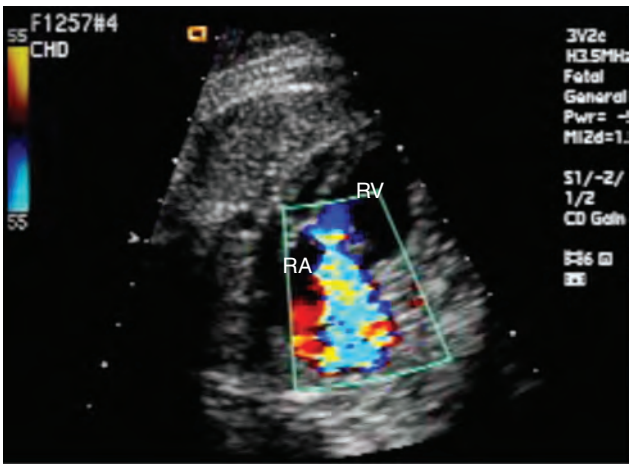
Figure 20.17 Color Doppler demonstrating flow across the fetal atrial stent and through a secondary hole just below the stent, likely created by the team as they maneuvered across the atrial septum to position the catheter. The demonstration of left atrial decompression suggests technical success of the fetal intervention. LA, left atrium; RA, right atrium; RV, right ventricle.



(a)



(b)



(c)

Figure 20.18 A fetal 4-chamber view demonstrating a thickened and dysplastic tricuspid valve in systole **(a)** and diastole **(b)**.The severity of the tricuspid insufficiency is apparent when a color Doppler sector is placed over the valve **(c)**.

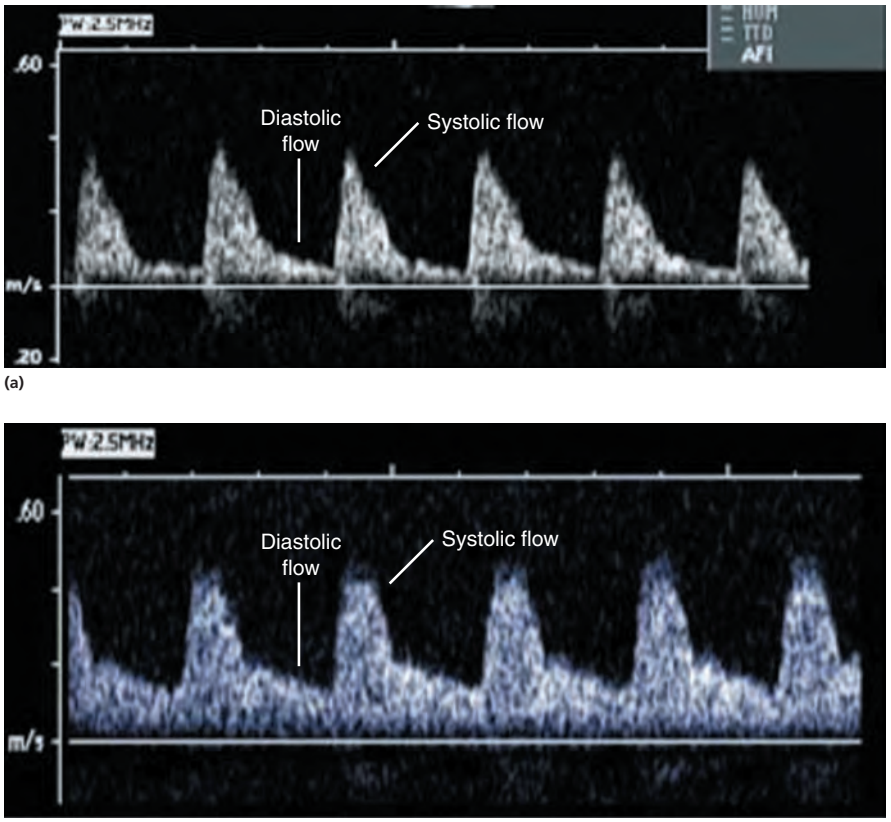


Figure 20.19 Flow pattern in the middle cerebral artery. **(a)** Normal flow pattern characterized by little diastolic flow due to high cerebral vascular resistance. **(b)** Flow pattern in hypoplastic left heart syndrome. Note the marked increase in diastolic flow, probably due to diminished vascular tone as part of a neurohormonal feedback circuit that encourages cerebral blood flow from the ductus arteriosus retrogradely through the arch.

afterload increases following separation from the low-resistance placental circuit and preload increases with the increase in pulmonary venous return to the heart once the lungs are expanded.

Serial echocardiographic evaluation during gestation is indicated in the fetus with HLHS as atrial level restriction or TR may newly develop or progress in later gestation, thereby affecting perinatal management. The evaluation includes Doppler sampling of flow in the ductus venosus, umbilical artery and middle cerebral artery, which provides useful information about the overall well-being of the fetus. Doppler analysis of normal flow in the ductus venosus demonstrates antegrade phasic flow throughout the cardiac cycle. Doppler evaluation of umbilical arterial flow demonstrates low systemic vascular resistance as evidenced by an abundance of diastolic flow, whereas evaluation of middle cerebral arterial flow demonstrates a relatively small amount of diastolic flow (Figure 20.19). This reflects the normal healthy state of an increased cerebrovascular resistance relative to placental resistance. However, in some fetuses with HLHS, an increase in middle cerebral artery diastolic flow relative to umbilical artery diastolic flow may indicate a lower cerebrovascular resistance. It is hypothesized that lower cerebrovascular resistance is a compensatory mechanism to increase cerebral blood flow in fetuses with anatomic obstruction due to a small aorta [69].

While flow patterns in the middle cerebral artery are intimately related to fetal circulatory characteristics, they may also have a predictive value for long-term neurodevelopmental outcome. Data from the Pediatric Heart Network suggests that those fetuses with low resistance in the middle cerebral artery have improved mid-term neurodevelopmental outcomes compared to peers with relatively elevated resistance [70]. This finding suggests that the vasoreactivity of the middle cerebral artery may be important in promoting normal intra-uterine brain development.

Postoperative assessment

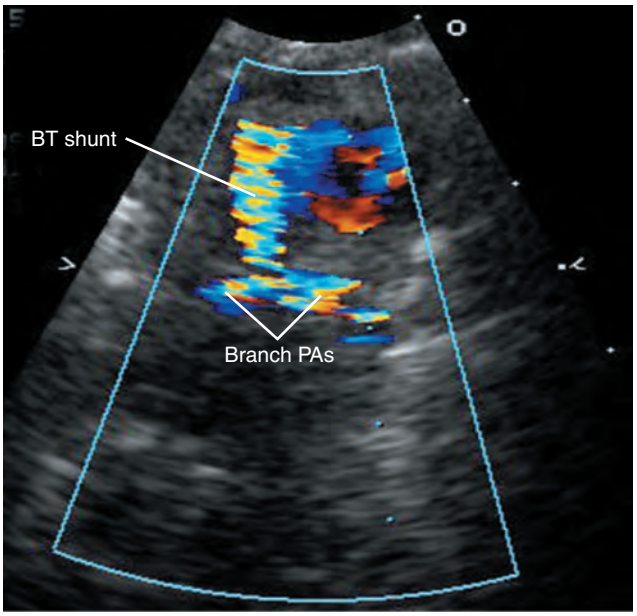
Assessment after stage 1 palliation for HLHS

In general, routine, non-question-directed echocardiography should be avoided in the early postoperative period after stage 1 reconstruction for HLHS as the stress of an unnecessary echocardiogram may disturb the fragile hemodynamics of the critically ill neonate. However, if specific targeted questions need to be answered, an echocardiogram can be a useful tool to help identify potential causes of acute decompensation.

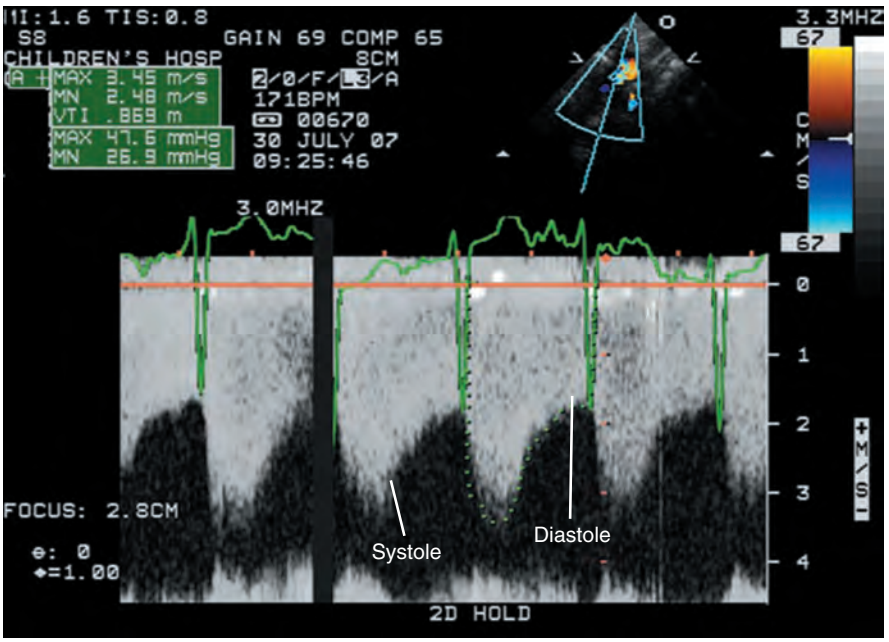
If a mediastinal drain or chest tube suddenly stops draining, an urgent echocardiogram may be warranted to rule out a pericardial effusion. Build-up of pericardial blood can lead to tamponade physiology and cardiovascular collapse. Ventricular dysfunction and TR can also cause acute hemodynamic compromise and can be quickly assessed at the bedside with echocardiography. Postoperative pulmonary overcirculation is another

potential cause of cardiovascular collapse [71]. A Doppler-derived aortic flow reversal ratio has been suggested as a means of assessing the ratio of pulmonary to systemic blood flow and may be clinically useful in some instances [72].

Unexpected cyanosis early after stage 1 reconstruction may be due to inadequate resection of the atrial septum or limited blood flow delivery to the pulmonary arteries due to shunt stenosis. Atrial septal anatomy and adequacy of the resection can be easily ascertained from subcostal imaging in the frontal or sagittal planes. A BT shunt can usually be seen and traced from the suprasternal frontal view with angulation slightly toward the right (Figure 20.20; Video 20.17). Flow through the shunt should be continuous throughout systole and diastole with a characteristic sawtooth Doppler spectral pattern, consistent with the continuous aortic to pulmonary pressure gradient present. Narrowing of the color jet through the shunt should raise concern for shunt narrowing or obstruction when clinical findings suggest decreased pulmonary blood flow. Shunt stenosis can be a challenging undertaking to confirm using echocardiography. Ultrasound scatter and artifact created by the shunt material itself



(a)



(b)

Figure 20.20 Evaluation of a modified Blalock–Taussig (BT) shunt. **(a)** Suprasternal coronal image demonstrating the course of the BT shunt from the right innominate artery to the RPA. Note the aliased color Doppler flow pattern. **(b)** Continuous-wave Doppler across the shunt demonstrating high-velocity continuous flow.

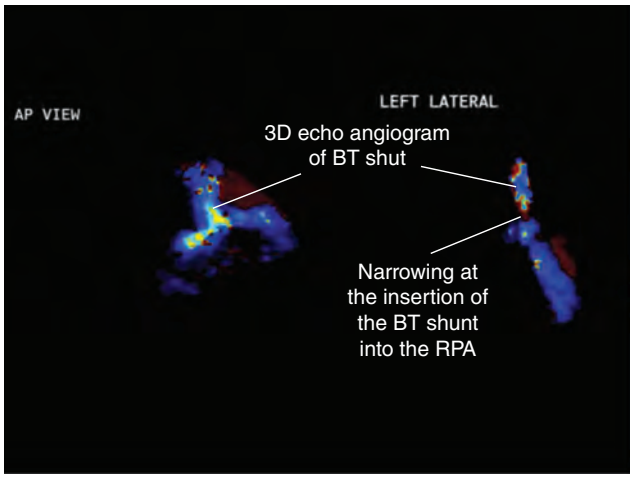


Figure 20.21 Examples of "angiograms" of modified Blalock–Taussig shunts using 3D echocardiography. The panel on the right demonstrates significant narrowing at the insertion of the superior vena cava into the right pulmonary artery. BT, Blalock–Taussig; RPA, right pulmonary artery.

may limit the ability to visualize directly the arterial origin, or pulmonary artery insertion site of the tube graft. In addition, Doppler interrogation and velocity data can underestimate the pressure gradient, as the modified Bernoulli equation is invalid in the case of a long-segment narrowing. Because the BT shunt originates from the innominate artery, one possible cause for limited pulmonary blood flow early after surgery may be torsion or kinking of the innominate artery itself. This can be identified on Doppler echocardiography by detection of turbulence and an increased velocity across the innominate artery at the site of shunt origin.

With the advent of 3D echocardiography, some centers have started to include "3D echo angiograms" (Figure 20.21; Videos 20.18 and 20.19) as part of their routine assessment of a BT shunt. This technique, while not yet validated against true angiograms, has the potential to identify specific areas of narrowing within the shunt and may become increasingly common as the technical aspects of 3D echo continue to evolve.

In patients with RV-to-PA conduit (Sano modification), postoperative cyanosis should prompt careful evaluation of the conduit at its origin from the RV, along its course, and into its insertion into the branch pulmonary arteries. Narrowing can occur at any site but is particularly common at the insertion of the conduit into the branch pulmonary arteries [73]. The conduit can usually be visualized in the subcostal sagittal view. In addition, an excellent view for examining the distal aspect of the conduit and the proximal branch pulmonary arteries can be achieved by a mid-left parasternal window angled superiorly (Figures 20.22 and 20.23; Video 20.20). This view is obtained by starting at the standard apical view and moving medially and slightly cephalad toward the mid-sternum. Color and PW Doppler sampling in the conduit and proximal branch pulmonary arteries demonstrate forward systolic flow and diastolic reversal back to the RV.

Inter-stage assessment

Once outside the immediate postoperative period, routine echocardiographic evaluation becomes an important tool for assessing the outcome of the first-stage palliation and the progression of inter-stage physiology. During this period, the echocardiogram should assess: (1) pulmonary venous return to rule out acceleration of flow, (2) the adequacy of the interatrial communication, (3) the degree of tricuspid valve regurgitation, (4) right ventricular size, hypertrophy, and function, (5) the neo-aortic outflow tract including neo-aortic valve competency, (6) the neo-aortic arch with specific attention to the proximal and distal anastomoses, and (7) the flow characteristics through the shunt or Sano conduit.

While an atrial septectomy is part of the Norwood procedure, progressive obstruction can occur at the atrial septal level, weeks to months after initial surgery. In a review at The Children's Hospital of Philadelphia, 4% of patients had a pressure gradient of ≥5 mmHg on routine echocardiography after stage 1 palliation. Severe restriction or an intact atrial septum before stage 1 surgery both correlated with the likelihood of postoperative obstruction [74]. As with the preoperative evaluation, PW and color Doppler are used to demonstrate acceleration of flow across the atrial septum and determine the presence and degree of obstruction. However, velocity information alone is not sufficient to assess the clinical significance of atrial-level obstruction, as an increased rate of pulmonary venous return is seen in patients with pulmonary overcirculation.

Assessment of the tricuspid valve remains a crucial part of any exam of a patient with single ventricle physiology. Color Doppler and 3D echo can provide insight into the degree and mechanism of regurgitation. Serial assessment of the tricuspid valve regurgitant jet can also give important clues about important RV dilation and diminished RV function.

Careful assessment of RV function is important and should be performed from a variety of angles and probe positions in order to assess global and regional performance of the RV. Apical and parasternal short-axis imaging are usually sufficient to evaluate qualitative RV wall shortening as these views provide orthogonal planes. Quantitative echocardiographic assessment of ventricular performance in HLHS is challenging due to the variable geometry of the systemic RV. For that reason, geometric formulae for measuring cavity volumes or myocardial mass are at best gross estimates and are frequently inaccurate compared with other imaging modalities. The role of 3D echocardiography, RV strain, tissue Doppler imaging, tricuspid annular planar systolic excursion, and the myocardial performance index are all potentially valuable as measures to follow in a serial manner. Given the heterogeneity of HLHS, it is not likely that a "normal range" will be identified for the disease as a whole, but many of these measures may be followed in a longitudinal manner in an individual patient to give a sense of RV function over time. Nevertheless, qualitative assessment of ventricular performance by an experienced echocardiographer remains the most commonly used means for evaluating RV function in HLHS.

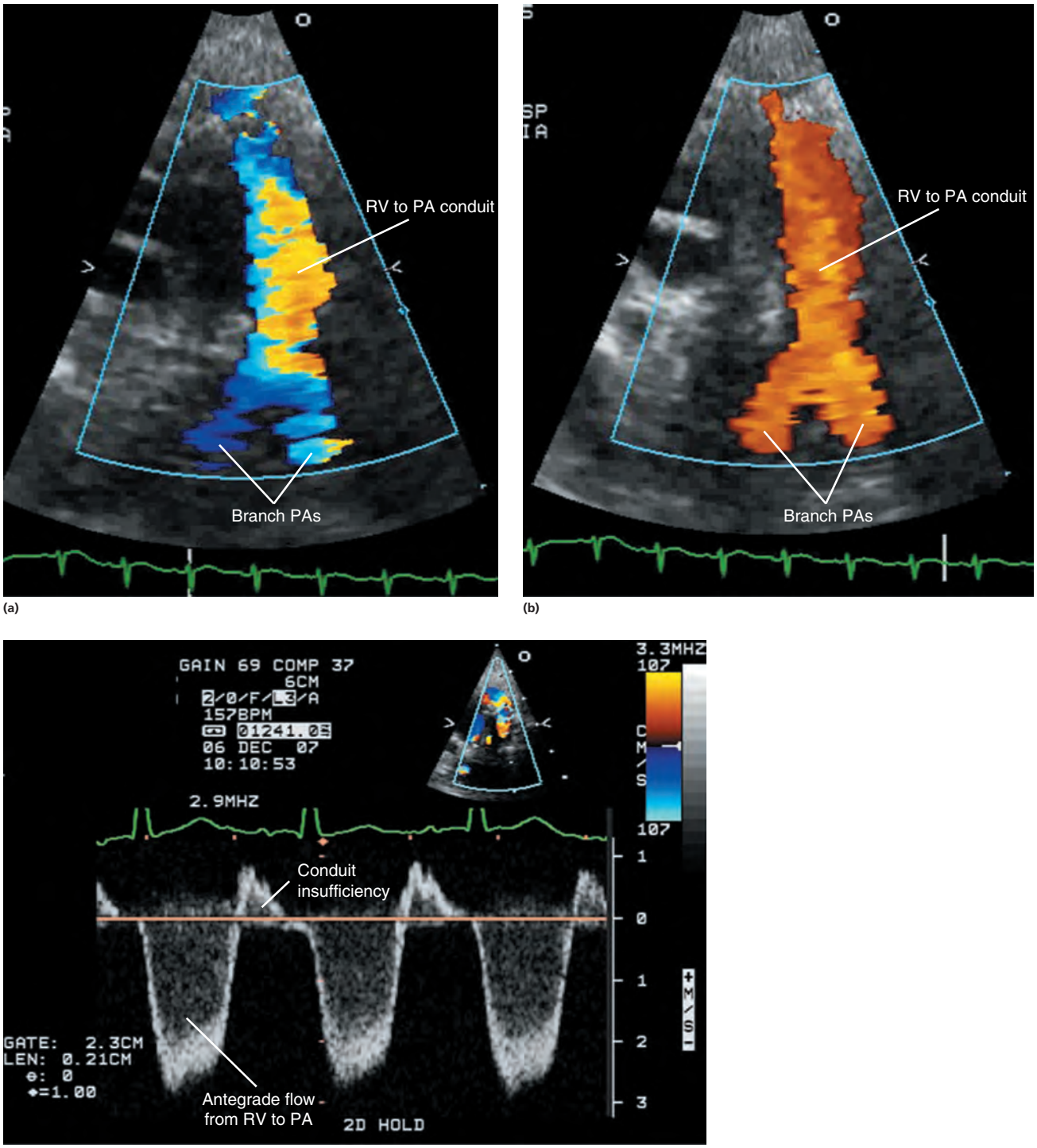


Figure 20.22 Stage 1 palliation of hypoplastic left heart syndrome with Sano modification. **(a)** Antegrade systolic flow in the right ventricle (RV)-to-pulmonary artery (PA) conduit. Note that blood flow is limited by the length and diameter of the conduit. **(b)** Conduit insufficiency in diastole. **(c)** Spectral Doppler interrogation of the conduit showing predominantly antegrade flow and a small amount of conduit regurgitation.

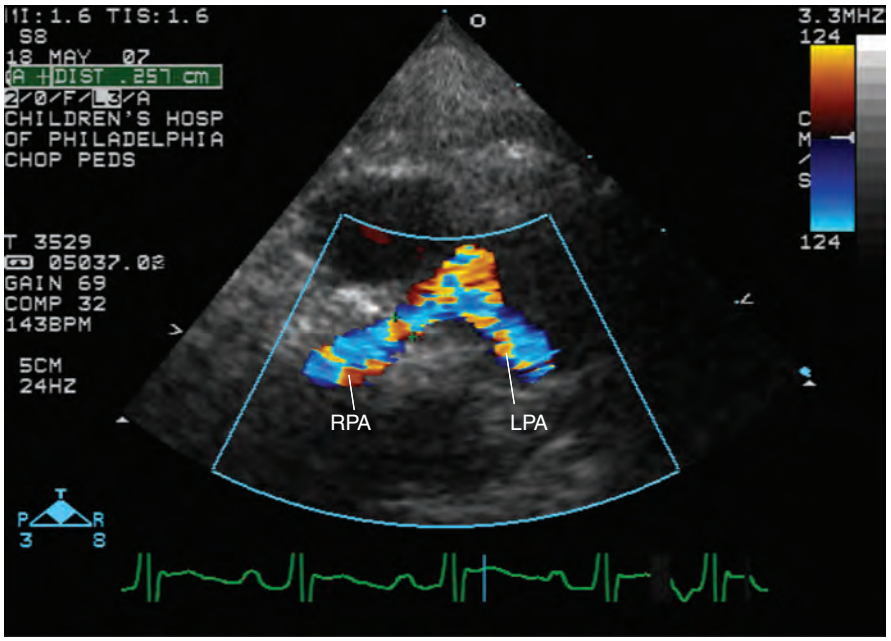


Figure 20.23 Distal attachment of a Sano conduit to the branch pulmonary arteries. LPA, left pulmonary artery; RPA, right pulmonary artery.

Narrowing of the neo-aorta following stage 1 palliation occurs primarily at the anastomosis of the reconstructed arch to the native pulmonary artery proximally or to the descending aorta distally (Figure 20.24; Video 20.21). Assessment of the proximal anastomosis is performed from subcostal, apical and parasternal imaging windows using color, PW and CW Doppler. If there is obstruction, it usually occurs at the supravalvar region at the suture line. Assessment of the distal neo-aortic anastomosis to the descending aorta is best done from the suprasternal sagittal view position.

After stage 1 palliation, there is often an increase in velocity through the distal arch, particularly at the site of distal anastomosis, as the caliber of the vessel decreases from the large, augmented transverse arch to the native descending aorta in a funnel-like manner (Figure 20.25). Whereas the altered geometry of the neo-aorta creates unique flow patterns, the diminished distensibility of the homograft patch further complicates the diagnosis of coarctation [75,76]. In the absence of normal aortic distensibility, the diastolic runoff pattern typically seen in classic coarctation of the aorta will not be present. In addition, if present, the modified BT shunt will drain blood away from the descending aorta during diastole, further diminishing the appearance of forward diastolic runoff. In an attempt accurately to predict clinically significant arch narrowing, a "coarctation index" was proposed [77]. While the initial index was a useful idea, it was not generally accepted into routine practice. Recently, a novel scoring system was identified in which two points were assigned for a peak velocity >2.5 m/sec and one point for either a change in qualitative systolic function (e.g. normal to mildly diminished) or a ratio of the narrowest portion of the arch reconstruction compared to the dimension of the descending aorta at the diaphragm of <0.7. Under this system, a score of 2 or higher was reported to be 100% sensitive and 85% specific for the diagnosis of clinically significant coarctation requiring catheter or surgical-based intervention [78].

A final approach to the identification of significant neo-aortic arch obstruction is the correlation of the tricuspid regurgitant jet velocity by CW Doppler to the systolic blood pressure. In the absence of obstruction the peak instantaneous pressure gradient across the tricuspid valve should come very close to mirroring the systolic blood pressure. If the peak instantaneous pressure gradient across the tricuspid valve is higher than the systolic blood pressure, coarctation should be suspected.

Inter-stage assessment after the hybrid procedure

As previously mentioned, the hybrid approach to HLHS involves securing systemic blood flow with a stent in the ductus arteriosus and limiting pulmonary blood flow by placing bands on the branch pulmonary arteries. The success of this operation depends on the balance of the circulations. If the bands are too loose, pulmonary overcirculation and high output heart failure can occur. If the bands are too tight, cyanosis may be a problem. An assessment of Doppler flow pattern in the ductus arteriosus can be helpful in assessing the degree of pulmonary blood flow and may be predictive of postoperative morbidity. Indeed the ductal regurgitant fraction, a ratio of retrograde flow VTI to antegrade flow VTI, has been correlated with a more complicated post-comprehensive stage 2 recovery [79].

The occurrence of "reverse coarctation" is another concern to be wary of in the interstage period following the hybrid. A reverse coarctation can result from obstruction to flow into the aortic arch from the ductal stent, or from progressive narrowing of the aortic isthmus. Risk factors for the development of

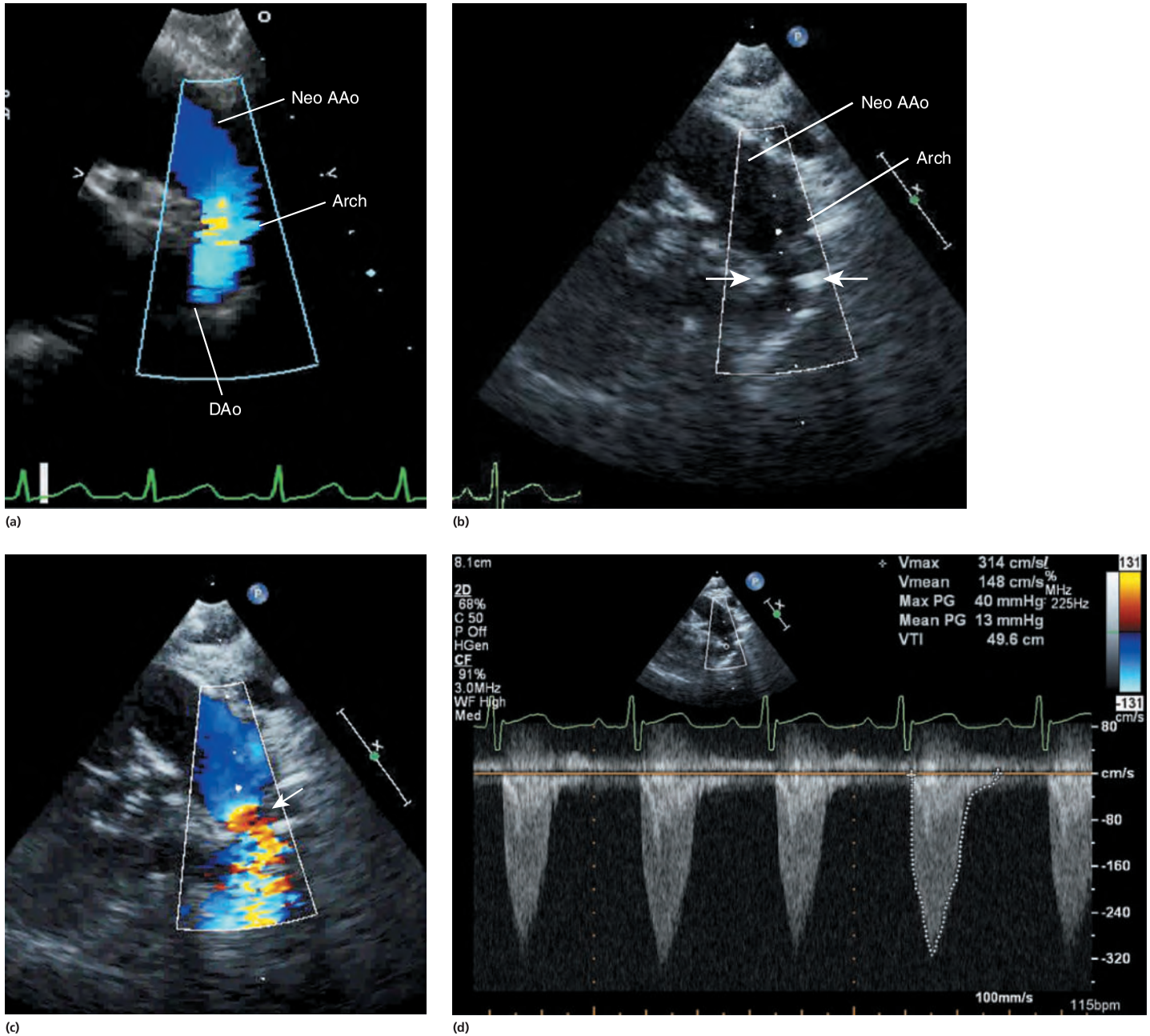


Figure 20.24 Aortic arch reconstruction after stage 1 hypoplastic left heart syndrome palliation. **(a)** Suprasternal sagittal image showing an unobstructed reconstructed aorta. **(b)** Similar view showing coarctation (arrows). **(c)** Color Doppler flow mapping showing aliasing at the suture line (arrow). **(d)** Spectral Doppler across the coarctation. Note that the usual diastolic runoff pattern of a coarctation is not present as a result of competitive runoff through a Blalock–Taussig shunt. Neo-AAo, neo-ascending aorta; DAo, descending aorta.

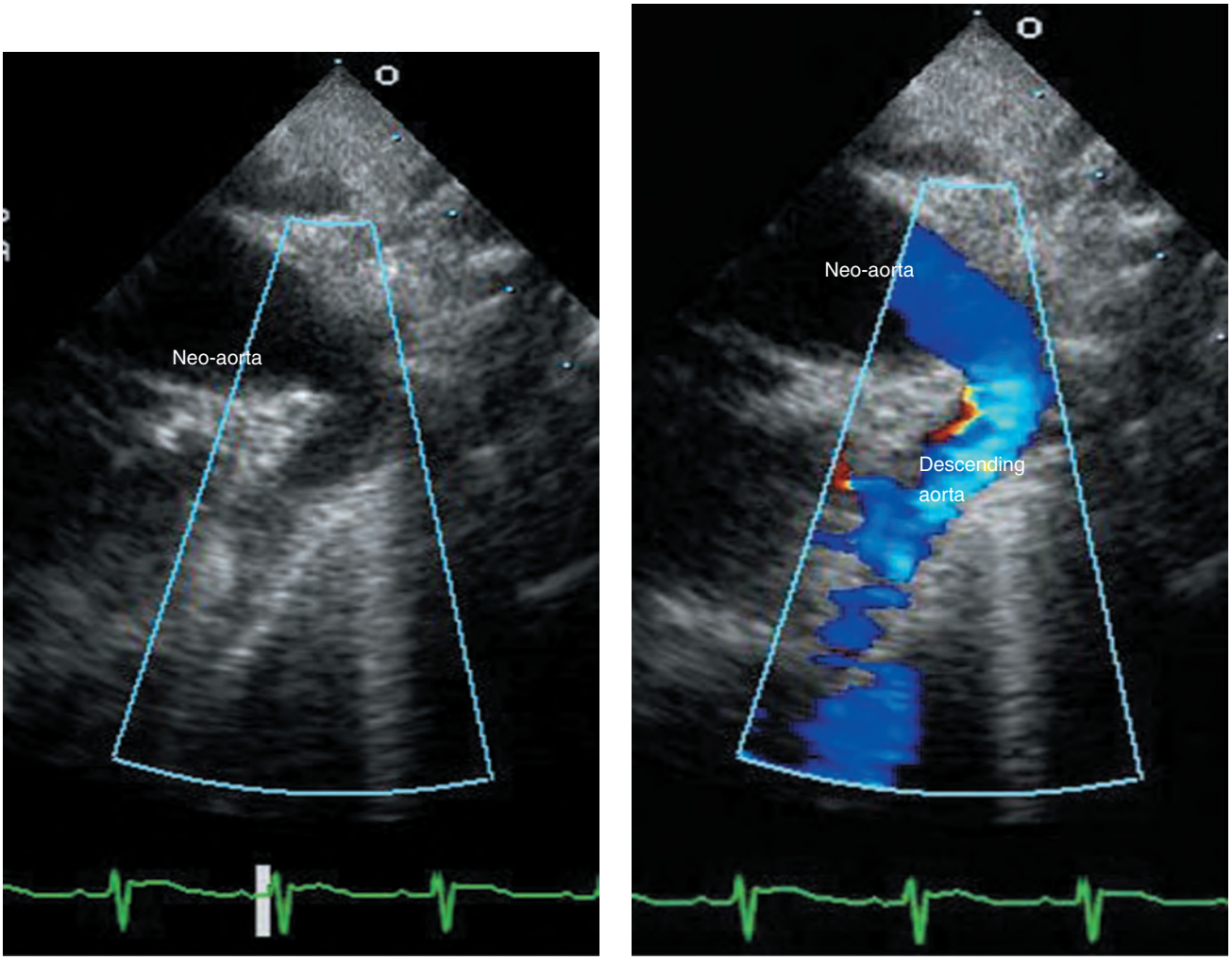


Figure 20.25 Funnel-like tapering of the distal neo-aorta often seen in patients after stage 1 reconstruction. **(a)** Two-dimensional imaging from the suprasternal notch. **(b)** Color Doppler shows no significant flow acceleration despite the narrowing seen by 2D imaging.

obstruction include a small ascending aorta and a steeper angle of insertion of the aortic isthmus into the ductal arch [80].

A final concern for the hybrid procedure is the development of restriction at the atrial septal level. This can occur at any point in the interstage period as the hybrid does not generally include an initial atrial septectomy. This should be monitored from routine imaging of the atrial septum and, if restriction is suspected, a referral for balloon septostomy or surgical atrial septectomy should be made.

Assessment before and after stage 2 of HLHS palliation

In the second stage of palliation for HLHS, superior caval blood is directed to the pulmonary arteries, either via a bidirectional Glenn [81] or a hemi-Fontan [82] procedure. In the bidirectional Glenn, the SVC is transected and the proximal portion is sewn directly into the superior aspect of the right pulmonary artery (Figure 20.26; Videos 20.22 and 20.23). In the hemi-Fontan, the posterior aspect of the superior vena cava is opened onto the anterior aspect of the right pulmonary artery. A patch is placed and then carried from the anastomosis out onto the proximal branch pulmonary artery to ensure wide patency. A dam is sewn into the entrance of the SVC into the RA, effectively separating the SVC from the heart. If a LSVC is present, the surgeon can elect to perform bilateral, bidirectional Glenn anastomoses or perform a hemi-Fontan on the right and a bidirectional Glenn on the left.

Echocardiography plays an important role in the diagnostic evaluation of patients prior to stage 2 surgery. RV function and TR should be assessed as a new, preoperative baseline. Examination of the atrial septum and pulmonary veins is helpful to rule out obstruction that may need to be addressed while in the operating room. The branch pulmonary arteries should be evaluated with echocardiography, although visualization may be limited

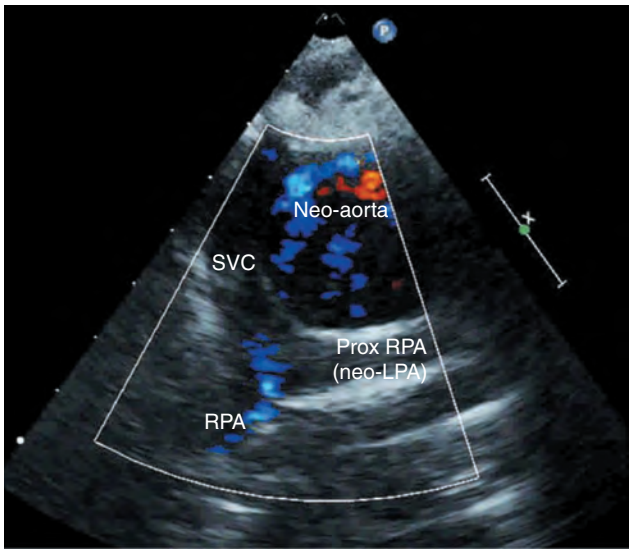


Figure 20.26 Imaging of superior cavopulmonary anastomosis from the suprasternal frontal position. The superior vena cava (SVC) is seen coursing alongside the neo-aorta. It has been transected and anastomosed to the right pulmonary artery (RPA). In this image the pulmonary arteries are widely patent.

to the proximal extraparenchymal portions. The portion of the pulmonary artery behind the reconstructed aorta is an important region for focus as a large bulbous reconstructed neo-aorta may compress the pulmonary artery causing stenosis and distal hypoplasia (Figure 20.27). The presence of a LSVC should be ascertained, as well as the presence and size of the innominate vein, as previously described. Even with optimal echocardiographic imaging, current practice in many institutions is to perform cardiac catheterization prior to the stage 2 surgery in order to determine safe candidacy for a cavopulmonary connection [83]. However, a randomized clinical trial found that a noninvasive approach utilizing echocardiography and cardiac MRI is a safe, effective and less costly alternative to routine catheterization in the evaluation of selected patients prior to bidirectional Glenn operation [84].

Assessment prior to the Fontan operation

In the not-too-distant past, cardiac catheterization was commonly performed as part of the evaluation prior to the Fontan operation; however, most centers have been moving toward a noninvasive imaging strategy in the low-risk subgroup of patients with HLHS. At The Children's Hospital of Philadelphia, we have identified a cohort of patients in whom cardiac catheterization is of no additional benefit above and beyond data derived from noninvasive imaging prior to the Fontan operation (Table 20.1) [85]. By applying these criteria we have been able to substantially reduce the number of patients undergoing invasive diagnostic testing and its associated potential complications. MRI techniques may advance our ability to reduce or nearly eliminate the need for diagnostic cardiac catheterization except in the most high-risk cases, relegating the role of catheterization to interventions once anatomic issues have been identified by noninvasive means [86].

Assessment after the Fontan operation

The Fontan operation is the final schedule surgical palliation for children with HLHS. This operation, an anastomosis of the inferior vena cava to the pulmonary arteries, effectively separates the systemic and pulmonary circulations. The "Fontan circulation" is a unique manmade construct that has allowed for the long-term survival of many children born with complex congenital

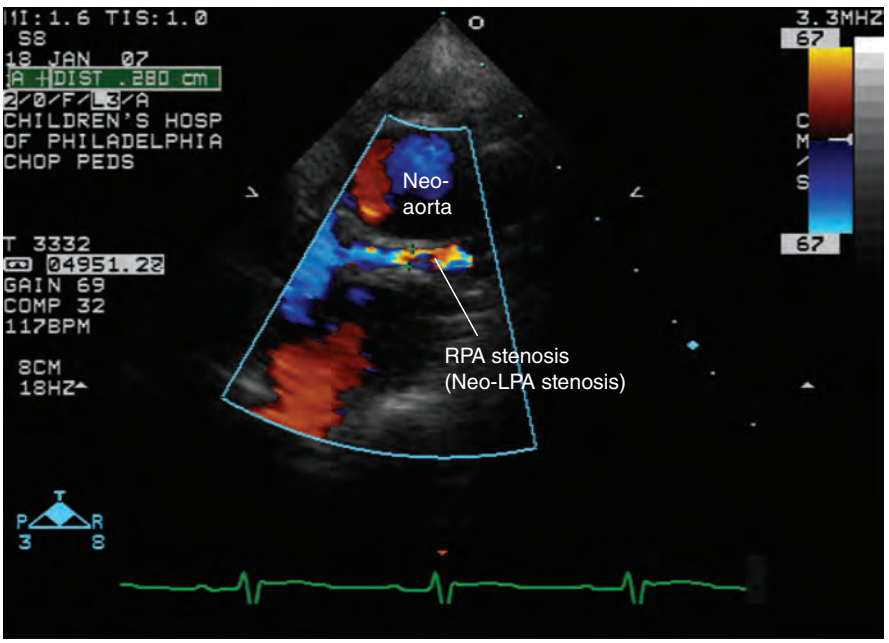


Figure 20.27 Severe stenosis of the proximal right pulmonary artery (RPA) as it courses under the bulbous neo-aorta.

Table 20.1 Criteria to forgo a cardiac catheterization prior to Fontan completion*

Clinical data
Room air pulse oximetry >76%
Hemoglobin <18 g/dL
Echocardiographic data
Left pulmonary artery visualized without stenosis
No significant atrioventricular valve insufficiency (<1+)
No significant ventricular dysfunction (qualitative)
No aortic coarctation
An unrestrictive atrial communication
No evidence of a decompressing vessel

*If the above criteria are met, there is no benefit to performing a cardiac catheterization prior to Fontan completion [85].

heart disease but is also associated with its own set of long-term morbidities. For a detailed discussion of imaging in the Fontan circulation see the discussion in Chapter 27.

Videos

To access the videos for this chapter, please go to www.laiecho.com.

Video 20.1 An apical 4-chamber view of hypoplastic left heart syndrome (HLHS). Note the hypertrophied right ventricle (RV), the redundant tricuspid valve tissue and the hypoplastic left ventricle (LV). The echo-bright left ventricular endocardium is consistent with endocardial fibroelastosis.

Video 20.2 In this apical 4-chamber view the numerous chordal attachments of the septal leaflet to the ventricular septum can be appreciated. These effectively "tether" the leaflet to the septum; a risk for abnormal tricuspid valve function and tricuspid regurgitation.

Video 20.3 This apical 4-chamber clip with color Doppler demonstrates severe tricuspid insufficiency resulting from a dysplastic tricuspid valve. This degree of tricuspid insufficiency may be a risk factor for poor outcome with staged palliation.

Video 20.4 A clip from the suprasternal sagittal position demonstrating the ascending aorta as it enters the transverse arch. In this case the ascending aorta is tiny and serves as a "common coronary" from which the right and left coronaries originate.

Video 20.5 This view is from the suprasternal sagittal position with color Doppler. In this example, the ascending aorta is more fully formed, but again the traverse arch is supplied retrograde from the patent ductus arteriosus (PDA).

Video 20.6 This view, from a high parasternal position, demonstrates the physiology after the "hybrid procedure." The struts of the ductal stent are well visualized stenting the patent ductus arteriosus (PDA) to allow for systemic perfusion. Note the retrograde flow within the PDA stent. An abundance of retrograde diastolic flow is a risk factor for poor outcome.

Video 20.7 In this view, from a high parasternal position, the physiology after the "hybrid procedure" is demonstrated. The pulmonary artery bands are crucial to ensure that the systemic and pulmonary circulations are well balanced.

Video 20.8 This view, from a high parasternal position, demonstrates the physiology after the "hybrid procedure." The pulmonary artery bands are crucial to ensure that the systemic and pulmonary circulations are well balanced.

Video 20.9 This high left parasternal view demonstrates the "ductal arch" from a standard "three-finger" ductal view. The patent ductus arteriosus (PDA) is quite large and transitions smoothly into the descending aorta. Both proximal branch pulmonary arteries are seen in this view.

Video 20.10 The same high left parasternal view as Video 20.9, with color Doppler applied to the image, antegrade systolic flow and retrograde diastolic flow are easily appreciated. Without surgical intervention, the balance and antegrade and retrograde flow can change as pulmonary vascular resistance drops creating a "steal" from the systemic circulation. For this reason, a surgical intervention (either a Norwood procedure or a hybrid procedure) is generally warranted within the first few days of life.

Video 20.11 This is an apical 4-chamber view from a fetal echocardiogram demonstrating a restrictive atrial septum by 2D imaging. Note that the septum bulges from the dilated left atrium toward the right atrial. In addition, the pulmonary veins are very dilated. This suggests elevated pulmonary venous pressure and is an ominous finding. If this is found early, a case like this may be a candidate for fetal intervention. If found later in gestation, an immediate postnatal procedure to compress the left atrium should be considered.

Video 20.12 This is another apical 4-chamber-type image from a fetal echocardiogram. In this image color Doppler has been applied. No flow is demonstrated traversing the atrial septum suggesting a severely restrictive or intact atrial septum.

Video 20.13 This two-dimensional image from the subcostal view demonstrates a stent well positioned across the atrial septum following a procedure performed in the immediate postnatal period. A stent can allow decompression of the left atrium in cases where the atrial septum is restrictive or intact.

Video 20.14 In this view with color Doppler, left-to-right flow across the atrial stent can be appreciated. The flow appears unobstructed and the left atrium appears adequately decompressed.

Video 20.15 This is an example of the result of a fetal intervention. The apical image from a fetal echocardiogram demonstrates a stent in position across the fetal atrial septum. The pulmonary veins in this image, while still dilated, appear less tense that prior to the procedure.

Video 20.16 In this example of the result of a fetal intervention, the application of color Doppler demonstrates flow across the stent and through a second defect at the inferior margin of the stent. The decompression of the atrial septum constitutes a technical success of the procedure.

Video 20.17 This suprasternal frontal view demonstrates the full length of a Blaylock–Taussig shunt. The shunt originates from the innominate artery and enters the right pulmonary artery. In this case the shunt and the branch pulmonary arteries appear to be widely patent.

Video 20.18 With the advent of 3D color Doppler flow mapping, a virtual angiogram can be created and can help to demonstrate clinically important narrowing within the Blaylock–Taussig shunt. This 3D image demonstrates a BT shunt as it enters the right pulmonary artery without suggestion of narrowing.

Video 20.19 This second 3D image demonstrating a Blaylock–Taussig shunt shows a significant narrowing at the insertion of the shunt into the right pulmonary artery along with a narrowing of the medial right pulmonary adjacent to the shunt insertion site. This technology is evolving and will become more clinically useful as the range of available 3D frequencies improves.

Video 20.20 In this view the Sano conduit is seen entering the branch pulmonary arteries. Note that the pulmonary arteries appear "tented" by the conduit. Branch pulmonary artery stenosis is a concern following stage 1 with Sano modification, and extensive branch pulmonary arterioplasty is common at the time of stage 2.

Video 20.21 This is an example of a reconstructed arch. The distal anastomosis of this neo-aorta does not have a smooth tapered contour and it appears that there is an area of discrete stenosis as demonstrated by color Doppler right at the distal suture line. This type of obstruction can lead to ventricular dysfunction and may have to be addressed in the interventional catheterization laboratory, or in the operating room.

Video 20.22 The branch pulmonary arteries are often difficult to see by echo after the second stage of reconstruction. This is a demonstration of a Glenn shunt connecting the superior vena cava to the right pulmonary artery. Notice that the portion of the native right pulmonary artery just to the left of the anastomosis to the SVC can be seen by 2D as it passes under the bulbous reconstructed aortic arch.

Video 20.23 The same view as Video 20.22. With the application of color Doppler, low-velocity flow can be demonstrated into the right pulmonary artery without evidence of obstruction.

References

1 Lev M. Pathologic anatomy and interrelationship of hypoplasia of the aortic tract complexes. *Lab Invest* 1952;**1**:61–70.

2 Noonan JA, Nadas AS. The hypoplastic left heart syndrome; an analysis of 101 cases. *Pediatr Clin North Am* 1958;**5**:1029–1056.

3 Hoffman JI, Kaplan S. The incidence of congenital heart disease. *J Am Coll Cardiol* 2002;**39**:1890–1900.

4 Natowicz M, Chatten J, Clancy R, et al. Genetic disorders and major extracardiac anomalies associated with the hypoplastic left heart syndrome. *Pediatrics* 1988;**82**:698–706.

5 Natowicz M, Kelley RI. Association of Turner syndrome with hypoplastic left-heart syndrome. *Am J Dis Child* 1987;**141**:218–220.

6 Glauser TA, Rorke LB, Weinberg PM, Clancy RR. Congenital brain anomalies associated with the hypoplastic left heart syndrome. *Pediatrics* 1990;**85**:984–990.

7 Licht DJ, Wang J, Silvestre DW, et al. Preoperative cerebral blood flow is diminished in neonates with severe congenital heart defects. *J Thorac Cardiovasc Surg* 2004;**128**:841–849.

8 Miller SP, McQuillen PS, Hamrick S, et al. Abnormal brain development in newborns with congenital heart disease. *N Engl J Med* 2007;**357**:1928–1938.

9 Hornberger LK, Sanders SP, Rein AJ, et al. Left heart obstructive lesions and left ventricular growth in the midtrimester fetus. A longitudinal study. *Circulation* 1995;**92**:1531–1538.

10 Dasgupta C, Martinez AM, Zuppan CW, et al. Identification of connexin43 (alpha1) gap junction gene mutations in patients with hypoplastic left heart syndrome by denaturing gradient gel electrophoresis (DGGE). *Mutat Res* 2001;**479**:173–186.

11 Garg V, Muth AN, Ransom JF, et al. Mutations in NOTCH1 cause aortic valve disease. *Nature* 2005;**437**:270–274.

12 McElhinney DB, Geiger E, Blinder J, et al. NKX2.5 mutations in patients with congenital heart disease. *J Am Coll Cardiol* 2003;**42**:1650–1655.

13 Lewin MB, McBride KL, Pignatelli R, et al. Echocardiographic evaluation of asymptomatic parental and sibling cardiovascular anomalies associated with congenital left ventricular outflow tract lesions. *Pediatrics* 2004;**114**:691–696.

14 Loffredo CA, Chokkalingam A, Sill AM, et al. Prevalence of congenital cardiovascular malformations among relatives of infants with hypoplastic left heart, coarctation of the aorta, and d-transposition of the great arteries. *Am J Med Genet A* 2004;**124**:225–230.

15 Hinton RB, Jr., Martin LJ, Tabangin ME, et al. Hypoplastic left heart syndrome is heritable. *J Am Coll Cardiol* 2007;**50**:1590–1595.

16 Bharati S, Lev M. The surgical anatomy of hypoplasia of aortic tract complex. *J Thorac Cardiovasc Surg* 1984;**88**:97–101.

17 Chin AJ, Weinberg PM, Barber G. Subcostal two-dimensional echocardiographic identification of anomalous attachment of septum primum in patients with left atrioventricular valve underdevelopment. *J Am Coll Cardiol* 1990;**15**:678–681.

18 Weinberg PM, Weindling S. Atrial septal anomalies differentiate types of hypoplastic left heart syndrome. *J Am Coll Cardiol* 1998;**12**(Suppl. A). [Abstract]

19 Rychik J, Rome JJ, Collins MH, et al. The hypoplastic left heart syndrome with intact atrial septum: atrial morphology, pulmonary vascular histopathology and outcome. *J Am Coll Cardiol* 1999;**34**:554–560.

20 Glatz JA, Tabbutt S, Gaynor JW, et al. Hypoplastic left heart syndrome with atrial level restriction in the era of prenatal diagnosis. *Ann Thorac Surg* 2007;**84**:1633–1638.

21 Seliem MA, Chin AJ, Norwood WI. Patterns of anomalous pulmonary venous connection/drainage in hypoplastic left heart syndrome: diagnostic role of Doppler color flow mapping and surgical implications. *J Am Coll Cardiol* 1992;**19**:135–141.

22 Bernstein HS, Moore P, Stanger P, Silverman NH. The levoatriocardinal vein: morphology and echocardiographic identification of the pulmonary-systemic connection. *J Am Coll Cardiol* 1995;**26**:995–1001.
23 Edwards JE, Du SJ, Alcott DL, Burchell HB. Thoracic venous anomalies. III. Atresia of the common pulmonary vein, the pulmonary veins draining wholly into the superior vena cava. *AMA Arch Pathol* 1951;**51**:446–460.
24 Fogel MA, Weinberg PM, Fellows KE, Hoffman EA. A study in ventricular-ventricular interaction. Single right ventricles compared with systemic right ventricles in a dual-chamber circulation. *Circulation* 1995;**92**:219–230.
25 Glatz JA, Fedderly RT, Ghanayem NS, Tweddell JS. Impact of mitral stenosis and aortic atresia on survival in hypoplastic left heart syndrome. *Ann Thorac Surg* 2008;**85**:2057–2062.
26 Jonas RA, Hansen DD, Cook N, Wessel D. Anatomic subtype and survival after reconstructive operation for hypoplastic left heart syndrome. *J Thorac Cardiovasc Surg* 1994;**107**:1121–1127; discussion 1127–1128.
27 Patel CR, Lane JR, Spector ML, et al. Prenatal diagnosis of ventriculocoronary arterial communication in fetuses with hypoplastic left heart syndrome. *J Ultrasound Med* 2006;**25**:245–249.
28 Barber G, Helton JG, Aglira BA, et al. The significance of tricuspid regurgitation in hypoplastic left-heart syndrome. *Am Heart J* 1988;**116**:1563–1567.
29 Checchia PA, McGuire JK, Morrow S, et al. A risk assessment scoring system predicts survival following the Norwood procedure. *Pediatr Cardiol* 2006;**27**:62–66.
30 Helton JG, Aglira BA, Chin AJ, et al. Analysis of potential anatomic or physiologic determinants of outcome of palliative surgery for hypoplastic left heart syndrome. *Circulation* 1986;**74**:I70–76.
31 Gaynor JW, Mahle WT, Cohen MI, et al. Risk factors for mortality after the Norwood procedure. *Eur J Cardiothorac Surg* 2002;**22**:82–89.
32 Stasik CN, Gelehrter S, Goldberg CS, et al. Current outcomes and risk factors for the Norwood procedure. *J Thorac Cardiovasc Surg* 2006;**131**:412–417.
33 Stamm C, Anderson RH, Ho SY. The morphologically tricuspid valve in hypoplastic left heart syndrome. *Eur J Cardiothorac Surg* 1997;**12**:587–592.
34 Jenkins PC, Flanagan MF, Jenkins KJ, et al. Survival analysis and risk factors for mortality in transplantation and staged surgery for hypoplastic left heart syndrome. *J Am Coll Cardiol* 2000;**36**:1178–1185.
35 Jenkins PC, Flanagan MF, Sargent JD, et al. A comparison of treatment strategies for hypoplastic left heart syndrome using decision analysis. *J Am Coll Cardiol* 2001;**38**:1181–1187.
36 Mahle WT, Cohen MS, Spray TL, Rychik J. Atrioventricular valve regurgitation in patients with single ventricle: impact of the bidirectional cavopulmonary anastomosis. *Ann Thorac Surg* 2001;**72**:831–835.
37 Michelfelder EC, Kimball TR, Pearl JM, et al. Effect of superior cavopulmonary anastomosis on the rate of tricuspid annulus dilation in hypoplastic left heart syndrome. *Am J Cardiol* 2002;**89**:96–98.
38 Reyes A, 2nd, Bove EL, Mosca RS, et al. Tricuspid valve repair in children with hypoplastic left heart syndrome during staged surgical reconstruction. *Circulation* 1997;**96**:II-341–343; discussion II-344–345.
39 O'Connor MJ, Elias MD, Cohen MS, Quartermain MD. Outcomes of infants undergoing superior cavopulmonary connection in the presence of ventricular dysfunction. *Pediatr Cardiol* 2012;**33**:547–553.
40 Hawkins JA, Doty DB. Aortic atresia: morphologic characteristics affecting survival and operative palliation. *J Thorac Cardiovasc Surg* 1984;**88**:620–626.
41 Machii M, Becker AE. Nature of coarctation in hypoplastic left heart syndrome. *Ann Thorac Surg* 1995;**59**:1491–1494.
42 Devloo-Blancquaert A, Titus JL, Edwards JE, et al. Interruption of aortic arch and hypoplastic left heart syndrome. *Pediatr Cardiol* 1995;**16**:304–308.
43 Lloyd TR, Evans TC, Marvin WJ, Jr. Morphologic determinants of coronary blood flow in the hypoplastic left heart syndrome. *Am Heart J* 1986;**112**:666–671.
44 Ito T, Niino M, Ishikawa J, et al. Hypoplastic left heart syndrome with a single coronary artery originating from the pulmonary artery. *Acta Paediatr Jpn* 1995;**37**:61–63.
45 Sarris GE, Drummond-Webb JJ, Ebeid MR, et al. Anomalous origin of left coronary from right pulmonary artery in hypoplastic left heart syndrome. *Ann Thorac Surg* 1997;**64**:836–838.
46 Cross RR, Harahsheh AS, McCarter R, Martin GR. Identified mortality risk factors associated with presentation, initial hospitalisation, and interstage period for the Norwood operation in a multi-centre registry: a report from the National Pediatric Cardiology Quality Improvement Collaborative. *Cardiol Young* 2013:1–10.
47 Rychik J, Gullquist SD, Jacobs ML, Norwood WI. Doppler echocardiographic analysis of flow in the ductus arteriosus of infants with hypoplastic left heart syndrome: relationship of flow patterns to systemic oxygenation and size of interatrial communication. *J Am Soc Echocardiogr* 1996;**9**:166–173.
48 Norwood WI, Lang P, Hansen DD. Physiologic repair of aortic atresia-hypoplastic left heart syndrome. *N Engl J Med* 1983;**308**:23–26.
49 Chrisant MR, Naftel DC, Drummond-Webb J, et al. Fate of infants with hypoplastic left heart syndrome listed for cardiac transplantation: a multicenter study. *J Heart Lung Transplant* 2005;**24**:576–582.
50 Galantowicz M, Cheatham JP. Lessons learned from the development of a new hybrid strategy for the management of hypoplastic left heart syndrome. *Pediatr Cardiol* 2005;**26**:190–199.
51 Akintuerk H, Michel-Behnke I, Valeske K, et al. Stenting of the arterial duct and banding of the pulmonary arteries: basis for combined Norwood stage I and II repair in hypoplastic left heart. *Circulation* 2002;**105**:1099–1103.
52 Honjo O, Benson LN, Mewhort HE, et al. Clinical outcomes, program evolution, and pulmonary artery growth in single ventricle palliation using hybrid and Norwood palliative strategies. *Ann Thorac Surg* 2009;**87**:1885–1892; discussion 1892–1893.
53 Sano S, Ishino K, Kado H, et al. Outcome of right ventricle-to-pulmonary artery shunt in first-stage palliation of hypoplastic left heart syndrome: a multi-institutional study. *Ann Thorac Surg* 2004;**78**:1951–1957; discussion 1957–1958.
54 Sano S, Ishino K, Kawada M, et al. Right ventricle-pulmonary artery shunt in first-stage palliation of hypoplastic left heart syndrome. *J Thorac Cardiovasc Surg* 2003;**126**:504–509; discussion 509–510.
55 Sano S, Ishino K, Kawada M, Honjo O. Right ventricle-pulmonary artery shunt in first-stage palliation of hypoplastic left heart

syndrome. *Semin Thorac Cardiovasc Surg Pediatr Card Surg Annu* 2004;**7**:22–31.
56 Rychik J, Szwast A, Natarajan S, et al. Perinatal and early surgical outcome for the fetus with hypoplastic left heart syndrome: a 5-year single institutional experience. *Ultrasound Obstet Gynecol* 2010;**36**:465–470.
57 Ohye RG, Sleeper LA, Mahony L, et al. Comparison of shunt types in the Norwood procedure for single-ventricle lesions. *N Engl J Med* 2010;**362**:1980–1992.
58 Remmell-Dow DR, Bharati S, Davis JT, et al. Hypoplasia of the eustachian valve and abnormal orientation of the limbus of the foramen ovale in hypoplastic left heart syndrome. *Am Heart J* 1995;**130**:148–152.
59 Kadletz M, Black MD, Smallhorn J, et al. Total anomalous systemic venous drainage to the coronary sinus in association with hypoplastic left heart disease: more than a mere coincidence. *J Thorac Cardiovasc Surg* 1997;**114**:282–284.
60 Ohta N, Sakamoto K, Kado M, et al. Surgical treatment of coronary sinus orifice atresia with hypoplastic left heart syndrome after total cavo-pulmonary connection. *Ann Thorac Surg* 2002;**73**:653–655.
61 Salminen JT, Hakala T, Pihkala J, et al. Coronary sinus orifice atresia with left superior vena cava in patients with univentricular heart. *Ann Thorac Surg* 2006;**81**:e16–17.
62 Takahashi K, Inage A, Rebeyka IM, et al. Real-time 3-dimensional echocardiography provides new insight into mechanisms of tricuspid valve regurgitation in patients with hypoplastic left heart syndrome. *Circulation* 2009;**120**:1091–1098.
63 Brann S, Brawn WJ, Raafat F, Sreeram N. Neonatal pulmonary vascular disease in hypoplastic left heart syndrome. *Ann Thorac Surg* 1995;**60**:433–434.
64 Gossett JG, Rocchini AP, Lloyd TR, Graziano JN. Catheter-based decompression of the left atrium in patients with hypoplastic left heart syndrome and restrictive atrial septum is safe and effective. *Catheter Cardiovasc Interv* 2006;**67**:619–624.
65 Vlahos AP, Lock JE, McElhinney DB, van der Velde ME. Hypoplastic left heart syndrome with intact or highly restrictive atrial septum: outcome after neonatal transcatheter atrial septostomy. *Circulation* 2004;**109**:2326–2330.
66 Chintala K, Tian Z, Du W, et al. Fetal pulmonary venous Doppler patterns in hypoplastic left heart syndrome: relationship to atrial septal restriction. *Heart* 2008;**94**:1446–1449.
67 Michelfelder E, Gomez C, Border W, et al. Predictive value of fetal pulmonary venous flow patterns in identifying the need for atrial septoplasty in the newborn with hypoplastic left ventricle. *Circulation* 2005;**112**:2974–2979.
68 Marshall AC, van der Velde ME, Tworetzky W, et al. Creation of an atrial septal defect in utero for fetuses with hypoplastic left heart syndrome and intact or highly restrictive atrial septum. *Circulation* 2004;**110**:253–258.
69 Kaltman JR, Di H, Tian Z, Rychik J. Impact of congenital heart disease on cerebrovascular blood flow dynamics in the fetus. *Ultrasound Obstet Gynecol* 2005;**25**:32–36.
70 Williams IA, Fifer C, Jaeggi E, et al. The association of fetal cerebrovascular resistance with early neurodevelopment in single ventricle congenital heart disease. *Am Heart J* 2013;**165**:544–550.e1.
71 Murdison KA, Baffa JM, Farrell PE, Jr., et al. Hypoplastic left heart syndrome. Outcome after initial reconstruction and before modified Fontan procedure. *Circulation* 1990;**82**:IV199–207.
72 Rychik J, Bush DM, Spray TL, et al. Assessment of pulmonary/systemic blood flow ratio after first-stage palliation for hypoplastic left heart syndrome: development of a new index with the use of Doppler echocardiography. *J Thorac Cardiovasc Surg* 2000;**120**:81–87.
73 Cardis BM, Fyfe DA, Ketchum D, Mahle WT. Echocardiographic features and complications of the modified Norwood operation using the right ventricle to pulmonary artery conduit. *J Am Soc Echocardiogr* 2005;**18**:660–665.
74 Mahle WT, Rychik J, Gaynor JW, et al. Restrictive interatrial communication after reconstructive surgery for hypoplastic left heart syndrome. *Am J Cardiol* 2001;**88**:1454–1457, A9.
75 Cardis BM, Fyfe DA, Mahle WT. Elastic properties of the reconstructed aorta in hypoplastic left heart syndrome. *Ann Thorac Surg* 2006;**81**:988–991.
76 Fraisse A, Colan SD, Jonas RA, et al. Accuracy of echocardiography for detection of aortic arch obstruction after stage I Norwood procedure. *Am Heart J* 1998;**135**:230–236.
77 Lemler MS, Zellers TM, Harris KA, Ramaciotti C. Coarctation index: identification of recurrent coarctation in infants with hypoplastic left heart syndrome after the Norwood procedure. *Am J Cardiol* 2000;**86**:697–699, A9.
78 Wellen SL, Glatz AC, Ravishankar C, Cohen MS. Abstract P1-76: Re-coarctation of the aorta after the Norwood operation can be accurately predicted using a composite score based on transthoracic echocardiography. *J Am Soc Echocardiogr* 2012;**25**:B28.
79 Birnbaum B, Berger G, Fenstermaker B, et al. Echocardiographic parameters that predict outcome in aortic atresia patients undergoing comprehensive stage II procedure. *Congenit Heart Dis* 2010;**5**:409–15.
80 Egan MJ, Hill SL, Boettner BL, et al. Predictors of retrograde aortic arch obstruction after hybrid palliation of hypoplastic left heart syndrome. *Pediatr Cardiol* 2011;**32**:67–75.
81 Bridges ND, Jonas RA, Mayer JE, et al. Bidirectional cavopulmonary anastomosis as interim palliation for high-risk Fontan candidates. Early results. *Circulation* 1990;**82**:IV170–176.
82 Douville EC, Sade RM, Fyfe DA. Hemi-Fontan operation in surgery for single ventricle: a preliminary report. *Ann Thorac Surg* 1991;**51**:893–899; discussion 900.
83 Brown DW, Gauvreau K, Moran AM, et al. Clinical outcomes and utility of cardiac catheterization prior to superior cavopulmonary anastomosis. *J Thorac Cardiovasc Surg* 2003;**126**:272–281.
84 Brown DW, Gauvreau K, Powell AJ, et al. Cardiac magnetic resonance versus routine cardiac catheterization before bidirectional glenn anastomosis in infants with functional single ventricle: a prospective randomized trial. *Circulation* 2007;**116**:2718–2725.
85 Ro PS, Rychik J, Cohen MS, et al. Diagnostic assessment before Fontan operation in patients with bidirectional cavopulmonary anastomosis: are noninvasive methods sufficient? *J Am Coll Cardiol* 2004;**44**:184–187.
86 Fogel MA. Is routine cardiac catheterization necessary in the management of patients with single ventricles across staged Fontan reconstruction? No! *Pediatr Cardiol* 2005;**26**:154–158.

CHAPTER 21

Aortic Arch Anomalies: Coarctation of the Aorta and Interrupted Aortic Arch

Jan Marek, Matthew Fenton, and Sachin Khambadkone
Cardiothoracic Unit, Great Ormond Street Hospital for Children and Institute of Cardiovascular Sciences, London, UK

Coarctation of the aorta

Definition

Coarctation of the aorta (COA) refers to narrowing of the aortic isthmus. Hypoplasia of the aortic arch and other associated cardiovascular anomalies are common. The term is also used to describe strictures of other segments of the thoracic or the abdominal aorta.

Incidence

The incidence of COA is approximately 36 (range 29 to 49) per 100,000 live births, representing the seventh most common, or approximately 5–7% of patients with congenital heart disease (CHD) [1,2]. In ~64% of patients COA manifests as the dominant CHD soon after birth, whereas in the remaining 36% it manifests at an older age. COA is 1.3–1.7 times more likely in males [3,4]. In prenatal series, COA constitutes 3–10% of all prenatal diagnoses of CHD [5].

Etiology

No single etiologic cause has been proven and evidence points to an interplay between genetic, environmental, and hemodynamic factors [4–8]. Abnormal flow distribution during fetal life with decreased aortic flow has long been suspected. This is supported by the observation that 71% of cases of aortic atresia also have COA [6]. The role of genetic factors is increasingly recognized. For example, COA occurs in 12% of patients with Turner syndrome (XO), and the incidence of chromosome 22q11 microdeletion is increased in patients with coarctation or interruption of the aortic arch [7,8].

Morphology and classification

The aortic arch is divided into three segments: (1) *proximal arch*, between the brachiocephalic (innominate) and the left carotid artery; (2) *distal arch*, between the left carotid and the left subclavian artery (known as transverse arch); and (3) *isthmus*, between the left subclavian and the ligamentum or ductus arteriosus (Figure 21.1). The anatomic criteria for defining arch hypoplasia is a proximal aortic arch of 60% of the ascending aortic diameter, or a distal aortic arch of 50% of the ascending aortic diameter, or isthmic narrowing of 40%. The commonly used echocardiographic definition determining transverse aortic arch hypoplasia in neonates is an internal diameter <1 mm for every 1 kg body weight [9]. Another commonly used criterion is diameter z-score <–2 standard deviations of the normal population's mean.

COA usually results from narrowing of the aortic isthmus at its junction with the proximal descending aorta at the insertion of the arterial duct (juxtaductal coarctation). The anatomic spectrum is wide but different morphologic patterns can be distinguished based on age at diagnosis – before birth, early infancy, and in older children and adults. In the fetus and infant, the distal transverse aortic arch between the left common carotid and left subclavian arteries is often elongated and hypoplastic (tubular hypoplasia), the angle between the ascending aorta and transverse arch is acute, and the aortic isthmus is diffusely hypoplastic [5], the arterial duct is almost always widely patent. In neonates, gradual development of COA is reported during closure of the ductus arteriosus and histologic studies have demonstrated ductal tissue circumferentially surrounding the juxtaductal portion of the aorta [10]. Although the stenotic site is typically located at the distal isthmus, other locations or multiple sites can be found (e.g., opposite or proximal to the origin of the left subclavian or any other brachiocephalic artery). In older children and adults, aortic arch hypoplasia is less common, the coarctation segment is usually discrete, and collateral arteries bypassing the COA are common. These collateral vessels develop from increased flow through the internal mammary, intercostals, and scapular arteries.

Regardless of age at diagnosis, the coarctation segment is characterized by luminal narrowing due to thickening of the intima

Echocardiography in Pediatric and Congenital Heart Disease: From Fetus to Adult, Second Edition. Edited by Wyman W. Lai, Luc L. Mertens, Meryl S. Cohen and Tal Geva.
© 2016 John Wiley & Sons, Ltd. Published 2016 by John Wiley & Sons, Ltd.
Companion website: www.lai-echo.com

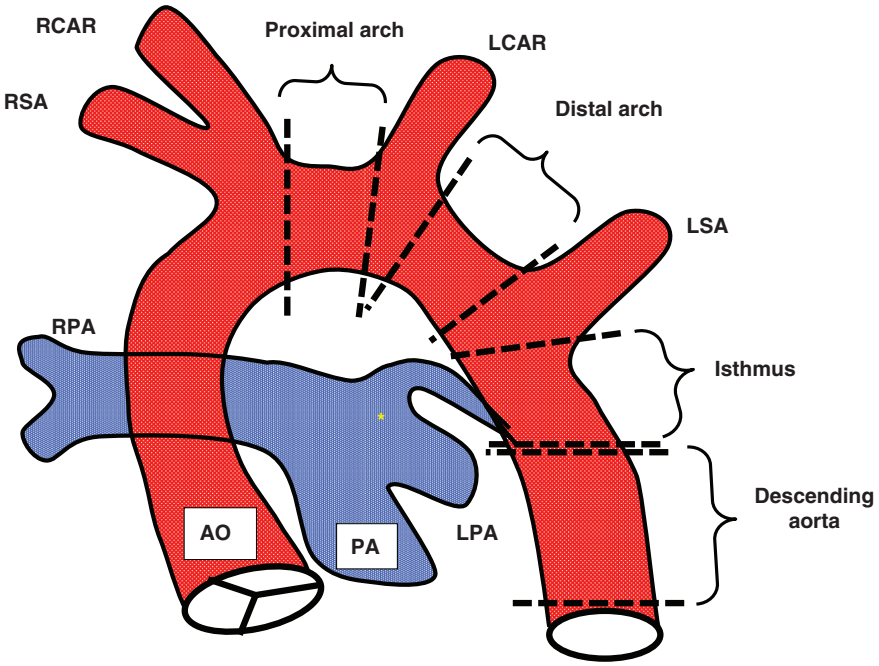


Figure 21.1 Schematic drawing of individual aortic arch segments in relationship to arterial duct or ligament (asterisk). AO, aorta; LCAR, left carotid artery; LPA, left pulmonary artery; LSA, left subclavian artery; PA, pulmonary trunk; RPA, right pulmonary artery; RCAR, right carotid artery; RSA, right subclavian artery.

and media layers, hypoplasia, and tortuosity. The endoluminal protrusion of the intimal–medial ridge (or "shelf") is typically circumferential but is often more prominent along the posterior and lateral wall of the aortic isthmus. The length of the stenotic segment varies from discrete (2–3 mm) to long-segment (7–20 mm). The proximal descending aorta immediately past the coarctation often exhibits poststenotic dilation, a feature more commonly found in older children and adults.

A high incidence (>50%) of associated cardiac abnormalities suggests that COA is a more complex defect than isolated narrowing of the aorta. COA is most commonly associated with bicommissural aortic valve, ventricular septal defect (VSD), subvalvar and valvar aortic stenosis, common atrioventricular canal, and others. COA is particularly common in patients with multiple left heart obstructive lesions and is part of Shone syndrome.

Rarely, COA affects other segments of the aorta. The morphology and pathophysiology of abdominal coarctation is different from coarctation of the aortic isthmus in that the involved segment is often long, the aortic media is markedly thickened, and involvement of the renal and mesenteric vessels is common. Involvement of the thoracic and abdominal aorta and branches has been reported in Takayasu aortitis, supravalvar aortic stenosis (Williams syndrome, familial aortic stenosis and sporadic supravalvar aortic stenosis), and mid-aortic syndrome.

"Pseudocoarctation" of the aorta refers to deformity of the aortic isthmus characterized by tortuosity but without luminal narrowing. The isthmus and part of the descending thoracic aorta are deformed, most frequently into the shape of the digit three ("3"). Internally, the caliber of the isthmus is not narrowed and blood flow is not obstructed.

Pathophysiology

Prenatal

The hemodynamic consequences of COA are usually tolerated well in the fetus because blood flow to the lower body and the placenta is supplied predominantly thorough the arterial duct with only ~10% of the combined cardiac output crossing the aortic isthmus. Narrowing of the aortic isthmus results in diversion of blood flow from the aorta to the pulmonary artery and the arterial duct. As a result, left ventricular afterload increases and its output decreases, whereas right ventricular output increases. Consequently, the right ventricle dilates while the left ventricle is pressure loaded [11], resulting in the ventricular size disproportion observed when COA is present in the fetus.

Postnatal

Neonatal coarctation

The pathophysiology of COA in the neonate depends on a complex interplay between the severity of aortic narrowing, the rate at which the COA progresses, patency of the arterial duct, pulmonary vascular resistance, and associated cardiac anomalies. The hemodynamic burden imposed by severe COA manifests after birth as the foramen ovale closes and the arterial duct constricts and ultimately closes. As a result, the left ventricle supplies the entire cardiac output and flow to the lower body must cross the narrow aortic segment(s). Under these conditions, the left ventricle faces pressure overload and systolic blood pressure in the upper body is increased. In contrast, distal to the COA the systolic blood pressure is low, clinically manifesting as reduced pulse amplitude in the femoral arteries. When the coarctation occurs proximal to the left subclavian artery, decreased pulse amplitude is noted in the left arm. In the rare circumstance

of COA proximal to the left subclavian artery associated with aberrant origin of the right subclavian artery, blood pressures and pulse volumes in the arms are similar to those in the lower extremities.

In neonates with severe COA, the increased impedance to left ventricular emptying leads to elevated end-diastolic pressure and left atrial, pulmonary venous, and pulmonary arterial hypertension. A widely patent arterial duct allows right-to-left systolic flow from the main pulmonary artery to the descending aorta, providing adequate perfusion to the lower body and normal volume of the femoral pulse. In the absence of an atrial-level right-to-left shunt or associated cardiac lesions, oxygen saturation in the upper extremities (preductal) is higher than that in the lower extremities (postductal), a phenomenon called *differential cyanosis*.

Constriction and ultimate closure of the arterial duct in neonates with severe or rapidly progressing COA lead to left ventricular dysfunction. Increased afterload due to the COA, decreased preload secondary to increased pulmonary vascular resistance and diastolic septal shift towards the left ventricle, and decreased myocardial perfusion contribute to left ventricular dysfunction. Failure of compensatory mechanisms ultimately leads to decreased cardiac output, lower body hypoperfusion, oliguria, acidosis, and shock. If the COA develops slowly and pulmonary vascular resistance normalizes, the left ventricular myocardium hypertrophies in response to the pressure load, wall stress is maintained, and systolic function is preserved.

Adult coarctation

Later in life coarctation is usually diagnosed either due to a heart murmur, low pulse amplitude in the lower extremities, or systemic hypertension. The clinical course of this type of coarctation is often insidious. This is usually due to development of collateral vessels between the high-pressure aortic branches proximal to the COA and the low-pressure distal aorta. When the collateral vessels are extensive, the pulse volume and blood pressure in the lower extremities can be near normal. Left ventricular pressure overload is gradual in onset and myocardial failure usually develops over decades in response to systemic hypertension and coronary artery disease. Another complication seen in adults with COA is cerebral aneurysm(s) [12].

Imaging

Echocardiography provides adequate diagnostic information in most newborns, infants, and young children. However, older children and adults often require other diagnostic modalities (e.g., MRI or CT), as echocardiographic imaging of the aortic isthmus and proximal descending aorta is difficult due to increased distance from the transducer and intervening airways. It is imperative that comprehensive evaluation of the aortic arch, arch branches, isthmus, and descending aorta is performed before selecting a management plan. Two-dimensional (2D) echocardiographic imaging as well as color and spectral Doppler techniques are used from suprasternal, right and left infraclavicular approaches to evaluate the anatomy and to quantify the degree of obstruction.

Key elements:

- Evaluation of heart situs and segmental cardiac anatomy.
- Doppler evaluation of flow profile in the descending aorta at or below the level of the diaphragm.
- Evaluation of aortic arch anatomy, origins of brachiocephalic vessels, aortic isthmus, and proximal descending aorta.
- Measurements of flow gradients in the transverse arch and at the COA site.
- Evaluation of flow in the arterial duct.
- Evaluation of morphology, size, and function of the left ventricular inflow and outflow, including the supramitral area, mitral valve, left ventricular outflow, aortic valves, and sinotubular junction.
- Measurements of left ventricular size (diameter, length, volume, thickness, and mass) and function.
- Evaluation of atrial communication(s), including direction of flow and measurement of mean pressure gradient.
- Estimation of the degree of pulmonary hypertension.
- Identification of associated anomalies.

Echocardiographic evaluation of neonatal coarctation

Imaging of the aortic arch and isthmus

The entire aortic arch, isthmus, arterial duct, and descending aorta are imaged from the suprasternal notch and from the right and left infraclavicular windows. Extension of the neck and upper thorax by placing a rolled towel under the shoulders facilitates imaging. Because the distance between the transducer and the aorta is short, we recommend using a transducer with frequencies ranging from 7.5 to 12 MHz to provide high-resolution imaging.

Imaging is first performed in the transverse plane, following the ascending aorta cranially, demonstrating the arch branching pattern, and imaging the transverse arch. This view is essential to characterize the anatomy and sidedness of the aortic arch and to exclude associated abnormalities such as right- or double aortic arch and aberrant origin of a subclavian artery (Figure 21.2; Video 21.1). The oblique sagittal plane is then used to visualize the long axis of the ascending aorta, arch, isthmus, and proximal descending aorta (Figure 21.3; Video 21.2). In neonates, the right infraclavicular area is particularly helpful for depicting most of the thoracic aorta in one plane. The distal aortic arch (between the left common carotid and left subclavian arteries) is often elongated and hypoplastic. The hypoplasia may extend from the origin of the brachiocephalic trunk or the left carotid artery up to the site of COA (Figure 21.4; Videos 21.3 and 21.4). Imaging of the coarctation site at the junction of the isthmus and proximal descending aorta can also be accomplished from the left subclavicular area in a sagittal plane. This view demonstrates the anatomy of the coarctation in detail and complements imaging from the right subclavicular area.

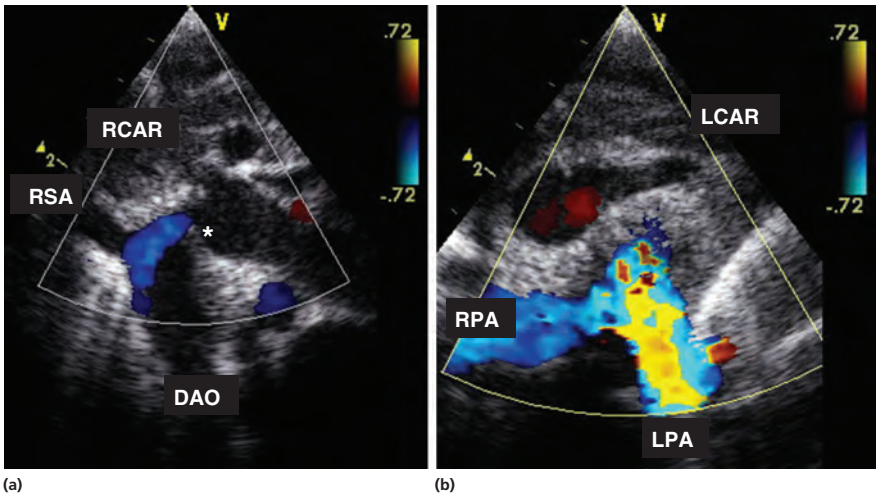


Figure 21.2 Unusual aortic coarctation in presence of right aortic arch with aberrant left subclavian artery. **(a)** Discrete narrowing (asterisk) seen between right carotid artery (RCAR) and right subclavian artery (RSA). **(b)** First non-bifurcating neck artery turning to the left suggested presence aberrant left subclavian artery. DAO, descendent aorta; LCAR, left carotid artery; LPA, left pulmonary artery; RPA, right pulmonary artery.

The site of maximal narrowing is determined by 2D imaging and color flow mapping and the diameter of the narrowest aortic segment is then measured on a 2D image. Using body surface area-adjusted normal values (see Appendix), the z-score of the narrowest arch segment is calculated. The arch is defined as hypoplastic if its diameter z-score is less than –2.0.

A protruding ridge is typically present at the site of COA but additional sites of obstruction can coexist due to the presence of another ridge, hypoplasia of the isthmus, or both. The ridge is directed from the lateral and posterior aspects of the isthmus towards the aortic end of the arterial duct (Figure 21.4). When assessing flow through the aortic isthmus, the suprasternal or right subclavicular windows usually provide an optimal angle for Doppler interrogation. The sample volume is placed at the site of maximum narrowing to avoid overlap with ductal flow. Flow across the isthmus is forward and continuous throughout the cardiac cycle, producing the characteristic appearance of a diastolic tail (Video 21.5). When the arterial duct is restrictive or closed and left ventricular systolic function is preserved, the blood pressure difference across the coarctation is high. The Doppler flow tracing shows a characteristic "serrated" pattern with rapid early acceleration and high-velocity systolic peak, followed by gradual deceleration throughout diastole

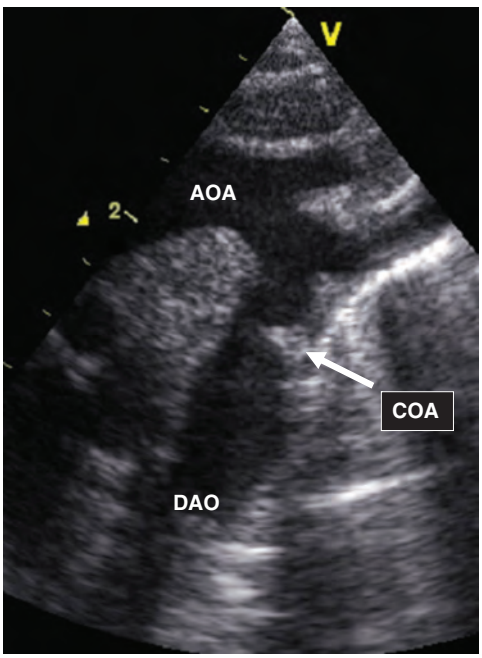


Figure 21.3 Imaging of neonatal COA from the suprasternal notch view. Coarctation ridge (COA) located ~5 mm below the origin of left subclavian artery. Descendent thoracic aorta (DAO) below obstruction is dilated. AOA, aortic arch.

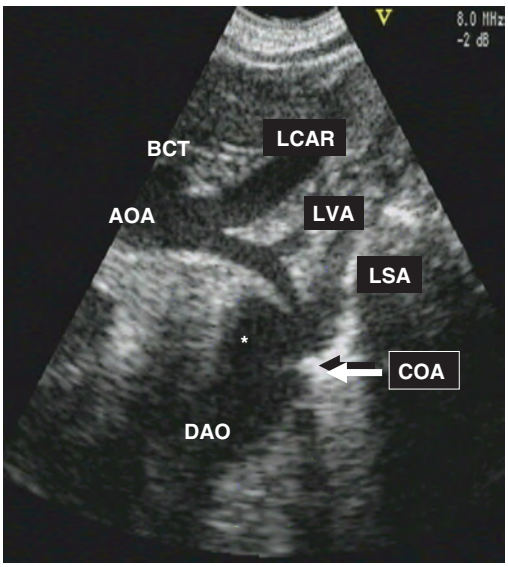


Figure 21.4 Neonatal coarctation (COA) with severe transverse aortic arch hypoplasia seen from the suprasternal view. Elongated, hypoplastic arch with maximal narrowing between the left carotid artery (LCAR), left vertebral artery (LVA), and left subclavian artery (LSA), which is predominantly supplied by arterial duct (asterisk). BCT, brachiocephalic trunk, DAO, descendent aorta.

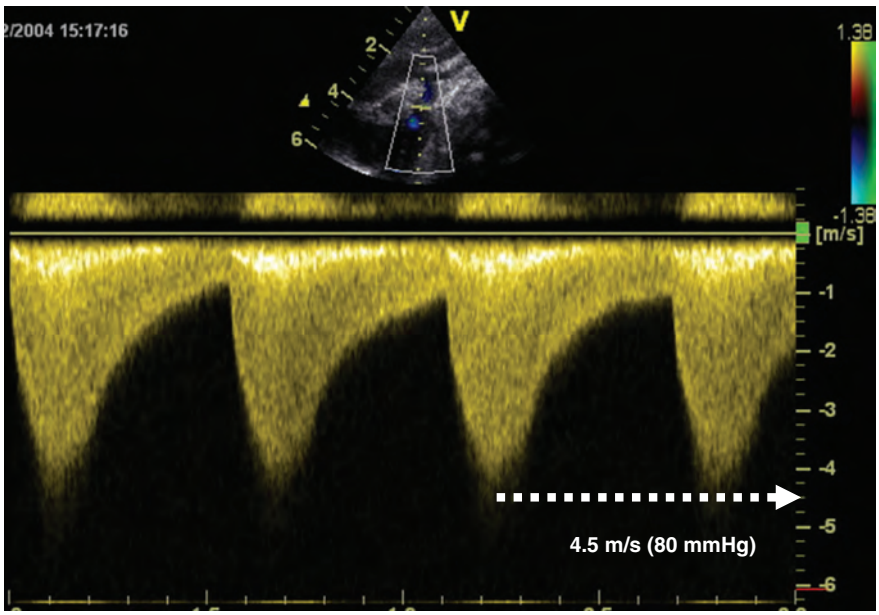


Figure 21.5 Continuous-wave Doppler through the aortic isthmus of a patient with severe COA. Note the high velocity systolic amplitude (4.5 m/s) with continuous antegrade flow throughout diastole.

(Figure 21.5). Evaluation of the severity of coarctation with preserved left ventricular systolic function is based on the peak and not the mean gradient because inclusion of the diastolic phase of the antegrade flow would not accurately reflect the systolic gradient. When multiple obstructions are present, usually in the context of associated aortic arch hypoplasia, the gradient measured by pulsed-wave (PW) Doppler proximal to the isthmus should be subtracted from the total coarctation gradient measured by continuous-wave (CW) Doppler (Figure 21.6).

Echocardiographic assessment in developing or mild COA may differ from the more severe forms (Figure 21.7). Instead of a typical coarctation ridge, 2D imaging demonstrates only mild isthmic narrowing. The Doppler signal in this situation shows only systolic acceleration rather than a typical "serrated" flow pattern.

Imaging of the arterial duct is performed from under the left clavicle, a position that provides an optimal angle for assessing ductal flow. When the COA is severe and pulmonary hypertension coexists, flow through the arterial duct is bidirectional – from the main pulmonary artery to the descending aorta during systole and from the aorta to the pulmonary artery during diastole (Figure 21.8; Videos 21.3 and 21.6). In patients without pulmonary hypertension flow is from the aorta to the main pulmonary artery throughout the cardiac cycle. The optimal position of the PW Doppler sample is in the middle of the arterial duct. Repeat echocardiographic examination should be

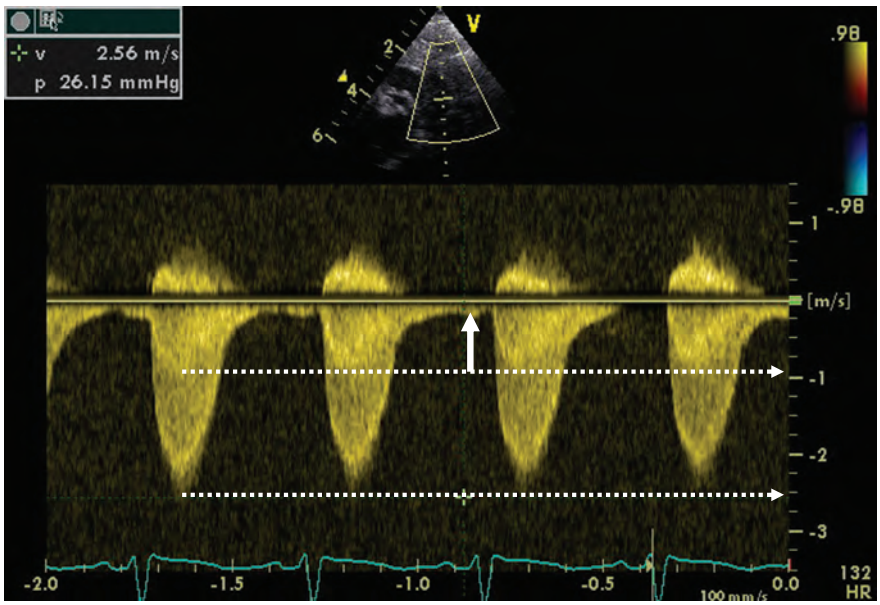


Figure 21.6 Flow characteristics in aortic isthmus in a neonatal coarctation. Summation of accelerated forward flow in systole across arterial duct (2.56 m/s) and lower velocity systolic flow (1 m/s) across aortic isthmus, and low velocity diastolic flow (arrow) with respiratory variation through the aortic isthmus as a result of reduction in diastolic blood pressure in the pulmonary artery.

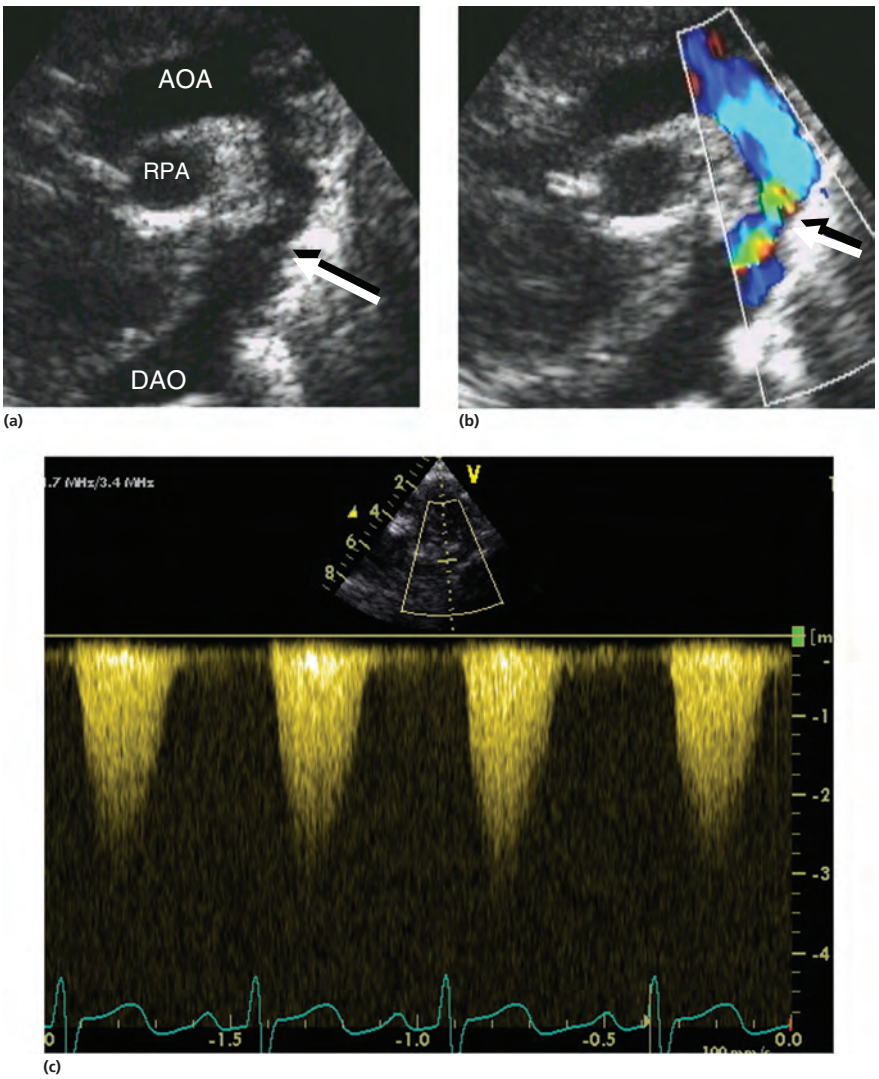


Figure 21.7 Evolving coarctation (arrows) in a 6-week-old infant. **(a)** 2D imaging; **(b)** color Doppler flow mapping; and **(c)** pulsed Doppler. Color aliasing indicates flow acceleration across mild isthmic narrowing in the absence of arterial duct. Pulsed Doppler technique indicated systolic acceleration (3 m/s) with no persistent diastolic flow. AOA, aortic arch; DAO, descendent aorta; RPA, right pulmonary artery.

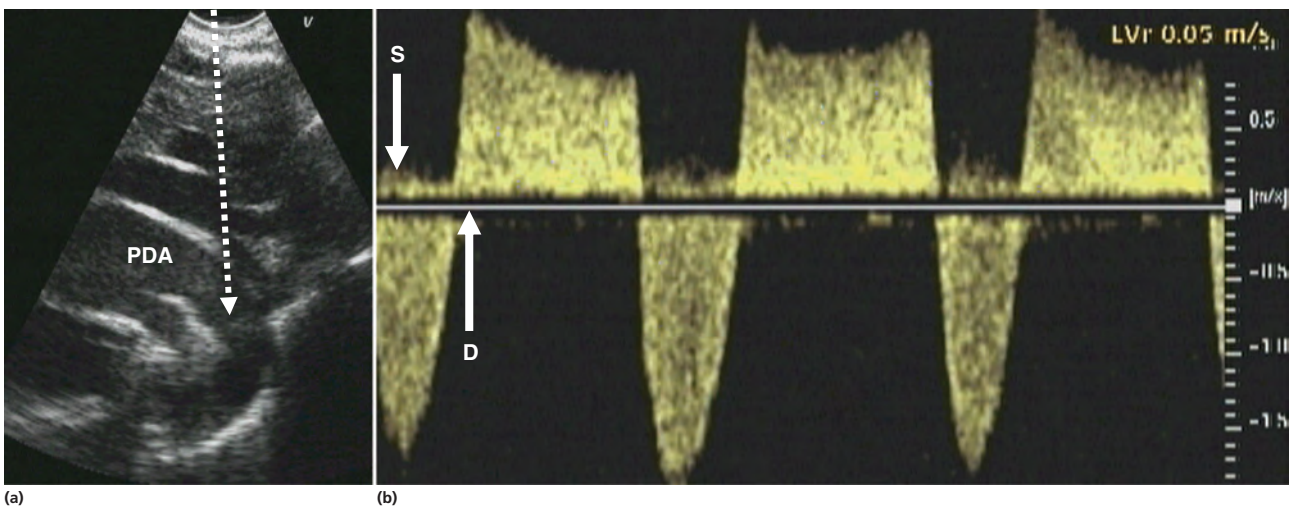


Figure 21.8 Ductal (PDA) flow patterns in severe neonatal coarctation. **(a)** The sample volume is placed in the middle of the arterial duct. **(b)** Bidirectional low-velocity flow with systolic right-to-left direction indicating high pulmonary arterial pressure. D, diastolic left-to-right flow; S, systolic right-to-left flow.

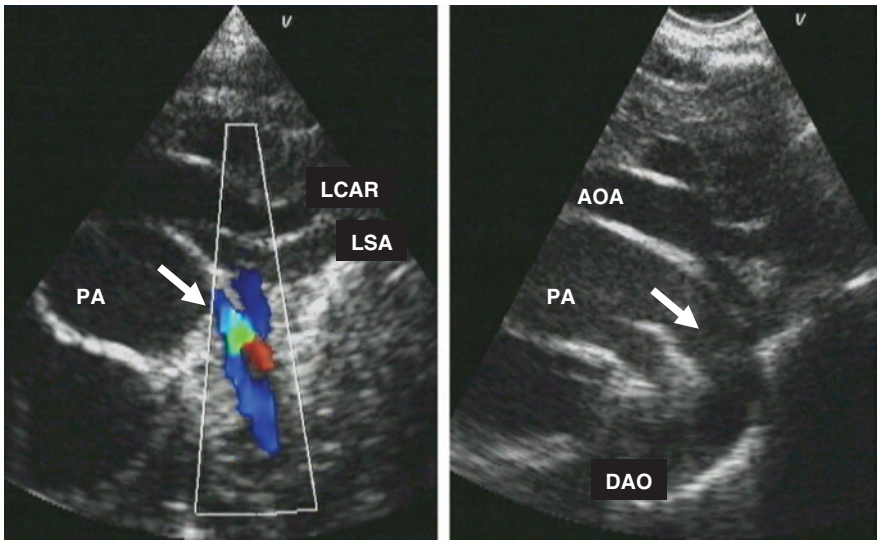


Figure 21.9 Serial echocardiograms in neonatal coarctation. **(a)** Restrictive arterial duct (arrow) demonstrated by color flow mapping prior to prostaglandin administration. **(b)** Significant ductal widening (arrow) after prostaglandin administration visualized by 2D imaging. AOA, aortic arch; DAO, descendent aorta; LCAR, left carotid artery; LSA, left subclavian artery; PA, pulmonary artery.

performed shortly after beginning prostaglandin administration to confirm ductal patency (Figure 21.9).

Subcostal views

Following determination of abdominal situs, cardiac position, and segmental evaluation of cardiac anatomy from the subcostal window, the characteristics of blood flow in the descending aorta at or below the level of the diaphragm are evaluated by PW Doppler. Care is taken to align the ultrasound beam with the long axis of the descending aorta. In neonates with severe COA, pulmonary hypertension, and patent arterial duct, the amplitude of the pulse wave is usually slightly decreased or normal and the diastolic component is absent or slightly reversed. This essentially normal flow profile results from unimpeded systolic flow from the right ventricle to the descending aorta through the arterial duct. The right ventricle thus generates the pulse wave, and when systolic function is preserved, normal velocity is demonstrated in the aorta below the diaphragm (~20–40 cm/s; no angle correction). In contrast, in neonates with severe COA and a closing or a closed arterial duct, the flow profile in the abdominal aorta is strikingly different; it typically exhibits low-velocity systolic–diastolic flow with minimal phasic variations (Figure 21.10). In addition to evaluation of the flow profile in the abdominal aorta, the entire aortic arch and the arterial duct can be viewed from the subcostal oblique sagittal plane (Video 21.7).

Imaging of the atrial septum from the subcostal long- and short-axis views almost always demonstrates a patent foramen ovale. The direction of shunt is depicted by color flow mapping and by PW Doppler in the foramen ovale. In neonates with severe pulmonary hypertension and elevated right atrial pressure, flow across the foramen ovale is bidirectional. In neonates with less severe pulmonary hypertension flow is predominantly left-to-right with velocity proportional to the pressure gradient

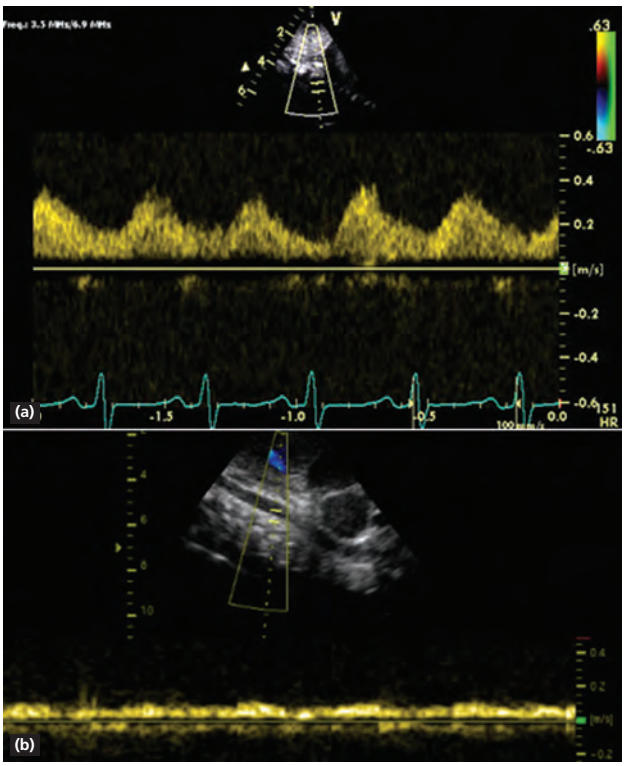


Figure 21.10 Pulsed Doppler flow pattern in abdominal aorta from subcostal sagittal view. **(a)** Coarctation with restrictive arterial duct and preserved systolic ventricular function in a 5-day-old neonate. Systolic waveform amplitude is low; antegrade diastolic flow indicates the obstruction proximal to sample volume. **(b)** Coarctation with closed arterial duct and impaired systolic ventricular function in 10-day-old neonate. The abdominal aorta flow velocity is very low over the cardiac cycle indicating extremely low lower body perfusion.

Table 21.1 Echocardiographic differences in neonatal (infant) coarctation of aorta with or without pulmonary hypertension.

		Left ventricle			PDA		
Neonatal COA	**PFO shunt**	**Volume**	**Wall**	**TR gradient**	**Dimension**	**Shunt**	**COA gradient**
With pulmonary hypertension	Bi-directional	Subnormal	Hypertrophy	>30 mmHg	Patent	Bi-directional (low velocity)	0–20 mmHg
Without pulmonary hypertension	Left-to-right	Enlarged	Hypertrophy and dilation	<30 mmHg	No (restrictive)	No Left-to-right (high-velocity)	30–70 mmHg (<30 mmHg with LV dysfunction)

Note: The indicated values of gradients are approximate.
COA, coarctation of aorta; PFO, persistent ovale foramen; TR, tricuspid regurgitation; PDA, persistent arterial duct.

between the atria. Finally, the subcostal approach also provides excellent imaging of the size and function of ventricles, the morphology and function of the AV valves, and the left and right ventricular outflow tracts.

Apical views

The apical 4-, 5- and 2-chamber views are important for assessment of left ventricular inflow and outflow, measurements of left ventricular volume and mass, and for determination of right ventricular systolic pressure by the tricuspid regurgitation jet velocity. The mitral annulus in isolated neonatal COA may be small; however, mitral valve function is usually normal. Color flow mapping and PW Doppler are used to evaluate the valve with particular attention to restriction of blood flow at the level of the annulus, leaflets, chordae tendineae, or at multiple levels (see Chapter 14 for further details). In an otherwise structurally normal mitral valve and nondilated left ventricle with preserved systolic function, significant mitral regurgitation is uncommon.

Evaluation of the left ventricular outflow from the apical window is particularly important due to the common association between COA and subvalvar and/or valvar aortic stenosis. Anterior apical 4-chamber and, in particular, apical long-axis views are used to evaluate the morphology and flow characteristics across the left ventricular outflow. Color flow mapping, PW, and CW Doppler are used to determine the presence and severity of obstruction and/or regurgitation (see Chapter 19 for further details).

Tricuspid regurgitation is often present due to annular dilation in neonates with severe pulmonary hypertension and a dilated right ventricle. Measurement of the peak tricuspid regurgitation jet velocity by Doppler provides an estimation of right ventricular systolic pressure.

Parasternal views

The parasternal long- and short-axis views are used to evaluate left ventricular size and function, mitral valve morphology and function, left ventricular outflow obstruction, aortic valve morphology, size, and mechanism of stenosis or regurgitation, tricuspid regurgitation, and right ventricular size and function. The right ventricular outflow tract, pulmonary valve, and pulmonary arteries are also evaluated from the precordial windows. Measurement of the pulmonary regurgitation end-diastolic flow velocity provides information on the pulmonary artery diastolic pressure.

Echocardiographic observations in neonates and infants with aortic coarctation, with and without pulmonary hypertension, are summarized in Table 21.1.

Adult coarctation

COA in older children and adults is caused by slow progression of the aortic ridge into the lumen of the aortic isthmus (Figure 21.11; Video 21.8). Presence of collateral arteries bypassing

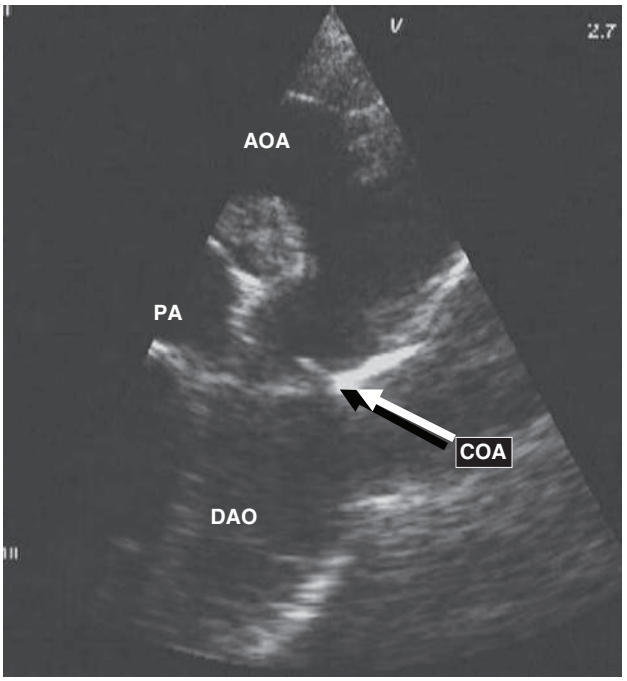


Figure 21.11 COA in a 12-year-old boy. Note the discrete shelf partly occluding the aortic isthmus (COA) and marked poststenotic dilation of thoracic aorta. AOA, aortic arch; DAO, descendent aorta; PA, pulmonary trunk.

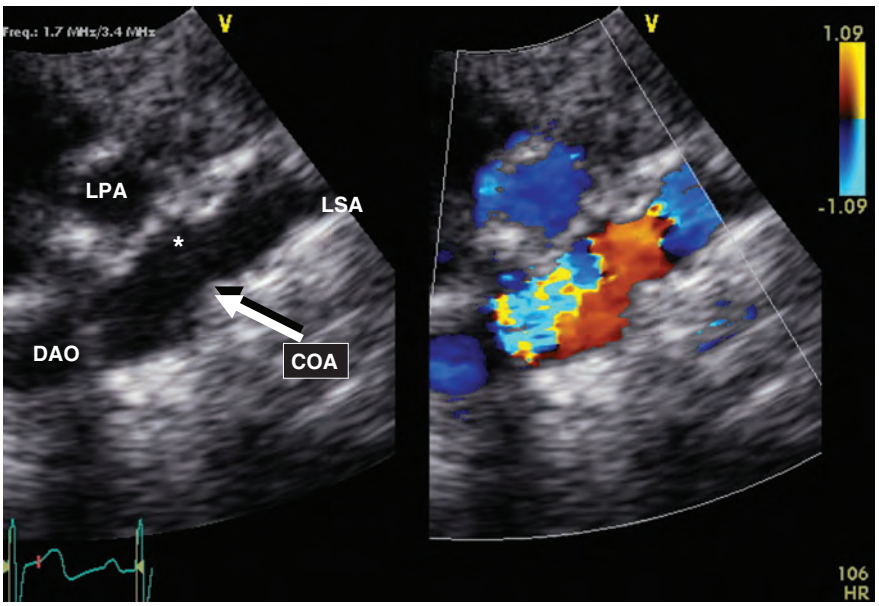


Figure 21.12 Left subclavicular approach in the sagittal plane showing mild isthmic narrowing (arrow) in 7-year-old child. **(a)** Coarctation shelf is opposite to aortic ampula of arterial duct (asterisk). **(b)** Flow acceleration across aortic isthmus seen by color Doppler flow mapping. DAO, descendent aorta; LPA, left pulmonary artery; LSA, left subclavian artery.

the COA is common. As mentioned earlier, suboptimal acoustic windows and a long distance from the transducer may hamper imaging of the distal aortic arch, isthmus, and proximal descending aorta. Adjustment of patient position (e.g., extension of the neck), use of a low-frequency transducer, and harmonic imaging are some of the tools that can aid in optimizing image quality. In addition, use of the left subclavicular window in the sagittal plane to visualize the aortic isthmus and the descending thoracic aorta is advised (Figure 21.12; Video 21.9). Placing the patient in the left lateral decubitus position aids in obtaining this view. Doppler assessment of COA severity is similar to that in the neonate (Figure 21.4). Optimal assessment of the velocity profile requires CW Doppler with a low-frequency filter to obtain a clear signal. As in neonatal COA, the gradient is estimated based on peak systolic velocity, not the mean gradient. When multiple obstructions of the aortic arch and isthmus coexist the contribution of each stenosis should be evaluated.

The abdominal aorta Doppler flow profile in adult COA is characterized by low-velocity systolic–diastolic flow, which can be visualized by PW Doppler and by color M-mode (Figure 21.13). When significant collateral vessels are present the difference between the amplitudes of the systolic and diastolic components of the flow curve is inversely proportional to the size of arterial collaterals. The entire thoracic as well as abdominal aorta should also be imaged to exclude distal coarctation, which can involve the origins of the celiac, mesenteric, and renal arteries (Figure 21.14; Video 21.10).

Similar to neonatal COA, comprehensive echocardiographic evaluation of cardiac anatomy and function is crucial in older children and adults due to the high frequency of associated anomalies. Bicommissural aortic valve and dilatation of the ascending aorta are common abnormalities in older children and adults with COA.

Prenatal assessment

COA diagnosed in the fetus is characterized by narrowing of the aortic isthmus and by a frequently associated transverse arch hypoplasia [5]. The main pulmonary artery communicates with the descending aorta through a widely patent arterial duct, creating a large ductal arch. Associated left heart obstructive lesions are also common.

Asymmetry of ventricular size (right ventricle larger than left ventricle) demonstrated in the 4-chamber view is frequently the first clue to prenatal diagnosis of COA (Figure 21.15; Video 21.11). The right ventricle is enlarged and tricuspid regurgitation is frequently detected. Right ventricular dilatation, however, is not specific for COA and is present in other forms of fetal cardiac and extracardiac anomalies. Ventricular function is usually normal and unlike other causes of right ventricular enlargement no other signs of fetal–placental circulatory failure are present. Despite progress in fetal echocardiography and heightened awareness, prenatal diagnosis of COA continues to be challenging. In a large nationwide epidemiologic study we confirmed that even in the current era, only 20% of patients with COA are diagnosed antenatally [13]. Head and colleagues found that in only one-third of patients suspected by fetal echocardiography to have COA was the diagnosis ultimately confirmed after birth [14].

Diagnosis of COA in the fetus requires detailed imaging of the aortic arch and isthmus and clear depiction of the aortic end of the arterial duct. The arch is visualized in the oblique sagittal plane either through the chest (Videos 21.12 and 21.13) or through the back of the fetus (Video 21.14). These views can depict the aorta along its entire length, including the root and ascending aorta, arch, origins of the brachiocephalic arteries, isthmus, and descending thoracic and abdominal aorta. The diameters of the aorta at different levels should be measured and

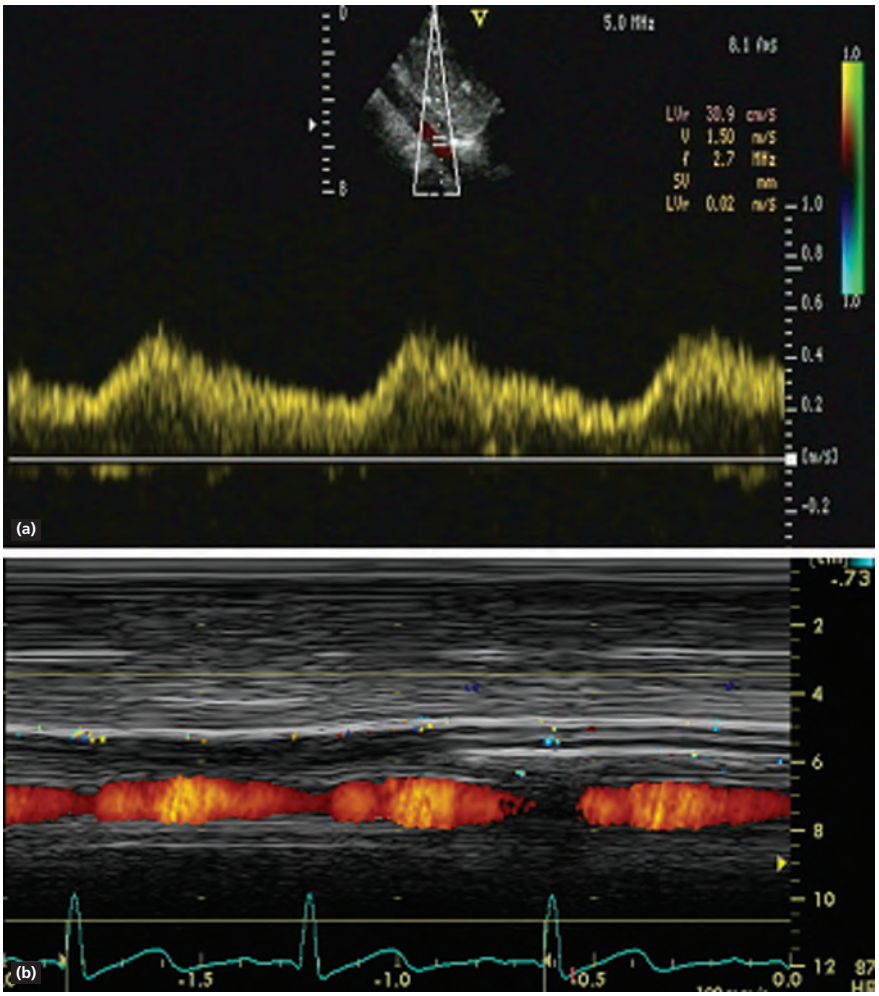


Figure 21.13 Flow profile in the abdominal aorta of a 6-year-old child with coarctation. **(a)** Pulsed-wave Doppler, and **(b)** color M-mode. Systolic velocity does not exceed 50 cm/s, and antegrade diastolic flow of 25 cm/s indicates proximal obstruction with presence of collaterals. Continuous, systolic–diastolic color flow Doppler superposed to 2D image in patient with COA and collaterals.

compared with gestational age-adjusted normal values [15,16]. The ascending aorta is often smaller than the main pulmonary artery. Reliable diagnosis of COA can be made when aortic arch hypoplasia is present (Figure 21.16; Video 21.15). Demonstration of hypoplasia and/or tortuosity of the aortic isthmus are paramount to the diagnosis of COA in the fetus (Figure 21.17). The width of the aortic isthmus is compared to the width of the aortic end of the arterial duct [15,17]. Color flow mapping can be useful in assessing the width of both segments. It is important, however, to use appropriate color gain and velocity scale (Nyquist limit) to avoid "bleeding" of the flow signal. With optimum settings, stenotic flow can be seen at the site of isthmus (Figure 21.18; Video 21.16), and color flow mapping can be used to assess the diameters of the isthmus and arterial duct.

Therapeutic interventions and long-term echocardiographic follow-up

Treatment options for correction of COA include surgery, percutaneous balloon angioplasty, and endovascular stent implantation. While surgery is the dominant treatment choice for native COA in neonates, balloon angioplasty and/or stent implantation are commonly used for treatment of recurrent or native COA in older children and adults [18,19]. The treatment of choice among surgical techniques for COA repair is resection and end-to-end anastomosis. When patent, the arterial duct is ligated and divided. In patients with aortic arch hypoplasia, the arch is augmented either by an extended anastomosis between the undersurface of the arch and the descending aorta or by reversed subclavian flap aortoplasty. Other, less commonly used, surgical techniques include subclavian flap aortoplasty, placement of a conduit bypassing the stenotic aortic segment, and patch plasty of the COA site. The latter technique has been associated with a high incidence of aneurysms at the repair site [20–22].

Echocardiographic evaluation after surgery or catheter-based treatment of COA is similar to that of native COA. Image quality is often hampered by postoperative changes and a larger body size, which restrict the acoustic windows available to image the distal arch, isthmus, and descending aorta. The importance of having detailed knowledge of the surgical or catheter procedure before the examination commences cannot be overemphasized. For example, following subclavian flap aortoplasty the proximal left subclavian artery is absent (Figure 21.18). After

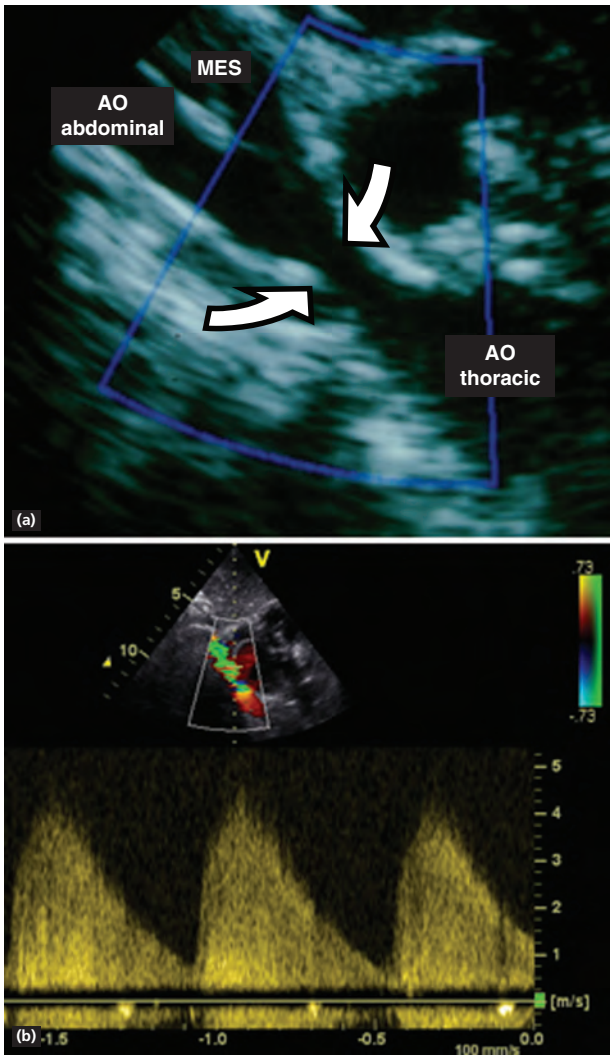


Figure 21.14 **(a)** Coarctation (arrows) of suprarenal abdominal aorta in subcostal sagittal view. Narrowing was localized just above the origin of the mesenteric artery (MES). **(b)** High-velocity (4.5 m/s) systolic–diastolic flow detected by continuous-wave Doppler. AO, aorta.

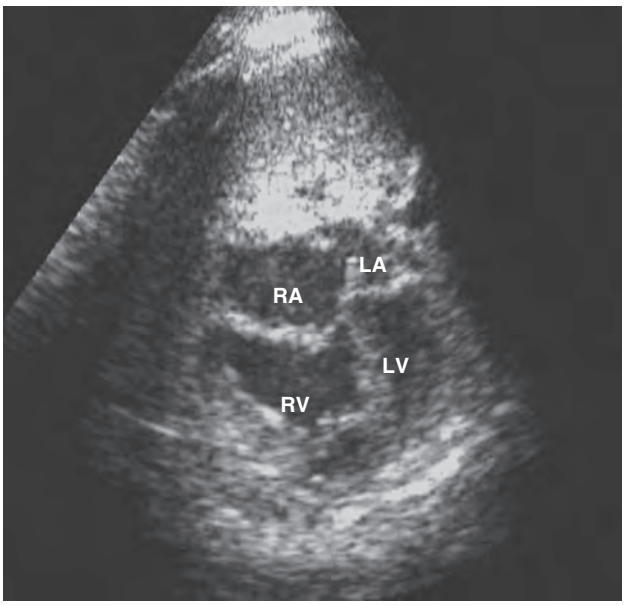


Figure 21.15 Ventricular size disproportion seen in this 4-chamber view in a 26-weeks' gestation fetus with COA. Right atrium (RA) and right ventricle (RV) are larger as compared with left atrium (LA) and left ventricle (LV). Left ventricle is not hypoplastic and forms the apex of the heart.

balloon dilatation of multilevel narrowing, restenosis between the brachiocephalic trunk and the left carotid artery, or between the left carotid and the left subclavian arteries can be seen. Visualization of a stent implanted in the aortic isthmus in adolescents and adults can be difficult due to artifacts produced by acoustic reflections from the stent but is often adequate in younger patients (Figure 21.19). Important potential complications after surgical or transcatheter treatment of COA that should be addressed by echocardiography include aneurysm formation and aortic dissection. Although difficult to image in detail in most patients, efforts should be made to evaluate vascular prostheses after extra-anatomic bypass (Figure 21.20). As with evaluation of native COA, comprehensive assessment of left ventricular inflow and outflow, mitral and aortic valve function, left ventricular size and function, diameters of the aortic root and ascending aorta is integral to echocardiographic follow-up after COA repair.

Although the relief of isthmic narrowing reduces the gradient across the aortic arch, associated arch shape irregularity such as Gothic geometry (Figure 21.21; Video 21.17) may result in systemic hypertension. This raises the concern about techniques used for primary repair to maintain adequate laminarity of the flow across the aortic arch in order to prevent or reduce the risk of systemic hypertension [23,24]. Other factors such as decreased compliance of the aortic wall and abnormal vascular reactivity may also contribute to systemic hypertension in these patients.

Interrupted aortic arch

Definition

Interruption of aortic arch (IAA) is a condition in which there is discontinuity between two adjacent segments of the aortic arch [25]. Aortic arch *interruption* should be distinguished from aortic arch *atresia* where there is anatomic continuity between the arch segments through a fibrous strand but the aortic lumen is completely obstructed. Because of their identical hemodynamic consequences, both conditions are discussed together in this chapter.

Incidence

In the New England Regional Infant Cardiac Program, the incidence of IAA was 19 per million live births or 1.3% of severe

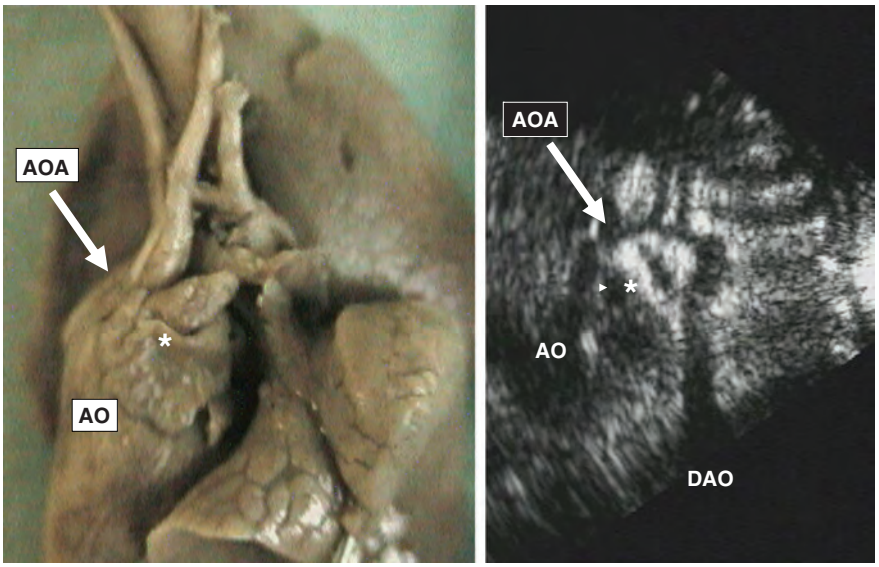


Figure 21.16 Fetal coarctation with hypoplastic aortic arch (AOA). **(a)** Postmortem; **(b)** prenatal echocardiogram. Hypoplastic transverse arch between left carotid and left subclavian artery (asterisks). AO, ascendent aorta; DAO, descendent aorta. Source: **(a)** Courtesy of Viera Povýšilová, Prague.

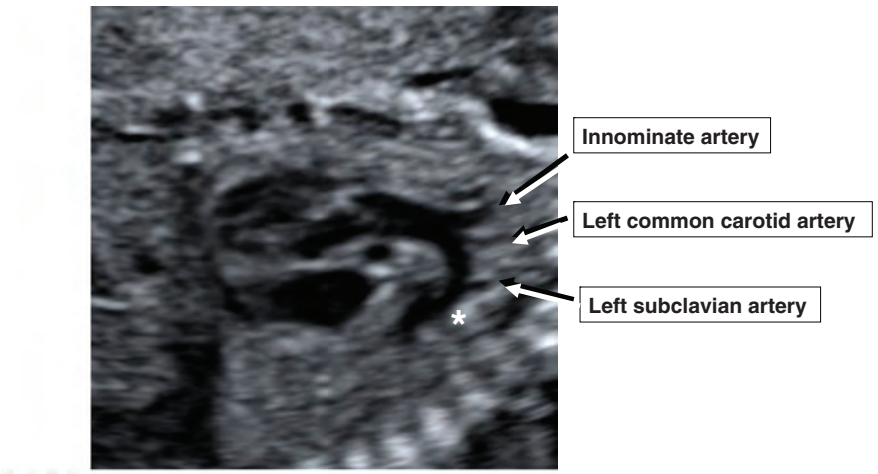


Figure 21.17 Isthmic narrowing in fetal coarctation (asterisk) as seen in fetal sagittal view. Origins of all three neck arteries are indicated, long segment transverse arch between left common carotid artery and left subclavian artery supports prenatal diagnosis of aortic coarctation (see in the text).

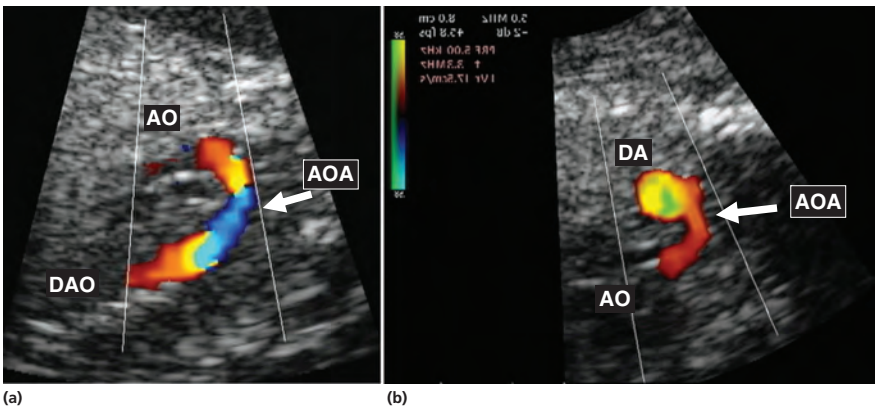


Figure 21.18 Flow acceleration across a narrow aortic isthmus (arrow) in a 33-weeks' gestation fetus with COA. **(a)** Color Doppler flow mapping shows aliasing with a Nyquist limit of 70 cm/s. **(b)** Hypoplastic aortic arch seen in the sagittal plane with the spine towards the transducer. Note the difference in size between the hypoplastic aortic arch (AOA) and the wide arterial duct (DA). AO, proximal aorta; DAO, distal aorta.

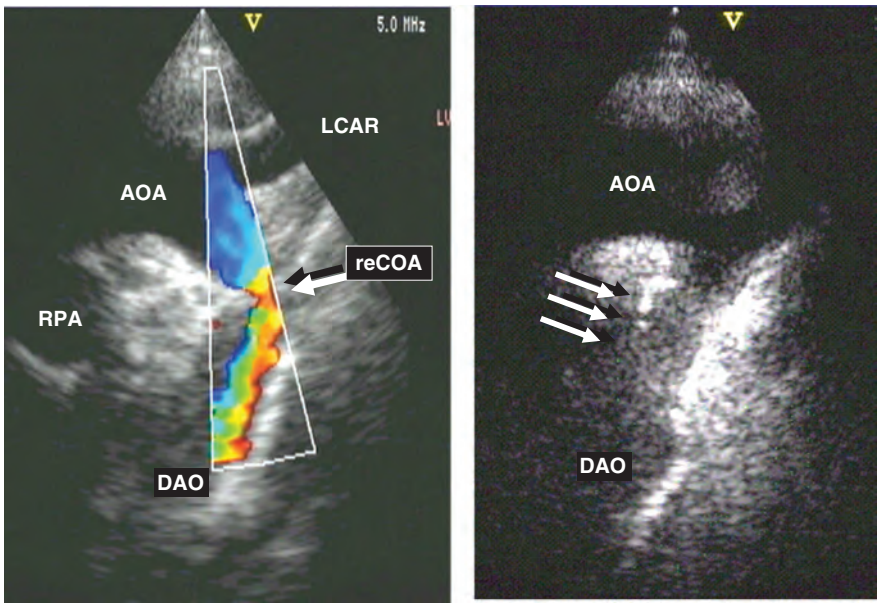


Figure 21.19 Recurrent coarctation of aorta (reCOA) in a patient after left subclavian flap aortoplasty (Waldhausen procedure). **(a)** Narrowing with flow acceleration seen by color Doppler flow mapping at the level of origin of the left subclavian artery, which was used to extend tubular aortic narrowing. **(b)** Stent implantation at the level of residual narrowing in a patient with recurrent coarctation (arrows). AOA, aortic arch; DAO, descendent aorta; LCAR, left carotid artery.

congenital heart disease [26]. In the Pediatric Cardiac Care Consortium, a registry of congenital heart disease from 35 centers, the incidence of IAA in the first year of life was 262 of 9154 (2.9%) [27]. Isolated IAA is rare and patency of the arterial duct and presence of VSD are common. In the National Fetal Heart Screening Program of the Czech Republic (1986–2006), IAA accounted for 0.8% of all 1604 heart lesions detected in utero [13].

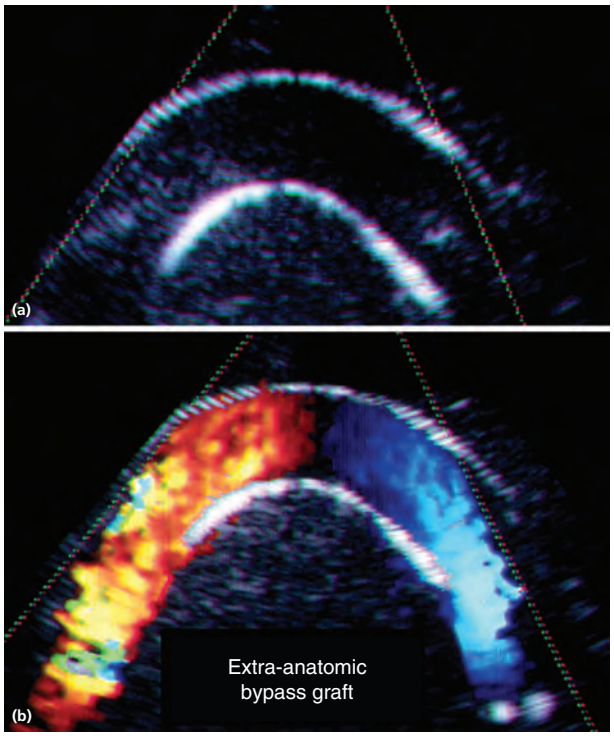


Figure 21.20 **(a)** Imaging of a Gore-Tex tube graft used to bypass tubular aortic arch hypoplasia from the left infraclavicular region. **(b)** Color Doppler flow mapping demonstrates laminar flow from ascending to descending aorta.

Etiology

The etiology of IAA remains incompletely understood. Based primarily on morphologic observations, several investigators proposed that interruption, atresia, or hypoplasia of the aortic arch are secondary to reduced flow in the ascending aorta during fetal life [28,29]. A growing body of evidence suggests an important role for genetic anomalies, including chromosome 22q11 microdeletion, DiGeorge syndrome, velocardiofacial (Shprintzen) syndrome, conotruncal face anomaly syndrome, and several other syndromes [28–31]. A particularly strong association between chromosome 22q11 microdeletion and type B IAA has been reported [32]. In mouse embryos deficient for *Gbx2* gene, aberrant cardiac neural crest cell patterning and defects in pharyngeal arch-derived structures are seen with abnormal development of the fourth pharyngeal arch arteries, including type B IAA, right aortic arch, and retroesophageal right subclavian artery [32]. In mice, conditional inactivation of GATA-6 – a transcription factor regulating morphogenetic patterning of the cardiac outflow tract and aortic arch – has resulted in perinatal mortality from a spectrum of cardiovascular defects, including IAA and truncus arteriosus [33]. Recent research has implicated β1 integrin in the development of aortic arch abnormalities. Mice deficient in β1 integrin developed ascending aorta, arch and carotid artery abnormalities [34].

Morphology and classification

Celoria and Patton classified IAA according to the site of interruption in relation to the arch branches [35].

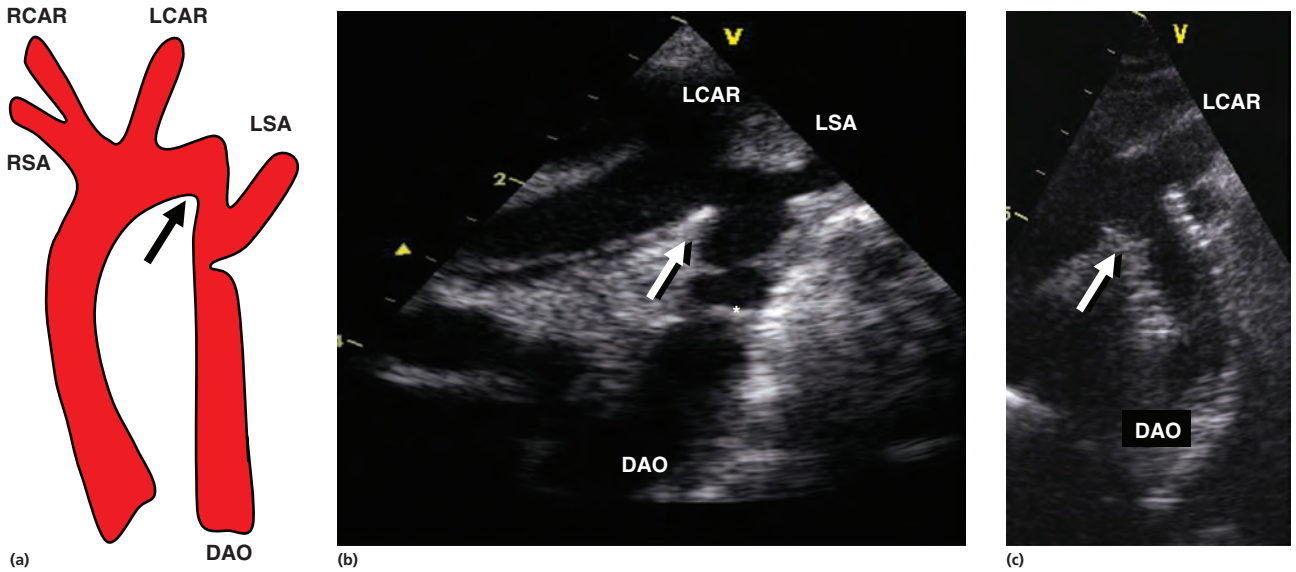


Figure 21.21 **(a)** Schematic drawing of angulated Gothic arch (arrow) in association with coarctation. **(b)** Corresponding 2D echocardiogram as seen from the suprasternal view. Note the sharp convexity (arrow) of the aortic arch causing the flow turbulence. **(c)** "Gothic" arch appearance (arrow) in stented arch narrowing following primary coarctation repair by reversal subclavian flap. DAO, descendent thoracic aorta; LCAR, left carotid artery; LSA, left subclavian artery; RCAR, right carotid artery; RSA, right subclavian artery.

Type A

Type A IAA involves interruption distal to the origin of the left subclavian artery (Figure 21.22). This type accounts for 30–37% of cases. The arterial duct supplies the lower body and the ascending aorta supplies the upper body. From the standpoint of morphogenesis, type A IAA can be explained by involution of both dorsal aortae distal to the fourth arches and proximal to the persistent sixth aortic arch on the same side of the interruption. The anatomy is essentially identical to extreme coarctation and differs only in the absence of luminal continuity of the aortic isthmus (called *aortic isthmus atresia*). The atretic segment may be very short or, in case of a longer isthmus, the distance between both stumps can be several millimeters long. Aberrant origin of the right subclavian artery from the descending aorta occurs in ~5% of patients.

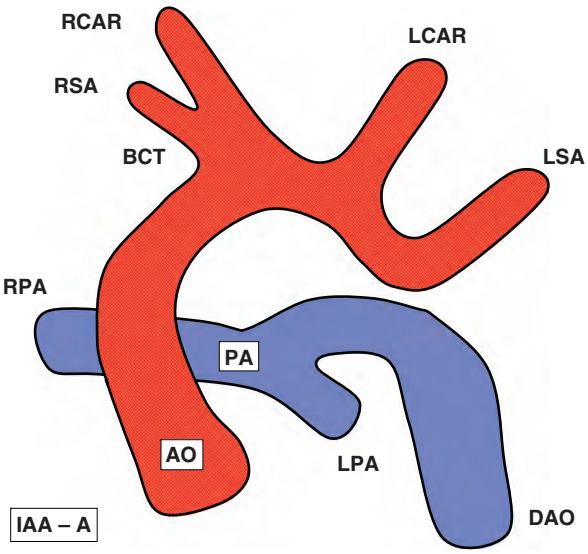


Figure 21.22 Type A interrupted aortic arch distal to the left subclavian artery (LSA). The descendent aorta (DAO) is supplied via the arterial duct (arrow). The proximal aorta (AO) gives rise to all brachiocephalic arteries. BCT, brachiocephalic trunk; LCAR, left carotid artery; LPA, left pulmonary artery; PA, pulmonary trunk; RCAR, right carotid artery; RPA, right pulmonary artery; RSA, right subclavian artery.

Type B

Type B IAA is defined by interruption between the left common carotid and left subclavian arteries (Figure 21.23). This type accounts for 62–70% of cases. The arterial duct supplies the left subclavian artery and the lower body. In ~50% of cases the right subclavian artery arises aberrantly from the descending aorta distal to the interruption (Figure 21.24). In these cases, the ascending aorta supplies only the head vessels. Type B IAA is likely due to involution or absence of the fourth aortic arch and of the dorsal aorta on the opposite side of the interruption. In cases with type B IAA and aberrant origin of the right subclavian artery, the morphology may be explained by involution of both fourth arches and the sixth arch on the side opposite to the interruption. The interruption is almost always complete and fibrous continuity between the arch segments is rare. The distance between the interrupted arch segments varies and may exceed 10 mm.

In type B IAA, the VSD is considered an integral part of the anomaly with an incidence of 94–100% [27,36]. It is described as a conoventricular defect with posterior malalignment of the

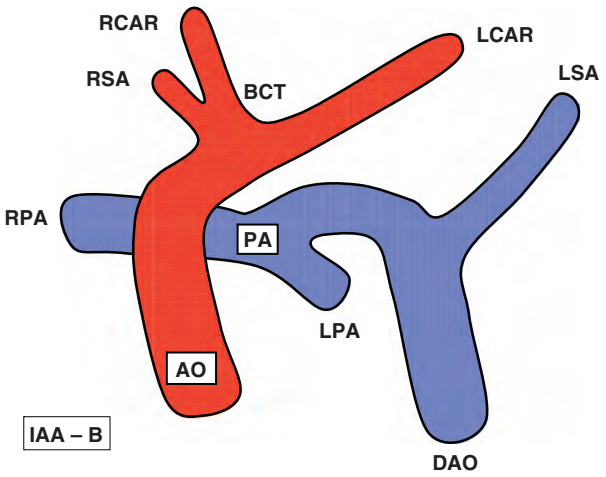


Figure 21.23 Type B interrupted aortic arch between the left carotid (LCAR) and left subclavian arteries (LSA). The descendent aorta (DAO) and left subclavian artery are supplied via arterial duct (arrow), brachiocephalic trunk (BCT), and left carotid artery (LCAR) supplied from the proximal aorta (AO). LPA, left pulmonary artery; PA, pulmonary trunk; RCAR, right carotid artery; RPA, right pulmonary artery; RSA, right subclavian artery.

conal (infundibular) septum. The term *conoventricular VSD* refers to its location between the conal septum superiorly and the Y of septal band inferiorly [37]. The designation *posterior malalignment* refers to the posterior, inferior, and leftward deviation of the conal (infundibular, outlet) septum towards the left ventricular outflow tract. When viewed from the right ventricular aspect, the space between the superior and inferior limbs of the cranial termination of septal band, normally filled by the conal septum, is wide open. This leads to the subpulmonary location of the VSD when viewed from the right ventricle. When viewed from the left ventricle, the conal septum can be seen protruding into the subaortic area. The conal septum in type B IAA is often hypoplastic and short. The posterior, inferior, and leftward malalignment of the conal septum into the left ventricular outflow tract leads to varying degrees of subaortic stenosis above the VSD [36]. Other anatomical variables that may contribute to subaortic stenosis in type B IAA include diffuse hypoplasia of the left ventricular outflow tract, an accessory anterolateral papillary muscle of Moulaert [38], and a discrete subaortic ridge or "membrane." The aortic valve annulus is often hypoplastic. Bi- or unicommissural aortic valves with varying degrees of hypoplasia and/or stenosis have been reported in IAA [36,39].

Type C

Type C IAA is defined as an interruption between the right and left common carotid arteries (Figure 21.25). The arterial duct supplies the left common carotid artery, left subclavian artery, and the descending aorta. This type accounts for 1% or less of cases [40,41].

IAA also occurs with other types of conotruncal anomalies, most commonly truncus arteriosus. In a series of 472 patients with IAA, 50 (11%) had truncus arteriosus [42]. The interruption was between the left common carotid and left subclavian arteries (type B) in 84% of the cases. IAA is also associated with other lesions such as aorto-pulmonary window [43], interrupted right aortic arch [44,45], interrupted cervical arch [46], and others.

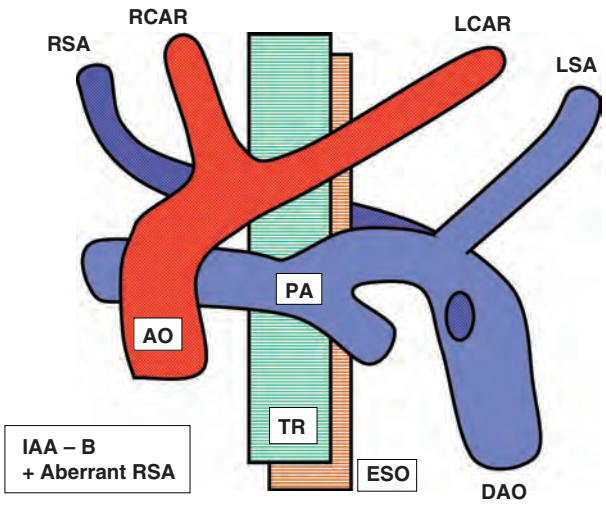


Figure 21.24 Type B interrupted aortic arch with aberrant right subclavian artery. Interruption between the left carotid arteries (LCAR) and the left subclavian artery (LSA). The descending aorta (DAO), left subclavian artery (LSA) as well as the aberrant right subclavian artery (RSA) are supplied via arterial duct (arrow); the aberrant subclavian artery courses behind the trachea (TR) and esophagus (ESO). The proximal aorta gives rise only to both carotid arteries. PA, pulmonary trunk.

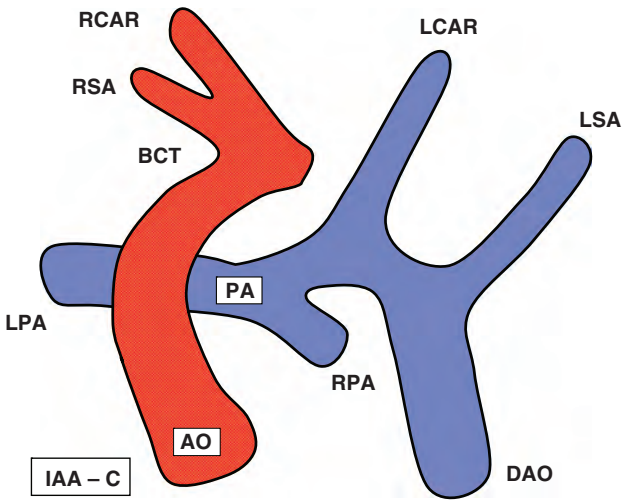


Figure 21.25 Type C interrupted aortic arch between the brachiocephalic trunk (BCT) and the left carotid artery (LCAR). The descending aorta (DAO), left carotid artery (LCAR) and left subclavian artery (LSA) are supplied by arterial duct (arrow). The proximal aorta (AO) supplies only the right subclavian (RSA) and carotid artery (RCAR). LPA, left pulmonary artery; PA, pulmonary trunk; RPA, right pulmonary artery.

Pathophysiology

Survival of newborns with IAA depends on a patent arterial duct. Spontaneous closure of the arterial duct leads to diminished perfusion of the systemic vascular bed distal to the interruption. Prompt initiation of prostaglandin infusion is lifesaving. The pathophysiology is identical to critical COA with pulmonary hypertension. In many patients, clinical deterioration with acute cardiovascular collapse progresses rapidly as the arterial duct closes and perfusion of major vascular beds rapidly decreases. Less commonly, patients with persistent arterial duct may present weeks or even months after birth with congestive heart failure, pulmonary overcirculation, and failure to grow. Without treatment, nearly 75% of patients die within the first month and almost 90% by the first year.

Imaging

Echocardiography allows comprehensive evaluation of the anatomy and hemodynamic manifestations of IAA and provides the information necessary for surgical planning in almost all patients [47–49]. Detailed description of the aortic arch, site of interruption, location of origins of brachiocephalic branches, distance between the interrupted aortic arch segments, status of the arterial duct, anatomy of the VSD, left ventricular outflow, aortic valve, and associated anomalies are important for planning surgical repair. The goals and imaging strategy of echocardiography in IAA are identical to those in COA (see earlier). Because of the frequent association between type B IAA and hypoplasia or agenesis of the thymus, particular attention is given to its presence and size [50]. The thymus is best seen from the subclavicular or suprasternal notch views as solid tissue. Its absence or markedly reduced size increases the likelihood of chromosome 22q11 microdeletion.

The aortic arch, brachiocephalic vessels, and arterial duct are imaged in the same way as in neonatal COA. Meticulous continuous sweeps of the transducer in the transverse plane (index mark points to the patient's left) demonstrate the ascending aorta in cross-section. From this view, the size of the ascending aorta (usually small) relative to the main pulmonary artery is determined. Further cranial angulations of the transducer demonstrate the origin of the first branch off the aortic arch (Figure 21.26). This branch is then followed towards the neck to determine its identity – right innominate artery or right common carotid artery. The caliber of the right innominate artery is approximately twice that of the left common carotid artery and it bifurcates into a right subclavian and right common carotid arteries. The latter has the same caliber as the left common carotid artery and can be followed to the neck without bifurcation (Figure 21.27). The site of interruption is then determined as the arch ends with the brachiocephalic artery proximal to the interruption – distal to the left subclavian artery in type A (Figure 21.28; Videos 21.18 and 21.19), distal to the left common carotid artery in type B (Figure 21.29; Videos 21.20 and 21.21) [51], and distal to the right common carotid artery in type C. The distance between the interrupted arch segments is measured at the origins of the corresponding brachiocephalic arteries (Figures 21.29 and 21.30).

The arterial duct is imaged similar to neonatal COA. In IAA, the arterial duct forms an arch that should not be confused with the aortic arch (Video 21.21). Careful imaging of the pulmonary origin and aortic termination confirms the anatomic identity of the arterial duct (Figure 21.30; Video 21.22). Color flow mapping and PW Doppler are used to determine the direction of flow through the duct (Figure 21.31; Video 21.21). Increased velocity of the right-to-left flow jet indicates restriction of the arterial duct.

The VSD in IAA is evaluated from the subcostal (Figure 21.32; Videos 21.23 and 21.24), apical, and parasternal windows. The posteriorly deviated infundibular septum can be seen in these views as a short ridge protruding into the left ventricular outflow tract immediately below a hypoplastic aortic valve, leaving no infundibular septal tissue below the pulmonary valve. From an anteriorly angled apical view (5-chamber view), color flow mapping demonstrates preferential flow from the left

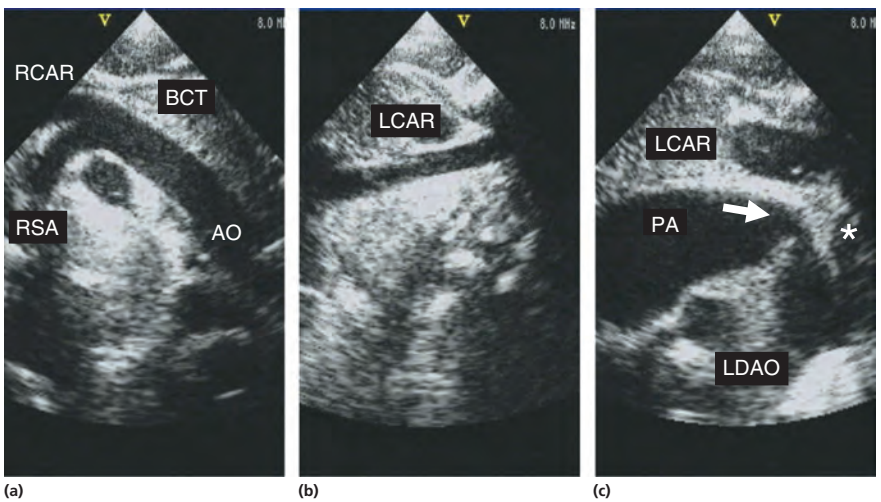


Figure 21.26 Serial views to visualize aortic arch anatomy in a neonate with type B interrupted aortic arch. **(a)** Sagittal view oriented towards the right shoulder (transducer marker at 4–5 PM) demonstrates the brachiocephalic trunk (BCT) with normal branching patterns. **(b)** Sagittal view oriented towards the left shoulder (transducer marker at 1–2 PM) shows only the left carotid artery (LCAR) with absent connection to the distal aorta. **(c)** Ductal view showing the distal aorta (LDAO) together with the left subclavian artery (asterisk) connected to the pulmonary trunk (PA) via restrictive arterial duct (arrow). AO, proximal aorta; RCAR, right carotid artery; RSA, right subclavian artery

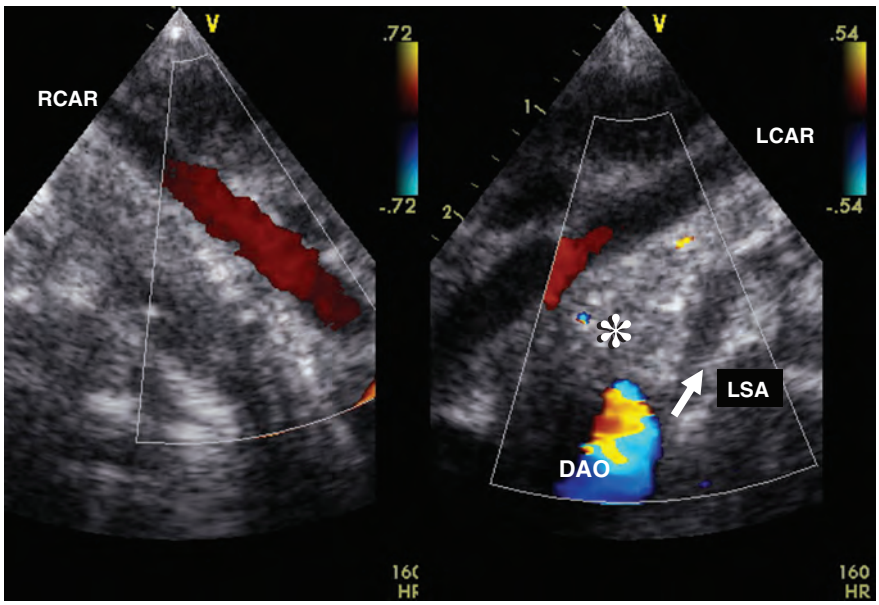


Figure 21.27 Serial views in a neonate with type B interrupted aortic arch and aberrant right subclavian artery. **(a)** Rightward orientation of the transducer shows the proximal aorta gives rise to the right common carotid artery. **(b)** The left common carotid artery. Note the long-segment interruption (asterisk). Both subclavian arteries connected to the distal aorta (DAO) are supplied by arterial duct. The image shows only the left subclavian artery (LSA); the aberrant right subclavian artery is not documented here.

ventricle to the right ventricle (Figure 21.33; Video 21.25). The flow velocity across the left ventricular outflow is usually not significantly accelerated despite the often narrowed subaortic region and the hypoplastic aortic valve. The reasons include decreased flow rate across the left ventricular outflow tract due to perfusion of only the head or the head and right arm (depending on IAA location and origin of the right subclavian artery) and due to ventricular dysfunction. The parasternal long-axis view is particularly helpful for depiction of the VSD and the left ventricular outflow (Figure 21.34; Videos 21.26 and 21.27). The width of the left ventricular outflow and the aortic valve annulus are measured in this view. The preoperatively measured cross-sectional area of the left ventricular outflow tract has been shown to be smaller in neonates with IAA who develop subaortic obstruction postoperatively, with a left ventricular outflow tract (LVOT) area of ≤ 0.7 cm^2/m^2 being a sensitive predictor [52]. A ratio of LVOT diameter to descending aorta diameter at the level of the diaphragm of ≤ 1.0 is a determinant of infundibular resection to prevent postoperative subaortic stenosis (ratio in normal infants 1.3 ± 0.14) [53]. Real-time 3D echocardiography allows visualization of left ventricular outflow obstruction (Figure 21.35; Videos 21.28, 21.29 and 21.30). This en face view can be useful when considering relief of obstruction either at the time of primary repair or before reoperation. Similar views can be obtained using a transesophageal approach [54]. Detailed imaging of the aortic valve from the parasternal short-axis view demonstrates its morphology (Video 21.31).

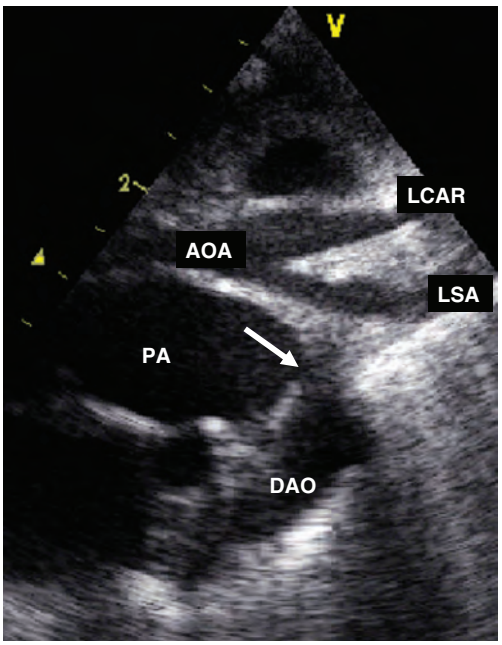


Figure 21.28 Type A interrupted left aortic arch distal to the left subclavian artery (LSA). The descendent aorta (DAO) is supplied via arterial duct (arrow). AOA, aortic arch; LCAR, left carotid artery; LSA, left subclavian artery; PA, pulmonary trunk.

Prenatal assessment

IAA does not usually adversely affect fetal physiology because the arterial duct bypasses the interruption. Prenatal echocardiographic examination of suspected IAA is conducted in the same way as in suspected COA (see afore-mentioned details). Similar to COA, however, prenatal diagnosis of IAA remains challenging (Figure 21.36). When imaging in the sagittal plane of the fetus, it is important to distinguish between the ductal arch and the aortic arch, especially when the latter is interrupted (Figures 21.37 and 21.38; Videos 21.32 and 21.33). However, careful imaging of the aorta in the oblique sagittal and transverse planes can demonstrate the relevant anatomy. Presence of a typical posterior malalignment VSD is an important clue to the

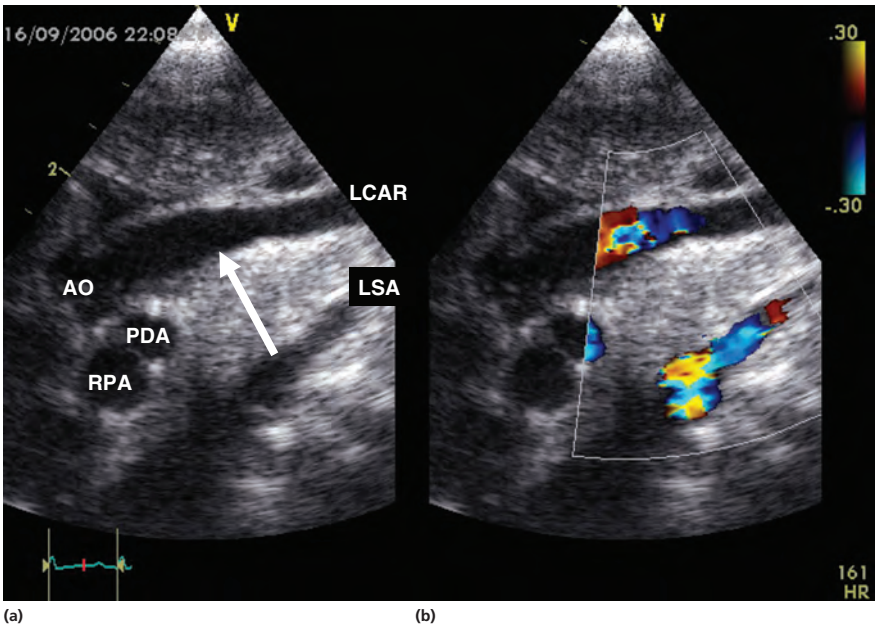


Figure 21.29 Type B interrupted aortic arch. **(a)** 2D imaging from a leftward-oriented high right parasternal view. **(b)** Color Doppler flow indicates the flow within the left carotid (LCAR) and left subclavian arteries (LSA). Note the long-segment discontinuity (arrow) between the left carotid and left subclavian arteries (LSA). PDA, arterial duct; RPA, right pulmonary artery.

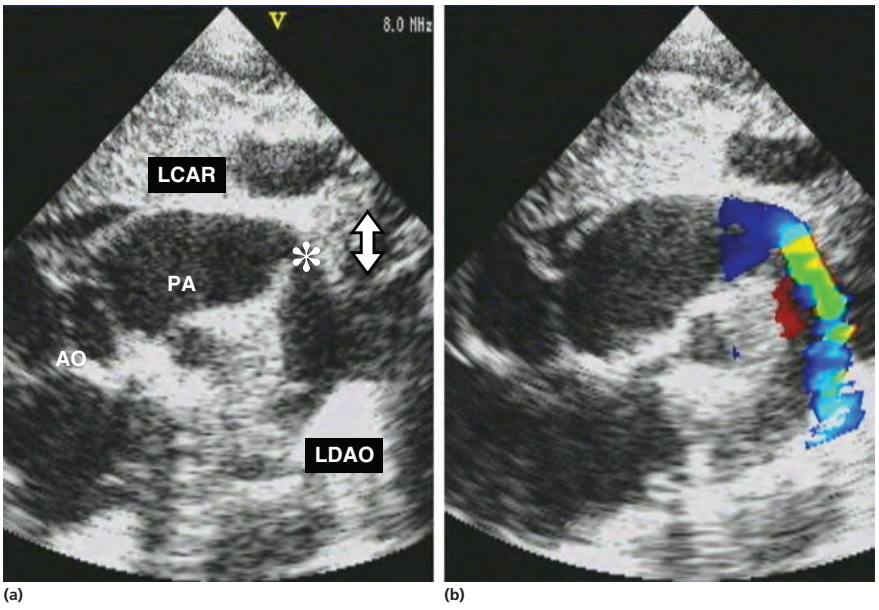


Figure 21.30 Imaging of type B interrupted aortic arch from the suprasternal window. The proximal aorta gives rise to the brachiocephalic trunk and left carotid artery (LCAR); the left distal aorta (LDAO) is supplied from the pulmonary trunk (PA) via restrictive arterial duct (asterisk). The short distance between the left carotid artery and distal aorta suggests a possible direct end-to-side anastomosis (arrows). AO, proximal aorta.

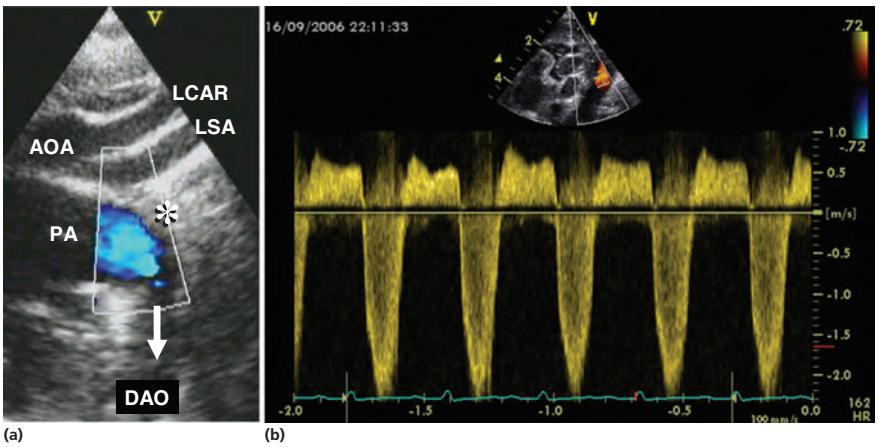


Figure 21.31 Type A interrupted aortic arch. **(a)** Absent connection between the distal arch past the left subclavian artery (LSA, asterisk) and descending aorta (DAO). Color flow mapping indicates a laminar right-to-left flow across the arterial duct (arrow). **(b)** Pulsed-wave Doppler tracing in the arterial duct shows a right-to-left shunt with peak velocity 2.3 m/s and diastolic left-to-right shunt. AOA, aortic arch; LCAR, left carotid artery; PA, pulmonary trunk.

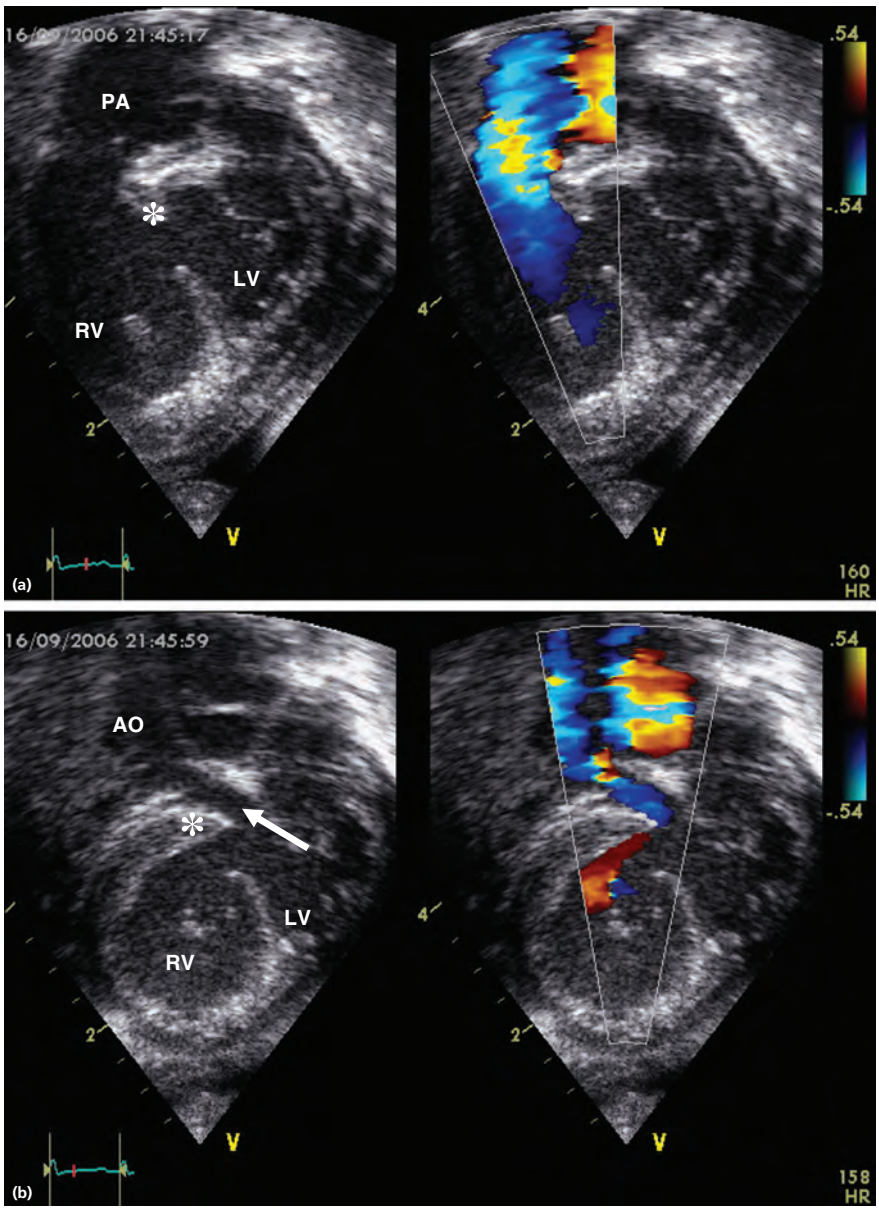


Figure 21.32 Subcostal views of the right ventricular outflow **(a)** and the left ventricular outflow **(b)** in a neonate with interrupted aortic arch. Unrestrictive conoventricular septal defect has muscular margins; infundibular septum (asterisk) is deviated posterior causing left ventricular outflow obstruction (arrow). AO, aorta; LV, left ventricle; PA, pulmonary trunk; RV, right ventricle.

diagnosis of IAA (Video 21.34). Color flow mapping with the Nyquist limit at 60–100 cm/s without filtering low velocities displays the bidirectional flow through the VSD. The defect is usually larger than the diameter of the aortic annulus. Unlike COA, however, the 4-chamber view is often normal because the large VSD allows free communication between the ventricles. Imaging in the sagittal plane can show the VSD and the size discrepancy between the smaller ascending aorta and the larger main pulmonary artery.

Therapeutic interventions and long-term echocardiographic follow-up

Surgery is the only treatment available for patients with IAA and primary corrective surgery in the neonatal period is the preferred approach [27,42,55,56]. In most cases, primary anastomosis between the interrupted segments is possible after resection of ductal tissue and extensive mobilization of the arch and descending aorta. When the gap between the interrupted aortic segments cannot be fully brought together, autologous pericardium or a prosthetic graft is used. However, every attempt is made to achieve connection between the proximal and distal segments through native tissue [57,58].

The goals and technique of the echocardiographic examination after IAA repair are identical to those after COA repair. The risk of postoperative left ventricular outflow obstruction is high after type B IAA repair but it is also an important consideration after COA repair (Figure 21.39; Video 21.35). Detailed imaging of the reconstructed aortic arch can be hampered

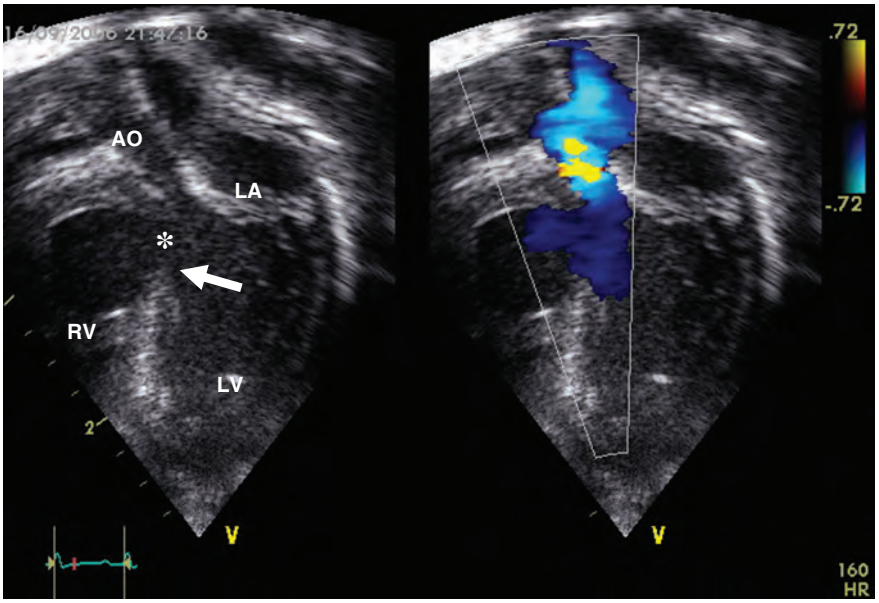


Figure 21.33 Apical 5-chamber view ((**a**) 2D imaging and **(b)** color Doppler) in a neonatal interrupted aortic arch demonstrating a large ventricular septal defect with unrestrictive left-to-right flow (arrow), posterior deviation of infundibular septum (asterisk), and narrow left ventricular outflow tract. AO, ascending aorta; LA, left atrium; LV, left ventricle; RV, right ventricle.

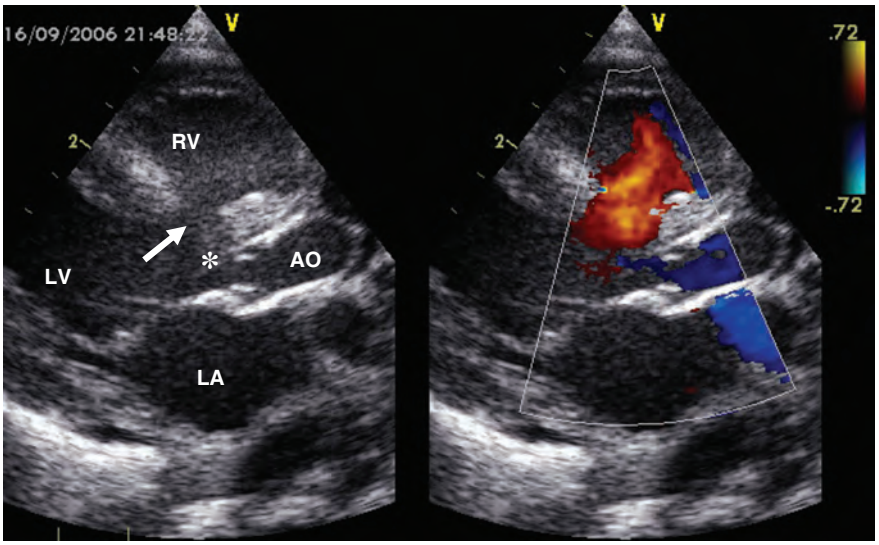


Figure 21.34 **(a)** Parasternal long-axis view in a neonatal interrupted aortic arch showing a large conoventricular septal defect (arrow) with unrestrictive left-to-right shunt seen by color Doppler flow mapping. **(b)** The asterisk indicates posterior deviation of the infundibular septum. Incomplete opening of the aortic valve is consistent with a bicuspid aortic valve. AO, aorta; LA, left atrium; LV, left ventricle; RV, right ventricle.

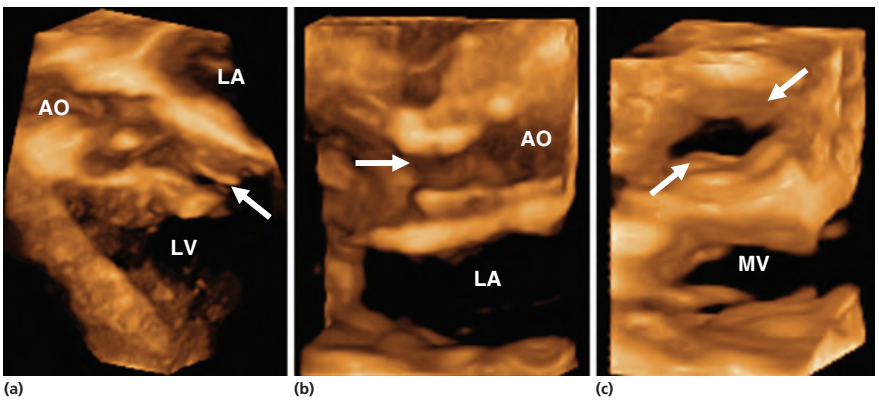


Figure 21.35 Subcostal real-time 3D echocardiogram in a neonate with interrupted aortic arch. **(a)** Left ventricular outflow tract obstruction indicated by arrows in a 5-chamber view; **(b)** long-axis view; and **(c)** en face view though the aortic valve as seen by the surgeon ("aortotomy view" from above). Obstruction is formed by complete subaortic conus with aortomitral discontinuity. AO, aorta; LA, left atrium; LV, left ventricle; MV, mitral valve.

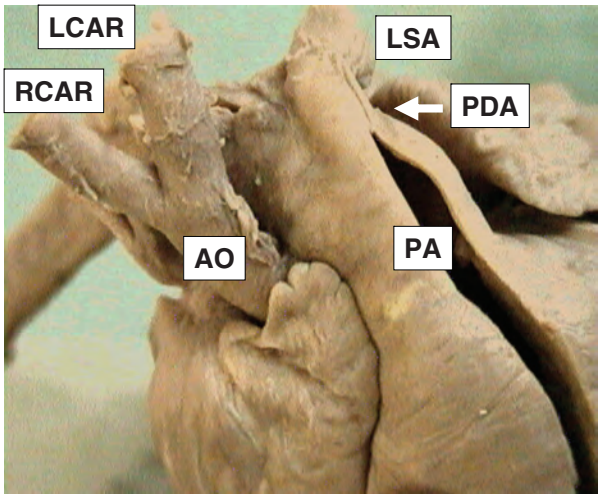


Figure 21.36 Postmortem finding in a 21-week-gestation fetus with type B interrupted aortic arch and aberrant right subclavian artery. The proximal aorta (AO) gives rise to the right (RCAR) and left (LCAR) carotid arteries; the left (LSA) and right subclavian arteries are connected to the junction of the large arterial duct and distal aorta (arrow). No connective tissue was found between the proximal and distal aorta. PA, pulmonary trunk. Source: Courtesy of Viera Povýšilová, Prague.

by postoperative changes and intervening airways. Alternative noninvasive imaging modalities (e.g., MRI, CT) should be considered when echocardiography does not provide adequate information.

Acknowledgment

All images used in this chapter were taken from imaging archives of Great Ormond Street Hospital, London, and University Hospital Motol, Prague. Some echocardiographic images were reproduced from Jan Marek: *Paediatric and Prenatal Echocardiography*, with permission of Triton Books (Prague, Czech Republic).

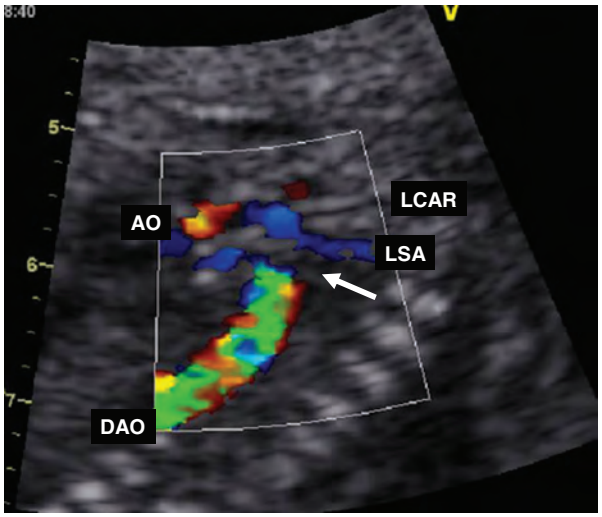


Figure 21.37 A type A interruption in a 22-week-gestation fetus: interruption (arrow) between left subclavian artery (LSA) and distal (DAO) aorta. LCAR, left common carotid artery.

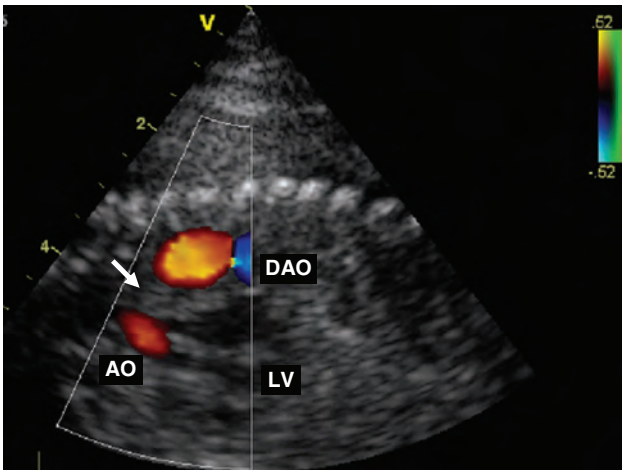


Figure 21.38 Aortic arch viewed through the spine of a 23-week-gestation fetus showing a type B interruption. The arrow indicates no flow continuity between the proximal (AO) and distal aorta (DAO). LV, left ventricle.

Videos

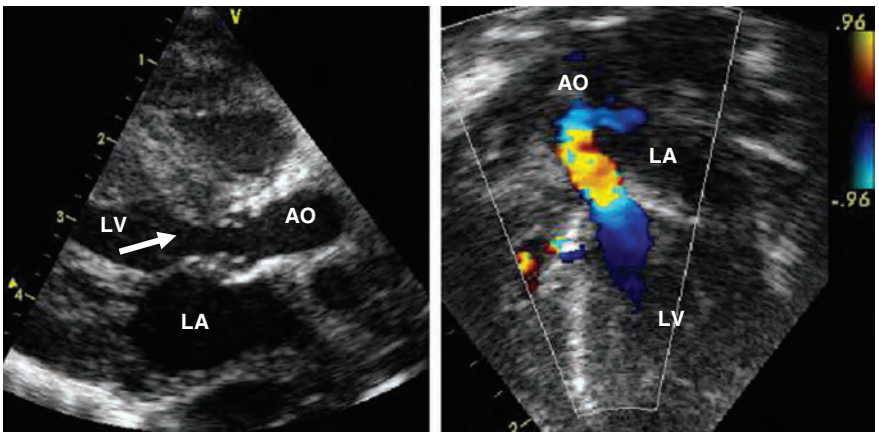
To access the videos for this chapter, please go to www.lai-echo.com.

Video 21.1 An unusual aortic coarctation in the presence of a right aortic arch with an aberrant left subclavian artery. Discrete narrowing is seen between the right carotid artery (RCAR) and right subclavian artery (RSA). The first nonbifurcating neck artery turning to the left suggests the presence of an aberrant left subclavian artery.

Video 21.2 Imaging of a neonatal coarctation of the aorta (COA) from the suprasternal notch view. A coarctation ridge is located ~5 mm below the origin of the left subclavian artery. An additional obstruction coexists at the aortic ampula of the arterial duct. Flow acceleration exceeding 1.24 m/s identified by color aliasing occurs at the site of aortic ductal tissue as well as at the level of the coarctation shelf.

Video 21.3 Neonatal coarctation with severe transverse aortic arch hypoplasia with juxtaductal COA shelf as seen from the suprasternal view. In contrast to low-velocity antegrade flow across hypoplastic aortic arch on color Doppler, there is high-velocity flow on the right-to-left systolic shunt across the arterial duct. Diastolic left-to-right flow across the arterial duct indicates lower diastolic pulmonary artery pressure compared to systemic diastolic pressure.

Video 21.4 A neonate with aortic arch hypoplasia and a large arterial duct connecting the pulmonary trunk and distal aorta. Note that



(a) (b)

Figure 21.39 Left ventricular outflow tract obstruction (LVOTO) after IAA repair. **(a)** 2D long-axis view; **(b)** flow acceleration visualized by color Doppler flow mapping. LVOTO formed by hypertrophied and posteriorly deviated infundibular septum (arrow) and incomplete systolic opening of aortic valve suggest a bicuspid valve. AO, aorta; LA, left atrium; LV, left ventricle.

the size of the arterial duct (9 mm) is nearly three times greater than the transverse aortic arch (3.5 mm).

Video 21.5 Tight preductal coarctation of the aorta (COA) with a very restrictive arterial duct in a 1-day-old critically ill neonate. Turbulent, high-velocity flow exceeding the Nyquist limit of 82 cm/s can be detected in both the severe isthmic narrowing and the patent arterial duct (PDA).

Video 21.6 Severe aortic isthmic hypoplasia (between the left subclavian artery and arterial duct) with minimal antegrade flow on color Doppler, in contrast to the high-velocity right-to-left shunt flow across the large arterial duct.

Video 21.7 Neonatal coarctation imaged from the subcostal sagittal approach, similarly to the prenatal transabdominal view.

Video 21.8 Coarctation of the aorta (COA) in a 12-year-old boy. Note the long aortic isthmus with a discrete shelf occluding the distal part of the aortic isthmus and the marked poststenotic dilation of the thoracic aorta.

Video 21.9 Left subclavicular approach in the sagittal plane showing mild isthmic narrowing in 7-year-old child. The coarctation shelf is opposite to the aortic ampula of a functionally closed arterial duct. Flow acceleration across the aortic isthmus is seen on color Doppler flow mapping.

Video 21.10 Coarctation of the abdominal aorta in an infant visualized from the subcostal sagittal view. Narrowing indicated by color Doppler flow is localized below the diaphragm and above the origin of the celiac arteries.

Video 21.11 Ventricular size disproportion seen in the 4-chamber view of a 26-week-gestation fetus with coarctation of the aorta (COA). The right atrium and right ventricle are larger compared with the left atrium and left ventricle. The left ventricle is not hypoplastic and forms the apex of the heart.

Video 21.12 Narrowing of the aortic isthmus is seen in this sagittal view of a 21-week-gestation fetus. The aortic ampula of the arterial duct is connected to the descendent thoracic aorta, whereas the transverse aortic arch is severely hypoplastic.

Video 21.13 Narrowing of the aortic isthmus is seen in this sagittal view of a 21-week-gestation fetus. Flow acceleration across the hypoplastic arch is low in contrast to the high-flow velocity exceeding the 60 cm/s Nyquist limit, across the arterial duct.

Video 21.14 Hypoplastic aortic arch in a 22-week-gestation fetus visualized from the sagittal view across the spine. Flow acceleration exceeding 75 cm/s starts between the left carotid and left subclavian arteries.

Video 21.15 Severe preductal aortic arch narrowing contrasted with a large postductal descendent thoracic aorta in a fetus scanned at 32 weeks' gestation.

Video 21.16 Isolated aortic coarctation in a 21-week-gestation fetus. Flow acceleration identified by color flow aliasing (Nyquist limit 89 cm/s) appeared underneath the origin of the left subclavian artery visualized distal to the prominent left carotid artery in an otherwise good-caliber transverse aortic arch.

Video 21.17 Neonatal aortic isthmic coarctation associated with a Gothic arch-shape irregularity as seen from the suprasternal view.

Video 21.18 Neonate with type A interrupted aortic arch distal to the left subclavian artery visualized from the suprasternal notch. The descendent aorta is connected to the pulmonary trunk via the arterial duct. The distance between the distal and proximal aorta is about 5 mm.

Video 21.19 Neonatal type A interrupted aortic arch with a common origin of the brachiocephalic trunk and left carotid artery, and with a hypoplastic short transverse aortic arch between the left carotid and subclavian arteries. The relatively long segment interruption between the left subclavian artery and distal aorta, which is supplied via the larger arterial duct with right-to-left shunt, is demonstrated on color Doppler.

Video 21.20 Type B interrupted aortic arch as seen from the suprasternal approach viewing the region of soft tissue between the left carotid and left subclavian arteries. The left carotid artery is supplied antegradely from the aorta, while the left subclavian artery is supplied via the arterial duct from the pulmonary trunk. The distance between the proximal and distal aorta exceeds 10 mm.

Video 21.21 Type B interruption in a neonate scanned shortly after delivery. The short interruption between the left carotid artery and the descendent thoracic aorta distal to the arterial duct is demonstrated on this 2D color Doppler echocardiogram. Note the left subclavian artery is not visualized because its origin is more posterior to the scan plane.

Video 21.22 High parasternal short-axis view in a neonate with an interrupted aortic arch. The large pulmonary trunk trifurcates ("Neptune's fork") giving rise to right and left pulmonary arteries as well as to the large arterial duct widely connected to the descendent thoracic aorta. A connection with the aortic arch could not be identified. Note that the bicuspid aortic valve is also visualized in the center of the clip.

Video 21.23 Ventricular septal defect in a neonate with an interrupted aortic arch visualized from a subcostal modified anterior 4-chamber view. The clip shows a large anterior muscular defect with posterior deviation of the infundibular septum and narrowed left ventricular outflow tract.

Video 21.24 Ventricular septal defect in a neonate with an interrupted aortic arch visualized from a subcostal modified anterior 4-chamber view. Color Doppler documented an important left-to-right systolic shunt across the nonrestrictive ventricular septal defect and laminar flow across the left ventricular outflow tract.

Video 21.25 Ventricular septal defect in a neonate with an interrupted aortic arch visualized from an apical 4-chamber view tilted anteriorly (5-chamber view). The two-dimensional clips show a muscular outlet defect with posterior deviation of the infundibular septum and a narrowed left ventricular outflow tract. Color Doppler documented a left-to-right systolic shunt across the nonrestrictive ventricular septal defect and laminar flow across the left ventricular outflow tract.

Video 21.26 Ventricular septal defect and left ventricular outflow track viewed from a parasternal long-axis view. A large ventricular septal defect was located in the outlet of the subaortic septum. The hypertrophied infundibular septum, together with the small (3.7-mm diameter) aortic valve, contributed to narrowing of the left ventricular outflow tract. Incomplete opening of the aortic leaflets suggests a bicuspid aortic valve.

Video 21.27 Ventricular septal defect and left ventricular outflow track viewed from a parasternal long-axis view. On the color Doppler clip, the laminar low-velocity flow across the left ventricular outflow tract suggests low systemic output due to high afterload in the presence of a large ventricular communication and lower postductal afterload.

Video 21.28 Subcostal real-time 3D echocardiography clip in a neonate with an interrupted aortic arch. Left ventricular outflow tract obstruction visualized in a 5-chamber view demonstrates complete subaortic conus, separating the aortic valve from the mitral valve.

Video 21.29 Subcostal real-time 3D echocardiography clip in a neonate with an interrupted aortic arch. Long-axis view through the aortic valve as seen by the surgeon ("aortotomy view" from above).

Video 21.30 Subcostal real-time 3D echocardiography clip in a neonate with an interrupted aortic arch. En face view through the aortic valve as seen by the surgeon ("aortotomy view" from above).

Video 21.31 Bicuspid aortic valve viewed from a parasternal short-axis view in a neonate with an interrupted aortic arch. Note that the ventricular septal defect is not seen as it is separated from the aortic, tricuspid and mitral valves by complete subaortic conus.

Video 21.32 Interrupted aortic arch (type A) in a 22-week-gestation fetus. Aortic arch visualized by 2D and color Doppler from leftward-oriented sagittal transabdominal view (magnified clip). Antegrade flow is clearly visible within the left carotid and left subclavian arteries, whereas flow imaged within the distal aorta is completely disconnected from the proximal aorta because the distal aorta is supplied from the arterial duct.

Video 21.33 Aortic arch viewed through the spine showing a type B interrupted aortic arch in a 23-week-gestation fetus. There is no continuity visible on color Doppler between the proximal and distal aorta.

Video 21.34 Left ventricular outflow tract, aortic root and ventricular septal defect in a 23-week-gestation fetus viewed from a 5-chamber projection. Already at an early stage, posterior deviation of the infundibular septum causing obstruction can be identified.

Video 21.35 Neonate after complete repair of an interrupted aortic arch, consisting of aortic arch reconstruction and closure of the ventricular septal defect. The left ventricular outflow remains small. Despite successful surgery, further echocardiographic follow-up is required to observe evolution of disease as progressive obstruction can develop with advancing age.

References

1 Hoffman JI, Kaplan S. The incidence of congenital heart disease. *J Am Coll Cardiol* 2002;**39**:1890–1900.
2 Šamánek M, Voříšková M: Congenital heart disease among 815,569 children born between 1980 and 1990 and their 15-year survival: a prospective Bohemia survival study. *Pediatr Cardiol* 1999;**20**:411–441.
3 Bower C, Ramsay JM. Congenital heart disease: a 10 year cohort. *J Paediatr Child Health* 1994;**30**:414–418.
4 Campbell M, Polani PE. The aetiology of coarctation of the aorta. *Lancet* 1961;**1**:463–468.

5 Sharland GK, Chan KY, Allan LD. Coarctation of the aorta: difficulties in prenatal diagnosis. *Br Heart J* 1994;**71**:70–75.

6 Mahowald JM, Lucas RV, Jr., Edwards JE. Aortic valvular atresia. Associated cardiovascular anomalies. *Pediatr Cardiol* 1982;**2**:99–105.

7 Ho VB, Bakalov VK, Cooley M, et al. Major vascular anomalies in Turner syndrome: prevalence and magnetic resonance angiographic features. *Circulation* 2004;**11**:1694–1700.

8 Goldmuntz E, Clark BJ, Mitchell LE, et al. Frequency of 22q11 deletions in patients with conotruncal defects. *J Am Coll Cardiol* 1998;**32**:492–498.

9 Machii M, Becker AE. Hypoplastic aortic arch morphology pertinent to growth after surgical correction of aortic coarctation. *Ann Thorac Surg* 1997;**64**:516–520.

10 Ho SY, Anderson RH. Coarctation, tubular hypoplasia, and the ductus arteriosus. Histological study of 35 specimens. *Br Heart J* 1979;**41**:268–274.

11 Rudolph A. *Congenital Diseases of the Heart*. Armonk, NY: Futura Publishing, 2001, pp. 378–393.

12 Curtis SL, Bradley M, Wilde P, et al. Results of screening for intracranial aneurysms in patients with coarctation of the aorta. *Am J Neuroradiol* 2012;**33**:1182–1186.

13 Marek J, Tomek V, Povýšilová V, et al. Prenatal ultrasound screening of congenital heart disease in an unselected national population: a 21-year experience. *Heart* 2011;**197**:124–130.

14 Head CE, Jowett VC, Sharland GK, Simpson JM. Timing of presentation and postnatal outcome of infants suspected of having coarctation of the aorta during fetal life. *Heart* 2005;**91**:1070–1074.

15 Hornberger LK, Weintraub RG, Pesonen E, et al. Echocardiographic study of the morphology and growth of the aortic arch in the human fetus. Observations related to the prenatal diagnosis of coarctation. *Circulation* 1992;**86**:741–747.

16 Matsui H, Mellander M, Roughton M, et al. Morphological and physiological predictors of fetal aortic coarctation. *Circulation* 2008;**118**:1793–1801.

17 Pfammatter JP, Ziemer G, Kaulitz R, et al. Isolated aortic coarctation in neonates and infants: results of resection and end-to-end anastomosis. *Ann Thorac Surg* 1996;**62**:778–782.

18 Grinda JM, Mace L, Dervanian P, et al. Bypass graft for complex forms of isthmic aortic coarctation in adults. *Ann Thorac Surg* 1995;**60**:1299–1302.

19 Redington AN, Booth P, Shore DF, Rigby ML. Primary balloon dilatation of coarctation of the aorta in neonates. *Br Heart J* 1990;**64**:277–281.

20 Rodes-Cabau J, Miro J, Dancea A, et al. Comparison of surgical and transcatheter treatment for native coarctation of the aorta in patients > or = 1 year old. The Quebec Native Coarctation of the Aorta study. *Am Heart J* 2007;**154**:186–192.

21 Dietl CA, Torres AR, Favaloro RG, et al. Risk of recoarctation in neonates and infants after repair with patch aortoplasty, subclavian flap, and the combined resection-flap procedure. *J Thorac Cardiovasc Surg* 1992;**10**:724–731.

22 Sciolaro C, Copeland J, Cork R, et al. Long-term follow-up comparing subclavian flap angioplasty to resection with modified oblique end-to-end anastomosis. *J Thorac Cardiovasc Surg* 1991;**101**:1–13.

23 Ou P, Bonnet D, Auriacomb L, et al. Late systemic hypertension and aortic arch geometry after successful repair of coarctation of the aorta. *Eur Heart J* 2004;**25**:1853–1859.

24 Sweeney MS, Walker WE, Duncan JM, et al. Reoperation for aortic coarctation: techniques, results, and indications for various approaches. *Ann Thorac Surg* 1985;**40**:46–49.

25 Tchervenkov CI, Jacobs JP, Sharma K, Ungerleider RM. Interrupted aortic arch: surgical decision making. *Semin Thorac Cardiovasc Surg Pediatr Card Surg Annu* 2005;92–102.

26 Fyler DC, Buckley DC, Hellenbrand WC, Cohn HE. Report of the New England Regional Infant Cardiac Program. *Pediatrics* 1980;**65**:375–461.

27 Powell CB, Stone FM, Atkins DL, et al. Operative mortality and frequency of coexistent anomalies in interruption of the aortic arch. *Am J Cardiol* 1997;**79**:1147–1148.

28 Van Mierop LHS, Kutsche LM. Interruption of the aortic arch and coarctation of the aorta: pathogenetic relations. *Am J Cardiol* 1984;**54**:829–834.

29 Rudolph AM, Heymann MA, Spitznas U. Hemodynamic considerations in the development of narrowing of the aorta. *Am J Cardiol* 1972;**30**:514–525.

30 Conley ME, Beckwith JB, Mancer JFK, Tenckhoff L. The spectrum of the DiGeorge syndrome. *J Pediatr* 1979;**94**:883–890.

31 Van Mierop LHS, Kutsche LM. Cardiovascular anomalies in DiGeorge syndrome and importance of neural crest as a possible pathogenetic factor. *Am J Cardiol* 1986;**58**:133–137.

32 Goldmuntz E, Clark BJ, Mitchell LE, et al. Frequency of 22q11 deletions in patients with conotruncal defects *J Am Coll Cardiol* 1998;**32**:492–498.

33 Lepore JJ, Mericko PA, Cheng L, et al. GATA-6 regulates semaphorin 3C and is required in cardiac neural crest for cardiovascular morphogenesis. *J Clin Invest* 2006;**116**:929–939.

34 Turlo KA, Noel O, Roshni V, et al. An essential requirement for β1 integrin in the assembly of extracellular matrix proteins within the vascular wall. *Dev Biol* 2012;**365**:23–35.

35 Celoria GC, Patton RB. Congenital absence of the aortic arch. *Am Heart J* 1959;**58**:407–413.

36 Kreutzer J, Van Praagh R. Comparison of left ventricular outflow tract obstruction in interruption of the aortic arch and in coarctation of the aorta, with diagnostic, developmental, and surgical implications. *Am J Cardiol* 2000;**86**:856–862.

37 Van Praagh R, Geva T, Kreutzer J. Ventricular septal defects: how should we describe, name and classify them? *J Am Coll Cardiol* 1989;**14**:1298–1299.

38 Moulaert AJ, Oppenheimer-Dekker A. Anterolateral muscle bundle of the left ventricle, bulboventricular flange and subaortic stenosis. *Am J Cardiol* 1976;**37**:78–81.

39 McCrindle BW, Tchervenkov CI, Konstantinov IE, et al. Risk factors associated with mortality and interventions in 472 neonates with interrupted aortic arch: a Congenital Heart Surgeons' Society study. *J Thorac Cardiovasc Surg* 2005;**129**:343–350.

40 Sim MM, Chen CC. Transthoracic echocardiographic diagnosis of a type C interrupted aortic arch in an adult. *J Am Soc Echocardiogr* 2007;**20**:1418.e1–4.

41 Fujii I, Ueno Y, Kurano R, Goto Y. Interrupted aortic arch type C associated with DiGeorge syndrome in 22q11.2 deletion: first case detected in Japan. *Pediatr Int* 2005;**47**:698–700.

42 Konstantinov IE, Karamlou T, Blackstone EH, et al. Truncus arteriosus associated with interrupted aortic arch in 50 neonates: a Congenital Heart Surgeons' Society study. *Ann Thorac Surg* 2006;**81**:214–222.

43 Konstantinov IE, Karamlou T, Williams WG, et al. Surgical management of aortopulmonary window associated with interrupted aortic arch: a Congenital Heart Surgeons' Society study. *J Thorac Cardiovasc Surg* 2006;**131**:1136–1141.
44 Pierpont MEM, Zollikofer CL, Moller JH, Edwards JE. Interruption of the aortic arch with right descending aorta: a rare condition and a cause of bronchial compression. *Pediatr Cardiol* 1982;**2**:153–159.
45 Geva T, Gajarski RJ. Echocardiographic diagnosis of type B interruption of a right aortic arch. *Am Heart J* 1995;**129**:1042–1045.
46 Kutsche LM, Van Mierop LHS. Cervical origin of the right subclavian artery in aortic arch interruption: pathogenesis and significance. *Am J Cardiol* 1984;**53**:892–895.
47 Kaulitz R, Jonas RA, van der Velde ME. Echocardiographic assessment of interrupted aortic arch. *Cardiol Young* 1999;**9**:562–571.
48 Tworetzky W, McElhinney DB, Brook MM, et al. Echocardiographic diagnosis alone for the complete repair of major congenital heart defects. *J Am Coll Cardiol* 1999;**33**:228–233.
49 Riggs TW, Berry TE, Aziz KU, Paul MH. Two-dimensional echocardiographic features of interruption of the aortic arch. *Am J Cardiol* 1982;**50**:1385–1390.
50 Moran AM, Colan SD, Mayer JE, Jr., van der Velde ME. Echocardiographic identification of thymic hypoplasia in tetralogy of Fallot/tetralogy pulmonary atresia. *Am J Cardiol* 1999;**84**:1268–1271.
51 Smallhorn JF, Anderson RH, Macartney FJ. Cross-sectional echocardiographic recognition of interruption of aortic arch between left carotid and subclavian arteries. *Br Heart J* 1982;**48**:229–235.
52 Geva T, Hornberger LK, Sanders SP, et al. Echocardiographic predictors of left ventricular outflow tract obstruction after repair of interrupted aortic arch. *J Am Coll Cardiol* 1993;**22**:1953–1960.
53 Minich LL, Snider AR, Bove EL, Lupinetti FM. Echocardiographic predictors of the need for infundibular wedge resection in infants with aortic arch obstruction, ventricular septal defect and subaortic stenosis. *Am J Cardiol* 1992;**70**:1626–1627.
54 Ge S, Warner JG, Jr., Fowle KM, et al. Morphology and dynamic change of discrete subaortic stenosis can be imaged and quantified with three-dimensional transesophageal echocardiography. *J Am Soc Echocardiogr* 1997;**10**:713–716.
55 Brown JW, Ruzmetov M, Okada Y, et al. Outcomes in patients with interrupted aortic arch and associated anomalies: a 20-year experience. *Eur J Cardiothorac Surg* 2006;**29**:666–673.
56 Schreiber C, Mazzitelli D, Haehnel JC, et al. The interrupted aortic arch: an overview after 20 years of surgical treatment. *Eur J Cardiothorac Surg* 1997;**12**:466–469.
57 Oosterhof T, Azakie A, Freedom RM, et al. Associated factors and trends in outcomes of interrupted aortic arch. *Ann Thorac Surg* 2004;**78**:1696–1702.
58 Serraf A, Lacour-Gayet F, Robotin M, et al. Repair of interrupted aortic arch: a ten-year experience. *J Thorac Cardiovasc Surg* 1996;**112**:1150–1160.

CHAPTER 22

Tetralogy of Fallot

Shubhika Srivastava[1], Wyman W. Lai[2], and Ira A. Parness[1]
[1]Division of Pediatric Cardiology, Mount Sinai Medical Center, New York, NY, USA
[2]Division of Pediatric Cardiology, Columbia University Medical Center, New York, NY, USA

Definition

In 1671, Niels Stenson first described the pathology of the syndrome now known as tetralogy of Fallot (TOF). Etienne-Louis Arthur Fallot, in his seminal 1888 paper, debunked the prevailing theory that cardiac cyanosis ("la maladie bleue") was due to right-to-left foramen ovale shunting. Fallot noted that most patients with cyanotic heart disease had an association of cardiac malformations that he coined "tetralogy" consisting of pulmonary stenosis, ventricular septal defect (VSD), dextroposition of the aorta, and right ventricular (RV) hypertrophy [1–3]. Abbott and Dawson [4], in 1924, named this malformation "tetralogy of Fallot."

In the nomenclature for TOF recommended by the Congenital Heart Surgeons' Society, TOF is classified into three main groups:

1 TOF with varying degrees of pulmonary stenosis
2 TOF with common atrioventricular (AV) canal
3 TOF with absent pulmonary valve.

TOF with pulmonary atresia was classified under the category of pulmonary atresia with VSD [5]. Nonetheless, in this chapter pulmonary atresia with VSD is categorized as the most severe morphologic variant of TOF.

Incidence

TOF is the most common cyanotic congenital heart defect, with an incidence of 32.6 per 100,000 live births [6,7]. Survival of patients with TOF improved dramatically with the introduction of the Blalock–Taussig shunt in 1944 as the first palliative procedure for cyanotic congenital heart disease [8]. The contributions of Vivien Thomas to the development of this procedure have been belatedly recognized [9]. In the 1980s, surgical management strategies evolved into early complete repair [10], although initial medical and surgical mortality was reported to be as high as 28% [11]. Current surgical practices involve a complete repair with an effort to minimize or avoid RV outflow tract scar and to maintain functional integrity of the pulmonary valve (PV). There is now a large population of adults with repaired TOF, which has necessitated advances in diagnostic techniques and management [12].

Embryology, genetics, and environmental factors

Embryology

The pathognomonic conotruncal abnormality of TOF has been attributed to arrest in neural crest cell migration [13]. Studies in chick and mouse embryos have demonstrated the key role of the secondary heart field (SHF) from the anterior mesoderm in cardiac embryogenesis [13–16], including a significant role in conotruncal and RV development in humans [17,18]. Following primary heart tube looping, committed precardiac cells from the SHF migrate to the anterior pole, where they are incorporated into the outflow tracts. Neural crest cells influence and modulate migration of the SHF. Ablation of the SHF or neural crest results in arrest of caudal migration of the committed precardiac cells toward the aortic sac [19–23]. The consequent short outflow tract [24], failure of normal rotation of the conotruncus, and abnormal coronary arteries are typical of TOF [25]. This embryologic theory supports the hypothesis proposed by Van Praagh and colleagues, who demonstrated that the primary morphologic abnormality in TOF is an underdeveloped subpulmonary infundibulum [3].

Genetics

The secondary precardiac mesoderm expresses NKX2.5 and GATA-4 transcription factors [16,19,20]. Gene defects affecting the expression of these transcriptional factors may explain the resultant conotruncal abnormality in TOF. Microdeletion of chromosome 22q11, seen in DiGeorge or velocardiofacial phenotype syndromes, is a common example of a single gene defect

Echocardiography in Pediatric and Congenital Heart Disease: From Fetus to Adult, Second Edition. Edited by Wyman W. Lai, Luc L. Mertens, Meryl S. Cohen and Tal Geva.
© 2016 John Wiley & Sons, Ltd. Published 2016 by John Wiley & Sons, Ltd.
Companion website: www.lai-echo.com

causing abnormal neural crest cell migration and resulting in TOF [18]. The prevalence of 22q11 deletions among patients with TOF is much higher in patients with associated pulmonary atresia than in patients with TOF and pulmonary stenosis [26].

Approximately 50 syndromes associated with TOF have been identified [27]. Known chromosomal anomalies, syndromes, or single gene defects are associated with approximately one-third of the cases with TOF [28,29]. In one study of 64 patients with TOF and associated common AV canal, 88% had a genetic syndrome and extracardiac abnormalities, 67% had Down syndrome, but none had 22q11 deletion [30]. Genetic syndromes in the absence of abnormal pulmonary artery architecture have not been shown to be an independent risk factor for mortality in TOF repair [31], but they may affect perioperative outcomes [32].

Environmental factors

Maternal diabetes, exposure to retinoic acid, maternal phenylketonuria, and trimethadione have been reported to be associated with TOF [33,34].

Recurrence risk

The recurrence rate of nonsyndromic TOF varies between 2.5% and 3% if one sibling is affected, and is 8% if more than one sibling is affected. The reported risk of recurrence is 1.4% from an affected father, and varies between 0.9% and 2.6% for an affected mother. The recurrence rate also depends upon associated syndromes and genetic or environmental factors [35,36].

Morphology

The conotruncus in TOF

Tetralogy of Fallot comprises conoventricular VSD, overriding aorta, RV outflow tract obstruction, and RV hypertrophy (Figure 22.1). However, the RV hypertrophy component is the consequence of prolonged systemic level RV pressures rather than being a primary morphologic feature. The principal developmental abnormality in TOF resulting in its components has been debated. There are two theories:

1 Van Praagh et al. advocated that the principal morphologic abnormality in TOF is hypoplasia of the subpulmonary infundibulum, the latter consisting of the parietal band and the muscle or conus (which may be considered synonymous with infundibulum) subtended under the pulmonary valve [3]. The combination of a small subpulmonary infundibulum, or conus, and absence of subaortic conus results in the anterocephalad deviation of the infundibular septum. According to Van Praagh, the normal aortic overriding of the ventricular septum is exaggerated by the presence of a VSD in TOF and by the dilated aorta. The relationship between the aortic valve and pulmonary valve in severe TOF is often altered, with significant clockwise rotation of the conotruncus (as viewed

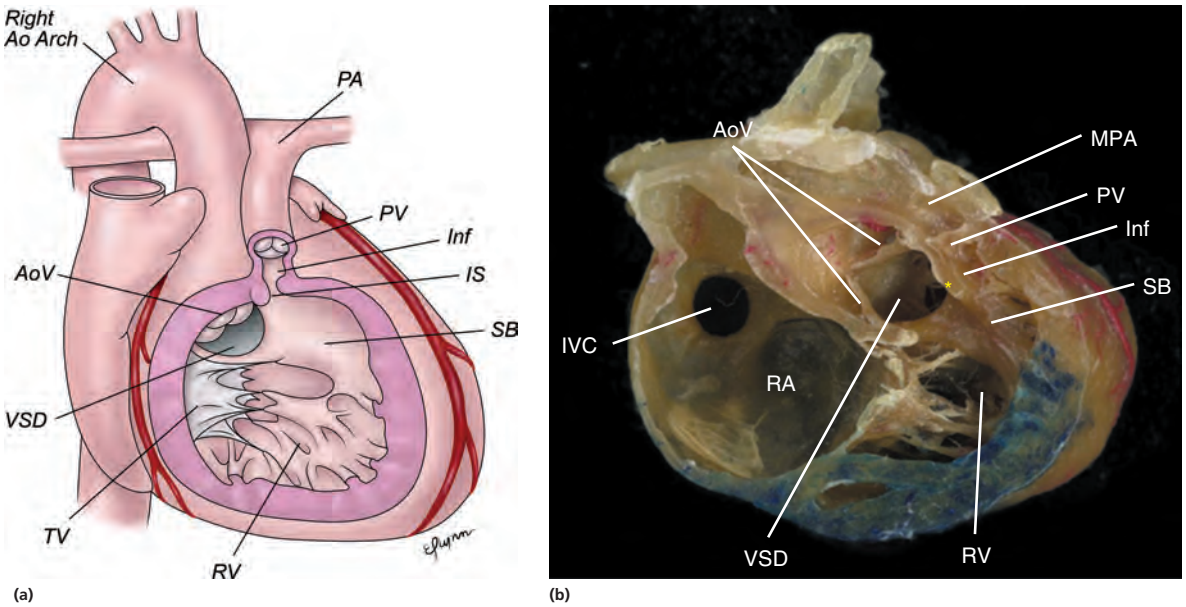


Figure 22.1 Tetralogy of Fallot (TOF) with pulmonary stenosis. **(a)** Diagram showing anterior-leftward deviation of the infundibular septum (IS) relative to the muscular ventricular septum, narrowed subpulmonary infundibulum (Inf), pulmonary valve (PV) stenosis, right ventricular (RV) hypertrophy, aortic override, and right aortic arch. The ventricular septal defect (VSD) is enclosed anteriorly and postero-inferiorly between the limbs of the septal band (SB) and superiorly by infundibular septum and the junction of the anterior limb of septal band and RV free wall. This anterior malalignment type of conoventricular septal defect is typical of TOF. **(b)** Waxed heart specimen showing the right side of the heart of an infant TOF with pulmonary stenosis. Source: Courtesy of Dr. Paul Weinberg, Children's Hospital of Philadelphia. AoV, aortic valve; IVC, inferior vena cava; MPA, main pulmonary artery; PA, pulmonary artery; RA, right atrium; TV, tricuspid valve; asterisk (*) denotes the infundibular septum.

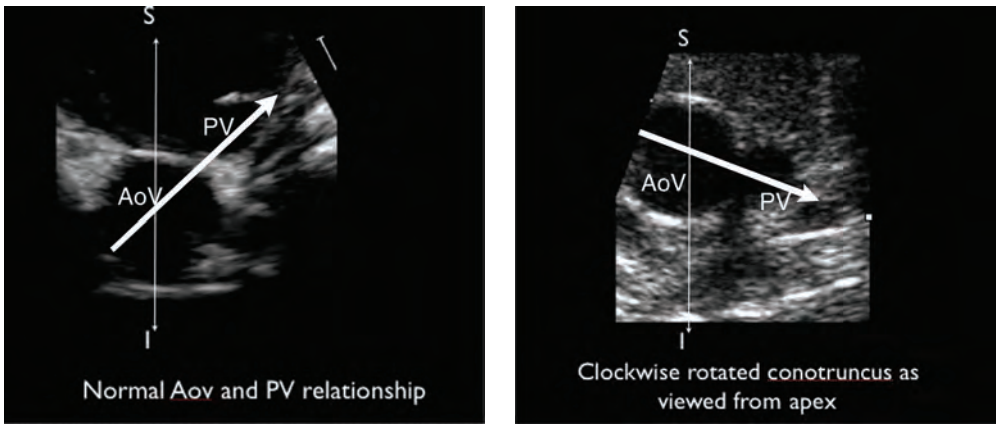


Figure 22.2 **(a)** Normal relationship of the pulmonary valve (PV) in relation to the aortic valve (AoV) as viewed from the apex. **(b)** Clockwise rotated conotruncus typical of TOF with increased rotation and more inferior displacement of the pulmonary valve (PV) that is correlated with severity of TOF and coronary anomalies.

from the cardiac apex) resulting in a rightward and more anteriorly located aortic valve, and a leftward and more posteriorly situated hypoplastic pulmonary valve [3] (Figure 22.2). The degree of clockwise rotation also correlates with the severity of TOF and associated coronary anomalies.

2 Becker et al. [1,37] and Anderson et al. [37,38] proposed that the principal abnormality in TOF is antero-superior deviation of the infundibular septum and not hypoplasia of the subpulmonary infundibulum. Because anterior deviation of the conal septum may be present without RV outflow obstruction as in Eisenmenger type VSD (Figure 22.3) [39–41], there must also be concomitant hypertrophy or hypoplasia of the subpulmonary infundibulum to produce TOF morphology. The infundibular septal deviation theory also does not easily explain the morphologic variant of TOF with doubly committed subarterial VSD, characterized by complete absence of the conal septum but hypoplasia of the pulmonary valve.

In either scheme, the embryonic morphologic abnormality of conal hypoplasia or conal septal malalignment results in failure of ventricular septation (VSD), subpulmonary or valvar pulmonary stenosis, and overriding of the aorta.

Ventricular septal defect morphology

The anterior malalignment type of conoventricular septal defect is typical of TOF [2,42]. Some authors have classified these defects as paramembranous or perimembranous [43]; however, most recognize the distinct nature of conal (infundibular or outlet) malalignment in TOF. The defect results from anterior, superior, and leftward deviation of the conal septum, which fails to align with the crest of the muscular septum (Figure 22.4). The malalignment of conal septum results in a wide communicating space between the ventricles rather than a deficiency, per se, in the "pars membranacea." The boundaries of the defect are formed by:

- Superiorly – the RV free wall and the aortic valve cusps, extending posteriorly to the tricuspid valve hinge point.
- Anteriorly – the parietal band of the crista supraventricularis.
- Inferiorly – the crest of the ventricular septum.
- Posteriorly – the muscle extending from septal band to the posterior muscular septum, also called the posterior limb of septal band. This muscle also separates the aortic valve from the tricuspid valve and is often referred to as the ventriculo-infundibular fold, which forms the inner heart curvature in a structurally normal heart. The width of this muscle is variable, at times being represented as a thin fibrous ridge allowing approximation of the tricuspid valve to the VSD [43].

The VSD is thus enclosed anteriorly and postero-inferiorly between the limbs of the septal band, and superiorly by the conal septum and the junction of the anterior limb of septal band and RV free wall [37] (Figure 22.1). Absence of the conal septum and associated hypoplasia of the subpulmonary infundibulum and hypertrophy of the septoparietal band results in a variant of TOF with doubly committed subarterial VSD (Figure 22.5; Video 22.1), overriding aorta, and pulmonary annular hypoplasia and stenosis [44].

The VSD in TOF is typically large but a restrictive defect has been reported in 1.5% of cases [45,46] (Figure 22.6). The mechanism of obstruction in nearly all the cases results from overlying abnormal or accessory tissue associated with the tricuspid valve. Rarely, myxomatous outpouching of the septal leaflet associated with Ebstein anomaly in TOF can result in a restrictive VSD [47]. Absolute small dimensions of the VSD caused by posterior deviation of the septal band and hypertrophy of the ventricular septum resulting in restriction to flow have also been described (Figure 22.7) [46].

TOF can also be seen in association with common AV canal defects characterized by an anteriorly malaligned conal septum in association with a predominantly Rastelli type C common AV valve (Figure 22.8) [37,48,49]. In the setting of complete

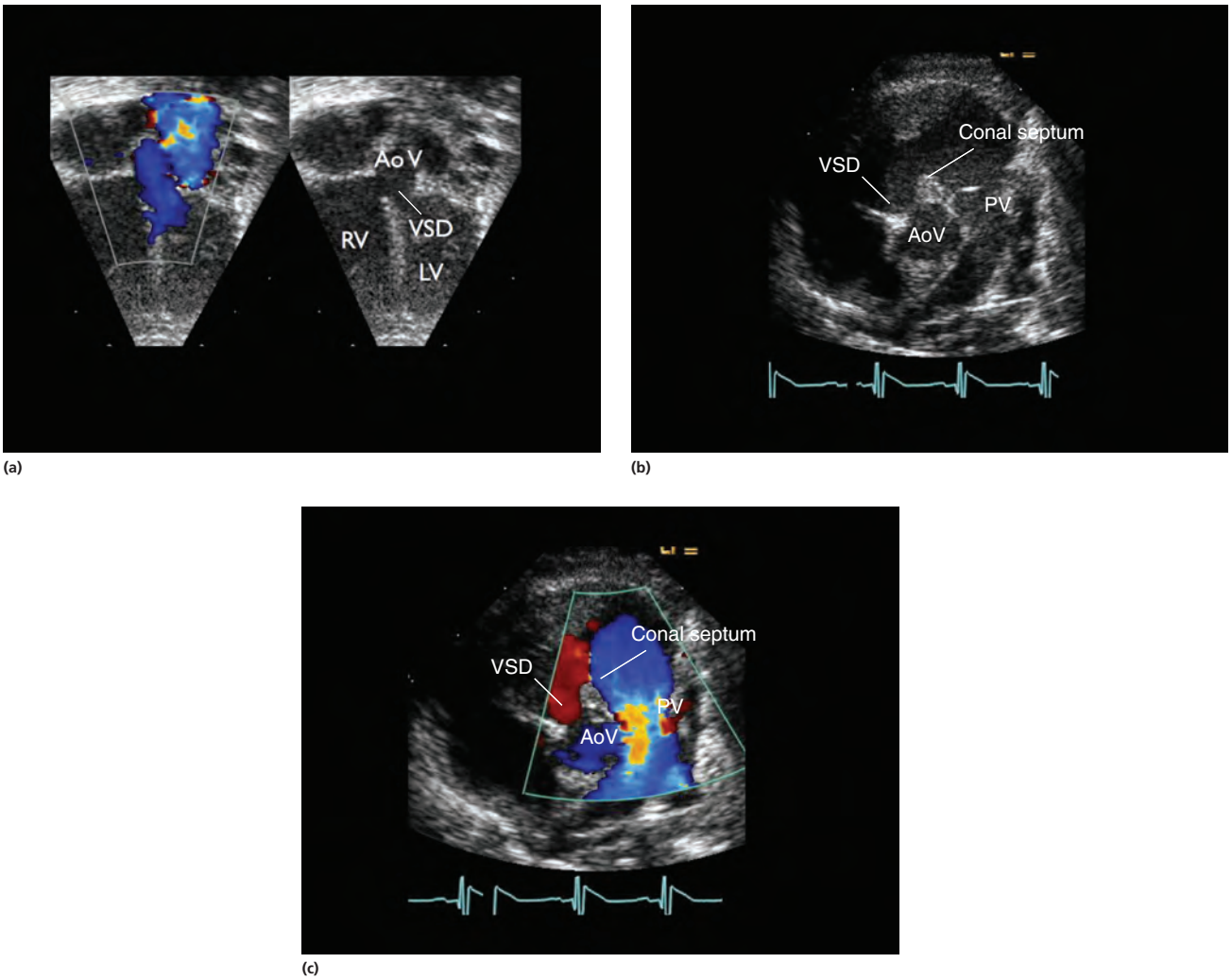


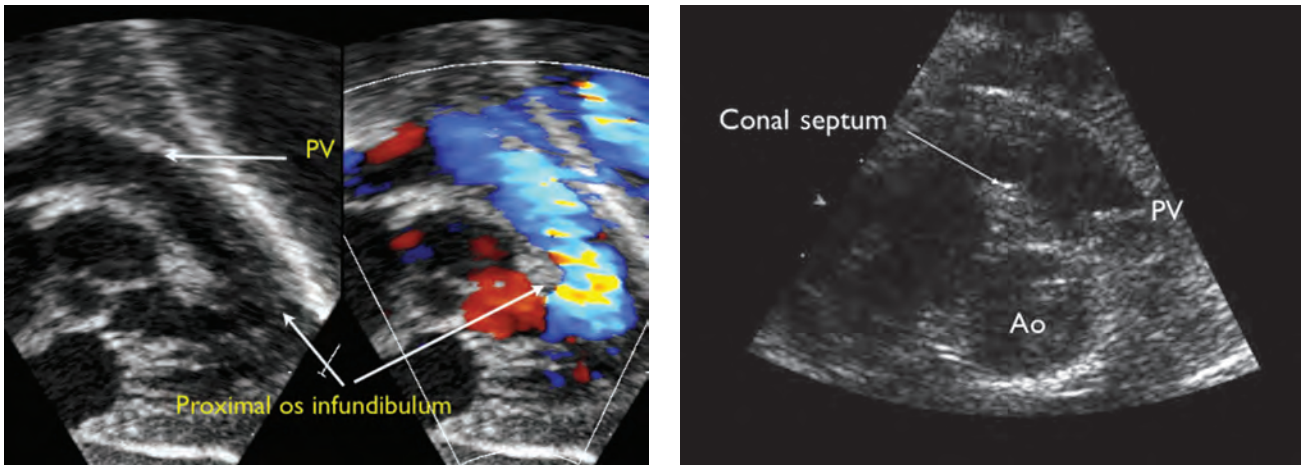
Figure 22.3 Eisenmenger VSD. **(a)** Apical view showing aortic valve (AoV) partially overriding the crest of ventricular septum and subaortic ventricular septal defect (VSD). **(b)** Parasternal short axis in 2D demonstrating anterior deviation of the conal septum and a widely expanded subpulmonary infundibulum. **(c)** Parasternal short axis with color flow mapping showing left-to-right flow across the VSD and absence of obstruction across the right ventricular outflow tract and pulmonary valve (PV). LV, left ventricle; RV, right ventricle.

common AV canal and TOF, VSD morphology is that of a single defect with confluent inlet and outlet components along with the typically anteriorly deviated conal septum. TOF may also occur in association with a rare variant of common AV canal in which there is an absent or diminutive atrial septal defect component [50].

Coronary arteries

Clockwise rotation of the aortic root (as viewed from the cardiac apex), and the resultant rotated origins of the coronary arteries, is typical in TOF (Videos 20.2 and 22.3). Anomalies in the branching pattern of the coronary arteries are reported in approximately 5% of all cases (Figure 22.9) [51]. The most common anomaly, occurring in 3%, is origin of the left anterior descending (LAD) coronary artery from the right coronary artery (RCA) (Videos 20.4 and 22.5); this is followed by dual LAD in 1.8%, single RCA in 0.3%, single left coronary artery (LCA) in 0.2%, and coronary-to-pulmonary artery fistula in 0.2%. In an angiographic study, anomalies of coronary artery branching pattern were more prevalent in patients with the most prominent aortopulmonary rotation [52]. The extraordinarily rare "isolated infundibuloarterial inversion" in TOF is associated with the RCA crossing anteriorly across the subpulmonary infundibulum. Anomalous origin of the LCA from the pulmonary artery has been reported in patients with TOF [53]. Origin of the LCA from the noncoronary cusp can also occur; its clinical implication thus far is unclear.

Coronary artery-to-pulmonary artery fistulae may rarely serve as a source of pulmonary blood flow in TOF with pulmonary valvar atresia or severe stenosis [54] (Figure 22.10; Video 22.6). Isolated coronary ostial stenosis or obstruction has also been reported in the absence of any other



(a) (b)

Figure 22.4 **(a)** Subxiphoid right anterior oblique view illustrating conal septal and RV free wall relationship. The RV outflow tract obstruction is due to conal septal deviation. Aliased flow at the os infundibulum is demonstrated by color flow Doppler. **(b)** Parasternal short-axis view to illustrate RV outflow tract obstruction. Ao, aorta; PV, pulmonary valve.

coronary anomaly [55]. Acquired coronary cameral fistulae may be observed following surgery [56].

Variants and associated lesions

TOF and double-outlet right ventricle

Some authorities have categorized extreme dextroposition, or aortic overriding with more than 50% of the aortic annulus over the RV, as double-outlet right ventricle (DORV) [37,38]. Nonetheless, according to Van Praagh et al., the maintenance of aortic-to-mitral valve fibrous continuity or normally related great arteries is pathognomonic for TOF irrespective of the degree of aortic override or dextroposition [2,37]. This approach recognizes a wide spectrum of aortic overriding within TOF without imposing an arbitrary dichotomous cutoff between TOF and DORV depending on the percentage of aortic override. Aortic–mitral fibrous continuity is also important in the prediction of postoperative left ventricular (LV) outflow tract obstruction: progressive subaortic obstruction following repair of typical TOF is rare [57]. However, progressive muscular hypertrophy causing subaortic obstruction may develop in cases of "TOF-like" DORV with retention of subaortic conus (see Chapter 25).

TOF and double-chambered right ventricle

Double-chambered right ventricle (DCRV) is an anomaly characterized by obstruction within the RV with or without an associated VSD (see Chapter 16). It can also present as a progressive lesion following corrective surgery for TOF [58]. DCRV is often misdiagnosed as TOF because both lesions have a VSD and subpulmonary stenosis [59]. However, in DCRV the primary morphologic abnormality resulting in subpulmonary stenosis is

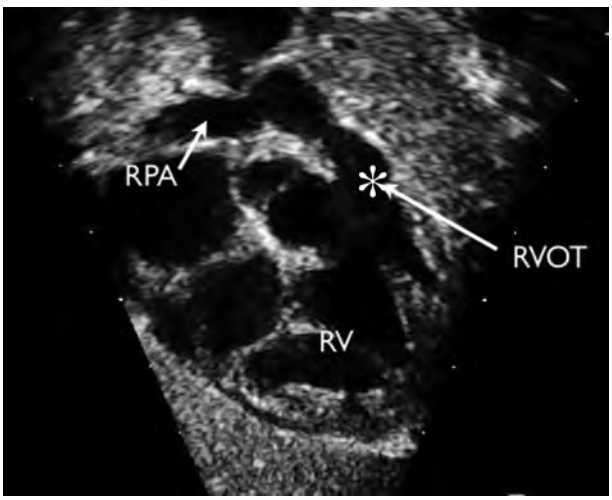


Figure 22.5 TOF with hypoplastic infundibulum and absent conal septum shown from the subxiphoid right anterior oblique view.

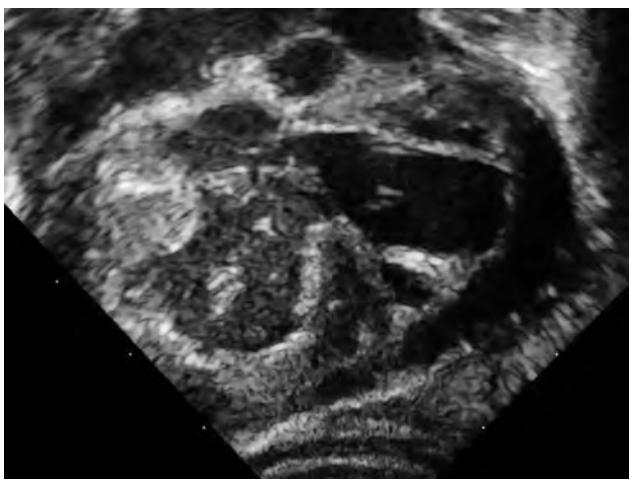


Figure 22.6 Restrictive ventricular septal defect is demonstrated in this patient with TOF and pulmonary atresia. Accessory tissue is billowing into the LV outflow tract.

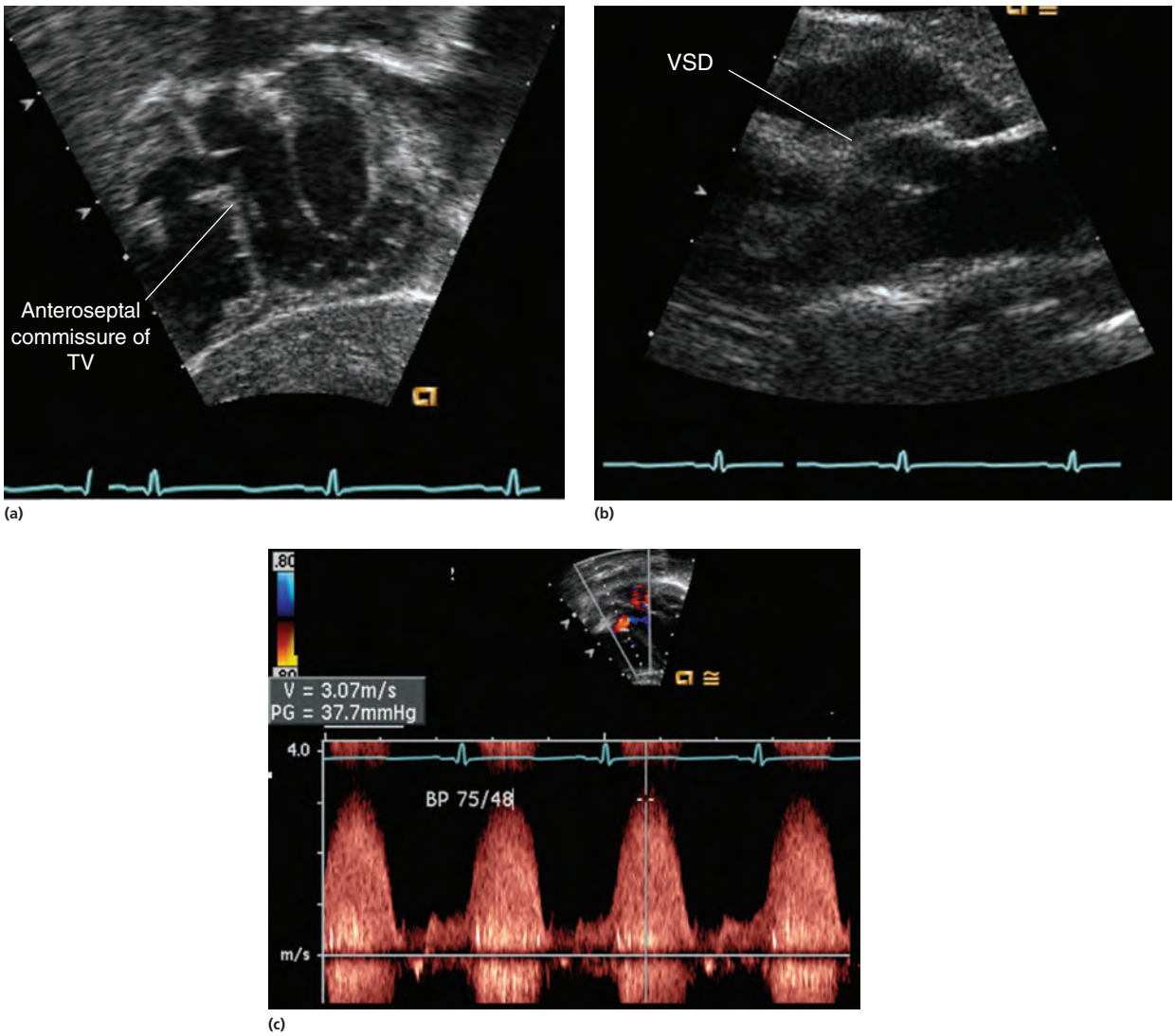
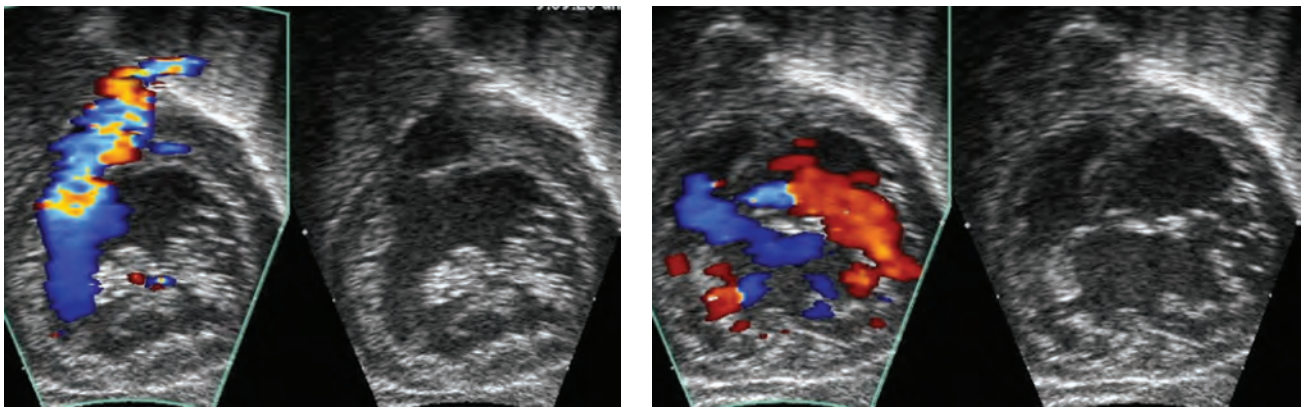


Figure 22.7 TOF with small, restrictive ventricular septal defect secondary to hypoplasia of the ventriculo-infundibular fold. **(a)** Subxiphoid short axis demonstrating the small dimensions of the defect in the superior-inferior plane. **(b)** Parasternal long axis demonstrating the small dimension in the base-to-apex plane. **(c)** Restrictive left-to-right shunting at the VSD demonstrated by continuous-wave Doppler interrogation.

either marked hypertrophy of the septoparietal trabeculations or moderator band, and/or abnormal displacement of the moderator band resulting in narrowing of the proximal infundibular ostium. Unlike TOF, DCRV is typically associated with normal size and morphology of the pulmonary valve and main and branch pulmonary arteries. Additionally, the VSD seen in DCRV is typically membranous rather than the malalignment type defect typical of TOF. However, there are overlap syndromes that share features of DCRV and TOF, such as those with an anterior malalignment type of VSD and aortic overriding but with a morphologically normal pulmonary valve and a well-developed infundibulum; in these cases, the subpulmonary obstruction is limited to the proximal os infundibulum (Figure 22.11; Video 22.7).

TOF with pulmonary atresia or extreme pulmonary hypoplasia

TOF with pulmonary atresia is a severe form of TOF. In addition to valvar atresia (short-segment atresia) or valve and main pulmonary artery absence (long-segment atresia), this condition is characterized by marked variability in the degree of pulmonary artery hypoplasia or absence and/or the presence of abnormal pulmonary arterial supply. The intracardiac anatomy, like other forms of TOF, typically consists of an enlarged and overriding aorta and an anterior malalignment VSD. In addition, there is marked infundibular hypoplasia or subvalvar atresia due to extreme leftward deviation of the conal septum, which may merge with the septal parietal band and RV free wall.



(a) (b)

Figure 22.8 **(a)** Subxiphoid short-axis view in systole showing TOF with complete common atrioventricular canal defect, Rastelli type C, with anterior deviation of conal septum and flow acceleration in the RV outflow tract. **(b)** Subxiphoid short-axis view in diastole demonstrating the common atrioventricular valve.

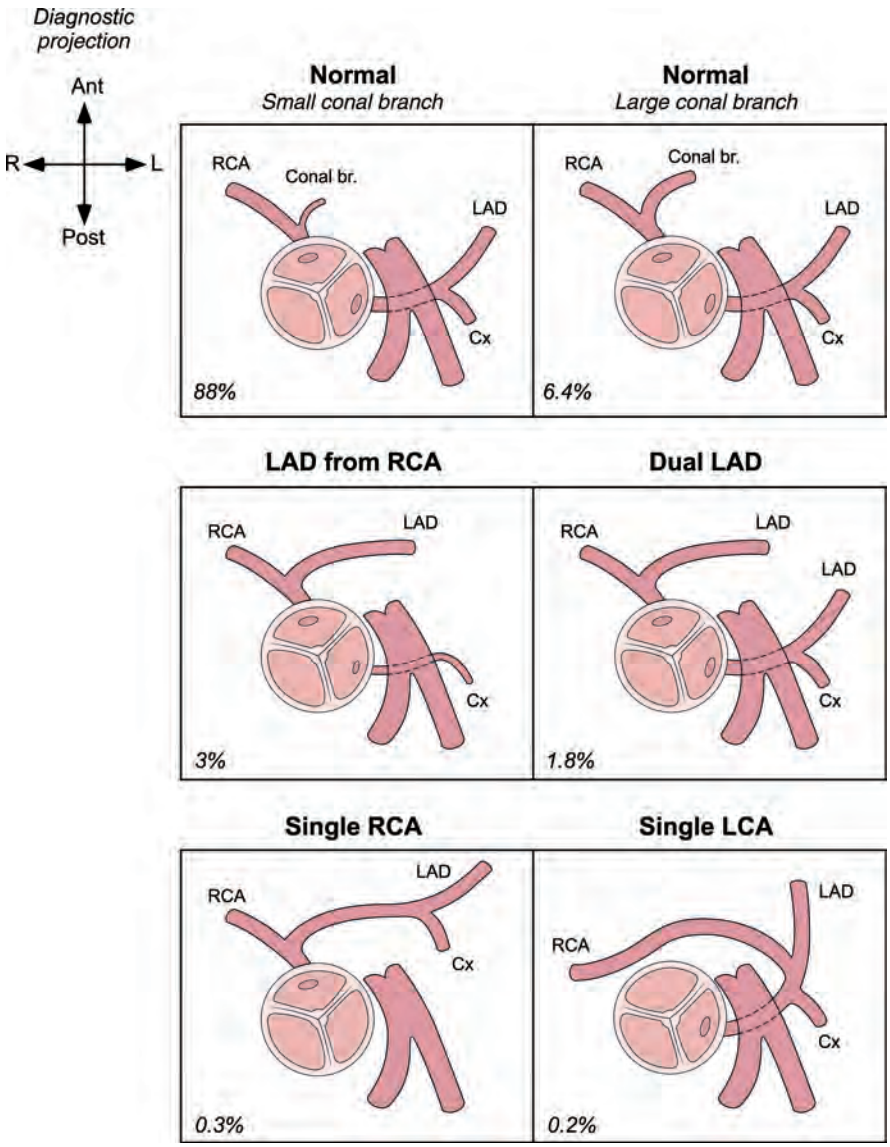


Figure 22.9 Diagram of coronary artery patterns in TOF. br., branch; Cx, circumflex artery; LAD, left anterior descending coronary artery; LCA, left coronary artery; RCA, right coronary artery.

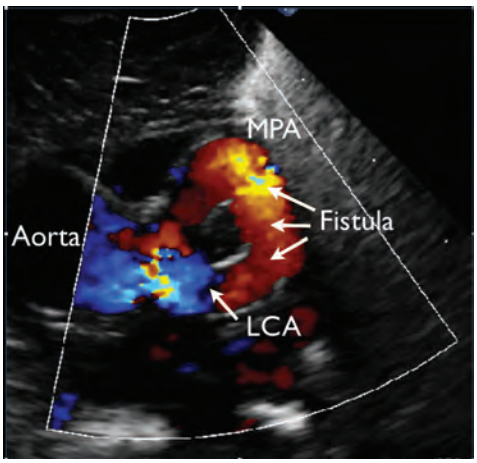


Figure 22.10 Parasternal short-axis image of a large left coronary-to-left pulmonary artery fistula in a patient with TOF. LCA, left coronary artery; MPA, main pulmonary artery.

This defect was initially misclassified as truncus arteriosus type IV in the classification of Collett and Edwards [60]. However, Van Praagh and Van Praagh correctly defined and classified this entity as TOF with pulmonary atresia. This entity was also described as "pseudotruncus" by Bharati et al. [61]. The Congenital Heart Surgeons' Society Nomenclature Committee classified TOF with pulmonary atresia under the umbrella of "Pulmonary atresia with VSD" [62]. The term "MAPCA(s)," or major aortopulmonary collateral artery, was coined by Macartney et al. [63].

TOF with pulmonary atresia can be further classified into three broad categories [62]:

1 Native confluent branch pulmonary arteries are present, which supply all lung segments; patency of the ductus arteriosus maintains pulmonary circulation. Interruption of antegrade pulmonary blood flow may be limited to the level of the valve, as in valvar atresia, or include the main pulmonary artery, as in long-segment pulmonary atresia.
2 Both native pulmonary arteries and MAPCAs are present; lung segments can have dual blood supply and the native pulmonary arteries may be supplied by either a ductus or MAPCAs. The pulmonary atresia may be long-segment with confluent mediastinal branch pulmonary arteries (Figure 22.12) or with discontinuous branch pulmonary arteries.
3 Native central pulmonary arteries are absent and MAPCAs supply the lung segments. Bronchial and pleural vessels can also be alternative sources of pulmonary blood flow.

The size of the branch pulmonary arteries is inversely proportional to the extent of MAPCAs and presence of a ductus arteriosus [64–67]. The angiographically determined Nakata index predicts good outcomes of complete repair of TOF with pulmonary artery hypoplasia if the index is greater than 100 mm^2/body surface area (BSA) [68].

Other rare variations in the morphology of TOF with pulmonary atresia have been reported, such as restrictive VSD [69,70], coronary artery-to-pulmonary artery fistula [49], and aortopulmonary window [69]. TOF with pulmonary atresia is associated with increased incidences of retroaortic innominate vein [71] and right aortic arch [61,72].

TOF with common atrioventricular canal defect

A common AV canal (CAVC) in association with TOF is an uncommon variant, seen in 1.7% of all cases of TOF and in 6.2% of cases with complete CAVC defects [48,49]. A very high incidence (87.5%) of genetic and extracardiac abnormalities is seen in this morphologic variant [73].

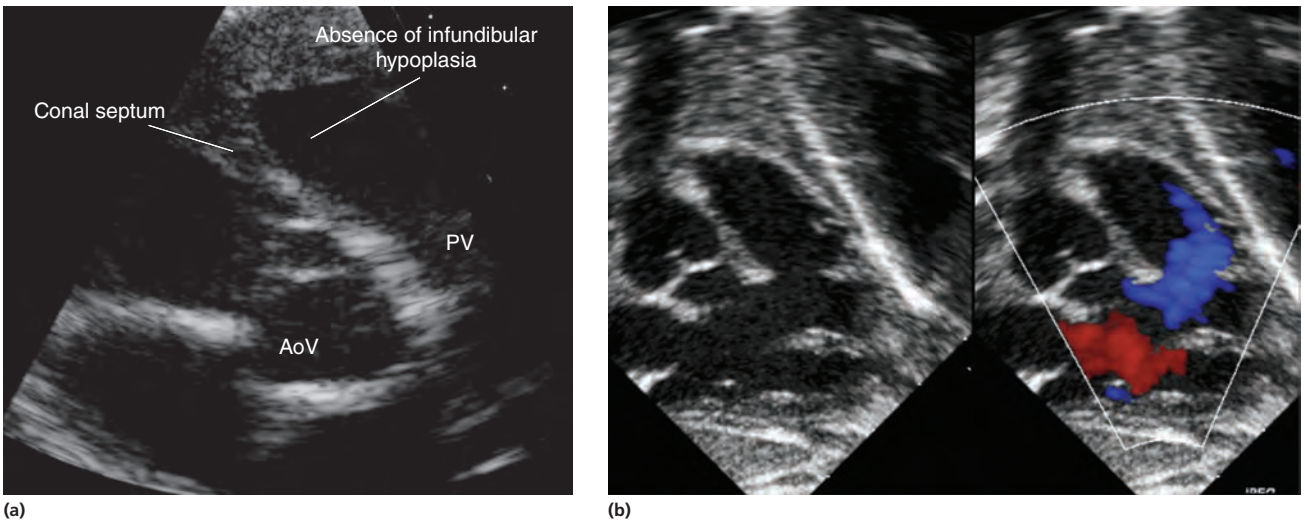


Figure 22.11 **(a)** Parasternal short-axis image of TOF with double-chambered RV variant. Note the deviated conal septum and prominent RV free wall muscle bundle resulting in narrowing of the proximal infundibular os but absence of infundibular hypoplasia and a normal pulmonary valve or distal infundibular os. AoV, aortic valve; PV, pulmonary valve. **(b)** Subxiphoid right anterior oblique view demonstrating the deviated conal septum and hypertrophied septal band resulting in double-chambered RV variant. Again note a well-expanded infundibulum and distal os infundibulum.

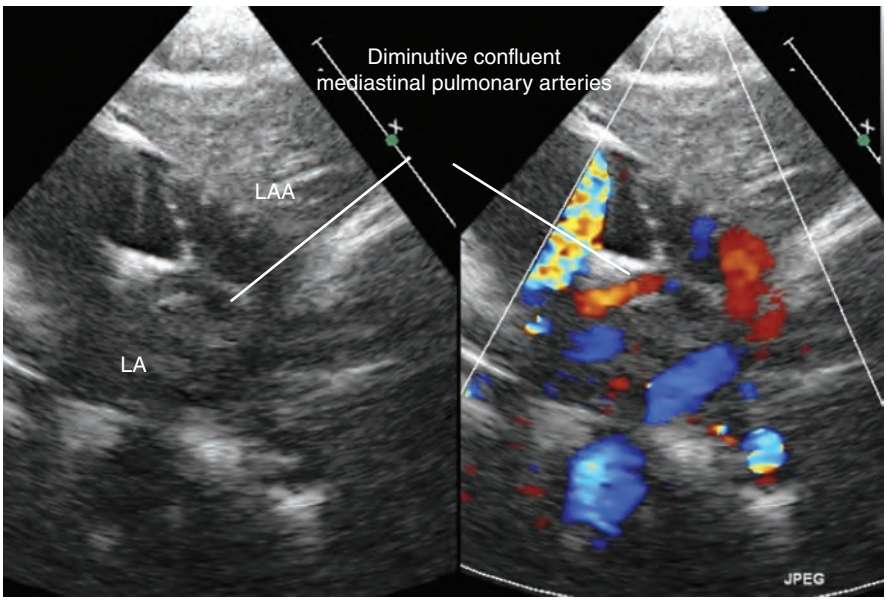


Figure 22.12 High left parasternal axial oblique color compare image showing diminutive, confluent mediastinal pulmonary arteries with retrograde flow in the right pulmonary artery on color flow mapping. LA, left atrium; LAA, left atrial appendage.

Rastelli type C morphology of the common AV valve has been reported in 85% of cases of TOF with CAVC [48] (Video 22.8). The diagnosis of type A common AV valve morphology in TOF has been questioned by Suzuki et al., who argued that attachments of the superior bridging leaflet to the crest of a malalignment VSD are unlikely [49]. We have observed concomitant absence of conal septum in the setting of otherwise typical morphology for TOF with CAVC. A small or absent primum ASD component can also occur in this morphologic variant, which can increase the challenge of surgical correction of this lesion [50,74]. TOF may also exist in conjunction with a cleft mitral valve without a primum ASD [75].

TOF with absent pulmonary valve syndrome

The prevalence of TOF with absent pulmonary valve is reported between 3% and 6% of TOF cases [76,77]. This anatomic variant is characterized by the typical anterior malalignment VSD and overriding aorta, but is differentiated by hypoplasia of the pulmonary valve annulus with rudimentary leaflets causing pulmonary stenosis and regurgitation. The main and/or one or both branch pulmonary arteries are typically aneurysmally enlarged [78,79]. This lesion is usually associated with absent patent ductus arteriosus (PDA), and prenatal absence of the PDA has been demonstrated by fetal echocardiography [78,80]. Marked dilation of the pulmonary arteries is associated with variable degrees of bronchial compression and intraparenchymal pulmonary arteriopathy, and may cause severe neonatal respiratory distress. In the fetus, severe forms may lead to hydrops fetalis or fetal demise.

Aortic arch anomalies

Right aortic arch (RAA) is seen in approximately 25% of patients with TOF [81,82], and is often associated with an aberrant left subclavian artery [72]. Double aortic arch, persistence of the fifth aortic arch, or other morphologic variations of vascular rings may also be associated with TOF [63,83,84].

Right aortic arch with isolation of the subclavian artery or with aberrant origin of the left subclavian artery from the ascending aorta have been reported [85,86]. The isolated left subclavian artery can be supplied by the left vertebral artery (in which case the direction of blood flow is reversed) and may cause a subclavian steal phenomenon. Alternatively, the isolated left subclavian artery may be connected via a PDA to the main pulmonary artery. In the latter case, the left vertebral artery supplies the main pulmonary artery resulting in a congenital pulmonary artery steal [87].

Aortopulmonary defects and variations in pulmonary artery origin and bifurcation

Aortic origin of branch pulmonary artery [88], unilateral absence of branch pulmonary artery, crossed pulmonary arteries [89], aortopulmonary window [90], and pulmonary artery slings [91] have been described in association with TOF. Crossed pulmonary arteries may be a marker for 22q11 deletion [92].

Left-sided lesions associated with TOF

Isolated reports of supramitral stenosis, LV outflow tract obstruction secondary to adherent anterior mitral valve leaflet, and cleft mitral valve have been described in patients with TOF [42,75,93]. Other associated left heart lesions include aortic valve abnormalities (bicommissural, stenosis, or regurgitation) [94–96], coarctation of the aorta [96], LV diverticulum [97], and cor triatriatum [98].

Systemic and pulmonary venous anomalies and atrial septal defects

In TOF, systemic and pulmonary venous anomalies may be seen independently or in association with heterotaxy syndrome

[99–101]. Subaortic (retroaortic) position of the innominate vein is more commonly seen in TOF with pulmonary atresia [71] (Video 22.9). Left superior vena cava to the coronary sinus (or rarely, to the left atrium) has been described in up to 11% of cases [102,103]. Left superior vena cava to left atrium without a connecting left innominate vein, if undiagnosed, can result in persistent hypoxemia following complete repair. Persistence of the levoatrial cardinal vein has also been reported [101]. Partially or totally anomalous pulmonary venous connection may be seen in association with TOF [104], rarely as part of scimitar syndrome [105]. Atrial septal defects, typically secundum type, are seen in 86% of cases [103]. Rarely, sinus venosus defects or coronary sinus septal defects occur in TOF [99,106].

Other rare associated malformations

In TOF associated with heterotaxy syndrome, small left-sided structures including mitral stenosis and left ventricular hypoplasia are often seen. Isolated infundibuloarterial inversion in the setting of atrial situs solitus, D-looped ventricles, and inversus normally related great arteries, or {S,D,I}, has been reported in TOF [107–109]. In the right side of the heart, Ebstein anomaly and double-orifice tricuspid valve (TV) have been reported [47,110]. The association of TOF with ectopia cordis (often in combination with other midline defects and ventricular diverticulum) is known as "pentalogy of Cantrell" [111].

Imaging

Detailed echocardiographic assessment has made diagnostic angiography nearly obsolete in the routine preoperative assessment of TOF. However, angiography and cardiac magnetic resonance (CMR) serve an important complementary role in the assessment of rare aortic arch anomalies as well as MAPCAs and hypoplastic branch pulmonary arteries in the setting of associated pulmonary atresia and in absent pulmonary valve syndrome. CMR provides unique information about pulmonary vessels *and* airway architecture, both of which are important for surgical planning.

Preoperative echocardiographic assessment

Key elements

In all cases, complete anatomic and functional examination by 2D and 3D imaging, as appropriate, and by color and spectral Doppler. In addition, the following elements of cardiovascular anatomy and function should be evaluated in detail and be given priority.

- Cardiac position and presence or absence of thymus.
- Visceral and atrial situs and segmental diagnosis; conotruncal anatomy.
- Pulmonary and systemic venous connections and atrial septal defects.
- AV valve morphology and function.
- VSD morphology, differentiating between malalignment, doubly committed subarterial, and AV canal types [112]. Rule out additional muscular ventricular septal defects. Assess for restriction to flow and determine the direction of VSD shunting.
- Degree and morphology of RV outflow obstruction: assess conal septal size and position as well as additional muscular obstruction, as in DCRV.
- Assess pulmonary valve annular diameter and valve morphology.
- Determine main and branch pulmonary artery size and flow. Rule out anomalous origin or course of branch pulmonary arteries [e.g., left pulmonary artery (LPA) sling]. Evaluate for branch pulmonary artery hypoplasia, discrete stenosis, or discontinuity, especially following ductal closure.
- Subaortic and aortic valve morphology and function.
- Image PDA origin from the aortic arch or from the brachiocephalic arteries and rule out additional sources of pulmonary blood flow such as aorto-pulmonary collaterals. Distinguish PDA from MAPCA.
- Determine aortic arch sidedness and branching pattern. Assess for vascular rings and other arch malformations.
- Image coronary artery origins, branching, and flow; rule out anomalous origin of the LCA from the main pulmonary artery, anomalous origin of the LAD from the RCA, or other large coronary branches crossing the RV outflow tract that may complicate transannular patch repair or conduit placement.

Organization of preoperative anatomic assessment

Organized, systematic, and detailed imaging starting with the subxiphoid long-axis window is our preferred approach for accurate diagnosis of congenital heart disease (see Chapter 4). In TOF with moderate stenosis, sedation imposes an additional risk for a hypercyanotic spell due to the combination of intravascular volume depletion [from being kept NPO (nil per os) for sedation] and systemic vasodilation. Hence, whenever possible the details of branch pulmonary artery anatomy, arch morphology, and coronary morphology should be defined during a newborn examination. Neonates will often sleep soundly after feeding, allowing a comprehensive and detailed examination without sedation.

Color flow mapping and spectral Doppler are crucial in refining the diagnosis, screening for subtle structural abnormalities (e.g., coronary, arch and branch pulmonary artery) and, of course, in assessing the hemodynamics, as described in Chapter 6.

Subxiphoid imaging

The initial *subxiphoid long-axis sweep* demonstrates visceral and atrial situs, systemic venous connections, coronary sinus, and atrial septal morphology [113] (Video 22.10). The descending aorta in its cross-section may be visualized to the left of the

spine, and through the course of the sweep it can be seen crossing over to the right of the thoracic spine. The VSD with overriding of the aorta may be seen as well as subpulmonary infundibular hypoplasia and stenosis. Branch pulmonary arteries may also be identified from subxiphoid long-axis imaging as the RPA traverses from left to right above the atrial mass; the LPA and ductus are often better imaged with color Doppler flow mapping (Video 22.11).

The *subxiphoid short-axis view* defines the atrial septum, the entrance of the right upper pulmonary vein into the left atrium, VSD, RV hypertrophy, and muscle bundles within the RV that could result in additional intracavitary obstruction, as in DCRV. Cleft mitral valve and common AV valve are also well imaged in this plane.

A modified *right anterior oblique subxiphoid view* is of exceptional benefit in viewing the subpulmonary infundibulum, inclusive of both the size of the conal septum and its displacement (Figure 22.11b; Video 22.12) [114]. This view is also useful for assessing additional muscle bundles contributing to RV outflow tract obstruction in the DCRV variant.

Apical views

Apical views demonstrate the AV valves, VSD, overriding aortic valve (Video 22.13). This view may also help identify other associated anomalies, such as left-sided obstructive lesions. Additionally, the mechanism of atypical restriction of the VSD may be visualized (Video 22.14).

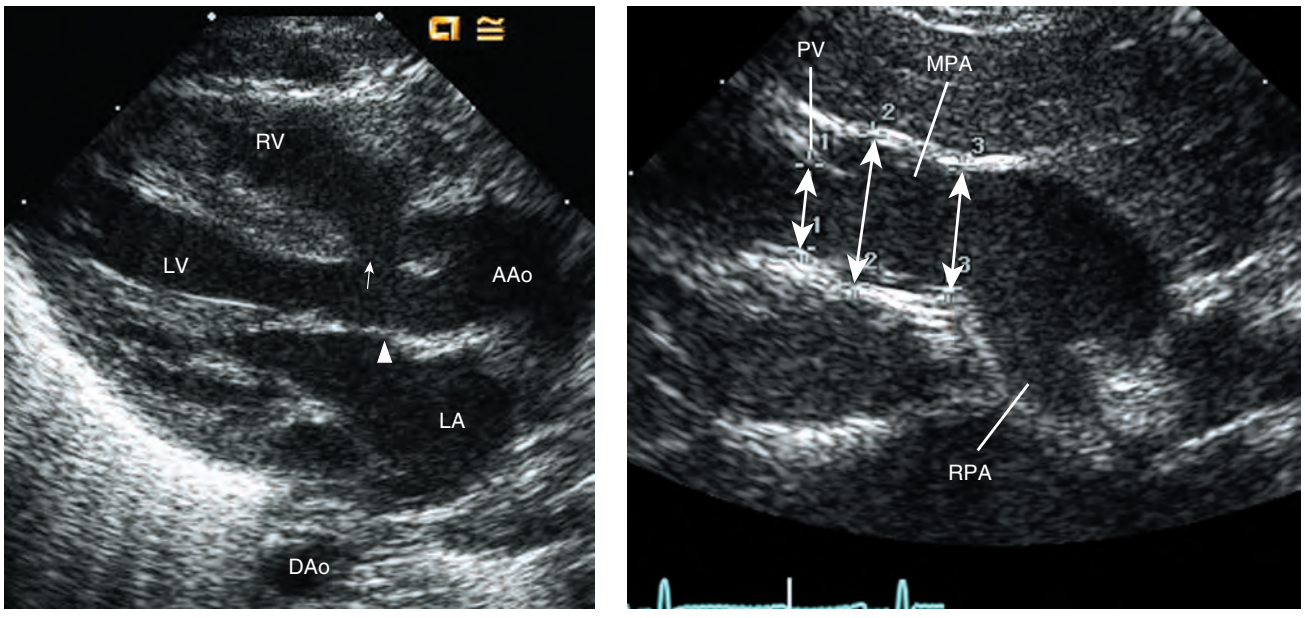
Parasternal imaging

Parasternal imaging may be limited if the thymus, which usually provides a reliably good acoustic window, is absent. The *parasternal long-axis view* demonstrates the overriding aorta, aortic-to-mitral valve fibrous continuity (distinguishing TOF from its related type of DORV) (Figure 22.13; Video 22.15), VSD morphology, and pulmonary valve morphology as the transducer sweeps leftward and anteriorly (Video 22.16).

The *parasternal short-axis view* further defines VSD morphology, subpulmonary obstruction, infundibular hypertrophy, and deviation of the conal septum (Video 22.17). Extension of the edge of the VSD beyond the intercoronary commissure under the right and noncoronary cusps and bordering the pulmonary valve annulus in the absence of the conal septum defines a doubly committed subarterial defect in TOF [44].

Ductal views

Imaging of the long axis of a ductus arteriosus is best performed from a high parasternal window in a sagittal plane or from the suprasternal notch long-axis view. At times, differentiating between a PDA and aorto-pulmonary collateral is difficult because both may arise from the same location in the proximal descending thoracic aorta. However, the termination of the vessel at the proximal branch pulmonary artery origin is consistent with a PDA, whereas aorto-pulmonary collaterals usually insert more distally into the branch pulmonary arteries at or distal to the hilum. Additionally, orthogonal imaging in a coronal plane from a high left parasternal view will demonstrate



(a) (b)

Figure 22.13 Parasternal long-axis view. **(a)** Image of the large conoventricular septal defect (arrow) with the aortic valve overriding the ventricular septum. Note the fibrous continuity between the aortic and mitral valve (arrowhead). **(b)** Tilting the transducer toward the left shoulder demonstrates the pulmonary valve (PV), main pulmonary artery (MPA) and proximal right pulmonary artery (RPA). Measurements of the pulmonary valve annulus and MPA are shown. AAo, ascending aorta; DAo, descending aorta; LA, left atrium; LV, left ventricle; RV, right ventricle.

the site of ductal insertion into the proximal branch pulmonary artery to evaluate the possibility for development of peripheral pulmonary artery stenosis or discontinuity consequent to ductal closure. Crossed pulmonary arteries are diagnosed when the RPA originates inferiorly from the left aspect of MPA and the LPA originates more superiorly from the right aspect of MPA (see Chapter 18).

High left parasternal imaging

The *high left parasternal view* helps to evaluate the main and branch pulmonary arteries (Video 22.18). It is important to align the beam perpendicular to the pulmonary artery being interrogated by altering the window of interrogation for each pulmonary artery. High (subclavicular) left sternal border windows are usually best for the main and left pulmonary arteries. High (subclavicular) right sternal border windows are usually best for the RPA. Larger branch pulmonary arteries have a lesser likelihood of concomitant presence of aorto-pulmonary collaterals. A branch pulmonary artery diameter z-score of less than −2.5 had a sensitivity of 88% and specificity of 100% for the presence of one or more MAPCAs [64].

Suprasternal notch imaging

Arch sidedness and branching pattern, retroaortic innominate vein (Video 22.9), partially anomalous venous connections to a systemic vein, double aortic arch, and vascular rings can be evaluated from this view. Left superior vena cava to coronary sinus or directly to left atrium with an unroofed coronary sinus are best seen from this view or from a left parasternal window in the sagittal plane.

Right parasternal views

Imaging from this acoustic window is best performed with the patient in a right decubitus position. This window allows clear imaging of the atrial septum, right superior vena cava, and the right pulmonary veins in right parasternal short-axis, sagittal, and transverse imaging planes, respectively. "En face" common AV valve morphology in patients with TOF and common AV canal can also be seen well from this window in short-axis planes.

Preoperative assessment by structures

Atrial septum

Color flow mapping of the atrial septum usually demonstrates the left-to-right shunting occurring in TOF even in the presence of severe pulmonary stenosis. Bidirectional or right-to-left shunting may be present in newborns.

Ventricular septal defect

The flow across the large VSD is usually nonrestrictive and bidirectional; only rarely it is restrictive. The degree of RV outflow tract obstruction determines the direction of flow across the VSD – less pulmonary stenosis allows predominantly left-to-right shunting, and the clinical scenario of "pink" TOF. More severe pulmonary stenosis results in predominant right-to-left shunting and cyanosis. In the typical setting of a nonrestrictive VSD, RV peak pressures cannot exceed systemic levels. Suprasystemic RV pressures in TOF can only occur in the setting of a restrictive VSD with pulmonary atresia or severe stenosis (Figures 22.6 and 22.7) [112]. Also, in the setting of a nonrestrictive malalignment VSD, additional muscular VSDs may be difficult to identify. Therefore, it is essential to interrogate the muscular septum by color flow mapping with a low Nyquist limit to identify low-velocity shunting across these small defects (Video 22.19).

In the rare preoperative TOF patient with pulmonary hypertension, as seen in Eisenmenger syndrome, the degree of right-to-left shunting across the VSD is affected by the presence of elevated pulmonary vascular resistance. Identification of a nonrestrictive source of pulmonary blood flow (such as an aortopulmonary window [115] or PDA [116]) is essential, as is the assessment for reversibility of pulmonary hypertension. Pulmonary venous obstruction has also been reported in association with TOF [117].

Right ventricular outflow tract and pulmonary arteries

The level of obstruction can be determined by imaging and by sequential pulsed Doppler interrogation starting from within the RV cavity to the pulmonary valve annulus. In severe stenosis, antegrade flow may be demonstrated using a lower-frequency transducer that achieves a higher Nyquist limit; this allows less "aliasing" of the color flow map of the high-velocity flow across the stenotic outflow tract. Continuous-wave (CW) Doppler interrogation is essential to estimate the total maximal instantaneous gradient, but accurate separation of the infundibular and valvar contributions to the total gradient is difficult with any Doppler interrogation technology (Figure 22.14). A double envelope is often noted with continuous-wave interrogation with the proximal late systolic peak representing proximal dynamic RVOT gradient.

The need for a transannular patch repair may be predicted by the size of the PV annulus and PV morphology. The decision for sparing the PV based on PV annulus size and associated supra-annular narrowing is surgeon- and institution-dependent. The following representative experiences have been reported: (i) PV annulus z-score ≥ -4, tricommissural PV, and RV/LV pressure ratio <0.7 associated with pulmonary valve-sparing procedures [118]; (ii) no association of PV annulus z-score with ability to preserve the pulmonary valve [119], and (iii) PV annulus z-score <-1.3 more likely to have postoperative pulmonary stenosis ≥ 30 mmHg [120].

In TOF with absent pulmonary valve syndrome, the severely dilated branch pulmonary arteries are readily apparent on subxiphoid imaging (Videos 20.20 and 22.21), and pulmonary regurgitation is easily demonstrated by color flow mapping (Videos 20.21–22.23) and may be associated with diastolic flow reversal in the branch pulmonary arteries.

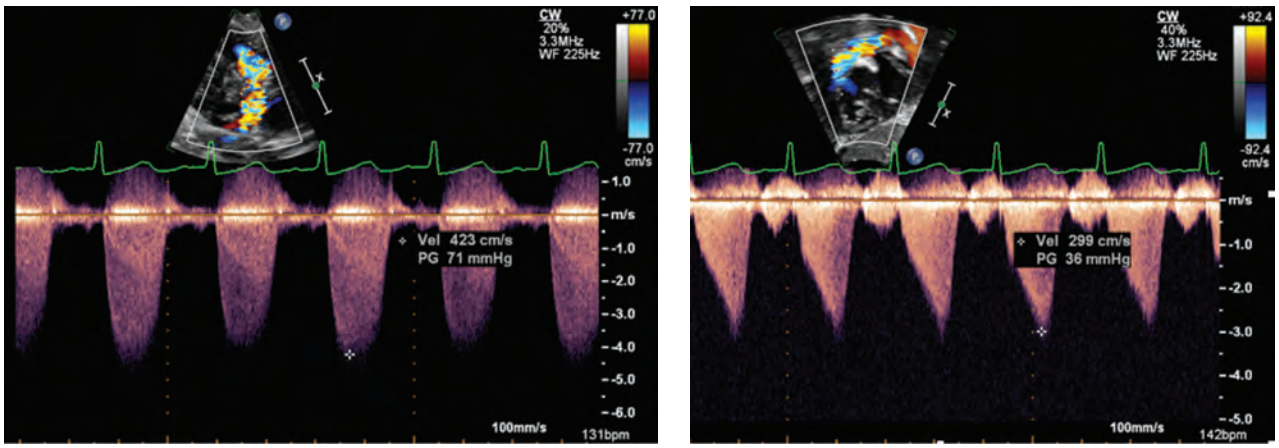


Figure 22.14 **(a)** RV outflow tract gradient by continuous-wave Doppler demonstrating a double envelope. The outer envelope with a parabolic shape reflects the total gradient. The envelope with a delayed systolic peak and the lower gradient is due to proximal RV outflow tract obstruction. **(b)** Pulsed-wave Doppler in the RV outflow tract demonstrates obstruction due to dynamic subpulmonary narrowing with a delayed maximal instantaneous gradient.

In patients with TOF and long-segment pulmonary atresia, the left atrial appendage can mimic the central main pulmonary artery segment (Video 22.24); this can be further delineated by careful imaging and by demonstration of low velocity to-and-fro flow by color and pulsed-wave (PW) Doppler. Because of its position under the aortic arch, the retroaortic innominate vein may mimic central confluent branch pulmonary arteries in pulmonary atresia. Doppler interrogation demonstrates the connection of the retroaortic innominate vein to the internal jugular vein or superior vena cava and demonstrates the typical multiphasic venous flow pattern of an innominate vein.

Atrioventricular valves

Color flow mapping from the apical window is used to assess the AV valve regurgitation that is usually seen in patients with associated malformations of the AV valves [e.g., Ebstein anomaly, double-orifice TV and mitral valve (MV), common AV valve, and cleft MV]. In the setting of significant mitral regurgitation without morphologic abnormalities and/or LV hypokinesis, associated anomalous origin of the LCA from the pulmonary artery must be excluded.

Aortic root dilation and regurgitation

Standard measurements in parasternal views will identify root and ascending aortic dilation, commonly seen in TOF, and allow serial follow-up of aortic size. Aortic regurgitation is uncommon preoperatively; it is most often acquired postoperatively or secondary to endocarditis.

Coronary arteries

The operator should employ the highest frequency transducers to achieve high-resolution coronary artery imaging. The Nyquist limit should be lowered on Doppler interrogation to accentuate low-velocity flow.

The origin of the coronary arteries can be demonstrated from the short-axis image. Clockwise rotation of the origins as viewed from the apex, a common finding in TOF, may be appreciated in this view. The left main coronary artery and its bifurcation are elongated by clockwise rotation of the transducer from the short-axis into a transverse plane (Videos 20.3–22.5). Evaluation for a LAD coronary artery origin from the RCA crossing the RV outflow tract requires a careful sweep from the standard reference view in the parasternal long axis, angling toward the left shoulder. Additional views that may be helpful include a high left parasternal cut in a transverse plane or a modified apical 4-chamber view angled anteriorly. Prominent crossing conal branches or dual LAD may be diagnosed in these sweeps, or occasionally from the most coronal extent of subxiphoid long-axis sweeps. Rare single RCA or LCA and anomalous origin of the LCA from the pulmonary artery may also be diagnosed. However, the echocardiographer must recognize that the turbulent pulmonary artery flow jets that characterize TOF may obscure the retrograde coronary flow emptying into the pulmonary artery.

With high-resolution parasternal imaging, color flow mapping with a low Nyquist limit is used to confirm the coronary origins and branching patterns, as well as to exclude anomalous origin of the left coronary artery from the pulmonary artery (ALCAPA). Depressed ventricular function is usually present in the setting of ALCAPA, but if there is associated pulmonary hypertension, as in cases of TOF with minimal pulmonary stenosis or with nonrestrictive PDA, ventricular function may be normal. Coronary–cameral fistulae may also be detected by color flow mapping but coronary–pulmonary artery fistulae may be obscured by aliased pulmonary artery flow patterns due to the pulmonary stenosis.

Intraoperative and postoperative assessment after TOF repair

Intraoperative echocardiographic assessment of TOF repair is almost always accomplished by using transesophageal echocardiography (TEE) or, in situations where esophageal access is not possible, utilizing an epicardial approach. The goal of the intraoperative TEE evaluation should be aimed at identification of hemodynamically significant lesions that can affect immediate postoperative management as well as long-term outcomes. Knowing the details of the surgical repair is essential to a successful intraoperative echocardiographic evaluation, and good communication between the surgeon and echocardiographer is paramount. Conventional echocardiography and TEE are important in the evaluation of the postoperative patient in the intensive care unit (ICU), especially to assess acute changes in clinical status. In addition to the TEE evaluation described in the following section, conventional echocardiography enables assessment of diaphragmatic motion and pleural or pericardial effusions. Conventional windows are often superior to TEE for assessment of the aortic arch and branch pulmonary arteries.

Goals for intraoperative TEE evaluation

- Residual VSD, including size, location, and gradient
- Residual RV outflow tract obstruction, including location and gradient
- PV regurgitation
- Main and proximal branch PAs
- Residual patent foramen ovale or ASD, including flow direction
- TV regurgitation, including gradient (for estimation of RV systolic pressure)
- Aortic valve regurgitation
- RV size and function
- LV size and function
- Residual PDA, including size, flow direction, and gradient.

Evaluation of the adequacy of TOF repair begins with the assessment of residual RV outflow tract obstruction, which can be achieved from transgastric longitudinal (Video 22.20) and mid-esophageal RV outflow tract imaging planes. Pulmonary valve function and branch pulmonary arteries can be evaluated from the appropriate mid-esophageal windows. Although RV systolic pressure can be estimated from Doppler interrogation of tricuspid regurgitation, RV outflow tract, or residual VSD, the angle of interrogation must be optimized. When necessary, Doppler data should be confirmed by direct pressure measurements.

The evaluation of surgical repair includes scanning for residual septal defects. The impact of residual atrial septal communications depends on the relative compliances of the right and left heart chambers. In the setting of RV dysfunction, which is common after TOF repair, right-to-left atrial-level shunting results in postoperative hypoxemia. In this setting, right-to-left diastolic shunting may also be noted across a residual VSD, even in the setting of left-to-right systolic shunting. Small residual VSDs with restrictive flow may have no impact on postoperative hemodynamics. The assessment of hemodynamic significance may be supplemented by direct intraoperative pressure and saturation data. Residual "intramural" VSDs occur when the VSD patch allows the blood to pursue a tortuous course within the myocardial trabeculations before exiting into the RV cavity. These defects are often quite small or unapparent initially, but may enlarge progressively on mid- to long-term follow-up. Occasionally, surgical closure of the large malalignment VSD may unmask previously undiagnosed additional small muscular VSDs.

It is important to assess tricuspid and aortic valve competence because either valve may be distorted by VSD patch closure. Postoperatively acquired small coronary fistulae are commonly seen following infundibular muscle resection; these hemodynamically insignificant fistulae often regress on follow-up examinations but may persist in the long term.

Adults with TOF

Unrepaired TOF in adults is rare. Surgical outcomes in adults with unrepaired TOF are generally good, with in-hospital mortality reported to be as low as 1.9% and significant functional improvement in the survivors. Evaluation of adults is different only in so far as obtaining adequate acoustic access may be more challenging. Otherwise, assessment should proceed as described earlier.

Repaired TOF

The evaluation of the adult with repaired TOF is focused at the assessment of factors that contribute to adverse outcomes. Increase in morbidity and mortality is attributed to the chronic hemodynamic burden imposed by residual pulmonary regurgitation, right ventricular outflow tract patch, right ventricular fibrosis, and ventricular dyssynchrony. This ultimately results in biventricular dysfunction and risk for arrhythmia or sudden death. The pathophysiology of pulmonary regurgitation and ventricular dysfunction is elegantly reviewed by Geva (Figure 22.15) [121].

Current standards for intervention for pulmonary valve replacement and risk stratification are based on CMR data. These include measures of severe RV dilation and RV systolic dysfunction. There is some variability in the recommended cutoffs used as an indication for surgery. A review of the literature yields cutoffs of RV EDV >150–170 mL/m^2, RV ESV >80–90 mL/m^2, and RV EF <45–48% [121]. In addition, evidence of LV systolic dysfunction has been shown to correlate with RV systolic dysfunction [122]. There are ongoing efforts to better define risk factors for adverse outcomes, including an international multi-institutional registry titled the INDICATOR cohort [123,124].

Late echocardiographic assessment of adolescents and adults with repaired TOF involves assessments of RV and LV functional surrogates that have been correlated with CMR data and

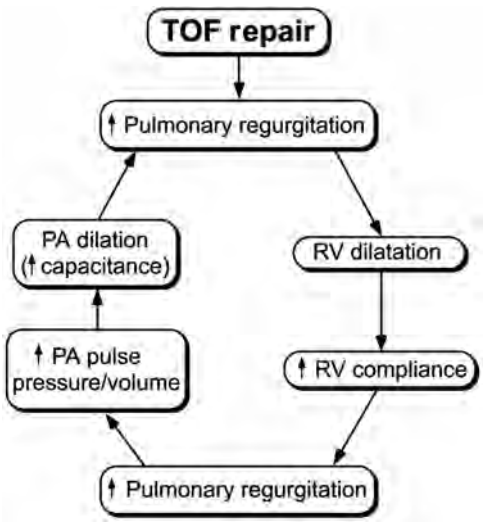


Figure 22.15 Pathophysiology of pulmonary regurgitation after TOF repair. Source: Geva T. Repaired tetralogy of Fallot: the roles of cardiovascular magnetic resonance in evaluating pathophysiology and for pulmonary valve replacement decision support. *J Cardiovasc Mag Reson* 2011;**13**.9. This is an Open Access article distributed under the terms of the Creative Commons Attribution License (http://creativecommons.org/licenses/by/2.0).

outcomes. The evaluation can be considered under the following three categories:

1 Assessment of physiologic and hemodynamic parameters that influence outcome, including
 - RV size and function
 - LV function
 - residual pulmonary stenosis or regurgitation
 - tricuspid regurgitation

 Serious derangements in the above categories have a significant impact on long-term outcomes, risk for ventricular arrhythmias, and sudden death [124].
2 Assessment of anatomic criteria of unknown significance on outcomes: RVOT aneurysm, DCRV, aortic dilation, and aortic regurgitation.
3 Echocardiography in pulmonary valve replacement (during and after transcatheter PV implantation, prosthetic PV, and RV-to-PA conduits).

Assessment of RV size and function in repaired TOF

RV size

Echocardiographic surrogates shown to have some utility in diagnosis of increased RV volumes include RV apical indexed end-diastolic area <22 cm^2/m^2, which identified patients with RV EDV by CMR <170 mL/m^2 and TV annular tilt of <20 degrees, which correlated well with RV indexed EDV <150 mL/m^2 [125]. Recently, 3D echocardiographic measurements of RV size and function have been correlated with CMR-derived RV values. However, because of systemic underestimation of RV dilation, 3D echocardiography cannot replace CMR for RV volumes in clinical decision making [126].

RV systolic function

Echocardiography has limited ability to accurately quantify RV function in repaired TOF [127], and recent guidelines published for the assessment of the RV in adults should be used with caution in the repaired TOF patient [128]. The more commonly used parameters for RV systolic function are TV annular peak systolic velocity (s′), isovolumic acceleration (IVA), tricuspid annular plane systolic excursion (TAPSE), myocardial performance index (MPI), and regional deformation indices such as strain and strain rate.

Published data suggest that the use of TV annular s′ <8.4 cm/s and IVA <95 cm/s^2 allowed identification of RV EF <45% [129]. In our experience [130], s′ had a very weak correlation with RV volumes and poor sensitivity and specificity in predicting RV EF. Correction of these variables for age improved identification of patients with low RV EF [130–132]. The utility of these indices as a screening tool to identify those with poor RV systolic function is only fair, but trending these indices in each patient over time may allow for using echocardiography as an adjunct and in spacing CMR evaluations.

Measures of RV longitudinal function, such as s′ and TAPSE, have been shown to be reduced in subjects with TOF compared with normal subjects. However, both s′ and TAPSE are affected by age, volume, and pressure load [133]. The value of TAPSE is also limited by the presence of the regional dysfunction commonly seen in this patient population [134,135]. A modified short-axis view has been proposed as being more sensitive for dysfunction in the evaluation of the postoperative RV [136].

There is a paradoxical decrease in MPI in the repaired TOF population with significant pulmonary regurgitation secondary to shortening of the isovolumic relaxation time. This "pseudonormalization" therefore decreases the sensitivity and clinical utility of this index [137].

Evaluation of RV regional function both by CMR and myocardial deformation imaging has allowed for a better understanding of the pathophysiology and evolution of RV dilation and biventricular dysfunction. RV free wall strain decreases with increasing pulmonary regurgitation as does RV apical function. Assessment of dyssynchrony may have a role in postoperative TOF evaluation. An increase in interventricular delay of >55 ms has been correlated with increased risk for ventricular arrhythmia [138,139]. Additionally intraventricular dyssynchrony defined as delay in time to peak systolic strain for the sinus compared to that of the RV infundibulum increases with increasing pulmonary regurgitation and is correlated with increased QRS duration and arrhythmic events [140].

Dobutamine stress echocardiography in combination with Doppler tissue indices (DTI) has been used to study RV functional reserve. A higher degree of pulmonary regurgitation (PR) has a negative impact on RV functional reserve [141, 142]. Decreased annular s′ and e′ DTI velocities correlate with decreasing peak oxygen consumption during exercise. Importantly, RV systolic velocity is predictive of exercise capacity in repaired TOF. Exercise stress echocardiography allows not only

for assessment of increase in RVOT gradients but also for assessment of decreased cardiac output and increased dyssynchrony. The potential use of stress echocardiography as an indication for PVR has yet to be evaluated.

RV diastolic function

Abnormal right atrial emptying and antegrade flow within the RV outflow tract or pulmonary artery at end-diastole (during atrial systole) throughout inspiration and expiration has been shown to represent RV diastolic dysfunction, with a correlation with worse clinical status [143]. Reduced early filling, impaired relaxation and increased RA volumes are prevalent and are adversely affected by an increase in RV volume [144]. Poor RV compliance also adversely affects LV filling and diastolic function [145].

Assessment of LV function

In addition to RV dilation and dysfunction, LV dysfunction – measured by CMR – has been shown to predict major adverse clinical events [122]. The demonstration of LV longitudinal dysfunction by echocardiography (longitudinal strain and mitral annular plane systolic excursion) has also been shown to predict life-threatening arrhythmia and death in patients with repaired TOF [146].

Impaired LV function may result from adverse ventricular interactions secondary to the shared myocardial band of the right and left ventricles. The findings of RV dilation and dysfunction, therefore, adversely impact LV performance in the repaired TOF population [147]. In a large multicenter, cross-sectional study with retrospective assessment of echocardiographic studies, LV systolic dysfunction (EF <55%) was reported in 21% of adults with repaired TOF [148].

Accurate quantification of LV function is limited by traditional echocardiographic methods because of abnormal chamber geometry in the postoperative patient. Conventionally derived shortening fractions are unreliable secondary to nearly universal diastolic septal flattening, which affects the geometric assumptions that underlie the measurement. RV dilation may interfere with apical windows, because the RV apex often replaces the LV apex as the acoustic window. The 5/6 area × length method for calculating ejection fraction (EF) has been demonstrated to more closely approximate CMR-derived LV EF than the biplane Simpson method [149].

Increased LV end-diastolic pressures are associated with increased RV end-diastolic volumes [150]. DTI indices are uniformly reduced in repaired TOF and this may be a function of smaller LV size in this cohort or inherent abnormalities in function secondary to ventricular interactions. Degree of impairment of RV compliance has been shown to correlate with larger RV dimensions and increase left atrial size and pronounced pulmonary venous reversal, which are surrogates of elevated LV end-diastolic pressures and left atrial pressures [145,151].

Assessment of pulmonary stenosis or regurgitation

Doppler estimates of RV outflow tract obstruction or peripheral branch pulmonary artery stenosis may be limited by suboptimal angle of interrogation or overestimation due to pressure recovery. Appropriate alignment with LPA flow can be achieved from the high right parasternal or suprasternal notch windows; and with the RPA flow from the high left parasternal window. A pattern of continuous antegrade diastolic flow with a "sawtooth" configuration is consistent with branch pulmonary artery stenosis.

The degree of pulmonary regurgitation (PR) is determined by (i) regurgitation orifice area; (ii) RV compliance; (iii) diastolic pressure difference between the main pulmonary artery (MPA) and the RV; (iv) capacitance of the pulmonary arteries; and (v) duration of diastole [121].

MRI is the currently accepted standard for quantification of PR. Echocardiographic features that have been validated for assessment of degree of PR have been compared to pulmonary regurgitant fractions and not to regurgitant volumes [152]. Echocardiographic evaluation of PR may include assessment by the following criteria (Figure 22.16):

1. Ratio of jet width/RV outflow diameter: mild <1/3; moderate 1/3–2/3; and severe >2/3.
2. Ratio of duration of PR/duration of diastole ≤0.77, which has been correlated with a PR regurgitant fraction ≥24.5% by CMR [153].
3. Pressure half-time <100 ms, which has been correlated with hemodynamically significant PR [154,155].
4. Presence of diastolic flow reversal in branch pulmonary arteries is associated with hemodynamically significant PR [156].

Right atrial function contributes significantly to overall RV output and performance. The atrial function comprises the following: reservoir, conduit, and pump function. Alterations and interdependence of right atrial filling, emptying, and RV EF have been demonstrated by speckle tracking and MRI. Clinical measures of right atrial function have yet to be determined and utilized in routine practice [157].

Assessment of tricuspid regurgitation and right atrial enlargement

Increased RV size due to PR can lead to annular dilation and an increase in tricuspid regurgitation that further aggravates RV volume overload. Tricuspid regurgitation is infrequently a major contributor to RV dilation in postoperative TOF unless there is an associated congenital tricuspid valve anomaly or inadvertent tricuspid valve damage during surgical repair.

Right atrial enlargement is considered a risk factor for arrhythmias, and its size should be evaluated during routine follow-up. Assessment of right atrial size and function are also now of increasing value since right atrial function and atrioventricular mechanical and functional synchrony are integral to RV function [143]. Right atrial enlargement in the absence of significant tricuspid regurgitation may signal the presence of restrictive RV physiology. Although current data suggests use of 18 cm^2

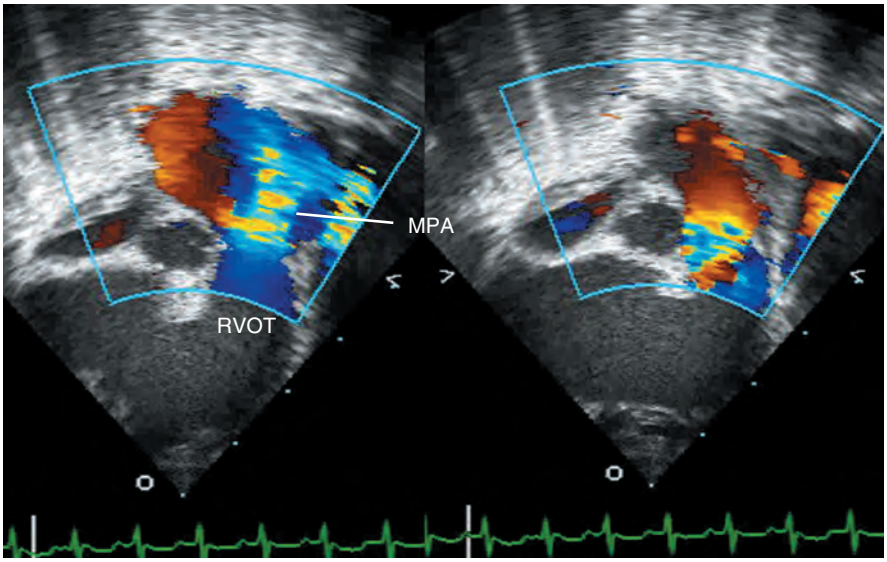


Figure 22.16 Color flow Doppler mapping of the RV outflow tract (RVOT) in an infant with TOF and absent pulmonary valve syndrome. The left panel shows a systolic frame with antegrade flow from the RVOT to the main pulmonary artery (MPA). The right panel shows a diastolic frame with a wide jet of retrograde flow from the MPA into the RVOT.

as an upper reference limit for RA end-systolic area [158], it should be noted that this cutoff value does not account for differences in body size.

Role of multimodality imaging

Comprehensive assessment of the anatomy and pathophysiology in the patient with repaired TOF often requires a combination of imaging modalities. The utility and limitation of each modality (echocardiography, MRI, CT, nuclear, etc.) is summarized by Valente et al. [159].

Echocardiographic assessment for transcatheter PV implantation

Assessment of suitability of RVOT morphology for transcatheter pulmonary valve implantation is an important component of follow-up care in most repaired TOF patients. The presence of conduit dysfunction with either stenosis or regurgitation is an appropriate indication for transcatheter PV implantation [160]. The following morphologic features should be assessed:

1. RVOT diameter, with current requirements of ≤22 mm for the Melody® valve, and >16 mm and <24 mm for the Edward Sapien® valve.
2. Presence of a transannular RV outflow tract patch.
3. Adherence of the conduit to the chest wall, which is a risk factor for early stent fracture.

Assessment of transcatheter implanted PV

A valve gradient of <15 mmHg and less than mild PR are acceptable results of transcatheter PV implantation. In a multicenter study of short- and medium-term outcomes, the only indication for reintervention following Melody valve placement was RV outflow tract obstruction [161]. Valve stent fracture and endocarditis have also been shown to be reasons for transcatheter-implanted valve failure.

Prenatal assessment

The diagnosis of TOF is often not obvious in the 4-chamber view. The LV outflow tract view or the 5-chamber view demonstrate aortic override, and on color flow mapping flow is directed from both ventricles into the aorta (Figure 22.17a). The basal short-axis view demonstrates the deviation of the conal septum, malalignment VSD, and subpulmonary stenosis (Figure 22.17b; Videos 22.25 and 22.26) The 3-vessel view (high axial cut of the superior vena cava, aorta, and main pulmonary artery) can demonstrate vessel size discrepancy, with the aorta being larger than the pulmonary artery (Figure 22.17c) [162]. The flow in the ductus arteriosus would be retrograde in case of severe pulmonic stenosis or atresia. Aortic arch sidedness and arch anomalies can be evaluated in the 3-vessel axial view, and the transmission qualities of the unexpanded fetal lungs can facilitate the prenatal diagnosis of vascular rings (Figure 22.18).

The following echocardiographic measurements have been reported to be useful in predicting severity of postnatal presentation and timing for intervention: poor PA growth, lower main PA, and PV z-scores; ascending aorta or PV/aortic valve ratio; elevation of Doppler velocities in the right ventricular outflow tract; and retrograde flow in ductus arteriosus [163–165]. Escribano et al. demonstrated that a pulmonary valve peak systolic velocity >87.5 cm/s predicted severity and timing of postnatal surgical intervention [165]. Recently, the absence of a patent ductus arteriosus and the degree of subpulmonary stenosis (defined as a ratio of the minimum dimension of the proximal os infundibulum to the descending aorta of <0.47) in the early second trimester had a high sensitivity and specificity in

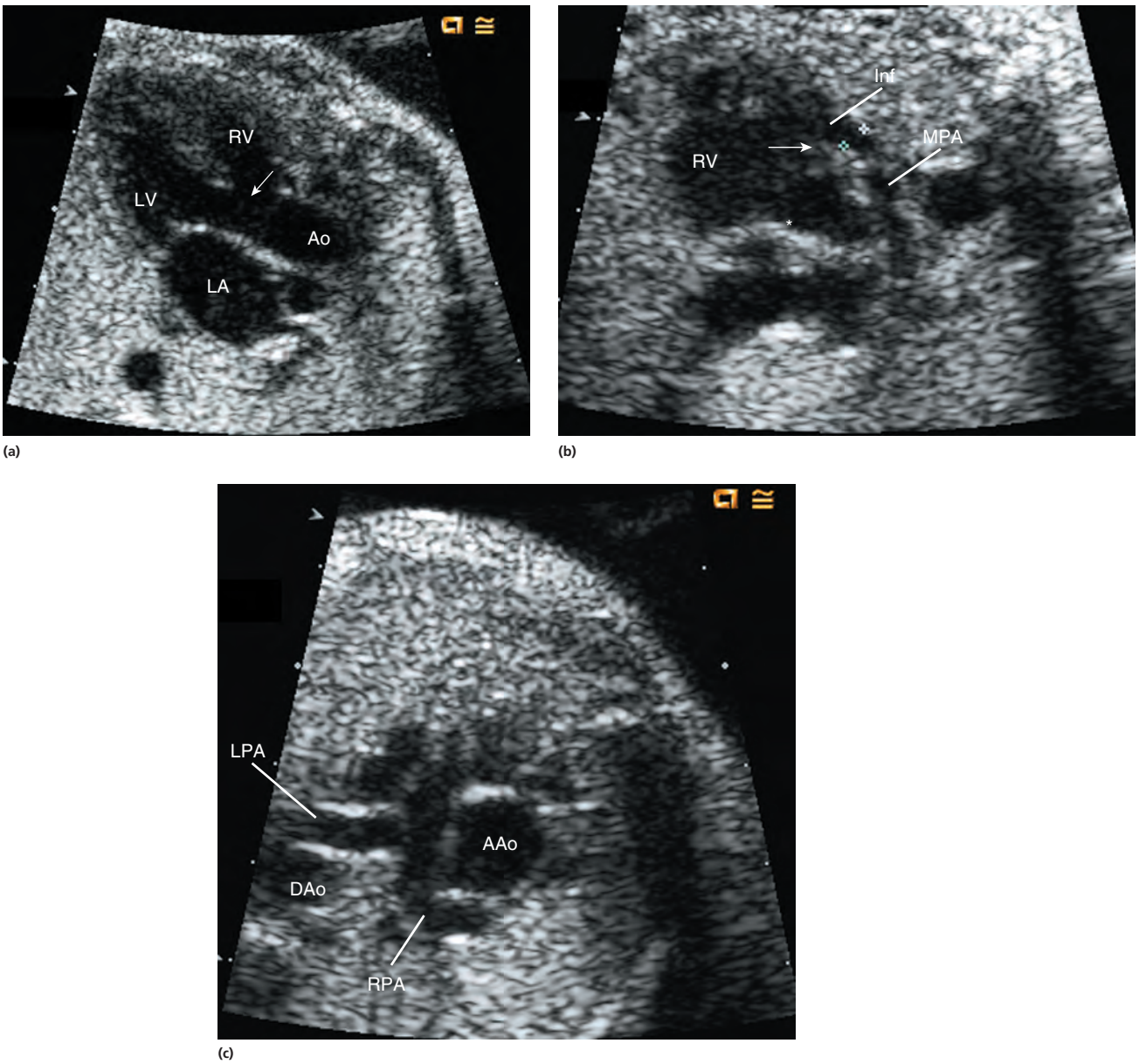


Figure 22.17 Fetal echocardiography in TOF with pulmonary stenosis. **(a)** Long-axis view of the left ventricular outflow demonstrates a large aortic root overriding a ventricular septal defect (arrow). **(b)** Imaging of the anteriorly deviated conal septum (arrow) and the conoventricular septal defect (∗). Note the hypoplastic infundibulum (Inf) and main pulmonary artery (MPA). **(c)** Transverse view of the fetal chest demonstrating the relatively small branch pulmonary arteries in relation to the dilated ascending aorta (AAo). DAo, descending aorta; LA, left atrium; LPA, left pulmonary artery; LV, left ventricle; RPA, right pulmonary artery; RV, right ventricle.

predicting severity of neonatal TOF [166]. Based on our institutional experience we would recommend using the RVOT gradient, degree of subpulmonary stenosis, and absence of a PDA in the early second trimester for counseling and directing delivery to a tertiary care center.

Serial fetal echocardiographic evaluations are recommended to screen for progression of pulmonary stenosis or branch pulmonary artery hypoplasia. Mild pulmonary stenosis in the early second trimester may progress to severe stenosis or atresia by the late third trimester [163]. This impacts upon neonatal management and counseling of the parents. Amniocentesis for associated chromosomal anomalies and fluorescence in situ hybridization (FISH) for microdeletion of chromosomal region 22q11 should be suggested routinely as this also bears a significant impact on neonatal outcome. The association of intrauterine growth retardation, polyhydramnios, increased nuchal translucency, and aortic arch anomalies with TOF can predict 22q11 deletion with a sensitivity of 88% [167,168]. The postnatal

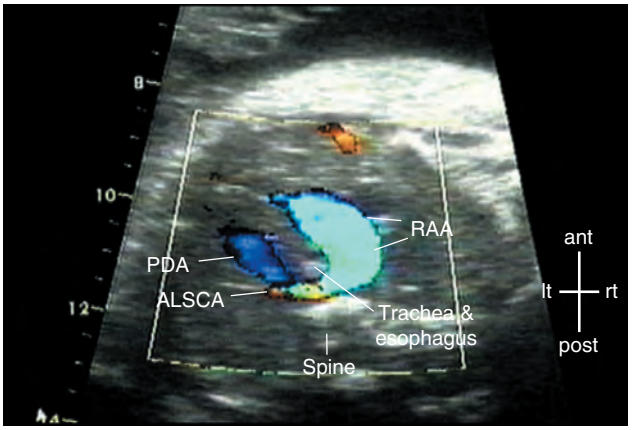


Figure 22.18 Prenatal echocardiographic diagnosis of TOF with a vascular ring. The ring comprises a right aortic arch (RAA), aberrant origin of the left subclavian artery (ALSCA), and left patent ductus arteriosus (PDA). ant, anterior; post, posterior; lt, left; rt, right.

prognosis of isolated TOF is good but outcomes of fetal diagnosis of conotruncal anomalies can be poor, mainly due to the frequent association with chromosomal or extracardiac anomalies, often leading to intrauterine or early neonatal death [169,170].

TOF with pulmonary atresia

Pulmonary atresia with TOF can be valvar, short-segment involving just the valve and proximal main pulmonary artery, or long-segment atresia in which the entire main pulmonary artery segment is missing. With long-segment atresia, it is prognostically essential to determine if there are central confluent mediastinal pulmonary arteries, and, if present, their degree of hypoplasia. Pulmonary stenosis can be progressive and evolve prenatally into pulmonary atresia [171,172]. Pulmonary blood supply from multiple aortopulmonary collaterals can be seen prenatally [171,172]. With short-segment pulmonary atresia, hypoplastic branch pulmonary arteries may be supplied by a tortuous PDA or, in the setting of a right aortic arch, from a PDA arising from the proximal left innominate artery.

TOF with pulmonary atresia may be mistaken for truncus arteriosus if the branch pulmonary artery origins are not clearly demonstrated. Both lesions share features of a large anterior malalignment VSD with overriding and enlarged semilunar root. Hence it is essential to image the origin or absence of branch pulmonary arteries when only one major vessel is seen overriding a malalignment VSD. It is also important to differentiate from truncus arteriosus the rare association of anomalous origin of a branch pulmonary artery from the ascending aorta with TOF. In the latter case, the contralateral branch pulmonary artery will be supplied by a separate, albeit small, pulmonary valve.

TOF with absent pulmonary valve

This lesion is easily diagnosed in utero because its key features stand out: the dysplastic pulmonary valve with stenosis and regurgitation and the aneurysmal main or branch pulmonary arteries (Figure 22.19; Videos 22.27–22.29). The ductus arteriosus is typically absent. Progressive RV and MPA dilation can be associated with hydrops fetalis due to RV dysfunction [80,173,174]. Neonatal outcome in published series was not predicted by the degree of pulmonary artery dilation but, as expected, outcome was poor in fetuses with hydrops [80]. Fetal MRI for assessment of associated lung and airway abnormalities may help predict postnatal outcome and management [175].

TOF with complete atrioventricular canal

In this lesion, the 4-chamber view is abnormal because the VSD extends from the inlet to the outlet septum. It is important to determine whether there is a balanced versus unbalanced AV canal defect as well as the degree of any associated AV valve regurgitation.

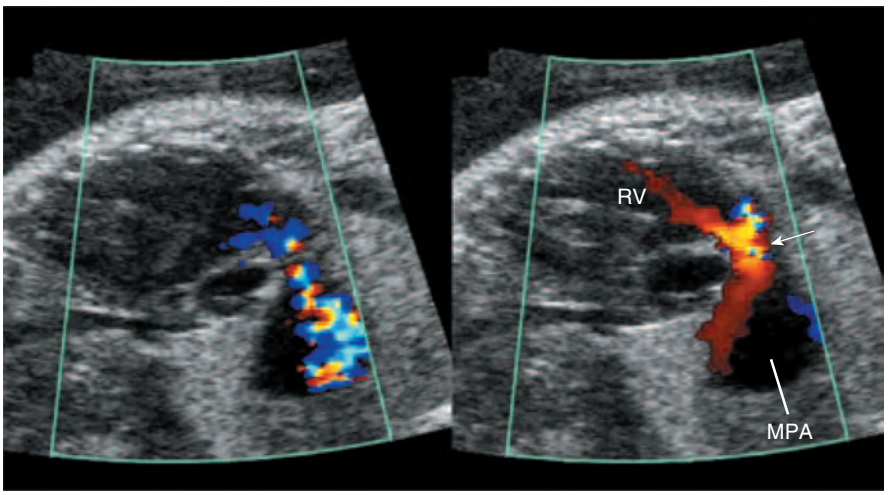


Figure 22.19 Fetal echocardiogram in TOF with absent pulmonary valve syndrome. The left panel shows a systolic frame with antegrade flow from the right ventricular outflow tract to a markedly dilated main pulmonary artery (MPA). The right panel shows a diastolic frame with pulmonary regurgitation jet into the right ventricle (RV). The arrow points to the location of the dysplastic pulmonary valve.

Associated genetic and extracardiac anomalies

Poon et al. reported their experience with fetal diagnosis of TOF at a mean gestational age of 20.6 weeks [170]. Increased nuchal translucency measurement >95th percentile was common (47%), but 19/37 fetuses had normal chromosomes. In their study cohort, 49% had chromosomal anomalies, including the 22q11 microdeletion in 15, with additional extracardiac malformations in 50% and additional cardiac malformations in 57%. In 70/129 (54%) cases, the parents chose termination of pregnancy.

Associated extracardiac anomalies can occur in up to approximately 30% of affected infants and children, and the incidence can be as high as 50–60% in fetal TOF. Important chromosomal and syndromic associations include microdeletion of chromosome 22q11, trisomies 21 and 18, pentalogy of Cantrell, VATER (vertebral anomalies, anal atresia, cardiac anomalies, tracheo-esophageal fistula, esophageal atresia, renal anomalies) or CHARGE (coloboma, heart defects, atresia of the choanae, retardation of growth, genital abnormalities, ear anomalies) association, tracheo-esophageal fistula, and omphalocele. Association with cleft palate may suggest velocardiofacial syndrome [162,167,170,176]. Appropriate prenatal evaluation and counseling for TOF requires careful high-level screening for noncardiac anomalies and chromosomal anomalies.

Videos

To access the videos for this chapter, please go to www.laiecho.com.

Video 22.1 Subxiphoid right anterior oblique 2D and color flow imaging of TOF with hypoplastic infundibulum and absent conal septum.

Video 22.2 Parasternal short-axis color compare images of prominent conal branch arising from the right coronary artery. AoV, aortic valve; PV, pulmonary valve.

Video 22.3 Parasternal short-axis color compare images with rotated origin of the left main coronary artery with antegrade flow well seen in the left anterior descending.

Video 22.4 Parasternal short-axis 2D image demonstrating a left anterior descending arising from the right coronary artery.

Video 22.5 Parasternal short-axis color compare images showing the left anterior descending coronary arising from the right coronary artery and coursing down to the anterior interventricular groove. Ao, aortic valve; PV, pulmonary valve.

Video 22.6 Parasternal short-axis color flow mapping of a large coronary artery-to-pulmonary artery fistula in a patient with pulmonary atresia in which the fistula serves as the source of pulmonary blood flow.

Video 22.7 Subxiphoid right anterior oblique color compare imaging of TOF with double-chambered right ventricle variant.

Video 22.8 Subxiphoid short-axis color compare of TOF with complete common atrioventricular canal defect (Rastelli type C).

Video 22.9 Suprasternal notch coronal 2D and color flow imaging of a small retroaortic innominate vein in a patient with tetralogy of Fallot and long segment pulmonary atresia. Ao, aorta; Inn Vn, innominate vein.

Video 22.10 Subxiphid long-axis 2D sweep demonstrating normal situs and normal cardiac segments in a patient with typical features of TOF.

Video 22.11 Subxiphoid long-axis color compare imaging of confluent branch pulmonary arteries with ductal flow into the left pulmonary artery in setting of long segment pulmonary atresia.

Video 22.12 Subxiphoid right anterior oblique color compare imaging demonstrating the anterior and superior deviation of conal septum (arrow).

Video 22.13 Apical 4-chamber color compare imaging with anterior angulation to demonstrate the overriding aorta.

Video 22.14 Apical 4-chamber color compare imaging showing aortic override and a restrictive, malalignment VSD with tricuspid valve-associated tissue partially obscuring the defect.

Video 22.15 Parasternal long-axis 2D and color flow mapping demonstrating a large, overriding aorta and fibrous continuity between the mitral and aortic valves. Also note the dilated coronary sinus.

Video 22.16 Parasternal long-axis image angled to the left and anteriorly to demonstrate the right ventricular outflow tract, pulmonary valve, and main pulmonary artery in this patient with TOF and multiple levels of obstruction starting at the proximal infundibular os, hypoplastic pulmonary annulus, sinotubular junction, and proximal main pulmonary artery.

Video 22.17 Parasternal short-axis 2D imaging demonstrating the deviated conal septum with significant dynamic obstruction of the right ventricular outflow tract.

Video 22.18 High left parasternal sagittal 2D imaging of the pulmonary valve and main pulmonary artery demonstrating infundibular narrowing. This is the preferred view for measurement of the pulmonary valve annulus and main pulmonary artery.

Video 22.19 Parasternal color flow mapping with a lowered Nyquist limit demonstrates multiple additional ventricular septal defects (VSDs) with bidirectional flow.

Video 22.20 Subxiphoid long-axis 2D imaging of TOF with absent pulmonary valve syndrome and massively dilated branch pulmonary arteries.

Video 22.21 Subxiphoid short-axis 2D imaging of TOF with absent pulmonary valve syndrome.

Video 22.22 Subxiphoid right anterior oblique color compare imaging in this patient with TOF with absent pulmonary valve

syndrome demonstrates aliased to-and-fro flow across the right ventricular outflow tract and proximal pulmonary arteries.

Video 22.23 Parasternal short-axis color compare imaging in this patient with TOF with absent pulmonary valve syndrome demonstrates pulmonary stenosis and regurgitation.

Video 22.24 Parasternal short-axis image of a patient with TOF with pulmonary atresia showing a normal left atrial appendage seen where one would typically expect to see the main pulmonary artery.

Video 22.25 Fetal echocardiogram – right ventricular basal short-axis or parasagittal "inflow–outflow" view.

Video 22.26 Fetal color flow imaging demonstrating antegrade flow across the hypoplastic pulmonary valve without pulmonary regurgitation.

Video 22.27 Fetal basal short-axis or parasagittal 2D image angled to show the dysplastic pulmonary valve in TOF.

Video 22.28 Fetal sagittal imaging with a bicaval view demonstrating massive dilation of the right pulmonary artery (rpa).

Video 22.29 Fetal basal short-axis ("axial oblique") color flow mapping angled to show significant pulmonary regurgitation in this patient with TOF/absent pulmonary valve syndrome.

References

1 Becker AE, Connor M, Anderson RH. Tetralogy of Fallot: a morphometric and geometric study. *Am J Cardiol* 1975;**35**:402–412.
2 Van Praagh R, Geva T, Kreutzer J. Ventricular septal defects: how shall we describe, name and classify them? *J Am Coll Cardiol* 1989;**14**:1298–1299.
3 Van Praagh R, Van Praagh S, Nebesar RA, et al. Tetralogy of Fallot: underdevelopment of the pulmonary infundibulum and its sequelae. *Am J Cardiol* 1970;**26**:25–33.
4 Abbott ME, Dawson WT. The clinical classification of congenital cardiac disease, with remarks upon its pathological anatomy, diagnosis and treatment. *Int Clin* 1924;**4**:156–188.
5 Jacobs ML. Congenital heart surgery nomenclature and database project: tetralogy of Fallot. *Ann Thorac Surg* 2000;**69**:S77–82.
6 Loffredo CA. Epidemiology of cardiovascular malformations: prevalence and risk factors. *Am J Med Genet* 2000;**97**:319–325.
7 Hoffman JI, Kaplan S. The incidence of congenital heart disease. *J Am Coll Cardiol* 2002;**39**:1890–1900.
8 Blalock A, Taussig HB. The surgical treatment of malformations of the heart in which there is pulmonary stenosis or pulmonary atresia. *JAMA* 1945;**128**:189–202.
9 Brogan TV, Alfieris GM. Has the time come to rename the Blalock-Taussig shunt? *Pediatr Crit Care Med* 2003;**4**:450–453.
10 Castaneda AR, Freed MD, Williams RG, Norwood WI. Repair of tetralogy of Fallot in infancy. Early and late results. *J Thorac Cardiovasc Surg* 1977;**74**:372–381.
11 Karr SS, Brenner JI, Loffredo C, et al. Tetralogy of Fallot. The spectrum of severity in a regional study, 1981–1985. *Am J Dis Child* 1992;**146**:121–124.
12 Marelli AJ, Mackie AS, Ionescu-Ittu R, et al. Congenital heart disease in the general population: changing prevalence and age distribution. *Circulation* 2007;**115**:163–172.
13 de la Cruz MV, Sanchez Gomez C, Arteaga MM, Arguello C. Experimental study of the development of the truncus and the conus in the chick embryo. *J Anat* 1977;**123**:661–686.
14 Mjaatvedt CH, Nakaoka T, Moreno-Rodriguez R, et al. The outflow tract of the heart is recruited from a novel heart-forming field. *Dev Biol* 2001;**238**:97–109.
15 Waldo KL, Kumiski DH, Wallis KT, et al. Conotruncal myocardium arises from a secondary heart field. *Development* 2001;**128**:3179–3188.
16 Kelly RG. Molecular inroads into the anterior heart field. *Trends Cardiovasc Med* 2005;**15**:51–56.
17 Ward C, Stadt H, Hutson M, Kirby ML. Ablation of the secondary heart field leads to tetralogy of Fallot and pulmonary atresia. *Dev Biol* 2005;**284**:72–83.
18 Towbin JA, Belmont J. Molecular determinants of left and right outflow tract obstruction. *Am J Med Genet* 2000;**97**:297–303.
19 Kelly RG, Brown NA, Buckingham ME. The arterial pole of the mouse heart forms from Fgf10-expressing cells in pharyngeal mesoderm. *Dev Cell* 2001;**1**:435–440.
20 Kelly RG, Buckingham ME. The anterior heart-forming field: voyage to the arterial pole of the heart. *Trends Genet* 2002;**18**:210–216.
21 Bajolle F, Zaffran S, Kelly RG, et al. Rotation of the myocardial wall of the outflow tract is implicated in the normal positioning of the great arteries. *Circ Res* 2006;**98**:421–428.
22 Kirby ML, Gale TF, Stewart DE. Neural crest cells contribute to normal aorticopulmonary septation. *Science* 1983;**220**:1059–1061.
23 Restivo A, Piacentini G, Placidi S, et al. Cardiac outflow tract: a review of some embryogenetic aspects of the conotruncal region of the heart. *Anat Rec A Discov Mol Cell Evol Biol* 2006;**288**:936–943.
24 Yelbuz TM, Waldo KL, Kumiski DH, et al. Shortened outflow tract leads to altered cardiac looping after neural crest ablation. *Circulation* 2002;**106**:504–510.
25 Tevosian SG, Deconinck AE, Tanaka M, et al. FOG-2, a cofactor for GATA transcription factors, is essential for heart morphogenesis and development of coronary vessels from epicardium. *Cell* 2000;**101**:729–739.
26 Gelb BD. Molecular genetics of congenital heart disease. *Curr Opin Cardiol* 1997;**12**:321–328.
27 Pierpont ME, Basson CT, Benson DW, Jr., et al. Genetic basis for congenital heart defects: current knowledge: a scientific statement from the American Heart Association Congenital Cardiac Defects Committee, Council on Cardiovascular Disease in the Young: endorsed by the American Academy of Pediatrics. *Circulation* 2007;**115**:3015–3038.
28 Formigari R, Michielon G, Digilio MC, et al. Genetic syndromes and congenital heart defects: how is surgical management affected? *Eur J Cardiothorac Surg* 2009;**35**:606–614.
29 Monaco M, Williams I. Tetralogy of Fallot: fetal diagnosis to surgical correction. *Minerva Pediatr* 2012;**64**:461–470.
30 Vergara P, Digilio MC, Zorzi AD, et al. Genetic heterogeneity and phenotypic anomalies in children with atrioventricular canal defect and tetralogy of Fallot. *Clin Dysmorphol* 2006;**15**:65–70.
31 Michielon G, Marino B, Oricchio G, et al. Impact of DEL22q11, trisomy 21, and other genetic syndromes on surgical outcome of

conotruncal heart defects. *J Thorac Cardiovasc Surg* 2009;**138**:565–570.
32 Mercer-Rosa L, Pinto N, Yang W, et al. 22q11.2 deletion syndrome is associated with perioperative outcome in tetralogy of Fallot. *J Thorac Cardiovasc Surg* 2013;**146**:868–873.
33 Levy HL, Guldberg P, Guttler F, et al. Congenital heart disease in maternal phenylketonuria: report from the maternal PKU collaborative study. *Pediatr Res* 2001;**49**:636–642.
34 Feldman GL, Weaver DD, Lovrien EW. The fetal trimethadione syndrome: report of an additional family and further delineation of this syndrome. *Am J Dis Child* 1977;**131**:1389–1392.
35 Calcagni G, Digilio MC, Sarkozy A, et al. Familial recurrence of congenital heart disease: an overview and review of the literature. *Eur J Pediatr* 2007;**166**:111–116.
36 Nora JJ, Nora AH. Familial risk of congenital heart defect. *Am J Med Genet* 1988;**29**:231–233.
37 Anderson RH, Weinberg PM. The clinical anatomy of tetralogy of Fallot. *Cardiol Young* 2005;**15**:38–47.
38 Anderson RH, Becker AE. Etienne-Louis Arthur Fallot and his tetralogy: a new translation of Fallot's summary and a modern reassessment of this anomaly. *Eur J Cardiothorac Surg* 1990;**4**:229–232.
39 Oppenheimer-Dekker A, Gittenberger-de Groot AC, Bartelings MM, et al. Abnormal architecture of the ventricles in hearts with an overriding aortic valve and a perimembranous ventricular septal defect ("Eisenmenger VSD"). *Int J Cardiol* 1985;**9**:341–355.
40 Gatzoulis MA, Soukias N, Ho SY, et al. Echocardiographic and morphological correlations in tetralogy of Fallot. *Eur Heart J* 1999;**20**:221–231.
41 Fukuda T, Suzuki T, Ito T. Clinical and morphologic features of perimembranous ventricular septal defect with overriding of the aorta–the so-called Eisenmenger ventricular septal defect. A study making comparisons with tetralogy of Fallot and perimembranous ventricular defect without aortic overriding. *Cardiol Young* 2000;**10**:343–352.
42 Van Praagh R, Corwin RD, Dahlquist EH, Jr., et al. Tetralogy of Fallot with severe left ventricular anomalous attachment of the mitral valve to the ventricular septum. *Am J Cardiol* 1970;**26**:93–101.
43 Rosenquist GC, Sweeney LJ, Stemple DR, et al. Ventricular septal defect in tetralogy of Fallot. *Am J Cardiol* 1973;**31**:749–754.
44 Capelli H, Somerville J. A typical Fallot's tetralogy with doubly committed subarterial ventricular septal defect. Diagnostic value of 2-dimensional echocardiography. *Am J Cardiol* 1983;**51**:282–285.
45 Faggian G, Frescura C, Thiene G, et al. Accessory tricuspid valve tissue causing obstruction of the ventricular septal defect in tetralogy of Fallot. *Br Heart J* 1983;**49**:324–327.
46 Flanagan MF, Foran RB, Van Praagh R, et al. Tetralogy of Fallot with obstruction of the ventricular septal defect: spectrum of echocardiographic findings. *J Am Coll Cardiol* 1988;**11**:386–395.
47 Davido A, Maarek M, Jullien JL, Corone P. Ebstein's disease associated with Fallot's tetralogy. Apropos of a familial case, review of the literature, embryologic and genetic implications. *Arch Mal Coeur Vaiss* 1985;**78**:752–756.
48 Delius RE, Kumar RV, Elliott MJ, et al. Atrioventricular septal defect and tetralogy of Fallot: a 15-year experience. *Eur J Cardiothorac Surg* 1997;**12**:171–176.
49 Suzuki K, Ho SY, Anderson RH, et al. Morphometric analysis of atrioventricular septal defect with common valve orifice. *J Am Coll Cardiol* 1998;**31**:217–223.
50 Kaur A, Srivastava S, Lytrivi ID, et al. Echocardiographic evaluation and surgical implications of common atrioventricular canal defects with absent or diminutive ostium primum defect. *Am J Cardiol* 2008;**101**:1648–1651.
51 Need LR, Powell AJ, del Nido P, Geva T. Coronary echocardiography in tetralogy of Fallot: diagnostic accuracy, resource utilization and surgical implications over 13 years. *J Am Coll Cardiol* 2000;**36**:1371–1377.
52 Chiu IS, Wu CS, Wang JK, et al. Influence of aortopulmonary rotation on the anomalous coronary artery pattern in tetralogy of Fallot. *Am J Cardiol* 2000;**85**:780–784, A9.
53 Meng CC, Eckner FA, Lev M. Coronary artery distribution in tetralogy of Fallot. *Arch Surg* 1965;**90**:363–366.
54 Krongrad E, Ritter DG, Hawe A, et al. Pulmonary atresia or severe stenosis and coronary artery-to-pulmonary artery fistula. *Circulation* 1972;**46**:1005–1012.
55 Shiraishi I, Yamagishi M, Toiyama K, et al. Coronary artery obstruction due to membranous ridge of the right sinus valsalva associated with tetralogy of Fallot: syncope mimics anoxic spell. *Ann Thorac Surg* 2004;**77**:321–322.
56 Chiu SN, Wu MH, Lin MT, et al. Acquired coronary artery fistula after open heart surgery for congenital heart disease. *Int J Cardiol* 2005;**103**:187–192.
57 Cicini MP, Giannico S, Marino B, et al. "Acquired" subvalvular aortic stenosis after repair of a ventricular septal defect. *Chest* 1992;**101**:115–118.
58 Moran AM, Hornberger LK, Jonas RA, Keane JF. Development of a double-chambered right ventricle after repair of tetralogy of Fallot. *J Am Coll Cardiol* 1998;**31**:1127–1133.
59 Galiuto L, O'Leary PW, Seward JB. Double-chambered right ventricle: echocardiographic features. *J Am Soc Echocardiogr* 1996;**9**:300–305.
60 Collett RW EJ. Persistent truncus arteriosus. A classification according to anatomic subtypes. *Surg Clin North Am* 1949;**29**:1245.
61 Bharati S, Paul MH, Idriss FS, et al. The surgical anatomy of pulmonary atresia with ventricular septal defect: pseudotruncus. *J Thorac Cardiovasc Surg* 1975;**69**:713–721.
62 Tchervenkov CI, Roy N. Congenital heart surgery nomenclature and database project: pulmonary atresia–ventricular septal defect. *Ann Thorac Surg* 2000;**69**:S97–105.
63 Macartney F, Deverall P, Scott O. Haemodynamic characteristics of systemic arterial blood supply to the lungs. *Br Heart J* 1973;**35**:28–37.
64 Acherman RJ, Smallhorn JF, Freedom RM. Echocardiographic assessment of pulmonary blood supply in patients with pulmonary atresia and ventricular septal defect. *J Am Coll Cardiol* 1996;**28**:1308–1313.
65 Hadjo A, Jimenez M, Baudet E, et al. Review of the long-term course of 52 patients with pulmonary atresia and ventricular septal defect. Anatomical and surgical considerations. *Eur Heart J* 1995;**16**:1668–1674.
66 Mackie AS, Gauvreau K, Perry SB, et al. Echocardiographic predictors of aortopulmonary collaterals in infants with tetralogy of Fallot and pulmonary atresia. *J Am Coll Cardiol* 2003;**41**:852–857.

67 Thiene G, Frescura C, Bortolotti U, et al. The systemic pulmonary circulation in pulmonary atresia with ventricular septal defect: concept of reciprocal development of the fourth and sixth aortic arches. *Am Heart J* 1981;**101**:339–344.

68 Nakata S, Imai Y, Takanashi Y, et al. A new method for the quantitative standardization of cross-sectional areas of the pulmonary arteries in congenital heart diseases with decreased pulmonary blood flow. *J Thorac Cardiovasc Surg* 1984;**88**:610–619.

69 Padmanabhan J, Varghese PJ, Lloyd S, Haller JA, Jr. Tetralogy of Fallot with suprasystemic pressure in the right ventricle. A case report and review of the literature. *Am Heart J* 1971;**82**:805–811.

70 Shinonaga M, Miyamura H, Watanabe H, et al. Tetralogy of Fallot with a restrictive ventricular septal defect caused by a membranous flap. *Nippon Kyobu Geka Gakkai Zasshi* 1994;**42**:1378–1381.

71 Ito M, Kikuchi S, Hachiro Y, Abe T. Anomalous subaortic position of the brachiocephalic vein associated with tetralogy of Fallot. *Ann Thorac Cardiovasc Surg* 2001;**7**:106–108.

72 Ramaswamy P, Lytrivi ID, Thanjan MT, et al. Frequency of aberrant subclavian artery, arch laterality, and associated intracardiac anomalies detected by echocardiography. *Am J Cardiol* 2008;**101**:677–682.

73 Vargas FJ, Kreutzer GO, Pedrini M, et al. Tetralogy of Fallot with subarterial ventricular septal defect. Diagnostic and surgical considerations. *J Thorac Cardiovasc Surg* 1986;**92**:908–912.

74 Uretzky G, Puga FJ, Danielson GK, et al. Complete atrioventricular canal associated with tetralogy of Fallot. Morphologic and surgical considerations. *J Thorac Cardiovasc Surg* 1984;**87**:756–766.

75 Van Praagh S, Porras D, Oppido G, et al. Cleft mitral valve without ostium primum defect: anatomic data and surgical considerations based on 41 cases. *Ann Thorac Surg* 2003;**75**:1752–1762.

76 Jekel L, Benatar A, Bennink GB, et al. Tetralogy of Fallot with absent pulmonary valve. A continuing challenge. *Scand Cardiovasc J* 1998;**32**:213–217.

77 Lev M, Eckner FA. The pathologic anatomy of tetralogy of Fallot and its variations. *Dis Chest* 1964;**45**:251–261.

78 Emmanoulides GC, Thanopoulos B, Siassi B, Fishbein M. "Agenesis" of ductus arteriosus associated with the syndrome of tetralogy of Fallot and absent pulmonary valve. *Am J Cardiol* 1976;**37**:403–409.

79 Lakier JB, Stanger P, Heymann MA, et al. Tetralogy of Fallot with absent pulmonary valve. Natural history and hemodynamic considerations. *Circulation* 1974;**50**:167–175.

80 Moon-Grady AJ, Tacy TA, Brook MM, et al. Value of clinical and echocardiographic features in predicting outcome in the fetus, infant, and child with tetralogy of Fallot with absent pulmonary valve complex. *Am J Cardiol* 2002;**89**:1280–1285.

81 Allen HD, Adams FH, Moss AJ. *Moss and Adams' Heart Disease in Infants, Children, and Adolescents: Including the Fetus and Young Adult*, 6th edn. Philadelphia, PA: Lippincott Williams and Wilkins, 2001.

82 Craatz S, Kunzel E, Spanel-Borowski K. Right-sided aortic arch and tetralogy of Fallot in humans–a morphological study of 10 cases. *Cardiovasc Pathol* 2003;**12**:226–232.

83 Donti A, Soavi N, Sabbatani P, Picchio FM. Persistent left fifth aortic arch associated with tetralogy of Fallot. *Pediatr Cardiol* 1997;**18**:229–231.

84 Emmel M, Schmidt B, Schickendantz S. Double aortic arch in a patient with Fallot's tetralogy. *Cardiol Young* 2005;**15**:52–53.

85 Chen MR, Yu CH. Subclavian and pulmonary steal phenomenon in isolated left subclavian artery with left lung agenesis. *Jpn Heart J* 2002;**43**:429–432.

86 Krishnan KG, Theodore S, Kiran S, Neelakandhan KS. Embryologic and surgical considerations in tetralogy of Fallot with right arch and aberrant left subclavian artery from the ascending aorta. *J Thorac Cardiovasc Surg* 2005;**130**:215–216.

87 Carano N, Piazza P, Agnetti A, Squarcia U. Congenital pulmonary steal phenomenon associated with tetralogy of Fallot, right aortic arch, and isolation of the left subclavian artery. *Pediatr Cardiol* 1997;**18**:57–60.

88 Soylu M, Demir AD, Tikiz H, et al. Left hemitruncus associated with tetralogy of Fallot: a case report. *Catheter Cardiovasc Interv* 2000;**51**:58–60.

89 Chaturvedi R, Mikailian H, Freedom RM. Crossed pulmonary arteries in tetralogy of Fallot. *Cardiol Young* 2005;**15**:537.

90 Castaneda AR, Kirklin JW. Tetralogy of Fallot with aorticopulmonary window. report of two surgical cases. *J Thorac Cardiovasc Surg* 1977;**74**:467–468.

91 Calder AL, Brandt PW, Barratt-Boyes BG, Neutze JM. Variant of tetralogy of Fallot with absent pulmonary valve leaflets and origin of one pulmonary artery from the ascending aorta. *Am J Cardiol* 1980;**46**:106–116.

92 Recto MR, Parness IA, Gelb BD, et al. Clinical implications and possible association of malposition of the branch pulmonary arteries with DiGeorge syndrome and microdeletion of chromosomal region 22q11. *Am J Cardiol* 1997;**80**:1624–1627.

93 Hohn AR, Jain KK, Tamer DM. Supravalvular mitral stenosis in a patient with tetralogy of Fallot. *Am J Cardiol* 1968;**22**:733–737.

94 Aru GM, Juraszek A, Moskowitz I, Van Praagh R. Tetralogy of Fallot with congenital aortic valvar stenosis: the tetralogy–truncus interrelationship. *Pediatr Cardiol* 2006;**27**:354–359.

95 Ermis C, Gupta-Malhotra M, Titus JL. An obstructive bicuspid aortic valve in the setting of tetralogy of Fallot with pulmonary atresia: a rare combination. *Cardiol Young* 2004;**14**:99–101.

96 Freedom RM, Benson LN, Mikailian H. Aortic coarctation in an infant with tetralogy and pulmonary atresia. *Cardiol Young* 2005;**15**:667–668.

97 Alayunt A, Yagdi T, Alat I, et al. Left ventricular diverticulum associated with Cantrell's syndrome and tetralogy of Fallot in an adult. *Scand Cardiovasc J* 2001;**35**:55–57.

98 Van Praagh R, Corsini I. Cor triatriatum: pathologic anatomy and a consideration of morphogenesis based on 13 postmortem cases and a study of normal development of the pulmonary vein and atrial septum in 83 human embryos. *Am Heart J* 1969;**78**:379–405.

99 Da Cruz E, Milella L, Corno A. Left isomerism with tetralogy of Fallot and anomalous systemic and pulmonary venous connections. *Cardiol Young* 1998;**8**:131–133.

100 Ferrin LM, Atik E, Aiello V, et al. Tetralogy of Fallot associated with left atrial isomerism. *Arq Bras Cardiol* 1996;**67**:249–253.

101 Fujiwara K, Naito Y, Komai H, et al. Tetralogy of Fallot with levoatrial cardinal vein. *Pediatr Cardiol* 1999;**20**:136–138.

102 Brzezinski M, Keller R, Grichnik KP, Swaminathan M. Persistent left superior vena cava in a patient with a history of tetralogy of Fallot. *Anesth Analg* 2005;**100**:1269–1270.

103 Rao BN, Anderson RC, Edwards JE. Anatomic variations in the tetralogy of Fallot. *Am Heart J* 1971;**81**:361–371.

104 Redington AN, Raine J, Shinebourne EA, Rigby ML. Tetralogy of Fallot with anomalous pulmonary venous connections: a rare but clinically important association. *Br Heart J* 1990;**64**:325–328.
105 Azhari N, Al-Fadley F, Bulbul ZR. Tetralogy of Fallot associated with scimitar syndrome. *Cardiol Young* 2000;**10**:70–72.
106 Quaegebeur J, Kirklin JW, Pacifico AD, Bargeron LM, Jr. Surgical experience with unroofed coronary sinus. *Ann Thorac Surg* 1979;**27**:418–425.
107 Foran RB, Belcourt C, Nanton MA, et al. Isolated infundibuloarterial inversion (S,D,I): a newly recognized form of congenital heart disease. *Am Heart J* 1988;**116**:1337–1350.
108 Santini F, Jonas RA, Sanders SP, Van Praagh R. Tetralogy of Fallot [S,D,I]: successful repair without a conduit. *Ann Thorac Surg* 1995;**59**:747–749.
109 Van Praagh R. Tetralogy of Fallot [S,D,I]: a recently discovered malformation and its surgical management. *Ann Thorac Surg* 1995;**60**:1163–1165.
110 Oppido G, Napoleone CP, Ragni L, et al. Double orifice tricuspid valve in an infant with tetralogy of Fallot. *Ann Thorac Surg* 2006;**81**:1121–1123.
111 Cantrell JR, Haller JA, Ravitch MM. A syndrome of congenital defects involving the abdominal wall, sternum, diaphragm, pericardium, and heart. *Surg Gynecol Obstet* 1958;**107**:602–614.
112 Musewe NN, Smallhorn JF, Moes CA, et al. Echocardiographic evaluation of obstructive mechanism of tetralogy of Fallot with restrictive ventricular septal defect. *Am J Cardiol* 1988;**61**:664–668.
113 Sanders SP, Bierman FZ, Williams RG. Conotruncal malformations: diagnosis in infancy using subxiphoid 2-dimensional echocardiography. *Am J Cardiol* 1982;**50**:1361–1367.
114 Marino B, Ballerini L, Marcelletti C, et al. Right oblique subxiphoid view for two-dimensional echocardiographic visualization of the right ventricle in congenital heart disease. *Am J Cardiol* 1984;**54**:1064–1068.
115 Carminati M, Borghi A, Valsecchi O, et al. Aortopulmonary window coexisting with tetralogy of Fallot: echocardiographic diagnosis. *Pediatr Cardiol* 1990;**11**:41–43.
116 Liang CD, Huang SC, Su WJ. Pulmonary vascular obstructive disease and hemoptysis in a child with tetralogy of Fallot and patent ductus arteriosus. *J Formos Med Assoc* 1997;**96**:121–124.
117 Lee ML, Wu MH, Lue HC. Infracardiac total anomalous pulmonary venous connection in tetralogy of Fallot with decreased pulmonary flow and masked pulmonary venous obstruction: report of one case. *Int J Cardiol* 1994;**47**:81–84.
118 Stewart RD, Backer CL, Young L, Mavroudis C. Tetralogy of Fallot: results of a pulmonary valve-sparing strategy. *Ann Thorac Surg* 2005;**80**:1431–1438; discussion 1438–1439.
119 Rao V, Kadletz M, Hornberger LK, et al. Preservation of the pulmonary valve complex in tetralogy of Fallot: how small is too small? *Ann Thorac Surg* 2000;**69**:176–179; discussion 179–180.
120 Awori MN, Leong W, Artrip JH, O'Donnell C. Tetralogy of Fallot repair: optimal z-score use for transannular patch insertion. *Eur J Cardiothorac Surg* 2013;**43**:483–486.
121 Geva T. Repaired tetralogy of Fallot: the roles of cardiovascular magnetic resonance in evaluating pathophysiology and for pulmonary valve replacement decision support. *J Cardiovasc Magn Reson* 2011;**13**:9.
122 Knauth AL, Gauvreau K, Powell AJ, et al. Ventricular size and function assessed by cardiac MRI predict major adverse clinical outcomes late after tetralogy of Fallot repair. *Heart* 2008;**94**:211–216.
123 Valente AM, Gauvreau K, Assenza GE, et al. Rationale and design of an international multicenter registry of patients with repaired tetralogy of Fallot to define risk factors for late adverse outcomes: the INDICATOR cohort. *Pediatr Cardiol* 2013;**34**:95–104.
124 Valente AM, Gauvreau K, Assenza GE, et al. Rationale and design of an international multicenter registry of patients with repaired tetralogy of Fallot to define risk factors for late adverse outcomes: the INDICATOR cohort. *Pediatr Cardiol* 2012 Jun 5.
125 Punn R, Behzadian F, Tacy TA. Annular tilt as a screening test for right ventricular enlargement in patients with tetralogy of Fallot. *J Am Soc Echocardiogr* 2010;**23**:1297–1302.
126 Dragulescu A, Grosse-Wortmann L, Fackoury C, et al. Echocardiographic assessment of right ventricular volumes after surgical repair of tetralogy of Fallot: clinical validation of a new echocardiographic method. *J Am Soc Echocardiogr* 2011;**24**:1191–1198.
127 Mercer-Rosa L, Yang W, Kutty S, et al. Quantifying pulmonary regurgitation and right ventricular function in surgically repaired tetralogy of Fallot: a comparative analysis of echocardiography and magnetic resonance imaging. *Circ Cardiovasc Imaging* 2012 Aug 7.
128 Lai WW, Gauvreau K, Rivera ES, et al. Accuracy of guideline recommendations for two-dimensional quantification of the right ventricle by echocardiography. *Int J Cardiovasc Imaging* 2008;**24**:691–698.
129 Kutty S, Zhou J, Gauvreau K, et al. Regional dysfunction of the right ventricular outflow tract reduces the accuracy of Doppler tissue imaging assessment of global right ventricular systolic function in patients with repaired tetralogy of Fallot. *J Am Soc Echocardiogr* 2011;**24**:637–643.
130 Srivastava S, Salem Y, Chatterjee S, et al. Echocardiographic myocardial deformation evaluation of right ventricular function in comparison with CMRI in repaired tetralogy of Fallot: a cross-sectional and longitudinal validation study. *Echocardiography* 2013;**30**:196–202.
131 Ko HH, Nielsen JC, Lytrivi ID, Srivastava S. Application of the recently published echocardiographic guidelines for assessment of right ventricular function in patients with repaired tetralogy of Fallot compared to those obtained by MRI. *J Am Soc Echocardiogr* 2011;**24–5**: B48–B49. [Abstract]
132 Lytrivi ID, Lai WW, Ko HH, et al. Color Doppler tissue imaging for evaluation of right ventricular systolic function in patients with congenital heart disease. *J Am Soc Echocardiogr* 2005;**18**:1099–1104.
133 Koestenberger M, Nagel B, Ravekes W, et al. Tricuspid annular peak systolic velocity (S′) in children and young adults with pulmonary artery hypertension secondary to congenital heart diseases, and in those with repaired tetralogy of Fallot: echocardiography and MRI data. *J Am Soc Echocardiogr* 2012;**25**:1041–1049.
134 Morcos P, Vick GW, 3rd, Sahn DJ, et al. Correlation of right ventricular ejection fraction and tricuspid annular plane systolic excursion in tetralogy of Fallot by magnetic resonance imaging. *Int J Cardiovasc Imaging* 2009;**25**:263–270.
135 Morcos M, Sheehan FH. Regional right ventricular wall motion in tetralogy of Fallot: a three-dimensional analysis. *Int J Cardiovasc Imaging* 2013 Jan 6.

136 Hui W, Abd El, Rahman MY, Dsebissowa F, et al. Comparison of modified short axis view and apical four chamber view in evaluating right ventricular function after repair of tetralogy of Fallot. *Int J Cardiol* 2005;**105**:256–261.

137 Abd El, Rahman MY, Abdul-Khaliq H, Vogel M, et al. Value of the new Doppler-derived myocardial performance index for the evaluation of right and left ventricular function following repair of tetralogy of Fallot. *Pediatr Cardiol* 2002;**23**:502–507.

138 Ortega M, Triedman JK, Geva T, Harrild DM. Relation of left ventricular dyssynchrony measured by cardiac magnetic resonance tissue tracking in repaired tetralogy of Fallot to ventricular tachycardia and death. *Am J Cardiol* 2011;**107**:1535–1540.

139 D'Andrea A, Caso P, Sarubbi B, et al. Right ventricular myocardial activation delay in adult patients with right bundle branch block late after repair of tetralogy of Fallot. *Eur J Echocardiogr* 2004;**5**:123–131.

140 Fernandes FP, Manlhiot C, Roche SL, et al. Impaired left ventricular myocardial mechanics and their relation to pulmonary regurgitation, right ventricular enlargement and exercise capacity in asymptomatic children after repair of tetralogy of Fallot. *J Am Soc Echocardiogr* 2012;**25**:494–503.

141 Baspinar O, Alehan D. Dobutamine stress echocardiography in the evaluation of cardiac haemodynamics after repair of tetralogy of Fallot in children: negative effects of pulmonary regurgitation. *Acta Cardiol* 2006;**61**:279–283.

142 Abd El, Rahman MY, Hui W, Yigitbasi M, et al. Detection of left ventricular asynchrony in patients with right bundle branch block after repair of tetralogy of Fallot using tissue-Doppler imaging-derived strain. *J Am Coll Cardiol* 2005;**45**:915–921.

143 Luijnenburg SE, Peters RE, van der Geest RJ, et al. Abnormal right atrial and right ventricular diastolic function relate to impaired clinical condition in patients operated for tetralogy of Fallot. *Int J Cardiol* 2012 Mar 3.

144 Friedberg MK, Fernandes FP, Roche SL, et al. Impaired right and left ventricular diastolic myocardial mechanics and filling in asymptomatic children and adolescents after repair of tetralogy of Fallot. *Eur Heart J Cardiovasc Imaging* 2012 Mar 30.

145 Ahmad N, Kantor PF, Grosse-Wortmann L, et al. Influence of RV restrictive physiology on LV diastolic function in children after tetralogy of Fallot repair. *J Am Soc Echocardiogr* 2012;**25**:866–873.

146 Diller GP, Kempny A, Liodakis E, et al. Left ventricular longitudinal function predicts life-threatening ventricular arrhythmia and death in adults with repaired tetralogy of Fallot. *Circulation* 2012 Apr 11.

147 Davlouros PA, Kilner PJ, Hornung TS, et al. Right ventricular function in adults with repaired tetralogy of Fallot assessed with cardiovascular magnetic resonance imaging: detrimental role of right ventricular outflow aneurysms or akinesia and adverse right-to-left ventricular interaction. *J Am Coll Cardiol* 2002;**40**:2044–2052.

148 Broberg CS, Aboulhosn J, Mongeon FP, et al. Prevalence of left ventricular systolic dysfunction in adults with repaired tetralogy of Fallot. *Am J Cardiol* 2011;**107**:1215–1220.

149 Lu JC, Ensing GJ, Yu S, et al. 5/6 area length method for left-ventricular ejection-fraction measurement in adults with repaired tetralogy of Fallot: comparison with cardiovascular magnetic resonance. *Pediatr Cardiol* 2013;**34**:231–239.

150 Schwartz MC, Rome JJ, Gillespie MJ, et al. Relation of left ventricular end diastolic pressure to right ventricular end diastolic volume after operative treatment of tetralogy of Fallot. *Am J Cardiol* 2012;**109**:417–422.

151 Koenigstein K, Raedle-Hurst T, Hosse M, et al. Altered diastolic left atrial and ventricular performance in asymptomatic patients after repair of tetralogy of Fallot. *Pediatr Cardiol* 2012 Nov 24.

152 Wald RM, Redington AN, Pereira A, et al. Refining the assessment of pulmonary regurgitation in adults after tetralogy of Fallot repair: should we be measuring regurgitant fraction or regurgitant volume? *Eur Heart J* 2009;**30**:356–361.

153 Li W, Davlouros PA, Kilner PJ, et al. Doppler-echocardiographic assessment of pulmonary regurgitation in adults with repaired tetralogy of Fallot: comparison with cardiovascular magnetic resonance imaging. *Am Heart J* 2004;**147**:165–172.

154 Schreiber C, Horer J, Vogt M, et al. A new treatment option for pulmonary valvar insufficiency: first experiences with implantation of a self-expanding stented valve without use of cardiopulmonary bypass. *Eur J Cardiothorac Surg* 2007;**31**:26–30.

155 Silversides CK, Veldtman GR, Crossin J, et al. Pressure half-time predicts hemodynamically significant pulmonary regurgitation in adult patients with repaired tetralogy of Fallot. *J Am Soc Echocardiogr* 2003;**16**:1057–1062.

156 Grothoff M, Spors B, Abdul-Khaliq H, Gutberlet M. Evaluation of postoperative pulmonary regurgitation after surgical repair of tetralogy of Fallot: comparison between Doppler echocardiography and MR velocity mapping. *Pediatr Radiol* 2008;**38**:186–191.

157 Riesenkampff E, Mengelkamp L, Mueller M, et al. Integrated analysis of atrioventricular interactions in tetralogy of Fallot. *Am J Physiol Heart Circ Physiol* 2010;**299**:H364–371.

158 Rudski LG, Lai WW, Afilalo J, et al. Guidelines for the echocardiographic assessment of the right heart in adults: a report from the American Society of Echocardiography endorsed by the European Association of Echocardiography, a registered branch of the European Society of Cardiology, and the Canadian Society of Echocardiography. *J Am Soc Echocardiogr* 2010;**23**:685–713; quiz 786–788.

159 Valente AM, Cook S, Festa P, et al. Multimodality imaging guidelines for patients with repaired tetralogy of Fallot: a report from the American Society of Echocardiography: developed in collaboration with the Society for Cardiovascular Magnetic Resonance and the Society for Pediatric Radiology. *J Am Soc Echocardiogr* 2014;**27**:111–141.

160 Zahn EM, Hellenbrand WE, Lock JE, McElhinney DB. Implantation of the Melody transcatheter pulmonary valve in patients with a dysfunctional right ventricular outflow tract conduit early results from the U.S. clinical trial. *J Am Coll Cardiol* 2009;**54**:1722–1729.

161 McElhinney DB, Cheatham JP, Jones TK, et al. Stent fracture, valve dysfunction, and right ventricular outflow tract reintervention after transcatheter pulmonary valve implantation: patient-related and procedural risk factors in the US Melody Valve Trial. *Circ Cardiovasc Interv* 2011;**4**:602–614.

162 Yoo SJ, Lee YH, Kim ES, et al. Three-vessel view of the fetal upper mediastinum: an easy means of detecting abnormalities of the ventricular outflow tracts and great arteries during obstetric screening. *Ultrasound Obstet Gynecol* 1997;**9**:173–182.

163 Hornberger LK, Sanders SP, Sahn DJ, et al. In utero pulmonary artery and aortic growth and potential for progression of pulmonary outflow tract obstruction in tetralogy of Fallot. *J Am Coll Cardiol* 1995;**25**:739–745.

164 Hirji A, Bernasconi A, McCrindle BW, et al. Outcomes of prenatally diagnosed tetralogy of Fallot: implications for valve-sparing repair versus transannular patch. *Can J Cardiol* 2010;**26**:e1–6.

165 Escribano D, Herraiz I, Granados M, et al. Tetralogy of Fallot: prediction of outcome in the mid-second trimester of pregnancy. *Prenat Diagn* 2011;**31**:1126–1133.

166 Kwon EN, Parness IA, Srivastava S, et al. Subpulmonary stenosis assessed in midtrimester fetuses with tetralogy of Fallot: a novel method for predicting postnatal clinical outcome. *Pediatr Cardiol* 2013 Feb 7.

167 Boudjemline Y, Fermont L, Le Bidois J, et al. Can we predict 22q11 status of fetuses with tetralogy of Fallot? *Prenat Diagn* 2002;**22**:231–234.

168 Boudjemline Y, Fermont L, Le Bidois J, et al. Prenatal diagnosis of conotruncal heart diseases. Results in 337 cases. *Arch Mal Coeur Vaiss* 2000;**93**:583–586.

169 Paladini D, Rustico M, Todros T, et al. Conotruncal anomalies in prenatal life. *Ultrasound Obstet Gynecol* 1996;**8**:241–246.

170 Poon LC, Huggon IC, Zidere V, Allan LD. Tetralogy of Fallot in the fetus in the current era. *Ultrasound Obstet Gynecol* 2007;**29**:625–627.

171 Azancot A, Eydoux P, Vuillard E, et al. Clinical spectrum of prenatal tetralogy of Fallot. *Arch Mal Coeur Vaiss* 2000;**93**:587–593.

172 Miyashita S, Chiba Y. Prenatal demonstration of major aortopulmonary collateral arteries with tetralogy of Fallot and pulmonary atresia. *Fetal Diagn Ther* 2004;**19**:100–105.

173 Berg C, Thomsen Y, Geipel A, et al. Reversed end-diastolic flow in the umbilical artery at 10–14 weeks of gestation is associated with absent pulmonary valve syndrome. *Ultrasound Obstet Gynecol* 2007;**30**:254–258.

174 Galindo A, Gutierrez-Larraya F, Martinez JM, et al. Prenatal diagnosis and outcome for fetuses with congenital absence of the pulmonary valve. *Ultrasound Obstet Gynecol* 2006;**28**:32–39.

175 Chelliah A, Berger JT, Blask A, Donofrio MT. Clinical utility of fetal magnetic resonance imaging in tetralogy of Fallot with absent pulmonary valve. *Circulation* 2013;**127**:757–759.

176 Chaoui R, Kalache KD, Heling KS, et al. Absent or hypoplastic thymus on ultrasound: a marker for deletion 22q11.2 in fetal cardiac defects. *Ultrasound Obstet Gynecol* 2002;**20**:546–552.

CHAPTER 23

Truncus Arteriosus and Aortopulmonary Window

Timothy C. Slesnick, Ritu Sachdeva, Joe R. Kreeger, and William L. Border
Noninvasive Cardiac Imaging Program, Children's Healthcare of Atlanta Sibley Heart Center, Emory University School of Medicine, Atlanta, GA, USA

Truncus arteriosus

In 1942 Lev and Saphir defined truncus arteriosus as an anomaly in which a single arterial trunk leaving the heart gives rise to the aorta, pulmonary arteries and coronary arteries [1]. This definition has persisted and is supported by other authors [2–5]. The earliest known descriptions of this defect were made by Wilson in 1798, as reported by Van Mierop et al. [6], and by Buchanan in 1864 [7]. Primary surgical repair in infants is the treatment of choice and is usually undertaken upon diagnosis. It is now common for many patients who underwent neonatal repair of truncus arteriosus to reach adulthood.

Definition

Truncus arteriosus is defined as an anomaly in which a single arterial trunk arises from the ventricles and gives rise to the aorta, pulmonary arteries and coronary arteries. Although not part of the definition, an associated subtruncal ventricular septal defect (VSD) is found in the majority of patients with truncus arteriosus.

Incidence

Truncus arteriosus is a congenital heart anomaly occurring in approximately 1–4% of patients with congenital heart defects [2,3,5,8]. The estimated incidence of truncus arteriosus is 9–11 per 100,000 live births [9]. Without surgical intervention, truncus arteriosus is usually fatal, with a mean age of death of 2.5 months [3]; 80% of children die during the first year of life [10].

Etiology

Investigations using chick and mammalian embryos [11,12], as well as human studies, implicate a microdeletion at the 22q11.2 locus as at least one factor in the genetic etiology of truncus arteriosus. This microdeletion manifests clinically as DiGeorge syndrome (also known as velocardiofacial syndrome) [13]. The responsible gene within the 22q11.2 locus has not yet been definitively identified. Although the relationship between a chromosome 22q11 deletion and conotruncal lesions, including truncus arteriosus, is well established, preliminary studies suggest other putative mechanisms [12]. The single tube that comprises the outflow tract in embryos undergoes septation into the aorta and the pulmonary trunk by means of a structure originating from the neural crest, the aortopulmonary septum. This structure is affected in DiGeorge syndrome, resulting in truncus arteriosus. However, the remainder of the septation occurs by a different, less well understood mechanism, involving mesenchymal cells. It has been speculated that bone morphogenetic proteins (BMPs) may be involved in this process, and mouse embryo studies have demonstrated mutations in BMP as causing truncus arteriosus and type B interrupted aortic arch [12]. Clearly, disruption of multiple embryologic steps is required for truncus arteriosus to develop.

Patients with conotruncal anomalies are at increased risk for a chromosome 22q11 microdeletion [14,15]. Fluorescence in situ hybridization (FISH) analysis for a chromosome 22q11 abnormality will detect a deletion in 35–40% of patients with truncus arteriosus [15–17]. Certain associated cardiac anomalies, such as right aortic arch, abnormal aortic arch branching pattern, or a combination of these two features, place these patients at even higher risk for the deletion [17].

In addition to the cardiac defects, DiGeorge syndrome can be characterized by facial dysmorphism, thymic hypoplasia, parathyroid hypoplasia resulting in hypocalcemia, learning disabilities and psychiatric disorders later in life. Patients with a 22q11 deletion and DiGeorge syndrome have been grouped under the unifying acronym CATCH 22 syndrome to emphasize their phenotypic components (*C*ardiac defects, *A*bnormal face, *T*hymic hypoplasia, *C*left palate and *H*ypocalcemia) [18]. Due to the high prevalence of a chromosome 22q11 microdeletion in patients with truncus arteriosus, the current recommendations are to screen all patients identified with this cardiac lesion.

Echocardiography in Pediatric and Congenital Heart Disease: From Fetus to Adult, Second Edition. Edited by Wyman W. Lai, Luc L. Mertens, Meryl S. Cohen and Tal Geva.
© 2016 John Wiley & Sons, Ltd. Published 2016 by John Wiley & Sons, Ltd.
Companion website: www.lai-echo.com

Morphology and classification

Developmental considerations

Two ridges that appear in the conotruncal segment of the 4–5-week embryo create the normal differentiation of the truncus into the aorta and pulmonary artery. These two ridges grow toward the midline and fuse to form the conotruncal septum, which divides the truncus into the proximal aorta and main pulmonary artery [19]. Ectomesenchymal cells derived from the cardiac neural crest contribute directly to aorticopulmonary septation [20]. The absence of conal cushion tissue, which during normal embryogenesis fuses with the muscular part of the interventricular septum to complete ventricular septation, results in the typical infundibular or outlet VSD. Ablation of the cardiac neural crest in chick embryos results in truncus arteriosus, and partial ablation results in other conotruncal abnormalities, such as double-outlet right ventricle, transposition of the great arteries, and tetralogy of Fallot [21]. The ectomesenchymal cells also contribute to the development of the pharyngeal arches and thus to the thymus and parathyroid glands. An alternative theory proposed by Van Praagh and Van Praagh [3] is that persistent truncus arteriosus is a form of tetralogy of Fallot combining pulmonary and infundibular atresia with failure of truncal separation – in essence an aortopulmonary window. Notably, neural crest abnormalities are found in tetralogy of Fallot, aortopulmonary window, and truncus arteriosus. However, in contrast to the aortic valve in tetralogy of Fallot, the truncal valve is often abnormal as described later in the chapter.

Classification

Collett and Edwards classified truncus arteriosus into four major types based on the sources of pulmonary blood supply (Figure 23.1, top panel) [21]:

Type I: short main pulmonary artery segment gives rise to both branch pulmonary arteries (Videos 23.1 and 23.2).

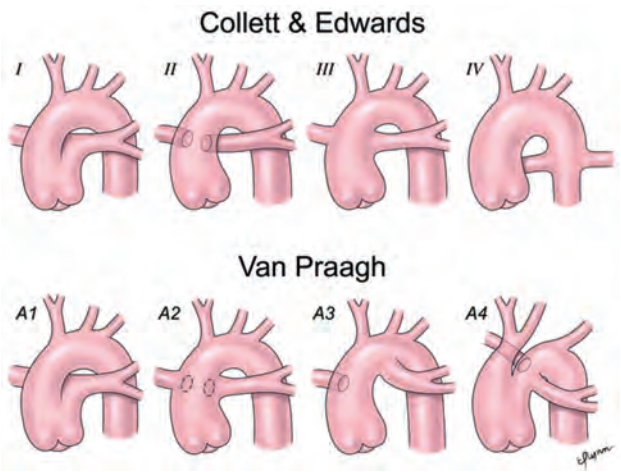


Figure 23.1 Classification of truncus arteriosus. **(Top panel)** Collett and Edwards. **(Bottom panel)** Van Praagh and Van Praagh. See text for details.

Type II: both branch pulmonary arteries arise from the common arterial trunk adjacent to one another with a rim of truncal tissue between them (Video 23.3).

Type III: the branch pulmonary arteries arise from either side of the truncus and are somewhat remote from one another.

Type IV (previously termed pseudotruncus): no pulmonary artery arises from the ascending segment of the truncus arteriosus; the pulmonary circulation is supplied by collateral vessels from the descending aorta. This anomaly is now considered a form of tetralogy of Fallot with pulmonary atresia rather than truncus arteriosus.

The classification of Van Praagh and Van Praagh [3] (Figure 23.1, bottom panel) modified the original classification of Collett and Edwards:

Type I: the branch pulmonary arteries arise from a short main pulmonary artery.

Type II: the branch pulmonary arteries arise directly from the arterial trunk through separate orifices.

Type III: only one branch pulmonary artery arises from the ascending segment of the arterial trunk. Collateral vessels usually supply the contralateral lung.

Type IV: truncus arteriosus with aortic arch hypoplasia, coarctation or interruption (usually type B interruption distal to the left common carotid artery). In this anatomic variant there is usually a well-formed main pulmonary artery and a small ascending aorta (Video 23.4).

In each of the above types of truncus arteriosus, a modifier "A" (with VSD) or "B" (intact ventricular septum) is used.

Morphology

Ventricular septal defect

In the majority of cases there is a subtruncal VSD over which the truncal valve sits, similar to tetralogy of Fallot (TOF). Rarely, the ventricular septum is intact [22,23]. The conal septum is usually absent and the truncal valve is in direct fibrous continuity with the mitral valve. In rare circumstances, the truncal valve may be supported by a complete infundibulum and relates exclusively to the right ventricle.

Truncal valve

The truncal valve leaflets are often thickened because of the expansion of the spongiosa and fibrosa layers, and the leaflets are often described as nodular [24–26]. The number and morphology of the leaflets are variable [2–5]: trileaflet valve in 65–70% of patients, quadricuspid in 9–24% (Figure 23.2; Video 23.5) and bicuspid in 6–23%. Rarely, unicuspid [27] or pentacuspid valves are present. Truncal valve stenosis has been reported in ~33% of patients, and some degree of regurgitation is present in ~50% of patients (Video 23.6) [28].

Pulmonary arteries

In the majority of patients, the branch pulmonary arteries arise from the posterior-left lateral aspect of the common trunk, either with a very short main pulmonary artery (type I; 48–68%

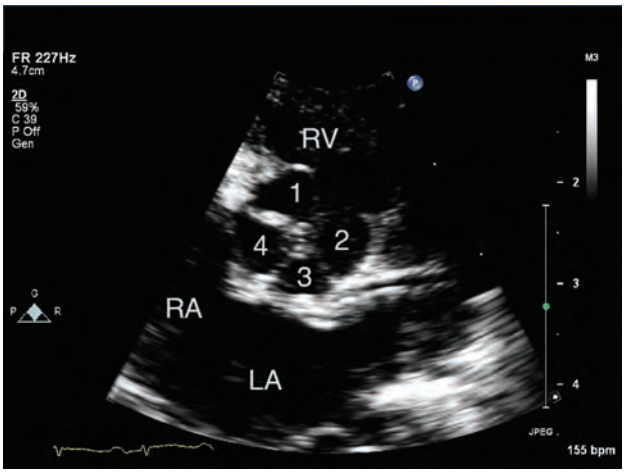


Figure 23.2 Parasternal short-axis imaging plane demonstrating the quadricuspid morphology of the truncal valve. LA, left atrium; RA, right atrium; RV, right ventricle.

of patients) or directly via two distinct orifices (type II; 29–48%) [2,4,5,27,29]. In ~6–10% of patients only one branch pulmonary artery arises from the ascending aspect of the common trunk (type III).

Coronary arteries

The coronary artery pattern in truncus arteriosus is variable. The most common abnormality includes a higher and more posterior origin of the left coronary artery, which may result in the origin being in close proximity to the origin of the pulmonary artery [30,31]. A single coronary artery has been reported in 13–18% of cases (Video 23.7). Importantly, the coronary ostia may be narrowed or slit-like, resulting in significant coronary artery stenosis. Despite their highly variable origin, the distal coronary branches tend to follow a normal course [32]. There have also been reports of prominent diagonal branches off the right coronary artery; they parallel the course of the conus branch but are further down the anterior surface of the right ventricle. In addition, the conal branch off the right coronary artery may be prominent, distributing a network of vessels to the right ventricular outflow tract. The presence of coronary arteries in the infundibular free wall can complicate placement of the right ventricle-to-pulmonary artery conduit as part of the surgical repair [33]. In addition to abnormalities of coronary ostial position, cases of an intramural course opening into the pulmonary artery have also been reported [34].

Associated cardiac lesions

The cardiac anomalies most frequently associated with truncus arteriosus involve the aortic arch. The aortic arch is right-sided in ~33% of patients [5]. Interrupted aortic arch occurs in approximately 19% of patients with truncus arteriosus (truncus type IV of Van Praagh) [35]. Conversely, approximately 12% of interrupted aortic arch anomalies have an associated truncus arteriosus. Type B interruption, between the left common carotid artery and the left subclavian artery, is the most common variant (Video 23.8). Other forms of interrupted aortic arch, such as type A, occur rarely (Video 23.4). An aberrant origin of the left or right subclavian artery (depending on aortic arch side) is common in patients with truncus arteriosus. A patent ductus arteriosus is almost uniformly absent in these patients except in those with an interrupted aortic arch.

Whereas a left superior vena cava is found in approximately 12% of patients with truncus arteriosus, other anomalies of systemic and pulmonary venous return are less common. Retroaortic position of the left innominate vein is an anatomic variant of systemic venous anatomy associated with truncus arteriosus, particularly in those with a right-sided aortic arch. Partial anomalous pulmonary venous return has been reported in approximately 1% of patients, and an associated total anomalous pulmonary venous connection is rare [3,4,36]. Other anomalies rarely reported to accompany truncus arteriosus include: secundum atrial septal defect, partial and complete atrioventricular canal defects, mitral atresia, mitral stenosis, tricuspid atresia, straddling tricuspid valve, Ebstein malformation, aortic atresia, hypoplastic left ventricle, double-inlet left ventricle, heterotaxy syndrome, and left pulmonary artery sling [37,38].

Pathophysiology

The clinical presentation of truncus arteriosus is variable, but in most cases the dominant physiology is that of a large left-to-right shunt with pulmonary overcirculation. Typically, this physiology becomes clinically apparent over the first few days to weeks of life as the pulmonary vascular resistance decreases. The resistances in the pulmonary and systemic vascular beds determine the relative proportion of systemic and pulmonary blood flow. A widening pulse pressure accompanies the worsening pulmonary overcirculation as the pulmonary vascular resistance decreases, and the diastolic runoff into the pulmonary arteries results in reduction of diastolic arterial pressure.

The oxygen saturation in patients with truncus arteriosus depends on the amount of pulmonary blood flow. Because the pulmonary blood flow is generally excessive, most infants with truncus arteriosus have only mildly reduced systemic oxygen saturation (typically ≥90%). In addition, the phenomenon of "streaming" can occur when there is a favorable spatial orientation of the branch pulmonary arteries relative to the VSD. This separates the oxygenated from the deoxygenated blood despite the absence of anatomic aortopulmonary septation, and can result in relatively normal oxygenation. If severe congestive heart failure develops, intrapulmonary right-to-left shunt due to inefficient gas exchange can lead to later cyanosis. If left unrepaired, increased pulmonary vascular resistance associated with obstructive pulmonary vascular disease may develop [39].

Abnormalities of the truncal valve, either regurgitation or stenosis, may play an important role in the clinical course of infants with truncus arteriosus. In most patients, the stenosis and/or regurgitation are not severe enough to alter the presentation and initial clinical course. If severe truncal stenosis is present, the dominant physiology is that of biventricular outflow obstruction. In patients with moderate or severe truncal valve regurgitation, the combination of left-to-right shunt and retrograde flow through the incompetent truncal valve results in severe left ventricular volume overload. In addition, the low diastolic blood pressure may result in compromised coronary perfusion resulting in myocardial ischemia.

The systemic circulation in infants with interrupted aortic arch or severe coarctation depends on flow through a patent ductus arteriosus and, therefore, requires prompt diagnosis and administration of intravenous prostaglandin E_1. Closure of the arterial duct will lead to low cardiac output and development of symptoms of shock.

Management

The management of truncus arteriosus consists of neonatal surgical repair. Improvements in surgical techniques and perioperative management have enabled successful early repair, with a reported mortality of 5–11% [34,40–43]. Delayed surgical repair can result in development of pulmonary vascular obstructive disease and myocardial dysfunction. Surgical repair is performed under deep hypothermia with either low-flow continuous cardiopulmonary bypass or intermittent periods of circulatory arrest [44]. The pulmonary arteries are removed from the truncus, and the resultant opening is either closed primarily or with a patch. The VSD is closed with a patch. Continuity between the right ventricle and the pulmonary arteries is established using a cryopreserved homograft, or a valved heterograft conduit. When significant truncal valve regurgitation is present in infancy, most surgeons now advocate repair of the truncal valve [42,44,45]. Replacement of the truncal valve at the time of initial repair is done only in the most severe cases [42,46]. Additional associated anomalies that have been identified as independent risk factors for surgical mortality include interrupted aortic arch, coronary artery anomalies, and truncal valve pathology necessitating truncal valve surgery at the time of initial repair [40,41,47,48]. Following repair, progressive obstruction of the right ventricle-to-pulmonary artery conduit requiring replacement is expected and truncal valve dysfunction is common [49–56].

Echocardiographic imaging

Key elements

The goals of the echocardiographic evaluation of truncus arteriosus depend upon the patient's age, physiologic state and temporal relationship to surgical intervention. The initial evaluation requires a thorough assessment of all components of the anatomic features. In addition, the examination must also assess any of the typical or unusual cardiac anomalies associated with truncus arteriosus. The older child and adult require evaluation of the underlying anatomy as well as the status of any surgical repair. In terms of the details of the components of each of these types of assessments, the following key elements must be delineated:

Neonatal echocardiogram

As part of a detailed, segmental evaluation of all aspects of cardiovascular anatomy and physiology, particular attention is focused on the following areas:

- Presence of atrial communication.
- Atrioventricular valve anatomy and function; presence of straddling chordae or valve tissue across the VSD.
- Location and size of VSD; presence of additional VSDs (Figure 23.3).
- Ventricular size and function.
- Morphology, location, and function of the truncal valve.
- Pulmonary artery anatomy, including presence or absence of a main pulmonary artery segment, pulmonary artery branch position and size (Video 23.9).
- Sources of pulmonary blood flow other than branch pulmonary arteries; e.g., ductus arteriosus and aortopulmonary collateral vessels (especially important when one of the branch pulmonary arteries does not arise from the ascending aorta).
- Aortic arch anatomy (evaluate arch sidedness, hypoplasia or interruption).
- Coronary artery origin and proximal course; relationships between coronary ostia and origin(s) of pulmonary arteries and truncal valve leaflets.
- Associated lesions (e.g., persistent left superior vena cava, anomalous pulmonary venous connection, aberrant origin of the left or right subclavian arteries).

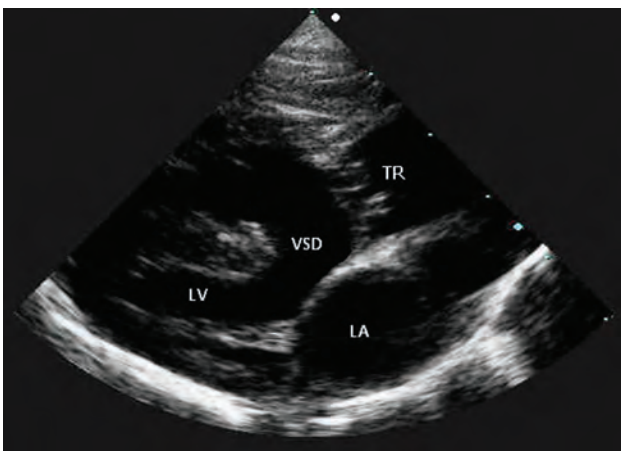


Figure 23.3 Parasternal long-axis imaging plane demonstrating truncal override of the ventricular septal defect. LA, left atrium; LV, left ventricle; TR, truncal root; VSD, ventricular septal defect.

Postoperative echocardiograms

Echocardiograms performed after the initial surgical intervention focus upon those aspects of cardiac anatomy and physiology that raised concern early on, or might be expected to develop over time. Areas of particular interest include:

- Presence, size and flow velocity through residual VSD(s).
- Truncal valve function and truncal root dimension.
- Right ventricle-to-pulmonary artery conduit stenosis/regurgitation.
- Branch pulmonary artery stenosis.
- Assessment of right ventricular systolic pressure.
- Atrioventricular valve function.
- Ventricular size and function.
- Aortic arch (if obstruction or interruption noted at presentation).

Imaging of truncus arteriosus

Truncus arteriosus can be accurately diagnosed using two-dimensional (2D) and Doppler echocardiography [57–60]. In most cases, echocardiography is sufficient to provide a complete preoperative assessment. In assessing truncus arteriosus by echocardiography it is crucial to have a clear understanding of the data required from the study, but also the limitations of this diagnostic modality so that alternative testing can be employed when needed.

The echocardiographic examination should be systematic and organized so that details are not missed. The subcostal view provides an image of all aspects of the anatomy and is the preferred initial imaging approach in many centers. In the parasternal long-axis view, the presence of an overriding single semilunar valve, often with thickened leaflets, and a malalignment-type VSD provides a clue to the diagnosis of truncus arteriosus (Figure 23.3). Often one can also image the pulmonary artery arising from the posterior aspect of the truncus from that view (Figure 23.4). The truncal valve is well seen, and truncal regurgitation can be assessed by color Doppler. In many instances truncal stenosis can be suggested by the anatomic appearance of the valve. When there is truncal stenosis, the valve appears thickened and leaflet excursion is reduced. This view is inadequate for assessing the severity of truncal stenosis, because the Doppler cursor cannot be aligned parallel to the direction of flow across the valve. If there is an associated interruption of the aortic arch, the ascending aorta can be seen arising from the rightward aspect of the truncus (Video 23.10). An enlarged coronary sinus may indicate a left superior vena cava.

From the parasternal short-axis view with the transducer angled superiorly above the level of the truncal valve, the origin of the pulmonary arteries from the left-posterior aspect of the truncus can be readily seen (Figure 23.5). This view is excellent to ascertain the type of truncus by imaging the branch pulmonary arteries. This view is also ideally suited for the assessment of truncal valve morphology, including its commissures and leaflets. Three-dimensional (3D) echocardiography may be particularly helpful for assessment of truncal valve

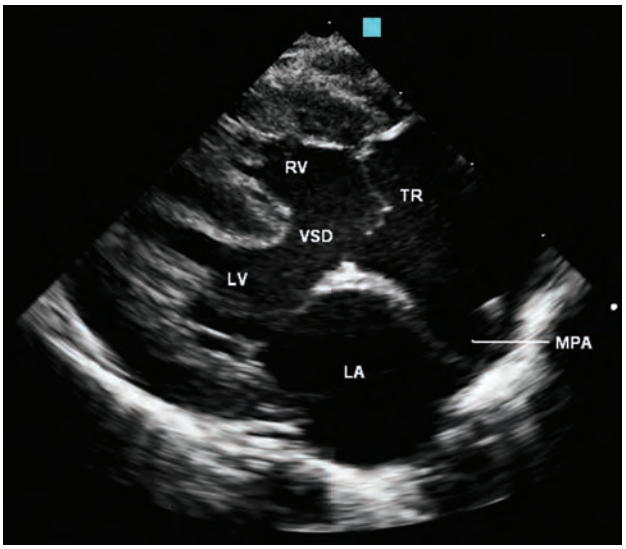


Figure 23.4 Parasternal long-axis view showing the truncal valve overriding the VSD, with the main pulmonary artery arising from the posterior aspect of the truncal root (TR). MPA, main pulmonary artery; TR, truncal root; VSD, ventricular septal defect; RV, right ventricle; LV, left ventricle; LA, left atrium.

anatomy. At the level of the truncal valve, the location of the VSD can be determined. The VSD is usually within or superior to the Y of septal band, and when this is the case, a rim of muscle appears adjacent to the tricuspid valve in the short-axis view. If the VSD extends to the tricuspid valve in this view, it involves the membranous septum. The coronary arteries may be imaged in this view by rotating the transducer clockwise. To image the

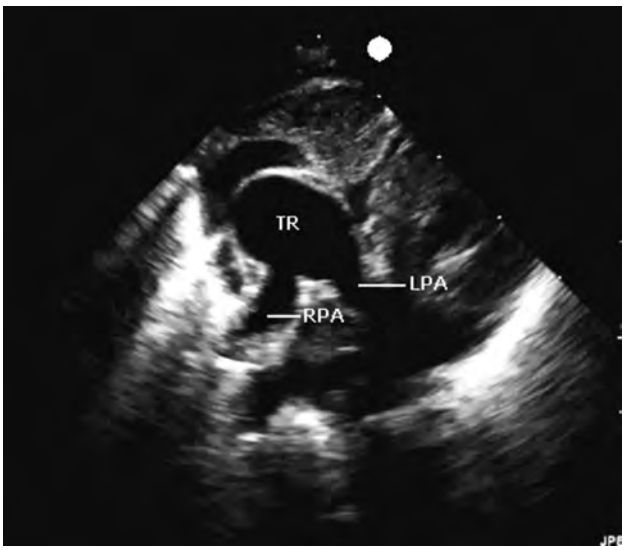


Figure 23.5 Parasternal short-axis view demonstrating separate origins of the pulmonary artery branches from the posterior aspect of the truncal root (truncus arteriosus type II). LPA, left pulmonary artery; RPA, right pulmonary artery; TR, truncal root.

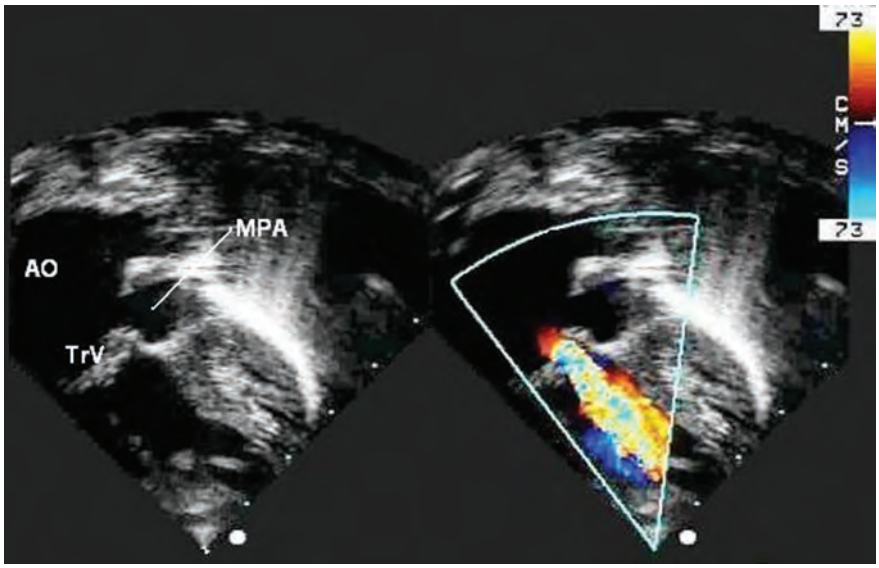


Figure 23.6 Apical 4-chamber view swept anteriorly to show the truncal valve (overriding the right ventricle). There is a broad jet of truncal regurgitation noted emanating from the truncal valve and extending deep into the right ventricle. AO, aorta; MPA, main pulmonary artery; TrV, truncal valve.

relationship of the coronary artery to the pulmonary artery, one must angle the transducer superiorly and inferiorly such that the coronary artery and the pulmonary artery are imaged in the same plane. The parasternal long-axis view and the subcostal coronal view are also helpful in imaging the relationship of the coronary artery to the pulmonary artery, as they can often be seen in the same plane.

Parasternal as well as suprasternal views allow assessment for the presence of a patent ductus arteriosus. Although typically a patent ductus arteriosus is only seen in the presence of aortic arch hypoplasia/interruption, rarely it may occur in those with a normal aortic arch [61].

The parasternal long-axis and apical 4-chamber views are most helpful in identifying additional muscular VSDs through the use of color Doppler. The typical large malalignment VSD is seen when the transducer is angled anteriorly toward the outflow tract, and the degree of truncal override can be assessed. This view is also particularly helpful for assessing truncal regurgitation and stenosis (Figure 23.6). The Doppler beam can be aligned parallel to the flow from this view, and an accurate Doppler gradient can be measured when truncal stenosis is present. The relationship between the pulmonary artery origin and the truncal root can be clearly imaged by angling anteriorly (Figure 23.7; Video 23.11).

The subcostal view provides an image of all aspects of the anatomy. At the atrial level the atrial septum can be imaged and the pulmonary veins can be seen entering the left atrium. As the transducer is swept anteriorly, the truncal valve overriding the VSD can be imaged. In addition, the branch pulmonary arteries and their origin from the truncus can be well seen (Figure 23.8; Video 23.12). The right pulmonary artery can usually be imaged just inferior and posterior to the truncus. The main pulmonary artery segment and the branch pulmonary arteries can be seen arising from the truncus, and the coronary arteries can be imaged in this view. The subcostal view provides an image of the ascending aorta when the aortic arch is interrupted. The ascending aorta arises slightly rightward and superior to the truncal valve. If one tilts the transducer superiorly, the bifurcation of the ascending aorta into the innominate and left carotid arteries can be imaged. Doppler interrogation of the abdominal aorta is utilized to detect diastolic flow reversal related to runoff into a low resistance pulmonary vascular bed and/or truncal valve regurgitation.

The suprasternal notch view provides the best imaging of the aortic arch and allows for determination of arch sidedness. Long-axis views can be very helpful in demonstrating aortic arch interruption (Video 23.4). However, careful suprasternal notch

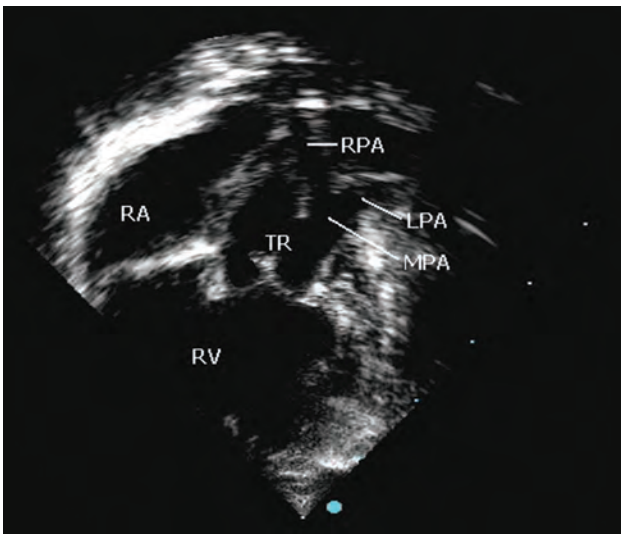


Figure 23.7 Apical 4-chamber view swept anteriorly to show the main pulmonary artery segment arising from the left lateral aspect of the truncal root, with subsequent bifurcation into left and right branch pulmonary arteries (LPA, RPA). MPA, main pulmonary artery segment; RA, right atrium; RV, right ventricle; TR, truncal root.

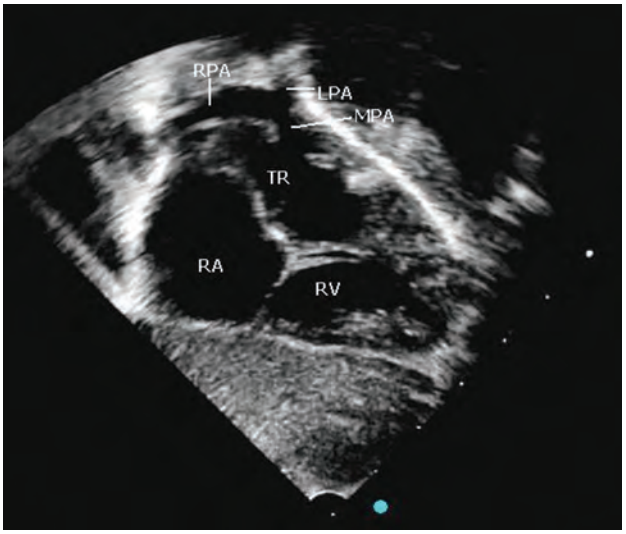


Figure 23.8 Subcostal coronal view swept anteriorly to show the truncal root and the origin of the main pulmonary artery segment from the left lateral aspect of the truncus, with subsequent bifurcation into right and left pulmonary arteries. LPA, left pulmonary artery; MPA, main pulmonary artery segment; RA, right atrium; RPA, right pulmonary artery; RV, right ventricle; TR, truncal root.

short-axis views are extremely helpful to document truncus with aortic arch interruption (Video 23.13). When the aortic arch is interrupted, the descending aorta is supplied by the ductus arteriosus, which forms a ductal arch. Tilting the transducer to the left of the patient's sagittal plane can image the ductal arch. The ductal arch can be differentiated from the aortic arch by sweeping to the right and left and imaging the ascending aorta as a separate structure. Doppler interrogation of the descending aorta typically elicits diastolic flow reversal related to flow into the pulmonary arteries and/or presence of truncal valve regurgitation.

Prenatal assessment

Many cases of truncus arteriosus are now diagnosed prenatally by fetal echocardiography. The pregnant woman in whom the diagnosis of a fetus with truncus arteriosus is considered may come to attention because of (i) a family history of congenital heart defect (typically a relative with a conotruncal defect); (ii) abnormal screening amniocentesis or chorionic villus sampling (often a 22q11 microdeletion by FISH); (iii) concern regarding a cardiac defect when the fetus is found on obstetrical ultrasound to have extracardiac anomalies (e.g., an abnormality of the palate in the patient with 22q11 deletion); or (iv) the identification of a cardiac anomaly on routine obstetrical ultrasound screening.

The frequency of prenatal diagnostic screening has increased dramatically over the past decade, as obstetrical ultrasonic cardiac screening techniques have become more standardized [62]. The accuracy of the identification of complex fetal cardiac anatomy has been well established. Tometzki et al. [63] reported their ability to diagnose a constellation of conotruncal defects, including fetuses with truncus arteriosus. Focused studies on the prenatal diagnosis of truncus arteriosus have also been performed, including the assessment of the associated cardiac anomalies [64,65]. These studies have shown a high degree of diagnostic accuracy for the overall identification of truncus arteriosus, including identification of VSD position, aortic arch anatomy, truncal valve pathology, and pulmonary artery architecture. However, the differentiation between truncus arteriosus (origin of the branch pulmonary arteries from the truncus) and tetralogy of Fallot with pulmonary atresia (no pulmonary arteries arising from the ascending aorta) continues to be challenging in the fetus. In addition, there are well-recognized variables in the accurate definition of fetal cardiac anatomy, including operator experience, fetal position, maternal body habitus, and gestational age. Nevertheless, the ability to provide accurate prenatal information to families and caregivers has greatly enhanced their options to make timely management decisions. The role of evolving technologies such as "real-time" 3D fetal echocardiography [66,67] and fetal cardiac magnetic resonance imaging (MRI) [68] awaits further technological refinements and clinical validation.

The data regarding postnatal outcomes of prenatally diagnosed truncus arteriosus is sparse. Duke and colleagues from the UK [64] reported that of 17 prenatal cases, pregnancy was terminated in 4 (24%), and 8 of the remaining 13 live births underwent neonatal surgery. Two newborns with severe truncal valve stenosis suffered preoperative sudden death. From this subset, 30-day surgical mortality was 25%.

Intraoperative assessment

Miniaturization of transesophageal echocardiographic (TEE) probes allows intraoperative and postoperative assessment of truncus arteriosus repair before and after cardiopulmonary bypass [69]. In this way, undetected anomalies may be clarified prior to cardiopulmonary bypass, and the adequacy of repair can be assessed for such lesions as residual VSDs, obstruction across the right ventricle-to-pulmonary artery conduit, and competency of the truncal valve [70]. As with other cardiac defects, TEE allows postoperative decision making to be made in a timely fashion so that the need for further interventions can be determined in the operating room.

Imaging of the adult

Echocardiographic imaging in the adult with repaired truncus arteriosus contains the essential components of the initial study with additional emphasis on evaluation of the truncal valve and right ventricle-to-pulmonary artery conduit. In addition, by adulthood there will be many patients who have developed such severe truncal valve dysfunction that valve replacement is required. The adult with progressive truncal valve disease is assessed in a manner similar to isolated aortic valve pathology. This involves evaluation of the severity of truncal regurgitation based upon color Doppler imaging, extent of diastolic flow reversal in the descending aorta, pressure half-time of the regurgitant jet, and left ventricular dilation and function. The

assessment of truncal valve stenosis is similar to that of aortic valve stenosis, including Doppler assessment of peak and mean gradient, valve morphology, and left ventricular hypertrophy and function.

Ancillary imaging modalities

There are instances in which additional diagnostic evaluation is necessary. As acoustic windows become restricted in older children and adults with repaired truncus arteriosus, cardiovascular MRI is the ideal alternative to echocardiography. This modality allows comprehensive anatomic and functional assessments, including accurate quantification of truncal valve regurgitation and biventricular size and function as well as anatomic evaluation of the pulmonary arteries and aorta [71]. Computed tomography (CT) can be used as an alternative modality (Figure 23.9) in patients with contraindications to MRI (e.g., pacemaker or implanted defibrillator). However, physicians recommending CT should carefully consider the risk of cancer due to ionizing radiation, which is considerably higher in young children [72]. In selected patients in whom conduit obstruction may be alleviated by transcatheter balloon angioplasty or stent placement, cardiac catheterization may be indicated for hemodynamic assessment and for possible intervention.

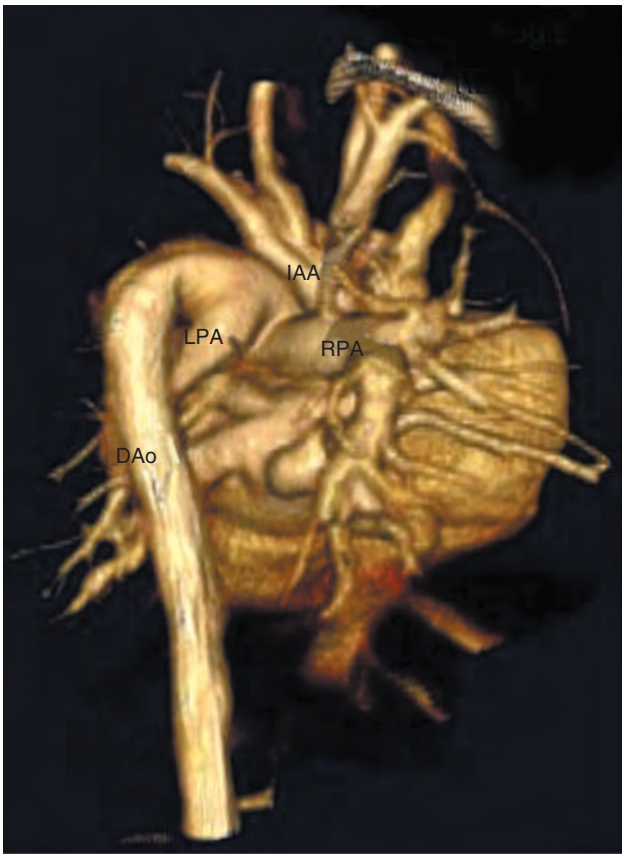


Figure 23.9 Three-dimensional volume reconstruction of computed tomography angiogram in a patient with truncus arteriosus and interrupted aortic arch type A. View of carotid and subclavian arteries (IAA) arising from the ascending aorta, with pulmonary artery branches (LPA, RPA) slightly offset in position as they arise from the truncal root. DAo, descending aorta.

Follow-up

Although there have been significant trends toward improved survival in the current era, ongoing morbidity related to conduit obstruction and/or regurgitation, truncal valve abnormalities, aortic root dilatation, and left and right ventricular dysfunction continue to dominate long-term outcomes. Interval echocardiographic imaging allows timely detection of progressive pathology prior to irreversible ventricular dysfunction, development of a life-threatening complication, or loss of opportunity to intervene via nonsurgical routes. As noted earlier, judicious use of other diagnostic modalities is particularly important during follow-up of patients with repaired truncus arteriosus.

Aortopulmonary window

Definition, incidence, morphology, and pathophysiology

An aortopulmonary window is a defect between the ascending aorta and the pulmonary artery above the semilunar valves. It is an extremely rare cardiac malformation accounting for only 0.1–0.2% of congenital heart defects [73,74]. Even though it can occur in isolation, more than half the patients have other associated cardiac anomalies [75]. These include type A interrupted aortic arch, right aortic arch, aortic origin of right pulmonary artery, anomalous origin of one or both coronary arteries from the pulmonary artery, tetralogy of Fallot, transposition of the great arteries, and ventricular septal defect.

Based on a classification proposed by Mori et al. [76] there are three types of aortopulmonary defects:

Type I (proximal defect): the defect is present midway between the semilunar valves and pulmonary bifurcation. This is the most common type (Figure 23.10).

Type II (distal defect): the defect is between the left posterior wall of ascending aorta and the junction of the right pulmonary artery and main pulmonary artery. This type is commonly associated with aortic origin of right pulmonary artery (Figure 23.11).

Type III (total defect): this is a very large defect involving the entire length of pulmonary trunk from immediately above the semilunar valves to the level of pulmonary bifurcation and the proximal portion of the right pulmonary artery.

All three types of aortopulmonary windows typically present with symptoms of a large left-to-right shunt due to the unimpeded flow from the ascending aorta into the pulmonary arteries. Less commonly, the communication may be smaller and pressure-restrictive, resulting in a lesser degree of left-to-right

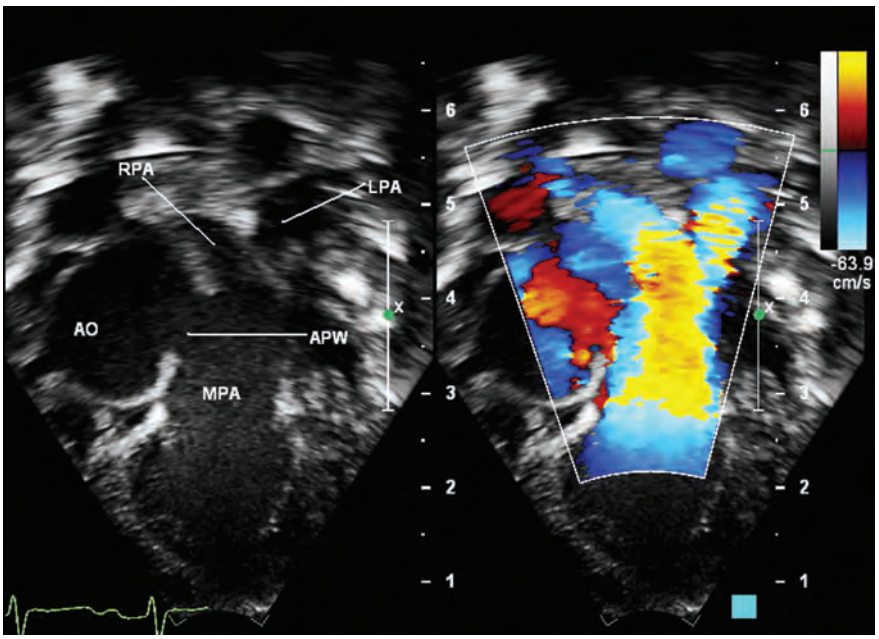


Figure 23.10 Apical 4-chamber view swept anteriorly to show the aortopulmonary window located proximally between the main pulmonary artery and the aorta (type I). AO, aorta; APW, aortopulmonary window; LPA, left pulmonary artery; MPA, main pulmonary artery; RPA, right pulmonary artery.

shunting and pulmonary overcirculation. Management may initially consist of pharmacologic therapy aimed at decreasing the pulmonary overcirculation. However, definitive therapy is provided by closure of the defect, either surgically or using a transcatheter device. In general, large defects and those associated with other cardiac malformations are closed surgically using a patch. Isolated small aortopulmonary windows or residual defects can be closed using transcatheter devices [77,78].

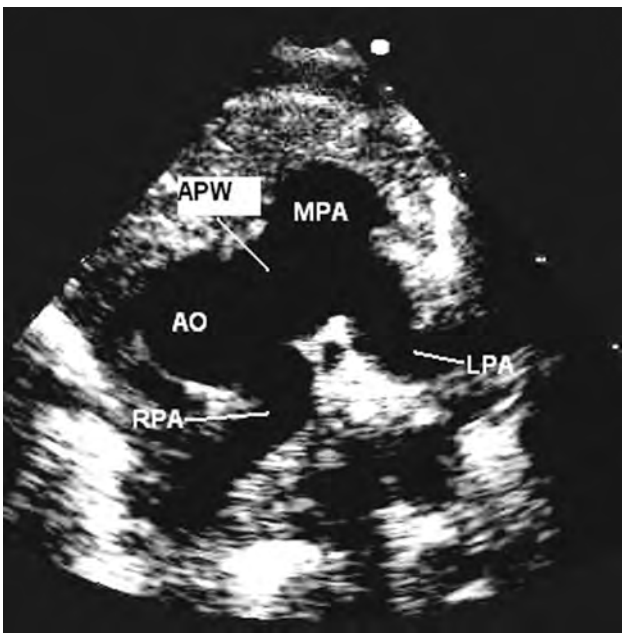


Figure 23.11 High parasternal short-axis showing a type II (distal) aortopulmonary window. Note the aortic origin of the right pulmonary artery. AO, aorta; APW, aortopulmonary window; LPA, left pulmonary artery; MPA, main pulmonary artery; RPA, right pulmonary artery.

Echocardiographic imaging

Key elements

The goals of the echocardiographic evaluation of patients with an aortopulmonary window are similar to those with other conotruncal defects, and are dependent upon the patient's age, physiologic state, and temporal relationship to surgical intervention. A complete evaluation of all anatomic features of the aortopulmonary window and any associated defects is required. In those who have undergone repair, follow-up evaluations focus primarily on residual lesions. The following key elements must be delineated:

Initial echocardiogram

As part of a detailed, segmental evaluation of all aspects of cardiovascular anatomy and physiology, particular attention is focused on the following areas:

- Presence of an atrial communication.
- Size of atria, and in particular evidence of left atrial enlargement suggestive of a large left-to-right shunt.
- Presence, size, and location of a ventricular septal defect.
- Ventricular size and function, including presence of left ventricular dilatation.
- Ventricular outflow tract obstruction, particularly right ventricular outflow tract obstruction as seen in tetralogy of Fallot with conal septal deviation.
- Morphology and function of the aortic and pulmonary valves.
- Coronary artery anatomy, with particular attention to their origins in relation to the aortopulmonary communication and ensuring that both arise from the aorta.

- Location, size, and type of aortopulmonary window.
- Pulmonary artery anatomy.
- Aortic arch anatomy (evaluation for arch sidedness, hypoplasia or interruption).
- Presence of a ductus arteriosus (uncommon except in the presence of significant arch hypoplasia or interruption).
- Associated anomalies (e.g., left superior vena cava, anomalous pulmonary venous connection, aberrant origin of the left or right subclavian arteries).

Postoperative echocardiograms

Echocardiograms performed after surgical or transcatheter intervention are focused on ensuring that there is no residual shunting and that both systemic and pulmonary pathways are unobstructed.

Imaging of aortopulmonary window

Aortopulmonary window can be diagnosed by 2D echocardiography from the parasternal short-axis, subcostal and suprasternal views. It is seen as a direct communication between the ascending aorta and the pulmonary artery and, unlike patent ductus arteriosus, it does not have any length to it. In the parasternal short-axis views with slight antero-superior angulation, the defect can be visualized and its extent into the pulmonary arteries can be defined (Figure 23.12; Video 23.14). This defect can be difficult to see from the standard parasternal long-axis views. In the subcostal coronal view, the defect can be seen when the plane of sound is swept anteriorly to open the right ventricular outflow tract (Figure 23.13; Video 23.15). Caution must be used in this view or any other view in which the ultrasound beam is parallel to where the great vessels crossover because a "dropout" can be mistaken for a defect [58]. A "T"-artifact at the edge of the defect can help distinguish a real defect from a "dropout" [75]. Special attention is paid to the coronary arteries, not only for any anomalies in their origin but also to define their proximity to the aortopulmonary window. The subcostal view is especially useful for determining the distance from the defect to the origin of the left coronary artery. In the suprasternal long-axis view, as the posterior border on the ascending aorta is followed superiorly, the aortopulmonary window is seen as a semicircle rather than the usual circle of the main pulmonary artery.

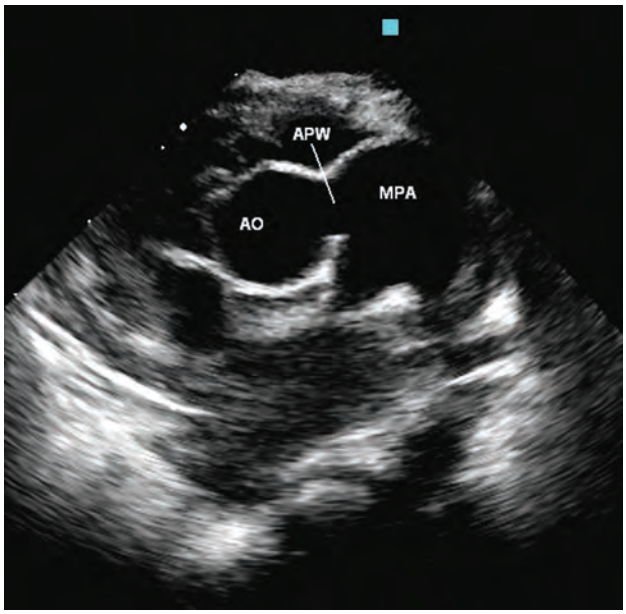


Figure 23.12 High parasternal short-axis view showing a moderate-sized type II aortopulmonary window. AO, aorta; APW, aortopulmonary window; MPA, main pulmonary artery.

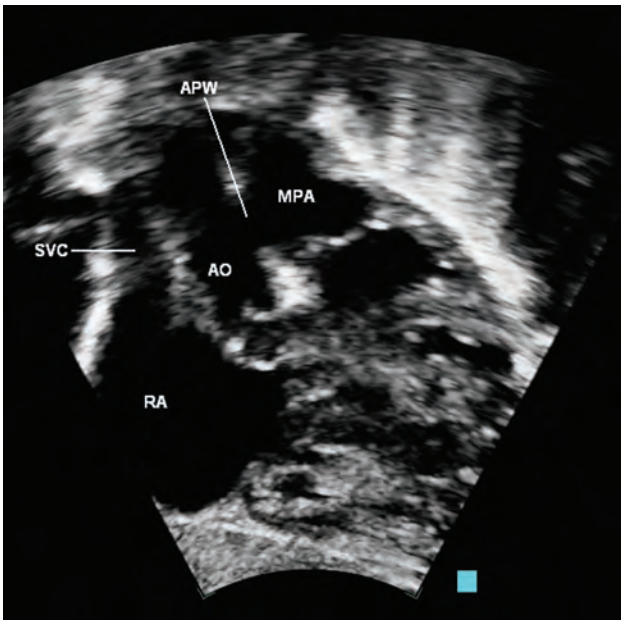


Figure 23.13 Subcostal coronal view swept anteriorly to show both outflow tracts, with a moderate-sized proximal aortopulmonary window (type I). AO, aorta; APW, aortopulmonary window; MPA, main pulmonary artery; RA, right atrium; SVC, superior vena cava.

The physiologic consequences of an aortopulmonary window result from the large left-to-right shunt. Color Doppler demonstrates increased pulmonary venous return and the left atrium and ventricle are dilated. There is increased flow across the mitral and the aortic valve. The pulmonary arteries distal to the defect are also dilated. The right ventricle can occasionally be hypertrophied. Due to the diastolic runoff from the aorta into the pulmonary artery, the thoracic aorta shows increased pulsatility when viewed from suprasternal or subcostal views.

Doppler echocardiography

In a small aortopulmonary window, color Doppler shows a continuous high-velocity turbulent jet from the aorta to the pulmonary artery. However, most of these defects are large and have unrestricted laminar flow from the aorta to the pulmonary artery. In those with normal pulmonary vascular resistance, continuous antegrade flow is seen in the pulmonary arteries distal

to the connection as a result of the large left-to-right shunt. In addition, an abnormal retrograde diastolic flow is seen in the ascending aorta, transverse arch and descending aorta due to runoff from the aorta into pulmonary arteries during diastole. This finding of diastolic flow reversal in the entire aorta can also be seen in cases with severe aortic regurgitation, an aorto-left ventricular tunnel or a ruptured sinus of Valsalva aneurysm [79]. In contrast, with a large left-to-right shunt across a ductus arteriosus, the retrograde diastolic flow is seen only in the descending aorta and not in the ascending aorta or transverse arch. If the defect remains unrepaired, pulmonary hypertension can develop over time. In such cases, a low-velocity bidirectional flow or an exclusive right-to-left flow will be seen across the defect.

Three-dimensional echocardiography

Availability of real-time 3D echocardiography allows for enhanced spatial resolution of the aortopulmonary window with an en face view of the entire defect. This technique can also be useful in assisting device closure of these defects.

Evaluation following closure of an aortopulmonary window

Both surgical and transcatheter closure of aortopulmonary windows can be complicated by residual defects or stenosis of the ascending aorta or pulmonary artery. In rare cases, the coronary circulation may also be compromised, resulting in regional or global dysfunction. These complications can be diagnosed and monitored using protocols similar to those described earlier for truncus arteriosus.

Videos

To access the videos for this chapter, please go to www.lai-echo.com.

Video 23.1 Parasternal long-axis view demonstrating origin of the main pulmonary artery from the truncal root (truncus arteriosus type 1).

Video 23.2 Color Doppler interrogation from the parasternal short-axis view demonstrating truncus arteriosus type I. The main pulmonary artery originates from the truncal root on the left lateral side and gives rise to two adequately sized confluent branch pulmonary arteries.

Video 23.3 Parasternal short-axis view demonstrating truncus arteriosus type II, with the origins of the pulmonary artery branches directly from the truncal root, adjacent to one another with a rim of truncal tissue between them.

Video 23.4 Suprasternal notch long-axis view and sweep showing truncus arteriosus with aortic arch interruption (type A). The ductal arch can be seen joining the common trunk to the descending aorta.

Video 23.5 Parasternal short-axis view showing an en face view of the quadricuspid truncal valve.

Video 23.6 Subcostal coronal view swept anteriorly shows moderate to severe truncal valve regurgitation. Note that the truncal valve overrides predominantly the right ventricle.

Video 23.7 Parasternal short-axis view in a type II truncus, showing a single coronary artery origin arising anteriorly from the truncal root and giving rise to left and right coronary systems.

Video 23.8 High parasternal short-axis view sweeping superiorly, showing the subtle separation of the relatively hypoplastic truncal root as it ascends (and interrupts, as a type B) from the ductal arch.

Video 23.9 Subcostal coronal view showing the truncal valve and truncal root. Note the main pulmonary artery segment arising from the left lateral aspect of the trunk and bifurcating into right and left pulmonary arteries (type I truncus).

Video 23.10 Parasternal long-axis view in a case of truncus arteriosus and type B aortic interruption. Note the ascending aorta arising from the anterior rightwards aspect of the truncal root.

Video 23.11 Apical 4-chamber view with color Doppler swept anteriorly to the truncal root, showing the origin of the MPA segment off the lateral aspect of the truncus (truncus type I), with subsequent bifurcation into right and left pulmonary arteries.

Video 23.12 Subcostal coronal view with color Doppler swept anteriorly to show the MPA segment arising from the left lateral aspect of the truncal root, and bifurcating into the right and left branch pulmonary artery.

Video 23.13 Suprasternal notch short-axis sweep in a patient with truncus type II and interrupted aortic arch type A. Note that the innominate artery, left carotid artery and left subclavian artery arise from the ascending aorta which then interrupts. The two branch pulmonary arteries can also be seen arising from the posterior aspect of the truncal root.

Video 23.14 High parasternal short-axis view with color Doppler showing a moderate-sized type II aortopulmonary window.

Video 23.15 Subcostal coronal view swept anteriorly to show both ventricular outflow tracts. Note is made of a moderate-sized proximal aortopulmonary window (type I).

References

1 Lev M, Saphir O. Truncus arteriosus communis persistens. *J Pediatr* 1942;**20**:74–88.
2 Collett RW, Edwards JE. Persistent truncus arteriosus; a classification according to anatomic types. *Surg Clin North Am* 1949;**29**:1245–1270.
3 Van Praagh R, Van Praagh S. The anatomy of common aorticopulmonary trunk (truncus arteriosus communis) and its

embryologic implications. A study of 57 necropsy cases. *Am J Cardiol* 1965;**16**:406–425.
4 Crupi G, Macartney FJ, Anderson RH. Persistent truncus arteriosus. A study of 66 autopsy cases with special reference to definition and morphogenesis. *Am J Cardiol* 1977;**40**:569–578.
5 Calder L, Van Praagh R, Van Praagh S, et al. Truncus arteriosus communis. Clinical, angiocardiographic, and pathologic findings in 100 patients. *Am Heart J* 1976;**92**:23–38.
6 Van Mierop LH, Patterson DF, Schnarr WR. Pathogenesis of persistent truncus arteriosus in light of observations made in a dog embryo with the anomaly. *Am J Cardiol* 1978;**41**:755–762.
7 Buchanan G. Malformation of heart: undivided truncus arteriosus heart otherwise double. *Trans Pathol Soc London* 1864;**15**:89.
8 Tandon R, Hauck AJ, Nadas AS. Persistent truncus arteriosus. A clinical, hemodynamic, and autopsy study of nineteen cases. *Circulation* 1963;**28**:1050–1060.
9 Hoffman JI, Kaplan S. The incidence of congenital heart disease. *J Am Coll Cardiol* 2002;**39**:1890–1900.
10 Locatelli G, Alfieri O, Villani M, et al. [Surgical treatment of truncus arteriosus in the 1st year of life]. *Chirurgie pediatrique* 1980;**21**:89–94. Traitement chirurgical du truncus arteriosus dans la première année de la vie. fre.
11 Kirby ML. Contribution of neural crest to heart and vessel morphology. In: Harvey R, Rosenthal N (eds.) *Heart Development*. San Diego, CA: Academic Press, 1999, pp. 179–193.
12 Delot EC, Bahamonde ME, Zhao M, Lyons KM. BMP signaling is required for septation of the outflow tract of the mammalian heart. *Development* 2003;**130**:209–220.
13 Driscoll DA, Budarf ML, Emanuel BS. A genetic etiology for DiGeorge syndrome: consistent deletions and microdeletions of 22q11. *Am J Hum Genet* 1992;**50**:924–933.
14 Marino B, Digilio MC, Toscano A, et al. Anatomic patterns of conotruncal defects associated with deletion 22q11. *Genet Med* 2001;**3**:45–48.
15 Goldmuntz E, Clark BJ, Mitchell LE, et al. Frequency of 22q11 deletions in patients with conotruncal defects. *J Am Coll Cardiol* 1998;**32**:492–498.
16 Iserin L, de Lonlay P, Viot G, et al. Prevalence of the microdeletion 22q11 in newborn infants with congenital conotruncal cardiac anomalies. *Eur J Pediatr* 1998;**157**:881–884.
17 McElhinney DB, Driscoll DA, Emanuel BS, Goldmuntz E. Chromosome 22q11 deletion in patients with truncus arteriosus. *Pediatr Cardiol* 2003;**24**:569–573.
18 Wilson DI, Burn J, Scambler P, Goodship J. DiGeorge syndrome: part of CATCH 22. *J Med Genet* 1993;**30**:852–856.
19 de la Cruz MV, Da Rocha JP. An ontogenetic theory for the explanation of congenital malformations involving the truncus and conus. *Am Heart J* 1956;**51**:782–805.
20 Kirby ML. Cellular and molecular contributions of the cardiac neural crest to cardiovascular development. *Trends Cardiovasc Med* 1993;**3**:18–23.
21 Kirby ML, Waldo KL. Role of neural crest in congenital heart disease. *Circulation* 1990;**82**:332–340.
22 Bain CW, Parkinson J. Common aorto-pulmonary trunk: a rare congenital defect. *Br Heart J* 1943;**5**:97–100.
23 Carr I, Bharati S, Kusnoor VS, Lev M. Truncus arteriosus communis with intact ventricular septum. *Br Heart J* 1979;**42**:97–102.
24 Becker AE, Becker MJ, Edwards JE. Pathology of the semilunar valve in persistent truncus arteriosus. *J Thorac Cardiovasc Surg* 1971;**62**:16–26.
25 Gelband H, Van Meter S, Gersony WM. Truncal valve abnormalities in infants with persistent truncus arteriosus. A clinicopathologic study. *Circulation* 1972;**45**:397–403.
26 Fuglestad SJ, Puga FJ, Danielson GK, Edwards WD. Surgical pathology of the truncal valve: a study of 12 cases. *Am J Cardiovasc Pathol* 1988;**2**:39–47.
27 Butto F, Lucas RV, Jr., Edwards JE. Persistent truncus arteriosus: pathologic anatomy in 54 cases. *Pediatr Cardiol* 1986;**7**:95–101.
28 Bengur AR. Truncus arteriosus. In: Garson A, Bricker JT, Fisher DJ, Neish SR (eds.) *Science and Practice of Pediatric Cardiology*, 2nd edn. Philadelphia, PA: Lippincott Williams and Wilkins, 1998, p. 1421.
29 Bharati S, McAllister HA, Jr., Rosenquist GC, et al. The surgical anatomy of truncus arteriosus communis. *J Thorac Cardiovasc Surg* 1974;**67**:501–510.
30 Suzuki A, Ho SY, Anderson RH, Deanfield JE. Coronary arterial and sinusal anatomy in hearts with a common arterial trunk. *Ann Thorac Surg* 1989;**48**:792–797.
31 Shrivastava S, Edwards JE. Coronary arterial origin in persistent truncus arteriosus. *Circulation* 1977;**55**:551–554.
32 de la Cruz MV, Cayre R, Angelini P, et al. Coronary arteries in truncus arteriosus. *Am J Cardiol* 1990;**66**:1482–1486.
33 Anderson KR, McGoon DC, Lie JT. Surgical significance of the coronary arterial anatomy in truncus arteriosus communis. *Am J Cardiol* 1978;**41**:76–81.
34 Bove EL, Lupinetti FM, Pridjian AK, et al. Results of a policy of primary repair of truncus arteriosus in the neonate. *J Thorac Cardiovasc Surg* 1993;**105**:1057–1065; discussion 65–66.
35 Van Mierop LH, Kutsche LM. Cardiovascular anomalies in DiGeorge syndrome and importance of neural crest as a possible pathogenetic factor. *Am J Cardiol* 1986;**58**:133–137.
36 Litovsky SH, Ostfeld I, Bjornstad PG, et al. Truncus arteriosus with anomalous pulmonary venous connection. *Am J Cardiol* 1999;**83**:801–804, A10.
37 Sharma D, Mehta AB, Bharati S, Lev M. Tricuspid atresia with persistent truncus arteriosus. *Chest* 1981;**79**:363–365.
38 Shapiro SR, Ruckman RN, Kapur S, et al. Single ventricle with truncus arteriosus in siblings. *Am Heart J* 1981;**102**:456–459.
39 Marcelletti C, McGoon DC, Mair DD. The natural history of truncus arteriosus. *Circulation* 1976;**54**:108–111.
40 Pearl JM, Laks H, Drinkwater DC, Jr., et al. Repair of truncus arteriosus in infancy. *Ann Thorac Surg* 1991;**52**:780–786.
41 Hanley FL, Heinemann MK, Jonas RA, et al. Repair of truncus arteriosus in the neonate. *J Thorac Cardiovasc Surg* 1993;**105**:1047–1056.
42 Thompson LD, McElhinney DB, Reddy M, et al. Neonatal repair of truncus arteriosus: continuing improvement in outcomes. *Ann Thorac Surg* 2001;**72**:391–395.
43 Jacobs JP, O'Brien SM, Pasquali SK, et al. Variation in outcomes for benchmark operations: an analysis of the Society of Thoracic Surgeons Congenital Heart Surgery database. *Ann Thorac Surg* 2011;**92**:2184–2191; discussion 91–92.
44 Imamura M, Drummond-Webb JJ, Sarris GE, Mee RB. Improving early and intermediate results of truncus arteriosus repair: a new

technique of truncal valve repair. *Ann Thorac Surg* 1999;**67**:1142–1146.
45 Jahangiri M, Zurakowski D, Mayer JE, et al. Repair of the truncal valve and associated interrupted arch in neonates with truncus arteriosus. *J Thorac Cardiovasc Surg* 2000;**119**:508–514.
46 McElhinney DB, Reddy VM, Rajasinghe HA, et al. Trends in the management of truncal valve insufficiency. *Ann Thorac Surg* 1998;**65**:517–524.
47 Brown JW, Ruzmetov M, Okada Y, et al. Truncus arteriosus repair: outcomes, risk factors, reoperation and management. *Eur J Cardiothorac Surg* 2001;**20**:221–227.
48 Russell HM, Pasquali SK, Jacobs JP, et al. Outcomes of repair of common arterial trunk with truncal valve surgery: a review of the Society of Thoracic Surgeons Congenital Heart Surgery database. *Ann Thorac Surg* 2012;**93**:164–169; discussion 9.
49 Yankah AC, Alexi-Meskhishvili V, Weng Y, et al. Accelerated degeneration of allografts in the first two years of life. *Ann Thorac Surg* 1995;**60**:S71–76; discussion 576–577.
50 Rajasinghe HA, McElhinney DB, Reddy VM, et al. Long-term follow-up of truncus arteriosus repaired in infancy: a twenty-year experience. *J Thorac Cardiovasc Surg* 1997;**113**:869–878; discussion 78–79.
51 Dearani JA, Danielson GK, Puga FJ, et al. Late follow-up of 1095 patients undergoing operation for complex congenital heart disease utilizing pulmonary ventricle to pulmonary artery conduits. *Ann Thorac Surg* 2003;**75**:399–410.
52 Lloyd TR, Marvin WJ, Jr., Mahoney LT, Lauer RM. Balloon dilation valvuloplasty of bioprosthetic valves in extracardiac conduits. *Am Heart J* 1987;**114**:268–274.
53 Ensing GJ, Hagler DJ, Seward JB, et al. Caveats of balloon dilation of conduits and conduit valves. *J Am Coll Cardiol* 1989;**14**:397–400.
54 Powell AJ, Lock JE, Keane JF, Perry SB. Prolongation of RV-PA conduit life span by percutaneous stent implantation. Intermediate-term results. *Circulation* 1995;**92**:3282–3288.
55 Bonhoeffer P, Boudjemline Y, Saliba Z, et al. Transcatheter implantation of a bovine valve in pulmonary position: a lamb study. *Circulation* 2000;**102**:813–816.
56 Hoerstrup SP, Sodian R, Daebritz S, et al. Functional living trileaflet heart valves grown in vitro. *Circulation* 2000;**102**:III44–49.
57 Rice MJ, Seward JB, Hagler DJ, et al. Definitive diagnosis of truncus arteriosus by two-dimensional echocardiography. *Mayo Clin Proc* 1982;**57**:476–481.
58 Smallhorn JF, Anderson RH, Macartney FJ. Two dimensional echocardiographic assessment of communications between ascending aorta and pulmonary trunk or individual pulmonary arteries. *Br Heart J* 1982;**47**:563–572.
59 Marin-Garcia J, Tonkin IL. Two-dimensional echocardiographic evaluation of persistent truncus arteriosus. *Am J Cardiol* 1982;**50**:1376–1379.
60 Riggs TW, Paul MH. Two-dimensional echocardiographic prospective diagnosis of common truncus arteriosus in infants. *Am J Cardiol* 1982;**50**:1380–1384.
61 Mello DM, McElhinney DB, Parry AJ, et al. Truncus arteriosus with patent ductus arteriosus and normal aortic arch. *Ann Thorac Surg* 1997;**64**:1808–1810.
62 Copel JA, Pilu G, Green J, et al. Fetal echocardiographic screening for congenital heart disease: the importance of the four-chamber view. *Am J Obstet Gynecol* 1987;**157**:648–655.
63 Tometzki AJ, Suda K, Kohl T, et al. Accuracy of prenatal echocardiographic diagnosis and prognosis of fetuses with conotruncal anomalies. *J Am Coll Cardiol* 1999;**33**:1696–1701.
64 Duke C, Sharland GK, Jones AM, Simpson JM. Echocardiographic features and outcome of truncus arteriosus diagnosed during fetal life. *Am J Cardiol* 2001;**88**:1379–1384.
65 Volpe P, Paladini D, Marasini M, et al. Common arterial trunk in the fetus: characteristics, associations, and outcome in a multicentre series of 23 cases. *Heart* 2003;**89**:1437–1441.
66 Sklansky M. Advances in fetal cardiac imaging. *Pediatr Cardiol* 2004;**25**:307–321.
67 Gotsch F, Romero R, Espinoza J, et al. Prenatal diagnosis of truncus arteriosus using multiplanar display in 4D ultrasonography. *J Matern Fetal Neonatal Med* 2010;**23**:297–307.
68 Muhler MR, Rake A, Schwabe M, et al. Truncus arteriosus communis in a midtrimester fetus: comparison of prenatal ultrasound and MRI with postmortem MRI and autopsy. *Eur Radiol* 2004;**14**:2120–2124.
69 Ungerleider RM, Kisslo JA, Greeley WJ, et al. Intraoperative echocardiography during congenital heart operations: experience from 1,000 cases. *Ann Thorac Surg* 1995;**60**:S539–542.
70 Muhiudeen IA, Roberson DA, Silverman NH, et al. Intraoperative echocardiography in infants and children with congenital cardiac shunt lesions: transesophageal versus epicardial echocardiography. *J Am Coll Cardiol* 1990;**16**:1687–1695.
71 Dorfman AL, Geva T. Magnetic resonance imaging evaluation of congenital heart disease: conotruncal anomalies. *J Cardiovasc Magnetic Res* 2006;**8**:645–659.
72 Brenner D, Elliston C, Hall E, Berdon W. Estimated risks of radiation-induced fatal cancer from pediatric CT. *Am J Roentgenol* 2001;**176**:289–296.
73 Kutsche LM, Van Mierop LH. Anatomy and pathogenesis of aorticopulmonary septal defect. *Am J Cardiol* 1987;**59**:443–447.
74 Abbot ME. *Atlas of Congenital Cardiac Disease*. New York, NY: American Heart Association, 1936.
75 Balaji S, Burch M, Sullivan ID. Accuracy of cross-sectional echocardiography in diagnosis of aortopulmonary window. *Am J Cardiol* 1991;**67**:650–653.
76 Mori K, Ando M, Takao A, et al. Distal type of aortopulmonary window. Report of 4 cases. *Br Heart J* 1978;**40**(6):681–689.
77 Stamato T, Benson LN, Smallhorn JF, Freedom RM. Transcatheter closure of an aortopulmonary window with a modified double umbrella occluder system. *Catheter Cardiovasc Diagn* 1995;**35**:165–167.
78 Naik GD, Chandra VS, Shenoy A, et al. Transcatheter closure of aortopulmonary window using Amplatzer device. *Catheter Cardiovasc Interv* 2003;**59**:402–405.
79 Mahle WT, Kreeger J, Silverman NH. Echocardiography of the aortopulmonary window, aorto-ventricular tunnels, and aneurysm of the sinuses of Valsalva. *Cardiol Young* 2010;**20**:100–106.

CHAPTER 24

Transposition of the Great Arteries

Luc Mertens[1], Manfred Vogt[2], Jan Marek[3], and Meryl S. Cohen[4]
[1]Cardiology, The Hospital for Sick Children, Toronto, ON, Canada
[2]Deutsches Herzzentrum, Munich, Germany
[3]Great Ormond Street Hospital, London, UK
[4]Children's Hospital of Philadelphia, Philadelphia, PA, USA

Definition

Transposition of the great arteries (TGA) is a conotruncal abnormality in which the aorta arises from the right ventricle (RV) and the pulmonary artery arises from the left ventricle (LV) resulting in discordant ventriculo-arterial connections. This anomaly can occur in isolation or in association with other cardiac defects. In this chapter we will focus on discordant ventriculo-arterial connections in the presence of concordant atrioventricular connections. Congenitally corrected transposition or ventriculo-arterial discordance with atrioventricular discordance will be discussed in a separate chapter. Transposition of the great arteries is also referred to as D-TGA. This is, however, a nonspecific term as the "D" may relate to the ventricular loop (D or L) or to the spatial position of the aortic and pulmonary valves. In the majority of patients with TGA, the aorta is malposed rightward and anterior to the pulmonary artery but there is a wide variability in the spatial relationships between the great vessels. Therefore the term D-TGA is better avoided; *D-loop TGA* may be more accurate where the D-loop refers to the ventricular looping. For the purpose of this chapter discordant ventriculo-arterial connections will be referred to as TGA. Physiologically, TGA results in parallel systemic and pulmonary circulations in which the deoxygenated systemic venous blood returns to the aorta via the RV and the oxygenated pulmonary venous blood returns to the pulmonary arteries through the LV (Figure 24.1). Clinical presentation generally occurs early in the neonatal period because of cyanosis.

Incidence

The incidence of TGA is approximately 31.5 per 100,000 live births (range 23.1 to 38.8 per 100,000 live births). It is the tenth most common congenital heart defect and the second most common cyanotic lesion after tetralogy of Fallot [1]. The incidence is likely higher in the fetal population since termination of pregnancy is not included in most population studies. TGA affects males more commonly than females with a ratio of over 2:1 [2]. Chromosomal anomalies in association with simple and complex forms of TGA are unusual. The incidence of TGA does not appear to be impacted by increased maternal age or increased parity [2].

Etiology

The etiology of TGA remains unknown; however, a genetic cause is probable in most cases. Familial recurrence occurs in TGA; 10% of afflicted individuals have a relative with a congenital heart defect. While 22q11 deletion is common in other conotruncal anomalies such as tetralogy of Fallot and common arterial trunk, it is quite rare in TGA [3]; however, single-gene mutations such as *CFC1* have been reported [4]. Of those affected, TGA is the most common recurrent lesion [5]. Environmental factors have been implicated and TGA has been associated with maternal diabetes [6] and exposure to the teratogen retinoic acid during gestation.

Morphology and classification

Developmental considerations

The developmental mechanisms leading to TGA have not been fully elucidated. The cardiac outflow tract, including the muscular conus and the arterial trunk, develop with contributions from neural crest cells and from the anterior heart field, which also forms large portions of the RV. Mesenchymal cells derived from the neural crest contribute to the septum that divides the common arterial trunk into the aorta and pulmonary artery. At early stages of gestation, the great vessels relate to each other similar to TGA. Conotruncal rotation associated with septation and

Echocardiography in Pediatric and Congenital Heart Disease: From Fetus to Adult, Second Edition. Edited by Wyman W. Lai, Luc L. Mertens, Meryl S. Cohen and Tal Geva.
© 2016 John Wiley & Sons, Ltd. Published 2016 by John Wiley & Sons, Ltd.
Companion website: www.lai-echo.com

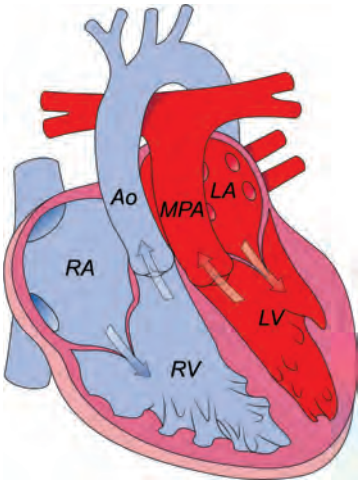


Figure 24.1 Diagram of D-loop transposition of the great arteries with atrioventricular concordance and ventriculo-arterial discordance. Ao, aorta; LA, left atrium; LV, left ventricle; MPA, main pulmonary artery; RA, right atrium; RV, right ventricle.

differential development of the infundibulum is required to align the aorta with the LV and the pulmonary artery with the RV. Abnormal conotruncal rotation during septation likely results in TGA. This is suggested in the perlecan-deficient mouse embryo model that develops TGA with intact ventricular septum. Perlecan is a heparin-sulfate proteoglycan expressed in the extracellular matrix. In this model, the mesenchyme of the outflow tract is disrupted. Outflow ridges normally twist in a counterclockwise pattern but in TGA this spiral likely does not occur, resulting in a "straight" outlet [7,8].

Anatomy

TGA with intact ventricular septum

In the commonest form of TGA, the segmental anatomy is typically situs solitus with atrioventricular concordance and ventriculo-arterial discordance with the aorta positioned anterior and to the right of the pulmonary artery. This has also been described as {S,D,D}: the situs of the visceral organs and the atrial is normal (solitus = S), the ventricles are D-looped (D), the atrioventricular alignment is concordant, and the ventriculo-arterial alignment is discordant with a rightward and anterior position of the aortic valve relative to the pulmonary valve (D, or dextro malposition). In some cases, the aorta is directly anterior to the pulmonary artery and in others the great vessels are side-by-side with the aortic valve to the right of the pulmonary valve. Rarely, the aorta can be leftward, in which case the segmental anatomy is {S,D,L}. This arrangement is typically associated with RV hypoplasia and superior-inferior ventricles. More rarely, the aortic valve can be located posterior and rightward relative to the pulmonary valve (TGA with posterior aorta) [9]. For each patient the spatial relationship between the great vessels needs to be clearly defined by echocardiography.

The anatomy of the ventricular outflow tracts in TGA is important for surgical management. In almost 90% of cases of TGA there is a subaortic conus (infundibulum) separating the aortic valve from the tricuspid valve and absence of a subpulmonary conus, resulting in fibrous continuity between the mitral and pulmonary valves [9,10]. Abnormalities in the outflow tracts can cause outflow tract obstruction, which is important when considering an arterial switch operation. Variants of outflow tract or conal anatomy are seen in ~12% of patients – bilateral subarterial conus in ~7%, subpulmonary conus without subaortic conus in ~3%, and bilaterally absent conus in ~2% of patients with TGA [11]. Atypical outflow tract anatomy can be associated with outflow tract obstruction, VSD, and unusual coronary anatomy. In the setting of TGA with intact ventricular septum, a left aortic arch without obstruction is the norm. However, rare cases of coarctation of the aorta have been reported [12]. Systemic and pulmonary venous connections are usually normal. Dynamic LV outflow tract obstruction can be seen when LV pressure is subsystemic. This usually resolves after anatomic correction (see later). Fixed anatomic subpulmonary stenosis is rare. Most patients with TGA have a patent ductus arteriosus (PDA) at birth. The foramen ovale is usually patent at birth but can be small or absent, resulting in severe cyanosis due to lack of atrial mixing. A true secundum atrial septal defect or other types of atrial defects are less common.

TGA with ventricular septal defect

Except for patent foramen ovale and PDA, VSD is the most commonly associated defect occurring in ~40–45% of cases. Similar to normally related great arteries, any type of VSD can be seen in association with TGA. Approximately 33% patients have a membranous (perimembranous) defect, ~30% have a malalignment defect (often associated with obstruction of one of the outflow tracts), ~25% have a muscular defect, and ~5% each have an atrioventricular (AV) canal-type (inlet) or outlet septal (doubly committed or subarterial) defect (Figure 24.2) [13]. Membranous defects may be large or restrictive and result in fibrous continuity between the tricuspid and the pulmonary valve leaflets. Spontaneous closure or restriction of the defect by tricuspid valve septal tissue is possible. Muscular defects can occur anywhere within the muscular septum (most commonly the midmuscular region) and are often multiple. Muscular defects can also close or decrease in size spontaneously. In those with AV canal-type VSD, the tricuspid valve may straddle the ventricular septum, usually with associated RV hypoplasia. Outlet septal defects (doubly committed type) are characterized by deficiency or absence of the outlet septum with little or no muscular separation between the aortic and pulmonary valves. Surgical closure of this type of VSD can be challenging because the sutures must be anchored into the fibrous rim between the aortic and pulmonary valves, potentially distorting one or both semilunar valves.

Malalignment VSDs are of particular surgical importance. In the setting of anterior malalignment of the outlet (conal) septum

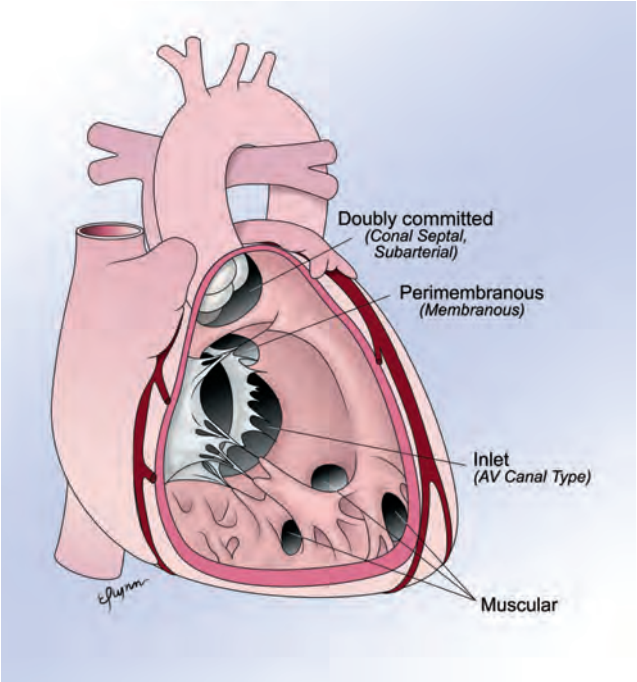


Figure 24.2 Different types of ventricular septal defects in the setting of transposition. AV, atrioventricular.

the VSD is generally large and unrestrictive. This anatomy typically results in impingement on the RV outflow tract with multiple levels of obstruction. Subaortic stenosis and aortic annulus hypoplasia are common; distal obstruction can include aortic arch hypoplasia, coarctation of the aorta, or interruption of the aortic arch. In contrast, posterior malalignment of the conal septum is often associated with LV outflow tract obstruction, including subvalvar and valvar pulmonary stenosis. In addition to posterior deviation of the conal septum into the LV outflow tract, other potential mechanisms of pulmonary outflow obstruction include a discrete fibrous ridge, muscular tunnel narrowing, abnormal mitral valve attachments, and redundant or straddling tricuspid valve tissue (Figure 24.3). The pulmonary valve annulus may be hypoplastic and the pulmonary valve leaflets and commissures are often abnormal (e.g., bicuspid or unicuspid pulmonary valve).

Coronary artery anatomy

Coronary artery anatomy is particularly important in TGA given that the majority of patients today undergo the arterial switch operation (ASO), which requires translocation of the coronary arteries to the neo-aorta. Although the origin and proximal course of the coronary arteries is variable, they originate from aortic sinuses facing the pulmonary valve in almost all cases. The aortic sinuses that face the pulmonary root are labeled according to their spatial location [14]. In the majority of patients in whom the aortic valve is anterior and rightward relative to the pulmonary valve, the sinuses are termed right-posterior- and left-anterior-facing sinuses. When the aortic valve is directly anterior the sinuses are termed right- and left-facing sinuses and when the great vessels are side-by-side the sinuses are termed posterior- and anterior-facing sinuses (Figure 24.4). Alternative taxonomies assign numbers or letters to the facing sinuses. The Leiden terminology describes the origin of the coronary arteries from the facing aortic sinuses of Valsalva as viewed from

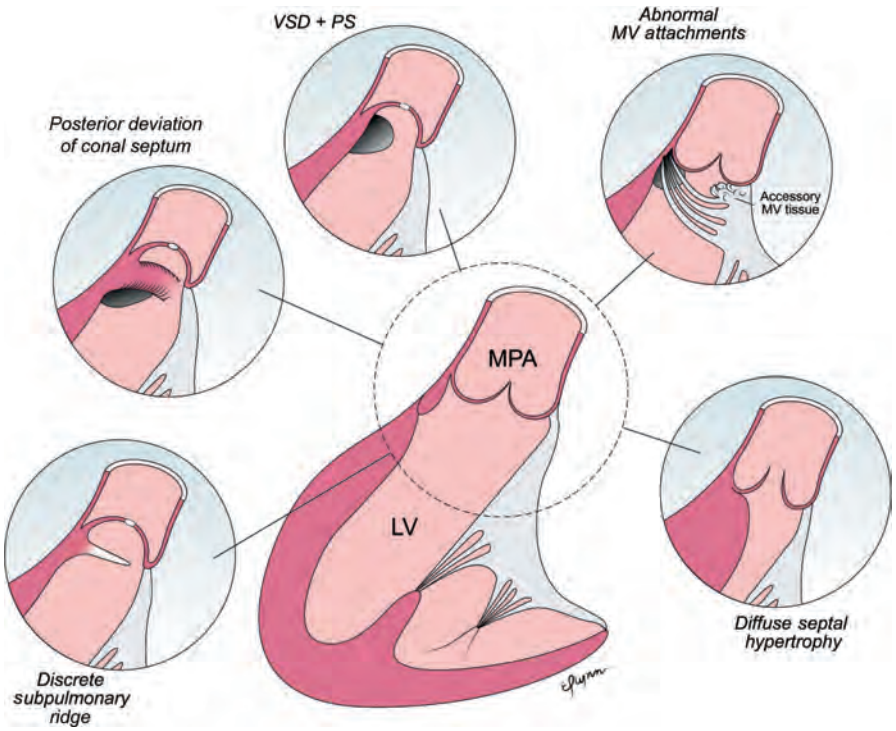


Figure 24.3 Different mechanisms of left ventricular outflow obstruction in D-loop transposition of the great arteries (TGA). More than one mechanism can be present. LV, left ventricle; MPA, main pulmonary artery; MV, mitral valve; PS, pulmonary stenosis; VSD, ventricular septal defect.

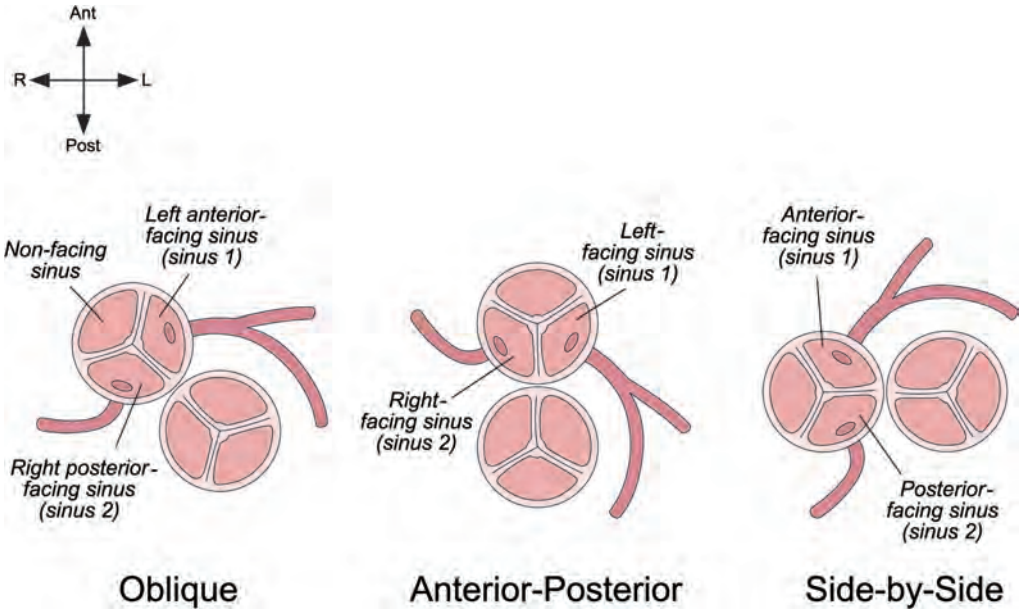


Figure 24.4 Designations of the aortic sinuses of Valsalva when the spatial orientation of the aortic and pulmonary roots is oblique, anterior-posterior, and side-by-side. Ant, anterior; Post, posterior; R, right; L, left.

the nonfacing sinus [15]. The observer takes a stance in the noncoronary sinus looking toward the pulmonary trunk (Figure 24.4). Viewed from this position, one sinus is always to the right of the observer (sinus 1) and the other sinus is always to the left of the observer (sinus 2). This definition holds irrespective of the relationship of the arterial trunks towards each other. While the Leiden classification is convenient for the surgeon who looks down on the aortic valve, this classification can be confusing for the echocardiographer who looks at the aortic valve from the opposite perspective. If uncertain about the description, a schematic drawing of the coronary origins as illustrated in Figure 24.5 may clarify the issue.

The eight major anatomic patterns of the coronary arteries in TGA are illustrated in Figure 24.5. Based on three studies encompassing 533 patients [16], the most common or "usual" pattern of coronary artery origin – left anterior descending (LAD) and left circumflex (LCx) arising from the left-facing sinus (sinus 1) and the right coronary artery (RCA) arising from the right-facing sinus (sinus 2) – is present in 65% of patients. The second most common form – LAD from the left-facing sinus (sinus 1) and RCA and LCx from the right-facing sinus (sinus 2) – is present in 13.6% of patients. The LCx courses posterior to the pulmonary root before reaching the left atrioventricular groove. The third most common pattern seen in 7.5% of cases is a single RCA arising from the right-facing sinus (sinus 2) where the left coronary artery (LCA) passes posterior to the pulmonary root before bifurcating into the LAD and LCx branches. Other variations include single LCA from the left-facing sinus (sinus 1) in 1.5% of cases, inverted coronary arteries (RCA from sinus 1 and LAD and LCx from sinus 2) in 2.6% of cases, and inverted RCA and LCx (RCA and LAD from sinus 1 and LCx from sinus 2) in 6% of cases. Intramural LCA and RCA are seen in 3% and 0.75% of patients, respectively. Based on analysis of nine studies from over two decades (total of 1942 patients), Pasquali et al. found that intramural or single coronary artery patterns were associated with an increased risk of death in patients undergoing an ASO [16].

Associated defects

In addition to patent foramen ovale, PDA, and VSD, TGA has been reported to be associated with a myriad of cardiovascular anomalies such as anomalies of the systemic (e.g., persistent left superior vena cava) and pulmonary veins (e.g., partially and totally anomalous pulmonary venous connections [17]), atrioventricular septal defect, anomalies of the atrioventricular valves (e.g., stenosis, cleft, abnormal attachments, straddling [18]), left and right ventricular outflow tract abnormalities, and anomalies of the great vessels (e.g., aortic arch hypoplasia, interruption [19], coarctation, and double aortic arch [20]). Leftward juxtaposition of the right atrial appendage occurs in approximately 2% of cases of TGA [21]. It is usually seen in association with other complex abnormalities such as dextrocardia and tricuspid atresia.

Pathophysiology

The parallel arrangement of the systemic and pulmonary circulations in TGA is tolerated well before birth due to mixing of oxygenated and deoxygenated blood through the foramen ovale and PDA. After birth, the decrease in pulmonary vascular resistance leads to increased pulmonary venous return to the left

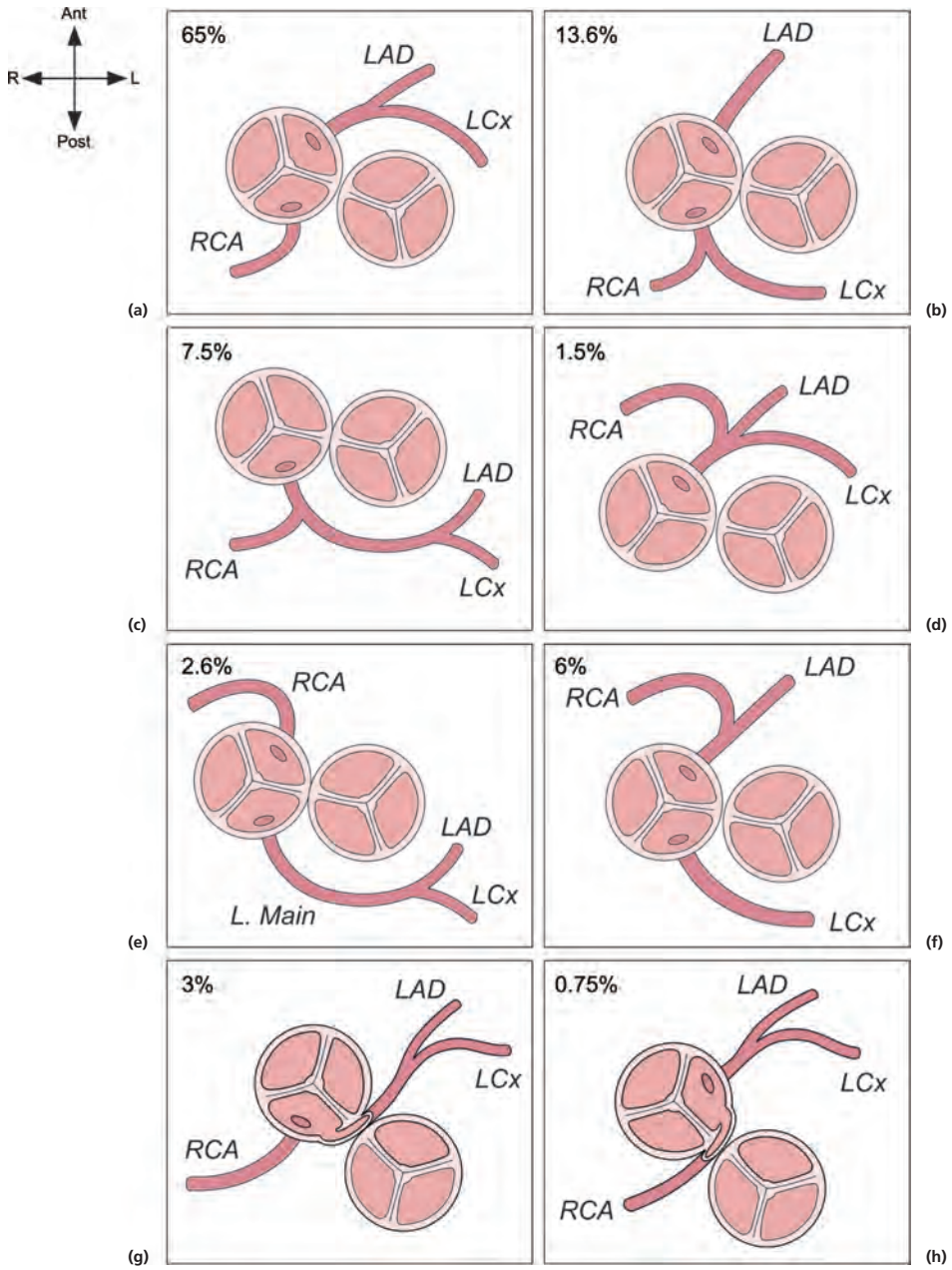


Figure 24.5 The most common patterns of coronary anatomy in patients with D-loop transposition of the great arteries (TGA). **(A)** Usual coronary anatomy with left coronary artery (LCA) coming from sinus 1 and right coronary artery (RCA) coming from sinus 2. **(B)** Left circumflex (LCx) from RCA (sinus 2) and left anterior descending (LAD) coming from sinus 1. **(C)** Single coronary coming from sinus 2. **(D)** Single coronary artery coming from sinus 1. **(E)** Inverted origins with RCA coming from sinus 1 and LCA coming from sinus 2. **(F)** LAD and RCA coming from sinus 1 and LCx coming from sinus 2. **(G)** Intramural LCA with origin of LCA and RCA both from sinus 2 and intramural course of LCA. **(H)** Intramural RCA with origin of RCA and LCA from sinus 1 and intramural course of RCA.

atrium, which is accentuated by flow from the aorta to the pulmonary artery through the PDA. If septum primum (valve of the fossa ovalis) effectively seals off the intra-atrial communication, severe hypoxia may occur within the first hours of life. In other cases, the foramen ovale remains open, allowing oxygenated blood returning to the left atrium to shunt from left-to-right mixing with the deoxygenated blood returning from the systemic veins. The presence of an adequate atrial communication is a requirement to obtain good aortic (preductal) saturations. If the atrial communication is small, a balloon atrial septostomy may be required. When present, a VSD provides another opportunity for mixing of blood between the left and right sides of the heart, although it may not provide enough effective pulmonary blood flow.

The RV (systemic ventricle) is generally larger compared to the LV. The difference in size is not striking in the neonatal period because the LV is initially at systemic pressure. In the weeks after birth, pulmonary vascular resistance decreases and, in the absence of a large VSD or outflow tract obstruction, the afterload on the LV decreases. This causes the LV to remodel with a thinner free wall and a smaller short-axis diameter. The RV meanwhile remains hypertrophied and dilated. Ultimately, LV mass decreases (deconditioning) to a level that precludes its ability to sustain the systemic circulation after the ASO. Thus, anatomic repair is performed in patients with TGA and intact ventricular septum or a small VSD within the first weeks of life in order to avoid LV remodeling. For patients presenting after age 2 months, careful assessment of LV size, wall thickness, and mass is required. Another factor that can lead to hemodynamic instability after birth is the presence of elevated pulmonary vascular resistance or persistent pulmonary hypertension. After the arterial switch operation, reduced pulmonary blood flow caused by pulmonary hypertension can lead to lower oxygenation and is seen in about 2% of all TGA patients.

Imaging

Echocardiography is the imaging modality of choice in children with TGA and currently most patients are referred for cardiac surgery based solely on echocardiographic diagnosis. Therefore, a comprehensive, detailed description of cardiovascular anatomy and suitability for surgical repair is paramount for successful management. In addition, echocardiography is often used as the primary imaging modality to guide balloon atrial septostomy.

Key elements

In all cases, complete anatomic and functional examination by 2D and 3D imaging, as appropriate, and by color and spectral Doppler. In addition, the following elements of cardiovascular anatomy and function should be evaluated in detail and be given priority.

- Segmental anatomy.
- Assessment of systemic and pulmonary venous connections.
- Evaluation of the atrial septum for interatrial communication(s): location, size, and flow direction and velocity; measure mean transseptal flow gradient.
- Rule out juxtaposition of atrial appendages.
- Evaluation of atrioventricular valve morphology (e.g., cleft, straddling, abnormal attachments) and function (e.g., stenosis, regurgitation).
- Determination of biventricular size and function.
- Determination of presence of VSD:
 - Single or multiple defects
 - Location and size
 - Restriction to flow
 - Direction of flow
- Ventriculo-arterial connections:
 - Position of aorta relative to the pulmonary artery at the level of the semilunar valves
 - Assessment of commissural alignment
 - Determination of presence and severity of outflow tract obstruction; if present, mechanism of obstruction
 - Semilunar valve anatomy and function (e.g., stenosis or regurgitation)
- Determination of coronary artery anatomy.
- Presence, size, and direction of flow through a PDA.
- Evaluation of aortic arch sidedness; rule out aortic arch hypoplasia or coarctation.

Imaging of TGA with intact ventricular septum

The subxiphoid acoustic window provides a wide-angle view of the heart and blood vessels and allows rapid diagnosis of TGA. After establishing the situs of the abdominal organs, a sweep of the transducer from the subxiphoid window in the oblique coronal plane demonstrates the systemic and venous connections to the heart, the atrial septum, atrioventricular and ventriculo-arterial connections and alignments, and the great vessels. As the transducer is swept from posterior-inferior to superior-anterior (Video 24.1), the main pulmonary artery is seen originating directly from the LV bifurcating into the left and right pulmonary arteries (Figure 24.6a). Further anterior tilt of the transducer demonstrates the origin of the aorta from the rightward and superior aspect of the RV (Figure 24.6b). Origin of the coronary arteries from the aortic root, often seen from this window, helps establish the identity of the aorta. Rotating the transducer clockwise ~90 degrees to the ventricular short axis (oblique sagittal plane) demonstrates the superior-inferior and anterior-posterior relations of the cardiovascular structures. The transducer is swept from right to left, beginning at the bicaval view and ending at the level of the ventricular apex. This view is particularly helpful in demonstrating the connection of the right upper pulmonary vein to the left atrium, the atrial septum, and the anatomy of the atrioventricular valves and their attachments and the outflow tracts of both ventricles. In TGA, this view demonstrates the parallel course of the great arteries (Figure 24.7). Interrogation of blood flow by color Doppler provides essential information about atrial and ventricular septal defects, valve function, outflow tract obstruction, semilunar valve function, and PDA. Evaluation of the atrial septum from the subxiphoid window includes determination of location and size of interatrial communications and assessment of the direction and velocity of blood flow. In most patients, atrial level flow is from left to right. The mean gradient of the flow across the atrial septum can be measured by spectral Doppler.

The apical window allows evaluation of the ventricular inflow and outflow tracts and the ventricular septum. This view is ideal for assessment of the atrioventricular valves for stenosis or regurgitation by color and spectral Doppler. Careful interrogation of the ventricular septum with particular attention to the

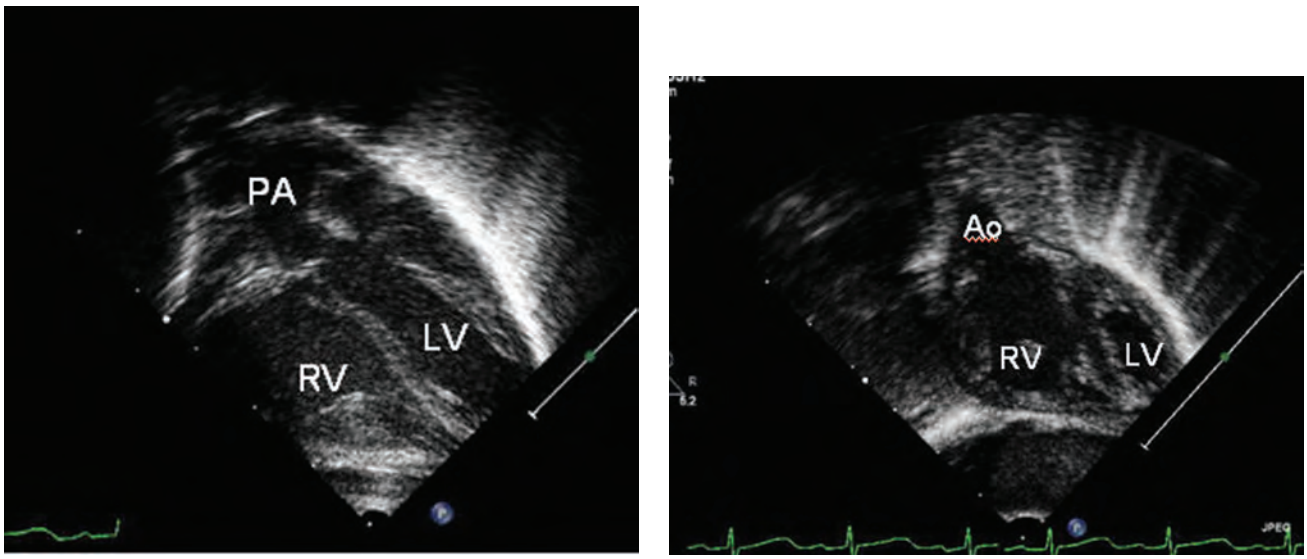


Figure 24.6 Subxiphoid long-axis views showing ventriculo-arterial discordance. **(a)** The main pulmonary artery (PA) is seen coming off the left ventricle (LV). **(b)** The aorta (Ao) is visible coming from the right ventricle (RV).

apex is important to exclude VSDs. In addition, the apical window provides an optimal angle for Doppler interrogation of the LV outflow tract for assessment of obstruction.

The parasternal window provides complementary anatomic and functional information. The parallel course of the great arteries is apparent in the parasternal long-axis view where both great vessels can be imaged longitudinally in the same plane (Figure 24.8; Video 24.2). Although parallel course of the aorta and main pulmonary artery in the same plane is not seen with normally related great vessels, it is important to recognize that it is not unique to TGA. For example, this anatomic arrangement is also seen in double-outlet right ventricle and



Figure 24.7 Subxiphoid short-axis view showing parallel great arteries off each ventricle with the aorta (Ao) anterior to the pulmonary artery (PA).

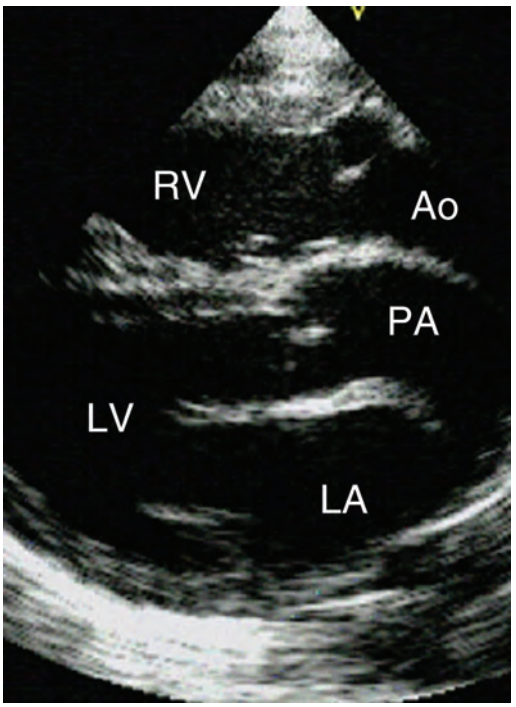


Figure 24.8 Parasternal long-axis view showing parallel great artery orientation off each ventricle. Also the fibrous continuity between the mitral and the pulmonary valve can be seen. Ao, aorta; LA, left atrium; LV, left ventricle; PA, pulmonary artery; RV, right ventricle.

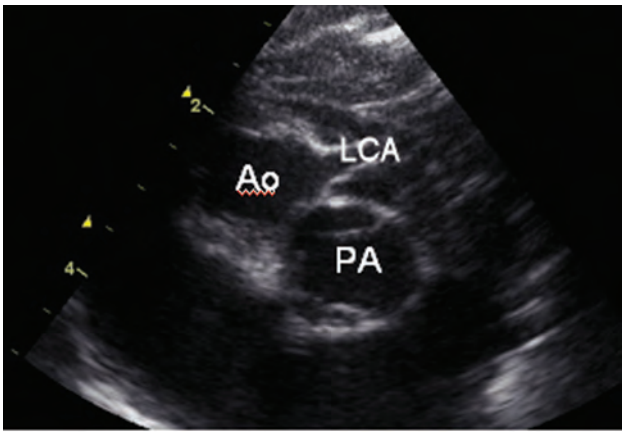


Figure 24.9 Parasternal short-axis view demonstrating the spatial position of the great arteries. The aorta with the left coronary artery (LCA) origin demonstrated is positioned rightward and anterior to the pulmonary artery (PA).

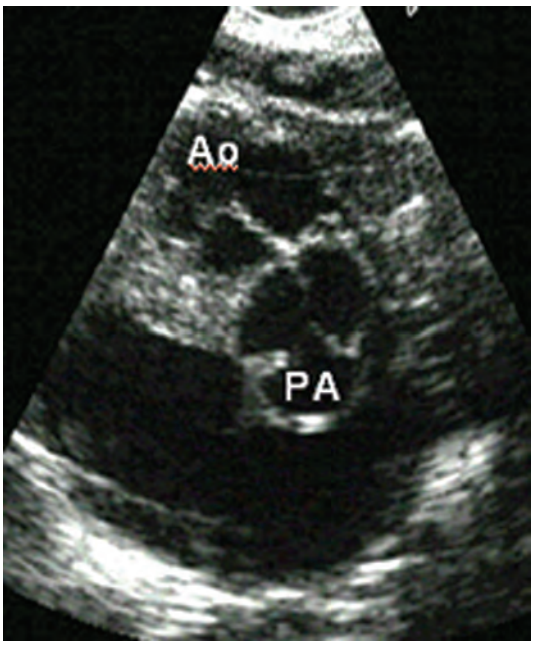


Figure 24.10 Parasternal short-axis view showing commissural alignment. Ao, aorta; PA, pulmonary artery.

congenitally corrected TGA. The parasternal long-axis view also demonstrates the fibrous continuity between the mitral and pulmonary valves. The aortic valve is seen anterior to the pulmonary valve and is supported by an infundibulum.

The parasternal short-axis plane is used to determine the spatial relationships between the semilunar valves and great vessels (Figure 24.9; Video 24.3). The parallel orientation of the aorta and main pulmonary artery accounts for their simultaneous appearance in cross-section as two circles in a parasternal short-axis plane. Most commonly, the aortic valve is anterior and to the right of the pulmonary valve but other relationships (e.g., side-by-side, anterior, leftward) are possible. Imaging from the high left parasternal position often optimizes this view. In most patients it is possible to obtain an image where the commissures between aortic and pulmonary valve leaflets can be viewed simultaneously (Figure 24.10). This is useful for assessing commissural alignment between the valve leaflets, which is important for coronary transfer during the ASO (Video 24.4). In some patients, this view cannot be obtained due to a more superior position of the aortic valve relative to the pulmonary valve.

Assessment of biventricular size and function can be performed in multiple views (Videos 24.5 and 24.6). Assessment includes ventricular dimensions, wall thickness, and measures of systolic and diastolic performance. Biventricular systolic function is usually preserved in infants with TGA unless severe hypoxia and metabolic acidosis is present.

Imaging of TGA with VSD

Description of the location of VSDs in TGA is identical to patients with concordant ventriculo-arterial alignments. A membranous VSD, the most common defect in TGA, may be imaged from several imaging planes, including subxiphoid long- and short-axis, apical, parasternal short-axis, and tilted long-axis views (Figure 24.11; Videos 24.7 and 24.8). In contrast to normally related great arteries, the parasternal short-axis view in TGA does not highlight membranous defects as well because of the abnormal relationship of the great arteries.

Imaging in multiple cross-sectional planes identifies muscular VSDs. The location of these defects is variable and requires detailed interrogation of the entire septum by 2D imaging and color Doppler. The apical 4-chamber view is particularly helpful for evaluation of the ventricular septum although the anterior-superior aspects of the septum are not seen optimally in this view. This view best depicts the basal (inlet or AV canal

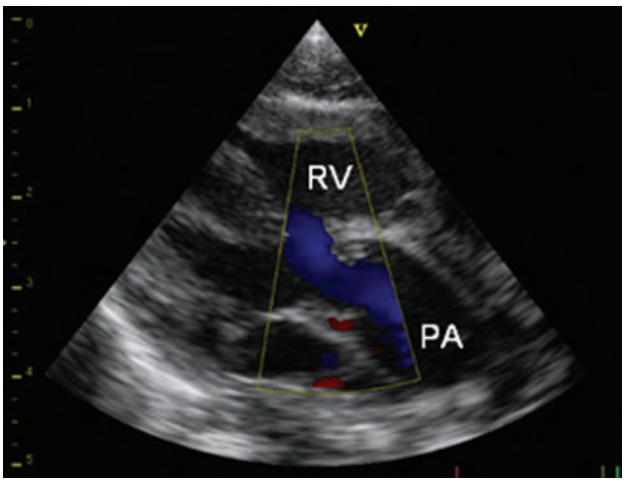


Figure 24.11 Parasternal long-axis view demonstrating the presence of a ventricular septal defect in the membranous area with shunting from the right ventricle (RV) to the left ventricle. PA, pulmonary artery.

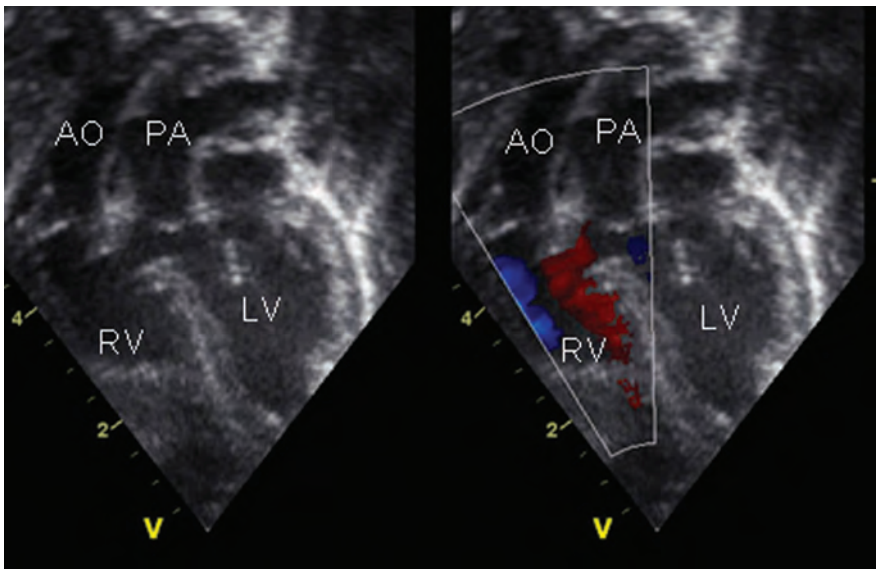
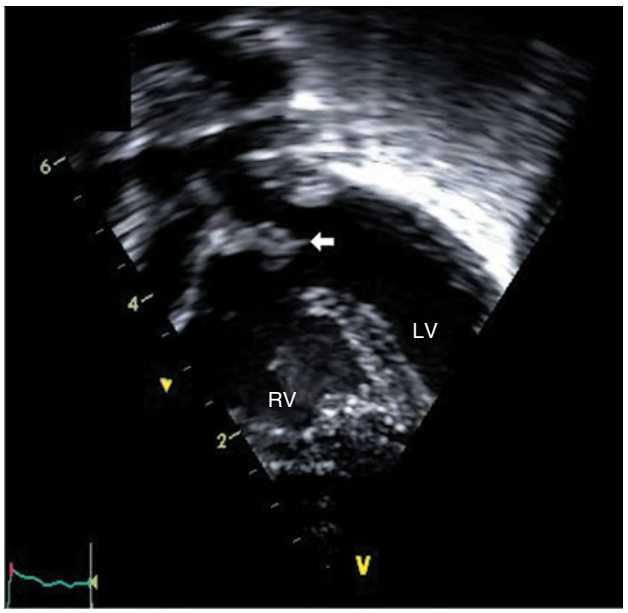


Figure 24.12 On this subcostal view long-axis view the parallel orientation of the great vessels is demonstrated. A membranous ventricular septal defect is visualized with the outlet part of the septum deviated anteriorly into the right ventricular outflow tract. AO, aorta; LV, left ventricle; PA, pulmonary artery; RV, right ventricle.

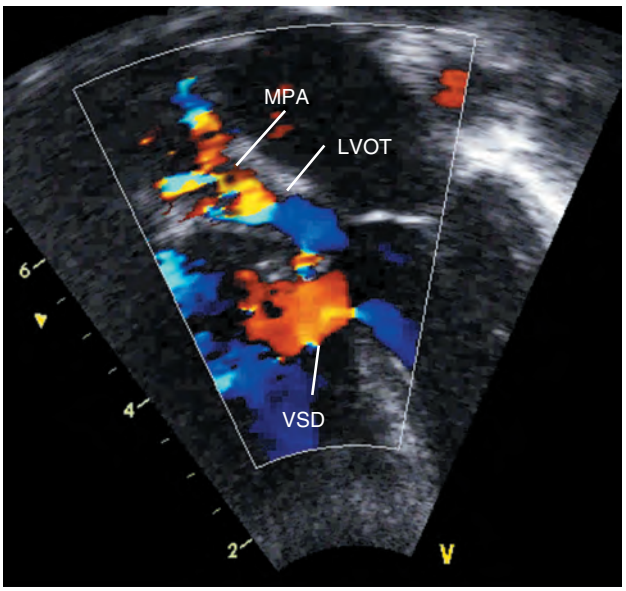
septum) and apical segments of the septum. The subxiphoid and parasternal short-axis views are helpful in evaluating the anterior-superior and posterior-inferior aspects of the septum as well as the mid-septum. Moderate–large defects can be easily detected using 2D imaging whereas small defects are usually best visualized using color Doppler. Lowering the Nyquist limit of the color Doppler scale is important to delineate VSDs in TGA given the often equal or near-equal pressures in the left and right ventricles.

Defects with anterior malalignment of the outlet (conal) septum are readily seen in most imaging planes (Figure 24.12; Videos 24.9 and 24.10). The subxiphoid sagittal view is particularly suitable to visualize the displaced outlet septum and associated RV outflow obstruction. This view is also used to measure the pressure gradient using pulsed (PW) and continuous-wave (CW) Doppler. Presence of RV outflow tract narrowing should prompt careful assessment of the aortic arch and isthmus for obstruction.

Defects with posterior malalignment are best viewed from the subxiphoid long- and short-axis views and from the parasternal long-axis view (Figure 24.13). Important elements of the echocardiographic evaluation include assessment of etiology



(a)



(b)

Figure 24.13 **(a)** Ventricular septal defect with posterior deviation of the outlet (conal) septum (white arrow) causing tunnel-like narrowing of the left ventricular outflow tract. **(b)** Color Doppler interrogation in the same patient shows flow across the ventricular septal defect (VSD) and acceleration of flow in the left ventricular outflow tract (LVOT) as a result of the posterior deviation of the outlet (conal) septum. MPA, main pulmonary artery.

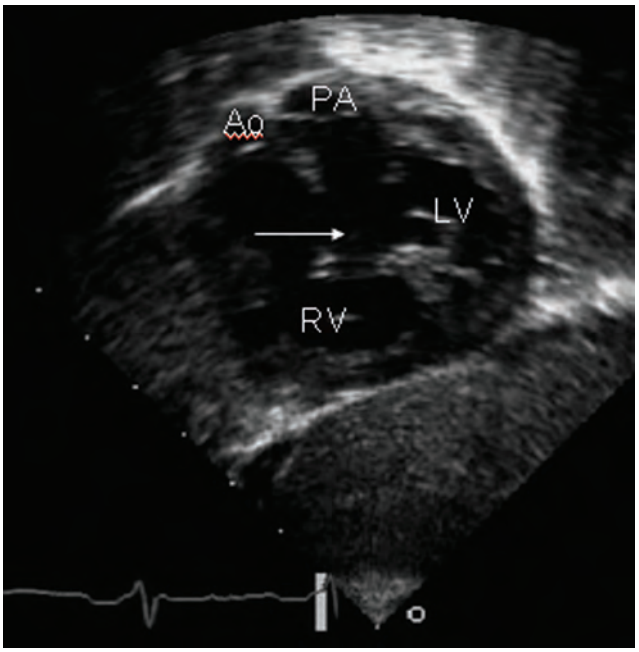


Figure 24.14 Subcostal apical 4-chamber view of TGA patient with large inlet VSD. A large ventricular septal defect (arrow) is seen at the inlet portion of the interventricular septum (AV canal-type VSD).

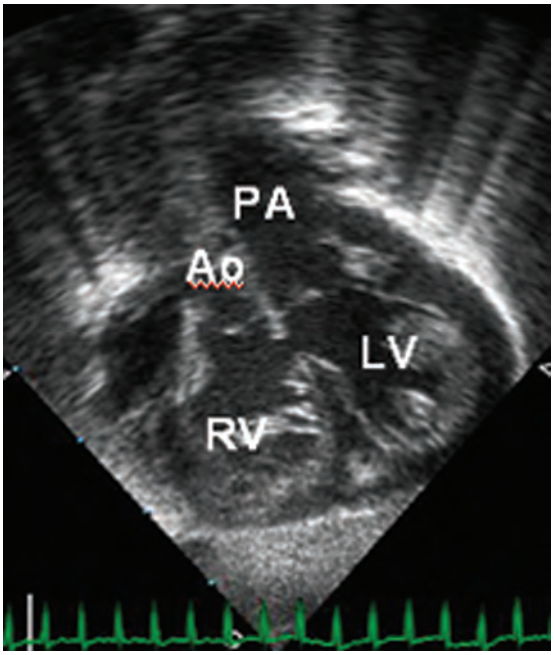


Figure 24.15 TGA with a ventricular septal defect extending to the outlet portion of the interventricular septum with absence of the outlet (conal) septum (doubly committed or subarterial VSD). In this subcostal view, the location of the VSD is just below the right-sided aortic valve and left-sided pulmonary valve.

and severity of LV outflow tract obstruction, which is commonly associated with this type of VSD. The gradient across the LV outflow tract can be measured by PW and CW Doppler from the apical window. It should be noted, however, that as long as the PDA is large and pulmonary hypertension persists the gradient can be small despite significant obstruction.

An inlet (AV canal-type) VSD can also be present in patients with TGA (Figure 24.14; Video 24.11). This type of defect is often associated with tricuspid valve anomalies including abnormal chordal attachments to the crest of the ventricular septum, overriding, and straddling of the valve. Straddling tricuspid valve can complicate surgical closure of the VSD and requires precise preoperative imaging. This type of VSD is best imaged in the apical 4-chamber view but can also been from other acoustic windows. A posteriorly angled apical 4-chamber view shows the defect at the base of the ventricular septum with the atrioventricular valve annulus forming the superior-posterior border of the defect. Abnormal tricuspid valve attachments or accessory tissue related to the valve can prolapse through the VSD causing variable degrees of LV outflow tract obstruction.

VSD with hypoplasia or absence of the outlet (conal) septum (doubly-committed defect) is rarely seen in TGA. Subxiphoid and parasternal images demonstrate absence or hypoplasia of the outlet (conal) septum with typically fibrous continuity between the aortic and pulmonary valve leaflets (Figure 24.15; Video 24.12).

Imaging of coronary arteries

Echocardiographic delineation of coronary artery anatomy in TGA can be challenging. Optimal imaging conditions, including proper position of the infant, removal of obstacles to imaging from the chest wall, and imaging when the patient is asleep are crucial for comprehensive evaluation of the origin and course of the coronary arteries. Imaging is performed predominantly from parasternal windows but complementary information is often gleaned from subxiphoid and apical views. The modified high parasternal short-axis view is used to image the origins of the coronary arteries (Figure 24.16). For viewing the origin and proximal course of the LCA a slight clockwise rotation is used, reaching a transverse view with the transducer's index mark at ~3 o'clock. For viewing the origin and proximal course of the RCA, a slight counterclockwise rotation of the transducer with the index mark at ~1 o'clock is helpful. In those with usual coronary anatomy, parasternal long-axis view through the aortic root helps to visualize the origin of the RCA from the posterior sinus. When sweeping the transducer in the long-axis view towards the left shoulder the bifurcation of the LCA into the proximal LAD and LCx can be imaged. When the LCx originates from the right posterior-facing sinus (sinus 2), the posterior course of the coronary relative to the pulmonary trunk can be seen in parasternal short-axis view and confirmed from the apical 4-chamber and subxiphoid views (Figure 24.17a,b). Anterior course of the coronary arteries, or combined anterior and posterior course relative to the aortic and pulmonary roots are present in cases of single

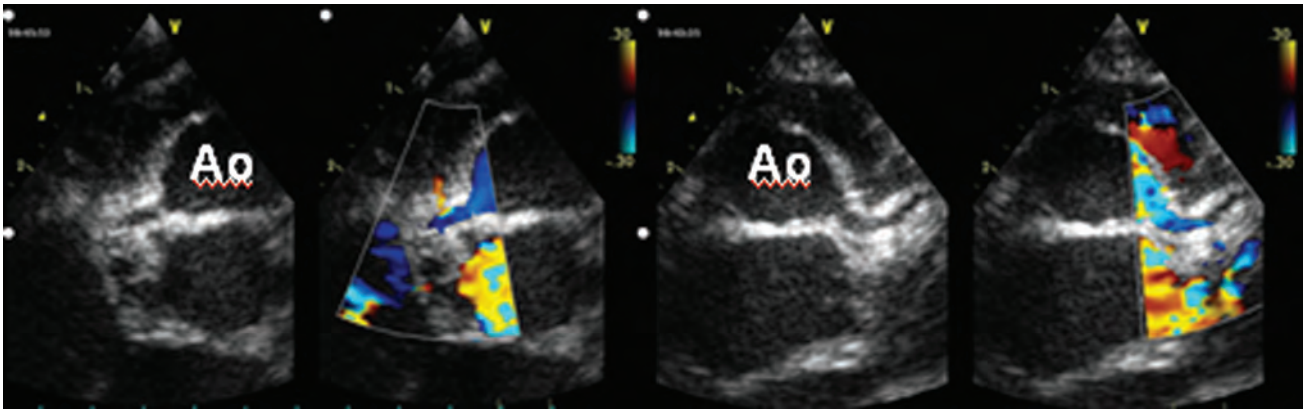
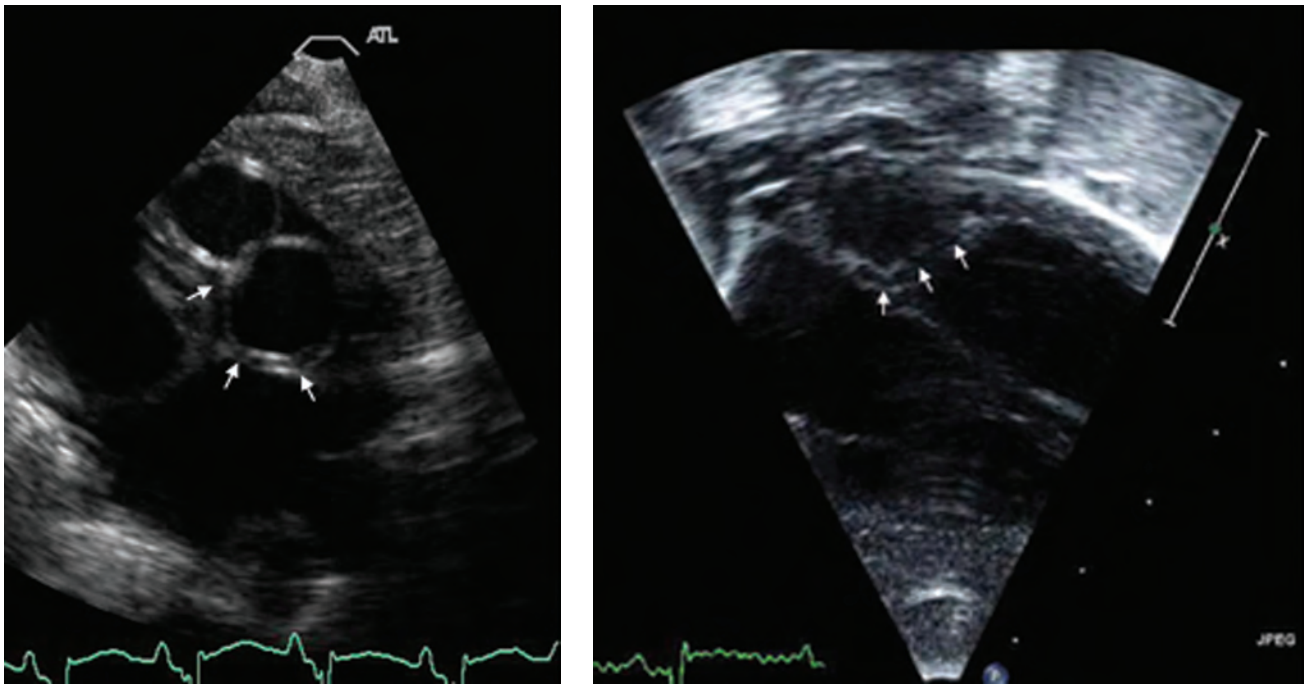


Figure 24.16 On these parasternal short-axis views the origin of the right coronary artery can be demonstrated originating from sinus 2 on the left-hand panel and the left coronary artery can be demonstrated coming from sinus one in the right-hand panel. Note that color Doppler can be helpful for identifying the coronary origins. Ao, aorta.

coronary arteries arising from one sinus or in the inverted patterns (Videos 24.13 and 24.14). Subxiphoid and apical views can also be helpful for delineating the relationship of the coronary arteries to the great vessels.

An intramural course of a coronary artery is associated with increased operative risk for the ASO and thus is important to try to identify preoperatively. An intramural coronary artery can generally be identified as a vessel originating from the opposite sinus of Valsalva in close proximity to the commissure that faces the pulmonary valve with a parallel proximal course within the aortic wall. The origin of most intramural coronary arteries is tangential to the aortic wall. From the parasternal short-axis view, the intramural coronary artery will often be seen coursing between the aorta and the pulmonary artery (Figure 24.18; Video 24.15). Every effort should be made to identify whether the origin of the intramural coronary artery is separate from the other coronary artery originating from the same aortic sinus of Valsalva (common orifice versus two separate orifices). Milder forms of intramural course are those coronary arteries that have a high takeoff relative to the sinotubular



(a) (b)

Figure 24.17 **(a)** Left circumflex from the RCA (from sinus 2). Parasternal short-axis view shows the proximal part of the RCA coming from sinus 2 with the circumflex artery originating from the RCA, coursing posterior to the pulmonary artery (arrows). **(b)** On a subcostal 4-chamber view tilted posterior to the pulmonary artery, the circumflex coronary artery is seen (arrows).

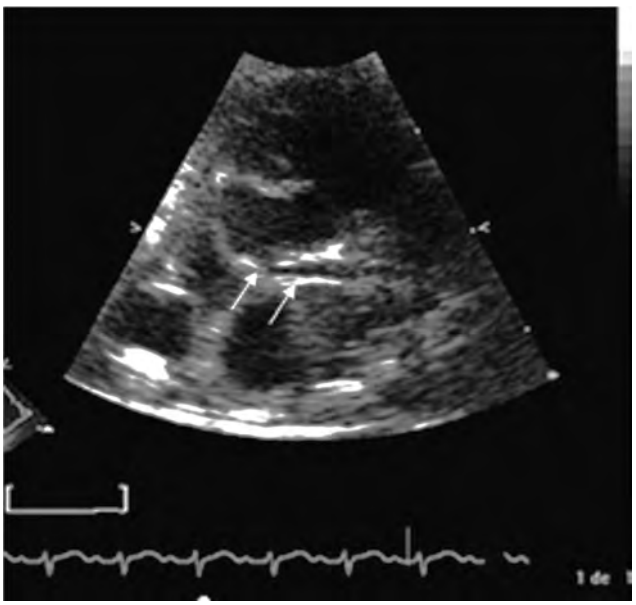


Figure 24.18 Intramural course of the left coronary artery. Note the abnormal origin of the LCA from the right posterior sinus with proximal intramural course (arrows).

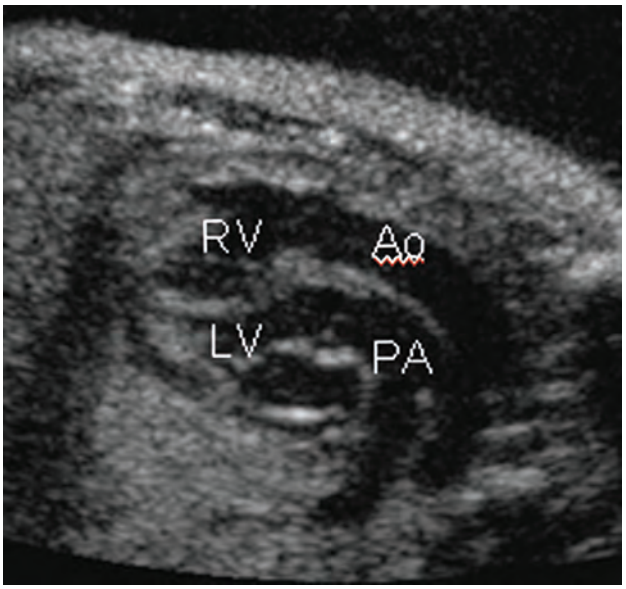


Figure 24.19 Fetal diagnosis of TGA. Fetal diagnosis of TGA relies on visualizing the outflow tracts where the parallel course of the great vessels can be appreciated. Ao, aorta; LV, left ventricle; PA, pulmonary artery; RV, right ventricle.

junction or when the artery has a proximal tangential course relative to the aortic wall. The origins of the coronary arteries should be imaged in detail because an intramural course can be missed when the artery does not cross the facing commissure in its proximal course.

Imaging of the PDA (arterial duct)

Presence of a PDA is important for mixing between the systemic and pulmonary circulations. In TGA, the orientation of the PDA is parallel to the long axis of the aortic arch and main pulmonary artery, allowing for imaging of the three vessels in one plane. The PDA is best seen from the suprasternal sagittal view, which demonstrates its aortic and pulmonary ends. Color and spectral Doppler demonstrate the direction of flow across the duct. In most newborns with TGA flow is from the main pulmonary artery to the descending aorta during systole and from the aorta to the main pulmonary artery during diastole (Video 24.16). In some patients pulmonary vascular resistance is increased due to abnormal development of the pulmonary vascular bed. In that circumstance flow through the PDA is predominantly right-to-left, which decreases effective pulmonary blood flow and results in severe cyanosis. Severe pulmonary hypertension can persist after the ASO and is associated with poor prognosis.

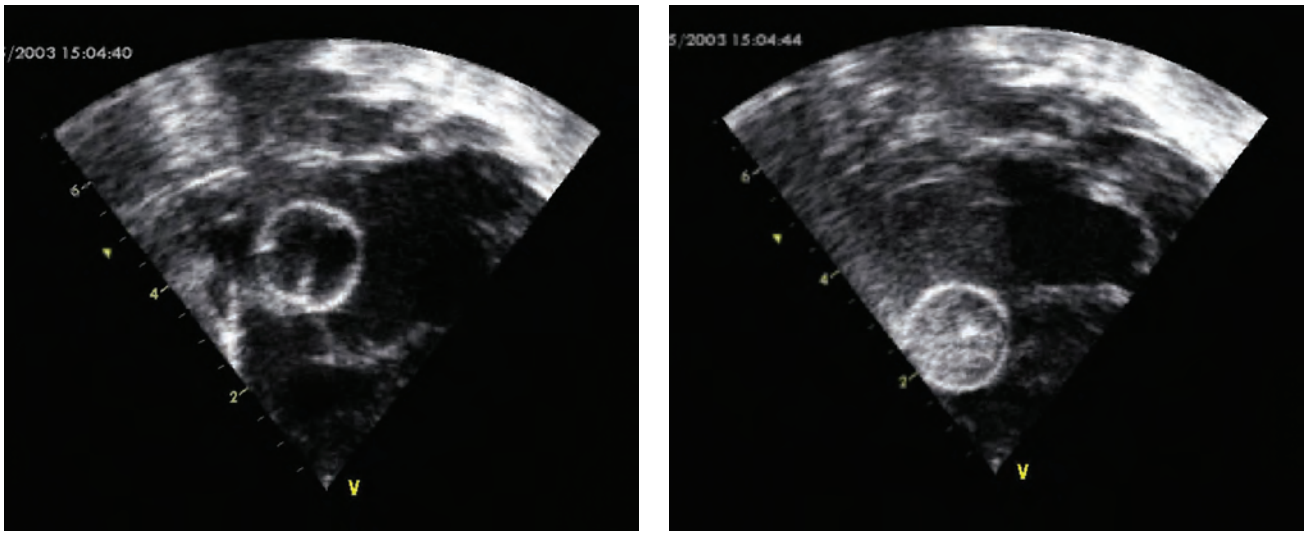
Prenatal assessment

Prenatal diagnosis of TGA can be made during the second trimester of pregnancy. Several studies have demonstrated that a screening ultrasound based solely on the 4-chamber view is inadequate for detection of conotruncal anomalies, including TGA [22–25]. In fact, the 4-chamber view may appear normal in a fetus with TGA unless there is a large VSD. More cephalad views that include the outflow tracts will readily identify the parallel orientation of the great vessels with origin of the main pulmonary artery from the LV and origin of the aorta from the anterior and rightwards aspect of the RV (Figure 24.19; Video 24.17). Associated VSDs can also be demonstrated but small defects might be missed, particularly if located in the muscular septum. Evaluation of the atrial septum is important for identification of a restrictive patent foramen ovale or intact atrial septum, conditions that may require balloon atrial septostomy immediately after birth. Significant atrioventricular or semilunar valve regurgitation is rare.

The data on the effects of prenatal diagnosis of TGA on postnatal morbidity and mortality rates are conflicting. Some studies suggest that prenatal diagnosis is associated with improved postnatal outcomes [26,27] whereas other studies have found no apparent benefit [28,29].

Balloon atrial septostomy

When balloon atrial septostomy is required, echocardiography can guide the procedure and instantly evaluate the results. The subxiphoid long-axis (coronal) view is generally the best to monitor the entire procedure. The position of the balloon before pulling it across the atrial septum should be assessed to assure it is free from the mitral valve, the left atrial appendage, and the pulmonary veins (Figure 24.20a,b; Video 24.18). The pull-back through the atrial septum can be imaged although the heart may shift momentarily when pulling the catheter. After septostomy, subxiphoid imaging evaluates the size of the new atrial



(a) (b)

Figure 24.20 Echocardiographic imaging of balloon atrial septostomy. Balloon atrial septostomy can be performed under echocardiographic guidance. Subcostal long-axis views of the atria are used to monitor the procedure. The position of the balloon in the left atrium can be checked prior to pulling the balloon back into the right atrium. **(a)** shows the balloon in the left atrium and **(b)** in the right atrium after having pulled the balloon through the atrial septum.

communication to determine whether the maneuver needs to be repeated and whether a pericardial effusion has developed.

Intraoperative assessment

Some centers perform transesophageal echocardiography (TEE) during surgery for TGA to evaluate the result immediately after coming off cardiopulmonary bypass. Epicardial echocardiography is an alternative approach preferred by some surgeons. Chapter 39 discusses the use of intraoperative TEE in detail. Here we summarize specific issues the echocardiographer needs to address by TEE after surgical procedures performed in patients with TGA. The ASO and the atrial switch are discussed as well as the Rastelli operation.

Arterial switch operation (ASO)

This operation is performed for TGA with intact ventricular septum as well as TGA with some types of VSD. In the operating room, particular attention is given to the following issues:

- Quantification of global and regional biventricular function as an indicator of the adequacy of coronary blood flow.
- Assessment of the implanted coronary arteries with color flow mapping and Doppler.
- Evaluation of the left and right ventricular outflow tracts for obstruction.
- Assessment of the neo-aorta, including evaluation of the neo-aortic valve function and neo-aortic anastomosis.
- Assessment of the neo-main pulmonary artery and proximal branch pulmonary arteries for stenosis after the Lecompte maneuver.
- Assessment for residual VSDs.

Atrial switch operation

In the present era, the atrial switch operation is rarely performed for TGA. It is generally reserved for patients with congenitally corrected TGA undergoing a double (atrial and arterial) switch operation. However, intraoperative TEE may be requested on the rare occasion that an atrial switch operation is performed in a patient with D-loop TGA. Particular attention is given to the following issues:

- Assessment of the pulmonary venous pathway to the tricuspid valve.
- Assessment of the systemic venous pathway to the mitral valve.
- Evaluation of residual shunt or baffle leak(s) at the atrial level.
- Assessment of atrioventricular valve function.
- Evaluation of systolic performance of the systemic RV and the subpulmonary LV.
- Assessment for residual VSD.

Rastelli operation

The procedure – LV-to-aortic valve baffle through the VSD and placement of a conduit from the RV to the pulmonary arteries – is performed in several cardiac anomalies, including TGA with posterior malalignment VSD with pulmonary outflow tract obstruction. Particular attention is given to the following issues:

- Detection of residual VSDs.
- Evaluation of the LV-to-aorta pathway.
- Evaluation of the RV-to-pulmonary artery pathway, including the proximal and distal conduit anastomoses.
- Assessment of atrioventricular valve function.
- Assessment of biventricular systolic performance.

Follow-up assessment

Follow-up assessment for TGA is usually performed using transthoracic echocardiography. TEE can sometimes be required, especially in adult patients with poor transthoracic acoustic windows.

After the arterial switch operation

Typical problems that require follow-up in the mid- and long term after the ASO are generally related to the great vessels and the coronary arteries. Late complications after the ASO include dilatation of the neo-aortic root, neo-aortic valve regurgitation, supravalvar pulmonary stenosis, and reduced coronary blood flow with or without impaired myocardial function.

Coronary arteries

Although early mortality after the ASO has decreased to ≤5% in experienced centers, rare events of myocardial infarction or sudden death have been reported during follow-up [30–32]. Most events occur within the first postoperative year and myocardial ischemia due to coronary insufficiency likely plays a major role. Careful monitoring of global and regional myocardial performance is important in the evaluation of patients after ASO (Videos 24.19 and 24.20). Identification of global or regional ventricular dysfunction on transthoracic echocardiography should prompt further investigation. Dobutamine stress echocardiography is an established method for detecting myocardial ischemia in adults with coronary artery disease. In patients who have undergone ASO, it can be used to identify stress-induced global and regional wall motion abnormalities that may not be detected at rest [33]. Exercise stress echocardiography is an alternative approach in patients who are able to cooperate with the test. Intracoronary blood flow measurements and positron emission tomography have been used to detect coronary flow abnormalities with variable results [34–36]. Both cardiac magnetic resonance (CMR) and computed tomography angiography (CTA) have been used successfully to image the coronary arteries after ASO [37,38]. However, the clinical significance of detecting coronary artery stenosis or occlusion by these and other diagnostic modalities remain uncertain because some patients develop an extensive network of collateral coronary circulation and are asymptomatic. In the largest series that evaluated coronary lesions after ASO as many as 5% of late survivors had coronary lesions [39]. Coronary angiography should be considered in patients in whom coronary stenosis or occlusion is highly suspected.

Neo-aortic root and valve

Long-term abnormalities of the neo-aortic root include dilation [40–42] and neo-aortic valve regurgitation [43]. A previous pulmonary artery band is risk factors for neo-aortic root dilatation and neo-aortic regurgitation. Additional risk factors include older age at ASO and presence of VSD. The diameter of the aortic root is measured from the parasternal long-axis during systole. Importantly, z-scores of the aortic root are used to follow patients over time to determine whether the root is dilating out of proportion to somatic growth.

A mild degree of neo-aortic valve regurgitation is common after the ASO with or without aortic root dilation (Video 24.21). Thus far, only 1–2% of patients after ASO have had evidence of hemodynamically important neo-aortic regurgitation. Neo-aortic incompetence can increase over time with 98% freedom from at least moderate neo-aortic regurgitation at 1 year, 96% at 5 years, and 93% at 10 years [42]. At present, surgical intervention on neo-aortic regurgitation is rare (1.4%), accounting for only 11.6% of all reoperations after ASO [44]. The apical 3- and 5-chamber views and the parasternal long- and short-axis views are best to estimate the severity of the neo-aortic regurgitation. The severity of the neo-aortic regurgitation is graded based on the diameter of the jet's vena contracta and the degree of diastolic retrograde flow in the abdominal aorta. The degree of LV dilation and dysfunction are important factors in the decision to operate on the neo-aortic valve for severe regurgitation.

Right ventricular outflow tract and pulmonary arteries

Stenosis of the RV outflow tract at any level is the most common cause for late reoperation after ASO [30,31,43,45]. Losay et al. reported a 4% incidence of reoperation for RV outflow tract obstruction within 15 years [43]. Obstruction can occur at any level but most commonly at the suture line of the neo-main pulmonary arterial anastomosis. The subxiphoid oblique sagittal and the parasternal short-axis views best demonstrate this type of obstruction and both views provide appropriate angles of interrogation for PW and CW Doppler. Severity of neopulmonary regurgitation can also be estimated from these views. A high parasternal long-axis view demonstrates the RV outflow tract from the RV to the pulmonary artery bifurcation anterior to the ascending aorta. A left-to-right orientation of the transducer (index mark at 3 o'clock) from a high parasternal or a suprasternal view demonstrates the pulmonary artery bifurcation with the proximal course of the branch pulmonary arteries anterior to the ascending aorta (as a result of the Lecompte maneuver) (Figure 24.21). Peak velocities ≤2 m/s (predicted maximum instantaneous gradient ≤16 mm Hg) across the distal main pulmonary artery and branch pulmonary arteries are within normal limits after ASO [46]. Trivial (gradient between 17 and 24 mmHg) supravalvar pulmonary stenosis is seen in up to 20% of patients with <4% developing gradients of more than 30 mmHg (Figure 24.22; Video 24.22). Evaluation of branch pulmonary artery stenosis by Doppler should take into account the distribution of blood flow to each lung. This information can be determined by a lung perfusion nuclear scan or by CMR flow measurements.

Ventricular size and function

Given the potential for myocardial ischemia related to coronary artery abnormalities and neo-aortic valve regurgitation after the ASO, long-term follow-up of left ventricular size and function is required. In the majority of patients, LV size and function continues to be within normal limits late after the ASO with a rapid

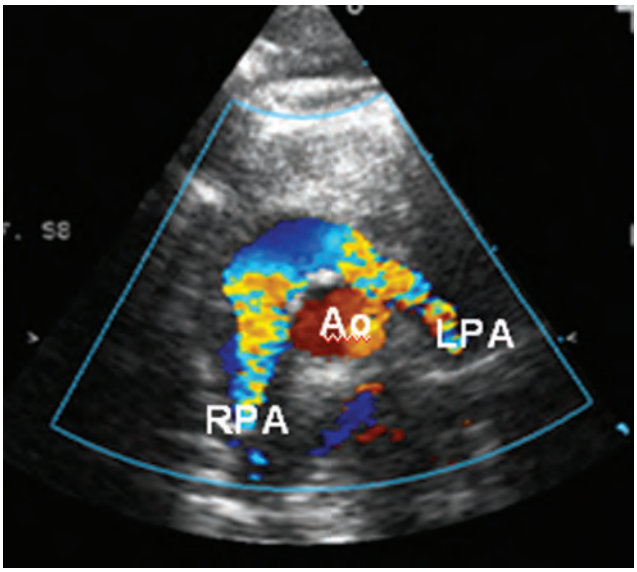


Figure 24.21 High parasternal short-axis view of the pulmonary arteries after the arterial switch operation with the Lecompte maneuver showing the position of the pulmonary artery bifurcation anterior to the aorta. Typically flow acceleration can be seen into the origins of the pulmonary arteries. Ao, aorta; LPA, left pulmonary artery; RPA, right pulmonary artery.

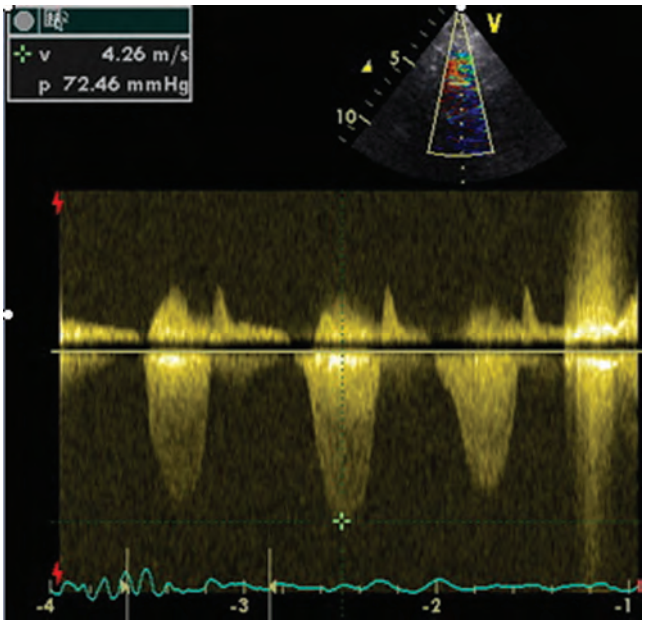


Figure 24.22 Continuous-wave (CW) Doppler interrogation of branch pulmonary artery stenosis after the arterial switch procedure. CW Doppler of the left pulmonary artery with moderate to severe stenosis at the origin of the pulmonary artery. A peak gradient of 72 mmHg is measured in this patient. As the narrowing typically is a long segment stenosis, Doppler gradients often overestimate catheter gradients.

two-stage procedure early in life being a risk factor for LV dysfunction [47]. Methods for assessment of systolic and diastolic function are discussed in detail in Chapters 7 and 8.

After the atrial switch operation

Complications after an atrial switch operation include stenosis of the systemic and/or pulmonary venous pathways, baffle leak, atrial arrhythmias, tricuspid regurgitation, and systemic (RV) ventricular dysfunction. Pathway obstruction occurs in 11–31% of patients and is more common after the Mustard procedure [48,49]. Transthoracic echocardiography allows evaluation of the venous pathways in patients with good acoustic windows. However, alternative modalities are required in those with poor acoustic windows. TEE has been used extensively in atrial switch patients but its invasive nature and narrow field of view are relative weaknesses as compared with CMR.

Transthoracic echocardiographic evaluation of the pulmonary and systemic venous pathways requires systematic imaging of each pathway from several views (Figure 24.23). Whenever possible, the subxiphoid window should be used. The apical window provides excellent views of the venous pathways even when other acoustic windows are suboptimal (Figure 24.24; Video 24.23). Systematic sweeps following each pathway with 2D and color Doppler can detect stenosis and spectral Doppler can measure the mean gradient. Imaging from parasternal windows can be helpful, especially imaging of the pulmonary venous

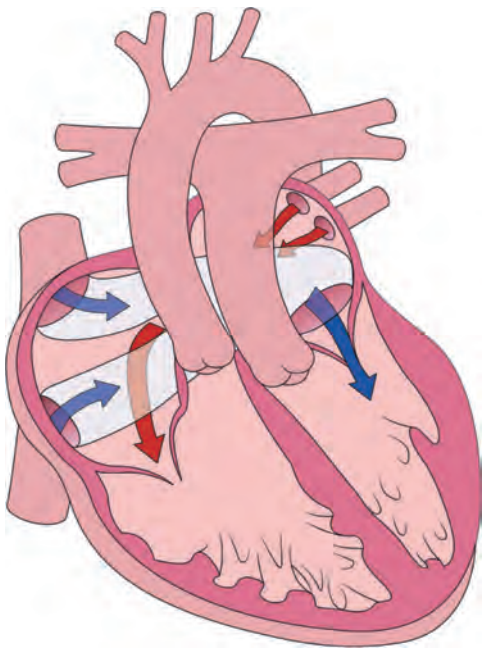


Figure 24.23 Diagram showing the atrial baffles after the atrial switch procedure.

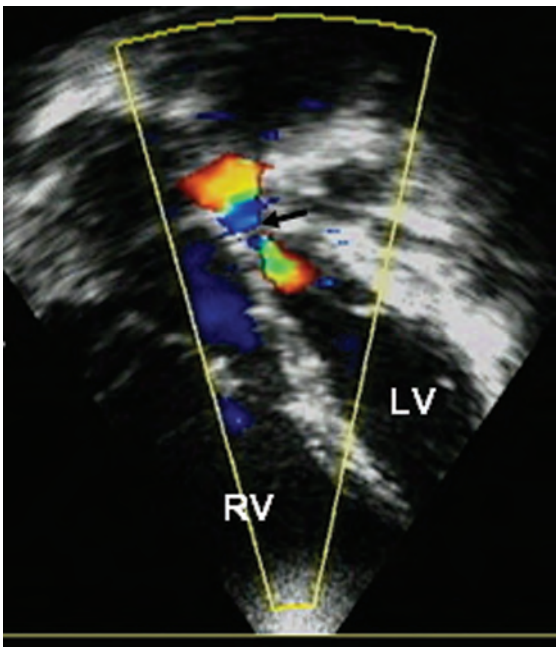


Figure 24.24 On this apical 4-chamber view the flow acceleration on the systemic venous baffle redirecting the blood towards the mitral valve can be detected. LV, left ventricle; RV, right ventricle.

and superior limb of the systemic venous pathways, but suboptimal parasternal acoustic windows are common late after atrial switch procedure. TEE allows detailed imaging of the venous pathways and is the ideal method for detection of baffle leaks (Video 24.24). Imaging is performed in multiple views, preferably using a multiplane probe (see Chapter 40 for details). Similar to transthoracic imaging, systematic sweeps of the transducer across each of the venous pathways using 2D and color Doppler allow detection of stenoses and leaks. TEE is also helpful for guidance of catheter-based treatment of pathway obstruction [50–52].

The sensitivity of TEE in the detection of baffle leaks is higher compared with transthoracic imaging because of the long distance from the transducer to the atrium with the latter approach. Contrast echocardiography with injection of agitated saline through a peripheral intravenous cannula can help confirm the presence and extent of baffle leaks. Presence of LV dilation should raise suspicion of an atrial baffle leak.

The LV in atrial switch patients is typically low pressure and wraps around the systemic RV (Video 24.25). Significant mitral regurgitation and LV dysfunction are uncommon. In contrast, tricuspid regurgitation and systemic RV dysfunction are common late complications (Video 24.26). Quantification of systemic RV function by echocardiography remains a challenge. In most clinical settings, assessment of global RV systolic function is qualitative. Quantitative methods include fractional area change [53] and tissue Doppler imaging. Meluzin et al. found that peak systolic tricuspid valve annular velocities <11.5 cm/s identified RV dysfunction with high sensitivity and specificity [54]. Isovolumic acceleration of the RV free wall is another measure that can be used for assessment of RV function after the atrial switch operation [55].

After the Rastelli operation

In the long-term assessment after the Rastelli operation, obstruction of the RV-to-pulmonary artery conduit is essentially inevitable, requiring conduit revision or replacement. Echocardiographic evaluation of the conduit and branch pulmonary arteries requires 2D, color, and spectral Doppler interrogations from several views. In infants and young children with good subxiphoid windows, the conduit can be imaged from short-axis views. This view is particularly helpful for evaluation of the proximal conduit anastomosis. However, even when good subxiphoid windows are present, the distal conduit anastomosis and branch pulmonary arteries are better seen from parasternal and suprasternal views. Optimizing patient position (e.g., lateral decubitus) and flexible use of nonstandard transducer position may allow visualization of the distal conduit and proximal pulmonary arteries even in patients with restricted transthoracic windows. Color Doppler is particularly helpful to identify flow through the conduit and to direct interrogation by spectral Doppler. Estimation of RV systolic pressure is based on the peak gradient across the conduit as well as the tricuspid regurgitation jet velocity and, when present, flow velocity across a VSD.

Obstruction of the LV-to-aortic valve pathway, aortic regurgitation, and LV dysfunction are potential late complications after the Rastelli operation. Another potential complication is residual VSD, including intramural defects that can develop years after surgery [56]. Detailed echocardiographic evaluation of these residual problems is integral to long-term follow-up of these patients (Video 24.27).

Imaging in the adult

Echocardiographic windows are often challenging in adults with TGA. Nevertheless, interval assessment of ventricular function, atrioventricular and semilunar valve function, venous pathways, and RV-to-pulmonary artery conduits is essential in the follow-up of the adult with TGA. Although transthoracic echocardiography is the first line of imaging in these patients, the importance of alternative diagnostic methods increases. Given the number of options available to practitioners caring for the adult with TGA (e.g., TEE, CMR, CTA, cardiac catheterization, single photon emission tomography, positron emission tomography, gated radionuclide angiography), judicious, patient-specific selection of techniques is paramount. TEE is ideally suited for evaluation of the venous pathways after the atrial switch operation [57] but is limited in its ability to assess the function of the systemic RV. There is a high incidence of atrial arrhythmias, particularly atrial flutter and fibrillation after the atrial switch.

TEE is often required prior to cardioversion to detect intra-atrial thrombus.

Among the alternative imaging modalities, CMR is particularly helpful in adults after surgery for TGA due to its excellent ability to noninvasively image all aspects of cardiovascular anatomy, accurately measure biventricular size and function, measure blood flow (e.g., shunts, valve regurgitation), image the proximal coronary arteries, and assess myocardial viability. Freedom from exposure to ionizing radiation with its attendant risk of cancer renders CMR optimal for long-term follow-up in this patient group. CTA provides high spatial resolution static images of cardiovascular anatomy, including the coronary arteries [37]. ECG-gated cine CT can be used to assess ventricular size and function in patients who cannot undergo a CMR examination (e.g., pacemaker) [58]. Cardiac catheterization is used selectively and its primary role is in catheter-based therapy. Radionuclide techniques have been used to address specific clinical or research questions in adults with TGA but they are not routinely employed.

Videos

To access the videos for this chapter, please go to www.lai-echo.com.

Video 24.1 Subcostal coronal sweep to demonstrate great artery relationships. The pulmonary artery with the bifurcation is seen originating from the left ventricle and the aorta from the right ventricle.

Video 24.2 Spatial relationship between the great arteries. Parasternal long-axis view with the typical parallel orientation of the great vessels. This view also demonstrates the fibrous continuity between the mitral valve and the pulmonary valve.

Video 24.3 Spatial relationship between the great arteries. Parasternal short-axis view demonstrating the spatial relationship between the great arteries, the aorta being anterior and to the right of the pulmonary artery.

Video 24.4 Commissural malalignment. Parasternal short-axis view demonstrating the commissural malalignment between the commissures of the aortic valve and pulmonary valve. In this example the commissures are clearly malaligned.

Video 24.5 Ventricular function and size. Parasternal long-axis view in a patient with transposition of the great arteries. A large and hypertrophied right ventricle (RV) and somewhat smaller left ventricle can be seen. There is bulging of the interventricular septum into the left ventricle during systole.

Video 24.6 Ventricular function and size. Parasternal short-axis view in a patient with transposition of the great arteries. A large and hypertrophied right ventricle (RV) and somewhat smaller left ventricle can be seen. The septum is flattening in systole.

Video 24.7 Perimembranous ventricular septal defect (VSD). Apical 5-chamber view demonstrating the presence of a large perimembranous VSD in a patient with transposition of the great arteries. The shunt goes from the right ventricle to the left ventricle.

Video 24.8 Perimembranous ventricular septal defect (VSD). Parasternal short-axis view demonstrating the presence of a large perimembranous VSD in a patient with transposition of the great arteries. The shunt goes from the right ventricle to the left ventricle.

Video 24.9 Transposition of the great arteries with anterior malalignment ventricular septal defect (VSD). On this apical view with anterior angulation, the parallel orientation of the great vessels is demonstrated. The VSD is visualized with the outlet part of the septum deviated anteriorly into the right ventricular outflow tract.

Video 24.10 Transposition of the great arteries with perimembranous-to-outlet ventricular septal defect (VSD) with anterior malalignment. On this long-axis view the parallel orientation of the great vessels is demonstrated. A perimembranous-to-outlet VSD is visualized with the outlet septum deviated anteriorly into the right ventricular outflow tract.

Video 24.11 Subcostal apical 4-chamber view of transposition of the great arteries with associated atrioventricular septal defect (AVSD). An inlet VSD with a single AV valve at the inlet of both ventricles can be noted on this clip.

Video 24.12 Subcostal view in a patient with transposition of the great arteries (TGA) and a doubly committed ventricular septal defect (VSD). In this subcostal sweep, the VSD can be located in the outlet part of the septum just below the pulmonary and aortic valves.

Video 24.13 Single coronary artery originating from sinus 1. The right coronary artery can be seen going anteriorly from the aorta (anterior loop).

Video 24.14 Single coronary artery originating from sinus 1. Short-axis color Doppler view. The right coronary artery can be seen going anteriorly from the aorta (anterior loop).

Video 24.15 Intramural course of left coronary artery (LCA). The LCA is originating from sinus 2 and has a proximal intramural course.

Video 24.16 Patent arterial duct in a patient with transposition of the great arteries is best viewed using the ductal view.

Video 24.17 Fetal image of patient with transposition of the great arteries. The outflow tracts from both ventricles are demonstrated with the parallel course of both great arteries, the aorta being anterior to the pulmonary artery.

Video 24.18 Subcostal view monitoring a balloon septostomy in a patient with transposition of the great arteries. The inflated balloon is viewed to cross the intra-atrial septum from the left atrium to the right atrium.

Video 24.19 Patient with single coronary artery after arterial switch operation presenting with sudden collapse 13 years after the procedure. The transesophageal echocardiogram shows severe global left ventricular dysfunction. Angiography demonstrated an occluded LCA with extensive collateral flow from the RCA to the LCA.

Video 24.20 Transesophageal echocardiogram in the same patient as in Video 24.19. The coronary ostium can be visualized with no flow to the left coronary artery (LCA) and flow exclusively to the right coronary artery (RCA). Angiography demonstrated an occluded LCA with extensive collateral flow from the RCA to the LCA.

Video 24.21 Parasternal long-axis view from a patient after the arterial switch operation. The dilation of the neo-aortic root can be appreciated with a mild degree of aortic regurgitation.

Video 24.22 High parasternal short-axis view of the pulmonary arteries after the arterial switch operation. Note that the pulmonary bifurcation is anterior to the aorta after the LeCompte maneuver. Also note the presence of turbulence at the origin of the right and left pulmonary arteries.

Video 24.23 Apical 4-chamber view in color compare mode in a patient after the Mustard operation with obstruction of the superior vena caval (SVC) baffle. Turbulence of the baffle can clearly be seen. Notice also the mild to moderate degree of tricuspid regurgitation.

Video 24.24 Parasternal short-axis view after the Senning operation for transposition of the great arteries. The dilated and hypertrophied right ventricle is demonstrated. The septum is flattened and bulges into the low-pressure left ventricle, causing the d-shape of the left ventricle.

Video 24.25 Apical 4-chamber view in color compare mode in a patient after the Mustard operation presenting with severe tricuspid regurgitation. Qualitatively there is a moderate degree of right ventricular dysfunction.

Video 24.26 Transesophageal echocardiogram in a patient with a baffle leak after the Mustard operation. The communication between the pulmonary venous chamber and the systemic venous atrium can be seen with left-to-right shunt.

Video 24.27 Patient with transposition of the great arteries, ventricular septal defect and pulmonary stenosis after the Rastelli operation. In this apical 5-chamber view, the left ventricular to aortic pathway can be visualized. The left ventricular outflow tract was unobstructed in this patient.

References

1 Hoffman JI, Kaplan S. The incidence of congenital heart disease. *J Am Coll Cardiol* 2002;**39**:1890–1900.

2 Pradat P, Francannet C, Harris JA, Robert E. The epidemiology of cardiovascular defects. Part I: a study based on data from three large registries of congenital malformations. *Pediatr Cardiol* 2003;**24**:195–221.

3 Goldmuntz E, Clark BJ, Mitchell LE, et al. Frequency of 22q11 deletions in patients with conotruncal defects. *J Am Coll Cardiol* 1998;**32**:492–498.

4 Goldmuntz E, Bamford R, Karkera JD, et al. CFC1 mutations in patients with transposition of the great arteries and double-outlet right ventricle. *Am J Hum Genet* 2002;**70**:776–780.

5 Digilio MC, Casey B, Toscano A, et al. Complete transposition of the great arteries: patterns of congenital heart disease in familial precurrence. *Circulation* 2001;**104**:2809–2814.

6 Wren C, Birrell G, Hawthorne G. Cardiovascular malformations in infants of diabetic mothers. *Heart* 2003;**89**:1217–1220.

7 Costell M, Carmona R, Gustafsson E, et al. Hyperplastic conotruncal endocardial cushions and transposition of great arteries in perlecan-null mice. *Circ Res* 2002;**91**:158–164.

8 Kirby ML. Embryogenesis of transposition of the great arteries: a lesson from the heart. *Circ Res* 2002;**91**:87–89.

9 Van Praagh R, Perez-Trevino C, Lopez-Cuellar M, et al. Transposition of the great arteries with posterior aorta, anterior pulmonary artery, subpulmonary conus and fibrous continuity between aortic and atrioventricular valves. *Am J Cardiol* 1971;**28**:621–631.

10 Wernovsky G. Transposition of the great arteries. In: Allen H, Driscoll D, Shaddy R, Feltes T (eds.) *Moss and Adams' Heart Disease in Infants, Children and Adolescents*, 7th edn. Philadelphia, PA: Wolters Kluwer, Lippincott, Williams and Wilkins, 2007.

11 Pasquini L, Sanders SP, Parness IA, et al. Conal anatomy in 119 patients with D-loop transposition of the great arteries and ventricular septal defect: an echocardiographic and pathologic study. *J Am Coll Cardiol* 1993;**21**:1712–1721.

12 Kurisu K, Yonenaga K, Furusho N, et al. [A case report of one-stage repair for transposition of the great arteries with intact ventricular septum and coarctation of the aorta in neonate]. *Nippon Kyobu Geka Gakkai Zasshi* 1997;**45**:1976–1980.

13 Kirklin JW, Barratt-Boyes B. Complete transposition of the great arteries. In: Kirklin JW, Barratt-Boyes B (eds.) *Cardiac Surgery*. New York, NY: Churchill Livingston, 1993, pp. 1383–1467.

14 Wernovsky G, Sanders SP. Coronary artery anatomy and transposition of the great arteries. *Coron Artery Dis* 1993;**4**:148–157.

15 Gittenberger-de Groot A, Sauer U, Oppenheimer-Dekker A. Coronary arterial anatomy in transposition of the great arteries: a morphologic study. *Pediatric Cardiol* 1983;**4**(Suppl. 1):15–24.

16 Pasquali SK, Hasselblad V, Li JS, et al. Coronary artery pattern and outcome of arterial switch operation for transposition of the great arteries: a meta-analysis. *Circulation* 2002;**106**:2575–2580.

17 Ueda Y, Miki S, Okita Y, et al. Transposition of the great arteries associated with total anomalous pulmonary venous return. *Ann Thorac Surg* 1994;**57**:470–472.

18 Fraisse A, del Nido PJ, Gaudart J, Geva T. Echocardiographic characteristics and outcome of straddling mitral valve. *J Am Coll Cardiol* 2001;**38**:819–826.

19 Tlaskal T, Hucin B, Kostelka M, Marek J. Primary repair of transposition of the great arteries with interrupted aortic arch. *Eur J Cardiothorac Surg* 1998;**13**:310–312.

20 Shirali GS, Geva T, Ott DA, Bricker JT. Double aortic arch and bilateral patent ducti arteriosi associated with transposition of the great arteries: missing clinical link in an embryologic theory. *Am Heart J* 1994;**127**:451–453.

21 Van Praagh S, O'Sullivan J, Brili S, Van Praagh R. Juxtaposition of the morphologically right atrial appendage in solitus and inversus atria: a study of 35 postmortem cases. *Am Heart J* 1996;**132**:382–390.

22 Bakiler AR, Ozer EA, Kanik A, et al. Accuracy of prenatal diagnosis of congenital heart disease with fetal echocardiography. *Fetal Diagn Ther* 2007;**22**:241–244.

23 Berghella V, Pagotto L, Kaufman M, et al. Accuracy of prenatal diagnosis of congenital heart defects. *Fetal Diagn Ther* 2001;**16**:407–412.

24 Rychik J, Ayres N, Cuneo B, et al. American Society of Echocardiography guidelines and standards for performance of the fetal echocardiogram. *J Am Soc Echocardiogr* 2004;**17**:803–810.

25 Randall P, Brealey S, Hahn S, et al. Accuracy of fetal echocardiography in the routine detection of congenital heart disease among unselected and low risk populations: a systematic review. *BJOG* 2005;**112**:24–30.

26 Bonnet D, Coltri A, Butera G, et al. Detection of transposition of the great arteries in fetuses reduces neonatal morbidity and mortality. *Circulation* 1999;**99**:916–918.

27 Jouannic JM, Gavard L, Fermont L, et al. Sensitivity and specificity of prenatal features of physiological shunts to predict neonatal clinical status in transposition of the great arteries. *Circulation* 2004;**110**:1743–1746.

28 Blyth M, Howe D, Gnanapragasam J, Wellesley D. The hidden mortality of transposition of the great arteries and survival advantage provided by prenatal diagnosis. *BJOG* 2008;**115**:1096–1100.

29 Bartlett JM, Wypij D, Bellinger DC, et al. Effect of prenatal diagnosis on outcomes in D-transposition of the great arteries. *Pediatrics* 2004;**113**:e335–340.

30 Brown JW, Park HJ, Turrentine MW. Arterial switch operation: factors impacting survival in the current era. *Ann Thorac Surg* 2001;**71**:1978–1984.

31 Daebritz SH, Nollert G, Sachweh JS, et al. Anatomical risk factors for mortality and cardiac morbidity after arterial switch operation. *Ann Thorac Surg* 2000;**69**:1880–1886.

32 Pretre R, Tamisier D, Bonhoeffer P, et al. Results of the arterial switch operation in neonates with transposed great arteries. *Lancet* 2001;**357**:1826–1830.

33 Hui L, Chau AK, Leung MP, et al. Assessment of left ventricular function long term after arterial switch operation for transposition of the great arteries by dobutamine stress echocardiography. *Heart* 2005;**91**:68–72.

34 Hauser M, Bengel FM, Kuhn A, et al. Myocardial blood flow and flow reserve after coronary reimplantation in patients after arterial switch and Ross operation. *Circulation* 2001;**103**:1875–1880.

35 Hauser M, Kuehn A, Hess J. Myocardial perfusion in patients with transposition of the great arteries after arterial switch operation. *Circulation* 2003;**107**:e126.

36 Oskarsson G, Pesonen E, Munkhammar P, et al. Normal coronary flow reserve after arterial switch operation for transposition of the great arteries: an intracoronary Doppler guidewire study. *Circulation* 2002;**106**:1696–1702.

37 Ou P, Mousseaux E, Azarine A, et al. Detection of coronary complications after the arterial switch operation for transposition of the great arteries: first experience with multislice computed tomography in children. *J Thorac Cardiovasc Surg* 2006;**131**:639–643.

38 Taylor AM, Dymarkowski S, Hamaekers P, et al. MR coronary angiography and late-enhancement myocardial MR in children who underwent arterial switch surgery for transposition of great arteries. *Radiology* 2005;**234**:542–547.

39 Raisky O, Bergoend E, Agnoletti G, et al. Late coronary artery lesions after neonatal arterial switch operation: results of surgical coronary revascularization. *Eur J Cardiothorac Surg* 2007;**31**:894–898.

40 Hourihan M, Colan SD, Wernovsky G, et al. Growth of the aortic anastomosis, annulus, and root after the arterial switch procedure performed in infancy. *Circulation* 1993;**88**:615–620.

41 Hutter PA, Thomeer BJ, Jansen P, et al. Fate of the aortic root after arterial switch operation. *Eur J Cardiothorac Surg* 2001;**20**:82–88.

42 Schwartz ML, Gauvreau K, del Nido P, et al. Long-term predictors of aortic root dilation and aortic regurgitation after arterial switch operation. *Circulation* 2004;**110**:128–132.

43 Losay J, Touchot A, Capderou A, et al. Aortic valve regurgitation after arterial switch operation for transposition of the great arteries: incidence, risk factors, and outcome. *J Am Coll Cardiol* 2006;**47**:2057–2062.

44 Losay J, Touchot A, Serraf A, et al. Late outcome after arterial switch operation for transposition of the great arteries. *Circulation* 2001;**104**:121–126.

45 Haas F, Wottke M, Poppert H, Meisner H. Long-term survival and functional follow-up in patients after the arterial switch operation. *Ann Thorac Surg* 1999;**68**:1692–1697.

46 Hovels-Gurich HH, Seghaye MC, Dabritz S, et al. Cardiological and general health status in preschool- and school-age children after neonatal arterial switch operation. *Eur J Cardiothorac Surg* 1997;**12**:593–601.

47 Colan SD, Boutin C, Castaneda AR, Wernovsky G. Status of the left ventricle after arterial switch operation for transposition of the great arteries. Hemodynamic and echocardiographic evaluation. *J Thorac Cardiovasc Surg* 1995;**109**:311–321.

48 Moons P, Gewillig M, Sluysmans T, et al. Long-term outcome up to 30 years after the Mustard or Senning operation: a nationwide multicentre study in Belgium. *Heart* 2004;**90**:307–313.

49 Dos L, Teruel L, Ferreira IJ, et al. Late outcome of Senning and Mustard procedures for correction of transposition of the great arteries. *Heart* 2005;**91**:652–656.

50 Asgar AW, Miro J, Ibrahim R. Recanalization of systemic venous baffles by radiofrequency perforation and stent implantation. *Catheter Cardiovasc Interv* 2007;**70**:591–594.

51 Mohsen AE, Rosenthal E, Qureshi SA, Tynan M. Stent implantation for superior vena cava occlusion after the Mustard operation. *Catheter Cardiovasc Interv* 2001;**52**:351–354.

52 Sharaf E, Waight DJ, Hijazi ZM. Simultaneous transcatheter occlusion of two atrial baffle leaks and stent implantation for SVC obstruction in a patient after Mustard repair. *Catheter Cardiovasc Interv* 2001;**54**:72–76.

53 Haddad F, Doyle R, Murphy DJ, Hunt SA. Right ventricular function in cardiovascular disease. Part II: Pathophysiology, clinical importance, and management of right ventricular failure. *Circulation* 2008;**117**:1717–1731.

54 Meluzin J, Spinarova L, Bakala J, et al. Pulsed Doppler tissue imaging of the velocity of tricuspid annular systolic motion; a new, rapid, and non-invasive method of evaluating right ventricular systolic function. *Eur Heart J* 2001;**22**:340–348.

55 Vogel M, Derrick G, White PA, et al. Systemic ventricular function in patients with transposition of the great arteries after atrial repair: a tissue Doppler and conductance catheter study. *J Am Coll Cardiol* 2004;**43**:100–106.

56 Preminger TJ, Sanders SP, van der Velde ME, et al. "Intramural" residual interventricular defects after repair of conotruncal malformations. *Circulation* 1994;**89**:236–242.
57 Ge S, Shiota T, Rice MJ, et al. Images in cardiovascular medicine. Transesophageal ultrasound imaging during stent implantation to relieve superior vena cava-to-intra-atrial baffle obstruction after Mustard repair of transposition of the great arteries. *Circulation* 1995;**91**:2679–2680.
58 Raman SV, Cook SC, McCarthy B, Ferketich AK. Usefulness of multidetector row computed tomography to quantify right ventricular size and function in adults with either tetralogy of Fallot or transposition of the great arteries. *Am J Cardiol* 2005;**95**:683–686.

CHAPTER 25

Double-Outlet Ventricle

Leo Lopez[1] and Tal Geva[2]
[1]The Pediatric Heart Center at the Children's Hospital at Montefiore, New York, NY, USA
[2]Department of Cardiology, Boston Children's Hospital, Boston, MA, USA

Introduction

Double-outlet ventricle exists when both great arteries are aligned with the right ventricle (RV: double-outlet right ventricle, or DORV), with the left ventricle (LV: double-outlet left ventricle, or DOLV), or with the infundibulum (double-outlet infundibulum). It is one type of ventriculo-arterial alignment within a classification system that describes the relationship of the semilunar valves and corresponding great arteries to the underlying ventricles (see Chapter 3). Other types of ventriculo-arterial alignments include concordant relationship, wherein the aorta arises from the LV and the pulmonary artery arises from the RV (such as normally related great arteries and anatomically corrected malposition of the great arteries); discordant relationship, wherein the aorta arises from the RV and the pulmonary artery arises from the LV (such as transposition of the great arteries, or TGA); and common outlet (such as truncus arteriosus). Because the spectrum of ventriculo-arterial alignments is in fact a continuum, any classification system must involve drawing sharp borders within transition zones between "discrete" groups. As a result, some anatomic variations may straddle distinct categories at these transition zones. Nevertheless, classification is indispensable in the study of congenital heart diseases, especially in terms of defining etiology, prevalence, natural history, and treatment outcome.

Double-outlet right ventricle

Definition

DORV occurs when both great arteries are completely or nearly completely aligned with the RV. Although this definition appears straightforward at first glance, the approach to making the diagnosis has been fraught with controversy [1–5]. Over the past several decades, the diagnostic debate over this so-called "morphogenetic monster" [3] has focused primarily on whether the term DORV refers to a specific morphologic entity or to a broader group of defects with the same abnormal ventriculo-arterial alignment. In addition, the extent that one of the semilunar valves overrides the ventricular septal plane has contributed significantly to the confusion over this definition. Some argue that the "50% rule" should be utilized, defining origin of a great artery from a ventricle if more than half of the semilunar valve is related to that ventricle over a ventricular septal defect (VSD) [2,3]. Many others argue that the diagnosis should be reserved for cases where the great arteries are completely or nearly completely aligned with the RV (absent or minimal override) [6–9], an approach that minimizes overlap among the ventriculo-arterial alignment categories. Assigning a percentage to the degree of override can be arbitrary and imprecise, especially given the complex three-dimensional (3D) relationship between the ventricles and great arteries, the curved geometry of the ventricular septum, and the rotational and translational motion of the heart during the cardiac and respiratory cycles. In addition, the aortic valve overrides the ventricular septum in a normal heart, and the degree of override is more pronounced in the setting of tetralogy of Fallot (TOF). Hence, the "50% rule" may classify many patients with TOF or with a VSD and normally related great arteries as DORV, an approach that by itself contributes little to the clinical tasks of choosing appropriate intervention and predicting outcome. Regardless of the debates over definitions and classification systems, however, the primary task when caring for this heterogeneous group of patients is to obtain a precise morphologic and functional description of the heart in order to formulate a rational surgical approach [10–13].

Historical perspective

In 1793, Abernathy provided one of the earliest descriptions of a heart where both great arteries originated from the RV [14]. However, during the nineteenth and early twentieth centuries, any abnormal relationship between the great arteries and ventricles was often considered as some form of TGA, and DORV was frequently classified as a subtype of TGA [15–17]. In 1949, Taussig and Bing described their famous heart with

Echocardiography in Pediatric and Congenital Heart Disease: From Fetus to Adult, Second Edition. Edited by Wyman W. Lai, Luc L. Mertens, Meryl S. Cohen and Tal Geva.
© 2016 John Wiley & Sons, Ltd. Published 2016 by John Wiley & Sons, Ltd.
Companion website: www.lai-echo.com

"transposition of the aorta and levoposition of the pulmonary artery" [18], noted over a decade later to be a case of DORV with a subpulmonary VSD, bilateral conus, and side-by-side great arteries [1,19]. The specific term "double-outlet right ventricle" was first introduced by Witham in 1957 [20]. Witham, however, still described DORV as a "partial transposition complex," and it was not until 1961 that McGoon utilized the term DORV on its own [9].

The role of the subarterial conus or infundibulum (outflow tract) in TGA and DORV has long been a focus of attention [1,5,18,21–23]. Van Praagh et al. highlighted the importance of abnormal conal development in the morphogenesis of abnormal great artery relationships [24]. They argued that DORV and TOF are separate entities with mutually exclusive diagnostic criteria, an important distinction when reporting surgical results [5]. Although earlier reports by Hallermann et al. [21] and by Baron [22] suggested that presence of both subaortic and subpulmonary conus defined DORV, Van Praagh et al. recognized that not all cases of DORV had bilateral conus and emphasized that the diagnosis is based not on the conal morphology but on the ventriculo-arterial alignment.

In 1972, Lev et al. proposed a classification system for DORV based on the anatomic position of the VSD relative to the great arteries, a system that is still widely used today [25]. In 1973, Kirklin used the percentage by which a semilunar valve is related to each ventricle over a VSD to determine the ventriculo-arterial alignment in cases of anatomically corrected malposition of the great arteries with a VSD [26]. Anderson et al. subsequently proposed the "50% rule" in an effort to synthesize a nomenclature for the various ventriculo-arterial connections [2,3,27]. In 2000, the Congenital Heart Surgery Nomenclature and Database Committee of the Society of Thoracic Surgeons defined DORV as "a type of ventriculo-arterial connection in which both great vessels arise either entirely or predominantly from the RV", a deliberately broad definition allowing for individual interpretation of how a great artery arises "predominantly" from the RV [28].

Incidence

DORV is an uncommon congenital heart disease with an estimated incidence of 12.7 per 100,000 live births, based on an analysis of 16 published articles spanning many decades [29]. However, the reported incidence per 100,000 live births has varied widely in individual reports: 3.2 in the New England Regional Infant Cardiac Program (1968–1974) [30]; 5.6 in the Baltimore-Washington Infant Study (1981–1982) [31]; 14.5 in the Alberta Heritage Pediatric Cardiology Program (1981–1984) [32]; and 22 in the Metropolitan Atlanta Congenital Defects Program (1995–1997) [33]. Among all the congenital heart lesions in the Baltimore-Washington Infant Study, DORV ranks 12th in frequency, representing 2% of all the cases [34]. Among all the cardiac diagnoses made at Boston Children's Hospital from 1988 to 2002, DORV ranks 16th in frequency [35].

Etiology

The etiology of DORV is not known and most cases are sporadic. A small number of familial cases have been reported [36]. A recent study of published case reports, epidemiologic analyses, and animal studies of DORV revealed distinct pathogenetic mechanisms associated with DORV [37]. Chromosomal abnormalities were present in up to 41% of the cases, mostly trisomies 13 and 18, and a significant percentage of these patients had hypoplasia of left heart structures in association with DORV. Population-based studies, including the Baltimore-Washington Infant Study, revealed a lower prevalence of associated chromosomal abnormalities (12%) [34,38,39]. Although frequently associated with other conotruncal anomalies, chromosome 22q11 deletion occurs rarely with DORV [37,40]. Mutations that have been described in association with the DORV phenotype in humans and animals include genes related to the neural crest (*NF-1*, *Pax-3*, *RXR*α) [41–44], genes controlling laterality (*CFC1*, *Pitx2*) [45,46], genes controlling transcriptional factors (*GATA-4*, *Nkx2.5*, *ZFPM2/FOG2*) [47–51], genes controlling cell proliferation and transformation from endothelial to mesenchymal cells (*TGF-*β_2) [52], genes controlling cell-to-cell communication (*Cx40*) [53], and genes controlling outflow tract myocardialization (*ECE-1*, *ECE-2*) [54] and polarization (*Vangl2* in the *Lp* mutant mouse) [55,56]. The large number and heterogeneity of genetic defects associated with DORV suggest that multiple developmental abnormalities may result in this phenotype. In addition, DORV has been produced in several experimental models, including surgical ligature of the chick embryonic conus to prevent its incorporation onto the LV after conal division [57], and surgical ablation of "cardiac" neural crest cells in the chick embryo [58]. Finally, several maternal risk factors have been associated with the development of DORV, including nongestational diabetes [59], assisted reproductive technology [60], exposure to solvents [36], and use of codeine [61], retinoic acid [62], and theophylline [63].

Morphology and classification

Developmental considerations

Knowledge of the normal development of the ventricular outflow tracts helps to elucidate some of the factors involved in the morphogenesis of DORV. A comprehensive review of cardiac embryology is beyond the scope of this chapter and can be found elsewhere [64–71]. At the conclusion of cardiac looping, the conotruncus relates exclusively to the developing RV. Shortly thereafter, pairs of internal ridges or cushions develop along the proximal and distal outflow tracts in a spiraling orientation. This is followed by migration of mesenchymal cells from the pharyngeal pouches into the distal outflow tract walls, contributing to their transformation from myocardial tissue to arterial tissue. At approximately the same time, there is also migration of cells derived from the neural crest into the developing cushions located in the distal segment of the conus and in the truncus arteriosus. The cushions with their neural crest-derived

cells begin to fuse distally within the truncus arteriosus, separating the future proximal aorta from the future pulmonary artery. The arterial valve leaflets and sinuses also evolve from the developing cushions at the base of the truncus arteriosus. The proximal (conal) cushions now begin to fuse, separating the subpulmonary outflow tract from the subaortic outflow tract, both of which are still committed to the developing RV. At around the same time, the endocardial cushion and muscular ventricular septum develop within the primordial ventricle. The fused proximal cushions eventually merge with the muscular ventricular septum, committing the pulmonary valve and artery to the RV, and the aortic valve and aorta to the LV. The subaortic outflow tract or conus is still present at this time, and its regression with consequent fibrous continuity between the mitral and aortic valves does not occur until approximately 12 weeks of gestation.

Although the exact mechanisms of morphogenesis in humans is unknown at this time, studies suggest that DORV can result from abnormalities in genetic and environmental signals for differentiation, proliferation, and migration of cardiogenic cells in the primary and secondary heart fields as well as neural crest-derived cells. As discussed previously, the marked heterogeneity that characterizes DORV morphology strongly suggests that several developmental mechanisms are involved. Developmental arrest at the embryonic stage when the conotruncus relates exclusively to the RV, disruption in the development of the proximal cushions, and abnormal ventricular development (such as hypoplasia and malposition) with or without abnormal conus are some of the proposed mechanisms.

Anatomy

Given the morphologic and physiologic diversity of DORV, the following anatomic features are crucial in understanding each case and determining the optimal interventional approach:

- VSD location and size and its relationship to the semilunar valves;
- conal morphology;
- spatial relationship of the great arteries to each other;
- associated cardiac lesions, including outflow tract obstruction, atrioventricular (AV) valve anomalies, ventricular hypoplasia and malposition, and abnormal coronary artery patterns.

VSD location and size

Description of the VSD location, especially in terms of its spatial relationship to the great arteries, has long been recognized as a clinically useful classification system for DORV [8,25,72–74]. When present, the VSD may fall into one of four categories [5,12,13,73,75–79]: subaortic, subpulmonary, doubly committed, or noncommitted (remote) VSD. It is important to recognize that the VSD in most cases of DORV is located between the antero-superior and postero-inferior limbs of the septal band. The only exceptions are cases with noncommitted (remote) VSD. The spatial relationship of the VSD to the semilunar valves is dictated by the presence, size, and position of the subarterial conus and by deficiency of adjacent septal segments such as the conal septum and AV canal septum. The size of the VSD, the distance from the VSD to the semilunar valves, and the presence of AV valve attachments along the VSD margins or within the defect are important variables when planning surgical repair. Occasionally, there are multiple VSDs [12], and rarely, the ventricular septum is intact [73,80].

It is worth noting that in contrast to hearts with concordant or discordant ventriculo-arterial alignments where the conal septum usually represents the superior border of a conoventricular septal defect, in hearts with DORV, the conal septum is a purely RV structure that does not contribute to the VSD margins. Thus, biventricular repair of DORV involves a baffle from the VSD to the closest semilunar root as opposed to simple patch closure of a VSD.

Subaortic VSD (42–57% of cases)

The defect is cradled between the limbs of septal band below the aortic valve. The postero-inferior margin may be in fibrous continuity with the tricuspid valve (confluent with the membranous septum), or it may consist of muscular extension of the posterior limb of the septal band [27,81]. This type of defect is termed *malalignment VSD* or *conoventricular septal defect* because the conal septum is malaligned with the underlying muscular septum. In DORV with D-malposition of the great arteries (aorta to the right of the pulmonary artery), the conal septum is rotated out of the plane of the ventricular septum and attaches to the antero-superior limb of the septal band (Figure 25.1) [81]. Pulmonary outflow tract obstruction is often present, and its severity is determined by the degree of anterior and leftward deviation of the conal septum and by associated pulmonary valve stenosis (Figure 25.2). In DORV with L-malposition of the great arteries (aorta to the left of the pulmonary artery), the subaortic VSD is situated more anteriorly and superiorly within the limbs of the septal band [82].

Subpulmonary VSD (24–37% of cases)

The defect is also cradled between the limbs of septal band. However, the conal septum is rotated out of the plane of the ventricular septum and attaches to the more posteriorly located ventriculoinfundibular fold rather than to the antero-superior limb of the septal band (Figure 25.3) [81]. As a result, the conal septum shields the aortic valve from the defect with only a short distance from the defect to the pulmonary valve. In 60% of cases, the postero-inferior margin of the defect is in fibrous continuity with the AV valves (confluent with the membranous septum); a muscular inferior border occurs in the other 40% [75]. The subaortic conus is usually well developed, and the aortic valve is rightward relative to the pulmonary valve with either a side-by-side or slightly anterior position. The subpulmonary conus varies in size. In some cases the subpulmonary conus is incomplete, allowing fibrous continuity between the pulmonary and tricuspid and/or mitral valves. The distinction between DORV and TGA in this scenario is dictated by the alignment between

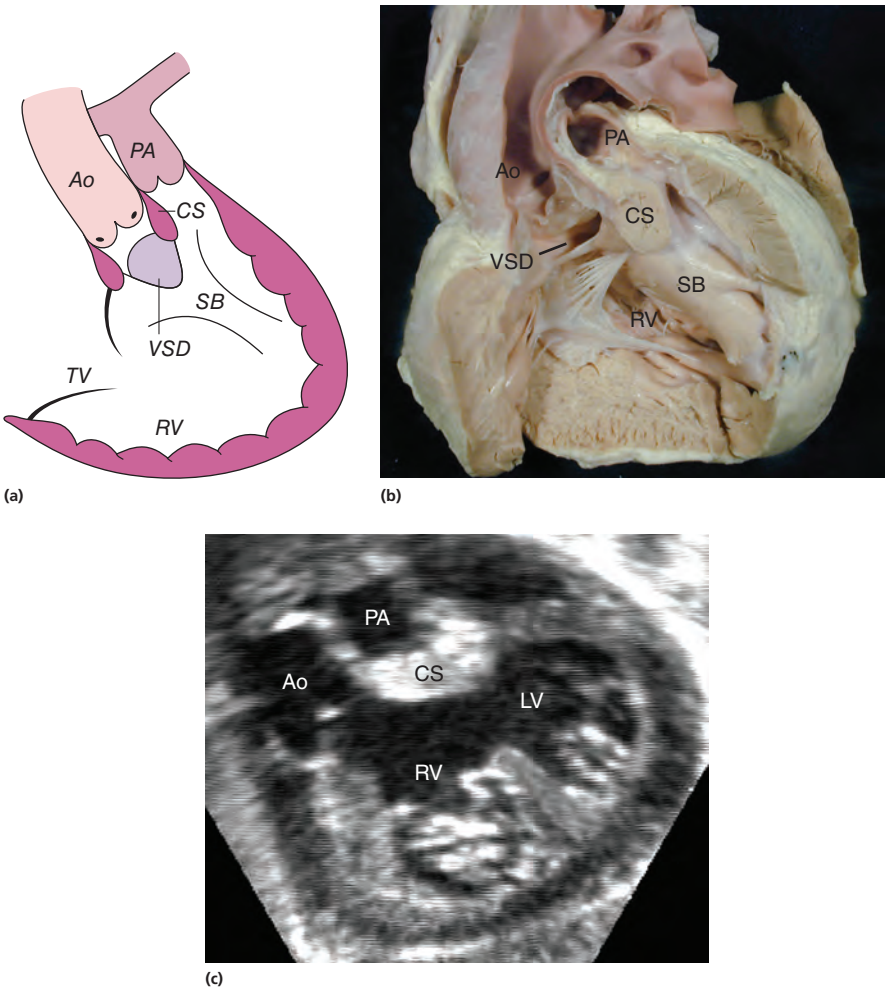


Figure 25.1 DORV with a subaortic VSD where the conal septum is attached to the antero-superior limb of the septal band in **(a)** diagram, **(b)** pathology specimen (reproduced with permission of Professor Robert H. Anderson, Institute of Child Health, London, UK), and **(c)** modified subxiphoid short-axis view. Ao, aorta; CS, conal septum; LV, left ventricle; PA, pulmonary artery; RV, right ventricle; SB, septal band; VSD, ventricular septal defect.

the pulmonary valve and the underlying ventricles: DORV is present when the pulmonary valve relates nearly exclusively to the RV, and TGA is present when the pulmonary valve relates nearly exclusively to the LV. Categorization of intermediate cases is challenging and one can describe such cases as having biventricular origin of the pulmonary artery.

Although many consider DORV with a subpulmonary VSD synonymous with the Taussig–Bing anomaly, it is worth noting that the original heart described by Taussig and Bing had DORV with a subpulmonary VSD, bilateral conus, and side-by-side great arteries [18]. In patients with this anatomy, hypertrophy and rightward deviation of the conal septum as well as hypertrophy of the subaortic conal free wall can result in varying degrees of subaortic stenosis, which in turn is associated with coarctation or aortic arch interruption. In addition, the mitral valve may straddle the VSD with attachments to the subpulmonary conus.

Doubly committed VSD (3–12% of cases)

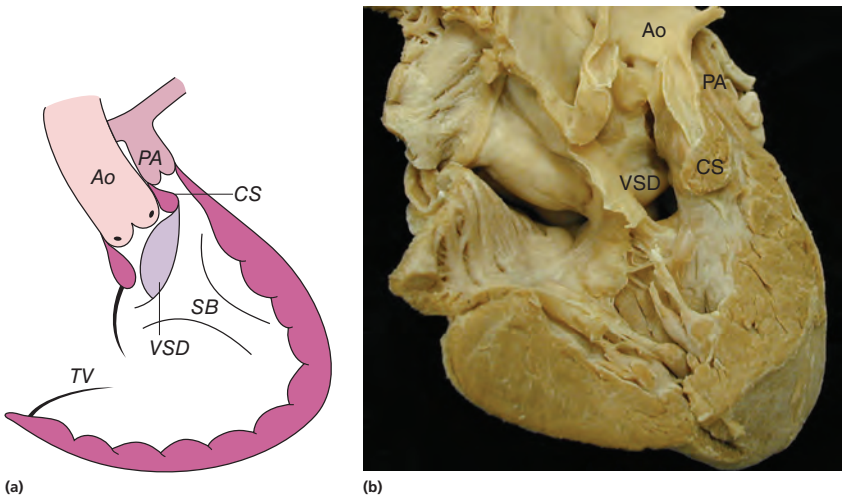
As a result of absent or markedly deficient conal septum, the defect is in close proximity or even contiguous with both semilunar valves (Figure 25.4). The VSD is located superiorly and is often large. The semilunar valves represent the antero-superior margin of the defect. Because the VSD is cradled between the limbs of septal band, this part of the septal band along with the right ventriculoinfundibular fold form the entire postero-inferior margin of the defect; occasionally, however, the defect extends into the fibrous area of the membranous septum. Infrequently, these defects are associated with pulmonary or aortic outflow tract obstruction [83] (Figure 25.4).

Noncommitted (remote) VSD (9–19% of cases)

The defect is not cradled between the limbs of septal band and thereby considered noncommitted or remote because of the distance from the semilunar valves (Figure 25.5). The defect can be located in the AV canal (inlet) septum, along the posterior aspect of the membranous septum, or within the muscular septum. It is important to recognize that some subaortic and subpulmonary VSDs cradled between the limbs of the septal band may appear remote because of elongated subarterial conus [81].

Conal morphology

Conal morphology is important in the comprehensive description of DORV cases, but it is important to note that it is



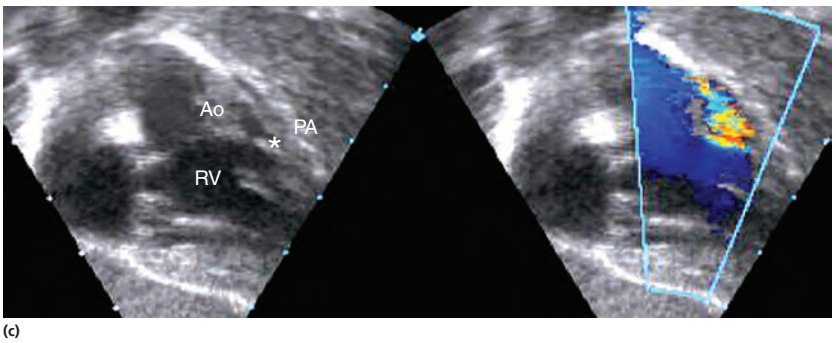
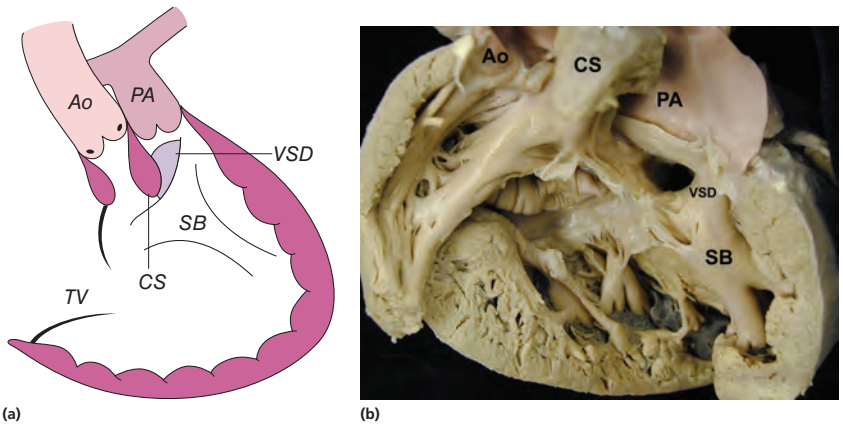


Figure 25.2 DORV with a subaortic VSD and pulmonary stenosis (TOF type) secondary to significant anterior malalignment of the conal septum **(a)** diagram, **(b)** pathology specimen (reproduced with permission of Professor Robert H. Anderson, Institute of Child Health, London, UK), and **(c)** modified subxiphoid long-axis view (right axial oblique view) where the asterisk represents the conal septum. Ao, aorta; CS, conal septum; PA, pulmonary artery; RV, right ventricle; VSD, ventricular septal defect.



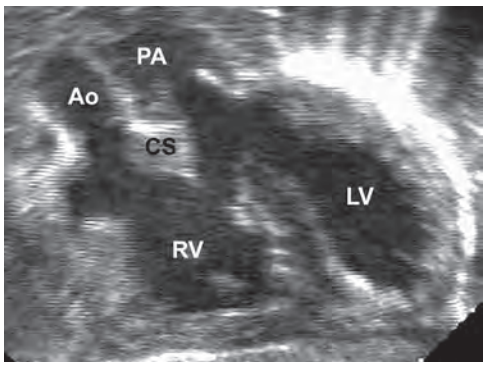
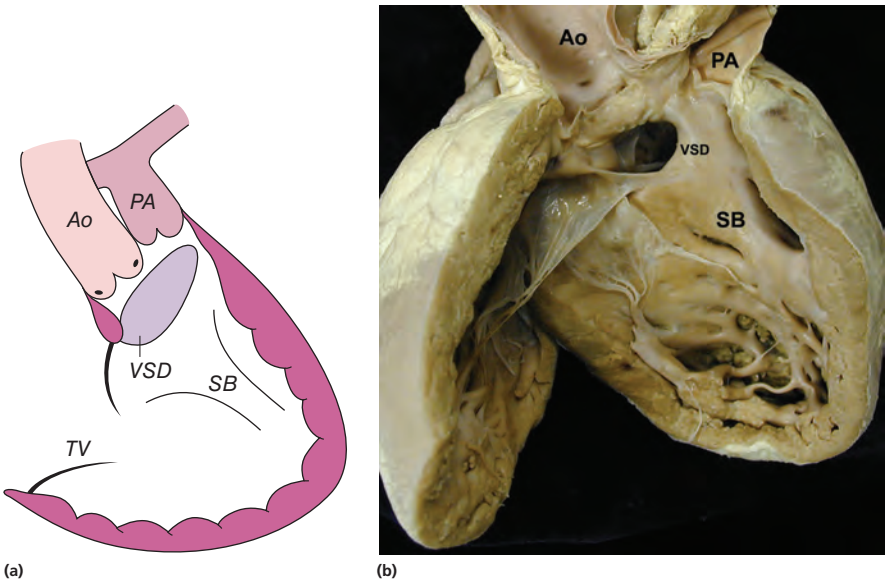


Figure 25.3 DORV with a subpulmonary VSD where the conal septum is attached to the right ventriculo-infundibular fold in **(a)** diagram, **(b)** pathology specimen (reproduced with permission of Professor Robert H. Anderson, Institute of Child Health, London, UK), and **(c)** subxiphoid long-axis view. Ao, aorta; CS, conal septum; LV, left ventricle; PA, pulmonary artery; RV, right ventricle; SB, septal band; VSD, ventricular septal defect.



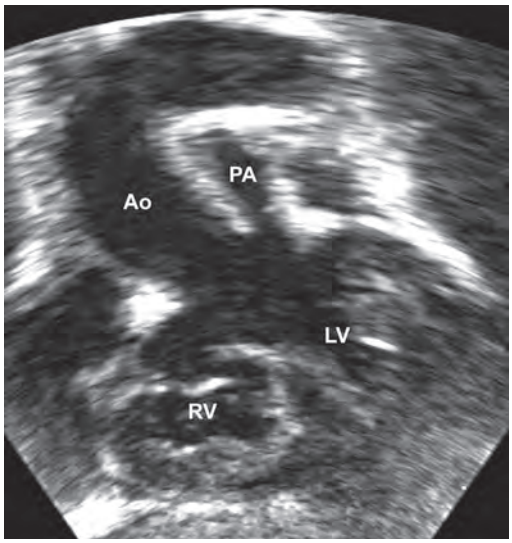


Figure 25.4 DORV with a doubly committed VSD and absent conal septum in **(a)** diagram, **(b)** pathology specimen (reproduced with permission of Professor Robert H. Anderson, Institute of Child Health, London, UK), and **(c)** subxiphoid short-axis view showing pulmonary stenosis. Ao, aorta; LV, left ventricle; PA, pulmonary artery; RV, right ventricle; SB, septal band; VSD, ventricular septal defect.

not a determining factor in the definition of DORV [10,84]. Many configurations of conal morphology occur in DORV cases (Figure 25.6), including bilateral conus, subpulmonary conus with absent subaortic conus, subaortic conus with absent subpulmonary conus, or bilaterally absent conus. Van Praagh et al. [5,24] as well as Kirklin [78] have suggested that conal morphology is the primary determinant of the various patterns of great artery relationships seen in DORV. This view, however, has not been endorsed unanimously [10]. Other classification schemes of conal anatomy have been proposed as well [85].

An important aspect of the description of conal morphology is the distance from the VSD to each semilunar valve. This is particularly relevant in the setting of bilateral conus where surgical repair involves a baffle from the LV through the VSD to the nearest semilunar valve (Figure 25.7). This distance has been shown to be predictive of adverse postoperative events such as residual LV outflow tract obstruction and death [86]. In patients with DORV and subaortic VSD, as the size of the subaortic conus increases, the distance from the tricuspid valve to the aortic valve increases and the distance from the tricuspid valve to the pulmonary valve decreases. Because the pathway from the LV to the aortic valve usually passes between the tricuspid and pulmonary valves, this distance is important in determining the feasibility of intraventricular baffling (Figure 25.8) [10,11,87]. Another important consideration in planning surgical repair is the morphology of the conal septum within the RV. The conal septum may be prominent with significant AV valve attachments, potentially hindering the course of an intraventricular baffle from the VSD to the closest semilunar valve. These attachments may also be problematic in cases where the semilunar valve adjacent to the VSD is hypoplastic and/or stenotic, and biventricular repair would require baffling from the VSD to the distant

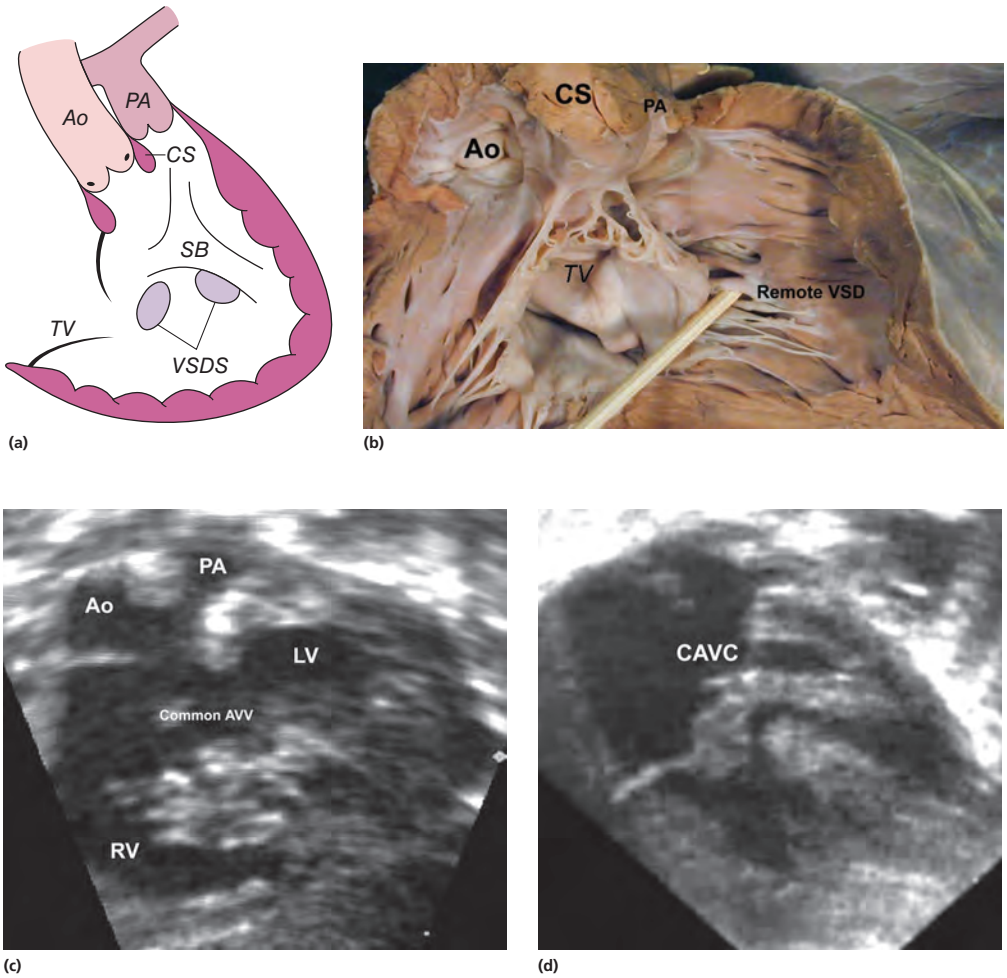


Figure 25.5 DORV with a remote VSD in **(a)** diagram, **(b)** pathology specimen (reproduced with permission of Professor Robert H. Anderson, Institute of Child Health, London, UK), **(c)** modified subxiphoid short-axis view showing the relationship of the great arteries to the VSD, and **(d)** an apical 4-chamber view showing the complete AV canal defect. Ao, aorta; AVV, atrioventricular valve; CAVC, complete atrioventricular canal defect; CS, conal septum; LV, left ventricle; PA, pulmonary artery; RV, right ventricle; VSD, ventricular septal defect.

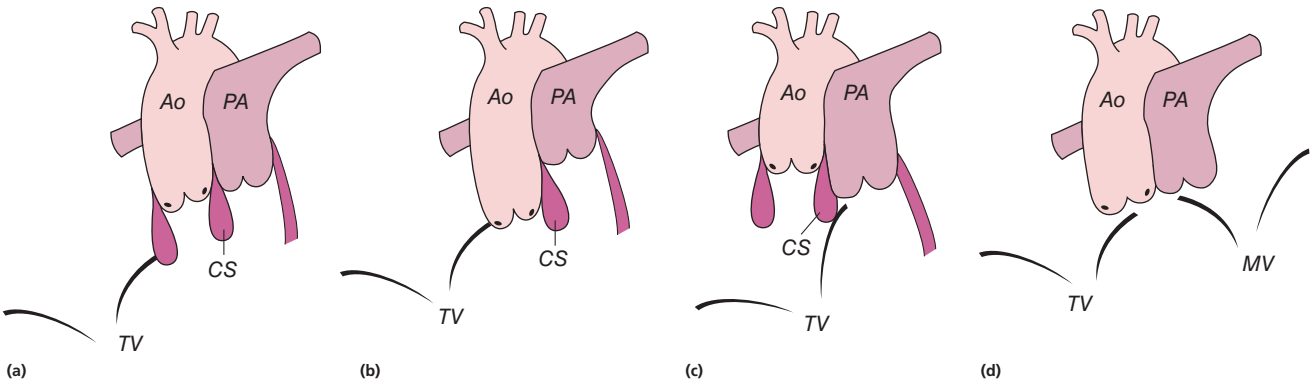


Figure 25.6 Diagrams depicting the four categories of conal morphology: **(a)** bilateral conus, **(b)** absent subaortic conus, **(c)** absent subpulmonary conus, and **(d)** bilaterally absent conus.

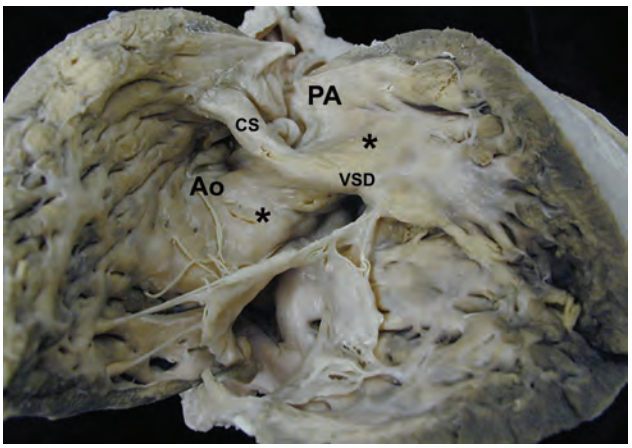


Figure 25.7 Pathology specimen of a DORV with bilateral conus (indicated by the asterisks). Ao, aortic valve; CS, conal septum; PA, pulmonary artery; VSD, ventricular septal defect. Source: Reproduced with permission of Professor Robert H. Anderson, Institute of Child Health, London, UK.

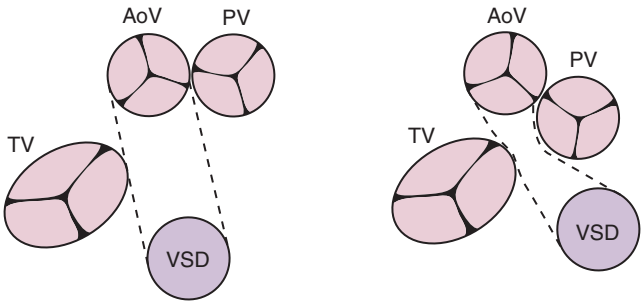
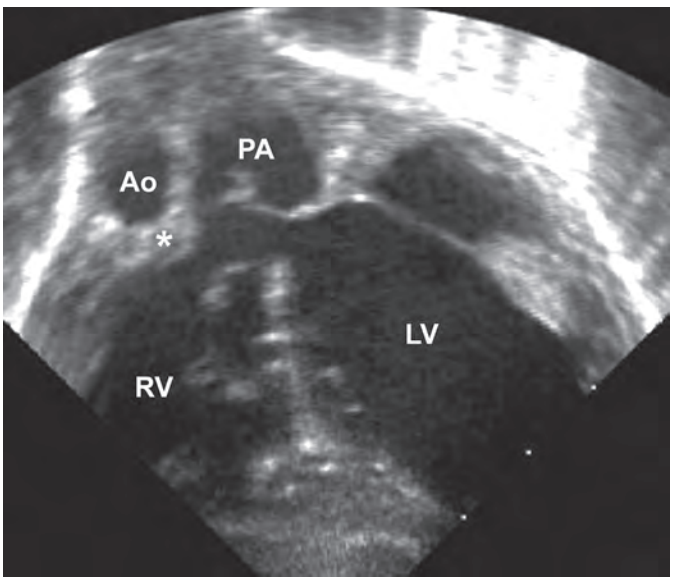


Figure 25.8 Diagram of how the distance from the tricuspid valve to the pulmonary valve can affect the potential baffle pathway from the LV to the aorta.

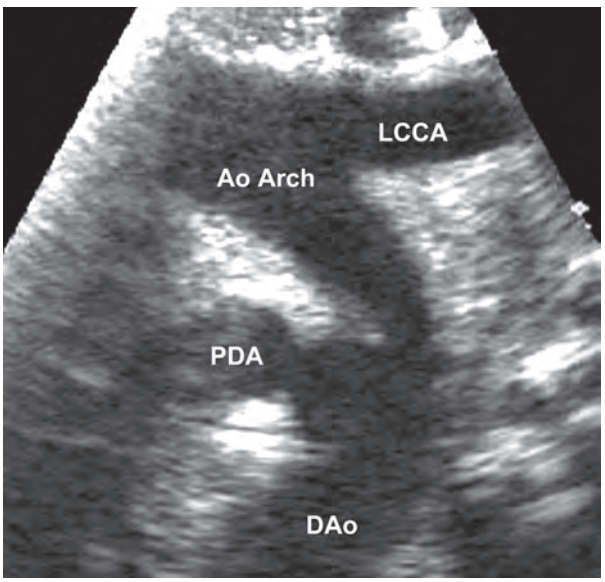
semilunar valve and resection of the conal septum. The conal septum may also deviate into one or the other subarterial outflow tract, resulting in subaortic or subpulmonary stenosis. In DORV with pulmonary outflow tract obstruction, this deviation may or may not be associated with subpulmonary conal hypoplasia (Figure 25.2). Often there is also pulmonary valve involvement with hypoplasia of the pulmonary annulus and pulmonary trunk as seen in TOF. In DORV with a subpulmonary VSD, the conal septum occasionally deviates into the subaortic region resulting in subaortic stenosis, coarctation, or aortic arch interruption (Figure 25.9).

Great artery relationships

The spatial relationships between the semilunar valves and their corresponding proximal great arteries vary markedly. Common examples include side-by-side great arteries with either D- or L-malposition of the aortic valve relative to the pulmonary valve, posterior and rightward aortic valve relative to the pulmonary valve (as in normally related great arteries), anterior and rightward aortic valve (as in D-malposition), aortic valve directly anterior to the pulmonary valve (as in A-malposition), posterior and leftward aortic valve (as in situs inversus totalis), or anterior and leftward aortic valve (as in L-malposition). The spatial orientation of the great arteries relative to each other can be crossed or parallel. In the most common variant of DORV with subaortic VSD, the aorta is often rightward and either slightly posterior or side-by-side relative to the main pulmonary artery. In DORV with subpulmonary VSD, the great arteries are generally side-by-side and parallel in their relationship, but the aorta can also



(a)



(b)

Figure 25.9 DORV with a subpulmonary VSD, narrow subaortic region, and coarctation in **(a)** subxiphoid long-axis (the asterisk represents the conal septum) and **(b)** suprasternal views. Ao, aorta; Dao, descending aorta; LCCA, left common carotid artery; LV, left ventricle; PA, pulmonary artery; PDA, patent ductus arteriosus; RV, right ventricle.

be anterior and rightward relative to the pulmonary artery at the base of the heart (similar to typical D-loop TGA). Notably, the spatial relationship of the great arteries does not always predict the VSD location [78] or the conal morphology [10].

Associated lesions

Outflow tract obstruction occurs in up to 70% of DORV cases [12,13,75,78,88]. This usually requires some modification to surgical management. The most common variant involves pulmonary outflow tract obstruction at the subvalvar and/or valvar level, often seen in DORV with a subaortic VSD (Figure 25.2). Subpulmonary stenosis results from similar anatomic abnormalities seen in TOF: leftward, anterior, and superior deviation of the conal septum relative to the muscular septum, and hypertrophy of the conal free wall. The subpulmonary conus is hypoplastic, usually with significant obstruction. In the most severe cases, there is pulmonary atresia. Although the term DORV with pulmonary atresia can be problematic, the pulmonary trunk in most cases is clearly anchored to the RV such that the absence of luminal continuity does not preclude determination of spatial alignment between the RV and the pulmonary trunk (Figure 25.10; Video 25.1). If the pulmonary artery segment is difficult to identify, the anatomy can be labeled as right ventricular origin of the aorta with pulmonary atresia. Along the aortic outflow tract, subaortic stenosis and/or aortic arch obstruction (coarctation or aortic arch interruption) can occur in up to 50% of DORV cases with a subpulmonary VSD (Figure 25.9) [85,89,90]. In these cases, subaortic stenosis usually results from muscular narrowing produced by the conal septum (which is deviated to the right), a hypertrophied right ventriculoinfundibular fold, and the RV conal anterior free wall.

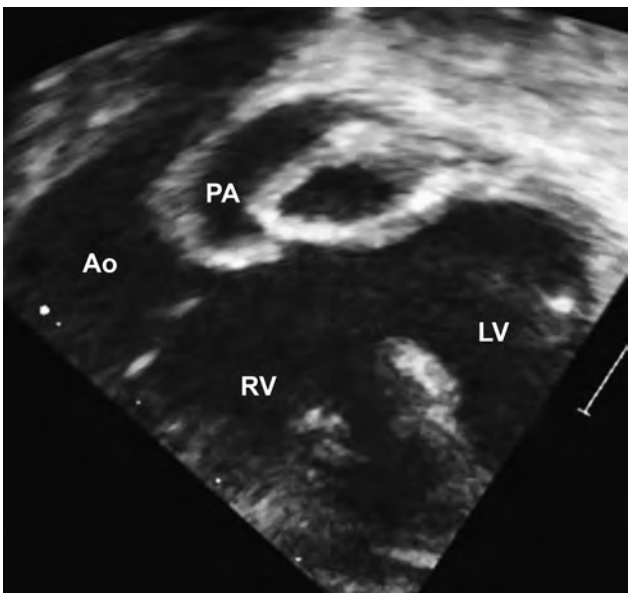


Figure 25.10 DORV with membranous pulmonary atresia in an apical view. Ao, aorta; LV, left ventricle; PA, pulmonary artery; RV, right ventricle.

AV valve anomalies, including a common AV valve in the setting of an AV canal defect, occur in up to 35% of DORV cases [75,88]. Anomalies of the mitral valve in DORV can pose a challenge for surgical repair [13,77,91]. In particular, a straddling mitral valve, which can occur in up to 20% of DORV cases with a subpulmonary VSD (Figure 25.11) [75,90,92], may complicate a biventricular repair [93,94] leading to a single ventricle palliation [95–97]. Parachute mitral valve, supramitral ring, mitral valve hypoplasia, and typical forms of mitral stenosis can also influence the surgical approach and may affect long-term prognosis. DORV with mitral atresia is a rare association that requires a single ventricle palliation. A straddling tricuspid valve can also occur in DORV with an AV canal-type VSD. Rarely, the AV valves are situated in a criss-cross orientation, resulting in a complex relationship between the VSD and the great arteries (Figure 25.12).

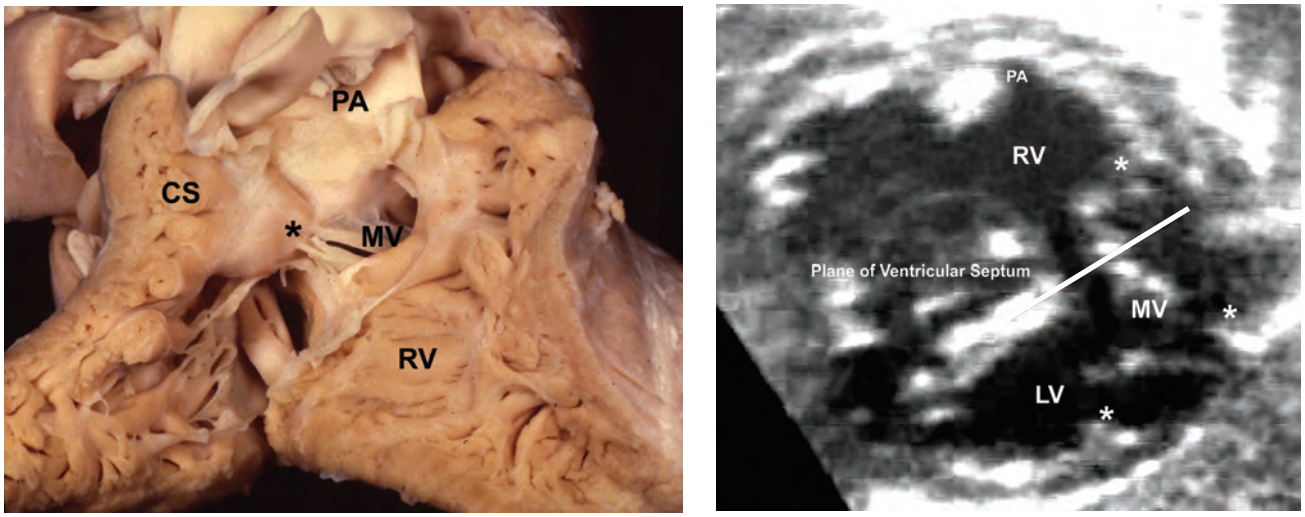
Other associated lesions include atrial septal defects, persistent left superior vena cava, and leftward juxtaposition of the atrial appendages, which occurs most frequently when the ascending aorta and pulmonary trunk are located along the extreme rightward aspect of the heart (Figure 25.13) [98]. DORV is common in patients with heterotaxy syndrome (usually of the asplenia type), often with associated systemic and pulmonary venous anomalies, common AV canal defects, and/or LV hypoplasia [99–101]. Many heterotaxy cases cannot support a biventricular circulation and must therefore undergo single ventricle palliation. A distinct constellation of cardiac anomalies involves a DORV with hypoplasia of the tricuspid valve and RV sinus, superior-inferior ventricles with criss-cross AV valves, and subvalvar and valvar pulmonary stenosis [5,102].

Coronary artery abnormalities occur in up to 30% of DORV cases [3] (Figure 25.14), with an increased frequency in those with a subpulmonary or a remote VSD [12,103,104]. Side-by-side great arteries is another risk factor for an abnormal coronary arterial pattern [105]. The coronary artery pattern can be an important determinant of surgical management. For example, in DORV with a subpulmonary VSD requiring an arterial switch operation, an intramural coronary artery can increase the complexity of the operation. In DORV with a subaortic VSD and pulmonary stenosis, a coronary artery crossing the RV outflow tract can influence surgical management of the pulmonary stenosis (Figure 25.15).

Pathophysiology

The variable clinical presentation and course of DORV patients reflect the anatomic and hemodynamic heterogeneity of this group [28]. The pathophysiology is determined primarily by VSD size, VSD relationship to the great arteries and the consequent effects of blood flow streaming, presence of pulmonary or aortic outflow tract obstruction, pulmonary vascular resistance, and associated cardiovascular anomalies. The most common pathophysiologic variants include:

- VSD physiology (DORV with a large subaortic VSD and no pulmonary stenosis);



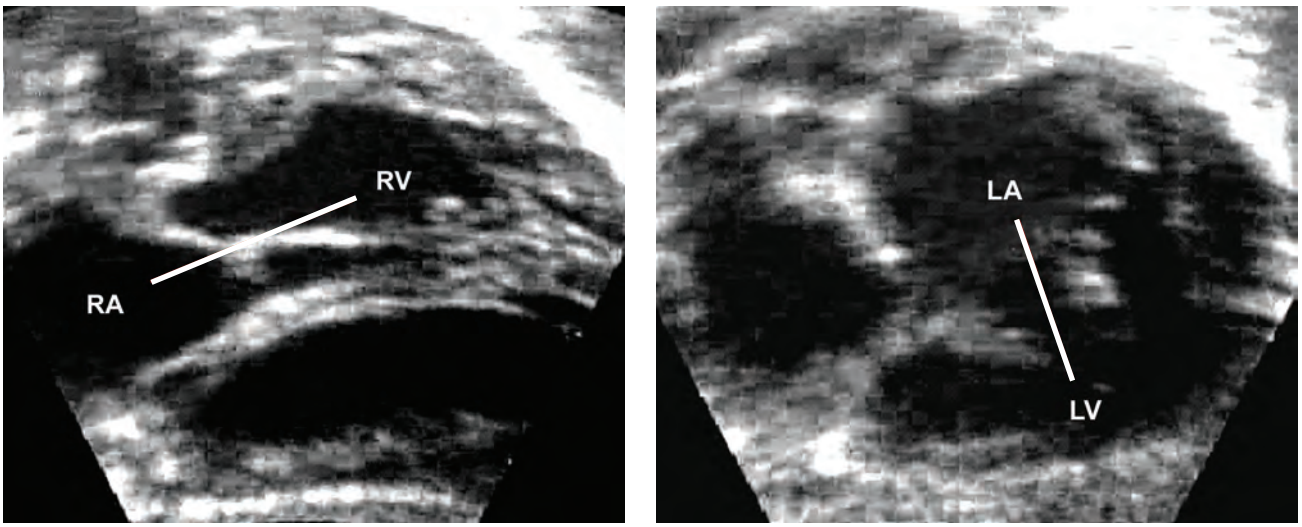
(a) (b)

Figure 25.11 DORV with a subpulmonary VSD and straddling MV in **(a)** a pathology specimen (the Ao is located behind the conal septum) (reproduced with permission from Professor Robert H. Anderson, Institute of Child Health, London, UK), and **(b)** a subxiphoid short-axis view (the asterisks represent MV attachments). CS, conal septum; LV, left ventricle; MV, mitral valve; PA, pulmonary artery; RV, right ventricle.

- TOF physiology (DORV with a subaortic VSD and pulmonary stenosis);
- TGA physiology (DORV with a subpulmonary VSD ± aortic outflow obstruction);
- single-ventricle physiology (DORV with mitral atresia or significant ventricular hypoplasia, often in association with an unbalanced AV canal defect and/or heterotaxy syndrome).

Imaging

The diagnosis of DORV is usually established by transthoracic echocardiography, which is the primary diagnostic tool used to determine the anatomic and physiologic features necessary for management decisions. Preoperative cardiac catheterization is seldom used in infants with DORV except when a transcatheter intervention is expected (e.g., balloon atrial septostomy). In selected cases with complex anatomy and uncertainty regarding complex venous or arterial anatomy or when a single versus biventricular approach is contemplated, cardiovascular magnetic resonance (CMR) may be used as an adjunct to transthoracic echocardiography. Intraoperative transesophageal echocardiography (TEE) is often performed at the conclusion of cardiopulmonary bypass to evaluate the repair.



(a) (b)

Figure 25.12 DORV with criss-cross AV valve orientation and superior-inferior ventricles in subxiphoid long-axis views showing **(a)** the right–left relationship of the right atrium to the superior RV, and **(b)** the postero-anterior relationship of the left atrium to the inferior LV. LA, left atrium; LV, left ventricle; RA, right atrium; RV, right ventricle.

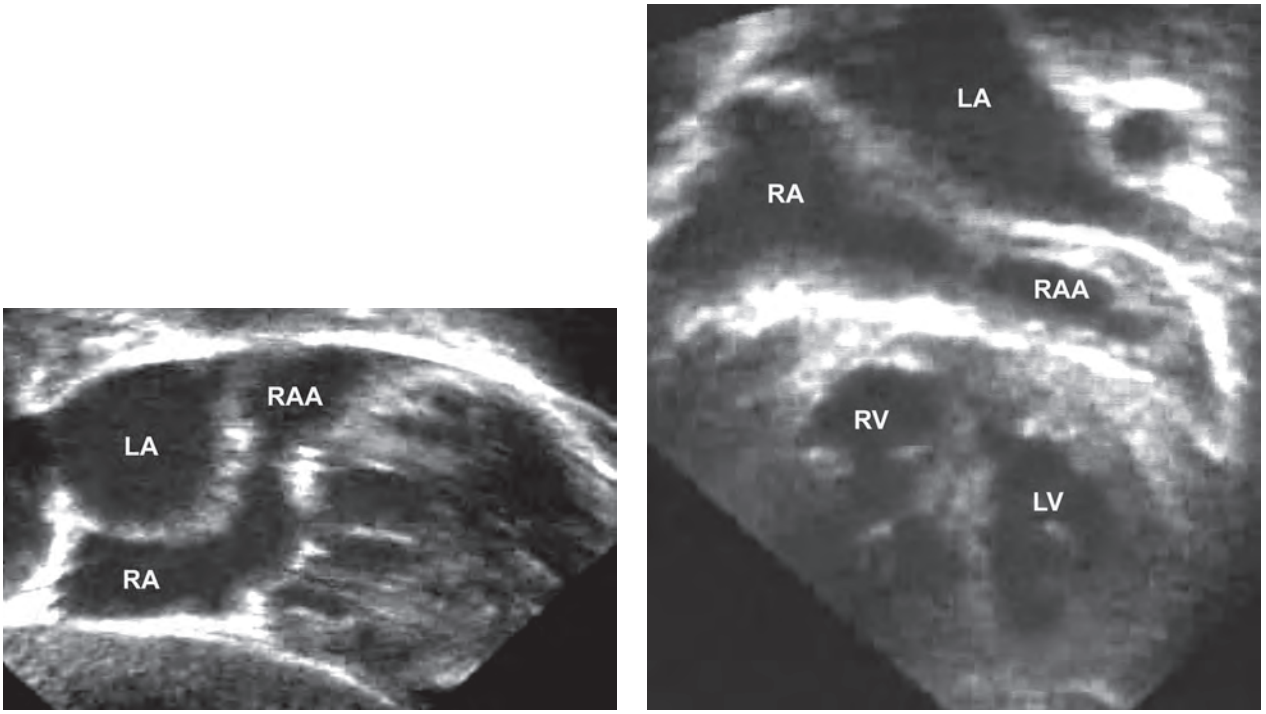


Figure 25.13 DORV with leftward juxtaposition of the atrial appendages in **(a)** subxiphoid long-axis and **(b)** apical views. LA, left atrium; LV, left ventricle; RA, right atrium; RAA, right atrial appendage; RV, right ventricle.

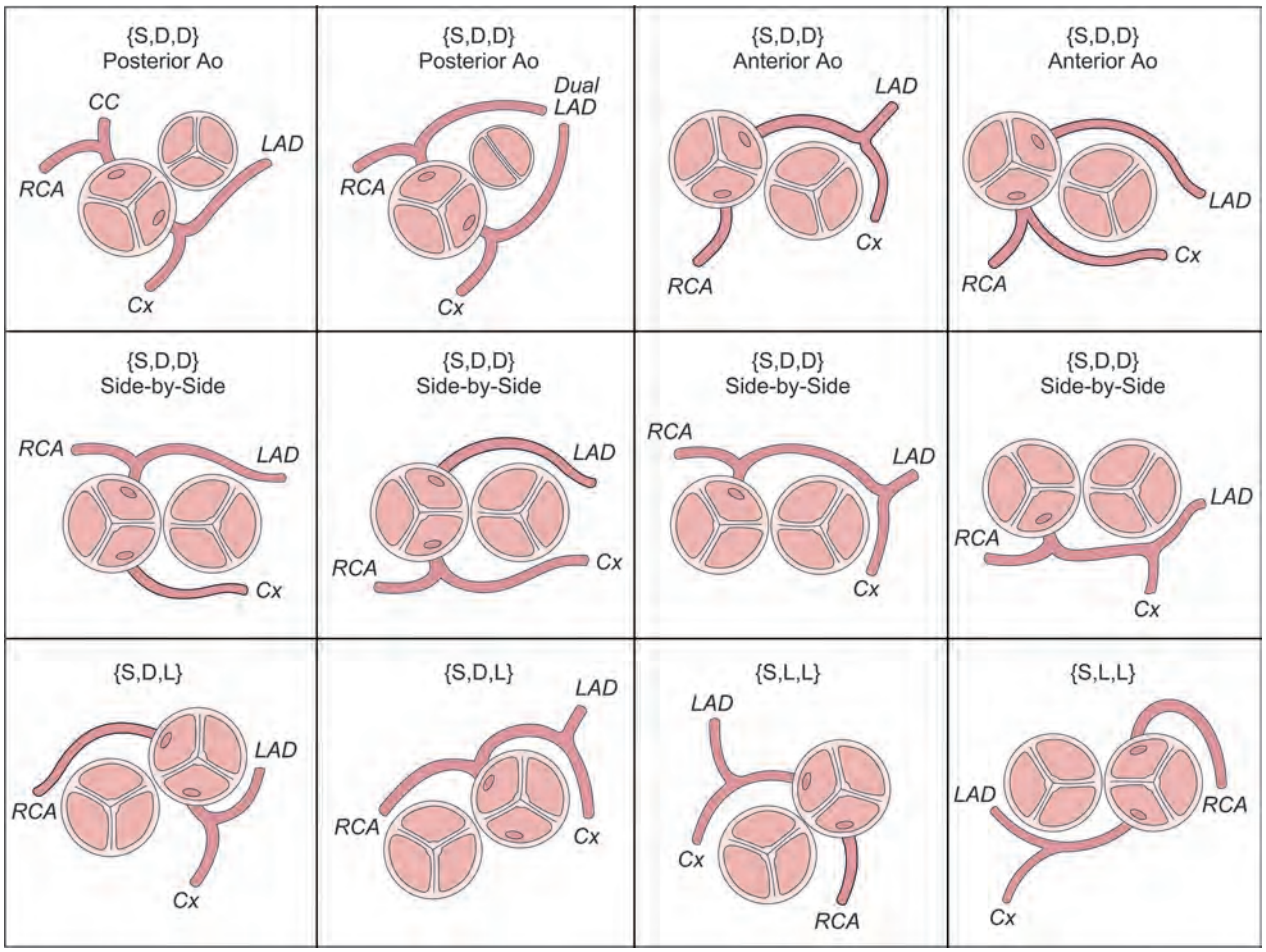


Figure 25.14 Diagram of the possible coronary artery patterns seen with DORV. Ao, aorta; CC, conal coronary artery; Cx, circumflex coronary artery; LAD, left anterior descending coronary artery; RCA, right coronary artery.

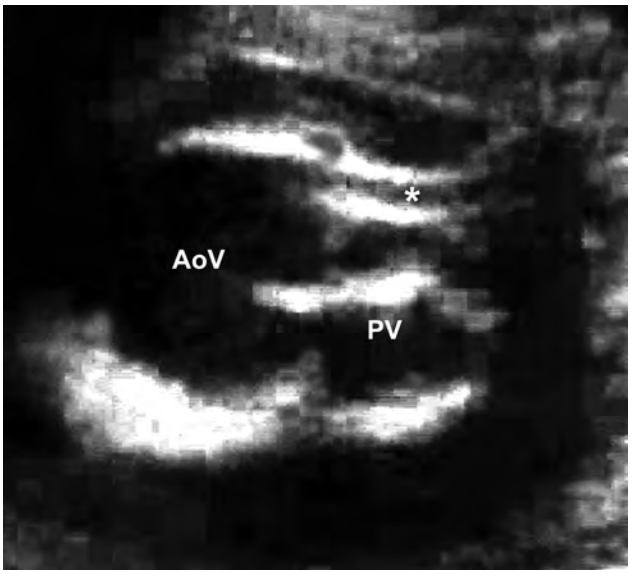


Figure 25.15 DORV, subaortic VSD, and pulmonary stenosis (TOF type) where the right coronary artery conal branch (asterisk) crosses in front of the pulmonary outflow tract and supplies the anterior descending coronary artery shown in a parasternal short-axis view. AoV, aortic valve; PV, pulmonary valve.

Key elements

Preoperative examination

The initial echocardiogram should establish the diagnosis and provide a comprehensive morphologic and physiologic description in order to determine the appropriate therapy. In addition to a detailed segmental approach (Chapter 3) [2,106–108], the evaluation should focus on the following features:

- Ventriculo-arterial alignment
 - Imaging of the spatial relationships (alignments) between the ventricles and the semilunar valves and arterial roots by 2D and color Doppler sweeps from the subxiphoid, apical, and parasternal long- and short-axis views (Video 25.2). Particular attention is given to delineation of the ventricular septal plane in relation to the positions of the semilunar valves. DORV is present when blood flow from the LV has to cross the VSD in order to reach the semilunar valves.
 - Parasternal short-axis sweep from the arterial roots to the apex to demonstrate the plane of the ventricular septum beyond the VSD and the imaginary line representing this plane as it transects the semilunar valves in order to delineate the degree of commitment to each ventricle.
 - When feasible, real-time 3D imaging.
 - Intraoperative pre-cardiopulmonary bypass TEE to confirm the preoperative diagnoses and to provide the surgeon and cardiologist another opportunity to review the planned surgical approach (Figure 25.16; Video 25.3).
- Systemic and pulmonary venous return and atrial morphology
 - Subxiphoid, apical, parasternal short-axis, high right parasternal border, and suprasternal views to evaluate the systemic and pulmonary venous connections as well as the atrial septum.
 - Subxiphoid long-axis, apical, and parasternal short-axis sweeps to display the relationship of the atrial appendages to the great arteries (Figure 25.13; Video 25.4); when the septal plane appears abnormally perpendicular to its usual location, one should consider leftward juxtaposition of the atrial appendages because the perceived "atrial septum" is

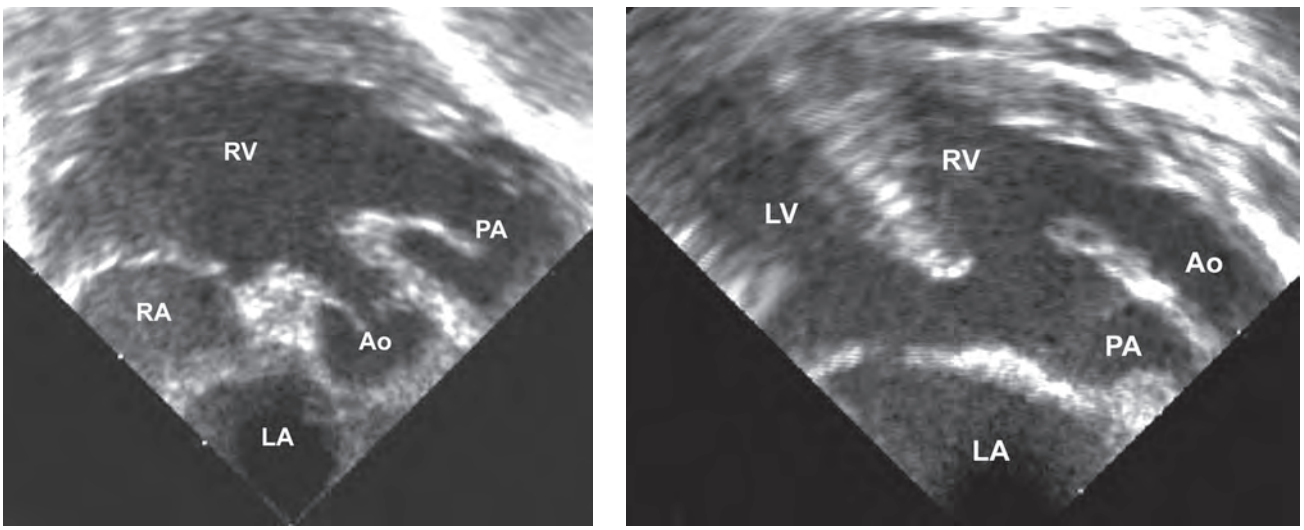
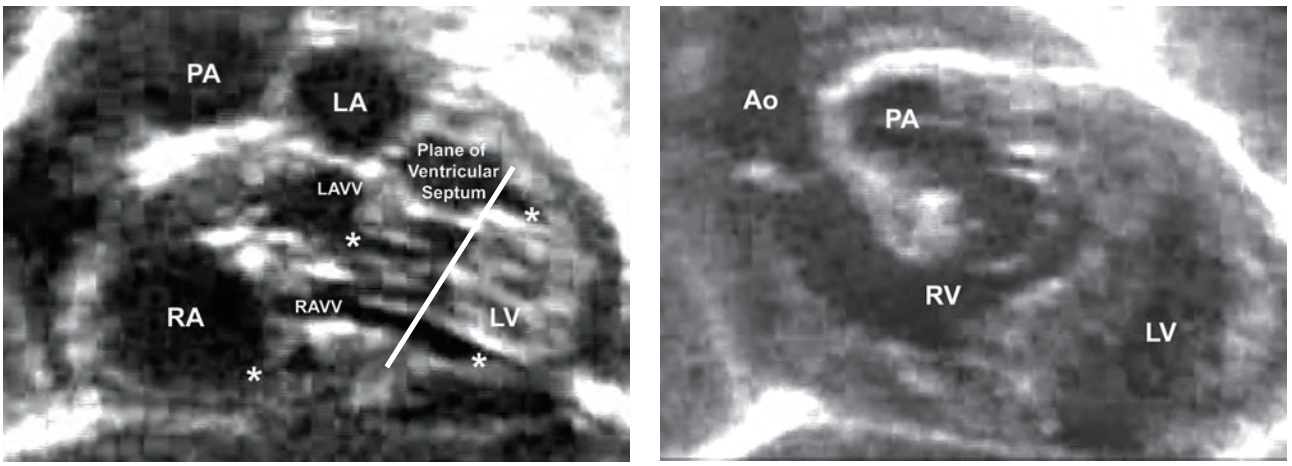


Figure 25.16 Preoperative TEE in a vertical (longitudinal) plane of **(a)** DORV with a subaortic VSD and bilateral conus, and **(b)** DORV with a subpulmonary VSD and mildly narrow subaortic region. Ao, aorta; LA, left atrium; LV, left ventricle; PA, pulmonary artery; RA, right atrium; RV, right ventricle.



(a) (b)

Figure 25.17 Unusual DORV with mild LV hypoplasia and bilateral straddling through a remote VSD in subxiphoid long-axis views showing **(a)** straddling of the right-sided and left-sided AV valves through the VSD where the asterisks represent the attachments of both AV valves to both ventricles, and **(b)** both great arteries originating from the RV. Ao, aorta; LA, left atrium; LAVV, left atrioventricular valve; LV, left ventricle; PA, pulmonary artery; RA, right atrium; RAVV, right atrioventricular valve; RV, right ventricle.

occasionally the plane of separation between the right atrial appendage and the left atrial chamber or appendage.

- Atrioventricular canal
 - Subxiphoid, apical, and parasternal views by 2- and 3D imaging to display the AV valves with particular attention to:
 - Stenosis and/or regurgitation;
 - Straddling chordae tendineae and leaflet tissue (Figures 25.11 and 25.17; Videos 25.5 and 25.6);
 - Other congenital anomalies of the mitral valve, such as a parachute deformity, short chordae, or supramitral ring (Figure 25.18; Video 25.7);
 - Criss-cross AV valves characterized by nearly perpendicular valve plane-to-ventricular apex axes associated with perpendicular AV valve planes (Figure 25.12; Video 25.8);
 - AV valve annular diameters.
- Ventricular morphology and size
 - Ventricular morphology is discussed in Chapters 3 and 4, and the methodology to measure ventricular volume and mass is discussed in Chapter 5.
- VSD location and size
 - Margins of subaortic, subpulmonary, and doubly-committed VSDs
 - Inferior margin – usually the crest of the muscular septum between the limbs of septal band;
 - Postero-inferior margin – usually the area of fibrous continuity between the tricuspid and mitral valves (when the defect is confluent with the membranous septum) or the muscular ventriculoinfundibular fold in continuity with posterior limb of the septal band;
 - Antero-superior margin – usually the adjacent semilunar valve or subarterial conus.
 - Subxiphoid, apical, and parasternal sweeps to delineate the location, extent, and boundaries of the VSD and its spatial relationship to great arteries (Figures 25.1, 25.3, 25.4, 25.5; Videos 25.9–25.12)
 - Subxiphoid short-axis sweeps to distinguish a subaortic VSD from a subpulmonary VSD in D-malposition (rightward aorta); if the VSD is seen before the conal septum during sweep from right to left, then it is likely a subaortic

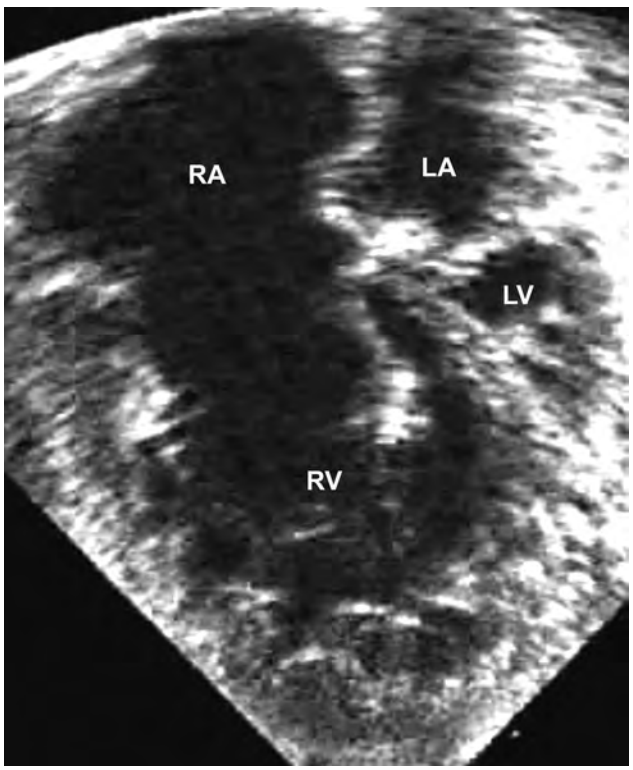


Figure 25.18 DORV with MS and LV hypoplasia in an apical 4-chamber view. LA, left atrium; LV, left ventricle; RA, right atrium; RV, right ventricle.

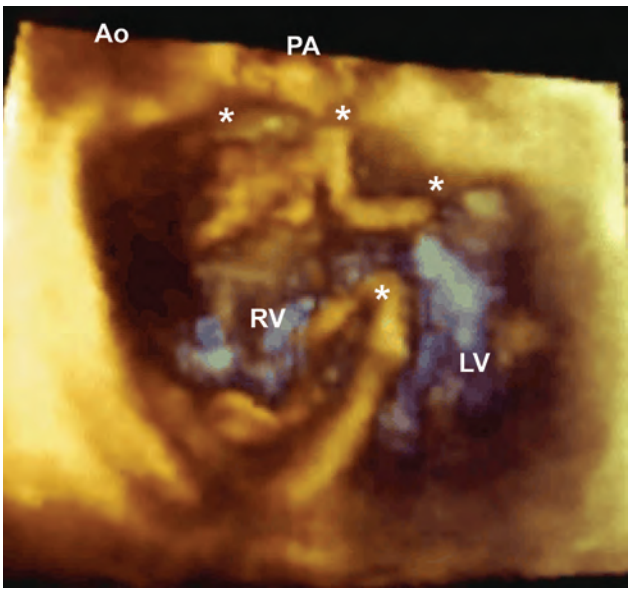


Figure 25.19 DORV with a subpulmonary VSD and tricuspid valve attachments to the conal septum and around the VSD (represented by asterisks) in a 3D apical view. Ao, aorta; LV, left ventricle; PA, pulmonary artery; RV, right ventricle.

VSD; if the VSD is seen after the conal septum, then it is likely a subpulmonary VSD;
 - Subxiphoid, apical, and parasternal views to evaluate the path from the VSD to the nearest semilunar valve and to exclude potential obstacles to a baffle (e.g., AV valve attachments) (Figure 25.19);
 - Subxiphoid, apical, and parasternal views to evaluate remote VSDs, which are usually located in the AV canal (inlet) septum or within the muscular septum. Exclude straddling AV valves and multiple muscular VSDs.
- Conal morphology and outflow tract obstruction
 - Subxiphoid, apical, and parasternal views to determine the type of conus (bilateral, subaortic, subpulmonary, or bilaterally absent) and presence and mechanism of outflow obstruction (Video 25.13). The subxiphoid view is particularly useful to determine muscular separation between the tricuspid valve and the nearest semilunar valve whereas the parasternal long-axis view is ideal for determining muscular separation between the mitral valve and the nearest semilunar valve.
 - Color-coded and spectral Doppler evaluation of outflow obstruction. When subaortic or subpulmonary stenosis is present, document the maximum instantaneous and mean gradients as well as the heart rate.
 - Subxiphoid, apical, and parasternal views to exclude tricuspid valve attachments to the conal septum.
 - Subxiphoid sweeps in DORV with a subpulmonary VSD to delineate the muscular tunnel produced by the conal septum (which is deviated to the right), a hypertrophied right ventriculoinfundibular fold, and the RV conal anterior free wall, all of which can contribute to subaortic stenosis (Figure 25.9a).
- Arterial roots
 - Subxiphoid long-axis sweeps with a transverse probe orientation (index mark at 3 pm) to assess the spatial relationship between the great arteries; the appearance of each great artery is noted during the sweep in order to determine their relative positions
 - Side-by-side great arteries will appear simultaneously during the sweep;
 - Great arteries in direct anterior-posterior relationship will not be visible at the same time but should appear separately in the same area during the sweep (Video 25.13);
 - Imaging of the spatial positions of the semilunar valves and arterial roots from a high left parasternal transverse plane (index mark at 3 pm).
- Coronary arteries
 - Parasternal short-axis views using a high frequency transducer to evaluate the origins and proximal courses of the coronary arteries. Imaging from other acoustic windows (e.g., parasternal long-axis, apical, and subxiphoid) is often helpful;
 - Coronary arteries should originate from the two aortic sinuses facing the pulmonary valve with bifurcation of the left main coronary artery into the anterior descending and circumflex coronary arteries;
 - Absent bifurcation of the left coronary artery can indicate abnormal origin of one or more of the branches, which may course anteriorly or posteriorly to the pulmonary root in order to reach its usual distribution site (such as inverted coronary arteries and origin of the anterior descending or circumflex coronary artery from the right coronary artery) (Figure 25.15; Video 25.14);
 - Rule out intramural coronary artery.
 - Subxiphoid long-axis and apical sweeps to display an abnormal posterior coronary artery (Figure 25.20).
- Aortic arch
 - Suprasternal long-axis views to evaluate aortic arch abnormalities such as coarctation and aortic arch interruption (Figure 25.9b). Measure the calibers of the distal transverse arch and isthmus. In interrupted aortic arch, measure the distance between the interrupted segments.
 - Suprasternal transverse view to determine the branching pattern of the aortic arch.
 - High left parasagittal view (also known as the ductal view), with the probe placed superiorly on the left chest in a vertical orientation, to display the aortic isthmus (at the level of the coarctation if present) and to evaluate a patent ductus arteriosus.
 - Doppler evaluation of the flow profile in the abdominal aorta from a subxiphoid parasagittal plane; a blunted upstroke and prolonged deceleration are suggestive of aortic coarctation.

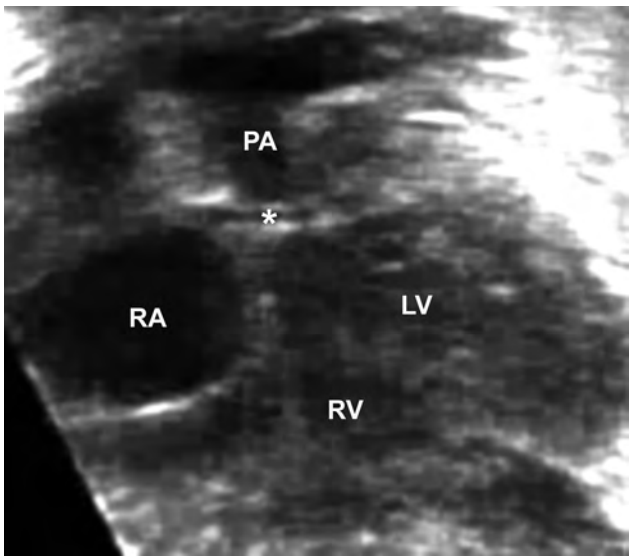


Figure 25.20 DORV with a subpulmonary VSD and a circumflex coronary artery (asterisk) which originates from the right coronary artery and courses behind the pulmonary trunk in a subxiphoid long-axis view. LV, left ventricle; PA, pulmonary artery; RA, right atrium; RV, right ventricle.

Postoperative examination

Surgical options for DORV include the following categories:

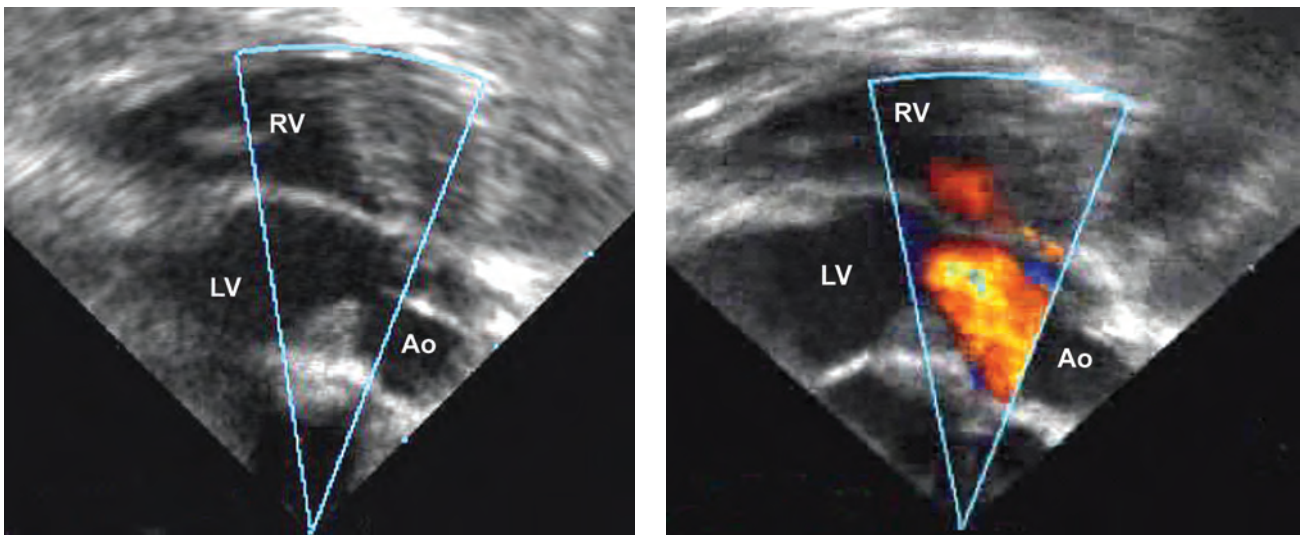
- Baffle from the LV to the aortic valve with or without resection of the conal septum while assuring unobstructed intracardiac flow from the RV to the pulmonary arteries.
- Baffle from the LV to the aortic valve with or without resection of the conal septum as well as placement of a homograft or conduit from the RV to the pulmonary artery (Rastelli procedure) or direct anastomosis of the pulmonary trunk to the RV free wall (*réparation à l'étage ventriculaire* or REV procedure).
- Baffle from the LV to the pulmonary valve and arterial switch operation.
- Aortic root translocation, baffle from the LV to the aortic valve, and placement of a homograft from the RV to the pulmonary artery [109].
- Single ventricle palliation.

The post-cardiopulmonary bypass TEE in patients undergoing biventricular repair should exclude the following postoperative problems:

- Residual VSD
 - Along the patch margins with the ventricular septum;
 - Along the patch margin at its attachment to the RV free wall (the so-called intramural VSD) [110];
 - In the muscular septum.
- Aortic outflow tract obstruction (Figure 25.21; Video 25.15), especially if the preoperative anatomy involved a small VSD, an elongated subaortic conus, or straddling AV valves.
- Pulmonary outflow tract obstruction.
- Pulmonary regurgitation, especially after a Rastelli or REV procedure.
- AV valve stenosis or regurgitation.
- Residual atrial septal defect or patent foramen ovale.
- Ventricular dysfunction.

The long-term sequelae of biventricular repair for DORV are as variable as the wide spectrum of preoperative morphologic and physiologic features. Some of the residual problems that may affect a patient's clinical status after biventricular repair include:

- Residual patch margin VSD.



(a) (b)

Figure 25.21 Postoperative TEE in a vertical (longitudinal) plane after biventricular repair of a DORV with a subaortic VSD, bilateral conus, and prominent muscle bundles in the subaortic conus now with **(a)** narrowing along the subaortic region and **(b)** turbulence in flow along this area by color flow mapping. Ao, aorta; LV, left ventricle; RV, right ventricle.

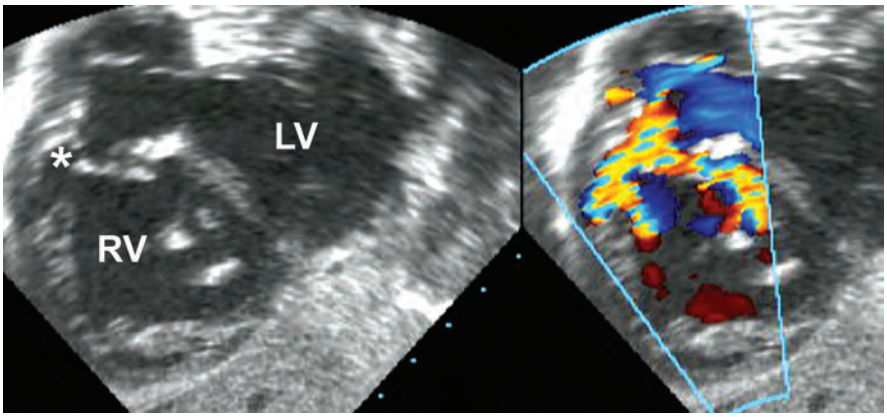


Figure 25.22 Subxiphoid short-axis view after biventricular repair of a DORV with a subaortic conus showing a small residual intramural VSD (asterisk) at the antero-superior patch margin where it is attached to the RV anterior free wall below the AoV. LV, left ventricle; RV, right ventricle.

- Intramural VSD (Figure 25.22; Video 25.16) [110]
 - Located at the margin between the patch and RV free wall, often just below the aortic valve;
 - Not always recognized because of its unusual location;
 - Not always present in the early postoperative period until associated RV hypertrophy regresses; can increase in size over time.
- Subaortic stenosis, particularly in patients who had a remote VSD or those whose VSD required enlargement (Video 25.17) [12,13].
- Neo-aortic valve regurgitation, supravalvar aortic stenosis, or neo-aortic root dilation after arterial switch operation.
- Aortic arch obstruction after coarctation repair or aortic arch reconstruction.
- Subvalvar pulmonary stenosis.
- Pulmonary stenosis, due to obstruction along the homograft or conduit after a Rastelli procedure or at the anastomosis of the pulmonary trunk to the RV in a REV procedure.
- Pulmonary regurgitation associated with a transannular RV outflow tract patch, pulmonary valvotomy, or homograft valve.
- Supravalvar pulmonary stenosis or branch pulmonary artery obstruction after arterial switch operation.
- Mitral or tricuspid valve regurgitation or stenosis in patients after AV canal defect repair.
- Ventricular dysfunction.

Some of these issues may be relevant for DORV patients requiring single ventricle palliation, but the long-term follow-up for this group of patients is discussed in other sections of this book.

Prenatal assessment

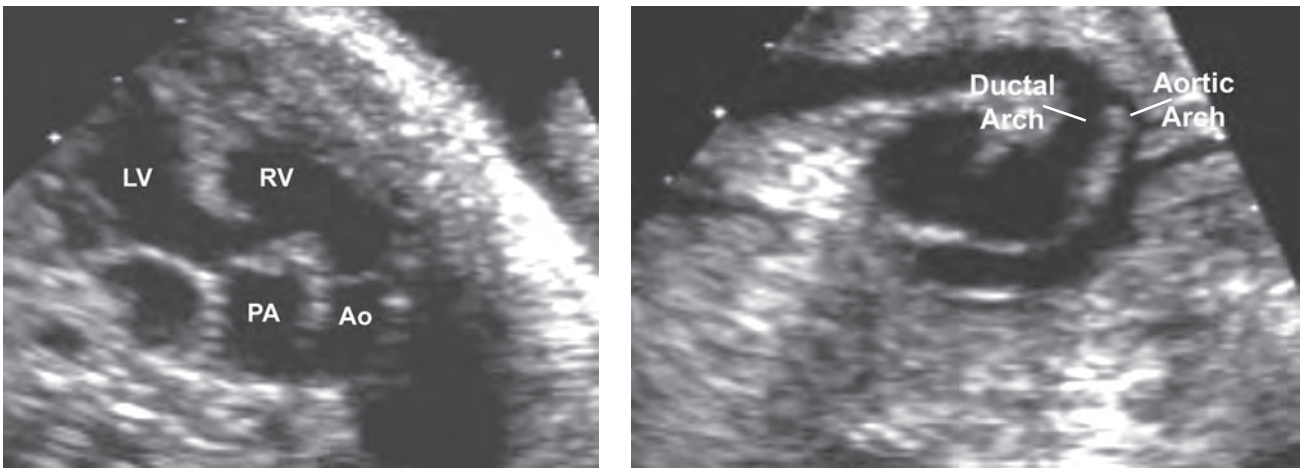
Similar to the postnatal data presented in the Baltimore-Washington Infant Study [34], DORV is the 12th most frequent diagnosis in a combined series of fetal cardiac malformations reported by Allan and Sharland [111], representing 62/2136 fetuses with congenital heart disease. In studies evaluating fetal detection of cardiac malformations [112,113], the prenatal incidence of DORV (1/6727 in low-risk and 1/3246 in high-risk pregnancies) is higher than the reported postnatal rates discussed previously [29–33]. This discrepancy may relate to high intra-uterine and neonatal mortality rates [114], variable diagnostic criteria, and selection bias.

DORV is often missed on routine obstetric ultrasound screening because the 4-chamber view is usually normal. Occasionally a ventricular or great arterial size discrepancy triggers the need for a fetal echocardiogram, during which the diagnosis can be made (Figure 25.23; Video 25.18). As in the postnatal assessment of DORV, the fetal study should evaluate the VSD, conal morphology, outflow tract obstruction, spatial relationship of the great arteries, anomalies of the aortic arch, and associated malformations. Pulmonary outflow tract obstruction in the fetus may not be associated with a significant pressure gradient by Doppler, but color flow mapping may reveal reversal of normal flow in the ductus arteriosus (from the aorta to the pulmonary arteries). Similarly, significant subaortic stenosis may be associated with reversal of flow in the aortic arch.

Prenatal diagnosis of DORV does not appear to affect outcome when compared to postnatally diagnosed patients [115]. However, when a DORV is detected in utero, counseling should include discussion of the anatomic and functional findings, treatment options, mortality and morbidity statistics, and neurodevelopmental outcomes data. It is also important to recognize that the fetal echocardiogram may not provide all the morphologic information needed to choose the appropriate surgical intervention. Amniocentesis should be recommended given the high frequency of chromosomal abnormalities associated with DORV [34].

Imaging of the adult

Although most adults with DORV have undergone surgical intervention, few patients survive to adulthood without intervention. Examples include patients with pulmonary stenosis and optimal balance between systemic and pulmonary blood flow and those without pulmonary stenosis and pulmonary vascular obstructive disease. Another small group of adult patients are those who underwent a palliative systemic-to-pulmonary artery shunt procedure in early childhood but no subsequent repair. Transthoracic echocardiographic evaluation is challenging



(a) (b)

Figure 25.23 Fetal echocardiogram of a DORV with a subpulmonary VSD showing **(a)** the parallel great arteries originating from the RV, and **(b)** the small aortic arch inserting onto the ductal arch suggestive of aortic coarctation. Ao, aorta; LV, left ventricle; PA, pulmonary artery; RV, right ventricle. Source: Courtesy of Dr. Jack Rychik, Children's Hospital of Philadelphia.

in adults with repaired or palliated DORV because most do not have good subxiphoid windows, and parasternal views are limited in the setting of postoperative scarring and highly reflective structures such as calcified valves, patches, and conduits. Although assessment of AV valve and LV function can usually be accomplished in apical and parasternal views, evaluation of complex baffle pathways in terms of residual outflow tract obstruction and intracardiac shunt can be difficult. Frequently, TEE, CMR, or cardiac catheterization is necessary to obtain adequate anatomic and physiologic data. CMR is a particularly useful adjunct to echocardiography in adolescent and adult patients with palliated DORV because this modality is not invasive, does not expose patients to ionizing radiation and its associated risk of cancer, and is capable of providing comprehensive morphologic and hemodynamic information irrespective of body size [116]. Computed tomography is a noninvasive alternative to CMR in patients with pacemakers or implanted defibrillators, though this modality provides little functional information.

Double-outlet left ventricle

Definition

Double-outlet left ventricle (DOLV) is a rare type of ventriculo-arterial alignment defined as complete or nearly complete origin of both great arteries from the LV. Similar to DORV, the Congenital Heart Surgery Nomenclature and Database Committee of the Society of Thoracic Surgeons has defined DOLV as "a type of ventriculo-arterial connection in which both great arteries arise entirely or predominantly from the morphologic LV" [117].

Historical perspective

Early reports suggested that DOLV is an embryologic improbability [118] or even an impossibility [119]. In 1967, Sakakibara et al. described the first DOLV patient undergoing surgical repair [120]. In 1970, Paul et al. published a report of an autopsy-proven case of DOLV with intact ventricular septum and bilaterally deficient conus [121]. Since the publication of these first cases over 40 years ago, over 200 cases of DOLV have been reported.

Incidence

DOLV is such a rare anomaly that all of the previously discussed studies reporting the incidence rates of congenital heart disease do not include DOLV in their analyses [29–33]. Wilkinson suggests that DOLV probably accounts for only 5% of all biventricular hearts with double-outlet connections, corresponding to an incidence of 1 in 200,000 births [75]. Among the 58,832 cases of congenital cardiac malformations diagnosed at Boston Children's Hospital from 1988 to 2002, only 3 patients had DOLV [35,88].

Etiology

Similar to DORV, the etiology of DOLV is unknown but likely relates to several mechanisms. Paul et al. suggested that DOLV results from deficient conal growth beneath both semilunar valves (rather than the normal deficient conal growth beneath only the aortic valve) [121]. Anderson et al., in their description of a case of DOLV in 1974, countered that errors in differential conal absorption or regression, rather than differential conal growth, provided a better explanation for the development of a DOLV [122]. Van Praagh et al., based on a study of 33 heart specimens with DOLV, speculated that a deficient subpulmonary conus associated with abnormal rotation of the outflow tract results in failure of normal alignment between the pulmonary valve and the RV [24]. Manner et al. used a chick embryo model to conclude that DOLV resulted not from errors in conal growth or absorption but from a malalignment

between the conal septum and the posterior wall of the RV outflow tract, isolating the proximal part of the RV conus from the great arteries [123]. They noted that the primordial conus and the primordial truncus arteriosus originate from different cardiogenic fields and that disruption in the normal development of the conal or proximal cushions may be the cause for this anterior malposition of the posterior RV conal wall.

Morphology and classification

Several classification schemes of DOLV have been proposed utilizing morphologic features that characterize the defect, determine the pathophysiology, and provide a rationale for surgical intervention [124,125]. Almost 75% of cases have two well-developed ventricles [125], and most are amenable to biventricular repair. A recent report of nearly 50 years of experience with DOLV at the Hospital for Sick Children in Toronto reveals that 13/19 patients had RV hypoplasia and 9/19 underwent single ventricle palliation [126]. Associated anomalies that preclude a biventricular outcome include tricuspid atresia and unbalanced common AV canal defect. Similar to DORV, the approach to the evaluation of DOLV includes:

- segmental anatomy;
- VSD location and size and its relationship to the great arteries;
- conal morphology;
- spatial relationship of the great arteries;
- ventricular hypoplasia;
- associated lesions (such as AV valve anomalies and outflow tract obstruction).

Segmental anatomy

In an analysis of 109 DOLV cases by Van Praagh et al. [125], patients with two well-developed ventricles presented with several distinct segmental patterns:

- DOLV with {S,D,D} segmental anatomy, visceral and atrial situs solitus, ventricular D-loop, a rightward aortic valve, and a subaortic VSD was the most common anatomic type with a frequency of 49%. In this group (n = 35), outflow tract obstruction occurred along the subpulmonary region (similar to TOF) in 83% and along the subaortic region in 11%; 6% had no outflow tract obstruction.
- DOLV {S,D,D} was associated with a subpulmonary VSD in 10.1% and with a doubly committed VSD in 6.4%.
- DOLV {S,D,L} with visceral and atrial situs solitus, ventricular D-loop, a leftward aortic valve, a subaortic VSD, and pulmonary stenosis occurred in 16.5%.
- DOLV {S,L,L} with visceral and atrial situs solitus, ventricular L-loop, and a leftward aortic valve occurred in 3.7%.
- DOLV {I,L,L} or {I,L,D} with visceral and atrial situs inversus, ventricular L-loop, and either leftward or rightward position of the aortic valve occurred in 2.8%. DOLV {I,D,D} with visceral and atrial situs inversus, ventricular D-loop, and a rightward aortic valve occurred in 1.8%.

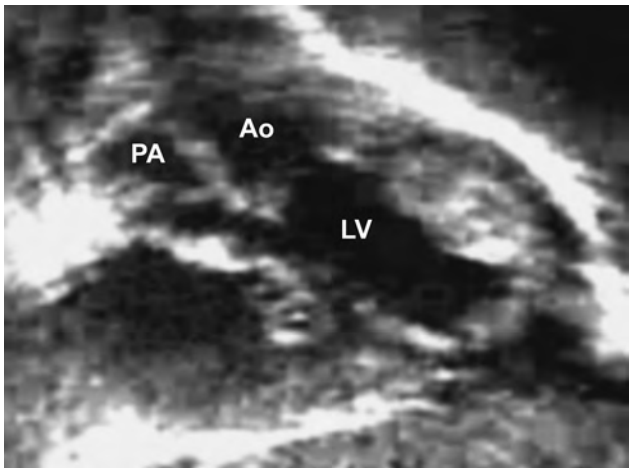


Figure 25.24 DOLV with a subaortic VSD in a subxiphoid long-axis view. Ao, aorta; LV, left ventricle; RV, right ventricle.

VSD location and size

The following types of VSD morphology have been reported in DOLV [124,125]:

- subaortic (70–75%) (Figure 25.24; Video 25.19);
- subpulmonary (15–17%);
- doubly committed (6–9%);
- noncommitted or remote (2%);
- intact ventricular septum (1–4%).

Interestingly, the study from the Hospital for Sick Children in Toronto revealed that up to 32% of their DOLV cases had an intact ventricular septum [126]. Similar to DORV, the subaortic, subpulmonary, and doubly committed VSDs are located between the limbs of septal band. The defect may be contiguous with the tricuspid valve as it extends into the membranous septum, or it may be separated from the tricuspid valve by muscular tissue. Cases with a doubly committed VSD are often difficult to distinguish from DORV, prompting some to label this diagnosis "double-outlet both ventricles" [127].

Conal morphology

Among 33 DOLV specimens described by Van Praagh et al. in another report [24]:

- 16 (48%) had a subpulmonary conus only (Figure 25.24; Video 25.19);
- 9 (27%) had a subaortic conus only;
- 4 (12%) had bilateral conus;
- 4 (12%) had bilaterally deficient conus.

Great artery relationship

The spatial relationships of the great arteries are variable [85]. In more than half of DOLV cases, the aortic valve is to the right and posterior, side-by-side, or anterior to the pulmonary valve. Approximately 40% have a leftward aortic valve (Figure 25.24; Video 25.19), and the aortic valve is directly anterior in another 8%.

Associated lesions

Among patients with biventricular hearts and a subaortic VSD, subvalvar and/or valvar pulmonary stenosis occurs in 90% (Figure 25.24; Video 25.19) [125]. Aortic outflow tract obstruction occurs frequently in cases with a subpulmonary VSD, often accompanied by coarctation or aortic arch interruption. A hypoplastic ventricle occurs in 27% in this series, though this number is higher in a clinical series that included patients undergoing single ventricle palliation [126]. Most hypoplastic ventricles are associated with a tricuspid valve anomaly (such as atresia, severe hypoplasia, or Ebstein malformation), whereas others are associated with mitral atresia, double-inlet LV, and heterotaxy syndrome.

Pathophysiology

The primary determinants of the pathophysiology in DOLV patients include VSD location and size (including its relationship to the semilunar valves), conal morphology, conal septum orientation, outflow tract obstruction, ventricular hypoplasia, AV valve anomalies, and segmental anatomy. In the absence of significant outflow tract obstruction, a patient with DOLV {S,D,D} and a subaortic VSD will present with symptoms of a large VSD. Cyanosis may result from significant pulmonary outflow tract obstruction or from streaming of blood from the RV to the aorta in the setting of a subaortic VSD, as was seen in 47% of the patients in the Toronto series [126]. Patients with aortic outflow tract obstruction and significant coarctation or arch interruption may present in critical condition requiring persistent flow through the ductus arteriosus.

Imaging

The techniques for preoperative, intraoperative, and postoperative imaging are similar to those outlined for DORV in the first section of this chapter. In addition, the long-term issues are also similar, and these need to be addressed using follow-up echocardiograms and/or other adjunct imaging modalities. Because of the rarity of this defect, the few reports regarding surgical repair have generally included the following options [128,129]:

- VSD closure and placement of a valved conduit from the RV to the pulmonary arteries.
- VSD closure with translocation of the pulmonary root to the RV.
- Intraventricular baffling of the RV to the pulmonary artery with or without VSD enlargement.
- Single ventricle palliation.

Videos

To access the videos for this chapter, please go to www.lai-echo.com.

Video 25.1 DORV with pulmonary atresia. Apical view of a DORV with membranous pulmonary atresia.

Video 25.2 DORV with subaortic VSD and pulmonary stenosis. Subxiphoid long-axis view showing a DORV with bilateral conus and subpulmonary stenosis secondary to leftward anterior deviation of the conal septum.

Video 25.3 Preoperative TEE of a DORV with a subaortic VSD. Preoperative TEE in horizontal (transverse) and vertical (longitudinal) planes of a DORV with a subaortic VSD and prominent muscle bundles within the subaortic conus.

Video 25.4 DORV with leftward juxtaposition of the atrial appendages. Apical view of a DORV with leftward juxtaposition of the atrial appendages.

Video 25.5 DORV with a straddling mitral valve. Subxiphoid short-axis view of a DORV with a straddling mitral valve.

Video 25.6 DORV with bilateral straddling AV valves. Modified subxiphoid short-axis view of a DORV with straddling of both AV valves across the remote VSD.

Video 25.7 DORV with mitral stenosis and LV hypoplasia. Apical view of a DORV with mitral stenosis and LV hypoplasia.

Video 25.8 DORV with criss-cross AV valves. Subxiphoid long-axis and short-axis sweeps of a DORV with criss-cross AV valves and superior-inferior ventricles where the tricuspid is oriented in a right–left direction towards the superior RV and the mitral valve is oriented in a postero–anterior direction towards the inferior LV.

Video 25.9 DORV with a subaortic VSD. Subxiphoid short-axis view showing DORV with a subaortic VSD and pulmonary stenosis.

Video 25.10 DORV with a subpulmonary VSD. Subxiphoid long-axis view of a DORV with a subpulmonary VSD and a rightward anterior aorta.

Video 25.11 DORV with a doubly committed VSD and pulmonary stenosis. Subxiphoid short-axis and parasternal short-axis views of a DORV with a doubly committed VSD, absent conal septum, and pulmonary stenosis.

Video 25.12 DORV with a remote VSD. Apical and modified subxiphoid long-axis views of a DORV with a complete AV canal defect.

Video 25.13 Great artery relationships in DORV. Subxiphoid long-axis sweeps showing two cases: the first case shows bilateral conus with side-by-side great artery relationship, and the second case shows a DORV in dextrocardia with ventricular inversion {S,L,L} where the aorta is almost directly anterior to the smaller pulmonary artery.

Video 25.14 DORV with dual supply to the anterior descending coronary artery. Parasternal short-axis view of a DORV with a subaortic VSD, pulmonary stenosis, and dual supply to the anterior descending coronary artery such that the conal branch supplying this coronary artery crosses in front of the RV outflow tract and may interfere with surgical repair of the pulmonary stenosis.

Video 25.15 Postoperative TEE of a DORV with a subaortic VSD after biventricular repair. Postoperative TEE in modified vertical

(longitudinal) planes showing persistence of the muscle bundles in the subaortic region and some turbulence in flow suggestive of residual subaortic stenosis.

Video 25.16 Residual intramural VSD after biventricular repair of a DORV with a subaortic VSD. Subxiphoid short-axis view with color depicting two small residual VSDs after biventricular repair of a DORV with a subaortic VSD; one of the VSDs is an intramural VSD and is located anteriorly at the attachment of the VSD baffle patch to the anterior RV free wall below the aortic valve.

Video 25.17 Residual subaortic stenosis after biventricular repair of a DORV with a subaortic VSD. Parasternal long-axis, subxiphoid short-axis, and apical views with color mapping as well as a real-time 3-dimensional apical view of a DORV with a subaortic VSD after biventricular repair depicting a narrow subaortic region secondary to some fibrosis associated with the VSD patch and prominent subaortic conal free wall muscle.

Video 25.18 Fetal echocardiogram showing a DORV with a subpulmonary VSD, parallel orientation of the great arteries as they exit the RV, and a hypoplastic aortic arch which inserts onto the ductal arch suggestive of aortic coarctation. Source: Courtesy of Dr. Jack Rychik, Children's Hospital of Philadelphia.

Video 25.19 Subxiphoid long-axis view of an unusual DOLV with a subpulmonary conus, absent or deficient subaortic conus, a subaortic VSD, pulmonary stenosis, an anterior and slightly leftward aorta, and {S,D,L} segmental anatomy.

References

1 Van Praagh R. What is the Taussig–Bing malformation? *Circulation* 1968;**28**:445–449.
2 Shinebourne EA, Macartney FJ, Anderson RH. Sequential chamber localization–logical approach to diagnosis in congenital heart disease. *Br Heart J* 1976;**38**:327–340.
3 Wilcox BR, Ho SY, Macartney FJ, et al. Surgical anatomy of double-outlet right ventricle with situs solitus and atrioventricular concordance. *J Thorac Cardiovasc Surg* 1981;**82**:405–417.
4 Edwards WD. Double-outlet right ventricle and tetralogy of Fallot. Two distinct but not mutually exclusive entities. *J Thorac Cardiovasc Surg* 1981;**82**:418–422.
5 Van Praagh S, Davidoff A, Chin A, et al. Double-outlet right ventricle: anatomic types and developmental implications based on a study of 101 autopsied cases. *Coeur* 1982;**13**:389–440.
6 Neufeld HN, Dushane JW, Wood EH, et al. Origin of both great vessels from the right ventricle. I. Without pulmonary stenosis. *Circulation* 1961;**23**:399–412.
7 Neufeld HN, Dushane JW, Edwards JE. Origin of both great vessels from the right ventricle. II. With pulmonary stenosis. *Circulation* 1961;**23**:603–612.
8 Neufeld HN, Lucas RV, Jr., Lester RG, et al. Origin of both great vessels from the right ventricle without pulmonary stenosis. *Br Heart J* 1962;**24**:393–408.
9 McGoon D. Origin of both great vessels from the right ventricle. *Surg Clin N Am* 1961;**41**:1113–1120.
10 Lecompte Y, Batisse A, Di Carlo D. Double-outlet right ventricle: a surgical synthesis. *Adv Cardiac Surg* 1993;**4**:109–136.
11 Sakata R, Lecompte Y, Batisse A, et al. Anatomic repair of anomalies of ventriculoarterial connection associated with ventricular septal defect. I. Criteria of surgical decision. *J Thorac Cardiovasc Surg* 1988;**95**:90–95.
12 Aoki M, Forbess JM, Jonas RA, et al. Result of biventricular repair for double-outlet right ventricle. *J Thorac Cardiovasc Surg* 1994;**107**:338–349; discussion 49–50.
13 Belli E, Serraf A, Lacour-Gayet F, et al. Biventricular repair for double-outlet right ventricle. Results and long-term follow-up. *Circulation* 1998;**98**:II360–365; discussion II5–7.
14 Abernathy J. *Surgical and Physiological Essays, Part II*. London: James Evans, 1793, p. 162.
15 Peacock TB. *On Malformations of the Human Heart*. London: John Churchill and Sons, 1866, p. 32.
16 Vierordt H. Die angeborenen Herzkrankheiten. Nothnagel's Handbuch der speziellen Pathologie und Therapie, Wien, 1898, p. 244.
17 Spitzer A. Uber den Bauplan des normalen und missbildeten Herzens. Versuch einer phylogenetischen theorie. *Virchows Arch F Path Anat* 1923;**243**:81–272.
18 Taussig HB, Bing RJ. Complete transposition of the aorta and levoposition of the pulmonary artery. *Am Heart J* 1949;**37**:551–559.
19 Beuren A. Differential diagnosis of the Taussig–Bing heart from complete transposition of the great vessels with a posteriorly overriding pulmonary artery. *Circulation* 1960;**21**:1071–1087.
20 Witham AC. Double outlet right ventricle. A partial transposition complex. *Am Heart J* 1957;**53**:928–939.
21 Hallermann FJ, Kincaid OW, Ritter DG, Titus JL. Mitral-semilunar valve relationships in the angiography of cardiac malformations. *Radiology* 1970;**94**:63–68.
22 Baron MG. Radiologic notes in cardiology. Angiographic differentiation between tetralogy of Fallot and double-outlet right ventricle. Relationship of the mitral and aortic valves. *Circulation* 1971;**43**:451–455.
23 Sridaromont S, Ritter DG, Feldt RH, et al. Double-outlet right ventricle. Anatomic and angiocardiographic correlations. *Mayo Clin Proc* 1978;**53**:555–577.
24 Van Praagh R, Layton WM, Van Praagh S. The morphogenesis of normal and abnormal relationships between the great arteries and the ventricles: pathologic and experimental data. In: Van Praagh R, Takao A (eds.) *Etiology and Morphogenesis of Congenital Heart Disease*. Mt. Kisco, NY: Futura, 1980, pp. 271–316.
25 Lev M, Bharati S, Meng CC, et al. A concept of double-outlet right ventricle. *J Thorac Cardiovasc Surg* 1972;**64**:271–281.
26 Kirklin JW, Pacifico AD, Bargeron LM, Jr., Soto B. Cardiac repair in anatomically corrected malposition of the great arteries. *Circulation* 1973;**48**:153–159.
27 Howell CE, Ho SY, Anderson RH, Elliott MJ. Fibrous skeleton and ventricular outflow tracts in double-outlet right ventricle. *Ann Thorac Surg* 1991;**51**:394–400.
28 Walters HL, 3rd, Mavroudis C, Tchervenkov CI, et al. Congenital Heart Surgery Nomenclature and Database Project: double outlet right ventricle. *Ann Thorac Surg* 2000;**69**:S249–263.
29 Hoffman JI, Kaplan S. The incidence of congenital heart disease. *J Am Coll Cardiol* 2002;**39**:1890–1900.
30 Fyler DC, Bucklet LP, Hellenbrand WE, Cohn HE. Report of the New England Regional Infant Cardiac Program. *Pediatrics* 1980;**65**:375–461.

31 Ferencz C, Rubin JD, McCarter RJ, et al. Congenital heart disease: prevalence at livebirth. The Baltimore-Washington Infant Study. *Am J Epidemiol* 1985;**121**:31–36.

32 Grabitz RG, Joffres MR, Collins-Nakai RL. Congenital heart disease: incidence in the first year of life. The Alberta Heritage Pediatric Cardiology Program. *Am J Epidemiol* 1988;**128**:381–388.

33 Botto LD, Correa A, Erickson JD. Racial and temporal variations in the prevalence of heart defects. *Pediatrics* 2001;**107**:E32.

34 Perry LW, Neill CA, Ferencz C, et al. Infants with congenital heart disease: the cases. In: Ferencz C, Rubin JD, Loffredo CA, Magee CA (eds.) *Perspectives in Pediatric Cardiology, Vol. 4: Epidemiology of Congenital Heart Disease: The Baltimore-Washington Infant Study (1981–1989)*. Mt. Kisco, NY: Futura, 1993, pp. 33–62.

35 Triedman JK. Methodological issues for database development: trends. In: Keane JF, Lock JE, Fyler DC (eds.) *Nadas' Pediatric Cardiology*, 2nd edn. Philadelphia, PA: Saunders Elsevier, 2006, pp. 323–336.

36 Ferencz C, Correa-Villasenor A, Loffredo CA, Wilson PD. Malformations of the cardiac outflow tract. In: Ferencz C, Correa-Villasenor A, Loffredo CA, Wilson PD (eds.) *Perspectives in Pediatric Cardiology, Vol. 5: Genetic and Environmental Risk Factors of Major Cardiovascular Malformations: The Baltimore-Washington Infant Study (1981–1989)*. Armonk, NY: Futura, 1997, pp. 59–102.

37 Obler D, Juraszek AL, Smoot LB, Natowicz MR. Double outlet right ventricle: aetiologies and associations. *J Med Genet* 2008;**45**:481–497.

38 Vuillemin M, Pexieder T, Winking H. Pathogenesis of various forms of double outlet right ventricle in mouse fetal trisomy 13. *Int J Cardiol* 1991;**33**:281–304.

39 Van Praagh S, Truman T, Firpo A, et al. Cardiac malformations in trisomy-18: a study of 41 postmortem cases. *J Am Coll Cardiol* 1989;**13**:1586–1597.

40 Goldmuntz E, Clark BJ, Mitchell LE, et al. Frequency of 22q11 deletions in patients with conotruncal defects. *J Am Coll Cardiol* 1998;**32**:492–498.

41 Brannan CI, Perkins AS, Vogel KS, et al. Targeted disruption of the neurofibromatosis type-1 gene leads to developmental abnormalities in heart and various neural crest-derived tissues. *Genes Dev* 1994;**8**:1019–1029.

42 Epstein JA. Pax3, neural crest and cardiovascular development. *Trends Cardiovasc Med* 1996;**6**:255–260.

43 Gruber PJ, Kubalak SW, Pexieder T, et al. RXR alpha deficiency confers genetic susceptibility for aortic sac, conotruncal, atrioventricular cushion, and ventricular muscle defects in mice. *J Clin Invest* 1996;**98**:1332–1343.

44 Bradshaw L, Chaudhry B, Hildreth V, et al. Dual role for neural crest cells during outflow tract septation in the neural crest-deficient mutant Splotch(2H). *J Anat* 2009;**214**:245–257.

45 Goldmuntz E, Bamford R, Karkera JD, et al. CFC1 mutations in patients with transposition of the great arteries and double-outlet right ventricle. *Am J Hum Genet* 2002;**70**:776–780.

46 Franco D, Campione M. The role of Pitx2 during cardiac development. Linking left-right signaling and congenital heart diseases. *Trends Cardiovasc Med* 2003;**13**:157–163.

47 Benson DW, Silberbach GM, Kavanaugh-McHugh A, et al. Mutations in the cardiac transcription factor NKX2.5 affect diverse cardiac developmental pathways. *J Clin Invest* 1999;**104**:1567–1573.

48 McElhinney DB, Geiger E, Blinder J, et al. NKX2.5 mutations in patients with congenital heart disease. *J Am Coll Cardiol* 2003;**42**:1650–1655.

49 Pu WT, Ishiwata T, Juraszek AL, et al. GATA4 is a dosage-sensitive regulator of cardiac morphogenesis. *Dev Biol* 2004;**275**:235–244.

50 De Luca A, Sarkozy A, Ferese R, et al. New mutations in ZFPM2/FOG2 gene in tetralogy of Fallot and double outlet right ventricle. *Clin Genet* 2011;**80**:184–190.

51 Scherptong RW, Jongbloed MR, Wisse LJ, et al. Morphogenesis of outflow tract rotation during cardiac development: the pulmonary push concept. *Dev Dyn* 2012;**241**:1413–1422.

52 Bartram U, Molin DG, Wisse LJ, et al. Double-outlet right ventricle and overriding tricuspid valve reflect disturbances of looping, myocardialization, endocardial cushion differentiation, and apoptosis in TGF-beta(2)-knockout mice. *Circulation* 2001;**103**:2745–2752.

53 Gu H, Smith FC, Taffet SM, Delmar M. High incidence of cardiac malformations in connexin40-deficient mice. *Circ Res* 2003;**93**:201–206.

54 Yanagisawa H, Hammer RE, Richardson JA, et al. Disruption of ECE-1 and ECE-2 reveals a role for endothelin-converting enzyme-2 in murine cardiac development. *J Clin Invest* 2000;**105**:1373–1382.

55 Henderson DJ, Phillips HM. Outflow tract remodeling–a role for tissue polarity? In: Artman M, Benson DW, Srivastava D, Nakazawa M (eds.) *Cardiovascular Development and Congenital Malformations: Molecular and Genetic Mechanisms*. Malden, MA: Blackwell Futura, 2005, pp. 155–157.

56 Phillips HM, Murdoch JN, Chaudhry B, et al. Vangl2 acts via RhoA signaling to regulate polarized cell movements during development of the proximal outflow tract. *Circ Res* 2005;**96**:292–299.

57 Arteaga M, de la Cruz MV, Sanchez C, Diaz GF. Double-outlet right ventricle: experimental morphogenesis in the chick embryo heart. *Pediatr Cardiol* 1982;**3**:219–227.

58 Kirby ML, Turnage KL, 3rd, Hays BM. Characterization of conotruncal malformations following ablation of "cardiac" neural crest. *Anat Rec* 1985;**213**:87–93.

59 Ferencz C, Rubin JD, McCarter RJ, Clark EB. Maternal diabetes and cardiovascular malformations: predominance of double outlet right ventricle and truncus arteriosus. *Teratology* 1990;**41**:319–326.

60 Tararbit K, Houyel L, Bonnet D, et al. Risk of congenital heart defects associated with assisted reproductive technologies: a population-based evaluation. *Eur Heart J* 2011;**32**:500–508.

61 Zierler S, Rothman KJ. Congenital heart disease in relation to maternal use of Bendectin and other drugs in early pregnancy. *N Engl J Med* 1985;**313**:347–352.

62 Lammer EJ, Chen DT, Hoar RM, et al. Retinoic acid embryopathy. *N Engl J Med* 1985;**313**:837–841.

63 Park JM, Schmer V, Myers TL. Cardiovascular anomalies associated with prenatal exposure to theophylline. *South Med J* 1990;**83**:1487–1488.

64 Arey LB. The heart and circulation changes. In: *Developmental Anatomy: A Textbook and Laboratory Manual of Embryology*, Revised 7th edn. Philadelphia, PA: WB Saunders, 1974, pp. 375–395.

65 Moore KL. The circulatory system: the cardiovascular and lymphatic systems. In: *The Developing Human: Clinically Oriented*

Embryology, 3rd edn. Philadelphia, PA: WB Saunders, 1982, pp. 298–343.
66 Manner J. Cardiac looping in the chick embryo: a morphological review with special reference to terminological and biomechanical aspects of the looping process. *Anat Rec* 2000;**259**:248–262.
67 de la Cruz MV, Markwald RR, Krug EL, et al. Living morphogenesis of the ventricles and congenital pathology of their component parts. *Cardiol Young* 2001;**11**:588–600.
68 Moorman A, Webb S, Brown NA, et al. Development of the heart: (1) Formation of the cardiac chambers and arterial trunks. *Heart* 2003;**89**:806–814.
69 Anderson RH, Webb S, Brown NA, et al. Development of the heart: (2) Septation of the atriums and ventricles. *Heart* 2003;**89**: 949–958.
70 Anderson RH, Webb S, Brown NA, et al. Development of the heart: (3) Formation of the ventricular outflow tracts, arterial valves, and intrapericardial arterial trunks. *Heart* 2003;**89**:1110–1118.
71 van den Hoff MJ, Moorman AF, Ruijter JM, et al. Myocardialization of the cardiac outflow tract. *Dev Biol* 1999;**212**:477–490.
72 Zamora R, Moller JH, Edwards JE. Double outlet right ventricle: anatomic types and associated anomalies. *Chest* 1975;**68**:672–677.
73 Sridaromont S, Feldt RH, Ritter DG, et al. Double outlet right ventricle: hemodynamic and anatomic correlations. *Am J Cardiol* 1976;**38**:85–94.
74 Patrick DL, McGoon DC. An operation for double-outlet right ventricle with transposition of the great arteries. *J Cardiovasc Surg* 1968;**9**:537–542.
75 Wilkinson JL. Double outlet ventricle. In: Anderson RH, Baker EJ, Macartney FJ, et al. (eds.) *Paediatric Cardiology*, 2nd edn. London: Churchill Livingstone, 2002, pp. 1353–1381.
76 Takeuchi K, Del Nido PJ. Surgical management of double-outlet right ventricle with subaortic ventricular septal defect. *Semin Thorac Cardiovasc Surg Pediatr Card Surg Annu* 2000;**3**:34–42.
77 Sondheimer HM, Freedom RM, Olley PM. Double outlet right ventricle: clinical spectrum and prognosis. *Am J Cardiol* 1977;**39**:709–714.
78 Kirklin JW, Barratt-Boyes BG (eds.). Double-outlet right ventricle. In: *Cardiac Surgery*, 2nd edn. New York, NY: Churchill Livingston, 1993, pp. 1469–1500.
79 Kleinert S, Sano T, Weintraub RG, et al. Anatomic features and surgical strategies in double-outlet right ventricle. *Circulation* 1997;**96**:1233–1239.
80 Troise DE, Ranieri L, Arciprete PM. Surgical repair for double outlet right ventricle and intact ventricular septum. *Ann Thorac Surg* 2001;**71**:1018–1019.
81 Anderson RH, McCarthy K, Cook AC. Double outlet right ventricle. *Cardiol Young* 2001;**11**:329–344.
82 Van Praagh R, Perez-Trevino C, Reynolds JL, et al. Double outlet right ventricle {S,D,L} with subaortic ventricular septal defect and pulmonary stenosis. *Am J Cardiol* 1975;**35**:42–53.
83 Uemura H, Yagihara T, Kadohama T, et al. Repair of double outlet right ventricle with doubly-committed ventricular septal defect. *Cardiol Young* 2001;**11**:415–419.
84 Pasquini L, Sanders SP, Parness IA, et al. Conal anatomy in 119 patients with D-loop transposition of the great arteries and ventricular septal defect: an echocardiographic and pathologic study. *J Am Coll Cardiol* 1993;**21**:1712–1721.
85 Snider AR, Serwer GA, Ritter SB. Double outlet right ventricle. In: *Echocardiography in Pediatric Heart Disease*, 2nd edn. St. Louis, MO: Mosby, 1997, pp. 323–342.
86 Fujii Y, Kotani Y, Takagaki M, et al. The impact of the length between the top of the interventricular septum and the aortic valve on the indications for a biventricular repair in patients with a transposition of the great arteries or a double outlet right ventricle. *Interact Cardiovasc Thorac Surg* 2010;**10**:900–905; discussion 5.
87 Castaneda AR, Jonas RA, Mayer JE, Hanley FL. Double-outlet right ventricle. In: *Cardiac Surgery of the Neonate and Infant*. Philadelphia, PA: WB Saunders, 1994, pp. 445–459.
88 Keane JF, Fyler DC. Double-outlet right ventricle. In: Keane JF, Lock JE, Fyler DC (eds.) *Nadas' Pediatric Cardiology*, 2nd edn. Philadelphia, PA: Saunders Elsevier, 2006, pp. 735–741.
89 Comas JV, Mignosa C, Cochrane AD, et al. Taussig-Bing anomaly and arterial switch: aortic arch obstruction does not influence outcome. *Eur J Cardiothorac Surg* 1996;**10**:1114–1119.
90 Takeuchi K, McGowan FX, Jr., Moran AM, et al. Surgical outcome of double-outlet right ventricle with subpulmonary VSD. *Ann Thorac Surg* 2001;**71**:49–52; discussion 52–53.
91 Serraf A, Belli E, Lacour-Gayet F, et al. Biventricular repair for double-outlet right ventricle. *Semin Thorac Cardiovasc Surg Pediatr Card Surg Annu* 2000;**3**:43–56.
92 Fraisse A, del Nido PJ, Gaudart J, Geva T. Echocardiographic characteristics and outcome of straddling mitral valve. *J Am Coll Cardiol* 2001;**38**:819–826.
93 Serraf A, Nakamura T, Lacour-Gayet F, et al. Surgical approaches for double-outlet right ventricle or transposition of the great arteries associated with straddling atrioventricular valves. *J Thorac Cardiovasc Surg* 1996;**111**:527–535.
94 Aeba R, Katogi T, Takeuchi S, Kawada S. Surgical management of the straddling mitral valve in the biventricular heart. *Ann Thorac Surg* 2000;**69**:130–134.
95 Russo P, Danielson GK, Puga FJ, et al. Modified Fontan procedure for biventricular hearts with complex forms of double-outlet right ventricle. *Circulation* 1988;**78**:III20–25.
96 Delius RE, Rademecker MA, de Leval MR, et al. Is a high-risk biventricular repair always preferable to conversion to a single ventricle repair? *J Thorac Cardiovasc Surg* 1996;**112**:1561–1568; discussion 8–9.
97 Serraf A, Jonas RA, Burke RP, et al. Univentricular repair for complex double right ventricle and transposed great arteries. *Cardiol Young* 1997;**7**:207–214.
98 Lai WW, Ravishankar C, Gross RP, et al. Juxtaposition of the atrial appendages: a clinical series of 22 patients. *Pediatr Cardiol* 2001;**22**:121–127.
99 Van Praagh S. Cardiac malpositions and the heterotaxy syndromes. In: Keane JF, Lock JE, Fyler DC (eds.) *Nadas' Pediatric Cardiology*, 2nd edn. Philadelphia, PA: Saunders Elsevier, 2006, pp. 675–695.
100 Rose V, Izukawa T, Moes CA. Syndromes of asplenia and polysplenia. A review of cardiac and non-cardiac malformations in 60 cases withspecial reference to diagnosis and prognosis. *Br Heart J* 1975;**37**:840–852.
101 Rubino M, Van Praagh S, Kadoba K, et al. Systemic and pulmonary venous connections in visceral heterotaxy with asplenia. Diagnostic and surgical considerations based on seventy-two autopsied cases. *J Thorac Cardiovasc Surg* 1995;**110**:641–650.

102 Geva T, Van Praagh S, Sanders SP, et al. Straddling mitral valve with hypoplastic right ventricle, crisscross atrioventricular relations, double outlet right ventricle and dextrocardia: morphologic, diagnostic and surgical considerations. *J Am Coll Cardiol* 1991;**17**:1603–1612.

103 Uemura H, Yagihara T, Kawashima Y, et al. Coronary arterial anatomy in double-outlet right ventricle with subpulmonary VSD. *Ann Thorac Surg* 1995;**59**:591–597.

104 Lacour-Gayet F, Haun C, Ntalakoura K, et al. Biventricular repair of double outlet right ventricle with non-committed ventricular septal defect (VSD) by VSD rerouting to the pulmonary artery and arterial switch. *Eur J Cardiothorac Surg* 2002;**21**:1042–1048.

105 Gordillo L, Faye-Petersen O, de la Cruz MV, Soto B. Coronary arterial patterns in double-outlet right ventricle. *Am J Cardiol* 1993;**71**:1108–1110.

106 Tynan MJ, Becker AE, Macartney FJ, et al. Nomenclature and classification of congenital heart disease. *Br Heart J* 1979;**41**:544–553.

107 Smallhorn JF. Double-outlet right ventricle: an echocardiographic approach. *Semin Thorac Cardiovasc Surg Pediatr Card Surg Annu* 2000;**3**:20–33.

108 Sanders SP, Bierman FZ, Williams RG. Conotruncal malformations: diagnosis in infancy using subxiphoid 2-dimensional echocardiography. *Am J Cardiol* 1982;**50**:1361–1367.

109 Bautista-Hernandez V, Marx GR, Bacha EA, del Nido PJ. Aortic root translocation plus arterial switch for transposition of the great arteries with left ventricular outflow tract obstruction: intermediate-term results. *J Am Coll Cardiol* 2007;**49**:485–490.

110 Preminger TJ, Sanders SP, van der Velde ME, et al. "Intramural" residual interventricular defects after repair of conotruncal malformations. *Circulation* 1994;**89**:236–242.

111 Allan L, Hornberger LK, Sharland G. Appendix A.2. In: Allan L, Hornberger LK, Sharland G (eds.) *Textbook of Fetal Cardiology*. London: Greenwich Medical Media, 2000, pp. 581.

112 Hafner E, Scholler J, Schuchter K, et al. Detection of fetal congenital heart disease in a low-risk population. *Prenatal Diagn* 1998;**18**:808–815.

113 Buskens E, Stewart PA, Hess J, et al. Efficacy of fetal echocardiography and yield by risk category. *Obstet Gynecol* 1996;**87**:423–428.

114 Kim N, Friedberg MK, Silverman NH. Diagnosis and prognosis of fetuses with double outlet right ventricle. *Prenatal Diagn* 2006;**26**:740–745.

115 Lagopoulos ME, Manlhiot C, McCrindle BW, et al. Impact of prenatal diagnosis and anatomical subtype on outcome in double outlet right ventricle. *Am Heart J* 2010;**160**:692–700.

116 Dorfman AL, Geva T. Magnetic resonance imaging evaluation of congenital heart disease: conotruncal anomalies. *J Cardiovasc Magn Reson* 2006;**8**:645–659.

117 Tchervenkov CI, Walters HL, 3rd, Chu VF. Congenital Heart Surgery Nomenclature and Database Project: double outlet left ventricle. *Ann Thorac Surg* 2000;**69**:S264–269.

118 Grant RP. The morphogenesis of transposition of the great vessels. *Circulation* 1962;**26**:819–840.

119 Van Mierop LHS, Wiglesworth FW. Pathogenesis of transposition complexes: II. Anomalies due to faulty transfer of the posterior great artery. *Am J Cardiol* 1963;**12**:226–232.

120 Sakakibara S, Arai T, Hashimoto A, Nogi M. Both great vessels arising from the left ventricle. *Bull Heart Inst Jpn* 1967:66–86.

121 Paul MH, Muster AJ, Sinha SN, et al. Double-outlet left ventricle with an intact ventricular septum: clinical and autopsy diagnosis and developmental implications. *Circulation* 1970;**41**:129–139.

122 Anderson R, Galbraith R, Gibson R, Miller G. Double outlet left ventricle. *Br Heart J* 1974;**36**:554–558.

123 Manner J, Seidl W, Steding G. Embryological observations on the formal pathogenesis of double-outlet left ventricle with a right-ventricular infundibulum. *Thorac Cardiovasc Surgeon* 1997;**45**:172–177.

124 Bharati S, Lev M, Stewart R, et al. The morphologic spectrum of double outlet left ventricle and its surgical significance. *Circulation* 1978;**58**:558–565.

125 Van Praagh R, Weinberg PM, Srebro JP. Double outlet left ventricle. In: Adams FH, Emmanoulides GC, Riemenschneider TA (eds.) *Moss's Heart Disease in Infants, Children, and Adolescents*, 4th edn. Baltimore, MD: Williams & Wilkins, 1989, pp. 461–485.

126 Imai-Compton C, Elmi M, Manlhiot C, et al. Characteristics and outcomes of double outlet left ventricle. *Congenit Heart Dis* 2010;**5**:532–536.

127 Kirklin JW, Barratt-Boyes BG (eds.). Double outlet left ventricle. In: *Cardiac Surgery*, 2nd edn. New York, NY: Churchill Livingston, 1993, pp. 1501–1509.

128 Freedom RM, Yoo S, Williams WG. Double-outlet ventricle. In: Freedom RM, You S, Makailian H, Williams WG (eds.) *The Natural and Modified History of Congenital Heart Disease*. New York, NY: Futura, 2004, pp. 370–380.

129 DeLeon SY, Ow EP, Chiemmongkoltip P, et al. Alternatives in biventricular repair of double-outlet left ventricle. *Ann Thorac Surg* 1995;**60**:213–216.

CHAPTER 26

Physiologically "Corrected" Transposition of the Great Arteries

Erwin Oechslin
Toronto Congenital Cardiac Centre for Adults, University Health Network/Toronto General Hospital, Toronto, ON, Canada

Definition

Physiologically "corrected" transposition of the great arteries is an uncommon congenital heart defect characterized by discordant atrioventricular (AV) and ventriculo-arterial (VA) connections (double discordance) (Figure 26.1). The systemic veins join the right atrium (RA), which is connected by a mitral valve to the subpulmonary left ventricle (LV). The left atrium (LA) receives pulmonary venous blood from the pulmonary veins and is connected by a tricuspid valve to the subaortic right ventricle (RV). The VA connections are also discordant wherein the aorta arises from the morphologic RV and the pulmonary artery from the morphologic LV. Discordant AV and VA connections can occur in isolation; however, associated congenital cardiac anomalies are common.

Incidence

Physiologically "corrected" transposition of the great arteries (TGA) is an uncommon congenital heart defect – too infrequent to deserve separate mention in a large study reporting the incidence of congenital heart defects [1]. It comprises less than 0.5% of all forms of congenital heart defects. Several sources have reported incidences ranging from 2 to 7 per 100,000 live births [2]. In a study of more than 800,000 children born between 1980 and 1990, the prospective Bohemia Survival Study yielded a prevalence of 3 per 100,000 live births; this accounted for 0.4% of all congenital heart defects in this study [3].

Developmental considerations and etiology

The etiology of physiologically "corrected" TGA is unknown. The primitive heart tube with the sinus venosus and the atrium at one end and the conotruncus at the other end does not loop to the right (D-loop) as in the normal heart with the usual arrangement of the atria (cardiac situs solitus); instead, it loops to the left (L-loop). This leftward looping brings the future RV to the left and the LV to the right. This abnormal looping is associated with discordant connections between the ventricles and great arteries.

Both genetic and environmental factors have been implicated in the etiology of this congenital heart defect [4–6]. The recurrence of TGA (concordant AV connection/discordant VA connection, D-loop TGA) and physiologically "corrected" TGA (discordant AV and VA connections, L-loop TGA) in the same family suggests a pathogenetic link between these two anatomically different malformations [5].

Morphology and classification

Common nomenclature

Rokitansky first described a cardiac malformation with inappropriate connections between the atria and ventricles and between the ventricles and great arteries, and noted the physiologic correction of this congenital heart defect [7]. Physiologically "corrected" TGA describes discordant AV and VA connections (i.e., double discordance): the atria connect to the inappropriate ventricles, which then connect to the inappropriate great arteries. Usual arrangement of the atria (atrial situs solitus) and L-loop transposition of the great arteries are present in the majority of patients (Figure 26.1a). Throughout this chapter, LV and RV refer to the morphologic left and right ventricles, respectively, regardless of their spatial position or topology.

A mirror-image arrangement of the atria (atrial situs inversus) is present in approximately 5% of patients with physiologically "corrected" TGA. Importantly, patients with a mirror-image arrangement of the atria have a rightward looping (D-ventricular loop) and not leftward looping of the primitive heart tube (Figure 26.1b).

Echocardiography in Pediatric and Congenital Heart Disease: From Fetus to Adult, Second Edition. Edited by Wyman W. Lai, Luc L. Mertens, Meryl S. Cohen and Tal Geva.
© 2016 John Wiley & Sons, Ltd. Published 2016 by John Wiley & Sons, Ltd.
Companion website: www.lai-echo.com

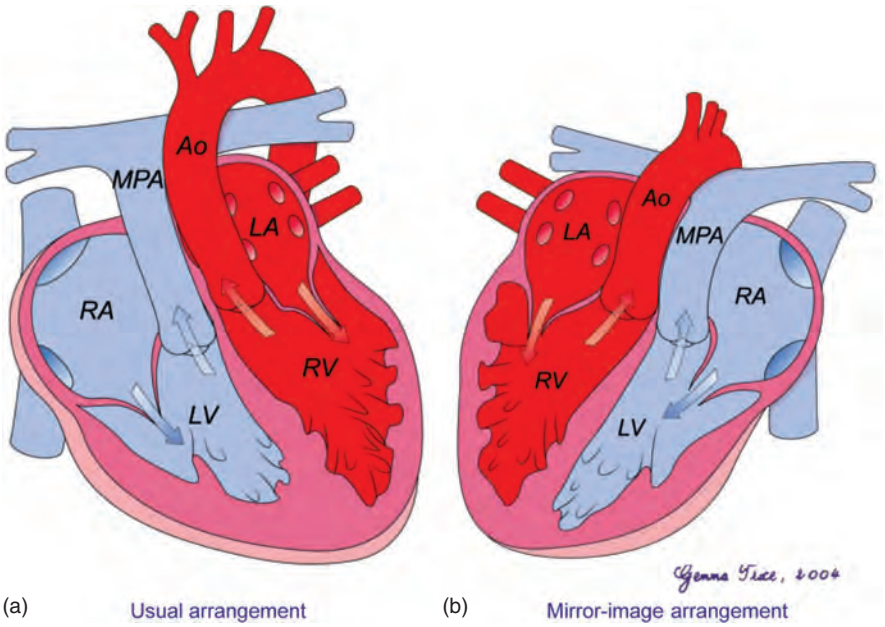


Figure 26.1 Diagram showing physiologically "corrected" transposition of the great arteries or discordant atrioventricular and ventriculo-arterial connections (double discordance). **(a)** Usual arrangement of the atria (atrial situs solitus) with **L**-ventricular loop and **L**-transposition of the great arteries. **(b)** Mirror-image arrangement of the atria (atrial situs inversus) with **D**-ventricular loop and **D**-transposition of the great arteries. Ao, aorta; LA, left atrium; LV, left ventricle; MPA, main pulmonary artery; RA, right atrium; RV, right ventricle.

There are a number of synonyms for physiologically "corrected" TGA, including double discordance, discordant AV and VA connections, congenitally corrected TGA, and L-TGA. It should be noted that the phrase L-TGA is a nonspecific term as the "L" may relate to the ventricular loop or to the spatial position of the great arteries [8]. Although in the majority of patients with physiologically "corrected" TGA in atrial situs solitus the aorta is positioned leftward and anterior to the pulmonary artery (L-malposition), there is wide variability in the spatial relationships between the great arteries in this condition. A minority of patients with physiologically "corrected" TGA in atrial situs solitus have an aorta that is anterior and to the right (D-malposition) of the pulmonary trunk [9]. Furthermore, leftward (L)-malposition of the aorta relative to the pulmonary trunk can be encountered in a variety of other complex congenital cardiac anomalies such as TGA with AV concordance and VA discordance, double-outlet right ventricle, crossed AV connections, univentricular hearts, and others [10,11]. Hence, L-TGA and physiologically "corrected" TGA are not the same and the term L-TGA is better avoided; *L-loop TGA* is more specific, where the L-loop refers to the ventricular looping [12].

Discordant AV and VA connections cannot be considered *anatomically* corrected because the RV is the subaortic ventricle supporting the systemic circulation and the LV is the subpulmonary ventricle giving rise to the pulmonary trunk [13,14]. The two discordant connections cancel each other with respect to the circulation; thus, *physiologically* "corrected" TGA is a more appropriate term indicating physiologic, but not anatomic, correction. However, the frequent association of other intracardiac defects makes physiologically "corrected" TGA far from being truly physiologically corrected. Other terms, such as ventricular inversion, dextroversion or L-TGA, were used in the past to describe combined abnormal segmental connections or discordant AV and VA connections. These terms are inappropriate and their use as a substitute for physiologically "corrected" TGA should be discouraged [9].

Discordant AV connections can only exist in the presence of discordant connection of the right and left atria to their inappropriate ventricles. Therefore, isomerism of the atrial appendages, atresia of an AV valve or univentricular atrioventricular connections (e.g., double-inlet left ventricle) exclude a discordant atrioventricular connection.

Van Praagh's classification

Van Praagh describes three types of segmental sets: the viscera and atria, the ventricular loop, and the great arteries (see Chapter 3 for details) [15,16]. The viscero-atrial situs can be solitus (S), inversus (I) or ambiguous (A), as shown {S,–,–} or {I,–,–}. The ventricular arrangement is either a D-loop ventricle (D) or an L-loop (L) ventricle, as described in {–,D,–} or {–,L,–}. The great arterial situs is solitus in normally related great arteries {–,–,S} or inversus {–,–,I}. When the spatial position of the great arteries is abnormal, the term "malposition" is applied: the right-sided aorta is symbolized as (D), the left-sided aorta as (L), and an anterior aorta as (A). According to the Van Praagh classification, physiologically "corrected" TGA is called {S,L,L} TGA in the presence of usual arrangement of the atria, or {I,D,D} TGA in the presence of a mirror-image arrangement of the atria. Other rare segmental combinations such as {S,L,D} and {I,D,L} TGA have been described.

Anatomy

There may be usual arrangement of the viscera and atria (situs solitus) or a mirror-image arrangement (situs inversus);

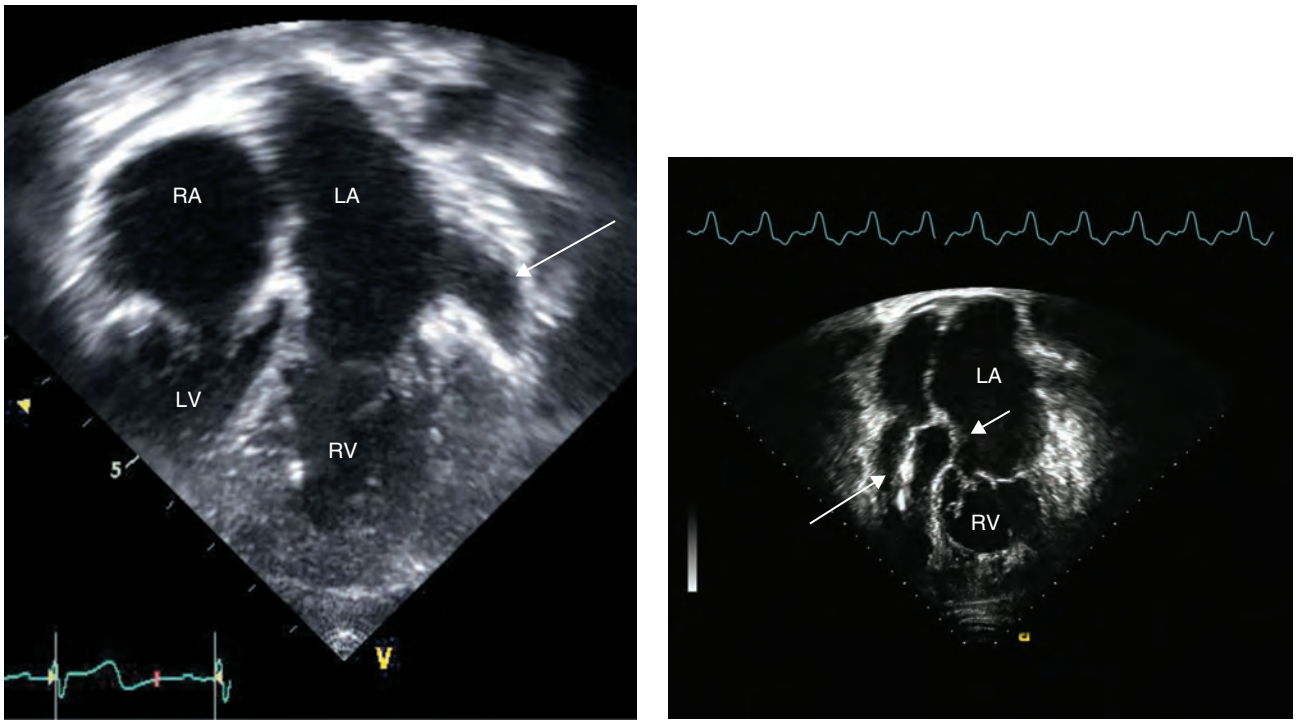


Figure 26.2 Usual arrangement of the atria (atrial situs solitus). **(a)** Apical 4-chamber view in a 9-year-old boy showing discordant atrioventricular (AV) connection. Note the characteristic morphology of the left atrial appendage (arrow) identifying the location of the morphologic left atrium, which lies on the left of the morphologic right atrium. The inflow of the morphologic right ventricle lies on the left of the morphologic left ventricle, which indicates L-ventricular loop. Source: Dr. Luc Mertens, Toronto, ON, Canada. Reproduced with permission of Dr. Mertens. **(b)** Usual arrangement of the atria (atrial situs solitus) with discordant atrioventricular connection in a 22-year-old man. Note eccentric hypertrophy and moderately reduced systolic function of the left-sided right ventricle and the presence of a pacemaker lead (arrow) in the right-sided left ventricle. Note the Ebstein-like malformation of the left-sided dysplastic tricuspid valve (small arrow) with malcoaptation of the leaflets due to prolapse of the anterior leaflet. LA, left atrium; LV, left ventricle; RA, right atrium; RV, right ventricle.

the cardiac orientation can be levocardia, dextrocardia, or mesocardia.

Usual arrangement of the atria (atrial situs solitus)

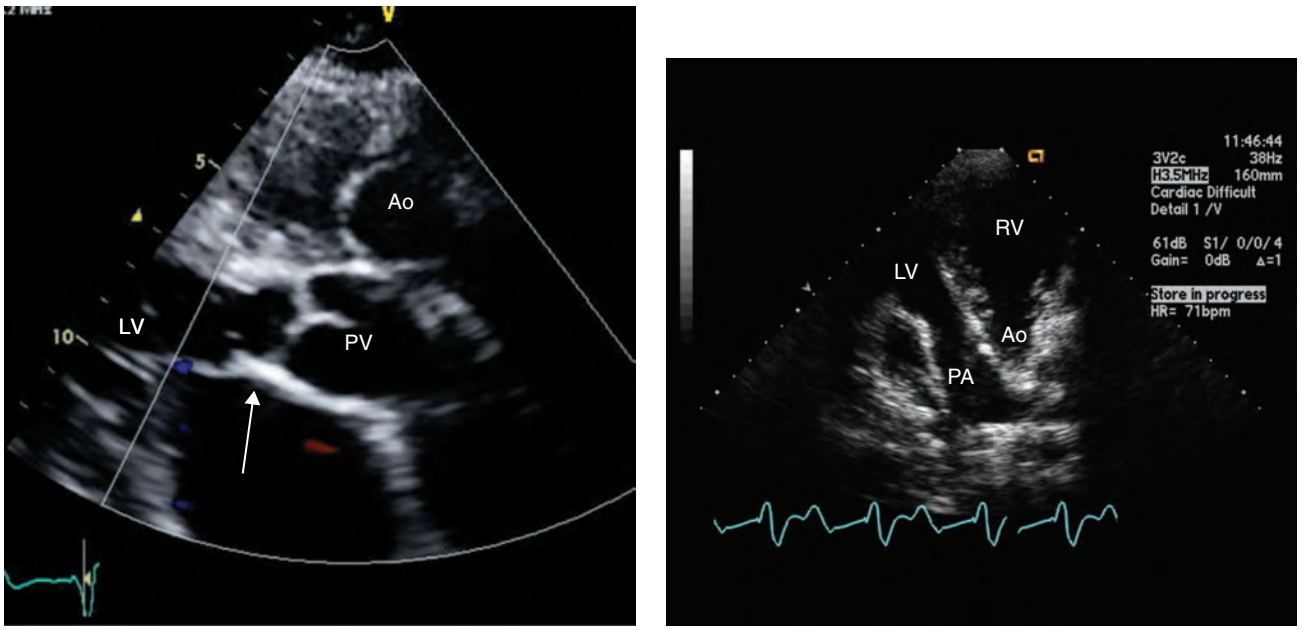
The majority (~95% of the patients) present with usual arrangement of the atria; that is, the right atrium lies to the right of the left atrium (Figure 26.1a). The right-sided superior vena cava and inferior vena cava connect to the right-sided right atrium, which empties through the mitral valve into the LV, which gives rise to a right-sided pulmonary trunk. The LV is L-looped and lies to the right of the RV (Figure 26.2a,b; Video 26.1). The mitral valve has two papillary muscles and is in fibrous continuity with the cusps of the pulmonary valve (Figure 26.3a,b; Video 26.2). The pulmonary veins are connected to the left-sided left atrium, which empties through the tricuspid valve into the subaortic L-looped RV, which lies to the left of the LV (Figure 26.2a,b; Video 26.1). In contrast to the normal heart, the left ventricular (pulmonary) and right ventricular (aortic) outflow tracts are in parallel, and the position of the ascending aorta is left and anterior (L-malposition) in relation to the pulmonary trunk (Figures 26.3b and 26.4; Videos 26.2 and 26.3).

Mirror-image arrangement of the atria (atrial situs inversus)

Approximately 5% of patients with physiologically "corrected" TGA present with a mirror-image arrangement of the atria (Figure 26.1b): the left-sided superior and inferior caval veins empty into the right atrium, which lies to the left of the left atrium (left-sided RA), and the pulmonary veins empty into the right-sided left atrium. As mentioned earlier, there are discordant AV and VA connections. However, the subaortic RV is not inverted and lies to the right of the subpulmonary LV (Figures 26.5 and 26.6; Video 26.4). The aorta is right-sided and anteriorly located in relation to the pulmonary trunk (D-malposition of the great arteries). The subxiphoid long-axis and apical 4-chamber windows are the best views to differentiate between D- and L-ventricular loops: the inflow of the RV lies to the *right* of the LV in the presence of *D-ventricular loop* (Figures 26.5 and 26.6; Video 26.4), whereas it lies to the *left* in the presence of *L-ventricular loop* (Figure 26.2a,b; Video 26.1).

Cardiac orientation

The axis between the base of the heart and the apex can point to the left (levocardia), to the right (dextrocardia) or it can be in



(a) (b)

Figure 26.3 Imaging the parallel position of the great arteries: the aorta is anterior and the pulmonary artery is posterior. **(a)** Parasternal long-axis view in a 41-year-old man without LV outflow tract obstruction. The arterial outflow tracts are parallel to each other. The AV valve is in fibrous continuity (long arrow) with the pulmonary valve. **(b)** Apical position of the transducer with an anterior sweep to image the parallel position of the great arteries in an 18-year-old man. Note the leftward position of the aorta in relation to the pulmonary artery with its bifurcation. Ao, aorta; LV, left ventricle; PA, pulmonary artery; PV, pulmonary valve; RV, right ventricle.

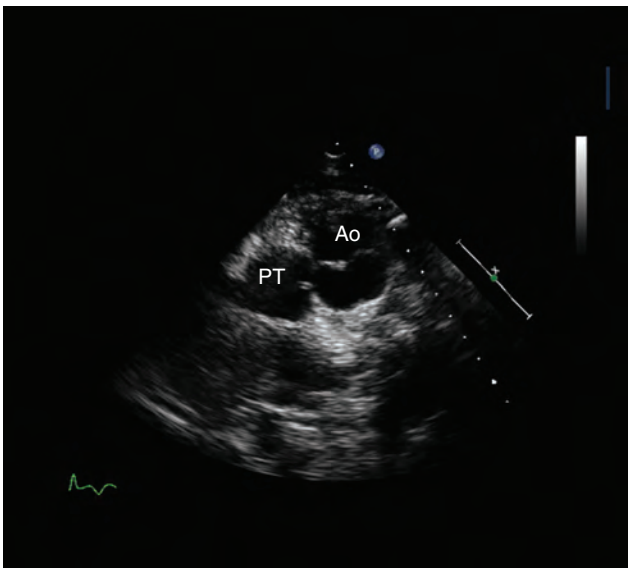


Figure 26.4 Parasternal short-axis view in a 25-year-old man showing the spatial relation of the aorta to the pulmonary trunk: the aorta (Ao) is anterior and leftward relative to the pulmonary trunk (PT) (L-malposition) in atrial situs solitus.

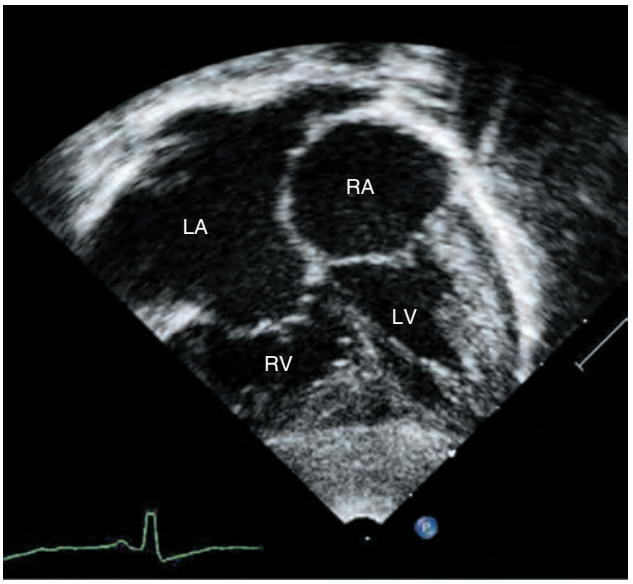


Figure 26.5 Mirror-image arrangement of the atria (situs inversus). Apical 4-chamber view in an 8-month-old boy with situs inversus and dextrocardia. The right atrium is to the left of the left atrium and the right ventricle is right-sided. LA, left atrium; LV, left ventricle; RA, right atrium; RV, right ventricle. Source: Dr. Luc Mertens, Toronto, ON, Canada. Reproduced with permission of Dr. Mertens.

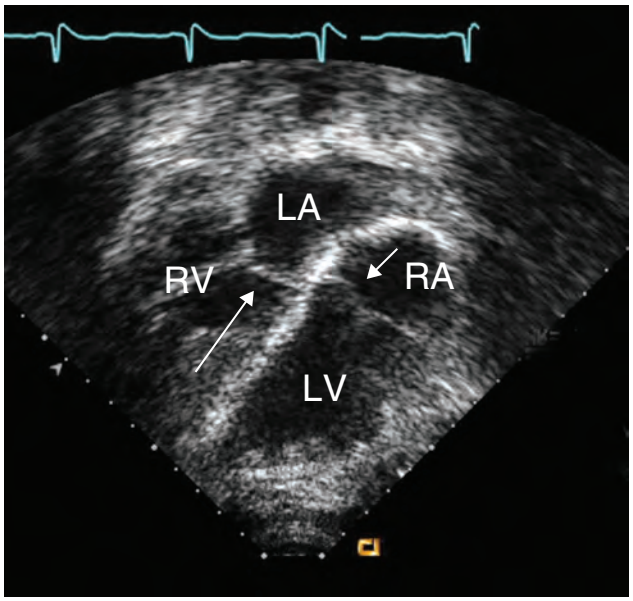


Figure 26.6 Subxiphoid view in a 26-year-old man with situs inversus and dextrocardia. The short arrow indicates the mitral valve; the long arrow denotes the tricuspid valve. LA, left atrium; LV, left ventricle; RA, right atrium; RV, right ventricle.

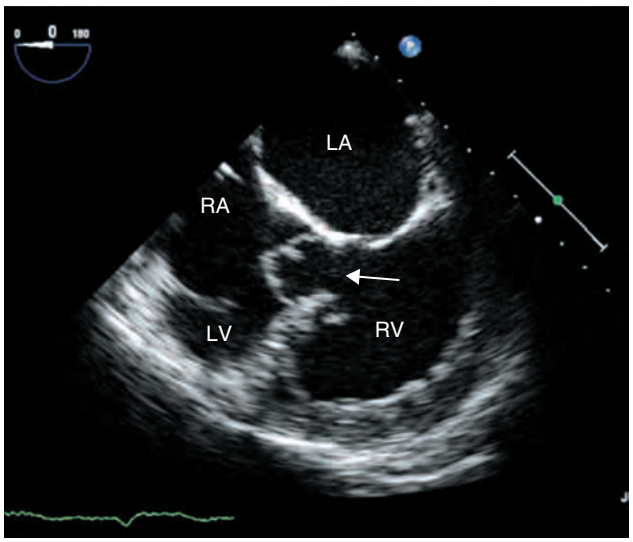


Figure 26.7 Transesophageal echocardiogram in a 41-year-old-man with atrial situs solitus and septal malalignment. The gap between the atrial and ventricular septum is filled with a large, redundant membranous septum (arrow). LA, left atrium; LV, left ventricle; RA, right atrium; RV, right ventricle.

the midline (mesocardia). Approximately 75% of patients with physiologically "corrected" TGA present with levocardia.

Ventricular topology

Ventricular topology describes the internal organization of the ventricles and the spatial relationship of one ventricle to the other; it can be right- or left-handed. The abnormal looping (L-loop) results in a left-hand pattern [12,16]: the left hand must be used to place the palm of the hand against the RV septal surface in such a way that the thumb points to the inlet and the fingers point to the outlet of the RV (in contrast to a D-loop or a normal heart where the right hand must be used; see Chapter 3 for details).

Atrioventricular valves

The mitral valve has two papillary muscles without insertion to the interventricular septum. However, one-fourth of the patients may present with abnormalities of the mitral valve [17]. The tricuspid valve, which is left-sided in usual arrangement of the atria, is frequently dysplastic (see "Associated lesions" later).

Septal malalignment

Malalignment between the atrial septum and the inlet part of the ventricular septum is a characteristic morphologic feature of discordant AV connection in patients with usual arrangement of the atria, and affects the position of the conduction system [18]. The AV septal malalignment results in a gap into which the subpulmonary LV outflow tract is wedged. This space is filled with a large membranous septum in patients without a ventricular septal defect (Figure 26.7; Video 26.5). In the presence of a ventricular septal defect (VSD), the septal malalignment has implications for the size and extent of the VSD, the severity of LV (pulmonary) outflow tract obstruction, and the position of the conduction system [19,20]. The degree of septal malalignment is less pronounced in hearts with a small or atretic pulmonary trunk or in patients with mirror-image arrangement of the atria than in those with severe left ventricular outflow tract obstruction or usual arrangement of the atria [20].

Coronary arteries

Coronary artery anatomy and distribution have gained more attention because of the potential of a double switch procedure in the surgical management of physiologically "corrected" TGA. The coronary arteries reflect ventricular topology. In patients with usual arrangement of the atria, there is a mirror-image distribution of the coronary arteries, which follow the corresponding ventricles [21,22]: the epicardial distribution of the right-sided coronary artery is that of a morphologically left coronary artery (circumflex and anterior descending coronary arteries); the left-sided coronary artery follows the left AV groove and supplies the RV [21,23–26]. Although the origin and course of the coronary artery show frequent variations [21,23,26,27], the origin and proximal branching pattern in physiologically "corrected" TGA appear to be more consistent than in D-loop TGA (concordant AV and discordant VA connection, D-transposition) [26].

Coronary sinus

Knowledge of the anatomy of the coronary sinus and coronary venous system is important as cardiac resynchronization therapy with implantation of pacemaker leads into the coronary sinus is increasingly considered a therapeutic option. In normal

anatomy, the coronary sinus courses posterior-inferior to the left atrium and connects to the right atrium [28,29]. In physiologically "corrected" TGA, the coronary sinus is expected to travel between the left atrium and the subaortic right ventricle (which it predominantly drains) [30,31]. The coronary sinus can usually be imaged by echocardiography in the pediatric population. However, alternative imaging modalities are required for preprocedural planning in this population to image the anatomy of the coronary venous system and its variations [29,30].

Associated lesions

Physiologically "corrected" TGA occurs in isolation (rarely) or can be complicated by associated congenital heart defects. More than 90% of patients have associated defects [32–35] and the following triad of associated malformations is common: (i) VSD; (ii) LV (pulmonary) outflow tract obstruction; and (iii) anomalies of the tricuspid valve. Any combination of these anomalies can coexist.

Ventricular septal defect

Ventricular septal defects are common, can occupy any position, and are described in the same way as in the normal heart and in D-loop TGA. The incidence ranges between 60% and 80% [22,32]. The VSD is frequently nonrestrictive and is the result of a malalignment between the atrial and ventricular septa. Membranous VSD is most common and is in fibrous continuity with the pulmonary and tricuspid valves. If the defect is located in the inlet (AV canal) septum, the offsetting of the attachment of both AV valves is lost; the septal and moderator bands allow identification of the RV (Figure 26.8).

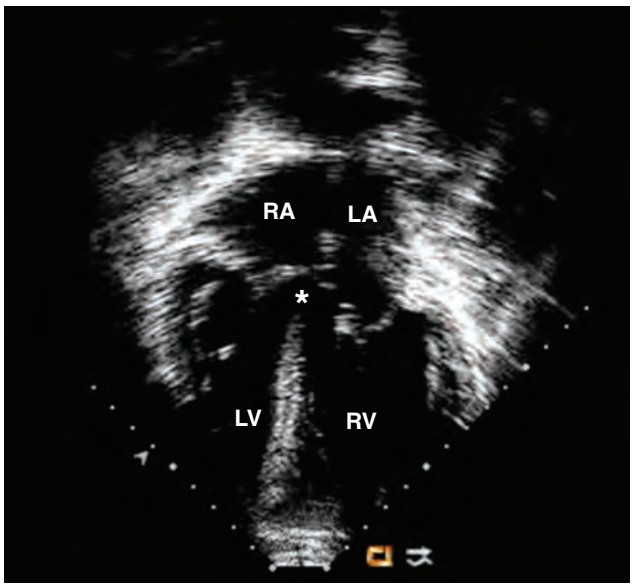


Figure 26.8 Apical 4-chamber view in a 27-year-old man with situs solitus showing a nonrestrictive ventricular septal defect extending from the outlet to the inlet septum (*). Note near-loss of the offsetting of the attachment of both AV valves. LA, left atrium; LV, left ventricle; RA, right atrium; RV, right ventricle.

Left ventricular outflow tract obstruction

Left ventricular outflow tract (subpulmonary) obstruction is observed in up to 50% of patients with usual arrangement of the atria and occurs at the subvalvar and/or valvar levels (Figure 26.9; Videos 26.6–26.9). Isolated valvar pulmonary stenosis is rare whereas combined subvalvar and valvar obstruction is common [32,33]. The subvalvar stenosis can be muscular or caused by a fibrous shelf, fibrous tissue tags originating from any of the valves near the outflow tract, or a fibrous ridge from the membranous septum. LV outflow tract obstruction can also result from a large aneurysm of the membranous septum in the presence of septal malalignment or from systolic anterior motion (SAM) of the mitral valve leaflets due to abnormal geometry of the LV. LV outflow tract obstruction is commonly associated with a VSD, and tricuspid valve abnormalities are frequently associated as well.

Abnormalities of the tricuspid valve

Abnormalities of the tricuspid valve are very common and occur in up to 90% in autopsy series; however, they are less frequently identified in the clinical setting [22,32,34–36]. The dysplastic tricuspid valve can occur with or without apical displacement of both the septal and posterior leaflets as in patients with concordant AV connection. Ebstein-like malformation of the tricuspid valve in physiologically "corrected" TGA is different from the classic Ebstein anomaly in patients with concordant connection (Figures 26.10 and 26.11; Videos 26.10–26.13). In contrast to a classic Ebstein malformation, in discordant AV connections there is usually no rotational displacement of septal and posterior leaflets, neither is the inlet portion of the RV myocardium dilated and thinned. The anterior tricuspid leaflet is usually not large and does not have a "sail-like" appearance, the adherence of the septal and posterior leaflets is limited, and the atrialized portion of the RV inflow is usually small. However, classic Ebstein anomaly of the left-sided tricuspid valve and RV inflow can infrequently be seen in physiologically "corrected" TGA. Other abnormalities of the left-sided tricuspid valve include hypoplasia and double orifice.

Other rare associated anomalies of the AV valves include straddling or overriding, anomalies that can significantly complicate surgical treatment [37].

Other associated anomalies

Aortic arch abnormalities (e.g., aortic atresia, coarctation, interrupted aortic arch) can be observed in hearts with discordant segmental alignments [38,39]. Subaortic obstruction should be suspected in these cases.

Pathophysiology

The discordant AV and VA connections cancel each other with respect to the circulation. In visceral-atrial situs solitus, deoxygenated blood returning to the RA reaches the pulmonary circulation through the right-sided LV, whereas the

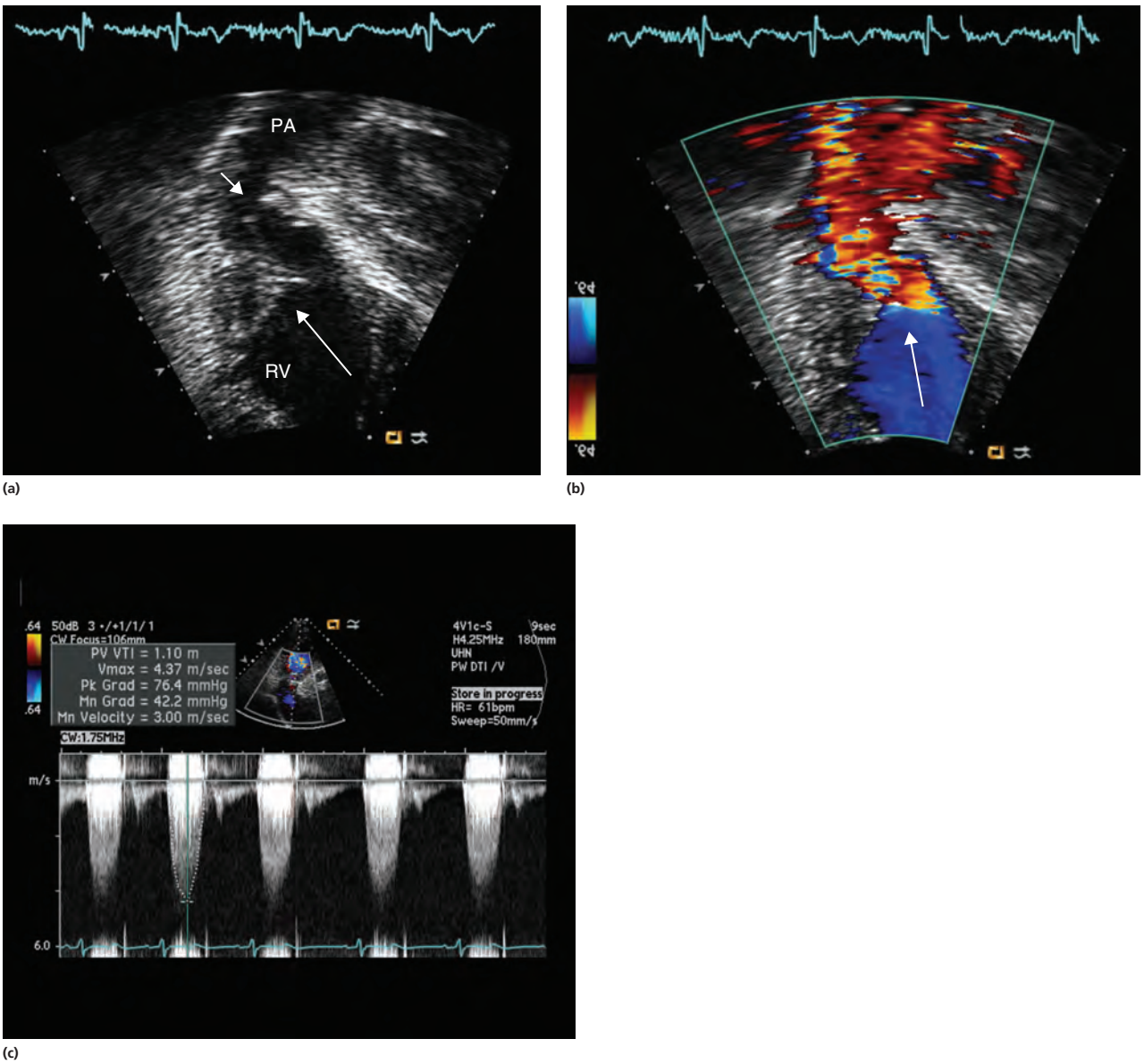


Figure 26.9 Modified apical 5-chamber view in a 27-year-old man showing subvalvar and valvar pulmonary stenosis. Same patient as in Figure 26.8. **(a)** Two-dimensional image showing fibrous tissue in the left ventricular outflow (long arrow). The small arrow indicates the thickened pulmonary valve with doming cusps. RV, right ventricule, PA, pulmonary artery. **(b)** Color Doppler flow mapping demonstrates flow acceleration (arrow) at the level of the subpulmonary left ventricular outflow (subpulmonic membrane). **(c)** Continuous-wave Doppler reveals a peak/mean systolic gradient of 76/42 mmHg across the LV (pulmonary) outflow tract.

oxygenated pulmonary venous blood returns to the LA and then, through the left-sided RV, reaches the systemic circulation (Figure 26.1a). In visceral-atrial situs inversus, deoxygenated blood returning to the left-sided RA reaches the pulmonary circulation through the left-sided LV whereas the oxygenated pulmonary venous blood returns to the right-sided LA and then, through the right-sided RV, reaches the systemic circulation (Figure 26.1b). Thus, in the absence of associated anomalies, patients with physiologically "corrected" TGA are acyanotic and the congenital heart defect can remain undiagnosed. Both complexity and severity of the associated intracardiac defects determine the pathophysiology, and the natural and "unnatural" history [32,40–47]. The subaortic RV supporting the systemic circulation remodels and develops concentric and eccentric hypertrophy, respectively. As the myocardium is aging, the subaortic RV may fail, with subsequent dilation and development of hemodynamically relevant tricuspid regurgitation due to malcoaptation of the tricuspid valve leaflets secondary to annular dilation and abnormal geometry of the RV (Figures 26.10 and 26.11; Videos 26.10–26.13) [32,40,42,44–46].

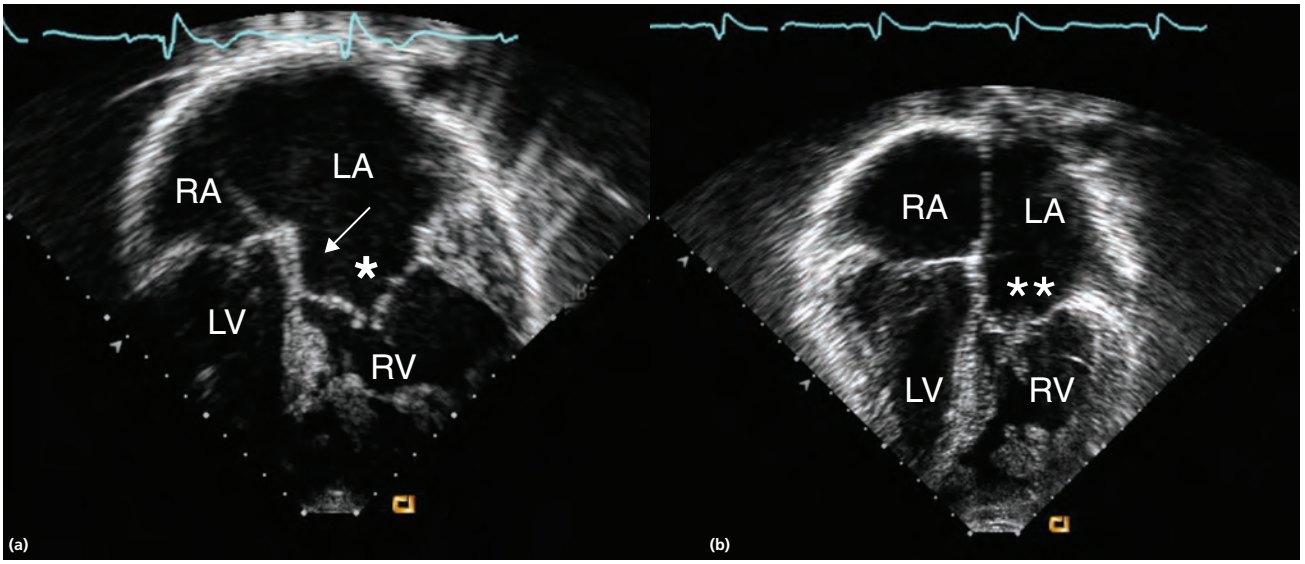


Figure 26.10 Two-dimensional imaging from the apical 4-chamber view in a 22-year-old man before **(a)** and after **(b)** banding of the main pulmonary artery for severe tricuspid regurgitation. Before banding **(a)**, note the dysplastic tricuspid valve leaflets with Ebstein-like malformation (apical displacement of the septal leaflet, arrow). Note that the anterior leaflet is not large as in classic Ebstein patients. Incomplete coaptation (∗) of the tricuspid valve leaflets is evident due to tricuspid annular dilation, abnormal geometry of the right ventricle, and shortened chordae tendineae secondary to severe dilation of the right ventricle. The interatrial septum shifts to the right, which reflects elevated pressure of the markedly enlarged left atrium due to severe tricuspid regurgitation. After the third banding **(b)**, note the remodeling of both ventricles and atria. The first pulmonary artery banding was performed at the age of 19 and the third at the age of 21. The images were taken 3 years apart. The interventricular septum has shifted to the left, which results in better coaptation of the tricuspid valve leaflet (∗∗) and less severe tricuspid regurgitation. The right atrium and left ventricle are larger, and the left atrium and right ventricle are significantly smaller. LA, left atrium; LV, left ventricle; RA, right atrium; RV, right ventricle.

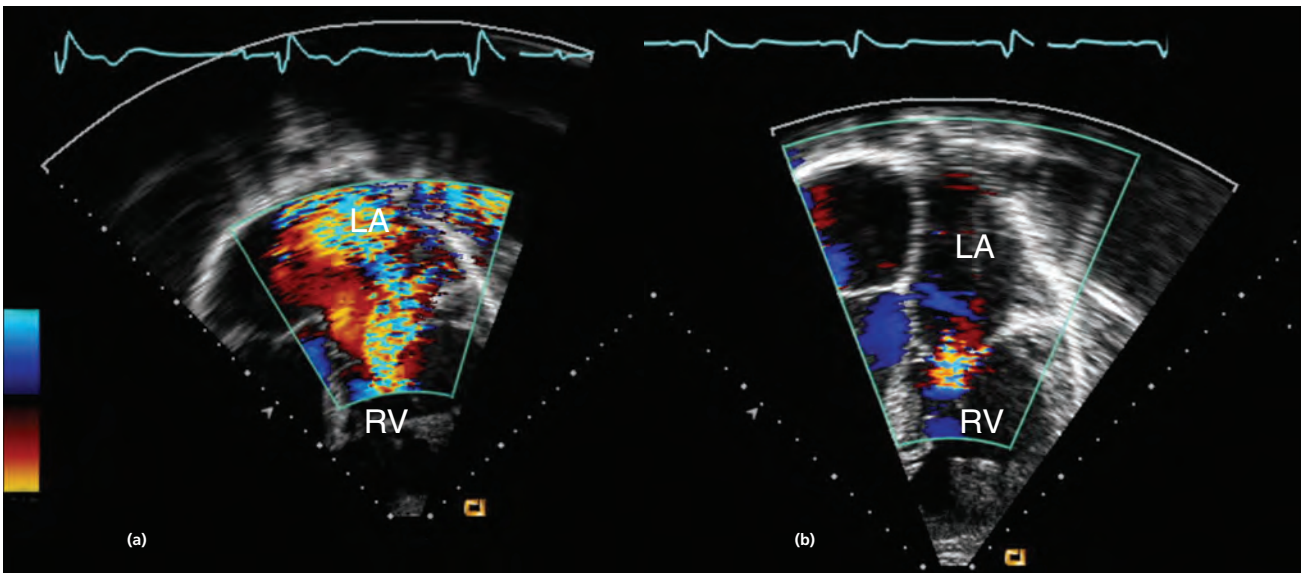


Figure 26.11 Color Doppler flow mapping in the apical 4-chamber view in the same patient as shown in Figure 26.10. **(a)** Severe tricuspid regurgitation before pulmonary artery banding. **(b)** Significant improvement in tricuspid regurgitation after pulmonary artery banding and ventricular remodeling. LA, left atrium; RV, right ventricle.

Associated intracardiac defects have different pathophysiologic effects on the subaortic RV and pulmonary blood flow. Volume load of the subaortic RV can be caused either by tricuspid regurgitation, or a nonrestrictive VSD, or both. Severe tricuspid regurgitation can be caused either by a pathology (dysplasia) of the tricuspid valve, or by malcoaptation of the tricuspid valve leaflets secondary to annular dilation and abnormal geometry of the RV as a consequence of a failing RV myocardium. Severe volume load of the RV can lead to heart failure symptoms during infancy, childhood or adulthood. Severe tricuspid regurgitation represents a major risk factor, appears to drive RV systolic dysfunction and heart failure and is linked to survival [44,46]. Hence, meticulous monitoring of RV systolic function and severity of tricuspid regurgitation is critical.

Left ventricular outflow tract (pulmonary) obstruction reduces pulmonary blood flow, alters the pressure load on the subpulmonary LV, alters the volume load of the subaortic RV, and modifies left and right ventricular interaction [45]. Tricuspid regurgitation is usually less severe in the presence of LV outflow tract obstruction because the interventricular septum shifts to the left (RV) secondary to the increased LV systolic pressure. The leftward shift of the interventricular septum impacts RV geometry, improves coaptation of the tricuspid valve leaflets, and reduces the severity of tricuspid regurgitation. Leftward shift of the interventricular septum and remodeling of the RV are illustrated by pulmonary artery banding performed for "training" the LV in preparation for a double switch procedure. A higher LV systolic pressure is associated with less severe tricuspid regurgitation as a consequence of RV remodeling (Figures 26.10 and 26.11; Videos 26.10–26.13) [45]. Hence, the presence of volume and/or pressure loads on both ventricles has an important impact on interventricular interaction and on morbidity and mortality [44–46].

Complete heart block due to abnormal location and course of the AV node and the bundle of His may be the first symptom in children, adolescents or adults [18,32,48]. Thus, physiologically "corrected" TGA must be excluded in all patients who present with conduction abnormalities, such as second- or third-degree AV block.

Imaging

Segmental analysis of cardiovascular anatomy by echocardiography (see Chapters 3 and 4) is crucial for comprehensive evaluation of patients with physiologically "corrected" TGA. A systematic, sequential approach helps in identifying the cardiac chambers, their alignments, connections, and the associated anomalies. Once the morphologic assessment is completed and the diagnosis of physiologically "corrected" TGA is confirmed, hemodynamic evaluation and biventricular function assessment are performed.

Key elements

In all cases, complete anatomic and functional examination by 2D and 3D imaging, as appropriate, and by color and spectral Doppler. In addition, the following elements of cardiovascular anatomy and function should be evaluated in detail and be given priority.

- Determine the arrangement of the abdominal aorta/inferior vena cava and atria (visceral-atrial situs): usual (situs solitus), or mirror-image arrangement (situs inversus).
- Cardiac orientation (base-to-apex axis) and position within the thorax: levocardia, mesocardia, dextrocardia.
- Determine the morphology and situs of the ventricles.
- Determine the morphology and spatial position of the great arteries.
- Determine the AV and VA alignments and connections.
- Determine the origin and proximal course of the coronary arteries (relevant for a double switch operation).
- Assess associated malformations:
 - tricuspid valve (dysplasia, Ebstein-like malformation).
 - straddling of the AV valves in the presence of a VSD.
 - ventricular septal defect(s): location, size, flow direction and velocity.
 - presence, mechanism, and degree of LV (pulmonary) outflow tract obstruction; determine which of the following mechanism(s) is present: (i) deviated outlet (conal) septum; (ii) accessory AV valve tissue; (iii) fibrous membrane; (iv) aneurysm of membranous septum; (v) hypoplastic pulmonary valve annulus; (vi) bicommissural pulmonary valve; (vii) narrowing of the pulmonary sinotubular junction; (viii) complex obstruction due to a combination of the above.
 - aneurysm of the membranous septum (LV outflow obstruction?).
 - atrial septal defect.
 - patent ductus arteriosus.
 - persistent left superior vena cava.
 - aortic arch obstruction.
- Biventricular size and function: evidence of pressure and/or volume load.
- Severity of mitral and tricuspid valve regurgitation.
- Gradient across the LV outflow tract.
- Estimation of LV systolic pressure based on mitral regurgitation jet velocity.

Transthoracic imaging

Subxiphoid views

The subxiphoid acoustic window provides the first view whereby the arrangement of the atria is defined. Usually, abdominal and atrial sidedness (situs) is concordant, which helps in determining the arrangement of the atria (atrial situs). The latter can be easily achieved by a cross-sectional view of the great vessels in the abdomen (see Chapters 3 and 4). In approximately 5% of patients with physiologically "corrected" TGA there is a mirror-image arrangement of the atria.

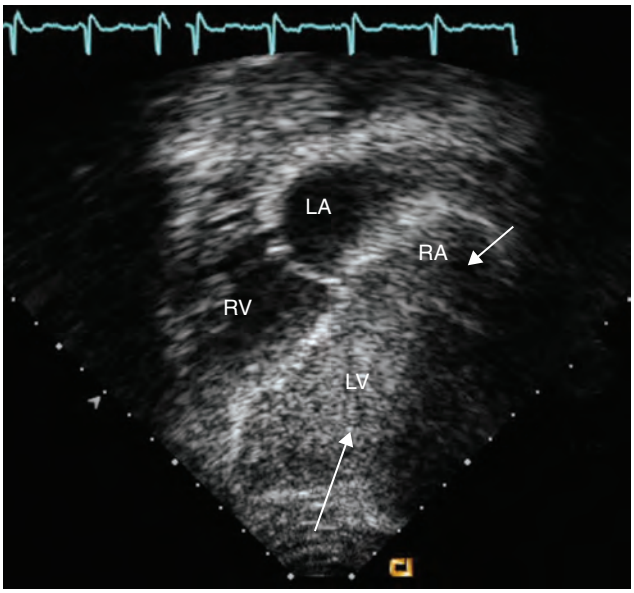


Figure 26.12 Subxiphoid view of the same 26-year-old man as shown in Figure 26.6. Agitated saline (arrows) appears in the left-sided chambers (right atrium [RA] and left ventricle [LV]) indicating situs inversus. The RV is to the right of the LV. Note that the base-apex axis points to the right (dextrocardia). LA, left atrium; RV, right ventricle.

Moving from the cross-sectional view of the great vessels below the diaphragm to the subxiphoid view of the heart, the examiner describes the connection of the inferior vena cava/hepatic veins and superior vena cava to the atrium. If the inferior vena cava is present, it usually connects to the morphologic RA. However, visualization of the connection between the inferior vena cava and the RA can be difficult or impossible in adults (Figure 26.6). Injection of agitated saline into an upper extremity vein can help in identifying the systemic venous connection to the right atrium (Figure 26.12).

Significant malalignment between the atrial and ventricular septum is common in patients with physiologically "corrected" TGA and can be the first hint of the presence of a discordant AV connection, as seen in the subxiphoid view or by transesophageal echocardiography (TEE) (Figure 26.7; Video 26.5). The morphology of the ventricles is described to identify the right and left ventricles by their intrinsic characteristic morphologic features (Figures 26.5, 26.8, and 26.10; Videos 26.4, 26.5, and 26.10–26.13). An anterior orientation of the transducer allows good visualization of the right and left ventricular outflow tracts. When present, the location(s) and mechanism(s) of LV outflow tract obstruction are delineated by 2D and 3D imaging and by color Doppler (Figure 26.13). The blood flow across the LV (pulmonary) outflow tract is usually well aligned (parallel) to the ultrasound beam, and the level of obstruction and gradients can be easily assessed by pulsed- (PW) and continuous-wave (CW) Doppler interrogation. LV-to-pulmonary artery conduits, which are implanted in some patients with complex LV (pulmonary) outflow tract obstruction, can be easily interrogated from the subxiphoid view with an anterior sweep of the transducer. The subaortic RV outflow tract can also be evaluated from this view (Figure 26.14).

The subxiphoid view is also used to image the pulmonary veins, atrial septum and morphology of the AV valves, and to assess the ventricular septum for the presence of a VSD.

Apical views

Apical views are obtained from the left lateral position (left chest) in patients with levocardia. However, acquisition of apical views may be challenging in the presence of dextrocardia, when the apical views are obtained in the right lateral position (right chest). Note that the transducer must be positioned on the chest according to standard guidelines to avoid any confusion or misinterpretation of the anatomy and sidedness (Figure 26.15). Specifically, the transducer is always positioned in such a fashion that it displays the patient's left side on the right side of the screen and the patient's right side on the left side of the screen (see Chapter 4).

The apical 4-chamber view is ideally suited to describe the morphology of the AV valves and to identify the morphologic right and left ventricles (Figures 26.2, 26.5, 26.8, and 26.10; Videos 26.1, 26.6, and 26.10–26.13). It is also a good view to describe ventricular looping (see Chapters 3 and 4). In L-ventricular loop the RV is positioned to the left of the LV.

An anterior position of the transducer in a modified apical 4- or 5-chamber view (the use of an "in-between" transducer angle) is encouraged to visualize the great arteries, which are usually arranged in parallel, and to identify the relation of the ascending aorta to the pulmonary artery (Figure 26.3b). This is an appropriate view to describe L- (leftward) or D- (rightward) malposition of the ascending aorta in relation to the pulmonary artery.

Hemodynamic assessment of both AV valves is performed from the apical view. The severity of mitral and tricuspid valve regurgitation is evaluated by color Doppler (Figure 26.11; Videos 26.11 and 26.13) and LV (pulmonary) systolic pressure can be estimated by measurement of the mitral valve regurgitation jet velocity. The apical views are also important to identify and to describe the morphology of obstructions across the left and/or right ventricular outflow tracts, and to confirm or to exclude VSDs. Alignment of the ultrasound beam parallel to the direction of blood flow across the LV (subpulmonary) outflow tract is possible in some patients by modified apical views (Figure 26.9; Videos 26.6–26.9), but it can be challenging in the standard apical view. Accurate assessment of the gradients can be difficult in some patients with restricted acoustic windows.

Parasternal views

A parallel position of the great arteries is readily apparent in the parasternal long- and short-axis views (Figures 26.3a and 26.4). The parasternal long-axis view proves very useful for identifying

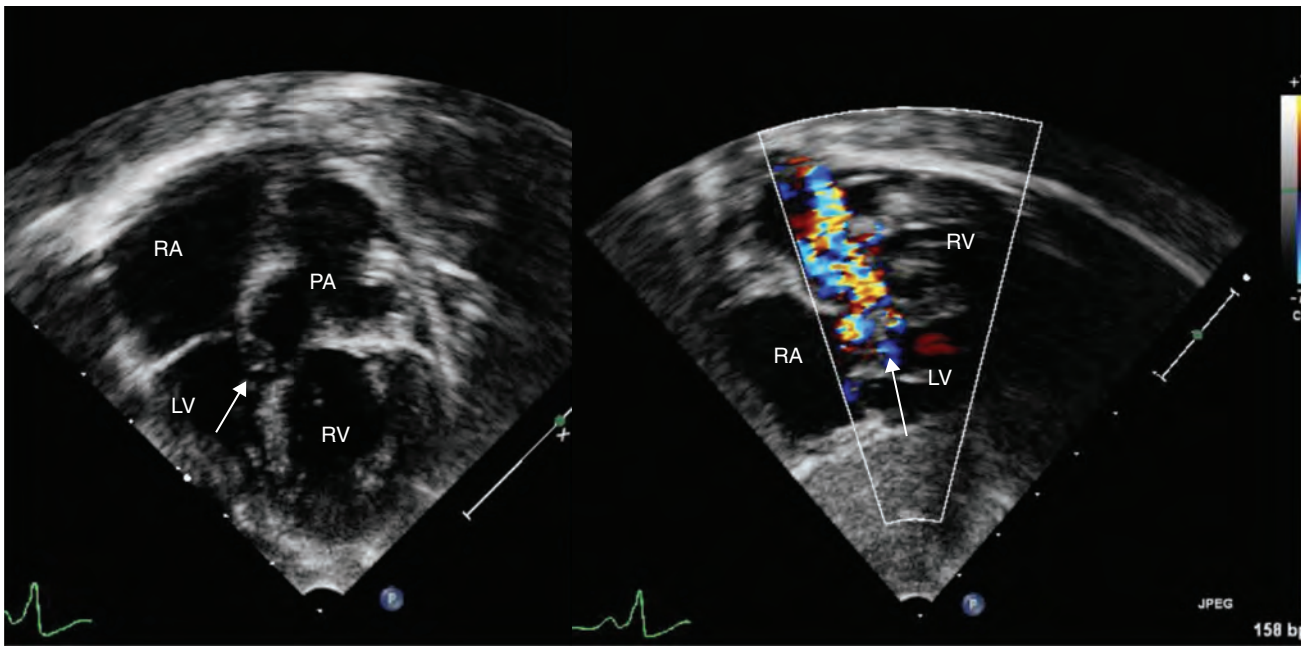


Figure 26.13 Imaging the left ventricular outflow tract from a subxiphoid view with an anterior sweep of the transducer in a 9-month-old boy with situs solitus and levocardia. **(a)** Two-dimensional imaging shows subpulmonary stenosis due to systolic anterior motion (SAM) of the mitral valve leaflets and ectopic fibrous tissue (arrow). LV, left ventricle; PA, pulmonary artery; RA, right atrium; RV, right ventricle. **(b)** Color Doppler flow mapping shows the origin of the turbulent flow at the subvalvar area (arrow). LV, left ventricle; RA, right atrium; RV, right ventricle. Source: Dr. Luc Mertens, Toronto, ON, Canada. Reproduced with permission of Dr. Mertens.

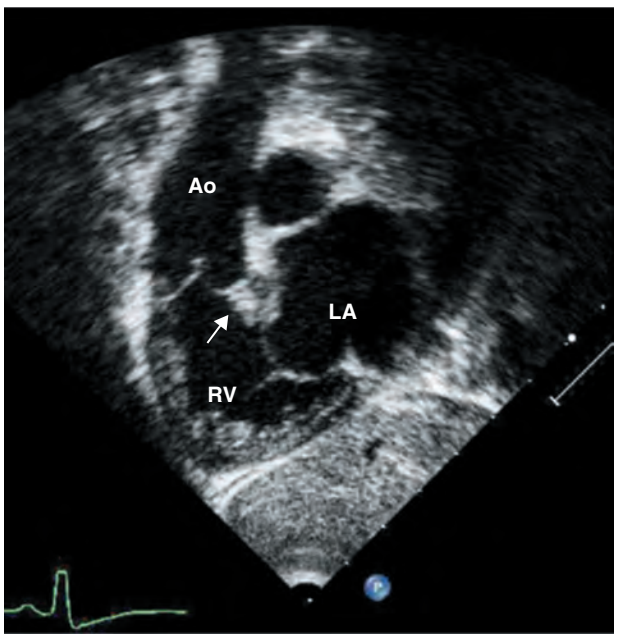


Figure 26.14 Imaging the right ventricular (aortic) outflow tract from a modified subxiphoid view in an 8-month-old boy with situs inversus and dextrocardia. Ventricular crest (arrow) between the AV valve and semilunar valve (aortic valve) helps in identifying the morphologic right ventricle (no fibrous continuity between the AV valve and semilunar valve). Ao, aorta; LA, left atrium; RV, right ventricle. Source: Dr. Luc Mertens, Toronto, ON, Canada. Reproduced with permission of Dr. Mertens.

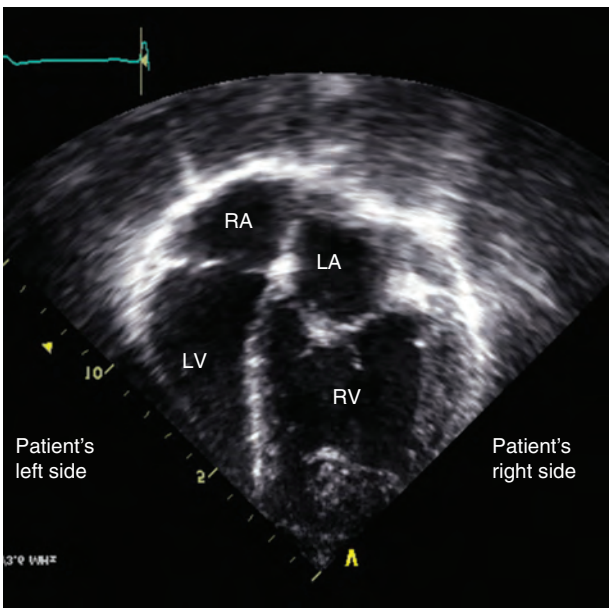


Figure 26.15 Apical 4-chamber view in a 22-year-old patient with situs inversus and dextrocardia. As a result of inappropriate (left–right reversal) transducer orientation the heart is displayed in a way that suggests atrial situs solitus and L-ventricular loop, whereas in fact the patient has atrial situs inversus and D-ventricular loop. This mistake resulted from an attempt to orient the transducer in a way that "corrects" the anatomy as opposed to keeping the left–right orientation according to standard guidelines (the patient's left is displayed on the right side of the screen). LA, left atrium; LV, left ventricle; RA, right atrium; RV, right ventricle.

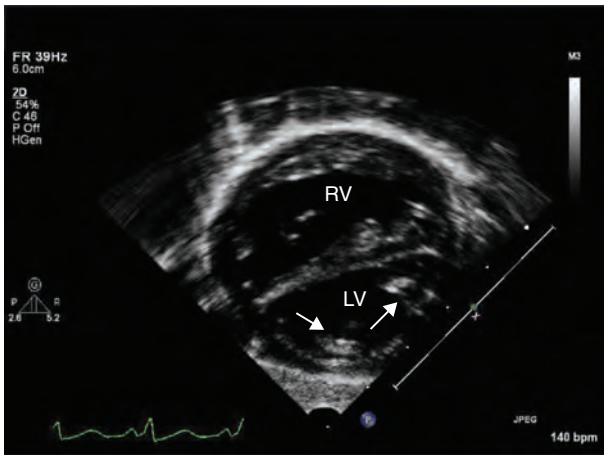


Figure 26.16 Parasternal short axis view of a 9-month-old boy with situs solitus, levocardia and L-ventricular loop. Two papillary muscles (arrows) help in identifying the anteriorly positioned left ventricle (LV). Note the eccentric hypertrophy of the anteriorly positioned right ventricle (RV) and flattening of the interventricular septum (d-shape). Source: Dr. Luc Mertens, Toronto, ON, Canada. Reproduced with permission of Dr. Mertens.

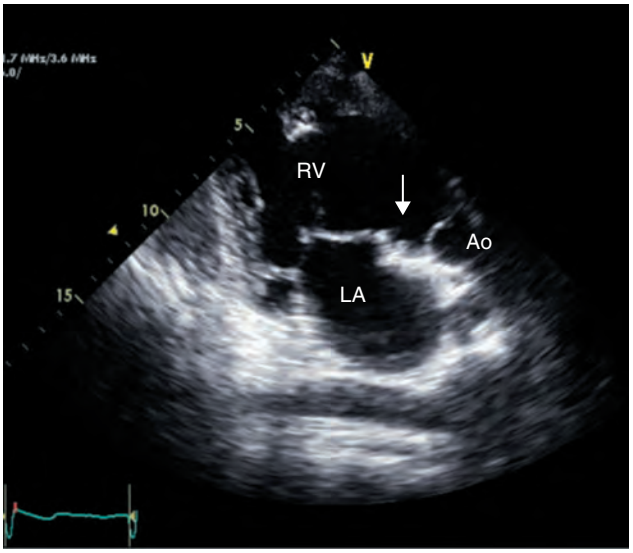


Figure 26.17 Imaging the ventricular crest (arrow) using a modified parasternal long-axis view in a 22-year-old man with situs inversus and dextrocardia. Ao, aorta; LA, left atrium; RV, right ventricle.

an obstruction across the LV (subpulmonary) outflow tract and for describing the mechanism(s) of obstruction.

The parasternal short-axis view describes the relation of the ascending aorta to the pulmonary trunk. The ascending aorta is usually found leftward and anterior in relation to the pulmonary trunk (Figure 26.4; Video 26.3). Although this relationship of the great arteries is typical, it is not uniform and cannot be used to describe ventricular looping.

The parasternal short-axis view also describes the orientation of the interventricular septum, the size and systolic function of both ventricles, and the morphology of the mitral and tricuspid valves and their corresponding papillary muscles (Figure 26.16). The VSD, when present, is usually located in the membranous septum and can be seen in the parasternal views. Muscular VSD(s) can be easily identified by color Doppler in parasternal short-axis views. When the pressure difference between the ventricles is low or absent (e.g., multiple VSDs, severe LV outflow obstruction), the Nyquist limit of the color Doppler velocity scale should be lowered to visualize low-velocity flow across the ventricular septum.

Suprasternal views

These views are best suited to describe the presence or absence of a patent ductus arteriosus, aortic arch sidedness and morphology, and to image the branching pattern of the aortic arch. They are also best suited to exclude the occasional association of aortic coarctation.

"In-between" views

Tailored "in-between" views or atypical views must frequently be obtained to complete a morphologic and hemodynamic assessment. In some patients the LV outflow tract obstruction cannot be fully assessed by standard views, and a nonstandard transducer position and/or orientation should be employed. Atypical parasternal, apical or subxiphoid views help in visualizing the anatomy of the left and right ventricular outflow tracts and in aligning the ultrasound beam parallel to the direction of blood flow. VSDs and straddling AV valves are frequently seen in atypical parasternal and apical views. Modified parasternal views can also help to identify the ventricular septal crest of the RV (Figure 26.17); this can be useful in the presence of an inlet (AV canal-type) VSD when the offset of the attachment of the AV valves is absent.

Transesophageal echocardiography (TEE)

Seldom does TEE add to the description of the underlying anatomy and pathophysiology in the pediatric population as transthoracic echocardiography usually provides the necessary diagnostic information. However, in older patients with suboptimal transthoracic windows, TEE is valuable to visualize endocarditis-related intracardiac vegetations; to exclude thrombus formation in the atrial appendages in patients with sustained supraventricular arrhythmias; to describe atrial septal defects; and to determine the morphology of the AV valves, the inlet ventricular septum, LV outflow tract obstruction, the membranous septum and associated aneurysm with or without LV outflow tract obstruction (Figure 26.18; Videos 26.14–26.17) [49]. The diagnosis by TEE of physiologically "corrected" TGA is aided by visualizing AV septal malalignment (Figure 26.7; Video 26.5) and parallel position of the great arteries. Injection of agitated saline (bubble study) into a peripheral systemic vein is helpful in identifying the right atrium, the subpulmonary LV,

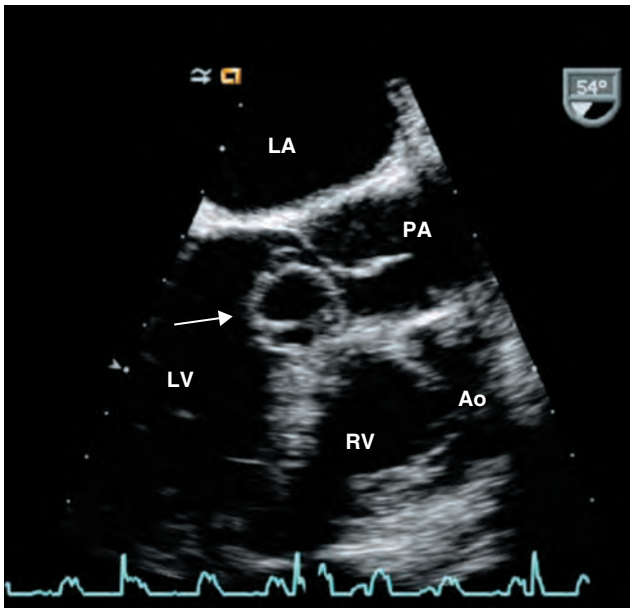


Figure 26.18 Transesophageal echocardiogram in a 41-year-old man with situs solitus shows an aneurysm of the membranous septum protruding into the left ventricular outflow tract (arrow). Ao, aortic valve; LA, left atrium; LV, left ventricle; PA, pulmonary artery; RV, right ventricle.

and the pulmonary arteries (Figure 26.19). In addition, TEE is performed routinely during intraoperative repair to monitor ventricular function, to determine severity of mitral and tricuspid regurgitation, to assess prosthetic tricuspid valves, and to detect residual atrial or ventricular septal defects. Assessment of conduits by TEE is usually difficult.

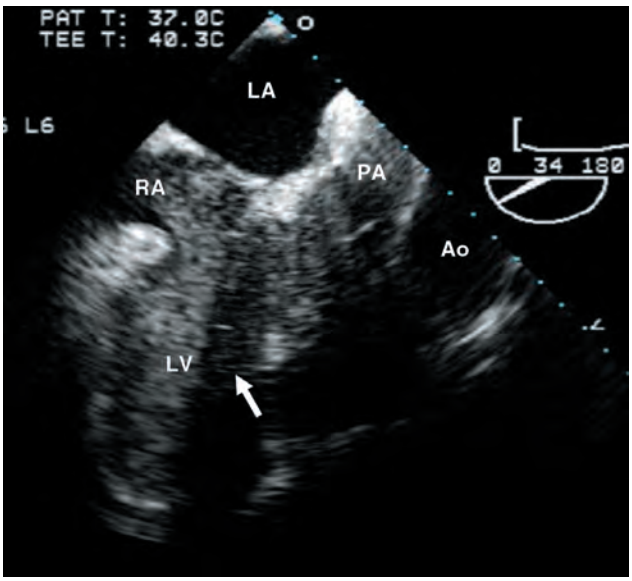


Figure 26.19 Transesophageal echocardiogram in a 69-year-old man with situs solitus and levocardia (due to poor quality of the transthoracic echocardiogram). Agitated saline injected into a right arm vein is seen in the right-sided right atrium (RA), the right-sided left ventricle (LV), and in the posteriorly positioned pulmonary artery (PA). There is a shadow caused by the mechanical valve in the tricuspid position (arrow). Ao, aorta.

Imaging of the fetus

Fetal diagnosis of physiologically "corrected" TGA is possible and depends on correct identification of the cardiac chambers and AV and VA connections (Figure 26.20a–c; Video 26.18). Diagnostic accuracy can be very high in specialized centers but the diagnosis may be more challenging in less experienced hands, especially during routine fetal screening. Associated lesions such as Ebstein-like malformation of the tricuspid valve, VSD, septal malalignment, or an absent AV connection often give a clue for the diagnosis. There are a number of echocardiographic features that help in establishing the diagnosis of physiologically "corrected" TGA in the fetus [50,51]. First, there is the reversed differential septal insertion of the tricuspid and mitral valve, with the tricuspid valve identified as being on the left side of the heart. Correct use of this anatomic feature depends on accurately identifying the left and right sides of the fetus and requires careful identification of fetal position. The reversed offset may be more difficult to identify in cases with an inlet (AV canal-type) VSD. A second, generally more reliable, sign is the presence of the septal-moderator band in the left-sided right ventricle. Identification of the septal-moderator band is one of the most consistent echocardiographic signs for identifying the RV during fetal life and its abnormal position helps in diagnosing physiologically "corrected" TGA. A third echocardiographic sign is the parallel orientation of the great arteries. In this context, the 3-vessel view is helpful to identify the abnormal spatial relationship of the great arteries. Also, a posterior-to-anterior sweep in a 4-chamber view can identify the first artery coming from the LV to be the pulmonary artery and the more anterior artery coming from the RV as being the aorta. Most fetuses with physiologically "corrected" TGA have associated lesions, the most common being tricuspid valve anomalies (Ebstein-like malformation), VSD, and pulmonary outflow tract stenosis or atresia. Severe tricuspid regurgitation, which can be present during fetal life, adversely affects fetal survival. Conduction abnormalities might already be present in fetal life, and cases with complete AV block have been reported [52,53]. In general, the short-term prognosis of the fetus with physiologically "corrected" TGA is good and is largely dependent on severity of associated lesions.

Imaging the adult

Technical challenges due to restricted echocardiographic windows resulting in poor image quality are major limitations in the evaluation of adults, especially in those who have undergone previous surgery. Hence, alternative imaging modalities such as cardiac magnetic resonance (CMR) imaging and multidetector computed tomography (MDCT) are widely used for structural and functional assessment of the heart and the right ventricle in particular [54–59].

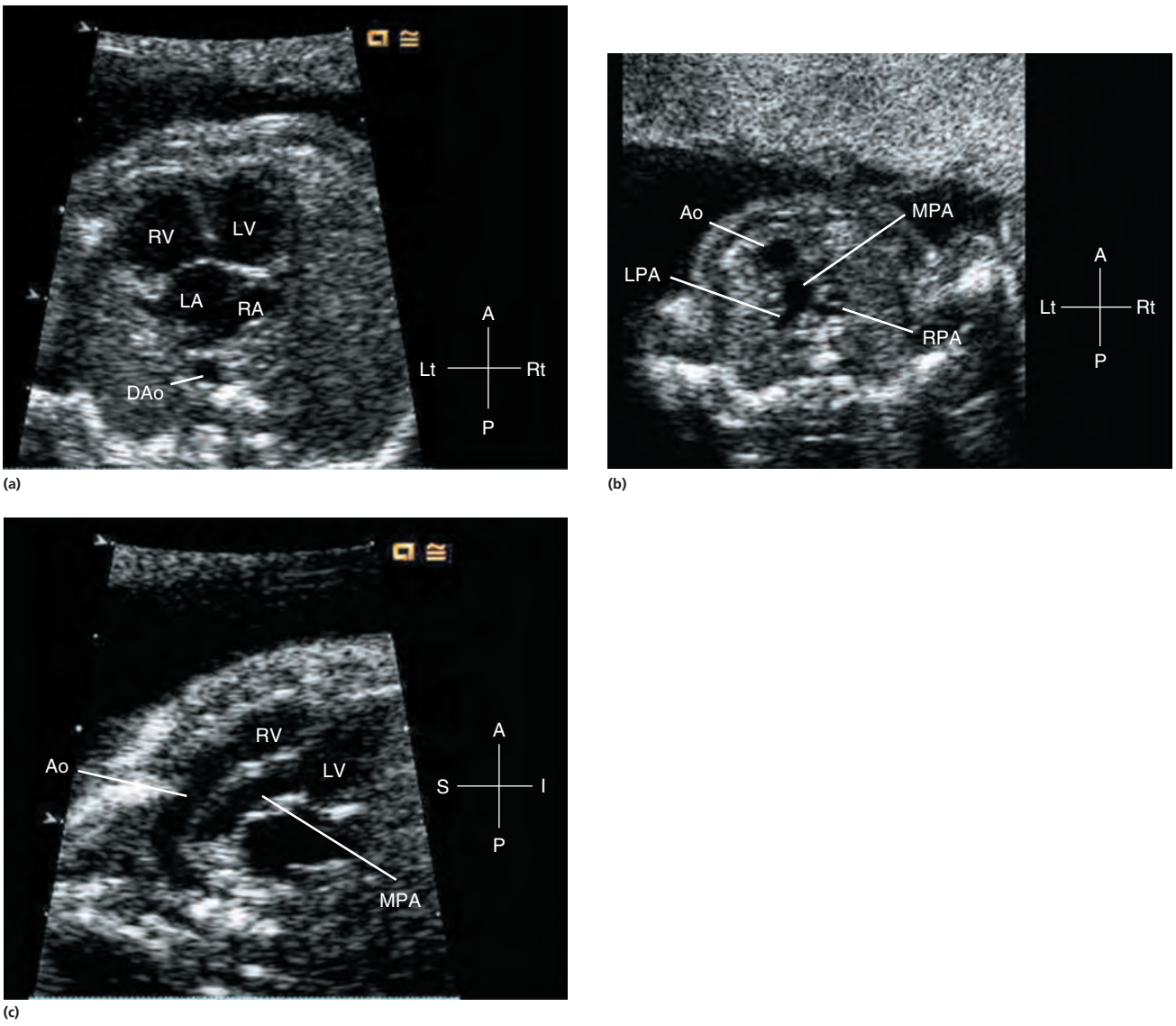


Figure 26.20 Fetal echocardiogram at 20 weeks' gestation showing levocardia, situs solitus and physiologically "corrected" transposition of the great arteries (TGA) with intact ventricular septum. **(a)** Transverse view of the fetal thorax demonstrating a 4-chamber view with atrioventricular (AV) discordance. **(b)** Transverse view of the superior aspect of the fetal thorax showing the leftward and anterior ascending aorta (Ao) and the posterior and rightward main pulmonary artery (MPA). The branch pulmonary arteries are seen at this level. **(c)** Parasagittal view of the fetus showing the parallel course of the great arteries with an anterior aorta (Ao) and a posterior MPA. DAo, descending aorta; LA, left atrium; LPA, left pulmonary artery; LV, left ventricle; RA, right atrium; RPA, right pulmonary artery; RV, right ventricle; A, anterior; P, posterior; Lt, left; Rt, right; I, inferior; S, superior. Source: Dr. Tal Geva from Children's Hospital Boston, MA, USA. Reproduced with permission of Dr. Geva.

The segmental approach to describe cardiovascular anatomy also applies to adults, as described earlier. TEE is an alternative to transthoracic echocardiography for delineating the intracardiac anatomy and the outflow tracts if the quality of the transthoracic images is inadequate [49,60]. Injection of agitated saline helps to identify the direction of blood flow and the chambers, as previously described.

Adults with physiologically "corrected" TGA and prior LV outflow tract obstruction can present with a conduit from the LV to the pulmonary artery (Video 26.14). Heart block may be the first symptom of physiologically "corrected" TGA in adults as acquired complete AV block continues to develop at a rate of 2% per year [61]. Thus, physiologically "corrected" TGA in such a patient should be excluded by echocardiography.

CMR imaging provides an excellent noninvasive alternative to TEE in adults with inadequate echocardiographic windows. CMR is ideally suited to describe the anatomy, to assess ventricular size and systolic function, and to measure valve regurgitation and shunts [54,55,59,62,63]. Computed tomography or radionuclide scintigraphy are alternatives in the presence of a

pacemaker or claustrophobia [59,64,65], although the role of radionuclide angiography to assess the subaortic RV is historical and minor. Radionuclide techniques have become of special interest for functional assessment of the heart, especially for assessing myocardial perfusion and metabolism [55]. Coronary angiography in patients at risk of coronary artery disease should be performed before any operative intervention if the patient is older than 40 years [56–58]. In addition, the coronary anatomy must be determined by any imaging modality in a patient who is considered for a double switch procedure.

Each imaging modality has its strengths and weaknesses/limitations to describe the anatomy/morphology, to provide the functional assessment of the heart, and to answer specific clinical questions. While echocardiography and CMR remain the commonly used imaging modalities in our clinical practice, radionuclide techniques play an inferior role in the current era and are used to answer very specific functional questions. The different imaging modalities are rather complementary than competitive.

Perioperative assessment

Surgical management of physiologically "corrected" TGA can be divided into two broad categories:

1 A physiologic-palliative approach, including repair of associated lesions such as VSD closure, LV-to-pulmonary artery conduit, tricuspid valve plasty/repair or replacement, pulmonary artery banding, and pacemaker.
2 Anatomic repair, including an atrial switch (Mustard or Senning) with either ventricular redirection (LV-to-aortic valve baffle and RV-to-PA conduit, also known as Rastelli procedure) or an arterial switch (also known as double switch operation).

The first approach leaves the RV as the subaortic ventricle whereas the second approach establishes the LV as the subaortic ventricle.

Miniaturization of multiplane TEE probes allows routine intraoperative assessment by echocardiography not only in adults and adolescents but also in most infants weighing more than 3 kg [66]. The pre-cardiopulmonary bypass echocardiogram aims to confirm preoperative diagnoses and to refine surgical planning. Three-dimensional TEE can be particularly helpful in planning tricuspid valve repair in patients with Ebstein-like anomaly. Goals of the post-cardiopulmonary bypass echocardiogram depend on the type of surgery performed. In all cases, assessment of ventricular size, global and regional systolic function, AV and semilunar valve function (stenosis and/or regurgitation), outflow tract obstruction, and exclusion of residual atrial or ventricular septal defects is performed. Special attention is given to evaluation of the systemic and pulmonary venous pathways for patency and leaks after an atrial switch procedure. Injection of agitated saline helps in identifying small shunts between the systemic and pulmonary venous pathways. The function of the semilunar valves and flow into the coronary arteries are evaluated after the arterial switch operation. Evaluation of conduits and prosthetic valves for a paravalvar leak or obstruction is performed when relevant.

Pulmonary artery banding

Patients undergoing banding of the pulmonary artery in preparation for a double switch procedure are followed serially by echocardiography. Severe tricuspid regurgitation is present in the majority of patients before banding, and is caused by malcoaptation of the tricuspid valve leaflets secondary to tricuspid annular dilation and abnormal RV geometry, in addition to dysplasia or Ebstein-like malformation of the tricuspid valve (Figures 26.10 and 26.11; Videos 26.10–26.13). Banding of the pulmonary artery leads to an increase in LV systolic pressure and to a shift of the interventricular septum toward the left-sided RV. The change in RV geometry improves the coaptation of the tricuspid valve leaflets and decreases the severity of tricuspid regurgitation (Figures 26.10 and 26.11; Videos 26.10–26.13) [45]. However, LV myocardial dysfunction and failure can occur if the pulmonary artery banding is too tight and the procedure is not carefully monitored by pressure-volume loop analysis and by intraoperative echocardiographic assessment of the LV. Echocardiographic assessment during and after pulmonary artery banding includes:

- evaluation of right and left ventricular systolic function;
- evaluation of tricuspid and mitral regurgitation;
- assessment of the gradient across the pulmonary artery band and LV systolic pressure by Doppler echocardiography.

Follow-up

Continued echocardiographic surveillance and periodic evaluations are integral to the long-term management of all patients with physiologically "corrected" TGA regardless of age [56–58,67]. These patients are at risk for late complications such as progressive tricuspid regurgitation, dysfunction and failure of the subaortic RV, LV outflow tract obstruction, AV block, endocarditis, prosthetic tricuspid valve dysfunction (Videos 26.19–26.22), conduit stenosis and/or regurgitation, and other abnormalities related to surgical procedures [32,40–44,46,47]. Careful assessment of RV systolic function and monitoring of the severity of tricuspid valve regurgitation and of the LV systolic pressure as a surrogate of the pulmonary artery pressure are essential during follow-up as they drive morbidity and mortality after tricuspid valve replacement [44,46]. A detailed, lifelong echocardiographic assessment aims to detect these and other complications [56–58].

Acknowledgement

The section on fetal echocardiography was contributed by Dr. Luc Mertens, Division of Cardiology, Hospital for Sick Children, Toronto, Canada.

Videos

To access the videos for this chapter, please go to www.lai-echo.com.

Video 26.1 Usual arrangement of the atria (cardiac situs solitus) with discordant atrioventricular (AV) connection in a 9-year-old boy. Note the characteristic morphology of the left atrial appendage identifying the location of the morphologic left atrium, which lies on the left of the morphologic right atrium. The inflow of the morphologic right ventricle (RV) lies to the left of the morphologic left ventricle (LV), which indicates L-ventricular loop. Source: Dr. Luc Mertens, Toronto, ON, Canada. Reproduced with permission of Dr. Mertens.

Video 26.2 Anterior sweep from an apical view imaging the parallel position of the great arteries in an 18-year-old man. The aorta is to the left of the pulmonary artery (the bifurcation identifies the pulmonary artery).

Video 26.3 Parasternal short-axis view of a 25-year-old man showing the spatial relationship of the aorta to the pulmonary trunk in physiologically "corrected" TGA. The aorta is anterior and slightly leftward to the pulmonary trunk in atrial situs solitus.

Video 26.4 Imaging situs inversus (mirror-image arrangement of the atria) with dextrocardia in an 8-month-old boy. Source: Dr. Luc Mertens, Toronto, ON, Canada. Reproduced with permission of Dr. Mertens.

Video 26.5 Transesophageal echocardiogram in a 41-year-old-man with atrial situs solitus and septal malalignment. The gap between the atrial and ventricular septum is filled with a large, redundant membranous septum protruding into the left ventricular outflow tract.

Video 26.6 Moderate to severe subvalvar pulmonary (left ventricular outflow tract) obstruction in a 9-month-old boy with situs solitus and levocardia. A modified 4-chamber view showing left ventricular outflow tract obstruction due to systolic anterior motion (SAM) of the mitral valve leaflet and ectopic fibrous tissue. Source: Dr. Luc Mertens, Toronto, ON, Canada. Reproduced with permission of Dr. Mertens.

Video 26.7 Moderate to severe subvalvar pulmonary (left ventricular outflow tract) obstruction in a 9-month-old boy with situs solitus and levocardia. Flow acceleration originates in the subvalvar area of the left ventricular outflow tract as shown by color Doppler. Same patient as in Video 26.6. Source: Dr. Luc Mertens, Toronto, ON, Canada. Reproduced with permission of Dr. Mertens.

Video 26.8 Moderate to severe subvalvar and valvar pulmonary (left ventricular outflow tract) obstruction in a 27-year-old man with situs solitus and levocardia. A modified 5-chamber view showing left ventricular outflow tract obstruction due to a subvalvar fibromuscular shelf and a thickened pulmonary valve with doming of the cusps.

Video 26.9 Moderate to severe subvalvar pulmonary (left ventricular outflow tract) obstruction in a 27-year-old man with situs solitus and levocardia. Flow acceleration originates in the subvalvar area of the left ventricular outflow tract as shown by color Doppler.

Video 26.10 Imaging Ebstein-like malformation of the tricuspid valve in a 22-year-old man with severe tricuspid regurgitation due to malcoaptation of the dysplastic leaflets. Images were obtained before (Videos 26.10 and 26.11) and after banding of the main pulmonary artery (Videos 26.12 and 26.13). Apical 4-chamber view before pulmonary artery banding showing apical displacement of the septal tricuspid valve leaflet, tricuspid annular dilatation and shortened chordae tendineae secondary to severe dilatation of the right ventricle, with lack of coaptation of the leaflets and severely dilated left atrium (LA) and right ventricle (RV).

Video 26.11 Ebstein-like malformation of the tricuspid valve with severe tricuspid regurgitation. Same patient as in Video 26.10 with color Doppler showing severe tricuspid regurgitation.

Video 26.12 Ebstein-like malformation of the tricuspid valve after pulmonary artery banding. Same patient as in Video 26.10 three years after pulmonary artery banding showing decreased LA and RV size, increased left ventricular (LV) size, and improved tricuspid leaflet coaptation.

Video 26.13 Ebstein-like malformation of the tricuspid valve after pulmonary banding. Same patient as in Video 26.12 with color Doppler showing markedly improved tricuspid regurgitation.

Video 26.14 Transesophageal imaging of a 25-mm Hancock valve conduit between the left ventricle (LV) and pulmonary artery showing LV outflow tract at the site of the proximal anastomosis of the conduit.

Video 26.15 Imaging an aneurysm of the membranous septum by transesophageal echocardiography in a 41-year-old man. A longitudinal view shows the aneurysm protruding into the LV outflow tract and located just below the pulmonary valve. Note the parallel position of the great arteries with the aorta anteriorly and the pulmonary artery posteriorly.

Video 26.16 Aneurysm of the membranous septum by TEE in the same patient as in Video 26.15. Color Doppler flow mapping shows no turbulence and mild pulmonary regurgitation.

Video 26.17 Aneurysm of the membranous septum by TEE. Injection of agitated saline appearing in the LV and pulmonary artery; there are no bubbles in the aneurysm of the membranous septum and there is no negative contrast, indicating absence of a ventricular septal defect. Same patient as in Video 26.15 and Video 26.16.

Video 26.18 Fetal echocardiogram at 20 weeks' gestation showing situs solitus, levocardia and physiologically "corrected" TGA with intact septum. A sweep through the fetal thorax in the transverse plane showing situs solitus, discordant atrioventricular (AV) and ventriculo-arterial (VA) connections with a leftward and anterior aorta relative to the main pulmonary artery. Source: Dr. Tal Geva

from Children's Hospital Boston, MA, USA. Reproduced with permission of Dr. Geva.

Video 26.19 Imaging the mechanical tricuspid valve in a 24-year-old woman at 12 weeks of pregnancy. Apical 4-chamber view shows eccentric hypertrophy of the left-sided subaortic right ventricle (RV) (L-ventricular loop) with reduced systolic function; only one disk of the CarboMedics mechanical tricuspid valve appears to move in the setting of an increased diastolic gradient across the valve. There is a pacemaker lead in the right-sided subpulmonic LV.

Video 26.20 Mechanical tricuspid valve in a 24-year-old woman at 12 weeks of pregnancy. Color Doppler demonstrates turbulent flow across the tricuspid valve with a mean diastolic gradient of 14 mmHg at a heart rate of 90 bpm.

Video 26.21 Mechanical tricuspid valve in a 24-year-old woman at 12 weeks of pregnancy. A transesophageal echocardiogram 4-chamber view reveals a left-sided dilated left atrium (LA) and RV. The medial disk of the CarboMedics valve is immobile due to pannus. There is no thrombus and the lateral leaflet opens normally.

Video 26.22 Mechanical tricuspid valve in a 24-year-old woman at 12 weeks of pregnancy. Color Doppler demonstrates absence of blood flow across the medial aspect of the CarboMedics valve. There is turbulent flow across the lateral aspect of the valve.

References

1 Hoffman JI, Kaplan S. The incidence of congenital heart disease. *J Am Coll Cardiol* 2002;**39**:1890–1900.
2 Keane JF, Fyler DC. Corrected transposition of the great arteries. In: Keane JF, Lock JE, Fyler DC (eds.) *Nadas' Pediatric Cardiology*, 2nd edn. Philadelphia, PA: Saunders Elsevier, 2006, pp. 791–797.
3 Samanek M, Voriskova M. Congenital heart disease among 815,569 children born between 1980 and 1990 and their 15-year survival: a prospective Bohemia survival study. *Pediatr Cardiol* 1999;**20**:411–417.
4 Kuehl KS, Loffredo CA. Population-based study of l-transposition of the great arteries: possible associations with environmental factors. *Birth Defects Res A Clin Mol Teratol* 2003;**67**:162–167.
5 Piacentini G, Digilio MC, Capolino R, et al. Familial recurrence of heart defects in subjects with congenitally corrected transposition of the great arteries. *Am J Med Genet A* 2005;**137**:176–180.
6 McElhinney DB, Geiger E, Blinder J, et al. NKX2.5 mutations in patients with congenital heart disease. *J Am Coll Cardiol* 2003;**42**:1650–1655.
7 Rokitansky CF. Die Defecte der Scheidewande des Herzens. *Wien: Wilhelm Braumuller*, 1875, pp. 81–86.
8 Van Praagh R, Van Praagh S, Vlad P, Keith JD. Anatomic types of congenital dextrocardia: diagnostic and embryologic implications. *Am J Cardiol* 1964;**13**:510–531.
9 Wilkinson JL, Cochrane AD, Karl TR. Congenital Heart Surgery Nomenclature and Database Project: corrected (discordant) transposition of the great arteries (and related malformations). *Ann Thorac Surg* 2000;**69**:S236–248.
10 Freedom RM, Harrington DP, White RI, Jr. The differential diagnosis of levo-transposed or malposed aorta. An angiocardiographic study. *Circulation* 1974;**50**:1040–1046.
11 Coto EO, Jimenez MQ, Cabrera A, et al. Aortic levopositions without ventricular inversion. *Eur J Cardiol* 1978;**8**:523–541.
12 Van Praagh R. Diagnosis of complex congenital heart disease: morphologic-anatomic method and terminology. *Cardiovasc Intervent Radiol* 1984;**7**:115–120.
13 Van Praagh R. What is congenitally corrected transposition of the great arteries? *N Engl J Med* 1970;**282**:1097–1098.
14 Warnes CA. Congenitally corrected transposition: the uncorrected misnomer. *J Am Coll Cardiol* 1996;**27**:1244–1245.
15 Van Praagh R. Segmental approach to diagnosis. In: Keane JF, Lock JE, Fyler DC (eds.) *Nadas' Pediatric Cardiology*, 2nd edn. Philadelphia, PA: Saunders Elsevier, 2006, pp. 39–46.
16 Schallert EK, Danton GH, Kardon R, Young DA. Describing congenital heart disease by using three-part segmental notation. *Radiographics* 2013;**33**:E33–46.
17 Penny DJ, Somerville J, Redington AN. Echocardiographic demonstration of important abnormalities of the mitral valve in congenitally corrected transposition. *Br Heart J* 1992;**68**:498–500.
18 Anderson RH, Becker AE, Arnold R, Wilkinson JL. The conducting tissues in congenitally corrected transposition. *Circulation* 1974;**50**:911–923.
19 Becker A, Anderson R. Conditions with discordant atrioventricular connections – anatomy and conducting tissues. In: Anderson RH, Macartney FJ, Shinebourne EA (eds.) *Pediatric Cardiology*. Edinburgh: Churchill Livingstone, 1978, pp. 184–197.
20 Hosseinpour AR, McCarthy KP, Griselli M, et al. Congenitally corrected transposition: size of the pulmonary trunk and septal malalignment. *Ann Thorac Surg* 2004;**77**:2163–2166.
21 Dabizzi RP, Barletta GA, Caprioli G, et al. Coronary artery anatomy in corrected transposition of the great arteries. *J Am Coll Cardiol* 1988;**12**:486–491.
22 Allwork SP, Bentall HH, Becker AE, et al. Congenitally corrected transposition of the great arteries: morphologic study of 32 cases. *Am J Cardiol* 1976;**38**:910–923.
23 Chiu IS, Wu, SJ, Chen SJ, et al. Sequential diagnosis of coronary arterial anatomy in congenitally corrected transposition of the great arteries. *Ann Thorac Surg* 2003;**75**:422–429.
24 Van Praagh R, Papagiannis J, Grunenfelder J, et al. Pathologic anatomy of corrected transposition of the great arteries: medical and surgical implications. *Am Heart J* 1998;**135**:772–785.
25 Shea PM, Lutz JF, Vieweg WV, et al. Selective coronary arteriography in congenitally corrected transposition of the great arteries. *Am J Cardiol* 1979;**44**:1201–1206.
26 McKay R, Anderson RH, Smith A. The coronary arteries in hearts with discordant atrioventricular connections. J *Thorac Cardiovasc Surg* 1996;**111**:988–997.
27 Ismat FA, Baldwin HS, Karl TR, Weinberg PM. Coronary anatomy in congenitally corrected transposition of the great arteries. *Int J Cardiol* 2002;**86**:207–216.
28 Malecka B, Bednarek J, Tomkiewicz-Pajak L, et al. Resynchronization therapy transvenous approach in dextrocardia and congenitally corrected transposition of great arteries. *Cardiol J* 2010;**17**:503–508.
29 Bottega NA, Kapa S, Edwards WD, et al. The cardiac veins in congenitally corrected transposition of the great arteries: delivery options for cardiac devices. *Heart Rhythm* 2009;**6**:1450–1456.

30 Uemura H, Ho SY, Anderson RH, et al. Surgical anatomy of the coronary circulation in hearts with discordant atrioventricular connections. *Eur J Cardiothorac Surg* 1996;**10**:194–200.
31 Pejkovic B, Krajnc I, Anderhuber F, Kosutic D. Anatomical variations of the coronary sinus ostium area of the human heart. *J Int Med Res* 2008;**36**:314–321.
32 Graham TP, Jr., Bernard YD, Mellen BG, et al. Long-term outcome in congenitally corrected transposition of the great arteries: a multi-institutional study. *J Am Coll Cardiol* 2000;**36**:255–261.
33 Anderson RH, Becker AE, Gerlis LM. The pulmonary outflow tract in classically corrected transposition. *J Thorac Cardiovasc Surg* 1975;**69**:747–757.
34 Silverman NH, Gerlis LM, Horowitz ES, et al. Pathologic elucidation of the echocardiographic features of Ebstein's malformation of the morphologically tricuspid valve in discordant atrioventricular connections. *Am J Cardiol* 1995;**76**:1277–1283.
35 Anderson KR, Danielson GK, McGoon DC, Lie JT. Ebstein's anomaly of the left-sided tricuspid valve: pathological anatomy of the valvular malformation. *Circulation* 1978;**58**:I87–91.
36 Horvath P, Szufladowicz M, de Leval MR, et al. Tricuspid valve abnormalities in patients with atrioventricular discordance: surgical implications. *Ann Thorac Surg* 1994;**57**:941–945.
37 Becker AE, Ho SY, Caruso G, et al. Straddling right atrioventricular valves in atrioventricular discordance. *Circulation* 1980;**61**:1133–1141.
38 Celermajer DS, Cullen S, Deanfield JE, Sullivan ID. Congenitally corrected transposition and Ebstein's anomaly of the systemic atrioventricular valve: association with aortic arch obstruction. *J Am Coll Cardiol* 1991;**18**:1056–1058.
39 Deanfield JE, Anderson RH, Macartney FJ. Aortic atresia with "corrected transposition of the great arteries" (atrioventricular and ventriculoarterial discordance). *Br Heart J* 1981;**46**:683–686.
40 Presbitero P, Somerville J, Rabajoli F, et al. Corrected transposition of the great arteries without associated defects in adult patients: clinical profile and follow up. *Br Heart J* 1995;**74**:57–59.
41 Lundstrom U, Bull C, Wyse RK, Somerville J. The natural and "unnatural" history of congenitally corrected transposition. *Am J Cardiol* 1990;**65**:1222–1229.
42 Connelly MS, Liu PP, Williams WG, et al. Congenitally corrected transposition of the great arteries in the adult: functional status and complications. *J Am Coll Cardiol* 1996;**27**:1238–1243.
43 Beauchesne LM, Warnes CA, Connolly HM, et al. Outcome of the unoperated adult who presents with congenitally corrected transposition of the great arteries. *J Am Coll Cardiol* 2002;**40**:285–290.
44 Prieto LR, Hordof AJ, Secic M, et al. Progressive tricuspid valve disease in patients with congenitally corrected transposition of the great arteries. *Circulation* 1998;**98**:997–1005.
45 Kral Kollars CA, Gelehrter S, Bove EL, Ensing G. Effects of morphologic left ventricular pressure on right ventricular geometry and tricuspid valve regurgitation in patients with congenitally corrected transposition of the great arteries. *Am J Cardiol* 2010;**105**:735–739.
46 Mongeon FP, Connolly HM, Dearani JA, et al. Congenitally corrected transposition of the great arteries ventricular function at the time of systemic atrioventricular valve replacement predicts long-term ventricular function. *J Am Coll Cardiol* 2011;**57**:2008–2017.
47 Oliver JM, Gallego P, Gonzalez AE, et al. Comparison of outcomes in adults with congenitally corrected transposition with situs inversus versus situs solitus. *Am J Cardiol* 2012;**110**:1687–1691.
48 Fischbach P, Law I, Serwer G. Congenitally corrected l-transposition of the great arteries: abnormalities of atrioventricular conduction. *Prog Pediatric Cardiol* 1999;**10**:37–43.
49 Sreeram N, Stumper OF, Kaulitz R, et al. Comparative value of transthoracic and transesophageal echocardiography in the assessment of congenital abnormalities of the atrioventricular junction. *J Am Coll Cardiol* 1990;**16**:1205–1214.
50 Sharland G, Tingay R, Jones A, Simpson J. Atrioventricular and ventriculoarterial discordance (congenitally corrected transposition of the great arteries): echocardiographic features, associations, and outcome in 34 fetuses. *Heart* 2005;**91**:1453–1458.
51 Chiappa E, Micheletti A, Sciarrone A, et al. The prenatal diagnosis of, and short-term outcome for, patients with congenitally corrected transposition. *Cardiol Young* 2004;**14**:265–276.
52 Costa P, Monterroso J, Areias JC. Prenatal diagnosis of complete heart block and congenitally corrected transposition of the great arteries. *Pediatr Cardiol* 2007;**28**:414–415.
53 Jaeggi ET, Hornberger LK, Smallhorn JF, Fouron JC. Prenatal diagnosis of complete atrioventricular block associated with structural heart disease: combined experience of two tertiary care centers and review of the literature. *Ultrasound Obstet Gynecol* 2005;**26**:16–21.
54 Kilner PJ, Geva T, Kaemmerer H, et al. Recommendations for cardiovascular magnetic resonance in adults with congenital heart disease from the respective working groups of the European Society of Cardiology. *Eur Heart J* 2010;**31**:794–805.
55 Valsangiacomo Buechel ER, Mertens LL. Imaging the right heart: the use of integrated multimodality imaging. *Eur Heart J* 2012;**33**:949–960.
56 Baumgartner H, Bonhoeffer P, De Groot NM, et al. ESC Guidelines for the management of grown-up congenital heart disease (new version 2010). *Eur Heart J* 2010;**31**:2915–2957.
57 Warnes CA, Williams RG, Bashore TM, et al. ACC/AHA 2008 Guidelines for the Management of Adults with Congenital Heart Disease: Executive Summary: a report of the American College of Cardiology/American Heart Association Task Force on Practice Guidelines (writing committee to develop guidelines for the management of adults with congenital heart disease). *Circulation* 2008;**118**:2395–2451.
58 Silversides CK, Salehian O, Oechslin E, et al. Canadian Cardiovascular Society 2009 Consensus Conference on the management of adults with congenital heart disease: complex congenital cardiac lesions. *Can J Cardiol* 2010;**26**:e98–117.
59 Prakash A, Powell AJ, Geva T. Multimodality noninvasive imaging for assessment of congenital heart disease. *Circ Cardiovasc Imaging* 2010;**3**:112–125.
60 Caso P, Ascione L, Lange A, et al. Diagnostic value of transesophageal echocardiography in the assessment of congenitally corrected transposition of the great arteries in adult patients. *Am Heart J* 1998;**135**:43–50.
61 Huhta JC, Maloney JD, Ritter DG, et al. Complete atrioventricular block in patients with atrioventricular discordance. *Circulation* 1983;**67**:1374–1377.
62 Schmidt M, Theissen P, Deutsch HJ, et al. Congenitally corrected transposition of the great arteries (L-TGA) with situs inversus totalis in adulthood: findings with magnetic resonance imaging. *Magn Reson Imaging* 2000;**18**:417–422.
63 Dodge-Khatami A, Tulevski II, Bennink GB, et al. Comparable systemic ventricular function in healthy adults and patients with

unoperated congenitally corrected transposition using MRI dobutamine stress testing. *Ann Thorac Surg* 2002;**73**:1759–1764.

64 Leschka S, Oechslin E, Husmann L, et al. Pre- and postoperative evaluation of congenital heart disease in children and adults with 64-section CT. *Radiographics* 2007;**27**:829–846.

65 Benson LN, Burns R, Schwaiger M, et al. Radionuclide angiographic evaluation of ventricular function in isolated congenitally corrected transposition of the great arteries. *Am J Cardiol* 1986;**58**:319–324.

66 Ayres NA, Miller-Hance W, Fyfe DA, et al. Indications and guidelines for performance of transesophageal echocardiography in the patient with pediatric acquired or congenital heart disease: report from the task force of the Pediatric Council of the American Society of Echocardiography. *J Am Soc Echocardiogr* 2005;**18**:91–98.

67 Rudski LG, Lai WW, Afilalo J, et al. Guidelines for the echocardiographic assessment of the right heart in adults: a report from the American Society of Echocardiography endorsed by the European Association of Echocardiography, a registered branch of the European Society of Cardiology, and the Canadian Society of Echocardiography. *J Am Soc Echocardiogr* 2010;**23**:685–713.

PART V

Miscellaneous Cardiovascular Lesions

CHAPTER 27

Hearts with Functionally One Ventricle

Stephen P. Sanders
Departments of Cardiology, Pathology and Cardiac Surgery, Boston Children's Hospital, Boston, MA, USA

Introduction

Hearts with functionally one ventricle comprise only a few percent of congenital heart defects [1], but patients with these hearts utilize a disproportionate amount of healthcare resources because of the complexity of management and the need for repeated interventions and lifelong care [2]. Optimal management depends on early recognition and careful observation and planning. Treatment principles include meticulous protection of the pulmonary vasculature, ongoing surveillance for and rapid treatment of systemic outflow obstruction, and maintenance of systemic ventricular function by avoiding volume and pressure overload as much as possible. Despite attentive and intelligent management strategies, the long-term outlook for these patients is guarded [3]. Palliation of patients with functionally one ventricle is likely to be effective for only two to four decades [4]. Most, perhaps all, such patients will eventually require an alternative management strategy such as transplantation or mechanical support.

Many hearts in this category have only one ventricular sinus or body, anatomically as well as functionally [5,6]. The other chamber usually present in the ventricular mass is an infundibulum or outlet chamber. These include double-inlet left ventricle (DILV), most double-inlet right ventricle (DIRV), most tricuspid atresia (TA), and many mitral atresia hearts. Others of this category, perhaps most, have two ventricular sinuses but one or both are unsuitable to function independently [7]. Most of these are discussed in other chapters and will only be listed here. Although not all cases of these defects have functionally one ventricle, many do and must be identified as soon as possible to maximize outcomes. Included are variants of hypoplastic left heart syndrome (Chapter 20), hypoplastic right heart syndrome (mostly pulmonary atresia with intact ventricular septum) (Chapter 17), straddling mitral valve (Chapter 14), straddling tricuspid valve (Chapter 13), unbalanced common atrioventricular (AV) canal (Chapter 15), congenitally physiologically corrected transposition of the great arteries (TGA) (Chapter 26), Ebstein anomaly (Chapter 14), heterotaxy syndromes (Chapter 28), and superior-inferior ventricles (SIV) and criss-cross heart.

Etiology

The genetic and/or environmental causes of these defects are poorly understood. Most cases appear to be sporadic although familial occurrences have been reported [8–10]. There are a few case reports of syndromic association of TA or other functionally single ventricle hearts [11–18]. The recurrence risk among first-degree relatives appears to be in the range associated with polygenic inheritance (2–5%) [19–22].

Embryologic development

Concepts about development of most congenital heart defects are speculative because no one has ever observed active, in vivo development of a defective human heart. However, it is possible to infer likely mechanisms from what is known about normal human development and abnormal development in animal models. The following brief description of normal development is provided for comparison with the proposed abnormal development in subsequent sections.

In early looping the heart tube is rather uniform with no clear demarcation of chambers. Cells from the second heart field are added to both ends of the heart tube as it elongates and loops [23]. The dorsal mesocardium, which initially joins the heart tube throughout its length to prepharyngeal mesoderm, degenerates in its mid portion [24] allowing the elongating heart tube to bend anteriorly and then rightward, called dextral or D-looping [25]. As the heart chambers begin expansile growth from the outer curvature of the looping heart tube [26], the AV canal becomes apparent as a constriction between the common atrial chamber and the developing left ventricle and the interventricular foramen as a constriction between the developing

Echocardiography in Pediatric and Congenital Heart Disease: From Fetus to Adult, Second Edition. Edited by Wyman W. Lai, Luc L. Mertens, Meryl S. Cohen and Tal Geva.
© 2016 John Wiley & Sons, Ltd. Published 2016 by John Wiley & Sons, Ltd.
Companion website: www.lai-echo.com

ventricles. The AV canal is exclusively aligned with the developing left ventricle and the outflow continues from the inner curvature of the heart tube at the rostral end of the developing right ventricle. As the heart chambers continue to enlarge, the right side of the AV canal and the right atrium grow faster than the left, allowing the AV canal to expand above the right ventricle and below the right atrium, creating a right ventricular inflow and establishing alignment of the right atrium with the right ventricle through the right side of the AV canal [27]. Swellings or cushions develop in the AV canal as well as the outflow [28]. At the same time, septation of the common atrium begins with downward growth of septum primum or the primary atrial septum from the superior wall and invasion of the dorsal mesenchymal protrusion or vestibular spine from the posterior-inferior wall [29]. These septal structures continue to grow into and septate the common atrium, finally fusing with the two main AV cushions. At that point the AV cushions fuse to each other as well, separating the AV canal into right and left halves, aligning the right atrium and ventricle and the left atrium and ventricle, respectively. Before completion of atrial septation, the septum primum, near its origin from the superior wall, breaks down forming ostium secundum and allowing continued communication between the right and left atria. The fused AV cushions then become draped over the muscular inflow ventricular septum that has developed on their ventricular side [30]. Meanwhile the outflow cushions fuse from distal to proximal under the influence of cardiac neural crest cells, dividing the outflow into aorta and pulmonary artery [31]. As this occurs the proximal outflow undergoes counterclockwise rotation, as viewed from the ventricles, so that the aorta which is anterior distally comes to lie rightward and posterior proximally, and the pulmonary artery which is posterior distally moves anteriorly and leftward proximally [32]. The outflow septum, which developed by fusion and muscularization of the proximal parts of the outflow cushions, then inserts into the limbs of the interventricular foramen, aligning the aorta with the left ventricle and the pulmonary artery with the right ventricle, and closing the interventricular foramen [33]. The AV valves develop from the AV cushions by a process that involves thinning, elongation and separation from underlying myocardium by apoptosis of cardiomyocytes [30]. The semilunar valves develop from the outflow cushions by excavation and thinning that also involves apoptosis probably initiated by neural crest cells [34].

Double-inlet left ventricle

DILV includes hearts in which both AV valves are aligned with and connected to one ventricular chamber of left ventricular morphology [6] (Figures 27.1–27.6; Videos 27.1–27.5).

Embryologic development

DILV is easily envisioned as an arrest of development at the stage where the AV canal is completely aligned with the developing left ventricle. Most often DILV is associated with leftward bending or looping (levo or L-looping) of the heart tube, although 30–35% of the time dextro or D-looping occurs. DILV is associated with failure of development and growth of the right ventricular sinus. As the AV canal expands toward the inner curvature of the heart tube it becomes aligned with the right atrium. However, the expanding edge does not cross the foramen between the left ventricle and outflow as it does in the normal heart. It is unclear if confinement of the AV canal to the left ventricle is primary and failure of RV development secondary, or the converse. In either case, atrial septation appears to proceed correctly with the septum primum and dorsal mesenchymal protrusion fusing with and inducing central fusion of the main AV cushions to form two AV valves. It is interesting that development of the AV valves proceeds rather normally despite lacking an underlying muscular ventricular septum over which to drape themselves. The infundibulum or outlet chamber derives from the outflow portion or ascending limb of the heart tube and maintains its primitive connection with the left ventricle, the outflow foramen, which would have been the interventricular foramen had the right ventricle developed. In fact, the size of the outlet chamber is somewhat variable and in some cases it appears that a small portion of right ventricular sinus might be present, especially in hearts where the outlet chamber extends inferiorly toward the diaphragmatic heart border. Alternatively, the larger size of the outlet chamber could be from expansion of the apical trabecular portion of the infundibulum or outlet chamber.

Abnormal ventriculo-arterial (VA) alignment, present in the great majority of these hearts, is most likely due to abnormal rotation of the outflow so that the proximal aorta remains anterior and the proximal pulmonary trunk posterior [35,36]. This abnormal rotation is also associated with persistence of the outflow foramen between the left ventricle and outlet chamber due to failure of the outlet septum to join the limbs of the outflow foramen [36]. Rarely, and essentially exclusively in D-loop hearts, the rotation of the outflow occurs correctly resulting in normally aligned great arteries. Even in these cases, however, the outflow septum rarely completely closes the outflow foramen.

Anatomy

The systemic and pulmonary veins and atria are usually normal (for situs solitus). Although reported in situs inversus [37,38], such hearts are extraordinarily rare because situs inversus and DILV are both rare conditions.

The AV valves are often recognizable as a mitral or tricuspid valve [39,40]. The valve near the septal wall of the left ventricle (see later) is often tricuspid in character and the one nearest the free wall more mitral (Figure 27.6). In other cases the valves are symmetrical, resembling each other more than either a mitral or tricuspid valve. Hypoplasia and stenosis of an AV valve is seen in up to 15–20% of hearts [40] (Figure 27.7). Rarely a common AV valve is aligned and connected to an isolated left ventricle.

The left ventricular chamber has a free wall on one side with multiple papillary muscles and a smooth wall on the other that

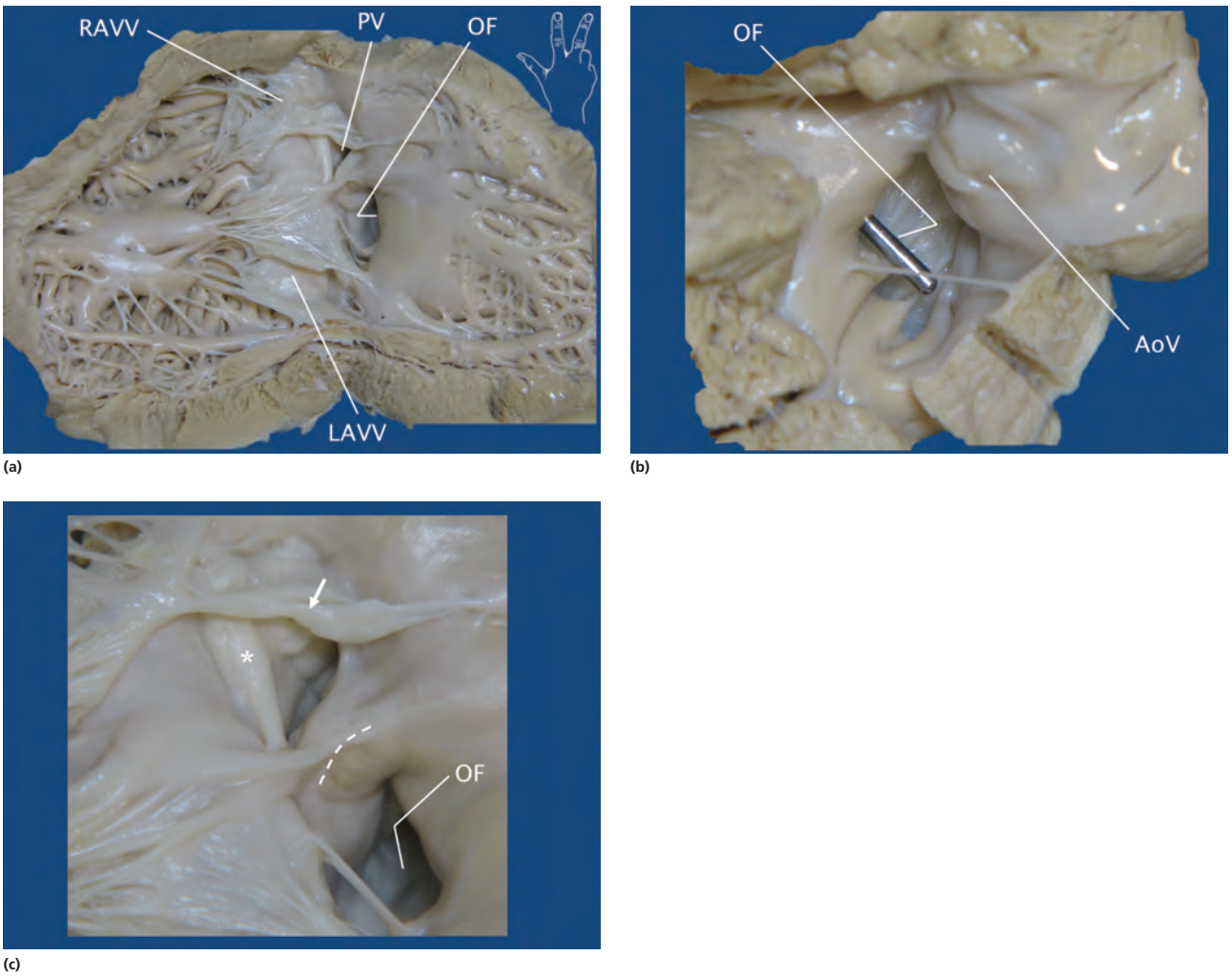


Figure 27.1 A heart specimen of DILV with transposition of the great arteries {S,L,L}. **(a)** Opened left ventricle. The smooth septal wall is to the right of the image and the free wall is to the left. The right AV valve (RAVV) is mitral-like with a deep medial leaflet and a shallow lateral leaflet while the left AV valve (LAVV) has three leaflets and attachments onto the inferior septal wall near the outflow foramen (OF), more like a tricuspid valve. The pulmonary valve (PV) is between the AV valves. Only a right hand (upper left) can describe this L-loop or inverted left ventricle, with the thumb in the AV valves, the fingers in the pulmonary valve and the palm against the septal wall. **(b)** Opened outlet chamber. The aortic valve (AoV) is supported by the ring of infundibular muscle that comprises the outlet chamber. Part of the LAVV is seen through the outflow foramen (OF) below the AoV. **(c)** Zoomed view of the PV and OF. Three mechanisms for subpulmonary obstruction are illustrated here: accessory AV valve tissue (arrow), fibromuscular ridge (∗), and deviation of the outlet septum (dashed line). Note that the outlet septum is nearly perpendicular to the plane of the muscular septum and does not occupy the OF.

is the left ventricular septal wall (Figures 27.1–27.3). Note that the septal wall is a characteristic feature of the left ventricle and is present even when there is no ventricular sinus on the other side. A large muscle bundle, the posterior median ridge, is often present on the inferior or diaphragmatic wall of the left ventricle running from base to apex between the AV valves (Figure 27.3a). An infundibulum or outlet chamber is uniformly associated with the left ventricle (Figures 27.1b and 27.2b) and the AV valve closer to the septum frequently straddles into it [6,40] (Figure 27.3). The connection between the left ventricle and outlet chamber is variously called a bulboventricular foramen, interventricular foramen, or ventricular septal defect. In fact, the type and location of the communication is variable [40,41]. Most often it is the persisting outflow foramen of the embryonic heart, between the conal or infundibular septum (outlet septum) and the left ventricular septal wall (Figures 27.1 and 27.3). The infundibular or outlet septum is readily identified between the semilunar valves because it is rarely correctly inserted into the muscular ventricular septum (Figures 27.1c and 27.2b). In other cases, the communication is a muscular defect between the mid or apical part of the outlet chamber and the left ventricle (Figure 27.7). The size of the communication is also variable [40–42]. A small communication is a frequent cause of obstruction to whichever semilunar root arises from the

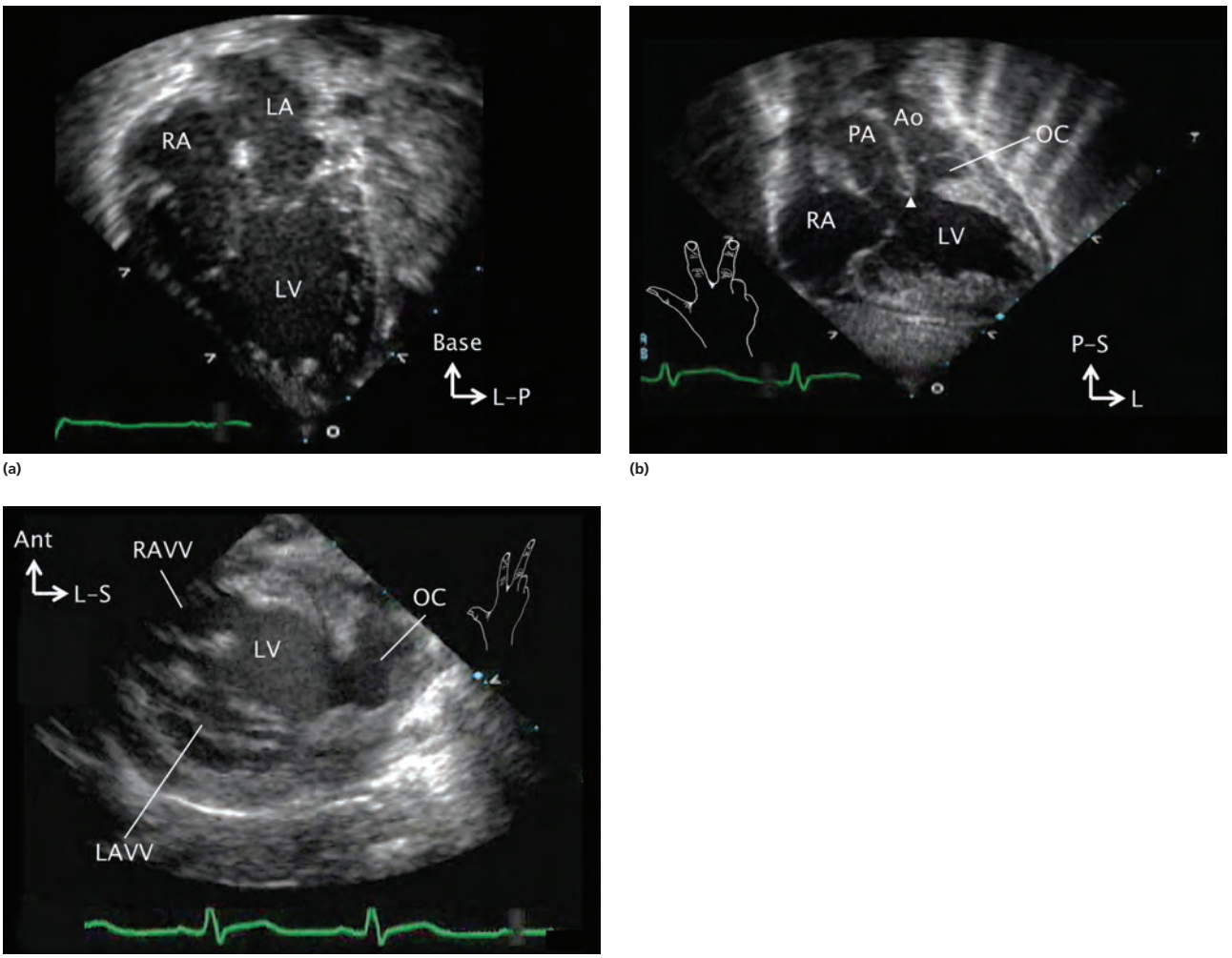
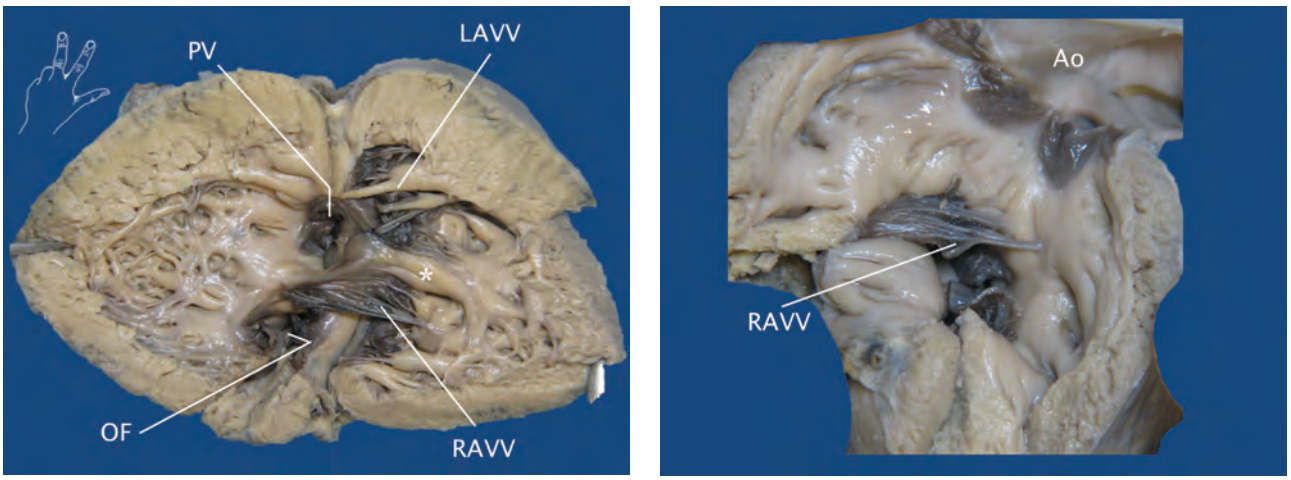


Figure 27.2 Three echocardiographic views of a heart with DILV and transposition of the great arteries {S,L,L}. **(a)** Apical 4-chamber view showing both AV valves entering the left ventricle (LV). **(b)** Subxiphoid long-axis view showing the right atrium (RA) aligned with the LV through the right AV valve, the posterior and rightward pulmonary artery (PA) aligned with the LV, and the anterior and leftward aorta (Ao) aligned with the outlet chamber (OC). The outlet septum (▲) is deviated posteriorly and leftward toward the PA. The space between the deviated outlet septum and the LV septal wall is the outflow foramen. **(c)** Parasternal short-axis view showing the left (LAVV) and right (RAVV) AV valves in the LV, the leftward and superior OC, and the outflow foramen connecting it to the LV. A right hand (right upper) is required to describe the LV with the thumb into the AV valves, the fingers in the outflow and the palm against the septal wall.

outlet chamber. A persistent outflow foramen is often large and unobstructed while more apical muscular communications are essentially always obstructed [40].

The situs or organization of the left ventricle can be either solitus or D-loop, or inversus or L-loop (Figures 27.1a, 27.2b, and 27.3a). The hand rule is useful to distinguish between the types of left ventricle [43]. One imagines placing the thumb in an AV valve, the palm against the septum, and the index finger in the outflow. If this can be done with the left hand, the left ventricle is solitus or D-loop. Alternatively, if a right hand is required, the left ventricle is inverted or L-loop. (Note that the handedness of the left ventricle is opposite to that of the right ventricle where the hand rule is more frequently applied.) The importance of determining ventricular situs or loop is threefold: first, the conduction system is usually superior to the outflow foramen in an inverted or L-loop left ventricle (with atrial situs solitus) but inferior in a solitus or D-loop left ventricle [44,45]; second, the VA alignment is essentially always transposition (discordance) when the left ventricle is inverted while in 10% or so of DILV with a solitus or D-loop left ventricle the great arteries are normally related (concordance) [40]; and third, the epicardial course of the coronary arteries is determined by the arrangement of the ventricles [46].

When the great arteries are transposed the pulmonary valve is typically wedged between the AV valves and is in fibrous continuity with both (Figures 27.1a and 27.3a) while the aortic valve is aligned with the outlet chamber and supported by infundibular muscle (Figures 27.1b and 27.3b). Conversely, in normally



(a) (b)

Figure 27.3 A heart specimen of DILV with transposition of the great arteries {S,D,D}. **(a)** Opened left ventricle. The smooth septal wall is to the left in this image and the free wall to the right. The left (LAVV) and right (RAVV) AV valves do not have clear mitral or tricuspid character, except that the right AV valve attaches to the septal wall. The RAVV also straddles through the outflow foramen (OF) into the outlet chamber. The pulmonary valve (PV) is between the AV valves. A posterior median ridge (*) courses down the free wall between the AV valves. Only a left hand (upper left) can describe this ventricle, with the thumb in the AV valves, the fingers in the PV and the palm against the septal wall. **(b)** Opened outlet chamber. The aortic valve (AoV) is supported by the infundibular muscle of the outlet chamber. A small part of the RAVV straddles into the outlet chamber through the outflow foramen.

related great arteries it is the aorta that is wedged between the AV valves and the pulmonary artery arises from the outlet chamber.

The coronary artery anatomy depends on the ventricular situs or loop because the epicardial coronary pattern seems to be determined by cues from the underlying ventricle. When the great arteries are malposed (transposition or double outlet), the arteries arise from the posterior, facing sinuses. In an L-loop DILV, the morphologically left coronary artery is right-sided and bifurcates into a small delimiting artery (analogous to the anterior descending artery) that runs in the groove between the left ventricle and outlet chamber and a circumflex artery that passes posteriorly in the right AV groove, giving off a variable number of atrial and ventricular branches along its course. The morphologically right coronary artery passes posteriorly in the left AV groove, giving off a posterior delimiting artery and a variable number of ventricular branches that run toward the apex. In D-loop DILV with abnormal VA alignment, the coronary pattern is just the mirror image of that described earlier. If the VA alignment is concordant (normally related great arteries), the coronary pattern is usually much like that seen in the normal heart where the ostia are in the anterior, facing sinuses.

The aortic arch is usually to the left and branching is usually normal. The orientation of a left aortic arch is often from left-anterior to right-posterior in L-transposed arteries simply because of the location of the ascending aorta. The branch pulmonary arteries are usually normal, even in hearts with subvalvar and/or valvar pulmonary stenosis.

The cardiotypes most frequently associated with DILV are: {S,L,L} (solitus atria, inverted L-loop left ventricle, leftward and anterior aorta) – 60%; {S,D,D} (solitus atria, solitus D-loop left ventricle, rightward and anterior aorta) – 20%; and {S,D,S} (solitus atria, solitus D-loop left ventricle, and solitus normally related great arteries) which carries the eponym Holmes heart – 15% [40].

A number of associated defects can be seen with DILV. A secundum atrial septal defect is occasionally present but the atrial septum is often intact. Abnormalities of the AV valves including hypoplasia or stenosis or regurgitation (Figure 27.6), are seen in a significant proportion [39–41]. Subvalvar obstruction of the posterior root – the one aligned with the left ventricle – can be due to posterior malalignment of the outlet septum, AV valve tissue, or a fibromuscular ridge (Figures 27.1c and 27.2c). The outflow foramen is frequently obstructed [40,41]. If the great arteries are transposed this results in subaortic stenosis and often hypoplasia of the aorta with coarctation or even arch interruption. Conversely, the obstruction is subpulmonary when the great arteries are normally related.

Physiology

DILV results in mixing of systemic and pulmonary venous blood in the left ventricle. If mixing is complete, the oxygen saturation is similar in the aorta and pulmonary artery and determined by the ratio of pulmonary to systemic blood flow (*Qp*/*Qs*). Occasionally there can be remarkable streaming that produces a marked difference between systemic and pulmonary arterial oxygen saturation. Obstruction of the outflow foramen with TGA favors pulmonary blood flow and diminishes systemic cardiac output but does the opposite with normally related great arteries.

Left ventricular volume overload is characteristic of essentially all forms of DILV because the left ventricle must pump both systemic and pulmonary blood flow. The higher the *Qp*/*Qs*

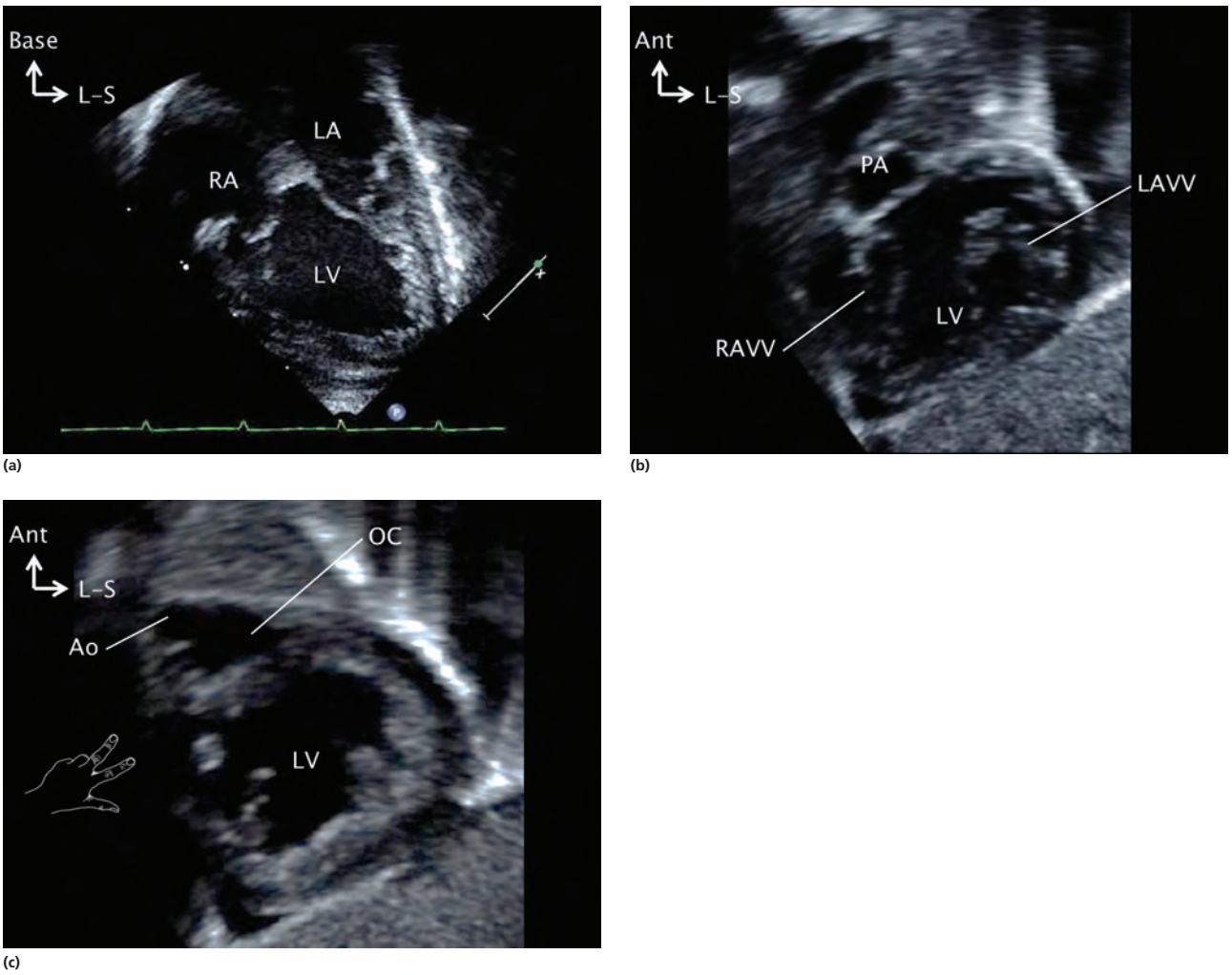


Figure 27.4 Three echocardiographic views of a heart with DILV and transposition of the great arteries {S,D,D}. **(a)** Apical 4-chamber view showing both AV valves aligned with the left ventricle (LV). **(b)** Subxiphoid short-axis view showing the right (RAVV) and left (LAVV) AV valve in cross-section. The pulmonary artery (PA) is aligned with the LV. **(c)** A more apical short-axis cut showing the aorta (Ao) arising from the outflow chamber (OC). The LV can only be described using the left hand, with the thumb in the AV valves, the fingers in the outflow and the palm against the LV septal wall.

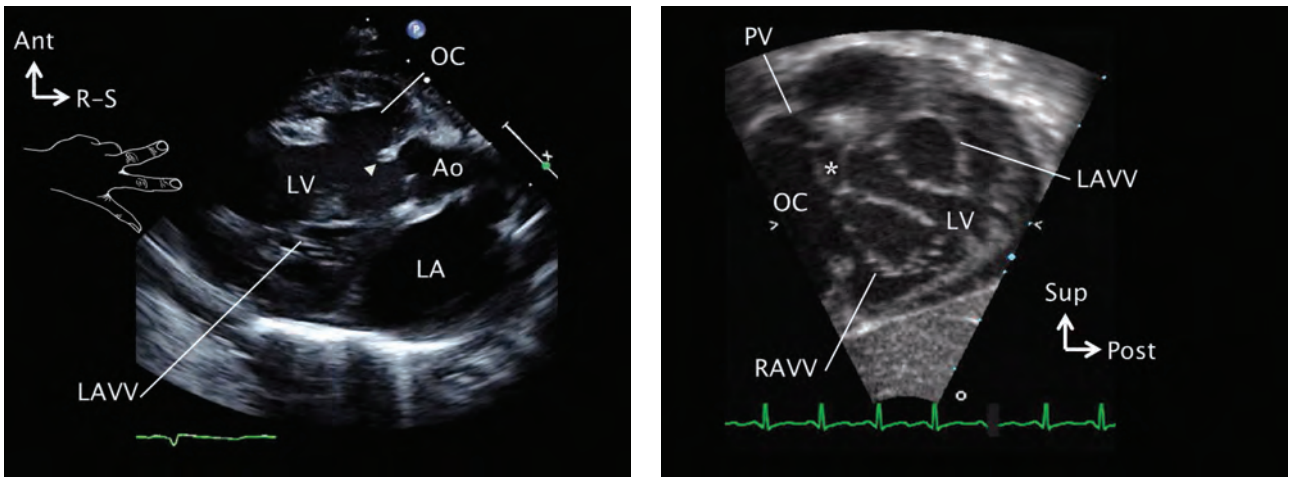
is, the greater the volume overload and the higher the systemic oxygen saturation. Chronic volume overload results in left ventricular dilation, eccentric hypertrophy, and eventually adverse remodeling. Obstruction to ventricular outflow or aortic arch obstruction causes concentric hypertrophy, myocardial fibrosis and diastolic dysfunction. Concentric hypertrophy further narrows the outflow resulting in a positive feedback loop that can quickly lead to ventricular failure.

Excessive pulmonary blood flow, especially with pulmonary hypertension, damages the pulmonary vascular endothelium and leads to progressive pulmonary vascular obstructive disease.

An atrial septal defect facilitates mixing and reduces streaming. AV valve regurgitation increases the ventricular volume overload. The effect of AV valve stenosis depends on which valve is involved and whether an atrial septal defect is present. In the absence of an atrial defect, stenosis of the left (pulmonary) AV valve causes pulmonary venous hypertension with pulmonary congestion and increased pulmonary arterial and venous smooth muscle. Conversely, right (systemic) AV valve stenosis causes systemic venous hypertension with liver engorgement, peripheral edema, and serous effusion.

Treatment strategies

Neonatal palliation is usually undertaken for systemic outflow and/or aortic arch obstruction. Amalgamation of the aorta and pulmonary trunk is frequently used to bypass obstruction of the outflow foramen between the left ventricle and outlet chamber [47]. Some type of systemic-pulmonary shunt is then necessary to provide pulmonary blood flow. Another approach is enlargement of the outflow foramen [45]. Extensive arch reconstruction may be necessary in cases of arch hypoplasia or interruption.



(a) (b)

Figure 27.5 Two echocardiographic views of a Holmes heart, DILV with normally related great arteries {S,D,S}. **(a)** Parasternal long-axis view showing the left AV valve (LAVV) entering the left ventricle (LV) and the aorta (Ao) normally aligned and connected to the LV. The outlet septum (▲) is small and mildly deviated posteriorly. The outflow foramen connects the LV with the outlet chamber (OC). This solitus or D-loop left ventricle can only be represented by a left hand with the thumb in the LAVV, the fingers in the Ao, and the palm against the septal wall. **(b)** Subxiphoid short-axis view through the base of the LV showing the LAVV and right AV valve (RAVV). The LAVV has a medial leaflet and a mural leaflet characteristic of a mitral valve. The RAVV has three leaflets, medial, inferior, and septal, characteristic of a tricuspid valve. The communication between the LV and outlet chamber (OC) extends from the outlet septum (*), seen just posterior to the pulmonary valve (PV), behind the septal leaflet of the RAVV. The size of the OC and the inferior extension of the outflow foramen suggest the presence of some RV sinus in this heart.

Severe pulmonary stenosis or atresia prompts creation of a systemic-pulmonary shunt. Patients with unrestricted pulmonary blood flow and no systemic outflow obstruction often undergo pulmonary artery banding within the first months of life to treat heart failure and improve outlook for Fontan palliation [48].

Patients with stenosis of an AV valve can benefit from creation of an atrial septal defect, either by interventional catheter procedure or surgery, to relieve systemic or pulmonary venous obstruction. Conversely, severe insufficiency of an AV valve may prompt plasty or even patch closure of the valve, with creation of an atrial defect, to relieve the volume overload.

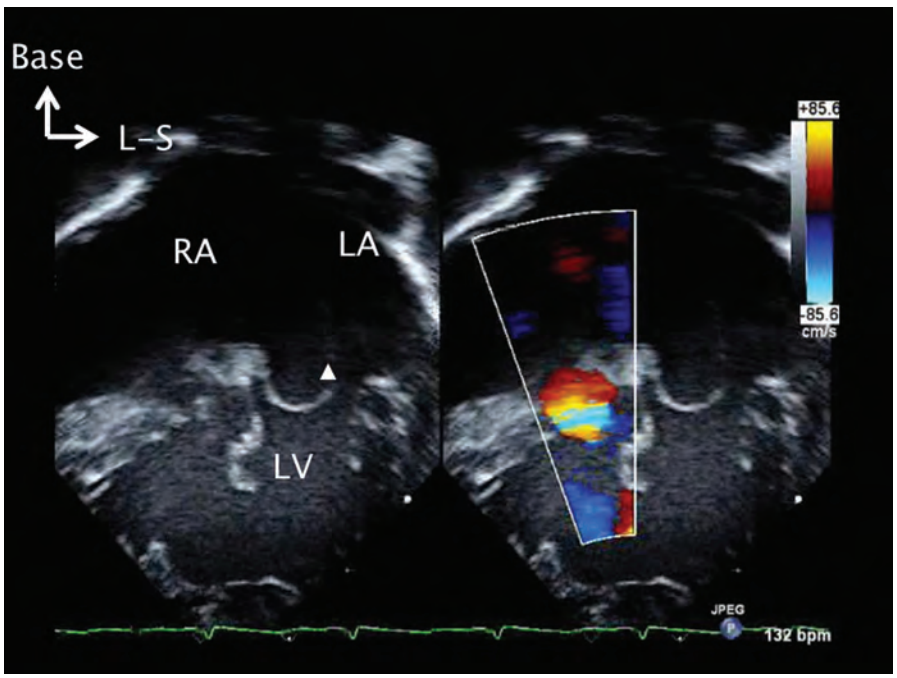


Figure 27.6 Apical 4-chamber view (left) and color flow map (right) of a heart with DILV, normally related great arteries {S,D,S}, and right AV valve hypoplasia. Note the aneurysm of septum primum (▲) bulging into the left AV valve.

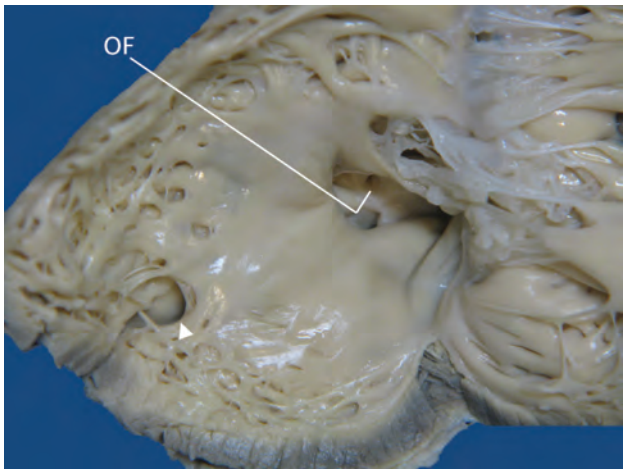


Figure 27.7 Opened left ventricle of a heart with DILV and double-outlet infundibulum {S,D,D}. There is a second, more apical communication (▲) between the left ventricle and the outlet chamber in addition to the outflow foramen (OF).

The long-term strategy for these patients is staging toward a Fontan procedure, with creation of a bidirectional cavopulmonary anastomosis around 6 months of age and completion of the Fontan procedure around 1 year of age [49].

Double-inlet right ventricle

DIRV is a rare heart defect (0.2% of cardiac autopsies and 1 in 11,000 patients seen by a cardiology service [50]) in which, analogous to DILV, both AV valves are aligned and connected with a ventricle of right ventricular morphology (Figures 27.8 and 27.9; Video 27.6). Some series [51,52] have described a preponderance of cases with heterotaxy syndrome, unbalanced common AV canal, and a hypoplastic left ventricle (see Chapter 28).

Embryologic development

The development of DIRV is more difficult to understand because there is never a time during normal development when the AV canal is completely aligned with the developing right ventricle. Even the direction of looping of the heart tube is uncertain in most cases because there is no clear septal wall of the right ventricle present and a rudimentary left ventricle is demonstrable in a minority [50]. In the few cases where a small LV cavity is present, the loop appears to have been dextral in most. Expansion of the AV canal appears to be normal or nearly so because it becomes normally aligned with the right atrium. Further, the combined size of the two AV valves is substantially larger than either a single mitral or tricuspid valve. What allows the AV canal to become situated completely above the developing right ventricle is unclear. Either the LV cavity is absent or small primarily or it becomes so after losing alignment with the AV canal. Atrial septation proceeds normally as in DILV resulting in division of the AV canal into two separate valves, both aligned with the right ventricle. Again, it is interesting that the AV valves develop relatively normally despite absence of the muscular inflow septum. The outflow then develops in broad continuity with the underlying right ventricle without interposition of an outflow foramen as seen in DILV. The infundibular or outlet septum divides the outflow into aortic and pulmonary components and comes to sit above the right ventricular cavity within the outflow muscular sleeve, which is the cranial continuation of the developing right ventricle. Outflow rotation appears to be abnormal in most cases resulting in double-outlet right ventricle with side-by-side or otherwise malposed great arteries. On the other hand, rotation may approximate normal in hearts with a rightward and posterior aorta and anterior and leftward pulmonary artery. Uneven division of the outflow, with or without deviation of the infundibular septum, likely explains the hypoplasia and obstruction of either the pulmonary or aortic outflow seen frequently in DIRV.

Anatomy

Persistence of a left superior vena cava to coronary sinus and secundum atrial septal defect appear to be frequent findings [50]. The morphology of the AV valves resembles a normal mitral or tricuspid valve less frequently than in DILV (Figures 27.8 and 27.9). Hypoplasia or stenosis of one AV valve, most frequently the left, occurs in 25% or more of cases (Figure 27.8b,c) but more than mild regurgitation is uncommon [50]. A tiny hip-pocket left ventricle (Figure 27.8c) is present in up to 20–25% of patients [50], although some series have reported a higher prevalence [51]. It is located posteriorly near the AV groove and usually communicates with the right ventricle through a ventricular septal defect. In these cases there are clearly two ventricular sinuses although the rudimentary left ventricle can never function independently. The right ventricle is often large, hypertrophied and bizarrely shaped with a few large muscle bundles. There is a prominent posterior-median ridge passing from base to apex between the AV valves (Figure 27.8b and 27.9) and which often receives attachments of the AV valves. This can give the appearance of a ventricular septum on clinical imaging studies and has resulted in an erroneous diagnosis of two ventricular sinuses with multiple ventricular septal defects. A characteristic feature of DIRV is absence of a septal wall with a smooth basal endocardial surface (the left ventricular septal wall) as seen in DILV. In addition the outflow of the heart continues broadly from the right ventricle with no constriction (outflow foramen) separating the outlet chamber from the ventricle as seen in DILV (Figures 27.8 and 27.9). The infundibular or outlet septum sits above the right ventricular cavity dividing the subarterial infundibular sleeve and does not usually join a wall of the ventricular body. Uneven division of the outflow into subpulmonary and subaortic infundibula, with or without deviation of the outflow septum, is a frequent cause of obstruction, especially subpulmonary obstruction (Figures 27.8a and

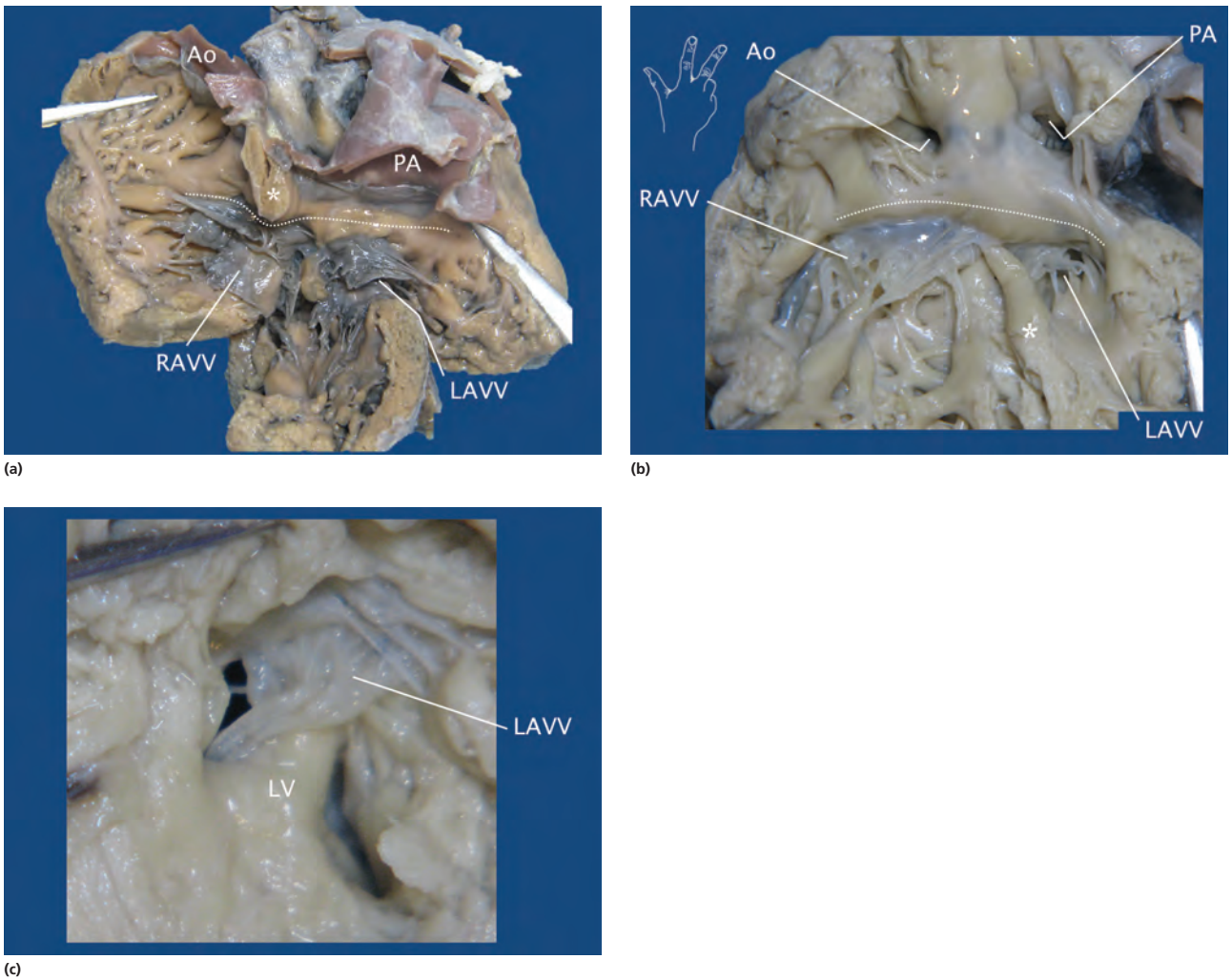


Figure 27.8 Two hearts with DIRV. **(a)** DIRV with double-outlet right ventricle {S,X,D}. The ventricular loop cannot be determined in this heart because the septal wall of the right ventricle cannot be identified, hence the "X" ventricular loop. The left (LAVV) and right (RAVV) AV valves enter the body of the right ventricle. The junction between the right ventricular body and outflow is broad (dotted line) and the infundibular or outlet septum (∗) sits directly above the right ventricular body with the aorta (Ao) and pulmonary artery (PA) on either side. **(b)** DIRV with double-outlet right ventricle {S,D,D}. The septal wall of the right ventricle can be identified in this heart because there is a small left ventricular chamber, seen in (c) behind the hypoplastic and straddling LAVV. Only a right hand (upper left) can be used to describe the right ventricle with the thumb in the AV valves, the fingers in the outflow, and the palm against the septal wall (under the LAVV). Here the hand rule is being applied to a right ventricle so that a right hand describes a solitus or D-loop right ventricle. Note the broad junction (dotted line) between the body of the right ventricle, with the LAVV and RAVV, and the outflow, with the Ao and PA. The outlet or infundibular septum is the muscular ridge between the Ao and PA. A posterior median ridge (∗) is seen between the LAVV and RAVV. **(c)** Opened hypoplastic left ventricle (LV) with a part of the LAVV straddling through a VSD. There are two ventricular sinuses present in this heart.

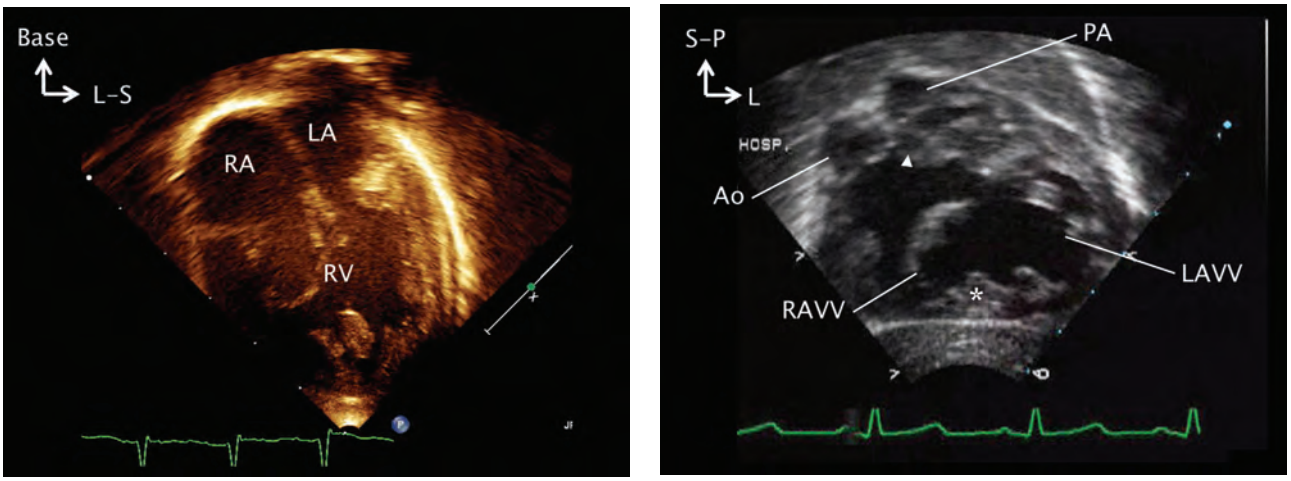
27.9). Aortic arch obstruction regularly accompanies subaortic stenosis.

Right aortic arch seems to be somewhat more frequent than expected [50,51]. Branch pulmonary arteries are usually normal despite the prevalence of subpulmonary obstruction. Coronary arteries arise from the aortic sinuses facing the pulmonary root and form circumflex arteries in their respective AV grooves, giving off descending branches at irregular intervals around the heart [46].

The cardiotypes most frequently associated with DIRV are: {S,X,D} (solitus atria, indeterminate ventricular loop, rightward and anterior aorta) – 50%; {S,D,D} (solitus atria, solitus D-loop left ventricle, rightward and anterior aorta) – 15%; and {S,X,L} (solitus atria, indeterminate ventricular loop, and leftward and anterior aorta) – 20% [50].

Physiology

The physiology of DIRV is rather similar to DILV in that both are common mixing lesions in the ventricle with the potential for outflow obstruction. Although the systemic and pulmonary arterial saturations are usually similar, and dependent on the *Qp*/*Qs*, considerable streaming can occur in some hearts. Right



(a) (b)

Figure 27.9 Two echocardiographic views in DIRV. **(a)** Apical 4-chamber view in a patient with DIRV and double-outlet right ventricle {S,X,D}. Both AV valves enter the right ventricle. Note the large muscle bundles in the right ventricle (RV). **(b)** Subxiphoid long-axis view in a heart with DIRV and double-outlet right ventricle {S,X,D} showing the left (LAVV) and right (RAVV) entering the body of the right ventricle which continues broadly as the outflow with the aorta (Ao) and pulmonary artery (PA). The infundibular or outlet septum (▲) is deviated under the PA causing subpulmonary obstruction.

ventricular volume overload is characteristic of DIRV because the right ventricle must pump both systemic and pulmonary blood flow. A higher Qp/Qs results in greater ventricular volume overload and higher systemic oxygen saturation. Chronic volume overload results in right ventricular dilation, eccentric hypertrophy, and eventually adverse remodeling. Conversely, very cyanotic patients have a low Qp/Qs and only a mild right ventricular volume overload. Obstruction to ventricular outflow or aortic arch obstruction causes concentric hypertrophy, myocardial fibrosis and diastolic dysfunction.

Although reduced pulmonary blood flow is the more frequent problem, excessive pulmonary blood flow, especially with pulmonary hypertension, leads to progressive pulmonary vascular obstructive disease.

As in DILV, in the absence of an atrial septal defect, stenosis of the right AV valve produces systemic venous obstruction and stenosis of the left AV valve results in pulmonary venous obstruction. Insufficiency of either AV valve compounds the right ventricular volume overload.

Pulmonary outflow obstruction occurs frequently and, if severe, results in a ductus-dependent pulmonary circulation. Systemic outflow obstruction is less common but can limit flow directly into the aorta. Marked limitation of aortic flow results in ductus-dependent systemic circulation. Aortic arch hypoplasia, coarctation or interrupted aortic arch often accompanies severe systemic outflow obstruction.

Treatment strategies

Initial palliation in DIRV is most often by creation of a systemic-pulmonary shunt for pulmonary stenosis or atresia [50,52]. A small proportion of patients, those with subaortic obstruction, undergo amalgamation of the aorta and pulmonary artery to bypass the obstruction with creation of a systemic-pulmonary shunt as a source of pulmonary blood flow [50,52]. Arch reconstruction is often needed in these patients as well. Creation of an atrial septal defect can improve mixing and is indicated if one AV valve is stenotic. Long-term palliation is staging toward a Fontan circulation with bidirectional cavopulmonary anastomosis around 6 months of age and completion of Fontan around 1–2 years of age [52].

Tricuspid atresia (TA)

TA is characterized by absence or impatency of the usual AV valve of the right ventricle (Figures 27.10–27.12; Videos 27.7–27.10). In addition, the right ventricular sinus or body is absent, or extremely hypoplastic. As in DILV, the small chamber present in the ventricular mass in addition to the left ventricle is an infundibulum or outlet chamber.

Embryologic development

The primary abnormality in TA is failure of expansion of the AV canal toward the inner curvature of the heart tube. Bending or looping of the heart tube is dextral in the majority of patients but is to the left (levo or L) in about 10%. As the chambers balloon out of the greater curvature of the heart tube, the atria and left ventricle appear to expand normally but the right ventricular sinus does not develop or remains quite hypoplastic. The AV canal remains confined to the left atrium and left ventricle, never becoming aligned with either the right atrium or right ventricle. Expansion of the AV canal is less than normal because the mitral valve that forms from it is substantially smaller than the combined sizes of the two AV valves that form in the normal heart or

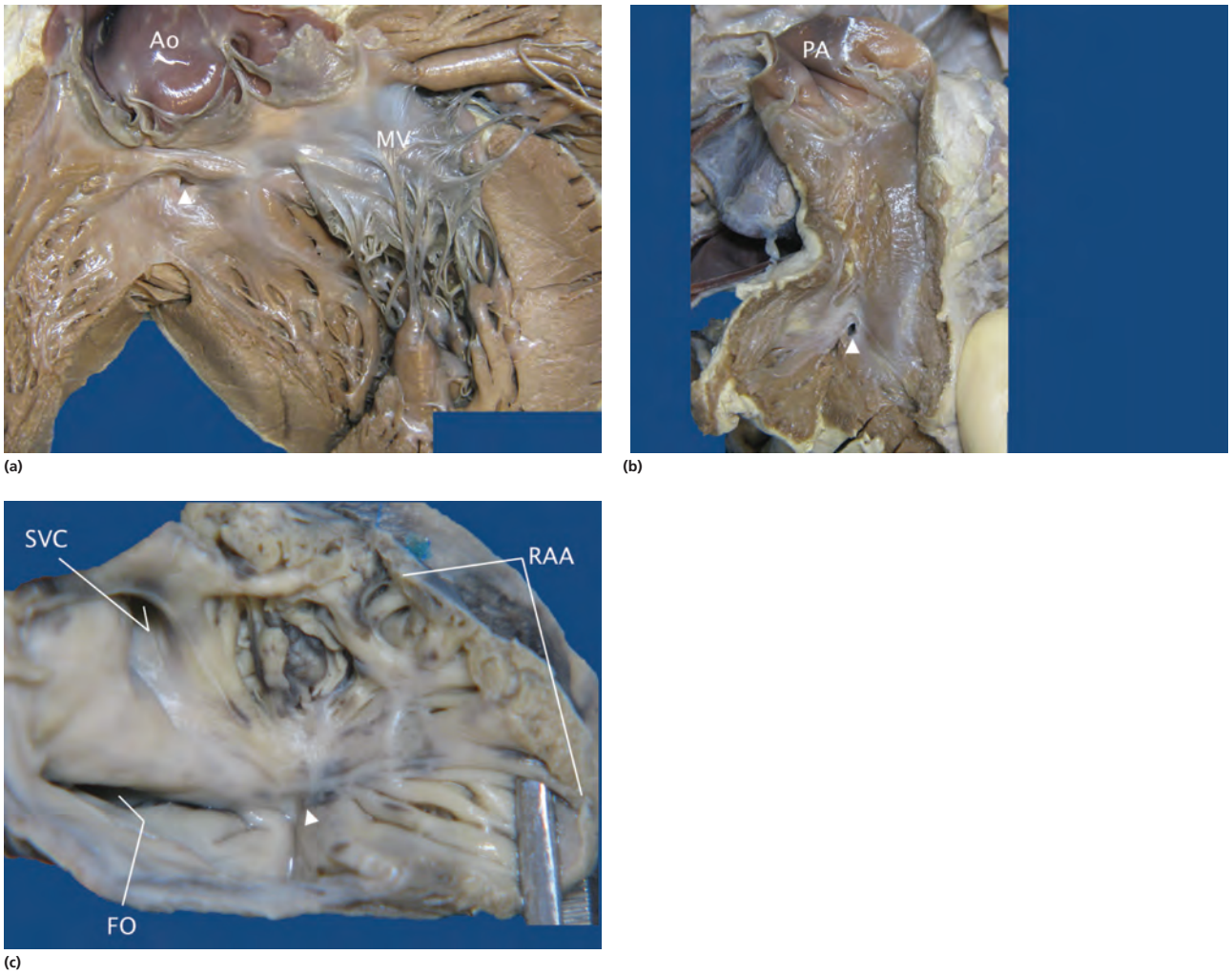


Figure 27.10 A heart with TA and normally related great arteries {S,D,S}. **(a)** The opened left ventricle with a smooth septal surface to the left of the image and the mitral valve (MV) attaching to free wall papillary muscles to the right. The aortic valve (Ao) is in fibrous continuity with the MV. There is a tiny communication (▲) between the left ventricle and the outlet chamber (seen in (b)). **(b)** The opened outlet chamber supporting the pulmonary artery (PA). The tiny communication (▲) with the left ventricle is seen. **(c)** The opened right atrium showing the orifice of the superior vena cava (SVC), the right atrial appendage (RAA) with pectinate muscles, and the foramen ovale (FO). Note the small depression in the floor of the right atrium (▲) marking the usual location of the absent tricuspid valve.

in double-inlet hearts. Atrial septation occurs normally except that the plane of the developing atrial septum, which appears normal with respect to the common atrium, is aligned with the edge of the AV cushions toward the inner curvature and not with the center of the cushions, apparently because of inadequate expansion of the AV canal. Consequently all of the AV cushion material goes toward making the mitral valve, with failure of development of direct communication between the right atrium and right ventricle. The left ventricle continues to communicate with the outflow part of the heart tube through the outflow foramen, which would have become the interventricular foramen had the right ventricle developed. Instead, only the infundibulum or outlet chamber develops. Rotation of the outflow seems to proceed normally in most hearts with TA resulting in normal alignment of the aorta with the left ventricle and the pulmonary trunk with the infundibulum or outlet chamber. In some of these hearts, the outflow foramen becomes completely closed by the outlet septum resulting in an intact septum between the left ventricle and outlet chamber. In most, however, the foramen is not closed allowing a communication of variable size between the left ventricle and the outlet chamber. In other hearts, including all of those with levo or L-loop left ventricle, outflow rotation is abnormal resulting in transposed or double-outlet alignment of the great arteries. In these hearts, the outflow foramen almost always remains open.

Anatomy

Persistence of a left superior vena cava draining to the coronary sinus occurs more frequently than in normal hearts [53].

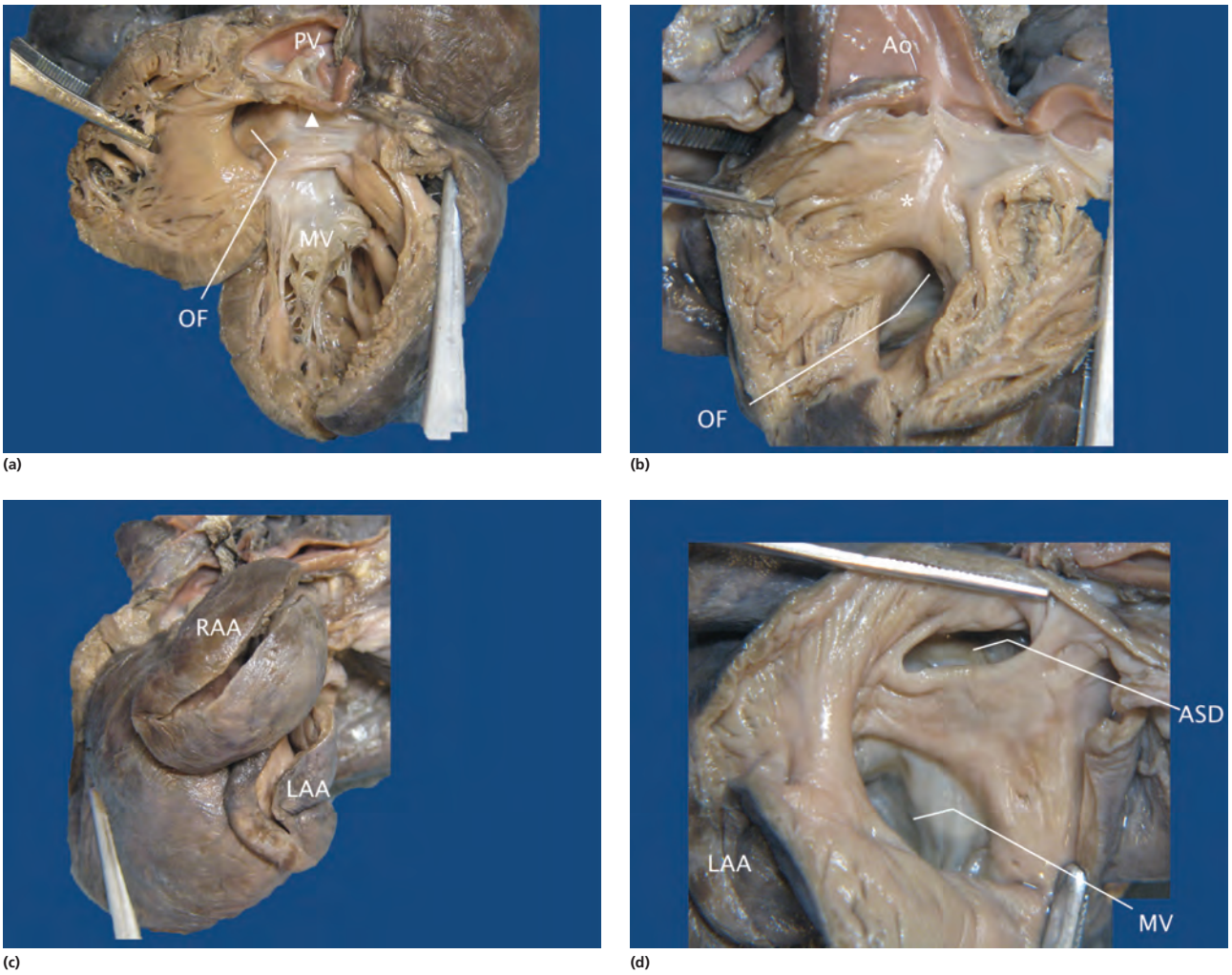


Figure 27.11 A heart with TA, transposition of the great arteries {S,D,D} and left-sided juxtaposition of the right atrial appendage. **(a)** Opened left ventricle with the smooth septal wall to the left of the image and the mitral valve (MV) with papillary muscle attachments to the free wall on the right side. The outflow foramen (OF) is seen in the septal wall. A small ridge of conal muscle (▲) separates the MV from the pulmonary valve (PV). **(b)** Outlet chamber comprised of conal or infundibular muscle supporting the aortic valve (Ao). The OF is seen just below the infundibular or outlet septum (∗). **(c)** Juxtaposed right (RAA) and left (LAA) atrial appendages at the left heart border. The RAA is always superior and anterior to the LAA in left-sided juxtaposition in situs solitus of the atria. **(d)** Opened left atrium showing the atrial septal defect (ASD) between septum primum below and septum secundum above. The mitral valve (MV) is between the atrial septum and the orifice of the LAA.

Left-sided juxtaposition of the atrial appendages in situs solitus (Figure 27.11c) is strongly associated with TA, occurring in about 10% of cases [54]. In hearts with this arrangement of the atrial appendages, a large atrial defect, associated with angulation of septum primum with respect to septum secundum, is the rule (Figure 27.11d). Otherwise, a patulous foramen ovale is the most frequent finding in the atrial septum (Figure 27.13). Pulmonary venous drainage is usually normal.

The tricuspid valve is completely absent in the majority of cases (Figures 27.10c and 27.12d). There is often a small depression in the muscular floor of the right atrium in the usual location of the tricuspid valve, but no valve apparatus. In most hearts with TA, the dimple in the floor of the right atrium is directed toward the left ventricular outflow and not toward the outlet chamber, further suggesting absence of the right ventricular sinus [55]. The right AV sulcus is very deep, reminiscent of the inner curvature of the early looping heart tube (Figure 27.14). In a minority of cases a tricuspid valve annulus, leaflets, and chordae, in varying stages of development, can be identified [53,55]. In these cases the leaflets are completely fused, preventing any flow of blood across the valve. Formed but atretic valves are associated with partial AV canal defects (primum atrial septal defect) [56], Ebstein anomaly [57], and congenital pulmonary valve regurgitation (absent pulmonary valve) with intact ventricular septum [58] (Figure 27.15).

The mitral valve is usually normally formed, but a cleft in the anterior leaflet (Figure 27.16) is seen in some hearts with TA and TGA [59]. The annulus diameter of the mitral valve is

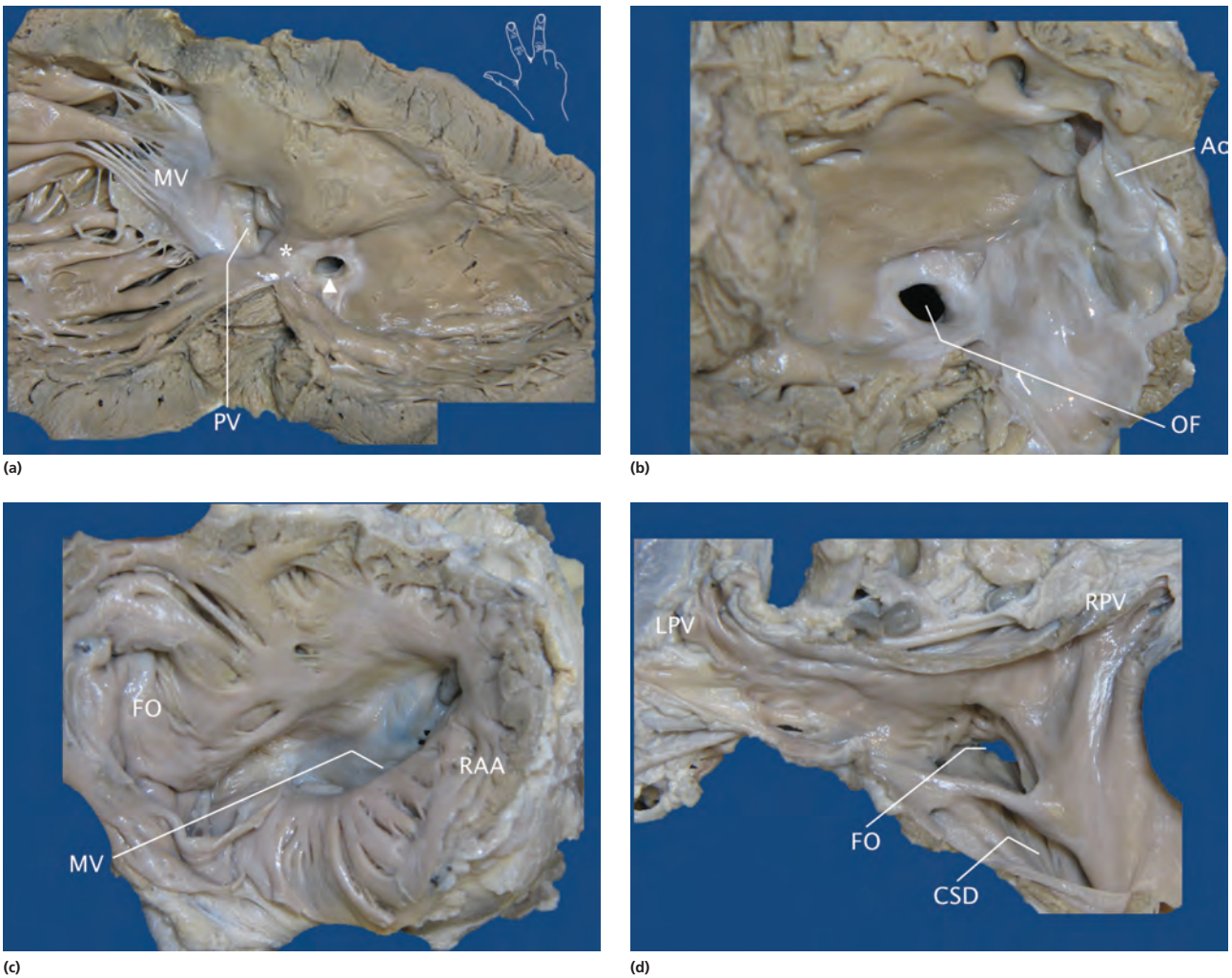


Figure 27.12 A heart with TA and transposition of the great arteries {S,L,L}. **(a)** Opened left ventricle with the smooth septal wall to the right of the image and the free wall with papillary muscle attachments of the mitral valve (MV) to the left. The MV is in fibrous continuity with the pulmonary valve (PV). The small outflow foramen is between the infundibular or outlet septum (∗) and the septal wall of the left ventricle. Only a right hand (upper right) can describe this left ventricle, with the thumb in the MV, the fingers in the PV and the palm against the septal wall, indicating that it is inverted or an L-loop. **(b)** Opened outlet chamber with the aortic valve (Ao) supported by infundibular or conal muscle. The orifice of the outflow foramen (OF) is surrounded by white, fibrous tissue extending onto the free wall under the Ao due to endothelial reaction to the high-velocity jet of blood crossing the OF. **(c)** Opened right atrium, with the right atrial appendage (RAA) and fossa ovalis (FO), draining through a mitral valve (MV) into the right-sided, inverted left ventricle. **(d)** Opened left atrium with left (LPV) and right (RPV) pulmonary veins entering. The only egress is through the foramen ovale (FO) or the coronary sinus defect (CSD) because the tricuspid valve is atretic.

usually somewhat greater than in normal controls [60], probably due to increased flow volume. The left ventricle is dilated but not excessively hypertrophied in the absence of outflow obstruction [61]. The infundibulum or outlet chamber is small and supports one or both great arteries. In cases where the outlet chamber extends inferiorly toward the diaphragmatic surface of the heart (Figure 27.17), some right ventricular sinus may be present. In any case, it is virtually always severely hypoplastic and has no inlet component. It is also possible that these larger chambers are simply an expanded infundibulum with no right ventricular sinus present. The left ventricle usually communicates with the outlet chamber through the primitive outflow foramen – often called a ventricular septal defect or bulboventricular foramen. In a few cases the septal wall of the left ventricle is intact. A small communication causes subvalvar obstruction of the arterial root that is supported by the outlet chamber.

The great arteries are normally related in most hearts with TA [53]. The aortic valve is aligned with the left ventricle and in fibrous continuity with the mitral valve. The pulmonary artery is aligned with the infundibulum or outlet chamber. The pulmonary valve, trunk and branches are remarkably well formed in most hearts despite severe subvalvar obstruction or even atresia (Figure 27.10). Only occasionally is there stenosis or atresia

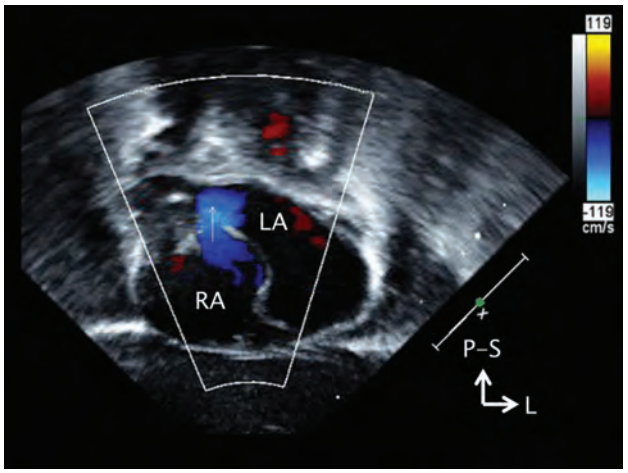


Figure 27.13 Color flow map in subxiphoid long-axis view in a patient with TA and normally related great arteries {S,D,S} showing right-to-left flow through the open foramen ovale (arrow).

of the pulmonary valve and very rarely discontinuity or obstruction of branch pulmonary arteries.

Abnormalities of VA alignment occur in a significant minority of TA hearts, most frequently transposition (discordance), with the pulmonary artery aligned with the left ventricle and mitral-pulmonary fibrous continuity and the aorta aligned with the outlet chamber [53]. In a few hearts there is double outlet from the infundibulum, with both great arteries arising from the outlet chamber. Extremely rare is double-outlet left ventricle with TA [62]. Hypoplasia of the aortic arch, coarctation and even aortic arch interruption are associated with obstruction of the outflow foramen when the great arteries are transposed (Figure 27.18). Other conotruncal anomalies, especially truncus arteriosus, occasionally accompany TA [63].

TA in the setting of an L-loop left ventricle is quite different anatomically and physiologically [53]. Here, because the ventricles are inverted, it is the left AV valve that is atretic (Figure 27.12). Because there is situs solitus of the atria, TA in this setting causes pulmonary venous outflow obstruction. The foramen ovale is often small, probably due to a higher pressure than normal in the left atrium in utero. There is usually a small cup-shaped indentation in the floor of the left atrium representing the atretic valve. The mitral valve and left ventricle are inverted (Figures 27.12 and 27.14) and usually somewhat larger than normal, but otherwise unremarkable. The infundibulum or outlet chamber is left-sided and small. The great arteries are virtually always transposed, with the pulmonary artery posterior and rightward and aligned with the left ventricle and the aorta anterior and leftward and aligned with the outlet chamber. Obstruction of the outflow foramen produces subaortic stenosis often associated with aortic arch obstruction. There are occasional cases of complete closure of the outflow foramen causing functional aortic atresia. As in DILV, when the ascending aorta is leftward, the aortic arch runs from left-anterior to right-posterior despite being a left aortic arch.

Physiology

TA is a common mixing lesion, producing complete mixing of systemic and pulmonary venous blood. In TA with a D-loop left ventricle this occurs in the left atrium and ventricle. The only egress for systemic venous blood from the right atrium is the foramen ovale or other interatrial communication. Although uncommon, the foramen ovale can become restrictive, resulting in systemic venous hypertension, liver enlargement and ascites

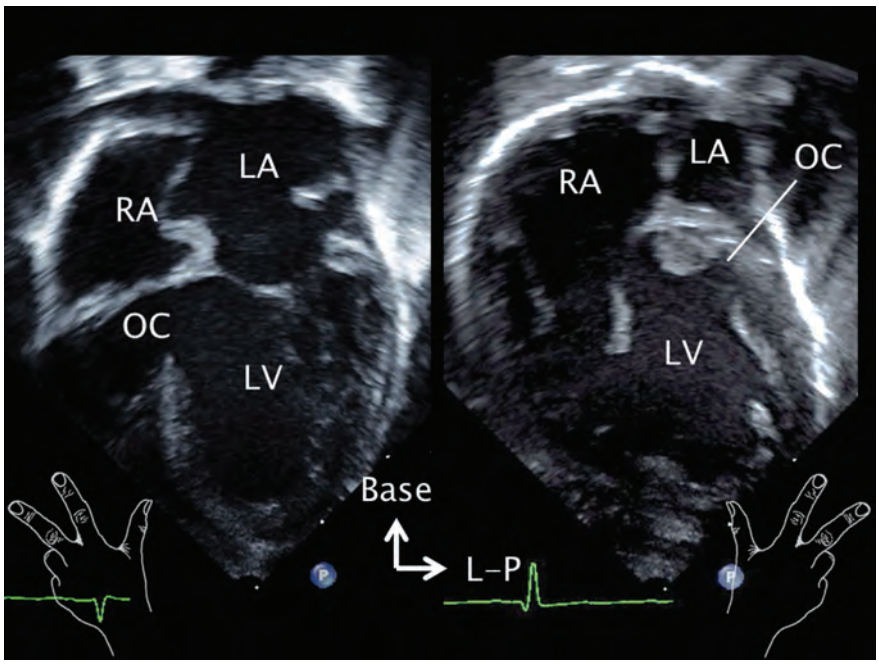


Figure 27.14 Apical 4-chamber views in two patients with TA are mirror images of each other. On the left is a D-loop or solitus left ventricle (LV) in a patient with TA and normally related great arteries {S,D,S}. The septal wall and outlet chamber (OC) are to the right and anterior so that only a left hand fits this LV. The deep AV groove on the right indicates right-sided tricuspid atresia. On the right is an L-loop or inverted LV with the septal wall and OC to the left and posterior. Only a right hand fits this LV. Here the deep AV sulcus is left-sided indicating atresia of the left AV valve. LA, left atrium; RA, right atrium.

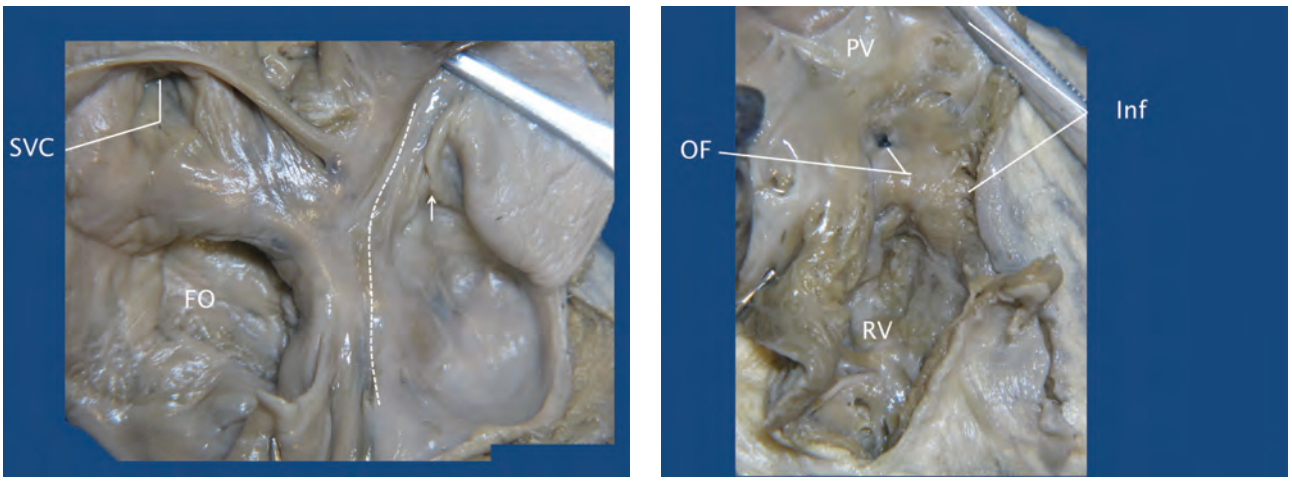


Figure 27.15 TA with associated Ebstein anomaly. **(a)** The opened right atrium (left side) and atrialized right ventricle (right side) in a heart with TA associated with Ebstein malformation. The anatomical tricuspid valve annulus (dashed line) indicates the AV junction. The superior vena cava (SVC) and foramen ovale (FO) are seen in the right atrium. The smooth-walled atrialized right ventricle ends blindly at rudimentary valve leaflets (arrow). **(b)** The opened apical trabecular portion of the right ventricle (RV) and the infundibulum or outflow (Inf) which supports the pulmonary valve (PV). There is no communication between the atrialized right ventricle and the apical trabecular segment. A small outflow foramen (OF) connects the infundibulum with the left ventricle.

[64]. Mitral regurgitation increases left ventricular volume overload and raises the pressure in both atria because the right atrial pressure must be at least as high as left atrial pressure for blood to flow across the foramen ovale. The left ventricle pumps both systemic and pulmonary blood flow, resulting in dilation and eccentric hypertrophy [61]. As in other common mixing lesions, the systemic oxygen saturation is proportional to the *Qp*/*Qs* ratio. In normally aligned great arteries, aortic outflow is rarely obstructed but pulmonary outflow often is [53]. Pulmonary obstruction can be due to restriction of the outflow foramen, obstruction within the infundibulum due to malalignment of the outflow septum or muscle bundles, or less frequently valvar stenosis. Although ductus-dependent pulmonary blood flow is uncommon, subpulmonary obstruction can progress rapidly so that intense cyanosis often supervenes within 3–6 weeks of birth [65]. Conversely, subaortic obstruction occurs in TA with transposed great arteries by the same mechanisms described earlier, except that valvar aortic stenosis is even less frequent than

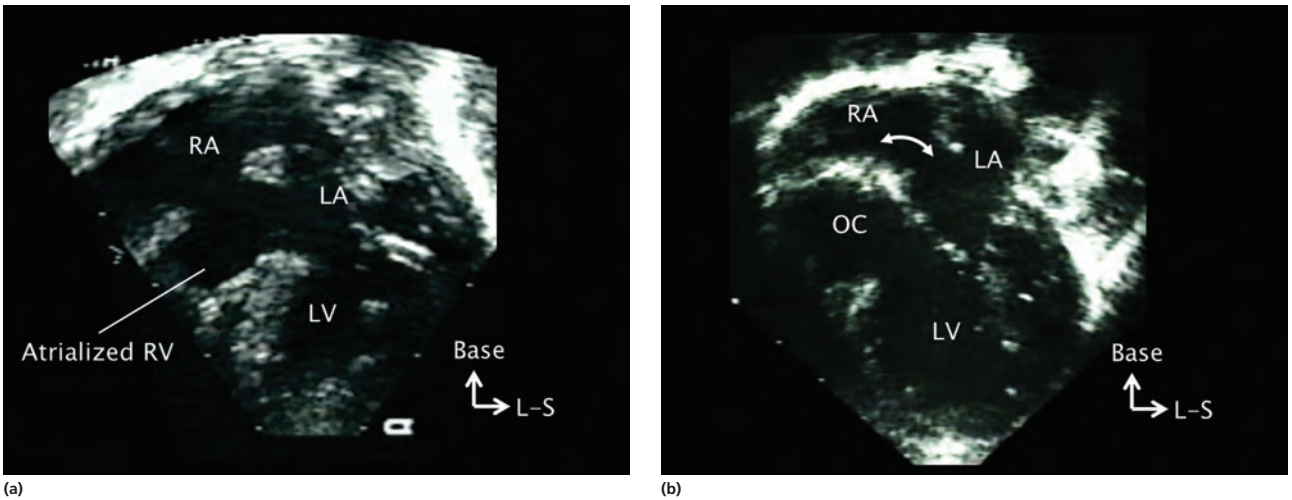


Figure 27.16 Echocardiographic views in hearts with TA associated with Ebstein anomaly and partial AV canal. **(a)** Apical 4-chamber view in a patient with TA associated with Ebstein anomaly and partial AV canal (primum atrial septal defect). The smooth-walled atrialized right ventricle (RV) ends blindly. A large primum atrial septal defect is apparent between the right (RA) and left (LA) atria. **(b)** Apical 4-chamber view in a patient with TA associated with partial AV canal or primum atrial septal defect. The deep AV sulcus characteristic of TA is seen on the right side between the right atrium (RA) and the outlet chamber (OC). The primum atrial septal defect (curved double arrow) is seen between the RA and LA. LV, left ventricle.

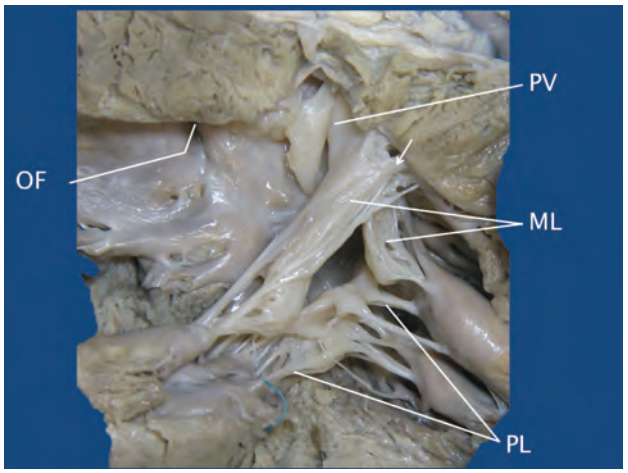


Figure 27.17 The base of the left ventricle in a patient with TA, transposition of the great arteries {S,D,D} and a cleft mitral valve. The medial leaflet (ML) of the mitral valve is divided into two parts by the cleft (arrow). The attachments around the cleft insert onto the left ventricular free wall lateral to the pulmonary valve (PV) rather than onto the septum as in an AV canal defect. The posterior or mural leaflet (PL) of the mitral valve is shorter than usual and runs between the postero-medial and antero-lateral papillary muscle groups. A restrictive outflow foramen (OF) is seen in the septal wall of the left ventricle.

valvar pulmonary stenosis. Ductus-dependent systemic circulation is seen in a significant proportion of patients with transposed great arteries. Even if the ductus has closed, a small outflow foramen is an unstable source of systemic blood flow and, without intervention, is likely to lead rapidly to heart failure or death. Subaortic obstruction is associated with aortic arch hypoplasia and/or obstruction.

In TA hearts with an L-loop left ventricle, the AV valve atresia is left-sided in situs solitus so that pulmonary venous egress is impeded. Because of the construction of the foramen ovale, flow from left atrium to right atrium is not favored. Consequently, left atrial pressure rises acutely with the rapid increase in pulmonary blood flow after birth. Unless treated, pulmonary edema with severe cyanosis and respiratory failure are likely. Otherwise, the physiology is similar to TA with D-loop left ventricle and transposed great arteries.

Treatment strategies

Some centers have advocated prophylactic balloon septostomy in TA with D-loop left ventricle to avoid restriction of the foramen ovale, but this is not necessary in most patients [64]. The few patients at risk can be identified based on the size of the foramen ovale and presence of an atrial septal aneurysm (see later) [64]. Conversely, creation of an atrial septal defect is essential in most patients with L-loop left ventricle to treat or prevent pulmonary venous hypertension [53]. Septostomy is often insufficient so that creation of a defect by septal puncture and dilation or stent placement is generally preferred. Alternatively, a surgical septectomy can be performed, particularly if some other surgical procedure is planned. Some patients with normally related great arteries have sufficient pulmonary blood flow to avoid any intervention until a bidirectional cavopulmonary anastomosis is performed at 4–6 months of age. Others undergo creation of a systemic-pulmonary shunt in the first weeks of life for progressive cyanosis.

Systemic outflow obstruction in TA with transposed great arteries is usually treated by amalgamation of the aorta and pulmonary artery with placement of a systemic-pulmonary shunt [66]. Enlargement of the outflow foramen is an alternative approach but can be difficult in small infants [45,66]. Aortic arch reconstruction is often necessary in these patients for coarctation or arch interruption.

Occasional patients with normally related great arteries and unobstructed pulmonary blood flow undergo pulmonary artery banding to treat heart failure in preparation for a bidirectional cavopulmonary anastomosis [48].

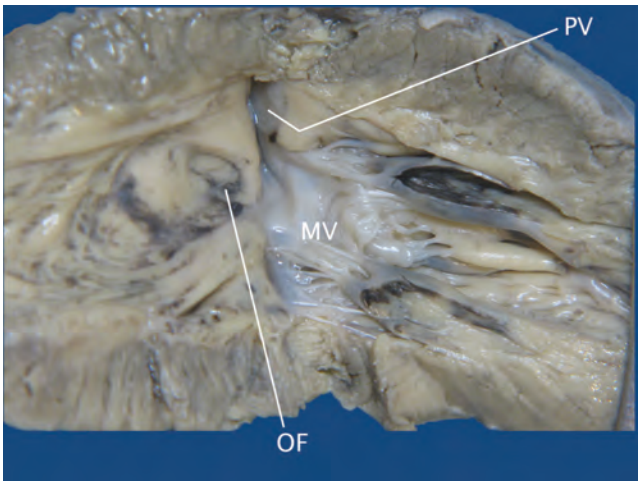
Long-term management is staged Fontan palliation with a bidirectional cavopulmonary anastomosis at 4–6 months of age and completion of Fontan at 1–2 years [49].

Superior-inferior ventricles and criss-cross heart

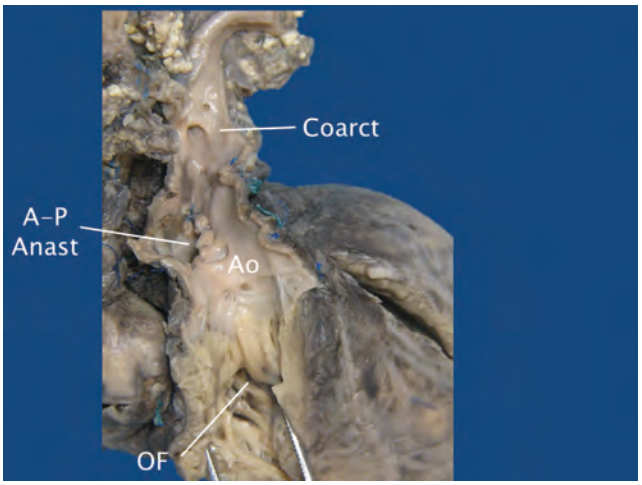
SIV hearts are those in which the two ventricles are stacked one on top of the other, rather than side-by-side, and the ventricular septum is horizontal (Figures 27.19–27.22; Videos 27.11 and 27.12). In criss-cross hearts the axes of the AV valves cross each other rather than being approximately parallel. These complex hearts challenge current understanding of heart development as well as diagnostic and therapeutic approaches. Superior-inferior ventricles are often but not uniformly associated with criss-cross AV valves; either can occur independently of the other. Although two ventricles are virtually always present, the right ventricle and tricuspid valve are often too small to permit a two-ventricle repair.

Embryologic development

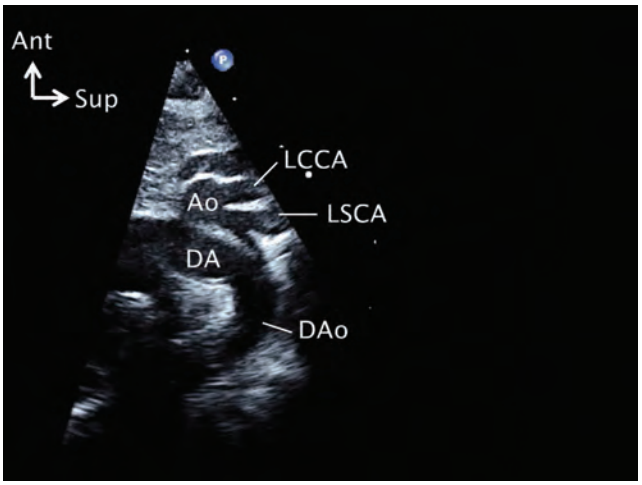
The mechanism for abnormal superior-inferior placement of the ventricles and that for crossing of the ventricular inflows are likely to be related but separate, and at least partially independent. Horizontal formation of the ventricular septum, with a superior right ventricle and inferior left ventricle, could be due to incomplete looping [25]. Interruption of looping after formation of the "C" loop but before completion of the "S" loop, would result in variable failure of caudal and ventral descent of the outflow limb of the heart tube. The outflow remains cranial to the developing left ventricle rather than descending to lie beside it. As the right ventricular sinus balloons out of the proximal outflow, it is cranial or superior to the left ventricle, rather than to the right or left of it, and the interventricular septum is horizontal. The ventricles can be either D-loop (solitus or right-handed)



(a)



(b)



(c)

Figure 27.18 A heart with TA, transposition of the great arteries {S,D,D} with a severely restrictive outflow foramen (OF) and coarctation of the aorta (Coarct). **(a)** Opened left ventricle showing the pulmonary valve (PV) in fibrous continuity with the mitral valve (MV) and a small outflow foramen (OF) in the septal wall. **(b)** The opened outlet chamber and ascending aorta (Ao). The small OF is seen below the aortic valve. The outlet chamber extends inferiorly to the diaphragmatic surface of the heart suggesting that some right ventricular sinus might be present. The obstructed OF was treated by creation of an anastomosis between the pulmonary trunk and the ascending aorta (A–P Anast). There is marked narrowing of the aortic isthmus (Coarct) creating coarctation of the aorta. **(c)** An echocardiogram in a high parasternal view in a similar patient showing severe coarctation of the aorta distal to the left subclavian artery (LSCA). A large ductus arteriosus (DA) continues from the pulmonary trunk to the descending aorta (DAo). LCCA, left common carotid artery.

or L-loop (inverted or left-handed) so "S" looping can begin in either direction before arresting.

The mechanism for crossing of the axes of the AV valves seems to be real or apparent twisting or axial rotation of the ventricles while the atria and AV valves remain relatively fixed. A mechanism for twisting of the ventricles is unknown and the timing of this process is unclear but seems likely to be near the end of or even after completion of looping. Clockwise twisting of the ventricles in a D-loop (and counterclockwise twisting in an L-loop), as viewed from the apex, would explain both the crossing of the AV valves and the large angle observed between the atrial and ventricular septa [67]. Usually the septa are nearly parallel with an angle of <10° between them. In criss-cross hearts, however, the angle can be as large 150°. Twisting of the ventricles with fixed atria and distal outflow also explains the curved elongation of the inflow and outflow tracts often observed in these hearts.

Hypoplasia of the tricuspid valve and right ventricle, seen in many cases of SIV and criss-cross heart, could be due to entrapment of the right side of the AV canal between the ventricular and atrial septa, limiting its capacity for expansion. More rotation of the ventricular septum would lead to a smaller tricuspid valve and right ventricular sinus. This concept is supported by the inverse relationship between the crossing angle of the AV

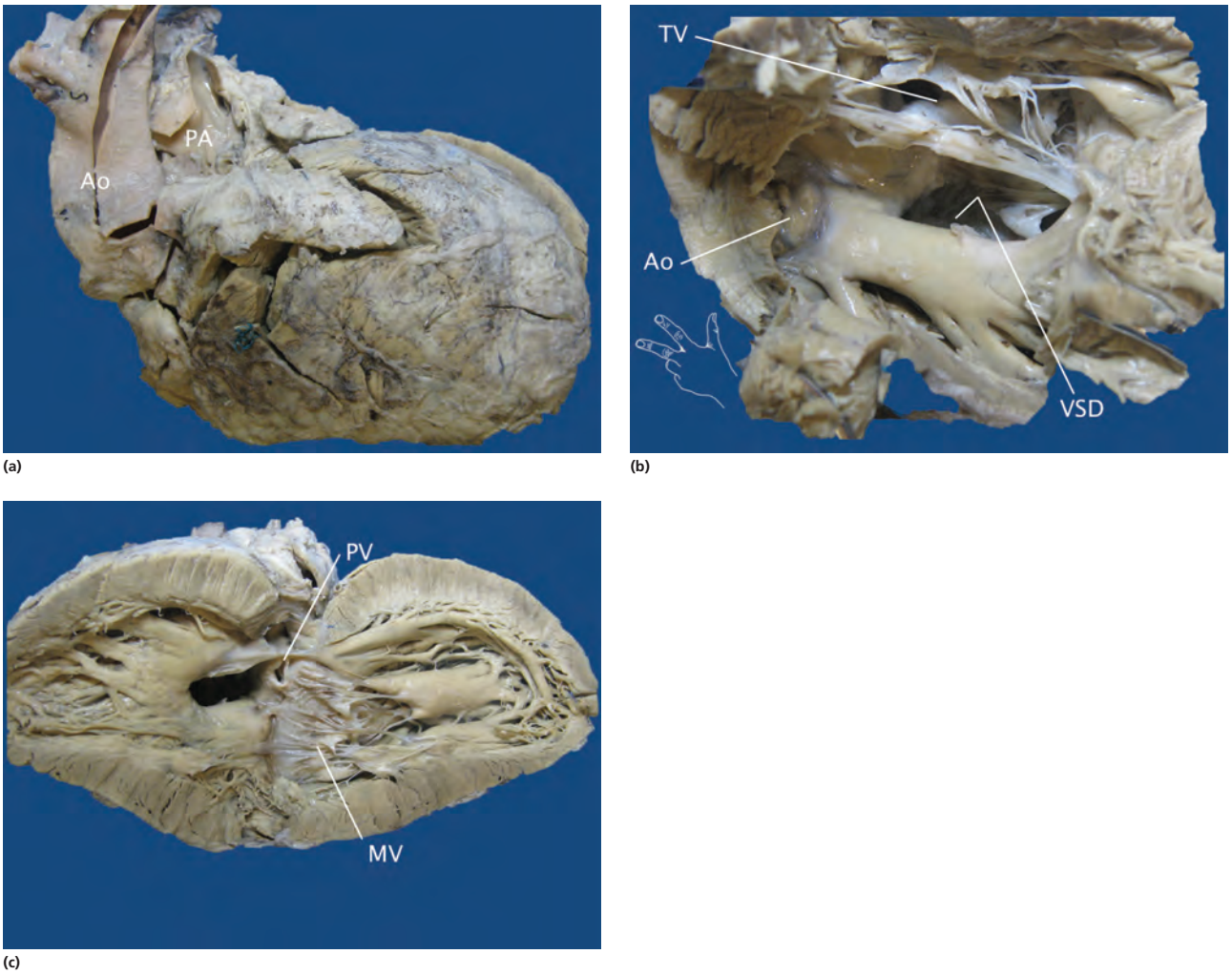


Figure 27.19 A heart with SIV and transposition of the great arteries {S,L,D}. **(a)** The aorta (Ao) is to the right and the pulmonary artery (PA) to the left. **(b)** The opened superior right ventricle showing the tricuspid valve (TV) entering from the left and the Ao exiting to the right. The large ventricular septal defect (VSD) is in the plane of the ventricular septum. This inverted or L-loop right ventricle is organized from left (inflow) to right (outflow) and can only be described using a left hand (lower left). **(c)** Opened left ventricle showing the mitral valve (MV) and pulmonary valve (PV).

valves, an indirect measure of twisting or rotation of the ventricles, and the size of the tricuspid valve and right ventricular sinus seen in infants with this condition [68]. However, it is not known if hypoplasia of the tricuspid valve and right ventricular sinus is primary, leading to abnormal placement of the ventricular septum, or secondary, resulting from the unusual location of the ventricular septum. The high prevalence of dextrocardia and mesocardia in patients with SIV and criss-cross heart is likely related to failure to complete the looping process and/or reduced growth capacity of the right ventricle [25].

The markedly abnormal outflow in these hearts is potentially explained by abnormal rotation of the outflow, as seen in many other types of abnormal VA alignment [32]. However, VA situs discordance frequently seen in these hearts (D-loop ventricles with L-malposition of the aorta or vice versa, see later) could also result from a rotation or twist of the ventricles that "pulls the outflow along." Rotation of the outflow along with the ventricles would have the effect of inverting the great arteries.

Anatomy

As indicated by the discussion of possible developmental mechanisms, the anatomy of SIV and criss-cross heart is complex and variable. In about half of cases these two anomalies occur together. Because of the abnormal position and shape of the ventricles in these hearts, use of the hand rule to establish chirality or topology is especially important [43].

In considering complex hearts like these, a brief review of segmental situs and alignments provides important background. In the majority of hearts the atria are either solitus (usual arrangement with the right atrium anterior and to the right and the left atrium posterior and to the left) or inversus (the mirror image

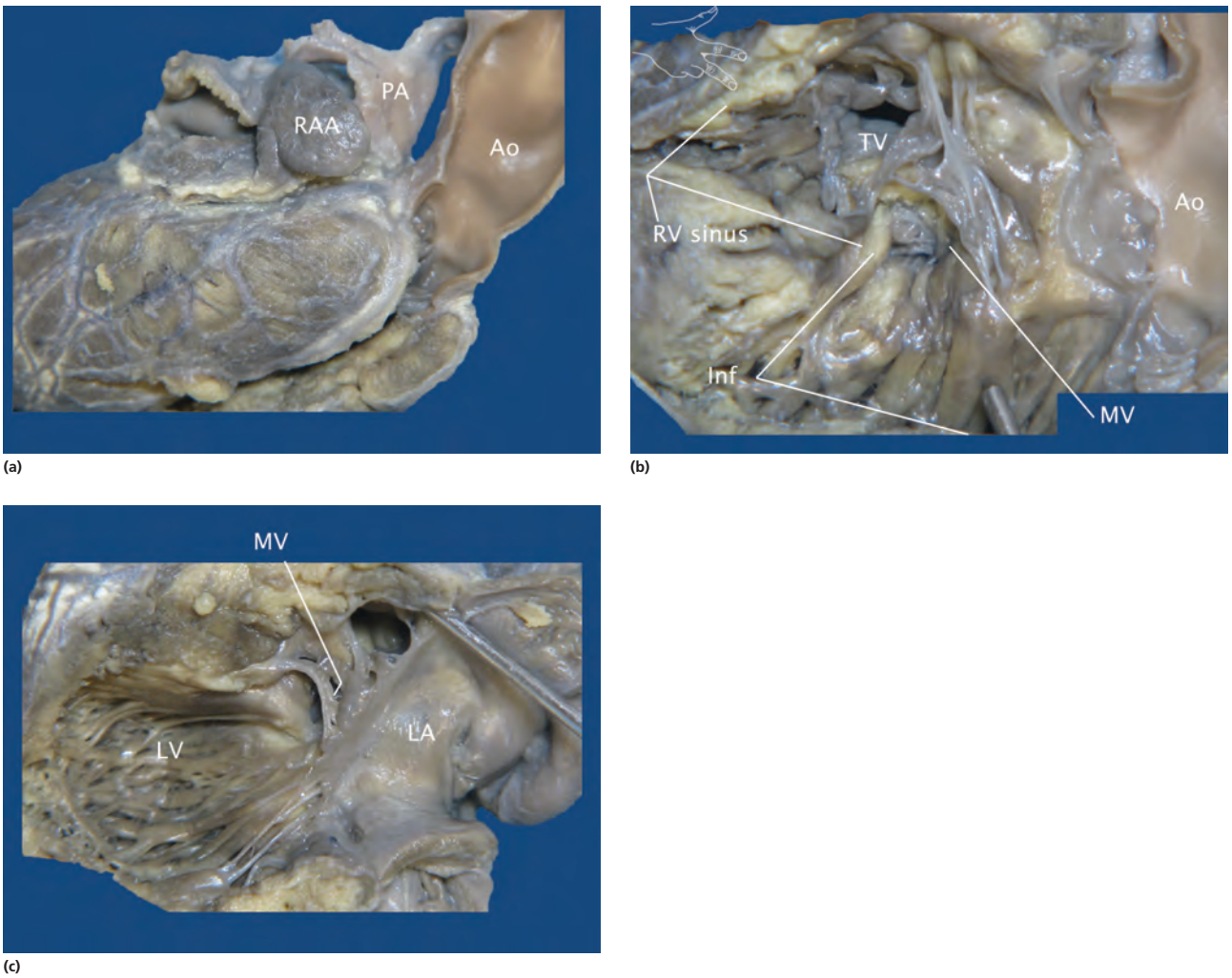


Figure 27.20 A heart with SIV, dextrocardia, transposition of the great arteries {S,D,L}, and straddling mitral valve. **(a)** The aorta (Ao) is to the left of the pulmonary artery (PA). The right atrial appendage (RAA) is to the right of the vascular pedicle. **(b)** The opened superior right ventricle, composed of the small right ventricular sinus (RV sinus) and larger infundibulum (Inf). The hypoplastic tricuspid valve (TV) enters the RV sinus. A part of the straddling mitral valve (MV) enters the Inf, which also supports the large aortic valve (Ao). A right hand (upper left) is required to describe this right ventricle, with the thumb into the TV, the fingers in the Ao, and the palm against the septum, the wall through which the MV straddles. The bizarre appearance of the right ventricle is due to marked clockwise rotation of the ventricles. About 150° of counterclockwise rotation of the image results in a much more usual orientation of the right ventricle. **(c)** The left atrium (LA) and inferior left ventricle (LV) which makes up the rightward apex of the heart.

of solitus). (We will ignore hearts with ambiguous situs or heterotaxy syndrome because they occur infrequently in this setting and are described in Chapter 28.) Similarly, the arrangement of the ventricles is generally either D-loop (solitus or right-hand topology) or L-loop (inverted or left-hand topology). Finally, in the arterial segment the aorta is either to the right or to the left of the pulmonary artery (and sometimes anterior). There is typically concordance or harmony between the atrial situs, the loop or situs of the ventricles, and the situs or position of the great arteries. When the atrial situs is solitus, there are usually D-loop ventricles and the aorta is usually to the right, either solitus normally related great arteries or some type of D-malposition of the great arteries. Conversely, in situs inversus there are usually L-loop ventricles and the aorta is usually leftward, inversus normally related great arteries or an L-malposition of the great arteries. In SIV and criss-cross hearts, one frequently sees segmental situs discordance or disharmony [69]. Review of a number of case series [67,68,70–74] shows that most of these hearts (>90%) occur with situs solitus of the atria and relatively normal systemic and pulmonary venous anatomy. About 75% have D-loop ventricles and about 25% have L-loop ventricles. Consequently, AV situs concordance occurs in about three-quarters and discordance in about one quarter of cases (Figures 27.21 and 27.22). Conversely, in about 75% of cases, D-loop ventricles are associated with L-malposition of the aorta and vice versa (Figures 27.21 and 27.22). So AV situs discordance is frequent while VA situs discordance is the rule.

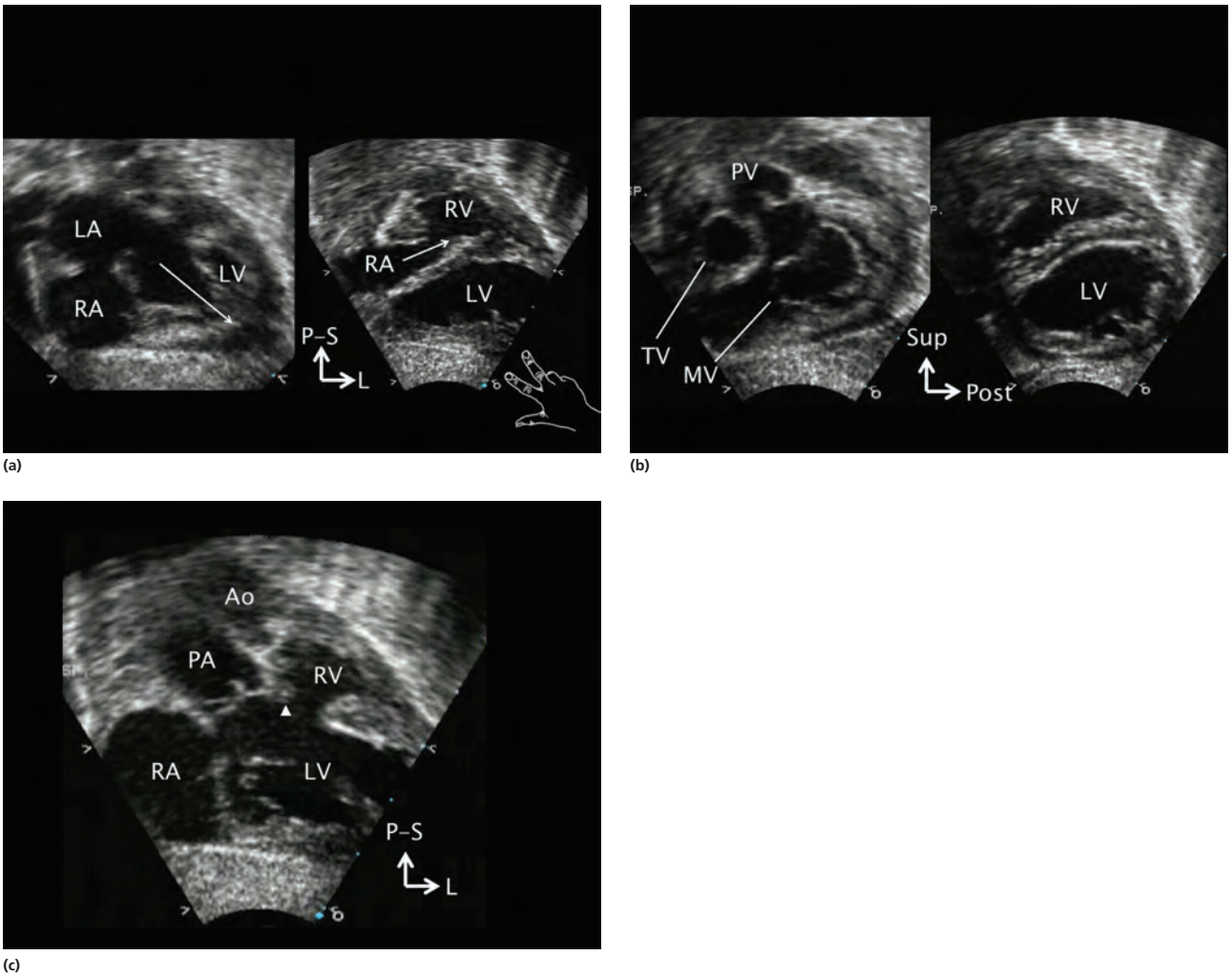


Figure 27.21 A series of echocardiographic views of a patient with SIV, criss-cross, and transposition of the great arteries {S,D,L}. **(a)** Subxiphoid long-axis views through the mitral (left) and tricuspid (right) valves. The left atrium (LA) is aligned with the left ventricle (LV) and the right atrium (RA) with the right ventricle (RV) – concordant AV alignments. The arrows indicate the axes of the AV valves which cross at nearly 90°. The tricuspid valve is superior and anterior, running from right to left while the mitral valve is inferior and posterior running posterior to anterior. The ventricles are D-loop or solitus even though the LV extends to the right of the RV. Only a right hand (bottom right) can describe the right ventricle with the thumb in the tricuspid valve, the fingers in the outflow and the palm against the septum. **(b)** Subxiphoid short-axis views through the base of the ventricles (left) and at mid ventricular level (right). The superior and anterior position of the small tricuspid valve (TV) in the right ventricle is again apparent. The pulmonary valve (PV) is aligned with the left ventricle (LV). The superior-inferior arrangement of the ventricles and the horizontal orientation of the ventricular septum (parallel to the diaphragm) are apparent. **(c)** A more anterior subxiphoid long-axis cut showing the outflow. The small infundibular septum (▲) is seen between the aortic and pulmonary valves. The conoventricular defect is between the conal or infundibular septum and the muscular septum.

Further, some of these hearts are characterized by discrepancy or disharmony between segmental situs and segmental alignments [69,74,75]. In the vast majority of hearts, when there is situs solitus of the atria and D-loop ventricles, or situs inversus and L-loop ventricles, the right atrium is aligned with (drains into) the right ventricle and the left atrium is aligned with the left ventricle. The situs of the segments correctly predicts the alignments. There is said to be concordance or harmony between situs and alignments. It is mostly in SIV and criss-cross hearts where one sees discordance or disharmony between situs and alignment: a solitus right atrium aligned with a D-loop left ventricle and a solitus left atrium aligned with a D-loop right ventricle (and the converse). Especially in these hearts one cannot assume that situs correctly predicts alignments; one must specifically elucidate and record both. Virtually all of the hearts with situs-alignment discordance that have been reported also have right juxtaposition of the atrial appendages [75].

The tricuspid valve is usually smaller than normal (Figure 27.21) and often severely hypoplastic [68,70]. The mitral valve is typically normal or large in size. In criss-cross hearts the tricuspid valve is anterior and oriented from right to left in D-loop ventricles (Figures 27.20 and 27.21) and from left to

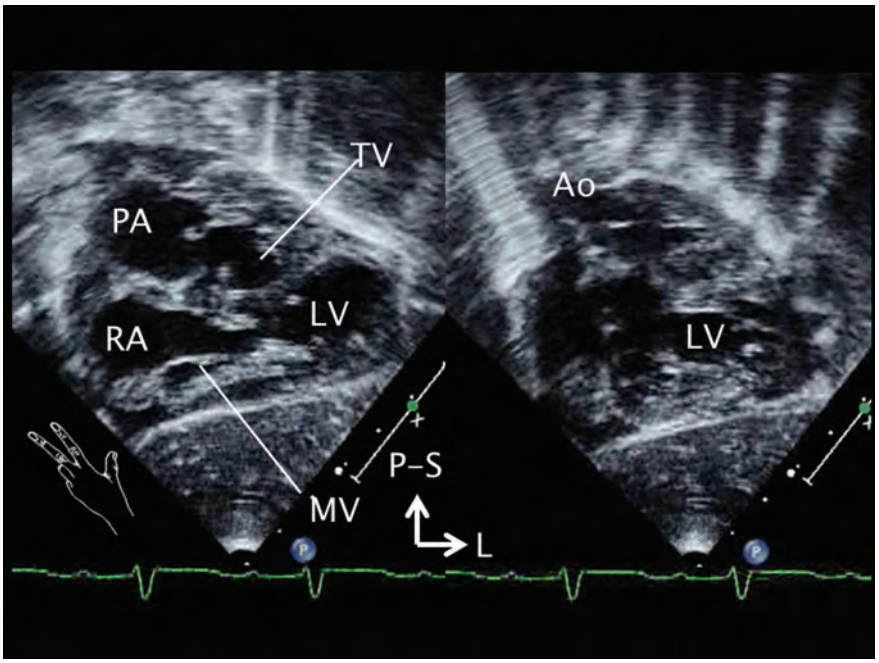


Figure 27.22 Subxiphoid long-axis views in a patient with SIV, criss-cross, and double-outlet right ventricle {S,L,D}. On the left is an inferior cut showing the right atrium (RA) aligned with the inferior left ventricle (LV) – AV discordance. The mitral valve (MV) is seen in long axis while the tricuspid valve (TV) is seen in cross-section, indicating that the valves cross at approximately 90°. The pulmonary artery (PA) is aligned with the right ventricle. The inverted or L-loop right ventricle can only be described using a left hand (lower left) with the thumb in the TV (into the plane of the image), the fingers in the PA, and the palm against the ventricular septum. A more superior and anterior cut (right panel) shows the aorta (Ao) also aligned with the right ventricle.

right in L-loop ventricles (Figures 27.19 and 27.22). The mitral valve is posterior and inferior to the tricuspid valve and is oriented from left-posterior to right-anterior in D-loop ventricles (Figure 27.21) and from right-posterior to left-anterior in L-loops (Figure 27.22). The crossing angle between the valves varies from 20–100° [68] and is inversely proportional to the size of the right ventricular sinus. In one type of criss-cross heart the mitral valve straddles into the infundibulum [67] (Figure 27.20). The right ventricular sinus is usually hypoplastic while the infundibulum is larger than normal, especially with a straddling mitral valve [68] (Figure 27.20). Criss-cross hearts with straddling mitral valve are associated with a larger angle between the atrial and ventricular septa indicating more apparent rotation of the ventricles with respect to the atria [67].

In virtually all hearts with SIV, and in most criss-cross hearts, the right ventricle is superior and the left ventricle inferior, but there is at least one published exception [76]. In D-loop ventricles the inferior left ventricle often extends to the right of the small, superior right ventricle giving the impression of inverted ventricles (Figure 27.21a). In fact, this characteristic of these hearts led Van Praagh and colleagues to emphasize the internal organization of the ventricles (chirality or topology) rather than spatial position as an indicator of ventricular loop or situs [43].

Although SIV and criss-cross hearts have been reported with an intact ventricular septum [77], most have one or more ventricular septal defects. The defect is often between the outlet or infundibular septum above and the muscular ventricular septum below (conoventricular) (Figure 27.21c). The outlet septum is often malaligned or deviated out of the plane of the muscular septum, most often producing or contributing to subpulmonary stenosis. Other types of defects, including membranous and AV canal type, have been reported as well.

Occasional patients have normally related great arteries (or nearly so) [78] but the great majority has either transposition (VA discordance) or double-outlet right ventricle. In most the pulmonary valve is posterior to the tricuspid valve (Figure 27.21b) and there is little or no subpulmonary infundibular muscle, leaving the pulmonary valve in continuity or near continuity with the AV valves. Proximity of the infundibular or outlet septum to the tricuspid valve is an important mechanism for subpulmonary stenosis. The aorta is usually large and unobstructed although there are occasional cases with subaortic stenosis and aortic arch obstruction [70].

Treatment strategies

The majority of these complex hearts are candidates for staged Fontan palliation [79,80] although most of those with an adequate right ventricle and tricuspid valve are candidates for a two-ventricle repair [81,82] or palliation [83]. Initial palliation often consists in a systemic-pulmonary shunt because of the prevalence of severe pulmonary stenosis. Some with less severe pulmonary stenosis can proceed directly to a bidirectional cavopulmonary anastomosis. Rare patients benefit from pulmonary artery banding because of pulmonary overcirculation. Completion of the Fontan is usually carried out by 1–2 years of age.

Imaging of hearts with functionally one ventricle

The initial exam is typically in utero (see Chapter 42) or in the neonatal period. Multiplane imaging is essential for a complete and accurate diagnosis. Subxiphoid views provide an excellent

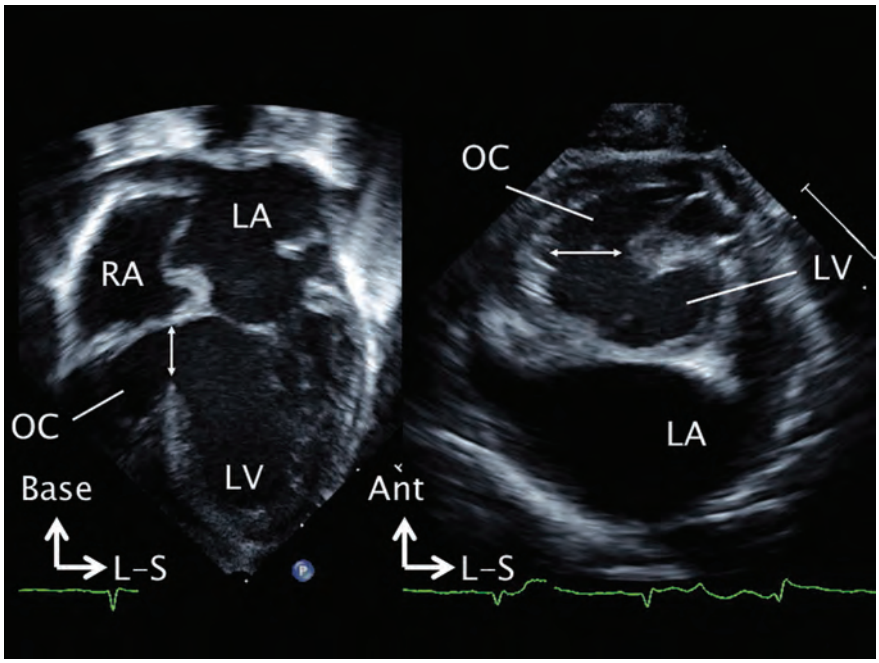


Figure 27.23 An apical 4-chamber (left panel) and a parasternal short-axis (right panel) view in a patient with TA and normally related great arteries {S,D,S}. Orthogonal dimensions (double-headed arrows) of the outflow foramen can be obtained in these views: apex-base dimension in apical 4-chamber and left–right dimension in parasternal short-axis view. LA, left atrium; LV, left ventricle; OC, outlet chamber; RA, right atrium.

overview of the heart, facilitating diagnosis of situs, alignments, and connections. In addition, these views afford excellent images of the veins, atria, atrial septum, AV valves and ventricle(s). The position of the ventricles in SIV and the crossing of the AV valves in criss-cross heart are also best appreciated from subxiphoid views [68,72] (Figures 27.21 and 27.22). Apical views are useful for examining and measuring the AV valves and can provide an apex-base dimension of the outflow foramen or ventricular septal defect (Figures 27.2a, 27.6, 27.14, and 27.23). Parasternal views provide a dimension of the AV valves orthogonal to that obtained from the apical views. The diameter of the semilunar valves, ascending aorta, and pulmonary trunk can be obtained from the parasternal long-axis and the valve morphology from the short-axis view. The parasternal long-axis is another view for obtaining an apex-base dimension of the outflow foramen or ventricular septal defect and the parasternal short-axis view provides the orthogonal dimension. The parasternal short-axis also shows the coronary artery anatomy. Suprasternal and high parasternal views show the aortic arch, isthmus, branch pulmonary arteries, and ductus arteriosus.

Color flow mapping and pulsed (PW) and continuous-wave (CW) Doppler are used to define the physiology. Subxiphoid and parasternal short-axis views show an interatrial communication as well as the communication(s) between the left ventricle and outlet chamber (Figure 27.24). Semilunar roots are often seen well in subxiphoid long- or short-axis views and these views usually afford a low-angle approach for spectral Doppler as well (Figure 27.25). Apical views allow interrogation of the AV valves and the semilunar root arising from the LV chamber. Parasternal long-axis views usually provide the best angle for assessing the gradient between the left ventricle and outlet chamber or across a ventricular septal defect in SIV (Figure 27.26). The function of the semilunar valves can be assessed in this view as well. High parasternal and suprasternal views provide the best vantage points for color and spectral Doppler exam of the branch pulmonary arteries, the aortic arch and the ductus arteriosus. Suprasternal axial or coronal views also show the pulmonary veins and allow Doppler interrogation.

The short-axis dimensions of the left ventricle and wall thickness can be measured from M-mode echo tracings. In the absence of regional wall motion abnormalities or unusual shape of the ventricle, function can be assessed using shortening fraction. The relationship between velocity of shortening and end-systolic wall stress has been used as a measure of contractility [84]. This technology is not useful for a functionally single right ventricle or an unusually shaped left ventricle or one with regional wall motion abnormalities. Ventricular volume and ejection fraction can be calculated using 2D echo views (Chapter 7), but the validity of these measures is unclear [85]. Recently, 3D echocardiography has been compared with magnetic resonance imaging (MRI) for estimation of volume and ejection fraction in patients with functionally single ventricle [86,87]. While size and function measures were highly correlated, 3D echocardiography produced lower (~10%) end-diastolic volume and ejection fraction estimates.

Systolic function can also be evaluated using myocardial velocity [88,89] and strain and strain-rate imaging [90,91]. Most experience has been in functionally single right ventricle associated with hypoplastic left heart syndrome [92,93]. Correlation between some of these functional measures, especially myocardial velocity measures, and other established function parameters has been poor in some reports [94]. These measures may be useful for serial evaluation although the meaning of a single measurement is unclear.

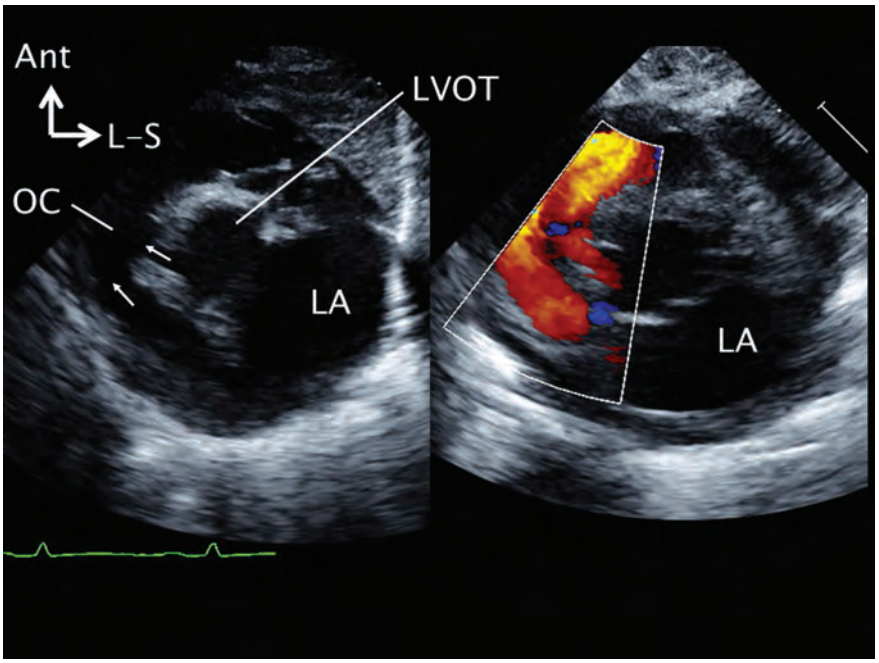


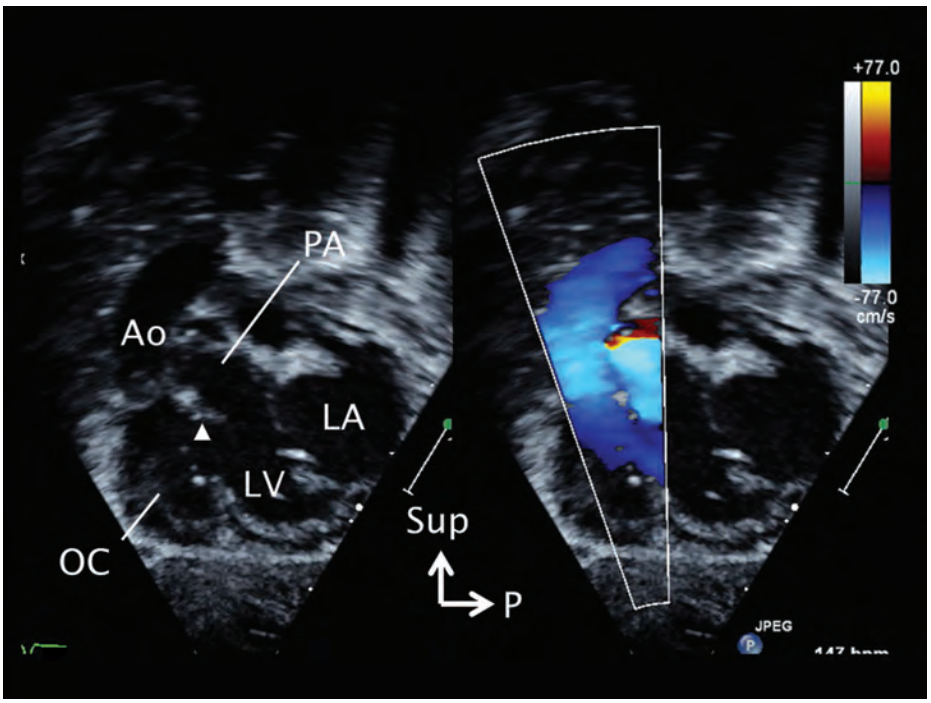
Figure 27.24 Parasternal short-axis view and color flow map in a patient with TA and normally related great arteries {S,D,S}. There are two communications (arrows) between the left ventricle and outlet chamber (OC). The color flow map shows unrestricted flow through the defects. LA, left atrium; LVOT, left ventricular outflow tract.

Dyssynchrony appears to be prevalent in hearts with functionally one ventricle [91,95] and is associated with systolic dysfunction and measures of myocardial fibrosis. Dyssynchrony is readily detectable by speckle deformation and 3D volumetric imaging and could have important implications for therapy (Figure 27.27). Although experience with resynchronization therapy is extremely limited in patients with functionally one ventricle, some patients appear to have benefited [96].

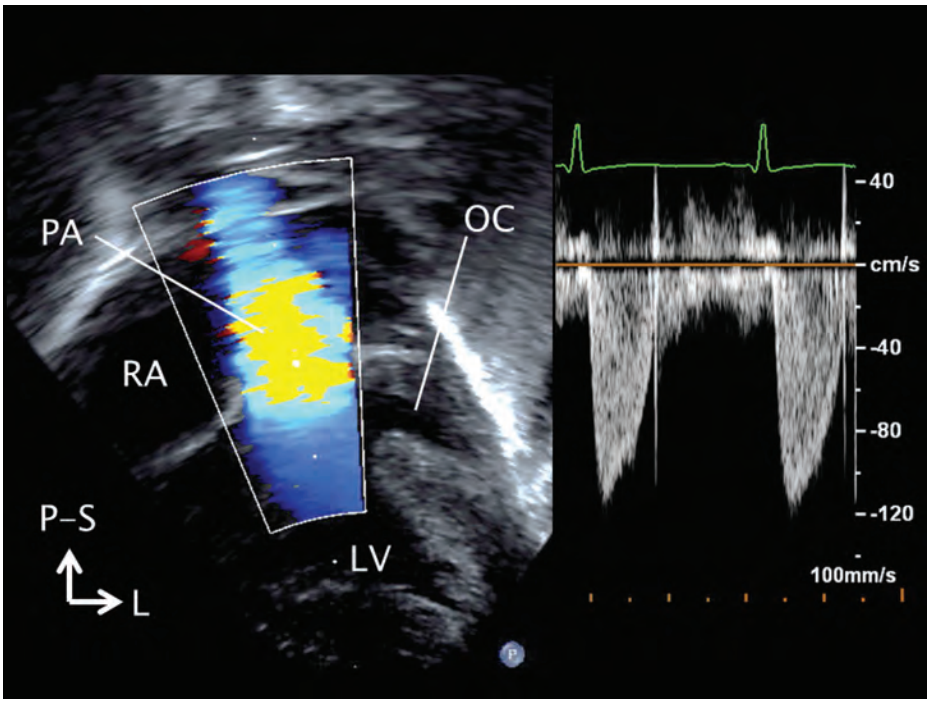
Diastolic function can be evaluated using blood-pool or myocardial velocity, but again the meaning of these measures is uncertain (Chapter 8).

The initial exam should specifically address the following points:

1 Systemic and pulmonary venous connections – DILV and DIRV are occasionally associated with heterotaxy syndrome (Chapter 28). TA is often associated with persistent left superior vena cava.
2 Condition of the atrial septum – this can affect mixing and venous pressure and is particularly important in TA. Factors that predispose to restriction of the atrial communication in TA are presence of an aneurysm of septum primum (Figure 27.28) or a maximum diameter of the foramen ovale <5 mm [64]. Juxtaposition of the atrial appendages, seen in up to 10% of patients with TA and some patients with SIV, is usually associated with a large atrial communication (Figures 27.11c, 27.11d, and 27.29). The foramen ovale or atrial septal defect should be measured in two planes and the mean gradient estimated by spectral Doppler guided by a color flow map.
3 AV valve anatomy and function – each valve annulus should be measured in orthogonal dimensions, any gradient recorded, and regurgitation graded (Chapter 6). The mean valve gradient can be measured from spectral Doppler tracings recorded in an apical or subxiphoid view. Color flow mapping in apical or parasternal views is useful for measuring the diameter of a regurgitant jet or for estimating the size of the flow jet (Chapter 6).
4 Number, location, size of, and gradient through communications between the left ventricle and the outlet chamber (DILV, TA) or across a ventricular septal defect (SIV, criss-cross) (Figures 27.24 and 27.26). The area of the outflow foramen in DILV and TA with TGA can be calculated from orthogonal dimensions using the formula for an ellipse [42] and is predictive of obstruction. Patients with an outflow foramen area index $<2\ cm^2/m^2$ in the first months of life are at high risk for developing obstruction early. The gradient can be estimated using spectral Doppler guided by a color flow map in parasternal or subxiphoid views (Figure 27.26).
5 Outflow anatomy and gradient – particularly in DIRV. Spectral Doppler guided by a color flow map is used to estimate the pressure gradient across the outflow using subxiphoid or apical views.
6 Semilunar valve diameter, anatomy and function. Parasternal long-and short-axis views are best for size and anatomy. Color flow in parasternal views allows measurement of the diameter or area of a regurgitant jet (Chapter 6).
7 Aortic arch anatomy, dimensions and gradient. Patients with systemic ventricular outflow stenosis are at most risk for aortic arch obstruction. The orientation of the arch is often unusual in patients with a leftward (L-malposed) aorta. A left arch is often directed from left anterior to right



(a)



(b)

Figure 27.25 TA and transposition of the great arteries {S,D,D}. **(a)** Subxiphoid short-axis view (left) and color flow map (right) in a patient with TA and transposition of the great arteries {S,D,D}. This view affords excellent alignment of the ultrasound beam with the arterial outflows for Doppler interrogation. Despite posterior deviation of the infundibular or outflow septum (▲), there is no flow disturbance in the pulmonary artery (PA). Similarly, the outflow foramen appears unobstructed. **(b)** Alignment of the spectral Doppler cursor. The spectral Doppler recording (right) allows estimation of the pressure gradient across the outflow. Ao, aorta; LA, left atrium; LV, left ventricle; OC, outlet chamber; RA, right atrium.

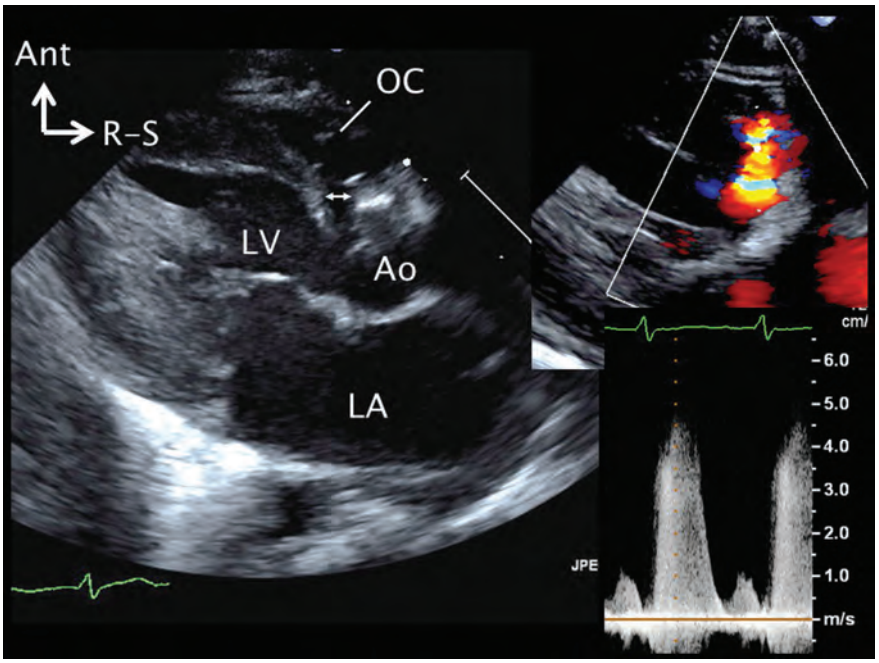


Figure 27.26 Parasternal long-axis view (left) in a patient with TA and normally related great arteries {S,D,S}. The outflow foramen (double arrow) is restrictive causing subpulmonary stenosis. The color flow map (upper right) facilitates proper alignment of the spectral Doppler cursor with the flow jet through the outflow foramen for estimation of the pressure gradient (lower right). Ao, aorta; LA, left atrium; LV, left ventricle; OC, outlet chamber.

posterior and the rare right aortic arch can be in an almost coronal plane. Coarctation is an anatomical diagnosis in infants with an open ductus arteriosus (Figure 27.18c). Absence of a gradient is not helpful in excluding coarctation. Diastolic anterograde flow across the isthmus can be a sign of coarctation but diastolic left-to-right flow across the ductus can produce the same finding.

8 Branch pulmonary artery anatomy, dimensions and gradient. These data are usually available from parasternal or suprasternal views with varying amounts of rotation to find the plane of the branch arteries.

9 Status of the ductus arteriosus and transductal gradient if patent. The ductus view usually allows estimation of the gradient using color-guided spectral Doppler (Figure 27.30).

10 Ventricular size, wall thickness, and systolic and diastolic function.

Coronary artery anatomy is rarely important in these patients, although readily available from parasternal views if of interest.

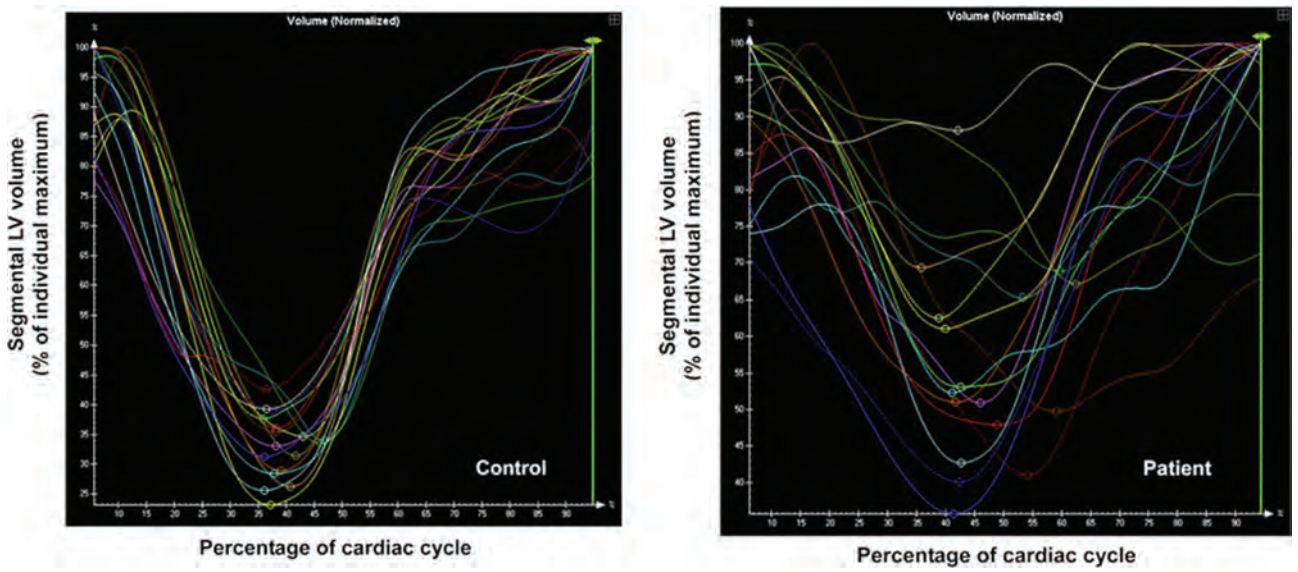
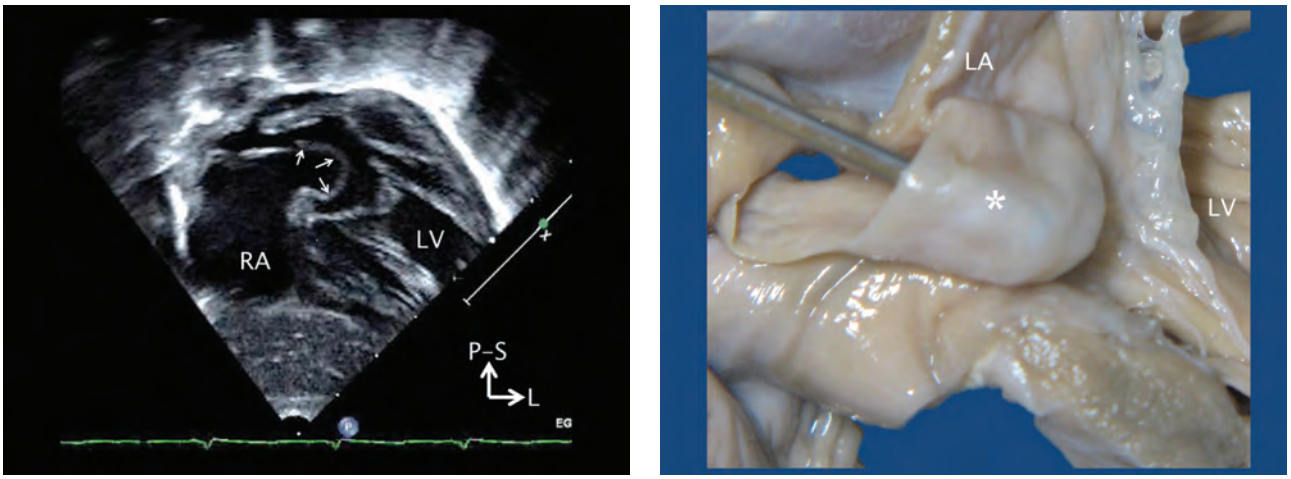


Figure 27.27 Regional left ventricular function analysis performed using semi-automated volume measurement from a 3D echocardiogram recorded from an apical view and divided into 16 segments. Synchronous regional function in a normal heart is shown in the left panel. Marked dyssynchrony, indicated by marked variation in the extent and timing of shortening, is seen in a patient with TA following a Fontan operation (right panel). Source: Ho P-K, et al. 2012 [95]. Reproduced with permission of Elsevier.



(a) (b)

Figure 27.28 TA and normally related great arteries {S,D,S}. **(a)** Subxiphoid long-axis view in a patient with TA and normally related great arteries {S,D,S}. There is an aneurysm of septum primum (arrows) bulging into the left atrium, a risk factor of restriction of the foramen ovale [64]. **(b)** Opened left atrium (LA) and left ventricle (LV) in a heart with an aneurysm of septum primum (∗) bulging toward the mitral valve. RA, right atrium.

It could be important if a palliative arterial switch operation is being considered [97].

Subsequent exams should re-address many of these points including status of the interatrial communication, AV valve function, size of and gradient across the outflow foramen, semilunar valve function, arch anatomy and gradient, and ventricular size and function.

If a pulmonary artery band has been applied, the band should be imaged in parasternal long-and short-axis views to measure the diameter, evaluate pulmonary valve function and assess the effect of the band on the branch pulmonary arteries. A gradient across the band should be measured from a parasternal, apical or subxiphoid projection (Figure 27.31). In the absence of systemic outflow obstruction, the pulmonary artery systolic pressure is the difference between the trans-band gradient and systemic systolic blood pressure. Patients with DILV or TA and TGA are at risk for development of systemic outflow obstruction following placement of a pulmonary artery band [48]. Careful evaluation of the outflow foramen and outlet chamber is especially important in these patients.

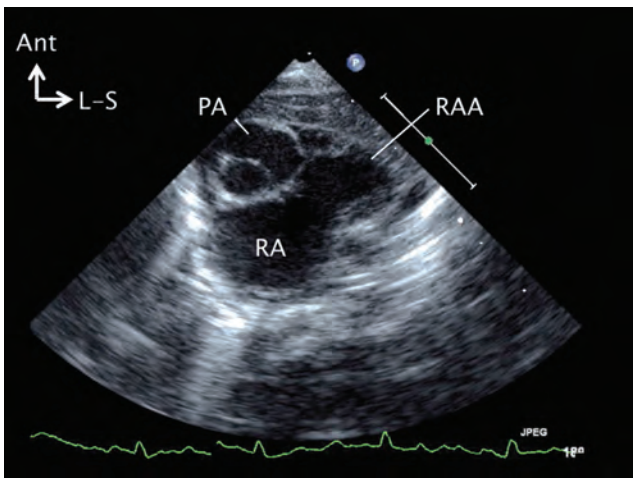


Figure 27.29 Parasternal short-axis view in a patient with TA, transpositions of the great arteries {S,D,D}, and left juxtaposition of the right atrial appendage (RAA). The juxtaposed RAA is seen as a leftward tubular extension of the right atrium (RA) behind the pulmonary artery (PA), the posterior arterial root.

A systemic-to-pulmonary shunt can be imaged and evaluated with color flow mapping in a suprasternal or high parasternal view (Video 27.13). The color flow map can be used to position the cursor for spectral Doppler. Systolic blood pressure minus the peak gradient across the shunt provides an upper limit estimate for systolic pulmonary artery pressure. Branch pulmonary arteries should be imaged carefully seeking stenosis or distortion due to the shunt, or spontaneous closure of the ductus arteriosus.

Many patients can undergo a bidirectional cavopulmonary anastomosis on the basis of comprehensive echocardiography (see earlier). Criteria for selecting patients for catheterization have been published [98]. Patients who have undergone a complete echo evaluation, including assessment of ventricular function, AV valve regurgitation, the atrial septum, the aortic arch (both ascending and descending), proximal branch pulmonary arteries, and pulmonary venous pathways (70% in this study) and in whom no abnormalities likely to prompt catheter intervention were discovered appear to be unlikely to benefit from catheterization. Judicious use of MRI for evaluation of the branch pulmonary arteries and reconstructed aorta – the two areas most likely to be inadequately imaged by echocardiography – could further reduce the need for diagnostic catheterization. However, echocardiography does not appear to be adequate in most patients prior to undertaking a Fontan procedure [99,100], largely because of its limited ability to image branch

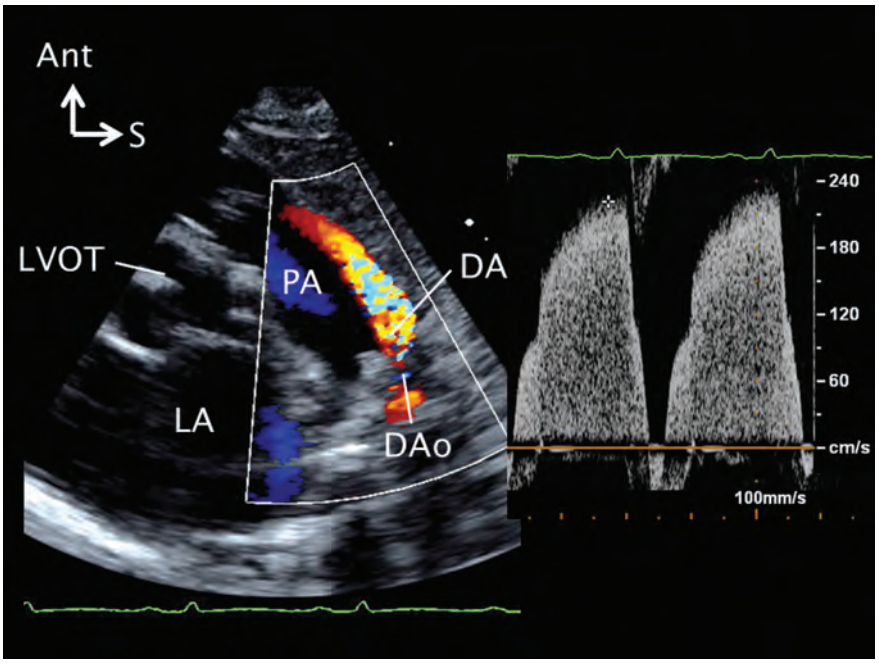


Figure 27.30 High left parasternal (ductus cut) view with color flow map in a patient with TA and normally related great arteries {S,D,S} illustrating flow through a ductus arteriosus (DA) from the descending aorta (DAo) to the pulmonary artery (PA). Spectral Doppler (right) is useful for estimation of the pressure gradient across the DA.

pulmonary arteries and the aortic arch. Additional study using MRI appears to suffice in a subset of patients but many seem to benefit from catheterization [101]. One apparent, but controversial, indication for interventional catheterization in these patients is the presence of significant aorto-pulmonary collateral vessels.

Echocardiography is the mainstay of long-term follow-up of patients with functionally single ventricle following Fontan palliation. Imaging in postoperative Fontan patients is further discussed in Chapter 28.

Videos

To access the videos and explanatory audio comments for this chapter, please go to www.lai-echo.com.

Video 27.1 Subxiphoid long-axis scan in DILV and TGA {S,L,L}.

Video 27.2 Parasternal short-axis scan in DILV and TGA {S,L,L}.

Video 27.3 Subxiphoid color map showing outflow tract evaluation in DILV and TGA {S,L,L}.

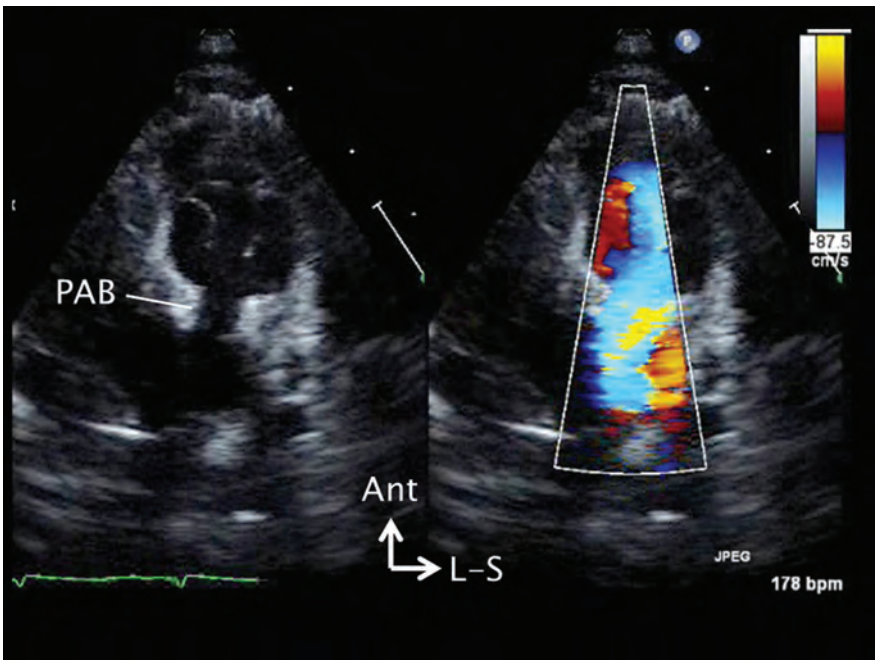


Figure 27.31 Parasternal short-axis view (left) and color flow map (right) of a patient with TA and normally related great arteries {S,D,S} after banding of the pulmonary artery. The pulmonary artery band (PAB) is seen just distal to the pulmonary valve. The color flow map shows flow disturbance through the band.

Video 27.4 Subxiphoid long-axis scan in DILV and TGA {S,D,D}.

Video 27.5 Parasternal short-axis scan in DILV with normally related great arteries {S,D,S}.

Video 27.6 Subxiphoid scan in DIRV and DORV {S,X,D}.

Video 27.7 Subxiphoid long-axis scan in TA with normally related great arteries {S,D,S}.

Video 27.8 Subxiphoid color map in TA with normally related great arteries {S,D,S}.

Video 27.9 Subxiphoid long-axis scan in TA with TGA {S,D,D}.

Video 27.10 Apical scan in TA with TGA {S,L,L}.

Video 27.11 Subxiphoid long-axis scan in SIV with criss-cross and TGA {S,D,L}.

Video 27.12 Subxiphoid short-axis scan in SIV with criss-cross and TGA {S,D,L}.

Video 27.13 Suprasternal color map showing a right modified Blalock–Taussig shunt.

References

1 Marelli AJ, Mackie AS, Ionescu-Ittu R, et al. Congenital heart disease in the general population: changing prevalence and age distribution. *Circulation* 2007;**115**:163–172.
2 Verheugt CL, Uiterwaal CSPM, van der Velde ET, et al. The emerging burden of hospital admissions of adults with congenital heart disease. *Heart* 2010;**96**:872–878.
3 Kirklin, J. K., et al. Is the "perfect Fontan" operation routinely achievable in the modern era? *Cardiol Young* 2008;**18**:328–336.
4 Khairy P, Fernandes SM, Mayer JE, Jr., et al. Long-term survival, modes of death, and predictors of mortality in patients with Fontan surgery. *Circulation* 2008;**117**:85–92.
5 Van Praagh R, David I, Van Praagh S. What is a ventricle? The single-ventricle trap. *Pediatr Cardiol* 1982;**2**:79–84.
6 Van Praagh R, Plett JA, Van Praagh S. Single ventricle. Pathology, embryology, terminology and classification. *Herz* 1979;**4**:113–150.
7 Silverman NH, McElhinney DB. Which two ventricles cannot be used for a biventricular repair? Echocardiographic assessment. *Ann Thorac Surg* 1998;**66**:634–640.
8 Bonnet D, Fermont L, Kachaner J, et al. Tricuspid atresia and conotruncal malformations in five families. *J Med Genet* 1999;**36**:349–350.
9 Kumar A, Victorica BE, Gessner IH, et al. Tricuspid atresia and annular hypoplasia: report of a familial occurrence. *Pediatr Cardiol* 1994;**15**:201–203.
10 Lin AE, Rosti L. Tricuspid atresia in sibs. *J Med Genet* 1998;**35**:1055–1056.
11 Sletten LJ, Pierpont ME. Variation in severity of cardiac disease in Holt–Oram syndrome. *Am J Med Genet* 1996;**65**:128–132.
12 Ruzic B, Bosnar B, Beleznay O. An unusual type of congenital heart disease associated with the Holt–Oram syndrome. *Radiologe* 1981;**21**:296–299.
13 Durairaj M, Chadha SK, Bhide M, et al. Noonan's syndrome associated with single ventricle (a case report). *Indian Pediatr* 1979;**16**:927–929.
14 Antonelli D, Antonelli J, Rosenfeld T. Noonan's syndrome associated with hypoplastic left heart. *Cardiology* 1990;**77**:62–65.
15 Marino B, Digilio MC, Novelli G, et al. Tricuspid atresia and 22q11 deletion. *Am J Med Genet* 1997;**72**:40–42.
16 Alva C, David F, Hernandez M, et al. Tricuspid atresia associated with common arterial trunk and 22q11 chromosome deletion. *Arch Cardiol Mex* 2003;**73**:271–274.
17 Hu P, Ji X, Yang C, et al. 22q11.2 microduplication in a family with recurrent fetal congenital heart disease. *Eur J Med Genet* 2011;**54**:e433–436.
18 Geva T, Ayres NA, Pignatelli RH, et al. Echocardiographic evaluation of common atrioventricular canal defects: a study of 206 consecutive patients. *Echocardiography* 1996;**13**:387–400
19 Gill HK, Splitt M, Sharland GK, et al. Patterns of recurrence of congenital heart disease: an analysis of 6,640 consecutive pregnancies evaluated by detailed fetal echocardiography. *J Am Coll Cardiol* 2003;**42**:923–929.
20 Weigel TJ, Driscoll DJ, Michels VV. Occurrence of congenital heart defects in siblings of patients with univentricular heart and tricuspid atresia. *Am J Cardiol* 1989;**64**:768–771.
21 Shapiro SR, Ruckman RN, Kapur S, et al. single ventricle with truncus arteriosus in siblings. *Am Heart J* 1981;**102**:456–459.
22 Whittemore R, Wells JA, Castellsague X. A second-generation study of 427 probands with congenital heart defects and their 837 children. *J Am Coll Cardiol* 1994;**23**:1459–1467.
23 Snarr BS, Kern CB, Wessels A. Origin and fate of cardiac mesenchyme. *Dev Dyn* 2008;**237**:2804–2819.
24 Drake CJ, Wessels A, Trusk T, et al. Elevated vascular endothelial cell growth factor affects mesocardial morphogenesis and inhibits normal heart bending. *Dev Dyn* 2006;**235**:10–18.
25 Männer J. The anatomy of cardiac looping: a step towards the understanding of the morphogenesis of several forms of congenital cardiac malformations. *Clin Anat* 2009;**22**:21–35.
26 Moorman AF, Christoffels VM. Cardiac chamber formation: development, genes, and evolution. *Physiol Rev* 2003;**83**:1223–1267.
27 Kanani M, Moorman AFM, Cook AC, et al. Development of the atrioventricular valves: clinicomorphological correlations. *Ann Thorac Surg* 2005;**79**:1797–1804.
28 Wessels A, Markman MW, Vermeulen JL, et al. The development of the atrioventricular junction in the human heart. *Circ Res* 1996;**78**:110–117.
29 Wessels A, Anderson RH, Markwald RR, et al. Atrial development in the human heart: an immunohistochemical study with emphasis on the role of mesenchymal tissues. *Anat Rec* 2000;**259**:288–300.
30 de Lange FJ, Moorman AFM, Anderson RH, et al. Lineage and morphogenetic analysis of the cardiac valves. *Circ Res* 2004;**95**;645–654.
31 Hutson MR, Kirby ML. Cardiac neural crest and conotruncal malformations. *Semin Cell Dev Biol* 2007;**18**:101–110.
32 Bajolle F, Zaffran S, Kelly RG. Rotation of the myocardial wall of the outflow tract is implicated in the normal positioning of the great arteries. *Circ Res* 2006;**98**:421–428.
33 Lamers WH, Moorman AFM. Cardiac septation. A late contribution of the embryonic primary myocardium to heart morphogenesis. *Circ Res* 2002;**91**:93–103.

34 Jain R, Engleka KA, Rentschler SL. Cardiac neural crest orchestrates remodeling and functional maturation of mouse semilunar valves. *J Clin Invest* 2011;**121**:422–430.

35 Lomonico MP, Bostrom MP, Moore GW, Hutchins GM. Arrested rotation of the outflow tract may explain tetralogy of Fallot and transposition of the great arteries. *Pediatr Pathol* 1988;**8**:267–281.

36 Bostrom MP, Hutchins GM. Arrested rotation of the outflow tract may explain double-outlet right ventricle. *Circulation* 1988;**77**:1258 –1265.

37 Shogan PJ, Folio L. Situs inversus totalis. *Mil Med* 2011;**176**:840–843.

38 Papagiannis J, Athanassopoulos G, Mavrogeni S, Rammos S. Double-inlet and double-outlet left ventricle in situs inversus. *Pediatr Cardiol* 1998;**19**:161–164.

39 Doherty A, Ho SY, Anderson RH, Rigby ML. Morphological nature of the atrioventricular valves in hearts with double inlet left ventricle. *Pediatr Pathol* 1989;**9**:521–529.

40 Bevilacqua M, Sanders SP, Van Praagh S, et al. Double-inlet single left ventricle: echocardiographic anatomy with emphasis on the morphology of the atrioventricular valves and ventricular septal defect. *J Am Coll Cardiol* 1991;**18**:559–568.

41 Shiraishi H, Silverman NS. Echocardiographic spectrum of double inlet ventricle: evaluation of the interventricular communication. *J Am Coll Cardiol* 1990;**15**:1401–1408.

42 Matitiau A, Geva T, Colan SD, et al. Bulboventricular foramen size in infants with double-inlet left ventricle or tricuspid atresia with transposed great arteries: influence on initial palliative operation and rate of growth. *J Am Coll Cardiol* 1992;**19**:142–148.

43 Van Praagh R, Weinberg PM, Matsuoka R, Van Praagh S. Malposition of the heart. In: Moss AJ, Adams FH, Emmanoulides GC (eds.) *Heart Disease in Infants, Children, and Adolescents*, 3rd edn. Baltimore, MD: Williams & Wilkins, 1983, pp. 422–458.

44 Cheung HC, Lincoln C, Anderson RH, et al. Options for surgical repair in hearts with univentricular atrioventricular connection and subaortic stenosis. *J Thorac Cardiovasc Surg* 1990;**100**:672–681.

45 Pass RH, Solowiejczyk DE, Quaegebeur JM, et al. Bulboventricular foramen resection: hemodynamic and electrophysiologic results. *Ann Thorac Surg* 2001;**71**:1251–1254.

46 Baraona F, Valente AM, Porayette P, et al. Coronary arteries in childhood heart disease: implications for management of young adults. *J Clinic Experiment Cardiol* 2012;**S8**:006.

47 Lotto AA, Hosein R, Jones TJ, et al. Outcome of the Norwood procedure in the setting of transposition of the great arteries and functional single left ventricle. *Eur J Cardiothorac Surg* 2009;**35**:149–155.

48 Jensen RA, Williams RG, Laks H, et al. Usefulness of banding of the pulmonary trunk with single ventricle physiology at risk for subaortic obstruction. *Am J Cardiol* 1996;**77**:1089–1093.

49 de Leval MR, Deanfield JE. Four decades of Fontan palliation. *Nat Rev Cardiol* 2010;**7**:520–527.

50 Saleeb SF, Juraszek A, Geva T. Anatomic, imaging, and clinical characteristics of double-inlet, double-outlet right ventricle. *Am J Cardiol* 2010;**105**:542–549.

51 Keeton BR, Macartney FJ, Hunter S, et al. Univentricular heart of right ventricular type with double or common inlet. *Circulation* 1979;**59**:403–411.

52 Kawahira Y, Uemura H, Yoshikawa Y, Yagihara T. Double inlet right ventricle versus other types of double or common inlet ventricle: its clinical characteristics with reference to the Fontan procedure. *Eur J Cardiothorac Surg* 2001;**20**:228–232.

53 Weinberg PM. Anatomy of tricuspid atresia and its relevance to current forms of surgical therapy. *Ann Thorac Surg* 1980;**29**:306–311.

54 Van Praagh S, O'Sullivan J, Brili S, Van Praagh R. Juxtaposition of the morphologically right atrial appendage in solitus and inversus atria: a study of 35 postmortem cases. *Am Heart J* 1996;**132**:382–390.

55 Orie JD, Anderson C, Ettedgui JA, et al. Echocardiographic-morphologic correlations in tricuspid atresia. *J Am Coll Cardiol* 1995;**26**:750–758.

56 Van Praagh S, Vangi V, Sul JH, et al. Tricuspid atresia or severe stenosis with partial common atrioventricular canal: anatomic data, clinical profile and surgical considerations. *J Am Coll Cardiol* 1991;**17**:932–943.

57 Anderson KR, Zuberbuhler JR, Anderson RH, et al. Morphologic spectrum of Ebstein's anomaly of the heart – a review. *Mayo Clin Proc* 1979;**54**:174–180.

58 Litovsky S, Choy M, Park J, et al. Absent pulmonary valve with tricuspid atresia or severe tricuspid stenosis: report of three cases and review of the literature. *Pediatr Dev Pathol* 2000;**3**:353–366.

59 Van Praagh S, Porras D, Oppido G, et al. Cleft mitral valve without ostium primum defect: anatomic data and surgical considerations based on 41 cases. *Ann Thorac Surg* 2003;**75**:1752– 1762.

60 Rydberg, BarAm S, Teien DE, et al. The abnormal contralateral atrioventricular valve in mitral and tricuspid atresia in neonates: an echocardiographic study. *Pediatr Cardiol* 1999;**20**:200–202.

61 Binotto MA, Higuchi ML, Aiello VD. Left ventricular remodeling in hearts with tricuspid atresia: morphologic observations and possible basis for ventricular dysfunction after surgery. *J Thorac Cardiovasc Surg* 2003;**126**:1026–1032.

62 Van Praagh R, Weinberg PM, Srebro JP. Double-outlet left ventricle. In: Moss AJ, Adams FH, Emmanouilides GC (eds.) *Heart Disease in Infants, Children, and Adolescents*, 3rd edn. Baltimore, MD: Williams & Wilkins, 1988, pp. 461–487.

63 Bonnet D, Fermont L, Kachaner J, et al. Tricuspid atresia and conotruncal malformations in five families. *J Med Genet* 1999;**36**:349–350.

64 Tzifa A, Gauvreau K, Geggel RL. Factors associated with development of atrial septal restriction in patients with tricuspid atresia involving the right-sided atrioventricular valve. *Am Heart J* 2007;**154**:1235–1241.

65 Rao PS. Natural history of the ventricular septal defect in tricuspid atresia and its surgical implications. *Br Heart J* 1977;**39**:276–288.

66 Lan Y-T, Chang R-K, Laks H. Outcome of patients with double-inlet left ventricle or tricuspid atresia with transposed great arteries. *J Am Coll Cardiol* 2004;**43**:113–119.

67 Geva T, Van Praagh S, Sanders SP, et al. Straddling mitral valve with hypoplastic right ventricle, crisscross atrioventrirular relations, double outlet right ventricle and dextrocardia: morphologic, diagnostic and surgical considerations. *J Am Coll Cardiol* 1991;**17**:1603–1612.

68 Marino B, Sanders SP, Pasquini L, et al. Two-dimensional echocardiographic anatomy in crisscross heart. *Am J Cardiol* 1966;**56**:325–333.

69 Van Praagh R. When concordant or discordant atrioventricular alignments predict the ventricular situs wrongly. I. Solitus atria, concordant alignments, and L-loop ventricles. II. Solitus atria,

discordant alignments, and D-loop ventricles. *J Am Coll Cardiol* 1987;**10**:1278–1279.
70 Freedom RM, Culham G, Rowe RD. The criss-cross and superoinferior ventricular heart: an angiocardiographic study. *Am J Cardiol* 1978;**42**:620–626.
71 Carminati M, Valsecchi O, Borghi A, et al. Cross-sectional echocardiographic study of criss-cross hearts and superoinferior ventricles. *Am J Cardiol* 1987;**59**:114–118.
72 Robinson PJ, Kumpeng V, Macartney FJ. Cross-sectional echocardiographic and angiocardiographic correlation in criss-cross hearts. *Br Heart J* 1985;**54**:61–67.
73 Héry E, Jimenez M, Didier D, et al. Echocardiographic and angiographic findings in superior-inferior cardiac ventricles. *Am J Cardiol* 1989;**63**:1385–1389.
74 Anderson RH, Smith A, Wilkinson JL. Disharmony between atrioventricular connections and segmental combinations: unusual variants of "crisscross" hearts. *J Am Coll Cardiol* 1987;**10**:1274–1277.
75 Geva T, Sanders SP, Ayres NA, et al. Two-dimensional echocardiographic anatomy of atrioventricular alignment discordance with situs concordance. *Am Heart J* 1993;**125**:459–464.
76 Porras D, Kratz C, Loukas M, et al. Superoinferior ventricles with superior left ventricle and inferior right ventricle: a newly recognized form of congenital heart disease. *Pediatr Cardiol* 2003;**24**:604–607.
77 Fontes VF, Malta de Souza JA, Pontes SC, Jr. Crisscross heart with intact ventricular septum. *Int J Cardiol* 1990;**26**:382–385.
78 Sato K, Ohara S, Tsukaguchi I, et al. A criss-cross heart with concordant atrioventriculo-arterial connections. Report of a case. *Circulation* 1978;**57**:396–400.
79 Nakada I, Nakamura T, Matsumoto H. Sezaki T. Successful repair of criss-cross heart using modified Fontan operation. *Chest* 1983;**88**:569–570.
80 Podzolkov VP, Ivanitsky AV, Makhechev OA, et al. Fontan-type operation for correcting complex congenital defects in a criss-cross heart. *Pediatr Cardiol* 1990;**11**:105–110.
81 Hibino N, Imai Y, Aoki M, et al. Double switch operation for superior-inferior ventricles. *Ann Thorac Surg* 2001;**72**:2119–2121.
82 Danielson GK, Tabry IF, Rirrer DG, Fulton RE. Surgical repair of criss-cross heart with straddling atrioventricular valve. *J Thorac Cardiovasc Surg* 1979;**77**:847–851.
83 Dunn JM, Donner R, Black I, Balsara RK. Palliative repair of transposition of the great arteries with criss-cross heart: ventricular septal defect and hypoplastic right (systemic) ventricle. *J Thorac Cardiovasc Surg* 1982;**83**:755–760.
84 Sluysmans T, Sanders SP, Van der Velde M, et al. Natural history and patterns of recovery of contractile function in single left ventricle after Fontan operation. *Circulation* 1992;**86**:1753–1761.
85 Margossian R, Schwartz ML, Prakash A, et al. Comparison of echocardiographic and cardiac magnetic resonance imaging measurements of functional single ventricular volumes, mass, and ejection fraction (from the Pediatric Heart Network Fontan Cross-Sectional Study). *Am J Cardiol* 2009;**104**:419–428.
86 Soriano BD, Hoch M, Ithuralde A, et al. Matrix-array 3-dimensional echocardiographic assessment of volumes, mass, and ejection fraction in young pediatric patients with a functional single ventricle. A comparison study with cardiac magnetic resonance. *Circulation*. 2008;**117**:1842–1848.
87 Friedberg MK, Su X, Tworetzky W, et al. Validation of 3D echocardiographic assessment of left ventricular volumes, mass, and ejection fraction in neonates and infants with congenital heart disease. A comparison study with cardiac MRI. *Circ Cardiovasc Imaging* 2010;**3**:735–742.
88 Hershenson JA, Zaidi AN, Texter KM, et al. Differences in tissue Doppler imaging between single ventricles after the Fontan operation and normal controls. *Am J Cardiol* 2010;**106**:99–103.
89 Menon SC, Gray R, Tani LY. Evaluation of ventricular filling pressures and ventricular function by Doppler echocardiography in patients with functional single ventricle: correlation with simultaneous cardiac catheterization. *J Am Soc Echocardiogr* 2011;**24**:1220–1225.
90 Singh GK, Cupps B, Pasque M, et al. Accuracy and reproducibility of strain by speckle tracking in pediatric subjects with normal heart and single ventricular physiology: a two-dimensional speckle-tracking echocardiography and magnetic resonance imaging correlative study. *J Am Soc Echocardiogr* 2010;**23**:1143–1152.
91 Moiduddin N, Texter KM, Zaidi AN, et al. Two-dimensional speckle strain and dyssynchrony in single left ventricles vs. normal left ventricles. *Congenit Heart Dis* 2010;**5**:579–586.
92 Petko C, Voges I, Schlangen J, et al. Comparison of right ventricular deformation and dyssynchrony in patients with different subtypes of hypoplastic left heart syndrome after Fontan surgery using two-dimensional speckle tracking. *Cardiol Young* 2011;**21**:677–683.
93 Moiduddin N, Texter KM, Zaidi AN, et al. Two-dimensional speckle strain and dyssynchrony in single right ventricles versus normal right ventricles. *J Am Soc Echocardiogr* 2010;**23**:673–679.
94 Rhodes J, Margossian R, Sleeper LA, et al. Non-geometric echocardiographic indices of ventricular function in patients with a Fontan circulation. *J Am Soc Echocardiogr* 2011;**24**:1213–1219.
95 Ho P-K, Lai CTM, Wong SJ, Cheung Y-F. Three-dimensional mechanical dyssynchrony and myocardial deformation of the left ventricle in patients with tricuspid atresia after Fontan procedure. *J Am Soc Echocardiogr* 2012;**25**:393–400.
96 Janousek J, Gebauer RA, Abdul-Khaliq H, et al., Working Group for Cardiac Dysrhythmias and Electrophysiology of the Association for European Paediatric Cardiology. Cardiac resynchronization therapy in paediatric and congenital heart disease: differential effects in various anatomical and functional substrates. *Heart* 2009;**95**:1165–1171.
97 Lacour-Gayet F, Serraf A, Fermont L, et al. Early palliation of univentricular hearts with subaortic stenosis and ventriculoarterial discordance: the arterial switch option. *J Thorac Cardiovasc Surg* 1992;**104**:1238–1245.
98 Brown DW, Gauvreau K, Moran AM, et al. Clinical outcomes and utility of cardiac catheterization prior to superior cavopulmonary anastomosis. *J Thorac Cardiovasc Surg* 2003;**126**:272–281.
99 Banka P, McElhinney DB, Bacha EA, et al. What is the clinical utility of routine cardiac catheterization before a Fontan operation? *Pediatr Cardiol* 2010:**31**:977–985.
100 Ro PS, Rychik J, Cohen MS, et al. Diagnostic assessment before Fontan operation in patients with bidirectional cavopulmonary anastomosis: are noninvasive methods sufficient? *J Am Coll Cardiol* 2004;**44**:184–187.
101 Ait-Ali L, De Marchi D, Lombardi M, et al. The role of cardiovascular magnetic resonance in candidates for Fontan operation: proposal of a new algorithm. *J Cardiovasc Magn Reson* 2011;**13**:69.

CHAPTER 28

Echocardiographic Assessment of Functionally Single Ventricles after the Fontan Operation

Marc Gewillig[1] and Luc Mertens[2]

[1]Pediatric Cardiology, University Hospitals Leuven, Leuven, Belgium

[2]Cardiology, The Hospital for Sick Children, University of Toronto, Toronto, ON, Canada

Introduction

For the majority of patients with different types of functionally univentricular hearts, the treatment goal is to achieve palliation through the creation of a total cavopulmonary anastomotic connection known as the Fontan operation [1]. This operation essentially bypasses the right heart by directing the systemic venous return into the pulmonary circulation without passing through a ventricular chamber. The Fontan operation causes a unique type of circulation, which requires a specific echocardiographic approach. In the current chapter we will first review the specific physiologic characteristics of a Fontan circulation followed by a discussion of the echocardiographic evaluation.

The Fontan circulation

A variety of cardiac malformations are characterized by the presence of a hypoplastic ventricle that is too small to sustain one of the circulations resulting in a functionally single ventricular (FSV) heart that has to support both circulations. During fetal life and immediately after birth the systemic and the pulmonary circulations in a FSV are connected in parallel with one ventricular chamber pumping to both circulations usually by way of the patent ductus arteriosus (Figures 28.1a,b). In the pre-Fontan era, these patients were palliated by an aortopulmonary artery shunt (e.g., Blalock–Taussig shunt) or pulmonary artery banding (both outflows unobstructed) which resulted in persistence of the parallel circuit. This palliation caused persistent arterial desaturation and chronic volume loading of the FSV. These procedures contributed to progressive ventricular dysfunction, leading to FSV failure, congestive heart failure and death with few survivors beyond the fourth decade. In 1971, Francis Fontan reported on a new surgical approach [1], separating the systemic and pulmonary circulations and redirecting the systemic venous blood directly to the pulmonary circulation. In the Fontan circulation, mixing of the circulations is avoided and the postcapillary energy and systemic venous pressure are used as the driving forces to push the blood through the pulmonary circulation (Figure 28.1c) [2]. Advantages of a Fontan circuit include separation of both circulations with normalization of the arterial saturation, and abolishment of chronic ventricular volume loading. The primary disadvantage is the resultant elevated systemic venous pressure and passive flow through the pulmonary vascular bed which causes chronic systemic venous hypertension, reduced cardiac output and a limited reserve during exercise (Figure 28.2).

By creating a cavopulmonary connection, a new portal system is created. In a portal system a capillary bed pools blood into another capillary bed through veins without passing through the heart. This is most typically seen in the normal gastrointestinal system where the superior mesenteric vein and splenic vein are connected via the portal vein to the hepatic veins. The Fontan portal system pools the systemic venous blood in the pulmonary circulation and limits the pulmonary venous return to the heart due to different static resistances and dynamic impedances in the circuit. The optimal Fontan circuit requires unobstructed Fontan connections, good-sized branch pulmonary arteries without stenosis, low pulmonary vascular resistance, and unobstructed pulmonary venous connection to the atrium and low atrial pressures. Atrial pressures are influenced by atrioventricular valve function and by FSV diastolic function. Good systolic FSV function is required to generate sufficient systemic output; chronic volume load (residual shunts, atrioventricular valve regurgitation, aortic regurgitation) and/or pressure load (outflow tract obstruction, residual coarctation of the aorta), even if mild can be very detrimental in patients with this physiology.

Echocardiography in Pediatric and Congenital Heart Disease: From Fetus to Adult, Second Edition. Edited by Wyman W. Lai, Luc L. Mertens, Meryl S. Cohen and Tal Geva.
© 2016 John Wiley & Sons, Ltd. Published 2016 by John Wiley & Sons, Ltd.
Companion website: www.lai-echo.com

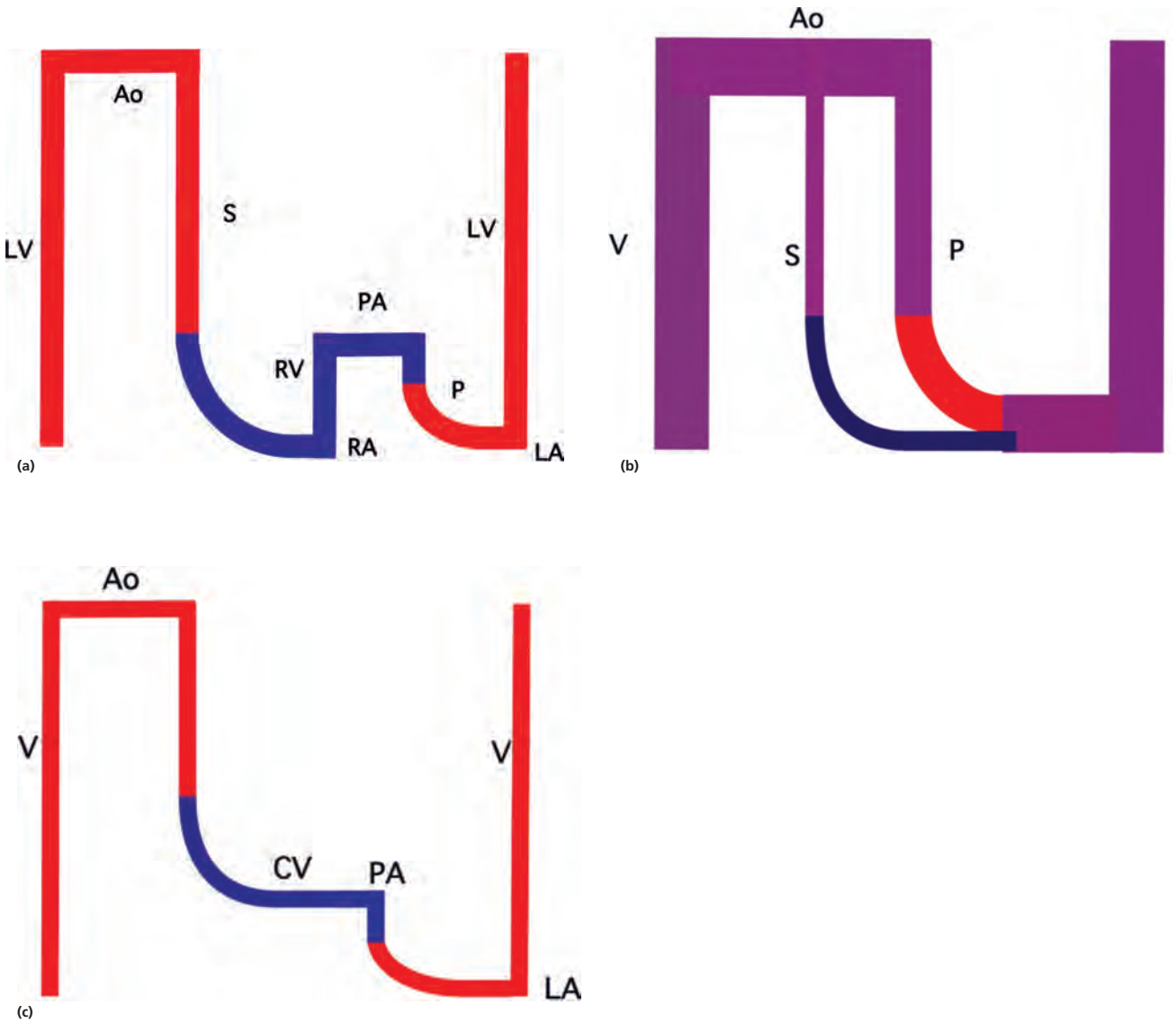


Figure 28.1 Schematic representation of **(a)** normal cardiovascular circulation, **(b)** shunted palliation, and **(c)** Fontan circulation. **(a)** The normal circulation: the pulmonary circulation (P) is connected in series with the systemic circulation (S). The right ventricle (RV) is more compliant than the left ventricle keeping the right atrial (RA) pressure lower than the left atrial (LA) pressure. The RV functions at lower pressure than the LV which is related to lower pressure and resistance in the pulmonary artery (PA). **(b)** Parallel circulation in a univentricular heart. The systemic (S) and pulmonary (P) circuits are connected in parallel with one dominant single ventricle (V) pumping blood into both circulations. There is complete admixture of systemic and pulmonary venous blood, causing arterial desaturation. **(c)** Fontan circuit. The systemic veins (CV) are connected to the pulmonary artery (PA), without a subpulmonary ventricle or systemic atrium: the lungs are hereby converted into a portal system which limits flow to the ventricle. In the absence of a fenestration, there is no admixture of systemic and pulmonary venous blood, but the systemic venous pressures are generally elevated. Ao, aorta; CV, caval veins; LA, left atrium; LV, left ventricle; PA, pulmonary artery; RV, right ventricle; V, single ventricle. Line thickness reflects output, color reflects oxygen saturation.

The functional single ventricle in a Fontan circulation

Ventricular dimensions and wall thickness

Figure 28.3 demonstrates the evolution of the FSV volume loading from fetal life until after completion of the Fontan circuit. During fetal life, the dominant ventricle is responsible for the combined output of the systemic and pulmonary circulations. This causes prenatal eccentric remodeling resulting in enlarged chamber dimensions in the single ventricle at birth [3]. After the initial neonatal palliation, (generally an aortopulmonary artery shunt or a pulmonary artery band), the parallel circulations cause a persistent, chronic volume load. The bidirectional Glenn shunt (a superior cavopulmonary anastomosis where only the

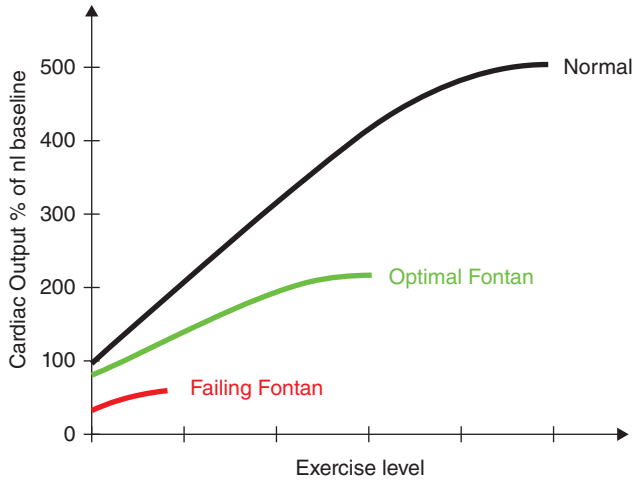


Figure 28.2 Cardiac output during exercise output: normal versus Fontan circulation. A normal subject with a biventricular circuit can increase output five times compared to baseline (black line). In Fontan patients output this is significantly impaired both at rest and during exercise. In optimal Fontan patients (green line) the output is mildly decreased at rest, with a moderately reduced capacity to increase cardiac output during exercise. This limits exercise capacity in almost all Fontan patients. In failing Fontan patients (red line), the output is significantly reduced at rest with very limited increase during exercise.

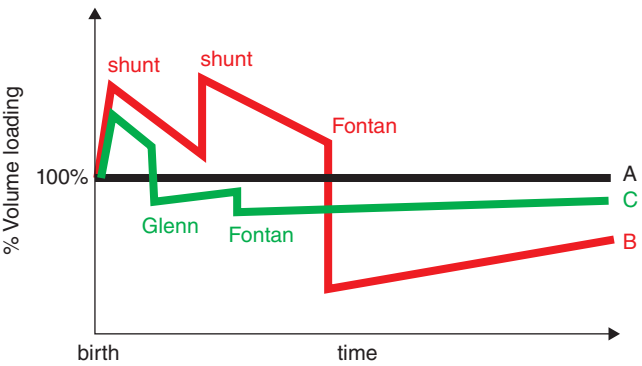


Figure 28.3 Effect of different pre-Fontan palliative strategies on volume loading. A: We assume a normal ventricle in a biventricular circulation functions on average at 100% of normal. Prior to birth the dominant single ventricle remodels and its size adjusts to the chronic volume loading. The patient with a UVH generally is born with an appropriate ventricular size adjusted for chronic volume load. Prior to the 1990s (B, red line), the volume loading to the ventricle was augmented shortly after birth by a shunt procedure to ±150%. The patient slowly outgrows his shunt, and adapts his ventricle, thereby gradually reducing the volume overload to ±100% for its size. A second shunt was created, augmenting the volume overload again to 150%. As this patient again outgrows his shunt, a Fontan circuit is made, acutely reducing the volume load to around 25% of the preload it was exposed to prior to the procedure. This sudden preload reduction was often poorly tolerated hemodynamically. This resulted in changes in management strategy. After the 1990s (C, green line), a small neonatal shunt was created for a short time (generally 6 months); the patient slowly outgrows the shunt; the ventricle is progressively volume unloaded in two separate steps: first, at the time of the bidirectional Glenn shunt, and a second time, at the time of the Fontan operation. This stepwise approach is generally hemodynamically better tolerated.

superior vena cava is connected to the pulmonary artery and the inferior vena cava remains connected to the right atrium) is generally performed at 4 to 8 months of age to address this issue. After this procedure, the chronic volume load is reduced. A recent serial follow-up study using cardiac MRI in patients scanned before the bidirectional Glenn and again before the Fontan operation, demonstrated that the bidirectional Glenn shunt resulted in a reduction of indexed ventricular volume with an increase in ejection fraction (i.e., reverse remodeling) [4]. Quantitative measurements by cardiac MRI have also demonstrated that flow through aortopulmonary collaterals contributes significantly to pulmonary blood flow and cardiac output after the bidirectional Glenn shunt [5]: up to one third of the cardiac output and up to 40% of the pulmonary blood flow comes from collateral flow. A higher burden of collateral flow adversely influences clinical outcomes immediately after the Fontan operation [5,6]. Despite the presence of collaterals, the FSV is volume unloaded after the Fontan operation due to a reduction in pulmonary venous return (with a reduced preload reserve being one of the characteristic features of the Fontan circulation). After the Fontan operation, further reverse remodeling occurs but the FSV is characterized by a detrimental decrease in ventricular dilation with persistence of an abnormal wall thickness and incomplete resolution of hypertrophy (eccentric remodeling), often termed increased mass-to-volume ratio [7]. Concentric hypertrophy may also develop in the FSV in response to increased afterload, defined as ventricular wall stress. Studies have shown that increased afterload (i.e., outflow tract obstruction, residual coarctation of the aorta or systemic hypertension) may persist after the Fontan operation [8,9]. Residual ventricular hypertrophy may contribute to diastolic dysfunction and eventually to failure of the Fontan circulation.

Effect of loading changes on parameters of systolic function

The most commonly used parameter to assess global pump function is ejection fraction. This parameter is sensitive to changes in preload and afterload. Recent serial data obtained with either MRI or echocardiography has demonstrated a decrease in ventricular volumes and ejection fraction immediately after the bidirectional Glenn shunt [4,10]. During the remodeling process a compensatory decrease in end-systolic volumes may result in an increase in ejection fraction just prior to the Fontan procedure [4]. Despite these findings, ejection fraction is generally preserved in the majority of patients after the Fontan operation suggesting that adaptation or further reverse remodeling occurs in the post-Fontan period [7]. It also indicates that systolic dysfunction is uncommon in pediatric Fontan survivors. In adult patients, ventricular dysfunction seems to be more common and is an important cause of failure of the Fontan circuit [11]. Systolic dysfunction may be intrinsic to the FSV or may be related to other comorbidities in adult life.

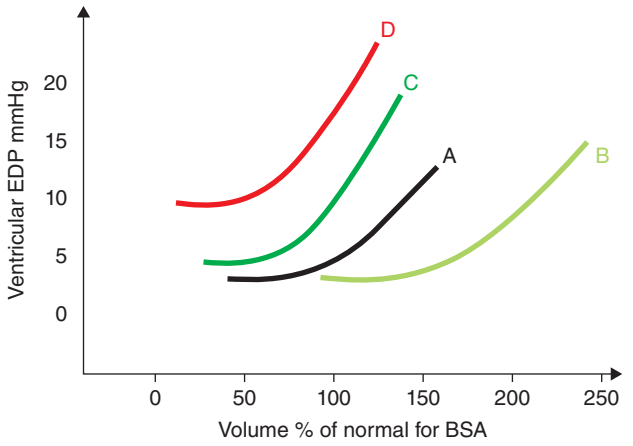


Figure 28.4 Diastolic pressure–volume relationship during different stages of palliation. A: the normal ventricle; B: shunted ventricle with chronic volume loading resulting in enhanced compliance; C: Fontan ventricle early after volume unloading; D: Fontan ventricle late after unloading; chronic volume unloading is thought to cause progressive stiffening of the ventricle with decreased compliance.

Diastolic function of the single ventricle

In the Fontan circuit, low atrial pressure is required for a low-pressure gradient across the pulmonary vascular bed (transpulmonary gradient). Atrioventricular valve regurgitation and single ventricular diastolic function are important determinants of atrial pressure. Diastolic function after the Fontan operation has been poorly studied due to the absence of good methods for assessment of ventricular filling in patients with this physiology. Experimental data have shown that acute volume unloading of the ventricle results in less recoil and decreased suction resulting in increased filling pressures (Figure 28.4) [12–15]. Echocardiographic studies in Fontan patients have suggested that the volume reduction associated with the Fontan operation results in early relaxation abnormalities and incoordinate wall motion abnormalities especially affecting the isovolumic relaxation period and early filling [13–15]. These diastolic changes have typically been observed in FSV patients who underwent a Fontan operation without a previous bidirectional Glenn shunt. In this era, the chronically volume-loaded ventricles were acutely unloaded and the observed diastolic and systolic abnormalities could be related to the ventricle being "too large" for the volume immediately after the procedure. In patients after the Fontan procedure, chronic volume reduction seems to cause a progressive decrease in ventricular compliance with a left upward shift in the end-diastolic pressure–volume relationship [16]. Moreover, the thicker myocardium may become stiffer with age. The FSV may enter a vicious cycle whereby the volume unloading results in adverse reverse remodeling, reduced compliance, reduced ventricular filling, and eventually declining cardiac output. A recent cohort study suggests that the majority of pediatric Fontan patients have abnormal diastolic function but the clinical and prognostic significance of these findings is currently unknown [7]. The primary issue regarding assessment of diastolic function is that the conventional echocardiographic parameters (atrioventricular valve inflow, pulmonary venous flow patterns, and tissue Doppler velocities) are difficult to interpret in Fontan patients. Progressive increase in ventricular stiffness and reduction in compliance may be one of the major mechanisms explaining Fontan failure with progressive age.

The pulmonary circulation limits cardiac output after the Fontan operation

A characteristic feature of the Fontan circuit is the lack of pulsatile pulmonary blood flow through the pulmonary vascular bed. In the normal biventricular circulation pulmonary blood flow is generally not a limiting factor for determining cardiac output. In ischemic heart disease and cardiomyopathy, decreased cardiac pump function limits cardiac output. After the Fontan procedure the pulmonary circulation limits the preload reserve to the FSV and determines the cardiac output response [8,17]. This is comparable to obstructed inflow after Mustard repair, primary pulmonary hypertension, constrictive pericarditis, and mitral stenosis.

Different factors influence the amount of pulmonary blood flow and cardiac output after the Fontan operation. The first limiting factor is the energy loss in the surgical connections. The presence of unobstructed surgical connections between the caval veins and the pulmonary arteries is a requirement for optimal Fontan function. Any degree of obstruction of the Fontan connections will reduce cardiac output. The pulmonary arteries need to be good-sized and unobstructed. Pulmonary vascular resistance (PVR) further determines pulmonary blood flow. Even a mild increase in PVR reduces pulmonary blood supply and cardiac output [18]. Recent data have shown that pulmonary vasodilators like sildenafil positively influence cardiac output and exercise capacity in Fontan patients [19,20]. Pulmonary venous obstruction is another important factor determining pulmonary blood flow. Some patients with FSV also have anomalous pulmonary venous connection that requires surgical intervention; they are at high risk for reobstruction. The extracardiac Fontan conduit may also compress the adjacent right pulmonary veins. Rarely, the left lower pulmonary vein may become compressed between the heart, the descending aorta and the spine.

In the Fontan circuit, pulmonary blood flow will increase with inspiration and decrease with expiration [21]. Studying respiratory variation in Fontan patients has provided interesting physiologic information. Increased intrathoracic pressure due to airway obstruction or positive pressure ventilation reduces pulmonary blood flow and is detrimental for Fontan physiology [22].

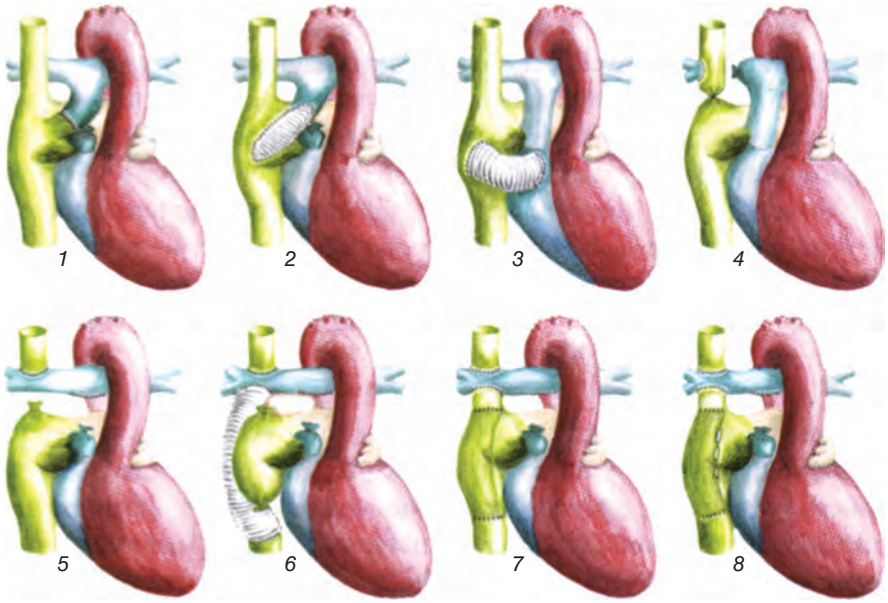


Figure 28.5 Different modifications of the Fontan operation.

Fontan modifications

Since its original description, the Fontan circuit has undergone several surgical modifications (Figure 28.5) [23,24]. The original Fontan operation included the hypoplastic right ventricle in the circuit. This required a valved surgical conduit to connect the hypoplastic ventricle with the pulmonary artery. These conduits degenerated and conduit obstruction was a major problem resulting in a high reoperation rate. This initial approach from Francis Fontan was quickly abandoned and was replaced by the atriopulmonary connection. This variation became the most commonly used modification as it was thought that including the right atrium in the connection would be beneficial for pulmonary hemodynamics due to the presence of the atrial kick. However, elevated atrial pressure caused progressive right atrial dilation, reducing the energetic efficiency and becoming a substrate for atrial arrhythmia. Experimental and computational modeling was subsequently performed which showed that a total cavopulmonary connection (TCPC) would be hemodynamically more favorable and would result in less energy and power loss in the conduit when compared to atriopulmonary connection [25,26]. In this circuit, the vena cavae are connected directly to the right pulmonary artery. The superior vena cava is connected to the right pulmonary artery (bidirectional Glenn shunt) and the inferior vena cava is connected through an intra-atrial (lateral tunnel) baffle or by an extracardiac conduit. The benefits of the lateral tunnel Fontan include use in small children and potential for growth. The possible drawback is that there is substrate for atrial arrhythmia as a result of the suture line in the atrium and the exposure of atrial tissue to high pressure. To avoid these problems, the extracardiac conduit was introduced. This procedure consists of a tube graft between the inferior vena cava and the pulmonary artery placed externally around the right atrium. This circuit leaves the entire atrium at low pressure, has minimal atrial suture lines, and can be performed without aortic cross-clamping. However, this tube graft has no growth potential and therefore is typically offered to larger patients (generally between 2–3 years of life). It remains to be determined whether the extracardiac conduit will ameliorate the arrhythmia risk. It is also more difficult to fenestrate (see later) this type of baffle. In most centers the extracardiac conduit is currently the preferred technique though some are returning to the lateral tunnel method. When assessing a patient with a Fontan circulation, it is essential to know which type of connection has been made.

Current strategy towards a Fontan circulation

At birth, it is fatal to create a Fontan circulation because the pulmonary vascular resistance remains elevated for several weeks to months. Even when resistance falls, a staged approach to Fontan completion is preferred, with the superior and inferior caval veins incorporated into the systemic venous chamber in two separate stages. Thus, the body adapts progressively to the new hemodynamic condition and eccentric hypertrophy, reducing the overall operative morbidity and mortality. In the neonatal period, clinical management aims at achieving unrestricted flow to the aorta (if required: arch repair, Damus–Kaye–Stansel, Norwood procedure), appropriately limited flow to the lungs (if required: pulmonary artery band, aortopulmonary artery shunt, stenting of the arterial duct), and unrestricted return of blood to the ventricle (if required: balloon septostomy, pulmonary venous connection). Between 4 to 8 months of age, the

bidirectional Glenn shunt is performed. After the Glenn shunt, the patient remains mildly cyanotic because the desaturated blood from the inferior vena cava still connects to the systemic ventricle and the aorta. Between 1 to 5 years of age, the Fontan circuit is completed, incorporating the inferior vena cava into the baffle.

Frequently a small fenestration or hole is created between the systemic venous pathway and the pulmonary atrium, either routinely or only in "high-risk" patients. The fenestration allows a residual right-to-left shunt, thereby reducing systemic venous pressure and increasing preload of the systemic ventricle at the expense of cyanosis. A fenestration has been shown to reduce operative mortality and morbidity (e.g., pleural drainage). It can be closed by a percutaneous intervention weeks or months after adaptation of the body to the new hemodynamic condition, particularly if marked cyanosis occurs with exercise.

Complications after the Fontan operation are common and relate to the increased systemic venous pressure and chronic low cardiac output. There may be clinical important early and late mortality, mild to moderate exercise intolerance, ventricular dysfunction, rhythm and conduction abnormalities, hepatomegaly with secondary liver dysfunction and potential for development of liver fibrosis or cirrhosis, lymphatic dysfunction, protein-losing enteropathy, plastic bronchitis, thrombus formation, ascites, and peripheral edema [1,2].

Echocardiographic assessment of the Fontan circulation

Before scanning a patient who has undergone a Fontan operation, it is essential to first review the underlying cardiac anatomy and previous surgical history. The ventricular morphology (left, right, or indeterminate) needs to be determined as this influences measurements and interpretation of functional information. It is important to establish the type of Fontan connection that has been performed as well as any additional cardiac surgery before starting to scan. This includes information regarding arch reconstruction, the presence of a Damus–Kaye–Stansel connection (between the ascending aorta and the pulmonary trunk), previous valve surgery, type of previous shunt if performed (modified Blalock–Taussig shunt or other), interventions on the pulmonary arteries (patch, balloon dilatation, or stent implantation) and intervention on the pulmonary veins. Additionally, the echocardiographer should know the clinical indication for the scan. When interpreting the images it helps to know the patient's clinical status and whether the study is being performed because of a concern or for routine follow-up. Some issues such as residual cyanosis, ascites, protein-losing enteropathy, or other signs of Fontan failure may require specific image acquisition. Access to previously performed imaging studies greatly facilitates interpretation of findings and detection of changes. Comparison between studies should be easy and should be routine in the review process. To facilitate this comparison, digital storage of clips and usage of standard scanning protocols is highly recommended. As these patients have frequently undergone multiple surgeries, acoustic windows may be challenging, especially with increasing age.

Goals of imaging

1 Assessment of the Fontan pathway
 - a Assess for presence and size of fenestration and transfenestration gradient
 - b Assess for presence and size of thrombus in Fontan pathway
 - c Assess for obstruction of Fontan pathway to pulmonary artery.
2 Assessment of pulmonary venous chamber
 - a Assess for adequate atrial communication
 - b Assess for pulmonary venous obstruction.
3 Assessment of atrioventricular valve function
 - a Severity of atrioventricular valve regurgitation, if present.
4 Assessment of single ventricular function
 - a Systolic and diastolic performance
 - b Hypertrophy and/or dilation.
5 Assessment of outflow tracts, semilunar valve(s), ascending aorta, and aortic arch
 - a Determine semilunar valve competency
 - b Assess for residual or recurrent arch obstruction.
6 Assessment of branch pulmonary arteries
 - a Determine narrowing, stenosis, competitive flow.

Assessment of Fontan connections, pulmonary arteries, and pulmonary veins

Typically it is recommended to initiate the scan with subxiphoid imaging. Coronal or subxiphoid sagittal views in particular allow for visualization of the inferior vena cava and its connection to the Fontan baffle. Color flow imaging and pulsed-wave (PW) Doppler tracings in this view are used to assess for obstruction (Figure 28.6; Videos 28.1 and 28.2). The inferior vena cava and hepatic veins are typically dilated and spontaneous contrast is often noted. Flow velocities should be low (generally <20–30 cm/s). For PW Doppler assessment, the sweep speed should be reduced in order to record flow throughout the respiratory cycle. Normally a low-velocity continuous systolic and diastolic flow pattern is detected (Figure 28.7). Usually, the flow increases with inspiration and decreases during expiration. The presence of respiratory variation suggests that intrathoracic pressure changes are well transmitted in the Fontan conduit, a sign that the Fontan connections are unobstructed. Absence of respiratory variation or the presence of reverse flow in the cardiac cycle is abnormal. Retrograde flow during systole may be seen in the setting of atrioventricular valve regurgitation or due to the presence of significant competitive collateral flow. Flow reversal during diastole may be present in the failing Fontan or in the presence of atrial arrhythmia (increased pressure in the Fontan circuit). Lack of respiratory variation should raise suspicion of conduit obstruction. In the intra-atrial tunnel or an extracardiac conduit, the connection between the

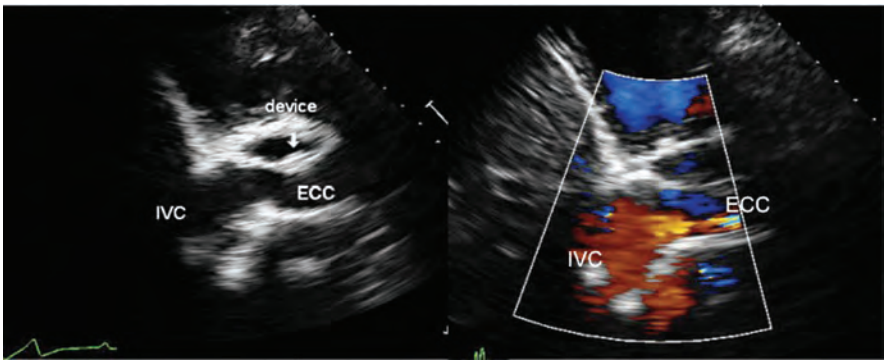


Figure 28.6 The connection between the inferior vena cava (IVC) and the extracardiac conduit (ECC). The connection between the inferior vena cava and the extracardiac conduit is demonstrated from a subxiphoid view. The IVC is dilated. The IVC–ECC connection is widely patent as seen by two-dimensional imaging (left panel) with laminar flow (right panel). The arrow points to a device that was used to close a fenestration between the ECC and the atrium.

inferior vena cava may be visualized well using a subxiphoid long- and short-axis sweep. Subxiphoid, apical and parasternal views should be combined to assess the Fontan baffle. This assessment includes looking for tunnel dilation, the presence of clots and residual fenestration or baffle leaks (Video 28.3). If a fenestration is present, a PW Doppler tracing of the fenestration flow should be acquired (Figure 28.8). An estimate of the pressure gradient between the systemic and pulmonary venous chambers can be determined by obtaining the mean gradient across the fenestration (transpulmonary gradient). If the fenestration has been closed with a device, the position of the device should be evaluated as well as the presence of a residual shunt.

The superior connection between the tunnel/conduit and the pulmonary artery is often more difficult to image. The apical and parasternal long-axis views but particularly the suprasternal view are helpful in visualizing this region (Figure 28.9; Video 28.4). In the atriopulmonary Fontan, the connection is variable depending on the anastomosis. Typically, the atriopulmonary connection results in progressive, marked atrial dilatation with low flow velocities, spontaneous contrast and potential for thrombus formation. Other types of connections involving valved conduits should be carefully inspected for valve dysfunction (especially stenosis) (Figure 28.10; Video 28.5) and thrombus. Color flow using low Nyquist settings should be used to visualize the surgical anastomosis sites of the Fontan connections. In the case of obstruction, the flow pattern in the baffle becomes continuous throughout the respiratory cycle as the gradient can persist during expiration. If TTE is insufficient, transesophageal echocardiography (TEE) may provide better imaging of the conduit, tunnel or atrium. Studies have demonstrated that thrombus that is present on TEE may not be visualized on TTE.

In patients with a lateral tunnel or extracardiac type Fontan connection, it is also important to evaluate the connection between the superior vena cava and the right pulmonary artery (Glenn anastomosis; Figure 28.11; Video 28.6). This can only be visualized from the suprasternal frontal view. In this view, the flow into the branch pulmonary arteries may be imaged although in older patients adequate images are challenging. The flow pattern in the superior vena cava resembles those in the inferior vena cava with increased flow with inspiration and decreased flow with expiration. If flow acceleration is noted at the anastomosis site, a PW Doppler tracing and mean gradient can be calculated. Thrombus may be present in the superior vena

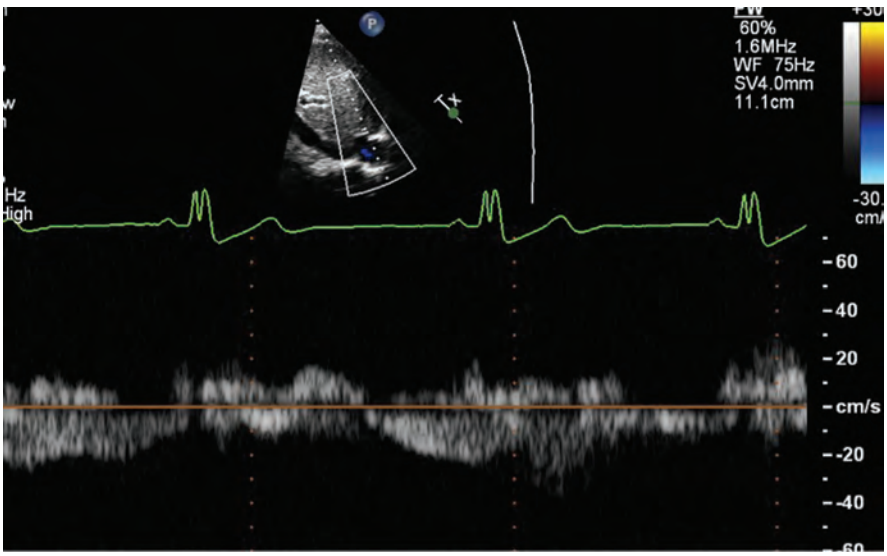


Figure 28.7 Venous flow pattern in the hepatic veins. Flow in the hepatic vein–inferior vena cava (IVC) junction. In this patient some systolic flow reversal can be noted which is related to a moderate to severe degree of tricuspid regurgitation.

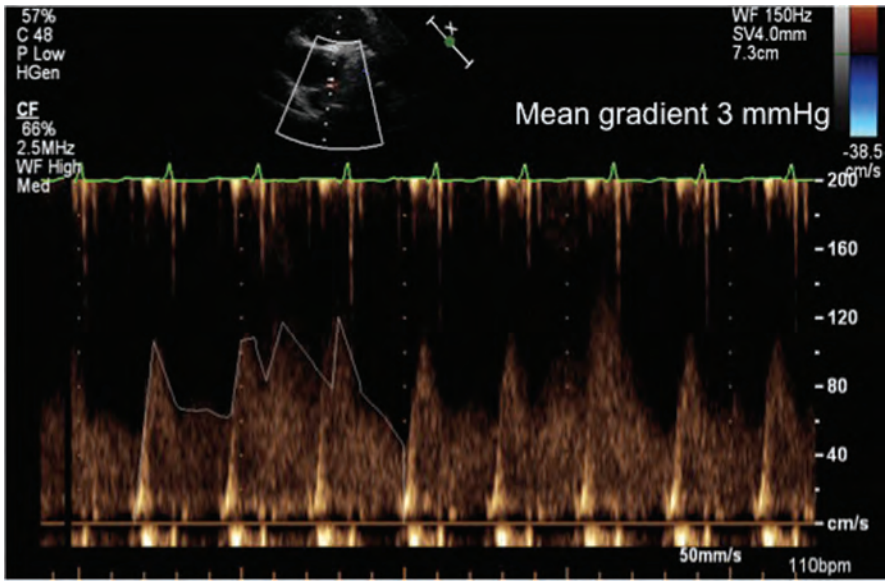


Figure 28.8 Doppler flow through the fenestration. A pulsed Doppler tracing is obtained to measure the flow through the fenestration between the extracardiac conduit and the atrium. The mean gradient between the fenestration and the atrium can be assessed. This reflects the pressure difference between the conduit and the atrium (transpulmonary gradient).

cava or the innominate vein, especially if a central line is present. In case of bilateral superior vena cavae, both anastomotic connections should be visualized. Generally, the left superior vena cava is smaller than the right, and obstruction of the left-sided anastomosis is more common. Also worth noting is that the pulmonary artery segment between both anastomoses sites may be small and become hypoplastic over time because it receives little flow.

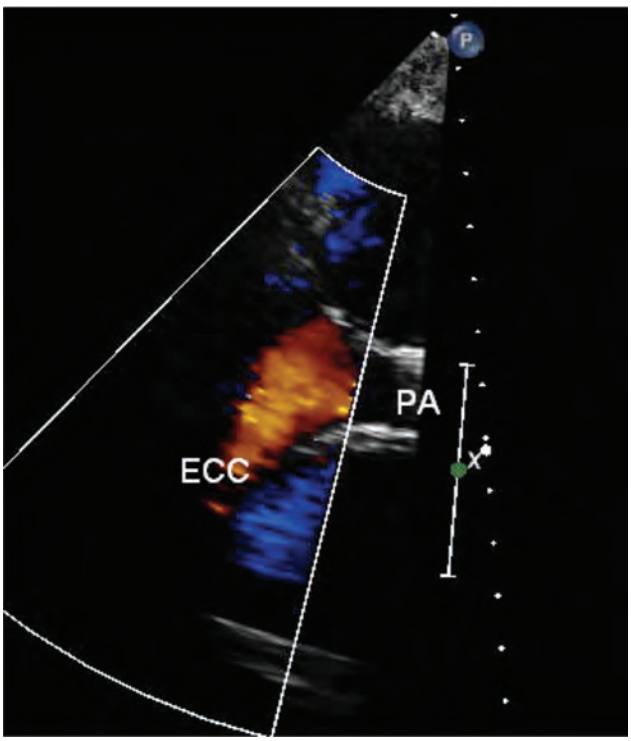


Figure 28.9 Connection between the extracardiac conduit and the pulmonary artery (PA). In this suprasternal image slightly tilted to the right and anteriorly, the connection between the extracardiac conduit (ECC) and the right pulmonary artery is nicely demonstrated. The red flow indicates the flow in the direction of the PA during inspiration.

The branch pulmonary arteries are also best visualized using suprasternal views (Figure 28.12; Videos 28.7 and 28.8). The proximal right pulmonary artery is visualized from the suprasternal frontal view. When moving the transducer into a sagittal (arch) view, the left pulmonary artery may be seen going towards the left hilum. Pulsed Doppler tracings should be obtained in both pulmonary arteries. If stenosis is present, a continuous flow pattern with an elevated mean gradient will be seen. If a pulmonary artery stent is present, the metal often causes shadowing and reverberations which can make it difficult to demonstrate flow. Color flow seen distal to the stent is reassuring. Flow reversal in the branch pulmonary arteries suggests increased pulmonary vascular resistance or the presence of significant aortopulmonary collaterals.

The pulmonary veins should also be interrogated after the Fontan procedure. An extracardiac conduit or significant atrial dilatation may cause compression of the pulmonary veins (Figure 28.13; Video 28.9). Pulmonary venous obstruction in a Fontan circuit can be difficult to detect by echocardiography and may require additional imaging by cardiac CT, magnetic resonance imaging, or cardiac catheterization.

Assessment of atrioventricular valve function

Careful evaluation of the atrioventricular valves should be performed in every Fontan patient. Significant atrioventricular valve regurgitation is associated with morbidity and mortality in this patient population.

Atrioventricular valve regurgitation is a common problem after the Fontan operation particularly in the presence of a common atrioventricular valve or a dominant tricuspid valve. Echocardiographic assessment should include evaluation of the

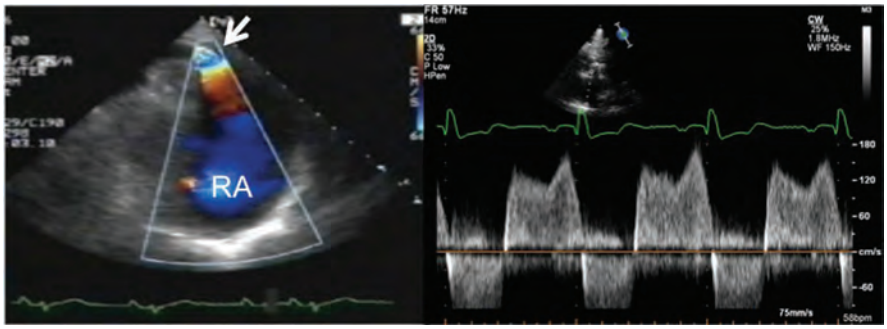


Figure 28.10 Stenosis on a conduit between the right atrium and a hypoplastic RV in a patient with tricuspid atresia who underwent a valved conduit insertion between the right atrium (RA) and the hypoplastic right ventricle. This is a right parasternal view. The conduit is located just below the sternum and can be very difficult to image. The Doppler tracing allows to quantify the degree of stenosis (mean gradient 5–6 mmHg). Also notice that there is regurgitation during systole. Source: Courtesy of Dr. F. Meijboom.

severity of atrioventricular valve regurgitation as well as identification of the mechanism (Figure 28.14; Videos 28.10 and 28.11). Evaluation of the severity of regurgitation is largely based on qualitative assessment using color flow. Different imaging planes should be used for assessing the size of the regurgitant jet in three dimensions. The jet width at the level of the leaflets generally is a good indicator of the severity of the regurgitation. Jet width assessment becomes more challenging when multiple jets are present. A combination of jet width, jet area and jet length into the atrium generally allows for subjective assessment as mild, moderate or severe. If more than mild, identifying the mechanism of regurgitation becomes important. A common mechanism for regurgitation is valve dysplasia with resultant valve leaflet irregularities at the zone of apposition and leaflet thickening [27]. Describing the mechanisms of regurgitation requires scanning the valve in multiple planes. Recent

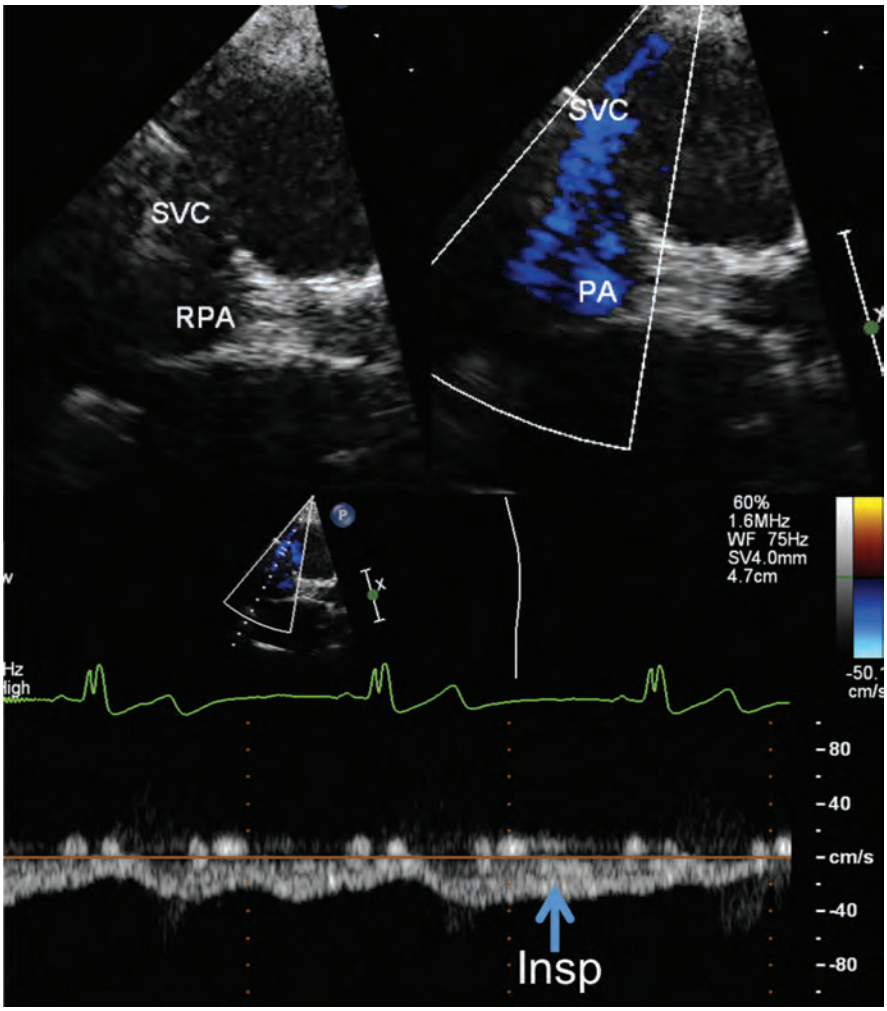


Figure 28.11 Anastomosis between the superior vena cava (SVC) and the right pulmonary artery (RPA). Suprasternal notch view demonstrating the connection between the SVC and the RPA. The connection is widely patent with laminar continuous flow increasing with inspiration (Insp).

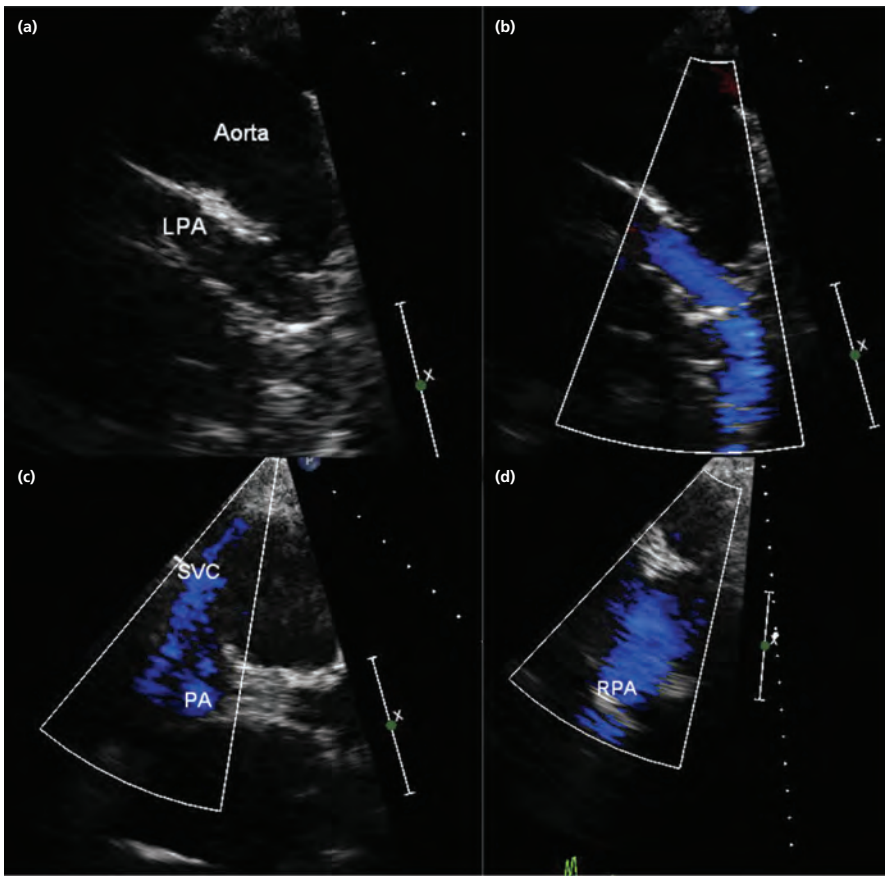


Figure 28.12 Imaging the pulmonary arteries. The suprasternal views are the best views to image the pulmonary arteries. The left pulmonary artery can be seen below the aorta when tilting the probe leftwards **(a)**. Color Doppler is very useful for identifying the pulmonary branches **(b)**. The right pulmonary artery (RPA) can be viewed from the suprasternal notch but by placing the probe more rightward. Figure **(c)** shows the superior vena cava (SVC) to RPA connection, while **(d)** shows the more distal RPA.

studies have suggested that 3D echocardiography may provide additional information on the atrioventricular valve in FSV [28]. Further improvements in spatial and temporal resolution of this technique will allow better defining of leaflet abnormalities and a more detailed description of the subvalvar apparatus.

After valve repair, careful follow-up of the surgical result is required. In case of prosthetic valve insertion, evaluation of prosthetic valve function is essential. Perivalvular leaks can be present and should be distinguished from regurgitation related to deficient prosthetic valve function. The low flow profile through the prosthetic valve makes it theoretically more prone to valve thrombosis. After valve repair, close monitoring of single ventricular function is required. The long-term outcome of patients undergoing atrioventricular valve repair in the context of single ventricle palliation is worse compared to case-matched patients not requiring valve surgery [29].

Atrioventricular valve stenosis is rare but can be present after atrioventricular valve repair or after prosthetic valve replacement. Inflow through the valve(s) should be assessed using color flow and PW Doppler from the apical views. If a gradient is present, CW Doppler should be obtained as aliasing may occur. The mean gradient should be calculated throughout the respiratory cycle. For prosthetic valves, a mean gradient is common and known for the specific valve types. If significant regurgitation is present, the mean inflow gradient may be overestimated due to increased flow.

Assessment of outflow tracts, ascending aorta, and aortic arch

In FSV, the outflow tract from the dominant ventricle connects the ventricle to the aorta. Outflow tract obstruction, if present, causes chronic pressure loading with secondary concentric hypertrophy, which is detrimental for the long-term preservation of ventricular function. It can further limit the output from the FSV. The mechanism causing outflow tract obstruction most commonly is subvalvar obstruction. The most typical example is double-inlet left ventricle with transposition of the great arteries where the VSD to the RV outlet chamber may become restrictive and thus, cause subaortic obstruction. In cases where a patient is at risk for this obstruction, a Damus–Kaye–Stansel (DKS) operation connecting both outflow tracts to the aorta is performed. The outflow tract needs to be imaged in all Fontan patients, especially in those who did not undergo a DKS procedure to assure unobstructed flow. Different acoustic windows (subxiphoid, apical views, and parasternal long-axis views) can be used to image the outflow tracts. Color Doppler, PW and CW Doppler traces should be obtained as well aligned with the outflow tract as possible. The peak and

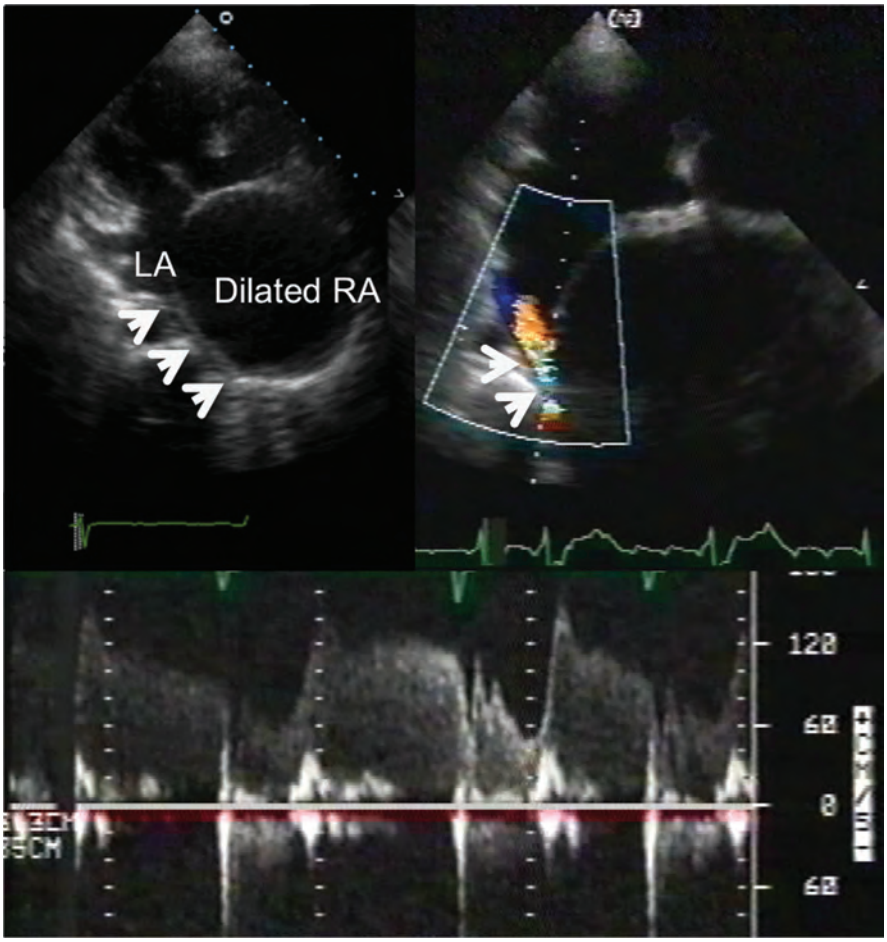


Figure 28.13 Pulmonary venous compression by dilated right atrium. This patient has an atriopulmonary connection with important dilation of the right atrium (RA), causing compression on the right upper pulmonary vein (arrows) with turbulent flow in the pulmonary vein and a mean gradient of 4–5 mmHg. Source: Courtesy of Dr. F. Meijboom.

mean gradients should be measured. If a gradient is detected, the mechanism causing the gradient should be defined. This can include subaortic obstruction due to a restrictive VSD, a membranous/fibrous ring, or valvar obstruction. In every patient the DKS connection between the ascending aorta and previous pulmonary trunk should be imaged. Obstruction at the connection between the aorta and the pulmonary can compromise coronary artery blood flow and result in ischemia and ventricular dysfunction. Semilunar valve function should also be evaluated. When the pulmonary valve is assigned to the aortic position (neo-aorta) regurgitation is prevalent. A DKS connection can distort one or both semilunar valves and cause regurgitation. Fortunately, important semilunar valve regurgitation is unusual in FSV. There have been reported cases of valve replacement.

In patients who underwent aortic arch reconstruction or coarctation surgery, assessment for residual arch obstruction is essential. Residual arch obstruction and coarctation of the aorta causes arterial hypertension and a significant increase in afterload to the FSV. Even a mild gradient can cause significant ventricular dysfunction. The suprasternal window is best to view the arch. Color Doppler and CW Doppler can be used to assess the peak gradient across the arch and the descending aorta. In a reconstructed arch, the proximal arch gradient should be incorporated into the Bernoulli equation to achieve the most accurate arch gradient. In adults the arch can be difficult to image. A good alternative for ruling out residual arch obstruction is obtaining a PW Doppler tracing of the abdominal aorta from the subxiphoid views. The absence of significant diastolic anterograde flow in the abdominal aorta rules out significant residual arch obstruction.

Assessment of single ventricular function

One of the most challenging parts of the echocardiogram in patients after the Fontan procedure is the assessment of ventricular function. Application of standard methods of assessment of the normal left ventricle to a FSV with variable ventricular morphology is a significant challenge. The FSV operates with reduced preload reserve and the pulmonary circulation is an important regulator of cardiac output. Assessment of ventricular function requires assessment of both systolic and diastolic function.

Systolic performance: The most widespread technique used to assess systolic ventricular function in patients after the Fontan operation, is *subjective assessment* or "eyeball technique." Most

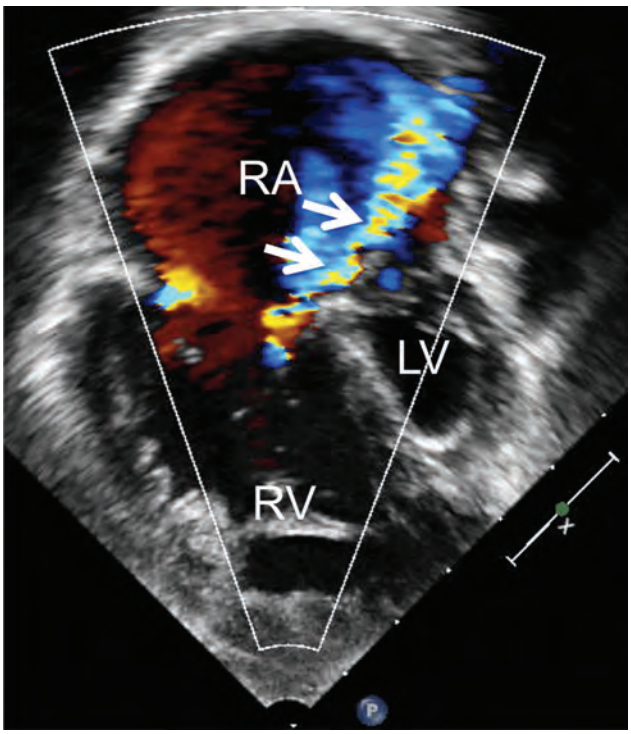


Figure 28.14 Tricuspid regurgitation in patient with hypoplastic left heart syndrome after the Fontan operation. Color Doppler image obtained from the apical 4-chamber view. There is a moderately wide jet of tricuspid regurgitation (arrows) coming from the zone of apposition between the anterior and septal leaflets. LV, left ventricle; RA; right atrium; RV, right ventricle.

echocardiography laboratories report ventricular function to be normal, mildly, moderately, or severely reduced based on subjective evaluation without any quantification. In two recent studies the qualitative assessment of FSV function was compared with MRI measurements of ejection fraction [30,31]. The studies looked at the reliability (intra- and inter-observer variability) as well as the accuracy (agreement between echocardiographic assessment and cardiac MRI quantification) of the assessment. The reproducibility of qualitative assessment was found to be moderate for LV morphology but weak for RV morphology. Also the agreement between qualitative assessment by echocardiography and quantitative assessment by cardiac MRI was weak. Both studies found that image quality and reader's experience influenced the results. In the mild to moderate range of dysfunction the disagreement is more pronounced. This is not surprising as most readers will be able to diagnose patients at the both extremes of the spectrum with either severely reduced function or a completely normal EF.

Quantitative approaches have been proposed and evaluated. A multicenter cohort study of the Fontan population used a *modified biplane Simpson's method* to quantify FSV volumes and ejection fraction [31]. The reproducibility of this method was found to be good amongst the core lab echocardiographers evaluating the studies, with better agreement for the LV than the RV measurements. The agreement between echocardiographic and MRI quantitative assessments was weak, however, with systematic underestimation of FSV volumes by echocardiography. This is probably related to the different geometry of FSV when applying the Simpson's formula. Given the relatively good reproducibility within the same laboratory, the biplane Simpson's technique may provide a reasonably good method for quantitative serial follow-up in the same patient. As most EF calculations are based on the geometric assumption of an ellipsoid LV, there will be relative inaccuracy in cases of more complex geometry. A reasonable alternative is the use of *fractional area change* from an apical 4-chamber view as an easy method for quantifying function (Figure 28.15). Lately *3D echocardiography* has been proposed as a potential emerging technique for evaluating FSV volumes and ejection fraction. The method of discs shows good reproducibility and accuracy [32]. However, it has recently been replaced by semi-automated (for the RV) or automated border detection and volumetric analysis programs that have been validated in biventricular hearts. These methods have yet to be validated for FSV [10]. A major issue with 3D echocardiography is that it can be very difficult to acquire a full volume of the entire FSV at reasonable frame rates; moreover, the anterior wall segments can be extremely difficult to visualize due to their anterior position in the chest just behind the sternum.

Since volumetric data are difficult to obtain in FSV, alternative nongeometric methods have been proposed. Using blood pool Doppler signals, d*P*/d*t* can be calculated. This preload-sensitive method is based on a valve regurgitation jet (Figure 28.16) or by using a modified method based on measurement of the isovolumic contraction time (IVCT) and aortic diastolic blood pressure and assuming FSV end-diastolic pressure (5 mmHg) [33]. The regurgitation method requires the presence of at least a mild to moderate amount of regurgitation in order to be able to acquire a reliable jet, which is not possible in every patient. The method based on IVCT requires measuring time intervals on the inflow tracing and the outflow tracing, which requires that there is no change in heart rate between the two traces. An additional problem with this method, is that the estimation of end-diastolic pressure may be inaccurate. The reproducibility of d*P*/d*t* measurements is high but the value of d*P*/d*t* correlates only weakly with MRI-based measurement of EF [33]. An alternative nongeometric Doppler-based method is the *myocardial performance index* (MPI) or Tei-index. This index of combined systolic and diastolic ventricular performance is calculated as follows:

$$\text{MPI} = (\text{IVRT} + \text{IVCT})/\text{ET}$$

where IVRT = isovolumic relaxation time and ET = ejection time. The index can be measured based on blood pool data (inflow and outflow) or tissue Doppler tracings. Tissue Doppler (Figure 28.17) has the advantage that the measurement can be performed on the same cardiac cycle [33,34]. The

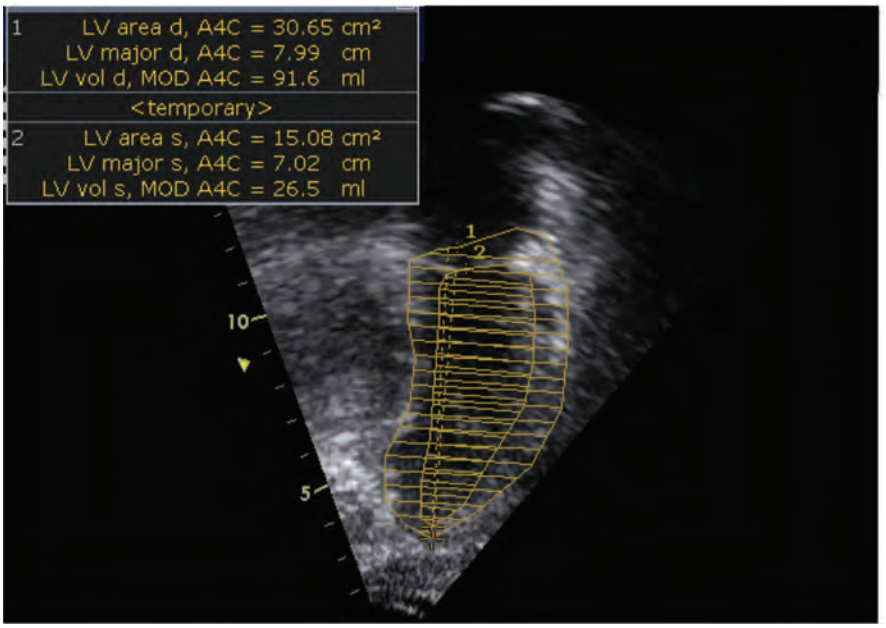


Figure 28.15 Quantification of single ventricular function. From an apical 4-chamber view fractional area change (FAC) can be measured by tracing the end-diastolic and end-systolic area and calculating the FAC. In this patient FAC was 50%. Using the Simpson's method volumes can be estimated and ejection fraction can be calculated. Ejection fraction in this patient was 72%.

reproducibility of this method has been moderately good. In Fontan patients, MPI has been reported to be prolonged but the degree of prolongation does not correlate with EF as measured by MRI. MPI is preload and afterload sensitive and this may affect the measure [35]. A potentially more attractive concept is *the ratio of systolic to diastolic duration* [36]. This measure requires an atrioventricular valve regurgitation jet and measuring the duration of the regurgitation jet as the systolic duration and the inflow duration as the diastolic duration. When ventricular dysfunction develops, systolic duration prolongs, shortening diastolic inflow duration. In severe dysfunction the heart spends most of the time in systole with only a very short time in diastole thus limiting diastolic filling. In normal children the S/D ratio varies between 0.4 and 1.6 and is largely determined by heart rate [37]. In patients with hypoplastic left heart syndrome the S/D ratio has been shown to be elevated and higher in patients with RV dysfunction compared to patients with normal RV function [36]. When corrected for heart rate, however, the values were shown to be in the normal range [34]. All these recent data illustrate that the use of nongeometric Doppler-derived timing parameters requires further investigation before they can be recommended in routine clinical practice.

Alternatively *tissue Doppler velocities* can be used. Tissue Doppler traces are relatively easy to obtain and are generally

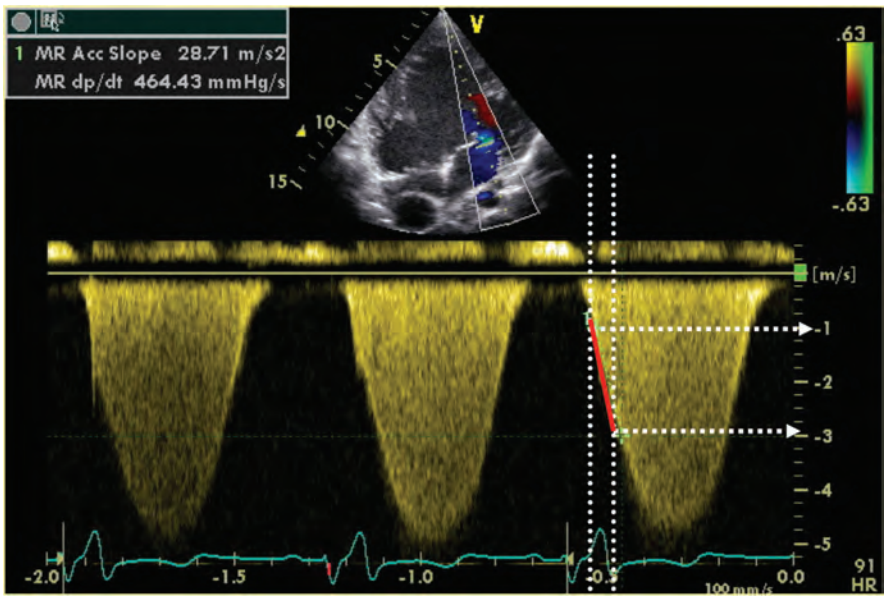


Figure 28.16 d*P*/d*t* as calculated from the atrioventricular valve regurgitation. In this patient with single ventricular dysfunction d*P*/d*t* was significantly reduced.

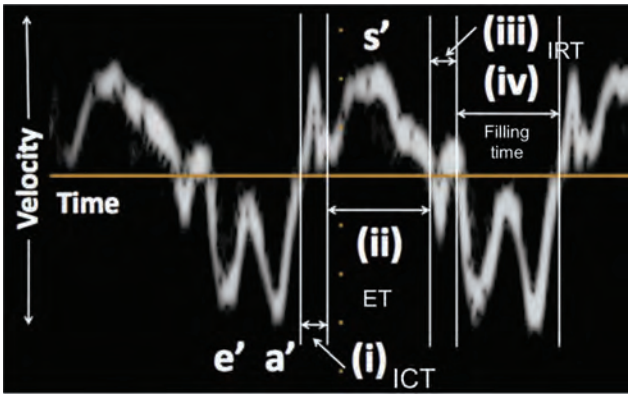


Figure 28.17 Measuring time intervals on tissue Doppler traces obtained in the AV-valve annulus. (i) represents the isovolumic contraction period with the IVA peak, (ii) is the ejection time, (iii) is the isovolumic relaxation time, and (iv) is the diastolic time or filling time. The myocardial performance index can be calculated by (ICT + IRT)/ET. (Bellsham-Revell EHJ-CVI 2012)

highly reproducible. Similar to other nonvolumetric methods, peak systolic velocity (S′ wave) is dependent on ventricular size, preload, afterload, and is also influenced by atrioventricular valve regurgitation. This can limit its use in clinical practice. In the Fontan population no correlation has be found between S′ and EF as measured by cardiac MRI [33]. S′ is a local parameter of myocardial function reflecting longitudinal contraction in the basal part of the ventricle. Thus, regional myocardial dysfunction may be present in other areas which can contribute to the lack of correlation. In serial follow-up studies, a reduction in S′ suggests a reduction in ventricular longitudinal function which may warrant closer follow-up or further investigation. The load-dependency of tissue Doppler velocities may be overcome by measuring the acceleration of the tissue Doppler spike present during the isovolumic contraction period [isovolumic acceleration (IVA)]. During this period, active force is developed in the fibers resulting in a shape change in the ventricle just prior to ejection. IVA appears to be a relative load-independent measurement of cardiac contractility. It is, however, highly heart rate dependent and difficult to measure.

Most recently, the introduction of speckle tracking technology has allowed the calculation of myocardial deformation or strain imaging in Fontan patients (Figure 28.18) [38]. This method was recently validated against myocardial strain measurements as obtained by MRI-based myocardial tagging [39]. Similar to other methods of function, strain measurements are dependent on loading conditions. Increased preload will increase myocardial deformation; increased afterload will result in decreased myocardial deformation. Presently, there is limited information on the clinical use of strain imaging in the Fontan population and how it can be used in clinical practice. The main application for this technology may be its use in detecting intraventricular dyssynchrony in patients who develop ventricular dysfunction in order to help to identify patients who might benefit from resynchronization therapy (Video 28.12) [40,41].

Diastolic performance

The development of diastolic dysfunction is probably one of the most important problems after Fontan palliation. Diastolic dysfunction has been shown to be highly prevalent with 72% of the patients having diastolic abnormalities in a large cohort study [7]. The study proposed a grading system for diastolic dysfunction with normal diastolic function defined as E/A between 1 and 2, DT ≥140 msec, and E/E′ ≤10. Impaired relaxation was defined on E/A ratio <1 only. Pseudonormalization was identified when E/A was between 1 and 2 but DT <140 msec or E/E′ >10 or (FP <55 cm/sec). Restrictive physiology was based on E/A >2. Of note, this grading system is extrapolated from adult data and has never been validated against invasive pressure data in Fontan patients. Moreover, there are limitations of these modalities related to nonsinus or paced rhythm, heart rate and atrioventricular valve function.

In the aging Fontan population, progressive decrease in ventricular compliance and increased end-diastolic pressure is often observed. This is difficult to detect using noninvasive methods. In the adult population with a biventricular circulation E/E′ has

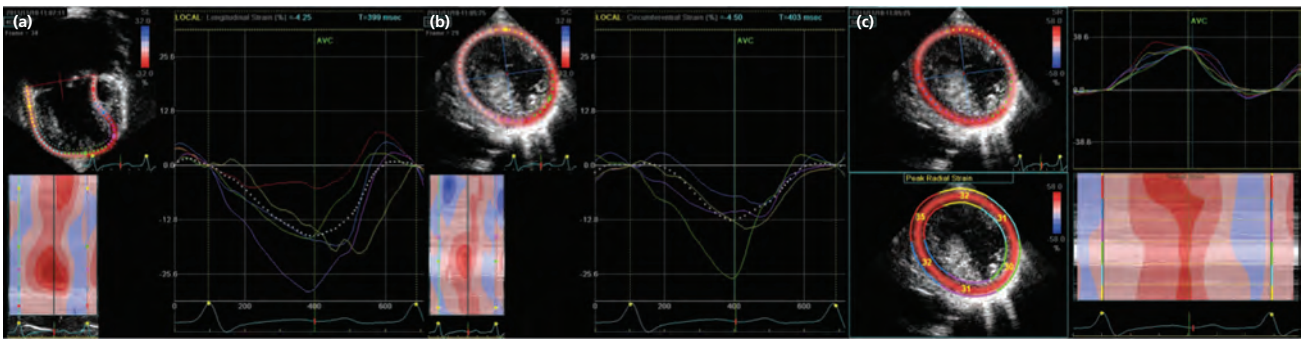


Figure 28.18 Strain measurements in the single right ventricle using speckle-tracking echocardiography. From an apical 4-chamber view, longitudinal strain can be estimated **(a)**. From a parasternal short-axis view circumferential **(b)** and radial strain measurements **(c)** can be obtained. Peak or end-systolic strain values can be measured.

been proposed as a useful parameter for identifying patients with increased filling pressures. In patients with FSV, the use of the E/E′ ratio is problematic because E velocities are influenced by atrioventricular valve size and E′ velocities are often preserved. Though diastolic dysfunction is a primary cause of Fontan failure, thus far current echocardiography techniques are not capable of identifying these patients based on any criteria. Identification of FSV patients with reduced compliance is one of the remaining challenges in congenital cardiology. Hopefully methods will soon be developed which will provide information on tissue characteristics, such as MRI-based T1-mapping.

Conclusion

Echocardiographic imaging in patients after the Fontan operation remains a significant challenge. It requires a full understanding of the underlying complex morphology, the surgical techniques and the unique physiology of the cardiac circuit. While echocardiography is the standard routine follow-up technique, patients with Fontan failure or suspected complications will likely require additional imaging by MRI, CT, or angiography.

Videos

To access the videos for this chapter, please go to www.lai-echo.com.

Video 28.1 The connection between the inferior vena cava (IVC) and the extracardiac conduit (ECC). The connection between the IVC and the conduit is nicely demonstrated from a subxiphoid view by two-dimensional imaging.

Video 28.2 The connection between the inferior vena cava (IVC) and the extracardiac conduit (ECC). The color flow image shows increased flow in the conduit with inspiration related to negative intrathoracic pressures during inspiration with increased blood flow in the Fontan circuit.

Video 28.3 Fenestrated extracardiac Fontan. In this subxiphoid view, color Doppler imaging demonstrates the presence of a continuous low-velocity jet through the fenestration.

Video 28.4 Connection between the extracardiac Fontan and the pulmonary artery. In this suprasternal image slightly tilted to the right and anteriorly, the connection between the extracardiac conduit (ECC) and the right pulmonary artery are nicely demonstrated. The red flow indicates the flow in the direction of the pulmonary artery during inspiration.

Video 28.5 Stenosis on a conduit between the right atrium and the hypoplastic RV. This patient with tricuspid atresia underwent a valved conduit insertion between the significantly dilated right atrium (RA) and the hypoplastic right ventricle which became significantly stenotic and regurgitant. Source: Courtesy of Dr. F. Meijboom.

Video 28.6 Suprasternal notch view demonstrating the connection between the superior vena cava (SVC) and right pulmonary artery (RPA). The connection is widely patent with laminar continuous flow increasing with inspiration.

Video 28.7 Imaging the left pulmonary artery (LPA). In a leftward tilted suprasternal view the LPA can be imaged below the aortic arch. The laminar continuous antegrade low velocity flow can be demonstrated in the proximal LPA.

Video 28.8 Imaging the right pulmonary artery (RPA) from a rightward tilted suprasternal notch view. The continuous low-velocity flow in the proximal RPA can be seen.

Video 28.9 Pulmonary venous obstruction caused by atrial dilatation. Atriopulmonary connection with important dilation of the right atrium (RA), causing compression on the right upper pulmonary vein with turbulent flow in the pulmonary vein and a mean gradient of 4–5 mmHg. Source: Courtesy of Dr. F. Meijboom.

Video 28.10 Tricuspid regurgitation in a patient with hypoplastic left heart syndrome after the Fontan operation. This clip shows a color Doppler image obtained from the apical 4-chamber view. There is a wide jet of tricuspid regurgitation coming from the zone of apposition between the anterior and septal leaflets.

Video 28.11 Tricuspid regurgitation in a patient with hypoplastic left heart syndrome after the Fontan operation. This clip shows an apical 2-chamber view of the RV with an additional jet coming from between the anterior and inferior leaflets of the tricuspid valve. Overall the regurgitation is severe in this patient with significant right atrial dilatation.

Video 28.12 Dyssynchrony in a patient with a single ventricle. Speckle tracking was used to quantify longitudinal deformation. From the images and curves it can be observed that the left lateral wall is being stretched at the time the right lateral wall contracts.

Video 28.13 Dyssynchrony in a patient with a single ventricle. This causes significant dysfunction of the single ventricle with the patient developing symptoms of heart failure. Resynchronization therapy resulted in significant improvement in global ventricular function and reverse remodeling.

References

1 Fontan F, Baudet E. Surgical repair of tricuspid atresia. *Thorax* 1971;**26**:240–248.
2 Gewillig M. The Fontan circulation. *Heart* 2005;**91**:839–846.
3 Brooks PA, Khoo NS, Mackie AS, Hornberger LK. Right ventricular function in fetal hypoplastic left heart syndrome. *J Am Soc Echocardiogr* 2012;**25**:1068–1074.
4 Bellsham-Revell HR, Tibby SM, Bell AJ, et al. Serial magnetic resonance imaging in hypoplastic left heart syndrome gives valuable

insight into ventricular and vascular adaptation. *J Am Coll Cardiol* 2013;**61**:561–570.
5 Grosse-Wortmann L, Al-Otay A, Yoo SJ. Aortopulmonary collaterals after bidirectional cavopulmonary connection or Fontan completion: quantification with MRI. *Circ Cardiovasc Imaging* 2009;**2**:219–225.
6 Odenwald T, Quail MA, Giardini A, et al. Systemic to pulmonary collateral blood flow influences early outcomes following the total cavopulmonary connection. *Heart* 2012;**98**:934–940.
7 Anderson PA, Sleeper LA, Mahony L, et al. Contemporary outcomes after the Fontan procedure: a Pediatric Heart Network multicenter study. *J Am Coll Cardiol* 2008;**52**:85–98.
8 Senzaki H, Masutani S, Ishido H, et al. Cardiac rest and reserve function in patients with Fontan circulation. *J Am Coll Cardiol* 2006;**47**:2528–2535.
9 Senzaki H, Masutani S, Kobayashi J, et al. Ventricular afterload and ventricular work in Fontan circulation: comparison with normal two-ventricle circulation and single-ventricle circulation with Blalock–Taussig shunts. *Circulation* 2002;**105**:2885–2892.
10 Kutty S, Graney BA, Khoo NS, et al. Serial assessment of right ventricular volume and function in surgically palliated hypoplastic left heart syndrome using real-time transthoracic three-dimensional echocardiography. *J Am Soc Echocardiogr* 2012;**25**:682–689.
11 Khairy P, Fernandes SM, Mayer JE, Jr., et al. Long-term survival, modes of death, and predictors of mortality in patients with Fontan surgery. *Circulation* 2008;**117**:85–92.
12 Gewillig M, Daenen W, Aubert A, Van der Hauwaert L. Abolishment of chronic volume overload. Implications for diastolic function of the systemic ventricle immediately after Fontan repair. *Circulation* 1992;**86**:II93–99.
13 Penny DJ, Redington AN. Diastolic ventricular function after the Fontan operation. *Am J Cardiol* 1992;**69**:974–975.
14 Penny DJ, Rigby ML, Redington AN. Abnormal patterns of intraventricular flow and diastolic filling after the Fontan operation: evidence for incoordinate ventricular wall motion. *Br Heart J* 1991;**66**:375–378.
15 Redington A, Penny D. Regional ventricular wall motion abnormalities in tricuspid atresia after the Fontan procedure: flawed methodology may lead to a spurious finding of hypokinesia. *J Am Coll Cardiol* 1994;**24**:271.
16 Cheung YF, Penny DJ, Redington AN. Serial assessment of left ventricular diastolic function after Fontan procedure. *Heart* 2000;**83**:420–424.
17 Schmitt B, Steendijk P, Ovroutski S, et al. Pulmonary vascular resistance, collateral flow, and ventricular function in patients with a Fontan circulation at rest and during dobutamine stress. *Circ Cardiovasc Imaging* 2010;**3**:623–631.
18 Khambadkone S, Li J, de Leval MR, et al. Basal pulmonary vascular resistance and nitric oxide responsiveness late after Fontan-type operation. *Circulation* 2003;**107**:3204–3208.
19 Giardini A, Balducci A, Specchia S, et al. Effect of sildenafil on haemodynamic response to exercise and exercise capacity in Fontan patients. *Eur Heart J* 2008;**29**:1681–1687.
20 Goldberg DJ, French B, Szwast AL, et al. Impact of sildenafil on echocardiographic indices of myocardial performance after the Fontan operation. *Pediatr Cardiol* 2012;**33**:689–696.
21 Penny DJ, Redington AN. Doppler echocardiographic evaluation of pulmonary blood flow after the Fontan operation: the role of the lungs. *Br Heart J* 1991;**66**:372–374.
22 Hsia TY, Khambadkone S, Redington AN, et al. Effects of respiration and gravity on infradiaphragmatic venous flow in normal and Fontan patients. *Circulation* 2000;**102**:III148–53.
23 de Leval MR, Deanfield JE. Four decades of Fontan palliation. *Nat Rev Cardiol* 2010;**7**:520–527.
24 de Leval MR. Evolution of the Fontan-Kreutzer procedure. *Semin Thorac Cardiovasc Surg Pediatr Card Surg Annu* 2010;**13**:91–95.
25 de Leval MR, Kilner P, Gewillig M, Bull C. Total cavopulmonary connection: a logical alternative to atriopulmonary connection for complex Fontan operations. Experimental studies and early clinical experience. *J Thorac Cardiovasc Surg* 1988;**96**:682–695.
26 Van Haesdonck JM, Mertens L, Sizaire R, et al. Comparison by computerized numeric modeling of energy losses in different Fontan connections. *Circulation* 1995;**92**:II322–326.
27 Bharucha T, Honjo O, Seller N, et al. Mechanisms of tricuspid valve regurgitation in hypoplastic left heart syndrome: a case-matched echocardiographic-surgical comparison study. *Eur Heart J Cardiovasc Imaging* 2013;**14**:135–141.
28 Takahashi K, Inage A, Rebeyka IM, et al. Real-time 3-dimensional echocardiography provides new insight into mechanisms of tricuspid valve regurgitation in patients with hypoplastic left heart syndrome. *Circulation* 2009;**120**:1091–1098.
29 Honjo O, Atlin CR, Mertens L, et al. Atrioventricular valve repair in patients with functional single-ventricle physiology: impact of ventricular and valve function and morphology on survival and reintervention. *J Thorac Cardiovasc Surg* 2011;**142**:326–335 e2.
30 Bellsham-Revell HR, Simpson JM, Miller OI, Bell AJ. Subjective evaluation of right ventricular systolic function in hypoplastic left heart syndrome: how accurate is it? *J Am Soc Echocardiogr* 2013;**26**:52–56.
31 Margossian R, Schwartz ML, Prakash A, et al. Comparison of echocardiographic and cardiac magnetic resonance imaging measurements of functional single ventricular volumes, mass, and ejection fraction (from the Pediatric Heart Network Fontan Cross-Sectional Study). *Am J Cardiol* 2009;**104**:419–428.
32 Soriano BD, Hoch M, Ithuralde A, et al. Matrix-array 3-dimensional echocardiographic assessment of volumes, mass, and ejection fraction in young pediatric patients with a functional single ventricle: a comparison study with cardiac magnetic resonance. *Circulation* 2008;**117**:1842–1848.
33 Rhodes J, Margossian R, Sleeper LA, et al. Non-geometric echocardiographic indices of ventricular function in patients with a Fontan circulation. *J Am Soc Echocardiogr* 2011;**24**:1213–1219.
34 Bellsham-Revell HR, Tibby SM, Bell AJ, et al. Tissue Doppler time intervals and derived indices in hypoplastic left heart syndrome. *Eur Heart J Cardiovasc Imaging* 2012;**13**:400–407.
35 Cheung MM, Smallhorn JF, Redington AN, Vogel M. The effects of changes in loading conditions and modulation of inotropic state on the myocardial performance index: comparison with conductance catheter measurements. *Eur Heart J* 2004;**25**:2238–2242.
36 Friedberg MK, Silverman NH. The systolic to diastolic duration ratio in children with hypoplastic left heart syndrome: a novel Doppler index of right ventricular function. *J Am Soc Echocardiogr* 2007;**20**:749–755.
37 Sarnari R, Kamal RY, Friedberg MK, Silverman NH. Doppler assessment of the ratio of the systolic to diastolic duration in normal children: relation to heart rate, age and body surface area. *J Am Soc Echocardiogr* 2009;**22**:928–932.

38 Friedberg MK, Mertens L. Deformation imaging in selected congenital heart disease: is it evolving to clinical use? *J Am Soc Echocardiogr* 2012;**25**:919–931.

39 Singh GK, Cupps B, Pasque M, et al. Accuracy and reproducibility of strain by speckle tracking in pediatric subjects with normal heart and single ventricular physiology: a two-dimensional speckle-tracking echocardiography and magnetic resonance imaging correlative study. *J Am Soc Echocardiogr* 2010;**23**:1143–1152.

40 Khoo NS, Smallhorn JF, Kaneko S, et al. Novel insights into RV adaptation and function in hypoplastic left heart syndrome between the first 2 stages of surgical palliation. *JACC Cardiovasc Imaging* 2011;**4**:128–137.

41 Friedberg MK, Silverman NH, Dubin AM, Rosenthal DN. Right ventricular mechanical dyssynchrony in children with hypoplastic left heart syndrome. *J Am Soc Echocardiogr* 2007;**20**:1073–1079.

CHAPTER 29

Cardiac Malpositions and Heterotaxy Syndrome

Irene D. Lytrivi[1] and Wyman W. Lai[2]

[1]Icahn School of Medicine at Mount Sinai, Division of Pediatric Cardiology, Mount Sinai Medical Center, New York, NY, USA
[2]Division of Pediatric Cardiology, Columbia University Medical Center, New York, NY, USA

Cardiac malpositions

Definitions

Cardiac malposition may be defined as any position of the heart other than situs solitus with levocardia [1]. The term is also used to describe abnormal spatial arrangements of the individual cardiac segments – atria, ventricles, and the great arteries – and thus encompasses a wider range of anomalies. This section covers malposition of the entire cardiac mass (dextro-/mesocardia) and isolated malposition of individual cardiac segments including juxtaposition of the atrial appendages [2,3], isolated ventricular inversion [4], and anatomically corrected malposition of the great arteries [5,6]. Heterotaxy syndromes [7] that are characterized by the presence of cardiac malposition, abnormal spatial organization of the thoraco-abdominal organs, and anomalies of multiple cardiac segments, are discussed separately. Cardiac malposition due to ectopia cordis is not addressed in this chapter.

Dextrocardia and *mesocardia* are terms indicating the position of the heart in the chest [8]. These terms generally define the direction of the major heart axis in the chest. In *levocardia* the base-to-apex axis points to the left, while it points to the right in dextrocardia, and more caudally in mesocardia [9]. *Situs inversus* refers to the mirror-image reversal of the normal thoraco-abdominal visceral arrangement (see Chapter 3). Situs inversus is generally associated with dextrocardia, referred to as *situs inversus totalis*, but may be rarely seen with levocardia.

The term *dextroposition* that refers to cardiac displacement to the right hemithorax by extracardiac factors such as hypoplastic right lung, and does not imply any intracardiac anomalies, has recently been replaced by the term *dextrocardia with levoversion* (Personal communication, ISNPCHD Meeting, Cambridge, UK, July 2015). Another term commonly used in the literature is *dextroversion*, or pivotal dextrocardia. It usually describes dextrocardia with situs solitus, where the cardiac apex appears as having been rotated from the left hemithorax to the right.

Juxtaposition of the atrial appendages (JAA) refers to malposition of one of the two atrial appendages. In situs solitus, juxtaposition of the morphologically right atrial appendage places both atrial appendages on the left side of the great arteries (commonly referred to as left JAA); in situs inversus, juxtaposition of the morphologically right atrial appendage places both atrial appendages to the right side of the great arteries [2]. Similar terminology applies to juxtaposition of the morphologically left atrial appendage [3]. Juxtaposition of the appendages can be complete when the entire appendage is juxtaposed, or partial when the appendage exhibits a bifid configuration with a small part in the normal position and the larger part in the juxtaposed position [10].

Isolated ventricular inversion is a term first used in 1966 [4] to describe a rare situation where ventricular inversion is not associated with transposition of the great arteries as in the usual case of "congenitally corrected" transposition of the great arteries. Instead, the case originally presented displayed thoraco-abdominal situs solitus, L-loop ventricles, atrioventricular discordance, and ventriculo-arterial concordance. The definition also applies to atrial situs inversus with D-loop ventricles and inversely normally related great arteries (ventriculo-arterial concordance with anterior and rightward PA; segmental set: {I, D, I}) [11]. "Isolated" ventricular inversion has also been described in patients with heterotaxy syndrome [12,13].

Anatomically corrected malposition of the great arteries (ACM), a term introduced by Van Praagh et al. [14] in 1971, is an equally rare anomaly with similarities to isolated ventricular inversion. In ACM, the great arteries arise from the appropriate ventricles (ventriculo-arterial concordance) but the spatial relationship between the two great arteries is abnormal with a parallel orientation instead of the normal spiraling relationship [5]. In D-loop ventricles, the aorta is typically positioned leftward and anterior to the pulmonary artery; in L-loop ventricles, the aorta is rightward and anterior to the pulmonary artery. Other spatial arrangements of the great arteries have also been described, and, currently, the diagnostic criteria include ventriculo-arterial

Echocardiography in Pediatric and Congenital Heart Disease: From Fetus to Adult, Second Edition. Edited by Wyman W. Lai, Luc L. Mertens, Meryl S. Cohen and Tal Geva.
© 2016 John Wiley & Sons, Ltd. Published 2016 by John Wiley & Sons, Ltd.
Companion website: www.lai-echo.com

concordance and parallel arrangement of the great arteries. The presence of bilateral conus, initially considered an integral part of the diagnosis, was later found to be nonessential [5,6,15].

Incidences

The incidence of fetal dextrocardia is reported as 220 to 830 per 100,000 fetuses referred for echocardiography [16,17]. Postnatally, dextrocardia is reported in 2.8% of cyanotic congenital heart disease and 0.4% of acyanotic heart disease [18]. The most common type of dextrocardia in the general population is associated with situs inversus totalis. The prevalence of situs inversus is approximately 1 in 10,000 for situs inversus totalis [19] and 1 in 22,000 for situs inversus with levocardia [20]. Dextrocardia with situs inversus (heart and stomach on the same side) is usually associated with normal intracardiac anatomy [17]. In contrast, dextrocardia with situs solitus, or levocardia with situs inversus (heart and stomach on opposite sides) are associated with a high rate of cardiovascular malformations.

The incidence of juxtaposition of the atrial appendages was 280 to 300 per 100,000 cases in clinical echocardiographic series [21,22] with juxtaposition of the right atrial appendage (JRAA) occurring more commonly, and 760 per 100,000 in an autopsy series [23]. Isolated ventricular inversion and ACM are very rare anomalies and only case reports or small case series exist in the literature.

Etiology

Unlike the genetics of situs inversus and heterotaxy syndrome, which have been extensively studied (see section "Heterotaxy syndrome" later), the genetic basis of dextrocardia and the rare forms of cardiac malposition is not well known. Mutations in genes defining laterality and left–right asymmetry influence cardiac position and ventricular looping causing laterality defects associated with congenital heart disease [24].

Morphology and classification

Developmental considerations

Dextrocardia in D-loop ventricles is probably related to arrested migration of the cardiac apex to the left hemithorax, a process that normally occurs between 23 and 35 days of gestation. L-loop ventricles, however, have a tendency to migrate to the right hemithorax, which explains the high incidence of dextrocardia in this type of looping.

During the early period of cardiac morphogenesis (at and prior to 23 days of gestation), left-sided JAA is normal. Between 23 and 27 days of gestation, the conotruncus migrates to the left of the right atrial appendage, as the ventricular D-loop slowly swings from right to left during the fourth and fifth week of fetal development. Failure of this leftward movement of the ventricular apex results in left JRAA and dextrocardia, and explains the high rate of concurrence of these two anomalies.

The embryogenesis of both isolated ventricular inversion [4] and ACM [25] is believed to be due to twisting of the ventricles and the great arteries in different directions during early cardiovascular development. Isolated ventricular inversion typically occurs with normal conotruncal development with a ventricular L-loop. In contrast, ACM occurs most commonly with leftward twisting of the conotruncus with a normal ventricular D-loop.

Anatomy

A broad spectrum of cardiac anomalies can be associated with dextrocardia, ranging from an isolated ventricular septal defect (VSD) to the most complex forms of congenital heart disease. In the presence of situs inversus and dextrocardia (segmental set: {I,L,I}), the most commonly associated congenital heart defects are tetralogy of Fallot and VSD [26], but rarer conditions such as single coronary ostium and hypoplastic left heart syndrome have been reported [27,28]. The aortic arch is usually right-sided [29].

Juxtaposition of the right atrial appendage (to the left in situs solitus, to the right in situs inversus) is often associated with significant congenital heart disease, including tricuspid atresia or severe tricuspid stenosis in 40–60%, right ventricular (RV) hypoplasia in 71–74%, subaortic or bilateral conus in 71–100%, pulmonary outflow tract obstruction in 52%, VSD in 88%, and secundum atrial septal defect (ASD) in 71% [2,30]. Abnormalities of the conus such as transposition of the great arteries and double-outlet right ventricle are particularly common [2,3,31]. Dextrocardia is another common association with JRAA, occurring twice as commonly in JRAA as in a control series without JRAA [30,32].

Juxtaposition of the left atrial appendage (JLAA; to the right in situs solitus, to the left in situs inversus) is more commonly associated with normal conus (normally related great arteries and subpulmonary conus) but a number of other major cardiovascular malformations are typically present: abnormalities of the left atrial outlet in the form of mitral valve or left-sided tricuspid valve atresia or severe stenosis in 69%, aortic outflow tract obstruction or atresia in 39%, common atrioventricular valve in 28%, and heterotaxy syndrome in 28% [3].

In isolated ventricular inversion (atrioventricular discordance with ventriculo-arterial concordance connections), although the ventriculo-arterial connections are normal, the spatial positioning of the great arteries relative to the ventricular chambers is not with a more inferior position of the great arteries [33,34]. Associated intracardiac defects include a VSD, hypoplastic tricuspid valve with RV hypoplasia, and coarctation of the aorta [34].

In ACM, the ventriculo-arterial connections are also concordant but the great vessel position and relationships are abnormal as they have a parallel course instead of the normal spiraling [32]. The circulation is potentially normal, depending on the atrioventricular alignments, but most described cases have additional intracardiac defects. These include VSD, JRAA, abnormal right atrioventricular junction with right heart hypoplasia, and subpulmonary or subaortic outflow tracts obstruction [35]. Another interesting observation is the high frequency of anomalies of the coronary artery origins (single coronary

artery or both coronary arteries arising from the right sinus of Valsalva) [5,36].

Pathophysiology

The presentation of dextrocardia depends on the associated cardiac anomalies and can vary from an incidental finding on a chest X-ray or echocardiography to symptoms of the underlying congenital heart defects. Juxtaposition of the atrial appendages does not cause any hemodynamic disturbance, yet it is frequently associated with complex cardiovascular abnormalities requiring intervention [22]. Because of the association of JAA with transposition of the great arteries, balloon atrial septostomy is a common procedure. Diagnosis of JAA prior to the procedure is important as positioning the balloon in the atrial appendage can cause rupture during balloon inflation and pull-back with potential catastrophic consequences [30,37]. Isolated ventricular inversion is associated with transposition physiology causing cyanosis in the neonatal period. The symptoms associated with ACM are determined by the associated intracardiac lesions which can be highly variable.

Imaging

Key elements

The main objectives of echocardiographic examination of cardiac malposition are:

- Determination of the location of the heart in the thorax and orientation of the cardiac apex.
- Identification of individual cardiac segments and their alignments.
- Identification of associated intracardiac anomalies.

As for every patient with suspected congenital heart disease a full segmental analysis has to be performed.

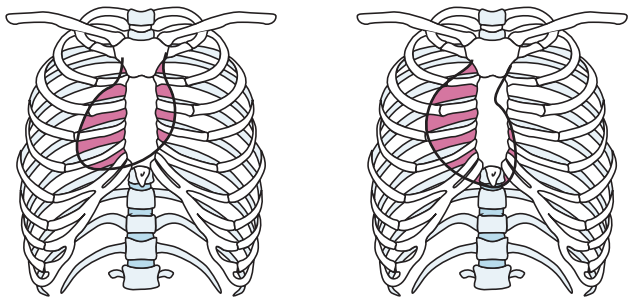


Figure 29.1 Dextrocardia **(a)** versus dextrocardia with levoversion **(b)**.

Dextrocardia

When the heart is in the right chest, a distinction should be made between a rightward apex (true or mirror-image dextrocardia) and a leftward orientation of the apex with rightward position (dextrocardia with levoversion) (Figure 29.1a,b). Crucial when imaging dextrocardia is to maintain the probe in the standard orientations. In the subxiphoid long-axis view the apex is oriented rightward (Figure 29.2a; Video 29.1). With clockwise rotation of the transducer the normal subxiphoid short-axis views are obtained, but to obtain the standard short-axis views, sweeping should be performed from left to right (base to apex) instead

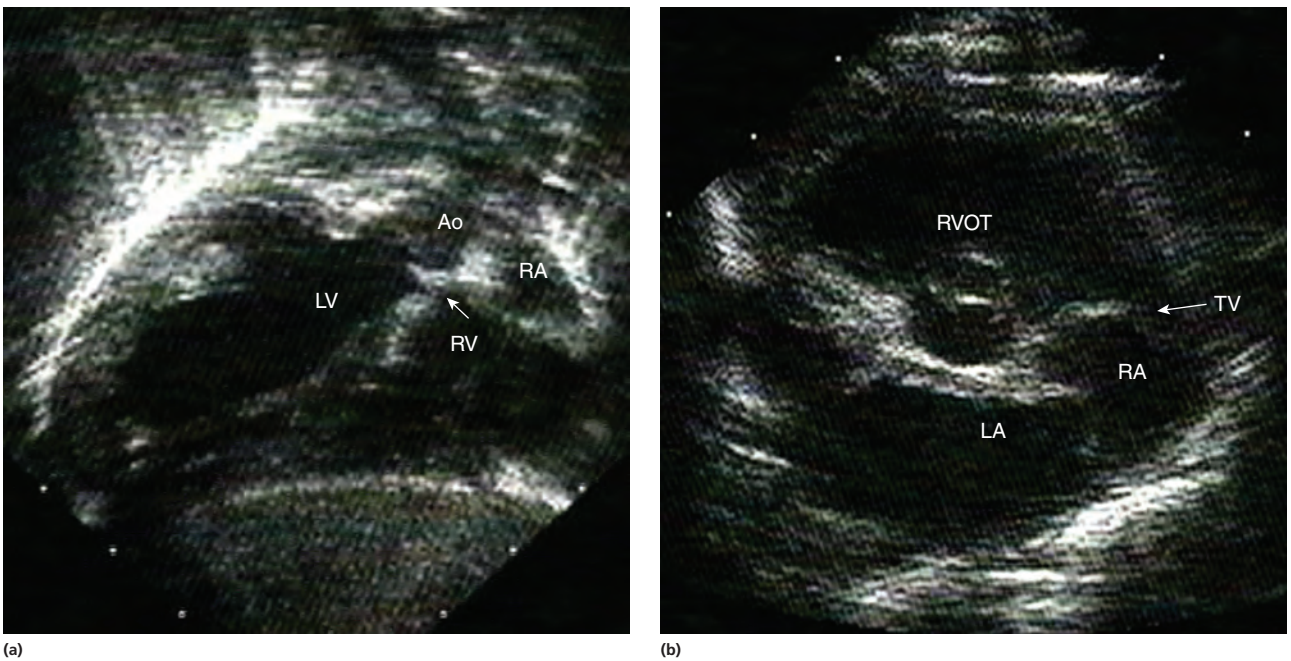


Figure 29.2 Situs inversus totalis. **(a)** Subxiphoid long-axis image of situs inversus totalis {I,L,I} with a membranous ventricular septal defect (arrowhead). **(b)** Right parasternal short-axis image of situs inversus totalis with a membranous ventricular septal defect (not shown). Ao, aorta; LA, left atrium; LV, left ventricle; RA, right atrium; RV, right ventricle; RVOT, right ventricular outflow tract; TV, tricuspid valve.

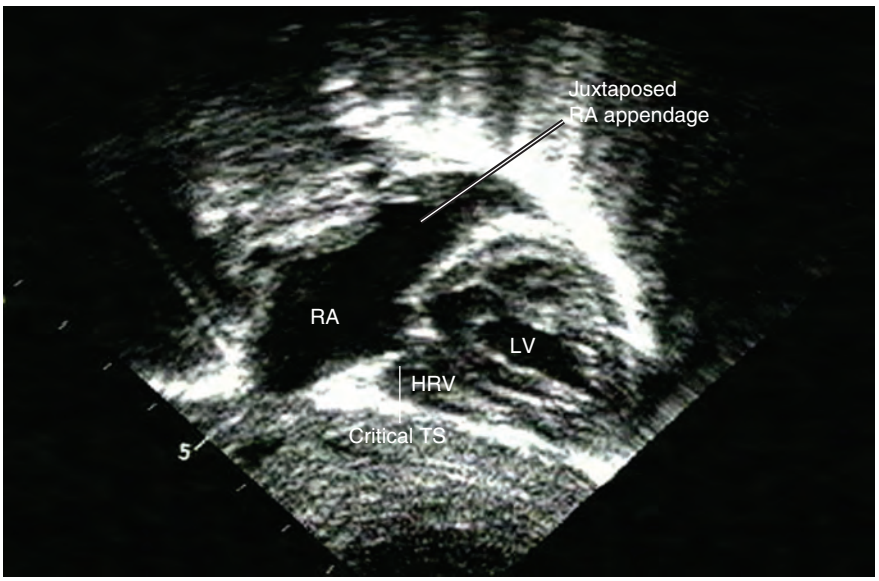


Figure 29.3 Subxiphoid image of leftward juxtaposition of the right atrial appendage in the setting of critical tricuspid stenosis (TS) and severely hypoplastic right ventricle (HRV). RA, right atrium; LV, left ventricle.

of right to left for levocardia. In the apical 4-chamber view the probe is placed on the right chest with the notch pointing to the left, resulting in a standard orientation. For the parasternal long-axis view the probe is placed on the right chest with the notch pointing to the left shoulder. This results in the normal display of the cardiac apex pointing to the left of the screen. To obtain the right parasternal short-axis view, the probe is rotated *clockwise* from the parasternal long axis, with the notch now pointing to the left hip (Figure 29.2b; Video 29.2). A common pitfall in the right parasternal short-axis view is the erroneous rotation of the probe counterclockwise toward the patient's right shoulder. Left parasternal long- and short-axis views can also be utilized and have been found helpful in delineating great artery relationships [9]. The segmental approach should be used to describe the entire cardiac anatomy and associated lesions.

Juxtaposition of the atrial appendages

Juxtaposition is best visualized from the subxiphoid long- and short-axis views (Figures 29.3 and 29.4; Video 29.3) as well as from the parasternal short-axis view (Figure 29.4; Video 29.4) [21]. The juxtaposed atrial appendage is always superior to the normally positioned appendage and adjacent to the great arteries. Abnormal spatial orientation of the atrial septum is frequently present [31,37]. Focused imaging of the juxtaposed atrial appendage is generally best from a coronal plane from a high thoracic or suprasternal window [22]. Transesophageal imaging can be useful in the diagnosis of JAA, especially in adult patients with poor transthoracic windows. Features include lateral deviation of the mid-portion of the atrial septum on the mid-esophageal 4-chamber view and a frontal orientation of the antero-superior portion with more cranial imaging [38].

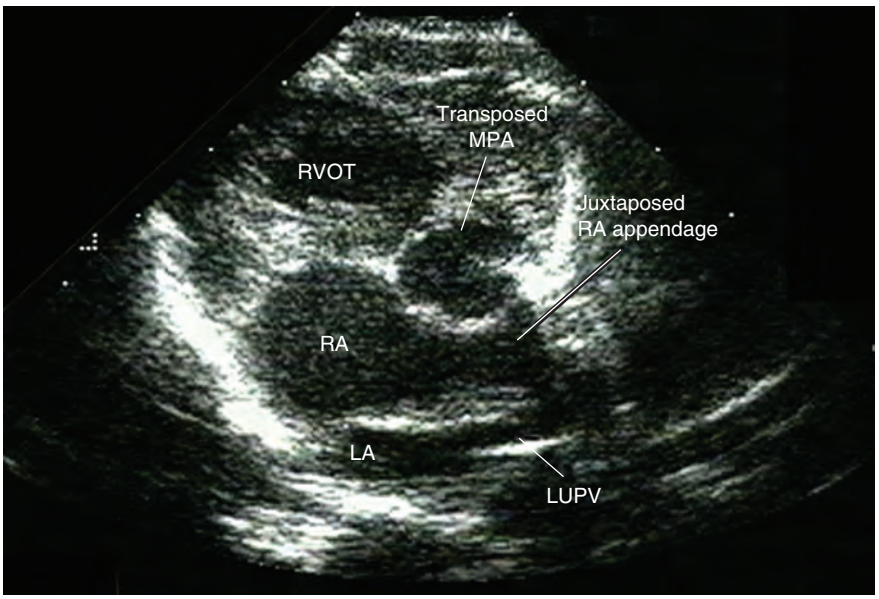


Figure 29.4 Parasternal image of leftward juxtaposition of the right atrial appendage (LJRAA). Horizontal orientation of the atrial septum is typically seen with the juxtaposed atrial appendages. In this case there is juxtaposition of the right atrial (RA) appendage in the setting of transposition of the great arteries. LA, left atrium; LUPV, left upper pulmonary vein; MPA, main pulmonary artery; RA, right atrium; RVOT, right ventricular outflow tract.

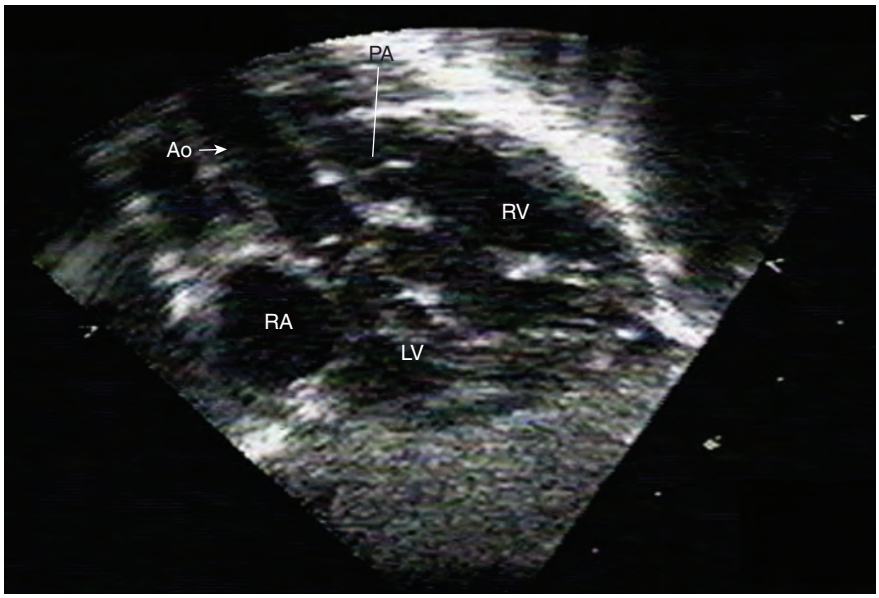


Figure 29.5 Subxiphoid long-axis image of isolated ventricular inversion with solitus atria, L-loop ventricles, and normally related great arteries with subpulmonary conus. Ao, aorta; LV, left ventricle; PA, pulmonary artery; RA, right atrium; RV, right ventricle.

The extension of the venous component of the atrial cavity to the juxtaposed atrial appendage may also be demonstrated.

Isolated ventricular inversion and ACM

For these more unusual and sometimes complex lesions, a full segmental approach using all standard imaging views should be used. Pasquini et al. [33] highlighted certain imaging findings specific to isolated ventricular inversion:

- The ventriculo-arterial alignments *and* connections are normal with aortic-mitral valve fibrous continuity and the presence of a subpulmonary conus.
- The infundibulum runs more vertical than in the normal heart and the great arteries appear to run more parallel from the subxiphoid long-axis views but they cross from parasternal long-axis views (Figures 29.5 and 29.6a,b; Videos 29.5 and 29.6).
- Interrogation of the atrial septum often reveals a closed or restrictive atrial communication [39], contributing to the severe cyanosis that is usually the presenting feature of this abnormality.

Detection of ACM is based on morphologic analysis of the individual cardiac segments and detailed imaging of the conotruncal region. ACM is recognized as ventriculo-arterial concordance with parallel arterial trunks (Figure 29.7a,b; Video 29.7).

Prenatal assessment

Identification of abnormal position of the heart in the thorax is generally obtained during the routine obstetrical ultrasound exam, and often is the main reason for referral for detailed fetal echocardiography. Differentiation between dextrocardia and dextroposition can be determined on the fetal echocardiogram. Intrathoracic abnormalities, including congenital diaphragmatic hernia, cystic adenomatoid malformation of the lung, bronchogenic cysts, and pericardial and pulmonary tumors, are the main causes for dextroposition. Dextroposition without an intrathoracic space-occupying lesion can be present [40]. This can occur in the context of right lung hypoplasia and hypoplasia of the right pulmonary artery, and the most common cardiac defect encountered is scimitar syndrome.

Fetal detection of JAA is generally made in the context of diagnosis of complex congenital heart disease. The position of the atrial appendages should be carefully evaluated in patients with dextrocardia, tricuspid atresia, transposition of the great arteries, and double-outlet right ventricle [22]. JAA is often first suspected on the 3-vessel view, where abnormal vascular structures are seen to the left or right of the cross-section of the arterial trunks [41] (Figure 29.8).

Isolated ventricular inversion and ACM have rarely been diagnosed in utero [42], but the diagnosis can be made by a detailed segmental analysis of the cardiac anatomy.

Pre- and postoperative assessment

Before surgical planning a full segmental evaluation is required with a complete description of the anatomy and physiology. Postoperative assessment is obviously determined by the type of surgical repair or palliation.

The importance of the diagnosis of JAA prior to balloon atrial septostomy has been stressed. In addition, identification of the juxtaposed appendages before intra-atrial baffle procedures is important because juxtaposition may require adaptation of the surgical atrial rerouting technique [43].

Isolated ventricular inversion can be managed surgically with an atrial switch procedure that corrects the transposition physiology and keeps the left ventricle connected with the aorta. Associated intracardiac defects like VSDs can be repaired during the same procedure. In cases of ventricular inversion the conduction

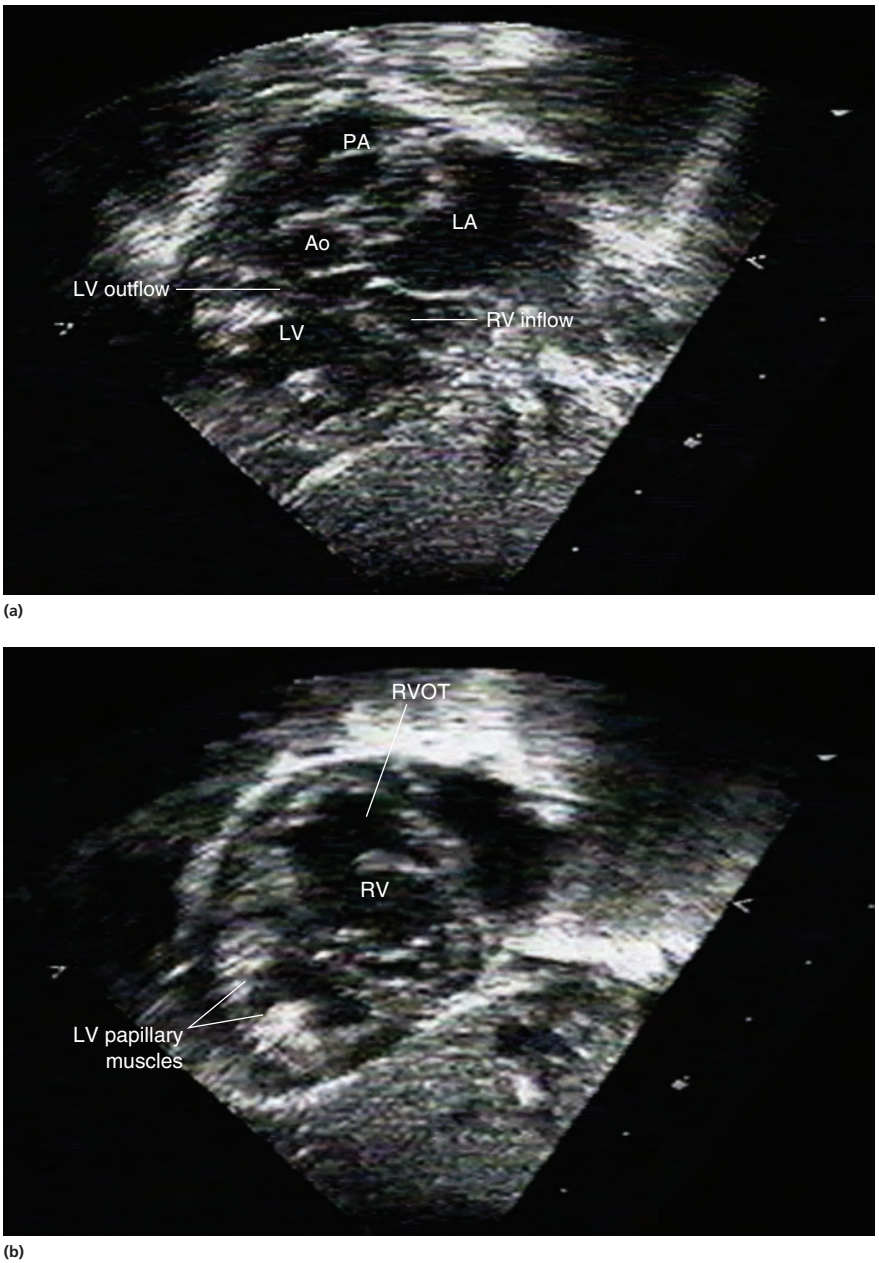


Figure 29.6 Subxiphoid short-axis images of isolated ventricular inversion at the level of the great arteries **(a)** and of the ventricles **(b)**, showing the abnormal spatial relationship of the L-looped ventricles with normally positioned great arteries. Ao, aorta; LA, left atrium; LV, left ventricle; PA, pulmonary artery; RV, right ventricle; RVOT, right ventricular outflow tract.

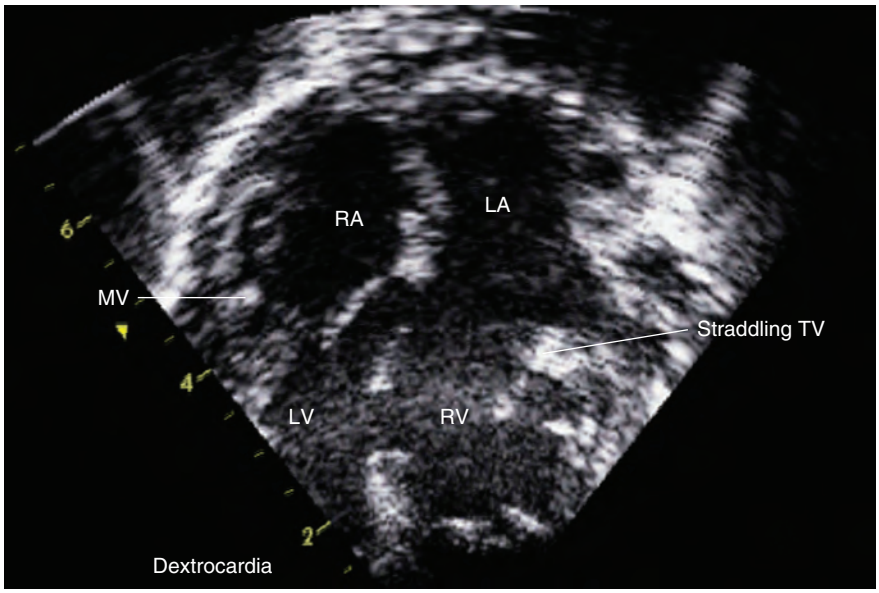
system runs on the right-sided left ventricular side of the septum so the patch needs to be placed on the left side [44].

In ACM, the atrioventricular connections should be identified first. The majority of reported cases have concordant atrioventricular connections and, thus, normal physiology. However, almost all have VSDs, and JAA and subpulmonary or subaortic outflow tract obstruction is frequently associated. A significant percentage of cases also have single coronary arteries. Less commonly, the atrioventricular connections are discordant and the patients present with transposition physiology. In those cases, the appendages are typically not malposed, but a VSD is almost always present and subaortic obstruction is frequent. A smaller percentage of the reported cases of ACM also have atresia of the right ventricular (RV) inflow or double-inlet left ventricle (LV) [36].

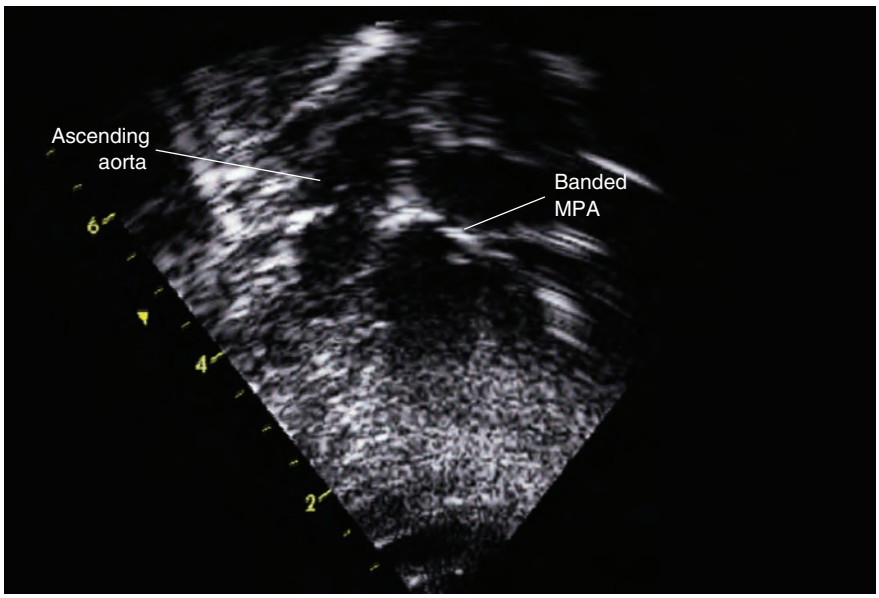
Heterotaxy syndrome

Definitions

In contrast to the remarkable external symmetry of all vertebrates, including humans, the internal organs normally are asymmetrically positioned along the left–right axis [45]. This asymmetry refers to both lateralization of unpaired organs (e.g., heart, liver, spleen, and stomach) as well as morphologic



(a)



(b)

Figure 29.7 Anatomically corrected malposition of the great arteries: apical 4-chamber views showing atrial situs solitus with atrioventricular discordance and ventriculo-arterial concordance in the setting of dextrocardia. There is a large ventricular septal defect, and the left-sided tricuspid valve (TV) is straddling over the defect **(a)**. Angled anteriorly the rightward and anterior aorta is shown to be aligned with the right-sided left ventricle, whereas the leftward and posterior main pulmonary artery (MPA) is aligned with the left-sided right ventricle. **(b)**. The segmental set is {S,L,D}, and the aorta is supported by a subaortic conus. LA, left atrium; LV, left ventricle; MV, mitral valve; RA, right atrium; RV, right ventricle.

differences of paired organs (lungs, bronchi, and atrial appendages) that do not allow them to be mirror images of each other. The term heterotaxy refers to the failure to generate normal left–right asymmetry, and it is defined as the presence of a pattern of spatial organization of the thoracic and abdominal viscera that is neither that of situs solitus nor that of situs inversus [7].

According to the definitions provided by the Working Group of the International Society for Nomenclature in Paediatric and Congenital Heart Disease [7], patients with heterotaxy syndrome can be stratified into the subsets of isomerism of the right atrial appendages/asplenia syndrome and isomerism of the left atrial appendages/polysplenia syndrome. Although right and left atrial isomerism are commonly used terms, it is important to note that atrial isomerism does not exist. It is only the atrial appendages that are isomeric (symmetrical mirror images of each other) in the setting of heterotaxy, and the terms right isomerism and left isomerism are used in this chapter as synonyms of asplenia syndrome and polysplenia syndrome, respectively. Those having isomeric right atrial appendages frequently have bilaterally tri-lobed lungs, each with a short bronchus, and absence of the spleen. Those having isomeric left atrial appendages frequently have bilaterally bi-lobed lungs, each with a long bronchus, and multiple spleens. There is also a smaller third category of patients with cardiac lesions common for right isomerism who, instead of asplenia, have a single, right-sided

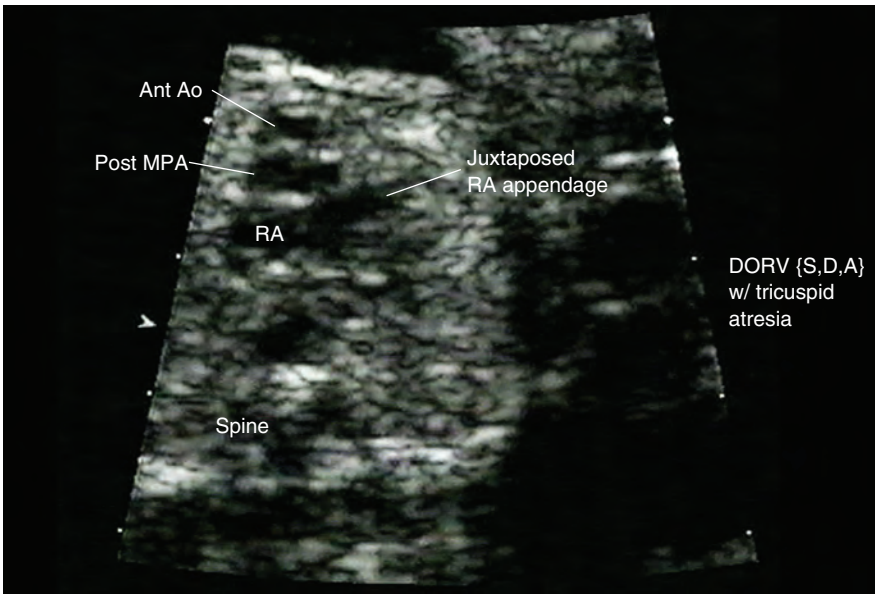


Figure 29.8 Fetal 4-chamber view of leftward juxtaposition of the right atrial appendage (LJRAA), angled anteriorly showing the abnormal spatial relationship of the great arteries – aorta rightward and anterior, pulmonary artery leftward and posterior. The juxtaposed right atrial appendage is seen traversing behind the pulmonary trunk to the left of the great vessels. Ant Ao, anterior aorta; DORV, double-outlet right ventricle; MPA, main pulmonary artery; RA, right atrium.

spleen [46]. The distinction between the groups is based on the common concurrence of different anomalies, although there is a wide variation and some overlap of the cardiac abnormalities found in any given patient. In general, the cardiac abnormalities in right isomerism/asplenia syndrome are more complex and the prognosis is poorer. Whatever classification system used, the imager should provide an accurate description of the thoracoabdominal visceral situs and of all cardiovascular abnormalities through a detailed segmental analytical approach.

Incidence

Despite the continuing problems with classification and terminology that make most series difficult to interpret, the majority of the published studies estimate the incidence of heterotaxy at 10–14 per 100,000 livebirths [47–51]. The relative frequency of heterotaxy syndrome is reported as 2.3–4.2% of congenital heart disease [47,49].

Etiology

Heterotaxy is due to a deficiency in the definition of left–right asymmetry which is controlled by different pathways resulting in complex genetics underlying the condition. Studies in humans and the *iv*/*iv* and *inv* mouse models suggest an autosomal recessive inheritance with variable penetrance, but polygenic or multifactorial causes have also been implicated [52–55]. Autosomal dominant, recessive and X-linked inheritance have all been described for this condition. Also environmental factors can influence the incidence of the disease as vertebrate studies have shown that maternal diabetes [50] and retinoic acid [56] exposure in utero can be potential factors contributing to the occurrence of the laterality defects.

A link between ciliary motility and the regulation of left–right asymmetry was proposed due to the association of primary ciliary dyskinesia with situs inversus totalis. Ciliary motion seems to be important for determining left–right asymmetry as malfunctioning cilia of afflicted humans can result in random generation of asymmetry (left–right or situs solitus or right–left or situs inversus, right–right or right isomerism or left–left or left isomerism) [57]. How cilia affect lateralization relates to the fetal node, which is a transient midline structure that is covered with specialized monocilia. The prevailing model hypothesizes that fluid flow directed by ciliary movement in the early embryonic stages determines left–right asymmetry by motion signaling proteins such as sonic hedgehog, fibroblast growth factor, or Nodal which are swept to the left side of the embryonic node where they initiate downstream signaling pathways [58]. Disruption of the midline barrier separating left from right may permit a mixing of molecules that are normally asymmetrically distributed in early embryos, resulting in abnormal organ sidedness later in development. Combinations of rare mutations in genes that control embryonic left–right patterning and environmental insults during early embryogenesis probably underlie most cases [59]. Nine genes have so far been linked to nonsyndromic human laterality disorders [45]. Despite these advances, the determinants of laterality are still not completely understood, and the correlation of genotype with phenotype remains at an early stage.

Morphology and classification

Developmental considerations

The major events in normal cardiac development that appear to be arrested or absent in heterotaxy syndrome occur largely during the fifth week of gestation [60], and the hearts of many patients with heterotaxy syndrome bear a remarkable resemblance to the heart of a normal embryo at 35 days of gestation. More specifically, the growth of the endocardial cushions, septation of the conotruncus, lobation of the lungs and rotation of the gut begin between days 28 and 35 of gestation [61] whereas

Table 29.1 Criteria for visceral heterotaxy and abnormal visceral symmetry

1	Thoraco-abdominal situs inconsistency
2	Abnormally symmetric lung lobes
3	Abnormally symmetric bronchial branching pattern
4	Abnormal symmetry of the liver
5	Unusual or abnormal systemic venous connections
6	Unroofed coronary sinus
7	Abnormal pulmonary venous connections or drainage
8	Similarities in the shape and morphology of the atrial appendages
9	Abnormal mesenteric attachments
10	Abnormal bowel location +/– malrotation
11	Asplenia, polysplenia or single right-sided spleen
12	Abnormal position and/or size of the pancreas

the spleen is present at about 32 days and is well demarcated by 35–36 days [60].

Anatomy

Heterotaxy syndrome is characterized by a wide spectrum of pathology, and its clinical diagnosis is not generally based on strict anatomic criteria. According to Van Praagh et al. [46] the fulfillment of at least 4 of the 12 criteria outlined in Table 29.1 correctly identifies patients with heterotaxy syndrome. The atrial appendages merit special mention as a diagnostic criterion, because they have been considered by many [62,63] to be the unifying link in the definition and classification of patients with heterotaxy syndrome. Whether isomerism accurately applies to the heart or not, it is true that both appendages frequently share characteristics of a right atrial appendage in asplenia syndrome and of a left atrial appendage in polysplenia syndrome. It has been suggested that the extent of the pectinate muscles relative to the muscular atrioventricular vestibule can reliably distinguish between left and right atrial appendages. In hearts with isomeric appendages, there is either bilateral extension of the pectinate muscles in cases of right isomerism, or continuity between the vestibule of the atrioventricular junction and the smooth-walled venous component of the atrium without interposition of pectinate muscles in cases of left isomerism [64]. Because the identification of internal anatomy, size and location of the appendages is not always feasible by echocardiography, we propose the combination of multiple criteria in order to classify correctly patients with heterotaxy/isomerism.

The usual combination of findings in right isomerism/asplenia syndrome includes: total anomalous pulmonary venous connection, usually to a systemic vein; bilateral superior venae cavae; unroofed/absent coronary sinus; common atrium; complete common atrioventricular canal (CCAVC); a high incidence of a functionally single ventricle, usually of dominant right ventricular morphology; pulmonary stenosis or atresia; and transposition of the great arteries (Figure 29.9a–d; Video 29.8). In left isomerism or polysplenia syndrome the cardiovascular anomalies are generally not as severe and usually consist of: interrupted inferior vena cava with azygos continuation; bilateral superior venae cavae; pulmonary veins draining to ipsilateral atria; CAVC in 50%; left ventricular outflow tract obstruction; rarely, transposition of the great arteries; and, uncommonly, pulmonary stenosis (Figure 29.10a,b; Video 29.9). The various cardiac anomalies frequently encountered in the heterotaxy syndrome and their incidences in reported series are listed in Table 29.2. Additional details of the encountered anomalies are given in the following sections.

Systemic venous connections

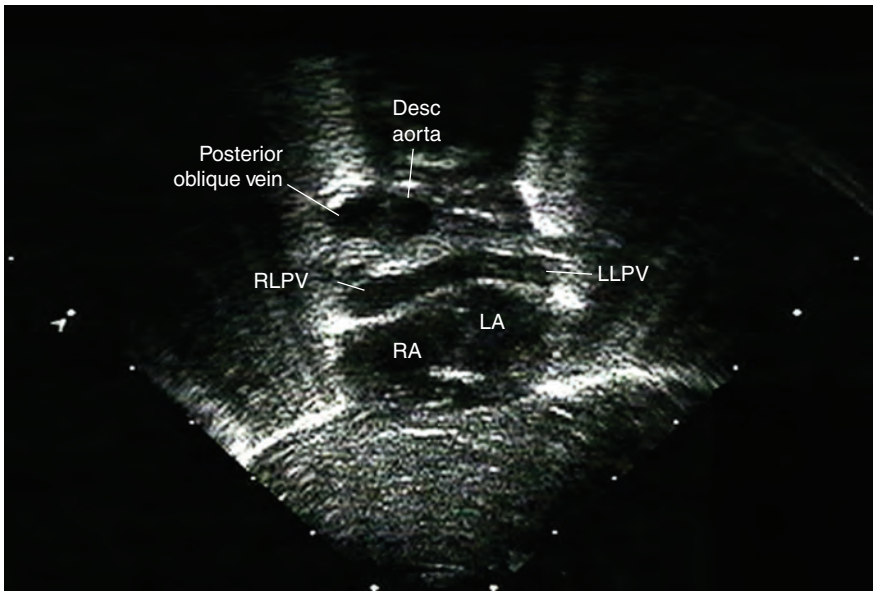
Interrupted inferior vena cava used to be considered pathognomonic for left isomerism/polysplenia syndrome, but recent case reports have shown that it can rarely be associated with right isomerism/asplenia syndrome [52,65]. In cases with interrupted inferior vena cava, the hepatic veins connect with the right-sided atrium directly, either as a single trunk – forming the suprahepatic segment of the inferior vena cava – or as separate connections of the left and right hepatic veins. When the inferior vena cava is intact, the hepatic veins drain in the IVC in the majority of cases, although in about a third of the cases, the hepatic veins draining the lobe of the liver opposite to the inferior vena cava can connect with the atrium directly (Figure 29.11). In any patient with suspected isomerism the hepatic venous drainage needs to be identified.

Pulmonary venous connections

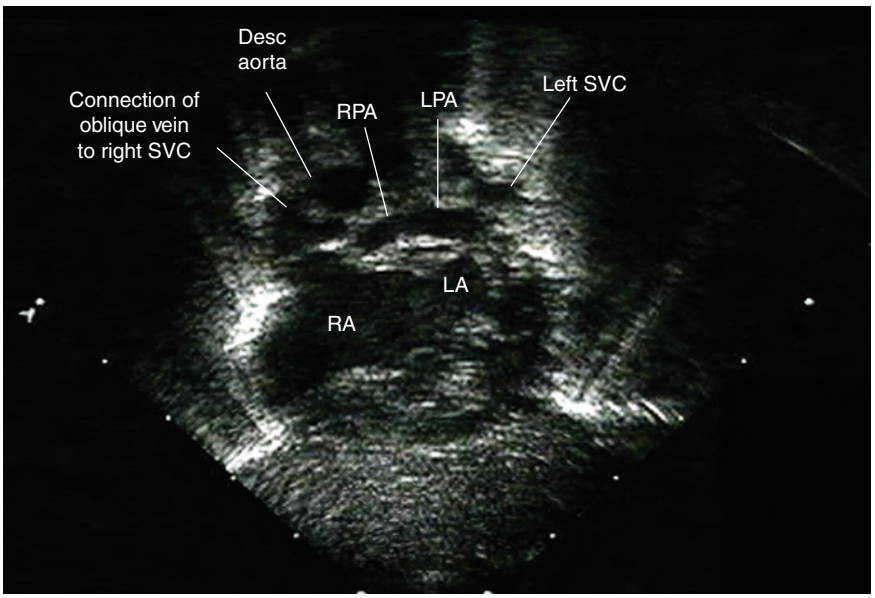
In right isomerism/asplenia syndrome total anomalous pulmonary venous drainage is very common with a collecting pulmonary venous chamber connected to a systemic vein. Pulmonary venous obstruction is frequently observed [66] and is associated with poor outcome. In left isomerism/polysplenia syndrome the pulmonary veins connect normally but drain anomalously due to malposition of the septum primum toward the anatomic left atrium (see later).

Atrial septum

A large atrial septal defect with a common atrium is frequently seen in both asplenia and polysplenia syndromes. Especially in right isomerism/asplenia syndrome, both septum secundum and septum primum may be absent, and only remnants of atrial septal tissue are recognized in these patients. This can be a fibromuscular strand that crosses the inferior aspect of the common atrium (inferior limbic band of the fossa ovale) or remnants of venous valve tissue. In left isomerism/polysplenia syndrome, it has been proposed that the partially or totally anomalous pulmonary venous connection to the contralateral atrium is due to malposition of septum primum, probably secondary to the absence of septum secundum [67]. The pulmonary veins appear to be connected normally to the left atrial wall externally but drain to the right atrium anomalously because of the malpositioned septum primum. There is usually an interatrial communication of variable size between the septum primum and the posterior atrial wall, which strictly speaking is not a foramen ovale [60]. A sinoseptal defect, frequently in the form of complete unroofing of the coronary sinus, is a common association, especially in patients with right isomerism/asplenia syndrome.



(a)



(b)

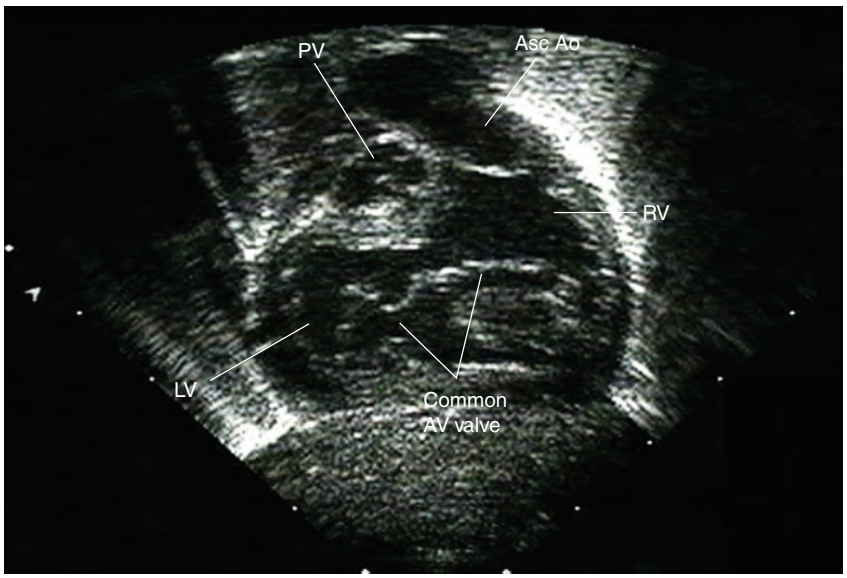
Figure 29.9 Heterotaxy syndrome most consistent with asplenia. **(a–d)** Sequential subxiphoid long-axis images from posterior/inferior to anterior/superior showing the typical constellation of findings in asplenia syndrome in a patient with double-outlet right ventricle {A,L,L}: bilateral superior venae cavae, totally anomalous pulmonary venous connections, nearly common atrium, complete common atrioventricular canal, and severe subpulmonary stenosis with bilateral conus. Asc, ascending; AV, atrioventricular; Desc, descending; LA, left atrium; LLPV, left lower pulmonary vein; LPA, left pulmonary artery; LV, left ventricle; MPA, main pulmonary artery; PV, pulmonary valve; RA, right atrium; RLPV, right lower pulmonary vein; RPA, right pulmonary artery; RV, right ventricle; SVC, superior vena cava.

Atrioventricular valves

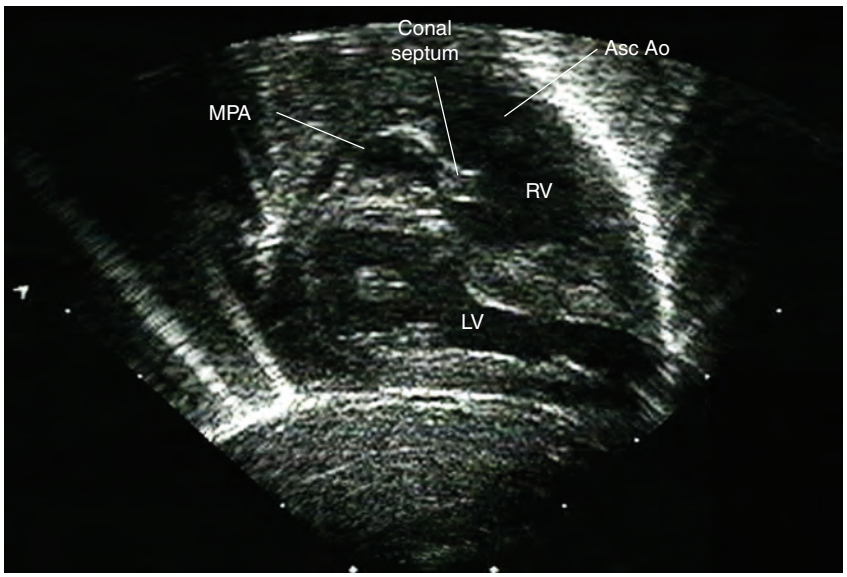
A partial or complete common atrioventricular (AV) canal is the most common cardiac malformation in all heterotaxy syndromes. In right isomerism/asplenia the defect is usually unbalanced with right ventricular dominance. In left isomerism/polysplenia, it is generally a balanced defect with two well-developed ventricles.

Ventricles

L-looped ventricles are encountered in 22–38% of patients with right isomerism/asplenia syndrome and in 12–30% of cases with left isomerism/polysplenia syndrome [68,69]. Preoperative recognition of ventricular looping is important because it can predict the location of the specialized conduction tissue. L-looped ventricles, irrespective of heterotaxy subgroup, usually have dual AV nodes, one situated anterolaterally and the other postero-inferiorly, occasionally with a "sling" of conduction tissue connecting them [70]. D-looped ventricles in the context of polysplenia syndrome usually possess a solitary AV node, situated where the ventricular septum meets the atrioventricular junction postero-inferiorly; the AV conduction axis is often discontinuous, providing the substrate for AV block that is common in left isomerism/polysplenia. Morphologic variations can be present in the AV valve that may further



(c)



(d)

Figure 29.9 (*Continued*)

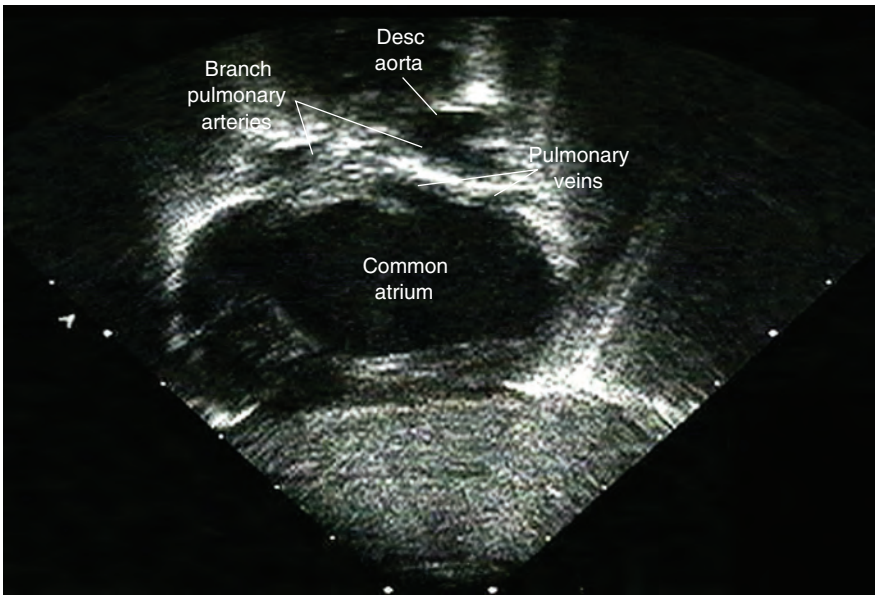
complicate surgical repair. More specifically, a study concentrating on cases of balanced CAVC in the setting of heterotaxy syndrome reports a higher frequency of solitary left-sided papillary muscles (Figure 29.12), shorter and deviated dual papillary muscles, and a smaller circumference of the mural leaflet of the morphologic left ventricle in asplenia syndrome compared with cases of CAVC in polysplenia syndrome or absence of heterotaxy [71].

Ventriculo-arterial connections

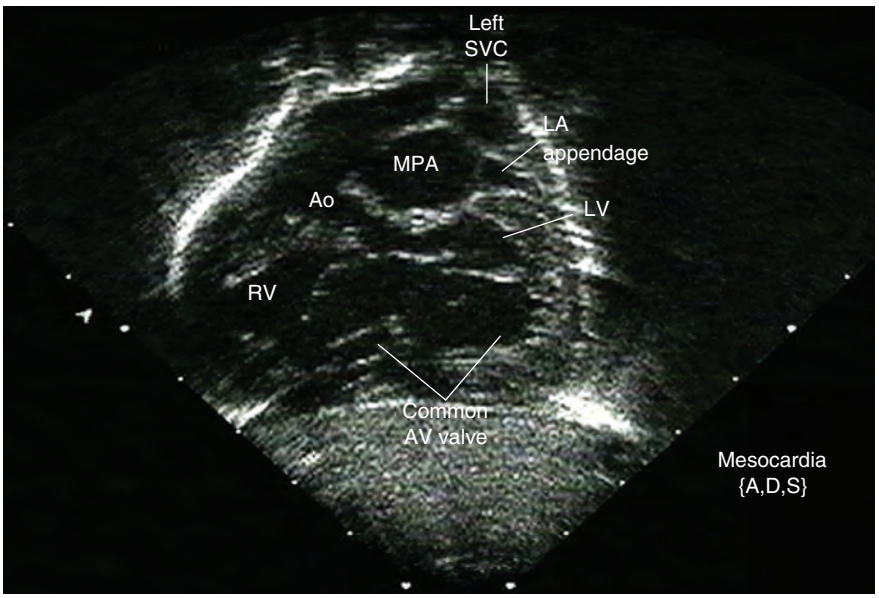
Significant abnormalities in ventriculo-arterial connections can be present in patients with heterotaxy syndrome. Generally in right isomerism/asplenia syndrome, there is double-outlet right ventricle or ventriculo-arterial discordance (transposed great arteries). One of the outflow tracts may be completely atretic as well (see later). In contrast, left isomerism/polysplenia syndrome is characterized by the absence of a subaortic conus, even in cases of transposition [68]. Ventriculo-arterial connections are more commonly concordant in this condition. Abnormal connection of the pulmonary veins to a systemic vein, irrespective of the heterotaxy subgroup, is almost always associated with abnormal infundibulum (either subaortic or bilateral) [68].

Pulmonary outflow tract obstruction

Pulmonary stenosis or atresia is very common, especially in right isomerism/asplenia syndrome, and, together with pulmonary venous obstruction, constitutes one of the most severe problems in the newborn period. A study of 72 postmortem cases



(a)



(b)

Figure 29.10 **(a,b)** Heterotaxy syndrome most consistent with polysplenia. Constellation of findings most consistent with polysplenia syndrome in a patient with mesocardia and abdominal visceral situs ambiguus (segmental set {A,D,S}): interrupted inferior vena cava with left azygos continuation to the left superior vena cava (SVC), common atrium, partial atrioventricular (AV) canal with a common AV valve, and normally related great arteries. Ao, aorta; Desc, descending; LA, left atrial; LV, left ventricle; MPA, main pulmonary artery; RV, right ventricle.

of asplenia syndrome [67] reported an interesting association between these two problems. Specifically, when the pulmonary artery branches were severely hypoplastic, stenotic or discontinuous, anomalous pulmonary venous connections were more probable (86% vs. 51% with pulmonary arteries that were only mildly hypoplastic or normal). Pulmonary venous obstruction was also more common (57% vs. 24%) in those patients.

Aortic outflow tract obstruction

In postmortem studies [69,72], subaortic obstruction was seen in 4–10% of patients with asplenia syndrome, and in 28–33% of patients with polysplenia syndrome. Van Praagh et al. described in detail the pathologic findings and clarified the anatomic basis of the malformation [72]. More specifically, there was no subaortic conus in any of their cases, and the obstruction was caused by the following lesions (Figure 29.13):

- redundant leaflet of the tricuspid valve;
- aneurysm of the membranous septum;
- excessive fibrous tissue from the mitral or common AV valve; or
- malposition of the conal septum.

Aortic arch, brachiocephalic vessels, and patent ductus arteriosus

Coarctation of the aorta and interrupted aortic arch are relatively uncommon, especially in asplenia syndrome (Figure 29.14a,b).

Table 29.2 Incidence of cardiac anomalies in heterotaxy syndrome

	Right isomerism/Asplenia syndrome (%)	Left isomerism/Polysplenia syndrome (%)
Dextrocardia	27–41 [46,61,64,69,76,115,116]	27–45 [46,48,64,69,115–117]
Interrupted IVC	0–3 [46,61,64,69,76,115,116]	65–92 [46,48,64,69,115–117]
Continuous IVC entering the RA	48–77 [46,64,76,115]	0–34 [46,64,115,117]
Continuous IVC entering the LA	20–52 [46,64,76,115]	0–16 [46,64,115,117]
Hepatic veins entering the atria directly	16–38 [46,61,64,69,76,115,116]	84–96 [46,48,64,69,115,116]
Unroofed coronary sinus	32–100 [46,61,64,69,115,116]	26–46 [46,48,64,69,115–117]
Bilateral superior venae cavae	38–71 [46,61,64,69,76,115,116]	33–50 [46,48,64,69,115–117]
TAPVC to a systemic vein	31–87 [46,61,64,69,76,115,116]	0–13 [46,48,64,115,117]
Pulmonary veins to RA (partial or total)	2–19 [46,64]	37–74 [46,48,64,115,117]
Common atrium	40–84 [61,64,69,76,116]	30–53 [46,48,64]
Atrial situs solitus	50 [46]	78 [46]
Atrial situs inversus	31 [46]	22 [46]
Atrial situs ambiguus	19 [46]	0 [46]
CAVC	69–92 [46,61,64,69,76,115,116]	16–66 [46,48,64,115,117]
Pulmonary stenosis/atresia	78–96 [46,61,64,69,76,115,116]	28–43 [46,48,64,115,117]
Aortic valve hypoplasia/ LVOT obstruction/coarctation	2–12 [46,61,64,69,76,116]	17–25 [46,48,69,117]
Single ventricle	29–73 [46,61,64,69,76,115,116]	26–43 [46,48,69,115]
TGA -D, -L/DORV	47–91 [46,61,64,69,76,115,116]	16–48 [46,48,69,115,117]
Abnormal coronary pattern	10–64 [61,64,69,115,116]	8–24 [69,117]
Aortic arch laterality		
– Left	56 [115]	33 [115]
– Right	32–49 [61,76,115]	67 [115]

CAVC, complete common atrioventricular canal; DORV, double-outlet right ventricle; IVC, inferior vena cava; LA, left atrium; LVOT, left ventricular outflow tract; RA, right atrium; TAPVC, totally anomalous pulmonary venous connection; TGA, transposition of the great arteries.

The incidence of right aortic arch is given in Table 29.2. In our database, out of 56 cases with heterotaxy syndrome, right aortic arch was diagnosed in 39% (all with mirror-image branching) [73]. Isolated left innominate artery has also rarely been described (three cases), with both subgroups of heterotaxy syndrome represented. Two of these three cases had associated aortic atresia [74]. Another reported association is the presence of bilateral ductus arteriosus in 25% of cases with pulmonary atresia and right isomerism/asplenia syndrome [75].

Noncardiac anomalies

In right isomerism/asplenia syndrome, in addition to the frequently encountered bronchial symmetry with bilateral trilobed lungs and eparterial bronchi, a midline liver is present in the

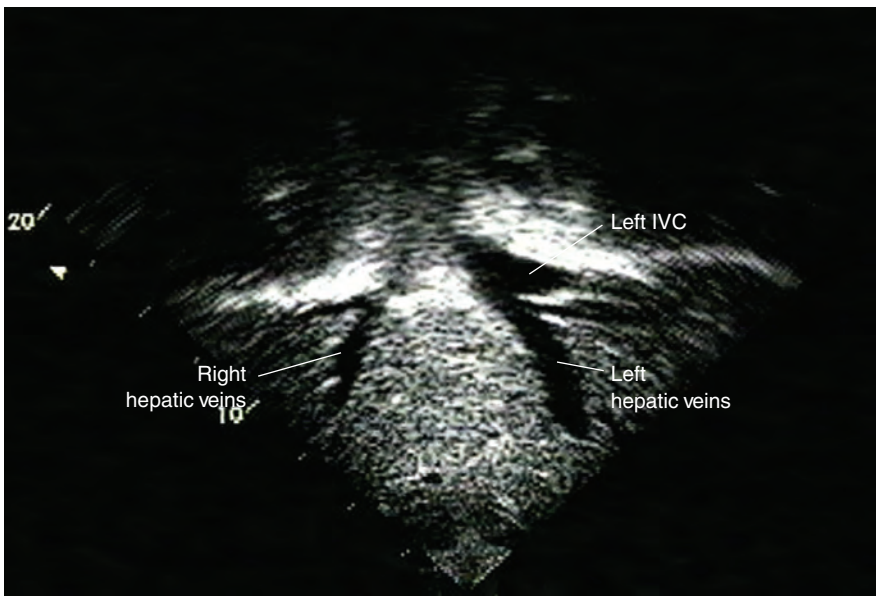


Figure 29.11 Ipsilateral hepatic veins. Subxiphoid long-axis view at the level of the diaphragm showing the left hepatic veins joining the left-sided intact inferior vena cava (IVC) and the right hepatic veins draining separately.



Figure 29.12 Single left ventricular papillary muscle. Subxiphoid short-axis image showing the well-balanced common atrioventricular valve and a single left ventricular (LV) posteromedial papillary muscle (arrow). RV, right ventricle.

majority of the cases whereas gastrointestinal and genitourinary anomalies are present in one-third and one-tenth of patients, respectively [76]. The most common gastrointestinal abnormality is intestinal malrotation.

In left isomerism/polysplenia syndrome, the incidence of extracardiac anomalies is higher, occurring in 36% of patients in the largest clinical series to date [48]. Gastrointestinal anomalies are common, with biliary atresia and intestinal malrotation occurring in 11% and 13% of patients, respectively, whereas genitourinary and neurologic abnormalities occur in 6% and 4% of patients.

Pathophysiology

Cyanosis in the newborn period is the presenting symptom in many patients with right isomerism/asplenia syndrome, due to the frequent presence of pulmonary stenosis or atresia, as well as common atrium and transposition physiology. In left isomerism/polysplenia syndrome, pulmonary stenosis or atresia

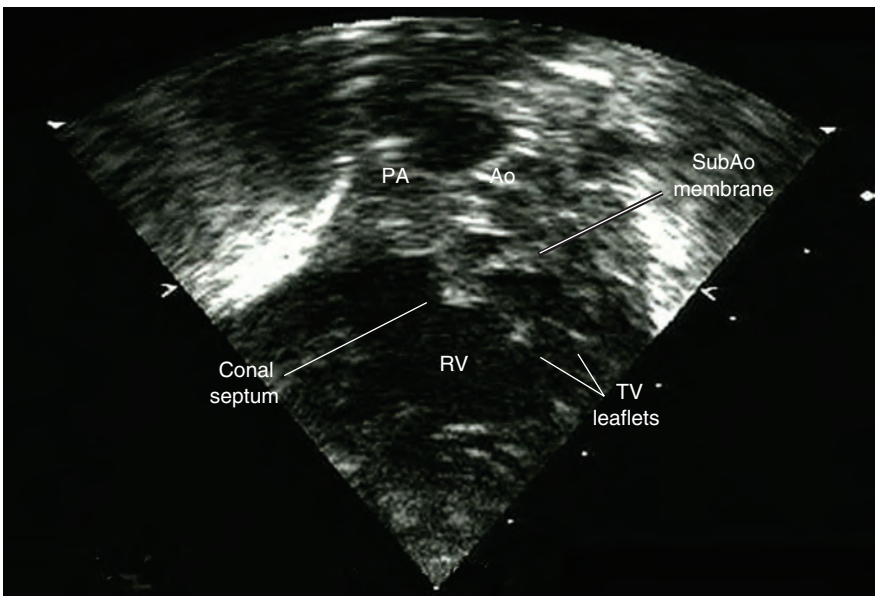
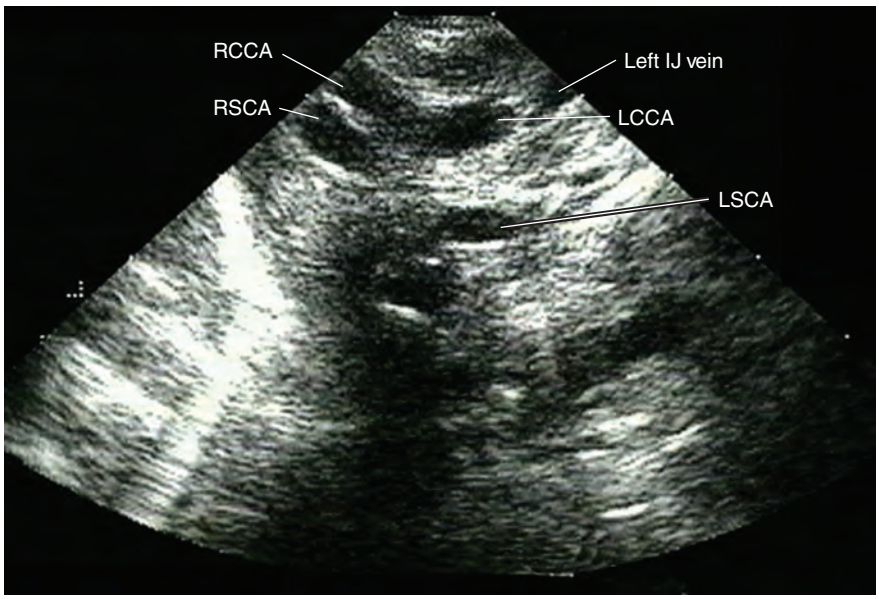
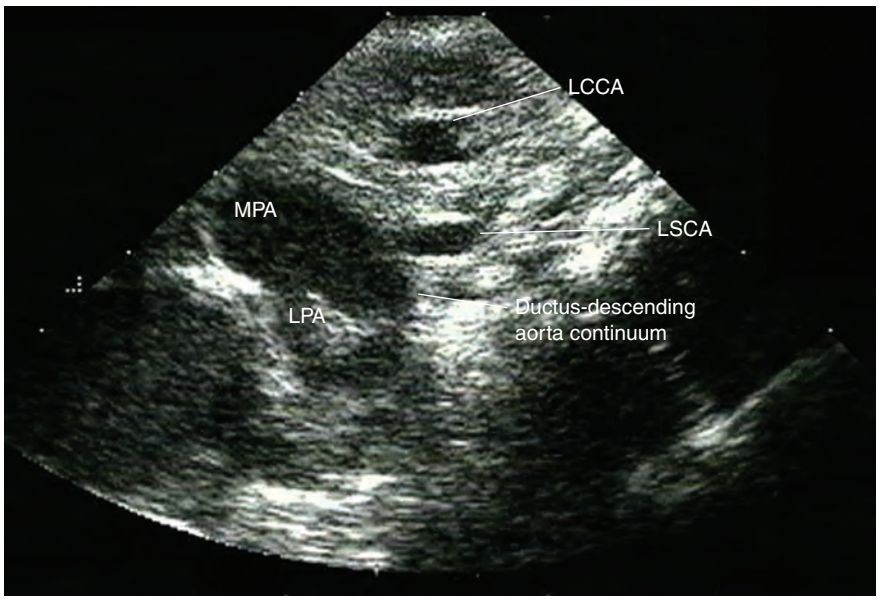


Figure 29.13 Mechanisms of ventricular outflow tract obstruction. Subxiphoid long-axis image angled anteriorly showing the different mechanisms of obstruction of the systemic outflow in heterotaxy syndrome, with critical obstruction in the systemic outflow due to posterior malalignment of conal septum, discrete subaortic membrane, tricuspid valve attachments and aortic valve hypoplasia. Ao, aorta; PA, pulmonary artery; RV, right ventricle; SubAo, subaortic; TV, tricuspid valve.



(a)



(b)

Figure 29.14 (a,b) Complex interrupted aortic arch type A in polysplenia syndrome. Short- and long-axis suprasternal notch images reveal a very unusual branching pattern of a probably left aortic arch: the first vessel is the left subclavian artery (LSCA), which arises from the ascending aorta, 15 mm above the level of the aortic annulus. The ascending aorta continues for another 8 mm before it trifurcates to the right subclavian (RSCA), right common carotid (RCCA) and left common carotid (LCCA) arteries. The distance between the distal ascending aorta and the descending aorta is measured at about 1 cm. IJ, internal jugular; LPA, left pulmonary artery; MPA, main pulmonary artery.

and transposition physiology are relatively uncommon, making symptoms of congestive heart failure from large left-to-right shunts the predominant presenting symptoms.

Rhythm abnormalities are common in both groups of heterotaxy syndrome. There are dual sinus nodes in the majority of right isomerism/asplenia syndrome patients, whereas in left isomerism/ polysplenia syndrome the sinus node tends to be hypoplastic or absent resulting in abnormal origin of the atrial rhythm (often low atrial rhythm) [70]. Complete atrioventricular block (CAVB) mainly affects patients with left isomerism/polysplenia syndrome and if this occurs during fetal life, fetal demise occurs in almost 100% of all cases. The high occurrence of CAVB has been attributed to discontinuity between the AV node and the ventricular conduction tissue [77]. Postnatally, it has been described in 7% of patients with left isomerism/polysplenia syndrome [48]; additionally, there is a small percentage of patients who develop complete AV block postoperatively.

The splenic abnormalities that accompany heterotaxy syndrome contribute significantly to morbidity and mortality. Asplenia can result in fulminant sepsis and patients require lifelong antibiotic prophylaxis. Splenic imaging is therefore important and can include abdominal ultrasound, CT, or magnetic resonance imaging. Because functional asplenia can develop with

age [78] it is recommended that patients with heterotaxy syndrome, even with documented multiple or solitary spleens, are monitored regularly for splenic function.

Imaging

The highly variable and often complex anatomy of heterotaxy requires a systematic segmental approach.

Key elements

Our proposed checklist involves determination of the following:

- Abdominal visceral situs
- Location of the heart in the thorax; orientation of the apex
- Systemic venous connections, including hepatic veins
- Coronary sinus septum
- Anatomy and drainage of pulmonary veins
- Atrial septum and atrial appendages
- Atrioventricular connections
- Ventriculo-arterial connections
- Atrioventricular valve anatomy and function
- Ventricular size, morphology, looping, and function
- Size and location of ventricular septal defect(s), potential LV-to-aorta or -pulmonary artery baffle pathway in cases of transposition of the great arteries with VSD or double-outlet right ventricle
- Sources of pulmonary blood flow (including branch pulmonary arteries, patent ductus arteriosus, and aortopulmonary collaterals)
- Systemic ventricular outflow tract for presence and type of obstruction
- Aortic arch sidedness and branching pattern.

The examination begins with subxiphoid imaging to evaluate the abdominal viscera and establish the sidedness of the abdominal aorta and inferior vena cava (Figure 29.15a–d). Subsequently, the location of the heart in the chest and the direction of the cardiac apex are determined. The same principles as described earlier for imaging dextrocardia should be applied. Following these initial steps, the cardiac segments (atria, ventricles, and great arteries) and their connections (AV junction and conotruncus) need to be analyzed independently and characterized in terms of situs and alignments following the principles of the segmental approach to diagnosis [79–81]. Starting with the

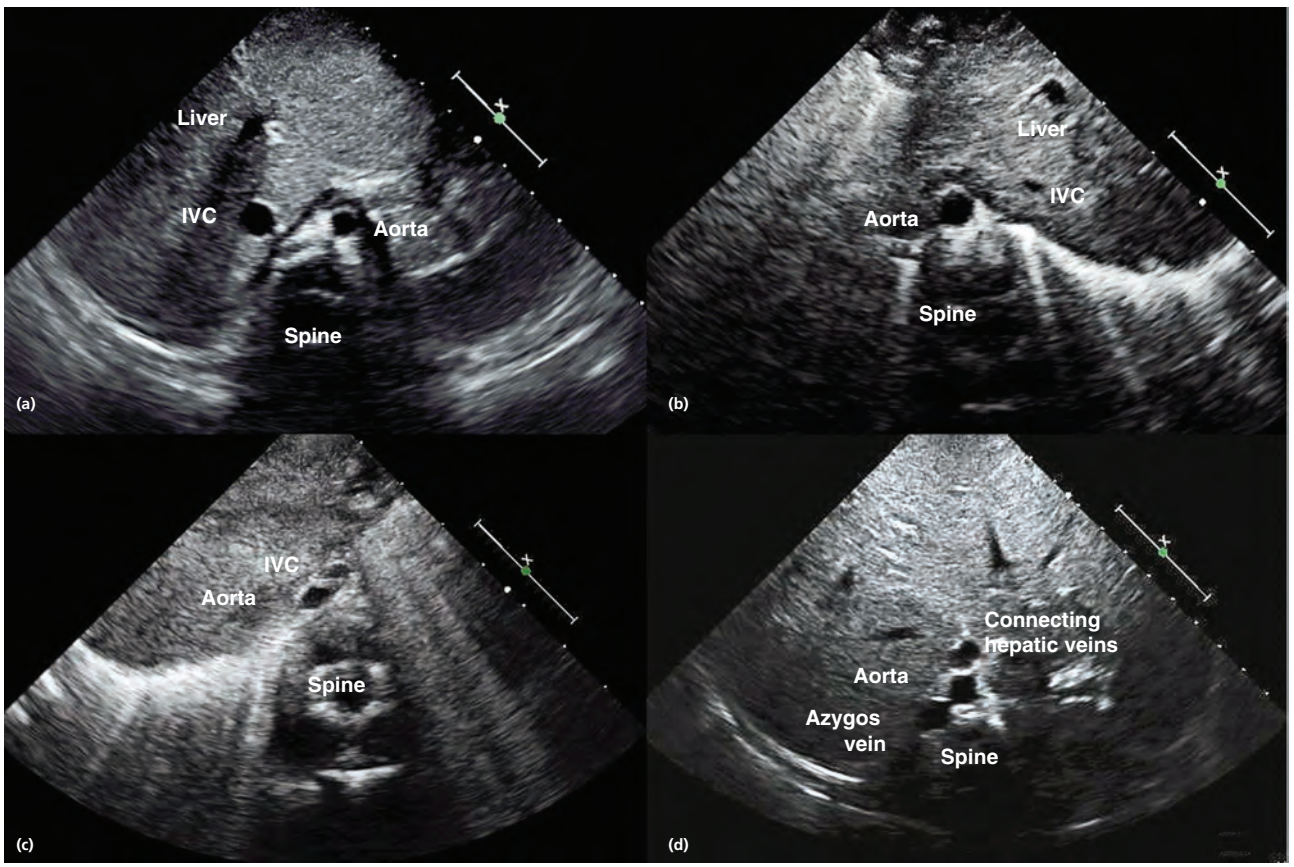


Figure 29.15 Abdominal visceral situs. **(a)** Normal. **(b)** Abdominal visceral situs inversus: left-sided liver with inferior vena cava (IVC), right-sided stomach and right-sided descending aorta. **(c)** Abdominal visceral situs ambiguus consistent with asplenia syndrome: midline liver with IVC and descending aorta on the same side. **(d)** Abdominal visceral situs ambiguus consistent with polysplenia syndrome: midline liver with interrupted IVC and dilated azygos vein.

atrial situs, the right atrium is identified based on the following characteristics:

1 The chamber receives a normal coronary sinus (not unroofed)
2 The chamber receives the venae cavae (the suprahepatic segment of the inferior vena cava, in cases of interruption)
3 The chamber has a larger, more anterior, broad-based, and triangular atrial appendage
4 The septal surface comprises the septum secundum
5 The chamber has an identifiable crista terminalis.

Based on the above criteria, Van Praagh and Van Praagh were able to correctly diagnose atrial situs in 100% of their postmortem cases of polysplenia syndrome, 100% of cases of right-sided spleen, and 81% of cases of asplenia syndrome [82]. In the remaining cases of asplenia syndrome, the inferior vena cava and the larger and more anterior appendage were contralateral; the diagnosis of situs ambiguus was made in those cases.

The inferior vena cava, hepatic veins, and their atrial connections as well as the abdominal aorta and the azygos vein termination to the superior vena cava are best seen from subxiphoid long- and short-axis views (Figure 29.16a,b) [83]. The hepatic vein connections can also be imaged from apical views angled inferiorly toward the abdomen. The superior vena cava on either side can be imaged using subxiphoid, suprasternal, and high parasternal views [84]. Subxiphoid views are also good for the imaging of pulmonary venous connections below the diaphragm (Figure 29.17a). Due to the high frequency of pulmonary venous obstruction, especially in asplenia syndrome, Doppler assessment of pulmonary venous flow is of paramount importance. To increase the sensitivity of the interrogation, filter settings should be low, and each vein should be interrogated by color flow mapping distal to the orifice for turbulent or high-velocity flow. In cases of pulmonary vein stenosis the Doppler flow pattern is no longer laminar and triphasic; instead, it becomes turbulent and continuous (Figure 29.17b) with a pattern reminiscent of a patent ductus arteriosus [85,86].

Imaging of the atrial appendages to determine their size and location can be attempted from subxiphoid and parasternal short-axis views, but the internal anatomy is difficult to ascertain. The malpositioned septum primum is seen well from subxiphoid long-axis and apical 4-chamber views [60].

Imaging of the AV canal area is described in detail in Chapter 15. The valve apparatus should be carefully evaluated for abnormalities of the number, size, and location of the papillary muscles, especially in right isomerism/asplenia syndrome [71]. Ventricular size and morphology need to be evaluated from all available views; the method for determining the identity of the ventricles and the ventricular looping has been described earlier (see Chapter 3). The outflow tracts can be imaged from subxiphoid views, apical views angled anteriorly and high parasternal views. The main pulmonary and branch pulmonary arteries should all be measured. If aortic outflow tract obstruction is present, coarctation should be suspected.

In cases with suboptimal transthoracic windows and an inconclusive diagnosis, transesophageal echocardiography is recommended [87,88]. In such cases, cardiac magnetic resonance imaging can also be considered as a noninvasive alternative [89,90] with the additional capability of delineation of the splenic status and the bronchial tree anatomy.

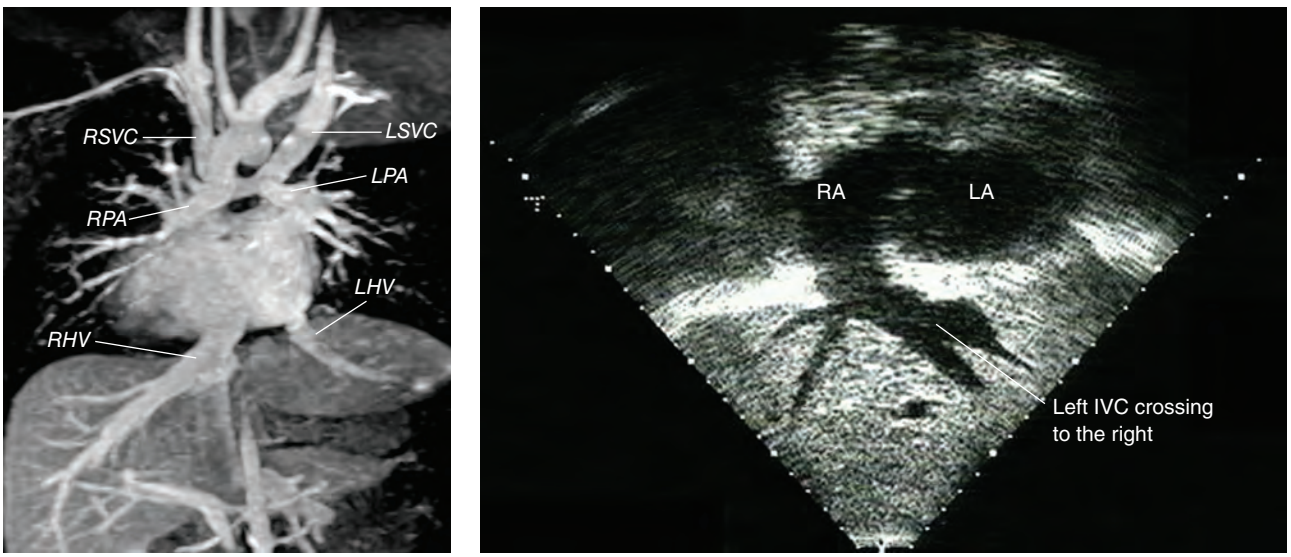
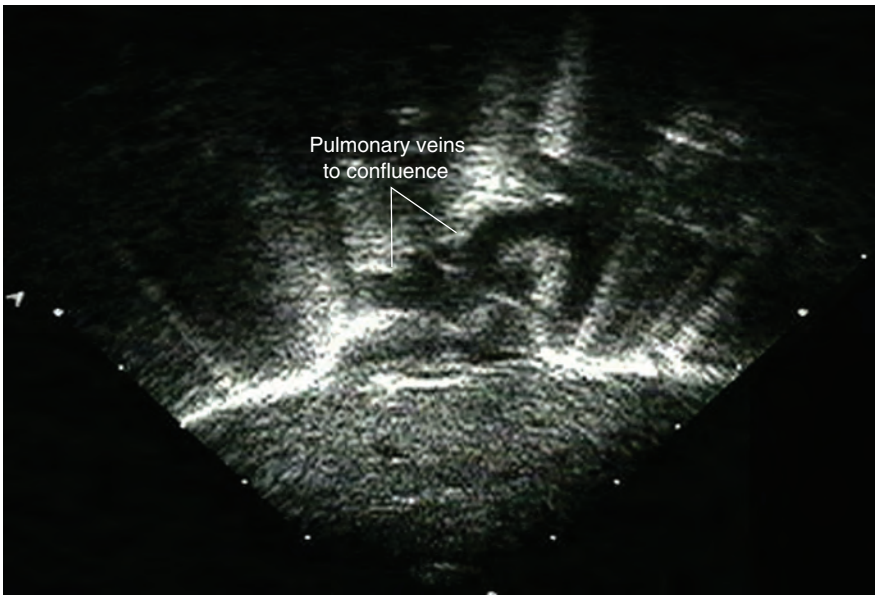
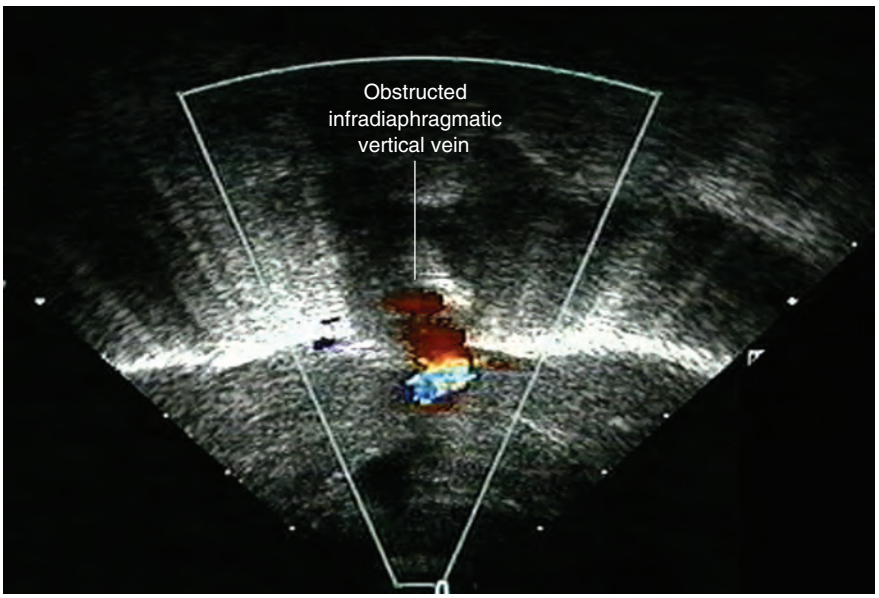


Figure 29.16 Systemic venous anomalies in heterotaxy. **(a)** Coronal maximal intensity projection of a magnetic resonance angiogram demonstrating dextrocardia, bilateral bidirectional Glenn anastomoses, and an interrupted inferior vena cava with separate connections of the right hepatic veins (RHV) and left hepatic veins (LHV) in a patient with asplenia syndrome, double-outlet right ventricle {S,L,L}, and right aortic arch. LPA, left pulmonary artery; LSVC, left superior vena cava; RPA, right pulmonary artery; RSVC, right superior vena cava. **(b)** Subxiphoid short-axis image showing a left-sided inferior vena cava (IVC) crossing to the right and receiving all hepatic veins. This is a case of asplenia syndrome with a single right ventricle and severe pulmonary stenosis, status post-Fontan takedown. LA, left atrium; RA, right atrium.



(a)



(b)

Figure 29.17 Infradiaphragmatic total anomalous pulmonary venous connections. **(a)** Subxiphoid long-axis 2D. **(b)** Color Doppler images of a vertical vein that accepts all pulmonary veins and is directed below the diaphragm into the hepatic portal venous system with mild flow acceleration (mean gradient of 4–5 mmHg).

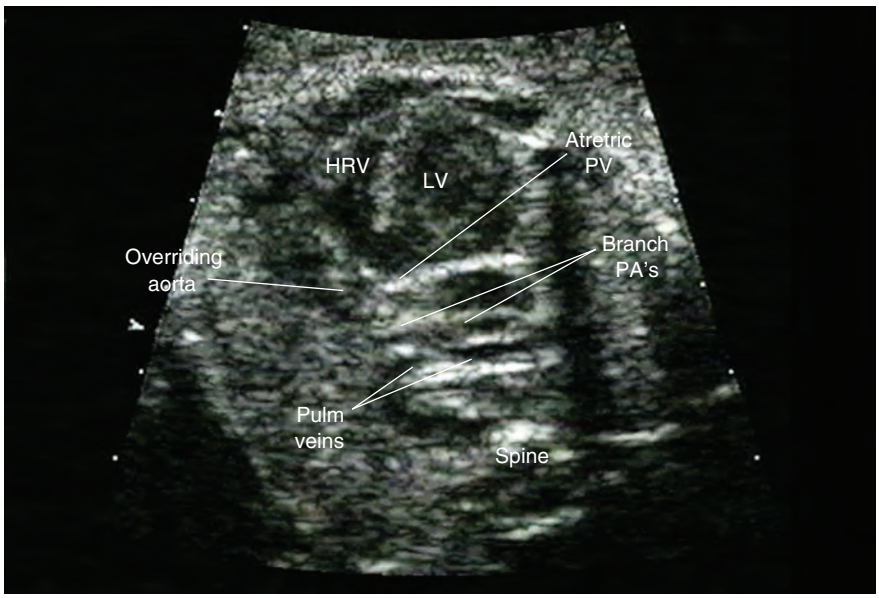
Prenatal assessment

The most common reasons for referral in cases of fetal heterotaxy syndrome are abnormal position of the stomach and/or heart, identified by obstetrical ultrasound examination, and fetal bradycardia. Prenatal diagnosis of heterotaxy syndrome has greatly improved over the last years, although the diagnosis of hepatic venous and inferior vena cava connections is still not as accurate, with correct diagnosis achieved in 62–67% of cases [91]. With respect to clinical outcomes, prenatal diagnosis does not appear to confer any survival advantage in either asplenia or polysplenia syndromes [91], but it offers prospective parents valuable time to reach an informed decision when they are faced with the diagnosis of severe cardiac anomalies.

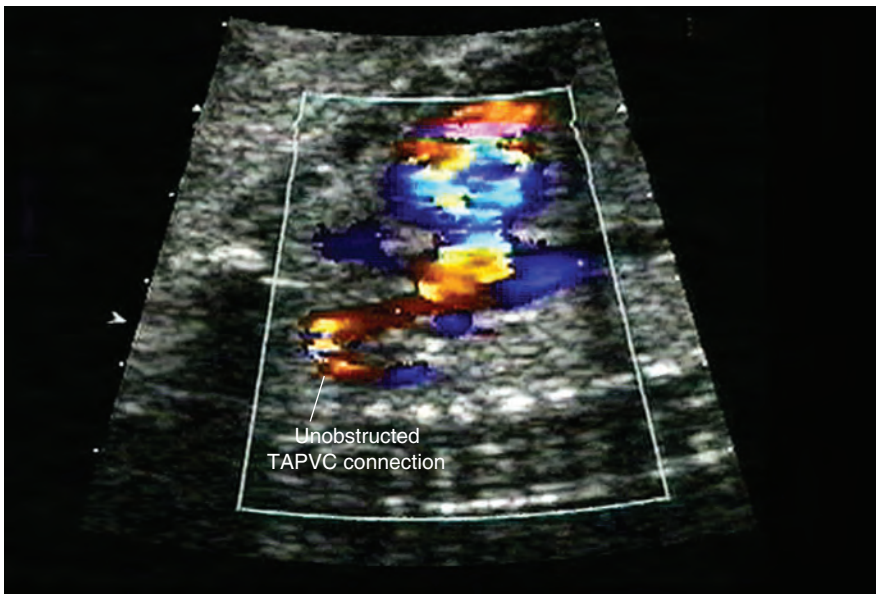
In cases of left isomerism/polysplenia syndrome, heart block and extracardiac anomalies (biliary atresia, gastric volvulus, bowel malrotation) are risk factors for fetal and neonatal loss, and long-term survival is reported at 14–52% [51,91,92]. It is known that heterotaxy syndrome patients with heart block have significantly lower ventricular rates compared with those with other structural lesions or patients with isolated CAVB. The lower ventricular rate in combination with the structural abnormalities appears to be a significant risk factor for perinatal loss [93]. In rare cases, association of left isomerism/polysplenia syndrome with ventricular noncompaction has been described both pre- [94] and postnatally [95,96]. In right isomerism/asplenia syndrome diagnosed prenatally, long-term survival is reported

at 13–16% [91,97], mainly due to the complex intracardiac anomalies and the high surgical mortality of neonatal repair.

In evaluating the fetus for possible heterotaxy syndrome, it is essential to follow the same comprehensive approach as for postnatal imaging. The first step is to determine the fetal lie and position and, thus, distinguish the left and right side of the fetus and the relative position of the thoracic and abdominal organs. Dextrocardia is relatively common in heterotaxy syndrome and should be ruled in or out early in the examination. Identification of atrial appendage morphology as well as the systemic venous connections will aid in differentiating between the two subgroups of heterotaxy syndrome. The atrial appendages [98] can be visualized from the 4-chamber view angled cranially. In left isomerism/polysplenia syndrome, the inferior vena cava is usually interrupted, and the dilated azygos can be identified posterior to the aorta; in right isomerism/asplenia syndrome the inferior vena is intact and typically on the same side of the spine as the aorta. Anomalous pulmonary venous connections, more commonly seen with right isomerism/asplenia syndrome, may be difficult to detect in utero, especially in cases with pulmonary stenosis or atresia (Figure 29.18; Video 29.10). With the color scale appropriately set to detect low flow rates and a narrowed sector to increase the frame rate, it is feasible to arrive at an accurate diagnosis (Figure 29.19; Video 29.11) of even the most complex forms of pulmonary venous abnormalities [99]. The intracardiac anomalies associated with heterotaxy syndrome are easy

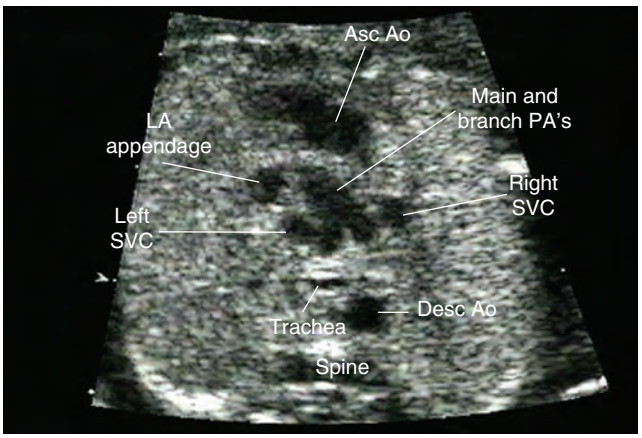


(a)

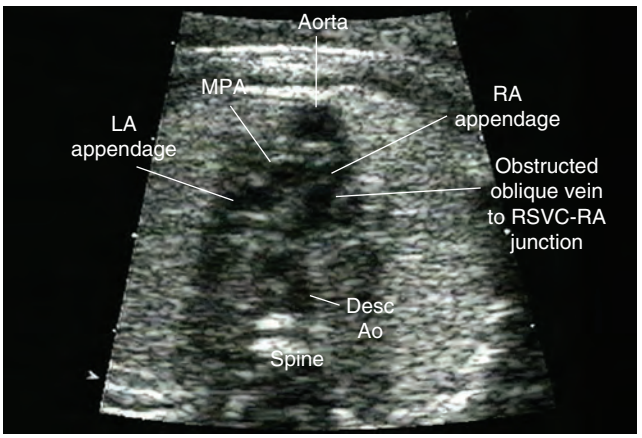


(b)

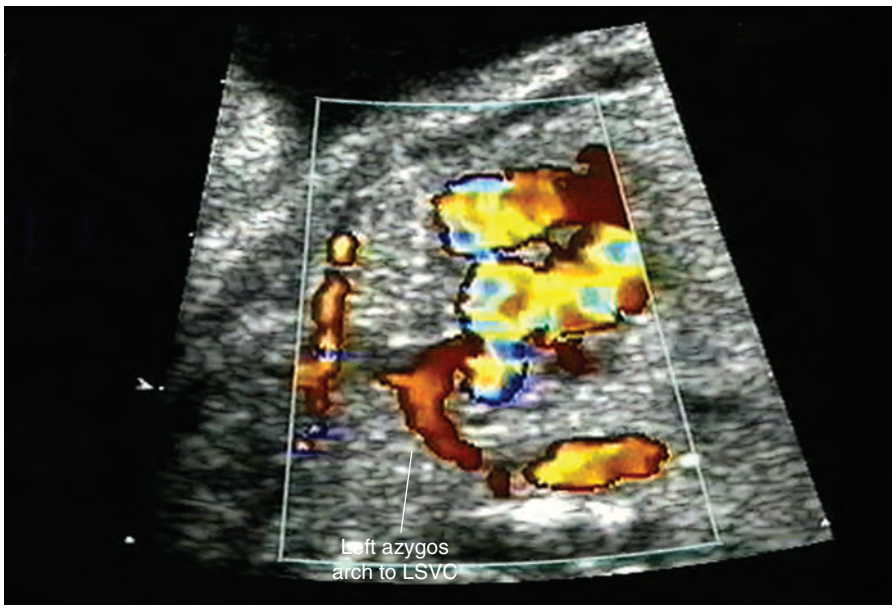
Figure 29.18 Fetal heterotaxy syndrome with total anomalous pulmonary venous connections (TAPVC). Fetal echocardiogram at 26 weeks' gestation with **(a)** 4-chamber **(b)** long-axis images demonstrating unobstructed TAPVC. The individual pulmonary veins form a confluence behind the left atrium and drain via a vertical vein to the left superior vena cava. In addition to TAPVC, this fetus was diagnosed as having levocardia with abdominal situs inversus, tricuspid atresia (segmental set {I,D,D}), pulmonary atresia, hypoplastic right ventricle (HRV) and systemic venous anomalies (left-sided intact inferior vena cava and bilateral superior venae cavae). PA, pulmonary artery; PV, pulmonary valve.



(a)



(b)



(c)

Figure 29.19 Fetal obstructed total anomalous pulmonary venous connections. **(a)** Fetal echocardiogram at 22 weeks' gestation with an axial image showing bilateral superior venae cavae, an anterior aorta, and a right-sided thoracic descending aorta. **(b)** Cranial angulation of the previous image reveals the obstructed oblique vein that drains the pulmonary veins to the right superior vena cava (RSVC)–right atrial (RA) junction. **(c)** Long-axis image shows a prominent azygos arch draining into the left superior vena cava (LSVC). The inferior vena cava was intact and left-sided. The diagnosis also included double-outlet right ventricle {I,D,D}, complete common atrioventricular canal and pulmonary stenosis. Ao, aorta; Asc, ascending; Desc, descending; LA, left atrial; MPA, main pulmonary artery; PA, pulmonary artery.

to identify (Figure 29.20), and ductal dependency can be accurately predicted. Complete heart block is readily identified in the fetus because of the fetal bradycardia (heart rate <110 beats per minute); the methods of assessment of fetal rhythm disturbances are described in Chapter 42. Briefly, utilizing pulsed Doppler and M-mode techniques, one can estimate atrial and ventricular contraction rates, ratio (normally 1:1, higher in cases of 2nd or 3rd degree AV block) and synchrony (dissociation in cases of complete heart block).

Detailed prenatal diagnosis allows for appropriate family counseling. Because right isomerism/asplenia syndrome, in particular, is currently considered one of the worst forms of congenital heart disease [100], it is very important to arrive at an accurate diagnosis in a timely manner and to be able to delineate all management options for the families.

Preoperative assessment

In the majority of cases, right isomerism/asplenia syndrome requires a single ventricular palliative approach due to the complex cardiovascular anatomy [101,102]. Biventricular repair is only feasible in the rare cases with two balanced ventricles and suitable anatomy. In cases of borderline ventricular hypoplasia, calculation of ventricular volumes is very important preoperatively, and a systemic–pulmonary shunt can be placed for the

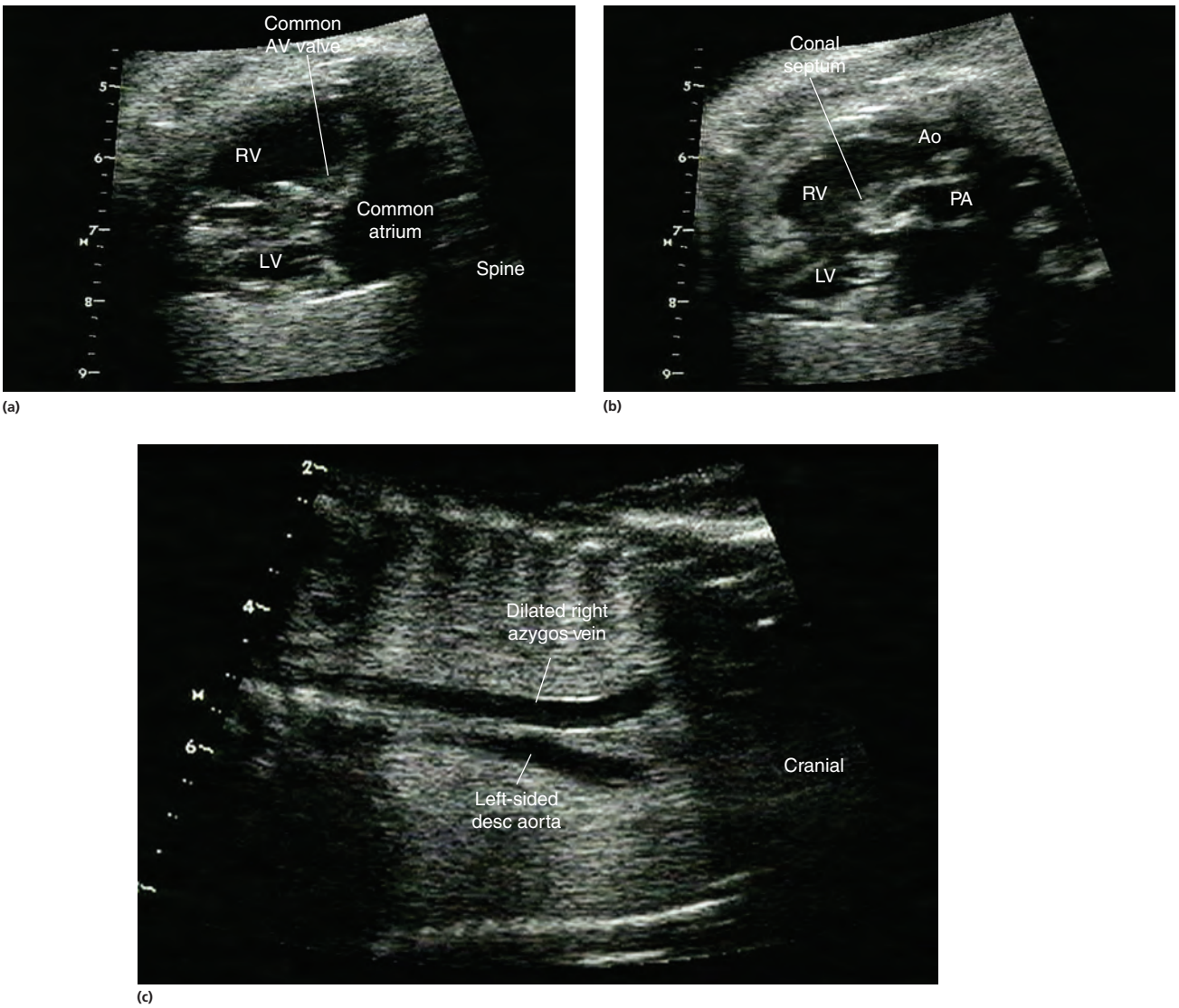


Figure 29.20 Fetal heterotaxy syndrome with severe pulmonary stenosis. **(a)** Fetal echocardiogram at 27 weeks' gestation with a 4-chamber view showing levocardia, common atrium and complete common atrioventricular canal. **(b)** Imaging of the ventricular outflows indicates the additional diagnoses of double-outlet right ventricle {A,D,D}, anterior aorta, and severe subvalvar and valvar pulmonary stenosis. **(c)** Coronal image demonstrates a dilated right azygos vein in the setting of an interrupted inferior vena cava. The cardiovascular findings in this fetus are most consistent with polysplenia syndrome. Ao, aorta; LV, left ventricle; RV, right ventricle; PA, pulmonary artery.

purpose of increasing the ventricular volume to facilitate intraventricular rerouting in addition to providing a stable source of pulmonary blood flow [103].

The systemic venous anatomy requires special attention in all preoperative patients with heterotaxy syndrome. An intact inferior vena cava with a dilated azygos needs to be differentiated from interrupted inferior vena cava with azygos continuation in order to decide whether the azygos should be ligated [67]. An interconnecting venous sinus between the inferior vena cava and the hepatic veins below their separate entry to the heart needs to be ruled out prior to the Kawashima procedure [67,104]. It is also critically important to evaluate for bilateral superior venae cavae, and the presence of an interconnecting vein should be determined before deciding whether to perform a bilateral bidirectional Glenn anastomosis. The exact location of the entrance of the systemic veins to the heart needs to be determined in cases where a biventricular repair will be attempted and atrial septation for separation of the pulmonary and systemic venous flow is necessary [105].

Totally anomalous pulmonary venous connection in right isomerism/asplenia syndrome often presents with obstruction and may warrant emergency operation in the newborn period, with a high mortality risk [66,102,106,107]. The techniques for diagnosis of pulmonary venous obstruction have been described earlier. Additionally, based on a study of totally anomalous pulmonary venous connection cases, the measurement of

individual pulmonary vein size and use of the indexed pulmonary vein sum can predict long-term survival and the probability of intrinsic pulmonary vein abnormalities preoperatively [108]. In cases of obstruction, the need for simultaneous shunt placement may be underestimated. The reverse is also true: the relief of critical obstruction of pulmonary blood flow may unmask obstructed total pulmonary venous connections in heterotaxy syndrome [109].

Before performing the Fontan operation, the degree of AV valve regurgitation needs to be assessed [110] because it affects surgical outcome. The ventricular septum should also be interrogated and the presence and type of VSD determined, especially in cases of double-outlet right ventricle, where the relation of the VSD to the aorta will determine the feasibility of an LV-aorta baffle repair.

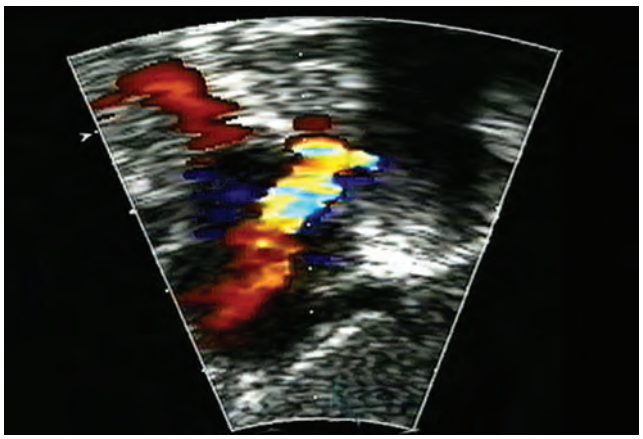


Figure 29.21 Postoperative obstructed totally anomalous pulmonary venous connections (TAPVC). Subxiphoid short-axis image showing moderate to severe obstruction at the pulmonary venous anastomosis after infradiaphragmatic TAPVC repair. A Doppler cursor is positioned at the anastomotic site.

Postoperative assessment and imaging in the adult

The main focus of the postoperative and follow-up examinations in patients with heterotaxy syndrome depends on the type of procedure performed. Because the majority of heterotaxy syndrome patients require staged single-ventricle palliation, the follow-up is as described in Chapter 27. The long-term prognosis is frequently dependent on the occurrence of complications related to obstruction of the pulmonary veins, distortion of the pulmonary arteries, elevated pulmonary vascular resistance, atrioventricular valve regurgitation, or depressed ventricular function. After correction of totally anomalous pulmonary venous connection, the individual pulmonary veins require special attention for evidence of stenosis, both at the anastomotic site (Figure 29.21) and more distally in the lumen of the veins. Transesophageal echocardiography may be necessary for pulmonary venous imaging in the adult.

The branch pulmonary arteries in the adult will frequently require imaging with cardiac magnetic resonance or computed tomography. Ventricular function and atrioventricular valve regurgitation (Figure 29.22) need to be carefully assessed and followed longitudinally to determine the timing and feasibility of surgical repair. Abnormalities of ventricular relaxation and compliance, easily detected with measurement of Doppler tissue imaging diastolic velocities, have been described both pre- and postoperatively, and can be present even before overt systolic dysfunction ensues [111,112]. Despite the improved success rate of corrective and palliative surgeries in recent years, mortality remains high with 5-year survival rates ranging from 30–74% for right isomerism/asplenia syndrome and 65–84% for left isomerism/polysplenia syndrome [48,76,113]. In case of severe AV valve regurgitation, ventricular dysfunction, or extracardiac complications such as protein-losing enteropathy, cardiac

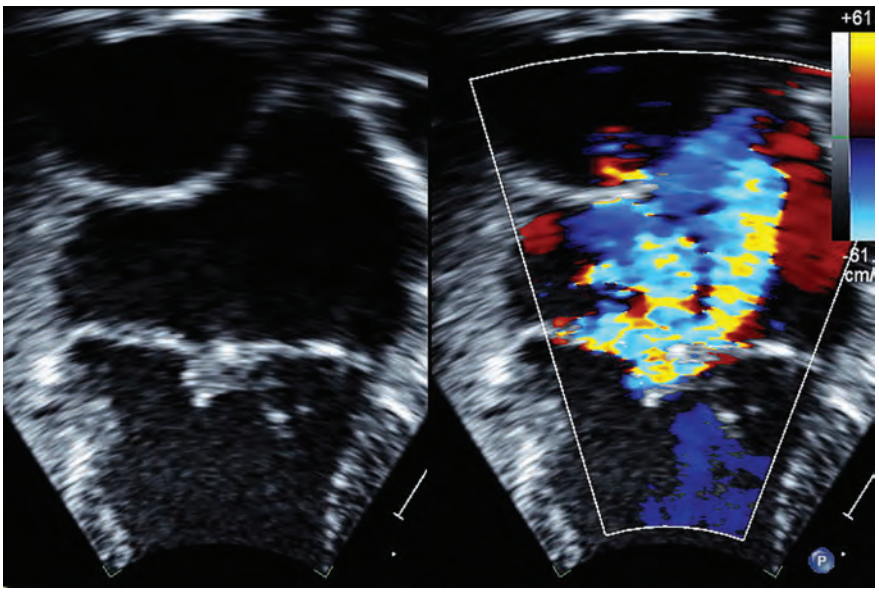


Figure 29.22 Apical 2D and color flow mapping focused on the common AV valve that shows severe regurgitation in this 20-year-old patient with heterotaxy syndrome {I,X,A(D)}, levocardia, common atrium, common ventricle, midline liver, bilateral superior venae cavae, left-sided inferior vena cava, totally anomalous pulmonary venous connections (TAPVC) to the base of the left superior vena cava, and severe pulmonary stenosis. Status post Blalock–Taussig shunt, TAPVC repair, bilateral bidirectional Glenn procedures with shunt takedown, and lateral tunnel Fontan procedure. This previously well patient presented with a one-year history of fatigue, chest pain, and palpitations.

transplantation may be the only surgical option, and results have been encouraging with reported 5-year survival that favorably compares with results of palliative procedures [114].

Videos

To access the videos for this chapter, please go to www.lai-echo.com.

Video 29.1 Subxiphoid long-axis sweep of situs inversus totalis {I,L,I} with a small membranous ventricular septal defect (arrow).

Video 29.2 Right parasternal long- and short-axis views of situs inversus totalis {I,L,I} and a small membranous ventricular septal defect with left-to-right flow by color flow mapping.

Video 29.3 LJRAA in the setting of double-outlet right ventricle {S,D,A}, critical tricuspid stenosis, RV hypoplasia, and severe subvalvar and valvar pulmonary stenosis.

Video 29.4 LJRAA in the setting of transposition of the great arteries {S,D,D}, small-to-moderate membranous ventricular septal defect, and small secundum atrial septal defect.

Video 29.5 Isolated ventricular inversion {S,L,S}. Transposition physiology is present due to atrioventricular discordance and ventriculo-arterial concordance. This infant presented shortly after birth with profound cyanosis.

Video 29.6 Isolated ventricular inversion {S,L,S} short-axis sweep.

Video 29.7 Anatomically corrected malposition apical 4-chamber and parasternal short-axis clips. Dextrocardia with anatomically corrected malposition of the great arteries {S,L,D}, atrioventricular discordance, ventricular septal defect, and straddling left-sided tricuspid valve, s/p main pulmonary artery band. There is bilateral conus. The rightward and anterior aorta is committed to the right-sided LV, and the leftward and posterior pulmonary artery is committed to the left-sided RV.

Video 29.8 Heterotaxy syndrome with cardiovascular findings most consistent with asplenia. Asplenia syndrome with double-outlet right ventricle {A,L,L} in the setting of levocardia and abdominal visceral situs ambiguus.

Video 29.9 Heterotaxy syndrome with cardiovascular findings most consistent with polysplenia. Polysplenia syndrome with common atrium and partial atrioventricular canal {A,D,S} in the setting of mesocardia and abdominal visceral situs ambiguus. There is second-degree heart block with 2:1 atrioventricular conduction and ventricular rates of 50–55 bpm.

Video 29.10 Fetal heterotaxy syndrome with total anomalous pulmonary venous connections (TAPVC). Fetal echocardiogram at 26 weeks' gestation. The individual pulmonary veins form a confluence behind the left atrium and drain via a vertical vein to the left superior vena cava. In addition to TAPVC, this fetus was diagnosed with levocardia with abdominal visceral situs inversus, tricuspid atresia (segmental set {I,D,D}), large conoventricular septal defect, pulmonary atresia, hypoplastic RV (HRV), and systemic venous anomalies (left-sided intact inferior vena cava and bilateral superior venae cavae).

Video 29.11 Fetal obstructed total anomalous pulmonary venous connection. Fetal echocardiogram at 22 weeks' gestation. Asplenia versus single right-sided spleen with double-outlet right ventricle {I,D,D}, complete common atrioventricular canal, and pulmonary stenosis. The pulmonary veins drain to the right superior vena cava–right atrial junction via an obstructed oblique vein. Despite the fact that the IVC is intact, there is a prominent azygos arch draining into the left superior vena cava.

References

1 Stanger P, Rudolph AM, Edwards JE. Cardiac malpositions. An overview based on study of sixty-five necropsy specimens. *Circulation* 1977;**56**:159–172.

2 Van Praagh S, O'Sullivan J, Brili S, Van Praagh R. Juxtaposition of the morphologically right atrial appendage in solitus and inversus atria: a study of 35 postmortem cases. *Am Heart J* 1996;**132**:382–390.

3 Van Praagh S, O'Sullivan J, Brili S, Van Praagh R. Juxtaposition of the morphologically left atrial appendage in solitus and inversus atria: a study of 18 postmortem cases. *Am Heart J* 1996;**132**:391–402.

4 Van Praagh R, Van Praagh S. Isolated ventricular inversion. A consideration of the morphogenesis, definition and diagnosis of nontransposed and transposed great arteries. *Am J Cardiol* 1966;**17**:395–406.

5 Cavalle-Garrido T, Bernasconi A, Perrin D, Anderson RH. Hearts with concordant ventriculoarterial connections but parallel arterial trunks. *Heart* 2007;**93**:100–106.

6 Van Praagh R, Durnin RE, Jockin H, et al. Anatomically corrected malposition of the great arteries {S, D, L}. *Circulation* 1975;**51**:20–31.

7 Jacobs JP, Anderson RH, Weinberg PM, et al. The nomenclature, definition and classification of cardiac structures in the setting of heterotaxy. *Cardiol Young* 2007;**17**:1–28.

8 Perloff JK. The cardiac malpositions. *Am J Cardiol* 2011;**108**:1352–1362.

9 Huhta JC, Hagler DJ, Seward JB, et al. Two-dimensional echocardiographic assessment of dextrocardia: a segmental approach. *Am J Cardiol* 1982;**50**:1351–1360.

10 Frescura C, Thiene G. Juxtaposition of the atrial appendages. *Cardiovasc Pathol* 2012;**21**:169–179.

11 Espino-Vela J, de la Cruz MV, Munoz-Castellanos L, et al. Ventricular inversion without transposition of the great vessels in situs inversus. *Br Heart J* 1970;**32**:292–303.

12 McElhinney DB, Reddy VM, Silverman NH, Hanley FL. Intraatrial baffle repair of isolated ventricular inversion with left atrial isomerism. *Ann Thorac Surg* 1996;**62**:1529–1532.

13 Park SC, Siewers RD, Neches WH, et al. Ventricular inversion with normal ventriculoarterial connection and left atrial isomerism: correction by the Mustard operation. *J Am Coll Cardiol* 1984;**4**:136–140.

14 Van Praagh R, Perez Trevino C, Lopez Cuellar M, et al. Transposition of the great arteries with posterior aorta, anterior pulmonary artery, subpulmonary conus and fibrous continuity between aortic and atrioventricular valves. *Am J Cardiol* 1971;**28**:621–631.

15 Loya YS, Desai AG, Sharma S. "Anatomically corrected malposition": a rare case with bilateral absence of a complete subarterial muscular infundibulum. *Int J Cardiol* 1991;**30**:131–134.

16 Bernasconi A, Azancot A, Simpson JM, et al. Fetal dextrocardia: diagnosis and outcome in two tertiary centres. *Heart* 2005;**91**:1590–1594.

17 Walmsley R, Hishitani T, Sandor GGS, et al. Diagnosis and outcome of dextrocardia diagnosed in the fetus. *Am J Cardiol* 2004;**94**:141–143.

18 Campbell M, Deuchar DC. Dextrocardia and isolated laevocardia. II. Situs inversus and isolated dextrocardia. *Br Heart J* 1966;**28**:472–487.

19 Splitt MP, Burn J, Goodship J. Defects in determination of left-right asymmetry. *J Med Genet* 1996;**33**:498–503.

20 Campbell M, Deuchar DC. Dextrocardia and isolated laevocardia. I. Isolated laevocardia. *Br Heart J* 1965;**27**:69–82.

21 Zhang YQ, Yu ZQ, Zhong SW, et al. Echocardiographic assessment of juxtaposition of the right atrial appendage in children with congenital heart disease. *Echocardiogr* 2010;**27**:878–884.

22 Lai WW, Ravishankar C, Gross RP, et al. Juxtaposition of the atrial appendages: a clinical series of 22 patients. *Pediatr Cardiol* 2001;**22**:121–127.

23 Sharma S, Devine W, Anderson RH, Zuberbuhler JR. The determination of atrial arrangement by examination of the appendage morphology in 1842 heart specimens. *Br Heart J* 1988;**60**:227–231.

24 Kathiriya IS, Srivastava D. Left-right asymmetry and cardiac looping: implications for cardiac development and congenital heart disease. *Am J Med Genet* 2000;**97**:271–279.

25 Zakheim R, Mattioli L, Vaseenon T, Edwards W. Anatomically corrected malposition of the great arteries (S,L,D). *Chest* 1976;**69**:101–104.

26 Merklin RJ, Varano NR. Situs inversus and cardiac defects. A study of 111 cases of reversed asymmetry. *J Thorac Cardiovasc Surg* 1963;**45**:334–342.

27 Turchin A, Radentz SS, Burke A. Situs inversus totalis and single coronary ostium: a coincidence or a pattern? *Cardiovasc Pathol* 2000;**9**:127–129.

28 Oppido G, Napoleone CP, Martano S, Gargiulo G. Hypoplastic left heart syndrome in situs inversus totalis. *Eur J Cardiothorac Surg* 2004;**26**:1052–1054.

29 Gutgesell HP. Cardiac malposition and heterotaxy. In: Garson A, Bricker JT, Fisher DJ, Neish SR (eds.) *The Science and Practice of Pediatric Cardiology*, 2nd edn. Baltimore, MD: Williams and Wilkins, 1998, pp. 1539–1561.

30 Melhuish BP, Van Praagh R. Juxtaposition of the atrial appendages: a sign of severe cyanotic congenital heart disease. *Br Heart J* 1968;**30**:269–284.

31 Chin AJ, Bierman FZ, Williams RG, et al. Two-dimensional echocardiographic appearance of complete left-sided juxtaposition of the atrial appendages. *Am J Cardiol* 1983;**52**:346–348.

32 Van Praagh R, Weinberg PM, Smith SD, et al. Malpositions of the heart. In: Adams FH, Emmanouilides GC, Riemenschneider TA (eds.) *Moss' Heart Disease in Infants, Children, and Adolescents*, 4th edn. Baltimore, MD: Williams and Wilkins, 1989, pp. 530–580.

33 Pasquini L, Sanders SP, Parness I, et al. Echocardiographic and anatomic findings in atrioventricular discordance with ventriculoarterial concordance. *Am J Cardiol* 1988;**62**:1256–1262.

34 Quero-Jimenez M, Raposo-Sonnenfeld I. Isolated ventricular inversion with situs solitus. *Br Heart J* 1975;**37**:293–304.

35 Oku H, Shirotani H, Yokoyama T, et al. Anatomically corrected malposition of the great arteries–case reports and a review. *Jpn Circ J* 1982;**46**:583–594.

36 Bernasconi A, Cavalle-Garrido T, Perrin DG, Anderson RH. What is anatomically corrected malposition? *Cardiol Young* 2007;**17**:26–34.

37 Rice MJ, Seward JB, Hagler DJ, et al. Left juxtaposed atrial appendages: diagnostic two-dimensional echocardiographic features. *J Am Coll Cardiol* 1983;**1**:1330–1336.

38 Stumper O, Rijlaarsdam M, Vargas-Barron J, et al. The assessment of juxtaposed atrial appendages by transesophageal echocardiography. *Int J Cardiol* 1990;**29**:365–371.

39 Snider AR, Enderlein MA, Teitel DF, et al. Isolated ventricular inversion: two-dimensional echocardiographic findings and a review of the literature. *Pediatr Cardiol* 1984;**5**:27–33.

40 Abdullah MM, Lacro RV, Smallhorn J, et al. Fetal cardiac dextroposition in the absence of intrathoracic mass: sign of significant right lung hypoplasia. *J Ultrasound Med* 2000;**19**:669–676.

41 Abdullah M, Yoo SJ, Lee YH, et al. Diagnosis of left juxtaposition of the atrial appendages in the fetus. *Cardiol Young* 2000;**10**:220–224.

42 Williams IA, Sharma J, Kleinman CS. Discordant anatomically corrected malposition of the great vessels and Ebstein's malformation: fetal and neonatal findings. *Ultrasound Obstet Gynecol* 2006;**28**:103–105.

43 Wood AE, Freedom RM, Williams WG, Trusler GA. The Mustard procedure in transposition of the great arteries associated with juxtaposition of the atrial appendages with and without dextrocardia. *J Thorac Cardiovasc Surg* 1983;**85**:451–456.

44 Baudet EM, Hafez A, Choussat A, Roques X. Isolated ventricular inversion with situs solitus: successful surgical repair. *Ann Thorac Surg* 1986;**41**:91–94.

45 Peeters H, Devriendt K. Human laterality disorders. *Eur J Med Genet* 2006;**49**:349–362.

46 Van Praagh S, Kreutzer J, Alday L, Van Praagh R. Systemic and pulmonary venous connections in visceral heterotaxy, with emphasis on the diagnosis of the atrial situs: a study of 109 postmortem cases. In: Clark EB, Takao A (eds.) *Developmental Cardiology: Morphogenesis and Function*. Mount Kisko, NY: Futura Publishing Co., 1990, pp. 671–727.

47 Fyler DC, Buckley LP, Hellenbrand WE, Cohn HE. Report of the New England Regional Infant Cardiac Program. *Pediatrics* 1980;**65**:375–461.

48 Gilljam T, McCrindle BW, Smallhorn JF, et al. Outcomes of left atrial isomerism over a 28-year period at a single institution. *J Am Coll Cardiol* 2000;**36**:908–916.

49 Ferencz C, Rubin JD, McCarter RJ, et al. Congenital heart disease: prevalence at live birth. The Baltimore-Washington Infant Study. *Am J Epidemiol* 1985;**121**:31–36.

50 Lin AE, Ticho BS, Houde K, et al. Heterotaxy: associated conditions and hospital-based prevalence in newborns. *Genet Med* 2000;**2**:157–172.

51 Lim JS, McCrindle BW, Smallhorn JF, et al. Clinical features, management, and outcome of children with fetal and postnatal diagnoses of isomerism syndromes. *Circulation* 2005;**112**:2454–2461.

52 Ruscazio M, Van Praagh S, Marass AR, et al. Interrupted inferior vena cava in asplenia syndrome and a review of the hereditary patterns of visceral situs abnormalities. *Am J Cardiol* 1998;**81**: 111–116.

53 Chen SC, Monteleone PL. Familial splenic anomaly syndrome. *J Pediatr* 1977;**91**:160–161.

54 Katcher AL. Familial asplenia, other malformations, and sudden death. *Pediatrics* 1980;**65**:633–635.

55 Chin AJ, Saint-Jeannet JP, Lo CW. How insights from cardiovascular developmental biology have impacted the care of infants and children with congenital heart disease. *Mech Dev* 2012;**129**:75–97.

56 Colbert MC. Retinoids and cardiovascular developmental defects. *Cardiovasc Toxicol* 2002;**2**:25–39.

57 Kennedy MP, Omran H, Leigh MW, et al. Congenital heart disease and other heterotaxic defects in a large cohort of patients with primary ciliary dyskinesia. *Circulation* 2007;**115**:2814–2821.

58 Bisgrove BW, Yost HJ. The roles of cilia in developmental disorders and disease. *Development* 2006;**133**:4131–4143.

59 Belmont JW, Mohapatra B, Towbin JA, Ware SM. Molecular genetics of heterotaxy syndromes. *Curr Opin Cardiol* 2004;**19**: 216–220.

60 Van Praagh S, Carrera ME, Sanders S, et al. Partial or total direct pulmonary venous drainage to right atrium due to malposition of septum primum. Anatomic and echocardiographic findings and surgical treatment: a study based on 36 cases. *Chest* 1995;**107**:1488–1498.

61 Phoon CK, Neill CA. Asplenia syndrome: insight into embryology through an analysis of cardiac and extracardiac anomalies. *Am J Cardiol* 1994;**73**:581–587.

62 Sapire DW, Ho SY, Anderson RH, Rigby ML. Diagnosis and significance of atrial isomerism. *Am J Cardiol* 1986;**58**:342–346.

63 Macartney FJ, Zuberbuhler JR, Anderson RH. Morphological considerations pertaining to recognition of atrial isomerism. *Consequences for sequential chamber localisation. Br Heart J* 1980;**44**:657–667.

64 Uemura H, Ho SY, Devine WA, et al. Atrial appendages and venoatrial connections in hearts from patients with visceral heterotaxy. *Ann Thorac Surg* 1995;**60**:561–569.

65 Anderson C, Devine WA, Anderson RH, et al. Abnormalities of the spleen in relation to congenital malformations of the heart: a survey of necropsy findings in children. *Br Heart J* 1990;**63**:122–128.

66 Heinemann MK, Hanley FL, Van Praagh S, et al. Total anomalous pulmonary venous drainage in newborns with visceral heterotaxy. *Ann Thorac Surg* 1994;**57**:88–91.

67 Rubino M, Van Praagh S, Kadoba K, et al. Systemic and pulmonary venous connections in visceral heterotaxy with asplenia. Diagnostic and surgical considerations based on seventy-two autopsied cases. *J Thorac Cardiovasc Surg* 1995;**110**:641–650.

68 Van Praagh S. Cardiac malpositions and the heterotaxy syndromes. In: Keany JF, Lock JE, Fyler DC (eds.) *Nadas' Pediatric Cardiology*, 2nd edn. Philadelphia, PA: Saunders Elsevier, 2006, pp. 675–695.

69 Uemura H, Ho SY, Anderson RH, Yagihara T. Ventricular morphology and coronary arterial anatomy in hearts with isomeric atrial appendages. *Ann Thorac Surg* 1999;**67**:1403–1411.

70 Smith A, Ho SY, Anderson RH, et al. The diverse cardiac morphology seen in hearts with isomerism of the atrial appendages with reference to the disposition of the specialized conduction system. *Cardiol Young* 2006;**16**:437–454.

71 Uemura H, Anderson RH, Ho SY, et al. Left ventricular structures in atrioventricular septal defect associated with isomerism of atrial appendages compared with similar features with usual atrial arrangement. *J Thorac Cardiovasc Surg* 1995;**110**:445–452.

72 Van Praagh S, Geva T, Friedberg DZ, et al. Aortic outflow obstruction in visceral heterotaxy: a study based on twenty postmortem cases. *Am Heart J* 1997;**133**:558–568.

73 Ramaswamy P, Lytrivi ID, Thanjan MT, et al. Frequency of aberrant subclavian artery, arch laterality, and associated intracardiac anomalies detected by echocardiography. *Am J Cardiol* 2008;**101**:677–682.

74 Papagiannis J, Kanter RJ, Vander Heide RS, et al. Isolated innominate artery in asplenia syndrome with aortic atresia: newly recognized cardiovascular complex. *Am Heart J* 1996;**131**: 1042–1044.

75 Formigari R, Vairo U, de Zorzi A, et al. Prevalence of bilateral patent ductus arteriosus in patients with pulmonic valve atresia and asplenia syndrome. *Am J Cardiol* 1992;**70**:1219–1220.

76 Hashmi A, Abu-Sulaiman R, McCrindle BW, et al. Management and outcome of right atrial isomerism: a 26-year experience. *J Am Coll Cardiol* 1998;**31**:1120–1126.

77 Ho SY, Fagg N, Anderson RH, et al. Disposition of the atrioventricular conduction tissues in the heart with isomerism of the atrial appendages: its relation to congenital complete heart block. *J Am Coll Cardiol* 1992;**20**:904–910.

78 Nagel BH, Williams H, Stewart L, et al. Splenic state in surviving patients with visceral heterotaxy. *Cardiol Young* 2005;**15**: 469–473.

79 Van Praagh R, Van Praagh S, Vlad P, Keith JD. Anatomic types of congenital dextrocardia. Diagnostic and embryologic implications. *Am J Cardiol* 1964;**13**:510–531.

80 Van Praagh R. The segmental approach to diagnosis of congenital heart disease. In: *Birth Defects: Original Article Series*, Vol. **8**. Baltimore, MD: Williams & Wilkins, 1972, pp. 4–23.

81 Anderson RH, Becker AE, Freedom RM, et al. Sequential segmental analysis of congenital heart disease. *Pediatr Cardiol* 1984;**5**:281–288.

82 Van Praagh R, Van Praagh S. Atrial isomerism in the heterotaxy syndromes with asplenia, or polysplenia, or normally formed spleen: an erroneous concept. *Am J Cardiol* 1990;**66**:1504–1506.

83 Huhta JC, Smallhorn JF, Macartney FJ. Two dimensional echocardiographic diagnosis of situs. *Br Heart J* 1982;**48**:97–108.

84 Huhta JC, Smallhorn JF, Macartney FJ, et al. Cross-sectional echocardiographic diagnosis of systemic venous return. *Br Heart J* 1982;**48**:388–403.

85 Smallhorn JF, Freedom RM, Olley PM. Pulsed Doppler echocardiographic assessment of extraparenchymal pulmonary vein flow. *J Am Coll Cardiol* 1987;**9**:573–579.

86 Smallhorn JF, Pauperio H, Benson L, et al. Pulsed Doppler assessment of pulmonary vein obstruction. *Am Heart J* 1985;**110**:483–486.

87 Stumper OF, Sreeram N, Elzenga NJ, Sutherland GR. Diagnosis of atrial situs by transesophageal echocardiography. *J Am Coll Cardiol* 1990;**16**:442–446.

88 Stumper O, Vargas-Barron J, Rijlaarsdam M, et al. Assessment of anomalous systemic and pulmonary venous connections by transesophageal echocardiography in infants and children. *Br Heart J* 1991;**66**:411–418.

89 Geva T, Vick W III, Wendt RE, Rokey R. Role of spin echo and cine magnetic resonance imaging in presurgical planning of heterotaxy syndrome. Comparison with echocardiography and catheterization. *Circulation* 1994;**90**:348–356.

90 Niwa K, Uchishiba M, Aotsuka H, et al. Magnetic resonance imaging of heterotaxia in infants. *J Am Coll Cardiol* 1994;**23**:177–183.

91 Taketazu M, Lougheed J, Yoo S-J, et al. Spectrum of cardiovascular disease, accuracy of diagnosis, and outcome in fetal heterotaxy syndrome. *Am J Cardiol* 2006;**97**:720–724.

92 Jaeggi ET, Hornberger LK, Smallhorn JF, Fouron JC. Prenatal diagnosis of complete atrioventricular block associated with structural heart disease: combined experience of two tertiary care centers and review of the literature. *Ultrasound Obstet Gynecol* 2005;**26**:16–21.

93 Schmidt KG, Ulmer HE, Silverman NH, et al. Perinatal outcome of fetal complete atrioventricular block: a multicenter experience. *J Am Coll Cardiol* 1991;**91**:1360–1366.

94 Friedberg MK, Ursell PL, Silverman NH. Isomerism of the left atrial appendage associated with ventricular noncompaction. *Am J Cardiol* 2005;**96**:985–990.

95 Ozkutlu S, Ayabakan C, Celiker A, Elshershari H. Noncompaction of ventricular myocardium: a study of twelve patients. *J Am Soc Echocardiogr* 2002;**15**:1523–1528.

96 Feldt RH, Rahimtoola SH, Davis GD, et al. Anomalous ventricular myocardial patterns in a child with complex congenital heart disease. *Am J Cardiol* 1969;**23**:732–734.

97 Lin JH, Chang CI, Wang JK, et al. Intrauterine diagnosis of heterotaxy syndrome. *Am Heart J* 2002;**143**:1002–1008.

98 Berg C, Geipel A, Kohl T, et al. Fetal echocardiographic evaluation of atrial morphology and the prediction of laterality in cases of heterotaxy syndromes. *Ultrasound Obstet Gynecol* 2005;**26**:538–545.

99 Yeager SB, Parness IA, Spevak PJ, et al. Prenatal echocardiographic diagnosis of pulmonary and systemic venous anomalies. *Am Heart J* 1984;**128**:397–405.

100 Freedom RM, Jaeggi ET, Lim JS, Anderson RH. Hearts with isomerism of the right atrial appendages – one of the worst forms of disease in 2005. *Cardiol Young* 2005;**15**:554–567.

101 Hirooka K, Yagihara T, Kishimoto H, et al. Biventricular repair in cardiac isomerism. Report of seventeen cases. *J Thorac Cardiovasc Surg* 1995;**109**:530–535.

102 Yun T-J, Al-Radi OO, Adatia I, et al. Contemporary management of right atrial isomerism: effect of evolving therapeutic strategies. *J Thorac Cardiovasc Surg* 2006;**131**:1108–1113.

103 Koh M, Yagihara T, Uemura H, et al. Biventricular repair for right atrial isomerism. *Ann Thorac Surg* 2006;**81**:1808–1816.

104 Kawashima Y, Kitamura S, Matsuda H, et al. Total cavopulmonary shunt operation in complex cardiac anomalies. A new operation. *J Thorac Cardiovasc Surg* 1984;**7**:74–81.

105 Vargas FJ, Mayer JE, Jonas RA, Castaneda AR. Anomalous systemic and pulmonary venous connections in conjunction with atriopulmonary anastomosis (Fontan-Kreutzer). Technical considerations. *J Thorac Cardiovasc Surg* 1987;**93**:523–532.

106 Sadiq M, Stumper O, De Giovanni JV, et al. Management and outcome of infants and children with right atrial isomerism. *Heart* 1996;**75**:314–319.

107 Cheung YF, Cheng VYW, Chau AKT, et al. Outcome of infants with right atrial isomerism: is prognosis better with normal pulmonary venous drainage? *Heart* 2002;**87**:146–152.

108 Jenkins KJ, Sanders SP, Orav EJ, et al. Individual pulmonary vein size and survival in infants with totally anomalous pulmonary venous connection. *J Am Coll Cardiol* 1993;**22**:201–206.

109 Freedom RM, Olley PM, Coceani F, Rowe RD. The prostaglandin challenge. Test to unmask obstructed total anomalous pulmonary venous connections in asplenia syndrome. *Br Heart J* 1978;**40**:91–94.

110 Zoghbi WA, Enriquez-Sarano M, Foster E, et al. American Society of Echocardiography. Recommendations for evaluation of the severity of native valvular regurgitation with two-dimensional and Doppler echocardiography. *J Am Soc Echocardiog* 2003;**16**:777–802.

111 Bassareo PP, Tumbarello R, Piras A, Mercuro G. Evaluation of regional myocardial function by Doppler tissue imaging in univentricular heart after successful Fontan repair. *Echocardiography* 2010;**27**:702–708.

112 Olivier M, O'Leary PW, Pankratz, VS, et al. Serial Doppler assessment of diastolic function after the Fontan operation. *J Am Soc Echocardiogr* 2003;**16**:1136–1143.

113 Serraf A, Bensari N, Houyel L, et al. Surgical management of congenital heart defects associated with heterotaxy syndrome. *Eur J Cardiothorac Surg* 2010;**38**:721–727.

114 Larsen RL, Eguchi JH, Mulla NF, et al. Usefulness of cardiac transplantation in children with visceral heterotaxy (asplenic and polysplenic syndromes and single right-sided spleen with levocardia) and comparison of results with cardiac transplantation in children with dilated cardiomyopathy. *Am J Cardiol* 2002;**89**:1275–1279.

115 Rose V, Izukawa T, Moes CAF. Syndromes of asplenia and polysplenia. A review of cardiac and non-cardiac malformations in 60 cases with special reference to diagnosis and prognosis. *Br Heart J* 1975;**37**:840–852.

116 Uemura H, Ho SY, Devine WA, Anderson RH. Analysis of visceral heterotaxy according to splenic status, appendage morphology, or both. *Am J Cardiol* 1995;**76**:846–849.

117 Peoples WM, Moller JH, Edwards JE. Polysplenia: review of 146 cases. *Pediatr Cardiol* 1983;**4**:129–137.

CHAPTER 30

Congenital Anomalies of the Coronary Arteries

J. René Herlong[1] and Piers C. A. Barker[2]
[1]Sanger Heart and Vascular Institute, Levine Children's Hospital, Charlotte, NC, USA
[2]Duke University School of Medicine, Durham, NC, USA

Definition

The term *coronary* derives from the Latin root *coronarius*, which means crown. Indeed, the coronary arteries sit on the heart as a crown and they are the "crowning subject" of adult cardiology due to the prevalence of acquired coronary artery disease. Although less of a preeminent subject in pediatric cardiology, coronary artery anomalies, with and without concomitant structural congenital heart disease, are an important topic for the pediatric cardiologist. This chapter reviews the echocardiography of congenital coronary artery anomalies of importance to the pediatric cardiologist. Material pertinent to all congenital coronary artery anomalies is presented first, followed by material particular to each important anomaly.

Developmental considerations

Before the development of the coronary arteries, the loosely packed myocardium of the embryonic heart is nourished from the cavities by sinusoids. As the myocardium becomes more compact, veins and arteries develop within the epicardial layer, with the intramyocardial circulation developing within the myocardium itself. The key feature in development, however, is the growth of the arterial channels into two of the developing aortic sinuses. It used to be thought that endothelial buds sprouted from the base of the developing arterial trunks to make contact with the epicardial network, itself derived from the proepicardial organ [1–5]. It was the elegant study of Bogers et al. [6], however, which showed that the arterial sprouts grow into the developing aortic sinuses rather than grow out from the arterial roots. This concept of ingrowth provides a much more rational basis for understanding the myriad patterns taken by anomalous coronary arteries. More recently, defects in *Tbx1* gene expression and development of the second heart field have been proposed as important to coronary artery patterning [7]. The development of the definitive coronary circulation begins at about 32 days' gestation and is complete by about 45 days' gestation.

Normal coronary anatomy

There are normally two major coronary arteries, which originate from the right and left aortic sinuses of Valsalva. These sinuses are small outpouchings of the aorta between the sinotubular junction and the aortic valve leaflets. There are normally three such sinuses; the third, or posterior, sinus of Valsalva is usually devoid of a coronary artery orifice. It is therefore called the noncoronary sinus of Valsalva.

The left coronary artery

The left main coronary artery arises from the left sinus of Valsalva and courses only a short distance (<4 cm in the adult) before dividing into the left circumflex and left anterior descending coronary arteries (Figure 30.1). The left circumflex coronary artery varies considerably in size depending on whether the posterior descending coronary artery is a branch of the right coronary artery (right-dominant coronary system) or a branch of the circumflex coronary artery (left-dominant coronary system). If the posterior descending coronary artery originates from the circumflex coronary artery (this occurs in about 10% of patients), the circumflex coronary artery is large. In some patients with a dominant right coronary artery, the circumflex coronary artery may be fairly small. The circumflex coronary artery travels under the left atrial appendage and along the left atrioventricular groove. In 50% of cases, the sinus node artery arises from the left circumflex coronary artery. The sinus node artery courses under the left atrial appendage, penetrates the interatrial septum, encircles the base of the superior vena cava, and supplies the sinus node. When the sinus node artery is not a branch of the left circumflex coronary artery, it is a branch of the right coronary artery. Kugel's artery may arise from the left circumflex coronary artery (alternatively, it may arise from

Echocardiography in Pediatric and Congenital Heart Disease: From Fetus to Adult, Second Edition. Edited by Wyman W. Lai, Luc L. Mertens, Meryl S. Cohen and Tal Geva.
© 2016 John Wiley & Sons, Ltd. Published 2016 by John Wiley & Sons, Ltd.
Companion website: www.lai-echo.com

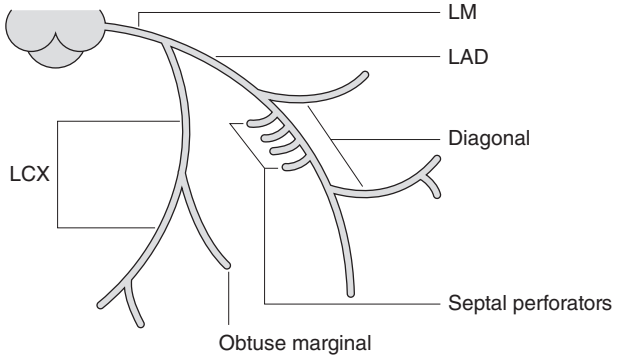


Figure 30.1 The normal left coronary artery system. LCX, left circumflex; LM, left main coronary artery; LAD, left anterior descending coronary arteries.

the right or left main coronary artery) and courses through the interatrial septum, anastomosing with the artery to the atrioventricular node. Marginal branches arise from the left circumflex coronary artery and supply areas of the lateral wall of the left ventricle. These are called obtuse marginal branches. The left atrial circumflex artery may arise from the left circumflex coronary artery and supply the left posterior atrial wall. Occasionally, the sinus node artery can arise from the left atrial circumflex coronary artery.

The left anterior descending coronary artery appears to be a direct continuation of the left main coronary artery rather than a branch of it. The left anterior descending coronary artery travels along the interventricular sulcus and may continue around the apex of the heart onto the posterior interventricular sulcus to anastomose with the posterior descending coronary artery. The left conus artery is the first branch of the left anterior descending coronary artery and may anastomose with the conal branch of the right coronary artery, forming the circle of Vieussens. Four to six septal branches of the left anterior descending coronary artery penetrate the ventricular septum and anastomose with posterior septal branches arising from the posterior descending coronary artery. The left anterior descending coronary artery gives rise to diagonal branches that supply the anterior surface of the right and left ventricles and the right ventricular infundibulum.

The right coronary artery

The right coronary artery arises from the right aortic sinus of Valsalva and courses behind the pulmonary artery beneath the right atrial appendage and along the right atrioventricular groove (Figure 30.2). At the acute margin of the heart, it turns posteriorly and caudally over the diaphragmatic surface of the heart. The branches of the right coronary artery include the right conal branch, the sinus node artery, an atrial branch, right ventricular muscle branches (acute marginal branches), posterior descending coronary artery, atrioventricular node artery, and septal branches. The right conus artery is the first branch of the right coronary artery in about 50% of cases; in the others, it arises

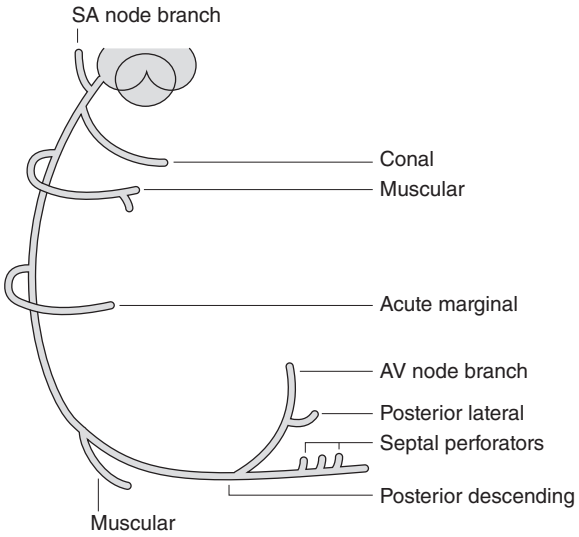


Figure 30.2 The normal right coronary artery system. SA, sinoatrial; AV, atrioventricular.

directly from the right aortic sinus of Valsalva. The sinus node artery arises from the right coronary artery in 50% of cases and from the left circumflex artery in the remainder. The right ventricular free wall is supplied by several branches of the right coronary artery. The largest of these branches is the acute marginal branch of the right coronary artery.

Around 90% of people have a dominant right coronary artery system, that is, the posterior descending coronary artery is a branch of the right coronary artery. In the remainder, the posterior descending coronary artery originates from the left coronary artery. The term "dominant right coronary artery system" refers only to the origin of the posterior descending coronary artery, not to the coronary artery that supplies most of the myocardium. Indeed, except in unusual circumstances, the majority of the myocardium is supplied by the left coronary artery regardless of the "dominance" of the coronary artery system.

The posterior descending coronary artery supplies the lower portion of the ventricular septum. The septal branches of the posterior descending coronary artery anastomose with the septal branches of the left anterior descending coronary artery. Muscular branches supplying the diaphragmatic portions of the right and left ventricles also arise from the posterior descending coronary artery. The artery to the atrioventricular node originates from the posterior descending coronary artery at or near the crux of the heart and travels cephalad to reach the atrioventricular node.

Physiology

The purpose of the coronary arteries is to provide a flow of oxygenated blood to the almost exclusively aerobic myocardium and a delicate balance is maintained between myocardial

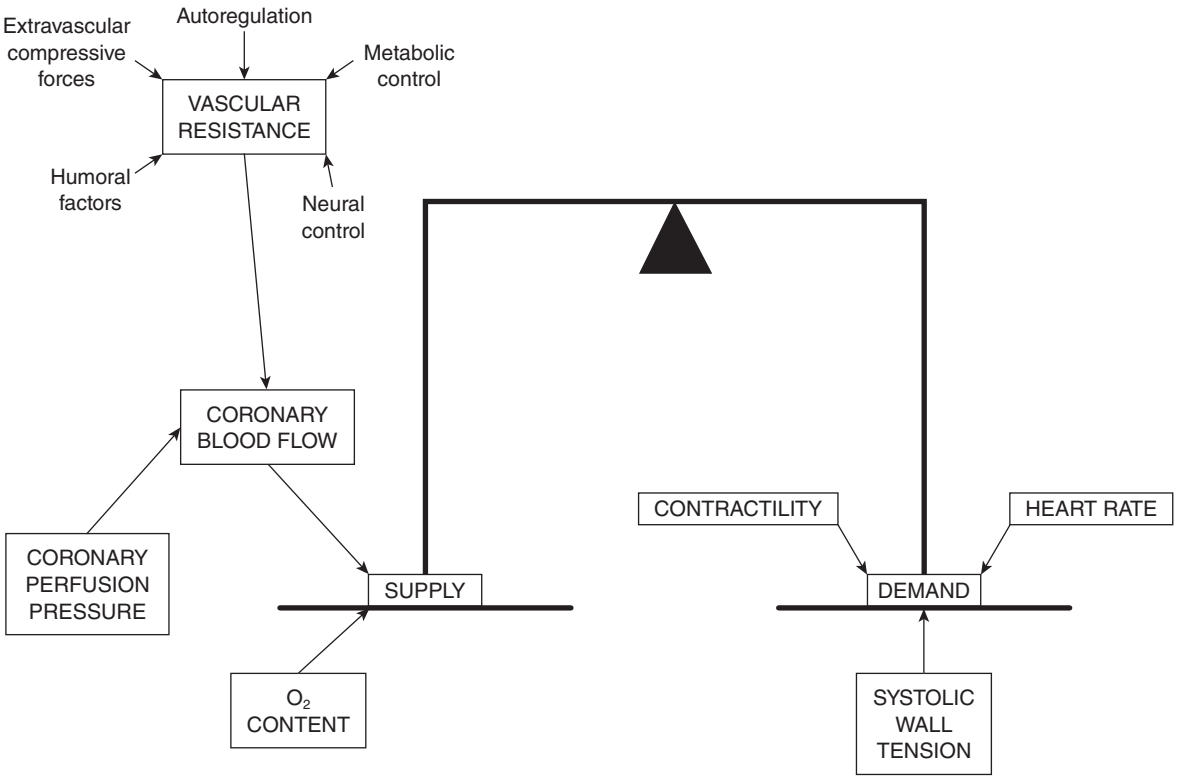


Figure 30.3 The delicate balance between myocardial oxygen supply and demand and the factors that influence this balance. Source: Adapted from Ardehali A, Ports TA. Myocardial oxygen supply and demand. *Chest* 1990;**98**:699–705, with permission from The American College of Chest Physicians.

oxygen supply and demand (Figure 30.3). Upsetting this balance produces myocardial ischemia and thus impaired ventricular contraction. The three primary determinants of myocardial oxygen demand are systolic wall tension, contractility, and heart rate. Pressure work increases myocardial oxygen consumption to a greater extent than does volume work. Myocardial oxygen supply is determined by the oxygen content of the blood and the coronary blood flow. Coronary blood flow is in turn determined by coronary perfusion pressure and by coronary vascular resistance.

Coronary perfusion pressure equals coronary artery pressure minus downstream pressure and is different for different regions of the myocardium. In the absence of a fixed or dynamic obstruction in the coronary circulation, coronary artery pressure equals aortic pressure. Distal to such an obstruction, coronary artery pressure and coronary perfusion pressure are reduced. Coronary vascular resistance is influenced by metabolic, humoral, and neural factors and also by autoregulation and by extravascular compressive forces.

The importance of extravascular compressive forces as determinants of vascular resistance is unique to the myocardium. Myocardial wall tension is so great in the left ventricle during systole that sufficient extrinsic compression is placed on the coronary arteries to cause coronary vascular resistance to approach infinity and coronary blood flow to approach zero. Thus, the vast preponderance of coronary blood flow to the left ventricle occurs during diastole. Compressive forces exerted by the right ventricle are ordinarily far less than those of the left ventricle; therefore, coronary blood flow to the right ventricle is not interrupted during ventricular systole. However, such flow interruption may occur with right ventricular hypertension [8].

Normally, coronary blood flow far exceeds the metabolic demands of the myocardium; there is therefore a large safety margin to protect the heart from ischemia. This concept has been expressed as coronary flow reserve, which is the difference between resting and maximal coronary blood flow at any given perfusion pressure. When coronary flow reserve is absent, ischemia ensues. Coronary flow reserve may be decreased if resting coronary blood flow increases or if maximal coronary blood flow decreases. Causes of an increase in resting coronary blood flow include exercise, anemia, hypoxemia, tachycardia, thyrotoxicosis, and ventricular hypertrophy. Causes of a decrease in maximal coronary blood flow include disease or occlusion of the large or small coronary arteries, an increase in left ventricular pressure without a corresponding increase in perfusion pressure, tachycardia, and polycythemia. All of these factors reduce coronary flow reserve and thereby increase the potential for myocardial ischemia [9].

The subendocardium is particularly susceptible to ischemia. This is due to this region's limited reserve for vasodilation, increased extrinsic compression from the higher wall stress to which it is subjected, and its resultant higher metabolic

demands. This region is therefore often the first to manifest ischemic changes.

Echocardiographic features pertinent to all anomalies

Goals of the examination and transthoracic imaging

Two-dimensional echocardiography with color Doppler has become an important tool in the diagnosis and functional evaluation of infants and children with suspected anomalies of the coronary arteries. In experienced hands, both transthoracic and transesophageal echocardiography can reliably image the proximal coronary arteries. Generally, coronary artery branches cannot be delineated well by echocardiography. Although transesophageal echocardiographic imaging of the coronaries is seldom performed as the initial diagnostic study in the pediatric population, it is important to include a careful assessment of the coronary artery anatomy as part of any complete intraoperative study, given the association of coronary anomalies with different congenital heart defects, the dramatic consequences that a new coronary diagnosis can have on the operative plan, and the potential to avoid serious morbidity to the patient [10–12].

The goals of the examination for both transthoracic and transesophageal imaging are as follows:

- Identify the origin of each major coronary artery (left anterior descending, circumflex and right).
- Identify the proximal course of each major coronary artery.
- Demonstrate direction of flow in each major coronary artery by color Doppler.
- Evaluate global and regional left ventricular function.
- Evaluate for mitral regurgitation.
- Identify associated defects.

Every echocardiographic examination should include evaluation of the origins and proximal courses of the coronary arteries [13]. Routine imaging of the coronary arteries in the course of an echocardiographic examination is important because coronary artery anomalies may be asymptomatic, they may be surgically important and prospectively identifying them may save lives. Decreasing the log compression of the instrument often allows more distinct identification of the coronary arteries. Most modern echocardiography machines have a factory preset that accomplishes this. The highest frequency probe that allows adequate penetration should be used. Often this will be a higher frequency probe than would typically be used for a particular view, as the coronary arteries are often in the near-field of the sector.

The proximal coronary arteries may be imaged best in the parasternal long- and short-axis views and from subcostal coronal images. The origins and proximal courses of the vessels may be reliably seen, hence abnormalities of branching may be appreciated. In the parasternal short-axis view at the base of the heart, both main coronary artery origins, often simultaneously, may be seen to arise from their respective sinuses of Valsalva (Figures 30.4 and 30.5). Clockwise rotation of the probe is often necessary for optimal imaging of the left coronary artery and either clockwise or counterclockwise rotation may be necessary for optimal imaging of the right coronary artery. These movements are very subtle.

One commonly performed practice that should be stringently avoided when imaging coronary arteries is that of obtaining still frames of the arterial origins and making diagnostic decisions based upon these still images. With the anomalous aortic origin of a coronary artery from the pulmonary trunk or the aorta, the proximal coronary artery often approaches the appropriate sinus of Valsalva very closely, and resolving the thin tissue between the coronary arterial and aortic lumens can be difficult or impossible in a still frame image. It is easy, therefore, to be falsely assured of a normal origin of the coronary artery when, in fact, the coronary artery arises anomalously from another location.

From the parasternal long-axis view, leftward angulation of the probe allows visualization of the bifurcation of the left coronary artery and also a long length of the left anterior descending coronary artery in its epicardial course down the interventricular septum (Figure 30.6). From the subcostal coronal (long-axis) view at the level of the aortic root, the proximal left and right coronary arteries may be visualized also (Figure 30.7).

The distal portions of the coronary arteries may also be visualized from several views. The distal right coronary artery may be seen in the posterior right atrioventricular groove from an apical 4-chamber view (Figure 30.8), whereas the distal circumflex coronary artery may be seen in the same view in the posterior left atrioventricular groove. The posterior descending coronary artery is often best seen from an inferiorly angled parasternal long-axis view (Figure 30.9).

In addition to the anatomic information discussed above, echocardiography may provide important functional information about the coronary arteries. The direction of flow in the coronary arteries may be demonstrated with color Doppler; this may provide pivotal information regarding anomalies of coronary artery origin from the pulmonary artery, as described later. Both systolic and diastolic function may be altered in certain forms of congenital coronary artery anomalies and these parameters may be readily evaluated with echocardiography. Finally, regional wall motion abnormalities may be appreciated and thereby point to a specific area of perfusion deficit. Newer modalities such as regional strain and dyssynchrony imaging may also prospectively identify an abnormal myocardial segment and be an important "clue" to further investigate coronary blood flow to that region [14].

Prenatal assessment

Rarely can the coronary arteries be seen well in fetal imaging. The exception would be congenital coronary artery anomalies that lead to significant dilation of the coronary arteries and/or lead to abnormal flow from the coronary arteries into a cardiac chamber or great vessel. These situations hold in cases of

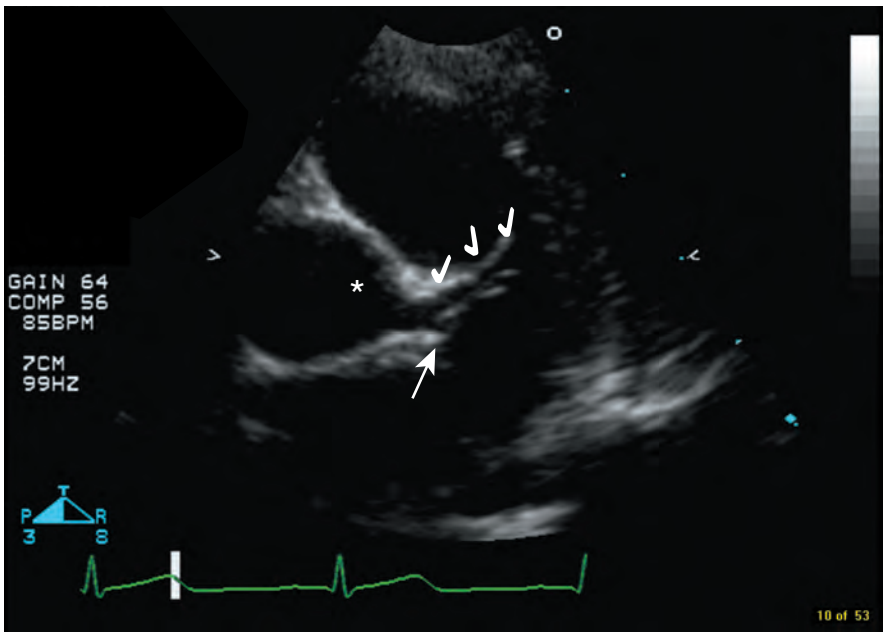


Figure 30.4 Parasternal short-axis image at the base of the heart. The left main coronary artery is seen arising from the aorta at the left sinus of Valsalva. The left anterior descending coronary artery (carets) and most proximal portion of the left circumflex coronary artery (arrow) are seen to arise from the left main coronary artery. The asterisk (∗) marks the position of the intercoronary commissure of the aortic valve.

coronary–cameral fistulae and these abnormalities have occasionally been noted on prenatal echocardiograms [15,16].

Imaging of the adult and alternative imaging techniques

Cardiac catheterization with aortic root angiography or selective coronary arteriography represents the gold standard in the diagnosis of many congenital coronary artery anomalies. It continues to have the highest spatial resolution (0.2 mm) of all imaging modalities, compared with multislice computed tomographic (CT) imaging (0.35 mm), cardiac magnetic resonance imaging (MRI) (varies by sequence), and echocardiography (variable depending on many factors) [17]. However, magnetic resonance coronary angiography and multislice CT imaging of the coronary arteries have become well-accepted noninvasive techniques for imaging coronary arteries in adults [18–20]. Magnetic resonance imaging has the advantage of providing additional information on cardiac function, differential coronary flow with adenosine stress testing, and presence of myocardial scar or infarction with delayed enhancement techniques. In contrast, cardiac CT angiography can provide a higher level of spatial resolution and an assessment of the presence of coronary

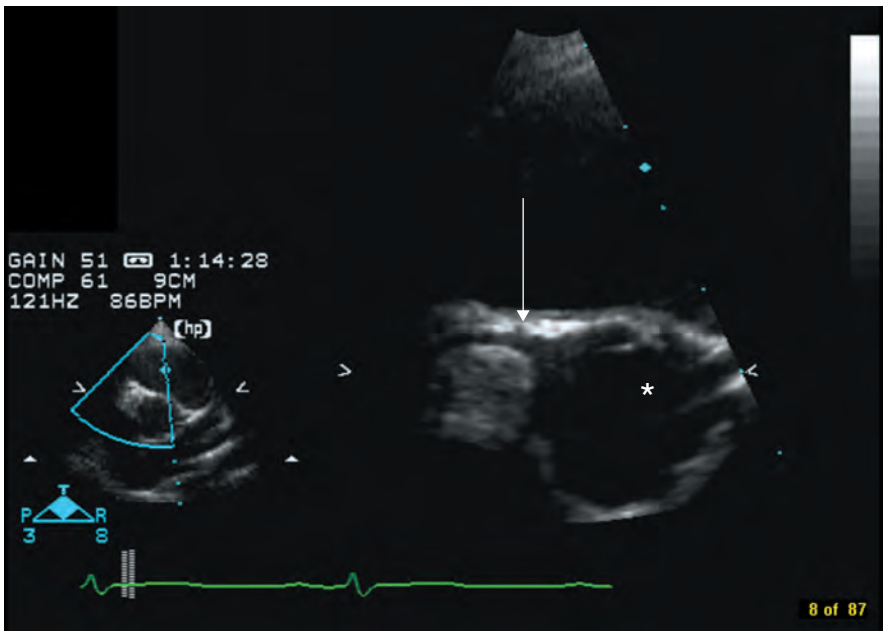


Figure 30.5 Parasternal short-axis image at the base of the heart. The proximal right coronary artery (arrow) is seen arising from the aorta at the right sinus of Valsalva. The asterisk (∗) marks the position of the intercoronary commissure of the aortic valve.

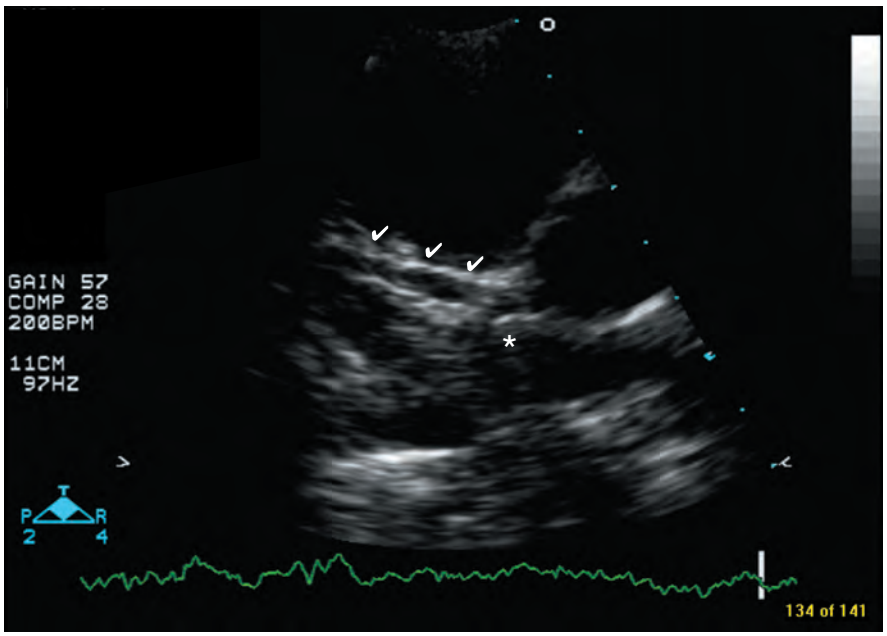


Figure 30.6 Parasternal long-axis image angled leftwardly and superiorly toward the right ventricular outflow tract. The left main coronary artery is seen to arise from the aorta and branch into left anterior descending (carets) and left circumflex (∗) coronary arteries.

calcium, while advances in scanner equipment and gating permit the use of progressively lower doses of ionizing radiation [17]. Both are rapidly expanding into the pediatric population [21–23], but their use remains limited owing to the requirement for a relatively motionless, cooperative patient with a slow heart rate for proper gating of the images. Ongoing work is therefore still needed for the younger pediatric population on scanning time, spatial and temporal resolution, and ionizing radiation dose reduction for these techniques to achieve their full potential usefulness.

Congenital coronary artery anomalies

A classification of congenital coronary artery anomalies is provided in Table 30.1. Many other classifications are available [24]. One of the more extensive of these has been proposed by the Society of Thoracic Surgeons and the Congenital Heart Surgeons' Society [25,26]. These anomalies are numerous. Some are minor and some are life threatening. Some are present in otherwise normal hearts and some are often associated with specific congenital heart lesions. Some are extremely rare, whereas

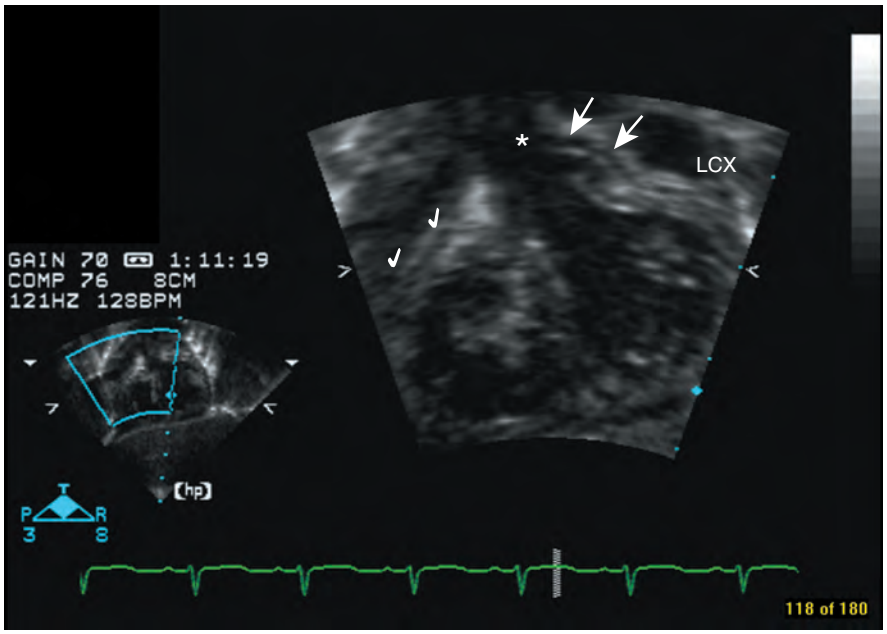


Figure 30.7 Subcostal long-axis image with some counterclockwise rotation at the level of the left ventricular outflow showing a high origin (∗) (just above the sinotubular junction) of the left main coronary artery (arrows) and a segment of the proximal right coronary artery in the anterior right atrioventricular groove (carets). The left circumflex coronary artery (LCx) is seen as a continuation of the left main coronary artery in the left atrioventricular groove.

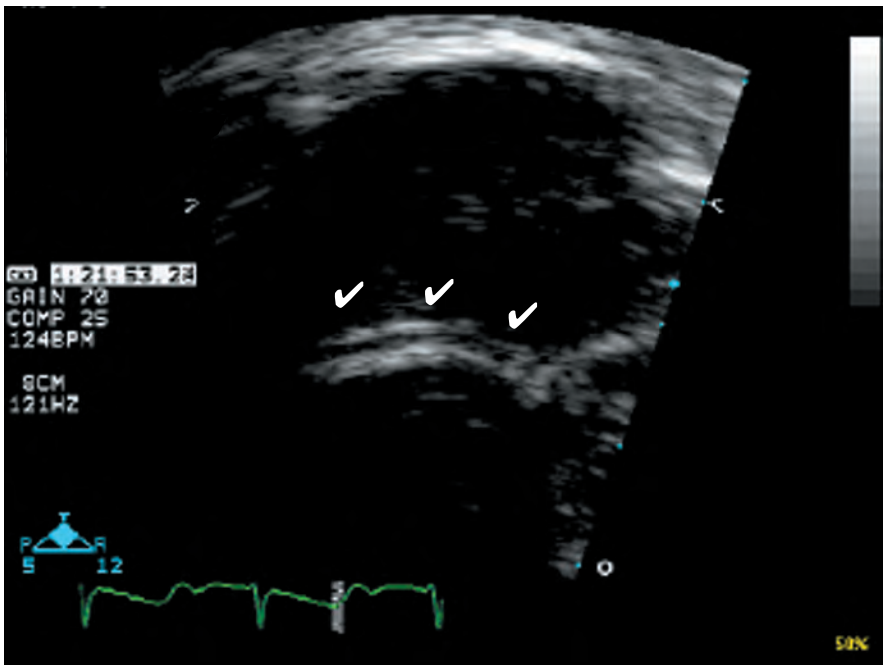


Figure 30.8 Apical 4-chamber view of the anterior right atrioventricular groove showing a long length of the proximal right coronary artery (carets).

others are relatively common. The remainder of this chapter discusses the congenital coronary artery anomalies that are most important to the pediatric cardiologist.

Minor variations in coronary artery anatomy

Minor variations in coronary artery anatomy are those that are hemodynamically insignificant and not associated with an increased risk of sudden death [27]. Their presence must nonetheless be recognized in order to interpret coronary arteriograms and echocardiograms properly, to avoid inadequate myocardial protection when cardioplegia is given selectively into the coronary orifices and to avoid injury to these anomalous arteries at the time of surgery.

The most common minor variation in coronary artery anatomy is the origin of the left circumflex coronary artery from the right aortic sinus. After its aberrant origin, this artery courses posterior to the aorta to reach its normal area of distribution. This anomaly occurs in about 0.5% of individuals undergoing coronary arteriography and is completely compatible with normal life. This anomaly is most often recognized echocardiographically by seeing a horizontal linear lucency (the proximal aberrant circumflex coronary artery)

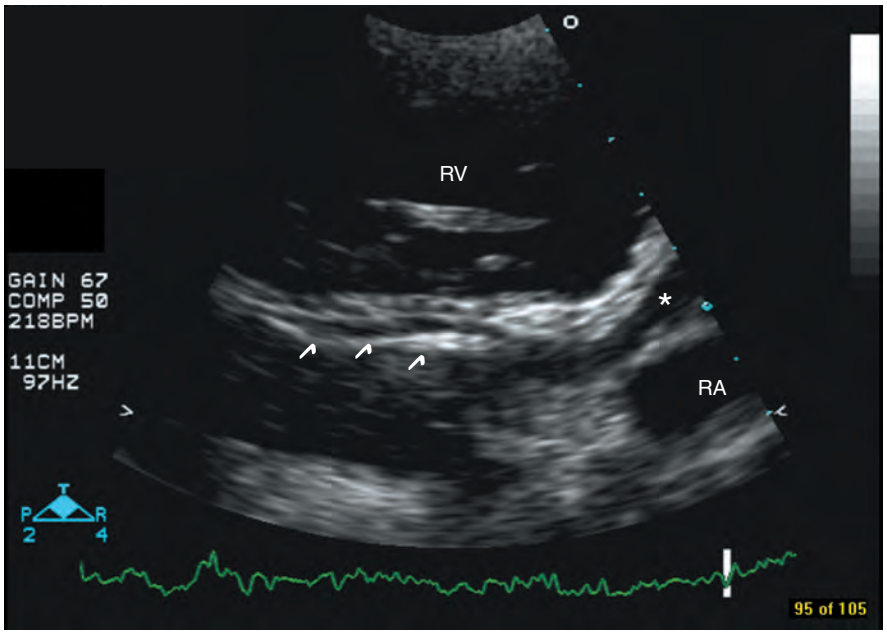


Figure 30.9 Parasternal long-axis view angled inferiorly to show the posterior descending coronary artery (carets). Asterisk (*) denotes the coronary sinus. RA, right atrium; RV, right ventricle.

Table 30.1 A classification of congenital coronary artery anomalies

I	**Anomalies of coronary artery origin**
A	Origin of one or more coronary arteries from the pulmonary artery (PA)
1	Left main coronary artery (LMCA) from PA
2	Right coronary artery (RCA) from PA
3	Left circumflex coronary artery (LC) from PA
4	Accessory coronary from PA
5	RCA and LMCA from PA
6	Single coronary artery from PA
7	Origin of a coronary artery from a branch pulmonary artery
B	Anomalous origin of one or more coronary arteries from the aorta
1	LMCA and RCA from right aortic sinus
2	LMCA and RCA from left aortic sinus
3	LMCA and RCA from posterior aortic sinus
4	RCA and LC from right aortic sinus (or LC from RCA) and left anterior descending coronary artery (LAD) from left aortic sinus
5	RCA and LAD from right aortic sinus (or LAD from RCA) and LC from left aortic sinus
6	RCA from posterior aortic sinus and LMCA from left aortic sinus
7	LMCA from posterior aortic sinus and RCA from right aortic sinus
8	LAD and LC from a separate ostium in the left aortic sinus (absence of LMCA) and RCA from right aortic sinus
C	Origin of only one coronary artery from the aorta without origin of a coronary artery from the PA (single coronary ostium)
1	From the right aortic sinus
2	From the left aortic sinus
3	From the posterior aortic sinus
D	Ostial anomalies
A	Abnormal number of ostia
B	Abnormal position of the ostia relative to the sinotubular junction
C	Intramural coronary artery
II	**Anomalies of coronary artery course or distribution or anomalies intrinsic to the artery**
A	Congenital coronary artery aneurysms
B	Congenital coronary artery stenosis
C	Congenital coronary artery hypoplasia
D	Coronary arterial loops
E	Myocardial bridges
III	**Anomalies of coronary artery termination**
A	Congenital coronary arteriovenous fistulae
B	Congenital coronary–cameral fistulae
IV	**Coronary artery anomalies associated with congenital heart disease**
A	Tetralogy of Fallot
B	D-transposition of the great arteries
C	L-transposition of the great arteries
D	Double-inlet left ventricle or univentricular heart
E	Double-outlet right ventricle
F	Truncus arteriosus
G	Pulmonary atresia with intact ventricular septum
H	Hypoplastic left heart syndrome

coursing posterior to the aorta from the apical 4-chamber view (Figure 30.10).

Variations in the number of coronary artery ostia are common. In approximately 50% of cases, the right conus artery originates from a separate orifice in the right coronary sinus. Less commonly, in approximately 1% of the general population, the left circumflex coronary artery has a separate orifice in the left coronary sinus [22,28]. Very rarely, these two anomalies occur together and produce four coronary ostia.

Finally, variations in the position of the coronary artery ostia are also common. Normally, in adults, the coronary artery ostia are located just below the junction of the sinus and tubular portions of the aorta or within 1 cm above this point. However, ostial positions above or below this occur in up to 40% of individuals undergoing coronary arteriography. Such variations appear to be benign [24].

Anomalies of coronary arterial origin

Anomalous left main coronary artery from the pulmonary artery

History, incidence, and anatomy

Anomalous left main coronary artery from the pulmonary artery (ALCAPA) is one of the most important congenital coronary artery anomalies for the pediatric cardiologist. Pulmonary artery origin of coronary arteries was first described by Brooks in 1886 [29] and was further discussed by Abbott in 1908 [30]. The first clinical description of this anomaly, however, was given eloquently by Bland, White, and Garland in 1933 [31] and the ALCAPA syndrome often bears the eponym *Bland–White–Garland syndrome*.

This anomaly is rather rare. It occurs approximately once per 300 000 live births and represents 0.5% of cases of congenital heart disease [32]. It generally occurs as an isolated anomaly but has been associated with patent ductus arteriosus, ventricular septal defects, atrioventricular canal defects, tetralogy of Fallot, coarctation of the aorta, hypoplastic left heart syndrome, and truncus arteriosus [33–40].

The left main coronary artery usually originates from either the left or the posterior sinus of the pulmonary artery. It can also originate more distally and even from the undersurface of the proximal right pulmonary artery. It then branches and distributes in a manner analogous to a normally arising left coronary artery. It is therefore only the origin of the coronary artery that is abnormal.

Physiology

The physiology of this anomaly depends on the status of blood flow in the left coronary artery (Figure 30.11). Classically, four hemodynamic phases have been described [41–43]. In the first phase, pulmonary vascular resistance and pulmonary arterial pressure are high and the anomalous coronary artery is supplied by blood from the pulmonary artery. This occurs in the newborn period and does not produce myocardial ischemia. The second phase is the transitional period during which pulmonary vascular resistance and pulmonary arterial pressure fall. During this time, flow into the left coronary artery begins to be retrograde, that is, from right coronary artery to left coronary artery via collaterals and left coronary perfusion pressure falls. Unless there is an extensive collateral circulation, signs and symptoms of myocardial ischemia occur during this time. The third, or

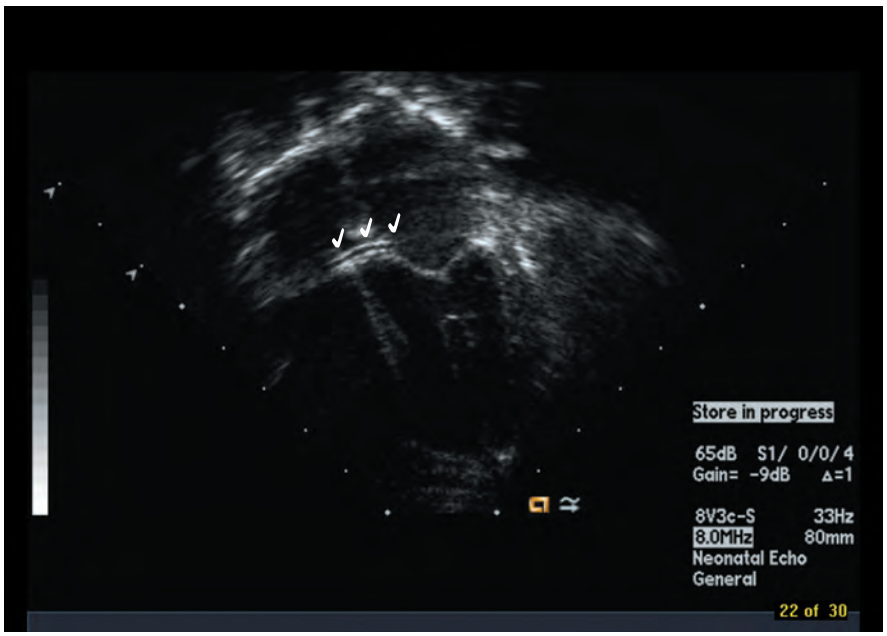


Figure 30.10 Apical 4-chamber view just posterior to the aortic root. An anomalous circumflex coronary artery arising from the right coronary sinus of Valsalva is seen crossing posterior to the aortic root (carets).

adult, phase is one in which there is an extensive collateral circulation and adequate perfusion of the myocardium supplied by the left coronary artery. Blood flows from the right coronary artery into the left coronary circulation and then into the pulmonary artery. There are no signs of myocardial ischemia in this phase. In the fourth phase, the left coronary artery no longer functions as a "feeding vessel" to the left ventricular myocardium but rather as a conduit from the right coronary artery to the pulmonary artery. That is, there is "steal" of oxygenated blood from the arteriolar and capillary vessels of the left coronary circulation. Myocardial ischemia is thus produced.

Not all patients pass consecutively through each of these phases. Indeed, most patients present in infancy during the transitional phase and never progress beyond this. A few patients have numerous collateral vessels between the right and left coronary arteries and pass unscathed through infancy to present in adulthood in phase three or four. The above schema nonetheless represents a useful framework for the

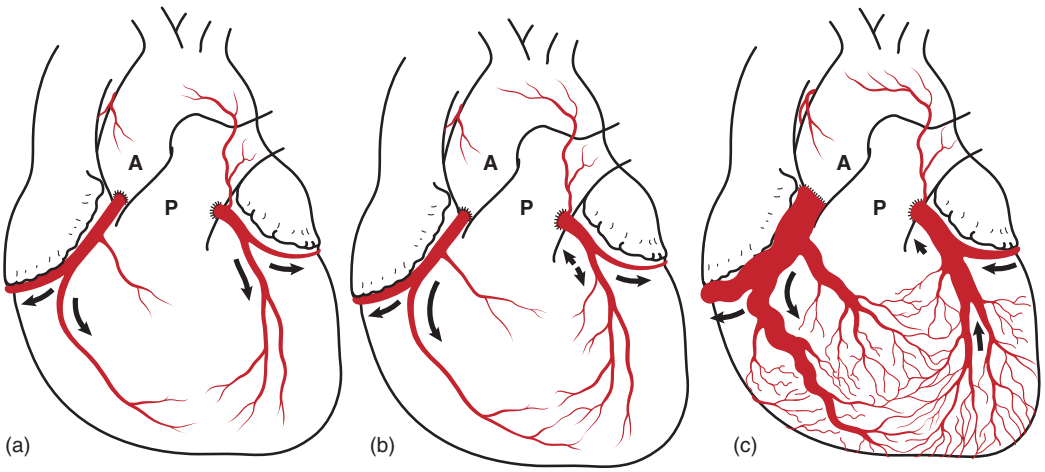


Figure 30.11 Diagrammatic portrayal of varying functional states in anomalous origin of the left coronary artery from the pulmonary trunk. **(a)** During fetal life aortic (A) and pulmonary arterial (P) pressures are essentially equal. Flow in the anomalous artery is from the pulmonary trunk into the myocardium. **(b)** In early postnatal life pulmonary pressure has fallen below levels that pertain during fetal life. Rich intercoronary collateral channels have not yet developed. In this phase, flow through the anomalous coronary artery is probably at a low level. The anomalous vessel may be perfused either from the pulmonary trunk or from the right coronary artery through developing collateral systems. **(c)** In the final phase a rich collateral system has developed between the two coronary arteries. Characteristics of an arteriovenous fistula now pertain, with the major contribution to fistulous flow coming from the right coronary artery. Mediastinal arteries, which make communication with the coronary arterial system, may also contribute to such flow. Source: Adapted from Edwards JE. The direction of blood flow in coronary arteries arising from the pulmonary trunk. *Circulation* 1964;**29**:164, with permission of Wolters Kluwer Health.

description of the varied physiologies with which these patients may present.

Clinical features

The majority of patients present in early infancy with failure to thrive, tachypnea, dyspnea, wheezing, diaphoresis, or angina-like episodes. In infantile cases, there is a 2:1 male to female preponderance [10]. Classically, infantile angina is brought on by feeding and consists of "paroxysmal attacks of acute discomfort precipitated by the exertion of nursing," and is sometimes also called "cardiac colic" [31]. Examination of such infants shows the signs of congestive heart failure. Either no systolic murmur or a very short grade 1–2 systolic murmur is heard. Occasionally, the murmur of mitral insufficiency may be the only presenting sign. The etiology of the mitral insufficiency is some combination of ischemia or infarction of the mitral valve papillary muscles and stretching of the mitral valve annulus due to the dilated cardiomyopathy that ensues from ischemia.

Occasionally, patients escape symptomatology in the infantile period. These are patients who have extensive collateral coronary arteries and they present either with a continuous murmur or with sudden cardiac death in later childhood or adulthood [12,44,45]. In one relatively large review of the adult experience with this lesion, the mean age at diagnosis was 41 years, with the oldest patient diagnosed at age 83 years. Most patients were symptomatic with congestive heart failure, ventricular arrhythmias, or sudden cardiac death and almost all had an abnormal ECG [46]. Another group of patients who escape symptomatology in the infantile period are those with ALCAPA syndrome and a concomitant congenital or acquired heart disease that preserves or produces pulmonary hypertension [47,48], or patients with left main ostial stenosis limiting the coronary "steal" [49]. These patients may present with catastrophic left ventricular dysfunction following repair of the associated lesion if the anomalous left coronary goes unrecognized.

Imaging preoperatively

Echocardiographically, the findings comprise a dilated, hypocontractile left ventricle and a dilated left atrium. There is left ventricular hypertrophy, but the ratio of myocardial volume to end-diastolic volume in the left ventricle is low, that is, the degree of volume expansion is out of proportion to the degree of hypertrophy. The left ventricular dysfunction is generally global with specific regional wall motion abnormality [50]. All of these findings may be seen with myocarditis and dilated cardiomyopathy in addition to the ALCAPA syndrome. Hence the coronary arteries must be diligently evaluated in any patient who presents with the above two-dimensional echocardiographic findings.

Two-dimensional imaging of the coronary arteries alone is inadequate to distinguish ALCAPA from these other conditions. The right coronary artery is often dilated in the ALCAPA syndrome [51], with one study reporting a right coronary artery to aortic root ratio of greater than 0.2 highly specific for this diagnosis [12,52], although this is not always appreciated. The left coronary artery may so closely approach the left aortic sinus of Valsalva that this coronary artery may appear to take its origin from the aorta even when ALCAPA is clearly present. This "dropout" of an intervening wall between the left coronary artery and aortic root due to the limitations of ultrasound lateral resolution is particularly confounding in the parasternal short-axis views. Color flow mapping of the coronary arteries, therefore, is crucial to adding diagnostic certainty to the echocardiographic examination in these conditions (Figure 30.12). The direction of flow in the various segments of the left coronary artery is the differentiating feature and must be evaluated in any patient with the findings of a dilated, hypocontractile left ventricle (Video 30.1). Demonstration of an abnormal flow jet into the pulmonary artery combined with detection of retrograde flow in at least two of the three segments of the left coronary artery is highly reliable for diagnosing the ALCAPA syndrome (Figure 30.13; Video 30.2). Furthermore, demonstration of antegrade flow in at least one segment of the left coronary artery is useful for excluding ALCAPA syndrome in patients with dilated cardiomyopathy [53]. Flow in the septal perforators is often prominent and represents one source of collateral coronary circulation (Figure 30.14). In patients in whom color Doppler is not conclusive, a brief (10 min) trial of supplemental oxygen can transiently increase the retrograde flow in the left coronary system and improve shunt visualization into the main pulmonary artery without compromising patient hemodynamic status [54].



Figure 30.12 Parasternal short-axis view at the base of the heart in a patient with anomalous left coronary artery from the pulmonary artery. Note how closely the left main coronary artery (carets) approaches the left aortic sinus of Valsalva (∗).

Imaging intraoperatively and postoperatively

Intraoperatively, transesophageal echocardiography is used to evaluate left ventricular function and mitral regurgitation. The anatomy is confirmed and the coronary artery origin is identified and the direction of coronary artery flow is demonstrated. Postoperatively, prograde flow from the aorta

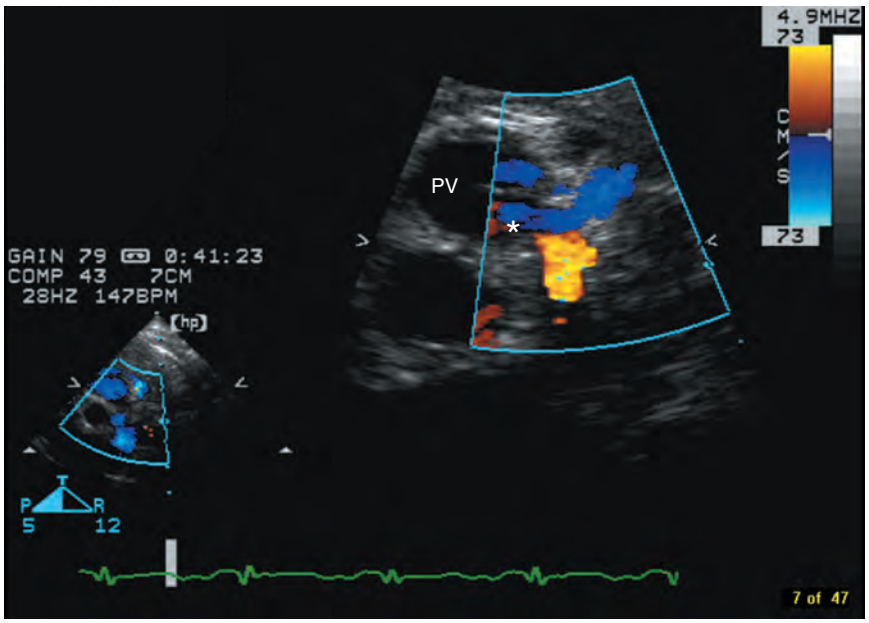


Figure 30.13 High parasternal axial image of the pulmonary valve (PV) and sinuses in a patient with anomalous left coronary artery from the pulmonary artery. Retrograde flow is seen in the left anterior descending coronary artery (blue) and in the left circumflex coronary artery (red) and flow is seen entering the left-facing pulmonary sinus (∗).

into the left main coronary artery is affirmed. Recovery of left ventricular function and improvement of mitral regurgitation are followed with serial examinations [50].

The clinical and echocardiographic findings associated with ALCAPA are presented in Table 30.2.

Table 30.2 Clues to ALCAPA diagnosis

Congestive heart failure presentation in early infancy
Severe left atrial and left ventricular dilation with abnormal systolic and diastolic function
Left ventricular endocardial fibroelastosis changes
Morphologically normal mitral valve with severe regurgitation
Dilated right coronary artery (right coronary artery diameter to aortic root diameter ratio >0.2)
Retrograde flow in 2 of 3 left coronary artery segments
Prominent flow in septal perforators mimicking muscular ventricular septal defect
Abnormal diastolic flow jet in main or right pulmonary artery, increased with supplemental oxygen trial

Anomalous right coronary artery from the pulmonary artery

Anomalous origin of the right coronary artery from the pulmonary artery (ARCAPA) is much less common than ALCAPA, occurring in approximately 0.002% of the general population (Figure 30.15; Video 30.3). However, it is more commonly

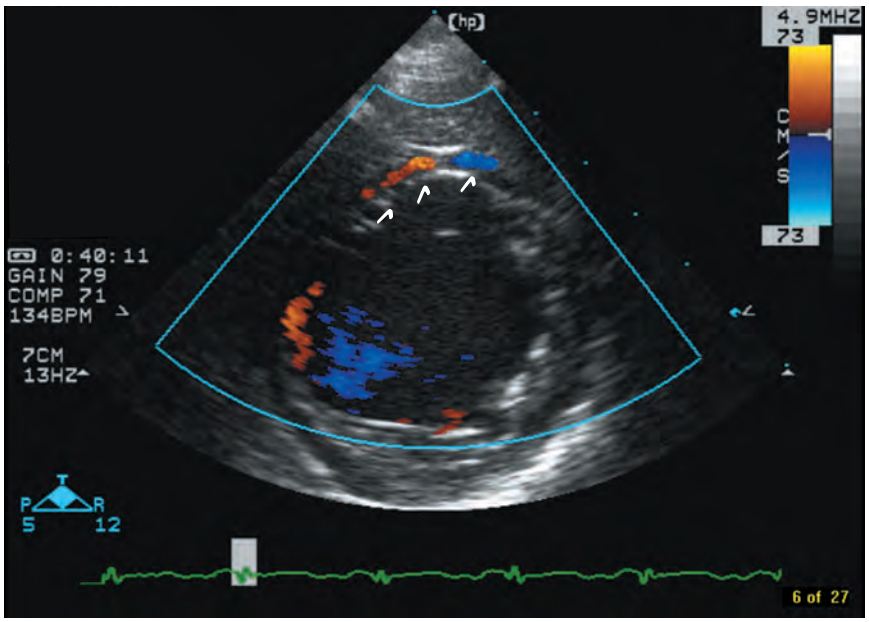
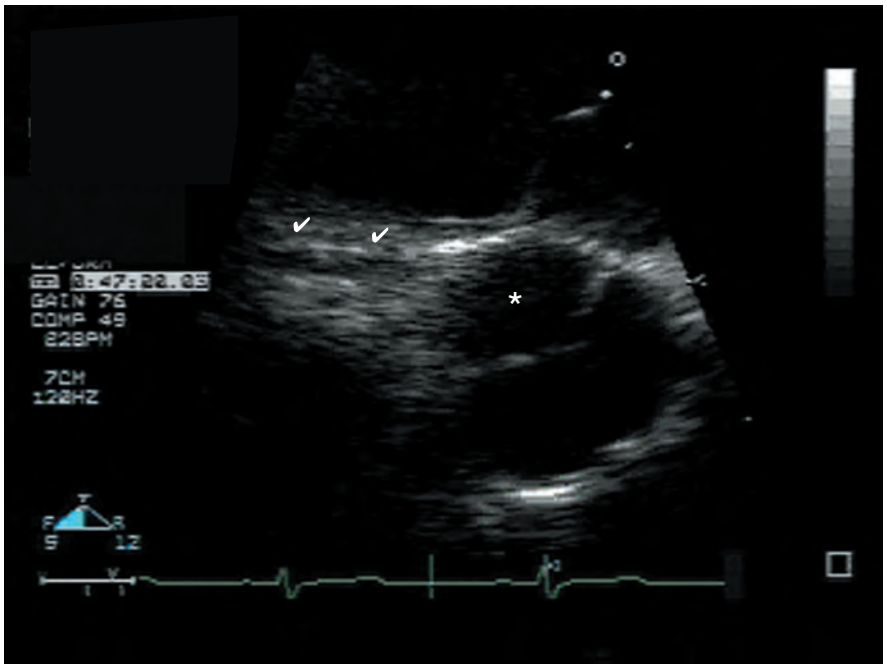
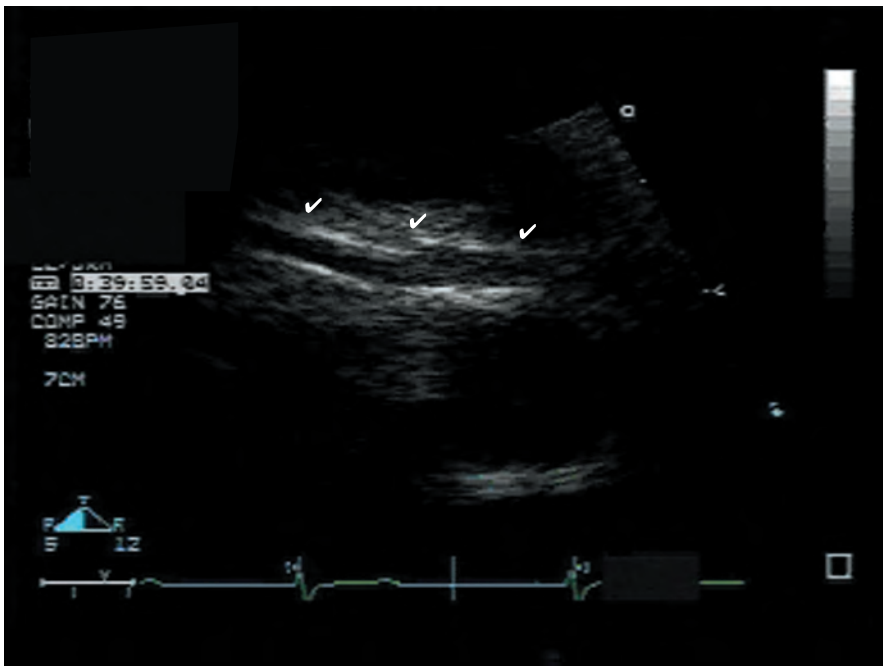


Figure 30.14 Parasternal short-axis view at mid-ventricular level in a patient with anomalous left coronary artery from the pulmonary artery and a dilated left ventricle. Note the prominent retrograde flow in the septal perforator coronary arteries (carets).



(a)

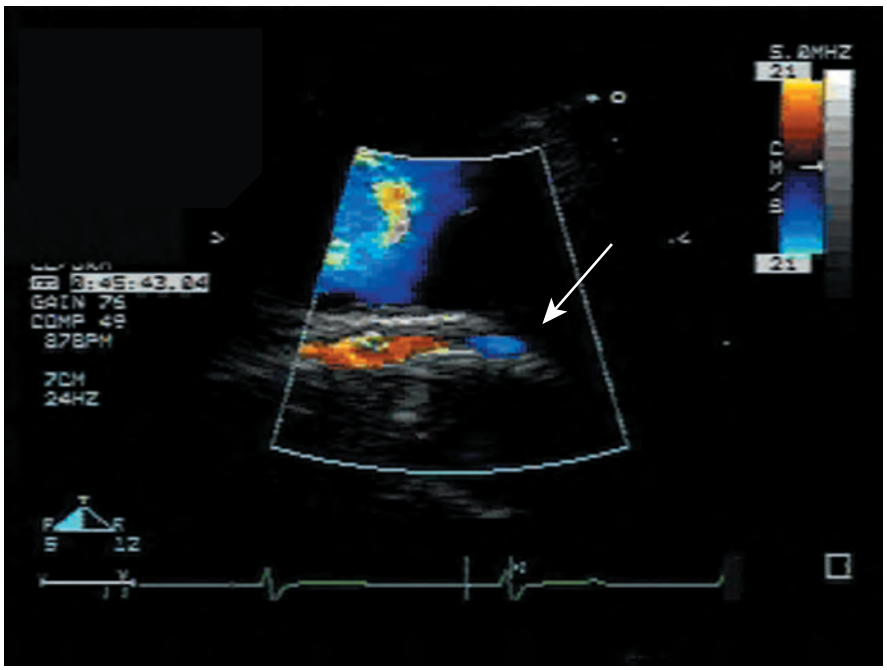


(b)

Figure 30.15 **(a)** Parasternal short-axis view at the base of the heart in a patient with anomalous origin of the right coronary artery from the pulmonary artery. Note how closely the right coronary artery (carets) approaches the right aortic sinus of Valsalva (∗). **(b)** Slightly more superior angulation shows that the right coronary artery (carets) bypasses the right aortic sinus of Valsalva to enter the pulmonary sinus of Valsalva. **(c)** Color Doppler in the right coronary artery shows retrograde flow in the coronary artery and flow entering the pulmonary artery (arrow).

associated with congenital heart disease (25–30% of cases) [55,56]; this makes it a clinically important addition lesion to diagnose. Reported associated congenital heart defects include aortopulmonary window, tetralogy of Fallot, ventricular septal defects, atrial and ventricular septal defects, double-outlet right ventricle, aortic coarctation, pulmonary stenosis, aortic stenosis, and patent ductus arteriosus [11].

There are many similarities between ARCAPA and ALCAPA in embryology, pathology, and physiology. The higher incidence of ALCAPA may be due to the closer proximity of the left coronary artery bud to the pulmonary artery sinus. On pathologic examination, the anomalous right coronary artery has been described as "thin-walled, dilated or vein-like," with origins from the right anterior pulmonary sinus of Valsalva,



(c)

Figure 30.15 (*Continued*)

right posterior pulmonary sinus of Valsalva, or anterior main pulmonary artery. Postnatal physiology may include similar "phases," with the presence of insufficient collateral vessels producing myocardial ischemia as pulmonary vascular resistance decreases or adequate collateral vessels producing a "steal" phenomenon. "Massive" collaterals may overcome a "steal" effect but produce a greater left to right shunt. Other factors that may influence physiology include ostial stenosis, which may be protective [57], at-risk myocardial territory, and the presence of other lesions that increase right ventricular myocardial oxygen demand [11,58].

The clinical spectrum of ARCAPA mirrors that of ALCAPA, although with a shift in the peak age of diagnosis to beyond infancy [11,55,59]. If no concurrent congenital heart disease is present, the diagnosis is most commonly made in childhood, with a murmur being the most common physical finding [11]. Almost half of patients are asymptomatic, with asymptomatic patients typically younger [59,60]. Symptoms, if present, may include angina, congestive heart failure, dyspnea, palpitations, myocardial infarction, myocarditis, and bradycardia [61]. However, sudden cardiac death may occur and has been reported at any age [11,59,60]. The approach to echocardiographic imaging, again similar to ALCAPA, hinges upon a high index of suspicion combined with meticulous imaging of the right coronary artery origin and direction of color flow in this vessel or evaluation of any abnormal flow signals within the pulmonary root or main pulmonary artery [24,62–64] (Figure 30.15; Video 30.3).

The clinical and echocardiographic findings associated with ARCAPA are presented in Table 30.3.

Table 30.3 Clues to ARCAPA diagnosis

Clinical presentation delayed beyond infancy, many asymptomatic with incidental murmur
Higher association with other congenital heart defects
Left atrial and left ventricular dilation with abnormal systolic and diastolic function
Right ventricular endocardial fibroelastosis changes
Dilated left coronary artery
Retrograde flow in right coronary artery system
Prominent flow in septal perforators mimicking muscular ventricular septal defect
Abnormal diastolic flow in region of right anterior or right posterior pulmonary sinus of Valsalva or main pulmonary artery

Coronary artery ostial atresia

Very rarely, the left main coronary artery and its branches can have a normally developed epicardial course but atresia of the ostium at the aortic sinus of Valsalva. Alternatively named congenital absence of the left main coronary artery ("CALM"), the resultant physiology is very similar to that for ALCAPA with collateral supply to the left coronary artery bed from the right coronary artery. The clinical presentation and clinical course are also similar to those for ALCAPA, with typical infantile heart failure and risk of myocardial infarction, arrhythmias, and sudden death. This lesion is exemplary of the need to combine 2D and color Doppler imaging for coronary artery assessment, as the left coronary system will appear normal by 2D imaging up to the aortic sinus, often with enough "dropout" to be convincing of a patent ostium, but with paradoxical retrograde flow in the left anterior or circumflex coronary arteries. As opposed to

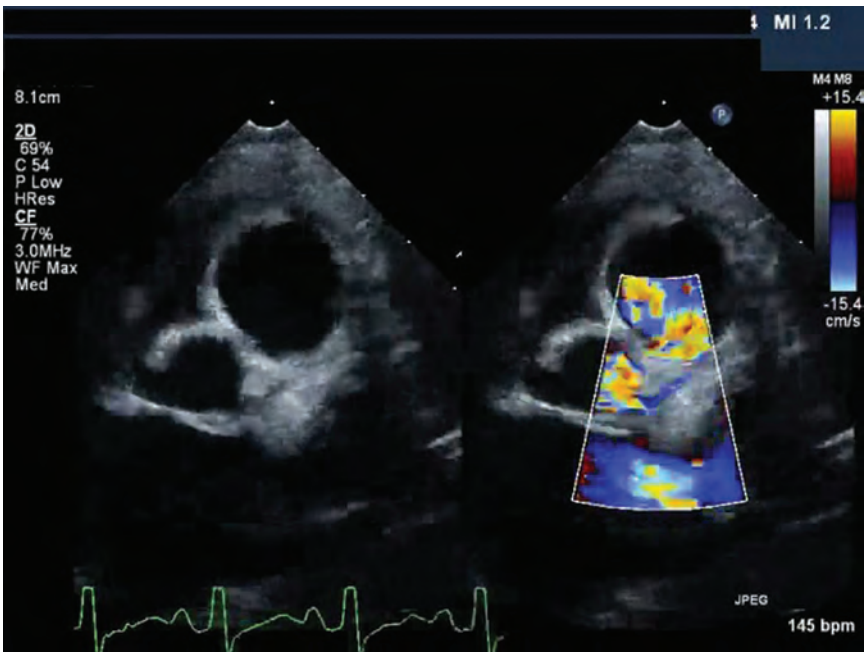


Figure 30.16 Parasternal short-axis view with color comparison demonstrating apparent "normal" origin of the left main coronary artery from the aortic root, but retrograde color flow highly suspicious for ostial atresia of the left main coronary artery. Source: Adapted from Cohen MS, Herlong JR, Silverman NH. Echocardiographic imaging of anomalous origin of the coronary arteries. *Cardiol Young* 2010;**20**(Suppl 3):26–34. Reproduced with permission of Cambridge University Press.

ALCAPA, no separate diastolic jet will be seen entering the pulmonary arteries. This abnormality has been associated with ventricular septal defects, supravalvar aortic stenosis, and left ventricular noncompaction and can be successfully managed surgically with long-term outcome dependent on the degree of preoperative myocardial infarction [65] (Figure 30.16; Video 30.4).

Other anomalies of pulmonary arterial origin of coronary arteries

Either the left anterior descending coronary artery or the circumflex coronary artery may take its origin from the pulmonary artery. Both anomalies are extremely rare but may be associated with signs of myocardial ischemia. An accessory coronary artery, most commonly a conus coronary artery, may also arise from the pulmonary artery; this is of no functional significance [66].

Origin of both coronary arteries from the pulmonary artery, either from separate orifices or as a single coronary artery, is another rare anomaly. Most of these infants present in the early neonatal period with profound heart failure and quickly succumb to this. Longer survival has been described in infants with concomitant congenital heart disease associated with elevations in pulmonary artery pressure, oxygen saturation, or both [67]. Until recently, this anomaly has been uniformly lethal. Urcelay et al. reported successful repair in two infants by direct reimplantation of the coronary arteries into the aortic root [68].

The left main coronary artery has also been found to originate from a branch pulmonary artery, and this has been successfully repaired [69].

Anomalous aortic origin of a coronary artery

This group of anomalies is currently attracting wide attention, and this upsurge in awareness has largely been due to the increased ability of echocardiography to assess the origins and proximal courses of the coronary arteries and the establishment of such imaging as standard in the pediatric and congenital populations. Much work remains to be done in understanding the incidence and clinical importance of these varied anomalies. A registry has recently been established by a working group of the Congenital Heart Surgeons' Society and prospective data are being obtained [70].

Anomalous aortic origin of the left coronary artery from the right coronary sinus

Anomalous aortic origin of the left main coronary artery from the right coronary sinus or from the proximal right coronary artery is a rare lesion, but one of great clinical importance because it has been associated with sudden cardiac death in children and adolescents [66,71–73]. After its anomalous origin, the left main coronary artery may take one of four different routes:

- anterior to the pulmonary artery
- posterior to the aorta
- in the interventricular septum beneath the right ventricular infundibulum (intraconal)
- between the aorta and pulmonary artery (interarterial).

Even rarer is anomalous origin of only the left anterior descending coronary artery from the right coronary artery or from the right sinus of Valsalva, but this anomaly probably has similar clinical behavior to anomalous origin of the entire left coronary artery system from the right coronary artery or the right sinus of Valsalva.

Patients in whom the anomalous left main coronary artery takes an interarterial course appear to be at greatest risk for sudden death (Figure 30.17). Most such coronary arteries also have an intramural course and the length of this course has

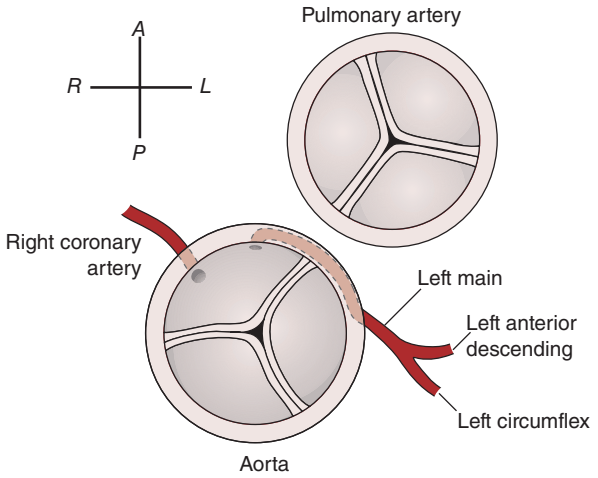


Figure 30.17 Anomalous origin of the left main coronary artery from the right aortic sinus of Valsalva with an intramural and interarterial course. Note the slit-like orifice of the left main coronary artery. A, anterior; P, posterior; R, right; L, left.

been correlated with symptoms [74]. The mechanism of such sudden death is acute myocardial ischemia, which is produced by embarrassment of flow in the left main coronary artery. This occurs most often during exercise, when myocardial oxygen demand is at its highest and the increased stroke volume causes outward expansion of the roots of both great vessels. The mechanism of obstruction to flow seems to be a combination of compression of the intramural portion of the left main coronary artery, compression of the left main coronary artery between the aorta and the pulmonary trunk, and worsening of the intrinsic narrowing or kinking at the anomalous ostium [66].

The most common presenting symptoms of individuals with anomalous aortic origin of the left main coronary artery from the right coronary sinus are syncope, presyncope, or chest pain associated with exercise. However, many patients with this anomaly are asymptomatic until sudden death occurs. In fact, coronary artery anomalies including anomalous left main coronary artery arising from the right coronary sinus join hypertrophic cardiomyopathy as the most common cardiac anomalies associated with sudden cardiac death in adolescents and young adults. Exercise stress testing of patients with this anomaly may show myocardial ischemia but also may be completely normal. Hence any evaluation of exercise-related syncope, presyncope, or chest pain must include definition of coronary arterial anatomy, and echocardiography is most often the imaging modality of choice [75].

Imaging

Excellent definition of the origin and proximal course of the anomalous coronary artery may most often be achieved with echocardiography. The parasternal short-axis view at the base of the heart is the best view to appreciate both the relationship of the origin of the left coronary artery to the intercoronary commissure and its often intramural course and also its relationship to the right ventricular outflow (Figure 30.18). Because of the extreme translation of the coronary artery origins during the cardiac cycle, the excellent temporal resolution of echocardiography (compared with that of other noninvasive techniques) makes this the diagnostic technique of choice in most cases [76]. The extreme translation of the coronary artery makes diagnosis in real time often difficult. Obtaining a loop that is one to several heartbeats in duration and then playing this back slowly is often of great help in visualizing the anomalous coronary artery and also discerning its relationship to the intercoronary commissure (Video 30.5). Color Doppler should be made to write in the intramural segment of the left main coronary artery. In fact, an abnormal jet seen during diastole over the space between the aorta and the pulmonary trunk often is the first indication of an abnormal coronary arterial course. A "diastolic hangup" of flow in this segment is characteristic. The interarterial course of the anomalous left main coronary artery can often be seen in the leftward-angled parasternal long-axis view (Figure 30.19; Video 30.6).

In older patients with slower heart rates, both MRI and multislice CT have also proven useful [77,78]. If any question remains, coronary angiography is recommended, although this technique does not allow for completely unambiguous delineation of the proximal course of the coronary artery.

Intraconal course of the left main coronary artery

An intraconal (also known as intraseptal or intramyocardial) course of an anomalous left main coronary artery from the right sinus of Valsalva is much rarer, but since it is generally considered benign, its recognition is important [71,79]. The key feature is seeing the "ground glass" appearance of muscle surrounding the proximal coronary artery. This may be accomplished from a parasternal short-axis view. Additionally, the course of the coronary artery inferior to the pulmonary annulus should be demonstrated. This may best be accomplished from a leftward-angled parasternal long-axis view. The "hammock sign" described in angiographic studies may be seen from a modified apical view. Color Doppler imaging should be obtained to rule-out any stenosis which may be present in the intraconal course (Videos 30.7 and 30.8).

Anomalous aortic origin of the right coronary artery from the left coronary sinus

Until recently, anomalous aortic origin of the right coronary artery from the left coronary sinus was considered a benign variant. It is reported less often than anomalous aortic origin of the left main coronary artery from the right coronary sinus, but its true incidence is probably greater than this better-recognized anomaly [66,80]. It is common for the anomalous right coronary artery to pass between the great vessels, although other courses are possible. Such a course provides the anatomic substrate for myocardial ischemia in an manner identical with that with anomalous aortic origin of the left coronary artery from the right sinus. Although presentation with sudden cardiac death

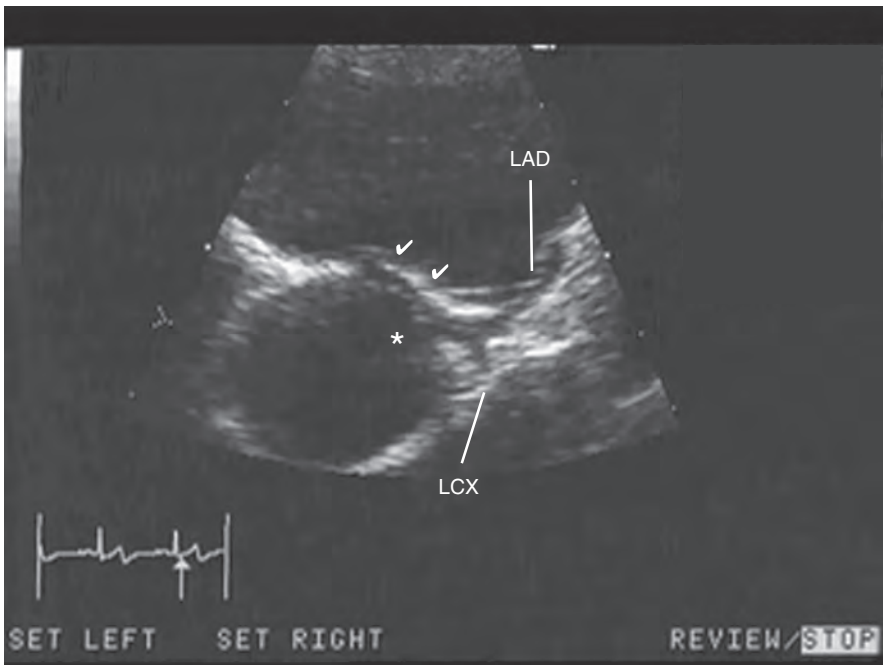


Figure 30.18 Parasternal short-axis view at the base of the heart in a patient with anomalous origin of the left main coronary artery from the right aortic sinus of Valsalva. The intramural and interarterial course of the left main coronary artery is apparent (carets). The asterisk (∗) marks the location of the intercoronary commissure. LAD, left anterior descending coronary artery; LCx, left circumflex coronary artery.

not preceded by other symptoms is less likely with this anomaly than with anomalous origin of the left coronary artery from the right sinus of Valsalva, up to one-fourth of individuals with an anomalous right coronary artery found at autopsy died suddenly and unexpectedly and almost one-third of them died of cardiac causes [81]. Operative intervention for anomalous origin of the right coronary artery from the left sinus in asymptomatic patients is controversial but is performed in a number of institutions [82–84].

Imaging

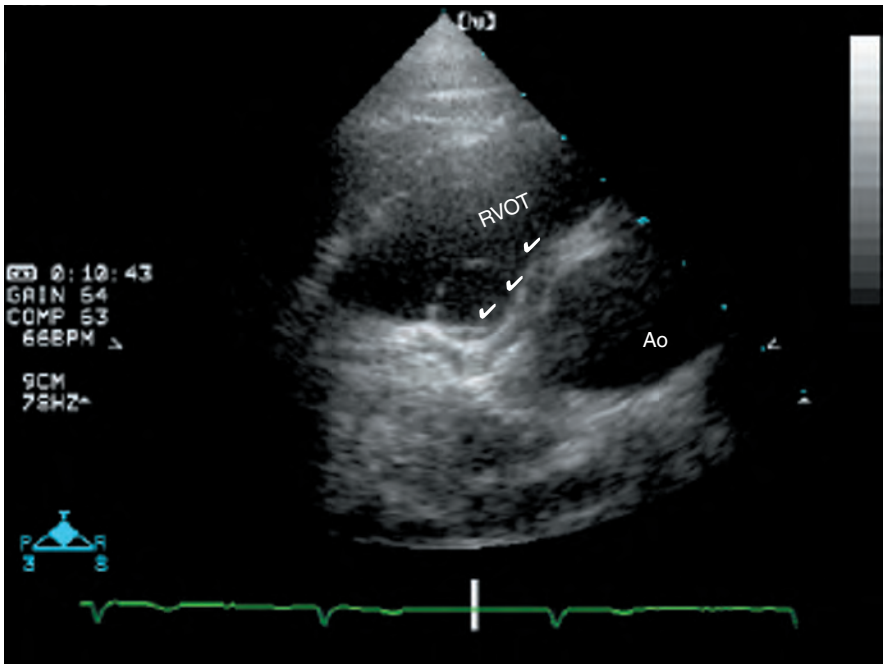
This anomaly is most often diagnosed by echocardiography either as an unexpected finding or as part of an evaluation for a patient with chest pain or exercised-induced syncope. It is found using the same principles as for anomalous aortic origin of the left coronary artery from the right coronary sinus of Valsalva in that the parasternal short-axis view allows the determination of the anomalous origin and proximal course of the right coronary artery. In this entity, an unusually high origin of the anomalous right coronary artery (at or slightly above the sinotubular junction) is common. It is the origin of the coronary artery with respect to the intercoronary commissure that determines the aortic sinus from which the coronary artery arises. When the origin is above the commissural post, sweeping superiorly from a view that shows the intercoronary commissure to a view that shows the coronary origin is necessary to demonstrate the sinus of origin from a short-axis view. When the origin is high, takedown of the intercoronary commissure during an unroofing procedure is usually not necessary; hence this identification is surgically important [85]. Identifying the origin in relation to the sinotubular junction is best accomplished in the parasternal long-axis view or in a long-axis transesophageal echocardiographic view (Figure 30.20; Video 30.9). We have found transesophageal echocardiography to be the imaging procedure of choice if anomalous aortic origin of a coronary artery is suspected but not definitively diagnosed by transthoracic imaging.

Postoperative imaging of anomalous aortic origin of a coronary artery

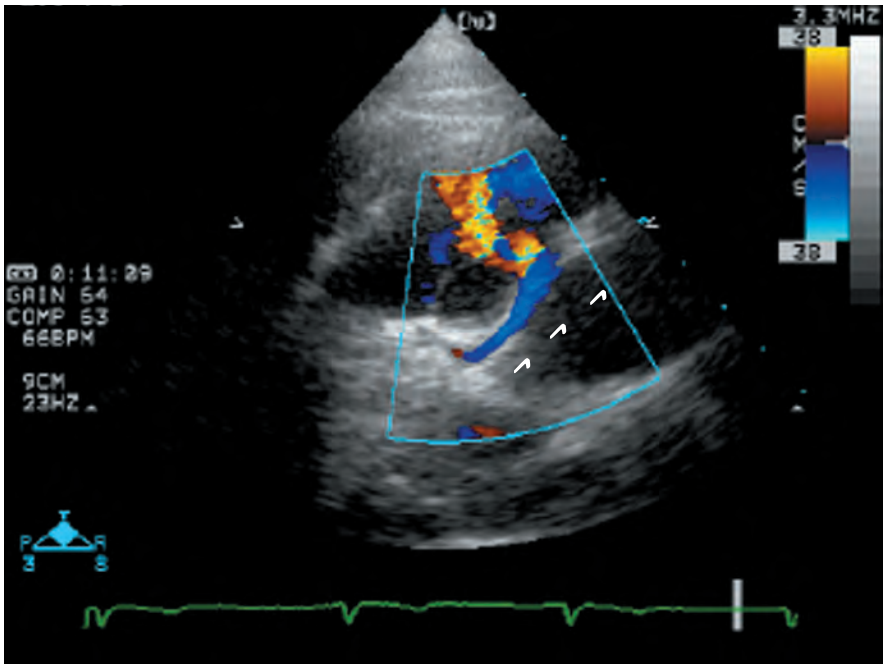
In patients who have had an unroofing procedure for repair of anomalous aortic origin of a coronary artery, it is necessary postoperatively to evaluate for aortic insufficiency due to potential distortion of the aortic valve. One should also demonstrate flow from the appropriate aortic sinus into the coronary artery (Figure 30.21).

Single coronary artery

This anomaly may be defined as one in which a single coronary artery arises from a single ostium in one of the aortic sinuses of Valsalva and follows the peripheral course and distribution of one or both right and left coronary arteries or follows an abnormal distribution [24]. This is a rare anomaly in individuals with an otherwise normal heart but was made publicly well known by the untimely death of "Pistol" Pete Maravich due to sudden cardiac death related to a single right coronary artery [86]. Classification schemes for single coronary artery have been proposed by Smith [87], Ogden and Goodyer [88], and Shirani and Roberts [89]. The last scheme is most complete and describes three features of the coronary circulation: the sinus of origin of the single coronary artery,



(a)



(b)

Figure 30.19 **(a)** Leftward-angled parasternal long-axis view of the left coronary artery in a patient with anomalous origin of the left main coronary artery from the right aortic sinus of Valsalva. The interarterial course is demonstrated (carets). RVOT, right ventricular outflow tract. **(b)** Color Doppler demonstrates prograde flow in the interarterial segment of the left main coronary artery (carets). Ao, aortic root; RVOT, right ventricular outflow tract.

the presence or absence of an aberrantly coursing coronary artery, and the course of the aberrantly coursing coronary artery if present. It is crucial to distinguish the presence of a single coronary artery, with normal prograde flow to all three major branches, from atresia of the left main coronary artery, in which there is collateral flow to the left coronary circulation and a much greater risk of left ventricular ischemia [65].

The majority of patients with a single right coronary artery are asymptomatic. Indeed, the anomaly is compatible with a normal life. Whether people with this anomaly are particularly prone to atherosclerotic disease is controversial [90]. Clearly,

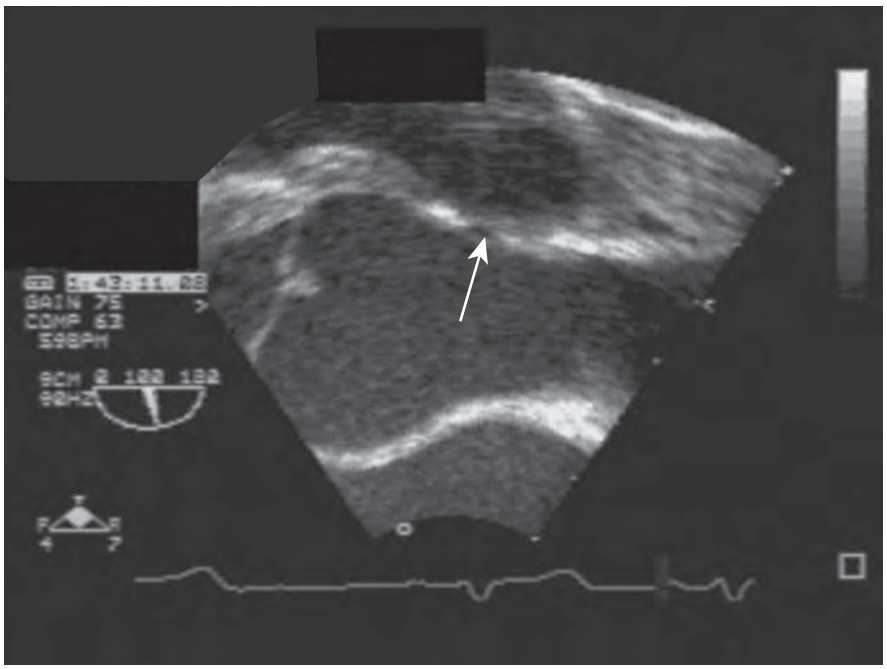


Figure 30.20 Long-axis transesophageal echocardiogram at the level of the ascending aorta in a patient with anomalous origin of the right coronary artery from the left aortic sinus of Valsalva. The origin of the right coronary artery (arrow) is seen just at the sinotubular junction.

however, the consequences of atherosclerotic occlusion of a single coronary artery are dire. Patients with a single right coronary artery with an aberrant left coronary artery (or branch of the left coronary artery) that courses between the great vessels seem to be at particular risk for sudden cardiac death. The pathophysiology of this phenomenon is probably the same as that for sudden death related to anomalous aortic origin of the left coronary artery from the right coronary artery, as discussed earlier.

A single coronary artery in a patient with an otherwise structurally normal heart is almost always an incidental finding. The origin and proximal course of each of the three major coronary arteries should be confirmed in multiple views when a single coronary artery is suspected.

Anomalies of coronary artery course or distribution and anomalies intrinsic to the artery

This heading encompasses a diverse group of coronary artery anomalies, each of which is rare, but all of which deserve mention because of their potential importance to the pediatric cardiologist.

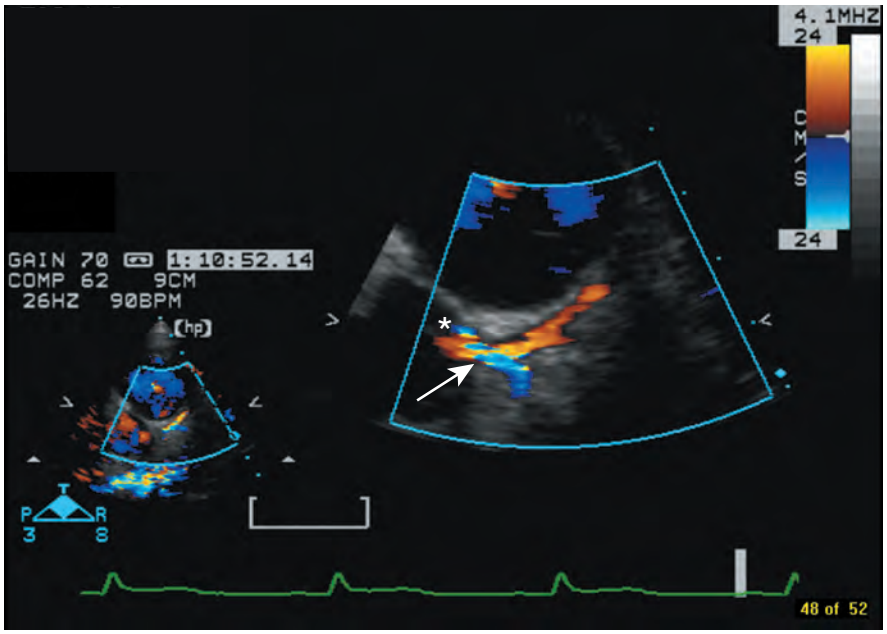


Figure 30.21 Parasternal short-axis view at the base of the heart in a patient who has undergone an unroofing procedure for repair of anomalous origin of the left main coronary artery from the right sinus of Valsalva. Color Doppler demonstrates prograde flow into the left main coronary artery from the left aortic sinus of Valsalva (arrow). The asterisk (*) denotes the position of the intercoronary commissure.

Congenital coronary artery aneurysm

Congenital aneurysm of a coronary artery accounts for roughly 17% of all coronary artery aneurysms [91]. The majority of coronary artery aneurysms are secondary to atherosclerotic disease, associated with congenital coronary–cameral fistulae, associated with Kawasaki disease, or of infectious or traumatic etiology. Congenital coronary artery aneurysm is thus a diagnosis of exclusion that may be made after these other more common etiologies have been ruled out.

Congenital coronary artery aneurysms are considered to be caused by a deficiency of the elastic elements in the media of the coronary arteries [92]. Patients with this anomaly present with signs and symptoms of myocardial ischemia, particularly during exercise. The diagnosis may be suggested on chest radiography by an abnormal bulge on the cardiac silhouette or by the presence of calcific rings along the distribution of the coronary arteries. Definitive diagnosis is made by coronary arteriography or with evolving CT or MRI techniques [93–95].

Complications of congenital coronary artery aneurysms include rupture of the aneurysm, myocardial infarction from embolization of clots from the aneurysm to the more distal coronary artery, and infective endocarditis. Such complications may be prevented by surgical therapy [24,96–99].

Echocardiographic evaluation of congenital coronary aneurysms is accomplished just as it is in the evaluation of coronary aneurysms associated with Kawasaki disease. This is covered in Chapter 38.

Anomalies of coronary artery termination

Congenital coronary–cameral and coronary–arteriovenous fistulae

These lesions have the same physiology and are therefore discussed together. A coronary–cameral fistula involves an abnormal fistulous connection between a coronary artery and a cardiac chamber, whereas a coronary–arteriovenous fistula involves such a connection between a coronary artery and one of the great veins entering the heart. Not strictly included under this nominal rubric but in the same category of lesions is a coronary artery-to-pulmonary artery fistula. Hereafter in this chapter, all of the above entities are called simply coronary arteriovenous fistulae (CAVFs).

History, incidence, anatomy, and embryology

Krause provided the first description of this anomaly in 1865 [100]. Although it is uncommon, CAVF is one of the more common congenital anomalies of the coronary arteries. This entity accounts for 0.2–0.4% of congenital cardiac anomalies and roughly half of congenital anomalies of the coronary arteries [101–103]. From a different perspective, CAVF may be found in up to 0.7% of adults with cardiac symptoms undergoing cardiac CT, with the majority of these fistulae draining to the pulmonary arteries [104].

About 60% of CAVFs originate from the right coronary artery and 40% from the left coronary artery; rarely, such a fistula may take its origin from both coronary arteries [24,101,105] or multiple fistulae may be present [106]. In most cases (about 90%), the CAVF terminates in the right side of the heart [107]. While the exact order of the most common sites of drainage is evolving due to the increased use of cardiac CT, the right ventricle, right atrium, and pulmonary artery are most frequently involved, followed by the coronary sinus, left atrium, and left ventricle [104,106,108,109]. The site of termination of the fistula may be a single entry site, multiple entry sites, a plexiform communication between the coronary artery and a cardiac chamber, or a side-to-side communication between the coronary artery and a cardiac chamber. The embryologic basis for CAVFs is postulated to be persistence of portions of the embryonic coronary sinusoids that connect the primitive coronary arteries to the cardiac chambers [24,110] or persistence of a connection between the splanchnic vascular bed and the embryonic lungs for coronary to pulmonary artery connections [111]. Approximately 20% of patients with CAVFs also have congenital heart disease, as varied as ventricular septal defects, bicuspid aortic valve and coarctation to tetralogy of Fallot, transposition of the great arteries, atrial septal defects, and most commonly pulmonary atresia with intact ventricular septum [107,112,113].

Physiology

The physiology of a coronary arteriovenous fistula varies with the chamber or vessel in which the fistula terminates. Coronary arteriovenous fistulae that terminate in the right atrium have the physiology of a pretricuspid left-to-right shunt, whereas those that terminate in the right ventricle or pulmonary artery have the physiology of a post-tricuspid left-to-right shunt. Those that terminate in the left atrium have a physiology similar to mitral regurgitation and those that terminate in the left ventricle have a physiology similar to aortic regurgitation.

In addition to the above varied physiologies of CAVFs, each such fistula has the potential to produce a coronary artery steal. That is, blood is stolen from the coronary arterial bed distal to the insertion of the fistula because of the runoff of coronary arterial blood into the chamber or vessel of termination. Such a steal may cause myocardial ischemia or rarely infarction, especially in the setting of coexisting coronary artery disease [114–116].

The clinical presentation for CAVFs similarly varies by size and age. Large CAVFs have been reported to cause abnormal chamber enlargement in fetal life and heart failure in childhood [117–119]. However, most CAVFs do not present until adulthood, with murmurs, dyspnea, and fatigue as frequent features [106,113]. Long-term consequences include the effects of chronic volume loading of the affected side of the heart, premature coronary artery disease postulated to be secondary to local shear stress, infective endocarditis, and pulmonary hypertension [106,108,113]. Both catheter-based and surgical closure techniques are feasible, although residual connections have been found in up to 30% of patients, placing patients at risk of distal thromboembolism or distal occlusion [107,115,120].

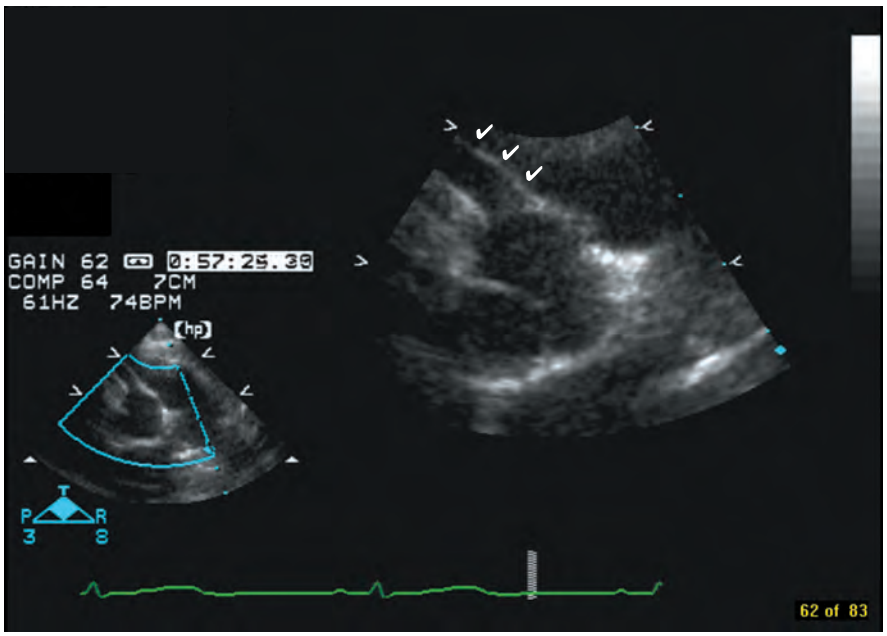


Figure 30.22 Parasternal short-axis view at the base of the heart in a patient with a coronary–cameral fistula from the right coronary artery to the right ventricle. The right main coronary artery (carets) is very dilated.

Imaging

Two-dimensional echocardiography shows dilation of the proximal portion of the coronary artery that feeds the fistula and chamber dilation consistent with the physiology of the particular fistula (Figure 30.22). Occasionally, the fistulous connection itself may be imaged, but fistula detection is greatly aided by color Doppler imaging [121] (Figure 30.23; Video 30.10). Often small CAVFs are first detected by abnormal diastolic flow into a right heart chamber or into the main or branch pulmonary arteries. These small fistulae are usually unexpected findings in an asymptomatic patient with no murmur and without dilation of any cardiac chamber or of the proximal coronary artery. Occasionally, coronary-to-right ventricle fistulae are acquired following operative muscle resection, typically for surgery to relieve right ventricular outflow obstruction [122].

Intervention upon CAVFs requires detailed definition of the distal coronary artery anatomy, and this is not possible by echocardiography. Typically, selective coronary angiography is

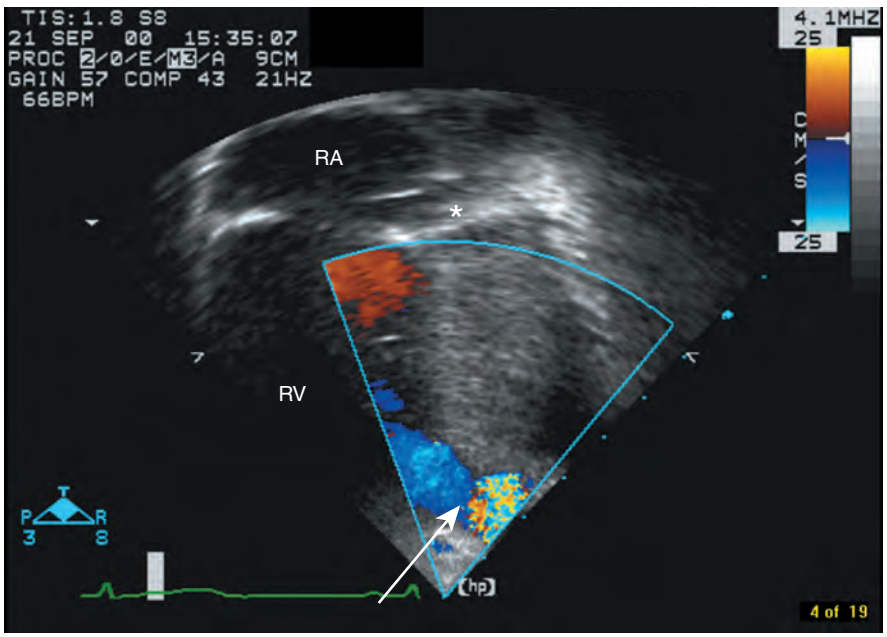


Figure 30.23 Apical 4-chamber view posteriorly at the level of the coronary sinus. Fistulous flow enters the right ventricular apex near the interventricular septum (arrow). The asterisk (*) indicates the coronary sinus. RA, right atrium; RV, right ventricle.

used, although CT or MRI angiography is becoming increasingly common. Transesophageal or intracardiac echocardiography may be used during or after transcatheter occlusion of a CAVF to document occlusion and to evaluate for potential wall-motion abnormalities related to ischemia as a complication of the occlusion [123].

Coronary artery anomalies associated with congenital heart disease

Anomalies of coronary arteries are surgically important in numerous types of congenital heart disease and these associations are discussed in the chapters on each individual lesion. It is worth emphasizing, though, that accurate delineation of the coronary artery anatomy is required in any patient who is to undergo surgery for congenital heart disease and remains important on subsequent examinations. It is necessary to make certain that a coronary artery anomaly does not place a major epicardial coronary artery in the region of surgical repair. Perhaps most important is the need to ensure that there is no abnormal origin of a coronary artery from the pulmonary artery [124], because the repair may change the physiology by decreasing the pulmonary artery pressure, thereby causing coronary steal and myocardial ischemia or infarction in the vulnerable period immediately upon weaning from cardiopulmonary bypass. One can avoid this catastrophic outcome by assiduous attention to coronary arterial anatomy in the preoperative echocardiogram.

Videos

To access the videos for this chapter, please go to www.lai-echo.com.

Video 30.1 Parasternal short-axis view at the base of the heart in a patient with anomalous left coronary artery from the pulmonary artery. Note how closely the left main coronary artery approaches the left aortic sinus of Valsalva. With the addition of color Doppler, retrograde flow is demonstrated in the left anterior descending coronary artery (LAD) and in the left circumflex coronary artery (LCCA). Ao, aortic valve; LCA, left main coronary artery; RVOT, right ventricular outflow tract. Source: Courtesy of Dr. Stephen Sanders.

Video 30.2 High parasternal view oriented in the axial plane in a patient with anomalous left coronary artery from the pulmonary artery. Retrograde flow is noted in the left anterior descending coronary artery and in the left circumflex coronary artery, and also from the left main coronary artery into the left-facing sinus of the pulmonary artery.

Video 30.3 Parasternal short-axis view in a patient with anomalous origin of the right coronary artery from the pulmonary artery. The proximal right coronary artery passes anterior to the right aortic sinus of Valsalva and enters the proximal pulmonary artery. The pulmonary sinus of origin cannot be determined from this view. With the addition of color Doppler, retrograde flow is demonstrated in the right coronary artery and also into the pulmonary artery. This movie demonstrates the value of obtaining a loop and slowing the playback to understand better the contiguity of the right coronary artery, which has a high amplitude of translation throughout the cardiac cycle.

Video 30.4 2D and color Doppler comparison of ostial atresia of the left main coronary artery.

Video 30.5 Parasternal short-axis view in a patient with anomalous origin of the left coronary artery from the right aortic sinus of Valsalva with an intramural and interarterial course. This movie again illustrates the utility of obtaining a cine loop and using a slow playback. In this way, the origin of the coronary artery with respect to the intercoronary commissure of the aortic valve is understood, and the interarterial and intramural course is shown to advantage. With the addition of color Doppler, prograde flow is demonstrated in the intramural segment.

Video 30.6 Anomalous aortic origin of the left main coronary artery from the right sinus of Valsalva (2). Leftward-angled parasternal long-axis view in a patient with anomalous aortic origin of the left main coronary artery from the right sinus of Valsalva with intramural and interarterial course. The interarterial course of the left main coronary artery is shown to advantage in this orientation, and color Doppler confirms prograde flow in this segment of the left main coronary artery. Note the typical "diastolic hangup" of color Doppler flow in the left main coronary artery.

Video 30.7 Parasternal short-axis view in a patient with anomalous aortic origin of the left main coronary artery from the right aortic sinus of Valsalva with an intraconal course. Note that the left main coronary artery travels within the conal septum (the muscle between and below the semilunar valves) and does not conform to the aortic root as it would if their course were intramural.

Video 30.8 Leftward-angled parasternal long-axis view in a patient with anomalous aortic origin of the left main coronary artery from the right aortic sinus of Valsalva with an intraconal course. Note the course of the left main coronary artery just proximal to the pulmonary valve. The "ground glass" appearance around the left main coronary artery is from muscle tissue. Source: Courtesy of Dr. Richard E. Lorber.

Video 30.9 Anomalous aortic origin of the right coronary artery from the left sinus of Valsalva. Transesophageal echocardiogram from behind the base of the heart in a patient with anomalous aortic origin of the right coronary artery from the left sinus of Valsalva. Imaging begins in the short-axis of the aortic valve. The intramural and interarterial course of the right coronary artery is demonstrated, and color Doppler shows prograde flow into this segment of the right coronary artery. The relationship of the origin of the right coronary artery to the intercoronary commissure is not demonstrated in this plane. This is because the origin is high; it is just at the sinotubular junction, as is illustrated in the next segment

of the clip, which depicts a longitudinal view of the aortic sinuses and ascending aorta.

Video 30.10 Subcostal long-axis and apical 4-chamber views in a patient with a coronary–cameral fistula from the right coronary artery to the right ventricle. In the subcostal long-axis view, color Doppler demonstrates luxurious flow in a tortuous right coronary artery along the acute margin and diaphragmatic surfaces of the right ventricle. In the apical 4-chamber view, color Doppler demonstrates the termination of the fistula into the right ventricular apex via the interventricular septum.

References

1 Abrikossoff A. Aneurysma des linken Herzeventrikels mit abnormer Abgangsstelle der linker Karonararterie von der Pulmonalis bei einem funfmonatichen Kinde. *Virchows Arch (Pathol Anat)* 1911;**203**:413–420.

2 Hackensellner HA. Uber akgessorische, von der Arteria pulmonalis abgehende Herzgfaesse und ihre Bedentung für das Verstaendnis der formalen Genese des Ursprunges einer oder beider Coronararterien von der Lungenschlagader. *Frankf Z Path* 1955;**66**:463–470.

3 Conte G, Pellegrini A. On the development of the coronary arteries in human embryos, stages 14–19. *Anat Embryol* 1984;**169**:209–218.

4 Hutchins GM, Kessler-Hanna A, Moore GW. Development of the coronary arteries in the embryonic human heart. *Circulation* 1988;**77**:1250–1257.

5 Conte G, Pellegrini A. On the development of the coronary arteries in human embryos, stages 14–1 9. *Anat Embryol* 1984;**169**:209–218.

6 Bogers AJJC, Gittenberger-de Groot AC, Poelmann RE, et al. Development of the origin of the coronary arteries, a matter of ingrowth or outgrowth. *Anat Embryol* 1989;**180**:437–441.

7 Theveniau-Ruissy M, Dandonneau M, Mesbah K, et al. The del22q11.2 candidate gene Tbx1 controls regional outflow tract identity and coronary artery patterning. *Circ Res* 2008;**103**:142–148.

8 Braunwald E, Sobel BE. Coronary blood flow and myocardial ischemia. In: Braunwald E (ed.) *Heart Disease: a Textbook of Cardiovascular Medicine*, 4th edn. Philadelphia, PA: Saunders; 1992, pp. 1161–1199.

9 Hoffman JIE. Maximal coronary flow and the concept of coronary vascular reserve. *Circulation* 1984;**70**:153–159.

10 Hlavacek A, Loukas M, Spicer D, Anderson RH Anomalous origin and course of the coronary arteries. *Cardiol Young* 2010;**20**:20–25.

11 Williams IA, Gersony WM, Hellenbrand WE. Anomalous right coronary artery arising from the pulmonary artery: a report of 7 cases and a review of the literature. *Am Heart J* 2006;**152**:1004.e9–1004.e17.

12 Zheng J, Ding W, Xiao Y, et al. Anomalous origin of the left coronary artery from the pulmonary artery in children: 15 years experience. *Pediatr Cardiol* 2011;**32**:24–31.

13 Lai WW, Geva T, Shirali GS, et al. Guidelines and standards for performance of a pediatric echocardiogram: a report from the Task Force of the Pediatric Council of the American Society of Echocardiography. *J Am Soc Echocardiogr* 2006;**19**:1413–1430.

14 Iriart X, Jalal Z, Derval N, et al. Two-dimensional strain as a marker of subclinical anterior ischaemia in anomaly of left coronary artery arising from pulmonary artery. *Eur J Echocardiogr* 2009;**10**:732–735.

15 Cotton JL. Diagnosis of a left coronary artery to right ventricular fistula with progression to spontaneous closure. *J Am Soc Echocardiogr* 2000;**13**:225–228.

16 Khan MD, Sivasubramonian S, Simpson JM. Prenatal diagnosis of tetralogy of Fallot associated with a fistula from the left coronary artery to the left atrium. *Cardiol Young* 2003;**13**:194–196.

17 Bardo DM, Brown P. Cardiac multidetector computed tomography: basic physics of image acquisition and clinical applications. *Curr Cardiol Rev* 2008;**4**:231–243.

18 Flamm SD, Muthupillai R. Coronary artery magnetic resonance angiography. *J Magn Reson Imaging* 2004;**19**:686–709.

19 Pannu HK, Flohr TG, Corl FM, Fishman EK. Current concepts in multi-detector row CT evaluation of the coronary arteries: principles, techniques and anatomy. *Radiographics* 2003;**23**: S111–25.

20 Dodd JD, Ferencik M, Liberthson RR, et al. Congenital anomalies of coronary artery origin in adults: 64-MDCT appearance. *Am J Roentgenol* 2007;**188**:W138–W146.

21 Fratz S, Hager A, Schreiber C, et al. Long-term myocardial scarring after operation for anomalous left coronary artery from the pulmonary artery. *Ann Thorac Surg* 2011;**92**:1761–1765.

22 Friedman AH, Fogel MA, Stephens P, et al. Identification, imaging, functional assessment and management of congenital coronary arterial abnormalities in children. *Cardiol Young* 2007;**17**(Suppl 2):56–67.

23 Olabiyi O, Kearney D, Krishnamurthy R, et al. First description of coronary artery ostial atresia with fistulous origin from a normal right ventricle. *Pediatr Cardiol* 2013;**34**:1877–1881.

24 Neufeld HN, Schneeweiss A. *Coronary Artery Disease in Infants and Children*. Philadelphia, PA: Lea and Febiger, 1983.

25 Dodge-Khatami A, Mavroudis C, Backer CL. Congenital Heart Surgery Nomenclature and Database Project: anomalies of the coronary arteries. *Ann Thorac Surg* 2000;**69**:S270–S297.

26 Jacobs ML, Mavroudis C. Anomalies of the coronary arteries: nomenclature and classification. *Cardiol Young* 2010;**20**: 15–19.

27 Shriki JE, Shinbane JS, Rashid A, et al. Identifying, characterizing and classifying congenital anomalies of the coronary arteries. *Radiographics* 2012;**32**:453–468.

28 Angelini P. Normal and anomalous coronary arteries: definitions and classification. *Am Heart J* 1989;**117**:418–434.

29 Brooks HS. Two cases of an abnormal coronary artery of the heart arising from the pulmonary artery: with some remarks upon the effect of this anomaly in producing cirsoid dilatation of the vessels. *J Anat Physiol* 1886;**20**:26–29.

30 Abbott M. Congenital cardiac disease. In: Osler W (ed.) *Modern Medicine: Its Theories and Practices*. Philadelphia, PA: Lea and Febiger; 1908, pp. 323–425.

31 Bland EF, White PD, Garland J. Congenital anomalies of the coronary arteries: report of an unusual case associated with cardiac hypertrophy. *Am Heart J* 1933;**8**:787–801.

32 Keith JD. The anomalous origin of the left coronary artery from the pulmonary artery. *Br Heart J* 1959;**21**:149–161.

33 Rao BN, Lucas RV, Jr, Edwards JE. Anomalous origin of the left coronary artery from the right pulmonary artery associated with ventricular septal defect. *Chest* 1970;**58**:616–620.

34 Pinsky WW, Gillette PC, Duff DF, et al. Anomalous origin of left coronary artery from the pulmonary artery with ventricular septal defect. *Circulation* 1978;**57**:1026–1030.

35 Hallman GL, Cooley DA, Singer DB. Congenital anomalies of the coronary arteries: anatomy, pathology and surgical treatment. *Surgery* 1966;**59**:133–144.

36 Wilcox WD, Hagler DJ, Lie JT, et al. Anomalous origin of left coronary artery from pulmonary artery in association with intracardiac lesions. Report of two cases. *J Thorac Cardiovasc Surg* 1979;**78**:12–20.

37 Driscoll DJ, Garson A, Jr, McNamara DG. Anomalous origin of the left coronary artery from the right pulmonary artery associated with complex congenital heart disease. *Cathet Cardiovasc Diagn* 1982;**8**:55–61.

38 Arciniegas E, Farooki ZQ, Hakimi M, Green EW. Management of anomalous left coronary artery from the pulmonary artery. *Circulation* 1980;**62**:I180–I189.

39 Nehgme RA, Dewar ML, Lutin WA, et al. Anomalous left coronary artery from the main pulmonary trunk: physiologic and clinical importance of its association with persistent ductus arteriosus. *Pediatr Cardiol* 1992;**13**:97–99.

40 Liu F, Huang G, Zhang J. Anomalous origin of a coronary artery from the right branchiocephalic trunk associated with complex congenital heart disease. *Pediatr Cardiol* 2010;**31**:163–165.

41 Edwards JE. The direction of blood flow in coronary arteries arising from the pulmonary trunk. *Circulation* 1964;**29**:163–166.

42 Askenazi J, Nadas AS. Anomalous left coronary artery originating from the pulmonary artery. Report on 15 cases. *Circulation* 1975;**51**:976–987.

43 Wright NL, Baue AE, Baum S, et al. Coronary artery steal due to an anomalous left coronary artery originating from the pulmonary artery. *J Thorac Cardiovasc Surg* 1970;**59**:461–467.

44 Wesselhoeft H, Fawcett JS, Johnson AL. Anomalous origin of the left coronary artery from the pulmonary trunk. Its clinical spectrum, pathology and pathophysiology, based on a review of 140 cases with seven further cases. *Circulation* 1968;**38**:403–425.

45 Irving C, Wren C. Asymptomatic anomalous origin of the left coronary artery from the pulmonary artery. *Pediatr Cardiol* 2009;**30**:385–386.

46 Yau JM, Singh R, Halpern EJ, Fischman D. Anomalous origin of the left coronary artery from the pulmonary artery in adults: a comprehensive review of 151 adult cases and a new diagnosis in a 53-year-old woman. *Clin Cardiol* 2011;**34**:204–210.

47 Awasthy N, Marwah A, Sharma R. Occult anomalous origin of the left coronary artery from the pulmonary artery with ventricular septal defect. *Ann Pediatr Cardiol* 2011;**4**:62–64.

48 Das M, Mahindrakar P, Das D, et al. Anomalous left coronary artery from pulmonary artery with mitral stenosis. *Ann Thorac Surg* 2011;**92**:735–737.

49 Legendre A, Ou P, Bonnet D. Ostial stenosis of an anomalous left coronary artery from the pulmonary artery in a teenager. *Pediatr Cardiol* 2009;**30**:1194–1195.

50 Rein AJ, Colan SD, Parness IA, Sanders SP. Regional and global left ventricular function in infants with anomalous origin of the left coronary artery from the pulmonary trunk: preoperative and postoperative assessment. *Circulation* 1987;**75**:115–123.

51 Schmidt KG, Cooper MJ, Silverman NH, Stanger P. Pulmonary artery origin of the left coronary artery: diagnosis by two-dimensional echocardiography, pulsed Doppler ultrasound and color flow mapping. *J Am Coll Cardiol* 1988;**11**:396–402.

52 Koike K, Musewe NN, Smallhorn JF, Freedom RM. Distinguishing between anomalous origin of the left coronary artery from the pulmonary trunk and dilated cardiomyopathy: role of echocardiographic measurement of the right coronary artery diameter. *Br Heart J* 1989;**61**:192–197.

53 Karr SS, Parness IA, Spevak PJ et al. Diagnosis of anomalous left coronary artery by Doppler color flow mapping: distinction from other causes of dilated cardiomyopathy. *J Am Coll Cardiol* 1992;**19**:1271–1275.

54 Blanco VM, Blalock SE, Ramaciotti C, et al. Oxygen supplementation is helpful for the echocardiographic detection of anomalous left coronary artery from the pulmonary artery. *J Am Soc Echocardiogr* 2010;**23**:1099–1102.

55 Gupta R, Marwah A, Shrivastva S. Anomalous origin of right coronary artery from pulmonary artery. *Ann Pediatr Cardiol* 2012;**5**:95–96.

56 Al-Ammouri IA, Berkwits KM, Fahey JT. Anomalous right coronary artery origin from the pulmonary trunk in an asymptomatic 4-year-old boy. *Pediatr Cardiol* 2009;**30**:1039–1040.

57 Bansal M, Golden AB, Siwik E. Images in cardiovascular medicine. Anomalous origin of the right coronary artery from pulmonary artery with ostial stenosis. *Circulation* 2009;**120**:e282.

58 Winner MW, III, Raman SV, Sun BC, Crestanello JA. Preoperative assessment of anomalous right coronary artery arising from the main pulmonary artery. *Case Rep Med* 2011;**2011**:642126.

59 Collins RT, Davis E, Stephens P. Asymptomatic anomalous right coronary artery from the pulmonary trunk. *Cardiol Young* 2009;**19**:391–392.

60 Bhatia SR, English RF. Anomalous right coronary artery arising from the pulmonary artery: case report and review of literature. *Cardiol Young* 2012;**22**:346–348.

61 Williams IA, Gersony WM, Hellenbrand WE. Anomalous right coronary artery arising from the pulmonary artery: a report of 7 cases and a review of the literature. *Am Heart J* 2006;**152**:1004.e9–1004.e17.

62 Tingelstad JB, Lower RR, Eldredge WJ. Anomalous origin of the right coronary artery from the main pulmonary artery. *Am J Cardiol* 1972;**30**:670–673.

63 Bregman D, Brennan FJ, Singer A, et al. Anomalous origin of the right coronary artery from the pulmonary artery. *J Thorac Cardiovasc Surg* 1976;**72**:626–630.

64 Lerberg DB, Ogden JA, Zuberbuhler JR, Bahnson HT. Anomalous origin of the right coronary artery from the pulmonary artery. *Ann Thorac Surg* 1979;**27**:87–94.

65 Cohen MS, Herlong RJ, Silverman NH. Echocardiographic imaging of anomalous origin of the coronary arteries. *Cardiol Young* 2010;**20**(Suppl 3):26–34.

66 Roberts WC. Major anomalies of coronary arterial origin seen in adulthood. *Am Heart J* 1986;**111**:941–963.

67 Heifetz SA, Robinowitz M, Mueller KH, Virmani R. Total anomalous origin of the coronary arteries from the pulmonary artery. *Pediatr Cardiol* 1986;**7**:11–18.

68 Urcelay GE, Iannettoni MD, Ludomirsky A, et al. Origin of both coronary arteries from the pulmonary artery. *Circulation* 1994;**90**:2379–2384.

69 Tanaka SA, Takanashi Y, Nagatsu M, et al. Origin of the left coronary artery from the right pulmonary artery. *Ann Thorac Surg* 1996;**61**:986–988.

70 Brothers JA, Gaynor JW, Jacobs JP, et al.; Anomalous Coronary Artery Working Group. The registry of anomalous aortic origin of the coronary artery of the Congenital Heart Surgeons' Society. *Cardiol Young* 2010;**20**:50–58.

71 Cheitlin MD, De Castro CM, McAllister HA. Sudden death as a complication of anomalous left coronary origin from the anterior sinus of Valsalva, a not-so-minor congenital anomaly. *Circulation* 1974;**50**:780–787.

72 Davia JE, Green DC, Cheitlin MD, et al. Anomalous left coronary artery origin from the right coronary sinus. *Am Heart J* 1984;**108**:165–166.

73 Barth CW, III, Roberts WC. Left main coronary artery originating from the right sinus of Valsalva and coursing between the aorta and pulmonary trunk. *J Am Coll Cardiol* 1986;**7**:366–373.

74 Kaushal S, Backer CL, Popescu AR, et al. Intramural coronary length correlates with symptoms in patients with anomalous aortic origin of the coronary artery. *Ann Thorac Surg* 2011;**92**:986–992.

75 Chu E, Cheitlin MD. Diagnostic considerations in patients with suspected coronary artery anomalies. *Am Heart J* 1993;**126**:1427–1438.

76 Turner II, Turek JW, Jaggers JJ, et al. Anomalous aortic origin of a coronary artery: preoperative diagnosis and surgical planning. *World J Ped Cong Heart Surg* 2011;**2**:340–345.

77 Bunce NH, Lorenz CH, Keegan J, et al. Coronary artery anomalies: assessment with free-breathing three-dimensional coronary MR angiography. *Radiology* 2003;**227**:201–208.

78 Deibler AR, Kuzo RS, Vohringer M, et al. Imaging of congenital coronary anomalies with multislice computed tomography. *Mayo Clin Proc* 2004;**79**:1017–1023.

79 Roberts WC, Dicicco BS, Waller BF, et al. Origin of the left main from the right coronary artery or from the right aortic sinus with intramyocardial tunneling to the left side of the heart via the ventricular septum: the case against clinical significance of myocardial bridge or coronary tunnel. *Am Heart J* 1982;**104**:303–305.

80 Brandt B, III, Martins JB, Marcus ML. Anomalous origin of the right coronary artery from the left sinus of Valsalva. *N Engl J Med* 1983;**309**:596–598.

81 Taylor AJ, Rogan KM, Virmani R. Sudden cardiac death associated with isolated congenital coronary artery anomalies. *J Am Coll Cardiol* 1992;**20**:640–647.

82 Frommelt PC, Frommelt MA, Tweddell JS, Jaquiss RD. Prospective echocardiographic diagnosis and surgical repair of anomalous origin of a coronary artery from the opposite sinus with an interarterial course. *J Am Coll Cardiol* 2003;**42**:148–154.

83 Mavroudis C, Dodge-Khatami A, Steward RD, et al. An overview of surgery options for congenital coronary artery anomalies. *Future Cardiol* 2010;**6**:627–645.

84 Peñalver JM, Mosca RS, Weitz D, Phoon CKL. Anomalous aortic origin of coronary arteries from the opposite sinus: a critical appraisal of risk. *BMC Cardiovasc Disord* 2012;**12**:83.

85 Jaggers J, Lodge AJ. Surgical therapy for anomalous aortic origin of the coronary arteries. *Semin Thorac Cardiovasc Surg Pediatr Card Surg Annu* 2005;122–127.

86 Choi JH, Kornblum RN. Pete Maravich's incredible heart. *J Forensic Sci* 1990;**35**:981–986.

87 Smith JC. Review of single coronary artery with report of 2 cases. *Circulation* 1950;**1**:1168–1175.

88 Ogden JA, Goodyer AV. Patterns of distribution of the single coronary artery. *Yale J Biol Med* 1970;**43**:11–21.

89 Shirani J, Roberts WC. Solitary coronary ostium in the aorta in the absence of other major congenital cardiovascular anomalies. *J Am Coll Cardiol* 1993;**21**:137–143.

90 Click RL, Holmes DR, Jr, Vlietstra RE, et al. Anomalous coronary arteries: location, degree of atherosclerosis and effect on survival – a report from the Coronary Artery Surgery Study. *J Am Coll Cardiol* 1989;**13**:531–537.

91 Daoud AS, Pankin D, Tulgan H, Florentin RA. Aneurysms of the coronary artery. Report of ten cases and review of literature. *Am J Cardiol* 1963;**11**:228–237.

92 Harris PN. Aneurysmal dilatation of the cardiac coronary arteries: review of the literature and report of a case. *Am J Pathol* 1937;**13**:89–98.

93 Choong AM, Clarke J, Marjot T, et al. Giant coronary artery aneurysm. *J Card Surg* 2013;**28**:51–52.

94 Sondej E, Burgess MI, Holemans JA, Pandya B. Giant left anterior descending artery aneurysm: the value of cardiac magnetic resonance imaging. *J Am Coll Cardiol* 2012;**59**:e5.

95 Tacke CE, Kuipers IM, Groenink M, et al. Cardiac magnetic resonance imaging for noninvasive assessment of cardiovascular disease during the follow-up of patients with Kawasaki disease. *Circ Cardiovasc Imaging* 2011;**4**:712–720.

96 Dawson JE, Jr, Ellison RG. Isolated aneurysm of the anterior descending coronary artery. Surgical treatment. *Am J Cardiol* 1972;**29**:868–871.

97 Ebert PA, Peter RH, Gunnells JC, Sabiston DC, Jr. Resecting and grafting of coronary artery aneurysm. *Circulation* 1971;**43**:593–598.

98 Ghahramani A, Iyengar R, Cunha D, et al. Myocardial infarction due to congenital coronary arterial aneurysm (with successful saphenous vein bypass graft). *Am J Cardiol* 1972;**29**:863–867.

99 Gray LA, Jr, McMartin DE. Surgical treatment of coronary artery aneurysm with rupture into the right atrium. *J Thorac Cardiovasc Surg* 1977;**74**:455–460.

100 Krause W. Uber den Ursprung einer Accessorischen A. coronaria cordis aus der A. pulmonalis. *Z Rationalle Med* 1865;**24**:225–227.

101 McNamara JJ, Gross RE. Congenital coronary artery fistula. *Surgery* 1969;**65**:59–69.

102 Fernandes ED, Kadivar H, Hallman GL, et al. Congenital malformations of the coronary arteries: the Texas Heart Institute experience. *Ann Thorac Surg* 1992;**54**:732–740.

103 Luo L, Kebede S, Wu S, Stouffer GA. Coronary artery fistulae. *Am J Med Sci* 2006;**332**:79–84.

104 Yun H, Zeng MS, Yang S, et al. Congenital coronary artery fistulas: dual-source CT findings from consecutive 6,624 patients with suspected or confirmed coronary artery disease. *Chin Med J (Engl)* 2011;**124**:4172–4177.

105 Neufeld HN, Lester RG, Adams PJ, et al. Congenital communication of a coronary artery with a cardiac chamber or the pulmonary trunk ("coronary artery fistula"). *Circulation* 1961;**24**:171–179.

106 Mangukia CV. Coronary artery fistula. *Ann Thorac Surg* 2012;**93**:2084–2092.

107 Latson LA. Coronary artery fistulas: how to manage them. *Catheter Cardiovasc Interv* 2007;**70**:110–116.

108 Canga Y, Ozcan KS, Emre A, et al. Coronary artery fistula: review of 54 cases from single center experience. *Cardiol J*. 2012;**19**:278–286.
109 Mitsutake R, Miura S, Shiga Y, et al. Coronary–pulmonary artery fistula with anomalous vessels arising from the right coronary sinus detected by 64-MDCT. *Intern Med* 2009;**48**:1893–1896.
110 Klein LW. A new hypothesis of the developmental origin of congenital left anterior descending coronary artery to pulmonary artery fistulas. *Catheter Cardiovasc Interv* 2008;**71**:568–571.
111 Sathanandam SK, Loomba RS, Ilbawi MN, Van Bergen AH. Coronary artery-to-pulmonary artery fistula in a case of pulmonary atresia with ventricular septal defect. *Pediatr Cardiol* 2011;**32**:1017–1022.
112 Anderson RH, Spicer D. Fistulous communications with the coronary arteries in the setting of hypoplastic ventricles. *Cardiol Young* 2010;**20**(Suppl 3):86–91.
113 Valente AM, Lock JE, Gauvreau K, et al. Predictors of long-term adverse outcomes in patients with congenital coronary artery fistulae. *Circ Cardiovasc Interv*, 2010;**3**:134–139.
114 Bishop JO, Mathur VS, Guinn GA. Letter. Congenital coronary artery fistula with myocardial infarction. *Chest* 1974;**65**:233–234.
115 Cason BA, Gordon HJ. Coronary steal caused by a coronary artery fistula. *J Cardiothorac Vasc Anesth* 1992;**6**:65–67.
116 Papadopoulos DP, Bourantas CV, Ekonomou CK, Votteas V. Coexistence of atherosclerosis and fistula as a cause of angina pectoris: a case report. *Cases J* 2010;**3**:70.
117 Burri M, Ackerman K, Malcic I, Horer J. Huge coronary fistula from the left anterior descending coronary artery to the right ventricle in a newborn: a rare congenital anomaly. *Pediatr Cardiol* 2012;**33**:1463–1465.
118 Hayashi G, Inamura N, Kayatani F, et al. Prenatal diagnosis of a left coronary artery to left atrial fistula. *Prenat Diagn* 2012;**32**:194–196.
119 Zhao X, Yang Y, Li RJ. A large hemodynamically significant right coronary artery fistula to right ventricle: prenatal detection and progression. *Echocardiography* 2012;**29**:E173–E175.
120 Anastacio MM, Lee AM, Lawton JS. Congenital fistula from the left main coronary artery to the left atrium presenting with an acute myocardial infarction. *J Thorac Cardiovasc Surg* 2012;**144**:e147–e148.
121 Velvis H, Schmidt KG, Silverman NH, Turley K. Diagnosis of coronary artery fistula by two-dimensional echocardiography, pulsed Doppler ultrasound and color flow imaging. *J Am Coll Cardiol* 1989;**14**:968–976.
122 Urcelay G, Ludomirsky A, Vermilion RP, et al. Acquired coronary artery fistulae after right ventricular myotomy and/or myomectomy for congenital heart disease. *Am J Cardiol* 1995;**75**:408–411.
123 Fischer G, Apostolopoulou SC, Rammos S, et al. Transcatheter closure of coronary arterial fistulas using the new Amplatzer vascular plug. *Cardiol Young* 2007;**17**:283–287.
124 Bafani E, Shukla AC, DiNardo JA. Unrecognized anomalous origin of the left coronary artery from the pulmonary artery as a cause of ventricular fibrillation after patent ductus arteriosus ligation in an infant. *Anesth Analg* 2007;**104**:81–83.

CHAPTER 31

Vascular Rings and Slings

Andrew J. Powell
Department of Cardiology, Boston Children's Hospital, Boston, MA, USA

Introduction

Airway obstruction in children and its accompanying symptoms of stridor and respiratory distress can be caused by intrinsic abnormalities of the tracheobronchial tree and/or extrinsic compression of the airway. Among the causes of the latter are selected abnormalities in the embryologic development of the aorta or pulmonary arteries that may be grouped together as vascular rings and slings.

Vascular rings

Definition

A vascular ring is an anomaly of aortic arch development that results in complete encirclement of the trachea and the esophagus by vascular structures. Some of the vascular components of the ring may not be patent but rather consist of fibrous remnants such as the ductal ligament or an atretic segment of the aorta [1].

Incidence

Because some vascular rings may not cause symptoms, their true prevalence is difficult to ascertain. They are clearly a rare anomaly and most evidence indicates that they represent approximately 1–3% of congenital cardiovascular anomalies [2]. In most but not all surgical case series, a double aortic arch is the most common vascular ring followed by a right aortic arch with an aberrant left subclavian artery and a left ductal ligament [3–8]. The latter type of vascular ring is likely the most common in the general population as it is typically looser and therefore patients may not meet criteria for surgery or may not be diagnosed. Usually, vascular rings are isolated abnormalities, although they may occur with other congenital heart disease, most commonly ventricular septal defect and tetralogy of Fallot [6].

Etiology

The etiology of most vascular rings is unknown. Chromosome 22q11 deletions are associated with isolated aortic arch anomalies, including vascular rings, and also with conotruncal cardiac defects and noncardiac abnormalities [9].

Morphology and classification

Developmental considerations

Knowledge of the morphogenesis of the aortic arch system provides a framework for understanding and classifying the wide variety of vascular rings [10,11]. In the early embryo, six paired arches form to connect the truncus arteriosus of the embryonic heart tube to the paired dorsal aortae, which fuse to form the descending aorta (Figure 31.1). In humans, the arches develop sequentially and persist or regress but are never all present simultaneously. In normal development, the first arches contribute to the external carotid arteries (Table 31.1). The second arches regress rapidly and only a portion remains to form the stapedial and hyoid arteries. The third arches become the common carotid arteries and the proximal portion of the internal carotid arteries. The left fourth arch forms that part of the definitive left aortic arch between the left carotid and left subclavian arteries. The right fourth arch is incorporated into the proximal right subclavian artery. The fifth arches regress. For the sixth arches, the proximal parts form the branch pulmonary arteries and the distal portions join the pulmonary vascular tree to the descending aorta via bilateral ductus, with the right usually regressing completely to leave a left ductus arteriosus. Between the sixth arches (the ductus) and the descending aorta are the paired dorsal aortae, which connect to the descending aorta. The seventh intersegmental arteries arise from the dorsal aortae and become the left subclavian and the distal right subclavian arteries. When the right dorsal aorta regresses, as is usual, the definitive left aortic arch is formed.

In conjunction with embryologic anatomy, the hypothetical double-arch model originally introduced by Edwards [12], and modified, simplified, and redrawn multiple times since, helps one to understand various arch anomalies (Figure 31.2). In this model, the ascending aorta divides into two arches, one passing to the right of the trachea and esophagus and the other to the left. These arches join posteriorly to form the descending aorta.

Echocardiography in Pediatric and Congenital Heart Disease: From Fetus to Adult, Second Edition. Edited by Wyman W. Lai, Luc L. Mertens, Meryl S. Cohen and Tal Geva.
© 2016 John Wiley & Sons, Ltd. Published 2016 by John Wiley & Sons, Ltd.
Companion website: www.lai-echo.com

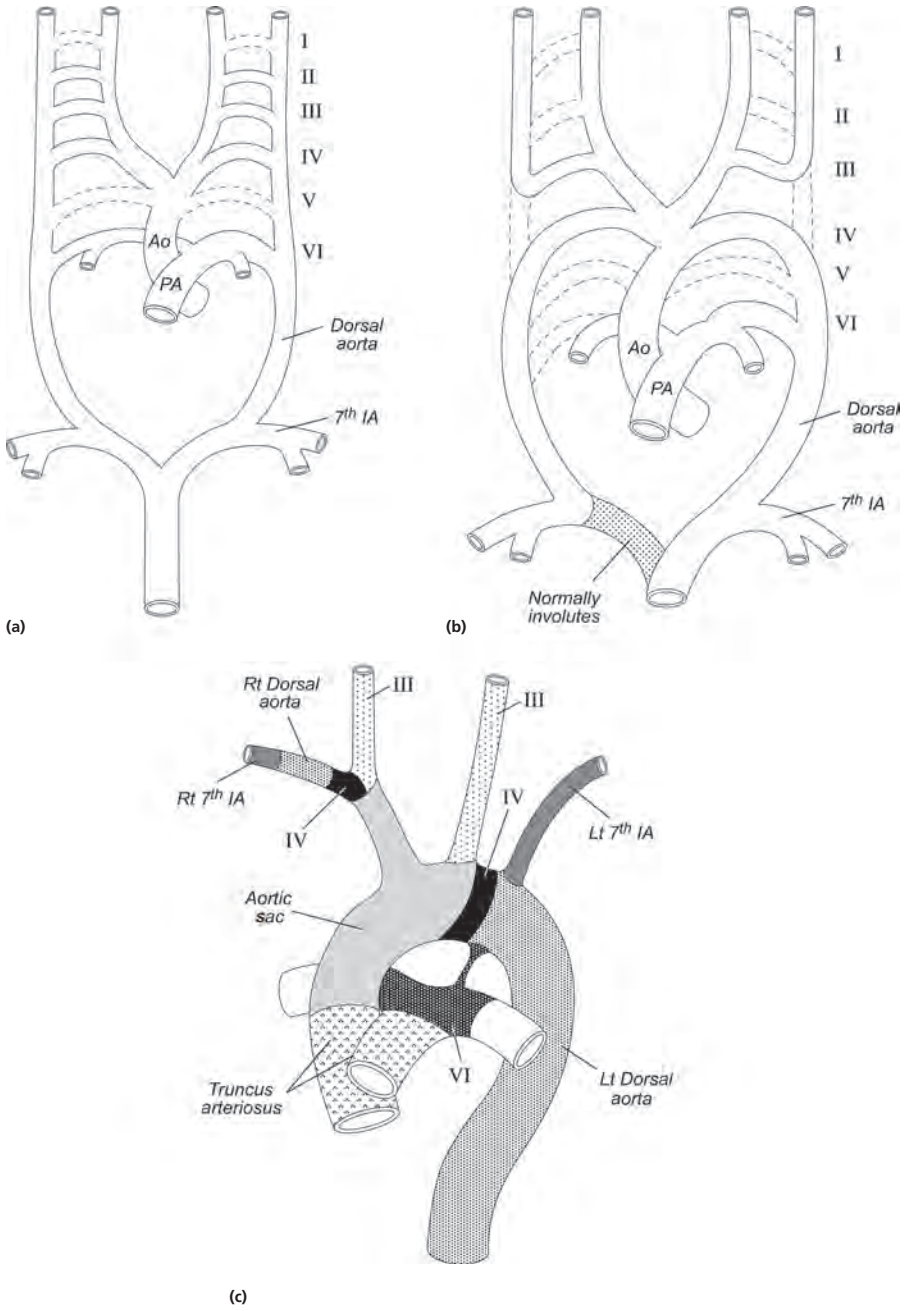


Figure 31.1 Diagrammatic representation of normal aortic arch development at **(a)** 5 weeks, **(b)** 7 weeks, and **(c)** maturity. Roman numerals enumerate the embryonic aortic arches. Ao, ascending aorta; Lt, left; PA, main pulmonary artery; Rt, right; 7th IA, seventh intersegmental artery.

From each arch there is a segment that gives rise to the right and left common carotids as the first branches on either side and the right and left subclavian arteries as the second branches on either side. A ductus arises from the proximal aspect of each subclavian segment. This model allows anomalies of the aortic arch to be conceptualized as variations in regression of segments of the hypothetical double arch. A further simplified line drawing is easily sketched and can be used in daily practice to depict almost every known arch anomaly (Figure 31.3).

Anatomy

Double aortic arch

In a double aortic arch, both of the embryonic right and left arches persist, arising from the ascending aorta, passing on both sides of the trachea and esophagus and joining posteriorly to form the descending aorta, thereby completely encircling the trachea and esophagus (Figures 31.3a, 31.4 and 31.5; Videos 31.1, 31.2, and 31.3). A ductal ligament usually contributes to the ring and is most often left-sided. The carotid

Table 31.1 Normal development of the embryonic aortic arches

Embryonic structure	Outcome
Truncus arteriosus	Proximal ascending aorta and pulmonary root
Aortic sac	Distal ascending aorta, innominate artery, and arch to the origin of the left common carotid artery (proximal aortic arch)
1st arch	Portion of the external carotid artery
2nd arch	Portions of the hyoid and stapedial artery
3rd arch	Common carotid artery and proximal internal carotid artery
4th arch	
Left	Aortic arch segments between the left common carotid artery and left subclavian arteries (distal aortic arch)
Right	Proximal right subclavian artery
5th arch	Complete involution
6th arch	
Left	Proximal portion becomes the proximal left pulmonary artery; distal portion becomes the ductus arteriosus
Right	Proximal portion becomes the proximal right pulmonary artery; distal portion involutes
Left dorsal aorta	Aortic isthmus distal to the left subclavian artery
Right dorsal aorta	Cranial portion becomes the right subclavian artery distal to the contribution from the right 4th arch; distal portion involutes
Left 7th intersegmental artery	Left subclavian artery
Right 7th intersegmental artery	Distal right subclavian artery

and subclavian arteries arise separately from each arch and are usually symmetrically positioned around the trachea. The right arch is larger than the left in approximately 75% of cases and also typically higher [13]. Occasionally, a segment of an arch (usually the left) may be atretic with a fibrous cord either between the carotid and subclavian arteries or distal to the left subclavian artery. In such cases, the aortic arch branching pattern evident on imaging studies may mimic other aortic anomalies.

Right aortic arch with an aberrant left subclavian artery

In the hypothetical double-arch paradigm, a right aortic arch with an aberrant left subclavian artery is the result of regression of the left aortic arch segment between the left common carotid and subclavian segments (Figure 31.3e). As a result, the left subclavian artery originates as the last branch from the aortic arch, at a relatively posterior location, coursing behind the esophagus to the left arm. A left ductal ligament originates from a bulbous dilation at the base of the left subclavian artery (termed the diverticulum of Kommerell) and attaches to the proximal left pulmonary artery, effectively pulling the diverticulum and left pulmonary artery towards each other, compressing the esophagus and trachea and forming a vascular ring (Figure 31.6; Videos 31.4, 31.5, and 31.6). Rarely, the ductus arteriosus is right-sided

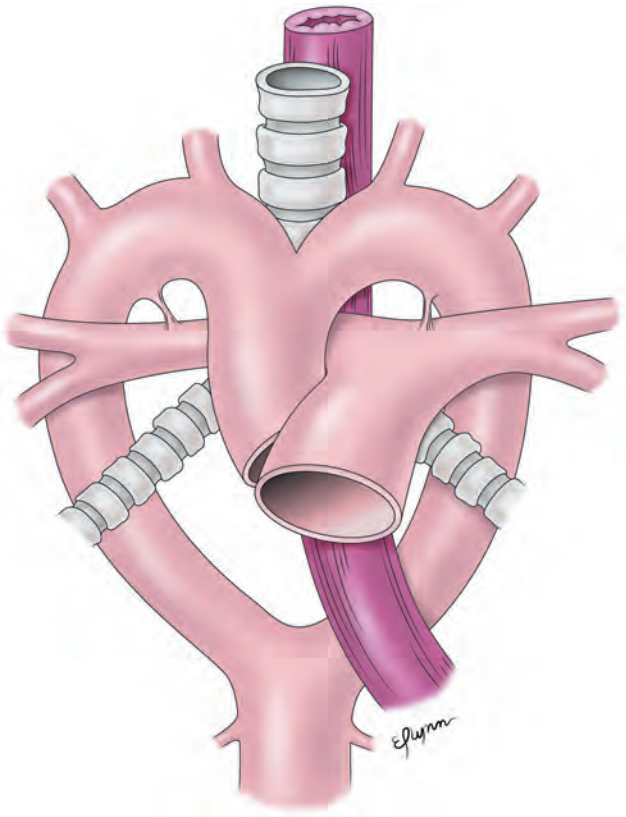


Figure 31.2 Edwards' hypothetical double aortic arch with bilateral ducti.

and connects the right pulmonary artery to the right-sided aortic arch and thus no vascular ring is formed. In such cases, there is no diverticulum of Kommerell and the caliber of the left subclavian artery is uniform throughout.

Right aortic arch with mirror image branching and a left ductus arteriosus

A right aortic arch with mirror image branching has the first branch off the arch as the innominate artery followed by the right carotid and the right subclavian arteries (Figure 31.3d; Video 31.7). Typically, this is the end to the mirror image symmetry of the normal left aortic arch as the ductus arteriosus usually is left-sided, arising anteriorly from the base of the innominate artery (Videos 31.8 and 31.9) rather than posteriorly from the descending aorta. Less frequently, the ductus will arise from the descending aorta and connect to the proximal right pulmonary artery, yielding the true mirror image of the normal left aortic arch. Because in both of these cases there is no left-sided encirclement of the trachea and esophagus, neither forms a vascular ring. On occasion, however, the ductus or ligament arises from the right-sided descending aorta, stemming from a retroesophageal diverticulum, courses leftwards, and then connects to the proximal left pulmonary artery. A vascular ring is thereby formed from the right aortic arch, retroesophageal ductal diverticulum, and left-sided ductal ligament (Figure 31.7). Embryologically, this ring results from regression of a segment of

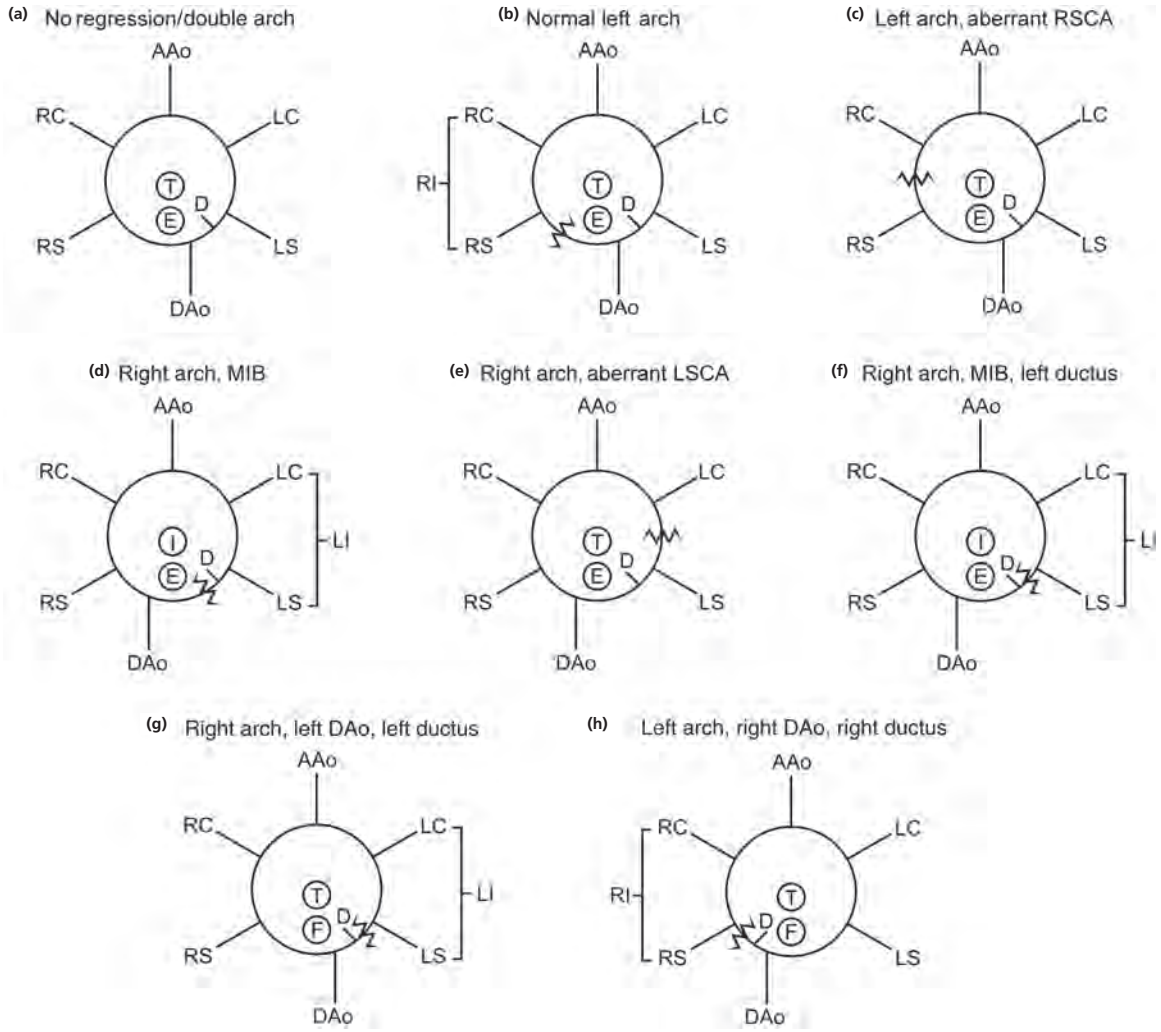


Figure 31.3 Simple line drawings illustrating how anomalies of the aortic arch can be conceptualized as variations in regression of segments of the hypothetical double arch. The jagged line indicates regression of that arch segment. AAo, ascending aorta; D, ductus; DAo, descending aorta; E, esophagus; LC, left carotid; LS, left subclavian; LSCA, left subclavian artery; MIB, mirror image branching; RC, right carotid; RS, right subclavian; RSCA, right subclavian artery; T, trachea.

left dorsal aorta between the left seventh intersegmental artery (destined to become the subclavian artery) and the left sixth arch (destined to become the ductus arteriosus as well as the right sixth arch) (Figure 31.3f).

Right aortic arch with a left descending aorta and a left ductus arteriosus

In this type of vascular ring, there is a right aortic arch that curves leftwards to pass posterior to the esophagus and trachea and then joins a left-sided descending aorta. A left ductus arteriosus or ductal ligament connects the descending aorta and the proximal left pulmonary artery, completing the vascular ring (Figure 31.8; Videos 31.10, 31.11, and 31.12). Note that unlike the more common type of right aortic arch in which the aorta descends to the right of the spine for some distance before gradually crossing to the left of the spine at about the level of the diaphragm, in this anomaly, the aortic arch itself crosses to the left and is posterior to the esophagus, after which it gives rise to the ductus arteriosus. Because of the course of the aorta, some authors have called this a "circumflex retroesophageal right aortic arch." The arch vessel branching pattern may be either the left carotid artery followed by the right carotid, right subclavian and left subclavian arteries or the left innominate followed by the right carotid and right subclavian arteries. Developmentally, depending on the branching pattern, this anomaly results from either regression of the left fourth arch or left dorsal aorta distal to the left subclavian artery (Figure 31.3g). The distal arch is composed of the retroesophageal right-sided dorsal aorta and the persistent left sixth arch (ductus) completes the ring.

Left aortic arch with a right descending aorta and right ductus arteriosus

This anomaly is nearly a mirror image version of the right aortic arch with a left descending aorta and left ductus arteriosus as

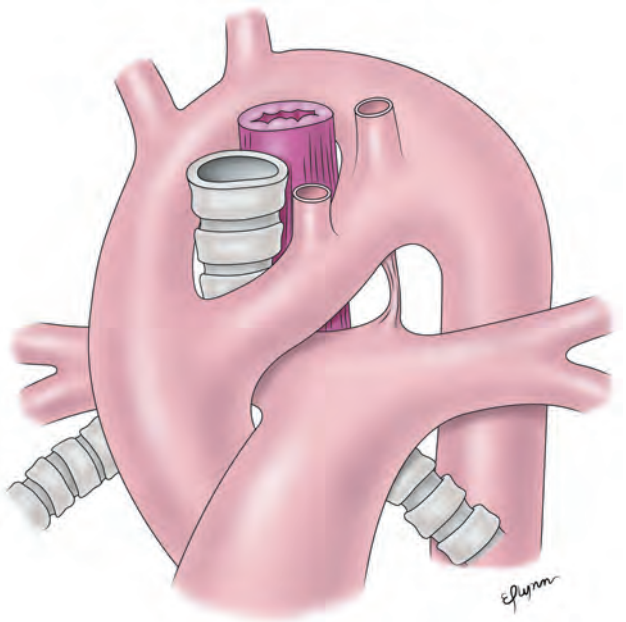


Figure 31.4 Drawing of a double aortic arch. The ring encircling the trachea and esophagus is comprised of the right and left aortic arches and the ductal ligament.

mentioned above, but is less common. A left aortic arch courses posterior to the esophagus and trachea and to the right, leading to a right-sided descending aorta. A ductus or ductal ligament connects the descending aorta and the proximal right pulmonary artery, completing the vascular ring (Figure 31.9). Developmentally, this anomaly results from the regression of the right fourth arch (segment between the right common carotid and right subclavian segments), persistence of the left dorsal aorta passing retroesophageally to a descending aorta beginning to the right of the spine and persistence of the right sixth arch (Figure 31.3h).

Pathophysiology

Vascular rings can cause varying degrees of compression of the trachea and esophagus. Mild tracheal compression may be asymptomatic. More significant involvement in younger patients may manifest as stridor, dyspnea, and a barking cough, all of which are worse during feeding or exertion [4–7]. "Reflex" apnea lasting seconds or even minutes may be triggered by feeding. Older children may have a history of chronic cough or wheezing misdiagnosed as asthma. Symptoms related to esophageal compression are less frequent and less well defined. They include vomiting, choking, and nonspecific feeding difficulties in infants and dysphagia and slow eating in older children.

Imaging

The diagnosis of vascular rings requires a high index of suspicion because of the relative infrequency of this entity compared with other conditions that cause respiratory distress in children, such as asthma, respiratory infection, and gastroesophageal reflux. Once suspected, diagnostic imaging studies should be obtained with the goals of (1) identifying the cause of a patient's symptoms by demonstrating the relevant vascular and airway anatomy and (2) preoperative planning. If video-assisted thoracoscopic surgery is available, it is important to determine whether the ring can be released by dividing ligamentous (nonpatent) or hypoplastic portions. This requires the diagnostician to have a high level of certainty regarding vessel caliber and patency throughout the ring. For both thoracoscopic and open surgery, the diagnosis must be established confidently enough to determine whether a right, left, or midline approach is appropriate.

Many imaging modalities are in use to evaluate vascular rings, including chest radiographs, barium contrast esophagograms, bronchoscopy, X-ray angiography, transthoracic echocardiography, computed tomography (CT), and magnetic resonance imaging (MRI). Development of a single universal diagnostic imaging algorithm is complicated by varying ages and modes of presentation and the numerous specialists involved in such cases. There are no reported studies that rigorously compared different imaging strategies with respect to accuracy, patient safety, and cost-effectiveness. In practice, a center's diagnostic testing algorithm is tailored to fit local expertise, experience, costs, and available technology. The approach is then individualized to the patient taking into account severity of symptoms, previous findings, age, and other medical conditions. It is important to note that no imaging modality except direct visualization can reliably show ligamentous or atretic structures. Their presence is typically inferred based on anatomic patterns, the position of vessels, and the presence of a diverticulum or dimple.

Echocardiography can provide a good depiction of the relevant vasculature and in many cases is sufficient for diagnosis and surgical planning [14,15]. It has the additional advantage of being able to define associated cardiovascular anomalies. Its principal weakness is poor visualization of the airway and esophagus. In addition, not infrequently portions of the dorsal aortic arch may be obscured by the trachea and posterior vessels such as aberrant subclavian arteries may be difficult to visualize in their entirety. Because of these limitations, the evaluation for a vascular ring with echocardiography may be incomplete and additional imaging with CT or MRI may be indicated (Figure 31.10; Videos 31.3 and 31.6).

In practice, if a left aortic arch with a normal branching pattern is clearly demonstrated by echocardiography, a vascular ring is excluded. Note, however, that simply demonstrating the presence of a right aortic arch with mirror image branching does not always exclude a vascular ring. This pattern may be seen in rings such as right aortic arch with mirror image branching and a left ductus or a double aortic arch with an atretic left arch segment distal to the left subclavian artery. Features that can help identify these uncommon vascular rings, such as tracheal narrowing and the presence of a dimple or diverticulum, are difficult or impossible to detect by echocardiography.

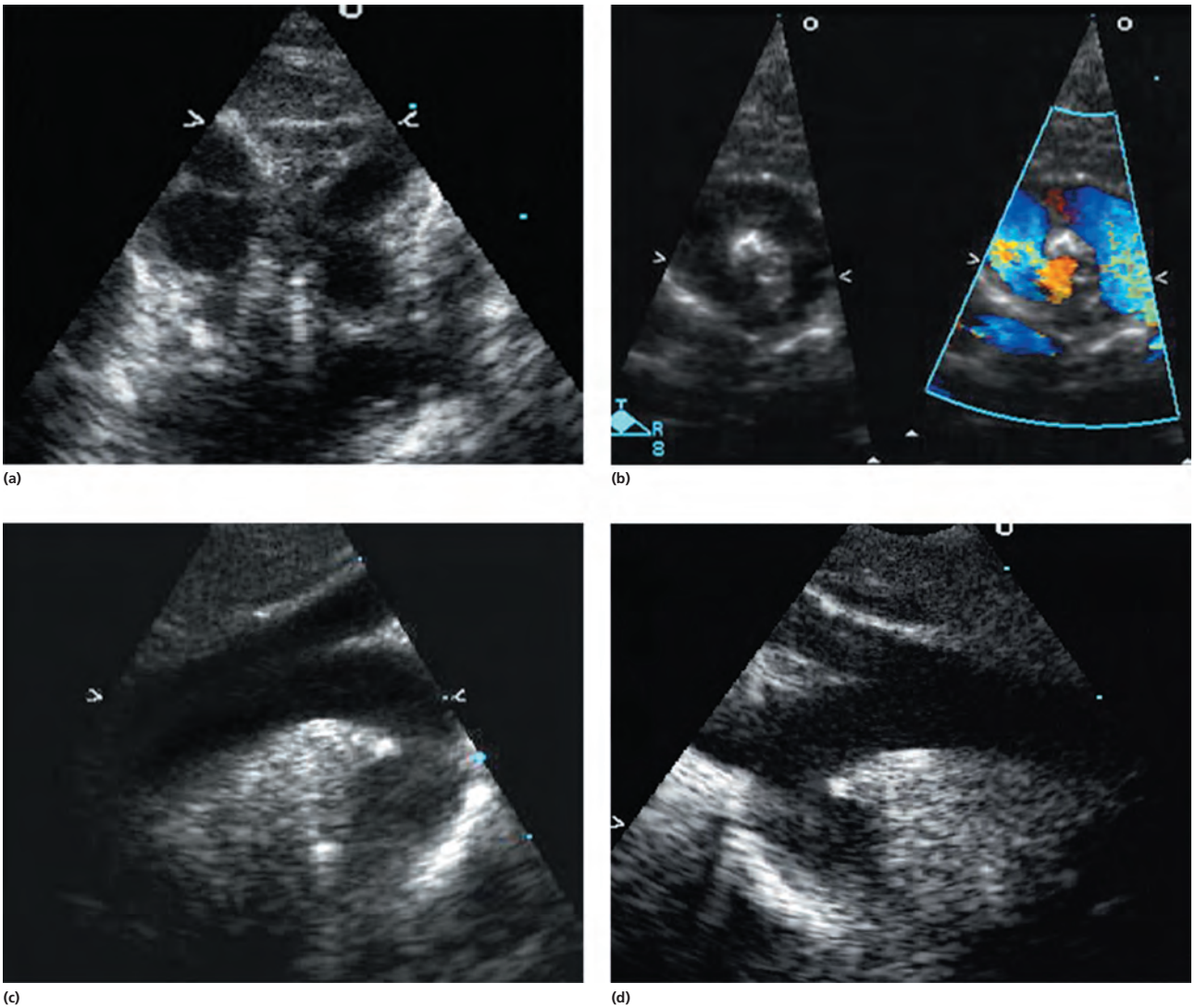


Figure 31.5 Echocardiographic imaging of a double aortic arch. Echocardiogram using a suprasternal notch window. **(a)** Transverse view superior to the arch level illustrating the symmetric origins of the right and left carotid and subclavian arteries from their respective arches. **(b)** Transverse view demonstrating the right and left aortic arches with two-dimensional and color Doppler imaging. **(c)** Long-axis view of the unobstructed left aortic arch. **(d)** Long-axis view of the unobstructed right aortic arch. Note that by convention, right aortic arches are displayed with the right–left screen orientation inverted so that superior structures are positioned to the left on the screen.

Echocardiography imaging protocol

As with all medical procedures, proper preparation is paramount and will maximize the likelihood of success. The medical history and prior imaging studies should be reviewed. Sedation with appropriate monitoring should be used in those patients who are not able to cooperate for a comprehensive echocardiogram and is well tolerated even in patients with moderate degrees of stridor [14]. The suprasternal notch and high parasternal windows are the most useful for examination of the aortic arch and, typically, elevating the patient's shoulders with a cushion so that the neck is extended approximately 30° optimizes the imaging. From either of these windows, it is useful to begin this portion of the examination with an axial (transverse) sweep of the transducer (i.e., marker directed to the patient's left). The sweep begins inferiorly, showing the ascending aorta and superior vena cava in cross-section, passing superiorly through the pulmonary arteries and continuing through the aortic arch and its branches (Video 31.13). It is often necessary to reposition the transducer to follow best the branching of the vessels arising from the aortic arch. From these images, arch sidedness can be determined based on whether the transverse arch courses to the left (left arch) or right (right arch) of the trachea. The trachea is identified as an echo-bright structure (because it is air filled) that runs vertically in the midline (Figure 31.11). A left aortic arch will curve to the left as it is followed distally to a descending aorta that is positioned left of the spine (Video 31.13). However, because the ascending aorta is positioned relatively rightwards to start, a right aortic arch will be primarily directed straight posteriorly,

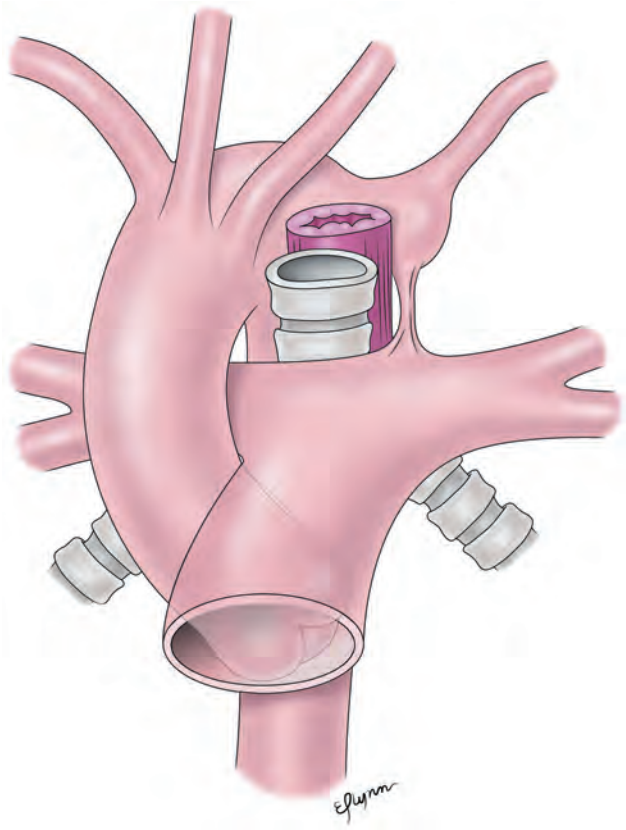


Figure 31.6 Drawing of a right aortic arch with an aberrant origin of the left subclavian artery. The ring encircling the trachea and esophagus is comprised of the right aortic arch, base of the left subclavian artery (diverticulum of Kommerell), and the left-sided ductal ligament.

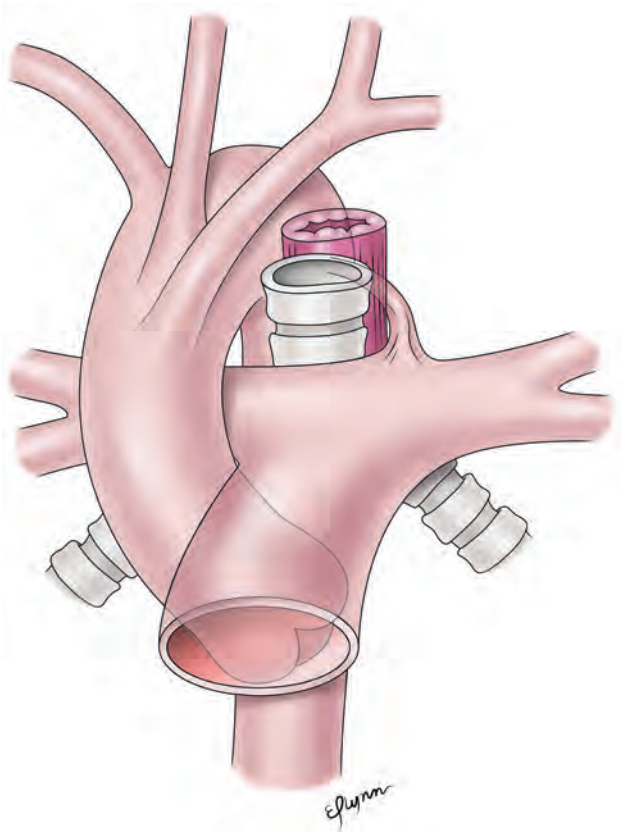


Figure 31.7 Drawing of a right aortic arch with mirror image branching and a left ductal ligament. The ring encircling the trachea and esophagus is comprised of the right aortic arch, retroesophageal ductal diverticulum, and left-sided ductal ligament.

rather than rightwards, as it is followed distally to a descending aorta that is usually positioned to the right of the spine (Figure 31.11; Videos 31.4, 31.7, and 31.8). In a double aortic arch, the ascending aorta is seen to split into two arch vessels that course to the right and left of the trachea (Figure 31.5; Videos 31.1 and 31.2). As the trachea can sometimes be difficult to identify, some echocardiographers have found it helpful to highlight the esophagus by having the patient drink a liquid (preferably carbonated) and then use this as a midline landmark and substitute for the trachea to determine whether the arch passes to the left or right.

The branching pattern of the aortic arch vessels should also be defined from the axial sweeps and can be of some help in identifying arch sidedness. One can begin by determining whether the first (i.e., most proximal) vessel off the arch is an innominate artery by following it superiorly and laterally and demonstrating that it bifurcates into two vessels of nearly equal caliber – a common carotid artery that continues into the neck and a subclavian artery that courses towards the shoulder (Videos 31.7 and 31.13). To demonstrate bifurcation, it may be helpful to rotate the transducer to image the suspected innominate artery and branches in long-axis. The innominate artery is also typically larger at its origin than the other vessels off the arch. One must be careful not to mistake the bifurcation of the superior vena cava into the subclavian and jugular veins for the innominate artery bifurcation. Demonstration of an arterial flow pattern in the vessels by pulsed-wave (PW) or color Doppler will help avoid this error. Note also that some patients, particularly those with a chromosome 22q11 deletion, may have an unusually distal bifurcation. If bifurcation of the first branch off the arch cannot be demonstrated (i.e., it is not an innominate artery), the branch is usually a carotid artery and the echocardiographer should suspect the presence of an aberrant origin of the subclavian artery from the descending aorta. Other possibilities in this situation include double aortic arch and isolation of the subclavian artery. Efforts should be made to visualize the aberrant subclavian artery by imaging the proximal descending aorta from a suprasternal notch window, aiming the transducer towards the feet in an oblique coronal imaging plane (Videos 31.5 and 31.14). The aberrant subclavian arises from the medial aspect of the descending aorta and crosses the midline and courses superiorly. Color Doppler imaging is useful in highlighting the vessel; blood flow in it will usually be towards the transducer (i.e., red).

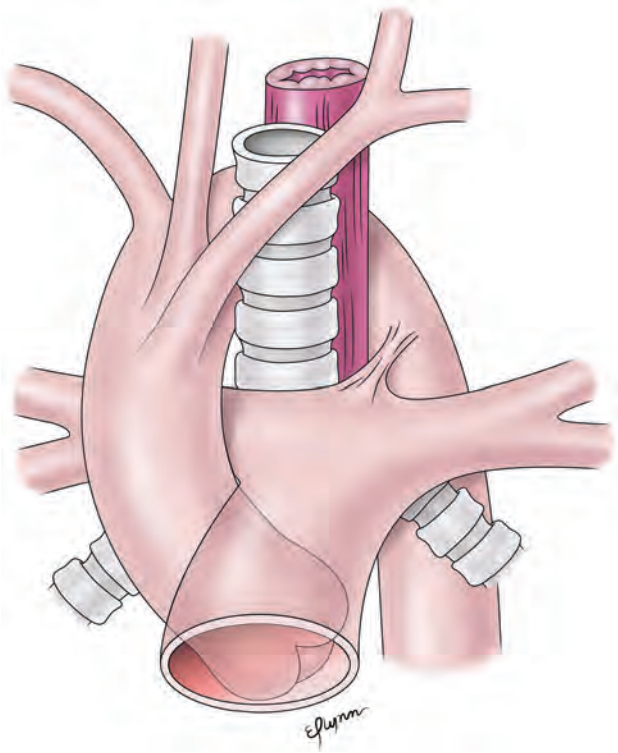


Figure 31.8 Drawing of a right aortic arch with mirror image branching, a left descending aorta, and a left ductal ligament. The ring encircling the trachea and esophagus is comprised of the right aortic arch, retroesophageal right-sided dorsal aorta, and left-sided ductal ligament.

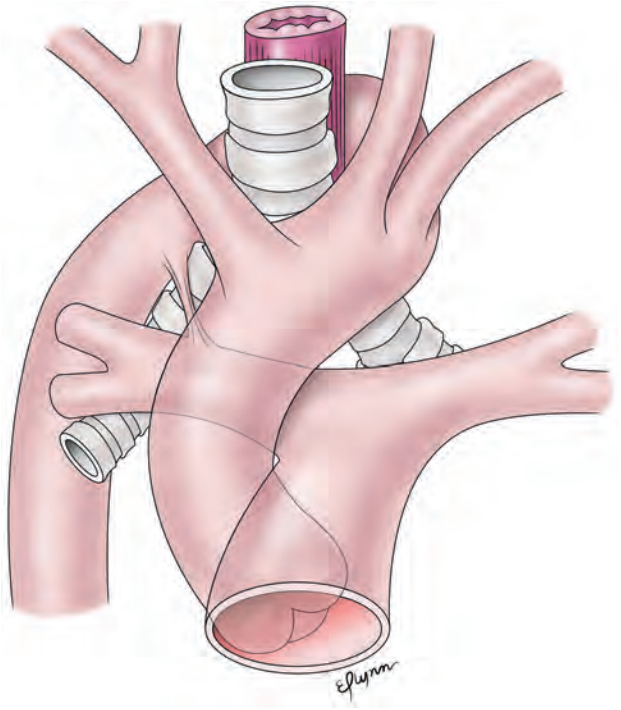


Figure 31.9 Drawing of a left aortic arch with mirror image branching, a right descending aorta, and a right ductal ligament. The ring encircling the trachea and esophagus is comprised of the left aortic arch, retroesophageal left-sided dorsal aorta, and right-sided ductal ligament.

After demonstrating the bifurcation of the first arch branch, the other arch vessels and the location of the proximal descending aorta should be identified. Echocardiographers should be familiar with two frequent normal variants of the left aortic arch. One is the common brachiocephalic trunk (also known as a bovine or ovine trunk) in which the innominate and left carotid arteries arise from a single origin [16]. The other is a separate origin of the left vertebral artery from the aortic arch proximal to the left subclavian artery rather than from the subclavian artery. Once the branching pattern of the aortic arch vessels is known, it can help confirm the sidedness of the arch. With the exception of the very rare isolated or aberrant innominate artery, the first arch vessel contains a carotid artery opposite to the side of the aortic arch [1]. Thus, in a right aortic arch, the first (i.e., most proximal) branch should course to the left and either bifurcate into left carotid and subclavian arteries as in mirror image branching (Video 31.7), or continue without bifurcating as the left carotid artery as in an aberrant origin of the left subclavian artery (Video 31.4). In a double aortic arch, the carotid and subclavian arteries arise separately from their respective arches. As a result, the initial axial sweeps often reveal a view of the aorta and its vessels with right–left symmetry that is characteristic of a double aortic arch (Figure 31.5a; Video 31.1).

Having established the basic anatomy of the aorta, long-axis imaging of the arch is then performed in oblique sagittal planes with particular attention to the caliber of the various arch segments and identifying obstruction. Some echocardiography laboratories by convention display long-axis images of right arches with the right–left orientation inverted so that superior structures are positioned to the left on the screen (Figure 31.5c and d). This presentation may be accomplished by rotating the transducer 180° or by selecting a right–left inversion option on the echocardiography machine. Assessment of the arch from long-axis views should be complemented by spectral and color Doppler imaging. In patients with a double aortic arch, it is important to interrogate completely both arches for obstruction as one will frequently be smaller or have an atretic portion. Differentiation of the right from the left arch may be facilitated by careful sweeps from side to side. An active effort should also be made to identify arterial ducts, keeping in mind the variety of potential locations and that they may be bilateral. Finally, subcostal imaging may be useful in identifying the position of the descending aorta relative to the spine.

Prenatal assessment

There are several reports describing the diagnosis of vascular rings by fetal echocardiography [17–24]. The overall approach to imaging is similar to that in postnatal echocardiography. Because the lumen of the trachea in the fetus is filled with fluid, it appears echo-dark and is often quite distinct. Another relative advantage in assessing the fetus is that the ductus arteriosus

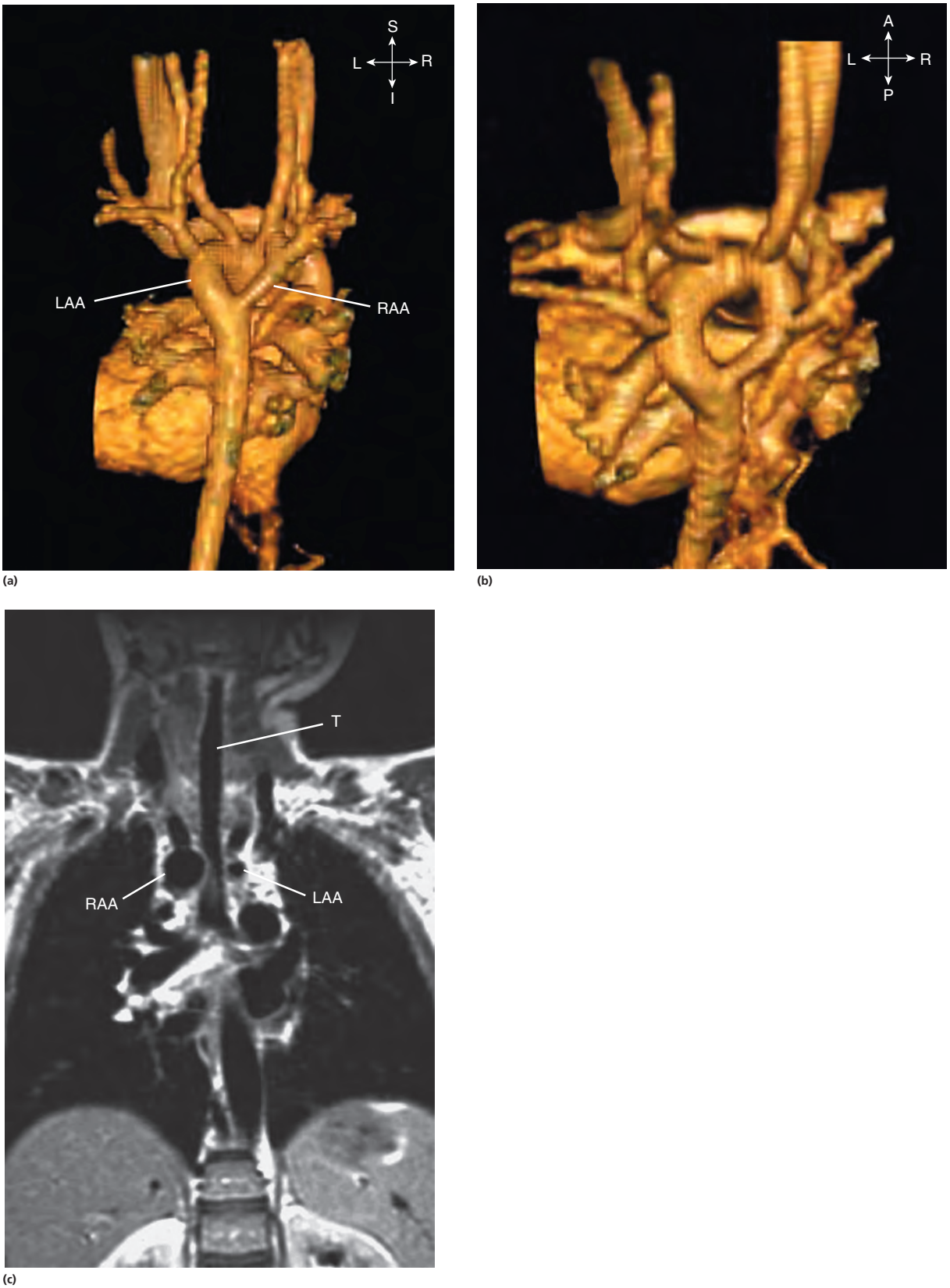


Figure 31.10 Double aortic arch with both arches patent. Volume rendered three-dimensional magnetic resonance angiogram viewed from **(a)** posterior and **(b)** superior vantage points. **(c)** MRI using fast spin-echo imaging and blood signal suppression in an oblique coronal plane illustrating tracheal compression by the right and left aortic arches which are seen in cross-section. LAA, left aortic arch; RAA right aortic arch; T, trachea.

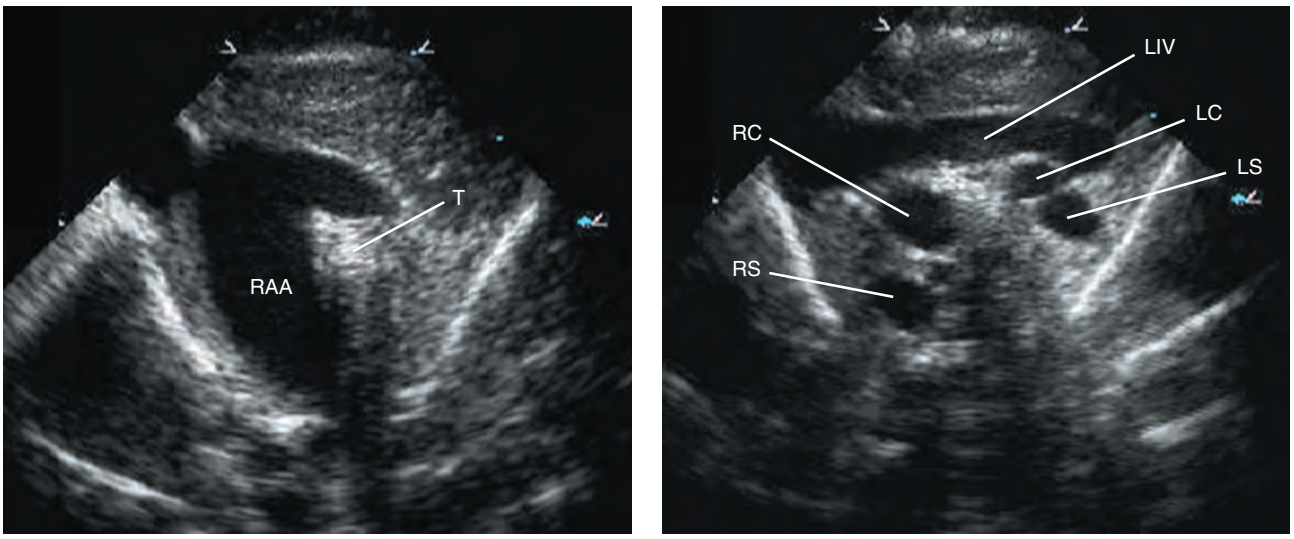


Figure 31.11 Right aortic arch and mirror image branching. Echocardiogram using a suprasternal notch window. **(a)** Transverse view showing the transverse aortic arch (RAA) positioned to the right of the echo-bright trachea (T). **(b)** Transverse view superior to the aortic arch showing the arch vessel branching pattern. LC, left carotid artery; LIV, left innominate vein; LS, left subclavian artery; RC, right carotid artery; RS, right subclavian artery.

is patent rather than ligamentous and therefore this component of the ring is easily visualized. A particularly careful assessment for a vascular ring should be made in any fetus with congenital heart disease or with a diagnosis of 22q11 deletion. Moreover, any fetus who has a vessel coursing posterior to the trachea has a high likelihood of a vascular ring [21].

Intraoperative assessment

Once the diagnosis has been established, echocardiography has little role in intraoperative assessment during surgical division of vascular rings.

Follow-up assessment

Complications related to vascular ring division are rare, and those which occur, such as nerve damage, chylothorax, or incomplete ring division, are difficult to assess by echocardiography. Similarly, clinical issues in follow-up usually relate to airway and swallowing symptoms and echocardiography is rarely helpful.

Pulmonary artery sling

Definition

Pulmonary artery sling, also known as anomalous left pulmonary artery from the right pulmonary artery, is a vascular anomaly in which the left pulmonary artery arises aberrantly from the proximal part of the right pulmonary artery and courses over the right mainstem bronchus, posterior to the trachea and anterior to the esophagus, to reach the left hilum (Figure 31.12). This arrangement creates a vascular "sling" hooked around and often compressing the trachea but not the esophagus.

Incidence

Pulmonary artery sling is a very rare congenital malformation; reliable data on its prevalence have not been published.

Etiology

Pulmonary artery sling is a developmental malformation. A genetic association (Mowat–Wilson syndrome) has been identified [25–28].

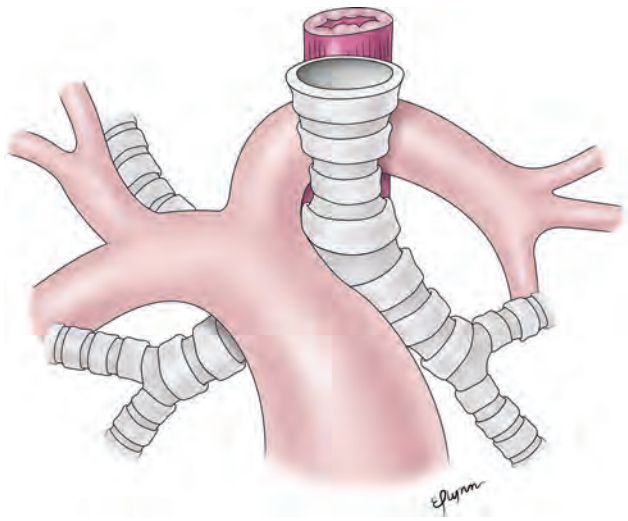


Figure 31.12 Drawing of a left pulmonary artery sling. The left pulmonary artery arises aberrantly from the proximal right pulmonary artery and courses posterior the trachea and anterior to the esophagus towards the left hilum.

Morphology and classification

Developmental considerations and anatomy

Normally, the distal pulmonary arteries arise for their respective lung buds and join the proximal pulmonary arteries that have formed from the sixth aortic arch [10]. The embryology of the pulmonary artery sling has not been definitively identified. It been hypothesized to occur when the proximal part of the left sixth arch regresses or fails to develop its normal connections to the left lung bud and a "collateral" vessel to the left lung develops. This vessel originates from the transverse portion of the right pulmonary artery, just to the right of the trachea, and then curves posteriorly and sharply to the left, superior and posterior to the right main bronchus and trachea, but anterior to the esophagus in its course to the left hilum and lung. The ductal ligament is positioned to the left of the trachea and connects the descending aorta to the distal main pulmonary artery. This anatomic arrangement causes constriction of the right main bronchus, the trachea, or both. In at least half of the cases, there are associated complete cartilaginous tracheal rings in which the posterior membranous portion of the trachea and proximal bronchi is absent and the tracheal cartilage is circumferential, the so-called "ring–sling" complex [29]. The complete cartilaginous rings may be localized to the area adjacent to the sling or extend throughout the trachea. Complete cartilaginous rings are often but not always associated with significant airway narrowing and may be an important source of airway symptoms in addition to the sling itself. Other abnormalities associated with left pulmonary artery sling include a tracheal origin of the right upper lobe bronchus (also known as bronchus suis), hypoplastic left pulmonary artery, right lung agenesis, and atrial and ventricular septal defects [30,31].

Pathophysiology

The airway narrowing associated with left pulmonary artery sling leads to respiratory stridor and distress that are often severe and typically manifest in the newborn period. In addition, left pulmonary artery hypoplasia can lead to decreased left lung perfusion and pulmonary hypertension.

Imaging

Echocardiography can usually demonstrate the abnormal origin of the left pulmonary artery and is sufficient to establish the diagnosis [14,15,32]. Because of the high incidence of tracheal anomalies other than simple compression by the sling, bronchoscopy is also warranted in most cases. This may be supplemented by CT or MRI as needed to ensure that the trachea, bronchi, and pulmonary arteries have been completely assessed (Figure 31.13) [33–35]. Angiography and bronchography are rarely indicated.

Echocardiography imaging protocol

Echocardiography for diagnosing pulmonary artery sling focuses on imaging of the pulmonary arteries. The suprasternal notch and high parasternal windows are the most useful; positioning the patient on their left side or elevating their shoulders with a cushion may improve visualization. The abnormal origin of the left pulmonary artery is best appreciated by imaging in an axial (transverse) orientation (i.e., marker directed to the patient's left). The origin of the left pulmonary artery is displaced to the right and appears as a vessel arising from the posterior or superior aspect of the right pulmonary artery (Figure 31.14; Video 31.15). The left pulmonary artery then curves leftwards and posterior to the echo-bright distal trachea and continues towards the left hilum. One should become suspicious for this lesion when the proximal left pulmonary artery does not have its typical course in which it travels primarily posteriorly and only slightly leftwards, appearing nearly as a continuation of the main pulmonary artery. Alternatively, a left pulmonary artery sling can be missed by mistaking the left atrial appendage or a patent ductus arteriosus for a normal left pulmonary artery [32]. Imaging from a subcostal window in the coronal plane may also be used to demonstrate the course of the pulmonary arteries. Once the diagnosis has been established, the size of the pulmonary arteries should be measured from 2D images. Color Doppler is often useful in delineating the course of the pulmonary arteries and spectral Doppler assessment should be performed to estimate the degree of obstruction. Note that the maximal instantaneous gradient may be low in the setting of significant anatomic obstruction if most of the flow is into the right pulmonary artery.

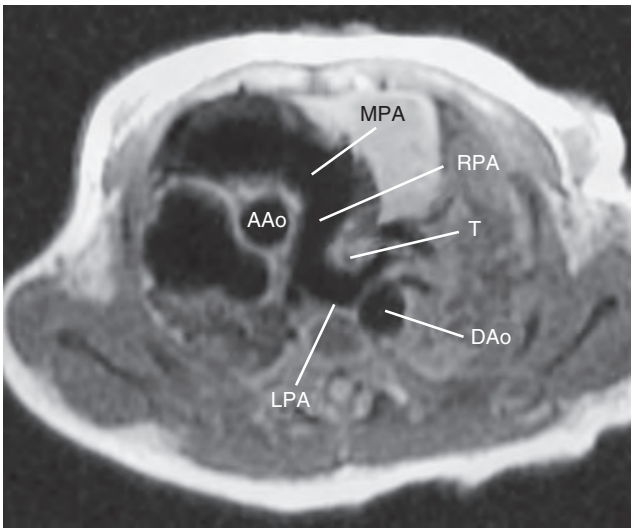


Figure 31.13 Left pulmonary artery sling. MRI using fast spin-echo imaging and blood signal suppression in an axial plane, illustrating the left pulmonary artery arising from the right pulmonary artery and coursing posterior to the narrowed trachea. Note also the right lung hypoplasia and secondary dextrocardia. AAo, ascending aorta; DAo, descending aorta; LPA, left pulmonary artery; MPA, main pulmonary artery; RPA, right pulmonary artery; T, trachea.

Prenatal assessment

Prenatal diagnosis of a left pulmonary artery sling is extremely rare. In principle, the same strategy as is applied to postnatal

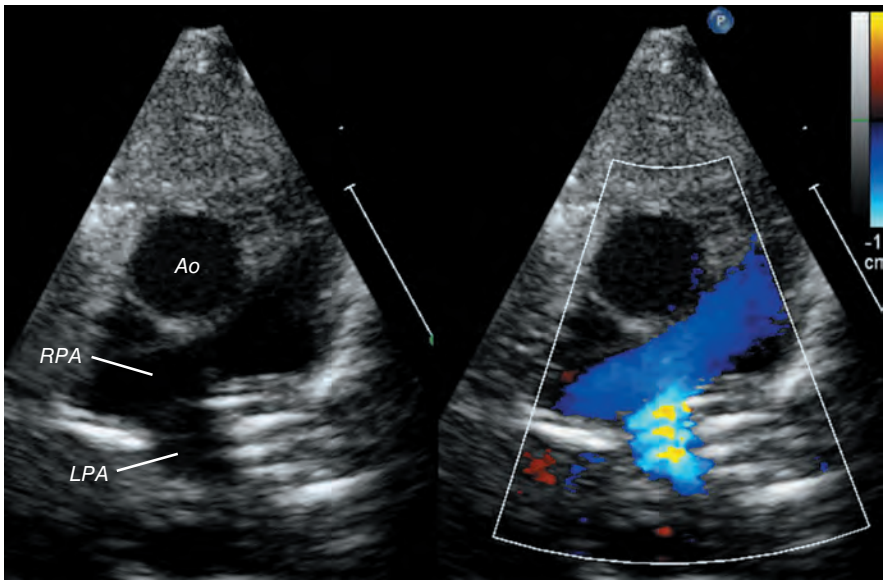


Figure 31.14 Left pulmonary artery sling. Echocardiogram using a high parasternal window, a transverse orientation, and two-dimensional and color Doppler imaging. Note that the left pulmonary artery (LPA) arises from the right pulmonary artery (RPA) and courses leftwards and posterior to the faintly seen echo-bright trachea.

assessment should be employed. One should make a concerted effort to visualize the main and branch pulmonary arteries in fetuses with pulmonary abnormalities.

Intraoperative assessment

Transesophageal echocardiography can be used intraoperatively to assess the branch pulmonary arteries. Particular attention should be paid postoperatively to evaluating the left pulmonary artery for obstruction.

Follow-up assessment

Patients who have undergone repair of a left pulmonary artery sling have a high incidence of left pulmonary artery stenosis [36]. Accordingly, the branch pulmonary arteries should be assessed with 2D imaging and Doppler techniques and the right ventricular pressure estimated using the tricuspid regurgitation jet velocity and ventricular septal position.

Innominate artery compression syndrome

Definition and etiology

Innominate artery compression syndrome refers to children with symptoms of airway obstruction who are found to have significant tracheal narrowing where the innominate artery passes anteriorly to it [37]. Typically, localized tracheomalacia with dynamic airway narrowing is found, but it remains controversial whether this is primarily an intrinsic airway problem. Some reports have attributed the tracheal narrowing to a more distal, posterior, and leftward origin of the innominate artery from the aortic arch; however, careful studies have not found this to be a consistent finding [38–40]. Others have proposed that mediastinal crowding and an enlarged thymus gland contribute to the pathology. Innominate artery compression syndrome is rarely associated with congenital heart disease.

Pathophysiology

Presentation is in infancy with stridor that may be sufficiently severe to cause apnea or syncope. Feeding difficulties (e.g., poor weight gain, gastroesophageal reflux) and a history of esophageal atresia and tracheoesophageal fistula are common.

Imaging

Because echocardiography is poorly suited for the evaluation the trachea, it has little role in establishing a diagnosis of innominate artery compression syndrome. Rather, this condition is best identified through a combination of bronchoscopy and CT or MRI. On bronchoscopy, there is a characteristic anterior pulsatile indentation of the trachea 1–2 cm above the carina. The trachea should be narrowed at least 50–75% during spontaneous respiration to attribute symptoms to this diagnosis. The imaging studies demonstrate the relationship of the aorta, innominate artery and thymus to the trachea (Figure 31.15).

Videos

To access the videos for this chapter, please go to www.lai-echo.com.

Video 31.1 Double aortic arch. Echocardiogram in a transverse orientation from a suprasternal notch window illustrating the symmetric origins of the right and left common carotid and subclavian arteries from their respective arches and left and right dorsal arches which are similar in size.

Video 31.2 Double aortic arch. Echocardiogram with two-dimensional and color Doppler imaging in a transverse orientation from a suprasternal notch window demonstrating right and left aortic arches which are similar in size. The echo-bright structure in the center of the arches is the air-filled trachea.

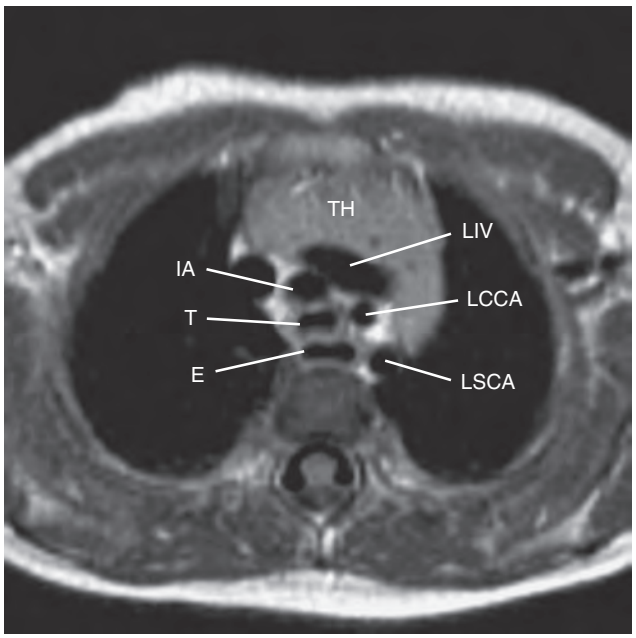


Figure 31.15 Innominate artery compression syndrome. MRI using fast spin-echo imaging and blood signal suppression in an axial plane, illustrating a narrow trachea with the innominate artery located anteriorly. E, esophagus; IA, innominate artery; LCCA, left common carotid artery; LIV, left innominate vein; LSCA, left subclavian artery; T, trachea; TH, thymus.

Video 31.3 Double aortic arch. Volume rendered three-dimensional magnetic resonance angiogram demonstrating approximately equal-sized left and right aortic arches. Note that the right arch is positioned slightly more superiorly than the left arch. The trachea and esophagus are not depicted in this rendering; they would both be positioned inside the ring formed by the aortic arches.

Video 31.4 Right aortic arch with an aberrant origin of the left subclavian artery. Echocardiogram in a transverse orientation from a suprasternal notch window demonstrating the transverse aortic arch coursing to the right of the echo-bright trachea. The first branch off the arch is the left common carotid artery. It courses leftwards and superiorly into the neck, where it is positioned just medially to the left jugular vein. The second and third branches off the arch are the right common carotid and right subclavian arteries, respectively. If, as in this case, there is a right aortic arch and the first branch off the arch fails to bifurcate into the left carotid and left subclavian arteries, this finding should raise suspicion for an aberrant origin of the left subclavian artery. The aberrant left subclavian artery itself is not depicted on this imaging sweep.

Video 31.5 Right aortic arch with an aberrant origin of the left subclavian artery. Echocardiogram with color Doppler showing a transverse to coronal sweep from a suprasternal notch window. The aberrant origin of the left subclavian artery from the proximal descending aorta is shown toward the end of the movie with its flow directed superiorly towards the transducer (red signal).

Video 31.6 Right aortic arch with an aberrant origin of the left subclavian artery. Volume rendered three-dimensional magnetic resonance angiogram. Note that the left subclavian artery has a broad base at its origin (diverticulum of Kommerell) and then tapers more distally.

Video 31.7 Right aortic arch with mirror image branching. Echocardiogram in a transverse orientation from a suprasternal notch window demonstrating the transverse aortic arch coursing to the right of the echo-bright trachea. The first branch off the arch is the left innominate artery, which is then seen to bifurcate into the left common carotid and left subclavian arteries. The second and third branches off the arch are the right common carotid and right subclavian arteries, respectively.

Video 31.8 Right aortic arch, mirror image branching, and a left-sided ductus arteriosus from the innominate artery. Echocardiogram in a transverse orientation from a suprasternal notch window demonstrating the transverse aortic arch coursing to the right of the echo-bright trachea and the left innominate artery bifurcating into the left common carotid and left subclavian arteries. The ductus arteriosus can be faintly seen coursing from the base of the left innominate artery to the proximal left pulmonary artery.

Video 31.9 Right aortic arch, mirror image branching, and a left-sided ductus arteriosus from the innominate artery. This is a similar imaging sweep to that in Video 31.8, now with color Doppler. The ductus arteriosus is demonstrated (blue signal) flowing from the base of the left innominate artery to the proximal left pulmonary artery.

Video 31.10 Right aortic arch with a left descending aorta and a left ductus arteriosus. Echocardiogram in a transverse orientation from a suprasternal notch window demonstrating the transverse aortic arch coursing to the right of the echo-bright trachea. The first branch off the arch is the left innominate artery, which is then seen to bifurcate into the left common carotid and left subclavian arteries. The second and third branches off the arch are the right common carotid and right subclavian arteries, respectively. Note that the transverse aortic arch courses not only posteriorly but also slightly leftwards and that the proximal descending aorta is positioned posterior to the trachea.

Video 31.11 Right aortic arch with a left descending aorta and a left ductus arteriosus. This is a similar imaging sweep to that in Video 31.10, now with color Doppler to highlight the anatomy.

Video 31.12 Right aortic arch with a left descending aorta and a left ductus arteriosus. This is similar imaging sweep to that in Video 31.11 but with the color Doppler box positioned more leftwards. The proximal descending aorta is positioned to the left of the trachea and the ductus arteriosus arises from it and courses to the left of the trachea to drain into the main pulmonary artery.

Video 31.13 Left aortic arch with normal branching. Echocardiogram in a transverse orientation from a suprasternal notch window demonstrating the transverse aortic arch coursing to the left of the

echo-bright trachea. The first branch off the arch is the right innominate artery, which is then seen to bifurcate into the right common carotid and right subclavian arteries. The second and third branches off the arch are the left common carotid and right subclavian arteries, respectively.

Video 31.14 Left aortic arch with an aberrant origin of the right subclavian artery. Echocardiogram with color Doppler in a coronal orientation from a suprasternal notch window. The aortic arch is positioned to the left of the trachea and the aberrant origin of the right subclavian artery from the medial aspect of the proximal descending aorta is shown with its flow directed superiorly towards the transducer (red signal).

Video 31.15 Left pulmonary artery sling. Echocardiogram with two-dimensional and color Doppler imaging in a transverse orientation from a high parasternal window. The left pulmonary artery arises from the right pulmonary artery and then courses posteriorly and leftwards. The trachea is located to the left of the left pulmonary artery origin but may be difficult to visualize by echocardiography.

References

1 Weinberg PM. Aortic arch anomalies. In: Allen HD, Gutgesell HP, Clark EB, Driscoll DJ (eds.) *Moss and Adams' Heart Disease in Infants, Children and Adolescents*, 6th edn. Philadelphia, PA: Lippincott Williams & Wilkins, 2001, pp. 707–735.

2 Marmon LM, Bye MR, Haas JM, et al. (1984) Vascular rings and slings: long-term follow-up of pulmonary function. *J Pediatr Surg* 1984;**19**:683–692.

3 Dodge-Khatami A, Tulevski II, Hitchcock JF, et al. Vascular rings and pulmonary arterial sling: from respiratory collapse to surgical cure, with emphasis on judicious imaging in the hi-tech era. *Cardiol Young* 2002;**12**:96–104.

4 van Son JA, Julsrud PR, Hagler DJ, et al. Surgical treatment of vascular rings: the Mayo Clinic experience. *Mayo Clin Proc* 1993;**68**:1056–1063.

5 Bonnard A, Auber F, Fourcade L, et al. Vascular ring abnormalities: a retrospective study of 62 cases. *J Pediatr Surg* 2003;**38**:539–543.

6 Woods RK, Sharp RJ, Holcomb GW, III, et al. Vascular anomalies and tracheoesophageal compression: a single institution's 25-year experience. *Ann Thorac Surg* 2001;**72**:434–438.

7 Backer CL, Ilbawi MN, Idriss FS, et al. Vascular anomalies causing tracheoesophageal compression. Review of experience in children. *J Thorac Cardiovasc Surg* 1989;**97**:725–731.

8 Ruzmetov M, Vijay P, Rodefeld MD, et al. Follow-up of surgical correction of aortic arch anomalies causing tracheoesophageal compression: a 38-year single institution experience. *J Pediatr Surg* 2009;**44**:1328–1332.

9 McElhinney DB, Clark BJ, III, Weinberg PM, et al. Association of chromosome 22q11 deletion with isolated anomalies of aortic arch laterality and branching. *J Am Coll Cardiol* 2001;**37**:2114–2119.

10 Larsen WJ. *Human Embryology.* New York: Churchill Livingstone, 1997.

11 Barry A. The aortic arch derivatives in the human adult. *Anat Rec* 1951;**111**:221–238.

12 Edwards JE. Anomalies of the derivatives of the aortic arch system. *Med Clin North Am* 1948;**32**:925–949.

13 Moes CAF. Vascular rings and related conditions. In: Freedom RM, Mawson JB, Yoo SJ, Benson LN (eds.) *Congenital Heart Disease: Textbook of Angiocardiography*, 1st edn. Armonk, NY: Futura Publishing, 1997, pp. 947–983.

14 Murdison KA, Andrews BA, Chin AJ. Ultrasonographic display of complex vascular rings. *J Am Coll Cardiol* 1990;**15**:1645–1653.

15 Lillehei CW, Colan S. Echocardiography in the preoperative evaluation of vascular rings. *J Pediatr Surg* 1992;**27**:1118–1120.

16 Katz JC, Chakravarti S, Ko HH, et al. Common origin of the innominate and carotid arteries: prevalence, nomenclature and surgical implications. *J Am Soc Echocardiogr* 2006;**19**:1446–1448.

17 Achiron R, Rotstein Z, Heggesh J, et al. Anomalies of the fetal aortic arch: a novel sonographic approach to in-utero diagnosis. *Ultrasound Obstet Gynecol* 2002;**20**:553–557.

18 Bronshtein M, Lorber A, Berant M, et al. Sonographic diagnosis of fetal vascular rings in early pregnancy. *Am J Cardiol* 1998;**81**:101–103.

19 Yoo SJ, Min JY, Lee YH, et al. Fetal sonographic diagnosis of aortic arch anomalies. *Ultrasound Obstet Gynecol* 2003;**22**:535–546.

20 Chaoui R, Schneider MB, Kalache KD. Right aortic arch with vascular ring and aberrant left subclavian artery: prenatal diagnosis assisted by three-dimensional power Doppler ultrasound. *Ultrasound Obstet Gynecol* 2003;**22**:661–663.

21 Patel CR, Lane JR, Spector ML, et al. Fetal echocardiographic diagnosis of vascular rings. *J Ultrasound Med* 2006;**25**:251–257.

22 Hsu KC, Tsung-Che HC, Chen M, et al. Right aortic arch with aberrant left subclavian artery – prenatal diagnosis and evaluation of postnatal outcomes: report of three cases. *Taiwan J Obstet Gynecol* 2011;**50**:353–358.

23 Li S, Luo G, Norwitz ER, et al. Prenatal diagnosis of congenital vascular rings and slings: sonographic features and perinatal outcome in 81 consecutive cases. *Prenat Diagn* 2011;**31**:334–346.

24 Jain S, Kleiner B, Moon-Grady A, et al. Prenatal diagnosis of vascular rings. *J Ultrasound Med* 2010;**29**:287–294.

25 Adam MP, Schelley S, Gallagher R, et al. Clinical features and management issues in Mowat–Wilson syndrome. *Am J Med Genet A* 2006;**140**:2730–2741.

26 Ishihara N, Yamada K, Yamada Y, et al. Clinical and molecular analysis of Mowat–Wilson syndrome associated with ZFHX1B mutations and deletions at 2q22–q24.1. *J Med Genet* 2004;**41**:387–393.

27 Zweier C, Thiel CT, Dufke A, et al. Clinical and mutational spectrum of Mowat–Wilson syndrome. *Eur J Med Genet* 2005;**48**:97–111.

28 Strenge S, Heinritz W, Zweier C, et al. () Pulmonary artery sling and congenital tracheal stenosis in another patient with Mowat–Wilson syndrome. *Am J Med Genet A* 2007;**143**:1528–1530.

29 Berdon WE, Baker DH, Wung JT, et al. Complete cartilage–ring tracheal stenosis associated with anomalous left pulmonary artery: the ring–sling complex. *Radiology* 1984;**152**:57–64.

30 Tesler UF, Balsara RH, Niguidula FN. Aberrant left pulmonary artery (vascular sling): report of five cases. *Chest* 1974;**66**:402–407.

31 Pu WT, Chung T, Hoffer FA, et al. Diagnosis and management of agenesis of the right lung and left pulmonary artery sling. *Am J Cardiol* 1996;**78**:723–727.

32 Yeager SB, Chin AJ, Sanders SP. Two-dimensional echocardiographic diagnosis of pulmonary artery sling in infancy. *J Am Coll Cardiol* 1986;**7**:625–629.

33 van Son JA, Julsrud PR, Hagler DJ, et al. Imaging strategies for vascular rings. *Ann Thorac Surg* 1994;**57**:604–610.
34 Newman B, Meza MP, Towbin RB, et al. Left pulmonary artery sling: diagnosis and delineation of associated tracheobronchial anomalies with MR. *Pediatr Radiol.* 1996;**26**:661–668.
35 Beekman RP, Hazekamp MG, Sobotka MA, et al. A new diagnostic approach to vascular rings and pulmonary slings: the role of MRI. *Magn Reson Imaging* 1998;**16**:137–145.
36 Goldstein BH, Bergersen L, Powell AJ, et al. Long-term outcome of surgically repaired unilateral anomalous pulmonary artery origin. *Pediatr Cardiol* 2010;**31**:944–951.
37 Gross RE, Neuhauser EB. Compression of the trachea by an anomalous innominate artery. An operation for its relief. *Am J Dis Child* 1948;**75**:570–574.
38 Fletcher BD, Cohn RC. Tracheal compression and the innominate artery: MR evaluation in infants. *Radiology* 1989;**170**:103–107.
39 Ardito JM, Ossoff RH, Tucker GF, Jr., et al. Innominate artery compression of the trachea in infants with reflex apnea. *Ann Otol Rhinol Laryngol* 1980;**89**:401–405.
40 Mustard WT, Bayliss CE, Fearon B, et al. Tracheal compression by the innominate artery in children. *Ann Thorac Surg* 1969;**8**:312–319.

CHAPTER 32

Connective Tissue Disorders

Julie De Backer
Department of Cardiology and Medical Genetics, University Hospital Ghent, Ghent, Belgium

Introduction

The spectrum of connective tissue disorders has expanded significantly over the past decade. With increasing knowledge of the underlying genetic defects, new insights into the pathophysiology and management have emerged. It has now been established that the clinical and genetic spectrum of "connective tissue disorders" is extensive. In addition to its structural role, the connective tissue is now known to be a key player in signal transduction and in maintaining tissue homeostasis in many organ systems, including the cardiovascular system. In this chapter, we first provide a summary of these pathophysiologic processes, then we describe the cardiovascular features associated with inheritable connective tissue disorders. Basic knowledge of these features is indispensable for correct diagnosis and hence for correct management of these patients.

Definition of connective tissue disorders

Connective tissue

"Connective tissue" refers to a complex structure or network present throughout the body, which is composed of cells (fibroblasts, smooth muscle cells) and the extracellular matrix (ECM). The ECM is a complex and highly heterogeneous structural entity. An important function of the ECM is to support and connect tissues and organs of multicellular organisms, but it is also a highly dynamic structure with diverse roles [1]. It can transmit specific environmental signals to cells, influencing their development, proliferation, migration, polarization, and metabolic functions. The ECM is also pivotal in regulating spatiotemporal bioavailability of growth factors and cellular signaling. Well-known examples are the ability to store TGF-β (transforming growth factor beta) and BMP7 (bone morphogenic protein 7) [2,3].

The constituents of the ECM are produced by cells specific to the tissue type. For instance, in the aorta they are synthesized by endothelial cells, smooth muscle cells, and fibroblasts. Variations in the amounts of different macromolecules and in their organization give rise to tissue-specific properties. For example, in the aortic media concentric layers of elastic fibers provide extensibility to the blood vessel, whereas in the eye parallel bundles of fibrillin-containing microfibrils enable anchorage of the lens to the ciliary body.

Connective tissue in the cardiovascular system

Although extracellular matrix molecules are diffusely present in the endocardial and myocardial layers, the major sites of deposition of cardiac connective tissue are at the fibrous annulus of the semilunar and atrioventricular valves. Also, the leaflets are composed of different layers of connective tissue, covered by endothelial cells. The adult human aortic valve leaflets, for example, are composed of around 10–15% elastin and 45–55% collagen [4]. The composition of the ECM in blood vessels varies between different types of blood vessels (elastic or muscular arteries; small, medium, or large veins). Within blood layers (tunica intima, media, and adventitia), the ECM is composed of different molecules, each playing a specific role in maintaining structural and functional homeostasis. It is beyond the scope of this chapter to go into much detail, but we believe that it is important to provide some basic concepts, focusing on those molecules relevant for cardiovascular disease.

The paradigm connective tissue disorder with cardiovascular involvement is Marfan syndrome (MFS); a detailed description of the cardiovascular features is provided in the following paragraph. Although the clinical recognition of the disease dates back to more than a century ago, it was not until the early 1990s that the causal gene defect in the fibrillin-1 gene (*FBN1*) was identified [5]. Fibrillin-1 had been identified shortly before through electron microscope studies as small-diameter fibrils (microfibrils) in the ECM located close to the basement membranes and also at the periphery of elastic fibers. Fibrillins are glycoproteins and were found to be long, flexible molecules [6]. Other proteins were identified as microfibril-associated proteins and overall, these molecules constitute the "fibrillin microfibril scaffold." From an evolutionary perspective, fibrillin predates all

Echocardiography in Pediatric and Congenital Heart Disease: From Fetus to Adult, Second Edition. Edited by Wyman W. Lai, Luc L. Mertens, Meryl S. Cohen and Tal Geva.
© 2016 John Wiley & Sons, Ltd. Published 2016 by John Wiley & Sons, Ltd.
Companion website: www.lai-echo.com

other microfibril proteins and was initially attributed a primarily structural role. Ongoing biochemical studies of molecular interactions in humans and mouse models of MFS, however, have nicely demonstrated that fibrillin also performs important functional roles, namely in regulating growth factors and in mechanotransduction. Fibrillins play an important role in regulating TGF-β and also bone morphogenic protein (BMP) bioavailability. The initial concept of TGF-β regulation was based on the knowledge that the fibrillin-1 protein is homologous with the family of latent TGF-β-binding proteins (LTBPs), which serve to hold TGF-β in an inactive complex in various tissues, including the extracellular matrix [7]. Fibrillin-1 was shown to bind TGF-β and LTBPs [8–10]. Based on this observation, it was hypothesized that mutations in fibrillin-1 could lead to perturbed sequestration of the inactive TGF-β complex [11], resulting in the observed increased TGF-β signaling in several tissues in MFS patients and murine models for MFS.

More recent studies demonstrated that an *Fbn1* mouse in which the LTBP binding site was deleted ($Fbn1^{H1\Delta}$) did not present features of MFS [12]. This observation refuted the importance of TGF-β sequestration by fibrillin-1 and an alternative hypothesis was proposed whereby mutant microfibrils influence TGF-β activation in a different way. Increased TGF-β signaling is now considered as a marker of a final common pathway in the disease process. Mechanisms leading to activation of TGF-β signaling in cardiovascular disease are now considered to be more complex than initially thought. The role of the pathway also shows variations during the dynamic transition from aortic aneurysm predisposition to end-stage disease, such as dissection [13].

Using MFS as a model, human and mouse studies have now revealed that the fibrillin microfibril structure is sensed by the cells (both fibroblasts and vascular smooth muscle cells). These will consequently send a signal through integrins and the cytoskeleton, resulting in inappropriate remodeling and aneurysm formation via a common pathway of inappropriate TGF-β signaling [14,15]. These concepts of "mechanosensing" and subsequent "mechanotransduction" through interaction with cellular receptors such as integrins are now believed to be one of the key mechanisms in many of the cardiovascular manifestations in MFS and related disorders. These concepts were nicely summarized by Sengle and Sakai [16] and Humphrey et al. [17] and are illustrated in Figure 32.1.

The initial concept of increased active TGF-β as a main driver of the disease led to the hypothesis of treating aneurysmal disease through inhibition of TGF-β. An initial experiment with TGF-β neutralizing antibodies in a mouse model for MFS showed a significant decrease in aortic root growth and restoration of normal aortic wall architecture. A seemingly very suitable candidate for TGFβ inhibition in humans was losartan, an angiotensin receptor-blocking agent known to inhibit TGF-β signaling. A trial with losartan in MFS mice showed a significant reduction of aortic root aneurysm progression and improvement of aortic wall architecture in MFS mice compared to treatment with either placebo or propranolol [18]. A small study in children with severe MFS showed promising preliminary human results [19].

Encouraged by these very promising results, at least 10 randomized trials ensued, recruiting more than 2000 patients in total, spanning all age ranges. The initial results from an open-label trial in a pediatric age group and also in an open-label study in adult MFS patients showed a beneficial effect of the combined treatment with a beta-blocker and losartan [20,21]. However, doubts arose with the publication of the results of a large randomized trial in a young (1 month–25 years of age) MFS cohort, conducted by the Pediatric Heart Network comparing atenolol and losartan, showing no difference in aortic root growth rate between the two groups [22–24]. Very recently, the synergistic effect of losartan added to beta-blockers could not be reproduced in a large double-blind randomized controlled trial, questioning the synergistic effect of these two drugs [25]. The current recommendations are to continue considering beta-blockers as primary medical therapy for aortic protection in MFS. Losartan may be considered as a reasonable alternative, especially in patients who cannot tolerate beta-blockers [26]. These results also further emphasize that the exact contribution of TGF-β in the process of aneurysm formation needs to be carefully reassessed.

From a clinical perspective, additional evidence for the involvement of the TGF-β pathway in aneurysmal disease was provided by the findings that mutations in several genes encoding different components of the TGF-β pathway result in aneurysmal diseases that have a significant clinical overlap with MFS. The Loeys–Dietz syndrome (LDS) was the first one to be identified and was shown to be caused by mutations in the TGF-β receptor 1 and 2 genes (*TGFBR1* and *TGFBR2*). In its most typical form, LDS is characterized by the triad of aortic root aneurysm/arterial tortuosity with bifid uvula/cleft palate and hypertelorism (widely spaced eyes). In 2011, mutations in the *SMAD3* gene involved in the TGF-β pathway were identified in patients with a very similar phenotype but also presenting osteoarthritis, hence the name "aneurysm–osteoarthritis syndrome" [27,28]. More recently, a family with juvenile polyposis associated with aortopathy and mitral valve disease was shown to be caused by *SMAD4* mutations [29]. Finally, mutations in both the TGF-β_2 and the TGF-β_3 ligands were identified in several families displaying very similar phenotypes [30–33]. Vascular disease in these more recently identified disease entities is not limited to the aorta and there may be a tendency for a more aggressive course of the lesions compared with patients with MFS – at least in a subset of patients [34]. Initially, these observations opened up useful opportunities for genotype-based treatment and management and it was recommended that patients carrying *TGFBR1/2* mutations be referred earlier for prophylactic aortic root surgery. More recent studies have revealed, however, that at least some patients with *TGFBR1/2* mutations show a less aggressive course with a phenotype indistinguishable from classic MFS [35]. Based on these contradictory observations, the

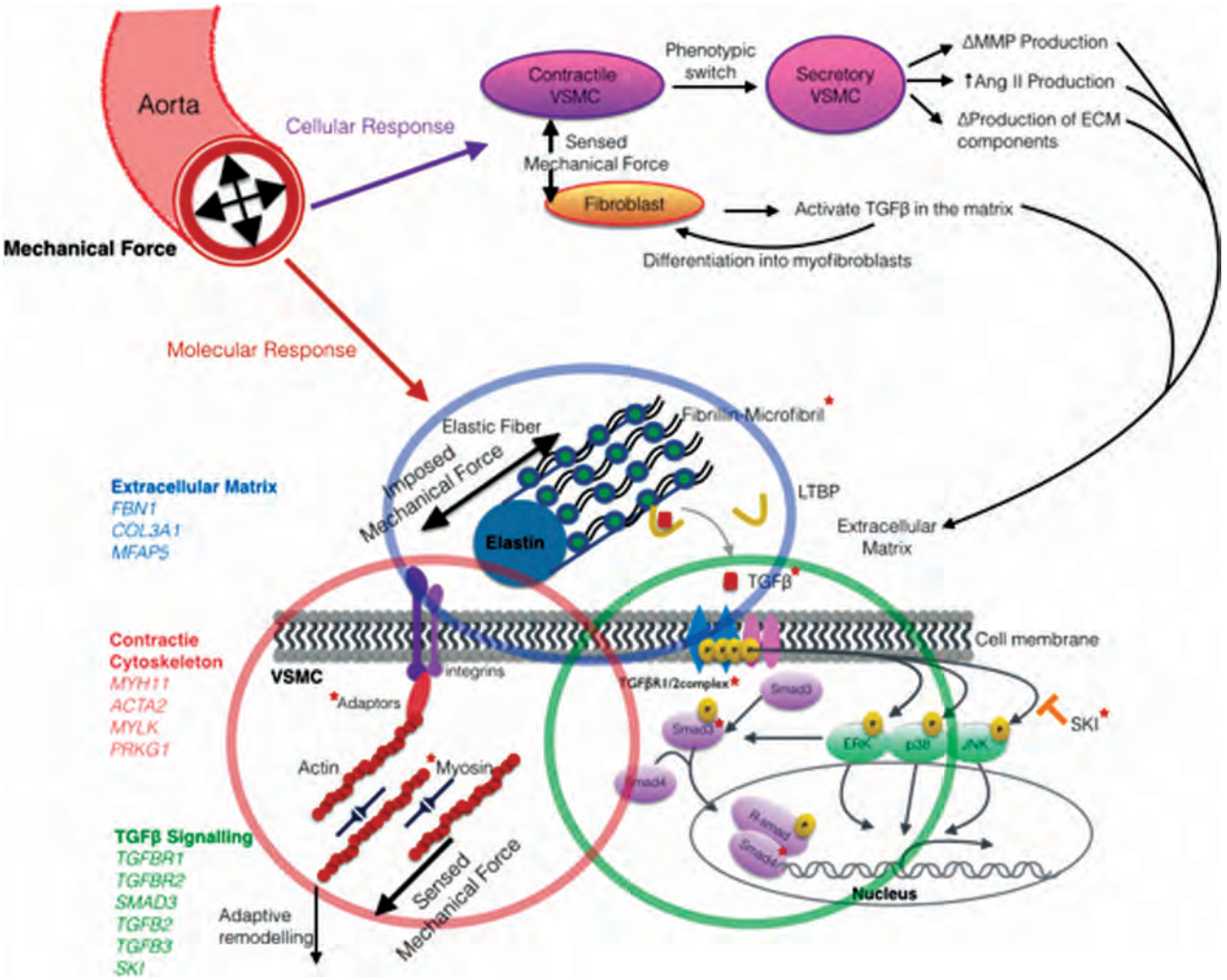


Figure 32.1 Concept of mechanobiology underlying homeostasis in the thoracic aorta. Mechanical forces (blood pressure) imposed on the aortic wall will lead to a cellular and a molecular response. Vascular smooth muscle cells will undergo a phenotypic switch, changing from a contractile to a secretory phenotype. This will induce altered secretion of extracellular matrix components. Fibroblasts in the aortic adventitia will differentiate into myofibroblasts under the impulse of activated TGF-β. Following its release from the ECM, TGF-β binds to its type II cell surface receptor (TβRII), which recruits and phosphorylates the type I receptor (TβRI). Subsequently both the canonical (Smad dependent, in purple) and noncanonical pathway (Erk dependent, in green) will be activated and will ultimately lead to the transcription of various TGF-β-dependent genes, such as connective tissue growth factor (CTGF), plasminogen activator inhibitor-1 (PAI-1) and multiple collagens. Extracellular matrix components will also interact with integrins on the cell surface and will subsequently transmit signals to the contractile apparatus consisting of actin and myosin filaments. Alterations, due either to higher imposed forces (hypertension) or to (genetic) alterations in the various components required for proper sensing and/or transduction of the signal may lead to aneurysms/dissections. The main molecular pathways related to thoracic aortic disease and their respective genes are listed on the left. Molecular components in which mutations lead to aortic aneurysms/dissections are marked with red asterisks.

European Society of Cardiology (ESC) 2014 guidelines on aortic disease have not adopted the recommendations for earlier surgery [36]. Very similar observations are true for genes identified later, including the *SMAD3* gene, the *TGF-β_2* gene and the *TGF-β_3* gene, with some patients presenting a severe phenotype reminiscent of LDS and others with much milder phenotypes such as "isolated thoracic aortic disease."

Other genes involved in isolated (familial) thoracic aortic aneurysms and dissections include genes encoding components of the smooth muscle cell contractile apparatus: the *ACTA2* gene, the *MYH11* gene, the *MLCK* gene, and the *PRKG1* gene [37–40]. The *ACTA2* gene [encoding α-smooth muscle actin (α-SMA)] and the myosin heavy chain 11 gene (*MYH11*) encode components of the smooth muscle cytoskeletal contractile apparatus. Increased TGF-β signaling has also been reported in human aortic specimens obtained in patients with these mutations [41]. The cytoskeleton influences different aspects of the TGF-β signaling pathway, including trafficking and activity of TGF-β receptors and signaling effectors [42,43].

The important clinical overlap between the different syndromic entities and the knowledge that mutations in all the

genes leading to syndromic TAD are also identified in patients and families with nonsyndromic forms led to the suggestion to group these entities under the term "heritable thoracic aortic disorders – H-TAD"[44]. In view of the difficulty in distinguishing these disorders clinically, it is recommended to perform panel testing of the known genes using next generation sequencing techniques. A recent study performed in our laboratory using this technique revealed a mutation detection rate of 13% in a series of 264 patients presenting with TAD. Importantly, in nonsyndromic TAD patients, mutations were found in the *FBN1*, *TGFBR1*, *SMAD3*, and *COL3A1* genes [45].

An overview of the different clinical entities and their underlying genetic defect is provided in Table 32.1. The gene pathways and their respective proteins involved in H-TAD are illustrated in Figure 32.1.

Cardiovascular lesions

Marfan syndrome

Marfan syndrome (MFS) is an autosomal dominant connective tissue disorder caused by mutations in the fibrillin-1 gene (*FBN1*). The diagnosis is based on clinical characteristics, although in some cases additional molecular testing with confirmation of an underlying *FBN1* mutation may be helpful. Criteria for diagnosis have been published as the "revised Ghent nosology" [46]. In the absence of a family history for MFS, the diagnosis is confirmed when

1 aortic root *z*-score ≥2 + ectopia lentis (EL);
2 aortic root *z*-score ≥2 + *FBN1* mutation;
3 aortic root *z*-score ≥2 + systemic score (≥7 points). The systemic score includes a list of clinical features involving different organ systems;
4 EL + *FBN1* mutation with known aortic root dilation.

In the presence of a family history, the diagnostic criteria are less strict:

5 EL + family history of MFS (as defined earlier);
6 systemic score ≥7 points + family history of MFS;
7 aortic root *z*-score ≥2 in adults, ≥3 in children + family history of MFS.

In the criteria, a lot of weight is put on aortic root *z*-scores, which underscores the importance of cardiovascular imaging in the diagnostic work-up (see later). Clinical manifestations in MFS vary widely both within and between families. Severe cardiovascular phenotypes exist with significant AV valve dysfunction and/or rapidly progressive aortic root dilation in infancy, so called "neonatal MFS" [47–49]. In the more common, classic MFS, cardiovascular manifestations generally develop in adolescence, although development of manifestations only later in life has also been reported [50,51].

Echocardiography plays a key role in the diagnostic work-up of cardiovascular manifestations and also in the follow-up and guidance of treatment.

Dilation of the ascending aorta

The primary cardiovascular manifestation in MFS is progressive dilation of the aortic root, eventually leading to aortic dissection or rupture. It is estimated that aortic root dilation is present in >80% of adult MFS patients [52].

Echocardiographic images should be obtained from the parasternal long-axis view visualizing the aortic root and the proximal ascending aorta (Videos 32.1 and 32.2). To optimize the view of the aortic root and the ascending aorta, the long-axis view is obtained at a higher intercostal space compared with the conventional long-axis view. Different transducer positions are often needed to optimize the images: a high left parasternal view located one or two rib interspaces superior to the standard location may be required. Alternatively, a high right parasternal view in a right lateral decubitus position is better at displaying the entire proximal aorta.

Measurements of the aortic root and the ascending aorta are taken at different levels: (1) the aortic valve annulus (defined as the hinge points of the aortic leaflets); (2) the maximal diameter at the sinuses of Valsalva; (3) the sinotubular junction (transition between the sinuses of Valsalva and the tubular portion of the ascending aorta); and (4) the ascending aorta at the level of the right pulmonary artery (see Figure 32.2).

When measuring the aortic diameter, it is important to obtain the maximum diameter measured perpendicular to the long axis of the vessel in that view. In the pediatric quantification guidelines from the American Society of Echocardiogaphy, the measurement is performed from inner edge to inner edge at end systole. This matches the measurements used by other imaging techniques, such as magnetic resonance imaging (MRI) and computed tomography (CT) scanning. For adults, the most recent guidelines from the American Society of Echocardiography recommend measuring at end diastole using the leading edge technique [53]. Absolute differences between the two techniques are small and further improvements in image resolution should minimize the difference between these measurement methods. Two-dimensional aortic diameter measurements rather than M-mode measurements should be obtained. Motion of the heart during the cardiac cycle and changes in M-mode cursor location relative to the maximum diameter of the sinuses of Valsalva can result in a systematic underestimation (by up to 2 mm) of aortic diameter by M-mode in comparison with the 2D aortic diameter [54]. Aortic root dilation in MFS is typically located at the level of the sinuses of Valsalva and is defined as an aortic root diameter above the upper limit of the 95% confidence interval of the distribution in a large reference population. Aortic dilation can easily be detected by plotting observed aortic root diameter versus body surface area on previously published nomograms [53]. Another possibility is the use of *z*-scores derived from the regression equation on the nomogram. A *z*-score ≥2 indicates a value exceeding 2SD (the 95% confidence interval). The *z*-scores are calculated on the basis of measured diameters obtained in the normal population. The clinical measurement method should match that used to generate the

Table 32.1 Overview of the clinical/genetic entities associated with aortic aneurysms; discriminating features are highlighted in bold.

Disorder		Gene(s)	Main cardiovascular features	Additional clinical features
Syndromic TAAD				
Marfan		*FBN1*	**Aortic root aneurysm**, aortic dissection, mitral valve prolapse, main pulmonary artery dilatation, left ventricular dysfunction	**Lens luxation**, skeletal features (arachnodactylia, pectus deformity, scoliosis, flat feet, increased armspan, dolichocephalia)
Ehlers–Danlos (vascular, valvular)		*COL3A1*, *COL1A2*	**Arterial rupture and dissection without preceding dilatation/aneurysm**, severe valvular insufficiency	**Thin, translucent skin**, dystrophic scars, facial characteristics (Madonna face, thin lips, deep-set eyes)
TGF-β	Loeys–Dietz	*TGFBR1/2*	**Aortic root aneurysm**, aortic dissection, arterial aneurysms and dissections, **arterial tortuosity**, mitral valve prolapse, congenital cardiac malformations[a]	**Bifid uvula/cleft palate, hypertelorism**, pectus abnormalities, scoliosis, club feet
	Aneurysm–osteoarthritis	*SMAD3*	**Aortic root aneurysm**, aortic dissection, arterial aneurysms and dissections, **arterial tortuosity**, mitral valve prolapse, congenital cardiac malformations[a]	**Osteoarthritis**, soft skin, flat feet, scoliosis, recurrent hernias, hypertelorism, pectus abnormalities
	$TGF\beta_2$, $TGF\beta_3$	*TGFB2, TGFB3*	**Aortic root aneurysm**, aortic dissection, arterial aneurysms and dissections, **arterial tortuosity**, **mitral valve prolapse**, congenital cardiac malformations[a]	Club feet, soft translucent skin
	Shprintzen–Goldberg syndrome	*SKI*	**Mild aortic root dilation,** mitral valve prolapse	Craniosynostosis, distinctive craniofacial features, skeletal changes, neurologic abnormalities, mild-to-moderate intellectual disability
Arterial tortuosity syndrome		*SLC2A10*	**Arterial tortuosity**, arterial stenoses and aneurysms	Hyperlax skin and joints
Cutis laxa syndromes		*FBLN4*, *ELN*	Arterial aneurysms and dissections, arterial tortuosity, arterial stenoses, BAV	Hyperlax skin and joints, mild emphysema
Nonsyndromic TAAD				
Familial thoracic aortic aneurysm syndrome (FTAA)		*TGFBR1/2* (3-5%)	Thoracic Aortic Aneurysm/Dissection	Lack of syndromal features
		ACTA2 (10-14%)	Thoracic Aortic Aneurysm/Dissection, BAV cerebrovascular disease, coronary artery disease	Lack of marfanoid skeletal features, **livedo reticularis, iris flocculi, coronary artery/cerebrovascular disease)**
		MYLK	Thoracic Aortic Aneurysm/Dissection	Gastrointestinal abnormalities
		SMAD3 (2%)	Intracranial and other arterial aneurysms	
		TGFB2, TGFB3	**Mitral valve prolapse**	
		PRKG1	Thoracic Aortic Aneurysm/Dissection, Arterial Aneurysms and Dissections, **Arterial Tortuosity**	
FTAA with bicuspid aortic valve (BAV)		*ACTA2*		Lack of marfanoid skeletal features, livedo reticularis, iris flocculi
		NOTCH1	**Highly calcified aortic Valve**	
FTAA with patent ductus arteriosus (PDA)		*MYH11*	**Patent ductus arteriosus**	

TAAD, thoracic aortic aneurysms and dissections.
[a]Congenital cardiac malformations including atrial septal defect, patent ductus arteriosus, ventricular septal defect, bicuspid aortic valve.

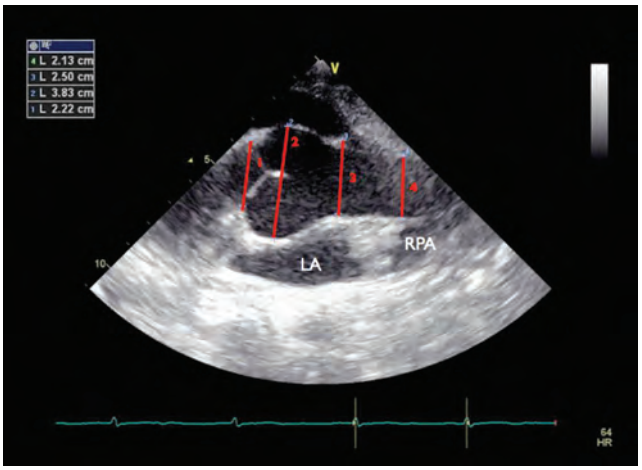


Figure 32.2 Echocardiographic image of ascending aortic aneurysm at the level of the sinus of Valsalva in MFS. Measurements are performed at end diastole using the "leading edge to leading edge" principle. LA, left atrium; RPA, right pulmonary artery.

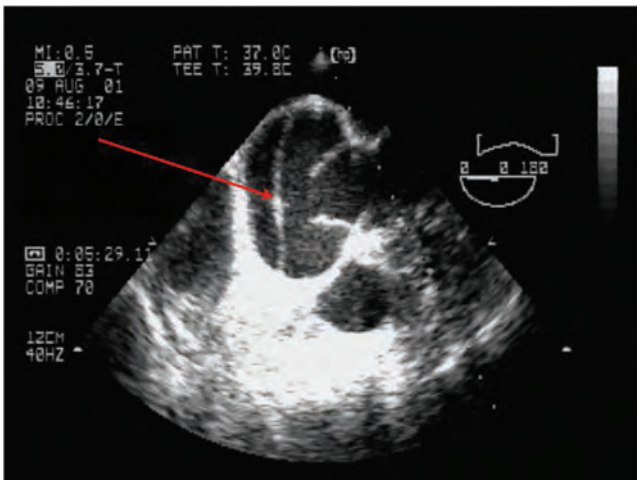


Figure 32.3 Dissection of the ascending aorta at the level of the sinuses of Valsalva. The arrow indicates the dissection flap.

normative data. For echocardiographic measurements made from inner wall to inner wall during systole in subjects aged ≤25 years, a *z*-score calculator can be found at http://www.marfan.org. For echocardiographic measurements made from leading edge to leading edge in diastole in all age groups, reference graphs and *z*-score equations are available. A useful equation has recently been published by Devereux et al. [55].

In some Marfan patients, aortic root dilation is asymmetric; therefore, measurement in the transverse plane of the aorta (parasternal short-axis view) may be important. A study by Meijboom et al. using MRI revealed the largest aortic root diameter between the right and left coronary cusps. For a given noncoronary to right coronary cusp diameter – which is the diameter assessed in the PSLAX view – the 95% confidence intervals revealed a variation of –20 to +20% in the aortic root area [56]. So far, no echocardiographic study has been performed confirming these results.

The predilection for the ascending aorta to dilate is a result of both structural and local hemodynamic factors. Both the aortic root and the proximal part of the pulmonary artery (which also dilates in MFS) are derived from neurologic crest cells, whereas the more distal arterial structures have a mesodermal origin. The elastic fiber content in the ascending aorta has been shown to be higher in the ascending aorta than in any other part of the arterial tree [57]. This can probably explain why diseases that affect elastic fiber integrity are more prominent in this part of the vascular system. Additionally, the ascending aorta is subject to the repetitive stress of left ventricular ejection, contributing progressive dilation [58,59]. As pressures in the aorta are significantly higher than those in the pulmonary artery, dilation is generally more pronounced in the aortic root.

In order to define indications for surgical intervention, absolute growth of the aortic root should be reported in addition to the diameter. Annual growth rates exceeding 0.5 cm/year are considered a risk factor for dissection.

Dissection of the ascending aorta

Dissection or rupture may occur as a consequence of the progressive dilation of the ascending aorta. Echocardiography is a very important tool in the diagnosis of aortic dissection. It can not only confirm the diagnosis but also identify complications such as pericardial tamponade or acute myocardial ischemia due to coronary artery obstruction or dissection. Although aortic dissection can be diagnosed using transthoracic echocardiography (TTE), transesophageal echocardiography (TEE) is the preferred technique in adults as it provides a better visualization of the ascending aorta, the aortic arch, and the descending aorta (Figure 32.3; Video 32.3).

Although most of the arch and origins of two of the great vessels can be seen in most patients, there is a blind spot in the upper ascending aorta and the proximal arch that cannot be seen by TEE because of the interposed tracheal bifurcation.

In patients with aortic aneurysms not associated with connective tissue disorders, the degree of aortic dilation correlates highly with the risk of aortic rupture or dissection [60]. The risk increases substantially when the diameter exceeds 55 mm.

In patients with MFS, the risk of aortic rupture or dissection is influenced by other factors and does not depend only on the degree of aortic dilation [61]. Some patients develop aortic dissection at diameters less than 55 mm [62,63]. Silverman et al. demonstrated that a family history of severe cardiovascular complications in MFS is associated with increased aortic diameter and decreased survival [64].

Other possible risk factors have been studied, such as central pulse pressure (pressure difference between systolic and diastolic pressure in the ascending aorta) [65] and aortic stiffness [66–69], but none of these have a higher predictive value than the absolute aortic diameter. Aortic stiffness appeared to have a

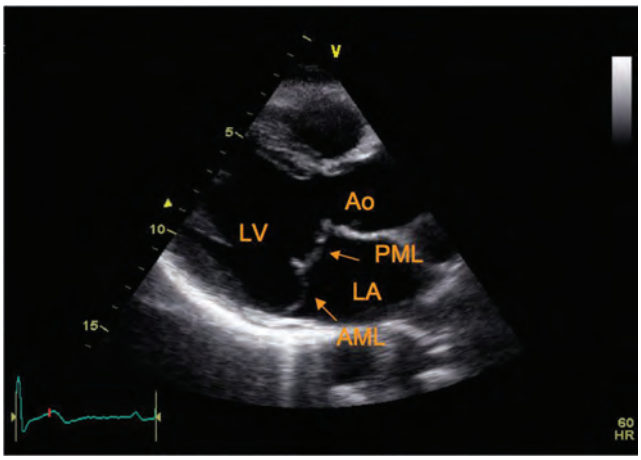


Figure 32.4 Echocardiographic picture of mitral valve prolapse (PSLAX window). AML, anterior mitral valve leaflet; PML, posterior mitral valve leaflet; LA, left atrium; LV, left ventricle; Ao, aorta.

diagnostic value in young patients in one study [70]. In clinical practice, these parameters are not easily applicable as no accurate cut-off values are available.

Mitral valve prolapse (MVP)

Two-dimensional echocardiography is the generally used tool for the identification of MVP. Both parasternal long axis and apical 4-chamber views may be used (Videos 32.4, 32.5, and 32.6) [71,72]. Classic prolapse is defined as leaflet displacement in systole exceeding the mitral valve annular plane by ≥2 mm with leaflet thickening exceeding 5 mm. Nonclassic prolapse refers to leaflet displacement without valve thickening. An example is illustrated in Figure 32.4. The prevalence of MVP in MFS patients varies between 40 and 66% (compared with 1–2% in the general population) [73]. In our own series, we observed MVP with echocardiography in 66% of MFS patients – 35% of whom had classic MVP [74].

A recent study by Rybczynski et al. showed that MFS patients have an increased risk of 28% for MV-related clinical events (endocarditis, surgery, heart failure) (compared with 13% in idiopathic MVP). The age at event was also significantly lower (35 versus 65 years in idiopathic MVP) [75].

Main pulmonary artery dilation

Main pulmonary artery (MPA) dilation was omitted from the revised diagnostic criteria, mainly owing to difficulties in assessment. Indeed, guidelines for the assessment of MPA dilation are scarce in the literature. CT or MRI may be better suited than echocardiography. Recently, Truong et al. suggested 27 and 29 mm as upper limits of normal for MPA diameter in men and women, respectively, using CT scanning [76]. Nollen et al. clearly demonstrated increased diameters in MFS patients assessed with MRI [77]. Using a cut-off value of 28 mm at the level of the MPA root, they reported a prevalence of MPA dilation of 74%. Recently, Lundby et al. reported main pulmonary artery dilation in 54% of MFS patients using a cut-off value of 30 mm [78]. In our own series with echocardiography, we proposed a cut-off value of 23 mm to define main pulmonary artery dilation in adult MFS patients [74]. The MPA is best viewed from the parasternal short-axis view. The largest diameter distal to the valve insertion should be measured. Complications arising from MPA dilation are generally limited. Pulmonary regurgitation is reported in many MFS patients [79]. Pulmonary artery dissection is very rare, however.

Dilation or dissection of the descending aorta

Complications in the descending aorta occur in only a minority of MFS patients. The incidence of descending thoracic aortic dissection may increase since medical and surgical treatments of ascending aortic complications have significantly improved, hence leaving the descending aorta at higher risk [80,81]. MFS patients presenting with thoracoabdominal aortic aneurysm/dissection have been reported in a few case reports [82,83]. Other reports on the descending aorta in MFS patients are mainly based on surgical follow-up data describing the occurrence of primary or secondary complications in the descending aorta necessitating surgical intervention. Finkbohner et al. reported that 15% of their patients had a first surgical intervention involving portions of the descending aorta [80]. Nollen et al. reported on increased growth (defined as ¿1 mm/year) in a small subset of patients (6% in the descending thoracic aorta and 7% in the abdominal aorta). They also identified aortic stiffness as an independent predictor of progressive abdominal aortic dilation [84]. Kawamoto et al. studied the progression of thoracoabdominal aortic diameters in MFS patients after surgical repair and defined a subgroup of patients showing progressive dilation of the distal aorta (¿3 mm/year) [83]. A recent study by Mimoun et al. demonstrated that dissection in the descending part of the aorta may occur whatever the diameter of the ascending aorta [86]. Schoenhoff et al. concluded that previous aortic dissection is a significant risk for recurrent interventions on the untreated aorta, a risk which was more pronounced in those with initial type B dissection compared with type A dissection [87]. In our own series of 29 MFS patients studied with MRI, we noted increased diameters at different levels of the descending aorta. However, there was too much overlap with normal controls to define cut-off values. We found no significant correlations with the proximal aortic diameter, although dilation occurred more frequently in patients with previous aortic root surgery [74].

About 8–15% of MFS patients require initial surgery in the descending aorta [80,87]. Patients with initial type B aortic dissection are at a significantly higher risk for reintervention (86% for previous type B dissection versus 42% for previous type A dissection). The majority of reinterventions are required in patients with previous dissection (48% versus 11% reintervention in the patients presenting with aortic aneurysm) [87]. A large contemporary series of 96 thoracoabdominal aortic aneurysm repairs in patients with MFS showed an excellent

survival rate of 97% [88]. Recommendations are slightly different from those applied for the aortic root (see below): repair at the thoracoabdominal level in MFS is recommended when the aneurysm diameter exceeds 5.5 cm [89].

Altered anatomic features in the aorta of MFS patients, such as dilation and/or dissection, are accompanied by functional impairment of the vessel, reflected in increased aortic stiffness in MFS patients. Abnormal elastic properties – pulse wave velocity and local aortic distensibility – are not confined to the ascending aorta, but are also detected in the normal-sized, more distal parts of the vessel [67,90], and this also in patients having previously undergone aortic root surgery as in unoperated MFS patients [91]. Interestingly, aortic stiffness seems to be an early marker of aortic disease as patients already demonstrate significantly decreased aortic distensibility at both proximal and distal levels of the aorta prior to dilation of the thoracic aorta [90]. Local distensibility of the descending thoracic aorta appeared to be an independent predictor of progressive descending aortic dilation [84]. Interestingly, increased augmentation index as an indirect maker of aortic stiffness has been found to predict progression of aortic disease in MFS independently of aortic root size [92]. Major determinants of the augmentation index are pulse wave velocity and the length of the arterial tree. Alterations in wave reflections seem to be more pronounced in younger MFS patients [93]. Although these data on functional alterations of the aorta are definitely worthy of further studies, they have not yet reached the level of clinical application. Larger scale studies are required to assess their validity in models for more robust risk stratification in MFS.

Guidelines for the assessment of distal aortic diameters and normal values for calculating *z*-scores are lacking. To view the distal ascending, arch, and descending aorta, TTE is feasible in many patients. Recommended views are provided in Figure 32.5. TEE may also be used although CT and MRI are

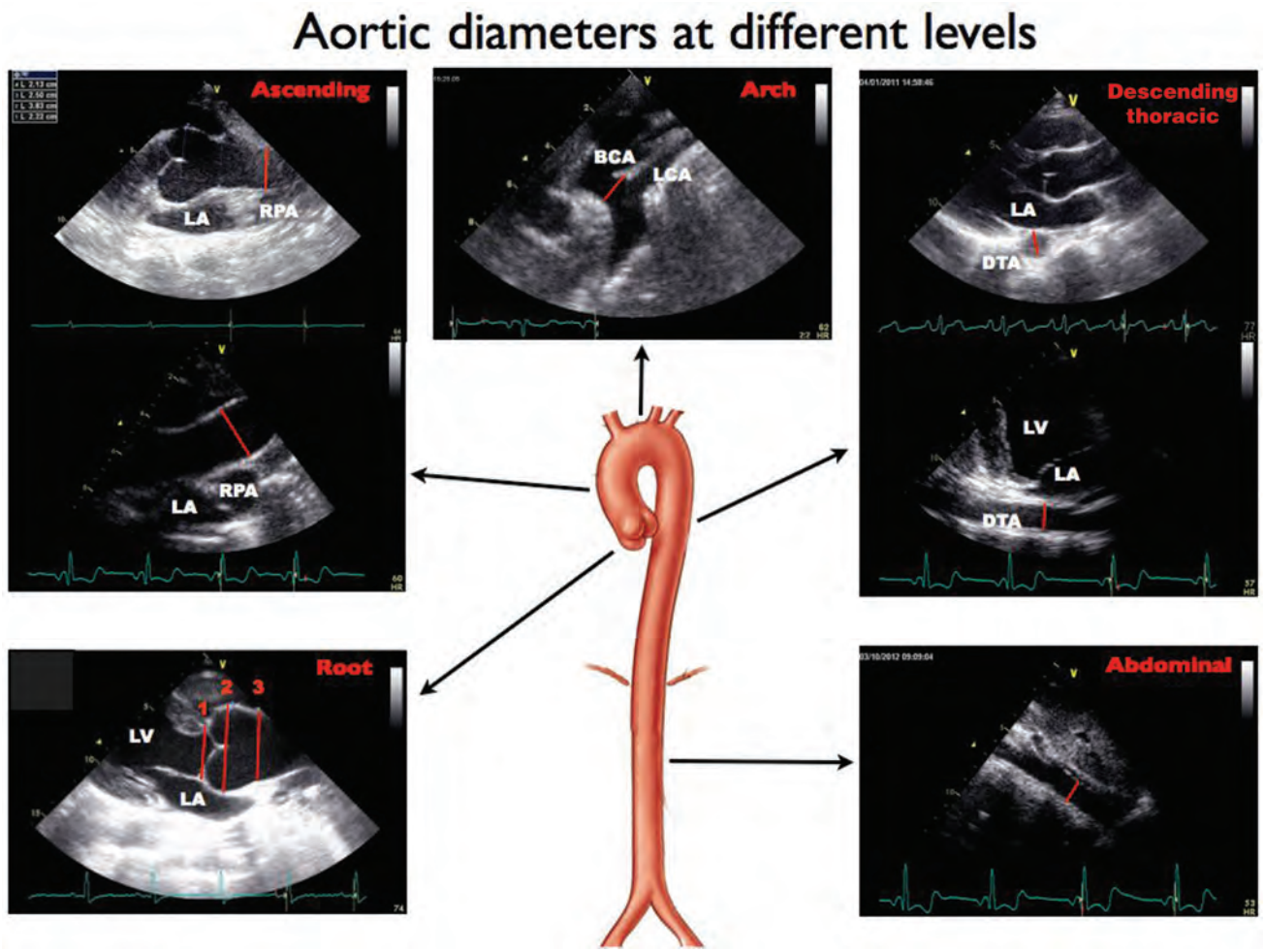


Figure 32.5 Recommended echocardiographic windows to assess the aorta at different levels. The aortic root is assessed from the PSLAX window. The ascending aorta is in most cases better viewed one intercostal space higher than the view for the root. Measurements are made at the level of the right pulmonary artery (RPA). The aortic arch is visualized from the suprasternal notch view. The descending thoracic aorta (DTA) can be viewed from the PSLAX window, located under the left atrium; a longitudinal view of the DTA is possible from a foreshortened apical 2-chamber view. The abdominal aorta is easily viewed from the subcostal window.

more convenient and informative techniques (Videos 32.7 and 32.8).

With our current knowledge of the existence of Marfan-like conditions, such as Loeys–Dietz syndrome (see later), it is important to note that some patients with Loeys–Dietz syndrome may have been included in older reports on MFS – especially patients with widespread vascular involvement should be carefully reconsidered.

Left ventricular dysfunction and arrhythmias

Although not commonly acknowledged in MFS, dilated cardiomyopathy, beyond that explained by aortic or mitral valve regurgitation, seems to occur with a higher prevalence, suggesting a role for the extracellular matrix protein fibrillin-1 in the myocardium. Significant LV dilation and dysfunction leading to heart failure and necessitating heart transplantation have been described in a few cases and seem to be a very rare complication [94]. Subclinical myocardial dysfunction, on the other hand, has been reported in larger subsets of MFS patients of various ages by several independent research groups [95–100], and mildly increased LV dimensions have been demonstrated in a subset of patients with MFS [101]. A study assessing genotype–phenotype correlations indicated that LV dilation was more frequently observed in patients with a non-missense *FBN*1 mutation [59,102,103]. Recently, studies in a mouse model for MFS provided interesting new insights into the pathophysiology of MFS cardiomyopathy, indicating altered muscle mechanosignaling as a trigger [74,78,104,105].

A feature that is closely related to ventricular dysfunction in MFS is an increased risk for adverse arrhythmogenic events, as evidenced by several groups [78,106–108]. Hoffmann and coworkers found an association with increased N-terminal pro-brain natriuretic peptide (NT-proBNP) levels [107,109].

Other syndromic heritable thoracic aortic disorders

The application of nosologic criteria has clearly facilitated the diagnosis of MFS but also permitted the identification of patients and families who present with thoracic aortic disease, but do not fulfill the diagnostic criteria for MFS and/or present with other clinical features that do not fit within the definition of MFS. Moreover, since the more widespread availability of molecular genetic testing in MFS, it became clear that subgroups of patients and families exist that do not carry an *FBN1* mutation, suggesting the involvement of other genes, as has been described earlier. Here we provide an overview of the other syndromic TAD entities.

Loeys–Dietz syndrome

Loeys–Dietz syndrome (LDS) is an autosomal dominant disorder caused by mutations in one of the TGF-β receptor genes (*TGFBR1* and *TGFBR2*). It is characterized clinically by aortic aneurysms and dissections, widespread arterial tortuosity/aneurysms, bifid uvula, and hypertelorism (wide-spaced eyes) [110]. The expression of the disease is variable between and within families.

Compared with MFS, the natural history of LDS patients in the initial reports was significantly worse and mainly related to the associated cardiovascular complications [34]. As mentioned earlier, initially, these observations opened up useful opportunities for genotype-based treatment and management and it was recommended that patients carrying *TGFBR1*/2 mutations be referred earlier for prophylactic aortic root surgery. More recent studies have revealed, however, that at least some patients with *TGFBR1/2* mutations show a less aggressive course with a phenotype indistinguishable from classic MFS [35]. Based on these contradictory observations, the recent ESC guidelines on aortic disease have not adopted these recommendations [36]. Large-scale prospective studies are required to gain better insight into the actual natural history of these disorders.

The lesions in LDS are generally also more widespread than in MFS. Aortic aneurysms and dissections in more distal parts of the aorta are more common in LDS. In LDS, aneurysms may also develop outside the aorta in large and mid-sized arteries, whereas aneurysm formation in MFS is generally confined to the aorta.

Finally, additional congenital cardiac anomalies, including patent ductus arteriosus (Video 34.9), bicuspid aortic valve, mitral valve prolapse, and atrial septal defects, are present with a higher than normal frequency in LDS patients [34]. Williams et al. demonstrated that the surgical outcome in LDS patients is good [111], which is in strong contrast to the vascular Ehlers–Danlos syndrome, known as a "surgical nightmare" owing to the extreme fragility of the vasculature and skin [112]. Many LDS patients in the study by Williams et al., however, required repeated interventions, usually in different parts of the aorta, with good outcomes.

In view of the extent of cardiovascular lesions in LDS, multiple imaging techniques are required. Echocardiography is useful for the assessment of aortic root dimensions and for the identification of associated lesions. Vascular studies such as magnetic resonance angiography (MRA) or CT scanning with 3D reconstruction from head to pelvis are required for the detection of distal aortic/arterial complications. Figure 32.6 demonstrates an MRA study in a patient with LDS. Figure 32.7 is an illustration of cerebral artery tortuosity in a patient with LDS.

Aneurysm–osteoarthritis syndrome

Aneurysm–osteoarthritis syndrome (AOS) is an autosomal dominant aneurysmal disease caused by mutations in the *SMAD3* gene [27]. Since many patients with AOS present some degree of osteoarthritis, this is a discriminating feature of the disease. Aneurysms, dissections, and tortuosity located in different parts of the arterial tree are the main cardiovascular-associated lesions. Arterial aneurysms may be large and are often are a presenting symptom [28,113,114] (Figure 32.8).

Other cardiovascular abnormalities include left ventricular hypertrophy, mitral valve disease, and atrial fibrillation [28].



Figure 32.6 MRA reconstruction of the aorta in a patient with Loeys–Dietz syndrome. Note the dilated ascending aorta distal to the aortic root prosthesis that was previously inserted (arrow), the tortuous aorta, and the tortuous and ectatic iliac and head and neck arteries.

Mild dysmorphic features, such as hypertelorism and bifid uvula, may also occur, as well as umbilical or inguinal hernias, varicose veins, velvety skin, and dermal striae [115]. Differentiation between AOS and LDS on clinical grounds may be difficult and molecular genetic studies are helpful in making the correct diagnosis.

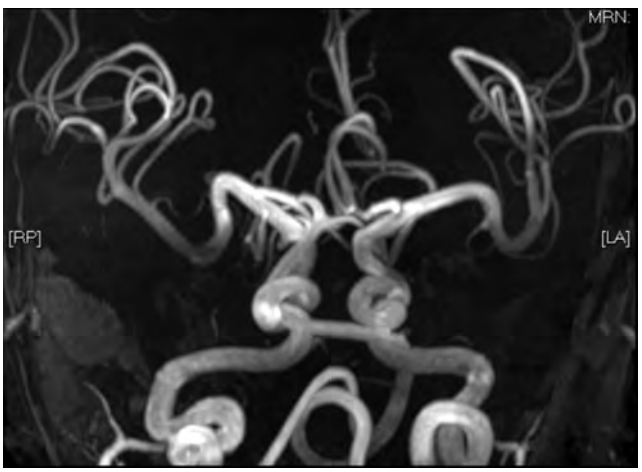


Figure 32.7 MRA reconstruction of the intracerebral vessels of an 8-year-old boy with Loeys–Dietz syndrome. Note the markedly tortuous vessels.

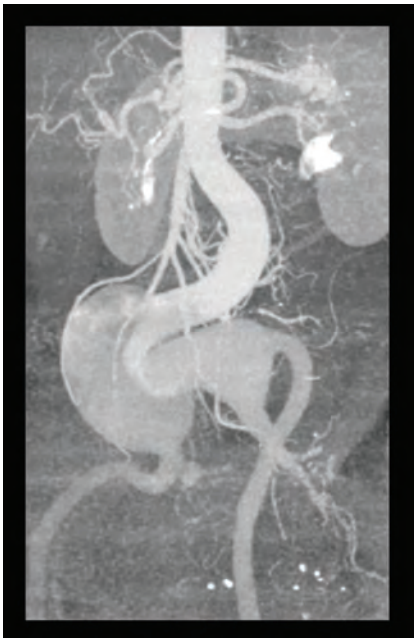


Figure 32.8 CT angiographic image of bilateral iliac artery aneurysms in a patient with AOS.

Aortic aneurysms caused by TGF-β_2 and TGF-β_3 mutations

Recently, mutations in two TGF-β ligands (TGF-β_2 and -β_3) were identified in several families with autosomal dominant aortic aneurysm disease [30,31]. The clinical phenotype shows overlap with other TGF-β signalopathies, including MFS, LDS and AOS. We found significant mitral valve involvement in TGF-β_2 mutation carriers, an observation that needs confirmation in larger series [32].

Vascular Ehlers–Danlos syndrome (EDS)

Vascular EDS is an autosomal dominant connective tissue disorder caused by mutations in the collagen type 3 gene (*COL3A1*). It is clinically characterized by joint hypermobility, skin abnormalities (cigarette paper scars, easy bruising, soft velvety skin), fragility of intestinal and genitourinary organs, and vascular fragility leading to dissection or rupture of medium to large muscular arteries. Typically in vascular EDS, dissections often occur without preceding dilation/aneurysm formation. In vascular EDS patients, complications in early childhood are rare. The average age at the time of a first complication in the large series reported by Pepin et al. was 23.5 years, with rupture of the gastrointestinal tract likely to occur at an earlier age than arterial rupture. About half of the arterial complications in vascular EDS involved the thoracic or abdominal arteries and the remainder were divided equally between the head, neck, and limbs [112]. In vascular EDS, the reported incidence of fatal complications during or immediately after vascular surgery is around 45% [112,116]. Clinical features in LDS and vascular EDS may be indistinguishable in some patients. So-called LDS type 2

patients have the same skin lesions as vascular EDS patients (easy bruising, wide and atrophic scars, translucent skin, velvety skin) and may also present with visceral rupture. Cardiovascular lesions (arterial tortuosity and/or aortic root aneurysm) are generally more pronounced in LDS patients. In those cases, genetic testing may be the only way to distinguish between the two diseases.

It is very difficult to define useful guidelines for cardiovascular imaging in vascular EDS since complications may occur unexpectedly and no specific treatment is currently available. Some authors advise not pursuing any additional investigation or surveillance, because a conservative approach will be adopted irrespective, and undue anxiety would be created [117]. Others recommend noninvasive cardiovascular imaging with echocardiography and vascular CT/MRI [116].

Arterial tortuosity syndrome (ATS)

ATS is an autosomal recessive disorder, caused by mutations in a glucose transporter gene (*GLUT10*) [118]. In ATS, arterial tortuosity is the most prominent clinical feature, along with large artery stenosis. Aneurysm formation of the aorta and large arteries occurs in ATS, although to a lesser extent than in LDS. ATS patients require imaging studies of the entire vascular tree such as with CT or MRI. Echocardiography is helpful in identifying pulmonary artery stenoses and aortic dilation or stenosis.

Smooth muscle cell dysfunction syndrome

A distinctive clinical phenotype is characterized by patent ductus arteriosus, aortic root dilation, pulmonary vascular hypertension, cerebrovascular abnormalities, congenital mydriasis, bladder hypotonia, and hypoperistalsis. This clinical syndrome is caused by specific mutations at the Arg179 position of the *ACTA2* gene. Clinical features are caused by generalized smooth muscle cell dysfunction [119].

Shprintzen–Goldberg syndrome

Recently, mutations in exon 1 of the *SKI* gene (a TGF-β repressor gene) were identified in patients with Shprintzen–Goldberg syndrome, characterized by mild aortic root dilation, mitral valve prolapse, and various clinical manifestations reminiscent of severe marfanoid habitus, including craniosynostosis, distinctive craniofacial features, skeletal changes, neurologic abnormalities, and mild-to-moderate intellectual disability [120,121].

Aortic aneurysms with cutis laxa

Cutis laxa is an acquired or inherited condition characterized by redundant, pendulous, and inelastic skin. Cutis laxa is a genetically heterogeneous disease and both autosomal dominant and autosomal recessive forms have been described. The autosomal dominant form is caused by mutations in the elastin gene (*ELN*). Recessive forms can be caused by mutations in the fibulin 4 (*FBLN4*), fibulin 5 (*FBLN5*) or *LTBP4* gene. Phenotypic features vary according to the underlying genetic defect. In families with mutations in the *ELN* gene, the clinical spectrum ranges from mild dilation to severe aneurysm requiring aortic root replacement or leading to aortic rupture early in adulthood. In a study by Szabo et al., one 5-year-old patient presented with significant dilation at the level of the sinuses of Valsalva [122]. Patients with fibulin-4 mutations may present with aortic aneurysms, arterial tortuosity, and stenosis [123].

Practical guidelines for cardiovascular imaging in connective tissue disorders are summarized in Table 32.2. We provide an overview of the recommended imaging studies and the anomalies described.

Nonsyndromic H-TAD

Thoracic aortic aneurysms and dissections (TAAD)

Familial TAAD is genetically heterogeneous, with two loci (TAAD1 at 5q13–14 and FAA1 at 11q23–24) and seven genes (*TGFBR1*, *TGFBR2*, *ACTA2*, *MYH11*, *MYLK*, *PRKG1*, and *SMAD3*) being identified so far. These genes account for disease in only 20% of FTAAD families, indicating that more genes are still to be determined.

By definition, the entity of TAAD is restricted to those cases presenting with "isolated" TAAD – as opposed to the known syndromes such as MFS and LDS. In practice, most reported families also exhibit some additional clinical features.

Pannu and co-workers reported the presence of *TGFBR2* mutations in four unrelated families with TAAD [124]. Imaging studies were limited to echocardiographic examination of the ascending aorta. Nevertheless, some patients included in the study did have vascular anomalies outside the aorta (two carotid artery aneurysms, three cerebral aneurysms, and two abdominal artery/popliteal artery aneurysms) or in the descending aorta (four patients with a type B dissection), and one patient with enlargement of the pulmonary artery, further raising the suspicion for LDS.

Guo et al. [37] reported on a family with TAAD whether or not in combination with livedo reticularis and iris flocculi, associated with mutations in the smooth muscle α-actin gene (*ACTA2*). The patients reported by Zhu et al. [125] with mutations in the *MYH11* gene had a strong association with patent ductus arteriosus and intracranial dissections and aneurysms, whereas manifestations in the distal aorta appeared less common.

The most important cardiovascular imaging study in TAAD is echocardiography for assessment of the proximal aortic diameters.

Thoracic aortic aneurysms and dissections associated with bicuspid aortic valve

The bicuspid aortic valve (BAV) affects 1–2% of the population and is associated with abnormalities of the aortic wall such as coarctation of the aorta, aortic dissection, and aortic aneurysm [126]. Aortic wall abnormalities associated with BAV are characterized by cystic medial necrosis [127], the same process as observed in the aorta of patients with MFS. Cystic medial

Table 32.2 Overview of the recommended cardiovascular imaging studies in diagnosis and follow-up of the clinical/genetic entities associated with aortic aneurysms.

Disorder	Diagnostic		Follow-up	
Marfan	Echocardiography	ARD, MVP	Echocardiography	ARD/descending aortic dilation
			CT/MRI	Descending aortic dilation
Loeys–Dietz, aneurysm–osteoarthritis	Echocardiography	ARD, PDA, ASD, BAV, MVP	Echocardiography	ARD/descending aortic dilation
	CT/MRI	Aortic/arterial tortuosity/dilation	CT/MRI	Aortic/arterial tortuostity/dilation
Vascular Ehlers–Danlos	Echocardiography?	ARD	Echocardiography?	ARD
	CT/MRI?	Aortic/arterial dilation	CT/MRI?	Aortic/arterial dilation
Arterial tortuosity	Echocardiography	ARD, PS	Echocardiography	ARD, PS
	CT/MRI	Arterial tortuosity/stenosis/dilation	CT/MRI	Arterial tortuosity/stenosis/dilation
Thoracic aortic aneurysm	Echocardiography CT/MRI	ARD, PDA, tortuosity	Echocardiography	ARD
Bicuspid aortic valve	Echocardiography	ARD, valvular morphology and function, coarctation	Echocardiography	ARD, valvular function
	CT/MRI	Ascending aortic dilation, coarctation	CT/MRI	Ascending aortic dilation

ARD, aortic root dilation; ASD, atrial septal defect; BAV, bicuspid aortic valve; MVP, mitral valve prolapse; PDA, patent ductus arteriosus; PS, pulmonary artery stenosis.

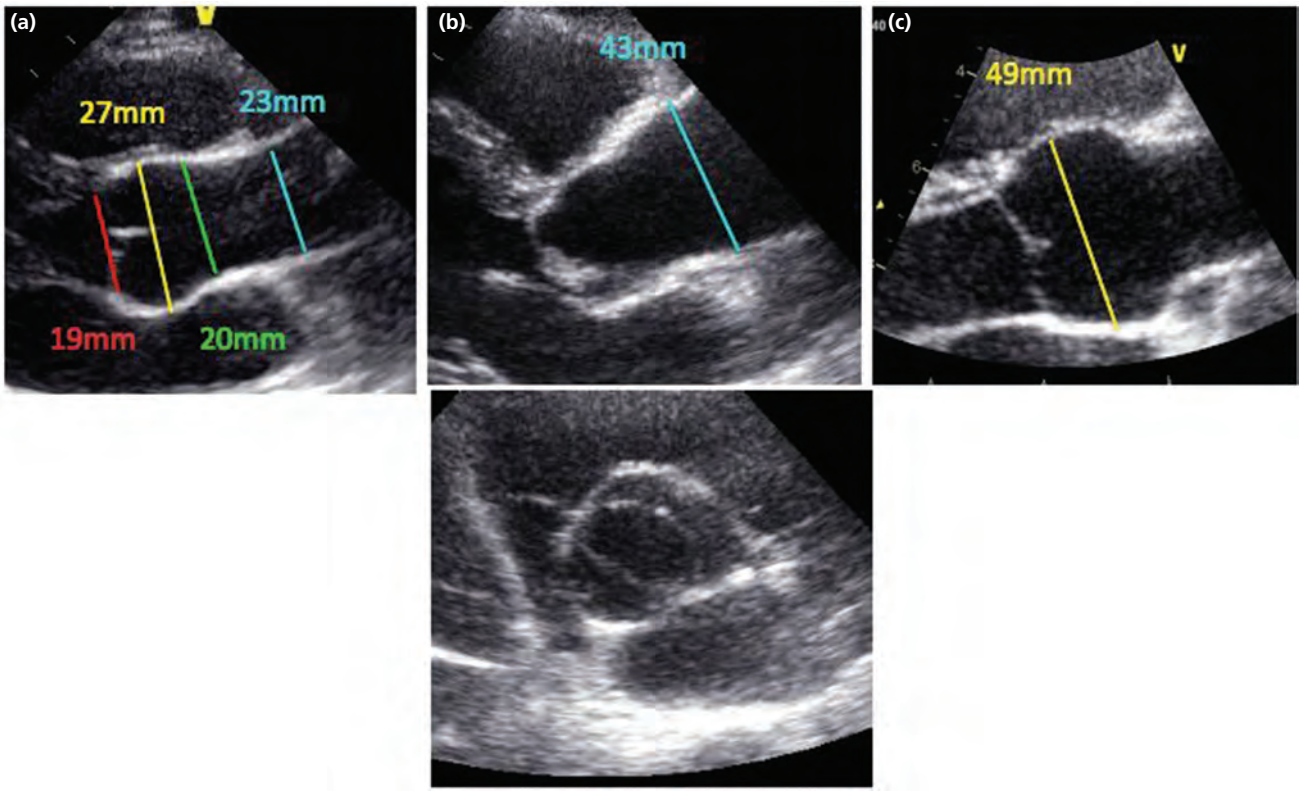


Figure 32.9 Echocardiographic views of the aortic root from the PSLAX window (upper row)and the aortic valve from the PSSAX window. **(a)** A normal aortic root with the various measurements as described previously. **(b)** The aortic root (upper) and valve (lower) from a BAV patient with anteroposterior valve morphology. **(c)** The aortic root from a Marfan syndrome patient. Note the different location of the aneurysm in the BAV patient (ascending aorta) compared with the Marfan patient (sinus of Valsalva).

necrosis in patients with BAV has been demonstrated in the aortic wall of patients with BAV, even without significant aneurysm formation. In patients with BAV, there is a ninefold increase in the risk of developing acute dissections compared with patients with normal aortic valves. Aortic aneurysms and dissections occur irrespective of altered hemodynamics or age [128]. In contrast to MFS, aortic root dilation in BAV patients is generally located in the ascending aorta, above the sinuses of Valsalva [129]. Even young children with BAV have aortic root dilation compared with controls [130,131]. Notably, the process of progressive dilation of the ascending aorta can continue after valve replacement. Patients with BAV require continuous surveillance to treat associated lesions and prevent complications. BAV may occur sporadic or familial. The minimal frequency of familial occurrence of bicuspid aortic valve ranges between 9.1 and 17.1% [132,133]. Analysis of these families indicated that the condition is inherited in an autosomal dominant manner with reduced penetrance. Goh et al. performed a comprehensive evaluation of multiple pedigrees segregating BAV with ascending aortic aneurysm, which revealed a high incidence of individuals with ascending aneurysm alone, suggesting that BAV and ascending aortic aneurysm are both primary manifestations of a single gene defect with variable expression [134]. Similar observations of isolated aortic aneurysm formation in family members of patients with BAV were reported by Loscalzo et al. [135]. Based on these findings, it is recommended that all family members, including those without BAV, should be followed up using imaging protocols that specifically assess aortic segments beyond the sinotubular junction. Echocardiographic evaluation includes both valvular evaluation (morphology and function) and evaluation of the ascending aorta (Figure 32.9). The latter is carried out from the parasternal long-axis view for assessment of the aortic root dimensions as described earlier. The ascending aorta may be better visualized from the high PSLAX view (one intercostal space more cranially), at the crossing of the right pulmonary artery. The aortic arch is visualized from the suprasternal notch view.

Conclusion

Echocardiography plays a key role in the management of patients with connective tissue disorders. Lesions vary widely according to the type of disorder and, even within one specific entity, the severity of the lesions may vary substantially. The most common lesions include aortic root aneurysm, mitral valve prolapse, pulmonary artery dilation, and bicuspid aortic valves. Echocardiography is indicated in every patient with proven or suspicious connective tissue disease and should be repeated life-long at regular intervals. In most patients, additional imaging studies are indicated to look for more distal lesions in the aorta and side branches.

Videos

To access the videos for this chapter, please go to www.lai-echo.com.

Videos 32.1 and 32.2 Aortic root aneurysm. Note the typical localization at the sinuses of Valsalva.

Video 32.3 Ascending aortic dissection in a 45-year-old female Marfan patient. Note the normal diameter distal to the root. Dissection flap seen in the center and division of flow seen with color M-mode.

Video 32.4 Mitral valve prolapse seen in the PSLAX view. Note the thickened valve leaflets and the displacement of the leaflets in the LA in systole.

Video 32.5 Mitral valve prolapse in the AP4Ch view without color Doppler. This 47-year-old female Marfan patient has a normal aortic root diameter.

Video 32.6 Mitral valve prolapse in the AP4Ch view with color Doppler. This 47-year-old female Marfan patient has a normal aortic root diameter.

Video 32.7 MRA image of descending aortic aneurysm in a 40-year-old female Marfan patient who previously underwent aortic root replacement and resection of an abdominal aortic aneurysm.

Video 32.8 Aneurysmatic dilation of the aortic arch (seen from the suprasternal notch view) in a 35-year-old male Marfan patient who previously underwent aortic root replacement.

Video 32.9 PSSAX view at the basal level showing a markedly dilated pulmonary artery and the presence of flow coming from a patent ductus arteriosus in a 27-year-old Loeys–Dietz patient.

References

1 Järveläinen H, Sainio A, Koulu M, et al. Extracellular matrix molecules: potential targets in pharmacotherapy. *Pharmacol Rev* 2009;**61**:198–223.

2 Rifkin DB. Latent transforming growth factor-beta (TGF-beta) binding proteins: orchestrators of TGF-beta availability. *J Biol Chem* 2005;**280**:7409–7412.

3 Charbonneau NL, Ono RN, Corson GM, et al. Fine tuning of growth factor signals depends on fibrillin microfibril networks. *Birth Defects Res C Embryo Today* 2004;**72**:37–50.

4 Schoen FJ. Aortic valve structure–function correlations: role of elastic fibers no longer a stretch of the imagination. *J Heart Valve Dis* 1997;**6**:1–6.

5 Dietz HC, Cutting GR, Pyeritz RE, et al. Marfan syndrome caused by a recurrent de novo missense mutation in the fibrillin gene. *Nature* 1991;**352**:337–339.

6 Sakai LY, Keene DR, Glanville RW, Bächinger HP. Purification and partial characterization of fibrillin, a cysteine-rich structural component of connective tissue microfibrils. *J Biol Chem* 1991;**266**:14763–14770.

7 Isogai Z, Ono RN, Ushiro S, et al. Latent transforming growth factor beta-binding protein 1 interacts with fibrillin and is a microfibril-associated protein. *J Biol Chem* 2003;**278**:2750–2757.

8 Dallas SL, Keene DR, Bruder SP, et al. Role of the latent transforming growth factor beta binding protein 1 in fibrillin-containing microfibrils in bone cells in vitro and in vivo. *J Bone Miner Res* 2000;**15**:68–81.

9 Dallas SL, Miyazono K, Skerry TM, et al. Dual role for the latent transforming growth factor-beta binding protein in storage of latent TGF-beta in the extracellular matrix and as a structural matrix protein. *J Cell Biol* 1995;**131**:539–549.

10 Saharinen J, Hyytiainen M, Taipale J, Keski-Oja J. Latent transforming growth factor-beta binding proteins (LTBPs) – structural extracellular matrix proteins for targeting TGF-beta action. *Cytokine Growth Factor Rev* 1999;**10**:99–117.

11 Neptune ER, Frischmeyer PA, Arking DE, et al. Dysregulation of TGF-beta activation contributes to pathogenesis in Marfan syndrome. *Nat Genet* 2003;**33**:407–411.

12 Charbonneau NL, Carlson EJ, Tufa S, et al. In vivo studies of mutant fibrillin-1 microfibrils. *J Biol Chem* 2010;**285**:24943–24955.

13 Dietz HC. TGF-beta in the pathogenesis and prevention of disease: a matter of aneurysmic proportions. *J Clin Invest* 2010;**120**:403–406.

14 Jeremy RW, Robertson E, Lu Y, Hambly BD. Perturbations of mechanotransduction and aneurysm formation in heritable aortopathies. *Int J Cardiol* 2013;**169**:7–16.

15 Horiguchi M, Ota M, Rifkin DB. Matrix control of transforming growth factor-β function. *J Biochem* 2012;**152**:321–329.

16 Sengle G, Sakai LY. The fibrillin microfibril scaffold: a niche for growth factors and mechanosensation? *Matrix Biol* 2015; May 7. (Epub ahead of print).

17 Humphrey JD, Schwartz MA, Tellides G, Milewicz DM. Role of mechanotransduction in vascular biology: focus on thoracic aortic aneurysms and dissections. *Circ Res* 2015;**116**:1448–1461.

18 Habashi JP, Judge DP, Holm TM, et al. Losartan, an AT1 antagonist, prevents aortic aneurysm in a mouse model of Marfan syndrome. *Science* 2006;**312**:117–121.

19 Brooke BS, Habashi JP, Judge DP, et al. Angiotensin II blockade and aortic-root dilation in Marfan's syndrome. *N Engl J Med* 2008;**358**:2787–2795.

20 Chiu HH, Wu MH, Wang JK, et al. Losartan added to beta-blockade therapy for aortic root dilation in Marfan syndrome: a randomized, open-label pilot study. *Mayo Clin Proc* 2013;**88**:271–276.

21 Groenink M, den Hartog AW, Franken R, et al. Losartan reduces aortic dilation rate in adults with Marfan syndrome: a randomized controlled trial. *Eur Heart J* 2013;**34**:3491–3500.

22 Lacro RV, Dietz HC, Wruck LM, et al. Rationale and design of a randomized clinical trial of beta-blocker therapy (atenolol) versus angiotensin II receptor blocker therapy (losartan) in individuals with Marfan syndrome. *Am Heart J* 2007;**154**:624–631.

23 Lacro RV, Guey LT, Dietz HC, et al. Characteristics of children and young adults with Marfan syndrome and aortic root dilation in a randomized trial comparing atenolol and losartan therapy. *Am Heart J* 2013;**165**:828–835.e3.

24 Lacro RV, Dietz HC, Sleeper LA, et al. Atenolol versus losartan in children and young adults with Marfan's syndrome. *N Engl J Med* 2014;**371**:2061–2071.

25 Milleron O, Arnoult F, Ropers J, et al. Marfan Sartan: a randomized, double-blind, placebo-controlled trial. *Eur Heart J* 2015; May 2. (Epub ahead of print).

26 Bowen J, Connolly H. Of Marfan's syndrome, mice, and medications. *N Engl J Med* 2014;**371**:2127–2128.

27 van de Laar IM, Oldenburg RA, Pals G, et al. Mutations in SMAD3 cause a syndromic form of aortic aneurysms and dissections with early-onset osteoarthritis. *Nat Genet* 2011;**43**:121–126.

28 van der Linde D, van de Laar IM, Bertoli-Avella AM, et al. Aggressive cardiovascular phenotype of aneurysms–osteoarthritis syndrome caused by pathogenic SMAD3 variants. *J Am Coll Cardiol* 2012;**60**:397–403.

29 Andrabi S, Bekheirnia MR, Robbins-Furman P, et al. SMAD4 mutation segregating in a family with juvenile polyposis, aortopathy, and mitral valve dysfunction. *Am J Med Genet A* 2011;**155A**:1165–1169.

30 Lindsay ME, Schepers D, Bolar NA, et al. Loss-of-function mutations in TGFB2 cause a syndromic presentation of thoracic aortic aneurysm. *Nat Genet* 2012;**44**:922–927.

31 Boileau C, Guo DC, Hanna N, et al. TGFB2 mutations cause familial thoracic aortic aneurysms and dissections associated with mild systemic features of Marfan syndrome. *Nat Genet* 2012;**44**:916–921.

32 Renard M, Callewaert B, Malfait F, et al. Thoracic aortic-aneurysm and dissection in association with significant mitral valve disease caused by mutations in TGFB2. *Int J Cardiol* 2013;**185**:584–587.

33 Bertoli-Avella AM, Gillis E, Morisaki H, et al. Mutations in a TGF-β ligand, TGFB3, cause syndromic aortic aneurysms and dissections. *J Am Coll Cardiol* 2015;**65**:1324–1336.

34 Loeys BL, Schwarze U, Holm T, et al. Aneurysm syndromes caused by mutations in the TGF-beta receptor. *N Engl J Med* 2006;**355**:788–798.

35 Attias D, Stheneur C, Roy C, et al. Comparison of clinical presentations and outcomes between patients with TGFBR2 and FBN1 mutations in Marfan syndrome and related disorders. *Circulation* 2009;**120**:2541–2549.

36 Erbel R, Aboyans V, Boileau C, et al. 2014 ESC Guidelines on the diagnosis and treatment of aortic diseases. The Task Force for the Diagnosis and Treatment of Aortic Diseases of the European Society of Cardiology (ESC). *Eur Heart J* 2014;**35**:2873–2926.

37 Guo DC, Pannu H, Tran-Fadulu V, et al. Mutations in smooth muscle alpha-actin (ACTA2) lead to thoracic aortic aneurysms and dissections. *Nat Genet* 2007;**39**:1488–1493.

38 Guo DC, Regalado E, Casteel DE, et al. Recurrent gain-of-function mutation in PRKG1 causes thoracic aortic aneurysms and acute aortic dissections. *Am J Hum Genet* 2013;**93**:398–404.

39 Wang L, Guo DC, Cao J, et al. Mutations in myosin light chain kinase cause familial aortic dissections. *Am J Hum Genet* 2010;**87**:701–707.

40 Pannu H, Tran-Fadulu V, Papke CL, et al. MYH11 mutations result in a distinct vascular pathology driven by insulin-like growth factor 1 and angiotensin II. *Hum Mol Genet* 2007;**16**:2453–2462.

41 Renard M, Callewaert B, Baetens M, et al. Novel MYH11 and ACTA2 mutations reveal a role for enhanced TGFbeta signaling in FTAAD. *Int J Cardiol* 2013;**165**:314–321.

42 Moustakas A, Heldin CH. The regulation of TGFbeta signal transduction. *Development* 2009;**136**:3699–3714.

43 Lindsay ME, Dietz HC. Lessons on the pathogenesis of aneurysm from heritable conditions. *Nature* 2011;**473**:308–316.

44 Pyeritz RE. Heritable thoracic aortic disorders. *Curr Opin Cardiol* 2014;**29**:97–102.

45 Campens L, Callewaert B, Muiño Mosquera L, et al. Gene panel sequencing in heritable thoracic aortic disorders and related entities – results of comprehensive testing in a cohort of 264 patients. *Orphanet J Rare Dis* 2015;**10**:9.

46 Loeys BL, Dietz HC, Braverman AC, et al. The revised Ghent nosology for the Marfan syndrome. *J Med Genet* 2010;**47**:476–485.

47 Tiecke F, Katzke S, Booms P, et al. Classic, atypically severe and neonatal Marfan syndrome: twelve mutations and genotype–phenotype correlations in FBN1 exons 24–40. *Eur J Hum Genet* 2001;**9**:13–21.

48 Kainulainen K, Karttunen L, Puhakka L, et al. Mutations in the fibrillin gene responsible for dominant ectopia lentis and neonatal Marfan syndrome. *Nat Genet* 1994;**6**:64–69.

49 Putnam EA, Cho M, Zinn AB, et al. Delineation of the Marfan phenotype associated with mutations in exons 23–32 of the FBN1 gene. *Am J Med Genet* 1996;**62**:233–242.

50 Black C, Withers AP, Gray JR, et al. Correlation of a recurrent FBN1 mutation (R122C) with an atypical familial Marfan syndrome phenotype. *Hum Mutat* 1998;(Suppl 1):S198–S200.

51 De Backer J, Loeys B, Leroy B, et al. Utility of molecular analyses in the exploration of extreme intrafamilial variability in the Marfan syndrome. *Clin Genet* 2007;**72**:188–198.

52 Judge DP, Dietz HC. Marfan's syndrome. *Lancet* 2005;**366**:1965–1976.

53 Roman MJ, Devereux RB, Kramer-Fox R, O'Loughlin J. Two-dimensional echocardiographic aortic root dimensions in normal children and adults. *Am J Cardiol* 1989;**64**:507–512.

54 Roman MJ, Devereux RB, Kramer-Fox R, Spitzer MC. Comparison of cardiovascular and skeletal features of primary mitral valve prolapse and Marfan syndrome. *Am J Cardiol* 1989;**63**:317–321.

55 Devereux RB, de Simone G, Arnett DK, et al. Normal limits in relation to age, body size and gender of two-dimensional echocardiographic aortic root dimensions in persons ≥15 years of age. *Am J Cardiol* 2012;**110**:1189–1194.

56 Meijboom LJ, Groenink M, van der Wall EE, et al. Aortic root asymmetry in Marfan patients; evaluation by magnetic resonance imaging and comparison with standard echocardiography. *Int J Card Imaging* 2000;**16**:161–168.

57 Apter JT. Correlation of visco-elastic properties with microscopic structure of large arteries. IV. Thermal responses of collagen, elastin, smooth muscle, and intact arteries. *Circ Res* 1967;**21**:901–918.

58 Pyeritz RE. Marfan syndrome: current and future clinical and genetic management of cardiovascular manifestations. *Semin Thorac Cardiovasc Surg* 1993;**5**:11–16.

59 Roman MJ, Rosen SE, Kramer-Fox R, Devereux RB. Prognostic significance of the pattern of aortic root dilation in the Marfan syndrome. *J Am Coll Cardiol* 1993;**22**:1470–1476.

60 Dapunt OE, Galla JD, Sadeghi AM, et al. The natural history of thoracic aortic aneurysms. *J Thorac Cardiovasc Surg* 1994;**107**:1323–1332; discussion 1332–1333.

61 Pyeritz RE. Genetics and cardiovascular disease. In: Braunwald E (ed.) *Cardiovascular Disease*. Philadelphia, PA: Saunders, 1992, pp. 1641–1643.

62 Groenink M, Lohuis TA, Tijssen JG, et al. Survival and complication free survival in Marfan's syndrome: implications of current guidelines. *Heart* 1999;**82**:499–504.

63 Legget ME, Unger TA, O'Sullivan CK, et al. Aortic root complications in Marfan's syndrome: identification of a lower risk group. *Heart* 1996;**75**:389–395.

64 Silverman DI, Gray J, Roman MJ, et al. Family history of severe cardiovascular disease in Marfan syndrome is associated with increased aortic diameter and decreased survival. *J Am Coll Cardiol* 1995;**26**:1062–1067.

65 Jondeau G, Boutouyrie P, Lacolley P, et al. Central pulse pressure is a major determinant of ascending aorta dilation in Marfan syndrome. *Circulation* 1999;**99**:2677–2681.

66 Adams JN, Brooks M, Redpath TW, et al. Aortic distensibility and stiffness index measured by magnetic resonance imaging in patients with Marfan's syndrome. *Br Heart J* 1995;**73**:265–269.

67 Groenink M, de Roos A, Mulder BJ, et al. Biophysical properties of the normal-sized aorta in patients with Marfan syndrome: evaluation with MR flow mapping. *Radiology* 2001;**219**:535–540.

68 Hirata K, Triposkiadis F, Sparks E, et al. The Marfan syndrome: cardiovascular physical findings and diagnostic correlates. *Am Heart J* 1992;**123**:743–752.

69 Jeremy RW, Huang H, Hwa J, et al. Relation between age, arterial distensibility, and aortic dilation in the Marfan syndrome. *Am J Cardiol* 1994;**74**:369–373.

70 Baumgartner D, Baumgartner C, Matyas G, et al. Diagnostic power of aortic elastic properties in young patients with Marfan syndrome. *J Thorac Cardiovasc Surg* 2005;**129**:730–739.

71 Freed LA, Levy D, Levine RA, et al. Prevalence and clinical outcome of mitral-valve prolapse. *N Engl J Med* 1999;**341**:1–7.

72 Levine R, Handschumacher M, Sanfilippo A, et al. Three-dimensional echocardiographic reconstruction of the mitral valve, with implications for the diagnosis of mitral valve prolapse. *Circulation* 1989;**80**:589–598.

73 Pyeritz RE, Wappel MA. Mitral valve dysfunction in the Marfan syndrome. Clinical and echocardiographic study of prevalence and natural history. *Am J Med* 1983;**74**:797–807.

74 De Backer J, Loeys B, Devos D, et al. A critical analysis of minor cardiovascular criteria in the diagnostic evaluation of patients with Marfan syndrome. *Genet Med* 2006;**8**:401–408.

75 Rybczynski M, Treede H, Sheikhzadeh S, et al. Predictors of outcome of mitral valve prolapse in patients with the Marfan syndrome. *Am J Cardiol* 2011;**107**:268–274.

76 Truong QA, Massaro JM, Rogers IS, et al. Reference values for normal pulmonary artery dimensions by noncontrast cardiac computed tomography: the Framingham Heart Study. *Circ Cardiovasc Imaging* 2012;**5**:147–154.

77 Nollen GJ, van Schijndel KE, Timmermans J, et al. Pulmonary artery root dilation in Marfan syndrome: quantitative assessment of an unknown criterion. *Heart* 2002;**87**:470–471.

78 Lundby R, Rand-Hendriksen S, Hald JK, et al. The pulmonary artery in patients with Marfan syndrome: a cross-sectional study. *Genet Med* 2012;**14**:922–927.

79 Dietz HC, Pyeritz RE. Marfan syndrome and related disorders. In: Scriver CR, Beaudet AL, Sly WS, Valle D (eds.) *The Metabolic and Molecular Bases of Inherited Diseases*, 8th edn. New York: McGraw-Hill, 2001, pp. 5287–5311.

80 Finkbohner R, Johnston D, Crawford ES, et al. Marfan syndrome: long-term survival and complications after aortic aneurysm repair. *Circulation* 1995;**91**:728–733.

81 Engelfriet PM, Boersma E, Tijssen JG, et al. Beyond the root: dilatation of the distal aorta in the Marfan syndrome. *Heart* 2006;**92**:1238–1243.

82 van Ooijen B. Marfan's syndrome and isolated aneurysm of the abdominal aorta. *Br Heart J* 1988;**59**:81–84.

83 Pruzinsky MS, Katz NM, Green CE, Satler LF. Isolated descending thoracic aortic aneurysm in Marfan's syndrome. *Am J Cardiol* 1988;**61**:1159–1160.

84 Nollen GJ, Groenink M, Tijssen JG, et al. Aortic stiffness and diameter predict progressive aortic dilation in patients with Marfan syndrome. *Eur Heart J* 2004;**25**:1146–1152.

85 Kawamoto S, Bluemke DA, Traill TA, Zerhouni EA. Thoracoabdominal aorta in Marfan syndrome: MR imaging findings of progression of vasculopathy after surgical repair. *Radiology* 1997;**203**:727–732.

86 Mimoun L, Detaint D, Hamroun D, et al. Dissection in Marfan syndrome: the importance of the descending aorta. *Eur Heart J* 2011;**32**:443–449.

87 Schoenhoff FS, Jungi S, Czerny M, et al. Acute aortic dissection determines the fate of initially untreated aortic segments in Marfan syndrome. *Circulation* 2013;**127**:1569–1575.

88 LeMaire SA, de la Cruz KI, Coselli JS. The thoracoabdominal aorta in Marfan syndrome. In: Bonser RS, Pagano D, Haverich A, Mascaro J (eds.) *Controversies in Aortic Dissection and Aneurysmal Disease*. London: Springer London, 2014, pp. 423–434.

89 Hiratzka LF, Bakris GL, Beckman JA, et al. 2010 ACCF/AHA/AATS/ACR/ASA/SCA/SCAI/SIR/STS/SVM guidelines for the diagnosis and management of patients with thoracic aortic disease. A report of the American College of Cardiology Foundation/American Heart Association Task Force on Practice Guidelines, American Association for Thoracic Surgery, American College of Radiology, American Stroke Association, Society of Cardiovascular Anesthesiologists, Society for Cardiovascular Angiography and Interventions, Society of Interventional Radiology, Society of Thoracic Surgeons, and Society for Vascular Medicine. *Circulation* 2010;**121**:e266–e369.

90 Teixido-Tura G, Redheuil A, Rodríguez-Palomares J, et al. Aortic biomechanics by magnetic resonance: early markers of aortic disease in Marfan syndrome regardless of aortic dilatation? *Int J Cardiol* 2014;**171**:56–61.

91 Nollen GJ, Meijboom LJ, Groenink M, et al. Comparison of aortic elasticity in patients with the Marfan syndrome with and without aortic root replacement. *Am J Cardiol* 2003;**91**:637–640.

92 Mortensen K, Aydin MA, Rybczynski M, et al. Augmentation index relates to progression of aortic disease in adults with Marfan syndrome. *Am J Hypertens* 2009;**22**:971–979.

93 Segers P, De Backer J, Devos D, et al. Aortic reflection coefficients and their association with global indexes of wave reflection in healthy controls and patients with Marfan's syndrome. *Am J Physiol Heart Circ Physiol* 2006;**290**:H2385–H2392.

94 Knosalla C, Weng Y-G, Hammerschmidt R, et al. Orthotopic heart transplantation in patients with Marfan syndrome. *Ann Thorac Surg* 2007;**83**:1691–1695.

95 Das BB, Taylor AL, Yetman AT. Left ventricular diastolic dysfunction in children and young adults with Marfan syndrome. *Pediatr Cardiol* 2006;**27**:256–258.

96 Savolainen A, Nisula L, Keto P, et al. Left ventricular function in children with the Marfan syndrome. *Eur Heart J* 1994;**15**:625–630.

97 Kiotsekoglou A, Moggridge JC, Bijnens BH, et al. Biventricular and atrial diastolic function assessment using conventional echocardiography and tissue-Doppler imaging in adults with Marfan syndrome. *Eur J Echocardiogr* 2009;**10**:947–955.

98 Alpendurada F, Wong J, Kiotsekoglou A, et al. Evidence for Marfan cardiomyopathy. *Eur J Heart Fail* 2010;**12**:1085–1091.

99 De Backer JF, Devos D, Segers P, et al. Primary impairment of left ventricular function in Marfan syndrome. *Int J Cardiol* 2006;**112**:353–358.

100 Rybczynski M, Koschyk DH, Aydin MA, et al. Tissue Doppler imaging identifies myocardial dysfunction in adults with Marfan syndrome. *Clin Cardiol* 2007;**30**:19–24.

101 Chatrath R, Beauchesne LM, Connolly HM, et al. Left ventricular function in the Marfan syndrome without significant valvular regurgitation. *Am J Cardiol* 2003;**91**:914–916.

102 Reed CM, Fox ME, Alpert BS. Aortic biomechanical properties in pediatric patients with the Marfan syndrome, and the effects of atenolol. *Am J Cardiol* 1993;**71**:606–608.

103 Aalberts JJJ, van Tintelen JP, Meijboom LJ, et al. Relation between genotype and left-ventricular dilatation in patients with Marfan syndrome. *Gene* 2014;**534**:40–43.

104 Keane MG, Pyeritz RE. Medical management of Marfan syndrome. *Circulation* 2008;**117**:2802–2813.

105 Cook JR, Carta L, Bénard L, et al. Abnormal muscle mechanosignaling triggers cardiomyopathy in mice with Marfan syndrome. *J Clin Invest* 2014;**124**:1329–1339.

106 Yetman AT, Bornemeier RA, McCrindle BW. Long-term outcome in patients with Marfan syndrome: is aortic dissection the only cause of sudden death? *J Am Coll Cardiol* 2003;**41**:329–332.

107 Hoffmann BA, Rybczynski M, Rostock T, et al. Prospective risk stratification of sudden cardiac death in Marfan's syndrome. *Int J Cardiol* 2013;**167**: 2539–2545.

108 Chen S, Fagan LF, Nouri S, Donahoe JL. Ventricular dysrhythmias in children with Marfan's syndrome. *Am J Dis Child* 1985;**139**:273–276.

109 Sheikhzadeh S, De Backer J, Gorgan N, et al. The main pulmonary artery in adults: a controlled multicenter study with assessment of echocardiographic reference values, and the frequency of dilatation and aneurysm in Marfan syndrome. *Orphanet J Rare Dis* 2014;**9**:203.

110 Loeys BL, Chen J, Neptune ER, et al. A syndrome of altered cardiovascular, craniofacial, neurocognitive and skeletal development caused by mutations in TGFBR1 or TGFBR2. *Nat Genet* 2005;**37**:275–281.

111 Williams JA, Loeys BL, Nwakanma LU, et al. Early surgical experience with Loeys–Dietz: a new syndrome of aggressive thoracic aortic aneurysm disease. *Ann Thorac Surg* 2007;**83**:S757–S763; discussion S785–S790.

112 Pepin M, Schwarze U, Superti-Furga A, Byers PH. Clinical and genetic features of Ehlers–Danlos syndrome type IV, the vascular type. *N Engl J Med* 2000;**342**:673–680.

113 van der Linde D, Verhagen HJM, Moelker A, et al. Aneurysm–osteoarthritis syndrome with visceral and iliac artery aneurysms. *J Vasc Surg* 2013;**57**:96–102. Available from: http://linkinghub.elsevier.com/retrieve/pii/S0741521412015935
114 Martens T, Van Herzeele I, De Ryck F, et al. Multiple aneurysms in a patient with aneurysms–osteoarthritis syndrome. *Ann Thorac Surg* 2013;**95**:332–335.
115 van de Laar IM, van der Linde D, Oei EH, et al. Phenotypic spectrum of the SMAD3-related aneurysms–osteoarthritis syndrome. *J Med Genet* 2012;**49**:47–57.
116 Oderich GS, Panneton JM, Bower TC, et al. The spectrum, management and clinical outcome of Ehlers–Danlos syndrome type IV: a 30-year experience. *J Vasc Surg* 2005;**42**:98–106.
117 Bergqvist D, Björck M, Wanhainen A. Treatment of vascular Ehlers–Danlos syndrome: a systematic review. *Ann Surg* 2013;**258**:257–261.
118 Coucke PJ, Willaert A, Wessels MW, et al. Mutations in the facilitative glucose transporter GLUT10 alter angiogenesis and cause arterial tortuosity syndrome. *Nat Genet* 2006;**38**:452–457.
119 Milewicz DM, Østergaard JR, Ala-Kokko LM, et al. De novo ACTA2 mutation causes a novel syndrome of multisystemic smooth muscle dysfunction. *Am J Med Genet A* 2010;**152**:2437–2443.
120 Carmignac V, Thevenon J, Adès L, et al. In-frame mutations in exon 1 of SKI cause dominant Shprintzen–Goldberg syndrome. *Am J Hum Genet* 2012;**91**:950–957.
121 Doyle AJ, Doyle JJ, Bessling SL, et al. Mutations in the TGF-β repressor SKI cause Shprintzen–Goldberg syndrome with aortic aneurysm. *Nat Genet* 2012;**44**:1249–1254.
122 Szabo Z, Crepeau MW, Mitchell AL, et al. Aortic aneurysmal disease and cutis laxa caused by defects in the elastin gene. *J Med Genet* 2006;**43**:255–258.
123 Renard M, Holm T, Veith R, et al. Altered TGFbeta signaling and cardiovascular manifestations in patients with autosomal recessive cutis laxa type I caused by fibulin-4 deficiency. *Eur J Hum Genet* 2010;**18**:895–901.
124 Pannu H. Mutations in transforming growth factor-beta receptor type II cause familial thoracic aortic aneurysms and dissections. *Circulation* 2005;**112**:513–520.
125 Zhu L, Vranckx R, Khau Van Kien P, et al. Mutations in myosin heavy chain 11 cause a syndrome associating thoracic aortic aneurysm/aortic dissection and patent ductus arteriosus. *Nat Genet* 2006;**38**:343–349.
126 Mills P, Leech G, Davies M, Leathan A. The natural history of a non-stenotic bicuspid aortic valve. *Br Heart J* 1978;**40**:951–957.
127 Fedak PW, Verma S, David TE, et al. Clinical and pathophysiological implications of a bicuspid aortic valve. *Circulation* 2002;**106**:900–904.
128 Hahn RT, Roman MJ, Mogtader AH, Devereux RB. Association of aortic dilation with regurgitant, stenotic and functionally normal bicuspid aortic valves. *J Am Coll Cardiol* 1992;**19**:283–288.
129 Cecconi M, Manfrin M, Moraca A, et al. Aortic dimensions in patients with bicuspid aortic valve without significant valve dysfunction. *Am J Cardiol* 2005;**95**:292–294.
130 Gurvitz M, Chang RK, Drant S, Allada V. Frequency of aortic root dilation in children with a bicuspid aortic valve. *Am J Cardiol* 2004;**94**:1337–1340.
131 Basso C, Boschello M, Perrone C, et al. An echocardiographic survey of primary school children for bicuspid aortic valve. *Am J Cardiol* 2004;**93**:661–663.
132 Huntington K, Hunter AG, Chan KL. A prospective study to assess the frequency of familial clustering of congenital bicuspid aortic valve. *J Am Coll Cardiol* 1997;**30**:1809–1812.
133 Emanuel R, Withers R, O'Brien K, et al. Congenitally bicuspid aortic valves. Clinicogenetic study of 41 families. *Br Heart J* 1978;**40**:1402–1407.
134 Goh DL, Han LF, Judge DP, et al. Linkage of familial bicuspid aortic valve with aortic aneurysm to chromosome 15q. *Am J Hum Genet* 2002;**71**(Suppl):211.
135 Loscalzo ML, Goh DLM, Loeys B, et al. Familial thoracic aortic dilation and bicommissural aortic valve: a prospective analysis of natural history and inheritance. *Am J Med Genet A* 2007;**143A**:1960–1967.

CHAPTER 33

Cardiac Tumors

Michele A. Frommelt
Division of Pediatric Cardiology, Medical College of Wisconsin, Children's Hospital of Wisconsin, Milwaukee, WI, USA

Introduction

Tumors of the heart in the pediatric age group are typically characterized by a proliferation of tissue normally present at the site of origin. Cardiac tumors can comprise muscle (rhabdomyoma), fibrous tissue (fibroma), vascular tissue (hemangioma), mixed tissue (teratoma), fatty tissue (lipoma) and, rarely, metastatic tissue. Tumors of the heart can be defined as primary or secondary to other disease processes, as well as benign or malignant. Primary cardiac tumors are much more common in children, with almost all being histologically benign. This is in contrast to adults, where most cardiac tumors are secondary and related to metastatic disease.

Incidence

Cardiac tumors are rare in children, with an estimated incidence of 0.03–0.4%. In a review of 11,000 pediatric autopsies from the Boston Children's Hospital, reported by Nadas and Ellison in 1968, cardiac tumors were present in 0.027% [1]. In the New England regional study of more than 2000 infants with congenital heart disease, nine had primary cardiac tumors (0.4%) [2]. In an 8-year review of more than 14,000 fetal echocardiograms, cardiac tumors were present in 19 pregnancies, an incidence of 0.14% [3]. The majority of cardiac tumors in all of these studies were benign, with the most common being rhabdomyoma.

Over the past few decades, the recognition of cardiac tumors has increased. This is likely not related to a true increase in their prevalence, but can be explained by the widespread availability and increased sensitivity of two-dimensional (2D) echocardiography. This is nicely demonstrated in a study by Beghetti et al., a 15-year review of more than 27,000 pediatric patients with cardiac disease [4]. The overall incidence of a primary cardiac tumor was 0.2%, with an increase in incidence over each successive 5-year period (from 0.06% in the first period to 0.32% in the last). More than half of the patients were less than 1 year old at the time of diagnosis, and 12 of the 56 patients were diagnosed prenatally. Two-dimensional (2D) echocardiography was the imaging modality of choice in 55/56 patients.

Rhabdomyoma is the most common primary pediatric cardiac tumor, comprising about 60–80% of all tumors (Table 33.1). Cardiac fibromas have the second highest incidence (6–25%), followed closely by the teratoma. Hemangiomas and lipomas are much less common. The cardiac myxoma is rarely seen in the pediatric population, despite being the most common primary cardiac tumor in adults [5–8].

Rhabdomyoma

Classification

Rhabdomyomas, also known as hamartomas, are defined as an anomalous, benign proliferation of primitive myocardial tissue displaying typical "spider cells" on histopathology [9]. They are the most common benign congenital tumor, and are frequently associated with the tuberous sclerosis complex (50–86%). The genetic mutation in the tuberous sclerosis complex leads to proliferation of embryonal myoblasts, most commonly yielding multiple solid masses, which may arise anywhere in the atrial or ventricular myocardium [10]. Of importance, spontaneous regression of these cardiac tumors after birth is the rule [11–14].

Echocardiography

Perhaps the most defining echocardiographic feature of the cardiac rhabdomyoma is the presence of multiple tumors (Figure 33.1; Video 33.1). The tumors appear nodular and embedded in the myocardium, but often protrude into the involved cardiac chamber (Figure 33.2). They are typically homogeneous and hyperechoic compared with normal myocardium (Figure 33.3). Cardiac rhabdomyomas also have a distinct preference for the ventricles. In a study by Nir et al., 109 patients with the diagnosis of tuberous sclerosis underwent a comprehensive 2D echocardiogram. Of these patients, 47 (43%) had cardiac rhabdomyoma. The tumors were most commonly located in the left and right ventricles (68 and 66%, respectively); only three patients (6%)

Echocardiography in Pediatric and Congenital Heart Disease: From Fetus to Adult, Second Edition. Edited by Wyman W. Lai, Luc L. Mertens, Meryl S. Cohen and Tal Geva.
© 2016 John Wiley & Sons, Ltd. Published 2016 by John Wiley & Sons, Ltd.
Companion website: www.lai-echo.com

Table 33.1 Characteristics of primary cardiac tumors in childhood.

Type	Rhabdomyoma	Fibroma	Teratoma	Hemangioma	Myxoma
Incidence (%)	60–80	6–25	6–25	<10	<1
Location	Ventricles	Ventricles	Pericardium	Right atrium	Left atrium
Appearance	Multiple	Large, solitary	Solitary	Solitary	Solitary
	Hyperechoic	Hyperechoic	Mixed echogenicity	Mixed echogenicity	Pedunculated
	Homogeneous	Heterogeneous (areas of calcification)	Solid/multicystic	Color Doppler signals	Mixed echogenicity
Age	Fetal/infancy	Any age	Fetal/infancy	Neonatal	Adolescence
Regression	Yes	No	No	Yes, in infancy	No
Associations	Tuberous sclerosis	Outflow obstruction	Pericardial effusion	Pericardial effusion	Emboli

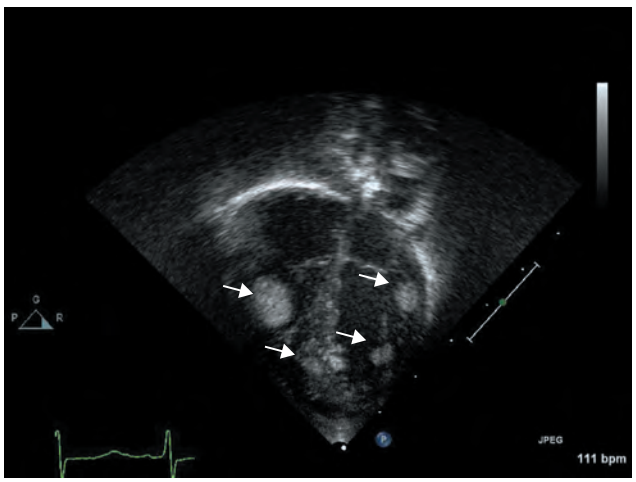


Figure 33.1 Apical 4-chamber view in a patient with tuberous sclerosis and rhabdomyomas. Multiple hyperechoic masses (arrows) are seen in the left and right ventricular free wall, and also the ventricular septum.

were found to have right atrial tumors. None were found in the left atrium [15].

Two-dimensional imaging and also color and pulsed-wave (PW) Doppler from standard acoustic windows should be performed. The goals of the examination should include determination of tumor size, location, and number. Hemodynamic abnormalities associated with the tumor should also be sought, with quantification of inflow or outflow tract obstruction, in addition to valvar insufficiency. Evaluation of ventricular function is also critical, as replacement of the ventricular muscle by noncontractile tumor tissue may mimic a cardiomyopathy [16]. In the fetus, it is also important to evaluate cardiac rhythm, and to investigate the serous cavities for effusions.

Serial echocardiographic evaluation of these patients is critical, both pre- and postnatally. Several studies have reported significant growth of cardiac rhabdomyoma in midgestation, suggesting that hormonal stimulation in utero plays a role in the

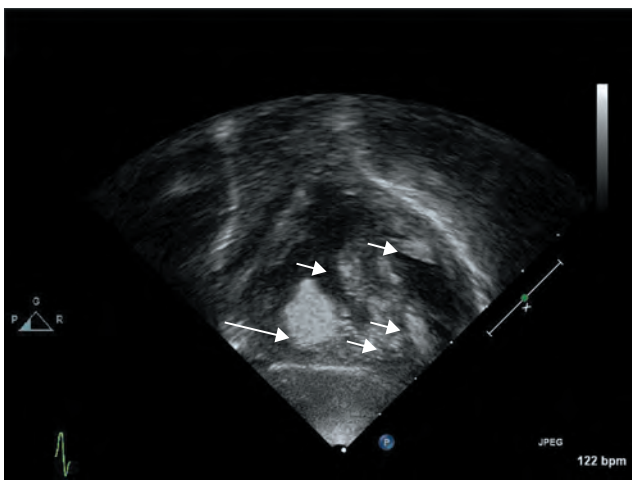


Figure 33.2 Subcostal 4-chamber view of the right ventricular outflow tract in a patient with tuberous sclerosis and rhabdomyomas. A large hyperechoic mass is seen just below the infundibulum (large arrow); multiple smaller masses are seen in the anterior muscular ventricular septum (small arrows).

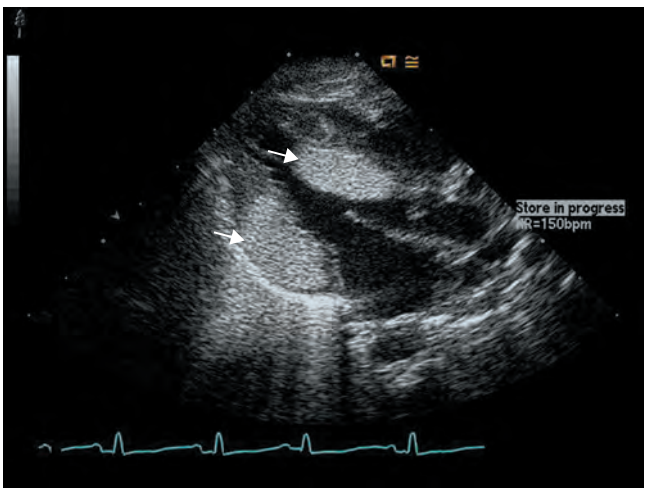


Figure 33.3 Parasternal long-axis view in a patient with tuberous sclerosis who presented with supraventricular tachycardia. Two large rhabdomyomas are seen in the left ventricular free wall and septum (arrows). The tumors appear embedded in the myocardium, and are hyperechoic and homogeneous.

growth process [3,17]. If there is a family history of tuberous sclerosis, it is important to remember that prenatal ultrasound rarely detects tumors prior to 20 weeks' gestation [18]. Therefore, an early screening ultrasound may be falsely reassuring. After birth, most cardiac rhabdomyomas will undergo spontaneous regression. This phenomenon has been extensively studied, and indeed, is one of the hallmarks of these tumors [11–14]. Surgery is recommended only for those patients with severe hemodynamic compromise or refractory arrhythmias. Of note, rapid tumor growth has been reported postnatally when the patient is treated with corticosteroids. The size of the cardiac rhabdomyoma should be followed carefully in those patients receiving this type of drug therapy [19].

Clinical course

The clinical course is generally benign and largely determined by tumor size and the presence of inflow or outflow tract obstruction. Rarely, global ventricular function may be depressed if there is significant tumor replacement of normal myocardium. Cardiac arrhythmias are well reported, and may be related to interruption of the normal conduction pathways. In several studies, the presence of Wolff–Parkinson–White syndrome was more frequent in patients with tuberous sclerosis compared with the normal population. Incessant ventricular arrhythmias, although rare, can be life threatening [20–22].

The timing of presentation also influences clinical course. In the older child referred to the echocardiography laboratory with a new diagnosis of tuberous sclerosis, it would be unusual to find a cardiac rhabdomyoma of clinical significance. However, when the diagnosis of tuberous sclerosis is suspected prenatally, the fetus may present with demise secondary to severe outflow tract obstruction or sustained arrhythmias. In a retrospective 7-year review by Geipel et al., 12 cases of cardiac tumors were observed prenatally. Eleven of the 12 were ultimately found to be rhabdomyomas, with one fibroma. Presenting symptoms were common in this age group, and included hydrops fetalis in five patients and arrhythmias in four patients. There were three elective terminations of pregnancy, one intrauterine demise related to severe left ventricular outflow tract (LVOT) obstruction, and three neonatal deaths, all related to massive tumor infiltration of the ventricular septum [23].

Fibroma

Classification

The cardiac fibroma is a benign connective tissue tumor derived from fibroblasts. It is the second most common type of primary cardiac tumor occurring in the pediatric age group. Cardiac fibromas are generally large tumors, averaging 5 cm in diameter, with the larger lesions able to obstruct outflow tracts and compress cardiac chambers. Their growth is typically within the myocardial mass itself, and they occur much more frequently within the anterior free wall of the left ventricle or the interventricular septum than in the posterior left ventricular wall or right ventricle. Although less common than the rhabdomyoma, fibromas are more often associated with symptoms, and more often require surgery. In contrast to the behavior of rhabdomyomas, spontaneous regression of fibromas is unusual [4–6,16].

Echocardiography

Cardiac fibromas are solitary lesions that arise from the ventricular septum or the free wall of the left or right ventricle (Figure 33.4). They often appear circumscribed, and are typically hyperechoic compared with normal myocardium. Calcification is frequent and an important diagnostic imaging feature. Areas of focal necrosis and cystic degeneration are common in the larger tumors. It is important to remember that a large septal fibroma may have the appearance of a hypertrophic obstructive cardiomyopathy. The absence of thickening/hypertrophy of other cardiac walls may suggest the diagnosis of fibroma. Also, calcification does not occur in hypertrophic cardiomyopathy. Fibromas can be massive, markedly distorting the cardiac muscle (Figures 33.5 and 33.6; Videos 33.2 and 33.3). This irregular appearance is also unusual for hypertrophic cardiomyopathy.

Two-dimensional imaging and color and pulsed Doppler interrogation from standard acoustic windows are important. In the symptomatic patient, severe LVOT obstruction may be profound and can mimic hypertrophic obstructive cardiomyopathy, with limited ventricular filling and dynamic outflow obstruction. In fact, the neonate who presents with severe LVOT obstruction may have ductal-dependent systemic blood flow. Doppler interrogation of the transverse arch should be performed to look for retrograde ductal supply of the transverse arch (Figure 33.7).

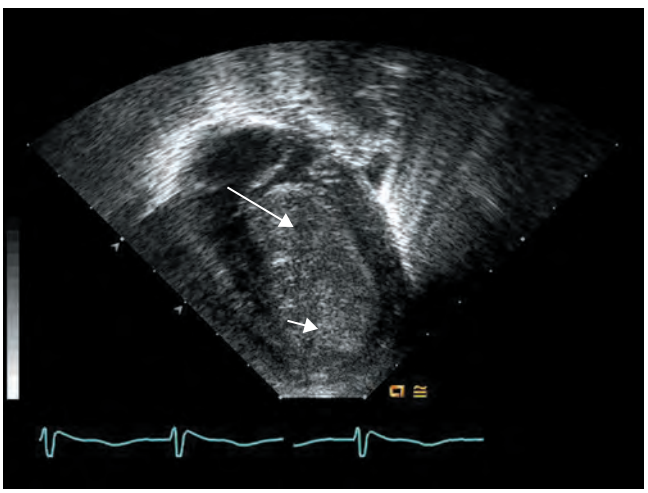


Figure 33.4 Apical 4-chamber view in a patient with a septal fibroma who presented with low cardiac output. A large hyperechoic mass is seen arising from the ventricular septum (large arrows), limiting mitral inflow and aortic outflow. The mass is heterogeneous, with areas of calcification (small arrow).

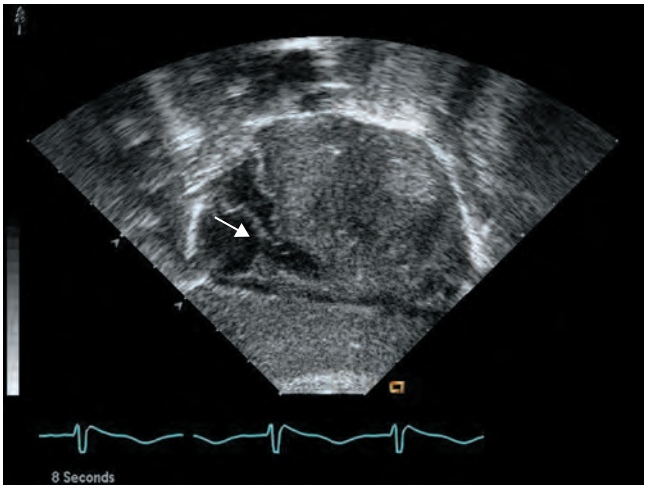


Figure 33.5 Subcostal 4-chamber view of the mitral inflow in a patient with a massive septal fibroma. The mass is irregular and heterogeneous, markedly distorting the cardiac architecture. Mitral inflow is compromised (small arrow).

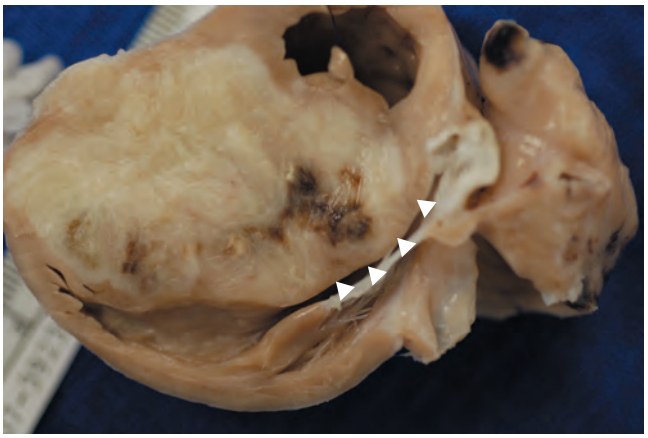


Figure 33.6 Pathologic specimen of the explanted heart in a patient with a massive septal fibroma who underwent cardiac transplantation. The fibrous mass occupies almost the entire ventricular septum, covered only by a thin rim of myocardium (arrows). The left ventricular cavity is small, with marked narrowing of the left ventricular outflow tract.

Clinical course

The age at presentation is variable, and often dependent on the presence of obstruction. Burke et al. identified 23 cases of cardiac fibroma from the files of the Armed Forces Institute of Pathology. The mean age at the time of diagnosis was 13 years; more than one-third of the patients were younger than 1 year of age [24]. Presentation in infancy heralds severe disease, with symptoms related to severe left or right ventricular outflow tract obstruction. The older child may be asymptomatic, but life-threatening arrhythmias and sudden cardiac death are well reported.

Spontaneous regression of the cardiac fibroma is rare. Therefore, in the patient with symptoms, surgical resection or palliation is often considered. Reports suggest that many ventricular fibromas can be completely resected with excellent early and late results [25,26]. However, cardiac transplantation may be a better option, especially in those patients with massive obstructive tumors [27]. Another approach has involved partial resection of a massive right ventricular fibroma with the addition of a bidirectional cavopulmonary shunt to provide a stable source of pulmonary blood flow [28].

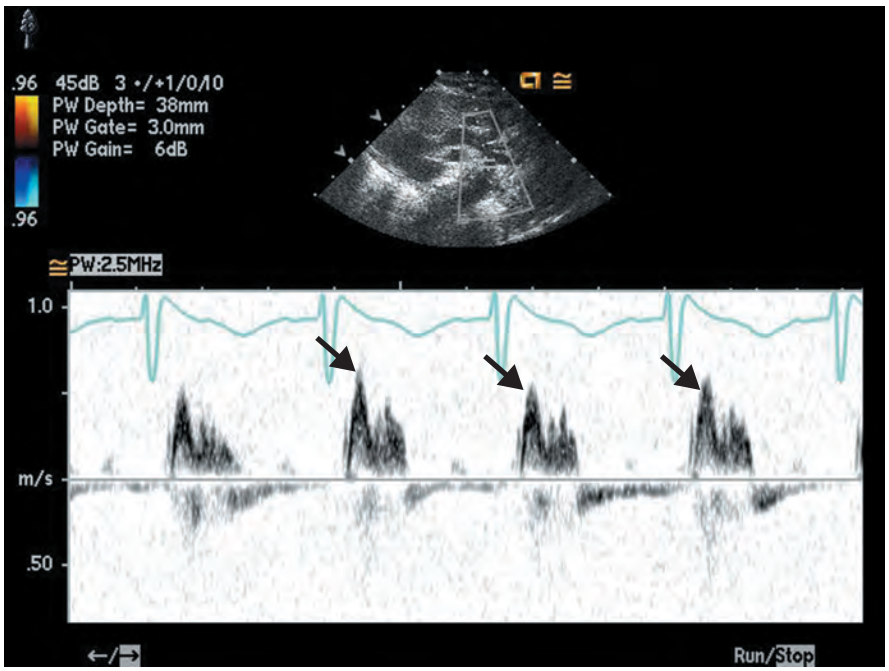


Figure 33.7 Suprasternal notch Doppler recording of the distal transverse arch in a newborn with a massive septal fibroma. There is no significant antegrade flow around the arch, with predominant retrograde systolic supply (arrow) of the arch from a patent ductus arteriosus. The patient presented with low cardiac output, but stabilized on prostaglandin therapy.



Figure 33.8 Pathologic specimen of a surgically removed pericardial teratoma. The teratoma has a predominantly solid surface with multiple microcysts filled with serous fluid. Microscopically, the tumor contained derivatives of all three germ layers, including elements of skin, gastrointestinal tract, respiratory tract, cartilage, liver, pancreas, and neural tissue.

Teratoma

Classification

Cardiac teratomas appear to be the third most common tumor type encountered in infants and children [4–7]. Nearly two-thirds are found in infants, and many more are detected antenatally than postnatally [29]. Cardiac teratomas most commonly originate in the pericardial cavity attached to the great vessels; pericardial effusion is present in almost all cases and may be significant. The tumor has a smooth external surface; cut sections reveal multiloculated cysts and solid areas (Figure 33.8). The tumor contains derivatives of all three germ layers, similar to the extrapericardial (i.e., sacrococcygeal) teratomas seen in the pediatric age group.

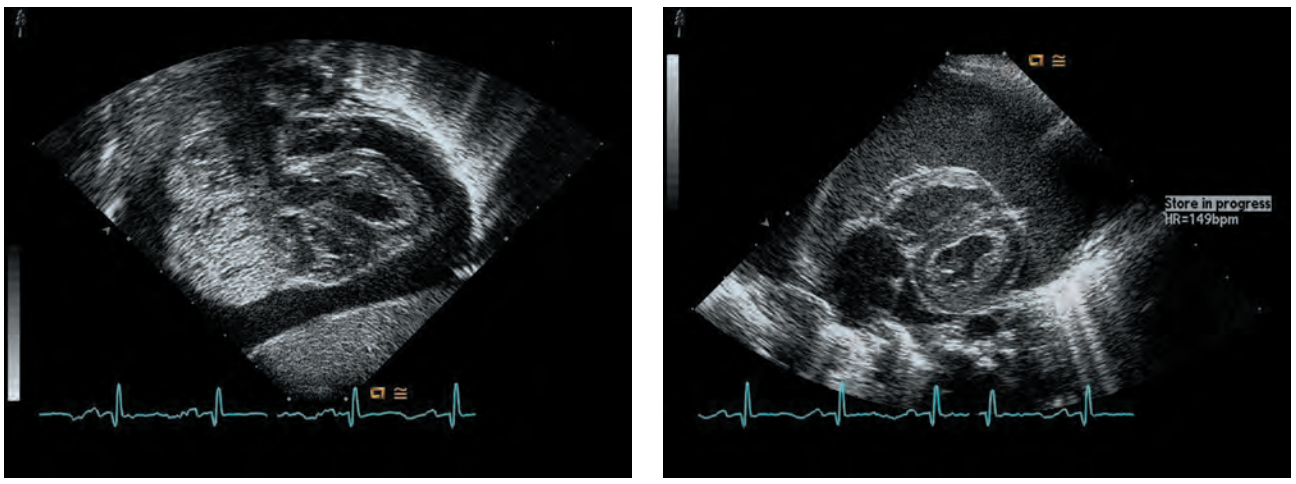
Echocardiography

Intrapericardial teratomas are attached to the root of the pulmonary artery or aorta, with both solid and multicystic areas (Figure 33.9a; Videos 33.4 and 33.5). Foci of calcification are also common. The presence of a pericardial effusion in association with a pericardial mass is almost diagnostic of a teratoma. The effusions can be large and hemodynamically important (Figure 33.9b). Intrapericardial teratoma in the fetus has also been well reported. Nonimmune hydrops is not uncommon, and may be related to cardiac tamponade or obstruction of systemic venous return from the tumor itself. In a literature review published by Bader et al., 31 cases of prenatal intrapericardial teratoma were identified. The diagnosis was typically suspected because of the presence of a pericardial effusion in the second or third trimester. Most tumors were located at the base of the heart. More than 75% of the fetuses developed hydrops. Fetal pericardial drainage was performed in 11 of the 31 reported cases with technical success, although reaccumulation of fluid was common [29].

Echocardiographic assessment of cardiac tamponade is critical in the patient with a large pericardial effusion. This should include 2D assessment of right atrial and right ventricular diastolic collapse, and also Doppler interrogation of respiratory variable cardiac filling and cardiac output.

Clinical course

Regression of teratomas is unusual. The majority of patients are symptomatic, either secondary to the large pericardial effusion or compression of the cardiac chambers and great vessels. Early recognition is important, as surgical resection is curative and can be accomplished with an excellent survival rate [4–7].



(a) (b)

Figure 33.9 **(a)** Subcostal 4-chamber view of the left ventricular outflow tract in a patient with a pericardial teratoma. The teratoma is heterogeneous, with multiple cystic areas. It appears to arise from the base of the heart, with an associated pericardial effusion. **(b)** Parasternal short-axis view in the same patient demonstrating the massive pericardial effusion. The 3-week-old infant presented with tachycardia and severe cardiomegaly on chest radiograph.

Myxoma

Classification

The cardiac myxoma is a benign tumor derived from cardiac multipotential mesenchymal cells [30]. It is the most common primary tumor of the heart in adults but is very rare in the pediatric age group [4–8]. Myxomas arise from the endocardium and form exophytic intracavitary masses. There are two distinct morphologies of myxoma: the solid myxoma appears firm and smooth whereas the papillary myxoma has a more cauliflower-like appearance [31,32]. The site of origin is usually the left atrium (Video 33.6) [33]. Presenting symptoms are common and include congestive heart failure, systemic emboli, and neurologic symptoms [8]. There are few reports in the literature describing myxomas in children. Interestingly, most myxomas described in the pediatric age group have occurred on the right side of the heart [34–36].

Echocardiography

Tumor location, size, attachment, and mobility can be assessed by echocardiography [37–40]. Approximately 75% of myxomas are found in the left atrium, with 20% in the right atrium and the remaining 5% equally distributed between the left and right ventricles (Figure 33.10). Typically myxomas are isolated, pedunculated tumors in the left atrium attached to the area of the foramen ovale by a stalk. If the tumor does not arise from the lower part of the interatrial septum, the diagnosis of myxoma should be questioned. Both hypoechoic and hyperechoic foci may be seen, reflecting areas of hemorrhage and calcification, respectively. Depending on the size, the tumor may prolapse through the mitral orifice in diastole, occasionally producing a tumor "plop" and accounting for the common misdiagnosis of mitral stenosis. Doppler echocardiography should be used to quantitate the degree of mitral stenosis or mitral insufficiency.

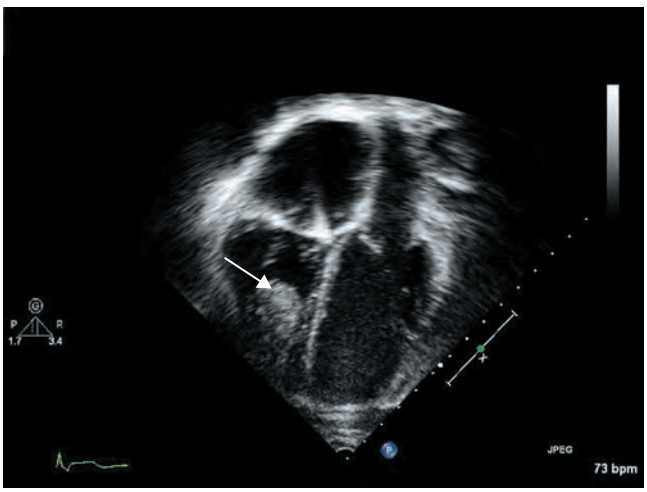


Figure 33.10 Apical 4-chamber view in a patient with a recurrent right ventricular myxoma (arrow). The myxoma is hyperechoic and appears to be involved with the tricuspid valve apparatus. The patient also had tricuspid valve repair at the time of the initial myxoma removal; a Carpentier ring is identified in the tricuspid annulus.

An atrial myxoma must be differentiated from a left atrial thrombus. A thrombus is usually situated in the posterior portion of the atrium, has a layered appearance, and extends into the left atrial appendage. Also, the formation of atrial thrombi is unusual in the pediatric setting, unless there is associated ventricular dysfunction or a history of atrial arrhythmias. Transthoracic echocardiography is usually sufficient to make the diagnosis, but if imaging is suboptimal, transesophageal echocardiography should be employed [41].

Clinical course

Symptoms of left heart inflow obstruction and/or embolic phenomena are almost inevitable in the setting of an atrial myxoma. In a study by Swartz et al., only 8% of patients were asymptomatic at the time of diagnosis [42]. Regression is atypical and, in fact, recurrence is likely if the tumor is not completely resected. Surgery has been successful, with little operative mortality and minimal morbidity [43–45].

Hemangioma

Classification

Hemangiomas are common benign congenital vascular lesions. They most commonly occur in the skin, but are occasionally found in internal organs. Cardiac hemangiomas comprise about 2.8% of all primary cardiac tumors and most are diagnosed in the neonatal period [46,47]. Cardiac hemangiomas are composed of endothelial cells that line interconnecting vascular channels. The main histologic types are based on the size of the vascular lumen. The cavernous hemangioma consists of large vascular channels, whereas the capillary hemangioma is composed of smaller vessels resembling capillaries. There are also mixed varieties.

Age at diagnosis appears to be predictive of histologic type, tumor location and clinical presentation. The fetus or young infant is much more likely to have a cavernous-type hemangioma located within the right atrium. Symptoms are common in this age group, generally related to the presence of a large pericardial effusion. The infantile tumor is more likely to regress spontaneously, and is responsive to antiangiogenic therapy. The older child with a vascular tumor is rarely symptomatic and much more likely to have a capillary-type hemangioma. Spontaneous regression is unusual in this setting [48].

Echocardiography

Cardiac hemangiomas can occur at any location in the heart, including the epicardial surface and pericardium (Figure 33.11). In the fetus and infant, the right atrium is the major primary site. The tumors are usually of mixed echogenicity. Cystic spaces can be identified, and have been attributed to both cavernous lakes and degeneration. Associated pericardial effusions are seen in most patients. Identification of color Doppler blood flow signals

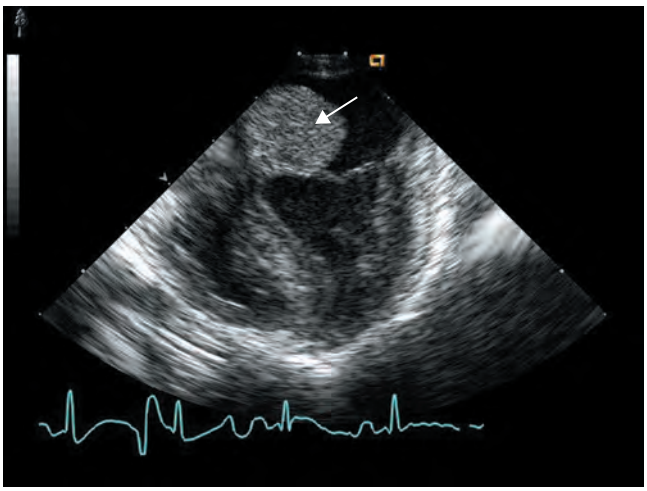


Figure 33.11 A transverse transesophageal image in a patient with a left atrial hemangioma. The absence of a stalk and a wide base of attachment to the anterior mitral valve leaflet help to differentiate this from a left atrial myxoma.

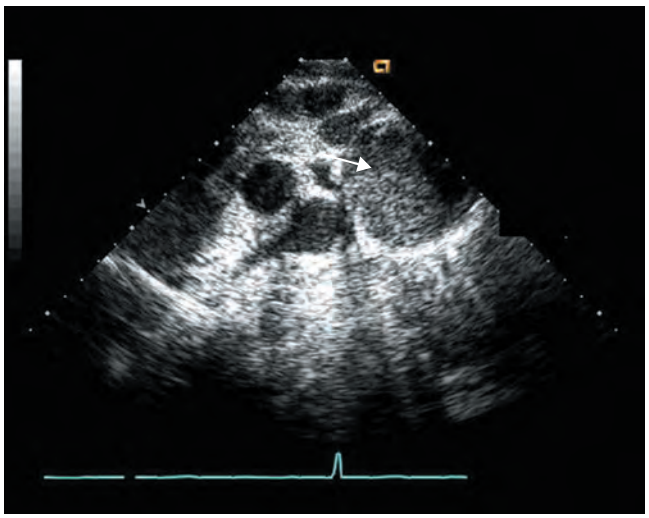


Figure 33.12 High left parasternal view of the branch pulmonary arteries in a patient with Hodgkin disease. The right pulmonary artery is of good size; the left pulmonary artery is compressed by a large, solid mediastinal mass (arrow).

in the mass helps make the diagnosis, although the absence of these signals is not uncommon. Unlike hemangiomas in other organs, such as the liver, significant blood flow is unusual; cardiac chamber enlargement and high-output congestive heart failure are rare.

Clinical course

Generally, vascular tumors have an excellent prognosis. The cavernous-type hemangioma has a tendency to regress spontaneously, but is also responsive to antiangiogenic therapy. In the older child, surgical resection can be accomplished with minimal morbidity/mortality.

Malignant cardiac tumors

Primary malignant cardiac tumors in children are rare. When they occur, they are almost exclusively sarcomas [4–7]. Rhabdomyosarcoma is the leading malignancy in the infant, whereas angiosarcoma is more common in the older child. The prognosis is bleak in all patients [49].

Secondary tumor involvement of the heart, by either distant metastasis or direct tumor extension, occurs in less than 2% of children with malignant solid tumors [50]. The tumors with the highest rate of cardiac metastasis include lymphoma and neuroblastoma, whereas direct tumor extension has been most often reported in patients with Wilms tumor [51,52]. External compression of cardiac structures can be seen with Hodgkin disease (Figure 33.12).

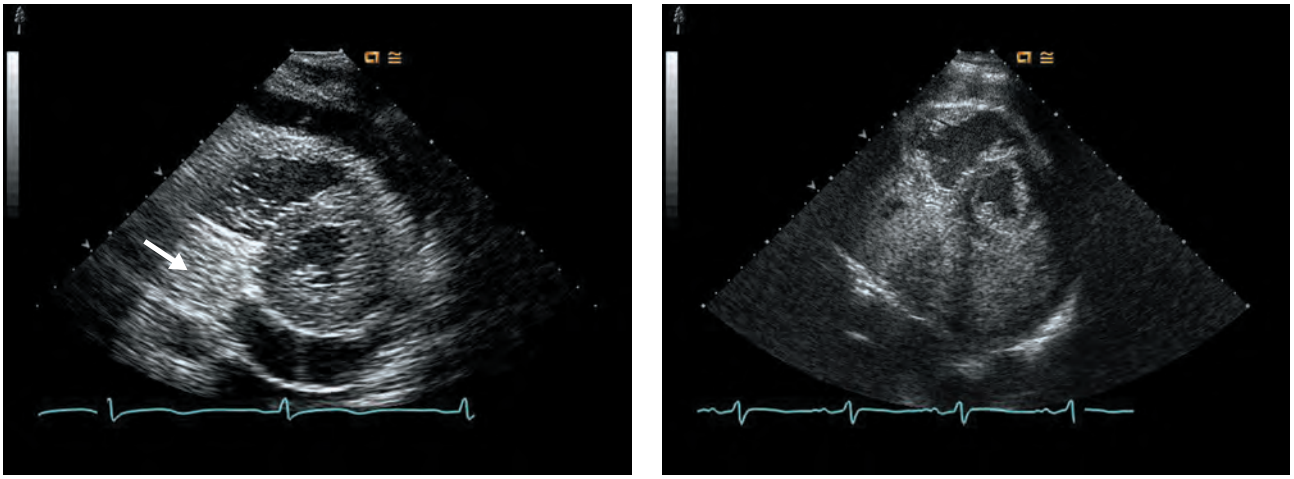
Echocardiography

The echocardiographic characteristics of primary malignant cardiac tumors are not substantially different from those of the benign tumors. The tumors behave more aggressively, and there are extensive metastases at the time of presentation. The cardiac angiosarcoma should be suspected when a hemorrhagic pericardial effusion is present, and the pericardium appears markedly thickened, with an irregular surface (Figure 33.13a,b).

Association with syndromes

It is important to remember that primary cardiac tumors in children can be associated with hereditary syndromes [53]. Perhaps the best-recognized association is that of cardiac rhabdomyoma and the tuberous sclerosis complex [4–7,10–17]. Tuberous sclerosis is a genetic disorder that affects cellular differentiation and proliferation, resulting in hamartoma formation in many organs, including the heart. Although it has an autosomal dominant inheritance pattern, more than half of the cases have been attributed to spontaneous mutations. There are two known genetic loci, one mapping to chromosome 9 and the other to chromosome 16 (also termed *TSC1* and *TSC2*). Defects in the affected proteins (tuberin and hamartin) lead to unregulated cellular growth and differentiation. It is currently thought that the majority of children with cardiac rhabdomyomas have tuberous sclerosis [54].

Although most cardiac fibromas in children occur as an isolated defect, approximately 3–5% of children with cardiac fibromas will have the nevoid basal cell carcinoma syndrome (Gorlin syndrome) [55]. Gorlin syndrome is an autosomal dominant disorder characterized by the development of basal cell carcinomas at an early age, jaw keratocysts, and palmar or plantar pits. Cardiac tumors that have been described in Gorlin syndrome include cardiac fibromas and fibrous histiocytomas. Of note, it is not unusual to have multiple cardiac fibromas in the



(a) (b)

Figure 33.13 **(a)** Parasternal short-axis view in a patient with a cardiac angiosarcoma. A hyperechoic circumscribed mass is seen in the pericardial sac (arrow); there is an associated moderate pericardial effusion. **(b)** Parasternal short-axis view in the same patient 1 month later. The pericardial sac now appears completely occupied by the angiosarcoma.

patient with Gorlin syndrome (Figure 33.14). The syndrome results from mutations in the *PTCH1* (patched) gene, which has been mapped to chromosome 9. This gene is thought to function primarily as a tumor suppressor. Cardiac myxomas are rare in children; however, they can be associated with Carney syndrome. Carney syndrome is characterized by cardiac myxomas, spotty pigmentation of the skin, and endocrine overactivity [56]. Although myxomas typically occur as an isolated lesion, there can be multiple tumors in patient with Carney syndrome. Several mutations have been identified in the PRK (protein kinase) gene on chromosome 17; this gene also functions as a tumor suppressor.

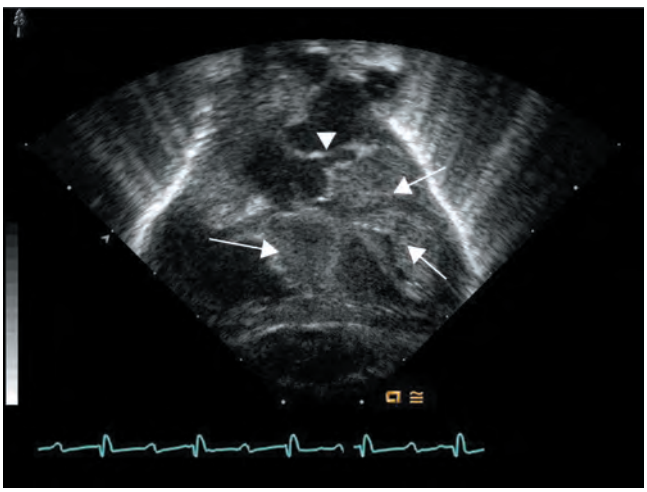


Figure 33.14 Subcostal 4-chamber view of the left ventricular outflow tract in a patient with Gorlin syndrome. Multiple fibromas are seen in the ventricular septum and left ventricular free wall (large arrows). The left main coronary artery appears dilated and is displaced by the mass (small arrow).

Videos

To access the videos for this chapter, please go to www.lai-echo.com.

Video 33.1 Neonate with multiple intracardiac tumors detected during fetal echocardiography, consistent with the diagnosis of rhabdomyomas. In this subcostal coronal view, multiple echodense tumors can be detected: one in the basal part of the right ventricle (RV) free wall, one very large one on the RV side of the mid- and apical portion of the interventricular septum, and one in the left ventricular outflow tract

Video 33.2 Newborn with a very large fibroma in the anterolateral left ventricular (LV) wall expanding inferiorly and superiorly to the level of the great vessels. Parasternal short-axis view: note the very large size and homogeneous aspect of the tumor, and how it affects LV function.

Video 33.3 Newborn with a very large fibroma in the anterolateral left ventricular (LV) wall expanding inferiorly and superiorly to the level of the great vessels. Subcostal view: the expansion of the mass to the level of the aorta can be appreciated.

Video 33.4 Neonate with pericardial teratoma. Parasternal long-axis right ventricular inflow view. Note the large mass anterior and lateral to the right atrium.

Video 33.5 Neonate with pericardial teratoma. High parasternal short-axis view of the mass. Note the presence of echodense and echolucent zones within the mass.

Video 33.6 Apical 4-chamber view of a patient with a left atrial myxoma. Note the large mobile mass moving with the mitral valve leaflets.

References

1 Nadas AS, Ellison RC. Cardiac tumors in infancy. *Am J Cardiol* 1968;**21**:363–366.
2 Fyler DC. Report of the New England Regional Infant Cardiac Program. *Pediatrics* 1980;**65**(Suppl):375–461.
3 Holley DG, Martin GR, Brenner JI, et al. Diagnosis and management of fetal cardiac tumors: a multicenter experience and review of published reports. *J Am Coll Cardiol* 1995;**26**:516–520.
4 Beghetti M, Gow RM, Haney I, et al. Pediatric primary benign cardiac tumors: a 15-year review. *Am Heart J* 1997;**134**:1107–1114.
5 Van der Hauwaert LG. Cardiac tumors in infancy and childhood. *Br Heart J* 1971;**33**:125–132.
6 Arciniegas E, Hakimi M, Farooki ZQ, et al. Primary cardiac tumors in children. *J Thorac Cardiovasc Surg* 1980;**79**:582–591.
7 Freedom RM, Lee KJ, MacDonald C, Taylor G. Selected aspects of cardiac tumors in infancy and childhood. *Pediatr Cardiol* 2000;**21**:299–316.
8 Reynen K. Cardiac myxomas. *N Engl J Med* 1995;**333**:1610–1617.
9 Fenoglio IJ, Jr., McAllister HA, Jr., Ferrans VJ. Cardiac rhabdomyoma: a clinicopathologic and electron microscopic study. *Am J Cardiol* 1976;**38**:241–251.
10 Jowiak S, Kotulska K, Kasprzyk-Obara J, et al. Clinical and genotype studies of cardiac tumors in 154 patients with tuberous sclerosis complex. *Pediatrics* 2006;**118**:e1146–e1151.
11 Farooki ZQ, Ross RD, Paridon SM, et al. Spontaneous regression of cardiac rhabdomyoma. *Am J Cardiol* 1991;**67**:897–899.
12 Alkalay AL, Ferry DA, Lin B, et al. Spontaneous regession of cardiac rhabdomyoma in tuberous sclerosis. *Clin Pediatr* 1987;**26**:532–535.
13 Smythe JF, Dyck JD, Smallhorn JF, Freedom RM. Natural history of cardiac rhabdomyoma in infancy and childhood. *Am J Cardiol* 1990;**66**:1247–1249.
14 Bosi G, Lintermans JP, Pellegrino PA, et al. The natural history of cardiac rhabdomyoma with and without tuberous sclerosis. *Acta Paediatr* 1996;**85**:928–931.
15 Nir A, Tajik AJ, Freeman WK, et al. Tuberous sclerosis and cardiac rhabdomyoma. *Am J Cardiol* 1995;**76**:419–421.
16 Isaacs H, Jr. Fetal and neonatal cardiac tumors. *Pediatr Cardiol* 2004;**25**:252–273.
17 Nir A, Ekstein S, Nadjari M, et al. Rhabdomyoma in the fetus: illustration of tumor growth during the second half of gestation. *Pediatr Cardiol* 2001;**22**:515–518.
18 Achiron R, Weissman A, Rotstein Z, et al. Transvaginal echocardiographic examination of the fetal heart between 13 and 15 weeks' gestation in a low-risk population. *J Ultras Med* 1994;**13**:783–789.
19 Hishitani T, Hoshino K, Ogawa K, et al. Rapid enlargement of cardiac rhabdomyoma during corticotrophin therapy for infantile spasms. *Can J Cardiol* 1997;**13**:72–74.
20 Wu CT, Chen MR, Hou SH. Neonatal tuberous sclerosis with cardiac rhabdomyomas presenting as fetal supraventricular tachycardia. *Jpn Heart J* 1997;**38**:133–137.
21 Case CL, Gillette PC, Crawford FA. Cardiac rhabdomyomas causing supraventricular and lethal ventricular arrhythmias in an infant. *Am Heart J* 1991;**122**:1484–1486.
22 O'Callaghan FJ, Clarke AC, Joffe H, et al. Tuberous sclerosis complex and Wolff–Parkinson–White syndrome. *Arch Dis Child* 1998;**78**:159–162.
23 Geipel A, Krapp M, Germer U, et al. Perinatal diagnosis of cardiac tumors. *Ultrasound Obstet Gynecol* 2001;**17**:17–21.
24 Burke AP, Rosado-de-Christenson M, Templeton PA, Virmani R. Cardiac fibroma: clinicopathologic correlates and surgical treatment. *J Thorac Cardiovasc Surg* 1994;**108**:862–870.
25 Cho JM, Danielson GK, Puga FJ, et al. Surgical resection of ventricular cardiac fibromas: early and late results. *Ann Thorac Surg* 2003;**76**:1929–1934.
26 Davies B, Oppido G, Brizard CP. Surgical management of symptomatic cardiac fibromas in children. *J Thorac Cardiovasc Surg* 2007;**133**:254–255.
27 Waller BR, Bradley SM, Crumbley AJ, III, et al. Cardiac fibroma in an infant: single ventricle palliation as a bridge to heart transplantation. *Ann Thorac Surg* 2003;**75**:1306–1308.
28 Beghetti M, Haney I, Williams WG, et al. Massive right ventricular fibroma treated with partial resection and a cavopulmonary shunt. *Ann Thorac Surg* 1996;**62**:882–884.
29 Bader R, Hornberger LK, Nijmeh LJ, et al. Fetal pericardial teratoma: presentation of two cases and review of literature. *Am J Perinatol* 2006;**23**:53–58.
30 Johansson L. Histogenesis of cardiac myxomas. An immunohistochemical study of 19 cases, including one with glandular structures, and review of the literature. *Arch Pathol Lab Med* 1989;**113**:735–741.
31 Heath D. Pathology of cardiac tumors. *Am J Cardiol* 1968;**21**:315–327.
32 St. John Sutton MG, Mercier LA, Giuliani ER, Lie JT. Atrial myxomas: a review of clinical experience in 40 patients. *Mayo Clin Proc* 1980;**55**:371–376.
33 Schaff HV, Mullany CJ. Surgery for cardiac myxomas. *Semin Thorac Cardiovasc Surg* 2000;**12**:77–88.
34 George KM, Przygodzki RM, Jonas RA, Di Russo GB. Resection of an obstructive neonatal cardiac myxoma of the infundibulum. *Pediatr Cardiol* 2006;**27**:369–371.
35 Balsara RK, Pelias AJ. Myxoma of right ventricle presenting as pulmonic stenosis in a neonate. *Chest* 1983;**83**:145–146.
36 Paladini D, Tartaglione A, Vassallo M, Martinelli P. Prenatal ultrasonographic findings of a cardiac myxoma. *Obstet Gynecol* 2003;**102**:1174–1176.
37 Goswami KC, Shrivastava S, Bahl VK, et al. Cardiac myxomas: clinical and echocardiographic profile. *Int J Cardiol* 1998;**63**:251–259.
38 Jelic J, Milici D, Alfirevi I, et al. Cardiac myxoma: diagnostic approach, surgical treatment and follow-up. A twenty year experience. *J Cardiovasc Surg (Torino)* 1996;**37**(6 Suppl 1):113–117.
39 Liu HY, Cheng KZ, Yang WY, et al. Diagnosis of intracardiac myxomas by echocardiography. *Chin Med J* 1983;**96**:421–428.
40 Tansel T, Harmandar B, Ugurlucan M, et al. Over 14 years of experience with cardiac myxomas. *Acta Cardiologica* 2006;**61**:285–288.
41 Perez de Isla L, de Castro R, Zamorano JL, et al. Diagnosis and treatment of cardiac myxomas by transesophageal echocardiography. *Am J Cardiol* 2002;**90**:1419–1421.
42 Swartz MF, Lutz CJ, Chandan VS, et al. Atrial myxomas: pathologic types, tumor location, and presenting symptoms. *J Cardiac Surg* 2006;**21**:435–440.
43 Bastos P, Barreiros F, Casanova J, Gomes MR. Cardiac myxomas: surgical treatment and long-term results. *Cardiovasc Surg* 1995;**3**:595–597.

44 Bortolotti U, Maraglino G, Rubino M, et al. Surgical excision of intracardiac myxomas: a 20-year follow-up. *Ann Thorac Surg* 1990;**49**:449–453.
45 Bortolotti U, Maraglino G, Rubino M, et al. Surgical excision of intracardiac myxomas: a 20-year follow-up. *Ann Thorac Surg* 1990;**49**:449–453.
46 Laga S, Gewillig MH, Van Schoubroeck D, Daenen W. Imminent fetal cardiac tamponade by right atrial hemangioma. *Pediatr Cardiol* 2006;**27**:633–635.
47 Tsend JJ, Chou MM, Lee YH, Ho ES. In utero diagnosis of cardiac hemangioma. *Ultrasound Obstet Gynecol* 1999;**13**:363–365.
48 Mackie AS, Kozakewich HP, Geva T, et al. Vascular tumors of the heart in infants and children: case series and review of the literature. *Pediatr Cardiol* 2005;**26**:344–349.
49 Booth AM, LeGallo RD, Stoler MH, et al. Pediatric angiosarcoma of the heart: a unique presentation and metastatic pattern. *Pediatr Dev Pathol* 2001;**4**:490–495.
50 Huh J, Noh CI, Kim YW, et al. Secondary cardiac tumor in children. *Pediatr Cardiol* 1999;**20**:400–403.
51 Szymik-Kontorowicz S, Urbanowicz W, Malec E, Kordon Z. Right atrial extension of Wilms' tumor. *Med Sci Monit* 2003;**9**:CS13–CS17.
52 Shamberger RC, Ritchey ML, Haase G, et al. Intravascular extension of Wilms' tumor. *Ann Surg* 2001;**234**:116–121.
53 Vidaillet HJ, Jr. Cardiac tumors associated with hereditary syndromes. *Am J Cardiol* 1988;**61**:1355.
54 Rosser T, Panigraphy A, McClintock W. The diverse clinical manifestations of tuberous sclerosis complex: a review. *Semin Pediatr Neurol* 2006;**13**:27–36.
55 Bossert T, Walther T, Vondrys D, et al. Cardiac fibroma as an inherited manifestation of nevoid basal-cell carcinoma syndrome. *Tex Heart Inst J* 2006;**33**:88–90.
56 Goldstein MM, Casey M, Carney JA, Basson CT. Molecular genetic diagnosis of the familial myxoma syndrome (Carney complex). *Am J Med Genet* 1999;**85**:62–65.

PART VI

Anomalies of Ventricular Myocardium

CHAPTER 34

Dilated Cardiomyopathy, Myocarditis, and Heart Transplantation

Renee Margossian
Department of Cardiology, Boston Children's Hospital, Boston, MA, USA

Introduction

Echocardiography is the primary diagnostic tool in the initial evaluation of children with suspected dilated cardiomyopathy (DCM) and myocarditis, and long-term management decisions rely in part on serial echocardiographic assessment. Echocardiography also plays an instrumental role in the evaluation of patients who undergo cardiac transplantation, from initial evaluation through long-term follow-up. Patients with DCM or myocarditis or who have undergone heart transplantation may also require interventions such as mechanical ventricular support or resynchronization therapy. In each of these situations, the focus of the examination is on myocardial performance, and the echocardiographic approach is similar, with a focus on systolic and diastolic function.

Dilated cardiomyopathy

Definition

In 1995, the World Health Organization defined cardiomyopathies as "diseases of the myocardium associated with cardiac dysfunction," and classified them according to morphology into four distinct types: dilated cardiomyopathy, hypertrophic cardiomyopathy, restrictive cardiomyopathy, and arrhythmogenic right ventricular dysplasia [1]. Specifically, DCM was defined as "dilation and impaired contraction of the left ventricle or both ventricles" [1]. The weakness of this approach has become more apparent as diagnostic advances in fields such as molecular genetics have broadened our understanding of cardiomyopathies in general: more than two dozen genes have been associated with the DCM phenotype, expressed through mitochondrial, X-linked, dominant, and recessive inheritance patterns [2]. Current debate continues as to the method of classification of cardiomyopathies, with a newer proposed classification recommending a cause-based approach (genetic, acquired, mixed) [3]. This classification system carries its own limitations, however: cardiomyopathies with the same genetic cause may exhibit different phenotypes among individuals, and phenotype can change over time within the same individual.

Regardless of the nomenclature difficulties faced by the field, echocardiographic establishment of the predominant phenotype (dilated, hypertrophic, or restrictive) is relatively straightforward, even in patients with mixed phenotypes. This has allowed large multicenter registries to evaluate the epidemiology and outcomes of cardiomyopathies in children [4,5].

Incidence

The true incidence of DCM has been difficult to ascertain, and may vary by geography, race/ethnicity, and socioeconomic status. Data from the Pediatric Cardiomyopathy Registry (PCMR) and Australia estimate the annual incidence of all forms of primary pediatric cardiomyopathy to be 1.13–1.24 cases per 100,000, with DCM accounting for approximately 50–60% of these cases [4,5]. These reports exclude patients with DCM due to congenital heart disease, arrhythmia, and/or chemotherapy exposure. This contrasts with an annual incidence of nonischemic DCM in the adult population of 6–7 cases per 100,000 [6,7]. Presentation with DCM is most common in children under 1 year of age. PCMR data indicate that in children with primary DCM, 66% of cases are idiopathic in nature, with myocarditis and neuromuscular diseases predominating among those with known causal etiology [8].

Etiology

As noted earlier, most cases of pediatric DCM are idiopathic in nature, with known causes identified 32–44% of the time [5,8,9]. Specific etiologies include genetic, metabolic, infectious, immune-mediated, mitochondrial, and environmental toxins (Table 34.1) [3]. In the PCMR group, myocarditis was the largest single cause of DCM in those under 18 years of age, accounting for 16–18% of all cases and 50% of cases with a known etiology

Echocardiography in Pediatric and Congenital Heart Disease: From Fetus to Adult, Second Edition. Edited by Wyman W. Lai, Luc L. Mertens, Meryl S. Cohen and Tal Geva.
© 2016 John Wiley & Sons, Ltd. Published 2016 by John Wiley & Sons, Ltd.
Companion website: www.lai-echo.com

Table 34.1 Classification of the dilated cardiomyopathies (modified phenotype-based classification).

Primary
Peripartum cardiomyopathy
Post-myocarditis
Primary familial dilated cardiomyopathy
Stress cardiomyopathy ("tako-tsubo")
X-linked cardiomyopathy (dystrophinopathy)
Metabolic
Endocrine
Fatty acid oxidation
Glycogenoses
Mucopolysaccharidoses
Sphingolipidoses
Secondary
Cardiovascular
Congenital heart disease
Tachycardia-induced
Valvar heart disease
Mitochondrial
Kearns–Sayre
Mitochondrial myopathy, encephalopathy, lactic acidosis, and stroke (MELAS)
Myoclonic epilepsy associated with ragged-red fibers (MERRF)
NADH–coenzyme Q reductase deficiency
Cytochrome *c* oxidase deficiency
Connective tissue disorders
Juvenile rheumatoid arthritis
Lupus erythematosis
Osteogenesis imperfecta
Polyarteritis nodosa
Reye syndrome
Sarcoidosis
Systemic sclerosis
Nutritional
Selenium deficiency (Keshan disease)
Thiamine deficiency (beri-beri)
Inflammatory (myocarditis)
Infectious: viral, bacterial, fungal parasitic, protozoal, rickettsial, spirochetal
Kawasaki
Neuromuscular
Dystrophinopathies (Duchenne, Becker dystrophies)
Emery–Dreifuss muscular dystrophy
Myotonic dystrophy
Polymyositis
Roussy–Lévy polyneuropathy
Scapulohumeral muscular dystrophy
Spinal muscular atrophy
Toxic
Alcoholic
Anthracyclines
Arsenic
Chloramphenicol
Cobalt
Iron (hemochromatosis)
Lead
Ischemic
Congenital coronary artery malformation
Acquired coronary artery disease

Source: Colan SD. Classification of the cardiomyopathies. *Prog Pediatr Cardiol* 2007;**23**:5–15. Reproduced with permission of Elsevier.

[8,9]. Other causes of DCM in the pediatric or adolescent population include neuromuscular disorders, familial DCM, and inborn errors of metabolism, accounting for 9, 5, and 4% of cases, respectively [8]. Additional etiologies include congenital heart disease, valvular heart disease, postpartum cardiomyopathy, pacemaker-induced DCM, arrhythmia-induced DCM, and coronary artery/ischemic disease; these will not be addressed in this chapter.

In familial DCM, most of the known mutations are associated with autosomal dominant inheritance. Familial cases of DCM are probably underestimated, as not all families undergo mutation analysis and some mutations may manifest incomplete penetrance. Mutations associated with autosomal dominant inheritance include those involving cytoskeletal proteins such as β- and δ-sarcoglycan and sarcomere proteins such as actin and cardiac troponin T. More than 50 single genes have been linked to DCM, with many of the same genes also linked to other forms of cardiomyopathy, particularly hypertrophic cardiomyopathy [3,10,11]. In addition, several genetic forms of DCM are associated with skeletal myopathy, including Duchenne/Becker muscular dystrophy, Barth syndrome, Emery–Dreifuss muscular dystrophy, and limb-girdle muscular dystrophy.

Pathophysiology

Myocardial damage and reduced cardiac function lead to decreased cardiac output; this results in a complex cascade of neurohormonal and vascular changes that increase preload and afterload, triggering a cycle of continued myocardial damage and remodeling. Stimulation of the sympathetic and renin–angiotensin systems leads to vasoconstriction, increased circulating catecholamines, stimulation of aldosterone secretion, and salt and water retention. Both the primary myocardial insult and the secondary effects of vascular and neurohormonal alterations result in myocardial cellular changes, including necrosis, apoptosis, and fibrosis. These changes lead to myocardial remodeling, with alterations in left ventricular (LV) geometry and compliance. A comprehensive review of these events is beyond the scope of this chapter, but can be found elsewhere [12,13].

Treatment and outcome

Current therapeutic strategies for treatment of cardiomyopathy are aimed at improving symptoms in addition to reversing the negative effects of maladaptive ventricular remodeling (e.g., LV dilation and myocyte hypertrophy). This phenomenon of improving cardiac geometry and function with various therapies is known as "reverse remodeling" and occurs at the molecular, cellular, tissue, and chamber levels. These therapies may be aimed at decreasing afterload (angiotensin-converting enzyme inhibitors or receptor blockers), decreasing preload (diuretics), and altering the neurohormonal profile (beta-blockers). Intravenous therapy with agents such as milrinone and dobutamine further decreases afterload and increases myocardial contractility. Additional interventions may include anticoagulation,

nutritional support, and the use of antiarrhythmic medication. Failure of maximal medical therapies necessitates other forms of support, including biventricular pacing [cardiac resynchronization therapy (CRT)], mechanical support [ventricular assist device (VAD)], extracorporeal membrane oxygenation (ECMO), and cardiac transplantation.

The clinical course of DCM in the pediatric population is variable, and a comprehensive risk stratification algorithm does not exist. Data suggest that the 1- and 5-year risks of death or transplantation in pediatric DCM are 28–31% and 37–46%, respectively [8,14]. In a systematic review of outcome predictors in pediatric DCM [15], younger age at diagnosis, higher LV shortening fraction (SF) and ejection fraction (EF), and the presence of myocarditis have been associated with better prognosis. Poor prognostic factors inconsistently identified in smaller studies have included the presence of a more spherically shaped LV [higher sphericity index (SI)], endocardial fibroelastosis, lack of improvement in cardiac function over time, arrhythmia, presence of intracardiac thrombus, thinning of the posterior wall, and significant mitral regurgitation (MR) [8,14,16–19]. Data also suggest that measures of myocardial velocities and right ventricular (RV) function may be predictive [20].

Fetal dilated cardiomyopathy

Fetal DCM is rare and accounts for a very small portion of heart disease discovered during fetal ultrasonography; it accounted for 0.2% of all fetal echocardiograms over a 20-year period in one large tertiary center [21]. Etiologies of DCM in the fetus are typically the same as in the neonate and include metabolic disease, myocarditis, tachycardia, familial/genetic and idiopathic. Other causes that may be seen predominantly in fetal life include anemia and endocardial fibroelastosis. Cardiac dysfunction secondary to structural heart disease (such as LV outflow tract obstruction) must be excluded. Fetal cardiac function may appear normal early in pregnancy, with evidence of DCM developing after 23 weeks [22]. Overall prognosis of DCM diagnosed in fetal life is poor, although fetuses with DCM secondary to treatable causes (such as arrhythmia) may have a better outcome [22]. Survival is less than 20% in fetuses with DCM and hydrops and approximately 50% in nonhydropic fetuses with DCM [21].

Myocarditis

Definition

Myocarditis is defined as an inflammatory disease of the myocardium diagnosed by established histologic, immunologic, and immunohistochemical criteria. Idiopathic, autoimmune, and infectious forms of inflammatory cardiomyopathy are recognized [1]. These inflammatory forms of cardiomyopathy are typically acquired, although some people may be genetically predisposed to these diseases. The Dallas criteria [23], which require histopathologic evidence of inflammatory infiltrate and myocardial cell damage, have been used to diagnose myocarditis. However, these criteria underestimate the incidence because of issues with sampling error, variations in interpretation, immune modulation in the heart, variable host immunologic response, and differences in patient selection for cardiac biopsy. Identification of viral DNA or evidence of systemic immune activation can aid in the diagnosis of myocarditis in the appropriate clinical setting. Clinical pathologic classification of myocarditis includes fulminant, chronic persistent, giant cell, and eosinophilic types [24]. In myocarditis, diagnostic echocardiographic findings are nonspecific; the distinction between DCM and myocarditis is often not possible. Cardiac magnetic resonance imaging (CMR) may be more sensitive and specific [25,26] in confirming the inflammatory nature of the disease, particularly in the acute setting [27].

Incidence

Myocarditis as a separate entity is typically sporadic and its incidence has been even more difficult to ascertain than DCM. Clinical manifestations are variable, the ability to confirm active or preceding viral infection is limited, and the initial presentation may be clinically silent. In a retrospective study, biopsy-proven myocarditis in children occurred at a rate of 2.5 cases per year in a population of 3 million people [28].

Etiology

The primary etiology of myocarditis in the pediatric population is viral or postviral. Viruses implicated include coxsackie B, adenovirus, cytomegalovirus, enterovirus, influenza A and B, varicella, picornavirus, parvovirus, HIV, and Epstein–Barr virus [7,29], with far fewer cases associated with bacterial, rickettsial, fungal, and parasitic infections. Giant cell myocarditis is an aggressive inflammatory myocarditis that is rare in children and associated with severe ventricular arrhythmia. Eosinophilic myocarditis is also rare and associated with hypersensitivity reactions. Chronic myocarditis may be due to chronic viral infection and autoimmune conditions.

Pathophysiology

The immunopathogenesis of inflammatory cardiomyopathy has been primarily studied in mice [30]. Host factors that play a role in susceptibility to infection and development of myocarditis include genetic factors (i.e., major histocompatibility complex), age, gender, and nutritional state [30]. Myocardial damage can result directly from infection or through immune-modulated mechanisms. Evidence indicates that the development and severity of myocarditis are related to cellular-mediated immune function, primarily associated with T-cell lymphocyte activity [30], with cytokine activation probably playing a major role in the inflammatory response [30,31]. Viral RNA can be detected using molecular techniques and viral persistence in the myocardium may play a role in chronic myocarditis [32]. There

is also evidence that viral myocarditis could be a trigger for apoptotic cell death [30].

Treatment and outcome

Supportive treatment similar to that discussed for DCM is also utilized for acute myocarditis. There is no consistent approach or recommendation for immune-modulated therapy for myocarditis. Some pediatric centers use intravenous gamma-globulin and/or steroids in the clinical setting of myocarditis; some patients with fulminant myocarditis require mechanical support with ECMO or VAD. There are some data to suggest that those with biopsy-proven myocarditis may have a better outcome than those with idiopathic disease [8,14,15].

Heart transplantation

The first successful pediatric heart transplant occurred in 1984; since then, more than 10,000 transplants in children have been reported to the International Society for Heart and Lung Transplantation [33]. Survival of pediatric post-transplant patients over this period has increased steadily and is now 90% at 1 year and 80% at 3 years [34]. This improvement has occurred primarily in early survival, with late survival rates remaining essentially unchanged for the last two decades. The most common causes of death early after transplant are infection and rejection. By 3 years, coronary artery vasculopathy and graft failure predominate [34].

The leading cause of heart transplantation in children over 1 year of age is DCM with end-stage heart failure. The PCMR data indicate that 40–45% of children with DCM died or were transplanted within 5 years of diagnosis [8]. Although timing and indications for transplant vary somewhat among centers, in general, patients are listed for transplant if they cannot be separated from inotropic and/or mechanical support. Outpatients with severely impaired quality of life or intractable growth failure may also be considered.

Myocarditis can present with acute, fulminant heart failure and marked hemodynamic compromise; however, many of these patients normalize systolic function over time, with relatively fewer deaths/transplants compared with DCM groups. The PCMR reported a death or transplant rate of 24% in patients with myocarditis compared with 47% in the DCM group [35]. In a registry report of ECMO centers, 7/255 patients with myocarditis underwent heart transplantation [36].

Even though allograft rejection is common following transplant, the incidence has been decreasing over time, from 34% in 2004 to 24% in 2011 [33]. The diagnosis of rejection is typically made by endomyocardial biopsy. Early signs and symptoms of acute rejection are often absent, necessitating frequent surveillance biopsies. Rejection can be classified as cellular or antibody-mediated. Acute cellular rejection is graded according to well-established histologic criteria, and is treated with increased immunosuppression. Antibody-mediated rejection is not as well characterized. Although the absence of standardized criteria for diagnosing antibody-mediated rejection leads to considerable heterogeneity in diagnosis and treatment, its incidence does appear to be increasing [37]: the incidence of biopsy-negative acute rejection is reported to be as high as 20% in adult transplant recipients [38].

In long-term follow-up, the most common causes of death in the child who has undergone cardiac transplantation are coronary artery vasculopathy and graft failure [39]. Clinical manifestations and symptoms of coronary vasculopathy may be subtle owing to the diffuse, multifocal nature of the vascular changes and denervation of the heart. Current methods used to detect graft vascular disease include angiography, often in combination with other modalities such as exercise or dobutamine stress echocardiography (DSE) [40,41] or intravascular ultrasound (IVUS) [42].

Imaging

Echocardiography is instrumental in the diagnosis, management, and follow-up of myocarditis and DCM. However, it is usually not helpful in determining the etiology of these disease processes. The key elements of the echocardiographic examination are summarized in the following.

Goals of imaging

In all first-time evaluations, a complete anatomic and functional evaluation by two-dimensional (2D), color, and spectral Doppler should be performed, with particular attention paid to assessing coronary artery origins with and without color Doppler.

General information to be obtained on all examinations (initial and follow-up):

- Height, weight, blood pressure (systolic, diastolic, and mean)
- Evaluation to exclude:
 - pericardial effusion
 - mitral regurgitation
 - pulmonary artery hypertension
 - intracardiac thrombi

Left ventricular size, geometry and systolic performance:

- Left ventricular dimensions, volumes
- 2D global function (ejection fraction, shortening fraction)
- Degree of sphericity
- Assessment of end-systolic wall stress

Left ventricular diastolic function:

- Left atrial size
- Pulsed-wave Doppler of mitral valve inflow
- Tissue Doppler imaging (TDI) of mitral annulus

Combined indices:

- Myocardial performance index
- d*P*/d*t*

Additional considerations for heart transplant recipients:

- Anastomosis sites
- Patent foramen ovale in the allograft
- Degree of tricuspid regurgitation
- Right ventricular systolic function (fractional area change)
- Consider intravascular ultrasound (IVUS) to assess presence of coronary artery vasculopathy

Additional considerations for assessment of ventricular synchrony:

- Interventricular mechanical delay by LV and RV outflow Doppler
- Consider TDI-derived timing intervals for intraventricular dyssynchrony
- Pulse wave of mitral inflow to assess for AV dyssynchrony, especially in paced rhythms

Additional considerations for assessment of mechanical support:

- Cannula positioning
- Doppler assessment of cannula flow
- Adequacy of LV decompression
- Presence of a patent foramen ovale
- Assessment of aortic regurgitation
- Assessment of RV function.

The presence of a dilated, poorly contractile ventricle is easily recognized with transthoracic imaging (Videos 34.1 and 34.2). Because afterload, preload, and contractility affect overall cardiac performance, volume- and/or pressure-loading lesions (e.g., aortic stenosis or regurgitation, coarctation, MR) must be excluded at the time of initial presentation. It is also critically important to exclude other surgically correctable lesions, particularly anomalous origin of the left coronary artery from the pulmonary artery (ALCAPA) (Figure 34.1a,b). In any patient presenting with features of DCM, the origin of the coronary arteries should be demonstrated by 2D imaging and *confirmed by color Doppler* in multiple views. Dilation of the right coronary also suggests that ALCAPA may be present. If the coronary artery origins are not demonstrated conclusively by color Doppler, then alternative imaging (i.e., angiography) is necessary.

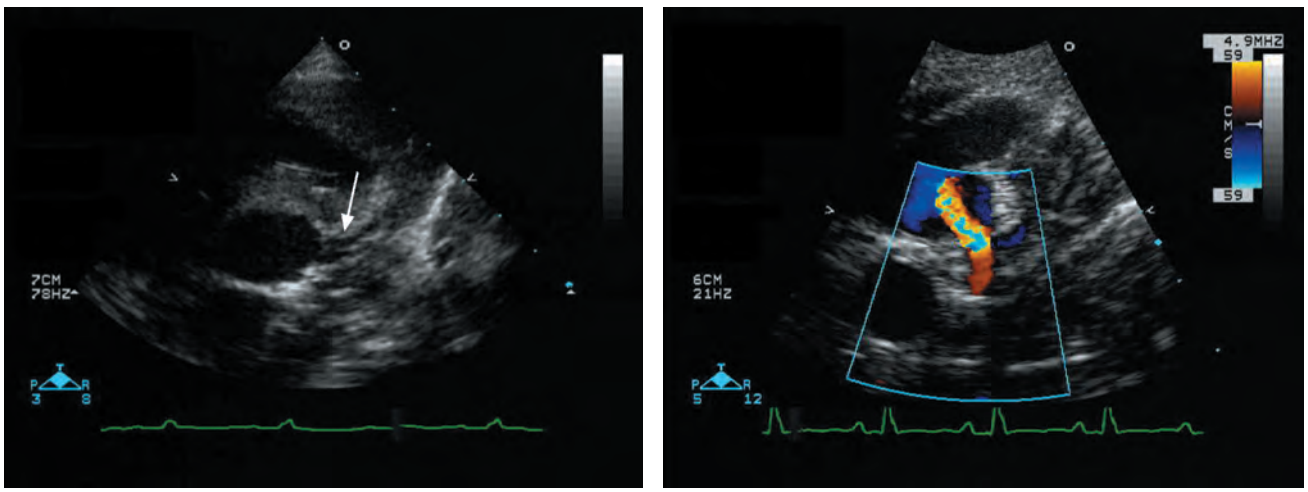
Useful echocardiographic assessment in the patient with DCM or myocarditis includes data regarding flow, pressures, volumes, and fiber shortening. Left ventricular dimensions, wall thickness, volumes, mass, SF, and EF are the echocardiographic cornerstones of DCM evaluation. Wall stress, rate-corrected velocity of circumferential fiber shortening (VCFc), and sphericity are also utilized in many institutions. Other parameters may add information, including assessment of diastolic function, myocardial performance index (MPI, or Tei index), and 3D imaging. Other findings associated with DCM and/or myocarditis should be evaluated (see the list at the start of the Goals of imaging section).

Most measures of LV size and function in the pediatric population are based on normal values derived from age- and body surface area-adjusted variables. Reporting these data as *z*-scores (number of standard deviations from the mean value) allows standardization of variables that change with age and growth [43]. Additional information on this topic can be found in Chapter 5.

Left ventricular size and geometry

Left ventricular size

Measures of LV size typically include LV end-diastolic and systolic dimensions from M-mode or 2D imaging, and LV end-diastolic and systolic volumes from 2D or 3D imaging. Often in DCM the heart is so large that the LV apex is difficult



(a) (b)

Figure 34.1 Anomalous origin of the left coronary artery (arrow) from the pulmonary artery (ALCAPA). By 2D imaging alone in parasternal short-axis view, the left coronary artery may appear to be normal **(a)**, but with color Doppler **(b)**, flow from the left coronary artery can be seen entering the pulmonary artery. In this patient, the pulmonary vascular resistance has dropped and there is coronary "steal" into the pulmonary artery.

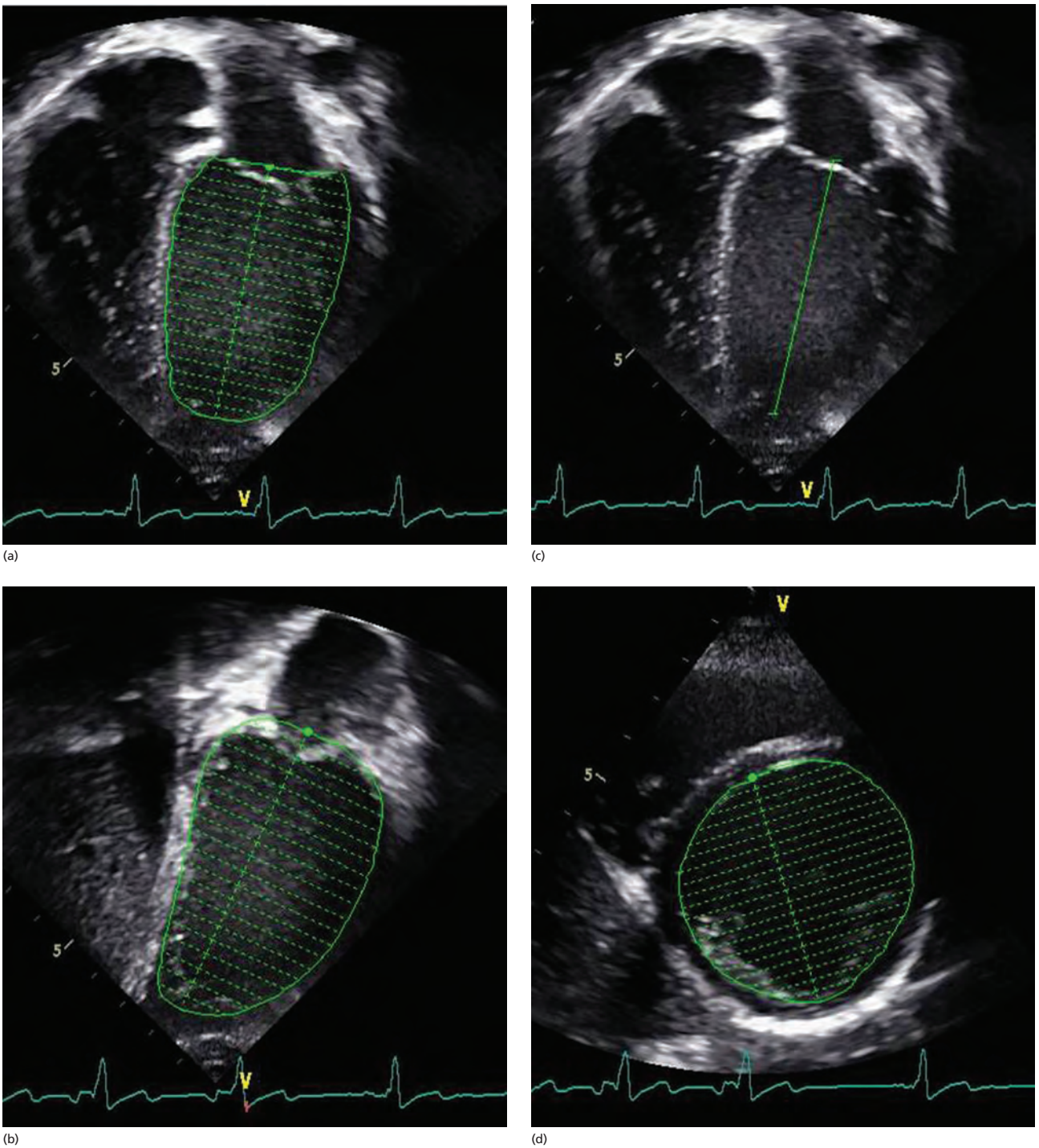


Figure 34.2 Common methods of calculating LV volume require images in two planes. The biapical Simpson method requires LV areas in apical 4-chamber **(a)** and 2-chamber **(b)** views. The 5/6 × area × length (5/6AL) method requires an apical 4-chamber view LV length **(c)** and a short-axis LV area **(d)**. LV, left ventricle.

to image, and care must be taken not to foreshorten the ventricle and to understand the limitations of the measurements under these conditions. From 2D imaging, common algorithms of determining LV volume include both the Simpson's biplane method (Figure 34.2a,b) and the 5/6 area–length method (Figure 34.2c,d) [44] It is critical that the same method of determining ventricular volumes be used across serial examinations in a given patient. It should also be the same method as that used in the *z*-score database, as these algorithms yield different values.

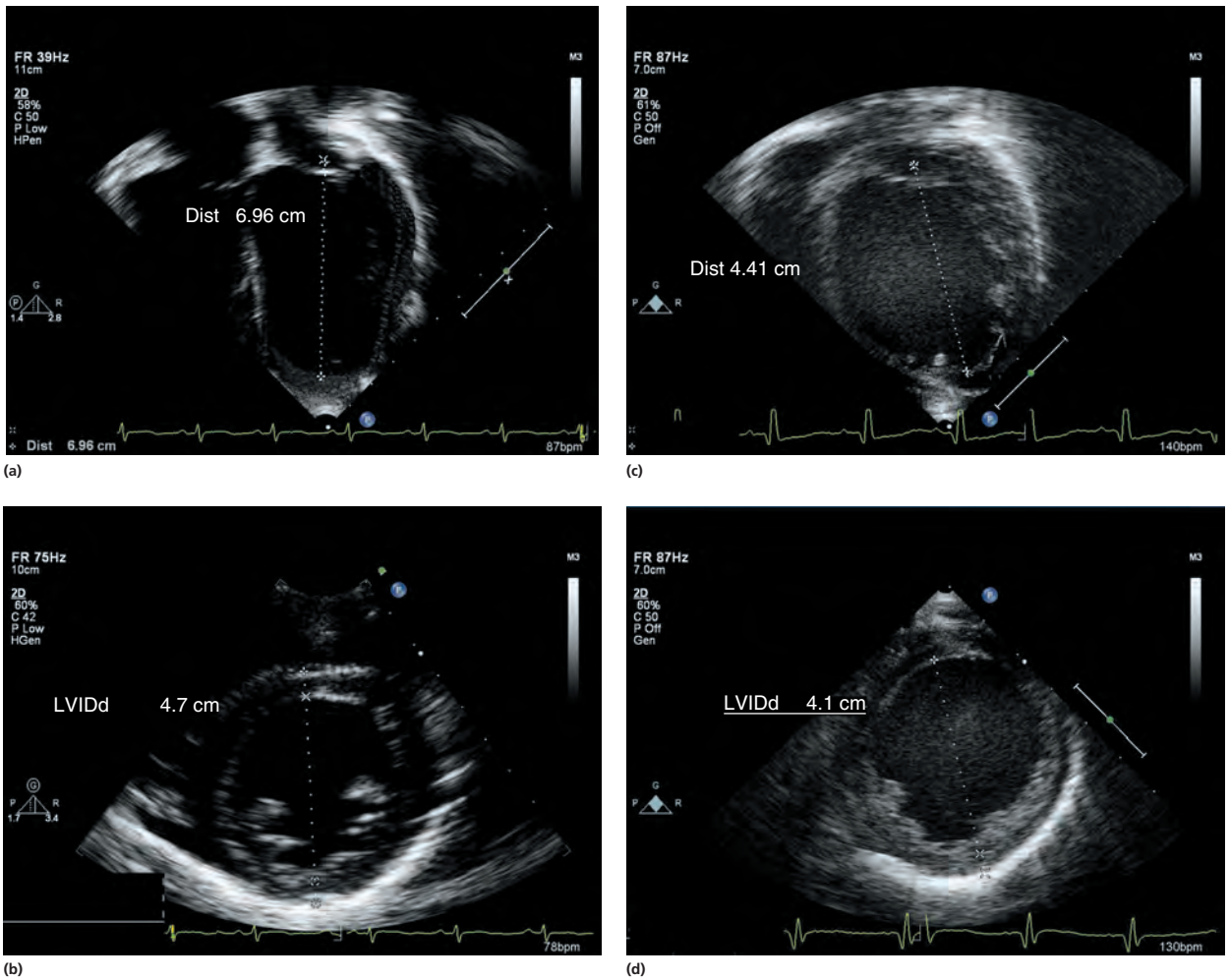


Figure 34.3 Apical 4-chamber view demonstrates the sphericity index in a normal patient **(a,b)** and in a patient with dilated cardiomyopathy (DCM) **(c,d)**. The sphericity indexes are 0.67 for the healthy patient and 0.93 for the patient with DCM. Dist, distance; LVIDd, left ventricular end-diastolic dimension.

Left ventricular geometry

The alteration in LV geometry in the setting of LV dysfunction is characterized by change from an ellipsoid shape to a spherical shape. This process is associated with increased thinning of the ventricular wall, increased end-systolic wall stress, decreased contractility and increased MR [45,46]. The SI is a measure of the LV geometry and is calculated as the LV diastolic short-axis dimension divided by the LV diastolic long-axis dimension; the SI approaches unity as the LV becomes more spherical (Figure 34.3a–d). It is useful only in structurally normal hearts. In a small group of children and adolescents, the mean SI has been reported as 0.66 ± 0.07 in healthy patients and 0.89 ± 0.10 in those with LV dysfunction [45]. The same study demonstrated a significant negative correlation between SI and measures of LV systolic function (SF and EF).

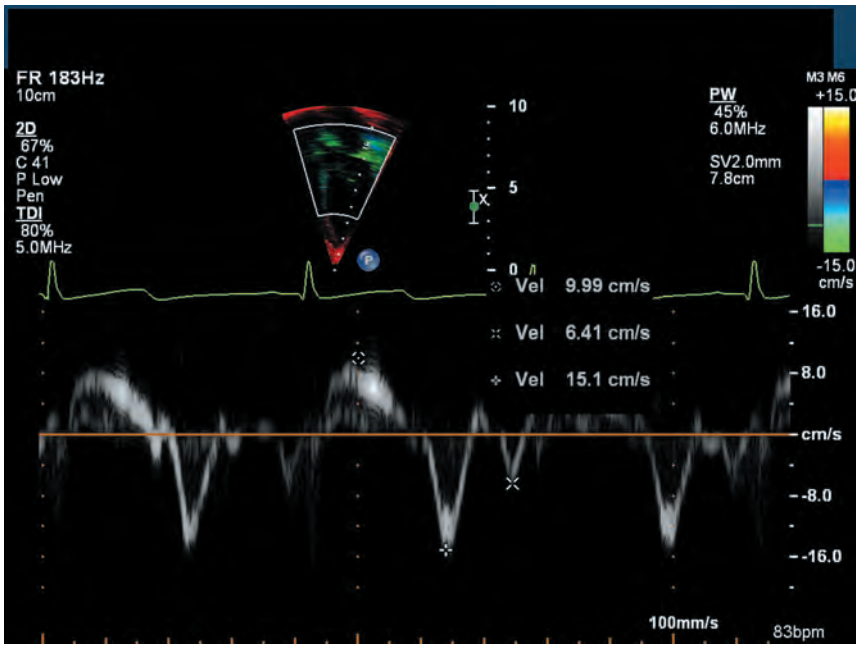
Left ventricular systolic performance

Shortening fraction and ejection fraction

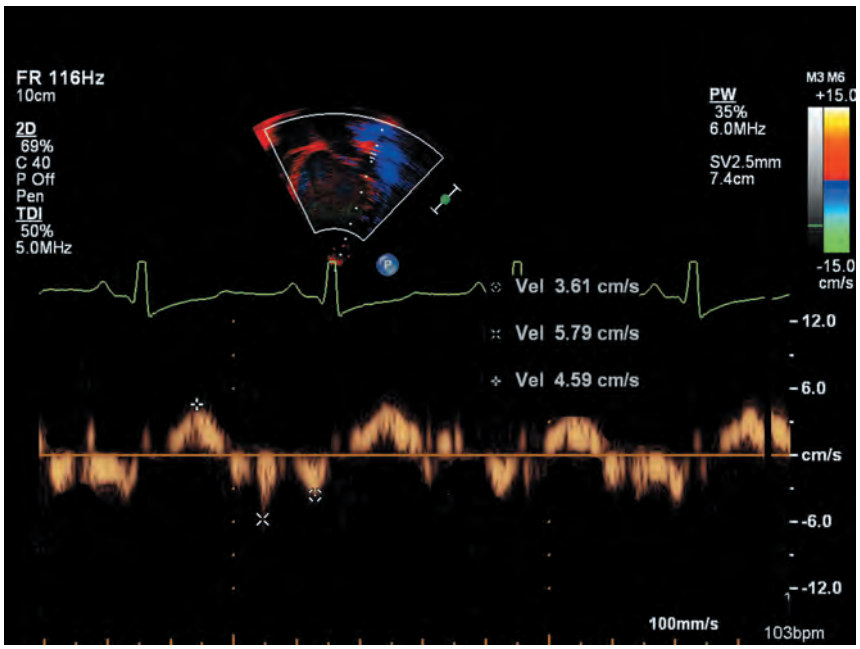
Measures of ventricular systolic function that are most commonly used in clinical practice include SF and EF. M-mode or 2D-derived LV dimensions are used to determine SF, and also the corrected velocity of circumferential fiber shortening (VCFc). 2D imaging and determination of ventricular volumes provide values for EF. VCFc, SF, and EF are sensitive to loading conditions and may not provide true reflections of underlying myocardial contractility. Despite these limitations, SF and EF are relatively easy to measure and are useful for comparing systolic function in the same patient over time.

Wall stress and measurement of afterload

Left ventricular wall stress can be calculated as a measure of afterload. Afterload is an important determinant of overall cardiac performance; end-systolic stress is the most relevant measurement with regard to systolic function [47]. The stress-adjusted shortening (relationship of wall stress to SF, dependent on preload) and stress-adjusted velocity (relationship of wall stress to VCFc, not dependent on preload) can then be used to adjust for preload and afterload, thus isolating true contractility. The method of measuring end-systolic wall stress is discussed in



(a)



(b)

Figure 34.4 Tissue Doppler imaging with myocardial velocities from the lateral mitral annulus in a normal subject **(a)** with normal myocardial velocities, and in a patient with severe DCM **(b)**, demonstrating significantly lower myocardial velocities.

Chapter 7. LV end-systolic wall stress is predictive of outcome in adult patients with DCM [48].

Left ventricular diastolic function

Assessment algorithms

Multiple algorithms have been proposed for comprehensive evaluation of LV diastolic function [49,50]. Much of the study of diastolic function in DCM, however, focuses more on individual parameters than on the results of complete algorithms.

Left atrial size

During diastole, the left atrium (LA) is exposed to the loading pressure within the LV, resulting in remodeling of the LA over time. Thus, LA size becomes a marker of the chronicity of LV diastolic dysfunction [49]. Robust normal adult data are available, and some pediatric normal data have also been published [51]. The presence and degree of MR should be taken into account when evaluating LA size.

Table 34.2 Myocardial performance index (MPI) and tissue Doppler imaging (TDI) data in patients with dilated cardiomyopathy and in control subjects.

	Dilated cardiomyopathy	Control subjects
N	80	80
Age (years)	7.2 ± 6.1	7.1 ± 5.7
LV SF (%)	21.6 ± 6.6**	38.1 ± 4.0
LV MPI	0.67 ± 0.20**	0.33 ± 0.06
Mitral TDI[a]		
MV-e′	11.8 ± 4.8***	16.8 ± 4.7
MV-a′	5.6 ± 3.0*	6.4 ± 1.9
MV-s′	6.5 ± 2.2***	9.1 ± 3.0
Septal TDI[a]		
IVS-e′	8.5 ± 2.9***	12.8 ± 2.7
IVS-a′	5.6 ± 1.8	5.9 ± 1.2
IVS-s′	5.7 ± 2.0***	7.8 ± 1.9
Tricuspid TDI[a]		
TV-e′	12.7 ± 3.9***	15.9 ± 3.2
TV-a′	9.2 ± 3.3*	10.3 ± 2.5
TV-s′	10.6 ± 2.9***	12.9 ± 2.2
Mitral e/e′ ratio	9.4 ± 6.5***	6.1 ± 2.1
Septal e/e′ ratio	11.7 ± 4.2***	7.8 ± 2.1
Tricuspid e/e′ ratio	4.5 ± 1.7*	3.9 ± 0.9

a′, Late diastolic velocity as measured by TDI; e, early diastolic velocity; e′, early diastolic velocity as measured by TDI; IVS, septal annulus; LV, left ventricle; MV, lateral mitral annulus; s′, systolic velocity as measured by TDI; SF, shortening fraction; TV, lateral tricuspid annulus. Data expressed as mean ± SD.

[a]Doppler velocity data expressed in cm/s.

*$p < 0.05$, **$p < 0.01$, and ***$p < 0.001$ compared with control subjects.

Source: Eidem et al. 2005 [56]. Reproduced with permission of Elsevier.

Mitral inflow velocity profile

The mitral inflow Doppler pattern contains several items for examination, including the E- and A-wave velocities and the deceleration time of the E wave. The load dependence of these measures limits their utility somewhat, but they are particularly useful when combined with tissue Doppler imaging.

Tissue Doppler imaging

Direct myocardial velocities can be measured using tissue Doppler imaging (TDI). This technique allows quantitative evaluation of regional myocardial function and is considered less load dependent than spectral Doppler of the mitral valve. Myocardial velocities at the level of the mitral or tricuspid valve annulus are indicative of longitudinal LV or RV function, respectively (Figure 34.4a,b). Systolic myocardial peak velocity (s′), early diastolic velocity (e′) and late diastolic velocity (a′) are typically measured. Normal values for children have been published [52–54]. Mitral annular velocities are decreased in adult [55] and pediatric [20,56] patients with DCM compared with healthy subjects (Table 34.2). Additional findings in DCM include increased MV pulsed-wave e to TDI e′ ratio (e/e′) compared with controls [56], and an indication that lower mitral and tricuspid annular e′ velocities may be predictive of worse outcome in pediatric DCM [20].

Isovolumic relaxation time

The isovolumic relaxation time (IRT) is the interval between aortic valve closure and mitral valve opening, and can be measured from an LV inflow–outflow Doppler tracing (Figure 34.5a) or from a TDI tracing (Figure 34.5b). The IRT varies with heart rate, hence values may not always be able to be dichotomized into normal and abnormal [49].

Combined systolic and diastolic indices

Myocardial performance index

The MPI, or Tei index, is a Doppler measure that assesses both systolic and diastolic function [57]. It can be measured by either pulsed-wave Doppler or TDI by determining the sum of the isovolumic contraction and isovolumic relaxation times divided by the ejection time (Figure 34.5a,b). With progressive LV dysfunction, the LV ejection time is decreased and the MPI becomes prolonged. The MPI in pediatric patients with dilated cardiomyopathy (0.78 ± 0.28) has been shown to be significantly increased compared with that in normal subjects (0.36 ± 0.07) [58], although it is not a strong predictor of death, transplantation, need for hospitalization or intravenous ionotropic support [20]. It is sensitive but not specific, and can reflect abnormalities in preload, afterload, contractility, diastolic function, and conduction. MPI has been more predictive of outcome in adult DCM and heart failure [59,60].

Change in LV pressure over time

If MR is present, change in LV pressure over time (d*P*/d*t*) can be calculated and reflects contractility. The normal time interval by this measure (the time difference between 1 and 3 m/s) is <27 ms. With significant LV dysfunction, the peak velocity of MR will occur in mid-to-late systole, as there is a slower rate of rise in LV pressure seen in the presence of reduced contractility (Figure 34.6) [61]. As with other measures of LV systolic function, d*P*/d*t* is both preload and afterload dependent and is also dependent on the presence and severity of MR.

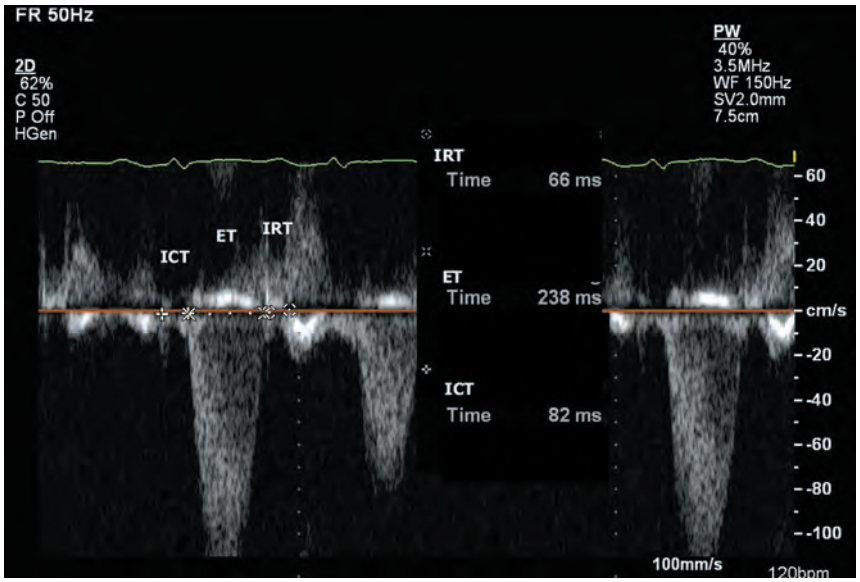
Other imaging modalities

Stress echocardiography

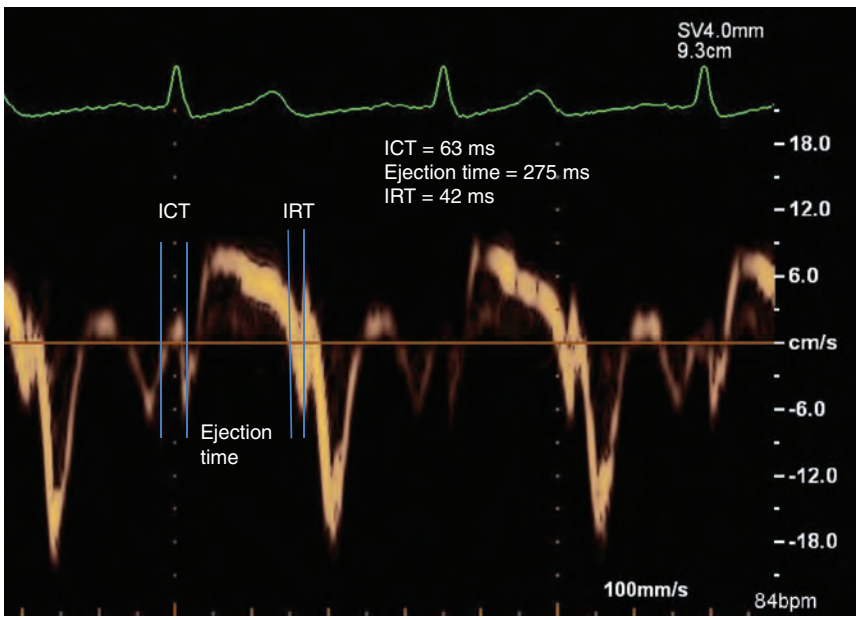
Stress echocardiography is an additional useful technique in the evaluation of contractile function in dilated cardiomyopathy. "Stress" is typically induced with exercise or pharmacologically, most commonly using dobutamine, although there is no consensus regarding method, protocol or measure of contractile reserve to use. Data indicate that dobutamine stress echocardiography has prognostic significance in adolescent patients with DCM, and may be of added benefit in clinical decision-making in conjunction with metabolic exercise testing in this group of patients [62].

3D Echocardiography

Ventricular volumes as measured by 3D echocardiography and volumetric methods more closely correlate with values



(a)



(b)

Figure 34.5 Measurement of the IRT (isovolumic relaxation time) and myocardial performance index (MPI, or Tei index) **(a)** in a patient with dilated cardiomyopathy, by LV inflow–outflow pulsed Doppler (MPI = 0.62, elevated) and **(b)** in a normal patient by tissue Doppler imaging (MPI = 0.38, normal). ET, ejection time; ICT, isovolumic contraction time; LV left ventricle.

obtained by CMR than those measured by 2D (biplane) methods, even given the altered ventricular geometry and morphology seen in DCM [63,64]. In very large ventricles, however, 3D echocardiography will also underestimate volumes, compared with CMR [64,65]. 3D echocardiography can be used to evaluate and quantify other cardiac chambers, including RV size and function and LA volumes, both of which may be important in patients with cardiomyopathy [66,67]. See Chapter 42 for additional comment on 3D evaluation.

Evaluation of the fetus with cardiomyopathy

Fetal echocardiography for assessment of cardiac function should include evaluation of both the RV and LV, including systolic and diastolic function, since both ventricles pump to the systemic circulation. Evaluation can include measurement of biventricular cardiac output, LV SF and EF, mitral and tricuspid inflow Doppler patterns, and evaluation of Doppler flow patterns in the vena cava, ductus venosus, and umbilical vein. Newer methods still being investigated in the fetus include

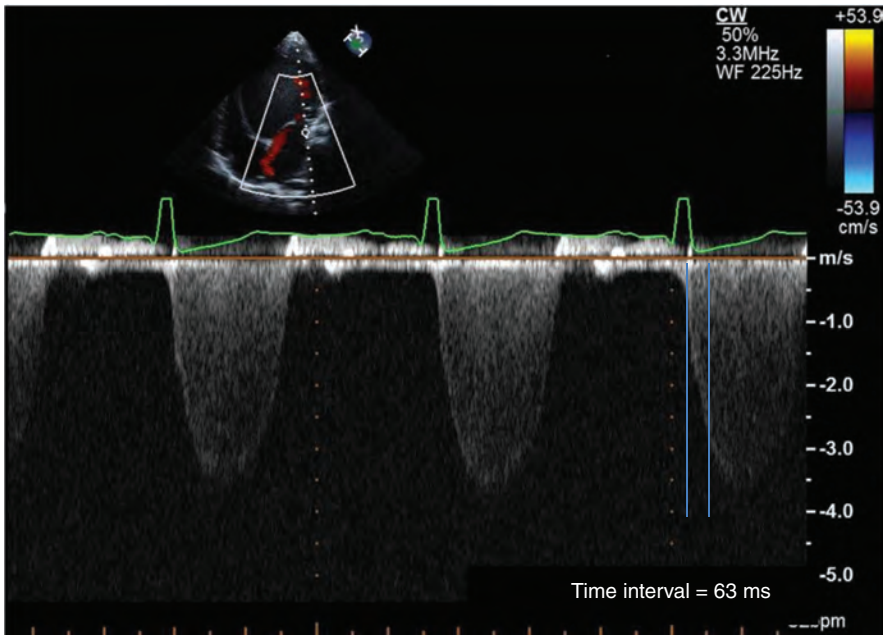


Figure 34.6 d*P*/d*t* measured from MR jet, = 32/time interval (seconds) between 1 and 3 m/s. In this patient with dilated cardiomyopathy, d*P*/d*t* is 508 mmHg/s. MR, mitral regurgitation.

determination of the MPI and the use of TDI to evaluate myocardial velocities [68–72]. Additionally, a fetal cardiovascular profile score has been developed to assess overall fetal cardiac well-being [68,73,74]. For fetuses at increased risk of DCM (family history, anemia, etc.), serial fetal echocardiograms may be useful given the evolving nature of the disease and the potential for late gestational presentation.

Special imaging considerations

Pericardiac transplant evaluation

Underlying congenital heart disease is a common indication for cardiac transplant in pediatrics [33], hence pre-transplant assessment requires complete understanding of the original anatomy. Post-transplant imaging evaluation also requires familiarity with the original cardiac morphology in addition to the type of transplant surgery performed. Although all cardiac transplants have anastomotic sites at the pulmonary artery and aorta, the venous anastomoses can be either biatrial or bicaval with pulmonary venous anastomoses. Biatrial anastomoses typically give the atria a significantly enlarged appearance (Figure 34.7). Each anastomotic site has the potential to become obstructed, particularly the superior vena cava after bicaval anastomosis-type procedures [75] (Figure 34.8a,b). Clinically significant RV dysfunction and tricuspid regurgitation in the allograft can occur due to increased pulmonary vascular resistance in the recipient [76,77]. The severity of tricuspid regurgitation on postoperative TEE at the time of cardiac transplantation has been shown to predict poor late survival in adult cardiac transplant recipients [77].

Cardiac allograft rejection surveillance by echocardiography

The current gold standard for diagnosing post-transplant rejection is endomyocardial biopsy, but because it is invasive, the search for noninvasive methods has been aggressively pursued. Although echocardiographic measures demonstrating a decrease in cardiac performance may have good specificity in predicting rejection in pediatric heart transplant patients,

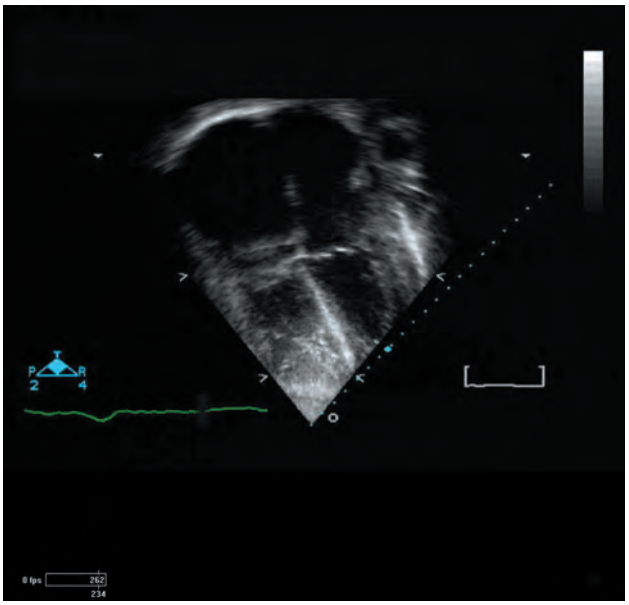


Figure 34.7 Apical 4-chamber view shows biatrial enlargement in a patient status post-heart transplant with a biatrial anastomosis.

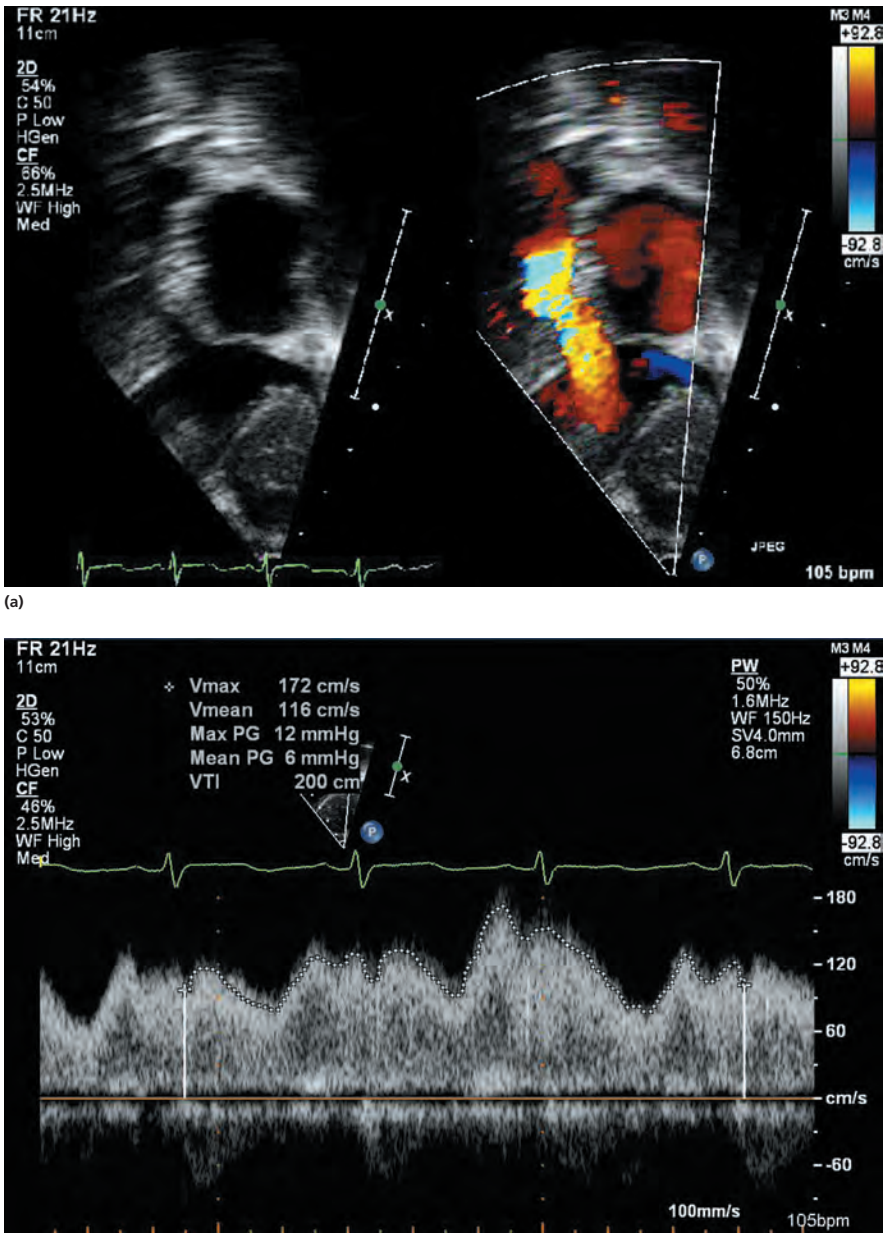
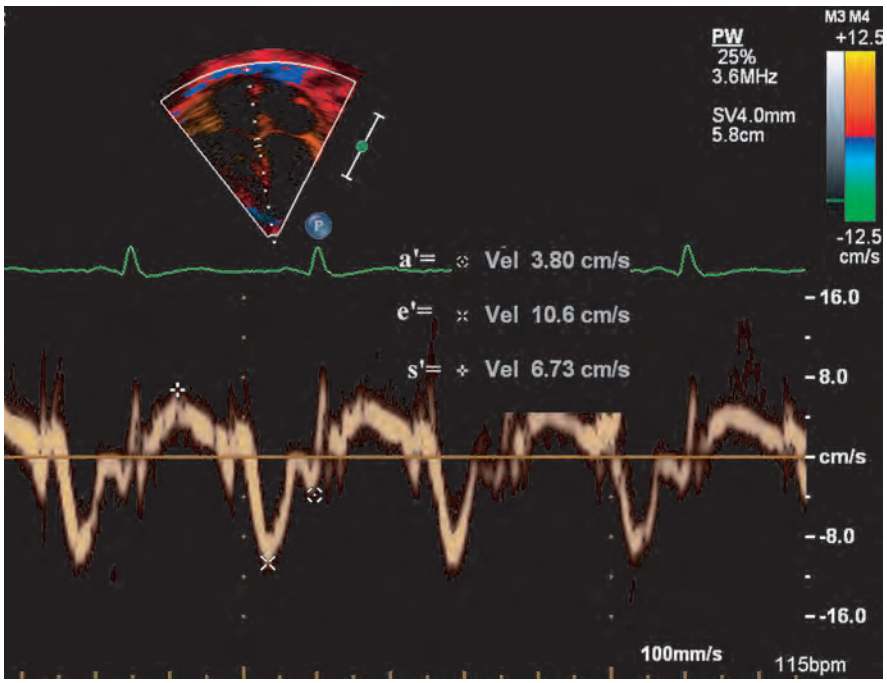


Figure 34.8 Subxiphoid sagittal view shows superior vena caval (SVC) obstruction in a patient status post-heart transplant. **(a)** Narrowing at the SVC anastomosis is demonstrated by 2D and color Doppler imaging; **(b)** spectral Doppler evaluation of the mean gradient across the obstructed region.

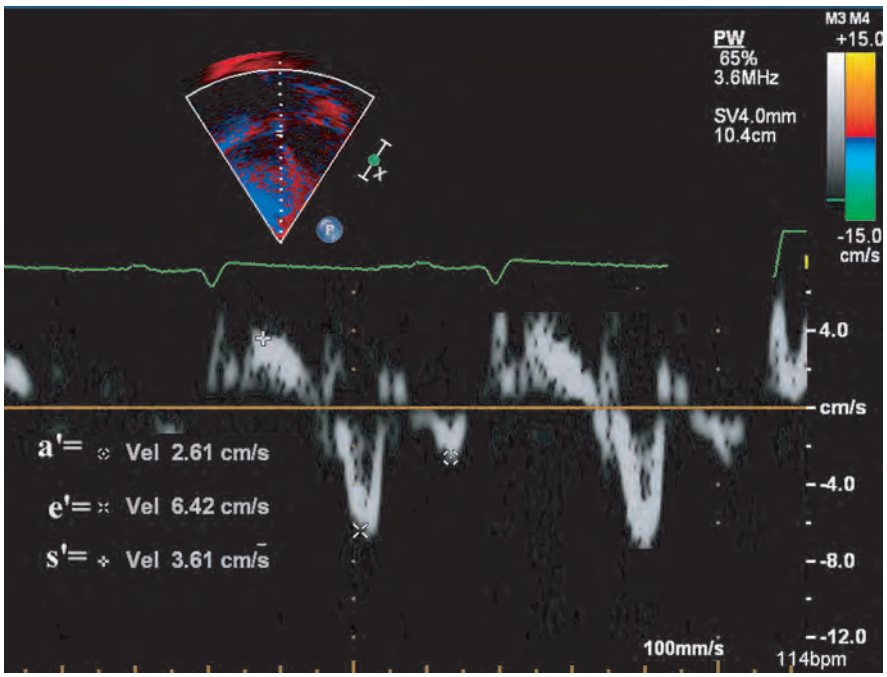
sensitivity remains limited [78]. Early after pediatric transplant, both systolic and diastolic longitudinal myocardial velocities, as assessed by TDI, are depressed. Velocities improve over the first 6 months after transplant but remain below control values [79]; LV MPI is more prolonged, and wall motion abnormalities are common [80]. During rejection, TDI velocities are further reduced (Figure 34.9a,b) and the MPI is prolonged [81]. Many echocardiographic measures have good negative predictive value for rejection [78,82]. Therefore, echocardiography may be more useful in excluding rejection as a diagnosis and potentially limiting the number of invasive myocardial biopsies.

Long-term surveillance for allograft vasculopathy is typically carried out through angiography. It may not, however, correlate with either pathologic findings or functional significance of the vasculopathy. IVUS is more sensitive than angiography, predicts morbidity and mortality in adult transplant patients [83,84] (Figure 34.10), and can be safely and effectively performed in pediatric patients [85,86]. There are also data in both children and adults indicating that conventional dobutamine stress echocardiography [42,87] is useful in detection of graft coronary vasculopathy.

Regardless of the length of time post-transplant, evaluation of tricuspid regurgitation remains important, as it may develop



(a)



(b)

Figure 34.9 **(a)** Septal myocardial velocities 1 month prior to severe rejection. **(b)** Further decreased myocardial velocities in the same patient with severe, acute rejection.

as a result of injury to the valve during catheterizations. Some clinicians have relied on real-time 2D and 3D echocardiography for echo-guided myocardial biopsies [88,89].

Cardiac resynchronization therapy for cardiomyopathy

Cardiac resynchronization therapy (CRT) has shown significant benefit in many adult patients with heart failure in terms of reducing hospitalizations and prolonging survival [90]. Despite this success, 25–35% of patients who receive CRT based on current criteria (NYHA functional class III–IV, QRS ≥120 ms and EF ≤35%) do not respond [91]. Many echocardiographic indices have been proposed to play a role in further identification of patients who might benefit from CRT.

Cardiac dyssynchrony in heart failure occurs at three levels: atrioventricular (prolonged left-sided atrioventricular delay),

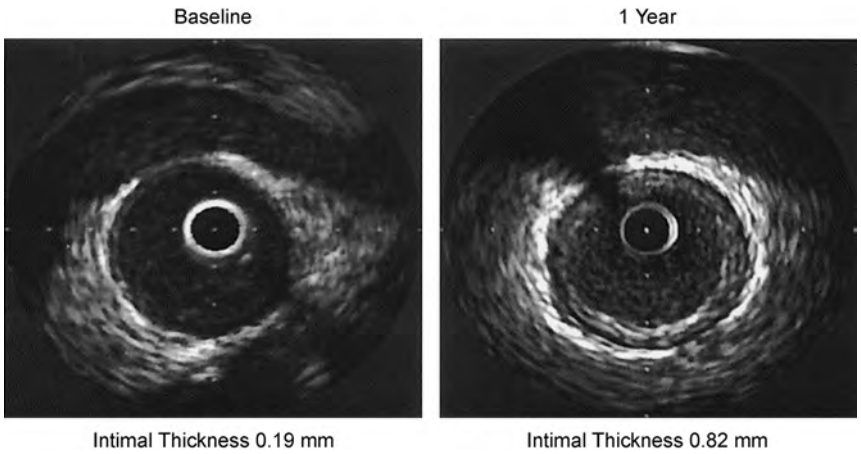


Figure 34.10 Intravascular ultrasound (IVUS) images showing a >0.5 mm difference between the intimal thickness observed at baseline and 1 year post-transplant, demonstrating rapidly progressive transplant vasculopathy. Source: Tuzcu et al. 2005 [83]. Reproduced with permission from Elsevier.

interventricular (discordant timing of contraction between the LV and RV) and intraventricular (delayed activation of one region of a ventricle relative to another region in the same ventricle). The end result of dyssynchrony is reduced cardiac efficiency and stroke volume, worsening MR, prolonged isovolumic phases, and impaired diastolic filling [92]. Currently there is no consensus on the best parameters to predict response or follow patients undergoing CRT.

In adults with heart failure, methods and parameters used to evaluate ventricular dyssynchrony have included the following.

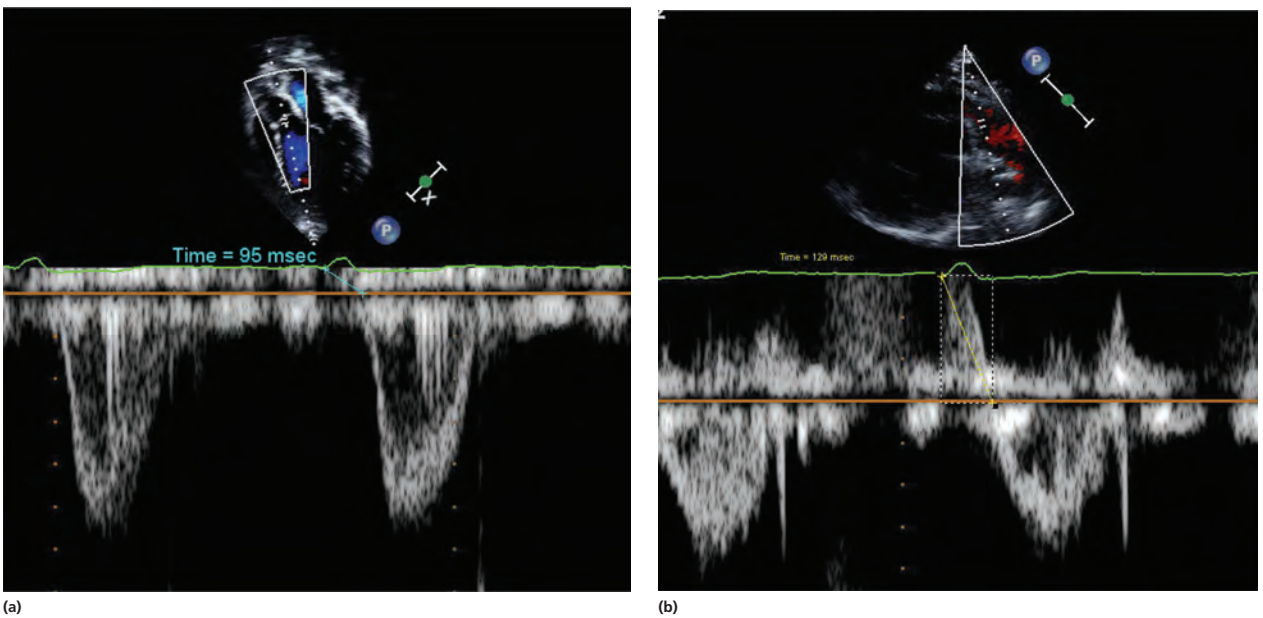
Interventricular dyssynchrony

- Interventricular mechanical delay (IVMD): the difference between the LV and RV pre-ejection intervals (measured from QRS to onset of flow across the aortic and pulmonary valves) A difference of >40 ms is considered abnormal in the adult population (Figure 34.11a,b) [93,94].

Intraventricular dyssynchrony

A multitude of parameters that measure intraventricular dyssynchrony have been used to predict response to CRT (Table 34.3). Some of the more common include:

- Septal-to-posterior wall motion delay: determined using parasternal short-axis M-mode by measuring the time from the maximal posterior displacement of the anterior septum to the maximum thickening of the posterior wall, with >130 ms being significant in adults [94–96].
- LV pre-ejection interval: measured as described earlier for IVMD (Figure 34.11a), with >140 ms considered prolonged in adults [94,95].



(a) (b)

Figure 34.11 Measurement of the interventricular mechanical delay (IVMD) **(a)** Left ventricular (LV) and **(b)** right ventricular (RV) pre-ejection intervals (PEIs), demonstrating a difference between the LV-PEI and RV-PEI of 34 ms.

Table 34.3 Measurements of regional delay to predict CRT response.

Study	Parameter	*N*	Population	Ischemic etiology (%)	Follow-up (months)	Response	Cut-off	Sensitivity (%)/specificity (%)
Pitzalis et al. [96]	SPWMD	20	NYHA III, QRS ≥140 ms, LVEF ≤35%, SR, LBBB	20	1	LVESV ≥15%	130 ms	100/63
Soliman et al. [109]	3D-SDI	90	NYHA ≥III, QRS ≥120 ms, LVEF ≤35%, SR	51	12	LVESV ≥15%	>10%	96/88
Bax et al. [110]	Ts-4	80	NYHA ≥III, QRS ≥120 ms, LVEF ≤35%, SR, LBBB	55	6	LVESV ≥15% NYHA ≥1	65 ms 65 ms	92/92 80/80
Yu et al. [97]	Ts-SD12	30	NYHA III, QRS ≥140 ms, LVEF ≤40%	40	3	LVESV ≥15%	32.6 ms	100/100
Yu et al. [111]	TSI-TS-SD12	56	NYHA ≥III, QRS ≥120 ms, LVEF ≤40%	50	3	LVESV ≥15%	34.4 ms	87/81
Suffolento et al. [112]	2D-RS	50	NYHA ≥III, QRS ≥120 ms, LVEF ≤35%, SR	62	8 ± 5	LVESV ≥15%	130 ms	89/83

2D-RS, speckle tracking radial strain; 3D-SDI, standard deviation of 16 time–volume peaks; LBBB, left bundle branch block; LVEF, left ventricle ejection fraction; LVESV, left ventricle end-systolic volume; NYHA, New York Heart Association class; SPWMD, M-mode septal to posterior wall motion delay; SR, sinus rhythm; TS-4, maximal velocity delay between four basal segments; TSI, tissue synchronization imaging; TS-SD12, standard deviation of velocity peaks in 12 basal and midventricular segments.
Source: Leenders et al. 2011 [92]. © The Author(s) 2010. Reproduced under open access.

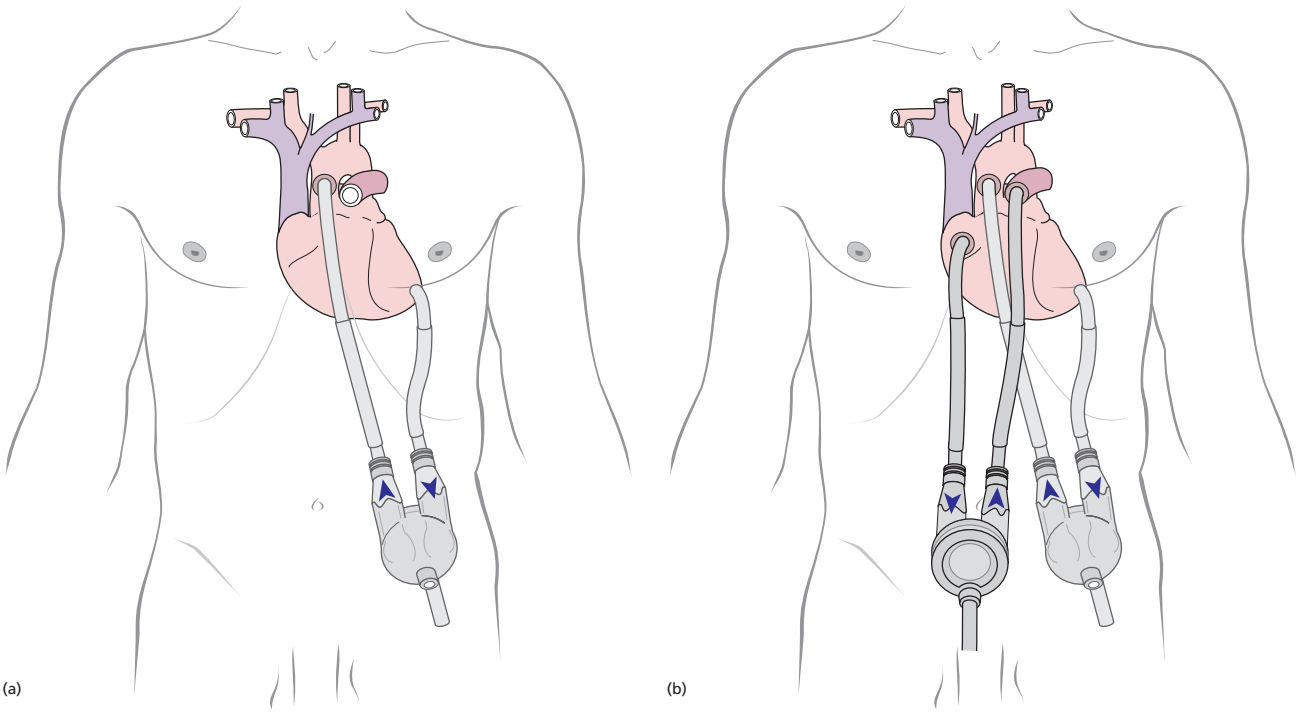


Figure 34.12 Placement of left ventricular assist device with apical cannulation **(a)** and biventricular assist device **(b)**. Source: Reproduced courtesy of Berlin Heart AG, Berlin, Germany.

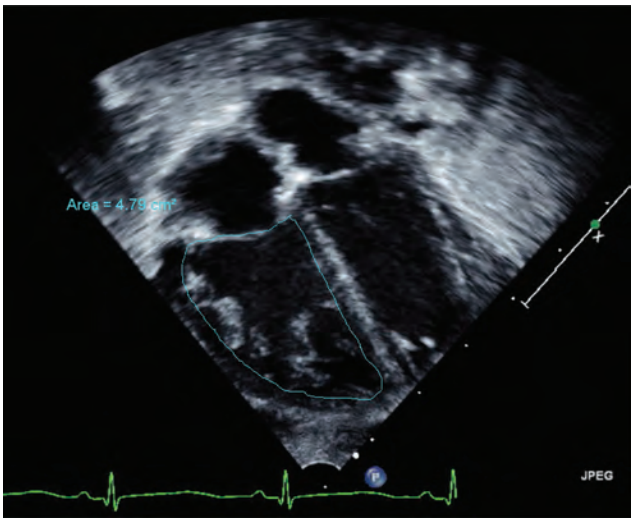
Table 34.4 Checklist for evaluation of patients receiving VADs.

Pre-VAD evaluation
- Cardiac anatomy
- Chamber dimensions and function
- Valvular abnormalities
 - Degree of regurgitation or stenosis
 - Annular dilation
- Intracardiac shunts (PFO, ASD, VSD); level, direction, and amount of shunt
- Intracardiac thrombus or spontaneous contrast
- Assessment of the ascending aorta

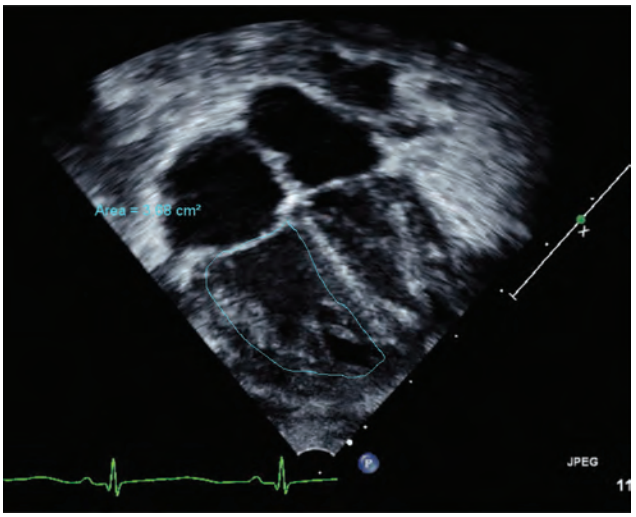
Intraoperative evaluation
- RV size and function (if LVAD alone)
- LV unloading
- Valvular abnormalities
- Intracardiac shunts: level, direction and amount of shunt
- Inflow and outflow cannula position and Doppler
 - LV inflow cannula: in LV apex
 - View in mid-esophageal 4-chamber and long-axis views
 - Parallel to septum and aligned with mitral inflow
 - Unidirectional flow from left ventricle into the cannula
 - LV outflow: in ascending aorta
 - View in mid-esophageal long-axis view
 - RV inflow: in the right atrium
 - View in mid-esophageal short-axis view and bicaval view
 - RV outflow
 - View in mid-esophageal 20–70°
- Cannula position before and after chest closure
- De-airing during the following phases of surgery:
 - From cannula placement until release of aortic cross-clamp
 - From release of aortic cross-clamp to the end of cardiopulmonary bypass
 - From the termination of cardiopulmonary bypass to the end of the operation

Assessment while on VAD support
- Biventricular size and function and septal position
- Valvular abnormalities
- Cannula position and Doppler
 - Malposition or obstruction
- Pericardial effusion and hematoma
 - Chamber collapse (an important marker of tamponade)
- Intracardiac thrombus
- Ascending aorta dissection
- Assessment of RV function

ASD, atrial septal defect; PFO, patent foramen ovale; VSD, ventricular septal defect.
Source: Sachdeva et al. 2013 [104]. Reproduced with permission of Elsevier.



(a)



(b)

Figure 34.13 RV focused apical 4-chamber view; the endocardium is traced in diastole **(a)** and systole **(b)**. The fractional area change (FAC) is 4.79–3.68/4.79 = 23.2%.

- TDI: TDI can be used to measure regional electromechanical delays, by measuring the time interval from QRS onset to the beginning, peak or end of the s′-wave in opposing basal and mid-LV segments [93,94,97]. Evaluating more segments will provide a better determination of LV dyssynchrony. However, TDI does not distinguish between active and passive myocardial motion; methods using strain-rate imaging (a measure of regional deformation) can be used to differentiate. Both strain and TDI methods require considerable post-processing time and are currently more suited to research trials than routine clinical practice.

Atrioventricular dyssynchrony

- Additional measures used to evaluate pacemaker therapy and CRT can include diastolic filling time [left ventricular filling time (LVFT)]. This is measured on the trans-mitral pulsed-wave Doppler from onset of mitral inflow (E-wave) to end of atrial contraction (A-wave) and is used as a measure of atrioventricular synchrony. In adults, an LV filling time of <40% of the cardiac cycle (RR interval) is evidence of atrioventricular dyssynchrony [93,95], although no such parameters currently exist for children. In the setting of pacemaker optimization, the most favorable setting is the atrioventricular delay that allows completion of the atrial contribution to diastolic filling [91].

Experience with CRT therapy in children with cardiomyopathy and heart failure is more limited than in adults.

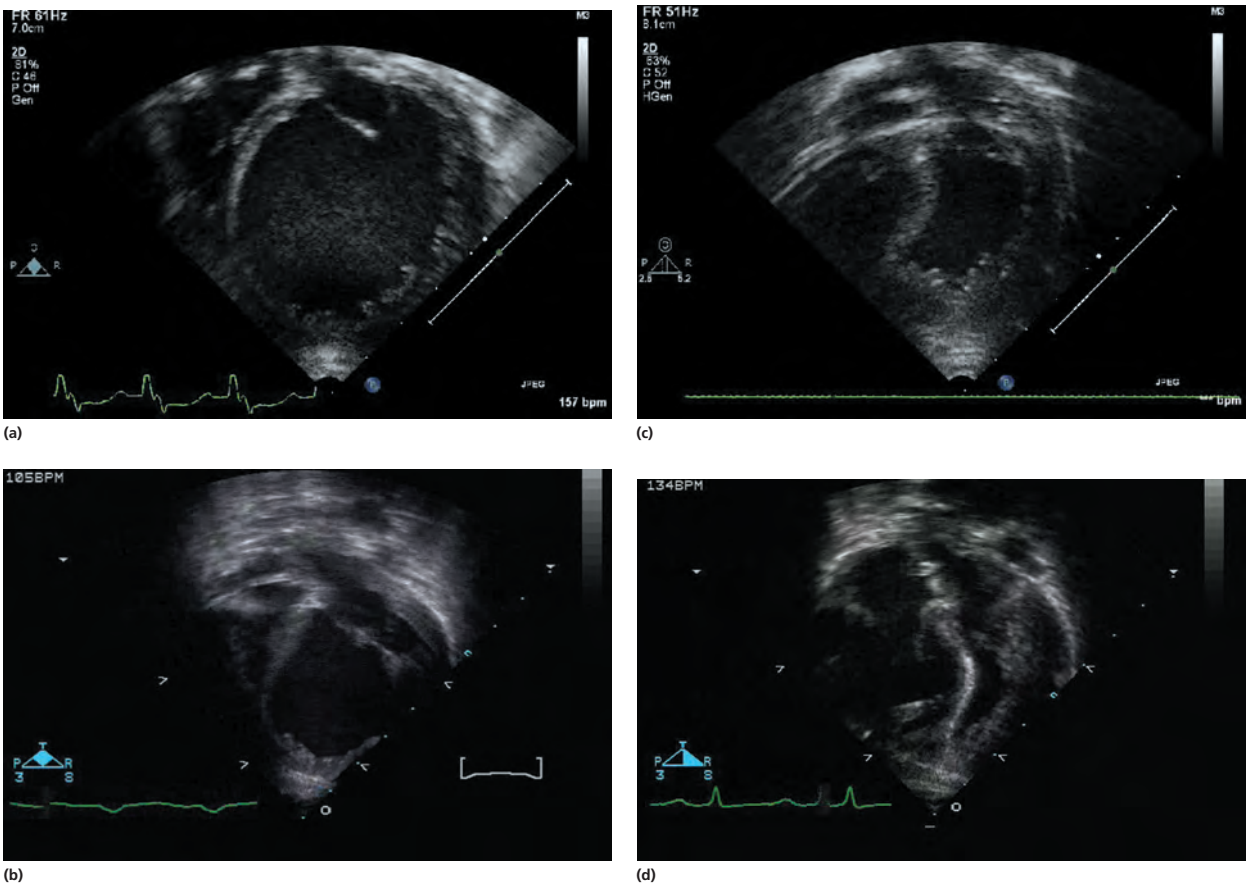


Figure 34.14 Ventricular geometry prior to and after left ventricular assist device (LVAD) placement; images taken within 36 h in the same patient. These images in the apical 4-chamber view demonstrate progressive decompression of the left ventricle (LV) with proper LVAD function. **(a)** Severe dilated cardiomyopathy (DCM) prior to LVAD placement; **(b)** just after LVAD placement without significant LV decompression; **(c)** some evidence of LV decompression; **(d)** significant decompression of the LV.

Preliminary evidence indicates that CRT is beneficial in children who have heart failure due to congenital heart disease and cardiomyopathy. Most pediatric patients do not have left bundle-branch block and therefore do not meet standard adult criteria for CRT. Interventricular dyssynchrony is more common in children given the higher incidence of right ventricular surgery, and less attention has been paid to the concept of diastolic dyssynchrony, although it has been shown to be prevalent in pediatric DCM, and may be related to increased risk of death or transplant [98].

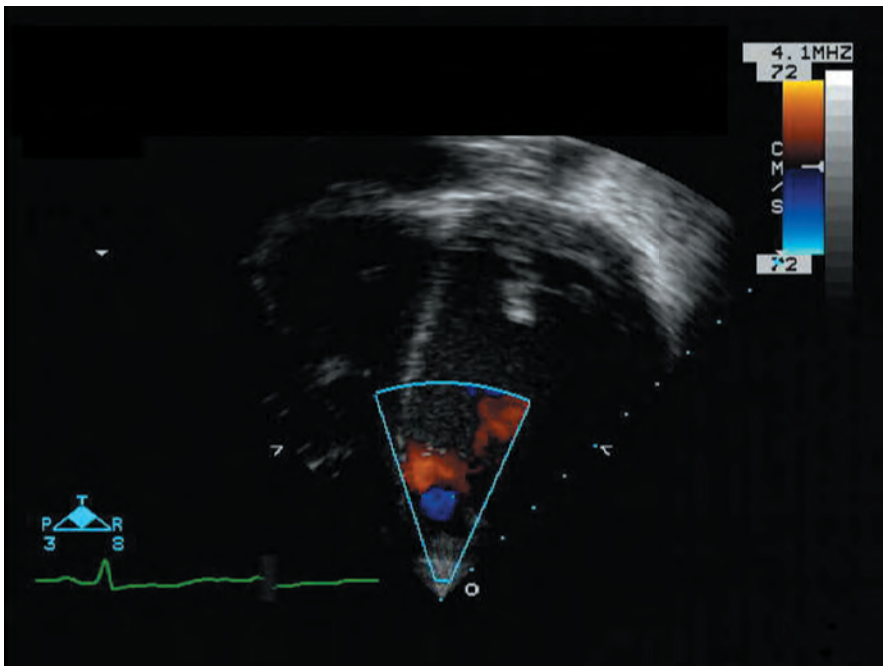
Echocardiography in cardiac mechanical support

Mechanical support for patients with heart failure can be used both as a bridge to transplantation and a bridge to recovery for myocarditis or other forms of acute, fulminant heart failure. In adults, it is being used as a destination therapy.

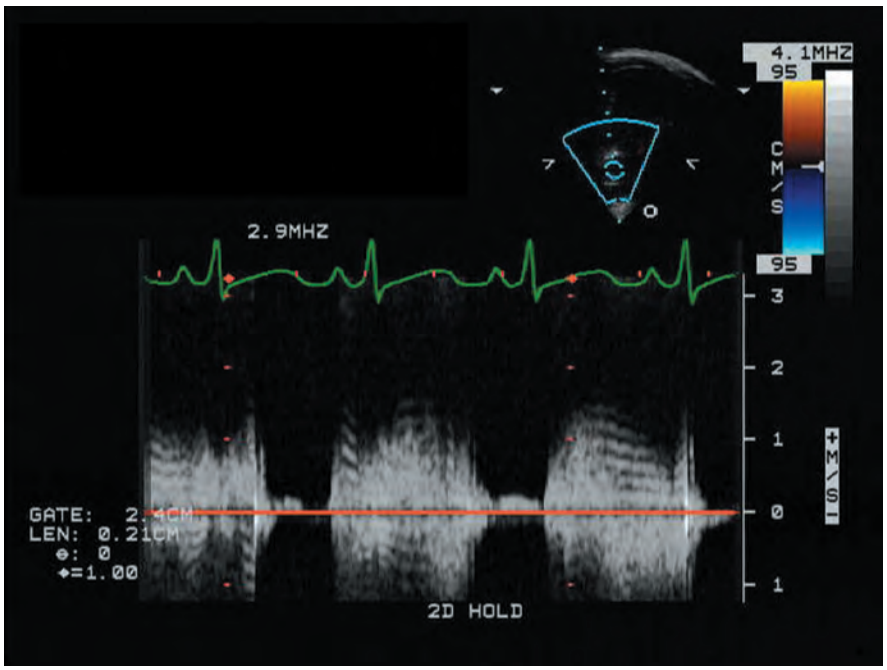
Echocardiographic evaluation of extracorporeal membrane oxygenation (ECMO)

ECMO has been used since the early 1970s to support neonates with cardiorespiratory derangements. Currently, its use is primarily as a bridge to recovery, in instances where mechanical support is expected to be necessary for no more than 14–21 days. It can provide pulmonary (through veno-venous cannulation) and/or cardiopulmonary (through veno-arterial cannulation) support, and can be rapidly deployed in children of almost any size. Typically, the venous cannula tip sits in the right atrium and the tip of the arterial cannula is in the aortic arch/innominate artery region. The primary modality of determining cannula position has been chest radiography, but in situations of abnormal cardiac anatomy or position (e.g., congenital diaphragmatic hernia) cannula position is often best determined and in some cases guided by echocardiography. Some take the position that echocardiography is superior in determining cannula position even in patients with normal anatomy and cardiac position [99].

Ongoing assessment for development of intracardiac thrombus should be undertaken at each opportunity (Video 34.3). Assessment of ventricular function in these patients, particularly with regard to determining timing of weaning/separating from support, remains difficult in the setting of the abnormal loading conditions, and there are few objective



(a)



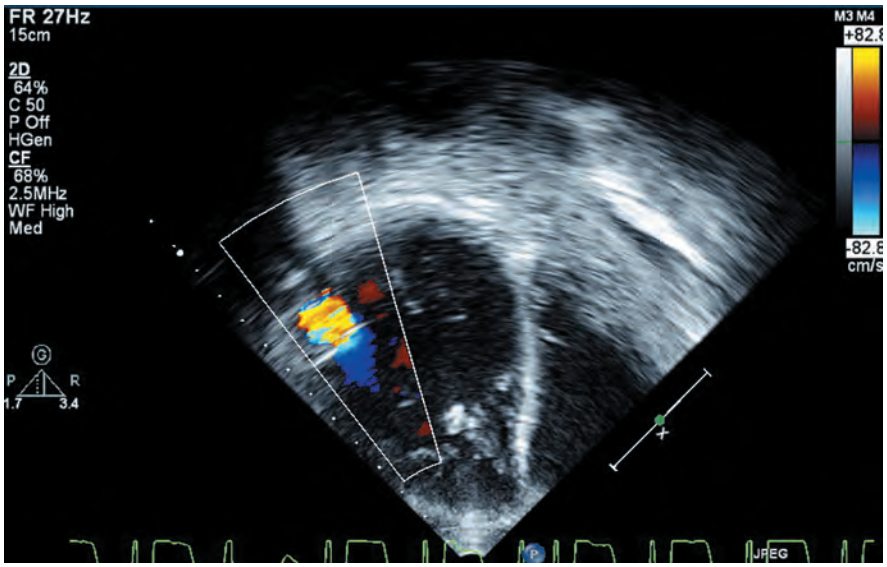
(b)

Figure 34.15 Transthoracic imaging of left ventricular assist device (LVAD) **(a,b)** and right ventricular assist device (RVAD) **(c,d)**, with flow seen in the LV apical inlet cannula by color Doppler (in apical 4-chamber view) (a) and spectral Doppler (b). In (c) the inlet cannula of the RVAD is seen (in apical view with anterior angulation) with blood flowing out of the ventricle and into the inlet cannula toward the VAD chamber; (d) demonstrates the gradient by spectral Doppler.

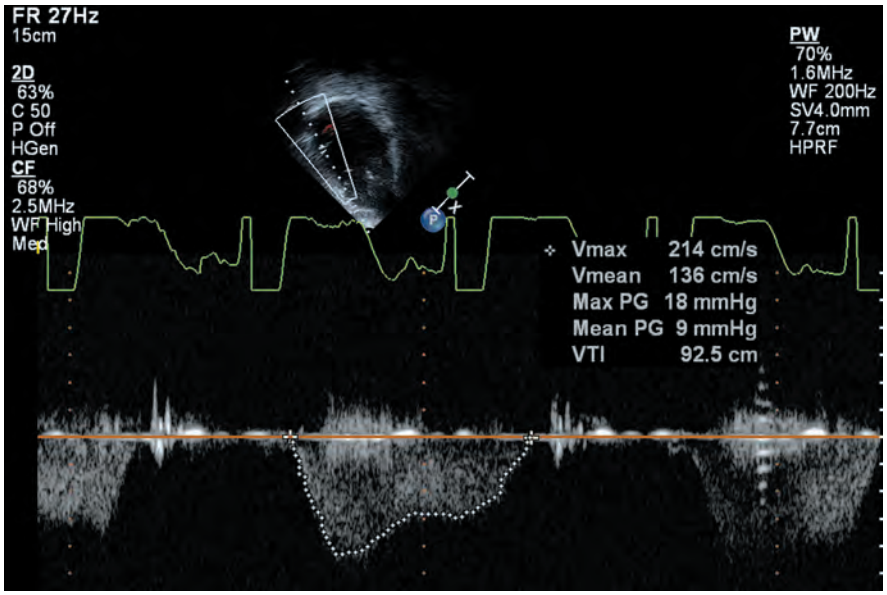
data to guide clinicians in these decisions. Currently, the most common parameters used are hemodynamic parameters and conventional echocardiographic measures (e.g., ejection fraction, aortic outflow velocity–time integrals) with perhaps some additional utility to be derived from tissue Doppler velocities and strain imaging [100].

Echocardiographic evaluation of ventricular assist devices (VADs)

In the recent past, ECMO has been the primary means of support for children with end-stage heart failure, chiefly because of the large size of VADs and the high incidence of thromboembolic events in children. Advances in pediatric-sized VADs



(c)



(d)

Figure 34.15 (*Continued*)

have led to increased utilization. The FDA recently approved the pulsatile-flow, pneumatic-driven device Berlin Heart EXCOR VAD (Berlin Heart AG, Berlin, Germany), following a trial performed with investigational device exemptions [101,102]. This review will focus on the imaging of extracorporeal pulsatile devices such as the EXCOR. Implantable, continuous-flow devices, such as the HeartWare HVAD, are being used with increasing frequency in children as small as 12 kg, but experience is more limited.

The use of biventricular systems is more common in pediatrics, particularly in patients with congenital heart disease [103]. For LVAD support, a cannula is typically placed through a hole made in the LV apex (inlet cannula), with unidirectional flow from the LV apical cannula into the device's blood chamber and then expulsion of blood into the ascending aorta through a long outlet cannula and graft (Figure 34.12a,b). RVAD cannulation occurs through the right atrium, with ejection of blood into the main pulmonary artery.

An overview of the suggested echocardiographic evaluation of patients receiving VADs is provided in Table 34.4 [104]. Preoperative or intraoperative echocardiography findings can greatly influence surgical and medical management in these patients. Such important findings may include the presence of a patent foramen ovale (PFO), aortic regurgitation, intracavitary thrombus, and RV dysfunction [105]. As the LV and LA pressures fall with initiation of VAD flow, right-to-left shunting at the PFO can result in systemic arterial desaturation and increased risk of embolus [105,106]. The PFO is typically closed surgically

or with a device in this setting. Aortic regurgitation can become an important phenomenon; with normal VAD function, the ventricular pressure is low and the aortic valve may remain closed (Video 34.4). Regurgitation creates a circulatory loop with increased device preload, decreased effective forward output, and alteration in pump function. The practice in some adult centers is to repair, replace, or oversew the aortic valve in the presence of aortic regurgitation [105,107,108]; this has not been reported in children. Pre- and intraoperative evaluation should also include careful evaluation for intracardiac thrombus. The most common locations for thrombus are in the LA appendage, and also the LV apex (which is typically the site of the inlet cannula placement).

Right ventricular function is assessed pre- and intraoperatively by both transthoracic and transesophageal echocardiography (TEE). Evaluation of RV function is often qualitative, although RV fractional area of change (FAC) may be used to quantitate RV systolic function (Figure 34.13a,b; Video 34.5). Those with an RV FAC of less than 20% may develop progressive RV failure with initiation of LVAD therapy [105]. Dilation of the RV with progressive tricuspid regurgitation as seen on intraoperative TEE is an indication of RV failure. This may lead to a sequence of decreased pulmonary venous return, collapse of the LA and LV, potential obstruction of the inflow cannula, and air in the aorta associated with continued VAD pumping [105]. Evidence of RV failure can be an indication for the addition of further ionotropic or pulmonary vasodilator therapy or institution of RV mechanical support.

Intraoperative assessment during VAD placement also includes evaluation for air in the outflow cannula and assessment of inlet cannula position [105]. Significant angulation of the inlet cannula can create inflow obstruction. Inlet cannula obstruction can be evaluated by color and spectral Doppler, with flow being laminar and unidirectional in the setting of normal inlet cannula function (Videos 34.6 and 34.7).

Postoperative evaluation of the patient with a VAD includes evaluation of LV decompression (Figure 34.14a–d). Additionally, images should include documentation of cannula position by 2D imaging, color flow, and spectral Doppler flow (Figure 34.15a–d; Video 34.6). Additional assessment includes RV function and evaluation for pericardial effusion/tamponade (Videos 34.8 and 34.9), in addition to assessment for aortic regurgitation.

Conclusion

Echocardiography remains the most commonly used modality to evaluate ventricular size and function. Advances in technology allow more information to be gained regarding cardiac performance in patients with DCM and myocarditis. Even with these advances in technology, it remains imperative to collect data on individual patients and the cardiomyopathy population as a whole in an organized, reproducible, and meticulous manner. Attention to detail in terms of technical considerations, image quality, measurements, and acquisition of quantitative data is critically important. Sonographers and cardiologists alike should strive to acquire information in a way that allows confidence in both clinical decision-making and research data analysis. Newer modalities that have a role in clinical research even now, and that may eventually become a larger part of clinical practice, include strain analysis by color Doppler and/or speckle-tracking and 3D imaging, as improvements in frame rate occur (especially important in pediatrics).

Videos

To access the videos for this chapter, please go to www.lai-echo.com.

Video 34.1 Two-dimensional and M-mode echocardiography in the parasternal short-axis view of a patient with dilated cardiomyopathy.

Video 34.2 Apical 4-chamber view of a patient with dilated cardiomyopathy.

Video 34.3 Apical 4-chamber view of a large thrombus in the left ventricular cavity, possibly also involving the left atrium. Note the decompressing cannula across the atrial septum, terminating in the left atrium.

Video 34.4 Imaging of the aortic valve in a patient with a left ventricular assist device. The aortic valve does not open and there is mild aortic regurgitation.

Video 34.5 Right ventricle focused apical 4-chamber view demonstrating a dilated right atrium and ventricle, with decreased right ventricular function.

Video 34.6 Imaging of the inlet cannula in the apex of the left ventricle in patient with a left ventricular assist device demonstrating color flow and Doppler evaluation of the inlet cannula.

Video 34.7 Imaging of the inlet cannula in the apex of the left ventricle in patient with a left ventricular assist device demonstrating color flow and Doppler evaluation of the inlet cannula.

Video 34.8 Imaging of a large pericardial thrombus in a patient with a left ventricular assist device: apical 4-chamber view.

Video 34.9 Imaging of a large pericardial thrombus in a patient with a left ventricular assist device: parasternal short-axis view.

References

1 Richardson P, McKenna W, Bristow M, et al. Report of the 1995 World Health Organization/International Society and Federation of Cardiology Task Force on the Definition and Classification of Cardiomyopathies. *Circulation* 1996;**93**:841–842.
2 Hershberger RE, Cowan J, Morales A, et al. Progress with genetic cardiomyopathies: screening, counseling, and testing in

dilated, hypertrophic, and arrhythmogenic right ventricular dysplasia/cardiomyopathy. *Circ Heart Fail* 2009;**2**:253–261.
3 Maron BJ, Towbin JA, Thiene G, et al. Contemporary definitions and classification of the cardiomyopathies: an American Heart Association Scientific Statement from the Council on Clinical Cardiology, Heart Failure and Transplantation Committee; Quality of Care and Outcomes Research and Functional Genomics and Translational Biology Interdisciplinary Working Groups; and Council on Epidemiology and Prevention. *Circulation* 2006;**113**:1807–1816.
4 Lipshultz SE, Sleeper LA, Towbin JA, et al. The incidence of pediatric cardiomyopathy in two regions of the United States. *N Engl J Med* 2003;**348**:1647–1655.
5 Nugent AW, Daubeney PE, Chondros P, et al. The epidemiology of childhood cardiomyopathy in Australia. *N Engl J Med* 2003;**348**:1639–1646.
6 Rakar S, Sinagra G, Di Lenarda A, et al. Epidemiology of dilated cardiomyopathy. A prospective post-mortem study of 5252 necropsies. The Heart Muscle Disease Study Group. *Eur Heart J* 1997;**18**:117–123.
7 Codd MB, Sugrue DD, Gersh BJ, et al. Epidemiology of idiopathic dilated and hypertrophic cardiomyopathy. A population-based study in Olmsted County, Minnesota, 1975–1984. *Circulation* 1989;**80**:564–572.
8 Towbin JA, Lowe AM, Colan SD, et al. Incidence, causes, and outcomes of dilated cardiomyopathy in children. *JAMA* 2006;**296**:1867–1876.
9 Cox GF, Sleeper LA, Lowe AM, et al. Factors associated with establishing a causal diagnosis for children with cardiomyopathy. *Pediatrics* 2006;**118**:1519–1531.
10 Towbin JA, Bowles NE. The failing heart. *Nature* 2002;**415**:227–233.
11 McNally EM, Golbus JR, Puckelwartz MJ. Genetic mutations and mechanisms in dilated cardiomyopathy. *J Clin Invest* 2013;**123**:19–26.
12 Colucci WS. Molecular and cellular mechanisms of myocardial failure. *Am J Cardiol* 1997;**80**:15L–25L.
13 Krum H, Abraham WT. Heart failure. *Lancet* 2009;**373**:941–955.
14 Daubeney PE, Nugent AW, Chondros P, et al. Clinical features and outcomes of childhood dilated cardiomyopathy: results from a national population-based study. *Circulation* 2006;**114**:2671–2678.
15 Alvarez JA, Wilkinson JD, Lipshultz SE. Outcome predictors for pediatric dilated cardiomyopathy: a systematic review. *Prog Pediatr Cardiol* 2007;**23**:25–32.
16 Burch M, Siddiqi SA, Celermajer DS, et al. Dilated cardiomyopathy in children: determinants of outcome. *Br Heart J* 1994;**72**:246–250.
17 Matitiau A, Perez-Atayde A, Sanders SP, et al. Infantile dilated cardiomyopathy. Relation of outcome to left ventricular mechanics, hemodynamics, and histology at the time of presentation. *Circulation* 1994;**90**:1310–1318.
18 Wiles HB, McArthur PD, Taylor AB, et al. Prognostic features of children with idiopathic dilated cardiomyopathy. *Am J Cardiol* 1991;**68**:1372–1376.
19 Azevedo VM, Santos MA, Albanesi Filho FM, et al. Outcome factors of idiopathic dilated cardiomyopathy in children – a long-term follow-up review. *Cardiol Young* 2007;**17**:175–184.
20 McMahon CJ, Nagueh SF, Eapen RS, et al. Echocardiographic predictors of adverse clinical events in children with dilated cardiomyopathy: a prospective clinical study. *Heart* 2004;**90**:908–915.
21 Sivasankaran S, Sharland GK, Simpson JM. Dilated cardiomyopathy presenting during fetal life. *Cardiol Young* 2005;**15**:409–416.
22 Yinon Y, Yagel S, Hegesh J, et al. Fetal cardiomyopathy – in utero evaluation and clinical significance. *Prenat Diagn* 2007;**27**:23–28.
23 Aretz HT, Billingham ME, Edwards WD, et al. Myocarditis. A histopathologic definition and classification. *Am J Cardiovasc Pathol* 1987;**1**:3–14.
24 Baughman KL. Diagnosis of myocarditis: death of Dallas criteria. *Circulation* 2006;**113**:593–595.
25 Mahrholdt H, Goedecke C, Wagner A, et al. Cardiovascular magnetic resonance assessment of human myocarditis: a comparison to histology and molecular pathology. *Circulation* 2004;**109**:1250–1258.
26 Skouri HN, Dec GW, Friedrich MG, et al. Noninvasive imaging in myocarditis. *J Am Coll Cardiol* 2006;**48**:2085–2093.
27 Lurz P, Eitel I, Adam J, et al. Diagnostic performance of CMR imaging compared with EMB in patients with suspected myocarditis. *JACC Cardiovasc Imaging* 2012;**5**:513–524.
28 English RF, Janosky JE, Ettedgui JA, et al. Outcomes for children with acute myocarditis. *Cardiol Young* 2004;**14**:488–493.
29 Amabile N, Fraisse A, Bouvenot J, et al. Outcome of acute fulminant myocarditis in children. *Heart* 2006;**92**:1269–1273.
30 Kawai C. From myocarditis to cardiomyopathy: mechanisms of inflammation and cell death: learning from the past for the future. *Circulation* 1999;**99**:1091–1100.
31 Pankuweit S, Portig I, Maisch B. Pathophysiology of cardiac inflammation: molecular mechanisms. *Herz* 2002;**27**:669–676.
32 Calabrese F, Thiene G. Myocarditis and inflammatory cardiomyopathy: microbiological and molecular biological aspects. *Cardiovasc Res* 2003;**60**:11–25.
33 Kirk R, Dipchand AI, Edwards LB, et al. The Registry of the International Society for Heart and Lung Transplantation: fifteenth pediatric heart transplantation report – 2012. *J Heart Lung Transplant* 2012;**31**:1065–1072.
34 Denfield SW. Cardiac transplant coronary allograft vasculopathy in children: Achilles' heel. *Congenit Heart Dis* 2012;**7**:301.
35 Foerster SR, Canter CE, Cinar A, et al. Ventricular remodeling and survival are more favorable for myocarditis than for idiopathic dilated cardiomyopathy in childhood: an outcomes study from the Pediatric Cardiomyopathy Registry. *Circ Heart Fail* 2010;**3**:689–697.
36 Rajagopal SK, Almond CS, Laussen PC, et al. Extracorporeal membrane oxygenation for the support of infants, children, and young adults with acute myocarditis: a review of the Extracorporeal Life Support Organization registry. *Crit Care Med* 2010;**38**:382–387.
37 Miller CA, Fildes JE, Ray SG, et al. Non-invasive approaches for the diagnosis of acute cardiac allograft rejection. *Heart* 2013;**99**:445–453.
38 Subherwal S, Kobashigawa JA, Cogert G, et al. Incidence of acute cellular rejection and non-cellular rejection in cardiac transplantation. *Transplant Proc* 2004;**36**:3171–3172.
39 Boucek MM, Aurora P, Edwards LB, et al. Registry of the International Society for Heart and Lung Transplantation: tenth official pediatric heart transplantation report – 2007. *J Heart Lung Transplant* 2007;**26**:796–807.
40 Di Filippo S, Semiond B, Roriz R, et al. Non-invasive detection of coronary artery disease by dobutamine-stress echocardiography in children after heart transplantation. *J Heart Lung Transplant* 2003;**22**:876–882.

41 Kimball TR, Witt SA, Daniels SR. Dobutamine stress echocardiography in the assessment of suspected myocardial ischemia in children and young adults. *Am J Cardiol* 1997;**79**:380–384.
42 Spes CH, Klauss V, Mudra H, et al. Diagnostic and prognostic value of serial dobutamine stress echocardiography for noninvasive assessment of cardiac allograft vasculopathy: a comparison with coronary angiography and intravascular ultrasound. *Circulation* 1999;**100**:509–515.
43 Sluysmans T, Colan SD. Theoretical and empirical derivation of cardiovascular allometric relationships in children. *J Appl Physiol* 2005;**99**:445–457.
44 Lopez L, Colan SD, Frommelt PC, et al. Recommendations for quantification methods during the performance of a pediatric echocardiogram: a report from the Pediatric Measurements Writing Group of the American Society of Echocardiography Pediatric and Congenital Heart Disease Council. *J Am Soc Echocardiogr* 2010;**23**:465–495; quiz 576–577.
45 Tani LY, Minich LL, Williams RV, et al. Ventricular remodeling in children with left ventricular dysfunction secondary to various cardiomyopathies. *Am J Cardiol* 2005;**96**:1157–1161.
46 Cohn JN, Ferrari R, Sharpe N. Cardiac remodeling – concepts and clinical implications: a consensus paper from an international forum on cardiac remodeling. *J Am Coll Cardiol* 2000;**35**:569–582.
47 Colan SD, Borow KM, Neumann A. Left ventricular end-systolic wall stress-velocity of fiber shortening relation: a load-independent index of myocardial contractility. *J Am Coll Cardiol* 1984;**4**:715–724.
48 Hara Y, Hamada M, Hiwada K. Left ventricular end-systolic wall stress is a potent prognostic variable in patients with dilated cardiomyopathy. *Jpn Circ J* 1999;**63**:196–200.
49 Lester SJ, Tajik AJ, Nishimura RA, et al. Unlocking the mysteries of diastolic function: deciphering the Rosetta Stone 10 years later. *J Am Coll Cardiol* 2008;**51**:679–689.
50 Nagueh SF, Appleton CP, Gillebert TC, et al. Recommendations for the evaluation of left ventricular diastolic function by echocardiography. *J Am Soc Echocardiogr* 2009;**22**:107–133.
51 Taggart NW, Cetta F, O'Leary PW, et al. Left atrial volume in children without heart disease and in those with ventricular septal defect or patent ductus arteriosus or hypertrophic cardiomyopathy. *Am J Cardiol* 2010;**106**:1500–1504.
52 Eidem BW, McMahon CJ, Cohen RR, et al. Impact of cardiac growth on Doppler tissue imaging velocities: a study in healthy children. *J Am Soc Echocardiogr* 2004;**17**:212–221.
53 Mori K, Hayabuchi Y, Kuroda Y, et al. Left ventricular wall motion velocities in healthy children measured by pulsed wave Doppler tissue echocardiography: normal values and relation to age and heart rate. *J Am Soc Echocardiogr* 2000;**13**:1002–1011.
54 Rychik J, Tian ZY. Quantitative assessment of myocardial tissue velocities in normal children with Doppler tissue imaging. *Am J Cardiol* 1996;**77**:1254–1257.
55 Mishiro Y, Oki T, Yamada H, et al. Evaluation of left ventricular contraction abnormalities in patients with dilated cardiomyopathy with the use of pulsed tissue Doppler imaging. *J Am Soc Echocardiogr* 1999;**12**:913–920.
56 Eidem BW, McMahon CJ, Ayres NA, et al. Impact of chronic left ventricular preload and afterload on Doppler tissue imaging velocities: a study in congenital heart disease. *J Am Soc Echocardiogr* 2005;**18**:830–838.
57 Tei C, Ling LH, Hodge DO, et al. New index of combined systolic and diastolic myocardial performance: a simple and reproducible measure of cardiac function – a study in normals and dilated cardiomyopathy. *J Cardiol* 1995;**26**:357–366.
58 Eto G, Ishii M, Tei C, et al. Assessment of global left ventricular function in normal children and in children with dilated cardiomyopathy. *J Am Soc Echocardiogr* 1999;**12**:1058–1064.
59 Dujardin KS, Tei C, Yeo TC, et al. Prognostic value of a Doppler index combining systolic and diastolic performance in idiopathic-dilated cardiomyopathy. *Am J Cardiol* 1998;**82**:1071–1076.
60 Harjai KJ, Scott L, Vivekananthan K, et al. The Tei index: a new prognostic index for patients with symptomatic heart failure. *J Am Soc Echocardiogr* 2002;**15**:864–868.
61 Bargiggia GS, Bertucci C, Recusani F, et al. A new method for estimating left ventricular d*P*/d*t* by continuous wave Doppler-echocardiography. Validation studies at cardiac catheterization. *Circulation* 1989;**80**:1287–1292.
62 Paraskevaidis IA, Adamopoulos S, Tsiapras D, et al. Prognostic usefulness of echocardiographic dobutamine in younger (14 to 25 years) and older (40 to 55 years) patients with idiopathic dilated cardiomyopathy. *Am J Cardiol* 2004;**93**:251–255.
63 Gutierrez-Chico JL, Zamorano JL, Perez de Isla L, et al. Comparison of left ventricular volumes and ejection fractions measured by three-dimensional echocardiography versus by two-dimensional echocardiography and cardiac magnetic resonance in patients with various cardiomyopathies. *Am J Cardiol* 2005;**95**:809–813.
64 Shiota T, McCarthy PM, White RD, et al. Initial clinical experience of real-time three-dimensional echocardiography in patients with ischemic and idiopathic dilated cardiomyopathy. *Am J Cardiol* 1999;**84**:1068–1073.
65 Chuang ML, Hibberd MG, Salton CJ, et al. Importance of imaging method over imaging modality in noninvasive determination of left ventricular volumes and ejection fraction: assessment by two- and three-dimensional echocardiography and magnetic resonance imaging. *J Am Coll Cardiol* 2000;**35**:477–484.
66 Papavassiliou DP, Parks WJ, Hopkins KL, et al. Three-dimensional echocardiographic measurement of right ventricular volume in children with congenital heart disease validated by magnetic resonance imaging. *J Am Soc Echocardiogr* 1998;**11**:770–777.
67 Poutanen T, Jokinen E, Sairanen H, et al. Left atrial and left ventricular function in healthy children and young adults assessed by three dimensional echocardiography. *Heart* 2003;**89**:544–549.
68 Aoki M, Harada K, Ogawa M, et al. Quantitative assessment of right ventricular function using doppler tissue imaging in fetuses with and without heart failure. *J Am Soc Echocardiogr* 2004;**17**:28–35.
69 Chan LY, Fok WY, Wong JT, et al. Reference charts of gestation-specific tissue Doppler imaging indices of systolic and diastolic functions in the normal fetal heart. *Am Heart J* 2005;**150**:750–755.
70 Eidem BW, Edwards JM, Cetta F. Quantitative assessment of fetal ventricular function: establishing normal values of the myocardial performance index in the fetus. *Echocardiography* 2001;**18**:9–13.
71 Friedman D, Buyon J, Kim M, et al. Fetal cardiac function assessed by Doppler myocardial performance index (Tei Index). *Ultrasound Obstet Gynecol* 2003;**21**:33–36.
72 Hernandez-Andrade E, Lopez-Tenorio J, Figueroa-Diesel H, et al. A modified myocardial performance (Tei) index based on the use of valve clicks improves reproducibility of fetal left cardiac function assessment. *Ultrasound Obstet Gynecol* 2005;**26**:227–232.

73 Falkensammer CB, Paul J, Huhta JC. Fetal congestive heart failure: correlation of Tei-index and cardiovascular score. *J Perinat Med* 2001;**29**:390–398.

74 Huhta JC. Guidelines for the evaluation of heart failure in the fetus with or without hydrops. *Pediatr Cardiol* 2004;**25**:274–286.

75 Shah M, Anderson AS, Jayakar D, et al. Balloon-expandable stent placement for superior vena cava–right atrial stenosis after heart transplantation. *J Heart Lung Transplant* 2000;**19**:705–709.

76 Romano P, Mangion JM. The role of intraoperative transesophageal echocardiography in heart transplantation. *Echocardiography* 2002;**19**:599–604.

77 Anderson CA, Shernan SK, Leacche M, et al. Severity of intraoperative tricuspid regurgitation predicts poor late survival following cardiac transplantation. *Ann Thorac Surg* 2004;**78**:1635–1642.

78 Moran AM, Lipshultz SE, Rifai N, et al. Non-invasive assessment of rejection in pediatric transplant patients: serologic and echocardiographic prediction of biopsy-proven myocardial rejection. *J Heart Lung Transplant* 2000;**19**:756–764.

79 Mahle WT, Cardis BM, Ketchum D, et al. Reduction in initial ventricular systolic and diastolic velocities after heart transplantation in children: improvement over time identified by tissue Doppler imaging. *J Heart Lung Transplant* 2006;**25**:1290–1296.

80 Pauliks LB, Pietra BA, Kirby S, et al. Altered ventricular mechanics in cardiac allografts: a tissue Doppler study in 30 children without prior rejection events. *J Heart Lung Transplant* 2005;**24**:1804–1813.

81 Leonard GT, Jr., Fricker FJ, Pruett D, et al. Increased myocardial performance index correlates with biopsy-proven rejection in pediatric heart transplant recipients. *J Heart Lung Transplant* 2006;**25**:61–66.

82 Putzer GJ, Cooper D, Keehn C, et al. An improved echocardiographic rejection-surveillance strategy following pediatric heart transplantation. *J Heart Lung Transplant* 2000;**19**:1166–1174.

83 Tuzcu EM, Kapadia SR, Sachar R, et al. Intravascular ultrasound evidence of angiographically silent progression in coronary atherosclerosis predicts long-term morbidity and mortality after cardiac transplantation. *J Am Coll Cardiol* 2005;**45**:1538–1542.

84 Kobashigawa JA, Tobis JM, Starling RC. Multicenter intravascular ultrasound validation study among heart transplant recipients: outcomes after five years. *J Am Coll Cardiol* 2005;**45**:1532–1537.

85 Dent CL, Canter CE, Hirsch R, et al. Transplant coronary artery disease in pediatric heart transplant recipients. *J Heart Lung Transplant* 2000;**19**:240–248.

86 Nicolas RT, Kort HW, Balzer DT, et al. Surveillance for transplant coronary artery disease in infant, child and adolescent heart transplant recipients: an intravascular ultrasound study. *J Heart Lung Transplant* 2006;**25**:921–927.

87 Pahl E, Crawford SE, Swenson JM, et al. Dobutamine stress echocardiography: experience in pediatric heart transplant recipients. *J Heart Lung Transplant* 1999;**18**:725–732.

88 Scheurer M, Bandisode V, Ruff P, et al. Early experience with real-time three-dimensional echocardiographic guidance of right ventricular biopsy in children. *Echocardiography* 2006;**23**:45–49.

89 Bedanova H, Necas J, Petrikovits E, et al. Echo-guided endomyocardial biopsy in heart transplant recipients. *Transpl Int* 2004;**17**:622–625.

90 Bradley DJ, Bradley EA, Baughman KL, et al. Cardiac resynchronization and death from progressive heart failure: a meta-analysis of randomized controlled trials. *JAMA* 2003;**289**:730–740.

91 Gorcsan J, III, Abraham T, Agler DA, et al. Echocardiography for cardiac resynchronization therapy: recommendations for performance and reporting – a report from the American Society of Echocardiography Dyssynchrony Writing Group endorsed by the Heart Rhythm Society. *J Am Soc Echocardiogr*.2008;**21**:191–213.

92 Leenders GE, Cramer MJ, Bogaard MD, et al. Echocardiographic prediction of outcome after cardiac resynchronization therapy: conventional methods and recent developments. *Heart Fail Rev* 2011;**16**:235–250.

93 Cazeau S, Bordachar P, Jauvert G, et al. Echocardiographic modeling of cardiac dyssynchrony before and during multisite stimulation: a prospective study. *Pacing Clin Electrophysiol* 2003;**26**:137–143.

94 Hawkins NM, Petrie MC, MacDonald MR, et al. Selecting patients for cardiac resynchronization therapy: electrical or mechanical dyssynchrony? *Eur Heart J* 2006;**27**:1270–1281.

95 Vitarelli A, Franciosa P, Conde Y, et al. Echocardiographic assessment of ventricular asynchrony in dilated cardiomyopathy and congenital heart disease: tools and hopes. *J Am Soc Echocardiogr* 2005;**18**:1424–1439.

96 Pitzalis MV, Iacoviello M, Romito R, et al. Cardiac resynchronization therapy tailored by echocardiographic evaluation of ventricular asynchrony. *J Am Coll Cardiol* 2002;**40**:1615–1622.

97 Yu CM, Fung WH, Lin H, et al. Predictors of left ventricular reverse remodeling after cardiac resynchronization therapy for heart failure secondary to idiopathic dilated or ischemic cardiomyopathy. *Am J Cardiol* 2003;**91**:684–688.

98 Friedberg MK, Mertens L. Echocardiographic assessment of ventricular synchrony in congenital and acquired heart disease in children. *Echocardiography* 2013;**30**:460–471.

99 Thomas TH, Price R, Ramaciotti C, et al. Echocardiography, not chest radiography, for evaluation of cannula placement during pediatric extracorporeal membrane oxygenation. *Pediatr Crit Care Med* 2009;**10**:56–59.

100 Aissaoui N, Guerot E, Combes A, et al. Two-dimensional strain rate and Doppler tissue myocardial velocities: analysis by echocardiography of hemodynamic and functional changes of the failed left ventricle during different degrees of extracorporeal life support. *J Am Soc Echocardiogr* 2012;**25**:632–640.

101 Fraser CD, Jr., Jaquiss RD, Rosenthal DN, et al. Prospective trial of a pediatric ventricular assist device. *N Engl J Med* 2012;**367**:532–541.

102 Morales DL, Almond CS, Jaquiss RD, et al. Bridging children of all sizes to cardiac transplantation: the initial multicenter North American experience with the Berlin Heart EXCOR ventricular assist device. *J Heart Lung Transplant* 2011;**30**:1–8.

103 Jefferies JL, Price JF, Morales DL. Mechanical support in childhood heart failure. *Heart Fail Clin* 2010;**6**:559–573, x.

104 Sachdeva R, Frazier EA, Jaquiss RD, et al. Echocardiographic evaluation of ventricular assist devices in pediatric patients. *J Am Soc Echocardiogr* 2013;**26**:41–49.

105 Scalia GM, McCarthy PM, Savage RM, et al. Clinical utility of echocardiography in the management of implantable ventricular assist devices. *J Am Soc Echocardiogr* 2000;**13**:754–763.

106 Liao KK, Miller L, Toher C, et al. Timing of transesophageal echocardiography in diagnosing patent foramen ovale in patients supported with left ventricular assist device. *Ann Thorac Surg* 2003;**75**:1624–1626.

107 Feldman CM, Silver MA, Sobieski MA, et al. Management of aortic insufficiency with continuous flow left ventricular assist devices: bioprosthetic valve replacement. *J Heart Lung Transplant* 2006;**25**:1410–1412.

108 Rao V, Slater JP, Edwards NM, et al. Surgical management of valvular disease in patients requiring left ventricular assist device support. *Ann Thorac Surg* 2001;**71**:1448–1453.

109 Soliman OI, Geleijnse ML, Theuns DA, et al. Usefulness of left ventricular systolic dyssynchrony by real-time three-dimensional echocardiography to predict long-term response to cardiac resynchronization therapy. *Am J Cardiol* 2009;**103**:1586–1591.

110 Bax JJ, Bleeker GB, Marwick TH, et al. Left ventricular dyssynchrony predicts response and prognosis after cardiac resynchronization therapy. *J Am Coll Cardiol* 2004;**44**:1834–1840.

111 Yu CM, Zhang Q, Fung JW, et al. A novel tool to assess systolic asynchrony and identify responders of cardiac resynchronization therapy by tissue synchronization imaging. *J Am Coll Cardiol* 2005;**45**:677–684.

112 Suffoletto MS, Dohi K, Cannesson M, et al. Novel speckle-tracking radial strain from routine black-and-white echocardiographic images to quantify dyssynchrony and predict response to cardiac resynchronization therapy. *Circulation*. 2006;**113**:960–968.

CHAPTER 35

Hypertrophic Cardiomyopathy

Colin J. McMahon[1] and Javiar Ganame[2]

[1]Department of Paediatric Cardiology, Our Lady's Hospital for Sick Children, Crumlin, Dublin, Ireland
[2]Department of Medicine, Division of Cardiology, McMaster University, Hamilton, ON, Canada

Introduction

Hypertrophic cardiomyopathy (HCM) is defined as myocardial hypertrophy that occurs in the absence of other disease capable of producing the magnitude of wall thickening that is evident. HCM, generally a disease of the sarcomere, represents the second most common cardiomyopathy in children [1]. It is genetic in origin and occurs in either sporadic or familial forms [2,3]. It is the most common cause of cardiac death in children and young adults [4]. The hallmark histologic findings of HCM are myocyte disarray and fibrosis [5]. Since its initial description, there have been significant advances in the diagnosis of HCM, in our understanding of its complex pathophysiology, and in its outcome and management. Echocardiography has played a crucial role in these advances. HCM represents a challenging condition given the marked genetic and phenotypic heterogeneity in clinical manifestations, disease course, age of onset, pattern and extent of left ventricular hypertrophy (LVH), degree of obstruction, and risk for sudden cardiac death.

HCM prevalence, etiology and genetics

Primary hypertrophic cardiomyopathy

The estimated prevalence of HCM among adults is reported to be 0.2% of the population [6]. Primary hypertrophic cardiomyopathy (also known as sarcomeric HCM) is an autosomal dominant condition characterized by LVH with occasional right ventricular involvement [1,7]. The first gene for familial HCM was localized to chromosome 14q11.2-q12 [8]. Over the past 20 years, more than 1000 distinct mutations have been identified in more than 20 genes [9–16]. Most mutations code for sarcomere proteins, including β-myosin heavy chain, cardiac myosin-binding protein C, myosin essential light chains, myosin regulatory light chain 2, cardiac troponin T, cardiac troponin I, α-tropomyosin, z-disc components, telethonin, muscle LIM protein, and actin. Sarcomere mutations are found in 60–70% of adult and pediatric patients with a family history of HCM, and also 30–40% of sporadic cases [17]. The identification of a pathogenic sarcomere gene mutation establishes a definitive diagnosis of HCM and the exact genetic etiology of disease. This information provides insight into the patient's prognosis and guidance in the management of their family. However, because of the genetic and clinical heterogeneity seen in HCM, robust prediction of outcome based on the genotype has proven elusive. Nonetheless, adverse outcomes appear more prominent in HCM patients with sarcomere mutations than in patients without an identifiable mutation [17,18].

Secondary hypertrophic cardiomyopathy

Specific metabolic, mitochondrial, and syndromic diseases (e.g., Noonan and Leopard syndromes) may manifest a "secondary HCM" [19]. In spite of the phenotypic similarities, secondary HCMs are very different from primary HCM. Secondary HCMs usually present in infancy (up to 15% of infants with HCM) and have a poor outcome. Typically, patients with secondary HCM develop concentric HCM, often accompanied by marked involvement of the right ventricle [20,21]. Metabolic screening and, in certain cases, muscle biopsy may help delineate the etiology. Metabolic diseases associated with secondary HCM include Fabry (glucocerebrosidase deficiency) disease, Danon disease, and Pompe (acid-maltase deficiency) disease [22–25].

Fabry disease is an X-linked recessive disorder that accounts for 4% of cases of unexplained LVH in young men [22]. Symptoms usually start in the first decade of life, with acroparesthesiae, heat intolerance, and development of cutaneous angiokeratomas. From the second decade onwards, patients develop proteinuria and neurologic manifestations, including vestibular and hearing disturbances and autonomic dysfunction. Cardiac involvement is present early in life but is usually not detected clinically until the third or fourth decade [23]. Early cardiomyopathy is characterized by concentric remodeling, progressing later to concentric biventricular hypertrophy, which causes diastolic dysfunction. The mitral and aortic valves are often

Echocardiography in Pediatric and Congenital Heart Disease: From Fetus to Adult, Second Edition. Edited by Wyman W. Lai, Luc L. Mertens, Meryl S. Cohen and Tal Geva.
© 2016 John Wiley & Sons, Ltd. Published 2016 by John Wiley & Sons, Ltd.
Companion website: www.lai-echo.com

thickened and distorted, resulting in regurgitation. Elevated serum levels of the enzyme α-galactosidase A confirm the diagnosis. This is of particular relevance because two recombinant enzyme preparations are approved for the treatment of Fabry disease.

Danon disease is an X-linked deficiency of lysosome-associated membrane protein type 2. It can present at variable ages as multisystemic disease with skeletal myopathy, mental retardation, and cardiomyopathy. Cardiac involvement is characterized by massive hypertrophy, ventricular pre-excitation, and heart failure. Disease clinically confined to the heart is described in some cases with later onset [24].

Pompe disease (acid-maltase deficiency) is an autosomal recessive disorder that may also result in HCM in infancy [25]. It is associated with severe skeletal muscle hypotonia, progressive weakness, hepatomegaly, and macroglossia. The electrocardiogram (ECG) typically shows broad, high-voltage QRS complexes and the concentric LVH is typically severe.

Mitochondrial diseases may also result in HCM [26]. Friedreich's ataxia is a progressive form of spinocerebellar degeneration that results from deficiency of the mitochondrial protein frataxin. Friedreich's ataxia typically gives rise to HCM, hence all young adults with this condition should undergo routine screening. The LVH seen is typically concentric [27,28]. LV cavity dilation and systolic dysfunction occur in the third and fourth decades, often leading to clinical deterioration [29].

Anatomy

There is marked heterogeneity in the pattern and extent of LVH in HCM. LVH involves the basal and mid-interventricular septum and is asymmetric with a ratio of septal to infero-lateral wall thickness of >1.3 in 60% of children and adolescents with primary HCM [2,3,30]. Up to 50% of infants with HCM demonstrate concentric LVH [20,21]. However, recently spiral forms of HCM with variable extension of hypertrophy have been described [31]. Less common forms of HCM are limited to the mid or apical segments. In HCM, the LV cavity is typically small. Hypertrophy can develop early in life or in childhood or adolescence depending on the etiology. The mitral valve may also be variably involved. The development of septal hypertrophy and anterior displacement of the mitral apparatus frequently leads to narrowing of the subaortic region and creation of a dynamic pressure gradient across the left ventricular outflow tract (LVOT) [33,34].

Pathophysiology

There continues to be considerable controversy about the cause and significance of the LVOT gradient in HCM. Whether there is true obstruction to LV ejection or whether the gradient is simply the consequence of vigorous LV emptying remains a matter of debate. Most now favor the view that a true mechanical impediment to LV ejection occurs when an outflow tract gradient is present, and that the pressure gradient results from anterior and apical displacement of the mitral valve apparatus contacting the interventricular septum in mid-systole [34,35].

One of the most important features of HCM is diastolic dysfunction. Abnormalities of diastolic filling are largely independent of the extent and distribution of myocardial hypertrophy. Even patients with mild localized hypertrophy may show marked diastolic dysfunction, suggesting that the myopathic process may occur in ventricular regions that are not visibly hypertrophied. Diastolic dysfunction occurs despite a normal or small LV cavity and appears to be related to abnormalities of LV relaxation and distensibility [36]. Abnormal early diastolic filling is thought to be related to a number of factors, including abnormal calcium transport, subendocardial ischemia, non-uniformity of load, and LVOT obstruction [37]. Late diastolic filling is altered when LV distensibility is impaired; as a consequence, ventricular filling pressures rise. Abnormal distensibility may result from myocardial fibrosis or cellular disarray [38].

Myocardial ischemia may also occur in patients with HCM. Proposed causes include impaired vasodilator reserve (perhaps related to the thickened and narrowed intramural coronary arteries), increased oxygen demand, and elevated LV diastolic pressures with resultant subendocardial ischemia [39]. In children in particular, compression of intramyocardial segments of the left anterior descending coronary artery (so-called myocardial bridging) may predispose to myocardial ischemia and sudden death [40].

Diagnosis

Clinical manifestations

Most patients with HCM are asymptomatic or only mildly symptomatic. Diagnosis is frequently made when a relative of an affected patient is screened or when a routine electrocardiogram is abnormal. Unfortunately, the first clinical manifestation in some individuals may be sudden cardiac death [3]. For this reason, it is crucial to identify the disease in childhood at the earliest possible time because the mortality rate is higher in younger individuals (1–2% per year). Syncope and sudden death are associated with recreational and competitive sports in patients with HCM, hence diagnosis typically results in exclusion from these activities.

The most common symptom in patients with HCM is dyspnea, which is secondary to elevated LV end-diastolic pressure. Syncope may be a precursor of sudden cardiac death. In infants with HCM, congestive heart failure and failure to thrive are frequently the first clinical manifestations [21]. Angina pectoris with exercise is present in 50% of symptomatic adult patients.

Differential diagnosis

A fundamental step in the evaluation of a child with suspected HCM is to rule out underlying conditions that may masquerade as HCM. LVOT obstruction secondary to subaortic, valvar or supravalvar aortic stenosis, or coarctation of the aorta must always be excluded. Differentiation between HCM and a fixed subaortic stenosis can be particularly challenging. The absence of a muscular (tunnel-like) or membranous subaortic narrowing adjacent to the aortic valve should be sought in multiple views [34,41]. In patients with fixed subaortic obstruction, Doppler echocardiography shows an early peak gradient generally associated with some degree of aortic regurgitation. Occasionally transesophegeal echocardiography (TEE) is needed to delineate the LVOT anatomy adequately.

Systemic hypertension may cause concentric LV hypertrophy and should be differentiated from HCM. Other conditions may mimic asymmetric septal HCM in children, including LV false tendons. Prominent false tendons may lead to overestimation of septal wall thickness, especially when performing measurements with M-mode echocardiography. Disproportionate asymmetric septal hypertrophy may be present in 10–15% of children with pulmonary hypertension secondary to congenital heart disease [42].

Athlete's heart

Diagnosis of HCM in athletes is particularly important given the high risk of sudden death in affected individuals engaging in competitive sports. The distinction between HCM and "athlete's heart" is often difficult. Table 35.1 outlines some of the distinguishing features of athlete's heart. The athlete's heart is characterized by LV hypertrophy, which may be difficult to differentiate from HCM [43,44]. However, athletes typically have a dilated LV with eccentric hypertrophy (Video 35.1). Importantly, reduced systolic and early diastolic myocardial velocities (<9 cm/s) are seen in patients with HCM but are normal or supranormal in athletes [45]. Exercise stress testing may help differentiate HCM from cardiovascular adaptation to training. Athletes frequently have a peak oxygen consumption >120% of predicted whereas the majority of patients with HCM have abnormally low indices. Finally, periods of deconditioning (3–6 months) will result in regression of LVH in athletes but not patients with HCM.

Table 35.1 Echocardiographic features of athlete's heart

End-diastolic septal thickness	
Adolescents	<12 mm (males) <11 mm (females)
Adults	<16 mm
Left ventricular cavity	>55 mm
Tissue Doppler velocities	Normal
Exercise testing MVO2	>120% normal
Deconditioning	Normalization of LV dimensions

Family screening and preclinical diagnosis

All first-degree relatives of patients with HCM should be screened for this condition, with detailed family history, 12-lead electrocardiogram, and an echocardiogram. Hypertrophy typically develops during puberty, so repeat imaging at yearly intervals during childhood and adolescence is recommended in relatives of affected individuals. In adults, repeat imaging can be performed at longer time intervals of 3–5 years because of the possibility of later development of hypertrophy [46]. Patients with HCM secondary to mutations in myosin-binding protein C generally develop hypertrophy in their fourth or fifth decade of life.

Performance of genetic testing in all those at risk remains controversial given the suboptimal diagnostic yield and only modest association between genotype and outcome. Genetic testing is very useful in relatives of those affected individuals in whom a mutation has been found because detection of the same mutation automatically leads to the diagnosis of HCM. Conversely, absence of the mutation excludes the disease and obviates the need for long-term surveillance.

The diagnosis of familial HCM in the absence of genetic mutation can be made when:

1. Maximal wall thickness is two standard deviations above the mean for age and body surface area.
2. Septal thickness is ≥15 mm or posterior wall thickness is ≥13 mm (in adults).
3. Electrocardiographic abnormalities and septal thickness ≥14 mm or posterior thickness ≥12 mm are present (in adults) [47].

Patients with HCM resulting from mutations in troponin T often manifest with only mild LVH but are at high risk of sudden death. Strict adherence to previous criteria would not permit the diagnosis of HCM in these individuals. Thus, care should be taken to assess the morphologic findings in the context of the family history. The electrocardiogram is usually abnormal in this setting [47]. Studies with cardiac magnetic resonance (CMR) have shown increased sensitivity over echocardiography for the preclinical diagnosis of HCM, especially when there is localized rather than diffuse hypertrophy [48].

Echocardiographic evaluation of HCM

Key elements

The goals of the echocardiographic examination in HCM are as follows:

- Assessment for structural cardiovascular disease that may cause ventricular hypertrophy.
- Accurate measurements of ventricular septal and free wall thickness.
- Assessment of LV global and regional systolic performance.
- Assessment of diastolic function.
- Assessment of presence and severity and mechanism of mitral regurgitation.

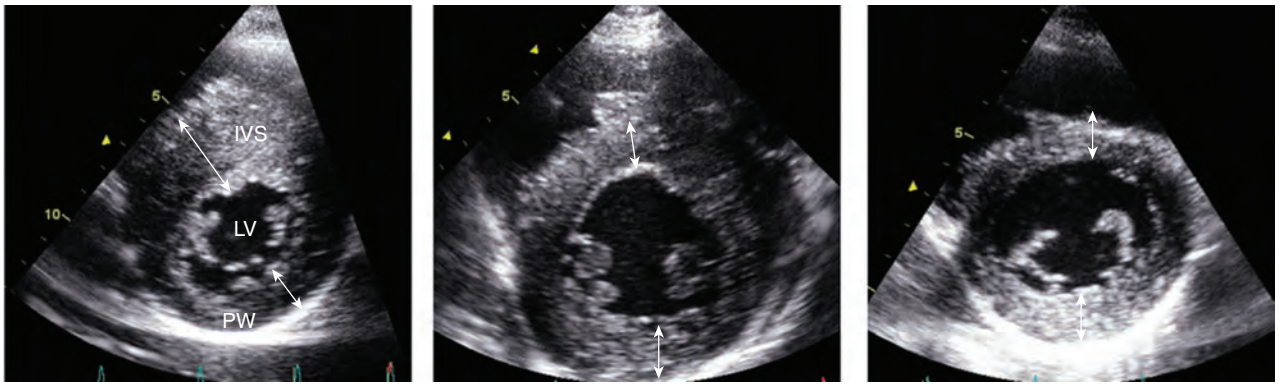


Figure 35.1 Series of parasternal short-axis views in three patients with different forms of hypertrophic cardiomyopathy (in each case, white arrows show the wall diameters). **(a)** Asymmetric septal hypertrophy with hypertrophy limited to the interventricular septum; the posterior wall is of normal thickness. **(b)** Diffuse concentric hypertrophy. (**c**) Hypertrophy is confined to the posterior wall. IVS, interventricular septum; LV left ventricle; PW posterior wall.

- Determination of etiology and severity of LVOT obstruction, if present.
- Doppler interrogation of the entire LVOT from apex to the aortic valve.
- Assessment for RV hypertrophy and RV function.
- Assessment for elevation of RV pressure.
- Detection of associated abnormalities.

Complete evaluation of the child with HCM includes M-mode, 2D imaging, Doppler evaluation of the mitral inflow and LVOT, tissue Doppler imaging (TDI), and strain rate imaging. Magnetic resonance imaging and cardiac catheterization may contribute additional information but will not be described in this chapter [49,50].

M-mode and 2D echocardiography

HCM may manifest as hypertrophy in various locations, including asymmetric septal, concentric, posterior LV (1–2%), midventricular (5%), or apical (2–3%) [30]. Many of these forms of LVH may be associated with obstruction to flow within the LV cavity and development of a gradient (Figures 35.1 and 35.2). Obstructive HCM occurs in only 30% of patients at rest [51]. The presence, magnitude, and distribution of LVH should be determined in the parasternal long-axis, short-axis, apical 4- and apical 2-chamber views in addition to subxiphoid views (Figures 35.3 and 35.4; Videos 35.2, 35.3, and 35.4). Measurements of wall thickness should be taken at end-diastole, indexed to body surface area with *z*-score measurements obtained [52]. A score system has been developed to quantify the extent of LVH (Table 35.2). This often provides additional crucial data where there is an uneven distribution of septal hypertrophy [2].

M-mode can be used to detect systolic anterior motion of the mitral leaflets and mid-systolic closure of the aortic valve (Figures 35.5 and 35.6). Although common, neither of these findings are pathognomonic of HCM as they have been described in other conditions (Table 35.3).

Assessment of diastolic function

Diastolic filling is impaired in HCM; this may result in breathlessness on exertion, elevated filling pressures, and left atrial enlargement [36,37]. Left atrial dilation as measured by left atrial volume reflects chronic left atrial hemodynamic burden from LV diastolic dysfunction and mitral regurgitation and correlates well with degree of myocardial fibrosis and degree of

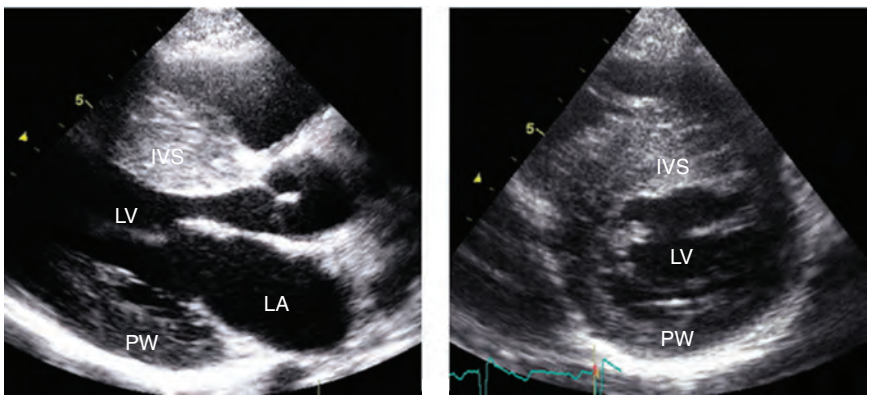


Figure 35.2 **(a)** Parasternal long-axis view at end-diastole in a patient with asymmetric septal hypertrophy. The interventricular septum is thickened and has increased reflectivity. **(b)** Parasternal short-axis view in the same patient shows similar findings. IVS, interventricular septum; LV left ventricle; LA, left atrium; PW, posterior wall.

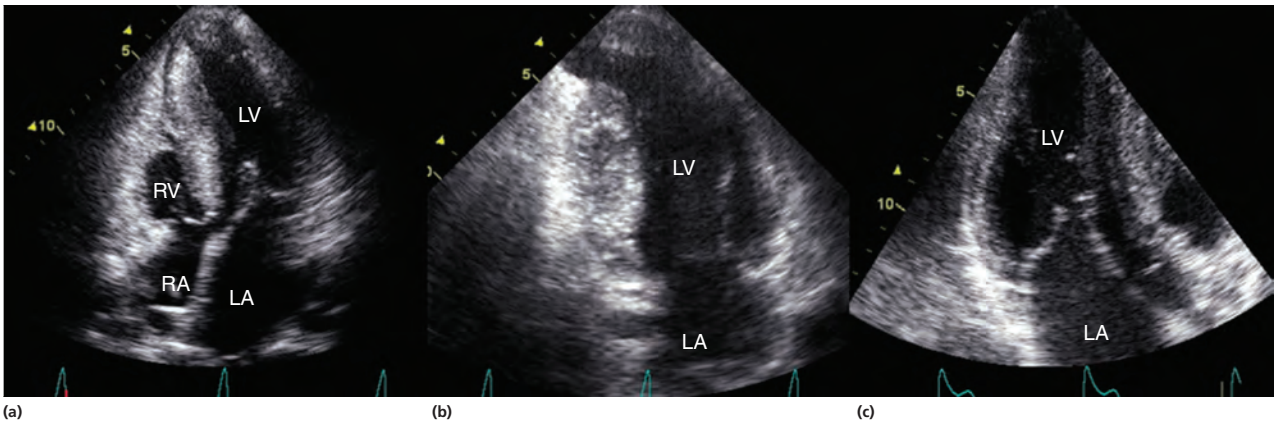


Figure 35.3 Apical 4-chamber **(a)**, 2-chamber **(b)**, and long-axis **(c)** views demonstrate the degree, extent, and distribution of hypertrophy. Considerable (25 mm) hypertrophy of the entire interventricular septum with extension onto the inferior wall is noted. In the 4-chamber view a dilated left atrium can be seen. The hypertrophied myocardium has increased reflectivity. LV left ventricle; LA, left atrium; RV, right ventricle; RA, right atrium.

Table 35.2 Extent of left ventricular hypertrophy (LVH) according to echocardiographic point score

Extent of hypertrophy	Points
Basal septal thickness	
15–19 mm	1
20–24 mm	2
25–29 mm	3
>30 mm	4
Extension to papillary muscles (basal 2/3 septum)	2
Extension to apex (all septum involved)	2
Anterolateral wall involvement	2
Total	10

Source: Wigle et al. 1985 [2]. Reproduced with permission of Elsevier.

exercise intolerance in children with HCM [53]. The transmitral inflow pattern should be carefully assessed with spectral Doppler in the apical 4-chamber view. The mitral E and A wave patterns typically show marked perturbations in diastolic relaxation with: reduced E wave velocity, increased A wave velocity [decreased E/A wave ratio (Figure 35.7)], prolonged E wave deceleration time, and prolonged isovolumetric relaxation time [49]. These findings suggest increased left atrial pressure. Pseudonormalization may occur with intermediate degrees of diastolic dysfunction when the mitral E/A wave ratio appears normal; A wave reversal and decreased lateral mitral TDI velocities will distinguish this from normal. During the Valsalva maneuver, there is typically a reduction of flow into the left heart; as a result, left atrial and diastolic ventricular pressures decrease along with E wave velocity reduction and reversal of pseudonormal E/A wave pattern [54]. Pulmonary vein Doppler recordings demonstrate a progressive decrease in systolic flow and an increase in A-wave reversal velocity and duration with increasing degrees of diastolic dysfunction (Figure 35.8). When left heart filling pressures are elevated, the pulmonary venous A wave duration may exceed the mitral A wave duration [55]. However, this may be difficult to measure in children because of increased heart rates and the small differences which may exist between these two measurements.

Mitral valve function

In the presence of significant LVOT obstruction, eddy currents are generated in the subaortic region. This hemodynamic abnormality results in displacement of the mitral valve leaflets or chords into the LVOT, known as "systolic anterior motion"

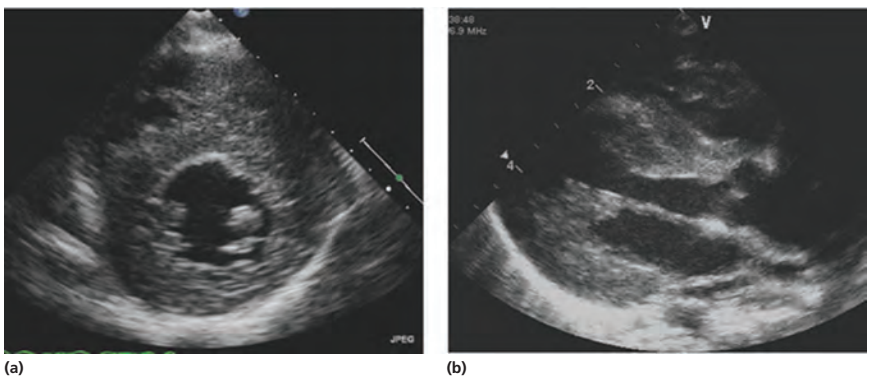


Figure 35.4 **(a)** Parasternal short-axis view in an infant with hypertrophic cardiomyopathy secondary to metabolic disease. Note the diffuse concentric biventricular hypertrophy. **(b)** Parasternal long-axis view shows similar findings. Note the involvement of the papillary muscles.

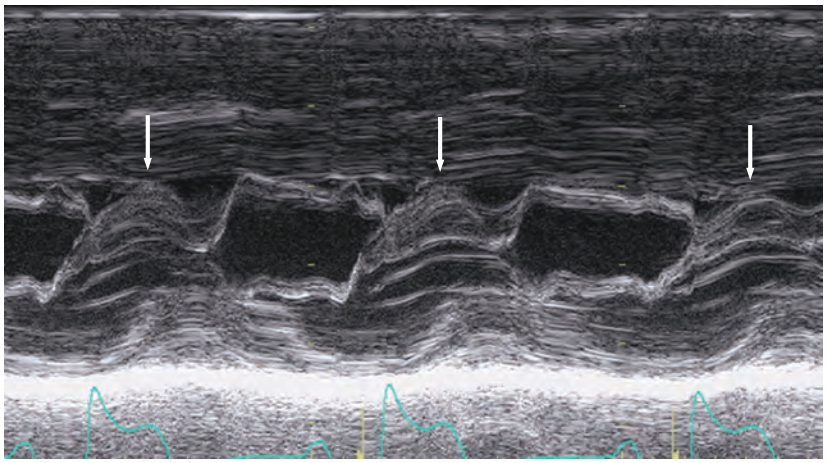


Figure 35.5 M-mode echocardiogram from parasternal long-axis view showing systolic anterior motion of the anterior mitral leaflet and septal contact (white arrows) during mid and late systole contributing to left ventricular outflow obstruction.

(SAM) of the mitral valve [56]. When present, the parasternal long-axis view demonstrates SAM very well (Figure 35.9). SAM often results in noncoaptation of the mitral valve leaflets with a jet of mitral regurgitation directed posteriorly along the left atrial wall (Figures 35.10 and 35.11). Similarly to the timing of LVOT obstruction, the mitral regurgitation that results from SAM is typically late in systole and may range from mild to severe (Videos 35.5, 35.6, and 35.7) [57]. Given the high LV systolic pressures, the mitral regurgitant jet velocity may be in supraphysiologic ranges [33]. When a direct measure of the LVOT gradient is difficult because of the angle of interrogation, the modified Bernoulli equation can be applied to the mitral regurgitation jet velocity to give an estimate of LV systolic pressure. Severe mitral regurgitation may result in retrograde flow into the pulmonary veins, contributing to pulmonary venous and arterial hypertension.

Table 35.3 Causes of systolic anterior motion (SAM) and dynamic left ventricular outflow tract (LVOT) obstruction

Hypertrophic cardiomyopathy with basal septal hypertrophy
Sigmoid basal septal hypertrophy of the elderly
Anomalous papillary muscle
After aortic valve replacement with hyperdynamic LV systolic function
After mitral valve repair
Apical ballooning
Apical myocardial infarction with hyperdynamic function of basal myocardial segments
Massive mitral annular calcification
Hypovolemia in patients with small LV cavity
Subpulmonic LV (after atrial switch operation, double discordance) with severe subaortic right ventricular dilatation causing septal shift to the LV

EF, ejection fraction; LVH, left ventricular hypertrophy.

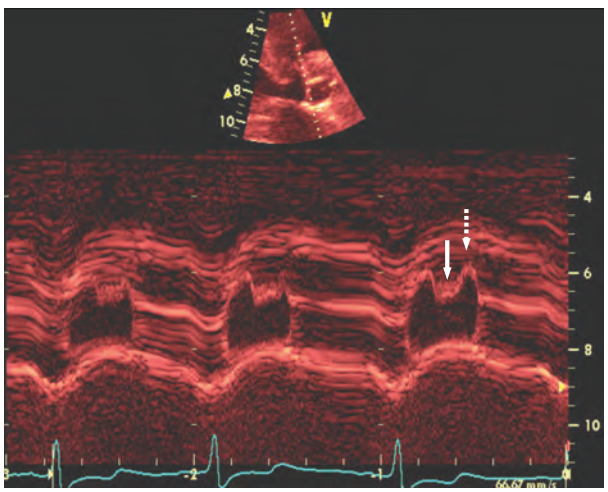


Figure 35.6 M-mode echocardiogram from parasternal long-axis view showing premature closure of the aortic valve (solid white arrow) secondary to systolic anterior motion and left ventricular outflow tract obstruction occurring in mid systole. Reopening of the aortic valve (dashed white arrow) occurs in late systole when systolic anterior motion ceases.

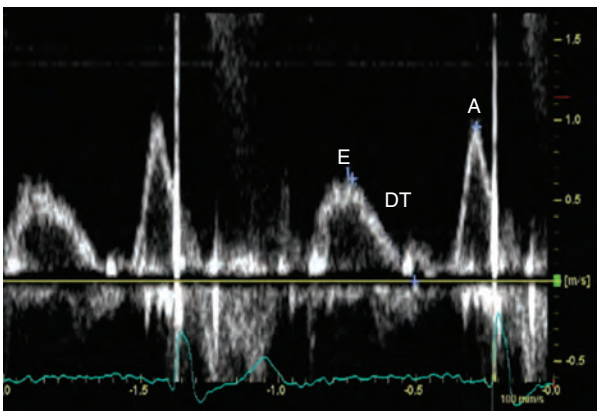


Figure 35.7 Mitral inflow pulsed-wave Doppler recording of a patient with HCM. The Doppler pattern shows abnormal relaxation. The early rapid filling velocity (E) is decreased (60 cm/s) and there is a prolonged deceleration time of the E wave (230 ms) and prominent atrial filling (A) velocity (94 cm/s).

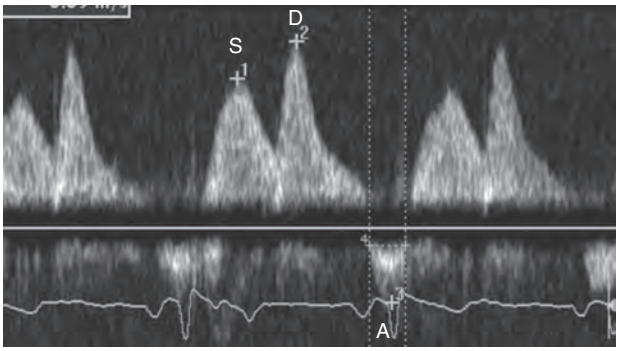


Figure 35.8 Pulmonary venous pulsed-wave Doppler recording from the same patient as in Figure 35.7. There is a blunted systolic component (S) and prominent and prolonged atrial flow reversal component (A). This is suggestive of increased left ventricular end-diastolic pressure.

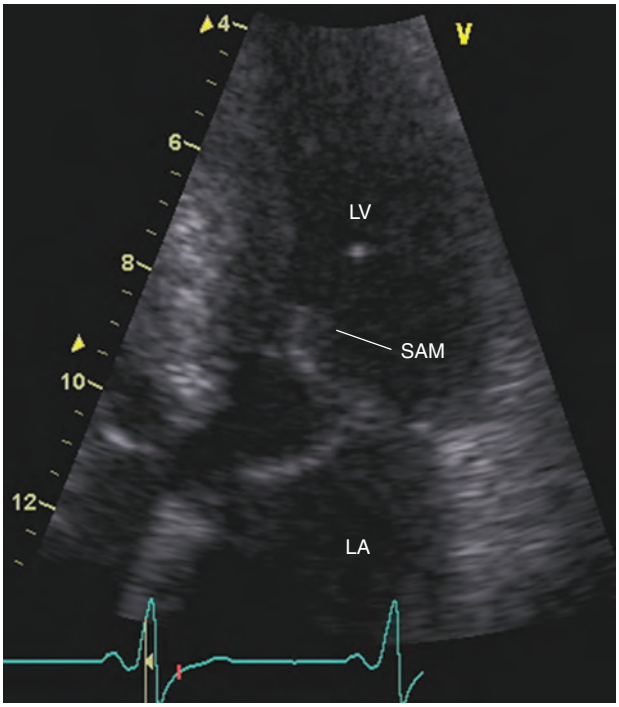


Figure 35.10 Apical 3-chamber view showing systolic anterior motion (SAM) of the anterior and posterior mitral leaflets producing septal contact. This contributes to left ventricular outflow tract obstruction. LA, left atrium; LV, left ventricle.

In approximately 40% of patients with HCM, mitral regurgitation may be secondary to intrinsic mitral valve disease. The anterior leaflet may be elongated and redundant. The presence of a nonposteriorly directed jet in apical or parasternal long-axis view suggests primary leaflet pathology independent of SAM [58]. Detection of intrinsic valve disease is particularly relevant in patients who are to candidates for surgical myomectomy as the presence of intrinsic mitral valve disease is associated with persistence of mitral regurgitation after surgery.

Left ventricular outflow tract (LVOT) assessment

The degree of LVOT obstruction is often multifactorial and dynamic. LVOT obstruction in HCM typically occurs in mid to late systole with no significant obstruction in early systole [34]. LV ejection typically diminishes during mid to late systole, resulting in partial closure of the aortic valve, with reopening with final ejection (Figure 35.6). The presence of SAM usually indicates some form of LVOT obstruction, particularly when SAM persists for >40% of systole [34,51].

The degree and location of LVOT obstruction is measured using color, pulsed-wave, and continuous Doppler, typically from the apical 5-chamber view. Color flow mapping often demonstrates aliasing due to outflow tract gradients exceeding the Nyquist limit and provides a visual impression on where flow acceleration occurs (Figure 35.11). Pulsed-wave Doppler traces are obtained sequentially at the LV apex, mid LV cavity, and proximal and distal LVOT (Figure 35.12). The peak velocity increases as the sample volume approaches the site of obstruction. Continuous-wave Doppler is then used to measure the peak gradient (Figure 35.13) [33]. In patients with a noncompliant left ventricle there may be evidence of presystolic forward flow in the LVOT obstruction secondary to atrial contraction as the A wave transmits to the LVOT. This is akin to the appearance of antegrade diastolic flow in the pulmonary arteries in patients with restrictive RV physiology. A dagger shape of the spectral wave pattern in the LVOT indicates a dynamic form of obstruction [59].

SAM and LVOT obstruction are dynamic phenomena. Therefore, a patient may have a pronounced gradient on one echocardiogram and essentially no gradient measured in the next study. Several physiologic manipulations may provoke or unmask a

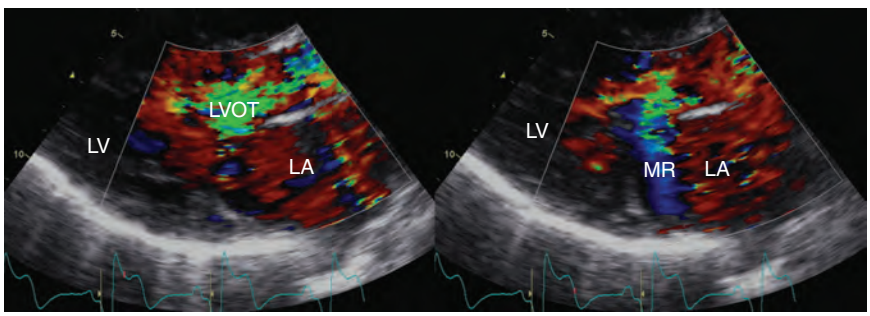


Figure 35.9 Parasternal long-axis view with color flow mapping showing the temporal relationship between left ventricular outflow tract obstruction and occurrence of mitral regurgitation. First obstruction to flow occurs; subsequently mitral regurgitation ensues. LA, left atrium; LV, left ventricle, MR, mitral regurgitation; LVOT, left ventricular outflow tract.

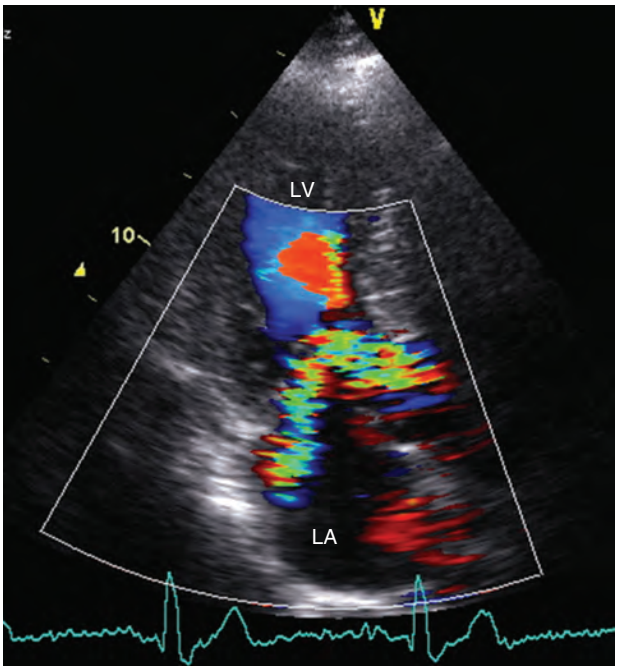


Figure 35.11 Apical long-axis view with color flow mapping demonstrates left ventricular outflow tract obstruction and eccentric, posteriorly directed mitral regurgitation occurring at mid systole. LA, left atrium; LV, left ventricle.

latent LVOT gradient, including squatting to standing or administering amyl nitrate. Stress echocardiography or dobutamine administration will increase contractility and may also unmask an LVOT gradient [60,61]. Significant (>50 mmHg) LVOT obstruction is present in only 25–30% of HCM patients under resting conditions but in up to 70% of HCM patients when they undergo exercise echocardiography. These high gradients may be associated with heart failure symptoms [51].

When assessing the LVOT, it is important to distinguish the high-velocity signal coming from the LVOT from the signal of the mitral regurgitation jet. The spectral signal of mitral regurgitation is characterized by an earlier onset, higher velocity (>6 m/s), and a more abrupt initial increase in velocity. Differentiation can also be accomplished by orienting the transducer more medially and anteriorly away from the mitral jet [34,62].

In some patients, the primary location of septal hypertrophy is mid-septal (Figure 35.14; Video 35.8). Consequently during mid to late systole there may be mid-cavitary obstruction with a marked decrease in stroke volume leading to syncope and sudden death [63]. Mid-cavitary obstruction is also associated with apical aneurysm formation possibly secondary to myocardial ischemia [64,65].

An apical form of HCM is unusual and is characterized by electrocardiograms with giant negative T waves in the precordial leads. It is associated with a good prognosis. Echocardiography in the apical and parasternal views shows increased wall thickness of one or more apical segments (Figure 35.15; Videos 35.9 and 35.10). The diagnosis may be missed if the true LV apex is not visualized (because of foreshortening) or if endocardial definition is limited due to poor acoustic windows [66]. Contrast echocardiography may be useful in enhancing endocardial definition for identification of apical HCM [67]. Long-term complications of apical HCM include the development of diastolic dysfunction, apical aneurysms, and/or mid-cavitary obstruction [68]. CMR imaging has better resolution than echocardiography to visualize the endocardial borders at the LV apex and has been shown to have higher sensitivity for the diagnosis of apical HCM [69].

Tissue Doppler imaging (TDI)

TDI employs spectral Doppler analysis to measure the velocity of myocardial contraction or relaxation, specifically early systolic (s′), early diastolic (e′) and late diastolic velocities (a′) [70]. Annular TDI velocities can be measured from the apical 4-chamber view. With increasing LV filling pressures, the transmitral e velocity increases and the early diastolic relaxation velocity (e′) reduces [71]. The relationship between the transmitral e velocity and e′ velocity (e/e′ ratio) allows an estimation of the LV filling pressure (atrial pressure). In adults, the normal e/e′ ratio is <10; e/e′ >15 has been reported to predict a filling pressure exceeding 15 mmHg (Figure 35.16) [72,73]. In a study of 80 consecutive children and adolescents with hypertrophic cardiomyopathy, the transmitral e/e′ ratio was most sensitive and specific in predicting children at risk for sudden cardiac death, arrhythmia, or need for transplantation [74]. Other studies have corroborated reduced tissue velocities in children with HCM [75,76]. For example, systolic myocardial velocity (s′), a measure of longitudinal systolic function, has been shown to be attenuated in HCM, even in nonhypertrophied ventricular segments.

Experimental data suggest that myocardial dysfunction likely occurs before the development of visible LVH in HCM. Myocardial velocities have been shown to be diminished in genotype-positive individuals with HCM in the absence of LVH [45,77]. Importantly, mutation-positive adults without evidence of LVH can be accurately identified by an s′ TDI velocity of <13 cm/s in the lateral mitral annulus with a sensitivity of 100% and a specificity of 93%. An additional study has shown that LVH eventually develops in those genotype-positive subjects with diminished myocardial velocities [78].

Assessment of systolic performance

Assessment of systolic function is routinely performed by measuring LV dimensions, shortening fraction (SF) and ejection fraction (EF). Most patients with HCM have small LV cavity dimensions and supranormal EF or SF [52]. In fact, the development of LV dilation and/or depressed systolic shortening are signs of poor prognosis that require institution of heart failure treatment. It is important to note that in HCM a normal EF or SF does not exclude myocardial dysfunction, which can be detected with more sensitive techniques such as myocardial velocities or strain rate imaging [79,80].

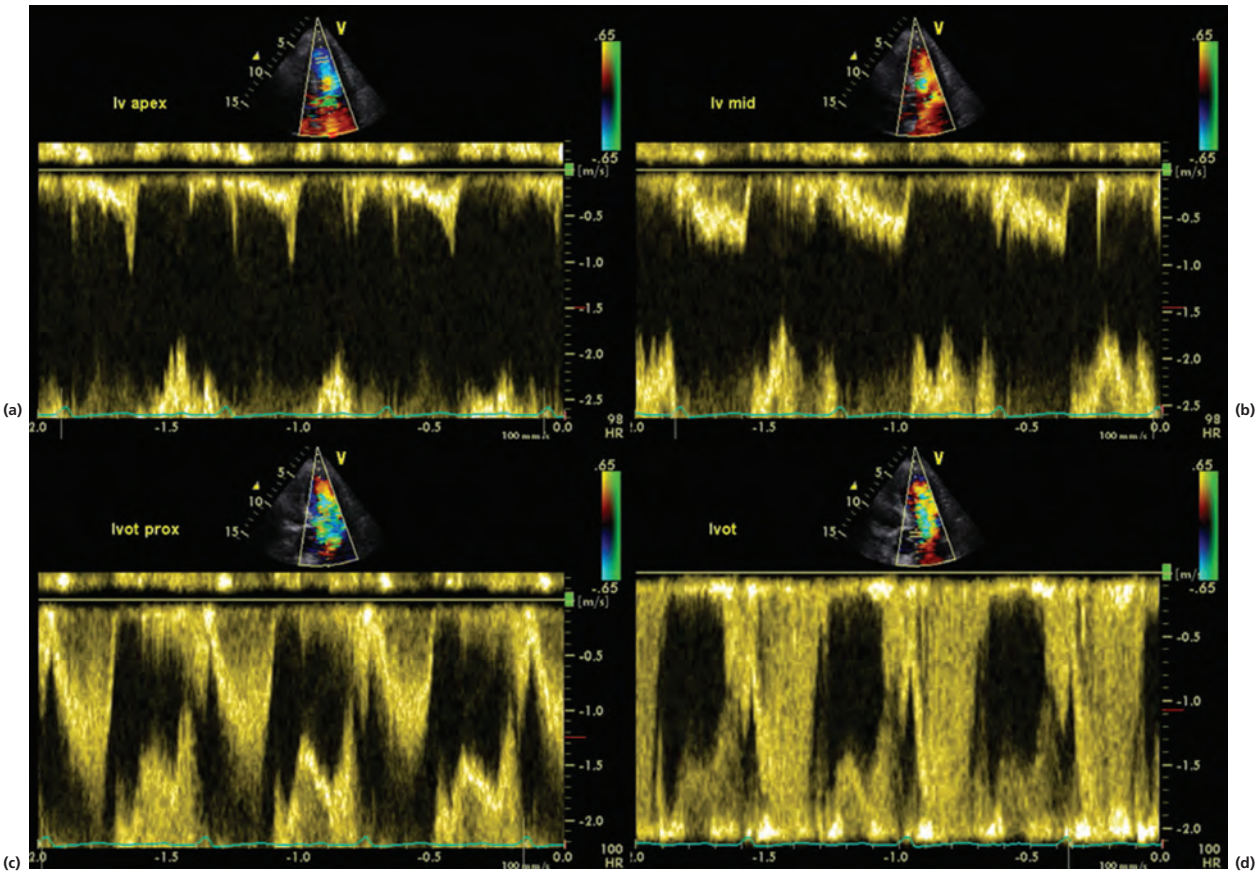


Figure 35.12 Pulsed-wave Doppler spectral tracing across the left ventricle to determine the site of obstruction to flow. Sampling at the left ventricular apex **(a)**, and at the mid-ventricular level **(b)**, show no flow acceleration. At the proximal left ventricular outflow tract **(c)**, there is mild flow acceleration, which becomes more pronounced with aliasing at the more distal left ventricular outflow **(d)**.

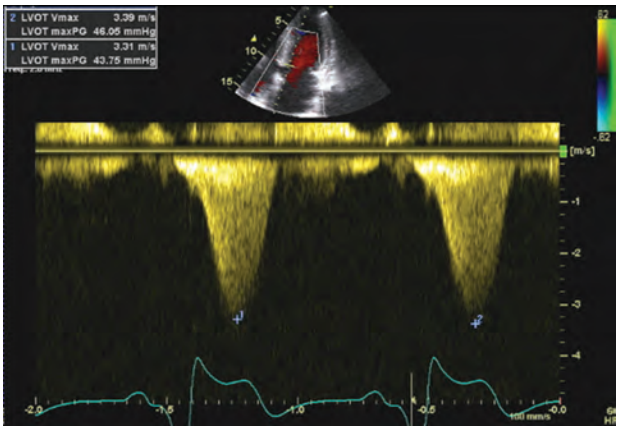


Figure 35.13 Continuous-wave Doppler spectral tracing from the apex in a patient with HCM demonstrates dynamic left ventricular outflow tract obstruction. Note the typical start after the QRS complex, which is preceded by a low-velocity presystolic signal and the late-peak configuration similar to a dagger. Peak velocity is 3.3 m/s, corresponding to a peak gradient of 44 mmHg.

Myocardial deformation imaging

Newer, more sensitive techniques might improve the diagnostic accuracy of HCM. HCM is a disease with marked nonuniformity in myocardial thickness and function. Myocardial deformation is closely related to myocardial contractility and can be measured regionally in different areas of the myocardium. Studies have shown that there is regional myocardial dysfunction with paradoxical systolic lengthening instead of shortening in up to 50% of basal and mid-septal myocardial segments of patients with asymmetric septal HCM (Figure 35.17) [81]. Also, severely reduced systolic deformation together with a septal to inferolateral wall thickness >1.4 can help distinguish patients with HCM from those with hypertension and LV hypertrophy [80].

The noninvasive study of radial, longitudinal, and circumferential myocardial deformation detects early abnormalities in myocardial function in patients with preserved global ventricular function [82]. Studies have shown myocardial deformation is more severely reduced in the more hypertrophied myocardial segments with values in those segments generally

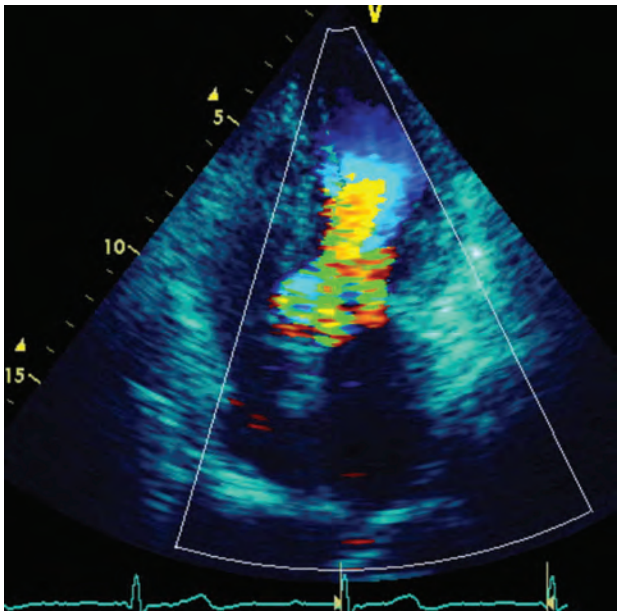


Figure 35.14 Apical 4-chamber view demonstrates mid-cavitary obstruction, characterized by prominent mid-septal hypertrophy, formation of a distinct apical chamber during systole, and appearance of a mosaic color jet at the mid-ventricular level in mid-systole.

below −10%. Interestingly, circumferential myocardial deformation is increased in HCM but rotation deformation is abnormal at the mid-ventricular level [83]. This may explain the normal or supranormal ejection fraction that is often observed.

Myocardial deformation imaging can also help characterize the pattern of LV hypertrophy [84]. Myocardial deformation is more reduced and is associated with post-systolic shortening in the more hypertrophied basal septum in patients with asymmetric septal HCM. This reduction is more uniformly distributed in patients with concentric HCM irrespective of whether HCM results from isolated or secondary HCM. Finally, reduced longitudinal myocardial deformation has been associated with nonsustained ventricular tachycardia and decreased exercise tolerance in HCM [85].

Three-dimensional (3D) echocardiography

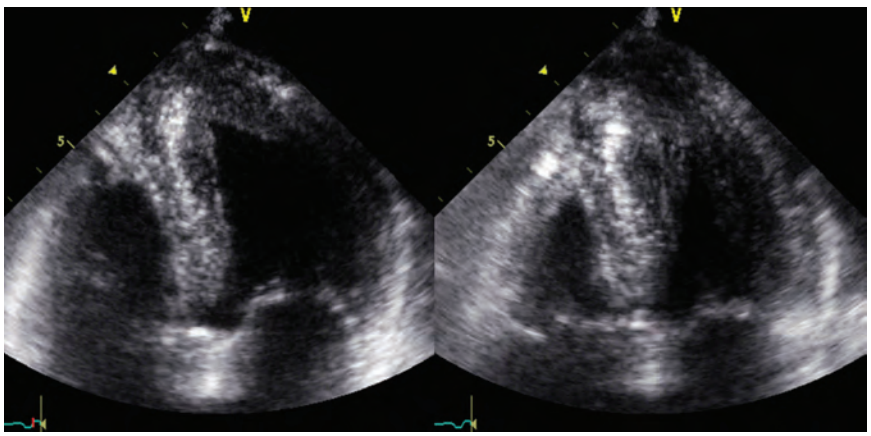
With 3D echocardiography, biventricular dimensions, wall thickness in all myocardial segments, and EF can be calculated without relying on geometric assumptions of uniform chamber size and shape [86]. This leads to higher accuracy in the measurements. Additionally, the heart can be visualized from any point of view. In HCM, this is particularly helpful in defining mitral valve anatomy and function in addition to LVOT anatomy before surgical or catheter-directed interventions [87]. However, this modality continues to be limited by spatial and temporal resolution [88].

Prognostic factors in children with HCM

The greatest challenge in the management of HCM is the identification of those patients at increased risk for sudden death. Reported risk factors include younger age at presentation, previously aborted sudden cardiac death, malignant family history, history of syncope, ventricular tachycardia on ambulatory monitoring, myocardial bridging, abnormal decrease in blood pressure with exercise, and presence of troponin T mutations [20,21,89–93]. Echocardiographic risk factors include marked and diffuse LVH defined as maximal end-diastolic wall thickness >30 mm [94,95]. An elevated e/e′ ratio was found to correlate with ventricular tachycardia, cardiac arrest, or death in a study of 80 consecutive children with HCM [73]. Left ventricular dilation and decreased ejection fraction are also associated with both symptoms of heart failure and reduced survival [96].

Stress echocardiography in HCM

Stress echocardiography can be performed using a cycle ergometer or treadmill or with dobutamine administration. Regional wall motion abnormalities may be revealed with increasing doses of dobutamine which are not apparent at rest. Although there are reports of stress echocardiography in children following cardiac surgical procedures and cardiac transplantation, there are limited data on stress echocardiography in children with HCM, likely because of the potential risk of an untoward event during the test. In some cases, stress echocardiography is



(a) (b)

Figure 35.15 **(a)** Apical 4-chamber view in a patient with apical hypertrophic cardiomyopathy showing increased thickness of all apical myocardial segments. **(b)** The same view in systole demonstrates the obliteration of the apical cavity at end-systole.

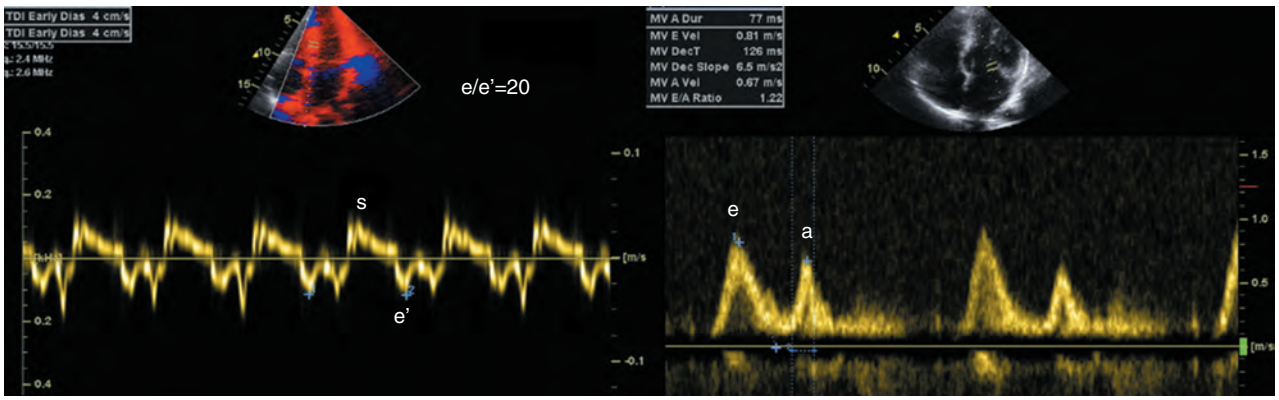


Figure 35.16 Tissue Doppler recording of the septal mitral annulus and pulsed-wave Doppler recording of the mitral inflow of a 12-year-old child with hypertrophic cardiomyopathy. Peak systolic (s) and early diastolic (e′) myocardial velocities are reduced. The mitral e/e′ = 20. This suggests elevated left atrial pressure.

used to unmask potential HCM although high LVOT gradients have been reported in the healthy pediatric population [97].

Echocardiography in the management of HCM

Management of HCM may be optimized by monitoring changes and the response to therapy with serial echocardiographic studies. Symptomatic patients are treated with three classes of pharmacologic agents: beta-blockers, disopyramide, and calcium channel blockers [1,62,95]. These agents potentially produce a decrease in contractility that results in decreased ejection velocity, delayed onset of SAM, and consequently decreased LVOT obstruction and mitral regurgitation. This may indirectly improve LV diastolic filling and improve symptoms.

Surgical myomectomy and septal catheter ablation

Septal reduction therapy is feasible with surgical myomectomy or intracoronary alcohol ablation. Patients with a dynamic gradient exceeding 30–50 mmHg at rest or exceeding 60 mmHg with exercise and a septal thickness greater than 15 mm may benefit from either procedure. It is important to determine the exact site of obstruction as patients with mid or distal ventricular obstruction generally do not benefit from basal septal reduction [98].

Septal myomectomy has been performed for more than four decades in patients who have significant LVOT obstruction and are symptomatic despite maximal medical therapy. This procedure consists of direct excision of the hypertrophied basal septum, which ideally results in widening of the LVOT,

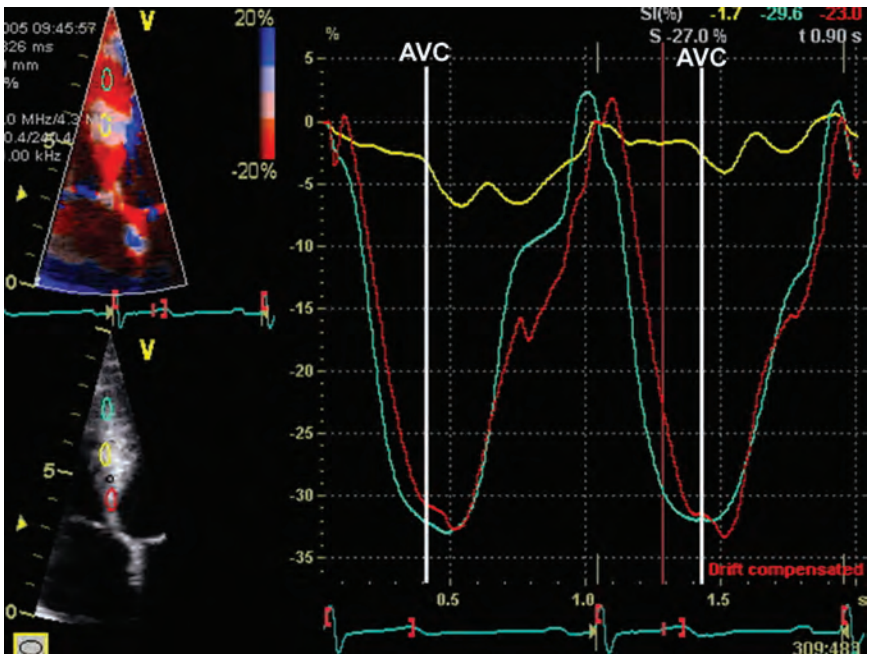


Figure 35.17 Myocardial deformation (strain) in a patient with asymmetric septal hypertrophic cardiomyopathy. The hypertrophied mid septum (yellow line) shows reduced and delayed deformation persisting after aortic valve closure (AVC, white line). The other septal myocardial segments (green and red lines) do not exhibit significant degree of hypertrophy and have preserved myocardial deformation.

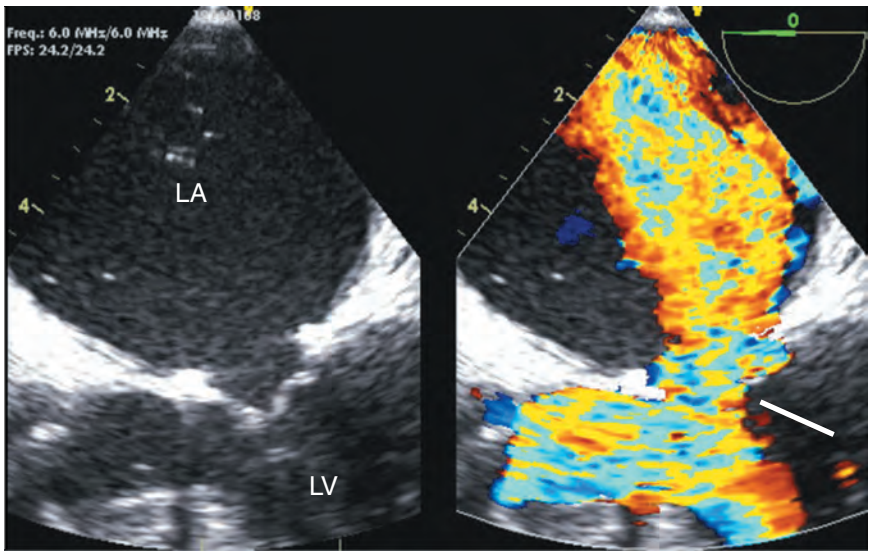


Figure 35.18 This intraoperative transesophageal echocardiogram in the 4-chamber view performed to assess success of mitral repair shows chordal and anterior leaflet systolic anterior motion of the mitral valve (SAM) leading to left ventricular outflow tract obstruction, malcoaptation of the mitral valve leaflets (white line), and severe, posteriorly directed mitral regurgitation. LA, left atrium; LV, left ventricle.

decreased dynamic obstruction of the LVOT, and decreased SAM. Perioperative complications of surgery include aortic regurgitation, ventricular septal defects, left bundle branch block and atrioventricular block requiring permanent pacemaker implantation.

Echocardiography is useful in defining patients suitable for surgical myomectomy. It is important to report maximal septal thickness and also distance of maximal septal thickness to aortic annulus because surgeons use these measures to determine extent of resection. The preoperative characteristics of patients who benefit from surgical myomectomy include asymmetric hypertrophy, severe SAM, and a high LVOT gradient at rest or provoked with exercise [99]. Preoperative echocardiographic evaluation also includes the assessment of intrinsic mitral valve disease that warrants surgery, and concomitant aortic valve disease in addition to the detection of additional sites of obstruction (mid-ventricular or right ventricular outflow tract). Some patients undergoing myomectomy will also require mitral valve replacement for severe mitral regurgitation.

Intraoperative TEE allows for delineation of the repair after myomectomy (Video 35.11). TEE can determine if there is residual LVOT obstruction residual mitral regurgitation or residual SAM (Figure 35.18) [100]. Surgical complications such as ventricular septal defects, aortic regurgitation, LV dysfunction, or pericardial tamponade can also be detected with intraoperative TEE. Echocardiographic studies performed at rest and with provocative maneuvers are important in the follow-up of patients after surgical myomectomy (Figure 35.19).

Septal catheter ablation consists of the selective injection of ethanol into the first septal perforator branch of the left anterior descending coronary artery. This leads to occlusion of the septal branch and a localized infarction of the hypertrophied

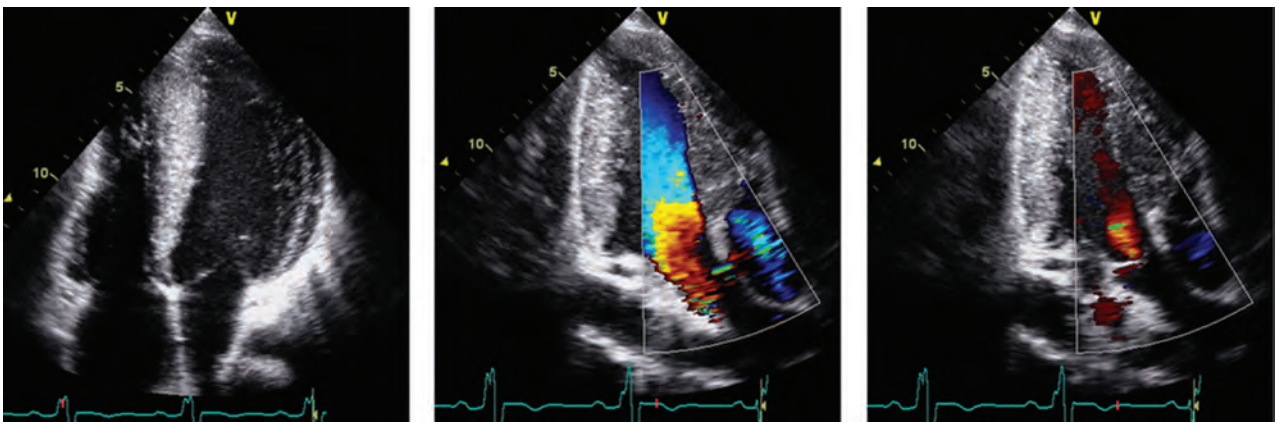


Figure 35.19 Transthoracic echocardiogram 3 months after surgical myomectomy to relieve left ventricular outflow tract obstruction. Various apical images are displayed. A. Apical 4-chamber view demonstrates thinning of the basal septum. B. Apical 5-chamber view with color flow mapping shows no significant residual left ventricular outflow tract obstruction. C. In the same view, mild to moderate aortic regurgitation is present.

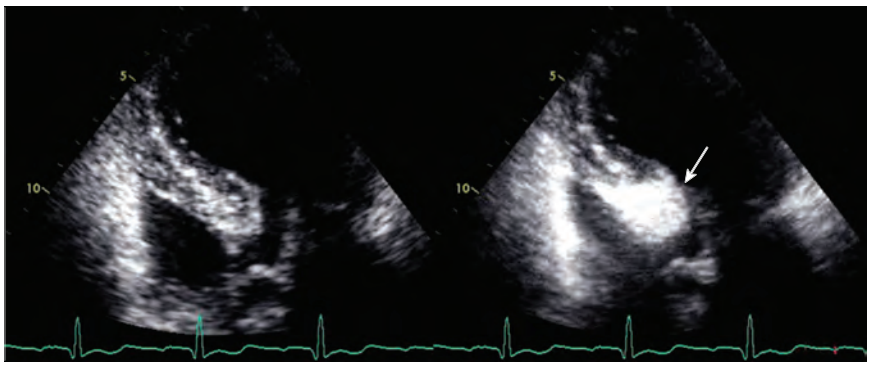


Figure 35.20 Transthoracic echocardiogram to guide alcohol septal ablation procedure. End-diastolic septal thickness was 18 mm and peak left ventricular outflow tract gradient was 65 mmHg. **(a)** Apical 4-chamber in adult view shows basal septal hypertrophy. **(b)** Myocardial perfusion imaging in the same view after administration of contrast agent into the first septal perforator branch shows that the contrast opacifies only the hypertrophied basal septum (white arrow) where there is mitral leaflet–septal contact. These findings make the patients eligible for alcohol septal ablation.

basal septum. The infarction results in thinning of the infarcted myocardial segment, decreased SAM, and immediate (generally modest) relief of the LVOT obstruction in the majority of patients. Chronic ventricular remodeling with further decrease in septal thickness, SAM, and enlargement of the LVOT leads to further decrease in LVOT obstruction over time [32].

Transthoracic imaging is used during septal ablation procedures. The intra-arterial injection of contrast agents allows the localization of the vascular beds perfused by individual septal perforators. After the injection of the contrast agent, the myocardial segments supplied by the septal branch become opacified (Figure 35.20). The extent of myocardial opacification can be evaluated from multiple views (Video 35.12). The vascular territory targeted by the procedure is the region of anterior mitral leaflet–septal contact adjacent to the zone of flow acceleration in the LVOT. If contrast opacification is seen in areas remote from the site of mitral leaflet–septal contact, this necessitates the selection of another vessel to be targeted. The injection of ethanol has the same distribution as that of the contrast agent and results in increased reflectivity of the targeted myocardial area [101]. It has been shown that the use of intraprocedural contrast echocardiography improves outcome after septal catheter ablation because it limits the number of vessels injected, lowers the volume of ethanol used, and causes fewer cases of atrioventricular block [102].

Videos

To access the videos for this chapter, please go to www.lai-echo.com.

Video 35.1 Athlete's heart. Two-dimensional apical 4-chamber image (in adult view) of a 15-year-old cyclist. There is mild biventricular hypertrophy. Ventricular cavities are enlarged and systolic function is normal.

Video 35.2 Asymmetric septal hypertrophic cardiomyopathy. Parasternal short-axis view at the papillary muscle level of a patient with asymmetric septal hypertrophic cardiomyopathy showing increased thickness of the interventricular septum with extension onto the anterolateral wall. The left ventricular cavity is small and there is hyperdynamic systolic function.

Video 35.3 Asymmetric septal hypertrophic cardiomyopathy. Parasternal long-axis view of a patient with asymmetric septal hypertrophic cardiomyopathy showing increased septal thickness, dilated left atrium, and systolic anterior motion of the mitral leaflets which contributes to left ventricular outflow obstruction.

Video 35.4 Biventricular hypertrophy. Subxiphoid view in a 6-month-old boy presenting with failure to thrive and dyspnea. There is marked biventricular hypertrophy. The boy was ultimately diagnosed with Pompe disease.

Video 35.5 Systolic anterior motion. Apical 5-chamber view of a patient with marked and extensive septal hypertrophy. Systolic anterior motion of the mitral leaflets and chordal tissue is demonstrated.

Video 35.6 Asymmetric septal hypertrophic cardiomyopathy. Parasternal long-axis view with color flow mapping showing basal septal hypertrophy with narrowing and obstruction of the left ventricular outflow tract and systolic anterior motion during systole. This leads to eccentric mid- to late-systolic mitral regurgitation.

Video 35.7 Asymmetric septal hypertrophic cardiomyopathy. Apical 4-chamber view with color flow mapping demonstrates basal septal hypertrophy. Aliasing demonstrates the location of the left ventricular outflow tract obstruction. The resultant mitral regurgitation is also seen.

Video 35.8 Mid-ventricular hypertrophic cardiomyopathy. Apical 4-chamber image (in adult view) demonstrates predominant mid-septal hypertrophy with cavity obliteration during systole.

Video 35.9 Apical hypertrophic cardiomyopathy. Apical 4-chamber view demonstrates hypertrophy of all apical myocardial segments and cavity obliteration at the apex during systole.

Video 35.10 Apical hypertrophic cardiomyopathy. Apical 4-chamber view showing hypertrophy of the apical myocardial segments. Myocardial deformation analysis shows reduced longitudinal shortening of the hypertrophied segments.

Video 35.11 Transesophageal echocardiogram demonstrating systolic anterior motion of the mitral valve. Left ventricular outflow

tract view demonstrates significant septal hypertrophy with systolic anterior motion of the mitral valve. The aortic leaflets flutter in systole as a result of the turbulent flow. The distance from the aortic valve and precise site of mitral–septal contact can be appreciated. Maximal septal thickness can be measured to determine extent of myomectomy.

Video 35.12 Contrast echocardiography to guide alcohol septal ablation. Apical 4-chamber image in adult view during alcohol septal ablation procedure. There is basal septal hypertrophy. Administration of agitated saline into the first septal branch opacifies only the basal interventricular septum, suggesting that alcohol septal ablation of the first septal perforator will lead to regression in basal septal hypertrophy and intraventricular gradients.

References

1 Moak JP, Kaski JP. Hypertrophic cardiomyopathy in children. *Heart* 2012;**98**:1044–1054.
2 Wigle ED, Sasson Z, Henderson MA, et al. Hypertrophic cardiomyopathy. The importance of the site and extent of hypertrophy. *Prog Cardiovasc Dis* 1985;**28**:1–83.
3 Maron BJ. Hypertrophic cardiomyopathy. *Lancet* 1997;**350**:127–133.
4 Marian AJ. On predictors of sudden cardiac death in hypertrophic cardiomyopathy. *J Am Coll Cardiol* 2003;**41**:1887–1896.
5 Chang AC, Towbin JA. *Heart Failure in Children and Young Adults: from Molecular Mechanisms to Medical and Surgical Strategies*. Philadelphia, PA: Elsevier Saunders, 2006, pp. 278–297.
6 Maron BJ, Peterson EE, Maron MS, et al. Prevalence of hypertrophic cardiomyopathy in an outpatient population referred for echocardiographic study. *Am J Cardiol* 1994;**73**:577–580.
7 Maron BJ, Towbin JA, Thiene G, et al. Contemporary definitions and classification of the cardiomyopathies: an American Heart Association Scientific Statement from the Council on Clinical Cardiology, Heart Failure and Transplantation Committee; Quality of Care and Outcomes Research and Functional Genomics and Translational Biology Interdisciplinary Working Groups; and Council on Epidemiology and Prevention. *Circulation* 2006;**113**:1807–1816.
8 Jarcho JA, McKenna W, Pare JA, et al. Mapping a gene for familial hypertrophic cardiomyopathy to chromosome 14q1. *N Engl J Med* 1989;**321**:1372–1378.
9 Watkins H, McKenna WJ, Thierfelder L, et al. Mutations in the genes for cardiac troponin T and alpha-tropomyosin in hypertrophic cardiomyopathy. *N Engl J Med* 1995;**332**:1058–1064.
10 Niimura H, Bachinski LL, Sangwatanaroj S, et al. Mutations in the gene for human cardiac myosin-binding protein C and late-onset familial hypertrophic cardiomyopathy. *N Engl J Med* 1998;**338**:1248–1257.
11 Thierfelder L, Watkins H, MacRae C, et al. Alpha-tropomyosin and cardiac troponin T mutations cause familial hypertrophic cardiomyopathy: a disease of the sarcomere. *Cell* 1994;**77**:701–702.
12 Morgensen J, Klausen IC, Pedersen AK, et al. Alpha-cardiac actin is a novel disease gene in familial hypertrophic cardiomyopathy. *J Clin Invest* 1999;**103**:R39–R43.
13 Arad M, Penas-Lado M, Monserrat L, et al. Gene mutations in apical hypertrophic cardiomyopathy. *Circulation* 2005;**112**:2805–2811.
14 Geier C, Perrot A, Ozcelik C, et al. Mutations in the human muscle LIM protein gene in families with hypertrophic cardiomyopathy. *Circulation* 2003;**107**:1390–1395.
15 Towbin J. Pediatric myocardial disease. *Pediatr Clin North Am* 1999;**46**:289–312.
16 MacRae CA, Ghaisas N, Kass S, et al. Familial hypertrophic cardiomyopathy with Wolff–Parkinson–White syndrome maps to a locus on chromosome 7q3. *J Clin Invest* 1995;**96**:1216–1220.
17 Ho C. Hypertrophic cardiomyopathy in 2012. *Circulation* 2012;**125**:1432–1438.
18 Van Driest SL, Ommen SR, Tajik AJ, et al. Sarcomeric genotyping in hypertrophic cardiomyopathy. *Mayo Clin Proc* 2005;**80**:463–469.
19 Colan SD. Clinical issues in the pediatric hypertrophic cardiomyopathies. *Prog Pediatr Cardiol* 2008;**25**:27–29.
20 Nugent AW, Daubeney PE, Chondros P, et al. Clinical features and outcomes of childhood hypertrophic cardiomyopathy: results from a national population-based study. *Circulation* 2005;**112**:1332–1338.
21 Colan SD, Lipshultz SE, Lowe AM, et al. Epidemiology and cause-specific outcome of hypertrophic cardiomyopathy in children: findings from the Pediatric Cardiomyopathy Registry. *Circulation* 2007;**115**:773–781.
22 Sachdev B, Takenaka T, Teraguchi H, et al. Prevalence of Anderson–Fabry disease in male patients with late onset hypertrophic cardiomyopathy. *Circulation* 2002;**105**:1407–1411.
23 Linhart A, Elliott PM. The heart in Anderson–Fabry disease and other lysosomal storage disorders. *Heart* 2007;**93**:528–535.
24 Yang Z, McMahon CJ, Smith LR, et al. Danon disease as an underrecognized cause of hypertrophic cardiomyopathy in children. *Circulation* 2005;**112**:1612–1617.
25 Arad M, Maron BJ, Gorham JM, et al. Glycogen storage diseases presenting as hypertrophic cardiomyopathy. *N Engl J Med* 2005;**352**:362–372.
26 Wallace DC. Mitochondrial defects in cardiomyopathy and neuromuscular disease. *Am Heart J* 2000;**139**(2 Pt 3):S70–S85.
27 Holmgren D, Wahlander H, Eriksson BO, et al. Cardiomyopathy in children with mitochondrial disease; clinical course and cardiological findings. *Eur Heart J* 2003;**24**:280–288.
28 Weidemann F, Rummey C, Bijnens B, et al. The heart in Friedreich ataxia: definition of cardiomyopathy, disease severity, and correlation with neurological symptoms. Mitochondrial Protection with Idebenone in Cardiac or Neurological Outcome (MICONOS) Study Group. *Circulation* 2012;**125**:1626–1634.
29 Dutka DB, Donnelly JE, Palka P, et al. Echocardiographic characterization of cardiomyopathy in Friedreich's ataxia with tissue Doppler echocardiographically derived myocardial velocity gradients. *Circulation* 2000;**102**:1276–1282.
30 Shapiro LM, McKenna WJ. Distribution of left ventricular hypertrophy in hypertrophic cardiomyopathy: a two-dimensional echocardiographic study. *J Am Coll Cardiol* 1983;**2**:437–444.
31 Florian A, Masci PG, De Buck S, et al. Geometric assessment of asymmetric septal hypertrophic cardiomyopathy by CMR. *JACC Cardiovasc Imaging* 2012;**5**:702–711.
32 Flores-Ramirez R, Lakkis NM, Middleton KJ, et al. Echocardiographic insights into the mechanisms of relief of left ventricular

outflow tract obstruction after nonsurgical septal reduction therapy in patients with hypertrophic obstructive cardiomyopathy. *J Am Coll Cardiol* 2001;**37**:208–214.
33 Panza JA, Petrone RK, Fananapazir L, et al. Utility of continuous wave Doppler in noninvasive assessment of the left ventricular outflow tract pressure gradient in patients with hypertrophic cardiomyopathy. *J Am Coll Cardiol* 1992;**19**:91–99.
34 Rakowski H, Sasson Z, Wigle ED. Echocardiographic and Doppler assessment of hypertrophic cardiomyopathy. *J Am Soc Echocardiogr* 1988;**1**:31–47.
35 Sherrid MV, Chu CK, Delia E, et al. An echocardiographic study of the fluid mechanics of obstruction in hypertrophic cardiomyopathy. *J Am Coll Cardiol* 1993;**22**:816–825.
36 Maron BJ, Spirito P, Green KJ, et al. Noninvasive assessment of left ventricular diastolic function by pulsed Doppler echocardiography in patients with hypertrophic cardiomyopathy. *J Am Coll Cardiol* 1987;**10**:733–742.
37 Nihoyannopoulos P, Karatasakis G, Frenneaux M, et al. Diastolic function in hypertrophic cardiomyopathy: relation to exercise capacity. *J Am Coll Cardiol* 199;**19**:536–540.
38 Betocchi S, Hess OM, Losi MA, et al. Regional left ventricular mechanics in hypertrophic cardiomyopathy. *Circulation* 1993;**88**:2206–2214.
39 Perrone-Filardi P, Bacharach SL, Dilsizian V, et al. Regional systolic function, myocardial blood flow and glucose uptake at rest in hypertrophic cardiomyopathy. *Am J Cardiol* 1993;**72**:199–204.
40 Yetman AT, McCrindle BW, MacDonald C, et al. Myocardial bridging in children with hypertrophic cardiomyopathy – a risk factor for sudden death. *N Engl J Med* 1998;**339**:1201–1209.
41 Prasad K, Atherton J, Smith GC, et al. Echocardiographic pitfalls in the diagnosis of hypertrophic cardiomyopathy. *Heart* 1999;**82**(Suppl 3):III8–III15.
42 Maron BJ, Clark CE, Henry WL, et al. Prevalence and characteristics of disproportionate ventricular septal thickening in patients with acquired or congenital heart diseases: echocardiographic and morphologic findings. *Circulation* 1977;**55**:489–496.
43 Sharma S, Maron BJ, Whyte G, et al. Physiologic limits of left ventricular hypertrophy in elite junior athletes: relevance to differential diagnosis of athlete's heart and hypertrophic cardiomyopathy. *J Am Coll Cardiol* 2002;**40**:1431–1436.
44 Pelliccia A, Maron BJ, Spataro A, et al. The upper limit of physiologic cardiac hypertrophy in highly trained elite athletes. *N Engl J Med* 1991;**324**:295–301.
45 Vinereanu D, Florescu N, Sculthorpe N, et al. Differentiation between pathologic and physiologic left ventricular hypertrophy by tissue Doppler assessment of long-axis function in patients with hypertrophic cardiomyopathy or systemic hypertension and in athletes. *Am J Cardiol* 2001;**88**:53–58.
46 Maron BJ, Seidman JG, Seidman CE. Proposal for contemporary screening strategies in families with hypertrophic cardiomyopathy. *J Am Coll Cardiol* 2004;**44**:2125–2132.
47 McKenna WJ, Spirito P, Desnos M, et al. Experience from clinical genetics in hypertrophic cardiomyopathy: proposal for new diagnostic criteria in adult members of affected families. *Heart* 1997;**77**:130–132.
48 Moon JC, Mogensen J, Elliot PM, et al. Myocardial late gadolinium enhancement cardiovascular magnetic resonance in hypertrophic cardiomyopathy caused by mutations in troponin I. *Heart* 2005;**91**:1036–1040.
49 Nagueh SF, Bierig SM, Budoff MJ, et al. American Society of Echocardiography Clinical Recommendations for Multimodality Cardiovascular Imaging of Patients with Hypertrophic Cardiomyopathy Endorsed by the American Society of Nuclear Cardiology, Society for Cardiovascular Magnetic Resonance, and Society of Cardiovascular Computed Tomography. *J Am Soc Echocardiogr* 2011;**24**:473–498.
50 Redwood DR, Scherer JL, Epstein SE. Biventricular cineangiography in the evaluation of patients with asymmetric septal hypertrophy. *Circulation* 1974;**49**:1116–1121.
51 Maron MS, Olivotto I, Zenovich AG, et al. Hypertrophic cardiomyopathy is predominantly a disease of left ventricular outflow tract obstruction. *Circulation* 2006;**114**:2232–2239.
52 Lopez L, Colan SD, Frommelt PC, et al. Recommendations for Quantification Methods During the Performance of a Pediatric Echocardiogram: A Report from the Pediatric Measurements Writing Group of the American Society of Echocardiography Pediatric and Congenital Heart Disease Council. *J Am Soc Echocardiogr* 2010;**23**:465–495.
53 Menon SC, Ackerman MJ, Cetta F, et al. Significance of left atrial volume in patients <20 years of age with hypertrophic cardiomyopathy. *Am J Cardiol* 2008;**102**:1390–1393.
54 Bruch C, Schmermund A, Marin D, et al. M-mode analysis of mitral annulus motion for detection of pseudonormalization of the mitral inflow pattern. *Am J Cardiol* 1999;**84**:692–697.
55 Rossvoll O, Hatle LK. Pulmonary venous flow velocities recorded by transthoracic Doppler ultrasound: relation to left ventricular diastolic pressures. *J Am Coll Cardiol* 1993;**21**:1687–1696.
56 Pollick C, Rakowski H, Wigle ED. Muscular subaortic stenosis: the quantitative relationship between systolic anterior motion and pressure gradient. *Circulation* 1984;**69**:43–49.
57 Schwammenthal E, Nakatani S, Shengqui H, et al. Mechanism of mitral regurgitation in hypertrophic cardiomyopathy. Mismatch of posterior to anterior leaflet length and mobility. *Circulation* 1998;**98**:856–865.
58 Panza JA, Petrone RK, Fananapazir L, Maron BJ. Coexistence of mitral valve prolapse in a consecutive group of 528 patients with hypertrophic cardiomyopathy assessed with echocardiography. *J Am Coll Cardiol* 1992;**20**:55–61.
59 Flores-Ramirez R, Lakkis NM, Middleton KJ, et al. Echocardiographic insights into the mechanisms of relief of left ventricular outflow tract obstruction after nonsurgical septal reduction therapy in patients with hypertrophic obstructive cardiomyopathy. *J Am Coll Cardiol* 2001;**37**:208–214.
60 Nellen M, Gotsman MS, Vogelpoel L, et al. Effects of prompt squatting on the murmur in idiopathic hypertrophic obstructive cardiomyopathy. *Br Heart J* 1967;**3**:140–143.
61 Marwick TH, Nakatani S, Haluska B, et al. Provocation of latent left ventricular outflow tract gradients with amyl nitrite and exercise in hypertrophic cardiomyopathy. *Am J Cardiol* 1995;**75**:805–809.
62 Woo A, Wigle ED, Rakowski H. Echocardiography in the evaluation and management of patients with hypertrophic cardiomyopathy. In: Otto C (ed.) *The Practice of Clinical Echocardiography*, 2nd edn. Philadelphia, PA: Saunders, 2002, pp. 588–610.
63 Shen AY, Gupta N, Napoor G. Severe intraventricular diastolic gradient due to hypertrophic cardiomyopathy and systolic left ventricular midcavitary obstruction. *Echocardiography* 2005;**22**:47–48.

64 Nakamura T, Matsubara K, Furukawa K, et al. Diastolic paradoxic jet flow in patients with hypertrophic cardiomyopathy: evidence of concealed apical asynergy with cavity obliteration. *J Am Coll Cardiol* 19921;**19**:516–524.
65 Sato Y, Matsumoto N, Matsuo S, et al. Mid-ventricular obstructive hypertrophic cardiomyopathy associated with an apical aneurysm: evaluation of possible causes of aneurysm formation. *Yonsei Med J* 2007;**48**:879–882.
66 Webb JG, Sasson Z, Rakowski H, et al. Apical hypertrophic cardiomyopathy: clinical follow-up and diagnostic correlates. *J Am Coll Cardiol* 1990;**15**:83–90.
67 Thanigaraj S, Pérez JE. Apical hypertrophic cardiomyopathy: echocardiographic diagnosis with the use of intravenous contrast image enhancement. *J Am Soc Echocardiogr* 2000;**13**:146–149.
68 Binder J, Attenhofer Jost CH, Klarich KW, et al. Apical hypertrophic cardiomyopathy: prevalence and correlates of apical outpouching. *J Am Soc Echocardiogr* 2011;**24**:775–781.
69 Moon JC, Fisher NG, McKenna WJ, et al. Detection of apical hypertrophic cardiomyopathy by cardiovascular magnetic resonance in patients with non-diagnostic echocardiography. *Heart* 2004;**90**:645–649.
70 McMahon CJ, Nagueh SF, Eapen RS, et al. Echocardiographic predictor of adverse clinical events in children with dilated cardiomyopathy: a prospective clinical study. *Heart* 2004;**90**:908–915.
71 Nagueh SF, Middleton KJ, Kopelen HA, et al. Doppler tissue imaging: a noninvasive technique for evaluation of left ventricular relaxation and estimation of filling pressures. *J Am Coll Cardiol* 1997;**30**:1527–1533.
72 Nagueh SF, Lakkis NM, Middleton KJ, et al. Doppler estimates of left ventricular filling pressures in patients with hypertrophic cardiomyopathy. *Circulation* 1999;**99**:254–261.
73 Nagueh SF, Miakti I, Kopelen HA, et al. Doppler estimation of left ventricular filling pressures in sinus tachycardia: a new application of tissue Doppler imaging. *Circulation* 1998;**98**:1644–1650.
74 McMahon CJ, Nagueh SF, Pignatelli RH, et al. Characterization of left ventricular diastolic function by tissue Doppler imaging and clinical status in children with hypertrophic cardiomyopathy. *Circulation* 2004;**109**:1756–1762.
75 Mohammed A, Mertens L, Friedberg MK. Relations between systolic and diastolic function in children with dilated and hypertrophic cardiomyopathy as assessed by tissue Doppler imaging. *J Am Soc Echocardiogr* 2009;**22**:145–151.
76 Cerrato F, Pacileo G, Limongeli G, et al. A standard echocardiographic and tissue Doppler study of morphological and functional findings in children with hypertrophic cardiomyopathy compared to those with left ventricular hypertrophy in the setting of Noonan and LEOPARD syndromes. *Cardiol Young* 2008;**18**:575–580.
77 Nagueh SF, Bachinski LL, Meyer D, et al. Tissue Doppler imaging consistently detects myocardial abnormalities in patients with hypertrophic cardiomyopathy and provides a novel means for an early diagnosis before and independently of hypertrophy. *Circulation* 2001;**104**:128–130.
78 Nagueh SF, McFalls J, Meyer D, et al. Tissue Doppler imaging predicts the development of hypertrophic cardiomyopathy in subjects with subclinical disease. *Circulation* 2003;**108**:395–398.
79 Carabello BA. Evolution of the study of left ventricular function: everything old is new again. *Circulation* 2002;**105**:2701–2703.
80 Kato TS, Noda A, Izawa H, et al. Discrimination of nonobstructive hypertrophic cardiomyopathy from hypertensive left ventricular hypertrophy on the basis of strain rate imaging by tissue Doppler ultrasonography. *Circulation* 2004;**110**:3808–3814.
81 Ganame J, Mertens L, Eidem BW, et al. Regional myocardial deformation in children with hypertrophic cardiomyopathy: morphological and clinical correlations. *Eur Heart J* 2007;**8**:2886–2894.
82 Serri K, Reant P, Lafitte M, et al. Global and regional myocardial function quantification by two-dimensional strain: application in hypertrophic cardiomyopathy. *J Am Coll Cardiol* 2006;**47**:1175–1181.
83 Carasso S, Yang H, Woo A, et al. Systolic myocardial mechanics in hypertrophic cardiomyopathy: novel concepts and implications for clinical status. *J Am Soc Echocardiogr* 2008;**21**:675–683.
84 Ganame J, Pignatelli RH, Eidem BW, et al. Myocardial deformation abnormalities in pediatric hypertrophic cardiomyopathy: are all aetiologies identical? *Eur J Echocardiogr* 2008;**9**:784–790.
85 Di Salvo G, Pacileo G, Limongelli G, et al. Non sustained ventricular tachycardia in hypertrophic cardiomyopathy and new ultrasonic derived parameters. *J Am Soc Echocardiogr* 2010;**23**:581–590.
86 Caiani EG, Corsi C, Sugeng L, et al. Improved quantification of left ventricular mass based on endocardial and epicardial surface detection with real time three dimensional echocardiography. *Heart* 2006;**92**:213–219.
87 Franke A, Schondube FA, Kuhl HP, et al. Quantitative assessment of the operative results after extended myectomy and surgical reconstruction of the subvalvular mitral apparatus in hypertrophic obstructive cardiomyopathy using dynamic three-dimensional transesophageal echocardiography. *J Am Coll Cardiol* 1998;**31**:1641–1649.
88 Cummisford KM, Manning W, Karthik S, et al. 3D TEE and systolic anterior motion in hypertrophic cardiomyopathy. *JACC Cardiovasc Imaging* 2010;**3**:1083–1084.
89 Spirito P, Chiarella F, Carratino L, et al. Clinical course and prognosis of hypertrophic cardiomyopathy in an outpatient population. *N Engl J Med* 1989;**320**:749–755.
90 Moolman JC, Corfield VA, Posen B, et al. Sudden death due to troponin T mutations. *J Am Coll Cardiol* 1997;**29**:549–555.
91 Maskatia SA, Decker JA, Spinner JA, et al. Restrictive physiology is associated with poor outcomes in children with hypertrophic cardiomyopathy. *Pediatr Cardiol* 2012;**33**:141–149.
92 Moak JP, Leifer ES, Tripodi D, et al. Long-term follow-up of children and adolescents diagnosed with hypertrophic cardiomyopathy: risk factors for adverse arrhythmic events. *Pediatr Cardiol* 2011;**32**:1096–1105.
93 Decker JA, Rossano JW, Smith EO, et al. Risk factors and mode of death in isolated hypertrophic cardiomyopathy in children. *J Am Coll Cardiol* 2009;**54**:250–254.
94 Spirito P, Maron BJ. Relation between extent of left ventricular hypertrophy and occurrence of sudden cardiac death in hypertrophic cardiomyopathy. *J Am Coll Cardiol* 1990;**15**:1521–1526.
95 Spirito P, Seidman CE, McKenna WJ, Maron BJ. The management of hypertrophic cardiomyopathy. *N Engl J Med* 1997;**336**:775–785.
96 Suda K, Kohl T, Kovalchin JP, Silverman NH. Echocardiographic predictors of poor outcome in children with hypertrophic cardiomyopathy. *Am J Cardiol* 1997;**80**:595–560.

97 Wittlieb-Webber C, Cohen MS, McBride MG, et al. Elevated left ventricular outflow tract velocities on exercise stress echocardiography may be a normal physiologic response in healthy youth. *J Am Soc Echocardiol* 2013;**26**:1372–1378.
98 Roberts R, Sigwart U. Current concepts of the pathogenesis and treatment of hypertrophic cardiomyopathy. *Circulation* 2005;**112**:293–296.
99 McCully RB, Nishimura RA, Bailey KR, et al. Hypertrophic obstructive cardiomyopathy: preoperative echocardiographic predictors of outcome after septal myectomy. *J Am Coll Cardiol* 1996;**27**:1491–1496.
100 Ommen SR, Park SH, Click RL, et al. Impact of intraoperative transesophageal echocardiography in the surgical management of hypertrophic cardiomyopathy. *Am J Cardiol* 2002;**90**:1022–1024.
101 Lakkis NM, Nagueh SF, Kleiman NS, et al. Echocardiography-guided ethanol septal reduction for hypertrophic obstructive cardiomyopathy. *Circulation* 1998;**98**:1750–1755.
102 Faber L, Seggewiss H, Gleichmann U. Percutaneous transluminal septal myocardial ablation in hypertrophic obstructive cardiomyopathy: results with respect to intraprocedural myocardial contrast echocardiography. *Circulation* 1998;**98**:2415–2421.

CHAPTER 36

Restrictive Cardiomyopathy and Pericardial Disease

Cecile Tissot[1,2] and Adel K. Younoszai[2]

[1]Pediatric Cardiology Unit, The University Children's Hospital of Geneva, Geneva, Switzerland
[2]The Heart Institute, Children's Hospital Colorado, Aurora, CO, USA

Restrictive cardiomyopathy

Introduction

Restrictive cardiomyopathy is a rare disorder in children characterized by abnormal diastolic filling or compliance with normal or decreased diastolic volume of the ventricular chamber, in the setting of normal or near-normal systolic function [1]. The natural history is variable and depends at least partially on the etiology. Once symptoms develop, the morbidity and mortality are high and the prognosis is poor. The probability of survival at 1, 2, and 5 years is 80.5, 39, and 20%, respectively [2]. The degree of hemodynamic abnormality and the risk of sudden death are significant [3], and heart transplantation is the treatment of choice once symptoms are present [4–6].

Incidence and etiology

Although the exact incidence is unknown, restrictive cardiomyopathy is the least common of all pediatric cardiomyopathies, representing approximately 5% of cases. No known racial predilection exists. Restrictive cardiomyopathy may be slightly more common in girls than in boys [7,8]. Idiopathic restrictive cardiomyopathy represents the majority of cases in children. In patients with a familial component to their restrictive cardiomyopathy, the mode of inheritance is predominantly autosomal recessive transmission [9]. Additionally, patients with hypertrophic cardiomyopathy and diabetic cardiomyopathy can also present with a restrictive component to their disease process. Restrictive cardiomyopathy is also seen with rare diseases [10], as summarized in Table 36.1.

Pathophysiology

The physiology of restrictive cardiomyopathy is characterized by impaired myocardial relaxation and ventricular compliance leading to atrial dilatation and dysfunction. As a result, ventricular filling is primarily limited to early diastole. Typical hemodynamic characteristics include increased ventricular end-diastolic pressures with equalization of diastolic pressure between the atrial and ventricular chambers.

Anatomic findings include atrial enlargement, normal ventricular size with normal wall thickness, or concentric hypertrophy. Histology reveals endocardial and interstitial fibrosis with increased collagen deposition, myocyte hypertrophy without myofiber necrosis or disarray, and without inflammatory infiltration. In children, endomyocardial biopsies are usually not helpful in the diagnosis, unless amyloidosis or hemochromatosis is suspected [11,12].

Imaging

Echocardiography is uniquely suited as a diagnostic tool to detect the anatomic and functional abnormalities associated with restrictive cardiomyopathy and remains the major noninvasive imaging modality employed in the initial assessment of restrictive and constrictive physiology [13,14]. A complete study composed of 2D imaging, M-mode, and Doppler interrogation of both systolic and diastolic function allows the examiner to identify specific features of restrictive physiology, correlate with left-sided and right-sided filling pressures, and importantly to differentiate and distinguish from constrictive physiology.

Goals of imaging

- Assessment of inferior vena cava size and collapse with inspiration.
- Assessment of atrial size, dimension and volume (if routinely performed).
- Assessment of ventricular size and function.
- Assessment of atrioventricular valve function.
 - Right ventricular pressure estimate as measured by tricuspid regurgitation jet.
- Inflow patterns of atrioventricular valves, pulmonary veins, hepatic veins.
- TDI investigation of mitral and tricuspid annuli to help distinguish from constrictive pericarditis (Table 36.2).
- Assessment for thrombus.

Echocardiography in Pediatric and Congenital Heart Disease: From Fetus to Adult, Second Edition. Edited by Wyman W. Lai, Luc L. Mertens, Meryl S. Cohen and Tal Geva.
© 2016 John Wiley & Sons, Ltd. Published 2016 by John Wiley & Sons, Ltd.
Companion website: www.lai-echo.com

Table 36.1 Etiologies of restrictive cardiomyopathy

Idiopathic
Amyloidosis
Hemosiderosis
Hemochromatosis
Hypereosinophilia:
Loeffler syndrome
Carcinoid syndrome
Endocardial fibroelastosis
Metabolic diseases:
Gaucher's disease
Fabry's disease
Hurler syndrome
Glycogen storage disease
Secondary to radiation therapy
Secondary to anthracycline administration

2D echocardiography

In restrictive cardiomyopathy, both ventricular cavities are typically small with decreased end-diastolic dimensions. Marked biatrial enlargement is pathognomonic (Figure 36.1; Video 36.1), with the atrial dimension in adults usually measuring >45 mm in apical 4-chamber view. A left atrial dimension greater than 60 mm has been associated with a poor prognosis [15]. Atrial thrombi may be seen, especially in the appendages. Concentric left ventricular hypertrophy with normal or slightly decreased systolic function is usual [16]. Thickening of the atrial septum and cardiac valves is also common. Valvar dysfunction is often present, especially atrioventricular valve regurgitation (Figure 36.2). In most cases, there is evidence of pulmonary hypertension including elevated right ventricular pressure estimate as measured by the tricuspid regurgitation jet (in 4-chamber view) or flattened or bowing ventricular septal position (Figure 36.3). Right ventricular pressure may be underestimated using the tricuspid regurgitation jet method because the atrial pressure (which must be included in the equation) is often fairly

Table 36.2 Echocardiographic parameters to distinguish between restriction, constriction and tamponade

Parameter	Tamponade	Constrictive pericarditis	Restrictive cardiomyopathy
RAP	↑	↑	↑
RV and LV filling pressures	↑ RV = LV	↑ RV = LV	↑ LV > RV
PAP	Normal	Mild↑	Moderate–severe↑
RV diastolic pressure plateau		RVSP <40 mm Hg >1/3 peak RV pressure	RVSP >40 mm Hg <1/3 RV pressure
2D echo	Pericardial effusion	Pericardial effusion Septal shudder Interventricular dependence: IVS diastolic shift toward LV during inspiration and toward RV during expiration	LVH No interventricular dependence
M-mode		Septal notch	No septal notch
Doppler MV and TV	Reciprocal respiratory changes in RV and LV filling ↑TV E during inspiration ↑MV E during expiration LV inflow: E > A	Respiratory variation (>10%) in RV and LV filling ↑MV E during expiration Respiratory variation in IVRT LV inflow: E > A	No respiratory variation in RV and LV filling No respiratory variation in IVRT LV inflow: early: E < A late: E ≫ A with ↓A velocity
Doppler Pv		↑TR peak velocity, VTI and duration during inspiration Respiratory variation in Pv flow: ↑D during expiration Pv flow: ↑AR ↓S	No respiratory variation in TR jet No respiratory variation in Pv flow Pv flow: ↑AR velocity and duration Early: ↑S and ↓D Late: normal S and ↑D
TDI		S/D >0.65 during inspiration e′ >8 cm/s E/e′ <15	S/D <0.4 e′ <8 cm/s E/e′ >15
Color M-mode		Vp >100 cm/s	Vp <45 cm/s

Source: Adapted from Otto CM. *Textbook of Clinical Echocardiography*, 3rd edn, p. 273. Elsevier Saunders, Philadelphia, PA, and from Tam JW, Shaikh N, Sutherland E. Echocardiographic assessment of patients with hypertrophic and restrictive cardiomyopathy: imaging and echocardiography. *Curr Opin Cardiol* 2002;**17**:470–477.

RAP, right atrial pressure; RV, right ventricle; LV, left ventricle; PAP, pulmonary artery pressure; RVSP, right ventricular systolic pressure; LVH, left ventricular hypertrophy; IVS, interventricular septum; MV, mitral valve; TV, tricuspid valve; IVRT, isovolumic relaxation time; Pv, pulmonary vein; TR, tricuspid regurgitation; AR, A reversal; Vp, propagation velocity

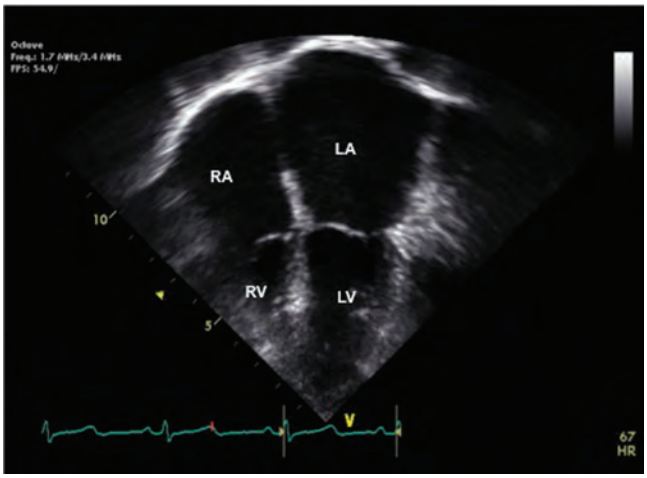


Figure 36.1 4-chamber view of a patient with restrictive physiology. Both ventricular cavities are small with decreased end-diastolic dimensions. The marked atrial enlargement ("ice cream cone heart") is pathognomonic.

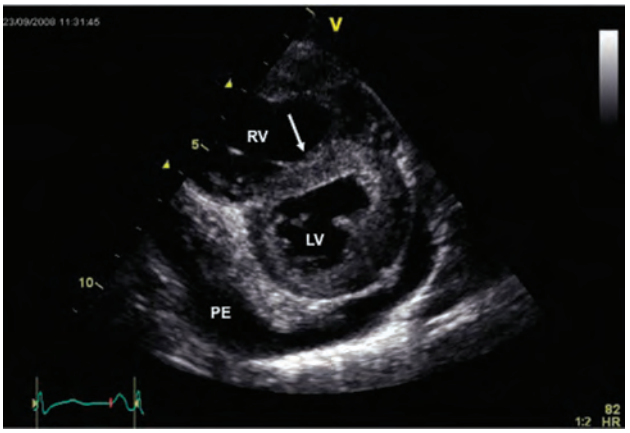


Figure 36.3 Parasternal short-axis view in restrictive cardiomyopathy demonstrating systolic flattening of the interventricular septum (arrow) indicative of pulmonary hypertension. This patient also has pericardial effusion from increased filling pressure. LV, left ventricle; PE, pericardial effusion; RV, right ventricle.

high. Subxiphoid imaging often reveals that the inferior vena cava is dilated and does not collapse with inspiration (plethora), reflecting increased right atrial pressure (Figure 36.4). A pericardial effusion may be present. Myocardial reflectance is usually increased. In the case of amyloidosis, the ventricular walls are thickened with a granular or sparkling myocardium on echocardiography, reflecting amyloid deposits. M-mode echocardiography provides basic assessment of cardiac structure and dimensional changes during the cardiac cycle [17]. When examined with this imaging modality, the ventricular chambers are typically small and mild concentric hypertrophy is usually seen.

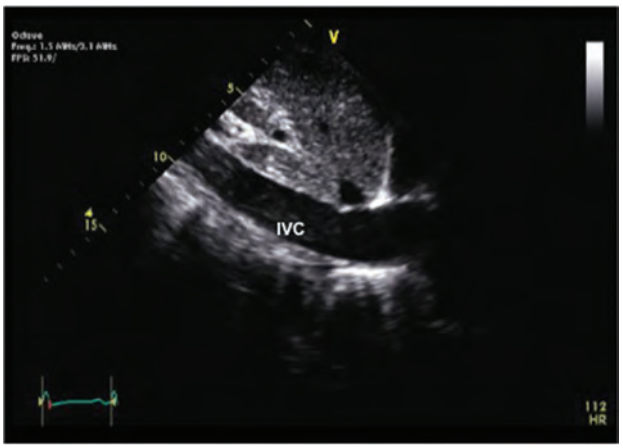
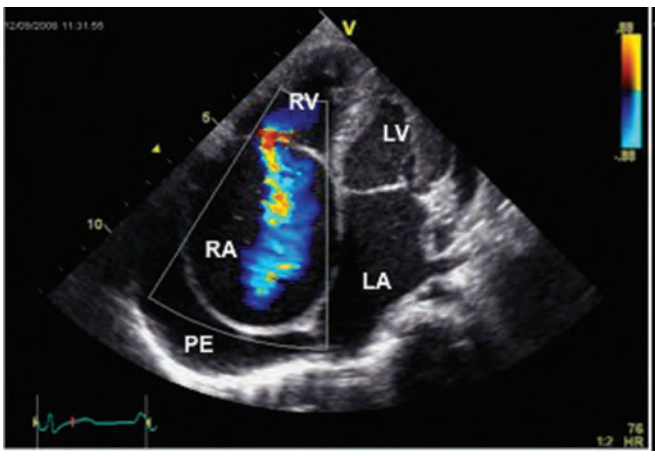


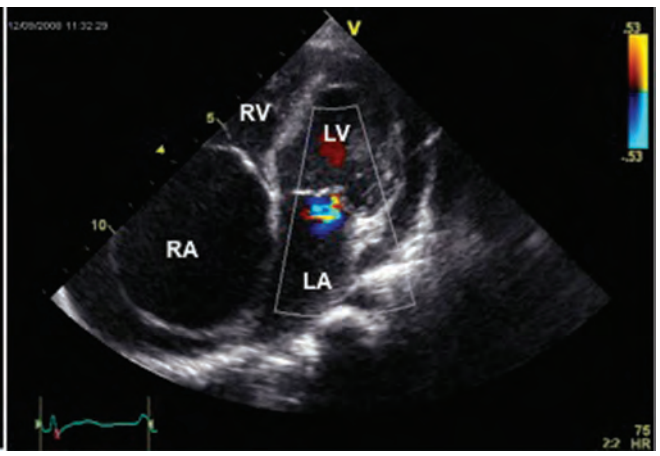
Figure 36.4 Subxiphoid view of a markedly dilated inferior vena cava, reflecting increased right atrial pressure. IVC, inferior vena cava.

Flow characteristics

Doppler echocardiography remains the primary clinical tool for providing reliable assessment of diastolic function. In the preliminary stages of restriction, an impaired relaxation pattern may be present before the onset of abnormal compliance.



(a)



(b)

Figure 36.2 Apical 4-chamber view of a child with restrictive cardiomyopathy: severe tricuspid regurgitation **(a)**, mild mitral regurgitation **(b)**, and pericardial effusion from increased filling pressure. LA, left atrium; LV, left ventricle; PE, pericardial effusion; RA, right atrium; RV, right ventricle.

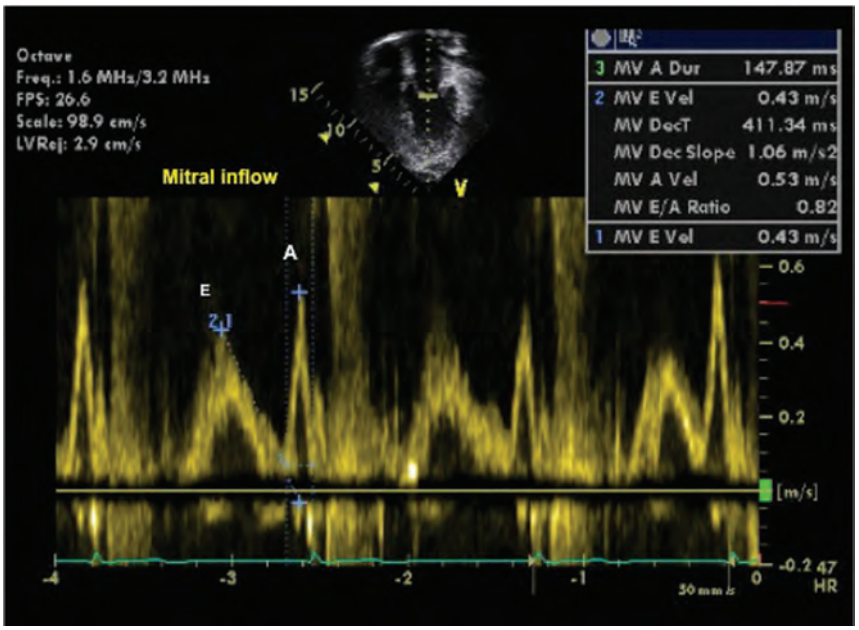


Figure 36.5 Mitral valve inflow Doppler showing predominantly late diastolic filling of the left ventricle, with E/A wave reversal (E < A). E, early diastolic wave; A, late diastolic wave.

Determination of severity of diastolic dysfunction is important not only for diagnostic but also for prognostic reasons, as the mortality rate is highly associated with a markedly restrictive pattern [18].

Evaluation of diastolic function is routinely comprised of measurement of mitral early (E wave) and late (A wave) diastolic inflow and pulmonary vein systolic (S wave), diastolic (D wave) and atrial reversal (AR wave) flow with the corresponding right-sided tricuspid and hepatic vein flow waves. Progressive impairment of diastolic function leads to different patterns of transmitral, pulmonary venous Doppler and mitral annular tissue Doppler velocities. Using these parameters, four stages of diastolic dysfunction may be determined [19].

The classic Doppler pattern of impaired relaxation is characterized by [13,18,20]:

1 *Mitral inflow:* In the initial phase of delayed relaxation, reversal of the normal transmitral E and A waves with E < A is noted (Figure 36.5). When restriction is present, a large E wave and small A wave with an E/A ratio >2 [21, 22], a shortened deceleration time (DT) (<150 ms), and a shortened isovolumic relaxation time (IVRT) (<60 ms) are noted (Figure 36.6). In contrast to constriction, there is no

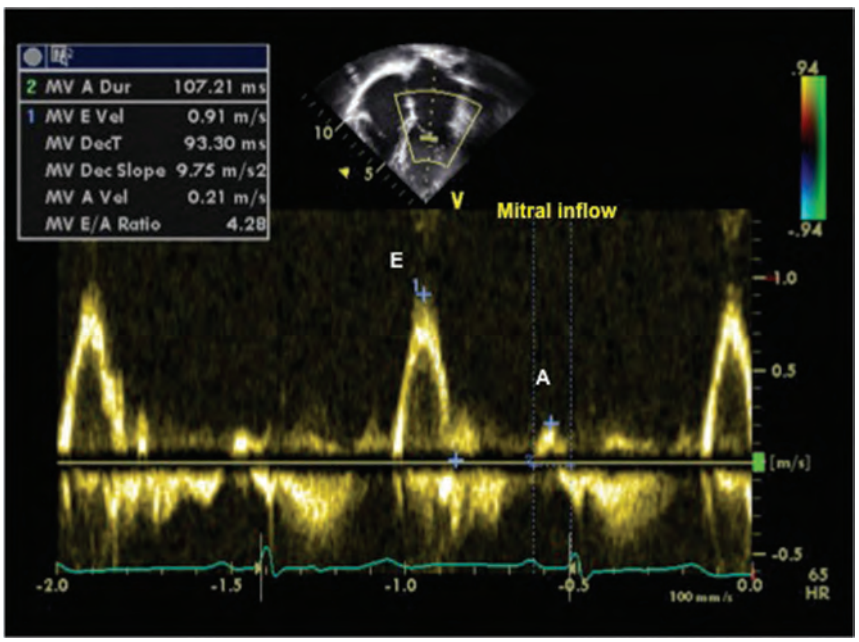


Figure 36.6 Mitral valve inflow Doppler of a patient with restrictive physiology. Large E wave and small A wave with an E/A ratio >2 and a short deceleration time (DT) of 93 ms are characteristic of a restrictive physiology.

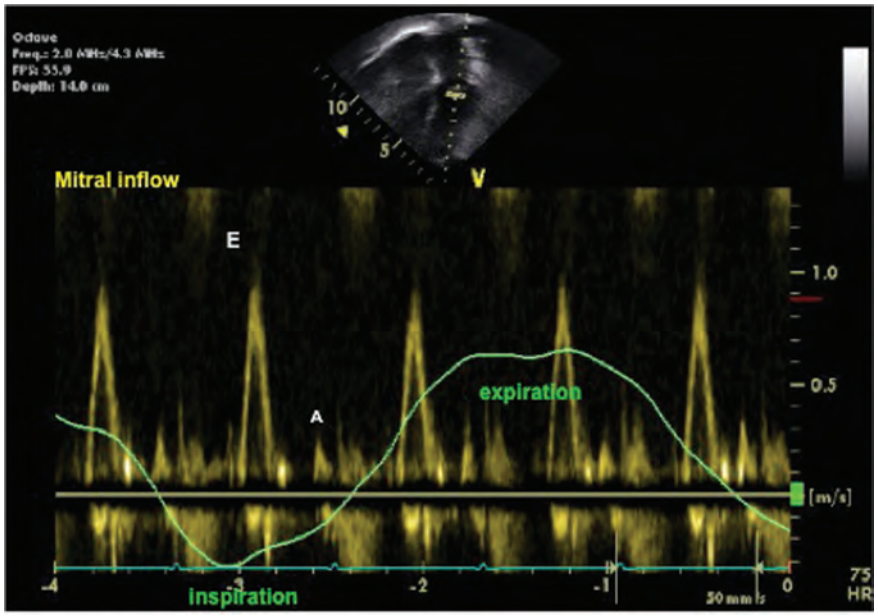


Figure 36.7 Mitral inflow Doppler showing no respiratory variation in restrictive physiology, as opposed to constrictive physiology.

significant change in mitral E wave, DT, or IVRT with respiration (Figure 36.7).

2 *Pulmonary veins:* The initial phase of delayed relaxation is characterized by reversal of the normal S and D waves with S > D in adults. Restriction is defined as a D-predominant flow pattern with small S wave and large D wave, with an S/D ratio <0.5. In young children in whom a dominant D wave is normally seen, evaluation of the S and D wave pattern is of little value. Prominent A reversal with both increased amplitude and prolongation is seen, with an A reversal width greater than the mitral A wave duration (Figure 36.8). In contrast to a constrictive pattern, there is no significant respiratory variation of the D wave.

3 *Tricuspid inflow:* The patterns are similar to mitral inflow with restriction characterized by an increased E/A ratio and a shortened DT (Figure 36.9). Further shortening of the DT is noted with respiration with minimal change in E/A ratio.

4 *Hepatic veins:* The patterns are similar to pulmonary vein flow. An S/D ratio <0.5 with prominent atrial and ventricular reversal is noted with restriction (Figure 36.10). There is increased prominence of reversal waves with respiration.

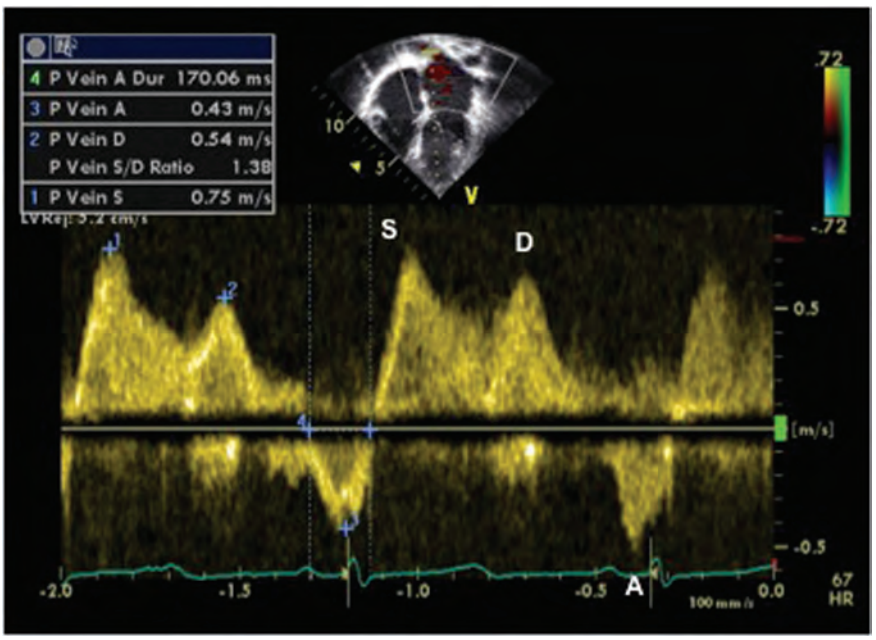


Figure 36.8 Note the prominent A reversal of the pulmonary vein Doppler with both increased amplitude and prolongation (corresponding to the numbers 3 and 4, respectively). The A reversal width is greater than the mitral A wave duration in the corresponding patient (Figure 36.5). S, systolic wave; D, diastolic wave; A, atrial reversal wave.

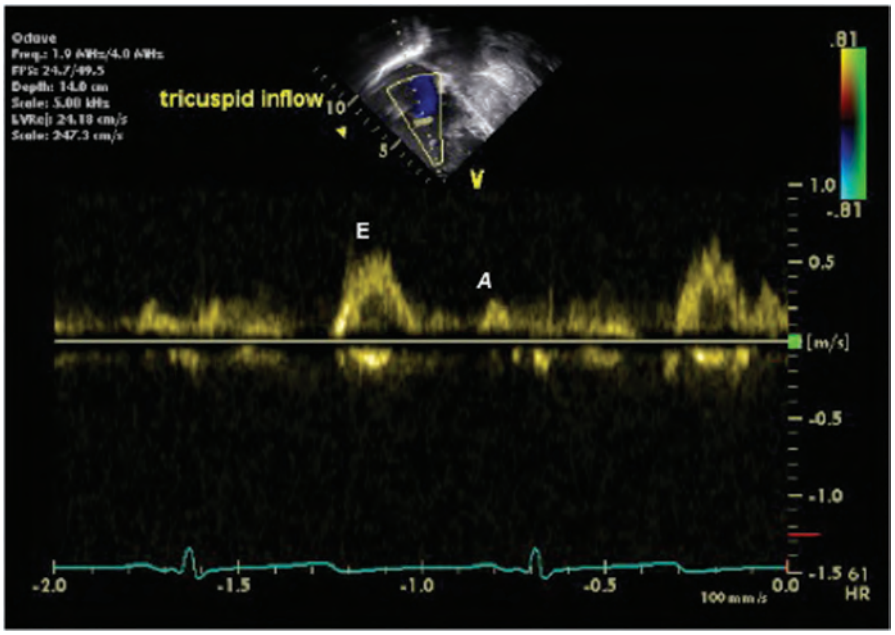


Figure 36.9 Tricuspid inflow of a patient with restrictive cardiomyopathy showing a large E wave and a small A wave.

It is important to remember that these measurements are dependent on loading conditions and assume that the patient is in sinus rhythm. As noted previously, and as opposed to constriction, there is no respiratory variation in mitral and tricuspid E wave and in left ventricular IVRT in restrictive physiology [23]. Unfortunately, Doppler echocardiographic findings still show overlap between restrictive and constrictive patterns. Intravascular volume expansion has been shown to be safe and effective in augmenting the diastolic impairment of restrictive physiology [24].

Color M-mode

Color M-mode offers a unique view into the fluid dynamics of left ventricular inflow. It assesses the flow propagation from the mitral valve into the left ventricle, which is dependent on intraventricular pressure gradients. The velocity of propagation (Vp), assessed by the slope of the color aliasing velocity at the leading edge of the E wave, is enhanced with rapid normal ventricular relaxation [25,26]. Vp provides a relatively preload-independent determination of relaxation and can be used in conjunction with the mitral inflow E wave to

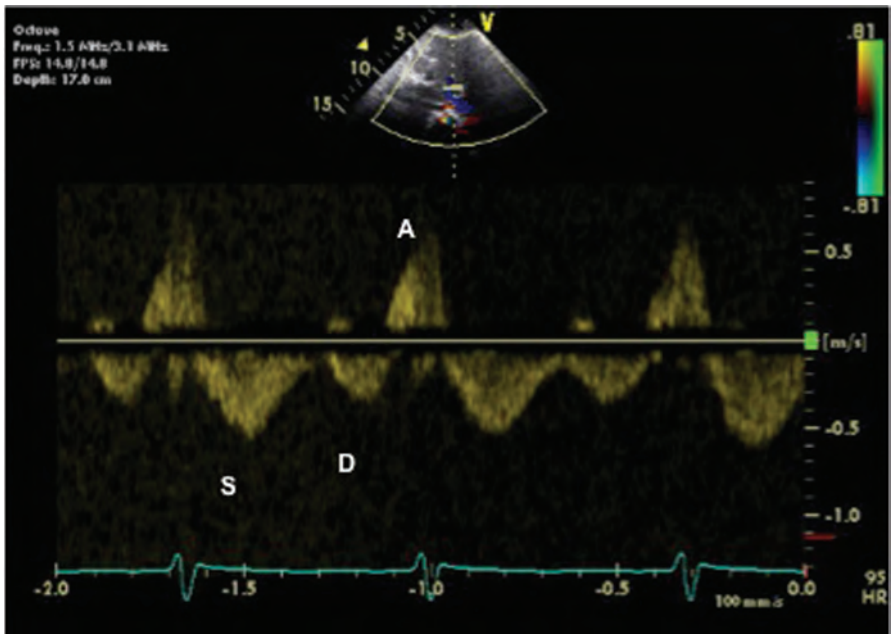
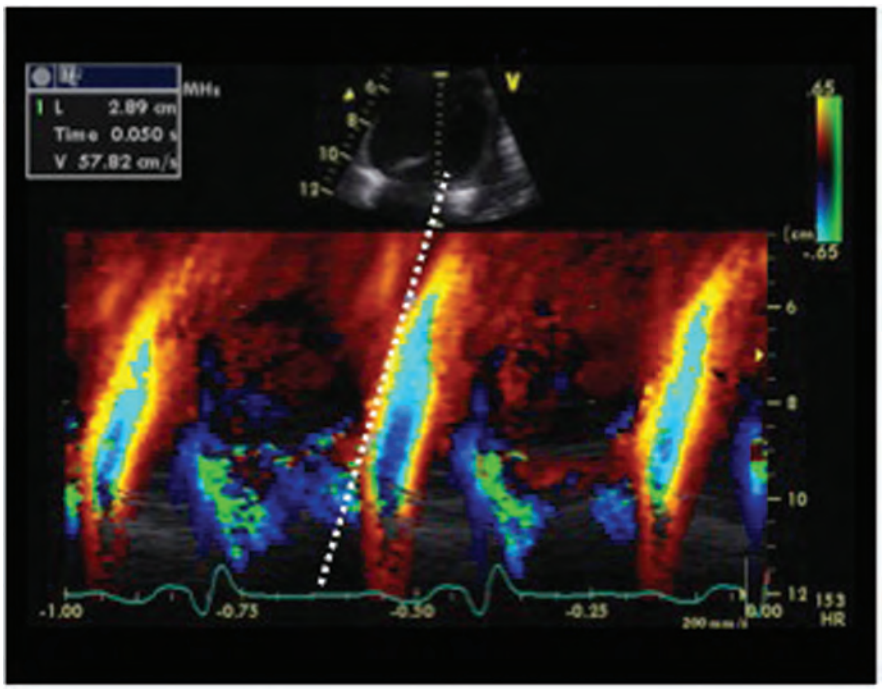
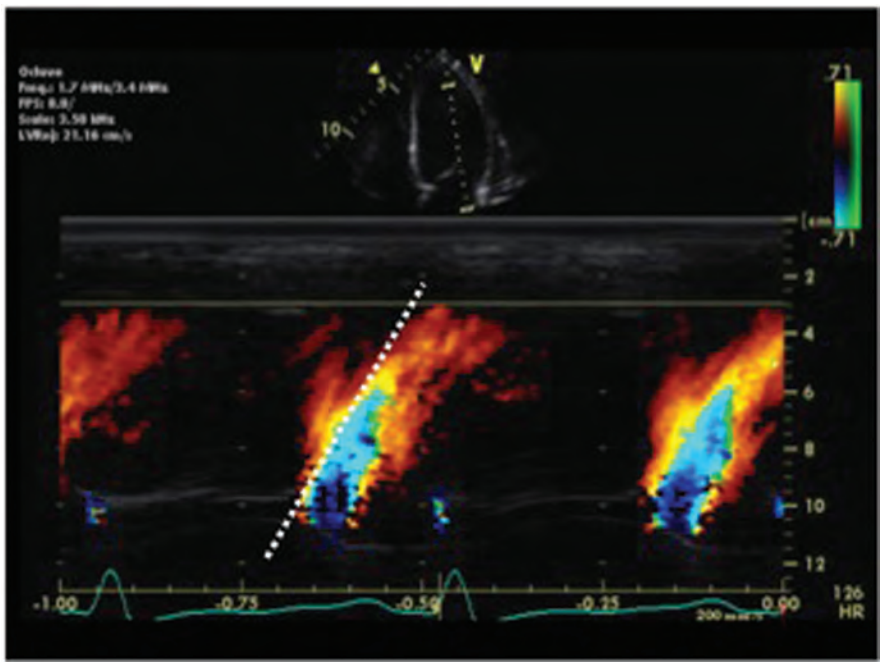


Figure 36.10 Hepatic venous Doppler in restrictive cardiomyopathy demonstrating prominent A wave reversal.



(a)



(b)

Figure 36.11 Color M-mode of a patient with restrictive cardiomyopathy **(b)**, demonstrating decreased inflow propagation velocity (Vp), compared with color M-mode in a normal patient **(a)**.

estimate pulmonary capillary wedge pressure [27]. In restrictive cardiomyopathy, Vp is decreased compared with constrictive pericarditis, where Vp is normal or increased (Figure 36.11) [28–30].

Tissue mechanics

Using either Doppler principles or tissue tracking technology, the movement of the myocardium can be evaluated in the assessment of restrictive cardiomyopathy. Tissue motion as measured by tissue Doppler imaging (TDI) is less load sensitive than blood flow. TDI helps distinguish constrictive from restrictive physiology. Patients with restrictive cardiomyopathy have an abnormality of both relaxation and compliance, whereas those with constrictive pericarditis have normal relaxation but impaired compliance. Early mitral annular velocity (e′ wave) is usually reduced in restriction (Figure 36.12), whereas it is normal or

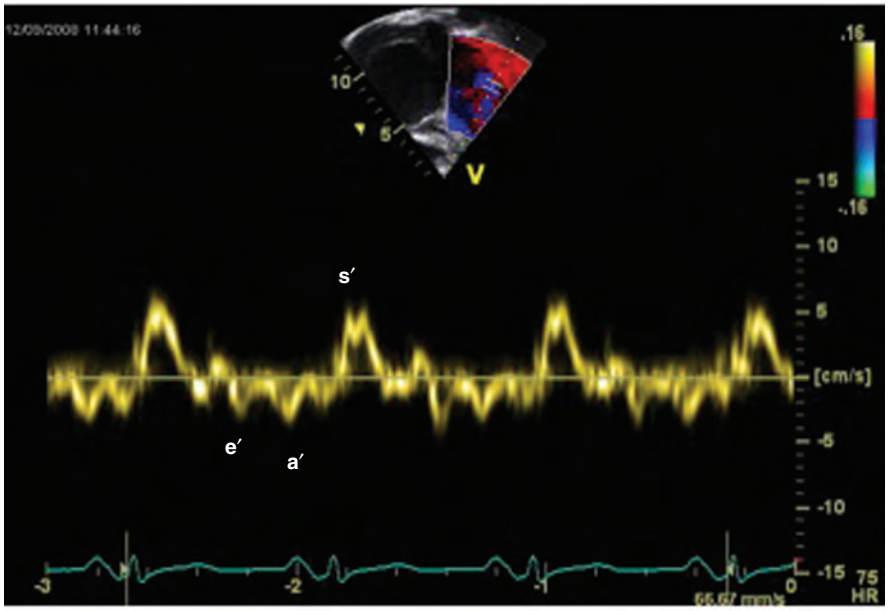


Figure 36.12 Decreased e′ velocity <8 cm/s **(a)** and prominent e′ and small a′ waves **(b)** by tissue Doppler imaging in a patient with restrictive cardiomyopathy. e′, early diastolic wave; a′, late diastolic wave; s′, systolic wave.

increased in constrictive pericarditis [30]. TDI of the mitral annulus reveals a similar reversal of the e′ and a′ pattern with e′ < a′ (Figure 36.13) and with velocities less than the normal 8 cm/s. However, with progressive diastolic dysfunction, early myocardial velocities remain depressed without the pseudonormalized pattern that confounds evaluation of color transmitral flow. Measurement of the ratio of the Doppler transmitral E wave to the tissue Doppler mitral e′ wave (E/e′ ratio) is useful in the assessment of left ventricular filling pressure. An E/e′ ratio >15 indicates elevated left ventricular filling pressure [28–33].

Additional methods of assessing myocardial mechanics in restrictive cardiomyopathy include strain and strain rate. Strain represents the relative deformation of myocardium and strain rate is defined as the speed of deformation of myocardium [34]. Strain is a dimensionless measure and is produced by application of stress. It represents the percentage change from the original or unstressed dimension and includes both lengthening or expansion (positive strain) and shortening or compression (negative strain). Compared with tissue velocities, these parameters are less influenced by cardiac motion and allow more accurate assessment of segmental myocardial function. Strain has been shown to correlate with both pulmonary arterial wedge pressure and end-diastolic pressure [20]. It is useful to demonstrate early impairment in systolic function at a time

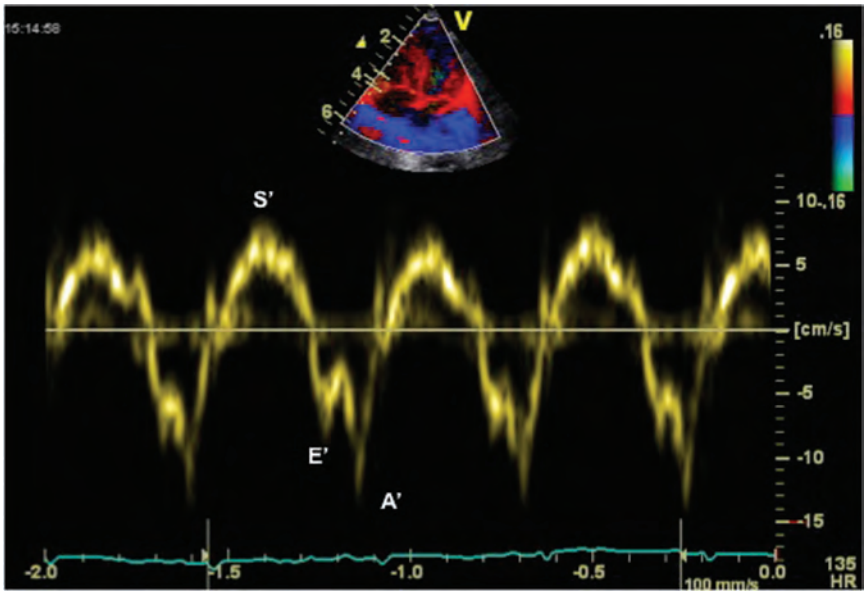


Figure 36.13 Tissue Doppler imaging showing reversal of e′ and a′ waves with e′ < a′.

when fractional shortening remains normal [35]. In patients with impaired relaxation, the subendocardial fibers demonstrate slower relaxation times in early diastole. Recently, tissue tracking techniques have been developed to eliminate the inherent angle dependency of conventional Doppler echocardiography. Tissue tracking of the myocardium has been used to evaluate both tissue velocities and deformation [36]. These novel applications should play an increasing role in future evaluation of restrictive physiology.

The different echocardiographic parameters of diastolic dysfunction in adults are summarized in Table 36.3 and Figure 36.14. It is important to remember that in young children, especially infants, the mature Doppler patterns of blood flow are not established, making the confident evaluation of diastolic function more challenging than in adults. Despite these limitations, with our growing understanding of myocardial mechanics, diastole should not be ignored in children. Evaluation of relaxation using all of the available tools is important to help identify isolated diastolic dysfunction – such as in restrictive cardiomyopathy – and monitor the patient's disease state. Further work to develop clear measures of diastolic function in children is ongoing.

Transesophageal echocardiography

Transesophageal echocardiography (TEE) affords improved imaging windows in the older patient and a superior angle of interrogation for analysis of the pulmonary vein flow. Additionally, the transgastric view offers a direct visualization of the pericardium. As described above, volume expansion has been shown to be effective in augmenting the diastolic impairment of restrictive physiology, increasing the likelihood of a positive diagnosis by TEE [24].

Table 36.3 Parameters and echocardiographic measures of diastolic function in children and adults

Parameters	Normal for youngsters	Normal for adults	Mild diastolic dysfunction (grade I)	Pseudonormal (grade II)	Restrictive pattern (grade III–IV)
LV relaxation	Normal	Normal	↓	↓↓	↓↓↓
LV stiffness	Normal	Normal	↑	↑↑	↑↑↑
LA contractility	Normal	Normal	↑	Normal	↓
Preload	Normal	Normal	Normal	↑	↑↑
E/A	>1	>1	<1	1–2	>2
DT (ms)	<220	<220	>220	150–200	<150
IVRT (ms)	<100	<100	>100	60–100	<60
S/D	<1	≥1	≥1	<1	<1
AR (cm/s)	<35	<35	<35	≥35	≥25
Vp (cm/s)	>55	>45	<45	<45	<45
e′ (cm/s)	>10	>8	<8	<8	<8

Source: Adapted from Garcia et al. [28].
LV, left ventricle; LA, left atrium; DT, deceleration time; IVRT, isovolumic relaxation time; AR, atrial reversal; Vp, propagation velocity.

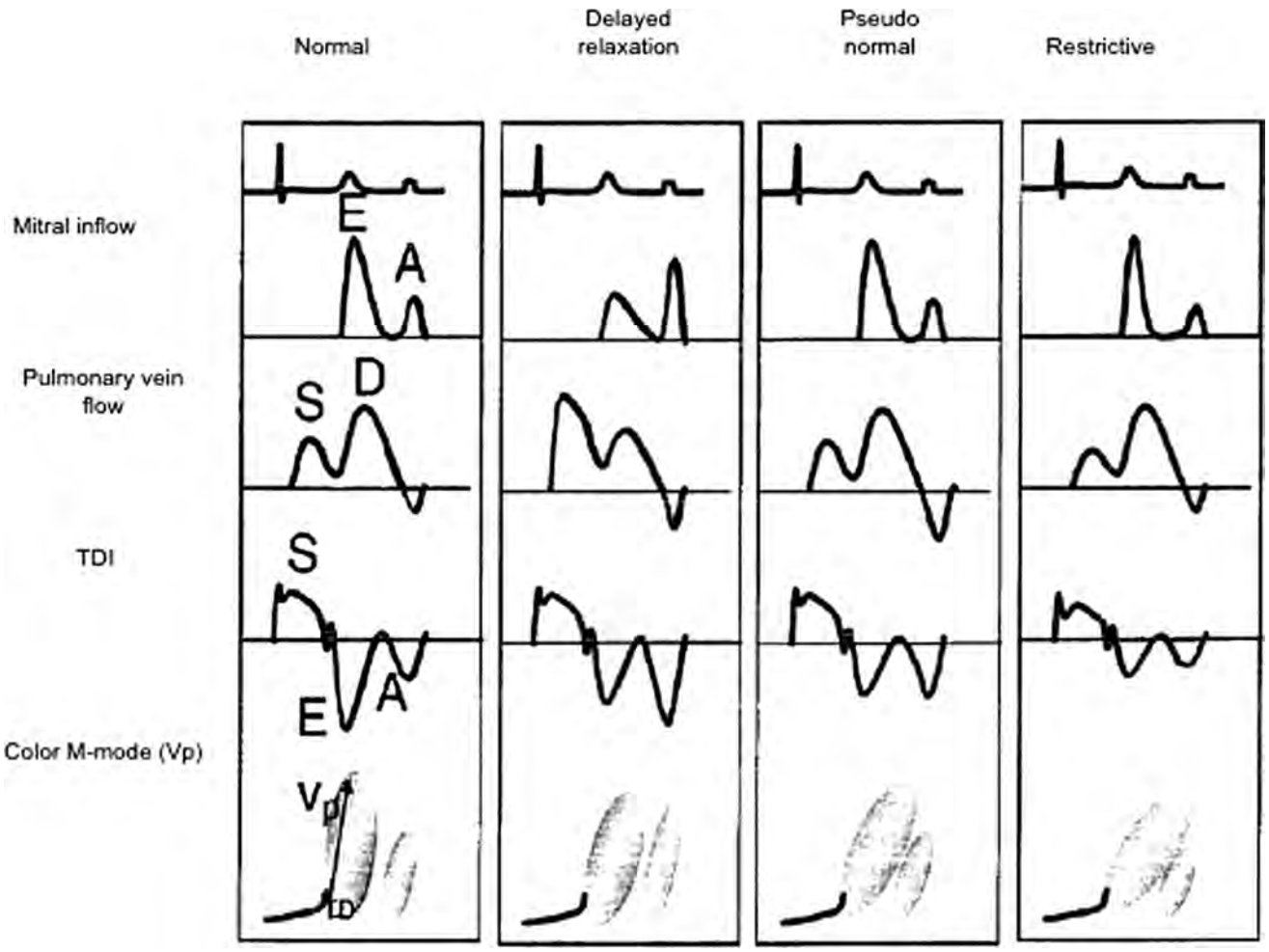


Figure 36.14 Comparison of the changes in mitral valve inflow Doppler, pulmonary vein Doppler, tissue Doppler, and color M mode found during evaluation of progressive stages of diastolic dysfunction. Source: Adapted from Garcia et al. 1998 [28].

Additional mModalities

Electrocardiography may help in distinguishing restrictive cardiomyopathy from constrictive pericarditis but is never diagnostic. The ECG may show depolarizing abnormalities such as a bundle branch block, ventricular hypertrophy, and impaired atrioventricular conduction. A chest X-ray may show cardiomegaly, enlarged atria with prominent right heart border, and enlarged carina angle. Cardiac catheterization can also help in the distinction.

Cardiac computed tomography and cardiac magnetic resonance imaging

Computed tomography (CT) and cardiac magnetic resonance (CMR) imaging are useful to help differentiate restrictive cardiomyopathy from constrictive pericarditis by assessing pericardial thickness, the hemodynamics of constriction, and any myocardial abnormalities. Some forms of restrictive cardiomyopathy are associated with characteristic CMR findings, such as endomyocardial fibrosis. CMR can reliably quantify iron loading in patients with hemochromatosis through the T2 mapping technique (shortened T2 relaxation time) [37].

Pericardial diseases

Constrictive pericarditis

Introduction

Constrictive pericarditis is defined as inflammation, thickening, and fusion of the thin and easily distensible parietal and visceral pericardial layers, resulting in impaired venous return and ventricular filling of the heart [38]. The process is typically indolent and slowly progressive, with clinical manifestation usually appearing months or even years after the initial inflammatory insult.

Incidence and etiology

Constrictive pericarditis is very rare and sporadic in the pediatric population [39]. The disease is most commonly a complication of acute pericarditis, either a single intense episode or

Table 36.4 Causes of constrictive pericarditis

Idiopathic
Post-acute pericarditis
Tuberculosis
Infectious:
Viral
Bacterial: staphylococci, streptococci
Fungal: histoplasmosis
Rheumatoid disease
Sarcoidosis
Mediastinal radiation (Hodgkin lymphoma)
Trauma (hemopericardium)
Status post-cardiac surgery (postpericardiotomy syndrome)
Uremia
Neoplasia with pericardial infiltration
Metabolic and genetic disorders

multiple recurrent flares [40]. The underlying inciting event frequently varies with the ethnicity and country of origin of the patient. Tuberculous pericarditis is the most frequent known cause of chronic constrictive pericarditis worldwide. Mediastinal irradiation and cardiac surgery are the most common causes of constriction in Europe and North America [41]. The diagnosis of constrictive pericarditis is often made after an extensive diagnostic work-up in the setting of failure of conventional medical therapy for congestive heart failure. Life expectancy is reduced in untreated children and in patients with relatively acute onset of symptoms [42]. There is no statistical difference between race and gender in the prevalence of the disease.

Constrictive pericarditis is rare in children. Different etiologies can produce variable clinical findings, depending on the rapidity and severity of development (Table 36.4). Chronic constrictive pericarditis develops insidiously and frequently no etiology is found.

Pathophysiology

In constrictive pericarditis, the size of the heart is usually normal. The pericardium typically shows inflammation, fibrosis, thickening and obliteration of the space between the visceral and parietal layers. Adhesions also occurs between the pericardium and myocardium. The pericardial thickening and adhesions may be focal or diffuse. Calcifications may also be present. Myocardial histologic findings include fibrotic thickening, chronic inflammation, granulomas, and calcification.

Conditions that lead to constrictive pericarditis result in decreased cardiac compliance associated with diminished ventricular distensibility, inability to maintain adequate preload, and biventricular diastolic dysfunction. As opposed to pericardial effusion, early ventricular filling is not altered in constrictive pericarditis. However, as the ventricles fill, they meet the inelastic resistance of the stiff, often calcified pericardium, at which time filling pressure rises rapidly to an elevated plateau. This late diastolic phenomenon is due to a change in the volume–elasticity curve, a small increase in volume results in a considerable increase in end-diastolic pressure. Atrial filling pressures are elevated, reflecting both ventricular noncompliance and atrial constraint by the thick pericardium. Since there is isolated encasement of the pericardium but not of the systemic veins or lungs, there is dissociation between intrathoracic and intracardiac pressures, with marked interventricular dependence, respiratory variation, and discordance in right and left heart filling [23,38,43].

Imaging

Echocardiography remains the best tool in the initial assessment of constrictive pericarditis [13]. A combination of 2D imaging, M-mode, and Doppler information is capable of diagnosing the anatomic and pathophysiologic features of constrictive pericarditis in most patients.

Goals of imaging

- Assessment of inferior vena cava size and collapse with inspiration.
- Assessment for pericardial thickening.
- Assessment of atrial and ventricular size and function.
- Doppler assessment of reciprocal respiratory variation of right and left heart flows.
- TDI assessment to help distinguish from restrictive cardiomyopathy (Table 36.2).

2D echocardiography

A thickened pericardium with some degree of pericardial effusion may be observed in various echocardiographic views [44]. However, 2D echocardiography is often insensitive, as mildly increased pericardial thickening may be missed and a false-positive finding may be obtained if the gains are set too high. Pericardial calcifications with localized tethering of atrial or ventricular cavities may be noted. Separation of the entire pericardium by a small fixed space is known as the "halo sign" (Figure 36.15). An abnormal echo contour at the reflection of the pericardium to the posterior left atrial wall may be seen. In subxiphoid view, the systemic veins are usually dilated, with the inferior vena cava exhibiting absent collapse with inspiration (plethora) (Figure 36.4).

Abnormal motion of the myocardium relative to the pericardium is best seen anterior to the right ventricular outflow tract or lateral to the apex in the 4-chamber view, with the myocardium appearing to pull the pericardium without altering the small echo-free separation of these two layers. Septal "bounce" is typical, defined as abrupt posterior movement of the interventricular septum in early diastole during inspiration (Video 36.2); this is caused by underfilling of the left ventricle and redistribution of blood from the left to the right ventricle. Septal "bounce" may represent the first and best clue for the presence of constriction [45]. The left ventricular posterior wall may show the same "bouncing" pattern.

In addition to these findings, most echocardiographic views will show that the right and left ventricular chamber sizes are decreased, and both atria are mildly enlarged, related to the

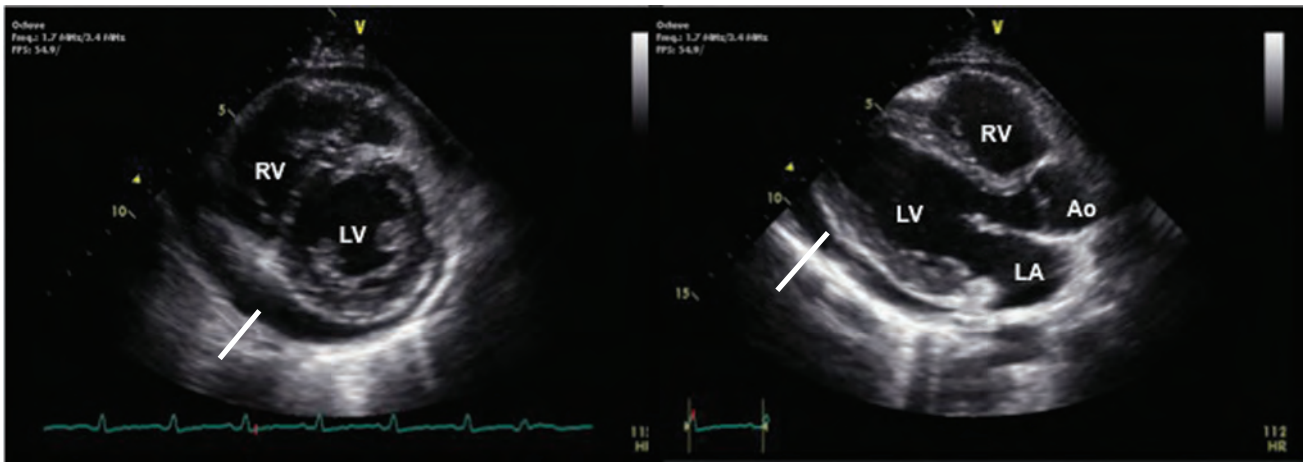


Figure 36.15 Parasternal short-axis and long-axis views of a patient with constrictive pericarditis and a small circumferential pericardial effusion (halo sign). Ao, aorta; LA, left atrium; LV, left ventricle; RV, right ventricle.

compliance abnormality of the ventricles. The ventricles often have an elongated appearance, giving the heart a tubular shape. The inspiratory increase in chamber size is larger in patients with constrictive pericarditis than in those with restrictive cardiomyopathy. The biventricular systolic function is usually normal. A typical feature of constrictive pericarditis is parallel motion of the epicardium and the parietal pericardium, as it is in the normal state, in contrast to the damping pattern of pericardial effusion. Interventricular septal motion, seen best with M-mode, may be paradoxical or flat as a sign of ventricular interdependence (Figure 36.16). A characteristic septal notch has been described in early diastole (Figure 36.17), corresponding to the pericardial knob which occurs between the second and third heart sounds and to the septal bounce seen by 2D echocardiography [46,47]. Extensive areas of adhesions seen posteriorly by 2D or M-mode provide evidence for generalized pericardial thickening and constriction (Figure 36.18).

Flow characteristics

The hallmark of Doppler examination in constrictive pericarditis is reciprocal respiratory variation of right and left heart flows caused by interventricular dependence. The classical Doppler pattern consists of the following (Figure 36.19) [20,48,49]:

1 *Mitral inflow:* During inspiration, a smaller E wave, longer IVRT, and shorter DT are noted. During expiration, there is larger E wave, shorter IVRT, and usually longer DT. The

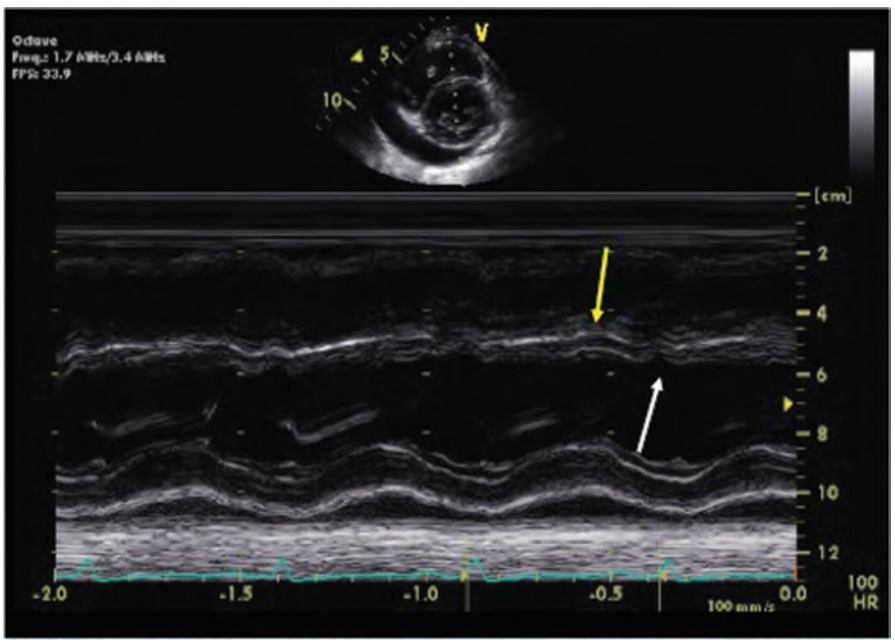


Figure 36.16 M-mode demonstrating paradoxical septal motion (yellow arrow) and septal notch (white arrow) in early diastole.

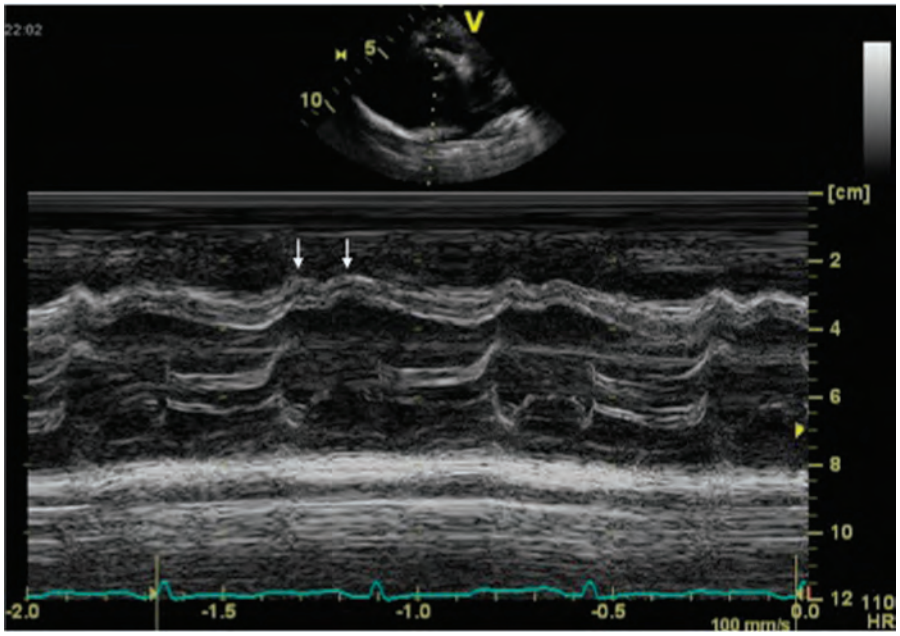


Figure 36.17 M-mode echocardiography in constrictive pericarditis: notched interventricular septum in early diastole (arrow).

E wave is typically increased more than 25% with expiration and the IVRT increases more than 25% with inspiration.

2 *Pulmonary veins:* During inspiration, S and D waves are near equal in size. During expiration, larger S and D waves are noted.

3 *Tricuspid inflow:* The tricuspid inflow shows the same pattern with reciprocal changes compared with the mitral inflow. During expiration, a smaller E wave, longer IVRT, and shorter DT is noted. During inspiration, there is larger E wave, shorter IVRT, and usually longer DT. The E wave is typically increased more than 40% with inspiration.

4 *Hepatic veins:* During inspiration, the S wave is greater than the D wave, with a small A reversal and ventricular reversal. During expiration, the S wave is greater than the D wave, with small or absent D wave and larger A reversal and ventricular reversal.

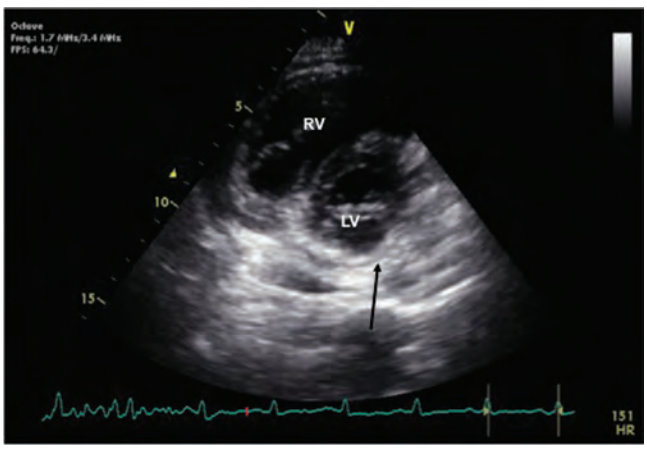


Figure 36.18 Parasternal short-axis view of a patient with constrictive pericarditis showing thickening of the posterior pericardium.

Also described in constrictive pericarditis is an inspiratory increase in the tricuspid regurgitant jet velocity and duration of the signal [50].

As opposed to restrictive cardiomyopathy, respiratory variation in the filling phases is more pronounced in constrictive pericarditis. It is important to note that no single Doppler measurement can fully characterize left ventricular diastolic function. Most of the parameters are dependent on load, heart rate, and age.

Color M-mode

Color M-mode is helpful in distinguishing constrictive pericarditis from restrictive cardiomyopathy. The propagation velocity (Vp) of early diastolic transmitral flow on color M-mode is normal or increased in constrictive pericarditis, in contrast to restrictive cardiomyopathy where the Vp is decreased (Figure 36.11) [28].

Tissue mechanics

The early mitral annular velocity (e′ wave) is usually normal or high in constrictive pericarditis, as opposed to reduced in restrictive cardiomyopathy [29]. The usually positive linear relation between mitral Doppler E and tissue Doppler e′ (E/e′), is useful to assess left atrial pressure and is found to be reversed (annular paradox) in constrictive pericarditis [51].

Transesophageal echocardiography

Although typically not performed in this setting in children, TEE offers a unique view of the pericardium, particularly from

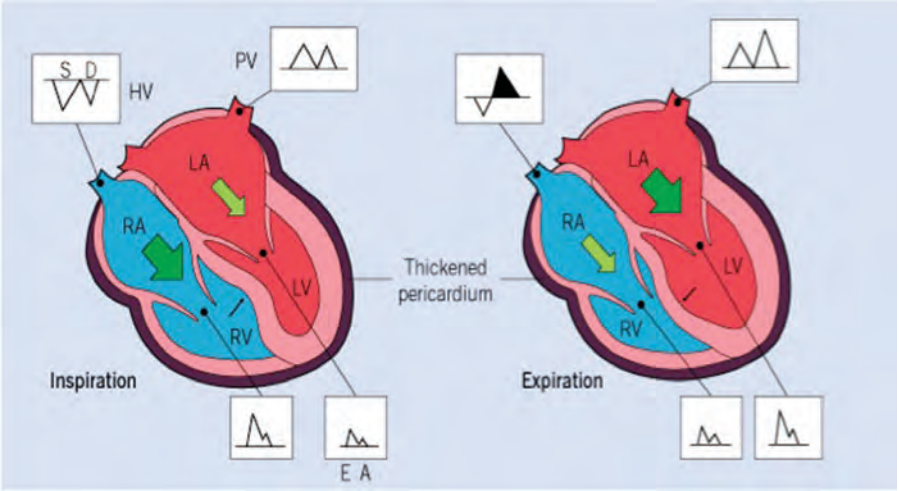


Figure 36.19 Ventricular interdependence and respiratory variation in transvalvar and central venous flow velocities in constrictive pericarditis. With inspiration, the driving pressure gradient from the pulmonary bed to the left cardiac chambers decreases, resulting in a decrease in mitral inflow and diastolic pulmonary venous velocities. Decreased left ventricular filling results in ventricular septal shift to the left, allowing increased flow to the right-sided cardiac chambers, resulting in increased tricuspid inflow and diastolic hepatic venous velocities. The opposite changes occur during expiration. A, late diastolic (atrial reversal) Doppler wave; D, diastolic Doppler wave; E, early diastolic Doppler wave; HV, hepatic vein; LA, left atrium; LV, left ventricle; PV, pulmonary vein; RA, right atrium; RV, right ventricle; S, systolic Doppler wave. Source: Adapted from Oh JK, Diagnostic role of echocardiography in constrictive pericarditis. *J Am Coll Cardiol* 1994;**23**:154–62.

the transgastric window [52,53]. Rapid volume expansion during TEE can be used for further separation of constrictive pericarditis from restrictive cardiomyopathy by significantly enhancing the respiratory variation of the pulmonary vein diastolic flow velocity in constrictive pericarditis [24].

Additional modalities

The electrocardiogram is never diagnostic and shows nonspecific ST-segment and T-wave changes. The chest X-ray may be unremarkable. Heart size is not enlarged but pericardial calcifications are present in up to 25–50% of patients (Figure 36.20), giving an "egg-shell" appearance to the cardiac silhouette [54]. The right superior mediastinum may appear enlarged due to dilation of the superior vena cava. Pleural effusions may be present, reflecting chronic right heart failure. Pulmonary infiltrates are uncommon. Cardiac catheterization may show cardiac calcifications on fluoroscopy (Figure 36.21) and allow assessment of hemodynamics.

Cardiac computed tomography and magnetic resonance imaging

Both CT and magnetic resonance imaging (MRI) can detect a thickened pericardium (≥4 mm), but this is an insensitive finding. An advantage of CT is the ability to detect calcification (Figures 36.22 and 36.23), indicative of constrictive pericarditis [54–56]. Failure of the immediate adjacent pulmonary structures to pulsate during the cardiac cycle in the presence of a thickened pericardium is highly suggestive of constrictive physiology. However, CT may have difficulty differentiating pericardial fluid from thickened pericardium, and the absence of pericardial thickening does not rule out hemodynamically significant constrictive pericarditis. Cardiac MRI may demonstrate pericardial thickening and right atrial dilation [57]. The



Figure 36.20 Chest X-ray demonstrating pericardial calcifications and an egg-shell appearance of the cardiac silhouette. Calcifications are present in 40–50% of patients with constrictive pericarditis.

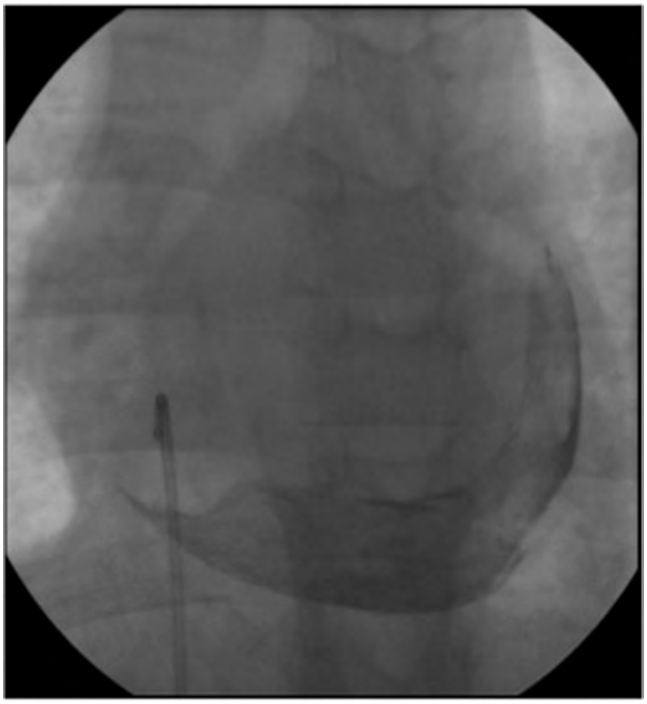


Figure 36.21 Cardiac catheterization with calcification of the pericardium in constrictive pericarditis.

pericardium can be delineated on black-blood imaging and inflammation can be imaged using late gadolinium enhancement. Tethering to the underlying myocardium and lack of slippage can be seen using tagging. Real-time cine-MRI may show ventricular–ventricular interaction (compression of the left ventricle by the right ventricle during inspiration) with a characteristic interventricular septal "bounce" in early diastole (early diastolic septal inversion occurring at the onset of inspiration) [37,58]). 3D reconstruction allows direct visualization of the calcified pericardium with its precise localization (Figure 36.24), and is often very useful for the surgeon before pericardiectomy.

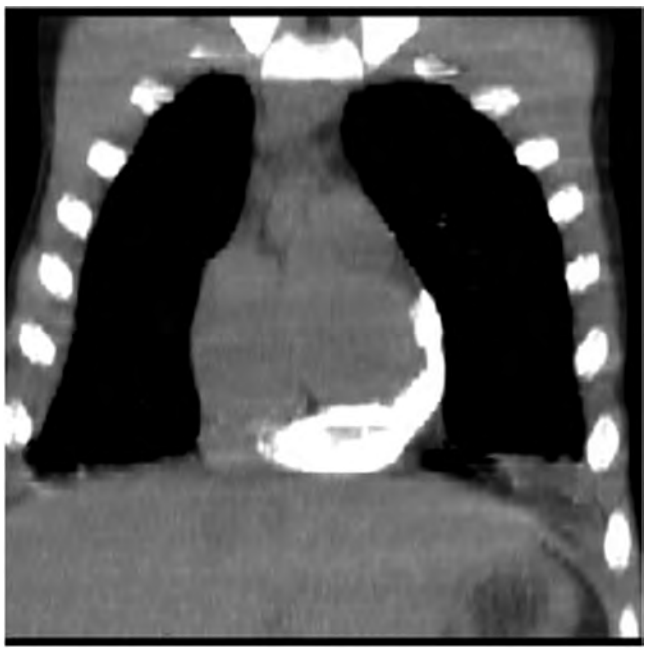


Figure 36.22 CT scan of the chest of the same patient demonstrating pericardial calcification (in white). Both CT and MRI can detect a thickened pericardium (≥4 mm), but an advantage of CT is the ability to detect calcification, indicative of constrictive pericarditis.



Figure 36.23 Cardiac computed tomography (CT) showing pericardial calcifications (arrows).

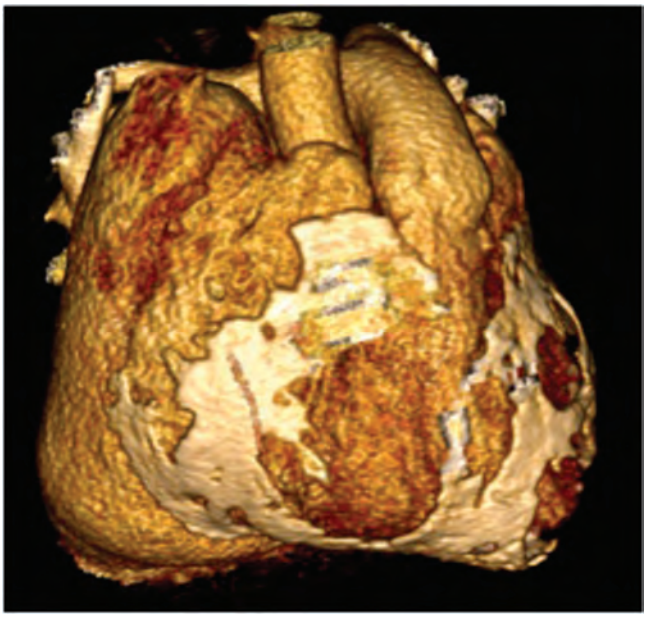


Figure 36.24 Cardiac computed tomography (CT) with 3D reconstruction: calcified pericardium.

Pericardial effusion and cardiac tamponade

Introduction

The pericardial space normally contains a small amount of fluid, which serves as lubrication between the visceral and parietal layers of the pericardium. This fluid is produced by the visceral pericardium and is essentially an ultrafiltrate of plasma. Pericardial effusion is defined as the presence of more than a physiologic amount of fluid in the pericardial space, usually as a result of inflammation. Cardiac tamponade (compression of the heart) results from a rapid or large amount of pericardial fluid accumulation, with subsequent restricted ventricular filling and hemodynamic compromise. Cardiac tamponade is a medical emergency with a rapid and universally fatal course if untreated. Chest X-ray will often identify a markedly enlarged cardiac silhouette in patients with large pericardial effusions and tamponade (Figure 36.25). This must be distinguished from cardiomegaly associated with cardiomyopathy or myocarditis.

Incidence and etiology

Acute pericarditis is the most common cause of pericardial effusion. The true incidence of pericardial effusion is unknown because it often goes unrecognized in mild cases. Some of the most common causes of pericardial effusions are summarized in Table 36.5 [59]. Up to 5–10% of children who have had cardiac surgery may develop postpericardiotomy syndrome, a pericardial fluid accumulation that occurs in the weeks after the repair. In children, cardiac tamponade is more common in boys than in girls, with a male-to-female ratio of 7:3.

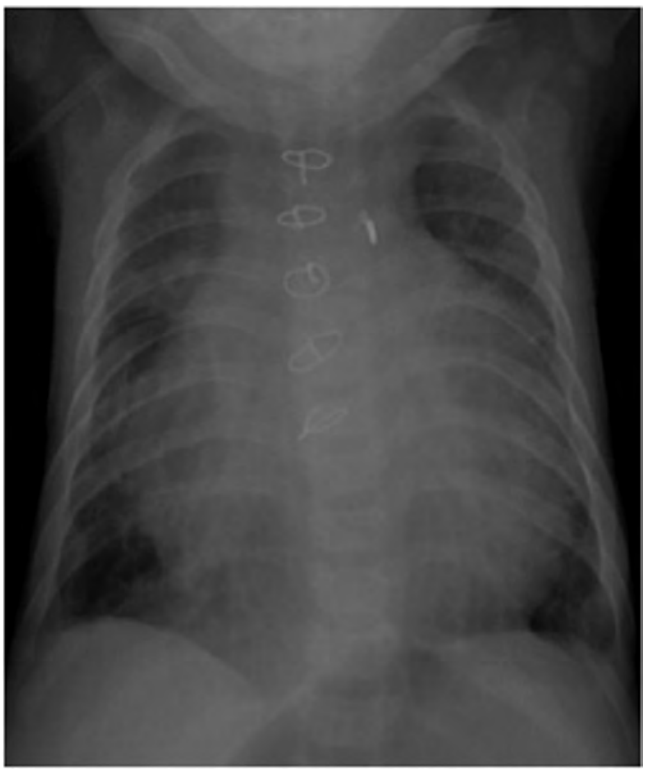


Figure 36.25 Chest X-ray revealing an enlarged cardiac silhouette with water-bottle-shaped heart in a patient with a large pericardial effusion post-cardiac surgery.

Table 36.5 Causes of pericardial effusion and acute pericarditis

Idiopathic Infectious	Viral (coxsackievirus, echovirus, mumps, varicella, Epstein–Barr, adenovirus, influenza, human immunodeficiency virus)
	Bacterial (streptococcus, pneumococcus, staphylococcus, *Neisseria* species, mycoplasmas, *Haemophilus influenzae* type b, *E. coli*, *Listeria*, *Legionella* species, *Pseudomonas*)
	Fungal (candidiasis, histoplasmosis, actinomycosis)
	Parasitic (toxoplasmosis, coccidiomycosis *Echinococcus*, *Entamoeba histolytica*, rickettsias)
	Tuberculosis
Uremia	
Hypothyroidism	
Neoplasia	Metastases
	Leukemia
	Lymphoma
Post-surgery (post-pericardiotomy syndrome)	
Acute myocardial infarction	
Aortic dissection	
Post-irradiation	
Rheumatic fever	
Collagen vascular disease and inflammatory	Rheumatoid arthritis
	Systemic lupus erythematosus
	Sarcoidosis
	Dermatomyositis
	Familial Mediterranean fever
Trauma	
Hypercholesterolemia	
Chylopericardium	
Whipple disease	
Drug-induced	Hydralazine, isoniazid, procainamide

Pathophysiology

Abnormal pericardial fluid production is usually secondary to injury or inflammation. Transudative fluid results from obstruction of fluid drainage, whereas exudative fluid is secondary to inflammatory, infectious, malignant, or autoimmune processes. Significant fluid accumulation can result in marked increases in pericardial pressure, leading to decreased cardiac output and hypotension (cardiac tamponade). The clinical manifestations of pericardial effusion are highly dependent upon the rate of accumulation of fluid in the pericardial sac. Rapid accumulation of pericardial fluid causes sudden increased intrapericardial pressure with hemodynamic compromise. Slowly progressing

effusions can be asymptomatic even when large fluid volumes are present [60].

The underlying pathophysiologic process for the development of tamponade is markedly diminished diastolic filling because transmural distending pressures are insufficient to overcome the elevated intrapericardial pressures. In tamponade, inspiration augments inflow to the right ventricle, causing an abrupt expansion of the right ventricle during diastole at the expense of the left ventricle [61]. The opposite happens during expiration, with left ventricular expansion causing right ventricular and atrial diastolic collapse. The reciprocating behavior of the ventricles during respiration is responsible for the physical examination finding of a pulsus paradoxus (an exaggerated decrease in systolic blood pressure during inspiration) [62].

Imaging

Goals of imaging

- Assessment of size and location of pericardial effusion.
- Assessment for cardiac tamponade.
 - Tricuspid and mitral inflow patterns.
 - Hepatic and pulmonary venous patterns.
 - Diastolic collapse of right-sided structures.

2D echocardiography

Pericardial effusion appears as an "echo-free" space between the visceral and parietal pericardium [63]. Early effusions tend to accumulate posterior and inferior to the left ventricle, owing to expandable posterior/lateral pericardium. Accumulation of fluid above the right atrium in the 4-chamber view is the most sensitive indication as it is the first place where a pericardial effusion is seen. Moderate effusions extend towards the apex of the heart, and large effusions circumscribe the heart (Figures 36.26 and 36.27; Videos 36.3 and 36.4) [64].

1 *Small effusion:* Seen along the length of the posterior wall, not anteriorly, and is defined as <10 mm in a mature heart.
2 *Moderate effusion:* Usually seen circumferentially. Weitzman criteria define a moderate effusion as 10–20 mm during diastole.
3 *Large effusion:* Seen circumferentially. Weitzman criteria define a large effusion as more than 20 mm [65].

The presence of a pericardial effusion does not necessarily cause hemodynamic compromise to the patient. The effects of the effusion must be evaluated by echocardiographic parameters of cardiac filling and transvalvar flow. The rapidity of fluid accumulation and the compliance of the pericardium influence the pressure elevation for any given fluid volume. As pericardial fluid accumulates, intrapericardial pressure increases until it exceeds the normal filling pressure of the heart, leading to tamponade.

The first sign of hemodynamic significance is expiratory right ventricular free wall collapse early in diastole (Figure 36.28), reflecting the brief period when intrapericardial pressure is greater than the right ventricular transmural distending pressure [66,67]. The echocardiogram shows flattening or even dynamic

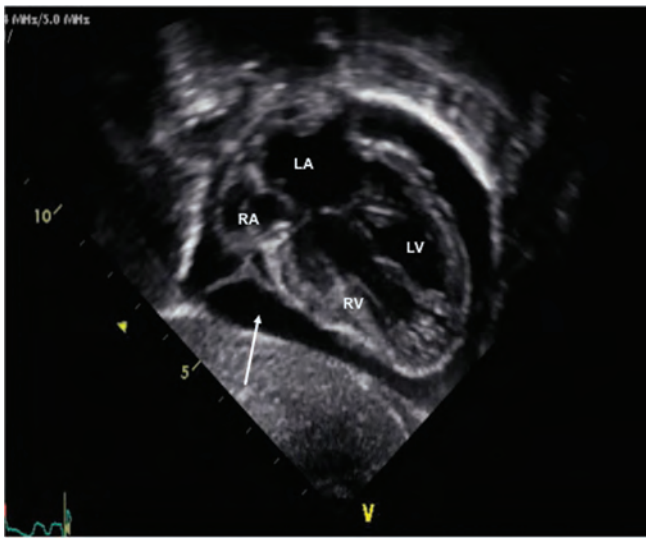


Figure 36.26 Subxiphoid echocardiographic image demonstrating a large circumferential pericardial effusion (arrow). LA, left atrium; LV, left ventricle; RA, right atrium; RV, right ventricle.

reversal of the concave outward curvature of the right ventricle. The right ventricle is the first to collapse, related to its lowest intracardiac pressure compared with the left ventricle. Although right ventricular collapse is generally a specific indicator of tamponade, the sensitivity can be reduced in conditions that have increased right ventricular pressure, such as pulmonary hypertension or unrepaired tetralogy of Fallot [68].

Expiratory right atrial collapse occurs in late diastole, seen by echocardiography as an indentation of the normally rounded anterosuperior right atrial wall (Figure 36.29). The sensitivity of expiratory right atrial collapse for diagnosing tamponade is low (55%), but the specificity is high (90%). Extension of

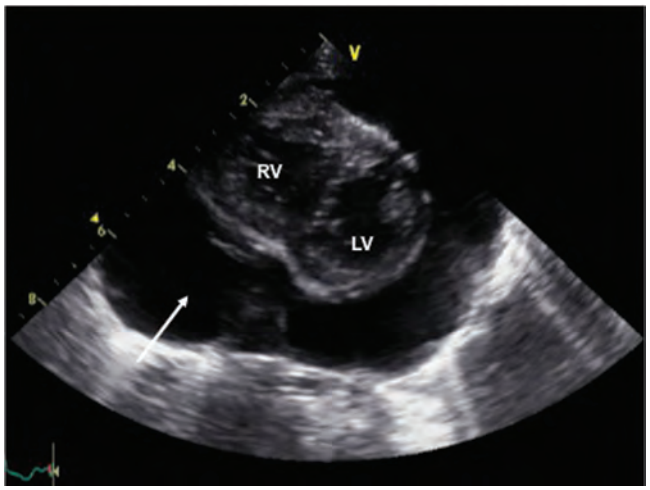


Figure 36.27 Subxiphoid echocardiographic image demonstrating a large circumferential pericardial effusion with tamponade physiology (arrow). LV, left ventricle; RV, right ventricle.

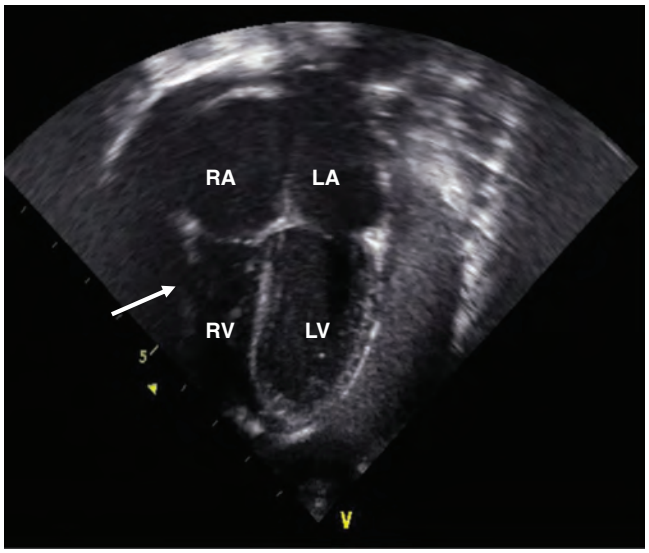


Figure 36.28 Four-chamber view demonstrating right ventricular collapse (arrow) as a finding of tamponade physiology. LA, left atrium; LV, left ventricle; RA, right atrium; RV, right ventricle.

collapse to greater than one-third of the cardiac cycle increases the sensitivity of this finding to more than 90% [69,70]. Therefore, absence of expiratory right atrial collapse virtually excludes tamponade.

As intrapericardial pressure increases further, the right-sided chamber volumes become markedly reduced. In adults, the inferior vena cava is dilated (Figure 36.4), exceeding 20 mm in diameter, and shows no inspiratory collapse (plethora), assessed by less than a 5 mm decrease in diameter during inspiration [71]. The sensitivity of inferior vena cava plethora is high (97%), but the specificity is low (66%), as it may be seen in other conditions such a right heart failure, pericardial constriction, and

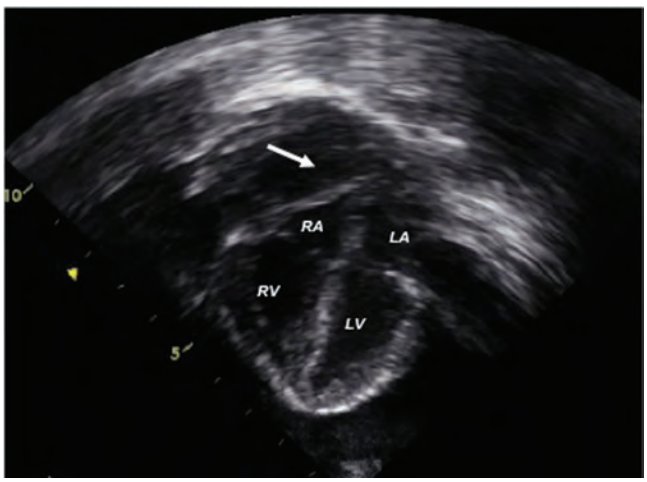


Figure 36.29 Subxiphoid view demonstrating right atrial collapse (arrows) in tamponade physiology. LA, left atrium; LV, left ventricle; RA, right atrium; RV, right ventricle.

mechanical ventilation. The cardiac chambers become small as a result of impaired filling. Decreased diastolic volume of the left atrium and left ventricle may occur during inspiration, related to the increased right heart inflow and abrupt expansion of the right ventricle. Nevertheless, left ventricular collapse is rarely seen because it is thicker walled and less compliant. The left ventricle usually shows signs of preload reduction but not frank free wall compression. In cardiac tamponade, the heart is swinging in the pericardial fluid on a beat-to-beat basis (Figure 36.27; Video 36.4). This is characterized as counterclockwise rotational movement, which occurs in addition to the triangular movement of the heart, producing a dance-like motion. The swinging heart correlates with electrical alternans on the electrocardiogram. The parietal pericardium shows "damping" (loss of parallel motion with the myocardium) and flattening while the motion of the visceral layer and the heart is exaggerated. When the effusion is large, it can be seen anterior to the right ventricle. In tense pericardial effusion, fluid can also be seen behind the left atrium. When assessed by M-mode echocardiography, a phasic decrease in right ventricular diameter synchronous with expiration is strongly suggestive of tamponade if <1 cm with the patient supine. M-mode can be used for assessment of expiratory right ventricular diastolic collapse, timing with the opening of the mitral valve or posterior wall motion. Changes in leaflet separation and in the E to F slope of the mitral valve during diastole is also useful, with the leaflet separation decreasing and the slope being reduced during inspiration, reflecting a decrease in mitral inflow.

Flow mechanics

The mitral and tricuspid inflow, the aortic and pulmonary outflow, and the hepatic vein flow show large swings in amplitude. Exaggerated respiratory variation in transvalvar flow is an important indicator of a hemodynamically significant effusion (Figure 36.30). Normally, there is no more than 10% variation in the amplitude of inflow and outflow signal, but variation exceeds 30% in tamponade.

The classic Doppler pattern of cardiac tamponade is [21,72]:

1. *Mitral inflow:* During inspiration, E wave decreases and IVRT increases by more than 30% compared with expiration (Figure 36.31).
2. *Pulmonary veins:* During inspiration, D wave decreases compared with expiration.
3. *Tricuspid inflow.* During inspiration, E wave increases more than 50% compared with expiration (Figure 36.32).
4. *Hepatic veins:* During inspiration, S is greater than D. During expiration, there is a very limited or absent D wave with prominent reversals.

These flow variations may precede chamber collapse.

Echocardiographically guided pericardiocentesis

Pericardiocentesis is considered the primary and definitive therapy for patients with clinically significant effusions [73,74]. The echocardiographic approach to pericardiocentesis is to assess the

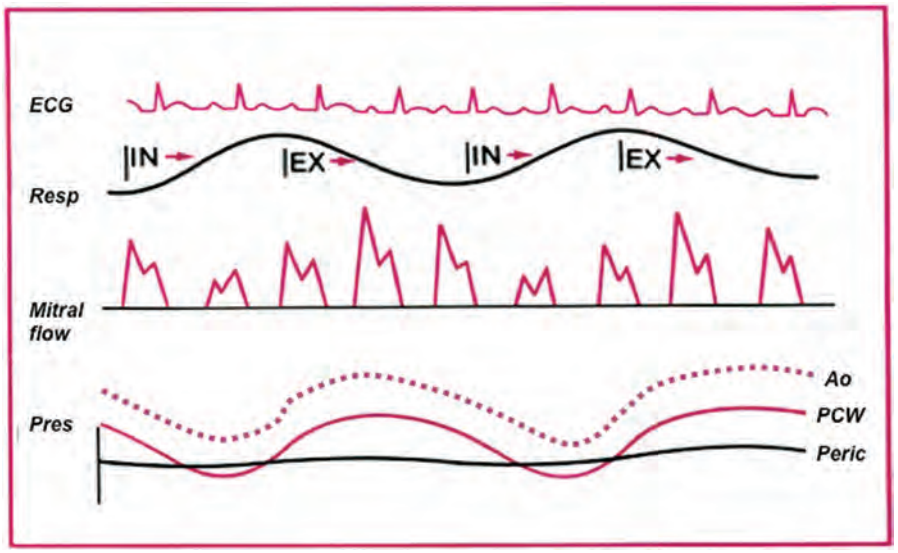


Figure 36.30 Respiratory variation in pericardial effusion and tamponade with exaggeration of inspiratory decrease in mitral inflow and blood pressure responsible for pulsus paradoxus. ECG, electrocardiogram; Resp, respiration; IN, inspiration; EX, expiration; Pres, pressure; Ao, aortic pressure; PCW, pulmonary capillary wedge pressure; Peric, intrapericardial pressure.

size, distribution, and ideal needle entry site and trajectory for the safest removal of fluid. The transducer is placed approximately 3–5 cm from the parasternal border and the area of maximal pericardial fluid accumulation. The needle trajectory is established by the angle of the transducer. Echo-guided pericardiocentesis has been proven to be a safe and effective procedure (Figure 36.33). Whenever required, a drain can be left in the pericardial space if there is a high risk of recurrence (Figure 36.34). Echocardiographic confirmation of diminished effusion is performed at the end of the case. This echo-guided procedure can be performed at a monitored bedside or in the cardiac catheterization laboratory.

Additional modalities

Several electrocardiographic changes are associated with tamponade, including sinus tachycardia and low-voltage QRS complex. Sometimes, ECG findings in acute pericarditis include widespread upward concave ST-segment elevation and PR-segment depression. Electrical alternans, defined as an alteration of the QRS complex amplitude or axis between beats, is specific but not sensitive for pericardial tamponade [60]. The chest X-ray may demonstrate an increased cardiac silhouette (Figure 36.25) with a water bottle-shaped heart when excessive pericardial fluid accumulation is present [75]. Another X-ray finding is a low-density pericardial fat stripe sign, which consists of epicardial fat

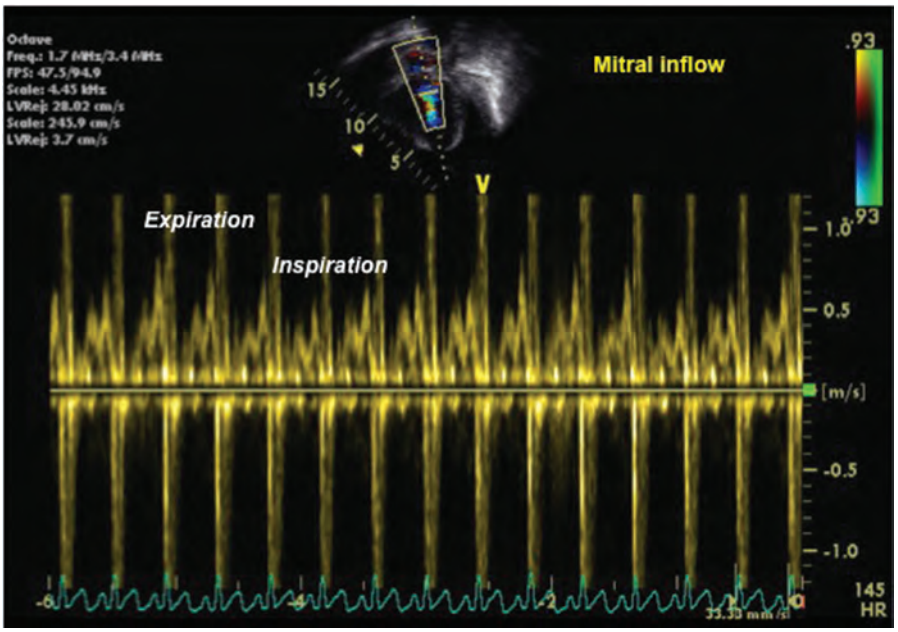


Figure 36.31 Respiratory changes in the mitral valve E wave Doppler patterns consistent with tamponade physiology. During inspiration, the mitral valve inflow E wave decreases by more than 30% compared with expiration. The tricuspid valve E wave inflow demonstrates the opposite and increases by more than 50% during inspiration compared with expiration.

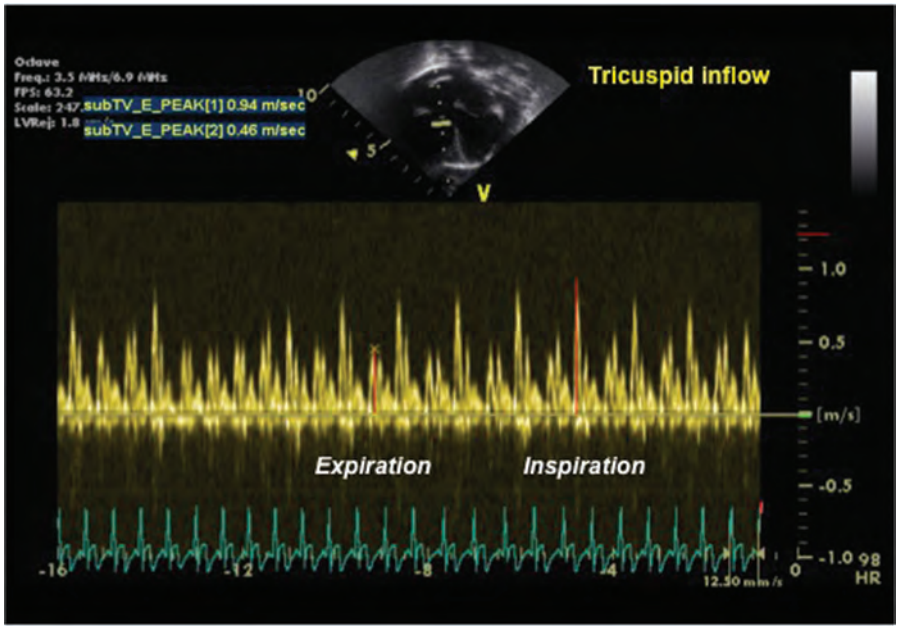


Figure 36.32 Respiratory changes in the tricuspid valve E wave Doppler patterns consistent with tamponade physiology. During inspiration, the mitral valve inflow E wave decreases by more than 30% compared with expiration. The tricuspid valve E wave inflow demonstrates the opposite and increases by more than 50% during inspiration compared with expiration (red lines).

visible between the myocardium and the pericardial effusion on the lateral view. The lung fields are usually oligemic but a pleural effusion may be associated, most often left-sided.

Cardiac computed tomography and magnetic resonance imaging

CT and CMR are usually not needed to diagnose pericardial effusion. CT can potentially determine compositions of fluids, may detect as little as 50 mL of fluid, and may be able to detect early signs of tamponade. Findings such as ventricular interdependence, right atrial and right ventricular collapse, and inferior vena cava and hepatic vein dilation can be detected. CT is sometimes useful for detecting loculated pericardial effusion or hematoma soon after cardiac surgery, as those often escape detection by echocardiography. CMR can detect as little as 30 mL of pericardial fluid, and may be able to distinguish hemorrhagic from nonhemorrhagic effusions [76].



Figure 36.33 Echo-guided pericardiocentesis: the arrow is pointing to the needle that has been advanced into the pericardial space to drain the fluid collection.

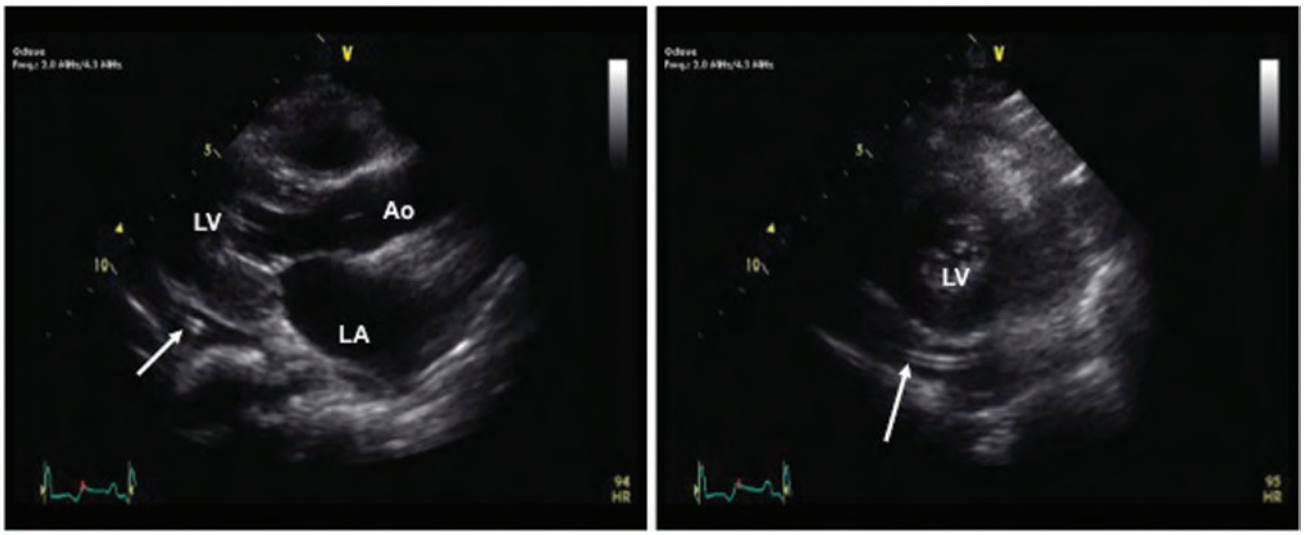
Differentiating restriction, constriction, and tamponade

Both restrictive cardiomyopathy and constrictive pericarditis are characterized by abnormal diastolic ventricular filling and elevated ventricular end-diastolic pressures. Distinguishing between the two diagnoses can be difficult, particularly in cancer patients who have received anthracycline chemotherapy in addition to thoracic radiation. As described earlier, Doppler echocardiography is generally helpful in distinguishing between these two disorders. Ventricular end-diastolic pressures in restrictive cardiomyopathy are generally discordant, with left ventricular end-diastolic pressure being higher than right ventricular end-diastolic pressure. In constrictive pericarditis, the end-diastolic pressures tend to be equal. Echocardiographically, there is evidence of significant respiratory variation in Doppler ventricular inflow signals in constrictive pericarditis compared with minimal respiratory variation in restrictive cardiomyopathy. The different characteristics of echocardiographic findings between restrictive cardiomyopathy, constrictive pericarditis and tamponade are summarized in Table 36.4.

Acute pericarditis

Introduction

Pericarditis is inflammation of the pericardium. When the pericardium becomes inflamed, the amount of fluid between the



(a) (b)

Figure 36.34 Pericardial tube: the arrow shows the drain in place. **(a)** Parasternal long-axis view; **(b)** Parasternal short-axis view.

two layers usually increases, leading to pericardial effusion. Pericarditis may be serous, fibrinous, purulent, hemorrhagic, or chylous.

Incidence and etiology

Most of the time, the cause is unknown and presumed to be a result of a viral infection [40,77]. The identified causes are summarized in Table 36.5. Since it may go undiagnosed, the true incidence is unknown. The pericardium serves as a protective barrier to the spread of infection or inflammation from adjacent structures and contains a physiologic amount of fluid. In case of inflammation or infection, effusion can accumulate in the pericardial space. The pericardium shows inflammation with infiltration of polymorphonuclear leukocytes and pericardial vascularization. Often, the pericardium manifests a fibrinous reaction with exudates and adhesions. A granulomatous pericarditis occurs with tuberculosis, fungal infections, rheumatoid arthritis, and sarcoidosis.

Imaging

2-D echocardiography

The echocardiogram is often normal, unless acute pericarditis is associated with pericardial effusion. While the finding of a pericardial effusion supports the diagnosis of acute pericarditis, its absence does not exclude it. In pericarditis, the pericardium may have a normal appearance.

Additional studies

An increase in cardiac troponin I levels has been described as detectable in acute pericarditis in about 30% of patients [78]. Moreover, markers of inflammation such as white blood cell count, erythrocyte sedimentation rate and C-reactive protein are usually elevated. Typical electrocardiogram changes include widespread upward concave ST-segment elevation and PR-segment depression. The chest X-ray is usually normal but sometimes cardiomegaly with clear lung fields may suggest associated pericardial effusion. CT and CMR are increasingly being used. Both are very sensitive in the detection of effusion and allow the measurement of pericardial thickness. The normal thickness of the pericardium as measured by CT scanning is less than 2 mm and by MRI less than 4 mm. The limitation of CT scanning is the difficulty in differentiating fluid from thickened pericardium. The most sensitive method for the diagnosis of acute pericarditis is delayed enhanced gadolinium uptake in the inflamed pericardium on CMR. Normally, the pericardium appears black because of a low water content; in patients with pericarditis, enhanced gadolinium uptake in the inflamed pericardium is delayed. CMR is also helpful in demonstrating concomitant myocardial involvement in patients with myopericarditis [76,79].

Miscellaneous diseases of the pericardium

Congenital absence of the pericardium

Congenital defects of the pericardium are rare (1/100,000 autopsies) and comprise partial left (70%), right (17%), or rarely total bilateral absence [80]. Most patients are asymptomatic but 30% of affected individuals have additional congenital abnormalities. The normal pericardium exerts a considerable influence on cardiac motion, provides stability of the heart in the chest, and limits dilation of the chambers. A shift of the heart to the left with right heart enlargement is common. Complete absence of the pericardium leads to enlargement of the right ventricle,

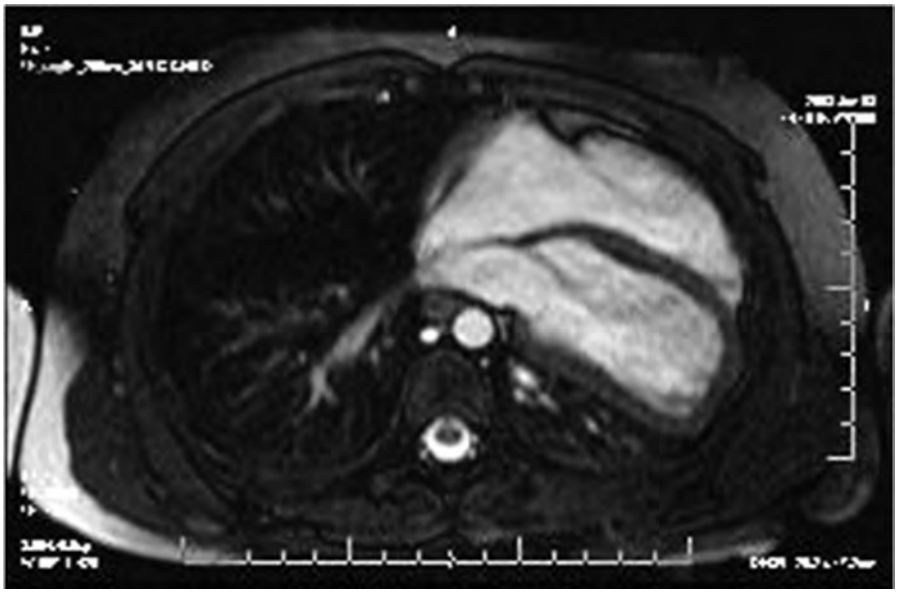


Figure 36.35 Cardiac MRI of absent pericardium includes unusual leftward and posterior shift of the heart and absence of a visible pericardium. On cine imaging, the ventricles are unusually mobile and the typically seen pericardial fluid (normally clearly visible during systole) is absent.

excessive motion of the posterior left ventricular wall, paradoxical motion of the interventricular septum, and a shift of the heart to the left, best seen in CMR (Figure 36.35). By echocardiography, this finding is best recognized when more of the right ventricle is seen on the left parasternal long-axis view by echocardiography mimicking right ventricular volume overload [81]. Homolateral heart displacement and augmented heart mobility impose an increased risk of traumatic aortic dissection. Complications of partial absence of the pericardium include herniation or cardiac chamber strangulation with the false appearance of wall motion abnormality. True wall motion abnormality is seen if a coronary artery is compressed.

Pericardial cyst

Pericardial cysts are rare, with an estimated incidence of 1 per 100,000 in the general population [82]. These cysts may be unilocular or multilocular with a diameter ranging from 1 to 5 cm [79]. Approximately 20 reported cases have presented before the age of 18 years [83]. Inflammatory cysts are caused by rheumatic pericarditis, tuberculosis, trauma, and surgery. Most patients are asymptomatic and cysts are detected incidentally. Congenital pericardial cysts most often occur at the right atrial border and are difficult to detect with transthoracic echocardiography [82]. They present as an echo-free space which is more localized (Figure 36.36; Video 36.5) and spherical than a pericardial effusion [84]. Additional imaging is often needed. Thoracic CMR (Figure 36.37) and contrast CT scanning are preferred methods to confirm a suspected diagnosis of pericardial cyst. On CT scan, pericardial cysts are thin-walled, sharply defined, oval homogeneous masses. Their attenuation is slightly higher than water density, 30–40 HU, and the cyst fails to enhance with intravenous contrast [85].

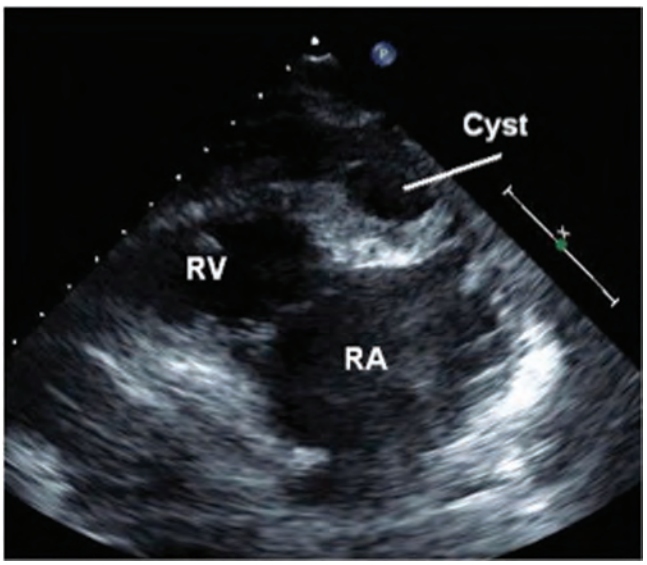


Figure 36.36 Echocardiography parasternal long-axis view of a pericardial cyst.

Videos

To access the videos for this chapter, please go to www.lai-echo.com.

Video 36.1 Apical 4-chamber view demonstrating markedly dilated left and right atria consistent with restrictive cardiomyopathy.

Video 36.2 Apical 4-chamber view demonstrating ventricular "septal bounce" seen in association with constrictive pericarditis.

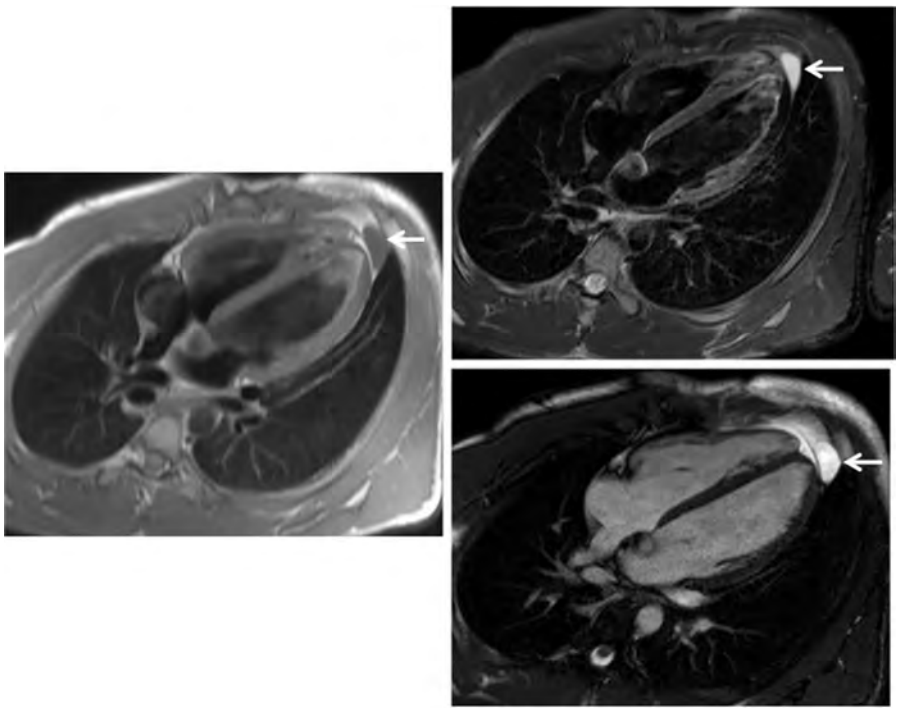


Figure 36.37 Cardiac MRI of a pericardial cyst (white arrow).

Video 36.3 Parasternal long-axis view demonstrating a moderate global pericardial effusion with the heart "swinging" in the fluid.

Video 36.4 Parasternal short-axis view demonstrating a large pericardial effusion with the heart "swinging" in the fluid.

Video 36.5 Parasternal long-axis view demonstrating multiple pericardial cysts seen along the anterior right ventricular wall.

References

1 Richardson P, McKenna W, Bristow M, et al. Report of the 1995 World Health Organization/International Society and Federation of Cardiology Task Force on the Definition and Classification of Cardiomyopathies. *Circulation* 1996;**93**:841–842.

2 Kimberling MT, Balzer DT, Hirsch R, et al. Cardiac transplantation for pediatric restrictive cardiomyopathy: presentation, evaluation, and short-term outcome. *J Heart Lung Transplant* 2002;**21**:455–459.

3 Weller RJ, Weintraub R, Addonizio LJ, et al. Outcome of idiopathic restrictive cardiomyopathy in children. *Am J Cardiol* 2002;**90**:501–506.

4 Lewis AB. Clinical profile and outcome of restrictive cardiomyopathy in children. *Am Heart J* 1992;**123**:1589–1593.

5 Cetta F, O'Leary PW, Seward JB, Driscoll DJ. Idiopathic restrictive cardiomyopathy in childhood: diagnostic features and clinical course. *Mayo Clin Proc* 1995;**70**:634–640.

6 Russo LM, Webber SA. Idiopathic restrictive cardiomyopathy in children. *Heart* 2005;**91**:1199–1202.

7 Denfield SW, Rosenthal G, Gajarski RJ, et al. Restrictive cardiomyopathies in childhood. Etiologies and natural history. *Tex Heart Inst J* 1997;**24**:38–44.

8 Rivenes SM, Kearney DL, Smith EO, Towbin JA, Denfield SW. Sudden death and cardiovascular collapse in children with restrictive cardiomyopathy. *Circulation* 2000;**102**:876–882.

9 Fitzpatrick AP, Shapiro LM, Rickards AF, Poole-Wilson PA. Familial restrictive cardiomyopathy with atrioventricular block and skeletal myopathy. *Br Heart J* 1990;**63**:114–118.

10 Kushwaha SS, Fallon JT, Fuster V. Restrictive cardiomyopathy. *N Engl J Med* 1997;**336**:267–276.

11 Angelini A, Calzolari V, Thiene G, et al. Morphologic spectrum of primary restrictive cardiomyopathy. *Am J Cardiol* 1997;**80**:1046–1050.

12 Yoshizato T, Edwards WD, Alboliras ET, et al. Safety and utility of endomyocardial biopsy in infants, children and adolescents: a review of 66 procedures in 53 patients. *J Am Coll Cardiol* 1990;**15**:436–442.

13 Asher CR, Klein AL. Diastolic heart failure: restrictive cardiomyopathy, constrictive pericarditis, and cardiac tamponade: clinical and echocardiographic evaluation. *Cardiol Rev* 2002;**10**:218–229.

14 Vaitkus PT, Kussmaul WG. Constrictive pericarditis versus restrictive cardiomyopathy: a reappraisal and update of diagnostic criteria. *Am Heart J* 1991;**122**:1431–1441.

15 Ammash NM, Seward JB, Bailey KR, et al. Clinical profile and outcome of idiopathic restrictive cardiomyopathy. *Circulation* 2000;**101**:2490–2496.

16 Gewillig M, Mertens L, Moerman P, Dumoulin M. Idiopathic restrictive cardiomyopathy in childhood. A diastolic disorder characterized by delayed relaxation. *Eur Heart J* 1996;**17**:1413–1420.

17 Mehta AV, Ferrer PL, Pickoff AS, et al. M-mode echocardiographic findings in children with idiopathic restrictive cardiomyopathy. *Pediatr Cardiol* 1984;**5**:273–279.

18 Klein AL, Hatle LK, Burstow DJ, et al. Doppler characterization of left ventricular diastolic function in cardiac amyloidosis. *J Am Coll Cardiol* 1989;**13**:1017–1026.

19 Zile MR, Brutsaert DL. New concepts in diastolic dysfunction and diastolic heart failure: Part I: diagnosis, prognosis, and measurements of diastolic function. *Circulation* 2002;**105**:1387–1393.

20 Fowler SJ, Narula J, Gurudevan SV. Review of noninvasive imaging for hypertrophic cardiac syndromes and restrictive physiology. *Heart Fail Clin* 2006;**2**:215–230.

21 Appleton CP, Hatle LK, Popp RL. Relation of transmitral flow velocity patterns to left ventricular diastolic function: new insights from a combined hemodynamic and Doppler echocardiographic study. *J Am Coll Cardiol* 1988;**12**:426–440.

22 Giannuzzi P, Imparato A, Temporelli PL, et al. Doppler-derived mitral deceleration time of early filling as a strong predictor of pulmonary capillary wedge pressure in postinfarction patients with left ventricular systolic dysfunction. *J Am Coll Cardiol* 1994;**23**:1630–1637.

23 Hatle LK, Appleton CP, Popp RL. Differentiation of constrictive pericarditis and restrictive cardiomyopathy by Doppler echocardiography. *Circulation* 1989;**79**:357–370.

24 Abdalla IA, Murray RD, Lee JC, et al. Does rapid volume loading during transesophageal echocardiography differentiate constrictive pericarditis from restrictive cardiomyopathy? *Echocardiography* 2002;**19**:125–134.

25 Rakowski H, Appleton C, Chan KL, et al. Canadian consensus recommendations for the measurement and reporting of diastolic dysfunction by echocardiography: from the Investigators of Consensus on Diastolic Dysfunction by Echocardiography. *J Am Soc Echocardiogr* 1996;**9**:736–760.

26 Garcia MJ, Palac RT, Malenka DJ, et al. Color M-mode Doppler flow propagation velocity is a relatively preload-independent index of left ventricular filling. *J Am Soc Echocardiogr* 1999;**12**:129–137.

27 Garcia MJ, Ares MA, Asher C, et al. An index of early left ventricular filling that combined with pulsed Doppler peak E velocity may estimate capillary wedge pressure. *J Am Coll Cardiol* 1997;**29**:448–454.

28 Garcia MJ, Thomas JD, Klein AL. New Doppler echocardiographic applications for the study of diastolic function. *J Am Coll Cardiol* 1998;**32**:865–875.

29 Rajagopalan N, Garcia MJ, Rodriguez L, et al. Comparison of new Doppler echocardiographic methods to differentiate constrictive pericardial heart disease and restrictive cardiomyopathy. *Am J Cardiol* 2001;**87**:86–94.

30 Garcia MJ, Rodriguez L, Ares M, et al. Differentiation of constrictive pericarditis from restrictive cardiomyopathy: assessment of left ventricular diastolic velocities in longitudinal axis by Doppler tissue imaging. *J Am Coll Cardiol* 1996;**27**:108–114.

31 Nagueh SF, Middleton KJ, Kopelen HA, et al. Doppler tissue imaging: a noninvasive technique for evaluation of left ventricular relaxation and estimation of filling pressures. *J Am Coll Cardiol* 1997;**30**:1527–1533.

32 Nagueh SF, Mikati I, Kopelen HA, et al. Doppler estimation of left ventricular filling pressure in sinus tachycardia. A new application of tissue Doppler imaging. *Circulation* 1998;**98**:1644–1650.

33 McMahon CJ, Nagueh SF, Pignatelli RH, et al. Characterization of left ventricular diastolic function by tissue Doppler imaging and clinical status in children with hypertrophic cardiomyopathy. *Circulation* 2004;**109**:1756–1762.

34 Sutherland GR, Di Salvo G, Claus P, et al. Strain and strain rate imaging: a new clinical approach to quantifying regional myocardial function. *J Am Soc Echocardiogr* 2004;**17**:788–802.

35 Koyama J, Ray-Sequin PA, Falk RH. Longitudinal myocardial function assessed by tissue velocity, strain, and strain rate tissue Doppler echocardiography in patients with AL (primary) cardiac amyloidosis. *Circulation* 2003;**107**:2446–2452.

36 Helle-Valle T, Crosby J, Edvardsen T, et al. New noninvasive method for assessment of left ventricular rotation: speckle tracking echocardiography. *Circulation* 2005;**112**:3149–3156.

37 Quarta G, Sado DM, Moon JC. Cardiomyopathies: focus on cardiovascular magnetic resonance. *Br J Radiol* **84**(Spec No 3): S296–S305.

38 Myers RB, Spodick DH. Constrictive pericarditis: clinical and pathophysiologic characteristics. *Am Heart J* 1999;**138**:219–232.

39 Gomes Ferreira SM, Gomes Ferreira A, Jr, do Nascimento Morais A, et al. Constrictive chronic pericarditis in children. *Cardiol Young* 2001;**11**:210–213.

40 Troughton RW, Asher CR, Klein AL. Pericarditis. *Lancet* 2004;**363**:717–727.

41 Haley JH, Tajik AJ, Danielson GK, et al. Transient constrictive pericarditis: causes and natural history. *J Am Coll Cardiol* 2004;**43**:271–275.

42 Chen CA, Lin MT, Wu ET, et al. Clinical manifestations and outcomes of constrictive pericarditis in children. *J Formos Med Assoc* 2005;**104**:402–407.

43 Shabetai R, Fowler NO, Guntheroth WG. The hemodynamics of cardiac tamponade and constrictive pericarditis. *Am J Cardiol* 1970;**26**:480–489.

44 Schnittger I, Bowden RE, Abrams J, Popp RL. Echocardiography: pericardial thickening and constrictive pericarditis. *Am J Cardiol* 1978;**42**:388–395.

45 Himelman RB, Lee E, Schiller NB. Septal bounce, vena cava plethora, and pericardial adhesion: informative two-dimensional echocardiographic signs in the diagnosis of pericardial constriction. *J Am Soc Echocardiogr* 1988;**1**:333–340.

46 Tei C, Child JS, Tanaka H, Shah PM. Atrial systolic notch on the interventricular septal echogram: an echocardiographic sign of constrictive pericarditis. *J Am Coll Cardiol* 1983;**1**:907–912.

47 Gibson TC, Grossman W, McLaurin LP, et al. An echocardiographic study of the interventricular septum in constrictive pericarditis. *Br Heart J* 1976;**38**:738–743.

48 Mehta A, Mehta M, Jain AC. Constrictive pericarditis. *Clin Cardiol* 1999;**22**:334–344.

49 Agatston AS, Rao A, Price RJ, Kinney EL. Diagnosis of constrictive pericarditis by pulsed Doppler echocardiography. *Am J Cardiol* 1984;**54**:929–930.

50 Klodas E, Nishimura RA, Appleton CP, et al. Doppler evaluation of patients with constrictive pericarditis: use of tricuspid regurgitation velocity curves to determine enhanced ventricular interaction. *J Am Coll Cardiol* 1996;**28**:652–657.

51 Ha JW, Oh JK, Ling LH, et al. Annulus paradoxus: transmitral flow velocity to mitral annular velocity ratio is inversely proportional to pulmonary capillary wedge pressure in patients with constrictive pericarditis. *Circulation* 2001;**104**:976–978.

52 Kronzon I, Tunick PA, Freedberg RS. Transesophageal echocardiography in pericardial disease and tamponade. *Echocardiography* 1994;**11**:493–505.

53 Ling LH, Oh JK, Tei C, et al. Pericardial thickness measured with transesophageal echocardiography: feasibility and potential clinical usefulness. *J Am Coll Cardiol* 1997;**29**:1317–1323.

54 Kameda Y, Funabashi N, Kawakubo M, et al. Heart in an eggshell – eggshell appearance calcified constrictive pericarditis demonstrated by three-dimensional images of multislice computed tomography. *Int J Cardiol* 2007;**120**:269–272.

55 Robles P, Rubio A, Olmedilla P. Value of multidetector cardiac CT in calcified constrictive pericarditis for pericardial resection. *Heart* 2006;**92**:1112.

56 Chen SJ, Li YW, Wu MH, et al. CT and MRI findings in a child with constrictive pericarditis. *Pediatr Cardiol* 1998;**19**:259–262.

57 Francone M, Dymarkowski S, Kalantzi M, et al. Assessment of ventricular coupling with real-time cine MRI and its value to differentiate constrictive pericarditis from restrictive cardiomyopathy. *Eur Radiol* 2006;**16**:944–951.

58 Spottiswoode B, Russell JB, Moosa S, et al. Abnormal diastolic and systolic septal motion following pericardiectomy demonstrated by cine DENSE MRI. *Cardiovasc J Afr* 2008;**19**:208–209.

59 Ilan Y, Oren R, Ben-Chetrit E. Etiology, treatment, and prognosis of large pericardial effusions. A study of 34 patients. *Chest* 1991;**100**:985–987.

60 Spodick DH. Acute cardiac tamponade. *N Engl J Med* 2003;**349**: 684–690.

61 Little WC, Freeman GL. Pericardial disease. *Circulation* 2006;**113**: 1622–1632.

62 Guntheroth WG, Morgan BC, Mullins GL. Effect of respiration on venous return and stroke volume in cardiac tamponade. Mechanism of pulsus parodoxus. *Circ Res* 1967;**20**:381–390.

63 Horowitz MS, Schultz CS, Stinson EB, et al. Sensitivity and specificity of echocardiographic diagnosis of pericardial effusion. *Circulation* 1974;**50**:239–247.

64 Pepi M, Muratori M. Echocardiography in the diagnosis and management of pericardial disease. *J Cardiovasc Med (Hagerstown)* 2006;**7**:533–544.

65 Weitzman LB, Tinker WP, Kronzon I, et al. The incidence and natural history of pericardial effusion after cardiac surgery – an echocardiographic study. *Circulation* 1984;**69**:506–511.

66 Schiller NB, Botvinick EH. Right ventricular compression as a sign of cardiac tamponade: an analysis of echocardiographic ventricular dimensions and their clinical implications. *Circulation* 1977;**56**:774–779.

67 Armstrong WF, Schilt BF, Helper DJ, et al. Diastolic collapse of the right ventricle with cardiac tamponade: an echocardiographic study. *Circulation* 1982;**65**:1491–1496.

68 Singh S, Wann LS, Schuchard GH, et al. Right ventricular and right atrial collapse in patients with cardiac tamponade–a combined echocardiographic and hemodynamic study. *Circulation* 1984;**70**:966–971.

69 Gillam LD, Guyer DE, Gibson TC, et al. Hydrodynamic compression of the right atrium: a new echocardiographic sign of cardiac tamponade. *Circulation* 1983;**68**:294–301.

70 Kronzon I, Cohen ML, Winer HE. Diastolic atrial compression: a sensitive echocardiographic sign of cardiac tamponade. *J Am Coll Cardiol* 1983;**2**:770–775.

71 Himelman RB, Kircher B, Rockey DC, Schiller NB. Inferior vena cava plethora with blunted respiratory response: a sensitive echocardiographic sign of cardiac tamponade. *J Am Coll Cardiol* 1988;**12**:1470–1477.

72 Klein AL, Cohen GI. Doppler echocardiographic assessment of constrictive pericarditis, cardiac amyloidosis, and cardiac tamponade. *Cleve Clin J Med* 1992;**59**:278–290.

73 Tsang TS, El-Najdawi EK, Seward JB, et al. Percutaneous echocardiographically guided pericardiocentesis in pediatric patients: evaluation of safety and efficacy. *J Am Soc Echocardiogr* 1998;**11**: 1072–1077.

74 Tsang TS, Freeman WK, Sinak LJ, Seward JB. Echocardiographically guided pericardiocentesis: evolution and state-of-the-art technique. *Mayo Clin Proc* 1998;**73**:647–652.

75 Eisenberg MJ, de Romeral LM, Heidenreich PA, et al. The diagnosis of pericardial effusion and cardiac tamponade by 12-lead ECG. A technology assessment. *Chest* 1996;**110**:318–324.

76 Khandaker MH, Espinosa RE, Nishimura RA, et al. Pericardial disease: diagnosis and management. *Mayo Clin Proc* 2010;**85**: 572–593.

77 Lange RA, Hillis LD. Clinical practice. Acute pericarditis. *N Engl J Med* 2004;**351**:2195–2202.

78 Imazio M, Demichelis B, Cecchi E, et al. Cardiac troponin I in acute pericarditis. *J Am Coll Cardiol* 2003;**42**:2144–2148.

79 Maisch B, Seferovic PM, Ristic AD, et al. Guidelines on the diagnosis and management of pericardial diseases executive summary; The Task Force on the Diagnosis and Management of Pericardial Diseases of the European Society of Cardiology. *Eur Heart J* 2004;**25**:587–610.

80 Miyazaki T, Zipes DP. Pericardial prostaglandin biosynthesis prevents the increased incidence of reperfusion-induced ventricular fibrillation produced by efferent sympathetic stimulation in dogs. *Circulation* 1990;**82**:1008–1019.

81 Payvandi MN, Kerber RE. Echocardiography in congenital and acquired absence of the pericardium. An echocardiographic mimic of right ventricular volume overload. *Circulation* 1976;**53**:86–92.

82 Patel J, Park C, Michaels J, et al. Pericardial cyst: case reports and a literature review. *Echocardiography* 2004;**21**:269–272.

83 Noyes BE, Weber T, Vogler C. Pericardial cysts in children: surgical or conservative approach? *J Pediatr Surg* 2003;**38**:1263–1265.

84 Hynes JK, Tajik AJ, Osborn MJ, et al. Two-dimensional echocardiographic diagnosis of pericardial cyst. *Mayo Clin Proc* 1983;**58**: 60–63.

85 Demos TC, Budorick NE, Posniak HV. Benign mediastinal cysts: pointed appearance on CT. *J Comput Assist Tomogr* 1989;**13**: 132–133.

CHAPTER 37

Other Anomalies of the Ventricular Myocardium

Rebecca S. Beroukhim and Mary Etta E. King
Massachusetts General Hospital, Boston, MA, USA

Introduction

A number of uncommon but important disorders that affect the left and right ventricular myocardium include (1) left ventricular noncompaction, (2) congenital left ventricular aneurysm and diverticulum, and (3) arrhythmogenic right ventricular cardiomyopathy/dysplasia. It is important that they be considered during echocardiographic evaluation of patients with ventricular dysfunction, arrhythmia, syncope, and/or thromboembolism. The echocardiographic findings may be subtle and easily missed if the examiner does not intentionally consider them in the differential diagnosis.

Left ventricular noncompaction

Definition

Left ventricular noncompaction (LVNC) is a myocardial disorder characterized by "spongy" myocardium with prominent trabeculae, separated by deep intertrabecular recesses; it typically affects the left ventricular apex and mid ventricle [1]. The intertrabecular recesses are lined with endothelium and communicate with the ventricular cavity, which distinguishes this feature from myocardial sinusoids. Although this anomaly typically affects the left ventricle (LV), involvement of the right ventricle (RV) has also been described [2,3]. LVNC can occur as an isolated anomaly (iLVNC) or in association with other structural heart defects (nonisolated, or ni-LVNC) such as ventricular septal defects and left or right ventricular outflow obstruction.

Incidence

The true incidence of LVNC is unknown, primarily as a result of inconsistent diagnostic criteria and nomenclature [4]. The diagnosis may be missed because of incomplete evaluation by echocardiography, or due to limited awareness of the pathologic features of LVNC. Studies in adult populations suggest that LVNC is fairly rare, with a prevalence of 0.014% [5]; however, these data may be confounded by technical imaging limitations in adult studies. A somewhat higher prevalence has been noted in pediatric populations, with a prospective study showing LVNC in 1.26% of all children referred for echocardiography at a single center over a $2^1/_2$-year period [6]. LVNC has been identified as the third most frequent cause of cardiomyopathy in children, representing 5–9% of cardiomyopathies seen among various studies [2,7,7a].

Etiology

LVNC is a genetically heterogeneous myopathy, occurring both sporadically and in familial forms. Many of the identified genetic mutations involve proteins in the common pathway that connects the extracellular matrix to the sarcolemma, sarcomere, and nuclear membrane. Isolated LVNC has been associated with mutations in the Xq28 region of the X chromosome, and specifically for the G4.5 gene encoding tafazzin in infants and children with X-linked familial LVNC. Mutations of this same locus are associated with Barth syndrome and other X-linked infantile cardiomyopathies [8,9]. A variety of mutations in the CYPHER/ZASP gene has been described in patients with isolated LVNC and in families with both dilated cardiomyopathy and LVNC [10]. Autosomal dominant familial LVNC in adulthood has been mapped to a locus on chromosome 11p15 [11]. In families with ni-LVNC associated with congenital heart disease, mutations in α-dystrobrevin and transcription factor NKX2.5 have been demonstrated [12]. iLVNC has also been described in the phenotypic spectrum of lamin A/C mutations, which have been mapped to human chromosomes 1q12.1-q23 and 10. The laminopathies are responsible for a number of other diseases, including dilated cardiomyopathy, Emery–Dreifuss muscular dystrophy, and limb girdle muscular dystrophy [13,14]. Associations have been noted with a variety of other genetic conditions such as Roifman syndrome, MIDAS syndrome, Melnick–Needles syndrome, nail–patella syndrome, DiGeorge syndrome, and trisomy 13 [2,15–19].

Echocardiography in Pediatric and Congenital Heart Disease: From Fetus to Adult, Second Edition. Edited by Wyman W. Lai, Luc L. Mertens, Meryl S. Cohen and Tal Geva.
© 2016 John Wiley & Sons, Ltd. Published 2016 by John Wiley & Sons, Ltd.
Companion website: www.lai-echo.com

Developmental considerations

During normal cardiac development, the ventricular myocardium begins as a spongy meshwork of myocardial fibers with intertrabecular recesses that communicate with the ventricular cavity. Compaction of the myocardium then progresses from epicardium towards endocardium and from base to apex, with vascular recesses becoming capillaries that eventually connect with the epicardial coronary artery system [20]. Arrest in this normal embryologic process of myocardial compaction is thought to be responsible for the findings in LVNC. This assumption is supported by the similarity in the appearance of the left ventricular myocardium in LVNC with that of embryonic myocardium, and by reports of prenatal diagnosis [21,22] and also symptomatic cases described in patients from infancy through adulthood. Countering this pathogenetic assumption are several documented cases in which LVNC was diagnosed but evidence of normal myocardial architecture had been demonstrated in previous echo studies [9,23]. It is possible, therefore, that the features of LVNC can be either a persistence of embryonic myocardial structure or a developmental pattern in a genetically impaired myocardium.

Clinical manifestations

The classic description of the clinical course in LVNC has included progressive heart failure, arrhythmia, and thromboembolism, with a poor long-term prognosis. The segments of the LV with noncompacted myocardium typically exhibit decreased systolic function as a result of hypoperfusion, ischemia, and fibrosis. These findings are confirmed by thallium imaging, positron emission tomography (PET) scanning and myocardial biopsy [3,24]. Impaired diastolic filling with restrictive physiology is also associated with hypertrabeculated myocardium [2]. Patients may present with clinical symptoms of heart failure during fetal life, infancy, childhood, or adult years. Although there can be some improvement in function with aggressive medical management of heart failure, progression of the cardiomyopathic process often leads to cardiac transplantation or death from heart failure, arrhythmia, or stroke. In a series of adult LVNC patients, the mortality rate was 47% over a 6-year follow-up period [25]. Based on a recent review of 155 cases of LVNC reported to the NHLBI pediatric cardiomyopathy registry, there was a combined endpoint of death or transplant of 33% for the entire group, with a much lower rate among those patients without ventricular dysfunction. Notably, 12% of patients with LVNC and normal ventricular function progressed to a cardiomyopathy phenotype within 2 years [7a].

The natural history of LVNC is further elucidated by the detection of asymptomatic cases during family or population screening studies. These more prospective investigations suggest that, at least in some patients, there may be a long preclinical phase with a much less dire natural history [3,26]. Electrocardiographic abnormalities are frequently observed in patients with LVNC, and may include left and right bundle branch block, ST- and T-wave abnormalities, pathologic Q waves or poor R-wave progression, biventricular hypertrophy, and Wolff–Parkinson–White syndrome. Arrhythmias are a common feature, with atrial fibrillation, supraventricular tachycardia, and ventricular tachycardia noted on baseline electrocardiogram (ECG) or Holter monitor [2,25]. Sudden death from presumed ventricular arrhythmia is a recognized complication of LVNC, and aggressive management of ventricular arrhythmia with pharmacologic therapy or an implantable defibrillator is often warranted. Thrombus formation within the deep intertrabecular recesses and associated arrhythmia is a likely explanation for the frequent occurrence of thromboembolic events in these patients. Adult series have reported up to 24% of patients suffering from transient ischemic attack, stroke, or peripheral emboli [5]. Anticoagulation is recommended in patients with documented thromboembolic episodes or with thrombus visualized by echocardiography; antiplatelet agents are often recommended as a prophylactic measure at the time of initial diagnosis.

Morphology

The anatomic features of LVNC include multiple trabeculations affecting the apex and the inferior and lateral walls at the midventricle, with deep intertrabecular recesses that communicate with the cavity of the LV and are lined with endocardial endothelium (Figure 37.1). The epicardial layer of the myocardium is thin and compact. There are often histologic areas of ischemia within the noncompacted endocardial layer, and subendocardial fibrosis and endocardial fibroelastosis have been described in autopsied hearts [5,27]. Electron microscopy has been inconsistent in findings related to myofiber and mitochondrial morphology. Trabeculation also affects the RV in less than 50% of cases,

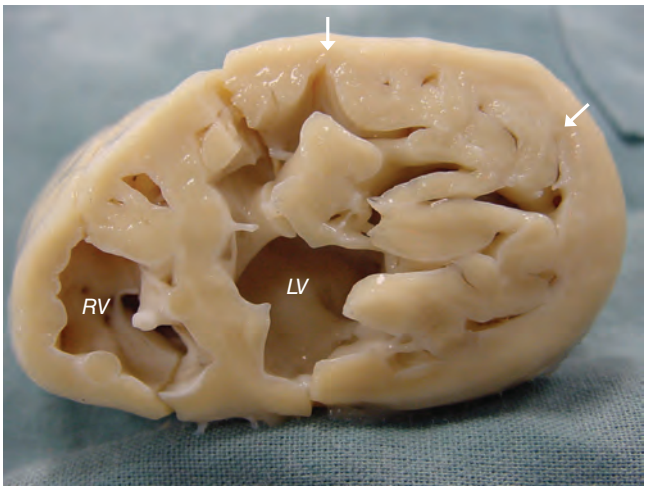


Figure 37.1 Pathologic specimen of left ventricular noncompaction. Explanted heart of a child with left ventricular noncompaction and severe left ventricular dysfunction. Note the dense trabeculations and deep recesses in lateral wall of the left ventricle (LV). The white arrows identify the demarcation between compact and noncompact myocardial layers. RV, right ventricle.

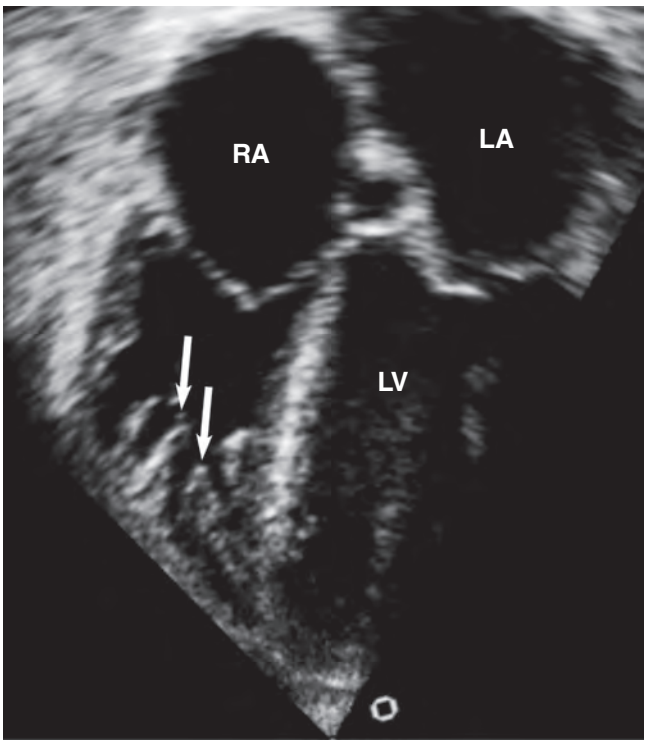


Figure 37.2 Apical 4-chamber view demonstrates right ventricular noncompaction. Prominent trabeculations (white arrows) fill the RV apex in this apical 4-chamber image. LA, left atrium; LV, left ventricle; RA, right atrium.

but differentiation of pathologic from normal degrees of RV trabeculation may be difficult (Figure 37.2). ni-LVNC occurs in association with ventricular septal defects (predominantly muscular), and with left or right ventricular outflow obstruction. Lesions affecting the left heart may include subaortic stenosis, valvar aortic stenosis, coarctation of the aorta, and hypoplastic left heart syndrome. Right heart obstruction may range from valvar pulmonary stenosis to pulmonary atresia and even tetralogy of Fallot [6]. LVNC has also been reported in association with heterotaxy syndrome particularly in the setting of complete heart block.

Classification

LVNC does not carry widespread recognition as a distinct form of cardiomyopathy. Whereas the American Heart Association defines it as a separate congenital cardiomyopathy, both the World Health Organization and the European Society of Cardiology consider it an unclassified cardiomyopathy [1,28,29]. This is based on multiple reasons, including heterogeneity in morphologic appearance, association with other forms of congenital heart disease, overlap with other forms of cardiomyopathy, range of clinical symptoms in patients with similar morphologic features, and genetic heterogeneity [30]. As more family and population screening studies have been reported, a larger number of asymptomatic individuals with LVNC have been identified [2].

Over the last 20 years, various authors have proposed imaging-based diagnostic criteria for LVNC [4,12,31,32]. Criteria have also been proposed for cardiac magnetic resonance (CMR) imaging [33]. More recently, investigators have questioned the validity of these criteria. One study compared three proposed criteria against a cohort of patients with ventricular dysfunction ($n = 199$) and a prospective cohort of normal controls ($n = 60$). They found that 24% of patients fulfilled one or more diagnostic criteria for LVNC. In that subgroup of 69 patients, only 30% fulfilled all three diagnostic criteria. Furthermore, there were racial differences in the degree of noncompaction, with a higher prevalence in normal black subjects. This suggests that the criteria are neither sensitive nor specific for the diagnosis of LVNC [34]. Furthermore, the measurements are poorly reproducible and not predictive of heart transplantation or death. Given a lack of consensus regarding these criteria, we propose that imaging should be focused on evaluating for the morphologic appearance of LVNC. The diagnosis of LVNC cardiomyopathy should incorporate not only these morphologic findings, but also any associated features of cardiomyopathy (e.g., features of restrictive, hypertrophic, or dilated cardiomyopathy).

Imaging

Key elements*

- Ventricular long- and short-axis imaging in the subxiphoid, apical, and parasternal views to determine the presence and location of myocardial trabeculations.
- Evaluation of the morphology of the papillary muscles, which are less differentiated in LVNC.
- Assessment of segmental and global ventricular systolic function.
- Verification of communication of the intertrabecular recesses with the ventricular blood pool by color Doppler or contrast (Video 37.1).
- Measurement of the diastolic transmitral flows and tissue Doppler annular velocities to assess diastolic function.
- Evaluation for associated structural heart disease.
- Evaluation of the recesses for thrombus formation.

Echocardiography is the first-line imaging modality used in the diagnosis of LVNC. The characteristics of LVNC are readily seen using 2D and color flow mapping. The hallmark feature is prominent trabeculations, typically along the lateral and apical walls of the LV (Figure 37.3). In LVNC, the noncompact, or trabeculated, inner layer is thicker than the compact layer. The trabeculations are more easily seen during diastole, whereas the two-layer appearance of the myocardium is better seen in systole [31]. Both contrast echocardiography and CMR can help define the continuity of the left ventricular cavity with the trabecular spaces, particularly when the quality of standard imaging is limited [33,36].

*Note the lack of consensus regarding strict diagnostic criteria for LVNC.

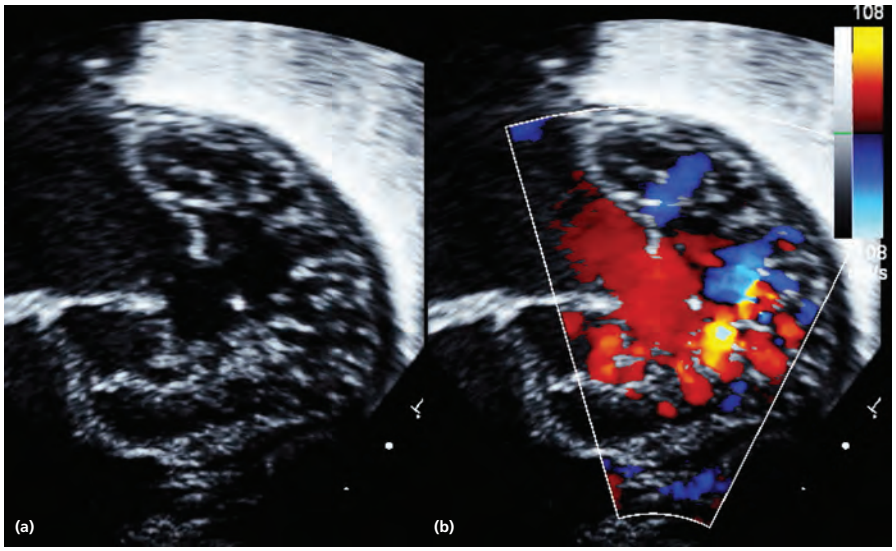


Figure 37.3 **(a)** Subxiphoid image in 2D of an infant with valvar aortic stenosis and left ventricular noncompaction. Deep intertrabecular recesses are seen. **(b)** Same image with color Doppler shows the color (blood flow) entering multiple small recesses within the LV cavity.

Speckle tracking is a novel marker that may help to distinguish LVNC from dilated cardiomyopathy. In a group of 10 patients with isolated LVNC, a solid body twist (or absent rotation) of the heart was found during systole, in contrast to an opposing twist direction from base to apex in those patients with normal hearts or in those with dilated cardiomyopathy [37]. However, speckle tracking has not gained widespread use because of limited reproducibility. Several imaging-based risk factors for adverse clinical outcome in LVNC have been proposed, including (1) ratio of noncompact to compact layers, (2) number of affected segments, (3) LV end-diastolic dimension, (4) abnormal echocardiographic lateral mitral annular early diastolic tissue Doppler velocity ($E < 7.8$ cm/s), and (5) ventricular dysfunction [5,35,38–42].

We propose that the most appropriate assessment of LVNC includes (1) two-layer appearance of the myocardium with a thin compact layer and thick non-compact layer, (2) increased number of trabeculations favoring the lateral wall and apex of the LV, (3) trabeculations that move synchronously with the myocardium, (4) perfusion of the intertrabecular recesses, and (5) abnormal ventricular function [4,12,31,32]. The diagnosis of LVNC cardiomyopathy should be made clinically by incorporating imaging features and other clinical parameters, such as the presence of heart failure and/or arrhythmias.

Prenatal assessment

Prenatal diagnosis of LVNC has been described [43]. Reported cases have involved ventricular dysfunction and right ventricular noncompaction [22]. A limitation of prenatal diagnosis is the difficulty in obtaining adequately high spatial resolution to detect trabeculations (Figure 37.4; Video 37.2). In the fetus with LVNC, there is a strong association with congenital heart disease, complete heart block, chromosomal/noncardiac abnormalities, and overall poor prognosis [43,44]. If ventricular function is poor, hydrops fetalis may develop. Color Doppler can be helpful to assess for flow within the trabecular recesses.

Congenital left ventricular aneurysm and diverticulum

Definition

Congenital LV aneurysms and diverticula have historically been mentioned interchangeably in discussion of protrusions from the LV cavity lacking any other etiologic explanation. As discussed by Van Praagh and colleagues [45], the two are distinct entities, beginning with the origin of their names: aneurysm is derived from the Greek root *eurys*, meaning "wide," whereas diverticulum is from the Latin word *deverticulum*, meaning a "byroad" with the connotation of a narrow, meandering pathway. LV aneurysms are characterized as protrusions from the myocardium with a wide mouth and consisting of thinned or abnormal myocardium or fibrous tissue. LV diverticula have a narrow communication with the functional ventricle and are composed of endocardium, myocardium, and epicardium [46]. Congenital LV aneurysms can have varying degrees of localized wall motion abnormality, whereas diverticula typically have normal contractile function [47]. Diverticula of the RV have also been reported, arising either from the conal region, the base, or the apex [48–50].

Incidence

Congenital LV aneurysm and diverticulum are both rare anomalies, mostly described in case reports and small case series. A frequency of 0.12% was reported for congenital LV aneurysm from a large cardiac pathology registry [39]. LV diverticulum was noted in 0.4% of an autopsy series of cardiac deaths and in 0.26% of nonselected patients undergoing cardiac catheterization [46,51].

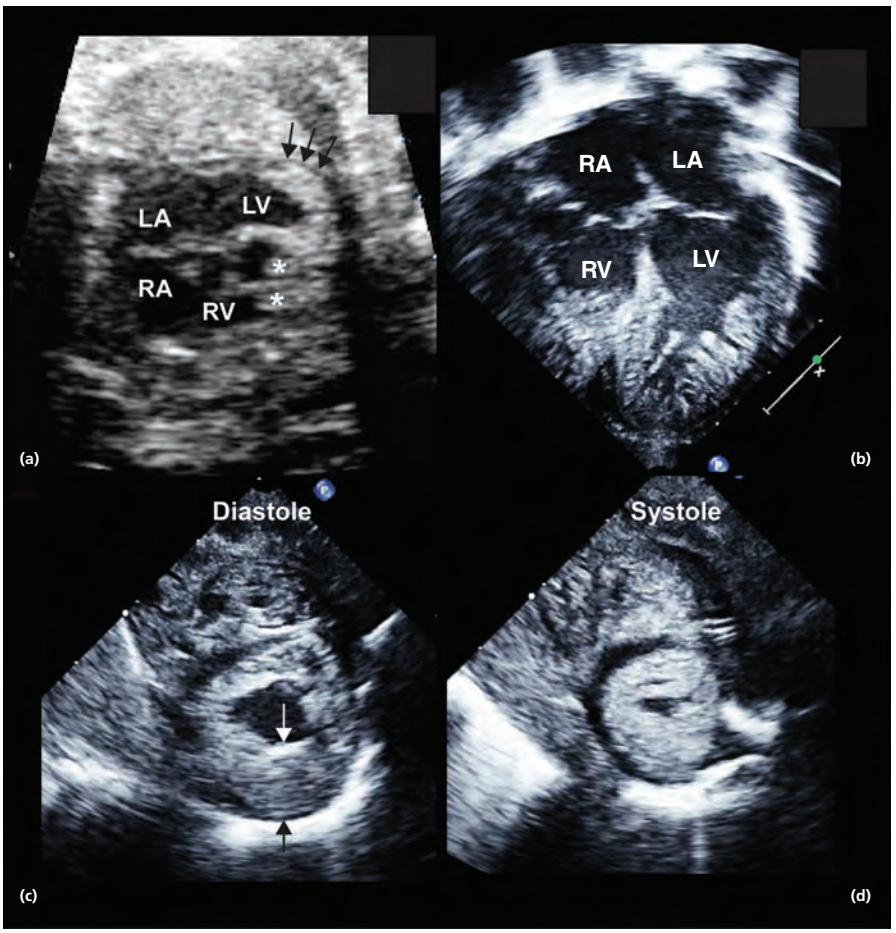


Figure 37.4 Multiple images of fetal left ventricular noncompaction. (a) Fetal 4-chamber view at 30 weeks' gestation demonstrates thickening of the left ventricular wall (black arrows), and increased trabeculations in the right ventricular apex (white asterisks). (b) Apical 4-chamber view of the postnatal echocardiogram in the same patient demonstrates features of noncompaction in the right ventricle (RV) and left ventricle (LV). Note the deep trabecular recesses of the left ventricular apical, lateral, and septal walls with relative sparing of the basal myocardium. (c) Parasternal short-axis view in the same patient in diastole shows the increased thickness of noncompact (white arrow) to compact myocardium (black arrow), with increased trabeculations in the RV. (d) Parasternal short-axis view in the same patient in systole demonstrates that the LV myocardium has a two-layered appearance. LA, left atrium; RA, right atrium.

Etiology

Congenital LV aneurysms and diverticula are both presumed to be idiopathic developmental abnormalities of the endomyocardium [39]. They are not associated with abnormalities of the coronary arteries or coronary insufficiency, and should be distinguished from aneurysms or pseudoaneurysms caused by ischemic, infective, or traumatic processes. A particular subtype of LV aneurysm, the submitral aneurysm, seen most often in patients from sub-Saharan Africa, is thought to result from a congenital deficiency in the fusion of myocardium with the cardiac fibrous skeleton (Figure 37.5; Video 37.3) [52]. Both aneurysms and diverticula have been described in utero, some resulting in fetal demise [53], and they occur in children and adults either as incidental findings or associated with clinical symptoms of arrhythmia, heart failure, mitral insufficiency, or thromboembolism. There is one report of the occurrence of LV diverticulum in siblings [54], but no genetic markers have yet been described. Apical LV diverticula occur in patients with pentalogy of Cantrell syndrome, a defect in the ventral mesoderm that results in abnormalities of the abdominal wall, sternum, anterior diaphragm, pericardium, and intracardiac anatomy (Figure 37.6; Video 37.4). It has been postulated that the diverticulum in this syndrome may be caused by an abnormal attachment of the heart tube to the yolk sac, causing the myocardium to be drawn out as the yolk sac recedes [55].

Clinical manifestations

Small aneurysms and diverticula are usually asymptomatic and found incidentally by echocardiography or angiography. Larger abnormalities may present as a deformity of the cardiac silhouette on chest X-ray. Systolic clicks or murmurs on auscultation have been described in patients with aneurysms and diverticula due to expansion of the lesion in systole or because of flow across the narrow diverticular neck. Mitral regurgitation may be the initial clinical feature in patients with submitral aneurysms or basilar congenital aneurysms that undermine the mitral support apparatus. Coronary compression with changes of ischemia or infarction has been reported with large aneurysms in the region of the left anterior descending or circumflex coronary arteries [46,56]. The ECG is frequently abnormal in patients with diverticula or other forms of congenital aneurysm, and includes findings of premature ventricular contractions, ventricular tachycardia, left axis deviation, and left bundle branch block [57]. The natural history of these disorders is variable.

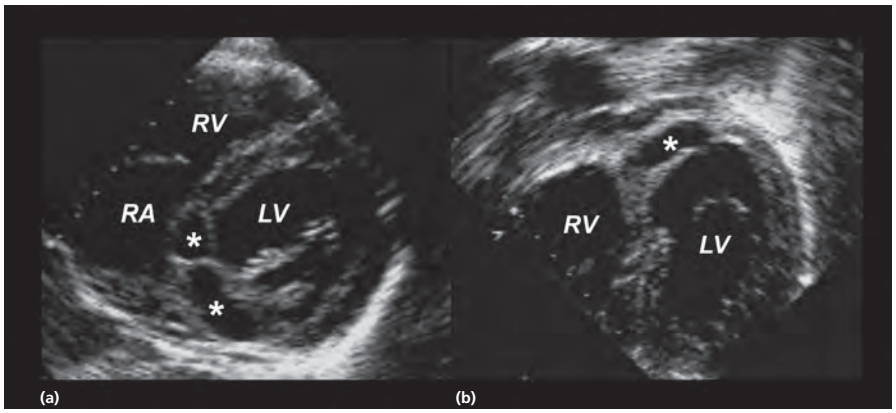


Figure 37.5 2D echocardiogram of a Bantu submitral aneurysm in a 44-year-old Nigerian male. **(a)** Parasternal short-axis view demonstrates the septated sonolucent areas in the posterior and inferior mitral annular region of the left ventricle (LV) (white asterisks). **(b)** Posteriorly angulated 4-chamber view in the same patient shows the submitral aneurysm (white asterisk) just inferior to the coronary sinus. RA, right atrium, RV, right ventricle.

Prenatal presentation of diverticula or aneurysms is variable. Some fetuses have had fetal or perinatal death from heart failure with hydrops, or from leaking and rupture of the aneurysm or diverticulum, presaged by fetal pericardial effusion. In other prenatal cases, the size of the diverticulum remains unchanged or decreases with growth of the surrounding myocardium. LV aneurysms may also continue to expand during gestation, with outcome related to the volume of the aneurysm relative to the ventricular cavity [39,58,59]. Postnatally, patients may present with symptoms related to arrhythmia or thromboembolism. Rupture of a thin-walled aneurysm or a high-pressure diverticulum can also result in tamponade and sudden death. Alternatively, some patients remain asymptomatic with no change in the size of the abnormal chamber over long-term follow-up [60]. In one case series of 26 patients with aneurysms or diverticula, 38% of patients had symptoms consisting of syncope, ventricular tachycardia, or heart failure. Larger aneurysm size is associated with larger LV end-diastolic volume and decreased ejection fraction. Apical aneurysms tend to be larger and are more commonly associated with symptoms, need for defibrillator placement, and surgical resection [47]. Management of these rare anomalies must be individualized depending on the size and

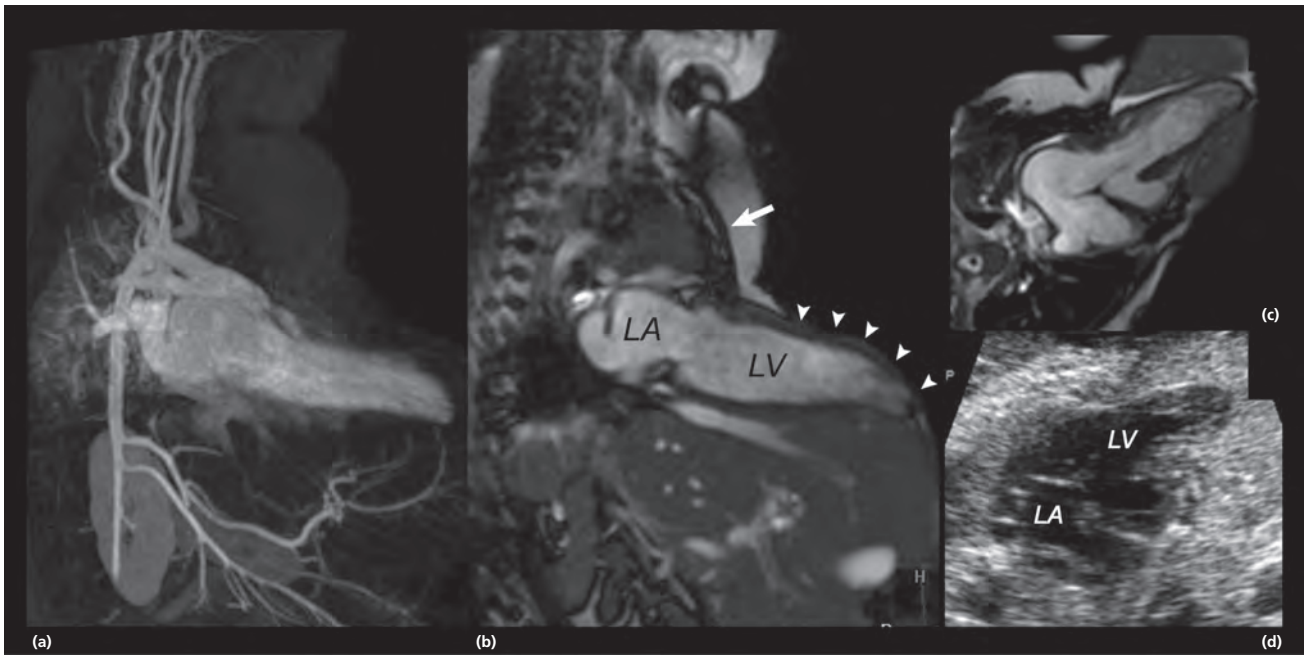


Figure 37.6 Multimodality imaging of congenital left ventricular diverticulum in the setting of pentalogy of Cantrell. Associated findings in this patient were tricuspid atresia, ectopia cordis, omphalocele, and sternal cleft. **(a)** CMR imaging shows the apex of the left ventricular (LV) cavity protruding from the thoracic cavity. **(b)** Cine SSFP imaging in the sagittal plane also shows protrusion of the LV from the thoracic cavity (thoracic cavity marked with white arrow) along with the abdominal contents (including the liver). The thin-walled LV diverticulum is denoted by white arrowheads. **(c)** Cine SSFP imaging in 4-chamber view demonstrates the anatomic abnormality of tricuspid atresia with ventricular septal defect and the LV diverticulum protruding from the thoracic cavity. **(d)** Fetal echocardiogram in 4-chamber view [equivalent view to **(c)**] also demonstrates tricuspid atresia with ventricular septal defect and LV diverticulum. LA, left atrium.

location of the defect and associated symptoms. Successful surgical repair with simple excision or modified Dor procedure has been reported [47,61,62]. Anticoagulation to prevent embolic complications should be considered if surgical resection is not feasible.

Morphology

Congenital ventricular aneurysms are wide-mouthed protrusions from the ventricle with varying degrees of wall motion abnormality (Figure 37.7; Video 37.5). The aneurysm consists of thinned or dysplastic myocardium and fibrous tissue [39]. Whereas aneurysms are seen most often at the LV apex, they may involve the LV free wall, the septum, or the submitral and subaortic annular regions. Subannular aneurysms may have one or more smaller entry sites from the LV around the mitral and aortic annuli. The extent of the aneurysm and its involvement of mitral supporting structures influences the degree of clinical symptoms.

Ventricular diverticula classically have a narrow orifice from the ventricle, are composed of endocardium, myocardium, and epicardium, and demonstrate intrinsic contractility. They may occur as single or multiple small protrusions from the left or right ventricle, or as a large meandering channel extending through a sternal or abdominal wall defect in patients with

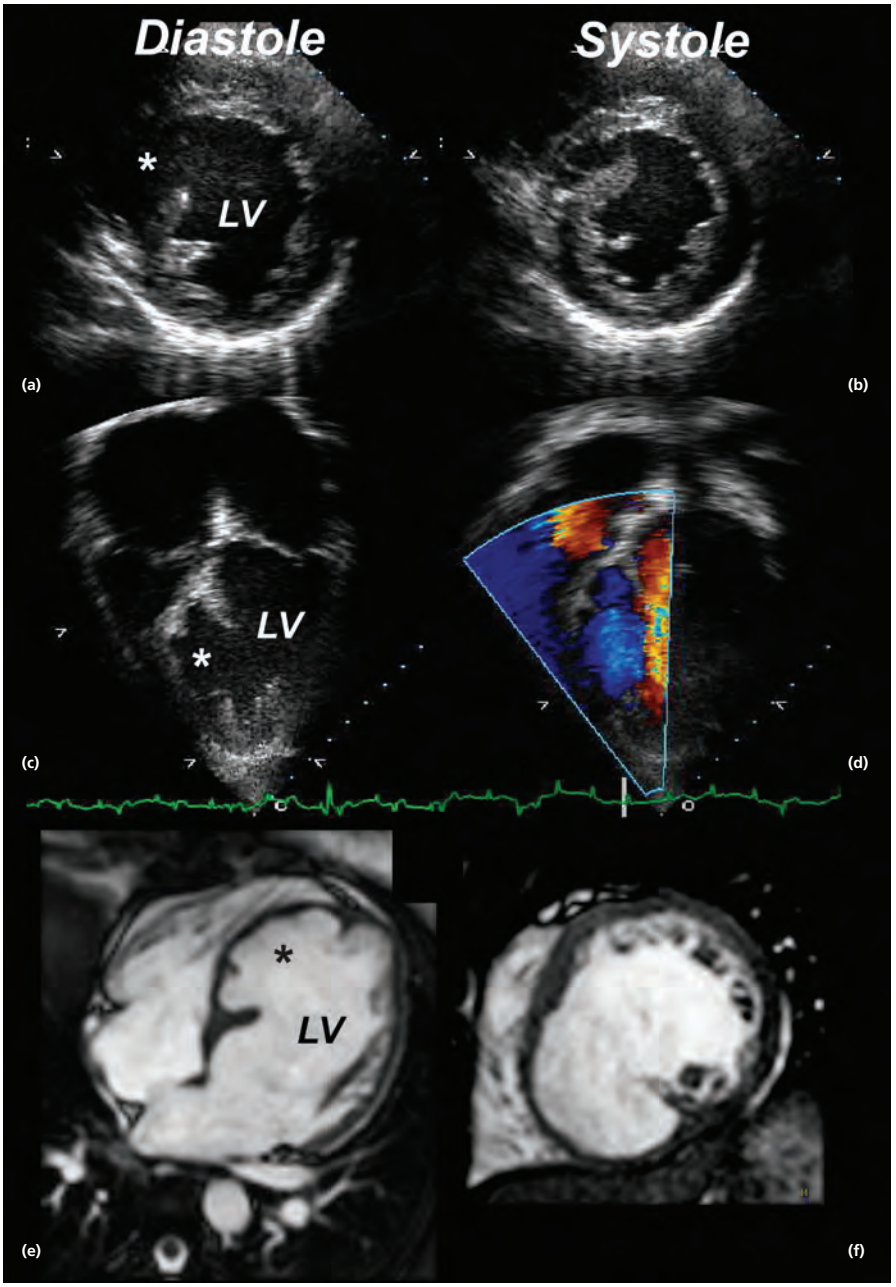


Figure 37.7 Multimodality imaging of a congenital aneurysm of the ventricular septum in a 19-year-old female with palpitations and frequent premature ventricular contractions. **(a)** Parasternal short-axis view demonstrates the aneurysm in the posterior portion of the ventricular septum in diastole (white asterisk). **(b)** In systole, the abnormal movement of the aneurysmal portion of the septum is seen. **(c)** Apical 4-chamber view in the same patient demonstrates the extent of the aneurysm with the wide neck noted and several septations (white asterisk). **(d)** Color Doppler imaging in the same patient in apical 4-chamber view demonstrates diastolic flow into the aneurysm. **(e, f)** CMR using cine SSFP imaging in the 4-chamber **(e)** and short-axis **(f)** views also shows the septal aneurysm. The wall of the aneurysm is thin walled and the LV appears dilated. LV, left ventricle.

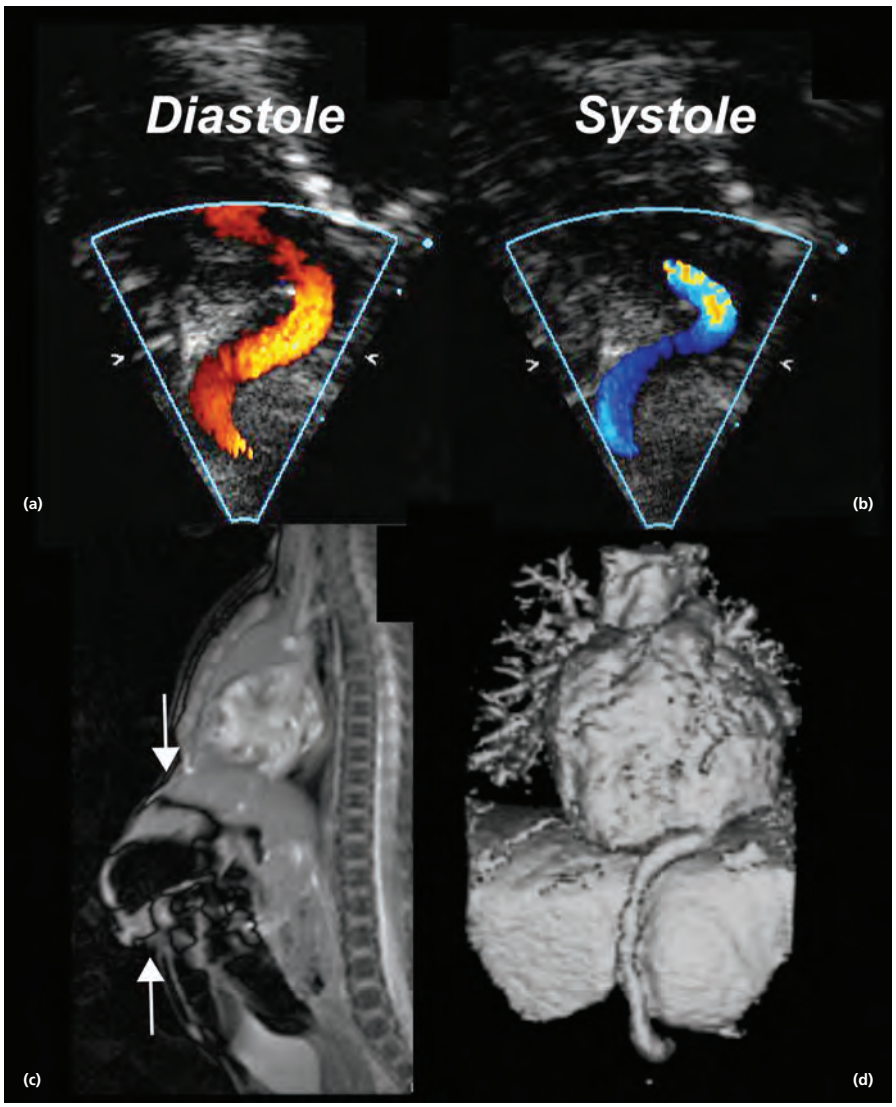


Figure 37.8 Multimodality imaging of a congenital left ventricular (LV) diverticulum in an infant with omphalocele and pulsatile mass over the abdomen. The heart was otherwise structurally normal. **(a)** Apical 4-chamber view with color Doppler in diastole demonstrates a long, finger-like protrusion from the apex of the LV with good contractility. **(b)** In systole, color flow is seen going in the opposite direction. **(c)** CMR in a sagittal plane demonstrates the abdominal wall defect (white arrows). **(d)** CMR angiography confirms a narrow appearance and long length of the diverticulum.

omphalocele or Pentalogy of Cantrell syndrome (Figure 37.8; Video 37.6) [55].

Imaging

Key elements

- Detection of distortion, deformity, or protrusion of ventricular cavities or subannular regions by 2D and if possible by 3D echocardiography (Figure 37.9; Video 37.7).
- Determination of the size of the communication between the cardiac chamber and the aneurysm or diverticulum.
- Assessment of the wall of the aneurysm or diverticulum for myocardial thickness and contractility.
- Evaluation of the aneurysm or diverticulum for the presence of thrombus.
- Quantification of global ventricular function.
- Investigation for associated structural cardiac anomalies and valvar function.

In children and adults, 2D echocardiography can detect outpouching of the ventricular cavity at the apex, from the LV free wall, the submitral region, or rarely from the RV free wall. Because imaging cannot evaluate for the histologic difference between aneurysm and diverticulum, the width of the neck of the anomaly is the main differentiating echocardiographic feature. Wall motion abnormalities are more common, but not the rule, in congenital aneurysms. Submitral and subaortic aneurysms will appear as spaces in the vicinity of the mitral annulus or intervalvar fibrosa that communicates with the ventricular cavity. Mitral and aortic regurgitation will be present when there is significant undermining of the valvar support or perforation of the aneurysmal space into the left atrium (Video 37.8). Segmental LV function should be assessed if coronary compromise is suspected from the location of the aneurysm. Thrombus may be present in the aneurysm or diverticulum. Contrast echocardiography may be helpful to

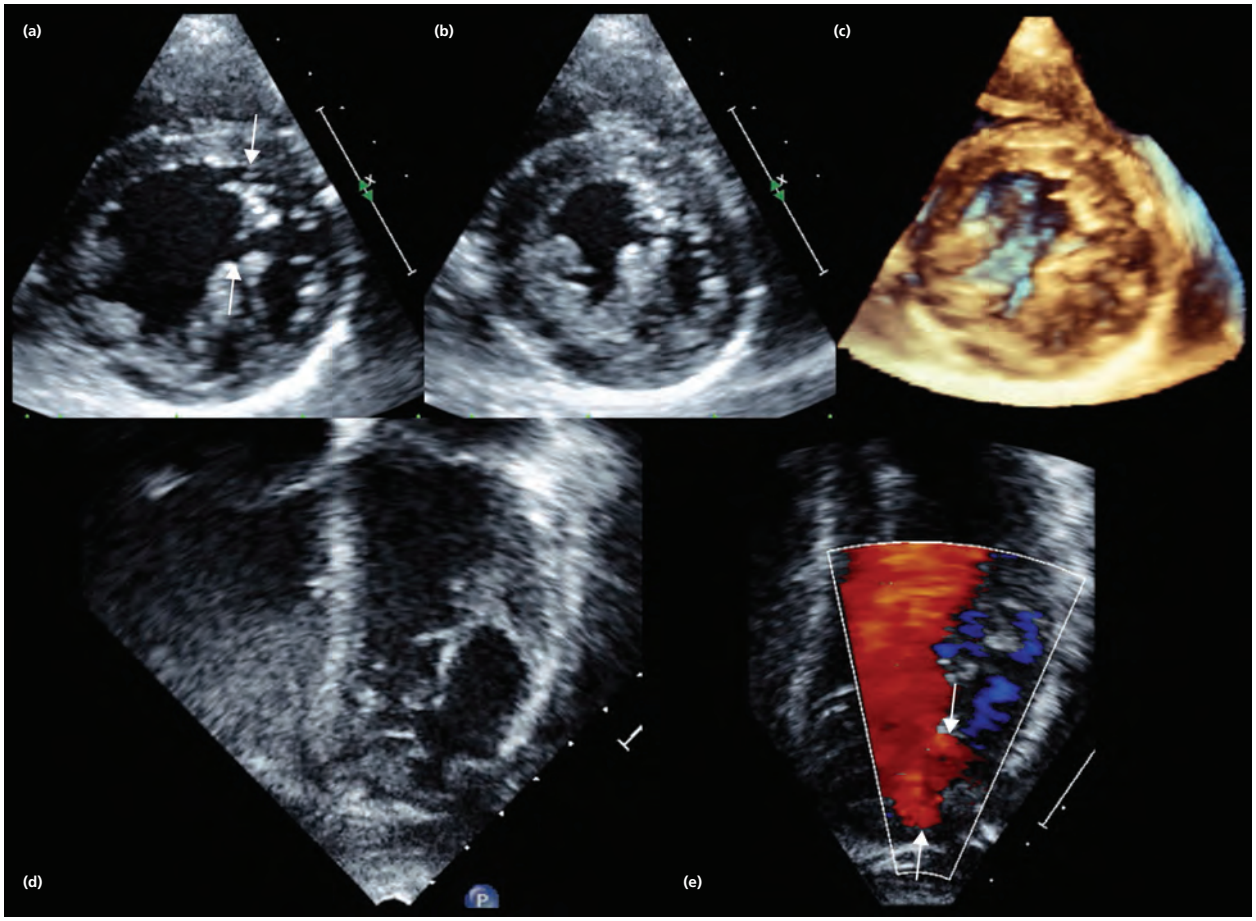


Figure 37.9 Multiple images of a congenital aneurysm of the left ventricular (LV) free wall. **(a)** In the parasternal short-axis view, the aneurysm has a broad base (white arrows) with several intervening trabeculations. **(b)** In systole, the aneurysm has good contractility. **(c)** 3D echocardiography confirms the presence of the aneurysm. **(d)** In the apical 4-chamber view, the aneurysm involves the mid-apical lateral wall of the left ventricle. **(e)** In the same view with color Doppler imaging, a broad diastolic flow jet is seen into the mouth of the aneurysm (white arrows).

define further the extent of the aneurysm or to demonstrate better the extra-cardiac extent of a diverticulum. This technique also permits differentiation of pooled blood from thrombus within the aneurysm (Figure 37.10) [63]. When defects in the anterior abdominal wall are present, LV diverticula should be sought in addition to structural cardiac anomalies including dextrocardia, atrial septal defect, ventricular septal defect, and tetralogy of Fallot. Other defects have also been described in this complex anomaly [50].

Prenatal Assessment

Left ventricular aneurysm or diverticulum should be considered in the prenatal assessment of cardiomegaly, fetal hydrops, arrhythmia, and pericardial effusion, and also in the complete evaluation of fetuses with midline thoraco-abdominal defects. Sizable aneurysms are easily detected during fetal echocardiography as distortions of the normal ventricular contour (Figure 37.11; Video 37.9). Attention should be directed to the width of the connection to the chamber of origin, the presence of contractility or expansion of the aneurysmal region, and the presence of thrombus within the abnormal segment. Diverticula may be more elusive, but investigation of the apical and submitral areas for irregular sonolucent regions may lead to the diagnosis. In some cases of large diverticula, hydrops fetalis may be present.

Postoperative assessment

Evaluation following repair of congenital aneurysm or diverticulum should include assessment of the effectiveness of the resection or exclusion method. Global and segmental ventricular function and mitral valve competence should be documented and followed over time. Patients with repair of associated structural congenital defects should be evaluated postoperatively as is lesion appropriate and discussed in other sections of the text.

Arrhythmogenic right ventricular cardiomyopathy/dysplasia

Definition

Arrhythmogenic right ventricular cardiomyopathy/dysplasia (ARVC/D) is an uncommon disorder classified as a primary

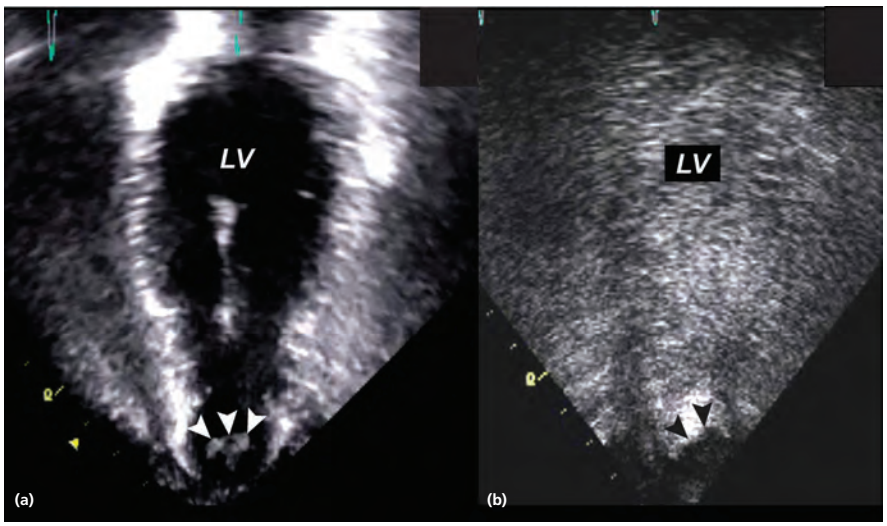


Figure 37.10 **(a)** Apical 4-chamber view demonstrating an apical aneurysm with thrombus (white arrowheads) in a 32-year-old female. **(b)** Image of the same patient with contrast opacification of the left ventricle (LV). Note that the apical aneurysm has a filling defect corresponding to the thrombus (black arrowheads). LV, left ventricle.

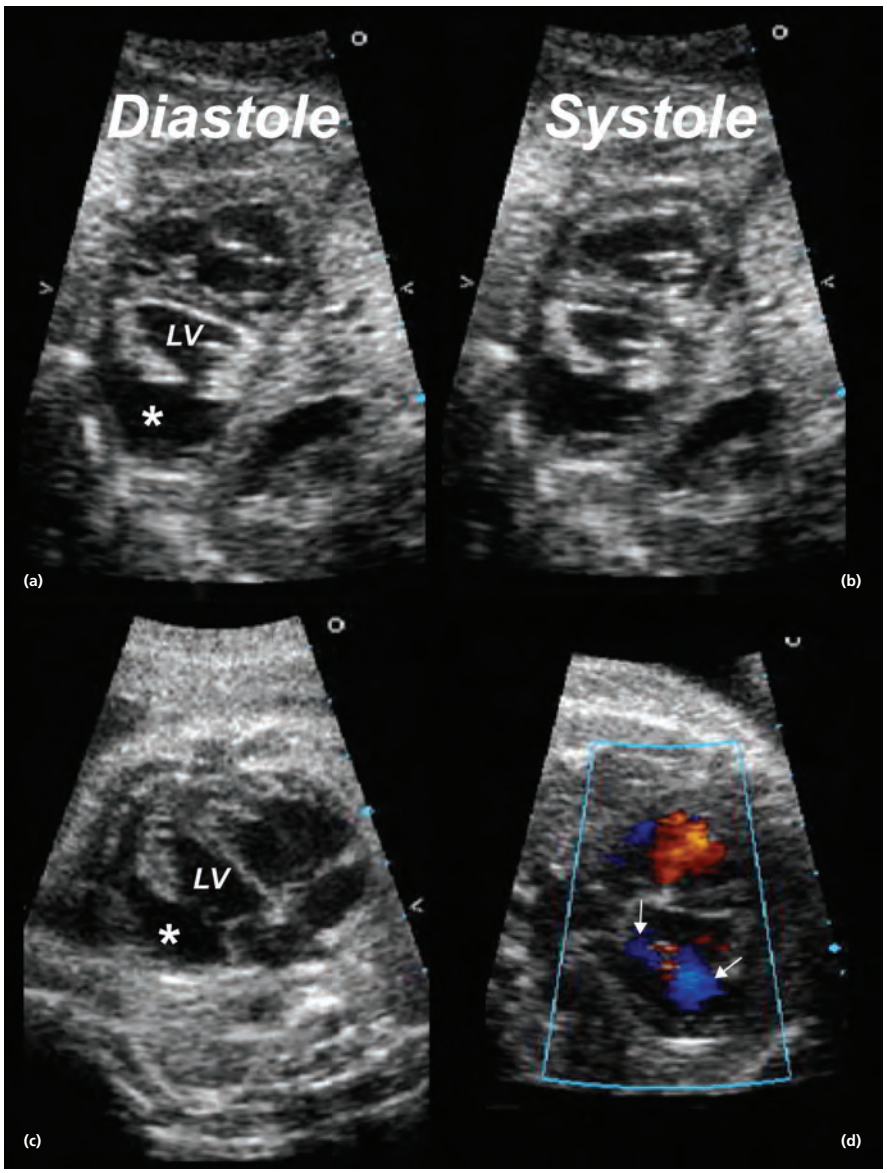


Figure 37.11 Fetal echocardiogram at 26 weeks' gestation demonstrates a congenital aneurysm arising from the basal lateral wall of the left ventricle (LV). **(a)** Short-axis view in diastole shows the large aneurysm (white asterisk). **(b)** Short-axis view in systole demonstrates poor contraction of the aneurysm. **(c)** 4-chamber view of the same fetus demonstrates that the aneurysm has a broad connection to the LV (white asterisk). **(d)** In an oblique short-axis view, diastolic flow jets pass into the mouth of the aneurysm (white arrows).

genetic cardiomyopathy [1]. It predominantly affects the RV and is characterized by fibrofatty replacement of myocardium leading to progressive myocardial dysfunction and potentially lethal ventricular arrhythmias. The diagnostic criteria were modified in 2010 to improve diagnostic sensitivity [64] (Table 37.1). These Task Force Criteria employ a series of major and minor criteria, which include structural and functional changes of the RV, electrocardiographic abnormalities and arrhythmia, family history, and tissue characterization of the myocardium by biopsy.

Incidence

Reports of the clinical description of ARVC/D appeared in the early 1980s, and since then the disorder has been recognized in Europe, Asia and the United States, with a prevalence of about 1 in 5000 persons [65–67]. The majority of cases manifest clinical symptoms between the ages of 15 and 40 years, with a male preponderance. ARVC/D is found in up to 20% of patients presenting with sudden death, and is a well-recognized cause of sudden death in young athletes [68,69].

Etiology

A familial occurrence of ARVC/D is reported, characterized by an autosomal dominant pattern of inheritance with incomplete penetrance, and accounting for about 30% of cases. Genetic studies have identified ARVC/D to be a genetically heterogeneous disorder of desmosomal dysfunction, with mutations discovered in genes encoding desmoplakin, plakophilin-2, plakoglobin, desmoglein-2, desmocollin-2, the cardiac ryanodine receptor RyR2, TMEM43, and regulatory sequences of transforming growth factor-β (TGF-β) [1,70–72]. ARVC/D has also been described in association with Naxos disease (palmoplantar keratoderma and woolly hair) and with Carvajal syndrome, both of which demonstrate autosomal recessive modes of inheritance [73]. Some sporadic cases of ARVC/D are isolated genetic mutations, but an association with infection by cardiotropic viral agents has also been reported, including coxsackievirus B3, enterovirus and adenovirus. The significance of this association is uncertain. It has been speculated that the disruption in myocardial function caused by ARVC/D may increase susceptibility to viral infection. Alternatively, the consequences of myocardial infection and inflammation may result in disruption of myocardial cellular junctions and ion channels, which leads to the clinical signs of ARVC/D [74].

Morphology

The hallmark of ARVC/D is fibrofatty replacement of myocardial cells in the RV. This abnormality results in thinning, localized aneurysmal bulging, and eventually RV dilation with global dysfunction. Specific areas of involvement of the RV are commonly seen and have been termed the "triangle of dysplasia" [66]: (1) the anterior infundibulum, (2) the RV apex, and (3) the inferior or diaphragmatic aspect of the RV. LV involvement also occurs and may be more frequent than previously recognized. When assessed by sensitive techniques such as CMR, 84% of patients with ARVC/D have been found to have evidence of LV involvement, including LV enlargement, decreased LV ejection fraction, LV intramyocardial fat, LV wall motion abnormalities, or late enhancement in a nonischemic pattern [71]. Microscopic study of the bundle of His and its branches has shown fibrous and fibrofatty infiltration in 68% of a series of ARVC/D patients with sudden death [69].

Clinical manifestations

Although ARVC/D classically makes its clinical appearance during adolescence and young adulthood, it has been identified both in utero and in a few case reports of younger children with ventricular tachycardia and evidence of RV and LV involvement with fibrofatty replacement [65,75,76]. The gradual appearance of clinical symptoms over a period of years may be attributed to a slow disruption of the myocardium, which is inherently flawed in its cellular structure. The added stress of vigorous exercise, particularly on the thinner-walled RV, may account for an earlier appearance of symptoms in individuals with ARVC/D who perform regular intensive sporting activities [77].

Patients with ARVC/D most commonly present with syncope, palpitations, or sudden death or near-death. ECG findings include frequent premature ventricular contractions, epsilon waves, inverted T-waves, prolongation of the QRS, and delayed S-wave upstroke in the right precordial leads. Ventricular tachycardia with left bundle branch morphology may be detected on Holter monitoring or exercise testing, and is often the proximate cause of sudden death. With progressive involvement of the RV myocardium, dysfunction may occur with signs of right heart failure. LV involvement with biventricular failure is a poor prognostic sign. The natural history reported for patients with symptomatic ARVC/D from a European population includes a high mortality from sudden death and progressive heart failure [78]. However, studies from populations including symptomatic probands and asymptomatic patients detected by family screening show a much more favorable long-term outcome with medical therapy and implantable cardiac defibrillator treatment for those at high risk for sudden death [79].

Imaging

Key elements*

- Assessment for RV wall aneurysms, global and regional dysfunction*.
- Measurement of the fractional area change of the RV by contouring the RV area in the apical 4-chamber view in diastole and systole*:

$$\text{fractional area change (\%)} = [(\text{RV area diastole} - \text{RV area systole})/\text{RV area diastole}] \times 100.$$

- Measurement of the dimension of the RV outflow tract at end-diastole*:
 - Parasternal long-axis view.
 - Parasternal short-axis view.

Table 37.1 2010 Revised Task Force Criteria for Diagnosis of Arrhythmogenic Right Ventricular Dysplasia/Cardiomyopathy.

I. Global and/or regional dysfunction and structural alterations

Major:

By 2D echo:
- Regional RV akinesia, dyskinesia, or aneurysm
- and 1 of the following (end diastole):
 - PLAX RVOT ≥32 mm (corrected for body size [PLAX/BSA] ≥19 mm/m^2)
 - PSAX RVOT ≥36 mm (corrected for body size [PSAX/BSA] ≥21 mm/m^2)
 - or fractional area change ≤33%

By MRI:
- Regional RV akinesia or dyskinesia or dyssynchronous RV contraction
- and 1 of the following:
 - Ratio of RV end-diastolic volume to BSA ≥110 mL/m^2 (male) or ≥100 mL/m^2 (female)
 - or RV ejection fraction ≤40%

By RV angiography:
- Regional RV akinesia, dyskinesia, or aneurysm

Minor:

By 2D echo:
- Regional RV akinesia or dyskinesia
- and 1 of the following (end diastole):
 - PLAX RVOT ≥29 to <32 mm (corrected for body size [PLAX/BSA] ≥16 to <19 mm/m^2)
 - PSAX RVOT ≥32 to <36 mm (corrected for body size [PSAX/BSA] ≥18 to <21 mm/m^2)
 - or fractional area change >33% to ≤40%

By MRI:
- Regional RV akinesia or dyskinesia or dyssynchronous RV contraction
- and 1 of the following:
 - Ratio of RV end-diastolic volume to BSA ≥100 to <110 mL/m^2 (male) or ≥90 to <100 mL/m^2 (female)
 - or RV ejection fraction >40% to ≤45%

II. Tissue characterization of wall

Major:
- Residual myocytes <60% by morphometric analysis (or <50% if estimated), with fibrous replacement of the RV free wall myocardium in ≥1 sample, with or without fatty replacement of tissue on endomyocardial biopsy

Minor:
- Residual myocytes 60–75% by morphometric analysis (or 50–65% if estimated), with fibrous replacement of the RV free wall myocardium in ≥1 sample, with or without fatty replacement of tissue on endomyocardial biopsy

III. Repolarization abnormalities

Major:
- Inverted T waves in right precordial leads (V1, V2, and V3) or beyond in individuals >14 years of age (in the absence of complete right bundle branch block QRS ≥120 ms)

Minor:
- Inverted T waves in leads V1 and V2 in individuals >14 years of age (in the absence of complete right bundle branch block) or in V4, V5, or V6
- Inverted T waves in leads V1, V2, V3, and V4 in individuals >14 years of age in the presence of complete right bundle branch block

IV. Depolarization/conduction abnormalities

Major:
- Epsilon wave (reproducible low-amplitude signals between end of QRS complex to onset of the T wave) in the right precordial leads (V1 to V3)

Minor:
- Late potentials by SAECG in ≥1 of 3 parameters in the absence of a QRS duration of ≥110 ms on the standard ECG
- Filtered QRS duration (fQRS) ≥114 ms
- Duration of terminal QRS <40 μV (low-amplitude signal duration) ≥38 ms
- Root-mean-square voltage of terminal 40 ms ≤20 μV
- Terminal activation duration of QRS ≥55 ms measured from the nadir of the S wave to the end of the QRS, including R′, in V1, V2, or V3, in the absence of complete right bundle branch block

V. Arrhythmias

Major:
- Nonsustained or sustained ventricular tachycardia of left bundle branch morphology with superior axis (negative or indeterminate QRS in leads II, III, and aVF and positive in lead aVL)

Table 37.1 (*Continued*)

Minor:
- Nonsustained or sustained ventricular tachycardia of RV outflow configuration, left bundle branch block morphology with inferior axis (positive QRS in leads II, III, and aVF and negative in lead aVL) or of unknown axis
- >500 ventricular extrasystoles per 24 h (Holter)

VI. Family history

Major:
- ARVC/D confirmed in a first-degree relative who meets current Task Force criteria
- ARVC/D confirmed pathologically at autopsy or surgery in a first-degree relative
- Identification of a pathogenic mutation[a] categorized as associated or probably associated with ARVC/D in the patient under evaluation

Minor:
- History of ARVC/D in a first-degree relative in whom it is not possible or practical to determine whether the family member meets current Task Force criteria
- Premature sudden death (<35 years of age) due to suspected ARVC/D in a first-degree relative
- ARVC/D confirmed pathologically or by current Task Force Criteria in second-degree relative

PLAX, parasternal long-axis view; RVOT, RV outflow tract; BSA, body surface area; PSAX, parasternal short-axis view; aVF, augmented voltage unipolar left foot lead; aVL, augmented voltage unipolar left arm lead; SAECG, signal averaged electrocardiogram.
Criteria for diagnosis of arrhythmogenic right ventricular dysplasia: definite diagnosis: 2 major or 1 major and 2 minor criteria or 4 minor from different categories; borderline: 1 major and 1 minor or 3 minor criteria from different categories; possible: 1 major or 2 minor criteria from different categories.
[a]A pathogenic mutation is a DNA alteration associated with ARVC/D that alters or is expected to alter the encoded protein, is unobserved or rare in a large non-ARVC/D control population, and either alters or is predicted to alter the structure or function of the protein or has demonstrated linkage to the disease phenotype in a conclusive pedigree.
Source: Marcus et al. 2010 [64]. Reproduced with permission of Oxford University Press.

- Assessment of LV size, global and regional function.
- Tricuspid annular plane systolic excursion (TAPSE).
- Myocardial performance index (MPI).

*Refer to the echocardiographic criteria in the 2010 Revised Task Force Criteria for diagnosis of arrhythmogenic right ventricular cardiomyopathy/dysplasia (Table 37.1) [64].

Although an uncommon disorder, ARVC/D should be considered in the differential diagnosis of all children, adolescents, and adults presenting with syncope or palpitations. The 2D echocardiographic study should focus carefully on RV wall thickness and segmental and global RV function (Figure 37.12; Videos 37.10 and 37.11). RV wall definition is often limited in standard 2D echocardiographic studies, and the examiner should intentionally focus on the RV outflow tract thickness and contractility, the subtricuspid annular region of the RV lateral wall, the inferior RV wall in short-axis views, and the apex. Subxiphoid views often provide optimal resolution of the subannular and diaphragmatic surface of the RV, whereas the best imaging of the lateral wall and apex may require off-axis apical views. It may be helpful to employ a high-frequency probe specifically to scan the RV free wall and apical myocardium.

Morphologic abnormalities that have been described in echocardiographic study of patients with ARVC/D include trabecular disarray of the RV, hyperreflectivity of the moderator band, and areas of focal RV wall thinning with saccular aneurysms (Figure 37.13; Video 37.12) [80,81]. Assessment of RV size and function is an important aspect of the evaluation of patients for ARVC/D. In a review of echocardiograms of patients from a multicenter registry for ARVC/D, the most common and readily quantified abnormality was dilation of the RV outflow tract, which was present in all patients who met Task Force criteria. An RVOT dimension of >30 mm for adult subjects, measured in diastole in the parasternal long-axis view, was a strong indicator of RV enlargement. Dimensional measurements of the RV sinus may also be abnormal; but because of the segmental nature of the myocardial process, dilation of the RV body is often a late feature in the course of the disease, and accompanies global RV dysfunction. Methods to quantify RV systolic function by echocardiography have traditionally been problematic. However, RV fractional area change (FAC) from the 4-chamber view, myocardial performance index (MPI), and tricuspid annular tissue Doppler imaging (TDI) measurements have all been used as measures of RV dysfunction in patients with ARVC/D [80,82]. In the multicenter registry study, an RV FAC >32% was considered normal RV function, FAC 27–32% was mildly impaired, and FAC <27% was severely impaired [80]. TDI and 2D strain deformation and strain rate may improve diagnostic sensitivity [83]. Of note, lower tricuspid annular plane systolic excursion (TAPSE) has also been found in the asymptomatic gene carriers [83].

CMR imaging is often recommended for patients with suspected ARVC/D for quantification of RV volume and segmental and global function, and for the ability to detect fatty replacement [84]. Contrast echocardiography may play a role in facilitating the definition of RV myocardial borders and chamber size, and assisting in the detection of regional wall motion abnormalities. One report has suggested that this technique can also detect altered areas of perfusion in regions where fatty replacement of

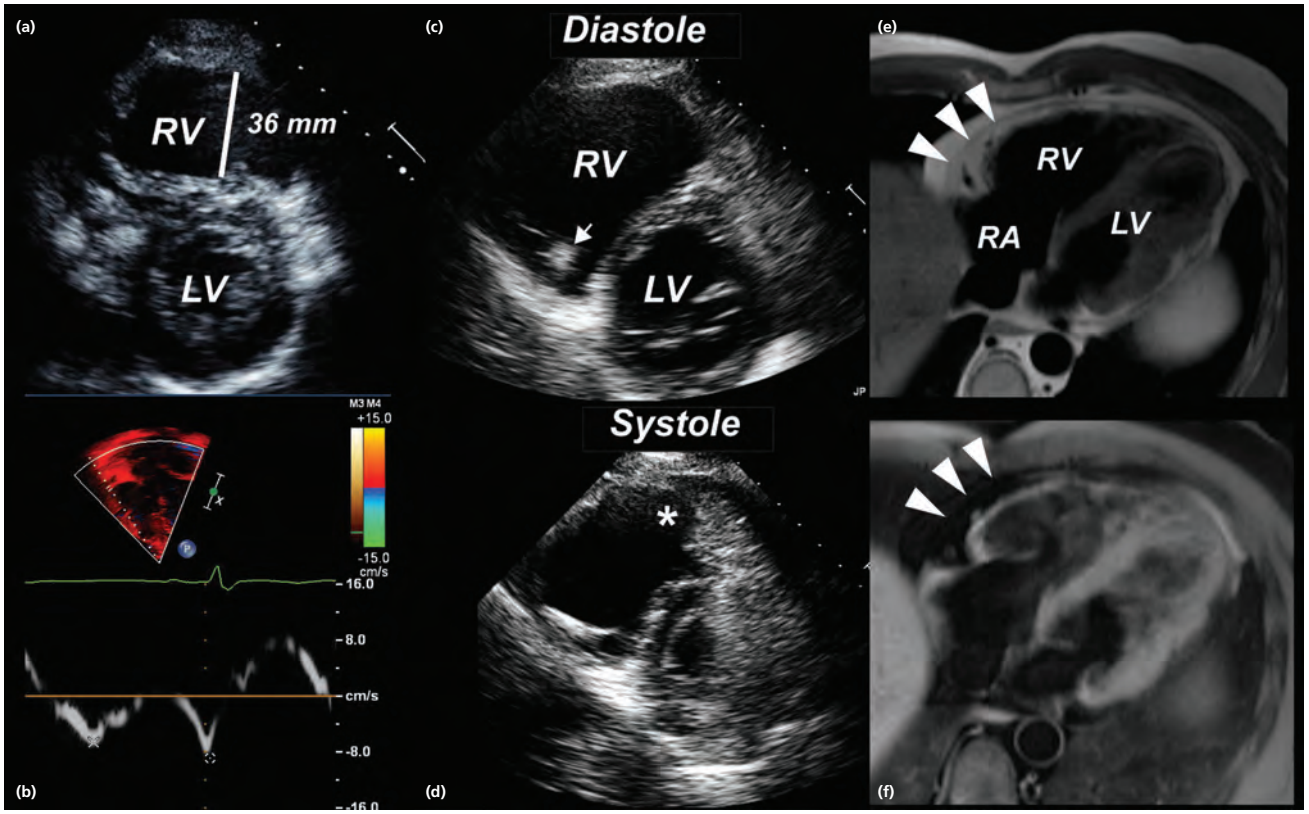


Figure 37.12 Multimodality imaging of arrhythmogenic right ventricular cardiomyopathy/dysplasia. **(a)** Parasternal short-axis view in a 16-year-old male with lightheadedness on exertion and ventricular tachycardia on exercise testing demonstrates right ventricular (RV) enlargement. **(b)** TDI of the RV free wall shows diminished tricuspid annular tissue Doppler velocities. **(c)** Parasternal short-axis view (in diastole) in the father of the previous patient demonstrates marked dilatation of the RV cavity. There is echobrightness within the posterior RV (white arrow) which represents a pacing wire. **(d)** Parasternal short-axis view (in systole) in the father demonstrates an aneurysm of the anterior RV free wall (white asterisk). **(e)** CMR imaging of the father demonstrates fatty infiltration of the RV free wall (white arrowheads). **(f)** CMR T1-weighted imaging with fat suppression highlights the dark region of fatty infiltration (white arrowheads). Both father and son have a plakophilin 2 mutation. RA, right atrium; LV, left ventricle.

myocardium has occurred [85,86]. Left ventricular chamber size and function should be measured, as LV involvement does occur with ARVC/D. Rarely, regions of thinning and segmental dysfunction may also be found in the LV.

Prenatal assessment

ARVC/D is extremely rare in the fetus, infant, and young child. One case of fetal ARVC/D has been reported in the literature. At 24 weeks' gestation, the fetus had an RV aneurysm and

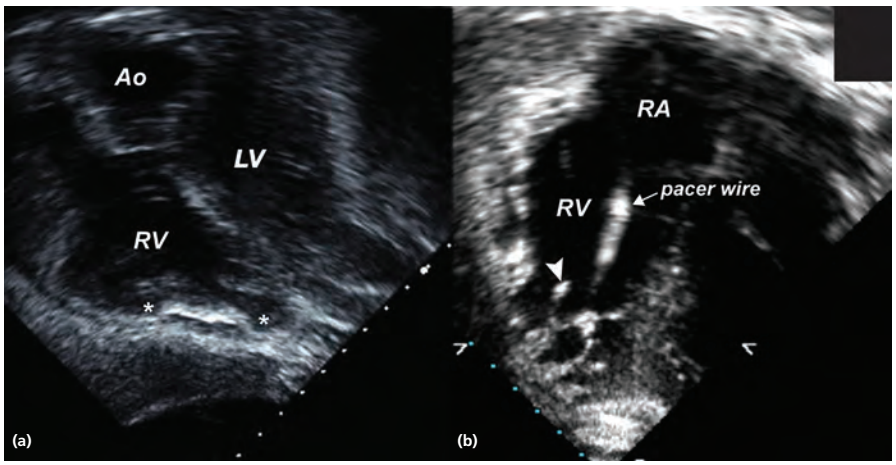


Figure 37.13 **(a)** Subxiphoid image in a patient with arrhythmogenic right ventricular cardiomyopathy/dysplasia demonstrates thinning and aneurysmal deformation of the right ventricular (RV) free wall (white asterisks). **(b)** Apical 4-chamber in a different patient with arrhythmogenic right ventricular cardiomyopathy/dysplasia shows prominent RV trabeculations in a distorted pattern (white arrowhead). Ao, aorta; LV, left ventricle.

ventricular dysfunction. After pregnancy termination at 27 weeks' gestation, pathology confirmed adipocytes interspersed with myocardial fibers, and no evidence of inflammation [76].

Videos

To access the videos for this chapter, please go to www.lai-echo.com.

Video 37.1 Neonatal left ventricular noncompaction. Subxiphoid view in color compare mode in an infant with valvar aortic stenosis and left ventricular noncompaction. Note the presence of a thick noncompact layer with deep intertrabecular recesses that fill with color on color Doppler echocardiography.

Video 37.2 Fetal left ventricular noncompaction. Fetal echocardiogram in the 4-chamber view in a 30-week gestation fetus demonstrates poor biventricular function, thickening of the left ventricular wall, and increased trabeculations in the right ventricular apex.

Video 37.3 Bantu submitral aneurysm. Parasternal short-axis view from a 44-year-old Nigerian male with a submitral aneurysm. Note the septated sonolucent area adjacent to the mitral annulus with significant dyskinetic wall motion in that region.

Video 37.4 Congenital left ventricular diverticulum in association with pentalogy of Cantrell. Fetal echocardiogram in the 4-chamber view demonstrates a left ventricular diverticulum protruding from the left ventricular apex, with good contractility. Associated findings in this patient include tricuspid atresia, ectopia cordis, omphalocele, and sternal cleft.

Video 37.5 Congenital aneurysm of the ventricular septum. A 19-year-old female with palpitations and frequent premature ventricular contractions. Magnetic resonance cine SSFP imaging in the short-axis plane demonstrates global left ventricular dysfunction with similar contractility of the aneurysm wall.

Video 37.6 Congenital left ventricular diverticulum in an infant with omphalocele and pulsatile mass over the abdomen. Subcostal view with color Doppler demonstrates the long, finger-like projection arising from the left ventricular apex with good contractility. Contrast fills the cavity in diastole, and washes back into the left ventricle in systole.

Video 37.7 Congenital aneurysm of the left ventricular wall. Dual view (parasternal short-axis on left, apical 4-chamber on right) 3D echocardiogram demonstrates a left ventricular aneurysm with a broad base and several intervening trabeculations. The apical view identifies a wall motion abnormality at the apical segment of the aneurysm.

Video 37.8 Bantu submitral aneurysm with mitral regurgitation. Apical 4-chamber view in color compare mode in a 44-year-old Nigerian male with a submitral aneurysm. Note the associated distortion of the posterior mitral leaflet with mitral regurgitation.

Video 37.9 Fetal left ventricular aneurysm. Fetal echocardiogram in 4-chamber view at 26 weeks' gestation demonstrates a large congenital aneurysm arising from the basal lateral wall of the left ventricle. Note the poor contraction of the aneurysm and decreased left ventricular function. The aneurysm has a broad connection to the left ventricle.

Video 37.10 Arrhythmogenic right ventricular cardiomyopathy/dysplasia. Parasternal short-axis view in a patient with arrhythmogenic right ventricular cardiomyopathy/dysplasia demonstrates right ventricular enlargement and systolic right ventricular dysfunction. A pacemaker lead is noted in the right ventricle.

Video 37.11 Arrhythmogenic right ventricular cardiomyopathy/dysplasia. This parasternal short-axis view demonstrates right ventricular enlargement with an aneurysm of the right ventricular free wall.

Video 37.12 Additional arrhythmogenic right ventricular cardiomyopathy/dysplasia findings. Subxiphoid image demonstrating thinning and aneurysmal deformation of the right ventricular wall along the free wall and the apex of the RV.

References

1 Maron BJ, Towbin JA, Thiene G, et al. Contemporary definitions and classification of the cardiomyopathies: an American Heart Association Scientific Statement from the Council on Clinical Cardiology, Heart Failure and Transplantation Committee; Quality of Care and Outcomes Research and Functional Genomics and Translational Biology Interdisciplinary Working Groups; and Council on Epidemiology and Prevention. *Circulation* 2006;**113**:1807–1816.

2 Pignatelli RH, McMahon CJ, Dreyer WJ, et al. Clinical characterization of left ventricular noncompaction in children: a relatively common form of cardiomyopathy. *Circulation* 2003;**108**:2672–2678.

3 Ichida F, Hamamichi Y, Miyawaki T, et al. Clinical features of isolated noncompaction of the ventricular myocardium: long-term clinical course, hemodynamic properties, and genetic background. *J Am Coll Cardiol* 1999;**34**:233–240.

4 Paterick TE, Tajik AJ. Left ventricular noncompaction: a diagnostically challenging cardiomyopathy. *Circ J* 2012;**76**:1556–1562.

5 Oechslin EN, Attenhofer Jost CH, Rojas JR, et al. Long-term follow-up of 34 adults with isolated left ventricular noncompaction: a distinct cardiomyopathy with poor prognosis. *J Am Coll Cardiol* 2000;**36**:493–500.

6 Lilje C, Razek V, Joyce JJ, et al. Complications of non-compaction of the left ventricular myocardium in a paediatric population: a prospective study. *Eur Heart J* 2006;**27**:1855–1860.

7 Nugent AW, Daubeney PE, Chondros P, et al. The epidemiology of childhood cardiomyopathy in Australia. *N Engl J Med* 2003;**348**:1639–1646.

7a Jefferies JL, Wilkinson JD, Sleeper LA, et al. Cardiomyopathy phenotypes and outcomes for children with left ventricular myocardial noncompaction: results from the Pediatric Cardiomyopathy Registry. *J Card Fail* 2015; Epub ahead of print.

8 Bione S, D'Adamo P, Maestrini E, et al. A novel X-linked gene, G4.5, is responsible for Barth syndrome. *Nat Genet* 1996;**12**:385–389.

9 Bleyl SB, Mumford BR, Brown-Harrison MC, et al. Xq28-linked noncompaction of the left ventricular myocardium: prenatal diagnosis and pathologic analysis of affected individuals. *Am J Med Genet* 1997;**72**:257–265.

10 Vatta M, Mohapatra B, Jimenez S, et al. Mutations in Cypher/ZASP in patients with dilated cardiomyopathy and left ventricular noncompaction. *J Am Coll Cardiol* 2003;**42**:2014–2027.

11 Sasse-Klaassen S, Probst S, Gerull B, et al. Novel gene locus for autosomal dominant left ventricular noncompaction maps to chromosome 11p15. *Circulation* 2004;**109**:2720–2723.

12 Ichida F, Tsubata S, Bowles KR, et al. Novel gene mutations in patients with left ventricular noncompaction or Barth syndrome. *Circulation* 2001;**103**:1256–1263.

13 Hermida-Prieto M, Monserrat L, Castro-Beiras A, et al. Familial dilated cardiomyopathy and isolated left ventricular noncompaction associated with lamin A/C gene mutations. *J Am Coll Cardiol* 2004;**94**:50–4.

14 Moric-Janiszewska E, Markiewicz-Loskot G. Genetic heterogeneity of left-ventricular noncompaction cardiomyopathy. *Clin Cardiol* 2008;**31**:201–204.

15 Happle R, Daniels O, Koopman RJ. MIDAS syndrome (microphthalmia, dermal aplasia, and sclerocornea): an X-linked phenotype distinct from Goltz syndrome. *Am J Med Genet* 1993;**47**: 710–713.

16 Wong JA, Bofinger MK. Noncompaction of the ventricular myocardium in Melnick-Needles syndrome. *Am J Med Genet* 1997;**71**:72–75.

17 McMahon CJ, Chang AC, Pignatelli RH, et al. Left ventricular noncompaction cardiomyopathy in association with trisomy 13. *Pediatr Cardiol* 2005;**26**:477–479.

18 Finsterer J, Stollberger C, Wanschitz J, et al. Nail–patella syndrome associated with respiratory chain disorder. *Eur Neurol* 2001;**46**:92–95.

19 Mandel K, Grunebaum E, Benson L. Noncompaction of the myocardium associated with Roifman syndrome. *Cardiol Young* 2001;**11**:240–243.

20 Sedmera D, Pexieder T, Vuillemin M, et al. Developmental patterning of the myocardium. *Anat Rec* 2000;**258**:319–337.

21 Winer N, Lefevre M, Nomballais MF, et al. Persisting spongy myocardium. A case indicating the difficulty of antenatal diagnosis. *Fetal Diagn Ther* 1998;**13**:227–232.

22 Moura C, Hillion Y, Daikha-Dahmane F, et al. Isolated noncompaction of the myocardium diagnosed in the fetus: two sporadic and two familial cases. *Cardiol Young* 2002;**12**:278–283.

23 Finsterer J, Stollberger C, Blazek G, et al. Cardiac involvement in myotonic dystrophy, Becker muscular dystrophy and mitochondrial myopathy: a five-year follow-up. *Can J Cardiol* 2001;**17**: 1061–1069.

24 Jenni R, Wyss CA, Oechslin EN, et al. Isolated ventricular noncompaction is associated with coronary microcirculatory dysfunction. *J Am Coll Cardiol* 2002;**39**:450–454.

25 Ritter M, Oechslin E, Sutsch G, et al. Isolated noncompaction of the myocardium in adults. *Mayo Clin Proc* 1997;**72**:26–31.

26 Murphy RT, Thaman R, Blanes JG, et al. Natural history and familial characteristics of isolated left ventricular non-compaction. *Eur Heart J* 2005;**26**:187–192.

27 Burke A, Mont E, Kutys R, et al. Left ventricular noncompaction: a pathological study of 14 cases. *Human Pathol* 2005;**36**:403–411.

28 Elliott P, Andersson B, Arbustini E, et al. Classification of the cardiomyopathies: a position statement from the European Society Of Cardiology Working Group on Myocardial and Pericardial Diseases. *Eur Heart J* 2008;**29**:270–276.

29 Richardson P, McKenna W, Bristow M, et al. Report of the 1995 World Health Organization/International Society and Federation of Cardiology Task Force on the Definition and Classification of Cardiomyopathies. *Circulation* 1996;**93**:841–842.

30 Oechslin E, Jenni R. Left ventricular non-compaction revisited: a distinct phenotype with genetic heterogeneity? *Eur Heart J* 2011;**32**:1446–1456.

31 Finsterer J, Stollberger C. No rationale for a diagnostic ratio in left ventricular hypertrabeculation/noncompaction. *Int J Cardiol* 2011;**146**:91–92.

32 Jenni R, Oechslin E, Schneider J, et al. Echocardiographic and pathoanatomical characteristics of isolated left ventricular noncompaction: a step towards classification as a distinct cardiomyopathy. *Heart* 2001;**86**:666–671.

33 Petersen SE, Selvanayagam JB, Wiesmann F, et al. Left ventricular non-compaction: insights from cardiovascular magnetic resonance imaging. *J Am Coll Cardiol* 2005;**46**:101–105.

34 Kohli SK, Pantazis AA, Shah JS, et al. Diagnosis of left-ventricular non-compaction in patients with left-ventricular systolic dysfunction: time for a reappraisal of diagnostic criteria? *Eur Heart J* 2008;**29**:89–95.

35 Saleeb SF, Margossian R, Spencer CT, et al. Reproducibility of echocardiographic diagnosis of left ventricular noncompaction. *J Am Soc Echocardiogr* 2012;**25**:194–202.

36 Lowery MH, Martel JA, Zambrano JP, et al. Noncompaction of the ventricular myocardium: the use of contrast-enhanced echocardiography in diagnosis. *J Am Soc Echocardiogr* 2003;**16**:94–96.

37 van Dalen BM, Caliskan K, Soliman OI, et al. Left ventricular solid body rotation in non-compaction cardiomyopathy: a potential new objective and quantitative functional diagnostic criterion? *Eur J Heart Fail* 2008;**10**:1088–1093.

38 Aras D, Tufekcioglu O, Ergun K, et al. Clinical features of isolated ventricular noncompaction in adults long-term clinical course, echocardiographic properties, and predictors of left ventricular failure. *J Card Fail* 2006;**12**:726–733.

39 McMahon CJ, Pignatelli RH, Nagueh SF, et al. Left ventricular noncompaction cardiomyopathy in children: characterisation of clinical status using tissue Doppler-derived indices of left ventricular diastolic relaxation. *Heart* 2007;**93**:676–681.

40 Punn R, Silverman NH. Cardiac segmental analysis in left ventricular noncompaction: experience in a pediatric population. *J Am Soc Echocardiogr* 2010;**23**:46–53.

41 Wald R, Veldtman G, Golding F, et al. Determinants of outcome in isolated ventricular noncompaction in childhood. *J Am Coll Cardiol* 2004;**94**:1581–1584.

42 Uribe S, Cadavid L, Hussain T, et al. Cardiovascular magnetic resonance findings in a pediatric population with isolated left ventricular non-compaction. *J Cardiovasc Magn Reson* 2012;**14**:9.

43 Arunamata A, Punn R, Cuneo B, et al. Echocardiographic diagnosis and prognosis of fetal left ventricular noncompaction. *J Am Soc Echocardiogr* 2012;**25**:112–120.

44 Karatza AA, Holder SE, Gardiner HM. Isolated non-compaction of the ventricular myocardium: prenatal diagnosis and natural history. *Ultrasound Obstet Gynecol* 2003;**21**:75–80.

45 Papagiannis J, Van Praagh R, Schwint O, et al. Congenital left ventricular aneurysm: clinical, imaging, pathologic, and surgical findings in seven new cases. *Am Heart J* 2001;**141**:491–499.

46 Baltaxe HA, Wilson WJ, Amiel M. Diverticulosis of the left ventricle. *AJR Am J Roentgenol* 1979;**133**:257–261.

47 McMahon CJ, Moniotte S, Powell AJ, et al. Usefulness of magnetic resonance imaging evaluation of congenital left ventricular aneurysms. *Am J Cardiol* 2007;**100**:310–315.

48 Cumming GR. Congenital diverticulum of the right ventricle. *Am J Cardiol* 1969;**23**:294–297.

49 Higgins CB, Hayden WG, Copeland J, et al. Congenital diverticulum of the right ventricle: clinical and angiographic features. *Br J Radiol* 1976;**49**:188–190.

50 Nicod P, Laird WP, Firth BG, et al. Congenital diverticula of the left and right ventricles: 3 cases. *Am J Cardiol* 1984;**53**:342–344.

51 Mardini MK. Congenital diverticulum of the left ventricle. Report of two unusual cases. *Br Heart J* 1984;**51**:321–326.

52 Chesler E, Joffe N, Schamroth L, et al. Annular subvalvular left ventricular aneurysms in the South African Bantu. *Circulation* 1965;**32**:43–51.

53 Tsujimoto H, Takeshita S, Kawamura Y, et al. Isolated congenital left ventricular diverticulum with perinatal dysrhythmia: a case report and review of the literature. *Pediatr Cardiol* 2000;**21**:175–179.

54 Shizukuda Y, Murakami H, Iwakura M, et al. Siblings with left ventricular diverticulum and hypertrophic cardiomyopathy. *J Cardiol* 1988;**18**:867–874.

55 Cantrell JR, Haller JA, Ravitch MM. A syndrome of congenital defects involving the abdominal wall, sternum, diaphragm, pericardium, and heart. *Surg Gynecol Obstet* 1958;**107**:602–614.

56 Simpson L, Duncan JM, Stainback RF. Perforated submitral left ventricular aneurysm resulting in severe mitral annular regurgitation. *Texas Heart Inst J* 2006;**33**:492–494.

57 Hamaoka K, Onaka M, Tanaka T, et al. Congenital ventricular aneurysm and diverticulum in children. *Pediatr Cardiol* 1987;**8**:169–175.

58 Bernasconi A, Delezoide AL, Menez F, et al. Prenatal rupture of a left ventricular diverticulum: a case report and review of the literature. *Prenatal Diagn* 2004;**24**:504–507.

59 McElhinney DB, Silverman NH. Left ventricular aneurysm in the fetus: a diagnosis with a mixed prognosis. *Cardiol Young* 1999;**9**:123–126.

60 Archbold RA, Robinson NM, Mills PG. Long-term follow-up of a true contractile left ventricular diverticulum. *Am J Cardiol* 1999;**83**:810–813, A11.

61 Yoshizumi K, Ishino K, Kawada M, et al. Dor procedure for left ventricular diverticulum with mitral regurgitation in an infant. *Ann Thorac Surg* 2005;**80**:332–333.

62 Pome G, Vignati G, Mauri L, et al. Isolated congenital left ventricular diverticulum. *Eur J Cardiothorac Surg* 1995;**9**:709–712.

63 Yalonetsky S, Agmon Y, Lessick J. Contrast echocardiographic imaging of left ventricular diverticulum in adult patients. *J Am Soc Echocardiogr* 2007;**20**:198.e1–198.e3.

64 Marcus FI, McKenna WJ, Sherrill D, et al. Diagnosis of arrhythmogenic right ventricular cardiomyopathy/dysplasia: proposed modification of the Task Force Criteria. *Eur Heart J* 2010;**31**:806–814.

65 Dungan WT, Garson A, Jr, Gillette PC. Arrhythmogenic right ventricular dysplasia: a cause of ventricular tachycardia in children with apparently normal hearts. *Am Heart J* 1981;**102**:745–750.

66 Marcus FI, Fontaine GH, Guiraudon G, et al. Right ventricular dysplasia: a report of 24 adult cases. *Circulation* 1982;**65**:384–398.

67 Peters S, Trummel M, Meyners W. Prevalence of right ventricular dysplasia–cardiomyopathy in a non-referral hospital. *Int J Cardiol* 2004;**97**:499–501.

68 Tabib A, Loire R, Chalabreysse L, et al. Circumstances of death and gross and microscopic observations in a series of 200 cases of sudden death associated with arrhythmogenic right ventricular cardiomyopathy and/or dysplasia. *Circulation* 2003;**108**:3000–3005.

69 Thiene G, Nava A, Corrado D, et al. Right ventricular cardiomyopathy and sudden death in young people. *N Engl J Med* 1988;**318**:129–133.

70 Sen-Chowdhry S, Syrris P, Ward D, et al. Clinical and genetic characterization of families with arrhythmogenic right ventricular dysplasia/cardiomyopathy provides novel insights into patterns of disease expression. *Circulation* 2007;**115**:1710–1720.

71 van Tintelen JP, Entius MM, Bhuiyan ZA, et al. Plakophilin-2 mutations are the major determinant of familial arrhythmogenic right ventricular dysplasia/cardiomyopathy. *Circulation* 2006;**113**:1650–1658.

72 Merner ND, Hodgkinson KA, Haywood AF, et al. Arrhythmogenic right ventricular cardiomyopathy type 5 is a fully penetrant, lethal arrhythmic disorder caused by a missense mutation in the TMEM43 gene. *Am J Hum Genet* 2008;**82**:809–821.

73 Protonotarios N, Tsatsopoulou A. Naxos disease and Carvajal syndrome: cardiocutaneous disorders that highlight the pathogenesis and broaden the spectrum of arrhythmogenic right ventricular cardiomyopathy. *Cardiovasc Pathol* 2004;**13**:185–194.

74 Bowles NE, Ni J, Marcus F, et al. The detection of cardiotropic viruses in the myocardium of patients with arrhythmogenic right ventricular dysplasia/cardiomyopathy. *J Am Coll Cardiol* 2002;**39**:892–895.

75 Atalay S, Imamoglu A, Gumus H, et al. Value of the echocardiographic findings of arrhythmogenic right ventricular dysplasia with left ventricular involvement in a child. *Pediatr Cardiol* 1996;**17**:40–42.

76 Rustico MA, Benettoni A, Fontaliran F, et al. Prenatal echocardiographic appearance of arrhythmogenic right ventricle dysplasia: a case report. *Fetal Diagn Ther* 2001;**16**:433–436.

77 Marcus F, Towbin JA. The mystery of arrhythmogenic right ventricular dysplasia/cardiomyopathy: from observation to mechanistic explanation. *Circulation* 2006;**114**:1794–1795.

78 Hulot JS, Jouven X, Empana JP, et al. Natural history and risk stratification of arrhythmogenic right ventricular dysplasia/cardiomyopathy. *Circulation* 2004;**110**:1879–1884.

79 Dalal D, Nasir K, Bomma C, et al. Arrhythmogenic right ventricular dysplasia: a United States experience. *Circulation* 2005;**112**:3823–3832.

80 Scognamiglio R, Fasoli G, Nava A, et al. Contribution of cross-sectional echocardiography to the diagnosis of right ventricular dysplasia at the asymptomatic stage. *Eur Heart J* 1989;**10**:538–542.

81 Yoerger DM, Marcus F, Sherrill D, et al. Echocardiographic findings in patients meeting task force criteria for arrhythmogenic right ventricular dysplasia: new insights from the multidisciplinary study of right ventricular dysplasia. *J Am Coll Cardiol* 2005;**45**:860–865.

82 Lindstrom L, Wilkenshoff UM, Larsson H, et al. Echocardiographic assessment of arrhythmogenic right ventricular cardiomyopathy. *Heart* 2001;**86**:31–38.

83 Teske AJ, Cox MG, Te Riele AS, et al. Early detection of regional functional abnormalities in asymptomatic ARVD/C gene carriers. *J Am Soc Echocardiogr* 2012;**25**:997–1006.

84 Tandri H, Castillo E, Ferrari VA, et al. Magnetic resonance imaging of arrhythmogenic right ventricular dysplasia: sensitivity, specificity, and observer variability of fat detection versus functional analysis of the right ventricle. *J Am Coll Cardiol* 2006;**48**:2277–2284.

85 Lopez-Fernandez T, Garcia-Fernandez MA, Perez David E, et al. Usefulness of contrast echocardiography in arrhythmogenic right ventricular dysplasia. *J Am Soc Echocardiogr* 2004;**17**:391–393.

86 Nemes A, Vletter WB, Scholten MF, et al. Contrast echocardiography for perfusion in right ventricular cardiomyopathy. *Eur J Echocardiogr* 2005;**6**:470–472.

PART VII

Acquired Pediatric Heart Disease

CHAPTER 38

Kawasaki Disease

Erik C. Michelfelder and Allison Divanovic
The Heart Institute, Cincinnati Children's Hospital Medical Center, Cincinnati, OH, USA

Introduction

Definition

Kawasaki disease is an acute systemic vasculitis of as yet unknown cause, first described in Japanese by Tomisaku Kawasaki in 1967 [1], and subsequently in English in 1974 [2]. Since its original description, mucocutaneous lymph node syndrome – or Kawasaki disease – has now come to be recognized as a common form of acquired heart disease in the pediatric population with a worldwide distribution, affecting children of all races. Kawasaki disease is diagnosed by recognition of its principal signs and symptoms (Table 38.1), which characteristically include fever, changes in the extremities, polymorphous skin exanthem, nonexudative conjunctivitis, changes in the lips and mucous membrane, and cervical lymphadenopathy. In addition to the "classical" clinical findings, there are multiple features associated with the illness that can be recognized, including (but not limited to) cardiac involvement, arthritis/arthralgia, vomiting, diarrhea, gall bladder hydrops, sterile pyuria, and irritability. Recent recommendations have addressed the diagnosis of "incomplete" Kawasaki disease, where persistent fever is identified in patients with only two or three classic clinical findings. In this setting, Kawasaki disease may be diagnosed when additional laboratory data and/or echocardiographic findings support the diagnosis [3].

Incidence

Kawasaki disease primarily affects young children, with 80% cases reported in children less than 5 years of age, and 90% of cases occurring in children less than 8 years of age [4]. In Japan, where the prevalence of Kawasaki disease is the highest, the disease occurs in 134 per 100,000 children less than 5 years of age. Outside Japan, prevalence ranges from 8 to 67 per 100,000 children less than 5 years of age, depending on the ethnicity of the population being studied [5]. The disease prevalence is highest in children of Asian descent, followed by African Americans, Hispanics, and Caucasians [6]. Males are affected more frequently than females, with a ratio of 1.5:1.

Etiology

The etiology of Kawasaki disease is unknown, although an infectious etiology is likely given its clinical and epidemiologic characteristics. In addition to its classic clinical characteristics, Kawasaki disease also features winter–spring predominance, a characteristic age distribution, evidence of community outbreaks, and evidence of prior epidemic periods. Laboratory data obtained during the illness also support an infectious agent as the cause. Prior theories, such as toxic exposures or bacterial superantigen-mediated inflammation, have not gained widespread acceptance. The exact pathogen responsible for Kawasaki disease, however, remains unidentified.

Pathophysiology

The acute febrile phase of the illness features a diffuse microvascular vasculitis, with endarteritis and perivascular inflammation of the coronary arteries [7]. The inflammatory process may also involve pericarditis, myocarditis [8], and endocarditis. The acute phase of the disease, therefore, can be associated with pericardial effusion, acute myocardial dysfunction, and valvar regurgitation. In the subacute clinical phase – following resolution of the fever – there is a persistent panvasculitis of the coronary arteries that may result in ectasia, aneurysm, and/or thrombosis. Pericarditis, myocarditis, and endocarditis are also frequently seen in this phase. In the convalescent and chronic phases of the disease, resolution of the microvascular angiitis is replaced by granulation and intimal thickening of the coronary arteries. Coronary artery scarring, stenosis, and calcification can be seen in later phases of the illness. Thrombosis of the coronary arteries may occur in all phases of the disease. Approximately 50–60% of coronary artery aneurysms will demonstrate evidence of regression over the first 3–5 years following acute Kawasaki disease [9,10]; however, the mechanism for regression of aneurysms may be detrimental, including myointimal proliferation with narrowing of the vessel lumen, or organization of endovascular thrombus [11]. Mitral regurgitation and

Echocardiography in Pediatric and Congenital Heart Disease: From Fetus to Adult, Second Edition. Edited by Wyman W. Lai, Luc L. Mertens, Meryl S. Cohen and Tal Geva.
© 2016 John Wiley & Sons, Ltd. Published 2016 by John Wiley & Sons, Ltd.
Companion website: www.lai-echo.com

Table 38.1 "Classic" clinical features of Kawasaki disease [3]

- Fever persisting ≥5 days
- Presence of *at least* 4 principal clinical features:
 - Changes in extremities
 - Acute: erythema of palms and/or soles, edema of hands and/or feet
 - Subacute: periungual desquamation of fingers and toes
 - Polymorphous exanthema
 - Bilateral, nonexudative conjunctival injection
 - Changes in lips and oral mucosa: erythema, cracked lips, strawberry tongue, diffuse injection of oral/pharyngeal mucosa
 - Cervical lymphadenopathy (>1.5 cm node), usually unilateral
- Exclusion of diseases with similar findings

myocardial dysfunction seen in later phases of the disease are usually due to myocardial and papillary muscle ischemia. In addition to these anatomic abnormalities, coronary vascular function may be abnormal in patients in the chronic phases of Kawasaki disease, with reduced coronary artery flow reserve and abnormal vascular reactivity [12–14].

Imaging

Key elements

Although the pathophysiology may change in acute, subacute, and chronic phases of the disease, echocardiography must focus on coronary artery abnormalities, valvar dysfunction, and myocardial function in all phases of the illness:

- Coronary artery assessment:
 - Identification of coronary artery abnormalities:
 - evidence of perivascular inflammation;
 - ectasia;
 - aneurysm (diameter and length, location, and number);
 - classification of severity of coronary artery abnormalities;
 - identification of coronary artery thrombus;
 - identification of coronary artery stenosis.
- Identification of valvar involvement:
 - Mitral and tricuspid valve regurgitation.
 - Aortic regurgitation.
 - Aortic root dilation.
- Identification of myocardial involvement:
 - Global myocardial dysfunction.
 - Regional myocardial dysfunction.
- Identification of pericardial involvement:
 - Pericardial effusion.

General principles

Kawasaki disease presents acutely (and subacutely) as a pancarditis, hence echocardiographic assessment must focus on the endocardium, myocardium, and pericardium in addition to assessment of coronary arteries. Identification of pericardial effusion, mitral regurgitation, or myocardial dysfunction may in fact be associated with an elevated risk of coronary artery changes [15,16]. These findings may also increase clinical suspicion of Kawasaki disease when clinical criteria are incomplete [3]. Recently, abnormalities in diastolic function – by tissue Doppler assessment of the left ventricle – have also been reported in association with acute and subacute Kawasaki disease [17]. In patients followed chronically with coronary artery abnormalities, the focus of the echocardiographic assessment shifts to assessment of coronary artery insufficiency, regional and global myocardial function, and ischemia-related atrioventricular valve dysfunction.

Consensus recommendations for echocardiographic imaging in Kawasaki disease

The pathophysiology of Kawasaki disease dictates that the acute cardiovascular sequelae of the disease appear with variable frequency during the acute and subacute phase of the illness (the first 6–8 weeks of the illness). During these phases, consensus guidelines published by the American Heart Association [3,18] recommend echocardiographic imaging at the time of diagnosis, at 2 weeks after diagnosis, and again at 6–8 weeks after diagnosis. During this period, acute changes in valvar or myocardial function, pericardial effusion, and acute coronary artery changes should be noted. In addition, imaging in the first 6–8 weeks of illness encompasses the period during which transient changes in coronary artery dilation and ectasia will often resolve. Alternatively, this is the period during which coronary artery aneurysms attain their maximum size [19]. In complex cases where coronary artery aneurysms and/or thrombosis, significant valvar regurgitation, effusion, or myocardial dysfunction occur, echocardiography during the acute and subacute phases should be performed as indicated by clinical circumstances. For patients with chronic – primarily coronary – abnormalities, annual follow-up with echocardiography is recommended. The focus of these follow-up evaluations is to assess for resolution of coronary artery abnormalities, evidence of coronary artery thrombosis/stenosis, valvar dysfunction, or myocardial dysfunction/ischemia. The proposed algorithm for long-term follow-up echocardiography, myocardial perfusion imaging, and angiography is summarized in Table 38.2.

General principles for coronary artery assessment

Coronary artery abnormalities are the most significant short- and long-term sequelae of Kawasaki disease. Echocardiography is a highly sensitive, specific, noninvasive means of assessing the coronary arterial system, and thus occupies a central role in the diagnostic work-up of children with Kawasaki disease. In general, coronary artery imaging should be performed at the highest feasible transducer frequency. Reducing 2D gain and dynamic range (i.e., compression) settings will often improve demonstration of the endovascular lumen and thereby improve coronary artery imaging. Imaging at lower depth will also enhance anatomic visualization.

Table 38.2 Consensus recommendations for follow-up imaging in Kawasaki disease

Risk level	Diagnostic imaging	Invasive testing
I (no CA changes at any stage of illness)	None	None
II (Transient CA ectasia resolving within the first 6–8 weeks)	None	None
III (1 small–medium CA aneurysm)	Echocardiogram, ECG yearly; biennial stress test, perfusion imaging	Angiography, if noninvasive imaging suggests ischemia
IV (≥1 large or giant CA aneurysm, or multiple/complex aneurysms in the same CA, no stenosis)	Echocardiogram, ECG twice yearly; annual stress test, perfusion imaging	Angiography at 6–12 months after diagnosis or as clinically indicated; repeated angiography if noninvasive testing suggests ischemia
V (CA obstruction)	Echocardiogram, ECG twice yearly; annual stress test, perfusion imaging	Angiography to evaluate therapeutic options

CA, coronary artery; ECG, electrocardiogram.
Source: Adapted from Newburger et al. 2004 [3].

Imaging of the left coronary artery system is best performed in the parasternal and apical windows. The left main coronary artery is most readily imaged in the parasternal short-axis window at the level of the aortic root. In the parasternal short-axis, the left anterior descending artery (LAD) and proximal left circumflex artery (LCx) can also be demonstrated. Often, a slight clockwise rotation of the transducer from the standard parasternal short-axis will increase visualization of a greater length of both LAD and LCx (Figure 38.1; Video 38.1). In the parasternal long-axis, sweeping the plane of sound between aorta and pulmonary artery – from right to left – will often demonstrate the proximal left coronary artery, LAD, and LCx (Figure 38.2; Video 38.2). In the apical 4-chamber view, anterior angulation of the plane of sound will demonstrate the more distal LCx in the anterior atrioventricular groove (Figure 38.3). Although technically more challenging, the LCx can also be demonstrated in subxiphoid windows, particularly when aneurysms are present (Figure 38.4; Video 38.3).

The right coronary artery (RCA) system can be visualized in several imaging windows. In the parasternal short-axis view at the aortic root, the proximal RCA can be imaged (Figure 38.5). A slight clockwise rotation of the plane of sound in this view will usually result in better visualization of a greater length of the proximal RCA. The proximal RCA can also be visualized in the anterior atrioventricular groove on either apical

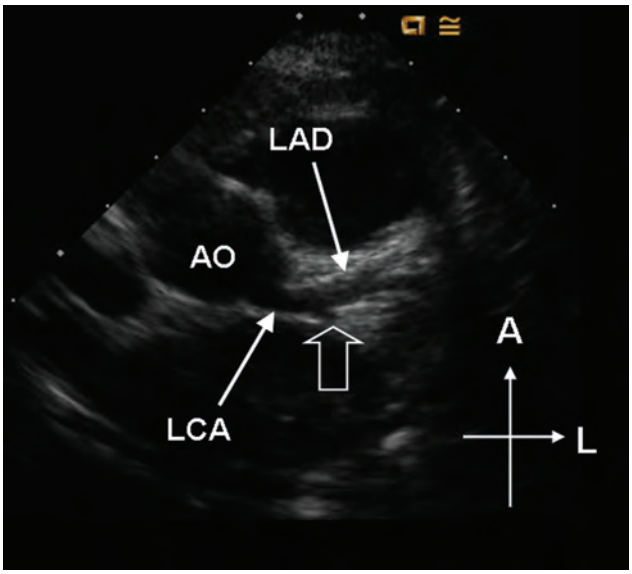


Figure 38.1 Parasternal short-axis view, with slight clockwise rotation, demonstrates the left main coronary artery (LCA), proximal left anterior descending artery (LAD), and proximal left circumflex coronary artery (open arrow). Note the diffuse enlargement of the LCA and LAD in this child with Kawasaki disease. A, anterior; Ao, aorta; L, left.

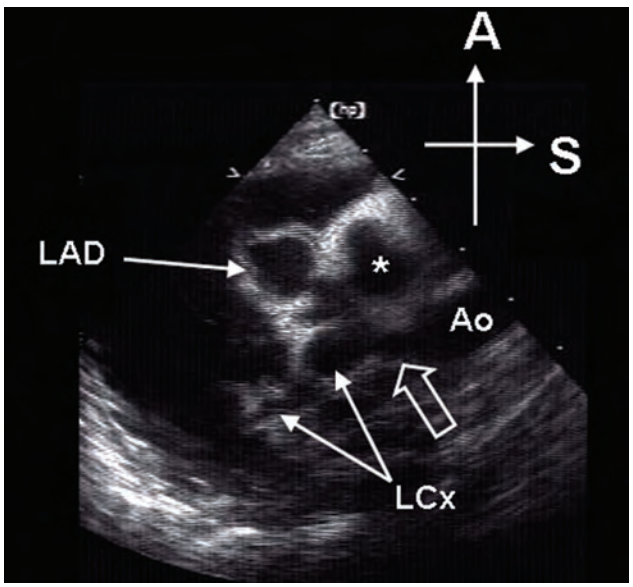


Figure 38.2 Parasternal long-axis view, with leftward angulation from standard view, highlights the aorta and the left main coronary artery (open arrow). Both the left anterior descending artery (LAD) and left circumflex (LCx) artery are seen; there are multiple saccular aneurysms involving both coronary arteries. Note the relationship of the aorta (Ao), LAD, and pulmonary artery (white asterisk) in this view. A, anterior; S, superior.

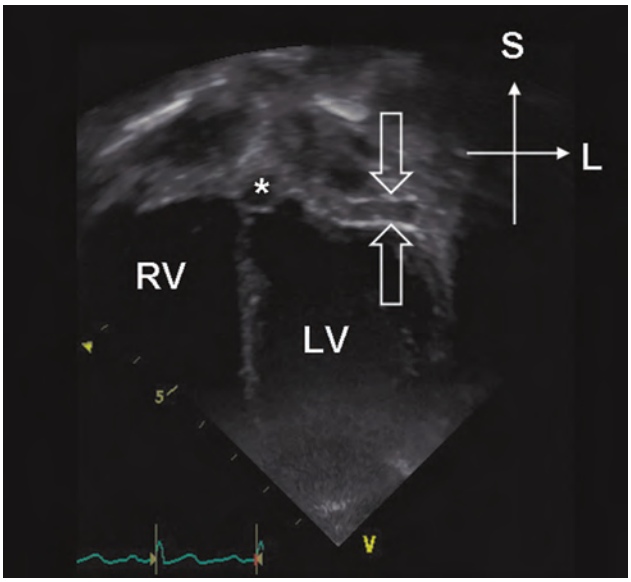


Figure 38.3 In apical 5-chamber view (anterior angulation), the left circumflex coronary artery can be demonstrated in the left anterior atrioventricular groove (open arrows). The aorta (asterisk) can also be seen on this image. Note the diffuse enlargement of the left circumflex artery and the increased perivascular echogenicity in a child with acute Kawasaki disease. L, left; LV left ventricle; RV, right ventricle; S, superior.

imaging (with anterior angulation of the plane of sound, Figure 38.6; Video 38.4), or in the subxiphoid long-axis (coronal) view (Figure 38.7; Video 38.5). The middle portion of the RCA can be visualized in cross-section in parasternal long-axis views, angulated towards the tricuspid valve and lateral

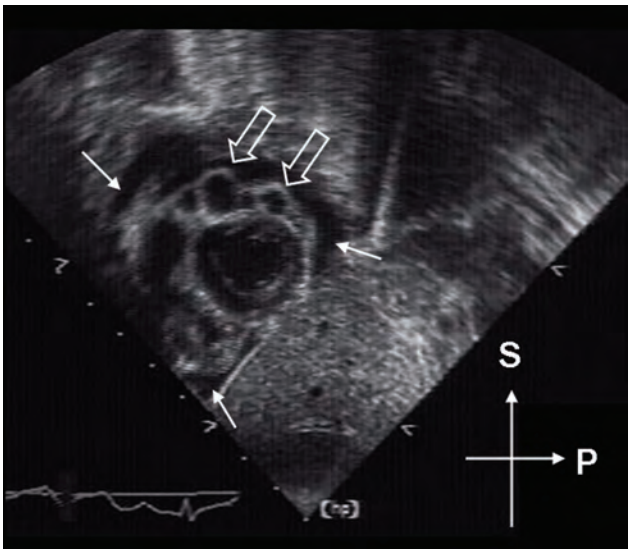


Figure 38.4 Subxiphoid sagittal view at the level of the left atrioventricular groove demonstrates multiple, saccular aneurysms of the left circumflex artery (open arrows). Note also the modest pericardial effusion (white arrows) seen in a patient with acute phase disease. P, posterior; S, superior.

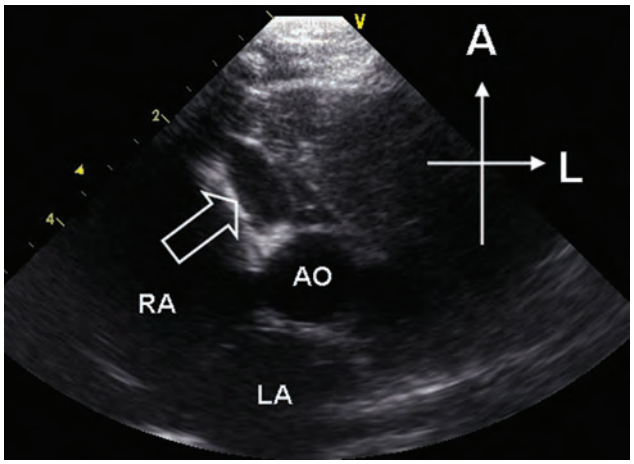


Figure 38.5 Parasternal short-axis view demonstrates a large, fusiform aneurysm of proximal right coronary artery (open arrow). A, anterior; Ao, aorta; L, left; LA, left atrium; RA, right atrium.

atrioventricular groove; it may also be visualized in subxiphoid short-axis (sagittal) view by angulation rightward into the lateral atrioventricular groove. The distal RCA and the junction of the RCA with posterior descending coronary artery can be imaged in the apical or parasternal long-axis view with posterior angulation into the posterior right atrioventricular groove. It can also be seen in the subxiphoid long-axis view with posterior angulation.

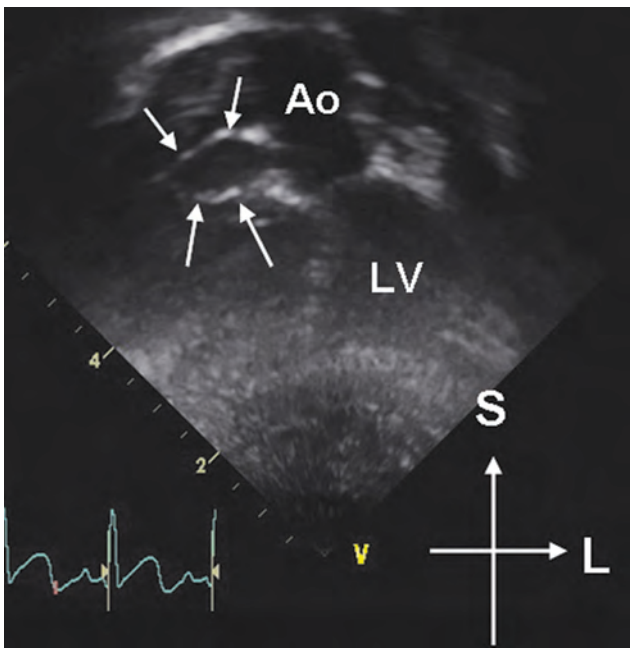


Figure 38.6 Apical 5-chamber view shows the proximal right coronary artery in the right anterior atrioventricular groove (arrows). Note the large, fusiform aneurysm in this image, which tapers proximally at the right coronary artery ostium. Ao, aorta; L, left; LV, left ventricle; S, superior.

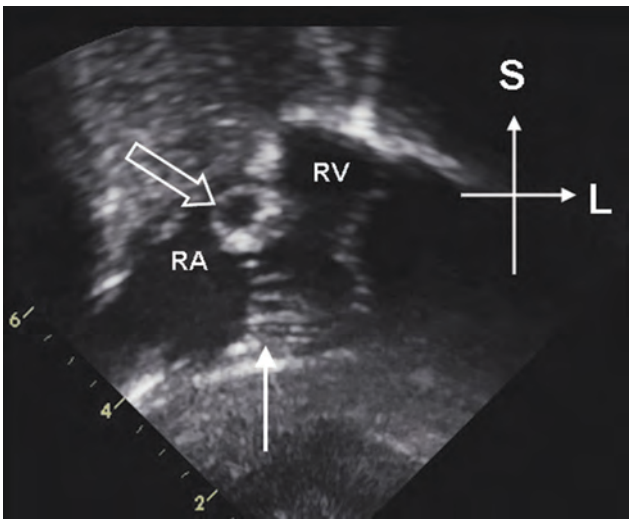


Figure 38.7 Subxiphoid coronal view demonstrates a right coronary artery aneurysm in the anterosuperior portion of the right atrioventricular groove. The right atrium (RA), tricuspid valve (white arrow), and right ventricle (RV) are also demonstrated. L, left; S, superior.

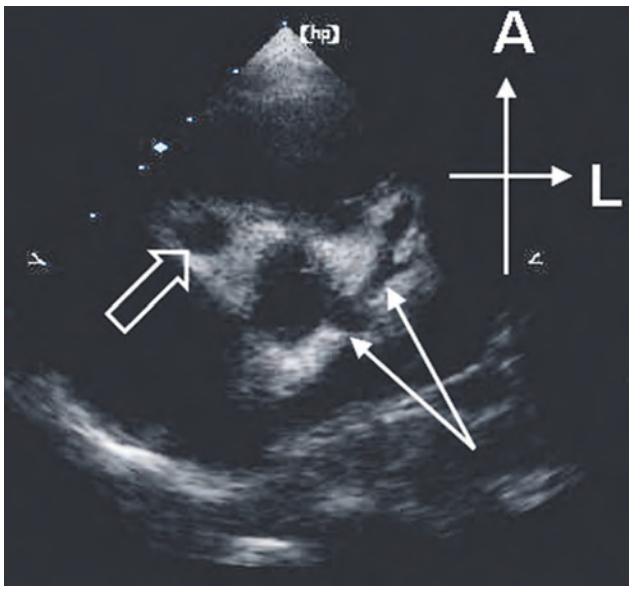


Figure 38.8 Parasternal short-axis image demonstrates diffuse ectasia of the left main and left anterior descending coronary arteries (white arrows). Note the moderate saccular aneurysm of the right coronary artery (open arrow). A, anterior; L, left.

It is important to make every effort to image each segment of the left and right coronary artery systems. The most common sites for coronary artery aneurysms are the proximal LAD and proximal RCA, followed in decreasing frequency by the left main coronary artery, LCx, distal RCA, and proximal posterior descending artery. Although isolated aneurysms of the left main coronary artery are relatively common, isolated RCA or LAD aneurysms are relatively uncommon, and isolated LCx lesions are rare. More commonly, multiple lesions involving both right and left coronary systems – particularly involving the LAD, RCA, and left main coronary artery – are seen [20].

Characterization of coronary artery abnormalities

Coronary artery aneurysms should be characterized both qualitatively and quantitatively by 2D echocardiography. Coronary artery *ectasia* is defined as coronary artery enlargement without aneurysm (Figure 38.8). Coronary artery aneurysms are described as *saccular* when the axial and longitudinal dimensions are nearly equal (Figures 38.7 and 38.9), or *fusiform*, when the axial dimension is less than longitudinal dimension, and the aneurysm tapers at its ends (Figures 38.5 and 38.6). Characterization of aneurysm type is of prognostic importance, as fusiform aneurysms are more likely than saccular aneurysms to regress over time [21]. In addition to frank coronary artery aneurysms, other more subtle changes have been reported in the acute phase of the illness, including perivascular echogenicity seen in the coronary arterial wall (Figure 38.3) and mild, diffuse coronary artery enlargement [5]. However, there are recent reports that suggest that perivascular echogenicity may be difficult to discriminate from normal control subjects [22].

Quantitative coronary artery assessment should be performed in all patients being evaluated for Kawasaki disease. In addition to having prognostic importance, recent management guidelines [3,18] are based on aneurysm size, number, and location. Internal vessel diameters should be measured by 2D echocardiographic images from inner edge to inner edge (Figure 38.10). The American Heart Association previously classified aneurysms by internal diameter as either small (<5 mm), medium (5–8 mm), or giant (>8 mm) [18]. Most recently,

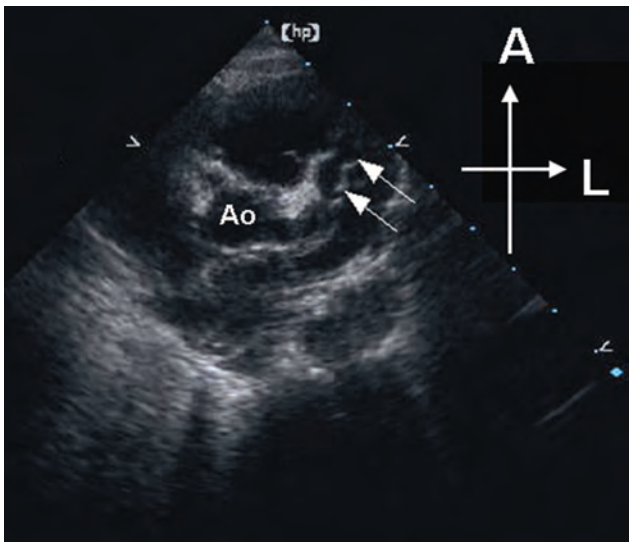


Figure 38.9 Parasternal short-axis view demonstrates two moderate-sized saccular aneurysms involving the left anterior descending coronary artery (arrows). A, anterior; Ao, aorta; L, left.

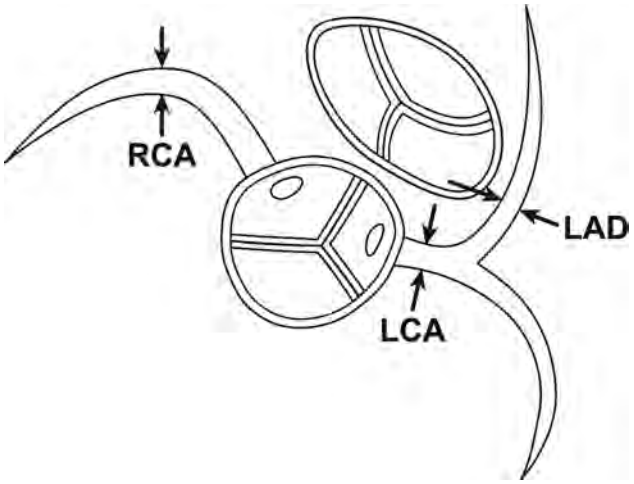


Figure 38.10 Standard locations for making quantitative measurements of left main coronary artery (LCA), left anterior descending artery (LAD), and right coronary artery (RCA) dimensions. Note that the LCA dimension should be measured distal to its ostium, and prior to its bifurcation into LAD and left circumflex artery. The RCA is measured after its initial turn rightward from the aortic sinus. The LAD is measured distal to its bifurcation from the LCA and prior to the takeoff of the first marginal branch. Source: de Zorzi et al. 1998 [24]. Reproduced with permission of Elsevier.

however, aneurysms have been reclassified as small–medium (>3 mm but <6 mm, coronary artery *z*-score of +3 to +7), large (≥6 mm), or giant (>8 mm) to reflect consensus suggestions for cardiovascular risk assessment [3]. Alternatively, the Japanese Ministry of Health has defined coronary artery dilation if (1) the internal diameter is >3 mm in children <5 years of age; (2) the internal diameter is >4 mm in children ≥5 years of age; (3) the internal diameter is at least 1.5 times the diameter of an adjacent coronary segment; or (4) the coronary artery lumen is clearly irregular [23]. These criteria, however, may result in under-recognition of coronary artery abnormalities if one compares patients with Kawasaki disease with body surface area-adjusted normal values for coronary artery dimensions [24,25]. It is therefore important also to assess coronary artery dimensions relative to published normal values (and *z*-score values) [24–26]. Understanding that published normal values exist only for the RCA, left main coronary artery, and LAD, it is also important to assess other coronary segments relative to their adjacent segments, as described above, using Japanese Ministry of Health criteria.

The location, number, and distribution of coronary artery aneurysms should also be noted, as the presence of multiple aneurysms (Figure 38.11) in one or more coronary artery results in higher risk stratification, more aggressive pharmacologic therapy, and the need for additional testing, such as coronary angiography and perfusion assessment.

The presence of thrombus within coronary artery aneurysms, particularly in giant aneurysms, should be evaluated (Figure 38.12; Video 38.6). Identification of stenosis or obstruction

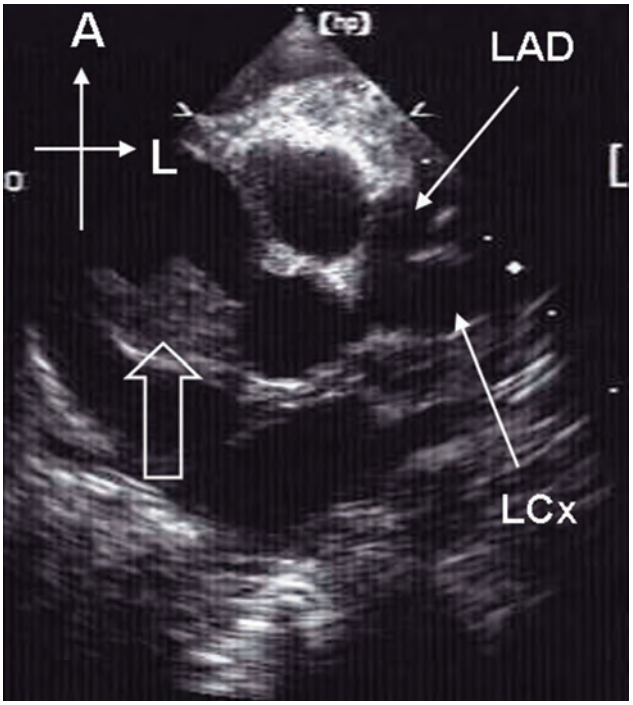


Figure 38.11 Parasternal short-axis view in a patient with multiple, complex coronary artery aneurysms. Large, saccular aneurysms involving the left anterior descending artery (LAD) and left circumflex artery (LCx) are present (white arrows); note also the giant right coronary artery aneurysm with thrombus (open arrow) formation. A, anterior; L, left.

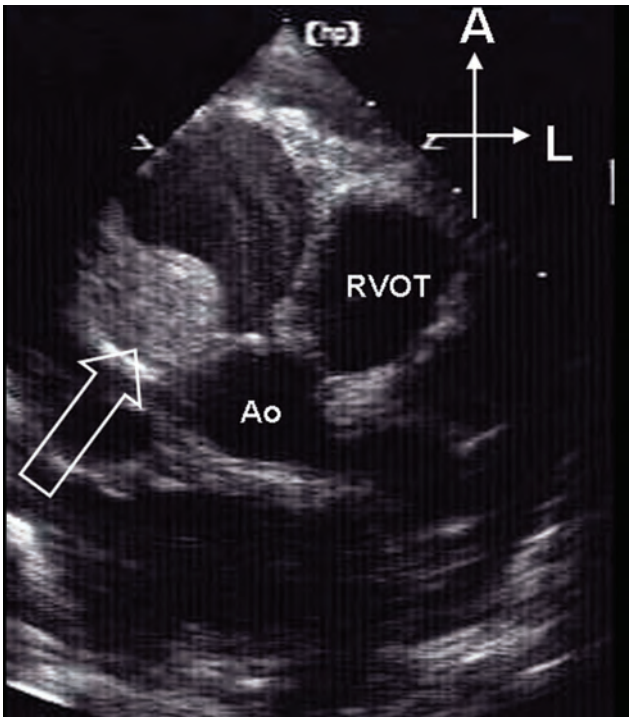


Figure 38.12 Parasternal short-axis view in a patient with a large thrombus (open arrow) within a giant right coronary artery aneurysm. Spontaneous contrast can also been seen within the aneurysm. A, anterior; Ao, aorta; L, left; RVOT, right ventricular outflow tract.

of the coronary arteries due to acute thrombosis or to chronic fibrosis and thickening of the vessel wall should be attempted, although it may be difficult by 2D echocardiography alone [27]. Identification of coronary artery stenoses may be improved by functional assessment of coronary artery perfusion but can also be confirmed by cardiac angiography.

Valvar dysfunction

In the acute phase of Kawasaki disease, color flow Doppler evaluation can often identify tricuspid and mitral valve regurgitation. Atrioventricular valve regurgitation in acute Kawasaki disease is usually mild, transient, and felt to be related to either valvulitis or myocarditis [28,29]. In one report, the presence of mitral regurgitation was associated with lower left ventricular ejection fraction in the acute phase of the illness [28]. In rare cases, acute mitral regurgitation can be severe [30]. Mitral regurgitation that persists long term has been associated with myocardial ischemia and papillary muscle dysfunction [29,31].

Aortic regurgitation may also occur, and is felt to be secondary to valvulitis and/or aortitis. Aortic regurgitation during the acute phase is also typically mild in severity and transient [31,32]. Aortic root dilation has been noted in Kawasaki disease [33], and may account in part for the development of aortic regurgitation. Aortic regurgitation may persist chronically and in rare cases require surgical intervention [34,35].

Myocardial involvement

Histologic evidence of myocarditis in the acute phase of Kawasaki disease is present in virtually all cases [7,8,36,37]. Echocardiographic assessment of ventricular function during the acute phases of Kawasaki disease is therefore an important component of initial and follow-up evaluations. Quantitative methods of assessing global ventricular chamber size and function are discussed elsewhere but generally include shortening fraction or ejection fraction. Evaluation of regional wall motion abnormalities should also be considered. Assessment of regional wall motion abnormalities is performed in the parasternal long- and short-axis, and apical 4- and 2-chamber views. These windows allow the examiner to assess 16 standard myocardial segments [38] and determine the specific coronary artery territory affected when segmental wall motion abnormalities are identified (Figure 38.13). Long-term imaging in patients with severe coronary artery involvement may reveal significant myocardial dysfunction, scarring, and mitral regurgitation related to papillary muscle ischemia (Videos 38.7 and 38.8).

Pericardial involvement

In the acute phase of Kawasaki disease, pericardial inflammation can produce modest pericardial effusions. Although rarely of hemodynamic significance, there have been reports of pericardial tamponade in association with severe acute Kawasaki disease [39,40]. Identification of pericardial effusion may also

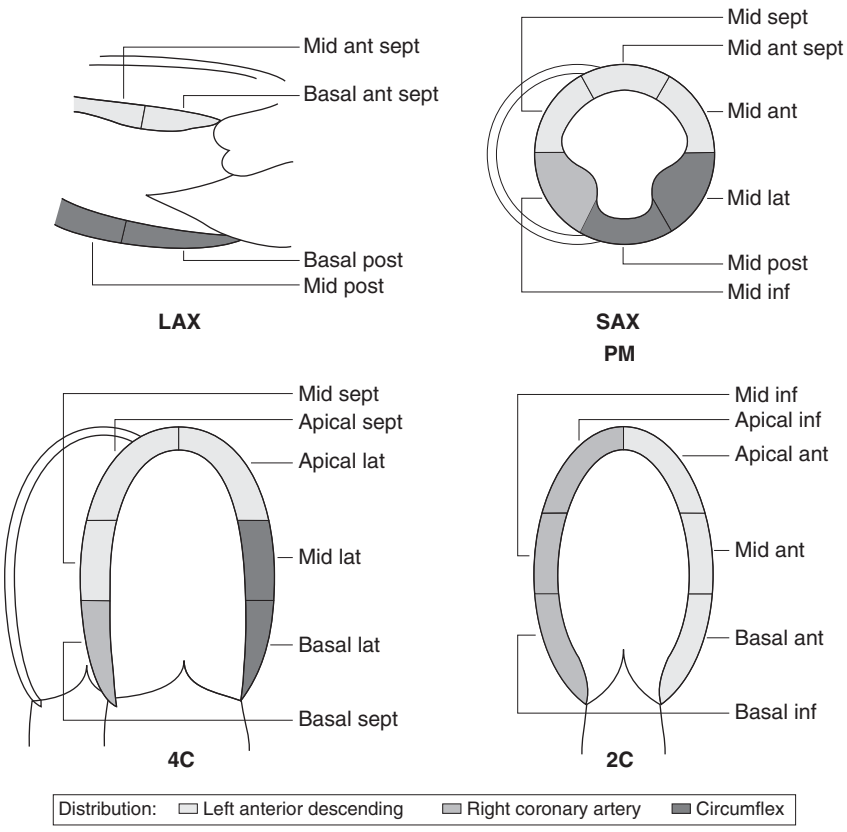


Figure 38.13 Sixteen myocardial segments demonstrated on parasternal and apical imaging of the left ventricle. Note the coronary artery supply to each specific segment. LAX, long axis; SAX, short axis; PM, papillary muscles; 2C, 2-chamber; 4C, 4-chamber; ant, anterior; inf, inferior; lat, lateral; post, posterior; sept, septum. Source: Segar et al. 1992 [57]. Reproduced with permission of Elsevier.

be a value in assessing risk of coronary artery changes [15] or in providing supportive diagnostic data in "incomplete" Kawasaki disease.

Assessment of coronary perfusion by echocardiography

In addition to anatomic imaging and identification of coronary artery abnormalities, *functional* imaging of the coronary arterial tree may be important in patients with Kawasaki disease, particularly in those who are known to have significant coronary artery aneurysms. Coronary artery dysfunction heralds atherosclerotic disease. Children with Kawasaki disease are at increased risk of developing early adult coronary artery disease. Stress echocardiography is an important tool that can be used to evaluate coronary artery function. Stress echocardiography is based on the presumption that a *stressor*—either dynamic, such as exercise, or pharmacologic, such as dobutamine—will induce relative ischemia in myocardial segments with inadequate coronary arterial blood supply. By increasing myocardial oxygen demand, stress echocardiography can produce, and subsequently demonstrate, ischemia-induced wall motion abnormalities – not present during resting imaging – in myocardial segments supplied by stenotic coronary artery branches. Stress echocardiography has the additional diagnostic advantage of focusing on regional wall motion abnormalities, which appear earlier during myocardial ischemia than either electrocardiographic changes or elevation of cardiac enzymes.

Exercise stress echocardiography, performed either immediately after or during exercise, has several disadvantages in the pediatric population, which are largely technical in nature. Exercise is usually performed in a graded, stepwise progression on either a treadmill or bicycle ergometer. Although the degree of physiologic stress reached with exercise is generally excellent, many children are not capable of performing these studies. Imaging either during or immediately after exercise can be technically challenging, due to movement and/or hyperpnea. Nonetheless, exercise stress echocardiography has successfully demonstrated angiographically confirmed coronary stenoses in patients following Kawasaki disease [41].

Pharmacologic stress echocardiography has several advantages over exercise stress echocardiography in the pediatric patient with Kawasaki disease. Use of pharmacologic stressors avoids the need for children (particularly the very young or those with disabilities) to perform graded exercise. Dobutamine, the most widely reported agent used in these studies [42–46], is generally safe. Mild side effects, including headache, nausea, hypertension, and atrial/ventricular ectopy, generally resolve rapidly with termination of the dobutamine infusion [44,46]. Serious arrhythmias and hypotension have been described, but are rare in the pediatric age group.

During dobutamine stress echocardiography, baseline images are obtained in the parasternal long- and short-axis, and in the apical 4- and 2-chamber views, in order to evaluate all 16 standard myocardial segments (Figure 38.13) [38]. Continuous dobutamine infusion is then administered in 3–5 min stages, at infusion rates of 10, 20, 30, 40, and 50 μg/kg/min. Continuous electrocardiographic and vital signs monitoring is performed, and images are repeated at the end of each infusion stage. Current cardiac ultrasound systems allow digital display of images in quad-screen format, which allows side-by-side comparison of either single views at multiple infusion rates or multiple views at a single infusion rate. Most laboratory protocols compare resting, low dose, and high dose, and recovery images for evidence of regional wall motion abnormalities. High (maximum) dose is typically reached either when target heart rate is attained or when maximum dose (30–50 μg/kg/min) is reached.

Data regarding the use of dobutamine stress echocardiography in children with Kawasaki disease suggest that it can be used safely to identify coronary artery stenosis [42,44,46]. In the largest such study, Noto et al. [44] demonstrated that dobutamine stress echocardiography identified coronary artery stenoses with a sensitivity of 90% and a specificity of 100%.

Alternative imaging modalities in Kawasaki disease

When significant coronary artery abnormalities are suspected, cardiac catheterization with coronary angiography is usually performed to fully evaluate the extent and distribution of coronary artery aneurysms (Table 38.2). Angiography fully delineates coronary artery anatomy, particularly in the distal vessels, but is invasive and not without clinical risk. Noninvasive alternatives to cineangiography are now available in the form of both cardiac magnetic resonance (CMR) imaging and computed tomography (CT). Studies using both CMR [47–50] and multidetector/ultrafast CT [51,52] have reported the accuracy of both modalities in identifying and characterizing coronary artery abnormalities in Kawasaki disease. Both CMR and CT may provide a noninvasive means of assessing coronary artery anatomy in the course of long-term follow-up of Kawasaki disease, particularly in patients with high-risk coronary artery abnormalities or patients with limited echocardiographic imaging windows.

For assessment of coronary artery perfusion, alternatives to stress echocardiography include stress nuclear perfusion studies [53–55] and stress CMR with regional perfusion assessment [56]. The method of assessing coronary artery perfusion in Kawasaki disease is likely to be determined by local experience, available resources, and clinical familiarity.

Acknowledgment

The authors thank Stacy Meredith RDCS for her help and assistance in preparing the images and figures for this chapter.

Videos

To access the videos for this chapter, please go to www.lai-echo.com.

Video 38.1 Parasternal short-axis image with slight clockwise rotation, demonstrating the left main coronary artery (LCA), proximal left anterior descending artery (LAD), and proximal left circumflex coronary artery. Note the diffuse enlargement of the LCA and LAD in this child with Kawasaki disease.

Video 38.2 Parasternal long-axis image in a patient with Kawasaki disease. Note that with leftward sweeping, both the proximal left anterior descending artery and left circumflex artery are seen and appear significantly ectatic on this image.

Video 38.3 Multiple, saccular left circumflex artery aneurysms seen on subxiphoid sagittal imaging at the level of the left atrioventricular groove. Note also the modest pericardial effusion seen in this patient with acute phase disease.

Video 38.4 In apical 5-chamber view, the proximal right coronary artery can be demonstrated in the right anterior atrioventricular groove. Note also the significant dilation of the left anterior descending coronary artery as it descends into the interventricular groove.

Video 38.5 Subxiphoid coronal view demonstrates a right coronary artery aneurysm in the anterosuperior portion of the right atrioventricular groove. The right atrium, tricuspid valve, and right ventricle are also demonstrated in this imaging plane.

Video 38.6 Parasternal short-axis view in a patient with a large thrombus within a giant right coronary artery aneurysm. Spontaneous contrast can also been seen within the aneurysm, consistent with sluggish blood flow.

Video 38.7 Apical 4-chamber view in a patient with left ventricular dysfunction secondary to coronary artery aneurysms (with stenosis) following Kawasaki disease. Note the global depression in left ventricular systolic performance, with regional hypokinesia, more severe in the interventricular septum when compared with the left ventricular free wall. In addition, there is thinning and increased echogenicity of the septal myocardium, consistent with myocardial fibrosis and scarring due to coronary ischemia in the left anterior descending artery distribution.

Video 38.8 Parasternal short-axis view in a patient with left ventricular dysfunction secondary to coronary artery aneurysms (with stenosis) following Kawasaki disease. Note the global depression in left ventricular systolic performance, with regional hypokinesia of the septal and inferior segments, consistent with both left anterior descending artery and right coronary artery involvement.

References

1 Kawasaki T. Acute febrile mucocutaneous syndrome with lymphoid involvement with specific desquamation of the fingers and toes in children. *Arerugi* 1967;**16**:178–222 (in Japanese).

2 Kawasaki T, Kosaki F, Okawa S, et al. A new infantile acute febrile mucocutaneous lymph node syndrome (MLNS) prevailing in Japan. *Pediatrics* 1974;**54**:271–276.

3 Newburger JW, Takahashi M, Gerber MA, et al. Diagnosis, treatment, and long-term management of Kawasaki disease: a statement for health professionals from the Committee on Rheumatic Fever, Endocarditis and Kawasaki Disease, Council on Cardiovascular Disease in the Young, American Heart Association. *Circulation* 2004;**110**:2747–2771.

4 Bell DM, Morens DM, Holman RC, et al. Kawasaki syndrome in the United States 1976 to 1980. *Am J Dis Child* 1983;**137**:211–214.

5 Newburger JW, Taubert KA, Shulman ST, et al. Summary and abstracts of the Seventh International Kawasaki Disease Symposium: December 4–7 2001, Hakone, Japan. *Pediatr Res* 2003;**53**:153–157.

6 Holman RC, Curns AT, Belay ED, et al. Kawasaki syndrome hospitalizations in the United States 1997 and 2000. *Pediatrics* 2003;**112**:495–501.

7 Fujiwara H, Hamashima Y. Pathology of the heart in Kawasaki disease. *Pediatrics* 1978;**61**:100–107.

8 Yutani C, Go S, Kamiya T, et al. Cardiac biopsy of Kawasaki disease. *Arch Pathol Lab Med* 1981;**105**:470–473.

9 Akagi T, Rose V, Benson LN, et al. Outcome of coronary artery aneurysms after Kawasaki disease. *J Pediatr* 1992;**121**:689–694.

10 Kato H, Ichinose E, Yoshioka F, et al. Fate of coronary aneurysms in Kawasaki disease: serial coronary angiography and long-term follow-up study. *Am J Cardiol* 1982;**49**:1758–1766.

11 Sasaguri Y, Kato H. Regression of aneurysms in Kawasaki disease: a pathological study. *J Pediatr* 1982;**100**:225–231.

12 Shinohara M, Sone K, Tomomasa T. Morphologic and functional assessment of coronary aneurysm after Kawasaki disease by repeated dipyridamole-loading coronary angiography. *Am J Cardiol* 1998;**82**:387–389.

13 Sugimura T, Kato H, Inoue O, et al. Vasodilatory response of the coronary arteries after Kawasaki disease: evaluation by intracoronary injection of isosorbide dinitrate. *J Pediatr* 1992;**121**:684–688.

14 Yamakawa R, Ishii M, Sugimura T, et al. Coronary endothelial dysfunction after Kawasaki disease: evaluation by intracoronary injection of acetylcholine. *J Am Coll Cardiol* 1998;**31**:1074–1080.

15 Gidding SS, Duffy CE, Pajcic S, et al. Usefulness of echocardiographic evidence of pericardial effusion and mitral regurgitation during the acute stage in predicting development of coronary arterial aneurysms in the late stage of Kawasaki disease. *Am J Cardiol* 1987;**60**):76–79.

16 Printz BF, Sleeper LA, Newburger JW, et al. Noncoronary cardiac abnormalities are associated with coronary artery dilation and with laboratory inflammatory markers in acute Kawasaki disease. *J Am Coll Cardiol* 2011;**57**:86–92.

17 Selamet Tierney ES, Newburger JW, Graham D, et al. Diastolic function in children with Kawasaki disease. *Int J Cardiol* 2011;**148**:309–312.

18 Dajani AS, Taubert KA, Takahashi M, et al. Guidelines for long-term management of patients with Kawasaki disease. Report from the Committee on Rheumatic Fever, Endocarditis, and Kawasaki Disease, Council on Cardiovascular Disease in the Young, American Heart Association. *Circulation* 1994;**89**:916–922.

19 Yanagisawa M, Yano S, Shiraishi H, et al. Coronary aneurysms in Kawasaki disease: follow-up observation by two-dimensional echocardiography. *Pediatr Cardiol* 1985;**6**:11–16.

20 Onouchi Z, Shimazu S, Kiyosawa N, et al. Aneurysms of the coronary arteries in Kawasaki disease. An angiographic study of 30 cases. *Circulation* 1982;**66**:6–13.

21 Takahashi M, Mason W, Lewis AB. Regression of coronary aneurysms in patients with Kawasaki syndrome. *Circulation* 1987;**75**:387–394.

22 Yu JJ, Jang WS, Ko HK, et al. Perivascular brightness of coronary arteries in Kawasaki disease. *J Pediatr* 2011;**159**:454.e1–457.e1.

23 Research Committee on Kawasaki Disease. *Report of Subcommittee on Standardization of Diagnostic Criteria and Reporting of Coronary Artery Lesions in Kawasaki Disease*. Tokyo: Ministry of Health and Welfare, 1984.

24 de Zorzi A, Colan SD, Gauvreau K, et al. Coronary artery dimensions may be misclassified as normal in Kawasaki disease. *J Pediatr* 1998;**133**:254–258.

25 Kurotobi S, Nagai T, Kawakami N, Sano T. Coronary diameter in normal infants, children and patients with Kawasaki disease. *Pediatr Int* 2002;**44**:1–4.

26 McCrindle BW, Li JS, Minich LL, et al. Coronary artery involvement in children with Kawasaki disease: risk factors from analysis of serial normalized measurements. *Circulation* 2007;**116**:174–199.

27 Fujiwara T, Fujiwara H, Ueda T, et al. Comparison of macroscopic, postmortem, angiographic and two-dimensional echocardiographic findings of coronary aneurysms in children with Kawasaki disease. *Am J Cardiol* 1986;**57**:761–764.

28 Suzuki A, Kamiya T, Tsuchiya K, et al. Tricuspid and mitral regurgitation detected by color flow Doppler in the acute phase of Kawasaki disease. *Am J Cardiol* 1988;**61**:386–390.

29 Takao A, Niwa K, Kondo C, et al. Mitral regurgitation in Kawasaki disease. *Prog Clin Biol Res* 1987;**250**:311–323.

30 Tomita H, Sawada Y, Higashidate Y, et al. Mitral regurgitation with gross deformity of a mitral leaflet due to Kawasaki disease. *Pediatr Cardiol* 1990;**11**:153–155.

31 Akagi T, Kato H, Inoue O, et al. Valvular heart disease in Kawasaki syndrome: incidence and natural history. *Am Heart J* 1990;**120**:366–372.

32 Nakano H, Nojima K, Saito A, Ueda K. High incidence of aortic regurgitation following Kawasaki disease. *J Pediatr* 1985;**107**:59–63.

33 Ravekes WJ, Colan SD, Gauvreau K, et al. Aortic root dilation in Kawasaki disease. *Am J Cardiol* 2001;**87**:919–922.

34 Fukunaga S, Egashira A, Arinaga K, et al. Aortic valve replacement for aortic regurgitation due to Kawasaki disease. Report of two cases. *J Heart Valve Dis* 1996;**5**:231–234.

35 Takahashi T, Taniguchi K, Matsuda H. Surgical treatment for aortic regurgitation and left ventricular dysfunction caused by Kawasaki disease. *Cardiol Young* 1998;**8**:123–125.

36 Amano S, Hazama F, Kubagawa H, et al. General pathology of Kawasaki disease. On the morphological alterations corresponding to the clinical manifestations. *Acta Pathol Jpn* 1980;**30**:681–694.

37 Landing BH, Larson EJ. Pathological features of Kawasaki disease (mucocutaneous lymph node syndrome). *Am J Cardiovasc Pathol* 1987;**1**:218–229.

38 Cerqueira MD, Weissman NJ, Dilsizian V, et al. Standardized myocardial segmentation and nomenclature for tomographic imaging of the heart: a statement for healthcare professionals from the Cardiac Imaging Committee of the Council on Clinical Cardiology of the American Heart Association. *Circulation* 2002;**105**:539–542.

39 Dahlem PG, von Rosenstiel IA, Lam J, Kuijpers TW. Pulse methylprednisolone therapy for impending cardiac tamponade in immunoglobulin-resistant Kawasaki disease. *Intensive Care Med* 1999;**25**:1137–1139.

40 Ozdogu H, Boga C. Fatal cardiac tamponade in a patient with Kawasaki disease. *Heart Lung* 2005;**34**:257–259.

41 Pahl E, Sehgal R, Chrystof D, et al. Feasibility of exercise stress echocardiography for the follow-up of children with coronary involvement secondary to Kawasaki disease. *Circulation* 1995;**91**:122–128.

42 Kimball TR, Witt SA, Daniels SR. Dobutamine stress echocardiography in the assessment of suspected myocardial ischemia in children and young adults. *Am J Cardiol* 1997;**79**:380–384.

43 Larsen RL, Applegate PM, Dyar DA, et al. Dobutamine stress echocardiography for assessing coronary artery disease after transplantation in children. *J Am Coll Cardiol* 1998;**32**:515–520.

44 Noto N, Ayusawa M, Karasawa K, et al. Dobutamine stress echocardiography for detection of coronary artery stenosis in children with Kawasaki disease. *J Am Coll Cardiol* 1996;**27**:1251–1256.

45 Pahl E, Crawford SE, Swenson JM, et al. Dobutamine stress echocardiography: experience in pediatric heart transplant recipients. *J Heart Lung Transplant* 1999;**18**:725–732.

46 Zilberman MV, Goya G, Witt SA, et al. Dobutamine stress echocardiography in the evaluation of young patients with Kawasaki disease. *Pediatr Cardiol* 2003;**24**:338–343.

47 Greil GF, Seeger A, Miller S, et al. Coronary magnetic resonance angiography and vessel wall imaging in children with Kawasaki disease. *Pediatr Radiol* 2007;**37**:666–673.

48 Mavrogeni S, Papadopoulos G, Douskou M, et al. Magnetic resonance angiography is equivalent to X-ray coronary angiography for the evaluation of coronary arteries in Kawasaki disease. *J Am Coll Cardiol* 2004;**43**:649–652.

49 Takemura A, Suzuki A, Inaba R, et al. Utility of coronary MR angiography in children with Kawasaki disease. *AJR Am J Roentgenol* 2007;**188**:W534–W539.

50 Tacke CE, Kuipers IM, Groenink M, et al. Cardiac magnetic resonance imaging for noninvasive assessment of cardiovascular disease during the follow-up of patients with Kawasaki disease. *Circ Cardiovasc Imaging* 2011;**4**:712–720.

51 Chu WC, Mok GC, Lam WW, et al. Assessment of coronary artery aneurysms in paediatric patients with Kawasaki disease by multidetector row CT angiography: feasibility and comparison with 2D echocardiography. *Pediatr Radiol* 2006;**36**:1148–1153.

52 Yu Y, Sun K, Wang R, et al. Comparison study of echocardiography and dual-source CT in diagnosis of coronary artery aneurysm due to Kawasaki disease: coronary artery disease. *Echocardiography* 2011;**28**:1025–1034.

53 Fukuda T, Akagi T, Ishibashi M, et al. Noninvasive evaluation of myocardial ischemia in Kawasaki disease: comparison between dipyridamole stress thallium imaging and exercise stress testing. *Am Heart J* 1998;**135**:482–487.

54 Fukuda T, Ishibashi M, Yokoyama T, et al. Myocardial ischemia in Kawasaki disease: evaluation with dipyridamole stress technetium 99m tetrofosmin scintigraphy. *J Nucl Cardiol* 2002;**9**:632–637.
55 Kondo C, Hiroe M, Nakanishi T, Takao A. Detection of coronary artery stenosis in children with Kawasaki disease. Usefulness of pharmacologic stress ^{201}Tl myocardial tomography. *Circulation* 1989;**80**:615–624.
56 Mühling O, Jerosch-Herold M, Näbauer M, Wilke N., et al. Assessment of ischemic heart disease using magnetic resonance first-pass perfusion imaging. *Herz* 2003;**28**:82–89.
57 Segar DS, Brown SE, Sawada SG, et al. Dobutamine stress echocardiography: correlation with coronary lesion severity as determined by quantitative angiography. *J Am Coll Cardiol* 1992;**19**:1197–1202.

CHAPTER 39

Rheumatic Fever and Rheumatic Heart Disease

Bo Reményi[1], Andrew Steer[2], and Michael Cheung[3]

[1]Menzies School of Health Research, Charles Darwin University, Darwin, NT, Australia

[2]Department of General Medicine, Royal Children's Hospital, Melbourne, VIC; Centre for International Child Health, Department of Paediatrics, Royal Children's Hospital, Melbourne, VIC; Group A Streptococcal Research Group, Murdoch Childrens Research Institute, Melbourne, VIC, Australia

[3]Department of Cardiology, Royal Children's Hospital, Melbourne, VIC; Department of Paediatrics, University of Melbourne, Melbourne, VIC; Heart Research Group, Murdoch Childrens Research Institute, Melbourne, VIC, Australia

Introduction

Rheumatic fever (RF) is a delayed autoimmune reaction that typically follows a group A β-hemolytic streptococcal throat infection. It is a multi-organ disease that affects the heart, joints, brain, skin, and subcutaneous tissue. The adverse effect on the cardiovascular system, rheumatic heart disease (RHD), is responsible for the mortality and the majority of morbidity relating to RF. Despite the virtual disappearance of RF/RHD from the developed world, its human, social, and economic costs remain a significant burden in many low- and middle-income countries.

Epidemiology

RF, once very common in North America and Europe, is now rarely seen by physicians who practice amongst affluent populations. However, in developing nations, RF remains the most common cause of acquired heart disease in children and young adults. In developed countries, the incidence of RF began to decline in the 19th century, preceding the availability of penicillin [1]. This change was attributed to decreased crowding, better personal hygiene, improved nutrition and overall improved living standards [1]. With the introduction of penicillin in the mid-20th century, the incidence of RF further decreased, and in many places it is now virtually nonexistent. Low- and middle-income countries and some indigenous populations of the developed world continue to struggle with the scourge of RF and its long-term consequences. A conservative estimate of 15 million people affected worldwide by RHD is likely the tip of the iceberg. The true prevalence of RHD would be several times this estimate if subclinical or echocardiography-positive disease were to be included [2–4]. Children aged between 5 and 15 years are at the greatest risk of a primary episode of RF [5]. Development of RF before this age period is almost nonexistent; onset of a primary episode is rare beyond the fourth decade of life. Although there is no established gender difference for RF, in most populations RHD occurs 1.5–2 times more commonly in females than in males, which may be due to increased exposure to streptococcal infections (related to child rearing), lack of access to preventive care, or different host susceptibility. RF also appears to follow a seasonal pattern, paralleling that of streptococcal pharyngitis.

Familial clustering of cases of RF is well described, and there is strong concordance in monozygotic twins [6]. It is thought that 3–6% of any population is at risk of developing RF [7,8]. Genetic predisposition to RF has been linked to human leukocyte antigen (HLA) class II alleles [9,10]. Polymorphisms in tumor necrosis factor alpha (TNF-α) and mannose-binding lectin genes have also been implicated. High-level expression of a particular alloantigen present on B cells, D8-17, has been reported to occur in patients with RF in some populations, implying that it may be a possible marker of susceptibility[11], but the expression of this marker is not consistent across all endemic populations [12].

Pathophysiology

The association between RF and group A β-hemolytic streptococcal upper respiratory tract infection is well established [1]. However, the exact pathogenesis of RF remains incompletely understood. The classical disease model is based on a complex interaction between a susceptible host, a virulent bacterium, and an environment conducive to bacterial infection. The current hypothesis attributes the delayed autoimmune reaction of RF to molecular mimicry between the host and the streptococcus [13]. Particular streptococcal proteins (e.g., M protein and *N*-acetylglucosamine) share homologous sequences with human

Echocardiography in Pediatric and Congenital Heart Disease: From Fetus to Adult, Second Edition. Edited by Wyman W. Lai, Luc L. Mertens, Meryl S. Cohen and Tal Geva.
© 2016 John Wiley & Sons, Ltd. Published 2016 by John Wiley & Sons, Ltd.
Companion website: www.lai-echo.com

Table 39.1 Comparison of AHA, WHO and Australian diagnostic criteria for RF

Manifestations	AHA (Jones) 1992 [16]	WHO 2004 [17]	Australia 2012 [18]	
			High risk	Low risk
Carditis	Major	Major	Major	
Subclinical carditis		n/a	Major	n/a
Prolonged PR interval	*Minor*	*Minor*	*Minor*	
Polyarthritis	Major	Major	Major	
Polyarthralgia	*Minor*	*Minor*	Major	*Minor*
Aseptic monoarthritis	n/a	n/a	Major	Minor
Monoarthralgia	n/a	n/a	Minor	n/a
Subcutaneous nodules	Major	Major	Major	
Sydenham's chorea	Major	Major	Major	
Erythema marginatum	Major	Major	Major	
Fever	*Minor*	*Minor*	*Minor*	
WBC, ESR, CRP	*Minor*	*Minor*	*Minor*	
Evidence of recent streptococcal infection	Required	Required	Required	

AHA, American College of Cardiology/American Heart Association; WHO, World Health Organization.
Source: Adapted from RHD Australia (RF/RHD Writing Group), National Heart Foundation of Australia, and the Cardiac Society of Australia and New Zealand 2012 [18]; http://www.rhdaustralia.org.au/resources/arf-rhd-guideline.

tissues such as myosin and laminin. As a result, the immune reaction that occurs in response to group A streptococcal infection can lead to the formation of cross-reactive antibodies and T cells in susceptible hosts. Cross-reactive antibodies attach to native laminin in valvar endothelium and to other tissues, allowing the entry of primed T helper cells to trigger an autoimmune reaction [14]. Inflammation then leads to neovascularization and further recruitment of T-cells.

Diagnostic criteria for rheumatic fever

The diagnosis of RF relies on clinical criteria as there are no specific tests that confirm or rule out the diagnosis. In 1944, Jones established diagnostic criteria for RF [15]. Over the latter part of the 20th century, the Jones criteria were modified and updated, most recently in 1992 (Table 39.1). On each occasion, the criteria were changed to become more specific and less sensitive for RF in response to the decline in RF in industrialized countries over that period. However, the Jones criteria may no longer be appropriate in regions where RF remains endemic, i.e. in populations with a high pretest probability of RF (Table 39.2). Authorities including the World Health Organization (WHO) and Australian disease control organizations that work in endemic areas have recently adjusted the Jones criteria to increase their sensitivity (Tables 39.1 and 39.2) [17,18].

Valvulitis is a clinical diagnosis based on the updated Jones and WHO criteria. However, it has been shown that auscultation is neither sensitive nor specific for mild mitral or aortic regurgitation. The 2012 Australian diagnostic guidelines modified the Jones criteria to include subclinical valvulitis as a major criterion for RF. Subclinical valvulitis refers to echocardiographic evidence of mild mitral and/or aortic valve regurgitation that is not audible.

Clinical course of rheumatic fever and rheumatic heart disease

Up to 80% of patients with a primary episode of RF have carditis. The overall risk of developing long-term RHD following the first episode of RF is approximately 60–65% [19]. Risk of progression to chronic severe RHD depends upon two factors: (1) the severity of carditis at presentation and (2) the number of RF recurrences following the primary episode [20–22]. Recurrence of RF is most common in the first 5 years after the initial episode and may occur in up to 75% of patients who do not receive regular secondary prophylaxis. Secondary prophylaxis is the continuous delivery of antibiotics to prevent recurrent episodes of RF, usually with monthly benzathine penicillin injections or daily oral penicillin. The benefits of secondary prophylaxis have been recognized since the 1960s [23–36]. Continuous adherence to secondary prophylaxis leads to a reduction in recurrent episodes of RF, improvement in the severity of RHD (including complete regression of mild valvulitis within 5–10 years in up to 70% of cases), and reduced mortality. Despite these preventive measures, RHD remains a common cause of morbidity and is one of the most frequent indications for valve intervention.

Imaging

Key elements

- Assessment of mitral valve anatomy:
 - For abnormal thickening, elongation of chordae and prolapse.
 - Measurement of mitral valve diameter and comparison with normal *z*-score measures.
 - Quantitation of mitral regurgitation:
 - Size and extent of regurgitant jet.
 - Assessment of regurgitant volume and regurgitant fraction if possible.
 - Measurement of effective regurgitant orifice area.
 - Assessing for volume overload by measuring left atrial and left ventricular size.
 - For mitral stenosis (in chronic disease):
 - Mean gradient across the valve.
 - Region in mitral apparatus where mitral stenosis begins.

Table 39.2 2012 updated Australian guidelines for the diagnosis of RF

	High-risk groups[a]	All other groups
Definite initial episode of RF	2 major or 1 major and 2 minor manifestations plus evidence of a preceding GAS infection[b]	
Definite recurrent episode of RF in a patient with known past RF or RHD	2 major or 1 major and 1 minor or 3 minor manifestations plus evidence of a preceding GAS infection[b]	
Probable RF (first episode or recurrence)	A clinical presentation that falls short by either 1 major or 1 minor manifestation, or the absence of streptococcal serology results, but one in which RF is considered the most likely diagnosis. Such cases should be further categorized according to the level of confidence with which the diagnosis is made: • Highly suspected RF • Uncertain RF	
Major manifestations	Carditis (including subclinical evidence of rheumatic valvulitis on echocardiogram)	Carditis (excluding subclinical evidence of rheumatic valvulitis on echocardiogram)
	Polyarthritis[c] or aseptic monoarthritis or polyarthralgia	Polyarthritis[c]
	Chorea[d]	Chorea[d]
	Erythema marginatum[e]	Erythema marginatum[e]
	Subcutaneous nodules	Subcutaneous nodules
Minor manifestations	Monoarthralgia	Fever[f]
	Fever[f]	Polyarthralgia or aseptic monoarthritis
	ESR ≥30 mm/h or CRP ≥30 mg/L	ESR ≥30 mm/h or CRP ≥30 mg/L
	Prolonged P–R interval on ECG[g]	Prolonged P–R interval on ECG[g]

CRP, C-reactive protein; ECG, electrocardiogram; ESR, erythrocyte sedimentation rate; GAS, group A streptococcal.
[a]High-risk groups are those living in communities with high rates of RF (incidence >30/100,000 per year in 5–14 year olds) or RHD (all-age prevalence >2/1000). Aboriginal people and Torres Strait Islanders living in rural or remote settings are known to be at high risk. Data are not available for other populations, but Aboriginal people and Torres Strait Islanders living in urban settings, Maoris and Pacific Islanders, and potentially immigrants from developing countries, may also be at high risk.
[b]Elevated or rising antistreptolysin O or other streptococcal antibody, or a positive throat culture or rapid antigen tests for GAS.
[c]A definite history of arthritis is sufficient to satisfy this manifestation. Note that if polyarthritis is present as a major manifestation, polyarthralgia or aseptic monoarthritis cannot be considered an additional minor manifestation in the same person.
[d]Chorea does not require other manifestations or evidence of preceding GAS infection, provided that other causes of chorea are excluded.
[e]Care should be taken not to label other rashes, particularly nonspecific viral exanthemas, as erythema marginatum.
[f]Oral, tympanic, or rectal temperature ≥38 °C on admission, or a reliably reported fever documented during the current illness.
[g]If Carditis is present as a major manifestation, a prolonged P–R interval cannot be considered an additional minor manifestation.

- Assessment of the aortic valve anatomy:
 - For effects on aortic valve leaflets:
 - Loss of leaflet height and retraction of leaflets.
 - Quantitation of aortic regurgitation:
 - Measurement of jet-width and cross-sectional area.
 - Assessment of regurgitant volume and regurgitant fraction if possible.
 - Measurement of pressure half-time.
 - Measurement of effective regurgitant orifice area.
 - Assessing for flow reversal in the abdominal aorta.
 - Assessing for volume overload by measuring left atrial and left ventricular size.
- Left ventricular function indices to assess for myocarditis.
- Estimation of right ventricular pressure using the tricuspid regurgitation jet to assess for pulmonary hypertension in the face of significant left-sided heart disease.
- Evaluation of pericardium for pericarditis.

In general, echocardiography in RF is a noninvasive diagnostic tool that allows for:

- Diagnosis of acute rheumatic carditis in an individual with suspected disease.
- Confirmation of the diagnosis of RHD in individuals without a clinical history of RF.
- Grading the severity of valve dysfunction.
- Monitoring disease progression.
- Determining the timing and method of treatment.
- 3D echocardiographic evaluation.
- Screening for latent and subclinical RHD in asymptomatic individuals in high-risk populations.

Acute rheumatic heart disease

Historically, acute rheumatic carditis was described as a pancarditis, affecting the endocardium, myocardium, and pericardium. In the echocardiographic era, it has been demonstrated that the predominant manifestation of RHD is valvulitis; myocardial dysfunction rarely occurs without significant valve involvement [27]. Acute valvulitis most commonly affects the mitral and aortic valves and typically manifests as regurgitation. Less commonly, the tricuspid and pulmonary valves are affected, but almost never in isolation. Valvulitis is usually evident at the time of presentation; however, it can be mild and its onset may be delayed by 2–6 weeks [28]. Repeated clinical and echocardiographic examinations may therefore be required to detect these changes. Pathologic mitral and aortic regurgitation can be difficult to distinguish from physiological regurgitation; the World Heart Federation has recently published minimal

Table 39.3 Echocardiographic criteria for subclinical valvulitis

Pathologic mitral regurgitation (all four Doppler criteria must be met)	Pathologic aortic regurgitation (all four Doppler criteria must be met)
Seen in two views	Seen in two views
In at least one view, jet length 2 cm[a]	In at least one view, jet length ≥1 cm[a]
Velocity ≥3 m/s for one complete envelope	Velocity ≥3 m/s in early diastole
Pan-systolic jet in at least one envelope	Pan-diastolic jet in at least one envelope

[a]A regurgitant jet length should be measured from the vena contracta to the last pixel of regurgitant color (blue or red).
Source: Reményi et al. 2012 [29]. Reproduced with permission of Nature Publishing Group.

echocardiographic diagnostic criteria for rheumatic mitral and aortic regurgitation [29] (Table 39.3).

Acute mitral valvulitis is characterized by leaflet thickening, annular dilation, and chordal elongation, leading to prolapse of the anterior and less commonly the posterior leaflet. As a result, mitral regurgitation occurs and the regurgitant jet is typically directed posterolaterally, causing thickening and calcification of the endocardium (otherwise known as MacCallum's patch). Mitral stenosis does not typically occur in the initial presentation of RHD. In extreme cases of mitral valvulitis, the primary chords of the anterior leaflet may rupture, resulting in a flail leaflet. To assess mitral valvulitis by echocardiography, the anterior mitral valve leaflet thickness should be measured during diastole at full excursion in the parasternal long-axis view. Measurements should be taken at the thickest portion of the leaflet, including focal thickening, beading, and nodularity. Abnormal thickening of the anterior leaflet is age specific and defined as follows: ≥3 mm for individuals ≤20 years of age; ≥4 mm for individuals 21–40 years of age; and ≥5 mm for individuals >40 years of age.

It is important to differentiate rheumatic mitral prolapse from the mitral prolapse seen in Barlow syndrome. In rheumatic mitral carditis, only the coapting portion of the anterior leaflet prolapses and there is no billowing of the medial portion. In contrast, billowing of the posterior or both leaflets of the mitral valve occurs in Barlow syndrome (mitral valve prolapse). Barlow syndrome is typically associated with a mid or late systolic mitral regurgitation, whereas prolapse associated with RHD typically causes pansystolic mitral regurgitation.

Several Doppler indices are of value in determining the degree of mitral regurgitation in the setting of acute rheumatic mitral valvulitis. These include signal intensity of the continuous-wave regurgitant jet, size and extent of the jet into the left atrium, and abnormal pulmonary venous flow patterns. The regurgitant jet width (vena contracta) measured from the parasternal long-axis or apical 4-chamber view is often used as a measure of regurgitant severity. The ratio of regurgitant jet area to left atrial area can be determined by color Doppler and can be used to discriminate between mild (<30%), moderate (30–50%), and severe (>50%) regurgitation. Regurgitant jet area indexed to body surface area has likewise been reported to correlate with the angiographic gradient of regurgitation. Moreover, systolic flow reversal in the pulmonary veins in the apical 4-chamber or parasternal long-axis view suggests significant mitral regurgitation. Increased left atrial pressure may limit this technique. Additional methods for determining the degree of mitral regurgitation include flow convergence and proximal isovelocity surface area (PISA); however, these methods have not gained widespread use in the pediatric population.

Quantification of mitral regurgitation severity can be accomplished by using a combination of 2D and Doppler techniques. Total stroke volume (TSV) is calculated by subtracting left ventricular end-systolic volume from the end-diastolic volume. Forward stroke volume (FSV) is obtained using pulsed Doppler to determine the mean velocity across the aortic valve, and multiplying this value by the vessel cross-sectional area. Mitral regurgitant volume (RV) can then be calculated as TSV – FSV, and the regurgitant fraction can be calculated as RV/TSV. The regurgitant fraction can be calculated by obtaining the stroke volume across the mitral valve and cardiac output across the aortic valve; however, this technique may be limited by the difficulty in measuring mitral annular dimensions accurately and obviously is not applicable if there is associated aortic regurgitation.

Acute aortic valvulitis occurs in 20% of cases of RHD but most commonly coexists with mitral valvulitis. Approximately 5% of children may have isolated aortic valve disease during the first presentation of RF. Aortic valvulitis is characterized by annular dilation, valve thickening, and, in more severe cases, prolapse of aortic cusp(s). Aortic valve disease is typically mild at its initial presentation but can progress over time to more regurgitation, stenosis, or both.

During the acute phase of RF, the aortic valve should be examined carefully by 2D imaging to exclude the possibility of a congenital bicuspid valve, which may result in incomplete closure and/or prolapse of the leaflets. M-mode echocardiography may demonstrate premature mitral valve closure. Doppler assessment of the aortic valve in the parasternal long-axis view reveals high-velocity turbulent flow below the aortic valve immediately after valve closure and throughout diastole. As with mitral regurgitation, several echocardiographic methods may be used to quantitate aortic regurgitation. Reliable predictors of aortic regurgitation severity include Doppler jet width normalized to left ventricular outflow tract (LVOT) width in the parasternal long-axis view and holodiastolic abdominal aortic flow reversal.

Pericarditis and myocarditis are rarely, if ever, isolated cardiac manifestations of RF [30]. Echocardiography can confirm the presence of pericardial effusion, evaluate its hemodynamic impact, and monitor resolution and progression (see Chapter 36). Myocarditis has not been clearly documented in

RHD without evidence of severe valvulitis [27]. Cardiac function on echocardiography in acute RF is more commonly hyperdynamic rather than depressed. If impairment of cardiac contractility is present, it is always in the setting of severe valvar dysfunction and recovery can be expected following improvement in valve function [31,32]. Therefore, modern imaging studies do not support the presence of clinically significant primary myocarditis in the setting of RF [27,33].

Chronic rheumatic heart disease

It is has been estimated that up to 46% of people with established RHD have not had a recognized episode of RF [7,34]. These individuals may present with cardiac symptoms resulting from advanced RHD and its complications (heart failure, arrhythmias, infective endocarditis, thromboembolic events, pregnancy-related complication, and premature death). To facilitate the diagnosis of RHD in individuals without a past history of RF, and to avoid misdiagnosis, the World Heart Federation established evidence-based echocardiographic guidelines in 2012 (Table 39.4) [29]. These echocardiographic criteria aim to guide physicians in the differentiation of mild RHD from normal or physiologic valvar regurgitation; they are specifically designed to be used in high-risk populations. The criteria divide echocardiographic findings into "definite" and "borderline" RHD. The "borderline" group is considered to display echocardiographic signs that overlap with normal individuals were they not at high-risk for the development of RHD. The clinical significance of "borderline RHD" has not been established, although clearly the concern is that it may represent early RHD in high-risk individuals. Ongoing follow-up and a lower threshold for prophylaxis might be considered appropriate in this group [29].

Chronic mitral valve disease is the most common manifestation of RHD. Over the course of decades, most patients with mitral regurgitation progress to mixed disease and then pure mitral stenosis [19,35]. RHD is responsible for over 95% of cases of mitral stenosis worldwide [36]. In some regions of the world where RF remains endemic, progression to severe mitral stenosis can be very rapid and affect children as young as 5–10 years of age. This has been referred to as "juvenile" or "malignant mitral stenosis" [37].

In children, isolated pure mitral regurgitation is the most common form of chronic RHD and occurs by the same mechanism as it does in the acute phase of RF. With time, scarring and fibrosis result in restricted movement of the leaflets (Figure 39.1; Video 39.1). Rheumatic mitral stenosis is the result, with gradual thickening, shortening and calcification of the chords and leaflets. (Figure 39.2; Video 39.2). Parasternal long- and short-axis views best demonstrate these changes in the mitral valve.

In mild mitral stenosis, some leaflet mobility may be preserved, resulting in diastolic doming of the anterior leaflet. This creates a characteristic "hockey-stick" appearance of the anterior leaflet (Video 39.1). As the disease progresses, the valve orifice becomes smaller and even more echo-dense in appearance. Calcification occurs at the leaflet tips, with later extension to the annulus. Over time, the leaflets become less pliable and more restricted in their mobility. The increased gradient across the mitral valve results in increased left atrial pressure and dilation. Pulmonary hypertension and right heart failure eventually develop.

Typical M-mode features of rheumatic mitral stenosis include thickening of the leaflets and decrease of the E–F slope. Two-dimensional imaging in the parasternal short-axis view provides "en face" visualization of the valve orifice (Figure 39.2). The

Table 39.4 World Heart Federation criteria for echocardiographic diagnosis of rheumatic heart disease

Echocardiographic criteria for RHD[a]

Definite RHD (either A, B, C or D):

- **A** Pathologic MR and at least 2 morphologic features of RHD of the mitral valve
- **B** MS mean gradient ≥4 mmHg
- **C** Pathologic AR and at least 2 morphologic features of RHD of the aortic valve
- **D** Borderline disease of both the aortic and mitral valves

Borderline RHD (either A, B or C):

- **A** At least 2 morphologic features of rheumatic mitral disease without pathologic MR or MS
- **B** Pathologic MR
- **C** Pathologic AR

Echocardiographic criteria for pathologic regurgitation

(all four Doppler criteria must be met)

Pathologic MR	*Pathologic AR*
1. Seen in 2 views	1. Seen in 2 views
2. In at least 1 view jet length 2 cm[b]	2. In at least 1 view jet length ≥1 cm[b]
3. Peak velocity ≥3 m/s	3. Peak velocity ≥3 m/s
4. Pan-systolic jet in at least 1 envelope	4. Pan-diastolic jet in at least 1 envelope

Morphologic features of RHD

Mitral valve	*Aortic valve*
1. AMVL thickening ≥3 mm[c]	1. Irregular or focal thickening
2. Chordal thickening	2. Coaptation defect
3. Restricted leaflet motion	3. Restricted leaflet motion
4. Excessive leaflet tip motion during systole	4. Prolapse

AMVL, anterior mitral valve leaflet; AR, aortic regurgitation; MR, mitral regurgitation; MS, mitral stenosis.
[a]Congenital anomalies must be excluded.
[b]A regurgitant jet length should be measured from the vena contracta to the last pixel of regurgitant color (blue or red) on nonmagnified (nonzoomed) images.
[c]AMVL thickness should be measured during diastole at full excursion. Measurement should be taken at the thickest portion of the leaflet and should be performed on a frame with maximal separation of chordae from the leaflet tissue.
Source: Reményi et al. 2012 [29]. Reproduced with permission of Nature Publishing Group.

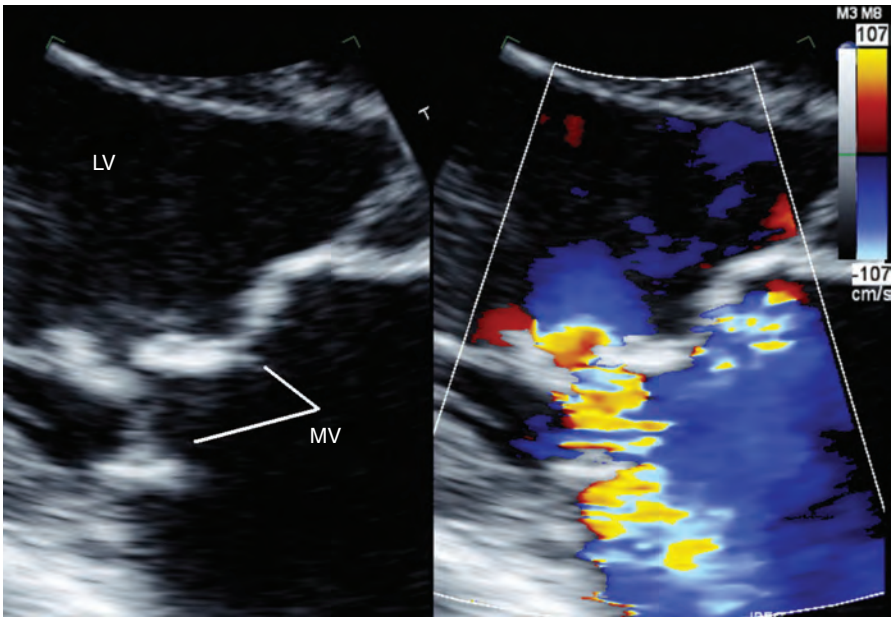


Figure 39.1 Parasternal long-axis view of mitral valve in zoomed color compare mode shows "hockey-stick" deformity of anterior leaflet. Color Doppler demonstrates the posteriorly directed jet of mitral regurgitation. LV, left ventricle; MV, mitral valve.

smallest orifice area during maximal diastolic leaflet separation may be traced by planimetry to estimate mitral valve area. The advantage of this method is that it is not significantly affected by heart rate or cardiac output. However, the technique is largely operator dependent.

The severity of mitral stenosis can be determined by noninvasive means using Doppler echocardiography. Several methods are used for quantification of mitral stenosis, including conversion of Doppler velocities to instantaneous and mean pressure gradients across the valve, calculation of mitral valve area by pressure half-time or flow convergence, the continuity equation, and PISA. Doppler flow patterns may vary according to severity of obstruction, presence of atrial fibrillation, and coexistence of mitral regurgitation. Over time, it is important to use the same method to determine severity of mitral stenosis for comparison purposes.

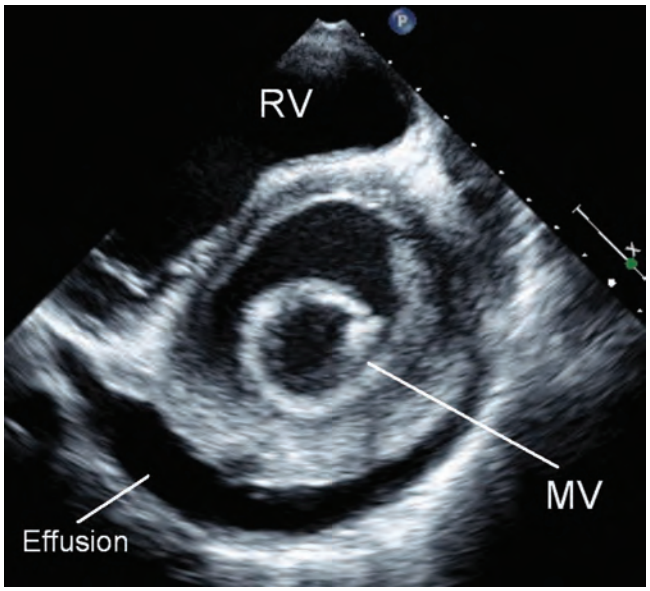
Chronic aortic valve disease manifests primarily as aortic regurgitation. Aortic disease most commonly coexists with mitral regurgitation, but in a small percentage of patients, aortic valve disease may be isolated [38]. The early disease process is characterized by leaflet prolapse, resulting in a loss of the height of the cusp and commissures [39]. With time, the leaflets thicken, retract, and the edges roll, giving rise to a central coaptation defect (Figure 39.3; Video 39.3). Leaflet thickening, commissural fusion, and later calcification all restrict the mobility of leaflets and may eventually lead to a mixed hemodynamic effect (stenosis and regurgitation). Over the course of decades, pure aortic stenosis may develop, although this is rare in children and adolescents. (Figure 39.4; Video 39.4).

The severity of aortic stenosis can be determined by noninvasive means using Doppler echocardiography. Several methods are used for quantification of aortic stenosis, including peak aortic flow velocity, mean pressure gradient, calculation of aortic valve area, and the LVOT/aortic valve time–velocity integral ratio. Measurement of LVOT velocity is typically performed from the apical 5-chamber view. When performing the examination, it is important to differentiate the aortic stenosis jet from other Doppler-associated findings, such as mitral regurgitation or sites of additional LVOT obstruction. Changes in left ventricular function and cardiac output may affect aortic peak velocity and mean aortic pressure gradient, such that the severity of aortic stenosis may be under- or overestimated.

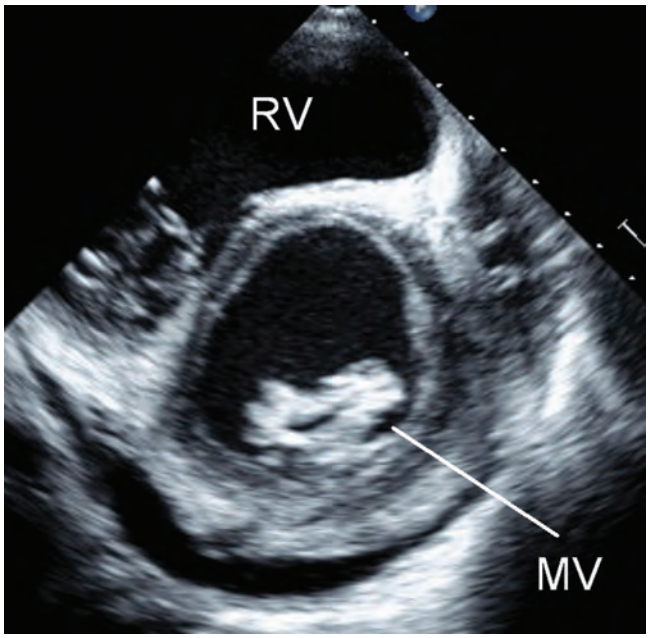
Tricuspid and pulmonary valve disease are less common in RHD. Significant tricuspid regurgitation is most often the result of advanced left-sided pathology and pulmonary hypertension. Organic tricuspid valve disease that results from direct rheumatic inflammation is less common, almost always coexists with mitral and/or aortic valve involvement, and is considered a marker of severity of RHD [40]. As with mitral regurgitation, tricuspid valve regurgitation may also progress to stenosis. Pulmonary valve involvement is extremely rare but has been reported in very severe cases of RHD [38]. As with tricuspid valve disease, it is likely to be functional rather than the result of direct rheumatic involvement.

Monitoring disease progression and resolution

Children and adolescents with mild to moderate RHD are generally asymptomatic. Even those with severe, compensated RHD frequently report no symptoms. As the disease progresses, reduced exercise tolerance, dyspnea, and congestive cardiac failure are likely to become apparent. Serial echocardiography permits monitoring for disease progression or resolution. In addition to assessing valve morphology and grading of the severity of the valve dysfunction, serial measurements of left atrial size and



(a)



(b)

Figure 39.2 **(a)** Parasternal short-axis view demonstrates thickened mitral valve (MV) leaflets with restricted motion, commissural fusion, and lack of coaptation. This image shows the maximal dimension of the MV in diastole. **(b)** Same image at end-systole shows thickened leaflets with a coaptation gap. Note the pericardial effusion in both images. RV, right ventricle.

left ventricular size and volume are recommended (Figure 39.5; Video 39.5). These measures can be graphed over time to assess for significant changes. It is important to note that in the setting of significant mitral and/or aortic regurgitation, dimension-based ejection phase indices such as fractional shortening or ejection fraction are poor surrogates for cardiac contractility due to altered loading conditions. These measures will likely underestimate cardiac impairment.

Valvar intervention

Echocardiography is useful in (1) guiding the timing of surgery in acute and chronic RHD, (2) evaluating suitability for percutaneous intervention, and (3) providing imaging during surgical repair. It is well documented that even severe acute rheumatic valvulitis can improve with medical management [30]. In the absence of fulminant heart failure or a flail leaflet, a conservative approach with careful clinical and echocardiographic re-evaluation is recommended.

In the setting of severe chronic *mitral valve regurgitation*, there are no clear guidelines to determine the timing of surgery in the pediatric population. However, symptoms of heart failure and/or impaired systolic left ventricular function are unequivocal indications for surgery in children and adults [41]. In well-compensated disease, ejection fraction or fractional shortening should be increased with hyperdynamic function. The altered loading conditions mask impaired cardiac contractility; a reduced or normal fractional shortening/ejection fraction suggests underlying dysfunction and carries a potentially poor prognosis. In the adult population, an LV end-systolic diameter (LVESD) of >50 mm has been associated with poor postoperative outcomes in the setting of severe mitral valve regurgitation. Thus, the American College of Cardiology/American Heart Association guidelines recommend surgery when the LVESD has reached 40 mm or LV ejection fraction <60%, even in asymptomatic patients (class 1 indication) [41]. New onset atrial fibrillation and pulmonary hypertension >50 mmHg are considered to be class IIa indications for valve surgery [41].

In the pediatric population, cut-off values based on LV size are not established; however, surgery should be considered when the left ventricular end-diastolic diameter *z*-score is >3 and if the LVESD *z*-score is increasing relative to the end-diastolic value. It is likely that over time, the indications for surgical intervention will change over time as expertise increases and risk of treatment decreases [42, 53]. One of the major determinants of surgery is its availability in different countries. Moreover, the level of compliance with antibiotic prophylaxis and/or anticoagulation are also important factors to consider.

Once intervention is required, the focus of echocardiography should be to determine the mechanism of valve dysfunction in order to guide valve intervention. Some valves, based on morphology and mechanism of dysfunction, will not be suitable for repair and will require replacement. Surgical options may also depend upon local expertise and resources. In the pediatric age group, valve repair remains the treatment of choice when factors such as ongoing somatic growth and the need for anticoagulation are considered.

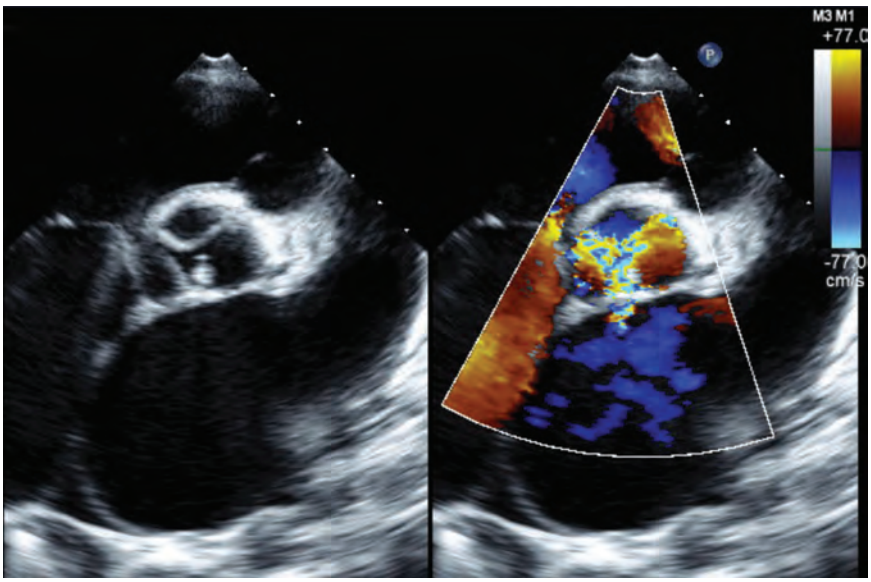


Figure 39.3 Parasternal short-axis view in color compare mode demonstrates thickened and retracted aortic valve leaflets. With color Doppler, regurgitation is seen at all commissures. Note the dilated left atrium and left atrial appendage.

For the mitral valve, true prolapse of the valve leaflet tips past the annulus or hinge points of the valve typically involves the anterior leaflet, resulting in a posteriorly directed jet of regurgitation. Prolapse of the posterior mitral valve leaflet is rare. The distance of leaflet tip excursion from the site of valve coaptation should be measured to guide surgical correction, which can be achieved using a number of different techniques that alter chordae and papillary muscle mobility [44].

Severe mitral stenosis is relatively uncommon in young children; however, it becomes more prevalent in late adolescence.

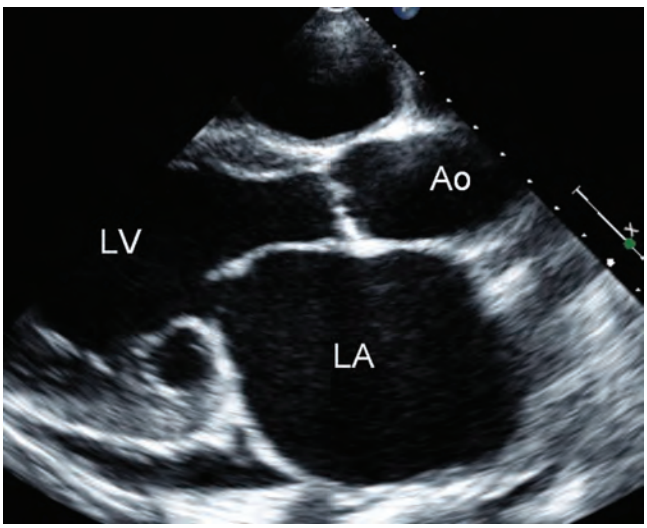


Figure 39.4 Parasternal long-axis view demonstrates predominant mitral and aortic valve stenosis in chronic rheumatic heart disease. Note the restricted opening of mitral valve and thickened aortic valve leaflets. The left atrium is markedly dilated. Ao, aorta; LA, left atrium; LV, left ventricle.

In those patients with primarily mitral stenosis and minimal regurgitation, guidelines to assist in the timing of interventions are extrapolated from adult data. Echocardiographic evidence of pulmonary hypertension >50 mmHg or a mitral valve area (MVA) of <1.5 cm^2 are considered to be indications for percutaneous balloon mitral valvotomy even in asymptomatic individuals, provided that anatomy on echocardiography appears favorable [41]. The echocardiographic Wilkins score [45] provides guidance regarding the suitability of the mitral valve morphology for percutaneous balloon mitral valvotomy (Table 39.5). It considers the degree of (1) valve calcification, (2) leaflet mobility, (3) leaflet thickening, and (4) disease of the subvalvar apparatus. Each item is graded on increasing severity from 0 to 4, with 0 being normal and 4 being the most abnormal. A score of 8 or less predicts a good result from mitral balloon valvotomy. In the pediatric population, indications are less clear-cut. Most children with mitral stenosis are asymptomatic even with moderate inflow gradients, Therefore, it is useful to ask about exercise limitation or to remeasure the mitral valve inflow gradient after a short burst of exercise.

Indications for surgery in adults with *severe aortic regurgitation* are symptomatic status, impaired ejection fraction (<50%), enlarged LVESD >55 mm and/or end-diastolic dimension >75 mm (class I indications) [41]. In young children, evidence of left ventricular dilation should be based on *z*-scores; however, cut-off values to help guide the timing of cardiac surgery have not been clearly defined. A retrospective study of patients undergoing the Ross procedure for nonrheumatic aortic valve disease determined that the recovery of LV function was less likely when the LVEDD had exceeded a *z*-score of +4 and that surgery should be considered when the *z*-score approaches or exceeds +3 [46]. Timing of aortic valve surgery in children is

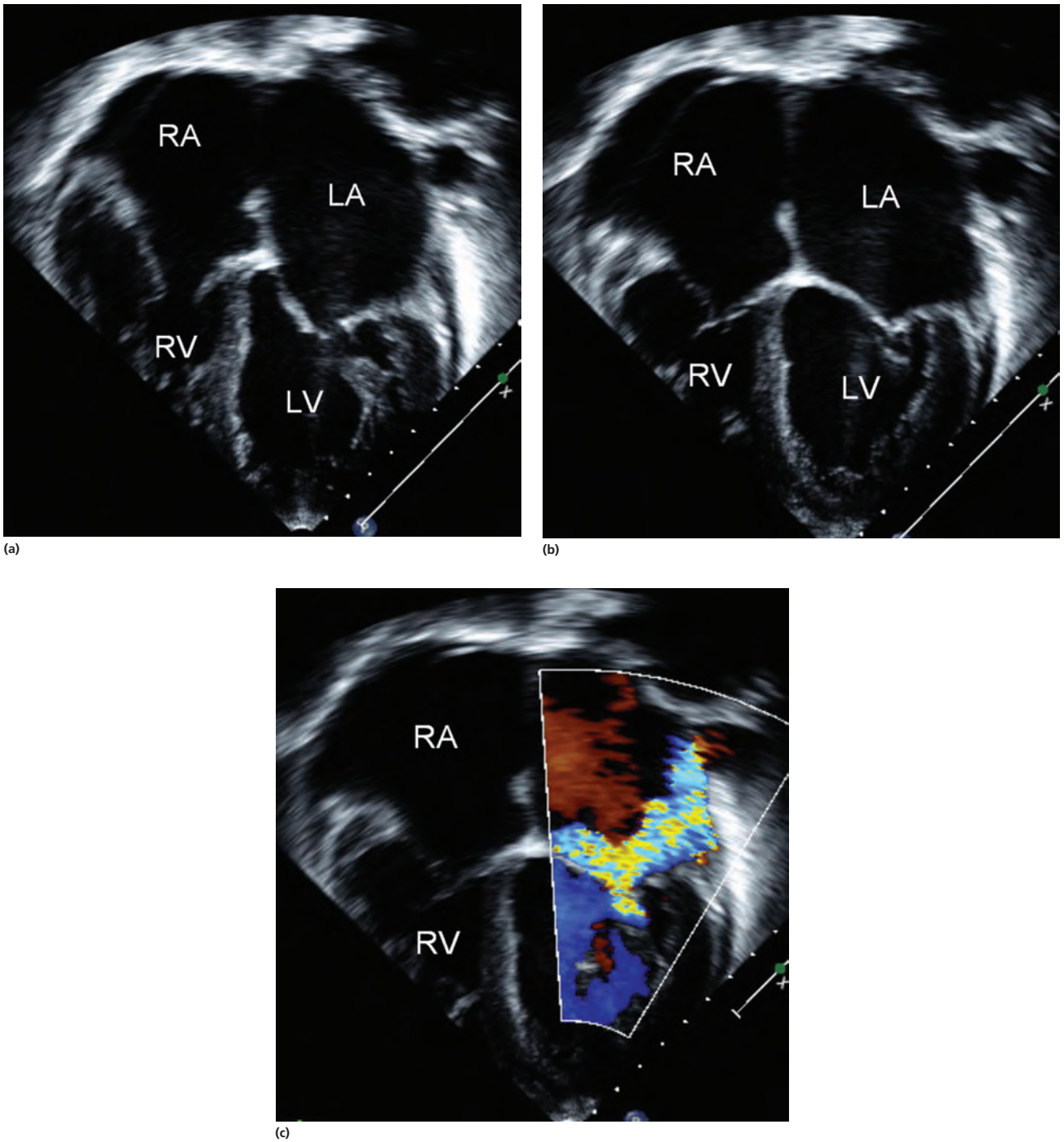


Figure 39.5 (a) Apical 4-chamber view at end-diastole demonstrates severely dilated left atrium and left ventricle with thickened mitral valve leaflets. (b) Same image in end-systole shows the immobile and retracted posterior leaflet. (c) Color Doppler of the same image demonstrates a jet of significant mitral regurgitation. LA, left atrium; LV, left ventricle; RA, right atrium; RV, right ventricle.

also impacted by whether the valve can be repaired or requires replacement. Rheumatic aortic valve disease typically results in leaflet retraction with loss of leaflet height. This loss of leaflet height draws the free edges of the leaflet away from the opposing leaflets, leading to aortic regurgitation. This abnormality may sometimes be corrected by patch augmentation of the leaflets [39,47].

RHD commonly manifests as *multi-valve disease*. A proximal valve lesion may modify the hemodynamic effects of the distal lesion by altering loading conditions. For example, severe

Table 39.5 Grading of mitral valve characteristics from the echocardiographic examination in adults

Grade	Mobility	Subvalvar thickening	Leaflet thickening	Calcification
1	Highly mobile valve with only leaflet tips restricted	Minimal thickening just below the mitral valve leaflets	Leaflets near normal in thickness (4–5 mm)	A single area of increased echo brightness
2	Mid and base portions of leaflet have normal mobility	Thickening of chordal structures extending up to one-third of the chordal length	Mid-leaflets normal, considerable thickening of margins (5–8 mm)	Scattered areas of brightness confined to the leaflet margins
3	Valve continues to move forward in diastole, mainly from the base	Thickening extending to the distal third of the chords	Thickening extending through the entire leaflet (5–8 mm)	Brightness extending into the mid-portion of the leaflets
4	No or minimal forward movement of the leaflets in diastole	Extensive thickening and shortening of all chordal structures extending down to the papillary muscles	Considerable thickening of all leaflet tissue (>8–10 mm)	Extensive brightness throughout much of the leaflet tissue

Source: Wilkins et al. 1988 [45]. Reproduced with permission of BMJ Publishing Group Ltd.

mitral stenosis may lead to underestimation of the significance of aortic valve stenosis. Conversely, significant mitral regurgitation may lead to overestimation of the severity of mitral stenosis. Currently, there are insufficient data available to make any specific recommendations in mixed-valve and multi-valve lesions. Generally, clinical symptoms and the nature of the predominant lesion should dictate the timing of cardiac intervention.

3D echocardiography

In addition to standard 2D imaging, 3D echocardiography may provide additional useful information to guide surgical repair. 3D datasets allow for better appreciation of some valve problems, such as extent and region of prolapse. It further permits the display of information to surgical colleagues in a more familiar format. Moreover, 3D allows the visualization of this information in the beating heart demonstrating the dynamic nature of such changes in vivo. (Figure 39.6; Video 39.6).

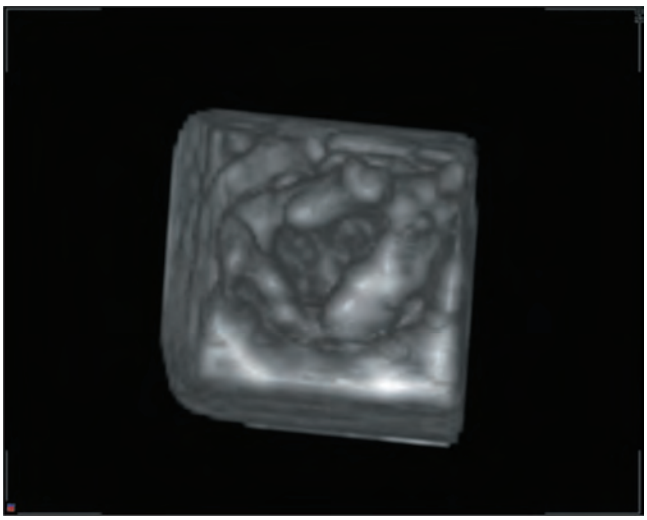


Figure 39.6 3D image en face view from the right ventricular side of the tricuspid valve in a patient with rheumatic tricuspid valve stenosis. Note the thickened leaflets with the "rolled" edges.

Secondary prophylaxis

Whenever possible, the duration of secondary antibiotic prophylaxis for the prevention of RF recurrences should be based on echocardiographic findings using local or regional guidelines. In general, prophylaxis is recommended until age 21 years in pediatric patients. Extension of prophylaxis is then based on severity of underlying residual disease. The Australian Guidelines are shown in Table 39.6.

Screening

In populations with a high burden of RF/RHD, echocardiographic screening may identify individuals during the subclinical phase of RHD, with the aim of initiating secondary prophylaxis. The 2012 World Health Federation echocardiographic guidelines were developed to facilitate this approach to RHD control by trying to differentiate the upper range of normal findings from mild RHD in children [29]. Prior to recommending population-based screening for RHD on the global stage, a number of issues must be addressed. These include, but are not limited to, achieving a better understanding of the natural history of subclinical disease, consideration of the cost-effectiveness of such programs, and overcoming the worldwide shortage of individuals who can perform echocardiograms. Perhaps most importantly, existing evidence-based practices that are known to improve outcome, such as register-based control programs and effective delivery of secondary prophylaxis, must be strengthened before routine RHD screening can be considered [48].

Table 39.6 Duration of secondary prophylaxis for patients with RHD

Category	Definition of category	Duration
All persons with RF or RHD[a]		Minimum 10 years after most recent episode of RF or until 21 years (whichever is longer)
Status after initial time period elapsed:		
No RHD	No pathologic mitral or aortic regurgitation, but may have minor morphologic changes to mitral or aortic valves on echocardiography	Discontinue at that time[b]
Mild RHD	Mild mitral or aortic regurgitation clinically and on echocardiography, with no clinical evidence of heart failure, and no evidence of cardiac chamber enlargement on echocardiography	Discontinue at that time
Moderate RHD	• Any valve lesion of moderate severity clinically (e.g., mild–moderate cardiomegaly and/or mild–moderate heart failure) or on echocardiography • Mild mitral regurgitation, together with mild aortic regurgitation clinically or on echocardiography • Mild or moderate mitral or aortic stenosis • Any pulmonary or tricuspid valve lesion coexisting with a left-sided valve lesion	Continue until 35 years of age
Severe RHD	• Any severe valve lesion clinically (e.g., moderate to severe cardiomegaly or heart failure) or on echocardiography • Any impending or previous cardiac valve surgery for RHD	Continue until 40 years of age, or longer[c]

[a]Patients >25 years of age who are diagnosed with RHD, without any documented history of prior RF, should receive prophylaxis until the age of 35 years. At this time they should be reassessed to determine whether prophylaxis should be continued.
[b]Decisions to cease secondary prophylaxis should be based on clinical and echocardiographic assessment.
[c]Risk of recurrence is extremely low in people aged >40 years. In some cases, for example, when the patient decides that they want to reduce even a minimal risk of recurrence, prophylaxis may be continued beyond the age of 40 years, or even for life.
Source: Adapted from RHD Australia (RF/RHD Writing Group), National Heart Foundation of Australia, and the Cardiac Society of Australia and New Zealand 2012 [18]; http://www.rhdaustralia.org.au/resources/arf-rhd-guideline.

Videos

To access the videos for this chapter, please go to www.lai-echo.com.

Video 39.1 Parasternal long-axis view in zoomed color compare mode shows "hockey-stick" deformity of anterior leaflet of the mitral valve, with immobile posterior leaflet, lack of leaflet coaptation and a dilated left atrium. Color Doppler demonstrates the posteriorly directed jet of mitral regurgitation.

Video 39.2 Parasternal short-axis view demonstrates mixed mitral valve disease. Note the thickened leaflets with restricted motion particularly of the posterior leaflet, and commissural fusion anteriorly. There is lack of coaptation with mitral regurgitation occurs along the entire length of the anterior/posterior leaflet commissure. Note also the small pericardial effusion.

Video 39.3 Parasternal short-axis view in color compare mode demonstrates thickened and retracted aortic valve leaflets especially affecting the noncoronary cusp. With color Doppler, regurgitation is seen at all commissures. Note the dilated left atrium and left atrial appendage.

Video 39.4 Parasternal long-axis view demonstrates predominant mitral and aortic valve stenosis in chronic rheumatic heart disease. Note the restricted opening of mitral and aortic valves. There is also a significant coaptation gap of the aortic valve. The left atrium is markedly dilated.

Video 39.5 Apical 4-chamber view shows a markedly dilated left atrium. Both leaflets of the mitral valve are thickened with an immobile and retracted posterior leaflet but greater excursion of anterior leaflet.

Video 39.6 3D image in the left atrial view of a rheumatic mitral valve demonstrating prolapse of A1–3 cusps with "rolled" edges.

References

1 Gordis L. The virtual disappearance of rheumatic fever in the United States: lessons in the rise and fall of disease. T. Duckett Jones memorial lecture. *Circulation* 1985;**72**:1155–1162.
2 Carapetis JR, Hardy M, Fakakovikaetau T, et al. Evaluation of a screening protocol using auscultation and portable echocardiography to detect asymptomatic rheumatic heart disease in Tongan schoolchildren. *Nat Clin Pract Cardiovasc Med* 2008;**5**:411–417.
3 Marijon E, Celermajer DS, Tafflet M, et al. Rheumatic heart disease screening by echocardiography: the inadequacy of World Health Organization criteria for optimizing the diagnosis of subclinical disease. *Circulation* 2009;**120**:663–668.
4 Paar JA, Berrios NM, Rose JD, et al. Prevalence of rheumatic heart disease in children and young adults in Nicaragua. *Am J Cardiol* 2010;**105**:1809–1814.
5 Parnaby MG, Carapetis JR. Rheumatic fever in indigenous Australian children. *J Paediatr Child Health* 2010;**46**:527–533.

6 Engel ME, Stander R, Vogel J, et al. Genetic susceptibility to acute rheumatic fever: a systematic review and meta-analysis of twin studies. *PLoS One* 2011;**6**:e25326.

7 Carapetis JR, Currie BJ, Mathews JD. Cumulative incidence of rheumatic fever in an endemic region: a guide to the susceptibility of the population? *Epidemiol Infect* 2000;**124**:239–244.

8 Rammelkamp CH, Wannamaker LW, Denny FW. The epidemiology and prevention of rheumatic fever. *Bull N Y Acad Med* 1952;**28**:321–334.

9 Guedez Y, Kotby A, El-Demellawy M, et al. HLA class II associations with rheumatic heart disease are more evident and consistent among clinically homogeneous patients. *Circulation* 1999;**99**:2784–2790.

10 Guilherme L, Kalil J. Rheumatic fever and rheumatic heart disease: cellular mechanisms leading autoimmune reactivity and disease. *J Clin Immunol* 2010;**30**:17–23.

11 Khanna AK, Buskirk DR, Williams RC, Jr, et al. Presence of a non-HLA B cell antigen in rheumatic fever patients and their families as defined by a monoclonal antibody. *J Clin Invest* 1989;**83**:1710–1716.

12 Bryant PA, Robins-Browne R, Carapetis JR, Curtis N. Some of the people, some of the time: susceptibility to acute rheumatic fever. *Circulation* 2009;**119**:742–753.

13 Guilherme L, Kalil J, Cunningham M. Molecular mimicry in the autoimmune pathogenesis of rheumatic heart disease. *Autoimmunity* 2006;**39**:31–39.

14 Roberts S, Kosanke S, Terrence Dunn S, et al. Pathogenic mechanisms in rheumatic carditis: focus on valvular endothelium. *J Infect Dis* 2001;**183**:507–511.

15 Jones T. Diagnosis of rheumatic fever. *JAMA* 1944;**126**:481–484.

16 Special Writing Group of the Committee on Rheumatic Fever, Endocarditis, and Kawasaki Disease of the Council on Cardiovascular Disease in the Young of the American Heart Association. Guidelines for the diagnosis of rheumatic fever. Jones Criteria, 1992 update. *JAMA* 1992;**268**:2069–2073.

17 World Health Organization. *Rheumatic Fever and Rheumatic Heart Disease: Report of a WHO Expert Consultation, Geneva, 29 Ocober–1 November 2001*. Geneva: World Health Organization, 2004.

18 RHDAustralia (ARF/RHD Writing Group), National Heart Foundation of Australia, and the Cardiac Society of Australia and New Zealand. *The Australian Guideline for Prevention, Diagnosis and Management of Acute Rheumatic Fever and Rheumatic Heart Disease*, 2nd edn. Darwin: Rheumatic Heart Disease Australia, 2012.

19 Bland EF, Jones TD. The natural history of rheumatic fever: a 20 year perspective. *Ann Intern Med* 1952;**37**:1006–1026.

20 Majeed HA, Yousof AM, Khuffash FA, et al. The natural history of acute rheumatic fever in Kuwait: a prospective six year follow-up report. *J Chronic Dis* 1986;**39**:361–369.

21 Sanyal SK, Berry AM, Duggal S, et al. Sequelae of the initial attack of acute rheumatic fever in children from north India. A prospective 5-year follow-up study. *Circulation* 1982;**65**:375–379.

22 Tompkins DG, Boxerbaum B, Liebman J. Long-term prognosis of rheumatic fever patients receiving regular intramuscular benzathine penicillin. *Circulation* 1972;**45**:543–551.

23 Feinstein AR, Spagnuolo M, Wood HF, et al. Rheumatic fever in children and adolescents. A long-term epidemiologic study of subsequent prophylaxis, streptococcal infections, and clinical sequelae. VI. Clinical features of streptococcal infections and rheumatic recurrences. *Ann Intern Med* 1964;**60**:(Suppl 5):68–86.

24 Padmavati S, Sharma KB, Jayaram O. Epidemiology and prophylaxis of rheumatic fever in Delhi – a five year follow-up. *Singapore Med J* 1973;**14**:457–461.

25 Stollerman GH, Rusoff JH, Hirschfeld I. Prophylaxis against group A streptococci in rheumatic fever; the use of single monthly injections of benzathine penicillin G. *N Engl J Med* 1955;**252**:787–792.

26 Wood HF, Simpson R, Feinstein AR, et al. Rheumatic fever in children and adolescents. A long-term epidemiologic study of subsequent prophylaxis, streptococcal infections, and clinical sequelae. I. Description of the investigative techniques and of the population studied. *Ann Intern Med* 1964;**60**(Suppl 5):6–17.

27 Veasy LG, Tani LY. A new look at acute rheumatic mitral regurgitation. *Cardiol Young* 2005;**15**:568–577.

28 Voss LM, Wilson NJ, Neutze JM, et al. Intravenous immunoglobulin in acute rheumatic fever: a randomized controlled trial. *Circulation* 2001;**103**:401–406.

29 Reményi B, Wilson N, Steer A, et al. World Heart Federation criteria for echocardiographic diagnosis of rheumatic heart disease – an evidence-based guideline. *Nat Rev Cardiol* 2012;**9**:297–309.

30 Kamblock J, N'Guyen L, Pagis B, et al. Acute severe mitral regurgitation during first attacks of rheumatic fever: clinical spectrum, mechanisms and prognostic factors. *J Heart Valve Dis* 2005;**14**:440–446.

31 Lewis BS, Geft IL, Milo S, Gotsman MS. Echocardiography and valve replacement in the critically ill patient with acute rheumatic carditis. *Ann Thorac Surg* 1979;**27**:529–535.

32 Strauss AW, Goldring D, Kissane J, et al. Valve replacement in acute rheumatic heart disease. *J Thorac Cardiovasc Surg* 1974;**67**:659–670.

33 Essop MR, Wisenbaugh T, Sareli P. Evidence against a myocardial factor as the cause of left ventricular dilation in active rheumatic carditis. *J Am Coll Cardiol* 1993;**22**:826–829.

34 Sliwa K, Carrington M, Mayosi BM, et al. Incidence and characteristics of newly diagnosed rheumatic heart disease in urban African adults: insights from the Heart of Soweto Study. *Eur Heart J* 2010;**31**:719–727.

35 Walsh B, Bland E, Jones T. Pure mitral stenosis in young persons. *Arch Int Med* 1940;**65**:321–327.

36 Iung B, Baron G, Tornos P, et al. Valvular heart disease in the community: a European experience. *Curr Probl Cardiol* 2007;**32**:609–661.

37 Roy SB, Bhatia ML, Lazaro EJ, Ramalingaswami V. Juvenile mitral stenosis in India. *Lancet* 1963;**ii**:1193–1195.

38 Chockalingam A, Gnanavelu G, Elangovan S, Chockalingam V. Clinical spectrum of chronic rheumatic heart disease in India. *J Heart Valve Dis* 2003;**12**:577–581.

39 Myers PO, Tissot C, Christenson JT, et al. Aortic valve repair by cusp extension for rheumatic aortic insufficiency in children: long-term results and impact of extension material. *J Thorac Cardiovasc Surg* 2010;**140**:836–844.

40 Sultan FA, Moustafa SE, Tajik J, et al. Rheumatic tricuspid valve disease: an evidence-based systematic overview. *J Heart Valve Dis* 2010;**19**:374–382.

41 Bonow RO, Carabello BA, Chatterjee K, et al. ACC/AHA 2006 guidelines for the management of patients with valvular heart disease: a report of the American College of Cardiology/American Heart Association Task Force on Practice Guidelines (Writing Committee to revise the 1998 guidelines for the management of patients

with valvular heart disease) developed in collaboration with the Society of Cardiovascular Anesthesiologists endorsed by the Society for Cardiovascular Angiography and Interventions and the Society of Thoracic Surgeons. *J Am Coll Cardiol* 2006;**48**:e1–e148.

42 Suri RM, Aviernos JF, Dearani JA, et al. Management of less-than-severe mitral regurgitation: should guidelines recommend earlier surgical intervention? *Eur J Cardiothorac Surg* 2011;**40**:496–502.

43 Bonow RO. Chronic mitral regurgitation and aortic regurgitation: have indications for surgery changed? *J Am Coll Cardiol* 2013;**61**:693–701.

44 Kalangos A. The rheumatic mitral valve and repair techniques in children. *Semin Thorac Cardiovasc Surg Pediatr Card Surg Annu* 2012;**15**:80–87.

45 Wilkins GT, Weyman AE, Abascal VM, et al. Percutaneous balloon dilatation of the mitral valve: an analysis of echocardiographic variables related to outcome and the mechanism of dilatation. *Br Heart J* 1988;**60**:299–308.

46 Cheung MM, Sullivan ID, de Leval MR, et al. Optimal timing of the Ross procedure in the management of chronic aortic incompetence in the young. *Cardiol Young* 2003;**13**:253–257.

47 Grinda JM, Latremouille C, Berrebi AJ, et al. Aortic cusp extension valvuloplasty for rheumatic aortic valve disease: midterm results. *Ann Thorac Surg* 2002;**74**:438–443.

48 Roberts K, Colquhoun S, Steer A, et al. Screening for rheumatic heart disease: current approaches and controversies. *Nat Rev Cardiol* 2013;**10**:49–58.

CHAPTER 40

Infective Endocarditis

Manfred Otto Vogt and Andreas Kühn
Department of Pediatric Cardiology and Congenital Heart Disease, Deutsches Herzzentrum München, Technische Universität München, Munich, Germany

Definition

Infective endocarditis (IE) is a subacute infectious disease of the heart and its surrounding vessels that carries a very high risk of morbidity and mortality. Unfortunately, a clear-cut diagnosis of IE is rare in patients with congenital heart disease (CHD) and is reserved for those who fulfill the classic Oslerian manifestations: bacteremia or fungemia, evidence of active vasculitis, and/or peripheral emboli (Figure 40.1) and immunologic vascular phenomena. In most cases the clinical presentation is quite variable and therefore the diagnosis is related to an evidence-based scoring system that includes clinical, microbiological and echocardiographic findings (Tables 40.1 and 40.2). The Duke criteria [1] and their modification in 2000 [2] have been validated not only in adults but also in children [3,4]. It should be kept in mind that the Duke criteria were developed primarily to facilitate epidemiologic and clinical research efforts so that data could be compared between different centers and countries. In present clinical practice these criteria serve as a guide for diagnosing IE but can never replace final clinical judgment.

Incidence

The incidence of IE in infancy and childhood is unknown as no data exist from a population-based cohort. Overall, the incidence of IE appears to be increasing but in absolute terms it is relatively rare in children. CHD now constitutes the predominant underlying condition for IE in children over the age of 2 years in developed countries [5]. Some of the cases in this age group are due to the complexity of neonatal and pediatric intensive care and may be related to indwelling catheters and instrumentation in this population (Video 40.1).

In pediatric hospitals, IE accounts for about 1 in 1280 pediatric admissions per year [6]. In patients with CHD, ventricular septal defect, patent ductus arteriosus, aortic valve abnormalities (e.g., bicuspid aortic valve), and tetralogy of Fallot are the most common underlying conditions in which IE occurs. IE may afflict such patients before surgical intervention, but an increasing proportion of patients have had previous corrective or palliative surgery [7–10].

Corrective surgery without residual defects essentially eliminates the increased risk of IE within 6 months of surgery for ventricular and atrial septal defects and/or patent ductus arteriosus. The highest annual risk for IE has been found in children with repaired or palliated cyanotic CHD [10]. Palliative shunt procedures (Video 40.2) or complex intracardiac repairs increase the risk for postoperative IE [8]. The risk is highest amongst patients who have had prosthetic aortic valve replacement (Figure 40.2; Video 40.3) or operations performed because of reduced pulmonary blood flow. In those patients with prosthetic valves or conduits, the risk for IE is high even in the immediate postoperative period (first 2 weeks after surgery) whereas for all other patients with residual defects the risk increases with time after surgery [11].

Children with congenital or acquired immunodeficiencies but without identifiable risk factors for IE (such as central venous catheters) do not appear to be at increased risk for IE compared with the general population [5]. Intravenous (IV) drug use is infrequent in childhood but the incidence is rising in adolescence and adulthood. The incidence of IE in IV drug users is unknown [12] but 1.5 to 3.3 cases per 1000 person-years [13,14] is a conservative estimate. IE is more frequent in HIV-seropositive IV drug users than in HIV-seronegative patients [15]. It may be difficult to diagnose IE correctly in febrile IV drug users because 35% do not present with a heart murmur on admission [16]. The predilective site of infection in this group is typically the tricuspid valve even in those with structurally normal hearts (Figure 40.3).

In the adult population, the incidence of IE is approximately 5 episodes/100,000 person-years if IV drug users are excluded [17]. Apart from pre-existing structural heart disease which accounts for three-quarters of all cases of IE, pacemaker and defibrillator implantations also account for a significant number of episodes of IE (Figure 40.4) [18]. In a recent large multicenter study of 2760 patients with proven IE, 6.4% (177) occurred in

Echocardiography in Pediatric and Congenital Heart Disease: From Fetus to Adult, Second Edition. Edited by Wyman W. Lai, Luc L. Mertens, Meryl S. Cohen and Tal Geva.
© 2016 John Wiley & Sons, Ltd. Published 2016 by John Wiley & Sons, Ltd.
Companion website: www.lai-echo.com



Figure 40.1 An Osler node of the first toe as a typical dermatologic sign of bacterial infective endocarditis.

patients with cardiac devices [19]. IE in patients who have septal defect occluder devices is rare but has been reported [20]. New interventional techniques such as percutaneous pulmonary valve implantation also denote risk of IE but long-term follow-up remains to be seen [21].

A particularly vulnerable group at risk for IE is the adult population with CHD. IE accounts for 4% of hospital admissions of adults with CHD in specialized centers [22]. In unoperated or palliated CHD, the most common sites of IE are ventricular septal defect, left ventricular outflow tract and mitral valve. In those with repaired CHD, IE is most commonly seen in those with repaired tetralogy of Fallot and atrioventricular canal defects (Figure 40.5; Video 40.4) [23]. An isolated atrial septal defect (unrepaired or later than 6 months after operation/catheter intervention) has not been associated with an increased risk for IE in any age group.

Etiology and pathogenesis

The pathogenesis of IE is characterized by the triad of endothelial damage, platelet adhesion and microbial adherence to the vegetation or intact valvar tissue [24]. An intact endothelium within the heart is generally a poor stimulator of blood coagulation and therefore not predestined for bacterial attachment [5]. However, in children with CHD, abnormal high-velocity jet streams of blood (as seen in such lesions as ventricular septal defect, patent ductus arteriosus, aortic or pulmonary valve stenosis, or regurgitant atrioventricular valves) lead to damage of the endothelium due to shear stress forces and activation of the prothrombotic cascade in the circulating blood. Subsequently, a sterile platelet–fibrin deposition on the endothelial lesion provides a milieu for bacterial colonization. In addition to CHD, the administration of indwelling intravenous catheters into the right side of a structurally normal heart may traumatize the endocardium or valvar endothelium by exposing the subendothelial collagen [25]. This is one of the major mechanisms resulting in IE of the newborn.

Once the inciting lesion has been formed, bacteremia must be present to colonize the vegetation. Even in the presence of an endothelial lesion and a sterile thrombus formation, not every bacteremia event leads to IE. Bacteria must be able to survive in the bloodstream in sufficient numbers and adhere to the platelet–fibrin–fibrinectin complex on the lesion. Organisms such as *Staphylococcus aureus*, *Streptococcus viridans*, *Streptococcus pneumoniae*, HACEK organisms and group A, C and

Table 40.1 Definition of terms used in the Duke criteria for the diagnosis of infective endocarditis (IE)*

Major criteria

1 Positive blood culture for IE
- Typical microorganism consistent with IE from two separate blood cultures: viridans streptococci, *Streptococcus bovis*, HACEK group, *Staphylococcus aureus*, or community-acquired enterococci in the absence of a primary focus† *OR*
- Microorganisms consistent with IE from persistently positive blood cultures defined as follows: at least two positive cultures of blood samples drawn >12 h apart, or all of three or a majority of four or more separate cultures of blood (with first and last samples drawn at least 1 h apart)
- **Single positive blood culture for *Coxiella burnetii* or anti-phase 1 IgG antibody titer >1:800**

2 Evidence of endocardial involvement
- Echocardiogram positive for IE defined as:
 [TEE is recommended for patients with: (i) prosthetic valves; (ii) at least "possible IE" by clinical criteria; or (iii) complicated IE (paravalvular abscess); TTE as first test in other patients]
 - Oscillating intracardiac mass on valve or supporting structures in the path of regurgitant jets, or on implanted material in the absence of an alternative anatomic explanation; *OR*
 - Presence of an abscess, *OR*
 - New partial dehiscence of prosthetic valve, *OR*
 - New valvar regurgitation (worsening or changing or pre-existing murmur not sufficient)

Minor criteria

1 Predisposition, predisposing heart condition, or intravenous drug use
2 Fever, temperature >38°C
3 Vascular phenomena including major arterial emboli, septic pulmonary infarcts, mycotic aneurysm, intracranial hemorrhage, conjunctival hemorrhages, and Janeway lesions
4 Immunologic phenomena: glomerulonephritis, Osler nodes, Roth spots, and rheumatoid factor
5 Microbiologic evidence: positive blood culture but does not meet a major criterion as noted above or serologic evidence of active infection with organism consistent with IE
6 **Echocardiographic minor criteria eliminated**

TEE, transesophageal echocardiography; TTE, transthoracic echocardiography.
*Modifications shown in bold typeface.
†Excludes single positive cultures for coagulase-negative staphylococci and organisms that do not cause endocarditis.
Source: Li JS, et al. 2000 [2]. Reproduced with permission of Oxford University Press.

Table 40.2 Definition of infective endocarditis (IE) according to modified Duke criteria*

Definitive IE

1 Pathological criteria
- Microorganisms demonstrated by culture or histologic examination of a vegetation, a vegetation that has embolized, or an intracardiac abscess specimen, *OR*
- Pathologic lesions: vegetation or intracardiac abscess present, confirmed by histology showing active endocarditis

2 Clinical criteria
- Two major criteria, or
- One major criterion and three minor criteria, or
- Five minor criteria

Possible IE

1 One major criterion and one minor criterion

2 Three minor criteria

Rejected

1 Firm alternative diagnosis explaining evidence of IE, *OR*

2 Resolution of IE syndrome with antibiotic therapy for <4 days, *OR*

3 No pathologic evidence of IE at surgery or autopsy, with antibiotic therapy for <4 days, *OR*

4 Does not meet criteria for possible IE as above

*Modifications shown in bold typeface.
Source: Li JS, et al. 2000 [2]. Reproduced with permission of Oxford University Press.

G streptococci as well as *Candida albicans* are known to have specific surface receptors for fibronectin that promote the adhesion of bacteria to the thrombus formation [26]. After adhesion, the microorganisms are trapped within the vegetation and thus protected from phagocytic cells and other host defense mechanisms [5]. Within the growing vegetation, proliferation is possible up to a maximum bacterial density of 10^7 to 10^{10} colony-forming units per gram of tissue [27,28].

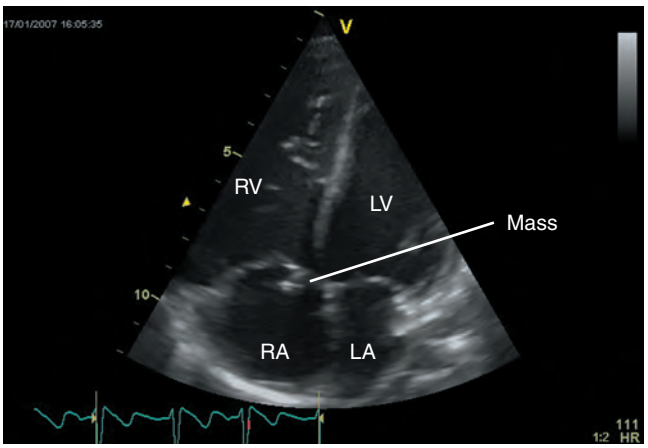


Figure 40.3 Transthoracic echocardiographic apical 4-chamber view showing a mass fixed to the atrial aspect of the septal leaflet of the tricuspid valve, as is typical in intravenous drug users. LA, left atrium; LV, left ventricle; RA, right atrium; RV, right ventricle.

Morphology and classification

The morphology of IE vegetations is dependent on the location of the endothelial lesion and typically follows the "pathologic" bloodstream. When IE occurs in association with a ventricular septal defect, the vegetation is typically visualized on the right ventricular aspect of the septum and/or on the site where the high-velocity jet strikes the right ventricular free wall (Figure 40.6). In the case of patent ductus arteriosus, the vegetation may float through the pulmonary opening of the ductus into the main pulmonary artery (Figure 40.7; Video 40.5). With regurgitant atrioventricular valves, the lesion is usually located on the atrial side (Figure 40.8; Video 40.6). Vegetations on valves may cause perforation (Figure 40.9; Video 40.7), or chordal

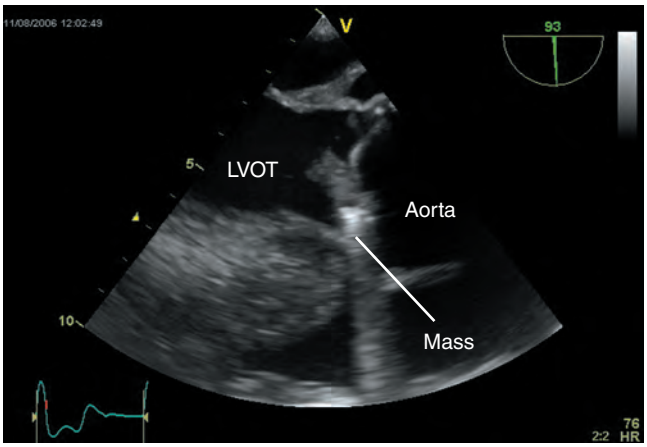


Figure 40.2 Transesophageal echocardiographic view of the left ventricular outflow tract (LVOT) after mechanical valve replacement, showing a subvalvular echogenic mass from the anterior portion of the valve ring indicating infective endocarditis.

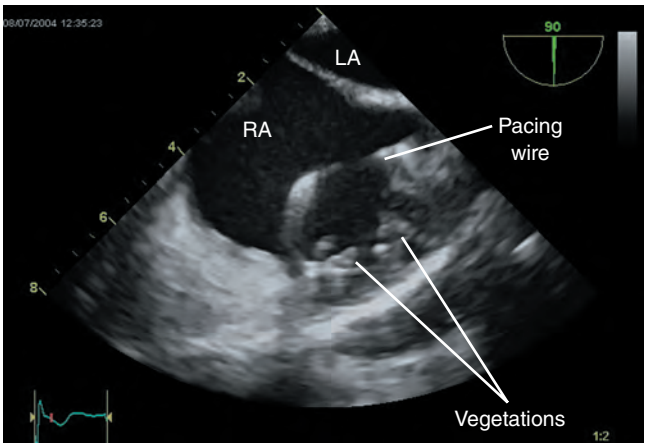


Figure 40.4 Transesophageal echocardiogram in the sagittal plane (90°) of an atrial pacemaker lead with fixation to the anterior wall of the right atrium. Multiple mobile vegetations can be seen adherent to the lead. LA, left atrium; RA, right atrium.

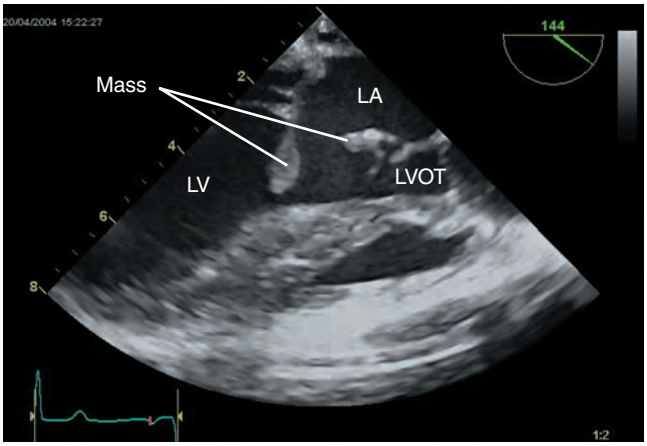


Figure 40.5 Transesophageal echocardiogram in the left ventricular outflow tract (LVOT) plane (120–140°) of a patient after repair of atrioventricular canal defect demonstrating a large echogenic mass adherent to the "posterior" leaflet of the left atrioventricular valve and another smaller mass fixed to the "anterior" leaflet. LA, left atrium; LV, left ventricle.

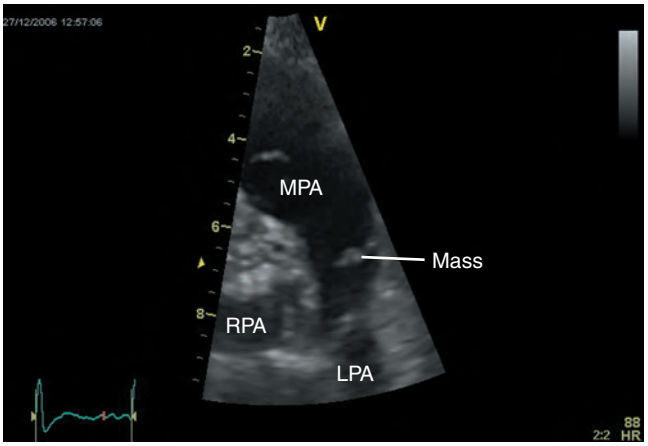


Figure 40.7 Transthoracic echocardiogram in the parasternal short-axis view demonstrates a thin vegetation originating from a small persistent ductus arteriosus. The mass is directed toward the main pulmonary artery (MPA) similar to the direction of blood flow. LPA, left pulmonary artery; RPA, right pulmonary artery.

rupture, but can also extend to the outside of the valve into surrounding structures (Figure 40.10). When semilunar valves are affected, the primary vegetation is typically on the ventricular surface of the valve (Figure 40.11) but may also extend more proximally through the valve into the supravalvar region in systole (Video 40.8). When the aortic valve is affected, perforation through the annulus into the myocardium or into either atria is possible. Newly acquired atrioventricular block (Figure 40.12) together with clinical suspicion of IE may be a strong indicator for the presence of para-aortic ring abscess (Figure 40.13) [29].

In a series of 153 patients [30], the major underlying cardiac lesion associated with IE in childhood was the unoperated ventricular septal defect (30%) (Figure 40.6) followed by mitral regurgitation (15%) (Figure 40.14) and bicuspid aortic valve (9%) (Figure 40.15; Video 40.9). In patients who undergo palliative surgery, infected aorto-pulmonary shunts (80%) predominate. In those who have corrective surgery, the most common sites for development of IE include right ventricle-to-pulmonary artery valved conduits (27%) (Figure 40.16; Video 40.10), prosthetic valves (22%) and ventricular septal defect patch (22%) (Table 40.3; Figure 40.17) [30,31]. Endocarditis on prosthetic valves usually initiates on the valvar cuff

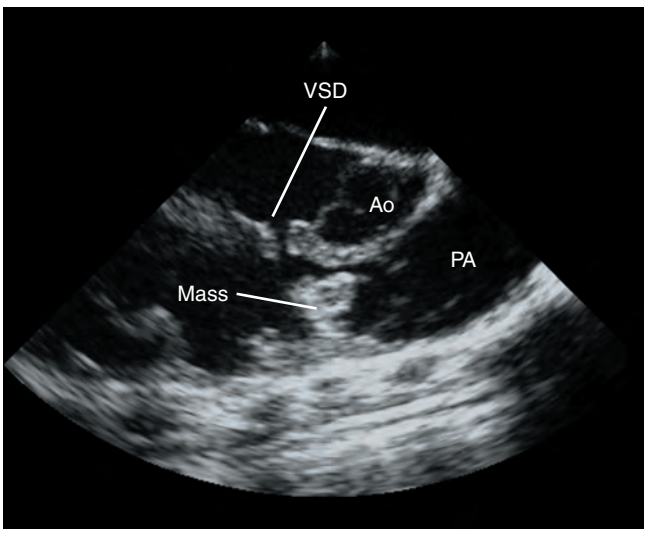


Figure 40.6 Transesophageal echocardiogram in the sagittal plane (90°) of a patient with a small restrictive ventricular septal defect (VSD) under the aortic valve. A large vegetation is seen at the site of the jet-lesion on the anterior right ventricular wall just below the pulmonary artery (PA). Ao, aorta.

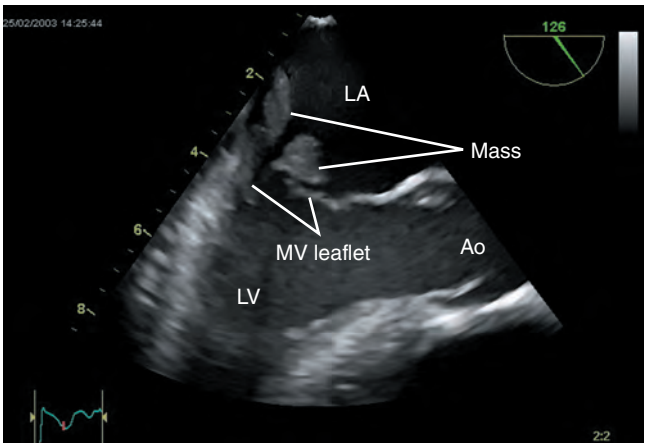


Figure 40.8 Transesophageal echocardiogram in the left ventricular outflow plane (120–140°) demonstrates multiple echogenic masses attached to the atrial side of the mitral valve leaflets. Ao, aorta; LA, left atrium; LV, left ventricle; MV, mitral valve.

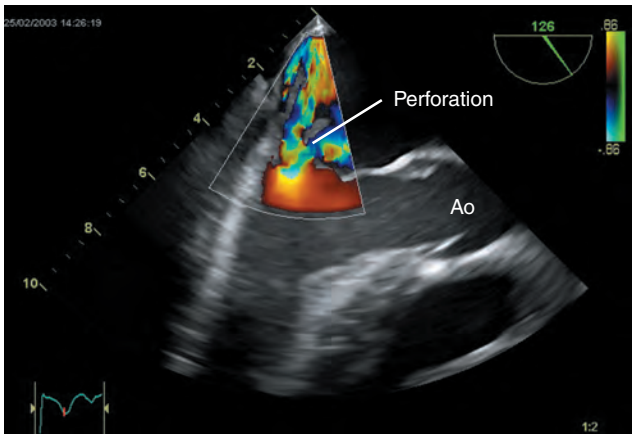


Figure 40.9 Transesophageal echocardiogram of the same patient as in Figure 40.8. Color Doppler shows newly acquired mitral regurgitation through a perforation in the posterior leaflet of the mitral valve. Ao, aorta.

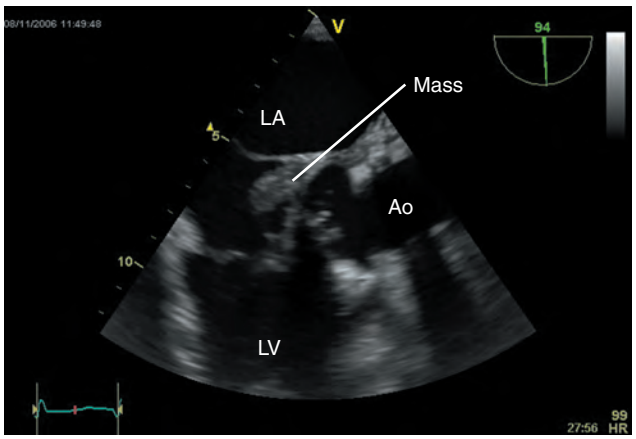


Figure 40.10 Transesophageal echocardiogram in the sagittal plane (90°) demonstrates an aortic ring abscess with perforation into the left atrium (LA). The underlying heart disease was a calcified stenotic aortic valve. Ao, aorta; LV, left ventricle.

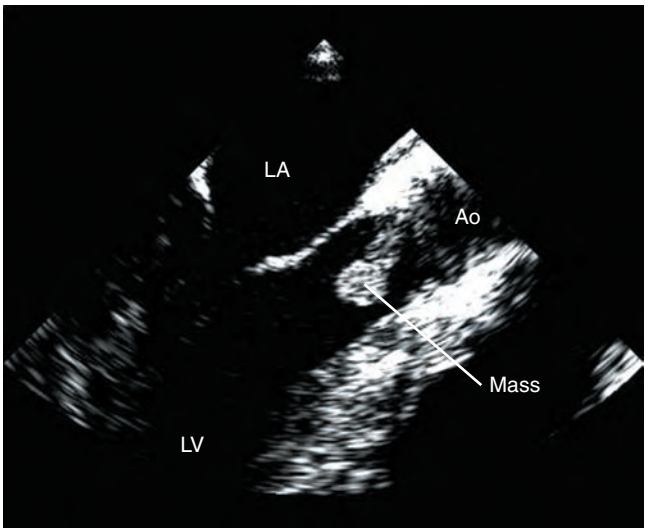


Figure 40.11 Transesophageal echocardiogram in the left ventricular outflow tract plane (120–140°) demonstrates native aortic valve endocarditis with a large globular vegetation on the ventricular side of the semilunar valve. Ao, aorta; LA, left atrium; LV, left ventricle.

(Figure 40.2; Video 40.3) and often extends outside the annulus, causing dehiscence (Figure 40.18; Video 40.11) and myocardial involvement [24]. Mechanical prosthetic valves appear to have higher risk for IE in the early period after surgery whereas the risk with bioprosthetic valves appears to be higher later on [32,33]. Implantable rings appear to have the lowest risk [34].

Pathophysiology

The pathophysiologic consequences of IE are primarily defined by the underlying CHD and the complications that arise from the insult, such as valvar obstruction, regurgitation and/or

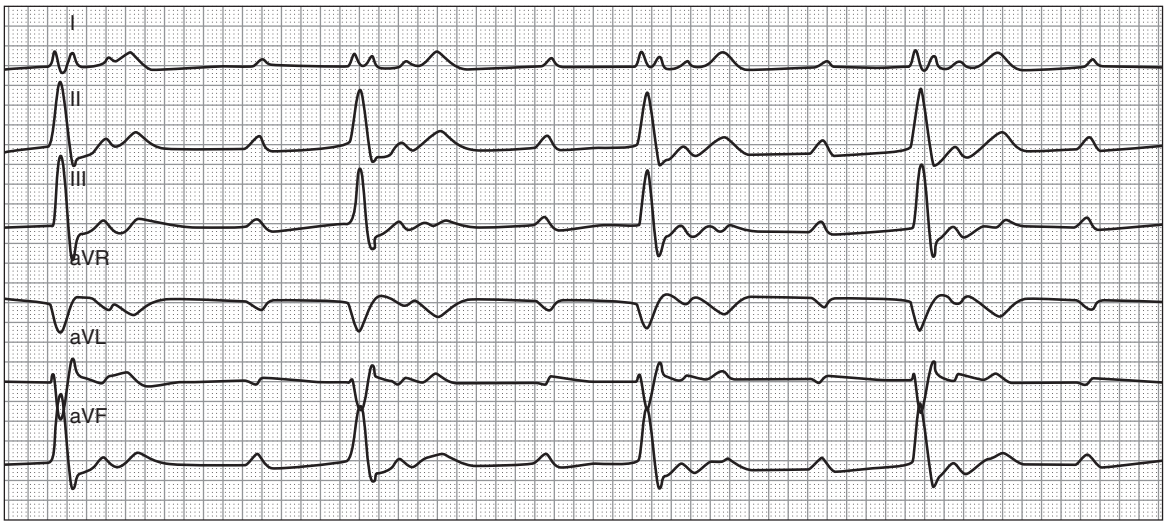


Figure 40.12 Electrocardiogram demonstrating newly acquired atrioventricular block in a patient with aortic valve replacement who developed a paravalvular abscess. A transesophageal echocardiogram of this patient is shown in Figure 40.13 and Video 40.14.

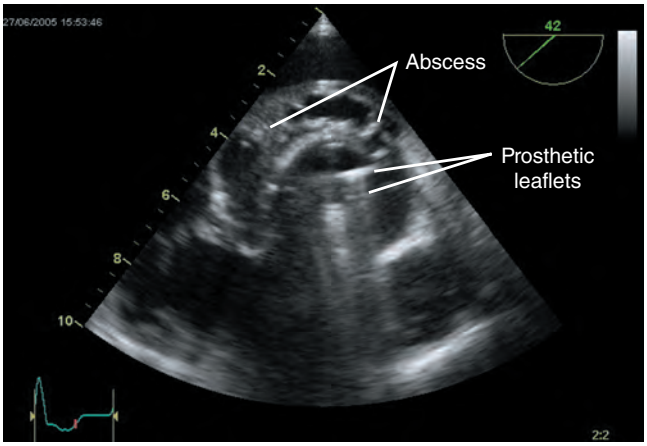


Figure 40.13 Transesophageal echocardiogram at 42° demonstrating a large paravalvular ring abscess years after aortic valve replacement with a mechanical St. Jude Medical valve.

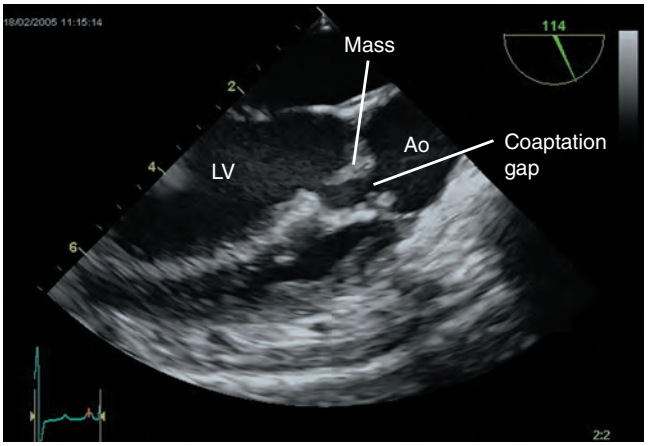


Figure 40.15 Transesophageal echocardiogram at 114° demonstrates a bicuspid aortic valve with a mobile vegetative mass on the posterior cusp and an immobile lesion on the anterior cusp such that the leaflets have a significant coaptation gap when closed. Ao, aorta; LV, left ventricle.

perforation, ventricular dysfunction, embolic phenomena and conduction disturbances. Age at presentation and location of IE (right-sided versus left-sided) also play a pivotal role. In newborns, symptoms are generally related to septicemia rather than cardiac failure [35,36]. In children with systemic–pulmonary artery shunts, increasing cyanosis may be the primary symptom together with pulmonary findings related to septic pulmonary embolization [37].

In adult patients with left-sided IE, congestive heart failure is one of the complications with greatest impact on prognosis [38–40]. Moderate to severe heart failure is identified as one of independent risk factors for 6-month mortality along with abnormal mental status, bacterial, etiology other than viridans streptococci and medical therapy without valve surgery [38]. The severity of symptoms is often not influenced by appropriate antibiotic therapy. Compensation of heart failure is dependent on the valve affected, with acute aortic regurgitation

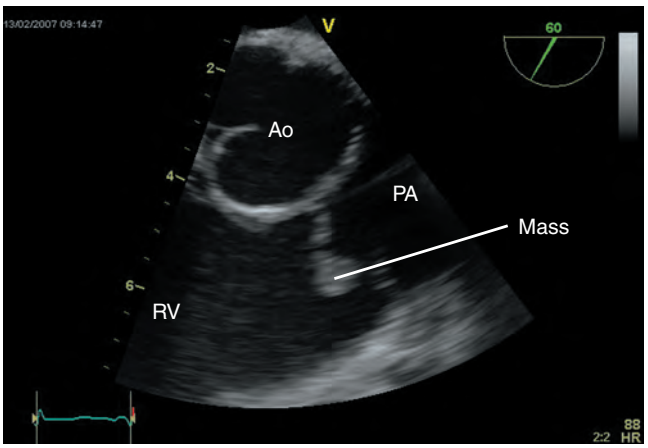


Figure 40.16 Transesophageal echocardiogram at 60° in a patient after the Ross operation with right ventricle (RV)-to-pulmonary artery (PA) conduit using a valved pulmonary homograft. There is a large vegetation attached to the homograft valve. Ao, aorta.

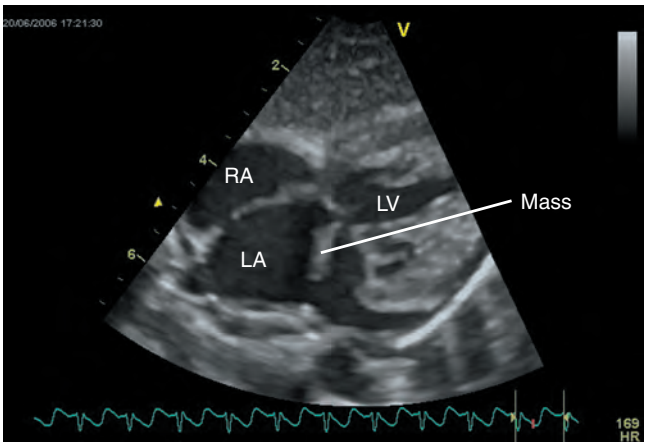


Figure 40.14 Transthoracic echocardiogram in the subcostal frontal view of a single mobile vegetation on the left atrial side of the anterior mitral leaflet. LA, left atrium; LV, left ventricle; RA, right atrium.

Table 40.3 Patients with congenital heart disease (CHD) at risk for infective endocarditis

Patients without surgery Ventricular septal defect, patent ductus arteriosus, atrioventricular canal defect, tetralogy of Fallot, mitral valve prolapse, bicuspid aortic valve, aortic valve stenosis, mitral valve regurgitation, pulmonary valve stenosis, complex CHD
Patients with previous palliation Aorto-pulmonary shunt, pulmonary banding, aortic/pulmonary conduit
Patients with corrective surgery – increasing risk with residual lesion Ventricular septal defect patch (simple and complex), tetralogy of Fallot repair, prosthetic valve implantation, atrioventricular canal repair, aortic/mitral valve surgery, coarctectomy, complex CHD, pacemaker implantation

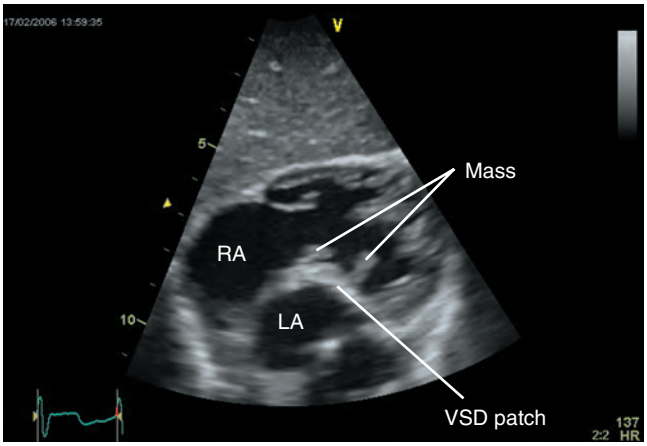


Figure 40.17 Transthoracic echocardiogram in a subcostal frontal view demonstrates a ventricular septal defect (VSD) that has been closed with a GORE-TEX patch. On the right ventricular surface, several finger-shaped vegetations can be seen. LA, left atrium; RA, right atrium.

being tolerated the least and acute tricuspid regurgitation being tolerated the best. Congestive heart failure will develop acutely when there is perforation of a native or bioprosthetic valve leaflet, acute valve dehiscence, rupture of an infected mitral chord, obstruction to outflow from a bulky vegetation, or sudden intracardiac shunt from a fistulous tract [12].

Imaging

Key elements

The objectives of echocardiographic examination in the setting of infective endocarditis can be summarized as follows:

- Identify masses/vegetation within the heart and/or its surrounding vessels.
- Determine the location, size, extent and number of IE lesions.
- Assess the severity of intracardiac damage as a result of the vegetation:
 - severity of valvar regurgitation;
 - perforation of valve leaflets;
 - development of paravalvular abscess or fistula formation;
 - for prosthetic valves, determine if dehiscence has occurred.
- Assess whether the vegetation is mobile or adherent.

Echocardiography is the gold standard of imaging in cases of suspected IE in any age group. However, echocardiography is not an appropriate screening test in the evaluation of patients with fever or a positive blood culture when IE is not suspected by any other clinical criteria. The classic echocardiographic findings defined as major criteria for IE in the Duke classification are vegetation, abscess, perivalvular involvement and new dehiscence of a prosthetic valve [12]. The vegetation as the hallmark lesion of IE typically presents as a high frequency oscillating mass attached to a valve, other endocardial structures or on implanted intracardiac material [2]. The motion of the vegetation during the heart cycle is typically independent to that of the structure to which it is attached. In some cases vegetations can also present as non-oscillating masses with atypical locations. From an imaging standpoint, abscesses present as thickened, nonhomogenous perivalvular areas with echodense or echolucent appearance [41]. Abscess formation may lead to other perivalvular complications such as perforation, pseudoaneurysm and fistula formation as well as conduction abnormalities. In pseudoaneurysms, color Doppler demonstrates blood flow between the cardiovascular lumen and a perivalvular cavity whereas fistulae are characterized by communications between two neighboring heart cavities through a perforation [41]. In prosthetic valves with dihiscence, echocardiography identifies paravalvular regurgitation with or without rocking motion of the prosthesis.

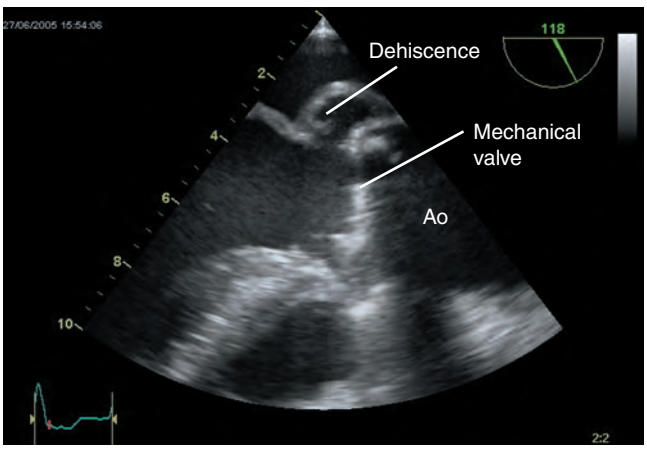


Figure 40.18 Transesophageal echocardiogram in the LVOT plane just prior to surgery for infective endocarditis of a mechanical valve prosthesis with aortic ring abscess and incomplete dissection of the valve. Intraoperatively, the valve was noted to be held in place by only two stitches. Ao, aorta.

Transthoracic versus transesophageal imaging

The first-line diagnostic tool should be a transthoracic echocardiogram (TTE) regardless of age. When the acoustic window is inadequate or the suspicion of IE is high but TTE does not demonstrate a lesion, then transesophageal echocardiography (TEE) should be performed without delay TTE can often visualize even small vegetations [42] but its sensitivity is estimated to be 81% [43–45]. In a small pediatric series of patients with IE, TTE was compared with TEE, and a sensitivity of 86% was found for detection of all events [46]. However, one of three patients with abscess formation and one of 14 with an intracardiac vegetation was missed on TTE. Even when TTE findings are positive, TEE may be required to assess for a paravalvular abscess. Almost every patient with suspected IE of a prosthetic valve should have a TEE.

In adults, TEE is superior in detecting vegetations measuring less than 5 mm, with a sensitivity of more than 90% [47]. It is also the best modality to diagnose prosthetic valve endocarditis and

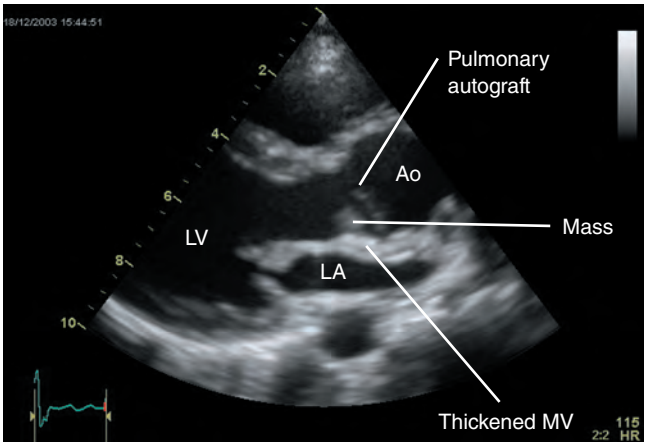


Figure 40.19 Parasternal long-axis view in a patient after the Ross operation demonstrating an echogenic mass on the ventricular side of the neo-aorta. There is also thickening of the mitral valve in the region of the mitral–aortic fibrous continuity as an indicator of infiltration. Ao, aorta; LA, left atrium; LV, left ventricle; MV, mitral valve.

paravalvular abscesses [48,49]. In patients with a high probability of IE but an initially negative TEE, a repeat TEE after an interval of 7–10 days may be indicated when clinical suspicion persists [50]. Some findings, like tricuspid vegetations (Video 40.12) or abnormalities of the right ventricular outflow tract may occasionally be better visualized with TTE than with TEE because of distance of finding from the focal point of the probe [51,52].

Initial screening by TTE in patients with CHD should focus on the underlying heart defect and the knowledge that IE is primarily located on the site of the endothelial jet lesion. Using the 2D modality, any unknown echogenic mass that moves faster than the surrounding cardiac structures is highly suspicious for IE (Figure 40.19; Video 40.13). In some patients with resolving IE, the vegetation may become calcified and thus, less mobile. New vegetations will typically move with a high frequency (i.e., an oscillating mass) whereas calcifications will usually have the same motion as the valve itself. Color Doppler is a sensitive modality for detecting pathologic flow patterns at the ventricular, valvar or vessel level, and is helpful in discriminating the site of a possible endothelial lesion, perivalvar leak or fistula.

Once the diagnosis is established and the site of the infection located, TTE/TEE is mandatory to describe the extent of valvar damage and to monitor cardiac function and the possible hemodynamic consequences of IE, such as pulmonary hypertension due to mitral regurgitation or acute volume load of the left ventricle due to aortic perforation (Table 40.4).

Imaging of the adult

Adults with CHD often present with limited TTE windows. Therefore, TEE is indicated as a first-line imaging modality when IE is suspected [53,54]. A rare localization of IE in the adult that may be easily missed on TTE is the Eustachian valve (Figure 40.20; Video 40.14) [55]. Pulmonary embolism may be the first clinical sign in this right-sided endocarditis; TEE is often performed in order to detect thrombus formation once pulmonary embolism is diagnosed.

Table 40.4 Goals of echocardiography for infective endocarditis (IE) in congenital heart disease

Diagnosis of IE
Site and extent of vegetation
Description of valvar function
Monitoring of hemodynamic consequences
Monitoring of cardiac function – ventricular performance
Detection of pericardial effusion – myocardial abscess
Therapeutic decision
Indication for surgery – based on vegetation size/location
Prediction of embolic events
Monitoring of treatment
Monitoring of conservative therapy
Intraoperative echocardiography
Post-treatment echocardiography

Preoperative assessment

Echocardiography should be performed in cases of systemic embolism such as brain (Figure 40.21) or other organ abscess (Figure 40.22) to assess for intracardiac vegetation. In addition to making the diagnosis of IE, echocardiography can diagnose high-risk complications such as pseudo-aneurysm, valvar perforation or valve or patch dehiscence, and can identify evidence of decompensated heart failure with a potential need for surgery [56]. The incidence of systemic embolism in IE ranges from 13% to 49% and may greatly influence mortality rate. In a prospective study, vegetation length exceeding 15 mm was an independent predictor of 1-year mortality [57].

When considering early surgery to avoid embolization, vegetation size and mobility must be taken into account, as well as bacteriologic and other clinical factors [58]. Early surgery in patients with left-sided IE, severe valve disease and large vegetations seems to reduce the risk of embolic events and death from

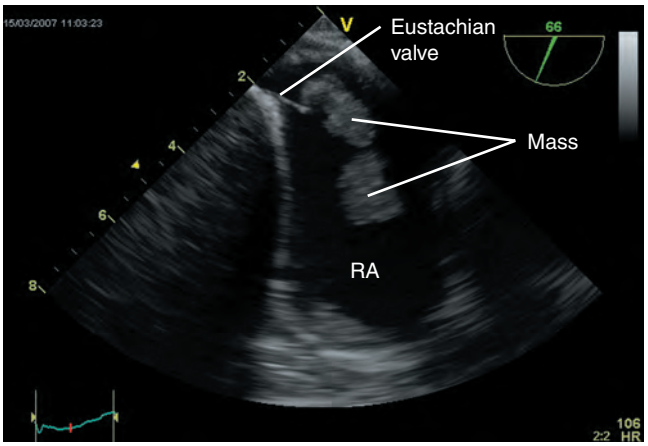


Figure 40.20 Transesophageal echocardiogram in the sagittal view (90°) of the inferior vena cava–right atrium (RA) junction showing two large vegetations attached to the Eustachian valve.

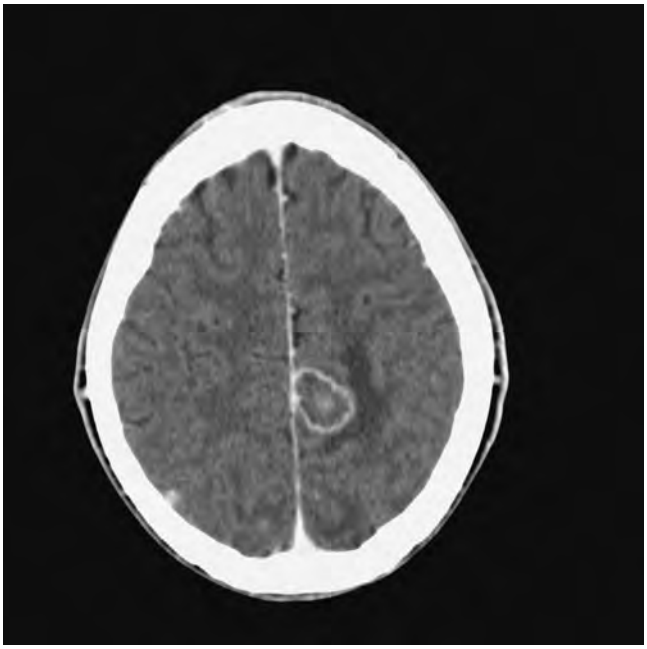


Figure 40.21 Cranial computed tomogram of a patient with *Staphylococcus aureus* endocarditis after mechanical aortic valve replacement. After contrast enhancement a 2-cm abscess is seen in the left parasagittal parietal region.

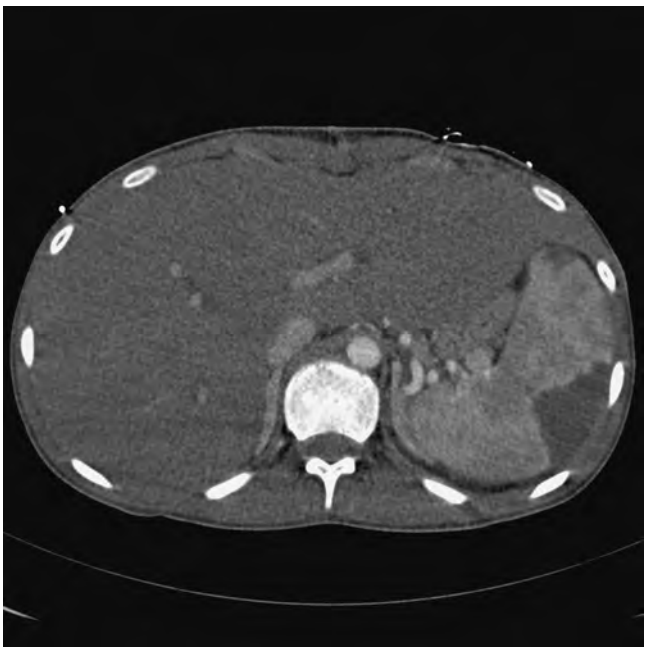


Figure 40.22 Computed tomogram of the abdomen of the same patient as in Figure 40.22 showing a triangular zone of infarction in the lateral portion of the spleen with another focus more caudal. Infarction was also demonstrated in both kidneys.

any cause [59]. Despite the wide acceptance of echocardiography for the diagnosis and management of IE, few published data support its use as a risk-stratification tool. A study has compared standard indications for surgery (such as heart failure, recurrent embolic events, severe valvar regurgitation and persistent bacteremia) with echocardiography-guided indications (such as vegetations >10 mm in length) [60]. The echocardiographic-based strategy reduced the risk for embolic stroke and death and was cost-effective [61].

Echocardiographic guidance of surgical treatment and postoperative assessment

Prior to surgery, intraoperative TEE is helpful in determining the mechanism, localization and degree of valvar dysfunction and/or region of myocardial disruption. It is also useful for excluding contamination of other valves and cardiac structures. The surgeon can then save time on cardiopulmonary bypass if he or she is sure that only right-sided or left-sided structures of the heart are infected. In cases where valves have to be replaced, preoperative determination of valve annulus size is mandatory.

Postoperative TEE should confirm the adequacy of the repair or valve replacement and document the successful closure of fistulous tracts [12]. Patients with previous IE are at high risk for a second bout of IE; thus surgical therapy should correct any residual defects, including paravalvular leaks, residual ventricular septal defects and/or residual fistulae. Postoperative TEE should also monitor hemodynamic changes after repair and assess ventricular performance, although alterations may occur once the patient is awake and extubated. In smaller children with an adequate acoustic window, a follow-up TTE may be sufficient; in all other cases a TEE prior to completion of medical therapy is indicated.

Nonbacterial thrombotic endocarditis

The pathognomonic feature of nonbacterial thrombotic endocarditis (NBTE) is an intracardiac vegetation consisting of a mesh of fibrin and platelets without an identified microorganism [62]. The primary pathogenetic mechanisms of this disorder are damage to the valvar endothelium and hypercoagulability. Both cancer and autoimmune diseases, such as systemic lupus erythematosus (i.e., Libman–Sacks endocarditis) are known to be associated with NBTE. The diagnosis, however, may be difficult in patients in whom the underlying disease is associated with fever. IE in this setting has to be ruled out carefully. NBTE is usually a postmortem diagnosis, with an incidence of 1.2% in autopsy patients. It has been reported to occur in all age groups but predominantly between the fourth and eighth decades of life [63]. Echocardiography cannot reliably distinguish between NBTE and IE. The NBTE vegetation usually grows on the atrial surface of the atrioventricular valves and the ventricular surface of the semilunar valves [64]. Although all valves may be affected, the mitral valve is most often involved [65]. Typically, NBTE has an indolent course, but systemic emboli may occur in 50% of the patients [64]. In very rare cases, surgical therapy is indicated

due to major valvar involvement with hemodynamic compromise [66].

Videos

To access the videos for this chapter, please go to www.lai-echo.com.

Video 40.1 Transesophageal echocardiographic view 109° of a central venous catheter as it enters the right atrium from the superior vena cava. It is adjacent to a large homogeneous echogenic mass, which is fixed to the Eustachian valve.

Video 40.2 Transesophageal echocardiogram of a central aorto-pulmonary GORE-TEX shunt to the main pulmonary artery. Color Doppler shows the direction of the accelerated flow into the pulmonary artery (jet lesion).

Video 40.3 Transesophageal echocardiogram of the same patient as in Video 40.2. An oscillating infective endocarditis mass is seen opposite to the entrance of the shunt into the pulmonary artery.

Video 40.4 Transesophageal echocardiogram of the left ventricular outflow tract after mechanical valve replacement demonstrating a subvalvular echogenic mass from the anterior portion of the valve ring, indicating infective endocarditis.

Video 40.5 Transthoracic echocardiogram in an apical 4-chamber view showing an oscillating mass fixed to the atrial aspect of the septal leaflet of the tricuspid valve, a finding typical in intravenous drug users.

Video 40.6 Transesophageal echocardiogram in the sagittal plane of an atrial pacemaker lead with fixation to the anterior wall of the right atrium. Multiple mobile vegetations can be seen adherent to the lead.

Video 40.7 Transesophageal echocardiogram in a patient after repair of atrioventricular canal defect demonstrating a large echogenic mass adherent to the "posterior" leaflet of the left atrioventricular valve mitral leaflet and another smaller mass fixed to the "anterior" leaflet.

Video 40.8 Transesophageal echocardiogram in a patient with a small, restrictive ventricular septal defect (VSD) under the aortic valve. A large vegetation is seen at the site of the jet-lesion on the anterior right ventricular wall just below the pulmonary artery.

Video 40.9 Transthoracic echocardiogram in a parasternal short-axis view demonstrating a very mobile, thin vegetation originating from a small persistent ductus arteriosus. The mass oscillates toward the main pulmonary artery, similar to the direction of blood flow.

Video 40.10 Transesophageal echocardiogram in the left ventricular outflow view demonstrating multiple echogenic masses attached to the atrial side of the posterior mitral valve leaflet.

Video 40.11 Transesophageal echocardiogram of the same patient as in Video 40.10. Color Doppler shows newly acquired mitral regurgitation through a perforation in the posterior leaflet of the mitral valve.

Video 40.12 Transesophageal echocardiogram demonstrating an aortic ring abscess with perforation into the left atrium. The underlying heart disease was a calcified stenotic aortic valve. Note the diminished mobility of the aortic valve leaflets.

Video 40.13 Transesophageal echocardiogram in a left ventricular outflow tract view shows aortic valve endocarditis with extension from the ventricular side through the valve into the sinotubular junction.

Video 40.14 Transesophageal echocardiogram demonstrating a large paravalvular ring abscess years after aortic valve replacement with a mechanical St. Jude Medical valve.

References

1 Durack DT, Lukes AS, Bright DK. New criteria for diagnosis of infective endocarditis: utilization of specific echocardiographic findings. Duke Endocarditis Service. *Am J Med* 1994;**96**:200–209.

2 Li JS, Sexton DJ, Mick N, et al. Proposed modifications to the Duke criteria for the diagnosis of infective endocarditis. *Clin Infect Dis* 2000;**30**:633–638.

3 Stockheim JA, Chadwick EG, Kessler S, et al. Are the Duke criteria superior to Beth Israel criteria for diagnosis of infective endocarditis in children. *Clin Infect Dis* 1998;**27**:1451–1456.

4 Del Pont JM, De Cicco LT, Vartalitis C, et al. Infective endocarditis in children: clinical analyses and evaluation of two diagnostic criteria. *Pediatr Infect Dis J* 1995;**14**:1079–1086.

5 Ferrieri P, Gewitz MH, Gerber MA, et al., Committee on Rheumatic Fever, Endocarditis, and Kawasaki Disease of the American Heart Association Council on Cardiovascular Disease in the Young. Unique features of infective endocarditis in childhood. *Circulation* 2002;**105**:2115–2127.

6 Van Hare GF, Ben-Shachar G, Liebman J, et al. Infective endocarditis in infants and children during the past 10 years: a decade of change. *Am Heart J* 1984;**107**:1235–1240.

7 Stull TL, LiPuma JJ. Endocarditis in children. In: Kaye D (ed.) *Infective Endocarditis*, 2nd edn. New York, NY: Raven Press, 1992, pp. 313–327.

8 Saiman L, Prince A, Gersony WM. Pediatric infective endocarditis in the modern era. *J Pediatr* 1993;**122**:847–853.

9 Martin JM, Neches WH, Wald ER. Infective endocarditis: 35 years of experience at a children's hospital. *Clin Infect Dis* 1997;**24**:669–675.

10 Morris CD, Reller MD, Menashe VD. Thirty-year incidence of infective endocarditis after surgery for congenital heart defect. *JAMA* 1998:**279**:599–603.

11 Karl T, Wensley D, Stark J, et al. Infective endocarditis in children with congenital heart disease: comparison of selected features in patients with surgical correction or palliation and those without. *Br Heart J* 1987;**58**:57–65.

12 Baddour LM, Wilson WR, Bayer AS, et al., Committee on Rheumatic Fever, Endocarditis, and Kawasaki Disease; Council on Cardiovascular Disease in the Young; Councils on Clinical Cardiology, Stroke, and Cardiovascular Surgery and Anesthesia; American Heart Association; Infectious Diseases Society of

America. Infective endocarditis: diagnosis, antimicrobial therapy, and management of complications: a statement for healthcare professionals from the Committee on Rheumatic Fever, Endocarditis, and Kawasaki Disease, Council on Cardiovascular Disease in the Young, and the Councils on Clinical Cardiology, Stroke, and Cardiovascular Surgery and Anesthesia, American Heart Association: endorsed by the Infectious Diseases Society of America. *Circulation* 2005;**111**:394–434.

13 Wilson LE, Thomas DL, Astemborski J, et al. Prospective study of infective endocarditis among injection drug users. *J Infect Dis* 2002;**185**:1761–1766.

14 Reisberg BE. Infective endocarditis in the narcotic addict. *Prog Cardiovasc Dis* 1979;**22**:193–204.

15 Sklaver AR, Hoffman TA, Greenman RL. Staphylococcal endocarditis in addicts. *South Med J* 1978;**71**:638–643.

16 Levine DP, Crane LR, Zervos MJ. Bacteremia in narcotic addicts at the Detroit Medical Center. II. Infectious endocarditis. A prospective comparative study. *Rev Infect Dis* 1986;**8**:374–396.

17 Berlin JA, Abrutyn E, Strom BL, et al. Incidence of infective endocarditis in the Delaware Valley, 1988–1990. *Am J Cardiol* 1995;**76**:933–936.

18 Sohail MR, Uslan DZ, Khan AH, et al. Management and outcome of permanent pacemaker and implantable cardioverter-defibrillator infections. *J Am Coll Cardiol* 2007;**49**:1851–1859.

19 Athan E, Chu VH, Tattevin P, et al. Clinical characteristics and outcome of infective endocarditis involving implantable cardiac devices. *JAMA* 2012;**307**:1727–1735.

20 Sievert H, Babic UU, Hausdorf G, et al. Transcatheter closure of atrial septal defect and patent foramen ovale with ASDOS device (a multi-institutional European trial). *Am J Cardiol* 1998;**82**:1405–1413.

21 Gillespie MJ, Rome JJ, Levi DS, et al. Melody valve implant within failed bioprosthetic valves in the pulmonary position: a multicenter experience. *Circ Cardiovasc Interv* 2012;**5**:862–870.

22 Borghi A, Ciuffreda M, Quattrociocchi M, Preda L. The grown-up congenital cardiac patient. *J Cardiovasc Med* 2007;**8**:78–82.

23 Li W, Somerville J. Infective endocarditis in the grown-up congenital heart (GUCH) population. *Eur Heart J* 1998;**19**:166–173.

24 Bashore TM, Cabell Ch, Fowler V. Update on infective endocarditis. *Curr Probl Cardiol* 2006;**31**:274–352.

25 Noel GJ, O'Loughlin JE, Edelson PJ. Neonatal *Staphylococcus epidermidis* right-sided endocarditis: description on five catheterized infants. *Pediatrics* 1988;**82**:234–239.

26 Moreillon P, Que YA, Bayer AS. Pathogenesis of streptococcal and staphylococcal endocarditis. *Infect Dis Clin North Am* 2002;**16**:297–318.

27 Durack DT, Beeson PB. Experimental bacterial endocarditis. I. Colonization of a sterile vegetation. *Br J Exp Pathol* 1972;**53**:44–49.

28 Durack DT, Beeson PB. Experimental bacterial endocarditis. II. Survival of bacteria in endocardial vegetation. *Br J Exp Pathol* 1972;**53**:50–53.

29 Graupner C, Vilacosta I, SanRoman J, et al. Periannular extension of infective endocarditis. *J Am Coll Cardiol* 2002;**39**:1204–1211.

30 Filippo SD, Delahaye F, Semiond B, et al. Current patterns of infective endocarditis in congenital heart disease. *Heart* 2006;**92**:1490–1495.

31 Awadallah SM, Kavey RE, Byrum CJ, et al. The changing pattern of infective endocarditis in childhood. *Am J Cardiol* 1991;**68**:90–94.

32 Karchmer A. Infective endocarditis. In: Zipes DP, Libby P, Bonow RO (eds.) *Heart Disease*. Philadelphia, PA: Elsevier Saunders, 2005, pp. 1633–1656.

33 Sexton DJ, Bashore TM. Infective endocarditis. In: Topol EJ (ed.) *Textbook of Cardiovascular Medicine*. Philadelphia, PA: Lippincott Williams & Wilkins, 2002, pp. 569–593.

34 Gordon SM, Serkey JM, Longworth DL, et al. Early onset prosthetic valve endocarditis: the Cleveland Clinic experience 1992–1997. *Ann Thorac Surg* 2000:**69**:1388–1392.

35 Oelberg DG, Fisher DJ, Gross DM, et al. Endocarditis in high-risk neonates. *Pediatrics* 1983;**71**:392–397.

36 Syndych PS, Krauss AN, Winchester P. Endocarditis following intracardiac placement of umbilical venous catheters in neonates. *J Pediatr* 1977;**90**:287–289.

37 Nucifora G, Badano L, Hysko F, et al. Pulmonary embolism and fever: When should right-sided infective endocarditis be considered? *Circulation* 2007;**115**:173–176.

38 Hasbun R, Vikram HR, Barakat LA, et al. Complicated left-sided native valve endocarditis in adults. *JAMA* 2003;**289**:1933–1940.

39 Vikram HR, Buenconsejo J, Hasbun R, Quagliarello VJ. Impact of valve surgery on 6-month mortality in adults with complicated left-sided native valve endocarditis. *JAMA* 2003;**290**:3207–3214.

40 Mills J, Utley J, Abbott J. Heart failure in infective endocarditis: predisposing factors, course and treatment. *Chest* 1974;**66**:151–157.

41 Habib G, Badano L, Tribouilloy C, et al. Recommendations for the practice of echocardiography in infective endocarditis. *Eur J Echocardiogr*. 2010;**11**:202–219.

42 Wilson W, Taubert KA, Gewitz M, et al. Prevention of Infective Endocarditis. Guidelines From the American Heart Association. A Guideline From the American Heart Association Rheumatic Fever, Endocarditis, and Kawasaki Disease Committee, Council on Cardiovascular Disease in the Young, and the Council on Clinical Cardiology, Council on Cardiovascular Surgery and Anesthesia, and the Quality of Care and Outcomes Research Interdisciplinary Working Group. *Circulation* 2007;**116**:1736–1754.

43 Habib G, Hoen B, Tornos P, et al. Guidelines on the prevention, diagnosis, and treatment of infective endocarditis (new version 2009): the Task Force on the Prevention, Diagnosis, and Treatment of Infective Endocarditis of the European Society of Cardiology (ESC). Endorsed by the European Society of Clinical Microbiology and Infectious Diseases (ESCMID) and the International Society of Chemotherapy (ISC) for Infection and Cancer. *Eur Heart J* 2009;**30**:2369–2413.

44 Roy P, Tajik AJ, Giuliani ER, et al. Spectrum of echocardiographic findings in bacterial endocarditis. *Circulation* 1976;**53**:474–482.

45 Kavey RE, Frank DM, Byrum CJ, et al. Two-dimensional echocardiographic assessment of infective endocarditis in children. *Am J Dis Child* 1983;**137**:851–856.

46 Humpl T, McCrindle BW, Smallhorn JF. The relative roles of transthoracic compared with transesophageal echocardiography in children with suspected infective endocarditis. *J Am Coll Cardiol* 2003;**41**:2068–2071.

47 Erbel R, Rohmann S, Drexler M, et al. Improved diagnostic value of echocardiography in patients with infective endocarditis by transesophageal approach. A prospective study. *Eur Heart J* 1988;**9**:43–53.

48 Daniel WG, Mugge A, Grote J, et al. Comparison of transthoracic and transesophageal echocardiography for detection of

abnormalities of prosthetic and bioprosthetic valves in the mitral and aortic positions. *Am J Cardiol* 1993;**71**:210–215.
49 Daniel WG, Mugge A, Martin RP, et al. Improvement in the diagnosis of abscesses associated with endocarditis by transesophageal echocardiography. *N Engl J Med* 1991;**324**:795–800.
50 Rohmann S, Erbel R, Darius H, et al. Prediction of rapid versus prolonged healing of infective endocarditis by monitoring vegetation size. *J Am Soc Echocardiogr* 1991;**4**:465–474.
51 San Roman JA, Vilacosta I, Zamorano JL, et al. Transesophageal echocardiography in right-sided endocarditis. *J Am Coll Cardiol* 1993;**21**:1226–1230.
52 San Román JA, Vilacosta I, López J, et al. Role of transthoracic and transesophageal echocardiography in right-sided endocarditis: one echocardiographic modality does not fit all. *J Am Soc Echocardiogr* 2012;**25**:807–814.
53 Miller-Hance WC, Silverman NH. Transesophageal echocardiography (TEE) in congenital heart disease with focus on the adult. *Cardiol Clin* 2000;**18**:861–892.
54 Gersony WM, Hayes CJ, Deiscoll DJ, et al. Bacterial endocarditis in patients with aortic stenosis, pulmonary stenosis, or ventricular septal defect. *Circulation* 1993;**87**:I121–126.
55 Pellicelli AM, Pino P, Terranova A, et al. Eustachian valve endocarditis: a rare localization of right side endocarditis. A case report and review of the literature. *Cardiovasc Ultrasound* 2005;**3**:30–35.
56 Bayer AS, Bolger AF, Taubert KA, et al. Diagnosis and management of infective endocarditis and its complications. *Circulation* 1998;**98**:2936–2948.
57 Thuny F, Di Salvo G, Belliard O, et al. Risk of embolism and death in infective endocarditis: prognostic value of echocardiography: a prospective multicenter study. *Circulation* 2005;**112**:69–75.
58 Erbel R, Rohmann S, Drexler M, et al. Improved diagnostic value of echocardiography in patients with infective endocarditis by transoesophageal approach: a prospective study. *Eur Heart J* 1988;**9**:43–53.
59 Kang DH, Kim YJ, Kim SH, et al. Early surgery versus conventional treatment for infective endocarditis. *N Engl J Med* 2012;**366**:2466–2473.
60 Olaison L, Pettersson G. Current best practices and guidelines. Indications for surgical intervention in infective endocarditis. *Cardiol Clin* 2003;**21**:235–251.
61 Liao L, Kong DF, Samad Z, et al. Echocardiographic risk stratification for early surgery with endocarditis: a cost-effectiveness analysis. *Heart* 2008;**94**:e18.
62 Eftychiou Ch, Fanourgiakis P, Vryonis E, et al. Factors associated with non-bacterial thrombotic endocarditis: case report and literature review. *J Heart Valve Dis* 2005;**14**:859–862.
63 Salem DN, Stein PD, Al-Ahmad A, et al. Antithrombotic therapy in valvular heart disease – native and prosthetic. The Seventh ACCP Conference on Antithrombotic and Thrombolytic Therapy. *Chest* 2004;**126**:457S–482S.
64 Lopez JA, Ross RS, Fishbein MC, Siegel RJ. Nonbacterial thrombotic endocarditis: a review. *Am Heart J* 1987;**113**:773–783.
65 Hesselink DA, Van Der Klooster JM, Schelfhout LJDM, Scheffer MG. Non-bacterial thrombotic (marantic) endocarditis associated with giant-cell arteritis. *Eur J Int Med* 2001;**12**:454–458.
66 Einav E, Gitig A, Marinescu M, et al. Valvulitis requiring triple valve surgery as an initial presentation of systemic lupus erythematosus. *J Am Soc Echocardiogr* 2007;**20**:1315.el–3.

PART VIII

Special Techniques and Topics

CHAPTER 41

Transesophageal and Intraoperative Echocardiography

Owen I. Miller, Aaron J. Bell, and John M. Simpson
Department of Congenital Heart Disease, Evelina London Children's Hospital; Guy's & St Thomas' NHS Foundation Trust, London, UK

Introduction

Transesophageal echocardiography (TEE) is an important imaging modality for the management of patients with congenital heart disease (CHD) [1–16]. Suitable TEE ultrasound probes have been developed which permit high resolution imaging of small infants [17–20] right through to adult patients. The major advantages of TEE are that it provides images of both high temporal and spatial resolution and avoids many of the issues of suitable acoustic windows that may limit a transthoracic approach. Furthermore, TEE lends itself to guidance of both surgical [14,21–30] and catheter procedures [31–37] because it can be performed without compromising access or the field of view for either the surgeon or the interventional cardiologist. The information sought by TEE, any patient-specific factors and the type of sedation or anesthesia that may be used during the procedure must all be carefully considered when planning the TEE.

Patient considerations

In approaching the patient to undergo TEE, the size and age of the patient are important considerations. For infants and children the procedure is usually performed under general anesthesia [38]. For airway protection, endotracheal intubation is performed which avoids the risk of TEE probe misplacement. This is preferred over the use of laryngeal masks because of the potential for the probe to dislodge the mask. In selected cases, particularly where spontaneous ventilation is deemed to be a hemodynamic advantage, the patient may be anesthetized/sedated with or without endotracheal intubation and remain spontaneously ventilating throughout the examination [39,40].

The patient's size determines the type of TEE probe to be used. In patients >25–30 kg an "adult" size multiplane TEE probe can be used for the examination. Multiplane pediatric probes are used below a patient weight of 25–30 kg, down to a weight of around 3–4 kg. Recently, smaller "micro" TEE probes have been developed which can be inserted in infants below 3 kg [19,20,41,42]. For patients who are "borderline" between the different probe sizes, both sizes should be prepared and be available at the start of the procedure in case the larger probe cannot be safely passed. Whatever type probe is employed, great care should be taken during probe insertion and vigorous or forcible probe insertion is strongly discouraged. Damage to teeth, mouth, esophagus and other structures have all been reported [42]. Appropriate positioning of the head and neck by the cardiologist and/or anesthesiologist is important [43] as well as slight flexion of the TEE probe to aid passage into the esophagus. During the insertion of the TEE probe, it is important to continue to monitor both the adequacy of ventilation as the TEE probe can compress the endotracheal probe [44,45], and heart rhythm, particularly bradycardia, as the TEE probe may cause an intense vagal stimulus. Detailed published guidance for the performance of pediatric TEE is available [16]. The probe can also compress posteriorly located cardiovascular structures such as a collecting chamber. This can cause hemodynamic instability after probe insertion.

TEE across the age range by definition encompasses children and young adults with varying body sizes. For this reason, the depth of probe insertion must be gauged by direct vision of the echocardiographic image during insertion and cannot rely on published standard probe depths at the mouth, or other probe-oriented marks. Before insertion, the probe must be connected to the echocardiogram machine, the TEE probe should be selected and the viewing angle set at zero degrees. Real-time imaging should be undertaken during insertion to gauge an adequate depth of insertion.

Both the cardiologist and the anesthesiologist need to understand the hemodynamics of the underlying cardiac lesion prior to the procedure. Anesthetic agents will cause systemic arterial vasodilation, thus, in patients with tetralogy of Fallot, for example, anesthesia may accentuate right-to-left shunting across the

Echocardiography in Pediatric and Congenital Heart Disease: From Fetus to Adult, Second Edition. Edited by Wyman W. Lai, Luc L. Mertens, Meryl S. Cohen and Tal Geva.
© 2016 John Wiley & Sons, Ltd. Published 2016 by John Wiley & Sons, Ltd.
Companion website: www.lai-echo.com

ventricular septal defect. Care is also necessary in patients with a total cavopulmonary connection in whom positive pressure ventilation may impede venous return to the heart [46]. Furthermore, clinical settings where the venous return to the left ventricle may be relatively fixed, such as patients with marked elevation of pulmonary vascular resistance or with severe mitral valve stenosis, can cause hemodynamic instability. Usually, such patients can be managed safely with appropriate use of intravascular volume expanders, vasopressor agents, oxygen (to reduce pulmonary vascular resistance), or minimizing the period of positive pressure ventilation depending on the individual situation. A discussion of possible issues prior to the procedure is central to pre-empting any problems and should be part of any preoperative briefing or checklist routine.

In some patients, TEE is contraindicated or at least seriously cautioned [16,47]. Patients who have had repair of esophageal atresia, portal hypertension or liver disease should have an endoscopic examination prior to consideration of TEE to exclude esophageal strictures or varices, or consideration should be given to other imaging modalities.

Available TEE probes and technical considerations

There have been major advances in the design of TEE probes over the past decade. In the past, pediatric-sized TEE probes were biplane only, which limited imaging planes in these smaller children. Currently, all major manufacturers produce multiplane TEE probes suitable for both adults and children [48]. "Micro" TEE probes have been developed that have the potential to extend TEE to low birth weight infants. The microprobes may also be used in older patients whilst they are awake because the passage of a small instrument, similar in size to a nasogastric tube, may be better tolerated [19,20,26,41]. The 3D TEE probes that are currently available are suitable for imaging patients who weigh more than 25–30 kg [25,49]. These probes have incorporated the real-time 3D "matrix" arrangement of ultrasound crystals into a very small footprint, appropriate for transesophageal use. Three-dimensional images can be obtained over several cardiac cycles providing a large field of view or else a smaller "live 3D" imaging field can be used. Applications of 3D TEE include both surgical and interventional applications, which are discussed later.

Whichever probe is selected for a particular patient, careful attention needs to be paid to the safety of the actual instrument. This includes careful inspection of the probe for surface cracks in the probe lining which may represent both an infection risk and an electrical risk. Manufacturers endorse various cleaning and maintenance protocols ranging from antiseptic immersion to surface cleaning. In our institution we use a strictly audited surface disinfection protocol before and after every use of the probe [50,51] in addition to a latex-free disposable sheath for each procedure. To assist any future audit for potential cross-infection, a detailed log is kept for each probe with date, time, patient demographics, and batch number for the disinfectant product.

Standard transesophageal views

Transthoracic echo (TTE) has evolved standard imaging planes based primarily on accessible sonographic windows. These standard imaging planes allow interoperator comparison and form the substrate for echocardiographic reporting of cardiac structure and function. TEE also has well described standard views [21]. These predefined views are, however, based on an assumption of levocardia and normal intracardiac connections. For the great majority of TEE done in the adult cardiovascular setting these tenets hold true. Indeed even for many pediatric patients these "standard" TEE views can be used. The standard views are well described and are particularly useful when imaging the valves [52–57], the interatrial septum [58–60] or when looking for intracardiac thrombi [61–63]. These predefined TEE views can reliably predict the cardiac structures seen at a particular probe depth or imaging angle. In patients with structural congenital heart disease, cardiac position and intracardiac connections can be highly variable, thus adaptation from standard views is frequently required to obtain adequate imaging of structures of interest. In the congenitally abnormal heart there may be both positional abnormalities such as dextrocardia, significant variation in connections, such as in congenitally corrected transposition and target structure such as the semilunar valves may not be seen in the standard planes. A comprehensive TEE may include up to 20 standard cross-sectional views to evaluate all heart structures in the adult patient with a normal cardiac anatomy. Despite anatomical variations across the spectrum of CHD, these standard views are still a good starting point for any comprehensive TEE examination in CHD.

The standard TEE views describe three probe depths: upper esophageal (UE), mid-esophageal (ME), and transgastric (TG). Additional descriptors relate to the probe controls and on a modern multiplane TEE probe these will include an ability to electronically vary the sector plane angle continuously from 0° to 180° and two further physical controls which allow the operator to induce a bend at the probe tip both in the antero-posterior and lateral planes. Using the convention of the patient being supine and the imaging surface at the tip of the probe facing forwards, inducing an anterior bend is termed anteflexion and inducing a posterior bend is called retroflexion. Finally, a lateral bend may be induced and is described as rightward or leftward in relation to the patient's right and left, respectively. Lateral flexion controls are usually present on standard-size adult probes but may not be present on all pediatric or other miniaturized probes.

Importantly TEE should be seen as adding additional information to existing TTE images. Although TEE indications may include poor TTE windows, the decision to proceed to TEE may more commonly relate to better sonographic windows for

certain specific cardiac structures such as the atrial septum, the atrioventricular valves, and the aortic valve. For this reason, the TTE and the TEE are not mutually exclusive; indeed it is our view that most TEE examinations should be preceded by a comprehensive TTE. TEE should be performed to obtain the missing diagnostic information that could not be obtained by TTE. When studies are performed under general anesthesia (GA), it is our usual practice to use the same GA to acquire 2D and 3D transthoracic images and then proceed with acquiring the relevant TEE images. For 3D TEE breath-holding allows the acquisition of higher frame-rate multibeat full volume 3D acquisitions without respiratory artifacts.

In many instances a full TEE study including all the different standard views is not feasible due to unstable patient hemodynamics or concurrent surgical or catheter interventions. Additionally, TEE performed under conscious sedation rather than general anesthesia will limit the duration of the study and may reduce the possibility of completing a comprehensive TEE. In these cases it may be advantageous to concentrate on the missing imaging information and on the structures of interest so that if the study is curtailed or study time is limited, then at least the most important TEE data would have been acquired.

Finally, expertise in TEE will require a high level of familiarity with both normal and abnormal cardiac structures, and for cases of congenital heart TEE, the operator will require expertise in the full range of CHD TTE to fully exploit the potential of TEE in this population [64–66] .

In both TTE and TEE, the imaging sector can be displayed both with the sector apex at the top but also inverted with the sector apex at the bottom of the screen. Although many non-congenital echocardiographers will perform all TTE and indeed TEE views without inverting the sector, it has become customary to invert the image for certain standard views when performing a congenital heart echocardiogram to allow more anatomically accurate projection of cardiac structures. In TTE this usually relates to subcostal and apical 4-chamber views where the cardiac apex is lowermost on the screen. When performing pediatric TEE for congenital heart disease it is our practice to invert the image for transgastric views to allow a more intuitive display of the ventricles with the left ventricle on the left and the outlets towards the top of the screen.

Although the TEE in CHD will need to be adapted to the morphology, the following standard views will be described with an initial assumption of a normally connected heart so that the core standard views can be understood and then adapted as required.

Mid-esophageal view, 0 degrees

Despite the possibility of cardiac malposition and abnormal connections in CHD, the ideal starting point for most TEE in CHD is still the mid-esophageal view, where at 0–20°; a view analogous to the TTE "4-chamber" view should be evident. Axial rotation of the probe may be required to center the sector immediately posterior to the atria, usually the morphologic left atrium.

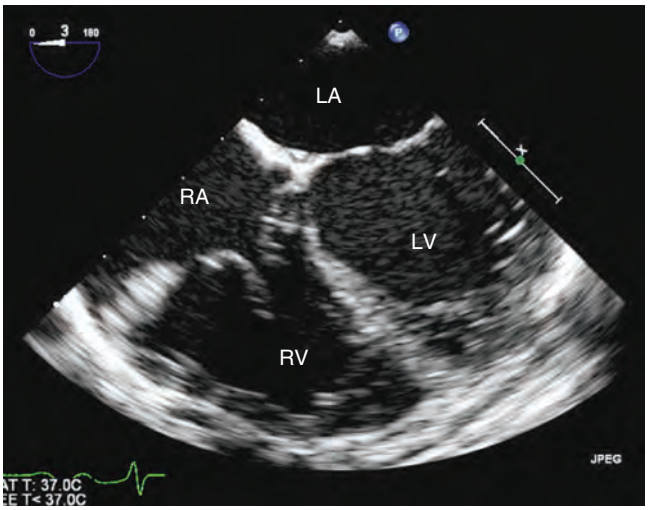


Figure 41.1 Transesophageal echocardiogram in a mid-esophageal position demonstrating a 4-chamber view. In this example the apex of the left ventricle is somewhat foreshortened by slight flexion of the probe, often necessary to maintain optimal probe contact. LA, left atrium; LV, left ventricle; RA, right atrium; RV, right ventricle.

The cardiac mass should be visible and the sector depth should be adjusted to include both the atrial and ventricular chamber(s).

The apex of the sector should be at the top of the screen, with the heart represented in anatomic format with the atrial mass uppermost and the ventricular mass toward the widest part of the imaging sector. Even in the presence of major structural problems, this starting view will allow orientation of left–right, posterior–anterior, and superior–inferior at the initial phase of a sequential examination (Figure 41.1). This starting view can be achieved by inserting the probe, already selected for live scanning, with the imaging surface of the probe tip facing anteriorly, the multiplane angle set at 0° and the probe depth assessed "live" during gentle introduction.

The echocardiographic sector at 0° from this ME depth will cut through the atrial mass, atrioventricular junction and ventricular mass from base to apex. However, as the cardiac apex is usually more inferior to the base, the ventricular chambers may appear foreshortened. Gentle retroflexion of the probe tip will allow the true apex of the heart to be visualized and this retroflexion manoeuver should be routine for the mid-esophageal 0° 4-chamber cut. Without retroflexion, there can be a misinterpretation of ventricular hypoplasia.

From this view, the intracardiac atrioventricular connections can be defined, the atrioventricular valves size and function can be described, and spectral Doppler assessment of the atrioventricular valve inflow and regurgitation can be achieved at generally acceptable insonation angles.

From this initial 4-chamber cut, one system of interrogation is to then perform a sequential segmental study starting at the venous connections.

Venous connections and the atrial septum

The superior caval vein can be seen in short axis by withdrawing the probe towards the upper esophagus whilst centering the image on the atrial septum. Advancing the probe into the lower esophagus until the inferior caval vein is seen also in cross-section will demonstrate the atrial septum from its inferior to the superior border (Video 41.1). The presence of any atrial septal abnormalities will be noted during this sweep and can then be displayed in closer detail at optimal depth and then at multiple sector angles. From the mid-esophageal depth, the atrial septum can then be displayed at 45° and then at 90° to provide multiple dimensions of any atrial septal communication. Preparation for device closure would also require detailed assessment of defect rims (see later). Note should be made of other identifying characteristics of the right atrium including the broad base of the right atrial appendage, the Eustachian valve, and any Chiari network. Failure to identify these right atrial structures should raise the possibility of a laterality defect.

Having demonstrated systemic venous connections and right atrial morphology, the operator can return to 0° at the mid-esophageal depth to then describe the pulmonary venous connections. Gross axial rotation of the probe, at the mid-esophageal depth and 0–20° multiplane angulation, will allow visualization of structures adjacent to the main cardiac mass. Pulmonary veins from the left and right can be seen at each heart border and may require gentle manipulation of the probe depth to bring in the inferior and superior pulmonary veins sequentially as these may not be visible at the same probe depth within the esophagus (Figure 41.2). Once visualized the pulmonary veins should be interrogated with color flow mapping (CFM) and pulsed-wave (PW) Doppler to establish a pulmonary vein flow profile. This is particularly important in pulmonary vein stenosis, mitral valve abnormalities, and in other forms of left heart dysfunction. As well as capturing a trace with cyclical ventilation, a second capture of the pulmonary venous Doppler trace should be obtained without artificial ventilation or positive end expiratory pressure (PEEP). For both right and left pulmonary veins, a long sweep usually at 0–20° will allow the operator to follow the pulmonary veins from their extra pericardial origin to their atrial entry (Video 41.2). Abnormalities of pulmonary venous return are best visualized during this sweep and confirmed following a 3D TTE or TEE acquisition. Failure to identify all pulmonary veins should prompt a detailed evaluation of possible sites for anomalous pulmonary venous drainage, including an evaluation of a longer length of the superior caval vein both at 0° and at 90°. Finally in the heart with atrial situs solitus, the left atrial appendage is best seen at the mid-esophageal depth with 60–90° multiplane angulation.

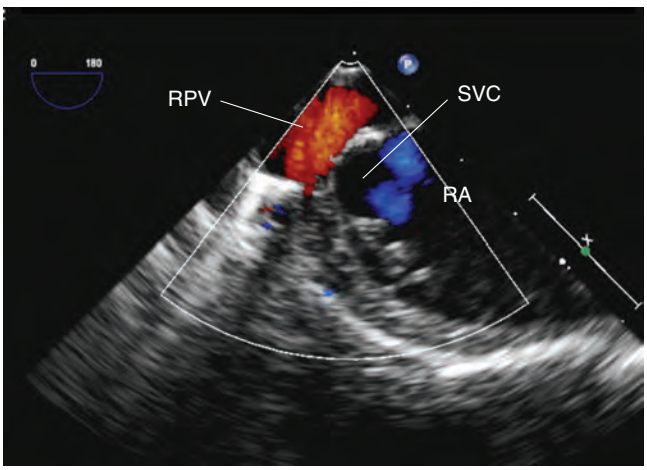


Figure 41.2 Transesophageal echocardiogram demonstrating the entry of the right upper pulmonary vein to the left atrium. The right pulmonary veins pass behind the superior vena cava which is cut in cross-section with the probe at 0° of rotation. RA, right atrium; RPV, right pulmonary vein; SVC, superior vena cava.

Atrioventricular junction

Demonstration of the atrioventricular junction can also start with the mid-esophageal 0° view. Axial rotation of the probe will allow specific visualization of the left and right atrioventricular junctions. In normally connected hearts, the tricuspid valve can be best seen with a slight clockwise rotation of the probe to improve the insonation angle for any color Doppler or spectral Doppler interrogation. The mitral valve is best seen with slight anticlockwise rotation of the probe and it is from this view that optimal real-time 3D imaging of the atrial aspect of the mitral valve is obtained. Further detail of 3D optimization will follow later.

Keeping the multiplane angle set at 0–20°, the probe can be gently withdrawn from the 4-chamber projection; this minor alteration in probe depth should allow visualization of the left ventricular outflow tract and the great artery connection arising from the center of the cardiac mass. In the normally connected heart this will be the aorta and keeping a low multiplane angle 0–20° will establish a quasi 5-chamber view of the left ventricular outflow tract. Despite this analogy to the TTE view, it is not always possible to obtain a reliable Doppler angle from this position and this view offers much less detail of other CHD lesions such as ventricular septal defects, subaortic stenosis or indeed aortic valve pathology, and therefore is of only limited value. All of these clinical/morphologic questions are better answered by further 2D TEE views described later or by a full volume 3D dataset acquisition.

Mid-esophageal view, 30 degrees

After completing the sequence of 0° views mentioned earlier, the operator can then maintain station at the mid-esophageal depth but select a multiplane angle of between 30–45° and withdraw the probe slightly, at all times watching the image display to see when the aortic valve comes into view. Rotation of the probe to position the aortic valve in the center of the sector and adjustment of the depth will allow fine detail of the aortic valve to be displayed. In this view, the aortic valve cusp aligned with the interatrial septum is the noncoronary cusp, the cusp to the

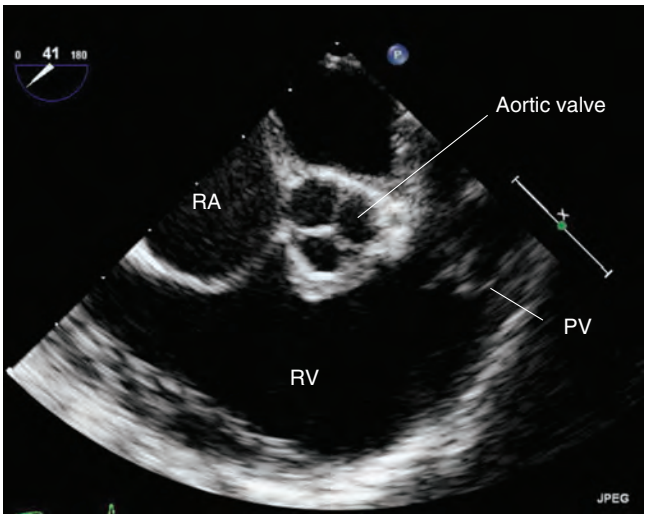


Figure 41.3 TEE view of the short axis of the aortic valve at 40° of rotation. The three leaflets of the aortic valve can be clearly identified and well as the right ventricular outflow tract wrapping around the aortic valve. PV, pulmonary valve; RA, right atrium; RV, right ventricle.

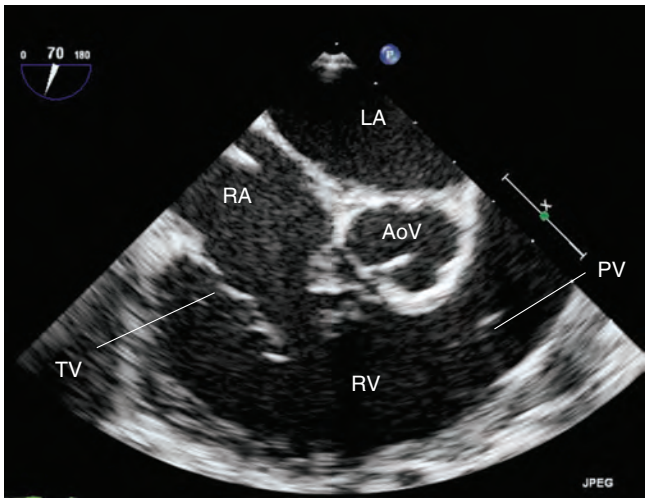


Figure 41.4 TEE of the right ventricular outflow tract which shows all components from the tricuspid valve through to the pulmonary artery. AoV, aortic valve; LA, left atrium; PV, pulmonary valve; RA, right atrium; RV, right ventricle; TV, tricuspid valve.

right and anterior (towards the bottom of the sector) is the right coronary cusp and the remaining cusp is the left coronary cusp (Figure 41.3).

Advancing the probe and rotation clockwise should bring the left atrial appendage into view to the left of the screen. As discussed earlier, this assumes normal atrial situs.

Mid-esophageal view, 60 degrees

Further angulation to a multiplane angle of 60–70° will bring the body of the right ventricle and the pulmonary valve into view.

This view also contains part of the perimembranous interventricular septum between the tricuspid valve on the left of the display screen and the aortic valve in the center (Figure 41.4). A perimembranous ventricular septal defect will be seen as a defect in the otherwise smooth outline of the aortic annulus and color flow mapping will clearly demonstrate the shunt. Once demonstrated, further definition will be possible at 120° (see later).

The pulmonary valve is an anterior structure and therefore not ideally demonstrated by TEE. It is, however, possible to visualize the valve annulus and any obvious dysplasia of the leaflets. Color flow mapping may show aliasing in cases of pulmonary valve stenosis but the Doppler angles are generally not useful for velocity estimation. Information about the pulmonary valve obtained by TEE should be compiled together with data obtained by TTE which is usually a better method for displaying this valve. The transgastric outflow tract view can also be used for better Doppler alignment. The pulmonary valve can be included in a 3D volume dataset; it is then our practice to display this postprocessed image in an anatomically correct orientation which requires the whole dataset to the rotated through 180° to show the pulmonary valve in its superior-anterior position.

Gentle withdrawal of the probe into the upper esophagus will demonstrate the origin and course of the right pulmonary artery but the left pulmonary artery is only poorly demonstrated. If more detailed imaging of the pulmonary arteries is required, epicardial imaging can be very useful. Especially after tetralogy of Fallot repair or after a cavopulmonary anastomosis, visualizing the branch pulmonary arteries is essential.

Mid-esophageal view, 90 degrees

Oriented with the transducer facing anteriorly, the mid-esophageal 90° view will allow composition of a "2-chamber view" of the left atrium and left ventricle. Anterior structures (left atrial appendage, anterior mitral valve leaflet) are to the left of the screen and posterior structures (inferior papillary muscle, posterior mitral valve leaflet) are to the right of the screen. Detailed descriptions of the standard multiplane and multidepth images of the complete TEE examination showing all three major scallops on both the anterior and posterior mitral valve leaflets in an anatomically normal mitral valve exist in the adult literature, and will not be further discussed here. These conventions describing which multiplane angle cuts through which part of the valve annulus can be useful even in congenital heart practice but cannot be relied upon to predefine any specific valve cusp in the congenitally malformed left atrioventricular valve. Once again, 3D TTE and TEE has proven more useful in the spatial description of atrioventricular valve abnormalities and anatomic relations [30,67,68].

Perhaps more important in congenital heart practice, the mid-esophageal 90° view when rotated axially to "look" posteriorly, clearly displays the atrial septum in long axis; with gentle withdrawal it can demonstrate the superior caval vein–right atrial junction (Figure 41.5) and when advanced can show the inferior

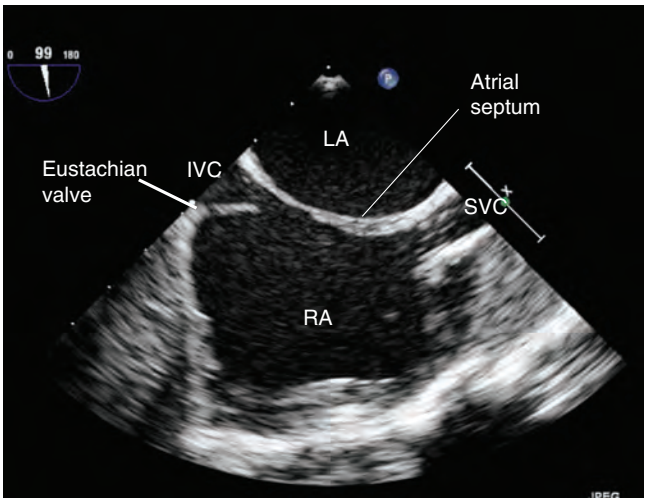


Figure 41.5 Bicaval view of the atriums showing the curved atrial septum. The left atrium is posterior and right atrium anterior. The Eustachian valve is seen close to the entry of the inferior vena cava to the right atrium. IVC, inferior vena cava; LA, left atrium; RA, right atrium; SVC, superior vena cava.

caval vein–right atrial junction albeit with less predictable image clarity. The presence and size of any atrial septal defect (ASD) already shown at 0° can be seen orthogonally and dimensions of both the defect and critical caval rims for possible device closure can be measured.

Mid-esophageal view, 120 degrees

In the normally connected heart, this view (110–130°) will demonstrate the left ventricular outflow tract, can confirm mitral-aortic continuity if present and will visualize a portion of the interventricular septum including the perimembranous region. The aortic valve cusp seen adjacent to the interventricular septum towards the bottom on the display is usually the right coronary cusp and this multiplane angle best demonstrates any coronary cusp prolapse or cusp involvement in any adjacent ventricular septal defect (Video 41.3). The other aortic valve cusp seen in this mid-esophageal long-axis view can be either the left or the noncoronary cusp depending on cardiac position and actual multiplane angle. Identification of the other cusp is best done by 3D or 2D sweep from short to long axis of the valve. Other aortic valve pathology and dysfunction including aortic valve incompetence is also best seen at 120° in augmented color Doppler, and in patients of an appropriate size by a 3D color acquisition to allow a multiplanar view of any regurgitant jet or indeed jets.

Transgastric views

Transgastric TEE views are best obtained by returning any flexion to neutral, reducing the multiplane angle to 0° and gently advancing the probe beyond the mid- or lower esophageal position until the heart is no longer seen. Once in the stomach, the probe is now anteflexed until the heart comes into view. Although the imaging sector could be left with the sector apex uppermost on the display, it is our practice to invert the imaging sector and allow a more intuitive anatomic projection of the cardiac chambers and outflow tracts.

At 0° from the transgastric window, the left ventricle will be seen in short axis with the postero-medial papillary muscle lowermost on the display, the right ventricle will be seen to the left of the screen which corresponds to the patient's right side. Axial rotation of the probe may be required to place the left ventricle on the center of the display. To optimize the short-axis cuts of the left ventricle it is important to check whether there is adequate anteflexion to avoid tangential cuts. This is best done by increasing the multiplane angle to 90° thereby obtaining a long-axis view of the left ventricle. More or less anteflexion is employed to display the left ventricle in an optimal horizontal orientation across the display. Advancing or withdrawing the probe to the apical, mid-portion of basal left ventricle and then sequentially obtaining a 0° apical, mid- and basal LV short axis can then be performed.

Apart from obtaining multiple short-axis LV cuts, the transgastric window will allow suitable Doppler angles for estimation of the left ventricular outflow tract velocity. From the mid-LV short-axis cut, the multiplane angle is increased to about 110–130° until the aortic valve appears to the right of the screen (Figure 41.6). Further axial rotation of the probe can optimize the placement of a Doppler cursor. Should the Doppler angle still be too shallow then a deeper transgastric view placing the probe

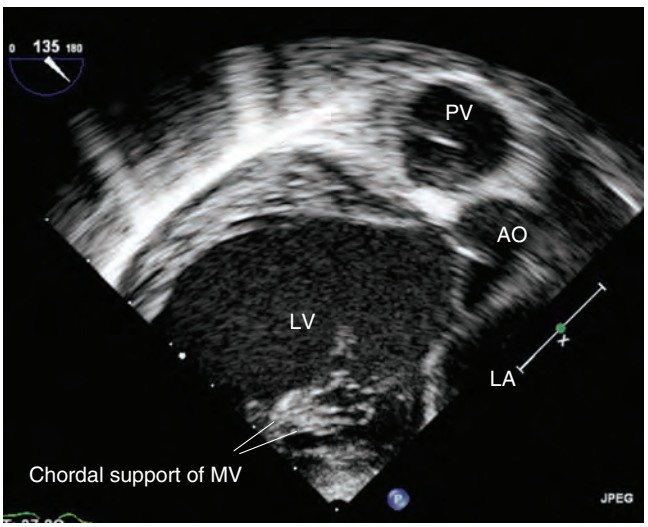


Figure 41.6 Transgastric TEE view of the left ventricular outflow tract (135°). The chordal support of the mitral valve is well seen in this projection. The left ventricular outflow tract is seen in long axis and the pulmonary valve in short axis. The projection also facilitates Doppler interrogation of the left ventricular outflow tract. AO, aorta; LA, left atrium; LV, left ventricle; MV, mitral valve; PV, pulmonary valve.

tip closer to the LV apex and more pronounced anteflexion may open up the left ventricular outflow tract towards the top of the display.

Transesophageal assessment for and guidance of interventional procedures

TEE guidance for catheter intervention can occur either by 2D TEE or 3D TEE using a real-time live acquisition mode [32,59]. Of fundamental importance, optimal TEE guidance of catheter intervention requires continuous dialogue between the echocardiographer and the catheter interventionalist. To facilitate this dialogue it is important for both the echocardiographer and the interventionalist to have simultaneous sight of both angiography and echocardiography displays. The actual screen positions will depend on catheter laboratory layout but as a minimum, three screens should be available to display both biplane catheter data and echocardiography. Once again depending on the layout and space available, it may also be advantageous for the echocardiographer to have a dedicated set of screens showing angiography in addition to the echo data viewable on the cart. Furthermore, it is also our view that the echocardiography images should be displayed as much as is possible in an anatomically intuitive projection so that catheter movements seen on both the angiography and echo screens concur in direction and make anatomic sense. When using real-time 3D it is our practice to orient the displayed image with reference to known external landmarks so that the image displayed mirrors an anatomic projection [69]. This is particularly relevant when using real-time 3D TEE guidance where a true representation of the anatomy will result in a projection understood by all. The echocardiographer should continuously update the catheter operator with positions of wires, sheaths and devices, but equally needs to assertively request time to optimize imaging or live 3D before moving to the next stage of the intervention.

Atrial septal defect

Routine TTE will give an indication about the need to close an atrial septal defect but actual suitability requires the added multiplanar definition provided by TEE [31,32,35,37,70].

Although many centers may perform the TEE assessment at the same time as or just before the planned catheter intervention, it is our practice to perform an independent assessment of suitability by an imaging cardiologist on a separate occasion. This independent TEE assessment will allow a careful and comprehensive study, time for detailed postprocessing of 3D datasets and an opportunity to explain the advantages and disadvantages of a planned procedure to the patient and family in any particular individual case based on the newly acquired TEE data.

The actual TEE assessment can use standard imaging views of the whole heart. Clearly specific attention will be paid to the atrial septum and adjacent structures that will form the anchoring rims for any device which will influence the stability of any implanted device. The proximity of adjacent vital structures including the pulmonary veins and mitral valve will be critical determinants of suitability.

Our exam sequence for TEE assessment for ASD device suitability will usually proceed in the following logical order:

A mid-esophageal 0° cut to confirm connections in the 4-chamber view, to review evidence of right heart volume overload, to assess the tricuspid valve for any intrinsic abnormality with Doppler assessment of any physiologic or pathologic tricuspid regurgitation to estimate right heart pressure. Two-dimensional and color assessment should also be made of the mitral valve as device deployment has potential to damage or impair the function of the mitral valve.

Maintain rotation of the probe at 0° to orient the atrial septum running approximately across the screen with the base to the left and cardiac apex to right. Depth is adjusted to include only as far as the tricuspid valve at the bottom right of the screen. Any obvious atrial septal defect or multiple defects at 0° are described and the diameters measured at 0°. Color flow mapping facilities identification of multiple or fenestrated defects. In our unit, we use the color flow diameter [33] as a guide to eventual device size rather than later relying on balloon sizing of the defect's stretched diameter. The total septal length is also measured at this stage. Finally, at 0°, the probe should be withdrawn until the superior caval vein is seen in cross-section and this caval vein should be followed into the heart by gradually advancing the probe whilst centering the image of the superior caval vein. A continuous luminal border of the cava will exclude superior sinus venosus type ASD. Advancing of the probe until the inferior caval vein is seen will address a similar question regarding inferior sinus venosus defects. Returning to the atrial septal defect(s), the probe is manipulated at 0° to place the atrial septum again in the center of the imaging display.

The multiplane angle is then advanced to 45° and the maximum diameter on 2D grayscale and on color flow mapping is recorded.

The multiplane angle is then further advanced to 90° and the probe rotated axially to obtain a bicaval view with superior caval vein to the right of the screen. Once again maximum diameters of any defects are recorded in 2D grayscale and color. Simultaneous, side-by-side 2D and color display, possible on most modern machines will ensure that the same defect is measured in the same phase of the cardiac cycle both on 2D and with color flow.

Having acquired all 2D diameters our usual practice is to now obtain a full volume 3D dataset in patients able to take a 3D TEE probe (>25–30 kg body weight). This 3D dataset is obtained at 0° with the depth set to include the tricuspid valve and the basal portion of the right ventricle (Video 41.4). This will allow image orientation at later post processing (see later).

Having described the defect size at three multiplane imaging angles (0, 45, and 90°), the operator can now focus on the surrounding tissue rims and adjacent vital structures.

At 0°, the pulmonary veins are imaged as described earlier and the pulmonary vein rim is the free-standing tissue with pulmonary vein lumen on one side and right atrial cavity on the other which extends from the right pulmonary vein entry to the left atrium and the ASD. In most series and for most devices, this rim must equal or exceed 5 mm in length to allow anchoring of the device but importantly the device should not obstruct pulmonary venous return. This latter aspect will be examined during actual device deployment.

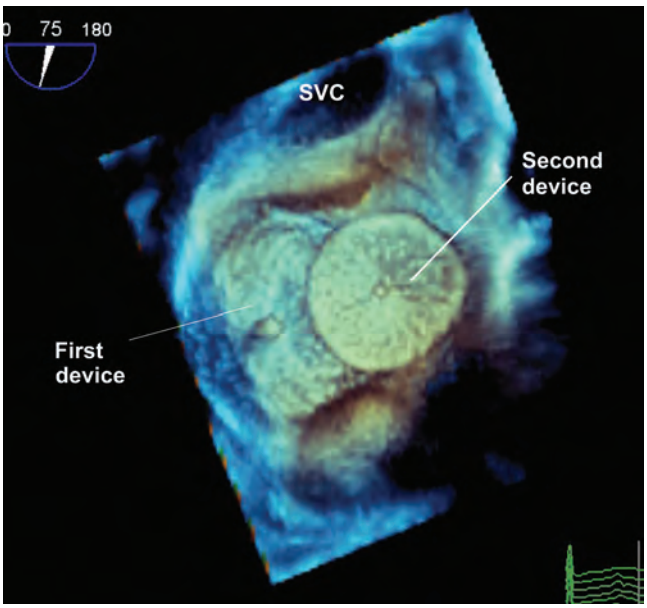
Still at 0°, the probe is rotated to develop a 4-chamber view and the distance between the atrial septal defect and the mitral valve hinge point is described as the mitral valve rim.

At 45°, the aortic valve is brought into view and the aortic rim is the often short tongue of tissue extending back from the aortic wall into the atrial cavity. Deficiency of the aortic rim continues to be of concern and has been the subject of a recent review by the Society for Cardiovascular Angiography and Interventions and reported to the FDA [71].

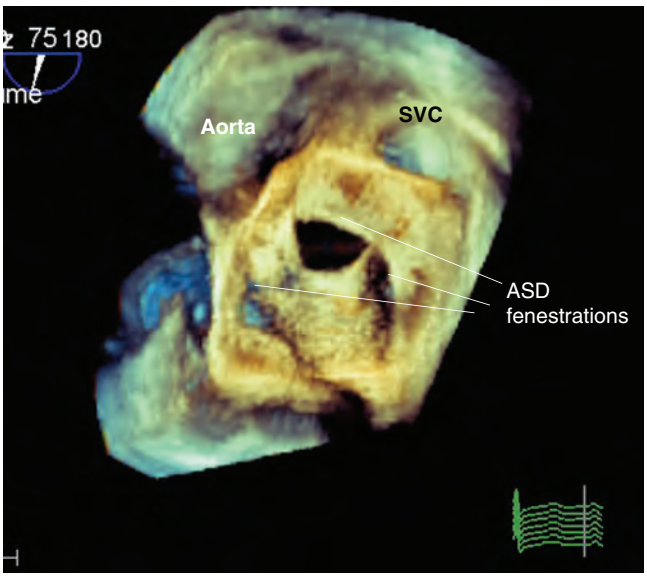
Finally, at a multiplane angle of 90°, the superior and inferior caval rims are documented. Of note the inferior caval rim is often difficult to define with TEE, and a correlation with TTE bicaval views should be made.

Once confirmed as likely suitable for device closure, catheter intervention for ASD can proceed also primarily under TEE guidance. Such catheter guidance by TEE has significant advantages, including a decreased radiographic screening time and radiation, a reduced total procedure time, and in cases of multiple fenestrations, the catheter interventionalist can confirm passage of the guide wire and subsequent deployment sheath via the target orifice, usually the largest of the defects (Videos 41.5 and 41.6). Catheter closure of multiple defects can also proceed with clear delineation that a second or subsequent device crosses the atrial septum via a different defect from the first or previous device or if using a single larger device to cover both defects then defect coverage can be confirmed before release (Figure 41.7a,b; Video 41.7). Device closure of atrial septal defects will usually employ a device with a component of the device on either side of the atrial septum. Real-time 2D TEE will allow confirmation that the right or left atrial component is sitting wholly within the correct atrium and is not straddling the defect.

When using 2D TEE, the optimal multiplane angle to guide initial deployment is often around 30–45°. However, once the left atrial disc is deployed the circumference of the defect will need to be surveyed again using standard multiplane angles or 0°, 45°, 90°. It is vital at this stage to confirm that the whole of the left atrial component of the device is within the left atrium and not through the defect into the right atrium. Once the position of the left atrial component is satisfactory, the right atrial component can be deployed and surveyed through all angles. The persistence of some color flow across the atrial septal defect at this stage is expected as there is still tension on the apparatus which will induce deformation. More importantly the role of the echocardiographer is to confirm correct placement of the device components and to reassess following any further manipulation of the device prior to release. Any gross size mismatch or interference with vital structure must be reported when seen. Before release the echocardiographers must reassess the rims, ensure that there is unobstructed pulmonary venous return, that the mitral valve motion is not impeded and that the defect is adequately covered.



(a)



(b)

Figure 41.7 Three-dimensional TEE showing two adjacent septal occluders visualized from the left atrium. SVC, superior vena cava.

Other catheter interventions

Catheter intervention for congenital heart disease is obviously not restricted to the closure of atrial septal defects. However, the general principles outlined earlier can be utilized for any echo-guided catheter procedure.

TEE is used to assess suitability for device closure of perimembranous ventricular septal defects and for mid-muscular defects, being particularly useful in defining the location of the defect in relation to the moderator band of the right ventricle and other potentially intervening structures. Actual procedural guidance of device closure for ventricular septal defects can then be guided by TEE without the potential complication of intracardiac echocardiography (ICE) or impracticality of transthoracic echo within the angiography field. A combination of 2D techniques (Video 41.8), real-time 3D guidance (Video 41.9), or simultaneous orthogonal plane projections (Video 41.10) are all utilized depending on the size of the patient and complexity of the case.

Catheter intervention for less common problems such as fistulas from a sinus of Valsalva aneurysm [72] and closure of paravalvular leaks after prosthetic valve surgery will be ideally guided by TEE to ensure device deployment does not compromise the leaflet function.

Three-dimensional TEE has the potential to further assist with interventional catheter procedures. The technique has been applied for many different indications including transseptal puncture [73], atrial septal defect closure [32,35], occlusion of the left atrial appendage, clipping of the mitral valve [74–76], paraprosthetic valve leaks [67], and VSDs [77]. Advantages of the technique include the ability to track the precise position of wires, catheters and devices as well as the ability to reconstruct views en face to septal structures, which is relevant for both ASD and VSD closure (Video 41.11). For procedures around the left atrium and mitral valve, the imaging position can be set so that the entirety of the left atrium can be visualized as well as the mitral valve leaflets. With respect to occlusion of septal defects, these can be imaged en face allowing for precise measurement of the defect and rims. This is particularly helpful for multifenestrated atrial septal defects or for positioning occlusion devices when other devices are in situ.

Intraoperative imaging

Although detailed multimodal preoperative imaging will facilitate surgical decision making and will form the substrate for a pre-surgical multidisciplinary surgical planning meeting, there is a still a role for further detailed echocardiography in the operating room immediately before cardiopulmonary bypass and certainly directly after coming off bypass and before leaving the operating suite.

Although the actual morphologic cardiac diagnosis is unlikely to change, refinement of the lesion detail may be enhanced, particularly if preoperative imaging outside the operating suite did not include TEE. TEE immediately before surgery may value-add by detecting additional minor lesions which may need surgical attention, that is, atrial septal communications, additional muscular ventricular septal defects.

Intraoperative echocardiography will either involve TEE or in selected patients an epicardial approach may be preferred. Although the advent of smaller multiplane TEE probes has reduced the need for direct 2D epicardial studies, the now routine use of 3D echocardiography has brought the epicardial approach back in to common use.

Epicardial echocardiography

Prior to the advent of small multiplane TEE, intraoperative echocardiography in small patients was limited to the epicardial approach. This is achieved by using a handheld high frequency probe in an appropriate sterile sheath manipulated directly by the surgeon within the sterile operating field; with image controls and interpretation performed by an advanced echocardiographer at the head of the operating table beyond the sterile field. Alternatively, the echocardiographer could gown and scrub-in with the surgeon to perform the actual probe manipulation with a second echocardiographer at the cart beyond the sterile field. In our experience, the best combination is a dedicated surgeon with appropriate training and experience manipulating the probe and the expert echocardiographer directing the study from the cart. The surgeon is most expert at dealing with the exposed heart and other cardiac structures with minimal risk of trauma to the surgical field. Using this approach the full range of echocardiography can be performed including 2D and 3D acquisition, Doppler and color flow.

The actual preparation of the epicardial probe requires the sterile sheath to be collapsed onto itself by the surgeon thus exposing the lumen; a generous amount of imaging gel is delivered to the distal end of the sheath and the cleaned but not sterile probe is carefully placed inside the lumen of the sheath without compromising sterility of the external surface. The sheath is then extended proximally to enclose the probe lead and the sheath handed over the anesthesiologist's drape to the echocardiographer. The sheath on the surgeon's side of the anesthesiologist's drape can be considered to be sterile and can be manipulated by the sterile operator. Our surgeons have developed a technique of placing a stay ligature around the outside of the sheath at the level of the probe to inhibit movement of the probe within the sheath at the distal end. This modification allows the operator to make minute manipulations of the actual probe without concern about the probe and sheath moving against each other.

The actual epicardial examination can either target the discrete area of interest or can include a comprehensive approach using established guideline views [78]. Our approach has been to target mainly the area of interest particularly as the heart is commonly congenitally malformed which may limit standard

views and the time for image acquisition should not unnecessarily extend the actual operation duration.

The established standard views can be considered analogous to standard TTE views and include an epicardial short-axis view at the level of the aortic valve, an aortic long-axis view obtained by rotating the probe through 90°, further short-axis views at the level of the mitral valve and mid-ventricular level displaying the LV papillary muscles, and an LV long-axis view which can be further developed to show the tricuspid valve in a similar fashion to TTE; an epicardial 2-chamber view can be developed from the LV long axis by further clockwise rotation of the probe. Finally, an epicardial RV outflow tract view can be obtained by manipulating the transducer over the RV outflow tract with the index mark toward the patient's left shoulder in the normally connected heart or along the axis of the main pulmonary artery in other morphologic permutations.

Following development of size-appropriate TEE probes that can be used on a larger proportion of congenital heart surgery patients, fewer intraoperative epicardial exams have been performed. However, despite the availability of TEE in smaller patients, there is still a major role for the epicardial approach in selected lesions. TEE is not ideal for the most anterior cardiac structures and does not provide optimal imaging of the main and branch pulmonary arteries. Direct epicardial examination allows very high-resolution imaging of these structures. Abnormalities of the atrioventricular junction including the complete atrioventricular septal defect (AVSD) and AVSD-tetralogy are routinely imaged by the epicardial approach particularly as this allows the use of 3D echocardiography in infants who are too small for a 3D TEE. Both real-time 3D and postprocessed full volume acquisitions can guide the surgeon when repairing the left AV valve and postoperative epicardial imaging will assess adequacy of the repair. Unusual presentations such as a flail mitral valve following repair of tetralogy of Fallot, also merit detailed 3D epicardial imaging. Video 41.12 shows a chordal rupture, which was subsequently repaired surgically. Surgical approaches to Ebstein's anomaly are difficult and often involve relocation of valve tissue across 2D planes; for this reason 3D epicardial echo support for the surgeon has been used with success [79]. The success of the arterial switch operation (ASO) for ventriculoarterial discordance is critically dependent upon successful relocation of coronary artery origin buttons and any kinking or undue tension may result in frank ventricular failure. As most ASO surgical candidates are newborns with a body weight of 2000–4000 grams, it is our practice to perform epicardial echocardiographic evaluation of LV systolic function at the end of every ASO to document good LV function and visualize the coronary anastomoses.

Intraoperative TEE

Despite the advantages offered by an epicardial approach as described earlier, an advantage of intraoperative TEE is that the probe can be placed preoperatively by the anesthesiologist and a baseline study can be performed to evaluate for any previously undetected additional lesion and to obtain optimal imaging windows for a direct comparison immediately after intracardiac repair on cardiopulmonary bypass. The intraoperative studies should ideally be performed by the same operator before, during, and after surgery to minimize interobserver bias when making subjective judgments about adequacy of repair, and the TEE operator must have sufficient expertise and seniority to make a difficult judgment call which may result in the patient going back on cardiopulmonary bypass (CPB) if the echocardiogram detects significant residual pathology. To accommodate this requirement, it is our practice for each intraoperative TEE to be supervised by an attending/consultant cardiologist with advanced TEE expertise. As an additional development, we have also installed a fixed telemedicine link between our operating suite echocardiography cart and the remote echo lab so that real-time guidance and reporting can occur even if the expert echocardiographer is not actually present in the operating suite.

Intraoperative TEE will use the same standard views described earlier but will more often concentrate on the lesion being operated. Optimization of the probe depth and multiplane angle before operation will allow rapid refocusing of the study during and after the surgery. It is important to de-select or disconnect the TEE probe during the actual surgery to minimize the risk of inadvertent thermal trauma to the esophageal mucosa. Our own practice is to leave the probe in the esophagus but disconnect from the cart to allow the cart to be moved out of the immediate anesthetic area. Depending on the machine characteristics and duration of start-up sequence, the operator may use a standby mode rather than full shutdown between the preoperative study and that done towards the end of the procedure.

The timing of any postoperative study is crucial to the interpretation of the data. For example, when evaluating an atrioventricular valve for regurgitation following repair, loading conditions are crucial. A TEE done on partial CPB will not replicate full loading conditions. Volume replacement, inotropes, vasodilators and rewarming will affect preload, afterload and contractility. Wherever possible a stable hemodynamic state after achieving systemic blood pressure and atrial filling pressure targets, at normothermia with a constant background rate of inotropes or vasodilators, will allow the most reliable estimate of valve function and systemic ventricular function. Similarly, outflow tract gradients can be significantly underestimated if the TEE is performed too early after coming off CPB.

Target lesions for transesophageal echocardiography in CHD

Intraoperative TEE is not indicated for every CHD surgery. Non-bypass extracardiac procedures such as pulmonary artery banding, coarctation repair or systemic to pulmonary artery shunts, do not merit routine intraoperative TEE. Simple intracardiac procedures on CPB such as surgical closure of a secundum atrial

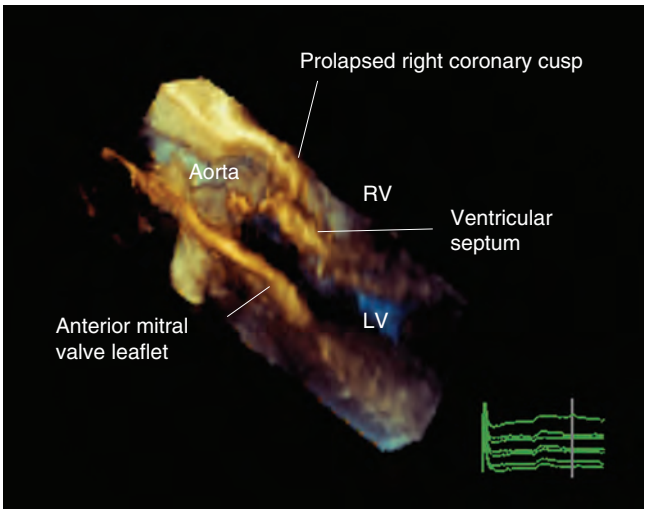


Figure 41.8 Three-dimensional TEE showing prolapse of the right coronary cusp into a perimembranous ventricular septal defect. LV, left ventricle; RV, right ventricle.

septal defect will also rarely merit TEE attention. Intraoperative TEE is, however, more likely to have a significant impact in certain lesions such as aortic valve repairs and surgery involving the atrioventricular valves. In a large single-center experience, Randolph et al. [15] were able to categorize clinical impact as minor or major, following pre- or post-bypass TEE and documented a combined major impact rate of 13.8%. Impact was greatest in patients undergoing reoperation. Finally, in many centers, routine post-bypass TEE is employed by the cardiac anesthetist to evaluate LV function and to look specifically for residual intracardiac air.

Three-dimensional TEE to assist surgical procedures

Standard cross-sectional 2D TEE techniques depend on the operator and surgeon using different planes to build up a picture of the lesion in question. This approach has many strengths including high image resolution and familiarity of most users with the technique. The use of color flow Doppler assists in detection of, for example, regions of valvar regurgitation or residual leaks across septal patches. In selected cases 3D TEE may assist as a complementary technique to inform the surgical approach [27,30,80,81]. Examples can include repair of atrioventricular valves, particularly on valves that have undergone previous surgical intervention or in patients in whom the position of the heart is abnormal where some cross-sectional imaging planes may be difficult to interpret. Lesions where the 3D geometry for repair is important are also potential targets for this approach such as re-suspension of the aortic valve following aortic valve cusp prolapse (Figure 41.8; Video 41.13). For repair of atrioventricular valves, the 3D technique can give unique views from the atrial aspect of the valve (Video 41.14) which cannot be achieved by cross-sectional techniques. In patients who are not large enough to accommodate the 3D TEE probe, we have utilized a 3D epicardial approach instead [68].

Conclusion

In congenital and pediatric cardiology 2D and 3D TEE are mainly used for intraoperative imaging and for guiding catheter interventions. Rarely, purely diagnostic TEE is performed for specific indications including detection of intracardiac thrombi or suspected vegetations. Currently no pediatric 3D TEE probe is available that limits the use of 3D TEE to children >25 kg. In smaller children epicardial perioperative imaging is an excellent alternative but requires coordination and collaboration with the surgical team.

Videos

To access the videos for this chapter, please go to www.lai-echo.com.

Video 41.1 TEE of the atrial septum at 0°. The probe is placed inferiorly and withdrawn, the coronary sinus is seen inferiorly and the entry of the SVC to the right atrium is viewed superiorly.

Video 41.2 TEE of the pulmonary veins in a patient with an atrial septal defect. The probe is rotated to demonstrate the left pulmonary veins and then right pulmonary veins as they enter the left atrium.

Video 41.3 TEE at 120° showing the left ventricular outflow tract. The right coronary cusp has prolapsed into a restrictive ventricular septal defect. There is mild aortic regurgitation.

Video 41.4 Three-dimensional TEE of the normal atrial septum viewed from the right atrial aspect. The tricuspid valve is seen opening to the right and the thin oval fossa tissue is seen centrally.

Video 41.5 Three-dimensional TEE showing a fenestrated atrial septal defect visualized from the right atrial aspect.

Video 41.6 Three-dimensional TEE of a catheter sheath passing across a large fenestration in the atrial septum. The depth of image permits visualization of the catheter course.

Video 41.7 Three-dimensional (3D) TEE of three septal occluder devices viewed from the left atrial aspect. The 3D technique facilitates visualization of the relative position of the devices.

Video 41.8 A catheter is seen crossing a muscular ventricular septal defect in a 4-chamber TEE projection.

Video 41.9 Three-dimensional TEE assists in delineating the course of catheters across the ventricular septum. The catheter is seen crossing from the left ventricle to the right ventricle.

Video 41.10 Cross-plane TEE imaging of a device placed in a muscular ventricular septal defect. This technique permits the operator to visualize two separate planes of insonation in a single projection to permit different perspectives on the VSD occlude device.

Video 41.11 Three-dimensional TEE of a perimembranous ventricular septal defect viewed from the right ventricular aspect of the ventricular septum. The defect is adjacent to the tricuspid valve and the pulmonary valve is in the far field.

Video 41.12 Epicardial 3D echocardiogram showing chordal rupture with a flail chord seen clearly within the left atrium during systole.

Video 41.13 Three-dimensional TEE of a ventricular septal defect with prolapse of the right coronary cusp.

Video 41.14 Atrial view of an atrioventricular septal defect. The trileaflet left AV valve is clearly seen as are the bridging leaflets between the left and right ventricles.

References

1 Kyo S, Koike K, Takanawa E, et al. Impact of transesophageal Doppler echocardiography on pediatric cardiac surgery. *Int J Card Imaging* 1989;**4**:41–42.

2 Kyo S, Omoto R, Matsumura M, et al. Intraoperative transesophageal echocardiography in pediatric patients. *J Thorac Cardiovasc Surg* 1990;**99**:373–375.

3 Stumper OF, Elzenga NJ, Hess J, Sutherland GR. Transesophageal echocardiography in children with congenital heart disease: an initial experience. *J Am Coll Cardiol* 1990;**16**:433–441.

4 Ritter SB. Transesophageal real-time echocardiography in infants and children with congenital heart disease. *J Am Coll Cardiol* 1991;**18**:569–580.

5 Stumper O, Kaulitz R, Elzenga NJ, et al. The value of transesophageal echocardiography in children with congenital heart disease. *J Am Soc Echocardiogr* 1991;**4**:164–176.

6 Fyfe DA, Kline CH. Transesophageal echocardiography for congenital heart disease. *Echocardiography* 1991;**8**:573–586.

7 Lam J, Neirotti RA, Nijveld A, et al. Transesophageal echocardiography in pediatric patients: preliminary results. *J Am Soc Echocardiogr* 1991;**4**:43–50.

8 Weintraub R, Shiota T, Elkadi T, et al. Transesophageal echocardiography in infants and children with congenital heart disease. *Circulation* 1992;**86**:711–722.

9 Stevenson JG, Sorensen GK, Gartman DM, et al. Transesophageal echocardiography during repair of congenital cardiac defects: identification of residual problems necessitating reoperation. *J Am Soc Echocardiogr* 1993;**6**:356–365.

10 Benheim A, Karr SS, Sell JE, et al. Routine use of transesophageal echocardiography and color-flow imaging in the evaluation and treatment of congenital heart disease. *Echocardiography* 1993;**10**:583–593.

11 Muhiudeen I, Silverman N. Intraoperative transesophageal echocardiography using high resolution imaging in infants and children with congenital heart disease. *Echocardiography* 1993;**10**:599–608.

12 Lam J, Neirotti RA, Lubbers WJ, et al. Usefulness of biplane transesophageal echocardiography in neonates, infants and children with congenital heart disease. *Am J Cardiol* 1993;**72**:699–706.

13 O'Leary PW, Hagler DJ, Seward JB, et al. Biplane intraoperative transesophageal echocardiography in congenital heart disease. *Mayo Clin Proc* 1995;**70**:317–326.

14 Loick HM, Scheld HH, Van Aken H. Impact of perioperative transesophageal echocardiography on cardiac surgery. *Thorac Cardiovasc Surg* 1997;**45**:321–325.

15 Randolph GR, Hagler DJ, Connolly HM, et al. Intraoperative transesophageal echocardiography during surgery for congenital heart defects. *J Thorac Cardiovasc Surg* 2002;**124**:1176–1182.

16 Ayres NA, Miller-Hance W, Fyfe DA, et al. Indications and guidelines for performance of transesophageal echocardiography in the patient with pediatric acquired or congenital heart disease: report from the task force of the Pediatric Council of the American Society of Echocardiography. *J Am Soc Echocardiogr* 2005;**18**:91–98.

17 Cromme-Dijkhuis AH, Djoa KK, Bom N, Hess J. Pediatric transesophageal echocardiography by means of a miniature 5-MHz multiplane transducer. *Echocardiography* 1996;**13**:685.

18 Mart CR, Fehr DM, Myers JL, Rosen KL. Intraoperative transesophageal echocardiography in a 1.4-kg infant with complex congenital heart disease. *Pediatr Cardiol* 2003;**24**:84–85.

19 Scohy TV, Gommers D, Jan ten Harkel AD, et al. Intraoperative evaluation of micromultiplane transesophageal echocardiographic probe in surgery for congenital heart disease. *Eur J Echocardiogr* 2007;**8**:241–246.

20 Pushparajah K, Miller OI, Rawlins D, et al. Clinical application of a micro multiplane transoesophageal probe in congenital cardiac disease. *Cardiol Young* 2012;**22**:170–177.

21 Shanewise JS, Cheung AT, Aronson S, et al. ASE/SCA guidelines for performing a comprehensive intraoperative multiplane transesophageal echocardiography examination: recommendations of the American Society of Echocardiography Council for Intraoperative Echocardiography and the Society of Cardiovascular Anesthesiologists Task Force for Certification in Perioperative Transesophageal Echocardiography. *Anesth Analg* 1999;**89**:870–884.

22 Mochizuki Y, Patel AK, Banerjee A, et al. Intraoperative transesophageal echocardiography: correlation of echocardiographic findings and surgical pathology. *Cardiol Rev* 1999;**7**:270–276.

23 Andropoulos DB. Transesophageal echocardiography as a guide to central venous catheter placement in pediatric patients undergoing cardiac surgery. *J Cardiothorac Vasc Anesth* 1999;**13**:320–321.

24 Smallhorn JF. Intraoperative transesophageal echocardiography in congenital heart disease. *Echocardiography* 2002;**19**:709–723.

25 Scohy TV, Ten Cate FJ, Lecomte PV, et al. Usefulness of intraoperative real-time 3D transesophageal echocardiography in cardiac surgery. *J Card Surg* 2008;**23**:784–786.

26 Scohy TV, Gommers D, Schepp MN, et al. Image quality using a micromultiplane transesophageal echocardiographic probe in older children during cardiac surgery. *Eur J Anaesthesiol* 2009;**26**:445–447.

27 Vegas A, Meineri M. Core review: three-dimensional transesophageal echocardiography is a major advance for intraoperative clinical management of patients undergoing cardiac surgery: a core review. *Anesth Analg* 2010;**110**:1548–1573.

28 Costa P, Moura C, Areias JC, Sousa AR. Intraoperative transesophageal echocardiogram using an intracardiac ultrasound catheter in a congenital heart surgery: a case report. *Pediatr Cardiol* 2013;**34**:1911–1913.

29 Scohy TV, Luthen C, McGhie J, Oei F. Three-dimensional transesophageal echocardiography: diagnosing intraoperative pulmonary artery thrombus. *Interact Cardiovasc Thorac Surg* 2011;**12**:840–841.

30 Hien MD, Rauch H, Lichtenberg A, et al. Real-time three-dimensional transesophageal echocardiography: improvements in intraoperative mitral valve imaging. *Anesth Analg* 2013;**116**:287–295.
31 Schubert S, Kainz S, Peters B, et al. Interventional closure of atrial septal defects without fluoroscopy in adult and pediatric patients. *Clin Res Cardiol* 2012;**101**:691–700.
32 Chen FL, Hsiung MC, Hsieh KS, et al. Real time three-dimensional transthoracic echocardiography for guiding Amplatzer septal occluder device deployment in patients with atrial septal defect. *Echocardiography* 2006;**23**:763–770.
33 Tzifa A, Gordon J, Tibby SM, et al. Transcatheter atrial septal defect closure guided by colour flow Doppler. *Int J Cardiol* 2011;**149**:299–303.
34 Van Der Velde ME, Perry SB. Transesophageal echocardiography during interventional catheterization in congenital heart disease. *Echocardiography* 1997;**14**:513–518.
35 Vaidyanathan B, Simpson JM, Kumar RK. Transesophageal echocardiography for device closure of atrial septal defects: case selection, planning, and procedural guidance. *JACC Cardiovasc Imaging* 2009;**2**:1238–1242.
36 Rigby ML. Transoesophageal echocardiography during interventional cardiac catheterisation in congenital heart disease. *Heart* 2001;**86**:II23–129.
37 Erdem A, Saritas T, Zeybek C, et al. Transthoracic echocardiographic guidance during transcatheter closure of atrial septal defects in children and adults. *Int J Cardiovasc Imaging* 2013;**29**:53–61.
38 Heard CM, Gunnarsson B, Heard AM, et al. Anaesthetic technique for transoesophageal echocardiography in children. *Paediatr Anaesth* 2001;**11**:181–184.
39 Mart CR, Parrish M, Rosen KL, et al. Safety and efficacy of sedation with propofol for transoesophageal echocardiography in children in an outpatient setting. *Cardiol Young* 2006;**16**:152–156.
40 Marcus B, Steward DJ, Khan NR, et al. Outpatient transesophageal echocardiography with intravenous propofol anesthesia in children and adolescents. *J Am Soc Echocardiogr* 1993;**6**:205–209.
41 Scohy TV, Matte G, van Neer PL, et al. A new transesophageal probe for newborns. *Ultrasound Med Biol* 2009;**35**:1686–1689.
42 Hilberath JN, Oakes DA, Shernan SK, et al. Safety of transesophageal echocardiography. *J Am Soc Echocardiogr* 2010;**23**:1115–1127; quiz 220–221.
43 Mart CR, Rosen KL. Optimal head position during transesophageal echocardiographic probe insertion for pediatric patients weighing up to 10 kg. *Pediatr Cardiol* 2009;**30**:441–446.
44 Stevenson JG. Incidence of complications in pediatric transesophageal echocardiography: experience in 1650 cases. *J Am Soc Echocardiogr* 1999;**12**:527–532.
45 Neema PK, Manikandan S, Vijayakumar A, et al. Resolution of airway compression induced by transesophageal echocardiography probe insertion in a pediatric patient after repair of an atrial septal defect and partial anomalous pulmonary venous connection. *J Cardiothorac Vasc Anesth* 2008;**22**:887–889.
46 Shekerdemian LS, Bush A, Shore DF, et al. Cardiopulmonary interactions after Fontan operations: augmentation of cardiac output using negative pressure ventilation. *Circulation* 1997;**96**:3934–3942.
47 Spier BJ, Larue SJ, Teelin TC, et al. Review of complications in a series of patients with known gastro-esophageal varices undergoing transesophageal echocardiography. *J Am Soc Echocardiogr* 2009;**22**:396–400.
48 Stevenson JG, Sorensen GK. Proper probe size for pediatric transesophageal echocardiography. *Am J Cardiol* 1993;**72**:491–492.
49 Kwak J, Andrawes M, Garvin S, D'Ambra MN. 3D transesophageal echocardiography: a review of recent literature 2007–2009. *Curr Opin Anaesthesiol* 2010;**23**:80–88.
50 Kanagala P, Bradley C, Hoffman P, Steeds RP. Guidelines for transoesophageal echocardiographic probe cleaning and disinfection from the British Society of Echocardiography. *Eur J Echocardiogr* 2011;**12**:i17–23.
51 Hernandez A, Carrasco M, Ausina V. Mycobactericidal activity of chlorine dioxide wipes in a modified prEN 14563 test. *J Hosp Infect* 2008;**69**:384–388.
52 Krivokapich J. Echocardiography in valvular heart disease. *Curr Opin Cardiol* 1994;**9**:158–163.
53 Singh GK, Shiota T, Cobanoglu A, et al. Diagnostic accuracy and role of intraoperative biplane transesophageal echocardiography in pediatric patients with left ventricle outflow tract lesions. *J Am Soc Echocardiogr* 1998;**11**:47–56.
54 Bach DS. Transesophageal echocardiographic (TEE) evaluation of prosthetic valves. *Cardiol Clin* 2000;**18**:751–771.
55 Shively BK. Transesophageal echocardiographic (TEE) evaluation of the aortic valve, left ventricular outflow tract, and pulmonic valve. *Cardiol Clin* 2000;**18**:711–729.
56 Zaroff JG, Picard MH. Transesophageal echocardiographic (TEE) evaluation of the mitral and tricuspid valves. *Cardiol Clin* 2000;**18**:731–750.
57 Miller AP, Nanda NC, Aaluri S, et al. Three-dimensional transesophageal echocardiographic demonstration of anatomical defects in AV septal defect patients presenting for reoperation. *Echocardiography* 2003;**20**:105–109.
58 Faletra FF, Nucifora G, Ho SY. Imaging the atrial septum using real-time three-dimensional transesophageal echocardiography: technical tips, normal anatomy, and its role in transseptal puncture. *J Am Soc Echocardiogr* 2011;**24**:593–599.
59 Pushparajah K, Miller OI, Simpson JM. 3D echocardiography of the atrial septum: anatomical features and landmarks for the echocardiographer. *JACC Cardiovasc Imaging* 2010;**3**:981–984.
60 Simpson JM, Anderson DR, Qureshi SA. Closed atrial septectomy with Brock punch aided by operative transesophageal echocardiography. *Ann Thorac Surg* 1995;**60**:1794–1795.
61 Aschenberg W, Schlüter M, Kremer P, et al. Transesophageal two-dimensional echocardiography for the detection of left atrial appendage thrombus. *J Am Coll Cardiol* 1986;**7**:163–166.
62 Fyfe DA, Kline CH, Sade RM, Gillette PC. Transesophageal echocardiography detects thrombus formation not identified by transthoracic echocardiography after the Fontan operation. *J Am Coll Cardiol* 1991;**18**:1733–1737.
63 Fyfe DA, Kline CH, Sade RM, et al. The utility of transesophageal echocardiography during and after Fontan operations in small children. *Am Heart J* 1991;**122**:1403–1415.
64 Quinones MA, Douglas PS, Foster E, et al. ACC/AHA clinical competence statement on echocardiography: a report of the American College of Cardiology/American Heart Association/American College of Physicians-American Society of Internal Medicine Task Force on clinical competence. *J Am Soc Echocardiogr* 2003;**16**:379–402.

65 Flachskampf FA, Badano L, Daniel WG, et al. Recommendations for transoesophageal echocardiography: update 2010. *Eur J Echocardiogr* 2010;**11**:557–576.
66 Flachskampf FA, Decoodt P, Fraser AG, et al. Guidelines from the Working Group. Recommendations for performing transesophageal echocardiography. *Eur J Echocardiogr* 2001;**2**:8–21.
67 Azran MS, Romig CB, Locke A, Whitley WS. Echo rounds: application of real-time 3-dimensional transesophageal echocardiography in the percutaneous closure of a mitral paravalvular leak. *Anesth Analg* 2010;**110**:1581–1583.
68 Rawlins DB, Austin C, Simpson JM. Live three-dimensional paediatric intraoperative epicardial echocardiography as a guide to surgical repair of atrioventricular valves. *Cardiol Young* 2006;**16**:34–39.
69 Simpson J, Miller O, Bell A, et al. Image orientation for three-dimensional echocardiography of congenital heart disease. *Int J Cardiovasc Imaging* 2012;**28**:743–753.
70 Abdel-Massih T, Dulac Y, Taktak A, et al. Assessment of atrial septal defect size with 3D-transesophageal echocardiography: comparison with balloon method. *Echocardiography* 2005;**22**:121–127.
71 Society for Cardiovascular Angiography and Interventions 2012. Written statement to the U.S. Food and Drug Administration's Circulatory System Devices Panel regarding the available published safety and effectiveness data for transcatheter Atrial Septal Defect occluders. Available from: http://www.fda.gov/downloads/AdvisoryCommittees/CommitteesMeetingMaterials/MedicalDevices/MedicalDevicesAdvisoryCommittee/CirculatorySystemDevicesPanel/UCM304929.pdf (last accessed May 22, 2015).
72 Arora R. Catheter closure of perforated sinus of Valsalva. In: Sievert H, Qureshi SA, Wilson N, Hijazi ZM (eds.) *Percutaneous Interventions for Congenital Heart Disease*, 1st edn. London: Informa Healthcare, 2007.
73 Hahn K, Gal R, Sarnoski J, et al. Transesophageal echocardiographically guided atrial transseptal catheterization in patients with normal-sized atria: incidence of complications. *Clinical Cardiology* 1995;**18**:217–220.
74 Siegel RJ, Luo H, Biner S. Transcatheter valve repair/implantation. *Int J Cardiovasc Imaging* 2011;**27**:1165–1177.
75 Altiok E, Becker M, Hamada S, et al. Optimized guidance of percutaneous edge-to edge repair of the mitral valve using real-time 3-D transesophageal echocardiography. *Clin Res Cardiol* 2011;**100**:675–681.
76 Slipczuk L, Siegel RJ, Jilaihawi H, et al. Optimizing procedural outcomes in percutaneous mitral valve therapy using transesophageal imaging: a stepwise analysis. *Expert Rev Cardiovasc Ther* 2012;**10**:901–916.
77 Fu YC, Bass J, Amin Z, et al. Transcatheter closure of perimembranous ventricular septal defects using the new Amplatzer membranous VSD occluder: results of the U.S. phase I trial. *J Am Coll Cardiol* 2006;**47**:319–325.
78 Reeves ST, Glas KE, Eltzschig H, et al. Guidelines for performing a comprehensive epicardial echocardiography examination: recommendations of the American Society of Echocardiography and the Society of Cardiovascular Anesthesiologists. *Anesth Analg* 2007;**105**:22–28.
79 Taktak A, Acar P, Dulac Y, et al. [A new approach to the tricuspid valve in Ebstein's anomaly by real-time 3D echocardiography]. *Arch Mal Coeur Vaiss* 2005;**98**:531–537.
80 Moustafa SE, Chandrasekaran K, Khandheria B, et al. Real-time three-dimensional transesophageal echocardiography assessment of the mitral valve: perioperative advantages and game-changing findings. *J Heart Valve Dis* 2011;**20**:114–122.
81 Gadhinglajkar S, Sreedhar R. Surgery for ruptured sinus of Valsalva aneurysm into right ventricular outflow tract: role of intraoperative 2D and real time 3D transesophageal echocardiography. *Echocardiography* 2010;**27**:E65–69.

CHAPTER 42

3D Echocardiography

Folkert Jan Meijboom[1], Heleen van der Zwaan[2], and Jackie McGhie[2]
[1]Department of Pediatrics and Cardiology, Academic Medical Centre Utrecht, Utrecht, The Netherlands
[2]Department of Cardiology, Erasmus University Rotterdam, Rotterdam, The Netherlands

A short history of 3D echocardiography

The first publication on 3D ultrasound dates from 1974 [1]. In the 1980s various research groups, such as the Tokyo and the Duke University groups, produced 3D ultrasound images of the heart [2–4]. In the early 1990s the Duke group developed the first real-time 3D (RT3D) matrix phased-array transducer, containing 512 elements, with a frame rate high enough to image cardiac motion (Figure 42.1) [5,6]. This technique remains the basis of all the 3D echo transducers currently commercially available. The rapid progression of computer technology, with increasing computational power of smaller microprocessors, allowed further improvements of the original transducer design [7,8]. Initially, the use of 3D echocardiography in pediatric cardiology was limited because only low-frequency transducers with large footprints were available. In recent years high-frequency pediatric probes have been developed for transthoracic use [9]. A major breakthrough for 3D echocardiography was the development of a 3D TEE probe which enables high-resolution images to be obtained due to its higher frequency and improved imaging windows. Unfortunately a specific pediatric 3D TEE probe is not yet available.

Current clinical applications of 3D echocardiography

3D TTE and congenital heart disease

Intuitively adding a third dimension is appealing for the diagnosis and management of congenital heart disease (CHD). Three-dimensional imaging replaces mental reconstruction based on 2D imaging for visualizing congenital cardiac anatomic abnormalities. However, despite the technological advances, 3D echocardiography still has a lower spatial and temporal resolution compared with 2D imaging, which limits its current use in clinical practice. The lower spatial resolution can be a limiting factor, especially when more detailed morphologic imaging is needed, for example in congenital and valvar heart disease. Despite these limitations, real-time 3D TTE can be used in addition to other echo modalities in selected cases for specific questions [10]. Three-dimensional echocardiography enables a unique surgical "en face view" of the valve morphology to be obtained, which can be used in surgical decision making. In complex congenital heart disease, it can be used to demonstrate the intricate 3D relationships of anatomic structures, as will be discussed later in this chapter [11–16].

3D TTE and LV function

For volume quantification of cardiac chambers image resolution is less crucial and this has been one of the first important applications of 3D echocardiography. A large number of studies have shown that volumes and ejection fraction calculated by 3D TTE correlate much better with CMR-derived volumes and EF compared to those obtained by 2D TTE [17,18]. The major limitation is the feasibility of the technique because a better image quality is required for 3D than for 2D analysis. In the adult population this is an important limitation as adequate images can only be obtained in approximately 60% of patients. Increasing automation of the 3D analysis enables very good reproducibility of the methodology, which is an advantage for clinical follow-up of patients. In oncology patients, it was recently demonstrated to be the method of choice in the clinical follow-up [19]. However, despite its proven superiority to 2D techniques, 3D LV volumetry has not been included as the preferred technique in the guidelines for echocardiographic chamber quantification.

3D TTE and RV function

RV function is an important prognostic clinical parameter, especially in congenital right heart disease, pulmonary hypertension, and in different types of left-sided heart disease. In recent years it has been shown that 3D TTE can assess RV volumes much more reliably than 2D TTE [20,21]. Further detail will be given in this chapter under the heading "RV function and 3D echo."

Echocardiography in Pediatric and Congenital Heart Disease: From Fetus to Adult, Second Edition. Edited by Wyman W. Lai, Luc L. Mertens, Meryl S. Cohen and Tal Geva.
© 2016 John Wiley & Sons, Ltd. Published 2016 by John Wiley & Sons, Ltd.
Companion website: www.lai-echo.com

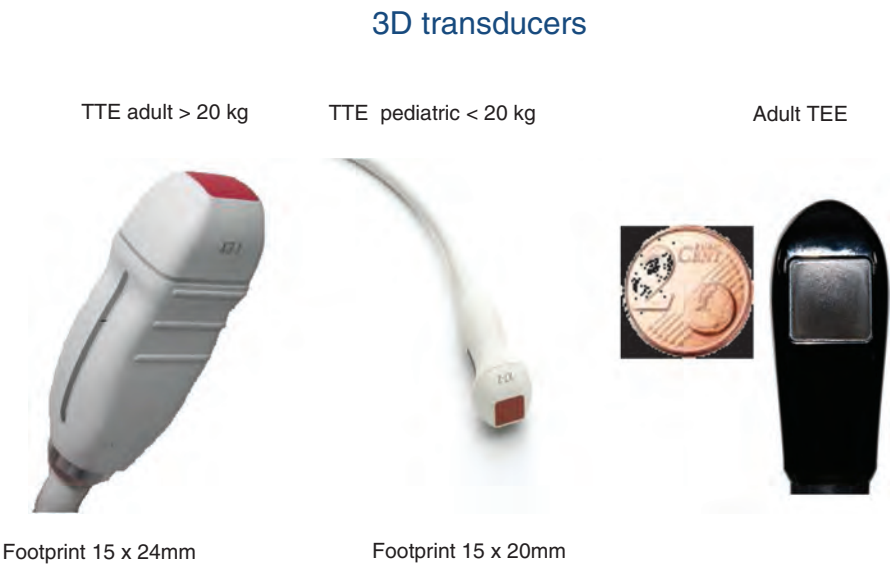


Figure 42.1 Three-dimensional transducers. TTE, transthoracic echo; TEE, transesophageal echo.

3D TEE and valve function

A breakthrough in clinical use of 3D echo was the introduction of the 3D TEE probe. Image quality is superior to that of 3D TTE and in a few years it has become part of routine clinical practice for some specific indications. In adult cardiology 3D TEE has become a very important tool in the assessment of the morphology and definition of the mechanisms of mitral [22] and aortic valve disease, the assessment of the dimensions of the aortic annulus and left ventricular outflow tract before transcatheter aortic valve implantation (TAVI), and for guiding different intracardiac interventions. Three-dimensional TEE monitoring is essential for percutaneous mitral valve repair [23] and for closure of paravalvular leaks [24]. It is also reported to be a very sensitive and efficient technique for excluding thrombi in the assessment of the left atrial appendage, which is important in atrial fibrillation. The technique uses either a real-time 3D image of the appendage, or multiplane imaging to simultaneously view two perpendicular cross-sections. Fewer reports have been published about the role of 3D TEE in congenital heart disease. Most articles focus on the advantages of RT 3D TEE during device closure of ASDs and there are some case reports on its value in a more detailed diagnosis of different congenital cardiac anomalies. The authors are convinced that the use of 3D TEE will expand quickly also in patients with more complex CHD.

How to do a 3D echo?

Due to technological advances incorporated into the latest matrix 3D transducers, the 2D image quality acquired with some of these probes is so good that the entire echo examination including 2D, 3D, and all Doppler modalities can be done using a single transducer [9].

This facilitates the integration of 3D echocardiography into daily clinical practice. The new transducer technology is also capable of providing a full volume acquisition in one single heart beat (at the expense of lower volume rates), as well as live 3D color Doppler imaging. Intermediate between 2D and 3D is biplane imaging. In this mode, two 2D images are acquired simultaneously in two planes perpendicular to each other. Additionally the ultrasound beam can be rotated electronically 360°, providing the examiner with a wide variety of 2D cross-sections without moving the transducer.

Image optimization at the time of acquisition

To optimize 3D image acquisition, we suggest the following:

1. Choose the optimal transducer frequency. In adults, penetration is important and lower-frequency transducers are preferred. In pediatric patients, penetration is less important and higher frequency transducers produce a superior spatial resolution.
2. Biplane or live 3D mode (with a narrow sector) can be used for orientation, before acquisition of a full-volume data set to check if the region of interest is within the pyramid size that you have selected.
3. First optimize the 2D image as much as possible because 3D image quality is critically dependent on 2D image quality; try to reduce noise and optimize gain settings. If necessary, increase the overall gain to ensure visualization of the structures in the planes that are not represented on the biplane mode or data not seen in the live 3D representation.
4. Choose the smallest sector size that will fit your whole region of interest (the smaller the angle, the higher the line density, and the higher the spatial resolution).
5. Note the importance of a regular heart rate if multiple beats are acquired. Most modern machines will allow single beat acquisitions but these generally have a relatively low frame rate. Multiple beat acquisition is based on reconstruction of a full volumetric data set based on a series of four to seven ECG-gated narrow data pyramids that are stitched together based on the ECG. This requires a regular heart rate; if the heart rate is irregular, stitching the subsegments into one data-pyramid

results in stitching artifacts, because the subsegments are not obtained in exactly the same phases of the cardiac cycle. Single beat full-volume acquisition is the only alternative for these patients.

6 If multibeat acquisition is used, breath-holding reduces artifacts when acquiring full volumetric data sets. Breath-holding can be very challenging in children. When children are intubated and ventilated obtaining a controlled breath hold may be easier and the opportunity should be considered.

7 For volumetric measurements, one single acquisition (from the apex) is often sufficient. If anatomic assessment is needed, multiple acquisitions from different scanning planes may be necessary. Ensure that the region of interest is in the center of the volume and perpendicular to the ultrasound beam for optimal resolution.

Image rendering

After image acquisition, one can choose to analyze datasets directly on the ultrasound scanner or perform offline analysis using dedicated software. LV volumes and EF can be calculated within seconds on the platforms. Direct visualization of cardiac structures is generally required during catheter interventions and in the operating theater. Three-dimensional TEE images can be shown real-time to guide the interventionalist or surgeon. For more complicated morphology offline analysis is recommended, as navigating through the data set often takes time and effort. Predefined 3D views are currently available, which enable fast processing of three data sets and allow the operator to obtain quickly certain views, such as an en face view on the mitral valve. When starting out with 3D echo analysis, it is possible to spend hours navigating through a single data set [25], but with training and experience, analyzing a specific region of interest can be achieved quickly. The essential "cropped views" and cross-section can be stored as "bookmarks" and included in the structured echo report [26]. Software for 3D echo analysis differs between vendors but most systems include a full volume pyramid data set encased in a cube, called a "crop box" (Figure 42.2; Video 42.1). Using a crop box, it is possible to go through the data set from each of the six sides of the cube, moving from the outer edge to the center or even crossing the center point to the opposite side. In terms of cutting planes, a coronal (or frontal) plane, that is, left-to-right and superior–inferior, a transverse (or horizontal) plane, that is, anterior–posterior and left-to-right, and a sagittal (or median) plane, that is, superior–inferior and anterior–posterior orientation can be presented, providing innumerable cross-sections along each plane [27]. The newer software versions have become more versatile and user-friendly compared with earlier versions, enabling faster manipulation of the data sets.

From the full volumetric data sets most systems will allow the operator to obtain multiple 2D cuts in different planes, and to scroll through the data sets obtaining multiple slices in different orientations (coronal, sagittal, and transverse). In complex hearts this enables a good definition of the spatial relationships of cardiac structures.

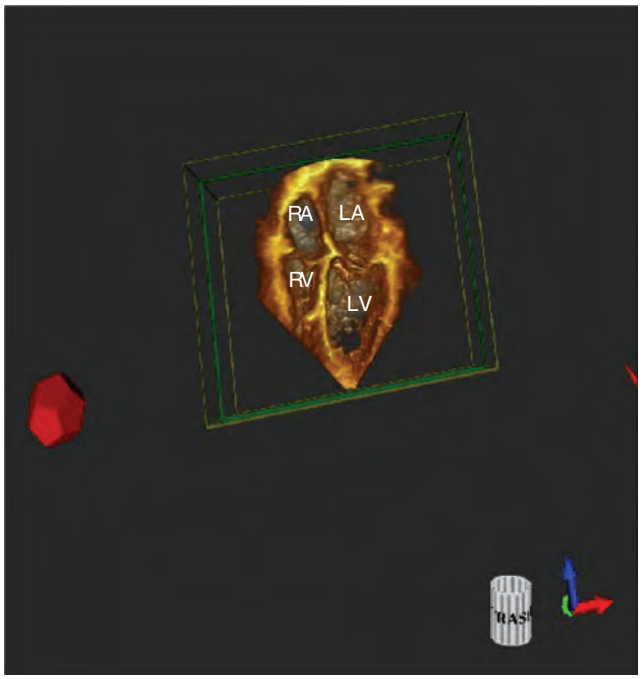


Figure 42.2 A crop box, with inside an anatomical representation of a normal heart. The apex is below, the atria above. LA, left atrium; LV, left ventricle; RA, right atrium; RV, right ventricle.

Volumetric quantification

Left ventricular function is important in clinical decision making and a reliable assessment of this function is required. In clinical practice, 2D echocardiography is the most widely used method for assessment of ventricular volumes and function. Atrial volume measurements are essential, because left atrial enlargement is associated with adverse cardiovascular outcomes [28]. Information on right ventricular function is especially important in patients with congenital heart disease, pulmonary hypertension, or heart failure [29–31]. Although 2D echocardiography is a widely used technique, the accuracy of the assessments of ventricular size and function, and atrial size, is hampered by foreshortened views and geometrical assumptions. Three-dimensional echocardiography overcomes some of the limitations of 2D echocardiography and is unquestionably superior to 2D echo for assessment of volumes and ejection fraction (EF) derived from these volumes [32,33].

Real-time 3D echocardiography for left ventricular function analysis

RT3D echocardiography can be used clinically for the assessment of left ventricular function, due to the relative ease of acquisition of volumetric data, that is, one 3D data set acquired from the LV apex (transducer in the apical 4-chamber view position), as well as the proven superiority of 3D echocardiography for volumetric quantification. RT3D echocardiography is

considered more accurate and more easily reproducible compared with M-mode or 2D echocardiography-derived calculations of LV volumes and function [34]. The currently used ultrasound systems have various imaging options for using RT3D echocardiography. To obtain information on ventricular function, full-volume RT3D echocardiography is needed. For left ventricular analysis, frame rates above 20 frames per heart beat are required and can be reached by either the single beat acquisition [35] or by using information from multiple cardiac cycles. The advantages of using single or two heart beats are that patient movement has less influence on acquisition and the technique may be applied in patients with irregular heart rhythms. Because ventricular filling varies during irregular heart rhythms, ventricular volumes and EF derived from one heart beat is not necessarily representative of ventricular function. Multiple data sets (at least three, and preferably more), with mean volumes (and ejection fraction derived from these) are needed for a more reliable estimation of cardiac function. After the acquisition of a data set, left ventricular volumes can be calculated online on the echo machine or offline, using the software installed on a workstation or personal computer. Different software packages for analysis are available which differ slightly in the way the analysis is performed. One of them is a centroid-based rotational algorithm. This produces an infinite number of long-axis views. Theoretically, the more cross-sections that are analyzed, the less dependent the technique will be on assumptions about shape and contours and the more reliable it will be. The newest software packages feature automatic contour detection based on 3D speckle-tracking algorithms. By indicating some landmark points, such as the lateral and medial mitral valve annulus, and the left ventricular apex, a dynamic 3D model of the left ventricular cavity is created (Figure 42.3; Video 42.2). Using automatic contour detection systems results in lower inter- and intra-observer values than manual contour detection [35,36]. This improved reproducibility facilitates application in clinical practice for the follow-up of individual patients. Population-based reference values have been obtained for RT3DE-derived measurements [37]. The newest software is also successfully used in congenital heart disease, with often abnormally shaped left ventricles due to an intrinsic abnormal geometry or secondary to right heart disease. In case of poor acoustic windows, endocardial blurring may affect the semi-automated tracking algorithm

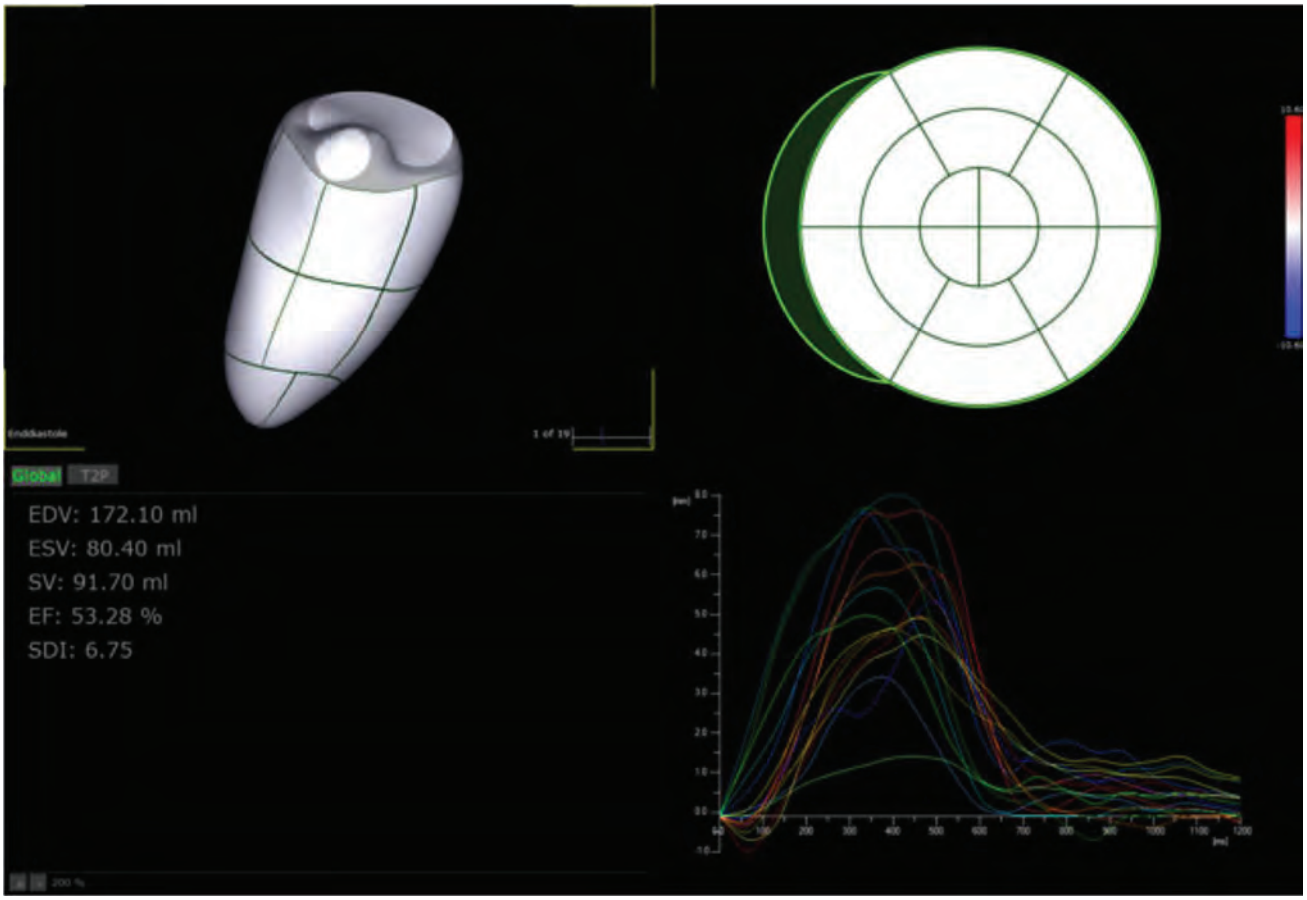


Figure 42.3 Left ventricular (LV) volume assessment with 3D echo. **(a)** A 3D hologram of the LV, including the LV outflow tract. **(b)** A "bull's eye" representation of 16 LV segments, which is valuable for assessment of regional wall motion abnormalities. The values of the automatically calculated LV volumes and ejection fraction are shown lower left.

used by the software and no reliable volumes can be traced. Poor image quality on 2D echo means even poorer 3D image quality.

Currently, CMR imaging is still considered the clinical standard for the assessment of volumes and function. The measurements are unaffected by geometric and spatial constraints, and have a good inter- and intra-observer variability [38] making them applicable for sequential assessment. Computed tomography (CT) can also be used for ventricular function assessment, but because it requires radiation and injection of iodinated contrast medium it is not commonly used for this indication. Importantly when comparing the different imaging modalities significant differences in LV volumes have been found [39,40]. CMR has the best correlation with real volumes (based on measurements of phantoms), RT3D significantly underestimates and CT overestimates LV volumes. Between the techniques, the agreement for ejection fraction is excellent.

Quantification of left ventricular mass

LV mass can be calculated using RT3D echocardiography. The acquisition of the data set for LV mass measurements is identical to that of left volumetric measurements. In contrast to the large number of studies on feasibility, accuracy, and reproducibility of LV volume assessment, there are only a few studies studying RT3D echocardiography for LV mass calculations [41,42]. When compared to 2D measurements, 3D mass calculations correlate better with CMR-derived LV mass with a lower inter- and intra-observer variability (Figure 42.4). Although the mean differences between CMR and RT3D echocardiography-derived values of LV mass are within acceptable limits, the standard deviation (SD) of the measurements is substantial in the different published studies. This means that the confidence limits of LV mass measurements are much wider compared to LV volume measurements. This is understandable, as a small error in, for example, endocardial border identification, will have relatively more impact when measuring a "smaller" structure such as the myocardial wall compared to the larger LV volume. The applicability of quantification of LV mass by RT3D echocardiography for use in clinical practice remains to be established.

Three-dimensional deformation imaging

By definition, 2D deformation imaging is hampered by through-plane motion of the heart: during the cardiac cycle the heart moves in various directions, through a fixed scanning plane. A further limitation is that obtaining myocardial wall motion in all segments during the same cardiac cycle is not possible in 2D imaging. Three-dimensional deformation imaging overcomes these limitations. Myocardial deformation imaging is currently based on speckle-tracking echocardiography. Myocardial reflectors or speckles can be tracked throughout the cardiac cycle and their relative displacement can be calculated allowing quantifying regional myocardial deformation or strain. When speckle-tracking analysis is performed in 3D data sets, the problem of through-plane motion is resolved. Three-dimensional tracking of speckle patterns in high volume rate data sets diminishes the need for assumptions on the expected motion pattern by the tracking algorithm, and thus theoretically increases the accuracy of measurements of deformation. Analysis of the immense amount of data, that is, all vectors of all defined speckles, is cumbersome. In the currently available software systems, assessment is simplified by reducing the analysis to three levels: basal, mid, and apical part of the LV walls. Despite its theoretical advantages over 2D deformation imaging, the relatively low volume rates of 3D echo limits temporal resolution and faster myocardial movements will be missed or will not be detected reliably [43,44]. This particularly limits its use in younger children, who often have high heart rates.

Quantitative assessment of right ventricular size and function

The RV is more difficult to image by echocardiography than the LV because of its crescent shape, retrosternal position, and thin, coarsely trabeculated wall [45]. Correlation between M-mode and 2D echocardiography-derived measurements of RV size and function and CMR-measurements [46–48] is generally poor. In patients with congenital heart disease this correlation is even lower [49]. None of the proposed geometric models using

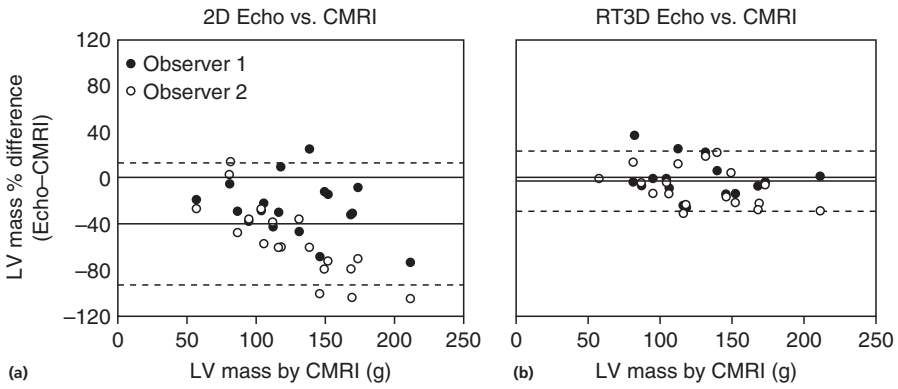
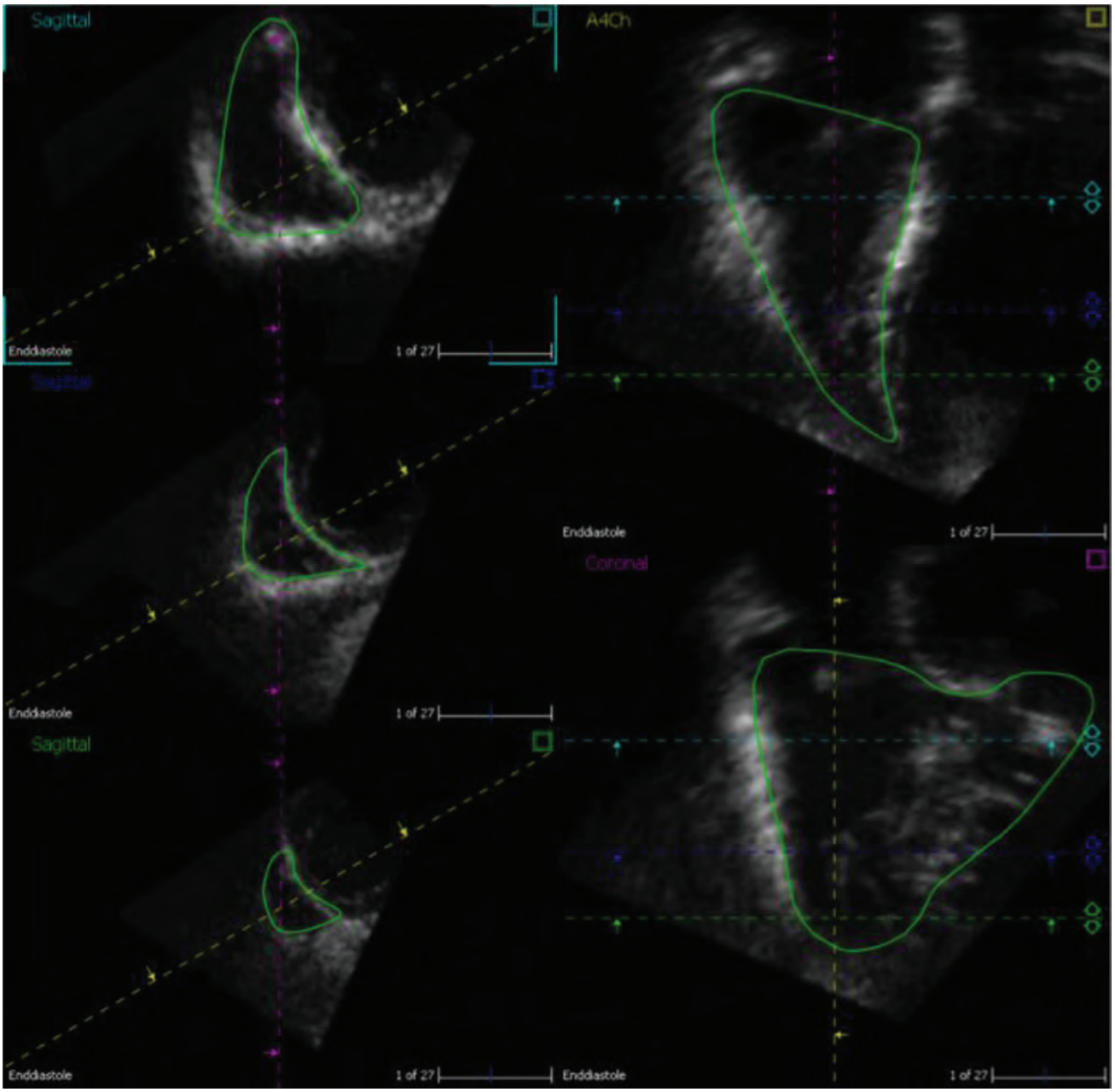


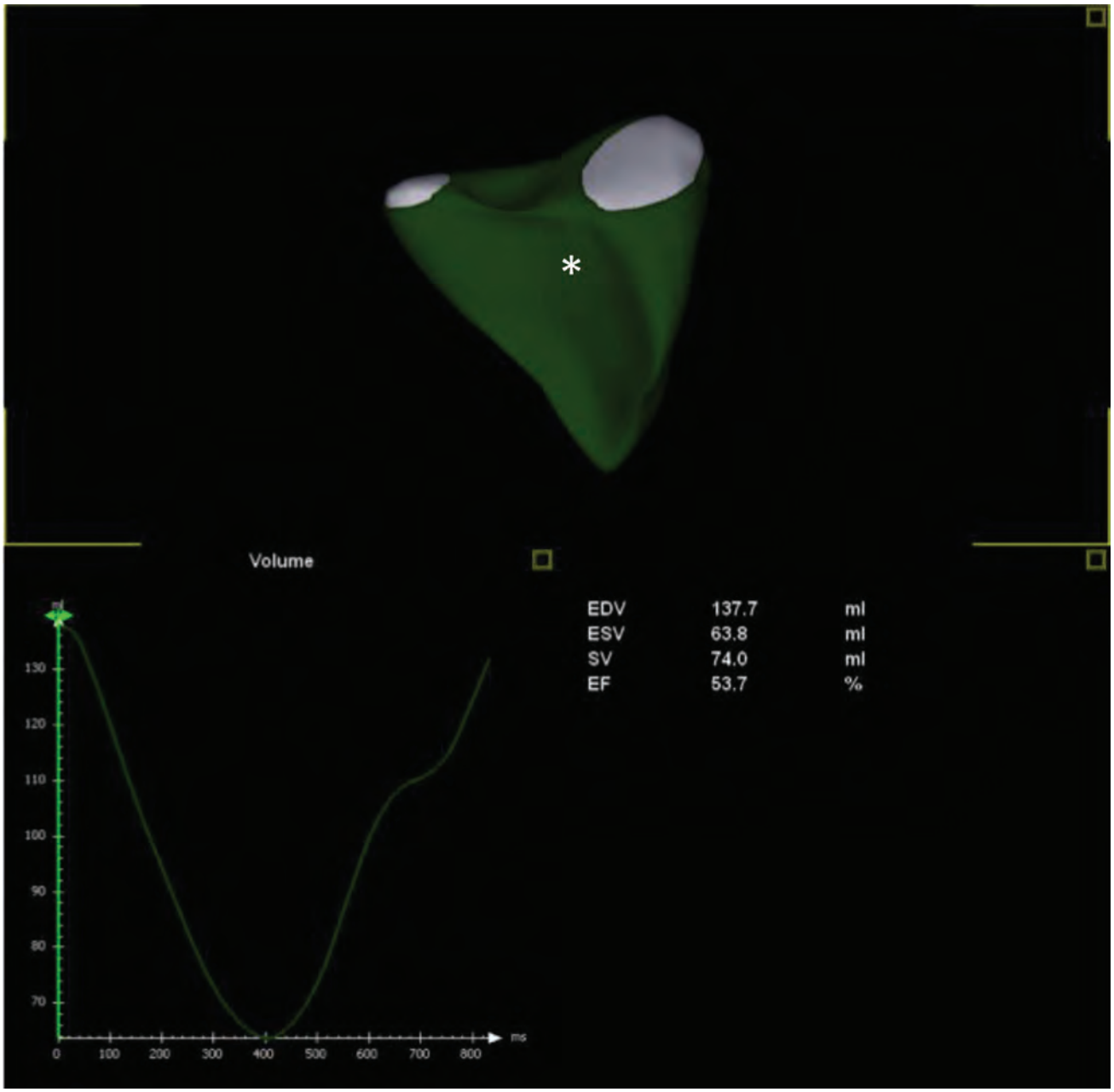
Figure 42.4 Left ventricular (LV) mass: comparison of inter-observer variability between **(a)** 2D echo versus cardiac magnetic resonance imaging (CMRI) and **(b)** real-time 3D (RT3D) echo versus MRI. Because the inter-observer difference with RT3D echo is less, it is a better, more robust way to assess LV mass than 2D echo.



(a)

Figure 42.5 **(a)** Contours of the RV can be traced in the transverse plane at three levels (three left-sided images), in the coronal view (upper left image) and the sagittal view (lower right). Contours should be traced in end-diastole and end-systole, and volume calculations are done automatically. Tracing of contours in the trabeculated RV is not straightforward, hence inter- and intra-observer variability is substantial. Robust automatic contour detection is essential for this application. **(b)** A 3D representation of a RV volume (a "beutel") is shown. TV, tricuspid valve; PV, pulmonic valve; ∗, the convexity of the interventricular septum – bulging into the RV – is nicely shown here. Bottom left shows a volume curve of the RV over time. Numeric representation of RV volumes are shown at the bottom right. EDV, end-diastolic volume; ESV, end-systolic volume; SV, stroke volume; EF, ejection fraction.

2D echocardiography have been found to reliably calculate RV volumes and EF [50]. Real-time 3D echo enables full volumetric data acquisition of the RV and subsequent offline analysis using dedicated software allows quantification of RV volumes and EF. Compared with LV volume analysis RV volumetric post-processing is semi-automated and still requires more extensive operator input (Figure 42.5; Videos 42.3 and 42.4). Several studies have demonstrated that RT3D echo assessment of the RV is a relatively reliable technique, with acceptable correlation between 3D echo measurements and CMR volumes, although – as in 3D echo assessment of LV volumes – a systematic underestimation of RV volumes compared to CMR is found [20]. The



(b)

Figure 42.5 (*Continued*)

underestimation becomes more important with increased RV size. Ejection fraction correlates well with CMR and it has shown to be a reliable screening tool to discriminate between normal and low RVEF [51]. Once familiar with the technology, analyses may only take a few minutes [24]; it is therefore considered to be fast enough for use in clinical practice [52].

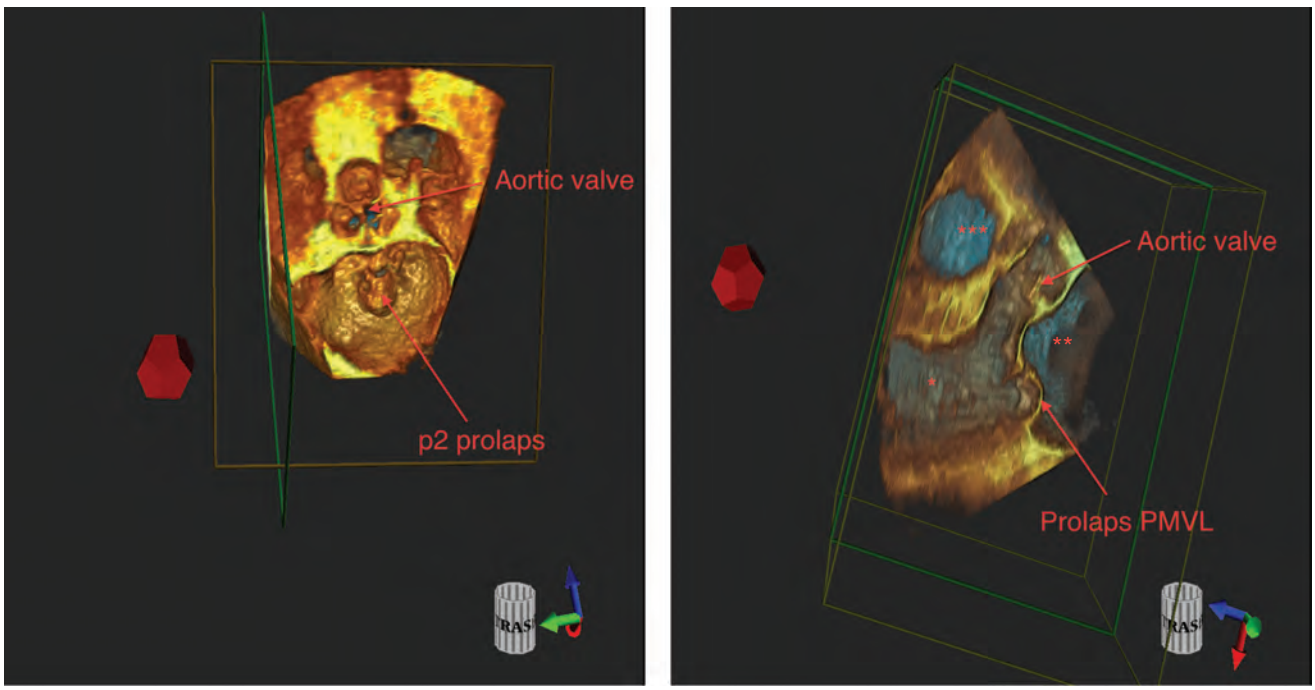
The relatively poor image quality of 3D echocardiography often makes contouring of the trabeculated RV difficult. Making use of the superior image quality of 2D echo, an alternative to 3D echo acquisition and measurement of RV volumes has been developed. A set of standardized 2D cross-sections of the RV are made. These 2D cross-sections are localized in the 3D space by a magnetic tracker attached to the probe. In these 2D data sets anatomic landmarks (e.g., the pulmonary valve annulus) are identified. These landmarks together with the spatial information are used to reconstruct the RV volume based on a data set of RV shapes obtained by CMR. The echo data are matched with CMR landmarks and contours of the same congenital anomaly as the patient (or normal anatomy) and a RV volume and shape are reconstructed in systole and diastole. As

a rule, dozens of CMR data sets are necessary for the reconstruction of one reconstructed 3D echo data set. First reports of this so-called "knowledge-based reconstruction" are encouraging and demonstrated very good correlation with CMR in terms of volumes – with less underestimation of volumes than RT3D echo – and EF [53,54]. This system may offer an alternative to RT3D echo of the RV, at least until image resolution of 3D echo improves to the level that is now obtained with 2D echo. This technique also overcomes the limitations in feasibility of the 3DRT techniques. The RV anterior wall and RV apex can be especially difficult to acquire in full volumetric data sets, particularly when the RV is dilated. In most patients it is feasible to obtain 2D data sets including important RV anatomic landmarks. The limitation of this technology is that it requires magnetic tracking and the availability of dedicated software.

Valve morphology and function

In adults, 3D TEE enables far more superior image quality making it the technique of choice for the assessment of mitral, aortic and tricuspid valve morphology and function in selected cases. In recommendations for imaging during transcatheter aortic valve implantation, 3D TEE is included as the preferred echo modality, considered to be superior to 2D TEE as it results in less underestimation of the LVOT dimension and aortic annulus, and hence less frequent undersizing of the implanted valve with a decreased incidence of subsequent paravalvular leaks [55–58]. Three-dimensional TEE also replaces 2D TEE for morphologic and functional assessment of the mitral valve. The "surgeon's view," looking from the left atrium into the mitral valve, is particularly useful [59] (Figure 42.6; Videos 42.5 and 42.6). A flail or prolapse can be seen directly [60] and even more difficult commissural regions are readily visualized. In combination with 3D color it allows identification [61] of the exact areas of regurgitation that can direct the surgeon to certain valve areas. Different techniques for transcatheter treatment of mitral regurgitation (Figure 42.7; Videos 42.7–42.9)have become available over the past few years, and without doubt, 3D TEE is the preferred imaging technique for monitoring and guiding these procedures [23,62,63]. Specific analysis software has been developed allowing quantification of the mitral valve and its subvalvar apparatus based on 3D TTE or TEE data sets.

As at the end of 2013, no pediatric 3D TEE probe is available. This precludes the use of this technique in smaller children. The better imaging windows in the pediatric population generally facilitate the use of 3D TTE. In particular, subcostal views can produce very good 3D images of cardiac valves in this patient population, for whom procedures and surgery present greater difficulties.



(a) (b)

Figure 42.6 **(a)** View from left atrium (LA) into the mitral valve (MV). A protruding part of the MV leaflet can be seen in the center of the posterior leaflet – at p2 level. **(b)** A left lateral cross-section of the MV showing a prolapse of the PMVL. The localization, extent, and severity of the MV prolaps can be assessed easily with 3D echo. PMVL, posterior mitral valve leaflet; ∗, en face view of LV side interventricular septum; ∗∗, left atrium; ∗∗∗, right ventricular outflow tract.

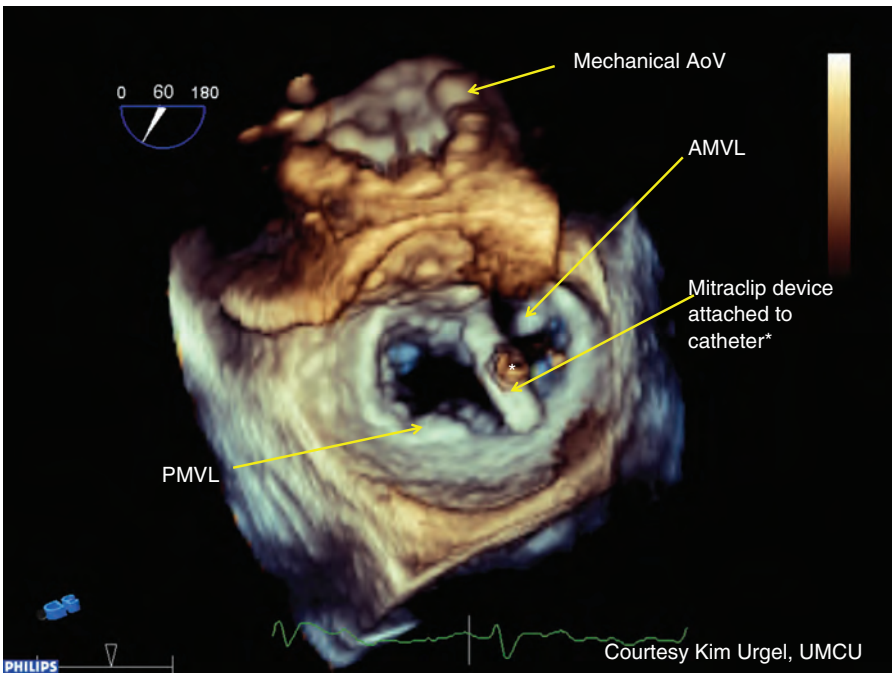


Figure 42.7 Transcatheter treatment of mitral regurgitation. TEE guidance of a MitraClip procedure. Left atrial view of mitral valve, with the MitraClip above the mitral valve, still in the left atrium. AMVL, anterior mitral valve leaflet; PMVL, posterior mitral valve leaflet; AoV, aortic valve; ∗, distal end of catheter, attached to the MitraClip. Source: Reproduced with permission of Kim Urgel, UMCU.

Congenital heart disease

In experienced hands, a 2D echo examination of a patient with congenital heart disease is almost always diagnostic. In contrast to volumetrics, for which the 3D technique is so obviously superior to 2D echo that it should replace it, the use of 3D in congenital heart disease is still relatively limited. It can be used in addition to 2D echo, which has a superior spatial and temporal resolution. Compared to high-quality 2D, 3D images have a much lower resolution. This is because the 3D line density is substantially lower than in 2D imaging, the interline space is wider and structures that are detected, appear to be thicker than they actually are. Despite these shortcomings, which will undoubtedly lessen as techniques advance in the coming years, 3D echo has some value in congenital heart disease. Viewing 3D images, makes the understanding of the anatomy easier and more intuitive. Instead of using multiple 2D cross-sections to make a mental reconstruction the anatomy is shown directly. With the en face view one can look onto (or into) either or valve or a septum as a whole. Also difficult spatial relationships can be studied well in volumetric datasets containing all cardiac structures of interest. Like in complex double-outlet right ventricle the relationship of the ventricular septal defect to the great vessels can be better defined in different planes. In standard TTE or TEE, a specific cross-section depends on the position of the ultrasound transducer, relative to the heart. In a 3D data set, any cross-section can be made, in any plane, in any direction, regardless of the original source of the data set. This means that all standard 2D cross-sections – from TTE or TEE – can be made in a 3D data set, as well as many more. Multiple 2D cross-sections and scrolling through 3D data sets in different planes can be very helpful. In the following section, examples of the use of 3D in various congenital cardiac malformations are given.

Atrial septal defect

In children, 2D TTE echocardiography is often diagnostic for different types of atrial septal defects (ASDs). The intra-atrial septum can be visualized from several transducer positions (especially subcostal views) and the ASD itself, its rims and distances to important intracardiac structures, can be measured. Generally the optimal 3D data set for an ASD is also acquired from the subcostal position, which is almost always feasible in infants and children [64], but rarely in adults. When the subcostal view is not possible, the transducer can best be positioned either on the site from where a foreshortened 4-chamber view is created, or from where a parasternal long-axis view angulated to the right (RV inflow view), is made. In adult congenital heart disease, 3D TTE data are more difficult to obtain and are not generally diagnostic. TEE enables better imaging of the interatrial septum and increasingly with 3D TEE is used to guide interventional closure of an ASD, especially when a more complex closure procedure is anticipated. Alternatively, intracardiac echocardiography can be used but this is a more expensive technique as it utilizes single-use ultrasound catheters.

The size of ASDs and their exact location and relationship to other cardiac structures has become more important since transcatheter closure of ASDs was introduced [65–68]. Not all defects are suitable for transcatheter closure; they should not be too large relative to the total septal size, the rims should be sufficient to provide "anchoring" of the device, and the defects should

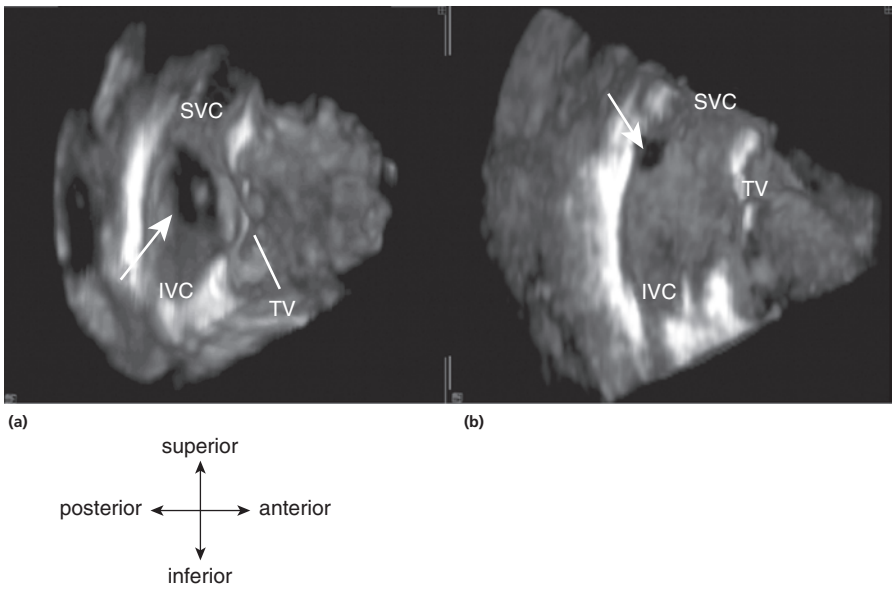


Figure 42.8 Right lateral view, looking on the right side of the interventricular and interatrial septum. The en face view allows assessment of size and localization of atrial septal defects (ASDs) (arrows). **(a)** A large secundum ASD is seen with good rims surrounding the defect. **(b)** A small secundum ASD is seen high in the interatrial septum, without a posterior rim. IVC, inferior vena cava; SVC, superior vena cava; TV, tricuspid valve.

not be too close to important intracardiac structures (mitral and tricuspid valves, coronary sinus or orifices of systemic/pulmonary veins). The advantage that RT3D echo has for analysis of an ASD is the possibility to create an en face view that looks at the interatrial septum [69]. The entire interatrial septum can be seen, with the defect within it (Figure 42.8). It can be viewed and measured, both from the left and right atrial sides, and the rims around the defect can be seen in one view. From the right-sided view, distances to important anatomic landmarks, such as the tricuspid valve, the ostium of the coronary sinus and the ostia of the caval veins, can be directly seen and measured (Figure 42.9; Video 42.10. Mathewson et al. [70] proposed a standardized orientation and nomenclature for the rims (Figure 42.10). If the data set is cropped from the left lateral side, the distance to the right pulmonary veins and mitral valve can be assessed. A good correlation between RT3D echo and surgical measurements and between RT3D echo and TEE is reported regarding measurements of the rim [71]. Most ASDs are not round but have an oval or even slit-like shape [72]. Something difficult to appreciate with 2D echo is the size change of the ASD during the cardiac cycle, but this is easy to see in the en face view using RT3D echo [73]. The area of the defect is largest during atrial relaxation, coinciding with ventricular systole, and smallest during atrial contraction. During this period, the area was reported to be 51 ± 15% smaller than during atrial relaxation. This information is important for the interventional cardiologist [74,75] who depends on these anatomic details when deciding on transcatheter closure [76]. A systematic step-by-step approach, both for diagnostic TEE and TEE guiding of ASD closurehas been proposed [77].

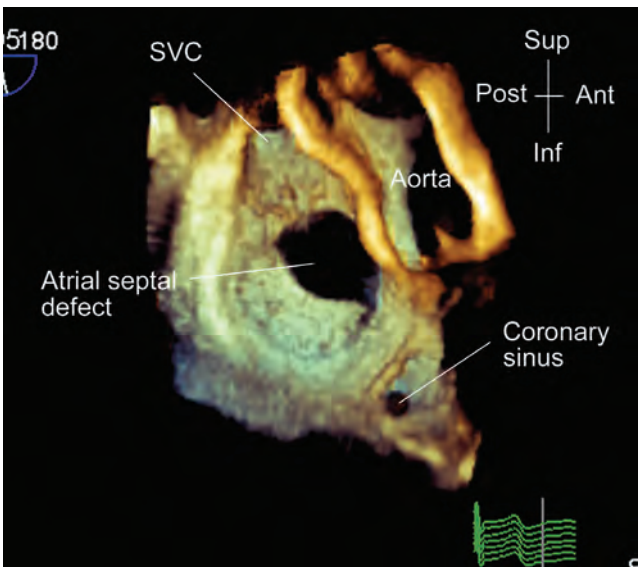


Figure 42.9 A right lateral view onto the intra-atrial septum with a large atrial septal defect. It is a fossa ovalis type defect with extension to antero–superior, the direction of the aortic root. SVC, superior caval vein.

Ventricular septal defects

Data sets are acquired from the apical 4-chamber position and from the parasternal long-axis view. In pediatric patients, the subcostal view is very useful. If cropped from the left side, the left-lateral view also reveals its relation (or distance) to the mitral and aortic valves. If the same data set is viewed from the right side, the ventricular septal defect (VSD) can be seen in relation to the tricuspid and pulmonary valves. Experience with 3D TEE for assessment of VSDs or for guiding device closure is anecdotal.

The interventricular septum (IVS) has a complex, spherical shape, which cannot be visualized in a single 2D plane. VSDs also change in size during the cardiac cycle. Muscular defects can even close entirely during ventricular systole. In perimembranous defects the size change is less striking, which can

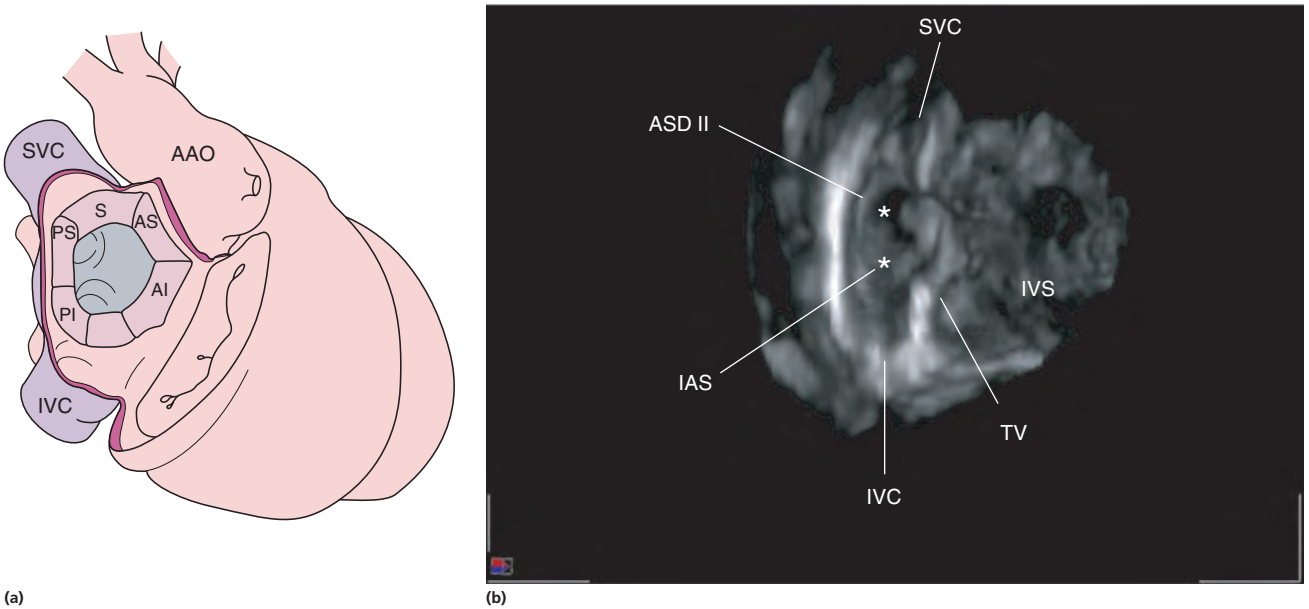


Figure 42.10 **(a)** A schematic presentation of the interatrial septum, the atrial septal defect (ASD) and surrounding rims, as proposed by Mathewson et al. AAO, ascending aorta; AI, antero-inferior; AS, antero-superior; IVC, inferior vena cava; PI, postero-inferior; PS, postero-superior; SVC, superior vena cava; S, superior. Source: Mathewson JW, et al. Absent posteroinferior and anterosuperior atrial septal defect rims: Factors affecting nonsurgical closure of large secundum defects using the Amplatzer occluder. *J Am Soc Echocardiogr* 2004;**17**:62–69. **(b)** A right lateral view of the interatrial and interventricular septum. The upper asterisk shows the atrial septal defect. The lower asterisk shows the inferior-posterior rim. ASD II, atrial septal defect secundum type; IAS, interatrial septum; IVC, inferior vena cava; IVS, interventricular septum; SVC, superior vena cava; TV, tricuspid valve.

probably be explained by the fact that such a defect is not entirely surrounded by contracting muscular tissue. It is again the en face view of the interventricular septum that brings the benefit, by showing the curved interventricular septum, the VSD within it and the relationship with other intracardiac structures (Figure 42.11; Video 42.11). The spatial relation of the VSD to other parts of the intracardiac anatomy can be assessed, either directly, during the data acquisition, or offline, in one 3D data set (Figure 42.12; Video 42.12) [78,79].

On the right ventricular side, a perimembranous VSD is often (partially) covered by the septal leaflet of the tricuspid valve, blocking the view from the right lateral side to the VSD. This tissue can be "cut away" electronically, thus exposing the entire VSD. This view is valuable because it mimics a surgical view used for VSD closure. Several authors have reported a better correlation between RT3D echo assessments of VSDs and surgical anatomy compared with 2D imaging [80–84]. This can be very helpful for the interventional cardiologist considering transcatheter closure of a VSD [85].

Atrioventricular septal defect (AVSD)

In infants and young children, both the subcostal and the apical 4-chamber views can provide good datasets that include the AV valve and the inlet septum. In adults, only the apical and foreshortened 4-chamber views are used.

Three-dimensional TTE is the only option for infants and smaller children. In larger children and adults 3D TEE should be considered prior to cardiac surgery of AVSD (mostly partial AVSD or primum defects). Epicardial RT3D echo before and directly after surgical repair, on a beating heart before closing the sternum, is reported as being useful in the immediate post-bypass assessment [86] in infants and children, who are too small to accommodate an adult-size 3D TEE probe.

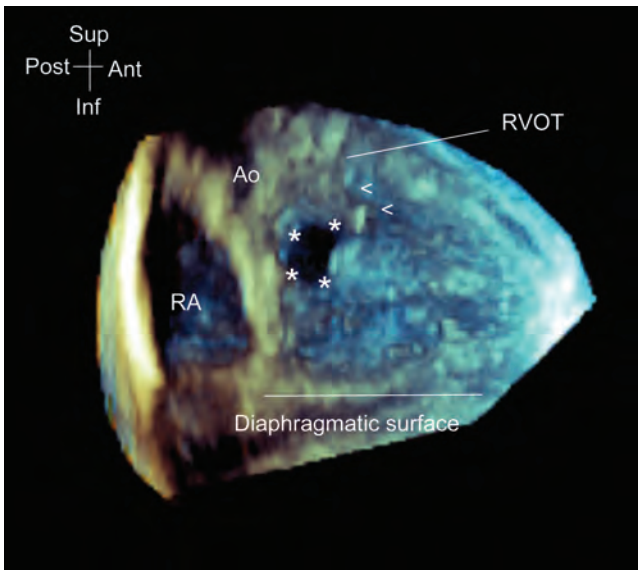


Figure 42.11 View from right lateral side of the heart, looking onto the right ventricular side of the interventricular septum. The contour of the VSD is indicated by the asterisks. AO, aorta; LV, left ventricle; RA, right atrium; RVOT, right ventricular outflow tract.

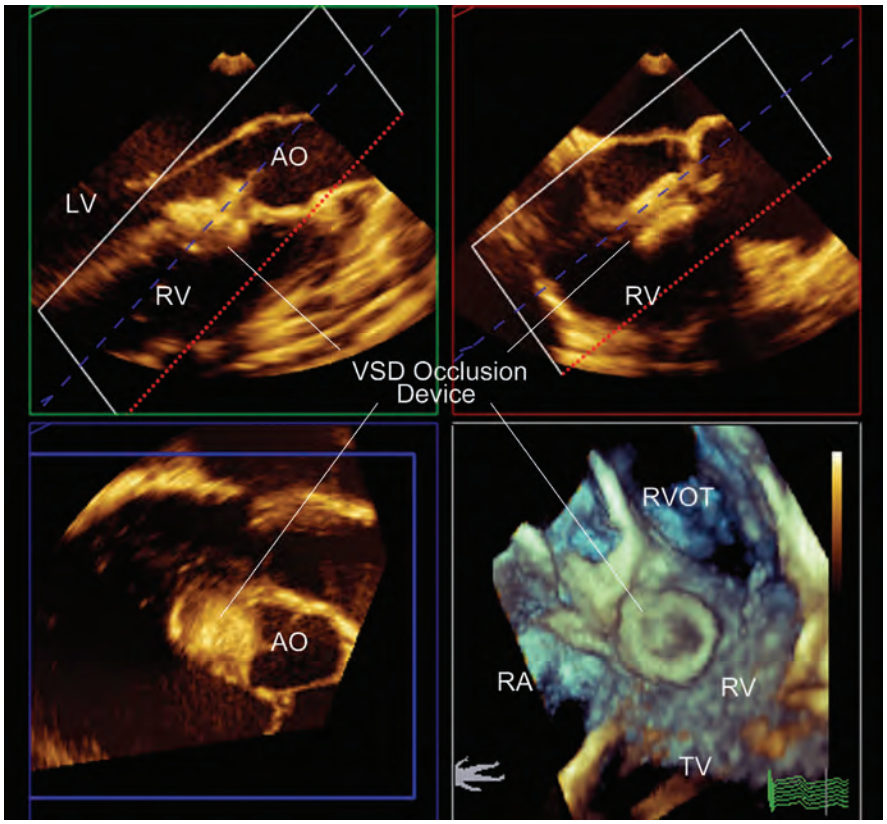


Figure 42.12 A "tile" view of a 3D data set of a closure device in a VSD. Three perpendicular planes are represented and a 3D hologram at the bottom right. In the 3D view it is obvious that the device has closed a perimembranous VSD, directly underneath the tricuspid valve, in the inner curvature of the right ventricle. In the two upper 2D cross-sections, the close relation of the device with the aortic valve can be appreciated. AO, aorta; LA, left atrium; LV, left ventricle; RA, right atrium; RV, right ventricle; RVOT, right ventricular outflow tract; TV, tricuspid valve.

Imaging the common atrioventricular valve in different types of AVSD is one of the main indications for the use of 3D echocardiography in congenital cardiology (Figure 42.13; Video 42.13). The anatomy of the AVSD is described in detail elsewhere (see Chapter 15). The anatomic hallmark of an AVSD is the presence of one common atrioventricular (AV) junction guarded by a common AV valve, most often consisting of five leaflets and this is readily seen with 3D echo (Figure 42.14). A complete AVSD has a single, undivided orifice. In a partial AVSD, the anterior and posterior bridging leaflets are attached to each other and to the interventricular septum. This results in two separate orifices in a partial AVSD. The annulus of the AVSD is a curved, saddle-shaped structure, which cannot be displayed in any 2D cross-section, but it can be well visualized with 3D echo.

The en face view of the atrioventricular valve is especially valuable as it allows visualizing of all leaflets in one image representation (Figure 42.15; Videos 42.14 and 42.15). The valve can be viewed directly from the, atrial side (the surgical view) as well as from the ventricular side. Because the entire valve is directly seen and also the subvalvar apparatus can be images, classification according to Rastelli is much easier than by using 2D echo. RT 3D echo, particularly the en face view, has contributed to a better understanding of the functioning of these abnormal valves [87–93]. Recent data suggest that 3D echocardiography better detects valve abnormalities like a double-orifice left AV valve and parachute-like abnormalities of the left AV valve. Assessment of the size of the individual leaflets and their movements, combined with assessment of the localization and severity of regurgitation by means of 3D color Doppler, allow a better preoperative estimation of the amount of valve tissue that is available for valve reconstruction. Also in the postoperative assessment 3DE can be extremely helpful in better defining the mechanisms causing residual AV-valve regurgitation [93]. This can be extremely helpful in preoperative planning of repeated surgery.

In adults, the most common presentations are either an unoperated patient with a partial or partitioned AVSD, or a patient who has undergone surgical repair in the past. Residual left-sided AV valve regurgitation and left ventricular outflow tract obstruction are the most common residual lesions after surgical repair. In a 3D TTE data set of an adult patient, obtained from an apical or foreshortened 4-chamber position, the atrial en face view is often disappointing when compared with this view in children or when compared with 3D TEE data. This way 3D TEE has become a first-choice imaging modality for patients in whom reintervention is being considered. The commissure between the superior and inferior bridging leaflets, often erroneously referred to as mitral valve with a cleft, is seen over its entire depth from the tip of the leaflets, toward the interventricular septum (Figure 42.16; Videos 42.16 and 42.17). With 2D echocardiography, it is sometimes difficult to distinguish left-sided and right-sided AV valves in an AVSD from normal mitral and tricuspid valves. With RT3D this confusion is impossible, because the marked difference of these AV valves from the normal anatomy can be readily visualized.

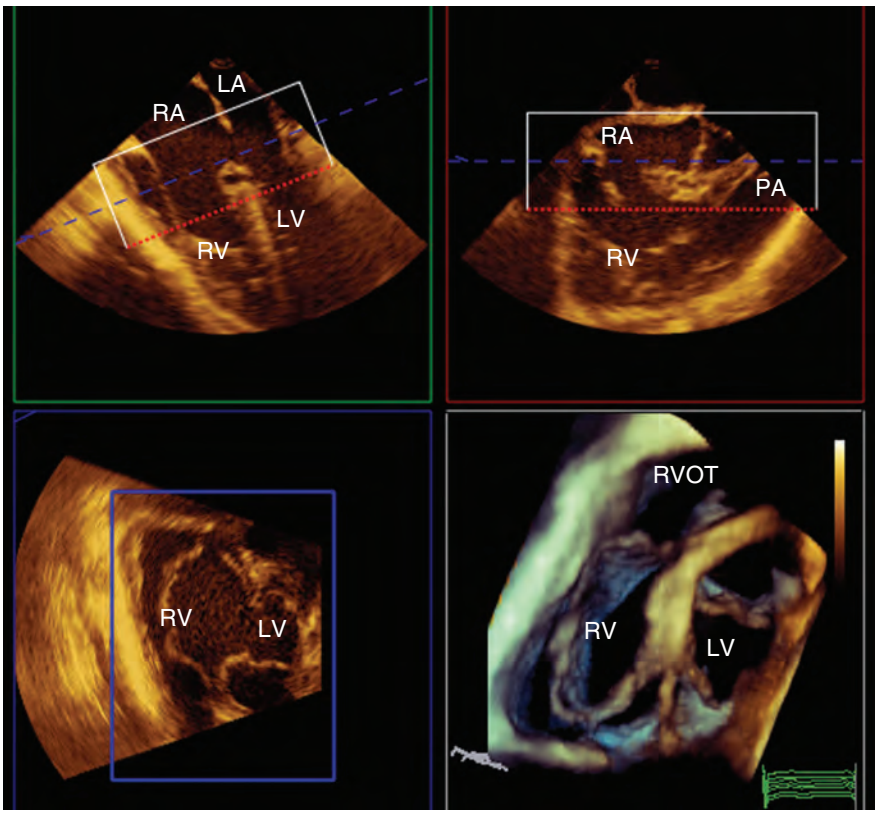


Figure 42.13 A "tile" view of an AVSD. The upper left tile shows an image comparable to that of an apical 4-chamber view. In the upper right tile, the red plane perpendicular to the green plane forms the neighboring 4-chamber view, a posterior to anterior orientation is shown at the same level, at the atrioventricular junction. The lower left tile shows a cross-section of the single atrioventricular orifice, where left and right atrioventricular valve leaflets can be seen. The lower right tile shows an unusual orientation of the 3D echo, from the apex rather than the more usual view toward the atrioventricular valve, through a part of the intact interventricular septum (IVS) into the right ventricular outflow tract (RVOT). LA, left atrium; LV, left ventricle; RA, right atrium; RV, right ventricle.

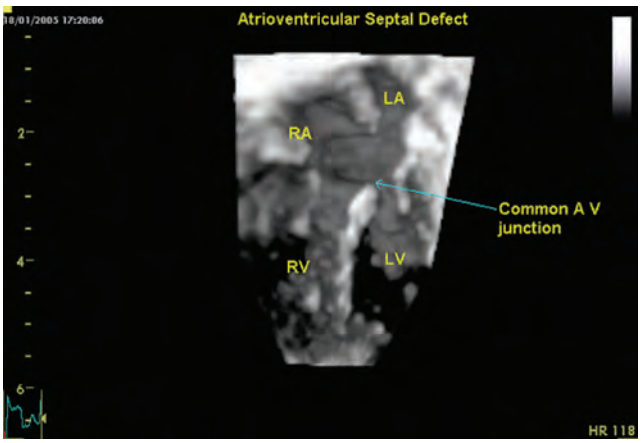


Figure 42.14 In this RT 3D TTE image of a newborn with AVSD, the size and shape of the AVSD is seen in one image. LA, left atrium; LV, left ventricle; RA, right atrium; RV; right ventricle. Source: Dr. Jan Marek, Great Ormond Street Hospital for Children, London. Reproduced with permission of Dr. Marek.

Tricuspid valve anomalies and Ebstein anomaly

Echocardiographic analysis of the tricuspid valve (TV) can be difficult and is generally limited by the fact that it can be extremely difficult to image the three leaflets of the TV in 2D. In the standard 2D echo views generally only two leaflets are visible, and it can be difficult to differentiate between the septal and the postero-inferior leaflets. TEE can be very helpful in the evaluation of the TV, but because the TV is positioned further away from the transducer located in the esophagus than the mitral valve, imaging can be more difficult. This is also true in case of Ebstein anomaly, the most common congenital malformation of the TV. The anatomy and echocardiographic workup of Ebstein disease (Chapter 13) is discussed extensively elsewhere in this book. An RT3D data set acquired from the subcostal view in children or from the apical or foreshortened 4-chamber position in adults will generally include the entire TV. A parasternal long-axis RV inflow view, can also provide excellent 3D data sets for viewing the TV. In one acquisition, the tricuspid annulus, the three leaflets with their attachments to the septum and to the anterior wall, and the degree of displacement of the functional TV orifice away from the annulus can be shown (Figure 42.17; Video 42.18). Assessment of the TV by TEE, including 3D TEE, is more challenging than assessment of the MV. A good transesophageal view on the entire TV can be especially difficult in Ebstein disease, and sometimes a 3D transgastric view will give a better image.

In order to assess the size and (often very irregular) shape of the TV orifice, an en face view is necessary. It can be a challenge to obtain a good en face view because of the wide variety of degree and direction of displacement of the TV opening [94]. One of the characteristics of Ebstein anomaly is the spiraling of the TV opening toward the right ventricular outflow tract. Once a good en face view is obtained, not only can the orifice be seen, but also the anterior-superior leaflet and the extent to

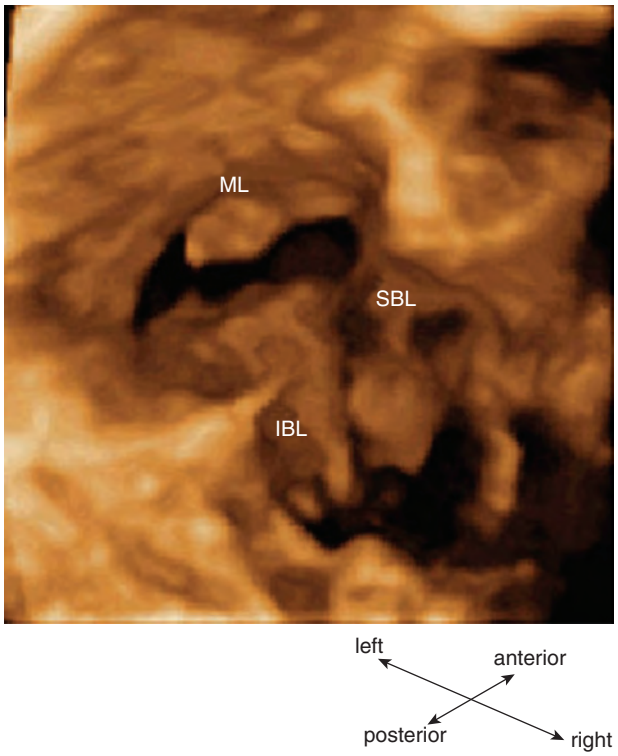


Figure 42.15 View from the atrial side down toward the common atrioventricular junction of a patient with a complete atrioventricular septal defect. In the single orifice, the superior and inferior bridging leaflets are visible in an en face view, as is the left mural leaflet. IBL, inferior bridging leaflet; ML, mural leaflet; SBL, superior bridging leaflet. Source: Dr. Jan Marek, Great Ormond Street Hospital for Children, London. Reproduced with permission of Dr. Marek.

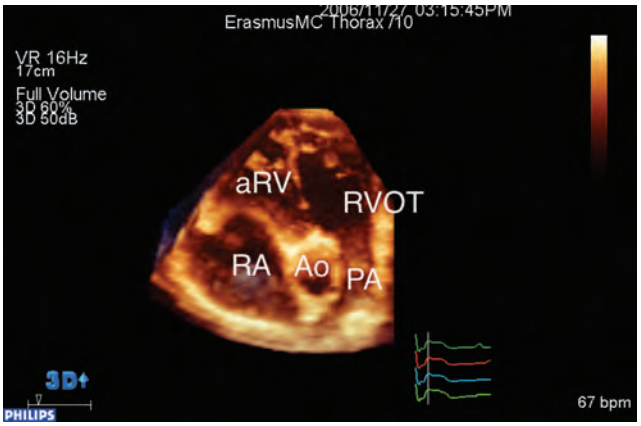


Figure 42.17 Transgastric view of Ebstein's anomaly, with tricuspid valve tissue extending far into the right ventricle. The remaining part of the right ventricle is small. The caliber pulmonary artery (PA) looks normal. Ao, aorta; aRV, atrialized part right ventricle; RA, right atrium; RVOT, right ventricular outflow tract.

which it is attached to the RV free wall can be appreciated (Figure 42.18; Video 42.19). In case of TV stenosis, the en face view can be used for planimetry of the orifice. Both the en face view and the right lateral view will provide extra anatomic information in addition to the 2D analysis. A combination of RT3D and (3D) color Doppler will provide more insight into the mechanism of tricuspid regurgitation.

In patients with hypoplastic left heart syndrome undergoing single ventricular palliation, tricuspid regurgitation is a common and can have significant hemodynamic impact. Recent data have demonstrated that 3D echocardiography can provide important insights into the mechanisms of valve regurgitation. Takahashi et al. demonstrated that annular dilatation together with valve prolapse and restricted valve motion are important contributory factors to at least moderate tricuspid regurgitation

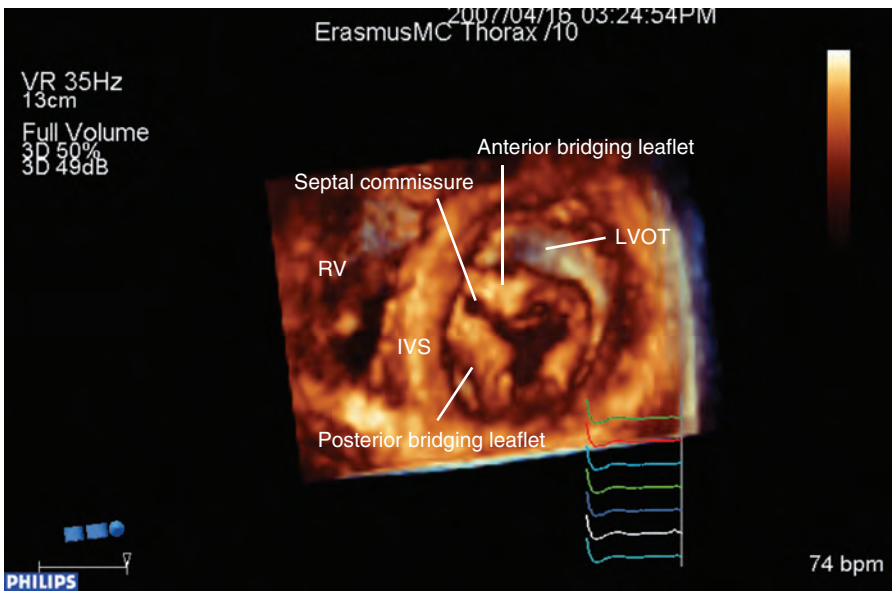


Figure 42.16 En face view from LV apex toward the left-sided atrioventricular valve. The commissure between anterior and posterior bridging leaflet runs from lateral toward the interventricular septum (this differs from a cleft in a mitral valve, which runs toward the aortic valve). AVSD, atrioventricular septal defect; IVS, interventricular septum; LVOT, left ventricular outflow tract; RV, right ventricle.

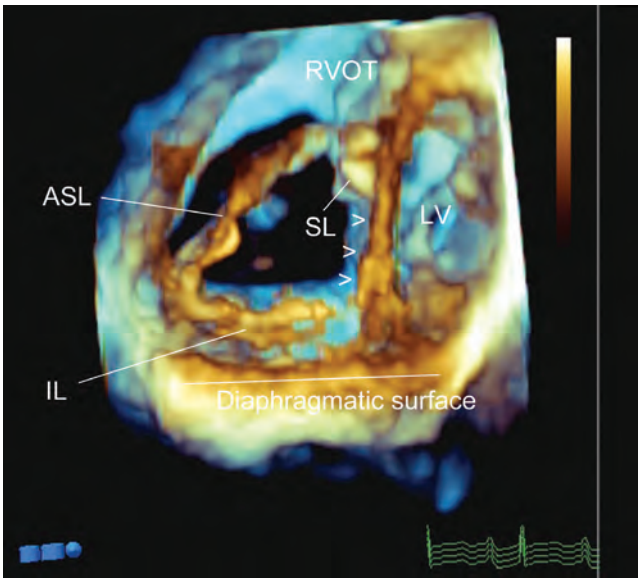


Figure 42.18 En face view of the displaced TV. The septal leaflet is seen attached to the interventricular septum. The large and sail-like anterior superior leaflet can also be seen. ASL, anterior-superior leaflet; IL, inferior (infero-posterior) leaflet; LV, left ventricle; RVOT, right ventricular outflow tract; SL, septal leaflet.

[92]. This with structural abnormalities of the tricuspid valve leaflets [93] contributes to the severity of tricuspid regurgitation after surgical palliation.

Transposition of the great arteries (TGA)

In the anatomic diagnosis of simple transposition of the great arteries (with no additional intracardiac abnormalities, RT3D echocardiography has no specific advantage over a 2D echo. Generally, with 2D echo the anatomy can be reliably depicted. In complex transposition, 3D visualization of the spatial relation of septal defects to other cardiac structures may sometimes be useful. In adult congenital heart disease, many patients with simple transposition of the great arteries have undergone an atrial switch procedure (either Mustard or Senning). In these patients the systemic venous blood is redirected to the left ventricle while the pulmonary venous blood is redirected to the right ventricle through complex intra-atrial tunnels. The right ventricle (RV) sustains the systemic circulation and is subject to systemic ventricular pressures, causing the ventricular septum to bulge to the left (Figure 42.19). RT 3D TTE is very helpful for imaging atrial tunnels, of which the anatomy is sometimes difficult to understand and image for non-experts. Figure 42.20 is a schematic drawing intended to help understanding of this aspect of the anatomy. A 3D acquisition from the apex is very valuable, but since the atrial tunnels are in the far field, ultrasound penetration and image resolution is often not optimal. Data sets acquired from a parasternal position can produce clear images of the atrial tunnels and pulmonary venous atrium. Experience with 3D TEE is anecdotal for this lesson.

Multiplane reconstruction ("quad tiling") is the first very helpful step in the analysis of a transposition after atrial switch. By scrolling through the oblique coronal plane from posterior to anterior, the inferior tunnel is seen first, with its course almost exclusively from right to left (Figure 42.21). At this level, the pulmonary venous atrium is seen, posterior from this inferior tunnel, with the left pulmonary veins draining from the left-lateral side into this compartment (Figure 42.22). On scrolling more anteriorly, the inferior tunnel disappears from this plane and the right pulmonary veins can now be seen entering the pulmonary venous atrium as well as the connection between pulmonary venous atrium and the right atrium, approximately at the level of the former interatrial septum (which has been removed during surgery). Going further anteriorly, the pulmonary venous atrium disappears from view and the superior tunnel is visualized, with a predominant superior-to-inferior course. Most of

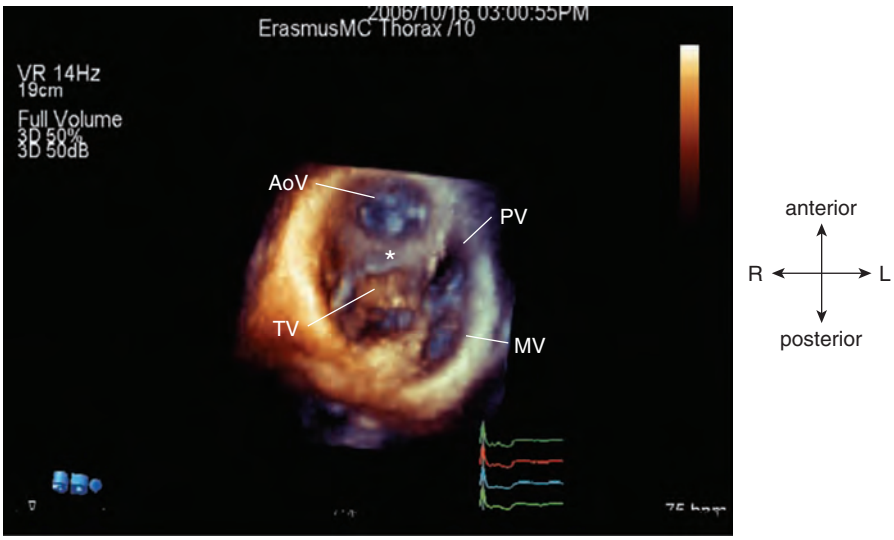


Figure 42.19 Transposition of the great arteries. Note the muscular band between tricuspid valve and aortic valve. View from the apex toward the atrioventricular and ventriculo-arterial valves. The aorta is anterior and to the right of the pulmonary valve. The asterisk (*) denotes the muscle band separating aortic valve (AoV) and tricuspid valve (TV). The left ventricle is flattened behind and to the left of the highly pressured right ventricle. MV, mitral valve; PV, pulmonary valve.

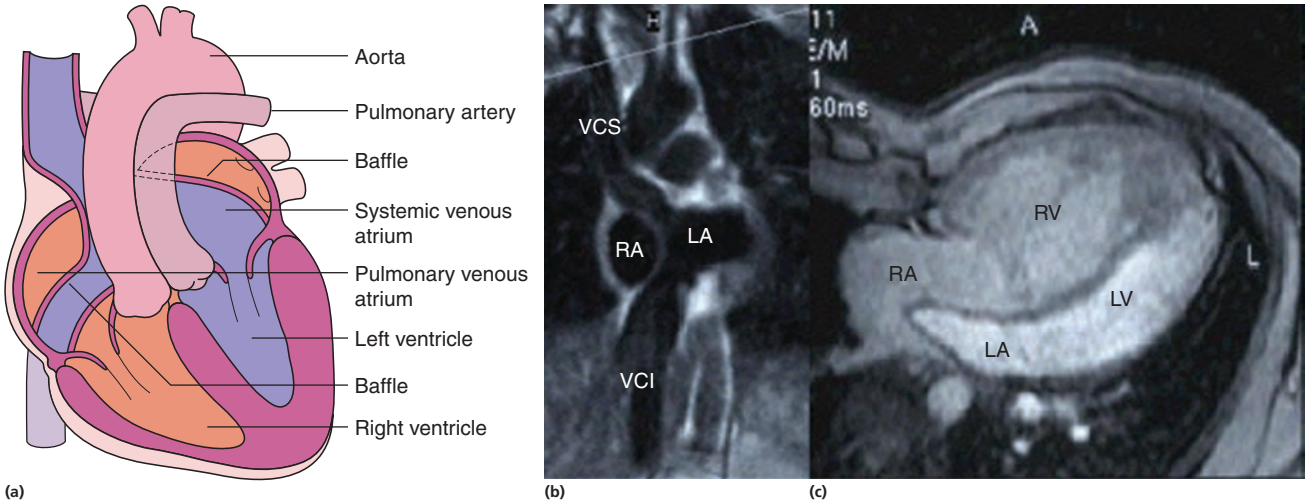


Figure 42.20 **(a)** Schematic drawing that does justice to both physiology and anatomy. Note that the superior and inferior baffles enter the anterior part of the left atrium (the posterior part is left free for drainage of the pulmonary veins) at an almost acute angle. This is also visible in **(b)**, a magnetic resonance image (MRI) with a coronal view of the heart. Image **(c)** is an axial cross section of the heart showing that the pulmonary veins in the posterior wall of the left atrium drain into the right atrium. The inferior baffle runs beneath this level from left to right; the superior baffle runs above the level of this cutting plane from inferior to superior. LA, left atrium; LV, left ventricle; RA, right atrium; RV, right ventricle; VCI, vena cava inferior; VCS, vena cava superior.

these 2D cross-sections can be acquired during the standard 2D echo workup, and it can therefore be argued that RT3D echo gives no real benefit. However, in our experience, the benefit consists in the possibility to show, offline, the exact orientation of these cross-sections in 3D space. Moreover, there is an excellent en face view of both superior and inferior tunnels, and their course from the caval veins to their entrance in the remnants of the original left atrium can be followed (Figures 42.23–42.25). If a tunnel stenosis is present, the area and length of a narrowed segment in the tunnel can be seen. A previously placed stent can also be assessed. When embarking for the first time on 3D analysis of patients with TGA after a Mustard- or Senning-type repair, it is helpful to start with a patient who has an endocardial pacemaker. The superior vena cava and the superior tunnel are identified easily because they contain a pacemaker wire. A stent can be helpful as well; if a patient has a stent in a superior or inferior tunnel, recognition of the anatomic structure that contains the stent makes orientation in the difficult 3D anatomy easier.

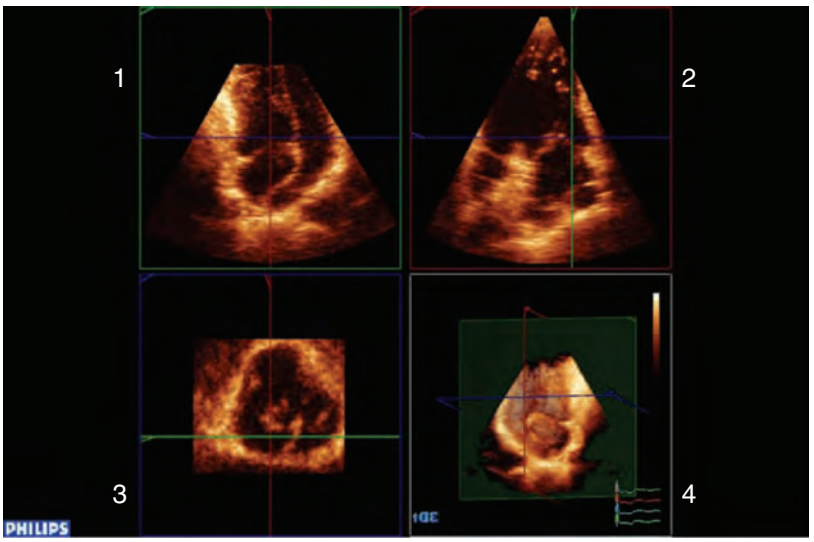
For patients with a complex transposition and a Rastelli-type repair, the intracardiac conduit from the left ventricle toward the anteriorly positioned aortic valve can be visualized and shown in relation to the adjacent structures. It is difficult, just as in 2D echo, to assess the anteriorly positioned conduit from right ventricle to the pulmonary artery.

Tetralogy of Fallot

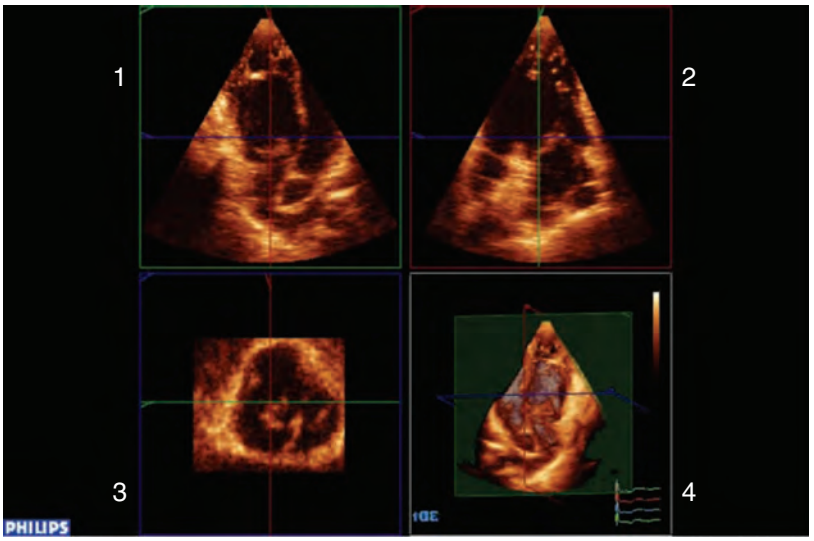
In infants, a dataset acquired from the subcostal position can contain the entire heart with tetralogy of Fallot. The whole anatomy, with the relation between the VSD, the aortic valve, the interventricular septum and the narrowed right ventricular outflow tract and pulmonary valve, can be shown (Figure 42.26). If the VSD has an uncommon shape or extension, for example, also toward the perimembranous or inlet part, this can be appreciated from both left lateral and right lateral views. The fact that the entire defect and its bordering structures can be visualized in one view is the most important benefit of 3D echo. Planimetry of the pulmonary annulus is sometimes feasible, but the outcomes rarely differ from what is known from 2D echo. The biggest challenge for the sonographer in tetralogy of Fallot after surgical correction is not morphology but the assessment of ventricular volumes and function. As described earlier, both LV and RV function can be assessed more reliably with RT3D echo than with 2D echo. 3DE has an important role in the postoperative assessment of TOF patients with residual pulmonary regurgitation.

Real-time 3D echo in other congenital cardiac malformations

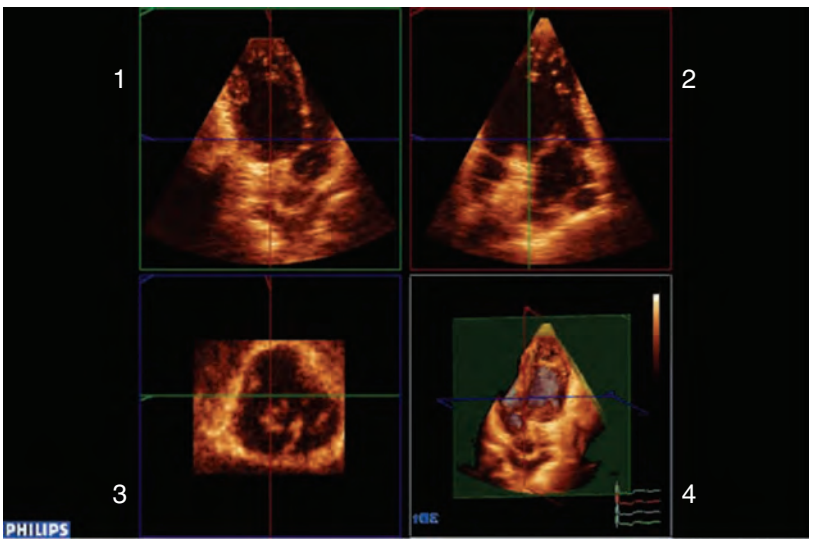
There is very little experience published so far about the benefits of RT3D echo in malformations other than the few described earlier. There have been case reports about its use in double-outlet right ventricle, subaortic stenosis [96] (Figure 42.27), double aortic arch [97], right atrial aneurysm [98], and infective endocarditis of a patent foramen ovale [99]. These are examples of the growing awareness of the potential of RT3D echo for use in congenital heart disease, but more experience is needed and the exact role of RT3D echo in the analysis of these complex congenital cardiac lesions remains to be established. The en face view on septa or valves and the possibilities for imaging abnormalities in relation to the surrounding anatomy are the most important aspects by which RT3D echo differs from 2D echo. The extent of the benefits that these views will have will differ for each abnormality, probably from virtually nothing to extremely helpful.



(a)



(b)



(c)

Figure 42.21 Three tile presentations each of a 3D image and three orthogonal 2D cross-sections. The images differ in the level of the cross-section through the 3D dataset, indicated in each case by the green plane in tile 4 (bottom right). The representation of the green section is shown in tile 1; the levels of the cross-sections are seen in tiles 2 and 3. The first level of the cross-section **(a)** is quite posterior and the connection with the inferior baffle is shown. Moving a bit more anteriorly **(b)**, the inferior baffle is out of this plane, but the connection of the pulmonary veins and pulmonary venous atrium to the right atrium can be seen. Moving even further anteriorly **(c)**, the pulmonary venous atrium disappears and the first part of the superior baffle is visible.

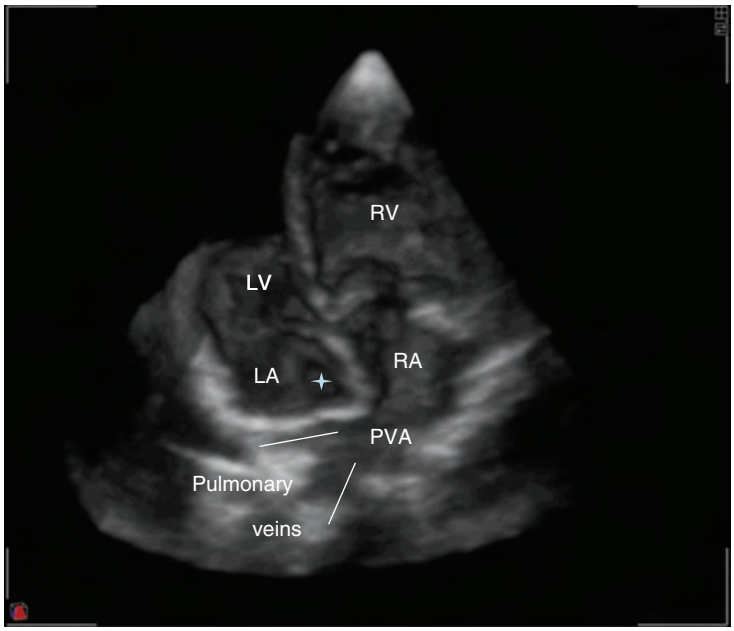


Figure 42.22 The anterior wall of the heart is cut away to give a view parallel to the interventricular septum in the heart. The "orifice" where the inferior baffle enters into the left atrium can be seen and is indicated with a star. Pulmonary veins from left and right can be seen entering the pulmonary vein atrium (PVA), which is connected without obstruction with the right atrium (RA). LA, left atrium; LV, left ventricle; RV, right ventricle.

Future applications

Improvement of image resolution, at least to the level of contemporary 2D echo, is expected in the coming years. This will overcome many of the objections against the current 3D echo systems. Better image resolution is likely to lead to better identification of the endocardial borders, which will allow more reproducible tracing of ventricular volumes. High-resolution images, comparable to that of 2D echo data, with accurate representation of even smaller and thinner intracardiac structures, will certainly result in better acceptance of 3D echocardiography in clinical practice. Another future development that will influence the use of 3D echocardiography for morphology is 3D viewing. When 3D imaging is used for assessment of morphology 3D rendering should be the standard. The current 3D imaging modes are represented as holograms on a flat 2D screen. The use of 3D screens, full holographic projection of 3D data sets and 3D printing techniques will change the field and take it to the next level.

Looking back over the short history of ultrasound, progressing from A-mode and M-mode, which were extremely expert-dependent techniques, to B-mode, which was substantially more

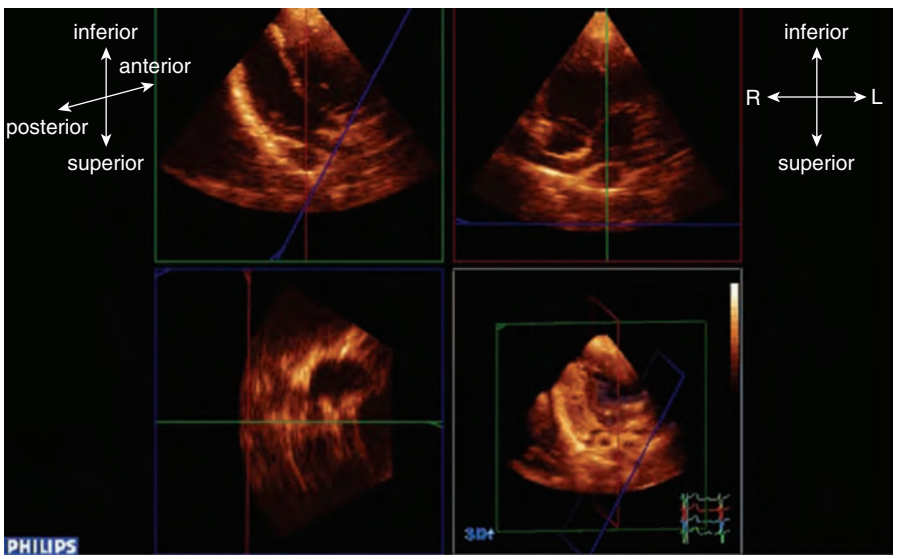


Figure 42.23 Tile presentation of a 3D dataset with three planes of cross-section. The red and green planes are perpendicular to each other, and the blue plane is modified to produce a good cross-section of the superior baffle. This plane can be moved from inferior to superior providing cross-sections of the superior baffle along its course. The diameter and circumference of the baffle can be measured reliably with planimetry in this way. The entire superior baffle is visualized within the green plane, and the entire inferior baffle is seen in the red plane. This demonstrates that the baffles have a course perpendicular to each other and enter the remains of the left atrium with separate orifices. This patient has a stent in the inferior baffle, making the entrance of the inferior baffle clearly visible.

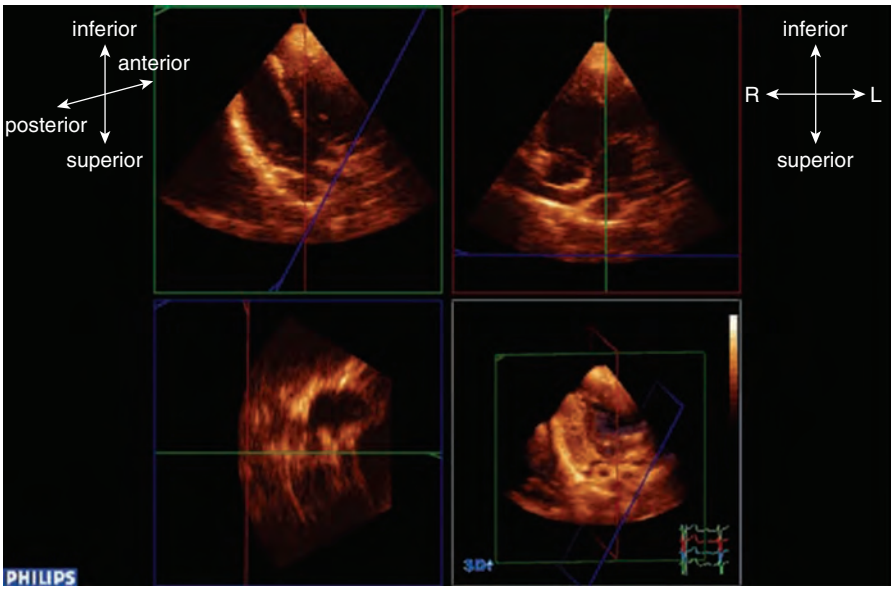


Figure 42.24 The same patient as in Fig. 42.23. Now the green plane is adjusted in such a way that it gives a cross-section of the inferior baffle. The blue plane still represents the plane perpendicular to the course of the superior baffle.

accessible but still expert-dependent in acquisition and interpretation, 3D echo has the potential to show the heart as a real 3D structure.

Videos

To access the videos for this chapter, please go to www.lai-echo.com.

Video 42.1 A crop box, showing inside an anatomical representation of a normal heart. The heart is cut through a coronal cross-section, moved first posteriorly and then anteriorly. The spatial relation between anatomical structures can be well appreciated in this way. Note the bulging of the interventricular septum to the right. At the end of the clip, the right ventricular outflow tract and pulmonary valve are seen, as structures that lie most anteriorly.

Video 42.2 On the left side, a 3D hologram of the left ventricular (LV), including the LV outflow tract, is shown. On the right side a "bull's eye" representation of 16 LV segments is shown, valuable for assessment of regional wall motion abnormalities. In the lower left, the values of the automatically calculated LV volumes and ejection fraction are shown. The color bar, at the far right of the clip, indicates the timing of the contraction. An even color during the cardiac cycle – as in this patient – indicates synchronous contraction and relaxation. In case of dyssynchrony of one or more segments, these segments will show immediately in a different color, enabling instantaneous recognition of delayed segments.

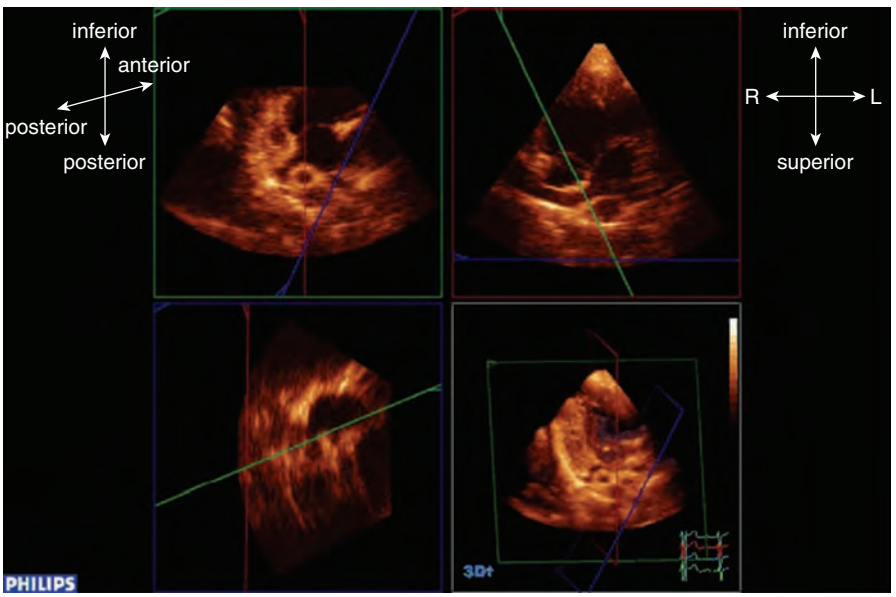


Figure 42.25 Again the same patient as in the previous figures. The green plane is adjusted to follow the course of the inferior baffle more to the right in the direction of the inferior caval vein. The inferior baffle can be followed this way along its course and planimetry can be done to measure surface and circumference.

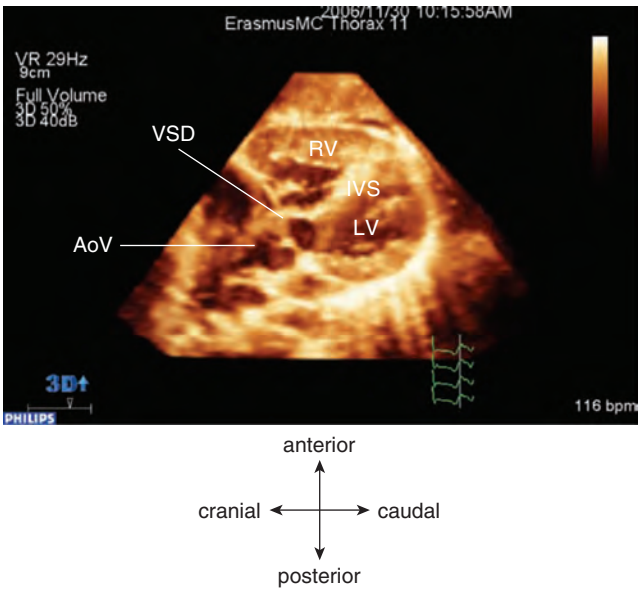


Figure 42.26 "Anyplane" cross-section in a patient with tetralogy of Fallot, showing left ventricle (LV), hypertrophic right ventricle (RV), ventricular septal defect (VSD) and overriding aorta. AoV, aortic valve; IVS, interventricular septum.

Video 42.3 The contours of the right ventricle (RV) can be traced in the transverse plane at three levels (the three left-sided images), in the coronal view (upper left), and the sagittal view (lower right). Contours should be traced in end-diastole and end-systole, and volume calculations are done automatically. Tracing of contours in the trabeculated RV is not straightforward, hence inter- and intra-observer variability is substantial. Robust automatic contour detection is essential for this application.

Video 42.4 A 3D representation of a RV volume (a "beutel") is shown in this clip. The convexity of the interventricular septum – bulging into the RV – shows well here. Bottom left shows a volume curve of the RV over time. The numeric representation of RV volumes is shown at bottom right. EDV, end-diastolic volume; EF, ejection fraction; ESV, end-systolic volume; SV, stroke volume.

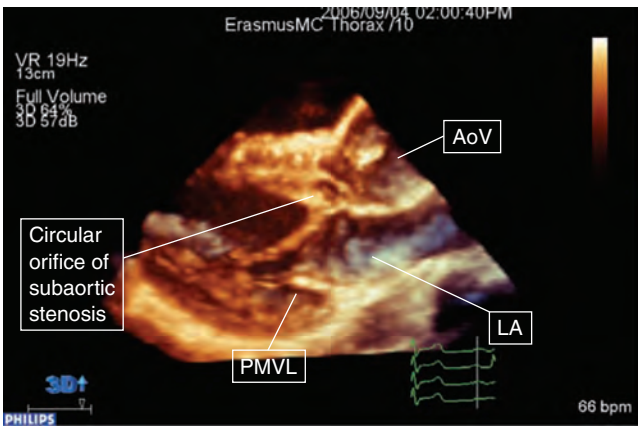


Figure 42.27 Left lateral view from a dataset acquired from a parasternal position. The left lateral wall of left atrium, left ventricle and ascending aorta are cut away. The circular opening of the subaortic stenosis is clearly visible. AoV, aortic valve; LA, left atrium; PMVL, posterior mitral valve leaflet.

Video 42.5 View from left atrium (LA) into the mitral valve (MV). A protruding part of the MV leaflet can be seen in the center of the posterior leaflet – at p2 level. In a left lateral cross-section of the MV (see Video 42.6) a prolapse of the PMVL is shown. The localization, extent, and severity of the MV prolaps can be assessed easily with 3D echo.

Video 42.6 Left lateral view of a mitral valve. The 3D data set can be turned in every direction, which enables viewing of the MV prolaps from all sides.

Video 42.7 TEE guidance of a MitraClip procedure. A left atrial view, with the MitraClip above the mitral valve, still in the left atrium. From the right side, the catheter through the interatrial septum is seen, attached to the MitraClip.

Video 42.8 TEE guidance of a MitraClip procedure. A left atrial view, with the MitraClip above the mitral valve, still in the left atrium. The clip has not been closed and the mitral valve is seen still with one orifice.

Video 42.9 A left atrial view of the mitral valve, with MitraClip in situ.The clip has been closed and the mitral valve is seen with two orifices.

Video 42.10 A right lateral view of the intra-atrial septum with a large atrial septal defect. It is a fossa ovalis-type defect with antero-superior extension, the direction of the aortic root.

Video 42.11 View from the right lateral side of the heart, looking onto the right ventricular side of the interventricular septum.

Video 42.12 A "tile" view of a 3D data set of a closure device in a VSD. Three perpendicular planes are represented and a 3D hologram at the bottom right. In the 3D view it is obvious that the device has closed a perimembranous VSD, directly underneath the tricuspid valve, in the inner curvature of the right ventricle. In the two upper 2D cross-sections, the close relation of the device with the aortic valve can be appreciated.

Video 42.13 A "tile" view of an atrioventricular septal defect (AVSD). The upper left tile shows an image comparable to that of an apical 4-chamber view. In the upper right tile, the red plane perpendicular to the green plane forms the neighboring 4-chamber view, a posterior to anterior orientation is shown at the same level, at the atrioventricular junction. The lower left tile shows a cross-section of the single atrioventricular orifice, where left and right atrioventricular valve leaflets can be seen. The lower right tile shows an unusual orientation of the 3D echo, from the apex rather than the more usual view toward the atrioventricular valve, through a part of the intact interventricular septum (IVS) into the right ventricular outflow tract (RVOT).

Videos 42.14 and 42.15 View from the apex toward the left-sided atrioventricular (AV) valve, from a transthoracic echo. Note that in an AVSD, the "cleft" is formed by the commissure between the anterior and posterior bridging leaflet. The direction is from the left toward the interventricular septum.

Video 42.16 View from the apex toward the single orifice of a complete atrioventricular septal defect (AVSD). The orientation is such that the anterior bridging leaflet is on top, the inferior bridging leaflet is at the bottom, the left mural leaflet is on the right side of the screen, and the two right-sided mural leaflets can be seen on the left side of the screen.

Video 42.17 En face view from the LV apex toward the left-sided atrioventricular valve. The commissure between the anterior and posterior bridging leaflet runs from lateral toward the interventricular septum (this is different from a cleft in a mitral valve, which runs toward the aortic valve).

Video 42.18 Transgastric view of Ebstein's anomaly, with tricuspid valve tissue extending far into the right ventricle (RV). The remaining part of the RV is small. The caliber pulmonary artery looks normal.

Video 42.19 En face view of the displaced tricuspid valve (TV). The septal leaflet is seen attached to the interventricular septum. The large and sail-like anterior superior leaflet can also be seen. The coaptation of the abnormal leaflets is not optimal, leaving an evident opening of the TV during systole, which leads to tricuspid regurgitation.

References

1 Dekker DL, Piziali RL, Dong E, Jr. A system for ultrasonically imaging the human heart in three dimensions. *Comput Biomed Res* 1974;**7**:544–553.

2 Matsumoto M, Inoue M, Tamura S, et al. Three-dimensional echocardiography for spatial visualization and volume calculation of cardiac structures. *J Clin Ultrasound* 1981;**9**:157–165.

3 Miwa H, Hayashi H, Shimura T, et al. 3-D envisioning by real time perpendicular bi-plane echocardiography (simultaneous multifrequency ultrasonography-III). *Ultrasound Med Biol* 1983;(Suppl 2):283–287.

4 Snyder JE, Kisslo J, von Ramm O. Real-time orthogonal mode scanning of the heart. I. System design. *J Am Coll Cardiol* 1986;**7**:1279–1285.

5 Sheikh, K., S. Smith, von Ramm OT, et al. Real-time, three-dimensional echocardiography: feasibility and initial use. *Echocardiography* 1991;**8**:119–125.

6 von Ramm OT, Smith SW. Real time volumetric ultrasound imaging system. *J Digit Imaging* 1990;**3**:261–266.

7 Salgo IS. Three-dimensional echocardiographic technology. *Cardiol Clin* 2007;**25**:231–239.

8 Gill EA, Klas B. Three-dimensional echocardiography: an historical perspective. *Cardiol Clin* 2007;**25**:221–229.

9 Acar P, Abadir S, Paranon S, et al. Live 3D echocardiography with the pediatric matrix probe. *Echocardiography* 2007;**24**:750–755.

10 Lang RM, Mor-Avi V, Sugeng L, et al. Three-dimensional echocardiography: the benefits of the additional dimension. *J Am Coll Cardiol* 2006;**48**:2053–2069.

11 Shirali GS. Three-dimensional echocardiography in congenital heart disease. *Echocardiography* 2011;**29**:242–248.

12 Simpson JM, Miller O. Three-dimensional echocardiography in congenital heart disease. *Arch Cardiovasc Dis* 2011;**104**:45–56.

13 Del Pasqua A, Sanders SP, de Zorzi A, et al. Impact of three-dimensional echocardiography in complex congenital heart defect cases: the surgical view. *Pediatr Cardiol* 2009;**30**:293–300.

14 Bleich S, Nanda NC, Hage FG. The incremental value of three-dimensional transthoracic echocardiography in adult congenital heart disease. *Echocardiography* 2013;**30**:483–494.

15 Zhang L, Xie M, Balluz R, Ge S. Real time three-dimensional echocardiography for evaluation of congenital heart defects: state of the art. *Echocardiography* 2012;**29**:232–241.

16 Hage FG, Raslan S, Dean P, et al. Real time three-dimensional transthoracic echocardiography in congenital heart disease. *Echocardiography* 2012;**29**:220–231. Erratum in: *Echocardiography* 2012;**29.**

17 Friedberg MK, Su X, Tworetzky W, et al. Validation of 3D echocardiographic assessment of left ventricular volumes, mass, and ejection fraction in neonates and infants with congenital heart disease: a comparison study with cardiac MRI. *Circ Cardiovasc Imaging* 2010;**3**:735–742.

18 Raedle-Hurst TM, Mueller M, Rentzsch A, et al. Assessment of left ventricular dyssynchrony and function using real-time 3-dimensional echocardiography in patients with congenital right heart disease. *Am Heart J* 2009;**157**:791–798.

19 Thavendiranathan P, Grant AD, Negishi T, et al. Reproducibility of echocardiographic techniques for sequential assessment of left ventricular ejection fraction and volumes: application to patients undergoing cancer chemotherapy. *J Am Coll Cardiol* 2013;**61**:77–84.

20 van der Zwaan HB, Helbing WA, McGhie JS, et al. Clinical value of real-time three-dimensional echocardiography for right ventricular quantification in congenital heart disease: validation with cardiac magnetic resonance imaging. *J Am Soc Echocardiogr* 2010;**23**:134–140.

21 Khoo NS, Young A, Occleshaw C, et al. Assessments of right ventricular volume and function using three-dimensional echocardiography in older children and adults with congenital heart disease: comparison with cardiac magnetic resonance imaging. *J Am Soc Echocardiogr* 2009;**22**:1279–1288.

22 Moustafa SE, Chandrasekaran K, Khandheria B, et al. Real-time three-dimensional transesophageal echocardiography assessment of the mitral valve: perioperative advantages and game-changing findings. *J Heart Valve Dis* 2011;**20**:114–122.

23 Swaans MJ, Van den Branden BJ, Van der Heyden JA, et al. Three-dimensional transoesophageal echocardiography in a patient undergoing percutaneous mitral valve repair using the edge-to-edge clip technique. *Eur J Echocardiogr* 2009;**10**:982–983.

24 Siddiqi N, Seto A, Patel PM. Transcatheter closure of a mechanical perivalvular leak using real-time three-dimensional transesophageal echocardiography guidance. *Catheter Cardiovasc Interv* 2011;**78**:333–335.

25 Jenkins C, Monaghan M, Shirali G, et al. An intensive interactive course for 3D echocardiography: Is "Crop Till You Drop" an effective learning strategy? *Eur J Echocardiogr* 2007;**9**:373.

26 Hare JL, Jenkins C, Nakatani S, et al. Feasibility and clinical decision-making with 3D echocardiography in routine practice. *Heart* 2008;**94**:440–445.

27 Nanda N, Hsiung MC, Miller AP, et al. *Live/Real Time 3D Echocardiography*. Oxford: Blackwell Publishing, 2010.

28 Nagueh SF. Noninvasive estimation of LV filling pressures in heart failure and reduced ejection fraction: revisited and verified. *JACC Cardiovasc Imaging* 2011;**4**:935–937.

29 Knauth AL, Gauvreau K, Powell AJ, et al. Ventricular size and function assessed by cardiac MRI predict major adverse clinical outcomes late after tetralogy of Fallot repair. *Heart* 2008;**94**:211–216.

30 van Wolferen SA, Marcus JT, Boonstra A, et al. Prognostic value of right ventricular mass, volume, and function in idiopathic pulmonary arterial hypertension. *Eur Heart J* 2007;**28**:1250–1257.

31 Ghio S, Gavazzi A, Campana C, et al. Independent and additive prognostic value of right ventricular systolic function and pulmonary artery pressure in patients with chronic heart failure. *J Am Coll Cardiol* 2001;**37**:183–188.

32 Ruddox V, Mathisen M, Bækkevar M, et al. Is 3D echocardiography superior to 2D echocardiography in general practice? A systematic review of studies published between 2007 and 2012. *Int J Cardiol* 2013;**168**:1306–1315.

33 Mor-Avi V, Jenkins C, Kuhl HP, et al. Real-time 3-dimensional echocardiographic quantification of left ventricular volumes: multicenter study for validation with magnetic resonance imaging and investigation of sources of error. *JACC Cardiovasc Imaging* 2008;**1**:413–423.

34 Soliman OI, Kirschbaum SW, van Dalen BM, et al. Accuracy and reproducibility of quantitation of left ventricular function by real-time three-dimensional echocardiography versus cardiac magnetic resonance. *Am J Cardiol* 2008;**102**:778–783.

35 Shibayama K, Watanabe H, Iguchi N, et al. Evaluation of automated measurement of left ventricular volume by novel real-time 3-dimensional echocardiographic system: validation with cardiac magnetic resonance imaging and 2-dimensional echocardiography. *J Cardiol* 2013;**61**:281–288.

36 Thavendiranathan P, Liu S, Verhaert D, et al. Feasibility, accuracy, and reproducibility of real-time full-volume 3D transthoracic echocardiography to measure LV volumes and systolic function: a fully automated endocardial contouring algorithm in sinus rhythm and atrial fibrillation. *JACC Cardiovasc Imaging* 2012;**5**:239–251.

37 Chahal NS, Lim TK, Jain P, et al. Population-based reference values for 3D echocardiographic LV volumes and ejection fraction. *JACC Cardiovasc Imaging* 2012;**5**:1191–1197.

38 Luijnenburg SE, Robbers-Visser D, Moelker A, et al. Intra-observer and interobserver variability of biventricular function, volumes and mass in patients with congenital heart disease measured by CMR imaging. *Int J Cardiovasc Imaging* 2010;**26**:57–64.

39 Greupner J, Zimmermann E, Grohmann A, et al. Head-to-head comparison of left ventricular function assessment with 64-row computed tomography, biplane left cineventriculography, and both 2- and 3-dimensional transthoracic echocardiography: comparison with magnetic resonance imaging as the reference standard. *J Am Coll Cardiol* 2012;**59**:1897–1907.

40 Sugeng L, Mor-Avi V, Weinert L, et al. Multimodality comparison of quantitative volumetric analysis of the right ventricle. *JACC Cardiovasc Imaging* 2010;**3**:10–18.

41 Teupe C, Takeuchi M, Yao J, Pandian N. Determination of left ventricular mass by three-dimensional echocardiography: in vitro validation of a novel quantification method using multiple equi-angular rotational planes for rapid measurements. *Int J Cardiovasc Imaging* 2002;**18**:161–167.

42 Schmidt MA, Freidlin RZ, Ohazama CJ, et al. Anatomic validation of a novel method for left ventricular volume and mass measurements with use of real-time 3-dimensional echocardiography. *J Am Soc Echocardiogr* 2001;**14**:1–10.

43 Atsumi A, Ishizu T, Kameda Y, et al. Application of 3-dimensional speckle tracking imaging to the assessment of right ventricular regional deformation. *Circ J* 2013;**77**:1760–1768.

44 Seo Y, Ishizu T, Enomoto Y, et al. Validation of 3-dimensional speckle tracking imaging to quantify regional myocardial deformation. *Circ Cardiovasc Imaging* 2009;**2**:451–459.

45 Mertens LL, Friedberg MK. Imaging the right ventricle–current state of the art. *Nat Rev Cardiol* 2010;**7**:551–563.

46 Hui W, Abd El Rahman MY, Dsebissowa F, et al. Comparison of modified short axis view and apical four chamber view in evaluating right ventricular function after repair of tetralogy of Fallot. *Int J Cardiol* 2005;**105**:256–261.

47 Koestenberger M, Nagel B, Ravekes W, et al. Systolic right ventricular function in pediatric and adolescent patients with tetralogy of Fallot: echocardiography versus magnetic resonance imaging. *J Am Soc Echocardiogr* 2011;**24**:45–52.

48 Puchalski MD, Williams RV, Askovich B. Assessment of right ventricular size and function: echo versus magnetic resonance imaging. *Congenit Heart Dis* 2007;**2**:27–31.

49 Lai WW, Gauvreau K, Rivera ES, et al. Accuracy of guideline recommendations for two-dimensional quantification of the right ventricle by echocardiography. *Int J Cardiovasc Imaging* 2008;**24**:691–698.

50 Jiang L, Levine RA, Weyman AE. Echocardiographic assessment of right ventricular volume and function. *Echocardiography* 1997;**14**:189–206.

51 Van der Zwaan HB, Helbing WA, Boersma E, et al. Usefulness of real-time three-dimensional echocardiography to identify right ventricular dysfunction in patients with congenital heart disease. *Am J Cardiol* 2010;**106**:843–850.

52 Van der Zwaan HB, Geleijnse ML, McGhie JS, et al. Right ventricular quantification in clinical practice: two-dimensional vs. three-dimensional echocardiography compared with cardiac magnetic resonance imaging. *Eur J Echocardiogr* 2011;**12**:656–664.

53 Sheehan FH, Kilner PJ, Sahn DJ, et al. Accuracy of knowledge-based reconstruction for measurement of right ventricular volume and function in patients with tetralogy of Fallot. *Am J Cardiol* 2010;**105**:993–999.

54 Sheehan FH, Ge S, Vick GW, 3rd, et al. Three-dimensional shape analysis of right ventricular remodeling in repaired tetralogy of Fallot. *Am J Cardiol* 2008;**101**:107–113.

55 Lang RM, Badano LP, Tsang W, et al. EAE/ASE Recommendations for image acquisition and display using three-dimensional echocardiography. *J Am Soc Echocardiogr* 2012;**25**:3–46.

56 Zamorano JL, Badano LP, Bruce C, et al. EAE/ASE recommendations for the use of echocardiography in new transcatheter interventions for valvular heart disease. *Eur J Echocardiogr* 2011;**12**:557.

57 Ng AC, Delgado V, van der Kley F, et al. Comparison of aortic root dimensions and geometries before and after transcatheter aortic valve implantation by 2- and 3 dimensional transesophageal echocardiography and multislice computed tomography. *Circ Cardiovasc Imaging* 2010;**3**:94 –102.

58 Jilaihawi H, Doctor N, Kashif M, et al. Aortic annular sizing for transcatheter aortic valve replacement using cross-sectional 3-dimensional transesophageal echocardiography. *J Am Coll Cardiol* 2013;**61**:908–916.

59 Izumo M, Shiota M, Kar S, et al. Comparison of real-time three-dimensional transesophageal echocardiography to two-dimensional transesophageal echocardiography for quantification of mitral valve prolapse in patients with severe mitral regurgitation. *Am J Cardiol* 2013;**111**:588–594.

60 La Canna G, Arendar I, Maisano F, et al. Real-time three-dimensional transesophageal echocardiography for assessment of mitral valve functional anatomy in patients with prolapse-related regurgitation. *Am J Cardiol* 2011;**107**:1365–1374.

61 Zhou ZW, Xu YW, Ashraf M, Sahn DJ. Three-dimensional echocardiography of colour Doppler flow. *Arch Cardiovasc Dis* 2010;**103**:333–339.

62 Lee AP, Lam YY, Yip GW, et al. Role of real time three-dimensional transesophageal echocardiography in guidance of interventional procedures in cardiology. *Heart* 2010;**96**:1485–1493.

63 Altiok E, Becker M, Hamada S, et al. Real-time 3D TEE allows optimized guidance of percutaneous edge-to-edge repair of the mitral valve. *JACC Cardiovasc Imaging* 2010;**3**:1196–1198.

64 Bilska KM, Kehrens CM, Riley G, et al. Subcostal real-time three-dimensional echocardiography of interatrial communications: reconstruction of an oval fossa defect, a superior sinus venosus defect with partially anomalous pulmonary venous drainage, an infero-posterior oval fossa defect, and a coronary sinus defect. *Cardiol Young* 2012;**22**:145–151.

65 McMahon CJ, Feltes TF, Fraley JK, et al. Natural history of growth of secundum atrial septal defects and implications for transcatheter closure. *Heart* 2002;**87**:256–259.

66 Cooke JC, Gelman JS, Harper RW. Echocardiologists' role in the deployment of the Amplatzer atrial septal occluder device in adults. *J Am Soc Echocardiogr* 2001;**14**:588–594.

67 Reddy SC, Rao PS, Ewenko J, et al. Echocardiographic predictors of success of catheter closure of atrial septal defect with the buttoned device. *Am Heart J* 1995;**129**:76–82.

68 Marx GR, Sherwood MC, Fleishman C, Van Praagh R. Three-dimensional echocardiography of the atrial septum. *Echocardiography* 2001;**18**:433–443.

69 van den Bosch AE, Ten Harkel DJ, McGhie JS, et al. Characterization of atrial septal defect assessed by real-time 3-dimensional echocardiography. *J Am Soc Echocardiogr* 2006;**19**:815–821.

70 Mathewson JW, Bichell D, Rothman A, Ing FF. Absent postero-inferior and antero-superior atrial septal defect rims: factors affecting nonsurgical closure of large secundum defects using the Amplatzer occluder. *J Am Soc Echocardiogr* 2004;**17**:62–69.

71 Lange A, Walayat M, Turnbull CM, et al. Assessment of atrial septal defect morphology by transthoracic three dimensional echocardiography using standard grey scale and Doppler myocardial imaging techniques: comparison with magnetic resonance imaging and intraoperative findings. *Heart* 1997;**78**:382–389.

72 Roberson DA, Cui W, Patel D, et al. Three-dimensional transesophageal echocardiography of atrial septal defect: a qualitative and quantitative anatomic study. *J Am Soc Echocardiogr* 2011;**24**:600–610.

73 Acar P. Three-dimensional echocardiography in children with atrial septal defect. *Minerva Pediatr* 2004;**56**:29–40.

74 Handke M, Schafer DM, Muller G, et al. Dynamic changes of atrial septal defect area: new insights by three-dimensional volume-rendered echocardiography with high temporal resolution. *Eur J Echocardiogr* 2001;**2**:46–51.

75 Xie MX, Fang LY, Wang XF, et al. Assessment of atrial septal defect area changes during cardiac cycle by live three-dimensional echocardiography. *J Cardiol* 2006;**47**:181–187.

76 Ojala T, Rosenthal E, Nugent K, et al. Live 3D echocardiography to guide closure of residual ASD. *JACC Cardiovasc Imaging* 2013;**6**:523–525.

77 Saric M, Perk G, Purgess JR, Kronzon I. Imaging atrial septal defects by real-time three-dimensional transesophageal echocardiography: step-by-step approach. *J Am Soc Echocardiogr* 2010;**23**:1128–1135.

78 Chen FL, Hsiung MC, Nanda N, et al. Real time three-dimensional echocardiography in assessing ventricular septal defects: an echocardiographic-surgical correlative study. *Echocardiography* 2006;**23**:562–568.

79 Mehmood F, Miller AP, Nanda NC, et al. Usefulness of live/real time three-dimensional transthoracic echocardiography in the characterization of ventricular septal defects in adults. *Echocardiography* 2006;**23**:421–427.

80 Cheng TO, Xie MX, Wang XF, et al. Real-time 3-dimensional echocardiography in assessing atrial and ventricular septal defects: an echocardiographic-surgical correlative study. *Am Heart J* 2004;**148**:1091–1095.

81 Hsu JH, Wu JR, Dai ZK, Lee MH. Real-time three-dimensional echocardiography provides novel and useful anatomic insights of perimembranous ventricular septal aneurysm. *Int J Cardiol* 2007;**118**:326–331.

82 Dall'Agata A, Cromme-Dijkhuis AH, Meijboom FJ, et al. Three dimensional echocardiography enhances the assessment of ventricular septal defect. *Am J Cardiol* 1999;**83**:1576–1579, A1578.

83 van den Bosch AE, Ten Harkel DJ, McGhie JS, et al. Feasibility and accuracy of real-time 3-dimensional echocardiographic assessment of ventricular septal defects. *J Am Soc Echocardiogr* 2006;**19**:7–13.

84 Mercer-Rosa L, Seliem MA, Fedec A, et al. Illustration of the additional value of real-time 3-dimensional echocardiography to conventional transthoracic and transesophageal 2-dimensional echocardiography in imaging muscular ventricular septal defects: does this have any impact on individual patient treatment? *J Am Soc Echocardiogr* 2006;**19**:1511–1519.

85 Charakida M, Qureshi S, Simpson JM. 3D echocardiography for planning and guidance of interventional closure of VSD. *JACC Cardiovasc Imaging* 2013;**6**:120–123.

86 Rawlins DB, Austin C, Simpson JM. Live three-dimensional paediatric intraoperative epicardial echocardiography as a guide to surgical repair of atrioventricular valves. *Cardiol Young* 2006;**16**:34–39.

87 Barrea C, Levasseur S, Roman K, et al. Three-dimensional echocardiography improves the understanding of left atrioventricular valve morphology and function in atrioventricular septal defects undergoing patch augmentation. *J Thorac Cardiovasc Surg* 2005;**129**:746–753.

88 Seliem MA, Fedec A, Szwast A, et al. Atrioventricular valve morphology and dynamics in congenital heart disease as imaged with real-time 3-dimensional matrix-array echocardiography: comparison with 2-dimensional imaging and surgical findings. *J Am Soc Echocardiogr* 2007;**20**:869–876.

89 van den Bosch AE, Ten Harkel DJ, McGhie JS, et al. Surgical validation of real-time transthoracic 3D echocardiographic assessment of atrioventricular septal defects. *Int J Cardiol* 2006;**112**:213–218.

90 van den Bosch AE, van Dijk VF, McGhie JS, et al. Real-time transthoracic three-dimensional echocardiography provides additional information on left-sided AV valve morphology after AVSD repair. *Int J Cardiol* 2006;**106**:360–364.

91 Hlavacek AM, Crawford FA, Jr., Chessa KS, Shirali GS. Real-time three-dimensional echocardiography is useful in the evaluation of patients with atrioventricular septal defects. *Echocardiography* 2006;**23**:225–231.

92 Takahashi K, Guerra V, Roman KS, et al. Three-dimensional echocardiography improves the understanding of the mechanisms and site of left atrioventricular valve regurgitation in atrioventricular septal defect. *J Am Soc Echocardiogr* 2006;**19**:1502–1510.

93 Singh A, Romp RL, Nanda NC, et al. Usefulness of live/real time three-dimensional transthoracic echocardiography in the assessment of atrioventricular septal defects. *Echocardiography* 2006;**23**:598–608.

94 Negoi RI, Ispas AT, Ghiorghiu I, et al. Complex Ebstein's malformation: defining preoperative cardiac anatomy and function. *J Card Surg* 2013;**28**:70–81.

95 Bharucha T, Honjo O, Seller N, et al. Mechanisms of tricuspid valve regurgitation in hypoplastic left heart syndrome: a case-matched echocardiographic-surgical comparison study. *Eur Heart J Cardiovasc Imaging* 2013;**14**:135–141.

96 Miyamoto K, Nakatani S, Kanzaki H, et al. Detection of discrete subaortic stenosis by 3-dimensional transesophageal echocardiography. *Echocardiography* 2005;**22**:783–784.

97 Sivaprakasam MC, Vettukattil JJ. 3-D echocardiographic imaging of double aortic arch. *Eur J Echocardiogr* 2006;**7**:476–477.

98 Guerra VC, Coles J, Smallhorn JF. Aneurysm of right atrium diagnosed by 3-dimensional real-time echocardiogram. *J Am Soc Echocardiogr* 2005;**18**:1221.

99 Acar P, Abadir S, Bassil R. Images in congenital heart disease. Infective endocarditis of the patent oval fossa assessed by three-dimensional echocardiography. *Cardiol Young* 2007;**17**:113.

CHAPTER 43

Pregnancy and Heart Disease

Anne Marie Valente
Department of Cardiology, Department of Pediatrics, Boston Children's Hospital;
Division of Cardiology, Department of Medicine, Brigham and Women's Hospital;
Harvard Medical School, Boston, MA, USA

Introduction

As the number of women with congenital heart disease (CHD) reaching childbearing age continues to grow, so does our understanding of the physiologic changes that occur during pregnancy and the effects that this physiology has on maternal heart disease. Profound hemodynamic changes occur during pregnancy, which are usually tolerated well by women with structurally normal hearts; however, these changes may not be tolerated so well in women with underlying cardiac conditions. It is important to understand these hemodynamic changes in order to predict the response of certain cardiac conditions. Echocardiography characterizes the ventricular and valvar function, as well as the extent of the disease in women and can be performed safely throughout pregnancy.

The 2014 American College of Cardiology/American Heart Association (ACC/AHA) Guidelines for Management of Patients with Valvular Heart Disease [1] includes a section on the management of valvar heart disease in pregnancy and the European Society of Cardiology has also published guidelines on the management of cardiovascular disease in pregnancy [2].

Echocardiography has an essential role in the evaluation and management of women with heart disease during pregnancy [3]. Chamber enlargement, valve annular dilation, and increased prevalence of trivial valve regurgitation are time-related events during normal pregnancy, resulting from a reversible cardiac remodeling process induced by physiologic volume overload. These aspects should be considered for correct interpretation of Doppler echocardiographic findings in pregnant women [4].

Many women experience symptoms of exercise intolerance, fatigue, and pedal edema during the later stages of pregnancy or develop a flow-related systolic murmur. However, occasionally previously unknown cardiac disease may be unmasked during pregnancy. Echocardiography should be considered in any pregnant women with a history of cardiac disease, concerning symptoms, arterial desaturation, or any new holosystolic or diastolic murmur [5].

The purpose of this chapter is to review the hemodynamic changes that occur with pregnancy and the echocardiographic changes that accompany this process with an emphasis on these changes in women with heart disease.

Physiologic hemodynamic changes in pregnancy and delivery

During pregnancy, dramatic changes in hemodynamics occur (Figure 43.1). On average, there is a 50% increase in the circulating blood volume that occurs during pregnancy [6]. There is up to a 50% increase in cardiac output in pregnancy, which peaks at the beginning of the third trimester [7]. This rise in cardiac output is due primarily to an augmentation in stroke volume with some contribution from a rise in heart rate [8]. The heart rate generally increases 10–20 beats per minute from pre-pregnancy values. At the same time, there is a dramatic decrease in systemic vascular resistance, due largely to the effects of uterine circulation and endogenous hormones [6]. There is a widening of the pulse pressure, with a disproportionate decrease in the diastolic blood pressure. Throughout pregnancy, the increase in venous tone increases preload, and decreases in aortic stiffness reduce afterload [9]. Body position can also influence the hemodynamics in pregnant women. In the supine position, women may experience decreased preload, stroke volume and cardiac output due to the compression of the inferior vena cava from the gravid uterus [10]. Therefore, women may be more comfortable in the left lateral decubitus position.

During labor and delivery, there is a further abrupt increase in cardiac output related in part to the associated pain and anxiety. Uterine contractions can lead to marked increases in both

Echocardiography in Pediatric and Congenital Heart Disease: From Fetus to Adult, Second Edition. Edited by Wyman W. Lai, Luc L. Mertens, Meryl S. Cohen and Tal Geva.
© 2016 John Wiley & Sons, Ltd. Published 2016 by John Wiley & Sons, Ltd.
Companion website: www.lai-echo.com

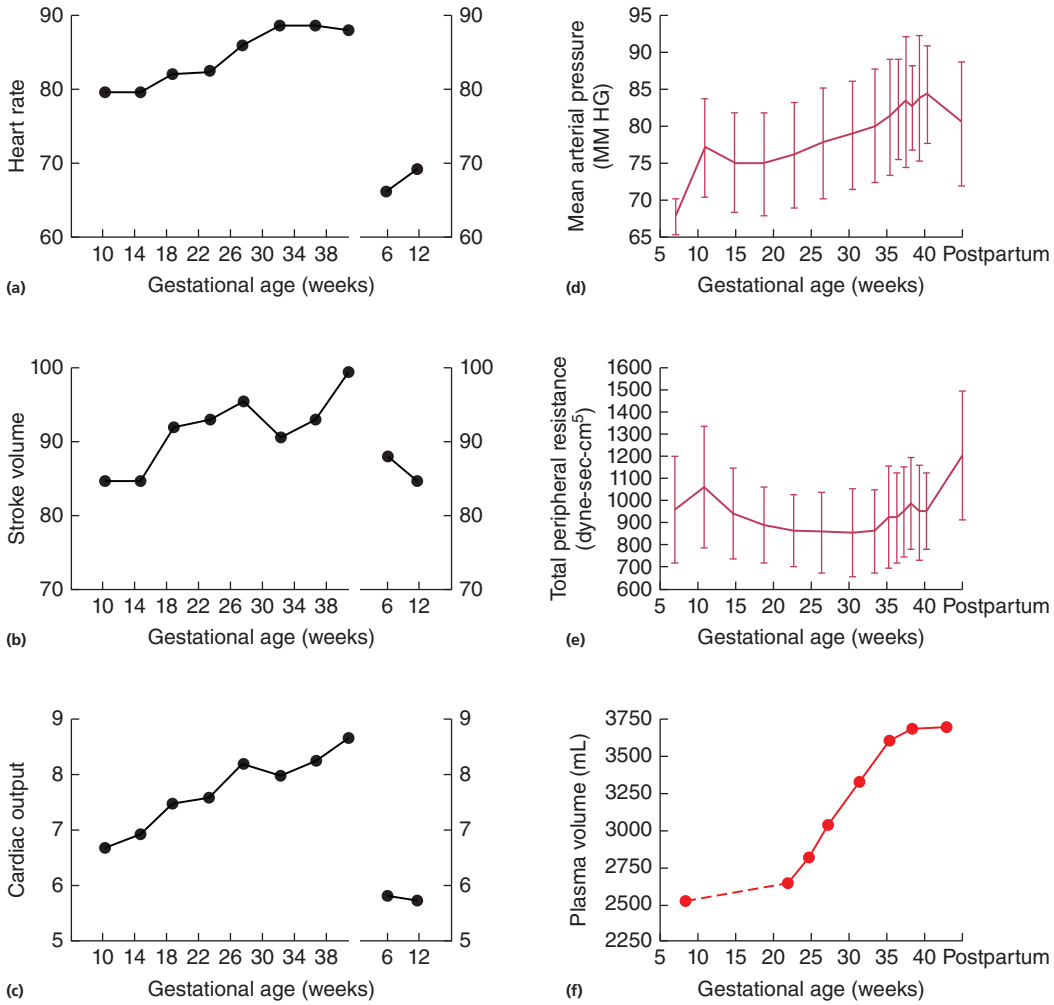


Figure 43.1 (**a–c**) Values on the *x* axis are from pulsed-wave Doppler. Normal hemodynamic changes with pregnancy. Source: Adapted from Mabie WC et al. A longitudinal study of cardiac output in normal human pregnancy. *Am J Obstet Gynecol* 1994;**170**:849–856. **(d,e)** Values on the *y* axis are represented as mean ± standard deviation. Source: Adapted from Stout K. Role of echocardiography in the diagnosis and management of heart disease in pregnancy. In: Otto C (ed.) *The Practice of Clinical Echocardiography*, 4th edn, 2012, Chapter 35, Figure 35-5, which was adapted from Easterling TR, et al. Maternal hemodynamics in normal and preeclamptic pregnancies: a longitudinal study. *Obstet Gynecol* 1990;**76**:1061–1069, Figures 1, 2, 3. **(f)** Source: Adapted from Silversides C. Physiological changes in pregnancy. In: Oakley C, Warnes CA (eds.) *Heart Disease in Pregnancy*, 2nd edn, BMJ Books, 2007, Chapter 2, Figure 2.1. ISBN: 978-1-4051-3488-0

systolic and diastolic blood pressure and surges in cardiac output [11]. After delivery, there is an initial surge in preload related to the autotransfusion of uterine blood into the systemic circulation and to inferior vena cava decompression. Stroke volume and cardiac output increase as much as 10% and persist for at least 24 hours following delivery. Hemodynamics usually normalize by 12 weeks postpartum, but there is some evidence that hemodynamics in women with underlying heart disease do not return to the pre-pregnancy baseline [12].

Pregnancy is also associated with a hypercoagulable state due to relative increases in fibrinogen, plasminogen activator inhibitors, clotting factors VII, VIII, X, von Willebrand factor, and platelet adhesion molecules; as well as relative decreases in protein S activity [13,14].

Normal echocardiographic changes with pregnancy

Echocardiography is an important imaging tool as it allows assessment of cardiac structure and function in women in various stages of pregnancy. There are challenges to determining the normal echocardiographic changes during pregnancy, as much of the reported data was not obtained in a standardized fashion. Differences in the position of the patient (supine versus left lateral decubitus), timing of gestation, and technical variables contribute to the discrepancies found in the literature. For example, during late pregnancy, significant increases in left ventricular (LV) ejection fraction (11%), end-diastolic volume (21%), stroke volume (35%), and cardiac output (24%) were

Table 43.1 Normal echocardiographic changes during pregnancy

Echocardiographic parameter	Changes during pregnancy
Left atrium	⇑ 3–4 mm
Left ventricular end-diastolic dimension	⇑ 2–3 mm
Left ventricular mass	⇑ 5–10%
Left ventricular ejection fraction	Unchanged or slightly ⇑
E/A ratio	⇓
E/e′ ratio	Unchanged
e′/a′ ratio	⇓
Valve annulus diameter	⇑ 1–2 cm
Valvar regurgitation	Physiologic TR, PR, MR (not AR)
Small pericardial effusion	Present in 25–40%

observed in the left lateral decubitus compared to the supine position [15]. There is a spectrum of cardiac responses to normal pregnancy, which adds to the difficulties in providing normal values for echocardiographic changes during pregnancy. A summary of the echocardiographic changes expected during pregnancy is listed in Table 43.1.

Throughout pregnancy, ventricular size and mass increase. On average, the LV end-diastolic dimension increases several mm [16]. The LV mass increases by 5–10% and is proportional to the increased workload of pregnancy. This results in eccentric hypertrophy, as the ratio of wall thickness to the ventricular radius does not change [17].

Left ventricular systolic function does not appear to significantly change during pregnancy. There have been reports of a transient increase in LV ejection fraction (EF) during the early stages of pregnancy which then falls in the third trimester. However, one confounder is that the Teichholz formula, which assumes an ellipsoid LV shape, is utilized for calculation of EF and may not be appropriate for pregnant patients due to the geometric changes of the ventricle. Bamfo and colleagues evaluated LV long-axis function and used tissue Doppler imaging in order to avoid geometric assumptions and reported that long-axis shortening decreased significantly at the septal but not the lateral margin of the mitral valve annulus. This may reflect that the changes in ventricular geometry affect the septum more than the lateral wall of the LV [18].

The data on the effects of pregnancy on myocardial contractility are conflicting. Geva et al. used a load-adjusted measure of contractility and reported a transient decrease in myocardial contractility due to a decrease in the end-systolic stress not matched by an increased rate in corrected velocity circumferential shortening [19]. Bamfo reported a progressive increase in the Tei index throughout pregnancy and the postpartum period, and postulated an intrinsic abnormality in contractility associated with pregnancy [18]. In contrast, others have reported no significant changes or increase in myocardial contractility during pregnancy [20,21].

Left ventricular diastolic function appears preserved despite increases in preload and left ventricular hypertrophy. Transmitral velocities are flow dependent and reflect the increase preload in pregnancy with peak mitral inflow velocity increases in early diastole (E) and atrial systole (A). As pregnancy progresses, there is an increased amount of atrial contraction contributing to LV filling resulting in higher A-wave velocities. The proportional change in A is greater than the change in E resulting in a diminished E/A ratio throughout pregnancy.

Using tissue Doppler as a load-independent assessment, investigators have shown that LV relaxation is preserved during pregnancy. The ratio of e′ to E remains within normal limits throughout pregnancy and reflects normal LV filling pressures [9]. The ratio of e′/a′ decreases throughout pregnancy, reflecting the enhanced atrial contraction. More recently, Savu and colleagues performed tissue Doppler strain and strain rate and 3D speckle tracking on 51 pregnant women and reported a significant, reversible decrease in global and segmental longitudinal deformation in both the LV and RV late in pregnancy. The decrease in longitudinal deformation was seen at all three levels in the LV (basal, mid, and apical) and most notably at the inferior, inferoseptal, and anteroseptal walls. In the RV, the decrease in longitudinal deformation was most notable at the apical level. These investigators also documented an increase in the cardiac globularity as defined by a decreased sphericity index [15].

The left atrium increases up to 10% in size during pregnancy [22]. Using 3D echocardiography, Yosefy et al. documented significant increases in the LA systolic volume, LA diastolic volume, and LA stroke volumes (all indexed to body surface area). These investigators confirmed the reduction in E/A ratio as pregnancy progresses with a decrease in the diastolic E wave, forcing the left atrium to increase the atrial kick (A wave) [23].

Pulmonary artery pressure remains normal during pregnancy due to the vascular recruitment in the highly capacitant pulmonary circulation resulting in decreased pulmonary vascular resistance [24]. There is a slight increase in valvar annular diameters during pregnancy and an increase in regurgitant flow velocities from the tricuspid, mitral, and pulmonary valves. The prevalence of right-sided heart valve velocities increase during pregnancy, but rarely exceed 2 m/sec. Physiologic valvar regurgitation is common in pregnancy, mainly involving right-sided valves in late gestational periods, occasionally persisting in the early puerperium [4]. Despite the increase in valvar regurgitation, women rarely are symptomatic from these changes [25]. Aortic root and left ventricular outflow tract dimensions increase by 1–2 cm during pregnancy and do not always return to pre-pregnancy baseline values [26].

Twenty-five to forty percent of women have small pericardial effusions during pregnancy. There is some evidence that women with greater weight gain during pregnancy have a higher incidence of effusions [27].

Echocardiographic changes in women with heart disease during pregnancy

In 1958, Lund reported the hemodynamic changes during pregnancy, labor, and the postpartum period in 25 women with congenital heart disease who delivered at the University of Minnesota [28]. Many of the observations that were made at that time still hold true today. The normal physiologic changes of pregnancy may exacerbate the underlying hemodynamics of women with heart disease, resulting in clinical symptoms and sometimes decompensation during pregnancy.

In contrast to the echocardiographic changes to pregnancy in women with structurally normal hearts, the hemodynamic adaptations to pregnancy in women with structural heart disease are less well studied. In a study of 29 women with structural heart disease utilizing echocardiography preconception, during pregnancy and postpartum, Cornette et al. confirmed increases in stroke volume and cardiac output. The magnitude of the increase, however, was lower than that described in normal populations and more comparable to patterns observed in pregnancies complicated by growth restriction. There was a significant increase in the E/e′ ratio and decrease in the EF after pregnancy compared to pre-pregnancy values, suggesting a negative influence of pregnancy on systolic function in women with cardiac disease [29]. These data are in contrast to Uebing et al. who did not find any deleterious effect of pregnancy on 53 women with heart disease who had undergone pregnancy. However, they did describe a persistent increase in subpulmonary ventricular size in patients with repaired tetralogy of Fallot (TOF) who had undergone pregnancy [30]. The potential for accelerated right ventricular (RV) remodeling was confirmed in a study with cardiac magnetic resonance imaging (MRI) in women with repaired TOF who had undergone pregnancy [31].

Risk stratification for women with congenital heart disease

There is an increase in morbidity and mortality in women with heart disease who undergo pregnancy and deaths attributable to maternal cardiac conditions have increased in the past decade [32,33]. The Cardiac Disease in Pregnancy (CARPREG) multicenter study addressing risk stratification included 13 Canadian centers and examined the outcomes of 599 pregnancies in women with heart disease, 74% with some form of CHD [34]. There was a 13% incidence of maternal cardiac complications and these investigators identified four predictors of adverse maternal cardiac outcomes, including prior cardiac event or arrhythmia; advanced New York Heart Association class or cyanosis defined as a resting oxygen saturation <90%; left heart obstruction, defined as a peak left ventricular outflow tract gradient of 30 mmHg or greater; and systemic ventricular dysfunction, defined as an ejection fraction <40% [34]. The presence of one predictor was associated with >25% change of a cardiac event and if a woman had more than one of these predictors, the chance of a cardiac event was above 70%. The majority of the cardiac outcomes were symptomatic heart failure or arrhythmias, but 1% of the pregnancies were complicated by maternal embolic stroke or cardiac death. In a single-center retrospective study of 90 pregnancies in 53 women with CHD, maternal cardiac complications occurred in 20%, including 17% heart failure and 3% arrhythmias [35]. This study validated the established CARPREG risk score, as well as identified several new risk factors including subpulmonary ventricular dysfunction, severe pulmonary regurgitation, and maternal smoking [35].

In a large literature review of 48 publications of outcomes in woman with CHD, totaling almost 2500 pregnancies, the ZAHARA investigators reported an ~5% risk of maternal cardiac complications. The risk was substantially increased in those women with more severe forms of congenital heart disease (e.g., ~1% risk of arrhythmias for women with atrial septal defects vs. ~15% risk for women with transposition or Fontan physiology) [36]. More recently, the European Society of Cardiology reported the results of pregnancies in 1321 women with heart disease (66% of whom had CHD) from 28 countries over a 4-year period. Fifteen percent of the women were hospitalized during their pregnancy, most commonly for management of heart failure symptoms. The investigators concluded that the majority of women with heart disease could delivery safely if they had undergone an adequate pre-pregnancy evaluation and received high-quality specialized care during pregnancy and the postpartum period [37]. Balint and colleagues have reported that women with CHD who suffer a cardiac event during pregnancy have a greater risk of long-term cardiac events [38]. Table 43.2 summarizes the established risk factors for adverse maternal cardiac outcomes in women with heart disease.

Maternal cardiac complications, however, are not the only adverse outcomes to consider when counseling women with heart disease regarding pregnancy risks. Neonatal and obstetric adverse outcomes must also be taken into account. Siu et al. reported a much higher rate of neonatal complications in 302 pregnancies in women with heart disease compared to 575 pregnancies in women without heart disease (neonatal complications 18% vs. 7%, $p < 0.001$). The neonatal complications included premature birth, small for gestational age, respiratory distress, and fetal or neonatal death [39]. Congenital heart disease was identified in 8% of the offspring of the 183 live births of mothers with CHD but not with a recognized genetic syndrome [39]. Khairy et al. reported 28% adverse neonatal outcomes in 90 pregnancies in 53 women with congenital heart disease. These outcomes included preterm delivery (21%), small for gestational age (SGA) (8%), respiratory distress syndrome (8%), intraventricular hemorrhage (1%), intrauterine fetal demise (3%), and neonatal death (1%) [35]. The ZAHARA literature review of 1302 women with CHD who had undergone pregnancy documented that women with more complex forms of CHD had a greater risk of premature labor and delivery and up to a four times increased risk of offspring mortality [36].

Table 43.2 Established risk factors for adverse maternal cardiac outcomes

Risk factor	Specific criteria
Events prior to pregnancy	Heart failure [1,2]
	TIA or CVA [1]
	Arrhythmia [1]
	Tobacco use [2]
	Cardiac medication use prior to pregnancy [3]
Decreased functional class	NYHA >II [1,3]
	NYHA ≥II [2]
	Cyanosis (defined as resting oxygen saturation <90%) [1]
Ejection fraction	Systemic ventricular EF >40% [1]
	Decreased subpulmonary ventricular EF [2]
Left heart obstruction	LVOT peak gradient >30 mmHg [1]
	LVOT peak gradient >50 mmHg
	MVA <2.0 cm^2 [1]
	AVA <1.5 cm^2 [1]
	AVA <1.0 cm^2 [3]
Other valvar lesions	Severe pulmonary regurgitation [2]
	Mitral regurgitation [3]
	Tricuspid regurgitation [3]
	Mechanical valve prosthesis [3]
Other conditions	Cyanotic heart lesions (repaired or unrepaired) [3]
	Pulmonary hypertension [4]
	Marfan syndrome [5]

[1] Siu SC, Sermer M, Colman JM, et al. Prospective multicenter study of pregnancy outcomes in women with heart disease. *Circulation* 2001;**104**:515–521.
[2] Khairy P, Ouyang DW, Fernandes SM, et al. Pregnancy outcomes in women with congenital heart disease. *Circulation* 2006;**113**:517–524.
[3] Drenthen W, Boersma E, Balci A, et al. Predictors of pregnancy complications in women with congenital heart disease. *Eur Heart J* 2010;**31**:2124–2132.
[4] Bassily-Marcus AM, Yuan C, Oropello J, et al. Pulmonary hypertension in pregnancy: critical care management. *Pulm Med* 2012;**2012**:709407.
[5] Hiratzka LF, Bakris GL, Beckman JA, et al. 2010 ACCF/AHA/AATS/ACR/ASA/SCA/SCAI/SIR/STS/SVM Guidelines for the Diagnosis and Management of Patients with Thoracic Aortic Disease: A Report of the American College of Cardiology Foundation/American Heart Association Task Force on Practice Guidelines, American Association for Thoracic Surgery, American College of Radiology, American Stroke Association, Society of Cardiovascular Anesthesiologists, Society for Cardiovascular Angiography and Interventions, Society of Interventional Radiology, Society of Thoracic Surgeons, and Society for Vascular Medicine. *Circulation* 2010;**121**:e266–369.

Obstetric complications appear to be higher in women with heart disease. In one report of 113 pregnancies in 65 women with CHD, adverse obstetric outcomes occurred in 32%. These events included preterm delivery, postpartum hemorrhage, and preterm premature rupture of membranes. Importantly, women who avoided the Valsalva maneuver during delivery had increased rates of postpartum hemorrhage, and third/fourth-degree vaginal lacerations [40].

In the past several years, there has been an emphasis on trying to define objective factors to identify the risk of maternal cardiac complications during pregnancy. For example, B-type natriuretic peptide (BNP) increases in response to increased volume loading with pregnancy; however, several investigators have shown an exaggerated BNP response in women with heart disease who suffer cardiac events. Tanous et al. reported that a BNP value of ≤100 pg/mL during pregnancy had a negative predictive value of 100% for identifying cardiac events in women with CHD during pregnancy [41]. In women with repaired TOF, Kamiya reported that the peak BNP after the second trimester was most useful in predicting adverse maternal cardiac events [42].

An inappropriate heart-rate response to exercise has also been associated with adverse maternal cardiac outcomes. This is particularly important in the group of women with repaired CHD, who may have sinus node dysfunction or atrioventricular block. The Alliance for Adult Research in Congenital Cardiology reported results from objective exercise testing in 83 women with CHD and determined that an abnormal chronotropic response correlates with adverse pregnancy outcomes [43].

Specific congenital heart lesions

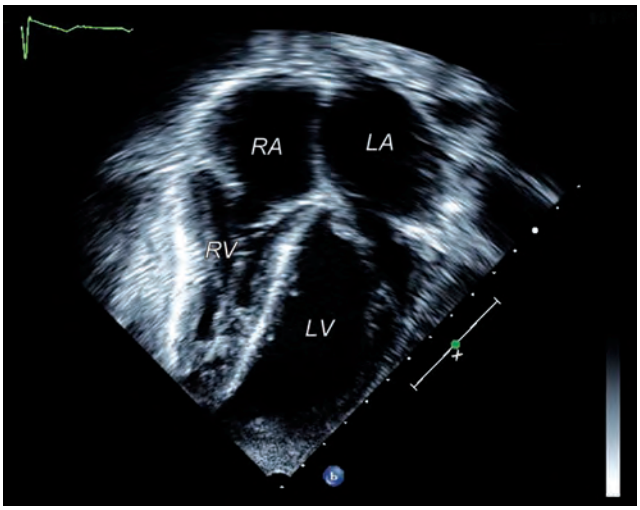
Due to the tremendous advances in the evaluation and management of CHD over the past several decades, the etiology of the majority of maternal heart disease in Western societies is congenital in origin.

Left-to-right shunts

In general, women with small left-to right shunts, normal exercise tolerance and oxygen saturation, and no history of arrhythmias tolerate pregnancy well. Women with atrial septal defects (ASDs) will have further volume loading of the right heart, and may develop increased volume retention and palpitations in pregnancy. Meticulous attention to intravenous line care is essential, as these women are at risk for paradoxical embolism and stroke. Women with small ventricular septal defects (VSDs) tolerate pregnancy well. Echocardiography, however, should be performed to confirm the high transseptal gradient across the defect, as any evidence of Eisenmenger syndrome would dramatically change the risk to the mother. Similarly, women with small patent ductus arteriosus remain asymptomatic in pregnancy, unless the flow is large enough to produce left ventricular dilation. There is some evidence that women with both repaired and unrepaired septal defects are at risk for adverse obstetric outcomes, including pre-eclampsia, premature labor, and SGA neonates [44,45].

Right ventricular outflow tract obstruction

The most common type of right ventricular outflow obstruction in women of childbearing age is pulmonary valve stenosis (PS). The majority of women with mild forms or PS tolerate pregnancy well, as mild forms of PS usually do not progress in adulthood [46]. Women may present with greater degrees of right ventricular outflow tract obstruction and have right ventricular hypertrophy (Figure 43.2). Women with severe right ventricular outflow tract obstruction who become pregnant must



(a)



(b)

Figure 43.2 **(a)** Apical 4-chamber view of severe right ventricular hypertrophy in a woman with Alagille syndrome and hypoplastic branch pulmonary arteries who presents with an unplanned pregnancy at 24 weeks' gestation. LA, left atrium; LV, left ventricle; RA, right atrium; RV, right ventricle. **(b)** Contrast injection in the proximal left pulmonary artery (arrow) confirming branch pulmonary artery stenosis. The patient underwent balloon angioplasty of this stenosis with immediate improvement in her pulmonary pressures. Source: Daniels CJ, Zaidi AN (eds.) *Color Atlas and Synopsis of Adult Congenital Heart Disease*, McGraw-Hill, 2015, Chapter 11, Figure 11-7. Reproduced with permission of McGraw-Hill Education.

be monitored closely for signs of right ventricular dysfunction. The incidence of maternal hypertensive disorders, particularly pre-eclampsia, may be increased in women with PS [47].

Ebstein anomaly

Many women with Ebstein anomaly have successfully carried full-term pregnancies. In a literature review of 127 pregnancies in women with Ebstein anomaly, 4% were complicated by arrhythmias and heart failure was reported in 3% [36]. Increased risk of complications are related to greater degrees of tricuspid regurgitation and worse right ventricular function [48]. Women with Ebstein anomaly and interatrial shunts are at increased risk for complications if they have arterial desaturation. They are also at risk for stroke from a paradoxical embolus. This condition is associated with an increased risk of prematurity, fetal loss, and CHD in the offspring [49].

Bicuspid aortic valve

A detailed echocardiographic examination should be performed in any woman with bicuspid aortic valve (BAV) considering pregnancy. Ascending aortic dilation or aneurysm may be present even in the presence of a normally functioning BAV. Due to the association with aortopathies in patients with BAV, the entire thoracic aorta should be investigated, with cardiac MRI if echocardiographic windows are limited. Cardiac MRI can accurately determine aortic dimensions and ventricular size and function, and it is considered safe in pregnancy, particularly after the first trimester is completed. Gadolinium contrast does cross the placenta and is not usually administered during pregnancy [50]. Aortic dissection may occur in pregnant women with BAV, but it is much less frequent than in those women with Marfan syndrome [51]. The 2008 ACC/AHA Guidelines for the Management of Adults with Congenital Heart Disease recommend that women with BAV and an ascending aortic diameter >4.5 cm should be specifically counseled regarding the increased risk in pregnancy [52].

Physiologically corrected transposition of the great arteries

Physiologically corrected transposition of the great arteries – also referred to as congenitally corrected TGA, L-loop TGA, or {S,L,L} TGA – is a congenital abnormality that may not be diagnosed until later in life. These patients have atrioventricular discordance and ventricular arterial discordance resulting in a systemic RV, which may become dysfunctional over time. Other associated cardiac anomalies include a VSD, PS, Ebstein anomaly, or dysplastic tricuspid valves. Maternal risk is often determined by the functional status, systemic ventricular function, presence of associated lesions, and arrhythmias. The Royal Brompton Hospital reported over four decades of experience with women with physiologically corrected TGA, which included 45 pregnancies and 27 live births. Cardiovascular complications occurred in 26% of these women including heart failure, worsening cyanosis, and cerebral vascular accident [53].

The Mayo Clinic experience over 17 years included 60 pregnancies with 83% live births, and a lower prevalence of maternal cardiac complications; one woman with significant tricuspid valve regurgitation developed heart failure symptoms; and multiple pregnancy-related complications (including toxemia, congestive heart failure, endocarditis, and myocardial infarction) were experienced by one woman who had a total of 12 pregnancies [54].

Cyanotic lesions

Any degree of cyanosis places both the mother and the fetus at significant risk. Maternal cyanosis is exacerbated during pregnancy, the fall in systemic vascular resistance increases right-to-left shunting. Additionally, hypoxia induces an erythrocytotic response, which will further increase the potential for thrombosis, and in the setting of an intracardiac shunt, risk for paradoxical embolism and stroke. In a study of 44 cyanotic women who underwent 96 pregnancies, only 12% of pregnancies resulted in live births when the maternal oxygen saturation was <85%. Maternal cardiac complications occurred in 32% and included heart failure, endocarditis, and thrombotic complications [55].

Pulmonary vascular disease

Regardless of the cause of elevated pulmonary artery pressures (pulmonary arterial hypertension, pulmonary emboli, elevated left-sided filling pressure, or CHD with systemic-to-pulmonary shunting), the mortality for these women is extremely high (up to 50% in some cases) [56,57]. Death often occurs in the early postpartum period, as abrupt decreases in preload and afterload, as well as vagal responses can be life threatening. Women with pulmonary vascular disease should be counseled to strongly adhere to contraceptive methods (non-estrogen-containing choices). If a woman with pulmonary vascular disease becomes pregnant and chooses not to terminate the pregnancy, she must be followed closely with particular attention to the delivery management. Spinal analgesia must be used with caution due to the potential for peripheral vasodilation. The mode of delivery should be determined in coordination with a multidisciplinary team of maternal fetal medicine specialists, cardiac anesthesiologists, and clinicians with expertise in pulmonary vascular management. Therapeutic options are limited, although nitric oxide, prostacyclin analogs, and phosphodiesterase inhibitors have been reported in selected cases [58].

Specific repaired congenital heart lesions

Tetralogy of Fallot

Women with repaired TOF represent one of the largest groups of women with repaired CHD who undergo pregnancy. With successful childhood definitive repair, cyanosis is relieved and women are often asymptomatic. However, residual hemodynamic lesions are common and may include pulmonary and tricuspid regurgitation, RV dilation, and possible RV dysfunction. Depending on the size and function of the RV, the additional volume load encountered with pregnancy may not be well tolerated [35,59,60]. Furthermore, the hemodynamic load of pregnancy may have long-term effects on subpulmonary ventricular size and function in women with repaired TOF [30,31]. Therefore, women with repaired TOF who have severe pulmonary regurgitation and RV dilation presenting for preconception evaluation should be counseled to consider undergoing pulmonary valve replacement prior to pregnancy [61].

Coarctation of the aorta

Similar to women with BAV, women with coarctation of the aorta should have the entire thoracic aorta imaged to evaluate for evidence of dilation, aneurysm, or dissection. A significant coarctation may cause decreased blood flow to the fetus resulting in a SGA newborn. Systemic hypertension in these women should be managed with antihypertensive therapies. Data from the National Inpatient Sample over a 9-year period in 697 women with coarctation of the aorta reported that women with coarctation are more likely to have hypertensive complications of pregnancy, delivery by cesarean section, have adverse cardiac outcomes, longer hospitalizations, and to incur higher hospital charges compared to women without coarctation [62]. Smaller descending thoracic aortic diameters (<12 mm), as measured by cardiac magnetic resonance angiogram, are associated with maternal cardiovascular events in women with coarctation of the aorta [63].

Transposition of the great arteries {S,D,D}TGA

Many women with transposition of the great arteries who are currently of childbearing age have undergone surgical correction with an atrial switch (Senning or Mustard procedure) in infancy. The atrial switch procedure directs deoxygenated blood to the LV to be pumped to the lungs and oxygenated blood to the RV to be pumped to the body. The RV in patients who have undergone the atrial switch procedure is the systemic ventricle and it becomes hypertrophied, dilated, and often dysfunctional. This may cause specific problems during pregnancy (Figure 43.3; Videos 43.1 and 43.2). The rigid atrial baffles are unable to increase stroke volume appropriately and many of these women have impaired ventricular filling [64]. They may also suffer from sinus node dysfunction, which impairs their ability to increase their heart rates. Therefore, they may be at increased risk for adverse maternal cardiac complications with the hemodynamic load of pregnancy. One report of 28 pregnancies in 16 women who had undergone Mustard procedure for TGA found that in 18 pregnancies, RV dimensions increased significantly in five patients, and this dilation persisted in all five at a mean of 2 years following pregnancy. Examining RV systolic function, 4 of 21 pregnancies had a significant decrease in the RV EF, and of those 4 patients, 3 had continued RV dysfunction when followed an average of 32 months following delivery. Lastly, there was an increase in tricuspid regurgitation in 8 of 20 pregnancies, and 3 of those 8 women had persistently increased regurgitation in follow-up [65].

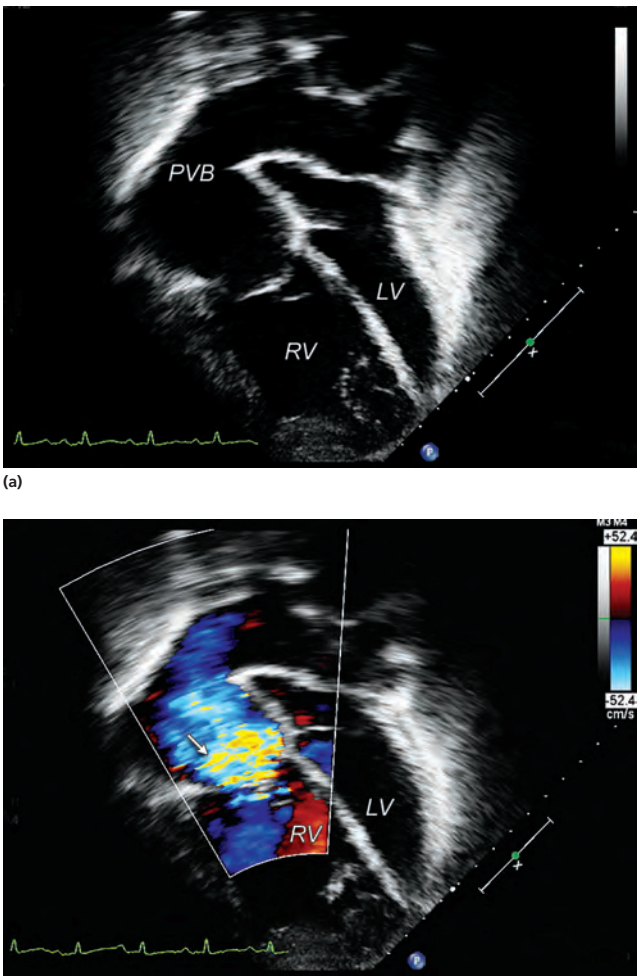


Figure 43.3 **(a)** Apical 4-chamber view in a woman with transposition of the great arteries and an atrial switch procedure demonstrating a dilated, hypertrophied systemic right ventricle who presented with heart failure in the postpartum period. LV, left ventricle; PVB, pulmonary venous baffle; RV, right ventricle. **(b)** Color Doppler revealing severe tricuspid valve regurgitation (arrow). LV, left ventricle; RV, right ventricle.

Successful pregnancies have also been reported in women who have undergone a Rastelli operation. However, any subaortic obstruction may worsen in pregnancy, and should be addressed prior to pregnancy [66].

Over the past three decades, the arterial switch procedure has become the surgical method of choice for transposition of the great arteries. A retrospective chart review from two tertiary care centers reported the pregnancy outcomes in 17 pregnancies from 9 women with arterial switch procedure. Two women developed cardiac complications during pregnancy; one woman with impaired left ventricular systolic function had nonsustained ventricular tachycardia; and one woman with a mechanical systemic atrioventricular valve developed postpartum valve thrombosis [67].

Fontan physiology

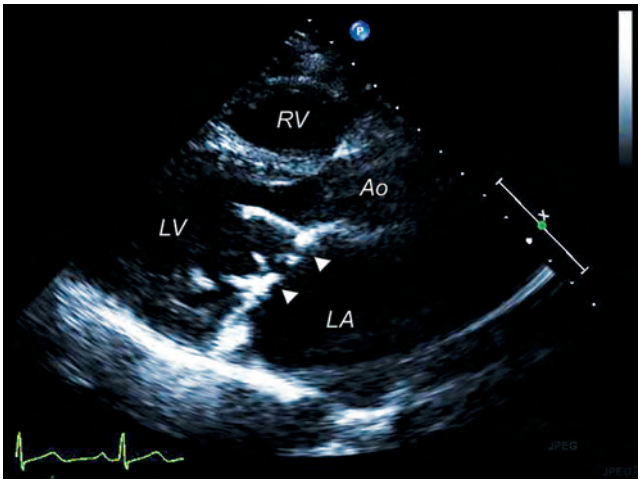
As the numbers of women with single ventricle physiology are reaching childbearing age, an increased number of women with Fontan palliation desire pregnancy. Although a select group of women with Fontan palliation may have a successful pregnancy and delivery, preconception counseling is critical, as these pregnancies are often high risk. Functional class, ventricular function, arrhythmia burden, and arterial oxygen saturation are important determinants of risk in women with Fontan physiology. The risk of thromboembolic complications in women with Fontan physiology during pregnancy is not known; however, the risks and benefits of anticoagulation should be considered on an individual basis. A multicenter report of 33 pregnancies in women with Fontan palliation resulting in 15 live births reported a low rate of maternal cardiac complications including heart failure and atrial flutter [68]. More recently, the CONCOR investigators reported 4 live births in 10 pregnancies of women with Fontan palliation of which maternal cardiac and obstetric complications were common [69]. Women with any degree of cyanosis, ventricular dysfunction, moderate or more atrioventricular valve regurgitation or those with protein-losing enteropathy should be counseled to avoid pregnancy [2].

Valvar heart disease

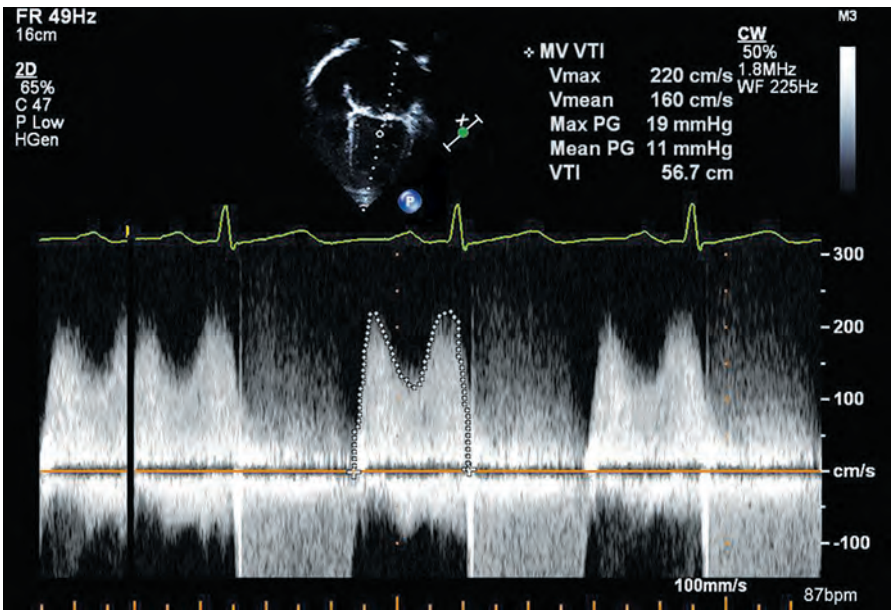
In general, stenotic lesions are less well tolerated in pregnancy than regurgitant lesions. Symptomatic patients with mitral and aortic stenosis tend to worsen during pregnancy, as the lower systemic vascular resistance will increase the transvalvular gradient [70].

Mitral stenosis

The most common cause of mitral stenosis in women of childbearing age remains rheumatic heart disease (Figure 43.4; Videos 43.3 and 43.4). The increased cardiac output and heart rate decreases the diastolic filling time and produces symptoms in previously asymptomatic women with mitral stenosis. Left atrial pressure may elevate due to decreased left atrial stroke volume, and atrial fibrillation may precipitate pulmonary edema. Management strategies include controlling the heart rate with beta-blockade which prolongs the diastolic filling time and usually improves symptoms [71]. Diuretics are used to control pulmonary edema; however, this should be done in consultation with the obstetric team, as high-dose diuretics may decrease the volume of amniotic fluid. Anticoagulants should be started if the patient has atrial fibrillation. In cases where medical management is ineffective in controlling symptoms, balloon valvuloplasty may be considered [72]. The timing of invasive evaluation must be carefully considered, and the obstetric team should be available in the event that premature labor develops during the procedure. Radiation exposure to the fetus may be minimized by lead screening of the mother's abdomen and pelvis and utilizing transesophageal echocardiography during the procedure to guide the valvar intervention [73].



(a)

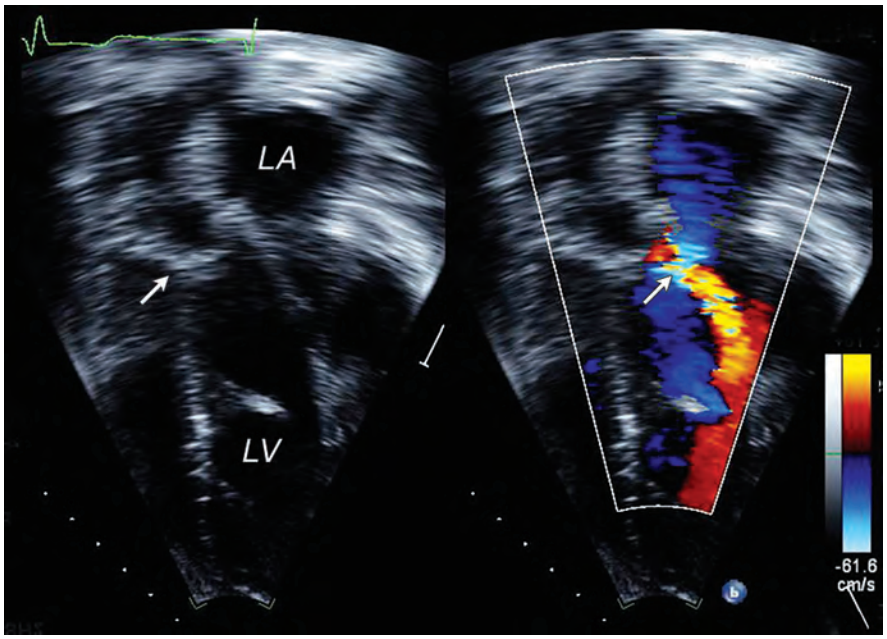


(b)

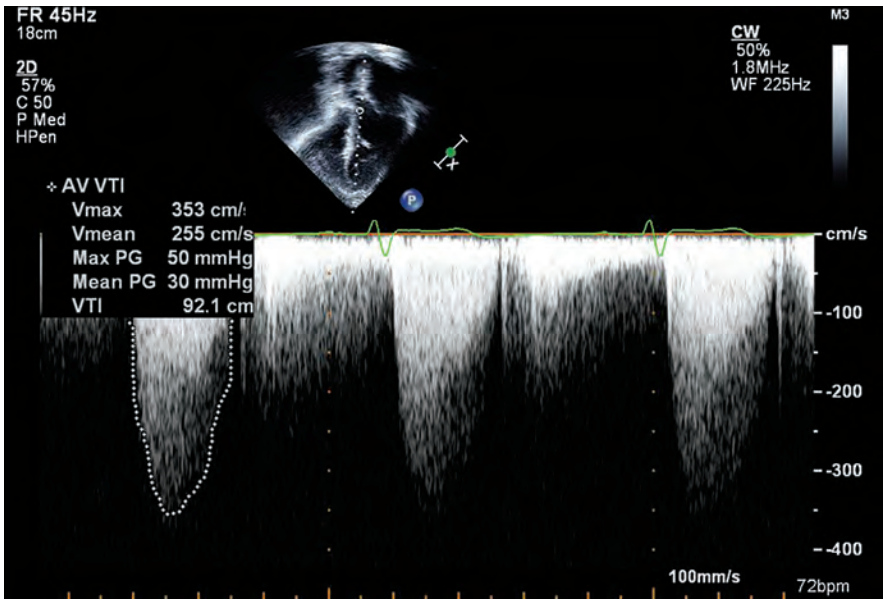
Figure 43.4 **(a)** Parasternal long-axis view demonstrating a thickened mitral valve (arrowheads) in a woman with rheumatic heart disease who presented at 21 weeks' gestation. Ao, aorta; LA, left atrium; LV, left ventricle; RV, right ventricle. **(b)** Continuous-wave Doppler demonstrating mitral stenosis with a mean gradient of 11 mmHg and a peak gradient of 19 mmHg.

Aortic stenosis

Many women with aortic stenosis who were asymptomatic prior to pregnancy become symptomatic during pregnancy due to the increased stroke volume and decreased ventricular compliance. The worse the left ventricular obstruction, the greater the chance of maternal cardiac complications, most commonly heart failure [74]. Echocardiographic changes that occur during pregnancy include an increase in the transvalvular velocity and pressure gradient (Figure 43.5). The aortic valve area does not significantly change. Silversides reported the outcomes of 49 pregnancies in 39 women with aortic stenosis, of which over half of the women had severe aortic stenosis. There were no maternal deaths. Serial echocardiograms were performed in nine women, and although the peak transvalvular gradients increased during pregnancy, the changes did not meet statistical significance (59 ± 13 vs. 68 ± 20; $p = 0.14$) [75]. Management of women with symptomatic aortic stenosis in pregnancy includes beta-blockade for control of heart rate and diuresis for volume control. Women with greater degrees of aortic stenosis are more likely to become symptomatic during pregnancy due to the decrease in the systemic vascular resistance that will increase the valvar gradient. In formulating the delivery plan, analgesia such as spinal blocks should be avoided due to the risk of hypotension. Additionally, women with aortic stenosis may experience clinical decompensation immediately following delivery, as abrupt decreases in preload and afterload may precipitate cardiovascular collapse. Invasive strategies should be reserved for severe clinical decompensation unresponsive to medical management.



(a)



(b)

Figure 43.5 **(a)** Three-chamber view of a pregnant woman with a bicuspid aortic valve with thickening of the aortic valve leaflets (arrow). Color Doppler demonstrates aortic stenosis and regurgitation. LA, left atrium; LV, left ventricle. **(b)** Continuous-wave Doppler demonstrates aortic stenosis with a peak gradient across the aortic valve of 50 mmHg, which is a known risk factor for a maternal event during pregnancy. She developed mild heart failure at the time of delivery.

Mitral regurgitation

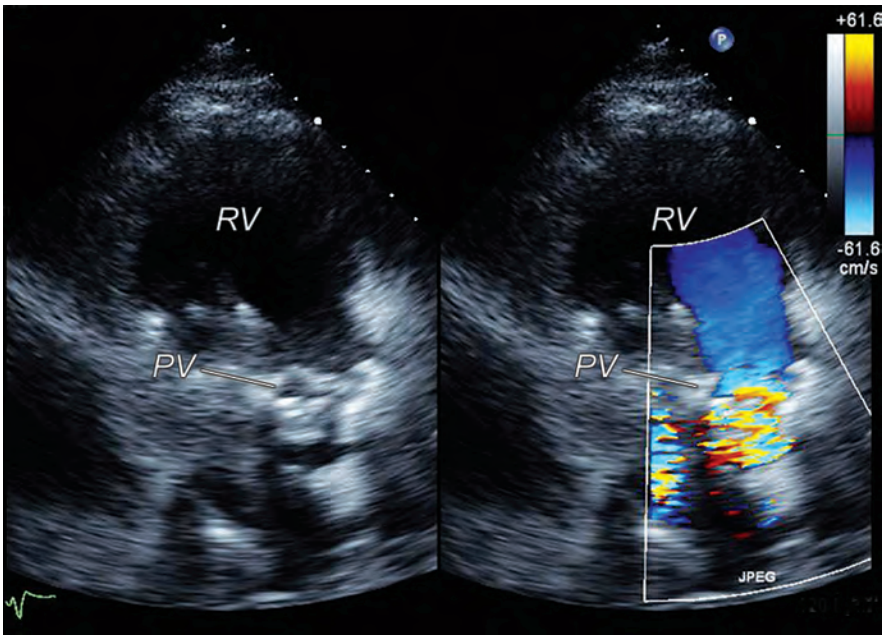
Moderate or less mitral regurgitation is usually well tolerated in pregnancy due to the afterload-reduced state that pregnancy imposes. Women with chronic, severe mitral regurgitation should be monitored closely for development of atrial fibrillation or pulmonary hypertension, which is not tolerated well.

Aortic regurgitation

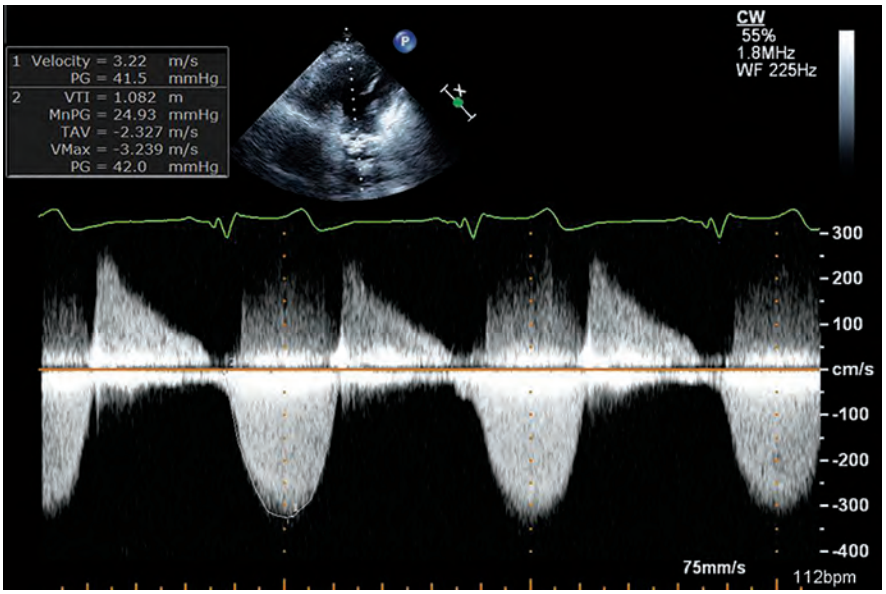
Similar to mitral regurgitation, women with aortic regurgitation often tolerate pregnancy well due to the low systemic vascular resistance. However, caution is warranted particularly if the left ventricle is dilated or dysfunctional.

Prosthetic heart valves

Women with prosthetic heart valves should be followed closely throughout pregnancy and the postpartum period. The transvalvular velocities increase throughout pregnancy (Figure 43.6; Videos 43.5 and 43.6), with little change in valve function or area. There is some data that suggests that bioprosthetic valves have a faster rate of degeneration in women who have undergone pregnancy [76]. Mechanisms postulated for



(a)

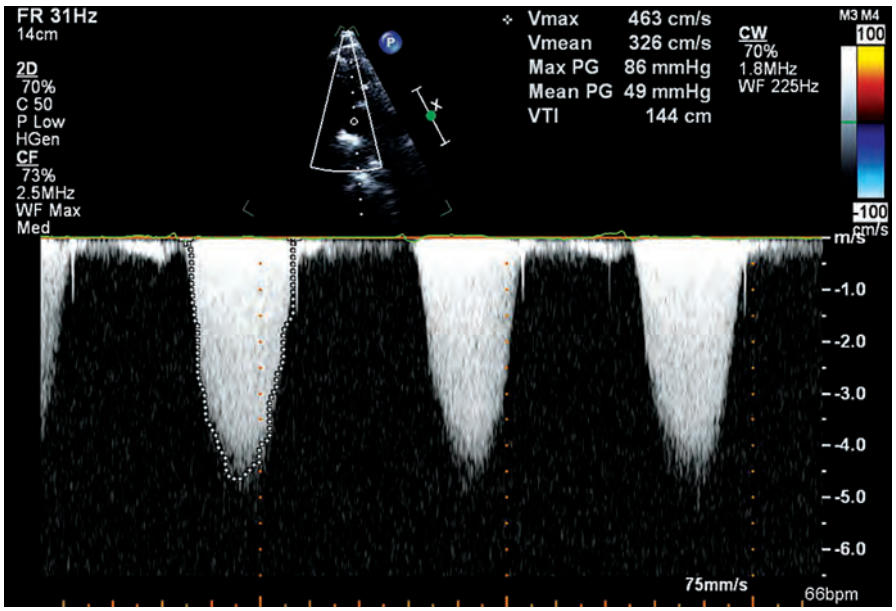


(b)

Figure 43.6 **(a)** Parasternal short-axis view of a woman with repaired tetralogy of Fallot and a bioprosthetic pulmonary valve (PV) with valvar degeneration during pregnancy. The color Doppler demonstrates turbulent flow across the pulmonary valve (arrow). **(b,c)** Continuous-wave Doppler demonstrating increasing gradients across the pulmonary valve and increasing right ventricular (RV) pressures as the pregnancy progresses. (b) Peak velocity 3.2 m/sec. (c) Peak velocity 4.6 m/sec.

rapid bioprosthetic valve degeneration include high calcium turnover and accelerated flow across the valve [77]. However, other reports have not confirmed a higher incidence of bioprosthetic valve degeneration in women who have undergone pregnancy [78].

Women with mechanical heart valves have several choices for anticoagulation during pregnancy, but no option is without significant risks to the mother and fetus. The risk of thromboembolic events and valve thrombosis depends on the type and location (mitral > aortic) of the mechanical valve, as well as other factors including history of a prior thrombotic event, atrial fibrillation, or multiple prosthetic valves [79]. The 2014 American Heart Association/American College of Cardiology Valvular Heart Disease Guidelines recommend frequent monitoring of anticoagulation in pregnant women with mechanical prostheses. Warfarin is recommended in pregnant patients with a mechanical prosthesis to achieve a therapeutic INR in the second and third trimesters, with discontinuation of warfarin and initiation of intravenous unfractionated heparin (UFH) prior to a planned delivery (Class I recommendation). Low-dose aspirin (75–100 mg) once daily is also recommended for pregnant patients with either a mechanical prosthesis or bioprosthesis in



(c)

Figure 43.6 (*Continued*)

the second and third trimesters (Class I recommendation). Class IIa recommendations include continuation of warfarin during the first trimester for pregnant women with a mechanical valve, after a discussion with the patient about risks and benefits, if the dose of warfarin to achieve a therapeutic INR is 5 mg per day or less. Dose-adjusted low molecular weight heparin at least twice daily (with a target anti-Xa level of 0.8–1.2 U/mL, 4–6 hours post-dose) or dose-adjusted continuous intravenous UFH (with an aPTT at least two times control) during the first trimester is reasonable for pregnant patients with a mechanical prosthesis if a warfarin dose of >5 mg per day is required to achieve a therapeutic INR [1].

Specific cardiac conditions

Marfan syndrome and other connective tissue disorders

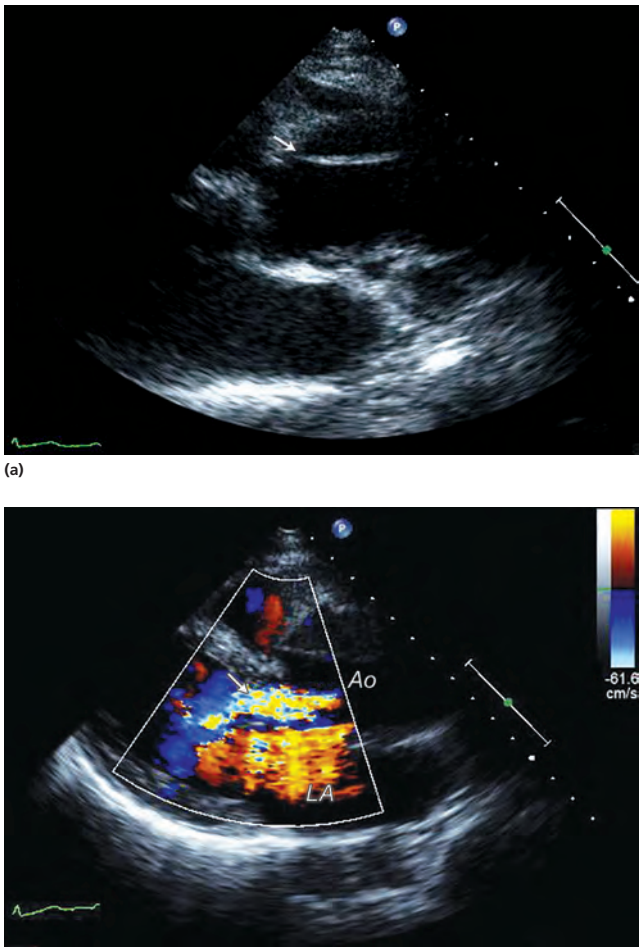
Women with connective tissue disorders should be followed closely during pregnancy with frequent imaging of the aorta. Pregnancy increases the risk of aortic dissection (Figures 43.7 and 43.8; Videos 43.7 and 43.8) through several mechanisms, including protease-mediated destruction of the extracellular matrix, altered signaling pathways, relaxin effects of decreasing collagen synthesis, and estrogen interference with collagen deposition [80]. The current guidelines for thoracic aortic disease recommend that any woman with aortic pathology from a connective tissue disorder should be counseled about the risk of aortic dissection as well as the heritable nature of the underlying condition. Strict blood pressure control should be maintained. From an imaging perspective, frequent echocardiograms (often monthly) should be performed for ascending aortic dimensions. For greater definition of aortic arch and descending aorta, MRI (without gadolinium) is recommended over computed tomography due to the exposure to ionizing radiation in the latter. Women with aortic aneurysms should be delivered where cardiothoracic surgery is available. Women with Marfan syndrome who are contemplating pregnancy should be counseled to consider replacement of the aortic root and ascending aorta if the diameter exceeds 4.0 cm prior to pregnancy [81].

Pregnancy increases the risk of aortic complications in the long term in these patients [82]. Donnelly et al. identified 98 women with Marfan syndrome at a single center, of which 69 (72%) experienced a total of 199 pregnancies resulting in 170 (86%) live births. The median number of pregnancies per women was three. Obstetric complications occurred in 17 (10%) and adverse fetal outcomes in 22 (13%). No woman experienced aortic dissection or required cardiac surgery during pregnancy. Aortic growth rate increased during pregnancy and did not return to baseline following pregnancy completion. Despite the lack of catastrophic peripartum complications, the prevalence of both aortic dissection and elective aortic surgery during long-term follow-up was higher in those women who had a prior pregnancy [82].

Infectious endocarditis

Infectious endocarditis (IE) is very rare in pregnancy, with an incidence reported to be 1.7–5.5 per 100,000. However, the maternal mortality rate is high, with reported rates between 22 and 33%, with the most deaths related to heart failure or an embolic event. The rate of fetal mortality ranges between 15 and 33% [83,84].

Echocardiography is particularly useful in the diagnosis of IE in pregnancy (Figure 43.9; Videos 43.9–43.12), identifying valvar lesions causing valve regurgitation and heart failure. In a literature review of 68 cases of IE in pregnancy, the valve-specific maternal mortality was 42% for aortic valves, 22% for mitral



(a)

(b)

Figure 43.7 **(a)** A postpartum 2D echocardiogram of a woman with Marfan syndrome and a dilated aortic root presenting with a type A aortic dissection. The parasternal long-axis view demonstrates the dissection flap (arrow) in the aortic root. **(b)** Color Doppler demonstrates severe aortic regurgitation. Ao, aorta; LA, left atrium; LV, left ventricle.

valve, and 10% for tricuspid valves [84]. In this review, underlying heart disease was noted in 31% of cases. Intravenous drug use and recent dental work were reported in 4% and 7% of cases, respectively [84].

Kawasaki disease

There are no guidelines for the management of women with Kawasaki disease and coronary artery aneurysms during pregnancy. Yet, increasingly women with this condition are reaching childbearing age. From the limited literature available on this topic, the outcomes of pregnancy in this group are favorable, regardless of anticoagulation strategy [85]. Delivery strategies generally should be based on obstetric indications.

Cardiomyopathies

Women with cardiomyopathies often have limited cardiovascular reserve which can be exacerbated by the hemodynamic changes of pregnancy and can result in clinical decompensation with worsening heart failure, arrhythmias, and rarely, maternal death [86]. Determining the etiology of any pre-existing cardiomyopathy (Figure 43.10; Video 43.13) is important in the management strategy.

Peripartum cardiomyopathy

Peripartum cardiomyopathy (PPCM) was first described in 1937, although heart failure in the puerperium has been recognized since the eighteenth century. This rare diagnosis is important to recognize and treat aggressively, as it remains one of the major causes of pregnancy-related death in the United States. Inherent in the definition of PPCM is the recognition that no other etiology for heart failure is known, and that there is no prior history of cardiac disease. The diagnosis of PPCM is restricted to the onset of heart failure in the last month of pregnancy through 5 months postpartum. There must be a demonstrable impairment of left ventricular function as documented by echocardiography with an ejection fraction <45% or a shortening fraction <30% [87,88]. The clinical presentation of these women is often indistinguishable from other forms of cardiomyopathy, with symptoms of shortness of breath, fatigue, and edema, which are often masked by pregnancy. The diagnosis is often made in the postpartum period [89]. Risk factors for PPCM include advanced maternal age, multifetal pregnancy, multiparity, pre-eclampsia or pregnancy-induced HTN, and use of tocolytic therapy [90]. Management strategies include diuretics for fluid retention, afterload reduction, beta-blockers for rate control, and consideration of delivery as soon as fetal lungs are mature. The prognosis of PPCM is variable, and generally if the left ventricular function improves, it does so in the first 6 months after diagnosis. However, even if the EF improves, women may continue to have decreased contractile reserve and limited exercise tolerance [90]. In one study of 92 women with PPCM, 26 recovered their LV function while 66 did not. There were no echocardiographic features identified that would predict which women with PPCM would have recovery of LV function [91].

Specific management issues

Hypertensive complications of pregnancy are common. At least 5% of pregnant women have pre-existing systemic hypertension (HTN). Gestational (pregnancy-induced) HTN is defined as an increase in systolic BP of at least 30 mmHg and diastolic BP by 15 mmHg that occurs after 20 weeks' gestation and resolves by 6 weeks postpartum [92]. In a large literature review of almost 25,000 pregnancies in women with CHD, hypertensive disorders related to pregnancy do not appear to be more prevalent for the whole CHD cohort [36].

Acute myocardial infarction (MI) in pregnancy is extremely rare. The case fatality rate, however, is between 5 and 37%. Pregnant women with acute MI should be evaluated urgently for coronary artery dissection. Risk factors for coronary artery dissection include systemic hypertension, diabetes, tobacco use, advanced maternal age (>30 years), thrombophilia, and

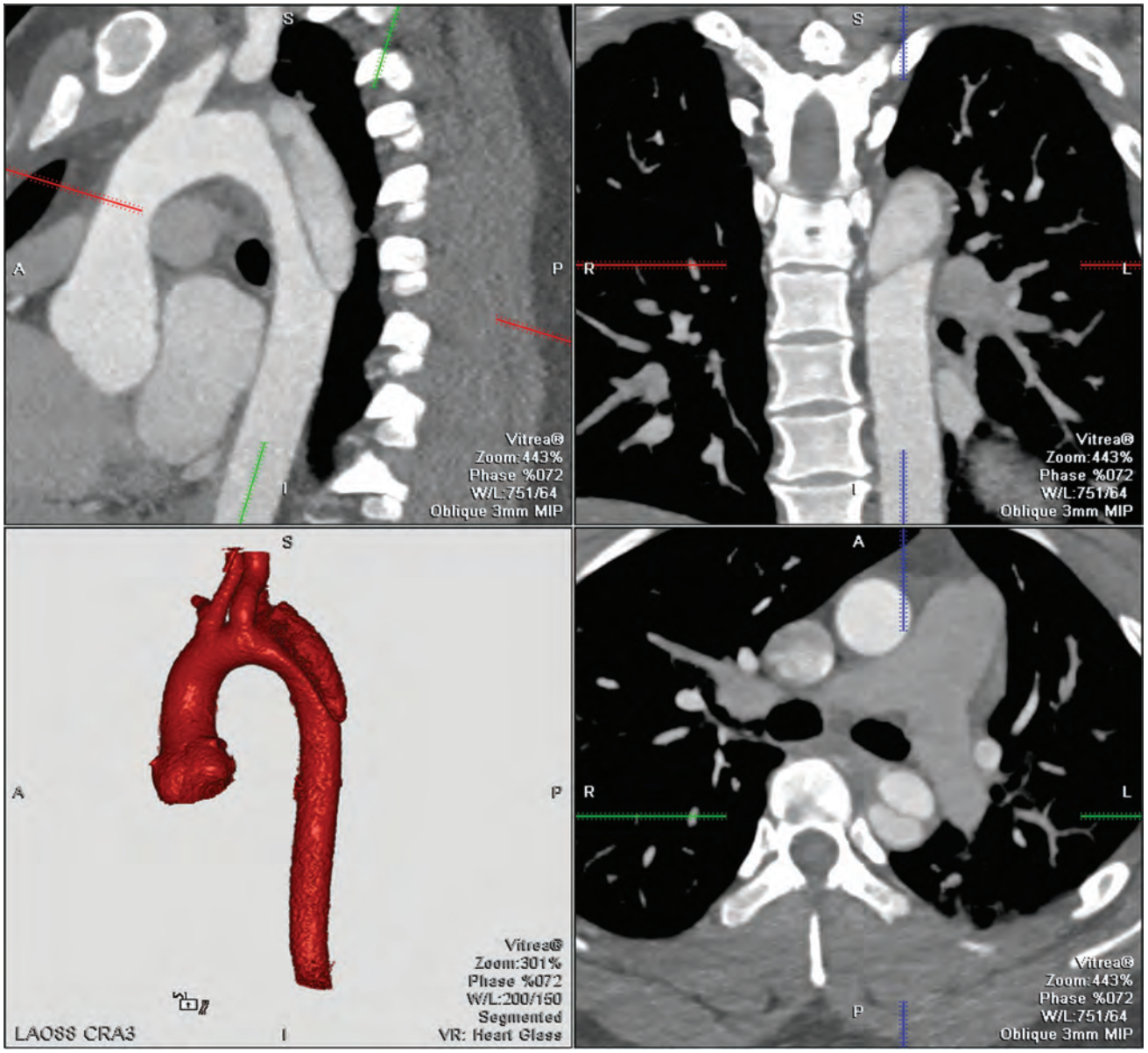


Figure 43.8 Cardiac CT reformatted images demonstrating a type B aortic dissection in a woman with Marfan syndrome at 28 weeks' gestation.

postpartum infections. Coronary artery dissection may occur up to 6 weeks postpartum [93,94].

Cardiovascular invasive strategies in women during pregnancy should be limited to severe clinical decompensation, unresponsive to medical interventions. Radiation doses >100 mGy are likely to cause dose-dependent developmental effects. Cardiac catheterization should be avoided in the first trimester if possible [95]. At the time of catheterization of any pregnant woman, abdominal shielding should be performed [95].

In rare cases where cardiac bypass surgery is required in pregnancy, maternal survival is good; however, fetal loss remains high [96].

Despite the rare occurrence of cardiac arrest as a complication of childbirth, guidelines exist for the management of this critical situation. Efforts should be made to place the patient in the full left-lateral position to relieve possible compression of the inferior vena cava. Intravenous access above the diaphragm should be established, and 100% oxygen administered. It is imperative to consider and treat any reversible cause of deterioration. Emergency cesarean section may be considered at 4 minutes after onset of maternal cardiac arrest if there is no return of spontaneous circulation (Class IIb, LOE C) [97].

An experienced multidisciplinary team should care for women with heart disease desiring pregnancy. The frequency of visits and diagnostic testing will be determined by the woman's

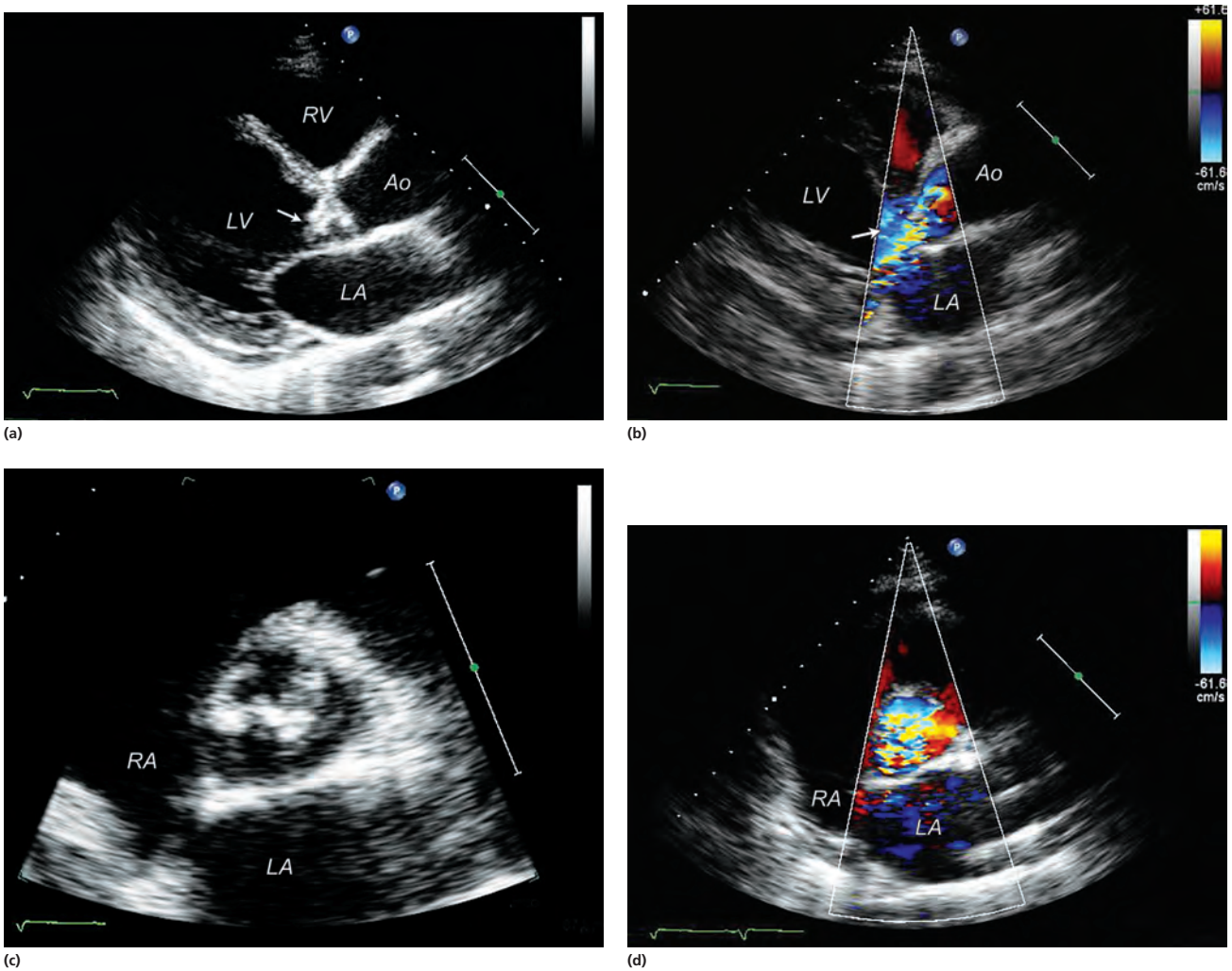


Figure 43.9 **(a–d)** Parasternal long- and short-axis views demonstrating a large vegetation (arrow) on a bicuspid aortic valve in a woman who presented with fever at 25 weeks' gestation. Color Doppler reveals severe aortic regurgitation. She went into premature labor at 36 weeks, and underwent replacement of her aortic valve one week after delivery. Ao, aorta; LA, left atrium; LV, left ventricle; RV, right ventricle.

underlying cardiac condition. Most women with heart disease should undergo a vaginal delivery, and cesarean section should be performed for obstetric indications [2]. Women with a history of CHD should be counseled to undergo fetal echocardiography at around 22–24 weeks' gestation (Figure 43.11). Many of the maternal cardiac complications in women with heart disease occur in the postpartum period, and women must be followed closely for adverse outcomes.

Videos

To access the videos for this chapter, please go to www.laiecho.com.

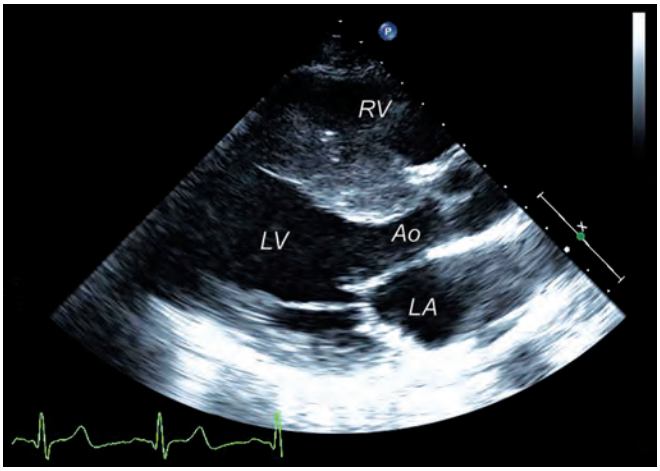
Video 43.1 Apical 4-chamber echocardiogram in a woman with transposition of the great arteries and an atrial switch procedure demonstrating a dilated, hypertrophied systemic right ventricle, who presented with heart failure in the postpartum period.

Video 43.2 Color Doppler in this same patient with transposition of the great arteries and an atrial switch demonstrating severe tricuspid regurgitation.

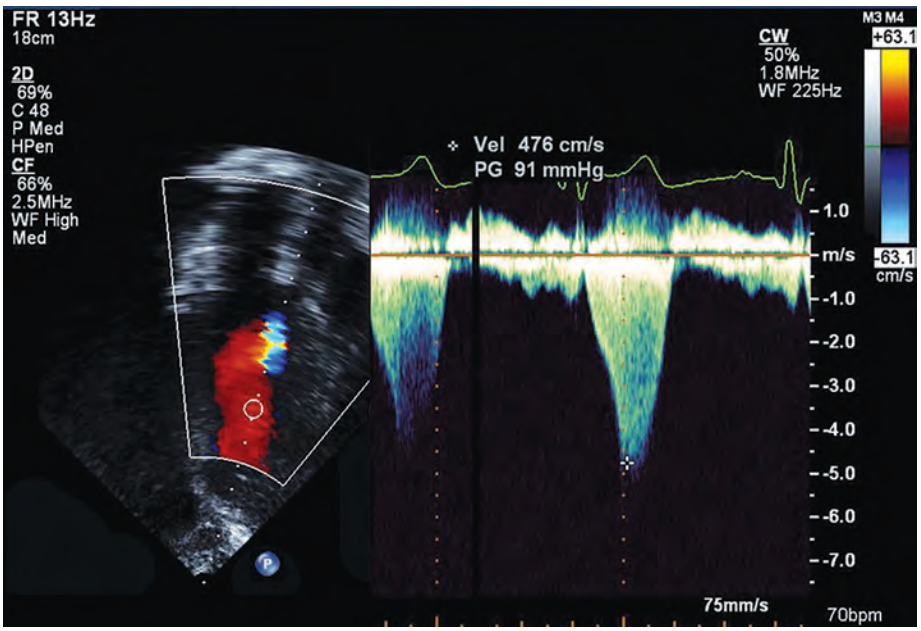
Video 43.3 Parasternal long-axis echocardiogram demonstrating a mitral stenosis in a woman with rheumatic heart disease who presented at 21 weeks' gestation.

Video 43.4 Parasternal short-axis 2D and color Doppler echocardiograms demonstrating a mitral stenosis and regurgitation in a woman with rheumatic heart disease who presented at 21 weeks' gestation.

Video 43.5 Parasternal short-axis view of a woman with repaired tetralogy of Fallot and a bioprosthetic pulmonary valve with valvar degeneration during pregnancy.



(a)



(b)

Figure 43.10 **(a)** Parasternal long-axis view of a woman with hypertrophic cardiomyopathy who presented in the second trimester of pregnancy with a left ventricular outflow tract gradient of 91 mmHg. **(b)** Ao, aorta; LA, left atrium; LV, left ventricle; RV, right ventricle.

Video 43.6 Color Doppler echocardiography in the same patient as in Video 43.5 demonstrates turbulent flow across the pulmonary valve.

Video 43.7 A postpartum 2D echocardiogram of a woman with Marfan syndrome and a dilated aortic root presenting with a type A aortic dissection. The parasternal long-axis view demonstrates the dissection flap in the aortic root.

Video 43.8 Color Doppler in the same patient as in Video 43.7 demonstrates severe aortic regurgitation.

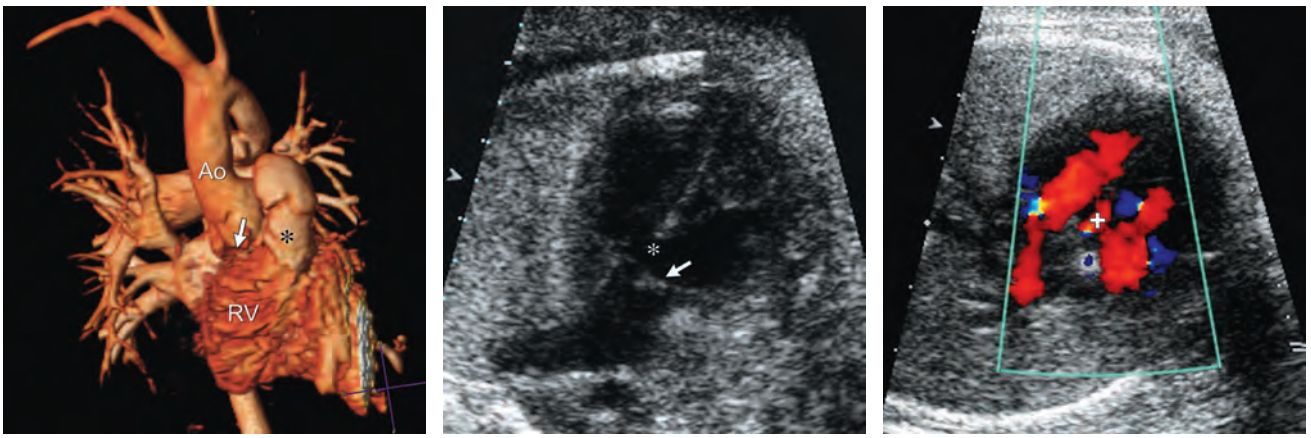
Video 43.9 Parasternal long-axis view demonstrating a large vegetation on a bicuspid aortic valve in a woman who presented with fever at 25 weeks' gestation.

Video 43.10 Parasternal long-axis view color Doppler reveals severe aortic regurgitation.

Video 43.11 Parasternal short-axis view of the same patient as in Video 43.10 with a large vegetation on a bicuspid aortic valve.

Video 43.12 Parasternal short-axis color Doppler on the same patient as in Video 43.10 with a large vegetation on a bicuspid aortic valve confirms severe aortic regurgitation. She went into premature labor at 36 weeks, and underwent replacement of her aortic valve one week after delivery.

Video 43.13 Parasternal long-axis echocardiogram of a woman with hypertrophic cardiomyopathy who presented in the second



(a) (b) (c)

Figure 43.11 A 3D reconstruction magnetic resonance angiogram of a woman with truncus arteriosus. **(a)** Ao, aorta; RV, right ventricle; arrow, single truncal valve; ∗, RV–PA conduit. At 20 weeks' gestation, she underwent a screening fetal echocardiogram that detected truncus arteriosus in the fetus. **(b)** Arrow, single truncal valve; ∗, ventricular septal defect. The fetal echocardiographic Doppler demonstrates truncal valve regurgitation in the fetus. **(c)** †, truncal valve regurgitation. Source: Daniels CJ, Zaidi AN (eds.) *Color Atlas and Synopsis of Adult Congenital Heart Disease*, McGraw-Hill, 2015, Chapter 11, Figure 11-3. Reproduced with permission of McGraw-Hill Education.

trimester of pregnancy with a left ventricular outflow tract gradient of 91 mmHg.

References

1 Nishimura RA, Otto CM, Bonow RO, et al. AHA/ACC Guideline for the Management of Patients With Valvular Heart Disease: a report of the American College of Cardiology/American Heart Association Task Force on Practice Guidelines. *Circulation* 2014;**129**:e521–643.

2 Regitz-Zagrosek V, Blomstrom Lundqvist C, Borghi C, et al. ESC Guidelines on the management of cardiovascular diseases during pregnancy. The Task Force on the Management of Cardiovascular Diseases during Pregnancy of the European Society of Cardiology (ESC). *Eur Heart J* 2011;**32**:3147–3197.

3 Tsiaras S, Poppas A. Cardiac disease in pregnancy: value of echocardiography. *Curr Cardiol Rep* 2010;**12**:250–256.

4 Campos O, Andrade JL, Bocanegra J, et al. Physiologic multivalvular regurgitation during pregnancy: a longitudinal Doppler echocardiographic study. *Int J Cardiol* 1993;**40**:265–272.

5 Mishra M, Chambers JB, Jackson G. Murmurs in pregnancy: an audit of echocardiography. *BMJ* 1992;**304**:1413–1414.

6 Gilson GJ, Samaan S, Crawford MH, et al. Changes in hemodynamics, ventricular remodeling, and ventricular contractility during normal pregnancy: a longitudinal study. *Obstet Gynecol* 1997;**89**:957–962.

7 Mabie WC, DiSessa TG, Crocker LG, et al. A longitudinal study of cardiac output in normal human pregnancy. *Am J Obstet Gynecol* 1994;**170**:849–856.

8 Capeless EL, Clapp JF. Cardiovascular changes in early phase of pregnancy. *Am J Obstet Gynecol* 1989;**161**:1449–1453.

9 Mesa A, Jessurun C, Hernandez A, et al. Left ventricular diastolic function in normal human pregnancy. *Circulation* 1999;**99**:511–517.

10 McLennan FM, Haites NE, Rawles JM. Stroke and minute distance in pregnancy: a longitudinal study using Doppler ultrasound. *Br J Obstet Gynaecol* 1987;**94**:499–506.

11 Hunter S, Robson SC. Adaptation of the maternal heart in pregnancy. *Br Heart J* 1992;**68**:540–543.

12 Robson SC, Dunlop W. When do cardiovascular parameters return to their preconception values? *Am J Obstet Gynecol* 1992;**167**:1479.

13 de Boer K, ten Cate JW, Sturk A, Borm JJ, Treffers PE. Enhanced thrombin generation in normal and hypertensive pregnancy. *Am J Obstet Gynecol*. 1989;**160**:95–100.

14 Brenner B, Grabowski EF, Hellgren M, et al. Thrombophilia and pregnancy complications. *Thromb Haemost* 2004;**92**:678–681.

15 Rossi A, Cornette J, Johnson MR, et al. Quantitative cardiovascular magnetic resonance in pregnant women: cross-sectional analysis of physiological parameters throughout pregnancy and the impact of the supine position. *J Cardiovasc Magn Reson* 2011; **13**:31.

16 Rubler S, Damani PM, Pinto ER. Cardiac size and performance during pregnancy estimated with echocardiography. *Am J Cardiol* 1977;**40**:534–540.

17 Kametas NA, McAuliffe F, Hancock J, et al. Maternal left ventricular mass and diastolic function during pregnancy. *Ultrasound Obstet Gynecol* 2001;**18**:460–466.

18 Bamfo JE, Kametas NA, Nicolaides KH, Chambers JB. Maternal left ventricular diastolic and systolic long-axis function during normal pregnancy. *Eur J Echocardiogr* 2007;**8**:360–368.

19 Geva T, Mauer MB, Striker L, et al. Effects of physiologic load of pregnancy on left ventricular contractility and remodeling. *Am Heart J* 1997;**133**:53–59.

20 Poppas A, Shroff SG, Korcarz CE, et al. Serial assessment of the cardiovascular system in normal pregnancy. Role of arterial compliance and pulsatile arterial load. *Circulation* 1997;**95**:2407–2415.

21 Vered Z, Poler SM, Gibson P, et al. Noninvasive detection of the morphologic and hemodynamic changes during normal pregnancy. *Clin Cardiol* 1991;**14**:327–334.

22 Sadaniantz A, Kocheril AG, Emaus SP, et al. Cardiovascular changes in pregnancy evaluated by two-dimensional and Doppler echocardiography. *J Am Soc Echocardiogr* 1992;**5**:253–258.

23 Yosefy C, Shenhav S, Feldman V, et al. Left atrial function during pregnancy: a three-dimensional echocardiographic study. *Echocardiography* 2012;**29**:1096–1101.

24 Robson SC, Hunter S, Boys RJ, Dunlop W. Serial changes in pulmonary haemodynamics during human pregnancy: a non-invasive study using Doppler echocardiography. *Clin Sci (Lond)* 1991;**80**:113–117.

25 Robson SC, Richley D, Boys RJ, Hunter S. Incidence of Doppler regurgitant flow velocities during normal pregnancy. *Eur Heart J* 1992;**13**:84–87.

26 Easterling TR, Benedetti TJ, Schmucker BC, et al. Maternal hemodynamics and aortic diameter in normal and hypertensive pregnancies. *Obstet Gynecol* 1991;**78**:1073–1077.

27 Ristic AD, Seferovic PM, Ljubic A, et al. Pericardial disease in pregnancy. *Herz* 2003;**28**:209–215.

28 Lund CJ. Maternal congenital heart disease as an obstetric problem. *Am J Obstet Gynecol* 1948;**55**:244–261.

29 Cornette J, Ruys TP, Rossi A, et al. Hemodynamic adaptation to pregnancy in women with structural heart disease. *Int J Cardiol* 2012;**168**:825–831.

30 Uebing A, Arvanitis P, Li W, et al. Effect of pregnancy on clinical status and ventricular function in women with heart disease. *Int J Cardiol* 2010;**139**:50–59.

31 Egidy Assenza G, Cassater D, Landzberg M, et al. The effects of pregnancy on right ventricular remodeling in women with repaired tetralogy of Fallot. *Int J Cardiol* 2013;**168**:1847–1852.

32 Berg CJ, Mackay AP, Qin C, Callaghan WM. Overview of maternal morbidity during hospitalization for labor and delivery in the United States: 1993–1997 and 2001–2005. *Obstet Gynecol* 2009;**113**:1075–1081.

33 Cantwell R, Clutton-Brock T, Cooper G, et al. Saving mothers' lives: reviewing maternal deaths to make motherhood safer: 2006–2008. The Eighth Report of the Confidential Enquiries into Maternal Deaths in the United Kingdom. *BJOG* 2011;**118**(Suppl. 1):1–203.

34 Siu SC, Sermer M, Colman JM, et al. Prospective multicenter study of pregnancy outcomes in women with heart disease. *Circulation* 2001;**104**:515–521.

35 Khairy P, Ouyang DW, Fernandes SM, et al. Pregnancy outcomes in women with congenital heart disease. *Circulation* 2006;**113**:517–524.

36 Drenthen W, Pieper PG, Roos-Hesselink JW, et al. Outcome of pregnancy in women with congenital heart disease: a literature review. *J Am Coll Cardiol* 2007;**49**:2303–2311.

37 Roos-Hesselink JW, Ruys TP, Stein JI, et al. Outcome of pregnancy in patients with structural or ischaemic heart disease: results of a registry of the European Society of Cardiology. *Eur Heart J* 2013;**34**:657–665.

38 Balint OH, Siu SC, Mason J, et al. Cardiac outcomes after pregnancy in women with congenital heart disease. *Heart* 2010;**96**:1656–1661.

39 Siu SC, Colman JM, Sorensen S, et al. Adverse neonatal and cardiac outcomes are more common in pregnant women with cardiac disease. *Circulation* 2002;**105**:2179–2184.

40 Ouyang DW, Khairy P, Fernandes SM, et al. Obstetric outcomes in pregnant women with congenital heart disease. *Int J Cardiol* 2010;**144**:195–199.

41 Tanous D, Siu SC, Mason J, et al. B-type natriuretic peptide in pregnant women with heart disease. *J Am Coll Cardiol* 2010;**56**:1247–1253.

42 Kamiya CA, Iwamiya T, Neki R, et al. Outcome of pregnancy and effects on the right heart in women with repaired tetralogy of Fallot. *Circ J* 2012;**76**:957–963.

43 Lui GK, Silversides CK, Khairy P, et al. Heart rate response during exercise and pregnancy outcome in women with congenital heart disease. *Circulation* 2011;**123**:242–248.

44 Yap SC, Drenthen W, Meijboom FJ, et al. Comparison of pregnancy outcomes in women with repaired versus unrepaired atrial septal defect. *BJOG* 2009;**116**:1593–1601.

45 Yap SC, Drenthen W, Pieper PG, et al. Pregnancy outcome in women with repaired versus unrepaired isolated ventricular septal defect. *BJOG* 2010;**117**:683–689.

46 Hameed AB, Goodwin TM, Elkayam U. Effect of pulmonary stenosis on pregnancy outcomes–a case-control study. *Am Heart J* 2007;**154**:852–854.

47 Drenthen W, Pieper PG, Roos-Hesselink JW, et al. Non-cardiac complications during pregnancy in women with isolated congenital pulmonary valvar stenosis. *Heart* 2006;**92**:1838–1843.

48 Donnelly JE, Brown JM, Radford DJ. Pregnancy outcome and Ebstein's anomaly. *Br Heart J* 1991;**66**:368–371.

49 Connolly HM, Warnes CA. Ebstein's anomaly: outcome of pregnancy. *J Am Coll Cardiol* 1994;**23**:1194–1198.

50 De Wilde JP, Rivers AW, Price DL. A review of the current use of magnetic resonance imaging in pregnancy and safety implications for the fetus. *Prog Biophys Mol Biol* 2005;**87**:335–353.

51 Immer FF, Bansi AG, Immer-Bansi AS, et al. Aortic dissection in pregnancy: analysis of risk factors and outcome. *Ann Thorac Surg* 2003;**76**:309–314.

52 Warnes CA, Williams RG, Bashore TM, et al. ACC/AHA 2008 Guidelines for the Management of Adults with Congenital Heart Disease: A report of the American College of Cardiology/American Heart Association Task Force on Practice Guidelines (Writing Committee to Develop Guidelines on the Management of Adults with Congenital Heart Disease). *Circulation* 2008;**118**:e714–833.

53 Therrien J, Barnes I, Somerville J. Outcome of pregnancy in patients with congenitally corrected transposition of the great arteries. *Am J Cardiol* 1999;**84**:820–824.

54 Connolly HM, Grogan M, Warnes CA. Pregnancy among women with congenitally corrected transposition of great arteries. *J Am Coll Cardiol* 1999;**33**:1692–1695.

55 Presbitero P, Somerville J, Stone S, et al. Pregnancy in cyanotic congenital heart disease. Outcome of mother and fetus. *Circulation* 1994;**89**:2673–2676.

56 Yentis SM, Steer PJ, Plaat F. Eisenmenger's syndrome in pregnancy: maternal and fetal mortality in the 1990s. *Br J Obstet Gynaecol* 1998;**105**:921–922.

57 Weiss BM, Zemp L, Seifert B, Hess OM. Outcome of pulmonary vascular disease in pregnancy: a systematic overview from 1978 through 1996. *J Am Coll Cardiol* 1998;**31**:1650–1657.

58 Bedard E, Dimopoulos K, Gatzoulis MA. Has there been any progress made on pregnancy outcomes among women with pulmonary arterial hypertension? *Eur Heart J* 2009;**30**:256–265.

59 Meijer JM, Pieper PG, Drenthen W, et al. Pregnancy, fertility, and recurrence risk in corrected tetralogy of Fallot. *Heart* 2005;**91**:801–805.

60 Veldtman GR, Connolly HM, Grogan M, et al. Outcomes of pregnancy in women with tetralogy of Fallot. *J Am Coll Cardiol* 2004;**44**:174–180.

61 Baumgartner H, Bonhoeffer P, De Groot NM, et al. ESC Guidelines for the management of grown-up congenital heart disease (new version 2010). *Eur Heart J* 2010;**31**:2915–2957.

62 Krieger EV, Landzberg MJ, Economy KE, et al. Comparison of risk of hypertensive complications of pregnancy among women with versus without coarctation of the aorta. *Am J Cardiol* 2011;**107**:1529–1534.

63 Juan-Jimenez L. Gadolinium-enhanced 3-dimensional magnetic resonance angiography of the aorta relates to pregnancy outcomes in women with coarctation of the aorta: a multicenter study. *Eur Heart J* 2013.

64 Fratz S, Hager A, Busch R, et al. Patients after atrial switch operation for transposition of the great arteries cannot increase stroke volume under dobutamine stress as opposed to patients with congenitally corrected transposition. *Circ J* 2008;**72**:1130–1135.

65 Guedes A, Mercier LA, Leduc L, et al. Impact of pregnancy on the systemic right ventricle after a Mustard operation for transposition of the great arteries. *J Am Coll Cardiol* 2004;**44**:433–437.

66 Radford DJ, Stafford G. Pregnancy and the Rastelli operation. *Aust N Z J Obstet Gynaecol* 2005;**45**:243–247.

67 Tobler D, Fernandes SM, Wald RM, et al. Pregnancy outcomes in women with transposition of the great arteries and arterial switch operation. *Am J Cardiol* 2010;**106**:417–420.

68 Canobbio MM, Mair DD, van der Velde M, Koos BJ. Pregnancy outcomes after the Fontan repair. *J Am Coll Cardiol* 1996;**28**:763–767.

69 Drenthen W, Pieper PG, Roos-Hesselink JW, et al. Pregnancy and delivery in women after Fontan palliation. *Heart* 2006;**92**:1290–1294.

70 Hameed A, Karaalp IS, Tummala PP, et al. The effect of valvular heart disease on maternal and fetal outcome of pregnancy. *J Am Coll Cardiol* 2001;**37**:893–899.

71 al Kasab SM, Sabag T, al Zaibag M, et al. Beta-adrenergic receptor blockade in the management of pregnant women with mitral stenosis. *Am J Obstet Gynecol* 1990;**163**:37–40.

72 Routray SN, Mishra TK, Swain S, et al. Balloon mitral valvuloplasty during pregnancy. *Int J Gynaecol Obstet* 2004;**85**:18–23.

73 Stoddard MF, Longaker RA, Vuocolo LM, Dawkins PR. Transesophageal echocardiography in the pregnant patient. *Am Heart J* 1992;**124**:785–787.

74 Easterling TR, Chadwick HS, Otto CM, Benedetti TJ. Aortic stenosis in pregnancy. *Obstet Gynecol* 1988;**72**:113–118.

75 Silversides CK, Colman JM, Sermer M, et al. Early and intermediate-term outcomes of pregnancy with congenital aortic stenosis. *Am J Cardiol* 2003;**91**:1386–1389.

76 Hung L, Rahimtoola SH. Prosthetic heart valves and pregnancy. *Circulation* 2003;**107**:1240–1246.

77 Badduke BR, Jamieson WR, Miyagishima RT, et al. Pregnancy and childbearing in a population with biologic valvular prostheses. *J Thorac Cardiovasc Surg* 1991;**102**:179–186.

78 El SF, Hassan W, Latroche B, et al. Pregnancy has no effect on the rate of structural deterioration of bioprosthetic valves: long-term 18-year follow-up results. *J Heart Valve Dis* 2005;**14**:481–485.

79 Traill TA. Valvular heart disease and pregnancy. *Cardiol Clin* 2012;**30**:369–381.

80 Wu D, Shen YH, Russell L, et al. Molecular mechanisms of thoracic aortic dissection. *J Surg Res* 2013;**184**:907–924.

81 Hiratzka LF, Bakris GL, Beckman JA, et al. 2010 ACCF/AHA/AATS/ACR/ASA/SCA/SCAI/SIR/STS/SVM Guidelines for the Diagnosis and Management of Patients with Thoracic Aortic Disease: A Report of the American College of Cardiology Foundation/American Heart Association Task Force on Practice Guidelines, American Association for Thoracic Surgery, American College of Radiology, American Stroke Association, Society of Cardiovascular Anesthesiologists, Society for Cardiovascular Angiography and Interventions, Society of Interventional Radiology, Society of Thoracic Surgeons, and Society for Vascular Medicine. *Circulation* 2010;**121**:e266–369.

82 Donnelly RT, Pinto NM, Kocolas I, Yetman AT. The immediate and long-term impact of pregnancy on aortic growth rate and mortality in women with Marfan syndrome. *J Am Coll Cardiol* 2012;**60**:224–229.

83 Montoya ME, Karnath BM, Ahmad M. Endocarditis during pregnancy. *South Med J* 2003;**96**:1156–1157.

84 Campuzano K, Roque H, Bolnick A, et al. Bacterial endocarditis complicating pregnancy: case report and systematic review of the literature. *Arch Gynecol Obstet* 2003;**268**:251–255.

85 Tsuda E, Kawamata K, Neki R, et al. Nationwide survey of pregnancy and delivery in patients with coronary arterial lesions caused by Kawasaki disease in Japan. *Cardiol Young* 2006;**16**:173–178.

86 Stergiopoulos K, Shiang E, Bench T. Pregnancy in patients with preexisting cardiomyopathies. *J Am Coll Cardiol* 2011;**58**:337–350.

87 Demakis JG, Rahimtoola SH. Peripartum cardiomyopathy. *Circulation* 1971;**44**:964–968.

88 Pearson GD, Veille JC, Rahimtoola S, et al. Peripartum cardiomyopathy: National Heart, Lung, and Blood Institute and Office of Rare Diseases (National Institutes of Health) workshop recommendations and review. *JAMA* 2000;**283**:1183–1188.

89 Homans DC. Peripartum cardiomyopathy. *N Engl J Med* 1985;**312**:1432–1437.

90 Elkayam U. Clinical characteristics of peripartum cardiomyopathy in the united states: diagnosis, prognosis, and management. *J Am Coll Cardiol* 2011;**58**:659–670.

91 Fett JD, Christie LG, Carraway RD, Murphy JG. Five-year prospective study of the incidence and prognosis of peripartum cardiomyopathy at a single institution. *Mayo Clin Proc* 2005;**80**:1602–1606.

92 Seely EW, Ecker J. Clinical practice. Chronic hypertension in pregnancy. *N Engl J Med* 2011;**365**:439–446.

93 James AH, Jamison MG, Biswas MS, et al. Acute myocardial infarction in pregnancy: a United States population-based study. *Circulation* 2006;**113**:1564–1571.

94 Ladner HE, Danielsen B, Gilbert WM. Acute myocardial infarction in pregnancy and the puerperium: a population-based study. *Obstet Gynecol* 2005;**105**:480–484.

95 Chambers CE, Fetterly KA, Holzer R, et al. Radiation safety program for the cardiac catheterization laboratory. *Catheter Cardiovasc Interv* 2011;**77**:546–556.

96 John AS, Gurley F, Schaff HV, et al. Cardiopulmonary bypass during pregnancy. *Ann Thorac Surg* 2011;**91**:1191–1196.

97 Vanden Hoek TL, Morrison LJ, Shuster M, et al. Part 12: Cardiac arrest in special situations: 2010 American Heart Association Guidelines for Cardiopulmonary Resuscitation and Emergency Cardiovascular Care. *Circulation* 2010;**122**:S829–861.

CHAPTER 44

Fetal Echocardiography

Darren P. Hutchinson[1] and Lisa K. Hornberger[2]

[1]Department of Pediatric Cardiology, The Royal Children's Hospital Melbourne, VIC, Australia
[2]Stollery Children's Hospital, Edmonton, AB, Canada

Fetal cardiology has evolved over the past two decades into a highly specialized clinical field that merges fetal–perinatal medicine and pediatric cardiology. At the center of this field is the fetal echocardiogram, which permits the evaluation of fetal cardiovascular anatomy, function, and rhythm. Fetal echocardiography continues to provide new insight into normal human cardiovascular growth and physiology otherwise only understood previously through fetal animal models. Improvements in ultrasound technology have made it possible to define in detail most forms of congenital heart disease (CHD), and to detect CHD even in the late first trimester. It has contributed significantly to our understanding of the prenatal and perinatal pathophysiology of structural and functional cardiovascular lesions. Serial observations have provided insight into the evolution and etiologies of the postnatal spectrum of CHD, improved prenatal counseling regarding prognosis, and even prompted development of fetal and perinatal interventions to alter the course of disease and thus improve outcome. Fetal echocardiography has provided a means of evaluating fetal arrhythmias which has led to the development of successful therapeutic strategies to prevent or reverse associated fetal heart failure. Finally, our ability to evaluate fetal heart function and to predict the potential for evolution of heart failure in primary cardiovascular lesions and in lesions that secondarily influence the fetal heart has continued to improve. Fetal echocardiography will continue to play a critical role in the management of a large spectrum of primary cardiac and noncardiac fetal pathologies.

Indications and timing of fetal echocardiography

With the growth and development of fetal cardiology and evolution of assisted reproduction and fetal therapy, the indications for a fetal echocardiography have grown concurrently (Table 44.1). These indications can be divided into maternal, fetal, and familial categories. Knowledge of the types and incidence of cardiac disease associated with a given risk factor, and the likelihood of diagnosis at a given gestational age are important in the approach to the examination, counseling, and follow-up of the pregnancy. An understanding of the incidence of extracardiac pathology in given cardiac pathology [1] is also essential as many associated lesions importantly impact the clinical outcome.

The most common reasons for referral for fetal echocardiography include maternal disease, maternal teratogen exposure, and family history of CHD or syndromes associated with CHD [2–4]. The referrals most associated with fetal heart disease, however, are based on an obstetric ultrasound that suggests an abnormality of the fetal heart (70–75% of affected pregnancies). Another 15–20% of affected pregnancies are referred for fetal echocardiography because of the diagnosis of extracardiac abnormalities on a routine obstetric ultrasound. As such, routine obstetric ultrasound screening in all pregnancies plays a critical role in the detection of fetal CHD.

The timing of the fetal echocardiogram depends partly upon the reason for referral. Most fetal echocardiograms are performed in the mid second trimester, between 18 and 23 weeks. This is typically the gestational age at which routine obstetric ultrasounds are performed, and prior to the gestational age limit for pregnancy termination in most countries where this is legalized. Occasionally, referral for fetal echocardiography occurs in the late second or third trimesters, for instance, when a follow-up ultrasound reveals a new anatomic finding or in cases where rhythm abnormalities with or without fetal hydrops are detected. With the advent of endovaginal transducers and the introduction of high-resolution linear and curvilinear probes, there has been an increasing interest in first trimester fetal echocardiography as early as at 10–11 weeks [5–12]. The latter has been prompted in part as a consequence of the development of nuchal translucency screening at 10–14 weeks which identifies the fetus at risk of aneuploidy [13–15] and congenital heart disease in the absence of aneuploidy [16–19].

Echocardiography in Pediatric and Congenital Heart Disease: From Fetus to Adult, Second Edition. Edited by Wyman W. Lai, Luc L. Mertens, Meryl S. Cohen and Tal Geva.
© 2016 John Wiley & Sons, Ltd. Published 2016 by John Wiley & Sons, Ltd.
Companion website: www.lai-echo.com

Table 44.1 Indications for fetal echocardiography

Maternal
Metabolic disorders
Diabetes mellitus
Gestational diabetes
Phenylketonuria
Autoimmune disease
Sjogren syndrome
Systemic lupus erythematosus
**Further elevated risk if concurrent maternal hypothyroidism or previous pregnancy with affected fetus
Teratogen exposure
Alcohol
Lithium
Vitamin A derivatives (retinoic acids)
Vitamin K antagonists
Anticonvulsants
SSRI antidepressants
ACE inhibitors
NSAIDs
Maternal/intrauterine infection
Maternal CHD
Pregnancy from assisted reproduction
Fetal
Suspected fetal heart abnormality by ultrasound
Extracardiac structural abnormalities
Central nervous system
Renal pathology
Abdominal wall defects
Gastrointestinal abnormalities
Diaphragmatic hernia
Skeletal anomalies
Cystic adenomatous malformation
Arteriovenous malformations
Increased nuchal translucency
Cystic hygroma
Single umbilical artery (two vessel cord)
Chromosomal abnormalities – confirmed or suspected
Fetal arrhythmia
Monochorionic twin gestation
Structural heart disease
Twin–twin transfusion syndrome
Acardiac twin gestation
Conjoined twins
Fetal nonimmune hydrops
Fetal conditions affecting fetal cardiac output
Fetal anemia
Familial
Previously affected child
Paternal CHD
Consanguinity
Mendelian syndromes (examples)
DiGeorge syndrome
Tuberous sclerosis
William syndrome
Ellis–van Creveld

CHD, congenital heart disease; SSRI, selective serotonin reuptake inhibitors.

Technical considerations

Diagnostic imaging of the fetal heart requires a technical approach that is different from that used in routine obstetric ultrasound and more akin to postnatal imaging of the heart. The dynamic nature and complexity of the heart requires high frame rates and optimal resolution. To obtain details of the diminutive fetal cardiovascular structures, a high-frequency transducer in the 6–10 MHz range with dynamic focusing capabilities is required in most cases. The highest frequency transducer that provides the needed penetration should be chosen. Frame averaging options or persistence is off or on low. A compress setting allowing for a narrow dynamic range (grayscale) has better sensitivity and defines the blood–tissue interfaces. While the fetal lungs do not interfere, the maternal abdominal wall may be thick and may have echogenic areas from adipose or scar tissue. Additionally, lotions and oils used on the skin, and fetal bone all contribute to reduced image quality and may limit imaging planes. Amniotic fluid provides a very useful interface between the maternal abdomen and the fetal chest, and low amniotic fluid levels reduce fetal image resolution significantly. Use of lower frequency transducers and harmonic imaging can facilitate the evaluation of third trimester patients or if the fetus is at a greater distance from the transducer. Finally, in late first trimester pregnancies, use of high-frequency, high-resolution endovaginal transducers, if available, may be required in some patients for even a basic evaluation of the fetal heart [6,7,11,12].

Color flow Doppler adds important information and should be used routinely. Color settings need to be optimized so that the color fills the desired vessel or chamber without causing significant "bleeding" of color outside of or across the structure being assessed. The Nyquist limit needs to be set just above the level at which aliasing is seen. The Nyquist limit, color gain, and color persistence needs to be modified regularly throughout the examination depending on what is being imaged. Power Doppler can be used to image particularly small vessels or vessels with low velocity flow. Traditionally power Doppler did not give direction of flow and hence was scarcely used in fetal echocardiography. However, power Doppler with high-definition (HD) flow has recently been introduced and allows bidirectional power Doppler imaging.

The screening fetal echocardiogram

A complete fetal echocardiogram should include two-dimensional (2D) imaging of the fetal cardiac anatomy, spectral and color Doppler interrogation of intracardiac, great arteries/arches and systemic and pulmonary venous blood flow, and a basic assessment of fetal heart function and rhythm (Table 44.2). Assessment of more remote blood flows, such as in the middle cerebral artery and umbilical artery and vein can provide useful information regarding fetal well-being, placental function, and the effect of cardiac disease on other

Table 44.2 Components of a complete fetal echocardiogram

- **Two-dimensional imaging**
 - Orientation to fetal position
 - Exclude obvious fetal hydrops
 - Pleural effusions
 - Pericardial effusion
 - Ascites
 - Skin edema
 - Visceral and atrial situs evaluation
 - Cross-sectional images
 - Four-chamber view sweeps
 - Cardiac axis
 - Cardiac size/cardiothoracic ratio
 - Cardiac position
 - Left and right atria
 - Atrial septal anatomy
 - Pulmonary veins (at least one right and one left)
 - Tricuspid valve
 - Mitral valve
 - Right ventricular morphology
 - Left ventricular morphology
 - Ventricular septal anatomy
 - Left ventricular outflow-aorta-pulmonary artery
 - Right ventricular outflow
 - Three-vessel view sweeps
 - 3-vessel view – normal great artery position and size relationship
 - Branch pulmonary arteries
 - Ductus arteriosus orientation and size
 - Aortic arch orientation and size
 - Trachea
 - Left innominate vein
 - Sagittal sweeps
 - Right superior vena cava
 - Right inferior vena cava
 - Left and right atria
 - Atrial septal anatomy
 - Aortic arch
 - Ductal arch
 - Tricuspid and mitral valve enface
 - Right and left ventricular morphology
 - Aortic and pulmonary outflow tracts
 - Basic RV and LV systolic function assessment
 - Ductus venosus and umbilical artery and vein anatomy
- **Color flow mapping**
 - Tricuspid and mitral valves
 - Ventricular outflows
 - Pulmonary veins
 - Aortic arch
 - Ductal arch
 - Inferior vena cava
 - Ductus venosus
 - Umbilical artery and vein
- **Pulsed Doppler assessment**
 - Ventricular inflows
 - Ventricular outflows
 - Ductus arteriosus
 - Aortic arch/isthmus
 - Pulmonary veins
 - Inferior vena cava or hepatic vein
 - Ductus venosus
 - Umbilical vein
 - Umbilical artery
- **Rhythm assessment**
 - Fetal heart rate
 - Relationship between atrial and ventricular contraction

organs. Obtaining measures of fetal size such as the biparietal diameter and femur length are important particularly when measurements of cardiac structures are not in keeping with gestational age. Assessment of the fetal heart is unique relative to postnatal evaluation of the pediatric patient in several ways. Orientation to fetal position within the mother is critical for deciphering right and left positions and the relationship of cardiovascular structures within the fetal chest and abdomen. The fetus is active, particularly prior to 16 weeks, and may shift many times during an examination requiring reorientation to fetal position. The diminutive structures at less than 16 weeks and the frequently prone position (spine-up) and relative oligohydramnios at >35 weeks may result in suboptimal image resolution. Classical imaging planes through the heart used after birth may be attempted in the fetus, but are frequently not available. As such one must be creative in deciphering particularly complex fetal structural heart disease. The unique aspects of the fetal circulation, including the parallel circulation and the presence of the foramen ovale and ductus arteriosus with equalization of pressures and redistribution of flow, must be taken into consideration and frequently results in the need for use of indirect observations such as discrepancy in ventricular or great artery size to determine the severity of a condition. Finally, the details gleaned must immediately be processed and synthesized in order to provide accurate counseling for a usually very stressed patient and her partner.

Two-dimensional imaging

Fetal echocardiographic assessment requires a systematic approach as is typically done after birth with determination of segmental anatomy, atrial–ventricular and ventricular–great artery connections, and assessment of aortic and ductal arch morphology and position. Cross-sectional, sagittal, and coronal images through the fetal chest, and short- and long-axis imaging of the fetal heart are valuable in the evaluation of both normal and abnormal fetal heart anatomy. The fetal heart and vascular structures are positioned within fluid-filled lungs that provide a unique opportunity to appreciate the normal and abnormal relationship of these structures to each other and their position within the thorax itself, much as is done after birth by cardiac magnetic resonance imaging.

Delineation of visceral and atrial situs requires an orientation to fetal position. This is probably the most challenging task of the fetal echocardiographer as there are innumerable potential fetal positions (e.g., supine, prone, transverse, vertex, etc.). This becomes even more difficult in multiple pregnancies. Techniques have been described to facilitate orientation, but none are without potential for error. Orientation of the transducer along the long axis, particularly the spine of the fetus at lower magnification will immediately provide information regarding the position of the head and the feet. The fetal spine helps distinguish the anterior and posterior aspects of the fetus. Use of a doll or model can facilitate recognition of the left and right sides

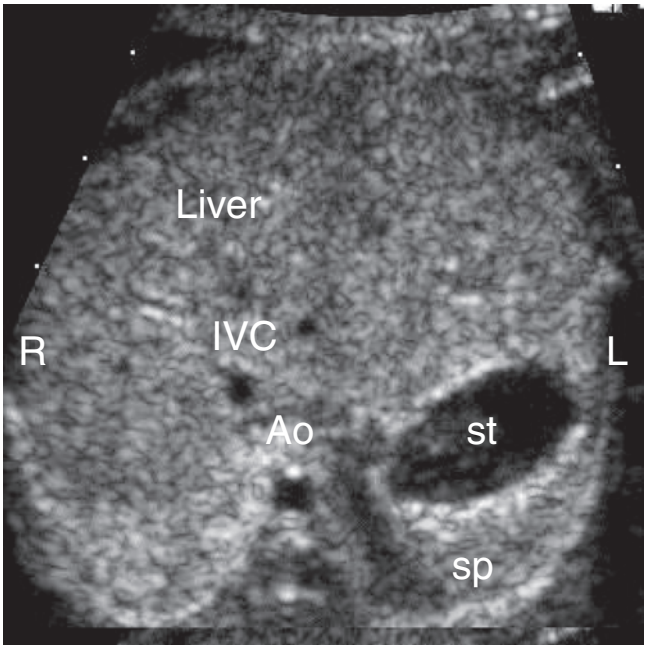


Figure 44.1 Cross-sectional image through the normal fetal abdomen. Ao, descending aorta; IVC, inferior vena cava; sp, spleen; st, stomach; L, left; R, right.

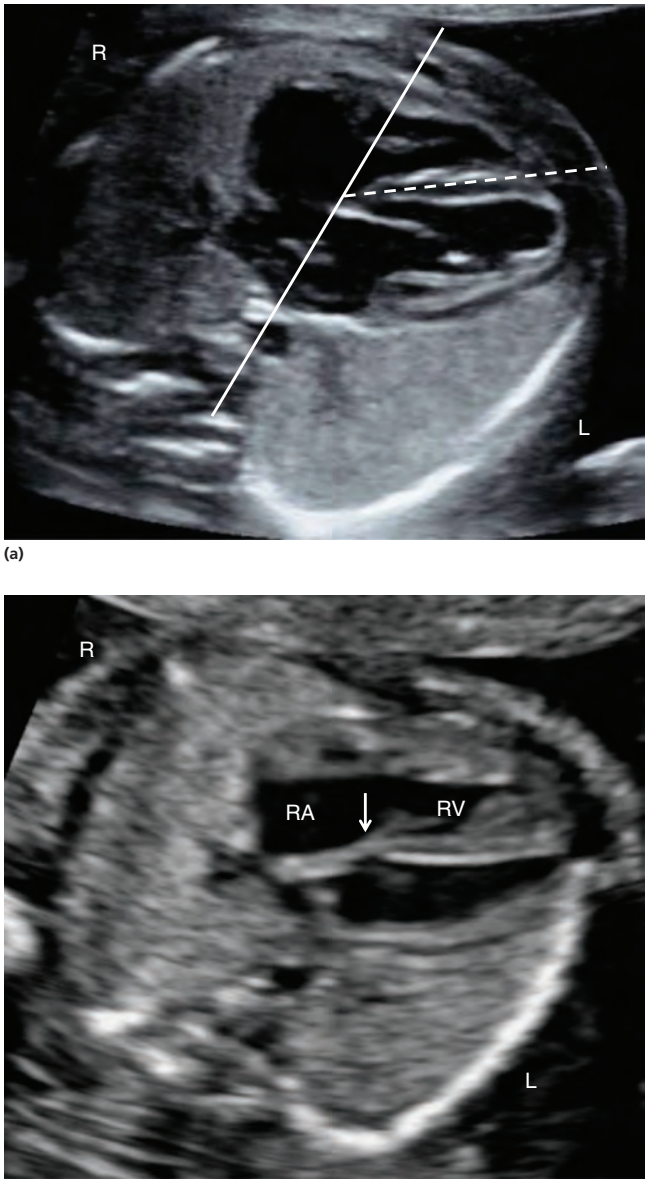


Figure 44.2 Cross-sectional image through the fetal thorax demonstrating **(a)** the cardiac axis – angle of the septum (dashed line) from the midline (solid line) – and **(b)** the 4-chamber view (the arrow demonstrates the offset of the atrioventricular valves). RA, right atrium; RV, right ventricle; L, left; R, right.

of the fetal body and help to better understand the fetal position and planes of imaging. In one technique, when the fetus is supine or prone, whether vertex or breech, orientation of the transducer orientation groove towards the fetal head along the long axis of the fetal body and clockwise rotation results in a cross-sectional image that displays the fetal left to the right of the screen (Video 44.1) [20]. This technique becomes more difficult to use when the fetus is in a transverse lie. Irrespective of the technique employed, if there is fetal cardiovascular pathology, it is critical that the responsible clinician put his/her hands on the transducer as the potential for error in determining the left and right sides of the fetus is significant and impossible to recognize with solely a review of images.

Once the fetal position is determined, cross-sectional imaging beginning at the level of the fetal abdomen with sweeping to the fetal chest provides information regarding visceral and atrial situs. A right-dominant liver, and left-sided stomach and spleen as well as a right-sided inferior vena cava suggests visceral situs solitus (Figure 44.1). Sweeping to the fetal chest, the inferior vena cava moves anteriorly to connect ultimately with the floor of the right atrium, just beneath the septum primum and the pathway to the foramen ovale. A cross-sectional image through the fetal chest provides images of the four chambers of the heart (Figure 44.2; Video 44.2). The heart should be roughly one third the size of the fetal chest. The cardiac axis, the axis of the ventricular septum relative to the midline of the fetal chest, is 43 +/– 7 degrees with little variation from 14 weeks to term (Figure 44.2a) [21]. Interestingly, the heart is much more mesocardic in the first trimester, rotating to the left by the 12th week [22]. In the normal fetus, the right atrium and a portion of the right ventricle are to the right of the midline (Figure 44.2b). The left ventricle, left atrium and a portion of the right ventricle are to the left of the midline. Any change in cardiac axis or position of the four chambers relative to the midline should prompt a search for either intracardiac or intrathoracic extracardiac pathology, the latter including unilateral lung hypoplasia [23,24], diaphragmatic hernia, pulmonary sequestrations, and cystic adenomatous malformations.

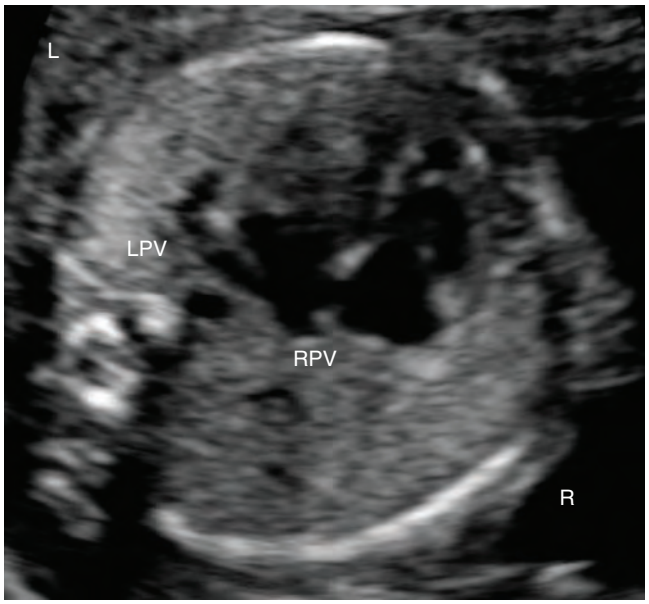
The left atrium is the most posterior 4-chamber structure, positioned just anterior to the descending aorta in the normal heart. At least one left and right pulmonary vein should be demonstrated at this level connecting with the left atrium with the left pulmonary veins coursing closest to the left-sided descending aorta. Color Doppler settings need to be optimized, with an appropriately reduced Nyquist limit, to show the low-velocity venous flow. Pulsed (PW) Doppler provides confirmation and assessment of the pulmonary venous flow pattern. (Figure 44.3; Video 44.3).

Evaluation of the fetal atrial and ventricular septa is best accomplished from planes of imaging perpendicular to the septum, thus preventing dropout of thinner structures including the septum primum and the membranous ventricular septum, which may almost appear absent when the plane of imaging is parallel to these structures. Assessment of the atrial septum should include imaging of septum secundum and primum and the foramen ovale (Figure 44.4). Sweeping posteriorly and inferiorly from the 4-chamber view, the thin coronary sinus is visualized as it courses within the left atrium just behind the inferior-posterior ring of the mitral valve. Dilation of the coronary sinus, which may be misinterpreted as an atrial septal defect at its mouth into the right atrium, suggests the presence of a persistent left superior vena cava.

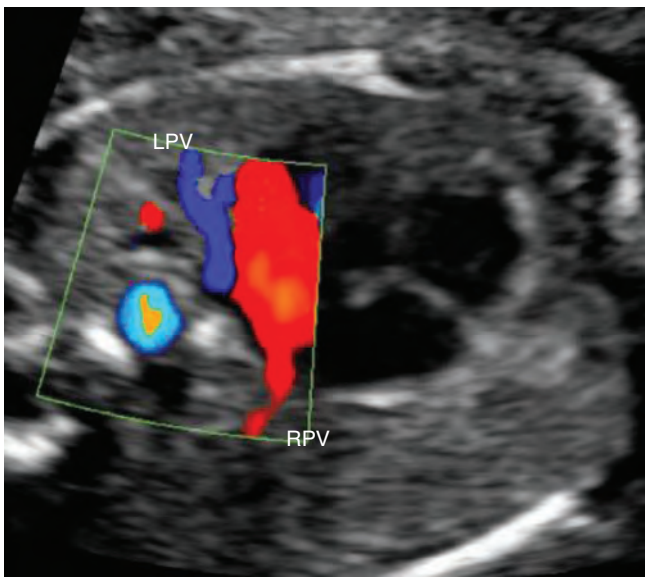
The mitral and tricuspid valves should be evaluated from both 4-chamber and short-axis imaging. In the normal heart, there is a subtle offset of the valves with a more apically displaced septal leaflet of the tricuspid relative to the anterior leaflet of the mitral valve (Figure 44.2b). A short-axis image through the inflow portion of the ventricles further delineates the AV valve morphology, with the anterior leaflet of the mitral valve shown away from the ventricular septum (Figure 44.5c; Video 44.4).

While postnatally, the trabeculation pattern of the ventricles may help in distinguishing the ventricles, prenatally this finding is less distinct, and thus other criteria should be used. The atrioventricular valves, when of normal morphology, can assist in defining the ventricles because a tricuspid valve is always part of a right ventricle and a mitral valve part of a left ventricle. The right ventricle has a more pyramidal shape with an inflow portion, a body and an outflow or infundibulum from which one or both great arteries arise. Identification of the moderator band, best recognized in a 4-chamber image, is also useful to identify the right ventricle. In contrast the more bullet-shaped, left ventricle has two papillary muscles best visualized in a short-axis or sagittal sweep through the heart (Figure 44.5d; Video 44.4), and continuity between the anterior mitral valve leaflet and the semilunar valve (usually aorta) can be demonstrated in a long-axis image through the fetal heart (Figure 44.6a).

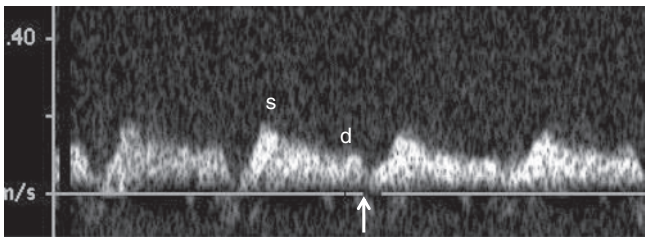
The ventricular septal anatomy includes an inlet, membranous, trabecular and outlet (conal septum) portion. They are typically evaluated through sweeping from the crux of heart just above the diaphragm to the ventricular outlets, or in a short-axis view sweeping from a more rightward aspect of the fetal heart leftward to the ventricular apex (Video 44.4). Slow sweeps with



(a)



(b)



(c)

Figure 44.3 **(a)** Four-chamber view demonstrating left and right pulmonary veins. **(b)** Color Doppler confirms the connection of left and right pulmonary veins with the left atrium. **(c)** Normal pulmonary vein flow is of low velocity with peaks in ventricular systole (s) and early diastole (d) and decreased flow during atrial systole (arrow). L, left; R, right; LPV, left pulmonary vein; RPV, right pulmonary vein.

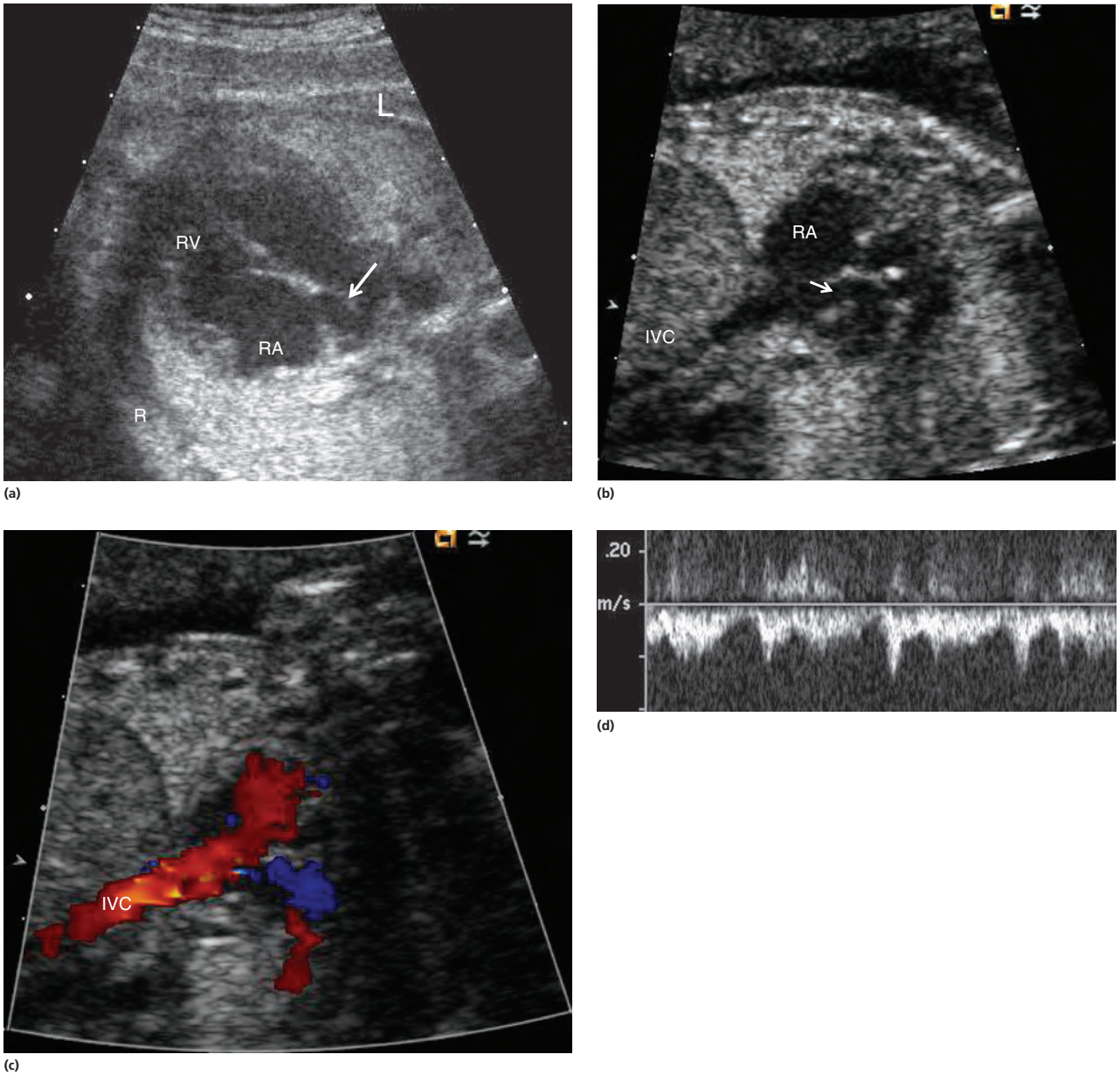


Figure 44.4 Atrial septal anatomy from the **(a)** 4-chamber and **(b)** sagittal views. The short arrow points to septum primum or the flap of the foramen ovale in both images. RA, right atrium; RV, right ventricle; IVC, interior vena cava. **(c)** Color Doppler demonstrates the path of the foramen ovale from right to left atrium. **(d)** Pulsed Doppler demonstrates the pulsatile flow pattern. IVC, inferior vena cava; RA, right atrium; RV, right ventricle; L, left; R, right.

color flow imaging at low-velocity settings can permit detection of even smaller ventricular septal defects.

Sweeping to the fetal head from a 4-chamber image, the ventricular outflow tracts and great arteries can be demonstrated (Figure 44.6; Video 44.2). The left ventricular outflow tract, begins more posterior and leftward relative to the right ventricular outflow tract and courses towards the right. The right ventricular outflow tract begins more anterior and courses leftward, wrapping around the left ventricular outflow meeting the pulmonary valve and main pulmonary artery. The main pulmonary artery is positioned to the left of the midline in the anterior – superior aspect of the fetal chest.

The "3-vessel view" facilitates recognition of normal and abnormal great artery, arch and airway anatomy [25]. It is a cross-sectional image obtained through the superior mediastinum that in normal fetuses consistently demonstrates the relationship of the right superior vena cava, ascending aorta and main pulmonary artery to each other and to other structures within the fetal chest (Figure 44.6). The main pulmonary artery is seen in this view in its long axis as the most anterior and

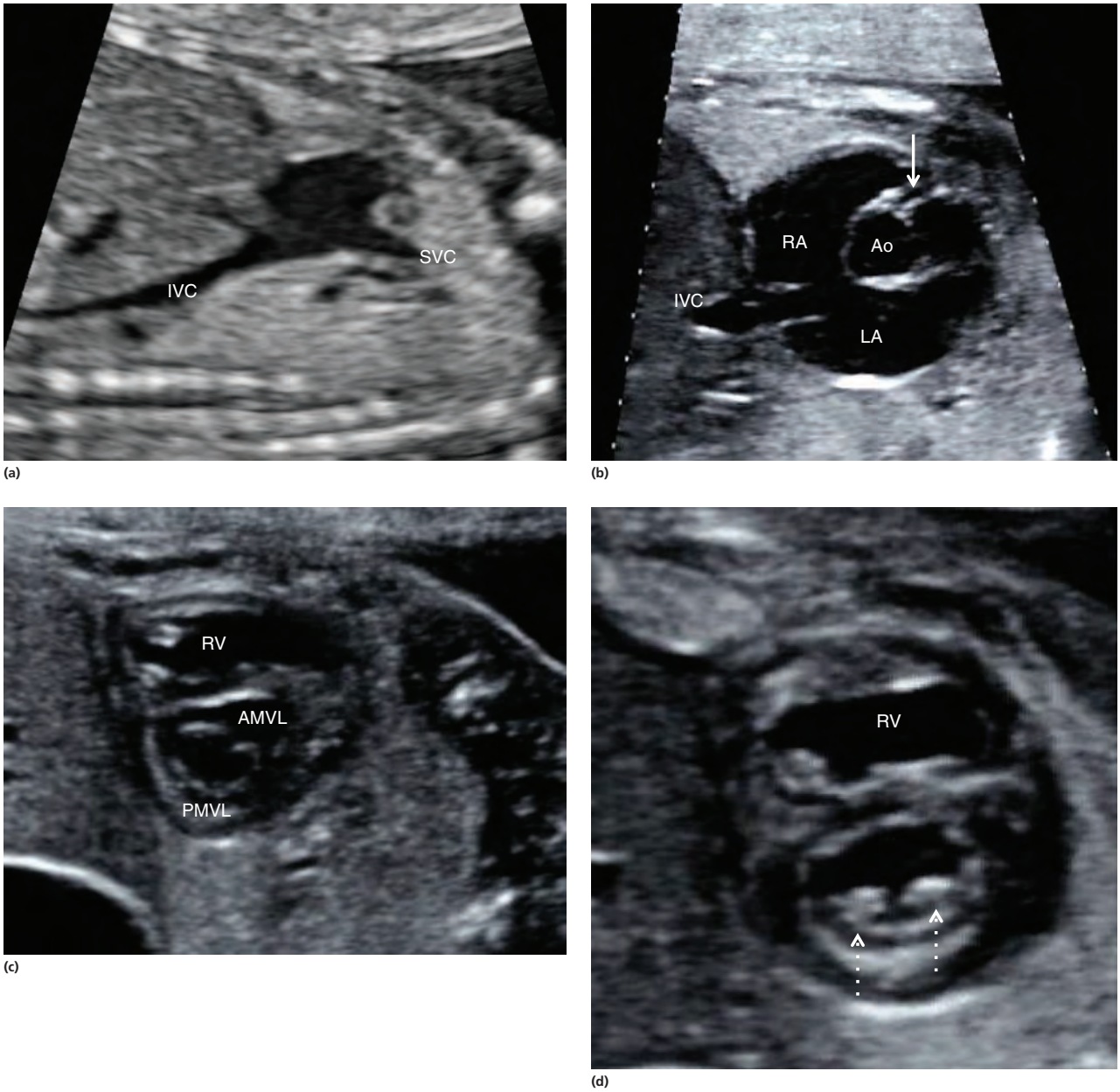


Figure 44.5 **(a–d)** Sagittal sweep through the fetal thorax. Ao, ascending aorta; IVC, inferior vena cava; LA, left atrium; AMVL, anterior mitral valve leaflet, PMVL; posterior mitral valve leaflet; RA, right atrium; LA, left atrium; RV, right ventricle; SVC, superior vena cava; solid arrow denotes left main coronary artery; dotted arrows denote left ventricular papillary muscles.

leftward vessel. The ascending aorta, in its short axis, is rightward and slightly more posterior relative to the main pulmonary artery. Finally, the right superior vena cava seen in its short axis is more rightward and posterior and usually has the smallest diameter compared to either great artery. Presence of an additional structure leftward of the main pulmonary artery and anterior to the left pulmonary artery may indicate a persistent left superior vena cava. Demonstration of a normal 3-vessel view quickly establishes the presence of normally related great arteries. The size relationship of the structures can assist in identifying altered flow or abnormal growth of the three vessels as may occur in left (including aortic coarctation) or right heart obstruction, the presence of semilunar valve insufficiency, altered flow through the left or right heart, and altered flow in the superior vena cava (e.g., interrupted inferior vena cava with azygous continuation or vein of Galen aneurysm). In the 3-vessel view the right pulmonary artery is seen coursing posterior in its long axis to the ascending aorta and superior vena cava (Figure 44.6d). Visualization of the left pulmonary artery often requires a slight rotation of the transducer from a straight cross-sectional plane as it

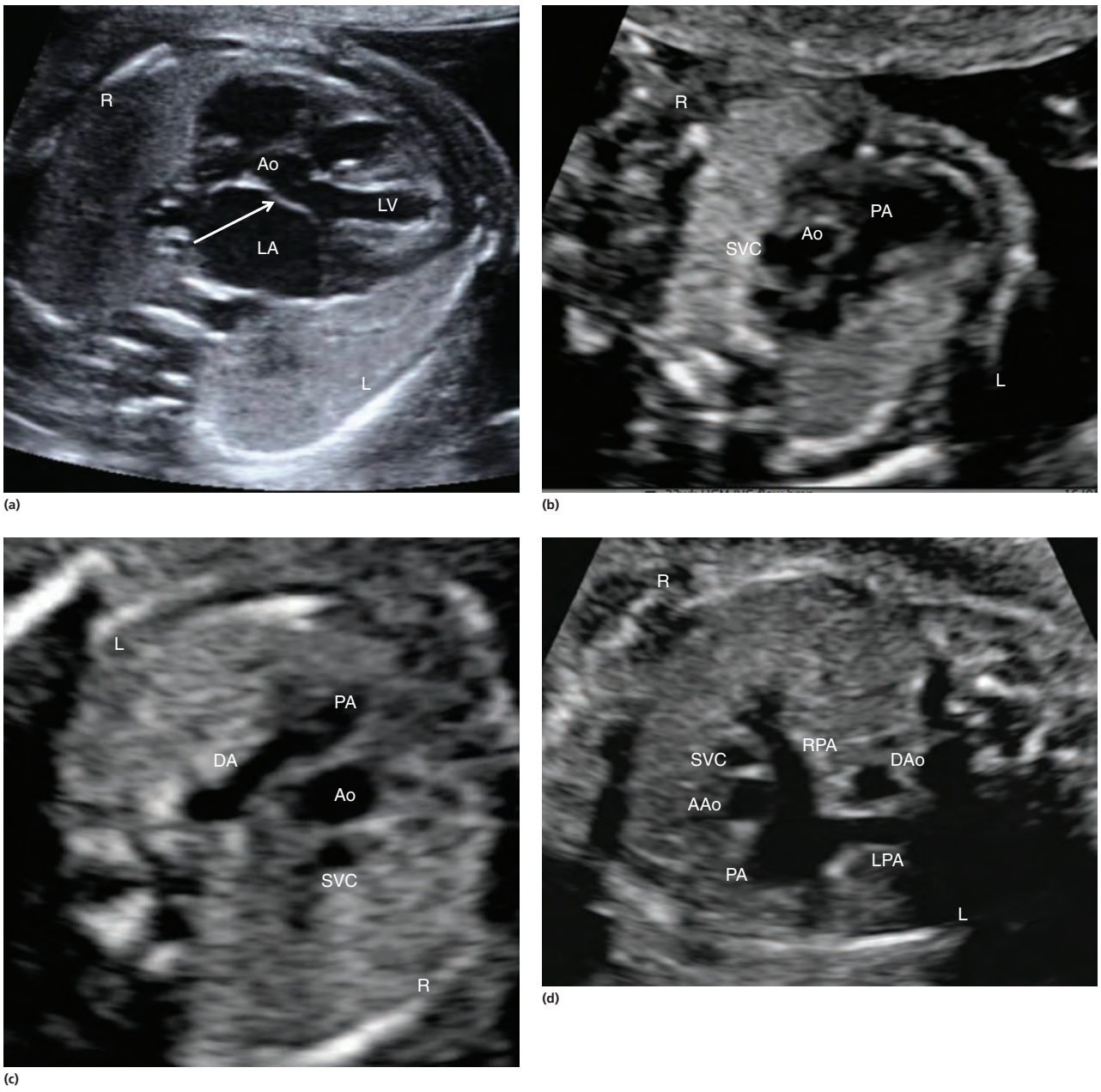


Figure 44.6 **(a,b)** Long-axis images through the fetal heart demonstrating crossing of the ventricular outlets and great arteries which can be only demonstrated through sweeping. **(c)** The normal 3-vessel view. **(d)** Both branch pulmonary arteries shown. The arrow in **(a)** shows area of continuity between anterior mitral valve leaflet and aortic arch. Ao, ascending aorta; DA, ductus arteriosus; DAo, descending aorta; LPA, left pulmonary artery; LV, left ventricle; PA, main pulmonary artery; RPA, right pulmonary artery; RV, right ventricle; SVC, superior vena cava; L, left; R, right.

courses slightly more inferiorly relative to the right pulmonary artery (Figure 44.6d).

In the 3-vessel view, the main pulmonary artery can be seen joining the arterial duct (Figure 44.7a) which dives straight back just to the left of the midline to meet the left-sided, descending aorta. Sweeping cephalad, the aortic arch can be seen coursing from right anterior to left posterior, crossing the midline towards the left of the trachea ultimately joining the descending aorta (Figure 44.7a). This confirms the presence of a left-sided aortic and ductal arches. From the 3-vessel sweeps, one can immediately orient the transducer to obtain a long axis of the arches. For instance, when the fetus is supine, rotating the transducer 90° along the plane of the ascending aorta (Figure 44.7b) (from right anterior to left posterior) produces a long-axis image of the fetal aortic arch (Figure 44.7c). The ascending aorta begins slightly more centrally courses anteriorly and curves posteriorly to meet the descending aorta, giving rise to the three brachiocephalic arteries. Its classic "cane handle" appearance (Figure 44.7c;

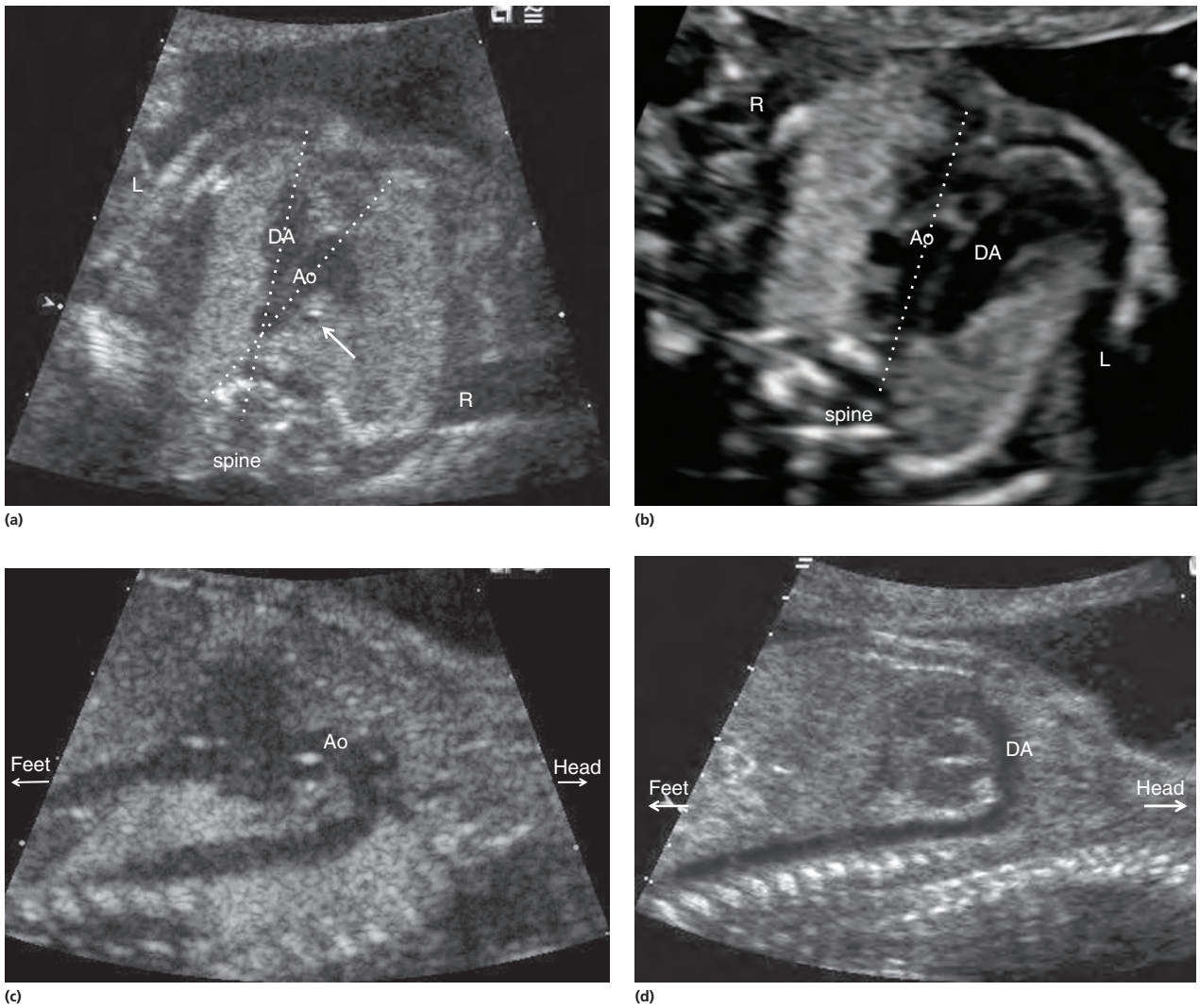


Figure 44.7 **(a)** A slightly rotated (clockwise) 3-vessel view demonstrating aortic and ductal arches. The arrow in **(a)** points to the trachea which, in the normal fetus, is to the right of both aortic and ductal arches. **(b)** Note change in fetal orientation from (a). By moving such that the cross-sectional image is aligned from the ascending aorta (Ao) to the descending aorta or the main pulmonary artery to the ductus arteriosus (DA) as shown in the dotted lines and rotating 90°, the long axis of the aortic **(c)** and ductal **(d)** arches, respectively, can be demonstrated. Ao, aorta; DA, ductus arteriosus; L, left; R, right.

Video 44.5) is readily distinguishable from the more flat, hockey-stick shape of the arterial duct (Figure 44.7d) with an almost 90° angle with the descending aorta.

Early in gestation, in the normal fetus, the left and right sides of the heart are usually symmetric or nearly symmetric particularly prior to 16 weeks. Later in gestation, however, the right atrium, right ventricle, main pulmonary artery, and even the arterial duct may be mildly larger than the left-sided structures [26,27]. Recognition of the normal degree of asymmetry is important in the detection of more subtle obstructive lesions including coarctation of the aorta [28,77]. Use of normograms for fetal cardiac dimensions, including inflow/outflow valve size and ventricular diameter and length, with generation of z-scores can be helpful in establishing size of structures relative to normal and in following growth [29].

Doppler interrogation

Spectral Doppler interrogation of the fetal heart requires the use of narrowed sample volumes and low-velocity settings for most assessments. While Doppler interrogation of the fetal heart with both color and PW Doppler is now routine in fetal echocardiography, much of the pathology can be detected from careful 2D imaging of the fetal cardiovascular anatomy. In this situation, Doppler confirms what is suspected based on the 2D images. Occasionally, though, new information such as valvar regurgitation or early pathology may be identified that warrants more detailed and ongoing assessment of the pregnancy. Color and PW Doppler may assist in the detection of certain aspects of normal anatomy where the image resolution is not sufficient. This is particularly true in very early pregnancy [7]. Color Doppler identifies abnormal flows including valve insufficiency

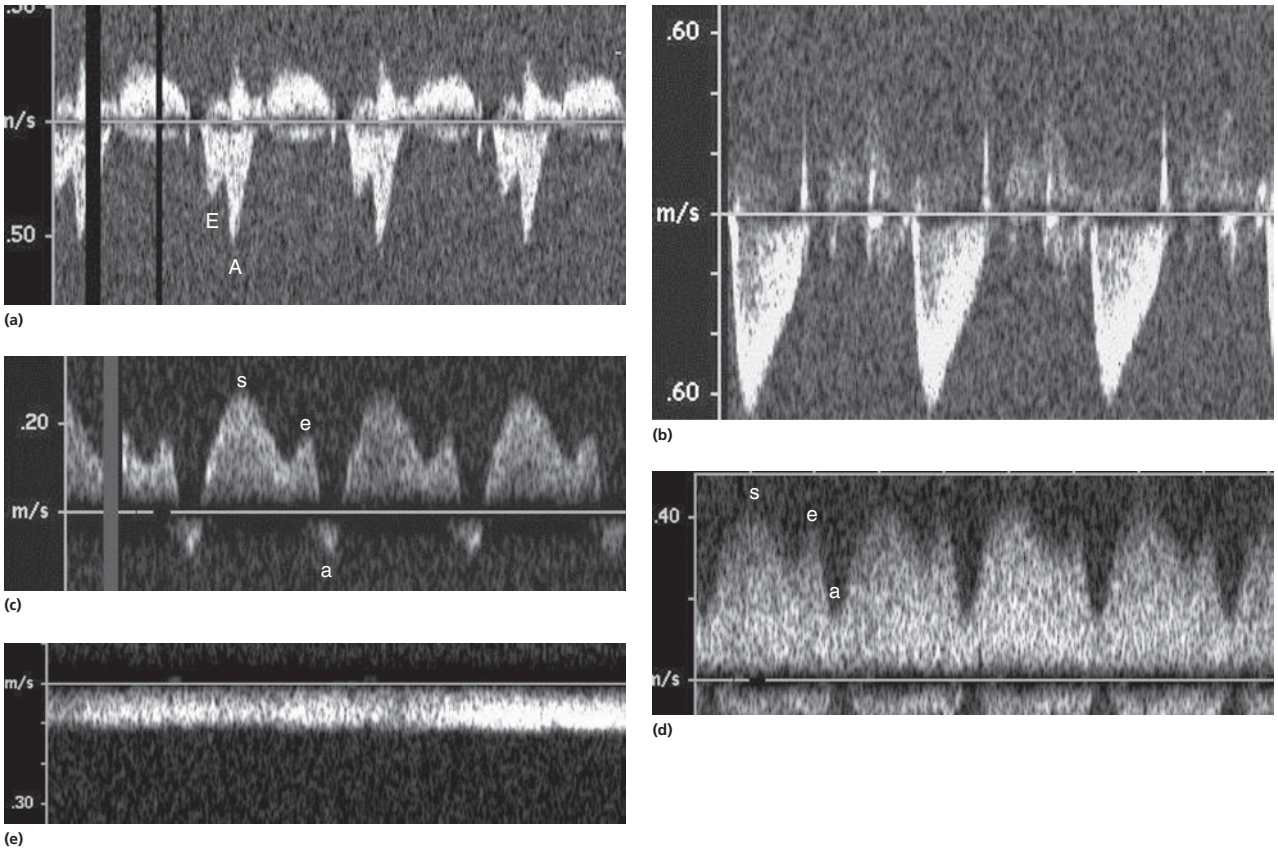


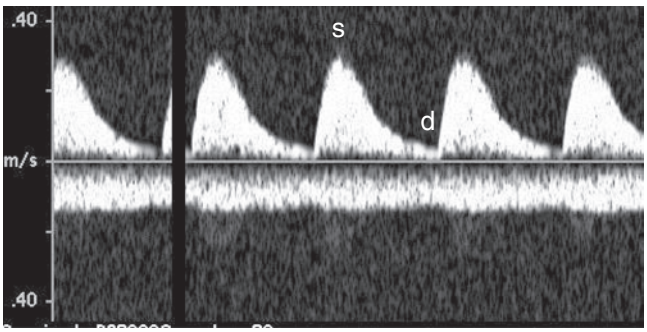
Figure 44.8 Pulsed Doppler spectra of **(a)** the left ventricular inflow and **(b)** outflow; **(c)** the inferior vena cava; **(d)** the ductus venosus; and **(e)** the umbilical vein. Inflow Doppler spectra are characterized from 12 weeks' gestation as biphasic and A-wave (atrial systole) dominant, with increasing E-wave (early ventricular diastole) velocities through gestation. Outflow velocities progressively increase during gestation as cardiac output increases. Inferior vena caval (IVC) **(c)** and ductus venosus (DV) **(d)** flows are phasic, with forward flow in ventricular systole (s) and early diastole (e), and flow reversal (IVC) or reduced velocities (DV) in atrial systole (a). **(e)** Umbilical vein (UV) flow is continuous and of low velocity and displays mild undulations during fetal breathing.

and obstruction, ventricular septal defects, and altered ductal and arch flow as observed in critical pulmonary or systemic outflow obstruction, respectively. Routine PW Doppler interrogation of both ventricular inflows and outflows, pulmonary venous, aortic and ductal arch, inferior vena cava, ductus venosus and umbilical arterial and vein flow is not only useful in confirming normal flows and function, but helps with the recognition of abnormal flows and altered fetal heart function (Figures 44.8 and 44.9).

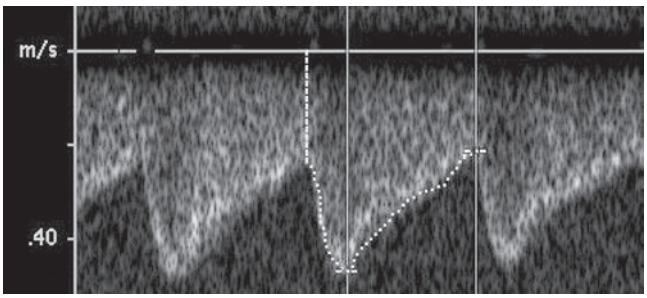
Fetal heart function

Evaluation of fetal heart function requires basic knowledge of normal fetal cardiovascular physiology and developmental changes that occur with gestation. It should consist of an evaluation of general features, as well as systolic and diastolic function parameters. Evaluation of fetal heart size or cardiothoracic ratio, wall thickness, inferior vena cava diameter, fetal heart rate and the presence or absence of features of fetal hydrops or heart failure can provide initial clues to the presence of normal or abnormal fetal heart function. Basic systolic function may be assessed through the measurement of ventricular shortening fraction using either 2D images or M-mode interrogation. In the normal fetus, left and right ventricular shortening fraction is 34 +/– 3% and it does not change from 17 weeks to term [30]. Although fetal ventricular ejection fractions have also been documented using Simpson techniques [31], the reproducibility of these volumetric measurements is poor [32]. Three-dimensional (3D) and four-dimensional (4D) echocardiography may ultimately provide the most accurate means of volumetric and mass assessment of the fetal heart [33–37].

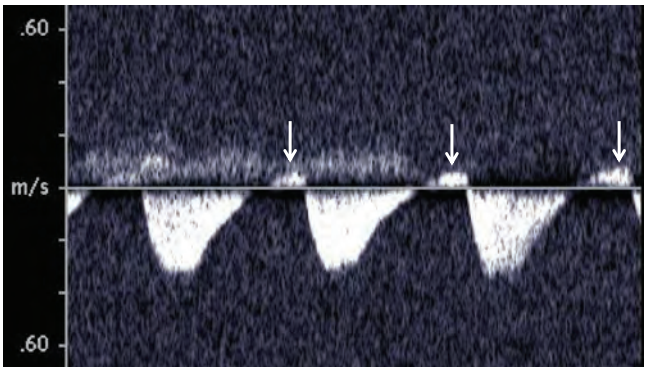
Stroke volume and cardiac output can also be assessed. The normal fetal left ventricular stroke volume and cardiac output is less than that of the right ventricle from the mid-trimester to term [38]. It requires accurate measures of semilunar valve diameters and that Doppler interrogation of outflows is with an angle of insonation of <20° to reduce errors in calculation. Documentation of fetal ventricular stroke volume and output is very useful in fetuses with hydrops fetalis, with or without a known etiology, to determine if increased output is contributing to the clinical picture. Increasing cardiac output has been



(a)



(b)



(c)

Figure 44.9 Umbilical arterial flow from **(a)** 14 weeks' gestation consists of systolic and diastolic flows, which increase with gestation. **(b)** The more dramatic increase in diastolic flow later in gestation reflects decreasing placental resistance. **(c)** Reversed flow in diastole (arrows) is never normal and may be seen where there is severe placental insufficiency. s, systole; d, diastole.

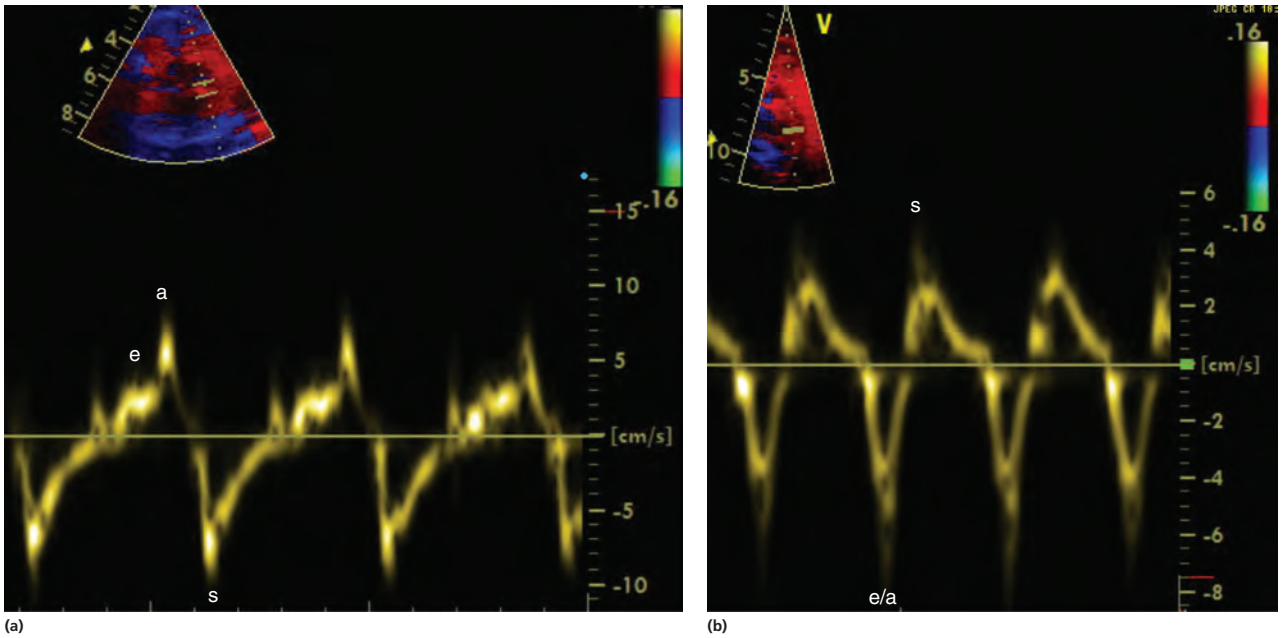
demonstrated, for instance, in such conditions as anemia, AV malformations, acardiac twin gestations and agenesis of the ductus venosus [39–41].

There has been a growing interest in the evaluation of fetal diastolic function in health and disease. PW Doppler assessment of ventricular inflow, inferior vena cava, ductus venosus and umbilical vein flow patterns and velocities have been useful in recognizing changes in diastolic or filling function that may place the fetus at greatest risk of heart failure and compromised umbilical flow through altered central venous pressures [42,43]. Changes that occur in left and right ventricular inflow Doppler flow patterns with increasing E-wave velocities during early ventricular diastole and minimal change in the A-wave velocity, reflect developmental changes in the diastolic properties of the fetal myocardium which may include both progressively more efficient relaxation and greater compliance [44,45]. Simultaneous assessment of left ventricular inflow and outflow velocities, permits measurement of the left ventricular isovolumic relaxation time which in the normal fetus is 43 +/– 8 ms (heart rate corrected) from 20 weeks gestation to term [46]. Finally, the so-called Tei index or myocardial performance index has been used to assess global myocardial function [47]. The Tei index equals the sum of the isovolumic relaxation and isovolumic contraction time over the ejection time. It can be calculated for either the left or right ventricle using the offset of ventricular inflow to the onset of the next inflow (*a*) less the ejection period (*b*) divided by *b*. In the normal second or third trimester fetus, the Tei index decreases with the gestational age, with the left ventricular index showing a greater decline than the right ventricular index [48,49]. The Tei index does not discriminate against changes in systolic, diastolic or combined cardiac dysfunction, and, as such, an abnormal Tei index should prompt further assessment to define the type, degree and possible cause of cardiac dysfunction.

Tissue Doppler imaging (TDI) has been described in the assessment of fetal heart function for over a decade [50,51]. Both pulsed-wave TDI (PW-TDI) and color TDI (C-TDI) have been used to assess systolic and diastolic fetal cardiac function (Figure 44.10). Normal values for PW-TDI, from 18 weeks gestational age, have been established for the left and right ventricular free walls and interventricular septum. LV and RV E/e′ normal values have also been published [50,52]. In clinical practice, fetal TDI can be obtained in the majority of cases. As is true for the postnatal patient, maximizing the frame rate, minimizing the angle of interrogation and using a small Doppler gate is essential. Generally PW-TDI values increase as gestational age increases, with E/e′ values steadily reducing [52]. More recently, C-TDI has been used to assess tissue strain and strain rate in the fetus [53]. The benefits of C-TDI include being able to choose any region of interest offline for assessment [53,54]; however, like PW-TDI, C-TDI remains angle-dependent.

More recently, 2D speckle tissue echocardiography (STE) has also been applied to the fetal heart [55–58]. The mechanics behind this method are described elsewhere in this textbook. One of the main benefits of STE is that, unlike TDI, it is angle-independent, which helps overcome some of the specific technical challenges that fetal position can pose (Figure 44.11). STE also allows for assessment of tissue motion not only at multiple sites, but also in multiple different planes (radial, longitudinal, etc.) [58]. STE using velocity vector imaging has recently been used in fetal HLHS to demonstrate that right ventricular remodeling with greater circumferential relative to longitudinal contraction akin to the normal left ventricle, begins in fetal life [59].

The clinical utility of both TDI and 2D STE imaging is still to be established [58,60]. As fetal cardiologists are increasingly



(a) (b)

Figure 44.10 Pulsed-wave tissue Doppler images obtained from the right ventricular free wall in **(a)** normal in a 34-week fetus and **(b)** a 21-week fetus with possible myocarditis showing short inflow duration with fusion of the E and A waves. a, atrial contraction; e, early diastolic filling; s, systole.

asked to assess fetuses with the potential for cardiac dysfunction, especially in its early stages, more advanced techniques to assess fetal cardiac function are needed. It is essential that these techniques are shown to be accurate and reproducible across observers before they come into mainstream use.

Fetal rhythm assessment

Finally, a complete screening fetal echocardiogram should include a limited assessment of fetal heart rate and rhythm. This can be accomplished routinely through the use of either M-mode or PW Doppler techniques [61,62] which demonstrate the mechanical events of atrial and ventricular contraction (wall motion or flow) from which electrophysiologic events are surmised. Figures 44.12 and 44.13 demonstrate techniques that are routinely used. Several PW Doppler techniques have been developed to assess flow during atrial and ventricular contraction including simultaneous left ventricular inflow and outflow, pulmonary artery and pulmonary vein [63], and superior vena cava and ascending aortic interrogation [64]. All of these techniques are limited to some extent by image resolution and fetal position. In addition they require some experience in interpreting the tracings. Color tissue Doppler with simultaneous evaluation of atrial and ventricular wall movement at multiple sites may prove to be the most effective echocardiographic technique for assessment of arrhythmias as it is less limited by image resolution and fetal position, and may be easier to interpret [65]. The use of tissue Doppler in this setting is still finding its place in routine clinical practice and is limited by availability of programs for offline analysis.

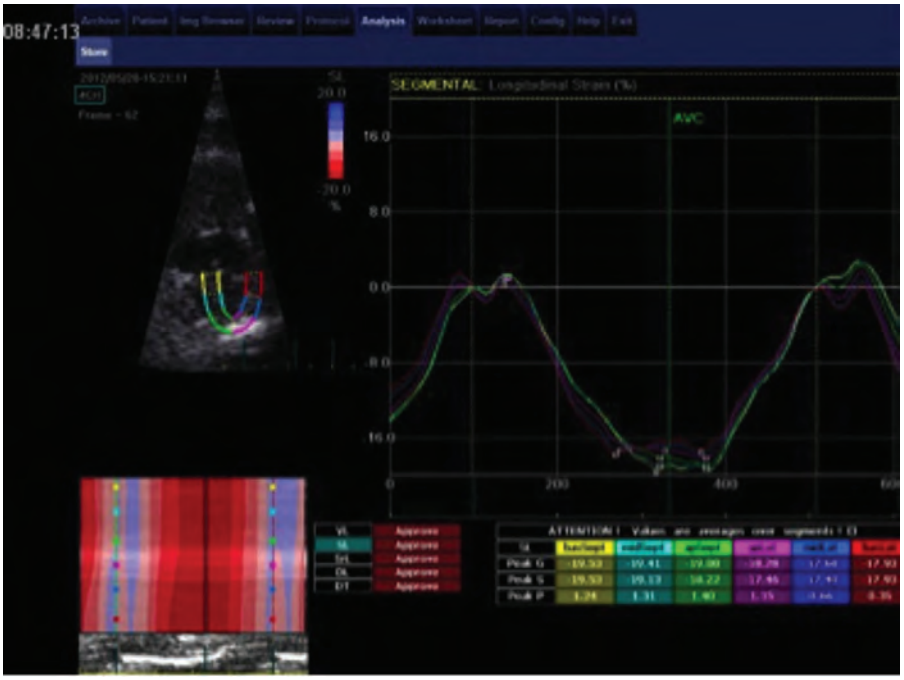
Fetal cardiovascular pathology

Fetal structural heart disease

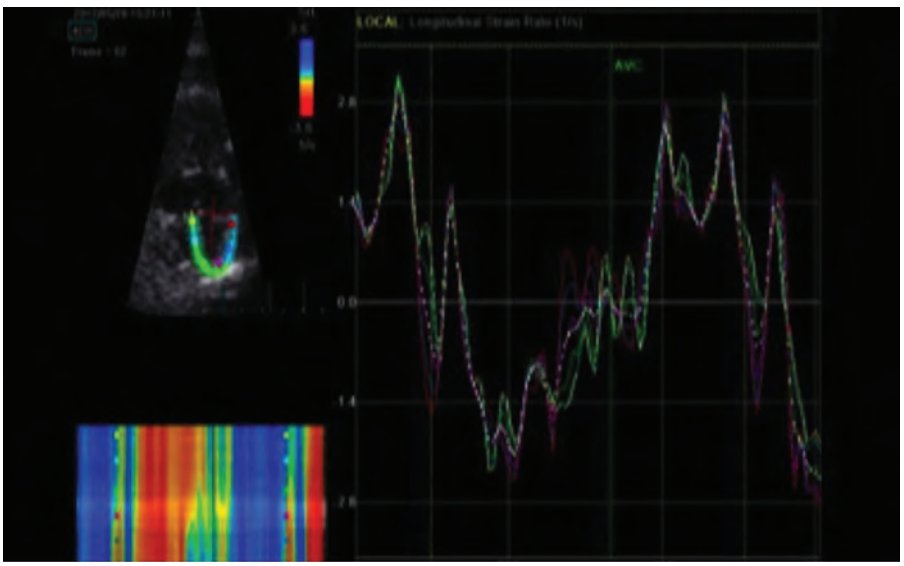
Definition of the segmental anatomy beginning with visceral and atrial situs, the atrioventricular and ventricular–arterial connections, and aortic and ductal arch position, morphology and flow becomes critically important when there is fetal cardiovascular pathology, particularly of a complex nature. Detailed assessment of cardiac pathology, with consideration of what can and cannot be confirmed, and knowledge of the potential for progression of fetal heart disease is critical for accurate counseling of an affected pregnancy and for perinatal management planning.

The cardiovascular pathology most often encountered prenatally tends to represent a more severe spectrum of pathology than is encountered after birth. This is due, at least in part, to referral bias with pathology most recognizable in the 4-chamber view (e.g., hypoplastic left heart syndrome) more often detected at routine obstetric ultrasound [66]. Cardiovascular lesions associated with extracardiac pathology, including aneuploidy are also more often detected [3,66]. A review of the prenatal features of specific forms of CHD are provided in the individual chapters devoted to the lesions. Additional examples of an approach to the evaluation of selected structural CHD in utero are provided in Figures 44.14 to 44.18.

Fetal echocardiography permits the diagnosis of all forms of CHD before birth [67–69].The accuracy of fetal diagnosis in the context of more complex structural heart disease has been best demonstrated in heterotaxy syndrome (Figure 44.14) where



(a)



(b)

Figure 44.11 Color tissue Doppler with post-acquisition processing in a 30-week fetus. Values for **(a)** strain and **(b)** strain rate can be obtained and compared to published normal values.

associated cardiac pathology includes abnormalities of visceral and atrial situs, systemic and pulmonary venous connections, A–V and V–A connections, abnormalities of the AV valves and outflows, abnormalities of the arches and even abnormalities of rhythm. In a large, single-center series of fetal heterotaxy, Taketazu et al. [69] demonstrated, at least in more recent years, that the majority of the cardiac pathology when compared to observations at autopsy or postnatal echocardiography was accurately defined (Table 44.3). There are some limitations, however, in fetal echocardiography, and the following features may still be missed or underappreciated: small to moderate-sized ventricular and atrial septal defects, minor valve abnormalities, complex apical muscular defects, partial anomalous pulmonary veins, coronary anomalies and cardiac lesions that evolve after birth.

Although most CHD is present after 5–7 weeks of gestation, there are many ways in which structural heart disease can evolve in utero as listed in Box 44.1 [70]. This is at least in part as a consequence of the unique features of the fetal circulation which

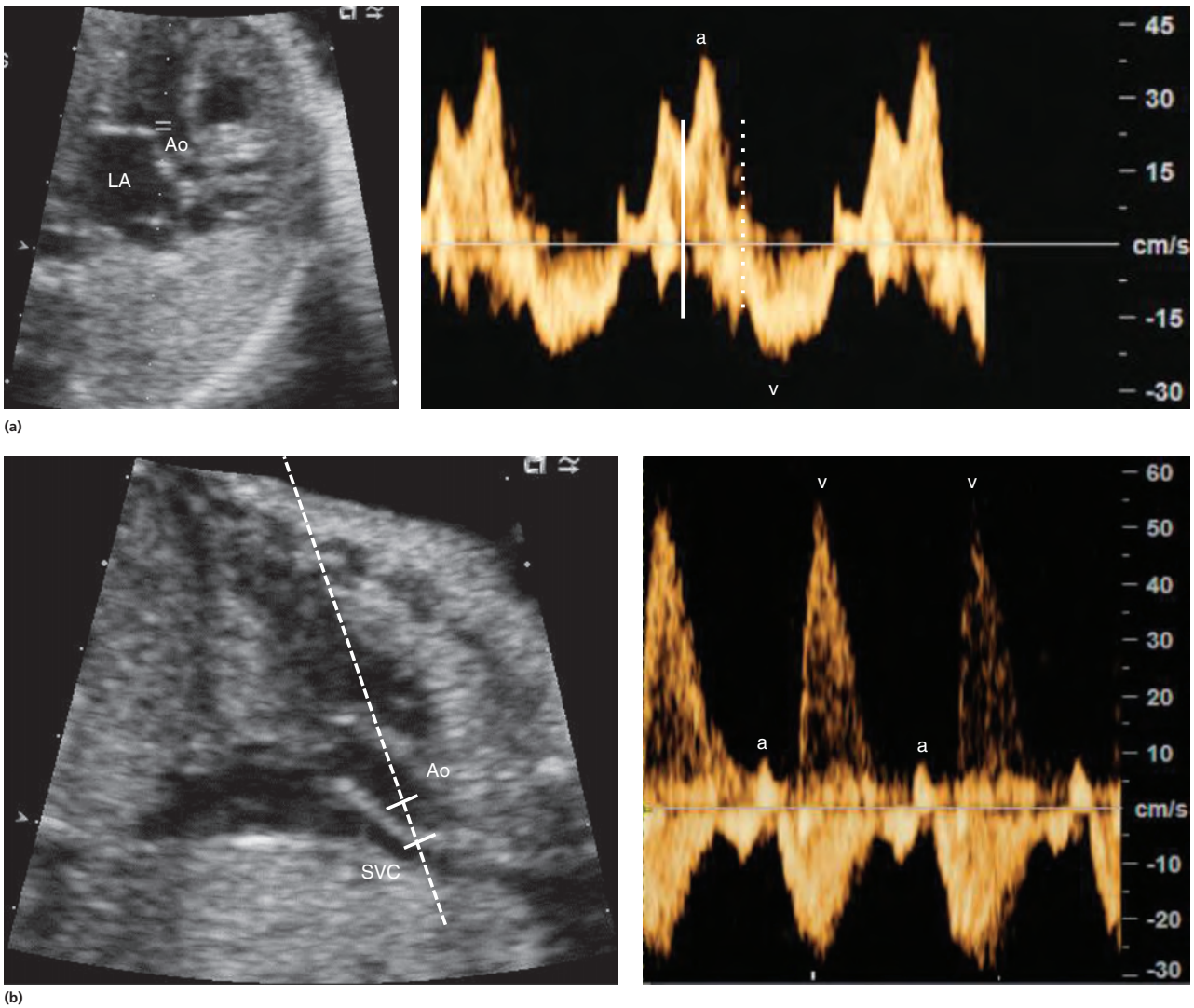


Figure 44.12 Rhythm assessment using simultaneous **(a)** left ventricular inflow and outflow, and **(b)** superior vena caval and ascending aortic pulsed Doppler interrogation. Doppler atrioventricular (A–V) intervals provide a rough estimate of the P–R interval. a, atrial systole; v, ventricular systole. Ao, aorta; LA, left atrium; SVC, superior vena cava. In **(a)** solid line denotes start of "a" wave and dotted line denotes start of "v" wave.

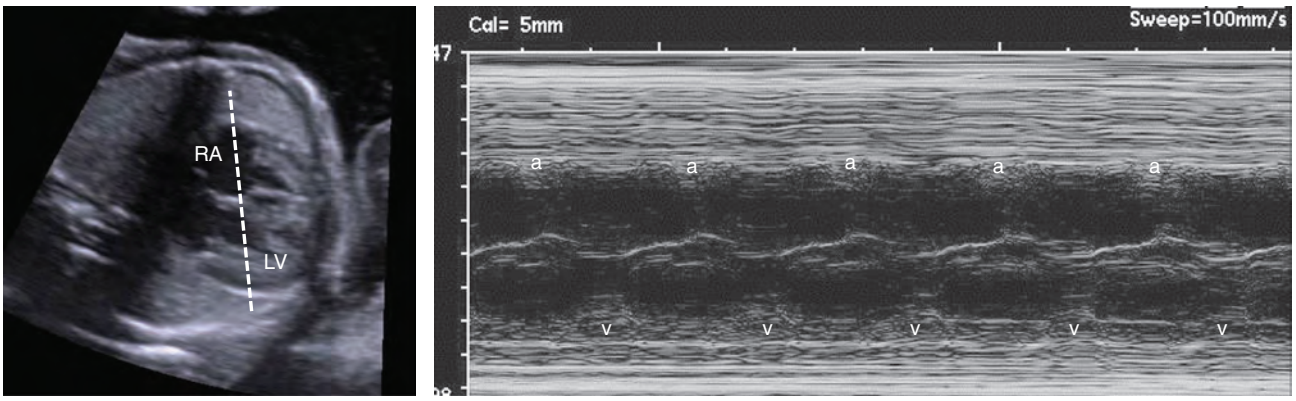


Figure 44.13 Fetal rhythm assessment using M-mode echocardiography. The M-mode cursor (dotted line) is directed through the right atrium and left ventricle to obtain the tracing. RA, right atrium; LV, left ventricle; a, atrial contraction; v, ventricular contraction.

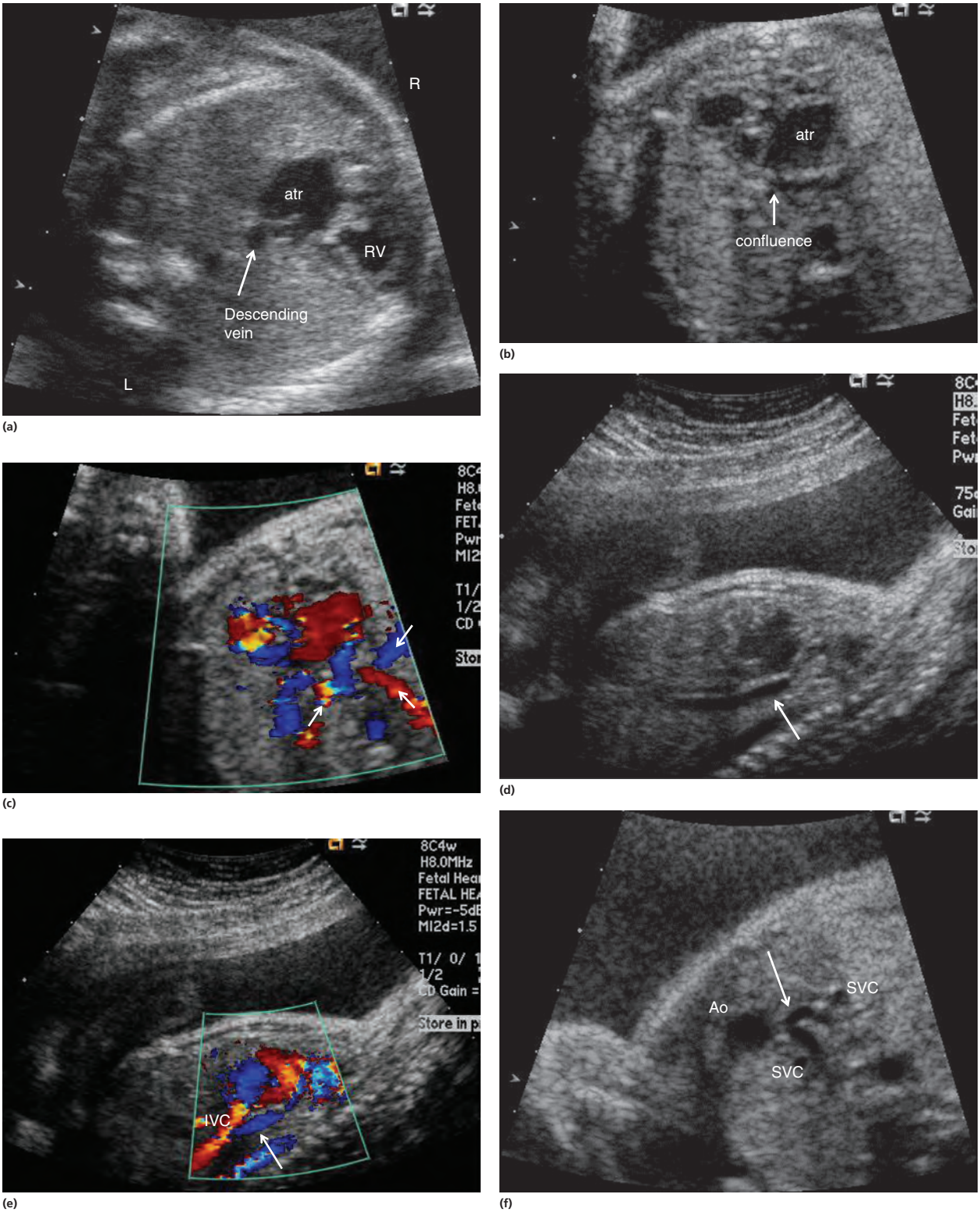


Figure 44.14 Fetal echocardiogram in a 27-week fetus with right atrial isomerism/asplenia syndrome – segmental anatomy {A,D,D}. **(a)** Four-chamber image demonstrating levocardia, an unbalanced atrioventricular (AV) septal defect and dominant D-looped right ventricle. The descending vertical vein which connects with all four pulmonary veins is seen immediately behind the common atrium. **(b)** The pulmonary vein confluence is seen coursing behind the posterior aspect of the atrium, and **(c)** color Doppler confirms pulmonary venous flow (arrows). **(d,e)** The pulmonary vein confluence joins a descending vein that descends through the diaphragm to join the portal venous system (arrow). **(f)** The "3-vessel view" demonstrating bilateral superior vena cava, a large anterior aorta and pulmonary atresia (branch pulmonary arteries indicated by arrow); the latter is confirmed by retrograde ductus arteriosus flow. Ao, aorta; atr, atrium; IVC, inferior vena cava; SVC, superior vena cava; L, left; R, right.

permits a redistribution of blood flow. There may be progressive atrioventricular or semilunar valve obstruction or insufficiency, abnormal growth of an AV valve, ventricle, semilunar valve, great artery and arch, abnormal growth of the branch pulmonary arteries, diminution in size or closure of a ventricular septal defect, foramen ovale restriction, ductus arteriosus constriction or aneurysm formation, tumor enlargement or regression, evolution of arrhythmias and the development of congestive heart failure. The potential for progression should prompt serial evaluation of most pregnancies with fetal CHD.

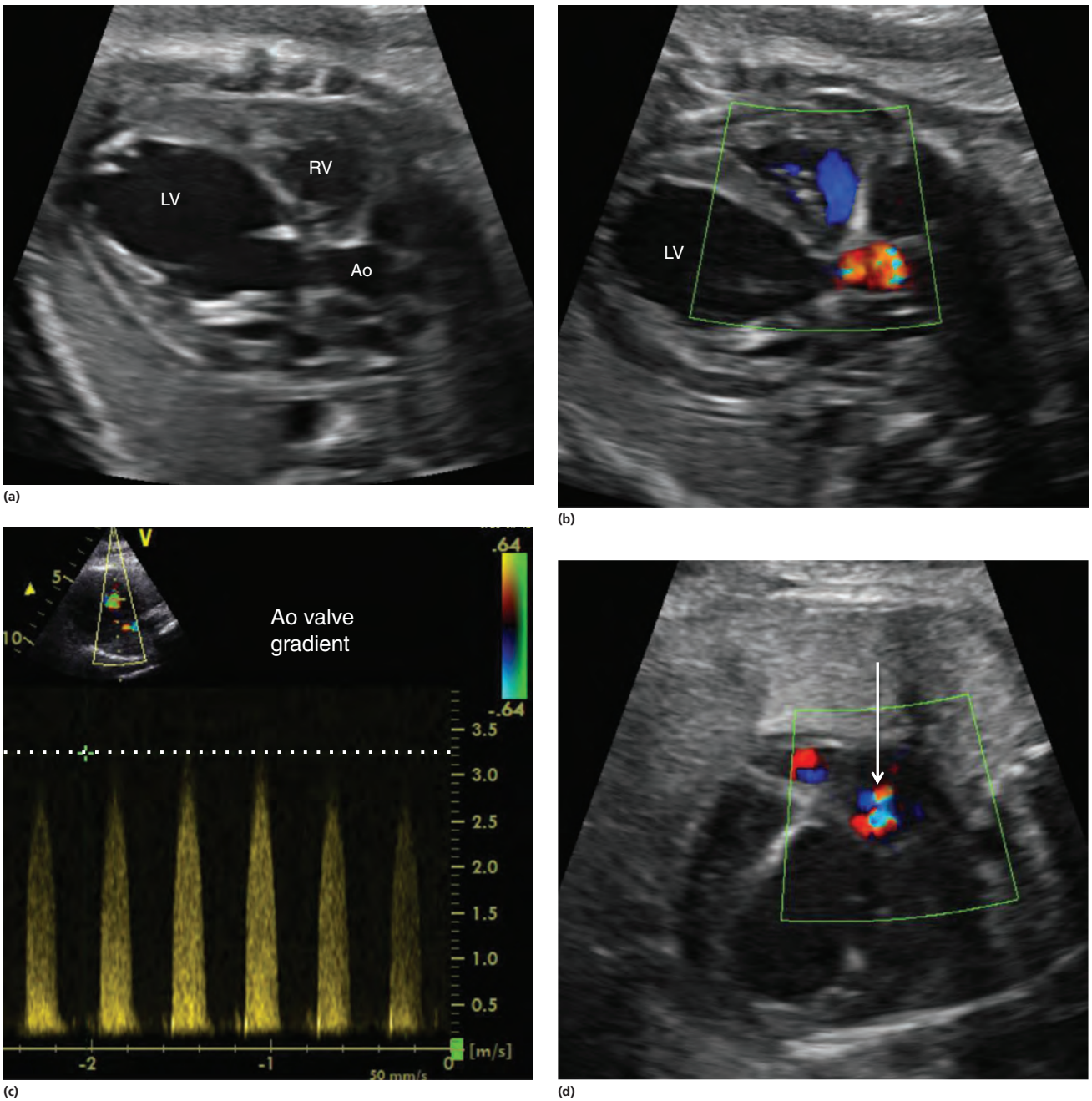
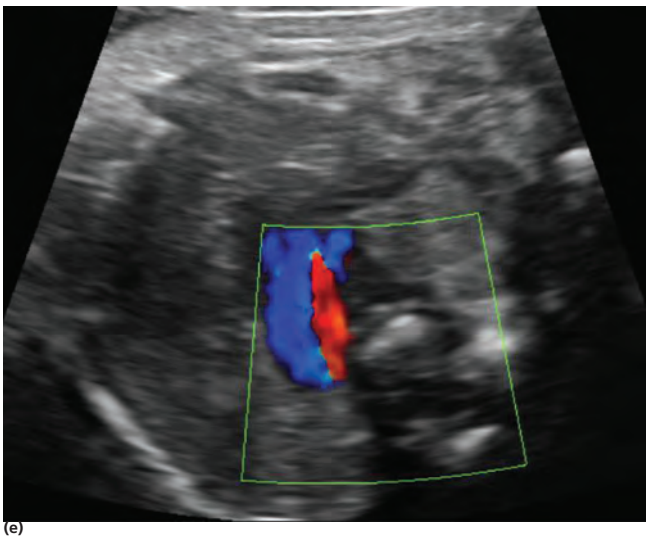


Figure 44.15 Critical aortic stenosis at 32 weeks' gestation. **(a)** Four-chamber view with dilated left ventricle and early endocardial fibroelastosis affecting the left ventricular apex and papillary muscles predominately. **(b,c)** Forward flow across the stenotic aortic valve (red) with significantly increased flow velocity. Peak instantaneous gradient approximately 44 mmHg. **(d)** Mild mitral regurgitation (arrow), the latter of which can be used to estimate and track changes in left ventricular systolic pressure. **(e)** Three-vessel arch view showing retrograde flow in the aortic arch (red) and antegrade flow in the ductal arch (blue) in keeping with critical aortic obstruction. Ao, aorta; LV, left ventricle; RV, right ventricle.



(e)

Figure 44.15 (Continued)

Box 44.1 Mechanisms of evolution of fetal heart disease

- Development/progression of ventricular inflow, outflow and arch obstruction [71–80]
- Development/progression of structural hypoplasia [71–74, 76,81–85]
- Development/progression of valvar regurgitation [75]
- Development/progression of dysrhythmia [69,75,86–90]
- Development of foramen ovale restriction [91,92]
- Diminution and closure of ventricular septal defect [93]
- Development of ductus arteriosus aneurysm or spontaneous constriction [94,95]
- Development of primary myocardial disease [41,96–99]
- Development of congestive heart failure [100–104]
- Development of, progression or regression of cardiac tumors [105–107]

Left and right heart obstructive lesions are among those of greatest interest given their risk of progression. More subtle abnormalities may be missed. Mild and moderate obstruction of either atrioventricular or semilunar valves may be associated with subtle ventricular or great artery size discrepancy. If mild or moderate semilunar valve obstruction is present early in gestation, there may be progressive obstruction that leads to more severe disease at birth. More severe obstruction of either semilunar valve may result in progressive hypertrophy of the ipsilateral ventricle and the development of AV valve insufficiency with increasing continuous-wave (CW) Doppler-demonstrated flow velocities suggesting increasing ventricular systolic pressures [71–74]. Eventually, when there is more critical obstruction, retrograde ductal or aortic arch flow confirms the diagnosis and need for prostaglandin therapy after delivery [108]. If severe obstruction occurs early in gestation, eventual failure of the ipsilateral ventricle or evolution of endocardial fibroelastosis observed in critical aortic valve stenosis may result in a redistribution of flow towards the contralateral heart as a consequence of the foramen ovale (Figure 44.15; Video 44.6). As long as the contralateral ventricle can sustain the equivalent of a biventricular output, the fetus can thrive but there is typically progressive hypoplasia of the ipsilateral ventricle, AV valve and great artery [71–74].

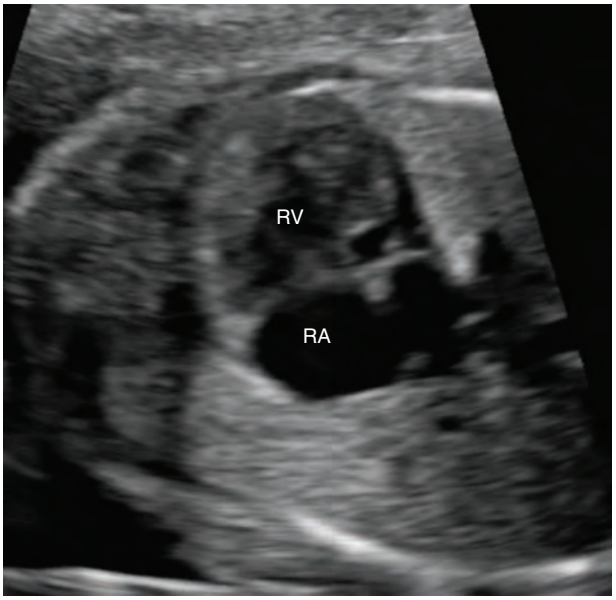
In severe left heart obstruction, progressive restriction of the foramen ovale may lead to severe left atrial hypertension, cyanosis and pulmonary edema at birth. Foramen ovale restriction may be suggested by the presence of a thickened atrial septum, a small atrial septal communication and turbulent flow through the atrial septum. It can be confirmed through the use of pulmonary venous Dopplers [109] (Figure 44.16). As the left atrial pressure increases, increasing flow reversal in atrial systole and decreasing early diastolic forward flow occurs. Ultimately, only to and fro flow may be seen with little net forward flow which places the infant at high risk for severe cyanosis at birth and ultimately very poor outcomes [109].

The evolution of more severe secondary pathology including hypoplastic left or right ventricles [78–85] in the presence of severe semilunar valve obstruction and restriction of the foramen ovale has prompted the development of invasive procedures to prenatally ameliorate the obstruction. To date, balloon aortic and pulmonary valvuloplasty [110–112] and atrial septoplasty and stent placement have been described with moderate success [113].

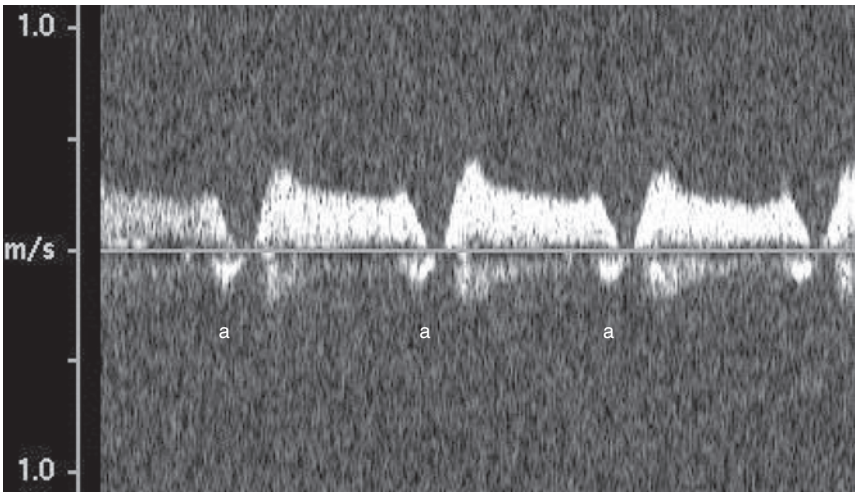
Some cardiovascular lesions are identified uniquely or more frequently before birth. Cardiovascular disease incompatible with the fetal circulation or associated with lethal extracardiac pathology which lead to fetal demise may be encountered. Ventricular aneurysms or diverticulum may be more common in prenatal series partly because more severe pathology is not tolerated by the fetal circulation [114–116] (Figure 44.17). Less severe lesions including some aneurysms and diverticuli as well as rhabdomyoma identified through imaging may not be associated with symptoms after birth. There are abnormalities of the fetal circulation, including restriction of the foramen ovale [91], ductus arteriosus constriction [94,117] and agenesis of the ductus venosus [41] which can cause cardiovascular compromise, for which the treatment is often delivery at a viable age.

Fetal heart failure

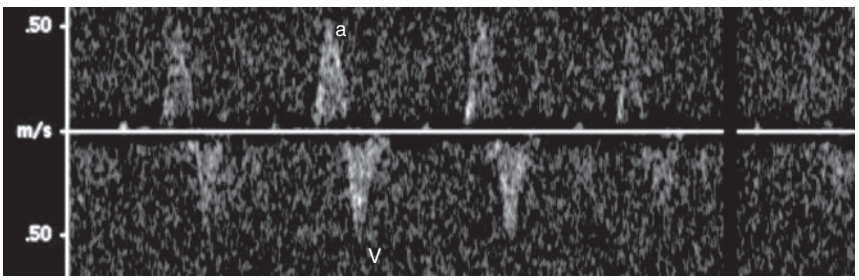
Umbilical venous return, which provides oxygenated blood from the placenta directed largely through the ductus venosus and across the foramen ovale, requires very low downstream systemic venous and atrial and ventricular filling pressures. Any pathology that influences central venous pressures can adversely affect the fetal circulation and lead to the evolution of hydrops, hypoxemia and demise. The fetal circulation requires at least one patent and competent AV and semilunar valve, a normally filling and ejecting ventricle and a well-functioning placenta. Many conditions can lead to the evolution of fetal heart failure which manifests in its worst state as hydrops with pleural and



(a)



(b)



(c)

Figure 44.16 (**a**) Four-chamber image obtained in a fetus with hypoplastic left heart syndrome. Pulmonary venous flow patterns are useful in such conditions to assess the severity of left atrial hypertension related to restrictive foramen ovale. Most affected fetuses have the pulmonary vein Doppler profile shown in **(b)** with low-velocity retrograde flow in atrial systole "a." **(c)** With severe left atrial hypertension, there is loss of forward flow in early diastole and reduced flow in ventricular systole (V) with increased retrograde flow in atrial systole. The fetus with the pulmonary vein flow depicted in (c) had a maximum P_aO_2 of 17 mmHg after birth. RA, right atrium; RV, right ventricle.

pericardial effusions, ascites, and skin edema. Hydrops occurs as a consequence of primary myocardial or structural heart disease that influences the function of both ventricles, fetal bradyarrhythmias or tachyarrhythmias that affect ventricular filling or ejection, and extracardiac abnormalities that affect the fetal cardiac output (Table 44.4). In the presence of primary myocardial disease (Figure 44.18; Video 44.7), systolic and diastolic function may be affected. The latter of which is most associated with the evolution of fetal heart failure [42]. PW Doppler evaluation of the fetal ventricular inflows, IVC, ductus venosus and umbilical venous flow patterns can help define the severity of altered central venous pressures and likelihood of evolution

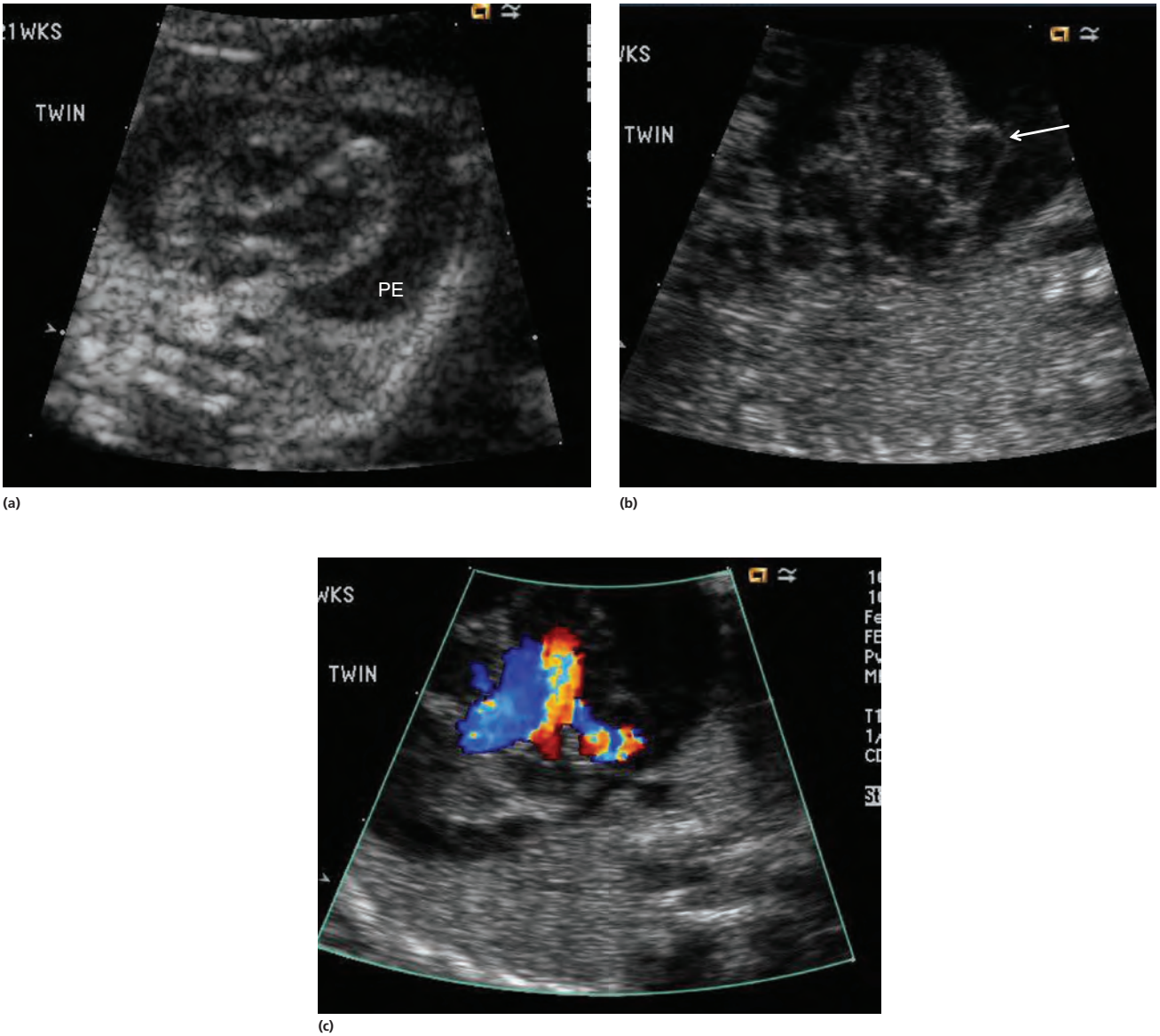


Figure 44.17 Echocardiogram findings in a 21-week fetus with a left ventricular (LV) free wall diverticulum. **(a)** Associated large pericardial effusion (PE) without other signs of hydrops. **(b)** Two-dimensional imaging of a thin-walled protrusion from the LV free wall that communicates through a narrow neck with the LV cavity (arrow); **(c)** color Doppler of same feature.

of fetal hydrops (Figure 44.18). Abnormalities of systemic venous Dopplers have been used to distinguish cardiovascular from noncardiovascular etiologies of hydrops.

An example of a structural heart defect that is among those least tolerated by the fetal circulation is that of severe tricuspid valve insufficiency (Figure 44.19; Video 44.8). In this condition, the right atrium and right ventricle become progressively dilated which further worsens the severity of tricuspid insufficiency. Eventually, the right ventricle is unable to generate sufficient pressure to open the pulmonary valve in systole. If the pulmonary valve is patent there may be pulmonary insufficiency which only adds to the right ventricular volume load. While initially there may be a redistribution of flow towards the left heart through the foramen ovale with the left ventricle sustaining the equivalent of a biventricular output, the right ventricular loading ultimately influences left heart function, particularly LV filling [118]. This can lead to increasing central venous pressures and eventually to hydrops. In addition, altered left ventricular filling and consequent reduced output [119], likely impact the ability of the fetus to respond to acute physiologic changes resulting in increased risk of sudden demise, particularly in the early third trimester. Associated supraventricular tachyarrhythmias compromise the fetal heart further by reducing the filling time of the left ventricle. Other volume loading conditions are similarly less tolerated by the fetal circulation including tetralogy of Fallot with absent pulmonary valve syndrome [120].

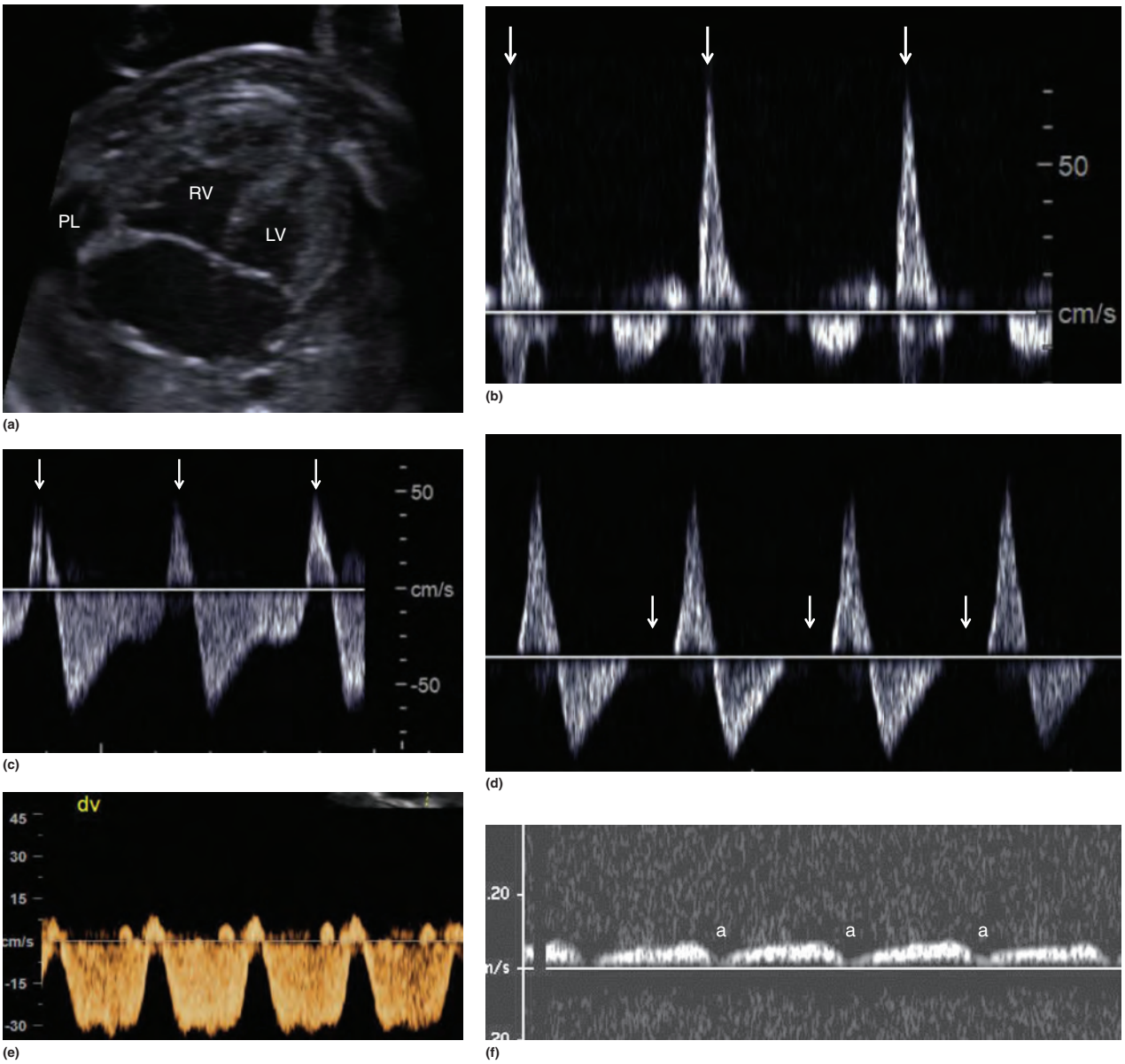


Figure 44.18 Fetal cardiomyopathy at 22 weeks. **(a)** Significant biventricular hypertrophy with severely depressed systolic and diastolic function was observed. Right-sided pleural effusion (PL) was present as well as ascites. Pulsed Doppler flow patterns with increased atrial and ventricular filling pressures and high central venous pressures. **(b)** Uniphasic (atrial systole), short-duration ventricular inflow pattern (arrows) seen in severe fetal myocardial disease. **(c)** Inferior vena caval flow (IVC) with increased A-wave reversal (arrows). **(d)** With higher atrial and ventricular filling and central venous pressures, there is loss of flow in early ventricular diastole (arrows). **(e)** In the ductus venosus (dv) there is cessation of forward flow in atrial systole and eventual A-wave reversal. **(f)** Eventually, umbilical venous (UV) pulsations develop with cessation of flow in atrial systole (a).

Fetal echocardiography, with opportunities to understand the etiology and pathophysiology of myocardial dysfunction, has played an increasingly more important role in the evaluation and noninvasive and invasive management of many fetal conditions that alter cardiac function. For instance, fetal echocardiography has been increasingly used in the care of monochorionic twin pregnancies complicated by twin–twin transfusion syndrome [121–123], and in the evaluation and treatment of lesions associated with high cardiac output states.

Evaluation of fetal arrhythmias

More than 90% of pregnancies referred for fetal arrhythmia are either found to have no arrhythmia at the time of fetal echocardiography or premature atrial beats [124]. Rarely, more important tachyarrhythmias or bradyarrhythmias may be identified that have the potential to lead to cardiovascular compromise and hydrops. Table 44.5 summarizes the fetal arrhythmias detected before birth and the fetal echocardiographic features. Figure 44.20 provides an example of Doppler and M-mode findings in

Table 44.3 Accuracy of specific structural pathology at fetal heterotaxy diagnosis and its evolution with study era [69]

Variable	Total ($n = 45$)	1991–1996 ($n = 18$)	1997–2002 ($n = 27$)	p
IVC connection in RAI*	5/9 (56%)	1/2 (50%)	4/7 (62%)	>0.99
Interrupted IVC in LAI	30/32 (94%)	11/12 (91%)	19/20 (95%)	>0.99
SVC anatomy†	37/43 (86%)	12/17 (71%)	25/26 (96%)	0.03
Intracardiac lesions	42/45 (93%)	15/18 (83%)	27/27 (100%)	0.06
Ventriculo-arterial connection	42/45 (93%)	16/18 (89%)	25/27 (93%)	>0.99
Outflow obstruction‡	39/44 (89%)	16/17 (94%)	23/27 (85%)	0.63
Pulmonary vein connection§	30/39 (77%)	4/12 (33%)	26/27 (93%)	<0.0001
Hepatic vein connection¶	20/31 (65%)	6/10 (60%)	14/21 (67%)	>0.99
Splenic lesion#	18/24(75%)	5/7 (71%)	13/17 (76%)	>0.99

The numerator/denominator indicates the number of lesions accurately diagnosed before birth/the number of lesions identified after birth or at postmortem. Accurate diagnosis ratio is showed as percent. IVC, inferior vena cava; SVC, superior vena cava (includes bilateral cava, unilateral SVC and left or right SVC to coronary sinus).

*includes inferior vena cava to the left side of the atrium or left-sided atrium, inferior vena cava to the right side of the atrium or right-sided atrium.

†includes isolated right or left superior vena cava to the atrium or coronary sinus or bilateral superior vena cava.

‡aortic, pulmonary or bilateral outflow obstruction.

§normal pulmonary venous connection or totally anomalous connection with details regarding specific location of return.

¶connection of all hepatic veins to the inferior vena cava, separate connection and to which atrium.

#no spleen, single left or right spleen or multi-lobed spleen.

a case of premature atrial beats with AV block. If they occur frequently as in a bigeminal pattern, fetal bradycardia may be the referring diagnosis as a result of either blocked AV conduction with the atrial extrasystoles or lack of detection of the lower stroke volumes with extrasystoles by clinically applied Doppler devices.

Tachyarrhythmias encountered before birth include supraventricular tachycardia (SVT), atrial flutter, junctional ectopic tachycardia, and ventricular tachycardia. Accurate delineation of the mechanism of the tachyarrhythmia is important in the management of affected pregnancies and counseling of the parents [61,64]. The relationship of the atrial and ventricular contractions, mode of onset and offset, and the atrial and ventricular rates all provide clues to the diagnosis. The most common form of fetal tachycardia is that of SVT in which there is 1:1 A–V contraction. SVT can be divided into short and long V–A types. With simultaneous Doppler interrogation of superior vena cava and ascending aortic flow, Fouron et al. showed that the relationship of the atrial and ventricular contractions can be demonstrated with measurement of A–V and V–A time intervals [64]. When the A–V interval is longer than the V–A interval, a short V–A SVT is present (Figure 44.21); whereas, a short A–V interval suggests the diagnosis of a long VA tachycardia. As is true after birth, short V–A SVTs include re-entrant tachycardias associated with an accessory AV pathway. Long V–A tachycardias include sinus tachycardia, ectopic atrial tachycardia and permanent junctional reciprocating tachycardia. In atrial flutter, the second most common fetal tachyarrhythmia, atrial rates may range from 350–500 bpm with usually variable AV conduction (Figure 44.22). In both ventricular and junctional ectopic tachycardia, rapid ventricular rates often with lack of V–A synchrony suggest these diagnoses. In the absence of fetal ECG or fetal magnetocardiography, however, delineation between these two arrhythmias can be difficult. In any arrhythmia, exclusion of important structural and primary functional cardiac abnormalities is important for counseling regarding prognosis, and planning treatment strategies and perinatal management.

Fetal bradycardia is diagnosed when the ventricular rates are <110 bpm after 16 weeks. The most common cause is sinus bradycardia which may occur in a healthy fetus intermittently during an exam. Most fetuses will have rapid return of a normal heart rate. Persistent fetal sinus bradycardia, however, could suggest more diffuse systemic disease and fetal distress. Persistent fetal bradycardia with ventricular rates of 35–120 bpm may also be caused by second- or third-degree AV block (AVB). AVB may be observed in the presence of structural heart disease (e.g., left atrial isomerism or polysplenia syndrome and lesions associated with L-ventricular looping) [86,87] or in isolation, which is largely the influence of maternal autoantibodies anti-Ro and anti-La [86,88]. With the development of normal AV time intervals in fetuses from 17 weeks to term using both PW and tissue Doppler techniques [125,126], even first-degree AV block can be diagnosed prenatally. Figure 44.23 demonstrates Doppler and M-mode examples of fetal AVB.

Evolving and future directions in fetal echocardiography

While there has been significant progress in fetal echocardiography over the past two to three decades, the future holds even more promise. Technological advances and ongoing experience will continue to enhance our ability to evaluate all forms of fetal heart disease, using a variety of techniques at increasingly earlier gestations.

Table 44.4 Cardiac causes of fetal heart failure

Primary cardiac causes
Myocardial disease
Intrinsic
Cardiomyopathies
Autosomal recessive
Autosomal dominant
X-linked
Mitochondrial
Aneuploidy
Extrinsic
Infectious – myocarditis
Maternal anti-Ro/anti-La mediated
Primary structural heart disease
Severe AV valve insufficiency
Ebstein's anomaly of the tricuspid valve
Tricuspid valve dysplasias
Severe aortic stenosis
Severe pulmonary stenosis
Atrioventricular septal defect
Severe semilunar valve insufficiency
Truncus arteriosus
Tetralogy of Fallot/absent pulmonary valve syndrome
Inflow obstruction
Severe right heart obstruction with foramen ovale restriction
Cardiac tumors
Outflow obstruction
Truncus arteriosus with truncal valve obstruction
Severe pulmonary outflow obstruction*
Severe aortic outflow obstruction*
Ductus arteriosus constriction
Cardiac tumors
Other
Ventricular aneurysm with biventricular dysfunction
Arrhythmias
Tachyarrhythmias
Supraventricular tachycardia (incessant, <32 weeks, structural disease)
atrial flutter
AV accessory pathway
long VA tachycardias
junctional ectopic tachycardia
Ventricular tachycardia
Bradycardias
Fetal AV block (structural heart disease, myocardial dysfunction)
Secondary causes
High-output states
Anemia
Acute twin–twin or fetal–maternal hemorrhage
Arteriovenous malformations
Agenesis of the ductus venosus
Acardiac twin gestation
High afterload
Twin–twin transfusion syndrome
Placental insufficiency
Reduced preload
Extracardiac/intrathoracic mass
Congenital cystic adenomatous malformation
Diaphragmatic hernia
Cystic hygroma
Pericardial effusion – teratoma

*Usually with severe atrioventricular valve insufficiency or dysfunction of the contralateral ventricle (at times from compression).

First trimester fetal echocardiography

Newer high frequency curvilinear probes, along with endovaginal ultrasound probes, are allowing for high-quality fetal echocardiography at earlier gestations. Endovaginal ultrasound transducers have been used in first trimester fetal imaging since the mid-to-late 1980s; however, very few centers have documented their use in late first and early second trimester fetal echocardiography[6–12,127] (Figures 44.24 and 44.25; Video 44.9). This has been in part due to the reluctance of fetal and pediatric cardiologists to use the technology. However, even transabdominal imaging of the fetal heart from 10–11 weeks has been shown to be successful in certain patients [6,7,116]. Color Doppler has contributed significantly to the definition of systemic venous and great artery anatomy as well as patency of ventricular inflows and outflows prior to 13 weeks [6,7,11,12].

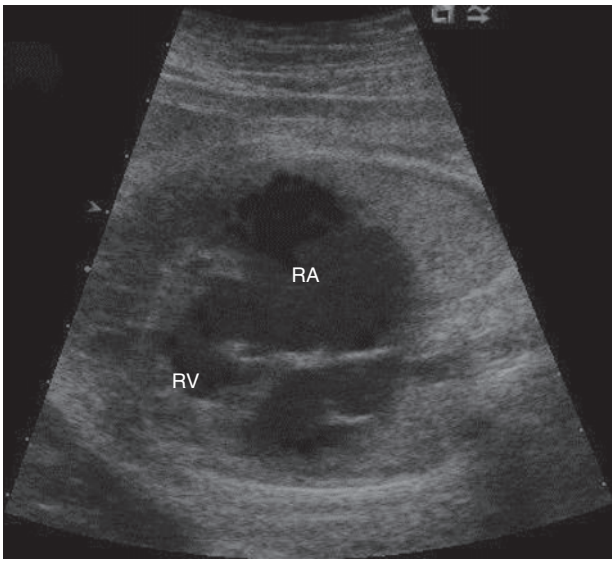
Earlier diagnoses, while a natural evolution of fetal echocardiography, are not without important limitations. Although fetal cardiac structure and function can be defined after 12 weeks' gestation, the diminutive size of the fetal heart prior to 12 weeks often creates difficulty in demonstrating all cardiac structures. However, with the introduction of high-frequency linear and curvilinear probes (up to 9 Hz) combined with high-frequency endovaginal probes (up to12 Hz), imaging of the fetal heart from 8 weeks GA has become possible in some patients [7]. Factors that influence the quality of imaging prior to 12 weeks include fetal position (depth from either the transabdominal or transvaginal probe) as well as maternal factors such as increased BMI and poor tissue characteristics. To gain satisfactory images, transvaginal imaging is currently needed in the majority prior to the 12th week gestation age [7–9].

Visualization of a 4-chambered heart as well as the outflow tracts (with the aid of color) is possible in more than 50% of patients from 8–11 weeks and in nearly all by 12 weeks [6, 7,10,128]. While more significant cardiovascular pathology may be detected at these earlier gestational ages, the details obtained at 18–22 weeks are not as consistently possible [128]. As such, more subtle pathology and associated cardiovascular lesions can be missed [10,128]. Still, the details in diagnosis are not unlike those experienced in the earlier era of fetal echocardiography.

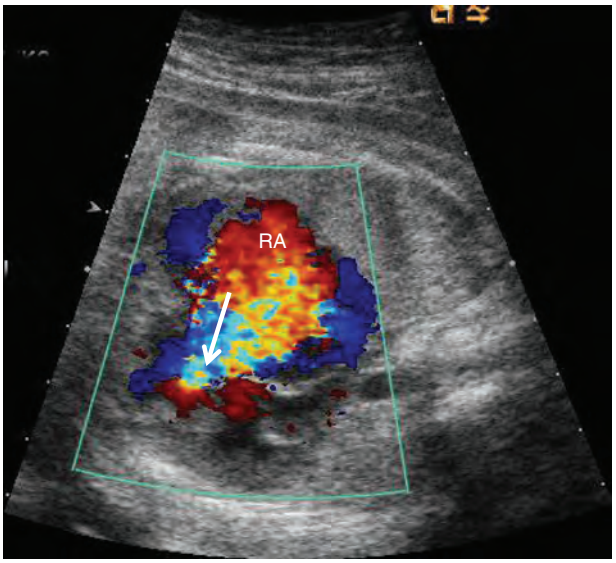
In the future, referrals for first trimester echocardiography will only continue to increase as screening methods such as nuchal translucency come into widespread use worldwide, and as the genes responsible for the development of a spectrum of cardiovascular pathology are identified. Serial observations from the first and early second trimester will provide further insight into the evolution of fetal cardiovascular disease during this period of very rapid fetal cardiovascular and general somatic growth [129]. Furthermore, first trimester observations of fetal heart function will help us to better understand the role of myocardial function in the viability of pregnancies.

3D and 4D fetal echocardiography

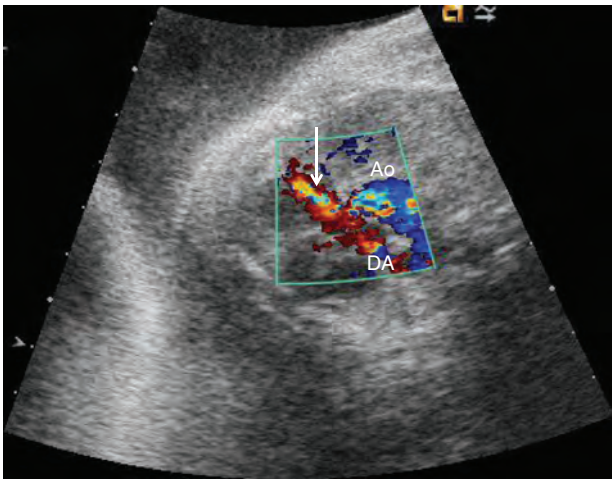
The use of high-resolution 3D and 4D fetal echocardiography is increasingly being used in fetal cardiology practice.



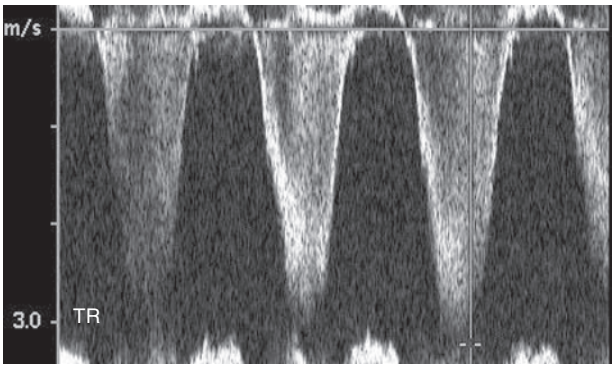
(a)



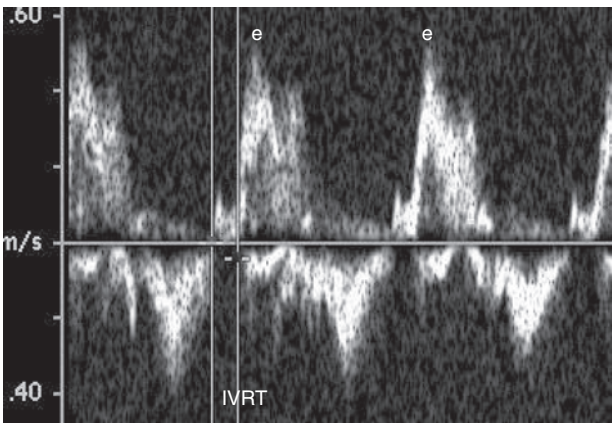
(b)



(c)



(d)



(e)

Figure 44.19 Ebstein anomaly of the tricuspid valve with severe tricuspid regurgitation in a 33-week fetus. **(a)** Significant cardiomegaly in the 4-chamber view. **(b)** Color Doppler confirms the presence of severe tricuspid insufficiency with failure of the leaflets to co-apt in systole (arrow). RA, right atrium. **(c)** Pulmonary regurgitation in systole (arrow), confirming patency of the pulmonary valve with retrograde ductus arteriosus flow. **(d)** Although the right ventricle (RV) cannot eject into the main pulmonary artery, the pressure generated (36 mmHg plus right atrial pressure) is very close to that of normal systemic systolic blood pressure and greater than half the systolic pulmonary pressure of a normal newborn. **(e)** Left ventricular (LV) inflow with dominant E wave (e) and prolonged IVRT. Ao, aorta; DA, ductus arteriosus; RA, right atrium; RV, right ventricle

Table 44.5 Fetal echocardiographic features of fetal arrhythmias

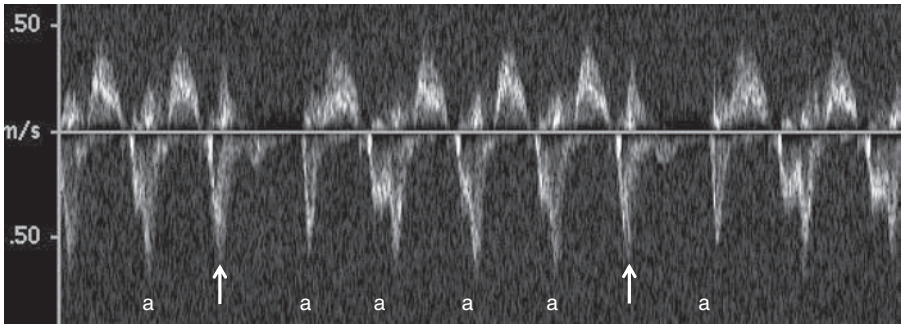
Rhythm	Atrial and ventricular rates	Atrial and ventricular intervals	Onset/offset	Associated lesions
Sinus rhythm	120–160 bpm	Normal A–V relationship	Gradual	Normal
Premature atrial contraction (PAC)	Variable	Short A–A from sinus to PAC but normal A–A interval from PAC to next sinus beat	Acute	Cardiac tumors,atrial dilation, redundant septum primum
Premature ventricular contraction(PVC)	Variable	Short V–V from preceding sinus beat to PVC	Acute	Cardiac tumors,myocardial disease, aneurysms, LAI
Sinus tachycardia	A and V rates 170–210 bpm	Long V–A relative to A–V	Gradual with beat–beat variability	Maternal thyrotoxicosis
Ectopic atrial tachycardia	A and V rates170–240 bpm	Long V–A relative to A–V	Gradual with beat–beat variability	Cardiac tumors, atrial dilation
PJRT	A and V rates 220–230 bpm	Long V–A relative to A–V	Typically incessant	
SVT with VA accessory pathway	A and V rates 220–300 bpm	Short V–A relative to A–V	Acute onset without beat–beat variability	Ebstein's anomaly
Atrial flutter	A-rates 300–500 bpm and variable V-rates	Often 2:1 or 3:1 A-V conduction	Acute onset without atrial beat–beat variability	Cardiac tumors, atrial dilation
Junctional tachycardia	V-rates 180–270 bpm	Usual V–A dissociation	Gradual or acute	
Ventricular tachycardia	V-rates 150–300 bpm	Usually A–V dissociation, rarely V–A conduction	Usually acute	Cardiac tumors, maternal autoantibodies anti-Ro and anti-La
Sinus bradycardia	A and V rates <110 bpm	Normal A–V relationship	Gradual	Fetal distress, umbilical cord compression
Second-degree AVB	A-rates 120–160 bpm V-rates 60–80 bpm	A–V synchrony present with conducted beats; often 2:1 A–V ratio	Intermittent or incessant	LAI, L-ventricular looping, maternal autoantibodies anti-Ro and anti-La, fetal cardiomyopathy with EFE
Third-degree AVB	A-rates 120–160 bpm V-rates 30–120 bpm	A–V dissociation	Usually incessant	LAI, L-ventricular looping, maternal autoantibodies anti-Ro and anti-La, fetal cardiomyopathy with EFE

A, atrial; AVB, atrioventricular block; bpm; beats per minute; EFE, endocardiofibroelastosis; LAI, left atrial isomerism or polysplenia syndrome; PJRT, permanent junctional reciprocating tachycardia; V, ventricular.

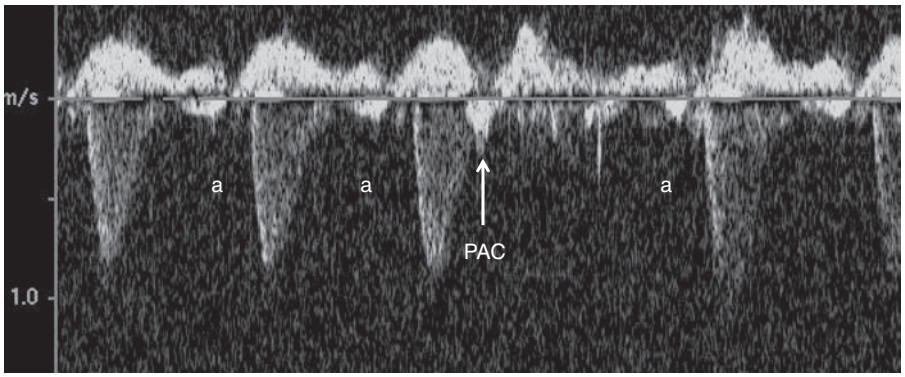
Three-dimensional fetal echocardiography refers to the acquisition of a 3D block of data whilst 4D adds the element of time and hence motion. Like 3D echocardiography postnatally, it is essential to have a high-quality 2D image from which 3D and 4D data are acquired. With the advent of specific 3D probes for obstetric imaging from multiple vendors, the process of acquiring a complete volume data set has become somewhat automated and possible with minimal additional training. Once a complete data volume has been acquired, extensive offline manipulation and analysis is possible.

Spatiotemporal image correlation (STIC) imaging is a well-established method of 3D/4D image acquisition and processing [33,130]. Mostly through the use of specialized 3D obstetric probes, an automated volume is acquired by the transducer making a slow sweep of the fetal heart. Both the angle that is swept and the time of acquisition can be modified to enhance the image. High B-mode frame rates, up to 150 FPS, are achieved with this method (Falkensammer GE Healthcare 2005). Once the volume data set is collected the cardiac motion is instantly analyzed and the images are arranged to represent one cardiac cycle. The data can be reviewed or manipulated on the machine or alternatively offline. The data set can also be obtained with the addition of either standard color Doppler or power Doppler. Once collected, the 3D/4D data set can be extensively manipulated offline and can aid in the detection and assessment of fetal heart disease [130–132].

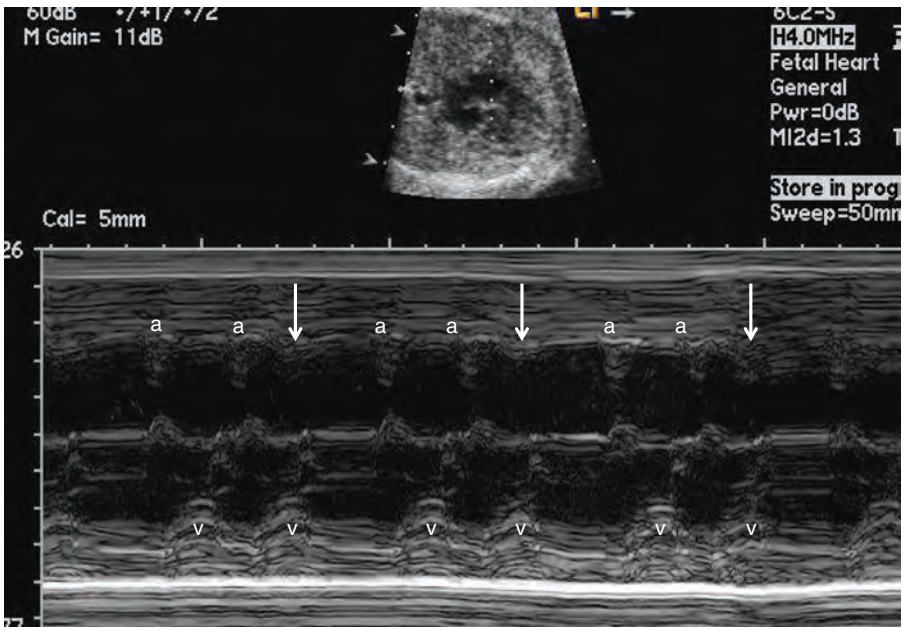
There are three commonly used modes to review the acquired 3/4D volume [33,132]. Sectional or multiplane reconstruction (MPR) allows the data set to be manipulated in three orthogonal planes (Figure 44.26). This allows imaging planes not traditionally possible with standard imaging to be displayed. Tomographic ultrasound imaging (TUI) displays multiple image slices



(a)



(b)



(c)

Figure 44.20 Premature atrial beats (arrows) with atrioventricular (AV) block demonstrated by **(a)** simultaneous left ventricular (LV) inflow and outflow Doppler; **(b)** superior vena cava–aortic Doppler and **(c)** in a trigeminal pattern by M-mode. a, normal atrial systole; RA, right atrium; v, ventricular systole.

either side of a selected image, somewhat akin to a CT set of images (Figures 44.27 and 44.28; Video 44.10). Any of the three orthogonal planes can be selected to be viewed and a single cardiac cycle can be viewed if 4D data has been obtained. Images incorporating slices starting from the 4-chamber view or sagittal aortic arch are commonly used. Multiple modifications to the image can be made, including altering the orientation in all three planes as well as varying the slice thickness to improve visualization of selected areas. Finally, surface rendering can allow viewing of any slice chosen from the MPR view with added

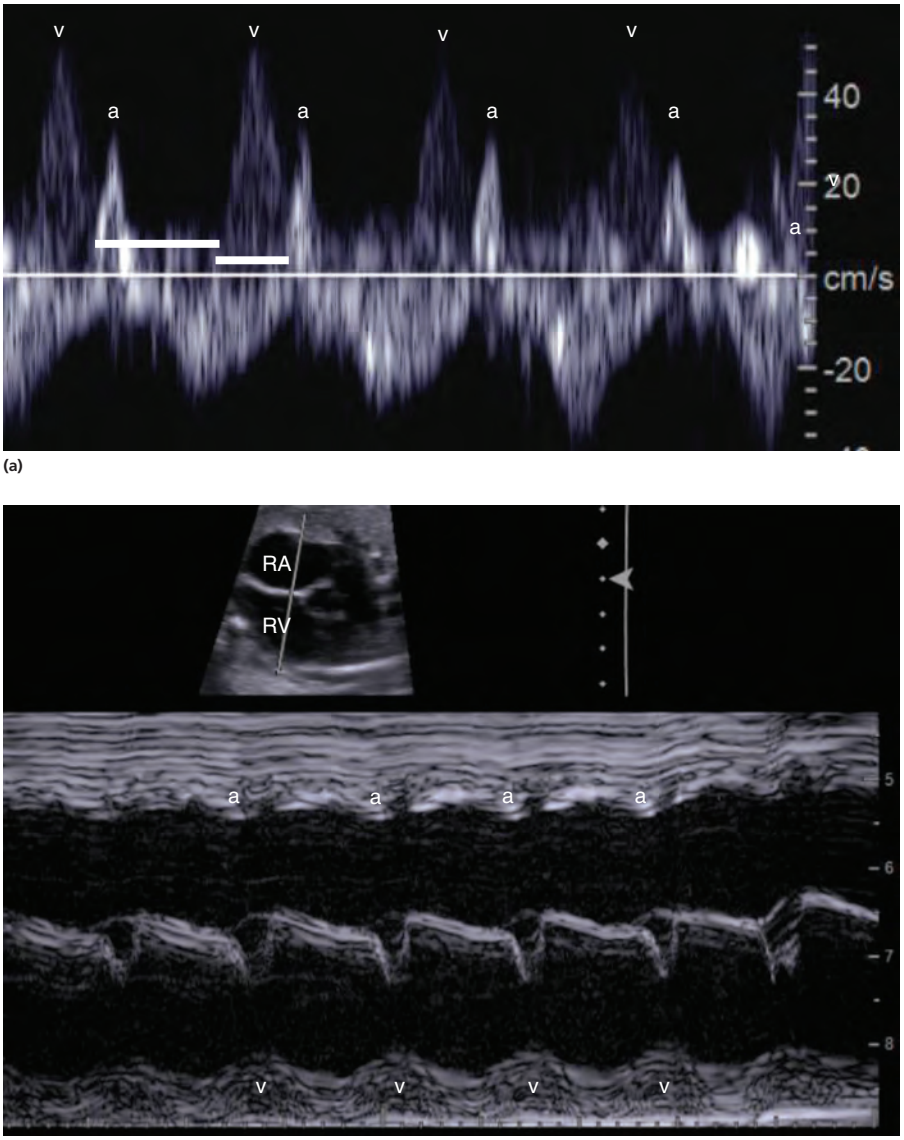


Figure 44.21 Short V–A (ventriculo-atrial) tachyarrhythmia with rate 220 bpm in a 36-week fetus. **(a)** The superior vena cava–aortic Doppler demonstrates a longer A–V interval (filled line) relative to the V–A interval (dotted line). **(b)** M-mode shows 1:1 AV relationship. a, atrial systole; RA, right atrium; RV, right ventricle; v, ventricular systole.

depth perception. For example, the AV valves can be viewed in short axis, with added depth aiding in the assessment of AV septal defects.

Using existing 3/4D ultrasound technologies, there are a number of more recently available techniques for assessment of ventricular volumes. Virtual Organ Computer-Aided Analysis (VOCAL) and Sonographic Automatic Volume Calculation (SonoAVC) are two examples [133,134]. These techniques can enable calculation of cardiac ventricular volumes and cardiac output using semi-automated methods. Early review of these newer techniques for assessment of fetal cardiac output shows less inter- and intraobserver variability than more traditional methods based of outflow Doppler[134].

There is much promise in the use of 3/4D fetal cardiac imaging. For the future, the hope is that these advanced techniques will reduce scanning times, increase the prenatal detection rate of congenital heart disease, reduce operator and window dependence as well as allows clinicians to review the information of patients who cannot be scanned locally. Future studies assessing the utility 3D/4D fetal echocardiography in detection of fetal heart disease during routine population screening will be essential.

Earlier prenatal detection, further delineation of the evolution of fetal heart disease and its etiologies, and ongoing experience should promote the development of more timely and effective fetal cardiovascular interventions. Fetal echocardiography

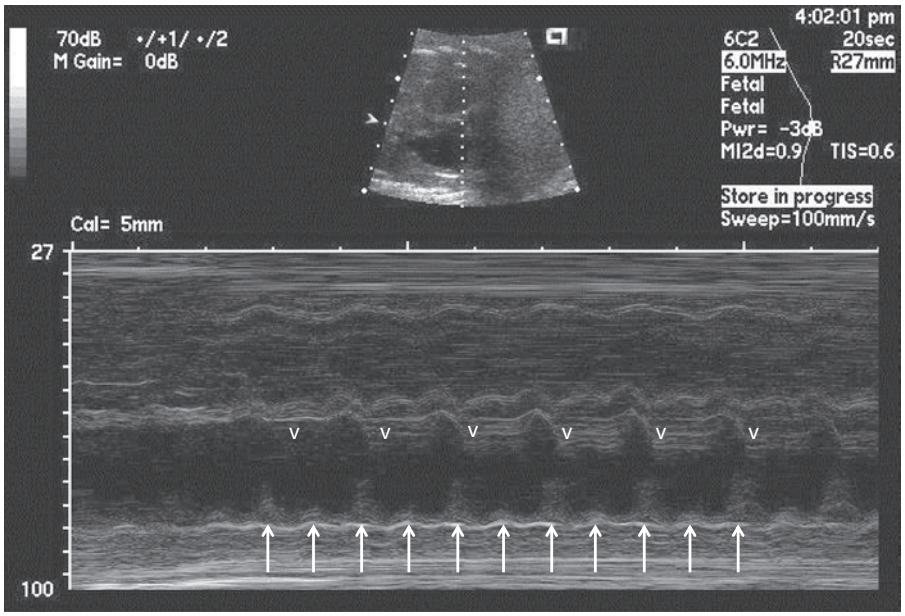


Figure 44.22 M-mode echocardiogram obtained in a 32-week fetus with atrial flutter. Atrial contractions (arrows) occurred at a rate of 450 bpm and ventricular contractions (v) at a rate of 225 bpm, consistent with 2:1 A–V (atrioventricular) conduction.

will play an increasingly more critical role in patient selection, planning of fetal cardiovascular and noncardiovascular interventions, directing therapy and evaluating the success of the therapy (Figure 44.29). Fetal echocardiography, for instance, is currently being used to evaluate lung growth through the measurement of branch pulmonary artery diameters which correlate with lung mass and PW Doppler interrogation of pulmonary arterial blood flow which reflects changes in pulmonary vascular resistance [135]. With the evolution of less invasive strategies to promote lung growth in such conditions as diaphragmatic hernia, the additional parameters of pulmonary vascular growth and resistance will no doubt enhance patient selection and be used in determining the subsequent success. Fetal echocardiography has already been employed in the evaluation and management of fetal conditions with potential for fetal hydrops and during fetal procedures [136].

Finally, fetal echocardiography and the prenatal diagnosis of fetal heart disease significantly impacts the outcome of affected pregnancies in many ways. It has led to improved perinatal and neonatal outcome of critical neonatal heart disease and heart disease associated with cardiovascular compromise before birth [137–140]. It has provided insight into the spectrum of postnatally encountered heart disease. Prenatal diagnosis of fetal heart disease provides time for the affected family to better understand and prepare for the delivery of their infant. Also importantly, it has begun to impact on the prevalence of more severe heart disease after birth [141]. Unfortunately, however, the impact of fetal echocardiography and prenatal diagnosis is severely limited by the generally low rates of detection of fetal heart disease at routine obstetric ultrasound [142–144]. This is despite the fact that the vast majority of major fetal heart disease is detectable before birth and that most pregnant women undergo at least one obstetric ultrasound at >16 weeks in the United States and most other countries internationally. For fetal echocardiography to reach its full potential, ongoing education and the development of either more objective screening tools for fetal heart disease and even greater regulation of the practices responsible for routine screening are critical.

Videos

To access the videos for this chapter, please go to www.lai-echo.com.

Video 44.1 Situs sweep and orientation. Initially the fetus is seen in its long axis with the transducer orientation groove oriented towards the fetal head. Fetal head is initially right of screen. The transducer is rotated 90° clockwise then showing the fetus in a transverse plane. With this maneuver, the fetal left will always be to the right of the screen at the end of the probe rotation. In this clip there is levocardia with a left-sided stomach. Even in this orientation sweep a 4-chambered heart and a normal 3-vessel view is seen.

Video 44.2 Four-chamber view sweeping to 3-vessel view. Normal fetal heart at 18 weeks starting with the 4-chambered view. The fetal left is to the right of the screen showing levocardia in this example. The transducer is tilted superiorly towards the fetal head showing the left ventricular outflow tract then right ventricular outflow tract and finally finishing with the normal 3-vessel view (pulmonary artery, aorta and SVC from left to right of the fetal chest). A symmetrical 4-chambered heart is seen with atrioventricular and

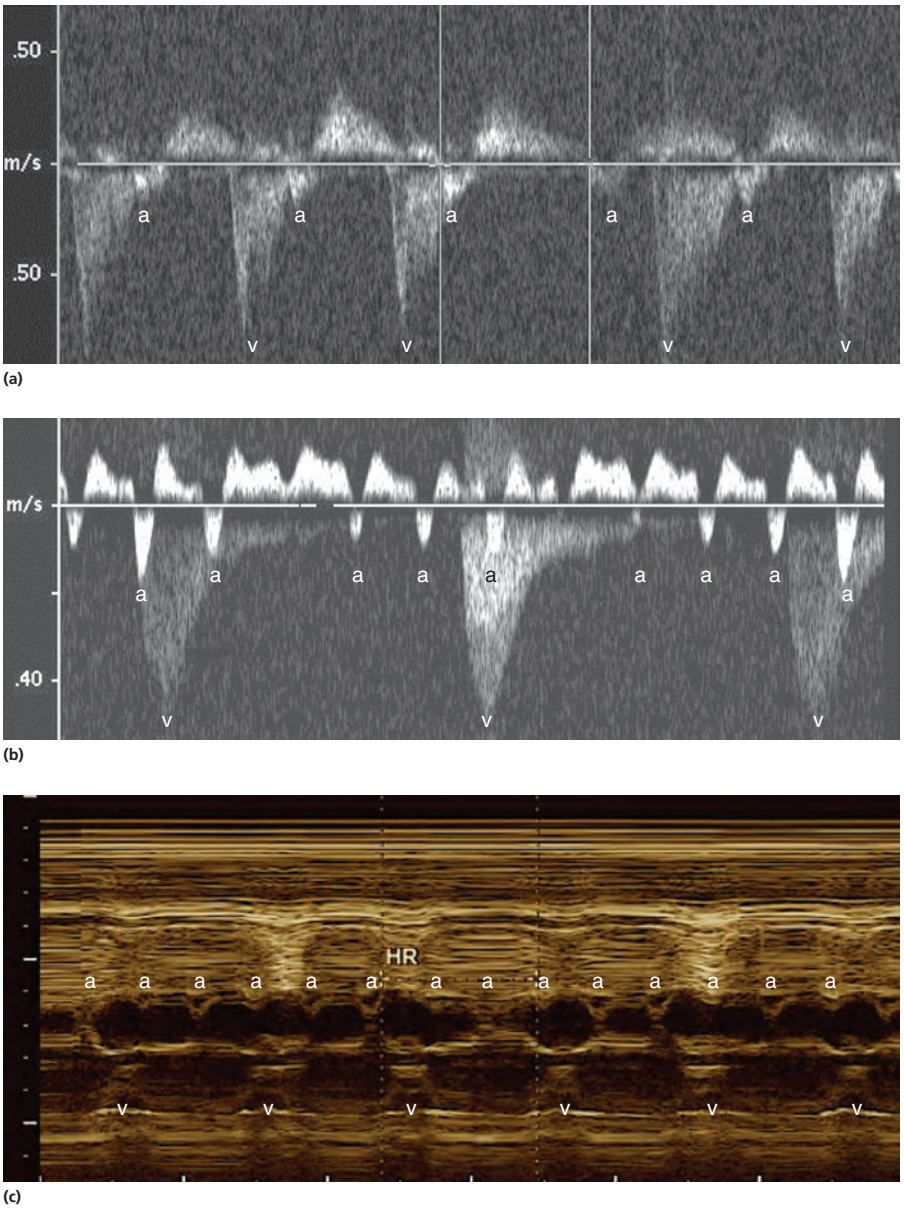


Figure 44.23 Doppler and M-mode methods demonstrating varying degrees of atrioventricular block (AVB). **(a)** Superior vena cava–aortic Doppler in a fetus with first-degree AVB (1° AVB) (A–V time interval 280 ms) and occasional episodes of second-degree AVB (2° AVB). **(b)** Simultaneous azygous and descending aortic flows in a fetus with complete AVB associated with polysplenia and a ventricular rate of 30–40 bpm. **(c)** Complete AVB demonstrated by M-mode. a, atrial systole; v, ventricular systole.

ventriculo-atrial concordance. On the initial image pulmonary veins are seen entering the left atrium.

Video 44.3 Pulmonary veins with color Doppler. Normal fetal heart at 18 weeks shown in the 4-chambered view to show pulmonary venous drainage. A color box is placed over the left atrium and shows one left (blue) and one right (red) pulmonary vein entering the left atrium. The pulsatile descending aorta is seen behind the left atrium and is spatially related to the left pulmonary artery.

Video 44.4 Short-axis sweep of the fetal heart from apex to base. Normal fetal heart at 19 weeks sweeping from cardiac apex to base, from left to right in a sagittal plane. The different morphology of the left and right ventricles is well seen and the mitral valve en face is shown. The tri leaflet aortic valve is shown in its short axis. The final image shows the aortic arch with three distinct head and neck vessels arising from it. These images were obtained using a 9 MHz transducer.

Video 44.5 Aortic arch 2D and color. Normal aortic arch in a 19-week fetus. The aortic arch is shown in the sagittal plane in 2D and with color Doppler. The aorta arises from the center of the fetal chest and has a "cane handle" appearance. The right pulmonary artery is

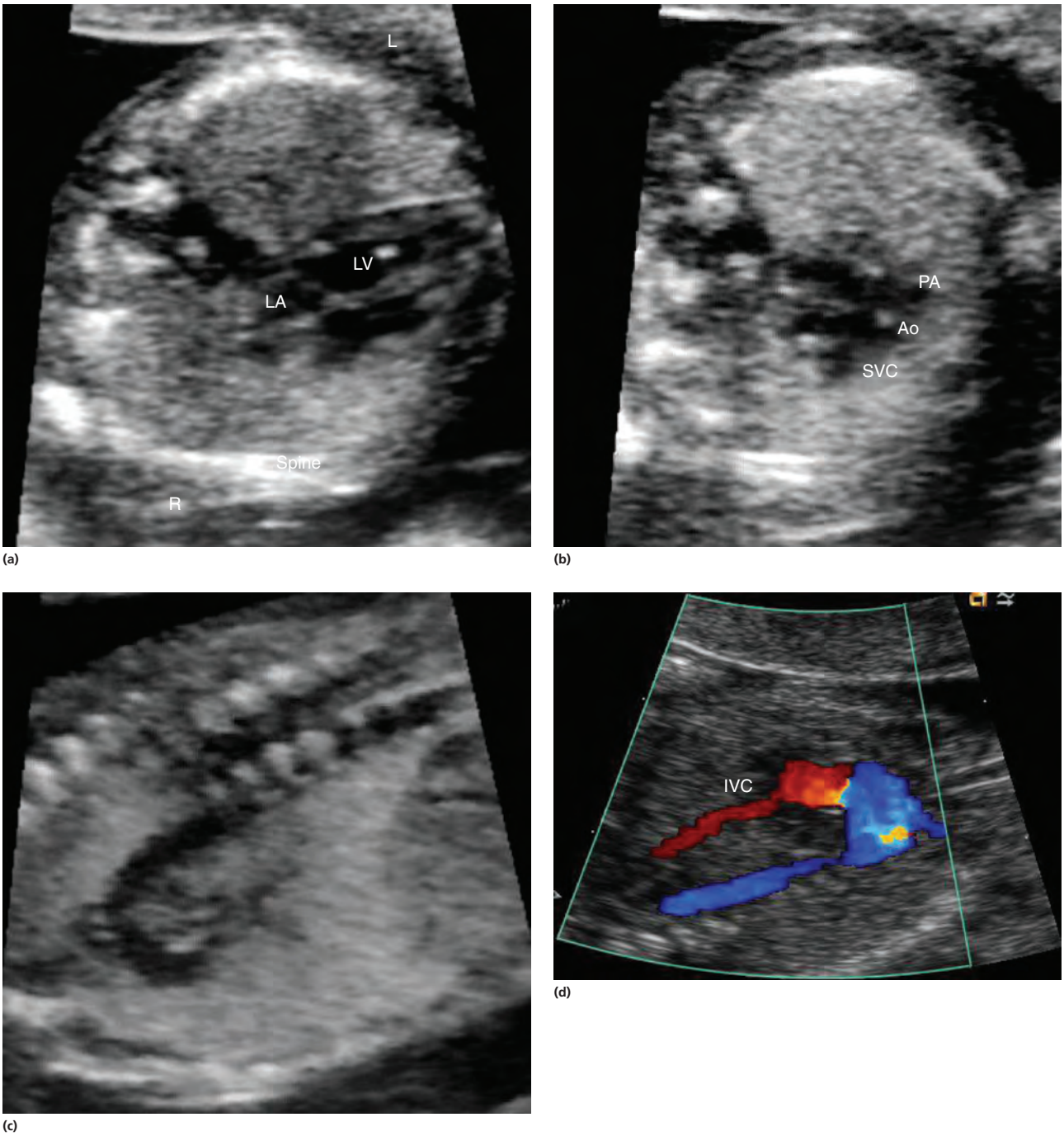


Figure 44.24 Echocardiographic assessment (transabdominal) of a 12-week fetus with no heart disease. **(a)** Four-chamber view; **(b)** sweeping cranially to 3-vessel view; **(c)** aortic arch. **(d)** Color Doppler confirms the presence of an intact inferior vena cava (IVC). Ao, aorta; LV, left ventricle; LA, left atrium; PA, main pulmonary artery; SVC, superior vena cava; L, left; R, right.

seen in cross-section under the aortic arch and the ductus arteriosus is seen joining the aorta at the junction of the distal aortic arch and descending aorta. Also seen in this image is the inferior vena cava entering the right atrium.

Video 44.6 Critical aortic stenosis. Significantly abnormal 4-chambered view in the setting of critical aortic stenosis. Normal cardiac connections. The left ventricle (LV) is severely dilated and has very reduced systolic function. There is evidence of endocardial fibro-elastosis, particularly affecting the LV apex and papillary muscles. The aortic valve is thickened and poorly opening. The right ventricle, near the top of the image, has preserved systolic function.

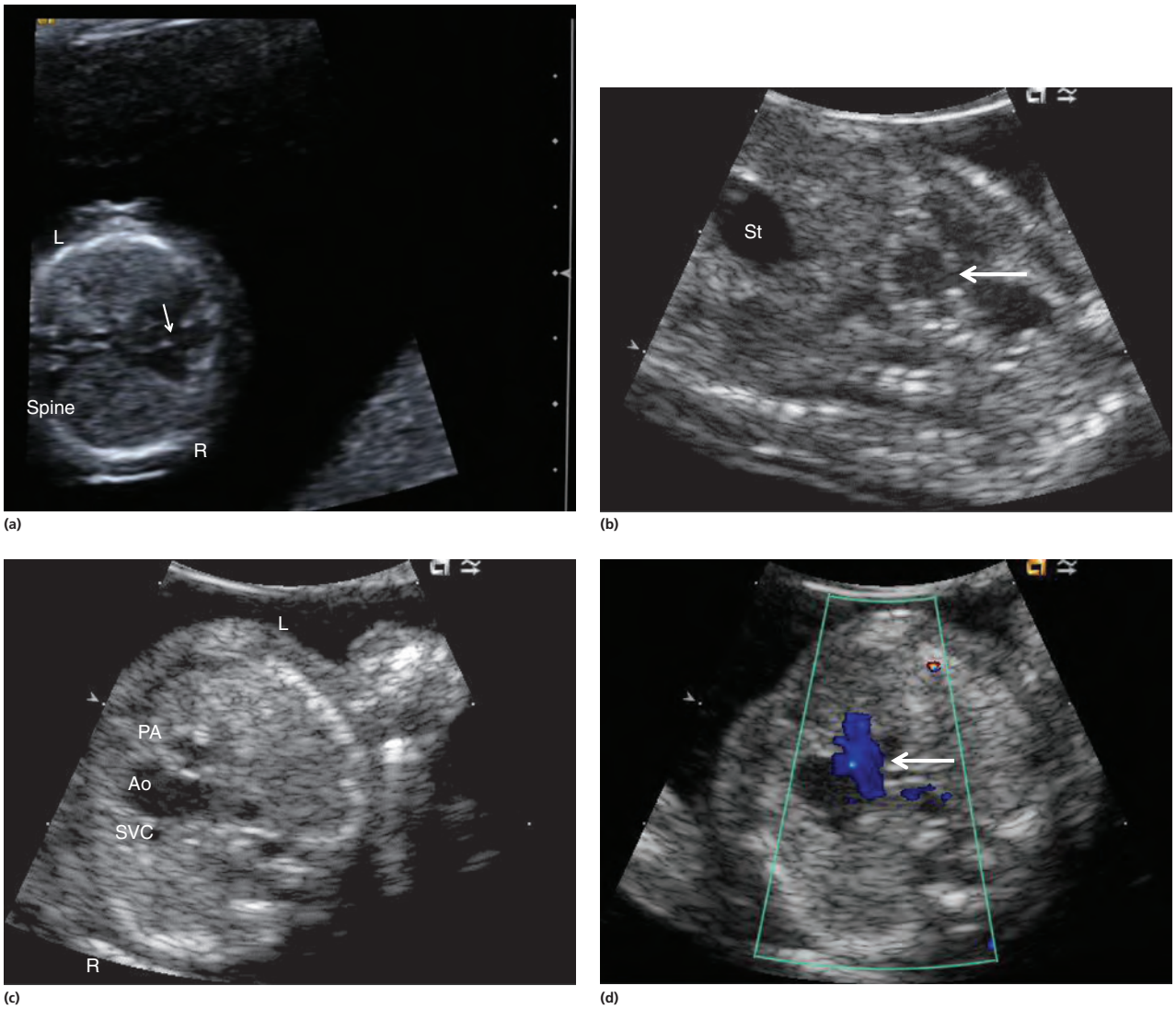


Figure 44.25 Transvaginal echocardiograms obtained in **(a)** an 11-week fetus with complete AVSD showing absence of the crux of the heart (arrow). Images (b–d) were also obtained by transvaginal echocardiography in a 14-week fetus with tetralogy of Fallot referred for increased nuchal translucency. **(b)** The sagittal view demonstrates the ventricular septal defect (arrow) and aortic override. **(c)** The 3-vessel view shows a large and anterior aorta and a smaller main pulmonary artery. **(d)** Patency of the pulmonary outflow tract was confirmed by color Doppler (arrow). Ao, aorta; PA, main pulmonary artery; St, stomach; SVC, superior vena cava; L, left; R, right.

Video 44.7 Fetal cardiomyopathy. Abnormal 4-chambered view in the setting of fetal cardiomyopathy in a 22-week fetus. Normal cardiac connections and levocardia. There is significant biventricular hypertrophy with a very reduced biventricular systolic function. A right-sided pleural effusion, likely indicating hydrops fetalis, is noted.

Video 44.8 Ebstein's with severe tricuspid regurgitation. Severe Ebstein's anomaly of the tricuspid valve in a 33-week fetus. Severe tricuspid regurgitation and massively dilated right atrium. Due to displacement of the septal leaflet of the tricuspid valve the regurgitant jet arises from near the RV apex. Left ventricular systolic function appears to be preserved at this time although there is mild mitral regurgitation (small red jet in diastole).

Video 44.9 Normal heart at 12 weeks GA. Structurally normal 4-chambered heart in a 12-week fetus using transabdominal imaging (9 MHz linear probe). The sweep begins showing a symmetrical 4-chambered heart. Fetal left is to the right of the image showing levocardia. The clip then sweeps cranially to first show the left outflow tract (aorta) followed by the right outflow tract (pulmonary artery) that arises more anteriorly. Crossing of the great vessels is confirmed. There is qualitatively normal biventricular systolic function.

Video 44.10 Ventricular short-axis TUI. A 20-week fetus. Tomographic ultrasound image (TUI) of the ventricular short axis acquired using gated STIC acquisition. One cardiac cycle is represented. The left and right ventricles are seen in short axis from the

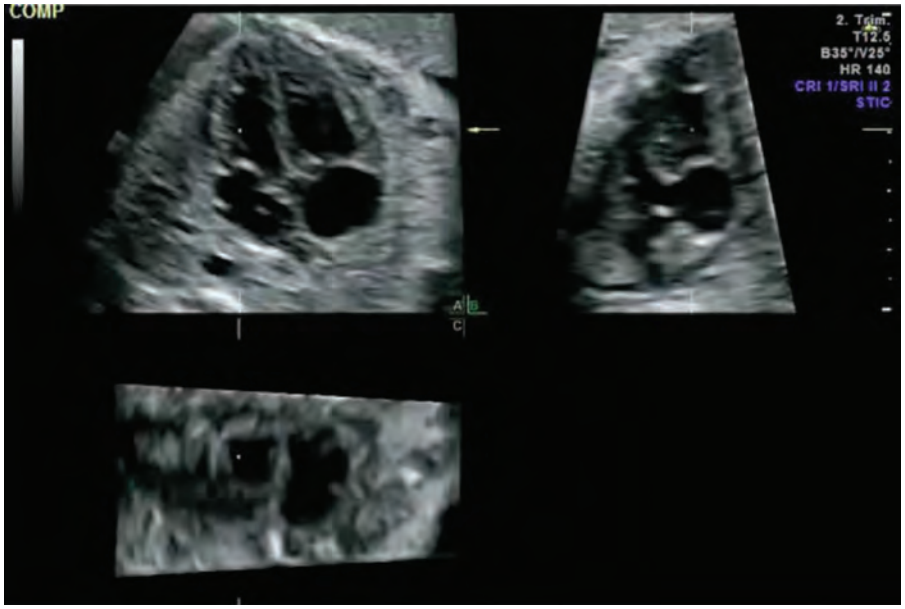


Figure 44.26 Multiplane reconstruction (MPR) image showing three orthogonal planes (4-chambered view, top left) acquired using spatiotemporal image correlation (STIC) technique from a 4-chambered view. All three planes can be manipulated offline.

cardiac apex (bottom right image) through to the base of the heart (top right image). The mitral valve and associate papillary muscles can be seen en face (center image). A trileaflet aortic valve is appreciated (top right image).

Video 44.11 Balanced AVSD TUI. A 28-week fetus. Tomographic ultrasound image (TUI) oriented to a 4-chambered view and showing one complete cardiac cycle. A complete atrioventricular septal defect is seen with a large atrial and ventricular septal defect. The defect appears to be balanced with similar size left and right ventricles. Source: Dr Julia Solomon. Reproduced with permission of Dr. Solomon.

References

1 Song MS, Hu A, Dyhamenahali U, et al. Extracardiac lesions and chromosomal abnormalities associated with major fetal heart defects: comparison of intrauterine, postnatal and postmortem diagnoses. *Ultrasound Obstet Gynecol* 2009;**33**:552–559.

2 Sharland GK, Lockhart SM, Chita SK, Allan LD. Factors influencing the outcome of congenital heart disease detected prenatally. *Arch Dis Child* 1991;**66**:284–287.

3 Friedberg MK, Silverman NH. Changing indications for fetal echocardiography in a University center population. *Prenat Diagn* 2004;**24**:781–786.

4 Carvalho JS. Improving the effectiveness of routine prenatal screening for major congenital heart defects. *Heart* 2002;**88**:387–391.

5 Wloch A, Rozmus-Warcholinska W, Czuba B, et al. Doppler study of the embryonic heart in normal pregnant women. *J Matern Fetal Neonatal Med* 2007;**20**:533–539.

6 Smrcek JM, Berg C, Geipel A, et al. Early fetal echocardiography. *J Ultrasound Med* 2006;**25**:173–182.

7 Hutchinson D, Hornberger LK, McBrien A, et al. Early first trimester fetal echocardiography: identification of cardiac structures by 2D imaging and color Doppler from six weeks gestation. *J Am Coll Cardiol* 2013;**61**:1–1.

8 Gembruch U, Knöpfle G, Bald R. Early diagnosis of fetal congenital heart disease by transvaginal echocardiography. *Ultrasound Obstet Gynecol* 1993;**3**:310–317.

9 Rustico MA, Benettoni A, D'Ottavio G. Early screening for fetal cardiac anomalies by transvaginal echocardiography in an unselected population: the role of operator experience. *Ultrasound Obstet Gynecol* 2000;**16**:614–619.

10 Carvalho JS. Clinical impact of first and early second trimester fetal echocardiography on high risk pregnancies. *Heart* 2004;**90**:921–926.

11 McAuliffe FM, Trines J, Nield LE, et al. Early fetal echocardiography–A reliable prenatal diagnosis tool. *Am J Obstet Gynecol* 2005;**193**:1253–1259.

12 Vimpelli T, Huhtala H, Acharya G. Fetal echocardiography during routine first-trimester screening: a feasibility study in an unselected population. *Prenat Diagn* 2006;**26**:475–482.

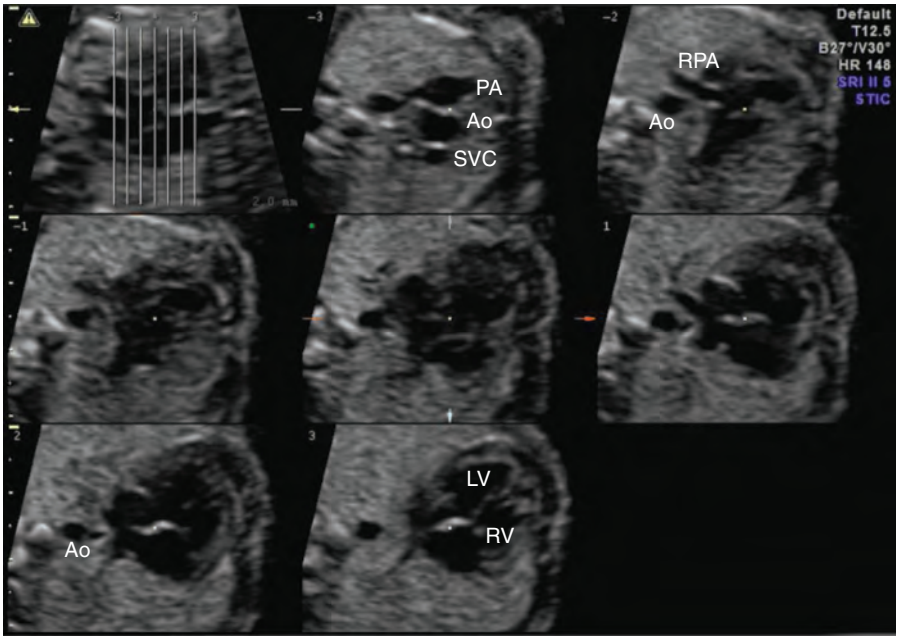
13 Ville Y, Lalondrelle C, Doumerc S, et al. First-trimester diagnosis of nuchal anomalies: significance and fetal outcome. *Ultrasound Obstet Gynecol* 1992;**2**:314–316.

14 Nicolaides KH, Brizot ML, Snijders RJM. Fetal nuchal translucency: ultrasound screening for fetal trisomy in the first trimester of pregnancy. *Br J Obstet Gynaecol* 1994;**101**:782–786.

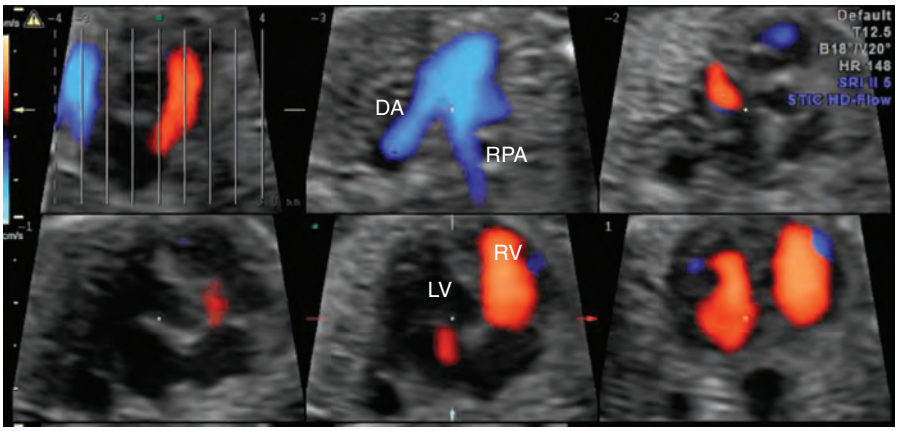
15 Pandya PP, Brizot ML, Kuhn P, et al. First-trimester fetal nuchal translucency thickness and risk for trisomies. *Obstet Gynecol* 1994;**84**:420.

16 Hyett J, Perdu M, Sharland G, et al. Using fetal nuchal translucency to screen for major congenital cardiac defects at 10–14 weeks of gestation: population-based cohort study. *BMJ* 1999;**318**:81–85.

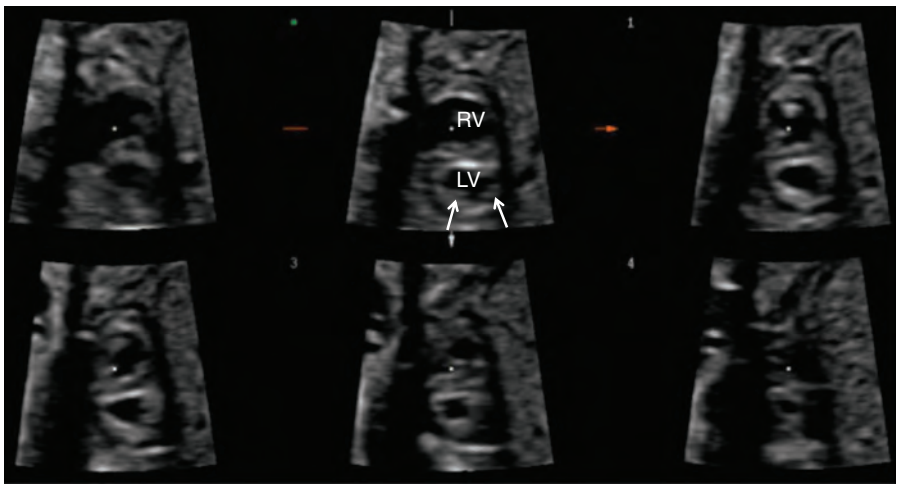
17 Souka AP, Krampl E, Bakalis S, et al. Outcome of pregnancy in chromosomally normal fetuses with increased nuchal



(a)

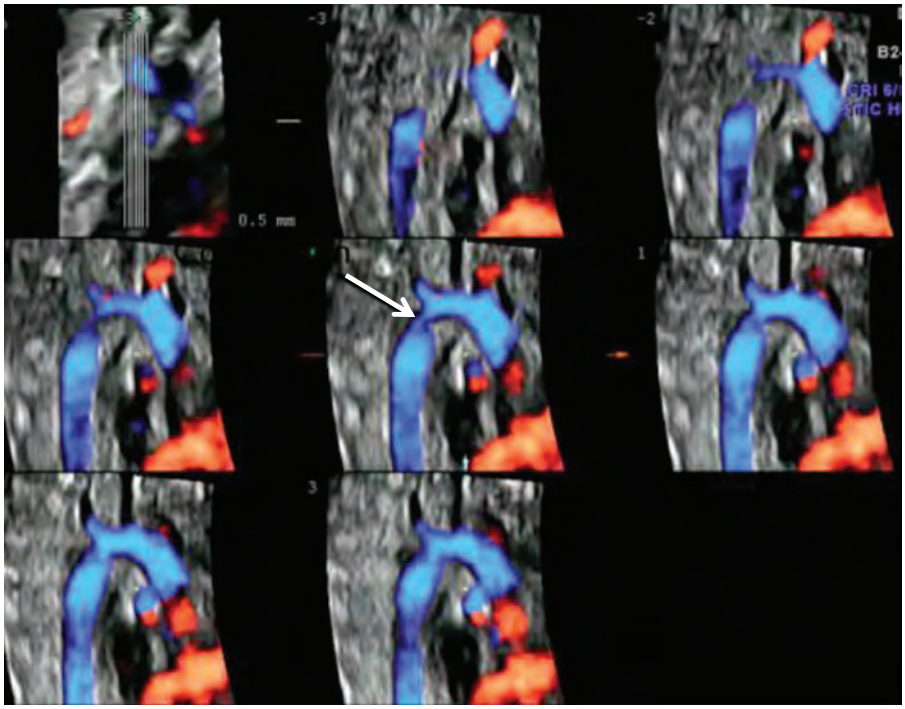


(b)

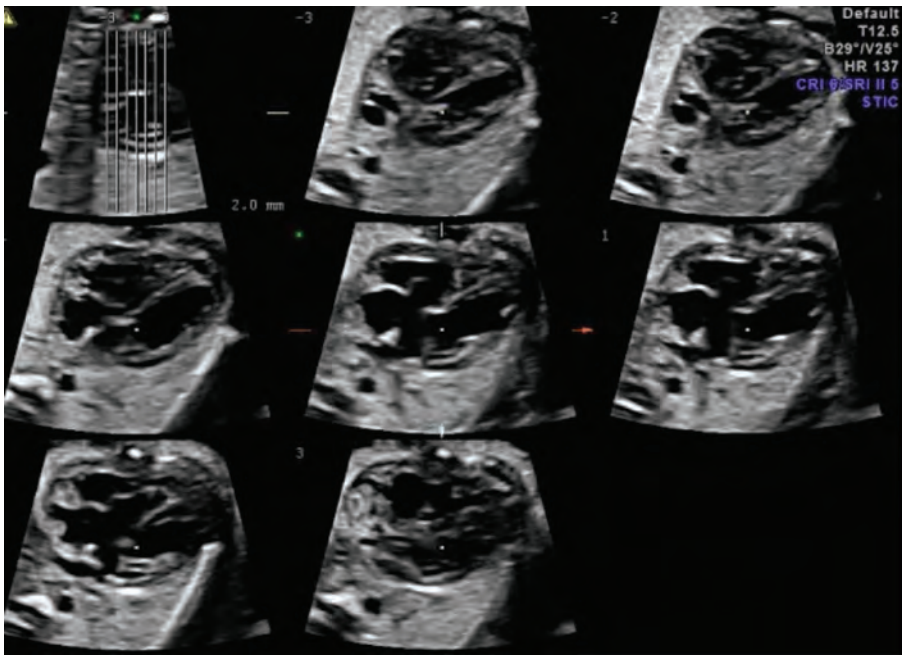


(c)

Figure 44.27 Tomographic ultrasound imaging (TUI) acquired using spatiotemporal image correlation (STIC) technique. **(a)** Multiple slices showing from the 4-chambered view (bottom) through to 3-vessel view and pulmonary arteries (top); **(b)** with addition of high-definition (HD) power Doppler (PD); **(c)** short-axis view of the heart from apex to base, including LV papillary muscles (arrows). Aortic arch in sagittal planes with HD PD showing coarctation (arrow). Ao, aorta; DA, ductus arteriosus; LV, left ventricle; PA, pulmonary artery; RPA, right pulmonary artery; RV, right ventricle; SVC, superior vena cava. Source (a): Dr. Julia Solomon. Reproduced with permission of Dr. Solomon.



(a)



(b)

Figure 44.28 Tomographic ultrasound imaging (TUI) acquired using spatiotemporal image correlation (STIC) technique. **(a)** Sagittal section through the aortic arch with high-definition power Doppler showing coarctation (arrow) at the aortic isthmus. **(b)** Axial image oriented to the 4-chambered view showing a complete atrioventricular septal defect. The ventricles appear to be balanced. Source: Dr. Julia Solomon. Reproduced with permission of Dr. Solomon.

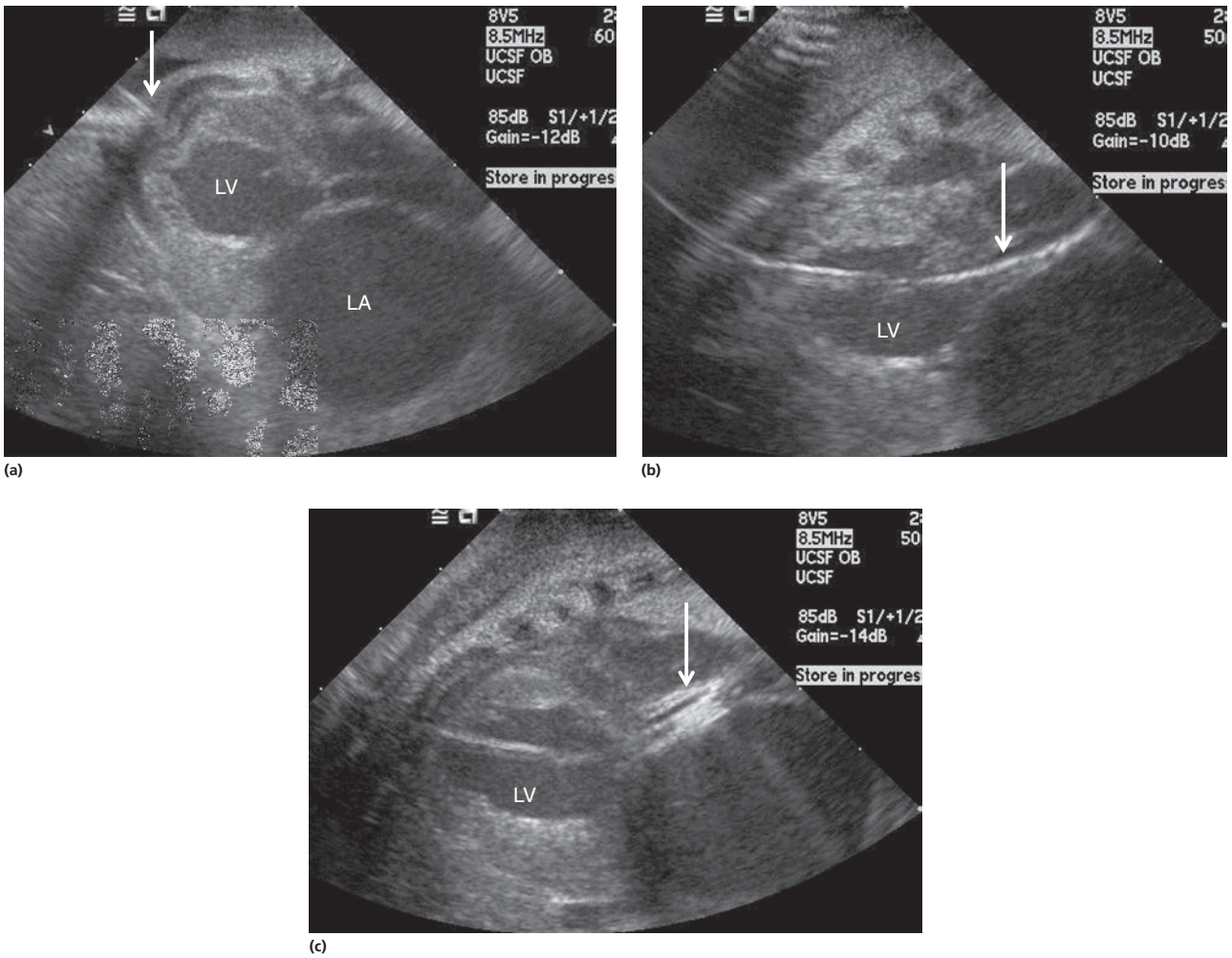


Figure 44.29 Balloon aortic valvuloplasty in a 27-week fetus with hydrops associated with critical aortic stenosis. The procedure is performed using a transuterine (maternal), transthoracic (fetal) approach following maternal laparotomy. **(a)** The introducing needle (arrow) can be seen indenting the left ventricular (LV) apex. **(b)** With the needle in the LV cavity, a wire (arrow) is passed through the needle and across the aortic valve. **(c)** The balloon is positioned through the aortic valve (arrow) and expanded. LA, left atrium; LV, left ventricle.

translucency in the first trimester. *Ultrasound Obstet Gynecol* 2001;**18**:9–17.

18 Hyett JA, Perdu M, Sharland GK, et al. Increased nuchal translucency at 10–14 weeks of gestation as a marker for major cardiac defects. *Ultrasound Obstet Gynecol* 1997;**10**:242–246.

19 Mavrides E, Cobian F, Tekay A, et al. Fetal nuchal translucency measurements in screening for major congenital cardiac defects in chromosomally normal fetuses. *Cardiol Young* 2000;**10**(Suppl. 2):9.

20 Cordes TM, O'Leary PW, Seward JB, Hagler DJ. Distinguishing right from left: a standardized technique for fetal echocardiography. *J Am Soc Echocardiogr* 1994;**7**:47–53.

21 Shipp T, Bromlet B, Hornberger LK, et al. Levorotation of the fetal cardiac axis: a clue for the presence of congenital heart disease. *Obstet Gynecol* 1995;**85**:97.

22 McBrien A, Howley L, Yamamoto Y, et al. Changes in fetal cardiac axis between 8 and 15 weeks' gestation. *Ultrasound Obstet Gynecol* 2013;**6**:653–658.

23 Bromley B, Benacerraf BR. Unilateral lung hypoplasia: report of three cases. *J Ultrasound Med* 1997;**16**:599–601.

24 Abdullah MM, Lacro RV, Smallhorn J, et al. Fetal cardiac dextroposition in the absence of an intrathoracic mass: sign of significant right lung hypoplasia. *J Ultrasound Med* 2000;**19**:669–676.

25 Yoo SJ, Lee YH, Cho KS. Abnormal three-vessel view on sonography: a clue to the diagnosis of congenital heart disease in the fetus. *Am J Roentgenol* 1999;**172**:825–830.

26 Sharland GK, Allan LD. Normal fetal cardiac measurements derived by cross-sectional echocardiography. *Ultrasound Obstet Gynecol* 1992;**2**:175–181.

27 Tan J, Silverman NH, Hoffman JIE, et al. Cardiac dimensions determined by cross-sectional echocardiography in the normal human fetus from 18 weeks to term. *Am J Cardiol* 1992;**70**:1459–1467.

28 Brown DL, Durfee SM, Hornberger LK. Ventricular discrepancy as a sonographic sign of coarctation of the fetal aorta: how reliable is it? *J Ultrasound Med* 1997;**16**:95–99.

29 Schneider C, McCrindle BW, Carvalho JS, et al. Development of Z-scores for fetal cardiac dimensions from echocardiography. *Ultrasound Obstet Gynecol* 2005;**26**:599–605.

30 Schmidt KG, Birk E, Silverman NH, Scagnelli SA. Echocardiographic evaluation of dilated cardiomyopathy in the human fetus. *Am J Cardiol* 1989;**63**:599–605.

31 Schmidt KG, Silverman NH, Hoffman JIE. Determination of ventricular volumes in human fetal hearts by two-dimensional echocardiography. *Am J Cardiol* 1995;**76**:1313–1316.

32 Simpson JM, Cook A. Repeatability of echocardiographic measurements in the human fetus. *Ultrasound Obstet Gynecol* 2002;**20**:332–339.

33 Yagel S, Cohen SM, Shapiro I, Valsky DV. 3D and 4D ultrasound in fetal cardiac scanning: a new look at the fetal heart. *Ultrasound Obstet Gynecol* 2007;**29**:81–95.

34 Gonçalves LF, Romero R, Espinoza J, et al. Four-dimensional ultrasonography of the fetal heart using color Doppler spatiotemporal image correlation. *J Ultrasound Med* 2004;**23**:473–481.

35 Bhat AH, Corbett V, Carpenter N, et al. Fetal ventricular mass determination on three-dimensional echocardiography. *Circulation* 2004;**110**:1054–1060.

36 Esh-Broder E, Ushakov FB, Imbar T, Yagel S. Application of free-hand three-dimensional echocardiography in the evaluation of fetal cardiac ejection fraction: a preliminary study. *Ultrasound Obstet Gynecol* 2004;**23**:546–551.

37 Messing B, Cohen SM, Valsky DV, et al. Fetal cardiac ventricle volumetry in the second half of gestation assessed by 4D ultrasound using STIC combined with inversion mode. *Ultrasound Obstet Gynecol* 2007;**30**:142–151.

38 Mielke G, Benda N. Cardiac output and central distribution of blood flow in the human fetus. *Circulation* 2001;**103**:1662–1668.

39 Barss VA, Doubilet PM, St John-Sutton M, et al. Cardiac output in a fetus with erythroblastosis fetalis: assessment using pulsed Doppler. *Obstet Gynecol* 1987;**70**(3):442.

40 Brassard M, Fouron JC, Leduc L, Grignon A. Prognostic markers in twin pregnancies with an acardiac fetus. *Obstet Gynecol* 1999;**94**:409–414.

41 Jaeggi ET, Fouron J-C, Hornberger LK, et al. Agenesis of the ductus venosus that is associated with extrahepatic umbilical vein drainage: prenatal features and clinical outcome. *Am J Obstet Gynecol* 2002;**187**:1031–1037.

42 Gudmundsson S, Huhta JC, Wood DC, et al. Venous Doppler ultrasonography in the fetus with nonimmune hydrops. *Am J Obstet Gynecol* 1991;**164**:33–37.

43 Pedra SRFF, Smallhorn JF, Ryan G, et al. Fetal cardiomyopathies. *Circulation* 2002;**106**:585–591.

44 Reed KL, Meijboom EJ, Sahn DJ, et al. Cardiac Doppler flow velocities in human fetuses. *Circulation* 1986;**73**:41–46.

45 Carceller-Blanchard AM, Fouron JC. Determinants of the Doppler flow velocity profile through the mitral valve of the human fetus. *Br Heart J* 1993;**70**:457–460.

46 Mori Y, Rice MJ, McDonald RW, et al. Evaluation of systolic and diastolic ventricular performance of the right ventricle in fetuses with ductal constriction using the Doppler Tei index. *Am J Cardiol* 2001;**88**:1173–1178.

47 Tei C, Lieng H, Hodge D, et al. New index of combined systolic and diastolic myocardial performance: a simple and reproducible measure of cardiac function–A study in normals and dilated cardiomyopathy. *J Cardiol* 1995;**26**:357–366.

48 Tsutsumi T, Ishii M, Eto G, et al. Serial evaluation for myocardial performance in fetuses and neonates using a new Doppler index. *Pediatr Int* 1999;**41**:722–727.

49 Friedman D, Buyon J, Kim M, Glickstein JS. Fetal cardiac function assessed by Doppler myocardial performance index (Tei Index). *Ultrasound Obstet Gynecol* 2003;**21**:33–36.

50 Harada K, Tsuda A, Orino T, et al. Tissue Doppler imaging in the normal fetus. *International J Cardiol* 1999;**71**:227.

51 Tutschek B, Zimmermann T, Buck T, Bender HG. Fetal tissue Doppler echocardiography: detection rates of cardiac structures and quantitative assessment of the fetal heart. *Ultrasound Obstet Gynecol* 2003;**21**:26–32.

52 Chan LY-S, Fok WY, Wong JT-H, et al. Reference charts of gestation-specific tissue Doppler imaging indices of systolic and diastolic functions in the normal fetal heart. *Am Heart J* 2005;**150**:750–755.

53 Larsen LU, Petersen OB, Norrild K, et al. Strain rate derived from color Doppler myocardial imaging for assessment of fetal cardiac function. *Ultrasound Obstet Gynecol* 2006;**27**:210–213.

54 Van Mieghem T, DeKoninck P, Steenhaut P, Deprest J. Methods for prenatal assessment of fetal cardiac function. *Prenat Diagn* 2009;**29**:1193–1203.

55 Peng Q-H, Zhou Q-C, Zeng S, et al. Evaluation of regional left ventricular longitudinal function in 151 normal fetuses using velocity vector imaging. *Prenat Diagn* 2009;**29**:1149–1155.

56 Van Mieghem T, Giusca S, DeKoninck P, et al. Prospective assessment of fetal cardiac function with speckle tracking in healthy fetuses and recipient fetuses of twin-to-twin transfusion syndrome. *J Am Soc* Echocardiography 2010;**23**:301–308.

57 Matsui H, Germanakis I, Kulinskaya E, Gardiner HM. Temporal and spatial performance of vector velocity imaging in the human fetal heart. *Ultrasound Obstet Gynecol* 2011;**37**:150–157.

58 Ishii T, McElhinney DB, Harrild DM, et al. Circumferential and longitudinal ventricular strain in the normal human fetus. *J Am Soc Echocardiogr* 2012;**25**:105–111.

59 Brooks PA, Khoo NS, Mackie AS, Hornberger LK. Right ventricular function in fetal hypoplastic left heart syndrome. *J Am Soc Echocardiogr* 2012;**25**:1068–1074.

60 Larsen LU, Petersen OB, Sloth E, Uldbjerg N. Color Doppler myocardial imaging demonstrates reduced diastolic tissue velocity in growth retarded fetuses with flow redistribution. *Eur J Obstet Gynecol Reprod Biol* 2011;**155**:140–145.

61 Hornberger LK. Echocardiographic assessment of fetal arrhythmias. *Heart* 2007;**93**:1331–1333.

62 Hornberger LK, Sahn DJ. Rhythm abnormalities of the fetus. *Heart* 2007;**93**:1294–1300.

63 Carvalho JS, Prefumo F, Ciardelli V, et al. Evaluation of fetal arrhythmias from simultaneous pulsed wave Doppler in pulmonary artery and vein. *Heart* 2007;**93**:1448–1453.

64 Fouron J-C. Fetal arrhythmias: the Saint-Justine hospital experience. *Prenat Diagn* 2004;**24**:1068–1080.

65 Rein AJJT, O'Donnell C, Geva T, et al. Use of tissue velocity imaging in the diagnosis of fetal cardiac arrhythmias. *Circulation* 2002;**106**:1827–1833.

66 Allan LD, Sharland GK, Milburn A, et al. Prospective diagnosis of 1006 consecutive cases of congenital heart disease in the fetus. *J Am Coll Cardiol* 1994;**23**:1452–1458.
67 Tometzki AJP, Suda K, Kohl T, et al. Accuracy of prenatal echocardiographic diagnosis and prognosis of fetuses with conotruncal anomalies. *J Am Coll Cardiol* 1999;**33**:1696–1701.
68 Gottliebson WM, Border WL, Franklin CM, et al. Accuracy of fetal echocardiography: a cardiac segment-specific analysis. *Ultrasound Obstet Gynecol* 2006;**28**:15–21.
69 Taketazu M, Lougheed J, Yoo S-J, et al. Spectrum of cardiovascular disease, accuracy of diagnosis, and outcome in fetal heterotaxy syndrome. *Am J Cardiol* 2006;**97**:720–724.
70 Trines J, Hornberger LK. Evolution of congenital heart disease in utero. *Pediatr Cardiol* 2004;**25**.
71 Hornberger LK, Sanders SP, Rein AJJT, et al. Left heart obstructive lesions and left ventricular growth in the midtrimester fetus. *Circulation* 1995;**92**:1531–1538.
72 Simpson JM, Sharland GK. Natural history and outcome of aortic stenosis diagnosed prenatally. *Heart* 1997;**77**:205–210.
73 Hornberger LK, Need L, Benacerraf BR. Development of significant left and right ventricular hypoplasia in the second and third trimester fetus. *J Ultrasound Med* 1996;**15**:655–659.
74 Mäkikallio K, McElhinney D, Levine J, et al. Fetal aortic valve stenosis and the evolution of hypoplastic left heart syndrome. *Circulation* 2006;**113**:1401–1405.
75 Hornberger LK, Sahn DJ, Kleinman CS, et al. Tricuspid valve disease with significant tricuspid insufficiency in the fetus: diagnosis and outcome. *J Am Coll Cardiol* 1991;**17**:167–173.
76 Hornberger LK, Benacerraf BR. Prenatal detection of severe right ventricular outflow tract obstruction: pulmonary stenosis and pulmonary atresia. *J Ultrasound Med* 1994;**13**:743–750.
77 Hornberger LK, Sahn DJ, Kleinman CS, et al. Antenatal diagnosis of coarctation of the aorta: a multicenter experience. *J Am Coll Cardiol* 1994;**23**:417–423.
78 Hornberger LK, Sanders SP, Sahn DJ, Rice MJ. In utero pulmonary artery and aortic growth and potential for progression of pulmonary outflow tract obstruction in tetralogy of Fallot. *J Am Coll Cardiol* 1995;**25**:739–745.
79 Lougheed J, Sinclair BG, Fung KFK, et al. Acquired right ventricular outflow tract obstruction in the recipient twin in twin-twin transfusion syndrome. *J Am Coll Cardiol* 2001;**38**:1533–1538.
80 McCaffrey FM, Sherman FS. Prenatal diagnosis of severe aortic stenosis. *Pediatr Cardiol* 1997;**18**:276–281.
81 Allan LD, Sharland G, Tynan MJ. The natural history of the hypoplastic left heart syndrome. *Int J Cardiol* 1989;**25**:341–343.
82 Danford DA, Cronican P. Hypoplastic left heart syndrome: progression of left ventricular dilation and dysfunction to left ventricular hypoplasia in utero. *Am Heart J* 1992;**123**:1712–1713.
83 Maeno YV, Boutin C, Hornberger LK, McCrindle BW. Prenatal diagnosis of right ventricular outflow tract obstruction with intact ventricular septum, and detection of ventriculocoronary connections. *Heart* 1999;**81**:661–669.
84 Scott RJ, Sullivan ID. Hypoplastic left heart syndrome in the second trimester. *Fetal Pediatr Pathol* 1996;**16**:543–548.
85 Sharland GK, Chita SK, Fagg NL, Anderson RH. Left ventricular dysfunction in the fetus: relation to aortic valve anomalies and endocardial fibroelastosis. *Heart* 1991;**66**:419–424.
86 Schmidt KG, Ulmer HE, Silverman NH, et al. Perinatal outcome of fetal complete atrioventricular block: a multicenter experience. *J Am Coll Cardiol* 1991;**17**:1360–1366.
87 Jaeggi ET, Hornberger LK, Smallhorn JF, Fouron JC. Prenatal diagnosis of complete atrioventricular block associated with structural heart disease: combined experience of two tertiary care centers and review of the literature. *Ultrasound Obstet Gynecol*. 2005;**26**:16–21.
88 Jaeggi ET, Hamilton RM, Silverman ED, et al. Outcome of children with fetal, neonatal or childhood diagnosis of isolated congenital atrioventricular block. A single institution's experience of 30 years. *J Am Coll Cardiol* 2002;**39**:130–137.
89 Simpson JM, Sharland GK. Fetal tachycardias: management and outcome of 127 consecutive cases. *Heart* 1998;**79**:576–581.
90 van Engelen AD, Weijtens O, Brenner JI, et al. Management outcome and follow-up of fetal tachycardia. *J Am Coll Cardiol* 1994;**24**:1371–1375.
91 Chobot V, Hornberger LK, Hagan-Ansert S, Sahn D. Prenatal detection of restrictive foramen oval. *J Am Soc Echocardiogr* 1990;**3**:15–19.
92 Bharati S, Patel AG, Varga P, Husain AN. In utero echocardiographic diagnosis of premature closure of the foramen ovale with mitral regurgitation and large left atrium. *Am J Heart* 1991;**122**;597–600.
93 Paladini D, Palmieri S, Lamberti A, et al. Characterization and natural history of ventricular septal defects in the fetus. *Ultrasound Obstet Gynecol* 2000;**16**:118–122.
94 Hofstadler G, Tulzer G, Altmann R, et al. Spontaneous closure of the human fetal ductus arteriosus–a cause of fetal congestive heart failure. *Am J Obstet Gynecol* 1996;**174**:879–883.
95 Dyamenahalli U, Smallhorn JF, Geva T, et al. Isolated ductus arteriosus aneurysm in the fetus and infant: a multi-institutional experience. *J Am Coll Cardiol* 2000;**36**:262–269.
96 Barrea C, Alkazaleh F, Ryan G, et al. Prenatal cardiovascular manifestations in the twin-to-twin transfusion syndrome recipients and the impact of therapeutic amnioreduction. *Am J Obstet Gynecol* 2005;**192**:892–902.
97 Fesslova V, Villa L, Nava S, et al. Fetal and neonatal echocardiographic findings in twin-twin transfusion syndrome. *Am J Obstet Gynecol* 1998;**179**:1056–1062.
98 Nield LE, Silverman ED, Taylor GP, et al. Maternal anti-Ro and anti-La antibody-associated endocardial fibroelastosis. *Circulation* 2002;**105**:843–848.
99 Sivasankaran S, Sharland GK, Simpson JM. Dilated cardiomyopathy presenting during fetal life. *Cardiol Young* 2005;**15**:409–416.
100 Allan L, Crawford D, Shridan R, Chapman M. Aetiology of non-immune hydrops: the value of echocardiography. *Br J Obstetr Gynaecol* 1986;**93**:223–225.
101 Kleinman CS, Donnerstein RL, DeVore GR, et al. Fetal echocardiography for evaluation of in utero congestive heart failure. *N Engl J Med* 1982;**306**:568–575.
102 Tsang W, van der Velde M, Windrim R, et al. Hydrops fetalis: primary cardiovascular etiologies and clinical outcome in 98 affected pregnancies. *J Am Coll Cardiol* 2002;**39**:415–415.
103 Naheed ZJ, Strasburger JF, Deal BJ, et al. Fetal tachycardia: mechanisms and predictors of hydrops fetalis. *J Am Coll Cardiol* 1996;**27**:1736–1740.

104 Silverman N, Kleinman C, Rudolph A, et al. Fetal atrioventricular valve insufficiency associated with nonimmune hydrops: a two-dimensional echocardiographic and pulsed Doppler ultrasound study. *Circulation* 1985;**72**:825–832.
105 Bader RS, Chitayat D, Kelly E, et al. Fetal rhabdomyoma: prenatal diagnosis, clinical outcome, and incidence of associated tuberous sclerosis complex. *J Pediatr* 2003;**143**:620–624.
106 Holley D, Martin G, Brenner J, et al. Diagnosis and management of fetal cardiac tumors: a multicenter experience and review of published reports. *J Am Coll Cardiol* 1995;**26**:516–520.
107 Nir A, Ekstein S, Nadjari M, et al. Rhabdomyoma in the fetus: illustration of tumor growth during the second half of gestation. *Pediatr Cardiol* 2001;**22**:515–518.
108 Berning RA, Silverman NH, Villegas M, et al. Reversed shunting across the ductus arteriosus or atrial septum in utero heralds severe congenital heart disease. *J Am Coll Cardiol* 1996;**27**:481–486.
109 Taketazu M, Barrea C, Smallhorn JF, et al. Intrauterine pulmonary venous flow and restrictive foramen ovale in fetal hypoplastic left heart syndrome. *J Am Coll Cardiol* 2004;**43**:1902–1907.
110 Kohl T. Fetal echocardiography: new grounds to explore during fetal cardiac intervention. *Pediatr Cardiol* 2002;**23**:334–346.
111 McElhinney DB, Tworetzky W, Lock JE. Current status of fetal cardiac intervention. *Circulation* 2010;**121**:1256–1263.
112 Viesca R, Huhta JC. Update in fetal cardiac intervention. *Curr Treat Options Cardio Med* 2006;**8**:379–86.
113 Marshall AC, Levine J, Morash D, et al. Results of in uteroatrial septoplasty in fetuses with hypoplastic left heart syndrome. *Prenat Diagn* 2008;**28**:1023–1028.
114 Hornberger LK, Dalvi B, Benacerraf BR. Prenatal sonographic detection of cardiac aneurysms and diverticula. *J Ultrasound Med* 1994;**13**:967–970.
115 Cavallé-Garrido T, Cloutier A, Harder J, et al. Evolution of fetal ventricular aneurysms and diverticula of the heart: an echocardiographic study. *Am J Perinatol* 2008;**14**:393–400.
116 McAuliffe FM, Hornberger LK, Johnson J, et al. Cardiac diverticulum with pericardial effusion: report of two new cases treated by in-utero pericardiocentesis and a review of the literature. *Ultrasound Obstet Gynecol* 2005;**25**:401–404.
117 Weichert J, Hartge DR, Axt-Fliedner R. The fetal ductus arteriosus and its abnormalities–a review. *Congenit Heart Dis* 2010;**5**:398–408.
118 Inamura N, Taketazu M, Smallhorn JF, Hornberger LK. Left ventricular myocardial performance in the fetus with severe tricuspid valve disease and tricuspid insufficiency. *Am J Perinatol* 2005;**22**:91–97.
119 Pavlova M, Fouron J-C, Drblik SP, et al. Factors affecting the prognosis of Ebstein's anomaly during fetal life. *Am Heart J* 1998;**135**:1081–1085.
120 Inamura N, Kado Y, Nakajima T, Kayatani F. Left and right ventricular function in fetal tetralogy of Fallot with absent pulmonary valve. *Am J Perinatol* 2005;**22**:199–204.
121 Barrea C, Hornberger LK, Alkazaleh F, et al. Impact of selective laser ablation of placental anastomoses on the cardiovascular pathology of the recipient twin in severe twin–twin transfusion syndrome. *Am J Obstet Gynecol* 2006;**195**:1388–1395.
122 Michelfelder E, Gottliebson W, Border W, et al. Early manifestations and spectrum of recipient twin cardiomyopathy in twin–twin transfusion syndrome: relation to Quintero stage. *Ultrasound Obstet Gynecol* 2007;**30**:965–971.
123 Rychik J, Tian Z, Bebbington M, et al. The twin–twin transfusion syndrome: spectrum of cardiovascular abnormality and development of a cardiovascular score to assess severity of disease. *Am J Obstet Gynecol* 2007;**197**:391.e1–8.
124 Kleinman CS, Nehgme RA. Cardiac arrhythmias in the human fetus. *Pediatr Cardiol* 2004;**25**:234–251.
125 Van Bergen AH, Cuneo BF, Davis N. Prospective echocardiographic evaluation of atrioventricular conduction in fetuses with maternal Sjögren's antibodies. *Am J Obstet Gynecol* 2004;**191**:1014–1018.
126 Nii M, Hamilton RM, Fenwick L, et al. Assessment of fetal atrioventricular time intervals by tissue Doppler and pulse Doppler echocardiography: normal values and correlation with fetal electrocardiography. *Heart* 2006;**92**:1831–1837.
127 Comas Gabriel C, Galindo A, Martínez JM, et al. Early prenatal diagnosis of major cardiac anomalies in a high-risk population. *Prenat Diagn* 2002;**22**:586–593.
128 Huggon IC, Ghi T, Cook AC, et al. Fetal cardiac abnormalities identified prior to 14 weeks' gestation. *Ultrasound Obstet Gynecol* 2002;**20**:22–29.
129 Yagel S, Weissman A, Rotstein Z, et al. Congenital heart defects: natural course and in utero development. *Circulation* 1997;**96**:550–555.
130 Gonçalves LF, Espinoza J, Lee W, et al. A new approach to fetal echocardiography: digital casts of the fetal cardiac chambers and great vessels for detect of congenital heart disease. *J Ultrasound Med* 2005;**24**:415–424.
131 Chaoui R, Heling KS. New developments in fetal heart scanning: three-and four-dimensional fetal echocardiography. *Semin Fetal Neonatal Med* 2005;**10**:567–577.
132 Yagel S, Cohen SM, Rosenak D, et al. Added value of three-/four-dimensional ultrasound in offline analysis and diagnosis of congenital heart disease. *Ultra in Obstet Gynecol* 2011;**37**:432–437.
133 Hamill N, Yeo L, Romero R, et al. Fetal cardiac ventricular volume, cardiac output, and ejection fraction determined with 4-dimensional ultrasound using spatiotemporal image correlation and virtual organ computer-aided analysis. *Am J Obstetr Gynecol* 2011;**205**:76.e1–76.e10.
134 DeKoninck P, Steenhaut P, Van Mieghem T, et al. Comparison of Doppler-based and three-dimensional methods for fetal cardiac output measurement. *Fetal Diagn Ther* 2012;**32**:72–78.
135 Sokol J, Bohn D, Lacro RV, et al. Fetal pulmonary artery diameters and their association with lung hypoplasia and postnatal outcome in congenital diaphragmatic hernia. *Am J Obstetr Gynecol* 2002;**186**:1085–1090.
136 Keswani SG, Crombleholme TM, Rychik J, et al. Impact of continuous intraoperative monitoring on outcomes in open fetal surgery. *Fetal Diagn Ther* 2005;**20**:316–320.
137 Eapen R, Rowland D, Franklin W. Effect of prenatal diagnosis of critical left heart obstruction on perinatal morbidity and mortality. *Am J Perinatol* 1998;**15**:237–242.
138 Kumar RK, Newburger JW, Gauvreau K, et al. Comparison of outcome when hypoplastic left heart syndrome and transposition of the great arteries are diagnosed prenatally versus when diagnosis of these two conditions is made only postnatally. *Am J Cardiol* 1999;**83**:1649–1653.

139 Bonnet D, Coltri A, Butera G, et al. Detection of transposition of the great arteries in fetuses reduces neonatal morbidity and mortality. *Circulation* 1999;**99**:916–918.
140 Tworetzky W, McElhinney DB, Reddy VM, et al. Improved surgical outcome after fetal diagnosis of hypoplastic left heart syndrome. *Circulation* 2001;**103**:1269–1273.
141 Allan LD, Sharland GK, Cook A, Sullivan I. Hypoplastic left heart syndrome: effects of fetal echocardiography on birth prevalence. *Lancet* 1991;**337**:959–961.
142 Garne E, Loane M, Dolk H, et al. Prenatal diagnosis of severe structural congenital malformations in Europe. *Ultrasound Obstet Gynecol* 2005;**25**:6–11.
143 Wong SF, Chan FY, Cincotta RB. Factors influencing the prenatal detection of structural congenital heart diseases. *Ultrasound in Obstet Gynecol* 2003;**21**:19–25.
144 Shima Y, Shindoh F, Nakajima M, et al. Prenatal diagnosis of congenital heart disease: clinical experience and analysis. *J Nippon Med Sch* 2004;**71**:328–332.

CHAPTER 45

The Echocardiographic Assessment of Pulmonary Arterial Hypertension

Lindsay M. Ryerson and Jeffrey F. Smallhorn
Division of Pediatric Cardiology, Stollery Children's Hospital, Edmonton, AB, Canada

Introduction

Pulmonary endothelial dysfunction promotes a triad of vasoconstriction, cell proliferation and thrombosis through the action of mediators such as thromboxane A_2, endothelin I and serotonin. Under normal circumstances these are counterbalanced by prostacyclin, nitric oxide and vasoactive intestinal peptide. The end result is irreversible vascular changes with intimal fibrosis, pulmonary arteriolar occlusion, and plexiform lesions [1].

Definition of pulmonary arterial hypertension

Pulmonary hypertension is defined as a resting mean pulmonary artery pressure >25 mmHg with a pulmonary arterial wedge pressure ≥15 mmHg [2]. Different classifications of pulmonary hypertension have been proposed, the most recent one being the Dana Point clinical classification (2008). In this approach, pulmonary arterial hypertension is divided into "idiopathic" when there is neither a family history nor an identifiable risk factor, "heritable" when PAH occurs in a familial context, "unknown," "drug or toxin induced," "associated with other diseases," or "persistent pulmonary hypertension of the newborn" [3]. Unfortunately, this classification is not readily applicable to pediatric disease, as it does not recognize the potential importance of developmental mechanisms including fetal origins, perinatal events including the transition period, and early childhood development. A specific classification for pediatric pulmonary hypertensive disease has been developed and is based on clinical practice [4]. Idiopathic pulmonary hypertension is a rare disorder in children. More commonly, secondary forms of pulmonary hypertension are diagnosed. Apart from the idiopathic group, pediatric patients with pulmonary hypertension represent a heterogeneous population, including:

1. Congenital heart disease with an associated large ventricular septal defect and an unobstructed pulmonary outflow tract or large shunts at great vessel level, that is, patent ductus arteriosus, aortopulmonary window and truncus arteriosus.
2. Congenital pulmonary venous abnormalities – encountered either in the newborn period with total anomalous pulmonary venous drainage, or in the form of congenital pulmonary vein stenosis, either in isolation or associated with other forms of congenital heart disease. Rarely, pulmonary hypertension may be seen with partial anomalous pulmonary venous drainage, usually in association with Scimitar syndrome and invariably associated with an intracardiac or extracardiac left-to-right shunt. Acquired pulmonary vein stenosis is most commonly seen post repair of total anomalous pulmonary venous drainage, particularly when there is an associated small pulmonary venous confluence or hypoplastic pulmonary veins.
3. Absence of a mediastinal left or right pulmonary artery may be associated with pulmonary hypertension, particularly when the other lung is exposed to an intracardiac or extracardiac shunt. In this setting the pulmonary arterial hypertension is often out of keeping with the magnitude of the left-to-right shunt.
4. Pulmonary arterial hypertension may be secondary to upper airway obstruction in cases with Down syndrome, sleep apnea, and/or obesity. Also, interstitial fibrosis, bronchopulmonary dysplasia secondary to premature birth, diaphragmatic hernia and chronic exposure to high altitudes may be associated with pulmonary arterial hypertension.
5. Pulmonary arterial hypertension in the newborn period in the absence of associated structural heart disease.
6. Less commonly encountered is pulmonary arterial hypertension secondary to systemic atrioventricular valve regurgitation, or left ventricular systolic and/or diastolic dysfunction.

Echocardiography in Pediatric and Congenital Heart Disease: From Fetus to Adult, Second Edition. Edited by Wyman W. Lai, Luc L. Mertens, Meryl S. Cohen and Tal Geva.
© 2016 John Wiley & Sons, Ltd. Published 2016 by John Wiley & Sons, Ltd.
Companion website: www.lai-echo.com

7 Pulmonary arterial hypertension secondary to left-sided obstructive lesions such as coarctation of the aorta, cor triatriatum, mitral stenosis, or relative hypoplasia of the systemic left ventricle is seen in the newborn period.
8 Pulmonary embolic disease is uncommon in pediatrics, but may be encountered in infants with chronic venous lines. Other embolic sources, such as infected vegetations, or thrombi secondary to acute myeloid leukemia, may be rarely encountered.
9 Residual pulmonary hypertension can be present after surgical repair of congenital heart defects in the early or late postoperative period.

Techniques and pitfalls of assessing the pediatric patient with suspected pulmonary arterial hypertension

In the pediatric population the diagnosis of idiopathic pulmonary arterial hypertension is made only after an exhaustive search for an underlying associated defect. Therefore, the exclusion of an associated intracardiac or extracardiac shunt lesion is essential. Whereas an associated perimembranous ventricular septal defect, atrial septal defect or patent ductus arteriosus is rarely overlooked, this is not the case with an aortopulmonary window. Frequent "dropout" in the area where the aorta and pulmonary artery cross may give the impression of an aortopulmonary window. However, inadequate interrogation of this region may result in the defect being missed, particularly in the child with a poor ultrasound window. As the majority of aortopulmonary windows are large, color Doppler interrogation may not be of great value, particularly as the direction of flow is invariably at right angles to the Doppler beam. Moreover, early increase in pulmonary vascular resistance can limit the degree of left-to-right shunting and remove the secondary clues of left-sided chamber enlargement. Therefore attention should be paid to the right-sided structures, such as secondary dilation of the main pulmonary artery and right ventricle.

A similar situation arises in cases where there is absence of a branch pulmonary artery and an associated intracardiac or extracardiac shunt, or in the setting of anomalous origin of a branch pulmonary artery from the aorta. In the latter case, the abnormally arising pulmonary artery may lie in close proximity to its counterpart, giving the impression that they are connected. It is therefore imperative to be sure that the branch pulmonary arteries and their origins are clearly defined. Also, when the mediastinal component of the right pulmonary artery is absent, there may be an echo-free space in its place that gives the appearance of the artery. In this setting, the clue is the absence of flow in this echo-free space.

Doppler interrogation of the pulmonary veins is an important component of the evaluation of any new referral with suspected congenital heart disease, even more so in the patient with suspected pulmonary arterial hypertension. This is readily achieved with the use of color Doppler in the apical and subcostal coronal views, with supplementary interrogation from the suprasternal coronal view in smaller patients. The normal pattern is that of low-velocity phasic flow [5–7], which is in marked contrast to an obstructive pattern of higher-velocity turbulent flow. It must be remembered that in some cases there is total occlusion of an extraparenchymal pulmonary vein, which is difficult to diagnose unless there is an excellent ultrasound window as seen in the newborn and small infant. Although the amount of pulmonary blood flow to the obstructed side of a pulmonary artery is reduced, it is usually still possible to detect the turbulent velocity pattern in the affected pulmonary vein. Interpretation of pulmonary venous velocity profiles may be difficult in cases with an associated large left-to-right shunt and associated mild pulmonary vein stenosis. In this setting, the left-to-right shunt increases the peak systolic and diastolic velocities, making interpretation difficult. It is therefore important for all such cases to undergo pulmonary vein interrogation after surgical repair, or following occlusion with an interventional device. Another area of confusion relates to the increased pulmonary venous Doppler velocity that is frequently observed in the left lower pulmonary vein. This profile is due to mild compression by the descending aorta (with a left aortic arch).

Echocardiographic techniques to evaluate the pulmonary vascular bed

Different echocardiographic techniques can be combined to assess right ventricular pressures and pulmonary arterial pressure. The techniques used may vary between different patients and is also determined by the underlying causes of elevated pulmonary arterial pressures. The techniques include:

- Peak velocity of the tricuspid valve regurgitation jet to estimate RV systolic pressure and pulmonary artery systolic pressure.
- End-diastolic Doppler velocity from the pulmonary regurgitant jet to estimate end-diastolic RV and PA pressure.
- Indirect assessment of pulmonary arterial hypertension looking at septal curvature.
- If ventricular septal defect is present the systolic Doppler gradient between the left and right ventricle can be measured and based on this difference the RV systolic pressure can be estimated. In the absence of associated right ventricular outflow tract obstruction this reflects systolic PA pressure. The same principle can be used in case of a patent arterial duct or systemic-to-pulmonary artery shunts. Doppler assessment can be performed for the assessment of systolic, diastolic and mean pulmonary artery pressure. Measurements of pulmonary capacitance and compliance can be made by combining Doppler interrogation techniques.

Tricuspid valve regurgitation

Tricuspid valve regurgitation provides the most consistent means for measuring right ventricular and pulmonary artery

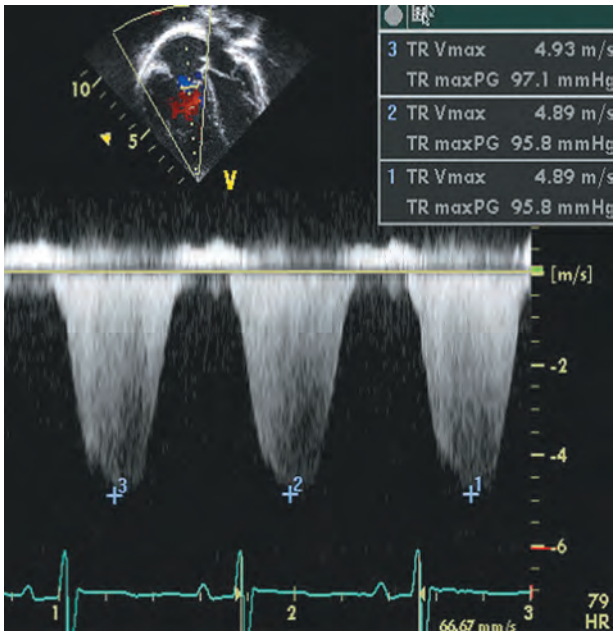


Figure 45.1 Doppler trace of tricuspid valve regurgitation indicating elevated right ventricular pressure.

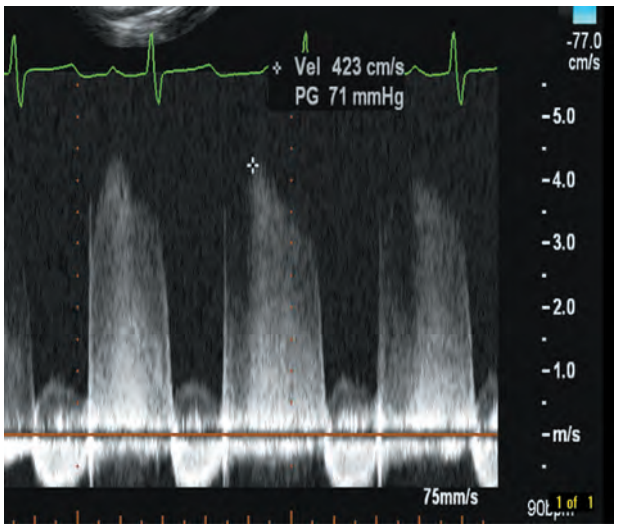


Figure 45.2 Pulmonary regurgitation Doppler trace in a patient with pulmonary hypertension. Note the peak Doppler velocity is 71 mmHg, with an associated high end-diastolic velocity.

systolic pressure, in the absence of right ventricular outflow tract obstruction [8]. To achieve this, an adequate spectral Doppler trace is essential to avoid underestimation of the maximum Doppler gradient. Color Doppler is helpful in ensuring that the Doppler interrogation is parallel to the regurgitant jet. It is important to interrogate the regurgitant jet from multiple views to ensure that the maximum velocity has been recorded (Figure 45.1). Also, in patients with a ventricular septal defect a left ventricle-to-right atrial shunt may contaminate the tricuspid regurgitant jet, which can result in erroneous RV pressure estimation. To estimate systolic right ventricular pressure (RVSP) based on the tricuspid regurgitant jet, determination of right atrial pressure (RAP) is necessary as RVSP = 4(peak TR velocity)^2 + RAP. In the absence of an absolute RA pressure measurement, an indirect assessment of RA pressure can be performed by cross-sectional imaging of the inferior vena cava. In general, if the right atrial pressure is less than 10 mmHg, the inferior vena cava should collapse during inspiration by more than 50% [9]. If this respiratory size variability cannot be detected this indicates that the RA pressure is greater than 10 mmHg. If the inferior vena cava is also dilated then the RA pressure probably exceeds 20 mmHg. This technique cannot be used if a patient is intubated and receives positive-pressure ventilation.

Pulmonary regurgitation for pulmonary artery end-diastolic pressure

Physiologic pulmonary regurgitation is present in a large number of normal individuals and the end-diastolic velocity of the Doppler signal obtained from the regurgitant jet can be used as an estimate of end-diastolic pulmonary artery pressure. As with tricuspid valve regurgitation, it can be difficult to obtain a reliable measurement. The Doppler acquisition needs to be aligned parallel to the angle of the regurgitant jet. This is usually possible, as the majority of jets are central and not entrained (Figure 45.2). When the signal is weak, it may be difficult to accurately measure the end-diastolic velocity. To overcome this limitation, the signal may be enhanced with the use of contrast agents and in one series an enhancement of weak signals could be obtained in 96% of cases [10]. For the estimation of end-diastolic pulmonary artery pressure, an indirect measure of right atrial pressure can be used as a surrogate for end-diastolic RV pressure. Apart from the end-diastolic velocity, it has been shown that there is a good correlation between invasive mean pulmonary artery pressure and the peak early diastolic velocity as measured from the pulmonary regurgitation Doppler signal [11]. This is a fortuitous relationship, as mean pulmonary artery pressure is a calculation, rather than a real physiologic event. This measurement is of value, as mean pulmonary artery pressure is an important component of calculated pulmonary vascular resistance.

Based on an excellent linear relationship between invasively measured systolic, diastolic and mean pulmonary artery pressures, it has been possible to reliably estimate mean and diastolic pulmonary artery pressure from tricuspid regurgitant Doppler echocardiography [12]. Using a regression equation, diastolic pulmonary artery (PA) pressure can be measured from the peak tricuspid regurgitant jet using the following formula:

$$\text{PA diastolic pressure} = 0.49 \times \text{PA systolic pressure (from peak TR gradient)}.$$

Interventricular septal shape

If direct pulmonary artery assessment is not possible, indirect clues can be used for the estimation of RV pressure. Elevation

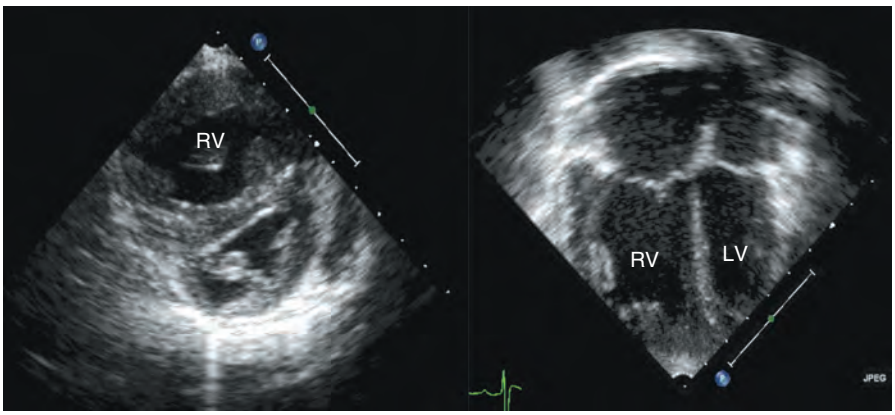


Figure 45.3 Montage from a case with pulmonary hypertension and systemic right ventricular pressure. Note the flat interventricular septum, as seen in systole. The right-hand panel shows dilation of the right ventricle. LV, left ventricle; RV, right ventricle.

of RV pressures affects RV size and thickness. Acute increase in RV pressure results in RV dilation as a compensatory mechanism to maintain RV output. Chronic increase in RV pressure causes RV remodeling with variable degrees of RV hypertrophy and dilation. Increased RV pressure typically affects interventricular interaction as reflected by the position of the interventricular septum. RV dilation causes flattening of the interventricular septal shape in diastole while elevated RV pressure also causes flattening of the septum in systole and eventually it can bulge into the LV cavity. Typically systolic flattening of the interventricular septum and D-shaping of the LV can be used as indicators for elevation of RV pressures (Figure 45.3) but obviously this does not yield absolute values.

Systolic time intervals

Time intervals can also be used as indirect techniques for the assessment of pulmonary artery pressure [13]. Most of the studies validating this methodology have been performed in adults, with slower and less variable heart rates. Almost every time interval is intrinsically influenced by heart rate which is problematic in the pediatric population. Different time intervals can be measured:

Pre-ejection period (PEEP) is measured from the onset of the "q" wave to the onset of the pulmonary artery systolic forward flow. The duration of PEEP is directly related to the pulmonary artery pressure and pulmonary arterial impedance but is inversely proportional to RV contractile function.

Pulmonary ejection time (ET) measures the duration of pulmonary forward flow during systole. As is PEEP, this is heart rate dependent. At a given heart rate, ejection time is directly related to stroke volume and inversely related to contractility.

Acceleration time (AT) is measured as the time interval from the onset to the peak of ejection. AT is directly related to RV systolic function, and is inversely related to pulmonary artery pressure and pulmonary vascular resistance. If AT is <100 ms, this suggests the presence of pulmonary arterial hypertension.

All of these parameters, namely PEEP, ET, and AT, assess the interaction between pressure and flow. Despite an overall good correlation in adult studies, there has been a considerable scatter when comparing individual values. In an attempt to overcome this limitation it has been suggested that the relationship between the pulmonary and systemic measurements be used, which takes into account the interaction between the two circulations [14].

Tricuspid and pulmonary valve time intervals

The time interval between pulmonary valve closure and tricuspid valve opening can also be used to indirectly assess systolic right ventricular pressure [15–17]. This period corresponds to the isovolumic relaxation period but in most patients this is not truly isovolumic as tricuspid regurgitation is present in the majority of patients. As pulmonary artery pressure increases this time period becomes longer. A similar technique can be used in cases where the duration of the tricuspid regurgitant (TR) jet can be measured, but not the peak. In cases with pulmonary hypertension and good systolic right ventricular function, there is a strong correlation between the time between pulmonary valve closure and the end of the tricuspid regurgitant jet and the right ventricular systolic pressure. As with most interval measurements this would be affected by heart rates that lie outside the normal range. Indeed, in the adult study that reported this technique, the heart rates were between 70 and 110 bpm [15]. Of note, this correlation did not appear to hold in cases with cardiomyopathy [15]. Using a similar technique, another group overcame this problem in patients with heart failure, by using the relationship between pulmonary valve opening and tricuspid regurgitation to assess pulmonary artery diastolic pressure [18]. This was achieved by measuring the time between the R wave on the electrocardiogram (ECG) and the opening of the pulmonary valve and superimposing this on the tricuspid regurgitant velocity profile. Measurement of the tricuspid regurgitant velocity at the time of pulmonary valve opening has been shown to correlate with the pulmonary artery diastolic pressure.

Ventricular septal defect and right ventricular systolic pressure measurement

Ventricular septal defects (VSDs) provide a window to the pulmonary vascular bed, either in the presence or absence of

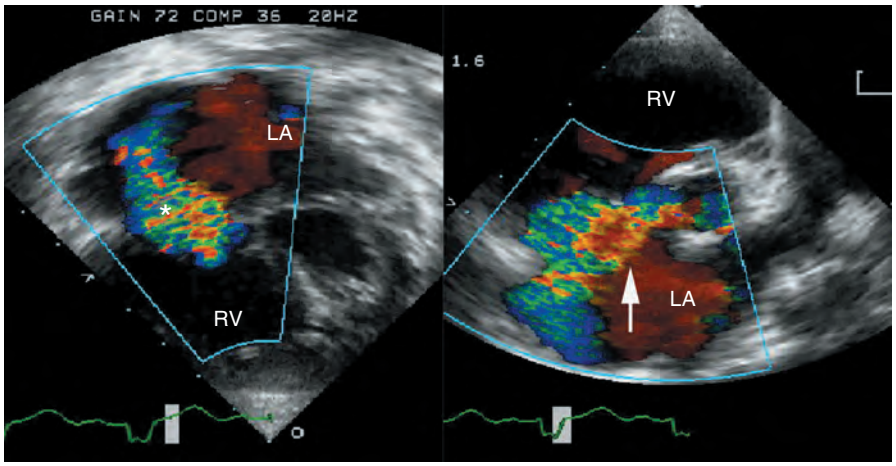


Figure 45.4 Ventricular septal defect with tricuspid valve regurgitation and an obligatory left ventricle (LV)-to-right atrium (RA) shunt, as indicated by the arrow in the right-hand panel. The asterisk represents the tricuspid regurgitant jet. LA, left atrium; RV, right ventricle.

associated pulmonary outflow tract obstruction. Continuous-wave (CW) Doppler techniques have been shown to provide an accurate assessment of right ventricular and systolic pulmonary artery pressures. Certain technical and theoretical considerations must be appreciated when using this approach. Maintaining a parallel angle between the VSD jet and Doppler beam is important to prevent underestimation of the true pressure drop. This is aided by using color Doppler and multiple views to obtain the maximum velocity. Although this is possible in the majority of cases, it can be somewhat challenging in those with a perimembranous inlet defect, where the color jet skirts the undersurface of the tricuspid valve in a lateral direction. Likewise, in a perimembranous inlet VSD there may be an associated obligatory left ventricular-to-right atrial shunt that contaminates the continuous-wave signal (Figure 45.4).

Although the correlation between Doppler assessment and absolute pressure differences between a fluid-filled catheter in the left and right ventricles has been very satisfactory in moderately sized defects, this has not been the case when the defect is small [19,20]. In this setting, there may be an underestimation of the true pressure drop between the left and right ventricles due to jets that are often at a large angle with the Doppler beam. Also, in small defects the maximum velocity can overestimate the true pressure drop across the VSD. Large VSDs with increased right ventricular and pulmonary artery pressures pose another problem. Some authors have reported an overestimation of the actual measured pressure drop across the VSD in this setting. It has been suggested that the proximal velocity be taken into consideration using the formula pressure gradient, $4(V_2 - V_1)^2$, to measure the absolute pressure drop across a large defect (V_2 is the velocity distal to and V_1 proximal to the obstruction). Moreover, it must be remembered that Doppler provides true peak instantaneous pressure gradients, whereas hemodynamic measurements represent peak-to-peak differences between the right and left ventricles. The contraction of the left and right ventricles also occurs at a slightly different time, which is exacerbated when there is complete right bundle branch block (Figure 45.5).

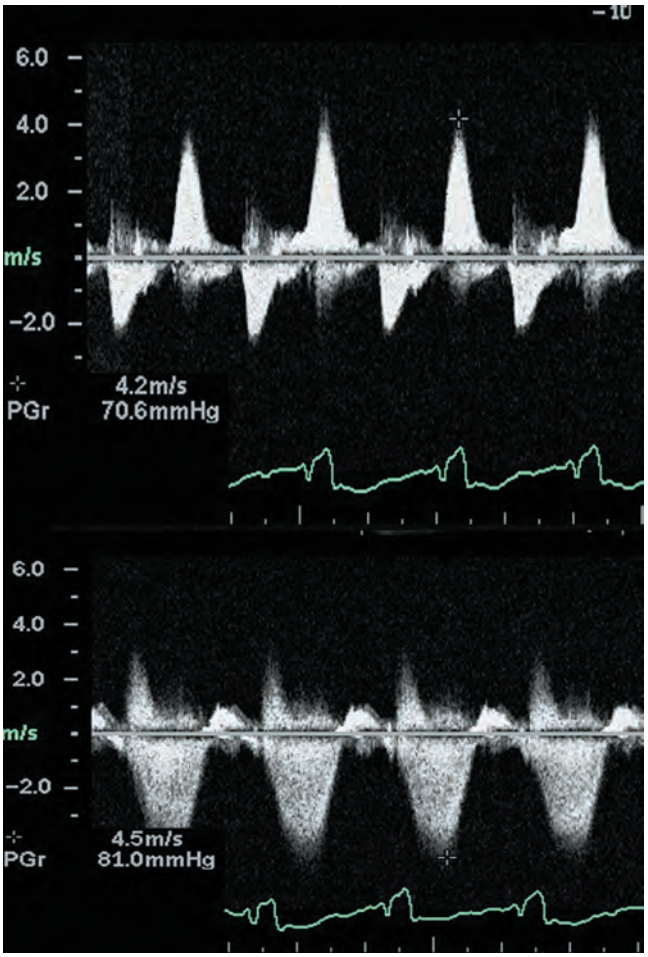


Figure 45.5 Doppler traces from an anterior ventricular septal defect. Note that the tricuspid valve regurgitation jet demonstrates a right ventricular (RV) pressure of 81 mmHg + right atrial pressure (RAP), whereas there is a 70 mmHg pressure drop across the ventricular septal defect. Note there is complete right bundle branch block, which probably accounts for the difference. In this case there was no obligatory left ventricle-to-right atrium shunt.

When using this technique to predict systolic right ventricular or pulmonary artery pressure an accurate systolic blood pressure measurement is also necessary. The pressure drop across the defect is then subtracted from the systolic blood pressure to provide an absolute value. Although this works in practice, it must be remembered that distal peripheral systolic blood pressure is higher than that measured centrally. Muscular VSDs frequently pose a challenge, as it may be difficult to obtain a Doppler beam parallel to the jet, resulting in underestimation. Also, muscular defects are frequently long and irregular, making measurements potentially inaccurate. Unlike perimembranous and subarterial defects, where the diameter remains fairly constant throughout systole, those in the muscular septum frequently become smaller throughout the cardiac cycle, which will affect the velocity measurements.

In the presence of a VSD and associated right ventricular outflow tract obstruction, a combination of the systolic blood pressure and velocity across the VSD and right ventricular outflow tract permits an assessment of systolic pulmonary artery pressure. This is of particular importance in those cases where it is felt appropriate to delay complete repair beyond the first 6 months of life. When the VSD is restrictive, it is sometimes difficult to separate a left-to-right jet directed toward the right ventricular outflow tract, from that across the obstruction, particularly when imaging from the precordium. If the child is young enough, a right anterior oblique view may help in separating the two jets, permitting a parallel angle between the Doppler beam and the right ventricular outflow tract. In the presence of tetralogy of Fallot with a long tunnel-like obstruction, there may be a problem with either overestimating the true pressure drop, or underestimating it if there is significantly reduced pulmonary blood flow.

Patent arterial duct and pulmonary artery pressure measurement

The patent arterial duct provides a valuable method for measuring pulmonary artery pressure, particularly in the younger patient where it is more likely to be encountered. Simultaneous hemodynamic and Doppler measurements have demonstrated that this is one of the few techniques that provide a measurement of mean pulmonary artery pressure [21] (Figure 45.6). As a result of jet entrainment, the majority of ductal left-to-right shunting hugs the anterior wall of the main pulmonary artery, providing a parallel angle for Doppler interrogation. If the mean and systolic blood pressures are obtained, then mean and systolic pulmonary artery pressures can be measured by subtracting the mean and peak pressure drop across the patent arterial duct from these measurements of blood pressure. The mean Doppler gradient across the patent arterial duct is obtained by planimetry of the spectral recording between two R–R intervals (Figure 45.7). This technique may not be applicable in several settings. Firstly, if the jet is very eccentric then parallel interrogation is difficult, resulting in an underestimation of the true pressure drop across the patent arterial duct. Secondly, if the patent arterial

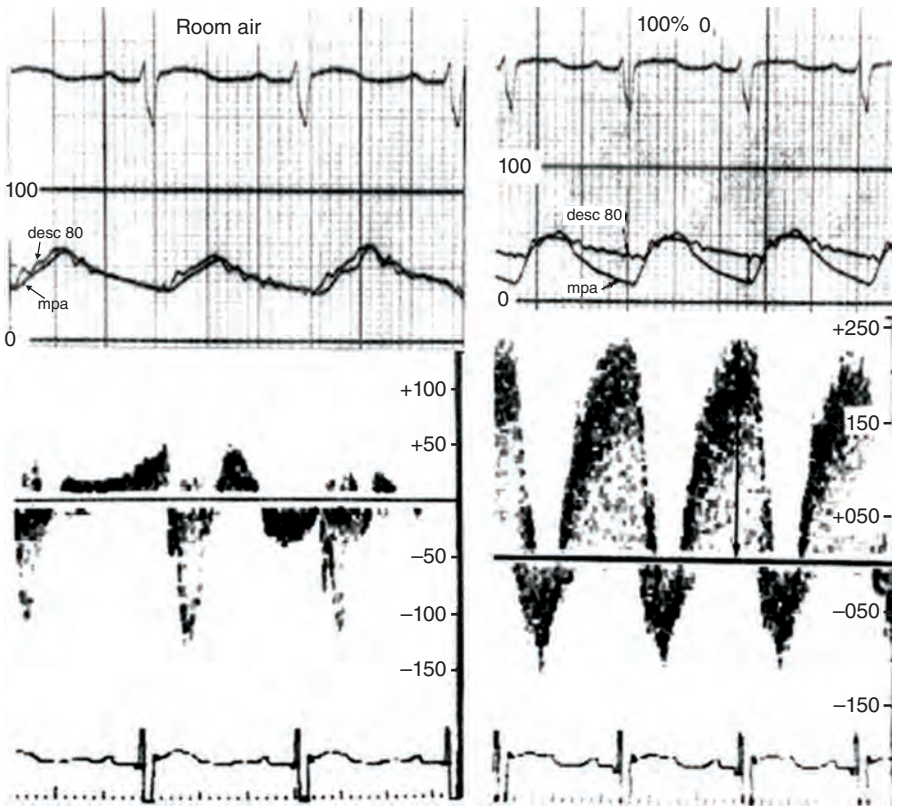


Figure 45.6 Demonstration of the use of the patent ductus arteriosus in the evaluation of pulmonary artery reactivity. The right-hand panel shows the drop in pulmonary artery pressure following the administration of oxygen.

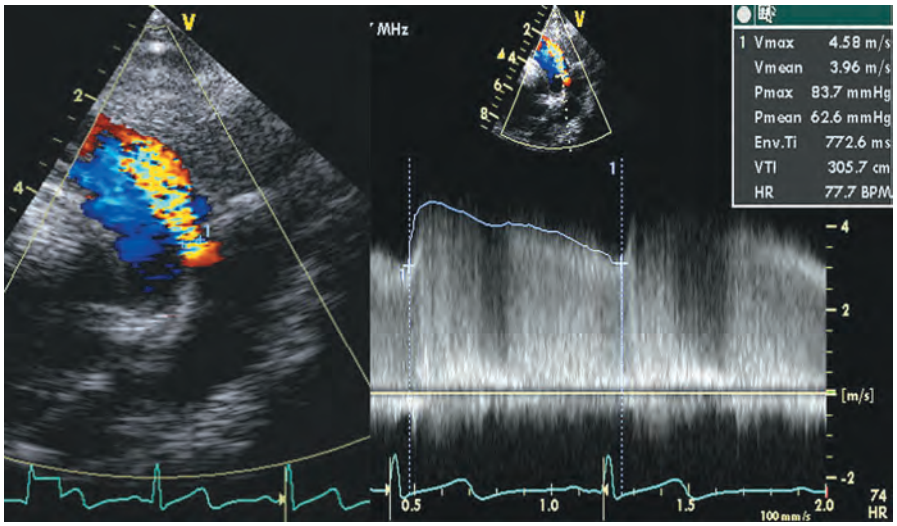


Figure 45.7 Doppler echocardiogram of a patent arterial duct. Note in the left-hand picture the entrainment of the jet toward the anterior wall of the main pulmonary artery. The right-hand panel demonstrates the calculation of mean and peak pulmonary systolic artery pressures.

duct is very small only abbreviated left-to-right shunting can be detected making measurements unreliable. Thirdly, if the patent arterial duct is tortuous, as seen in cases with severe right ventricular outflow tract obstruction, then parallel Doppler interrogation is difficult.

In cases with bidirectional shunting across the patent ductus arteriosus there is usually left-to-right shunting in diastole, with right-to-left in systole, making planimetry difficult. The presence of bidirectional shunting indicates a high pulmonary artery pressure and, more importantly, the duration of right-to-left shunting provides important insight into the pulmonary vascular bed. In general, a greater degree of right-to-left shunting in systole and into diastole indicates suprasystemic pulmonary artery pressure. This observation is seen more frequently in cases with pulmonary hypertension in the newborn period with a normal heart [22], hypoplastic left heart syndrome and a restrictive atrial septal defect or obstructed total anomalous pulmonary venous drainage.

Measurement of pulmonary artery pressure from systemic-to-pulmonary artery shunts

Another technique for assessing pulmonary artery pressure has been the use of Doppler gradients across systemic-to-pulmonary artery shunts, which are still a common occurrence in the small child with congenital heart disease. Although this is relatively simple to do, its validity has been questioned using the simplified modified Bernoulli equation [23].

Measurements of pulmonary artery capacitance by Doppler

Background

Pulmonary vascular resistance is the resistance in the small vessels and the pulmonary vascular cross-sectional area, but does not account for the large and medium vessels, nor the pulsatile elements in the pulmonary circulation. Pulmonary vascular capacitance is a measure of workload on the right ventricle. When the capacitance is low all of the forward blood goes to the peripheral vessels, whereas when it is high the blood is initially stored in the large-capacitance vessels, which decreases the load on the heart. A wide pulse pressure, seen in those with low capacitance is a known risk factor on the left side of the heart [24]. The workload on a pump is proportional to forward output and the impedance of the vascular bed. Impedance is proportional to resistance and inversely proportional to capacitance. Pulmonary compliance represents the stretch of the vessel walls and how much they will increase in volume for a given pressure.

Pulmonary vascular capacitance measures how much the vascular tree dilates with each contraction of the right ventricle. Therefore, capacitance = stroke volume (mL)/pulse pressure (mmHg). By echocardiography the stroke volume can be calculated from the left or right ventricular outflow tracts, for example:

$$\text{right ventricular stroke volume (mL)} = \text{pulmonary valve diameter (cm/2)}^2 \times \pi \times \text{VT I (cm)}$$

(VTI stands for velocity time integral). The pulse pressure is the peak systolic gradient from tricuspid valve regurgitation (TR) minus the end-diastolic pressure from pulmonary regurgitation (PR), that is:

$$\text{SV (mL)}/4 \times (\text{TR}^2 - \text{PR}^2)$$

(SV stands for stroke volume). This noninvasive measurement of pulmonary vascular capacitance was found to be the best predictor of adverse events in a group of adults with pulmonary hypertension, with a risk ratio of 3:1 [24]. This measurement also was a better predictor of adverse events than systolic, diastolic and mean pulmonary artery pressures; however, in a multivariate model pulmonary vascular resistance added to prognostic value. The measurement of pulmonary vascular

capacitance is probably a strong predictor of adverse events, as it takes into consideration the load on the right side of the heart and the status of the lung parenchyma. To measure pulmonary vascular capacitance it is necessary to have a measurement of pulmonary diastolic pressure from pulmonary regurgitation. As not all patients have pulmonary valve regurgitation, other authors have used data derived from invasive techniques. This is based on the relationship between pulmonary artery diastolic and systolic pressures [25]:

$$\text{pulmonary artery diastolic pressure} = 0.49 \times \text{pulmonary artery systolic pressure.}$$

Pulmonary arterial compliance and Doppler

Pulmonary vascular resistance is a steady-state parameter and measures opposition to continuous flow. However, this ignores the very nature of pulmonary flow, which is pulsatile in nature. Flow into the pulmonary vascular bed requires a coordinated effort from the right ventricular pump in systole and the pulmonary vascular bed in diastole. In an attempt to measure this variation throughout the cardiac cycle, a combination of change in pulmonary artery wall diameter throughout the cardiac cycle using color M-mode Doppler tissue imaging, coupled with systolic pressure as measured from tricuspid valve regurgitation, has been used [26]. Color M-mode Doppler tissue imaging has high spatial (1.6–1.9 mm) and temporal resolution (5 ms) and overcomes some of the limitations of other techniques used to detect instantaneous changes in the vessel diameter over time. There appears to be a very good correlation between the changes in diameter of the pulmonary artery as measured by this technique compared with intravascular ultrasound:

$$\text{compliance (dynes)} = [(D(s) - D(d))/(D(d) \times P(s))] \times 10^4$$

where D(s) = systolic diameter, D(d) = diastolic diameter, and P(s) = systolic pressure.

This technique may play a role in evaluating treatment regimens for pulmonary hypertension. For example, increased pulmonary artery pressure may produce a stiffer vessel on the basis of the strain-stiffness effect, rather than being secondary to abnormalities of the vessel wall. With vasodilator therapy, if it is a strain-stiffness effect then the response to treatment will be different than if there is a true abnormality in the vessel wall. In one study it was found that a >40% change in right pulmonary artery diameter per 100 mmHg was consistent with a compliant vessel, whereas a value of <40% indicated a stiffer vessel [26]. This technique is not applicable if there is significant pulmonary regurgitation. Of note, the authors commented that the 40% cutoff value may change through further studies in which a wider variation of pressures could be assessed. Also, the technique required further validation through challenging with high pressure-high flow and high pressure-low flow situations.

The impact of pulmonary arterial hypertension on the right ventricle

The ability of the right ventricle to function under increased afterload is an important determinant of illness severity. Right ventricular dysfunction is a powerful predictor of adverse outcomes. Additionally, right ventricular dilation and dysfunction may impair left ventricular function due to ventricular interdependence. Adult patients with a right ventricular diameter >36.5 mm had an increased death rate compared to patients with a right ventricular diameter ≤36.5 mm. However, patients with a right ventricular diameter >36.5 mm associated with a right ventricular wall thickness >6.6 mm was not associated with a poorer prognosis suggesting that the accompanied hypertrophy decreased the abnormally high right ventricular wall tension [27]. Unfortunately, the complex geometry of the right ventricle makes it unsuitable for geometric measurements of ventricular function. As a result, other echocardiographic predictors of right ventricular function have been evaluated.

Tricuspid annular plane systolic excursion (TAPSE)

TAPSE is the systolic excursion of the tricuspid annulus measured by M-mode through the tricuspid annulus. It reflects longitudinal function of the RV free wall and is an indirect measurement of right ventricular function. TAPSE is reproducible and easy to obtain regardless of heart rate. Normal values for children have been published. TAPSE is a highly sensitive and specific indicator of depressed right ventricular stroke volume index and cardiac index (measured by cardiac catheterization) at a cutoff of 1.8 cm in adult pulmonary hypertension patients [28]. For the pulmonary arterial hypertension cohort, patients with TAPSE <1.8 cm had significantly shorter survival than patients with TAPSE ≥1.8 cm. Another study examining the prognostic value of right ventricular function indices found that patients with TAPSE <15 mm combined with a diastolic left ventricular eccentricity index ≥1.7 had the highest event rate including death and emergency lung transplantation [29]. There has been minimal evaluation of TAPSE in the pediatric population. Pediatric patients with pulmonary hypertension had decreased TAPSE values compared to normal controls, but there was no correlation with outcomes [30].

Myocardial performance index (Tei index)

The Tei index, which measures global ventricular function, has been used to assess the impact of increased pulmonary artery pressure in a pediatric population [31]. It is defined as the (isovolumic relaxation time + isovolumic contraction time)/ejection time. Its relative independence of heart rate makes it theoretically attractive in the pediatric population. It has been used to assess the response to pulmonary vasodilator therapy both in children and adults. Compared with controls, the right ventricular Tei index was higher in those with pulmonary arterial

hypertension, with a reduction in the value following a fall in pulmonary artery pressure [32]. The Tei index is not an index of RV contractility or intrinsic RV systolic function. In animal experiments it has been demonstrated to be very sensitive to acute changes in afterload [33]. It probably reflects ventricular–vascular interactions which explains why it has been shown to be a predictor of outcome in adults with pulmonary hypertension [24]. One of the major difficulties using the Tei index in the RV is its poor reproducibility. It is based on measuring multiple timing intervals obtained on two different Doppler signals (pulmonary outflow and tricuspid inflow).

The use of tissue Doppler and strain imaging in pulmonary hypertension

Tissue Doppler imaging (TDI) allows quantitative assessment of right ventricular systolic and diastolic function by means of measurement of myocardial velocities. Tricuspid annular tissue Doppler velocities represent RV longitudinal function. Systolic velocities are afterload and preload dependent, which makes their interpretation difficult. In children the velocities change with age and are influenced by growth. Finally they should be considered as a regional parameter of RV function. Tricuspid annular TDI has been used to assess the Tei index in combination with peak early mitral inflow velocity to calculate an M-index (mitral inflow velocity/Tei) in patients with idiopathic and secondary pulmonary arterial hypertension due to pulmonary emboli [34]. Those with an embolus had a lower M-index compared with controls or those with primary pulmonary hypertension. By combining the tissue Doppler-derived Tei index with mitral inflow velocity there was a better receiver–operator curve than with the Tei index alone. The advantage of tissue Doppler Tei index measurements is that is easier and more reproducible compared to blood pool Doppler methods.

Another way to measure RV longitudinal function is by measuring RV longitudinal strain and strain rate. This can be done by using tissue Doppler-derived methods but more commonly by speckle-tracking echocardiography. This has been used in adult patients with pulmonary hypertension [35] and there appears to be a good correlation between 2D RV longitudinal strain and strain rate and pulmonary artery pressure and RV ejection fraction. The inter- and intra-observer variability for 2D strain is acceptable. The methodology has been applied to patients with pulmonary arterial hypertension who were shown to have lower longitudinal right ventricular free wall strain compared to normal controls [36]. Moreover reduced strain and SR values were detected in patients with normal Tei index, TAPSE and right ventricular fractional area change.

These techniques have also been used before and after treatment with the pulmonary vasodilators [37]. In this study the basal segment of the right ventricle had a strain of -8.8 ± 4.1 prior to treatment, compared with a normal value of -24.3 ± 4.7 ($p < 0.001$). After treatment, the RV basal strain increased to -13.3 ± 6.2 ($p < 0.001$). There was a weaker correlation with tissue Doppler-derived strain in the same segment ($p < 0.2$), and also a weak correlation with isovolumic acceleration, pre- and post-treatment ($p < 0.2$). The Tei index was also evaluated, and in a similar fashion to tissue Doppler had a weaker correlation with treatment of the pulmonary hypertension. There was a significant drop in pulmonary vascular resistance ($p < 0.001$) with an increase in the 6-minute walk ($p < 0.002$) pre- and post-treatment. Two-dimensional strain ($p < 0.03$) and tricuspid annular excursion ($p < 0.02$) had a weak correlation with the 6-minute walk. Finally, in a study involving 80 adult patients with PAH, average right ventricular longitudinal free wall strain independently predicted right-sided heart failure, clinical deterioration, and mortality [38].

Pericardial effusion

In a prospective, echocardiography study of 82 adult patients with PAH, the presence of a pericardial effusion was significantly associated with mortality. In multivariable analyses, pericardial effusion and an enlarged right atrial indexed area remained predictors of adverse outcomes including mortality [39]. The presence of a pericardial effusion was an independent predictor of mortality in the recent, large REVEAL registry [40].

The impact of pulmonary hypertension on the left ventricle

Left–right ventricular interaction in patients with pulmonary hypertension with an intact ventricular septum may result in an abnormal left ventricular diastolic inflow pattern. This was initially felt to be related to abnormal diastolic function, but more recently has been attributed to altered left ventricular preload. This latter view has been supported by alterations in the mitral E/A pattern, pulmonary venous flow and mitral annular tissue Doppler [41]. In this study, an observed increase in the mitral E/A ratio and pulmonary venous Doppler velocity, with relatively normal mitral tissue Doppler parameters, was observed post-thromboendarterectomy in adults with secondary pulmonary arterial hypertension and preserved right ventricular systolic function. A similar finding of decreased left ventricular filling rate and stroke volume has also been observed by magnetic resonance imaging (MRI) in adults with primary pulmonary hypertension [42]. The role of pericardial constraint, as a cause for abnormal left–right ventricular interaction in pulmonary arterial hypertension, is somewhat controversial. In an acute model of pulmonary hypertension secondary to pulmonary embolus, the observed decrease in left ventricular stroke volume can be reversed by opening the pericardium. However, in a similar chronic model this increase has not been observed, thus questioning the role of pericardial constraint.

References

1 Fox DJ, Khatter RS. Pulmonary arterial hypertension: classification, diagnosis and contemporary management. *Postgrad Med J* 2006;**82**:717–722.

2 Badesch DB, Champion HC, Gomez Sanchez MA, et al. Diagnosis and assessment of pulmonary arterial hypertension. *J Am Coll Cardiol* 2009;**54**:S55–66.

3 Simonneau G, Robbins IM, Beghetti et al. Updated clinical classification of pulmonary hypertension. *J Am Coll Cardiol* 2009;**54**;S43–S54.

4 Cerro MJ, Abman S, Diaz G, et al. A consensus approach to the classification of pediatric pulmonary hypertensive vascular disease: report from the PVRI Pediatric Taskforce, Panama 2011. *Pulm Circ* 2011;**1**:286–298.

5 Keren G, Sherez J, Megidish R, et al. Pulmonary venous flow pattern–its relationship to cardiac dynamics. A pulsed Doppler echocardiographic study. *Circulation* 1985;**71**:1105–1112.

6 Smallhorn JF, Freedom RM, Olley PM. Pulsed Doppler echocardiographic assessment of extraparenchymal pulmonary vein flow. *J Am Coll Cardiol* 1987;**9**:573–579.

7 Smallhorn JF, Burrows P, Wilson G, et al. Two-dimensional and pulsed Doppler echocardiograpy in the postoperative evaluation of total anomalous pulmonary venous connection. *Circulation* 1987;**76**:298–305.

8 Yock PG, Popp RL. Noninvasive estimation of right ventricular systolic pressure by Doppler ultrasound in patients with tricuspid regurgitation. *Circulation* 1984;**70**:657–662.

9 Kircher BJ, Himelman RB, Schiller NB. Noninvasive estimation of right atrial pressure from the inspiratory collapse of the inferior vena cava. *Am J Cardiol* 1990;**66**:493–496.

10 Tanabe K, Asanuma T, Yoshitomi H, et al. Doppler estimation of pulmonary artery end-diastolic pressure using contrast enhancement of pulmonary regurgitant signals. *Am J Cardiol* 1996;**78**:1145–1148.

11 Masuyama T, Kodama K, Kitabatake A, et al. Continuous-wave Doppler echocardiographic detection of pulmonary regurgitation and its application to noninvasive estimation of pulmonary artery pressure. *Circulation* 1986;**74**:484–492.

12 Friedberg MK, Feinstein JA, Rosenthal DN. A novel echocardiographic Doppler method for estimation of pulmonary arterial pressures. *J Am Soc Echocardiogr* 2006;**19**:559–562.

13 Morera J, Hoadley SD, Roland JM, et al. Estimation of the ratio to systemic pressures by pulsed-wave Doppler echocardiography for assessment of pulmonary arterial pressure. *Am J Cardiol* 1989;**63**:862–866.

14 Sorrell VL, Reeves WC. Noninvasive right and left heart catheterization: taking the echo lab beyond an image-only laboratory. *Echocardiogr* 2001;**18**:31–41.

15 Brecker SJD, Xiao HB, Maissouroum M, Gibson DG. Assessment of the peak tricuspid regurgitant velocity from the dynamics of retrograde flow. *Int J Cardiol* 1992;**34**:267–271.

16 Burstin L. Determination of pressure in the pulmonary artery by external graphic recordings. *Br Heart J* 1967;**29**:396–404.

17 Hatle L, Angelsen BAJ, Tromsdal A. Non-invasive estimation of pulmonary artery systolic pressure with Doppler ultrasound. *Br Heart J* 1982;**45**:157–165.

18 Lanzarini L, Fontana A, Campana A, Kletsy C. Two simple echo-Doppler measurements can accurately identify pulmonary hypertension in the large majority of patients with chronic heart failure. *J Heart Lung Transplant* 2005;**24**:745–754.

19 Zhiming G, Yun Z, Weiqiang K, et al. Noninvasive evaluation of interventricular pressure gradient across ventricular septal defect: a simultaneous study of Doppler echocardiography and cardiac catheterization. *Am Heart J* 1992;**124**:176–182.

20 Zhiming G, Yun Zhang, Weiqiang Kang, et al. Noninvasive evaluation of right ventricular and pulmonary artery systolic pressures in patients with ventricular septal defects: simultaneous study of Doppler and catheterization data. *Am Heart J* 1993;**125**:1073–1081.

21 Musewe NN, Smallhorn JF, Benson LN, et al. Validation of Doppler-derived pulmonary arterial pressure in patients with ductus arteriosus under different hemodynamic states. *Circulation* 1987;**76**:1081–1091.

22 Musewe NN, Poppe D, Smallhorn JF, et al. Doppler echocardiographic measurement of pulmonary artery pressure from ductal Doppler velocities in the newborn. *J Am Coll Cardiol* 1990;**15**:446–456.

23 DeGroff CG, Shandas R, Kwon J, Valdes-Cruz L. Accuracy of the Bernoulli equation for estimation of pressure gradient across stenotic Blalock–Taussig shunts: an in vitro and numerical study. *Pediatr Cardiol* 2000;**21**:439–447.

24 Mahapatra S, Nishimura RA, Oh JK, McGoon MD. The prognostic value of pulmonary vascular capacitance determined by Doppler echocardiography in patients with pulmonary arterial hypertension. *J Am Soc Echocardiogr* 2006;**19**:1045–1050.

25 Friedberg MK, Feinstein JA, Rosenthal DN. Noninvasive assessment of pulmonary arterial capacitance by echocardiography. *J Am Soc Echocardiogr* 2007;**20**:186–190.

26 Dyer K, Lanning C, Das B, et al. Noninvasive Doppler tissue measurement of pulmonary artery compliance in children with pulmonary hypertension. *J Am Soc Echocardiogr* 2006;**19**:403–412.

27 Ghio S, Pazzano AS, Klersy C, et al. Clinical and prognostic relevance of echocardiographic evaluation of right ventricular geometry in patients with idiopathic pulmonary arterial hypertension. *Am J Cardiol* 2011;**107**:628–632.

28 Forfia PR, Fisher MR, Mathai SC, et al. Tricuspid annular displacement predicts survival in pulmonary hypertension. *J Am Respir Crit Care Med* 2006;**174**:1034–1041.

29 Ghio S, Klersy C, Magrini G, et al. Prognostic relevance of the echocardiographic assessment of right ventricular function in patients with idiopathic pulmonary arterial hypertension. *Int J Cardiol* 2010;**140**:272–278.

30 Arce OX, Knudson OA, Ellison MC, et al. Longitudinal motion of the atrioventricular annuli in children: reference values, growth related changes, and effects of right ventricular volume and pressure overload. *J Am Soc Echocardiogr* 2002;**15**:906–916.

31 Dyer KL, Paulkis LB, Das Bibhuti, et al. Use of myocardial performance index in pediatric patients with idiopathic pulmonary hypertension. *J Am Soc Echocardiogr* 2006;**19**:21–27.

32 Dambrauskaite V, Delcrois M, Claus P, et al. The evaluation of pulmonary hypertension using right ventricular myocardial isovolumic relaxation time. *J Am Soc Echocardiogr* 2005;**18**:1113–1120.

33 Cheung MM, Smallhorn JF, Redington AN, Vogel M. The effects of changes in loading conditions and modulation of inotropic state on the myocardial performance index: comparison with conductance catheter measurements. *Eur Heart J* 2004;**25**:2238–2242.

34 Shih-Hung Hsiao, Shu-Mei Chang, Chiu-Yen Lee, et al. Usefulness of tissue Doppler parameters for identifying pulmonary embolism in patients with signs of pulmonary hypertension. *Am J Cardiol* 2006;**98**:685–690.

35 Pirat B, McCulloch ML, Zoghbi WA. Evaluation of global and regional right ventricular systolic function in patients with pulmonary hypertension using a novel speckle tracking method. *Am J Cardiol* 2006;**98**:699–704.

36 Kittipovanonth M, Bellavia D, Chandrasekaran K, et al. Doppler myocardial imaging for early detection of right ventricular dysfunction in patients with pulmonary hypertension. *J Am Soc Echo* 2008;**21**:1035–1041.

37 Borges AC, Knebel F, Eddicks S, et al. Right ventricle function assessed by two-dimensional strain and tissue Doppler echocardiography in patients with pulmonary arterial hypertension and effect of vasodilator therapy. *Am J Cardiol* 2006;**98**:530–534.

38 Sachdev A, Villarraga HR, Frantz RP, et al. Right ventricular strain for prediction of survival in patients with pulmonary arterial hypertension. *Chest* 2011;**139**:1299–1309.

39 Raymond RJ, Hinderliter AL, Willis PW, et al. Echocardiographic predictors of adverse outcomes in primary pulmonary hypertension. *J Am Coll Cardiol* 2002;**39**:1214–1219.

40 Benza RL, Miller DP, Gomberg-Maitland M, et al. Predicting survival in pulmonary arterial hypertension: insights from the Registry to Evaluate Early and Long-Term Pulmonary Arterial Hypertension Disease Management (REVEAL). *Circulation* 2010;**122**:164–172.

41 Gurudevan SV, Malouf PJ, Auger WR, et al. Abnormal left ventricular diastolic filling in chronic thromboembolic pulmonary hypertension–true diastolic dysfunction or left ventricular underfilling? *J Am Coll Cardiol* 2007;**49**:1334–1339.

42 Gan Tji-Joong, Lankhaar Jan-Willem, Marcus JT, et al. Impaired left ventricular filling due to right to left ventricular interaction in patients with pulmonary arterial hypertension. *Am J Physiol Heart Circ Physiol* 2006;**290**:H1528–1533.

APPENDIX

Normal Echocardiographic Values for Cardiovascular Structures

Steven D. Colan
Department of Pediatrics, Harvard Medical School; Department of Cardiology, Boston Children's Hospital, Boston, MA, USA

The normal population on which these measurements are based and the methods of derivation of the regression equations and confidence intervals are described in Chapter 5 and in Sluysmans and Colan [1].

M-mode methods. The methods used in the recording and measurement of the M-mode normative data for the left ventricle (LV) that are presented in Figures A.1–A.6 and the calculation of the derived values of percent fractional shortening (Figure A.7), and rate-corrected velocity of circumferential fiber shortening (Figure A.8) are presented in detail in [2].

Two-dimensional (2D) dimension data. The methods used in the recording and measurement of the 2D normative data for the LV that are presented in Figures A.9–A.14 and the calculation of the derived values of percent fractional shortening (Figure A.15), and rate-corrected velocity of circumferential fiber shortening (Figure A.16) are described in [3].

Vascular and valvar dimensions and areas. The dimensions of all vascular and valvar structures (Figures A.17–A.35) were measured from inner surface to inner surface at the moment of maximal expansion during the cardiac cycle (mid-systole for arterial measurements and early diastole for atrioventricular valve annuli).

LV mass and volume measurements. The end-diastolic endocardial and epicardial, and the end-systolic endocardial short-axis cross-sectional area of the LV were measured from parasternal short-axis images. The end-diastolic endocardial (Figure A.36) and epicardial, and the end-systolic (Figure A.37) endocardial long-axis lengths of the LV were measured on 4-chamber apical views. End-diastole for these measurements was defined as the frame following mitral valve closure and end-systole was defined as the frame preceding mitral valve opening (Figure A.38). The end-diastolic endocardial (EDV, Figure A.39) and epicardial, and the end-systolic endocardial (ESV, Figure A.40) volumes were then calculated from their respective lengths and areas using the formula [3]:

$$\text{volume} = 5/6 \times \text{area} \times \text{length}.$$

Left ventricular mass (LVM) was calculated as the difference between the epicardial and endocardial volumes multiplied by the specific gravity of the myocardium (1.05). Ejection fraction was calculated as (EDV – ESV)/EDV.

Mitral and tissue Doppler measurements. The mitral inflow velocities and the left ventricular basilar lateral wall and septal tissue velocities were obtained as described in [3].

Echocardiography in Pediatric and Congenital Heart Disease: From Fetus to Adult, Second Edition. Edited by Wyman W. Lai, Luc L. Mertens, Meryl S. Cohen and Tal Geva.
© 2016 John Wiley & Sons, Ltd. Published 2016 by John Wiley & Sons, Ltd.
Companion website: www.lai-echo.com

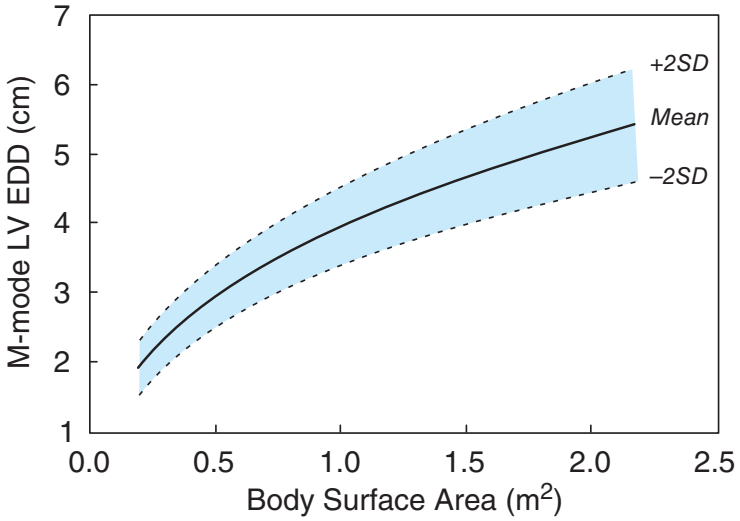


Figure A.1 M-mode left ventricular (LV) end-diastolic dimension (EDD) versus body surface area.

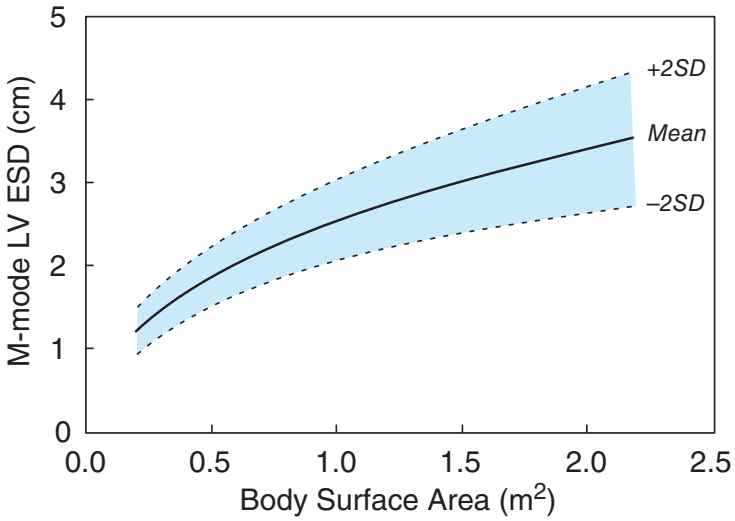


Figure A.2 M-mode left ventricular (LV) end-systolic dimension (ESD) versus body surface area.

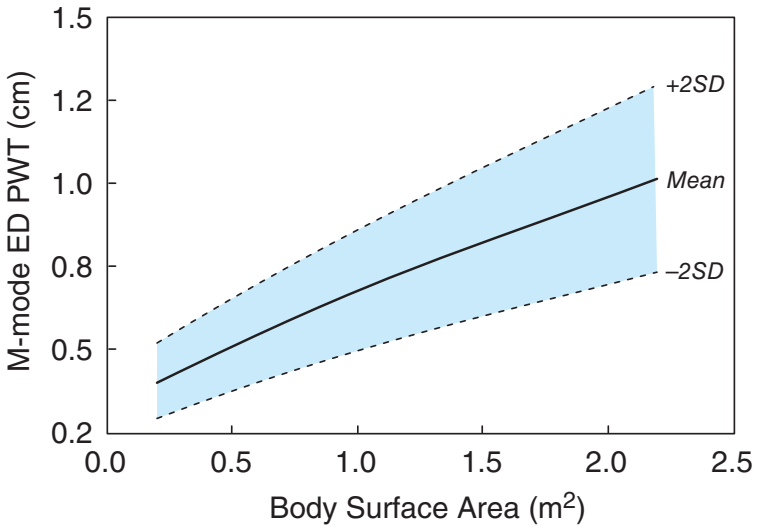


Figure A.3 M-mode left ventricular end-diastolic (ED) posterior wall thickness (PWT) versus body surface area.

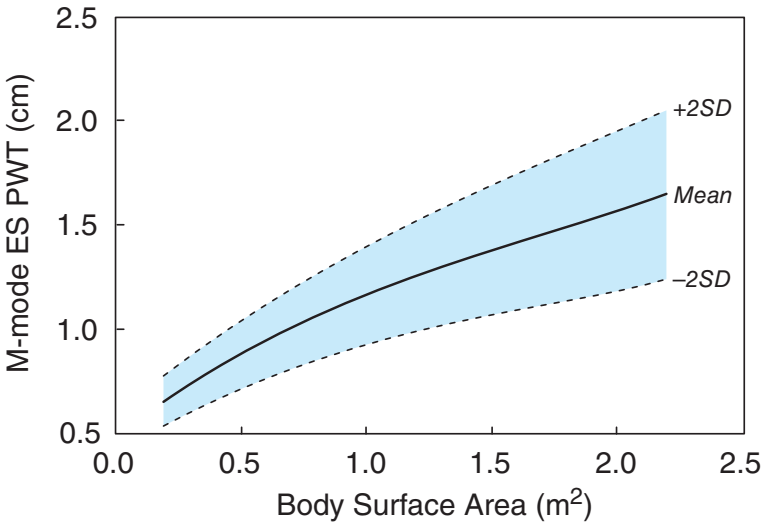


Figure A.4 M-mode left ventricular end-systolic (ES) posterior wall thickness (PWT) versus body surface area.

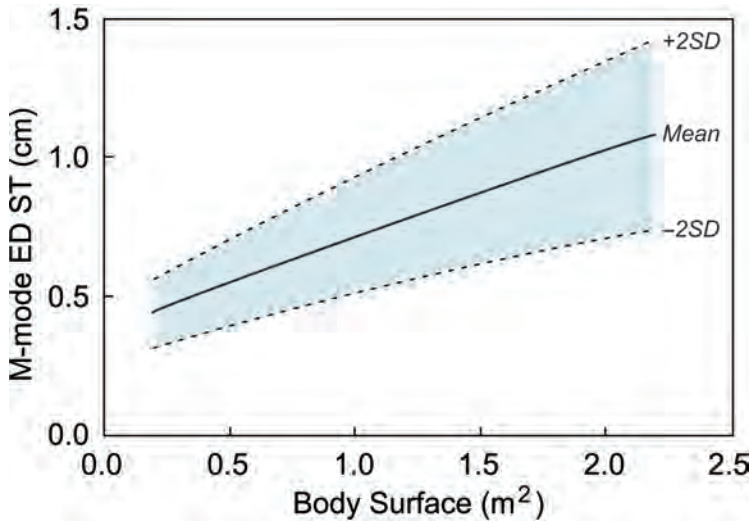


Figure A.5 M-mode end-diastolic (ED) septal thickness (ST) versus body surface area.

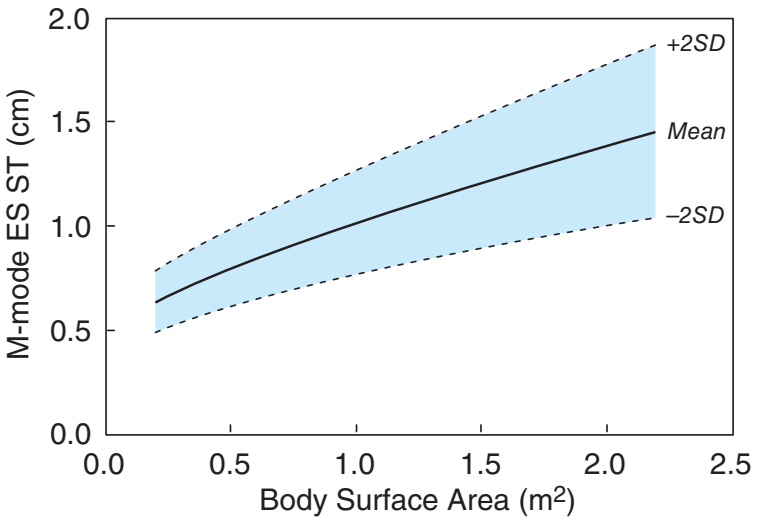


Figure A.6 M-mode end-systolic (ES) septal thickness (ST) versus body surface area.

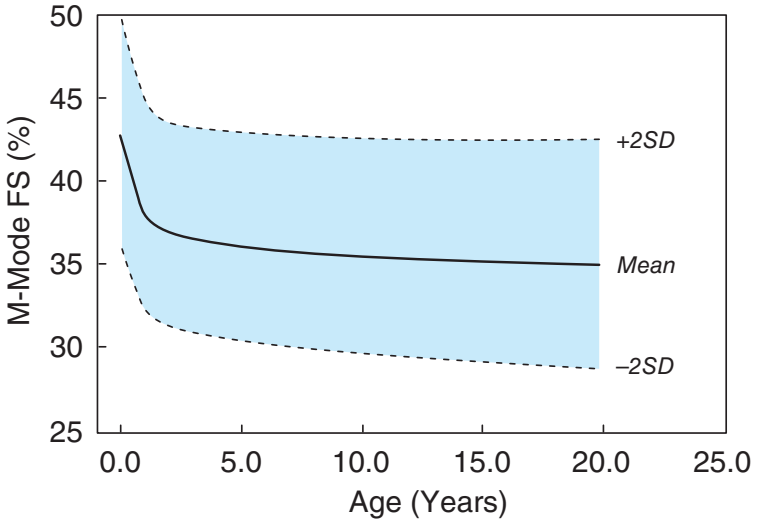


Figure A.7 M-mode left ventricular endocardial percent fractional shortening (FS) versus age. Percent fractional shortening (FS) is calculated as 100∗(EDD – ESD)/EDD where EDD = end-diastolic dimension and ESD = end-systolic dimension.

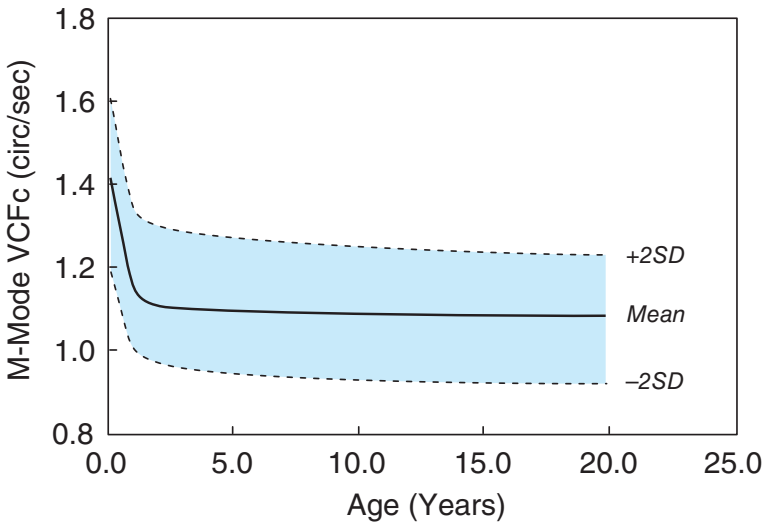


Figure A.8 M-mode left ventricular endocardial rate-corrected velocity of circumferential fiber shortening (VCFc) versus age. VCFc was calculated as FS/ETc, where FS is fractional shortening and ETc is ejection time divided by the square root of the Q–Q interval on the electrocardiogram.

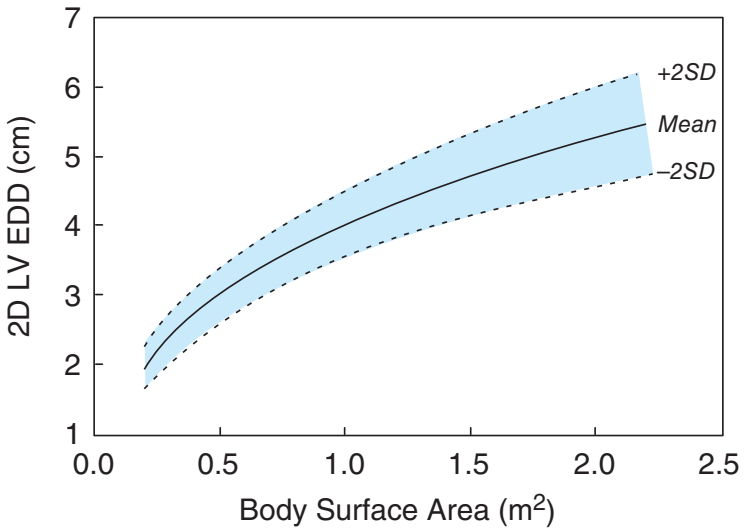


Figure A.9 Two-dimensional (2D) left ventricular (LV) end-diastolic dimension (EDD) versus body surface area.

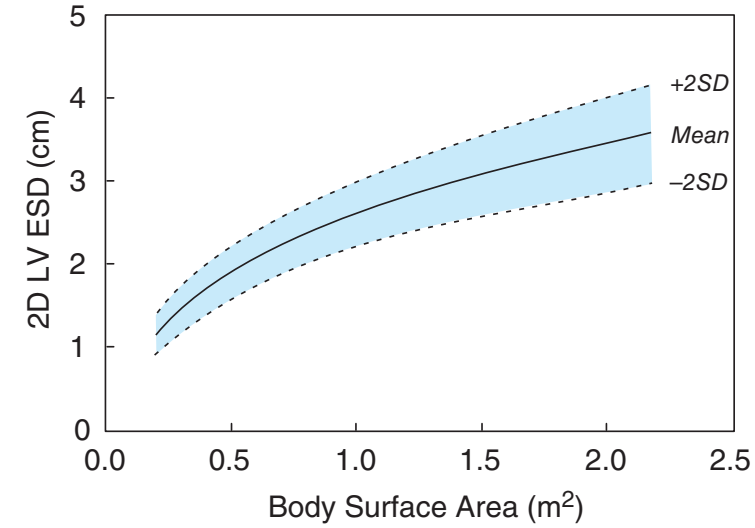


Figure A.10 Two-dimensional (2D) left ventricular (LV) end-systolic dimension (ESD) versus body surface area.

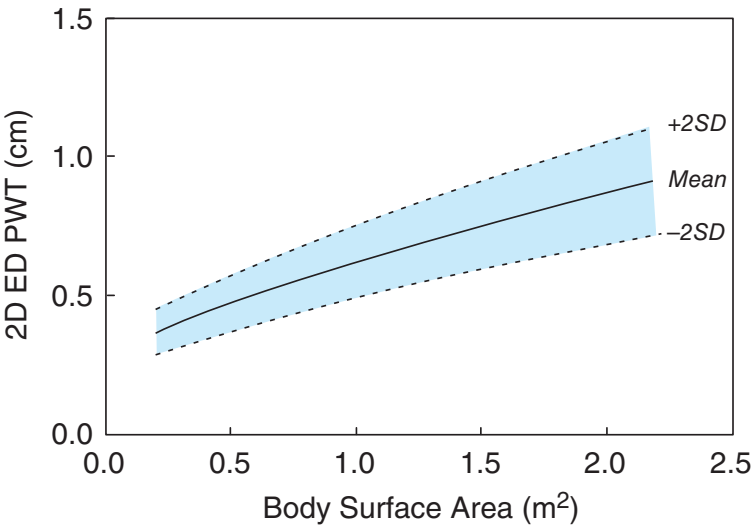


Figure A.11 Two-dimensional (2D) left ventricular end-diastolic (ED) posterior wall thickness (PWT) versus body surface area.

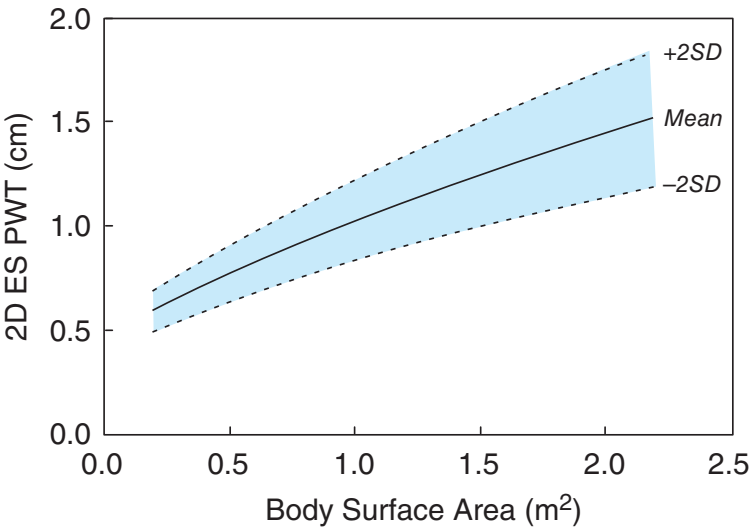


Figure A.12 Two-dimensional (2D) left ventricular end-systolic (ES) posterior wall thickness (PWT) versus body surface area.

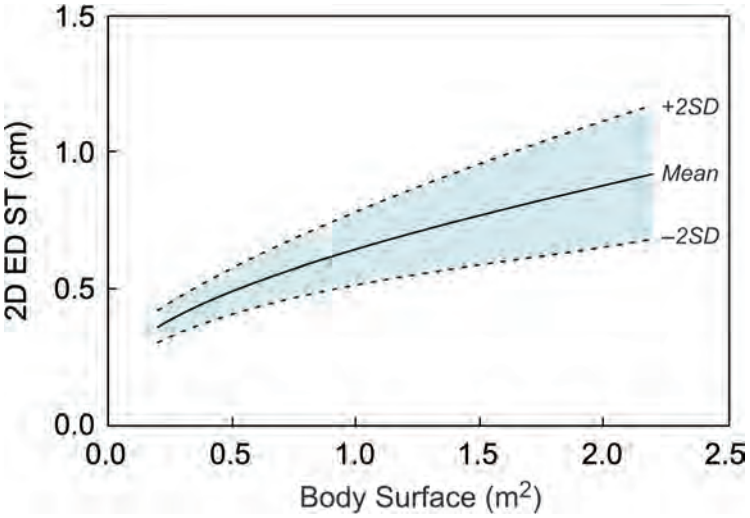


Figure A.13 Two-dimensional (2D) end-diastolic (ED) septal thickness (ST) versus body surface area.

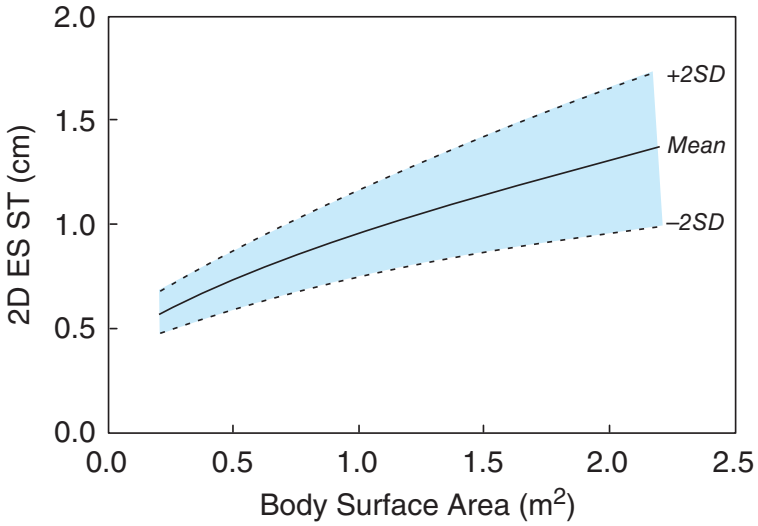


Figure A.14 Two-dimensional (2D) end-systolic (ES) septal thickness (ST) versus body surface area.

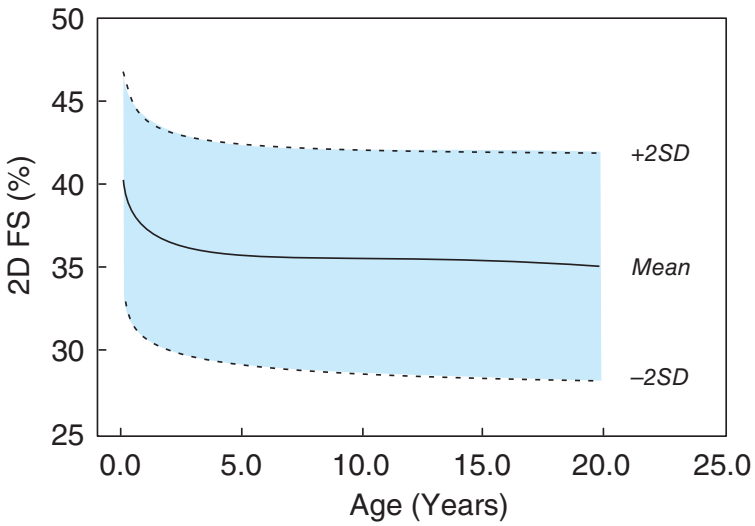


Figure A.15 Two-dimensional (2D) left ventricular endocardial percent fractional shortening (FS) versus age. Percent fractional shortening (FS) is calculated as 100∗(EDD – ESD)/EDD where EDD = end-diastolic dimension and ESD = end-systolic dimension.

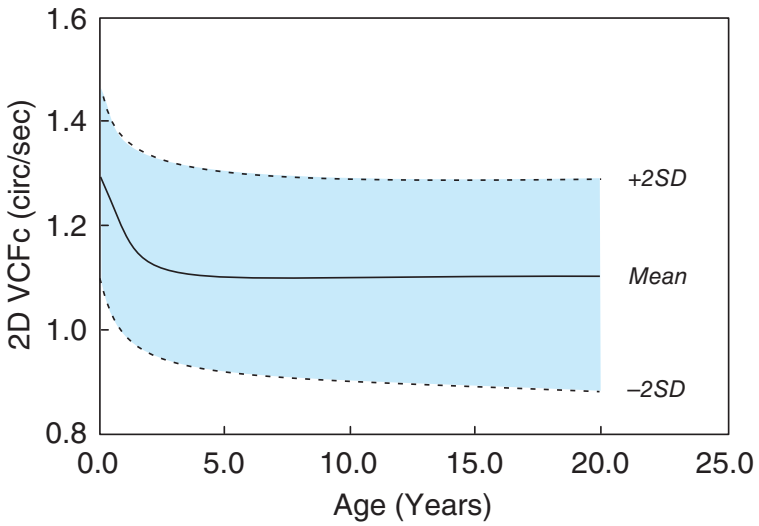


Figure A.16 Two-dimensional (2D) left ventricular endocardial rate-corrected velocity of circumferential fiber shortening (VCFc) versus age. VCFc was calculated as FS/ETc, where FS is fractional shortening and ETc is ejection time divided by the square root of the Q–Q interval on the electrocardiogram.

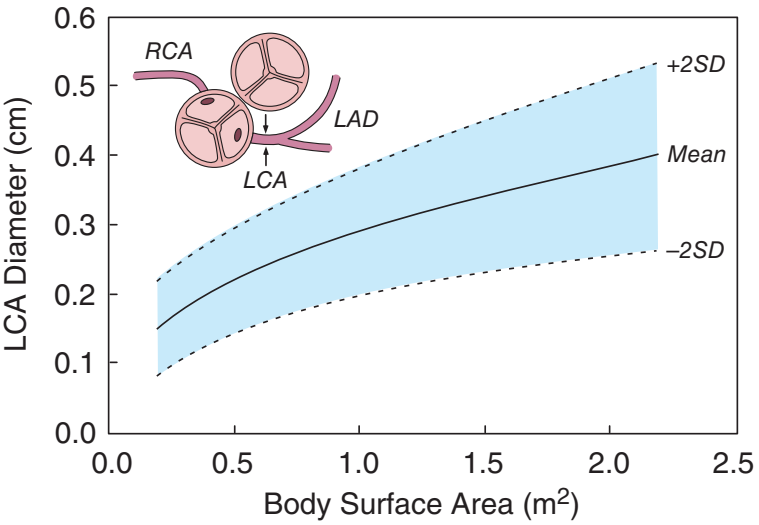


Figure A.17 Inner-edge to inner-edge left main coronary artery (LCA) diameter versus body surface area.

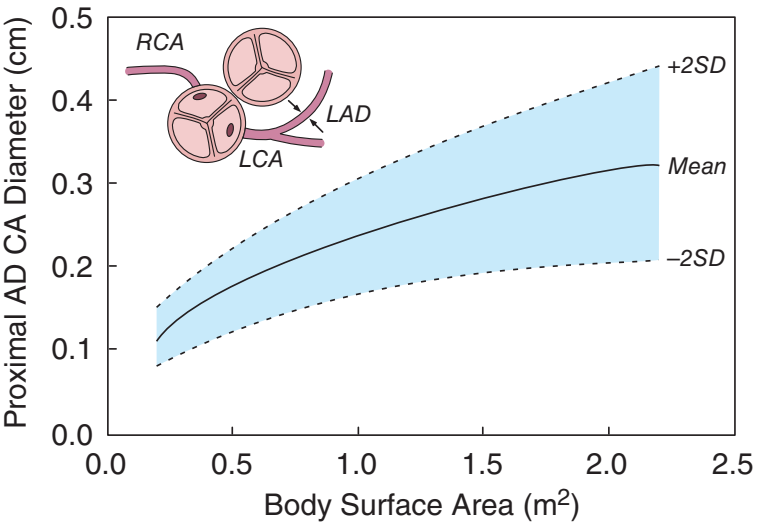


Figure A.18 Inner-edge to inner-edge proximal anterior descending (AD) coronary artery (CA) diameter versus body surface area.

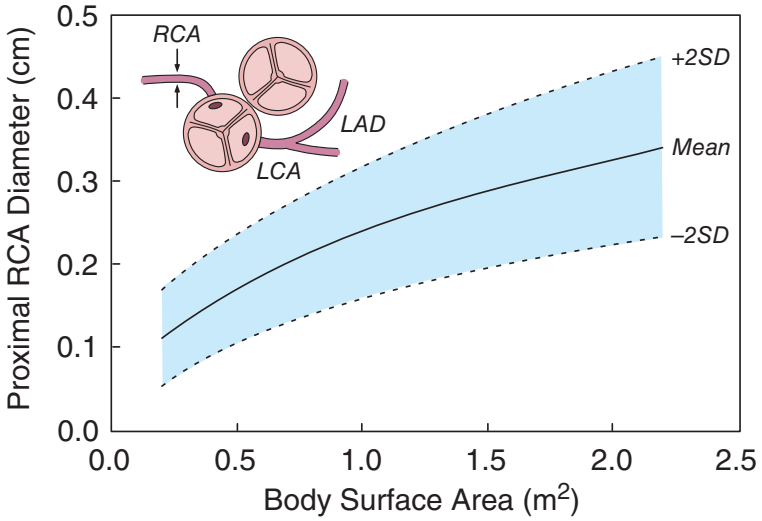


Figure A.19 Inner-edge to inner-edge proximal right coronary artery (RCA) diameter versus body surface area.

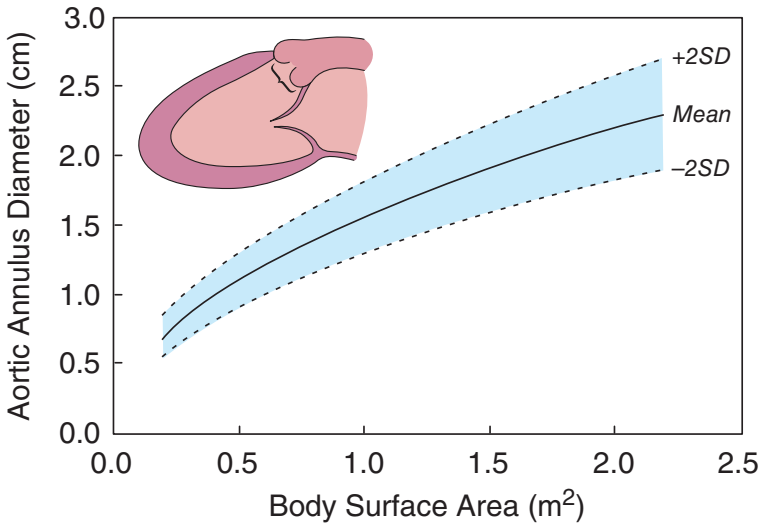


Figure A.20 Inner-edge to inner-edge, mid-systolic aortic valve annulus diameter versus body surface area.

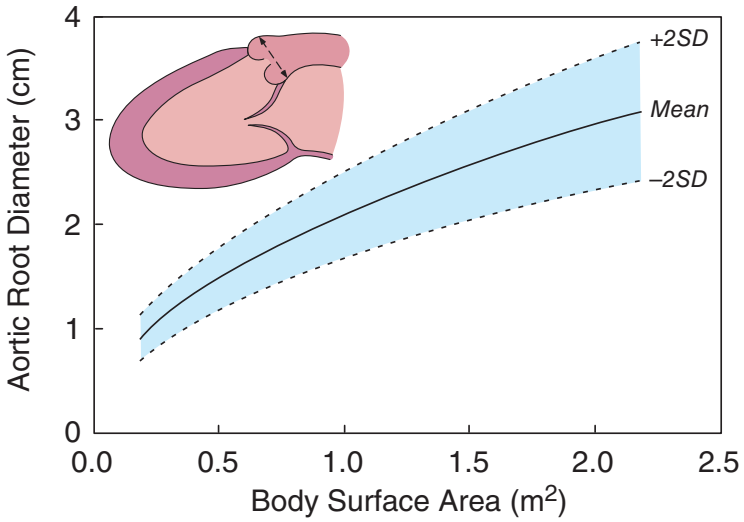


Figure A.21 Inner-edge to inner-edge, mid-systolic aortic root diameter versus body surface area.

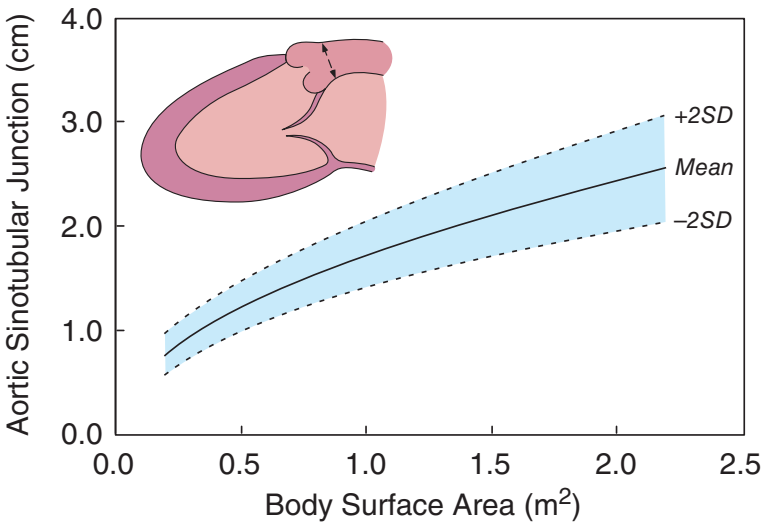


Figure A.22 Inner-edge to inner-edge, mid-systolic aortic sinotubular junction diameter versus body surface area.

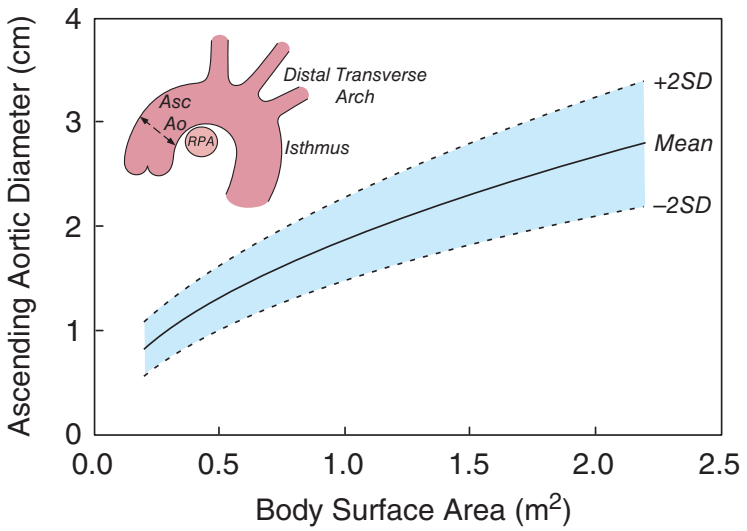


Figure A.23 Inner-edge to inner-edge, mid-systolic ascending aortic diameter versus body surface area, measured directly anterior to the crossing of the right pulmonary artery.

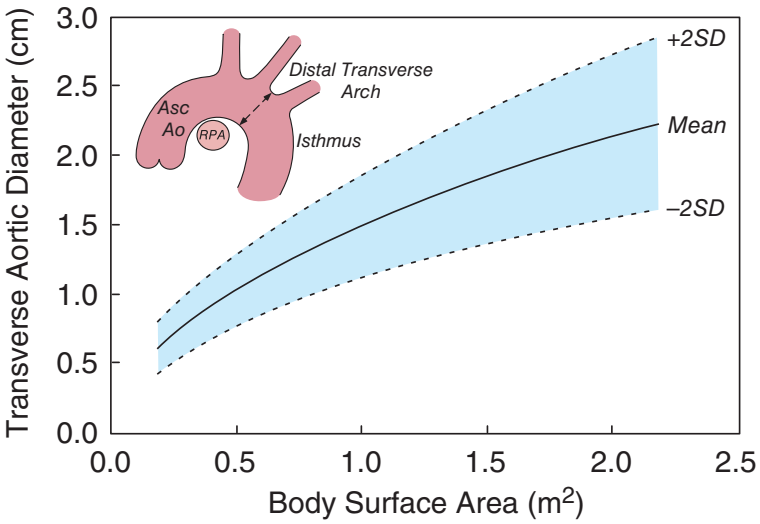


Figure A.24 Inner-edge to inner-edge, mid-systolic distal transverse aortic diameter versus body surface area, measured at the mid-point between the origin of the left carotid and left subclavian arteries.

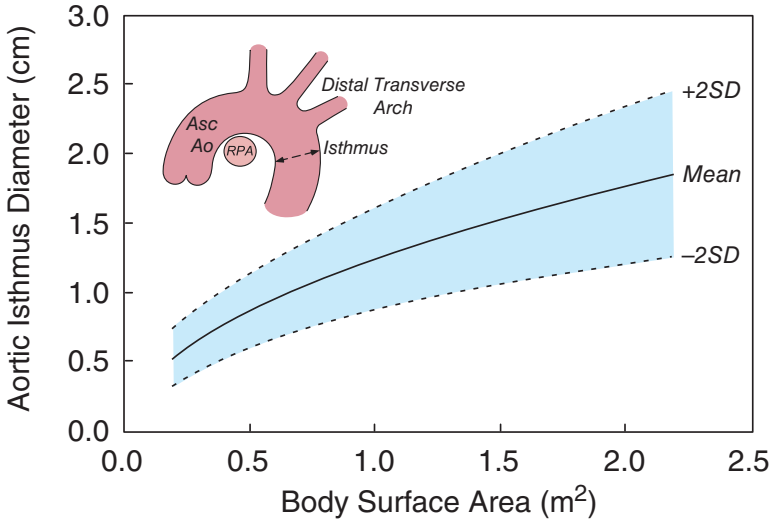


Figure A.25 Inner-edge to inner-edge, aortic isthmus diameter versus body surface area, measured just distal to the origin of the left subclavian artery.

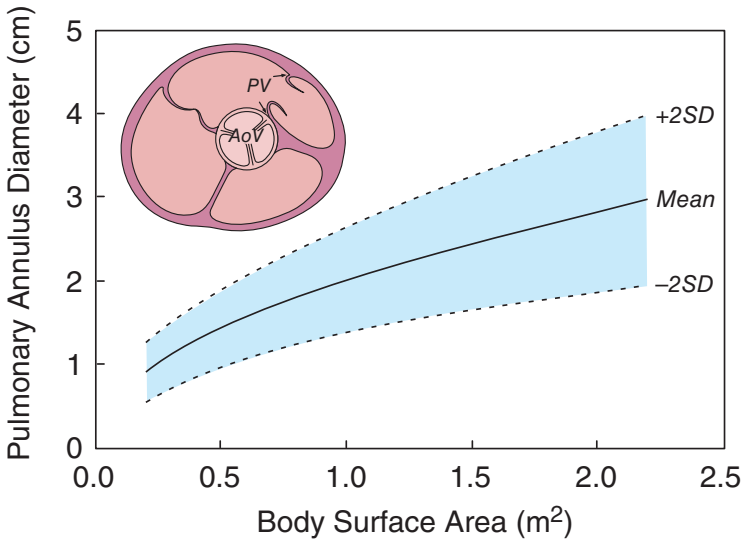


Figure A.26 Inner-edge to inner-edge, mid-systolic pulmonary valve annulus diameter versus body surface area.

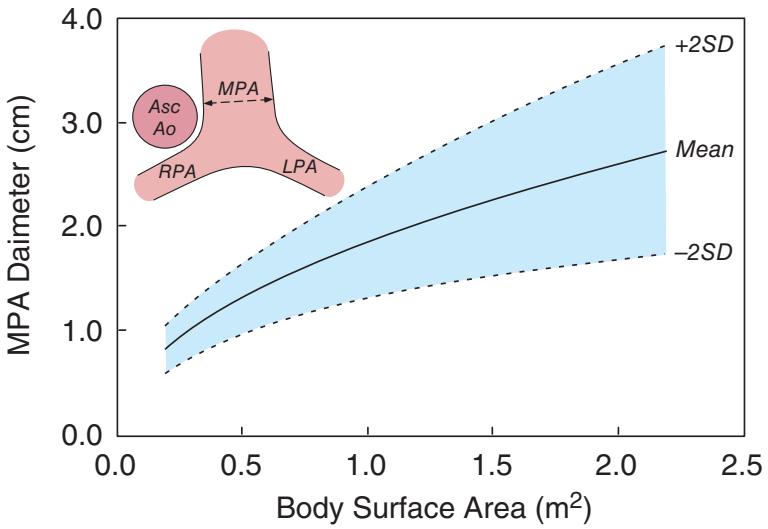


Figure A.27 Inner-edge to inner-edge, mid-systolic main pulmonary artery (MPA) diameter versus body surface area.

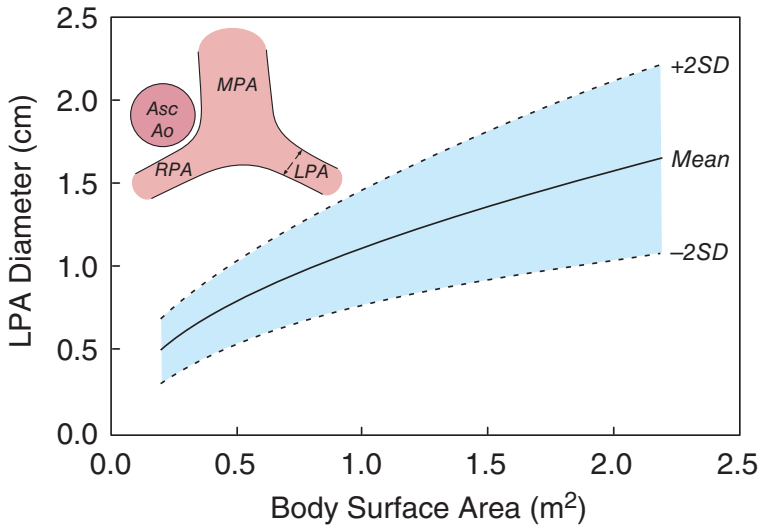


Figure A.28 Inner-edge to inner-edge, mid-systolic left pulmonary artery (LPA) diameter versus body surface area.

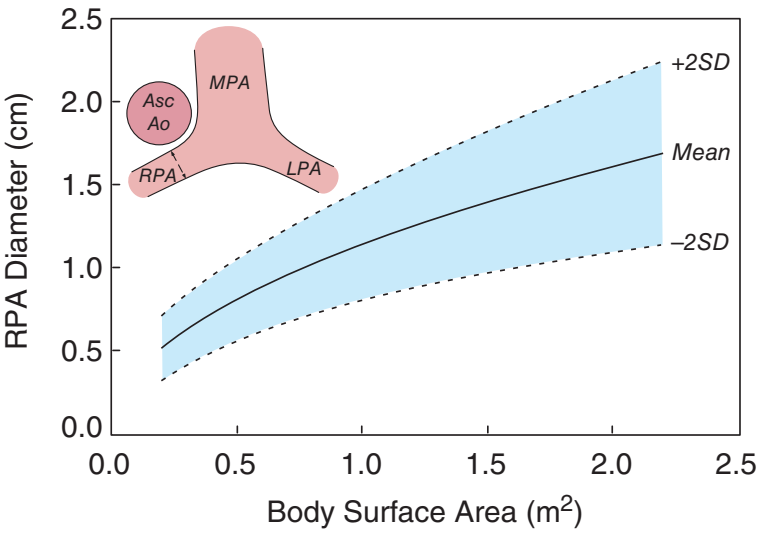


Figure A.29 Inner-edge to inner-edge, mid-systolic right pulmonary artery (RPA) diameter versus body surface area.

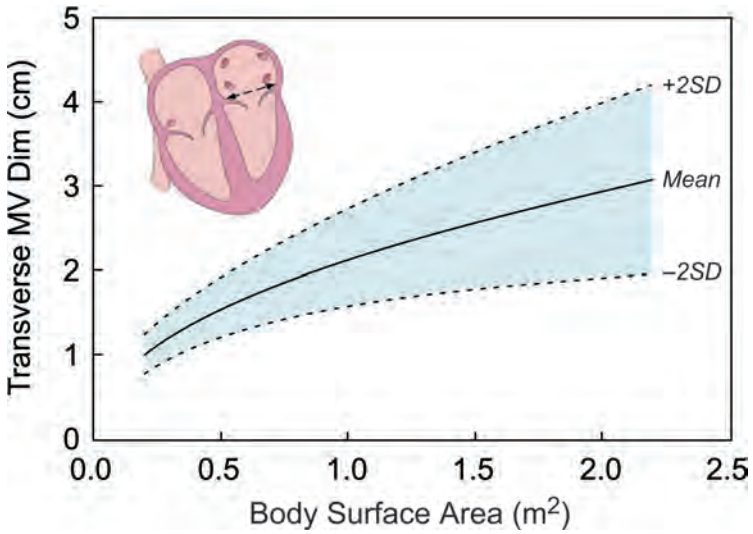


Figure A.30 Inner-edge to inner-edge, mid-diastolic transverse mitral valve (MV) annulus diameter versus body surface area, measured from the apical 4-chamber view.

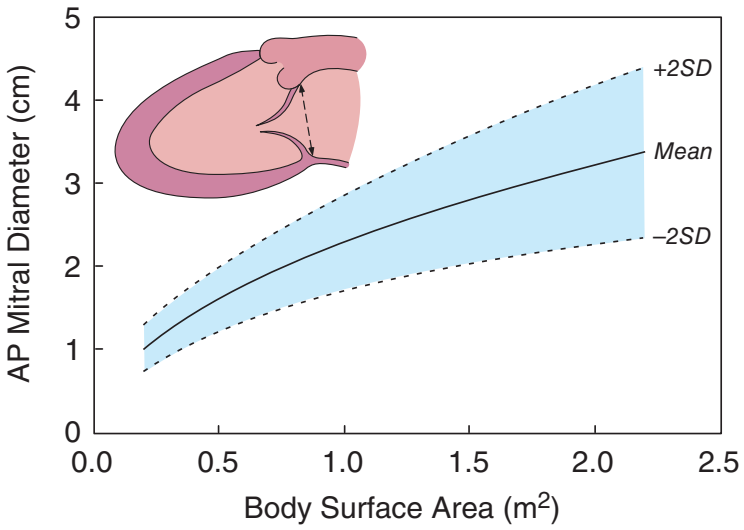


Figure A.31 Inner-edge to inner-edge, mid-diastolic anteroposterior (AP) mitral valve (MV) annulus diameter versus body surface area, measured from the parasternal long axis view.

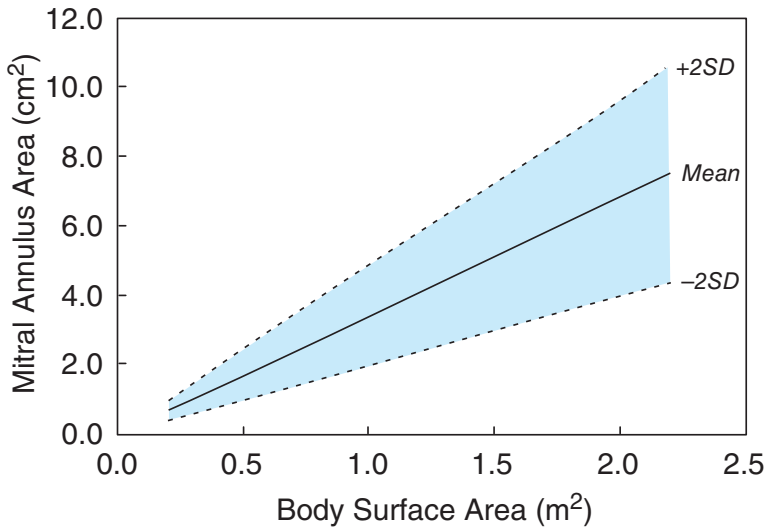


Figure A.32 Mitral valve annulus cross-sectional area versus body surface area, calculated as an ellipse from the transverse and anteroposterior annulus dimensions.

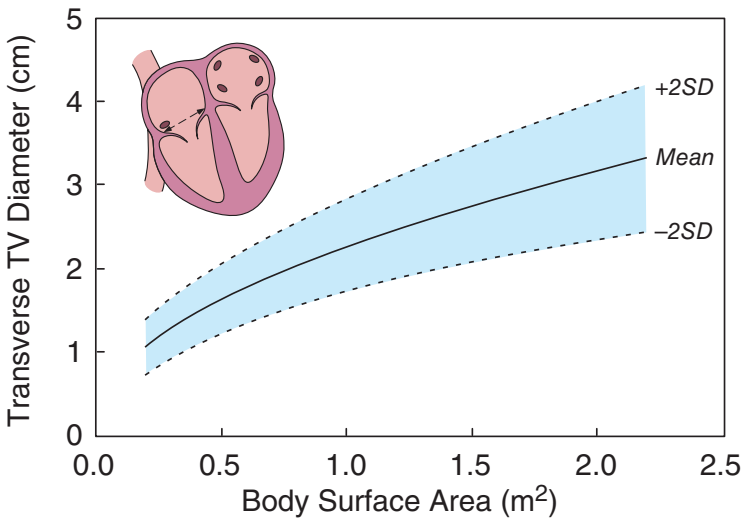


Figure A.33 Inner-edge to inner-edge, mid-diastolic transverse tricuspid valve (TV) annulus diameter versus body surface area, measured from the apical 4-chamber view.

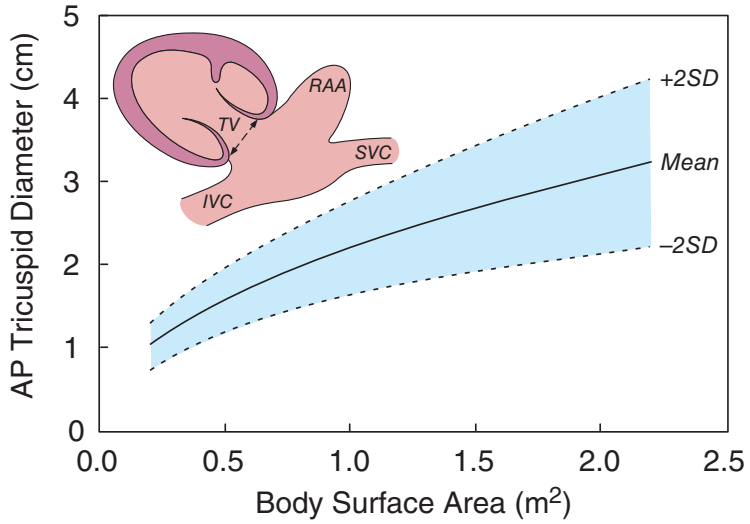


Figure A.34 Inner-edge to inner-edge, mid-diastolic anteroposterior (AP) tricuspid valve (TV) annulus diameter versus body surface area, measured from the parasternal long-axis view. IVC, inferior vena cava; RAA, right atrial appendage; SVC, superior vena cava.

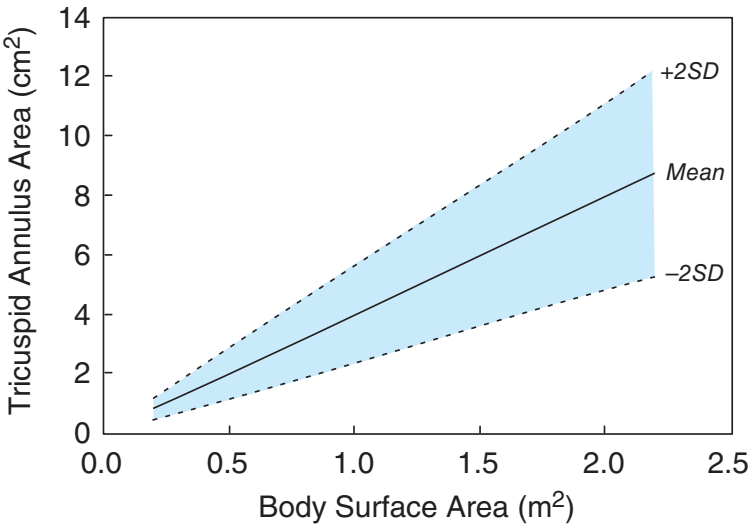


Figure A.35 Tricuspid valve annulus cross-sectional area versus body surface area, calculated as an ellipse from the transverse and anteroposterior annulus dimensions.

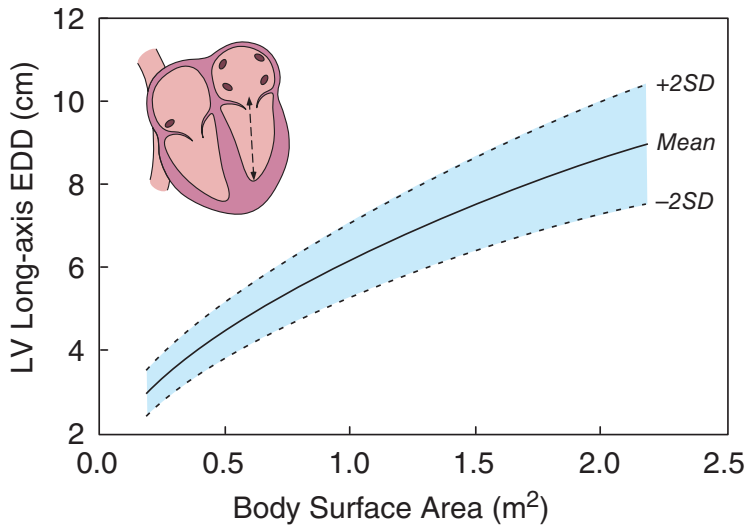


Figure A.36 Left ventricular (LV) long-axis end-diastolic dimension (EDD) versus body surface area. End diastole is defined as the frame on which the mitral valve closes.

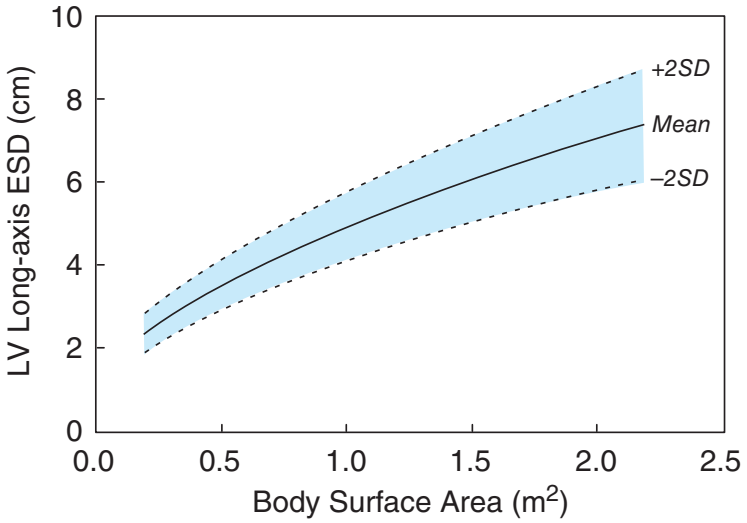


Figure A.37 Left ventricular (LV) long-axis end-systolic dimension (ESD) versus body surface area. End systole is defined as the frame preceding mitral valve opening.

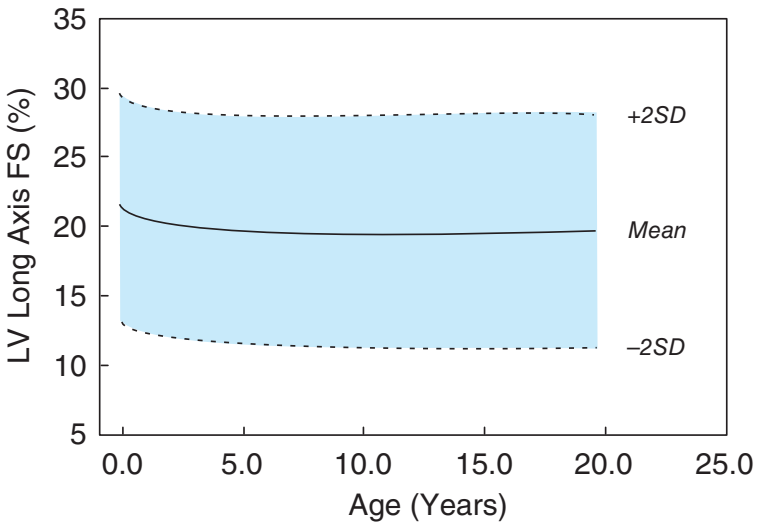


Figure A.38 Left ventricular (LV) endocardial long-axis percent fractional shortening (FS) versus age. Percent long-axis fractional shortening is calculated as 100∗(EDDla – ESDla)/EDDla where EDDla = long-axis end-diastolic dimension and ESDla = long-axis end-systolic dimension.

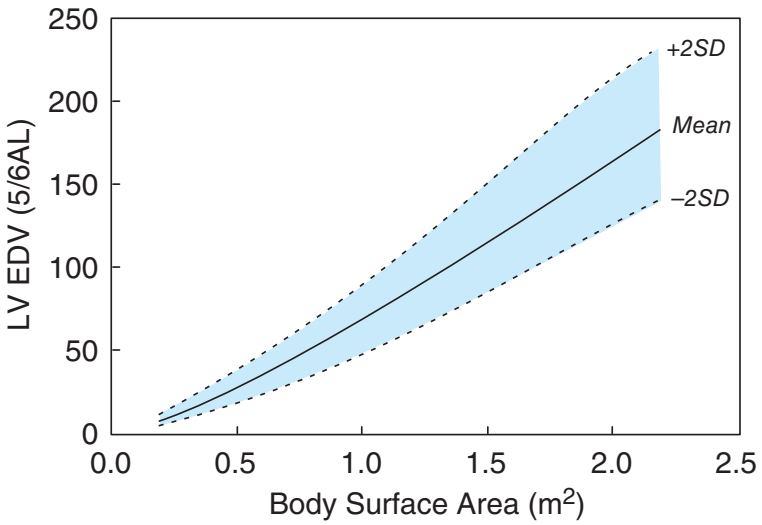


Figure A.39 Left ventricular (LV) end-diastolic volume (EDV) using the 5/6∗area∗length algorithm (5/6AL) versus body surface area.

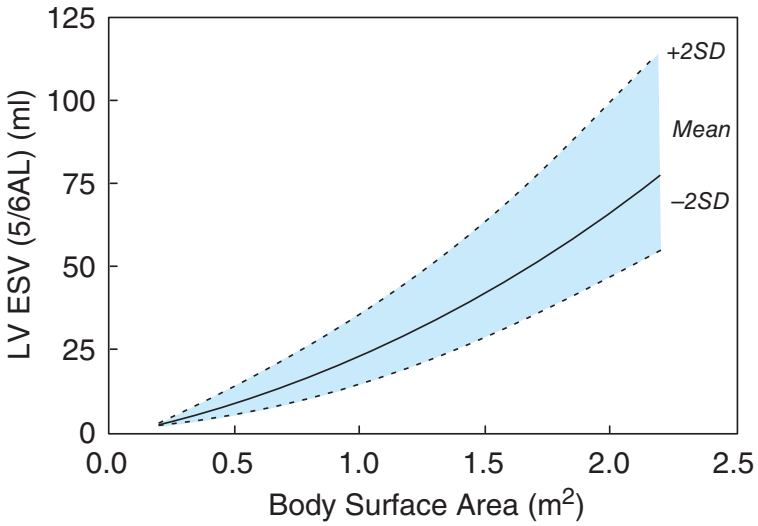


Figure A.40 Left ventricular (LV) end-systolic volume (ESV) using the 5/6∗area∗length algorithm (5/6AL) versus body surface area.

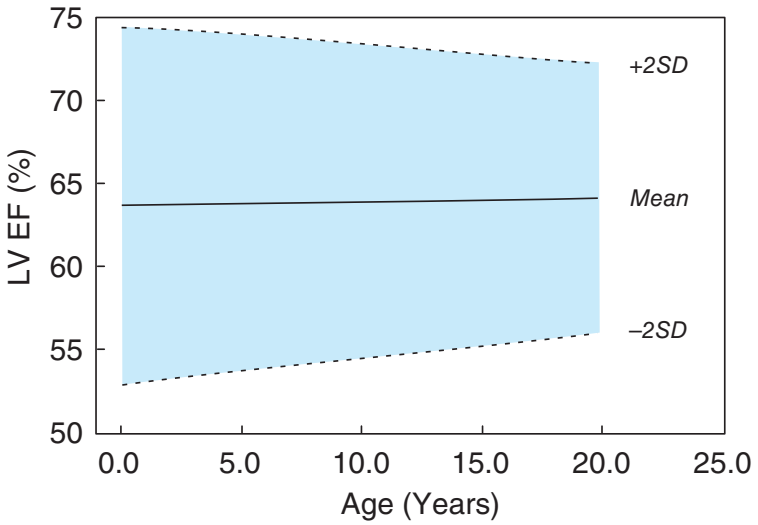


Figure A.41 Left ventricular (LV) percent ejection fraction (EF) versus age. Percent ejection fraction was calculated from the end-diastolic (EDV) and end-systolic volume (ESV) as 100∗(EDV – ESV)/EDV.

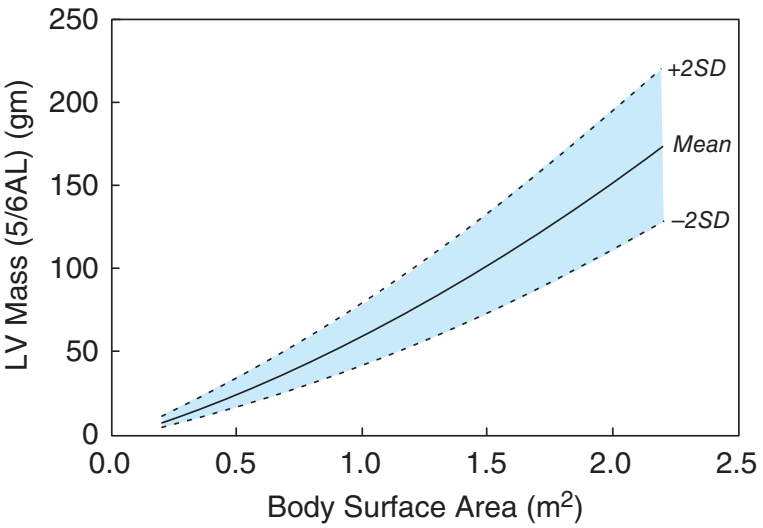


Figure A.42 Left ventricular (LV) mass using the 5/6∗area∗length algorithm (5/6AL) versus body surface area. LV mass was calculated as the difference between the epicardial and endocardial volumes multiplied by the specific gravity of the myocardium (1.05).

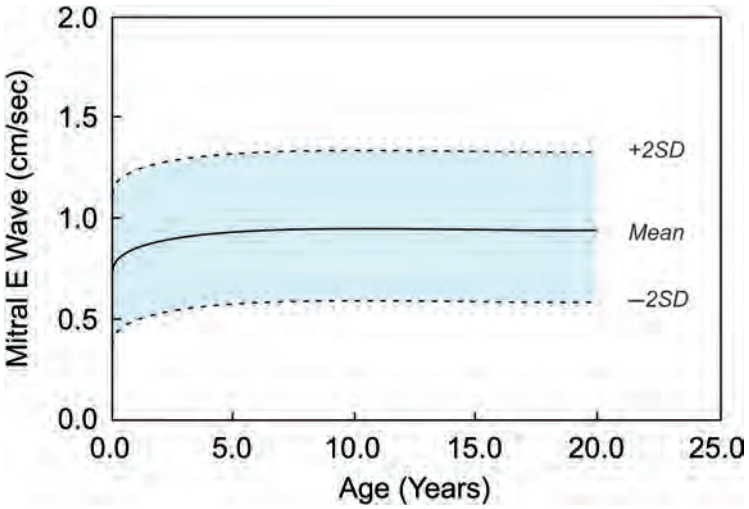


Figure A.43 Mitral valve early diastolic peak inflow velocity (E wave) versus age.

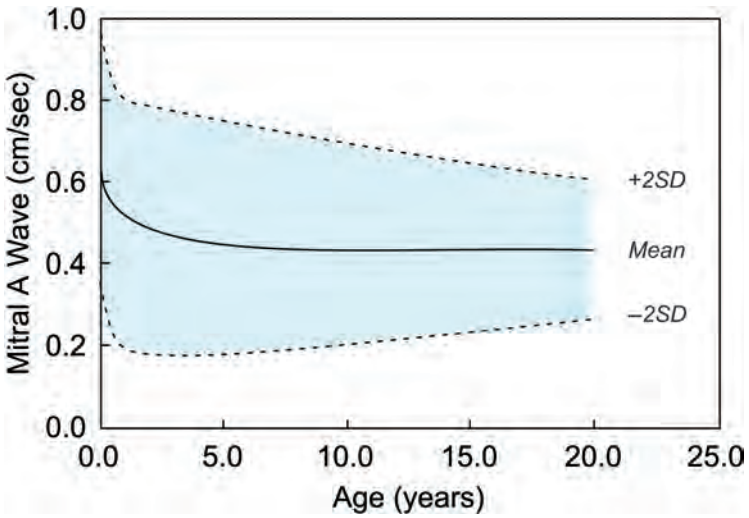


Figure A.44 Mitral valve late diastolic peak inflow velocity (A wave)
versus age.

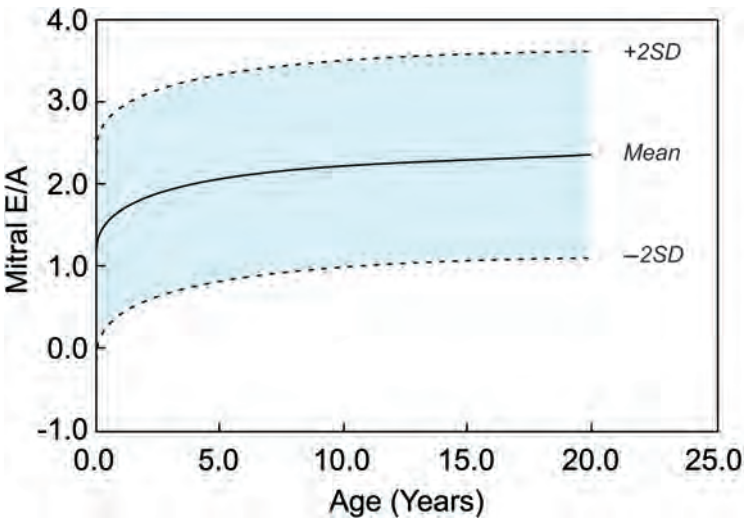


Figure A.45 Ratio of the mitral valve early to the late diastolic peak inflow velocities (E/A) versus age.

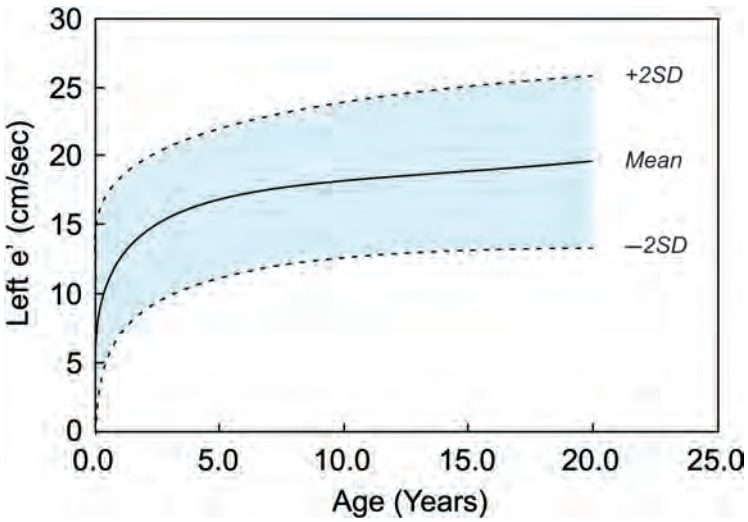


Figure A.46 Left basilar lateral wall peak early diastolic tissue velocity
(Left e′) versus age.

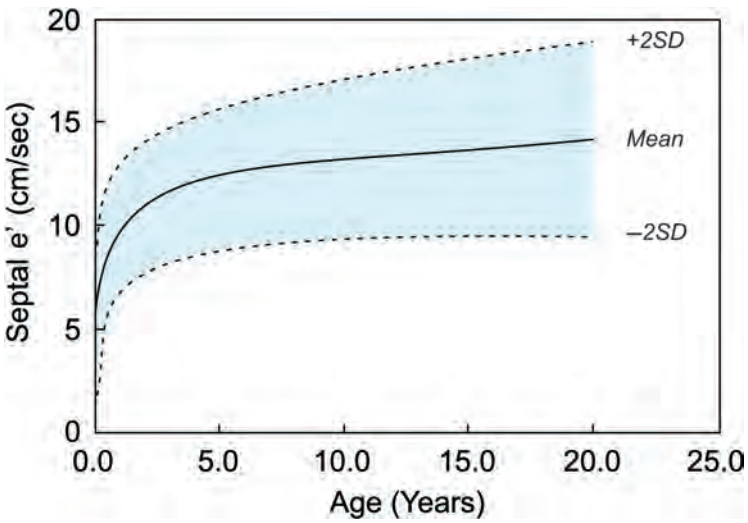


Figure A.47 Basilar septal peak early diastolic tissue velocity (Septal e′) versus age.

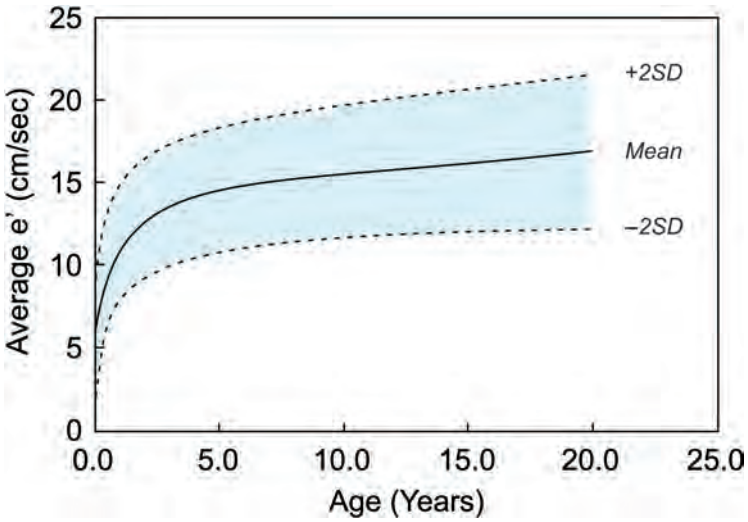


Figure A.48 Average of the left lateral and the basilar septal peak early diastolic tissue velocities (e′) versus age.

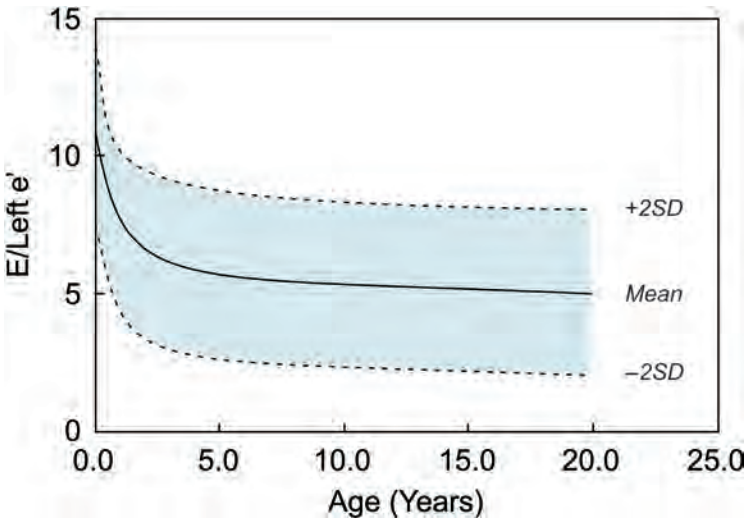


Figure A.49 Ratio of the peak early diastolic mitral inflow velocity to the left basilar lateral wall peak early diastolic tissue velocity (E/Left e′) versus age.

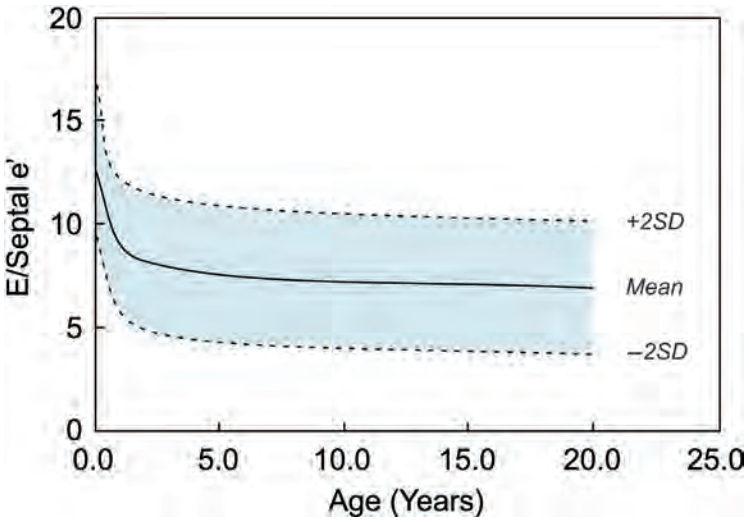


Figure A.50 Ratio of the peak early diastolic mitral inflow velocity to the basilar septal peak early diastolic tissue velocity (E/Septal e′) versus age.

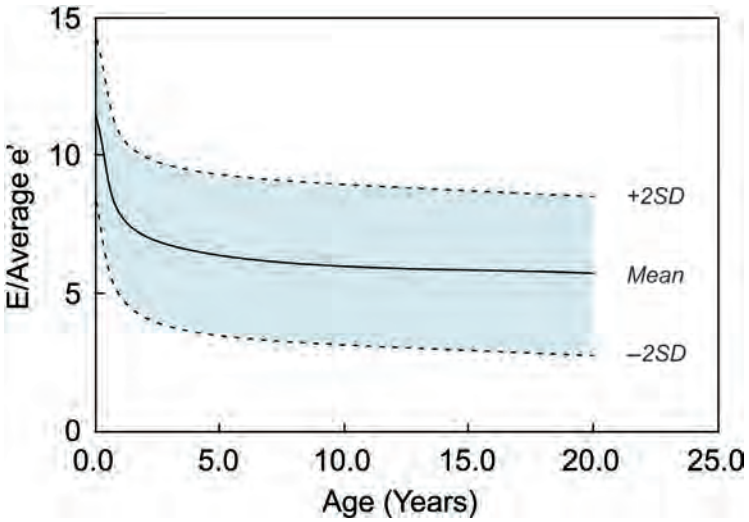


Figure A.51 Ratio of the peak early diastolic mitral inflow velocity to the average of the left lateral and the basilar septal peak early diastolic tissue velocities (E/Average e′) versus age.

References

1 Sluysmans T, Colan SD. Theoretical and empirical derivation of cardiovascular allometric relationships in children. *J Appl Physiol* 2005;**99**:445–457.

2 Colan SD, Parness IA, Spevak PJ, et al. Developmental modulation of myocardial mechanics: age- and growth-related alterations in afterload and contractility. *J Am Coll Cardiol* 1992;**19**:619–629.

3 Lopez L, Colan SD, Frommelt PS, et al. Recommendations for quantification methods during the performance of a pediatric echocardiogram: a report from the Pediatric Measurements Writing Group of the American Society of Echocardiography Pediatric and Congenital Heart Disease Council. *J Am Soc Echocardiogr* 2010;**23**:465–495.

Index

Page numbers in *italics* denote figures, those in **bold** denote tables.

A-mode imaging 5, *6*
Abbott, Maude 31, 297
absent pulmonary valve syndrome 290–292, *291*, *292*
 and Fallot's tetralogy 415, 425, *425*
accreditation **21**, 28
acoustic pressure 3, *4*
acoustic wave 3, *6*
acute pericarditis 713–716
 causes **709**
 imaging 714
 incidence and etiology **709**, 714
adults
 atrial septal anomalies 207
 atrioventricular canal defects 270–271, *274*
 coarctation of aorta 384, 389–390, *389–392*
 congenital coronary artery anomalies 588–589
 double-out ventricle 481–482
 ductus arteriosus anomalies 324
 Fallot's tetralogy 420
 heterotaxy syndromes 579–580, *579*
 infective endocarditis 770, *770*
 mitral valve anomalies 254–255
 pulmonary venous anomalies 174–175
 subpulmonary stenosis 290
 transposition of great arteries 461–462
 physiologically "corrected" 501–502
 truncus arteriosus 439–440
 ventricular septal defect 226
afterload 97, 657
 correcting dimensional changes for 105
Alagille syndrome 281, 326, *820*
ALCAPA syndrome 591–594, *592–594*, **594**, 657, *657*
aliasing 15, *15*
allometric modeling 63–69
 choice of normalizing variable 67–68
 heteroscedasticity 68
 "indexing" methods 65–66, *66*
 per-BSA method 64–65, *64–66*
 z-score methods 66–67
anatomic orifice area (AOA) 75
anatomic segments of heart *32*
anatomic vise 183, 185
anatomically corrected malposition of great arteries 558
 imaging 562, *562*, *563*
anatomy *see individual conditions*
aneurysm
 aortic **628**, *629*, 633, **635**
 with bicuspid aortic valve **628**
 with cutis laxa 634
 with patent ductus arteriosus **628**
 coronary artery
 congenital 602
 Kawasaki disease 740, *741–743*
 ductal 319
 imaging 323–324, *323*, *324*
 left ventricular 722–727
 sinus of Valsalva 348–350, *350*, *351*
 thoracic artery 634, 636
aneurysm-osteoarthritis syndrome 632–633
anomalous origin of left coronary artery from pulmonary artery *see* ALCAPA syndrome
anomalous origin of right coronary artery from pulmonary artery *see* ARCAPA syndrome
anthracycline cardiotoxicity 148
aorta
 aneurysm **628**, *629*, 633, **635**
 ascending *see* ascending aorta
 coarctation *see* coarctation of aorta
 descending, dilation/dissection 630–632, *631*
 diameter *891*, *892*
 hypoplastic left heart syndrome 359–360, *361*
 imaging 365, *365*
 thoracic *see* thoracic aorta
aortic arch anomalies
 double aortic arch 610–611, *612–614*
 double-outlet right ventricle 478
 Fallot's tetralogy 415
 heterotaxy syndromes 569–570, *572*
 left aortic arch
 patent ductus arteriosus 307, 318, *318*, *319*
 with right descending aorta and right ductus arteriosus 612–613, *616*
 right aortic arch
 with aberrant left subclavian artery 611, *612*, *615*
 with left descending aorta and left ductus arteriosus 612, *616*
 with mirror image branching and left ductus arteriosus 611–612, *612*, *615*
 truncus arteriosus 434, 435
 see also coarctation of aorta; interrupted aortic arch
aortic arch development *610*, *611*, **611**
aortic atresia *40*
aortic blood flow velocity 106
aortic cusp prolapse 347–348, *348*, *349*
aortic isthmus atresia 395
aortic outflow tract obstruction 569, *571*
aortic regurgitation *88*, 745
 pregnancy 824
 rheumatic heart disease **753**, 757–758
aortic root
 diameter *890*
 dilation 419
 regurgitation 419
aortic sinotubular junction diameter *891*
aortic stenosis 340–345
 fetal 344–345, *344*, *345*, *849*
 imaging 341–345, *341–345*
 morphology 340, *340*
 pathophysiology 340–341
 pregnancy 823, *824*
aortic valve
 bicuspid (bicommissural) 347, 634, **635**, 636
 pregnancy 820
 chronic disease 755, *756*, *757*
 diameter *890*
 flutter 338, *339*
 regurgitation *see* aortic regurgitation
 stenosis *see* aortic stenosis
aortic valvulitis in rheumatic heart disease 753, **753**
aortico-left ventricular tunnel 350–353, *351*, *352*
aortopulmonary defects 415
aortopulmonary window 440–443
 definition, incidence, morphology and pathophysiology 440–441, *441*
 imaging 441–443, *441*, *442*
apical views **45**, 49–50, *50*, *51*
ARCAPA syndrome 594–596, *595*
arrhythmias
 Doppler echocardiography 135
 fetal 853–854, **857**, *858–861*
arrhythmogenic right ventricular dysplasia 727, 729–733
 clinical manifestations 729
 definition 727, 729
 diagnostic criteria **730–731**
 etiology 729

Echocardiography in Pediatric and Congenital Heart Disease: From Fetus to Adult, Second Edition. Edited by Wyman W. Lai, Luc L. Mertens, Meryl S. Cohen and Tal Geva.

© 2016 John Wiley & Sons, Ltd. Published 2016 by John Wiley & Sons, Ltd.

Companion website: www.lai-echo.com

arrhythmogenic right ventricular dysplasia (*Continued*)
imaging 629–631
prenatal assessment 732–733
incidence 729
morphology 729
arterial switch operation 458
follow-up 459–460, *460*
arterial tortuosity syndrome **628**, 634, **635**
ascending aorta
diameter *891*
dilation 627, 629, *629*
dissection 629–630, *629*
asplenia syndrome 187, 564, *567–568*
see also heterotaxy syndromes
athletes, diastolic function 143–145
athlete's heart 679, **679**
atria
common 201–202
filling 132
left *see* left atrium
right *see* right atrium
see also entries under atrial
atrial septal anomalies 197–214
definition 197
etiology 197
imaging 202–210
adults 207
coronary sinus defects 206–207, *206*
echocardiographic guidance of transcatheter ASD closure 207–209, *208–211*
follow-up assessment 210
intraoperative assessment 209–210, *210*
postoperative/postdevice examination 202–203
prenatal assessment 207
preoperative evaluation 202
secondum ASDs 203–204, *203*, *204*, *208*, *209*
sinus venosus defects 204–206, *205*, *206*
incidence 197
morphology and classification 197–202
anatomy 198–202, *200*, *201*
developmental considerations 197–198, *198*, *199*
pathophysiology 202
atrial septal defect (ASD) 197
3D echocardiography 799–800, *800*, *801*
and Fallot's tetralogy 415–416
heterotaxy syndromes 566
secundum 198, *200*
imaging 203–204, *203*, *204*, *208–210*
transcatheter closure, imaging 207–209, *208–211*
atrial septum
hypoplastic left heart syndrome 358, *359*
imaging 364, *364*, 418
transesophageal echocardiography 780, *780*
atrial situs *see* situs
atrial switch operation 458
follow-up 460–461, *460*, *461*
atrioventricular alignments and connections 38, *39*
atrioventricular canal
imaging 478, *478*
morphology 477
atrioventricular canal defects 259–278
common atrioventricular canal 414–415
definition 259
etiology 259
and Fallot's tetralogy 414–415
imaging 264–275
adults 270–271, *274*
complete CAVC defect 265–267, *266–268*
follow-up assessment 272–275, *275*, *276*
incomplete and transitional CAVC defect 267–268, *269–271*
intraoperative assessment 271–272, *274*
key elements 265
left ventricular outflow tract 268, *271*
prenatal assessment 269–270, *273*
three-dimensional assessment 272, *275*
unbalanced CAVC defect 268–269, *271–273*
incidence 259
morphology and classification 259–264
anatomy 259–264, *260–264*
developmental considerations 259
pathophysiology 264
VSDs 219–220, *220*, 225–226, *226*
atrioventricular junction, imaging 780
atrioventricular regurgitation *86*
atrioventricular septal defect, 3D echocardiography 801–802, *803*, *804*
atrioventricular valves
annular displacement **100**
Fontan circulation 548–550, *552*
heterotaxy syndromes 567
imaging 419
insufficiency 135
stenosis 135
transposition of great arteries 493
see also mitral valve; tricuspid valve
attenuation correction 5
AVSD *see* atrioventricular septal defect
axial resolution 10
azygos veins **181**

B-mode imaging 7, *7*
B/A parameter 10
backscatter 3
balloon atrial septostomy 457–458, *458*
Baltimore-Washington Infant Study 215
Barlow syndrome 753
basilar lateral wall peak early diastolic tissue velocity *899*
Bazett's correction 105
Bernoulli equation 79–80, *80*, 285
bicuspid (bicommissural) aortic valve 347
pregnancy 820
bilateral ductus arteriosi 319
Blalock–Taussig shunt *308*, *309*, 363, *363*, *371*, *372*
Bland-White-Garland syndrome 591–594, *592–594*, **594**
blood flow 73–88
Coanda effect 75, *75*
Doppler insonation angle 73
narrow orifice 75–76, *75*, *76*
pressure gradients 79–83, *79–82*
profiles 73–74, *74*
prosthetic valves 88–93, *90–92*, **93**
quantification 76–79, *77*, *78*
regurgitation 83, **83**, 84–88
valvar stenosis 83–84, **83**
blood pool Doppler indices 105–111, **105**, *106*, *107*, **108**, *109*, *111*
body surface area 64
bone morphogenetic proteins in truncus arteriosus 433
boundary layer attachment *see* Coanda effect
brachiocephalic vessels in heterotaxy syndromes 569–570, *572*
bronchus suis 619
BSA *see* body surface area
Budd-Chiari syndrome 197
bulboventricular foramen 513

cardiac CT
constrictive pericarditis 707–708, *708*
pericardial effusion 713
restrictive cardiomyopathy 703
cardiac function at ventricular level 97–98, *98*
cardiac index 64
cardiac malpositions 558–563
anatomy 559–560
definitions 558–559
dextrocardia *34*, 35, 167, 491, *493*, *499*, 558, 560–562, *560*
etiology 559
imaging 560–563
dextrocardia 560–562, *560*
goals 478
juxtaposition of atrial appendages 561–562, *561*
pre/postoperative assessment 562–563, *563*
prenatal assessment 562
ventricular inversion 562, *562*
incidences 559
juxtaposition of atrial appendages 561–562, *562*, *565*
mesocardia 33, *34*, 167, 491, 558
morphology and classification 559
pathophysiology 560
situs inversus 32, *34*, *36*, 558, *560*
cardiac MRI
constrictive pericarditis 707–708, *708*
pericardial effusion 713
restrictive cardiomyopathy 703
cardiac output 97
measurement 76–79, *77*, *78*
cardiac position 33, *34*, 35
see also cardiac malpositions
cardiac resynchronization therapy 665–669, *666–669*, **667**
atrioventricular dyssynchrony 668–669
interventricular dyssynchrony 666, *666*
intraventricular dyssynchrony 666, *666*
cardiac tamponade 709–713
echocardiographic parameters **695**
imaging 710–713, *710–713*
flow mechanics 711, *712*, *713*
two-dimensional 710–711, *710*, *711*
incidence and etiology 709, **709**
pathophysiology 709–710
cardiac translation 108, 109
cardiac transplantation 656
allograft rejection surveillance 663–666, *665*, *666*
imaging 663, *663*, *664*
cardiac tumors 641–650, **642**
association with syndromes 647–648, *648*
fibroma *550*, **642**, 643–644, *643*, *644*

hemangioma **642**, 646–647, *647*
incidence 641
malignant 647, *647*
myxoma **642**, 646, *646*
rhabdomyoma 641–643, *642*, **642**
teratoma **642**, 645, *645*
cardinal vein, levoatrial 185–186, *186*, 364–365
cardiomyopathy
dilated 653–655
hypertrophic 337, 677–693
inflammatory *see* myocarditis
peripartum 827
restrictive *see* restrictive cardiomyopathy
cardiovascular dimensions 69–70
growth adjustment 70
minimum work principle 69–70, *70*, *71*
Carney syndrome 648
cat-eye syndrome 157
cerebral artery blood flow *370*
CHARGE syndrome 426
Chiari network 240, *240*
children
annular tissue Doppler imaging values **144**
diastolic function 143–146, **702**
age-related changes in diastolic filling 143, **143**, **144**
healthy children/athletes 143–145
chirality 38
chloral hydrate **25**
chronic renal disease 147
circle of Vieussens 585
circumferential fiber shortening (Vcf), velocity of 101
circumflex retroesophageal right aortic arch 612, *616*
Coanda effect 75, *75*
coarctation of aorta 382–392
definition 382
etiology 382
imaging 384–392
adult coarctation 389–390, *389–392*
key elements 384
long-term follow-up 391–392, *394*, *395*
neonatal coarctation 383–389, *385–388*, **389**
prenatal assessment 390–391, *392*, *393*
incidence 382
morphology and classification 382–383, *383*
pathophysiology 383–384
pregnancy 821
collagen 624
color flow imaging 16, *16*
color M-mode imaging
constrictive pericarditis 706
flow propagation 137, *137*
left ventricular inflow 699–700, *700*
restrictive cardiomyopathy 699–700, *700*
common atrioventricular canal defects (CAVC) *see* atrioventricular canal defects
common atrium 158, 201–202
complete echocardiogram **28**
conal morphology
double-outlet left ventricle 483, *483*
double-outlet right ventricle 469, 471, *472*, 473, *473*
pathophysiology 484
conal septal VSDs 219, *219*, 224–225, *225*
congenital heart disease 31–43, 148–149
3D echocardiography 799–809
coronary arteries *see* coronary arteries, congenital anomalies
mitral stenosis 243, 250, 251–253, *253*
risk stratification in pregnancy 818, **819**, *820*, *822–828*
segmental analysis 31–32, *32*, *33*
atrial situs 35–37, *35*, *36*, **36**
atrioventricular alignments and connections 38, *39*
cardiac position 33, *34*, 35
semilunar valve relationships 41, *41*
thoraco-abdominal situs 32–33, *34*
type of infundibulum (conus) 40–42, *41*
ventricular loop 37–38, *37–39*
ventriculo-arterial alignments 38, 40, *40*
see also individual conditions
connective tissue 624–627, *626*
connective tissue disorders 624–640
aortic aneurysms with cutis laxa 634
arterial tortuosity syndrome 634
classification **628**
definition 624
Ehlers-Danlos syndrome 243, 633–634
imaging *635*, **635**
Loeys-Dietz syndrome 632, *633*
Marfan syndrome 243, 253, 624–625, 627–632, **628**, *629–631*
Shprintzen-Goldberg syndrome **628**, 634
smooth muscle cell dysfunction syndrome 634
thoracic aortic aneurysms/dissection 634, 636
with bicuspid aortic valve 634, 636
conotruncal face anomaly syndrome 394
conotruncus in Fallot's tetralogy 408–409, *408*, *409*
conoventricular/perimembranous VSDs 217, *217*, 222–223, *222*
constrictive pericarditis 703–708
echocardiographic parameters **695**
imaging 704–708, *705–708*
2D echocardiography 704–705, *705*, *706*
color M-mode 706
flow characteristics 705–706, *707*
goals 704
tissue mechanics 706
transesophageal echocardiography 706–707
incidence and etiology 703–704, **704**
pathophysiology 704
continuous-wave Doppler 12–13, *13*
aortic regurgitation *88*
contrast imaging 10
conus 40–42, *41*
cor triatriatum
dextrum 240
imaging 165–166, *166*, *167*
sinister 159, *159*, *166*
coronary arteries
anatomy 584–585, *585*
left coronary artery 502–503, 584–585, *585*
right coronary artery 585, *585*
congenital anomalies 584–608
ALCAPA 591–594, *592–594*, **594**
anomalous aortic origin 597
ARCAPA 594–596, *595*, *596*
association with congenital heart disease 604
classification **591**
congenital coronary artery aneurysm 602
coronary-cameral/coronary-arteriovenous fistulae 602–604, *603*
definition 584
developmental considerations 584
imaging 587–589, *588–590*
left coronary artery origin from right coronary sinus 597–598, *598–600*
minor anatomical variations 590–591, *592*
ostial atresia 596–597, *597*
physiology 585–587, *586*
pulmonary arterial origin 597
right coronary artery origin from left coronary sinus 598–599, *601*
single coronary artery 599–601
diameter *889*, *890*
double-outlet right ventricle 479, *480*
in Fallot's tetralogy 410–411, *413*
hypoplastic left heart syndrome 359–360
imaging 365–366, 419
in Kawasaki disease 740–745, *741–745*
neo-aortic root and valve 412
pulmonary atresia
with right ventricular dilatation 301
with right ventricular hypoplasia 299
transposition of great arteries 448–449, *449*, *450*
imaging 455–457, *456*, *457*
physiologically "corrected" 493
truncus arteriosus 435
coronary ectasia 743
coronary fistula *299*
coronary sinus 181, **181**
anomalies 190–191
dilatation 190–191
ostium atresia or stenosis 191
defects 201, *201*
imaging 206–207, *206*
coronary sinus septum 198
coronary-arteriovenous fistula 602–604, *603*
coronary-cameral fistula 602–604, *603*
'crab view' 162
criss-cross heart 511, 526–531, *528–531*
cross-fiber shortening 96
CT, cardiac
constrictive pericarditis 707–708, *708*
pericardial effusion 713
restrictive cardiomyopathy 703
cutis laxa syndromes **628**, 634
cyanotic lesions in pregnancy 821

Damus-Kaye-Stansel operation 550
Danon disease 677, 678
deformation imaging *see* myocardial deformation imaging
depth-gain compensation 5
dexmedetomidine **25**
dextrocardia *34*, 35, 167, 491, *493*, *499*, 558, *560*
imaging 560–562, *560*
dextroposition 558, *560*
dextroversion 558
diabetes mellitus type 1 147–148
diastasis 132
diastole, definition and physiology 132–133, *133*

diastolic disease 139–143
abnormal relaxation
with elevated atrial pressure 140–141, *141*
with normal atrial pressure 139–140, *140*
abnormal ventricular compliance 141–143, *142*, **143**
acquired/systemic 146–149
anthracycline cardiotoxicity 148
chronic renal disease 147
diabetes mellitus type 1 147–148
left ventricular hypertrophy 146–147, *147*
obesity 147
obstructive sleep apnea 148
cardiomyopathy
dilated 145–146
hypertrophic 145, *145*
restrictive 146, *146*
congenital anomalies 148–149
echocardiography 149–150, *150*, **702**
patterns of 139, **140**
diastolic filling, age-related changes 143, **143**, **144**
diastolic function 132–153
adults **702**
cardiomyopathy
dilated 660–661
hypertrophic 680–681, *682*, *683*
children 143–146, **702**
age-related changes in diastolic filling 143, **143**, **144**
healthy children/athletes 143–145
infants **143**, **144**
color M-mode flow propagation 137, *137*
deformation imaging 137–139
left atrial volume 138–139, *139*
strain rate/strain imaging 137–138, *138*
Doppler electrocardiography 133–135
mitral inflow 133–134, **133**, *134*
pulmonary venous inflow 97–98, *97*
tricuspid and systemic venous inflow 135
Fallot's tetralogy 422
Fontan circulation 544–545, *544*
tissue Doppler imaging 135–137, *136*
Doppler indices **136**, **137**
DiGeorge syndrome 394
truncus arteriosus 433
dilated cardiomyopathy 145–146, 653–655
classification **654**
definition 653
etiology 653–654
imaging 656–672
cardiac mechanical support *667*, *668–671*, **668**, 669–672, *670*, *671*
cardiac resynchronization therapy 665–669, *666–669*, **667**, **668**
change in left ventricular pressure over time 661, *663*
fetal dilated cardiomyopathy and myocarditis 655, 662–663
goals 656–657, *657*
left ventricular diastolic function 660–661
left ventricular size/geometry 657–659, *658*, *659*
left ventricular spherical index *659*
left ventricular sphericity index *659*
left ventricular systolic function 659–660
myocardial performance index 657, **661**
shortening fraction and ejection fraction 659
stress echocardiography 661
three-dimensional imaging 661–662
tissue Doppler *660*, 661, *662*
wall stress and afterload 659–660
incidence 653
pathophysiology 654
treatment and outcome 654–655
displacement index 231, *233*, 235
Doppler effect 12, *12*
Doppler imaging 12–18
aliasing 15, *15*
aortopulmonary window 442–443
cardiomyopathy **661**
dilated *660*, 661, *662*
hypertrophic 684, *687*
color flow imaging 16, *16*
continuous-wave 12–13, *13*
diastolic function 133–137, *136*
Doppler indices **136**, **137**
mitral inflow 133–134, **133**, *134*
pulmonary venous inflow **133**, 134–135, *134*, *135*
tricuspid and systemic venous inflow 135
left ventricular myocardial function 108–110, **108**, *109*
myocardial velocity imaging 17–18, *17*
pulmonary arterial hypertension 880
pulsed-wave Doppler 13–15, *14*, *15*
regurgitation 85, *85*
velocity resolution 14–15
Doppler insonation angle 73
DORA *see* double-outlet right atrium
double aortic arch 610–611, *612–614*
double-inlet ventricle *40*
left 512–518
anatomy 512–515, *518*
embryology 512
physiology 515–516
treatment strategies 516–518
right 518–520, *519*, *520*
see also functionally univentricular heart
double-orifice mitral valve 243, 246
imaging 249, *250*, *254*
double-outlet left ventricle 482–484
associated lesions *483*, 484
definition 482
etiology 482–483
great artery relationships 483, *483*
history 482
imaging 484
incidence 482
morphology and classification 483–484, *483*
double-outlet right atrium (DORA) *39*, 262, *263*
double-outlet right ventricle (DORV) *40*, 411, 466–482
anatomy 468–475
conal morphology 469, 471, *472*, 473, *473*
great artery relationships 473–474
ventricular septal defect 468–469, *469–471*
associated lesions 474, *474–477*
definition 466
etiology 467
history 466–467
imaging 475–482
adult 481–482
goals, key elements 477–481, *477–481*
postoperative examination 480–481, *481*
prenatal assessment 481, *482*
preoperative assessment 477–480, *477–480*
incidence 467
morphology and classification 467–468
pathophysiology 474–475
Down syndrome 197, 215
atrioventricular canal defects 264
Fallot's tetralogy 263
Down syndrome cell adhesion molecule (DSCAM) 259
dropout artifacts 8
ductal aneurysm 319
imaging 323–324, *323*, *324*
ductus arteriosus
bilateral 319
hypoplastic left heart syndrome 359–360, *361*
imaging 365, *366*
left 611–612, *612*, *615*, *616*
right 612–613
ductus arteriosus anomalies 317–325
definition 317
embryology 317
etiology 317
imaging 319–325, *320–325*
adults 324
ductal aneurysm 323–324, *323*, *324*
echocardiography 324–325, *325*
goals *318–322*, 319–321
patent ductus with left aortic arch 321–322
patent ductus with right aortic arch 322–323
post-closure 324
post-stenting 324–325, *326*
reverse-oriented patent ductus 323
incidence 317
morphology 317
patent ductus arteriosus *see* patent ductus arteriosus
pathophysiology 317–319, *318*, *319*

Ebstein anomaly 231–240, 494
associated features 234
clinical presentation 233–234, *234*, **234**
fetus *856*
imaging 234–239
echocardiography 234–237, *235–237*
preoperative examination 239
three-dimensional 803–805, *804*, *805*
tricuspid valve repair 237–239, *238*
morphology and development 231–232, *232*, *233*
pathophysiology 232–233
pregnancy 820
ectopia cordis 35
effective orifice area (EOA) 75
Ehlers-Danlos syndrome, vascular 243, **628**, 633–634, **635**
Eisenmenger syndrome 182, *274*
ejection fraction 99, *101*, 659
elastin 624
elevation resolution 11
endocarditis
infective 763–774
pregnancy 826–827, *829*
nonbacterial thrombotic 771–772
envelope detection 5, *6*
epicardial echocardiography 785–786
etomidate **25**
Eustachian valve 240, *240*

extracellular matrix 624
extracorporeal membrane oxygenation (ECMO) 669–670

Fabry disease 677–678
Fallot, Etienne-Louis Arthur 407
Fallot's tetralogy *81*, 148–149, *148*, 182, 263, 269, 407–432
 definition 407
 embryology, genetics and molecular basis 407–408
 environmental factors 408
 imaging 416–426
 3D echocardiography 806, *810*
 adults 420
 anatomic two-dimensional assessment 416–418, *416*, *417*
 diastolic function 422
 intraoperative/postoperative assessment 420
 left ventricular function 422
 multimodal 423
 prenatal assessment 423–426, *424*, *425*
 preoperative assessment 416–419, *417*, *419*
 pulmonary stenosis/regurgitation 422, *423*
 repaired TOF 420, *421*
 right atrial enlargement 422–423
 right ventricular size and function 421–422
 systolic function 421–422
 transcatheter techniques 423
 tricuspid regurgitation 422–423
 incidence 407
 morphology 408–416
 absent pulmonary valve syndrome 415
 aortic arch anomalies 415
 aortopulmonary defects and variations in pulmonary artery origin and bifurcation 415
 atrial septal defect 415–416
 common atrioventricular canal 414–415
 conotruncus 408–409, *408*, *409*
 coronary arteries 410–411, *413*
 double-chambered right ventricle 411–412, *414*
 double-outlet right ventricle 411
 left-sided lesions 415
 pulmonary atresia and/or extreme pulmonary hyperplasia 412, 414, *415*
 systemic and pulmonary venous anomalies 415–416
 ventricular septal defect 409–410, *410–413*
 pregnancy 821
 recurrence risk 408
 right aortic arch 318
false tendons 353
familial thoracic aortic aneurysm syndrome (FTAA) **628**
fetal echocardiography 24, 26, **27**, 834–871
 cardiovascular pathology 845–854
 fetal arrhythmias 853–854, **857**, *858–861*
 fetal heart failure 850–853, *853*, **855**, *856*
 fetal structural heart disease 845–846, *848–853*, 849–850, **854**
 components of **836**
 evolution and future directions 854–855, 857–860
 3D and 4D echocardiography 855, 857–860, *864–867*
 first trimester echocardiography 855, *862*, *863*
 indications and timing 834–835, **835**
 screening 835–845, **836**
 2D imaging 836–842, *837–842*
 Doppler interrogation 842–843, *843*
 fetal heart function 843–845, *844–846*
 fetal rhythm assessment 845, *847*
 technical considerations 835
fetus
 absent pulmonary valve 291
 aortic stenosis 344–345, *344*, *345*, *849*
 arrhythmias 853–854, **857**, *858–861*
 arrhythmogenic right ventricular dysplasia 732–733
 atrial septal anomalies 207
 atrioventricular canal defects 269–270, *273*
 cardiac malpositions 562
 coarctation of aorta 390–391, *392*, *393*
 congenital coronary artery anomalies 587–588
 dilated cardiomyopathy 655, 662–663
 double-outlet right ventricle 481, *482*
 Ebstein anomaly *856*
 echocardiography *see* fetal echocardiography
 Fallot's tetralogy 423–426, *424*, *425*
 heart failure 850–853, *853*, **855**, *856*
 heart function 843–845, *844–846*
 heart rhythm 845, *847*
 heterotaxy syndrome 575–577, *576–578*
 hypoplastic left heart syndrome 366–370, *367–370*, *851*
 interrupted aortic arch 398, 400, *402*
 juxtaposition of atrial appendages *565*
 left ventricular aneurysm/diverticula 727, *728*
 left ventricular noncompaction 722, *722*, *723*
 mitral valve anomalies 253–254, *254*
 myocarditis 662–663
 pulmonary artery sling 619–620
 pulmonary valve anomalies
 atresia 302, 303–304, *303*, *304*
 regurgitation *856*
 stenosis 283, *283*
 pulmonary venous anomalies 173–174, *175*
 structural heart disease 845–846, *848–853*, 849–850, **854**
 subpulmonary stenosis 289
 transposition of great arteries 401, 457, *457*, *502*
 truncus arteriosus 439
 vascular rings 616, 618
 ventricular septal defect 226, *226*
 see also congenital heart disease
fibrillin 624, 625
fibroma **642**, 643–644, *643*, *644*
fistula
 coronary *299*
 coronary-arteriovenous 602–604, *603*
 coronary-cameral 602–604, *603*
"flank" view 56, *58*
flow *see* blood flow
flow velocity profile 74, *74*
Fontan circulation 541–557, *541*, *542*
 current strategy 545–546
 functionally univentricular heart 542–544
 diastolic function 544, *544*
 limitations on cardiac output 544
 systolic function 543
 ventricular dimensions and wall thickness 542–543, *543*
 imaging 546–555, *547–554*
 atrioventricular valves 548–550, *552*
 diastolic function 554–555
 goals 546
 outflow tracts, ascending aorta and aortic arch 550–551
 pulmonary arteries/veins 546–548, *547–549*
 single ventricular function 551–554, *553*, *554*
 pregnancy 822
 surgical modifications 545, *545*
Fontan operation 309, *311*, 377–378, **378**
foramen ovale, patent 197, 198, *200*
foramen primum 197, *198*
foramina secundi 197
"force–frequency relation" 98
fossa ovalis, limbus of 197
four-dimensional imaging of fetus 855, 857–860, *864–867*
fractional shortening 78, *100*
Frank-Starling relationship 97
Friedreich's ataxia 678
functionally univentricular heart 511–540
 anatomy
 double-inlet left ventricle 512–518
 double-inlet right ventricle 518–520, *519*, *520*
 tricuspid atresia 511, 520–526, *521–527*
 definition 511
 embryology 511–512
 etiology 511
 Fontan circulation 541–557
 diastolic function 544, *544*
 imaging 546–555, *547–554*
 limitations on cardiac output 544
 systolic function 543
 ventricular dimensions and wall thickness 542–543, *543*
 imaging 531–537, *532–537*
 superior-inferior ventricles 526–531, *528–531*
 criss-cross heart 526–531, *528–531*

general anesthesia **25**
Gerbode VSDs 220
giant left atrium 243
 imaging 250
Glenn shunt procedure 183, 302, 376–377, 542
goose-neck deformity 265, *266*, 269–270
Gorlin equation 84
Gorlin syndrome 647
grayscale encoding 5–7, *6*, *7*
Gross, Robert 31
growth, adjustment for 63–72

haemodynamic measurements 73–95
 blood flow 73–88
 Coanda effect 75, *75*
 Doppler insonation angle 73
 narrow orifice 75–76, *75*, *76*
 pressure gradients 79–83, *79–82*
 profiles 73–74, *74*
 prosthetic valves 88–93, *90–92*, **93**
 quantification 76–79, *77*, *78*
 regurgitation 83, **83**, 84–88
 valvar stenosis 83–84, **83**
 symbols and abbreviations **74**
halo sign 704, *705*
hand rule 514, 528

heart failure in fetus 850–853, *853*, **855**, *856*
heart rate 98
hemangioma **642**, 646–647, *647*
hemiazygos veins **181**
hemitruncus 327
hepatic veins 181–182, **181**
 anomalies 189–190, *191*
 flow patterns
 cardiac tamponade 711
 constrictive pericarditis 706
 diastolic disease **702**
 restrictive cardiomyopathy 698, *699*
 ipsilateral *570*
heteroscedasticity 68
heterotaxy syndromes 37, 158, 529, 533, 563–580
 anatomy 566–571, **566**, *569–572*, **570**
 aortic arch, brachiocephalic vessels and patent ductus arteriosus 569–570, *572*
 aortic outflow tract obstruction 569, *571*
 atrial septum 566
 atrioventricular valves 567
 noncardiac anomalies 570–571
 pulmonary outflow tract obstruction 568–569
 pulmonary venous connections 566
 systemic venous connections 566, *570*
 ventricles 567–568, *571*
 ventriculo-arterial connections 568
 definitions 563–565
 etiology 565
 imaging 573–580
 adults 579–580, *579*
 key elements 573–575, *574*, *575*
 postoperative assessment 579–580, *579*
 prenatal assessment 575–577, *576–578*
 preoperative assessment 577–579
 incidence 565
 morphology and classification 565–566
 pathophysiology 571–573
hockey-stick deformity 754, *755*
Holmes heart 515
Holt-Oram syndrome 157, 197, 215, 357
Hunter, John 297
hydrops fetalis 843
hypertrophic cardiomyopathy 145, *145*, 337, 677–693
 anatomy 678
 athlete's heart 679, **679**
 clinical manifestations 678
 differential diagnosis 679
 etiology 677–678
 family screening and preclinical diagnosis 679
 imaging 679–689
 diastolic function 680–681, *682*, *683*
 key elements 679–680
 left ventricular outflow tract 683–684, *684–686*
 M-mode and 2D echocardiography 680, *680–682*, **681**, **682**
 mitral valve function 681–683, *683*, *684*
 myocardial deformation 685–686
 stress echocardiography 686–687
 systolic function 684
 three-dimensional 686
 tissue Doppler 684, *687*
 management
 echocardiography 687
 surgical myomectomy and septal catheter ablation 687–689, *688*, *689*
 pathophysiology 678
 prevalence 677–678
 primary 677
 secondary 677–678
hypoplastic left heart syndrome 263, 357–381
 anatomy 358–361, *359–361*
 definition 357, *358*
 etiology 357
 imaging 363–378
 goals 363
 postoperative assessment 370–378, *371–378*, **378**
 prenatal assessment 366–370, *367–370*, *851*
 preoperative 363–366, *364–366*
 incidence and associated anomalies 357
 management 361–363, *362*, *363*
 pathophysiology 361
 types 358

image artifacts 7–8, *7*, *8*
 reverberation 8, *8*
 shadowing and dropout 8
 side lobe 7, *7*
image construction 7, *7*
image creation 3–5, *4*, *5*, *7*
image optimization 11–12
image resolution 10–11, *11*
 axial 10
 elevation 11
 lateral 11
 temporal 11
imaging
 acute pericarditis 714
 aortic valve stenosis 341–345, *341–345*
 arrhythmogenic right ventricular dysplasia 729, 731–733, *732*
 prenatal assessment 732–733
 atrial septal anomalies 202–210
 coronary sinus defects 206–207, *206*
 secondum ASDs 203–204, *203*, *204*, *208*, *209*
 sinus venosus defects 204–206, *205*, *206*
 atrioventricular canal defects 264–275
 cardiac malpositions 560–563
 cardiac tamponade 710–713, *710–713*
 cardiomyopathy
 dilated 656–657
 hypertrophic 679–689
 restrictive 694, **695**, *696–703*, **702**
 coarctation of aorta 384–392
 congenital coronary artery anomalies 587–589, *588–590*
 constrictive pericarditis 704–708, *705–708*
 ductus arteriosus anomalies 319–325, *320–325*
 Ebstein anomaly 234–239
 echocardiography 234–237, *235–237*
 preoperative examination 239
 tricuspid valve repair 237–239, *238*
 equipment 20–22, **22**
 Fallot's tetralogy 416–426
 Fontan circulation 546–555, *547–554*
 functionally univentricular heart 531–537, *532–537*
 heterotaxy syndromes 573–580
 infective endocarditis 769–772, *769–771*
 innominate artery compression syndrome 620, *620*
 Kawasaki disease 740–747
 left ventricular aneurysm/diverticula 726–727, *727*, *728*
 postoperative evaluation 727
 prenatal assessment 727, *728*
 left ventricular noncompaction 721–722, *723*
 prenatal assessment 722, *723*
 left ventricular outflow tract 683–684, *684–686*
 mitral valve anomalies 247–255
 pericardial effusion 710–713, *710–713*
 pulmonary artery abnormalities 328–333, *328–332*
 pulmonary artery sling 619–620, *619*, *620*
 pulmonary valve stenosis 283–285, *283–285*
 pulmonary venous anomalies 162–177
 rheumatic fever 751–759, **753**, **754**, *755–759*, **759**
 subaortic stenosis 338–340, *339*, *340*
 subpulmonary stenosis 288–290, *289*
 supravalval aortic stenosis 345–347, *346*, *347*
 transesophageal echocardiography *see* transesophageal echocardiography
 transposition of great arteries 451–462
 physiologically "corrected" 497–503, *498–502*
 truncus arteriosus 436–440, *436–440*
 vascular rings 613–618, *617*, *618*
 ventricular septal defect 221–228
 transthoracic 221–226, *222–226*
 see also individual modalities
"indexing" methods 65–66, *66*
indications for echocardiography 27–28
infants
 annular tissue Doppler imaging values **144**
 diastolic function **143**, **144**
infective endocarditis 763–774
 definition 763, **765**
 diagnostic criteria **764**
 etiology and pathogenesis 764–765
 imaging 769–772, *769–771*
 adult 770, *770*
 goals **770**
 key elements 769
 nonbacterial thrombotic endocarditis 771–772
 preoperative assessment 770–771, *771*
 surgical treatment and postoperative assessment 771
 transthoracic vs transesophageal 769–770
 incidence 763–764, *764*, *765*
 morphology and classification 765–767, *766–769*
 pathophysiology 767–769
 pregnancy 826–827, *829*
 risk factors **768**
inferior vena cava 181–182, **181**
 anomalies 187–190
 bilateral IVCs 189, *189*
 interrupted IVC with azygos/hemiazygos continuation 187–189, *188*, *189*
 left IVC to right atrium 189, *190*
 pathophysiology and clinical significance 151, *151*
 right IVC to left atrium 189
innominate artery compression syndrome 620, *621*
innominate veins **181**
 anomalies 191–192, *192*
 retroaortic innominate vein 192

instrumentation 20–22, **22**
echocardiography 20–22, **22**
storage format and reporting 22–23
system settings 21–22
interrupted aortic arch 392, 394–402
definition 392
etiology 394
imaging 397–402, *397–403*
long-term follow-up 400, 402, *402*, *403*
prenatal assessment 398, 400, *402*
incidence 392, 394
morphology and classification *352*, 394–396, *395*, *396*
pathophysiology 397
type A 395, *395*
type B 395–396, *396*
type C 356, *396*
Intersocietal Accreditation Commission (IAC) 28
Intersocietal Commission for the Accreditation of Echocardiography Laboratories (ICAEL) **28**
interventricular septum 874–875, *875*
intracardiac echocardiography 26
intrinsic contractility 98

Jacobsen syndrome 357
Jarcho-Levine syndrome 197
juxtaposition of atrial appendages 558
fetal *565*
imaging 561–562, *561*, *565*

Kawasaki disease 602, 739–749
clinical features **740**
definition 739
etiology 739
imaging 740–746
alternative modalities 746
consensus recommendations 740, **741**
coronary artery abnormalities 743–745, *743*, *744*
coronary artery assessment 740–743, *741–743*
coronary perfusion *745*, 746
key elements 740
myocardial involvement 745, *745*
pericardial involvement 745–746
valvar involvement 745
incidence 739
pathophysiology 739–740
pregnancy 827, *830*
Kommerell's diverticulum 611
Kugel's artery 584

laboratory
facility 20–22, **21**, *22*
structure/organization 19–23
see also specific aspects
Laplace's law 97, *98*
lateral resolution 11
LeCompte maneuver 458
left anterior oblique view 55–56, *58*
left atrial anomalies 243–258
see also mitral valve anomalies
left atrial pressure *133*
left atrium
giant 243
imaging 250
hypoplastic left heart syndrome 358
size 660
left ventricle
diastolic function 660–661
double-inlet 512–518
double-outlet *see* double-outlet left ventricle
ejection fraction *897*
end-diastolic dimension *884*, *886*, *887*, *895*
end-diastolic posterior wall thickness *887*
end-diastolic septal thickness *885*, *888*
end-diastolic volume *896*
end-systolic dimension *896*
end-systolic posterior wall thickness *885*, *887*
end-systolic volume *897*
fractional shortening *886*, *888*, *896*
hypertrophic 146–147, *147*
hypoplastic left heart syndrome 358–359
imaging 365
longitudinal function 104–105
mechanical dyssynchrony 124
noncompaction 146
pulmonary arterial hypertension 880
sphericity index *659*
systolic function 114–115, **114**, *115*, 659–660
velocity of circumferential fiber shortening *886*, *889*
see also left ventricular
left ventricular aneurysm/diverticula 722–727
clinical manifestations 723–725
definition 722
etiology 723, *724*
imaging 726–727, *727*, *728*
incidence 722
morphology 725–726, *725*, *726*
left ventricular assist devices *see* ventricular assist devices
left ventricular diastolic dysfunction **140**
left ventricular function 98–99
Marfan syndrome 632
left ventricular mass *897*
left ventricular noncompaction 719–722
classification 721
clinical manifestations 720
definition *620*, 719
developmental considerations 720
etiology 719
imaging 721–722, *722*, *723*
prenatal assessment 722, *723*
incidence 719
morphology 720–721, *720*, *721*
left ventricular outflow tract 77, 268, *271*
anomalies 336–356
aortic cusp prolapse 347–348, *348*, *349*
aortic valve stenosis 340–345
aortico-left ventricular tunnel 350–353, *351*, *352*
bicuspid (bicommissural) aortic valve 347
definitions 336
etiology 336
false tendons 353
incidence 336
sinus of Valsalva aneurysm 348–350, *350*, *351*
subaortic stenosis 337–340
supravalval aortic stenosis 345–347
imaging *400*, 683–684, *684–686*
obstruction, transposition of great arteries 494
left ventricular pressure *133*
changes with time 661, *663*
left ventricular volume 657–659, *658*, *659*
left-to-right shunt 220
pregnancy 819
Leopard syndrome 677
levoatrial cardinal vein 185–186, *186*, 364–365
levocardia 33, *34*, 491, *501*
limited echocardiogram **28**
Loeys-Dietz syndrome **628**, 632, *633*, **635**
log-compression 5
logarithmic compression curve *6*

M-mode imaging
constrictive pericarditis 706
diastolic function 137, *137*
hypertrophic cardiomyopathy 680, *680–682*, **681**, **682**
restrictive cardiomyopathy 699–700, *700*
malalignment VSDs 217–218, *218*, 223–224, *223*, *224*
Marfan syndrome 243, 253, 624–625, 627–632, **628**, **635**
dilation/dissection of ascending aorta 627, 629–630, *629*
dilation/dissection of descending aorta 630–632, *631*
left ventricular dysfunction 632
main pulmonary artery dilation 630
mitral valve prolapse 630, *630*
pregnancy 826, *827*, *828*
mechanical dyssynchrony
detection of 116–117, *117*
left ventricular 124
mesocardia 33, *34*, 167, 491, 493, 558
midazolam **25**
minimum work principle 69–70, *70*, *71*
mitral atresia *39*
mitral inflow
cardiac tamponade 711, *712*
constrictive pericarditis 705–706
dilated cardiomyopathy 661
Doppler imaging 133–134, **133**, *134*
restrictive cardiomyopathy 697–698, *697*, *698*, *703*
diastolic dysfunction **702**
mitral regurgitation 756–757
pregnancy 824
rheumatic heart disease **753**
mitral stenosis 246
congenital 243
flow orifice assessment 251–253, *253*
pregnancy 822, *823*
rheumatic heart disease 757
mitral valve
annulus diameter *893*, *894*
chronic disease 754–755, **754**, *755*, *756*
diastolic peak inflow velocity *898*, *900*
Doppler imaging values **144**
hypertrophic cardiomyopathy 681–683, *683*, *684*
hypoplastic left heart syndrome 358–359
imaging 365
straddling *39*
mitral valve anomalies 243–258
cleft mitral valve 245, 248–249, *248*
double-orifice mitral valve 246, 249, *250*, *254*
etiology 243–244

mitral valve anomalies (*Continued*)
imaging 247–255
adults 254–255
key elements 247–248
postoperative assessment 254–255
prenatal assessment 253–254, *254*
transcatheter and surgical treatment 254
incidence 243
morphology and classification 244–246
giant left atrium 246, *246*
parachute mitral valves 250, *252*
pathophysiology 247
regurgitation *see* mitral regurgitation
stenosis *see* mitral stenosis
straddling mitral valve *221*, 245–246, 249, *249*
supravalvar mitral ring 250, *251*
mitral valve prolapse *86*, 243, 244–245, *244*, *245*
imaging 248, *248*
Marfan syndrome 630, *630*
mitral valvulitis 753, **753**
Mowat-Wilson syndrome 618
MRI
cardiac
constrictive pericarditis 707–708, *708*
pericardial effusion 713
restrictive cardiomyopathy 703
multi-valve disease 758–759
muscular VSDs 218–219, *219*
myocardial deformation imaging 111–114, *112*, *113*, **114**, 685–686
clinical applications 114–117, *115–117*
early myocardial dysfunction 115–116, *116*
mechanical dyssynchrony 116–117, *117*
regional left ventricular function 114–115, **114**, *115*
diastolic function 137–139
left atrial volume 138–139, *139*
strain rate/strain imaging 137–138, *138*
tissue Doppler 121–124, *122*, **122**, *123*, **124**
ultrasonic strain rate/strain imaging 111–113, *112*, *113*
myocardial function
left ventricular 108–110, **108**, *109*
tissue Doppler imaging 108–110, **108**, *109*
myocardial performance index 106, *107*, 121, 661, **661**, *662*
pulmonary arterial hypertension 879–880
myocardial velocity imaging 17–18, *17*
myocarditis 653, 655–656
fetus 662–663
see also cardiomyopathy
myocardium in Kawasaki disease 745, *745*
myxoma **642**, 646, *646*

neo-aortic root 459
neo-aortic valve regurgitation 459
neonates
coarctation of aorta 383–389, *385–388*, **389**
interrupted aortic arch *397*
truncus arteriosus 436, *436*
nonbacterial thrombotic endocarditis 771–772
Noonan syndrome 157, 197, 281, 677
normal echogram 44–60
additional/supplemental imaging 55–56
apical views **45**, 49–50, *50*, *51*
examination principles 44–45, **45**
"flank" view 56, *58*
left anterior oblique view 55–56, *58*
measurements 56–58
orthogonal views 45–55, *46*
parasternal (left parasternal) views **45**, 50–53, *51–53*
reporting 58–59, **59**
right anterior oblique view 55, *57*
right parasternal views **45**, 50–53, *51–57*
subxiphoid (subcostal) views **45**, 46–49, *46–49*
suprasternal notch views **45**, 53–55, *54*, *55*
normalizing variable 67–68
Norwood reconstruction 363, *363*

obesity 147
obstructive sleep apnea 148
orifice
anatomic area (AOA) 75
effective area (EOA) 75
narrow, blood flow *75–76*, *75*, *76*
see also specific heart valves
Osler's nodes *764*

pacemaker therapy *see* left ventricular assist device
PAPVC *see* partial anomalous pulmonary venous connection
parachute mitral valves 250, *252*
parajet area *76*
parasternal (left parasternal) views **45**, 50–53, *51–54*
pars membranacea 409
partial anomalous pulmonary venous connection (PAPVC) 159–160, *160*
imaging 166–168, *166–168*
partial anomalous pulmonary venous drainage 159
patent ductus arteriosus 221, 269
with aortic aneurysm **628**
heterotaxy syndromes 569–570, *572*
imaging 457
with left aortic arch 318
imaging 321–322
pulmonary arterial hypertension 877–878, *877*, *878*
reverse-oriented 319
imaging 323
with right aortic arch 318
imaging 322–323
see also ductus arteriosus anomalies
patent foramen ovale 197, 198, *200*, 298, *307*, 447
patient preparation 23, *23*
sedation 23–24, **25**
patient safety 23
pentalogy of Cantrell 35
pentobarbital **25**
per-BSA method 64–65, *64–66*
pericardial disease 703–716
absence of pericardium 714–715, *715*
acute pericarditis 713–716
constrictive pericarditis 703–708
pericardial cyst 715, *715*, *716*
pericardial effusion and cardiac tamponade 709–713
pericardial effusion 709–713, *709*
causes **709**
imaging 710–713, *710–713*
flow mechanics 711, *712*, *713*
two-dimensional 710–711, *710*, *711*
incidence and etiology 709
pathophysiology 709–710
pulmonary arterial hypertension 880
pericardiocentesis, echocardiographically guided 711–712, *714*
pericarditis
acute 713–716
constrictive 703–708
pericardium
absence of 714, *715*
in Kawasaki disease 745–746
peripartum cardiomyopathy 827
personnel 19–20
phased array transducers 9, *9*
physicians, training 19–20, **20**, **21**
PISA *see* proximal isovelocity area (PISA) method
polysplenia syndrome 564, *569*, *572*
see also heterotaxy syndromes
Pompe disease 677, 678
pregnancy 815–833
aortic regurgitation 824
aortic stenosis 823, *824*
bicuspid (bicommissural) aortic valve 820
coarctation of aorta 821
cyanotic lesions 821
Ebstein anomaly 820
echocardiographic changes
heart disease 818
normal 816–817, **817**
Fallot's tetralogy 821
Fontan circulation 822
infective endocarditis 826–827, *829*
Kawasaki disease 827, *830*
left-to-right shunt 819
Marfan syndrome 826, *827*, *828*
mitral regurgitation 824
mitral stenosis 822, *823*
physiologic hemodynamic changes 815–816, *816*
prosthetic heart valves 824–826, *825*, *826*
pulmonary vascular disease 821
right ventricular outflow tract obstruction 819–820, *820*
risk stratification for congenital heart disease 818, **819**, *820*, *822–828*
specific management issues 827–829
transposition of great arteries 821–822, *822*
preload 97
prenatal assessment *see* fetus; pregnancy; and individual conditions
pressure gradients 79–83, *79–82*
pressure measurement error 82
pressure recovery 75–76, *75*, *76*, 83
primary ring 215
primum atrial septal defect 198
propofol **25**
prosthetic heart valves
blood flow 88–93, *90–92*, **93**
in pregnancy 824–826, *825*, *826*
protocols
patient safety 23
research 27
proximal isovelocity area (PISA) method 84, 86–87, *87*
pseudotruncus 414
pulmonary arterial hypertension 872–882
assessment in pediatric patients 873
definition 872–873

interventricular septum shape 874–875, *875*
left ventricle effects 880
patent ductus arteriosus 877–878, *877*, *878*
pericardial effusion 880
pulmonary regurgitation 874, *874*
right ventricle effects 879–880
myocardial performance index 879–880
systolic pressure 875–877, *876*
tissue Doppler and strain imaging 880
tricuspid annular plane systolic excursion 879
secondary 872
systemic-to-pulmonary artery shunts 878
systolic time intervals 875
tricuspid and pulmonary valve time intervals 875
tricuspid valve regurgitation 873–874, *874*
ventricular septal defect 875–877, *876*
pulmonary artery
abnormalities 325–333
definition 325
imaging 328–333, *328–332*
morphology 325–326
banding 503
branch, aortic origin 327, 330, *330*
capacitance 878–879
compliance 879
crossed 327–328
imaging 330, *330*
diameter *892*, *893*
dilation in Marfan syndrome 630
discontinuous 327
imaging 329
end-diastolic pressure 874, *874*
Fontan circulation 546–548, *547–551*
imaging 418–419
post-atrial switch 459
pressure measurement 877–878, *877*, *878*
stenosis 292–293, *292*, *293*
truncus arteriosus 434–435
variations in origin and bifurcation 415
pulmonary artery sling 618–620
definition 618, *618*
etiology 618
imaging 619–620, *619*, *620*
incidence 618
morphology and classification 619
pathophysiology 619
pulmonary atresia *40*
and Fallot's tetralogy 412, 414, *415*, 425
fetal heart in 302, 303–304, *303*, *304*
with intact ventricular septum 297–316
definition 297
etiology 297–298
history 297
imaging 302–311, *303–311*
incidence 297
morphology 298–301, *298–301*
pathophysiology 301–302
treatment 302
with right ventricular dilatation 300–301, *301*
treatment 302
with right ventricular hypoplasia 298–299, *298*
treatment 302
pulmonary outflow tract obstruction 568–569
pulmonary regurgitation 286, 422, *423*
fetus *856*
imaging 422, *423*
pulmonary arterial hypertension 874, *874*
pulmonary stenosis 281–287, 422, *423*
congenital branch 326–327, 329–330, *329*
imaging 283–285, *283–285*, 422, *423*
key elements 283
long-term sequelae 286–287, *287*
postnatal assessment 283–286, *284*, *285*
postprocedure assessment 286–287, *287*
prenatal assessment 283, *283*
pulmonary valve regurgitation 286
transcatheter and surgical treatment 286
incidence 281
morphology and classification 281
pathophysiology 281–282, *282*
pulmonary valve
absent *see* absent pulmonary valve syndrome
annulus diameter *892*
chronic disease 755
pulmonary atresia
with right ventricular dilatation 301
with right ventricular hypoplasia 298–299, *298*
time intervals 875
pulmonary vascular bed 221
pulmonary vascular disease in pregnancy 821
pulmonary vascular resistance 220–221
pulmonary veins
abnormal number 158, *158*
imaging 162, *163*
flow patterns
cardiac tamponade 711
constrictive pericarditis 706
diastolic disease **702**
restrictive cardiomyopathy 698, *698*
Fontan circulation 546–548, *547–551*
hypoplastic left heart syndrome 358
imaging 365
pulmonary venous anomalies 157–179
definition 157
etiology 157
imaging 162–177
abnormal number of pulmonary veins 162, *163*
adults 174–175
cor triatriatum 165–166, *166*, *167*
goals of 162
PAPVC 166–168, *166–168*
postoperative assessment 176–177
prenatal assessment 173–174, *175*
pulmonary venous connections with anomalous drainage 163–164, *164*
pulmonary venous stenosis *128*, 164–165, *165*
TAPVC 168–173, *168–174*
transcatheter/surgical treatment 175–176, *176*, *177*
incidence 157
morphology and classification 157–162
anatomy 158–160, *158–160*
developmental considerations 157–158
pathophysiology 160–162
pulmonary venous atresia 159
pulmonary venous connections 566
anomalous drainage 158, *158*
imaging *128*, 163–164, *164*
heterotaxy syndromes 566
partial anomalous 159–160, *160*
total anomalous *161*
total anomalous (TAPVC) 160
pulmonary venous drainage
partial anomalous 159
total anomalous 158, *158*
pulmonary venous inflow, Doppler echocardiography **133**, 134–135, *134*, *135*
pulmonary venous stenosis *159*
imaging 164–165, *165*
pulse-echo experiment 3–4, *4*
pulsed-wave Doppler 13–15, *14*, *15*
aortic regurgitation *89*
regurgitation 85

quality assurance 16–17
quality improvement 28–29, **29**

radio-frequency signal 4, *5*, *6*
Raghib anomaly 185
Raghib syndrome 201, 202, 207
Rastelli operation 339, *339*, 458
follow-up 461
regurgitation 83, **83**, 84–88
aortic *88*, 745
pregnancy 824
rheumatic heart disease **753**, 757–758
aortic root 419
assessment of 84–88
2D echocardiography 84
Doppler echocardiography 85, *85*
jet area 85, *86*
PISA 86–87, *87*
vena contracta 85–86, *86*
volumetric 84–85
atrioventricular *86*
mitral 756–757
pregnancy 824
rheumatic heart disease **753**
neo-aortic valve 459
pulmonary 286, 422, *423*
fetus *856*
imaging 422, *423*
pulmonary arterial hypertension 874, *874*
tricuspid *79*, 422–423
pulmonary arterial hypertension 873–874, *874*
see also individual valves
reporting 23
research protocols 27
restrictive cardiomyopathy 146, *146*, 694–703
echocardiographic parameters **695**
imaging 694, **695**, *696–703*, **702**
2D echocardiography 695–696, *696*
color M-mode 699–700, *700*
flow characteristics 696–699, *697–699*
goals 694
tissue mechanics 700–702, *701*, *702*, **702**
transesophageal echocardiography 702
incidence and etiology 694, **695**
pathophysiology 694
reverberation artifacts 8, *8*
rhabdomyoma 641–643, *642*, **642**
rheumatic fever/rheumatic heart disease 750–762
clinical course 751
definition 750

rheumatic fever/rheumatic heart disease (*Continued*)
diagnostic criteria 751, **751**, **752**
epidemiology 650
imaging 751–759
3D echocardiography **758**, 759, *759*
acute rheumatic heart disease 752–754, **753**
chronic rheumatic heart disease 754–755, **754**, *755*
disease progression/resolution 755–756, *758*
key elements 751–752
valvar intervention 756–759
Jones criteria **751**
pathophysiology 750–751
screening 759
secondary prophylaxis 759, **760**
right anterior oblique view 55, *57*
right atrium
anomalies 240, *240*
double-outlet *39*, 262, *263*
enlargement 422–423
hypoplastic left heart syndrome 358
imaging 363–364
pulmonary atresia
with right ventricular dilatation 300–301, *301*
with right ventricular hypoplasia 298
size 422–423
right parasternal views **45**, 50–53, *51–57*
right ventricle
arrhythmogenic dysplasia 727, 729–733
double-chambered 411–412, *414*
double-inlet 518–520, *519*, *520*
double-outlet *see* double-outlet right ventricle
functional parameters 120–121, *120*, *121*
hypoplastic left heart syndrome 358
imaging 365
pulmonary arterial hypertension 879–880
myocardial performance index 879–880
tissue Doppler and strain imaging 880
tricuspid annular plane systolic excursion 879
systolic function 118–124, *118*, *119*, **120**
systolic pressure 875–877, *876*
right ventricular assist devices *see* ventricular assist devices
right ventricular dilatation
with pulmonary atresia 300–301, *301*
treatment 302
right ventricular hypoplasia, with pulmonary atresia, treatment 302
right ventricular outflow tract 459
imaging *400*, 418–419, *419*
obstruction *410*
pregnancy 819–820, *820*
right ventricular outflow tract anomalies 281–296
absent pulmonary valve 290–292, *291*, *292*
pulmonary artery stenosis 292–293, *292*, *293*
pulmonary valve stenosis 281–287
subpulmonary stenosis 287–290
right ventricular stroke volume 291, 878, 879
ring-sling complex 619
Ross-Konno operation 339
rubella, congenital 281

Sano modification *373*, *374*
sarcomere shortening 96
scheduling 22
Schprintzen syndrome 394
scimitar syndrome 160, *160*, 167
second harmonic imaging 9–10, *9*
secundum atrial septal defect 198, *200*
imaging 203–204, *203*, *204*, *208*, *209*
sedation 23–24, **25**
segmental analysis 31–32, *32*, *33*
atrial situs 35–37, *35*, *36*, **36**
atrioventricular alignments and connections 38, *39*
cardiac position 32, *34*, 35
semilunar valve relationships 41, *41*
thoraco-abdominal situs 32–33, *34*
type of infundibulum (conus) 40–42, *41*
ventricular loop 37–38, *37–39*
ventriculo-arterial alignments 38, 40, *40*
semilunar valve relationships 41, *41*
septal ablation for hypertrophic cardiomyopathy 687–689, *688*, *689*
septal malalignment 493, *493*
septum primum 198
malposition/malattachment 158, *158*
septum secundum 197, 198
sevoflurane **25**
shadowing artifacts 8
Shone syndrome 383
shortening fraction 101, 659
Shprintzen-Goldberg syndrome **628**, 634
side lobe artifacts 7, *7*
single ventricle 149
sinus of Valsalva 584
aneurysm 348–350, *350*, *351*
sinus venosus
defect 158, 199–200, *201*
imaging 204–206, *204*, *205*
septum 198
situs
ambiguous 33, *34*, *36*
ambiguus *569*, *573*
atrial 35–37, *35*, *36*, **36**
inversus 32, *34*, *36*, 489, *490*, 491, *492*, *499*, 558, 559, *560*, *576*
totalis 558, *560*
solitus 32, *34*, *36*, 489, *490*, 491, *493*, *501*
ventricular 37–38, *37–39*
Smith-Lemli-Opitz syndrome 357
smooth muscle cell dysfunction syndrome 634
sonographers 20, **21**
space requirements 20
speckle tracking 17–18, *17*, 123
spectrogram 12
specular reflection 3
stenosis
aortic 340–345
fetal 344–345, *344*, *345*, *849*
imaging 341–345, *341–345*
morphology 340, *340*
pathophysiology 340–341
pregnancy 823, *824*
atrioventricular valves 135
coronary sinus 191
flow measurement 83–84, **83**
Coanda effect 75, *75*
parajet area *76*
pressure recovery 75–76, *75*, *76*, 83
vena contracta 75–76, *75*, *76*, 85–86, *86*
mitral 246
congenital 243
flow orifice assessment 251–253, *253*
pregnancy 822, *823*
rheumatic heart disease 757
pulmonary 281–287, 422, *423*
congenital branch 326–327, 329–330, *329*
imaging 283–285, *283–285*, 422, *423*
incidence 281
morphology and classification 281
pathophysiology 281–282, *282*
pulmonary venous *159*
imaging 164–165, *165*
subaortic 337–340
imaging 338–340, *339*, *340*
morphology and classification 337–338, *337*
pathophysiology 338
subpulmonary 287–292
imaging 288–290, *289*
morphology and classification 288
pathophysiology 288
supravalval aortic 345–347, *346*, *347*
Stenson, Niels 407
storage format 22–23
straddling
mitral valve *39*, 243, 245–246
imaging 249, *249*
tricuspid valve *39*
strain imaging 137–138, *138*
strain rate 111–113, *112*, *113*, 137–138, *138*
stress echocardiography
dilated cardiomyopathy 661
hypertrophic cardiomyopathy 686–687
stroke volume 97
structural measurements 63–72
allometric modeling 63–69
choice of normalizing variable 67–68
heteroscedasticity 68
"indexing" methods 65–66, *66*
per-BSA method 64–65, *64–66*
z-score methods 66–67, 68
cardiovascular dimensions 69–70
growth adjustment 70
minimum work principle 69–70, *70*, *71*
subaortic stenosis 337–340
imaging 338–340, *339*, *340*
morphology and classification 337–338, *337*
pathophysiology 338
subclavian artery, left, aberrant 611, *612*, *615*
subpulmonary stenosis 287–292
imaging 288–290, *289*
adults 290
echocardiographic guidance of surgical treatment 290
key elements 288–289
postoperative assessment 290
prenatal assessment 289
preoperative assessment 289–290, *289*
morphology and classification 288
pathophysiology 288
subxiphoid (subcostal) views **45**, 46–49, *46–49*

superior vena cava 181, **181**
 anomalies 182–187, *182–186*
 left SVC to coronary sinus 182–184, *182–184*
 with atretic right SVC 184, *184*
 left SVC to left atrium 184–185, *184*
 levoatrial cardial vein 185–186, *186*
 right SVC to left atrium/both atria 186, *186*
supervision 19–20, **20**
suprasternal notch views **45**, 53–55, *54*, *55*
supravalval aortic stenosis 345–347
 imaging 345–347, *346*, *347*
 morphology 345, *346*
 pathophysiology 345
supravalvar mitral ring 250, *251*
surgical myomectomy for hypertrophic cardiomyopathy 687–689, *688*, *689*
surgical techniques, imaging 175–176, *176*, *177*
Swiss cheese septum 219
systemic veins
 hypoplastic left heart syndrome 358
 imaging 363–364
systemic venous anomalies 180–196
 coronary sinus 190–191
 embryology and etiology 180–181, **181**
 hepatic vein 189–190, *191*
 inferior vena cava 187–190
 bilateral IVCs 189, *189*
 interrupted IVC with azygos/hemiazygos continuation 187–189, *188*, *189*
 left IVC to the right atrium 189, *190*
 right IVC to left atrium 189
 innominate veins 191–192, *192*
 prevalence 180
 superior vena cava 182–187, *182–186*
 left SVC to coronary sinus 182–184, *182–184*
 left SVC to coronary sinus with atretic right SVC 184, *184*
 left SVC to left atrium 184–185, *184*
 levoatrial cardial vein 185–186, *186*
 right SVC to left atrium/both atria *149*, 186, *186*
systemic venous connections 566, *570*
systemic venous inflow, Doppler echocardiography 135
systemic venous valve anomalies 240, *240*
systemic-to-pulmonary artery shunts 878
systolic function 96–131
 blood pool Doppler indices 105–111, **105**, *106*, *107*, **108**, *109*, *111*
 cardiac function at ventricular level 97–98, *98*
 deformation imaging 111–114, *112*, *113*, **114**
 dilated cardiomyopathy 659–660
 dimensional changes 99–105, *100*, **100**, *102–104*
 Fallot's tetralogy 421–422
 Fontan circulation 543
 hypertrophic cardiomyopathy 684
 left ventricular function 98–99, 114–115, **114**, *115*
 mechanics 96
 regional myocardial function 108–110, **108**, *109*
 right ventricle 118–124, *118*, *119*, **120**
 tissue Doppler velocities 110, *111*
systolic time intervals 875

Takayasu aortitis 383
TAPVC *see* total anomalous pulmonary venous connection
telemedicine 27
temporal resolution 11
teratoma **642**, 645, *645*
tethering 110, *360*
Thebesian valve 240
thoracic aortic aneurysms/dissection **628**, 634, **635**, 636
 with bicuspid aortic valve **628**, 634, 636
 with cutis laxa **628**, 634
 with patent ductus arteriosus **628**
thoraco-abdominal situs 32–33, *34*
three-dimensional imaging 791–814
 clinical application 791–792
 congenital heart disease 791, 799–809
 atrial septal defect 799–800, *800*, *801*
 atrioventricular septal defect 801–802, *803*, *804*
 Ebstein anomaly 803–805, *804*, *805*
 Fallot's tetralogy 806, *810*
 transposition of great arteries 805–806, *805–809*
 tricuspid valve anomalies 803–805, *804*, *805*
 ventricular septal defect 800–801, *801*, *802*
 deformation imaging 795
 examination protocol 792–793
 image optimisation 792–793
 image rendering 793, *793*
 fetal 855, 857–860, *864–867*
 future applications 808–809
 history 791, *792*
 hypertrophic cardiomyopathy 686
 intraoperative 787
 left ventricular function 791, 793–795, *794*
 left ventricular mass 795, *795*
 rheumatic fever **758**, 759, *759*
 right ventricular size/function 791, 795–798, *796*, *797*
 valve morphology/function 792, 798, *798*, *799*
 volumetric quantification 793
time-gain compensation 5
tissue Doppler imaging *see* Doppler imaging
tissue Doppler velocities 110, *111*
 in children 110, *111*
total anomalous pulmonary venous connection (TAPVC) 160, *161*
 cardiac *161*
 imaging 168–173, *168–174*
 infradiaphragmatic *161*
total anomalous pulmonary venous drainage 158, *158*
training 19–20, **20**, **21**
transcatheter techniques
 mitral valve anomalies 254
 pulmonary stenosis 286
 transesophageal echocardiography 784–785, *784*
 ventricular septal defect 227–228, *227*
transesophageal echocardiography 24, 162, 226, 777–790
 atrial septal defect 783–784
 constrictive pericarditis 706–707
 epicardial 785–786
 infective endocarditis *766–768*, 769–770
 interventional catheterization 784–785, *784*
 interventional procedures 783
 intraoperative 786–787, *787*
 target lesions for CHD surgery 786–787
 three-dimensional 787
 intraoperative imaging 785
 patient considerations 777–778
 probes 778
 restrictive cardiomyopathy 702
 standard views 778–783
 atrioventricular junction 780
 mid-esophageal 0 degrees 779, *779*
 mid-esophageal 30 degrees 780–781, *781*
 mid-esophageal 60 degrees 781, *781*
 mid-esophageal 90 degrees 781–782, *782*
 mid-esophageal 120 degrees 782
 transgastric 782–783, *782*
 venous connections and atrial septum 780, *780*
 technical considerations 778
 training **26**
 transposition of great arteries 500–501, *501*
transforming growth factor-beta 625
transposition of great arteries 245, *248*, 446–465
 3D echocardiography 805–806, *805–809*
 anatomy 447–449
 coronary artery anatomy 448–449, *449*, *450*
 intact ventricular septum 447
 ventricular septal defect 447–448, *448*
 associated defects 449
 definition 446, *447*
 double-inlet left ventricle *513–516*
 etiology 446–447
 follow-up assessment 459–462, *460*, *461*
 arterial switch operation 459–460, *460*
 atrial switch operation 460–461, *460*, *461*
 Rastelli operation 461
 imaging 451–462
 adults 461–462
 arterial switch operation 458, 459–460, *460*
 atrial switch operation 458, 460–461, *460*, *461*
 balloon atrial septostomy 457–458, *458*
 coronary arteries 455–457, *456*, *457*
 intact ventricular septum 451–453, *452*, *453*
 intraoperative assessment 458–459
 key elements 451
 patent ductus arteriosus 457
 prenatal assessment 457, *457*
 Rastelli operation 458, 461
 ventricular septal defect 453–455, *453–455*
 incidence 446
 pathophysiology 449–451
 physiologically "corrected" 489–507
 anatomy 490–494, *491–494*
 definition 489
 developmental considerations 489
 follow-up 503
 imaging 497–503, *498–502*
 incidence 489
 morphology and classification 489–494, *490–494*
 pathophysiology 494–496, *495*
 perioperative assessment 503
 pregnancy 820–821
 Van Praagh's classification 491
 pregnancy 821–822, *822*
transthoracic echocardiography 24
 infective endocarditis *765*, *768*, 769–770
transthoracic imaging of VSDs 221–226, *222–226*
tricuspid annular plane systolic excursion (TAPSE) 120–121, *121*, 879

tricuspid atresia *39*
and functionally univentricular heart 511, 520–526, *521–527*
anatomy 521–524, *521–527*
embryology 520–521
physiology 524–526
treatment strategies 526
and transposition of great arteries *534*
tricuspid inflow
cardiac tamponade 711, *713*
constrictive pericarditis 706
restrictive cardiomyopathy 698, *699*
tricuspid regurgitation *79*, *360*, 422–423
pulmonary arterial hypertension 873–874, *874*
tricuspid valve
3D echocardiography 803–805, *804*, *805*
chronic disease 755
diameter *894*, *895*
Doppler imaging values **144**
dysplasia 231, 239–240, *239*, 359, *360*
hypoplastic left heart syndrome 359, *360*
imaging 365
morphology and development 231–232, *232*
pulmonary atresia
with right ventricular dilatation 300, *301*
with right ventricular hypoplasia 298–299, *298*
repair 237–239, *238*
straddling *39*
time intervals 875
tricuspid valve anomalies
Ebstein anomaly 231–240
regurgitation *see* tricuspid regurgitation
transposition of great arteries 494, *496*
truncal valve 434, *435*
truncus arteriosus *40*, 433–440
definition 433
etiology 433
follow-up 440
imaging 436–440, *436–440*
adult 439–440
ancillary modalities 440, *440*
intraoperative assessment 439
key elements 436–437, *436*
neonates 436, *436*
postoperative assessment 437
prenatal assessment 439
incidence 433
management 436
morphology and classification 434–435, *434*, *435*
coronary arteries 434
pulmonary arteries 434–435
truncal valve 434, *435*
ventricular septal defect 434
pathophysiology 435–436
Turner syndrome 157, 357, 382
two-dimensional imaging
acute pericarditis 714
cardiac tamponade 710–711, *710*, *711*
constrictive pericarditis 704–705, *705*, *706*
fetus 836–842, *837–842*
hypertrophic cardiomyopathy 680, *680–682*, **681**, **682**
pericardial effusion 710–711, *710*, *711*
restrictive cardiomyopathy 695–696, *696*

ultrasound
image
artifacts 7–8, *7*, *8*
construction 7, *7*
creation 3–5, *4*, *5*, *7*
optimization 11–12
resolution 10–11, *11*
physics 3–7
technology 3–7, 9–12
contrast imaging 10
phased array transducers 9, *9*
second harmonic imaging 9–10, *9*
umbilical arterial flow *844*

valvar stenosis 83–84, **83**
see also individual valves
vascular rings 609–618
anatomy 610–613, *612–614*
double aortic arch 610–611, *612–614*
left aortic arch with right descending aorta and right ductus arteriosus 612–613, *616*
right aortic arch with aberrant left subclavian artery 611, *612*, *615*
right aortic arch with left descending aorta and left ductus arteriosus 612, *616*
right aortic arch with mirror image branching and left ductus arteriosus 611–612, *612*, *615*
definition 609
etiology 609
imaging 613–618, *617*, *618*
follow-up assessment 618
intraoperative assessment 618
prenatal assessment 616, 618
protocol 614–616
incidence 609
morphology and classification 609–613, *610–614*, **611**
pathophysiology 613
vascular ultrasound *see* ultrasound
VATER syndrome 426
velocardiofacial syndrome 426
truncus arteriosus 433
velocity measurement error 82
velocity resolution 14–15
vena contracta 75–76, *75*, *76*, 85–86, *86*
ventricles
double-inlet *39*
heterotaxy syndromes 567–568, *571*
left *see* left ventricle/ventricular
right *see* right ventricle/ventricular
single ventricle *see* functionally univentricular heart
superior-inferior 526–531, *528–531*
see also entries under ventricular
ventricular assist devices *667*, **668**, *669*, 670–672, *670–671*
ventricular compliance, abnormal 141–143, *142*, **143**
ventricular inversion 558
imaging 562, *562*
ventricular loop 37–38, *37–39*
ventricular septal defect (VSD) 215–230
atrioventricular canal 219–220, *220*, 225–226, *226*
conal septal 219, *219*, 224–225, *225*
conoventricular/perimembranous 217, *217*, 222–223, *222*
definition 215
double-outlet left ventricle 483, *483*
double-outlet right ventricle 468–469, *469–473*
doubly committed 469, *471*
etiology 215
and Fallot's tetralogy 409–410, *410–413*
Gerbode type 220
imaging 221–228, 418
3D echocardiography 800–801, *801*, *802*
adults 226
echocardiographic guidance of transcatheter techniques 227–228, *227*
postoperative assessment 228
postoperative/follow-up 221
prenatal assessment 226, *226*
preoperative 221, 227, *227*
transthoracic 221–226, *222–226*
incidence 215
location and size 468
malalignment 217–218, *218*, 223–224, *223*, *224*
morphology and classification 215–216
anatomy 216–220, *217*
development 215–216
muscular 218–219, *219*
noncommitted 469, *472*
pathophysiology 220–221
associated defects 221
left-to-right shunt 220
pulmonary vascular resistance 220–221
pulmonary arterial hypertension 875–877, *876*
subaortic 468, *469*, *470*
subpulmonary 468–469, *470*
terminology **216**
transposition of great arteries 447–448, *448*
imaging 453–455, *453–455*
physiologically "corrected" 444
truncus arteriosus 434, *435*
ventricular size, post-atrial switch 459–460
ventricular-ventricular interactions 124
ventriculo-arterial alignment 38, 40, *40*
ventriculo-arterial connections 568
Venturi effect 348
Venturi tube *76*
vertical veins 160, *160*

wall stress 97–98, 659–660
wavelength 3
Williams syndrome 281, 383
Williams-Beuren syndrome 326, 336
Wolff–Parkinson–White syndrome 643
working environment 16

z-scores 66–67
parametric vs. statistical derivation 68

WILEY END USER LICENSE AGREEMENT

Go to www.wiley.com/go/eula to access Wiley’s ebook EULA.